



UNITED NATIONS
UNIVERSITY



ORKUSTOFNUN

Geothermal Training in Iceland *2013*



Reports of the 6-month UNU Fellows
at the United Nations University
Geothermal Training Programme, 2013



**UNITED NATIONS
UNIVERSITY**

GEOHERMAL TRAINING PROGRAMME
Orkustofnun, Grensásvegur 9
IS-108 Reykjavík, Iceland

Geothermal Training in Iceland 2013

**Reports of the 6-month UNU Fellows at the
United Nations University
Geothermal Training Programme in 2013**

*Edited by
Málfríður Ómarsdóttir,
Ingimar G. Haraldsson and
Lúdvík S. Georgsson*

**ISBN 978-9979-68-342-1
ISSN 1670-7400**

The photo on the front page shows the Fellows of the 35th annual UNU Geothermal Training Programme in 2013 at Hjalteyri, low-temperature production field, Eyjafjörður, N-Iceland.

Back row from left: Tufwane Mwagomba (Malawi), Angel Monroy (El Salvador), Shakhin-Uz-Zaman (Bangladesh), Yussuf Mohamud (Kenya), Behailu Woldesemayet (Ethiopia), Ammon Omiti (Kenya), Vijay Chauhan (India), Ferdinand Wakana (Burundi), Tharanga Munasinghe (Sri Lanka), Abdirasak Omar (Djibouti), Jean Pascal Niyigena (Rwanda), Loice Kipchumba (Kenya), Ronald Verave (Papua New Guinea), Farah Omar (Djibouti).

Mid row: Tito Lopeyok (Kenya), Samuel Kinyanjui (Kenya), Kristine Antonio (Philippines), Claudia Pichardo (El Salvador), Carolyn Kipsang (Kenya), Idalia Matus (Nicaragua), Grace Lajwe (Uganda), Joyce Okoo (Kenya), Jane Uwera (Rwanda), Long Hui (China).

Front row: Wondwossen Redie (Ethiopia), Anthony Ponce (Philippines), Kennedy Kamunya (Kenya), Jefferson Africa (Philippines), Isaac Makuk (Kenya), Eric Rop (Kenya), Li Shengtao (China), Lilian Okwiri (Kenya), Daniel Saitet (Kenya), Mohammed Masum (Bangladesh).

INTRODUCTION

The 35th annual session of the UNU-GTP was held from April to October 2013. A record thirty four UNU Fellows from fifteen countries in four continents completed the traditional six month courses. They came from Bangladesh (2), Burundi (1), China (2), Djibouti (2), El Salvador (2), Ethiopia (2), India (1), Kenya (12), Malawi (1), Nicaragua (1), Papua New Guinea (1), Philippines (3), Rwanda (2), Sri Lanka (1) and Uganda (1). The UNU Fellows were trained in eight lines of specialization in 2013, in: Reservoir Engineering (6 Fellows), Geothermal Utilization (6), Geophysical Exploration (5), Drilling Technology (5), Borehole Geology (4), Chemistry of Thermal Fluids (4), Geological Exploration (2) and Borehole Geophysics (2). They were all on fellowships from the Icelandic Government and the UNU. Three UNU Fellowships were co-funded by the Energy Development Company (EDC) in the Philippines, and ten by the Geothermal Development Company (GDC) and Kenya Electricity Generating Company (KenGen) in Kenya. For the first time UNU-GTP gave a similar training in a cooperation country, through courses and advanced training, sponsored by KenGen, with 5 borehole geologists trained on site in Kenya. Consequently, they have been given a similar status to the 6-month UNU Fellows in Iceland, meaning that in all 39 trainees completed this kind of training in 2013. Their training reports have been published separately. Kenya's drive for fast geothermal development has led to an urgent need for geothermal training on a large scale. No new countries were added for the 6-month training in 2013. Thus, during 1979-2013, 554 scientists and engineers from 53 countries have completed the annual six month courses, or equivalent. Of these, 39% have come from countries in Asia, 34% from Africa, 15% from Latin America and the Caribbean, 11% from Central and Eastern Europe, and 1% from Oceania which was represented for the first time at the UNU-GTP in 2012. Among them have been 109 women (20%). Over 90 professionals have received shorter training in Iceland (2 weeks to 4 months).

Twelve former UNU Fellows (from El Salvador 2, Kenya 7, Nicaragua 1, Rwanda 1 and Tanzania 1), undertook MSc studies in 2013 under a cooperation agreement with the University of Iceland. The traditional six month courses at the UNU-GTP constitute 25% of the MSc studies. Two (one from El Salvador and one from Kenya) defended their MSc thesis, and seven started their MSc studies in 2013, 2 in January and 5 in September. A milestone was reached when the first UNU-GTP PhD Fellow defended her thesis in February. She was also the first African to receive a PhD degree from the University of Iceland. Two others continued their PhD studies in 2013. All are from Kenya.

Our annual UNU Visiting Lecturer this year was Dr. Kevin Brown, a chemist and one of New Zealand's foremost geothermal experts. He gave a series of fascinating lectures on geothermal development. It has to be noted that rarely have we seen such interest and attendances at similar occasions.

The sixth event in the UN Millennium series of Short Courses / Workshops for the Americas was the "*Short Course V on Conceptual Modelling of Geothermal Systems*" which was organized and conducted by the UNU-GTP and LaGeo S.A. in Santa Tecla, El Salvador on February 24 - March 2, 2013. The lecturers came from El Salvador (10), Iceland (5), Costa Rica (4), Mexico (2), Nevis (1) and USA (1). The number of registered participants (apart from lecturers) was 61 in all, from Chile (5), Colombia (4), Costa Rica (2), Dominica (1), Ecuador (3), Guatemala (2), Honduras (4), Mexico (6), Nevis (2), Nicaragua (11), Peru (3) and the host country El Salvador (18). This was the first official UNU-GTP event for Peru to participate in.

The ninth annual Millennium event in Africa, "*Short Course VIII on Exploration for Geothermal Resources*", was held in Kenya, October 31 - November 22, 2013. This was a record-breaking event with 70 participants from 18 African countries (including Yemen) plus 50 lecturers and field instructors (mostly from Kenya, but four from Iceland (ISOR and UNU-GTP), and six from the neighbouring countries (Ethiopia (2), Eritrea, Tanzania, Rwanda and Uganda). New countries participating for the first time in UNU-GTP events were Cameroon and Niger. The Short Course was co-hosted by the UNU-GTP, KenGen and GDC. The course was very well received by the participants, who were also impressed by the great development of geothermal taking place in Kenya.

UNU-GTP's activities in customer-designed courses continued in 2013. The year started with the last 4 weeks (January 7 – February 2) of the “*Advanced Training in Borehole Geology*” tailor-made for 5 KenGen borehole geologists. Two, 3-4 day “*Short Courses for Decision Makers in Geothermal Development*” were held in Naivasha, Kenya, the first one in September for Burundi, DR Congo and Rwanda, the other one in November for Malawi, Tanzania and Zambia. These events were financed by ICEIDA and the Nordic Development Fund (NDF). Finally, ICEIDA and NDF contracted UNU-GTP to give a Short Course, and then be responsible for on-site training in borehole geology, environmental sciences and drilling supervision in Rwanda during the geothermal drilling project in Karisimbi in Rwanda. This project was on-going for most of the second half of 2013, into 2014.

The year 2013 marked a milestone in the operations of the Geothermal Training Programme, as the director from its foundation in late 1978, and for most of the 35 years, Dr. Ingvar Birgir Fridleifsson, my close colleague for the last 25 years, stepped down from his post at the end of July into a well-earned retirement. The international geothermal community all knows what Ingvar has stood for, and the activities of the UNU-GTP from 1979 bear witness to his great pioneering work in geothermal.

The teaching and research supervision of the UNU-GTP in 2013 was carried out as follows: by geothermal specialists from ISOR (Iceland GeoSurvey) 70%, the University of Iceland and Reykjavik University (10%), and specialists at other institutions, energy utilities and consulting engineering offices about 20%. Many thanks are due to the teachers and supervisors and their institutions. The availability of top quality supervisors for the various lines of studies offered is of vital importance to the UNU-GTP operations. Warm thanks are also due to the permanent staff, Thórhildur Ísberg, Ingimar G. Haraldsson, Málfríður Ómarsdóttir and Markús A.G. Wilde.

Finally, we want to remind the readers that the reports presented here are written as a part of an academic exercise, and in most cases under a considerable time pressure. The reports have been written under close guidance of the supervisors. We are grateful for the dedication of the UNU Fellows and the teachers in their work at the UNU Geothermal Training Programme. Furthermore, we would like to point out that all the reports of the UNU-GTP from the start in 1979 are available through our website: www.unugtp.is, where they are published in colour.

With warmest regards from Iceland,
Lúdvík S. Georgsson, director

Information about the UNU Geothermal Training Programme

The Geothermal Training Programme of the United Nations University has operated at Orkustofnun (the National Energy Authority) in Iceland since 1979 with six months annual courses for professionals who mostly come from the developing countries. Candidates must have a minimum of one year practical experience in geothermal work in their home countries prior to the training, and, preferably, they should be within 40 years of age. Specialized training is given in geological exploration, borehole geology, geophysical exploration, borehole geophysics, reservoir engineering, environmental studies, chemistry of thermal fluids, geothermal utilization, and drilling technology. Each trainee attends only one specialized course. The training is conducted in English.

The trademark of the training is to give university graduates engaged in geothermal work very intensive on-the-job training in their chosen fields of specialization. The trainees work side by side with geothermal professionals in Iceland, mostly staff members of ISOR – Iceland GeoSurvey, an agency actively working on most aspects of geothermal exploration and development. The training is tailor-made for the individual and the needs of his institution/country. The aim is to assist developing countries with significant geothermal potential to build up groups of specialists that cover most aspects of geothermal exploration and development. Priority is given to candidates from institutions where geothermal work is already under way. All candidates are selected by private interviews and receive scholarships (covering tuition, per diem and international travel) financed by the Government of Iceland and the UNU, or others. Upon completion of their training the participants receive a UNU Certificate. Further description can be found at our internet home page: www.unugtp.is.

TABLE OF CONTENTS

5.	Africa J.R.: 1D inversion of MT and TEM data with application of soundings from Krýsuvík, SW-Iceland and a review of MT/TEM data from Bacman geothermal project, Central Philippines.....	1
6.	Antonio, K.E.S.: Comparison of simulations of the Tanawon sector simultaneous discharge test in Bacon-Manito geothermal field in the Philippines	35
7.	Chauhan, V.: Geothermal space heating and thermal storage using phase change material in Chumathang, India.....	65
8.	Kamunya, K.M.: Scaling potential during production in Hverahlíð field, Hengill high-temperature geothermal area, SW-Iceland	91
9.	Kinyanjui, S.: Direct use of geothermal energy in Menengai, Kenya: Proposed geothermal spa and crop drying	109
10.	Kipchumba, L.J.: Borehole geology and hydrothermal alteration of wells MW-08 and MW-11, Menengai geothermal field, Kenya.....	143
11.	Kipsang, C.: Cost model for geothermal wells	177
12.	Lajwe, G.: Comparison, characterization, and interpretation of geothermal fluid geochemistry in the sedimentary environments of Kibiro, Panyimur, and Öxarfjörður..	201
13.	Li Shengtao: Production capacity assessment of the Hoffell low-temperature geothermal system, SE-Iceland.....	235
14.	Long Hui: Comparison of borehole and surface resistivity at Theistareykir, NE-Iceland.....	261
15.	Lopeyok, T.P.: Borehole geology and hydrothermal mineralisation of wells MW-09 and MW-12, Menengai geothermal field, Kenya	289
16.	Makuk, I.K.: Reducing geothermal drilling problems to improve performance in Menengai.	325
17.	Masum, M.: Geothermal gradient and geology of Hoffell low-temperature field, SE-Iceland	359
18.	Matus Pravia, I.A.: Volumetric, lumped and 2-D numerical models of the Momotombo reservoir, Nicaragua	383
19.	Mohamud, Y.N.: 1D joint inversion of TEM and MT data: Suswa geothermal field, Rift Valley, Kenya	411
20.	Monroy Parada, A.F.: Geothermal binary cycle power plant principles, operation and maintenance.....	443
21.	Munasinghe, M.M.T.N.B.: Geothermal exploration in Gufudalur, Hveragerdi, SW-Iceland .	477
22.	Mwagomba, T.: Comparative analysis of geothermal power plant designs suitable for Malawi's Chiweta geothermal field.....	501

23.	Niyigena, J.P.: Geochemistry of thermal water from the Theistareykir geothermal field in NE-Iceland compared to that of the geothermal prospects in NW-Rwanda.....	531
24.	Okoo, J.A.: Borehole geology and hydrothermal alteration mineralogy of well OW-39A, Olkaria geothermal project, Naivasha, Kenya	547
25.	Okwiri, L.A.: Geothermal drilling time analysis: A case study of Menengai and Hengill.....	577
26.	Omiti, A.O.: Resistivity structure of the Eburru geothermal field, Kenya, depicted through 1D joint inversion of MT and TEM data	599
27.	Omar F., F.: Directional well design, trajectory and survey calculations, with a case study in Fiale, Asal Rift, Djibouti	625
28.	Omar M., A.: Geothermal well design	659
29.	Pichardo López, C.M.: Borehole geology and hydrothermal alteration of well SV-5A, San Vicente geothermal field, El Salvador, C.A.	691
30.	Ponce, A.S.: Analysis of geothermal casing thinning rate of Leyte geothermal production field.....	717
31.	Redie K., W.: Injection and production well testing in the geothermal fields of southern Hengill and Reykjanes, SW-Iceland and Theistareykir, N-Iceland	747
32.	Rop, E.: Interpretation of recent temperature and pressure data and updated conceptual model of the Greater Olkaria geothermal system, Kenya	769
33.	Saitet, D.S.: Synthesis of well test data and modelling of Olkaria South East production field.....	807
34.	Uwera, J.: Design of a cooling system for storage of agricultural products with emphasis on Irish potatoes.....	845
35.	Verave, R.T.: Detection and delineation of geothermal resources using 1D joint inversion of MT and TEM data with practical applications from Reykjanes geothermal field, SW-Iceland.....	873
36.	Wakana, F.: Preliminary study of binary power plant feasibility comparing ORC and Kalina for low-temperature resources in Rusizi Valley, Burundi.....	901
37.	Woldesemayet, B.: Processing and 1D inversion of magnetotelluric data from Dubti area in Tendaho geothermal field, Ethiopia.....	933
38.	Shakhin-Uz-Zaman, M.: Chemical assessment of Icelandic geothermal fluids for direct applications.....	957



**UNITED NATIONS
UNIVERSITY**

GEOTHERMAL TRAINING PROGRAMME
Orkustofnun, Grensasvegur 9,
IS-108 Reykjavik, Iceland

Reports 2013
Number 5

1D INVERSION OF MT AND TEM DATA WITH APPLICATION OF SOUNDINGS FROM KRÝSUVÍK, SW-ICELAND AND A REVIEW OF MT/TEM DATA FROM BACMAN GEOTHERMAL PROJECT, CENTRAL PHILIPPINES

Jefferson R. Africa

Energy Development Corporation - EDC
38/F One Corporate Centre Building
Julia Vargas corner Meralco Avenue
Ortigas Center, Pasig City, 1605
PHILIPPINES
africa.jr@energy.com.ph

ABSTRACT

1D joint inversion and a study of selected MT and TEM soundings from the Krýsuvík high-temperature area, SW-Iceland and the Bacon-Manito geothermal project, Central Philippines was carried out using the TEMTD program. The two areas show a significant down shifting of MT apparent resistivity curves as a result of near-surface inhomogeneity. Joint inversion sections show a good correlation of the resistivity structure with the mineral alterations seen in the intersected wells although relic alteration was observed in both cases.

Inversion results highly depend on the initial model used and the parameters imposed. There exists a basement depth value where the fit of the inverted 1D model of the TEM and MT data varies significantly as depth becomes shallower or deeper than that value. The reliability of 1D joint inversion is highly dependent on the overlap of the TEM and MT data such that the downward bias of the MT apparent resistivity curve and the 3D structure effect of TEM data is reduced.

1. INTRODUCTION

Rapid industrialization demands an equally advancing technology. With this increasing technological capability, human beings can now automate a lot of things. But a huge amount of manageable energy is needed to keep up with the demands which human beings, we ourselves, have initially imposed. A lot of energy sources are now being utilized worldwide but only a small percentage is accounted for by renewable sources. Nonetheless, with the pressing issue of global warming, shifting towards renewable energy sources has been a long-term goal for humanity.

Among the renewable sources, geothermal energy has been utilized by people since time immemorial for direct utilization, but it plays a younger role in electricity generation. And, interestingly enough, only a small portion of the world's population is allocating work for geothermal energy development, which is to say that only 212 people per year per country (where countries considered are: 51% in Europe, 28% in Asia, 16% in America and 5% in Africa and Oceania) from the period of 2005-2009

expended time and effort on geothermal work (Lund et al., 2011). Nonetheless, geothermal development has progressed over the past few decades from a relatively small workforce.

In terms of geothermal developmental work, geo-scientific surface exploration has been mostly employed as a frontline procedure. The speculative work of exploration geoscientists like geophysicists resulted in a deep subsurface model, a reconstruction of data collected at the surface or near the surface of the ground. A lot of effort was made to improve the capability of scientists to “see through” the earth. There are a number of material properties like phase, density, conductivity, permeability and temperature and they play interdependently with one another. And the thin line that connects our devised models from the actual earth properties is our measuring and computing devices. The challenge for scientists is how to make sense out of the measured values and relate them to the intended subject, here a geothermal resource.

Cumulative work to improve scientific procedures and interpretation has culminated in today’s capabilities. This report presents just a few of the geophysical tools which have contributed a lot in the geothermal industry. It presents some applications of electromagnetic methods and their processing schemes for geothermal prospecting.

2. PRINCIPLES

2.1 Resistivity of rocks

Electrical resistivity surveying is found to be the most useful tool in geothermal prospecting as it has a direct relationship with other material properties significant to a hydrothermal environment such as salinity, temperature and alteration (Hersir and Árnason, 2009). For the sake of simplicity, electrical resistivity/conductivity will be termed solely as resistivity/conductivity from now on and the terms will be used interchangeably. Most often, rocks behave as an Ohmic conductor/resistor having this simple relationship:

$$\rho = \frac{1}{\sigma} = \frac{|\vec{E}|}{|\vec{j}|} \quad (1)$$

where ρ = Resistivity (Ωm);
 σ = Conductivity (S/m or $1/\Omega\text{m}$);
 $|\vec{E}|$ = Electric field magnitude (V/m) (arrow on top signifies a vector quantity while vertical bars signify the magnitude component of the corresponding vector);
 $|\vec{j}|$ = Current density (A/m^2).

Equation 1 states that under the constant influence of an electric field, the amount of charges passing through a section of rock at an interval of time decreases by the same factor that resistivity has increased or in the same way that its conductivity has decreased.

In a normal state, rocks behave as good resistors since electrons or ions within them are relatively bound. However, in a more natural setting, rocks interact with a lot of other substances like water and air and factors like temperature and pressure. Rock interactions with these other variables make their bulk resistivity highly variable.

Water plays a big role in altering the resistivity of rocks especially when it is saline and contains dissolved ions. Saline water is highly conductive compared to dry rock. As charges always flow through the region of least resistance, a rock in contact with saline water will, in effect, make the bulk resistivity lower since current will favour its flows with the ions dissolved in the water. In relation to this, the porosity of the rock matrix and its pore connectivity or effective porosity has a large effect on the

resistivity. Porosity itself can be defined as primary where interstices are originally present in the rock matrix and secondary where void spaces are created as a result of external factors such as pressure and erosion (Todd and Mays, 2005). At this point, it is noteworthy to include Archie's law (Archie, 1942) in the discussion which states that on a bi-logarithmic scale conductivity increases by a determined empirical factor with porosity.

$$\log \sigma = n \log \Phi_t + \log \sigma_w / a \quad (2)$$

where n = Cementing factor which is empirically determined; usually around 1-2;
 Φ_t = Fractional porosity of the rock matrix;
 σ_w = Conductivity of the fluid in the rock matrix (S/m);
 a = Parameter depending on porosity type; empirically determined and usually around 1.

Temperature also plays a role in altering the bulk resistivity of the rock material and, again, an aqueous environment present in the rock matrix contributes much to this effect. The temperature is a measure of the average kinetic energy of a material such that, at higher temperatures, ionic movement is greatly enhanced, and thus conductivity in the same way. This relationship is more accurately defined by Dakhnov (1962):

$$\sigma_w = \sigma_{w0} [1 + \alpha(T - T_0)] \quad (3)$$

where σ_w = Conductivity of pore fluid (S/m) at temperature of T (°C);
 σ_{w0} = Conductivity of pore fluid (S/m) at reference temperature of T_0 (°C);
 T = Temperature at which σ_w is formed (°C);
 α = Temperature coefficient of resistivity, i.e. $\alpha = 0.023/^\circ\text{C}$ for $T_0 = 25^\circ\text{C}$

Equation 3 is valid only for a temperature range of 0-200°C and the behaviour starts to reverse as the temperature increases further. The Arrhenius formula shows this reverse change of a rock's electrical characteristics as the temperature approaches the melting point of the material. Thus, when approaching the heat source of a geothermal system where more than 400°C can be expected, one would observe an increase in the conductivity of the rock (Flóvenz et al., 2012).

In any case, the factors that can significantly alter the bulk resistivity of a rock in any hydrothermal environment are effective porosity of the rock matrix, salinity of the pore fluid and temperature.

In the instance that hot groundwater comes into contact with rock, the surface that is in direct contact with the hot fluid experiences secondary mineralization. This happens in such a way that as fluid flows through pores, some of their components are left in the rock or vice versa, restructuring them in the process. This is often referred to as hydrothermal alteration. It has a relevant effect on the conductivity of the rock being altered. Interestingly enough, alteration minerals vary depending on the temperature of the water coming into contact with it. Figure 1 shows the range of temperature values at which different alteration materials can be formed.

It has been found out that these alteration minerals contribute to a lot of differences in the bulk resistivity of the rock matrix as they themselves have different resistivity values. In a general sense, rock resistivity is affected by three main conduction mechanisms. The first

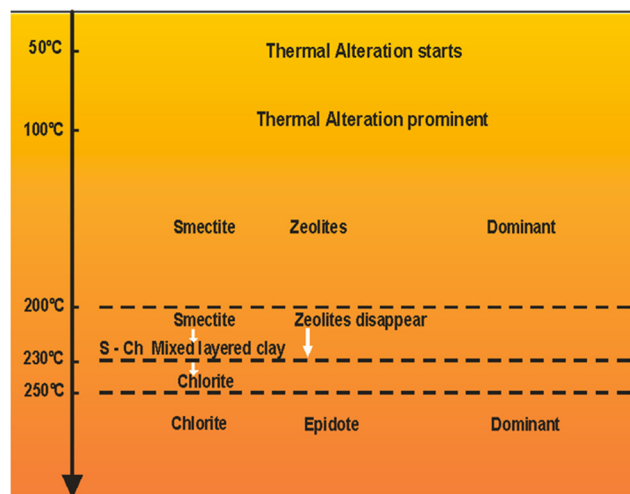


FIGURE 1: Formation temperature of different alteration minerals (adapted from Hersir and Árnason, 2009)

one is mineral conduction and has the least effect of conducting electrical current in a rock. This is contributed by the dry solid rock matrix itself. The next mechanism is pore fluid conduction; this is caused by moving ions within the heated saline groundwater. The last is surface conduction which is contributed mostly by the alteration minerals attached to the pore surface of the rock matter.

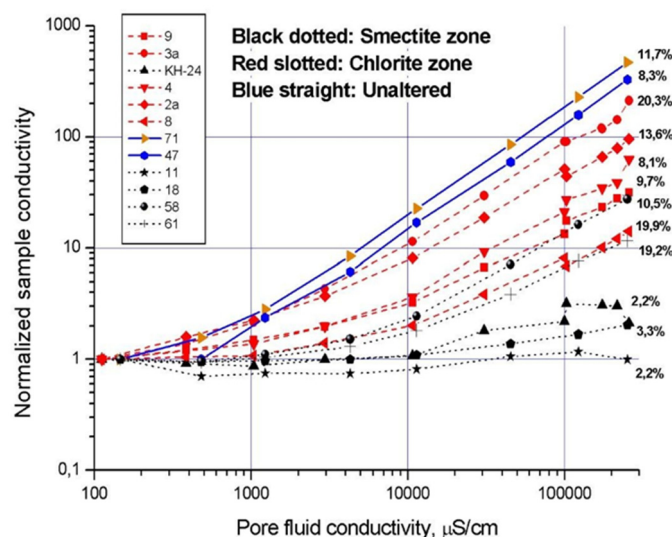


FIGURE 2: Bulk resistivity versus fluid conductivity at varying porosities (Flóvenz et al., 2005)

in Figure 2. As the conductivity of the pore fluid in a rock is increased, its bulk conductivity is likewise increased. But the rate of increase is dictated by the type of minerals attached to the rock, whereby conductivity of the unaltered rock unit has higher sensitivity with the conductivity of the fluid than rocks with chlorite and smectite attached to them. The bulk conductivity of rock with smectite is least responsive to the change in the conductivity of the contained fluid.

The resistivity signature of rocks in a high-temperature geothermal environment may show three types of circumstances with reference to their temperature conditions. The existing temperature of the rocks can be in exact accordance with the formation temperatures of their secondary minerals and the measured resistivity. This means that the resistivity information can practically tell the present temperature distribution in the rocks. However, this is not always the case. The other two cases pertain to the temperature conditions of rocks which are not in accordance with the present mineral alterations in them. There may be cooling whereby the resistivity information will show an overestimate of the temperature distribution compared to the existing condition, or there may be a rise in heat where the resistivity shows an underestimate of the temperature value with the actual one since newer mineral alterations are still building up.

2.2 Resistivity methods

The heat from underneath the earth's surface can be utilized effectively by a convection mechanism using a mobile flowing medium and the most abundant material that can transfer this huge amount of energy is groundwater. Hot water interacting with rocks can significantly alter their resistivity. Measuring the resistivity of rocks has been the straightforward means of geophysical exploration work in geothermal prospecting. There are other parameters which aid in any geothermal exploration studies such as temperature and thermal conductivity, the magnetization of rocks, density and seismic velocity but they are not tackled in this report.

Subsurface resistivity data can correlate both with temperature and the alteration of rocks which are key determinants in a geothermal resource study. A number of resistivity methods have been used for

In a high-temperature geothermal environment, it is the alternating role of the last two conducting mechanisms that gives the contrast of resistivity at depth. The so-called "high-low-high" resistivity signature in this environment is caused by the presence of different alteration minerals which are formed and attached to the host rock at different temperatures. The low-temperature forming alterations like smectite and zeolite contain loosely bound ions contributing more to the surface conduction, hence to the bulk conductivity of the rock, than fluid conduction, while the high-temperature forming alterations like chlorite and epidote which have more bound ions contribute less to the conduction mechanism than pore fluid conduction itself. This behaviour is clearly illustrated

geothermal resource exploration. The oldest one is direct current (DC) measurement but in terms of practicality it is not commonly used nowadays (Georgsson, 2012). The most recent commonly utilized methods are the transient electromagnetic and the magnetotelluric methods. For the purpose of this report, the latter two methods will be discussed.

2.3 TEM theory

The transient electromagnetic method (TEM) is an active method which uses controlled current source to measure resistivity in the ground. The method basically works under two of Maxwell's equations on electromagnetism; one is Faraday's Law which states that the induced electromotive force or the voltage in a closed circuit is caused by the time changing magnetic flux going through the circuit. The other one is Ampere's Law which states that a changing electric field or current would induce a magnetic field around it. Putting these physical laws into geological perspective, the set of conductors where the induced current would flow corresponds to the layers of the earth and the changing magnetic field and magnetic flux corresponds to the effect brought about by Ampere's Law as the controlled current from the loop of wire installed on the earth's surface changes. In mathematical form, we can state the two governing laws of TEM as:

Faraday's law:

$$\oint_{\partial\Sigma} \vec{E} \cdot d\vec{l} = -\frac{d}{dt} \iint_{\Sigma} \vec{B} \cdot d\vec{S} \quad (4)$$

Ampere's law:

$$\oint_{\partial\Sigma} \vec{H} \cdot d\vec{l} = \iint_{\Sigma} \left(\vec{J}_f + \frac{\partial \vec{D}}{\partial t} \right) \cdot d\vec{S} \quad (5)$$

where $\vec{E}; \vec{J}_f$ = Electric field (V/m); free current density (A/m²);
 $\vec{B}; \vec{H}$ = Magnetic induction (T); Magnetic field (A/m);
 \vec{D} = Electric displacement field (C/m²);
 Σ = Arbitrary open surface with boundary defined by $\partial\Sigma$.

As the controlled current in the source loop at the surface of the earth is turned off, it induces current down into the earth (Figure 3). If the ground is horizontally layered, then the current would flow along these layers as it widens and deepens with time. A series of cylindrical smoke rings centred along the vertical axis of the surface source loop can be depicted to represent the flow of the total current in a given horizontal layer. The area of this loop is generally a simplified representation from the net magnetic flux due to the magnetic field over an infinitely extending earth layer. Each single layer of the smoke ring contributes to an induced magnetic field at the surface at any given time which is dependent on the current density, radius and the depth from the surface (Christiansen et al., 2006). In a more complex earth model where resistivity is no longer horizontally layered, the current rings will then be oriented at different axes and may obtain different geometries deviating away from the shape of the source loop. There is often a sensitivity function which indicates the effective depth of penetration of the smoke rings at certain time periods.

This is obtained by summing up the amplitude contributions from the total current density of a layer and

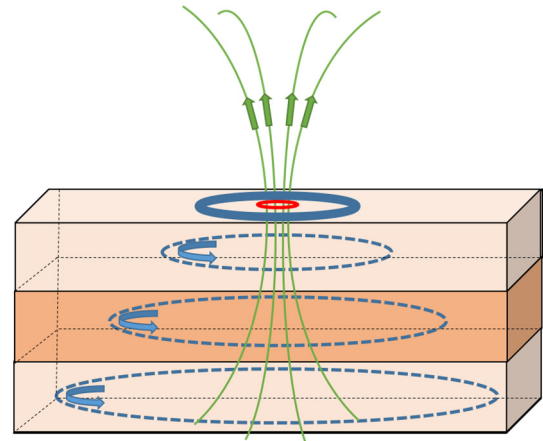


FIGURE 3: TEM working principle where dashed circles represent the net induced ground currents from source loop (dark blue circle on top); green lines represent induced magnetic field which then induces another current in the receiving loop (red circle on top)

the reduced contributions of each of these in every layer as the ground is penetrated. But this depends on the resistivity of the layers since the induced current systems tend to stay longer in conductive layers than do the resistive ones.

The current rings, immediately after the source current at the surface goes down to zero, would decay in amplitude, thus inducing a secondary magnetic field which in turn induces current in any conducting loop nearby. This is how the receiving loop works. The voltage values read by the receiving coil is directly related to the decaying secondary magnetic field from the current rings. At deeper penetration depth, the vertical component of a secondary magnetic field (B_{2z}) at the centre of the source loop can be approximated to be:

$$\frac{\partial B_{2z}}{\partial t} \approx \frac{-I\mu_0^{5/2} a^2 \pi^{-1/2}}{20t^{5/2} \rho^{3/2}} \quad (6)$$

where I = Maximum current (A);
 a = Radius of the source loop (m);
 ρ = Resistivity at the penetration depth (Ωm);
 t = Time after current turn off (s);
 μ_0 = Magnetic permeability in vacuum (H/m).

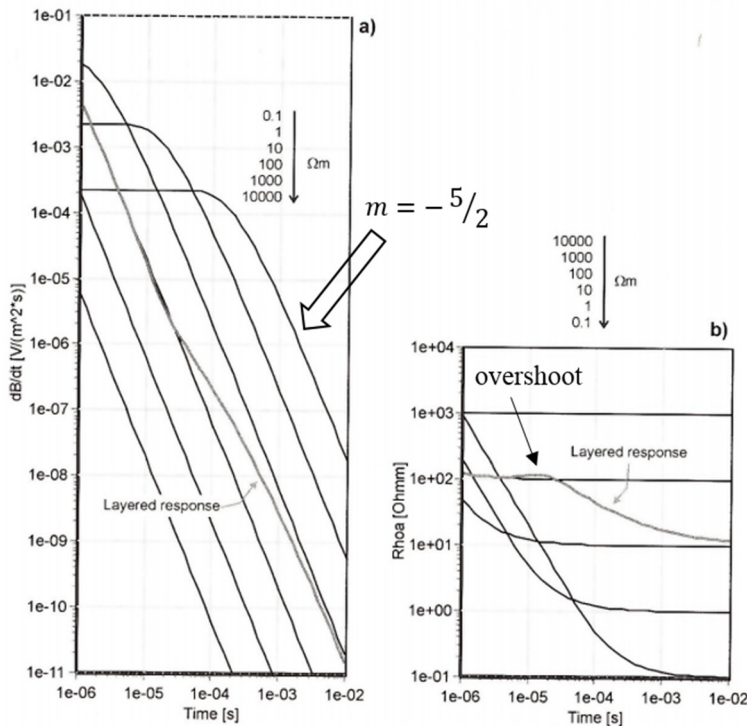


FIGURE 4: a) Impulse responses of the secondary magnetic field with different homogeneous earth models and a sample response of a two-layer earth with 100 Ωm above a 10 Ωm ;
 b) calculated apparent resistivity based on a)
 (modified from Christiansen et al., 2006)

down compared with the lower ones as seen in Figure 4. We iterate here that at the early time stage of the magnetic field response or equivalently the voltage response, the plot does not in any way reconstruct the real earth layer but only the linear behaviour of the curve and so the apparent resistivity curve starts at an unreliable value at that early stage. Likewise, there is also the unavoidable overshoot of the calculated apparent resistivity from the induced voltage response curve when it shifts from one to the other line with a higher y-intercept, i.e. when the upper layer has higher resistivity than the layer below

Equation 6 only simplifies the mathematics involved in obtaining the changing secondary magnetic field i.e. it is only an equation derived by assuming a large value of time (t) where the ratio $\sqrt{\mu_0 \sigma / 4t}$ approaches zero (Christiansen et al., 2006). This now separates the secondary magnetic field response into two major time segments we call early time and late time. This is clearly seen in Figure 4 where early time is approximated with a horizontal line and late time by a negative-sloping line. The equation also tells us that for a homogeneous earth with a source loop having a given current and a constant area, the logarithm of the induced voltage (as related to the time-changing magnetic field) would decay by a constant factor on a logarithmic time scale. Thus, we would expect that at later time, a homogenous earth with different resistivity will have all approaching lines with a $-5/2$ slope but vertically shifted, i.e. higher resistivity values have lines shifted

it. This overshoot value should not be interpreted as another earth layer. However, this behaviour does not happen the other way around.

Rearranging Equation 6 and using Faraday's Law of induction, we can calculate the resistivity, or properly termed the late-time apparent resistivity, as a function of the voltage of the receiving loop and time:

$$\rho_a \approx \frac{\mu_0}{4\pi} \left[\frac{2\mu_0 A_r n_r A_s n_s I}{5t^{5/2} V(t, r)} \right]^{\frac{2}{3}} \quad (7)$$

where $A_r n_r$ = Effective area: cross-sectional area multiplied by the number of turns of the receiver loop (m^2);
 $A_s n_s$ = Effective area: cross-sectional area multiplied by the number of turns of the source loop (m^2);
 $V(t, r)$ = Measured induced voltage (V) of the receiving loop as a function of time and radius of the source loop.

The secondary magnetic field is only present when the source current from the loop is turned off. But turning off the source current requires a certain range of time since abrupt current turn off is physically impossible, i.e. it will induce an infinite voltage. In such a time, the receiving loop at the centre of the current loop will create a different signature of electromotive force in the wire depending on whether the current is fully turned off or not. The induced current is exponentially increasing at the time the current approaches zero value but exponentially decreasing from the time when the current is absolutely zero. It is only during the time when the current has been fully turned off that the induced voltage values give a more workable representation of the subsurface resistivity. Thus, turn-off time must be fully determined.

It is also noteworthy to discuss the turn-on effect brought about by switching the current on. In the same principle that the current can never abruptly change, then turning the current on at every instant would similarly create an exponentially increasing electromotive force with opposite polarity. This will linger and may cause additional effect even after current turn off. This is emphasized more as the interval between current turn-on and turn-off becomes shorter, i.e. at higher frequency of the source current.

The actual current source in the transmitter loop is a half-duty square wave with varying input frequencies and signal amplitude. The voltage values are measured after the current is fully turned off. It is read on a logarithmic time scale which is called log-gating (Figure 5). This way, the random noise decreases proportional to $t^{-1/2}$ (Christiansen et al., 2006). The current is cyclic and moves from a

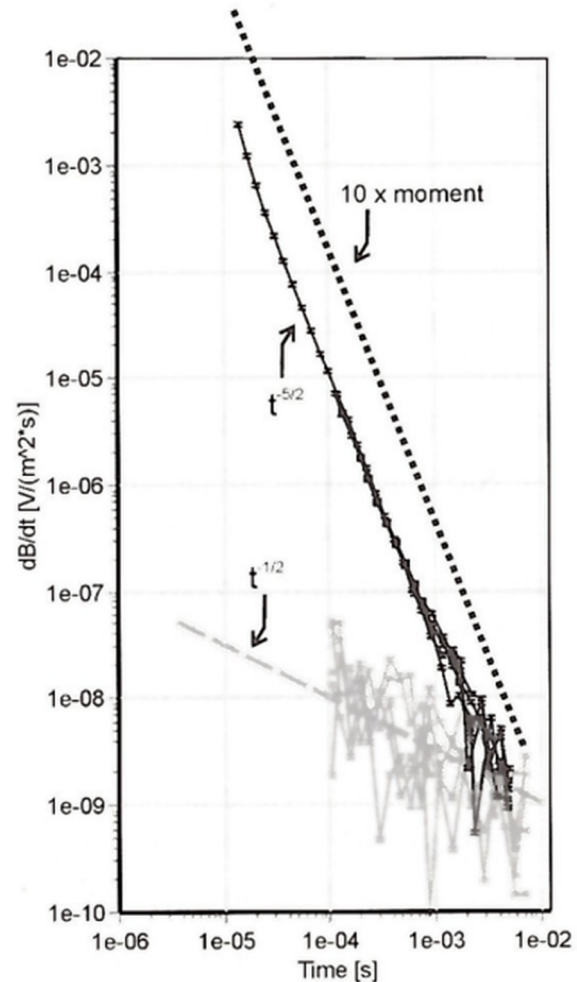


FIGURE 5: Earth response from a TEM sounding (black curve) and the same sounding with 10 times higher moment (dashed lines) with noise level (grey curve) measured in a logarithmic time scale (adapted from Christiansen et al., 2006)

positive current value to a negative one so as to prevent the ground from building up self-potential and thus preventing an unwanted current source. And to be more statistically confident of the measured data and to improve its quality, voltage values are measured and stacked over a number of current cycles. In the same way, increasing the signal source or the magnetic moment of the source loop can help increase the signal to noise ratio. This also helps the late time voltage readings from drowning too much from the noise level.

2.4 MT theory

The magnetotelluric (MT) method is a passive electromagnetic sounding method which uses naturally occurring electromagnetic sources as they propagate into the earth. As these waves penetrate into the earth's material, they induce a current into the ground, called telluric current, which generates secondary magnetic fluctuations. As these two fields are interdependent with one another as expressed by Ampere's and Faraday's Laws in Equations 4 and 5, they are able to delineate the subsurface conductivity as they penetrate into the earth. The transfer function which translates the fluctuation of

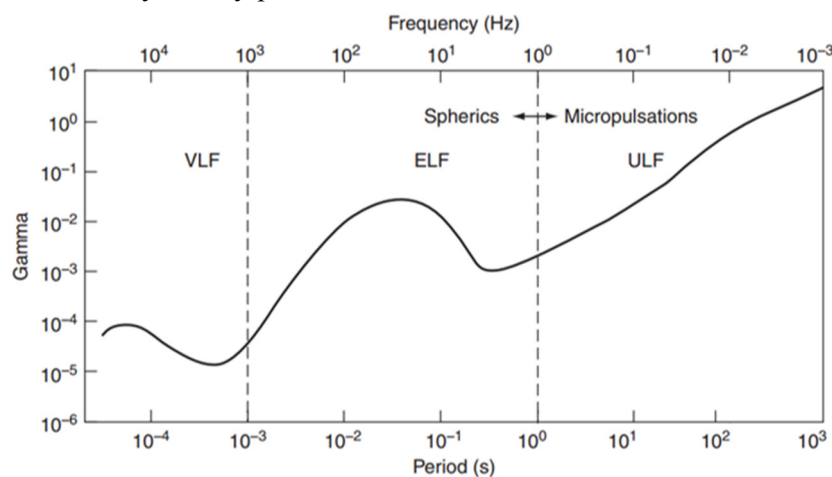


FIGURE 6: Mean amplitude of the magnetic field spectrum which MT uses as a function of period or frequency; note the two local minima of the curve which signify the dead band of the spectrum (from Flóvenz, et al., 2012)

one field to the other best describes the electrical property of the medium into which they are propagating. MT uses electric and magnetic fields from a period of 0.0025-1000 s and even up to a value of 10,000 s (Figure 6) (Flóvenz et al., 2012). It practically uses two different wave sources. The long period fluctuations of >1 s come from micro-pulsations as a result of solar wind from the sun interfering with the magnetosphere of the earth. The short period fluctuations of <1 s come from lightning activities which are usually generated near the equatorial region of the earth and are distributed throughout the globe via total internal reflection. This source is often called spherics. The period of MT covers, at most, two known ranges having the minimum signal amplitude and are called dead bands. The first one is approximately between the period of 0.0002 and 0.001 s while the other one is between 0.2 and 2 s. The latter has the largest impact for geothermal prospecting since it belongs to the period range where the probed depth usually reaches a hydrothermal resource.

In actual terms, an electromagnetic field is propagating in all directions from its source but behaves more like a plane wave when it gets farther away from it. For simplicity of mathematical computation and analysis, MT assumes electromagnetic fluctuations as plane waves propagating down the earth and since there is a big contrast of refractive index between the atmosphere and the ground, it is likewise simpler to consider that these waves penetrate at normal to the ground surface. Some other assumptions of the earth as discussed by Cagniard (1953) and Keller and Frischknecht (1966) (in Simpson and Bahr, 2005) are considered in MT so as to make calculations straightforward yet acceptable so as not to move far away from the real earth; they are discussed here:

1. The earth absorbs electromagnetic waves but does not generate any or at least in the frequency range where MT works.

2. Accumulation of free charges, specifically at boundary regions, is minimal or not present at all. Otherwise this can mask the actual resistivity value of the earth and can give unreliable interpretations. This is what is known as static shift.
3. The material where MT propagates is entirely ohmic, i.e. the current density passing through a medium is proportional to the electric field present in it.
4. Displacement current is negligible compared to conduction current; and electric permittivity and magnetic permeability do not vary as much as bulk conductivity of the rock material does.

Now, with waves assumed to be uniformly planar in propagation, we demand that both the source electric and magnetic fields be of the form:

$$|\vec{V}| = V_0 e^{i\omega t - kz} \quad (8)$$

where $|\vec{V}|$ = Electric (V/m) or magnetic (T) field magnitudes;
 V_0 = Maximum amplitude of both electric (V/m) or magnetic (T) field;
 ω = Angular frequency of wave oscillation (rad/s);
 t = Time (s);
 k = Wave number (m^{-1});
 z = Depth (m).

The wave oscillation has to be small enough compared with the earth's curvature so as not to deviate too much from the plane wave assumption and it occurs for electromagnetic signals having a period of less than a day (Srivastava, 1965).

Putting Equation 8 into Equations 4 and 5 (in differential form), we further assume that the source wave is vertically incidental to the earth, i.e. $\partial \vec{V} / \partial x = \partial \vec{V} / \partial y = 0$ and that it is composed generally of linear, isotropic and homogenous media i.e. $|\vec{D}| = \epsilon |\vec{E}|$ and $|\vec{H}| = \mu^{-1} |\vec{B}|$. Then, we can proceed to obtain the equation below:

$$\frac{\partial^2 E_y}{\partial z^2} = i\omega\mu \frac{\partial H_x}{\partial z} = i\omega\mu(\sigma + i\omega\epsilon)E_y \quad (9)$$

$$\frac{\partial^2 E_x}{\partial z^2} = -i\omega\mu \frac{\partial H_y}{\partial z} = i\omega\mu(\sigma + i\omega\epsilon)E_x \quad (10)$$

where $H_{x,y}$ = Horizontal components of \vec{H} along 2 arbitrary \perp directions;
 $E_{x,y}$ = Horizontal components of \vec{E} along 2 arbitrary \perp directions;
 μ, ϵ = Magnetic permeability (H/m) and electric permittivity (F/m) of a rock material.

For simplicity, it is assumed that conductivity, σ , is much higher by around a factor of ten compared with the electrical permittivity at the highest possible angular frequency (rad/s) i.e. $\sigma \gg \omega\epsilon_{max}$. Starting from Equations 9 and 10, we can find a unique solution such that the fields will practically diminish to zero when the depth (z) goes to infinity. Finally, we can get the general solution or the transfer function of MT in a 1D earth:

$$H_x = -\frac{k}{i\omega\mu} E_y \quad (11)$$

$$H_y = \frac{k}{i\omega\mu} E_x \quad (12)$$

where $k = \sqrt{i\omega\mu\sigma}$

From Equations 11 and 12, it is straightforward to obtain the apparent resistivity and phase from the complex transfer function. These are expressed in generalized form as:

$$\rho_{ij}(T) = \frac{1}{\omega\mu} \left(\frac{E_i^* E_j}{H_j^* H_i} \right) = \frac{1}{\omega\mu} (Z_{ij}) \quad (13)$$

$$\theta_{ij} = \tan^{-1} \frac{\text{Im}(Z_{ij})}{\text{Re}(Z_{ij})} \quad (14)$$

where i and j stands for any of the x and/or y components of the electric and magnetic fields.

It is often convenient to express the impedance values in a matrix notation. The conventional matrix form of Equations 13 and 14 is often referred to as the impedance tensor. It represents apparent resistivity and phase values at different orientations in space and at a particular frequency value. We also want to point out another independent tensor called the Tipper vector which shows the relationship of the horizontally propagating magnetic field with the measured vertical magnetic field.

This vector indicates the presence of lateral variations in the ground.

$$\begin{bmatrix} E_x \\ E_y \end{bmatrix} = \begin{bmatrix} Z_{xx} & Z_{xy} \\ Z_{yx} & Z_{yy} \end{bmatrix} \begin{bmatrix} H_x \\ H_y \end{bmatrix} \quad (15)$$

$$H_z = [T_x \quad T_y] \begin{bmatrix} H_x \\ H_y \end{bmatrix} \quad (16)$$

where Z_{ij} = Impedance element at different orientations in space;

T_x, T_y = Tipper vector along \perp and horizontal magnetic fields.

An electromagnetic method such as MT is actually a volume sounding (Simpson and Bahr, 2005). Using the compact matrix form, it is relatively easy to distinguish the geo-electrical dimensionality of the earth as well as to apply the rotation to the values as needed.

In a 1D case as seen in Equations 11 and 12, Z_{xx} and Z_{yy} which are the diagonal components, are always zero, thus, only perpendicular magnetic and electric fields interplay with each other. The impedances from the off diagonal elements of the Z matrix, Z_{xy} and Z_{yx} , have equal magnitude components but opposite signs. It lags a constant value of π for their phases. In terms of the geomagnetic transfer function, or the Tipper, there is no net vertical magnetic effect from the horizontally propagating magnetic fields, since lateral variations in a 1D earth are not present. It is also noteworthy to discuss here that this simplified earth model assumes a rotationally invariant impedance value which may take the form:

$$Z_{det} = \sqrt{(Z_{xx}Z_{yy} - Z_{xy}Z_{yx})} \quad (17)$$

where Z_{det} = Determinant of the impedance matrix in Equation 15.

In a 2D case, the Z matrix can be rotated to a certain angle whereby the diagonal elements are reduced to zero and at the same time maximize the values for both the off diagonal elements. However, in this instance, the latter pair is not necessarily equal. This reoriented Z matrix gives new definition to Z_{xy} becoming the transverse electric (TE) impedance element which runs parallel with the major geo-electric strike in the area as demanded by the 2-dimensionality assumption. The Z_{yx} now becomes the transverse magnetic (TM) impedance element and runs perpendicular to the defined geoelectric strike. It is also important to note from here that the two different impedance signatures should be inverted in a profile direction along with their defined orientations such that profile sections should be made along the geo-electric strike if inverting for TE impedances and perpendicular to the strike if inverting for TM impedances. This dimensionality also demands that the Tipper vector is non-zero along the TE mode, i.e. since it has the magnetic field H_y which “sees” the lateral conductivity contrast of the earth. And, thus, the induction arrows, both imaginary and real, orient themselves perpendicular to the strike direction (Figure 7) (Castells, 2006).

In the generalized 3D case, the impedance and the Tipper tensors are all non-zero at any given rotation.

2.4.1 MT penetration depth

The MT resistivity sounding method has the capability of probing very deep, even up to hundreds of kilometres depth (Flóvenz et al., 2012). This depth of penetration is dependent on two variables: the period of the waves and resistivity where the wave is propagating. In a general case, the signal having a longer period can probe deeper. However, the resistivity of the material itself limits the capability of the MT signal to propagate downwards, i.e. if the earth is conductive, the signal tends to decrease at a faster rate than when the earth is less conductive. It is considered that when the signal decreases to $1/e$ of its maximum value, which is at the surface, then it has achieved its effective penetration depth. In mathematical terms, the skin depth of MT in metres is:

$$\delta(T) = 500\sqrt{\rho T} \quad (18)$$

where T = Period of the propagating electromagnetic wave (s).

2.4.2 Remote referencing

MT data, just like any other geophysical data, are measured with noise. Different types of noises disturb an MT signal but it is usually the coherent noises that are easy to minimize aside from systematic noises. To illustrate, we take one of the extended forms of the element of the Z-matrix defined in Equation 15:

$$Z_{xy} = \frac{(E_x H_y^*)(H_x H_x^*) - (E_x H_x^*)(H_x H_y^*)}{(H_x H_x^*)(H_y H_y^*) - (H_x H_y^*)(H_y H_x^*)} \quad (19)$$

where H_x^*, H_y^* = Conjugates of H_x and H_y respectively.

The details of how Equation 19 was derived is not shown here but by assuming that the noise is relatively more significant in the electric than in the magnetic field, we basically add to Equation 15 an error function matrix. By minimizing this error function, we arrive at each of the solutions for the impedance elements like the one shown in Equation 19. It is reasonable to assume that the horizontal magnetic field does not vary significantly from a site to a certain remote location which is usually several kilometres away but only the inherent noises in their respective places. Thus, it is valid to replace conjugates of the magnetic field in Equation 19 with the conjugate values of the equivalent magnetic field at a remote site. Hence, we have:

$$Z_{xy} = \frac{(E_x H_{ry}^*)(H_x H_{rx}^*) - (E_x H_{rx}^*)(H_x H_{ry}^*)}{(H_x H_{rx}^*)(H_y H_{ry}^*) - (H_x H_{ry}^*)(H_y H_{rx}^*)} \quad (20)$$

where H_{rx}^*, H_{ry}^* = Conjugates of H_x and H_y of the remote site, respectively.

This eliminates auto powers from reducing the effect from the coherent noises in the magnetic signals of both stations since the uncorrelated noises are now multiplied. As an effect, it reduces the downward tendency of the apparent resistivity curves or the bias, especially at high frequency signals where the stacks are plentiful. The technique discussed was proposed by Gamble et al. (1979).

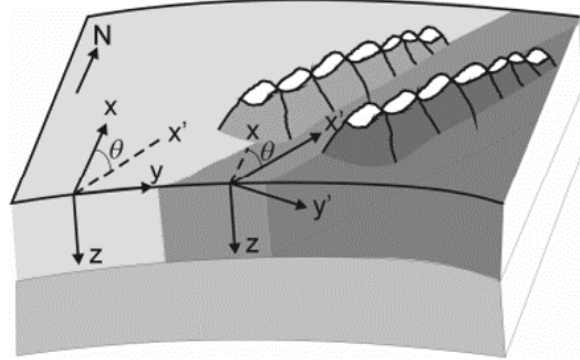


FIGURE 7: Sketch of the 2D dimensionality case of the earth where θ is the rotation of the axis of the impedance tensor from x to x' , moving the latter to orient along the strike direction as indicated by surface conditions (adapted from Castells, 2006)

2.4.3 Static shift problem

MT measurements are done on the surface of the earth. The earth itself has a lot of inhomogeneities which in one way or another alter the path of the telluric currents but not so much as to significantly change magnetic fluctuations. When a field encounters a relatively small shallow body, either resistive or conductive, it changes the value of the electric field at all frequency ranges. This, in effect, multiplies a factor to specific impedance elements as seen in Equation 15, depending on where in space the inhomogeneity is located. In a way, it alters the computed apparent resistivity from this by multiplying it with a constant scalar factor. But this never alters the phase since it is computed as a ratio of the components of the complex impedance. The value of the shift depends upon the contrast of the resistive/conductive inhomogeneity with the surrounding layer. Other means of static shift are caused by changes in topography where the current is redistributed, thus altering the current density and by the presence of lateral structures/boundaries which change the effective voltage drop between measurement poles. All of them contribute to the same effect of vertically shifting the apparent resistivity curves on a logarithmic scale and altering the computed skin depth as well.

However, the reality is that the actual earth layers are not known beforehand. And for the sake of argument, having knowledge of it can always correct for the static shift problem of MT but will defeat the purpose of the survey per se. Thus, at any point in doing the MT survey or even at a processing stage, a geophysicist may not be fully aware of how to correct it, although a lot of computational methods have been proposed to overcome these offsets. One is through spatial averaging at selected frequencies (Bostick, 1986; Sternberg et al., 1982 & 1985; Vozoff, 1990). Another one works out the shift correction with the statistical assumption that the product of the shift multipliers of a large number of MT soundings over a significantly wide area is close to unity (DeGroot-Hedlin, 1991). There is also another study which corrects for static offsets in a sedimentary environment using modal estimates by considering a fixed earth layer at a certain known value (Jones, 1988).

It was pointed out by Árnason et al. (2010) that the DeGroot-Hedlin (1991) assumption was not empirically verified by collating the static shift multiplier values of processed data from Hengill and

TABLE 1: Product of static shift multipliers of a large number of soundings in Hengill, Krafla and Asal Rift areas (modified from Árnason et al., 2010)

Area	Number of Soundings	Product
Hengill	149	1.089×10^{-10}
Krafla	124	1.683×10^{-10}
Asal Rift	64	1.045×10^{-16}

Krafla in Iceland and the Asal Rift in Djibouti. It was shown that these three cases produced a product of the shift values in the order of 10^{-20} - 10^{-10} which are quantities closer to zero than unity. The static shift problem in MT has been its weakness but TEM can effectively correct for the offset. In TEM there are no direct measurements of the electric field from the ground but only through measurement of the voltage produced by induction mechanisms, which is independent of any near-surface inhomogeneity (Table 1).

2.5 Inversion theory

The apparent resistivity curve is not the actual form of the earth's layered resistivity but only reflects the response of an electromagnetic signal from the layered earth. Thus, through inversion, the apparent resistivity is translated into true resistivity or as close to it as possible. In actual terms, there is no single layered earth solution to an apparent resistivity curve. The uncertainties introduced in the data set give a problem of equivalence whereby combinations of layers' resistivity and thickness values can produce curves that are within the bounds of the uncertainties in the data. In an Occam inversion, which was mostly employed in this report, the approach considers that electromagnetic soundings are not sensitive to sharp boundaries or to significantly thin layers of the earth (Constable et al., 1987).

The inversion works by iteratively adjusting the model parameters such that its forward curve fits well with the measured data. Iteration means that the previous models serve as the basis on how the next parameters should be adjusted based on the fit. As discussed by Arnason (1989), one of the approaches of electromagnetic inversion is by implementing a non-linear least square method whereby the model parameters must be forced to adjust such that the misfit function χ^2 of the response curve against the measured data, apparent resistivity in our case, be at a minimum, i.e. by taking the first-order derivative of all components of model parameters, say j in total, to zero.

$$\chi^2(\mathbf{m}) = \sum_{i=1}^M [y_i - f(x_i, \mathbf{m})]^2 / \sigma_i^2 \quad (21)$$

where $\chi^2(\mathbf{m})$ = Misfit as a function of the model parameters;
 y_i = Data vector as apparent resistivity (Ωm);
 $f(x_i, \mathbf{m})$ = Forward response as a function of abscissa variables x_i e.g. time (s) and model parameters \mathbf{m} as resistivity (Ωm) and thickness (m);
 σ_i = Standard deviation of response values;
 M = Number of data points considered in a response curve.

The tedious process of minimization for a non-linear $f(x_i, \mathbf{m})$ can be done by iteration. And the process itself needs to have an initial \mathbf{m} value which is intended not to move far away from the hypothesized actual earth model. Now, applying minimization to χ^2 with respect to all j model parameters by assuming that the selected model \mathbf{m} varies from the actual model by a step value of $\delta\mathbf{m}$, then we can say that:

$$\sum_{i=1}^M \frac{1}{\sigma_i^2} \left[y_{0i} - f(x_i, \mathbf{m}) - \sum_{k=1}^N \frac{\partial f(x_i, \mathbf{m})}{\partial m_k} \delta m_k \right] \frac{\partial f(x_i, \mathbf{m})}{\partial m_j} = 0 \quad (22)$$

where N = Number of partial derivative terms considered in the Taylor expansion of the forward response curve.

From this point, only N numbers of $\delta\mathbf{m}$ are unknown. But the solution is done by implementing the Levenberg-Marquardt method which robustly treats outliers while solving for these small steps in model parameters and updates them every iteration such that this \mathbf{m} vector will confidently converge to the empirical or expected value.

3. MEASUREMENT PROCEDURES

3.1 TEM sounding

The central loop TEM measurements are done by placing a loop of wire which is usually a square with a variable area of around 40,000-90,000 m² (but can go down to less than 10,000 m² for shallower soundings). Alternating half-duty square wave current is applied to the loop with repetition rates that are harmonics of the electrical environment used in the area. This is controlled by the TEM transmitter instrument. The current in the wire can be implemented with an amplitude of around 20-25 A using an electrical generator, but can go to less than 10 A if portable batteries are used. However, we note here that there is a great chance of acquiring data with lower signal-to-noise ratio when using lower current.

Initially, the TEM receiver instrument is calibrated using a known signal source. In the case of Geonics PROTEM digital receiver, a built-in calibration circuit generates an exponentially decaying signal to the instrument that can have four options of time constants and can automate its calibration (Geonics, 1999). Since TEM works with very rapid signal transitions, it is necessary to precisely synchronize the transmitter and the receiver instruments so that the receiver can have the information of the actual turn-off time interval of the transmitter and can start recording from there. Synchronization can come in two

options either by reference cable or by crystal clocks. The two instruments must work at the same repetition rates. Now, a receiving loop is placed near the centre. Different loop areas can be practically used here but the higher the effective loop area, the higher the signal-to-noise ratio of the data gets, especially at late time gates. However, it can be argued here that at higher repetition rates, a smaller loop area should be used to avoid saturation of voltage records. The integration time of the receiver instrument must be taken into account for greater stacking and thus higher data confidence. A particular instance can be illustrated here whereby a 10 m × 10 m square loop with several windings (effective area of around thousands of square metres) is used at a 2.5 Hz repetition rate and another set of measurements using the same repetition rate but with a smaller circular loop of 1 m² with 100 windings (100 m² effective area). This was done to get quality value of voltage stacks for the later gates using the former set-up and the same for the earlier gates using the latter set-up. In the case of a higher repetition rate of 25 Hz, the same small circular loop was used to acquire good quality data at shallow regions, while the later gates in this case are usually less significant since there is some good overlap with the previous set-up using 2.5 Hz.

3.2 MT sounding

MT measurements are done by setting up perpendicularly oriented electric lines which have electrode pots at the ends, usually composed of lead-chloride with a porous ceramic bottom for measuring telluric currents. The opposite ends must be connected with the N-S and E-W connections in the data logger, although the orientations of these lines might not necessarily follow the cardinal directions. But the choice of it may depend on the terrain or the discretion of the field-man. The endpoints of the electric lines are important and they should be in good contact with the ground. A good strategy is to use a solid water-bentonite mixture as an intermediary between the electrodes and the ground. This is done so that telluric current can easily flow from the ground directly to the measuring instrument or data logger which is commonly placed at the junction point of the telluric lines. A ground electrode is also placed somewhere near the middle or the junction point in order to obtain relative voltage drops for each end of the line and possibly troubleshoot for any anomalous readings. But the ground electrode does not participate in the data collection per se.

Two magnetic sensors, which commonly are elongated coils, should be placed along the orientations of the perpendicular telluric lines. Another coil must be placed normal to the ground. These three coils measure the three independent components of the magnetic field. Hence, they must be stable enough to prevent them from unnecessary movements. This is often done by housing them under a considerable amount of ground which is done by digging. The polarity of these coils must be taken into account and in the case of Phoenix instruments (Phoenix manual), the connected ends of the horizontally oriented coils should face the southern and the western ends of the electric lines as indicated by their connections in the data logger. We note here that the orientation in space of the entire set-up does not matter as long as the relative directions of the component are well established. However, it is a necessity to record the direction of the set-up and the coils used for each line as well as the distances of the electrodes since they will be used for later data processing. The data logger is set to record for at least a day. And it is advisable to acquire data at night-time rather than at daytime since the signal from the former is stronger than the latter (Simpson and Bahr, 2005).

4 GEOLOGICAL SETTING AND PREVIOUS WORK

4.1 Krýsuvík high-temperature area

The Krýsuvík high-temperature area is located on the Reykjanes peninsula, SW-Iceland. As the peninsula is an elevated portion of the diverging Mid-Atlantic Ridge, it has considerable manifestations of post-glacial lava fields with protrusions of hyaloclastites and pillow lavas and breccias, all basaltic in composition (Arnórsson et al., 1975). Krýsuvík area is within the NE-SW oriented volcanic zones

characterized by fissure swarms with intense alteration clays and hydrothermal manifestations like boiling springs and explosion craters. This area along with high-temperature areas in the peninsula deviate from most other high-temperature areas in Iceland, e.g. no indications of volcanic centres are seen (Hersir et al., 2013), but there are indications of intrusions in the base of a buried caldera as argued by Saemundsson in Hersir et al. (2013).

Early exploration studies were done in the area in 1975 (Arnórsson et al., 1975) employing DC measurements as their resistivity method but complications arose in the drilling of exploratory wells. Eventually, MT and TEM measurements were employed in the area in 2007-2008, and then these new data sets were multi-dimensionally inverted into 1D, 2D and 3D cases (Hersir et al., 2010; Lemma, 2010; Hersir et al., 2013).

4.2 Bacon-Manito geothermal project

The Bacon-Manito or Bacman geothermal project is located in the southeast region of Luzon Island which is one of the major islands located in the central part of the Philippines. It is part of the NW-SE trending volcanic belt and is overlain by Pliocene up to younger andesitic and basaltic volcanoes (Panem and Alincastre, 1985). It is situated between two major tectonic zones. To its east is the Philippine trench which is the collision boundary between the Philippine Sea plate and the Eurasian plate. To its west is the Philippine Fault system which runs through the country in a NW-SE direction. The splay of the Philippine fault, which is considered active (Lagmay et al., 2005) in the region of Bacman, is of considerable interest since it affects the structural dynamics in the area. One of them is called the Bacman fault zone (BFZ), predominantly WNW-ESE (Braganza, 2011). Another band lies NW-SE of the region, the Pocdol belt, and has several permeable structures. Likewise, as seen in Figure 8, the region of intersection of the two mentioned zones coincides with the identified and developed geothermal system. Several TEM and MT measurement were done. These data were 2D inverted and a resistivity map of this area has been made recently.

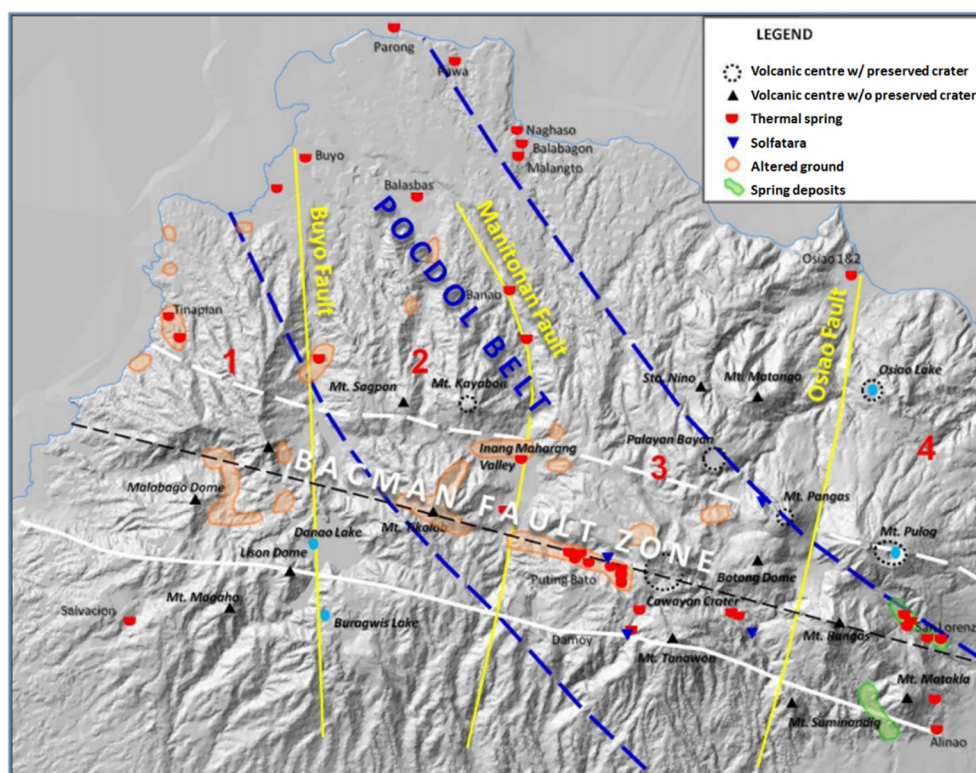


FIGURE 8: Elevation map of the Bacman area with delineated major structures, altered grounds and other thermal manifestations (modified from Braganza, 2011)

5. TEM AND MT DATA PROCESSING FROM KRÝSUVÍK

5.1 TEM processing and 1D inversion

Raw TEM data, which contain the induced voltage values acquired by a 20-gate TEM receiver at different repetition rates of 25 and 2.5 Hz, were inputted into a Linux-based software called TemX (Árnason, 2006a). This was done to convert these values to their equivalent apparent resistivity curves. This graphical-user interface software permits one to remove outlying data points visually. The output format of the files from this software are text files which we conventionally call inv files (since we attach a suffix of .inv at the end).

The inv files were then inputted to an inversion program called TEMTD (Árnason, 2006b). The inversion produces a layered model with resistivity and thickness values for each of the inv files. This program can perform either layered earth or Occam inversion which assumes relatively smoother and

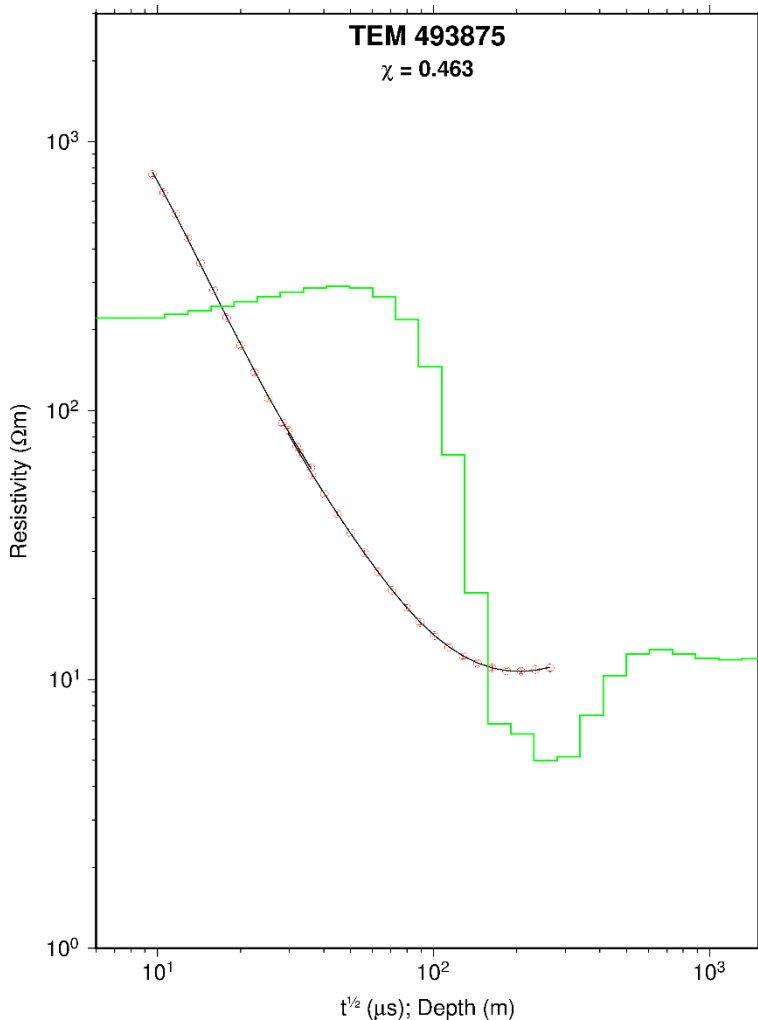


FIGURE 9: 1D inversion results from a TEM sounding; the red dots are the calculated apparent resistivity points from voltage data; the green line shows the layered model generated by TEMTD; the black line is the response from the model

continuous resistivity changes of the earth. The latter inversion works with fixed layer thicknesses and assumes numerous earth layers for "smoothness". Additionally, the program permits greater control on the generated models by allowing different constraints to be manually adjusted like smoothness of the model's resistivity, which henceforth is referred to as R (applies the same for layer thicknesses but only used with layered earth inversion), or a damping parameter for regulating oscillation of the model resistivity which from here on is referred to as S (applies the same for layer thicknesses but only with layered earth inversion), a scaling factor for uncertainties in the data, top layer thickness, depth to basement and suppression of some of data points (details in Árnason, 2006b). Inversion was done not only to minimize the misfit but also arrive at an acceptable 1D earth model. An example of an inversion output is shown in Figure 9. It shows an Occam inversion model of 40 layers with R and S equal to 3.2 and 2.6, respectively. A total of 11 TEM sounding data in this area were inverted for voltage values and all resulted in a low misfit value as presented in Appendix I (Africa, 2013).

The quality of the fit is one of the best determinants of an inversion output, aside from geophysically assessing the sensibility of the experimental data and the generated model. This is one thing that modern-age computers do well - performing routine minimization. There can be no simpler way to

invert an apparent resistivity curve than by assuming a simple layered earth model by representing the measured resistivity using the minimum possible number of layers. With the data presented in Figure 9, we vary the number of earth layers starting from a three layered earth model until reaching up to less than a hundred layers. We compared the quality of the fit that each of these layered models produced. This was done by successively adding a layer at every turn of inversion starting from the simple 3 layered earth. The previously generated model was used as the initial model for the next run until reaching the highest attainable number of layers. The procedure was implemented under a constant set of parameters, i.e. 5 iterations per Occam inversion with a basement depth of 1000 m, top layer thickness of 5 m, R and S were equal and the rest of the parameters were set as default.

The plot in Figure 10 generally shows a decrease in the misfit value as the number of layers is increased. For all three cases of R and S values, curves were observed to significantly relax and gradually decrease in misfit after around 30 layers. In the case where R and S parameters were not considered, i.e. both R and S were zero, the misfit approached its minimum with a lower number of layers than in the case when R and S were non-zero, especially when they were both set to 10. This suggests that having more layers in the model can more easily make the inversion approach a better fit but adding constraints to the model limits its freedom to allow equivalent models to be noticed, thus hampering fitting or making the misfit higher. Given reliable data, a model with low misfit values may not necessarily be acceptable, but an acceptable model should always have a low misfit. In the end, the choice of an acceptable model relies on the discretion of the geophysicist.

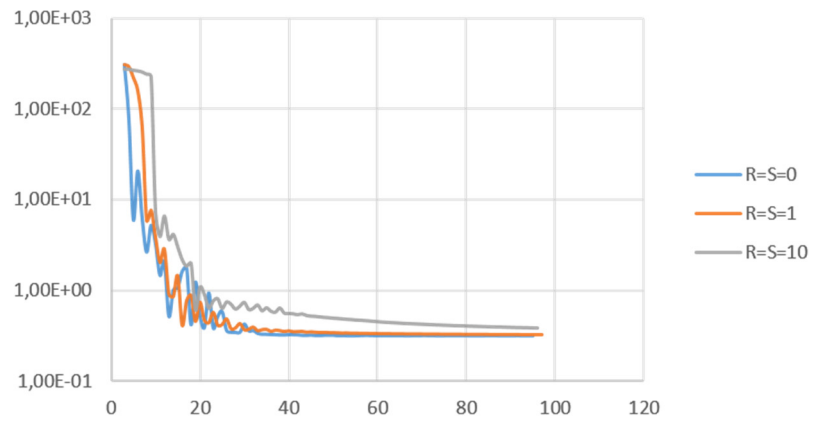


FIGURE 10: χ^2 misfit value of the forward response with the measured data as a function of number of layers of the model; plots were obtained from inverting a single TEM sounding data using constant parameters but only varying resistivity smoothness and oscillation

5.2 MT processing, static shift and joint 1D inversion

Raw MT data are time series data containing two electric and three magnetic field readings (if a 5 channel set-up is used) at 3 different sampling frequencies to serve as low-pass filters and sampling intervals to serve as high-pass filters. These data are inputted to the software provided by Phoenix Geophysics (as we are using their manufactured MT instruments) in order to convert these time series values to auto- and cross-powers where impedance, Tipper, coherency, Z-strike, skew and other desired values are embedded. This is implemented first in SSMT2000 by segmenting the series and applying Fourier transformation to extract the frequency components of each segment, remote referencing the calculated values of the overlapping segments and applying robust estimation. The rest of editing is visually done using the graphical-user interface software called MTeditor where unwanted outliers are further removed from the data. The final output file is called an EDI file where EDI stands for electrical data interchange (SEG, 1991).

From the EDI files generated, it is recomputed to obtain the needed impedance values or the apparent resistivity and phase and the strike. Since we are processing data in a 1D dimension case, then only the determinant of the impedance tensor is used to make it rotationally invariant.

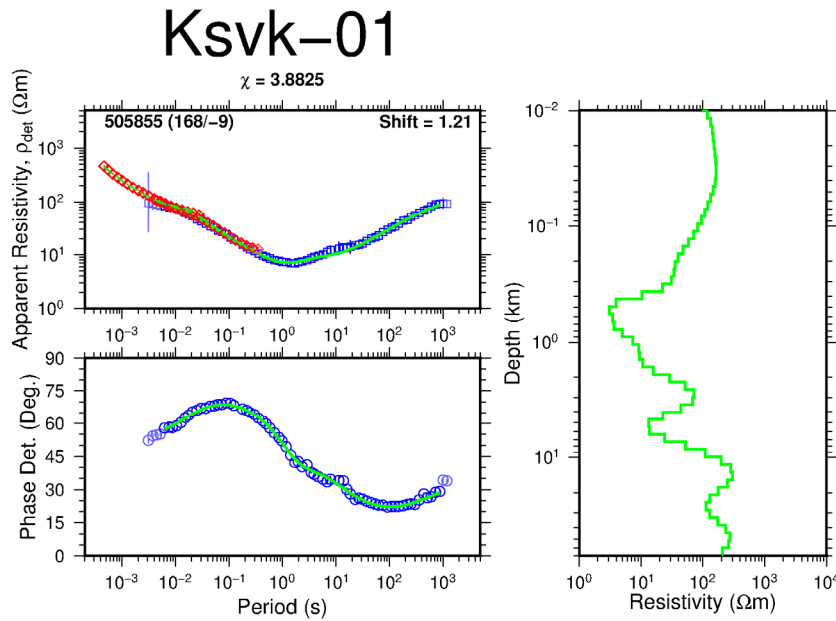


FIGURE 11: 1D joint inversion result of TEM and MT sounding; red diamonds are TEM apparent resistivity points transformed to pseudo-MT points; blue squares are MT apparent resistivity and blue circles are MT apparent phase points which are derived from the determinant of MT impedance tensor; Green lines on the right represent 1D joint inversion model and on the left represent the model's MT apparent resistivity and phase response. The name on top of the plot is the MT station name with the misfit value of the model; the data is given by the equation below it. The shift value implemented to MT data so that it would fit the TEM data is 1.21. The name of the TEM sounding is 505855 with an aerial distance of 168 m from the MT sounding and elevation difference of 9 m

at Figure 12, we see that the fit of the response goes well with the measured data but a slight off is seen in the period range of around 10 s. This could be due to the 3D behaviour of the impedance data at that particular period range.

5.3 Sensitivity-to-depth test

MT penetration depth can be best approximated by skin depth as seen in Equation 18. Here we test the sensitivity to depth of a joint TEM and MT sounding in Krýsuvík. First, depth to basement was reduced to around 6 km as modified from the best generated model having a depth of 45 km. This new model was inputted as an initial model in the joint inversion with all other parameters kept the same as with the best model. Figure 12a shows the result. It produces an acceptable fit with a chi square value of 4.84. The best model generated a misfit of 4.79 which gives a very close value with the shallower model. In the second case, depth to basement was cut to a shallower depth of around 5.1 km as modified from the same best model. Inversion results as seen in Figure 12b give a model with a significantly larger misfit of 10.30 from the initial 4.79. The response noticeably misfits the highest frequency periods of the data as expected. It means that at this depth range of 5-6 km and for this particular sounding, there is a significantly high sensitivity in the fitting capability of 1D joint inversion, especially at the highest frequency points of the MT data. However, extending further down from this basement depth of 6 km can result in a slightly better fit, but the reliability of the resulting model below 6 km is another thing to look at.

After calculating and editing the apparent resistivity curves for both the TEM and MT, they are ready for joint inversion. This was implemented using TEMTD software but this program can also do inversion of TEM or MT separately. TEMTD considers the MT apparent resistivity shift as part of the parameters that is inverted for, although "force shifting" was also possible. Figure 11 shows a sample of the best fitted model, where the data were inverted for voltage of the TEM data, and for the apparent resistivity and phase of the MT data. Unwanted data points were disregarded in the inversion. All data were inverted using Occam inversion method with varying first and second order derivatives of the resistivity layers such that the model will be optimized for resistivity smoothness and avoid unnecessary oscillations in their values. Looking closely

5.4 Model results

A total of 21 MT sounding data and 20 TEM sounding data were jointly inverted, meaning two MT stations used a single TEM sounding. This data set produced two profiles cutting SE-NW through the survey area. Three boreholes with hydrothermal alteration data were used on the profiles. Figure 13 shows the map of the Krýsuvík high-temperature area together with the location of the TEM and MT soundings as well as the profile trace generated from them.

The two profiles run from NW-SE and cut through the fissure structures. The profiles shown in Figure 14 extend down to 10,000 m below sea level; these same profiles are shown in Figure 15 at a shallower depth of 2000 m below sea level. Both of the profiles exhibit low resistivity values of $<10 \Omega\text{m}$ at shallow depths of up to around 1500 m, but deepen considerably at the southeast end of profile 2 and the northwest end of profile 1 which are seen farthest from the fissure swarms. Updoming configuration of the low resistivity region is pronounced in the central region of profile 2. The defined low resistivity zone can be interpreted as rocks having extensive amounts of low-temperature secondary alterations like smectite or zeolite. The moderately high resistivity of less than a $100 \Omega\text{m}$, as seen underneath the low resistive cap, suggests the presence of secondary alterations like chlorite and epidote. The presence of some highly resistive regions of around $200 \Omega\text{m}$ below the identified clay cap (mostly seen on profile 1) is most probably related to impermeable rock regions where lesser amounts of groundwater can come into contact, thus maintaining its high resistivity characteristic compared to its immediate surroundings. The surface and near-surface high resistivity regions of several hundreds of Ωm in value are represented by the young volcanics covering the region which are fresh unaltered rocks and mostly above the water table. Low resistivity values are also seen close to the surface where fumaroles are located.

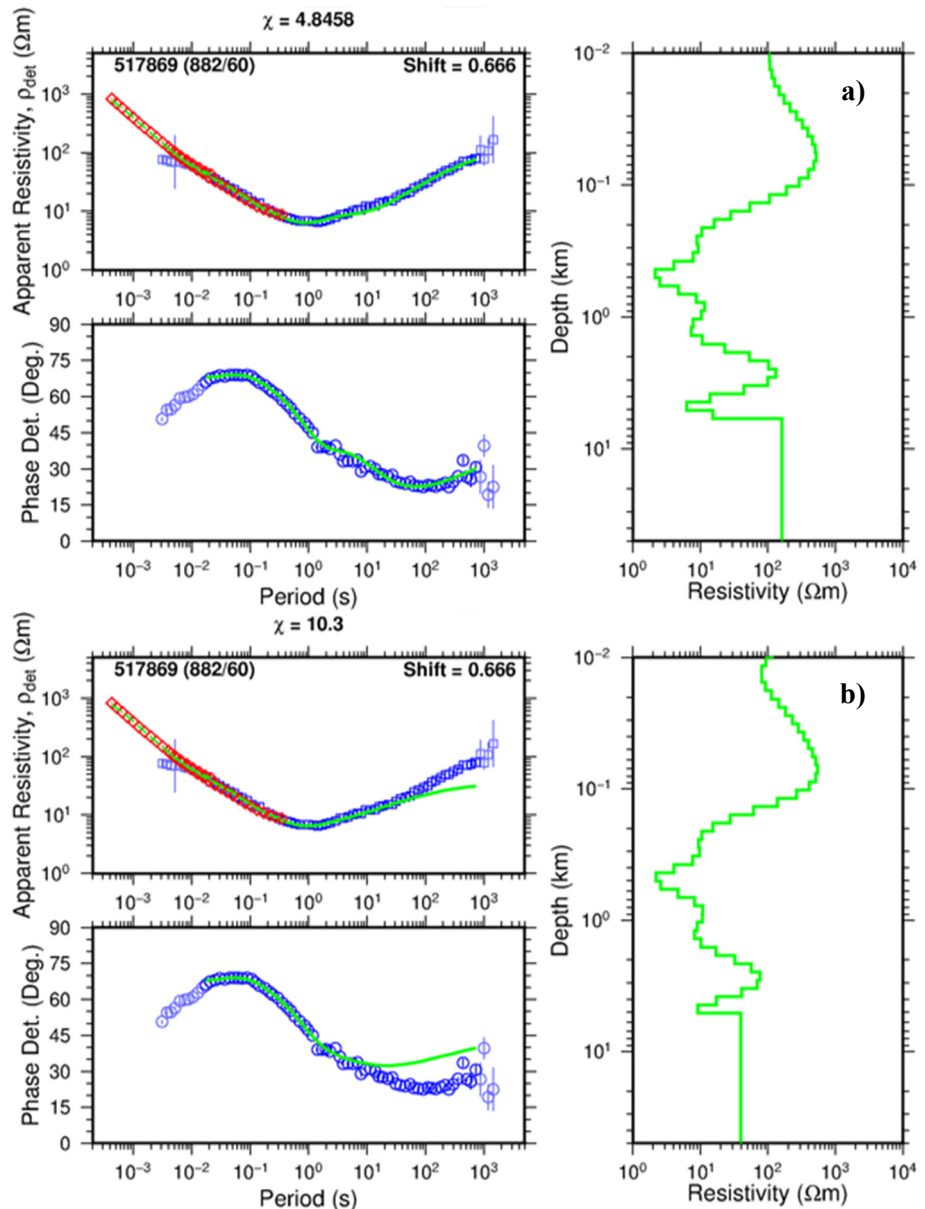


FIGURE 12: In a) basement depth of the best model was reduced to 6 km; this initial model produced an inversion result with 4.84 as misfit; b) basement depth of the best model reduced to 5.1 km which produced a result of 10.30 as misfit

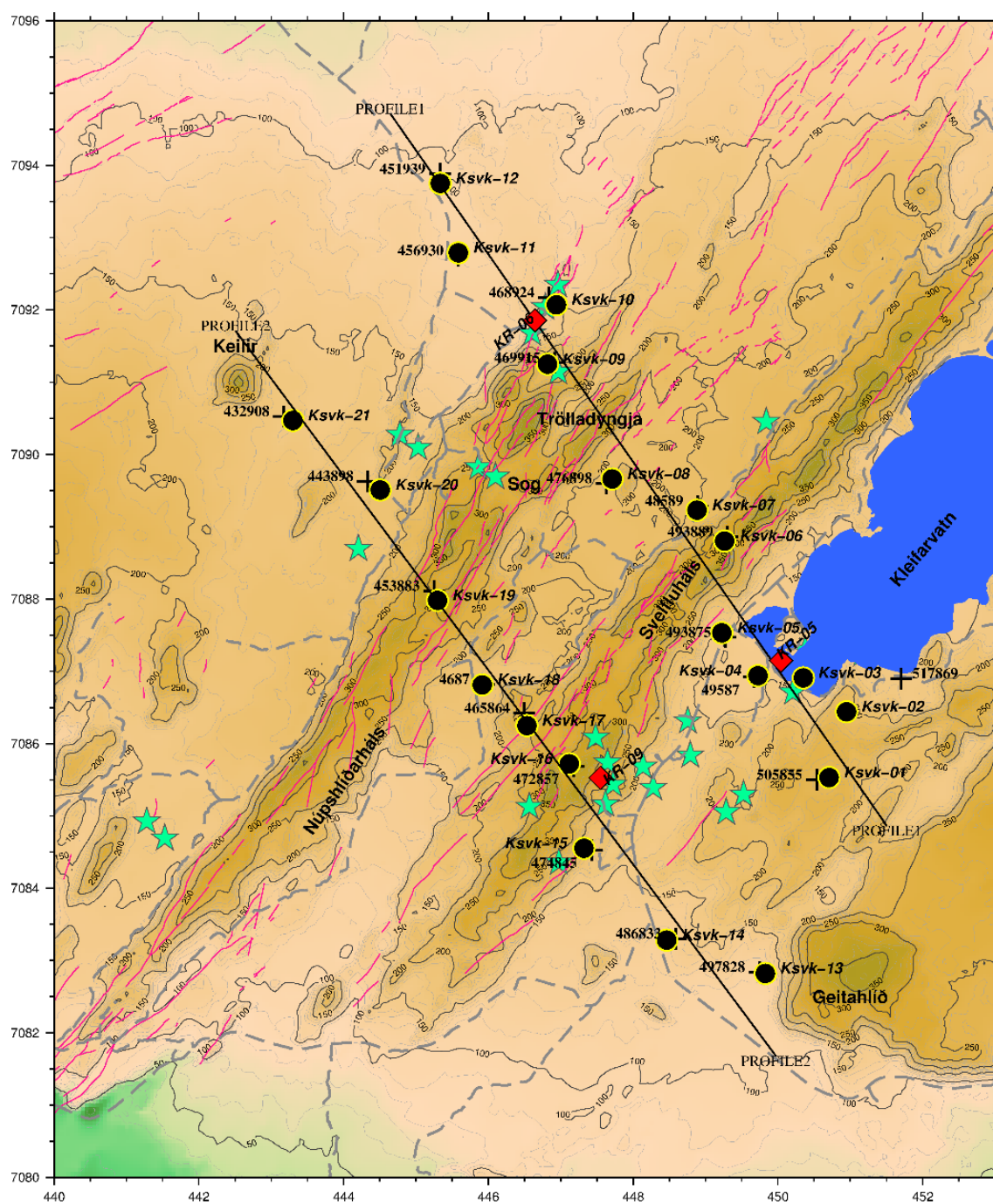


FIGURE 13: Map of Krýsuvík high-temperature area, SW-Iceland; shows locations of MT soundings represented by black dots, TEM soundings by crosses, fumaroles by green stars, boreholes by red diamonds and identified faults by red lines

The two profiles also intersect three wells. Well KR-05, at around 820 m depth, intersects profile 1. In it, chlorite alteration is found at around 100 m depth. In well KR-06, smectite-zeolite alteration is found between 50 and 450 m depth and chlorite is dominant from 450 down to 840 m which is the final depth of the well (Hersir et al., 2010, and references therein). There is quite a good correlation of smectite as it is mostly found within the decreasing resistivity of the region, having values of less than 6 Ωm . The chlorite below it overlaps well with the increasing resistivity. There seems to be a good correspondence between the dominant alterations in the wells with the resistivity structure of the profile. However, looking at the well temperature data, the system suggests fossil alteration since the rock temperature

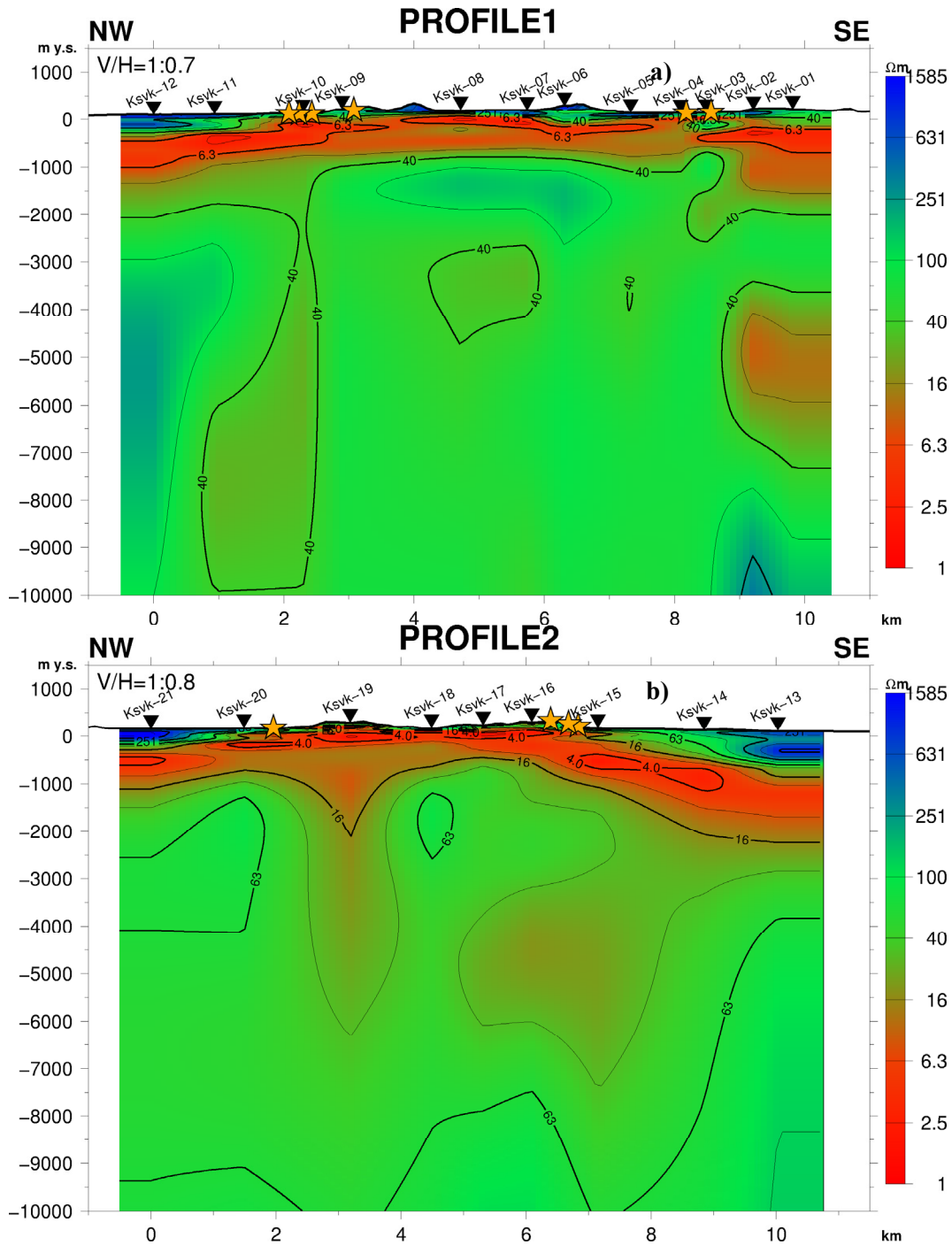


FIGURE 14: The 11 km long a) Profile 1 and b) Profile 2 both cutting NW-SE through the region of Krýsuvík; inverted triangles on the surface are MT stations and orange stars are intersected fumaroles; locations of these profiles shown in Figure 13

shows lesser values than the expected formation temperature of the alteration minerals. There is also an evident temperature inversion in the system.

Well KR-09, at around 330 m in depth, intersects profile 2. A smectite-zeolite zone found at the top 130 m depth of the well intersects with the identified low-resistivity cap. Mixed clay from 130 m down to the final depth of the well is seen and overlaps the increasing values of the identified low-resistivity cap (Hersir et al., 2010, and references therein). However, values of $<10 \Omega\text{m}$ are considerably low for the existence of mixed clay alterations. This may still be reasonable since this well is around 400 m away from profile 2.

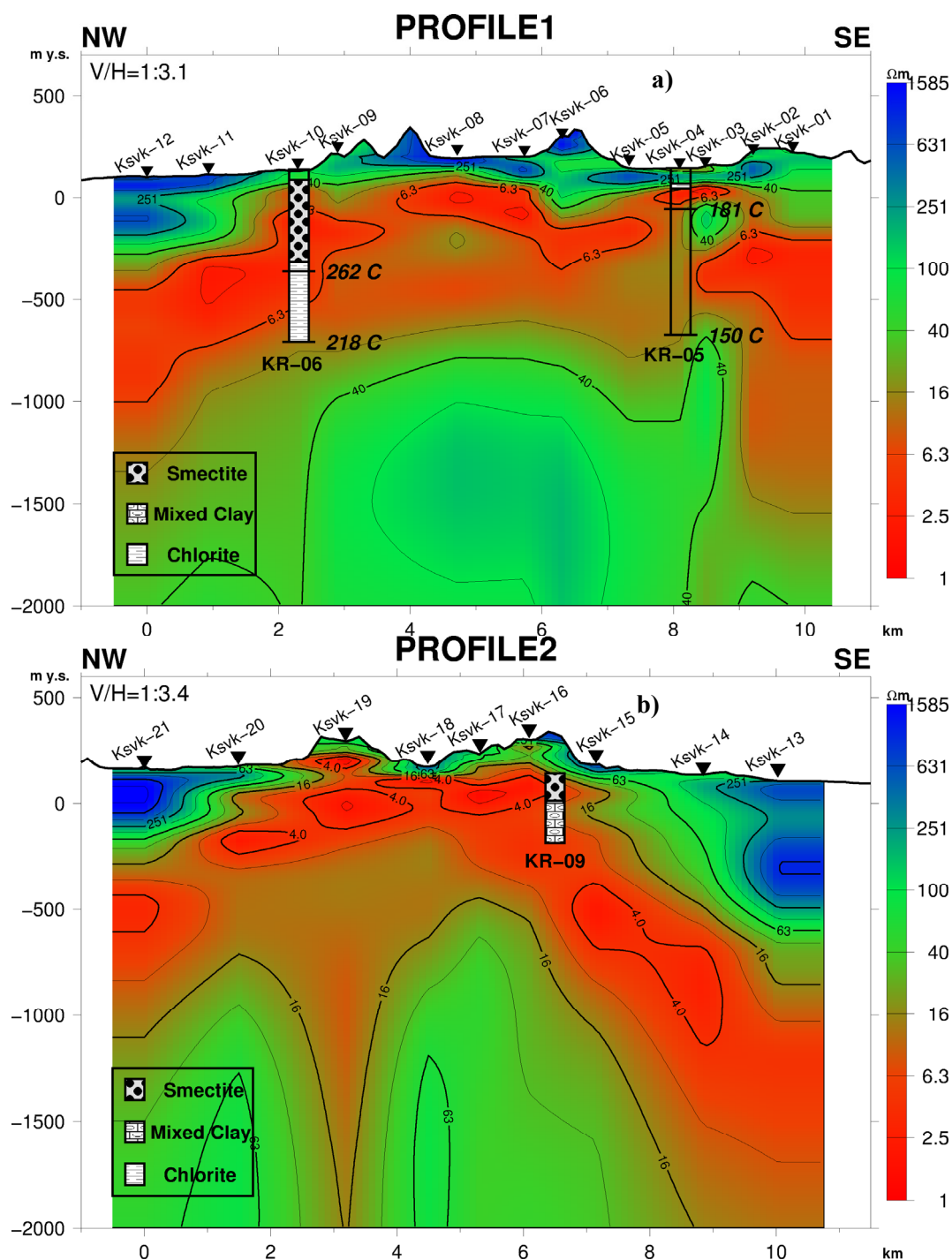


FIGURE 15: a) Profile 1 and b) Profile 2 shown down to 2000 m depth with nearby wells projected into them; good correlation of resistivity seen with indications of alteration minerals in both profiles which mostly intersects the observed low-resistivity cap: locations of profiles is shown on Figure 13

In terms of the shift offset of the MT apparent resistivity data, it can be observed that most of them are shifted down by a factor between 0.5-0.9 as seen in the histogram plot in Figure 16. Looking at the corresponding distribution of the shift on the contour map in the same figure, it can be observed that the area where down shifts occur are mostly found within the region where a lot of thermal manifestations are located. This is a good confirmation of how static shift is affected by shallow resistivity inhomogeneities whereby, in this scenario, low-resistivity alterations from surface thermal manifestations shift MT apparent resistivity down to a lower value.

The Tipper strike from different period ranges was obtained. It can be observed from the rose diagram of the T-strike at a period range of 0.01-0.1 s in Figure 17a that there is a significant resistivity contrast along the NW-SE direction at a very shallow depth. Some of the soundings do not show T-strike information since there was no vertical component magnetic sensor installed during data acquisition. This alignment is consistent with the presence of the shallow low resistivity seen in the central region of profiles 1 and 2 which happens to coincide with the locations of the fissure structure. It is clearly shown by the real component of the Tipper arrow at 0.05 s period as shown in Figure 17b. As these arrows point away from conductive bodies, there are apparent indications of low-resistivity structures lying within the fissure system.

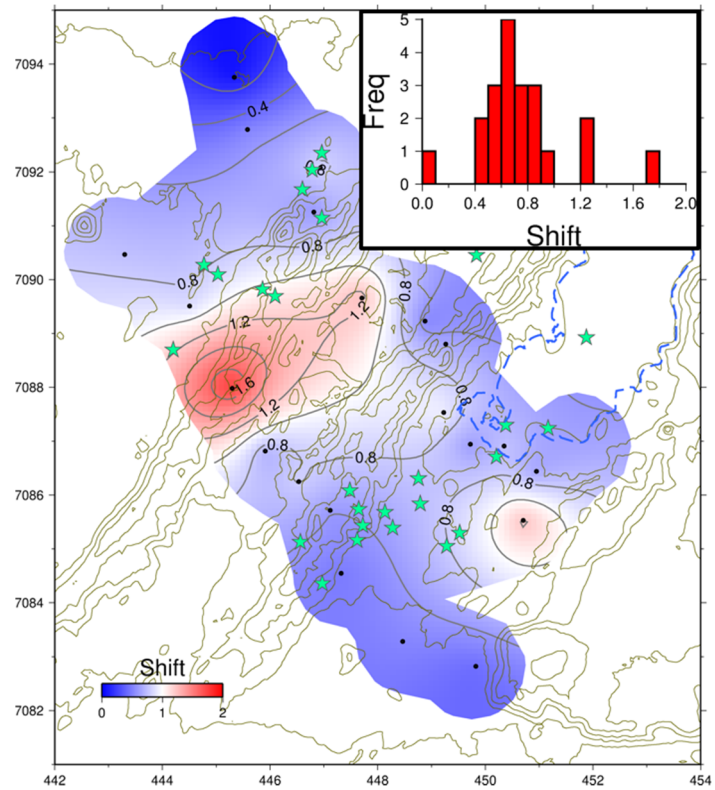


FIGURE 16: Shift histogram of all the inverted MT soundings in Krýsuvík with their contoured values overlain in a topographic map; shift values of less than unity are found within the regions where thermal manifestations are located

Looking at greater depth corresponding to an MT period range of 10-100 s, T-strike starts to align well with the sea water located immediately south of the area, as seen in Figure 18a.

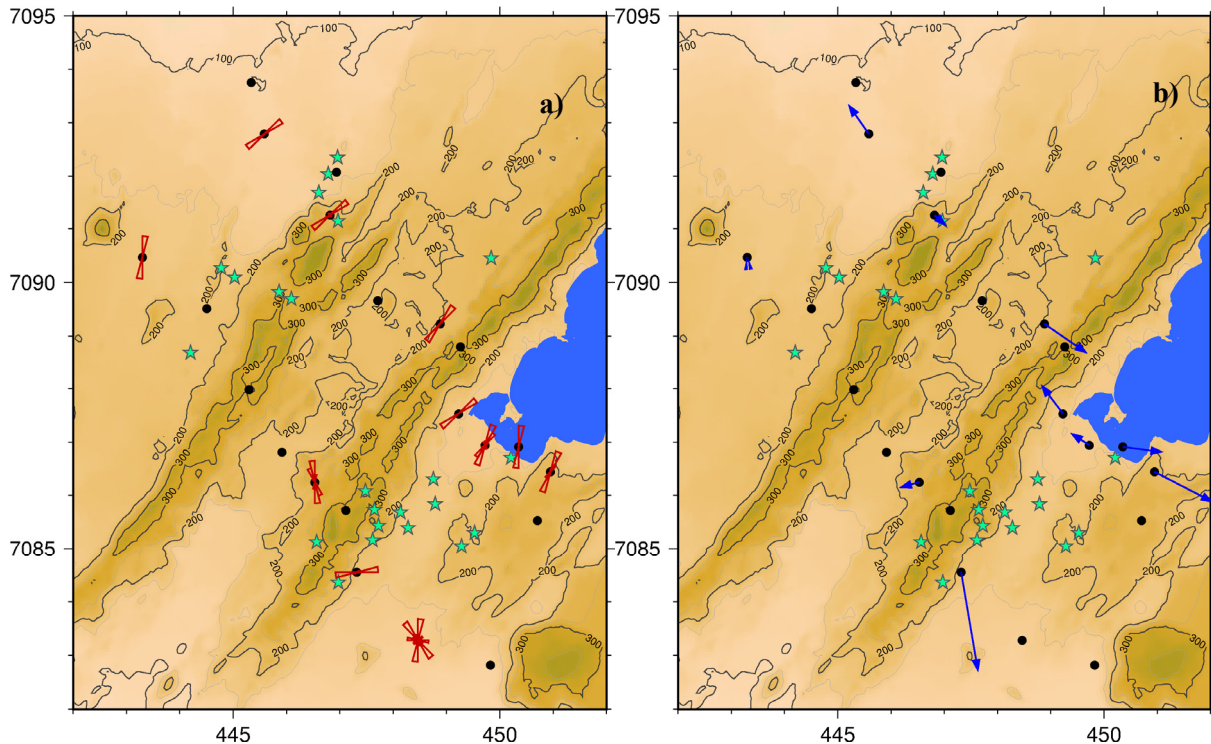


FIGURE 17: a) Tipper strike between period range of 0.01 and 0.1 s;
b) real part of the induction arrows at period of 0.05 s

The presence of the highly conductive sea, with an average resistivity of $0.3 \Omega\text{m}$, makes the real component of the Tipper arrow point away from it (see Figure 18b). The shallower and more resistive fresh water from the lake is negligible.

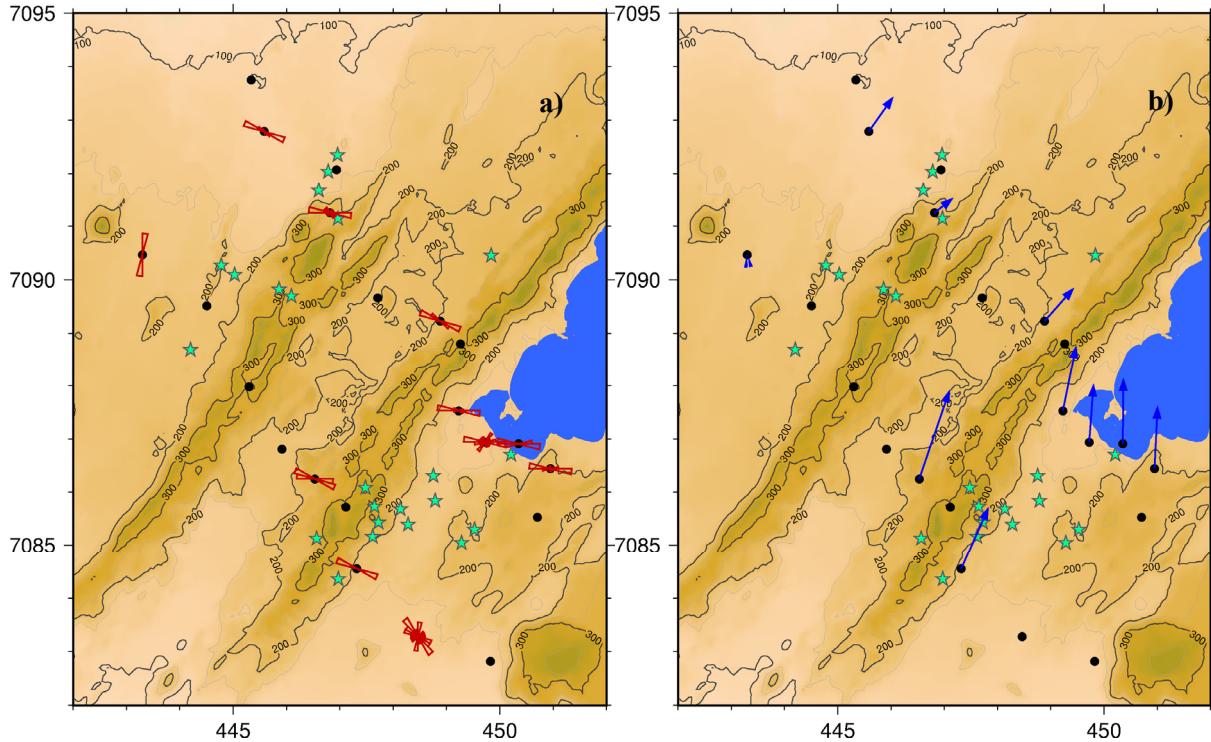


FIGURE 18: a) Tipper strike between period range of 10 and 100 s;
b) real part of the induction arrow at period of 30 s

Due to the 90° ambiguity of the Z-strike, it is more often reliable to assess lateral resistivity variations using the Tipper information. This is another independent data set which relies on the relationship of the vertically changing magnetic field with the horizontally oscillating magnetic fields as shown in Equation 16 which, in a way, confirms the resistivity structure produced by inverting the apparent resistivity and phase values of MT derived from the transfer function (impedance tensor in Equation 15) relating the horizontally oscillating electric and magnetic fields.

6. REVIEW OF RESISTIVITY DATA FROM BACMAN

Over a hundred MT and TEM soundings have already been done in BacMan area. Joint inversion for several soundings was not possible due to the poor overlap of TEM with the MT data. In this report, only 10 pairs of MT and TEM sounding data were considered for inversion. Figure 19 shows the location of some of the MT and TEM data in the area with the three sections considered in the joint inversion.

6.1 TEM inversion

TEM data were collected using the Geonics PROTEM 47D system under 60 Hz at the survey area; the country, as a whole, uses the same power line frequency. The transmitter instrument generated current with repetition rates of 285 and 75 Hz and maximum current of 2-4 A. The transmitter loop was set-up to a $40 \text{ m} \times 40 \text{ m}$ area. The soundings were done in two configurations: in-loop and out-loop. A current of 2 A was deployed in an in-loop configuration while a current of 4 A was deployed in an out-loop

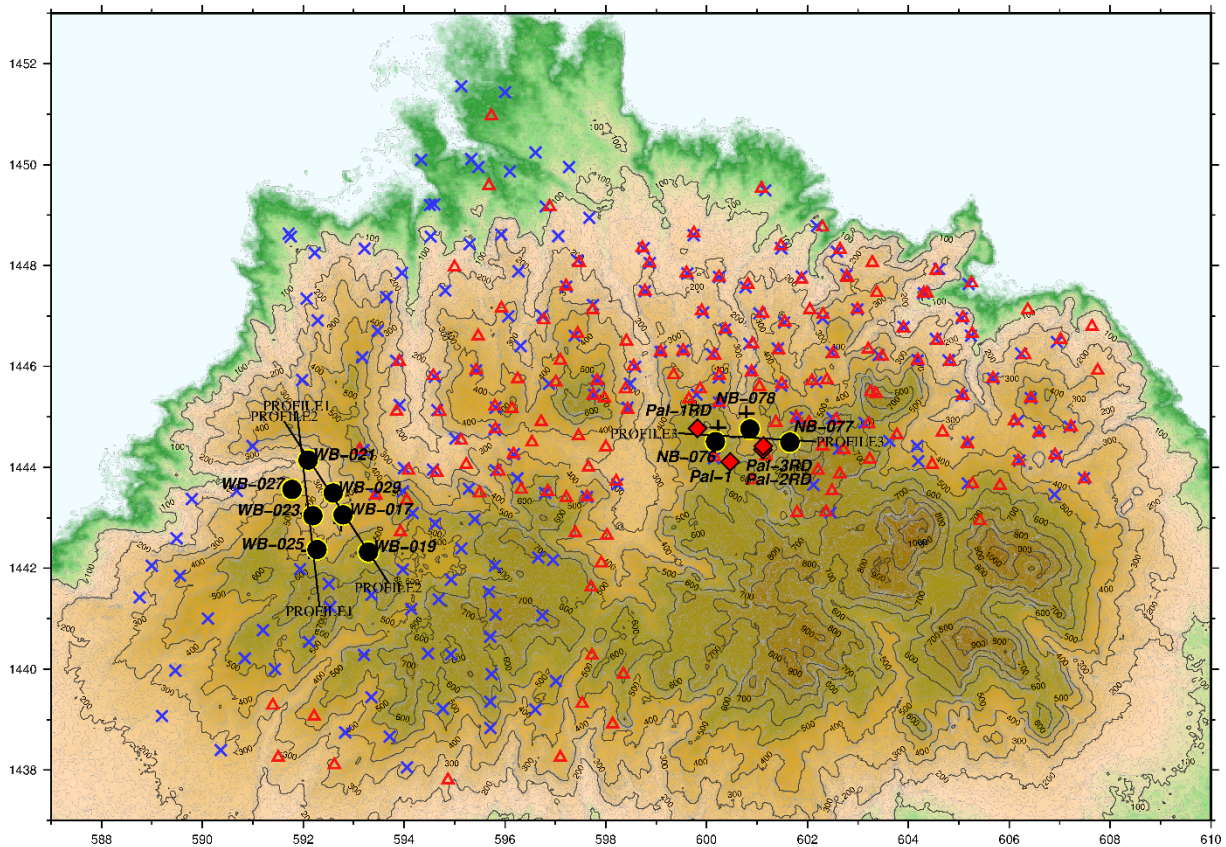


FIGURE 19: Map of Bacon-Manito geothermal area; black dots and black crosses are the inverted MT and TEM sounding data, respectively, with profile lines shown running across these points; red diamonds are location of some wells in the area; blue crosses are MT and red triangles are TEM soundings done in the area (but not processed in this report)

configuration. However, the TemX program only calculates the apparent resistivity data from an in-loop configuration of TEM. Thus, processing and inversion was done using the in-loop TEM data only. At this point, it is noteworthy to point out that in terms of the calculated apparent resistivity, the in-loop and out-loop TEM configurations will have different signatures at early measurement times but will virtually converge at later times. This is caused by the presence of different orientations of the secondary magnetic fields inside the offset loop when the smoke rings are in the early and shallow stage, but at late and deeper propagation, the expanded smoke rings will consider the offset receiver to be almost identical with the in-loop receiver, i.e. the secondary magnetic field is passing through these loops with similar orientations, i.e. vertically when the earth has very small or no lateral resistivity variations.

Several of the TEM soundings have low signal-to-noise ratio since low current amplitude of 2 A was used and little data stacking was done. Since the decay falls off in the order of $t^{-5/2}$, then small amplitude signals can easily be drowned in noise after a short time. Out of these, a number of good TEM soundings were inverted and compared. Using the set-up described above, sounding depth reliably reaches up to around 200 m. This shallow profiling can well resolve the upper layer resistivity of an area. However, for the purpose of geothermal exploration, resolution of shallow earth is usually not considered significant. The very shallow resistivity structure of the earth is usually not observed when a lower frequency of the source current is used since this earth layer is seen at its early time measurements and normally shows a shoot up response in the apparent resistivity. There may also be the possibility of coupling of several of the poor quality TEM data which made the data points oscillate or deviate from the true value even after multiple stacking (Christiansen et al., 2006). This problem causes a large deviation of the inverted model from the actual earth structure if not considered beforehand since it may also represent an undisturbed response. But there can be no straightforward means of validating the sounding unless obvious evidence of the source of noise is recognized in the field or a tightly spaced

TEM sounding is employed. Figure 20 shows the measured apparent resistivity of two different areas in BacMan. A good fit was established for both of the soundings. The entirely different shallow resistivity profiles produced from the inversion may suggest different local resistivity conditions in the area. Significantly, the increasingly deeper end of the apparent resistivity seen in Figure 20b may suggest two possibilities for the model at deeper levels, i.e. higher resistivity is present below the lower one as shown in the generated model or an even conductive layer is present below the resistive top layer similar to what was shown in Figure 4b.

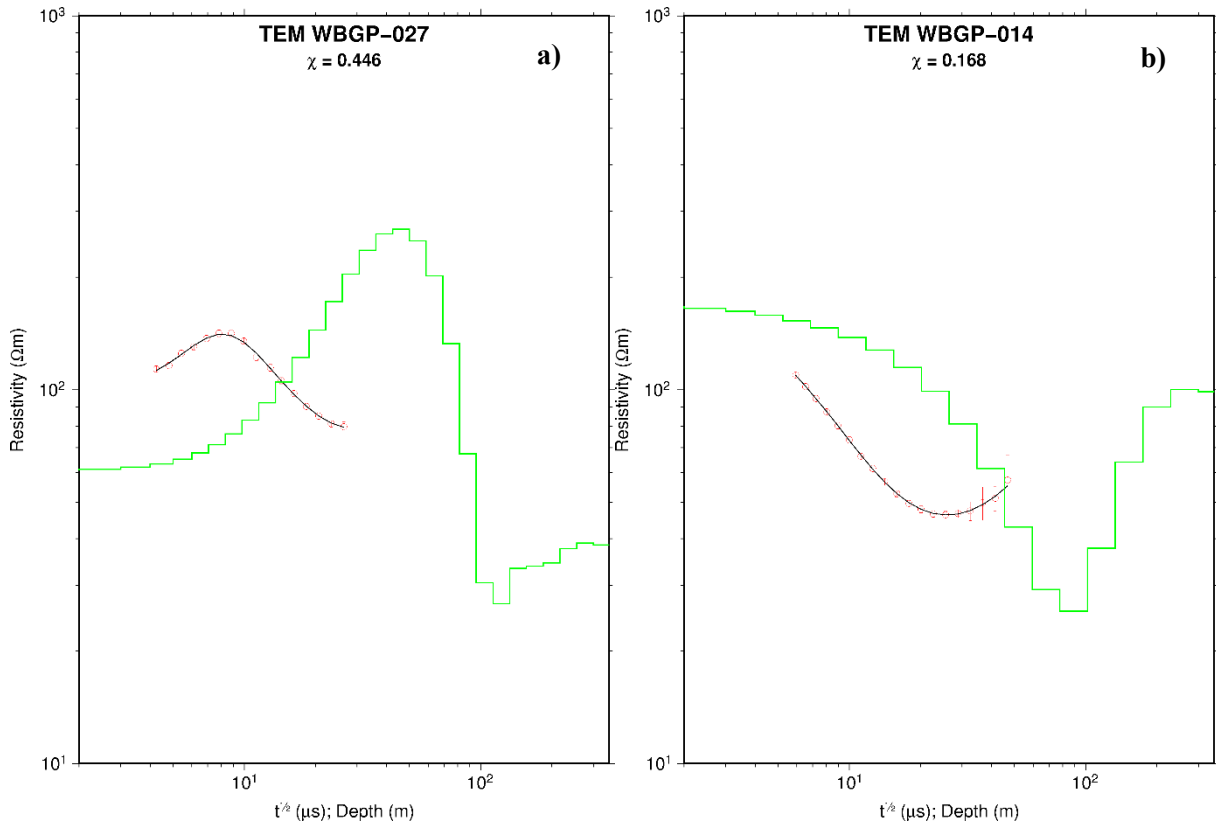


FIGURE 20: Sample of the inverted TEM data in Bacon-Manito area; soundings were inverted up to a basement depth of around 300 m

6.2 MT and TEM joint inversion

1D joint inversion, specifically TEMTD, considers the MT shift value as one of its unknown parameters such that the generated model is able to fit exclusively both TEM and MT data. Hence, a considerable number of overlapping TEM and MT data points must be present in order to have a reliable joint inversion. The high frequency apparent resistivity of MT data may usually have downward bias even after remote referencing since this only reduces the effect of coherent noise. TEM data, which in our case only considers induction from the vertical secondary magnetic field, may see lateral resistivity or 3D effects and display the deeper end of the apparent resistivity curve up which overestimates the actual resistivity value since the horizontally measured induced voltage is always less than the actual one (secondary magnetic field is no longer perpendicular to the surface). But it should also be pointed out that the same behaviour can be observed if the earth is 1D only if the horizontal components of the secondary magnetic fields are almost zero. In the end, distinction from this effect is often difficult unless non-horizontally induced voltages are measured. These two independent issues of the methods may result in an unreliable calculation of the shift parameter or even fitting if few overlapping points are established. One particular instance is shown in Figure 21. Figure 21a shows a case of inverting MT and TEM data where the program looked for the most probable shift parameter such that the misfit was

at a minimum. We can observe that the model produced a response where late time points of TEM and the high frequency of the MT do not overlap. Here, the program tried to find a model that could satisfy the linkage between TEM data with MT data curve as dictated by the phase information which anticipates the resistivity behaviour at a shallower depth where TEM is supposed to coincide. Figure 21b shows the inversion result of the same data set where the MT shift value was fixed and the scaling factor was set to a higher value so that the response could have a larger range of values to play around with as iteration proceeded. There is an observed overlap of points between the MT and TEM data but since the high-frequency phase data sees a higher value of resistivity at shallower depth, it forces the response curve in the TEM range to shoot up. Figure 21c shows the inversion result of the force-shifted MT data but with less of a leeway range for the response, i.e. allowable models are more restricted than the previous one. The result is a good overlap of the response with the apparent resistivity curve of both MT and TEM but a poor fit with the high-frequency phase points as expected. It can be noticed that the three models produced significant changes in resistivity values at depth corresponding to the junction region of these two data. Hence, a deeper TEM sounding with a considerable overlap with the MT data could possibly improve the reliability of the inversion results.

Now, we look at the profiles generated in the western part of the area as seen in Figure 19. It can be observed that the near surface resistivity extending down to 1500 m depth has a low-resistivity signature from around 10-20 Ωm . This is prominently seen on profile 1 (Figure 22a), less so on profile 2 (Figure 22b). This low resistivity can be associated with a highly loose or scattered mineral alteration since the area where the section is located has a considerably altered ground but no thermal springs, as shown in Figure 8. The water table might also contribute to lowering the resistivity structure at shallow layers of both profiles. A relatively elevated water table in this area can be inferred from the nearby Danao Lake (shown in Figure 8) which is located on the southeast end of these sections and has a surface elevation of roughly 400 m above sea level. The highly resistive signature on the

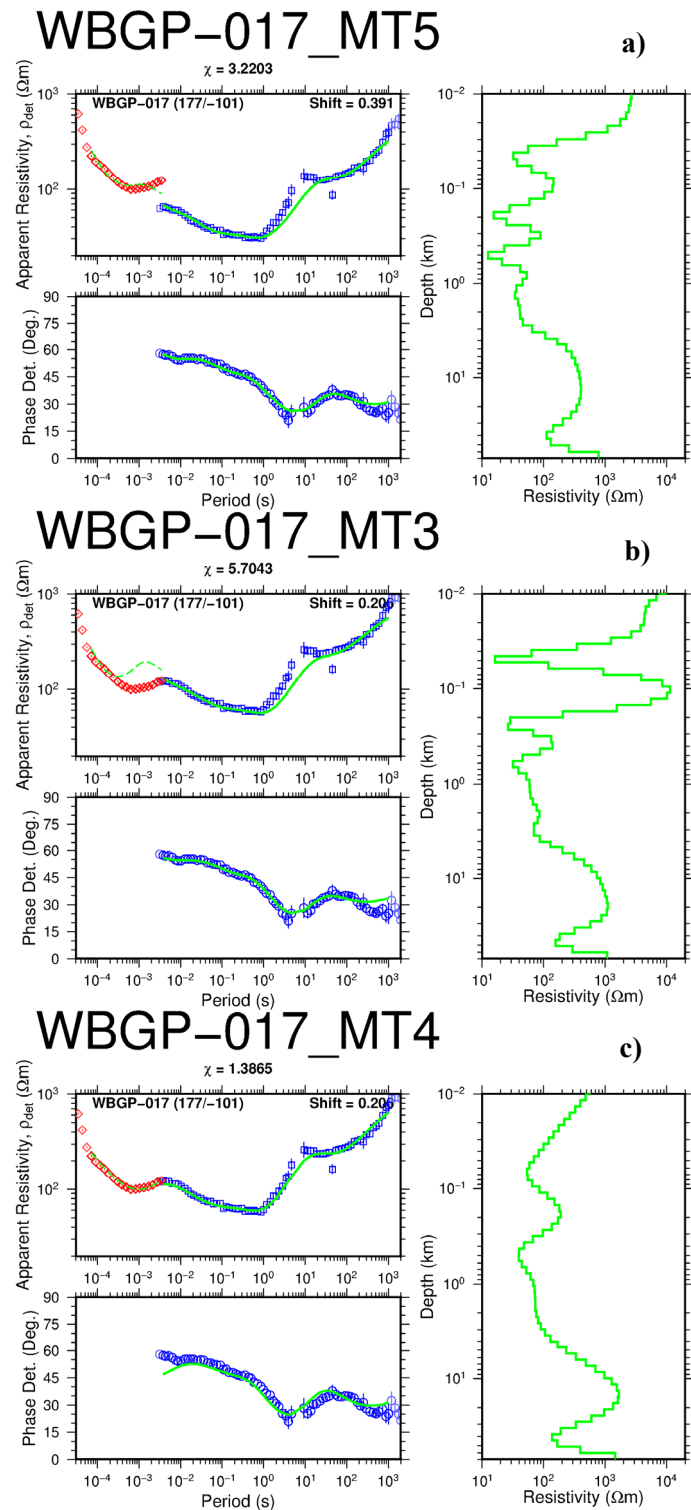


FIGURE 21: Three cases of joint inversion results:
a) Shift parameter was determined by the program;
b) Shift parameter was set by used with high scaling factor for data uncertainty; c) Same as b but scaling factor is further reduced

A relatively elevated water table in this area can be inferred from the nearby Danao Lake (shown in Figure 8) which is located on the southeast end of these sections and has a surface elevation of roughly 400 m above sea level. The highly resistive signature on the

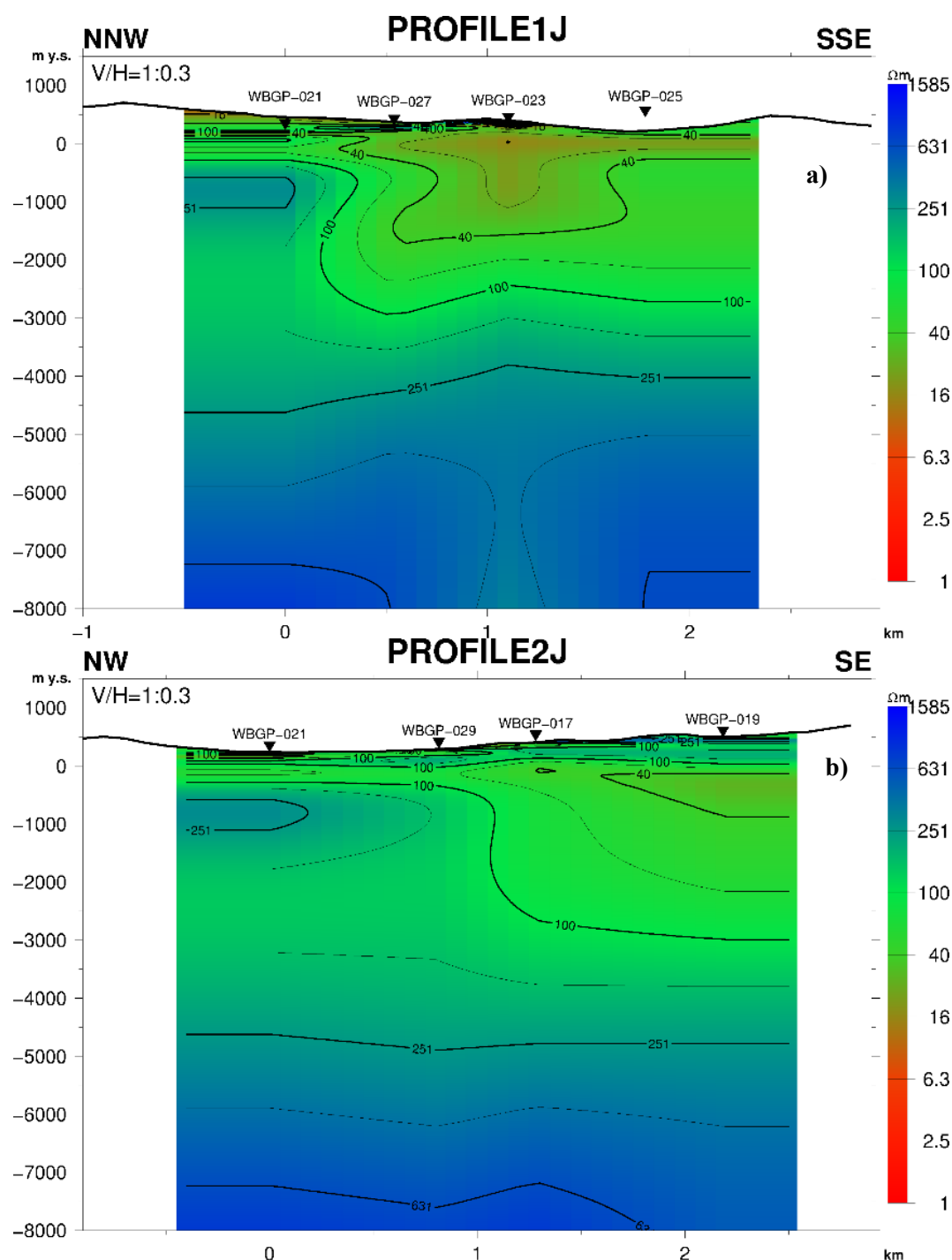


FIGURE 22: Jointly inverted 3 km a) profile 1 located on the far western part of Bacman geothermal project running NNW-SSE, and b) profile 2 located also on the same part of the area running NW-SE and intersecting profile 1 at the northwest end (see Figure 19 for location)

northwest side of both profiles suggests the presence of unaltered and possibly less permeable structures since we take notice that this end of the profile is nearest to the sea and it could have an extensively low resistivity value if this end was permeable. The very resistive layer at the bottom can be interpreted to be another impermeable rock structure, the Manitohan volcanic centre, which may be part of the oldest volcanic system in the area (Braganza, 2011). This may indicate part of the western periphery of the geothermal resource.

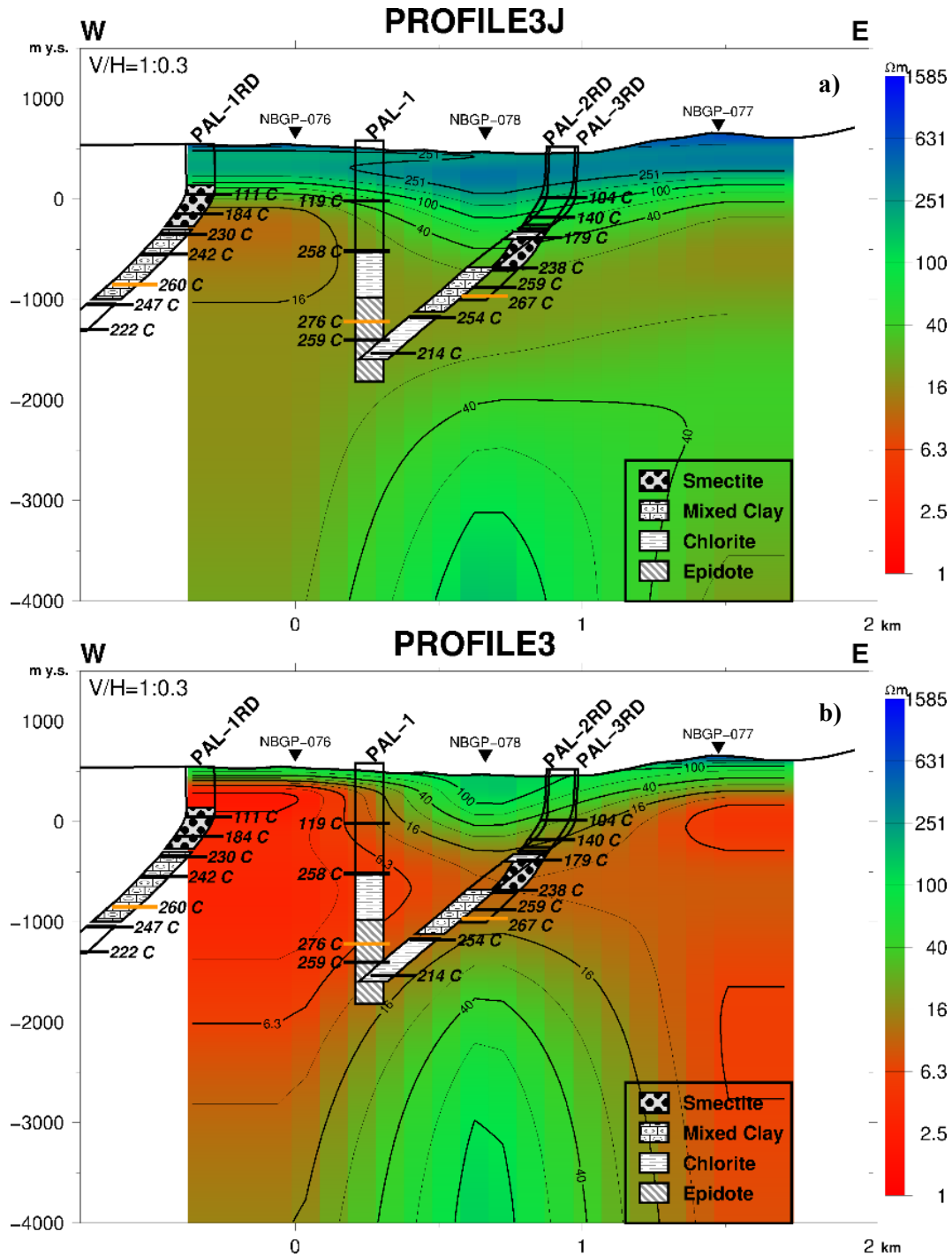


FIGURE 23: a) Jointly inverted b) MT inverted profile 3 running W-E extending up to a depth of 4000 m with 4 projected wells; better correlation of well alteration data observed in the jointly-inverted case than in the non-joint case (see Figure 19 for location)

We took a 2 km profile in the eastern part of the area where some wells are located. Profile 3, shown in Figure 19, considers 4 nearby wells which are mostly reinjection wells except for one, i.e. Well PAL-1, which is also farthest from the profile (around 500 m). Figure 23 shows two cases of inversion done in the same profile. The model generated from joint inversion is shown in Figure 23a (referred to from here on as joint case) while the model from MT inversion is shown in Figure 23b (referred to from here on as non-joint case). There is temperature inversion in the area with relic alteration observed mostly in the deeper regions of the wells. The maximum temperature reaches to around 270°C at 1500 m depth. The two sections show a big dissimilarity in their resistivity values at different depths. Joint case shows

severe shifting (~ 0.2 - 0.3) on both ends of the profile. The non-joint case indicates significantly thick and low-resistivity values of less than $10 \Omega\text{m}$ extending up to 4000 m depth while the joint case indicates a thinner low-resistivity layer reaching up to $20 \Omega\text{m}$. Alteration minerals in the wells were also correlated with both of the profiles. In PAL-1RD, a relatively good overlap of smectite is seen with the decreasing resistivity region for both cases. However, the range of resistivity is much lower in the non-joint case but extends further on top of the identified smectite layer. The rest of the well's alteration information cannot possibly be correlated due to lack of sounding data. In PAL-1, better correlation of chlorite and epidote at depth of 1000 - 2500 m with resistivity is observed with the joint case than with the non-joint case where it intersects the profile at a low-resistivity value of around $10 \Omega\text{m}$. The first 350 m of the well is composed of unaltered andesitic lava flows (Reyes, 1982) and is distinctly identified by the joint case as a high-resistivity top layer of several hundreds of ohm-metres in value. In PAL-2RD and PAL-3RD (alteration data from Barnett, 1985), there is better overlap of smectite on the resistivity structure with the non-joint case but the relic chlorite found at shallower depth fits suitably with the joint case. Mixed clays and chlorite found at 1200 - 2100 m depth coincide more appropriately with the 20 - $40 \Omega\text{m}$ range in the joint case than $<16 \Omega\text{m}$ range in the non-joint case. In this case, it can be considered that the resistivity profile of the jointly inverted data matches the alteration data of the nearby wells. But, it is good to realize that TEM data collected along this profile are shallow and there is no good overlap in the inversion. But the best model generated gave a considerably low misfit.

7. CONCLUSIONS AND RECOMMENDATIONS

1D joint inversion of the TEM data and the determinant of MT data in both Krýsuvík high-temperature area and Bacman geothermal area were done. It was observed that apparent resistivity offset is vulnerable in the areas. This has a lot of effect in the later inversion and interpretation if not considered beforehand. Highly probable areas of resistivity offset in a high-temperature geothermal environment are sites of altered grounds, thermal manifestations, huge topographic contrast, intrusive bodies and fractures occurring at the surface or the near-surface. A considerable amount of overlap of the late time TEM and the high-frequency MT data points must be established in order to obtain reliable inversion results, especially with the static shift parameter determination. This is done to increase confidence in the input data by reducing/removing unwanted 3D structure effects on the TEM data at late time and the downward bias at the high frequency range of MT data. The final model from a joint inversion using TEMTD satisfies a minimum misfit of the response curve with both TEM data and the shifted apparent resistivity MT data and its phase. A static shift parameter was also considered by the inversion in its model generation. The convergence to a best and acceptable fit is usually dependent on the initial model and the parameters imposed in the inversion.

The TEM method is unaffected by static shift but may produce data deviating from the true value even after multiple stacking. This may be caused by coupling, especially from nearby man-made electrical structures or some disturbances from communication equipment or facilities (Christiansen et al., 2006). Random noises from natural electromagnetic activity like spherics can also influence TEM data collection although they have very little effect (Christiansen et al., 2006). Some TEM data in Bacman were viewed as highly suspicious of being affected by some of these influences.

Shallow TEM soundings have been proven to be as important as deeper MT soundings in geothermal exploration. It is, thus, a good practice to have deeper TEM soundings by implementing larger transmitter loop areas, if possible, and applying a lower repetition rate to the transmitter current (30 Hz or less, in a 60 Hz power line environment). The depth of TEM sounding also relies on the subsurface resistivity such that TEM probes deeper in a resistive earth than a conductive earth, the same as with MT soundings. In order to have an increased signal to noise ratio of a TEM sounding, especially at late times, it is beneficial to increase the moment of the source loop by increasing its area, loop turns and/or the current amplitude but this, in general, is limited by the power rating of the transmitter instrument. It

is also a good strategy to implement different receiver loop areas to accommodate good quality data at various gate locations.

In implementing 1D joint inversion of MT and TEM data, it is always good to keep in mind that the unavoidable presence of 3D effects in the soundings are considered as noise just like electromagnetic disturbances. Thus, models generated from this inversion serve as a coarse model of the earth's resistivity structure.

ACKNOWLEDGEMENTS

I would like to express my warmest thanks to UNU-GTP staff for making the training as enjoyable and worthwhile as it can get. Your hospitality, patience and professionalism made this training a success. Best regards is also expressed to Dr. Ingvar Fridleifsson (retired UNU-GTP founding Director) for sharing a huge part of his life in honing geothermal talents all over the world and to Mr. Lúdvik S. Georgsson (current UNU-GTP Director) for keeping up the same vision that made this institution. I'm really humbled by your dedication. I am also deeply thankful to have as my supervisors Mr. Gylfi Páll Hersir and Mr. Andemariam Teklesenbet for their tireless encouragement and support during our project period. I salute your bountiful patience towards us, geophysical exploration trainees. I also greatly appreciate the efforts of the rest of my mentors in ÍSOR, Orkustofnun, especially Mr. Knútur Árnason, Mr. Arnar Már Vilhjálmsson, Mr. Gudni Karl Rosenkjaer and, again, Mr. Gylfi Páll Hersir for a handful of knowledge I gained regarding MT, TEM and all that comes along with it. You made me realize that geophysicists must think more than usual.

I also thank my employer, Energy Development Corporation Philippines, and my supervisor, Mr. Domingo Layugan, for giving me this opportunity to undergo geothermal training in Iceland. I am likewise grateful for the Filipino community in Iceland, especially the Torres family and relatives, who have helped me through the rest of my life here in this country. I will treasure our times together.

I thank my family for giving me unending support and inspiration to pursue my career as a geophysicist. You have always been and will be my sturdy foundation. Utmost gratitude will forever be expressed to God, our Grand Designer, for giving me life.

REFERENCES

Africa, J.R., 2013: Appendices to the report: "*1D inversion of MT and TEM data with application of soundings from Krýsuvík, SW-Iceland and a review of MT/TEM data from Bacman geothermal project, Central Philippines*". UNU-GTP, Iceland, report 5 appendices, 50 pp.

Archie, G.E., 1942: The electrical resistivity log as an aid in determining some reservoir characteristics. *Tran. AIME*, 146, 54-67.

Árnason, K., 1989: *Central loop transient electromagnetic sounding over a horizontally layered earth*. Orkustofnun, Reykjavík, report OS-89032/JHD-06, 129 pp.

Árnason, K., 2006a: *TemX short manual*. ÍSOR – Iceland GeoSurvey, Reykjavík, internal report, 17 pp.

Árnason, K., 2006b: *TEM TD (Program for 1D inversion of central-loop TEM and MT data)*. ÍSOR – Iceland GeoSurvey, Reykjavík, short manual, 16 pp.

Árnason, K., Eysteinnsson, H., and Hersir, G.P., 2010: Joint 1D inversion of TEM and MT data and 3D inversion of MT data in the Hengill area, SW Iceland. *Geothermics*, 39, 13-34.

Arnórsson, S., Björnsson, A., and Gislason, G., 1975: *Systematic exploration of the Krýsuvík high-temperature area, Reykjanes Peninsula, Iceland*. Orkustofnun, Reykjavik, report OS-JHD-7528, 20 pp.

Barnett, P.R., 1985: Memorandum: *Petrology report Bacman well PAL-3RD*. KRTA, report, 23 pp.

Bostick, F.X.Jr., 1986: Electromagnetic array profiling (EMAP). *56th Annual SEG Meeting, Houston, Texas, Expanded abstract, EM 2.1*, 60–61.

Braganza, J.S., 2011: *Resource assessment update of Bacon-Manito geothermal resource*. Energy Development Corporation, Philippines, report, 66 pp.

Cagniard, L., 1953: Basic theory of the magneto-telluric method of geophysical prospecting. *Geophysics*, 18, 605-635.

Castells, A.M., 2006: *A magnetotelluric investigation of geoelectrical dimensionality and study of the Central Betic crustal structure*. University of Barcelona, Department of Geodynamics and Geophysics, PhD thesis, 45 pp.

Christiansen A.V., Auken E., and Sørensen K., 2006: The transient electromagnetic method. In: Kirsch R. (ed.), *Groundwater geophysics: a tool for hydrogeology*. Springer, NY, 179-225.

Constable, S.C., Parker, R.L., and Constable, C.G., 1987: Occam's inversion: A practical algorithm for generating smooth models from electromagnetic sounding data. *Geophysics*, 52-3, 289-300.

Dakhnov, V.N., 1962: Geophysical well logging. *Q. Colorado Sch. Mines*, 57-2, 445 pp.

DeGroot-Hedlin, G., 1991: Removal of static shift in two dimensions by regularized inversion. *Geophysics*, 56, 2102–2106.

Flóvenz, Ó.G., Hersir, G.P., Saemundsson, K., Ármannsson, H., and Fridriksson Th., 2012: Geothermal energy exploration techniques. In: Syigh, A. (ed.), *Comprehensive renewable energy*, vol. 7. Elsevier, Oxford, 51-95.

Flóvenz, Ó.G., Spangerberg, E., Kulenkampff, J., Árnason, K., Karlsdóttir, R., Huenges, E., 2005: The role of electrical interface conduction in geothermal exploration. *Proceeding of the World Geothermal Congress 2005, Antalya, Turkey*, 9 pp.

Gamble, T.D., Goubau W.M., and Clarke, J., 1979: Magnetotellurics with a remote magnetic reference. *Geophysics*, 44, 53-68.

Geonics Ltd., 1999: *Operating manual for PROTEM 67 D*. Geonics Ltd, Ontario, 58 pp.

Georgsson, L.S., 2012: Geophysical methods in geothermal exploration. *Paper presented at "Short Course VII on Exploration for Geothermal Resources", organized by UNU-GTP and KenGen, at Lake Bogoria and Lake Naivasha, Kenya*, 16 pp.

Hersir, G.P., and Árnason K., 2009: Resistivity of rocks. *Paper presented at "Short Course on Surface Exploration for Geothermal Resources", organized by UNU-GTP and LaGeo, Santa Tecla, El Salvador*, 8 pp.

Hersir, G.P., Árnason, K., and Vilhjálmsson, A.M., 2013: 3D inversion of magnetotelluric (MT) resistivity data from Krýsuvík high temperature geothermal area in SW Iceland. *Proceedings of the 38th Workshop on Geothermal Reservoir Engineering, Stanford University, Stanford, Ca*, 14 pp.

Hersir, G.P., Vilhjálmsson, A.M., Rosenkjaer, G.K., Eysteinnsson, H., and Karlsdóttir, R., 2010: “*The Krýsuvík geothermal field. Resistivity soundings 2007 and 2008*”. ÍSOR – Iceland GeoSurvey, report ÍSOR-2010/025 (in Icelandic), 263 pp.

Jones, A.G., 1988: Static shift of magnetotelluric data and its removal in a sedimentary basin environment. *Geophysics*, 53-7, 967-978.

Keller, G.V., and Frischknecht, F.C., 1966: *Electrical methods in geophysical prospecting*. Pergamon Press Ltd., Oxford, 527 pp.

Lagmay, A.M.F, Tengonciang, A.M.P., and Uy, H.S., 2005: Structural setting of the Bicol basin and kinematic analysis of fractures on Mayon Volcano, Philippines. *J. Volcanology & Geothermal Research*, 144, 1-14.

Lemma Didana, Y., 2010: *Multidimensional inversion of MT data from Krýsuvík high-temperature geothermal field, SW-Iceland, and study of how 1D and 2D inversion can reproduce a given 2D/3D resistivity structure using synthetic MT data*. University of Iceland, MSc thesis, UNU-GTP, report 4, 94 pp.

Lund, J.W., Freeston, D.H., and Boyd, T.L., 2011: Direct utilization of geothermal energy 2010 worldwide review. *Geothermics*, 40, 159-180.

Panem, C.C., and Alincastré, R.S., 1985: *Surface geology of the Bacon-Manito geothermal reservation*. Philippine National Oil Corporation – Energy Development Corporation, report.

Reyes A.G., 1982: *Petrological report: well Palayangbayan-I, Bacon-Manito Albay/Sorsogon*. Philippine National Oil Company- Energy Development Corporation, Philippines, memorandum, 6 pp.

SEG, 1991: *MT/EMAP data interchange standard*. Society of Exploration Geophysicists, 112 pp.

Simpson, F., and Bahr, K., 2005: *Practical magnetotellurics*. Cambridge University Press, Cambridge, UK, 254 pp.

Srivastava S.V., 1965: Methods of interpretation of magnetotelluric data when the source field is considered. *J. Geophys. Res.*, 70, 945-954.

Sternberg, B.K., Buller, P.L., Kisabeth, J.L., and Mehreteab, E., 1982: Electrical methods for hydrocarbon exploration: II. Magnetotelluric (MT) method. *Proceedings Southern Methodist University Symposium III, Unconventional Methods in Exploration for Petroleum and Natural Gas*. SMU Press, 1984, 202-230.

Sternberg, B.K., Washburne, J.C., and Anderson, R.G., 1985: Investigation of MT static shift correction methods. *55th SEG meeting, Washington DC, Expanded Abstracts*, 264-267.

Todd, D.K., and Mays, L.W., 2005: *Groundwater hydrology* (3rd ed.). John Wiley & Sons, Inc., NY, 636 pp.

Vozoff, K., 1990: Magnetotellurics: principles and practice. *Proceedings of the Indian Academy of Sciences-Earth and Planetary Sciences*, 99, 441-471.

COMPARISON OF SIMULATIONS OF THE TANAWON SECTOR SIMULTANEOUS DISCHARGE TEST IN BACON-MANITO GEOHERMAL FIELD IN THE PHILIPPINES

Kristine Eia S. Antonio

Energy Development Corporation - EDC
38/F One Corporate Center Building
Julia Vargas corner Meralco Avenue
Ortigas Center, Pasig City, 1605
PHILIPPINES
antonio.kes@energy.com.ph

ABSTRACT

The Tanawon simultaneous discharge test pressure monitoring data was simulated using lumped parameter, numerical reservoir models, and then with the same models coupled with wellbore simulator HOLA. Ten-year forecasts were run using the various models and the results were compared. The wellbore simulator was used to check whether the wells could produce, assuming the pressure drawdown forecasted by the lumped parameter models. The wellbore simulator was also implicitly coupled with a BGPF numerical reservoir model, which resulted in the extension of the life of the wells in the model due to boiling.

1. INTRODUCTION

Geothermal wells are essential to geothermal research and resource management because they allow access to the resource fluid for study and are the closest measurement points to the reservoir. The testing of geothermal wells or boreholes is, therefore, a vital part of geothermal reservoir management as it provides crucial information regarding the condition of the reservoir (Axelsson, 2013a). Wellbore pressure is one of the first measurements reviewed and analysed by reservoir engineers. Pressure provides information not only about the well that is being measured, but also about the hydrothermal structure of the reservoir (Grant, 1988). Looking at the pressure distribution within a field can provide information on the location of the water table or the existence of flow barriers and resistances throughout the field. Also significant to the reservoir engineer are the pressure changes against time, which can characterize the fluid flow properties that affect a field's production, recharge and, consequently, sustainability. Testing a single well can give knowledge regarding the well's productivity and can be used as a guide for the permeability distribution of the reservoir. Testing multiple wells can produce results which are applicable for a wider area. Ideally, the pressure monitoring data used for sustainability assessment is taken from a well within the producing field over an extended period of time (Bixley, 1988; Ramey, 1988). A type of multi-well test conducted by the Energy Development Corporation (EDC) is a simultaneous discharge test wherein all existing wells in the field being assessed are discharged and the pressure is monitored from one or more shut monitoring wells.

The wellhead pressure, mass flow, enthalpy, and chemistry of the discharging wells are also closely monitored. The objective of simultaneous discharge tests is to study the production capacity of the field in a situation that closely mimics full-scale production. The monitoring data collected during a simultaneous discharge test may be analysed through the use of reservoir models. By calibrating the models against the reservoir pressure and discharge changes through time, the characteristics of the reservoir can be inferred. By simulating long-term production using the calibrated models, the sustainable production level of the field can be estimated from the calculated pressure drawdown and fluid enthalpy in the simulated reservoir. Ironically, most models used to analyse well tests were developed to model the bulk flow through the porous reservoir rocks and the dynamics of the geothermal fluid flowing up the well are simply not part of the modelling process. Pruess (2002) suggested that the interaction of the wellbore and the reservoir be simulated through coupling of a reservoir and wellbore model. This added layer of complexity not only increases computational cost, but requires more data and analysis time to set up. The effect of coupling a wellbore model to a reservoir model must, therefore, be examined.

As a first step in reviewing coupling wellbore and reservoir models, the Tanawon simultaneous discharge test was modelled using standard reservoir models and coupled models. The models were used to forecast 10 years of production and the results of the different forecasts were then compared. The focus of this study is to assess the reservoir modelling techniques used in forecasting and to determine whether incorporating wellbore effects will drastically change the forecast results.

2. BACKGROUND OF THE TANAWON SECTOR

Tanawon is a geographical sector of the Bacon-Manito (BacMan) geothermal production field (BGPF), one of the high-temperature geothermal fields in the Philippines managed by EDC. Tanawon Sector is one of the expansion fields under development, but not yet in full operation in BGPF (EDC, 2013). It is projected to contribute 40 MWe to the geothermal project (DOE, 2013).

2.1 Overview of the BacMan resource

2.1.1 Geologic setting of BacMan

The Philippines is an archipelagic country that was formed at the convergence of the Sundaland-Eurasia and the Philippine Sea Plates. The country is thus surrounded by subduction zones of various microplates, resulting from the stresses on the deforming major plate boundaries; most related to this study is the Philippine Trench to the east of the country (Figure 1). The Philippine Fault Zone, a left lateral strike slip fault that traverses most of the country in a generally north to south manner, relieves whatever stresses the subduction zones cannot accommodate (Yumul et al., 2008). The presence of many fracture-dominated geothermal reservoirs in the country can be attributed to the main Philippine Fault Zone, its splays, and subsidiary faults (Yumul et al., 2008; Malapitan and Reyes, 2000). The fractures and faults not only provide conduits for hydrothermal fluids, but are also responsible for the intrusion of young plutonics throughout the country. The subduction of the Philippine Sea plate into the Philippine trench is said to be responsible for the magmatism in the East Philippine Volcanic Arc (Yumul et al., 2008) that stretches from the Bicol Peninsula to Mindanao. The East Philippine Volcanic Arc hosts some of the largest geothermal developments in the country, including BGPF (Malapitan and Reyes, 2000).

BGPF is located within the Pocdol volcano or Pocdol Mountains, a cluster of small eruptive craters belonging to the Bicol Belt (EDC, 2003). Like most geothermal systems within the country, the major source of permeability in the BGPF geothermal wells are faults (Malapitan and Reyes, 2000). The major geologic structure in the area is the WNW-ESE trending San Vicente-Linao fault, whose trace cuts

through the Pocdol Mountains as a 5-km wide shear zone dubbed the BacMan fault zone (Figure 2). It is inferred that the San Vicente-Linao fault is a splay of the Philippine fault because the movement of the two faults is related.

Other geologic structures in BGPF follow four major structural trends: WNW-ESE, NW-SE, E-W, and NE-SW. The NW-SE trending structures, labelled the Pocdol belt (Figure 2), are said to control the deep south-eastward flow of geothermal fluids (EDC, 2003; Braganza, 2011).

The development area of BGPF is located within the intersection of the BacMan fault zone and the Pocdol belt (Braganza, 2011). While the most recent volcanic activity in the Pocdol Mountains is estimated to have occurred 40,000 years ago. Reyes et al. (1995) used the presence of kaipohans - ground discharge of H_2S and CO_2 that are related to high-temperature hydrothermal systems with an acidic core - and solfataras in rugged terrains as evidence of a young heat source. The subsurface stratigraphy of the field as derived from well cuttings is divided into the Late Pliocene-Late Pleistocene Pocdol volcanics and the Late Miocene-Early Pliocene Gayong sedimentary formation (Ramos, 2002).

2.1.2 BacMan resource and development

BGPF was one of the geothermal prospects identified by the Commission on Volcanology (COMVOL) in the 1970s and is one of the actively producing geothermal projects in the country. Logistically, the main production field can be divided into two developmental units: the Palayang Bayan sector, which supplies steam to the 110 MWe BacMan I turbines, and all other fields outside of the Palayang Bayan sector, collectively known as BacMan II. The development of BGPF began with an initial geoscientific exploration study in September, 1977 with shallow depth vertical electrical soundings, semi-detailed geological mapping, detailed geochemical investigations, and, eventually, the drilling of medium-depth exploration wells Manito 1 and 2 (Tolentino and Alcaraz, 1986). BacMan I was eventually

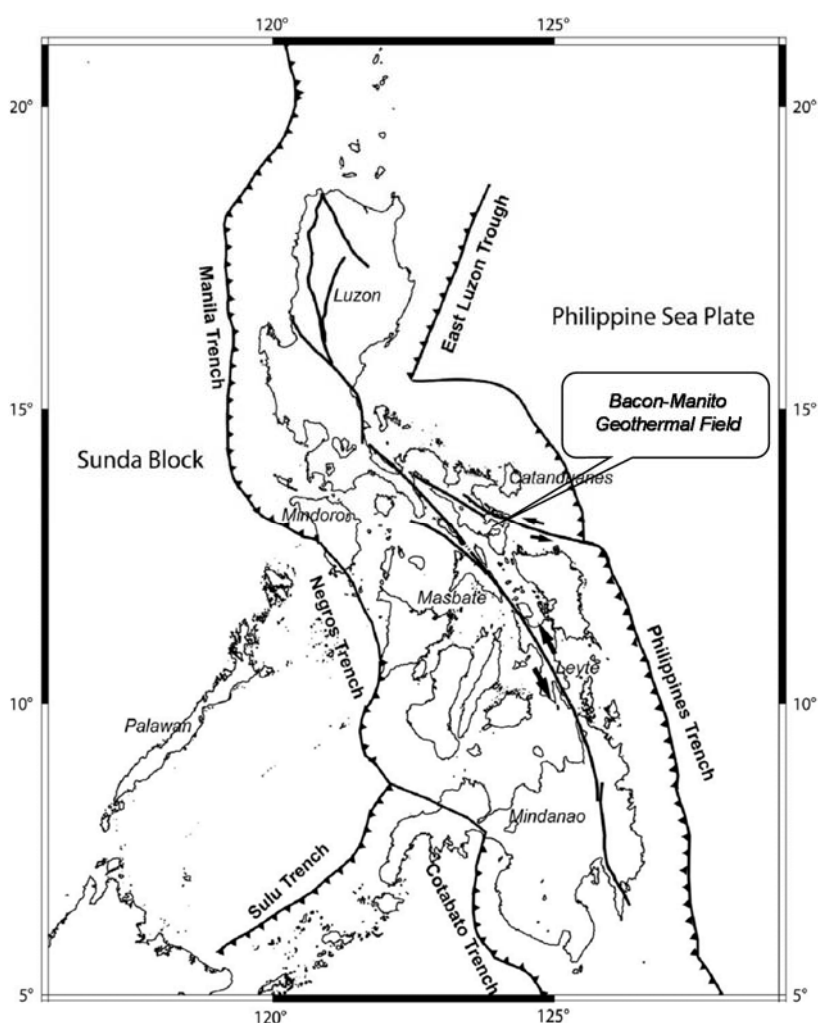


FIGURE 1: BGPF Location on Philippine tectonic setting map (modified from Yu, et al., 2013)

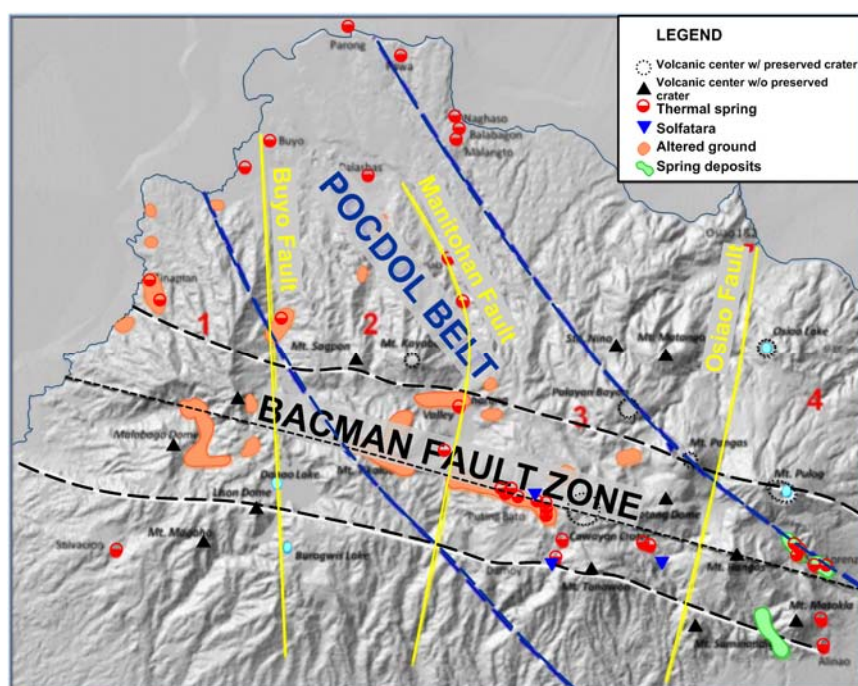


FIGURE 2: BGPf relief contrasts showing the BacMan fault zone (black) and Pocdol belt (blue) (modified from Braganza, 2011)

commissioned in 1993, Cawayan in 1994, and Botong in 1998. To date, BacMan II has two 20 MWe turbines commissioned, one each for Botong and Cawayan sectors. Based on the Philippine Department of Energy list of private sector initiated power projects, as of 12 August 2013, three additional power projects in Tanawon, Rangas, and Kayabon sectors have been indicated for BacMan II at 40 MWe each. All projects are undergoing feasibility studies. Tanawon has a target commissioning date on December 2018, while Rangas and Kayabon are aiming to be commissioned by 2019 (DOE, 2013).

The latest hydrogeological model of the BacMan resource puts the main upflow of the field beneath Palayang Bayan and Botong where the highest temperatures have been found (Ramos and Santos, 2012). The high temperatures exceeding 300°C that are indicated by a closed isothermal contour of secondary biotite (Ramos and Santos, 2012) are corroborated by both measured temperatures (Austria, 2008) and quartz temperatures (Ruaya, et al., 1994) in wells drilled in the general direction of the upflow (Figure 3). The preferential outflow direction is towards the northwest where the 240-280°C isothermal contours based on hydrothermal alteration dip gently (Ramos and Santos, 2012). The elongation of T-quartz temperature contours towards Inang Maharang indicates the same preferred outflow direction (Ruaya, et al., 1994). Exploration well IM-1 and the injection wells in the Inang Maharang region exhibit a downflowing profile which is typical of wells drilled along resource boundaries (Austria, 2008). A minor outflow is directed towards Rangas in the southeast. Steeply dipping isotherms based on hydrothermal alterations and a high pressure anomaly northeast of Palayang Bayan suggest a geologic boundary that acts as a flow barrier from the main field to the Osiao-Pangas-Botong area (Ramos

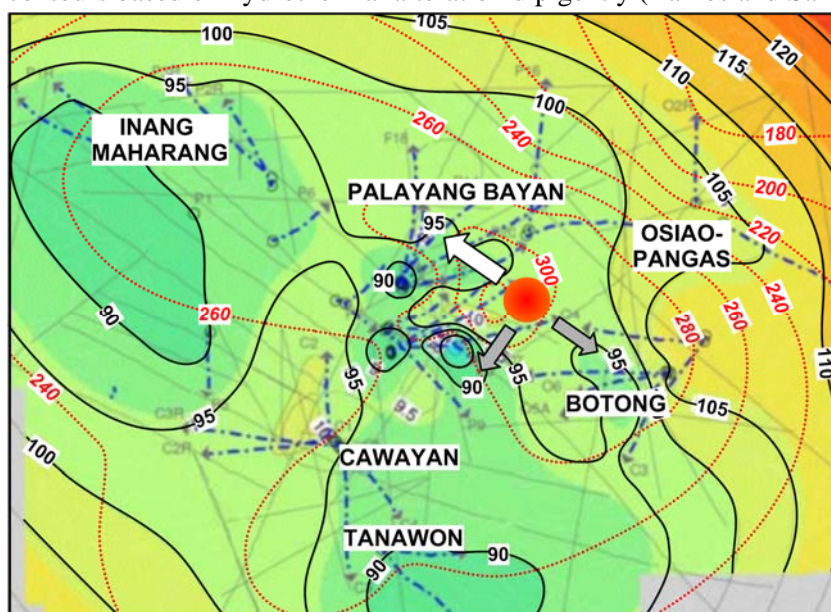


FIGURE 3: BGPf pressure (solid, black) and temperature contours (dotted, red) (modified from Austria, 2008)

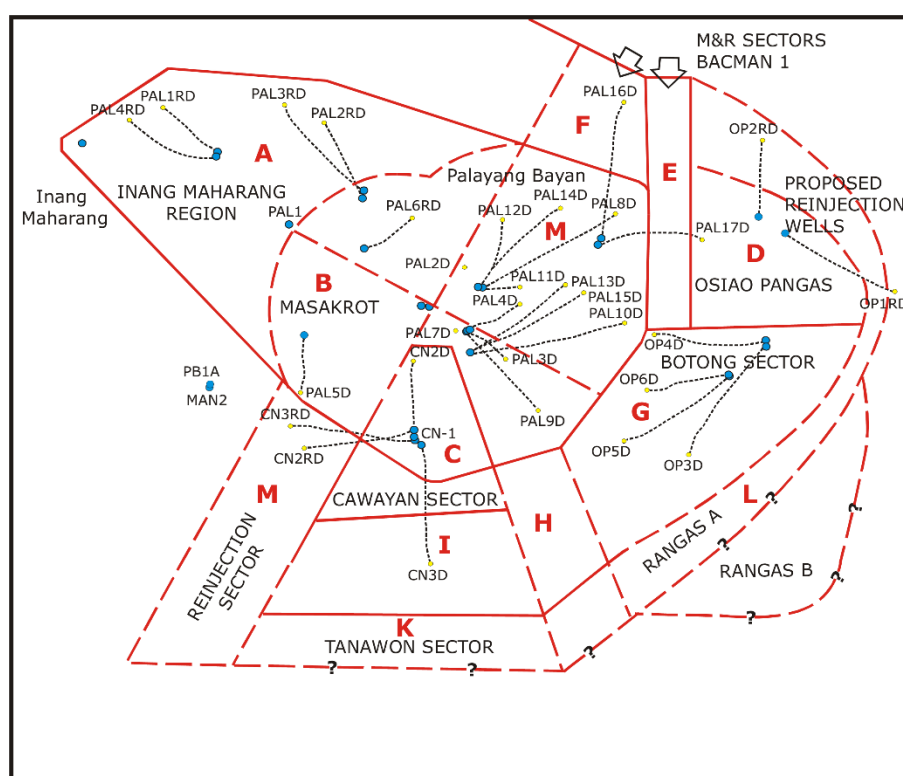
and Santos, 2012). The elongation of T-quartz temperature contours towards Inang Maharang indicates the same preferred outflow direction (Ruaya, et al., 1994). Exploration well IM-1 and the injection wells in the Inang Maharang region exhibit a downflowing profile which is typical of wells drilled along resource boundaries (Austria, 2008). A minor outflow is directed towards Rangas in the southeast. Steeply dipping isotherms based on hydrothermal alterations and a high pressure anomaly northeast of Palayang Bayan suggest a geologic boundary that acts as a flow barrier from the main field to the Osiao-Pangas-Botong area (Ramos

and Santos, 2012; Austria, 2008). A third outflow is towards the southwest to Cawayan and then Tanawon. The existence of a minor localized upflow in the Cawayan area was also suggested on the basis of fluid inclusion studies (Reyes, et al., 1995). The latest data from drilling have shown a low-temperature gradient and poor permeability associated with fine-grained clastics towards the southwest of Tanawon, possibly demarcating the boundary of the BacMan resource in that direction (Ramos and Santos, 2012).

Austria's 2008 resource assessment of BGPF, a volumetric assessment, shows a 90% probability of BacMan I producing 94.1 MWe and BacMan II producing 106.3 MWe from 2006 to 2031, while dynamic modelling techniques indicated that BacMan I and BacMan II combined can sustainably produce 150 MWe.

2.2 Brief history of Tanawon sector development

The Tanawon sector is at the periphery of the BacMan resource and is located within a high resistivity block identified during the initial geoscientific studies of the area. Interest in the sector began after the drilling of Well CN3D in 1990. Well CN3D was originally meant to be a reinjection well drilled within sector C of the BacMan field (Figure 4). It was converted to a production well due to its good permeability, productivity, and temperatures reaching 270°C. The results of drilling Well CN3D led to the recontouring of the resource boundaries and the addition of resource blocks I and K. Resource block I is an extension of the Cawayan resource block while resource block K is the Tanawon sector (Figure 4). Thus, development in the Tanawon field is fairly recent in comparison to the developmental history of BGPF, which started commercial operation in 1993; its main production area is within 2 km south of the production area of the Cawayan sector whose 20 MWe plant was commissioned in 1994.



2.3 Tanawon simultaneous discharge test

The simultaneous discharge test was conducted to gain an understanding about the possible response of the Tanawon field to full production. Three production wells within the Tanawon field, Wells TW-1D, TW-2D, and TW-4D, were simultaneously allowed to discharge while pressure response was monitored from monitoring Well TW-3DA using a Pruett-type tool (Pruett, 2013). The main objectives of the test were to determine the steam available, the behaviour of the discharging and nearby wells, monitor possible changes in the physical and chemical properties of the discharge fluid, and obtain additional data for Tanawon resource assessment. Pressure monitoring data is available for most of the test except for a break from day 79 to 107 while the tool was being recalibrated after the retrieved data for the preceding 15 days proved to be erratic. The discharge of the wells in Tanawon was monitored using the James lip pressure method (Grant, 1982).

The goal was to discharge the wells at full capacity throughout the discharge test period; however, due to the deteriorating reinjection capacity of Tanawon's reinjection well, Wells TW-1D and TW-4D were shut from days 59 to 66. Due to reinjection issues, Well TW-4D was often throttled to maintain the wellhead pressure in the reinjection well. Wells TW-1D and TW-4D were eventually shut on the 179th day. All Tanawon wells were closed on the 209th day. Pressure monitoring continued until the 229th day to recover pressure lost during the shutdown of the field. Figure 5 illustrates the pressure trends against the significant events during the simultaneous discharge.

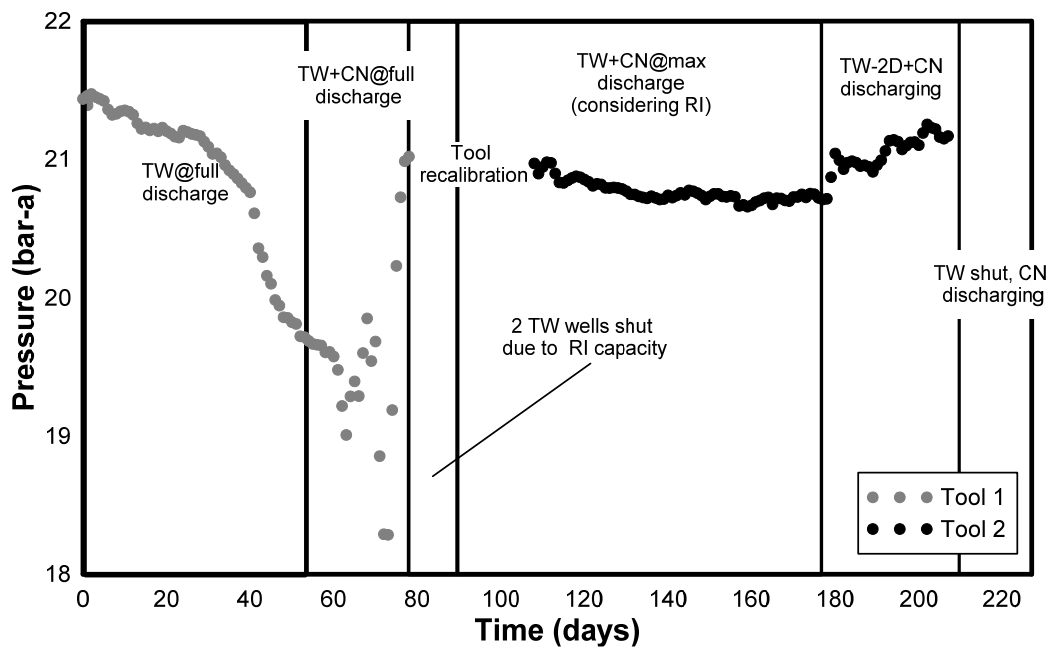


FIGURE 5: Simultaneous discharge test: average daily pressure measurements with annotations

Because an intimate connection between Tanawon and Cawayan had been observed, during the Tanawon discharge test, Cawayan was also monitored. To ensure that the behaviour captured was as close as possible to actual production behaviour, Cawayan was discharged at its full load of 20 MWe from day 55 to the end of the test. BacMan I was also kept under production throughout the test.

3. MODELLING IN GEOTHERMAL SYSTEMS

The mathematical modelling of the different aspects of geothermal systems has become a standard analysis technique in the study of geothermal reservoirs. Most models have a two-fold purpose: first to characterize the system being modelled and second to predict the response of the system to changes in utilization (Axelsson, 2013b). Two aspects that can be modelled in geothermal systems are the geothermal reservoir and the geothermal wellbore. Geothermal reservoir models describe the resource and can be used to characterize the reservoir rock while geothermal wellbore models describe the flow up the wellbore pipe and the portion of the reservoir feeding fluid into the wellbore. While the wellbore and the reservoir are closely connected and deal with the same fluid, because of the difference in the flow equations and time-scale involved, they are often modelled separately.

3.1 Reservoir modelling

Geothermal reservoir models can be used to quantify reservoir parameters and forecast reservoir response and output based on a given utilization scenario. Reservoir models have been used extensively throughout the geothermal industry as part of resource management. Models range from simple heat in place models based on the area of the resource to complex numerical reservoir models. In 2001, an informal survey by O'Sullivan et al. (2001) found that there are over a hundred geothermal fields with developed reservoir models. Two years later, Pruess (2003) put the number at several hundred fields. The growing number of fields utilizing geothermal reservoir models stresses the importance of geothermal reservoir modelling to project development.

There are several reservoir modelling techniques available for geothermal reservoir assessment and the modelling technique to be used should be determined by the availability of data and the objective of the modelling study (Axelsson, 1989). There are two main categories of modelling techniques used in the geothermal industry. Static modelling techniques use the amount of heat contained by the reservoir to estimate the output without taking into account changes in time; while dynamic modelling techniques look at the nature and response of the geothermal reservoir to disturbances due to utilization and exploitation and the corresponding output of the reservoir based on these (Axelsson, 2013b).

The list of the main modelling methods below was adapted from Axelsson (2013b):

Static modelling techniques

- Deep temperature estimates
- Surface thermal flux
- Volumetric method

Simple dynamic modelling techniques

- Decline curve analysis
- Simple mathematical modelling
- Lumped parameter modelling
- Detailed numerical modelling

The principal static modelling method is the volumetric method (Axelsson, 2013b). The volumetric method is used when surface data is available. Volumetric methods use the least subsurface information and thus have the greatest amount of uncertain, albeit educated, assumptions. Unfortunately, it is rare that sufficient subsurface data is available at the stage of geothermal development where financial commitments are obtained. Grant (1997) makes the point that initial resource assessments are often extremely optimistic, not because of calculation errors, but because of changes in the understanding of the reservoir being assessed. The output of such assessments should, therefore, be presented in such a way that explicitly recognizes the presence of such uncertainty. For this reason, the volumetric method is often coupled with a Monte Carlo simulation that can create a probability distribution of reservoir outputs.

The principal methods of dynamic modelling can be further subdivided into simple dynamic modelling techniques and the detailed numerical reservoir models. Simple models do not consider or reduce the spatial heterogeneity and variations in response of the reservoir in order to obtain a closed analytic form that describes the reservoir response. The lumped parameter modelling of water level or pressure changes is the principal simple dynamic method for studying the long-term response of low-temperature geothermal systems to utilization (Axelsson, 2013b). The Theis model is another simple mathematical model which is extensively used, but mostly for analysis of geothermal well tests which are on a much shorter time scale than a full production history. Detailed numerical models, in contrast to simple models, attempt to represent the geometry and spatial heterogeneity of the reservoir and determine the response of the reservoir through calculating the flow of fluid and heat through it. Numerical models require a significant amount of time and data for set up and calibration, but a model with sufficient detail can be instrumental in studying the physical and chemical processes that control the behaviour of the geothermal system (Axelsson, 2013b).

3.1.1 Lumped parameter models

Lumped parameter modelling of geothermal systems simplifies the geothermal system as a network of tanks and fluid conductors. Each tank in the network is characterized by a storage coefficient, κ , such that when liquid of mass m is injected into the tank, the pressure in the tank is the response $p = m/\kappa$. Pairs of tanks are connected by conductors which are described by conductance, σ , which transmits a mass flow $q = \sigma \nabla P$ where ∇P is the pressure difference between the tanks. Flow between tanks is always from the tank with a higher pressure to the tank with a lower pressure. The network can be modelled as either closed where flows are only between tanks and there is no external recharge or open wherein the network is connected to a constant pressure infinite source analogous to an electrical ground which acts as a recharge boundary. The derivation of the analytical solution to this problem is detailed by Axelsson (1989).

The main problem when performing lumped parameter modelling is the calculation of the tank and conductor parameters. LUMPFIT is a program that automates this calculation by treating it as an inverse modelling problem. For simplicity, fluid extraction or injection is limited to one tank which represents the main production or injection field. Pressure monitoring is also assumed to be within this tank. The pressure response in an N -tank system is given by

$$p(t) = - \sum_{j=1}^N Q(t) \frac{A_j}{L_j} (1 - e^{-L_j t}) - Q(t) B t \quad (1)$$

where A_j , L_j , and B are functions of the corresponding κ 's and σ 's.

Assuming a constant production, Q , pressure response of the tank would be declining. The magnitude of the lowering pressure is controlled by the amplitude coefficient, A 's while the L 's coefficient most strongly influences the rate of decay over time. Parameter B introduces boundary conditions wherein a closed system with no recharge would have a linear pressure decline over time for constant production. For an open system with recharge, $B = 0$, meaning the pressure in the tank would eventually stabilize (Axelsson and Arason, 1992).

Axelsson et al. (2005) presented cases from Iceland wherein the results of lumped parameter modelling were validated against actual monitoring data. It was found that the models were quite reliable and that the actual pressure response was expected to fall between the open and closed model forecasts. One of the goals of using lumped parameter modelling is, therefore, to find an optimistic open model and a pessimistic closed model (Liu, 2011).

Other significant findings during this validation process are that the most reliable models were those based on a long production history and that uncertainty in predictions increased with an increasing

forecasting period. As a final note, it was stressed that lumped parameter modelling assumes isothermal single-phase conditions and that changes in reservoir conditions such as boiling and changes in reservoir properties such as an increase in permeability due to seismic activity could make the results unreliable (Axelsson et al., 2005).

3.1.2 Numerical reservoir models

Detailed numerical reservoir models are one of the most powerful tools for studying geothermal reservoirs and numerical modelling has been a standard practice since the 1990s. The main steps of developing a geothermal reservoir model have been established and the list below was adapted from Axelsson (2013b):

- Dividing the reservoir into small semi-homogenous sub-volumes called grid-blocks;
- Assigning hydrological and thermal properties to the grid-blocks;
- Adding sources to represent fluid and heat entering the reservoir and sinks to represent fluid and heat exiting the reservoir; and
- Specifying appropriate boundary conditions.

Assigning grid-block properties can be a time consuming process and requires a well-developed conceptual model that describes the location of the upflowing heat and fluid source, the flow paths of the fluids, and the exit points from the field or outflows. The grid-block properties must be consistent with the conceptual model and produce flows that are consistent with well test data. The calibration process of finding the appropriate grid-block properties is a two-step process which involves natural state modelling followed by matching production history. Natural state modelling allows the model to evolve over geologic model time until the pre-exploitation temperature and pressures of the reservoir are matched. Production state matching, on the other hand, involves matching the measured response of wells to the production such as pressure drawdown and enthalpy and mass flow trends. These two steps, though often called stages of model calibration, are an iterative process of adjustments made to the grid-block properties, which if done during the production history matching phase should cause a deterioration of the matches made with the natural state model. Today, the calibration process has been made more efficient by the development of inverse modelling software such as iTOUGH2 and PEST; but, even with such technologies, the most complex reservoir models can take a long time to calibrate.

Setting up the boundary conditions is another part of the calibration process. The model can cover only a finite area, but its boundaries must be set so as not to affect the main reservoir. In many cases, this involves setting up very large grids that encompass an area much larger than the actual geothermal field being modelled. The large grids required for such simulations often lead to large grid-blocks, which are not suitable for capturing the behaviour of flow within fractures or through wells. For geothermal systems, flow through fractures are often dominant, and many solutions to the large grid-block sizes have been put forward, including dual-porosity models, process models, and sub-grids.

O'Sullivan et al. (2001) opined that the technology of geothermal reservoir modelling was already mature during the early 2000s. Despite borrowing and adapting many technologies and techniques from groundwater and oil and gas modelling, geothermal reservoir engineering lagged behind its counterparts in related industries because geothermal systems tend to involve multiphase and multi-component fluids moving in a highly heterogeneous environment. While there are numerous multiphase-multi-component simulators available, their capabilities are often limited compared to the problem they need to solve. In addition to this, as geothermal technology evolves, so do the requirements of the reservoir models. Modelling of enhanced geothermal systems, for example, requires modelling of dynamic changes in fracture permeability which most hydrothermal modelling software cannot easily simulate. In the recent past, the primary barrier to the development of numerical models was the amount of computing power that was available, making simulation time and the calibration process prohibitive. Today, this barrier is being overcome both by advancement in computing technology and in development of more efficient

computing algorithms; the current trend of geothermal reservoir modelling, therefore, is to create a fully-coupled thermo-hydro-mechanical-chemical simulation code for the reservoir itself (IPGT, 2012).

3.2 Wellbore modelling

Geothermal wellbore models are flow within pipe models that can be used to assess how fluids flow in from the reservoir and subsequently travel up the wellbore. In wellbore models, fluids enter the well through localized productive zones called feedzones. The highly localized inflow is common in wells that are drilled through fractured volcanic rocks of low porosity (Björnsson, 1987) where fluid flows are mainly through fractures. Flow properties are calculated given pressure conditions either at the wellhead or at the feedzone depth. Properly set-up models can be used to estimate the change in the output of the well with variations in wellbore and reservoir conditions.

Wellbore models are comprised of two main parts: the wellbore geometry and the feedzone properties. The most basic wellbore geometry describes the configuration of the well via the well depth and the inner diameter of the casings and liners or open hole. Some simulators allow for deviated wells and, thus, the location of the kick-off point and the deviation angle are also used. Feedzones also need to be described by their mass flow contribution, q , and enthalpy. The mass flow contribution may be provided either as productivity and reservoir pressure or a fixed mass flow. The productivity of a feedzone is often given as a productivity index, PI (Equation 2), which is a proportionality constant relating the mass flow contribution of a feedzone and the pressure difference, ΔP , between the wellbore at the feedzone depth and the reservoir.

$$PI = \frac{q}{\Delta P} \quad (2)$$

The more advanced wellbore simulators also consider dissolved salts and CO_2 . Wellbore simulators can be run either from the top down to the deepest feedzone, in which case the wellhead pressure, enthalpy, and mass flow need to be supplied to the simulator; or from the deepest feedzone to the wellhead, in which case the wellbore pressure at the deepest feedzone is needed. Wellbore models that use productivity indices can be used to create bore output curves by running the model with varying deepest feedzone wellbore pressures. Figure 6 shows an example of a wellbore profile calculated by HOLA.

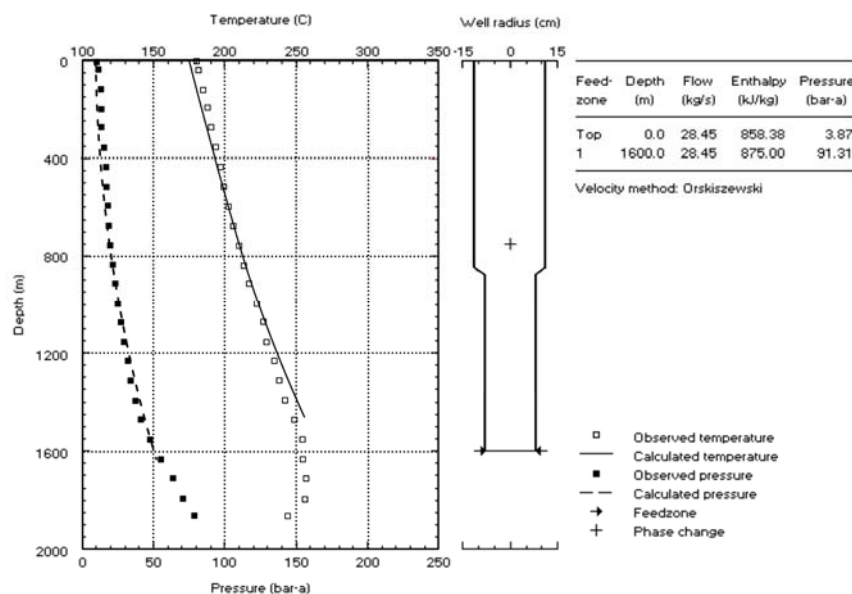


FIGURE 6: HOLA wellbore model example

Figure 6 shows an example of a wellbore profile calculated by HOLA.

Accurate wellbore geometry is sometimes easily obtained from the drilling information; but, in many cases, wells have blockages, scaling, or thinning. Blockage surveys or multi-finger caliper surveys will provide useful information, though often the modeller has to make assumptions about the length of the affected section and its diameter. Creating a wellbore geometry that is as close as possible to reality is important because the pressure drop from the feedzone to the wellhead is significantly affected by this.

Calibration of feedzone properties involves matching discharge pressure and temperature profiles of wells at a corresponding mass flow. If the information is available, relative velocity profiles can also be matched. Accurate wellhead parameters are, therefore, important in this part of the process. For various reasons, it is not unusual to find that the wellhead pressure read from the wellhead is not consistent with the 0-depth pressure read by the pressure survey tool. The modeller will, therefore, have to make assumptions regarding the correct wellhead pressure, mass flow, and enthalpy.

Freeston and Gunn (1993) observed that wellbore simulations have also become important not only as a tool to optimize the utilization of wellbores, but also as a means to improve reservoir models. Wellbore modelling can be used to gain insights on the optimum well design, determining minimum wellhead pressure that would prevent scaling in the casing (Björnsson, 1987), estimating improvements after acidizing (Fajardo and Malate, 2005) or clearing, and gauging the effects of drawdown. Aragon et al. (1999) stated that when calibrated correctly, wellbore simulations can sometimes reduce the need for Pressure-Temperature-Mass Flow (PTQ) logs, which are most often used to determine the distribution of mass flow contributions amongst feedzones. While most wellbore simulators are steady state simulators that assume stabilized discharge, there are transient wellbore simulators available.

3.3 Coupling of reservoir and wellbore models

Representing wellbore flow within a reservoir model has long been a subject of computational studies. Though simplified well “models” are included in most reservoir simulators in the form of mass sinks, the complexity of the two-phase flow inside the well is ignored (Murray and Gunn, 1993). The reservoir model limitations that are addressed by considering wellbore flow in reservoir simulations include ensuring that the mass extracted from the reservoir reaches the surface with sufficient wellhead pressure, interaction between the different feedzones of the well, and possibly simulating reduced discharge capability of a well that is wellbore-related and not reservoir related as in the case of blockages.

Many methods have been proposed in order to perform this task and these methods can be divided into two groups: methods that integrate wellbore flow into the model, and methods that couple a wellbore simulator with a reservoir simulator. Some examples of wellbore models integrated into a wellbore simulator are the T2Well module for TOUGH2 (Pan and Oldenburg, 2012), the work of Marcolini and Battistelli (2012), and the work of Hu et al. (2007). Developing the integrated wellbore and reservoir simulators involves adding to or changing the code of the reservoir simulator, as in the case of Pan and Oldenburg and Marcolini and Battistelli or programming a new simulator altogether as did Hu et al. Coupling of simulators, on the other hand, utilizes existing simulators and linking them by feeding the outputs of one as inputs to the other. This input-output cycle can be done either explicitly or separately through the creation of well tables.

Explicitly coupling a wellbore simulator and a reservoir simulator is the most straightforward approach to including wellbore effects into a reservoir simulation (Pruess, 2002). Murray and Gunn (1993) credit Hadgu et al. (2007) for the first explicit coupling of a wellbore simulator and reservoir model. This study linked Hadgu’s WFSa wellbore simulator with a TOUGH reservoir model. The modeller provided the required wellhead pressure and wellbore geometry, TOUGH supplied reservoir properties such as reservoir pressure and fluid enthalpy required by WFSa, and WFSa would iterate over different wellbore pressures until the required wellhead pressure was matched (Murray and Gunn, 1993). More recently, Rivera (2010) coupled HOLA with TOUGH2 using shell scripts, and Gudmundsdóttir (2012) coupled FloWell with TOUGH2 via iTOUGH2-PEST.

One approach that is fairly simple to implement is coupling simulators via well tables. Assuming a fixed wellhead pressure, the wellbore pressure at a feedzone required to discharge the fluid at this wellhead pressure would be a function of mass flow and enthalpy. A well table would give the required wellbore pressure at the feedzone of the well given a specific mass flow and enthalpy pair. Creating a well table involves running the wellbore simulator repeatedly over varying mass flow and enthalpy

conditions. The reservoir simulator would then interpolate using the well tables as to which wellbore pressure it would give a well, provided the enthalpy of the block. Well tables are a facility of certain reservoir simulators such as TOUGH2 and TETRAD.

4. HOLA WELLBORE MODELS OF TANAWON WELLS

As part of the study of the discharge properties of the Tanawon wells, Pressure-Temperature-Spinner profiles of Wells TW-2D and TW-4D were taken. Well TW-1D was not surveyed due to a shallow blockage, but an older discharge profile was available. In order to determine the productivity indices of the wells, calibrated wellbore models were developed using HOLA wellbore simulator to match the discharge profiles of the Tanawon wells. From the wellbore models, the productivity indices and wellbore pressures at the feedzone were derived and incorporated into the AUTOUGH2 input file of the BacMan reservoir model.

4.1 HOLA wellbore simulator

The earliest version of wellbore simulator HOLA was developed and validated by Björnsson in 1987 as a “Multi-Feedzone Geothermal Wellbore Simulator”. The simulator treats the flow within the wellbore as a one-dimensional steady state flow within a vertical pipe. The pipe is thus divided into a series of grid points and HOLA solves the mass, momentum, and energy flow through the pipe using an explicit finite difference method. The fluid inside the wellbore is assumed to be pure water, but it can occur as a two-phase fluid. To calculate the flow of the two-phase fluid, HOLA uses the method of separated flow models which calculates the flow of the steam and liquid separately, then correlates the two using phase velocity correlations, which have been empirically derived (Björnsson, 1987).

HOLA allows for modelling of multiple feedzones inside the wellbore and each feedzone is modelled as a feed point that is located on one of the grid points (Björnsson, 1987). The feed point properties that are required by the simulator are depth, enthalpy, reservoir pressure at the depth of the feed point, and a productivity index.

The HOLA version used in this study is HOLA version 3.3 compiled in September 1994. This version allows for six simulation modes. The mode most utilized for this study was mode 2 which finds discharge profiles for a required wellhead pressure given the feed point properties. Mode 2 varies the pressure at the deepest feed point until a pre-defined wellhead pressure is achieved. Four-phase velocity methods can be used: Armand, Orkiszewski, Chisholm, and Björnsson. All simulations in this work were done using the Orkiszewski correlation. Though based on empirical behaviour of oil and gas wells, the use of the Orkiszewski correlation for geothermal wells was recommended in the early days of geothermal wellbore simulators. In a pair of companion papers by Ambastha and Gudmundsson (1986a; 1986b) it was demonstrated by matching the flow in the production casing that the Orkiszewski correlation has a general applicability for modelling geothermal wellbore flow and good matches between the measured and calculated pressures and temperatures were obtained, particularly if the steam mass flux was above 100 kg/s-m^2 (Ambastha and Gudmundsson, 1986a). Further research regarding flow correlations was recommended by the authors as flow within the slug regime was not well matched (Ambastha and Gudmundsson, 1986b). Since the development of HOLA, new flow correlations have been developed and utilized in other wellbore simulators. The flow correlation is an important part of geothermal wellbore modelling because the pressure loss due to friction is strongly determined by the flow adjacent to the walls of the well, which is a matter dictated by the flow correlation used (Hsu and Graham, 1976).

4.2 Tanawon wellbore models

The three Tanawon wells that were modelled were Wells TW-1D, TW-2D, and TW-4D. Two models were created for each well. The base model is a multi-feed zone model which attempts to match the behaviour of the well. This base model is used to select the feedzone that contributes the most to the overall mass flow of the well. A single feedzone “TOUGH Model” is then constructed by selecting the depth in the wellbore model closest to the major feedzone that has a corresponding block centre in the AUTOUGH2 model.

Wells TW-1D and TW-2D were drilled in 2000 through a joint venture of Kyushu Electric Power Company of Japan and PNOC-EDC. The drilling of both wells suffered persistent fills, tight spots, stuck pipes and eventually premature termination. Post-drilling well tests suggested formation damage as indicated by positive skin and this was attributed to large amounts of viscous mud lost-in-hole and cement injected into the formation through cement plugging. The wells were thus given acid treatment to cure the formation damage (Fajardo and Malate, 2005).

Well TW-1D is a standard diameter wellbore. Its stable discharge at fully opened conditions has a discharge enthalpy of 1400 kJ/kg while throttling the well brings the enthalpy to about 1200 kJ/kg. The difference in enthalpy is attributed to flashing in the formation, resulting from significant pressure drawdown caused by large mass extractions (Fajardo and Malate, 2005).

The base line model for Well TW-1D is a two feedzone model based on a throttled condition survey done in 2001. The feedzones are a liquid enthalpy, low productivity feed at the bottom to model the observed temperature inversion, and a higher productivity index feedzone 100 m from the bottom. The base model matched the pressure slightly better than the temperature (Figure 7). The calculated temperatures tended to be slightly higher than the measured values, with a maximum deviation of +2°C close to the wellhead. The temperature trend at the bottom was also not well captured as the calculated temperature showed a step change while the measured temperatures had a more gradual change. The largest temperature deviation from measured temperatures of -18°C occurred near the bottom of the well between the two simulated feedzones. The feedzone depth in the TOUGH model is set between the feedzones of the base model and given an enthalpy closer to the major feedzone enthalpy. The TOUGH model overlaps with the base model except at its bottom where the base model only has low enthalpy flow from its deepest feedzone.

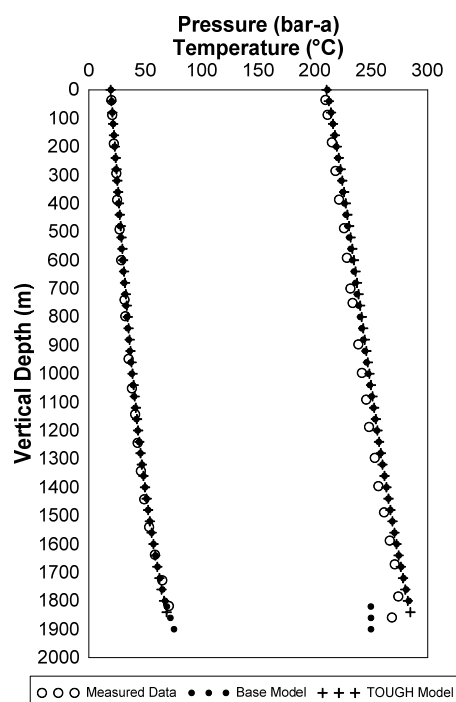


FIGURE 7: Well TW-1D discharge profile

Well TW-2D was drilled as a large diameter well in the hopes of overcoming the drilling problems encountered by Well TW-1D (Fajardo and Malate, 2005). The discharge characteristics of Well TW-2D were low enthalpy of about 1090 kJ/kg. Fully open discharge mass flow and wellhead pressure were also lower than in Well TW-1D.

The base model of Well TW-2D was calibrated against the throttled condition profile because HOLA could not calculate a discharge profile for the fully-opened condition, which had a low wellhead pressure (Figure 8). The base model for Well TW-2D was similar to the base model of Well TW-1D, and had a low enthalpy, low productivity feedzone at the bottom and a higher enthalpy, higher productivity feedzone 100 m above the bottom. In order to match the discharge profile, measured enthalpy at the wellhead was adjusted by +50 kJ/kg. This shift in enthalpy was necessary to discharge the well in

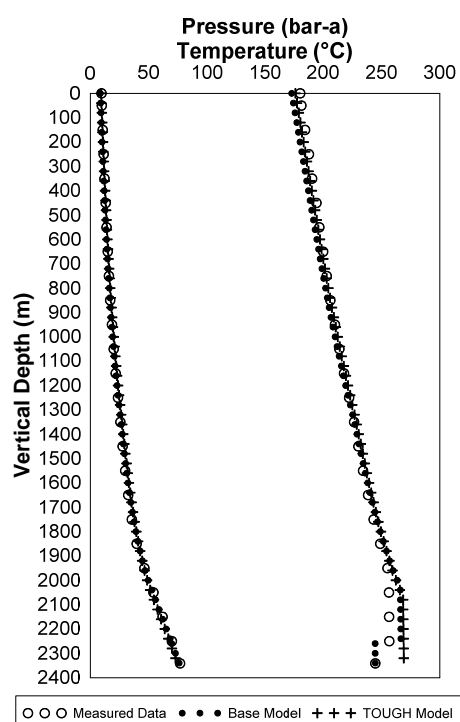


FIGURE 8: Well TW-2D
discharge profiles

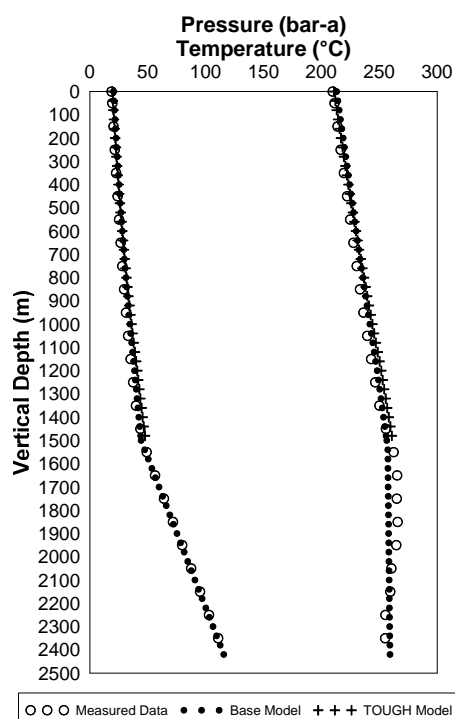


FIGURE 9: Well TW-4D
discharge profiles

HOLA, which was calculating a too large pressure drop and consequently choking the well when the measured enthalpy was used. It was the same as Well TW-1D; the TOUGH model feedzone was set between the two base model feedzones.

Well TW-4D was recently drilled, designed to be a large diameter well. Drilling problems encountered during its drilling led to a configuration that is similar to a large diameter well at the top, but then tapers to a standard well at the bottom, resulting in a hybrid configuration. After drilling, Well TW-4D underwent a stimulation programme that involved perforation of its blank liner and acidizing it. The discharge characteristics of Well TW-4D are similar to the discharge characteristics of Well TW-1D, albeit at a higher enthalpy even when throttled. The higher enthalpy of Well TW-4D is attributed to the feedzones from its perforated section which is shallower.

The base model of Well TW-4D puts the major feed at the perforated section of the well, which is consistent with findings from spinner surveys. The match between the base model and the measured data is good for pressure and acceptable for temperature (Figure 9). A better match for the temperature profile can be made by adding more feedzones, but for the purpose of identifying the major zones in the well, it was deemed unnecessary. The enthalpy at this feedzone was set to 1400 kJ/kg.

In modelling the Tanawon wells, some compromises had to be made to work around some of the limitations of HOLA. First off, the Tanawon wells are all deviated wells and had to be converted to vertical wells. This led to a shorter pipe because the vertical depths of the wells were used instead of the measured depth. The shorter depth and the lack of a deviation angle affected the pressure and enthalpy drop as the fluid rose to the top of the wellbore. The simulated profiles were sensitive to fluid enthalpy and the presence of non-condensable gases (Ambastha and Gudmundsson, 1986a). The Orkiszewski correlation was also found to be less reliable under the slug flow regime, which is the dominant flow regime in the Tanawon wells (Ambastha and Gudmundsson, 1986b). It must be stressed that pressure drop as the fluid rises from the bottommost feedzone is an important consideration when dealing with the calibration of multi-feed wellbores in HOLA. Feedzones in HOLA are characterized by productivity indices so that the mass flow contribution of the shallower feedzones is dependent on the pressure of the fluid at that depth. For the same productivity index, a lower pressure drop from the bottom will result in a lower contribution at the shallower feedzone. In terms of calibration, this may result in unnecessarily increasing the productivity index at the shallow feedzone to get the appropriate feedzone contribution.

5. LUMPED PARAMETER MODELLING OF PRESSURE MONITORING DATA

To get an analytic solution for the pressure response of the reservoir to the extraction at Tanawon sector, LUMPFIT was used to find an appropriate lumped parameter model for the pressure monitoring data of Well TW-3DA. As there was missing data in the middle of the data set due to the replacement of the pressure monitoring tool, the data before the 110th day were excluded from the modelling process to prevent LUMPFIT from interpolating production history within the gap. However, data from day 1 were loaded into LUMPFIT so that the corresponding production history would be considered in the modelling process. The dataset from the later part of the test was favoured because it has more data points and included the pressure response to the shutdown of Tanawon.

Modelling the pressure response against Tanawon extraction produced good matches indicating that the extraction in the Tanawon production area is well correlated with the pressure in Well TW-3DA. For the different Tanawon extraction models, the change in the fit is marginal as can be seen by the nearly overlapping plots in Figure 10. This insensitivity to the number of tanks can be attributed to very small conductivity values which means the production tank is not well connected to its surroundings. The main difference between the one- and two-tank models is that the two-tank model is more sensitive to fluctuations in production.

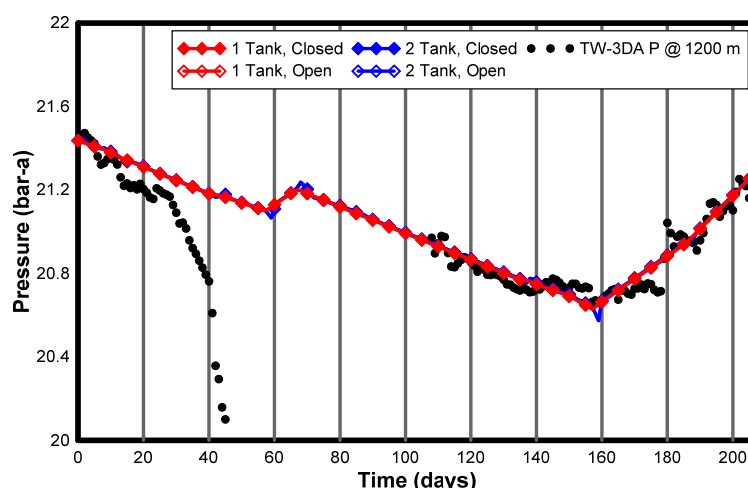


FIGURE 10: LUMPFIT model using Tanawon extraction against monitoring data

While the general drawdown and recovery trends are well represented by the Tanawon extraction model, there are portions of the data that cannot be explained by Tanawon extraction alone, which is an indication that there are other processes in the field affecting the pressure response in Well TW-3DA. Suspected, of course, is the extraction in the Cawayan sector.

The pressure cannot be modelled using Cawayan extraction alone because at the time of the pressure recovery, Cawayan extraction was constant. But by adding Cawayan extraction to Tanawon extraction (Figure 11), two features of the pressure response were better reflected by the model. The curvature of the drawdown while Tanawon was at maximum extraction was better matched and the change in slope due to the increase in Cawayan discharge was mimicked, though not matched. The pressure recovery was not as well captured as in the Tanawon extraction only model, because the step decrease around day 179 due to the shutdown of two of the wells was a smaller percentage of the total extraction. This increase in Cawayan production could also be attributed to the shutdown of Tanawon. In the Cawayan plus Tanawon extraction model, there were also marginal

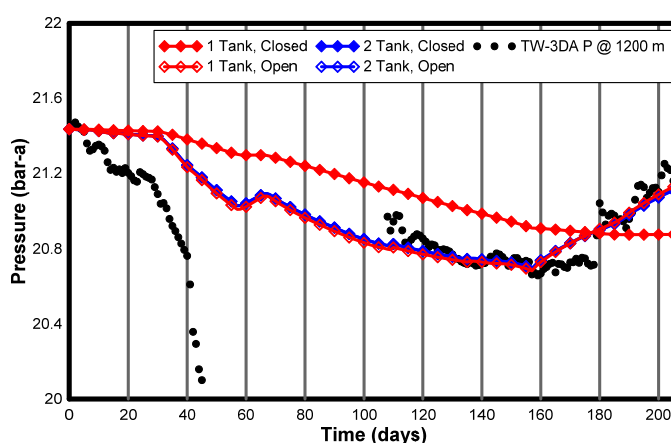


FIGURE 11: LUMPFIT model using Tanawon+Cawayan extraction against monitoring

differences between the one-tank, open and two-tank models. The recovery and drawdown of the two-tank models were slightly slower than that of the one-tank, open model. The one-tank, closed model was unable to match the recovery which is an indication that there is recharge coming into the area. Most likely due to the short duration of the test, it is unclear whether this recharge is merely from the periphery of the reservoir like from the second tank of a two tank model or true recharge from a constant pressure source.

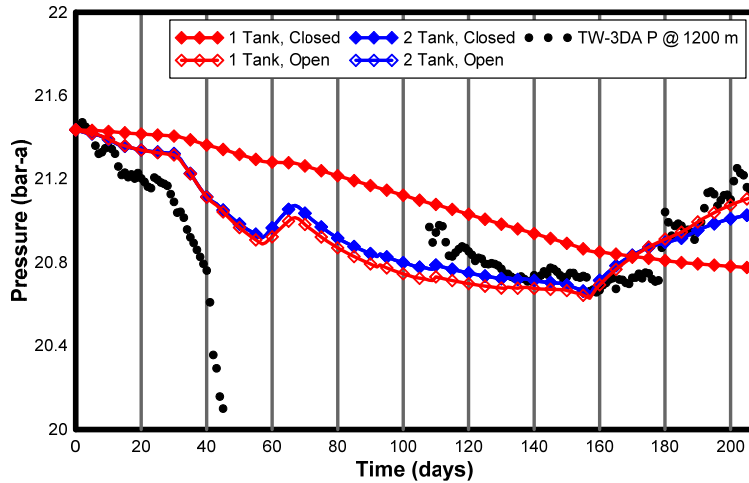


FIGURE 12: LUMPFIT model using Tanawon+Cawayan net extraction against monitoring

The last scenario considered was the scenario wherein the pressure response is influenced by injection in the area; however, when reinjection was considered, the matches did not improve (Figure 12). This does not mean that reinjection does not affect the monitoring well; rather, the effects of reinjection are not as strongly felt or not as immediately observed in the monitoring well.

The strong relationship between the pressure response in Tanawon and the extraction in Cawayan suggests that north to south may be the dominant flow direction. The seemingly weak correlation of

Tanawon with the Cawayan + Tanawon reinjection, on the other hand, points towards the idea that the NW to SE trending flow that would have been driven by the Pocdol belt may be a less prominent process. It is also possible that because the reinjection sector is a bit further away from the monitoring well than the Cawayan production area, the effects of reinjection have not yet been observed.

Looking at the statistical measures of fit given by LUMPFIT, the best fitting model was the one that utilizes Tanawon extraction on its own; however, in terms of capturing features of the pressure response, the Tanawon combined with the Cawayan extraction without injection was better. This illustrates that despite the statistical measures provided by LUMPFIT, it is still important to plot the results and examine whether they make sense. Table 1 summarizes the LUMPFIT parameters used for the best-fitting models.

TABLE 1: LUMPFIT parameters

Production data used	Model		A1	L1	A2	L2	B
	No. tanks	Boundary					
Tanawon Extraction	1	Closed	-	-	-	-	16.68
	1	Open	16.69	0.21E-05	-	-	0.00
	2	Closed	16.39	0.46E-06	-	-	0.16
	2	Open	16.39	0.46E-06	0.16	0.46E-07	0.00
Tanawon and Cawayan Total Extraction	1	Closed	-	-	-	-	4.10
	1	Open	18.21	0.24E-01	-	-	0.00
	2	Closed	16.94	0.23E-01	-	-	0.18
	2	Open	16.94	0.23E-01	0.18	0.13E-02	0.00
Tanawon and Cawayan Total Net Extraction	1	Closed	-	-	-	-	12.66
	1	Open	84.73	0.39E-01	-	-	0.00
	2	Closed	86.73	0.59E-01	-	-	4.50
	2	Open	90.73	0.59E-01	4.50	0.74E-03	0.00

Because the one- and two-tank, open models have almost the same results, the one-tank, open model may be selected as representative of this system. These results differ from the results of Fajardo (2000), which models the Cawayan area as a two-tank, open model. However, the complexity of the applicable lumped parameter model is known to be dependent on the length of time covered by the monitoring data (Axelsson, et al., 2005) and, so, the test duration may have the effect that the second tank is not yet clearly observable. The difference in best-fitting models may also be due to the difference in the location of the monitoring wells. The choice of monitoring wells that is able to represent the processes in the geothermal system of interest is important to the modelling process (Sarak et al., 2005). Fajardo's monitoring well, Pal-7D, is located close to the central production area and directed towards Cawayan sector, making it a good monitoring well for Cawayan. Based on the results of the lumped parameter modelling in this study, the Tanawon monitoring well is isolated from most external reservoir processes and is, thus, able to capture the response of the Tanawon reservoir to the simultaneous discharge test more clearly with less interference from the main production area.

Table 2: LUMPFIT parameters for model with turbulence

Production data used	Model		Turbulence coefficient	A1	L1	A2	L2	B
	No. tanks	Boundary						
Tanawon and Cawayan Total Extraction	2	Closed	0	16.94	0.23E-01	-	-	0.18
		Open		16.94	0.23E-01	0.18	0.13E-02	0.00
	2	Closed	0.35	26.50	0.32E-01	-	-	0.27
		Open		27.50	0.32E-01	0.55	0.96E-01	0.00

The model can be further improved by changing the turbulence coefficient (Table 2, Figure 13), which would normally be used to correct the pressure response of the well for skin losses close to the wellbore due to turbulence resulting from the sudden decrease in the effective flow cross-section from the reservoir to the wellbore. The effect of the turbulence can be observed in the relationship between the mass flow entering a feedzone Q and the difference between the reservoir pressure and the wellbore pressure at the feedzone. The expected behaviour for laminar flow is linear as characterized by the first-degree term in Q and coefficient, A . The turbulent effects are expressed by the squared term and coefficient, B . Note that when $B = 0$, A is equivalent to the productivity index, PI .

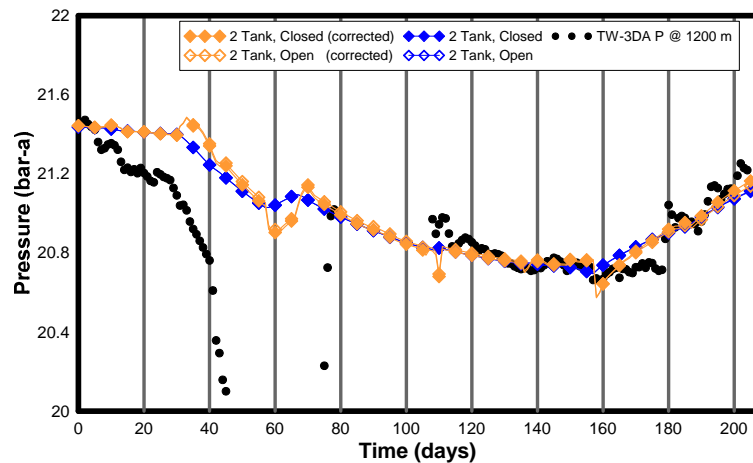


FIGURE 13: LUMPFIT model using Tanawon+Cawayan extraction with turbulence

The turbulent effects are expressed by the squared term and coefficient, B . Note that when $B = 0$, A is equivalent to the productivity index, PI .

$$p_{\text{reservoir}} - p_{\text{well@FZ}} = AQ + BQ^2 \quad (3)$$

Because the monitoring well was not being discharged during the test, the turbulence effect could not be quantified. For purposes of this study, it was just an additional parameter to adjust in order to improve the model fit.

A cursory validation of the models can be done using idealized storage conditions for liquid reservoirs. The reservoir is known to have a two-phase cap based on the discharge of the wells, thus a free surface model was used. Table 3 summarizes the tank and fluid conductor properties from the first tank of the two-tank open models and the corresponding calculated areas.

Table 3: LUMPFIT-derived properties

Model	κ_1 (kg/Pa)	σ_1 (kg/s-Pa)	A_{free} (km ²)
Tanawon extraction (2-tank, open)	5176.60	0.12E-06	1.02
Tanawon + Cawayan extraction (2-tank, open)	5046.73	0.13E-02	0.99
Tanawon + Cawayan extraction with turbulence (2-tank, open)	3080.21	0.32E-01	0.60

The calculated areas are smaller than the actual assessment for Tanawon based on combined geoscientific and well testing data. Sarak et al. (2005) and Axelsson (1989) enumerated the possible reasons why such a calculation might be unreliable. These include pressure response influences that were not considered in the modelling, the short production history used, problems with data accuracy, and the fact that the system is actually two-phase. Another thing to look at it is the possible weighting of the influences. Summing up the production and injection from the different sectors assumes that each sector has equal influence on the pressure response, which is rarely the case in such a heterogeneous system. Finally, the assumption of all production coming from a single tank may not be fully applicable in this situation because during the simultaneous discharge test, the rest of BacMan was not shut down or discharging at a constant rate. This extraction would most likely not fall within the “first tank”.

6. NUMERICAL SIMULATION OF THE SIMULTANEOUS DISCHARGE TEST

The main weakness of the lumped parameter modelling is that it ignores the spatial geometry of the geothermal system. While lumped parameter modelling can be reliable for gauging pressure drawdown, it cannot model many of the other phenomena in geothermal utilization that should be considered when looking at sustainable production. Distributed parameter modelling or numerical reservoir modelling is able to look at a wider range of parameters.

The simultaneous discharge test was modelled using an AUTOUGH2 program developed for BGPF. The test was modelled by programming the model to extract mass from the reservoir equivalent to the extraction during the test itself. It was then determined whether with this extraction the pressure response observed in TW-3DA could be simulated.

6.1 TOUGH and AUTOUGH

TOUGH and its current incarnation TOUGH2 is one of the programs available for numerical reservoir modelling. It is a member of the multi-phase, multi-component family of codes referred to as MULKOM that is being developed in the Lawrence Berkeley National Laboratory (LBNL) (Reeves, et al., 1994). The name TOUGH is an acronym for “transport of unsaturated groundwater and heat” and was developed for problems that involve “strongly” heat-driven flow that is an effect of vaporization taking place at high water temperatures (Pruess, 1987). TOUGH2 was developed to extend the capabilities of TOUGH and was set up in such a way that future developments to the code would be encouraged (Reeves, et al., 1994). AUTOUGH2 is one of the customized versions of TOUGH2, developed by the University of Auckland. The main thrusts of the AUTOUGH2 development are to improve ease of use, increase execution speed, and extend TOUGH2 capabilities and options (Yeh et al., 2012).

The main problem solved by TOUGH and all its subsequent versions is solving the mass and energy balance for every grid-block in the model. The form of the mass balance and energy balance equations for the n^{th} grid-block with volume V_n and surface area A_n is the same and is given by

$$\frac{d}{dt} \int_{V_n} M^{(k)} dv = \int_{A_n} \mathbf{F}^{(k)} \cdot \mathbf{n} d\Gamma + \int_{V_n} q^{(k)} dv \quad (4)$$

where k is the component of interest, which can be heat, water, air, and more; M is the accumulation term, which accounts for how much of a component is contained in the grid-block; \mathbf{F} is the flux term, which refers to the amount of each component passing through the surface of the grid-block; and q is a term which is applicable for blocks that are sources or sinks of heat or mass. The differential equation is solved in space via integral finite differences and time evolution is solved through a fully implicit finite difference scheme, which would ensure unconditional stability to the numerical solution (Pruess, 1987). The flow of the fluid is governed by a multiphase extension of Darcy's Law while heat flows via convection and conduction (Pruess, et al., 1999). TOUGH is distributed as a series of separate equations of state (EOS) modules, which all solve Equation 4, but for different sets of components (Pruess et al., 1999). In AUTOUGH2, all the EOS modules are compiled together and are run on a single executable. To run the correct module, in addition to standard TOUGH2 inputs, the simulator or EOS to be used can be specified at the beginning (Yeh et al., 2012).

One of the most noticeable extensions made in AUTOUGH2 is the addition of new generator types. Generators, or sinks and sources, in TOUGH2 (Pruess, et al., 1999) were enumerated as follows:

- HEAT generator to act as heat sources;
- Injection generators (COM1/WATE, COM2 to COMn) to act as mass sources;
- MASS generator, which injects or withdraws a fixed amount of mass from the source or sink block;
- Wells on DELiVerability (DELV) sink, which simulates the feedzone of a well and withdraws fluid from a block based on a given productivity index, a given fixed wellbore pressure, and the calculated block pressure using $PI = Q/(p_{block} - p_{well@FZ})$; and
- F-type wells on deliverability sink, which like DELV simulates the feedzone of a well and withdraws fluid from the block based on a given productivity index and the calculated block pressure, but solves for the wellbore pressure based on a well table provided in a file. The F-type generator is useful for implicit coupling of wellbore simulators and TOUGH2.

The DELV and F-type generators are used in simulating wells with a fixed wellhead pressure, which is often the case when wells are utilized for power production. The DELV generator assumes that the wellbore pressure required to discharge at the set wellhead pressure will be constant throughout production, which is only applicable when wellbore geometry, mass flow produced, and enthalpy are held constant. On the other hand, the F-type generator calculates this required wellbore pressure using the provided well table based on a fixed wellhead pressure. The MASS generator is useful when simulating production history, where actual extraction is known. Because the actual mass extraction is provided, the pressures within and near the wellbore are not taken into consideration.

AUTOUGH2 incorporates most of the TOUGH2 generators and introduced new generators, mostly variations of the DELV generator of TOUGH2. The F-type well was replaced by WFLO, which retrieves a well table from a file called WFLO. The main difference between the F-type and WFLO wells is that only one WFLO file can be used per simulation while any number of F-type wells can be called. Another generator type in AUTOUGH2 that can be used in a way that is similar to the F-type well is the geothermal well on DELiVerability (DELG), which has two modes of operation. Either DELG can be used to model a time-varying productivity index by providing a table of times and productivity index values or to give a wellbore pressure against enthalpy table. The second mode of operation is similar to F-type except the mass flow is not included in the well table. There are other new generator types in AUTOUGH2 described in Yeh et al. (2012), but they will not be discussed here as this study only utilized MASS, DELV, and DELG.

6.2 The 2010 BGPF reservoir model

The base model used for this study is the BGPF 3D reservoir model developed by Villacorte, Colina and others in 2010 using the Petra Sim graphical interface for TOUGH2 (Colina et al., 2011). The model is a single-porosity model with a rectangular grid that spans a total area of 1677 km² and 37 layers. The total number of grid blocks utilized by the model is 85,100, with finer meshing at the centre where the production area is located. Two convective systems were included in the model (Colina et al., 2011). Of interest is the main BacMan production area, which is outlined in white in Figure 14.

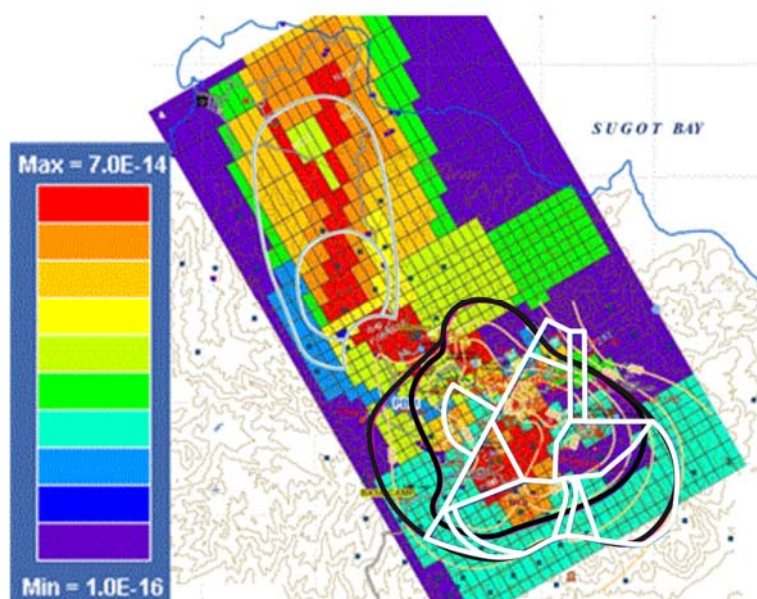


FIGURE 14: Permeability distribution at -1125mRSL (modified from Colina et al., 2011)

The model was calibrated against all available natural state temperatures and pressures in 2010 and over 17 years of production history. Production history data used were the discharge enthalpies of the wells and the pressure drawdown from 13 monitoring wells. Most wells in the field had good natural state temperature and pressure matches. The model was then converted to an AUTOUGH2 model for the simulation of CO₂ in the field. Profiles calibrated with CO₂ were similar to the profiles without CO₂ (Colina et al., 2011).

Two heat sources were used in the model, one for each of the modelled convective systems. The calibrated permeability distribution replicated the boundaries inferred from geophysical surveys (black lines in Figure 14). High permeability pathways were assigned towards the outflow regions (Colina et al., 2011).

At the time of the model's calibration, only Wells TW-1D and TW-2D had been drilled and neither had been produced for extended periods of time. While no Tanawon wells were used during the production history calibration of the model, four Cawayan wells were part of the calibration process. Enthalpy was not well matched in Cawayan with only two out of the four wells having a good match (Colina et al., 2011). The modelled pressure drawdown in Cawayan was also higher than the measured pressure drawdown.

During the model's development, Well TW-4D was included as a make-up well and its configuration did not include the perforated section, so a new sink was added to the model to include this feedzone.

6.3 Numerical simulation results

The time resolution needed to capture the pressure response during the simultaneous discharge test is fairly fine; however, if complex numerical models are being run, it is also not practical to impose a prohibitively small time step in order to create an "accurate" picture. Because Darcy is numerically stable when an implicit finite-differencing scheme is utilized, as it is in TOUGH2 and AUTOUGH (LBNL, 2013), the problem of large step sizes in the numerical model is not so much about achieving a stable solution, but more a problem of smoothing out fluctuations that should have otherwise been resolved by the model had a small time step been utilized. Using the fixed MASS model, three time

steps were tested and compared. The finest time step of $1.44\text{E}+5\text{s}$ (1.67 days) used was based on a maximum Courant number of 1. The Courant number is a stability criterion for numerical solutions to partial differential equations. Keeping the Courant number below 1 is a stability criterion for explicit finite difference schemes, and is, admittedly, too tight a restriction for TOUGH2. The largest time step of $2.59\text{E}+6\text{ s}$ is equivalent to one month. The third time step of $5.26\text{E}+5\text{ s}$ (6.1 days) was calculated based on the condition that the bulk fluid does not “skip over” blocks within one time step. The finer time steps are dependent on the average permeability in the area of interest. Mathematically, high permeability areas would require smaller stepping on account of faster breakthrough of fluids. Table 4 provides the details of the time step calculation.

The simulated pressure response was not compared with the actual pressure response using standard statistical regression methods because the monitoring block in the model is at a deeper depth than the actual monitoring depth within Well TW-3DA, resulting in a much higher pressure. While there is a block at the same depth as the pressure probe in the real monitoring well, the block is set within the caprock of the model, making it insensitive to the short-term changes induced by the simultaneous discharge test. The simulated pressure response is, therefore, only graphically compared with the actual pressure response.

Time step size does not affect the maximum pressure drop within the simulation period (Figure 15). The general trends of pressure lowering due to high extraction during the simultaneous discharge and recovery when the Tanawon wells were shut were all captured by the model regardless of the time step. The main feature that was smoothed out in the large time step was the recovery in pressure when Wells TW-1D and TW-4D were temporarily shut. A notable side effect of the fine time steps was that pressure recovery due to the shutdown of Tanawon occurred almost a full month earlier.

This premature recovery is because AUTOUGH/TOUGH2 interpolated a linear decrease in production between full production and the shutdown period. AUTOUGH2 settings can be adjusted to remedy this. The initial pressure recovery at the beginning of the simulation can be related to changes in Cawayan production. It is unclear whether the real system responds in the same way due to the truncated data set. To balance between computational economy and time resolution, all other simulations utilized the $5.26\text{E}+5\text{ s}$ maximum time step.

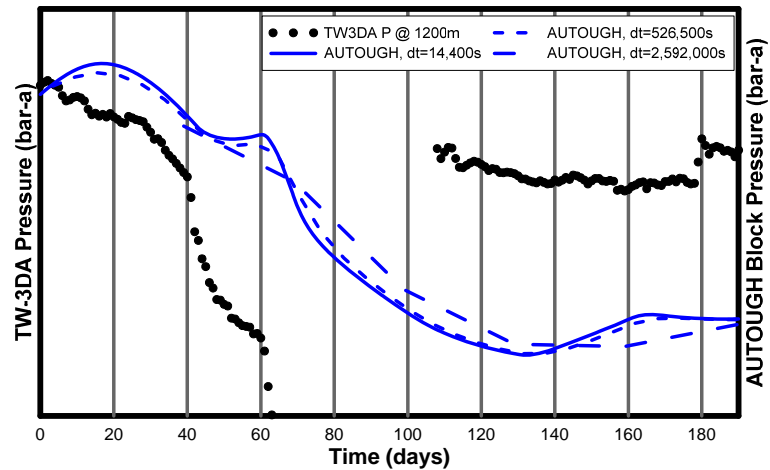


FIGURE 15: Comparison of fixed mass simulations with different time steps

TABLE 4: Comparison of time steps

Time step calculation	Time step (s)	No. of iterations	Minimum pressure (bar)
$C_{max} = 1 \geq \Delta t \left(\frac{u_x}{\Delta x} + \frac{u_y}{\Delta y} \right)$	14,400	1267	58.20
$\Delta t = \frac{\Delta x}{u_x}$	526,500	36	58.21
$\Delta t = 1 \text{ month}$	2,592,000	6	58.26

When compared against wells on DELV and the coupled model with wells on DELG, the wells discharging at predefined MASS followed the average monthly trend of the extraction as it was programmed to and hence followed the general pressure trends better but exhibited a larger drawdown than actually occurred (Figure 16). This is consistent with the observation regarding the pressure drawdown calibration for Cawayan. For the wells on DELV, the production was limited by the block pressure. The Tanawon blocks had pressures lower than what was actually measured in the reservoir, probably due to the simulated pressure drawdown in Cawayan being higher than actual. Because Cawayan is part of the flow path to Tanawon from the upflow, its pressures would affect the recharge in the Tanawon sector, as well. Thus, despite using the HOLA-simulated productivity index, the block pressures are too low to discharge at the same level as the real wells. For the wells on DELG, both enthalpy and block pressure affected the discharging conditions. The wells on DELG produced even less than the wells on DELV due to the enthalpy in the feed blocks being less than actual. Because of the low extraction in Tanawon in the DELV and DELG reservoir models, the pressure response in these models was dominated by extraction in other fields. Pressure recovery was not observed in either the DELV or DELG models. There was, however, a change in the pressure response slope at the point in time when the production in Tanawon was reduced, showing that the pressure monitoring block is not insensitive to Tanawon production and thus could be used as a monitoring block for forecasting.

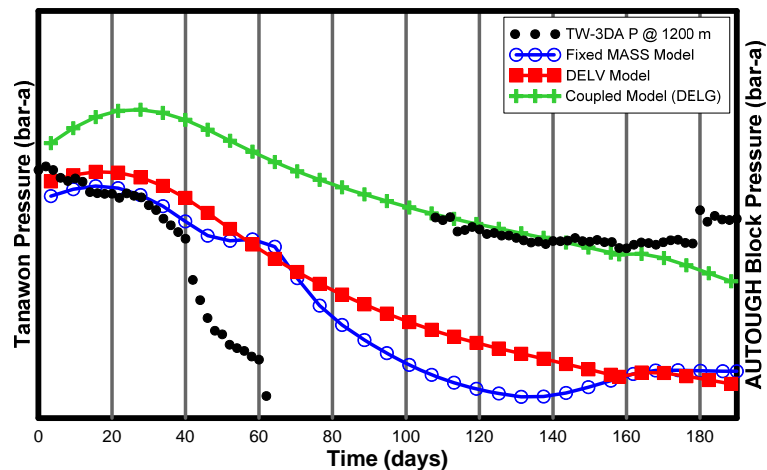


FIGURE 16: Comparison of simulations of the simultaneous discharge test using different sink types

7. LONG TERM FORECASTING

The purpose of long term forecasting is to gain a perspective on the impact of the different modelling schemes. Simulations for a ten-year production period were conducted and compared.

7.1 LUMPFIT forecasts

The ten-year forecast was performed assuming constant discharge for ten years at the level of the simultaneous discharge test maximum production. For Tanawon extraction models, the forecasts assumed that the field would be producing at the highest sustained production of Tanawon during the discharge test, while for the Tanawon + Cawayan extraction models, the forecasts assumed Tanawon extraction as detailed above plus the 20 MWe Cawayan production. Figure 17 shows a comparison of the different LUMPFIT forecasts.

The forecasts using Tanawon extraction models overlapped, all with linearly decreasing pressure, effectively acting like one-tank closed models. The addition of a second tank slightly reduced the drawdown rate, but the decay was still linear. The behaviour of the Tanawon extraction model forecasts can be attributed to low conductivity values.

Collectively, the forecast from the Tanawon extraction models can be seen as a pessimistic forecast, which disconnects the Tanawon reservoir from the rest of the BacMan resource. Given what is known

about the field and the results of other LUMPFIT models, this scenario is unlikely. The pessimistic models could not sustain the set discharge level for ten years. Negative pressures were calculated by year 7.

HOLA was used to determine at what date the wells would stop discharging at operating wellhead conditions. Figure 18 shows the bore output curves of the Tanawon wells. As drawdown increases, the output curves shift towards the left. It is apparent that the maximum discharge pressure of the wells decreased with increasing drawdown in the reservoir. Figure 17 shows that the higher enthalpy wells could tolerate significant drawdown, but the wells with liquid enthalpy could only discharge at the minimum operating wellhead pressure if drawdown stayed below 10.95 bar. Based on the rate of drawdown, low enthalpy wells like TW-2D can only be discharged for two years.

The forecasts using the Tanawon+Cawayan extraction on the other hand, suggest that the reservoir can sustain the combined production of the two fields for ten years. For the open and closed models, drawdown is negligible after a 1-bar pressure drop that occurs in the first year. Figure 17 shows that all wells can discharge under these conditions.

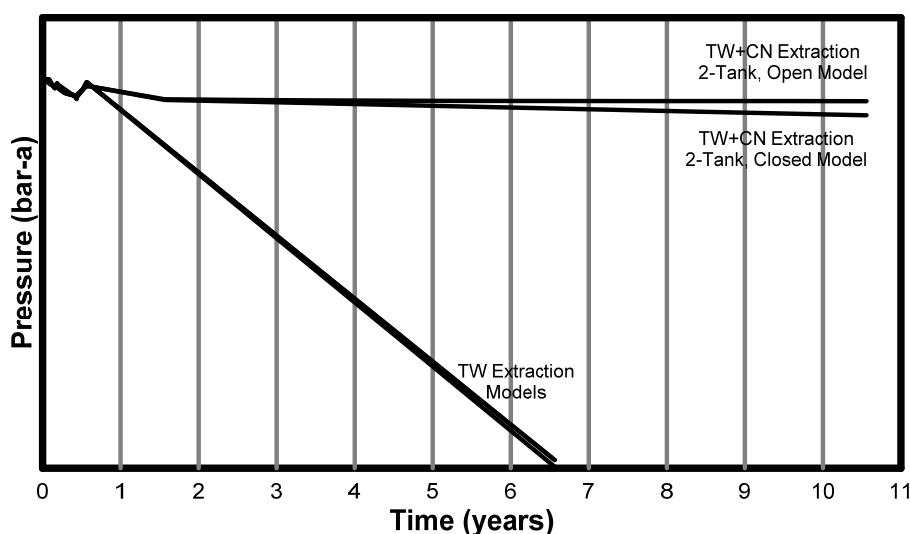


FIGURE 17: Comparison of LUMPFIT forecast results

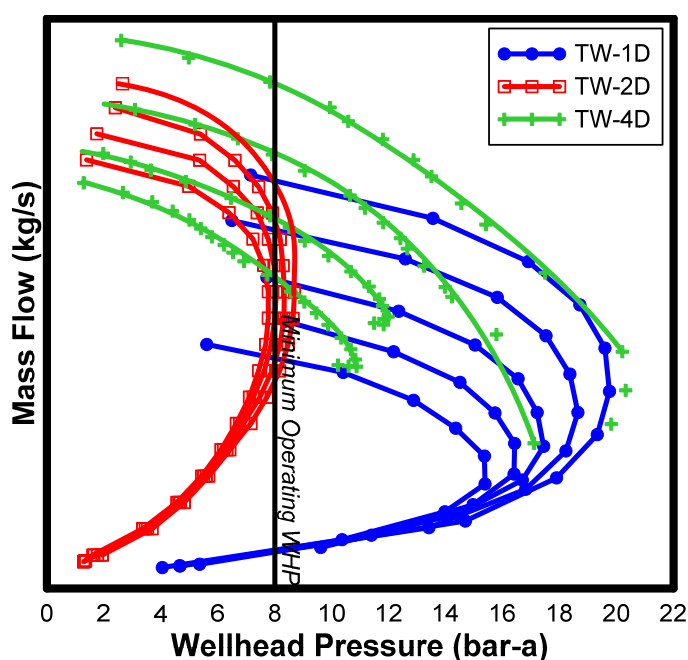


FIGURE 18: Bore output curves for varying reservoir pressure drawdown

Note that the basis for discharging was simply that the HOLA-calculated maximum discharge pressure be beyond the minimum operating wellhead pressure for the field. No changes were made to the wellbore configuration, which means it was assumed that there would be no scaling in the well. Scaling would reduce the flow diameter and increase friction losses as the fluid rises up the wellbore reducing the maximum discharge pressure for the same reservoir conditions. It was also assumed that the enthalpy would not change, which ignores boiling. Boiling would prolong the life of the well as higher enthalpy wells can keep discharging

7.2 Numerical model forecast

The effect of the different well types can only be seen with a simulation that covers a long period of time. Figure 19 illustrates the monitored pressure response for the various AUTOUGH2 models.

For fixed mass wells, the mass flows are based on the average production of the wells during the simultaneous discharge test. While the fixed mass well type produced results that most closely mimicked reality in the simulation of the simultaneous discharge test, it produced the most unrealistic results in the long term simulation. Blocks were forced to produce at a fixed rate regardless of block pressure, resulting in rapid drawdown. Before the second year of production, Well TW-1D began boiling due to over extraction while Well TW-4D enthalpies continuously rose beyond 3000 kJ/kg (Figure 20).

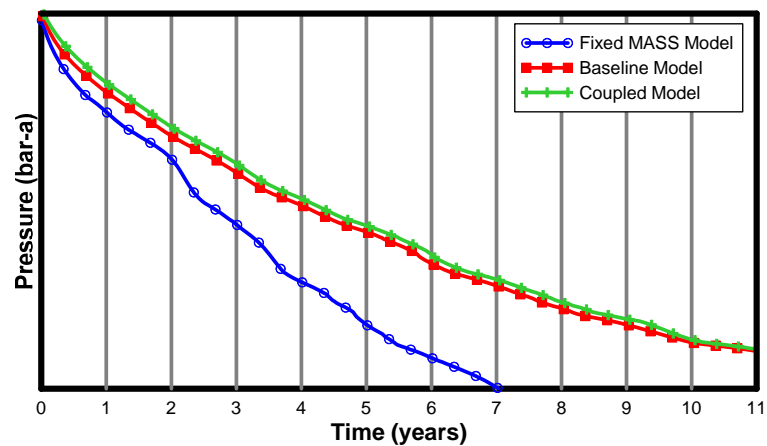


FIGURE 19: Comparison of AUTOUGH2 forecast results

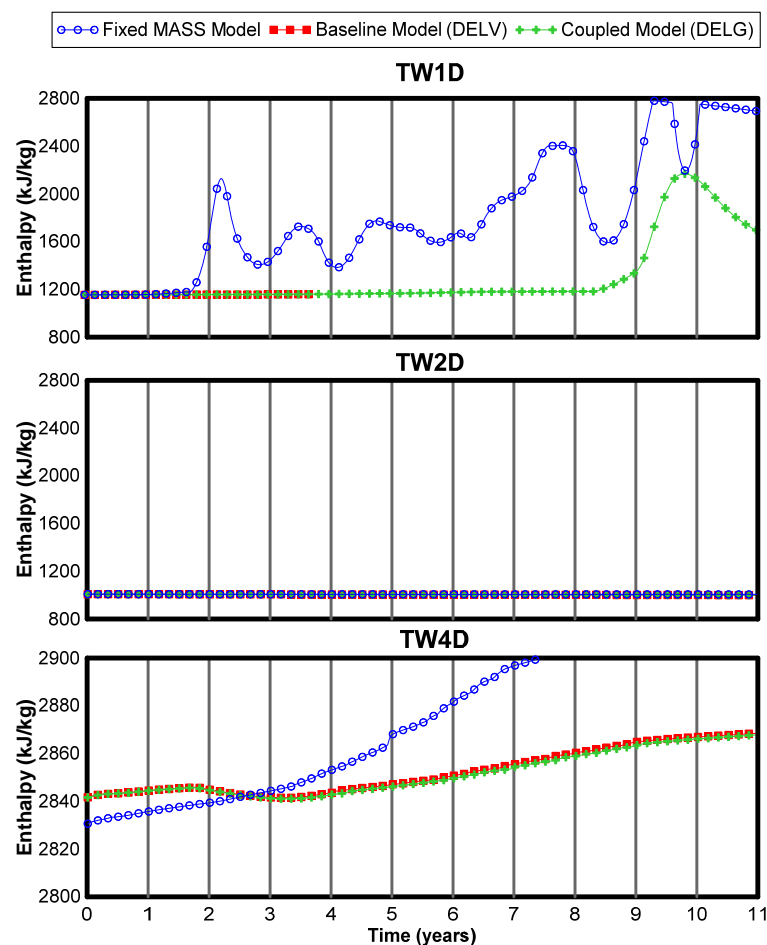


FIGURE 20: Discharge enthalpy trends for AUTOUGH2 forecasts

Tanawon, Well TW-1D became capable of production again. While the phenomenon of resurrecting Well TW-1D is not necessarily a realistic scenario, the capability of the coupled model to adjust its cut-

The baseline model used wells on DELV. This is more realistic than fixed MASS when it comes to simulation of production rates which are not yet available. In the baseline model, the blocks are not forced to produce more than what the reservoir is capable of discharging. If the block pressure is sustained, so is the level of production. The fixed wellbore pressure at depth acts as a cut-off pressure for production. If the block pressure drops below this cut-off pressure, then the well in the model stops discharging. In the baseline model, the cut-off pressure caused Well TW-1D to stop discharging before the fourth year. The coupled model, which uses wells on DELG, adjusted the cut-off pressure based on enthalpy. As illustrated in the bore output curves of Figure 18, higher enthalpy wells are more tolerant to drawdown. Because both the baseline model and the coupled model depend on a set productivity index, the two forecasts have similar behaviours in general. The main difference in the two models is that in the coupled model, when extraction created boiling in

off pressure based on the enthalpy of the discharge brings the simulation closer to a more accurate depiction of production.

From the perspective of the monitoring block, the difference between the baseline and the coupled model is negligible. However, the Tanawon wells are a small fraction of the total BacMan production so the effect of the coupling would not be as observable. Also, boiling in the area had just begun towards the end of the forecast; so the pressure response might deviate a bit more, further into the future.

7.3 Comparison of forecasts

In the long-term, the pressure drop in the AUTOUGH2 models agrees with the pressure drop simulated by LUMPFIT in the sense that the AUTOUGH2 simulated drawdown falls between the optimistic and pessimistic LUMPFIT forecasts. Figure 21 shows the comparison of the simulated pressure drawdown of the different forecast models.

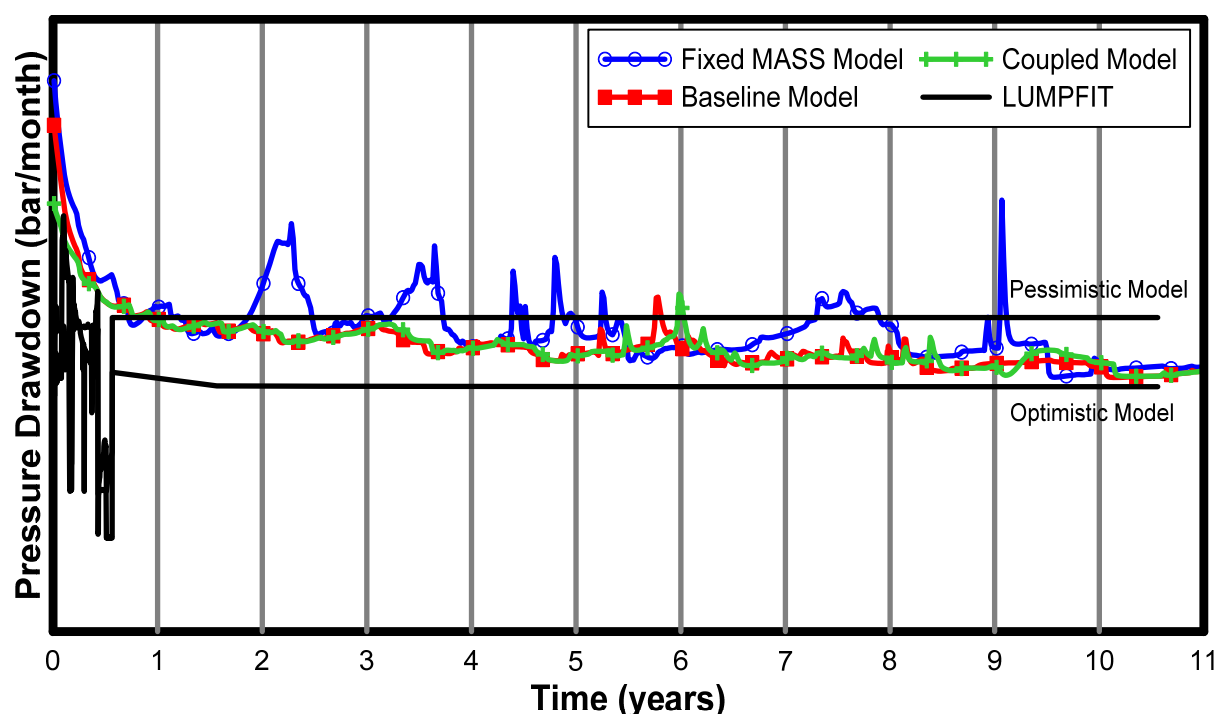


FIGURE 21: Comparison of pressure drawdown of different forecast models

It is expected that the LUMPFIT pessimistic model will always forecast the highest pressure drawdown, but this limit is crossed by the fixed MASS simulated drawdown, especially in the first four years of the forecast. Recall that based on wellbore simulations, Well TW-2D should stop discharging after two years if the pessimistic LUMPFIT drawdown applies. Since Figure 20 does not show any significant changes in Well TW-2D enthalpy, extraction in Well TW-2D should have stopped by the second year. But, since the fixed MASS simulation is blind to this, it keeps extracting via Well TW-2D, making the results of this simulation unfeasible.

On the other hand, the drawdown for the baseline and coupled models falls neatly between the optimistic and pessimistic LUMPFIT predicted drawdown. At the beginning of the forecast period, the AUTOUGH2 drawdown is comparable to the pessimistic model drawdown, but as the discharge of the wells is decreased by drawdown, the AUTOUGH2 drawdown falls closer to the LUMPFIT optimistic model drawdown.

8. SUMMARY

The Tanawon simultaneous discharge test and ten-year forecast were modelled using various methods and the model results and forecasts were compared. Simultaneous discharge testing was done to simulate production conditions and gain information about the field. The simultaneous discharge test data was analysed through LUMPFIT and AUTOUGH2 to look at the reservoir characteristics and through HOLA to examine wellbore characteristics. LUMPFIT was paired with HOLA simulations to determine whether the stable reservoir pressure would actually allow the wells to discharge. LUMPFIT was also paired with HOLA to find when the wells would stop discharging.

For the lumped parameter models, though the model ignores the spatial geometry of the reservoir, the relative influence of neighbouring fields could be gauged by modelling the pressure response with different extraction data. Because only drawdown is given by the lumped parameter model, wellbore simulators could be used to check whether the wells would still discharge given the calculated drawdown. This is especially important when wells in the area have an inherently low enthalpy or are affected by a cold recharge.

For the numerical models, coupling the model with a wellbore simulator extended the life of the wells that underwent boiling, but would stop low enthalpy wells from discharging earlier. In the 10 year forecast, the effect of coupling on the drawdown was negligible, though this was expected because coupling was only applied to a few of the wells whose cumulative output is a small fraction of the discharge from neighbouring fields. Because the coupled model is more sensitive to pressure drawdown and enthalpy than the baseline model, it is important that the reservoir model be recalibrated to get reasonable forecasts.

ACKNOWLEDGEMENTS

I would like to extend my sincere gratitude to Mr. Lúdvík S. Georgsson for the opportunity to participate in the six-month training programme. To Dr. Ingvar Fridleifsson and all the other UNU-GTP lecturers who took time to mentor us and share with us their experiences in the geothermal industry, thank you and be assured that what you have invested in us is not for naught. To the UNU-GTP staff, Ingimar, Frída, Thórhildur, and Markús, who assisted and guided us through life in Iceland and made sure we got through the six months in one piece, no words can express how much your efforts are valued.

To my supervisors Ms. Sigríður Sif Gylfadóttir and Dr. Andri Arnaldsson, this project would not have been completed had it not been for your direction and expertise. To my EDC supervisor, Sir Jericho Omagbon, thank you for sharing your ideas for the project and for always being there to check my work and encourage me. To my colleagues, Daryl Gamez, Christine Espartinez, Bryan Cacho, Thor Sazon, and Jeff Africa, thank you for sending me the data and references that I needed. Jefferson Villacorte and Raquel Colina, this project would not have been possible without your reservoir model. Thank you all very much for your patience with me.

Special thanks have to be extended to the management of the Energy Development Corporation, EDC President Richard Tantoco and TSS SVP Manny Ogena for not only allowing me to take part, but also for supporting me in this training programme. Sir Francis Sta. Ana, Sir Dave Yglopaz, and Sir Jericho, thank you for nominating me for this training.

To my family and my friends your love and prayers helped me pull through. *Ad maiorem dei gloriam.*

REFERENCES

- Ambastha, A.K., and Gudmundsson, J.S., 1986a: Pressure profiles in two-phase geothermal wells: comparison of field data and model calculations, *Proceedings of the 11th Workshop on Geothermal Reservoir Engineering, Stanford University, Stanford, Ca*, 183-188.
- Ambastha, A.K., and Gudmundsson, J.S., 1986b: Geothermal two-phase wellbore flow: pressure drop correlations and flow pattern transitions, *Proceedings of the 11th Workshop on Geothermal Reservoir Engineering, Stanford University, Stanford, Ca*, 277-281.
- Aragon A., Garcia, A., Baca, A., and Gonzáles, E., 1999: Comparison of measured and simulated pressure and temperature profiles in geothermal wells. *Geofísica Internacional*, 38-1, 35-42.
- Austria, J.J.C., 2008: *Production capacity assessment of the Bacon-Manito geothermal reservoir, Philippines*, University of Iceland, MSc thesis, UNU-GTP, Iceland, report 2, 62 pp.
- Axelsson, G., 1989: Simulation of pressure response data from geothermal reservoir by lumped parameter models. *Proceedings of the 14th Workshop on Geothermal Reservoir Engineering, Stanford University, California*, 257-263.
- Axelsson, G., 2013a: *Geothermal well testing*. UNU-GTP, Iceland, unpublished lecture notes.
- Axelsson, G., 2013b: *Dynamic modelling of geothermal systems*. UNU-GTP, unpublished lecture notes.
- Axelsson, G., and Arason, Th., 1992: *LUMPFIT, automated simulation of pressure changes in hydrological reservoirs. Version 3.1, user's guide*. Orkustofnun, Reykjavík, 32 pp.
- Axelsson, A., Björnsson, G., and Quijano, J.E., 2005: Reliability of lumped parameter modelling of pressure changes in geothermal reservoir. *Proceedings of the World Geothermal Congress 2005, Antalya, Turkey*, 8 pp.
- Bixley, P.F., 1988: Downhole measurements in geothermal wells. In: Okandan, E. (editor), *Geothermal reservoir engineering*. Kluwer Academic Publishers, Dordrecht, 41-53.
- Björnsson, G., 1987: *A multi-feedzone geothermal wellbore simulator*. Lawrence Berkeley Laboratory, report LBL-23546, 8-19.
- Braganza, J.S., 2011: *Geology of Bacon-Manito geothermal resource, resource assessment update of Bacon-Manito geothermal resource*. EDC internal report (unpublished), 66 pp.
- Colina, R.N., Villacorte, J.D., Ledesma, S.C., Omagbon, J.B., Austria, J.J.C., and Sta. Ana, F.X.M., 2011: *Update of the Bacon-Manito geothermal production field reservoir model*. EDC Resource Management, meeting report (unpublished), 15 pp.
- DOE, 2013: *Private sector initiated power projects*, Republic of the Philippines – Department of Energy, website, www.doe.gov.ph/power-and-electrification/private-sector-initiated-power-projects.
- EDC, 2003: *Environmental Impact Statement 50-80 MW Tanawon geothermal project (in Bacon-Manito geothermal production field)*, European Investment Bank, website, www.eib.org/attachments/pipeline/20090372_eis_en.pdf.
- EDC, 2013: *Our projects*. Energy Development Corporation, webpage, <http://www.energy.com.ph/our-projects/geothermal/>.

Fajardo, V.R, 2000: Lumped parameter model of the Bacon-Manito geothermal production field, Albay, Philippines. *Proceedings of the World Geothermal Congress 2000, Kyushu-Tohoku, Japan*, 2551-2554.

Fajardo, V.R., and Malate, R.C.M., 2005: Estimating the improvement of Tanawon production wells for acid treatment, Tanawon sector, BacMan geothermal production field, Philippines. *Proceedings of the World Geothermal Congress 2005, Antalya, Turkey*, 7 pp.

Freeston, D., and Gunn, C., 1993: Wellbore simulation – case studies, *Proceedings of the 18th Workshop on Geothermal Reservoir Engineering, Stanford University, Stanford, California*, 261-266.

Grant, M.A., 1982: A modified gas correction for the lip-pressure method, *Proceedings, 8th Workshop Geothermal reservoir engineering, Stanford University, Stanford, California*, 133-136.

Grant, M.A., 1988: Reservoir physics and conceptual modelling. In: Okandan, E. (editor), *Geothermal reservoir engineering*. Kluwer Academic Publishers, Dordrecht, 23-40.

Grant, M.A., 1997: Risk and resource assessment. *Proceedings of the PNOC-EDC 18th Geothermal Conference, Makati, Philippines*, 142-145.

Gudmundsdóttir, H., 2012: *A coupled wellbore-reservoir simulator utilizing measured wellhead conditions*. University of Iceland, MSc thesis, Reykjavik, Iceland, 90 pp.

Hsu, Y., and Graham, R.W., 1976: *Transport processes in boiling and two-phase systems*, Hemisphere Publishing Corporation, USA, 559 pp.

Hu, B., Sagen, J., Chupin, G., Haugset, T., Ek, A., Sommersel, T., Xu, Z.G., and Mantecon, J.C., 2007: Integrated wellbore/reservoir dynamic simulation. *SPE Asia Pacific Oil & Gas Conference and Exhibition 2007, Jakarta, Indonesia*, 9 pp.

IPGT, 2012: *Geothermal reservoir modelling*. International Partnership for Geothermal Technology, recommendations for research and development, August 2012, 25 pp.

Liu Junrong, 2011: Well test interpretation and production prediction for well SD-01 in the Skarddalur low-temperature field, Siglufjörður, N-Iceland. Report 19 in: *Geothermal training in Iceland 2011*. UNU-GTP, Iceland, 391-416.

LBNL, 2013: *TOUGH2 software*. Lawrence Berkeley National Laboratory, Earth Sciences Division, website, esd.lbl.gov/research/projects/tough/software/tough2.html.

Malapitan, R.T and Reyes, A.N., 2000: Thermal areas of the Philippines. *Proceedings of the World Geothermal Congress 2000, Kyushu -Tohoku, Japan*, 1395-1400.

Marcolini, M., and Batistelli, A., 2012: Modelling of wellbore flow within geothermal reservoir simulations at field scale. *Proceedings of the TOUGH Symposium 2012, Lawrence Berkeley National Laboratory, Berkeley, California*, 9 pp.

Murray, L., and Gunn, C., 1993: Toward integrating geothermal reservoir and wellbore simulation: TETRAD and WELLSIM. *Proceedings of the 15th NZ Geothermal Workshop, Auckland*, 279-284.

O’Sullivan, M.J., Pruess, K., Bodvarsson, G.S., and Lippmann, M.J., 2001: State of the art of geothermal reservoir simulation. *Geothermics*, 30-4, 395-429.

Pan, L., and Oldenburg, C.M., 2012: T2WELL – An integrated wellbore-reservoir simulator. *Proceedings of the TOUGH Symposium 2012, Lawrence Berkeley National Laboratory, Berkeley, California*, 8 pp.

Pruess, K., 1987: *TOUGH user's guide*. Lawrence Berkeley Laboratory, 73 pp.

Pruess, K., 2002: *Mathematical modeling of fluid flow and heat transfer in geothermal systems – an introduction in five lectures*. UNU-GTP, Iceland, report 3, 84 pp.

Pruess, K., 2003: Preface to TOUGH Symposium 2003, *Geothermics*, 33, 399-400.

Pruess, K., Oldenburg, C., and Moridis, G., 1999: *TOUGH2, user's guide version 2.0*. Lawrence Berkeley National Laboratory, 197 pp.

Pruett Tech Inc., 2013: *Pruett Tech Inc.* Pruet Tech Inc., website, <http://pruettech.com/>

Ramey, J.R., 1988: Transient pressure testing in geothermal reservoirs. In: Okandan, E. (editor), *Geothermal reservoir engineering*. Kluwer Academic Publishers, Dordrecht, 55-62.

Ramos, S.G., 2002: Potential constraints to the development of the Rangas sector based on petrologic evaluation of the BacMan geothermal field, Philippines. *Proceedings 27th Workshop on Geothermal Reservoir Engineering, Stanford University, Stanford, California*, 9 pp.

Ramos, S.G., and Santos, B.N.A., 2012: Updated hydrogeological model of the Bacon-Manito geothermal field, Philippines. *Proceedings of the 37th Workshop on Geothermal Reservoir Engineering, Stanford University, Stanford, Ca*, 4 pp.

Reeves, M., Baker, N.A., and Duguid, J.O., 1994: *Review and selection of unsaturated flow models*. Report prepared for US Department of Energy, Yucca Mountain Site Characterization Project, Las Vegas, Nevada.

Reyes, A.G., Zaide-Delfin, M.C., and Bueza, E.L., 1995: Petrological identification of multiple heat sources in the Bacon-Manito geothermal system, the Philippines. *Proceedings of the World Geothermal Congress 1995, Florence, Italy*, 2, 713-717.

Rivera A., M.A., 2000: *Coupled geothermal reservoir-wellbore simulation with a case study for the Námafjall field, N-Iceland*. University of Iceland, MSc thesis, UNU-GTP, Iceland, report 2, 74 pp.

Ruaya, J.R., Buenviaje, M.M., Solis, R.P., and Gonfiantini, R., 1994: *Chemical and isotopic studies of fluids in the Bacon-Manito geothermal field, Philippines*. IAEA-TECDOC Series, 185-209.

Sarak, H.E., Korkmaz, E.D., Onur M., and Satman A., 2005: Problems in the use of lumped-parameter reservoir models for low-temperature geothermal fields, *Proceedings of the World Geothermal Congress 2005, Antalya, Turkey*, 9 pp.

Sarmiento, Z.F., 1993: *Geothermal development in the Philippines*. UNU-GTP, report 2, 99 pp.

Tolentino, B.S., and Alcaraz, A.P., 1986: Strategies relating to the exploration and development of a geothermal field: A case for Bacon-Manito geothermal project, Albay/Sorsogon provinces Philippines. In: Tolentino, B. (lect.), *Lectures on geothermal energy in the Philippines*. UNU-GTP, Iceland, Report 12, 91-121.

Yeh, A., Croucher, A.E., and O'Sullivan, M.J., 2012: Recent developments in the AUTOUGH2 simulator, *Proceedings of the TOUGH Symposium 2012*. Lawrence Berkeley National Laboratory, Berkeley, California, 8 pp.

Yu, S., Ya-ju H., Bacolcol, T., Chia-Chu, Y., and Solidum, R., 2013: Present-day crustal deformation along the Philippine fault in Luzon, Philippines. *J. Asian Earth Sciences*, 65, 64-74.

Yumul, G.P., Dimalanta, C.B., Maglambayan, V.B., and Marquez, E.J., 2008: Tectonic setting of a composite terrain: A review of the Philippine island arc system. *Geosciences J.*, 12-1, 7-17.



**UNITED NATIONS
UNIVERSITY**

GEOTHERMAL TRAINING PROGRAMME
Orkustofnun, Grensasvegur 9,
IS-108 Reykjavik, Iceland

Reports 2013
Number 7

GEOTHERMAL SPACE HEATING AND THERMAL STORAGE USING PHASE CHANGE MATERIAL IN CHUMATHANG, INDIA

Vijay Chauhan

School of Engineering
Indian Institute of Technology, Mandi-175001
Himachal Pradesh
INDIA
vijay30008@gmail.com

ABSTRACT

The present work discusses utilization of geothermal energy for space heating in combination with a phase change energy storage system. The thermodynamics and thermoeconomics of the combined heating and thermal storing system were studied to show the scope of energy storage and cost savings. The analysis was done taking the second law of efficiency into consideration since the second law represents the true flow of energy. Results show the scope of utilization of phase change material for low ambient temperature conditions.

1. INTRODUCTION

Space heating has been a well-known application of geothermal energy utilization for decades. The usage of geothermal energy for space heating provides an economical and a non-polluting way for achieving human comforts. Chumathang, located in the Northwest Himalayan region, has good geothermal potential in the form of hot springs. This has also been confirmed by drilling exploration wells. The climate in the region is very cold, such that temperatures below zero are recorded during the night for almost six months of the year. Due to a lack of natural resources in the area required for the construction of houses, insulation is insufficient, thus requiring more space heating to maintain human comfort. A demonstration project for space heating has been undertaken by the Norwegian Geotechnical Institute (NGI), funded by the Research Council of Norway in collaboration with the Government of India, for heating a restaurant, which includes three rooms, in Chumathang. The project will help promote geothermal utilization for space heating on a larger scale in the area. The design for the demonstration project will also help in learning about the various factors to be considered for large scale applications since the conditions involved for the design are demanding due to local house construction and the climatic and geographical conditions prevalent in the area. The present work focuses on designing a room heating system in Chumathang. The design involves heat load calculation, equipment selection and sizing while considering the climatic conditions and the geothermal resource potential that is available.

In order to study a thermodynamic system's performance, which can either involve heating or power generation, the second law of thermodynamics plays an important role. The second law helps to better understand the energy flow processes in addition to the first law of thermodynamics. Several studies have been conducted on exergy analysis of buildings. The concept of low exergy systems for heating and cooling have been proposed in IEA ECBCS Annex 37 (2000). An exergetic life cycle assessment

for resource evaluation in the built environment was conducted by Meester et al. (2009). Shukuya and Komuro (1996) applied concepts of entropy and exergy for investigating the relationship between buildings, passive solar heating and the environment. Various results about patterns of human exergy consumption in relation to various heating and cooling systems were given by Saito and Sukaya (2001). Conclusions about the inadequacy of the concept of energy conservation in understanding important aspects of energy utilization processes were made by Yildiz and Gungör (2009). The second law analysis is important in order to have an efficient utilization of the available resource.

It is a well-known fact that thermal heating systems have low second law efficiency. In geothermal systems, water exiting after passing through heat exchangers and radiators still has sufficient exergy required for human comfort and could be stored for off peak requirements. Another important concern about storage is when available flow rate is limited and heat requirements are high. Saving energy during off peak heating can help to fulfil the peak load requirements. Such applications are practiced well with other renewable energy sources such as solar energy. The application of energy storage in geothermal energy utilization can also help reduce the major capital investment required for drilling purposes. The present work focuses on the application of energy storage systems in geothermal energy utilization. Thermodynamic analysis was done for a geothermal heating system in combination with phase change material storage added parallel to the geothermal exit flow from a heat exchanger for making efficient utilization of geothermal energy. Exergoeconomic analysis of the combined heating and storage was also done in order to find the scope of cost savings.

1.1 Chumathang geothermal field

Chumathang is located in the Ladakh district of Jammu and Kashmir State of India. The place is situated across the Northwest Himalayan range along the banks of the Indus River and at an altitude of 4300 m above mean sea level. A thick sequence of shallow marine to fluvial sediments deposited over a granitic basement is found in the area. Chumathang field is located in this belt. Spring deposits in the form of carbonate plateaus can be found in the area. Thermal manifestations can be seen on the northern bank of the river in an area of about 1 square kilometre. The area has around 73 hot springs with a discharge of about 200 litres per minute and a temperature range varying from 30 to 87°C (Razdan et al., 2008).

Geochemistry

The pH value of the water in Chumathang field ranges from 6.9 to 8.6. The water has high SO_4 concentration and low Cl, Na, HCO_3 and K. The fluid is classified as sodium bicarbonate and sulphate type. The base temperatures calculated using Na-K, Na-K-Ca and SiO_2 thermometry are found to be 145-166°C, 160-184°C and 148-174°C, respectively.

1.2 Houses in Chumathang

Figure 1 shows the general construction of a house in Chumathang, which is constrained by limited local resources. A common house has three floors. The ground floor walls are made of stone and the upper floor walls are comprised of sun dried mud bricks plastered with clay. The roofs are constructed from poplar beams, willow branches, mud and earth. Roofs are flat as there is little rain and snow can be removed easily. Grass is piled on the roof over walls to protect from precipitation.

The above mentioned materials used for construction makes houses in Chumathang less insulated than normal houses. The cold climate lasts for more than half of the year, adding to high heat losses from the houses.



FIGURE 1: A house in Chumathang

1.3 Weather analysis

The heat load of a building mainly depends upon the outdoor ambient temperature. The other factors influencing heat load are wind velocity and solar radiation. Figure 2 shows the monthly average, minimum and maximum temperature in the Chumathang region. The figure shows that the outside maximum temperature reaches the room temperature required for human comfort, 20°C, only one month in a year. Temperatures below zero prevail in the area for more than six months a year, reflecting the requirement for space heating in the region.

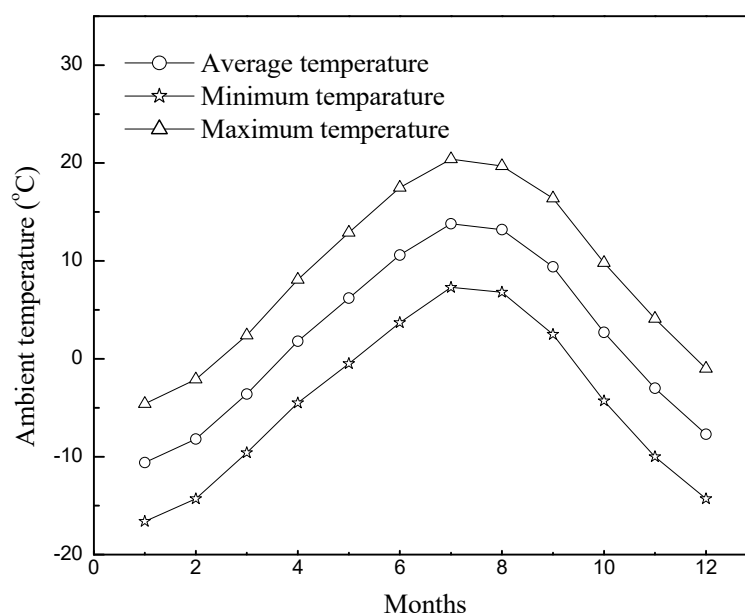


FIGURE 2: Monthly outdoor temperature in Chumathang

1.4 Phase change material (PCM)

One of the best solutions for the problem when demand and supply are out of phase is the use of energy storage materials. The key to effective utilization of alternative energy sources is efficient and economical energy storage systems. Energy storage systems which are currently being researched by the scientific community are mainly of three types, classified on the basis of the principle under which they work. The first one consists of an energy storage system utilizing chemical heat reaction for absorbing and emitting heat energy. The second class of storage devices is that of utilizing sensible heat capacity for storage such as storing in tanks. The third and most useful energy storage system utilizes phase change materials (PCM). Such systems absorb and release heat energy as latent heat of the storing material with a change of phase. Various advantages of PCM over other storage systems have emphasized its importance over the years. The studies done by Adebiyi and Russell (1987) concluded two advantages derived from using a phase change material in a thermal energy storage system design. The first advantage was an increase in the second law of efficiency of the system as compared to the one using sensible heat storage system. The second major advantage was the reduced amount of storage material required. Since PCM is based on the principle of storing heat as latent energy of phase change, the energy stored is far higher than that stored by sensible heating systems which store energy according to their specific heat capacity.

Analysis of latent heat storage based on the first law of thermodynamics can be found in various literatures. The first law analysis helps us to obtain a workable design but not an optimum one. In order to consider the effects of time and the temperature at which heat is supplied, analysis of the second law is required. According to Bejan et al. (1996) an optimal system which a designer can develop, having the least irreversibility, is based on minimization of entropy generation. The application of second law analysis for studying latent heat storage was studied by Bjurström and Carlsson, 1985; Adebiyi and Russell, 1987; and later by Bejan (1996). A study (El-Dessouky and Al-Juwayhel, 1997) was done for investigating the effects of different variables on the entropy generation number defined by Bejan (1996). The analysis considered the case of storage material exchanging heat at a constant melting point. Two commonly available storing materials, paraffin wax and calcium chloride, were considered with air or water as the heating fluid.

A number of materials exist which can be used as PCM over a wide range of temperatures. A list of such materials can be found in the literature (Abhat, 1983). The selection of a PCM for energy storage

is based on the fulfilment of criteria such as high latent heat capacity, non-corrosiveness, high thermal conductivity, and it should be non-toxic, without deposition or super cooling. The transition temperature of the phase change material is decided by the room temperature required.

1.5 Importance of PCM to geothermal energy storage

Studies on the analysis of PCM, both numerical and experimental, have been reported in the literature (Farid et al., 2004). The work is mainly focused on the relationship to solar energy storage. The present work proposes the use of PCM for storage of geothermal energy used for direct heating applications. It is important to know how the stored geothermal energy will be utilized when the mass flow itself can be controlled. The answer depends upon the conditions for storage application. For an existing heating system using radiators and heat exchangers, an important fact also discussed in literature is the variation of geothermal exit temperature with outside ambient temperature for a fixed design network (Karlsson and Ragnarsson, 1995). It is found that as the ambient temperature decreases, the exit temperature of a geothermal heating network increases. The increase in exit temperature reflects an increase in useful heat loss. In terms of the second law of efficiency, the decrease in ambient temperature causes an increase in exergy loss to the atmosphere. Surely the application of energy storage can provide a means of saving energy which can be used in the off peak time when demand is low. Stored heat from the geothermal exit fluid at night can be used for fulfilling daytime requirements. The other advantage of thermal storage for geothermal application is found in areas with limited flow and high heat demand. Heat energy in such cases could be stored during off peak or daytime and utilized for peak load demands during the night.

The advantage of PCM over a sensible storage system is the low volume requirement of the storage material. Since the latent heat of PCM is generally many times greater than the specific heat of water, it requires far less space for storage than for storing water. Another advantage of PCM is its ability to absorb and release heat at a constant temperature. This is not possible in storing heat using sensible heating, and heat loses its quality with time as temperature decreases. The PCM, on the other hand, provides constant temperature heating.

1.6 Thermoeconomics

Thermoeconomic or exergoeconomic analysis considers both thermodynamic and economic principles for improving system performance. Exergoeconomic analysis helps in quantifying the exergy losses in terms of monetary losses. According to Bejan et al. (1996) thermoeconomics is defined as the branch of engineering that combines exergy analysis and economic principles to provide the system designer or operator with information not available through conventional energy analysis and economic evaluations, but crucial to the design and operation of the cost effective system. Exergetic cost analysis for space heating using a ground source heat pump system was done by Jingyana et al. (2010). The work shows the sensitivity of various sub systems to unit exergy cost. Application of exergoeconomic analysis for geothermal district heating systems was presented by Oktay and Dincer (2009) and reviewed by Hepbasli (2010) using energy, exergy and economic aspects. The effect of reference temperature on the thermoeconomic evaluation of geothermal heating system was studied by Keçebaş (2013).

For making economical use of a thermodynamic system, attention should be given to the cost paid for inefficiencies. The calculation of such costs helps in governing the final cost of the product in addition to improving the effectiveness of the system. The economic costs required for thermoeconomic analysis are obtained from relationships which represent cost as a function of design and geometrical parameters such as length and volume.

2. HEAT LOAD CALCULATION

Several different tools for evaluating the performance of a building's heat load exist (Crawley et al., 2008). Many parameters about the geometry, thermo-physical properties and construction are required in order to make use of these simulation tools for evaluating building performance. For evaluating the energy consumption of a building, envelope parameters and air changes are the major parameters to be evaluated (Budaiwi, 2011). Comparison of different existing methods for building calculation was done by Carlos and Nepomuceno (2004) focusing on the energy use of space heating for a standard case. A simplified model for calculating the heat load was also proposed in the paper. The model used fewer input parameters and required little time for making calculations. Comparison of the simplified model with pre-existing models gave good similar results.

The present work makes use of the model proposed by Carlos and Nepomuceno (2004) for heat load calculation for the application required. The input parameters required for the heat load calculation were in accordance with the existing conditions and requirements. For the present analysis, steady state conditions were assumed. Also the internal conditions were assumed to be constant and the effects of solar radiation on the building neglected. The approach for calculating the heat load requirement is described as follows:

Overall heat transfer coefficient

The overall heat transfer coefficient U (W/m² K) is calculated as (for definitions see Nomenclature):

$$\frac{1}{U} = \frac{1}{h_{int}} + \frac{x}{\lambda_{surf}} + \frac{1}{h_{ext}} \quad (1)$$

The wall has the thickness x (m) and thermal conductivity λ_{surf} (W/mK). The value of the heat transfer coefficient h_{int} (W/m² K) of the inside wall is assumed constant, equal to 8. The convective heat coefficient outside the wall, h_{ext} (W/m² K), is calculated as given by Mirsadeghi et al. (2013):

Windward side:

$$h_{ext} = 8.07 \times V_w^{0.605} \quad (2)$$

Leeward side:

$$h_{ext} = 18.64 \times (0.3 + 0.05V_w)^{0.605} \quad (3)$$

where V_w = Wind velocity in m/s (assumed 10 m/s).

Building heat loss

Transmission heat loss:

$$Q_{transmission} = U \times A_{exp} \times \Delta T \quad (4)$$

Ventilation heat loss:

$$Q_{ventilation} = \frac{C_a \times \rho_a \times Volume \times air\ changes/hour \times \Delta T}{3600} \quad (5)$$

where $\Delta T = T_{room} - T_{amb}$.

Total heat loss:

$$Q_{loss} = Q_{transmission} + Q_{ventilation} \quad (6)$$

Internal heat gain

The internal heat gain occurs from the occupants and the heat emitting objects in a room. Since the number of occupants and objects varies, the heat gain is calculated from an estimated heat gain per floor area:

$$Q_{gain} = \nu \times A_{floor} \quad (7)$$

where ν = Heat gained per unit floor area, assumed to be 4 W/m².

Seasonal useful heat gain:

$$Q_u = \eta Q_{gain} \quad (8)$$

where η = Utilization factor for the heat gain.

The utilization factor is used for taking the thermal inertia of a building into account. For the calculation of the utilization factor, different factors need to be calculated as follows.

The ratio of heat gain and heat loss given as:

$$\phi = \frac{Q_{gain}}{Q_{loss}} \quad (9)$$

Time constant of the building in seconds given as:

$$Z = \frac{K}{H} \quad (10)$$

where K = Internal heat capacity of building (J/K); and

H = Coefficient for the heat loss through ventilation and transmission (W/K).

For easy calculation, the time constant for different building compositions was adapted from Kalema and Pylsy (2008).

The utilization factor can be found as:

$$\eta = \frac{1 - \phi^n}{1 - \phi^{n+1}} \quad \text{if } \phi \neq 1 \quad (11)$$

$$\eta = \frac{\phi}{\phi + 1} \quad \text{if } \phi = 1 \quad (12)$$

The value of n in the above equation depends on the time constant given as:

$$n = n_o + \frac{Z}{Z_o} \quad (13)$$

The value of parameter n_o is 1 if the calculation is made on a monthly basis and 0.8 for a seasonal basis. Z_o is the reference time constant having a value of 16 hours for monthly calculation and 28 hours for seasonal calculation.

Upon obtaining all the above parameters for a building, the net heat load can be found as:

$$Q = Q_{loss} - \eta Q_{gain} \quad (14)$$

Results of heat load calculation are given in Section 5.

3. THERMODYNAMIC MODELLING

Figure 3 shows the schematic diagram of the combined space heating and thermal storage system. The geothermal water is first passed through a heat exchanger giving heat to the secondary fluid. The secondary fluid passes through the radiator heating system giving heat to the room and then returns to the heat exchanger, forming a closed loop. The geothermal fluid, after exiting the heat exchanger, passes

into a phase change thermal storage system. The geothermal fluid gives heat to the phase change material and then exits the system. Thermodynamic modelling of the combined system is described below:

3.1 Heating system

Space heating using geothermal fluid is generally done using one of two methods, by sending geothermal fluid directly through space heating radiators or by using a heat exchanger which transfers heat from the geothermal fluid to the secondary fluid which then passes through the radiators for giving heat. Where geothermal fluid is unsuitable for direct use, the latter technique is applied. Also for cases where the minimum ambient temperature goes below the freezing point of water, anti-freeze is used in the secondary loop.

The present analysis assumes use of the indirect method of space heating such that the geothermal fluid gives heat to the secondary fluid which is passed through radiators for room heating. The radiators are designed for fixed design conditions at assumed room temperature. For ambient temperatures other than the design temperature, the heat load is calculated as:

$$\dot{Q}_T = \dot{Q}_{des} \left(\frac{T_{amb} - T_{room}}{T_{des} - T_{room}} \right) \quad (15)$$

The amount of heat transferred from a radiator is given as:

$$\dot{Q}_T = A_R \times U_R \times LMTD_R \quad (16)$$

The value of the logarithmic mean temperature difference between the radiator and the room air can be found using the following relationship:

$$LMTD_R = \frac{T_{R,in} - T_{R,out}}{\ln \left(\frac{T_{R,in} - T_{room}}{T_{R,out} - T_{room}} \right)} \quad (17)$$

It is found from experience that the logarithmic mean temperature difference varies with the radiator heat load as follows:

$$\frac{\dot{Q}_T}{\dot{Q}_{des}} = \left(\frac{LMTD_R}{LMTD_{R,des}} \right)^n \quad (18)$$

The value of exponent n is 1.3 (Anon, 1977).

Combining Equations 17 and 18, the radiator exit temperature can be found for a heat load other than the design load. Since the combined equation is an implicit function of the radiator exit temperature, any numerical technique such as the Newton Raphson method can be used for solving the equation.

On obtaining the temperature at the radiator outlet, the mass flow rate of fluid required through the radiator is given as:

$$\dot{m}_{rad} = \frac{\dot{Q}_T}{C_{R,f}(T_{R,in} - T_{R,out})} \quad (19)$$

The calculation of the above parameters for radiators requires full definition of the radiator side parameters. The output parameters from the radiator and the geothermal fluid inlet parameters (flow

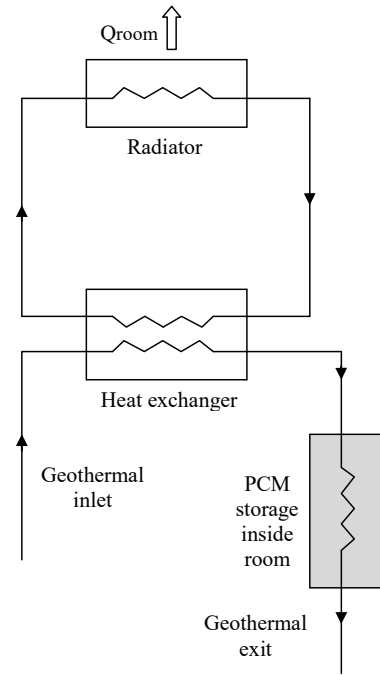


FIGURE 3: Schematic diagram of combined heating and storing system

rate and temperature), are the input parameters for the heat exchanger. In general, plate type heat exchangers are used for residential heating due to the advantages of low heating space, high heat transfer rate and ease in construction and maintenance over shell and tube type heat exchangers. With limited information for calculation of heat transfer coefficients through plate heat exchangers, the present analysis uses the relationship suggested by Incropera et al. (2007) for flow through circular pipes with diameter equal to the hydraulic diameter of a non-circular channel of the heat exchanger through which geothermal and secondary fluid passes. The relationship is given as:

$$Nu = 0.0296 Re^{0.8} Pr^{0.333} \quad (20)$$

where Nu = Dimensionless Nusselt number;
 Pr = Dimensionless Prandtl number; and
 Re = Dimensionless Reynolds number.

The Nusselt number and the Reynolds number are calculated as:

$$Nu = \frac{hD_h}{\lambda_f} \quad (21)$$

$$Re = \frac{\rho_f v_f D_h}{\mu_f} \quad (22)$$

The value of the Prandtl number (Pr) can be found from literature as a material property at different temperatures.

On finding the values of the heat transfer coefficient for both geothermal water and radiator fluid, the overall heat transfer coefficient for the heat exchanger is found as follows:

$$\frac{1}{U_{HX}} = \frac{1}{h_g} + \frac{x_{HX}}{\lambda_{HX}} + \frac{1}{h_R} + R_{HX} \quad (23)$$

The amount of heat transferred through the heat exchanger is given as:

$$\dot{Q}_T = A_{HX} \times U_{HX} \times LMTD_{HX} \quad (24)$$

Knowing the value of the heat exchange required and the area for which the heat exchanger is selected for a specific design, the logarithmic mean temperature difference of the heat exchanger can be calculated from the above equation. The geothermal exit temperature from the heat exchanger can then be calculated from the following equation:

$$LMTD_H = \frac{(T_{g,in} - T_{R,in}) - (T_{g,out} - T_{R,out})}{\ln\left(\frac{T_{g,in} - T_{R,in}}{T_{g,out} - T_{R,out}}\right)} \quad (25)$$

The above equation signifies the logarithmic mean temperature difference as an implicit function of geothermal water return temperature; hence, it needs to be solved numerically. Knowing the return water temperature, the mass flow rate of the geothermal fluid can then be found as:

$$\dot{m}_{geo} = \frac{\dot{Q}_T}{C_{g,f}(T_{g,in} - T_{g,out})} \quad (26)$$

3.2 Phase change material

The present work focuses on the analysis of PCM combined with a geothermal space heating system. The aim of the study is to calculate the amount of energy and exergy saved using PCM combined with geothermal space heating. The amount of PCM to be used for thermal storage depends upon the building heat load requirement and the difference in ambient temperature during storage and discharging. Since

the ambient temperature difference varies from season to season, the analysis assumed the mass phase change material to be 400 kg. The storage material mass and other physical properties were kept constant during the analysis. The heat storage system was assumed to consist of two concentric cylinders with inner and outer diameter of 0.02 and 0.045 m such that the heat source fluid flowed through the inner periphery and the storage material was filled between the cylinders as shown in Figure 4. The calculated length required for storage was found to be 186 m.

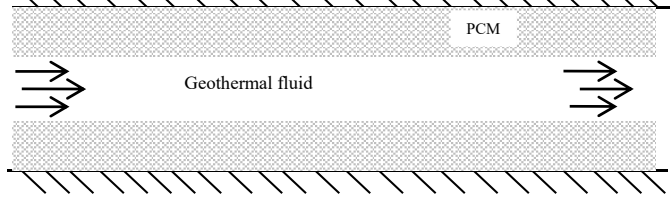


FIGURE 4: Configuration of thermal storage system

The PCM material used was calcium chloride. The properties of the PCM material and the heating fluid, water, were taken from El-Dessouky and Al-Juwayhel (1997). Analysis for the PCM, using air and water as the heating fluid, was discussed in the corresponding literature, considering water and air as the ideal fluid. For calculation of exergy terms, this assumption did not validate fully for water. Another important exergy analysis for phase change material was done by Bjurström and Carlsson (1985). Relations were derived for the amount of exergy stored in PCM and the final temperature of storage material. The present work uses the equations derived in Bjurström and Carlsson (1985) for analysing the system. The assumptions used in the analysis are:

- There is no heat exchange between the storage system and the surroundings during the charging process;
- The heat exchanger wall is assumed to have no resistance to heat transfer;
- Thermophysical properties of PCM and flowing fluid are assumed to be constant; and
- Since the analysis was done using phase change material with low transition temperature, the temperature difference between the transition temperature and the room temperature was small, hence all stored exergy was assumed to be used for room heating.

The heat transfer coefficient, h_f , between the heat transfer fluid and the wall is calculated from Equation 21. For turbulent flow, Equation 20 is used to obtain the Nusselt number, whereas for laminar flow $Nu = 3.66$.

The heat transfer coefficient between the wall and the storage material were calculated according to the relationships developed by Yanadori and Masuda (1989), based on experimental data.

$$h_m = \frac{2\lambda_s}{0.4 \left(D_{inner} \ln \left(\frac{D_{outer}}{D_{inner}} \right) \right)} \quad (27)$$

After obtaining the convective heat coefficient for the geothermal fluid and the phase change material, the overall heat transfer coefficient for PCM storage is calculated as:

$$\frac{1}{U_s} = \frac{1}{h_f} + \frac{1}{h_m} \quad (28)$$

In the above equation, resistance due to the wall is neglected as it is small in comparison to the convective heat transfer coefficients.

When the available information for calculating the heat transfer is insufficient, the Number of Transfer Units is used. This method helps to calculate heat transfer when all the inlet and exit temperatures are not given. The Number of Transfer Units on the fluid side is given by:

$$NTU = \frac{U_s \pi D_{inner} L_s}{\dot{m}_{geo} c_{g,f}} \quad (29)$$

For analysis, the initial temperature of the storage material and the inlet temperature of the heat source are assumed. The procedure used for calculating the final storage temperature and the amount of exergy stored is found from equations given by Bjurstrom and Carlsson (1985), as follows:

A dimensionless time Ω is defined as:

$$\Omega = \frac{\dot{m}_{geo} c_{g,f}}{M_{pcm} C_{pcm}} t \quad (30)$$

For analysis, temperatures are made dimensionless using the following equation:

$$\theta = \frac{T - T_o}{T_o} \quad (31)$$

The temperature efficiency (r) of the heat exchanger is given as:

$$r = 1 - \exp(-NTU) \quad (32)$$

The phase change material exhibits three stages of heat absorption: (1) sensible heat in solid phase from initial temperature to transition stage; (2) Latent heat during transition phase, and (3) Sensible heat in liquid phase. An equivalent heat capacity C_{pcm} is defined by the relationship:

$$M_{pcm} C_{pcm} (T_l - T_b) = M_{pcm} C_s (T_m - T_b) + M_{pcm} H + M_{pcm} C_l (T_l - T_m) \quad (33)$$

or

$$\theta_l - \theta_b = \alpha(\theta_m - \theta_b) + \omega(\theta_l - \theta_b) + \sigma(\theta_l - \theta_m) \quad (34)$$

The constants α , ω and σ are given as:

$$\alpha = \frac{C_s}{C_{pcm}} \quad (35)$$

$$\omega = \frac{H}{C_{pcm} (T_l - T_b)} \quad (36)$$

$$\sigma = \frac{C_l}{C_{pcm}} \quad (37)$$

For heating at a temperature below the phase transition temperature, the instantaneous storage temperature as a function of time is given as:

$$\theta_s = \theta_b + (\theta_i - \theta_b)(1 - \exp^{-r\Omega'}) \quad (38)$$

where Ω' is given as:

$$\Omega' = \frac{\Omega}{\alpha} \quad (39)$$

For heating the PCM above the transition temperature, the equations for instantaneous storage temperature and geothermal fluid outlet temperature are given as:

$$\theta_s = \theta_m + (\theta_i - \theta_m)(1 - \exp^{-r\Omega''}) \quad (40)$$

$$\theta_e = \theta_i(1 - r) + \theta_m r \quad (41)$$

where Ω'' is given as:

$$\Omega'' = \frac{1}{\sigma} \left(\theta - \left(\frac{\alpha}{r} \ln \left(\frac{\theta_i - \theta_b}{\theta_i - \theta_m} \right) \right) - \frac{\omega}{r} \left(\frac{\theta_l - \theta_b}{\theta_i - \theta_m} \right) \right) \quad (42)$$

The second and third terms in the parenthesis representing the dimensionless times required for bringing PCM to phase transition temperature and its completion.

For PCM where the storage temperature exceeds the transition temperature, the amount of energy stored in PCM is given by:

$$Q_{stored} = M_{pcm}C_s(\theta_m - \theta_b) + M_{pcm}H + M_{pcm}C_l(\theta_s - \theta_m) \quad (43)$$

Discharging

The phase change material storage is the cylindrical tanks or heat exchanger having phase change material in the annulus and hot water flowing inside. Such an arrangement can act as a radiator when placed in a room. The discharging of heat, stored during the night when the geothermal flow rate and temperature to phase change inlet is high, takes place during the daytime. As the daytime heat load requirement in rooms is low, the mass flow rate of the geothermal fluid is less and the inlet temperature of the geothermal fluid is low. Stopping the flow of geothermal water through phase change material makes the phase change storage system start to discharge heat since the phase change storage temperature is higher than the room temperature. The phase change storage system initially discharges heat at a higher rate since the initial storage temperature is much higher than the room temperature. On reaching the transition temperature, the phase change material gives heat at a constant rate because of a constant storage temperature equal to the phase change transition temperature. The low value of the convective heat transfer coefficient between the storage wall and the room does not permit the storage system to lose heat fast, hence allowing a longer period of discharge.

4. SYSTEM ANALYSIS

4.1 Exergy analysis

4.1.1 Room envelope system

On determining the total heat load for the room, the amount of exergy required for the heat load is determined. In order to determine the exergy required, the quality factor of the room air must be estimated. The quality factor describes the maximum energy that can be converted into useful work. Since heat energy is a form of low grade energy, the amount of exergy present in the heat energy is determined by the quality factor which is estimated by means of the Carnot efficiency, given as:

$$Y_{q,room} = 1 - \frac{T_{amb}}{T_{room}} \quad (44)$$

The amount of exergy required for satisfying the heat load demand is given as:

$$\dot{E}_{room} = Y_{q,room} \times \dot{Q}_T \quad (45)$$

4.1.2 Heating system

The radiator system is used for heating the room. In order to calculate the exergy load of the radiator system, the inlet and outlet temperatures of the system play important roles. The radiator surface temperature is calculated as the logarithmic mean temperature of the emission system as defined by Moran and Shapiro (1998):

$$T_{rad} = T_{room} + \frac{1}{2} \left(\frac{T_{R,in} - T_{R,out}}{\ln \left(\frac{T_{R,in} - T_{room}}{T_{R,out} - T_{room}} \right)} \right) \quad (46)$$

The amount of exergy given by the radiator is then given as:

$$\dot{\epsilon}_{rad} = \dot{Q}_T \left(1 - \frac{T_{amb}}{T_{rad}} \right) \quad (47)$$

In order to calculate exergy changes in a component along a flow line, the exergy flow rate at point i is calculated using the equation given by Bejan et al. (1996):

$$\dot{\epsilon}_i = \dot{m}_{in} [(h_{in} - h_o) - T_o(s_{in} - s_o)] \quad (48)$$

The values of enthalpy and entropy of the heating and radiator fluid as a function of temperature and pressure are calculated using the relationships given by Cooper and Dooley (2007).

The amount of exergy given by the geothermal fluid is calculated as:

$$\dot{\epsilon}_{geo} = \dot{m}_{geo} [(h_{geo,in} - h_o) - T_{amb}(s_{geo,in} - s_o)] \quad (49)$$

4.1.3 Storage system

The amount of exergy stored in the PCM is given by Bjurstrom and Carlsson (1985) as:

$$\begin{aligned} \epsilon_{stored} = M_p C_{pcm} T_{amb} \left\{ \alpha \left[(\theta_m - \theta_b) - \ln \left(\frac{1 + \theta_m}{1 + \theta_b} \right) \right] + \omega (\theta_l - \theta_b) \frac{\theta_m}{1 + \theta_m} \right. \\ \left. + \sigma \left[(\theta_s - \theta_m) - \ln \left(\frac{1 + \theta_s}{1 + \theta_m} \right) \right] \right\} \end{aligned} \quad (50)$$

4.2 Piping system design and pump selection

Design of the piping system requires the integration of mechanical, thermal and economic aspects. The material used for a pipe system depends upon the fluid flowing through it. Fluid conditions such as high temperature, high pressure, corrosive and hazardous are some of the factors that need to be taken into account while selecting pipe material. For applications requiring hot fluid to flow through pipes, thermal expansion should be taken into consideration.

Head loss

The head loss in a pipe due to friction is calculated using the Bernoulli equation. It can be estimated using the following equation:

$$h_l = \frac{4fL_p v_f^2}{2gD_p} + k \frac{v_f^2}{2} \quad (51)$$

where the first term represents head loss due to pipe friction and the second term represents head loss due to bending and resistance.

The value of the factor for different fittings, k , can be found from the table given in Bejan et al. (1996). The factor f represents the Fanning friction factor. The value of the Fanning friction factor is a function of the Reynolds Number and pipe roughness and is given as:

$$\frac{1}{\sqrt{f}} = -4 \log \left(\frac{e_p/D_p}{3.7} + \frac{1.256}{(\sqrt{f})Re} \right) \quad (52)$$

The above implicit function can be solved using a numerical technique to obtain the value of the friction factor.

On knowing the head loss through the pipe and the required head, the pump power requirement is calculated as:

$$P_{pump} = \frac{\dot{m}_f g (h_l + h_s)}{\eta_{pump}} \times 100 \quad (53)$$

Pipe selection

Various types of pipe materials exist with varying costs and durability. Different types of pipe materials used for geothermal applications include: various types of steel, polyvinyl, polybutylene, polyethylene and fibre glass. In addition to cost, temperature and the chemical properties of the geothermal fluid decide the type of pipeline material to be used.

For pipes carrying geothermal fluid for longer distances, some form of insulation is required. The insulation can be provided by using a pre insulating piping system, field applied methods or backfill methods. A pipe having a pre insulating system will have an insulation layer covering the carrier pipe. Many different combinations of insulation jacket and carrier pipe materials are available in the market, the most common using polyurethane as an insulation material. Almost 50% of the distribution cost is associated with pipe insulation. Much of the pipe cost can be saved by using uninsulated pipes. The heat loss due to no insulation is compensated for by increasing the flow rate of the fluid.

4.3 Exergoeconomic analysis

The exergy transformation process in a system is represented in Figure 5. The total exergy given to a system includes fuel exergy which is transformed into product exergy, some part of which includes exergy destruction and exergy loss. The increase in efficiency causes an increase in exergy output for a given input but also causes an increase in the costs required to improve the system.

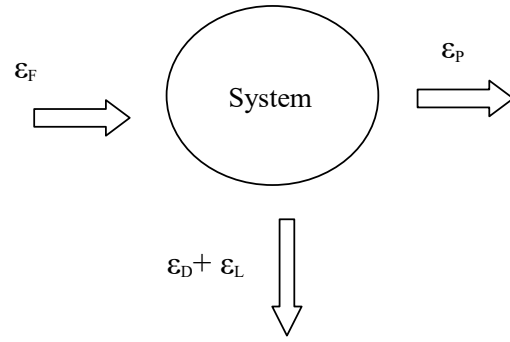


FIGURE 5: Exergy flow in a system

For exergoeconomic analysis, cost is assigned for every exergy flow in a system. The cost is proportional to the amount of exergy the flow contains. The product cost is defined according to the fuel cost, capital expenditure and other operating and maintenance costs required for production or services. The general equation is given as:

$$\dot{C}_p = \dot{C}_F + \dot{Z}^{cl} + \dot{Z}^{OM} \quad (54)$$

The equation signifies that the total cost associated with the product is the sum of the fuel cost, capital investment and the other costs related to the operation and maintenance of the system producing the product.

A general cost balance equation in terms of cost per unit exergy for an i^{th} component having heat and work interaction with the surroundings can be represented in terms of costs per unit exergy:

$$\sum (c_{out,i} \dot{E}_{out,i} + c_{w,i} \dot{W}_i) = \sum (c_{in,i} \dot{E}_{in,i} + c_{Q,i} \dot{E}_{Q,i} + \dot{Z}_i^{cl} + \dot{Z}_i^{OM}) \quad (55)$$

The inlet cost in the above equation is obtained from that of the exit cost of the previous component. For the first component, the inlet cost is the cost at which the fuel is supplied. Hence, the above equation can be solved for the unknowns.

4.3.1 Purchase equipment cost

For real life applications, equipment cost can be obtained from a vendor's catalogue. Generally it is not possible to obtain detailed costs of every component for every design condition. For such cases, the literature provides some useful sources. Mathematical charts and relationships built from past experiences are available giving cost values in terms of different parameters such as design and geometry. The simplest way for estimating product cost is by using an exponential law which defines the product cost as an exponential function of the size of the component. The relationship is given as follows:

$$I = I_r \left(\frac{S}{S_r} \right)^e \quad (56)$$

Such a relationship is assumed to be valid for a given range of equipment sizes. A general sixth-tenth rule is used for any equipment by taking the value of exponent to be 0.6. Different values of reference costs and their size along with the type of component are given by Boehm (1987).

Because of various economic factors, the cost always changes with time. The above relationship is for finding the cost with the reference cost of the indexed year. The obtained cost is brought to the current year cost by using the conversion relationship given as:

$$\text{Reference year cost} = \text{Original cost} \times \frac{\text{Reference year cost index}}{\text{Cost index for year for which calculation was made}} \quad (57)$$

The cost index used in the above equation takes into consideration inflation in the cost of the material, equipment and labour. Various cost indices are available in the literature. The present analysis uses Marshall et al. (2009) for indexing the equipment cost. The exergoeconomic analysis requires levelized costs of the equipments. For converting investment cost into levelized costs, a Capital Recovery Factor (CRF) is used, given by following equation:

$$CRF = \left(\frac{i(1+i)^N}{(1+i)^N - 1} \right) \quad (58)$$

The other factor to be taken into consideration while calculating component cost is operation and maintenance cost. The analysis assumes an annual 2% of the investment cost of each component as the operation and maintenance cost (β). The total cost flow rate associated with the component a with t hours of annual operation is then calculated as:

$$\dot{Z}_i = \frac{I_i(CRF + \beta)}{t \times 3600} \quad (59)$$

4.3.2 Exergy costs

Guidelines for obtaining equations for different streams can be found in the literature (Bejan et al., 1996). The present case mainly involves the usage of heat exchanging components. The balancing equations for the components used are described as:

Heat exchanger

In this system a heat exchanger is used to deliver heat coming from a geothermal inlet stream to a radiator exit stream which is the product stream. Hence, the following equations are obtained:

$$\dot{C}_{g,in} - \dot{C}_{HX,out} + \dot{C}_{R,out} - \dot{C}_{R,in} = -\dot{Z}_{HX} \quad (60)$$

Also, since the fuel side is that of the geothermal stream, its cost per unit exergy remains constant. The equation is given as:

$$\frac{\dot{C}_{g,in}}{\dot{E}_{g,in}} = \frac{\dot{C}_{HX,out}}{\dot{E}_{HX,out}} \quad (61)$$

Radiator

The cost associated with the radiator is charged to the product which is the exergy flowing out from the radiator for room heating. The equation obtained is:

$$\dot{C}_{R,in} - \dot{C}_{R,out} - \dot{C}_{heating} = -\dot{Z}_R \quad (62)$$

Also, no exergy is added to the inlet stream, hence the cost per unit exergy remains the same; the equation obtained is:

$$\frac{\dot{C}_{R,in}}{\dot{E}_{R,in}} = \frac{\dot{C}_{R,out}}{\dot{E}_{R,out}} \quad (63)$$

Storage system

The cost associated with storage is charged to the product, which is the exergy stored in the system. The equation obtained is:

$$\dot{C}_{HX,in} - \dot{C}_{g,out} - \dot{C}_{storage} = -\dot{Z}_{storage} \quad (64)$$

Also, no exergy is added to the inlet stream, hence the cost per unit exergy remains the same; the equation obtained is:

$$\frac{\dot{C}_{HX,out}}{\dot{E}_{HX,out}} = \frac{\dot{C}_{g,out}}{\dot{E}_{g,out}} \quad (65)$$

The above linear equations can be solved simultaneously to obtain the unknown variables.

5. RESULTS AND DISCUSSIONS

5.1 Heating system design

Tables 1 and 2 show the overall heat transfer coefficient for the different structures of room and restaurant. The calculation assumes that the larger side of the rooms is the windward side. Since the restaurant is surrounded by other building on three sides, only the glass window side is assumed to be the windward side.

The proposed system was analysed for variable radiator inlet temperature at different ambient conditions. The design conditions for the heating system assumes -15°C ambient temperature and 20°C room temperature. The fluid used in the secondary loop was assumed to be water. Table 3 shows the values of the different variables for the geothermal heating system.

Radiator

Different sizes of radiators can be selected from the manufacturer's catalogue depending upon the heat load requirement and the space available for installation. The catalogue specifies the radiator size and power output for particular models for given logarithmic temperature differences of the radiator and room temperature. Correction factors are available in the catalogue for getting heat output at other logarithmic temperature differences for a selected model. For the present design, radiators with a 40° logarithmic mean temperature difference design were selected, supplied by BYKO. The radiator models selected are given in Table 4.

TABLE 1: Overall heat transfer coefficient for rooms

Wall (windward)	3.1 W/m ² K
Wall (leeward)	2.8 W/m ² K
Glass	6.1 W/m ² K
Door	1.7 W/m ² K
Roof	4.1 W/m ² K
Floor	0.56 W/m ² K

TABLE 2: Overall heat transfer coefficient for restaurant

Wall (leeward)	2.8 W/m ² K
Glass	6.1 W/m ² K
Door	1.7 W/m ² K
Roof	4.1 W/m ² K
Floor	0.5 W/m ² K

TABLE 3: Design parameters and their values

Parameter	Value
Q_{load}	34.2 kW
\dot{m}_{geo}	0.25 kg/s
\dot{m}_{rad}	0.25 kg/s
$T_{R,in}$	75.0°C
$T_{R,out}$	42.5°C
$T_{g,in}$	80.0°C
$T_{g,out}$	47.5°C

TABLE 4: Radiator selection

Building	Required heat load (kW)	Model	No of radiators	Radiator heat capacity (kW)	Size
Rooms	11.43	E-33	3	3.85	0.6 m × 2.0 m
Restaurant	22.67	E-33	4	3.96	0.4 m × 2.8 m
		E-33	3	2.29	0.3 m × 2.0 m

Heat exchanger

For geothermal heating, generally plate type heat exchangers are preferred. The plate type heat exchangers offer many advantages over other types of heat exchangers. The nominal approach temperature of plate type heat exchangers is less than for other heat exchangers. In addition, the overall

TABLE 5: Heat Exchanger Specifications

Plate material	Stainless steel type AISI 316
Heat capacity	35 kW
Plate thickness	0.00035 m
Fouling Factor	0.075 m ² K/kW
Thermal conductivity	15.0 W/mK
Plate spacing	0.002 m
Plate width	0.1 m
Number of plates	81
Heat transfer area/plate	0.025 m ²

heat transfer coefficient of plate type heat exchangers is three to four times higher than shell and tube units. The construction of plate type heat exchangers makes them easier to maintain also. The plate type heat exchangers also permit expansion by the addition of extra plates as required. In addition, the compactness of the plate type heat exchangers also adds to its preference for selection.

For the present heat load requirement, a 4/4 brazed plate heat exchanger manufactured by Cetetherm AB was selected. The heat exchanger specifications are given in Table 5.

Pump and pipe

The cycle length of pipe for the secondary loop is around 110 m. The pressure head at the pipe end is kept at 2 bar. The amount of pressure loss in heating system components varies from one specification to another. The calculation assumes one radiator in each room. The calculation assumes pressure losses as shown in Table 6. Figure 6 shows the variations of pump power requirements with pipe diameter. The pipe diameter was selected to be a standard 0.025 m pipe, commonly available since the pump power does not decrease much as we increase the diameter further as shown in Figure 5. The corresponding pump power requirement was found to be 148 W.

TABLE 6: Pressure losses in heating system components

Component	No. of components	Pressure loss
Heat exchanger	1	20 kPa
Radiator	10	0.5 kPa
Radiator valve	10	10 kPa

Valve

Valves are used for switching and control of flow in the piping system to the radiator. The radiator valves can be of thermostatic type or manual. Thermostatic valves can be of two types. The first type controls the flow rate of hot water in accordance to the room temperature. The other type of thermostatic valves controls the flow rate in accordance to the return water temperature. On the other hand, manual valves need to be operated by human effort for controlling the flow rate depending upon the heating requirements. Thermostatic valves controlling the flow rate according to the return water temperature were used in the present design.

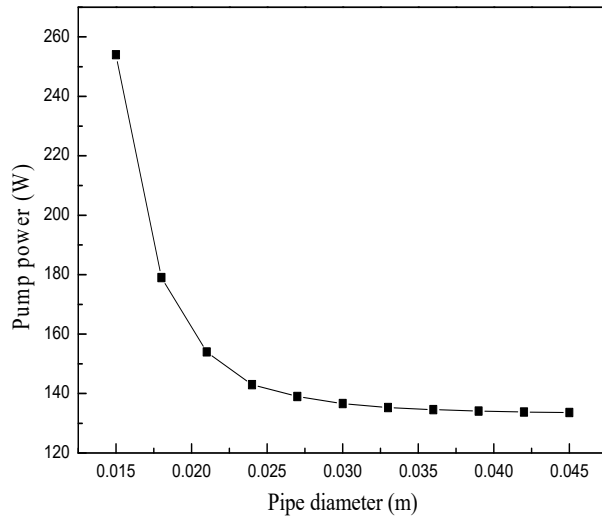


FIGURE 6: Variation of pump power with pipe diameter

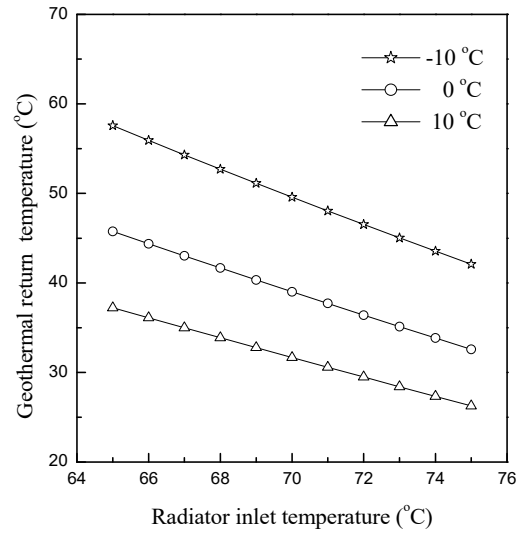


FIGURE 7: Variations of geothermal return temperature with radiator inlet temperature

5.2 Analysis

In order to have an optimized heating system, low temperature of the geothermal fluid exiting the heat exchanger is required, signifying high heat exchange in the radiator. Figure 7 shows the variation of geothermal outlet temperature from the heat exchanger at different radiator inlet temperature at three different ambient temperatures. Two important conclusions can be drawn from the graph, also reported in the literature (Karlsson and Ragnarsson, 1995). The first is the decrease in the geothermal fluid outlet temperature with an increase in the radiator inlet temperature. This is due to the fact that for a constant heat load, the logarithmic temperature difference remains constant for which the radiator outlet temperature decreases for a given increase in inlet temperature. Radiator inlet temperature is decided by the pinch point difference at the heat exchanger's geothermal water inlet. The second important conclusion is the increase in the geothermal fluid exit temperature with a decrease in ambient temperature. As the ambient temperature decreases, the heat load increases which causes an increase in the logarithmic temperature difference. For a constant inlet temperature, the outlet temperature from the radiator increases for a given increase in the logarithmic temperature difference. The increase in the geothermal fluid exit temperature with a decrease in ambient temperature results in a decrease in efficiency of the heating system with concerns about heat wastage at lower ambient temperatures.

Figure 8 shows the variation of the first and second laws of efficiency for room heating with ambient temperature. With the increase in ambient temperature, the first law of efficiency increases. Increase in the ambient temperature causes the radiator exit temperature to decrease as explained before. Decrease in the outlet temperature causes high heat removal per unit mass from the hot fluid passing through the radiator, with a subsequent increase in efficiency. The second law of efficiency also increases with ambient temperature as the exergy removal per unit mass through hot fluid increases with a decrease in the radiator outlet temperature. The increase in exergy removal from the hot fluid is then offset by a decrease in the exergy output as the reference temperature approaches the mean radiator temperature, hence causing the second law of efficiency to decrease.

The heating system was simulated by parallel additions of heat storage using phase change material for different ambient temperatures and for different time durations of the heat storage process in the phase change material. The storage material mass and other physical properties were kept constant during the analysis.

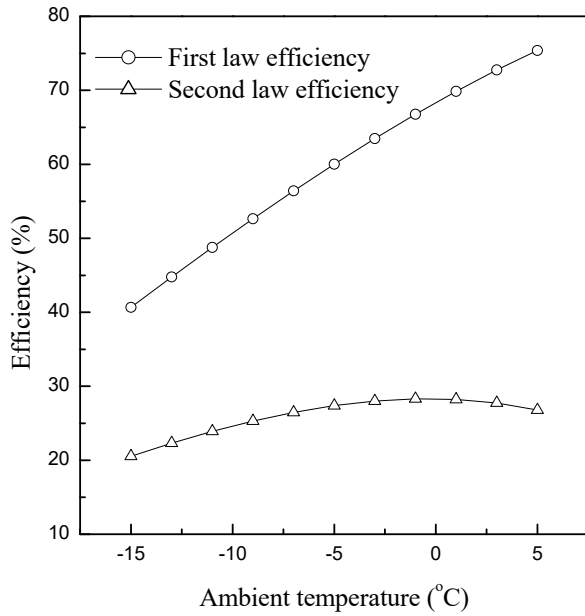


FIGURE 8: Variation of thermal efficiencies with ambient temperature

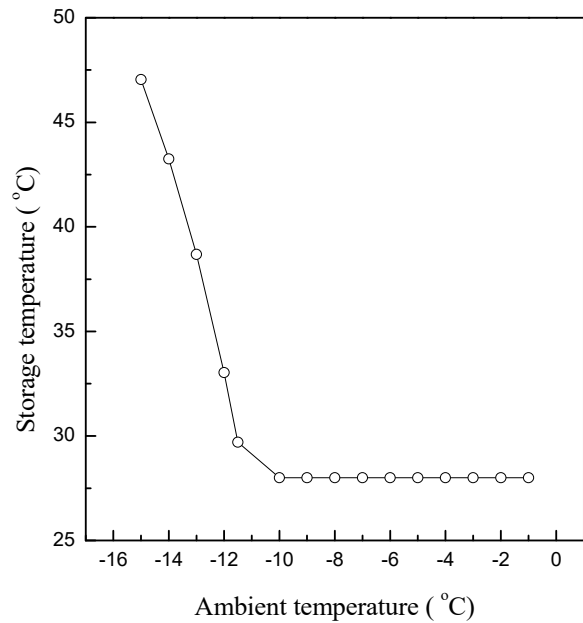


FIGURE 9: Variation of storage temperature with ambient temperature after an hour of operation

Figure 9 shows the variation of storage temperature with ambient temperature after an hour of the heat transfer process. It was found that at lower ambient temperature, heat gained by the phase change material was high enough that the phase change material was above the transition temperature earlier than expected. This occurred because of the high temperature and mass flow rate of the geothermal fluid at the storage inlet. With an increase in the ambient temperature, the heat exchanger or storage inlet temperature and mass flow rate of the geothermal fluid decreased causing a smaller heat transfer rate between the geothermal fluid and the phase change material. This caused the phase change material to remain in the transition stage after the same interval of time as that for a lower temperature.

Figure 10 shows the variation of heat transferred for different ambient temperatures after an hour of the heat storing process, keeping all other parameters constant. With the increase in ambient temperature, heat input from the geothermal fluid decreased. This occurred due to low geothermal fluid exit temperature at the heat exchanger exit. The required mass flow rate of the geothermal fluid also decreased with the increase in ambient temperature which also caused a decrease in the heat input from the geothermal fluid. Room heat load showed a continuous decrease as the ambient temperature increased. The amount of heat gained by phase change storage was higher at lower temperature and decreased with an increase in the ambient temperature. At lower ambient temperature, the phase change material was above the transition stage. The amount of heat stored was high, as the mass flow rate of the geothermal fluid at lower temperature also added to the high heat storage. The amount of heat stored at lower ambient temperature was the sum of latent heat of the material and the sensible heat stored at the storage temperature of the material at that time period. The exergy changes also showed similar trends as shown in Figure 11. Figures 10 and 11 show significant contribution made by phase change storage in energy savings at low ambient temperature. The graphs show that the energy and exergy stored were small in comparison to the total input but were significant in comparison to the room heat load.

Thermodynamic analysis of the storage system was done for different periods of charging, assuming -10°C ambient temperature. Figure 12 shows the variation of phase change material storage temperature with time during charging. The initial temperature of the phase change material was assumed to be equal to the room temperature. With an increase in the storage time, storage temperature increased until the transition temperature occurred. Since the temperature difference between the heat source fluid and the storage temperature was high, heat transferred rapidly causing a rapid increase in the storage

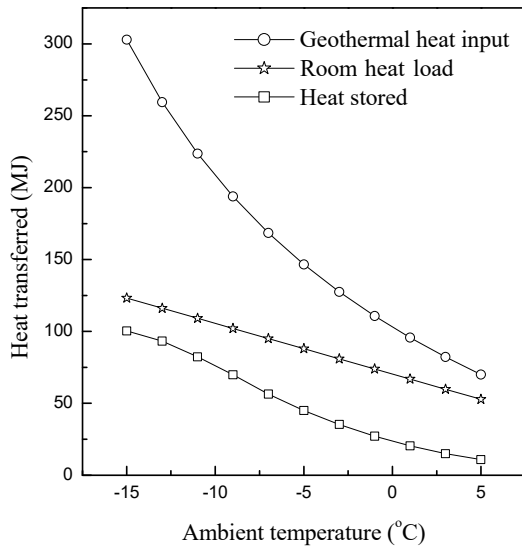


FIGURE 10: Variation of heat transfer with ambient temperature after an hour of operation

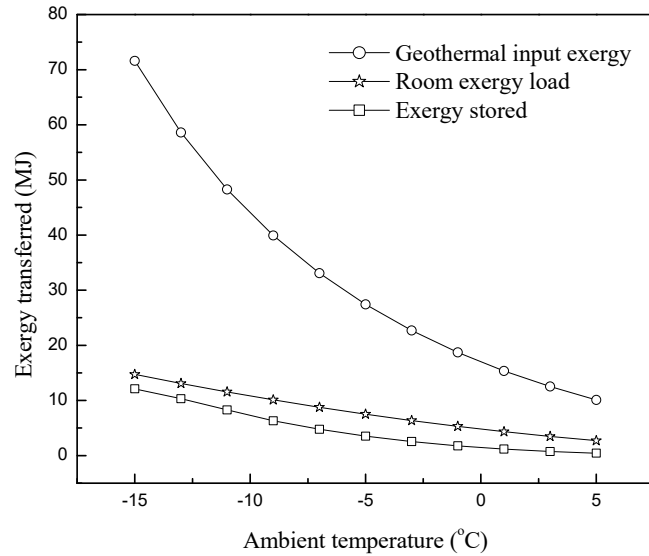


FIGURE 11: Variation of exergy transferred with ambient temperature after an hour of operation

temperature. On reaching the transition temperature heat transfer occurred at a constant temperature until the latent heat of the material was absorbed. After the transition phase was over, the storage temperature again started to increase, first at a high rate and then more slowly as the storage temperature became closer to the heat transfer fluid inlet temperature.

Figure 13 shows the variation of total heat transferred by the geothermal heat source fluid, room heat load and stored heat with time. With an increase in time duration, the total room heat increased constantly as the ambient temperature was fixed, hence, a fixed heat load. Total geothermal heat input from geothermal heat source also increased linearly since for a constant room heat load mass, the flow rate of the geothermal fluid also remained constant and the inlet hot fluid temperature was also fixed. The constant increase is reflected by the constant slopes of the geothermal heat input and room heat load in Figure 13. On the other hand, the total heat stored increased constantly till the transition stage was complete and then increased at a lower rate till the total heat stored became constant. The total heat

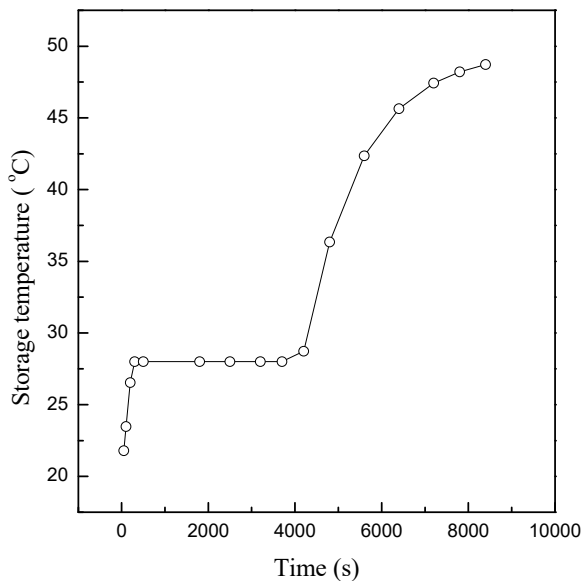


FIGURE 12: Variation of storage temperature with time at -10°C ambient temperature

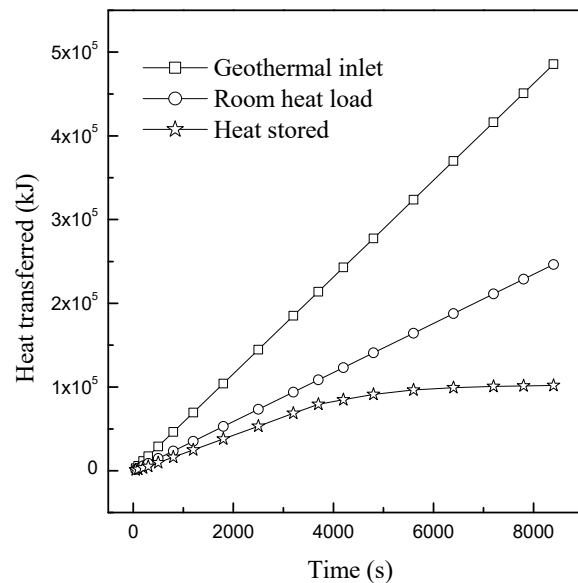


FIGURE 13: Variation of total heat transferred with time at -10°C ambient temperature

stored showed a constant slope during the latent heat absorption. After that, sensible heat storage started taking place and the rate of heat storage decreased as the storage temperature started approaching the heat source fluid temperature. It can be seen from the graph that the room heat load requirement was much smaller than the total heat input from the geothermal fluid. The addition of a phase change storage system increased significantly the heat savings compared to the room heat load requirement. The significant amount of heat stored could be enough to satisfy the heat load requirement during the daytime when the heat load is less.

Figure 14 shows the variation of total exergy stored in the phase change material with time. The initial phase of the storage process showed a constant increase in exergy accumulation in the phase change storage process. This exergy accumulation process increased constantly until latent heat storage took place. After the phase transition was complete, sensible heating started. The rate of exergy accumulation in the phase change storage material then started decreasing as the storage temperature approached the geothermal fluid inlet temperature.

Figure 15 shows the variation of fractional exergy stored as a function of the fractional heat stored. The initial and end part of the graph represents heat storage due to sensible heating and the middle constant range represents latent heat storage. It is seen from the graph that major exergy accumulation took place in the latent heat change process and sensible heating of the phase change material did not contribute much to exergy storage. Hence, it can be concluded from the graph that latent heat storage makes more of a contribution to heat storage than sensible heat.

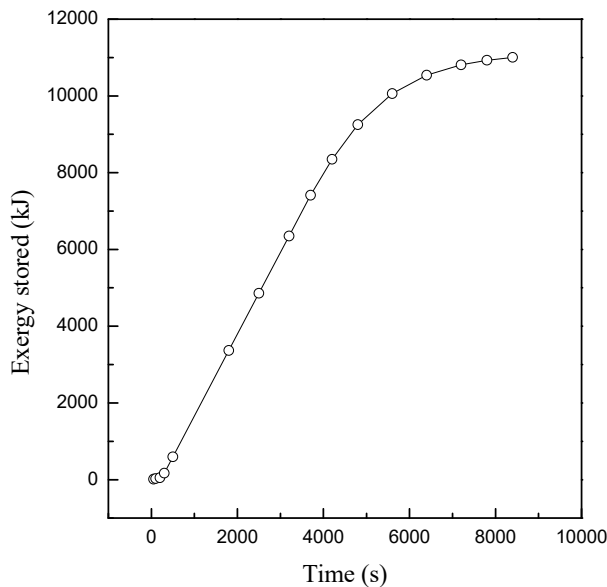


FIGURE 14: Variation of total exergy stored with time at -10°C ambient temperature

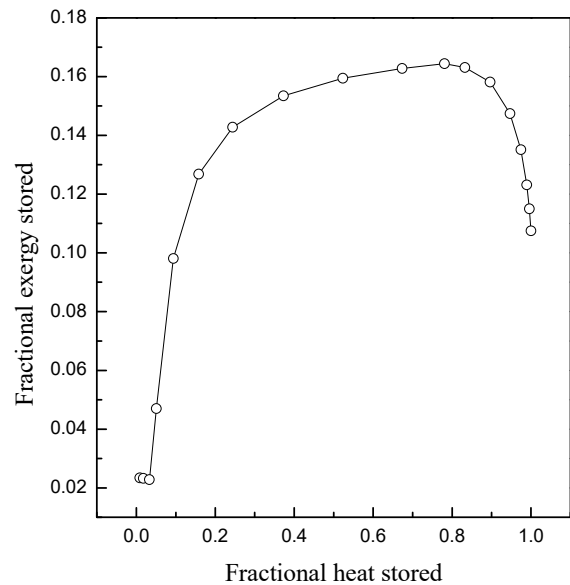


FIGURE 15: Variation of fractional exergy stored with fractional heat stored

Figure 16 shows the variation of cost flow rate per unit exergy (\$/kJ/hr) at different ambient temperatures. The inlet cost flow rate of the geothermal fluid is associated with that of the well and pumping costs. Since the well cost varies from place to place, the present analysis assumed a well cost of 0.5 million USD and 0.1 USD/kWh for the pumping cost with a total required head of 200 m from pump and an annual 7000 hours of operation. The discharge from the well was assumed to be 12 kg/s. The exergy flow rate from a geothermal fluid depends upon the ambient temperature. With an increase in ambient temperature, exergy per unit mass flow rate of geothermal fluid decreases as the reference temperature increases. Also the increase in ambient temperature causes a decrease in the mass flow rate through the well as the heat load decreases. These two factors cause the cost flow rate of the geothermal fluid to increase with ambient temperature. The cost flow rate of exergy supplied by radiators to a room increases with ambient temperature. As the ambient temperature increases, the heat load required

decreases causing the required exergy flow rate to decrease. The decrease in the exergy flow rate does not affect the purchase cost associated with the heat exchanger and radiator since the size of the equipment depends upon the design conditions for the minimum ambient temperature. Similar variations were found for the cost flow rate of exergy stored in the phase change storage system. The increase was found to be greater at higher ambient temperature. This occurs because as the ambient temperature increases, the heat exchanger exit temperature and mass flow rate decrease causing less exergy flow rate at the heat exchanger exit. The decrease in the exergy flow rate causes an increase in the cost flow per unit exergy as the purchasing cost remains the same as that for minimum ambient design conditions. An important observation from the graph is the difference in cost flow rates of the radiator heating and the stored exergy. It can be seen from the graph that the cost flow rate of stored exergy is lower than the radiator heating at lower ambient temperature. Since with the increase in ambient temperature the cost flow rate of the radiator heating increases, the amount of exergy stored at lower temperature with a low cost flow rate could be used at higher temperatures, resulting in cost savings.

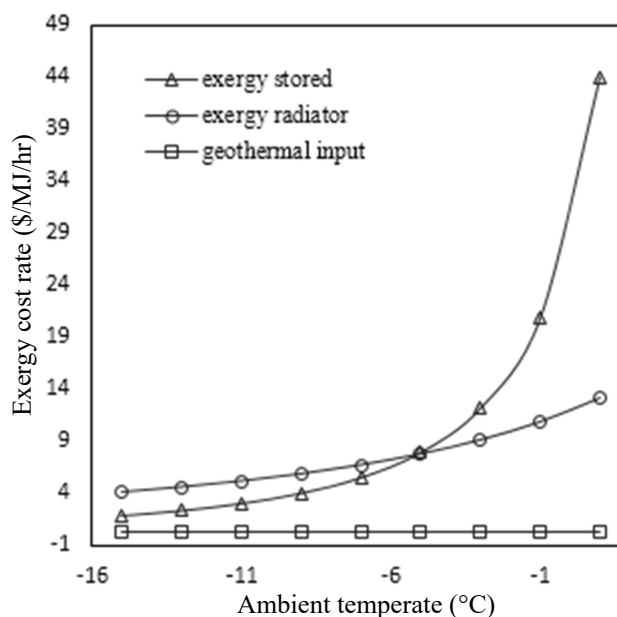


FIGURE 16: Variation of exergy cost flow rate per unit exergy with ambient temperature

Table 7 shows the exergy and cost flow rate per unit exergy at different state points in the combined heating and storing system at -5°C ambient temperature. The values of the cost flow rates per unit exergy show that each system, including a geothermal well and pumping, a heating system and a heat storage system, makes a significant contribution to the overall product cost rate, that is the cost of room heating and storing exergy. Also the low value of exergy storage cost in comparison to room heating using a radiator system at higher temperature shows the advantage of storing exergy at low ambient temperature.

TABLE 7: Exergy and cost flow rates at -5°C ambient temperature

State points	Exergy flow rate (kW)	Cost per unit exergy (USD MJ ⁻¹ hr ⁻¹)
Geothermal inlet	7.61	0.32
Storage inlet	2.73	0.32
Storage exit	1.6	0.32
Radiator inlet	6.04	0.69
Radiator exit	1.77	0.69
Room heating	2.08	7.83
Storage	0.69	7.98

6. CONCLUSIONS

Thermodynamic and exergoeconomic analysis of space heating using geothermal energy was done for a building in Chumathang, India. Due to the extreme cold conditions and poor insulation of the houses, the heat load requirement is high as calculated. The cost involved with drilling and pumping also

contributes to the total cost for space heating. The cost becomes significant when the flow rate requirement is high due to high heat load requirements.

Variations of heating system efficiency with ambient temperature were studied. Heating system efficiency was found to be low at lower ambient temperature. Hence, thermal losses become significant at lower temperatures.

A parallel combination of a phase change storage system with a heating system was studied. Heat supply to the storage system was provided from heat exiting the heat exchanger. Thermodynamic studies of the heat storage process at different times and ambient temperatures were done. Higher heat storage was observed at low ambient temperature. The rate of exergy storage during the latent heat transition period was found to be larger than for sensible heat storage. A sufficient amount of exergy was stored during the charging period at low temperature which could be used to fulfil the daytime heat load requirements.

Exergoeconomic analysis of the combined heating and storage system was done. At low ambient temperature, the cost flow rate of exergy storage was found to be lower than the radiator heating cost flow rate. For the assumed value of investment cost rates, heat storage using phase change material was found to be more economical than radiator heating till -5°C . Another important conclusion drawn was the increase in the cost flow rate of radiator heating exergy with ambient temperature. The usage of exergy storage at low ambient temperature for heating at higher ambient temperature could make significant contributions in cost savings.

Thermodynamic and exergoeconomic analysis of heating using geothermal energy in combination with a phase change storage system was done. Parametric analysis was done using a selected storage phase change material. Results showed both thermodynamic and exergoeconomic feasibility and scope for optimization. Future work must concentrate on the application of phase change materials with different transition temperatures and their combinations in order to optimize the storage process both thermodynamically and thermoeconomically.

ACKNOWLEDGEMENTS

I thank the United Nations University, the Indian Institute of Technology, Mandi, and the Government of Himachal Pradesh for giving me the opportunity to attend this program. My sincere gratitude goes to Dr. Ingvar Birgir Fridleifsson, Mr. Lúdvík S. Georgsson, Ms. Málfríður Ómarsdóttir, Mr. Ingimar Gudni Haraldsson, Ms. Thórhildur Ísberg, Mr. Markús A.G. Wilde and Ms. Rósa S. Jónsdóttir for all their guidance and services.

I wish to express my sincere thanks to my supervisor Dr. Árni Ragnarsson and my teachers Dr. P. Anil Kishan, Dr. Sateesh Gedupudi, Dr. Ashan Absar, Prof. B.N Banergee and Prof. Deepak Khemani. I would like to thank my parents and elder brother. They were always supporting me and encouraging me with their best wishes. I also place on record my sense of gratitude to one and all who, directly or indirectly, have lent their helping hand in this venture.

Above all, I am grateful to The Almighty God for enabling me to complete my geothermal training Programme.

NOMENCLATURE

A_{exp}	= area exposed (m ²);
A_{HX}	= area of heat exchanger (m ²);
A_R	= radiator area (m ²);
$c_{in,i}$	= inlet flow cost per unit exergy (\$/kJ);
$c_{out,i}$	= outlet flow cost per unit exergy (\$/kJ);
$c_{Q,i}$	= heat flow cost per unit exergy (\$/kJ);
$c_{w,i}$	= work flow cost per unit exergy (\$/kJ);
\dot{C}_F	= fuel cost flow rate (\$/s);
$\dot{C}_{g,in}$	= geothermal inlet cost flow rate (\$/s);
$\dot{C}_{g,out}$	= geothermal outlet cost flow rate (\$/s);
$\dot{C}_{heating}$	= heating cost flow rate (\$/s);
$\dot{C}_{HX,in}$	= heat exchanger inlet exergy cost flow rate (\$/s);
$\dot{C}_{HX,out}$	= heat exchanger outlet exergy cost flow rate (\$/s);
\dot{C}_p	= product cost flow rate (\$/s);
$\dot{C}_{R,out}$	= radiator outlet exergy cost flow rate (\$/s);
$\dot{C}_{R,in}$	= radiator inlet exergy cost flow rate (\$/s);
$\dot{C}_{storage}$	= storage exergy cost flow rate (\$/s);
C_a	= specific heat capacity of air (kJ/kgK);
$C_{R,f}$	= specific heat capacity of radiator fluid (kJ/kgK);
$C_{g,f}$	= specific heat capacity of geothermal fluid (kJ/kgK);
C_l	= specific heat capacity of phase change material in liquid phase (kJ/kg);
C_{pcm}	= latent heat capacity of phase change material (kJ/kg);
C_s	= specific capacity of phase change material in solid phase (kJ/kg);
D_h	= hydraulic diameter (m);
D_{inner}	= inner diameter (m);
D_{outer}	= outer diameter (m);
e	= exponent for cost;
D_p	= pipe diameter (m);
r_p	= pipe roughness factor (m);
f	= friction factor;
g	= acceleration due to gravity (m/s ²);
h	= convective heat transfer coefficient (W/m ² K);
h_m	= convective heat transfer coefficient of storage side (W/m ² K);
h_g	= convective heat transfer coefficient of geothermal fluid side (W/m ² K);
h_f	= convective heat transfer coefficient of fluid flowing side (W/m ² K);
h_R	= convective heat transfer coefficient of radiator fluid side (W/m ² K);
$h_{geo,in}$	= specific enthalpy of geothermal inlet fluid (kJ/kg);
h_o	= specific enthalpy of fluid at reference state (kJ/kg);
h_l	= head loss (m);
h_s	= static head required (m);
H	= latent heat capacity of storage material (kJ/kg);
i	= interest rate per annum (%);
I	= cost of equipment (\$);
I_r	= cost of reference equipment (\$);
k	= bending loss coefficient;
L_p	= length of pipe (m);
L_s	= length of phase change storage (m);
$LMTD_{HX}$	= logarithmic mean temperature difference of heat exchanger (K);

$LMTD_R$	= logarithmic mean temperature difference of radiator/room (K);
$LMTD_{R,des}$	= logarithmic mean temperature difference of radiator/room at design conditions (K);
\dot{m}_f	= mass flow rate (kg/s);
\dot{m}_{geo}	= geothermal water mass flow rate (kg/s);
\dot{m}_{rad}	= radiator fluid mass flow rate (kg/s);
M_{pcm}	= phase change material mass (kg);
N	= number of years of operation;
P_{pump}	= pump power (kW);
\dot{Q}_{des}	= design heat load (kW);
\dot{Q}_T	= heat load (kW);
\dot{R}_{HX}	= resistance due to fouling in heat exchanger ($m^2 K/W$);
$s_{geo,in}$	= geothermal water inlet entropy (kJ/K);
s_o	= reference state entropy (kJ/K);
S	= size of equipment;
S_r	= size of reference equipment;
t	= time (s);
T	= temperature (K);
T_o	= reference ambient temperature (K);
T_{amb}	= ambient temperature (K);
T_{des}	= design ambient temperature (K);
T_l	= final temperature of the phase change material (K);
T_b	= initial temperature of the phase change material (K);
T_m	= temperature in transition phase (K);
T_{rad}	= mean radiator temperature (K);
T_{room}	= room temperature (K);
$T_{R,in}$	= radiator fluid inlet temperature (K);
$T_{R,out}$	= radiator fluid outlet temperature (K);
$T_{g,in}$	= geothermal water inlet temperature (K);
$T_{g,out}$	= geothermal water outlet temperature (K);
U_{HX}	= heat exchanger overall heat transfer coefficient ($W/m^2 K$);
U_R	= radiator overall heat transfer coefficient ($W/m^2 K$);
U_s	= storage system overall heat transfer coefficient ($W/m^2 K$);
v_f	= fluid velocity (m/s);
\dot{W}_i	= rate of work for i^{th} component (kW);
x_{HX}	= thickness of heat exchanger plate (m);
$Y_{q,room}$	= exergy quality factor;
\dot{Z}^{cl}	= levelized capital cost (\$/s);
\dot{Z}^{OM}	= levelized operation and maintenance cost (\$/s);
\dot{Z}_{HX}	= total cost rate of heat exchanger (\$/s);
$\dot{Z}_{storage}$	= total cost rate of storage system (\$/s);
\dot{Z}_R	= total cost rate of radiator (\$/s);
ρ_f	= density of fluid (kg/m^3);
ρ_a	= density of air (kg/m^3);
v_f	= velocity of fluid (m/s);
β	= annual operation and maintenance cost (%);
μ_f	= dynamic viscosity of fluid ($N s/m^2$);
θ_b	= dimensionless temperature at initial state;
θ_e	= dimensionless exit temperature of geothermal fluid;
θ_i	= dimensionless inlet temperature of geothermal fluid;
θ_l	= dimensionless temperature in liquid phase;
θ_m	= dimensionless phase transition temperature;

θ_s	= thermal storage temperature;
\dot{E}_D	= exergy destruction rate (kW);
\dot{E}_F	= fuel exergy flow rate (kW);
\dot{E}_L	= exergy loss rate (kW);
\dot{E}_P	= product exergy flow rate (kW);
$\dot{E}_{Q,i}$	= exergy flow rate due to heat flow in i^{th} component (kW);
$\dot{E}_{out,i}$	= outlet exergy flow rate from i^{th} component (kW);
$\dot{E}_{g,in}$	= geothermal water inlet exergy flow rate (kW);
$\dot{E}_{g,out}$	= geothermal water outlet exergy flow rate (kW);
$\dot{E}_{HX,out}$	= exergy flow rate from heat exchanger outlet (kW);
$\dot{E}_{in,i}$	= inlet exergy flow rate to i^{th} component (kW);
\dot{E}_{room}	= exergy required for heating (kW);
\dot{E}_{rad}	= exergy given by the radiator (kW);
\dot{E}_i	= exergy flow rate at i^{th} component (kW);
\dot{E}_{geo}	= exergy given by the geothermal fluid (kW);
\dot{E}_{stored}	= exergy stored in the PCM (kW);
λ_f	= thermal conductivity of fluid (W/mK);
λ_s	= thermal conductivity of heat storage material (W/mK);
λ_{surf}	= thermal conductivity of wall material (W/mK);
λ_{HX}	= thermal conductivity of heat exchanger plate (W/mK);
η_{pump}	= efficiency pump (%);
Ω	= dimensionless time.

REFERENCES

- Abhat, A., 1983: Low temperature latent heat thermal energy storage: heat storage materials. *Solar Energy*, 30, 313–332.
- Adebiyi, G.A., and Russell, L.D., 1987: Second law analysis of phase-change thermal energy storage systems. *Proceedings of the ASME, WA-HTD-80, Boston, MA*, 9-20.
- Anon, 1977: *DIN 4703 Part 3. Heat transport of bodies at room temperature* (in German). Beuth Verlag, Berlin, Germany.
- Bejan, A., 1996: Entropy generation minimization: The new thermodynamics of finite size devices and finite time processes. *J. Applied Physics*, 79, 1191-1218.
- Bejan, A., Tsatsaronis, G., and Moran, M., 1996: *Thermal design and optimization*. John Wiley & Sons, NY, 542 pp.
- Bjurstrom, H., and Carlsson, B., 1985: An exergy analysis of sensible and latent heat storage. *J. Heat Recovery Systems*, 5, 233-250.
- Boehm, R.F., 1987: *Design and analysis of thermal systems*, John Wiley and Sons, NY, 259 pp.
- Budaiwi, I.M., 2011: Envelope thermal design for energy savings in mosques in hot humid climate. *J. Building Performance Simulation*, 4, 49-61.
- Carlos, J.S., and Nepomuceno, M.C.S., 2004: A simple methodology to predict heating load at an early design stage of Dwellings. *Energy Conversion and Management*, 45, 1597-1615.
- Cooper, J.R., and Dooley, R.B., 2007: *Revised release on the IAPWS industrial formulation 1997 for the thermodynamic properties of water and steam*. IAPWS, Lucerne, Switzerland, 49 pp.

- Crawley, D.B., Hand, J.W., Kummert, M., and Griffith, B.T., 2008: Contrasting the capabilities of building energy performance simulation programs. *Building and Environment*, 43, 661-673.
- El-Dessouky, H., and Al-Juwayhel, F., 1997: Effectiveness of a thermal energy storage system using phase change materials. *Energy Conversion and Management*, 38, 601-617.
- Farid, M.M., Khudhair, A.M., Razack, S.A.K., and Al-Hallaj, S., 2004: A review on phase change energy storage: materials and applications. *Energy Conversion and Management*, 45, 1597-1615.
- Hepbasli, A., 2010: A review on energetic, exergetic and exergoeconomic aspects of geothermal district heating systems (GDHSs). *Energy Conversion and Management*, 51, 2041-2061.
- IEA ECBCS Annex 37, 2000: *Low exergy systems for heating and cooling of buildings. Annex 37, Conservation in buildings and community systems*. VTT, webpage: www.vtt.fi.
- Incropera, F.P., Dewitt, D.P., Bergman, T.L., Lavine, A.S., and Middleman, S., 2007: *Fundamentals of heat and mass transfer: an introduction to mass and heat transfer* (6thed.). John Wiley and Sons Inc., NY, 1720 pp.
- Jingyana, X., Juna, Z., and Na, Q., 2010: Exergetic cost analysis of a space heating system. *Energy and Buildings*, 42, 1987-1994.
- Kalema, T., and Pylsy, P., 2008: Accuracy of the calculation of heating and cooling energy needs in Nordic conditions. *Proceedings of the 8th Symposium on Building Physics in the Nordic Countries, Copenhagen*, 535-542.
- Karlsson, Th., and Ragnarsson, Á., 1995: Use of very low temperature geothermal water in radiator heating system. *Proceedings of the World Geothermal Congress 1995, Florence, Italy*, 2193-2198.
- Keçebaş, A., 2013: Effect of reference state on the exergoeconomic evaluation of geothermal district heating systems. *Renewable and Sustainable Energy Reviews*, 25, 462-469.
- Marshall, R.J., Lozowski, D., Ondrey, G., Torzewski, K., and Shelley, S.A., (eds.) 2009: Marshall and Swift cost index. *Chemical Engineering Magazine, February*, 64 pp.
- Meester, B.D., Dewulf, J., Verbeke, S., Janssens, A., and Langenhove, H.V., 2009: Exergetic life cycle assessment (ELCA) for resource consumption evaluation in the built environment. *Build Environment*, 44, 11-17.
- Mirsadeghi, M., Cóstola, D., Blocken, B., and Hensen, J.L.M., 2013: Review of external convective heat transfer coefficient models in building energy simulation programs: Implementation and uncertainty. *Applied Thermal Engineering*, 56, 134-151.
- Moran, M.J., and Shapiro, H.N., 2007: *Fundamentals of engineering thermodynamics*. John Wiley and Sons, NY, 944 pp.
- Oktay, Z., and Dincer, I., 2009: Exergoeconomic analysis of the Gonen geothermal district heating system for buildings. *Energy and Buildings*, 41, 154-163.
- Razdan, P.N., Agarwal, R.K., and Singh, R., 2008: Geothermal energy resources and its potential in India. *e – J. Earth Science India*, 1, 30-42.
- Saito, M., and Shukuya, M., 2001: The human body consumes exergy for thermal comfort. *LowExNews*, 2, 6-7.
- Shukuya, M., and Komuro, D., 1996: Exergy-entropy process of passive solar heating and global environmental systems. *Sol Energy*, 58, 25-32.
- Yanadori, M., and Masuda, T., 1989: Heat transfer study on a heat storage container with phase change materials: Part 2. *Solar Energy*, 42, 27-34.
- Yildiz, A., and Gungör, A., 2009: Energy and exergy analyses of space heating in buildings. *Applied Energy*, 86, 1939-1948.



SCALING POTENTIAL DURING PRODUCTION IN HVERAHLÍD FIELD, HENGILL HIGH-TEMPERATURE GEOHERMAL AREA, SW-ICELAND

Kennedy Mativo Kamunya

Kenya Electricity Generating Company - KenGen

P.O. Box 785-20117, Naivasha

KENYA

kennedy.mativo@gmail.com, kkamunya@kengen.co.ke

ABSTRACT

Hverahlíd high-temperature geothermal field is one of four high-temperature geothermal fields of the Hengill geothermal area. It is located southeast of the Hengill central volcano. It has not been developed yet, but it shows a field capacity of 90 MWe. Scaling potential with respect to amorphous silica, calcite and anhydrite was assessed for the Hverahlíd system through processes of adiabatic boiling and conductive cooling of the deep aquifer fluid, during steam production, utilization, separation and reinjection. The scaling potential was studied based on mineral saturation. The calculations were conducted using the WATCH program. Amorphous silica scaling shows a potential to occur in well fluids upon boiling at temperatures below 205°C in production wells, during utilization, in reinjection wells and in aquifers receiving the reinjected fluid. Calcite has the potential to cause scaling in production wells upon extensive boiling but is not considered a risk during utilization at lower temperatures in reinjection and the receiving aquifer. Anhydrite poses no risk of scaling for any of the processes of boiling and conductive cooling that were considered.

1. INTRODUCTION

Utilization of high-temperature geothermal resources usually comes with challenges. Among these challenges is mineral scaling in production and injection wells as well as in pipes transporting the geothermal brine. Potential scaling formation is largely governed by the concentrations of dissolved components in the geothermal fluids and changes in fluid chemistry upon boiling, cooling and mixing as well as by temperature and pressure dependent minerals and other solids' solubility. Mineral formation kinetics also plays an important role. It has been concluded that the concentration of major elements in geothermal fluids at depth is controlled by the close approach to equilibrium with common geothermal minerals (e.g. Giggenbach et al., 1980, 1981; Arnórsson et al., 1982). However, during utilization of geothermal fluids, the fluids are brought to the surface. This results in changes in the physical state of the fluid including temperature and pressure drop and fluid phase separation into water and steam. In turn, these changes disrupt the equilibrium conditions, potentially causing chemical reactions including mineral precipitation.

Scaling potential assessment for a production field prior to production is important. Through such an assessment, a potential scaling problem may be overcome by changing the P-T conditions of utilization

or fluid handling of mineral supersaturated geothermal brine. The three processes that may cause mineral scaling during geothermal fluid utilization are boiling, cooling and mixing. Depressurization boiling and the removal of steam from a geothermal fluid increases the concentration of non-volatile dissolved constituents in the residual boiled water as the same amount of solutes are dissolved in less amounts of water. Removal of heat through the heating of a secondary fluid leads to lowering of the temperature of the geothermal brine. The solubility of certain dissolved components like silica is related to the temperature of the fluid. Scales of various types form during exploitation. These include sulphides, calcite, silica, dolomite, and clays among others. Scales of greatest concern on surface installations and injection wells are sulphide and silica scales and calcite in production wells and the pressure reduction zones around them.

The extent to which utilization of high-temperature geothermal fluid can be put to use is mostly limited by the saturation state of silica in the fluid (Gunnarsson et al., 2010; Brown, 2011). Dissolved silica and pH value set the lower temperature at which a geothermal fluid can be safely used without the risk of silica scaling. This can set a limit to the amount of heat that can be extracted from the geothermal fluid and, therefore, the efficiency of the geothermal power plant. If set at a lower temperature, silica precipitation can clog valves, transport pipes (and other surface installations), reinjection wells and the receiving aquifer of the re-injected, spent geothermal waters. The solubility of quartz controls the amount of silica dissolved in the fluid in most geothermal systems (Fournier, 1982) and hot geothermal water extracted from geothermal systems corresponds to the solubility of quartz at reservoir temperature (Bohlman et al., 1980; Brown, 2011). Quartz precipitation has very slow kinetics in temperatures below 300°C (Bohlman et al., 1980) and, because of this, it is not readily precipitated from solutions upon utilization of the geothermal fluid.

If heat is extracted from the geothermal fluid beyond the point of amorphous silica solubility by second stage boiling or conductive cooling, the fluid becomes silica supersaturated. Two processes have a tendency to take place in silica supersaturated solutions. One is direct deposition of monomeric silica on an existing surface and the other is a homogenous formation of silica polymers (Gunnarsson and Arnórsson, 2005). Depending on the chemical composition of the fluid, these polymers either stay in solution or settle out of solution to form scales (Gallup 2011; Brown 2011). If the salinity of the fluid is low, the silica polymers stay in solution; the net outcome of polymerization is lowering the risk of silica scaling (Gunnarsson and Arnórsson, 2005).

Upon boiling of geothermal fluids, volatile components partition fully or partially into the steam phase. Among these volatiles are CO₂ and H₂S that are generally the two main acids in geothermal fluids. The loss of acid from the water to steam phase results in a pH increase of the boiled water which may trigger mineral precipitation of carbonates. Indeed, calcite scaling often takes place upon boiling. Chemical inhibitors have been used to prevent such scaling (Ngothai et al., 2010). Also, high wellhead pressures have to be maintained at the wellhead to prevent boiling within the production wells and to prevent scaling (Mroczek and Graham, 2001).

Anhydrite (CaSO₄) is precipitated from solution upon a drop in temperature. It exhibits retrograde solubility. Ca and SO₄ are both non-volatiles and their concentrations increase in the water phase upon boiling, possibly leading to supersaturation.

In this report, potential scaling associated with geothermal fluids from the Hverahlíd geothermal field of Hengill geothermal area, SW-Iceland, was investigated. Hverahlíd is a high-temperature geothermal field that is at production drilling stage. Several wells have been drilled and the field shows good potential for further development. The scaling potential was assessed in the production wells. Also, scaling potentials upon fluid mixing and phase separation (boiling) to form steam and waste water were carried out; scaling potentials upon re-injection, after electricity production treatment of the separated waters to enhance heat extraction after separation, were done for other low pressure uses. Modelling for scaling in spent water for reinjection was carried out and potential for scaling in the reinjection wells and receiving aquifer was assessed.

2. HENGILL GEOTHERMAL SYSTEM

2.1 General settings

The Hengill geothermal system is situated ~30 km east of Reykjavík in SW Iceland (Figure 1). It hosts four high-temperature geothermal fields: Hverahlíð, Hellisheidi, Nesjavellir, and Bitra. It is one of the most important geothermal fields in Iceland for district heating and electricity for Reykjavík city. As of today, of the four, Hellisheidi and Nesjavellir have been developed whereas Hverahlíð and Bitra have not. The production capacity at Nesjavellir power plant is 300 MWt and 120 MWe and at Hellisheidi the capacity is 133 MWt and 303 MWe. Four wells have been drilled in Hverahlíð and there is a plan to drill more wells (Níelsson and Franzson, 2010).

High-temperature geothermal resources in Iceland are associated with the North Atlantic Ridge and a mantle plume (Ágústsson and Flóvenz, 2005; Hardarson et al., 2009). The mantle plume has migrated over the course of geological history to the southeast relative to the North Atlantic Ridge, and a subsequent movement to the east. This caused shifts in the spreading axis over Iceland towards the east. In the Hengill area, the spreading axis is joined by a minor transform component, forming a triple junction. Micro seismic events occur in this transform component and may be influential especially on keeping permeability structures open (Hardarson et al., 2010).

The Hengill geothermal system comprises the Hengill central volcano, fissures swarms and lava flows. The system is in a graben with a NE-SW strike, extending up to 40 km NE of Hengill Mountain and a width of 3-5 km. It has a throw of 300 m to the west of Hengill. The same amount of throw is thought to occur in the east, though this is not apparent (Franzson et al., 2010). It is thought that the throw to the east may be in a series of small normal step faults. Within this graben is a series of dyke swarms and faulting with Hengill volcano as the loci of highest volcanic accumulation (Hardarson et al., 2009). The age of the Hengill system has been placed at 300,000 years from geologic studies in wells in the Nesjavellir field in the north, though studies in the south at Hellisheidi revealed an age of 400,000 years. The age at Hellisheidi has been placed as the maximum age of the geothermal system (Franzson et al., 2005).

The Hengill Mountain is built up of hyaloclastites and lava flows with the lava flows occurring in the interglacial periods. Hyaloclastites are rocks erupted in the base of glaciers allowing them to accumulate and form the highlands. The hyaloclastites are of limited extent and because of this they do not serve as good marker horizons for geological correlation. Felsic rocks can also be found to the southwest of the mountain; these are more evolved rocks. During interglacial periods, lava flows from the central volcano flowed to the surrounding lowlands. Basaltic fissure eruptions have occurred since the last glacial period of Holocene. Dates of these post glacial eruptions have given rise to three ages of 9, 5 and 2 thousand years ago for the lava flows (Níelsson and Franzson, 2010). Hverahlíð lies in the lowlands southwest of Hengill and outside of the central volcano. Although there is no seismic evidence

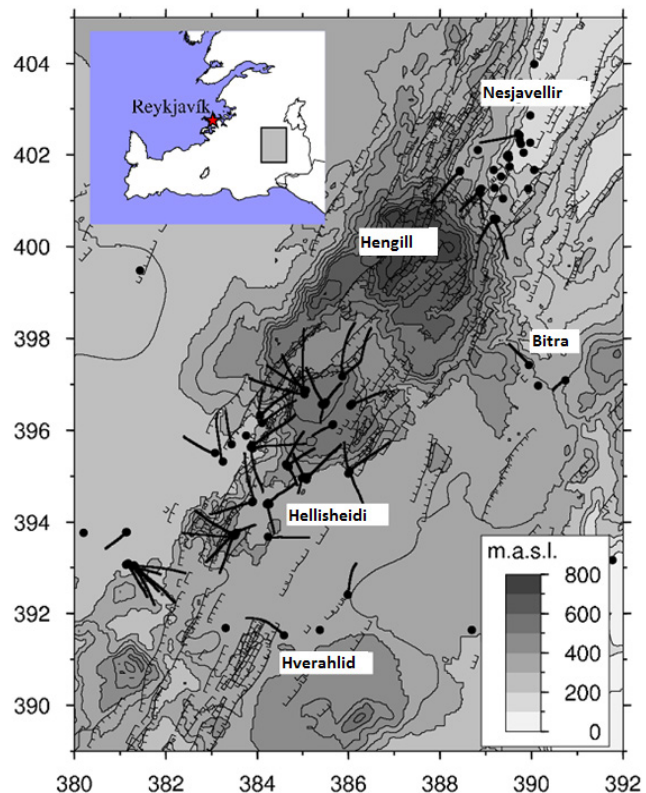


FIGURE 1: Location of Hverahlíð geothermal field; the NE-SW line are faults conforming to the Iceland neovolcanic zone that hosts high-temperature resources in the country (Gunnarsson et al., 2010)

of a magma chamber underlying the root of Hengill central volcano (Franzson et al, 2010), periodic injections of shallow crustal magma chambers or dyke swarms are thought to be the source of heat driving the system (Hardarson et al., 2010).

2.2 Hverahlíð geothermal field

Hverahlíð field is located southeast of Hengill volcano and associated with the NE-SW structures of the Hengill system. Surface manifestations are reported there (Níelsson and Franzson, 2010) and are manifested in a structure that is a few metres wide, stretching 400 m with a strike in a NE-SW direction. The first well drilled in this field, HE-21, was drilled to target structures feeding the surface manifestations. Injection tests, carried out later for this first well, induced micro-seismic events in the area to the west. Well HE-36 was sited 1 km west of Well HE-21 to test the structures to the west of the field. Other wells have been drilled to test various structures in the field. They are vertical and direction wells.

Information on the geology and subsurface mineral alteration obtained from the analysis of drill cuttings taken at 2 m intervals are considered in this section. Studies from well cuttings for Well HE-36 reveal the geology of Hverahlíð. It shows post glacial lavas are found at the top 100 m with a pillow basalt formation below that. Below the pillow basalts are tuffaceous formations extending to a depth of 450 m below sea level. Lava formations continue from the base of the tuffaceous formation to 1000 m b.s.l. This has been interpreted as the base of the Hengill volcano (Níelsson and Franzson 2010). There are intrusive bodies at depth that have been identified in the well cuttings. These are of basaltic and andesitic composition and they are identified from their compact nature and the alteration in their margins.

Permeable zones have been interpreted as occurring where there is a loss of circulation during drilling, from temperature logs and hydrothermal alteration mineralogy. Well HE-36 shows feed zones at 750-950 m b.s.l. (Níelsson and Franzson, 2010). Though pillow basalts are highly porous, they have rather poor permeability, especially when they are altered (Franzson et al., 2005).

Alteration mineralogy encountered in wells drilled in Hverahlíð show a suite of alteration from low-temperature zeolites to amphibole at high temperatures. Major alteration horizons are marked by the appearance of quartz at temperatures of 180°C, epidote at temperatures above 250°C and amphibole above 280°C. Comparison of alteration mineralogy with present day formation temperature reveal recent heating in some parts of the field as observed in temperature reversal with depth for Well HE-36.

From studies of the Hengill geothermal field, the wells discharge water of Na-Cl-HCO₃ composition with considerably low chloride content of below 200 ppm (Scott, 2011). The source of the fluids for Nesjavellir has been inferred to come from Langjökull glacier while that of Hellisheidi is from local precipitation from isotope studies (Mutonga et al., 2010). Waters from Nesjavellir and Hellisheidi plot mostly on the partial equilibrated waters on the Na-K-Mg ternary plot but within mature waters on a Cl-SO₄-HCO₃ ternary plot.

3. METHODS AND RESULTS

3.1 Sampling and analysis of geothermal water and steam

The samples from Hverahlíð used in this report were obtained from Wells HE-21, HE-36, HE-53 and HE-54. The sampling methods have been outlined in detail by Arnósson et al. (2006). Steam and water from two-phase well discharges were separated using a Webre separator. It is important that the separator is well insulated to prevent steam condensation. Pressure and/or temperature of separation need to be measured. Sampling of high enthalpy fluids poses a particular challenge due to the high

steam to water ratio and problems of steam condensation in the water phase. The water phase was cooled using a stainless steel coil. A liquid water phase, free of steam contamination, was collected by ensuring that there were no gas bubbles in the liquid after cooling.

The pH of the water phase was measured on site and samples for the determination of dissolved inorganic carbonate (DIC) were collected into air tight amber glass bottles for later determination in the laboratory. Samples for H₂S analysis were collected in a similar way for on-site analysis. Samples for determination of major cations including Si, B, Na, K, Mg, Ca, Al, and Fe were filtered through a 0.2 µm pore cellulose acetate membrane into high density polyethylene plastic bottles and acidified to 0.5% using Suprapur HNO₃. Samples for F and Cl determination were filtered as described above but not further treated. Samples for SO₄ analysis were also filtered as described above, followed by the addition of 2 ml of 0.2 M Zn-acetate in order to precipitate H₂S out of solution. A further sample for SiO₂ analyses was collected; this sample was not filtered and was diluted on site with deionized water at a 1:10 ratio.

Steam samples were collected into pre-evacuated gas bulbs containing 10-15 mL 50% KOH solution. During sampling, the gas-bulb was continuously cooled to condense the steam. In addition, H₂S and CO₂ were dissolved into the alkaline steam condensate whereas the other non-condensable gases including N₂, H₂, CH₄, Ar and O₂ were enriched in the gas phase.

The chemical analyses were carried out according to standard methods for geothermal fluid analysis. For the water phase, the H₂S concentration was determined on-site using Hg-acetate titration (Arnórsson et al., 2000; Arnórsson et al., 2006). Other chemical analyses were carried out in the laboratory. The pH was analysed using a combination glass electrode and the DIC concentration was determined using modified alkalinity titration (Arnórsson et al., 2000; Stefánsson et al., 2007) within 1-2 days of sampling. The major cations, Si, B, Na, K, Mg, Ca, Al, and Fe, were analysed using ICP-OES, whereas the major anions Cl and F were determined in filtered and untreated samples, SO₄ in filtered samples and Zn-acetate treated samples by using ion chromatography.

The concentration of H₂S and CO₂ in steam samples was analysed in the steam condensate using Hg-acetate and modified alkalinity titration, respectively (Arnórsson et al., 2000). The non-condensable gases were analysed using gas chromatography.

3.2 Calculation of aquifer fluid composition

Fluid composition was calculated beyond the level of boiling from the samples of two-phase well discharges collected at the surface. In addition, the fluid composition was simulated upon boiling and mixing from the parent aquifer fluids. These calculations were carried out using the WATCH program (Arnórsson et al., 1982; Bjarnasson, 2010). For these calculations, conservation of enthalpy and mass was assumed. For conservation of enthalpy we have:

$$h^t = Xh^v + (1 - X)h^l \quad (1)$$

and

$$X = \frac{h^t - h^l}{h^v - h^l} \quad (2)$$

Where h^t is the total enthalpy of the fluid, h^v is the enthalpy of the vapour phase, h^l is the enthalpy of the liquid water and X is the steam fraction.

Similarly, the conservation of mass for the i -th component may be defined:

$$m_i^t = X m_i^v + (1 - X) m_i^l \quad (3)$$

where m_i^t is the concentration of the i -th component in the total fluid, m_i^v is the concentration of the i -th component in the steam phase and m_i^l is the concentration of the i -th component in the liquid water phase.

For non-volatiles that do not enter into the steam phase upon boiling, m_i^v is equal to zero and the concentration in the total aquifer fluids becomes:

$$m_i^t = (1 - X)m_i^l \quad (4)$$

where X is the steam fraction of the discharge fluids at sampling.

For volatile components that only partition in the steam phase we have:

$$m_i^t = m_i^v x \quad (5)$$

Some components partition both in the water and the vapour phase. These are usually gases (CO_2 and H_2S). An equation for calculating the concentration of the two phases is given by:

$$D_s = \frac{n_v^s}{n_l^s} \quad (6)$$

where D_s is the distribution coefficient for water and steam phase, n_v^s is the molal concentration of the gas in the steam fractions and n_l^s is the molal concentration of the gas in the water fractions.

The calculations of aquifer fluid composition beyond the level of boiling require the selection of an aquifer temperature. In the present study, the aquifer temperatures were calculated assuming equilibrium with quartz, i.e. using the quartz geothermometry temperature. Alternatively, the measured temperatures of the producing aquifers may be used when available.

3.3 Aqueous speciation and mineral saturation

Aqueous speciation and mineral saturation were calculated with the aid of the WATCH program (Arnórsson et al., 1982; Bjarnasson, 2010).

The mineral saturation index (SI) is defined as the logarithm of the ratio of the reaction quotient (Q) to the equilibrium solubility (K) of a particular mineral reaction:

$$SI = \log(Q/K) \quad (7)$$

where Q is defined as the activity product of the respective water,

$$Q = \prod a_i^v \quad (8)$$

where a_i is the activity of the aqueous species to the stoichiometric power for the reaction. The stoichiometric power is negative for reactants and positive for products.

The three major mineral reactions considered in this study are silica, carbonate and anhydrite scaling. The dissolution for solid silica is defined according to:



The equilibrium constant for this reaction may be defined for various polymorphs of silica including amorphous silica, chalcedony and quartz (Gunnarsson and Arnórsson, 2000). The reaction quotient for the reaction is defined as:

$$Q = a_{\text{H}_4\text{SiO}_{4(aq)}} \quad (10)$$

For calcium carbonate, the dissolution is defined according to:



and the reaction quotient is defined as:

$$Q = aCa^{2+} aCO_3^{2-} \quad (12)$$

For anhydrite, the dissolution is defined according to:



and the reaction quotient is defined as:

$$Q = aCa^{2+} aSO_4^{2-} \quad (14)$$

The equilibrium solubility of calcite and anhydrite was taken from Arnórsson et al. (1982).

From the activities of the respective species and the mineral solubilities, the mineral saturation states may be determined. At equilibrium $SI = 0$, whereas if $SI > 0$, the fluids are supersaturated with respect to the mineral and if $SI < 0$ the fluids are undersaturated with respect to the mineral.

3.4 Boiling, mixing and mineral scaling

The potential calcite and silica scaling were assessed in this study along the production line from the data on aquifer fluids and well discharges. After the steam separation pressure for the field was chosen, the steam fraction at the separation pressure was obtained and used to calculate the liquid fraction. The discharge rate for each well was used to compute the water discharge rate after separation. The separated water was then boiled to 2 bars absolute and conductively cooled to 60°C. This water was subsequently diluted with condensate. The chemistry of the condensate was obtained from experience in the other fields of Nesjavellir and Hellisheidi in Hengill geothermal area. Mixing ratios for the separated water was done with the condensate from 90% separated water and 10% condensate to 30% separated water and 70% condensate. The mixture was then heated to 250°C to simulate re-injection. For each step the SI for amorphous silica, calcite and anhydrite were computed using the same method described above for amorphous quartz, but the SI for calcite and anhydrite was computed by the program using $\log K$ and $\log Q$.

Some analysis was done in the lab to measure the total concentration of the component in the solution. Another analysis was made of the active part of the component that was sensitive to the method applied. The components, however, for example C and Si in a geothermal fluid, can exist in several forms in solution which are $H_2CO_3^0$, HCO_3^- or CO_3^{2-} for carbon and $H_4SiO_4^0$, $H_3SiO_4^-$, and $NaH_3SiO_4^0$ for silica. The distribution of various species in a geothermal fluid is a function of pH, the ionic strength and redox potential of the fluid. As a result, care must be taken in the measurement of the pH as pH is a function of temperature for calculations in other temperatures. The sum of the ions of weak acids was taken to be constant at all temperatures (Arnórsson et al., 1982). The sum of the ions of weak acid can be used to derive the pH at a different temperature deduced from that of measured pH. The sum of weak acid used in this report was calculated as follows:

$$\sum weak\ acids = mOH^- + mH_3SiO_4^- + 2mH_2SiO_4^{2-} - mH_2BO_3^- + mHCO_3^- + 2mCO_3^{2-} + mHS^- + 2mS^{2-} \quad (15)$$

where m is the *molal* concentration of the charged species contributing to the weak acids in the fluid.

3.5 Results

3.5.1 Sampled fluid composition

The results of chemical analysis for Hverahlíð wells carried out in the lab are presented in Table 1. The waters show typical composition of high-temperature geothermal waters that have undergone boiling.

The pH is alkaline and major elements in the water phase include SiO₂, Na and Cl, whereas the major gases in the vapour phase include CO₂, H₂S and H₂.

3.5.2 Aquifer fluid calculations

The composition of deep aquifer fluid beyond the zone of boiling was calculated for individual wells based on the chemical composition of the water and vapour at the wellhead. The calculations were carried out with the aid of the WATCH speciation program. The temperatures were calculated assuming equilibrium with quartz, i.e. the quartz geothermometry temperatures were used, and deep liquid enthalpy was used to estimate possible aquifer steam fraction and aquifer vapour composition. The results are listed in Table 2. The aquifer fluids discharged by various wells at Hverahlíð show very similar composition for non-volatiles, including Na, Cl and SiO₂ with the expectation of Well HE-36 being much lower in SiO₂ than the other wells. However, the volatile concentration is somewhat variable. The main reason for this is considered to be the difficulties in calculating the exact mass of the aquifer vapour; the volatile concentrations are very sensitive to aquifer vapour fraction.

TABLE 1: Well discharge fluid composition of Hverahlíð geothermal field

Well	HE-36	HE-21	HE-54	HE-53
Well head pressure	19	25	30.2	35
Sample no.	08-5119	11-5096	11-5185	11-5062
Sampling pressure	7.2	5.1	18.8	8
Water (ppm)				
pH/°C	9.31/23	7.87/24	8.06/24	7.87/19
CO ₂	3.10	34	30.4	3.79
H ₂ S	77.4	6.63	21.6	15.6
B	0.863	2.13	1.22	1.30
SiO ₂	557	1035	964	1071
Na	220	276	245	266
K	33.8	65.4	65.7	66.0
Mg	0.030	0.019	0.007	0.001
Ca	2.03	0.596	0.569	0.513
F	1.48	0.965		0.833
Cl	252	448	378	430
SO ₄		6.49	3.26	3.80
Al	1.52	1.25	0.972	1.17
Fe	0.060	0.069	0.015	0.007
Vapour				
L gas/kg condensate			0.172	0.399
CO ₂ (ppm)	1572	4199	2966	1472
H ₂ S (ppm)	1180	355	792	630
H ₂ (%)			60.54	71.25
N ₂ (%)			38.75	26.40
CH ₄ (%)			0.70	0.52
O ₂ (%)				0.1

4. DISCUSSION

Utilization of geothermal fluids poses several challenges. Among these challenges is scaling. Scaling is the precipitation of minerals from the fluid which coat the surfaces inside equipment in geothermal installations, from the well bore casing inside the well, steam gathering systems, feeding separator stations, in separator stations and in pipes carrying separated water to reinjection wells. Scaling inside wells leads to a reduction in output of production wells; there may be a sharp decline or a gradual fall in output. Spent geothermal fluids are re-injected in many geothermal fields in the world today. Re-injection wells and the receiving aquifer may suffer scaling and mineral precipitation. The potential for scaling in geothermal fluid can be evaluated through speciation programs.

4.1 Scaling potential evaluation of Hverahlíð during production

Evaluation for scaling was taken in steps from production wells to reinjection. The processes that contribute to the processes of scaling that were looked at in this evaluation include adiabatic boiling and conductive cooling. For evaluation of scaling potential in production wells, stepwise adiabatic boiling

of individual well aquifer fluids was done. The boiling process assumed conservation of mass and enthalpy. At each temperature step, the solubility quotient of amorphous silica, calcite and anhydrite was obtained. Similarly, the solubility constant for the 3 minerals was obtained. The saturation index (SI) for each mineral was calculated according to Equation 7.

4.1.1 Amorphous silica saturation state

Evaluation for scaling was taken in steps from production wells to reinjection. The processes that contribute to the processes of scaling that were looked at in this evaluation include adiabatic boiling and conductive cooling. For evaluation of scaling potential in production wells, stepwise adiabatic boiling of individual well aquifer fluids was done. The boiling process assumed conservation of mass and enthalpy. At each temperature step, the solubility quotient of amorphous silica, calcite and anhydrite was obtained. Similarly, the solubility constant for the 3 minerals was obtained. The saturation index (SI) for each mineral was calculated according to Equation 7.

The saturation index of amorphous silica in production wells in Hverahlid is shown in Figure 2. In all cases, the fluids are undersaturated at aquifer conditions. The degree of undersaturation is, however, variable. It is lower in Well HE-36 compared with Wells HE-21, HE-53 and HE-54. Consequently, the fluids became amorphous silica saturated at a much lower temperature for Well HE-36 or at 122°C compared to the other three wells which became saturated with amorphous silica as follows: Well HE-21 at 198°C, Well HE-54 at 201°C and Well HE-53 at 204°C. In order to avoid amorphous silica saturation and prevent scaling, a separation temperature was chosen above these temperatures or at 205°C. This

TABLE 2: Aquifer fluid chemistry of Hverahlid geothermal field for wells

	HE-36	HE-21	HE-54	HE-53
Temperature (°C) (T^{qlz})	247	304	312	315
Liquid phase (ppm)				
pH	7.40	7.21	7.37	7.08
B	0.717	1.42	0.911	0.887
SiO ₂	463	692	721	729
Na	183	185	183	181
K	28.1	43.8	49.1	44.9
Mg	0.025	0.013	0.005	0.001
Ca	1.69	0.40	0.43	0.35
F	1.23	0.649		0.565
Cl	209	300	283	293
SO ₄		4.34	2.44	2.59
Al	1.26	0.838	0.727	0.794
Fe	0.050	0.046	0.011	0.005
CO ₂	44.6	204	160	76.4
H ₂ S	140	41.3	100	74.2
H ₂			0.13	0.37
O ₂			0	0.01
CH ₄			0.01	0.02
N ₂			1.02	1.62
Vapour phase (ppm)				
CO ₂	3672	6713	4327	1998
H ₂ S	2339	523	150	813
H ₂			13.2	33.2
O ₂				0.74
CH ₄			1.21	1.85
N ₂			118	171

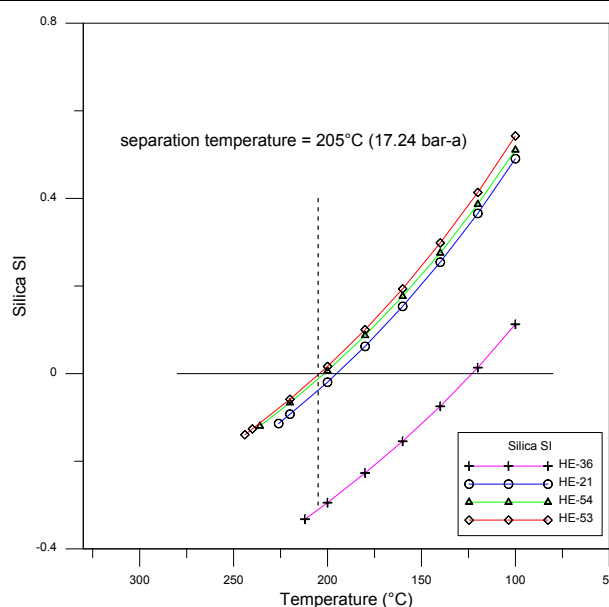


FIGURE 2: Amorphous silica scaling potential of Hverahlid production wells upon boiling of aquifer fluid

temperature corresponds to the liquid and steam pressure value of 17.24 bars absolute.

4.1.2 Calcite saturation state

The potential for calcite scaling was assessed in a similar manner as for amorphous silica. For these calculations CO_2 degassing was assumed to be at equilibrium or less, i.e. degassing coefficients of 0.1, 0.5 and 1.0 were used. The results are shown in Figure 3. Calcite exhibits retrograde solubility as the temperature of water rises. Boiling enhances the removal of CO_2 from solution. At the same time, the main acids CO_2 and H_2S enter the vapour phase and the resulting boiled water becomes alkaline. This results in an increase of HCO_3^- and CO_3^{2-} species concentration. The combination of these effects lead to calcite supersaturation upon boiling. However, extensive boiling eventually leads to calcite undersaturation.

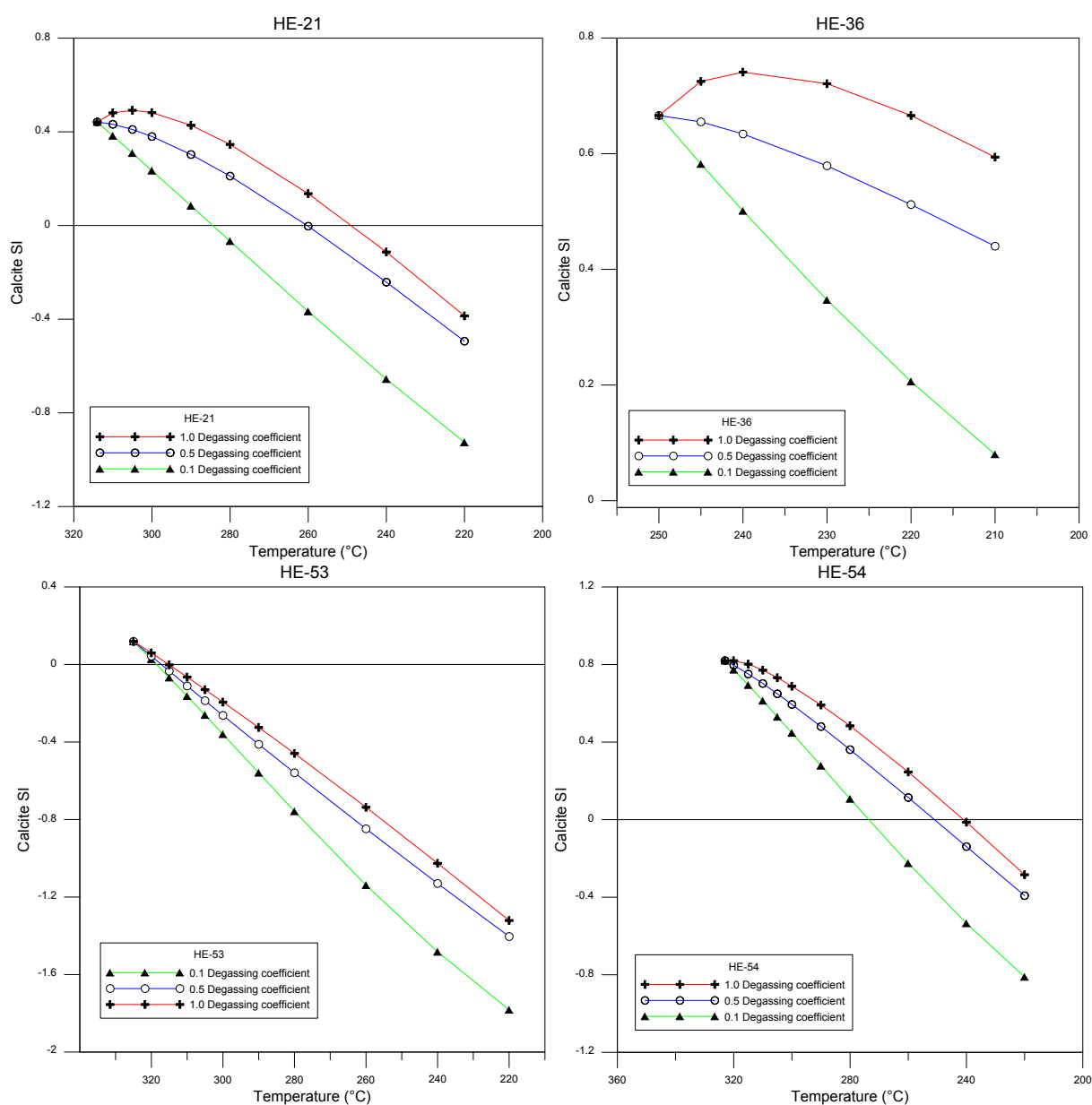


FIGURE 3: Calcite scaling potential of Hverahlíð production wells upon boiling of aquifer fluid

4.1.3 Anhydrite saturation state

All the wells considered for Hverahlid show anhydrite undersaturation with respect to the aquifer fluids and upon boiling. Anhydrite scaling in the production wells is, therefore, not considered a potential risk (Figure 4). The SI for anhydrite for Well HE-36 was not evaluated due to missing results for SO_4 analysis.

4.2 Mixing of production wells separated water

The composition of the separated water mixture was calculated based on the fluid discharge mass of each production well (Table 3). The steam fraction at the separation pressure for individual wells was subtracted from the total mass of the wells to obtain the water fraction. The water fractions from various wells was then added together to obtain the respective water mixture. The concentration of the various components in the mixture is given in Table 4. The pH for the mixture was modelled based on conservation of alkalinity. A model for the calculation of the pH for the separated well water mixture is shown in Figure 5.

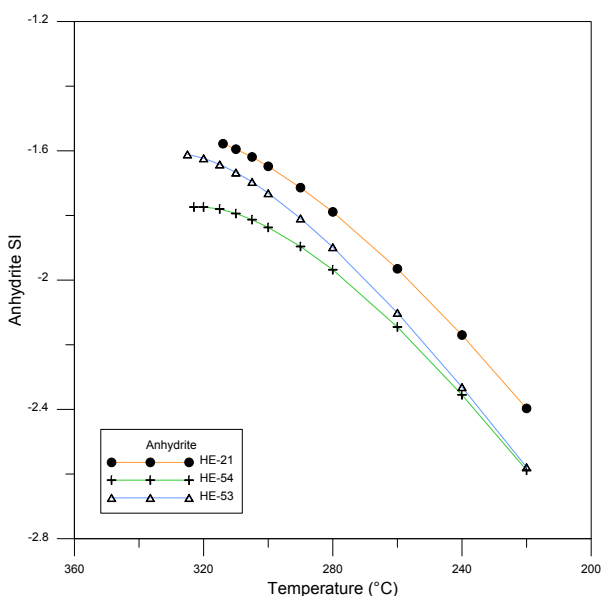


FIGURE 4: Anhydrite scaling potential in Hverahlid production wells upon boiling of aquifer fluid

TABLE 3: Well discharge characteristics of Hverahlid geothermal field

	HE-36	HE-21	HE-54	HE-53
Discharge Q (total) kg/s	22.9	59.5	85.1	46.5
Steam fraction separation (205°C/17.24 bar-a)	0.19	0.49	0.49	0.58
Water discharge (kg/s)	18.59	30.35	43.15	19.60

TABLE 4: Separated water composition in ppm

Water pH/T (°C)	7.15/ 205
B	1.33
SiO ₂	888
Na	239.7
K	57.5
Mg	0.01
Ca	0.76
F	0.60
Cl	365
SO ₄	3.5
Al	1.11
Fe	0.03
CO ₂	19.8
H ₂ S	34.5

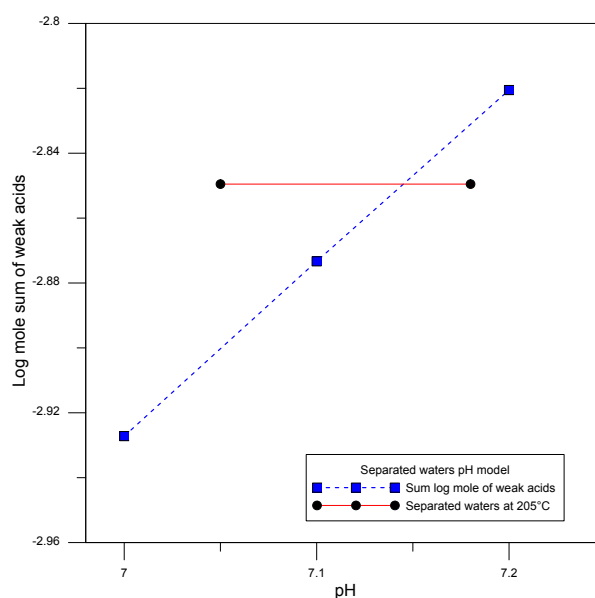


FIGURE 5: Log mole sum of weak acids calculated at 205°C at guessed pH values of 7, 7.1 and 7.2; Log mole sum of weak acids calculated for the separated water is fitted into this model to find the true pH of separated water

4.3 Scaling potential during reinjection

The fluid reinjection experience at Hengill area is that separated water reinjected at wells at high temperatures is more likely to cause scaling problems in the receiving aquifer, reducing its permeability due to silica scaling, than when reinjection is done for fluids at a lower temperature (Hardarson et al., 2010). As a result, the temperature of the separated waters was reduced through adiabatic boiling of the well mixture at 205°C. The separated water mixture at 17.24 bar-absolute was adiabatically boiled to 2 bar-a. The purpose of this was to maximise the usage of the heat from the water to run a possible low pressure turbine. The fluid was conductively cooled from 2 bar-a (Table 5) to 60°C. At each step of the two processes, scaling potential for all three minerals was evaluated. Figures 6, 7 and 8 show the saturation index of amorphous silica, calcite and anhydrite, respectively, upon boiling and conductive cooling.

TABLE 5: Separated water composition in ppm, adiabatically boiled to 120°C

Water pH/T (°C)	7.717/ 120
B	1.6
SiO ₂	1068
Na	288
K	69.1
Mg	0.012
Ca	0.91
F	0.7
Cl	439
SO ₄	4.16
Al	1.34
Fe	0.04
CO ₂	0.8
H ₂ S	4.7

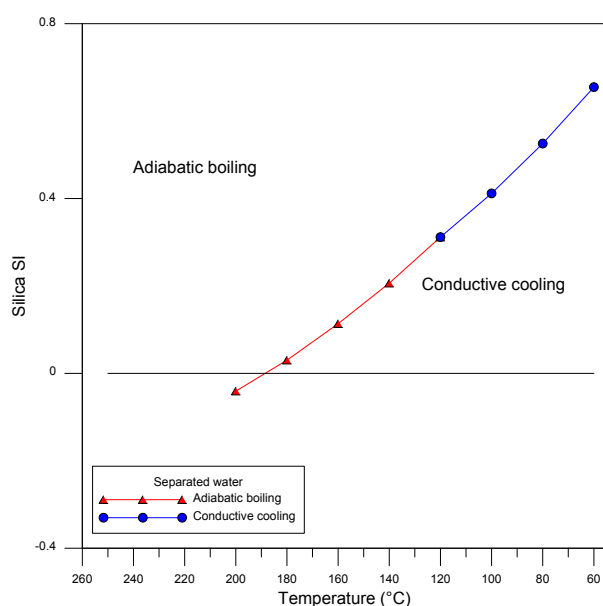


FIGURE 6: Amorphous silica saturation index of separated waters upon adiabatic boiling from 205°C to 120°C and subsequent conductive cooling to 60°C

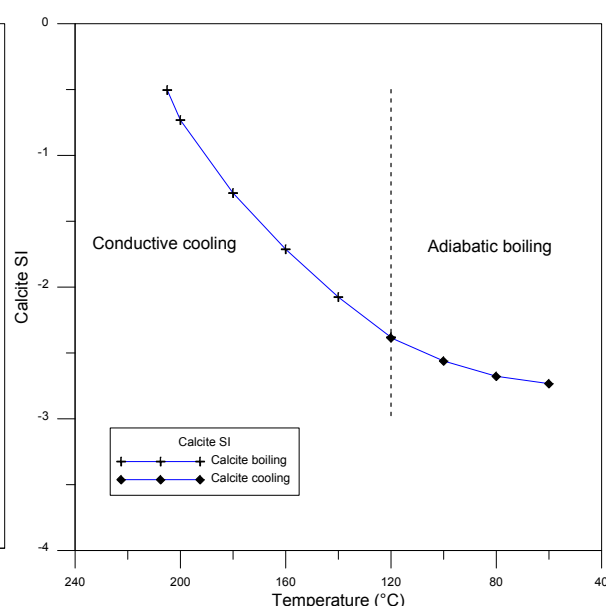


FIGURE 7: Calcite saturation index of separated waters upon adiabatic boiling from 205°C to 120°C and subsequent conductive cooling to 60°C

4.4 Dilution of separated water with condensate

To prevent possible scaling upon re-injection, steam condensate and separation water may be mixed with waste water. Condensate was added to the separated water mixture at various ratios. This was done at 7 ratios as follows: 90% separated water 10% condensate, to 30% separated water 70% condensate. The composition for each of the mixtures was then computed based on the ratio of the separated water to the condensate as described for the mixture after separation. The condensate essentially is steam condensed after expansion in the turbine and consequent cooling in the condenser and cooling tower in geothermal power stations and has no non-volatile components dissolved in it except for condensable gases (CO₂ and H₂S) at 1 ppm. The pH of each of the mixtures was then modelled as described above for separated water from production wells (Figure 9). Table 6 shows the

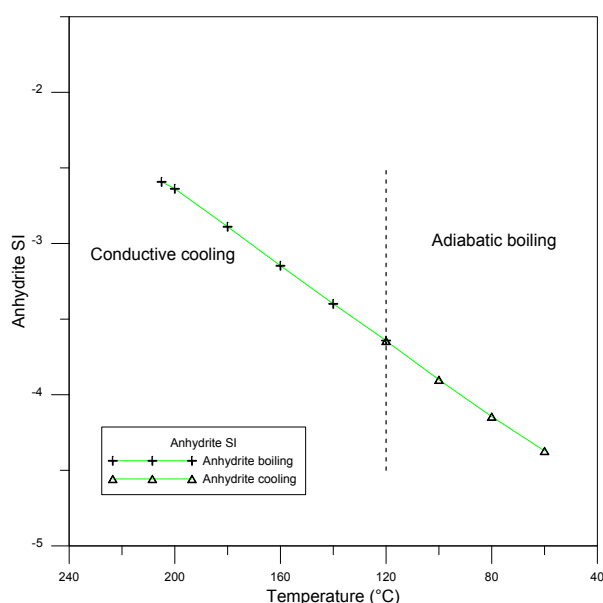


FIGURE 8: Anhydrite saturation index of separated waters upon adiabatic boiling from 205°C to 120°C and subsequent conductive cooling to 60°C

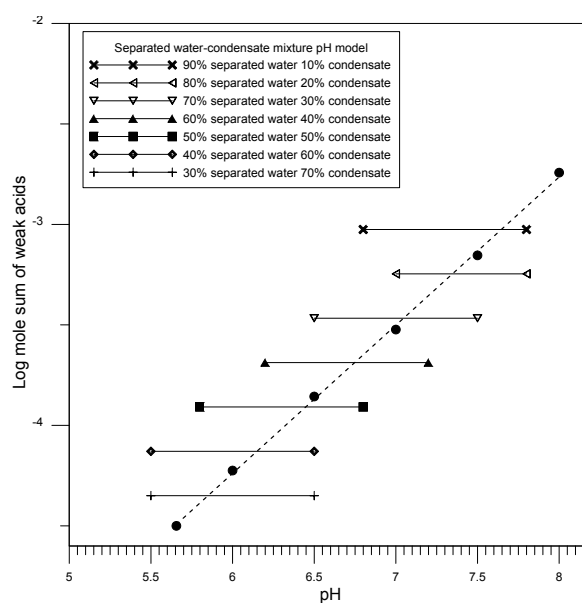


FIGURE 9: Log mole sum of weak acids calculated for separated waters-condensate mixture at 25°C with fits of actual sum log mole of weak acids for the mixture at various ratios

composition of the condensate-separated water at various ratios. The change in the saturation index of the minerals in the fluid upon mixing the separated water with condensate at the various ratios was evaluated. Figures 10, 11 and 12 show the saturation index of amorphous silica, calcite and anhydrite, respectively, upon this dilution.

TABLE 6: Separated water-condensate mixture composition at various mixing ratios in ppm

Separated water-condensate mixture	90% brine 10%cond.	80% brine 20%cond.	70% brine 30%cond.	60% brine 40%cond.	50% brine 50%cond.	40% brine 60%cond.	30% brine 70%cond.
pH/T (°C)	7.63/25	7.33/25	7.04/25	6.74/25	6.45/25	6.15/25	5.86/25
T _{Mixture} (°C)	94.5	89	83.5	78	72.5	67	61.5
B	1.44	1.28	1.12	0.96	0.80	0.64	0.48
SiO ₂	961	854	748	641	534	427	320
Na	260	231	202	173	144	115	86
K	62.2	55.3	48.4	41.5	34.6	27.6	20.7
Mg	0.01	0.01	0.008	0.007	0.006	0.005	0.004
Ca	0.82	0.73	0.64	0.55	0.46	0.36	0.24
F	0.65	0.58	0.51	0.43	0.36	0.29	0.22
Cl	395	351	307	263	220	176	133
SO ₄	3.7	3.3	2.9	2.5	2.1	1.7	1.2
Al	1.2	1.1	0.9	0.8	0.7	0.5	0.4
Fe	0.03	0.03	0.03	0.02	0.02	0.01	0.01
CO ₂	0.82	0.84	0.86	0.88	0.9	0.92	0.94
H ₂ S	4.34	3.97	3.60	3.23	2.86	2.48	2.11

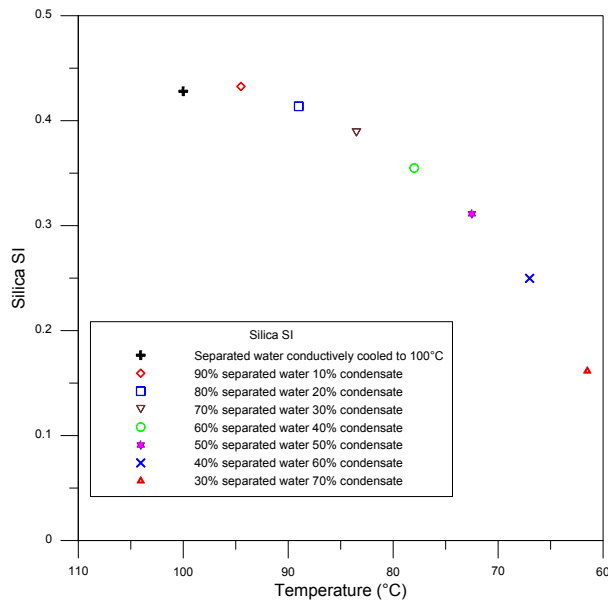


FIGURE 10: Amorphous silica saturation index of separated water after conductive cooling to 100°C and mixing with condensate at 45°C at various ratios of separated water to condensate

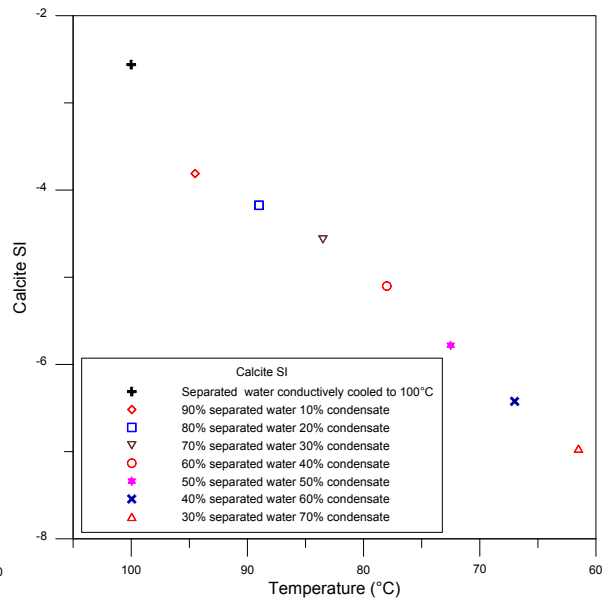


FIGURE 11: Calcite saturation index of separated water after conductive cooling to 100°C and mixing with condensate at 45°C at various ratios of separated water to condensate

4.5 Mineral saturation state in reinjection aquifer

To simulate for reinjection, the condensate separated water mixture was heated in steps of 25°C up to 250°C to simulate reinjection reservoir conditions. The calculations were carried out with the aid of the WATCH program (Bjarnason, 2010). Generally, calcite and anhydrite were undersaturated in the condensate mixture throughout and in the reinjection wells and with subsequent heating to 250°C (Figures 13 and 14). However, amorphous silica was found to be supersaturated at temperatures below 100-200°C, depending on the separated water to condensed steam mixing ratio (Figure 15).

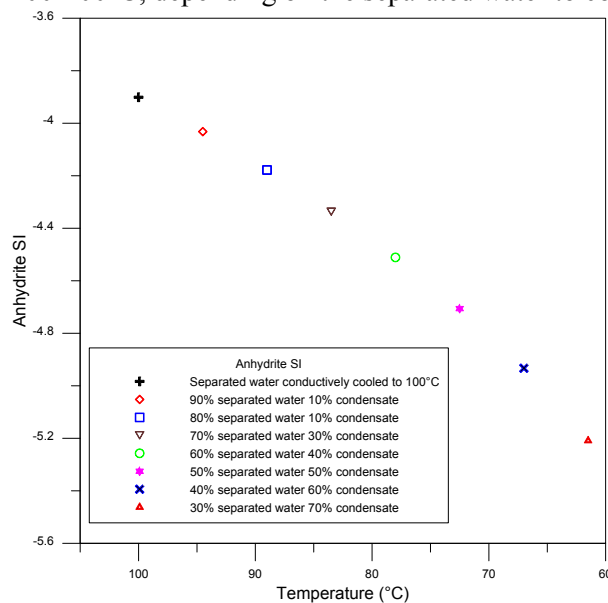


FIGURE 12: Anhydrite saturation index of separated water after conductive cooling to 100°C and mixing with condensate at 45°C at various ratios of separated water to condensate

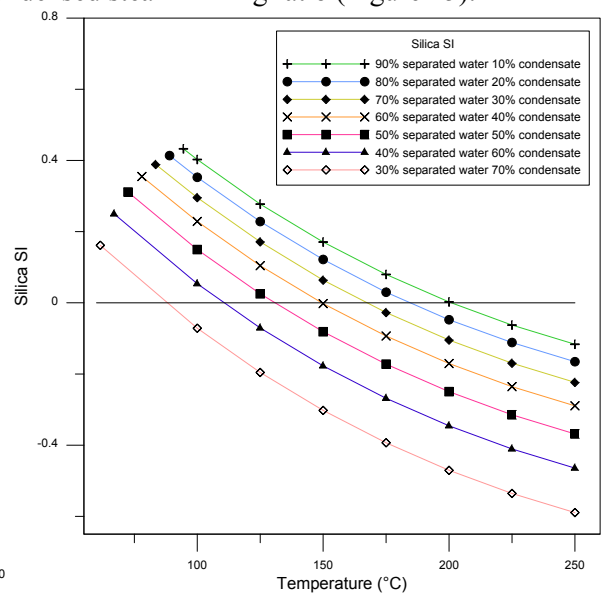


FIGURE 13: Amorphous silica saturation index of separated water-condensate mixture heated to 250°C to simulate heating at reinjection aquifer

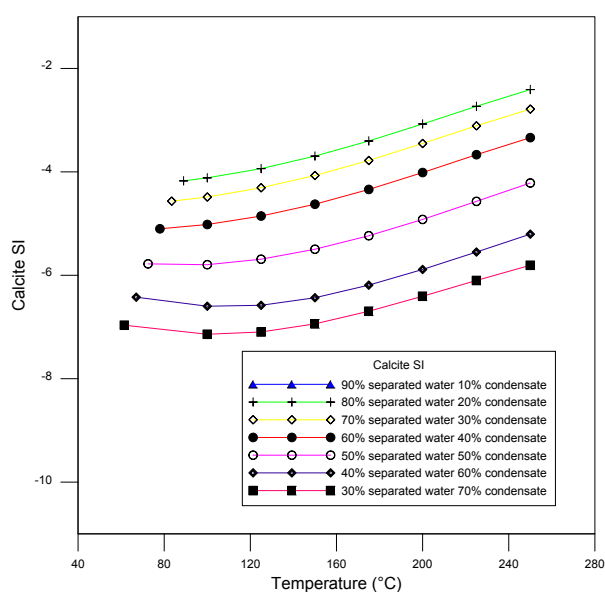


FIGURE 14: Calcite saturation index of separated water-condensate mixture heated to 250°C to simulate heating at reinjection aquifer

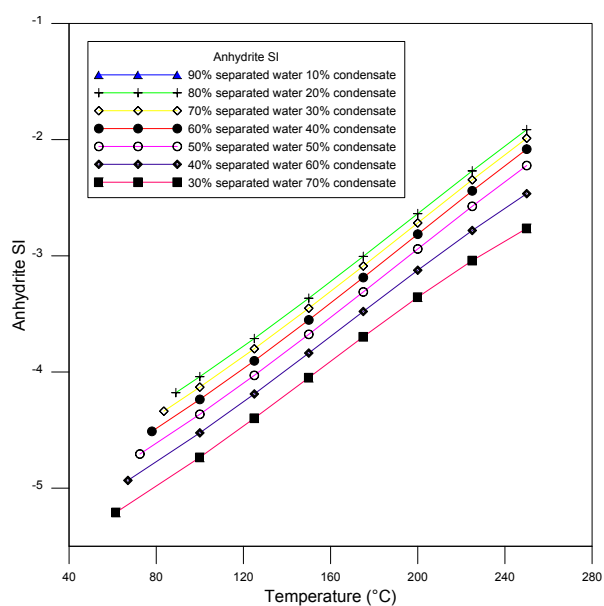


FIGURE 15: Anhydrite saturation index of separated water-condensate mixture heated to 250°C to simulate heating at reinjection aquifer

4.6 Summary

In summary, of greatest concern is silica scaling since it has the potential to occur in all the cases considered from production wells, separated water mixing and in reinjection. Figure 16 gives a summary of the silica saturation index at the various stages during utilization of the Hverahlid fluids for the wells that were considered for this study.

Fluids with high dilution ratios of steam condensate were found to be less supersaturated than less steam diluted separated water.

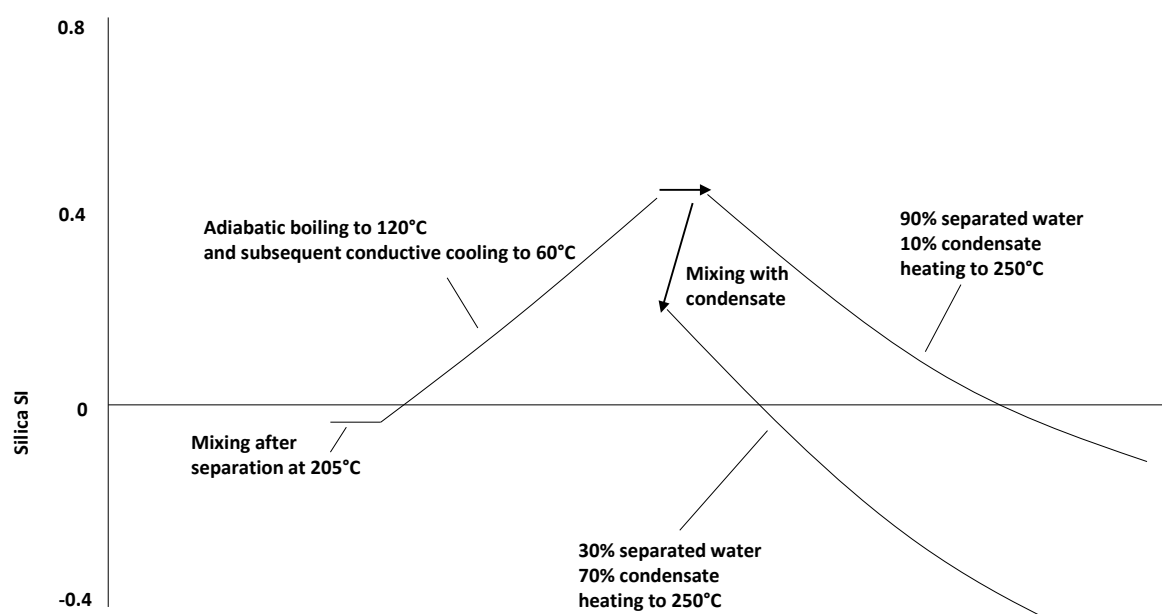


FIGURE 16: Silica saturation index of Hverahlid high-temperature geothermal field from production wells, mixing of separated well fluids, utilization, dilution with condensate and reinjection

5. CONCLUSIONS

- Amorphous silica oversaturation was attained for the geothermal separated waters for Hverahlid wells considered in this study. Steps should be taken to avoid silica scaling on surface installations upon use of the fluids after separation.
- There is a potential for downhole calcite scaling for Wells HE-21, HE-54 and HE-53. Monitoring for calcite scaling for the wells during production should be considered.
- There is no danger posed by anhydride scaling for any of the wells considered.
- The best reinjection composition for spent geothermal fluids is the composition of 30% separated water and 70% condensate. However, this may prove a challenge considering the availability of condensate water to meet the mixing ratio.

ACKNOWLEDGEMENTS

I would like to thank the Government of Iceland and the United Nations University Geothermal Training Programme for giving me a scholarship to take part in the six months course. I would also like to thank KenGen for granting me a six months study leave to undertake this training.

I am greatly indebted to Dr. Ingvar Birgir Fridleifsson, former UNU-GTP director, and current director, Mr. Lúdvík S. Georgsson, for their guidance and their time during the training. I would like to thank all the lecturers of UNU-GTP for sharing their knowledge throughout the training period. My warmest regards go to Mr. Markús A.G. Wilde, Mr. Ingimar G. Haraldson and Ms. Málfríður Ómarsdóttir for making the six months a great learning experience. To Ms. Thórhildur Ísberg, thank you for welcoming me to Iceland and making sure that my stay here in Iceland was ok. To Ms. Rósa S. Jónsdóttir, thank you for availing study material in time whenever I needed them. I would also like to thank the UNU class of 2013 fellows for sharing your knowledge and experience during the course of the six months training.

To my supervisors Dr. Andri Stefánsson of the University of Iceland and Mr. Ingvi Gunnarsson of Reykjavik Energy, thanks for your patience and taking your time to guide me throughout the project period. Your comments and shared knowledge are greatly appreciated.

I would like to give thanks to my family and my mum for keeping contact through calls to check up on me and their patience while I was away. I would like to thank God for his grace and blessings upon my life.

REFERENCES

- Ágústsson, K., and Flóvenz, Ó.G., 2005: The thickness of the seismogenic crust in Iceland and its implications for geothermal systems. *Proceedings of the World Geothermal Congress 2005, Antalya, Turkey*.
- Arnórsson, S., D'Amore, F., and Gerardo-Abaya, J., 2000: Isotopic and chemical techniques in geothermal exploration, development and use. In: Arnórsson, S. (ed.), *Isotopic and chemical techniques in geothermal exploration, development and use. Sampling methods, data handling, interpretation*. International Atomic Energy Agency, Vienna, 351 pp.

- Arnórsson, S., Bjarnason, J.Ö., Giroud, N., Gunnarsson, I., and Stefánsson, A., 2006: Sampling and analysis of geothermal fluids. *Geofluids*, 6, 203-216.
- Arnórsson, S., Sigurdsson, S., and Svavarsson, H., 1982: The chemistry of geothermal waters in Iceland I. Calculation of aqueous speciation from 0°C to 370°C. *Geochim. Cosmochim. Acta*, 46, 1513-1532.
- Bjarnason, J.Ö., 2010: *The speciation program WATCH, Version 2.4, user's guide*. The Iceland Water Chemistry Group, Reykjavík, 9 pp.
- Bohlmann, E.G., Mesmer, R.E., and Berlinski, P., 1980: Kinetics of silica deposition from simulated geothermal brines. *Soc. Pet. Eng. J.*, 20, 239-248.
- Brown, K.L., 2011: Thermodynamics and kinetics of silica scaling. *Proceedings of the International Workshop on Mineral Scaling 2011, Manila, Philippines*, 1-8.
- Fournier, R.O., 1982: A method of calculating quartz solubilities in aqueous sodium chloride solutions. *Geochim. Cosmochim. Acta*, 47, 579-586.
- Franzson, H., Gunnlaugsson, E., Árnason, K., Saemundsson, K., Steingrímsson, B., and Hardarson, B.S., 2010: The Hengill geothermal system, conceptual model and thermal evolution. *Proceedings of the World Geothermal Congress 2010, Bali, Indonesia*, 9 pp.
- Franzson, H., Kristjánsson, B.R., Gunnarsson, G., Björnsson, G., Hjartarson, A., Steingrímsson, B., Gunnlaugsson, E., and Gíslason G., 2005: The Hengill Hellisheidi geothermal field. Development of a conceptual geothermal model. *Proceedings of the World Geothermal Congress 2005, Antalya, Turkey*, 7 pp.
- Gallup, D.L., 2011: pH modification scale control technology. *Proceedings of the International Workshop on Mineral Scaling 2011, Manila, Philippines*, 39-46.
- Giggenbach, W.F., 1980: Geothermal gas equilibria. *Geochim. Cosmochim. Acta*, 44, 2021-2032.
- Giggenbach, W.F., 1981: Geothermal mineral equilibria. *Geochim. Cosmochim. Acta*, 45, 393-410.
- Gunnarsson, I., and Arnórsson, S., 2000: Amorphous silica solubility and the thermodynamic properties of $\text{H}_4\text{SiO}_4^\circ$ in the range of 0° to 350°C at P_{sat} . *Geochim. Cosmochim. Acta*, 64, 2295-2307.
- Gunnarsson, I., and Arnórsson, S., 2005: Impact of silica scaling on the efficiency of heat extraction from high-temperature geothermal fluids. *Geothermics*, 34, 320-329.
- Gunnarsson, I., Ívarsson, G., Sigfússon, B., Thrastarson, E.Ö., and Gíslason, G., 2010: Reducing silica deposition potential in waste waters from Nesjavellir and Hellisheidi power plants, Iceland. *Proceedings of the World Geothermal Congress 2010, Bali, Indonesia*, 5 pp.
- Hardarson B.S., Einarsson G.M., Franzson H., and Gunnlaugsson, E., 2009: Volcano-tectonic-geothermal interaction at the Hengill triple junction, SW Iceland. *GRC Transactions*, 33, 49-54.
- Hardarson, B.S., Einarsson, G.E., Kristjánsson, B.R., Gunnarsson, G., Helgadóttir, H.M., Franzson, H., Árnason, K., Ágústsson, K., and Gunnlaugsson, E., 2010: Geothermal reinjection at the Hengill Triple junction, SW Iceland. *Proceedings of the World Geothermal Congress, Bali, Indonesia*, 7 pp.
- Mroczek, E.K., and Graham, D.J., 2001: Calcite scaling field experiments to 120°C at Wairakei. *Proceedings of the 23rd New Zealand Geothermal Workshop, Auckland, NZ*, 33-37.

Mutonga, M.W., Sveinbjörnsdóttir, Á., Gíslason, G., and Ármannsson, H., 2010: The isotopic characteristics of geothermal fluids in Hengill area, SW-Iceland (Hellisheidi, Hveragerdi and Nesjavellir fields). *Proceedings of the World Geothermal Congress 2010, Bali, Indonesia*, 13 pp.

Ngothai, Y., Yanagisawa, N., Pring, A., Rose, P., O'Neill, B., and Brugger, J., 2010: Mineral scaling in geothermal fields: A review. *Proceedings of the Australian Geothermal Conference 2010, Adelaide*, 5 pp.

Nielsson S., and Franzson H, 2010: Geology and hydrothermal alteration of the Hverahlid HT-system, SW-Iceland. *Proceedings of the World Geothermal Congress 2010, Bali, Indonesia*, 6 pp.

Scott, S.W., 2011: *Gas chemistry of the Hellisheidi geothermal field*. REYST / University of Iceland, Faculty of Science, MSc thesis, 81 pp.

Stefánsson, A., Gunnarsson, I., and Giroud, N., 2007: New methods for the direct determination of dissolved inorganic, organic and total carbon in natural waters by Reagent-Free™ ion chromatography and inductively coupled plasma atomic emission spectrometry. *Analytical ChimicaActa*, 582, 69-72.



UNITED NATIONS
UNIVERSITY

GEOTHERMAL TRAINING PROGRAMME
Orkustofnun, Grensasvegur 9,
IS-108 Reykjavik, Iceland

Reports 2013
Number 9

DIRECT USE OF GEOTHERMAL ENERGY IN MENENGAI, KENYA: PROPOSED GEOTHERMAL SPA AND CROP DRYING

Samuel Kinyanjui

Geothermal Development Company

P.O. Box 100746 Nairobi 00101

KENYA

skinyanjui@gdc.co.ke, samuelkinyanjui@gmail.com

ABSTRACT

Direct use of geothermal heat as an energy source has significant economic and environmental benefits. Its use increases the utilisation efficiency of geothermal resources compared to electricity generation only. The use of geothermal heat in Menengai, Kenya, for bathing and drying of agricultural crops is proposed in this report. A geothermal spa of 2800 m² in water surface area, requiring 35 kg/s of geothermal flow is designed. Three location scenarios of the lagoon in Menengai field are evaluated with regard to pipeline cost. Conventionally heated swimming pools including an outdoor pool, indoor pool, steam room, wading pool and three hot tubs with a total water surface of 700 m² utilising 55 kg/s of 130°C geothermal fluid are analysed.

Utilisation of geothermal heat for drying is demonstrated through the design of a 30 m³ mobile grain crop dryer comprised of a drying chamber, water-air heat exchanger and a blower. For air re-circulation purposes, a diversion valve from the tunnel to the bed dryer is provided for. The dryer requires 2 kg/s of 130°C geothermal water and has a capacity of 3 ton/hr of grains.

1. INTRODUCTION

Direct use of geothermal hot water as an energy source has significant economic and greenhouse gas emission benefits and also reduces the demand for electricity. Geothermal heat has been utilized since ancient times, mainly for bathing purposes. In Kenya, direct use has been on a relatively small scale, primarily in heating greenhouses, crop drying and bathing. In recent years, the government of Kenya has given more priority to the development of the geothermal resources in Kenya, and Menengai is one of the fields under development.

Menengai geothermal field is a high-temperature field located along the Kenya Rift valley, north of Lake Nakuru and south of Lake Bogoria. The Geothermal Development Company (GDC) has been carrying out drilling activities in the field and the first well, MW-01, successfully discharged in May 2011. The field is characterised by an elliptical caldera of 11.5 km in major axis (Kipng'ok, 2012), mainly covered by volcanic rocks which erupted from centres associated with the Menengai volcano. The field is in Nakuru, the fourth largest town in Kenya and a major agricultural centre in the country.

The agricultural sector is the largest contributor to the country's GDP. It accounts for 24% of the country's GDP (FAO, 2011) with seventy five per cent of the population directly or indirectly employed in this sector (Government of the Republic of Kenya, 2013). The food crops subsector contributes up to 32% of the agricultural GDP, with maize crops contributing about 15%. The other subsectors are industrial crops, horticulture, livestock and fisheries. Sixty five per cent of the total agricultural export is coffee and tea as the principal exports (KNBS, 2008). Flowers and horticultural products are also important foreign exchange income.

Drying of maize, tea and vegetables is done for storage purposes. The government of Kenya, through the National Cereals and Produce Board in Nakuru, dries maize in silo bins using diesel while tea is dried in major tea factories using wood or diesel. Coffee seeds have been majorly dried in the sun.

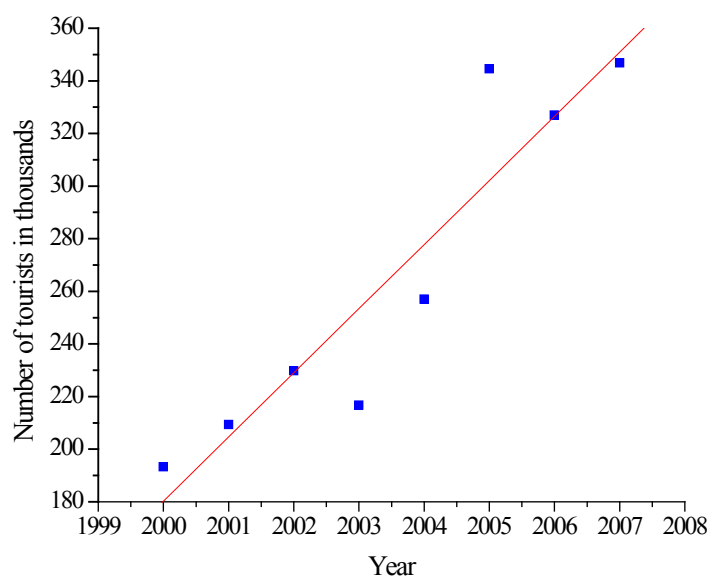


FIGURE 1: Tourists visiting Lake Nakuru
(Source: Ministry of tourism, 2010)

Tourism is the third largest contributor to the country's GDP after agriculture and manufacturing, providing 10% of the country's GDP (KNBS, 2008). The main tourist attractions are the country's world renowned national parks and beaches. Lake Nakuru, which is near Menengai geothermal field, is also a major tourist site, hosting over 300,000 foreign tourists annually, as shown in Figure 1.

Menengai caldera and Lake Nakuru National Park are the major tourist attraction sites in Nakuru County. The caldera peak offers a panoramic view of the surrounding areas including Nakuru Town. Lake Nakuru, a Ramsar site, located a few kilometres south of the Caldera, is famous for being the first successful Rhino Sanctuary in Kenya and

a habitat for flamingos. There is a potential to package Lake Nakuru National Park together with the Menengai caldera and Lord Egerton Fort as tourist attraction sites under an ecotourism project. Menengai caldera is already attracting many local and foreign non-paying visitors.

The possibilities for direct utilization around Menengai are diverse and depend to a large extent on the economic activities in the area. Crop drying and bathing are some of the potential applications.

The aim of this project is twofold:

- 1) To propose a design for a geothermal spa in Menengai; and
- 2) To evaluate the use of geothermal heat in drying agricultural crops and to design a pilot grain dryer.

2. GEOTHERMAL SPAS AND SWIMMING POOLS

2.1 Background

Bathing is one of the earliest known uses of geothermal heat. Bathing in geothermal water is not only known to be a recreational activity today, but has therapeutic effects on the human body. Relaxation and stress relief, cleansing, socialization and musculoskeletal disorders are among the many factors as

to why millions of people around the world visit and enjoy the benefits of hot water in spas. Apart from offering these benefits, the spa is also a viable business venture.

Other health benefits derived from bathing in geothermal water include treatment of high blood pressure, skin diseases, diseases of the nervous system and relieving the symptoms of rheumatism. The mineral composition of geothermal waters, especially silica, has also been proven to have considerable healing effects for psoriasis skin disease (Pétursdóttir and Kristjánsson, 1995). Different guests visit and take baths in public bathing places and meet others from different quotas, hence enriching their social lives.

Steam baths and saunas have also been designed to utilize geothermal fluids. Relaxing in these facilities is associated with enormous health benefits including:

- Improved blood circulation;
- Cleaning and rejuvenating the skin;
- Eased muscle tension;
- Promotes feeling of relaxation and well-being; and
- Enhances detoxification processes.

The use of geothermal energy to heat swimming pools is a common practice, especially in cold countries such as Iceland where over 90% of the swimming pools are geothermally heated all year round (Orkustofnun, 2013).

2.2 Icelandic Blue Lagoon and Olkaria geothermal spa

The Icelandic Blue Lagoon, located in Svartsengi geothermal field, has an average temperature of 37°C, pH 7.5 and about 2.5% salinity (Pétursdóttir and Kristjánsson, 1995). It was gradually formed as an accident from disposed geothermal water. Currently, it gets the geothermal water from reservoirs with temperatures of 240°C in Svartsengi geothermal field, composed of 65% sea water and 35% fresh water (Ólafsson and Sigurgeirsson, 2003). The lagoon covers a water surface area of 4000 m² and the brine at 150°C flows at a rate of 40 l/s. It has a health clinic and, in total, the lagoon receives over 500,000 guests a year (internal communication).

In Olkaria field, a recently constructed geothermal spa utilises brine from a re-injection pipeline. It is comprised of two interconnected lagoons for cooling and flow regulation, a main bathing lagoon, 70 m in diameter, and a fourth children's pond, 10 m wide. The brine temperature is maintained at 30-35°C (Mangi, 2012) in the bathing pond.

The Mývatn baths in north Iceland utilise geothermal water from shallow wells. The water is cooled in a tank and then flows by gravity to the bathing lagoon. The temperature is regulated and maintained at 37°C. The baths cover a surface area of 2000 m² and are supplied by hot geothermal water at 15-20 l/s.

2.3 Proposed geothermal spa in Menengai

2.3.1 Source of geothermal water

The source of geothermal water for bathing in the spa is considered to be Well MW-03 which has a low wellhead pressure and a flow rate of 16 kg/s (GDC, 2013). Utilizing brine from Well MW-01 is also a possibility or from central separators in the future.

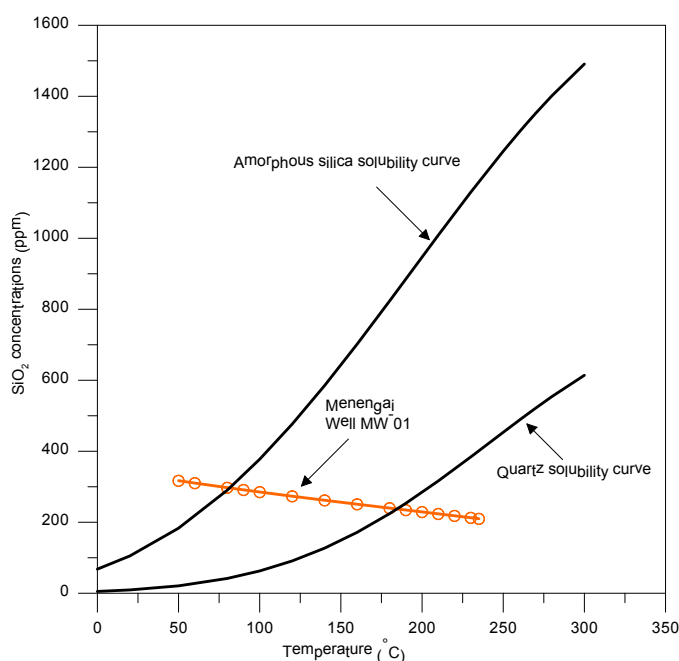


FIGURE 2: Silica concentrations in Well MW-01 during one step adiabatic boiling (Kipng'ok, 2011)

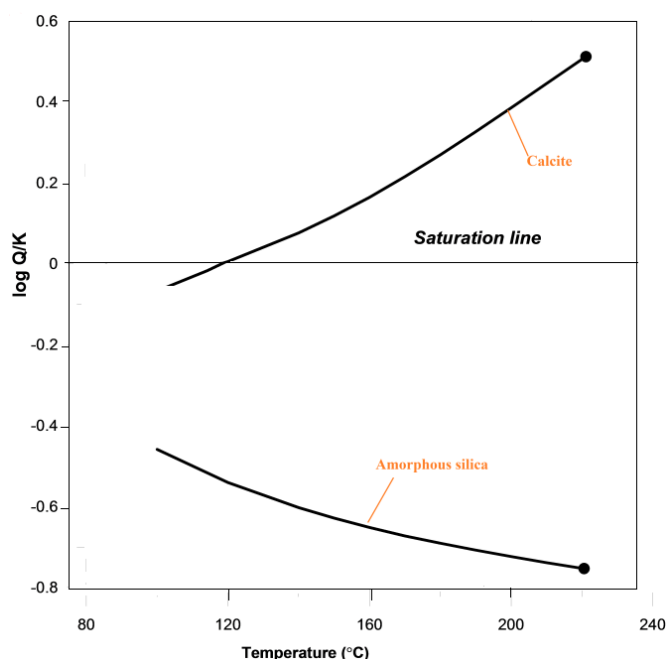


FIGURE 3: Calcite and amorphous silica saturation state during one step adiabatic boiling of Well MW-03 (GDC, 2013)

Menengai field are considered in this report, as shown in Figure 4: locations A, B and C. The hot water delivery pipeline, cooling pond, main bathing pond and the pumping pond are designed for the three scenarios. The pipeline design and pumping for both the brine supply and the re-injection pipelines are evaluated for the different scenarios.

The sizes of the ponds are the same for all three scenarios.

The assumptions made are:

2.3.2 Silica scaling

Silica scaling is a universal challenge in the exploitation of geothermal fields producing brines and has largely inhibited the use of waste heat from discharge waters in these fields (Jamieson, 1984).

The solubility of silica decreases with a decrease in temperature. As opposed to carbonate, silica deposition is controlled by kinetics and can begin on the surface in several minutes or hours after reaching super saturation (Kashpura and Potapov, 2000). Similarly, silica scales are harder to remove mechanically.

Results based on Well MW-01 (Kipng'ok, 2011) indicate that amorphous silica precipitation will not occur until it is cooled below 88°C (Figure 2). If the temperature of the transported brine in the pipeline is maintained above this amorphous silica saturation temperature, then problems of silica scaling are avoided.

Analysis done on Well MW-03 (GDC, 2013) indicate that the water is under saturated with respect to amorphous silica even at lower temperatures, and there is no calcite scaling for temperatures below 120°C (Figure 3). Chemical analyses for Well MW-03, carried out in October 2012 at ambient temperature, indicate a fluid pH of 8.6 and a silica concentration of 362 mg/kg (Table 1).

Calcite deposition is predicted to occur, in minimal amounts only, according to chemical analysis and interpretation done on Well MW-03 (GDC, 2013).

2.3.3 Location of the geothermal spa in the field

Three location scenarios for the spa in the field are considered in this report, as shown in Figure 4: locations A, B and C. The hot water delivery pipeline, cooling pond, main bathing pond and the pumping pond are designed for the three scenarios. The pipeline design and pumping for both the brine supply and the re-injection pipelines are evaluated for the different scenarios.

- The source of the geothermal fluid is assumed to be from Well MW-03 and no pumping will be required to supply the geothermal water to the spa;
- For all the scenarios, the re-injection point is near Well MW-02; and
- The cost of the pipes used is estimated from prevailing market prices in Kenya.

TABLE 1: Chemicals results for Well MW-03 carried out in October 2013 at 20°C (GDC, 2013)

Parameter	Value	Unit
pH	8.6	
SiO ₂	362	mg/kg
TDS	6580	ppm
WHP	0.7	bar-g

Scenario A:

The spa is located at point A (Figure 4). This is approximately 3 km from the cold water pump site, near the main entrance to the field. The proposal for this location is based on the fact that this is close to the main entrance and, therefore, convenient for visitors to the spa. The area is fairly flat and has ample space to accommodate the bathing facilities envisaged.

Scenario B:

Under this scenario, the bathing lagoon is located at point B near the caldera rim next to the road exiting into Kabarak, about 1.5 km away from Well MW-01. This location provides a relatively good view of the crater and the caldera. The location has lava outcrops on the surface, creating a more serene and natural atmosphere. This location has about 3000–4000 m² of relatively flat surface area available.

Scenario C:

The bathing lagoon is located at point C, about 1 km away from Well MW-02. Since the assumed re-injection point is at Well MW-02 then there is no requirement for a brine supply pipeline, should the spa get its supply from the separated brine. A provision for tee-off along the brine pipeline is sufficient. However in this design, a supply pipeline route is considered from Well MW-03.

An area of 7000 m² is proposed for the spa, including the changing rooms, shopping space, restaurant and parking area.

The X and Y co-ordinates indicated in Table 2 are generated from an AutoCAD map used in the distance transform method to calculate the pipe length and the best possible pipeline route.

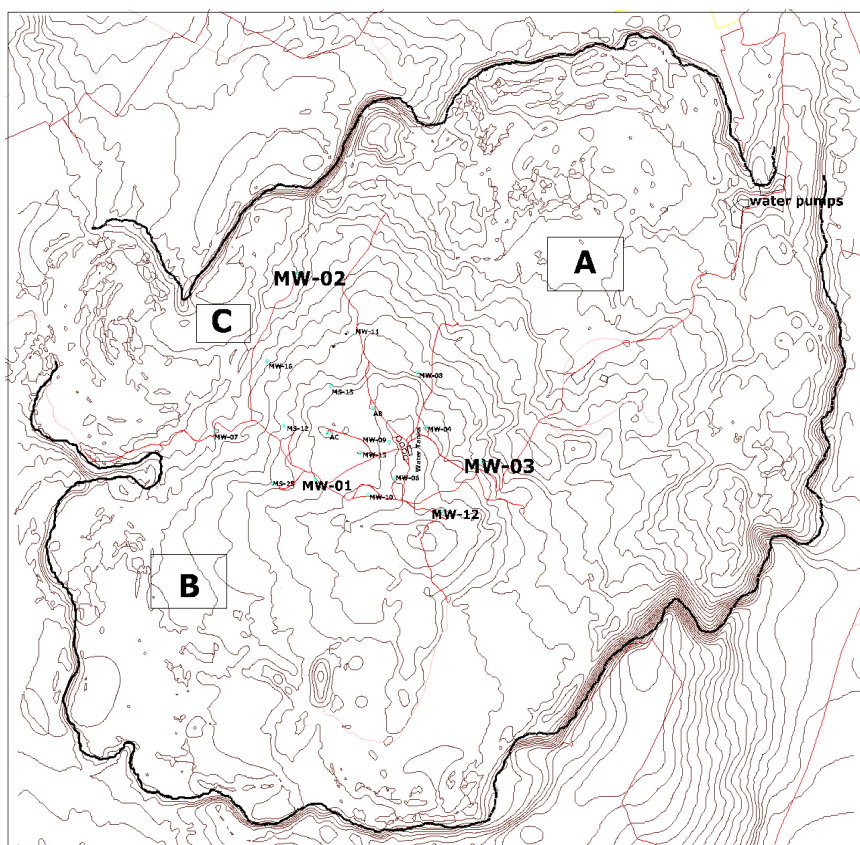


FIGURE 4: A map of Menengai caldera showing possible spa locations, labelled A, B and C

2.3.4 Spa size and layout

The pipelines, both for supply and re-injection, were designed and an optimum pipe diameter obtained. The geothermal fluid is first delivered into a cooling pond and then into the bathing pond before it is pumped to the cold re-injection point. A stainless steel heat exchanger coil is installed in the cooling pond. This offers two advantages: it will aid in cooling the pond as well as in heating up fresh cold water to be used in the steam room, showers and at the waterfall.

A surface area of water of 2800 m² is considered in this design to accommodate 1000 bathers, allowing each bather 2.8 m² of water surface area. The average depth of the deepest section is 1.5 m while the shallow section is 0.5 m, hence an average depth of 1 m. The brine exits the pond at approximately 33°C.

TABLE 2: Coordinates of the proposed locations and elevations (see Appendix I)

	Coordinates		Elevations (m)
	X	Y	
Scenario A	8509	9728	1820
Scenario B	3082	5626	2000
Scenario C	3805	9010	1940
MW-02 (proposed for re-injection)	4630	9493	1900
MW-03	7096	7062	1940

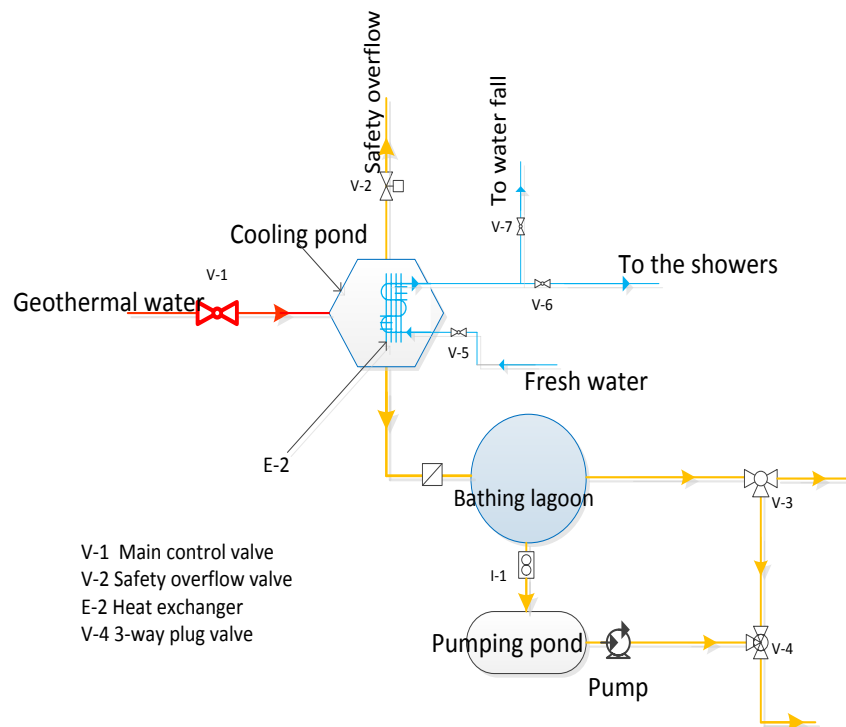


FIGURE 5: Proposed design layout of the geothermal spa

The cooling pond shall be 16 m in diameter and 2 m deep. The layout is as shown in Figure 5.

TABLE 3: Summary of monthly weather data for Nakuru (Source: RETScreen, 2011)

2.3.5 Pipeline design

Pipe diameter optimization, based on minimum cost, topology and route selection was considered. Route selection was done using the distance transform method. An upward flow of up to 30% was allowed for a pipe route going uphill. Heat losses were calculated assuming an insulation thickness of 0.05 m rock wool and a pipe setup as shown in Figure 6. The summary of monthly weather data for Nakuru used in this report is indicated in Table 3.

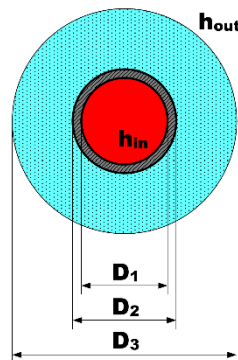


FIGURE 6: An insulated pipe

Month	Air Temp. °C	Relative Humidity %	Wind Speed m/s
Jan	18.45	57.6	3.809
Feb	19.2	51.9	3.792
Mar	19.95	56.9	3.965
Apr	18.75	71.4	2.37
May	17.3	74.2	1.811
Jun	17.85	73.4	1.556
Jul	16.8	72.9	1.515
Aug	17.1	72.3	1.616
Sep	17.3	68.6	2.237
Oct	17.5	70.8	1.893
Nov	17.2	74.6	3.154
Dec	16.8	65.7	1.926
Average	17.85	67.5	2.47

The total cost of a pipeline is a parameter used for selecting the optimum diameter. Increase in pipe diameter results in an increase in the total capital cost and, at the same time, decreases the pumping cost.

Optimum pipe diameter was obtained from the following cost calculations:

$$C_t = C_c + C_a(1/(1+i)^T)/i \quad (1)$$

where C_t = Total cost;
 C_c = Capital cost;
 C_a = Annual cost;
 i = Interest rate; and
 T = Life time.

The capital costs were calculated from:

$$C_c = L_p k_p + n_b k_b + n_c k_c + n_u k_u + n_v k_v + n_d k_d + L_p k_i \quad (2)$$

where L_p = Pipe length (m);
 k_p = Cost of pipe (USD/m);
 n_b = Number of bends;
 k_b = Cost of a bend (USD/bend);
 n_c = Number of connections;
 k_c = Cost of a connection (USD/connection);
 n_u = Number of expansion units;
 k_u = Cost of an expansion unit (USD/expansion unit);
 n_v = Number of valves;
 k_v = Cost of a valve (USD/valve);
 n_d = Number of pumps;
 k_d = Cost of a pump (USD/pump); and
 k_i = Cost of insulation material (USD/m).

Annual cost was calculated from:

$$C_a = k_e O_h P \quad (3)$$

Where O_h = Operating hours in a year;
 k_e = Cost of electrical energy (USD/kWh); and
 P = Power of the pump (kW).

Pump power was calculated from:

$$P = g \rho H_{tot} Q / \eta \quad (4)$$

where g = Acceleration due to gravity (m/s²);
 ρ = Density of the fluid (kg/m³);
 H_{tot} = Total head (m);
 Q = Volumetric flow rate (m³/s); and
 η = Pump efficiency.

The total head is given from the sum of pressure drop caused by friction and the static head due to the elevation difference:

$$H_{tot} = (H_f + \Delta Z) \quad (5)$$

where H_f = Friction head (m); and
 ΔZ = Elevation difference between end and start points (m).

The velocity, v had to be calculated, in order to determine H_f :

$$v = Q / \left(\frac{\pi D_{in}^2}{4} \right) \quad (6)$$

where D_{in} = Inner pipe diameter (m).

The equivalent length, taking into account the pressure drop in fittings and valves, was calculated from:

$$L_e = L_p + n_b h_b D_{in} + n_c h_c D_{in} + n_u h_u D_{in} + n_v h_v D_{in} \quad (7)$$

where L_p = Pipe length (m);
 h_b = Ratio of equivalent length to pipe diameter for bends;
 h_c = Ratio of equivalent length to pipe diameter for connections;
 h_u = Ratio of equivalent length to pipe diameter for expansion units; and
 h_v = Ratio of equivalent length to pipe diameter for valves.

The Reynolds number was calculated from:

$$Re = \frac{\rho v D_{in}}{\mu} \quad (8)$$

where μ = Dynamic viscosity of the fluid (kg/ms).

If $Re \leq 2100$, then

$$f = 64/Re \quad (9)$$

If $Re \geq 5000$, then

$$f = 0.25 / \left(\log_{10} \left[\frac{\epsilon}{3.7 D_{in}} + \frac{5.74}{Re^{0.9}} \right] \right)^2 \quad (10)$$

where f = Friction factor; and
 ϵ = Absolute roughness of the pipe (m).

The friction head was calculated from:

$$H_f = f v^2 L_e / (2g D_{in}) \quad (11)$$

2.3.6 Energy requirements for the spa

The heat transfer from the open pond occurs in the following ways:

- Convection;
- Evaporation;
- Radiation;
- Conduction; and
- Rain.

Heat loss due to convection, Q_c , in W/m²:

$$Q_c = h_{co}(T_w - T_a) \quad (12)$$

where h_{co} = Heat transfer coefficient (W/m²°C);
 T_w = Water temperature (°C); and
 T_a = Air temperature (°C).

From Rimsha-Doncenko equations, h_{co} :

$$h_{co} = K + 1.88V \quad (13)$$

where K = Constant dependent on the temperatures ($W/m^2\text{°C}$); and
 V = Wind speed at 2 m height (m/s).

$$K = 3.89 + 0.17(T_w - T_a) \quad (14)$$

Heat loss due to evaporation, Q_e in W/m^2 :

$$Q_e = (1.56K + 2.93V)(e_w - e_a) \quad (15)$$

where e_w = Partial pressure of steam at surface (mbar); and
 e_a = Partial pressure of steam in air (mbar).

Heat loss due to radiation, Q_r in W/m^2 :

$$Q_r = (4.186((13.18 * 10^{-9}T_a^4(0.46 - 0.06e_a^{0.5}) - G_o(1 - a))(1 - 0.012N^2) + 13.18 * 10^{-9}(T_w^4 - T_a^4)) \quad (16)$$

where G_o = Sun's radiation in clear weather;
 a = Natural reflection of water; and
 N = Cloudiness factor (0-8).

For design purposes we consider the case giving highest energy requirements which is when $G_o = 0$ and $N = 0$.

Heat loss due to *conduction* is calculated by estimating the heat loss through the walls and bottom of the pool. Heat loss due to *rain* is calculated as the amount of energy needed to heat the rain from the ambient temperature to the pool temperature. These losses are expected to be relatively small.

Heat loss from pipes:

An insulated pipe, as shown in Figure 6, was considered. Heat loss per unit length from insulated pipes is given by:

$$Q = \pi D_3 U * (T_{in} - T_{out}) \quad (17)$$

where D_3 = Outer diameter including insulation (m);
 U = Overall heat transfer coefficient based on outside of the insulated pipe ($W/m^2\text{°C}$);
 T_{in} = Fluid temperature ($^{\circ}\text{C}$); and
 T_{out} = Outside air temperature ($^{\circ}\text{C}$).

$$\frac{1}{U} = \left\{ \left(\frac{D_3}{D_1 h_{in}} \right) + \left[\frac{D_3 \ln \left(\frac{D_2}{D_1} \right)}{2k_{pipe}} \right] + \left[\frac{D_3 \ln \left(\frac{D_3}{D_2} \right)}{2k_{ins}} \right] + \frac{1}{h_{out}} \right\} \quad (18)$$

where h_{in} = Heat transfer coefficient inside the pipe;
 D_1, D_2, D_3 = Diameters as shown in Figure 6 (m);
 k_{pipe} = Thermal conductivity of the pipe material ($W/m^{\circ}\text{C}$);
 k_{ins} = Thermal conductivity of the insulation material ($W/m^{\circ}\text{C}$); and
 h_{out} = Heat transfer coefficient outside the pipe ($W/m^2\text{°C}$).

2.4 Results of pipeline design

A pipeline from MW-03, which is a liquid dominated well (GDC, 2013), was designed to the proposed spa locations in the three scenarios. The supply pipeline is insulated while the re-injection pipeline from the pumping pond is not. In this report, the cost of pumping to a distance of 1 km to a high point from

Well MW-03, requiring one pumping unit at 60 kg/s, was estimated and used to obtain the optimum diameter at the minimum cost for the supply pipeline which was found to be 200 mm (Figure 7).

Temperature drop, with and without insulation of the supply pipeline in scenario C, the longest pipeline in the three scenarios, was calculated using Equations 17 and 18. This was found to be over 17°C without insulation and 2°C with 50 mm thick insulation, for the 4600 m as shown in Figure 8; therefore, there is a need for insulation.

Using the X and Y co-ordinates from Table 2, the distance transform algorithm was used to obtain the shortest appropriate pipeline route (Appendix I) and the pipeline cost was determined.

Table 4 shows the results of the pipeline cost analysis for the three scenarios. Scenario C has the lowest cost because of its location near the assumed re-injection point, hence a shorter pipeline needed for re-injection. A comparison of the supply, re-injection and the total pipeline costs for the three scenarios is shown in Figure 9. Scenario B has the highest total pipeline cost. Scenario A is 12% cheaper than B while scenario C is 32% cheaper than scenario B.

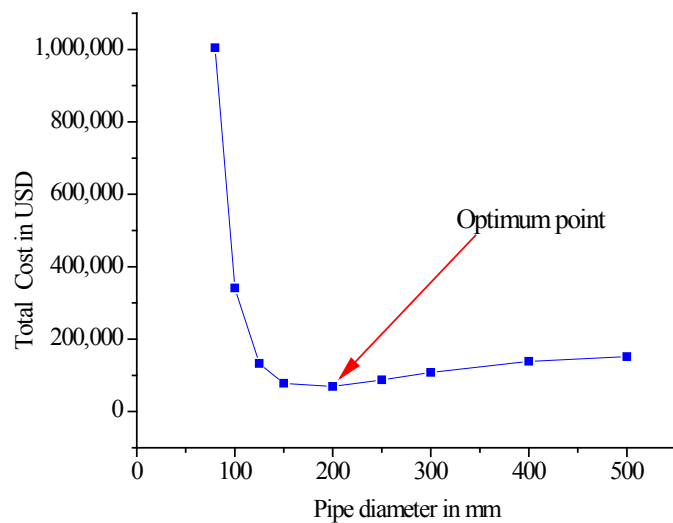


FIGURE 7: Optimum diameter selection based on minimum cost

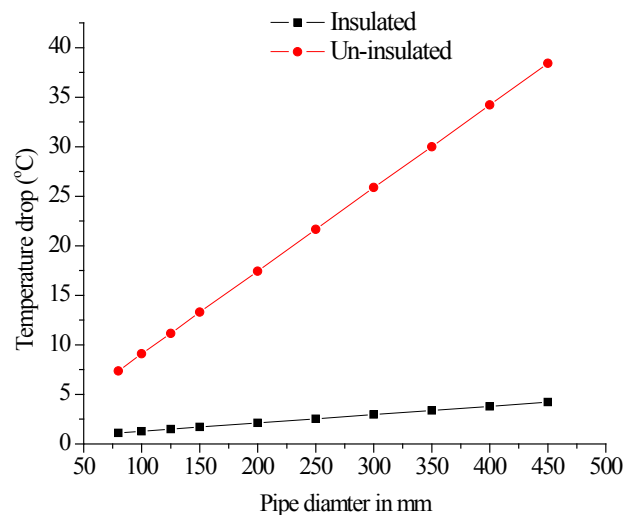


FIGURE 8: Temperature drop in insulated and un-insulated pipes of different diameter

TABLE 4: Pipeline length, diameter and capital cost for the three scenarios

	Supply pipeline (Insulated)			Re-injection (Un-insulated)			Total cost (USD)
	Length (m)	Pipe diameter (m)	Cost (USD)	Length (m)	Pipe diameter (m)	Cost (USD)	
Scenario A	3000	0.2	210,000	4700	0.2	290,000	500,000
Scenario B	4500	0.2	305,000	4200	0.2	260,000	565,000
Scenario C	4600	0.2	320,000	1000	0.2	65,000	385,000

Scenario A requires a pump between the spa and the re-injection point. The cost of the pump and pipe supports cost is not included in the pipeline cost analysis shown in Table 4 and Figure 9.

Calculations were done for heat transfer in the cooling and bathing ponds, using Equations 12 to 16, and the results are as shown in Table 5.

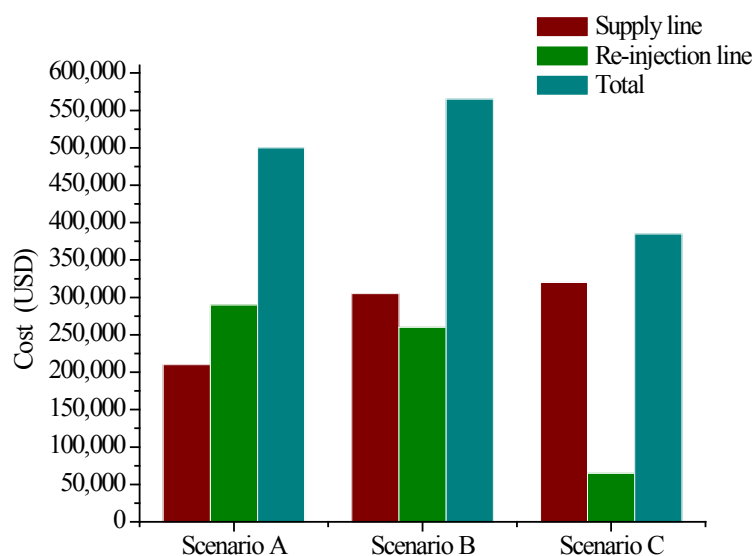


FIGURE 9: Comparisons of pipeline costs for the three scenarios

TABLE 5: Main geothermal spa parameters

Mass flow bathing pond (kg/s)	Area bathing pond (m ²)	Area cooling pond (m ²)	Retention time bathing pond (hrs)	Retention time cooling pond (hrs)	Temp bathing pond (°C)	Temp geo in (°C)
33.8	2827	201.1	23	2.9	35	130

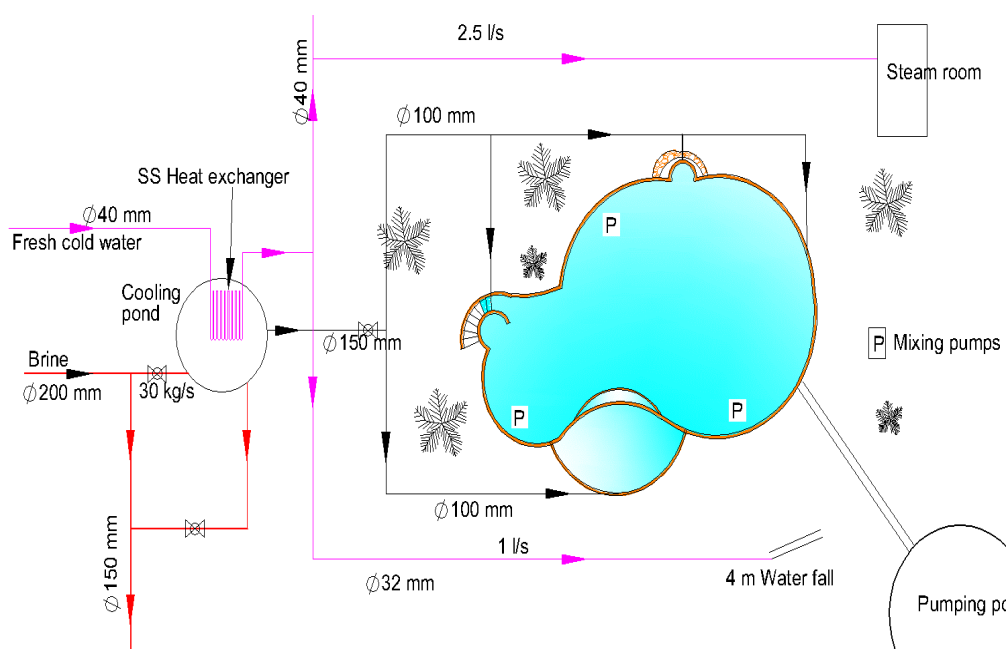


FIGURE 10: Designed spa layout and pipe work

A stainless steel pipe loop, 30 m long and 40 mm in diameter, is installed in the cooling pond as a heat exchanger to heat up cold water from 18°C to 55°C at a flow rate of 8 l/s. This heated fresh water is pumped through the steam jets in the steam room and is also used in the showers before the visitors can take a bath in the lagoon. Scale deposits on the stainless steel loop are expected on the outer side of the pipes and will be cleaned regularly. The piping into the shower is done using high pressure PVC pipes.

Geothermal hot water flows into the cooling pond at a 130°C and drops to a 100°C where it is retained for 3 hours. It flows by gravity through a 150 mm diameter pipe at 35 l/s to the bathing pond. Three submersible drainage pumps (Figure 10) are installed in the bathing pond to re-circulate and mix the water, preventing it from forming layers along the depth of the lagoon, with varying temperatures and therefore, assisting in achieving uniform temperatures in the lagoon. The retention time in the main lagoon is found to be 23 hours at 35°C; flow is by gravity into the pumping pond.

A 15 kW pump is used to pressurize the heated fresh water through the steam jets in the steam room. Table 6 shows the designed details of the spa and the steam room.

TABLE 6: Designed details and specifications of the spa

Facility		Parameter	Units	Value
Bathing lagoon		Temperature	°C	35
		Retention time	hours	23
		Flow rate	kg/s	35
Steam room		Dimensions	m	2.1 by 3 by 2
		Material	-	Concrete
	Pumps	Motor rating	kW	15
		Flow rate	m³/hr	15
	Steam jets	Pressure	bar	2
		Flow rates	l/s	0.6
		Number	-	9
Water fall		Flow rate	l/s	1
		Dimensions	m	4 m high

The retention time in the cooling pond is 3 hours while in the bathing pond it is 23 hours. This allows for aging of the water allowing polymerisation. Various sampling points will be provided in the pipeline between the cooling pond and the bathing lagoon.

3. GEOTHERMAL POOL HEATING

Open-air swimming pools are heated to extend the swimming time or to maintain a temperature that is comfortable to the swimmer. Heating of swimming pools by solar energy has existed for many decades with the technology now well established (Ruiz and Martinez, 2009). However, solar heating is limited due to its intermittence and its un-availability at night. The collectors have to be exposed to the sun, thus requiring relatively large installation areas on the surface, which is not appealing to nature. Control of solar heating is also a challenge.

The size of a swimming pool is largely guided by the number of bathers it can support. According to Halldórsson (1975), the space required for each individual is dependent upon pool depth. International standards for training professional swimmers and swimming competitions also give a guide on the minimum size requirements of a pool (Perkins, 1988).

In Iceland the total annual water consumption in geothermal heated swimming pools is estimated to be 6.9 million m³ which corresponds to an energy use of 1,300 TJ per year. The specific water and energy demand is about 220 m³ of geothermal water or 40,000 MJ of energy for heating 1 m² pool surface area (Orkustofnun, 2013).

3.1 Water re-circulation and cleaning

Re-circulation of the pool water is the only means that ensures it is cleaned of dirt, that pathogenic bacteria are removed, and that an even pH is maintained in the pool. A range of recommended parameters for swimming pools is shown in Table 7. Most pools are fitted with skimmers or have a deck level channel to help skim the top layer of floating debris. By use of hand held nets and strainer baskets, big solid particles can be mechanically removed. Many particles are not removed using this method, so filtration is required. The filter is made of multiple layers of sand that vary in size. When the water flows through the sand, solid particles are filtered out.

Swimming pools need to be chemically treated to maintain pool water balance and hygiene. Chemicals for swimming pools include various kinds of sanitizers and disinfectants which control the growth of bacterial and algae matter in the pool water. The pH is controlled using either an acid or a basic compound. Chlorine is added to control algal and bacterial growth, waterborne illnesses, cloudy water and insufficient sanitation of the water. A balance tank is provided for in all swimming pools to hold the excess water from the pool and provide a pumping point for re-circulating the water, as shown in Figure 11.

TABLE 7: Recommended range of swimming pool water parameters (EUSSA, 2010)

Parameter	Range
Appearance	Clear and free from suspended matter
pH	7.2 – 8.0
Total hardness	50 – 400 mg/l
Total alkalinity	75 – 200 mg/l
Total dissolved solids	Less than 500 mg/l

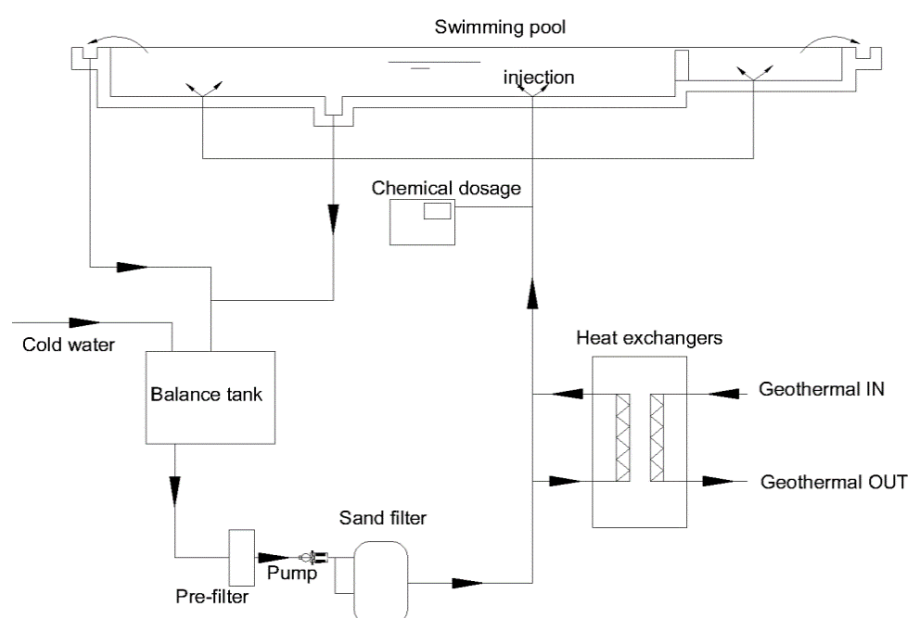


FIGURE 11: Swimming pool circulation layout

The swimming pools considered in this design include a main outdoor swimming pool, an indoor swimming pool, three hot baths, a wading pool, a steam room, a shallow pool and a waterfall (Figure 12), all heated geothermally. All the water is re-circulated. The physical location of the swimming pools is different from the location of the geothermal spa described earlier. The location is not stated in this report, but a

location that could suit these swimming pool facilities is in the geothermal complex headquarters.

The significant heat loss from the swimming pools due to evaporation, conduction, convection and rain is calculated as described in chapter 2.3.6. The calculations are based on monthly average climate conditions, given in Table 3. Figure 13 shows a pie which indicates the highest heat loss from a swimming pool is due to evaporation losses, while loss due to rain is the least.

The turnover of the pool water is 4 hours based on the standards and other parameters shown in Table 7 (Perkins, 1988). Heating a swimming pool is largely dependent on weather conditions and the size of the pool.

The total energy required for heating the swimming pools is dependent largely on the wind speed rather than air temperature. The months of January to March and November require the most heating energy. The least required thermal energy is in the month of July as shown in Figure 14.

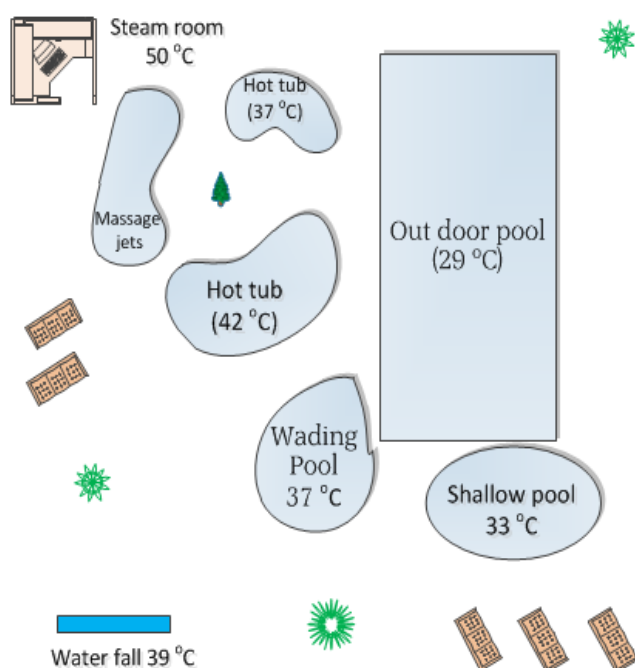


FIGURE 12: Various swimming pools

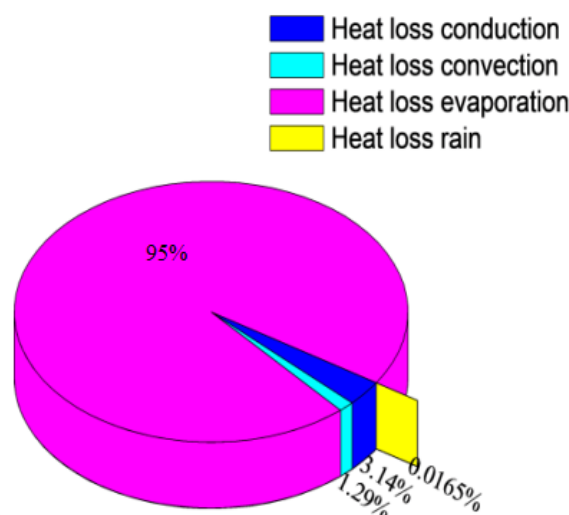


FIGURE 13: Various means of heat loss from the swimming pool

Figure 15 shows the required geothermal flow rates for various designed swimming pools. The geothermal flow rate required for heating the indoor pool water is the least and remains constant throughout the year. This is because the indoor pool is not affected by the outside wind which varies throughout the year. The geothermal flow required for heating the waterfall is constant throughout the year because the water is more exposed than the pool water as it falls down and this exposure factor has more influence than the wind. The outdoor main pool is the most affected by weather variations.

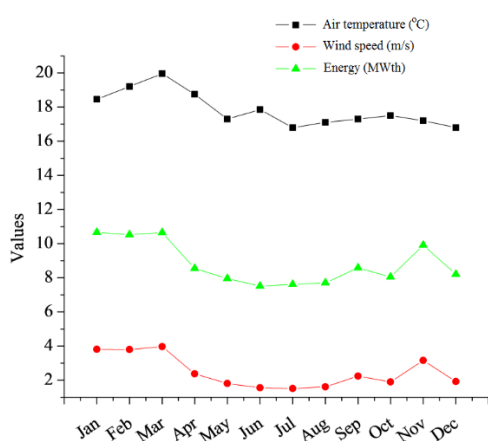


FIGURE 14: Variations of air temperature and wind speed and energy requirements for pool heating in a year

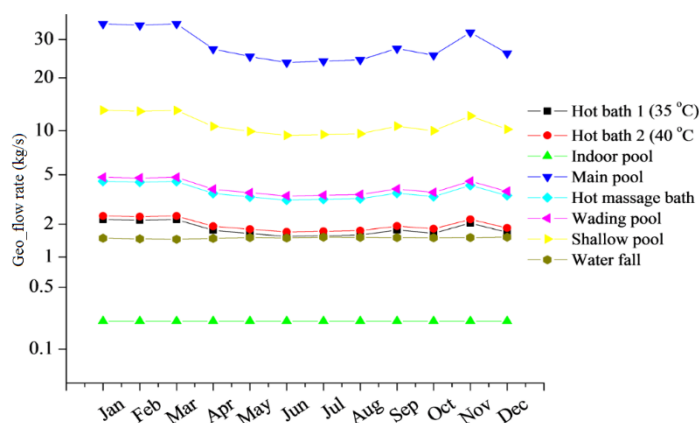


FIGURE 15: Flow rate requirements in the various pools in a year

The average thermal power required to heat all the swimming facilities is 9 MWth. This energy is extracted through heat exchangers from geothermal water at 130°C, exiting at 90°C. The highest thermal power required is 11 MWth between January and March which are the windiest months of the year. The total mass flow required is 55 kg/s.

Table 8 shows the main accessories and equipment for the various swimming pools considered and designed in this report. The turnover mainly depends on the type of facility and its volume.

TABLE 8: Main accessories and equipment for the swimming pool installations

	Main	Shallow	Wading	Indoor	Hot tub 1	Massage tub	Hot tub 2
Area (m ²)	313	113	38	113	18	36	18
Volume (m ³)	469	79	1	101	18	36	18
Turnover (hr)	4.0	4.0	0.2	3.0	1.0	1.0	1.0
Flowrate (m ³ /hr)	117	20	5	34	18	36	18
Sand filters	4No CX900	1No CX800	1No CX500	2No CX800	1No CX800	2No CX800	1No CX800
No. of inlets	17	3	1	5	3	6	3
Vol. balance tank (m ³)	24	4	1	6	1	2	1
Pumps	2No 28kw DE65/20	1No 1.2kw SLL 400	1No 0.6kw DM3	2No 1kw SLL 300	1No 1kw SLL 300	2No 1kw SLL 300	1No 1kw SLL 300
Chlorinator (gms/hr)	79	14	4	23	13	25	13
Type of chlorinator	M4921 1.kw	BMSC20 120w	BMSC20 120w	BMSC26 160w	BMSC20 120w	BMSC26 160w	BMSC20 120w

Table 9 shows the details of the swimming pools. The total combined water surface area of all the swimming facilities is 670 m².

TABLE 9: The details of the swimming pool facilities designed

General details: Total land area 4700 m ² Total water surface area 670 m ²		
Main outdoor pool	L: 25 m W: 12.5 m Area 313 m ² Volume 469 m ³	Maximum depth 2 m Minimum depth 1 m Temperature 29°C
Indoor pool	L: 15 m W: 7.5 m Area 113 m ² Volume 101 m ³	Uniform depth 0.9 m Temperature 30°C
Shallow/game pool	Radius: 6 m Area 113 m ² Volume 79 m ³	Uniform depth 0.7 m Temperature 33°C With a water slide of 51 m track length
Wading pool	Radius: 3.4 m Area 38 m ² Volume 1 m ³	Uniform depth 0.25 m Temperature 37°C
Hot tubs: 1. 35°C 2. 36°C 3. 40°C	Radius: 2.4 m, kidney shaped Radius: 3.4 m, kidney shaped Radius: 2.4 m, kidney shaped	Depth of 1 m With 6 massage jets High temperature
Steam room	L: 4 m, W: 3 m	Temperature 55°C 9 steam jets
Waterfall	Height: 4 m, width: 3 m	Temperature 39°C

3.2 Heat exchangers

Heat exchangers are usually designed to maximize the surface area that exists between two fluids. Selection of heat exchangers in this design is done by considering the flow rates and temperature differences. Water-water plate heat exchangers are designed for each pool having a separate heating and cleaning system. Table 10 shows the various specifications for heat exchangers for each swimming facility considered in this report

4. COST ANALYSIS OF THE GEOTHERMAL SPA AND CONCLUSIONS

4.1 Cost analysis

The main parameters usually evaluated in an economic analysis include PV (Present Value), NPV (Net Present Value), and IRR (Internal Rate of Return). These are based on two basic adages of finance, according to Bradley et al. (2011) which are “a dollar today is worth more than a dollar tomorrow” and “a risky dollar is worth less than a safe one”. In any investment, there is the opportunity cost which is foregone by investing in the project rather than in another one. The rate of return of the foregone project is called the discount rate, r .

TABLE 10: Water-water heat exchanger details

Pool type	Side	Temp. in (°C)	Temp. out (°C)	Pressure drop (kPa)	Water volume / Unit (l)	Max. working pressure (bar)	Max. working temp. (°C)	LMTD (K)	Surface area (m ²)
Hot bath 1 (37°C)	A	120	90	4.74	0.063	25	180	78.32	0.13
	B	18	35	9.33	0.084	25	180		
Hot bath 2 (42°C)	A	120	90	6.58	0.063	25	180	75.93	0.13
	B	18	40	8.05	0.084	25	180		
Indoor pool	A	120	90	0.12	0.063	25	180	80.2	0.13
	B	18	31	0.44	0.084	25	180		
Main pool	A	120	90	188.61	0.24	16	180	81.13	0.19
	B	18	29	932.22	0.3	16	180		
Massage tub	A	120	90	16.5	0.063	25	180	77.85	0.13
	B	18	36	30.37	0.084	25	180		
Wading pool	A	120	90	19.68	0.063	25	180	77.37	0.13
	B	18	37	32.75	0.084	25	180		
Shallow pool with slide	A	120	90	125.63	0.063	25	180	79.26	0.13
	B	18	33	313.56	0.084	25	180		
Waterfall	A	120	90	6.58	0.063	25	180	74.96	0.13
	B	18	42	6.83	0.084	25	180		

The Present Value (PV) of a delayed payoff is found by multiplying the payoff (C_1) by a discount factor as:

$$PV = \text{Discount factor} * C_1 \quad (19)$$

The discount factor is expressed as:

$$\text{Discount factor} = 1/(1 + r) \quad (20)$$

To calculate the present value, the expected future payoffs are discounted by the rate of return offered by comparable investment alternatives (i.e. the discount rate). To calculate the Present Value, the cash flows every year (C_1, C_2, C_3) are discounted by an appropriate discount rate:

$$PV = \frac{C_1}{(1 + r_1)} + \frac{C_2}{(1 + r_2)^2} + \frac{C_3}{(1 + r_3)^3} + \dots \quad (21)$$

To find the Net Present Value we have:

$$NPV = C_0 + PV \quad (22)$$

where C_0 = Initial investment.

Internal Rate of Return (IRR) is the value of the discounted cash flow (DCF) rate of return that forces the NPV to zero in the period considered. IRR is evaluated by means of iterative calculation from the equation:

$$NPV_{IRR} = C_0 + \sum_{i=1}^n \frac{C_i}{(1 + IRR)^i} = 0 \quad (23)$$

where n = Number of years considered (project life).

The economic analysis is done for the geothermal spa with an assumed project life of 10 years. In this cost analysis, the following assumptions were made:

- An average price of a ticket for an adult bather is 6 US dollars per visit and increases at 5% per year.
- The spa operates 330 days, paying for 30 days of maintenance in a year.
- The average number of visitors in a year increases by 30%. Visitors in the first year of operation number 25% of the annual number of tourists currently visiting Lake Nakuru National Park.
- The variable and running costs increase at 15% annually.
- The cost of exploration and well drilling is not considered. The price of hot geothermal is assumed to be charged per volume consumed, irrespective of temperature drop. In this report it was assumed as 0.5 USD/m³. This is a very rough estimation of the price of fresh water in Kenya when sold in bulk for industrial use.
- The discount rate in this report is assumed to be 12%. This is based on the central bank of Kenya Treasury bond coupon rate for a 10 year maturation period, as of August 2013. Treasury bonds are considered as the opportunity cost in this report work.
- This analysis does not consider the main pipeline costs.

The spa project is assumed to generate revenue after one year of initial capital expenditures for construction work. If the start-up year is 2015, then the following financial analysis is done.

The preliminary analysis indicates that the cash flow will be positive after running the project for 2 years (Figure 16). The NPV curve at a 12% discount rate returns a positive value in the year 2019, five years after the assumed project start. This is according to a cumulative present value analysis (Figure 17). With a project life of 10 years, the indication is that the project is viable.

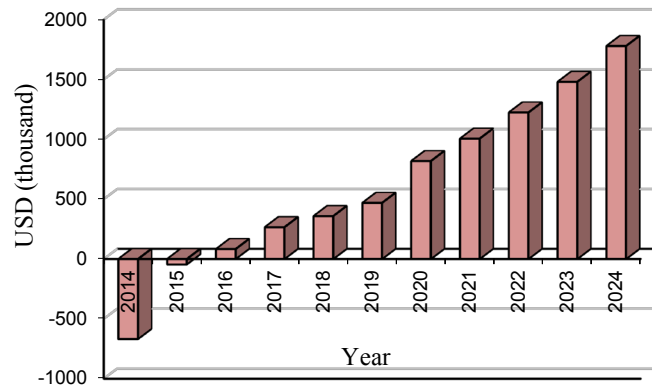


FIGURE 16: Cash flows

According to the analysis, the IRR is 40% for a project life of 10 years. This is higher than the discount rate, indicating the viability of the project. After the 5th year, the IRR analysis indicates a higher rate than the discount rate, as shown in Figure 18.

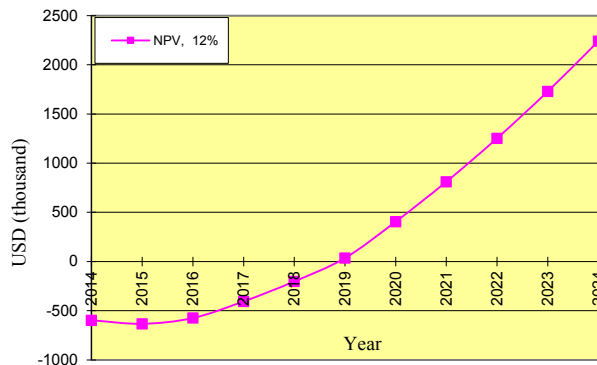


FIGURE 17: Cumulative present values

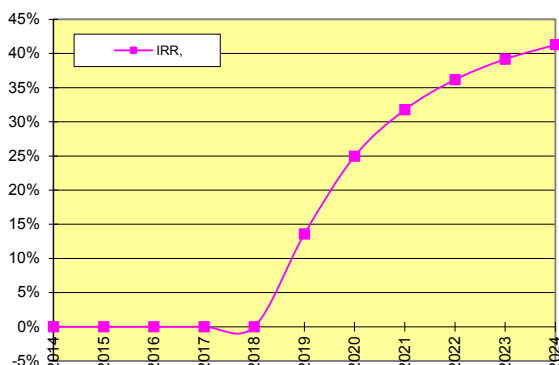


FIGURE 18: Internal rate of return

4.2 Conclusions

A geothermal spa was designed for Menengai geothermal field. There are other factors that may contribute to the site location of the spa other than the pipeline cost alone as considered in this report. Financial gains, leisure as well as utilisation of the available resources which could not otherwise have been utilised, are some of the advantages in the construction of a spa. The nearness of Menengai geothermal field to Lake Nakuru provides an opportunity to attract more visitors as the distance between is relatively short. The fact that Menengai already attracts visitors, students, scholars and other professionals is a key indicator of the potential that exists in the field. This preliminary research work indicates that design and construction of a spa in Menengai is possible and could offer various benefits, among them financial. Health tourism will be greatly promoted whereby the tourists spend their spare time improving their health and wellbeing. With geothermal sites and power plants attracting visitors, scholar and students, this forms a potential for many tourists to visit the health spa. Heating of a conventionally circulated swimming pool was also discussed.

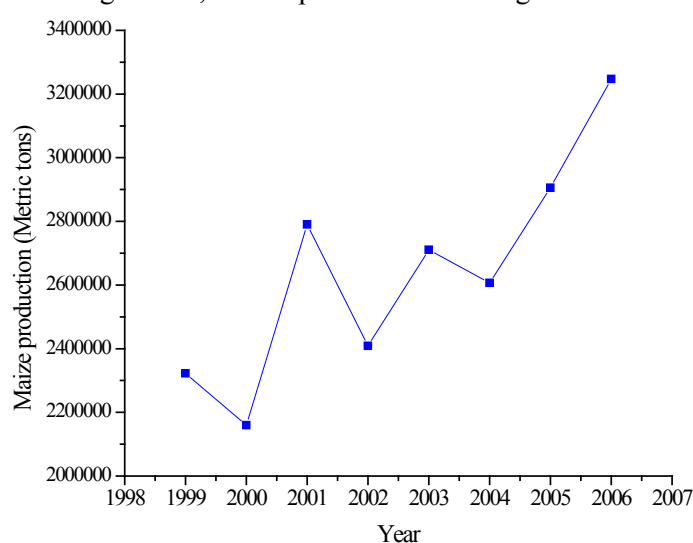
Further research on silica scaling, the financial perspective and additional sources of geothermal water is recommended.

5. GEOTHERMAL CROP DRYING

5.1 Background

Drying is one of the oldest methods of preserving food, and it is fairly simple, safe and can be done all year round if it done indoors under controlled conditions. It entails the removal of moisture from the product. Each type of crop has its own drying requirements. Some of the crops which require drying are cereals, tea, vegetables and fruits which are extensively grown in Kenya and are dried to a moisture content of below 13%. In addition to crops, fish and meat products also require drying for preservation purposes.

Maize is the largest cereal grain grown in the Rift Valley regions and is sun dried on a small scale, while on a large scale, diesel power is used at government or privately owned grain drying and storage facilities.



Maize has continued to be the most important food crop in Kenya, playing an integral role in national food security. Kenya produces around 3 million tonnes of maize per year (Figure 19); about 15% is sold directly to the National Cereals and Produce Board and large millers. The total area under maize cultivation as of the end of 2003 stood at 1.6 million hectares (KNBS). Maize growing in Kenya is concentrated in the Rift Valley districts of Trans Nzoia, UasinGishu and Nakuru (Figure 20). The region is often referred to as the 'Granary of Kenya' (EPZA, 2005).

FIGURE 19: Maize production in Kenya (KNBS, 2012)

Tea and coffee are dehydrated as part of their manufacturing process. This is done at the processing factories. Vegetables are dehydrated to enhance their storage, minimise losses and enhance their availability during dry weather spells.

The Ministry of Agriculture has the overall responsibility of the grains sector, with the National Cereals and Produce Board, established in 1985 to regulate and offer drying, marketing and storage services in the sector.

5.2 Crop drying in Kenya

5.2.1 Sun drying

Maize dries partially on the farms through solar drying. For storage purposes, further drying is required to reduce the moisture content from 27% to a 13% dry basis. The small scale farmers achieve this through sun drying for relatively many days (5 to 45 days), where maize is dried on the ground on spread canvas (Figure 21). This is done along the roadsides or in open fields. Dust, laden with fungal spores, can easily be deposited on the maize. Furthermore, sun drying is weather dependent, unreliable and impractical for large volumes of maize. In this case, commercial dryers are utilised.

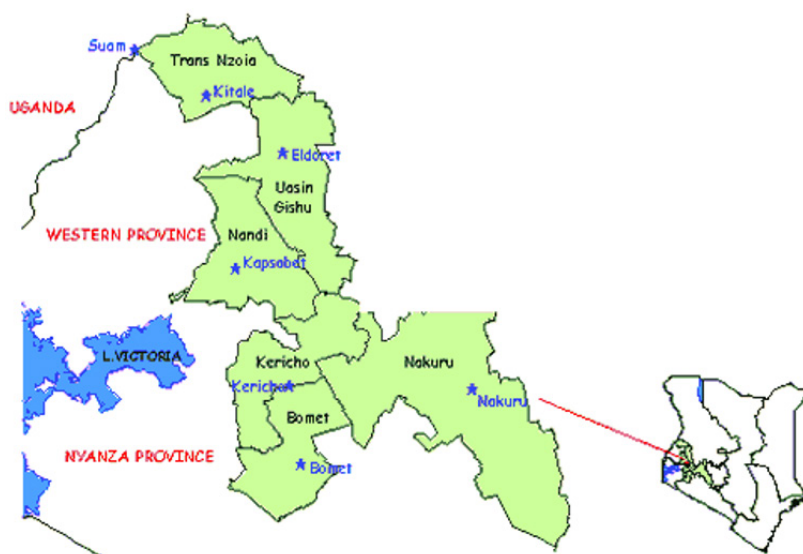


FIGURE 20: Map of Kenya showing grain growing areas (MOA, 2001)

5.2.2 Geothermal drying

A pyrethrum crop dryer, which utilizes geothermal heat, exists at Eburru, near Naivasha. The steam from a shallow well is piped through galvanized iron pipes and is used to dry flowers and maize, as shown in Figure 22. The well was drilled in the 1940s and farmers utilized the geothermal energy to dry pyrethrum flowers (Mwangi, 2005).

5.2.3 Fossil fuel use in drying

The National Cereals and Produce Board of Kenya, owned by the government, operates its own dryers and charges for drying and storage of maize, wheat and barley. The dryers are powered by industrial diesel oil heaters. Use of fossil fuels leaves a negative carbon footprint on the environment. Thus, there exists significant potential to utilize clean geothermal heat for drying operations.



FIGURE 21: Sun drying of grains



FIGURE 22: Pyrethrum drying using geothermal heat in Eburru, Kenya

A privately owned drying firm, Lesiolo Grain Dryers, also based in Nakuru, provides drying services and post-harvest management of grains including wheat, maize, barley and sorghum. It has a combined storage capacity of 80,000 metric tons and 6 dryers of capacities ranging from 10 to 100 tons, all using industrial diesel oil. In addition, it has two mobile dryers of 13 tons capacity each, which are either operated from a tractor PTO or diesel powered with a 200 litre fuel tank capacity, operating in a temperature range of 40 to 60°C.

5.3 Theory of grain drying

The main objective of drying agricultural products is to reduce the moisture content to certain levels that allow safe storage over an extended period of time. It also brings about a reduction in weight and volume, minimizing packaging, storage and transportation costs (Kavak Akpinar et al., 2006). Thermal drying is most commonly used and involves the vaporisation of moisture within the product by the application of heat with subsequent evaporation from the product. Thus, in thermal drying, there is simultaneous heat and mass transfer.

Drying is an energy intensive operation. In most industrialized countries, the energy used in drying accounts for 7–15% of the nation's industrial energy, often with relatively low thermal efficiencies ranging from 25% to 50% (Kavak Akpinar et al., 2006). Agricultural crop drying has been reported to account for about 12 to 20% of the energy consumption in the agricultural sector (Liviu and Badea, 2009).

During the drying process, food materials undergo physical, chemical, and biological changes which can affect some natural attributes like texture, colour, flavour, and nutritional value. Changes in colour and flavour are most important to crops like tea, fruits and vegetables. The drying process influences these factors and, therefore, the quality of the final product. Drying of grains is mainly divided into four broad categories: low-temperature drying using unheated air; medium-temperature drying, below 43°C for seeds and below 60 °C for grains to be milled; high-temperature drying where kernel temperatures are maintained below 82°C for animal feeds; and combination drying using both low and high temperatures (FAO, 2008). The optimum grain drying temperature depends on the dryer type, the grains species and the grain quality requirements.

The importance of a dryer is to supply the product with more heat than is available under ambient conditions, thereby increasing the vapour pressure of the moisture held within the crop and decreasing significantly the relative humidity of the drying air and increasing its moisture carrying capacity, ensuring sufficiently low equilibrium moisture content.

5.3.1 Drying kinetics

Thermal drying involves two simultaneous actions: a heat transfer process by which the moisture content of the solid is reduced and a mass transfer process where there is fluid displacement within the structure of the solid towards its surface and evaporation. The quality and quantity of energy as well as heat and mass transfer should be investigated throughout the drying processes.

5.3.2 Water activity

Water activity (a_w) is the ratio of the vapour pressure of water in a material to the vapour pressure of pure water at the same temperature. The water activity of a sample is equal to the relative humidity of air, when there is equilibrium of vapour pressure and temperature. Water activity is temperature dependent. Temperature changes water activity due to changes in water binding, dissociation of water, solubility of solutes in water, or the state of the matrix.

$$a_w = \frac{p}{p_o} \quad (24)$$

where p = Vapour pressure of water in the product; and
 p_o = Vapour pressure of pure water at the same temperature.

Water activity affects the shelf life, safety, texture, flavour, and smell of foods and it is the most important factor in controlling spoilage.

5.3.3 Moisture content

Moisture content of a substance is expressed as a percentage by weight on a wet or dry basis. The moisture content is presented as relative to dry basis, because the dry basis concept is the common basis in the drying research area. A commonly used simple model, assuming that the resistance for water transport is all over the surface of the particle, is represented by an equation analogous to Newton's law of cooling, the Lewis equation (Lewis, 1921):

$$\frac{dM}{d\theta} = -k(M - M_{eq}) \quad (25)$$

where M = Moisture content;
 M_{eq} = Equilibrium moisture content;
 θ = Time; and
 k = Drying constant dependent on the product.

The moisture content attained by a product with respect to a set of atmospheric temperatures and relative humidity is called the equilibrium moisture content. In such conditions, the grain moisture is in equilibrium with the surrounding air. Moisture storage requirements for some grains is shown in Table 11.

TABLE 11: Moisture requirement for storage of grains

Crop	Moisture content for storage (% w.b)	
	For one year storage	For two year storage
Maize	13	11
Wheat	13-14	11-12
Barley	13	11

According to Henderson and Pabis (1961):

$$\frac{M_{final} - M_{eq}}{M_{initial} - M_{eq}} = e^{-k\theta} \quad (26)$$

where $M_{initial}$ = Initial moisture content; and
 M_{final} = Final moisture content.

5.4 Grain dryers

Grain dryers can either be unheated air dryers or heated air dryers:

Unheated or natural air-drying is usually performed in a storage bin for a relatively small volume of grain. The period of drying is very much dependent on the weather and could take relatively long to completely dry. Turning of grains is usually performed to ensure uniform and continuous drying.

Heated air dryers can be deep bed dryers or thin layer dryers. In deep bed drying, the condition of the drying air at any point in the grain mass changes with time and the depth of the grain bed. The rate of drying is slower when compared to thin layer drying of grain. The heat should not be more or less than the required amount for evaporation to avoid hardening, discolouration or other unsuitable outcomes (Tesha, 2006).

The most common shapes in deep bed drying are round or rectangular. For efficient operation of deep bed dryers, the air flow rate of 2.94 - 3.92 m³/minute per tonne is recommended. An air flow rate that

is above 3.92 m³/minute per tonne may result in uneven drying and is expensive in operation. If the moisture content of grains is up to 18%, the layer depth of grain should be limited to 3 m and, above 18%, the moisture depth recommended is 2.5 m. The net perforated area of the floor should be 15% of the total floor area. An air velocity of 300 m/minute through opening is preferable.

Thin layer drying refers to the grain drying process in which all grains are fully exposed to the drying air under constant drying conditions. Most commercial dryers are designed on thin layer drying principles. In this case, two periods of drying are usually encountered: the constant drying rate where the rate of evaporation under any given set of air condition is independent of the solid and is essentially the same as the rate of evaporation from a free liquid surface under the same conditions; the falling rate period enters after the constant drying rate period and corresponds to the drying cycle where the product surface is no longer wet and continually decreases until the surface is dry.

5.5 Factors influencing the quality of dried product

Several factors affect the quality of dried product. These include quality of raw material, drying rate and drying temperature.

5.5.1 Raw material quality

Agricultural materials can be either hygroscopic (absorbing moisture from the air) or non-hygroscopic. The quality of the dried product can only be as good as the material from which it was derived. Food products like fish and meat products are usually sensitive and heavily dependent on the raw material quality. Fruit products can be sliced to obtain better and more evenly dried products.

5.5.2 Drying rate

A very fast drying rate can cause shrinkage while a slow rate could result in loss rehydration capacity or increase costs. The drying rate is dependent upon several factors, namely air temperature, air flow rate, relative humidity, exposure time, variety and size of grain, initial moisture content, and grain depth.

The rate of drying increases with the rise of air temperature. According to Henderson and Pabis (1961) the air rate has no observable effect on thin layer drying of wheat when air flow is turbulent. However, for paddy rice and maize, it has been found that the air rate has an effect on the rate of drying. Increasing air humidity decreases the rate of drying while the increase in exposure time of drying air in a single pass increases the drying rate.

The empirical drying equation for maize is:

$$M_{eq} = 0.01 * \left[\frac{LN(1 - rh_{amb})}{-8.65 \cdot 10^{-5}(T_{amb} + 49.810)} \right]^{\frac{1}{1.8634}} \quad (27)$$

where rh_{amb} = Relative humidity of ambient air; and
 T_{amb} = Ambient temperature (°C).

5.5.3 Drying temperature

Different products have an optimum drying temperature. Very high temperatures lead to distortion of the chemical composition or may even result in 'cooking' the product. The optimum temperature for maize drying is 49°C. Tea is dried at a temperature range of 60-100°C, depending on the desired flavour.

A very high drying temperature for fish can also lead to case hardening, which may be prevented by controlling the relative humidity and temperature of the drying air (Sotocinal, 1992).

5.6 Mass and heat balances

The rate of air flow required for drying may be calculated by making a heat balance. The heated air drying system is represented in Figure 23.

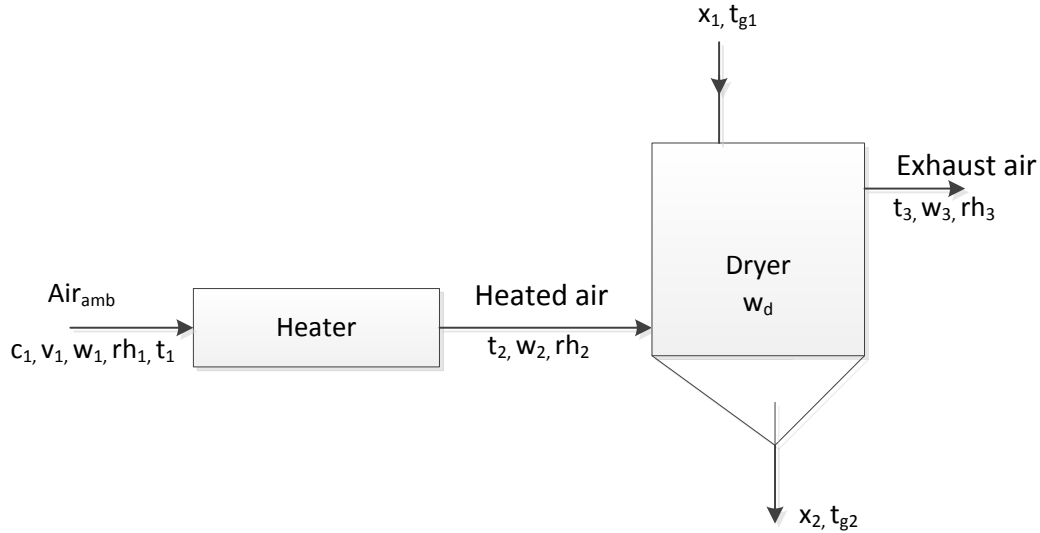


FIGURE 23: Heated air drying system

where c_1 = Air flow rate (m^3/hr);
 w_1, w_2, w_3 = Humidity ratios of ambient, heated and exhaust air, respectively (kg/kg);
 rh_1, rh_2, rh_3 = Relative humidity of ambient, heated and exhaust air, respectively;
 t_1, t_2, t_3 = Temperature of ambient, heated and exhaust air, respectively;
 w_d = Weight of bone dry grain in the dryer (kg);
 x_1, x_2 = Initial and final moisture contents of grain (kg/kg);
 t_{g1}, t_{g2} = Initial and final grain temperatures ($^\circ\text{C}$); and
 v_1 = Specific volume of air (m^3/kg).

Heat supplied by drying air, q_a is given by:

$$q_a = ((0.24 + 0.45w_1) * G_o(t_3 - t_2)\theta) * 4.187 \quad (28)$$

where q_a = Heat supplied by air (kJ);
 θ = Drying time (hours); and
 G_o = Rate of air supply (kg/hr).

Heat required for evaporation of moisture from the grain, q_1 is given by:

$$q_1 = w_d(x_1 - x_2)\lambda \quad (29)$$

where q_1 = Heat required for operation (kJ); and
 λ = Average value of latent heat of vaporisation of moisture from the grain (kJ/kg).

Sensible heat required to raise the grain temperature is given by:

$$q_0 = w_d c_g(t_{g2} - t_{g1}) + w_d c_w(t_{g2} - t_{g1})x_1 \quad (30)$$

where q_0 = Sensible heat required to raise the temperature of the grain and its moisture (kJ); and
 c_g, c_w = Specific heats of grain and water, respectively ($\text{kJ}/\text{kg}^\circ\text{C}$).

The overall mass and energy balances in a drying system give information on dryer performance and parameters of dryer design.

Using energy and mass balance:

$$q_a = q_1 + q_0 \quad (31)$$

And solving for G_o :

$$G_o = \frac{W_d[(x_1 - x_2)\lambda + c_g(t_{g2} - t_{g1}) + c_w(t_{g2} - t_{g1})x_1]}{((0.24 + 0.45w_1) * (t_3 - t_2)\theta) * 4.187} \quad (32)$$

and

$$G = G_o * v_1 \quad (33)$$

where v_1 = Specific volume of humid air (m^3/kg).

Fuel consumption rate:

$$rate_{diesel} = \frac{q_a}{\eta * \eta_b * \eta_{ex} * C_n} \quad (34)$$

where $rate_{diesel}$ = Fuel rate (kg/hr);
 C_n = Calorific value of fuel (kJ/kg);
 η = Efficiency of the heating system;
 η_b = Efficiency of boiler; and
 η_{ex} = Efficiency of the heat exchanger.

Design of fan and blowers

Selection and design of a centrifugal blower is done for a given airflow rate and static pressure. Specific speed (N_s) for the specific static pressure, air flow rate and designed motor speed are found by:

$$N_s = \frac{N\sqrt{Q}}{P_s^{0.75}} \quad (35)$$

where N = Speed of the motor (rpm);
 Q = Air flow rate (cubic feet/min); and
 P_s = Static pressure (inches of water).

The type of air moving unit which would operate at high efficiency is determined at or near peak efficiency at the calculated specific speed, from fan efficiency curves (Appendix II). If more than one type of air moving unit has good efficiency, a final selection can be based on other factors such as relative cost, size and shape of space available and the characteristics of the air flow path (Shirbhate, 2013).

The typical value of the pressure coefficient, Ψ , is found by interpolation, for the type of fan or blower selected and the value of specific speed, N_s . The impeller diameter is found from:

$$\Psi = \frac{2.35 \cdot 10^8 P_s}{N^2 d^2} \quad (36)$$

where Ψ = Pressure coefficient; and
 d = Diameter of the impellor (inches).

The typical value of the flow coefficient is found from the fan characteristics table and the width is calculated as follows:

$$W = \frac{175Q}{\Phi N d^2} \quad (37)$$

where W = Width of the impellor (inches); and
 Φ = Flow coefficient.

Geothermal heating requirement

The heat supplied by air is equivalent to the heat energy from geothermal. The total amount of geothermal supplied, Geo_{amount} is given by:

$$Geo_{amount} = q_a * (T_{in} - T_{out}) * c_w \quad (38)$$

where Geo_{amount} = Total amount of geothermal utilised (kg);
 T_{in} = Entry temperature of geothermal in the heat exchanger; and
 T_{out} = Exit temperature of geothermal in the heat exchanger.

The geothermal flow rate, \dot{m} in kg/s is given by:

$$\dot{m} = \left(\frac{Geo_{amount}}{3600 * \theta} \right) \quad (39)$$

For diesel use, the total cost of diesel fuel in USD is given by:

$$Cost_{diesel} = rate_{diesel} * \theta * price_{diesel} \quad (40)$$

where $price_{diesel}$ = Price of diesel (USD/l).

The cost of geothermal in USD is calculated from:

$$Cost_{geo} = Geo_{amount} * price_{geo} \quad (41)$$

where $price_{geo}$ = Price of geothermal (USD/kg).

5.7 Design of a geothermal crop dryer

5.7.1 Type, size and shape

The design of a heated grain dryer varies with the method of drying, whether a static deep bed batch dryer or the continuous flow batch dryers (mixing or non-mixing type). A static batch dryer is designed in this research work. The components include the drying chamber, air distribution system, indirect air heating system and the blower. The capacity of the dryer is 20 tons of maize at ambient air conditions. The tunnel/bed type of the dryer is adopted in this design in order to accommodate a wide variety of agricultural products, with minimal modification to the air flow duct and temperature regulation. The thickness of the grain layer exposed is limited to the depth of each tray and fixed to 10 cm. The dryer shall be a tunnel type where the air is blown from the side of the drying chamber and flows along the trays. This is appropriate when drying high moisture products and air re-circulation is necessary. When the air direction is vertical from below, then it is a bed dryer and the choice depends on the type of crop being dried. This also allows for comparing the efficiency of the heat exchanger for both air flow types. An air diversion valve is provided for changing the air flow from tunnel to the bottom of the drying trays.

5.7.2 Drying tea, fruits and vegetables

The processing steps in manufacturing black tea are plucking, withering, maceration, fermentation and drying. Withering reduces the moisture content to about 70% wet basis. It is then dried for about 1 or 2 hours depending on the desired flavour, at a temperature range of 70 to 120°C to a moisture content of 3% (Temple et al., 2000). According to Panchariya et al. (2002), the air velocity is considered to be 0.25 to 0.65 m/s or less.

Fruits and vegetables are considered shrinkable products after drying. The drying kinetics used in this design are based on experimental work by Kowalski and Mierzwa (2013), with an air temperature of 50°C and air flow velocity of up to 1.2 m/s. These parameters for drying tea and vegetables are used to predict the energy requirements by using the model of the designed tunnel dryer.

5.7.3 Air recirculation

The drying temperature depends upon the characteristics of the products. The air can be circulated with the help of a fan and blown in counter-current direction to the flow of the solid (Maharjan, 1995). If the temperatures are too high, the food products may cook or may cause case hardening where moisture is trapped inside the product. On the other hand, too low drying temperatures slow down the drying time and may lead to spoilage of moisture sensitive products like fish and meat products. During the initial drying stages, the moisture evaporates quickly from the product. When the surface moisture is lost, the outside begins to feel dry and the rate of evaporation slows down as the product warms up. It becomes important to recirculate the relatively humid air and prevent case hardening. In drying at a temperature of 49°C and air exiting at 43°C, we have the air properties during the drying process shown in Appendix III. The ambient air is 19°C with 67% relative humidity. The recirculated air properties are as shown in the process labelled “B” in Appendix III at 49°C and 42% relative humidity. This will require 25% fresh ambient air resulting in energy saving while maintaining the product. The designed pilot dryer for drying maize is shown in Figure 24 and the details for the trays are shown in Figure 25.

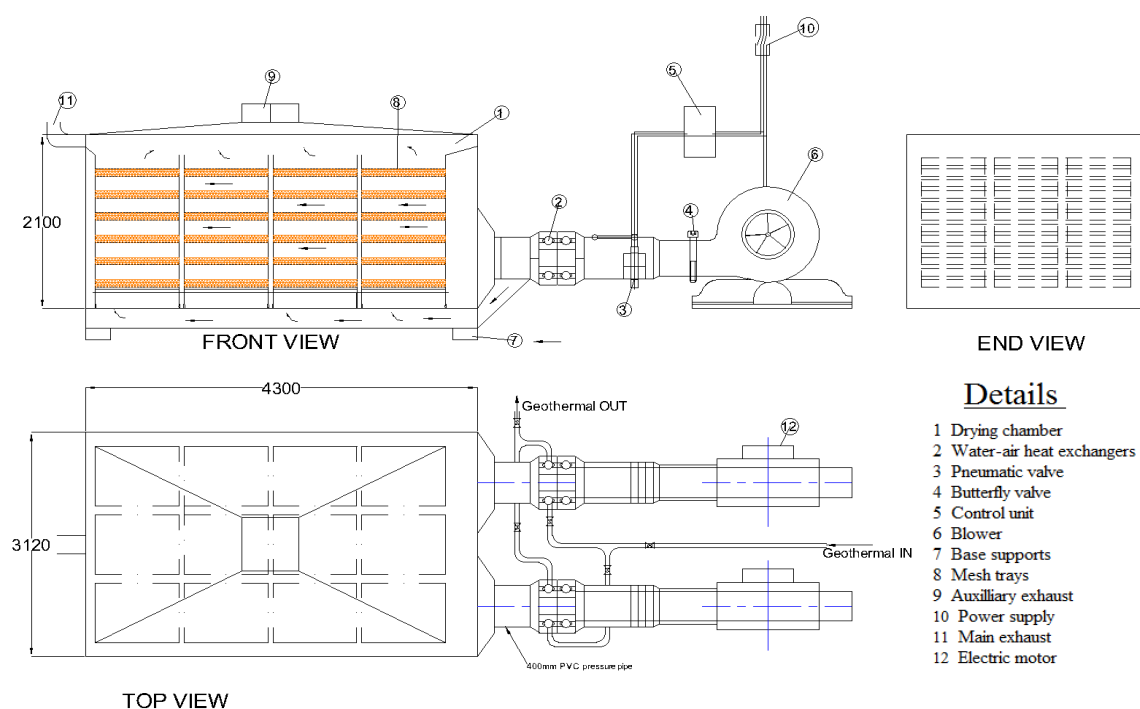


FIGURE 24: Designed crop dryer

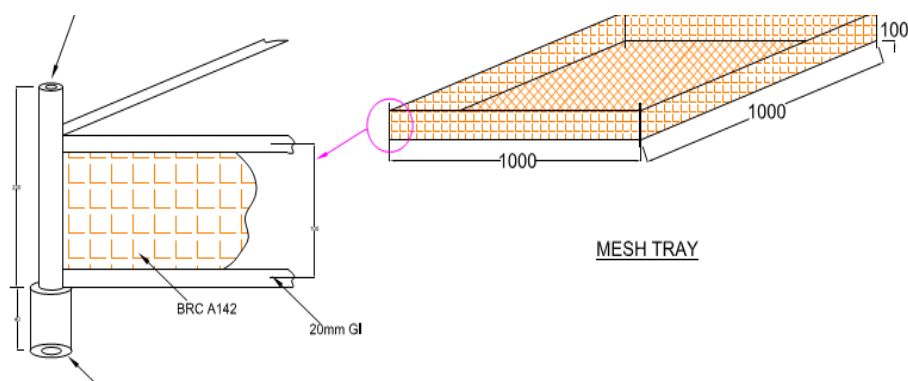


FIGURE 25: Details of the designed drying trays

In drying maize, air is blown into the heat exchanger at an ambient temperature of 19°C and heated to 65°C, and exits the drying chamber at 49°C. Control of geothermal flow into the water-air heat exchanger is then necessary, depending on the product being dried.

The design model was run for different maize capacities and different drying hours to determine the variations in the required flow rate as shown in Figures 26 and 27.

Figure 26 shows the variation of geothermal flow rate for different drying times for maize grains. Drying time is dictated by the amount of moisture to be removed and the type of product. For a higher volume of products, it is recommended to use a longer drying time when using relatively small pipe diameters or when the geothermal mass flow is not sufficient. The geothermal flow rate decreases exponentially with an increase in drying time as shown in Figure 27. The amount of heat energy required for various weights of maize is shown in Figure 28.

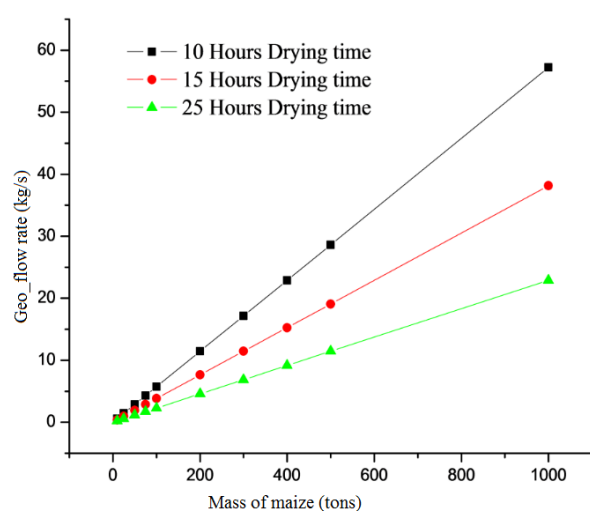


FIGURE 26: Variation of mass flow for different masses of maize

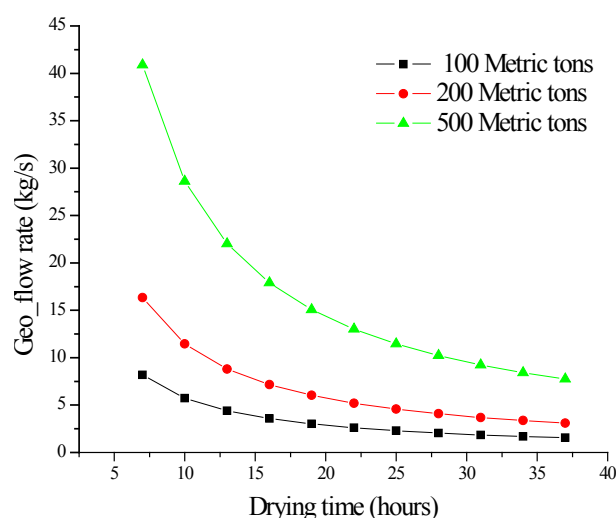


FIGURE 27: Mass flow against time for various grain capacities

Both the rates of geothermal usage and diesel usage increase lineally with an increase in the mass of grains being dried as shown in Figure 29.

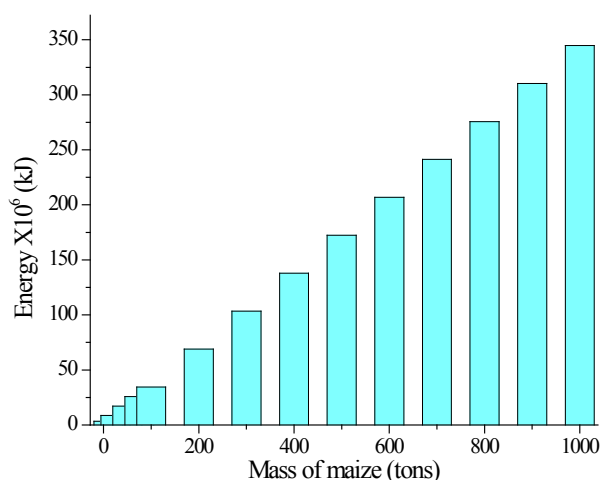


FIGURE 28: Heat energy requirement for various masses of grains

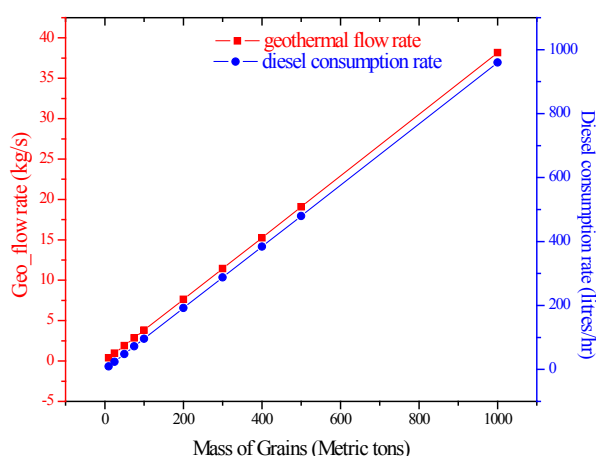


FIGURE 29: Geothermal flow rate and diesel consumption rates for drying different masses of grains

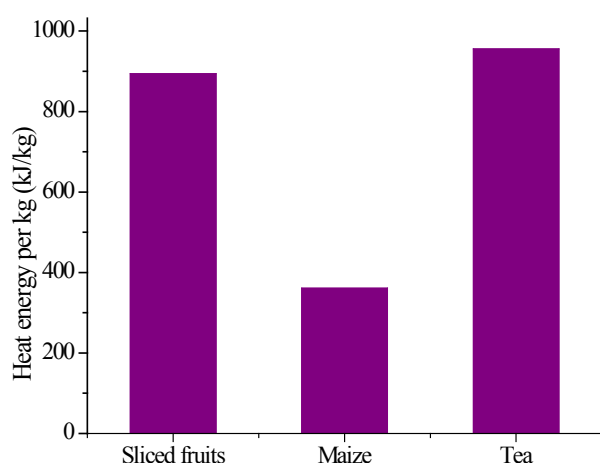


FIGURE 30: Heat energy per kg for drying different crops

The dryer can be used to dry other agricultural products. A test on drying tea and vegetables (tomatoes) was done in the design model and is shown in Figure 30. The energy per kilo of dried product for sliced tomatoes and tea is higher than that of maize, mainly because of higher moisture content in these products. The design parameters are summarised in Table 12.

TABLE 12: Designed dryer inputs and calculated outputs

Inputs			
	Parameter	Units	Value
Grain	Initial moisture content (db)	%	27
	Final moisture content (db)	%	13
	Grain drying temperature	°C	49
	Grain density	kg/m ³	721
Dryer	Volume	m ³	30
	Type : Tunnel/tray	-	-
Air	Ambient temperature	°C	19
	Relative humidity	-	0.68
	Atmospheric pressure	kPa	88
Geothermal	Entry temperature	°C	130
	Exit temperature	°C	93
	Flow rate	kg/s	2
Calculations			
Dryer	Mass of grain dried	tonnes	15
	Evaporated moisture	tonnes	2
	Thermal energy	kWt	250
	Drying time	hours	7
	Quantity of geothermal used	tonnes	40
	Air velocity	m/s	0.5
	Static pressure	mm H ₂ O	300
Heat exchanger (water-air)	Max. operating pressure	bars	24
	Number of fins	-	12
Centrifugal blower	Air flow rate	cubic ft/min	14000
	Static pressure	mm H ₂ O	400
	Motor rating	HP	30
	Operating temperature	°C	150

6. CONCLUSIONS

A geothermal crop dryer was designed and the energy required to dry grains was evaluated. The same dryer can be used for drying more crop varieties and can be experimented upon. Air re-circulation is a means of saving energy and maintaining high drying quality and can be implemented as indicated in this report.

The recommendation from this work, is to evaluate the drying efficiency of this dryer against drying various crops and do a cost comparison with diesel. The quality of the dried crops with regard to nutrients and shrinkage properties should be analysed and reported. Cascaded application with drying should be studied further among other applications.

ACKNOWLEDGEMENTS

I would like to thank my employer, Geothermal Development Company, for granting me the opportunity to attend this training programme. I am also grateful to the former director, Dr. Ingvar B. Fridleifsson and the current director Mr. Lúdvík S. Georgsson, for the successful organization of the programme. Many thanks go to my supervisors, Dr. Árni Ragnarsson and Prof. Sigurjón Arason for their good guidance, for sharing their knowledge and for supervision of this work. My thanks also go to Mr. Jóhann F. Kristjánsson for his assistance. Sincere thanks to Ms. Thórhildur Ísberg, Mr. Ingimar G. Haraldsson, Ms. Málfríður Ómarsdóttir and Mr. Markús A.G. Wilde for their useful help during the training period. I am grateful to the UNU Fellows for the time we have had together.

Special thanks to my wife Dorcas M. Ndirangu for her support, love, encouragement, prayers and endurance during my stay in Iceland.

Thanks to Almighty God for giving me wisdom and the strength.

NOMENCLATURE

KNBS	= Kenya National Bureau of Statistics;
MOA	= Ministry of Agriculture;
EUSPA	= European Union of swimming pool and spa associations;
GDC	= Geothermal Development Company;
GDP	= Gross Domestic Product;
FAO	= Food and Agriculture Organisation;
NCPB	= National Cereals and Produce Board; and
USD	= US dollars.

REFERENCES

Breadley, R., Myers S., and Allen 2011: *Principles of corporate finance* (10thed.). McGraw-Hill, Ltd., NY, 969 pp.

EPZA, 2005: *Grain production in Kenya 2005*. Export Processing Zone Authority, website: www.epzakenya.com.

EUSSA, 2010: *Domestic swimming pool water 2010*. European Union Swimming and Spa Association, website: www.eusaswim.eu/Documentation/downloads/Paper-on-water-quality.pdf.

FAO, 2008: *Basic principles of grain drying*. Food and Agriculture Organisation, website: www.fao.org/home/en/.

FAO, 2011: *Situation analysis: improving food safety in the maize value chain in Kenya*. Food and Agriculture Organisation, website: www.fao.org/home/en/.

GDC, 2013: *Well MW-03 discharge chemistry report*. Geothermal Development Company, Kenya, unpublished report, 12 pp.

Government of the Republic of Kenya, 2013: *Kenya Vision 2030*. Website: www.vision2030.go.ke

Halldórsson, G., 1975: *Heating and cleaning of water in swimming pools*. Sigurdur Thoroddsen Consulting Engineers, report ST 75 071 (in Icelandic), 63 pp.

Henderson, S.M., and Pabis, S., 1961: Grain drying theory I. Temperature effect on drying coefficient. *J. Agriculture Engineering Res.*, 6-3, 169-174.

Jamieson, R.E., 1984: Simulation of the silica scaling process. *Proceedings of the 6th New Zealand Geothermal Workshop, Auckland University, Auckland, NZ*, 135-140.

Kashpur, V.N., and Popatov, V.V., 2000: Study of the amorphous silica scales formation at the Mutnovskoe hydrothermal field (Russia). *Proceedings of the 25th Workshop on Geothermal Reservoir Engineering Stanford University, Stanford, Ca*, 7 pp.

Kavak Akpınar, E., Bicer, Y., Cetinkaya, Y., 2006: Modelling of thin layer drying of parsley leaves in a convective dryer and under open sun. Research Gate, website: www.researchgate.net.

Kevin, D., Rafferty, P.E., and Gene, C., 1991: Heat exchangers. In: Lienau, P.J., and Lunis, B.C. (editors), *Geothermal direct use engineering and design guidebook*. Geo-Heat Centre, Institute of Technology, Klamath Falls, 247-261.

Kipng'ok, J.K., 2011: Fluid chemistry, feed zones and boiling in the first geothermal exploration well at Menengai, Kenya. Report 15 in: *Geothermal training in Iceland 2011*. UNU-GTP, Iceland, 281-302.

KNBS, 2012: *Maize production in Kenya*. Kenya Bureau of Statistics, website: www.knbs.or.ke/.

Kowalski, S.J., and Mierzwa, D., 2013: Numerical analysis of drying kinetics for shrinkable products such as fruits and vegetables. *J. Food Engineering*, 114-4, 522-529.

Lewis, W.K., 1921: The rate of drying of solid materials. *Ind. Eng. Chem.*, 13-5, 427-432.

Liviu, G., and Badea, L., 2009: Aspects into the use of renewable energy sources in cereals drying process. *Proceedings of the 8th WSEAS International Conference on Signal Processing, Robotics and Automation 2009*, 74-77.

Maharjan R., 1995: Design of a dryer and a swimming pool using geothermal water. Report 7 in: *Geothermal training in Iceland 1995*. UNU-GTP, Iceland, 155-184.

Mangi P., 2012: Geothermal resource optimization: a case of the geothermal health spa and demonstration centre at the Olkaria geothermal project. *Presented at Short Course VII on Exploration*

for Geothermal Resources, organized by UNU-GTP, GDC and KenGen, at Lake Bogoria and Lake Naivasha, Kenya, 10 pp.

MOA, 2001: *Grain growing areas in Kenya*. Ministry of Agriculture, Kenya.

Mwangi, M., 2005: *Lectures on geothermal in Kenya and Africa*. UNU-GTP, Iceland, Report 4, 58 pp.

Ólafsson, J.H., and Sigurgeirsson, B., 2003: *The Blue Lagoon and psoriasis*. Blue Lagoon Ltd., 12 pp.

Orkustofnun, 2013: *Bathing and recreation*. Website: www.nea.is/geothermal/direct-utilization/bathing--recreation.

Panchariya, P.C., Popovic, D., and Sharma, A.L., 2002: Thin-layer modelling of black tea drying process. *J. Food Engineering*, 52-4, 349-357.

Perkins, P.H., 1988: *Swimming pools*. Elsevier Applied Science Publishers Ltd., London, 370 pp.

Pétursdóttir, S., and Kristjánsson, J.K., 1995: The relationship between physical and chemical conditions and low microbial diversity in the Blue Lagoon geothermal lake in Iceland. *FEMS Microbiology Ecology*, 19-1, 39-45.

RETScreen, 2011: *Retscreen international – Empowering cleaner energy decisions*. Natural Resources Canada, website: <http://www.retscreen.net/ang/home.php>

Ruiz, E., and Martinez, P.J., 2009: *Analysis of an open-air swimming pool solar heating system by using an experimentally validated TRNSYS model*. Universidad Miguel Hernandez, Edificio Torreblanca, Elche, Spain, 8 pp.

Shirbhate, D.V., 2013: *Design and study of grain dryer*. Scribd, website: www.scribd.com/doc/7370568/Design-Study-of-Grain-Dryer, 101 pp.

Sotocinal, A.S., 1992: *Design and testing of a natural convection solar fish dryer*. McGill University Montreal, Department of Agricultural Engineering, MSc thesis, 202 pp.

Temple S.J., Tambala S.T., and Boxel A.J.B., 2000: Monitoring and control of fluid-bed drying of tea. *Control Engineering Practice*, 8, 165-173.

Tesha, 2006: Utilization of brine water for copra drying in Lahendong geothermal field, Indonesia. Report 20 in: *Geothermal training in Iceland 2006*. UNU-GTP, 453-470.

APPENDIX I: Results of variable distance transform for pipe route selection

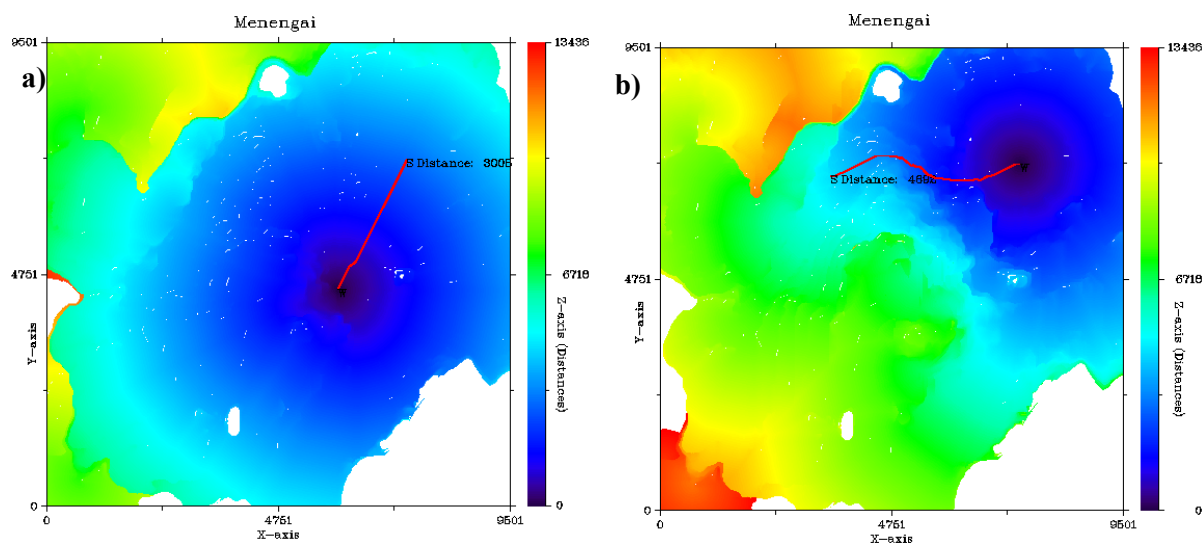


FIGURE 1: Map showing pipe route for supply (a) and re-injection (b) under scenario A

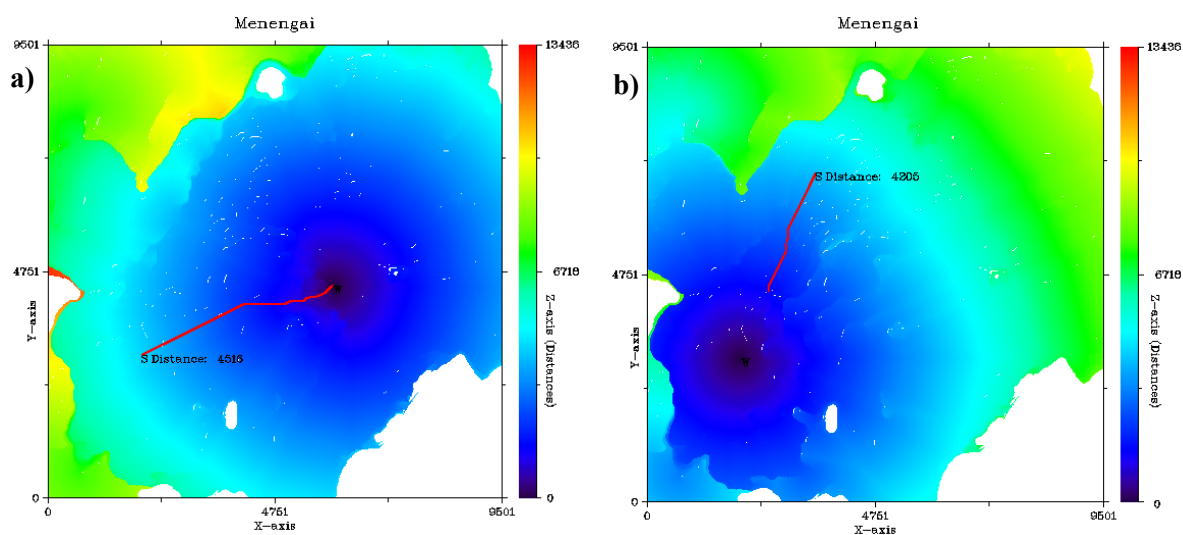


FIGURE 2: Map showing pipe route for supply (a) and re-injection (b) under scenario B

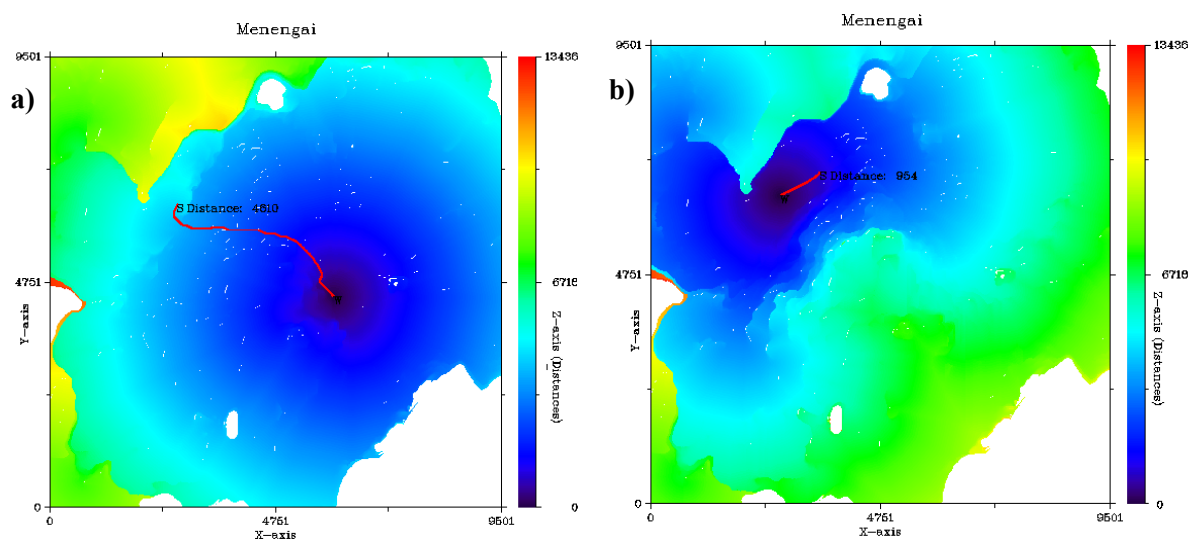


FIGURE 3: Map showing pipe route for supply (a) and re-injection (b) under scenario C

APPENDIX II: Shedd's curve showing resistance of grains to air flow

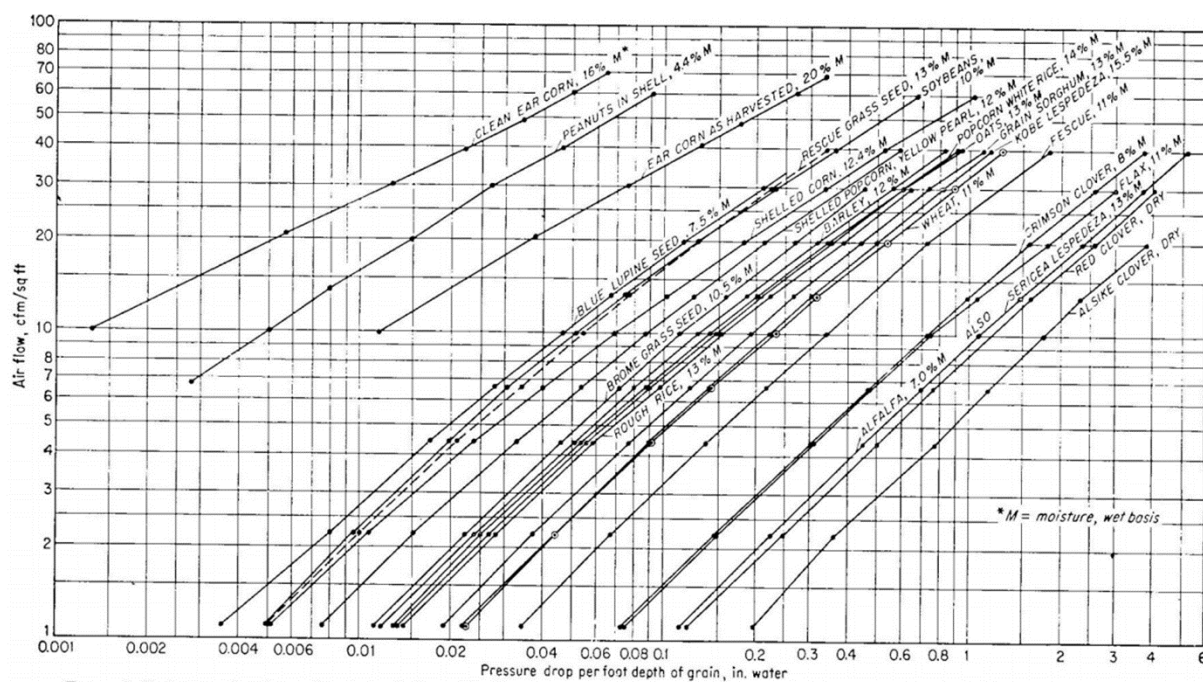


FIGURE 1: Resistance of grains to airflow (Shedd's characteristic curve, 1953)

APPENDIX III: Air properties during the drying process

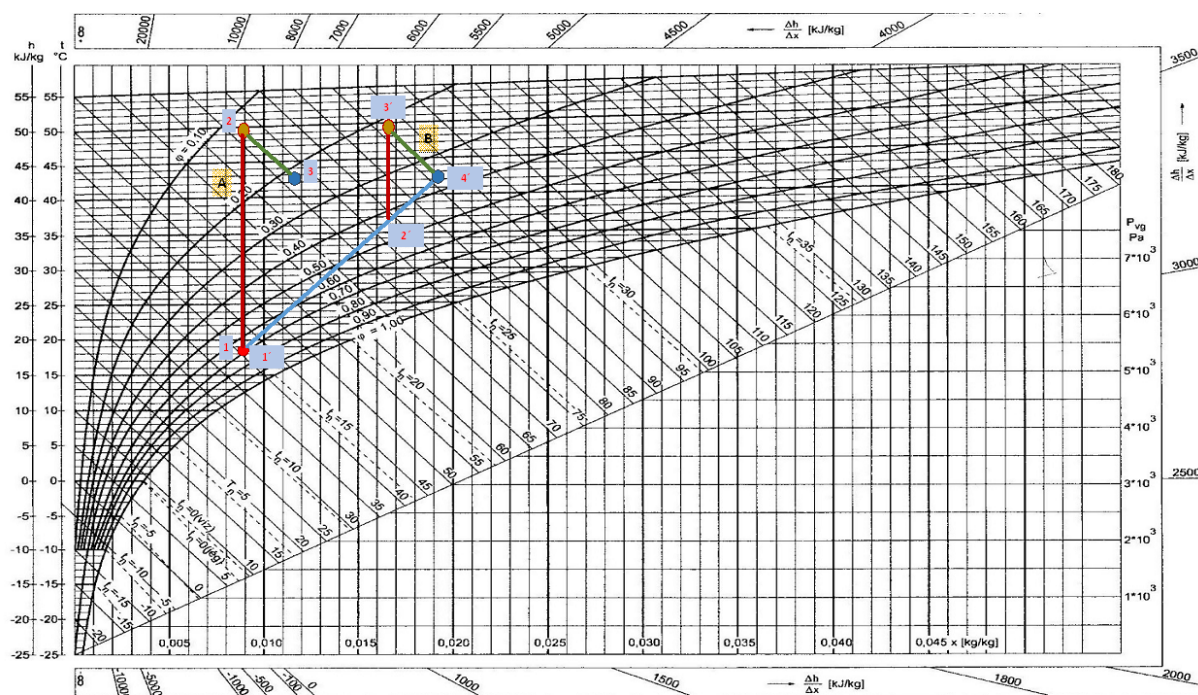


FIGURE 1: Psychrometric chart indicating air properties under re-circulation



BOREHOLE GEOLOGY AND HYDROTHERMAL ALTERATION OF WELLS MW-08 AND MW-11, MENENGAI GEOTHERMAL FIELD, KENYA

Loice Jemutai Kipchumba

Geothermal Development Company – GDC

P.O. Box 17700-20100,

Nakuru

KENYA

lkipchumba@gdc.co.ke

ABSTRACT

In order to understand the subsurface geology in any geothermal field, drilling is essential. The borehole geologists use the cuttings obtained during drilling to study the subsurface formation so as to identify the lithology, hydrothermal alteration mineralogy and probable location of aquifers. However, it is from the drilled wells that the temperature of the reservoir is measured. With such data, the dynamics of the geothermal system can be evaluated.

This paper presents the stratigraphic sequence and the hydrothermal alteration of Wells MW-08 and MW-11, drilled in the Menengai geothermal field. The stratigraphic column is made up of four rock units. They include: pyroclastics, trachyte, tuff and basalt. These dissected rocks conform to the Pre-, Syn- and Post-caldera volcanic activities that started shortly before 0.18 Ma. The highly altered basalt penetrated by the wells at greater depths is presumed to be older than the caldera and is linked to the pre-caldera volcanics. The main hydrothermal alteration minerals encountered include: zeolites, chalcedony, quartz, pyrite, calcite, smectite, illite, chlorite, epidote, wollastonite, and actinolite. From the hydrothermal alteration, four alteration zones have been identified below a zone of no alteration: a zeolite-illite zone appears followed by a quartz-illite zone, an epidote-quartz-illite zone and finally an epidote-illite-wollastonite-actinolite zone. Aquifers in the wells are associated with fractures, lithological contacts and loss of returns. A correlation of the hydrothermal alteration, fluid inclusion analysis and measured temperatures of the wells indicates that Well MW-08 is at equilibrium or slightly heating below 1700 m depth, whereas cooling is observed in Well MW-11.

1. INTRODUCTION

1.1 General information

Menengai geothermal field is one of the high-temperature fields located within the central segment of the Kenya Rift Valley. It is presumed to be at the triple junction where the failed junction Nyanzian Rift joins the main Kenya Rift Valley (Figure 1). The Kenya Rift is a volcano-tectonic feature that transects the country from Lake Turkana in the north to Lake Natron in Tanzania and is part of the East

African Rift System, an active continental-continental divergence zone where the Somali and Nubian plates are drifting apart at a rate of 2 cm per year (1 cm in each direction) resulting in crustal thinning (e.g. Lagat, 2003). The segment is host to several Quaternary to recent volcanic complexes. Some of the volcanic centres are dotted with hydrothermal activity and are envisaged to host extensive geothermal systems driven by their still hot magma. Studies show that these volcanic centres have positive indications of a geothermal resource that could be commercially exploited (GDC, 2010).

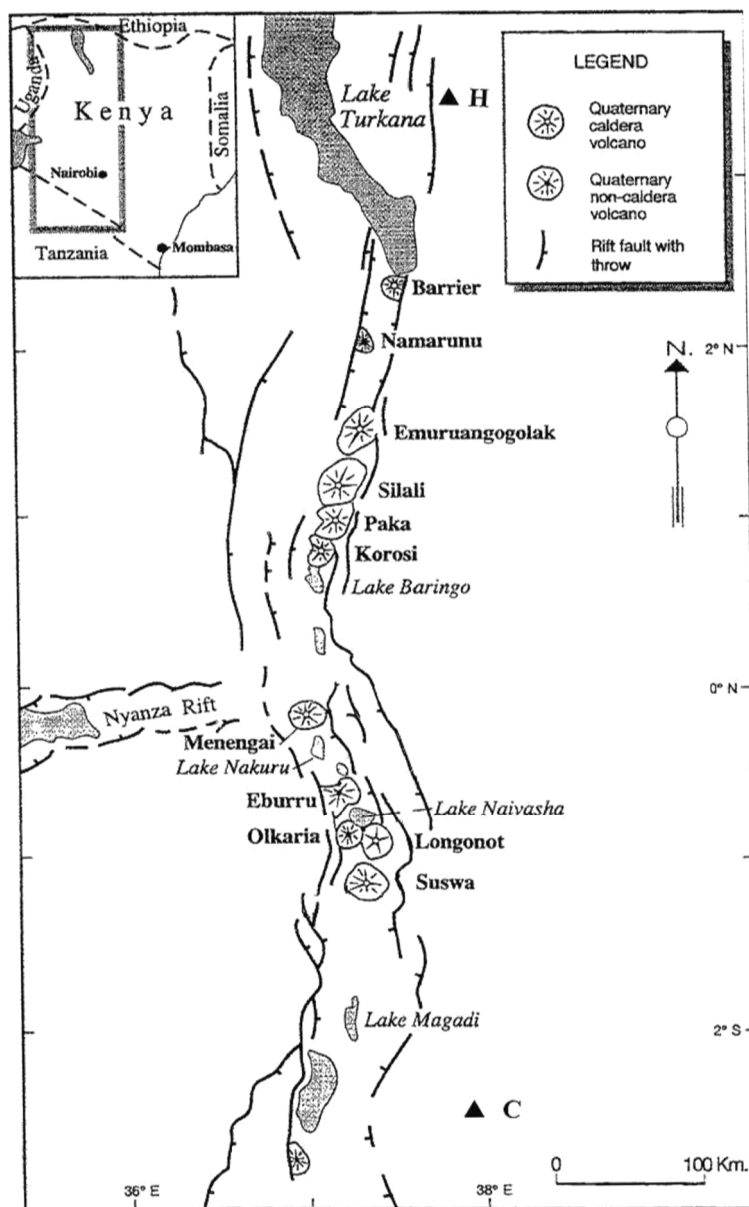


FIGURE 1: Quaternary volcanoes in the Kenya Rift (from Scott and Skilling, 1999 in Macdonald, 2003)

purposes/objectives including academically based research, regional geological mapping for government institutions and regional mapping with interests in natural resources, including geothermal. Some of the most relevant publications/reports include mapping by McCall (1967) in which the geology of area around Menengai is described. Leat (1983) carried out a very comprehensive study on the petrochemistry and evolution of the Menengai volcano, which was presented in a PhD thesis. Jones and Lippard authored and co-authored a number of papers in which the geologic evolution of Menengai volcano was discussed (Jones, 1985; Jones and Lippard, 1979). Geotermica Italiana (1987) carried out

Exploration drilling to prove steam, determine the resource extent, nature and chemical characteristics in Menengai geothermal field is ongoing since its commencement in February 2011; at the time of writing this report, 15 wells have been drilled, among them Wells MW-08 and MW-11.

1.2 Objective of the project

The aim of the project is to study the borehole geology and hydrothermal alteration mineralogy of Wells MW-08 and MW-11 by analysing drill cuttings taken at 2 m intervals in both wells. This is to describe the subsurface lithological formations, feed zones or aquifers, the hydrothermal alteration mineral assemblage and to delineate how they relate to the formation temperatures of the wells.

This project report was carried out and submitted as a partial fulfilment of the six months course in Borehole Geology at the United Nations University Geothermal Training Programme (UNU-GTP) attended in Iceland in 2013.

1.3 Previous work

Previously, Menengai geothermal field has been studied by different geoscientists for different

work with an interesting discussion on the occurrence of geothermal potential under the GoK/ UNDP geothermal reconnaissance project that covered the region between Menengai and Bogoria. The report described the geological and hydrogeological features of the region and attempts to interpret the relationship with the occurrence of geothermal manifestations. KenGen (2004) later carried out detailed surface exploration with the purpose of evaluating the geothermal systems and, in their results, indicated that Menengai had a potential for a geothermal resource that could be commercially exploited. In 2010, GDC conducted a detailed study in the Menengai prospect to confirm all geological observations recorded in previous work that might be associated with development and occurrences of geothermal resources in the prospect area. From this study, the geophysical analysis indicated a heat source underlying the caldera structure in Menengai and a similar one in the Ol'rongai geothermal area with reservoir temperatures $>250^{\circ}\text{C}$, deduced from gas geothermometry. Based on these findings, exploratory wells were sited and a decision to commence drilling was reached. At the time of writing this report, drilling is ongoing and a total of 15 wells have been drilled since commencement in February 2011.

2. GEOLOGY AND STUCTURAL SETTING

2.1 Regional geology

The high-temperature geothermal prospects in Kenya are located within, and are associated with, the development of the Kenya Rift. The Kenya Rift is part of the eastern arm of the East African Rift System, an incipient continental divergence zone where thinning of the crust is occurring with consequent eruption of lavas and associated volcanic activities (Lagat, 2004). The development of the Rift was initiated by rift faults within the Late Proterozoic basement of the Mozambique belt and close to the eastern margin of the Tanzania craton (Hetzel and Strecker, 1994; Smith and Mosely, 1993). The geological evolution of the Rift started during the late Oligocene (30-35 Ma) in the area known as the Turkana Rift (MacDonald, 2003). During the Miocene period, volcanism associated with the rifting began. The activity was accompanied by domal uplift of about 300 m on the crest of erupted phonolites, which were subsequently faulted (Baker and Wohlenberg, 1971; Williams, 1972; Hay and Wendlandt, 1995).

The Pliocene eruptions that followed the Miocene volcanics and the subsequent faulting are divided into four principal phases (Baker et al., 1988). These phases were coupled with faulting episodes, during which time most of the structural features evolved. The first phase was the wide-spread Mau-Kinangop tuff ash flows (3.7-3.4 Ma). Major faulting occurred following the ignimbrite eruptions, which converted an earlier half graben into a graben. The second phase was the eruption of the Limuru flood trachyte (2.0-1.8 Ma) which was initiated by the progressive inward migration of the fault zones. This migration resulted in the formation of step-faulted platforms (Mau escarpments) and the fissure eruptions of the Limuru trachyte flood lavas. Basalts and basaltic trachy-andesites form the third and fourth phases, respectively (1.65-0.9 Ma). These last two phases were triggered by faulting that followed the Limuru flood trachytes. This faulting was triggered by a convecting mantle, opening up fractures which served as conduits for Quaternary volcanic activity and the development of many large shield volcanoes of silicic composition in the axis of the rift (Baker et al., 1988). These volcanoes, most of which are geothermal prospects, include Suswa, Longonot, Olkaria, Eburru, Menengai, Korosi, Paka, Silali, Emuruaogolak, and the Barrier Complex (Omenda, 2007).

Geothermal manifestations like fumaroles, hot springs, hot and altered grounds are abundant within the Rift and most of them are associated with the young Quaternary volcanoes (Omenda, 1998). Thinning of the crust in the Rift is also responsible for the general high heat flow within the Rift, with a geothermal gradient of over $200^{\circ}\text{C}/\text{km}$ (Wheildon et al., 1994).

2.2 Geology of the Menengai volcanic complex

Menengai is a large caldera volcano located on the floor of the Kenyan Rift Valley and is within an area with complex tectonic activity characterized by a confluence of two tectono-volcanic axes, Molo and Solai (Omenda, 2007). The caldera is of the Krakatau type, formed as a result of rapid emptying of a magma chamber (McCall, 1957). Leat et al. (1984), Macdonald and Scaillet (2006), and Macdonald et al. (1970) described the surface geology of Menengai to be composed of silica-oversaturated, peralkaline, metaluminous trachytes or pantellerite. Its evolution and surface geology have been described and linked to the Pre-, Syn- and Post caldera volcanic activities (Figure 2).

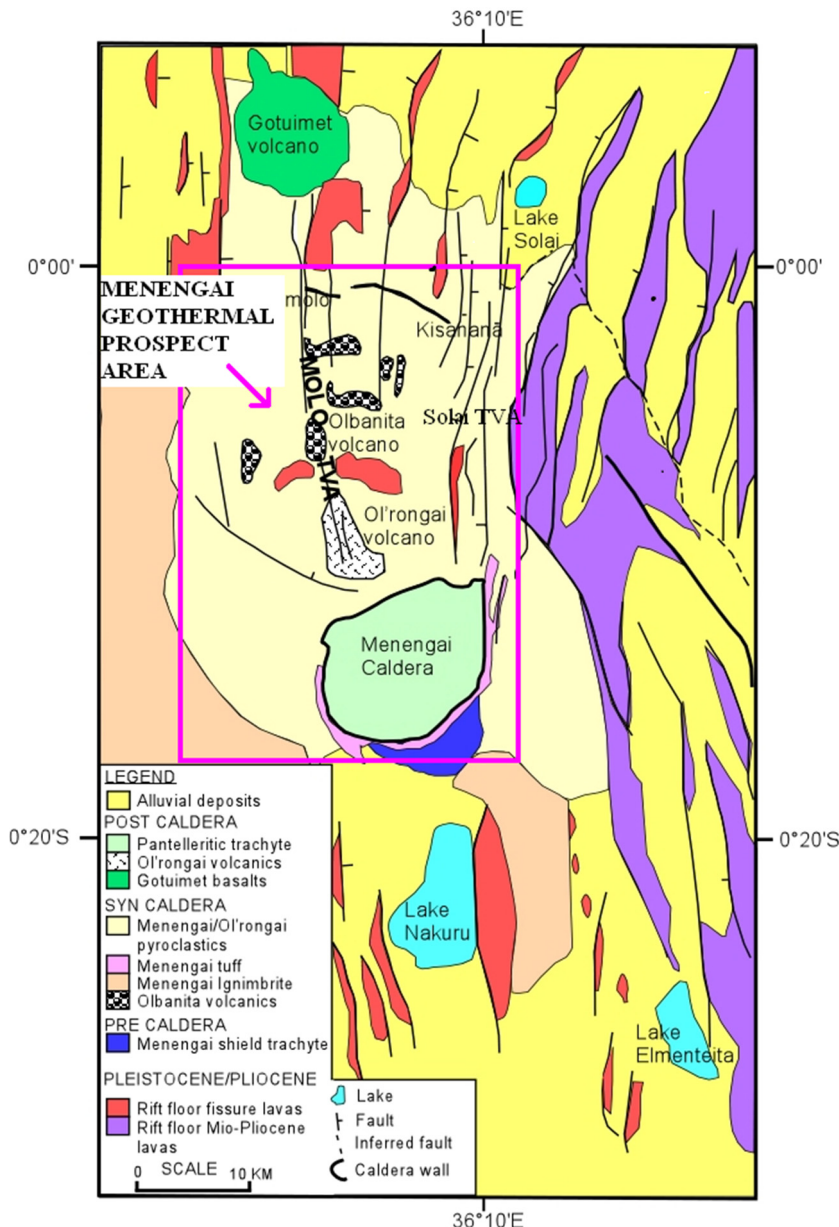


FIGURE 2: Geological map of Menengai geothermal prospect (GDC, 2010)

the failed rift arm at the point where the Nyanzian Rift joins the main East African Rift (GDC, 2010). Within the embayed ring-fracture, an eruption of two ash flow tuffs occurred, representing a combined magma volume of about 50 km³. The eruption of both tuffs was preceded by an air-fall phase. During post-caldera times, secondary eruptions of mainly lavas, sheet-forming air-fall pumice, and cinder cones took place. About seventy lava flows cover the caldera floor, with many flows showing both blocky

Activity started shortly before 0.18 Ma and continued in the Pleistocene with the formation of the caldera and more recent activity has given rise to the flows on the caldera floor (Leat, 1984; Macdonald et al., 1970). The volcano evolved from the growth of a broad low-angle trachyte lava shield, which probably sloped gently (10 m per Km) northward from south of Menengai (Leat, 1984). The flanks of this early structure remain intact and form low hills which slope away from the rim of the caldera while its central part foundered during the caldera collapse. The thickness and sequences of the pre-caldera volcanics, which are associated with the formation of the shield volcano, have been exposed by the caldera wall.

Isopach maps of the pre-caldera volcanics illustrate that the volcano was shield-like, with flanks dipping 1.5-8° away from the summit and had a broadly oval plane with a major axis of 22 km trending NE-SW (Leat, 1984).

A Krakatau-style collapse which formed a 77 km² caldera occurred as a result of

and ropy features (McCall, 1957; Leat, 1984). The air-fall beds are interbedded with the lavas and the cinder cones up to 50 m high, composed of unconsolidated scoria.

To the northwest of Menengai caldera the Ol'rongai and Ol'banita calderas are found. These are thought to be older than the Menengai caldera due to the presence of ignimbrite deposits whose age suggests an older date than the lava pile of the embryonic stage of Menengai. Through extrapolation of the existing arcuate remnant scarps, a caldera that occurs at the centre of Ol'rongai volcano, and one that extends to El Bonwala ridge north of Ol'banita swamp have been proposed (GDC, 2010).

2.3 Structural setting of Menengai geothermal field

From the surface geology, three main geological structures (Figure 3), which include the Molo TVA, the Solai TVA and the Menengai caldera/ring faults, can be described.

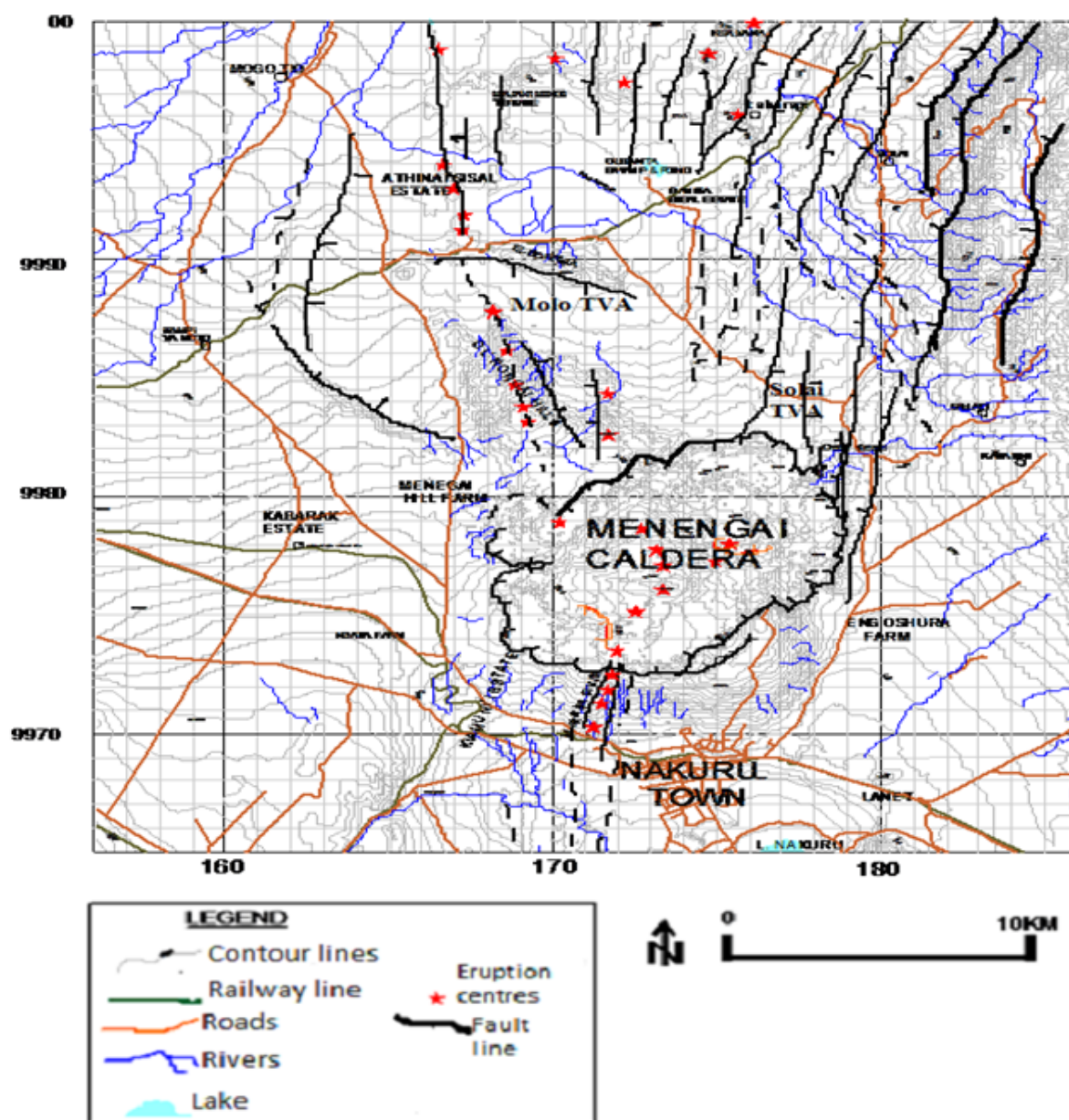


FIGURE 3: Structural map of Menengai geothermal prospect (modified from GDC, 2010)

Molo TVA is a prominent volcano-structural feature represented on the surface by a zone with a high concentration of faults and fractures along which volcanic eruptions have taken place. The Ol'Rongai structural system represents a part of the larger Molo TVA that has had significant volcanic activity, including eruptions in the early Pleistocene epoch that resulted into a build-up of a NNW-SSE trending ridge referred to as the Ol'Rongai volcano. The apparent high volcanism indicated by numerous eruption centres in the western part of Menengai caldera is probably due to the intersection of the caldera structures and the Molo TVA/Ol'Rongai fracture system.

Solai TVA is a narrow (4 km wide on average) tectonic axis graben that runs in a NNE-SSW trend through Lake Solai. It extends into the Menengai caldera system and probably even beyond, giving rise to the Makalia fault system which passes through the western part of Nakuru Town. It is comprised of numerous fault/fractures systems trending NNE-SSW. The western boundary of the graben is associated with the Makalia fault (Mibei and Lagat, 2011). Since it is cutting through the caldera, these faults are considered younger than the Menengai caldera.

Lagat and Ngenoh (2010) described the *Menengai caldera/ring faults* as an elliptical depression with minor and major axes measuring about 8 and 12 km. Its existence is proof of the presence of a heat source beneath Menengai. The circular rim of the caldera ring fault is well preserved with a vertical cliff at some places measuring up to about 400 m. The ring structure has only been disturbed by the Solai graben faults at the northeast end. The caldera is partially filled with post caldera lavas such that it is not possible to estimate the collapse depth or any structures that may be marking the caldera floor.

3. METHODOLOGY

3.1 Sampling

Rock cutting samples were collected at a 2 m interval during drilling except at points where a partial or total loss was experienced. Binocular analysis was performed at the rig site with the aim of developing a preliminary litho-stratigraphy and to estimate the down-hole temperatures from alteration mineralogy. This was to help in the casing depth determination and in advising drillers on geotechnical aspects. The samples were taken to the laboratory for further detailed analysis and storage. Cores were not collected in these wells; hence all the descriptions and interpretations are based on the rock cuttings.

3.2 Analytical techniques

3.2.1 Binocular microscope analysis

Binocular analysis was done using an Olympus SZX12 stereo microscope. It involved washing the samples thoroughly with tap water to remove dust and impurities and to enhance visibility. The small sample holder boxes containing the cleaned 2 m interval samples were then mounted on the stage of the binocular microscope, one at a time, for analysis. The physical properties of the rock cuttings were the main features which include the rock type, colour, texture and grain size, rock fabric, primary mineralogy, and secondary/alteration mineralogy. Other features like oxidation, intensity of alteration, vein fillings, intrusions, probable aquifers and various litho-stratigraphic boundaries were identified through this method of analysis. Representative samples from the lithological units penetrated by the wells were selected and prepared for further analysis using other analytical techniques.

3.2.2 Petrographic microscope analysis

A total of seventy thin sections, prepared from the selected representative samples, were analysed using the LeitzWetzlar petrographic microscope. These analyses were done so as to confirm the rock type and alteration minerals noted in the binocular analysis. In addition, the analyses helped to identify additional alteration minerals not observed by the binocular microscope and clearly identified the depositional sequence of the alteration minerals.

3.2.3 X-ray diffractometer analysis

Thirty six samples were prepared for XRD analysis. Each sample was prepared and analysed in three conditions: untreated, glycolated, and heated. The peaks recorded from the analyses were interpreted and the types of clay present in the selected cuttings were identified. Identification of various types of clays in the wells' lithological columns was important in the sense that the alteration zone boundaries could be determined, hence estimating the alteration temperatures in the geothermal system through the wells' stratigraphy.

3.2.4 Fluid inclusion analysis

Fluid inclusion analysis is simply an analysis of fluids trapped in vacuoles inside mineral grains during growth or recrystallization. The trapped fluids, termed as fluid inclusions, give an approximate temperature from the time when the fluid was trapped in the mineral grain. This is measured by heating the crystal until the fluid inclusion reaches the homogenization temperature (Th). For this study, the procedure involved careful selection and polishing of secondary quartz and calcite grains from specific depths of the study wells. Upon confirmation by use of the petrographic microscope of the presence of clear fluid inclusions, the grains, each at a time, were slowly heated on a Linkam THSMG 94 freezing and heating stage, focusing on the trapped bubble/inclusion until the fluid homogenized into a single phase (i.e. bubble disappears) and the Th was measured. Comparing the results from this analysis with the measured temperatures of the wells brings to light the thermal evolutionary history of the geothermal system.

Finally, findings from all the analyses were integrated and compiled using LogPlot 2007 (RockWare, 2007) for ease of conclusive analysis and interpretation.

4. BOREHOLE GEOLOGY

4.1 Drilling of wells MW-08 and MW-11

Wells MW-08 and MW-11 are the eighth and eleventh exploration/production wells drilled in Menengai geothermal field. Their locations are E 173231.3, N 9978225.3 at an elevation of 2015 m above sea level and E 172374, N 9978707 at 1993 m above sea level, respectively (Figure 4). The wells were aimed at tapping from the NE-SW striking faults and the NNW-SSE structures associated with the Molo and Solai TVA. The specific objective for drilling the wells was to further explore and determine the subsurface geology, hydrothermal alteration, and chemical characteristics of the geothermal reservoir at Menengai.

4.1.1 Drilling of Well MW-08

Well MW-08 was spudded on 17th February, 2012 at 1315hrs and completed on 20th June, 2012 (Figure 5) after which the rig was released for demobilization. The drilling was conducted in the following four main stages:

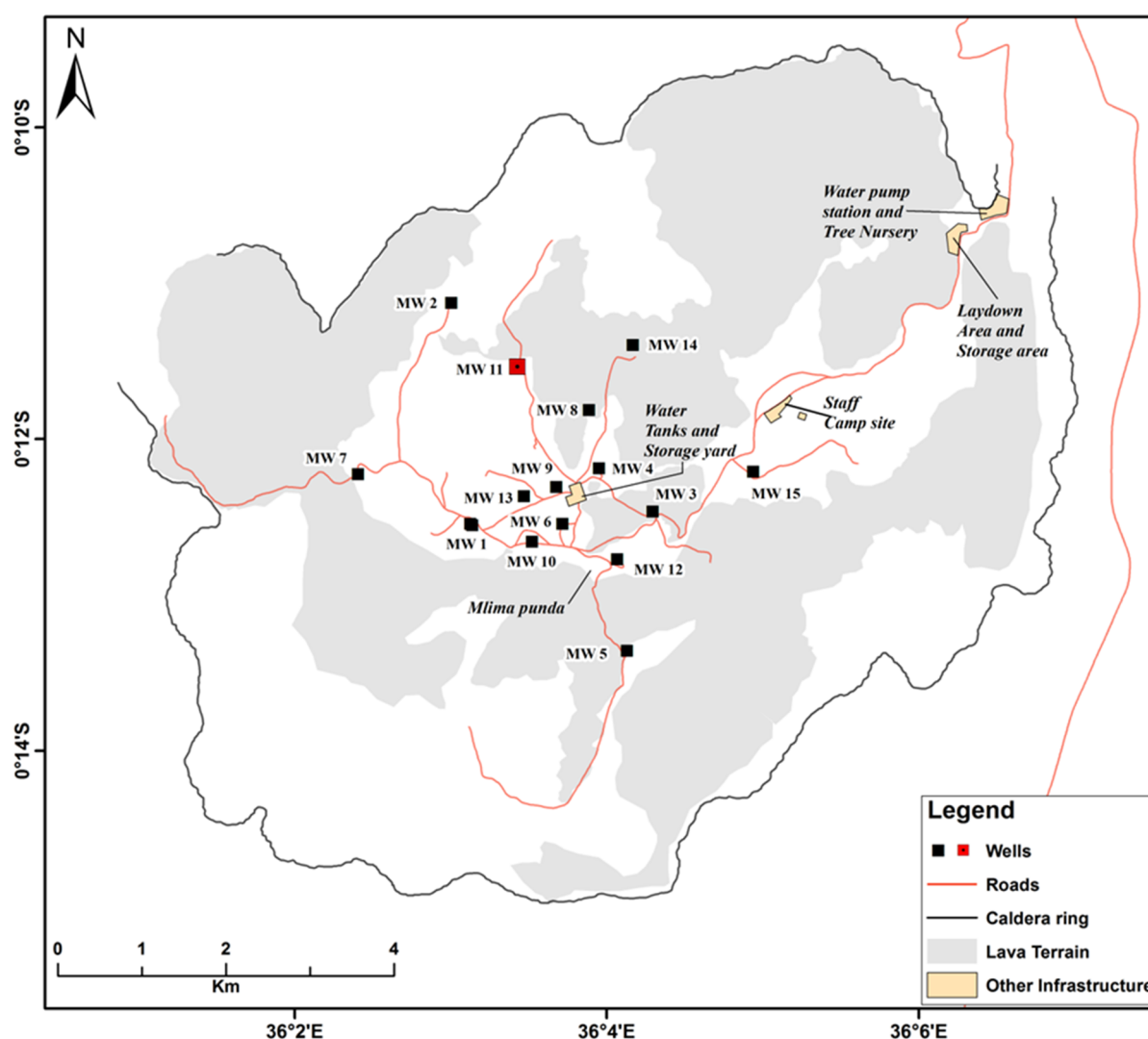


FIGURE 4: Location of Wells MW-08 and MW-11 (GDC, 2013)

Stage one (Drilling of 26" hole): The 26" hole was drilled to a depth of 65.03 m. This section was drilled with water complemented by mud gel sweeps. Circulation of returns was good for the entire section. A 20" casing was run in hole at 63.25 m RKB and was cemented with 10.33 m³ of cement slurry of density 1.73 g/cm³. Cement returns were not received on the surface. Therefore, a backfill job was done with 4.5 m³ of cement slurry with successful returns.

Stage two (Drilling of 17½" hole): Drilling of the 17½" hole commenced on 29th February, 2012. At a depth of 179 m, a cross over failed when shearing occurred at the box end, leaving behind the 17½" bit, bit sub, 17½" stabilizer, the crossover and two stands of 8" drill collars, necessitating a fishing job. After a successful retrieval, drilling progressed with water, complemented with mud sweeps, to a depth of 378.9 m. Returns were full with alternately partial returns at depths 230-263 m. The 13⅜" casing was run in hole to a depth of 366.22 m followed by primary cementing using 38 m³ of cement. After three backfill jobs with 34.7, 19.2, and 1.9 m³ of cement slurry for the first, second and third backfills, cement returns were received on the surface. A slurry density of 1.72 g/cm³ for primary and 1.65 g/cm³ for backfills was used.

Stage three (Drilling of 12¼" hole): The 12¼" hole was drilled to a depth of 932.25 m. The drilling fluid used included water and mud. Most of the time there were full returns, but total losses occurred at depths of 636, 638, 716, 722, 762, 859, and 861 m. The 9⅝" casings were run in the hole, landing at

928.08 m. A cementing operation followed with primary cementing taking in 34 m³ of cement slurry of density 1.72 g/cm³. The first and second backfills took 43 and 7 m³, respectively, both with a density of 1.65 g/cm³.

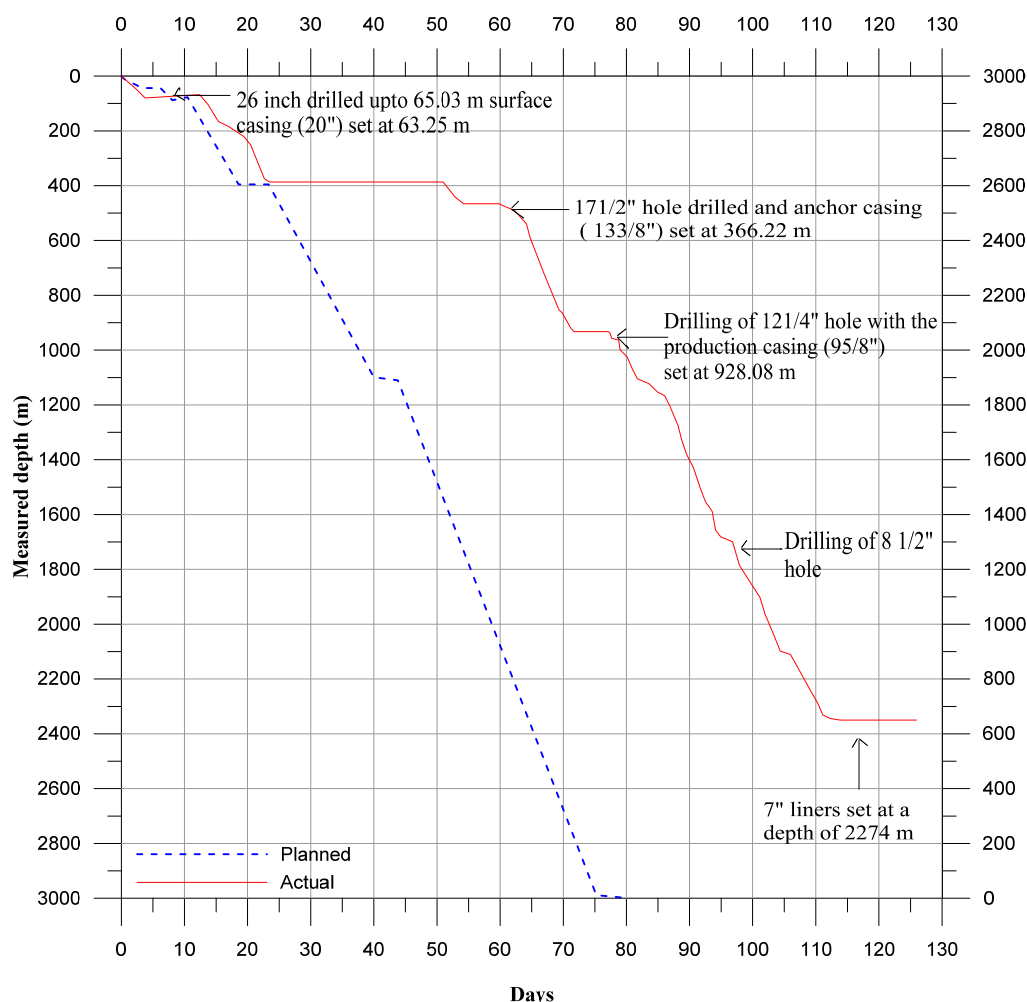


FIGURE 5: Drilling progress of Well MW-08

Stage four (Drilling of 8 1/2" hole): The drilling fluid used in this section was aerated brine and foam with continuous returns received on the surface. The target depth of 2355.56 m was attained. However, on pulling out to run in 7" liners, it was realized that the 8 1/2" bit, 6 1/2" bit sub, 8 1/2" blade stabilizer, and three 6 1/2" drill collars were left down the hole. The total length of the tools left down the hole is 29.73 m. The fishing operation was called off after several unsuccessful attempts. The liner was then run in the hole and set at a depth of 2274 m, i.e. hanging at 51.83 m from the fish top on 17th June, 2012, followed by well completion tests from 18th June to 19th June, 2012. The well was capped on 20th June, 2012 with a 10" expandable Master valve.

4.1.2 Drilling of Well MW-11

On 28th September, 2012 at 1700hrs, Well MW-11 was spudded. The four main stages during the drilling of this well included:

Stage one (Drilling of 26" hole): A 26" bit was used to spud the well. The 26" diameter hole was drilled to a depth of 70.5 m RKB. This section of the hole was drilled with water with returns received on the surface throughout. Mud sweeps were done twice per single drill pipe. A total of 7 joints of 20" 94

PPF BTC casings were run in, followed by primary cementing of 9.2 m³ of cement and two backfills of 3.5 m³ each. The total neat cement consumed was 12.8 m³.

Stage two (Drilling of 17½" hole): The intermediate hole was drilled with a 17½" bit to a depth of 278.6 m. Generally, this section was drilled blind with water with partial returns from 90 to 156 m and total losses from 156 to 268 m. Efforts to regain circulation by use of LCM and plugging bore no fruit. Due to the failure to regain circulation and a relatively hard formation, the 13⅜" casing depth was set at 273.96 m. Primary cementing of 5 m³ of neat cement was done followed by 4 backfills of 17.67, 14.88, 28.8 and 4 m³ of neat cement, respectively.

Stage three (Drilling of 12¼" hole): The third drilling stage for the production casing was drilled with a 12¼" bit to a depth of 899 m. The main drilling fluid in this section was aerated water and foam. Intermittent losses were encountered at depths of 304, 307 m and from 315 to 326 m. However, several pluggings were done due to a problem of a parted (anchor) casing that caused an obstruction at 563.78 m. The 9⅝" casing was set at a depth of 888.29 m with a total of 42.75 m³ for the plug jobs and 85.5 m³ was used in cementing the production casing.

Stage four (Drilling of 8½" hole): The production section was drilled to a depth of 1842.37 m using an 8½" bit for the entire section; aerated water and foam were used as the drilling fluid. Sweeps with high viscosity mud were employed after every 5 m to ensure thorough removal of cuttings. At 1842.37 m depth, the drill string was pulled out for inspection. A tight spot encountered at 1840 m when running in the drill string called for reaming, and it was while reaming at a depth of 1841 m that the drill string got stuck. Several attempts were made to free the string but all were unsuccessful (Figure 6). It was, therefore, decided to mechanically back off the drill string. Two stands of 6½ inch drilling collars, stabilizer, and bit were left in hole. A total of eighty 7" liners were run and set at 1784.28 m and a master valve was installed.

4.2 Stratigraphy

The evolution and surface geology of Menengai geothermal field have been described and linked to the Pre-, Syn- and Post caldera volcanic activities (Leat 1984; GDC, 2010). The two meter interval collected sample cuttings from Wells MW-08 and MW-11 were subjected to both binocular and petrographic microscope analysis with the aim of identifying the formations penetrated by both wells and to find if they were related to the evolutionary history of the geothermal field.

From the analysis, five types of rock units were found to form the litho-stratigraphy of Wells MW-08 and MW-11. They include: pyroclastics, trachyte, tuff, syenite, and basalt. Syenite occurred as an intrusive. Pyroclastics formed the top 20 m column from the ground surface. It is made up of grey to brownish grey vesicular fragments of pumice lapilli particles, obsidian, and glass and lithics of trachytic composition. Trachyte was the most dominant rock penetrated by both wells. It was encountered from 4 m to the bottom of the wells, alternating with lenses of tuff, basalt and syenite. The rock ranges from light to dark grey, brownish grey and green in colour. The texture ranged from fine to coarse grained and porphyritic with prismatic sanidine phenocrysts embedded in the feldspar rich groundmass. This textural and grain size variation could be linked to different episodes of lava eruptions during the Pre-, Syn- and Post caldera volcanic activity.

Tuff is the second most abundant rock (after trachyte) encountered in both wells. In Menengai, tuff has been identified as the marker horizon separating the pre-caldera and post-caldera volcanic stages. Wells MW-08 and MW-11 saw this formation at depths of 474 and 280 m, respectively. Significant tuff layers were also at depths of 850 m, 962-1022 m and 1198-1222 m. It mainly occurred as a grey to brownish, poorly crystalline, vesicular rock. From the binocular analysis, the vesicles at the 300-490 m range were seen to be partially filled with chalcedony. Calcite, quartz, and clays filled both the vesicles and veins

in the rocks at greater depths. In all the occurrences, the tuff was bleached and moderately to highly altered.

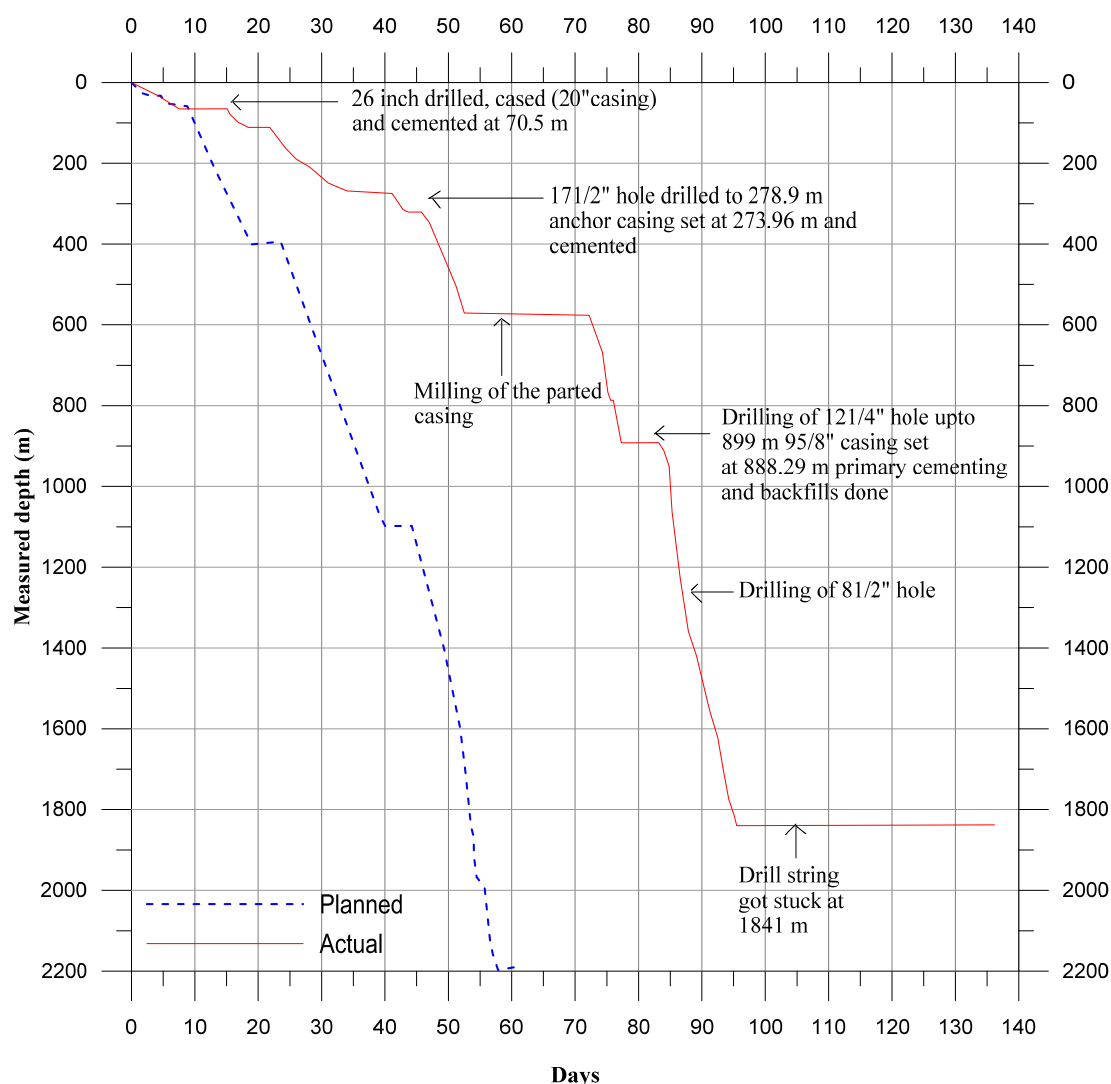


FIGURE 6: Drilling progress of Well MW-11

Syenite was only encountered in Well MW-08 at depths of 1830-1854 m, 1926-1948 m and 1978-2002 m, respectively. It appeared as thin lenses between the thick trachytic lavas. The rock is grey, coarse grained and porphyritic, consisting primarily of alkali feldspars together with some mafic minerals. The rock is hard and compact when encountered, deduced from the low penetration rates recorded during drilling and the disappearance of pyrite.

A thick column of basalt was encountered at 1558-1810 m in Well MW-08 and from 1680 m to the bottom of the well in Well MW-11. In both occurrences, three types of basalt were identified: Glassy grey fine-grained, greyish fine-grained porphyritic and a more crystalline, dark, fine-grained type of basalt. These three types occurred in one column and systematically with the glassy, fine grained on top, fine-grained porphyritic in the middle, and the more crystalline fine grained basalt at the bottom. Importantly noted was the degree of alteration: the glassy type was extensively altered and marked by the first appearance and abundant deposition of high-temperature alteration minerals of epidote, wollastonite, and actinolite. The fine-grained porphyritic and the more crystalline types of basalt appeared compact and less altered compared to the host basalt. In Well MW-11, the greyish fine-grained porphyritic type of basalt was not seen. Below is a detailed description of the lithological units seen in Wells MW-08 and MW-11.

4.2.1 Well MW-08

Post-caldera volcanics:

0-12 m: *Pyroclastics*. It is made up of grey to brownish grey, vesicular fragments of pumice lapilli particles, obsidian, and glass and lithics of trachytic composition. The bulk of the pyroclastic is poorly sorted and unconsolidated. The alteration minerals observed are opaque (oxides) and clays, indicating an interaction due to precipitation.

12-62 m: *Fine-grained trachyte*. Grey to greenish grey, hypocrySTALLINE fine-grained trachyte with trachytic texture. Greenish-yellow pleochroic clinopyroxenes appear scattered in the feldspar-rich matrix. Pyrite is seen disseminated in the groundmass.

62-66 m: *Loss of returns*

66-188 m: *Fine-grained trachyte*. The formation is light to dark grey, fine grained and porphyritic. Sanidine phenocrysts are elongated and scattered in the rock matrix. The rock is slightly oxidized but becomes intensely oxidized between 124-150 m. Chalcedony at 68 m is seen as a vesicle infill.

188-304 m: *Loss of returns*

304-474 m: *Fine-grained trachyte*. Green to bluish, equi-granular rock. Alteration intensity is low, with the feldspars and pyroxenes starting to alter slightly to clays and abundant segregates of fully grown primary quartz are found at this depth.

Possible syn-caldera volcanics

474-494 m: *Tuff*. Reddish brown, vesicular tuff with large phenocrysts of sanidine. At 488 m scolesite and chalcedony are seen filling veins and vesicles.

Possibly pre-caldera volcanics

494-532 m: *Fine-grained trachyte*. Brownish grey to grey, fine-grained porphyritic formation. Mixing is evident at this depth.

532-544 m: *Loss of returns*

544-912 m: *Fine- to medium-grained trachyte*. Grey to brownish grey, fine- to medium-grained porphyritic lava with feldspars, pyroxenes and amphiboles as primary minerals. Abundant quartz vein filling at depths 666 m and 754 m is evident. Pyrite is disseminated in the groundmass.

912-936 m: *Loss of returns*

936-962 m: *Fine-grained trachyte*. The rock is moderately altered and shows mild bleaching. It is grey to brownish, fine-grained feldspar porphyritic lava. Pyrite crystals are still dominant in veins and the groundmass.

962-1022 m: *Tuff*. The colour ranges from grey to bluish-greenish, with lithics of trachytic components embedded in a fine-grained groundmass. Minor pyrite and calcite and greenish clays form the alteration minerals at this depth.

1022-1198 m: *Fine-grained trachyte*. Grey moderately altered fine-grained, sanidine porphyritic lava. Bleaching on the fractured surface is evident. Veins are filled with quartz, calcite and pyrite at 1060-1080 m, 1100-1108 m and 1144-1154 m.

1198-1222 m: *Tuff*. Grey vesicular rock that has been highly altered to whitish clays. Calcite is abundant in this unit and quartz and silica infilling veins are noted.

1222-1406 m: *Fine-grained trachyte*. Brownish grey, moderately altered and fractured trachyte. Calcite, pyrite, clays, and quartz were the main alteration minerals observed. Epidote coloration is observed, starting at depth of 1242 m and continues downhole.

1406-1558 m: *Fine-grained trachyte*. Light grey to grey, fine-grained rock. It appears fractured and highly altered. High-temperature minerals characterize this formation. These include quartz, chlorite, wollastonite, and actinolite.

1558-1728 m: *Glassy fine-grained basalt*. Greenish grey, glass rich, fine-grained hypocrySTALLINE rock. It is highly altered and characterized by the first appearance of epidote and an abundance of wollastonite, actinolite, and calcite.

1756-1782 m: *Fine-grained porphyritic basalt*. Fine-grained, more crystalline basalt with large phenocrysts of plagioclase and pyroxene. Epidote, wollastonite and actinolite still characterize this unit though not as abundantly as in the glassy basalt type.

1782-1810 m: *Fine-grained basalt*. Dark grey to almost black in colour. It is hypocrySTALLINE and relatively fresh showing chilled margins at the depth of 1810 m.

1810-1854 m: *Syenite*. The rock unit is grey, medium to coarse grained and porphyritic, consisting primarily of alkali feldspars together with some mafic minerals. The rock is hard and compact with little permeability, deduced from the low penetration rates recorded during drilling and the disappearance of pyrite and the high-temperature alteration minerals.

1854-1926 m: *Fine-grained trachyte*. Greyish, fine-grained and porphyritic. It is moderately altered into whitish and greenish clays. Minor veins are filled up with quartz and calcite.

1926-1948 m: *Syenite*. Light grey and coarse-grained with phaneritic texture, and appears relatively fresh.

1948-1978 m: *Fine-grained trachyte*. Dark grey, fine-grained trachyte. The rock is highly altered with quartz, wollastonite, epidote, and abundant calcite characterizing this unit.

1978-2002 m: *Syenite*. Light grey, medium to coarse-grained and porphyritic consisting primarily of alkali feldspars together with some mafic minerals. It is moderately altered and fractured, but veins are filled with quartz and calcite.

2002-2344 m: *Fine-grained trachyte*. Brownish grey, fine-grained feldspar porphyritic lava. The rock is moderately altered into greenish clays. Deposition of clays, quartz, and calcite on the fractured surfaces was noted. At depths from 2338- 2344 m, the rock becomes fresher with only slight alteration, indicating reduced or no permeability.

4.2.2 Well MW-11

Post-caldera volcanics:

0-14 m: *Pyroclastics*. Grey to dark grey, fine-grained and highly vesicular rock. The vesicles are unfilled.

14-52 m: *Fine-grained trachyte*. Black brownish, fine-grained felsic rock. Iron oxide precipitates are observed at the margins and interstices of mafic crystals such as clinopyroxene.

52-60 m: *Loss of returns*

60-74 m: *Tuff*. This is fine-grained, vesicular rock exhibiting moderate oxidation and minor calcite.

74-102 m: *Loss of returns*

102-140 m: *Fine-grained trachyte*. The rock is grey, fine-grained, exhibiting slight oxidation. Sanidine phenocrysts are scattered in needle-like lath shaped crystals. Abundant opaque iron oxides, appearing brown to deep brown, are precipitated between crystals in the groundmass. Prismatic aegirine-augite microphenocrysts are seen in the crossed polars.

140-152 m: *Loss of returns*

152-162 m: *Fine-grained trachyte*. Grey, fine grained exhibiting slight oxidation. The sanidine phenocrysts are scattered in needle-like lath shaped crystals. Abundant opaque iron oxides, appearing brown to deep brown, are precipitated between crystals in the groundmass. Prismatic yellow-green sodium-pyroxene microphenocrysts are seen in the crossed polars.

162-268 m: *Loss of returns*

268-280 m: *Medium-grained trachyte*. Dark grey, medium-grained lava. The primary minerals are mainly sodium-pyroxene embayed with smaller sanidine laths. The rock appears relatively fresh.

Possible syn-caldera volcanics

280-304 m: *Tuff*. Dark green to bluish, fine-grained, poorly crystalline vesicular rock, with fully grown quartz crystals in the matrix. The vesicles and veins are filled up with chalcedony, clays and zeolites. This rock unit is possibly related to the syn-caldera.

304-374 m: *Loss of returns*

Possibly pre-caldera volcanics

374-480 m: *Medium-grained sanidine porphyritic trachyte*. Sanidine phenocrysts are scattered in a slightly oxidized feldspar rich groundmass. Scattered microphenocrysts of yellowish-green aegirine-augite crystals are present at this depth. The feldspars are seen altering to albite.

480-510 m: *Loss of returns*

510-604 m: *Medium-grained trachyte*. Grey, medium-grained phyric lava exhibiting slight alteration with minor calcite and clays.

604-666 m: *Loss of returns*

666-714 m: *Fine-grained trachyte*. Dark grey to greenish grey, fine-grained trachyte mixed with minor amounts of a vesicular, poorly crystalline tuff. Chlorite is seen forming in the rock matrix.

714-728 m: *Tuff*. This formation is grey to greenish, poor crystalline and vesicular with fragments of trachytic composition. It is moderately altered with yellowish- green illite clays and chlorite infilling the vesicles.

728-778 m: *Loss of returns*

778-822 m: *Fine-grained trachyte*. Grey, fine-grained, porphyritic lava with sanidine phenocrysts embedded in the matrix. Chlorite and abundant calcite characterize this unit.

822-852 m: *Loss of returns*

852-894 m: *Tuff*. This formation is grey to greenish, poorly crystalline and vesicular with fragments of trachytic composition. It is moderately altered with yellowish-green illite clays and chlorite infilling the vesicles.

894-1170 m: *Loss of returns*

1170-1222 m: *Fine-grained trachyte*. Light grey, fine-grained lava. It is highly altered to yellowish-grey clays. Pyrite at this depth is abundant in the groundmass and vein fillings between 1172-1210 m. Partial circulation losses at depths of 1174-1194 m due to minor fractures. First appearance of epidote at 1178 m was noted.

1222-1542 m: *Loss of returns*

1542-1680 m: *Medium-grained trachyte*. Dark-grey, porphyritic lava, moderately altered with abundant calcite. Pyrite is seen disseminated in the matrix. Minor losses were encountered at 1582-1642 m depth.

1680-1772 m: *Glassy fine-grained basalt*. Greenish grey, glass rich, fine-grained hypocrySTALLINE rock. It is highly altered and characterized by the first appearance of wollastonite and an abundance of epidote, calcite and chlorite in the rock matrix.

1772-1832 m: *Fine-grained basalt*. Dark grey to almost black in colour. Large plagioclase phenocrysts, showing albite twinning, are embedded in the groundmass. Alteration minerals of epidote, wollastonite, and calcite characterize this zone.

4.3 Stratigraphic correlations of wells MW-08, MW-11, MW-09 and MW-12

A stratigraphic cross-section across Wells MW-08, MW-11 and neighbouring Wells MW-09 and MW-12 (Lopeyok, 2013) is highlighted in Figure 7. From the figure it can be deduced that the subsurface geology of Menengai geothermal field is predominantly trachytic with intercalations of tuff and pyroclastics. The tuff formation dissected by the wells at depths between 220-480 m conforms to the syn-caldera volcanics. Mibei (2012) described it as a greenish brown to brownish tuff layer at 320-400 m.

This formation separates the post caldera volcanics from the pre-caldera volcanics. The blocky nature of the post-caldera volcanics described by Leat (1984) has been reflected by severe circulation losses and drilling challenges encountered during drilling of the top 300 m of the wells. The pre-caldera volcanics, predominantly trachytes, form the largest part of the stratigraphic column. The trachytes show varied textures, fine-, medium- and coarse-grained, which could represent different episodes of lava eruptions during the pre-caldera stage. The basalts encountered at greater depths of Wells MW-08 and MW-11 are highly altered and are presumed to link with the Pliocene and Pleistocene subordinate basalts overlying the Miocene phonolites, resting on the Precambrian metamorphic basement (Leat, 1984).

Circulation losses between depths 100-300 m in Wells MW-08, MW-09 and MW-11 could be linked to the syn-caldera tuffs encountered at the same depth range in Well MW-12, deduced from the increase in penetration rates at this unit of the column. However, a correlation of the tuffs reveals possible normal faults between Wells MW-12/ MW-09, MW-09 / MW-08 and MW-08 / MW-11 (Figure 7).

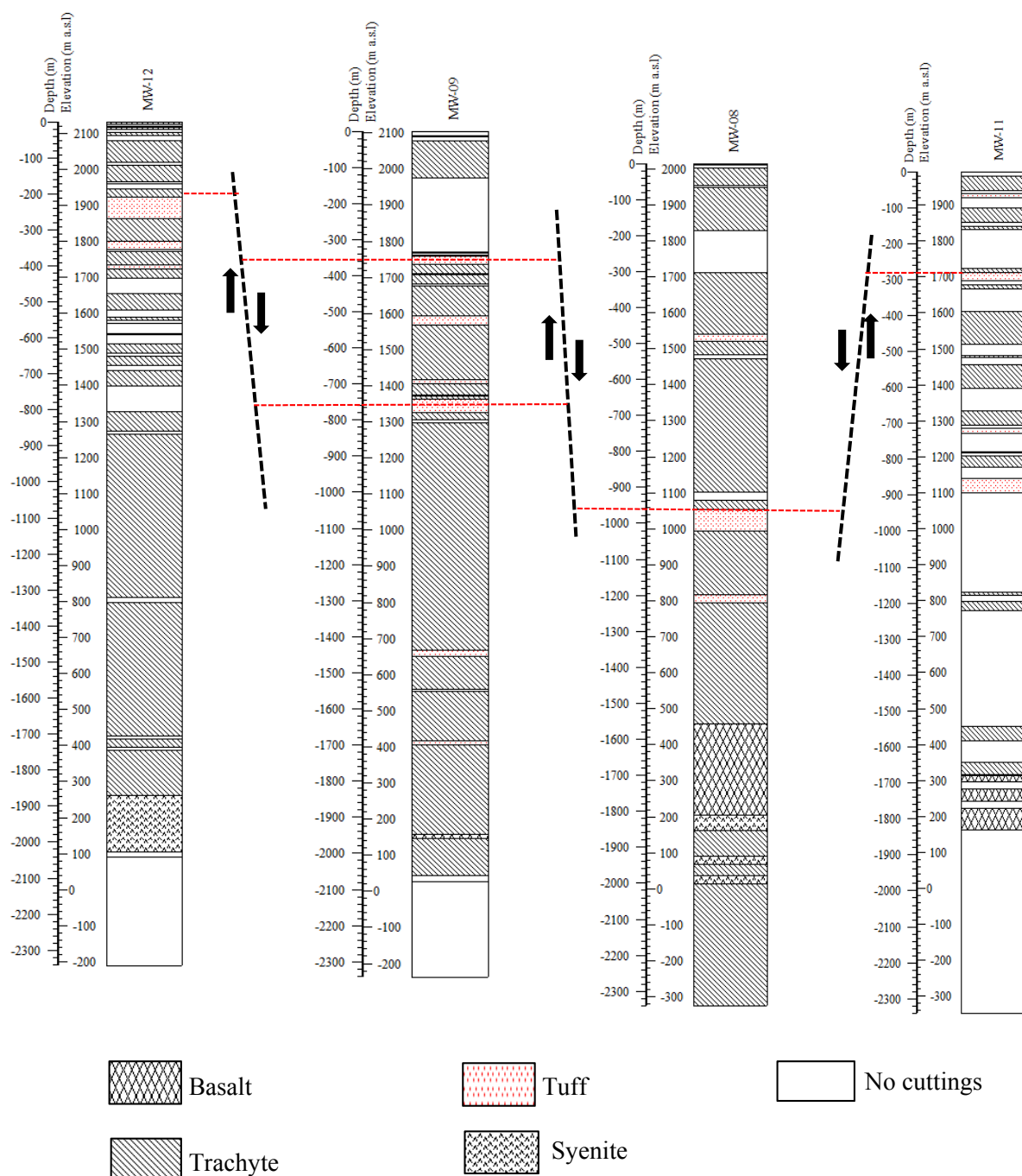


FIGURE 7: Stratigraphic correlation of wells MW-08, MW-11, MW-09 and MW-12

4.4 Aquifers

For a hydrothermal system to exist, permeable formations or structures should exist to allow water to percolate through. These permeable zones form the aquifers (Lagat, 2004). Typically, aquifers are located at the intersection of faults, fractures, intrusions and lithological contacts. In a geothermal system, aquifers can either be cold or hot. The cold aquifers, which are usually encountered in the upper parts of the wells, are cased off and carefully cemented to prevent them from cooling the hot aquifers in the deeper part of the wells. The location of aquifers in Wells MW-08 and MW-11 was based on various parameters which include: temperature logs, circulation losses, changes in penetration rate during

drilling, lithological contacts, and hydrothermal alteration minerals present, but the abundance of calcite, pyrite and high alteration intensity in the wells may be correlated with permeability.

4.4.1 Well MW-08

In Well MW-08, circulation losses were noted only in small sections (Figure 8); the losses in these sections are attributed to fractures, which act as feeder zones. The shallow feeders, between the surface and 900 m, were cased off by the anchor and production casings as they are associated with cold inflows. The deeper sections are associated with hot inflows and were not cased off as the production casing was set at 928 m. The permeability of Well MW-08 is low in the production section. Eight aquifers were located in the well but, out of these, four small aquifers were identified between 990 and 2000 m depths in the production section. They are associated with highly altered basalt, tuff, fractured trachyte formations, syenitic intrusions and lithological contacts between trachyte and tuff as described below:

Aquifer 1 occurs at a loss zone starting from 200 m and is characterised by a total loss of circulation and an increase in the drilling penetration rate.

Aquifer 2 is a small aquifer encountered at 560 m at a loss zone. It is characterised by an increase in the penetration rate and the temperature, as recorded in the temperature logs.

Aquifer 3 is located at 780 m and is associated with a fractured trachyte. The zone is marked by an increase in alteration and pyrite.

Aquifer 4 forms the main aquifer in this well. It is located at 960 m just below the production casing. It is characterised by a break in the temperature profile associated with a very permeable tuff formation.

Aquifer 5 is a small aquifer at 1360 m, associated with a highly fractured and altered trachytic formation.

Aquifer 6 is associated with a boundary between trachyte and a highly altered basaltic formation at 1550 m. The zone is marked by increased intensity of alteration and the presence of the high-temperature alteration minerals, epidote and wollastonite. Temperature profiles show a break in the curve which characterises a coldpoint.

Aquifer 7 occurs at 1980 m, a contact between a trachyte and a syenite intrusion. The temperature profile at this zone shows a break in the curve due to more cooling around the aquifer.

4.4.2 Well MW-11

Well MW-11 is a very permeable well exemplified by the significant circulation losses experienced. At shallow depths, i.e. 0-200 m, the losses experienced were due to a highly fractured blocky trachyte. There is almost no alteration at this zone, but the rocks are highly oxidized probably because of the effects of shallow underground water and/or because of closely spaced contact zones due to the post-caldera lavas. Geothermal aquifers are observed at varying depths from 490 m to the bottom of the well. Their identification is based on circulation losses, lithological characteristics, and measured temperatures. Nine aquifers were mapped in the well, all of them associated with loss zones (Figure 9). These zones are characterized by an increase in the measured temperature logs and correlate with geological observations.

Aquifers 1 and 2 are associated with losses at 220 and 340 m, respectively. These aquifers are associated with the groundwater and were cased off.

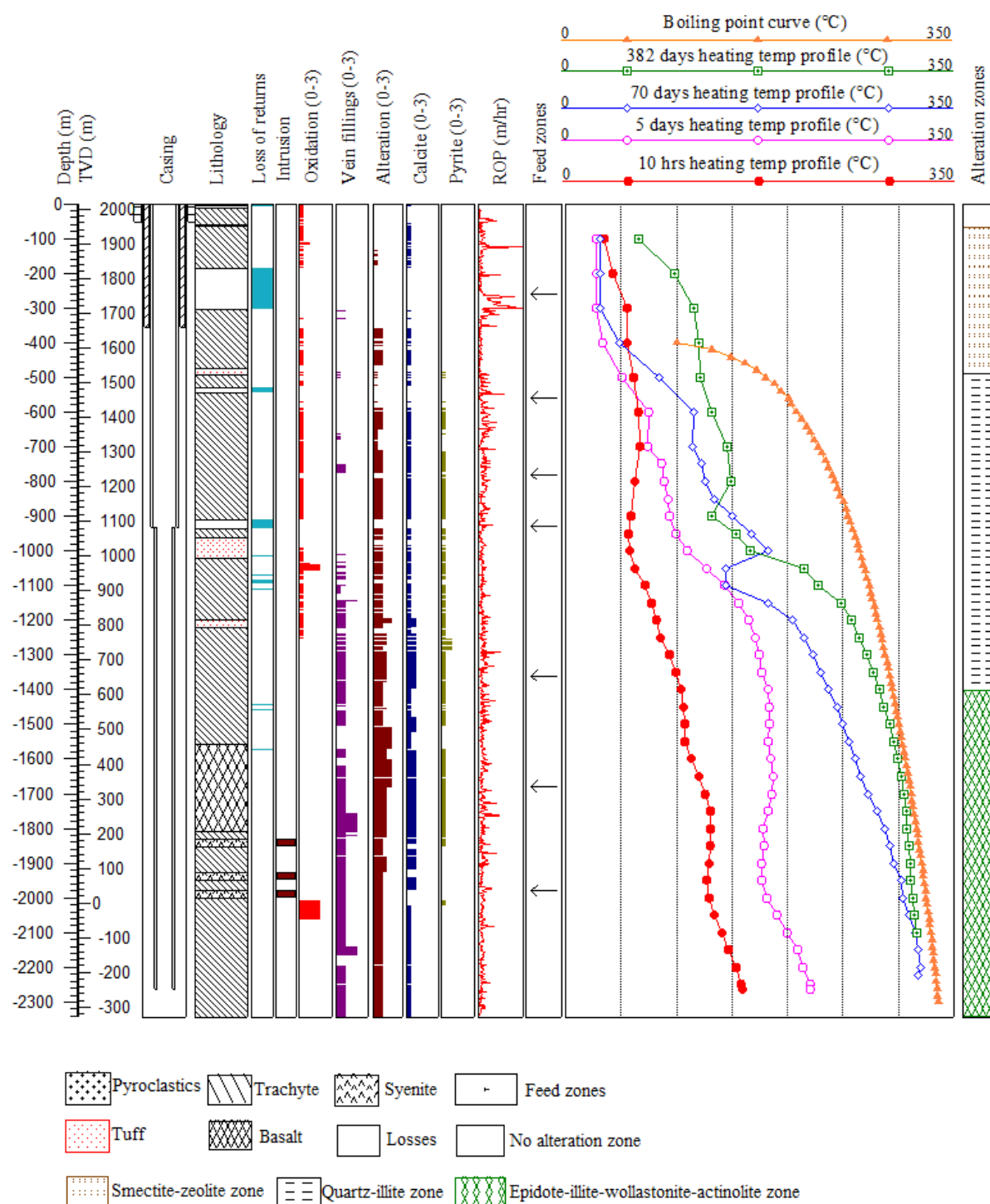


FIGURE 8: Lithology, selected alteration minerals and temperature logs in correlation with aquifers in Well MW-08

Aquifer 3 was located at 650 m. It is a medium aquifer characterised by an increased rate of penetration and the temperature profile shows a break in the curve which indicates a cold point.

Aquifers 4 and 5 form the major aquifers in the well. They are located at 1000 and 1240 m, respectively, and are characterised by a break in temperature profile, associated with a circulation loss with high rates of penetration recorded.

Aquifers 6 and 7 are intermediate aquifers at 1420 and 1460 m, respectively, associated with loss zones. The temperature profile at this zone shows a break in the curve due to more heat around the aquifer.

Aquifers 8 and 9 were identified from a break in the temperature curves and increased rates of penetration and are located at a loss zone at depths 1620 and 1720 m, respectively.

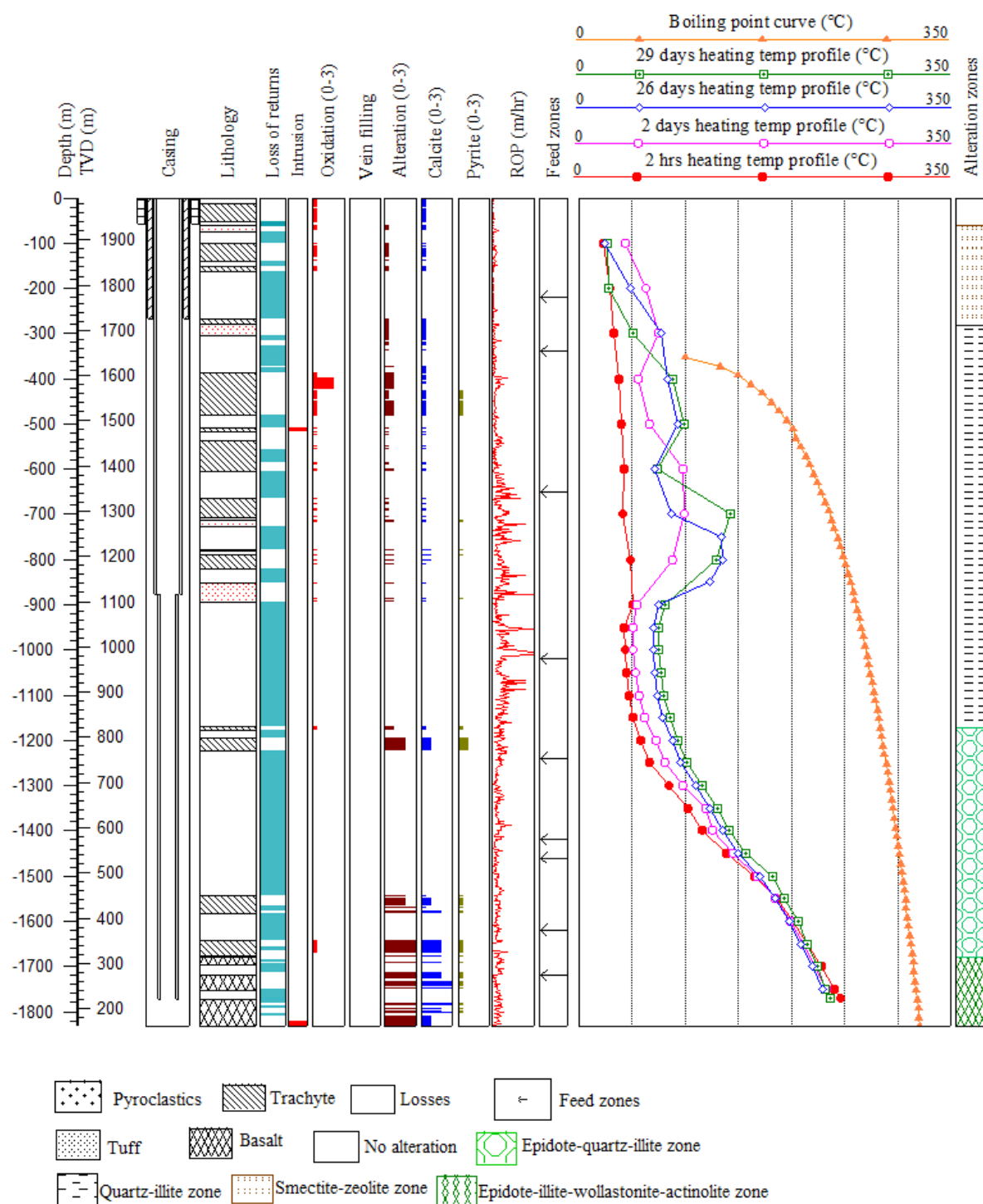


FIGURE 9: Lithology, selected alteration minerals and temperature logs in correlation with aquifers in Well MW-11

5. HYDROTHERMAL ALTERATION

Hydrothermal alteration involves the change in mineralogy, texture, and chemistry of a rock due to interaction of the rock with hydrothermal fluids (hot water, steam, or gases). Primary minerals are replaced by different secondary minerals upon interaction of the rocks with the minerals. The formation and distribution of these secondary mineral assemblages is influenced by various factors which include permeability, temperature, composition of the geothermal fluid, lithology, tectonic setting and time (Browne, 1978).

Analysis of hydrothermal alteration mineralogy from rock cuttings in a geothermal field is an important tool from which we acquire information about the dynamics of the geothermal system. It is also important during the drilling process, e.g. when it comes to determining the setting depth of the production casing. Apart from estimating the fluid pH, hydrothermal alteration minerals can be used to predict scaling and corrosion tendencies in fluids, measure permeability, possible cold water influx, and as a guide to the hydrology (Reyes, 1990).

5.1 Alteration of primary minerals

The primary minerals found in Wells MW-08 and MW-11 include volcanic glass, olivine, pyroxene, amphibole, feldspars, and opaque minerals (FeTi-oxides). In a geothermal environment, the interaction of the invading hydrothermal fluid with the rock leads to partial or complete rock alteration. The primary minerals are gradually replaced by alteration minerals as follows:

Volcanic glass in Wells MW-08 and MW-11 was encountered in the top 300 m column of the wells from the ground surface. It is transparent to translucent, exhibiting conchoidal fracturing and a vitreous lustre. It is altered into clays, zeolites, chalcedony, and may even be replaced by calcite. In thin section, it appears brown and anisotropic due to alteration to clays.

Olivine is one of the primary minerals in basaltic rocks and is very susceptible to alteration. In the study wells, basalt was encountered at 1558 m in Well MW-08, and at 1680 m in Well MW-11. At this depth, olivine had been completely altered and replaced by calcite and clays.

Pyroxene is the mineral most resistant to alteration. It appears as dark and shiny with a metallic lustre, embedded in a feldspar-rich groundmass. It was easily identified in thin section by its high relief and good cleavage. In Well MW-08, pyroxenes start to alter at 774-900 m depth and alter less than 10% to clays. It appears fresh again at 1180 m. From 1180 m to the bottom of the well, it shows 10-50% alteration into illite, chlorite, actinolite, and calcite. On the other hand, pyroxenes in Well MW-11 start to alter at 390 m to illite and continues to the bottom of the well.

Feldspars, both sanidines and plagioclases, occurred as the major groundmass component as well as phenocrysts. Sanidine is the most abundant associated with trachytes, while plagioclase is associated with basalts. In thin sections, the sanidines appear fine grained and elongated, exhibiting the trachytic texture. It also occurs both in the groundmass and as phenocrysts in rocks exhibiting porphyritic textures. The sanidine phenocrysts were readily identified by low relief and simple twinning. At shallow depths, the feldspars are relatively unaltered but become altered progressively with depth into albite and occasionally to clays, calcite, and epidote. Alteration of feldspars in Well MW-08 starts at 666-1544 m, where 10-30% of feldspar has altered mainly to clay, calcite, albite, and quartz. Medium to high alteration intensity 50-80% is found at 1544-2318 m where the feldspar alters to chlorite and epidote. In Well MW-11, albite is first seen at 538 m and, like in Well MW-08, medium to high alteration intensity of plagioclase to epidote, illite, and calcite is seen from depths 1680 m to the bottom of the well, in association with the basaltic formation.

Opaque minerals appear opaque in transmitted light. They occur as idiomorphic, disseminated or irregularly shaped aggregates within the groundmass. They are generally resistant to alteration but when altered, sphene (titanite) is the main alteration product of these minerals. Sphene is first seen in Well MW-08 at 1558 m and disappears after 1810 m. In Well MW-11, sphene was first encountered at 668 m and then again at 1680-1832 m.

In general, the order of decreasing susceptibility to alteration is volcanic glass, olivine, feldspars, pyroxene and opaques.

5.2 Hydrothermal minerals in Wells MW-08 and MW-11

A number of hydrothermal minerals were found in both Well MW-08 and Well MW-11. They occurred in two ways: either as replacements, replacing the primary rock-forming minerals, or as depositions infilling fractures, vesicles and vugs.

Analyses of drill cuttings from the two wells has shown that the hydrothermal minerals occurring in the wells include zeolites, chalcedony, quartz, pyrite, calcite, smectite, illite, albite, epidote, wollastonite, titanite (sphene), chlorite, and actinolite. The occurrence of these minerals with depth is shown in Figures 10 and 11.

In the study wells, *zeolites* were positively identified by petrographic analysis. The types encountered are thomsonite and scolecite. Thomsonite was first and only observed in Well MW-11 at 282 m, infilling vesicles and veins in tuff. In Well MW-08, zeolites were first encountered at 488 m as scolecite infilling vesicles. They indicate low-temperature alteration (approximately < 120°C).

Chalcedony was first seen in both wells filling in cavities and vesicles. Chalcedony was first encountered at 94 m in Well MW-08 and at 62 m depth in Well MW-11. It appeared as a milky white, smooth and perfectly circular deposition. It began to be replaced by quartz at 288 m in Well MW-11.

Secondary *Quartz* appeared mainly as a precipitation mineral filling vesicles and fractures. It was easily identified in cuttings by its typical euhedral shape, transparency and forming a regular hexagonal pyramid shape. Some of the euhedral grains of quartz were noted growing in clusters while others grew individually. In the study wells, quartz was seen both in binocular and petrographic analysis. Quartz was first identified at 390 m in Well MW-11 and at 666 m in Well MW-08 and persisted to the bottom of the wells.

Calcite is a common alteration mineral with a formation temperature extending from 50 and up to 290°C (Kristmannsdóttir, 1979). It was encountered all through the well columns but showed a wide range of occurrences from little in the fresh un-altered trachyte to abundant in the fractured and highly altered trachyte, basalt and tuff formations. In binocular analysis, calcite was identified using dilute hydrochloric acid. In rock cuttings, calcite was seen to be directly precipitated in fractures and vesicles. In thin section, it occurred as radial, euhedral, and platy and could be easily distinguished by its rhomboid cleavage and high order interference colours.

Pyrite occurs as euhedral cubic crystals with a brassy yellow lustre in reflected light. Pyrite is seen mainly disseminated in the feldspar-rich groundmass in both wells. It was encountered first at 480 m in Well MW-08 and at depth 420 m in Well MW-11 and was regularly identified throughout the well columns. A relative increase of pyrite in the groundmass at depths 1160-1220 m in both wells was observed. The abundance of pyrite conforms to a fractured trachyte, and is hence an indicator of permeability.

Albite occurs as an alteration product of sanidine and plagioclase. The first appearances of albite in the study wells was identified in thin section at 538 m and 1790 m in Wells MW-08 and MW-11, respectively, where it replaced sanidine; its formation destroys the feldspar twinning habit.

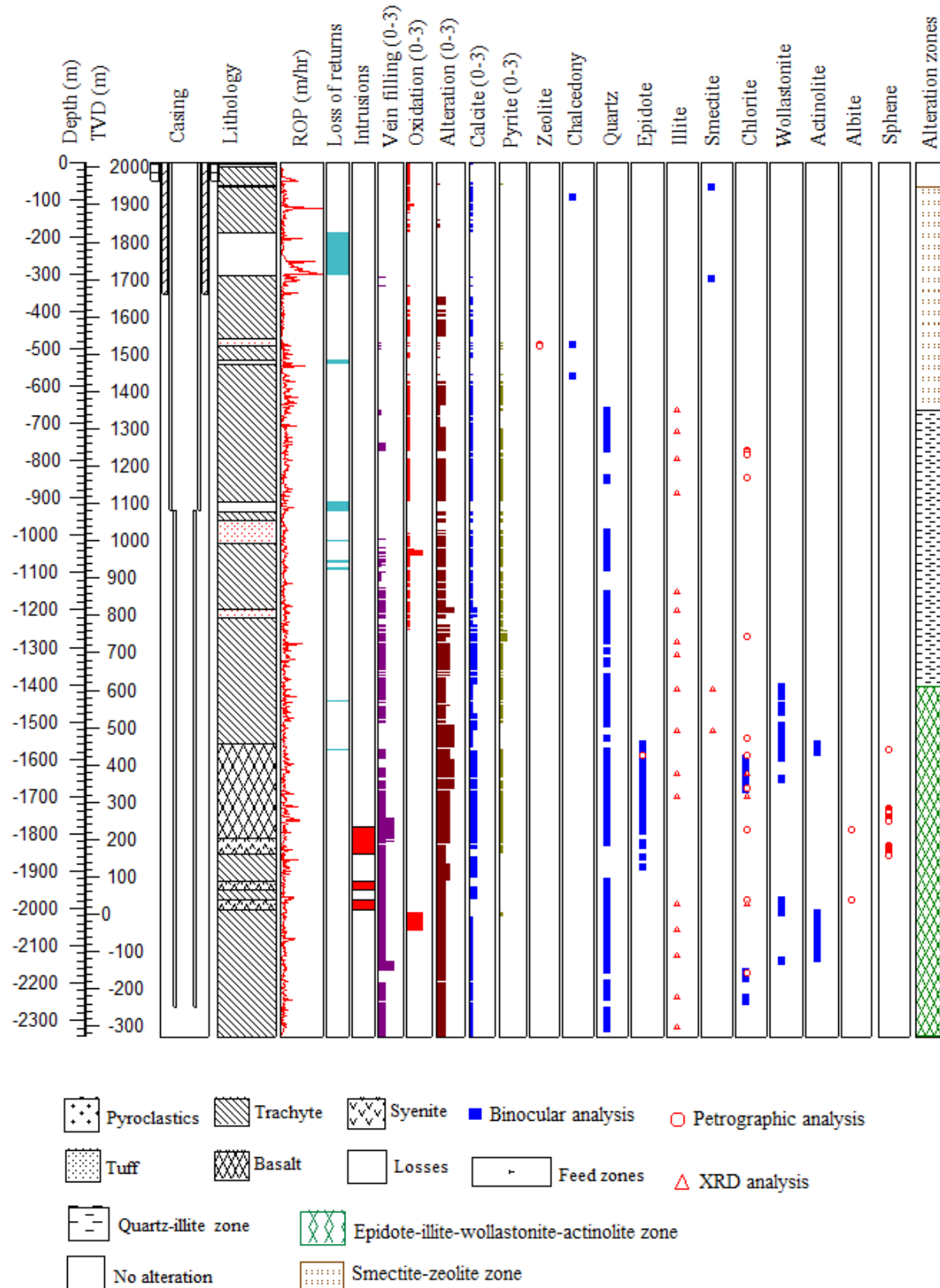


FIGURE 10: Distribution of hydrothermal alteration minerals in Well MW-08

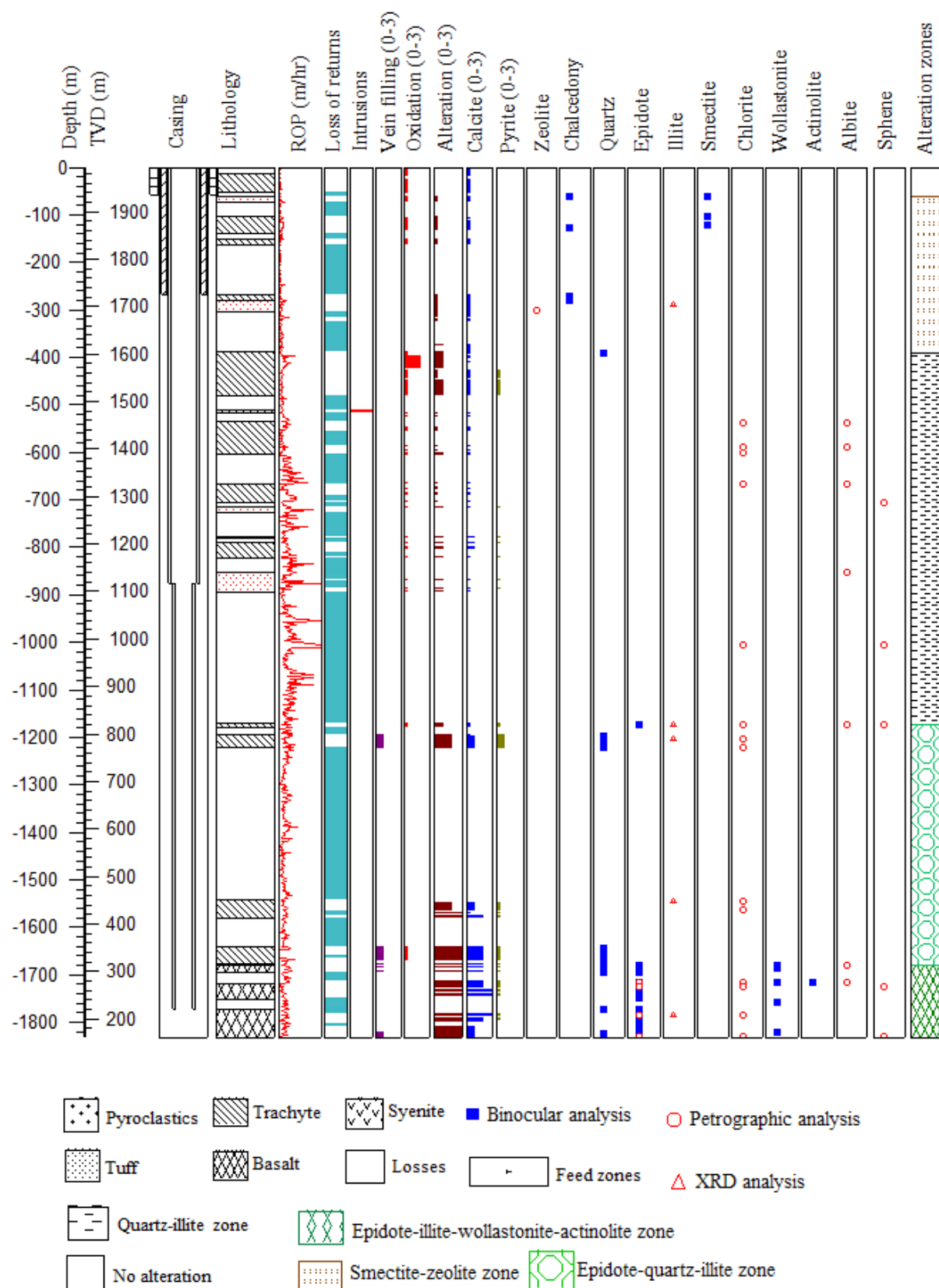


FIGURE 11: Distribution of hydrothermal alteration minerals in Well MW-11

Epidote was first noted in Wells MW-08 and MW-11 at depths of 1558 m and 1172 m, respectively, as yellowish green radiating prismatic crystals growing in vesicles and also replacing plagioclase and

pyroxene. It occurs in association with quartz, wollastonite and actinolite. In thin section, it is yellow green with high interference colours and parallel extinction. The appearance of epidote typically correlates with a formation temperatures that of more than 240°C.

Wollastonite was identified in the rock cuttings by its whitish colour and fibrous, hairy structure. It was mainly observed deposited in vesicles and occurred in association with quartz, epidote, and actinolite. It was first encountered in Wells MW-08 and MW-11 at depths of 1404 m and 1680 m, respectively. The first appearance of wollastonite marks a temperature of 270°C and can be stable at temperatures above 300°C.

Actinolite appeared greenish to whitish in colour with a vitreous lustre, growing in fibrous aggregates in the cuttings. It forms at temperatures above 280°C and was first encountered at 1716 m in Well MW-11 and 1558 m in Well MW-08 and occurred intermittently down to 2180 m.

Titanite (sphene) was identified in both petrographic and binocular analysis in the study wells. It appeared as white, small, and ball-like in the rock cuttings. In thin section, it is brown in colour with a very high relief and occurs as irregular anhedral grains replacing opaque minerals.

Clays are common products of hydrothermal alteration of rocks. The formation of clay minerals involves chemical reactions and the physical movement of hydrothermal fluids and, in many cases, there is a zonal arrangement of the clay minerals around the source of alteration, depending on the parent rock and the nature of the hydrothermal solutions. Hence, different types of clays could be seen to occur throughout the wells' columns ranging from low-temperature smectites occurring at the surface and shallower depths, to chlorite occurring at deeper and higher temperatures. X-ray diffraction analysis was done on 36 selected samples in addition to the petrography and binocular microscope analysis to better identify the types of clay minerals as these different types of clay minerals can be used as temperature indicators (Kristmannsdóttir, 1979; Franzson, 1998). Three types of clay were identified and they are:

Smectite was mainly observed under the petrographic microscope as light green in plane-polarized light and slightly pleochroic and was found as vesicle and vein fillings. On XRD analysis, it showed peaks commonly occurring between 12.8 and 15 Å when untreated, 13 to 17 Å when treated with glycol and collapsing to 10.3 Å when heated (Figure 1 in Appendix I). Smectite is a low-temperature clay and its occurrence is an indication of temperatures lower than 200°C. In thin section, smectite was first seen at depth of 148 m in Well MW-08 and at 122 m in Well MW-11, respectively, whereas XRD analysis indicated smectite at greater depths of 796 and 1784 m in Wells MW-08 and MW-11, respectively.

Chlorite was identified in all three analyses, i.e. binocular, petrographic and X-ray diffraction. In the cuttings, chlorite had a light to dark green colour and was often associated with high-temperature alteration minerals like epidote, actinolite, and wollastonite. In thin-section it was characterised as fine to coarse grained, light green coloured and fibrous in plane polarized light. It appeared light grey to white in cross polarized light, showing a feather texture and sometimes radial forms. It occurred both as a replacement of primary minerals in the rocks and as a vesicle filling. In thin-section it was first identified at 538 m depth in Well MW-11 and at 774 m in Well MW-08 and extended to the bottom of the well. Chlorite is an indicator of temperatures exceeding 200°C. In XRD it showed peaks at 14.4 Å and 7.1 Å, which did not change upon glycolation and heating (Figure 2 in Appendix I). It is only in Well MW-08 that chlorite was identified in the XRD analysis at depths of 1640-1988 m.

Illite was identified through X-ray diffraction analysis. Illite forms at temperature of 200°C and above. XRD analysis showed its first appearance at depths of 666 and 288 m in Wells MW-08 and MW-11, respectively, and prevailed down to depths of 2314 and 1734 m, respectively. From the analysis, illite showed peaks between 10.2 to 10.3 in untreated, glycolated, and heated samples (Figure 3 in Appendix I).

5.3 Vesicles and vein fillings

Vesicles are small cavities in volcanic rocks that are formed by the expansion of gases as they are exsolved from the lava as it solidified. Vein fillings, on the other hand, are fractures that have been filled with minerals deposited from hydrothermal fluids. They dictate the porosity and permeability which are two of the primary factors that control the movement and storage of fluids in rocks, leading to the deposition of secondary minerals either in veins or vesicles. Identification of vesicle and vein fillings in this study was crucial as it reveals the sequence of mineral deposition which can be used to study the temperature conditions and the palaeo-thermal history of the geothermal system.

In the top 60 m of both the well columns, vesicles were identified but were empty. At depths between 280-490 m, chalcedony, zeolites, calcite and quartz and clays were seen infilling the vesicles. At greater depths of 900-1540 m in Well MW-08, veins and minor vesicles infilled with quartz, calcite, and pyrite were noted. At this depth in Well MW-11, significant losses occurred. The high-temperature minerals, epidote, wollastonite, and actinolite, at depths of 1558 m in Well MW-08 and 1680 m in Well MW-11, were seen to fill the vesicles and veins.

5.4 Sequence of mineral deposition

Minerals are formed at their characteristic physico-chemical conditions during the history of geothermal systems (Gebrehiwot, 2010). The distribution and deposition of alteration minerals in a well gives information about the formation temperature of the well at their time of formation. From the analysis of the mineral depositional sequence, information as to whether the geothermal system has been heating up, cooling or is in thermal equilibrium can be obtained. Petrographic analysis was the main method used to obtain the highlighted mineral deposition sequence.

In Well MW-08, at a shallow depth of 490m, zeolites were deposited in the vesicles, which disappeared at 666 m where secondary quartz was first seen. This indicates a temperature rise in the geothermal system. At depths from 900-1404 m in the well, veins were filled by pure quartz, but some examples were found where quartz formed first and calcite was deposited later. Vesicles were rare in this section of the column. However, vesicles at the 1404-1980 m depth range showed a number of sequences where the high-temperature minerals started with epidote, then wollastonite, and actinolite forming last (Table 1). This indicates that the system is evolving from low-temperature to high-temperature conditions.

TABLE 1: Sequence of mineral deposition in Well MW-08

Depth (m)	Alteration sequence (early-late)	Filling type
1270 (MW-08)	Quartz-calcite	Vein
1416 (MW-08)	Quartz-wollastonite	Vesicle
1476 (MW-08)	Calcite-quartz	Vesicle
1588 (MW-08)	Quartz-epidote-wollastonite	Vesicle
1920 (MW-08)	Epidote-wollastonite	Vesicle
1978 (MW-08)	Quartz-chlorite-actinolite	Vesicle

The mineral deposition sequence in Well MW-11 was rarely observed. However, from the few noted sequences (Table 2), the deposition sequences showed that at 282 m, zeolite was seen to form later than low-temperature smectites (yellowish green) at shallow depths.

TABLE 2: Sequence of mineral deposition in Well MW-11

Depth (m)	Alteration sequence (early-late)	Filling type
282 (MW-11)	Clays-zeolite	Vein
1680 (MW-11)	Epidote-calcite	Vesicle
1716 (MW-11)	Epidote-quartz-wollastonite	Vesicle

The disappearance of zeolite and the formation of secondary quartz at 380 m indicates a progressive evolution in the geothermal system. However, at a greater depth of 1680 m, calcite was deposited later

than epidote, an indication of cooling in the system at this depth in the reservoir. This is also been reflected by the 220°C measured temperature at this depth.

5.5 Mineral alteration zones

From examination of the hydrothermal alteration mineralogy of the cuttings for Wells MW-08 and MW-11, four hydrothermal alteration zones were identified in addition to the top unaltered zone. They are:

Unaltered zone which consists mainly of pyroclastics and trachytes showing a high level of oxidation; the rocks are unaltered. Vesicles in this zone are empty.

Smectite - zeolite zone is marked by the presence of chalcedony, smectite, calcite, and zeolites of mainly thomsonite and scolecite. This zone indicates temperatures below 200°C.

Quartz-illite zone: It is characterised by assemblages of calcite, quartz, albite, and illite. This zone is marked by the first appearance of secondary quartz and illite at 666 and 390 m in Wells MW-08 and MW-11, respectively.

Epidote-quartz- illite zone: The first appearance of epidote at a depth of 1158 m in Well MW-08 and at 1558 m in Well MW-11 marks this zone. However, it is only in Well MW-11 that this zone is identified. This zone in Well MW-08 was not identified, as wollastonite was encountered at a shallower depth than epidote. This zone indicates an alteration temperature of more than 240°C.

Epidote- illite- wollastonite –Actinolite zone is characterised by the first appearance of wollastonite at 1404 m in Well MW-08 and at 1680 m in Well MW-11. This zone extends to the bottom of the wells and is characterised by the presence of epidote, actinolite, illite, and chlorite. Temperatures in this zone exceed 270-290°C.

5.6 Fluid inclusion geothermometry

A fluid inclusion analysis was carried out using quartz and calcite grains obtained from Wells MW-08 and MW-11. This was carried out in order to measure the temperature of alteration mineral formation (homogenization temperatures) within the reservoir rocks and for comparison with current measured temperatures.

5.6.1 Well MW-08

Fluid inclusion measurements were done in this well at 1746 m depth. A quartz crystal was used for the analysis and the homogenisation temperature was recorded. Seventy three fluid inclusions both of primary and secondary origin were analysed and a homogenisation temperature, ranging from 265 to 315°C, was observed. These results were drawn on a histogram (Figure 12), which showed two populations. Secondary fluid inclusions were seen aligned along fractures in the crystal and gave a recorded temperature range of 275-280 and 285-290°C. The primary fluid inclusions gave a higher temperature, ranging from 295 to 315°C. The histogram was incorporated

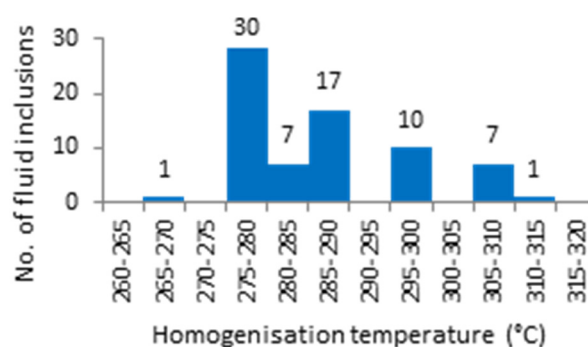


FIGURE 12: Histogram showing the results of fluid inclusion analysis in Well MW-08

together with the measured, alteration and boiling point temperature curves so as to understand how the geothermal system has evolved with time.

From the relationships (Figure 13), the four parameters show that between 400 to 1200 m, the measured temperature is lower than the alteration temperature, indicating cooling in this section of the well. At 1400 m depth, equilibrium exists between measured temperature and alteration, but deeper in the well below 1700 m depth, measured temperature is slightly higher (310°C) than temperature measured with fluid inclusion analysis (275-310°C), suggesting stable or maybe even slightly increasing temperature conditions at this depth in the well.

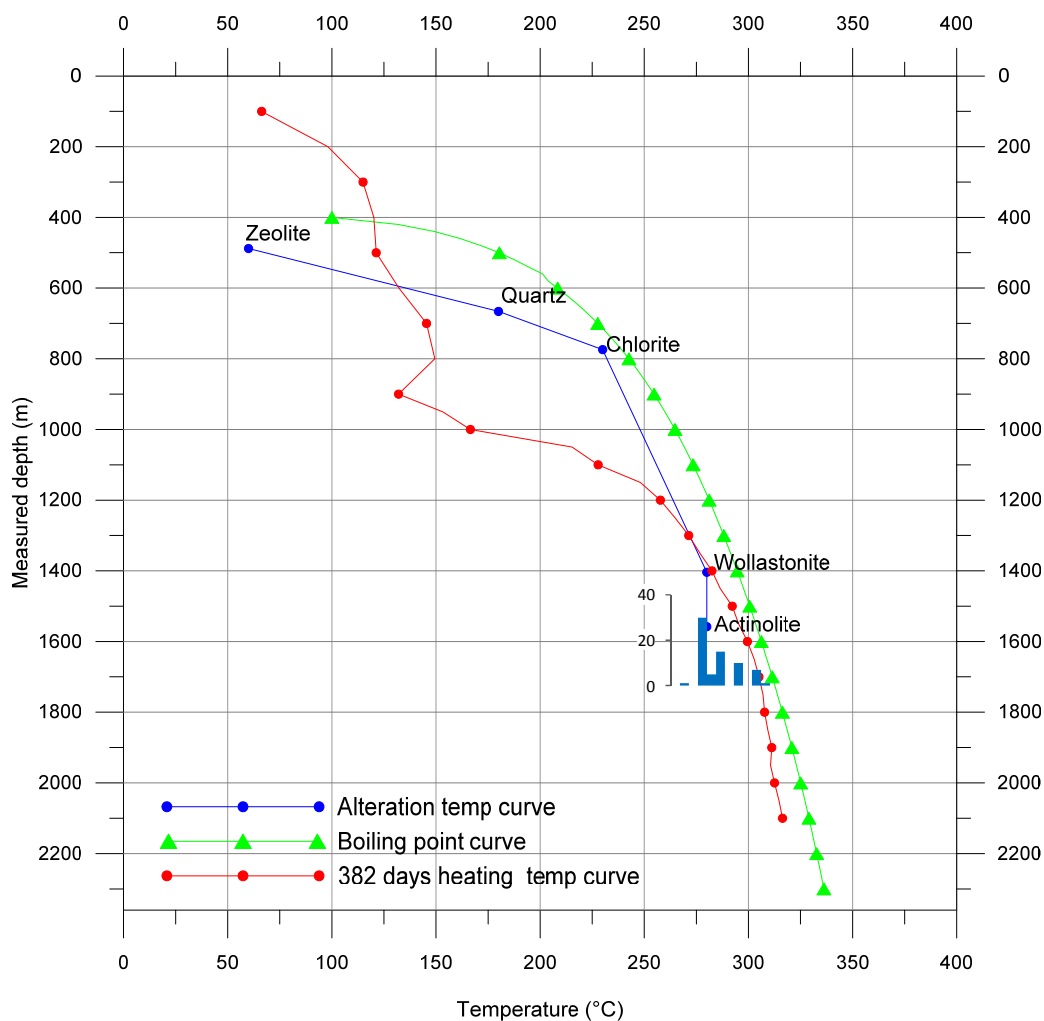


FIGURE 13: Relationship between fluid inclusion temperatures, alteration temperatures, boiling point curve and 382 days heating temperature curve for Well MW-08

5.6.2 Well MW-11

In this well both calcite and quartz crystals were picked for fluid inclusion analysis at a depth of 1720 m. A total of fifty four fluid inclusions were identified and analysed and a histogram was drawn showing the temperatures at which inclusions homogenised (Figure 14). From the histogram, two populations were recorded. The first population ranged from 255 to 285°C with most of the inclusions homogenising between 275 and 280°C. From the analysis of the quartz crystal, the primary inclusions identified recorded higher temperatures of 300 and 325°C, forming the second population. The calcite crystal showed a higher temperature range from 305 to 335°C with the highest temperatures plotting at 310 to

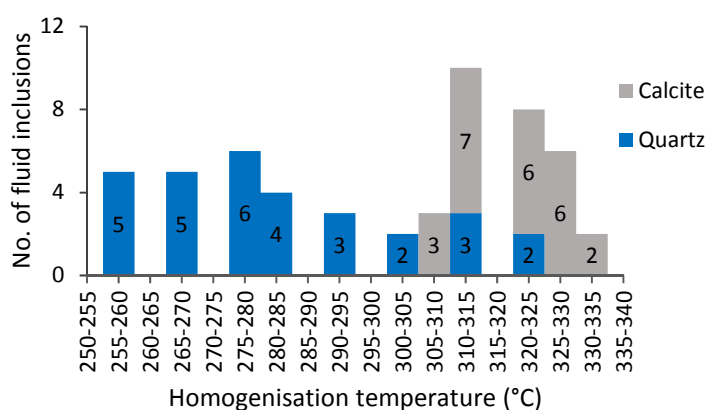


FIGURE 14: Histogram showing the results of fluid inclusion analysis in Well MW-11

315°C. This implies that the system had at a time been at boiling conditions, but has since then experienced some cooling.

A comparison of the fluid inclusion, alteration temperature and measured temperature after 29 days of heating is highlighted in Figure 15. It should be noted that measured temperature after only 29 days does not reflect the formation temperature. The comparison indicates cooling by $\approx 55^\circ\text{C}$ at 1680 m. This was estimated from comparison of the measured temperature with the first appearance of wollastonite. The homogenisation fluid inclusion

temperature at 1720 m reflects that temperatures have been at the boiling point, $\sim 310^\circ\text{C}$, in the past, but since then cooling has been experienced. The lowest temperature measured in the fluid inclusions at this depth is 255°C , slightly higher than the estimated measured temperature at 250°C . More fluid inclusion measurements are recommended at shallower depths to ascertain the cooling of this well.

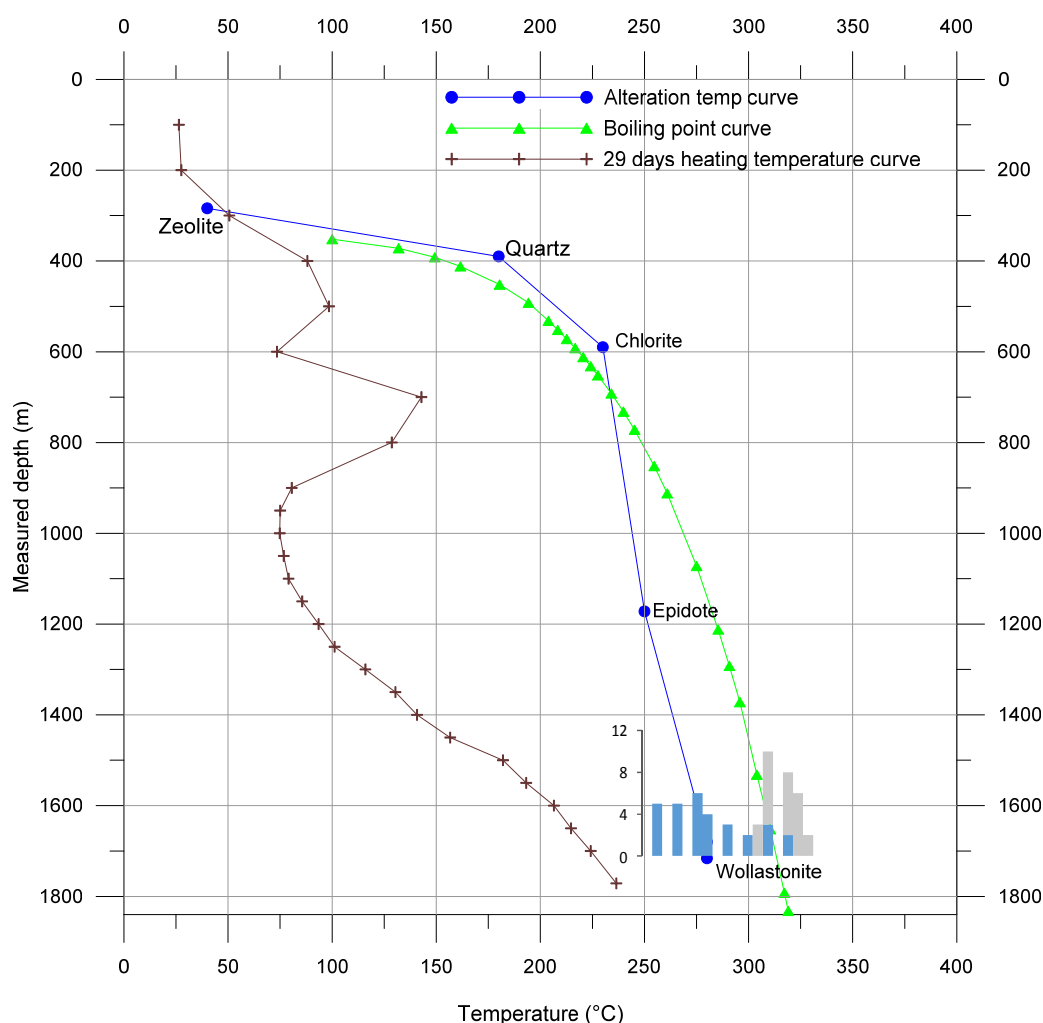


FIGURE 15: Relationship between fluid inclusion temperatures, alteration temperatures, boiling point curve and 29 days heating temperature curve for Well MW-11

6. DISCUSSION

The litho-stratigraphic successions in Menengai geothermal field are predominantly trachytes. However, in the sub surface geology, a few lenses of tuff, syenite and basalt were encountered in the study wells. Based on the analysis of the drill cuttings, five rock units were found to form the litho-stratigraphy of Wells MW-08 and MW-11. They include: pyroclastics, trachyte, tuff, syenite, and basalt. These formations are classified based on their texture and mineralogy. The penetrated rock units correlate well with the surface geology and the three evolutionary stages: Pre-, Syn- and Post- caldera volcanic activities that started shortly before 0.18 Ma ago (Leat, 1984).

Leat (1984) described the post-caldera volcanics to be composed of mainly blocky lavas, sheet-forming air-fall pumice and cinder cones composed of unconsolidated scoria. The blocky nature of these rocks was illustrated by the drilling challenges and significant losses encountered during the drilling of the top 300 m of the wells.

The brown to greenish brown tuff formation encountered at 490 and 288 m in Wells MW-08 and MW-11, respectively, conforms very well to the Syn-caldera formation and its identification has aided in mapping out faults that were buried by the post-caldera volcanics as indicated in Figure 7. The pre-caldera forms the major part of the stratigraphic column of the wells. It is predominantly trachytic but has a few lenses of tuff, and intrusions of syenite were encountered. The trachyte showed varied textures in this column, which could indicate different episodes of lava eruptions during the pre-caldera volcanic stage. Worth noting is the highly altered basalt penetrated at depths of 1558 and 1680 m in Well MW-08 and Well MW-11, respectively, which is presumed to be the Pliocene and Pleistocene subordinate basalts overlying the Miocene phonolites resting on the Precambrian metamorphic basement (Leat, 1984). This can be used as a marker horizon for the pre-caldera lava sequence. However, further analyses on the composition of the basalt are needed to ascertain this.

Aquifers in Wells MW-11 and MW-08 are mainly associated with tuff formations and highly fractured trachyte. However, in Well MW-08 vein fillings are abundant from 1000 m to the bottom of the well, which is in contradiction with the poor permeability of the well. However, the veins are filled with alteration minerals, thus, this could indicate that the fractures have been sealed. A comparison between the two wells shows that the major feed zone in the wells is between 990 and 2000 m, tied to faults, lithological contacts and highly permeable tuff.

There is a similarity in the trend and occurrence of hydrothermal alteration minerals with depth in both wells. Low-temperature minerals were noted at shallow depths and subsequently higher-temperature alteration minerals occurred with an increase in depth. The hydrothermal minerals include: chalcedony, zeolite, smectite, calcite, illite, pyrite, quartz, albite, sphene, epidote, chlorite, wollastonite, and actinolite. Their pro-grade distribution with depth indicates a history of heating in the geothermal system around the wells. However, in Well MW-11 at 1680 m, calcite was seen forming after epidote in the vesicles. This may be an indication of temperature reversal in the well and is consistent with the temperature measurements and fluid inclusion analyses at this depth. The cooling may be attributed to the closeness of the well to the caldera ring structure, which could be channelling cold fluids, hence cooling the well. Therefore, deeper production casing of the wells closer to the caldera ring needs to be considered.

On the basis of hydrothermal alteration minerals and their variations with depth, four hydrothermal mineral zones were located in order of increasing temperature and depth. They include: (1) smectite-zeolite zone, (2) quartz-illite zone, (3) epidote-quartz-illite zone, and (4) epidote-illite-wollastonite-actinolite zone. The unaltered zone formed the uppermost 60 m in both wells.

Fluid inclusion studies indicate that the geothermal system around Well MW-08 is in thermal equilibrium below 1400 m depth, or may be heating slightly below 1700 m depth. From the seventy three fluid inclusions analysed at 1746 m, the homogenisation temperature ranges from 265 to 315°C

but with an average temperature of the analyses being 282°C; the measured temperature is about 310°C at this depth, which is at the high end of the temperature range measured in the fluid inclusions. In Well MW-11, on the other hand, comparison of measured temperature with alteration temperature and fluid inclusion analyses indicate cooling in the well. The homogenisation fluid inclusion temperature at 1720 m ranged from 255-335°C while measured temperature was 250°C. High temperatures recorded from the fluid inclusion analyses indicate boiling conditions at one point of time in the system within Well MW-11, but the temperature has since then cooled and is approximately 250°C today at this depth. It must be noted, however, that the measured temperature available was logged only 29 days after the well was completed.

7. CONCLUSIONS

From the analysis of the sample cuttings and data for Wells MW-08 and MW-11, the following conclusions can be drawn:

1. The lithostratigraphy of Wells MW-08 and MW-11 is similar and is composed of five rock types: pyroclastics, trachyte, tuff, basalt, and syenite. They conform to the stratigraphy of previous wells in the area.
2. Hydrothermal alteration minerals in Menengai geothermal field are controlled by rock type, permeability, and temperature.
3. The major source of permeability in the wells is mainly fractures/faults; other sources of permeability in the wells include: lithological contacts between formations and permeable tuffs.
4. Four alteration zones were identified, based on hydrothermal mineral assemblages; they include: (1) smectite-zeolite zone, (2) quartz-illite zone, (3) epidote-quartz-illite zone, and (4) epidote-illite-wollastonite-actinolite zone. The unaltered zone formed the uppermost 60 m in both wells.
5. Comparison of fluid inclusion analysis, measured temperature, and the hydrothermal alteration curves indicates that the geothermal system around Well MW-08 is at equilibrium at 1400 m depth, but may be slightly heating below 1700 m depth. However, analysis of alteration and temperature measurements from Well MW-11 seems to indicate cooling of the geothermal system around this well. This could be attributed to the closeness of the well to the caldera ring structure, which could be channelling cold fluids, hence cooling the well.

ACKNOWLEDGEMENTS

I owe sincere appreciation to the UNU-GTP and the Government of Iceland for granting me this scholarship to participate in this six months training programme. My gratitude goes to the UNU Geothermal Training Programme staff, Dr. Ingvar Birgir Fridleifsson, Mr. Lúdvík S. Georgsson, Ms. Thórhildur Ísberg, Mr. Ingimar Gudni Haraldsson, Mr. Markús A.G. Wilde, and Ms. Málfríður Ómarsdóttir, for their guidance, assistance and care throughout the course. My special thanks goes to my supervisors, Ms. Anette K. Mortensen, Dr. Björn S. Hardarson, and Dr. Hjalti Franzson for their dedicated support and guidance during project preparation, research and writing which made it possible for me to complete this report.

I am grateful to my employer, the Geothermal Development Company, Ltd. for nominating and granting me leave to attend this vital course.

To the 2013 UNU Fellows, thank you for the shared experience and supportive ideas; your friendship is immeasurable. Special thanks to my fellow borehole geologists Joyce Okoo, Tito Lopeyok and Claudia M. Pichardo Lopez for their continuous support with information and ideas whenever needed. Above all, I express my deepest gratitude to my relatives and family. To my dear husband and daughters, thanks for your encouragement, sacrifice and unconditional love during my six months of study.

This far the Lord has been Ebenezer.

REFERENCES

Baker, B.H., and Wohlenberg, J., 1971: Structural evolution of the Kenya Rift Valley. *Nature*, 229, 538-542.

Baker, B.H., Mitchel, J.G., and Williams, L.A.J., 1988: Stratigraphy, geochronology and volcanotectonic evolution of the Kedong-Naivasha-Kinangop region, Gregory Rift Valley, Kenya. *Geological Society of London*, 145, 107-116.

Browne, P.R.L., 1978: Hydrothermal alteration in active geothermal fields. *Annual Review Earth & Planetary Sciences*, 6, 229-250.

Franzson, H., 1998: Reservoir geology of the Nesjavellir high-temperature field in SW-Iceland. *Proceedings of the 19th Annual PNOC-EDC Geothermal Conference, Manila*, 13-20.

GDC, 2010: *Menengai geothermal prospect, an investigation for its geothermal potential*. GDC, Nakuru, Kenya, Geothermal Resource Assessment Project, internal report, 66 pp.

GDC, 2013: *Borehole geological report of Well MW-11*. GDC, Nakuru, Kenya, internal report, 16 pp.

Gebrehiwot M., K., 2010: *Subsurface geology, hydrothermal alteration and geothermal model of northern Skardsmýrarfjall, Hellisheidi geothermal field*. University of Iceland, MSc thesis, UNU-GTP, report 5, 65 pp.

Geotermica Italiana Srl., 1987: *Geothermal reconnaissance survey in the Menengai- Bogoria area of the Kenya Rift Valley*. UN (DTCD)/GOK, report.

Hay, D.E., and Wendlandt, R.F., 1995: The origin of Kenya rift plateau-type flood phonolites: Results of high-pressure/high-temperature experiments in the system's phonolite-H₂O and phonolite-H₂O-CO₂. *J. Geophys. Res.*, 100, 401-10.

Hetzel, R., and Strecker, M.R., 1994: Late Mozambique Belt structures in western Kenya and their influence on the evolution of the Cenozoic Kenya Rift. *J. Structural Geology*, 16-2, 189- 201.

Jones, W.B., 1985: Discussion on geological evolution of trachytic caldera and volcanology of Menengai volcano, Rift Valley, Kenya. *J. Geol. Soc. Lon.*, 142, 711 pp.

Jones, W.B., and Lippard, S.J., 1979: New age determination and geology of Kenya rift – Kavirondo Rift Junction, West Kenya. *J. Geol. Soc. Lond.*, 136, 63 pp.

KenGen, 2004: *Menengai volcano: Investigations for its geothermal potential*. KenGen, Kenya, Geothermal Resource Assessment Project, unpubl. report,

Kristmannsdóttir, H., 1979: Alteration of basaltic rocks by hydrothermal activity at 100-300°C. In: Mortland, M.M., and Farmer, V.C. (editors), *International Clay Conference 1978*. Elsevier Scientific Publishing Co., Amsterdam, 359-367.

Lagat, J., 2003: Geology and the geothermal systems of the southern segment of the Kenya Rift. *Proceedings of the International Geothermal Conference IGC 2003: "Multiple integrated uses of geothermal resources"*, Reykjavík, S12, 33-40.

Lagat, J.K., 2004: *Geology, hydrothermal alteration and fluid inclusion studies of the Olkaria Domes geothermal field, Kenya*. University of Iceland, MSc thesis, UNU-GTP, Iceland, report 2, 71 pp.

Lagat, J.K., and Ngenoh, D., 2010. *Menengai geothermal prospect*. GDC, Kenya, internal report.

Leat, P.T., 1983: *The structural and geochemical evolution of Menengai caldera volcano, Kenya Rift Valley*. University of Lancaster, UK, PhD thesis, 482 pp.

Leat, P.T., 1984: Geological evolution of the trachytic caldera volcano Menengai, Kenya Rift Valley. *J. Geol. Soc. London*, 141, 1057-1069.

Leat, P.T., MacDonald, R., and Smith, R.L., 1984: Geochemical evolution of the Menengai caldera volcano, Kenya. *J. Geophys. Res.*, 89, 8571-8592.

Lopeyok, T.P., 2013: Borehole geology and hydrothermal mineralization of wells MW-09 AND MW-11, Menengai geothermal field, Kenya. Report 15 in: *Geothermal training in Iceland 2013*. UNU-GTP, Iceland.

MacDonald, R., 2003: Magmatism of the Kenya Rift Valley: A review. *Earth Sciences*, 93, 239- 253.

MacDonald, R., Bailey, D.K., and Sutherland, D., 1970: Oversaturated peralkaline glassy trachyte from Kenya. *J. Petrology*, 11, 507-517.

MacDonald, R., and Scaillet, B., 2006: The central Kenya peralkaline province: insights into the evolution of peralkaline salic magmas. *Lithos*, 91, 59-73.

McCall, G.J.H., 1957: The Menengai caldera, Kenya colony. *Proceedings of the 20th International Geol. Congress, Section 1*, 55-69.

McCall, G.J.H., 1967: *Geology of the Nakuru-Thomson's Falls-Lake Hannington area*. Geological Survey of Kenya, report 78, 122 pp.

Mibei, G., 2012: Geology and hydrothermal alteration of Menengai Geothermal field. Case study: Wells MW-04 and MW-05. Report 21 in: *Geothermal training in Iceland 2013*. UNU-GTP, Iceland, 437-465.

Mibei, G., and Lagat, J.K., 2011: Structural controls in Menengai geothermal field. *Proceedings of the Kenya Geothermal Conference – KGC2011, Nairobi, Kenya*, 28-37.

Omenda, P.A., 1998: The geology and structural controls of the Olkaria geothermal system, Kenya. *Geothermics*, 27-1, 55-74.

Omenda, P.A., 2007: The geothermal activity of the East African rift. *Presented at Short Course II on Surface Exploration for Geothermal Resources, organised by UNU-GTP and KenGen, at Lake Naivasha, Kenya*, 12 pp.

Reyes, A.G., 1990: Petrology of Philippine geothermal systems and the application of alteration mineralogy to their assessment. *J. Volc. Geoth. Res.*, 43, 279-309.

RockWare, 2007: *LogPlot program*. RockWare, Inc., USA.

Scott, S.C., and Skilling, I.P., 1999: The role of tephrochronology in recognising synchronous caldera-forming events at the Quaternary volcanoes Longonot and Suswa, south Kenya Rift. In: Firth, C.R and McGuire, W.J. (eds): *Volcanoes in the Quaternary*, Geological Society, London, Spec. Publ., 61, 47-67.

Smith, M., and Mosley, P., 1993: Crustal heterogeneity and basement influence on the development of the Kenya Rift, East Africa. *Tectonics*, 12, 591-606.

Wheildon, J., Morgan, P., Williamson, K.H., Evans, T.T., and Swanberg, C.A., 1994: Heat flow in the Kenya Rift zone. *Tectonophysics*, 236, 131-149.

Williams, L.A.J., 1972: The Kenya rift volcanics: a note on volumes and chemical composition. *Tectonophysics* 15, 83-96.

APPENDIX I: XRD diffractograms of samples

MW-08 #10 UNT (796 m)

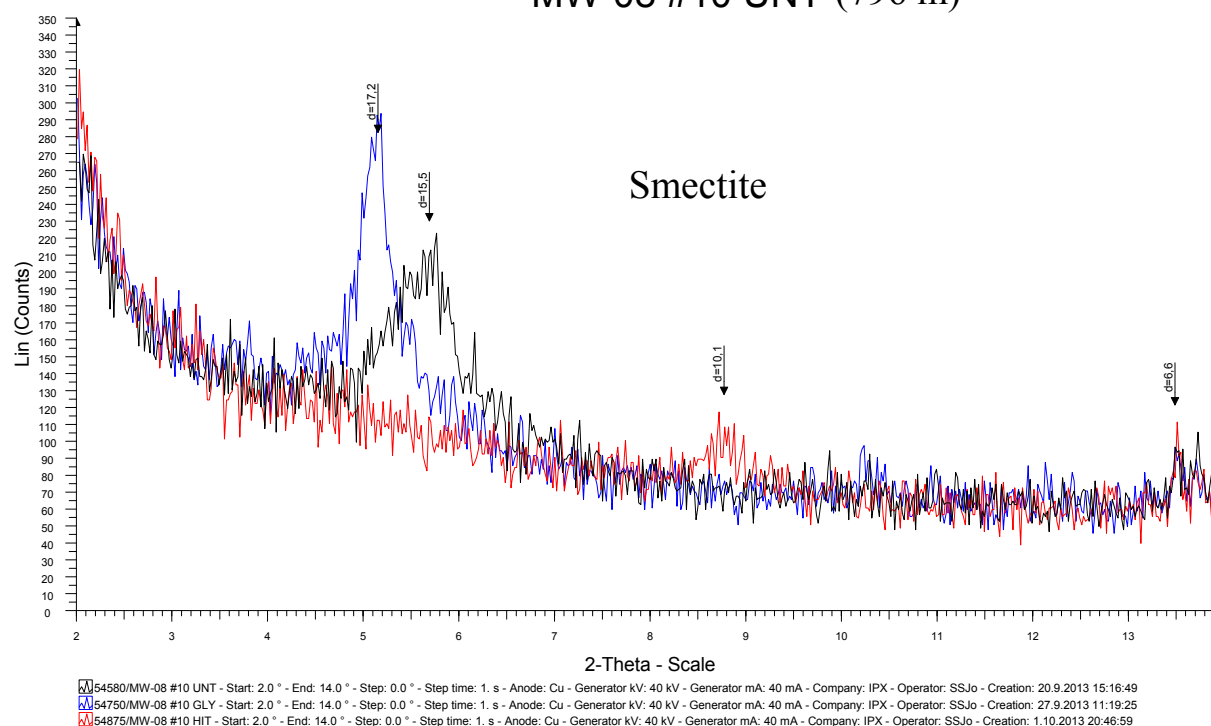


FIGURE 1: Diffractograms of smectite and illite clays at 796 m in Well MW-08

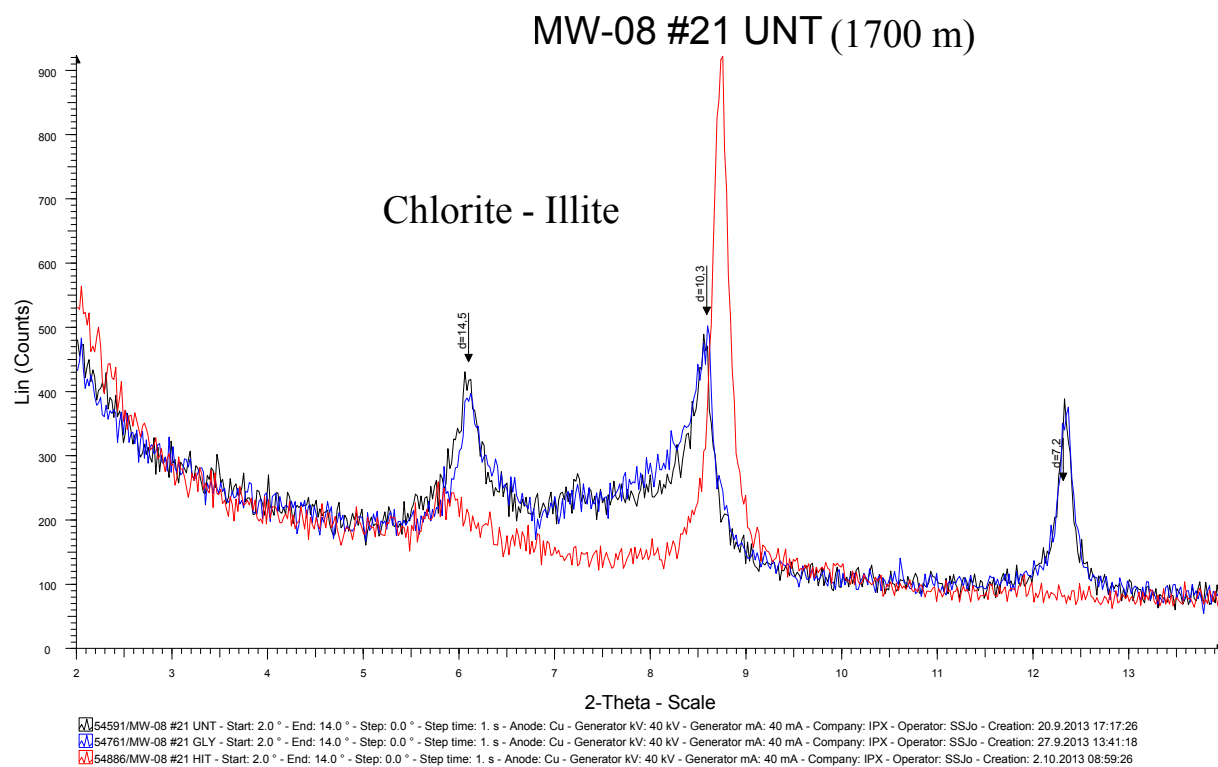


FIGURE 2: Diffractograms of chlorite and illite clays at 1700 m in Well MW-08

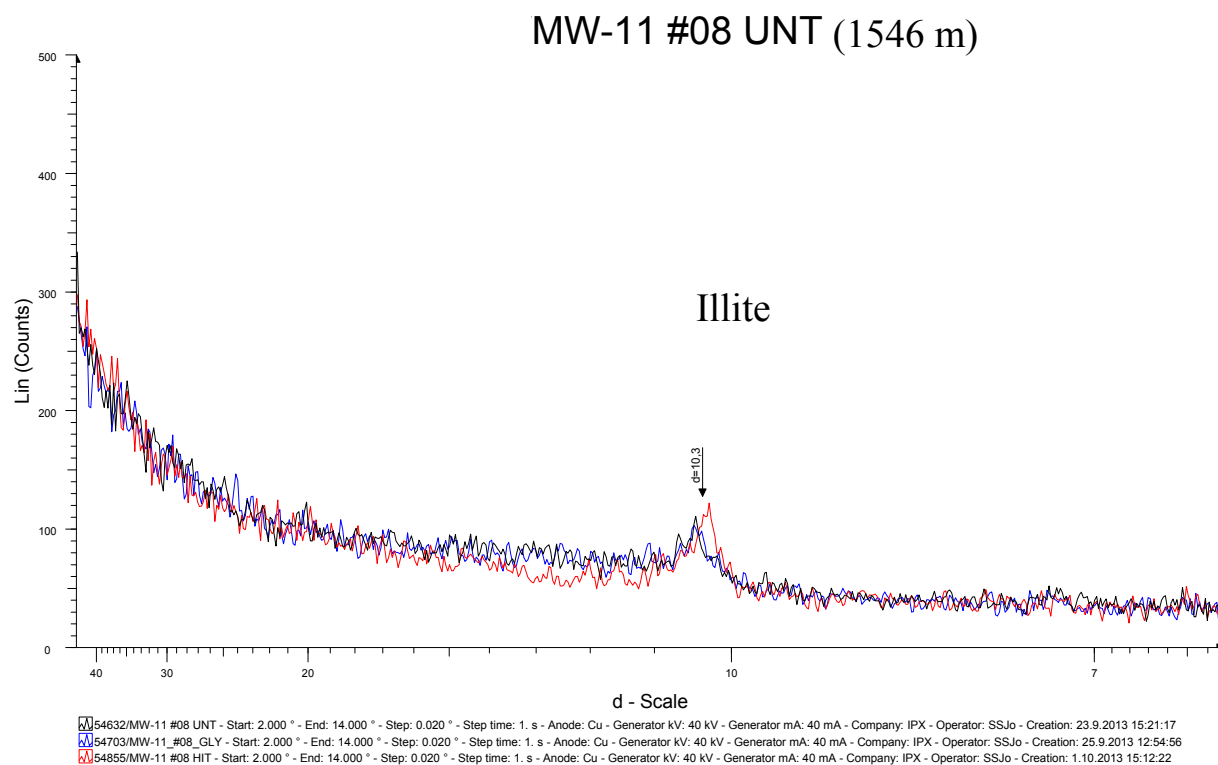


FIGURE 3: Diffractograms of illite at 1546 m in Well MW-11



**UNITED NATIONS
UNIVERSITY**

GEOTHERMAL TRAINING PROGRAMME
Orkustofnun, Grensasvegur 9,
IS-108 Reykjavik, Iceland

Reports 2013
Number 11

COST MODEL FOR GEOTHERMAL WELLS

Carolyn Kipsang

Kenya Electricity Generating Company Limited
Geothermal Resource Development
P.O. Box 785 20117 Naivasha
KENYA
carolynkipsang@gmail.com

ABSTRACT

The cost of drilling geothermal wells is estimated to be about 40% of the total investment cost for a new high temperature geothermal plant. This makes geothermal plants more expensive to build than conventional fuel fired power plants, and as a result the cost of the wells becomes a key consideration when determining the economic viability of a geothermal field. Obtaining accurate costs for geothermal wells is, therefore, very important as it quantifies a substantial percentage of the cost of the geothermal project. This will help in future planning and budgeting of geothermal projects. Accurate well cost records also make it possible to carry out an analysis of drilling-cost-with-depth and evaluate the benefits of selecting different drilling technologies and materials for various geothermal fields and regions and, further, couple them with the energy-recovery-with-depth for the field. The purpose of this paper is to develop a cost model for high temperature geothermal wells that allows for the estimation of well costs from a few key input variables such as well depth, number and size of casing intervals, and well trajectory. The model uses two input parameters, the criteria where the well design is established and a price book where all the unit costs are listed. The cost model then calculates the drilling materials required to drill each section of the specified well to completion. The cost of these materials is then automatically calculated using the unit cost that is automatically picked from the price book. The summary sheet then gives the total cost of the well. The paper also describes the well cost structure, the factors that affect the cost of the well and items considered when pricing a geothermal well. There is surprisingly little published data available on the breakdown of geothermal drilling costs due to the competitive nature of the geothermal drilling industry and confidentiality clauses. As a result, the data used for the price book for this model are estimated based on best guess values. The cost model divides the well cost into three major parts: pre-spud, drilling, and completion costs. The pre-spud costs include all the costs prior to spud-in, while the drilling costs are all the costs incurred while making the hole. This includes the rig rental cost, materials and the supervision cost. This is where the bulk of the cost lies. Finally the completion costs are the costs incurred after achieving total depth, prior to rig release. The model does not include the cost of monitoring the well after drilling nor that for flow testing.

1. INTRODUCTION

The goal of any geothermal drilling project is to drill the well to completion as per the drilling programme while ensuring the safety of the drilling staff, the drilling rig and to complete the well with minimum cost. The drilling programme includes the geoscientific studies which are conducted to determine the location of the well and the targets to be reached, the design of the well, the drilling technology to be applied and the well measurements and logging to be conducted while drilling and upon completion.

Drilling geothermal wells is a complex process that uses expensive drill rigs, a wide range of drilling experts and a lot of financial muscle. It is also a labour intensive operation with most of the jobs being performed 24 hours a day, seven days a week, in all weather conditions. The work is strenuous and hard and in Kenya is performed in a traditional 12 hour shift on a two-week on and off rotation. Only extreme weather, mechanical failure or lack of supplies will warrant the shutting down of these operations. Although the physics of drilling is the same everywhere in the world, wells vary widely in complexity and type, depending on the geological conditions. Accurate costing of these geothermal wells is, therefore, very important.

Several factors affect the cost of geothermal wells. These factors include well design, the total depth of the well, the type of drill rig and the methods used. Other parameters may include the efficiency of the drilling operation and the optimization of the drilling variables. These translate to the total time taken to drill the well. The total well time constitutes both the drilling and the non-drilling time. There are several factors and events which influence the well drilling time. Measurable factors include the physical characteristics of the well, geology of the area and the drilling parameters employed. The indirect factors, on the other hand, include well planning, drilling operator experience, execution team communication and organisation, leadership and project management skills. These indirect factors will, however, be considered to be beyond the scope of analysis for this paper.

Many advances have been made with the aim of reducing well drilling costs. The realization that the drilling process with the bit on the bottom takes about 50% of the total time, and the rate of penetration cannot be significantly increased, has led to the option of trying to reduce the non-drilling time. The challenge is to increase rig availability and reduce the time of “flat spots” where there is no depth progress. The “flat spots” are due to rig-up time, running in and cementing the casing, and solving drilling problems mainly caused by loss of circulation or a stuck pipe. One success story has been the development of drill bits which can stay in the hole longer and drill more depth, thereby reducing the rig time.

2. GEOTHERMAL PROJECT DEVELOPMENT

Geothermal projects have seven key development phases before the actual operations and maintenance phase commences. It is said to take approximately seven years to develop a typical full size geothermal project with, for example, a 50 MWe turbine as a first step (ESMAP and World Bank, 2012). However the project development time may vary, depending on the country's geological conditions, available information about the resource, institutional and regulatory climate, and access to suitable funding, among other factors. The phases as outlined by Mwangi (2005) are as follows;

i. Studies of surface manifestation: This phase involves the collection of information from previous geoscientific studies made in the area and analysing it. It also involves conducting surface exploration by mapping the geothermal manifestation in the area to determine the existence of a commercially viable geothermal reservoir and to estimate its exploitable potential.

ii. Detailed exploration: The detailed exploration phase consists of surveys to further confirm the findings from the preliminary resource assessment. An exploration plan is generated. This plan includes the geochemical, geological and geophysical exploration, heat flow measurements, hydrogeological and baseline environmental studies. Interpretation of old information and results from new surveys are used to develop the first basic conceptual model.

iii. Exploratory well drilling: This is the last phase of the exploratory phases. Based on the environmental studies done and the developed conceptual model, 3 to 5 exploratory drill sites are selected and the first wells are drilled and tested. This is followed by drilling the appraisal wells. The appraisal wells are mainly drilled in order to determine the size, characteristics and potential of a reservoir and, therefore, the size of the power plant to be developed.

iv. Feasibility studies: The results from the test drilling will enable the completion of the feasibility study, including all the financial calculations. At this point it is considered possible to determine the most economically advantageous project size and the investment necessary.

v. Developmental phase: This marks the beginning of the actual development of the power project. It consists of drilling production and re-injection wells. The time needed to drill a geothermal well not only depends on a well's total depth, but also on the geology of the area and the capability and capacity of the drilling rig being used. Production drilling is a time consuming and expensive activity. Delays during the drilling phase can, therefore, seriously affect the financial viability of a project. The environmental impact assessment for the project is carried out concurrently with the detailed power plant design.

vi. Construction, start-up and commissioning: This phase comprises the installation of a steam gathering system and the separators, installation, start-up and commissioning of the power plant with the turbine, generator and the cooling system. The cooling system consists mainly of a condenser, cooling tower, and a re-injection system.

vii. Operation and maintenance: This includes the operation and maintenance of both the steam field which includes the geothermal wells, steam pipelines and infrastructure and the power plant which includes the turbine, generator and cooling system. Proper maintenance of all of these facilities is crucial as it ensures availability of the power plant and steady steam production from the geothermal wells.

3. PHASES OF GEOTHERMAL DRILLING

The entire drilling project from well planning, designing, and drilling right to the delivery of a geothermal well can be divided into three main phases: the pre-spud phase, drilling phase and the completion phase as summarized in Figure 1:

3.1 Pre-spud phase

The pre-spud phase constitutes mainly the designing, planning and preparation of the infrastructure. It extends from the start of a drilling contract to the well spud. The pre-spud phase has several sub-phases as discussed below.

Well design: The number of casing strings, casing diameter selection and casing setting depths are important factors to consider when designing a geothermal well. The depth of each casing string is determined by several factors including: the geological properties of the area, the total depth of the well, formation fluids as well as well control considerations. When selecting the type of casing to be run in the hole, several parameters are considered as well. These parameters include:

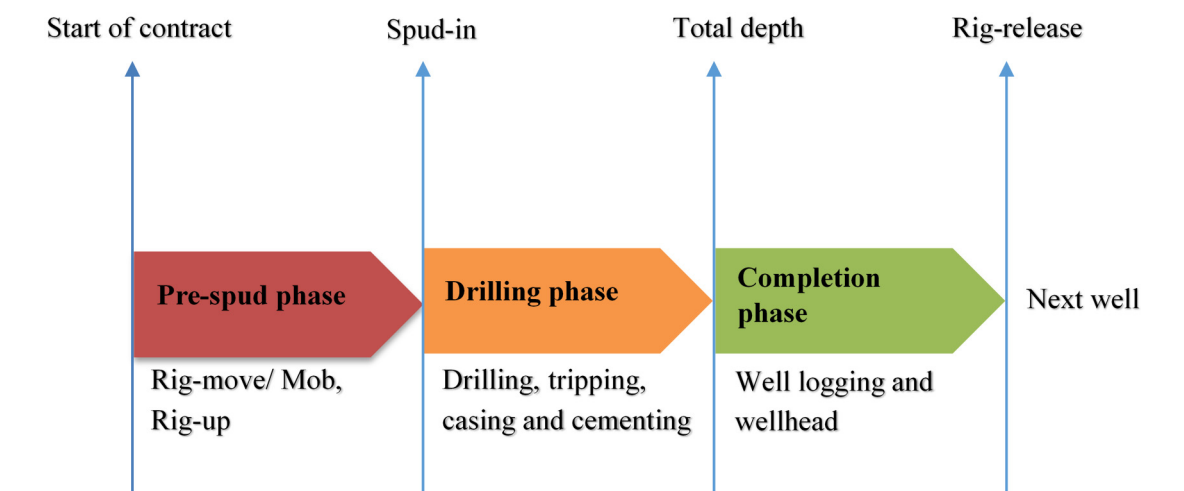


FIGURE 1: Summary of geothermal drilling phases

- i. The nominal production rate from the well and the casing diameter implied by that flow rate;
- ii. The depth of the production zone and expected temperature;
- iii. Well trajectory;
- iv. Length of individual casing interval;
- v. Brine chemistry; and
- vi. The need for special casing material or connections.

Wells are generally designed from the bottom up to the surface casing, which is to say that the expected depth of the production zone and the expected flow rate will determine the casing programme. Most of the drilling equipment requirements will follow from these criteria.

The next important step is the preparation of a drilling programme. This programme contains the primary objective of drilling the well and a step by step schedule giving detailed procedures on how to carry out each activity when drilling the well. It also outlines most of the anticipated drilling problems and how best to handle them (Karewa, 2012). Other factors put into consideration may include other drilling materials and consumable specifications and selection, for example the wellhead, drilling fluid, cement and cement additives.

Construction of access roads: Construction of the access roads follows. It involves clearing vegetation, removal of the top soil, excavation, grading, murrum dumping, final grading and compacting and provision of drainage. Earth moving equipment is used for this purpose. In new geothermal fields this can take quite a long time and can also be expensive.

Well pad preparation: This is the preparation of a stable, well compacted drilling site that will accommodate the drilling rig, its associated equipment, all the offices and accommodation facilities and the drilling crew. A large discharge pond which is big enough to accommodate the discharged fluids is also prepared. This is done according to a designed access road route and well pad layout. The process involves marking the sites, clearing the vegetation and removing the top soil, taking spot heights and fixing depth of cut while excavating the pad area. The process of levelling, dumping of murrum, final grading, and compacting of the pad using earth moving equipment follows:

Cellar construction: A cellar is a concrete structure that provides working space for well head equipment for the rig such as the blow out preventer (BOP) and later for the production wellhead. Construction of the cellar includes marking the cellar area, excavation and either bringing in a precast cellar or by making it on site from concrete, and laying drainage pipe. The cellar design usually depends on the size of the drill rig and the rig floor height.

Laying water lines: Water for the drill fluid is key during the drilling of geothermal wells although its availability close to drilling sites is limited in most geothermal fields in the world. The water is mostly sourced from nearby rivers, lakes or boreholes. This water has to be pumped from the source to the drill site. The pipeline route is first surveyed and approved. The length of pipeline can be more than 10 km and the change in elevation several hundred metres. This is followed by laying the pipe, installing the pumps and arranging for water storage. The flow meters are then installed and finally the water line is tested for any leakages.

Rig mobilization/ demobilization: This involves the transportation of the drill rig to a new geothermal field. This is usually a one off cost. The cost may be borne entirely by the first well drilled or shared amongst several wells to be drilled. Mobilization cost is, therefore, highly variable.

Rig move, rig up and transport costs: Rig move is the transport of the drill rig from one drill site to the next. It includes the rig down, rig move and rig up on the new site. This is usually the case when the drill rig is drilling within the same geothermal field or different fields within the same region.

3.2 Drilling phase

The drilling phase includes all the activities carried out from when the well is spudded until the total depth is reached. Typically, geothermal wells today are drilled to depths ranging from 400 to 2000 m depth for low to medium temperature systems and from 700 to 3000 m depth for high temperature systems. Both vertical and directional wells are drilled. An example of a typical regular diameter well profile and trajectory for wells drilled in Olkaria geothermal field is shown in Figure 2.

Drilling geothermal wells is carried out in a series of stages with each stage being of smaller diameter than the previous stage, and each being secured by steel casings, which are cemented in place before drilling the subsequent stage. The final section of the well uses a perforated uncemented liner which allows the geothermal fluids to pass into the pipe (Semancik and Lizak, 2009).

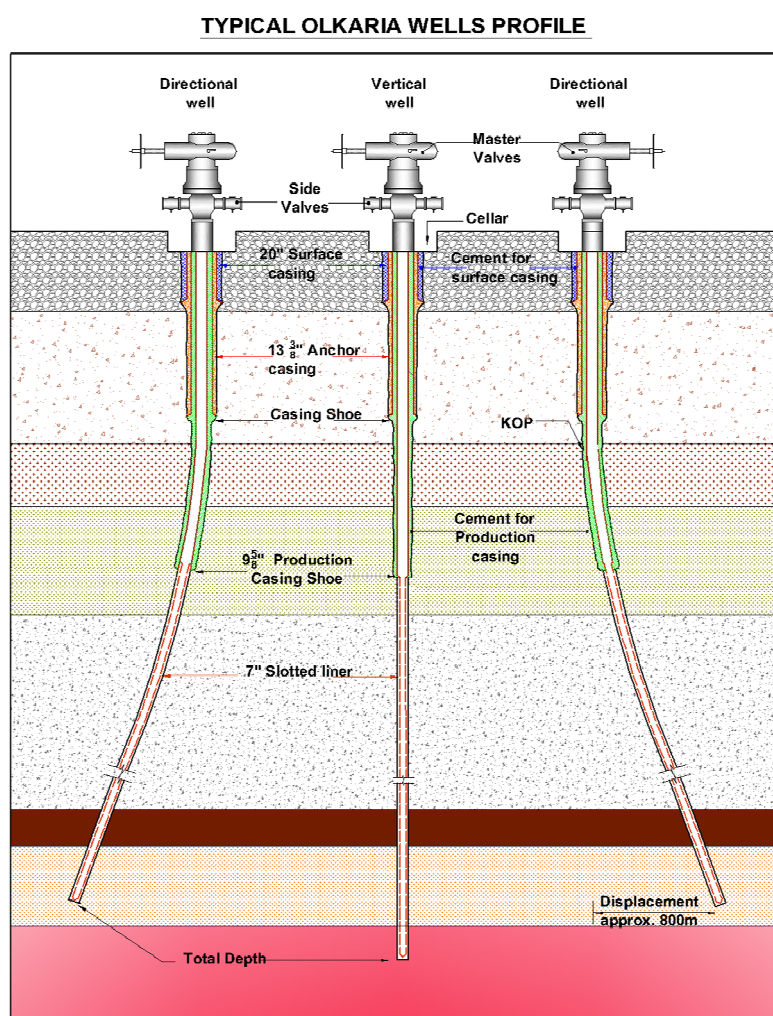


FIGURE 2: Typical regular diameter well profile in Olkaria

3.2.1 Casing programme

The first design task in preparing the well plan is selecting the depths to which the casings will be set and cemented. These depths are determined such that the casings can safely contain all well conditions encountered as a result of surface operations and from the behaviour of the formations and fluids encountered as drilling proceeds. Casing shoe depths are determined by analysing data from adjacent wells. This includes rock characteristics, formation and formation temperatures, fluid types, composition and pressures and, in particular, the fracture gradient data that is gathered from nearby wells. Figure 3 illustrates how the shoe depth may be chosen as per the New Zealand Standard 2403:1991. It assumes a boiling point for depth fluid pressure conditions from a nominal water level at 200 m depth; and a uniform formation fracture gradient (overburden) from the surface to the total depth of 2400 m. From this model, the production casing shoe would need to be set at about 800 m, the anchor casing shoe at approximately 350 m, and a surface casing at around 50 m depth.

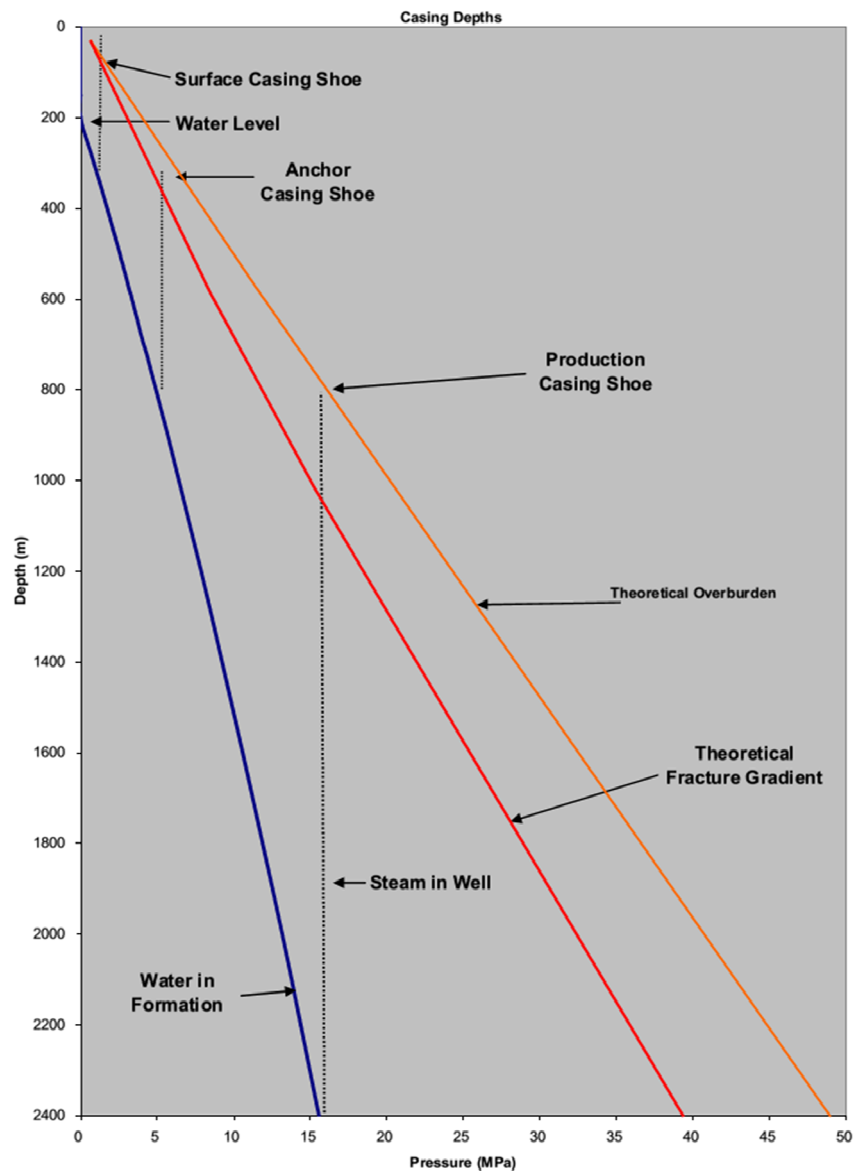


FIGURE 3: Theoretical minimum casing depth selection (Hole, 2008a)

Casing diameters:

The casing diameters will be dictated by the desired open hole production diameter. A typical regular diameter geothermal well as discussed by Thórhallsson (2013) would include:

i. Surface casing (20" or 18-5/8" casing): These are the largest casings which are set at a shallow depth and are used to prevent loose near surface materials from collapsing into the hole. They are also utilized to support the initial drilling wellhead or blow out preventer and to contain the circulation drilling fluid. The setting depth of the casing shoe will be estimated from geological deductions but may be altered to reflect conditions found during the course of drilling.

sii. Intermediate or anchor casing (13-3/8" casing): This string of casing isolates the surface aquifer from contamination while providing anchorage for the wellhead. It also seals off loss zones and protects the shallow formation from deep reservoir pressure, thus preventing blowouts. The setting depths are

usually chosen from expected formation rock and fluid conditions to provide adequate permanent anchorage and additional security against drilling problems, including blowouts.

iii. Production casing (9-5/8" casing): This casing is smaller in diameter and is set at greater depth than the previous casing. It primarily acts as the conduit for the reservoir fluid to the surface, protecting the shallow formation from deep reservoir pressure, thus preventing blowouts, and isolating the cooler shallow water from degrading the reservoir fluids. The depth of this casing string is chosen on the basis of the expected depths and temperatures of fluids to be included and excluded from production. A common criterium for high temperature wells is to accept only fluids above 210°C, as the inflow of lower temperature fluid may have an unstable flow or even no self-flow.

iv. Slotted liner (7" casing): This is primarily run to prevent the reservoir wellbore from collapsing and blocking the well flow path. The liner depth is from 10-20 m up into the production casing (overlap) and to the well's total depth.

The competence of the rock and the incidence of drilling circulation fluid losses are likely to govern final casing depths. The final decision on casing depths is, however, made on site, considering the actual well conditions and the design.

Casing material and connections:

The casing material is determined in two steps. First, the operational scenarios which will result in burst, collapse and axial loads are defined and their magnitude calculated. From the calculated values, the casing thickness which has a higher burst and collapse resistance than the calculated value is selected. The casing material most commonly used is steel, based on the petroleum industry standard API SPEC 5CT. The preferred API steel grades are K-55, L-80, and C-75 (Thórhallsson, 2013).

Casing connections:

The compressive stress imposed on a casing string undergoing heating after well completion is extreme. As an example, an 800 m length of casing undergoing heating from the cement setup temperature of about 60°C to the final formation temperature of about 210°C would freely expand. If uniformly constrained over the full length, the compressive strength induced would be about 360 MPa; the minimum yield strength of grade K-55 casing steel is 379 MPa. This illustrates that the axial strength is critical and it is, therefore, important that the casing connection exhibits a compressive strength at least equivalent to that of the casing body. It is usual, therefore, for a square section thread form to be chosen; this is typically the API Buttress threaded connection (Hole, 2008b).

3.2.2 Cementing programme

Geothermal well cementing is the process of mixing and pumping a cement slurry down the casing and then up the annulus to totally fill the annular space between the casing string and the formation. Upon setting, the cement will establish a bond between the casing and the formation. The slurry is made by mixing cement with water and other additives. The additives are used to tailor cement for a specific application. They are dry mixed into the cement to alter the properties of both the slurry and the hardened cement. These additives adjust the density, thickening time, and viscosity of the cement slurry. Sometimes mica flakes are added to form bridging for lost circulation. The cement is usually mixed with 35-40% silica flour for temperature resistance. This ensures longevity of the cement (Bett, 2010).

Other additives besides the silica flour may include:

i. Retarders are used to prolong the thickening time of the cement slurry, thus avoiding premature setting at elevated temperatures. The retarder concentration is based on the expected or measured bottom hole circulation temperature (BHCT) and the pumping time. The exact retarder concentration is, however, decided upon after a cement laboratory test on the same batch of cement.

ii. *Lightweight additives* or extenders are used to reduce the slurry density for cementing jobs where the hydrostatic head of the cement slurry may exceed the fracture strength of the formation. In reducing this slurry density, the ultimate compressive strength and thickening time is reduced. The most commonly used extender is expanded perlite or glass microspheres and bentonite.

siii. *Friction reducer* includes dispersants used to lower the yield point of the slurry, thereby allowing the cement slurry to go into turbulent flow at a lower velocity.

iv. *Fluid loss control* additives are used to prevent dehydration of cement slurry and premature setting.

v. *Loss of circulation* additives are used to prevent the loss of slurry into the formation. Mostly used are the mica flakes.

vi. *Accelerators* are added to the cement slurry to shorten the setting time. These are mostly used when cementing the surface casing where temperature is low, resulting in the cement taking too long to set. An example is calcium chloride.

3.2.3 Bit selection

The drill bit is the most critical part of the bottom hole assembly. Drilling efficiency largely depends on the drill bit's life and the rate of penetration. There is a relationship between the bit cost, bit life and the bit performance. For a drill bit to have a longer drilling life, more advanced technology needs to be applied during manufacturing, thereby resulting in higher bit costs. Most drill bit manufacturers tend to play with these factors to strike a balance between cost effectiveness and bit performance. For geothermal wells, drill bits with tungsten carbide inserts, gauge protection and journal bearing are most commonly used (Cherutich, 2009). The factors that affect bit life are lithology, the bottom hole assembly design, well trajectory and the drilling parameters employed. Although one has no control over the lithology of the area, the bit life can be significantly improved by making intelligent changes in the latter three factors.

3.2.4 Drilling fluids

Drilling fluids are very important when drilling geothermal wells as they contribute to the success of the drilling project. They are required in order to remove cuttings from the well, cool and lubricate the bit and the drill string and control the formation pressures during drilling. Various drilling fluids are selected depending on the diameter of the well, loss of circulation, temperature and the technique of drilling employed. It is important, therefore, to select a drilling fluid that will provide the best results in terms of cost, safety and performance so as to attain the desired depth and output of the well. The drilling fluids most commonly used when drilling geothermal wells include water-based mud, water alone, aerated mud or water and foam. The upper section of a geothermal well is usually drilled with water-based bentonite mud, thereby maintaining the pH above 9. As drilling proceeds and temperature increases, the viscosity of the mud is controlled with the addition of dispersants. If loss of circulation is encountered above the production casing shoe depth, attempts will be made to seal these losses with loss of circulation materials (LCM), and cement plugs if the loss persists. If none of these methods work, then drilling blind or drilling with aerated fluid commences. Once the production casing shoe has been run in hole and cemented, and drilling into the production part of the well commences, mud is no longer used as drilling fluid, as it has the potential to damage the permeability and, thus, the production potential of the well (Chemwotei, 2011). In the open hole section, water alone is used as the drilling fluid and, in many areas, compressed air is added to achieve a pressure balance, especially after encountering losses. High viscosity polymer pill sweeps are used, especially before adding a new drill pipe, to aid in hole cleaning should there be a large fill-in.

3.2.5 Directional drilling

Directional drilling is a special drilling operation used when a well is intentionally curved to reach a bottom location. It is the most widely used method of drilling geothermal wells due to its various advantages. Drilling multiple wells in the same well pad allows for fewer drill sites, less surface area disturbance as well as making it easier to exploit the resources being drilled. Additional equipment and expert services from “directional drillers” are, however, required when drilling a directional well as opposed to a vertical well. They include:

i. Tools for changing the course of the well bore from vertical to the desired direction, such as downhole motors. They are of two types, either having a bent-sub above the “straight” motor, or the mud motor housing itself having a bend a short distance above the bit. The latter type is more versatile as it can either be deployed in a “sliding” mode to increase the angle or “rotation” to drill straight to stay on track, but the straight motor and bent-sub can only increase the angle and then the bent sub has to be removed to drill straight with a new BHA.

ii. Surveying equipment run on a wireline such as magnetic-single shot equipment, magnetic multi-shot equipment and the gyroscopic multi-shot. Measurement while drilling tools (MWD) are used in the BHA above the motor to transmit by mud pulse technology the toolface, inclination and azimuth.

These tools enable a change in the course of the wellbore from vertical to the desired direction and inclination while allowing the driller to know the position and course of the hole as drilling progresses. The principle is to orient the drill bit in the required direction at the kick-off point (KOP). The factors that determine the choice of tool to use is identified by Miyora (2010) as the degree of deflection needed, formation hardness, depth of the well, encountered temperature and economics.

3.2.6 Hole problems

These are any occurrences which may cause a time delay in the progression of planned drilling operations. Included are the time required to solve the problems and the time it takes to bring the operation back to the point or depth at which the event occurred. It is very common to experience these problems when drilling geothermal wells. The ultimate goal of any drilling organization is to improve drilling performance by reducing unscheduled events and thereby reducing well costs. That is not to say that actual times cannot be reduced by eliminating inefficiencies. The most common down-hole problems when drilling geothermal well are discussed below.

Loss of circulation

This is one of the most expensive problems routinely encountered when drilling geothermal wells. It is the loss of drilling fluid to pores or fractures in the rock formation being drilled. Ideally the well should have no losses until the casings have been cemented, but in the open hole section big losses indicate good future production potential and are, thus, highly desirable. Loss of circulation is quite harmful for the drilling process for several reasons:

i. Drilling without returns can leave the formation pressure unbalanced, which can allow the hole wall to fall in. Also, the cuttings that do not enter the fracture accumulate inside the well cavities. At breaks in circulation, for example when adding a new pipe and without much warning, the material can jam the drill string. This can cause a stuck pipe, twist offs, or even loss of the well.

ii. Flow of the drilling fluid with cuttings into the formation can damage the formation’s permeability and reduce well productivity.

iii. Lost circulation that occurs during the cementing of the well can cause incomplete cement jobs that can in turn lead to casing failure.

iv. The drilling fluid used, for example bentonite, is usually quite expensive and losing it into the formation instead of re-circulating it is costly.

vi. Lost circulation can suddenly lower the fluid level in a well. Decreasing the static head of drilling fluid in a hot formation can allow the formation fluids to enter the wellbore, causing loss of well control.

vii. Placement of cement plugs is made difficult because the top and bottom of the loss zone are often not well known.

viii. Time lost in attempts to regain circulation adds to the cost of the well.

Stuck pipe

This refers to the mechanical sticking of a drill string. It is caused by chips and cuttings collecting on top of the drill string. The pipe can also be held against the wellbore wall by the differential between the drilling fluid pressure and the pore pressure. Sticking directly affects the cost of the well as it can extend the time it takes to complete the well.

Fishing

A fishing operation is an attempt made to remove stuck or broken objects from the well which prevent further drilling. Fishing may take up to 20% of the time incurred when drilling a geothermal well. Each rig is equipped with various fishing tools. Fishing jobs require high skill and specialized equipment. Most companies find it more economical to rely on service companies to furnish the tools and specialized personnel when the need arises (Ngugi, 2008).

Other well problems may include twist-offs (broken drill string), hole stability problems, well control problems, cementing, casing problems and directional drilling problems.

3.3 Completion phase

The completion phase covers the time from when the total depth is achieved to rig release. Immediately after a geothermal well is drilled to total depth, a slotted liner is run into the open hole production section of the well. It is a usual practise to carry out a series of completion tests on the well, utilising the drilling rig and equipment, and in particular the rig pumps before rigging down and releasing the rig from the drill site. These completion tests and measurements are designed to identify potential feed zones in the well, provide an estimate of the total effective permeability of the well, and to establish a baseline dataset of the casing conditions (Hole, 2008c). In addition, these tests determine the physical properties of the reservoir. A significant amount of information, which will add to the characterization of the reservoir and the well, can only be obtained in the period during and immediately after drilling activities are completed. The activities during the completion phase include: injection tests, well logging, running in the slotted liner and installation of the master valve.

3.4 Rig release, rigging down and rig move

After the master valve is installed, the rig is released and rig down is commenced. The rig components are dismantled and loaded to trucks for transportation to the next drill site. The time taken to rig down, transport and finally rig up on the new site determines the cost of a rig move operation. This time will vary from 5 to 14 days, mainly depending on the type and size of the rig and the distance involved. Drilling companies usually charge a fixed price for the rig move to the next well.

4. WELL COSTS

4.1 Elements of well costs

Well costs are a major component of the total cost of developing any geothermal project. It is estimated to be about 40% of the total investment cost for a new high temperature geothermal plant (Thórhallsson and Sveinbjörnsson, 2012). There are several factors that affect these well costs. They include the depth of the geothermal resource together with the nature, structure and hardness of the rock formation. These parameters automatically influence the initial and final well diameter, the number of casing strings required, the rate of penetration and drilling speed, and eventually the total time required to complete the well. Deeper wells also require larger and thus more expensive drilling rigs. Other factors that influence well cost may include the geographical location of the drill site, well design, whether vertical or directional, the down hole problems encountered and finally the well measurements and well logging employed.

Well costs are divided into three major items: the pre-spud, the drilling and the completion costs. The pre-spud costs are the costs incurred during the pre-spud phase for infrastructure and rig mobilization. The drilling cost, on the other hand, is the sum of the total costs incurred when making the hole. This includes the cost of the drilling rig rental, drilling materials and consumables and the cost of services offered depending on the contract. The drilling cost, although quite predictable, can vary according to the drilling contract, the size and rating of the drilling rig being used, the well design and, to a lesser extent, the remoteness of the drill site and proximity to suppliers.

Drilling costs are further categorized into four components, namely:

i. Daily operating costs: These are the costs incurred when operating the drilling rig on a day to day basis. It includes the daily rig rate which is the rental charge for the rig with crew and associated equipment. This rig rate varies depending on the type and size of rig, length of contract, and of course the market conditions as reflected in a tender. The well design will dictate the type of rig to be hired and the extra equipment that comes with it. It may also include the costs for the water supply, catering and accommodation, drill site maintenance and waste disposal.

ii. Drilling consumables costs: These are the costs inclusive of VAT and transport and handling of the drilling consumables that are used when drilling a geothermal well. These consumables include the rock bits, drilling detergent, diesel, lubricating oil, cement and cement additives and drilling mud. The quantity of these consumables will entirely depend on the well design and the working days.

iii. Casing and wellhead costs: These are the cost of the steel casing, casing accessories and wellhead equipment inclusive of VAT and transport to the drilling site. The cost of these drilling materials can be easily estimated. The purchasing of materials is usually by an open tender process or integrated in the drilling contract. When calculating the cost of casings for a particular well, for example, each casing string for each hole size is costed and the total is summed up to give the total casing costs for the well.

iv. Services costs: There are several services provided during the drilling of a geothermal well. These services vary depending on the well design and the drilling contract in place. These services include drilling supervision, planning and logistics, civil engineering, geological services, cementing services, directional drilling services, air drilling services and well logging.

v. Non-productive costs: These are the costs incurred from delays due to encountered downhole problems.

The total drilling cost is, therefore, the sum of all of these costs. The costs incurred during the completion phase include the well logging and equipment rental and the associated service charge. These costs depend primarily on the type of well measurements and logging programme employed.

4.2 Drilling time

Drilling time is a key measure of the technical performance when drilling a geothermal well. The total time spent on a well consists of both productive and non-productive time. It is a sum of the following:

- i. The time spent on making the hole. This includes the actual drilling time and the associated activities for example circulation, directional drilling, wiper trips and reaming or hole opening.
- ii. The “flat time” that is spent on tripping, running in casing and cementing it in place, making up BOPs and wellheads.
- iii. The time spent on conducting the well completion tests.
- iv. Time taken to move the rig to location, rig up and rig down once the well is drilled to completion and the rig released.
- v. The non-productive time.

A graph of well depth is plotted against the total drilling time, usually in days, as shown in Figure 4. The detailed time estimate is then prepared for each section of the well by considering the individual operations involved. The drilling time is affected by several factors as discussed below.

i. Drilling rate - rate of penetration (ROP)

This refers to the rate at which the drill bit penetrates the formation. This drill rate depends primarily on rock type and the type of bit selected. Hard-rock drilling needs significantly more drilling time than soft rock drilling. Other factors may include the type of bit used, weight on the bit, the rotary speed, bottom hole cleaning and the type of drilling fluid being used. A study done by Miyora (2010), a UNU fellow, in which he compared the time required to drill 12 directional wells from the Olkaria geothermal field in Kenya to 14 similar wells of regular diameter from the Hengill geothermal field in Iceland shows an overall advance from start to finish of drilling to be about 57 m per day when drilling in Iceland versus 48 m per day when drilling in Olkaria.

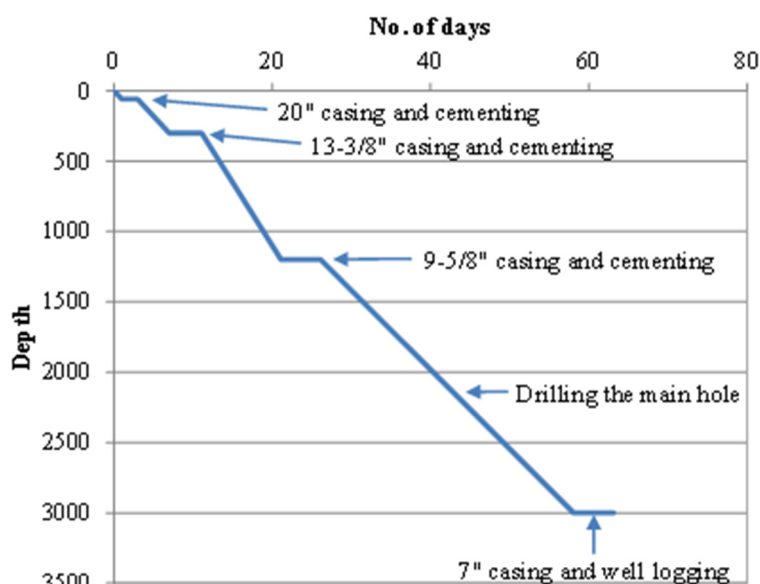


FIGURE 4: Drilling time - depth vs. days

ii. Well design

The target total depth and design of the well will have an effect on the drilling time. It takes a shorter time to drill a shallow well to total depth than a deep well. The time to drill a “regular” geothermal well and a “large” diameter geothermal well is, however, virtually the same.

iii. Casing and cementing

This is the time required to run the casing into the well, and cement it in place. The casing and cementing time is highly dependent on the casing size and length, hole conditions and crew efficiency. From the study done by Miyora (2010), cementing wells takes about one and a half times longer in Kenya than in Iceland. This could be due to the large number of backfill jobs required if cement returns are not received on the surface in Kenya as compared to Iceland. Another possible cause deduced was the cementing programme, where no calliper logging was done in Kenya to accurately ascertain the capacity of the

annulus, unlike in Iceland where the calliper logging is carried out to estimate the cement volume and temperature logs to locate the main loss zones.

iv. Directional drilling

Directional control of a well requires an increase in the drilling time, whether it is an attempt to drill a well directionally or in maintaining directional control of a well that has deviation tendencies. This increase in time in Kenya is usually from the many directional surveys conducted and the need to correct well angle and azimuth if need be by changing the BHA, compared to Iceland where a MWD tool and a steerable motor is used, allowing the drilling to go on without interruption.

v. Completion logging

Well completion test and logging for geothermal wells vary in complexity and, therefore, have a significant variation in the duration. The most common well logging done are the temperature, pressure and lithological logging. These measurements aid in obtaining information which lead to a better understanding of subsurface conditions. The efficiency of the associated personnel and their experiences with the type of well logging being done have a major impact on the required completion time.

vi. Rig move

Rig transportation is an important part of the drilling process. There are two types of rig transportation: rig mobilisation and rig move. Rig mobilisation is where the rig is transported either from the rig manufacturers workshop or overseas contractor yard, whereas rig-move refers to the movement of the rig from one completed well to the next drilling site within the same geothermal field (Cherutich, 2009).

Rig move-in and rig-up occur before the well is spudded-in while rig-down and rig move-out occur after completion of the well. The size of the drilling rig, therefore, is a major determinant of the rig moving costs. For the present model, the cost for the rig move is a fixed sum.

4.3 Drilling contracts

Geothermal drilling contracts mainly fall under four main categories:

i. Day rate contracts

This is the most commonly used contract worldwide. The drilling contractor in this case is paid a specified sum by the company for each day that he spends on the well. Most drilling contractors prefer this type of contract as there is little downside for them. The day rates are usually broken down into three: Operating day rate, which is applied to the day rate when the contractor's equipment and personnel are fully utilized; The second is the standby day rate in which case the contractor's equipment and personnel are not being fully utilized. This rate is usually a slightly lower than the operating rate: Finally, the zero day rate is when no payment is made at all to the drilling contractor, e.g. if rig maintenance exceeds agreed limits.

ii. Footage contracts (metre rates)

In this case, a specified rate per metre drilled is negotiated for a well of a certain design. Certain operations are, however, charged at a day rate or a fixed rate. With this type of contract, the contractor has an incentive to drill the well faster. This type of contract has been employed in mature geothermal fields which are reasonably well known, for example in Iceland.

iii. Integrated drilling contracts

An integrated contract is made with the drilling contractor for the provision of all drilling services and materials, under one contract.

iv. Turnkey contracts

With this type of contract, the company pays the contractor a lump sum to drill a well of a certain depth in a given field. It is, therefore, up to the drilling contractor to procure all the drilling materials and to organise the required third party services in order to deliver the well. The company has no input on the day to day drilling operations unless of course if it is stated in the contract.

The scope of work of a drilling service contract will define the split of responsibility between the owner and the contractor. Operational responsibility, control and risk are all interlinked. Operational responsibility implies operational risks, but imposes operational risk, as depicted by Hole (2006) in Figure 5.

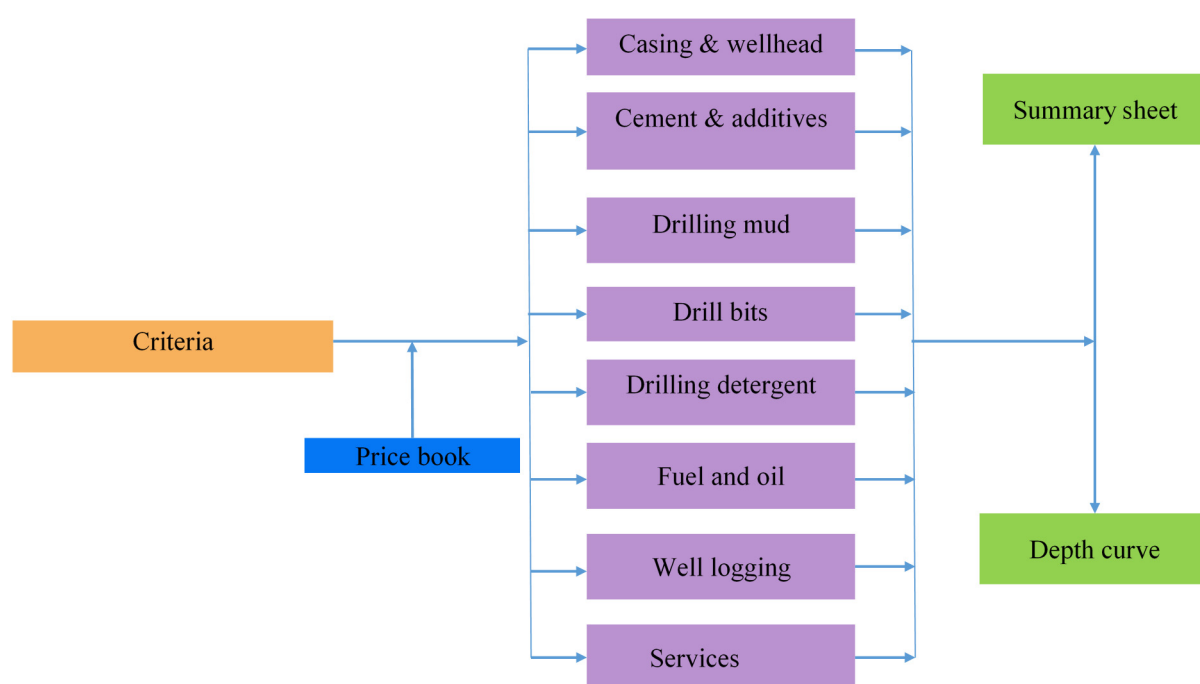


FIGURE 5: Summary of cost model parameters (Hole, 2006)

5. COST MODEL STRUCTURE AND PARAMETERS

The need to make an accurate estimation of well costs led to the development of a well cost model known as the Wellcost Lite in the United States of America. This model was used to determine the most important factors behind drilling costs for geothermal wells. The model allows for the input of a casing design programme, rate of penetration, bit life and trouble map for each well interval. The model then calculates the time to drill each interval including rotating time, trip time, mud, and related costs and the end of interval costs such as casing and cementing and well evaluation. The cost of materials and the time required to complete each interval is calculated. The time is then multiplied by the hourly cost for all rig time –related cost elements such as tool rental, blow out preventers (BOP), and supervision. Each interval is then summed to obtain a total cost. The cost components of the well are presented in a descriptive breakdown and on the typical authorization for expenditure (AFE) form used by many companies to estimate drilling costs (Augustine and Petty, 2006). The Wellcost Lite model is, however, not yet available.

The EXCEL based spreadsheet cost model developed as a part of this study divides well costs into six major components: the pre-spud costs, daily operating costs, drilling consumables, casing, wellheads,

and services costs. For this case study, a 3000 m deep regular diameter well (9 5/8" production casing) was selected, similar to wells drilled in Kenya. The general design of the well is as described in the criteria in Table 1. With the case of a large diameter well or a slim hole, the various casing diameters and setting depths need to be entered into the criteria inputs. The number of days taken to drill each section of the well is inputted, based on best knowledge, and the rate of penetration is then automatically calculated. This is summarised in Figure 6.

TABLE 1: Criteria showing each depth interval, duration and calculated rate of penetration

Criteria inputs	Depth (m)		Duration	ROP
	From	To	Days	(m/day)
Drill 26" hole	0	60	1	60
20" casing and cementing	0	58.5	2	-
Drill 17-1/2" hole	60	300	4	75
13-3/8" casing and cementing	0	298.5	4.1	-
Drill 12-1/4" hole	300	1,200	10	120
9-5/8" casing and cementing	0	1,198.5	5	-
Drill 8-1/2" hole	1,200	3,000	32	93.8
7" casing	1,174.5	3,000	2	
Completion tests			2	
Breaking Tubulus/Rig release			1	
TOTAL			63.1	

5.1 Pre-spud costs

The pre-spud costs consist of the drillsite preparation cost, which is a fixed cost, and the rig mobilization, rig demobilization and rig move costs. This is, however, a day rate cost and therefore depends on the number of days taken to move the rig. These actual costs vary depending on the location of the geothermal field and the size of the drilling rig being used. These costs were input into the price book for this model as a fixed cost based on recent experience.

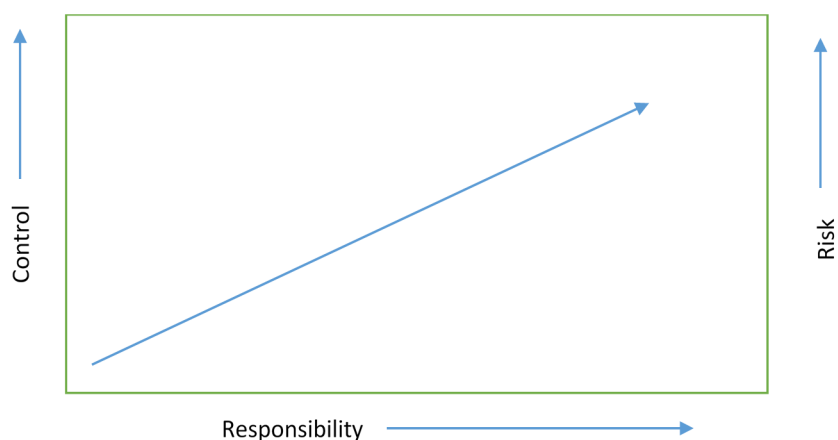


FIGURE 6: Responsibility, control and risk matrix

5.2 Daily operating costs

The daily operating costs consist of the rig rental, together with the drilling crew and all the associated rig equipment, but not such equipment as the cementing equipment, directional drilling, air compressor and fishing tools. Most of these items are day rate based except for the drill stem inspection which is a fixed one-off cost and is done on a contract basis. This cost was, therefore, calculated by multiplying the total drilling time from spud in to total depth by the unit daily costs.

5.3 Drilling consumables

The cost of the drilling consumables includes the cost of rock bits, drilling detergent, diesel, lubricating oil, cement and cement additives and finally drilling mud or bentonite. The unit price for all of these materials is the cost of the material on site that is inclusive of VAT, transport and handling costs and shipping. Although VAT, shipping and transport and handling vary greatly, the example in this model used the estimated values assuming the field to be in Olkaria, Kenya and the port to be Mombasa. This was worked out in the price book for the final price used for the various drilling materials.

TABLE 2: Cost of bits used

Rock bits	Life (m)	No.	Unit cost (USD)	Total cost (USD)
26"	180	1	30,000	30,000
17-1/2"	300	1	25,000	25,000
12-1/4"	350	3	15,000	45,000
8-1/2"	400	5	8,000	40,000
Stabilizers add 30% to bit cost				42,000
SUM	182,000			

i. Rock bits

The total number of bits required to drill each section of the well was calculated by dividing the depth of the well section, which was picked from the criteria, by the expected depth life of the respective bit size as shown in Table 2. The depth life of bits is assumed as shown in Table 2. It may vary, however, depending on the formation and type of bit being used.

ii. *Drilling mud*

For this example, an assumption was made that bentonite mud was only utilized when drilling the top sections of the well down to about 300 m and a reserve is kept in the mud tanks when drilling the next section, just in case there is need for the drilling mud for sweeps.

When calculating the total amount of drilling mud required, the capacity of the hole which was obtained from Gabolde and Nguyen (2006) was multiplied by the depth of the well and an excess added. The excess is added because the actual volume of drilling mud required is assumed to be twice the theoretical value for the well, to cover losses into the formation. This was added to the amount of drilling mud reserved on the two mud tanks. As a rule of thumb, the total capacity of mud tanks on rigs should be about three times the well volume. Table 3 below shows how the calculations were made.

TABLE 3: Cost of drilling mud

[illegible]

iii. Drilling detergent

Drilling detergent (drilling soap) is added to the compressed air for pressure balance drilling after loss of circulation is encountered during drilling. It is quite difficult to estimate how much drilling detergent is needed for a particular well. The amount depends on the geological conditions encountered and the amount of aerated drilling employed and, therefore, varies from location to location. For this example, however, it was approximated that two drums with a capacity of 210 litres each were used daily. This is a very rough estimation. This was then multiplied by the time it takes to drill that section of the well, as shown in Table 4.

TABLE 4: Cost calculation for drilling detergent

	From (m)	To (m)	Usage (L/day)	Total usage	No. of drums	Unit cost	Total cost
Drilling 26" hole	0	60	420	0	0	500	0
Drilling 17-1/2" hole	60	300	420	1680	8	500	4,000
Drilling 12-1/4" hole	300	1,200	420	4200	20	500	10,000
Drilling 8-1/2" hole	1,200	3,000	420	13440	64	500	32,000
SUM				19320	92	500	46,000

iv. Cement and cement additives

The amount of cement required for each well section was then calculated. This was done by first calculating the total theoretical annulus volume in litres. To obtain this volume, the hole capacity which was obtained from Gabolde and Nguyen, (2006) was multiplied by the depth of the section of the well to be cemented. To cover losses and volume in cavities and washouts, an excess was added. The excess depends on the geology of the area and the losses encountered during drilling. For the cost model an excess of 120 % is used (theoretical volume of the open hole * 2.2, but with no excess in the casing-casing annulus). The amount of dry neat cement required was then calculated as shown in Equation 1 below, based on a slurry yield of 75.8 L/100 kg.

$$\text{Amount of cement} = \frac{\text{Volume in litres} * 100}{75.8} \quad (1)$$

This was then divided by 1000 to get the weight of cement in tonnes as shown in Table 5.

TABLE 5: Cost calculation for neat cement

	Depth (m)	Capacity (l/m)	Excess (%)	Total vol. /L	Neat cement (Tonne)	Cost/tonnes (USD)	Total cost (USD)
26" x 20"	60	139.8	120	18,454	24.35	250	6,100
Backfill	25	139.8	50	5,243	6.92	250	1,800
Plug job	10	342.5	20	4,110	5.42	250	1,400
17-1/2" x 13-3/8"	300	64.5	120	42,570	56.16	250	14,100
Backfill	100	64.5	20	7,740	10.21	250	2,600
Plug job	30	155.2	20	5,587	7.37	250	1,900
12-1/4" x 9-5/8"	1,200	29.1	80	62,856	82.92	250	20,800
Backfill	600	29.1	0	17,460	23.03	250	5,800
Plug job	100	76.04	120	16,729	22.07	250	5,600
SUM				180,748	193.35		60,100

For the cement additives, the amount by weight of blended cement used was calculated. For this example, the cement additives considered were retarder and water loss with 0.3 and 0.5 percent by weight of cement (BWOC), respectively. This was calculated as shown in Table 6.

TABLE 6: Cost of cement additives

	% BWOC	Cement w. additives (Tonne)	Total weight (Tonne)	Unit cost (USD)	Total cost (USD)
Water loss	0.5	163	0.82	12,000	9,900
Retarder	0.3		0.49	8,000	4,000
SUM					13,900

v. *Diesel and Lubricating oil*

The daily consumption of diesel fuel will greatly vary with the horsepower rating of the drilling rig. For this model, it was estimated that about 4 tonnes of diesel is required on average per day under normal drilling operations and 6 tonnes per day when using the air compressors. The total cost of lubricating oil required for the rig and associated equipment during the entire period from spud-in to rig release was estimated to be about 5 percent of the cost of diesel. Table 7 shows the calculations for the cost of diesel and lubricating oil.

TABLE 7: Cost of diesel and lubricating oil

	Volume/day (L)	Tot. volume (L)	Unit cost (USD)	Total cost (USD)
Diesel	5000	315500	1.5	473,300
Lubricating Oil	-	-	-	23,700
SUM				497,000

5.4 Casing and wellhead

This includes the cost of the casing, casing accessories and consumables and the wellhead equipment, together with the associated consumables. For the casing, the length of casing required for each well section was determined from the criteria. The number of the different casing accessories and consumables were identified and input into the table, and the cost calculated. What constituted the total cost of the casings, casing accessories and consumables and wellhead equipment is shown in Tables 8, 9 and 10, respectively.

TABLE 8: Cost of casing

	Depth (m)	Length (m)	Unit cost (USD)	Total cost (USD)
20" casing	60	58.5	375	22,000
13-3/8" 54.5 lb/ft casing	300	298.5	150	44,800
13-3/8" 68 lb/ft casing, top two casings	24	24	195	4,700
9-5/8" 47 lb/ft casing	1,200	1198.5	135	161,800
7" 26 lb/ft casing slotted	3,000	1,826	105	191,700
7" 26 lb/ft casing plain inside prod. casing	24	24	75	1,800
SUM				426,800

TABLE 9: Casing accessories and consumables

	Number	Unit cost (USD)	Total cost (USD)
For 20" casing:			
Casing shoe	1	900	900
Float collar	1	1800	1,800
Cement plugs, Top/bottom	1	200	200
Casing dope	1	150	150
For 13-3/8" casing:			
Casing shoe	1	800	800
Float collar	1	1500	1,500
Cement plugs, Top/bottom	1	200	200
Centralizer	13	200	2,600
Casing dope	1	150	150
For 9-5/8" casing:			
Casing shoe	1	700	700
Float collar	1	1300	1,300
Cement plugs, Top/bottom	1	150	150
Centralizer	43	150	6,450
Casing dope	1	150	150
For 7" casing:			
Casing hanger	1	12000	12,000
Guide shoe	0		
Casing dope	2	150	300
SUM			29,400

TABLE 10: Wellhead equipment

	Number/Sets	Unit cost (USD)	Total cost (USD)
Master valve 10" Class 900	1	45000	45,000
Casing head flange	1	10000	10,000
Adaptor flange	1	3000	3,000
2-1/16" Side valve, 5000psi	1	4500	4,500
Adaptor spool	2	8000	16,000
Ring gasket and bolts	3	350	1,050
SUM			79,600

5.5 Services

Various services are required during the drilling of any geothermal well regardless of the contract type. For this example, the service costs were as follows:

- i. Drilling supervision;
- ii. Civil construction supervision;
- iii. Directional services;
- iv. Air drilling services;
- v. Mud engineering services;
- vi. Cementing services;
- vii. Geological services including site geologist;

- viii. Reservoir engineering / well logging;
- ix. Maintenance engineering;
- x. Planning and logistics.

These activities and processes may be provided to the well owner under a large number of totally separate service contracts, under one lead contract, integrated with the drilling contract, or any mix of these.

6. DISCUSSION

This paper has discussed the various elements of well costing and the various factors that affect these elements. The well costs for this model were divided into three major costs and may be summarised as follows:

$$\text{Cost of well} = \text{Pre pud costs} + \text{drilling costs} + \text{completion costs}$$

The pre-spud costs were described to be the costs incurred during site preparation and rig mobilisation, rig move and rig-up. It can be summarised as follows:

$$\text{Pre – spud costs} = \text{site preparation} + \text{Rig mobilisation} + \text{Rig move} + \text{Rig up}$$

For a mature geothermal field this can be summarised as:

$$\text{Pre – spud costs} = \text{Rig move} + \text{Rig up}$$

The drilling costs were described as the total cost incurred when making the hole. The cost can be summarised as follows:

$$\text{Drilling costs} = \text{daily operating costs} + \text{cost of drilling materials} + \text{service costs}$$

The daily operating costs are mainly day rate costs which are multiplied by the total well time. Drilling materials were subdivided into drilling consumables, casing and wellhead.

The completion costs were identified to include the well logging tools rental charge and the associated service charge. They are often said to be a day rate charge for the period of time the well logging and measurements will last. The completion costs can be summarised as follows:

$$\text{Cost of well} = \text{Pre – spud costs} + \text{drilling costs} + \text{completion costs}$$

where

$$\text{Completion costs} = (\text{daily charge} \times \text{completion time}) + \text{service cost}$$

The primary objective was to come up with a cost model that allows the estimation of well costs from a few key input variables such as well depth, number and size of casing intervals, and well trajectory. The model has two input parameters, the criteria where the well design is established and the price book where all the costs are listed. The cost model then calculates the amount of all the drilling materials required to drill the specified well to completion. The cost of these materials is then automatically calculated using the unit cost that is automatically picked from the price book. The summary sheet then gives the total cost of the well as shown in Table 11.

7. CONCLUSION

Costing geothermal wells can be a fairly simple task if one has a clear understanding of all activities and operations involved from well planning up to when it is completed, and knowing the unit prices, so as to obtain an accurate figure of the total well cost. For this study, an Excel spreadsheet model was created.

By defining the casing programme and time required for drilling each section, the model calculates the material requirements and total well cost. The unit costs for materials and services are entered centrally in a “Price Book” so they can easily be updated later to reflect actual costs. The cost numbers shown in this report are not based on actual prices but are approximate values and used for the creation of the model only, and do not reflect KenGen prices.

TABLE 11: Summary sheet

	Unit	Total (USD)
Pre-spud costs		
Drillsite preparation	Fixed	400,000
Rig mobilisation and transport (1/5)	One-off	400,000
Sum		800,000
Daily operating costs		
Rig rental with crew	Day rate	2,208,500
Rig rental with crew-standby	Day rate	210,000
Air compressors, balanced drilling	Day rate	16,000
Cementing equipment	Day rate	24,000
Maintenance Engineering	From table	24,000
Drill stem inspection	Fixed	300,000
Transportation and cranes	Day rate	12,000
Directional drilling equipment rentals	Day rate	157,800
Water Supply	Day rate	126,200
Waste disposal, clean up and site maintenance	Day rate	12,620
Lodging, catering (camp and food)	Day rate	151,500
Sum		3,242,700
Drilling consumables		
Rock bits	From table	182,000
Drilling detergent	From table	46,000
Diesel & lubricating oil	From table	497,000
Cement	From table	60,100
Cement additives	From table	13,900
Drilling mud	From table	18,900
Sum		817,900
Casing and wellhead		
Casing	From table	426,800
Casing accessories and consumables	From table	29,400
Wellhead Equipment	From table	79,600
Sum		535,800
Services		
Drilling supervision	From table	24,000
Civil engineering	From table	6,000
Site geologist	From table	12,000
Geological services	From table	9,000
Reservoir engineering	From table	6,000
Planning and logistics	From table	12,000
Logging services	Fixed	30,000
Sum		99,000
TOTAL		5,495,400
TOTAL +10% CONTINGENCY		549,600
PROJECT TOTAL		6,045,000

It is also imperative to note that proper and reliable data is vital when costing geothermal wells. This, therefore, calls for systematic accounting to make the unit costs available internally within the company for such modelling. Only then will the estimation of the well cost become as accurate as possible.

Accurate well costing helps quantify the substantial costs associated with the development of geothermal projects. It will also help to investigate the costs of drilling and the completion of wells and relate these costs to the economic viability of the geothermal project.

ACKNOWLEDGEMENTS

My sincere gratitude goes to the Government of Iceland and the United Nations University, Geothermal Training Programme (UNU-GTP), under the leadership of former director, Dr. Ingvar Birgir Fridleifsson and current Director, Mr. Lúdvík S. Georgsson, for offering me the chance to take part in the 2013 UNU-GTP Fellowship. My sincere appreciation goes to my supervisor, Mr. Sverrir Thórhallsson, for his guidance and for sharing his valuable knowledge. Many thanks go to Mr. Ingimar Haraldsson, Ms. Málfríður Ómarsdóttir, Mr. Markús A. G. Wilde and Ms. Thórhildur Ísberg for their assistance during my stay in Iceland.

I acknowledge my employer, KenGen, for granting me permission to attend this vital course.

I give special appreciation to my family, Lebo, Mark and Netai for their unwavering support and encouragement throughout the six months and especially for enduring my absence for six months. This report is dedicated to you.

Finally, I thank the Almighty for His divine favour and blessings and for making all things possible.

REFERENCES

Augustine, C., and Petty, S., 2006: A comparison of geothermal with oil and gas well drilling costs. *Paper presented at 31st Workshop on Geothermal Reservoir Engineering*, Stanford University, Stanford, Ca, 7 pp.

Bett, E.K., 2010: Geothermal well cementing, materials and placement techniques. Report 10 in: *Geothermal training in Iceland 2010*. UNU-GTP, Iceland, 99-130.

Chemwotei, S.C., 2011: Geothermal drilling fluids. Report 10 in: *Geothermal training in Iceland 2011*. UNU-GTP, Iceland, 149-177.

Cherutich, S.K., 2009: Rig selection and comparison of top drive and rotary table drive system for a cost effective drilling project in Kenya. Report 8 in: *Geothermal training in Iceland 2009*. UNU-GTP, Iceland, 65-84.

ESMAP and World Bank, 2012: *Geothermal handbook: Planning and financing power generation*. Energy Sector Management Assistance Program (ESMAP) and World Bank, technical report 002/12, 150 pp, website: www.esmap.org.

Gabolde G., and Nguyen, J.P., 2006: *Drilling data handbook* (8th edition). Institut Francais du Pétrole Publications, Paris, 576 pp.

Hole, H., 2006: Geothermal well drilling service contracts. Lecture 4 in: *Lectures on geothermal drilling and direct uses*. UNU-GTP, Iceland, report 3, 21-26.

Hole, H., 2008a: Geothermal well design-casing and wellhead. *Paper presented at "Petroleum Engineering Summer School", Dubrovnik, Croatia, Workshop 26*, 7 pp.

Hole, H., 2008b: Geothermal deep well drilling practices – an introduction. *Paper presented at "Petroleum Engineering Summer School", Dubrovnik, Croatia, Workshop 26*, 6 pp.

Hole, H., 2008c: Geothermal well completion tests. *Paper presented at "Petroleum Engineering Summer School", Dubrovnik, Croatia, Workshop 26*, 5 pp.

Karewa, N.O., 2012: Reporting and efficiency analysis in geothermal well drilling. Report 16 in: *Geothermal training in Iceland 2012*. UNU-GTP, Iceland, 293-328.

Miyora, T.O., 2010: Controlled directional drilling in Kenya and Iceland. Report 20 in: *Geothermal training in Iceland 2010*. UNU-GTP, Iceland, 365-390.

Mwangi, M., 2005: Phases of geothermal development in Kenya. *Papers presented at "Workshop for Decision Makers on Geothermal Projects and Managements", UNU-GTP and KenGen, Lake Naivasha, Kenya*, 11 pp.

Ngugi, P., 2008: Geothermal well drilling. *Paper presented at "Short Course III on Exploration for Geothermal Resources" UNU-GTP and KenGen, Lake Naivasha, Kenya*, 19 pp.

Semancik, P., and Lizak, F., 2009: Geothermal resources. *Paper presented "Environmental Impacts of Power Industry", Pernink, University of West Bohemia, Czech Republic*, 6 pp.

Thórhallsson, S., 2013: *Geothermal drilling technology*. UNU-GTP, Iceland, unpublished lecture notes.

Thórhallsson, S., and Sveinbjörnsson, B., 2012: Geothermal drilling cost and drilling effectiveness. *Paper presented at "Short course on Geothermal Development and Geothermal Wells" organized by UNU-GTP and LaGeo, in Santa Tecla, El Salvador*, 10 pp.



UNITED NATIONS
UNIVERSITY

GEOTHERMAL TRAINING PROGRAMME
Orkustofnun, Grensasvegur 9,
IS-108 Reykjavik, Iceland

Reports 2013
Number 12

COMPARISON, CHARACTERIZATION, AND INTERPRETATION OF GEOTHERMAL FLUID GEOCHEMISTRY IN THE SEDIMENTARY ENVIRONMENTS OF KIBIRO, PANYIMUR, AND ÖXARFJÖRDUR

Grace Lajwe

Ministry of Energy and Mineral Development
Department of Geological Survey and Mines
P.O. Box 9, Entebbe
UGANDA
gracelajwe@yahoo.com

ABSTRACT

Geochemical data interpretation of representative chemical, analytical, and isotopic results for geothermal waters and gas in sedimentary environments obtained by standard analytical methods were studied in this research work. Techniques like chemical geothermometers (silica and cation geothermometers) and gas geothermometers were used in predicting the variation in temperatures in three geothermal systems, i.e. Kibiro and Panyimur in the East Africa Rift System, and Öxarfjörður in Iceland. The speciation programme WATCH was used to calculate the activity of the different species of anions and cations, Na/K, Quartz and Chalcedony temperatures, a Ternary diagram for Na/1000-K/100- $\sqrt{\text{Mg}}$ based on the equilibration conditions for these cations in these waters at particular temperatures, and a Cl-SO₄-HCO₃ ternary plot were constructed. Different mixing models and plots of different constituent relationships were used in the comparison, characterization and interpretation of the geochemistry of these different geothermal areas. The geochemistry of magmatically driven geothermal systems may be used to develop effective exploration techniques for the geothermal systems that are driven by temperature gradients like the East African Rift System (EARS), the western branch of which Kibiro and Panyimur are part.

The chemical and isotopic composition of the water samples from Kibiro, Panyimur and Öxarfjörður, suggest mixing of cold groundwater with geothermal waters. Major ions and isotope parameters were used to characterize the waters from Kibiro and Panyimur as Na-Cl-HCO₃ waters, and water from Öxarfjörður as Na-Cl water. The main processes affecting the geothermal system in the sedimentary geological environment are: dilution and conductive cooling.

1. INTRODUCTION

For future exploration, building a conceptual model, and deciding on the utilization of geothermal resources in the area where they exist, a sound understanding of the chemistry of the geothermal fluids needs to be established in the beginning of the exploration phase for better facilitation and approaches

(Bruhn et al., 2010). Water and gas chemistry have been used for the last decades to: find the origin of the geothermal fluids, understand the mixing effects in the geothermal system, evaluate subsurface temperature, and predict corrosion and scaling problems during the use of these fluids (Fournier, 1977; Rybach, and Muffler, 1981; Arnórsson, et al., 1983; Arnórsson, 2000; Giggenbach, 1988).

The chemical composition of geothermal steam and water from natural manifestations provides initial constraints on reservoir temperature, and helps identify production properties and potential environmental concerns related to the utilization of the geothermal fluid. These can only be attained by carrying out geochemical exploration, one of the exploration techniques applied in the search for any geothermal resource for any utilization.

This project aims to investigate the geochemical relationship of the geothermal waters of Kibiro and Panyimur geothermal areas in East Africa and compare them with the low temperature geothermal system of the Öxarfjörður geothermal field which is located in North Iceland. The formation conditions of the geothermal fluids differ from one area to another (Hjartarson et al., 2005); this can only be proven by analysing the chemical characteristics and comparing the findings with the different formation conditions. The geology of these geothermal areas is briefly described, together with a classification of the geothermal waters. The speciation program WATCH (Bjarnason, 2010), and geothermometers were mainly used for the determination of the reservoir temperatures and equilibrium conditions.

Geothermal systems all over the world are mostly associated with a rift system where a powerful heat source is close to the surface of the earth (Björnsson et al., 2005). The geothermal activity in Kibiro and Panyimur is largely restricted to the rift system (Figure 1) of the western branch of the EARS, with geothermal manifestations like fumaroles, hot springs and travertine occurring along some of the border faults of the rift valley and within the volcanic fields (Data and Bahati, 2003). The geothermal system of the Öxarfjörður area in north Iceland is also within a major graben which is associated with current volcanic activity.

1.1 Objectives of the study

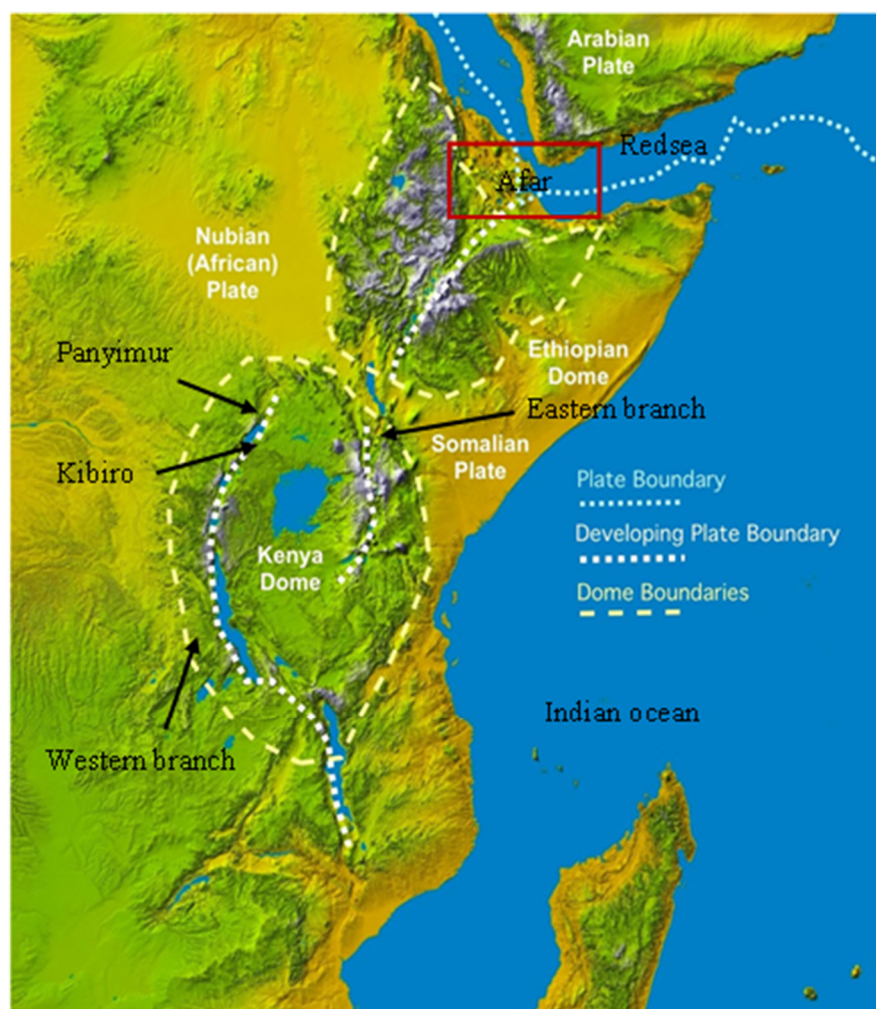
There are two objectives: 1) to understand the geochemical evolution of geothermal waters in two different sedimentary geological environments by carrying out a classification and an interpretation of their geochemical analytical results; 2) to develop better geothermal exploration and exploitation methods and techniques for geothermal waters occurring in sedimentary environments.

2. LITERATURE REVIEW

2.1 Geology of the Western branch of the East African Rift System

The western arm of the EARS, where the Kibiro and Panyimur areas of this study are located, has Cenozoic rift faults (Atekwana et al., 2004) starting from the north along the Sudan border, and then curving to the west and southwest along the border with the Democratic Republic of Congo, and south to Rwanda and Burundi for about 100 km. The western branch of the EARS is considered to be at an early stage of development, and is younger, that is Late Miocene to Recent, than the more mature eastern branch (Morley, 1999). The rifting region has a higher heat flow than the surrounding Pre-Cambrian terrain. Two different *en echelon* strands are found in the Western Rift, separated by the Rwenzori Mountains which rise from a base of less than 1000 m in the Rift to over 5000 m elevation. Within the rift valley there are thick layers of late Tertiary and Quaternary sediments, fresh water and saline crater lakes, volcanics, and plutonic bodies identified beneath L. Albert and L. Edward (EDICON, 1984). The majority of the geothermal areas of Uganda are found in the Western Rift Valley (Figure 1).

The western branch of the rift runs along the western side of Lake Victoria and along the edge of the East African plateau (Figure 1). The geography of the western branch is typically half grabens characterized by high angle normal rift faults. The rift is characterized by a paucity of volcanism relative to the Kenyan and Ethiopian rifts (Ebinger et al., 1989). The Lake Albert Rift was initiated in early Miocene and is dominated by a thick sequence of sediments. It is characterized by an abundance of potassic alkaline rocks that consist of basalts, carbonatites, ultrapotassic mafic rocks and potassic mafic-felsic lava.



2.1.1 Geology of Kibiro

FIGURE 1: Modified EARS (Wood and Guth, 2012)

The area (Appendix I) has some volcanic rocks injected through Pleistocene lacustrine rocks in the rift valley and granitic gneisses on and above the escarpment at Kibiro; big dykes of basic intrusive rocks can be traced in some cases for miles in the argillites and gneisses trending NNE to SSW. The mineralogical composition of the rocks in this area is: porphyritic augites, pyroxenes, ilmenite, and titaniferous minerals. In addition to the more basic intrusives, there are also other granitic types like charnockites found 4.8 km southeast of Kibiro in a very large intrusion running east and west, presumed to be a late date intrusion related to faults (Kato, 2003).

The geology of the Kibiro geothermal area (Figure 2) is quite unique in its tectonic setting (Gíslason et al., 2005). Geological and geophysical studies carried out in this area revealed that the geothermal activities may be associated with the block faulted granites some distance from the main rift system.

2.1.2 Geology of Panyimur

The area (Appendix I) is characterized by fractured crystalline basement rocks such as coarse hornblende gneisses, coarse hornblende garnet rocks, talcose rocks and pegmatitic veins in a gorge that dips into the escarpment. In the area there is foliation/basement schistose trending- NNE-SSW. In addition, there is another schistose trend almost NE, parallel to the major local faults (Natukunda, 2013). The major rocks in the area include crystalline basement rocks, which are coarsely jointed granitic-gneiss with outcrops to the west and Pleistocene sediments to the east of the Rift fault boundary. There are some mylonite gneisses which are intruded by pegmatitic dykes, quartz veins and garnetiferous amphibolite dykes on

the escarpment, with the minor faults cross cutting the rift faults (upper Panyimur fault and the lower Panyimur fault, both striking northeast).

2.2 Geology of Öxarfjörður

The Öxarfjörður area in NE-Iceland is characterized by historical lavas of younger to older age, with thick sediment of about 1000 m (Georgsson et al., 2000) from a glacial river and by fissure swarms from active central volcanoes further inland (Figure 2). It is located at the junction between the NE-SW spreading zone which crosses Iceland, and a right – lateral transform zone, the Tjörnes Fracture Zone (Ólafsson, et al., 1993). Today the waters around the island are oxygen saturated. This could be due to the fact that major climate changes during the Pleistocene could have changed the paths of ocean currents and maybe that of the oxygen cycle, too.

The Öxarfjörður sedimentary graben falls in a transform zone of lateral transform movement, spreading, and volcanism in the zone between the North Iceland Volcanic Zone in Öxarfjörður and the spreading axis along the Kolbeinsey Ridge, (Jónsson et al., 1991).

The geological model of the Öxarfjörður sedimentary trough, based on the tectonic settings and geophysical data, indicates that it is younger than 1 Ma, with a probable thickness of up to 1 km at the shore inside the Krafla and Theistareykir fissure swarms, while thinning southwards where the sediments are expected to be more frequently interbedded with lavas and hyaloclastites (Georgsson et al., 2000).

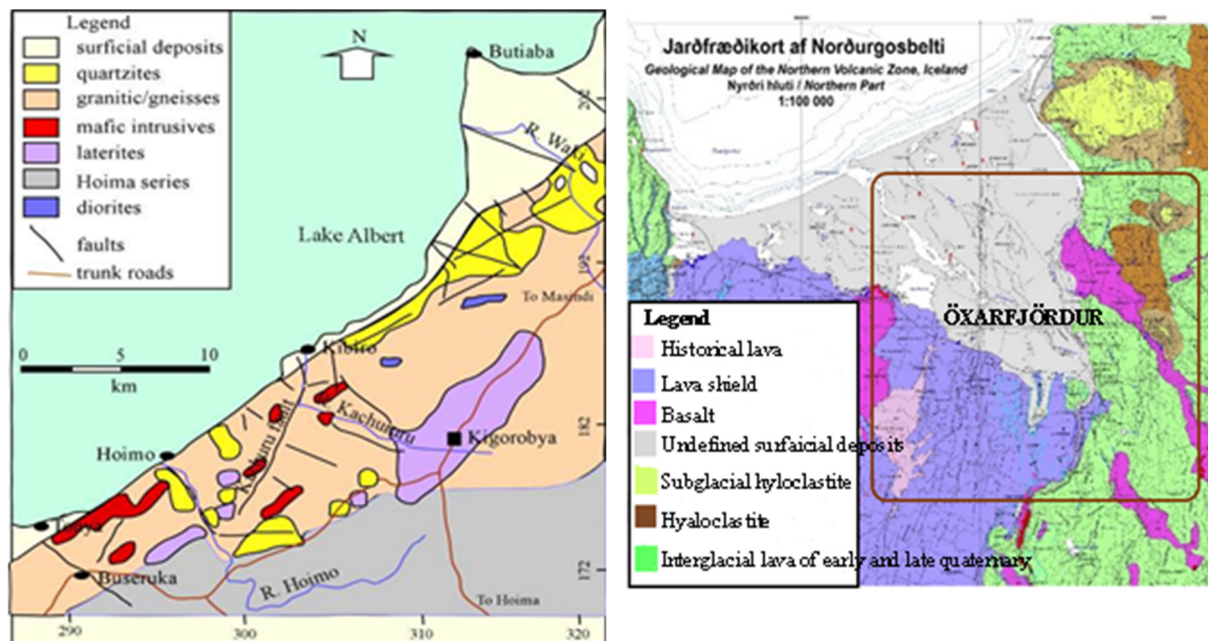


FIGURE 2: Geological maps of Kibiro and Öxarfjörður (DGSM, 2013 and ISOR)

2.3 Surface geothermal manifestations in Kibiro, Panyimur and Öxarfjörður

2.3.1 Surface geothermal manifestations in Kibiro and Panyimur

The hot springs in the Panyimur geothermal area are located within a stretch about 1.5 km along the main fault (Data and Bahati, 2003) and all are aligned in a northeast direction in the western escarpment of the Rift Valley, which probably means that they are controlled by the intersection of the traverse fault

together with the main rift. In addition to that, deposits of travertine, sulphurous algae, the smell of hydrogen sulphide and all the discharges are characterized by gas bubbling (Bahati, 2007).

The manifestations of Kibiro are mainly concentrated at Kibiro and Kachuguru, west of the escarpment, on the shores of Lake Albert; some fumarolic activity can be seen at Kachuru and along the escarpment for approximately 1.5 km from the intersection of the Kachuguru fault and the main escarpment to the Kibiro hot springs (Bahati, 2012). There are some calcite deposits observed in cracks and fissures in many locations along the escarpment, the Kachuguru fault, the Kitawe fault and in the crystalline rocks located south-southeast of Kibiro, indicating extinct thermal fluid discharges. The hot springs at Kibiro are apparently related to a secondary fault, oblique to the main Rift fault, and most likely controlled by their intersection (Figure 2). The total flow measured from the hot springs is approximately 7 l/s and the maximum surface temperature is 86.4°C (Gíslason et. al., 1994).

2.3.2 Surface geothermal manifestations in Öxarfjörður

The surface geothermal manifestations in the Öxarfjörður region are meagre, mainly in the form of warm springs and warm ground within the active fissure swarms. Geothermal manifestations are known at 13 locations, which can be divided into 3 groups (Georgsson et al., 1993). These groups are: 1) The Krafla fissure swarm which has the most important sites like Skógalón where water at a shallow level has temperatures up to 100°C, covering an area of several hundred square metres, and Bakkahlaup with warm ground covering a wide area with temperatures of up to 80°C in the uppermost part, considerably lower before the Krafla fires. 2) The Theistareykir fissure swarm in the western part of the Öxarfjörður area, with the most important one at Ytra Lón close to the coast, with recently measured temperatures of 50°C; older records show temperatures above 80°C. 3) Geothermal sites found outside the active fissure swarms.

2.4 The chemistry of the geothermal fluids

2.4.1 Brief overview of geothermal fluid chemistry

The chemistry of geothermal fluids is diverse and largely reflects the geological setting of a particular area (Henley and Ellis, 1983). Most of these chemical differences depend upon the source of recharge waters with some contribution of gases from magmatic or metamorphic sources. Geothermal fluids contain a number of different constituents with varying concentrations (Ármannsson, 2013), with important chemical parameters which characterize geothermal fluids, such as pH which describes the acidity or alkalinity of the fluid, and TDS which gives a measure of the amount of chemical constituents dissolved in the fluids.

The constituents of geothermal water can be grouped into two categories with respect to their properties, i.e.:

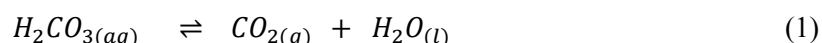
- 1) Reactive constituents, which are also used as geo-indicators due to the fact that they tend to equilibrate with some of the minerals in the geothermal system (Arnórsson, 2000a). Information on temperature and the steam fraction, which together constitute the physical state of the geothermal system, may be provided by these constituents.
- 2) Conservative constituents such as Br, Cl, B, N₂, ²H, ¹³C, ⁴⁰Ar, and ¹⁸O (Arnórsson, 2000a) may be used to trace the origin and flow of the geothermal fluids, as they do not take part in water-rock interaction.

The geothermal fluids or natural waters may be classified using the Cl-SO₄-HCO₃ ternary plot diagram (Giggenbach, 1991). This diagram is used to distinguish a number of different types of thermal waters like: immature unstable waters, giving an indication of the mixing relationships or the geological groupings; steam heated waters; volcanic waters; and peripheral waters. And this leads to the provision

of a trend and preliminary statistical evaluation of the grouping of geothermal waters (Giggenbach, 1988). Water circulating in high-enthalpy geothermal reservoirs is mostly of meteoric origin but, in some geothermal systems, it may be oceanic or evolved connate waters (Bruhn et al., 2010). For geothermal systems which are located along the convergent plate boundaries and are close to the volcanic-magmatic association, the deep magmatic heat source tends to add some acidic gases like CO₂, SO₂, HF, H₂S and HCl, with some andesitic waters in the system.

In high-enthalpy geothermal systems, four different types of geothermal waters have been classified (Truesdell, 1991; Giggenbach, 1988; Henley et al., 1984; Ellis and Mahon, 1977):

- 1) Acid sulphate water: this is the type of thermal water which is mainly found in the upflow part of the geothermal system, (Bruhn et al., 2010). This type of geothermal water is characterized by a low pH of 0 to 3 and a low concentration of chloride. It reacts very fast with the host rocks, mainly giving advanced argillic alteration paragenesis. Composed of alunite and kaolinite. CO₂ and H₂S are the two main types of gases in this geothermal environment. The H₂S may undergo oxidization in the upflow zone to form SO₄ near the surface and contains constituents mostly dissolved from the surrounding rock with which it is in contact (Ármannsson, 2009).
- 2) Sodium – chloride water: water with a chloride concentration of up to 10,000 mg/kg, and pH of approximately ± 1 or ± 2 units to a neutral pH at depth, for example 5.5-5.6 at a temperature of 200°C to 300°C. This type of water contains the following constituents in higher concentrations than in cold water: Na, B, F, Li, Si, K, Ca, but with low Mg and with CO₂ and H₂S as the main dissolved gases (Bruhn et al., 2010).
- 3) Acid chloride – sulphate water: this type of water is found in the deepest part of the connecting neutral pH that is a NaCl system, there and in the inflow of magmatic gases rich in sulphur and hydrochloride species, namely H₂S and SO₂; this produces a very reactive aqueous solution that dissolves the rock or leaches the cations from them, leading to the deposition of pyrite, alunite, kaolinite and anhydrite (look at the chapter in Ármannsson, 2010). The acid Chloride – Sulphate water is mainly found in crater lakes (Bruhn et al., 2010). The interaction of the magmatic gases with rock masses and water is greater at depth, with higher temperatures and lasts for a longer period than in the crater lakes. This leads to the formation of neutral NaCl waters (Reed, 1991; Giggenbach, 1997), due to more neutralization in the system.
- 4) Sodium bicarbonate water: found in: the zone of condensation for a vapour-dominated geothermal reservoir; the marginal regions of the liquid-dominated geothermal reservoirs; in the deep geothermal reservoir located in sedimentary rocks and/or metamorphic rocks. The condensation of geothermal steam in a free oxygen groundwater in a relatively deep zone may be the dissolution of CO₂, present in some of the gases in the system, which can lead to the origin of bicarbonate rich waters (Bruhn et al., 2010). The lack of oxygen in this system prevents the oxidation of H₂S, meaning that the acidity in the aqueous solution is from the dissociation of the H₂CO₃ as shown in Equation 1.



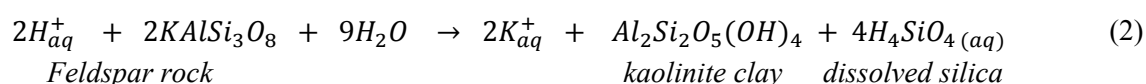
The conversion of feldspars to clay is aided by this weak acid, especially in medium to high temperature geothermal reservoirs, gives rise to neutral aqueous solutions.

2.4.2 Water-rock interaction

Geological processes are mostly a result of reactions which take place between the minerals in the rock and the fluids (Driesner, 2013). When geothermal water or fluids move through the rock, they may chemically react with the rock with which they come into contact, (and some of the rocks themselves are chemically complex). This may lead to the following: 1) dissolution of some selective minerals

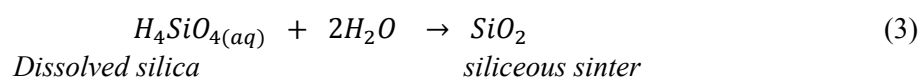
from the rock; 2) Precipitation of some minerals from the solution; and 3) substitution of certain chemical elements in the fluids by other elements in the minerals. All three processes may lead to secondary mineral formation by depletion or enrichment of some of the chemical components from the fluids (Rodríguez, 2011), or removal of chemical components from the rock due to the dissolution of the primary minerals. A series of chemical reactions, associated with the interactions between the water, the chamber rock and the path by which the water reaches the earth's surface (Arnórsson et al., 2007) may occur, for example reactions which typically involve sulphur and /or metal cations. Water - rock interactions generally take place slowly, that is primary rock dissolves very slowly in water but, like most reactions, the process is faster at higher temperatures. The changes in the chemical and/or mineralogical composition may or may not lead to volume changes in the rock (Arnórsson et al., 2002). If the volume of the rock is changed, then porosity and permeability may be affected, too. When the reaction between water and rock is prolonged, some of the ionic species and saturated silica are dissolved (Equation 2). $\text{Na}^+(\text{aq})$ and $\text{Ca}^{2+}(\text{aq})$ also dissolve in the geothermal water.

Physico-chemical conditions like temperature may, if decreased, lead to the precipitation of minerals due to low solubility (Equation 4). Boiling, upon pressure decreases, may cause re-partitioning of the forces between the vapour and the liquid phase leading to solubility decreases for some metals, for example, gold.



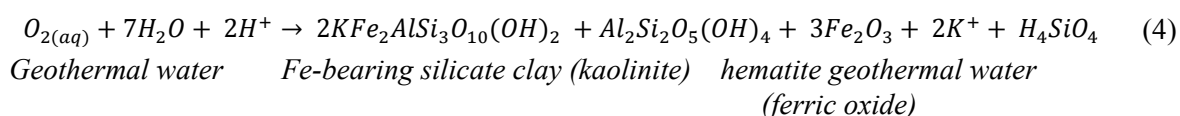
Water may be in equilibrium with the rock for sufficiently long to be used to calculate the temperature of the water. In effect, the ratios of the concentrations of the liberated cations like: Ca^{2+} , Na^+ , Mg^{2+} and K^+ are temperature dependent. The most important process governing their relative contents is rock dissolution and equilibration (Giggenbach, 1984).

The solubility of silica is also temperature dependent, but this equilibrium is attained rather more rapidly than the dissolution of most other silicate minerals.



This reaction may be used as the basis of a geothermometer (Afeworki, 2010). Any difference in temperatures obtained from the two geothermometers is related to the sampling of the water relative to the deep aquifer: waters that have moved away from the aquifer are likely to have lower temperatures derived from silica concentrations than temperatures derived from concentrations of Na, K and Ca. This may either be due to faster equilibration in the silica dissolution than the ion-exchange reactions or to mixing with dilute water. Some ion exchange reactions are, however, very fast such as the K-Mg reaction, and a geothermometer based on it may even show a lower temperature than a silica geothermometer.

Iron and manganese ions may be liberated from silicate minerals and ultimately precipitate as their highly coloured oxides. The example below shows the oxidative liberation of iron from a silicate mineral under acid conditions. Iron (II) is oxidized to iron (III).



As the water rises to the surface it cools, and silica minerals are precipitated along with other minerals. This may help "cap" the aquifer, and prolong the geothermal system's existence. Water that does reach

the surface through faults and fractures will cool further and produce the sinter mounds and terraces that are typical around geysers and hot springs.

When water in a geothermal system has attained a high temperature that is above 100°C, it will react with the rock to a greater extent, leading to the production of significant oxygen shift, which can be proven by Equation 4 (Arnórsson, 2000b); this may tell us if the geothermal water shows precipitation which fell during the present day climate or under different climatic conditions.

2.4.3 Mixing in the upflow zones

Geothermal waters may be mixed with cold water after a certain period of conductive cooling of the hot water, before, after or during boiling (Arnórsson, 2000b). Depending on pressure and temperature conditions, the main component of geothermal fluids, H₂O, can be present in different physical states (Bruhn et al., 2010). The presence of a single liquid phase in the geothermal reservoir is the most frequent situation, but it is not the only one, since either a two-phase liquid vapour mixture or a single vapour phase can be present in the reservoir. These possibilities can be ascertained by accurate enthalpy data or by gas geochemistry (Giggenbach, 1980; Bertrami et al., 1985).

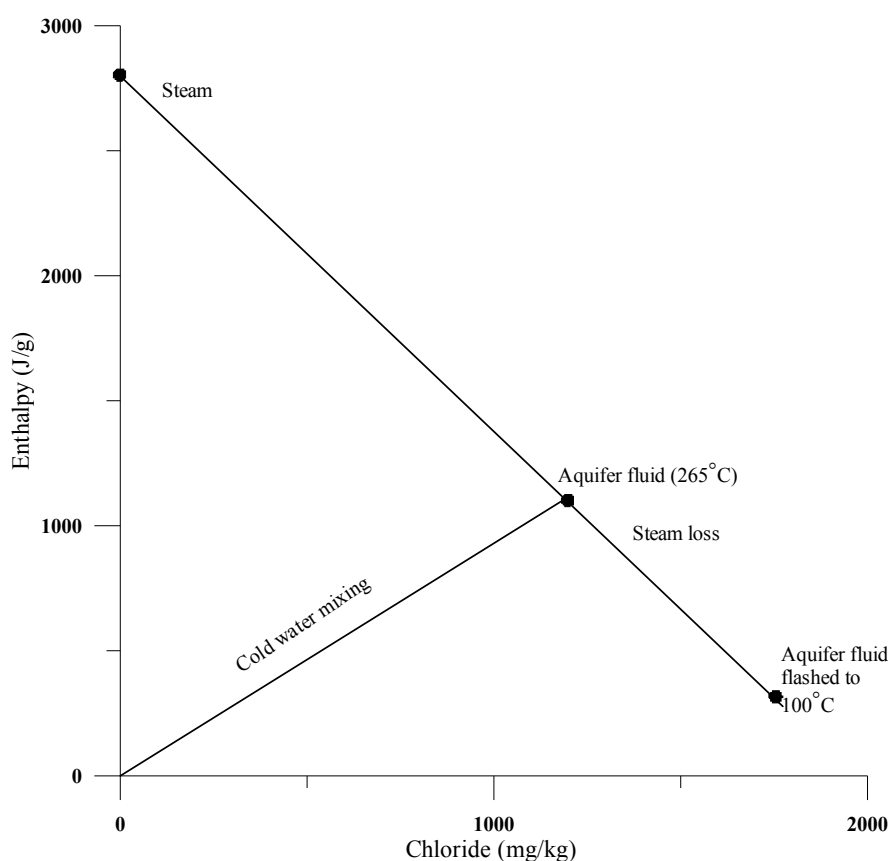


FIGURE 3: Enthalpy versus chloride for boiling and dilution (Fournier, 1979)

Large variations in the temperature and flow rates of thermal springs in a particular field that can be linked with the parallel variations in the concentrations of the non-reactive components in the water, like Cl, usually constitute the best evidence that mixing has taken place (Marini and Cioni, 1985). Mixing models have been developed to allow the estimation of the hot water component in mixed waters emerging in springs or discharged from shallow drill holes (Truesdell and Fournier, 1977). Three mixing models are most frequently applied: 1) the chloride-enthalpy model; 2) the silica-enthalpy mixing model; and 3) the silica – carbonate mixing model.

The enthalpy versus chloride plot is a suitable tool for distinguishing the effects of boiling (steam loss) and mixing, since both steam and cold waters, which generally have low chloride contents, are characterized by very different enthalpy values (Fournier, 1979). The enthalpy-chloride plot (Figure 3) shows that boiling moves the liquid from the point representative of the 265°C geothermal liquid towards higher chloride contents and lower enthalpies, whereas the addition of cold, dilute waters causes a decrease in both enthalpy and chloride. If the discharged water is cooled, mainly through conductive heat loss, the chloride concentration of the deep hot water remains unchanged (Bruhn et al., 2010).

The linear relationship between the concentrations of conservative components like Cl and B or Cl and $\delta^2\text{H}$ are generally considered to constitute the best evidence for mixing (Bruhn et al., 2010). The magnitude of the oxygen shift depends on the extent of the water - rock interaction. Generally, increasing temperature enhances chemical reaction rates (Stefánsson, et al., 2007) including reactions involving water and rock, hence increasing the ^{18}O isotope shift (see Chapter 2.4.5). Mixing of geothermal waters with local groundwater may manifest itself in a linear relationship between the δ values for ^2H and ^{18}O or between these values and the aqueous concentrations of conservative elements such as Cl.

Hot water ascending to the surface from the geothermal reservoir tends to have a relatively high concentration of total dissolved solids (Árnason and Gislason, 2009), but cold groundwater contains relatively low total dissolved solids, so if such cold groundwater mixes with the hot water, it leads to dilution which reduces the concentration of the total dissolved solids (Rodríguez, 2011). Chloride, which is a non-reactive component in water, tends to give the best evidence of mixing in water systems, depending on the variation of temperature and the flow rates of the geothermal hot or cold water.

In many geothermal hot springs, mixing of the hot and cold water leads to dilution and cooling (Noda and Shimada, 1993); to prove this by using the different mixing model techniques, the chemical composition of each component in the geothermal water needs to be evaluated thoroughly. And for better use of mixing models, to establish whether there is mixing in the up flow zone of a geothermal system, a large number of samples from the geothermal area is required. The chloride enthalpy plot is used in mixing prediction because chloride concentration increases gradually with continuous rock dissolution with an increase in temperature (Yohannes, 2004).

2.4.4 Mineral saturation

This is one of the techniques used in the evaluation of mineral equilibrium, using the assumption of mineral dissolution in solution, taking into account the different physical conditions in which this mineral dissolves (Arnórsson and Bjarnason, 2007). Determining the chemical equilibrium between the aqueous solution and the mineral in any natural system needs to be carried out with an idea of the activities of the different species present in that solution (Arnórsson et al., 2002).

2.4.5 Isotope chemistry of geothermal fluids

Isotopic chemistry is one of the most important tools used in the exploration for geothermal resources today. To gain representative results for a particular geothermal system, the isotope values need to be interpreted in conjunction with other chemical techniques (Giggenbach et al., 1984; Giggenbach., 1991; Craig., 1963). It is used mainly to establish the isotopic characteristics (that is $\delta^{18}\text{O}$ and $\delta^2\text{H}$) of the precipitation in relation to the altitude and latitude, together with continental effects. There is a general decrease in the values of the $\delta^{18}\text{O}$ and $\delta^2\text{H}$ for samples collected from geothermal areas that are further inland, at a higher elevation and at higher latitudes. And these values are more closely related to the meteoric water line through the equation:

$$\delta^2\text{H} = 8 \delta^{18}\text{O} + d \quad (5)$$

where $d = 10$ and for each isotope $\delta = [(R_{\text{sample}} - R_{\text{SMOW}})/R_{\text{SMOW}}] \times 1000$, reported in ‰, and R = the ratio of the number of atoms of a given isotope to the number of atoms of the element's most abundant isotope, i.e. $R = ^{18}\text{O}/^{16}\text{O}$ for oxygen-18 and $R = ^2\text{H}/^1\text{H}$ for deuterium and SMOW is the Standard Mean Ocean Water as defined by the IAEA.

In a high-temperature geothermal system, there may be isotopic exchange between rock minerals which are rich in $\delta^{18}\text{O}$ and water, causing the $\delta^{18}\text{O}$ values to increase and fall to the right of the world meteoric line, or the so called oxygen isotope shift (Giggenbach, 1991). Along the convergent plate boundaries of a volcanic system, Giggenbach (1992) showed that there is a linear relationship between the values of $\delta^{18}\text{O}$ and $\delta^2\text{H}$, which is also the case in numerous geothermal systems showing a mixing trend in

common with a magmatic source with $\delta^2\text{H}$ of about $-20 \pm 10\text{‰}$ and $\delta^{18}\text{O}$ of about $+10 \text{‰}$. This phenomenon is common in subduction systems and explains the isotope signature of andesitic waters, but is unlikely to be applicable in the systems presently studied.

2.4.6 Geothermometers in geothermal exploration

This has proved to be one of the major exploration tools used in the search for geothermal energy. This method is based on the isotopic and the chemical composition of the fluids that discharge from natural hot springs, cold springs and wells (D'Amore and Arnórsson, 2000b). They are used for the following: 1) to predict or estimate the subsurface temperature of the geothermal system which is expected to be encountered in case of any drilling in the area for exploration or production purposes; 2) during the late stages of geothermal development and utilization, especially in establishing the horizons in productive wells; and 3) the chemical state of the recharging water in the vicinity of a well as a result of cooling or boiling, due to depressurization, can be determined by this technique (Bruhn et al., 2010).

In a geothermal system, most of the chemical reactions are temperature dependent (Ármannsson, 2009) and their kinetics are not fast at a relatively low temperature, hence the equilibrium characteristics are preserved even when the water flows to the surface and cools down. Using the assumption of the conservation of mass and heat and determining the chemical composition of the surface geothermal fluid, the subsurface temperature may be determined.

Geothermometers are divided into basically three categories:

1. Isotope geothermometers

These are based on the fractionation of the isotopes of light elements (given by Equation 5) between gaseous and aqueous portions of the geothermal fluids. This is mainly temperature dependent making it very important:

$$1000 \ln \alpha_{AB} = \delta_A - \delta_B \quad (6)$$

where $\ln \alpha_{AB}$ = Isotopic fractionation in two phases;

δ_A = Concentration of constituent A;

δ_B = Concentration of constituent B.

2. Water or solute geothermometers

These are based on the fact that the concentration and any ion ratio for an aqueous species may be used as a geothermometer, taking into consideration that equilibration is attained for the reaction (Arnórsson and Svavarsson, 1985). The most common types of such geothermometers are the silica (quartz and chalcedony), the Na–K and the Na–K–Ca (Fournier, 1973; Fournier and Truesdell, 1973; Ellis and Mahon, 1977; D'Amore and Arnórsson, 2000). For this particular research work, the water or solute geothermometers used are shown by the equations below.

Arnórsson et al., 1983 (Cation):

$$T(^{\circ}\text{C}) = \frac{933}{0.993 + \log\left(\frac{Na}{K}\right)} - 273.13 \quad (7)$$

Truesdell and Fournier, 1976 (Cation):

$$T(^{\circ}\text{C}) = \frac{856}{0.857 + \log\left(\frac{Na}{K}\right)} - 273.13 \quad (8)$$

Giggenbach et al., 1994 (Quartz):

$$T(^{\circ}\text{C}) = \frac{4410}{14.0 + \log\left(\frac{K^2}{Mg}\right)} - 273.13 \quad (9)$$

Fournier, 1977 (Quartz):

$$T(^{\circ}\text{C}) = \frac{1522}{5.75 - \log S} - 273.13 \quad (10)$$

Fournier, 1977 (Quartz):

$$T(^{\circ}\text{C}) = \frac{1309}{5.19 - \log S} - 273.13 \quad (11)$$

Arnórsson et al., 1983 (Quartz):

$$T(^{\circ}\text{C}) = \frac{1112}{4.91 - \log S} - 273.13 \quad (12)$$

Fournier, 1977 (Quartz):

$$T(^{\circ}\text{C}) = \frac{1032}{4.69 - \log S} - 273.13 \quad (13)$$

Fournier and Truesdell, 1973 (Cation):

$$T(^{\circ}\text{C}) = \frac{1647}{\log \frac{Na}{K} + \beta \left[\log \left(\frac{\sqrt{Ca}}{Na} \right) + 2.06 \right] + 2.47} - 273.13 \quad (14)$$

Arnórsson, 2000 (Quartz):

$$T(^{\circ}\text{C}) = -55.3 + 0.36590S - 5.3954 \times 10^{-4}S^2 + 5.5132 \times 10^{-7}S^3 + 74.360 \quad (15)$$

Fournier and Plotter, 1982 (Quartz):

$$T(^{\circ}\text{C}) = -53.5 + 0.11236S - 0.5559 \times 10^{-4}S^2 + 0.1772 \times 10^{-7}S^3 + 88.390 \log S \quad (16)$$

Arnórsson, 2000 (Quartz):

$$T(^{\circ}\text{C}) = -66.9 + 0.13780S - 4.9727 \times 10^{-5}S^2 + 5.5132 \times 10^{-8}S^3 + 87.841 \log S \quad (17)$$

Verma and Santoyo, 1997 (Quartz):

$$T(^{\circ}\text{C}) = -44.119 + 0.24469S - 1.7414 \times 10^{-4}S^2 + 79.305 \log S \quad (18)$$

$$Na - \text{feldspar} + K^+ = K - \text{feldspar} + Na^+ \quad (19)$$

$$\begin{aligned} 2.8 K - \text{feldspar} + 1.6 \text{ water} + Mg^{2+} \\ = 0.8 K - \text{mica} + 0.2 \text{ chlorite} + 5.4 \text{ silica} + 2 K^+ \end{aligned} \quad (20)$$

$$T_{K-Mg} = 4410par + K^+ = K - \text{feldspar} + Na^+ \quad (21)$$

3. Gas geothermometers

These are applicable for gas and steam samples since in many geothermal fields there are fumaroles, hot ground and acidic surface waters. These types of geothermometers are grouped into three as follows:

- 1) The mineral gas equilibria geothermometers;
- 2) Gas – gas equilibria geothermometers; and
- 3) Mineral – gas equilibria geothermometers involving CO₂, CH₄ and H₂S, which need to be externally fixed, using empirical methods.

3. METHODS

3.1 Data sources

The geochemical data of selected hot springs used in this research work were collected from the department of geological survey and mines in Uganda, (GSMD). These data were acquired during the UNDP/UNDESD project funded by OPEC and the Iceland Government, and data for the Öxarfjörður area were collected from Iceland GeoSurvey, (ISOR), by the geochemistry department; these results were acquired as part of the early studies for the search for oil. The data set includes analysed samples from selected hot springs, a cold spring and wells listed in Table 1.

3.2 Field sampling methodology

In all these areas of research work, geochemical sampling of the hot springs, and the wells was carried out by the GSMD geochemistry team, together with Dr. Halldór Ármannsson from the Iceland GeoSurvey, in Uganda (GSMD, 2008), while the sampling from the Öxarfjörður area, north Iceland, was carried out by the Iceland GeoSurvey geochemistry team. Measurements of the physical parameters and an analysis of the volatile components of the water samples collected were carried out in the field. Rock samples were collected for mineralogy analysis to determine the source of salinity in the geothermal waters from Kibiro and Öxarfjörður, although these were not used in this research work.

Untreated samples were collected for pH, carbonate, H₂S and conductivity measurements and also for the analysis of Mg and SiO₂. During the sampling, the concentrations of SiO₂ were expected to be more than 100 ppm, so the samples were diluted with distilled or deionized water to bring the concentrations into the range of 30 to 100 ppm in triplicate and the dilution factor was recorded. Samples were also collected and anions were filtered; for the cations, the filtered samples were acidified with nitric acid. All the samples used in the determination of sulphate were precipitated with Zn (CH₃COO)₂ and then the sulphate was analysed after filtration of the samples. For the analysis of stable isotopes ($\delta^2\text{H}$, $\delta^{18}\text{O}$), the isotope laboratory needed 60 ml of filtered sample. A summary of the sample treatment is given in Table 2 and the preservation method for the sampling of hot spring and hot water wells are presented in Table 3.

These samples had to be preserved both by chemical and physical processes, as shown in Table 3, in order to ensure no changes in the chemical and physical characteristics of these waters and the gases. Preservation techniques were carried out both in the field and in the laboratory, depending on the handling of the different constituents in these samples.

TABLE 1: Chemical composition (mg/kg) of selected samples from the Öxarfjörður, Kibiro and Panyimur and (isotope values in ‰ SMOW)

LOC	T(°C)	PH	CO ₂	H ₂ S	NH ₃	Cl	SO ₄	F	Br	Na	K	Ca	Mg	Al	Fe	SiO ₂	B	Li	TDS	δ ² H	δ ¹⁸ O
ÖXA																					
ISK	95.7	7.mar	30.mar	0.05	0.00	3539	232	0.41	12.jan	1818	98	400	júl.14	0.00	0.00	148	jan.77	0.00	6401	-87.8	-9.3
ISG	92.0	8.júl	30.jún	0.05	0.00	1807	85.9	0.33	6.feb	950	55	186	0.07	0.00	0.00	123	jan.40	0.00	3326	-88.5	-9.6
IEK	78.5	8.apr	30.ágú	<0.05	0.00	658	46.1	0.39	2.feb	427	41	17	jan.47	0.00	0.00	100	0.53	0.00	1283	-90.0	-12.0
IA1	98.0	9.mai	12.apr	<0.05	0.00	2460	138	0.65	<0.0	12.50	77	259	0.18	0.00	0.00	139	<0.0	0.00	4630	0.0	-10.0
IA3	96.0	7.sep	24.mar	0.07	0.00	1534	96.6	0.27	5.mar	833	44	154	0.42	0.00	0.00	129	1.00	0.00	2709	-100.4	-10.9
IA4	132.0	8.jún	5.jan	<0.03	0.00	2110	150	0.12	ágú.23	1222	67	185	0.65	0.00	0.00	214	jan.36	0.00	4085	-114.1	-11.1
IJÖ	2.sep	7.ágú	42.1	<0.03	0.00	6.sep	7.sep	0.16	<0.0	19.ágú	1.apr	6.jan	mar.62	0.00	0.00	16.ágú	<0.0	0.00	104	-98.7	-13.9
ISW	4.0	8.jan	105	<0.03	0.00	18288	2545	0.70	<0.0	10113	396	378	1162	0.00	0.00	1.jún	<0.0	0.00	36110	-7.1	-0.8
KIB																					
KN1	86.5	7.jún	146	10.apr	0.00	2500	46.6	5.des	16.júl	1530	169	62.0	8.jan	0.037	0.00	129	feb.26	1.500	4576	-11.3	-2.01
KN2	81.1	júl.14	155	13.0	0.00	2450	26.apr	5.feb	16.apr	1490	164	62.9	júl.96	0.041	0.02	125	feb.23	1.480	4436	-11.8	-2.08
KN3	71.8	júl.14	155	17.mar	0.00	2440	15.apr	apr.74	16.feb	1480	165	66	sep.21	0.044	0.00	122	feb.21	1.460	4384	-10.6	-1.98
KN4	39.5	8.mai	115	<0.0	0.00	2580	49.9	mai.37	17.mar	1570	182	76	ágú.71	0.029	0.03	135	feb.47	1.530	4548	-3.9	-1.01
KN4	29.ágú	jún.89	367	<0.0	0.00	31.2	139	0.37	0.26	87.5	7.júl	76	39.5	0.010	jan.50	90.5	<0.0	0.02	662	-15.2	-3.58
KN6	23.jún	jún.26	130	<0.0	0.00	5.feb	5.mar	0.12	0.04	12.apr	2.jún	15	8.mar	0.007	0.74	70.8	<0.0	0	124	-4.1	-1.57
KN7	24.sep	jún.72	232	<0.0	0.00	123	227	0.12	0.64	50.6	7.mai	138	39.5	0.014	0.72	76.1	<0.0	0.02	680	-5.2	-2.08
KN8	30	ágú.93	236	<0.0	0.00	24.feb	19.mar	0.83	0.13	72.3	49	9.ágú	27.mar	0.015	0.07	0.5	<0.0	0.01	338	39.8	mai.47
PAN																					
PA1	58	ágú.66	71	mai.61	2.jan	470	26	5.feb	1.mai	352	11	4.mai	0.36	0.47	0.1	73	0.65	0.12	890	-7.7	-3.5
PA2	45	ágú.45	109	feb.48	1.jún	379	36	4.júl	0.93	321	9.mai	8.mai	0.68	0.17	0	69	0.58	0.00	794	-5.5	-3.3
PA3	35	júl.56	142	<0.0	0.25	83	19	2.apr	0.17	138	7.mar	8.apr	3.jan	0.21	0.2	54	0.22	0.00	337	1.sep	-2.5
PA4	49	9.jún	95.5	<0.0	0.12	53	4.apr	6.jún	0.29	110	2.jún	1.apr	0.04	0.17	0	70	<0.1	0.00	nd	-1.9	-2.5
PA5	48	ágú.23	91.1	<0.0	<0.1	51	73	8.0	0.45	111	3.sep	6.jún	0.76	0.21	0.2	68	0.2	0.00	nd	2.mai	-2.0
PA6	60	ágú.35	216	<0.0	<0.1	95	341	13.0	<0.2	322	18	24	2.júl	<0.1	0.1	118	0.18	0.19	815	-4.9	-18.8
PA7	42	ágú.39	207	<0.0	<0.1	97	343	13.ágú	<0.2	323	19	21	1.mai	<0.1	0.2	129	<0.1	0.2	812	-4.8	-17.2
PA8	38	ágú.44	207	<0.1	<0.1	96	352	13.0	<0.02	342	22	21	1.mai	<0.1	0.3	129	0.76	0.22	825	-16.6	-4.9

TABLE 2: Treatment and sub-samples from hot springs and hot water wells
(Ármansson and Ólafsson, 2012)

Specification	Container	Capacity (ml)	Treatment	Used for
Ru	Glass	250-300	None; amber glass bottle with ground glass stopper	pH, CO ₂ , H ₂ S (if not in field) and conductivity
Ru	Plastic	200	None	Mg, SiO ₂ if < 100ml
Rd (1:1)	Plastic	3×100	Dilution; 0ml of sample added to 50 ml of distilled, deionized water	SiO ₂ if < 100ml
Fu	Plastic	200	Filtration	Anions
Fa	Plastic	200	Filtration; 0.8ml of conc. HNO ₃ acid added to 200 ml of sample	Cations
Fp, Fpi	Plastic	200, >500	Filtration; 2ml of 2M ZnAc ₂ added to sample in 100 ml volumetric glass flask and ≥10 ml to ≥500 ml bottle containing ≥25mg SO ₄ to precipitate sulphide	SO ₄ , δ ³⁴ S and δ ¹⁸ O in SO ₄
Fui, Fuc, Fut	Glass	60, 1000	Filtration; 1, 60ml, and 2, 1000ml amber glass bottles	δ ² H, δ ¹⁸ O, ¹³ C and ³ H

Note: Fp =Filtered precipitated; Fpi =Filtered precipitated for isotope; Fui =Filtered untreated; Fu =Filtered untreated; Fa =Filtered acidified; Ru =Raw untreated; Rd =Raw diluted.

TABLE 3: Preservation methods for geothermal samples (Ármansson and Ólafsson, 2006)

Type	Method	Purpose	Used for
Physical	Filtration with 0.45 or 0.22 μ membrane filter	Prevent interaction with suspended matter	Anions, Cations, TDS
	Freezing	Prevent biological activity	Nutrients
	Airtight container	Prevent interaction with atmospheric air	Reactive constituents
	On-site analysis	Prevent reactions of reactive constituents	
Chemical	Base addition	Absorption of acid gases	CO ₂ , H ₂ S in steam, δ ³⁴ S in H ₂ S in vapour
	Acidification	Prevent adsorption on the walls of containers	Cations
	Precipitation	Prevent a constituent from reaction to change the concentration of another constituent	Sulphate to fix Sulphide
	Sterilization	Prevent biological activity, using HgCl or formaldehyde	
	Dilution	Prevent polymerization and precipitation	Silica
	Redox	To change oxidation state of volatile constituent to make it less volatile	Hg
	Ion exchange	Concentrate and further prevent adsorption on the walls of container of trace constituents	Trace cations
	Extraction	Concentrate and further prevent adsorption on the walls of container of trace constituents	Trace cations

3.3 Analytical methods

The Department of Geological Survey and Mines carried out the determination of the TDS and conductivity of the geothermal waters in their laboratory at Entebbe. The samples were then divided into different portions for analysis. Then the samples were sent for complete chemical analysis to the Institute of Geological and Nuclear Science, New Zealand (Ármannsson, 2010), but the samples collected from Öxarfjörður area were analysed in the Orkustofnun Laboratory. The methods and instruments summarized in Table 4 were used in the analysis of these samples.

TABLE 4: Analytical methods (Ármannsson and Ólafsson, 2006)

Constituents	Laboratory	Method	LOD	PR RSD%
Conductivity	GSMD	4 electrode		
pH	GSMD	GE		
CO ₂ and H ₂ S	GSMD	Titration	0.02 – 1.0	3.8 – 13.7
SiO ₂ , B and NH ₃	OS and GSMD	SP	0.01- 0.5	0.7 – 8.3
Na, K, Ca, Mg, Sr, Li	OS	AAS	0.0005-0.1	1.5 – 2.7
SO ₄ , Cl and Br	OS	IC	0.02 – 0.025	0.8 – 5.4
TDS	OS	GR	2.5	3.4
F	OS	ISE	0.05	0.9
Fe, Al and Mn	OS	FAAS	0.001	
δ ¹⁸ O and δ ² H	USI	MS		
CO _{2, n.c.} , H ₂ S, n.c., CH ₄ , H ₂ , N ₂ , Ar, and C ₂ H ₆	OS	GC	0.01 – 0.02	

4. RESULTS AND DISCUSSION

4.1 The aqueous chemistry of the geothermal fluids in these areas

The results for selected hot springs and hot water wells presented in Table 1 from Kibiro, Panyimur and Öxarfjörður are generally in the range of neutral – alkaline with pH of 6.7- 9.5. A general summary of the different chemical component ranges in the samples from Kibiro, Panyimur and Öxarfjörður are presented in Table 5. Samples from Öxarfjörður contain very low H₂S (<0.03 – 0.07 mg/kg), CO₂ (5.1 – 30.8 mg/kg); the δ¹⁸O is -12 - -9.3 ‰, and δ²H -114.1 - -87.8 ‰, and TDS is relatively high (1283 – 6401 mg/kg). Samples from Kibiro also contain relatively high CO₂ (115 – 367 mg/kg) and H₂S (0.0 – 17.3 mg/kg). Panyimur samples, in general, contain relatively low concentrations of all the chemical components. And, in general, the samples from Panyimur and Öxarfjörður contain lower concentrations of Mg than the samples from Kibiro. There is a relatively higher concentration of fluoride in some of the samples from Panyimur, compared to the samples from Kibiro and Öxarfjörður. The chemistry of these water samples differs mainly in the samples from Öxarfjörður which, in general, contain almost none or very little H₂S, but contain the highest amount of Na, K, TDS, and concentrations of SiO₂, Na, Cl, CO₂, Mg and TDS.

TABLE 5: Summary of the different constituents in mg/kg and stable isotopes in ‰ SMOW of water samples of Öxarfjörður, Kibiro and Panyimur

	T(°C)	PH	CO ₂	H ₂ S	Cl	SO ₄
Gen	24 -132	6.26-9.5	5.1-367	<0.03-17.3	5.2-3539	1.9-352
Öxa	78.5-132	7.3-9.5	5.1-30.8	<0.03-0.07	658-3539	46.1-232
Kib	23.6-86.5	6.26-8.93	115-367	0-17.3	5.2-2580	5.3-227
Pan	35-60	7.56-9.06	71-216	<0.1-5.61	51-470	4.4-352
	K	Ca	Mg	SiO ₂	B	TDS
Gen	2.6-169	1.4-400	0.07-39.5	54-214	<0.1-16.7	124-6401
Öxa	41-98	6.1-400	0.18-1162	1.6-214	0.53-1.77	104-36110
Kib	2.6-470	9.75-75.9	0.99-39.5	0.5-147	2.0-2.47	124-4810
Pan	2.6-19.2	1.4-24	0.04-3.1	54-129	<0.1-0.76	337-890
	Na	Br	δ ² H	δ ¹⁸ O	F	
Gen	12.4-10113	<0.02-17.3	-100.5-39.8	-0.8-5.47	0.12-13.8	
Öxa	427-10113	2.2-12.1	-100.5-7.1	-12--0.8	0.12-0.7	
Kib	12.4.2163	0.13-17.3	-3.9-39.8	-1.01-5.47	5.12-7.2	
Pan	110-352	<0.02-1.5	-16.6-2.5	-18.8--2.0	2.4-13.8	

4.2 Use of ternary diagram in classifying geothermal waters of Kibiro, Panyimur and Öxarfjörður

4.2.1 Cl-SO₄-HCO₃ ternary diagram

The Cl-SO₄-HCO₃ ternary plot diagram has been used in the classification of geothermal and natural waters (Giggenbach, 1991). Composition of many water types is shown as one of the following in the triangular plot (Figure 4): mature waters, steam-heated waters, volcanic waters and peripheral waters. From the Cl-SO₄-HCO₃ ternary plot, the degree of separation of the plotted points for high-chloride and bicarbonate waters shows some indication of a relative degree of interaction of the fluids at lower temperature with CO₂, and of the HCO₃ contents increasing with time and distance travelled by the waters underground (Giggenbach, 1988).

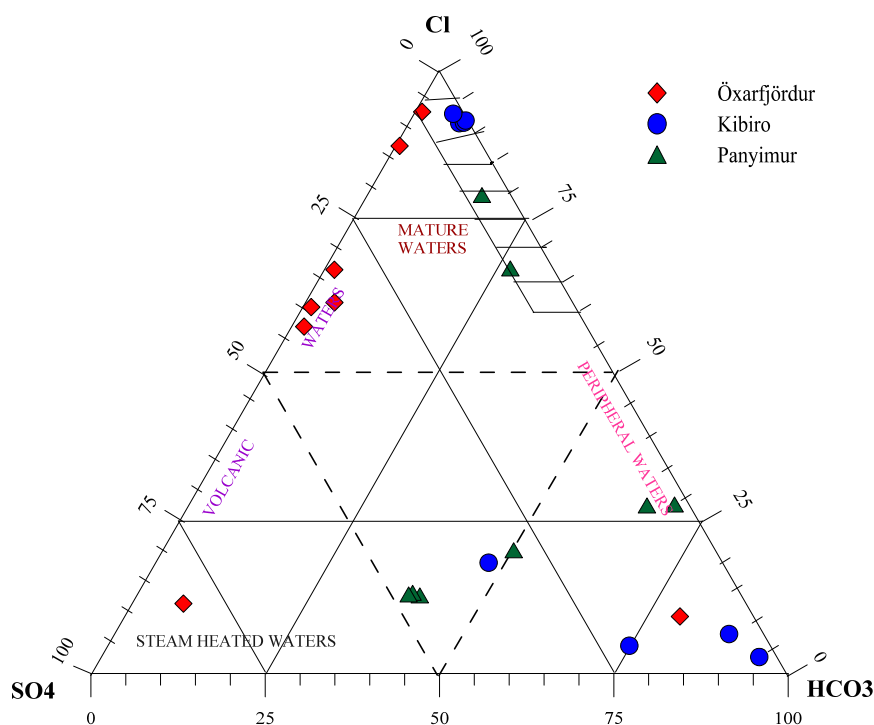


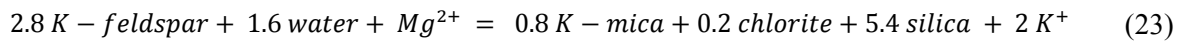
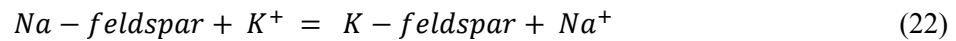
FIGURE 4: Cl-SO₄-HCO₃ ternary plot (Giggenbach, 1991) for water samples from Kibiro, Panyimur and Öxarfjörður

In Figure 4, for the waters from Kibiro, Panyimur and Öxarfjörður, there is a great degree of variation among the HCO₃ and Cl waters. The waters from the Öxarfjörður area plotted in the volcanic region of the diagram, with two samples in the Cl portions, one in the SO₄ and another one in the HCO₃ part. Four of the Kibiro samples plotted in the chloride portion of the diagram, and three in the HCO₃ region, but

more towards the SO_4 and the HCO_3 section. Two of the Panyimur samples plotted in the Cl area, and two in the peripheral water zone.

4.2.2 The Na-K-Mg triangular diagram

This technique for the derivation of Na-K-Mg-Ca geothermometers was initiated by Giggenbach (1988) as one of the classification techniques for different kinds of water depending on whether they are: 1) immature water; 2) partially equilibrated water; or 3) fully equilibrated water. Using the plots, one may apply geothermometers to the equilibrated and partially equilibrated water only. The triangular diagram, which is temperature dependent, is based on two reactions, Equations 17 and 18.



Equations 22 and 23 are used in the derivation of the geothermometer used.

In the triangular plot, the area of partial equilibrium indicates that there could be some mineral that has dissolved, though it has not yet attained equilibrium or it may be that it is geothermal water, but has been diluted with water that has not yet reached equilibrium, for example cold groundwater. Points which plotted close to the $\sqrt{\text{Mg}}$ corner indicate that there is a very high proportion of relatively cold groundwater mixed in the water system.

In Figure 5, 4 samples from Panyimur and 6 samples from Öxarfjörður plotted close to the full equilibrium line but 4 samples from Panyimur and 1 sample from Öxarfjörður plotted in the partially equilibrated region of the diagram, probably meaning that there may be some recharge from cold groundwater into the geothermal systems in those areas. In Kibiro, two of the samples plotted in the immature region, hence contain cold groundwater, while six of the samples plotted in the partially equilibrated portion. The t_{km} temperature for samples from Kibiro varied, ranging between 160°C to 140°C , and then 100°C to $<100^\circ\text{C}$; the t_{kn} was from 100°C to 240°C ; for Panyimur, the t_{km} ranged from 120°C to 70°C and the t_{kn} from 100°C to 160°C ; for Öxarfjörður, t_{km} varied in the range of $<100^\circ\text{C}$ to 200°C and the t_{kn} from 100°C to 200°C . The t_{km} temperature for all these samples varied considerably. This could be due to the fact that the K-Mg geothermometer tends to react faster to change than the K-Na geothermometer in the same system.

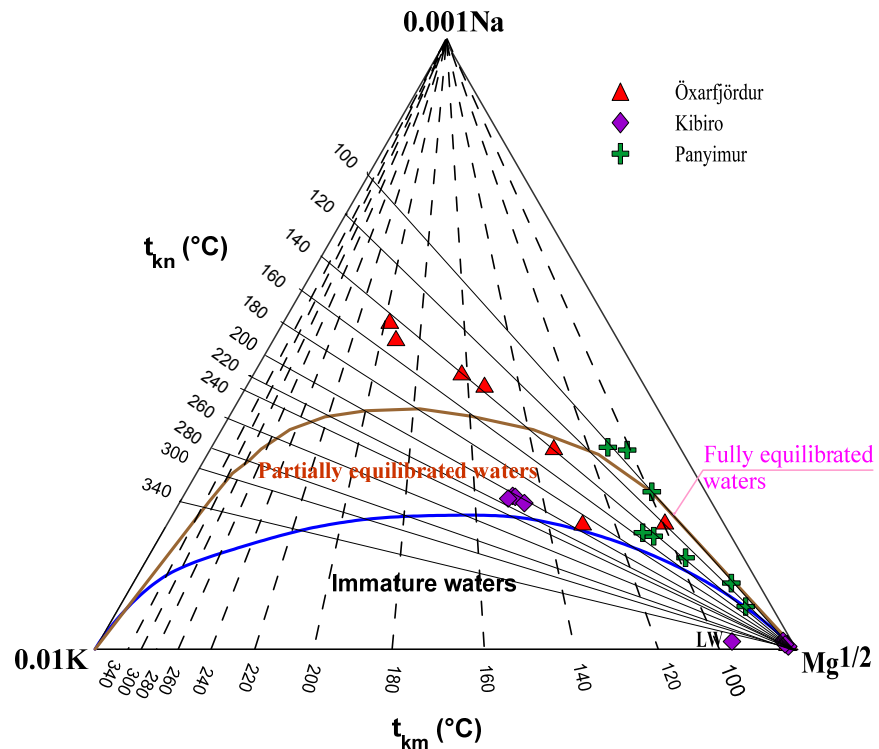


FIGURE 5: Na-K-Mg triangular diagram for samples from Kibiro, Panyimur and Öxarfjörður

4.3 Geothermometer data output

Sixteen different geothermometer Equations (eight for quartz geothermometers, two for chalcedony, three each for Na/K, K-Mg and Na-K-Mg) were applied in the prediction of the subsurface temperatures of the geothermal water from Kibiro, Panyimur and Öxarfjörður. The calculated geothermometer temperatures for eleven geothermometers out of the sixteen are presented in Table 6. The average calculated quartz geothermometer temperature for hot springs and wells in Öxarfjörður was 150°C, in Kibiro samples it was 123°C and in Panyimur it was 129°C. The Na-K geothermometer temperatures for Kibiro and Panyimur were high while the Na-K-Ca geothermometer gave very high temperatures for Öxarfjörður. This may due to loss of CO₂ leading to calcite precipitating out of the solution. This affects the concentration of calcium in the solution, leading to abnormally high geothermometer temperatures. The calculated chalcedony geothermometer temperatures for these samples were: for Öxarfjörður 116°C, for Kibiro 114°C, and for Panyimur 101°C. The calculated Na-K geothermometer temperatures were: for Öxarfjörður 148°C, for Kibiro 197°C and for Panyimur 116°C. Appendix II shows comparison plots of calculated temperature results obtained from sixteen different equations of geothermometers for Öxarfjörður, Kibiro and Panyimur.

TABLE 6: Calculated values for 11 equations for solute geothermometers temperatures (in °C) for samples from Öxarfjörður, Kibiro and Panyimur

	T_{Na-K}	$T_{Na-K\ 1}$	T_{K-Mg}	$T_{qz\ 1}$	$T_{qz\ 2}$	$T_{qz\ 3}$	$T_{qz\ 4}$	$T_{ch\ 1}$	$T_{ch\ 2}$	$T_{qz\ 5}$	$T_{qz\ 6}$
LOC											
ISK	139.6	129.77	132.6	152	153.80	150.2	143.08	136.42	132.7	160.33	160.39
ISG	144.4	134.79	197.4	142.6	144.1	137.82	132.77	123.60	121	148.95	148.94
IBK	191.1	183.73	130	132.9	134.1	125.35	122.23	110.68	109.2	137.36	137.39
IA1	150.3	140.89	191.9	148.8	150.5	145.97	139.57	132.03	128.7	156.46	156.48
IA3	136.9	127.01	153.1	145.1	146.7	141.10	135.5	126.99	124.1	151.98	151.98
IA4	140.8	131.01	161.5	171.9	174.2	176.99	165.12	164.22	157.9	185.61	185.08
IJÖ	162.1	153.24	35.97	63.23	56.68	41.81	43.03	24.71	28.64	57.01	57.12
ISW	115.6	104.91	98.38	1.29	-35.28	-39.53	-48.75	-43.10	-36.85	-10.61	-27.54
KIB											
KM1	205.36	198.79	148.7	145.1	146.7	141.05	135.47	126.94	124.1	151.93	151.93
KM2	204.98	198.39	148.00	143.5	145.1	139.01	133.76	124.83	122.1	150.05	150.04
KM3	206.4	199.84	145.7	142.3	143.8	137.45	132.46	123.22	120.7	148.61	148.60
KM4	210.6	204.31	150.1	147.3	149.00	144.03	137.95	130.03	126.90	154.67	154.69
KM4	182.30	174.43	45.87	131.7	131.9	131.85	131.85	128.08	103.4	104.41	131.77
KM6	285.1	284.34	40.18	118.8	119.00	119.00	119.00	117.11	90.25	90.24	119.05
KM7	238.90	234.54	45.34	122.5	122.7	122.69	122.69	120.27	94.02	94.29	122.70
KM8	532.3	564.09	92.86	-34.8	65.25	65.25	65.25	-21.62	-59.76	-66.38	-67.87
PAN											
PA1	99.73	88.62	110.9	118.4	119.1	107.31	106.58	91.94	91.84	120.34	120.59
PA2	96.83	85.64	98.15	116	116.5	104.30	103.90	88.81	88.93	117.46	117.77
PA3	137.9	128.06	72.33	105.7	105.5	91.79	92.57	75.78	76.80	105.44	105.97
PA4	83.04	71.54	101.5	116.6	117.2	105.06	104.58	89.6	89.67	118.19	118.48
PA5	108.1	97.21	74.13	115.4	115.9	103.53	103.21	88.01	88.18	116.72	117.04
PA6	141	131.22	96.34	140.7	142.2	135.34	130.68	121.03	118.7	146.66	146.64
PA7	147.3	137.81	106.7	145.1	146.7	141.05	135.47	126.94	124.1	151.93	151.93
PA8	153.9	144.70	110.6	145.1	146.7	141.05	135.47	126.94	124.1	151.93	151.93

Note: T_{Na-K} =Na-K cation geothermometer; T_{K-Mg} =K-Mg cation geothermometer;
 $T_{qz\ (1-6)}$ =Quartz geothermometers; $T_{ch\ (1\ and\ 2)}$ =Chalcedony geothermometer.

In many instances there was not a good agreement between the Na-K temperatures and the silica temperatures for samples from Öxarfjörður, but the cation geothermometers seemed to agree quite closely. The quartz geothermometer temperatures for Kibiro seemed to agree quite well, and for the Panyimur samples, there were great variations in all the calculated geothermometer temperatures. The magnesium concentrations were high in these samples, suggesting a substantial influence of cold

groundwater, rendering the Na/K geothermometer unreliable; at low temperatures, the silica geothermometers are not dependable either.

The anomalously high estimates from the Na-K-Ca geothermometer for all the samples could be due to calcium carbonate deposited during the ascent which prevents aqueous K and Na from interacting with the country rock (Fournier and Truesdell, 1973).

Geothermometers take advantage of specific mineral –solute reactions (Karingithi, 2009) which are slow to equilibrate at cooler temperatures, especially under conditions where the fluid is effectively separated from the minerals which control the equilibria. The result is that a hot equilibrium temperature is “frozen in” to the fluid, reflected by solute concentrations or solute ratios.

4.4 Mixing model interpretations

Assuming that the silica has not precipitated before or after mixing and that there has been no conductive cooling of the water, then the dissolved silica concentration of a mixed water and a silica – enthalpy diagram may be used to determine the temperature of the hot water component. However, it is not easy to determine whether a given spring is a mixture of hot and cold spring water and also to prove that silica has not precipitated or that conductive cooling has not occurred (Truesdell and Fournier, 1977).

From the enthalpy – silica mixing model (Figure 6), the samples from Kibiro indicate a geothermal system with a temperature of about 191-220°C; samples from Panyimur indicate temperatures of about 150-160°C, and samples from Öxarfjörður show temperatures of 190-220°C.

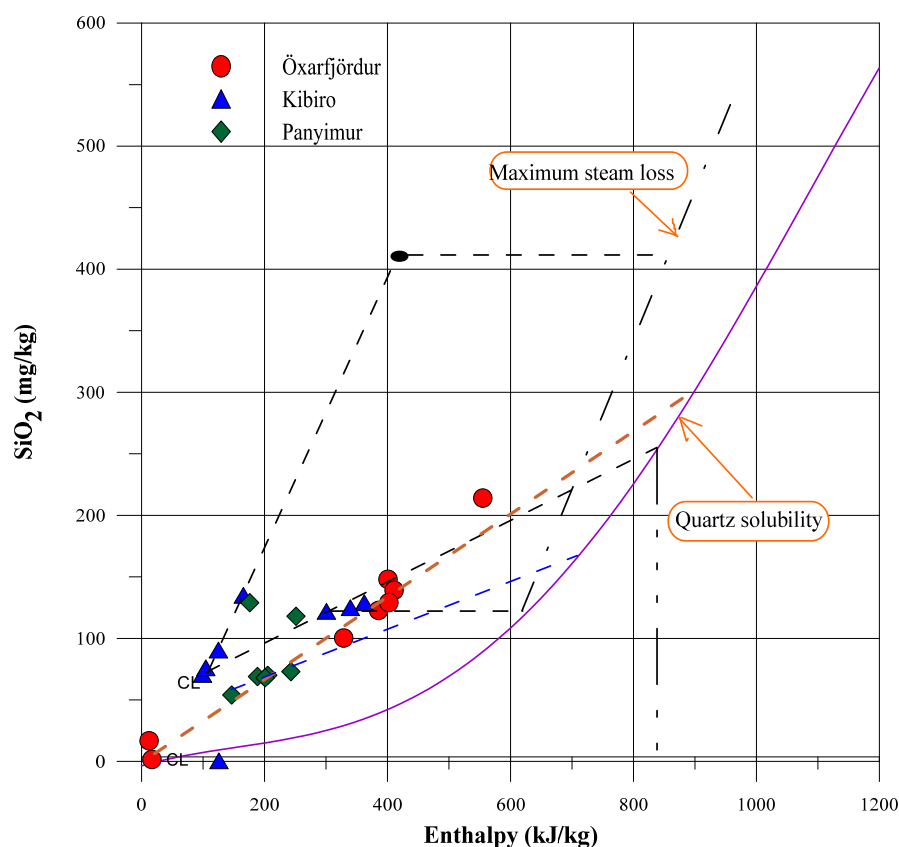


FIGURE 6: Silica-enthalpy mixing model applied to water samples from Kibiro, Panyimur and Öxarfjörður

The silica – carbonate plot (Figure 7) for all the samples from Panyimur indicates that boiling has not occurred; for Kibiro, two of the samples showed boiling in the hot spring while some showed equilibration and others suggested no boiling or mixing. Samples from Öxarfjörður suggested that boiling had occurred, meaning that some of the CO₂ had been lost in the steam phase, hence lowering the CO₂ concentrations in some of those samples.

4.5 Gas geothermometer temperature results based on this analysis

Gas geothermometer temperatures were calculated for one sample from Kibiro and the results were: $T_{\text{CO}_2} = 199^\circ\text{C}$, $T_{\text{CH}_4/\text{C}_2\text{H}_6} = 208^\circ\text{C}$ and $T_{\text{H}_2/\text{Ar}} = 221^\circ\text{C}$. For the samples from Öxarfjörður, the following estimates of $T_{\text{CH}_4/\text{C}_2\text{H}_6}$ were made on three well samples; these showed the following temperature ranges: Well AER-01 = $150\text{--}170^\circ\text{C}$; Well AER-03 = $175\text{--}180^\circ\text{C}$; and Well AER-04 = $200\text{--}220^\circ\text{C}$. This was done basically to confirm the variations of gas geothermometers and the chemical or solute geothermometers.

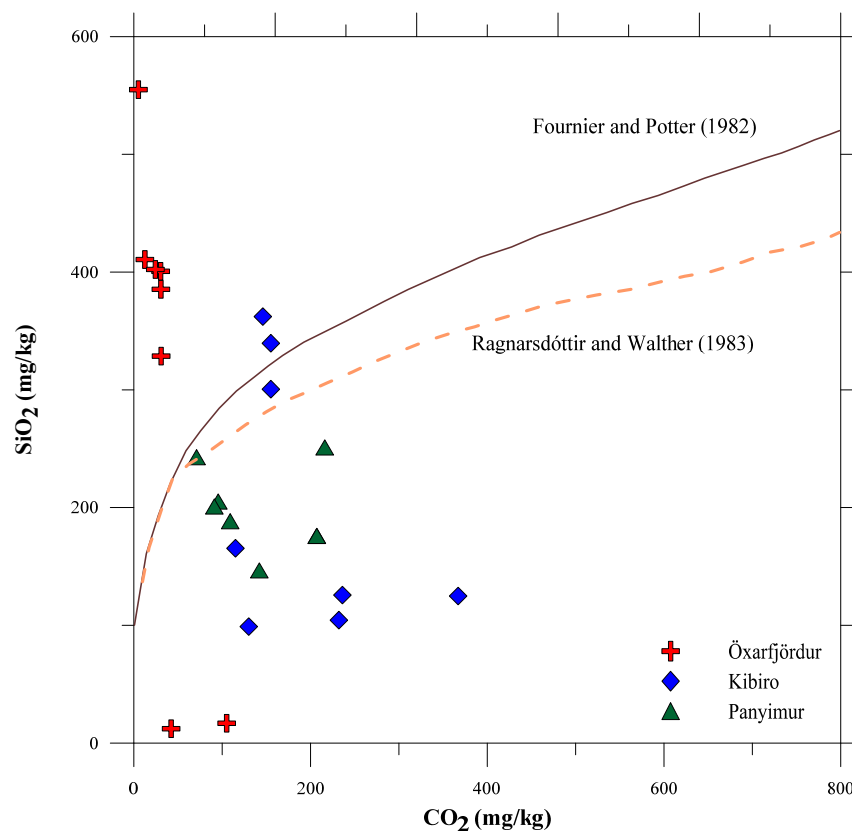


FIGURE 7: Silica versus carbon dioxide

4.6 Binary plots

A mixing trend can be clearly seen in all the areas under study as shown in Figure 8a, K^+ vs. Cl^- and in Figure 8b, Na^+ vs. Cl^- , with positive correlations for Öxarfjörður and Kibiro, which may mean that there is a high Cl^- concentration possibly being added into these systems. In Öxarfjörður, it could be that seawater is mixing with the geothermal waters. In Kibiro, the source may be from the salt mining in that area and/or sodium chloride geothermal waters. For Panyimur, sodium chloride geothermal waters may be mixing at depth.

The concentration of HCO_3^- , shown in Figure 8c, in four samples from Kibiro and in two samples from Panyimur is relatively higher than in other samples, suggesting that there could be CO_2 absorption from the gases that the fluid carries or from the condensation of geothermal steam containing CO_2 in the particular geothermal water samples containing high concentrations of HCO_3^- . There is an increase in the concentration of chloride in the samples from Öxarfjörður which may mean that there is either mixing of the geothermal waters with sea water or with deep geothermal fluids.

Looking at the relationships of different elements in the geothermal waters from Kibiro, Panyimur and Öxarfjörður (Figure 9), the following conclusions may be drawn from these results. There are some linear relationships between B and Cl (Figure 9a) which may mean that there is mixing of cold water with hot geothermal fluid in the upflow zones in these systems. For the Kibiro samples, there seems to be a linear relationship between Li and Cl (Figure 9b) that may be due to the uptake of lithium from the waters by the surrounding rocks in the area, suggesting that there could be some water rock interaction in the system.

The relationships between Na – B and Ca – B (Figures 9c and d) in which B is a conservative element, and a linear relationship in the plots of these samples may mean that Ca and Na are present in the environment in which these waters occur; the increase in the B concentration suggests that there is water-

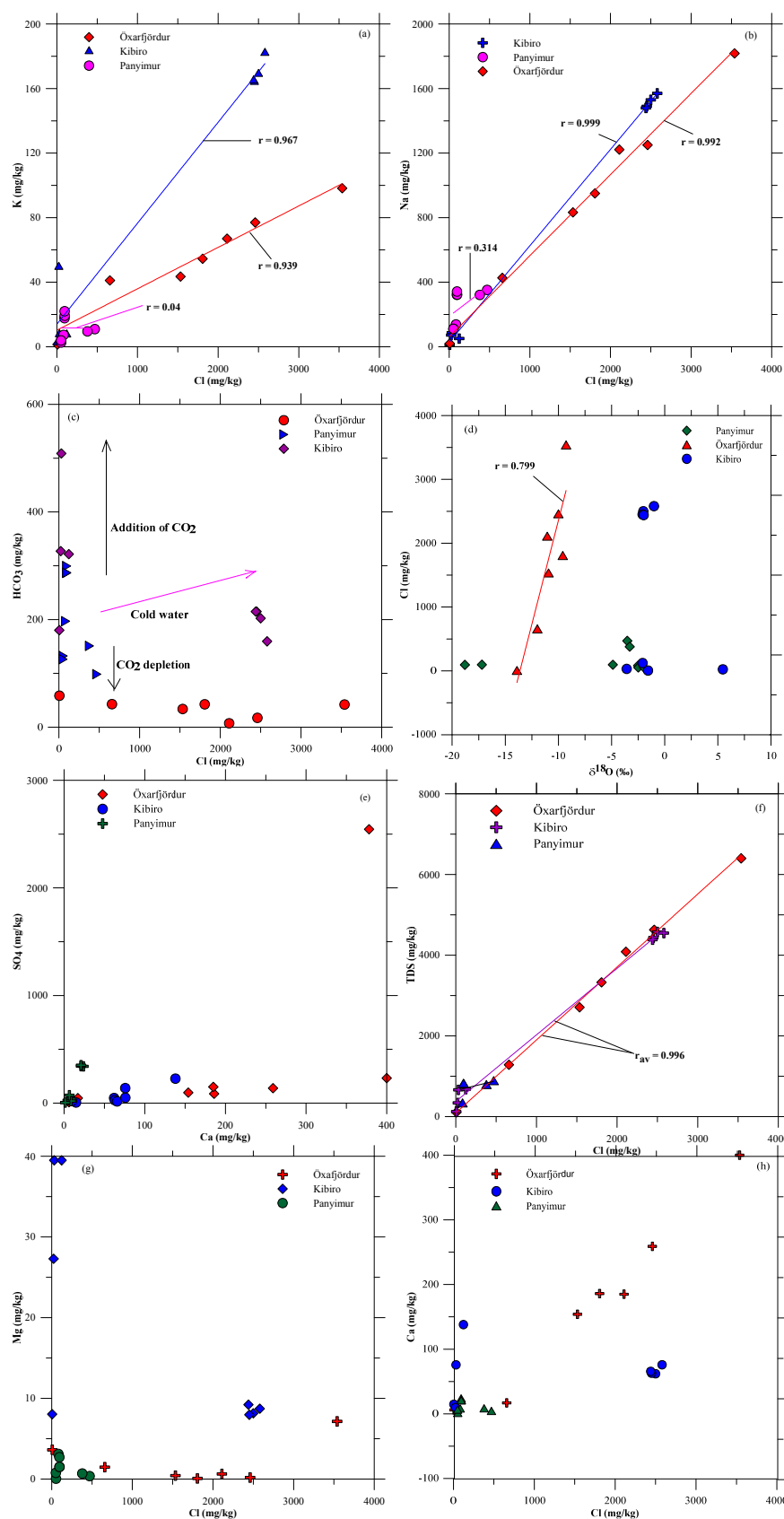


FIGURE 8: Binary plots of K vs. Cl, Na vs. Cl, HCO_3 vs. Cl, Cl vs. $\delta^{18}\text{O}$, SO_4 vs. Ca, TDS vs. Cl, Mg vs. Cl, and Ca vs. Cl

rock interaction since Ca and Na are less mobile compared to B, and may be removed from the water during secondary mineral precipitation out of the solution.

Clear linear relationships are observed for $\delta^{18}\text{O}$ and Cl in samples from Öxarfjörður (Figure 8d) which may be due to mixing of saline and non-saline component and/or water-rock interaction and B and Cl in samples from all three areas (Figure 9a) suggesting water-rock interaction.

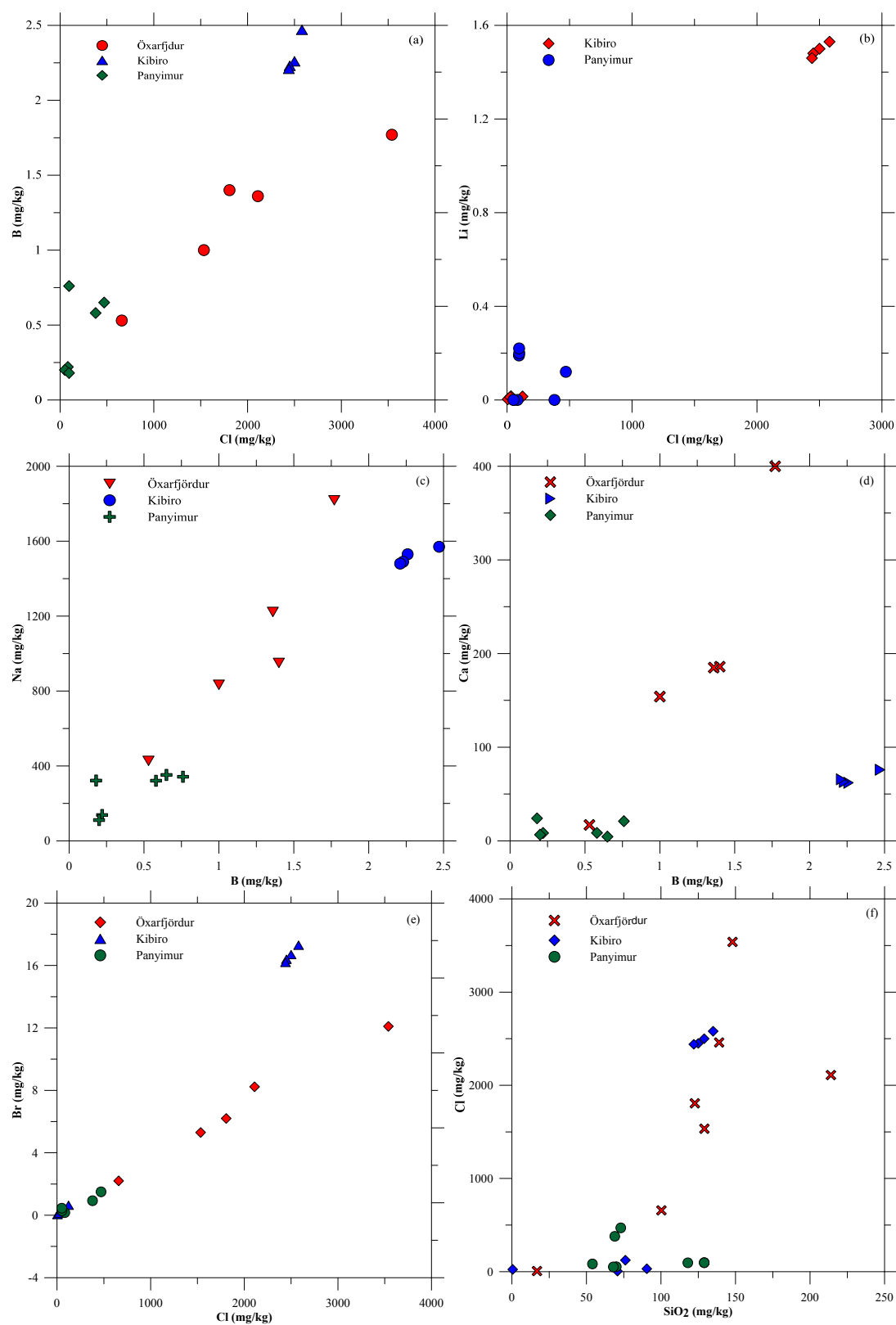


FIGURE 9: Binary plots of B vs. Cl, Li vs. Cl, Na vs. B, Ca vs. B, B vs. Cl and Cl vs. SiO₂

4.7 Mineral saturation

In the log (Q/K) plots showing the equilibrium state of some of the minerals calculated by the WATCH programme for Kibiro samples (Figure 10), most of the curves intersect the line of log (Q/K) equal to zero for Kibiro area in the temperature range 140 – 160°C, and some of the minerals converge below the log (Q/K) equal to zero line at 180 –>200°C. For Panyimur, most of the curves cross the log (Q/K) equal to zero line at 120 – 160°C and converge below it at 180 –> 200°C. For Kibiro and Panyimur, it may be inferred that there is some mixing of cold water with a geothermal component. The anhydrite in the samples from Kibiro and Panyimur are undersaturated. Samples from Öxarfjörður (Figure 11) show that most of the minerals have not yet reached equilibrium. The curves for the different minerals intersect the log (Q/K) line equal to zero at temperatures of about 120 – 150°C. And some of the curves converge below the log (Q/K) line equal to zero at temperatures of about 90 – 180°C, with some curves converging above 200°C. There is some mixing of cold water with a geothermal component in the Öxarfjörður area. And most of the minerals are undersaturated, that is their solubility, for example, of hydrate, talc, and calcite decreases (Stefánsson et al., 2000) with increasing temperature leading to their being precipitated out of the solution. This may be due to mixing of hot water with cold water in the area.

4.7.1 More output from the WATCH programme

The WATCH speciation program (Bjarnason, 2010; Arnórsson et al., 1983a) was used in the calculation of the mineral equilibria, based on the fact that different minerals have different reaction quotients and equilibrium constants. The ionic balance values for two samples from Öxarfjörður, four samples from Kibiro and two samples from Panyimur are above 5%, but the rest are below 5%.

4.8 Isotope data interpretation

In the Öxarfjörður area, the $\delta^{18}\text{O}$ ranges from -12.0 to -0.8 ‰ and $\delta^2\text{H}$ from -100.4 to -7.1 ‰; in Kibiro: $\delta^{18}\text{O}$ from 5.5 to -1.0 ‰ and $\delta^2\text{H}$ from +39.8 to -3.9 ‰, and for Panyimur: $\delta^{18}\text{O}$ values range from -18.8 to -2.0 ‰, then $\delta^2\text{H}$ from 2.5 to -16.6 ‰. There is a significant variation in the $\delta^{18}\text{O}$ values of these three areas.

All Kibiro samples plotted close to: the WML, KRL and CARL lines, with some slight shift from the WML line (Figure 12) which may mean that there is some oxygen shift due to water rock interaction within the system as a result of a low water rock ratio or a high temperature. All samples from Panyimur plotted above the lines, suggesting that there could be some good permeability in the area; this could also mean that there is excess deuterium.

The samples from Öxarfjörður all plotted below the KRL and CARL lines, but close to the WML line. This could mean that the water samples from Öxarfjörður have undergone water rock interaction for a relatively long time and there may be a high temperature at depth, hence leading to oxygen shift due to the exchange of oxygen between water and the rock.

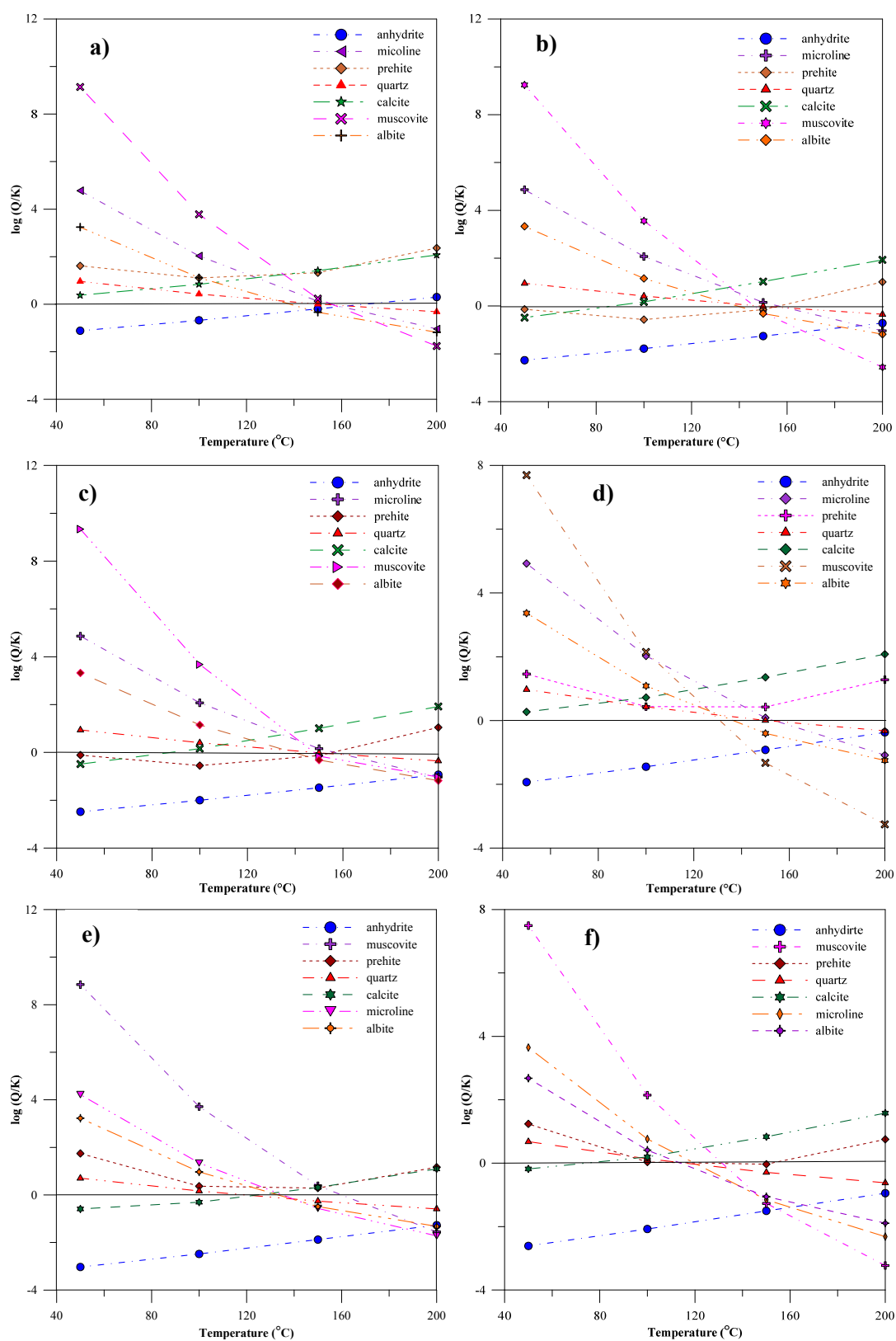


FIGURE 10: Mineral equilibrium plots for Kibiro samples (a – d) and Panyimur samples (e and f)

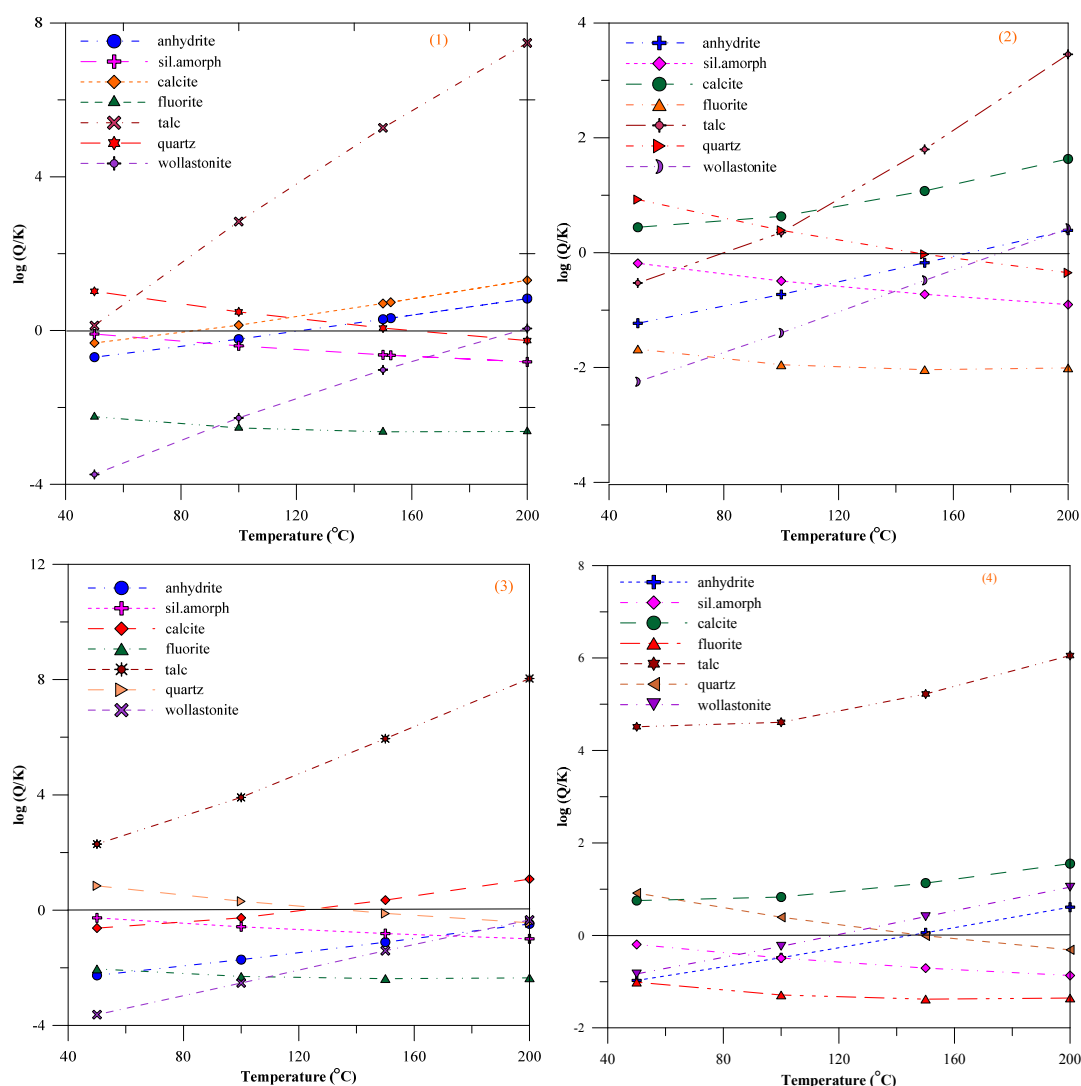


FIGURE 11: Mineral equilibrium plots for Öxarfjörður

5. CONCLUSIONS

- The geothermal waters of Kibiro, Panyimur and Öxarfjörður are classified as sodium-chloride-bicarbonate waters. The geothermal samples from Öxarfjörður are more mature than the water samples from Kibiro and Panyimur.
- From geothermometer temperature prediction and interpretation, quartz and Na/K geothermometers are applicable in a very wide range of geological environments, for example from rhyolitic, classic sediments to a basaltic geological setting.
- The mineral saturation plots for Kibiro and Panyimur showed that all waters had almost reached equilibration with most minerals, but in Öxarfjörður they have not yet attained equilibrium.
- The chemical composition of the water samples from Kibiro, Panyimur and Öxarfjörður, with different sedimentary geological settings, is much affected by the strata through which these fluids flow.
- Despite the fact that the Öxarfjörður geothermal system is located in a sedimentary graben, there is considerable water- rock interaction at depth beneath the sedimentary system compared to the situation at Kibiro and Panyimur.

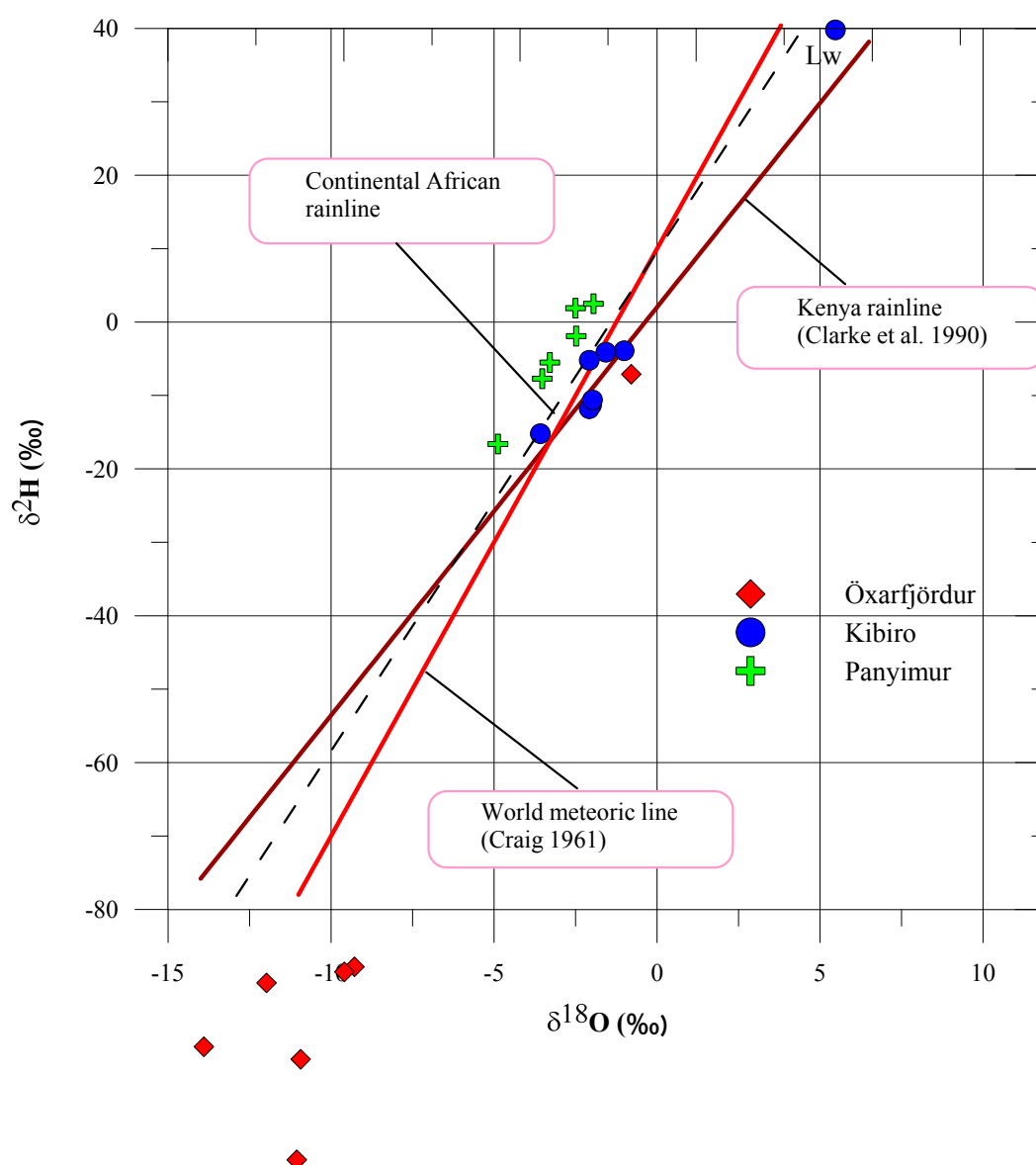


FIGURE 12: Plot of $\delta^{2}\text{H}$ vs $\delta^{18}\text{O}$ for samples from Kibiro, Panyimur and Öxarfjörður

5.1 Recommendations and future research work

- More geochemical exploration work needs to be carried out in geothermal systems occurring in sedimentary geological settings for better interpretation of the geochemistry of these systems.
- Combined geochemical, geological and geophysical studies are required for better understanding of geothermal systems in sedimentary settings.
- A distribution map for deuterium ratios and full geological maps of the geothermal systems in Kibiro and Panyimur are required.
- The geochemistry of the hot spring discharges in Kibiro and Panyimur may be controlled by the interaction of the fluids with the crystalline basement, and is characterized by low B/Cl conservative element ratios and a high pH. This needs more research.

- From this study, the application of geothermometry techniques clearly differ from one place to another due to the different environmental conditions, such as physical processes like conductive cooling and mixing with cold water. Boiling during upflow may affect possible water-rock equilibria in the deep reservoir, and this can result in unreliable temperature predictions. Furthermore, it is very useful to employ different geothermometers and methods for studying equilibrium states in order to check each and to exclude unreliable samples and non-applicable geothermometers.

ACKNOWLEDGEMENTS

To the United Nation University Geothermal Training Program together with the Government of Iceland, I hereby express my gratitude for the opportunity granted to me for the participation in this six months Geothermal Training Programme. I am indebted to former Director, Dr. Ingvar B. Fridleifsson and the new Director, Mr. Lúdvík S. Georgsson, for UNU, for their undivided dedication to the success of this training.

Special thanks to my supervisors, Dr. Halldór Ármannsson and Mr. Dadi Thorbjörnsson for their assistance and critical advice including provision of data, both analytical and literary information during the preparation of this report. I would like to thank all the ISOR staff, especially those who gave lectures in the different fields that build up the geothermal training programme.

I am grateful to the following: Ms. Thórhildur Ísberg, Mr Ingimar G. Haraldsson, Ms. Málfríður Ómarsdóttir and Mr. Markús A.G. Wilde for the commitment that they offered us during this training period. And not forgetting all the other UNU staff for their coordination of the training activities and for guidance that led to the successful completion of this training.

To my late mum and my son (Obiro Anthony Claret), I dedicate this small piece of my work to you. And I thank the Department of Geological Survey and Mines for allowing me to come for this training.

Finally, I would like to give thanks to the Almighty God for his generous support and encouragement in all that I do.

NOMENCLATURE

EARS = East Africa Rift System
ISOR = Iceland GeoSurvey
MEMD = Ministry of Energy and Mineral Development
CARL = Continental African rain line
WML = World meteoric line
KRL = Kenyan rain line
GSMD = Geological Survey and Mines Department
UNU = United Nations University
TDS = Total dissolved solids
OS = Orkustofnun
ICEIDA = Icelandic International Development Agency
IAEA = International Atomic Energy Agency
LOC = Location
KIB = Kibiro
ÖXA = Öxarfjörður
PAN = Panyimur

AAS = Atomic absorption spectrophotometry
IC = Ion chromatography
ISE = Ion specific electrode
FAAS = Flameless atomic absorption spectrophotometry
GC = Gas chromatography
USI = University of Iceland science institute, Reykjavik
n.c. = non-condensable
MS = Mass spectrometry
T = Temperature in (°C)
Tqz (1-8) = Temperature obtained using quartz geothermometer
Tch (1-2) = Temperature obtained using chalcedony geothermometer
TK-Mg, TNa-K, TNa-K and Na-K-Ca are different cation geothermometers used to obtain the temperature

REFERENCES

Afeworki O., M., 2010: Analysis of temperature and pressure characteristics of the Hverahlid geothermal field in the Hengill geothermal system, SW-Iceland. Report 20 in: *Geothermal training in Iceland 2010*. UNU-GTP, Iceland, 1-28.

Ármannsson, H., 2009: Application of geochemical methods in geothermal exploration. *Proceedings of the "Short Course IV on Exploration for Geothermal Resources" organized by UNU-GTP, KenGen and GDC, at Lake Naivasha, Kenya*, 8 pp.

Ármannsson, H., 2010: *Investigations of geothermal areas in Uganda other than Katwe-Kikorongo, Buranga and Kibiro*. ÍSOR – Iceland GeoSurvey, prepared for ICEIDA, report ÍSOR-2010/003, 1-17 pp.

Ármannsson, H., 2013: *Fluid chemistry and utilization*. UNU-GTP, Iceland, unpublished lecture notes, 22 pp.

Ármannsson, H. and Ólafsson, M., 2006: *Collection of geothermal fluids for chemical analysis*. ÍSOR – Iceland GeoSurvey, Reykjavik, report ISOR-2006/016, 17 pp.

Árnason, K., and Gíslason, G., 2009: Geothermal surface exploration. *Paper presented at "Short Course on Surface Exploration for Geothermal Resources", organized by UNU-GTP and LaGeo, Santa Tecla, El Salvador*, 7 pp.

Arnórsson, S. (ed.), 2000a: Isotopic and chemical techniques in geothermal exploration, development and use. *Sampling methods, data handling, and interpretation*. International Atomic Energy Agency, Vienna, 351 pp.

Arnórsson, S., 2000b: The quartz and Na/K geothermometers. I. New thermodynamic calibration. *Proceedings of the World Geothermal Congress 2000, Kyushu-Tohoku, Japan*, 929-934.

Arnórsson, S., and Bjarnason, J.Ö., 2007: Fluid-fluid interaction in geothermal systems. *Reviews in Mineralogy & Geochemistry*, 65, 229-312.

Arnórsson, S., and Svavarsson, H., 1985: Application of chemical geothermometry to geothermal exploration and development. *Geoth. Res. Council, Transactions*, 9-1, 293-298.

Arnórsson, S. (ed.), D'Amore, F., and Gerardo-Abaya, J., 2000: *Isotopic and geochemical techniques in geothermal exploration, development and use: Sampling methods, data handling, and interpretation*. International Atomic Energy Agency, Vienna, 351 pp.

Arnórsson, S., Gunnarsson, I., Stefánsson, A., Andrésdóttir, A., and Sveinbjörnsdóttir, Á.E., 2002: Major element chemistry of surface- and ground waters in basaltic terrain, N-Iceland. I. Primary mineral saturation. *Geochim. Cosmochim. Acta*, 66, 4015-4046.

Arnórsson, S., Gunnlaugsson, E., and Svavarsson, H., 1983: The chemistry of geothermal waters in Iceland. III. Chemical geothermometry in geothermal investigations. *Geochim. Cosmochim. Acta*, 47, 567-577.

Atekwana, E.A., Hogan, J.P., Kampunzu, A.B., and Modisi, M.P., 2004: Early structural evolution of the nascent Okavango rift zone, NW Botswana. *Proceedings of the East African Rift System: Geodynamics, Resources, and Environment Conference, Addis Ababa*, 12-16.

Bahati, G., 2007: Status of geothermal energy exploration in Uganda. *Paper presented at "Short course II on surface exploration for geothermal resources, Naivasha Kenya", organized by UNU-GTP, Iceland, and KenGen, Naivasha, Kenya*, CD SC-05, 10 pp.

Bahati, G., 2012: Status of geothermal exploration and development in Uganda. *Paper presented at "Short Course VII on Exploration for Geothermal Resources, organized by UNU-GTP, GDC and KenGen, at Lake Bogoria and Lake Naivasha, Kenya*, 14 pp.

Bertrami, R., Cioni, R., Corazza, E., D'Amore, F., and Marini, L., 1985: Carbon dioxide in geothermal gases. Reservoir temperature calculations at Larderello (Italy). *Geothermal Research Council, Transactions*, 9, 299-303.

Bjarnason, J.Ö., 2010: *The speciation program WATCH, Version 2.4*. The Iceland Water Chemistry Group, Reykjavík.

Björnsson, A., Eysteinnsson, H., and Beblo, M., 2005: Crustal formation and magma genesis beneath Iceland: magnetotelluric constraints. In: Foulger, G.R., Natland, J.H., Presnall, D.C., Anderson, D.L. (eds.), *Plates, plumes and paradigms*. Geological Society of America, Spec. Pap. 388, 665-686.

Bruhn, D., Manzella, A., Vuataz, F., Faulds, J., Moeck, I., and Erbas, K., 2011: Exploration methods. In: Huenges, E. (ed.), *Geothermal energy systems*. Wiley-VCH Verlag GmbH, Weinheim, 465 pp.

Craig, H., 1963: The isotopic geochemistry of water and carbon in geothermal areas. In: Tongiorgi, E. (ed.), *Nuclear geology on geothermal areas*. Consiglio Nazionale delle Ricerche, Laboratorio di Geologia Nucleare, Pisa, 17-53.

D'Amore, F., and Arnórsson, S., 2000: Geothermometry. In: Arnórsson, S. (ed.), *Isotopic and chemical techniques in geothermal exploration, development and use. Sampling methods, data handling, interpretation*. International Atomic Energy Agency, Vienna, 152-199.

D'Amore, F., Krajca, J., Michard, G., Nuti, S., Ólafsson, M., Paces, T., Zhaoli, S., Wei, T., and Zhifei, Z., 1991: *Fluid sampling for geothermal prospecting*. UNITAR/UNDP Centre on Small Energy Resources, Rome, 93-117 pp.

Data, G., and Bahati, G., 2003: The chemistry of geothermal waters from areas outside the active volcanic belt, SW-Uganda. *Proceedings of the 2nd KenGen Conference, Nairobi, Kenya, April 2003*, 24-29.

Driesner, T, 2013: Geothermal activities in the Main Ethiopian Rift: Hydrogeochemical characterization of geothermal waters and geothermometry applications (Dofan-Fantale, Gergede-Sodere, Aluto-Langano). *Geothermics*, 47, 1-12.

Ebinger, C.J., Deino, A.L., Drake, R.E., and Tesha, A.L., 1989: Chronology of volcanism and rift basin propagation: Rungwe volcanic province, East Africa. *J. Geophys. Res.*, 94-B11:15, 785-803.

EDICON, 1984: *Aeromagnetic interpretation of Lake Albert/Edward portion of the Western Rift Valley*. EDICON, Inc., Denver, Colorado, unpublished report.

Ellis, A.J., and Mahon, W.A.J., 1977: *Chemistry and geothermal systems*. Academic Press, New York, 392 pp.

Fournier, R.O., 1977: Chemical geothermometers and mixing model for geothermal systems. *Geothermics*, 5, 41-50.

Fournier, R.O., 1979: A revised equation for Na-K geothermometer. *Geoth. Res. Council, Trans.*, 3, 221-224.

Fournier, R.O., and Potter, R.W., 1982: An equation correlating the solubility of quartz in water from 25° to 900°C at pressures up to 10,000 bars. *Geochim. Cosmochim. Acta*, 46, 1969-1973.

Fournier, R.O., and Truesdell, A.H., 1973: An empirical Na-K-Ca geothermometer for natural waters. *Geochim. Cosmochim. Acta*, 37, 1255-1275.

Georgsson, L.S., Árnason, K., and Karlsdóttir, R., 1993: Resistivity sounding in high-temperature areas in Iceland, with examples from Öxarfjörður, N-Iceland and Brennisteinsfjöll, SW-Iceland. *Proceedings of the 14th PNOC-EDC Geothermal Conference, Manila*, 9 pp.

Georgsson, L.S., Fridleifsson, G.Ó., Ólafsson, M., and Flóvenz, Ó.G., 2000: The geothermal exploration of the Öxarfjörður high-temperature area, NE-Iceland. *Proceedings of the World Geothermal Congress 2000, Kyushu-Tohoku, Japan*, 1157-1162.

Giggenbach, W.F., 1980: Geothermal gas equilibria. *Geochim. Cosmochim. Acta*, 48, 2693-2711.

Giggenbach, W.F., 1984: Mass transfer in hydrothermal alteration systems – A conceptual approach. *Geochim. Cosmochim. Acta*, 48, 2693–2711.

Giggenbach, W.F., 1988: Geothermal solute equilibria. Derivation of Na-K-Mg-Ca geothermometers. *Geochim. Cosmochim. Acta*, 52, 2749-2765.

Giggenbach, W.F., 1991: Chemical techniques in geothermal exploration. In: D'Amore, F. (coordinator), *Application of geochemistry in geothermal reservoir development*. UNITAR/UNDP publication, Rome, 119-144.

Giggenbach, W.F., 1992: Isotope shift in waters from geothermal and volcanic systems along convergent plate boundaries and their origin. *Earth and Planetary Sci. Lett.*, 113, 495-510.

Giggenbach, W.F., Sheppard, D.S., Robinson, B.W., Stewart, M.K., and Lyon, G.M., 1994: Geochemical structure and position of the Waiotapu geothermal field, New Zealand. *Geothermics*, 23, 599-644.

Gíslason, G., Ngobi, G., Isabirye, E., and Tumwebaze, S. 1994: *An Inventory of three Geothermal Areas in West and Southwest Uganda*. Prepared by the United Nations for a Project of the UNDP.

Gíslason, G., Ívarsson, G., Gunnlaugsson, E., Hjartarson, A., Björnsson, G., and Steingrímsson, B., 2005: Production monitoring as a tool for field development; A case history from the Nesjavellir field, Iceland. *Proceedings of the World Geothermal Congress 2005, Antalya, Turkey*, 9 pp.

GSMD, 2008: *Exploration report by the geological team of DGSM*. DGSM, Entebbe, unpublished report.

Henley, R.W. and Ellis, A.J. 1983: Geothermal systems ancient and modern: a geochemical review. *Earth Science and Reviews*, 19, 1-50.

Henley, R.W., Truesdell, A.H., and Barton, P.B. Jr., 1984: *Fluid-mineral equilibrium in hydrothermal systems*. Society of Economic Geologists, Reviews in Economic Geology, 1, 267 pp.

Hjartarson, A., Axelsson, G., and Xu Y., 2005: Production potential assessment of the low-temperature sedimentary geothermal reservoir in Lishuiqiao, Beijing, P.R. of China, based on a numerical simulation study. *Proceedings of the World Geothermal Congress 2005, Antalya, Turkey*, 12 pp.

Jónsson, G., Kristjánsson, L., and Sverrisson M., 1991: Magnetic surveys of Iceland. *Tectonophysics* 189, 229-247.

Kato, V., 2003: *Chemistry of thermal springs in Uganda*. Geological Survey and Mines Department, Entebbe, report KVK/14, 2 pp.

Karingithi, C.W., 2009: Chemical geothermometers for geothermal exploration, *Paper presented at Short Course IV on Exploration for Geothermal Resources, organized by UNU-GTP, KenGen and GDC, at Lake Naivasha, Kenya*, 12 pp.

Marini, L., and Cioni, R., 1985: A chloride method for the determination of the enthalpy of steam/water mixtures discharged from geothermal wells. *Geothermics*, 14, 29-34.

Mosley, P.N., 1993. Geological evolution of the late Proterozoic “Mozambique belt” of Kenya. *Tectonophysics*, 221, 223-250.

Natukunda.J.F., 2013: *Exploration report on the follow up of the geology of Panyimur by the geological team of DGSM*.DGSM, Entebbe, unpublished report.

Noda, T., and Shimada K., 1993: Water mixing model calculation for evaluation of deep geothermal water. *Geothermics*, 22, 165-180.

Ólafsson, M., Fridleifsson, G.Ó., Eiríksson, J., Sigvaldasson, H., and Ármannsson, H., 1993: *On the origin of organic gas in Öxarfjörður, NE-Iceland*. Orkustofnun, Iceland, report OS-93015/JHD-05, 76 pp.

Reed, M.H., 1991: Computer modelling of chemical processes in geothermal systems: Examples of boiling, mixing and water-rock reaction. In: D’Amore, F. (coordinator), *Applications of geochemistry in geothermal reservoir development*. UNITAR/UNDP publication, Rome, 275-297.

Rodríguez, A., 2011: *Water-rock interaction of silicic rocks: an experimental and geochemical modelling study*. University of Iceland, MSc thesis, UNU-GTP, Iceland, report 1, 44 pp.

Rybach, L., and Muffler, L.J.P. (eds.), 1981: *Geothermal systems, principles and case histories*. John Wiley & Sons, Ltd., Chichester, 359 pp.

Stefánsson, A., Gíslason, S.R., and Arnórsson, S., 2000: Dissolution of primary minerals in natural waters II. Mineral saturation state. *Chemical Geology*, 172, 251-276.

Stefánsson, A., Gunnarsson, I., and Giroud, N., 2007: New methods for the direct determination of dissolved inorganic, organic and total carbon in natural waters by Reagent-Free™ IonChromatography and inductively coupled plasma atomic emission spectrometry. *Analytical ChimicaActa*, 582, 69-72.

Truesdell, A.H., 1991: Origin of acid fluids in geothermal reservoirs. *Geotherm. Res. Counc., Trans.*, 15, 289-296.

Truesdell, A.H., and Fournier, R.O., 1976: Calculations of deep temperatures in geothermal systems from the chemistry of boiling spring waters of mixed origin. *Proceedings of 2nd U.N. Symposium on the Development and Use of Geothermal Resources, San Francisco*, 1,837-844.

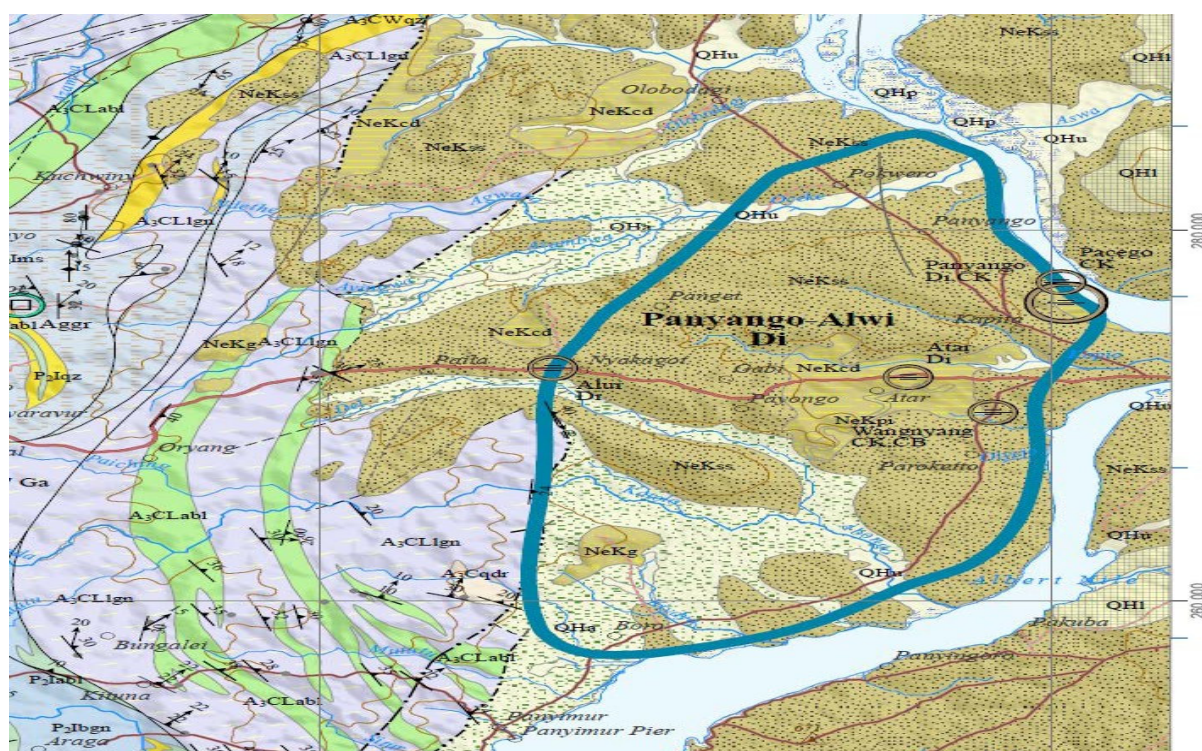
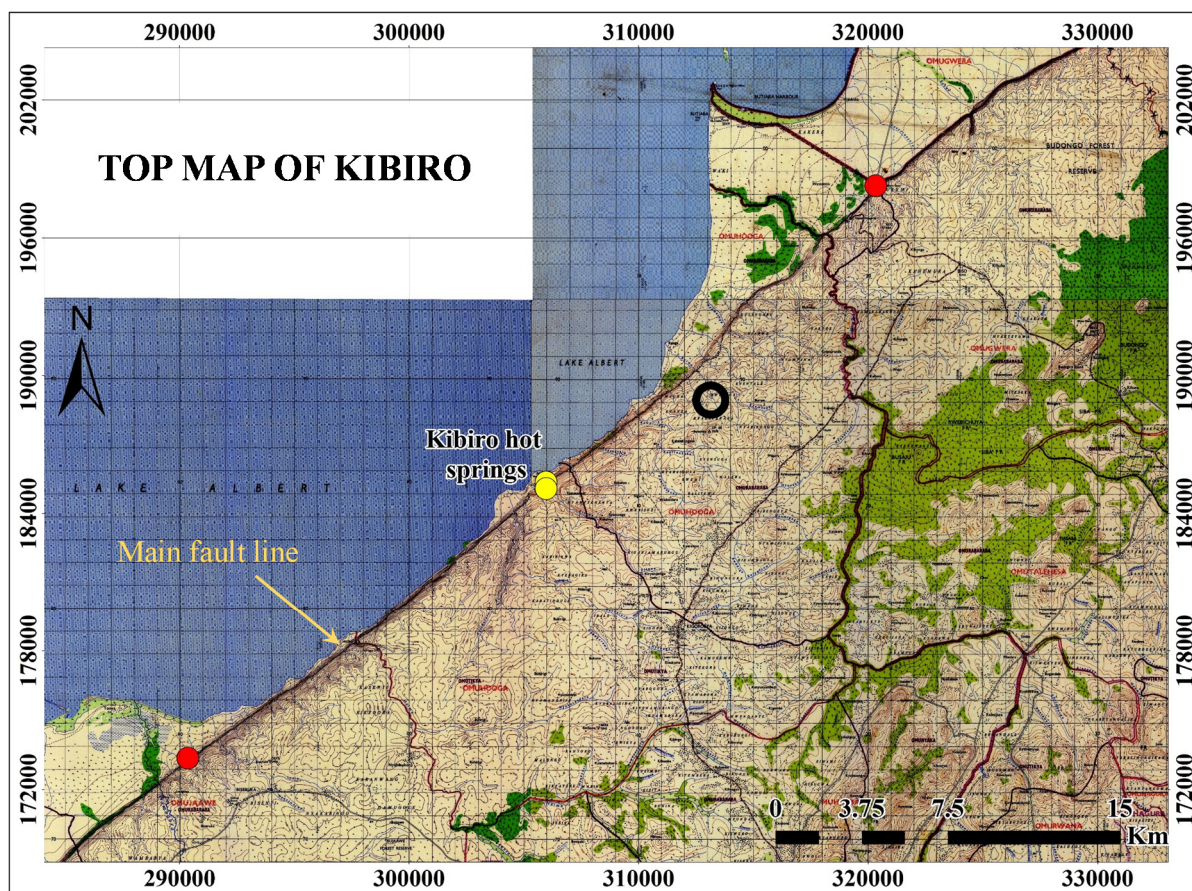
Truesdell, A.H., and Fournier, R.O., 1977: Procedure for estimating the temperature of a hot water component in a mixed water using a plot of dissolved silica vs. enthalpy. *U.S. Geol. Survey J. Res.*, 5, 49-52.

Verma, S.P., and Santayo, E., 1997: New improved equations for Na/K, Na/Li and SiO₂ geothermometers by outlier detection and rejection. *J. Volcanol. Geotherm. Res.*, 79, 9-23.

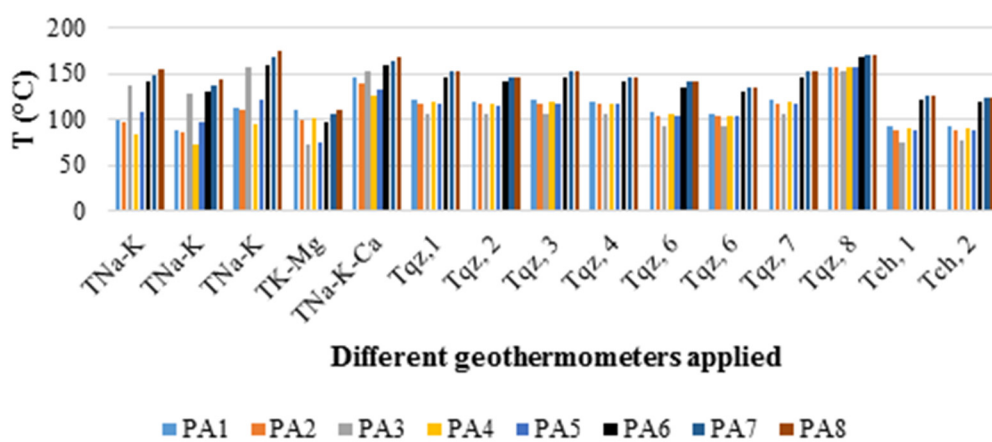
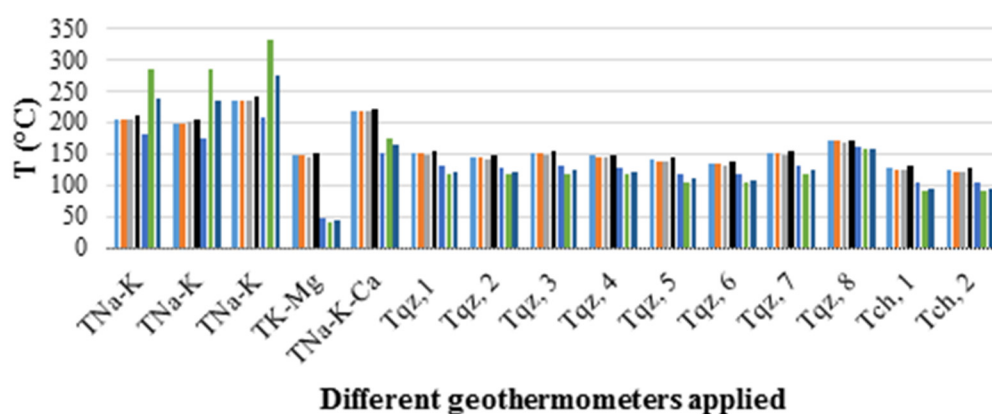
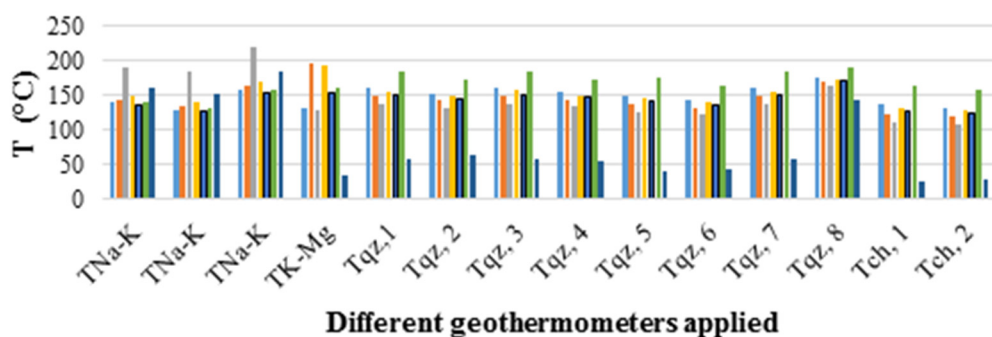
Wood, J., and Guth, A., 2012: *East Africa's Great Rift Valley, a complex rift system*. Geology.com, webpage: geology.com/articles/east-africa-rift.shtml.

Yohannes B., E. 2004: Geochemical interpretation of thermal water and gas samples from Krýsuvík, Iceland and Alid, Eritrea. Report 18 in: *Geothermal training in Iceland 2004*. UNU-GTP, Iceland, 403-438.

APPENDIX I: Maps of Kibiro and Panyimur (source DGSM, 2013)



APPENDIX II: Comparison plots of calculated temperature results obtained from sixteen different equations of geothermometers for Öxarfjörður, Kibiro and Panyimur





PRODUCTION CAPACITY ASSESSMENT OF THE HOFFELL LOW-TEMPERATURE GEOTHERMAL SYSTEM, SE-ICELAND

Li Shengtao

Centre for Hydrogeology and Environmental Geology Survey
China Geological Survey
Qiyi Middle Road 1305
Baoding 071051
CHINA
lishengtao@chegs.cn

ABSTRACT

Recently a new geothermal well named HF-1 was drilled for the purpose of space heating in the low-temperature geothermal field at Hoffell, Nesjar, in southeast Iceland. To evaluate the production capacity of the geothermal system a conceptual model of the system was established and a volumetric assessment performed. Based on the analysis of the conceptual model and the volumetric assessment, together with the Monte Carlo method, the total energy in the system is estimated as 46.9 TJ (most likely), the recoverable energy as 9.4 TJ (most likely) and the thermal power for 50 and 100 years is estimated as 6.0 and 3.0 MW_{th} (most likely), respectively. Well test data from two step-rate tests were analysed with WellTester to estimate the parameters of the system. Permeability was, thus, estimated to be around 4.8-7.0 mDarcy. The well's skin factor was around -0.1 after the well was deepened. Lumped parameter modelling was consequently used to simulate the behaviour of the reservoir to exploitation during a long-term test from April 9 to September 8, 2013. A two-tank closed model and a two-tank open model (using Lumpfit) could simulate the monitoring data very well. The parameters resulting from the Lumpfit and WellTester evaluations are quite comparable, with the permeability thickness of the reservoir around Well HF-1 estimated to be in the range of 2-5 Darcy·m. Finally, future water level predictions were calculated to estimate the probable response of the reservoir to different production scenarios for the next 10 years, both with a conservative and an optimistic model. It seems that if the system is closed, Well HF-1 can only sustain around 10 l/s for the next 10 years and if it is open, Well HF-1 will sustain around 30 l/s for 10 years. It is unlikely that the system is completely closed so 15-20 l/s seems to be the most likely production range. If the system is closed, reinjection will be necessary to increase and maintain the production capacity.

1. INTRODUCTION

Recently a new deep geothermal well, HF-1, was drilled in the Hoffell area in the Nesjar region of Skaftafellssýsla in southeast Iceland. The area is characterised by a large outlet glacier from Vatnajökull, Hoffellsjökull, and gabbroic rock, which is very uncommon in Iceland but was originally

formed deep in the earth's crust. The gabbroic rock is now visible due to uplift of the area and glacial erosion. The Hoffell area is 15 km from the town of Höfn (Figure 1).



FIGURE 1: Location of the Hoffell area in SE-Iceland (modified from Landmaelingar Íslands, 2012)

Systematic geothermal exploration in this area began in 1992. The results of the exploration, which consisted of surface geology, magnetic measurements, chemical analysis of the water and geothermal gradient exploration drilling, showed that there is good likelihood of exploitable low-temperature geothermal resources. The temperature gradient of eastern Skaftafellssýsla is generally low, but at Hoffell and Midfell it shows abnormal values of up to 186°C/km (Figure 2), and chemical composition of the water indicated a 70-80°C temperature deep in the water system (Stapi Geological Services, 1994).

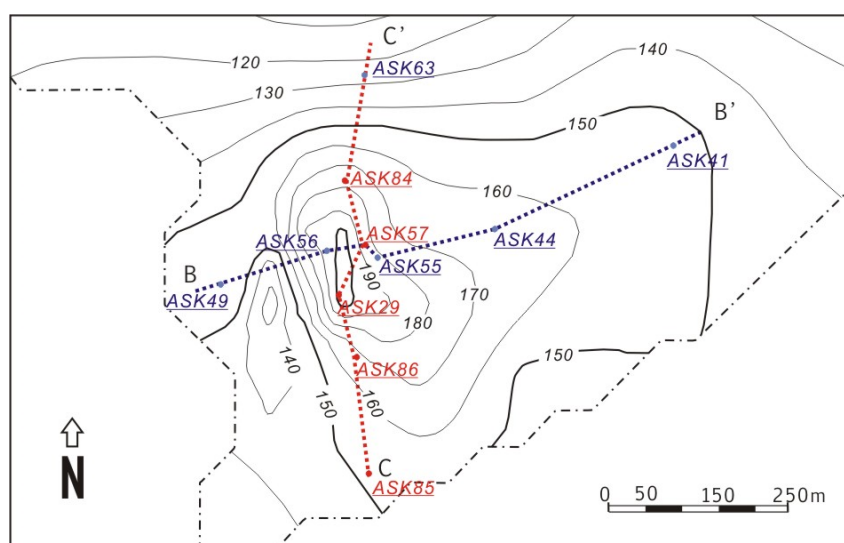


FIGURE 2: Temperature gradient map (°C/km) for the Hoffell area, showing locations of cross-sections in Figures 4 and 5 (modified from Árnadóttir et al., 2013)

RARIK (Iceland State Electricity) drilled Well HF-1, but before the well was drilled in 2012 there were already 33 boreholes in the area with a cumulative total drilling depth of 3594 metres (Figure 3). Most of the wells (20 holes) are shallow, actually shallower than 60 m, but four of the wells are over 300 m in depth.

The drilling of the borehole HF-1 (B73061) at Hoffell in Nesjar started in early November 2012 and lasted until 11 January 2013. The hole was first drilled down

to 1208 m depth. However, ÍSOR experts met with the representatives of RARIK and suggested deepening the hole by at least 200 m to see further down into the approximately 80°C hot geothermal system. Following this the hole was deepened twice before 19 February 2013, first to 1404 m and finally to 1608 m depth (Kristinsson et al., 2013a, 2013b; Kristinsson and Ólafsson, 2013).

To estimate the parameters of the aquifers intersected by the well, well tests were performed by air-lifting with the drill-string in the well, blowing out air at different depths, on three occasions. Two of these are evaluated here. The first of these was conducted on January 12-13, lasting around 10 hours with temperature of 68-69°C, and the second one on February 19-20 lasting around 12 hours with temperature of 72-73°C (Kristinsson et al., 2013a, 2013c).

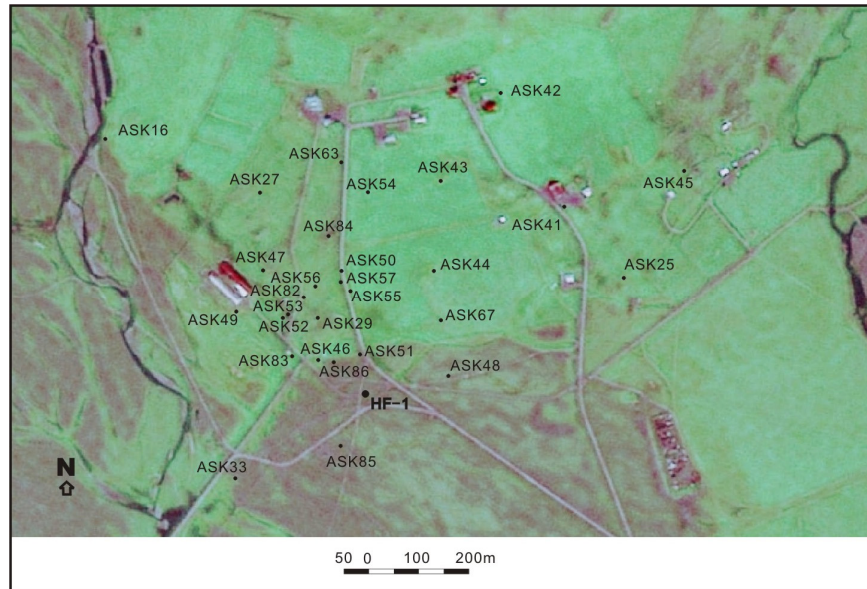


FIGURE 3: Location of borehole HF-1 and some of the exploration wells (Hjartarson et al., 2012)

After drilling was completed, long term production testing was performed to understand the reservoir behaviour and to estimate its production potential. The test started April 9, 2013. Water-level drawdown, production flow rate and temperature were monitored and recorded continuously. By September 8, 152 days of monitoring data had been collected.

This report presents the results of an assessment of the production capacity of the Hoffell low-temperature geothermal system. After a simple conceptual model was established, based on the geological background and the temperature distribution in the system, a volumetric assessment was performed to estimate the total energy and thermal power of the system, using the Monte-Carlo method. And then, well test interpretations were carried out to estimate the parameters of the reservoir. Finally, lumped parameter modelling was used to simulate the behaviour of the reservoir to exploitation and to predict the probable response of the reservoir to different production scenarios, including scenarios with reinjection.

2. CONCEPTUAL MODEL

Mountain-belt strata, which tilt steeply to the northwest, extend to the southeast of Vatnajökull glacier. The Hoffell area is located on the southern margin of the mountain belt. According to borehole and geological exploration, the bedrock of Hoffell and Midfell are mostly composed of basalt and gabbro. Several dykes, veins, cracks and faults exist in the area, but most of them are unclear. Magnetic surveying shows some small faults and cracks, which are not clearly related to the boundary of the geothermal system.

The temperature gradient was measured in 33 gradient exploration holes. According to the results, an isoline map was plotted by ISOR. It shows that typically the temperature gradient of this area is high, or up to 150°C/km and, in the core of the area the gradient is up to 200°C/km and even more (Figure 2).

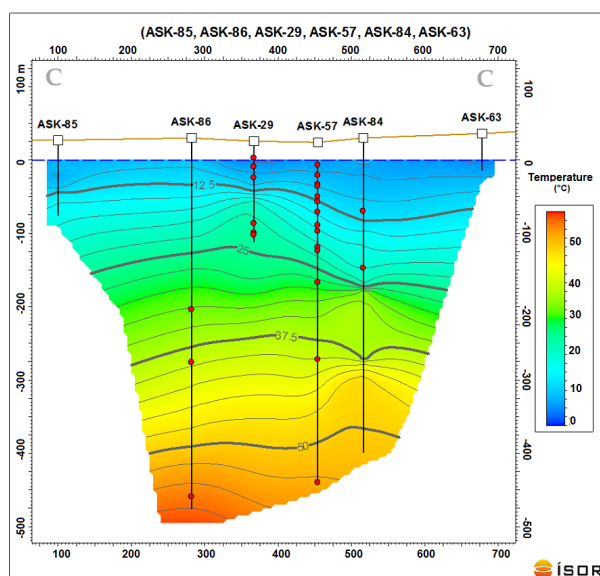


FIGURE 4: N-S temperature cross-section C-C' (Árnadóttir et al., 2013)

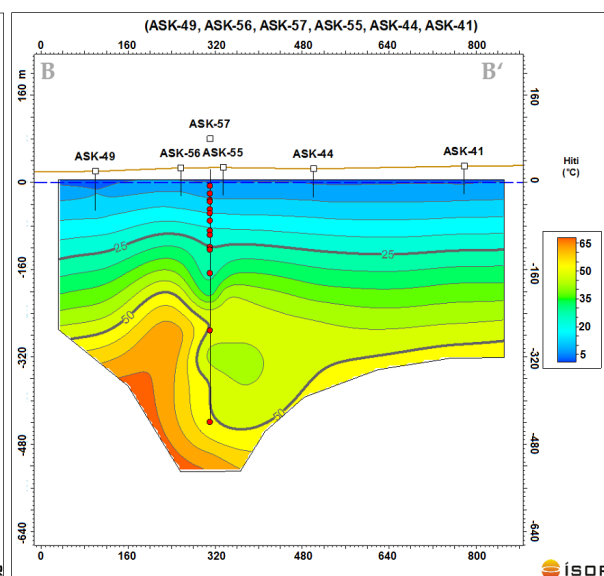


FIGURE 5: WSW-ENE temperature cross-section B-B' (Árnadóttir, et al., 2013)

Temperature cross-sections, also plotted by ISOR (Figures 4 and 5), show that the formation temperature is higher than 25°C under 100 m.b.s.l (metres below sea level), and it is higher than 50°C below around 400 m.b.s.l. The cross-sections do not reveal clearly the boundaries of the reservoir. The boundaries seem to be controlled by some geological structures at the outer edge of the geothermal system. They are likely controlled by diminishing permeability of fractures.

Temperature logs were measured in Well HF-1 from the beginning to the end of drilling (Figure 6). The estimated formation temperature of the well is about 80°C at 1000-1600 m depth. In addition, about 7.0 l/s free flow of 70°C hot water were delivered from the borehole after drilling. Considering the vertical distribution of the temperature versus depth, the main feedzones of the well must be confined above and the thermal water cools as it flows upward.

From the information above, a simple conceptual model of the Hoffell geothermal system could be established (Figure 7). It includes these main features: It is a liquid-dominated low-temperature geothermal system with about 80°C thermal groundwater in a deep confined aquifer below 600-1000 m depth. There seems to be 25-60°C thermal water in shallower layers, but it plays no major role. The reservoir seems to extend much deeper, and the boundaries of the system are still unknown. The main permeability of the system is provided by several near-vertical faults and/or fractures and the core of the system appears to be associated with the intersection of some of these.

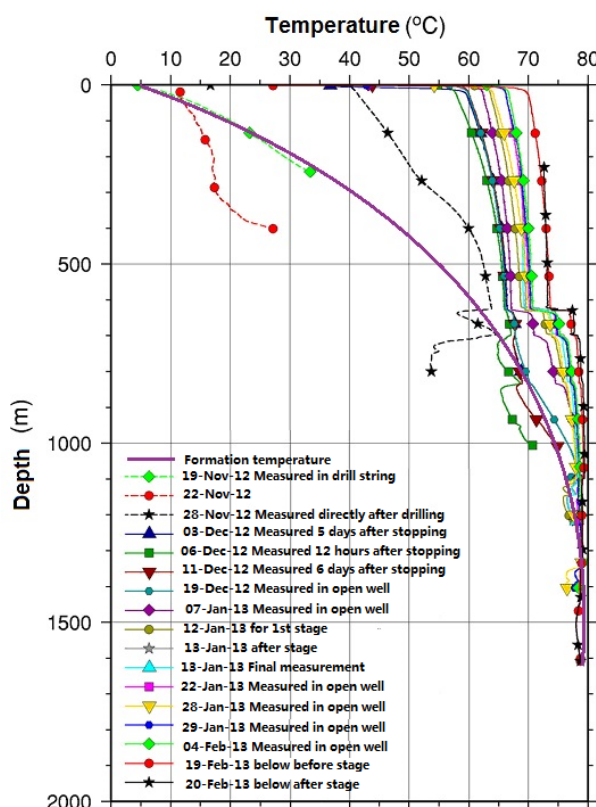


FIGURE 6: All temperature logs measured in Well HF-1 along with the deduced formation temperature profile

3. VOLUMETRIC ASSESSMENT

3.1 Theoretical background

3.1.1 Volumetric method

The volumetric method refers to the calculation of thermal energy in the rock and the fluid of a geothermal system, which could be extracted based on specified reservoir volume, reservoir temperature, and reference or final temperature. This method was originally patterned from the work applied by the USGS to the Assessment of Geothermal Resources of the United States (Muffler, 1979). In their work, the final or reference temperature is based on the ambient temperature, following the exhaust pressures of the turbines. Many, however, choose a reference temperature equivalent to the minimum or abandonment temperature of the geothermal fluids for the intended utilization of the geothermal reservoir. For space heating, as in the case under study here, the abandonment temperature is typically 30-40°C, but for electricity generation the reference temperature is usually up to 180°C for conventional power plants but lower for binary plants.

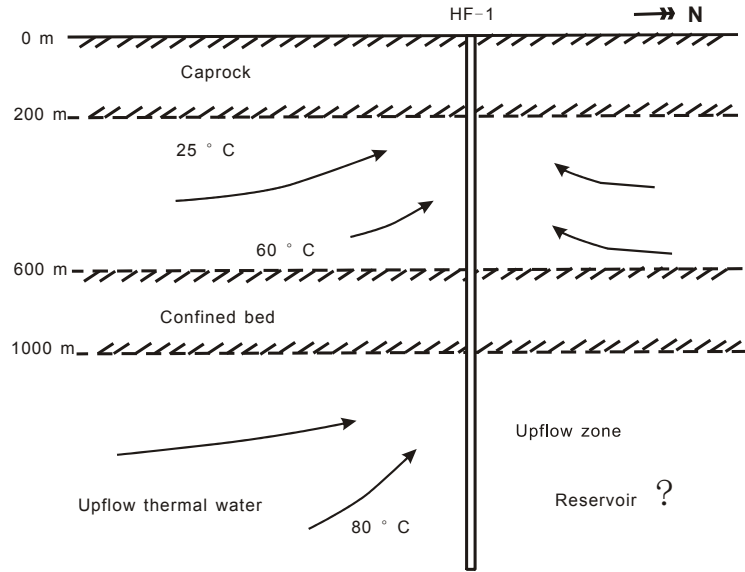


FIGURE 7: A sketch of the conceptual model of the Hoffell geothermal system

The equation used in calculating the thermal energy for a liquid dominated reservoir is as follows:

$$Q_T = Q_r + Q_w \quad (1)$$

and

$$Q_r = A \cdot h \cdot [\rho_r \cdot C_r \cdot (1 - \phi) \cdot (T_i - T_f)] \quad (2)$$

$$Q_w = A \cdot h \cdot [\rho_w \cdot C_w \cdot \phi \cdot (T_i - T_f)] \quad (3)$$

where Q_T = Total thermal energy (kJ/kg);
 Q_r = Heat in rock (kJ/kg);
 Q_w = Heat in water (kJ/kg);
 A = Area of the reservoir (m²);
 h = Average thickness of the reservoir (m);
 C_r = Specific heat of rock at reservoir conditions (kJ/kg·K);
 C_w = Specific heat of liquid (usually water) at reservoir conditions (kJ/kg·K);
 ϕ = Porosity (dimensionless);
 T_i = Average temperature of the reservoir (°C);
 T_f = Abandonment /cut-off temperature (°C);
 ρ_w = Liquid (usually water) density (kg/m³); and
 ρ_r = Rock density (kg/m³).

The volumetric method can also incorporate equations for two-phase zones and for power generation capacity estimation. However, those equations will neither be explained nor used here.

The equations presented above only apply to the total thermal energy existing in the reservoir. But it is impossible to extract the total energy from the reservoir. In order to estimate the energy that can be extracted from the system, we need to introduce a recovery factor, R , which refers to the fraction of

the stored heat in the reservoir that may be extracted to the surface. It depends on the fraction of the reservoir that is considered permeable and on the efficiency by which heat can be swept from these permeable channels, as well as on whether reinjection is applied during the utilization, and indirectly on the boundary conditions (open or closed) of the geothermal system. Using this factor, the thermal energy recoverable from the system can be calculated as follows:

$$Q_R = R \cdot Q_T \quad (4)$$

where Q_R = Recoverable thermal energy (kJ/kg); and
 R = Recovery factor (dimensionless).

The recovery factor is a measure of how easily the heat contained in the system can be extracted. It depends mostly on permeability. For fractured reservoirs, the factor has a range of 2-25% (Williams, 2007). A linear correlation between porosity and recovery factor has been proposed where, for example, porosity of 10% responds to a recovery factor of 25% (Muffler, 1979). Such a relationship is not considered realistic for volcanic rocks.

3.1.2 Monte Carlo calculation

The variables used in the volumetric method are always uncertain. What we can estimate for the reservoir are often probable values of the variables rather than certain values. To deal with the uncertain situation, a numerical calculation technique, named Monte Carlo, can be used. It is a technique that uses a random number generator to produce and extract an uncertain variable from within a distribution model for calculation in a given formula or correlation. Monte Carlo simulation became popular with the advent and power of computers.

The Monte Carlo method selects the occurrence of an unknown variable as through the random behaviour in a game of chance, for a single calculation. The calculation is repeated over and over again until the specified iteration cycle is completed. In playing dice, 1, 2, 3, 4, 5 or 6 are possible outcomes, but we don't know which outcome is the result of each roll. The same is true for the various parameters used in calculating the geothermal reserves (e.g. area, thickness, porosity, reservoir temperature, recovery factors). They all vary within a certain range of values that is uncertain for a particular sequence in the calculation. To produce the desired results, unknown variables for each reservoir property are fitted into a chosen model distribution (e.g. normal, triangular, uniform and log normal) based on predetermined conditions or criteria of the area being evaluated. The simulation then proceeds by extracting numbers representing the unknown variable and using these as input into the cells in the spread-sheet used until the process is completed (Sarmiento and Steingrímsson, 2007).

3.2 Volumetric assessment for the Hoffell geothermal system

3.2.1 Parameters and variables

The parameters used in the Monte Carlo volumetric assessment model for the Hoffell geothermal system are presented in Table 1.

Area (km²)

Because of the lack of information on the boundaries of the geothermal system, we use the temperature gradient isoline of 150°C/km as the boundary. Thus, the area should be at least 0.1 km² in area. But the actual area is likely to be larger than this. In the Monte Carlo input cell, we use the most likely: 0.15 km²; minimum: 0.1 km²; maximum: 0.2 km².

Cut-off temperature (°C)

As the well will be used for space heating we use 25°C as the cut-off temperature.

TABLE 1: Parameters and variables used in the Hoffell Monte Carlo volumetric assessment

Input parameters	Units	Minimum	Most likely	Maximum	Distribution	Random pick
Surface area	km ²	0.1	0.15	0.2	Triangle	0.2
Thickness	m	1000	2000	2500	Triangle	1776
Rock density	kg/m ³	2700	2850	2900	Triangle	2824
Porosity	%	8	10	12	Triangle	8.1
Rock specific heat	J/kg°C	910	950	980	Triangle	953
Temperature	°C	70	80	90	Triangle	74
Fluid density	kg/m ³	958.1	971.6	977.7	Triangle	972.0
Fluid specific heat	J/kg°C		4200		Fixed	4200
Recovery factor	%	15.0	20.0	22.0	Triangle	18.5
Cut-off temperature	°C		25		Fixed	25

Reservoir temperature (°C)

The formation temperature of the well seems to be about 80°C in the 1000-1600 m depth-range. In the Monte Carlo input cell, we use the most likely: 80°C; minimum: 70°C; maximum: 90°C.

Thickness (m)

The formation temperature is higher than 25°C below 100 m.b.s.l., and it grows with increasing depth. The bottom of the geothermal system is unknown. But with modern drilling techniques, at least 2500 m can be reached, and in Well HF-1 the thickness of the feedzone-interval is about 1000 m. In the Monte Carlo input cell, we use the most likely: 2000 m; minimum: 1000 m; maximum: 2500 m.

Rock density (kg/m³)

The type of rock is mostly basalt, which has a density of around 2850 kg/m³. Therefore, we use the most likely: 2850 kg/m³; minimum: 2700 kg/m³; maximum: 2900 kg/m³.

Porosity (%)

The average porosity is assumed to be 10%, as is common for basaltic rocks in Iceland. In the Monte Carlo input cell, we use the most likely: 10%; minimum: 8%; maximum: 12%.

Rock specific heat (J/kg°C)

Usually, it is about 950 J/kg°C. In the Monte Carlo input cell, we use the most likely: 950 J/kg°C; minimum: 910 J/kg°C; maximum: 980 J/kg°C.

Fluid density (kg/m³)

Water density is 971.6 (most likely), 977.7 (maximum), and 958.1 kg/m³(minimum) at 80°C, 70°C, and 90°C, respectively.

Fluid specific heat (J/kg°C)

It is about 4200 J/kg°C for pure water at a temperature of 70-100°C.

Recovery factor (%)

According to Muffler's research referred to above a porosity of 10% corresponds to a recovery factor of 25%, which seems to be a little large during actual utilization. In the Monte Carlo input cell, we use the most likely: 20%; minimum: 15%; maximum: 22%.

3.2.2 Results for Hoffell

The results obtained for Hoffell by the Monte Carlo method are presented in Table 2. According to the Monte Carlo volumetric assessment results, the total energy in the system is most likely 46.9 TJ (1 TJ = 10¹² J) and the total recoverable energy is estimated to be most likely 9.4 TJ. If the heating

system is used for 50 years, it would yield a most likely average thermal power of 6.0 MW_{th}. And if the heating system was used for 100 years, the thermal power is estimated to be most likely 3.0 MW_{th}.

The frequency distribution and cumulative frequency of the thermal power, as calculated by the Monte Carlo model, are presented in Figure 8. The mean thermal power, the median thermal power, the standard deviation, 90% upper limit, and 90% lower limit could also be extracted from the results, shown in Table 3.

TABLE 2: Most likely estimated results of the Monte Carlo volumetric assessment for Hoffell

Results	Units	Most likely	Random pick
Total Energy	TJ	46.9	38.6
Total Recoverable Energy	TJ	9.4	7.1
Thermal Power / 50 years	MW _{th}	6.0	4.5
Thermal Power / 100 years	MW _{th}	3.0	3.4

TABLE 3: Summarized results of the thermal power estimation for Hoffell according to the Monte Carlo volumetric assessment

Results	Units	Thermal power / 50 years	Thermal power / 100 years
Mean thermal power	MW _{th}	6.0	3.0
Median thermal power	MW _{th}	6.0	3.0
Standard deviation	MW _{th}	1.0	1.0
90% above (lower limit)	MW _{th}	3.3	1.7
90% below (upper limit)	MW _{th}	6.8	3.3

In addition to estimating the thermal power presented above, we need to know the corresponding average thermal water flow rate for well HF-01, which can then be compared with other results later in this report. As $Q = q \cdot c \cdot \Delta T$, where Q is the thermal power (W), c is specific heat of water

(4200 J/kg·°C), ΔT is the difference between the water flow temperature and the cut-off temperature (75 – 25 = 50°C), we can estimate q , which is the average thermal water flow rate.

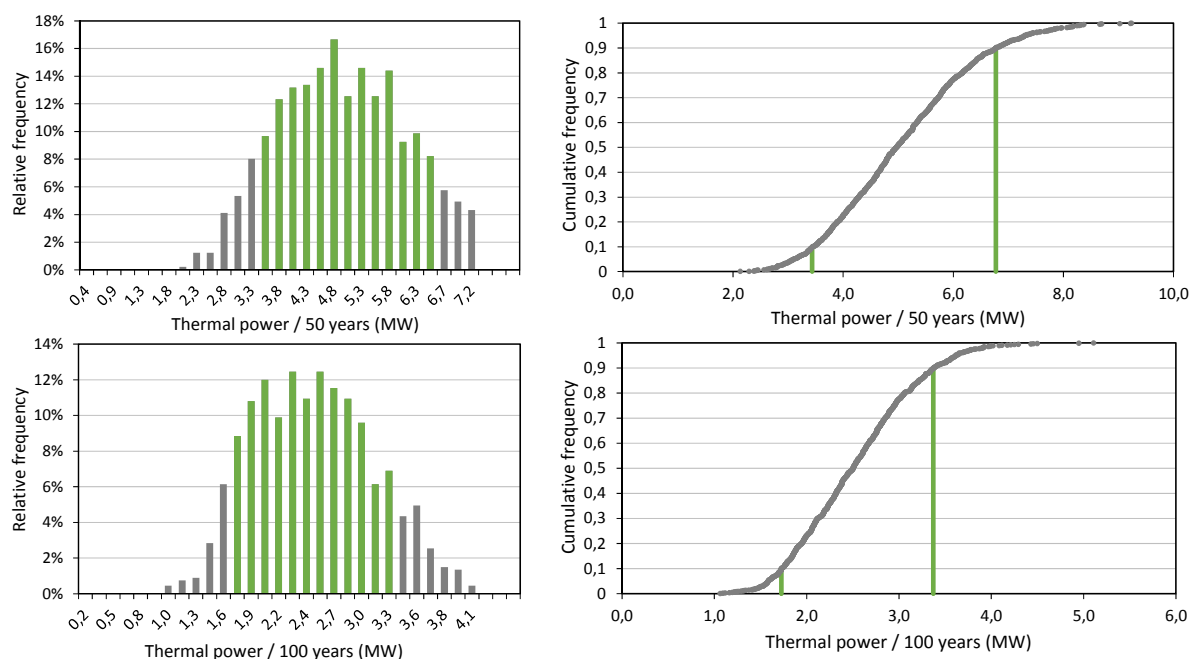


FIGURE 8: The outcome of the Monte Carlo volumetric assessment of the Hoffell system presented as probability and cumulative probability distributions for thermal power for 50 and 100 years utilization. The green columns on the left indicate the 90% probability range while the vertical green lines on the right indicate the 90% upper and lower limit of the cumulative distribution.

If the heating system will be used for 50 years with average thermal power of 6.0 MW_{th}, we need a thermal water flow rate of 28.6 l/s. And if the heating system will be used for 100 years with a thermal power of 3.0 MW_{th}, we need a thermal water flow rate of 14.3 l/s.

4. WELL TEST INTERPRETATION

4.1 Theoretical background

As an effective way to understand the hydrological conditions of a reservoir, well test analysis is, in fact, synonymous with pressure transient analysis. Pressure transients are caused by the changes in production or injection of fluids; hence, the flow rate is treated as a transient input and the pressure as a transient output (Horne, 1995). Usually, the traditional well test interpretation method does not consider the effect of temperature change during the test. On the other hand, the temperature often changes in reality due to variations in injection or flow rate, so the density of the water changes, therefore affecting the pressure. Under these conditions, a combination of the pressure response and the temperature change may give a more reasonable result (Liu, 2011).

4.1.1 Pressure diffusion equation

The basic equation of well testing theory is the pressure diffusion equation. The most commonly used solution of the pressure diffusion equation is the Theis solution, or the line source solution. Three governing laws are needed in deriving the pressure diffusion equation:

Conservation of mass inside a given control volume (in radial coordinates):

Mass flow in – Mass flow out = Rate of change of mass within the control volume

$$\rho Q - \left(\rho Q + \frac{\partial(\rho Q)}{\partial r} dr \right) = 2\pi r dr \frac{\partial(\phi \rho h)}{\partial t}$$

or

$$-\frac{\partial(\rho Q)}{\partial r} = 2\pi r \frac{\partial(\phi \rho h)}{\partial t} \quad (5)$$

Conservation of momentum, expressed by Darcy's law:

$$Q = -2\pi r h \frac{k}{\mu} \frac{\partial P}{\partial r} \quad (6)$$

where Q = Volumetric flow rate (m³/s);
 h = Reservoir thickness (m);
 k = Formation permeability (m²);
 P = Reservoir pressure (Pa);
 r = Radial distance (m); and
 μ = Dynamic viscosity of fluid (Pa·s).

Fluid compressibility (at constant temperature):

$$c_f = \frac{1}{\rho} \left(\frac{\partial \rho}{\partial P} \right)_T \quad (7)$$

where c_f = Compressibility of fluid (Pa⁻¹);
 ρ = Density of fluid (kg/m³); and
 T = Temperature (°C).

Additionally, some simplifying assumptions are needed:

- Isothermal flow;
- Homogeneous and isotropic reservoir;
- Production well completely penetrating the reservoir thickness; and
- Reservoir completely saturated with single phase fluid.

Based on these equations and assumptions, the pressure diffusion equation can be expressed as (in radial coordinates):

$$\frac{1}{r} \frac{\partial}{\partial r} \left(\frac{r \partial P(r, t)}{\partial r} \right) = \frac{\mu c_t}{k} \left(\frac{\partial P(r, t)}{\partial t} \right) = \frac{S}{T} \frac{\partial P(r, t)}{\partial t} \quad (8)$$

where c_t = Total compressibility of rock and water, $\phi c_f + (1 - \phi) c_r$, (Pa^{-1});
 c_t = Compressibility of fluid (Pa^{-1});
 c_r = Compressibility of rock (Pa^{-1});
 ϕ = Porosity (-);
 S = Storativity, $c_t h$, ($\text{m}^3/(\text{Pa} \cdot \text{m}^2)$);
 T = Transmissivity, kh/μ , ($\text{m}^3/(\text{Pa} \cdot \text{s})$);
 h = Effective reservoir thickness (m);
 k = Permeability of the rock (m^2);
 μ = Dynamic viscosity of the fluid ($\text{Pa} \cdot \text{s}$);
 $P(r, t)$ = Reservoir pressure at a distance r and time t (Pa); and
 t = Time (s).

4.1.2 Theis solution

The radial pressure diffusion equation is a partial differential equation. To solve this equation, initial and boundary conditions are required in addition to assumptions on the geometry of the reservoir (aquifer) in question. For an infinite acting, homogeneous reservoir of constant thickness, with a line-source at $r = 0$ simulating a production well, the initial and boundary conditions are (Liu, 2011):

a) Initial conditions

$$P(r, t) = P_i \quad \text{for } t = 0 \text{ and for all } r > 0 \quad (9)$$

where P_i = Initial reservoir pressure (Pa).

b) Boundary conditions

$$P(r, t) \rightarrow P_i \quad \text{for } r \rightarrow \infty \text{ and for all } t > 0 \quad (10)$$

$$2\pi r h \frac{k}{\mu} \frac{\partial P}{\partial r} \rightarrow Q \quad \text{for } r \rightarrow 0 \text{ and for all } t > 0 \quad (11)$$

The solution to the radial diffusion equation with these boundary and initial conditions is given by:

$$P(r, t) = P_i - \frac{Q\mu}{4\pi kh} W \left(\frac{\mu c_t r^2}{4kt} \right) = P_i - \frac{Q}{4\pi T} W \left(\frac{Sr^2}{4Tt} \right) \quad (12)$$

where $W(x)$ is the well function or the exponential integral function defined by:

$$W(x) = -E_i(-x) = \int_x^\infty \left(\frac{e^{-u}}{u} \right) du$$

For small values of x , i.e. $x < 0.01$, $W(x) \approx -\ln(x) - \gamma \approx -\ln(x) - 0.5772$, where γ is the Euler constant. Therefore, if (infinite acting period):

$$t > 25 \frac{\mu c_t r^2}{k} = 25 \frac{Sr^2}{T}$$

the Theis solution can be expressed as:

$$P(r, t) = P_i + \frac{2.303Q}{4\pi T} \left[\log \left(\frac{Sr^2}{4Tt} \right) + \frac{\gamma}{2.303} \right] \quad (13)$$

Equation 13 is the most commonly used equation in well test analysis. It describes pressure at a distance r at time t when producing at constant rate Q with radial flow of single phase fluid in a homogeneous reservoir model.

4.1.3 Semi-logarithmic well test analysis

By monitoring pressure changes with time, it may be possible to fit the observed pressure history to the theoretical results and identify two important parameter groups, the permeability-thickness (kh) and the storage coefficient, or storativity-thickness, ($c_t h$). By rearranging Equation 9, the solution can be written as:

$$\Delta P = P_i - P(r, t) = \frac{2.303Q}{4\pi T} \log \left(\frac{2.246T}{Sr^2} \right) + \frac{2.303Q}{4\pi T} \log(t) \quad (14)$$

The above equation is in the form of $\Delta P = \alpha + m \log(t)$. Plotting ΔP vs. $\log(t)$ gives a semi-log straight line response for the infinite acting radial flow period of a well, and this is referred to as a semi-log analysis. The line is characterized by the slope m and an intercept α , where

$$\Delta P = P_i - P(r, t), \quad \alpha = \frac{2.303Q}{4\pi T} \log \left(\frac{2.246T}{Sr^2} \right), \quad m = \frac{2.303Q}{4\pi T}$$

By determining m , the formation transmissivity can be estimated by:

$$T = \frac{kh}{\mu} = \frac{2.303Q}{4\pi m} \quad (15)$$

If the temperature is known, then the dynamic viscosity μ can be found from steam tables, thus the permeability-thickness (kh) can be calculated as follows:

$$kh = \frac{2.303Q\mu}{4\pi m} \quad (16)$$

And the storage coefficient can be obtained by:

$$S = c_t h = 2.246 \left(\frac{kh}{\mu} \right) \left(\frac{t}{r^2} \right) 10^{-\frac{\Delta P}{m}} = 2.246T \left(\frac{t}{r^2} \right) 10^{-\frac{\Delta P}{m}} \quad (17)$$

from any point on the semi-log straight line ($t, \Delta p$). The semi-log analysis is based on the location and interpretation of the semi-log straight line response that represents the infinite acting radial flow behaviour of the well. However, as the wellbore has a finite volume, it becomes necessary to determine the duration of the wellbore storage effect and the time at which the semi-log straight line begins (Horne, 1995).

Pressure propagation does not take place uniformly throughout the reservoir because it is affected by local heterogeneities. Usually, due to the ineffective pressure control during drilling or completion, some external fluids (such as mud, cement) invade into the original formation around the well and form a zone with lower permeability. Some methods (such as acidizing, hydraulic stimulation/fracturing) are often used to stimulate the reservoir next to a well so that during production a permeability improved zone can be formed. Such zones are called skin zones. It causes

an additional pressure drop ΔP_s near the wellbore in addition to the normal reservoir pressure change due to production (Horne, 2010).

$$\Delta P_s = \frac{Q\mu}{2\pi kh} \times s \quad (18)$$

where s = Skin factor (dimensionless).

A negative skin factor indicates that the near-well permeability is improved while a positive skin factor indicates that the near well surroundings are damaged (reduced permeability). The skin due to a damaged zone of radius r_s and reduced permeability k_s can be calculated from:

$$s = \left(\frac{k}{k_s} - 1 \right) \ln \frac{r_s}{r_w} \quad (19)$$

where k = Permeability of undamaged zone (m^2);
 k_s = Permeability of damaged zone (m^2);
 r_s = Radius of damaged zone (m); and
 r_w = Radius of wellbore (m).

Since the skin has a similar effect as changing the effective radius of the well, the effective well radius is $r_{w\text{eff}}$ given by:

$$r_{w\text{eff}} = r_w e^{-s} \quad (20)$$

In a well with skin, the total pressure change at the well is given by:

$$\Delta P = P_i - P(r_w, t) \approx \frac{2.303Q}{4\pi T} \left[\log(t) + \log\left(\frac{T}{Sr_w^2}\right) + 0.3514 + 0.8686s \right] \quad (21)$$

The skin effect does not change the evaluation of permeability-thickness in a semi-log analysis, but it does influence the evaluation of the storage coefficient, as shown in the following equation (the storage coefficient and skin are directly linked):

$$Se^{-2s} = 2.246T \left(\frac{t}{r^2} \right) 10^{-\frac{\Delta P}{m}} \quad (22)$$

4.1.4 Derivative plot

A derivative plot is a useful diagnostic tool for examining the effects of wellbore storage, recharge and barrier boundaries, leakage, and delayed gravity response and fracture flow. The derivative plot provides a simultaneous presentation of $\log(\Delta P)$ vs. $\log(\Delta t)$ and $\log(tdP/dt)$ vs. $\log(\Delta t)$ and provides many separate characteristics in one plot that would otherwise require different plots. Selecting an appropriate calculating method of the derivative is very important when performing derivative analysis. A straightforward numerical differentiation using adjacent points will produce a very noisy derivative (Horne, 1995).

$$t \left(\frac{\partial P}{\partial t} \right) = t_i \left[\frac{(t_i - t_{i-1})\Delta P_{i+1}}{(t_{i+1} - t_i)(t_{i+1} - t_{i-1})} + \frac{(t_{i+1} + t_{i-1} - 2t_i)\Delta P_i}{(t_{i+1} - t_i)(t_i - t_{i-1})} - \frac{(t_{i+1} - t_i)\Delta P_{i-1}}{(t_i - t_{i-1})(t_{i+1} - t_{i-1})} \right] \quad (23)$$

Here t is the time, P is the pressure, and index $(i - 1)$ and $(i + 1)$ refer to the two adjacent points to i .

If the data are distributed in a geometric progression, then the numerical differentiation with the logarithm of time can be used to remove noise from the calculations (Horne, 1995).

$$t \left(\frac{\partial P}{\partial t} \right) = \left[\frac{\ln(t_i/t_{i-1})\Delta P_{i+1}}{\ln(t_{i+1}/t_i)\ln(t_{i+1}/t_{i-1})} + \frac{\ln(t_{i+1} \times t_{i-1}/t_i^2)\Delta P_i}{\ln(t_{i+1}/t_i)\ln(t_i/t_{i-1})} - \frac{\ln(t_{i+1}/t_i)\Delta P_{i-1}}{\ln(t_i/t_{i-1})\ln(t_{i+1}/t_{i-1})} \right] \quad (24)$$

If this method still leads to a noisy derivative, the best method to reduce the noise is to use data points that are separated by at least 0.2 of a log cycle. Hence:

$$t \left(\frac{\partial P}{\partial t} \right) = \left[\frac{\ln(t_i/t_{i-k}) \Delta P_{i+j}}{\ln(t_{i+j}/t_i) \ln(t_{i+j}/t_{i-k})} + \frac{\ln(t_{i+j} \times t_{i-k}/t_i^2) \Delta P_i}{\ln(t_{i+j}/t_i) \ln(t_i/t_{i-k})} - \frac{\ln(t_{i+j}/t_i) \Delta P_{i-k}}{\ln(t_i/t_{i-k}) \ln(t_{i+j}/t_{i-k})} \right] \quad (25)$$

$$\ln(t_{i+j}) - \ln(t_i) \geq 0.2 \quad (26)$$

$$\ln(t_i) - \ln(t_{i-k}) \geq 0.2 \quad (27)$$

The value of 0.2 (known as the differentiation interval) can be replaced by smaller or larger values (usually between 0.1 and 0.5), with consequent differences in the smoothing of the noise.

4.2 HF-1 well tests during drilling

Three production well tests were performed during, and at the end of, drilling. Two of them are used in the project to estimate the parameters of the reservoir intersected by the well. The testing was done by air-lifting, i.e. with the drilling string blowing out air at different depths. The first test used for interpretation was performed January 12-13 lasting around 10 hours with a water temperature of 68-69°C when the well was at depth 1214 m, and the second was done February 19-20 lasting around 12 hours with a water temperature of 72-73°C, when the well was 1608 m deep (Kristinsson et al., 2013b; 2013c).

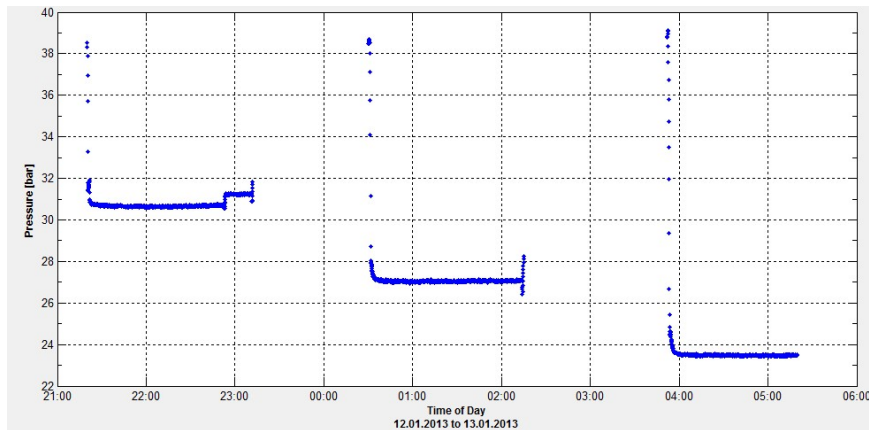


FIGURE 9: Pressure transients measured at 400 m depth in well HF-1 during the first well test, January 12 - 13, 2013

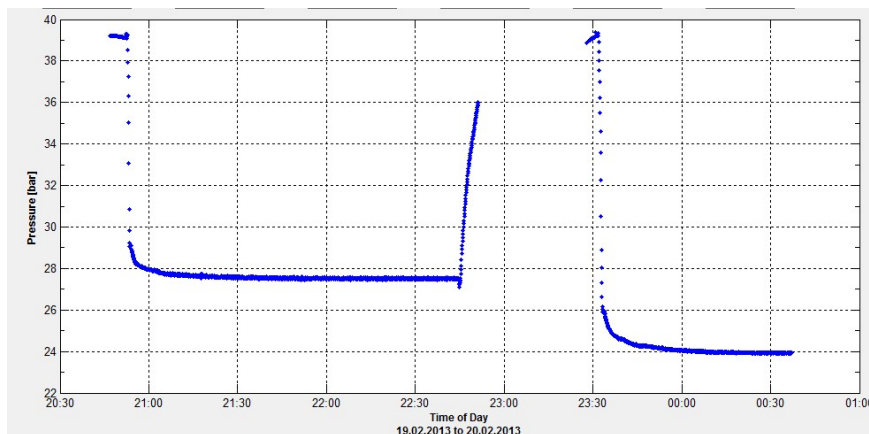


FIGURE 10: Pressure transients measured at 400 m depth in well HF-1 during the second well test, February 19 - 20, 2013

The first production test included 3 effective drawdown steps (Figure 9). Step 1 lasted from 21:20 to 23:12 on January 12, 2013, with an average production rate of 13 l/s. Step 2 lasted from 00:30 to 02:15 on January 13, 2013, with an average production rate of 15.5 l/s. Step 3 lasted from 03:52 to 05:20 on January 13, 2013, with an average production rate of 19 l/s. What should be mentioned is that the well had a free flow rate of 4.6 l/s before testing. The pressure transients in the well were measured with a pressure sensor at 400 m depth.

The second production test included 2 effective drawdown steps (Figure 10). Step 1 lasted from 20:47 to 22:44 on February 19, 2013, with an average production

rate of 25 l/s. Step 2 lasted from 23:28 February 19 to 00:37 February 20, 2013 with an average production rate of 29 l/s. The pressure was also measured with a sensor at 400 m depth. But the free flow rate of the well was 7 l/s before this test.

4.3 Well test interpretation and results

Computer software, WellTester, which was developed by ISOR (Júliússon et al., 2007), was used for the well test interpretation. To obtain a better fit between the data and theory with WellTester, each step of the two production tests was interpreted separately.

4.3.1 The first production well test

The initial parameters given in WellTester are values that are assumed to be known approximately. It is not essential for all of these parameters to be correct (with the exception of the wellbore radius) to get meaningful results from the well test analysis, but having good estimates helps in deducing information from the well test beyond the standard output. The initial parameter values used for this analysis are shown in Table 4.

The 3 steps were modelled separately to estimate the parameters of the reservoir. By trying different flow models to fit each of the steps with WellTester, the best model appeared to be a dual porosity reservoir model, with a constant pressure boundary, constant skin and wellbore storage.

In order to obtain realistic results, the reservoir thickness was set between 500 and 1000 m, the storativity was set between $3.33 \cdot 10^{-8}$ and $6.65 \cdot 10^{-8}$ m³/ (Pa·m²), the skin factor was set between -1 and 1, and the radius of investigation was set between 75 and 80 m, because there is no effect in other wells, except a slight effect in Well ASK-86 which is 75 m north of HF-1

(Kristinsson et al., 2013b). A summary of the output from WellTester, i.e. the estimated reservoir and well parameters, is listed in Table 5 and the output plots for each step with sampled data and model results are shown in Figures 11-13.

4.3.2 The second production well test

Initial parameters used for the analysis of this production well test are shown in Table 6.

The two production steps were modelled separately to estimate the parameters of the reservoir. By trying different flow models to fit each of the steps with WellTester, the best fitting model also turned out to be the dual porosity reservoir model with a constant pressure boundary, constant skin and

TABLE 4: Summary of initial parameters used for analysis of the first production well test with WellTester

Parameter Name	Values	Unit
Estimated reservoir temperature (T_{est})	69	°C
Estimated reservoir pressure (P_{est})	38	bar
Wellbore radius (r_w)	0.14	m
Porosity (ϕ)	0.10	-
Dynamic viscosity of reservoir fluid (μ)	$4.09 \cdot 10^{-4}$	Pa·s
Compressibility of reservoir fluid (c_w)	$4.45 \cdot 10^{-10}$	Pa ⁻¹
Compressibility of rock matrix (c_r)	$2.44 \cdot 10^{-11}$	Pa ⁻¹
Total compressibility (c_t)	$6.65 \cdot 10^{-11}$	Pa ⁻¹

TABLE 5: Summary of the WellTester results for the first HF-1 well test of Well HF-1 January 12-13

Parameters	Step 1	Step 2	Step 3	Units
Transmissivity (T)	$1.19 \cdot 10^{-8}$	$1.04 \cdot 10^{-8}$	$0.99 \cdot 10^{-8}$	m ³ /(Pa·s)
Storativity (S)	$5.81 \cdot 10^{-8}$	$5.65 \cdot 10^{-8}$	$5.65 \cdot 10^{-7}$	m ³ /(Pa·m ²)
Radius of investigation (r_e)	75	75	75	m
Skin factor (s)	0.60	0.67	0.67	-
Reservoir thickness(h)	873.11	849.89	850.00	m
Wellbore storage (C)	$4.52 \cdot 10^{-7}$	$2.55 \cdot 10^{-7}$	$4.24 \cdot 10^{-7}$	m ³ /Pa
Effective permeability (k)	5.57	5.00	4.76	mD

wellbore storage, as in the case of the first well test interpretation. The ranges of reservoir thickness, storativity, skin factor and radius of investigation were set the same as in the first test. The resulting parameter estimates are listed in Table 7 and the output plots for each step with sampled data and model results are shown in Figures 14-15.

Based on the results of the two interpretations, transmissivity (T) can be assumed to be in the range of $0.99 \cdot 10^{-8} - 1.45 \cdot 10^{-8} \text{ m}^3/(\text{Pa} \cdot \text{s})$; storativity (S) is in the range of $5.36 \cdot 10^{-8} - 5.81 \cdot 10^{-8} \text{ m}^3/(\text{Pa} \cdot \text{m}^2)$; permeability is in the range of 4.76-7.04 mD, which is quite low compared to other geothermal systems in Iceland. Skin factors changed from around 0.60 - 0.67 to $-0.03 \sim -0.09$ from the first well test to the second. This shows that the well is improved after deepening between the two tests.

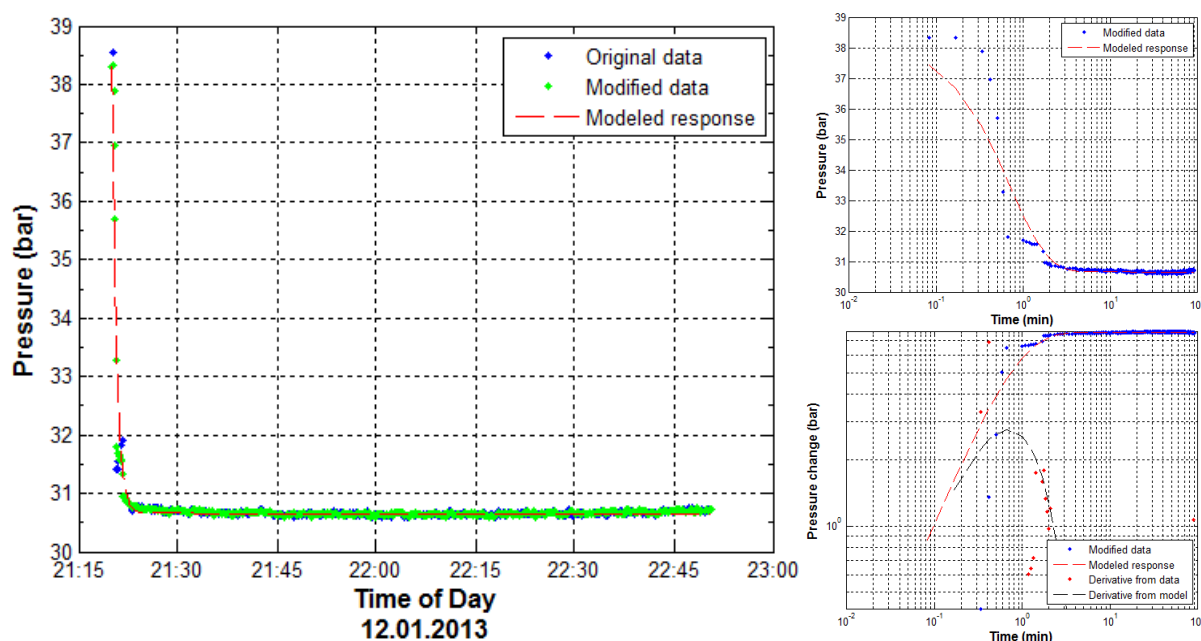


FIGURE 11: Fit between model and collected data for step 1 in the first well-test of HF-1; Left: Linear time-scale; Upper right: Logarithmic time scale; Lower right: Log-log scale

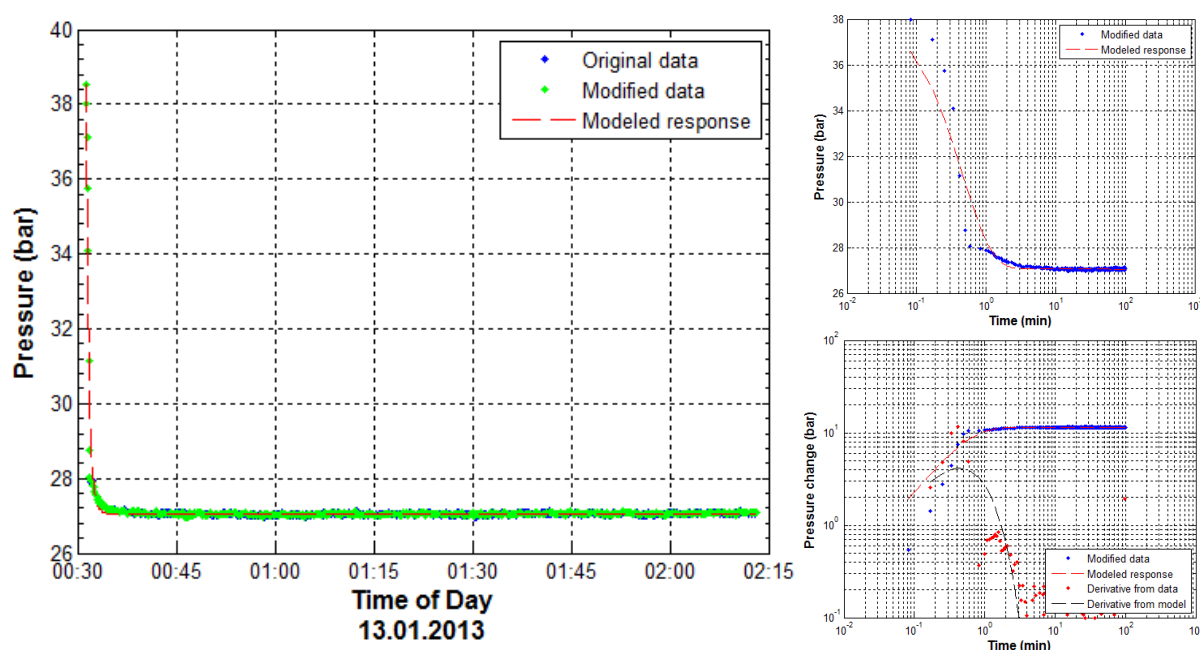


FIGURE 12: Fit between model and collected data for step 2 in the first well-test of HF-1; Left: Linear time-scale; Upper right: Logarithmic time scale; Lower right: Log-log scale

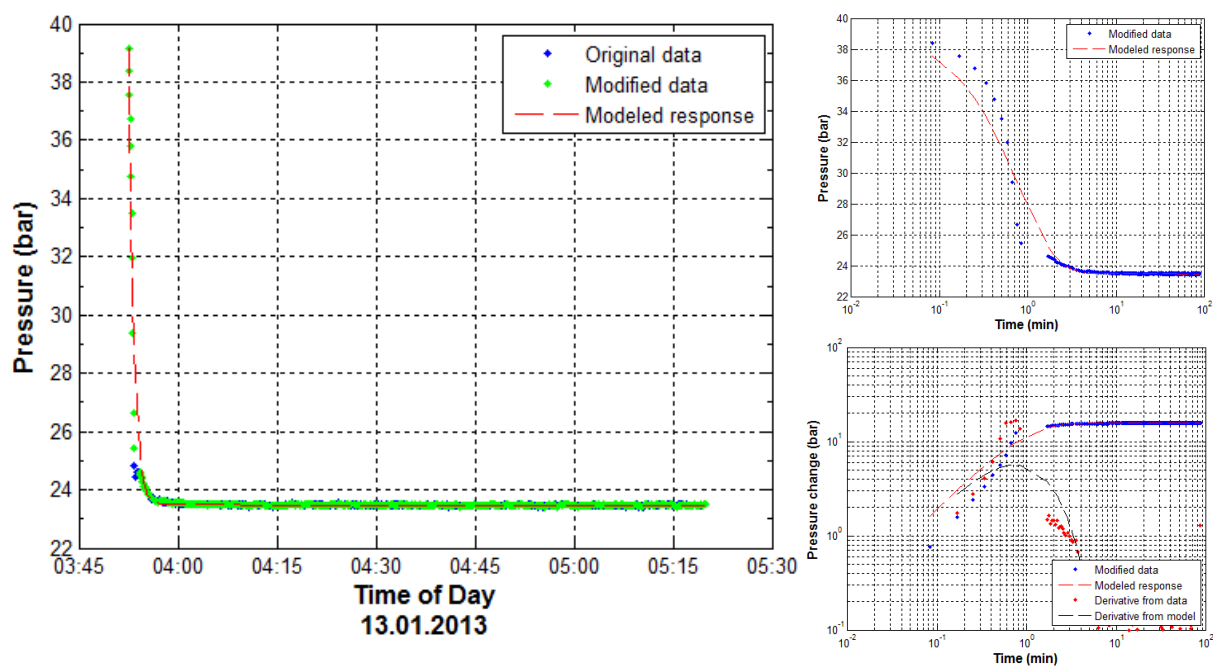


FIGURE 13: Fit between model and collected data for step 3 in the first well-test of HF-1; Left: Linear time-scale; Upper right: Logarithmic time scale; Lower right: Log-log scale

TABLE 6: Summary of initial parameters used for analysis of the second production well test with WellTester

Parameter name	Values	Unit
Estimated reservoir temperature (T_{est})	73	°C
Estimated reservoir pressure (P_{est})	39	Bar
Wellbore radius (r_w)	0.14	M
Porosity (ϕ)	0.10	-
Dynamic viscosity of reservoir fluid (μ)	$3.89 \cdot 10^{-4}$	Pa·s
Compressibility of reservoir fluid (c_w)	$4.48 \cdot 10^{-10}$	Pa ⁻¹
Compressibility of rock matrix (c_r)	$2.44 \cdot 10^{-11}$	Pa ⁻¹
Total compressibility (c_t)	$6.68 \cdot 10^{-11}$	Pa ⁻¹

TABLE 7: Summary of the WellTester results for the second HF-1 well test, February 19-20

Parameters	Step 1	Step 2	Units
Transmissivity (T)	$1.45 \cdot 10^{-8}$	$1.28 \cdot 10^{-8}$	m ³ /(Pa·s)
Storativity (S)	$5.36 \cdot 10^{-8}$	$5.49 \cdot 10^{-8}$	m ³ /(Pa·m ²)
Radius of investigation (r_e)	75	75	m
Skin factor (s)	-0.03	-0.09	-
Reservoir thickness(h)	801.74	822.10	m
Wellbore storage (C)	$5.82 \cdot 10^{-7}$	$9.55 \cdot 10^{-7}$	m ³ /Pa
Effective permeability (k)	7.04	6.06	mD

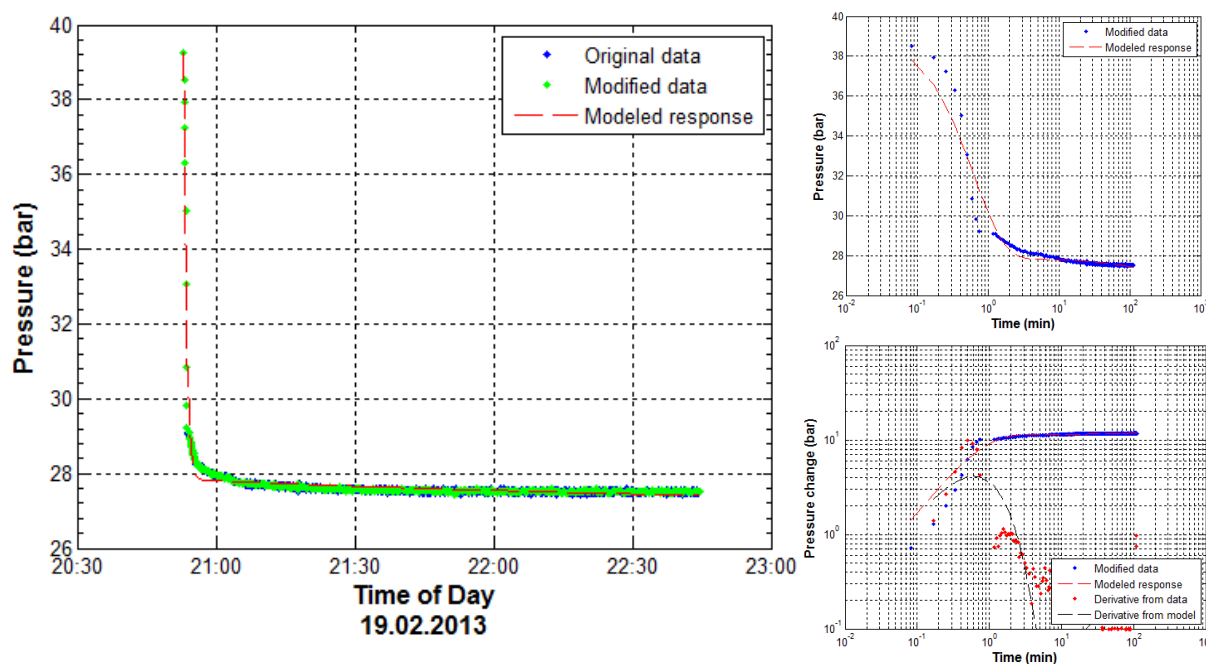


FIGURE 14: Fit between model and collected data for step 1 in the second well test of HF-1; Left: Linear time-scale; Upper right: Logarithmic time scale; Lower right: Log-log scale

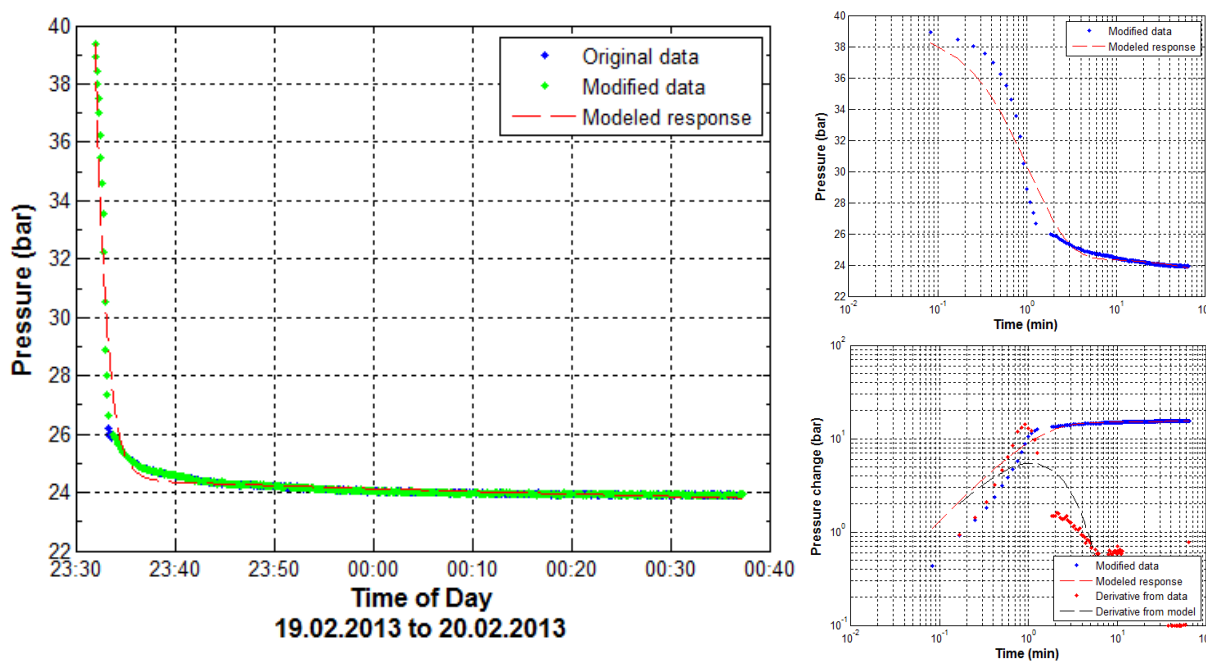


FIGURE 15: Fit between model and collected data for step 2 in the second well test of HF-1; Left: Linear time-scale; Upper right: Logarithmic time scale; Lower right: Log-log scale

5. LONG-TERM PRODUCTION TEST AND FUTURE PREDICTIONS

5.1 Theoretical background

To estimate production capacity of geothermal systems based on the prediction of changes in reservoir conditions (chiefly pressure and temperature), reservoir modelling needs to be brought in to help.

Reservoir modelling plays such an important role in geothermal assessment and management, because a lot of information can be obtained through it. It is an effective tool not only in obtaining information on physical conditions and properties of a reservoir, but also in simulating and predicting its response to exploitation.

Various modelling methods are used in geothermal research such as simple analytical modelling, lumped parameter modelling and detailed numerical modelling. Among these the lumped parameter modelling methods, which ignore geometry and integrate all the properties into lumped values, have been extensively used to simulate data on pressure (water-level) changes in geothermal systems in Iceland as well as in the P.R. China, Central America, Eastern Europe, Philippines, Turkey and many other countries during the past few decades (Axelsson, 2005). They can simulate such data very accurately, if the data quality is sufficient. Compared to other simple models, lumped parameter modelling can be the most precise. And compared to detailed numerical modelling, it is not very time consuming and does not require such comprehensive field data.

A general lumped parameter model is shown in Figure 16. It consists of a few tanks (capacitors) that are connected by flow resistors (conductors). The tanks simulate the storage capacity of different parts of the reservoir and the resistors, or conductors, simulate the permeability. A tank in a lumped model has a storage coefficient (capacitance) κ when it responds to a load of liquid mass m with a pressure increase, $p = m/\kappa$. The resistors (conductors) simulate the flow resistance in the reservoir, controlled by the permeability of the rocks. The mass conductance (inverse of resistance) of a resistor is σ when it transfers $Q = \sigma \Delta p$ units of liquid mass per unit time at the pressure difference, Δp . The pressures in the tanks simulate the pressures in different parts of the reservoir, whereas production from the reservoir is simulated by withdrawal of water from only one of the tanks (Axelsson, 1989).

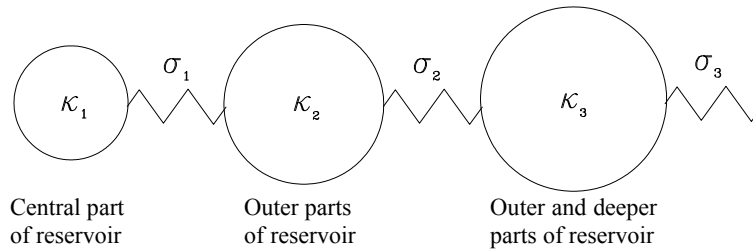


FIGURE 16: A general lumped parameter model used to simulate water level or pressure changes in a geothermal system (Axelsson et al., 2005)

Lumped models can be either open or closed. Open models are connected by a resistor to an infinitely large imaginary reservoir which maintains a constant pressure, and it can be considered optimistic since equilibrium between production and recharge is eventually reached and the water level will stabilize during long term production. On the other hand, closed lumped models are isolated from any external reservoir and can be considered pessimistic since no recharge is allowed for such models and the water level declines steadily with time during long term production. Actual reservoirs can most generally be represented and simulated by two- or three-tank closed or open lumped parameter models (Axelsson, 1989). The pressure response, $\Delta p(t)$, of a single-tank open model for production Q , assuming a step response since time $t = 0$, is given by the following equation (Axelsson and Arason, 1992):

$$\Delta p(t) = -\left(\frac{Q}{\sigma_1}\right)\left(1 - e^{-\frac{\sigma_1 t}{\kappa_1}}\right) \quad (28)$$

The pressure response of a more general open model with N tanks, to Q , assuming a step response, from time $t = 0$, is given by:

$$\Delta p(t) = - \sum_{j=1}^N Q \left(\frac{B_j}{L_j} \right) (1 - e^{-L_j \times t_i}) \quad (29)$$

The pressure response of a general closed model with N tanks is given by:

$$\Delta p(t) = - \sum_{j=1}^N Q \left(\frac{B_j}{L_j} \right) (1 - e^{-L_j \times t_i}) + Q \times C \times t_i \quad (30)$$

Coefficients B_j , L_j and C are functions of the storage coefficients of the tanks (κ_j) and the conductance coefficients of resistors (σ_j) of the model, and can be estimated by the LUMPFIT program which uses an iterative non-linear inversion technique to fit a corresponding solution to the observed pressure or water level (Axelsson, 1989).

After developing a model which matches the observed data very well with LUMPFIT, the size and properties of the different parts of the reservoir can be estimated by the conductance and capacitance coefficients obtained from the model (Vitai, 2010).

The surface area of the different parts of the system A_j can be calculated by the following equation:

$$A_j = \frac{\kappa_j}{s \cdot h} \quad (31)$$

where κ_j = Storage coefficient or capacitance (kg/Pa) or ($\text{m} \cdot \text{s}^2$);
 s = Storativity of the reservoir ($\text{kg}/(\text{Pa} \cdot \text{m}^3)$) or (s^2/m^2);
 h = Reservoir thickness (m); and
 j = 1, 2, 3, referring to the innermost, the deeper or outer and the recharge part of the reservoir, respectively, (this is valid only for a 3-tank model; for a 1-tank model, $j = 1$ and for a 2-tank model $j = 1, 2$).

Conductance σ_j can be used to estimate the permeability k_j (or permeability thickness $k_j h_j$) of the different parts of the reservoir. For 1-dimensional flow, it can be calculated as:

$$k_j = (\sigma_j L_j v) / A_{\perp j} \quad (32)$$

where k_j = Permeability of the reservoir (m^2);
 v = Kinematic viscosity of the geothermal fluid (m^2/s);
 σ_j = Conductance coefficients of resistor ($\text{m} \cdot \text{s}$) or ($\text{kg}/(\text{Pa} \cdot \text{s})$);
 $A_{\perp j}$ = Area of the reservoir perpendicular to the flow path (m^2); and
 L_j = Length of the flow path between adjacent reservoir parts, of the outermost part of the system and the surroundings (m).

For 2- dimensional flow, the permeability can be expressed as:

$$k_j = \left(\sigma_j v \ln \frac{r_{j+1}}{r_j} \right) / 2\pi h_j \quad (33)$$

where r_j = Defined in Table 8; and
 h_j = Thickness of the reservoir (m).

The radius of each tank and the equations for calculating distances from the centre to the relevant edge are listed in Table 8. The tanks in LUMPFIT may be thought of as concentric volumes where R_1 is the radius of the innermost one, R_2 the radius of the second one and R_3 of the outermost one. In the

formulas in Table 8, r_1 , r_2 , r_3 and r_4 are the distances from the centre of a tank to the outside of the relevant edge.

TABLE 8: The radius of each tank and equations to calculate distances from the centre to the relevant edge for different lumped parameter models, for 2-dimensional flow (Liu, 2011)

Model type	Equations
1-tank open model	$r_1 = R_1/2; r_2 = 3 R_1/2$
2-tank closed model	$r_1 = R_1/2; r_2 = R_1 + (R_2 - R_1)/2$
2-tank open model	$r_1 = R_1/2; r_2 = R_1 + (R_2 - R_1)/2; ; r_{2+1} = R_2 + (R_2 - R_1)/2$
3-tank closed model	$r_1 = R_1/2; r_2 = R_1 + (R_2 - R_1)/2; r_3 = R_2 + (R_3 - R_2)/2$
3-tank open model	$r_1 = R_1/2; r_2 = R_1 + (R_2 - R_1)/2; r_3 = R_2 + (R_3 - R_2)/2; r_4 = R_3 + (R_3 - R_2)/2$
	$V_1 = \kappa_1/S; V_2 = \kappa_2/S; V_3 = \kappa_3/S; R_1 = (V_1/\pi h)^{0.5};$ $R_2 = [(V_1 + V_2)/\pi h]^{0.5}; R_3 = [(V_1 + V_2 + V_3)/\pi h]^{0.5}$ where V_j is the volume of the j -th tank (m^3) and R_j is the radius of the first j tanks combined (m).

5.2 Lumped parameter modelling for the Hoffell geothermal system

After drilling of Well HF-1 was completed, a long term production test with a down-hole pump was started on April 9, 2013. The test is was still on-going at the time of writing of this report. Water-level drawdown, production flow rate and water temperature have been monitored and recorded simultaneously. Up until September 8, 152 days of monitoring data had been collected. These data provide the basis for lumped parameter modelling of the geothermal system and interpretation.

During the 152 day production process, production started with a flow rate of 20 l/s, and was later changed to 15 l/s (on August 2, 2013). The water level in the well varied in the range of -80 to -140 m depth (below surface level) while the water temperature was constant at 72°C. As was referred to in Section 4.2, Well HF-1 had a free flow rate of 7.0 l/s when it was measured on February 19, 2013. Considering this background condition, the production test/process can be assumed to be extended from 49 days to 201 days in total, from February 19 to September 8, 2013. The flow rate of the test was assumed to be 7.0 l/s with a water level of 0 m, constantly from February 19 to April 9, 2013.

During the long time production test, a step rate test was performed on May 7-8, 2013 to estimate the relationship between the water level and the production rate. According to the plot of the results (Figure 17), a trend line and its equation were calculated which show that the well has a turbulence coefficient of 0.16 $\text{m}/(\text{l/s})^2$.

Two lumped parameter models, a two-tank closed model and a two-tank open model, were used to simulate the long term monitoring data from Well HF-1, assuming an initial water level of 85 m above surface. The modelling results are shown in Figure 18. The coefficient of determination for the fit of the two-tank closed model is 98.7% while that of the two-tank open model is 99.3%. The parameters of the two models are listed in Table 9.

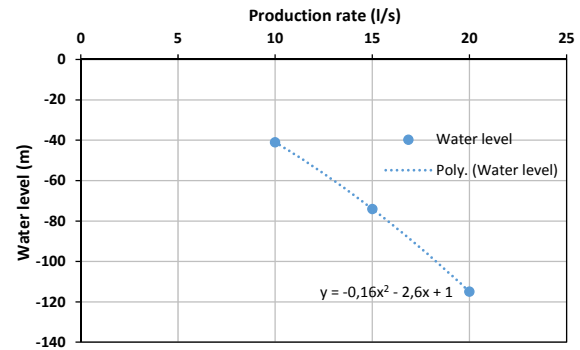


FIGURE 17: Relationship between water level and production rate during a step-rate test of Well HF-1

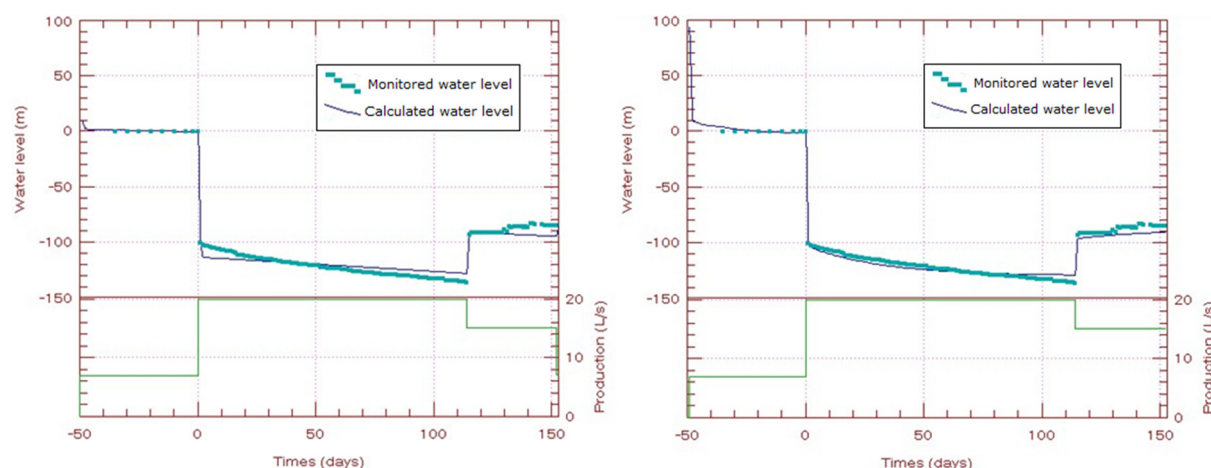


FIGURE 18: Monitored and calculated water level of Well HF-1 during the long-term production test; calculated values are those of the lumped parameter models (Left: Two-tank closed model; Right: Two-tank open model); Time $t = 0$ corresponds to April 9, 2013

Assuming a confined liquid-dominated geothermal system with 2-dimensional flow, storativity of 5.43×10^{-8} and reservoir thickness of 810 m (average of the second well test), the surface area and permeability thickness of different parts of the reservoir could be estimated according to the theoretical background. The results are listed in Table 10.

Based on the results, it is reasonable to conclude that the permeability thickness of the reservoir around Well HF-1 is around 1.9 - 2.2 D·m. This is further supported by the fact that this range is quite similar to that estimated for the short-term test analysed by WellTester.

TABLE 9: Parameters of lumped parameter models for Well HF-01

Parameters	Two-tank closed model	Two-tank open model
A_1 (data units)	32.3	52.9
L_1 (data units)	2.49	4.40
A_2 (data units)	-	0.0596
L_2 (data units)	-	0.0315
B (data units)	0.00645	-
κ_1 (kg/m ³ Pa)	0.273	0.166
κ_2 (kg/m ³ Pa)	1370	150
σ_1 (kg/sPa)	0.00000784	0.00000845
σ_2 (kg/sPa)	-	0.0000547
Root mean square misfit	5.30	3.80
Estimate of standard deviation	5.35	3.85
Coefficient of determination	98.7%	99.3%

TABLE 10: Reservoir properties of the lumped parameter models for the Hoffell reservoir

Properties	Two-tank closed model	Two-tank open model
Reservoir volume V_1 (km ³)	0.00502	0.00306
Reservoir volume V_2 (km ³)	25.2	2.76
Surface area A_1 (km ²)	0.00620	0.00378
Surface area A_2 (km ²)	31.1	3.41
Permeability thickness $k_1 h_1$ (D·m)	2.2	1.9
Permeability k_1 (mD)	2.7	2.3

5.3 Future water-level predictions

Based on the lumped parameter models established above, future predictions could be calculated to estimate the response of the water level (reservoir pressure) to exploitation. The monitoring period was relatively short, only 201 days, which is not long enough to make accurate long term predictions. However, 10 year predictions were calculated to help gain an understanding of the general water-level changes for different production flow rates.

As estimated in Chapter 3, the average thermal water flow rate was estimated to be 28.6 l/s if the heating system was used for 50 years and 14.3 l/s if the heating system was used for 100 years. These

results form the basis for the prediction production scenarios; the production rates were set as 28.6 l/s, 21.4 l/s, 14.3 l/s and 7.15 l/s.

Since we do not know whether the geothermal system is closed or open, i.e. with no recharge or with recharge equilibrating with the production, two models were adopted for the predictions. The two-tank closed model was used to get conservative predictions while the two-tank open model was used to get optimistic predictions. The prediction results of the two models are shown in Figure 19.

The results (Figure 19, Table 11) show that the water level behaves quite differently in the two models. Over the next 10 years, the water level is predicted to decline very sharply in the closed system while in the open system it reaches equilibrium. With an increasing production rate, the difference between the two becomes more obvious. The difference between the two models varies from 180 m to 658 m after 10 years with the production rates changing from 7.15 l/s to 28.6 l/s. The water level in a closed system had a greater response to large production rates than that in an open system. A large production rate (e.g. 21.45 and 28.6 l/s) would lead to a very great water level decline, if the geothermal system was a closed system. A large rate such as 28.6 l/s would cause the water level to drop down to -841 m after 10 years, which is not realistic.

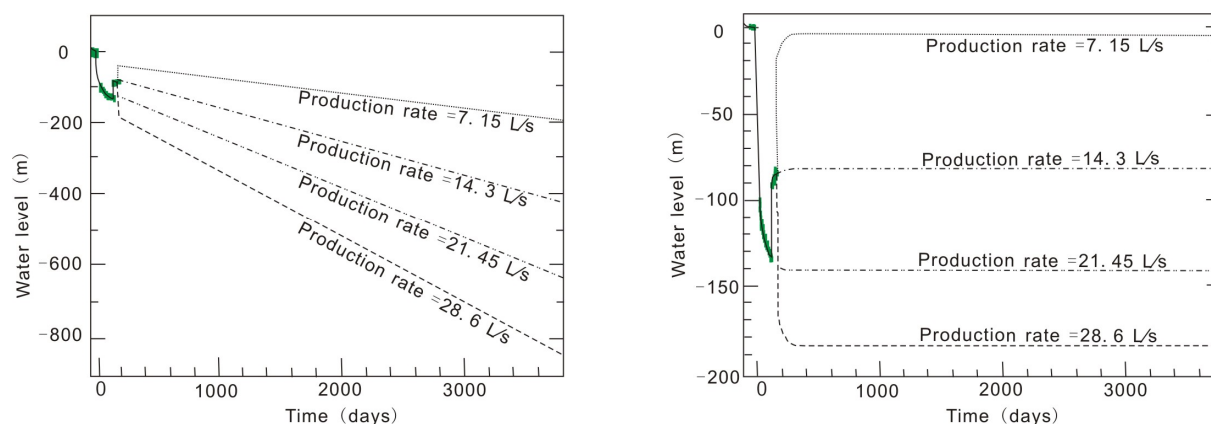


FIGURE 19: Predicted water levels in Well HF-1 for the next 10 years for different production rates (Left: Conservative predictions using two-tank closed model; Right: Optimistic predictions using two-tank open model)

TABLE 11: Predicted water levels in Well HF-1 after 10 years production (m)

Production flow rate (l/s)	Conservative model (closed system)	Optimistic model (open system)	Difference between the two models
7.15	-187	-6.5	180
14.3	-421	-81.6	339
21.45	-639	-140	499
28.6	-841	-183	658

Based on the results, it seems that if the system is open, Well HF-1 will sustain around 30 l/s for 10 years; if the system is closed, the well can only sustain around 10 l/s for the next 10 years (pump at depth of about 200 m). It is also very unlikely that the system is completely closed; maybe its behaviour will be somewhere in-between the two models, which means 15 to 20 L/s is the most likely production range. However, to reduce negative influence, reinjection will be necessary, especially for large production rates if the system turns out to be relatively closed.

6. CONCLUSIONS

The purpose of this research project was to perform a production capacity assessment for the Hoffell low-temperature geothermal system in SE-Iceland, using three different reservoir engineering research methods. The conclusions of the work can be summarized as follows:

- Based on the geological background and subsurface temperature distribution of the system, a simple conceptual model was established. The system is a liquid-dominated low-temperature geothermal system with about 80°C thermal groundwater existing in deep confined aquifers below 600-1000 m depth, with flow controlled by near-vertical fractures.
- A volumetric assessment was performed using the Monte Carlo method. The total energy of the system was estimated to most likely be 46.9 TJ and the total recoverable energy was estimated to most likely be 9.4 TJ. If the energy was used for a heating system for 50 years or 100 years, it corresponds to a most likely thermal power of 6.0 MW_{th} or 3.0 MW_{th} with a production flow rate of 28.6 l/s or 14.3 l/s, respectively.
- Interpretation of two well tests performed in Well HF-1 was carried out with the software WellTester to estimate the parameters of the reservoir. The transmissivity (T) was estimated to be in the range of $0.99 \cdot 10^{-8} - 1.5 \cdot 10^{-8} \text{ m}^3/(\text{Pa} \cdot \text{s})$ and the permeability in the range 4.8 – 7.0 mDarcy. The skin factor of the well improved from around 0.6 to -0.1 from the first well test to the second. This shows that the well was obviously improved by deepening between the two tests.
- Lumped parameter modelling was used to simulate the behaviour of the reservoir to exploitation, based on the results of a 5 month production test, using the software Lumpfit. A two-tank closed model and a two-tank open model were used to simulate the long term monitoring data from Well HF-1, and a good fit between the data and the models was achieved. Permeability, estimated on the basis of the Lumpfit-results and from WellTester, was quite comparable, indicating that the permeability thickness of the reservoir around Well HF-1 was about 2 – 5 Darcy·m.
- Predictions were calculated to estimate the probable response of the water level in Well HF-1 to different production rates for the next 10 years. It seems that if the system is open, Well HF-1 will sustain around 30 l/s for 10 years. If the system is closed, the well will only sustain around 10 l/s for the next 10 years, according to the present predictions. It is very unlikely that the system is completely closed, however; maybe the behaviour will be between the two possibilities, which means that 15 – 20 l/s is the most likely production range. Reinjection will be necessary if the system turns out to be relatively closed.
- It should be noted that the future predictions are quite uncertain, as witnessed by the great discrepancy between the open and closed predictions. As more production experience is gained, this discrepancy will diminish. It may also be mentioned that an unusually great turbulence pressure-drop occurred in well HF-1, corresponding, for example, to about 65 m at 20 l/s production. If more successful production wells are drilled in the area, the production capacity of the system would likely increase as the turbulence pressure loss would decline as production was distributed among more wells.
- Further research is highly necessary in the Hoffell area as the geothermal system needs to be described in more detail for a more accurate assessment and with precise locations of new wells. The sustainable production capacity of the reservoir should be revealed if more wells are drilled in the future. Once exploitation starts, monitoring and comprehensive management of this valuable resource should be performed carefully and scientifically.

ACKNOWLEDGEMENTS

I wish to extend my gratitude to the United Nations University - Geothermal Training Programme, in particular to Dr. Ingvar B. Fridleifsson and Mr. Lúdvík S. Georgsson, for offering me the opportunity to participate in the 35th session of the training programme. I am grateful to Mr. Ingimar G. Haraldsson, Ms. Thórhildur Ísberg, Mr. Markús A. G. Wilde and Ms. Málfríður Ómarsdóttir for their kind assistance and arrangements. I express my wishes to the other 2013 UNU Fellows for our friendship without borders.

Sincere thanks to my supervisor Dr. Gudni Axelsson for his intelligent advice and support. Special thanks go to Dr. Svanbjörg H. Haraldsdóttir, Mr. Sigurdur G. Kristinsson, Mr. Magnús Ólafsson and Ms. Sigrún Gunnarsdóttir for their patient guidance and help in the research project. I would also like to thank all the lecturers and staff of the UNU-GTP, ÍSOR and Orkustofnun for their excellent lectures, generous sharing, and efficient assistance. RARIK (Iceland State Electricity) is acknowledged for allowing use of the Hoffell data.

I am also grateful to my employer, China Geological Survey and Ministry of Land and Resources, for supporting me with the opportunity to study abroad. Particular thanks to Dr. Li Wenpeng, Dr. Guo Jianqiang, Dr. Tong Yuanqing, and Ms. Li Hongying for their recommendations.

Deepest thanks go to my family, my wife and my daughter, for their love and support during the last six months.

REFERENCES

Axelsson, G., 1989: Simulation of pressure response data from geothermal reservoir by lumped parameter models. *Proceedings of the 14th Workshop on Geothermal Reservoir Engineering, Stanford University, Stanford, CA, United States*, 257-263.

Axelsson, G., and Arason, Th., 1992: *LUMPFIT, automated simulation of pressure changes in hydrological reservoirs. Version 3.1, user's guide*. Orkustofnun, Reykjavík, 32 pp.

Axelsson, G., Björnsson, G., and Quijano, J., 2005: Reliability of lumped parameter modelling of pressure changes in geothermal reservoirs. *Proceedings of the World Geothermal Congress 2005, Antalya, Turkey*, 8 pp.

Árnadóttir, S., Egilsson, Th., Blischke, A., Stefánsson, H.O., and Jóhannesson, H., 2013: *Televiwer and well measurements at Hoffell and Midfell in Nesjar and the location of well HF-1*. ÍSOR – Iceland GeoSurvey, Reykjavík, report ÍSOR-2013/017 (in Icelandic), 81 pp.

Hjartarson, Á., Flóvenz, Ó.F., and Ólafsson, M., 2012: *Probability of geothermal resources near Hoffell and Midfell in Nesjar: research and material examined*. ÍSOR – Iceland GeoSurvey, Reykjavík, report ÍSOR-2012/002 (in Icelandic), 23 pp.

Horne, R.N., 1995: *Modern well test analysis, a computer aided approach* (2nd edition). Petroway Inc., USA, 257 pp.

Horne, R.N., 2010: *Geothermal well testing*. UNU-GTP, Iceland, unpublished Visiting Lecturer's notes.

Júlíusson, E., Grétarsson, G., Jónsson, P., 2007: *Well Tester 1.0b. User's guide*. ÍSOR – Iceland GeoSurvey, Reykjavík, report ÍSOR-2008/063, 26 pp.

Kristinsson, S.G., Helgadóttir, H.M., Stefánsson, H.O., Tryggvason, H., Pétursson, F., and Ólafsson, M., 2013a: *Drilling well HF-1: drilling history, geology and capacity measurements*. ÍSOR – Iceland GeoSurvey, Reykjavík, report ÍSOR-013/030 (in Icelandic), 49 pp.

Kristinsson, S.G., and Ólafsson, M., 2013: *Hoffell in Nesjar, performance measurement for well HF-1 with depth at 1404 m*. ÍSOR – Iceland GeoSurvey, Reykjavík, report ÍSOR-13013 (in Icelandic), 8 pp.

Kristinsson, S.G., Ólafsson, M., Stefánsson, H.O., and Tryggvason, H., 2013b: *Performance measurements for well HF-1 in Hoffell*. ÍSOR – Iceland GeoSurvey, Reykjavík, report ÍSOR-13006 (in Icelandic), 10 pp.

Kristinsson, S.G., Stefánsson, H.O., Pétursson, F., Hafstad, Th.H., and Ólafsson, M., 2013c: *Hoffell in Nesjar: the third air-lift testing of well HF-1, preliminary results*. ÍSOR – Iceland GeoSurvey, Reykjavík, report ÍSOR-13020 (in Icelandic), 8 pp.

Liu Jiurong, 2011: Well test interpretation and production prediction for well SD-01 in the Skarðdalur low-temperature field, Siglufjörður, N-Iceland. Report 19 in: *Geothermal training in Iceland 2011*. UNU-GTP, Iceland, 391-416.

Muffler, L.P.J. (editor), 1979: *Assessment of geothermal resources of the United States - 1978*. USGS Circular 790, Arlington, VA, United States, 163 pp.

Sarmiento, Z.F., and Steingrímsson, B., 2007: Computer programme for resource assessment and risk evaluation using Monte Carlo simulation. *Paper presented at "Short Course on Geothermal Development in Central America – Resource Assessment and Environmental Management", organized by UNU-GTP and LaGeo, Santa Tecla, El Salvador*, 11 pp.

Stapi Geological Services, 1994: *Geothermal exploration in East-Skaftafellssýsla in the years 1993-1994*. County committee of East-Skaftafellssýsla, report, 200 pp.

Vitai, Z.M., 2010: *Sustainable use of low-temperature geothermal reservoirs in Iceland*. University of Iceland and University of Akureyri, School for Renewable Energy Science, MSc thesis, 95 pp.

Williams, C.F., 2007: Updated methods for estimating recovery factors for geothermal resources. *Proceedings of the 32nd Workshop on Geothermal Reservoir Engineering*. Stanford University, Stanford, CA, United States, 6 pp.



COMPARISON OF BOREHOLE AND SURFACE RESISTIVITY AT THEISTAREYKIR, NE-ICELAND

Long Hui

Centre for Hydrogeology and Environmental Geology Survey
China Geological Survey
Qiyi Middle Road 1305, Baoding 071051
CHINA
longhui@chegs.cn

ABSTRACT

Resistivity logs from five boreholes in the Theistareykir high-temperature geothermal field and resistivity from surface exploration are compared in this report. The resistivity is also compared to the first appearance of alteration minerals. The available resistivity logs from each section of drilling are combined for each well and inserted into Petrel, a 3D modelling software, for viewing geological and geophysical data. A 3D model of the resistivity which had previously been found by 3D inversion of MT soundings from field work performed by ÍSOR had previously been inserted into Petrel. The resistivity well logs are averaged to the same resolution as the TEM and MT model. The previous study of TEM and MT resistivity from Theistareykir shows a conventional resistivity structure for a high-temperature geothermal system in Iceland, consisting of a low resistivity cap underlain by a high-resistivity core in the uppermost 2 km and a deep seated low-resistivity layer. The resistivity in boreholes and resistivity from the inversion of TEM and MT have slight differences but, in general, show a very good correlation in all of the studied wells. The study also confirmed what had previously been shown that lower resistivity was linked with smectite-zeolite zonation and the higher resistivity with chlorite and epidote-amphibole deeper down in the wells, which show alteration with increasing temperature, respectively.

1. INTRODUCTION

The Theistareykir high-temperature geothermal field is located in the volcanic zone in NE-Iceland and has abundant geothermal surface manifestations (Figure 1). The active part of the geothermal area is located in the eastern part of the Theistareykir fissure swarm. Hydrothermal alteration is also evident on the western side of the swarm, but surface thermal activity seems to have died out there some 1000 years ago (Grönvold and Karlsdóttir, 1975). The geothermal activity covers a 10.5 km² area; the most intense activity is on the northwest and northern slopes of Mt. Baejarfjall and in the pastures extending from there northwards to the western part of Mt. Ketilfjall. If the old alteration in the western part of the swarm is considered to be a part of the thermal area, its coverage is nearly 20 km² (Ármannsson et al., 1986; Saemundsson, 2007).

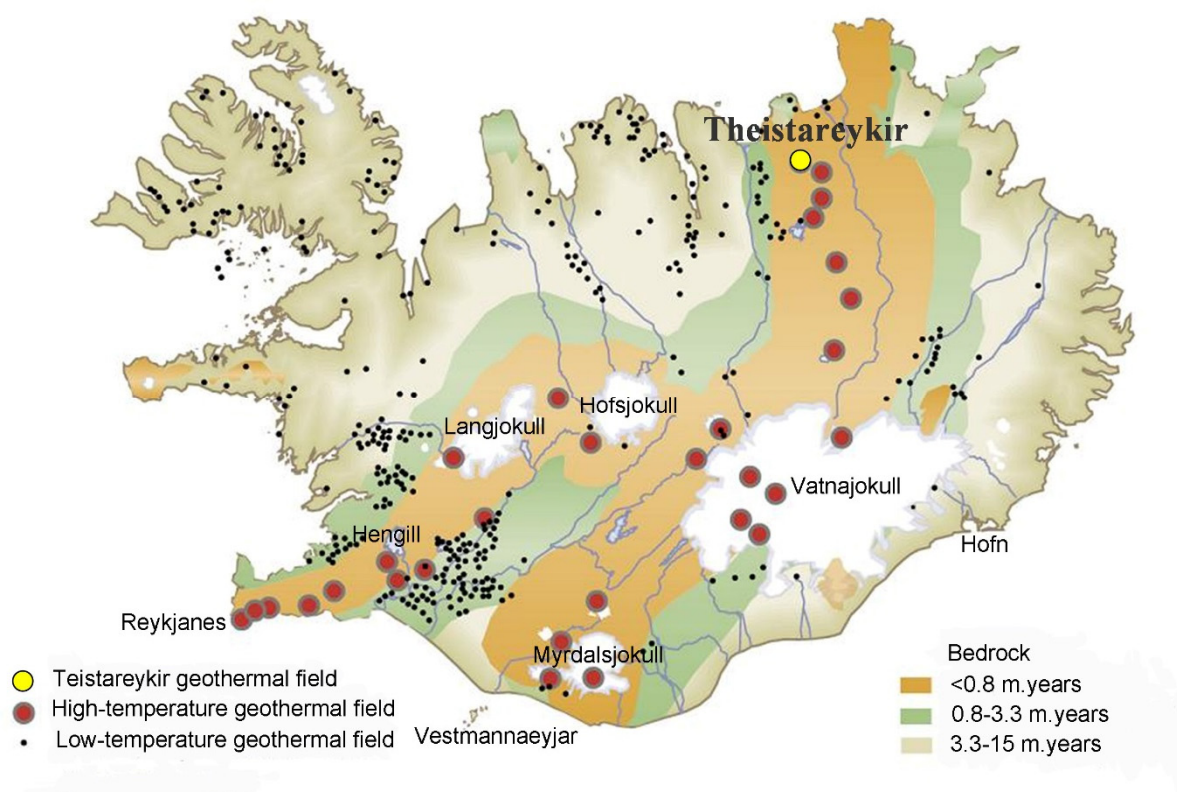


FIGURE 1: The location of Theistareykir high-temperature field in NE-Iceland in the eastern

There are nine geothermal exploration wells in the Theistareykir geothermal field, five of which are involved and processed in this project, ThG-01, ThG-02, ThG-03, ThG-04 and ThG-09. ThG-01, ThG-02, ThG-03 and ThG-09 are vertical wells and ThG-04 is a directional well.

The main purpose of this project was to compare resistivity in boreholes to resistivity from surface exploration at Theistareykir in NE-Iceland (Figure 2). The well logs were compared to a 3D resistivity model from a previous study found by inversion of TEM and MT electromagnetic soundings (Karlsson et al., 2012). The well logs in the five boreholes which had been collected in different sections of drilling were depth corrected and combined to form a continuous well log for the relevant wells. The resistivity of the basaltic rock was found to have a strong relationship to hydrothermal alteration which is mainly dependent on formation temperature (e.g. Arnason et al., 1987; 2000). Therefore, the relationship between hydrothermal alteration and resistivity was also studied.

2. BACKGROUND

2.1 Geology of Iceland

The world's known geothermal resources are mainly located in three main areas: 1) Circum Pacific geothermal belt, from the Mid-Atlantic ridge eastwards across the Mediterranean; 2) the Middle East to Yunnan, China, Tibet geothermal belt; and 3) the African Great Rift Valley and the Red Sea Rift Valley geothermal belt (Lu et al., 2012). These zones are active crustal anomalies, including volcanoes and earthquakes. Iceland belongs to the Mid-Atlantic ridge geothermal belt in the North Atlantic area near the Arctic Circle. This is the boundary between the North American and Eurasian tectonic plates. The two plates are moving apart at a rate of about 2 cm per year. As a result of its location, Iceland is one of the most tectonically active places on Earth, resulting in a large number of volcanoes and hot springs.

Earthquakes are frequent, but rarely cause serious damage due to strict building regulations. More than 200 volcanoes are located within the active volcanic zones (Björnsson et al., 2010) stretching through the country from the southwest and south to the northeast, shown in Figure 1. At least 30 of them have erupted since the country was settled. In the western belt 12 high-temperature geo-thermal fields are located from Reykjanes to Langjökull and Hofsjökull; 17 high-temperature geothermal fields are located in the eastern belt from Vestmannaeyjar, Mýrdalsjökull, and Vatnajökull to Krafla and Theistareykir.

In the volcanic zones there are at least 20 high-temperature areas containing steam fields with underground temperatures reaching 200°C within 1000 m depth (Figure 1). These areas are directly linked to the active volcanic systems. About 250 separate low-temperature areas with temperatures not exceeding 150°C in the uppermost 1000 m are found mostly in the areas flanking the active zone. To date, over 600 hot springs with temperature over 20°C have been located (Björnsson et al., 2010). It can be seen from Figure 1 that all of the high-temperature geothermal fields are located within the active volcanic zones passing through Iceland (shown in brown colour) where the bedrock is very young geologically or less than 0.8 million years. The low-temperature geothermal fields are located outside the active volcanic zones. The most exploited fields are crowded together in the southwest of Iceland and the others are found almost all over the country. The bedrocks in the low temperature areas are older than the active volcanic zones where the high-temperature geothermal areas are located.

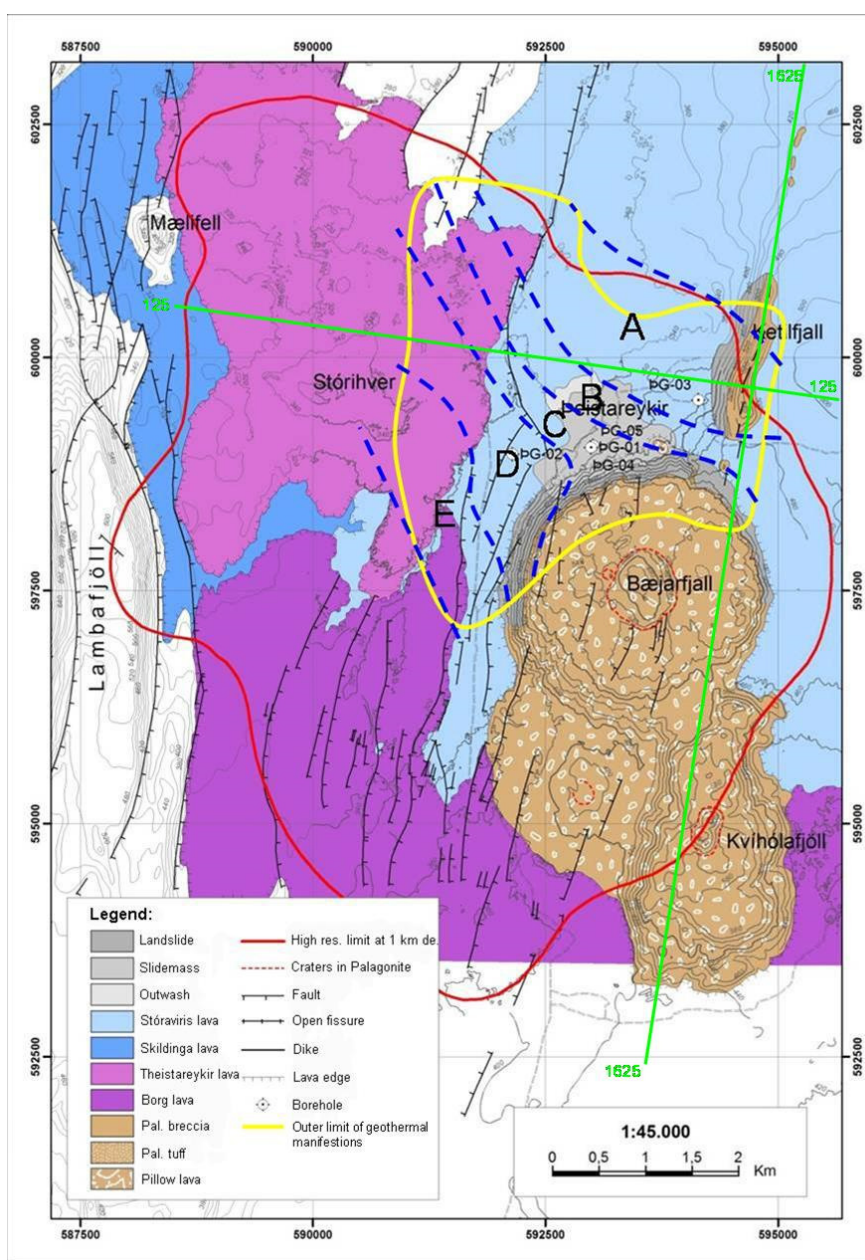


FIGURE 2: A geothermal map of the Theistareykir geothermal system and division into five sub-areas (adapted from Saemundsson, 2007; and Ármannsson et al., 1986)

2.2 Geology at Theistareykir

The regional geology has been described in detail by Saemundsson (2007) that added to, and expanded on, the work of Torfason in Gíslason, et al. (1984). The local geology is summarized in Figure 2, adapted from Saemundsson (2007). The area is covered in lavas all of which, except for one, which originate from eruptions in the last stages of the Ice Age or shortly afterwards. The bedrock at Theistareykir area is divided into breccia (hyaloclastites) ridges formed by sub-glacial eruptions during the ice age, interglacial lava flows, and recent lava flows (younger than 10,000 years), all of which are basaltic (Ármannsson et al., 1986). The oldest hyaloclastite formations in the region are exposed in the west in Lambafjöll. In the vicinity of the geothermal centre at Theistareykir, Ketilfjall is the oldest hyaloclastite formation. It formed in a fissure eruption underneath the Quaternary ice-sheet on a 4 km long fissure, stretching from Lake Mývatn in the south and to the ocean in Öxarfjörður in the north (Saemundsson, 2007). Baejarfjall and Kvihólafjöll are younger lavas or table-mountains formed by eruptions on short fissures or single volcanic events. The recent flows in the area are surprisingly old as only one of the flows is considered to be younger than 10,000 years old. This is Theistareykir lava (Figure 2) which is considered to be over 2500 years old. The lava flows have partially buried the sub-glacial table-mountains and ridges so their “roots” are hidden. The absence of younger volcanic products is intriguing when considering potential heat sources for the geothermal activity. Presumably intrusions at depth are providing the heat to drive the hydrothermal system.

Ármannsson et al. (1986) divided the surface area with abundant geothermal manifestations into five sub-areas, shown in Figure 2, three of which (A, C and D) appeared promising for drilling; nine wells, five of which are included in this project, were drilled in these three sub-areas.

2.3 Borehole logging

Geophysical well logging is done at the end of each drilled section of a borehole. In this project, 64" resistivity and 16" resistivity were mainly processed and studied while temperature, Caliper, gamma and Neutron-Neutron were partly processed and used to compare, and partly for depth correction.

Two simultaneous resistivity measurements were made during the logging, 16" resistivity and 64" resistivity. The resistivity of the formation can be measured with several different measuring techniques at present. ÍSOR uses the so called normal configuration. The setup consists of four electrodes, two of which are fixed on the logging probe in the well (Stefánsson and Steingrímsson, 1990); the third one is placed at the surface (mud pit), and the armour of the logging cable is used as the fourth electrode. The two electrodes used for measuring the resistivity indirectly were located at 16" and 64" above a current electrode which was at the end of the cable (Haraldsdóttir et al., 2010). The 16" resistivity and 64" resistivity were calculated from a uniform current and measured the potential at the relevant electrode. The 16" resistivity was often higher than the 64" resistivity. The well logs penetrated the wall rock of the borehole, where the 64" resistivity showed a deeper penetration a little further into the formation than the 16" resistivity. The results were stored in two files as measured depth and a signal.

Temperature logs were measured during and after drilling which were applied to locate feed zones and feed points and detect cross flow between aquifers. An important purpose of the temperature logs during drilling is to evaluate cooling due to injection of cold water into the well, and thereby obtain information to prevent other temperature sensitive logging tools from damage. In this project, formation temperatures from the ÍSOR database were used for getting a rough overview of the temperature in the area and view it in context with the results in the project. The formation temperatures had already been prepared by analysing the warm up temperature logs.

The Caliper log is a measurement which can show information about a wells' true diameter. The diameters from the Caliper log have often been shown to be larger than what the drill bit size would predict (Steingrímsson, 2011a). The Caliper logging probes are of many different types. The most

common probes are with 3, 4 or 6 arms and up to tens of arms are used in special cases, for example inspection of the casing. The applications of the Caliper log are very extensive, such as for the locations of cavities, evaluation of cementing, casing corrosion and casing damages, comparison of the Caliper logs with the lithological section of the borehole, and for finding the end of the casing in the logs to depth correct them in the presented project. ÍSOR uses 3 and 4 arms Caliper tools. From the 3 arms Caliper tool, the output is the averaged diameter at each depth, but the output from a 4 arms tool is X and Y diameters and can reveal if the well is elliptical and if possibly casing damages exist at some depth.

The gamma ray log is a passive measurement, where a detector is lowered into the well to register the natural radiation from the surrounding geological formations (Steingrímsson, 2011b). The purpose of gamma ray logging is to distinguish between rock formations, while acidic rocks contain more radioactive isotopes or elements than basaltic rocks and sometimes an increase in gamma can be a sign of metamorphosed rocks. The neutron-neutron has one neutron source and one or two detectors, the latter one is called a dual neutron device (far and near sensors).

Before processing the data, the units of gamma and neutron-neutron logs should first be checked for consistency in units, after which the logs are depth corrected. The logs are plotted in a graph with other geological wire line logs from the same well for evaluating the porosity of the formation and the geological sections found in the drill cuttings, distinguishing different rock types, determining the stratigraphy of the lithological section, thus identifying important information by comparing the different logs.

2.4 Boreholes at Theistareykir

Extensive surface manifestations such as fumaroles, mud pools and sulphur deposition (Ármannsson, 2011) have been studied previously in the Theistareykir area (Figure 3). Detailed geological and geophysical surveys were carried out prior to drilling. A number of shallow wells were drilled to the depth of 100-200 m to survey groundwater patterns and to obtain a suitable source of cold water before drilling the deep exploration wells. Figure 3 reveals the locations and trajectories of drilled wells in the Theistareykir field at present and Table 1 shows information about the wells in the presented study, such as if the well is vertical or directional, time of drilling, total measured depth, elevation of the well top and finally the highest measured temperature and the corresponding measured depth in the well.

Icelandic borehole reports show that Wells ThG-01, ThG-02 and ThG-03 are vertical wells drilled in 2002, 2003 and 2006 to the depth of 1953, 1723 and 2659 m, respectively. Well ThG-04 was drilled directionally in 2007, from the same well pad as Well ThG-01, towards the southeast beneath Mt. Baejarfjall, with a final depth of 2239 m. Wells ThG-05 to ThG-08 were not included in this project. Well ThG-09 was drilled as a vertical well with a final depth of 2194 m in 2012. The highest temperature and the corresponding depths are shown in Table 1, where it is clear that Well ThG-02 is the coldest of the wells in this study, but it is also shallow while the others have fairly similar temperatures.

TABLE 1: Information about boreholes in Theistareykir geothermal field

Well name	ID	Type	Drill time	Depth (m)	Elevation (m a.s.l.)	Highest temp(°C)/Depth(m)
ThG-01	60401	Vertical	2002	1953	352	331.6/1933
ThG-02	60402	Vertical	2003	1723	330	241.6/1697
ThG-03	60403	Vertical	2006	2659	400	380.1/2633
ThG-04	60404	Directional	2007	2239	352	319.5/2213
ThG-09	60409	Vertical	2012	2194	350	345.0/2163

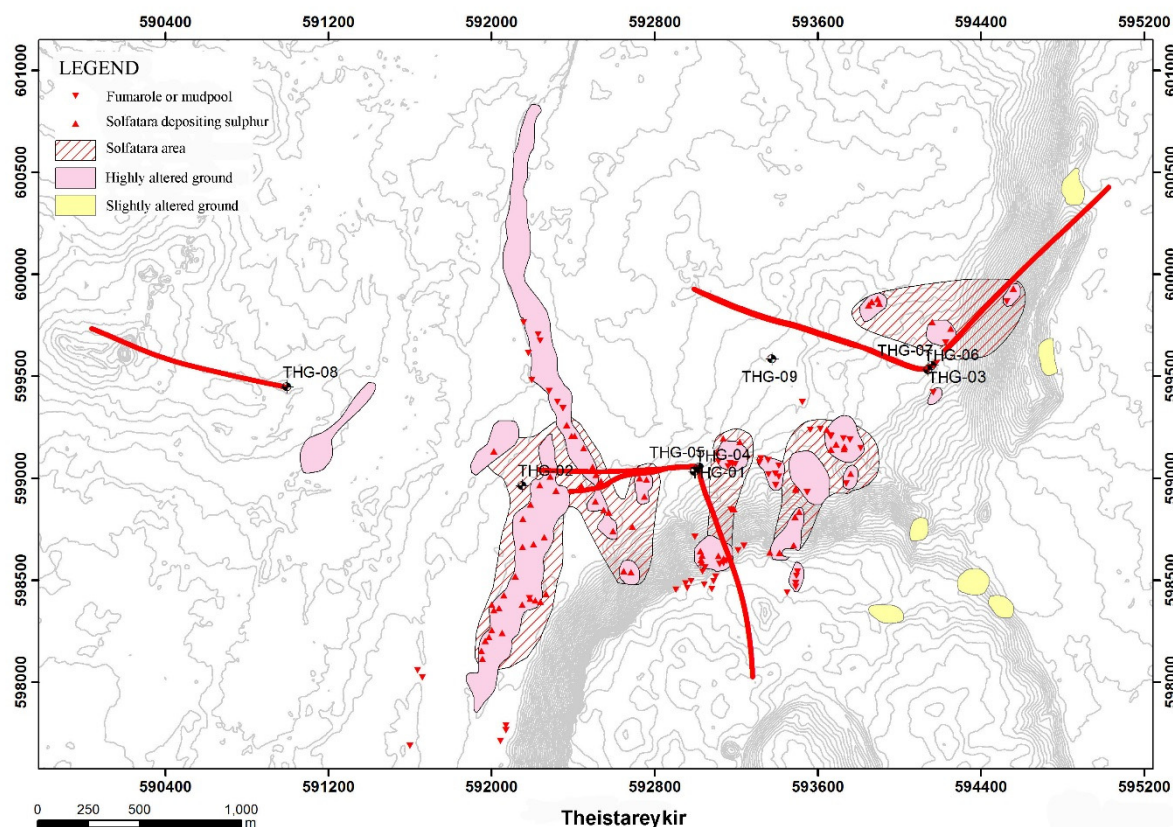


FIGURE 3: The trajectories of boreholes at Theistareykir geothermal field; A dot indicates a vertical well and red lines show the trajectories of directional wells (adapted from Ármannsson, 2011)

3. PREVIOUS STUDIES

3.1 Surface exploration

Surface exploration started in the 1970s and continued intermittently to the middle of the 1980s (Gíslason et al., 1984). In the late 1990s, interest in the field increased again and the first deep exploratory well was drilled in the summer of 2002 (Table 1). Concomitant with exploratory drilling, additional field surveys were undertaken including TEM (Karlsdóttir et al., 2006) and MT (Karlsdóttir et al., 2012), and resistivity surveys (Gudmundsson et al., 2008). In addition, geological mapping in greater detail led to a much improved understanding of the age relationships of late quaternary and recent formations (Saemundsson, 2007).

Mapping of fumaroles, mud-pools and gas-seeps and monitoring of gas and fluids in terms of abundances and isotopic constitution, has been an ongoing effort for the last three to four decades (e.g. Ármannsson et al., 2000; Ármannsson, 2004; and Ármannsson, 2011; Darling and Ármannsson, 1989). On the basis of the chemical and isotopic data, the geothermal field was subdivided into five distinct subfields, three of which were considered suitable for exploitation (Figure 2). The oxygen and hydrogen isotopic composition of steam condensates suggested that the fluid is recharged from further inland with a contribution from local precipitation (Darling and Ármannsson, 1989).

3.2 Mineral alteration

Primary minerals usually tend to alter to secondary minerals due to hydrothermal alteration that are either stable or meta-stable in geothermal environments. Hydrothermal alteration is affected by permeability, temperature, duration of hydrothermal activity, rock type, pressure and fluid composition. It has been shown that the stability of many hydrothermal alteration minerals is highly dependent upon temperature through a large number of studies in different areas. Identification of temperature dependent alteration minerals during drilling gives very useful evidence regarding the temperature range to be expected in a well. Mineral alteration indicates the temperature at the time of formation at which they were formed (Kristmannsdóttir, 1979; Franzson, 1994). Geothermal systems are, however, dynamic with repeated cycles of warming and cooling, so there is not always a perfect match between mineral alteration and the present formation temperature. The analytical methods used to identify the alteration minerals are stereo microscope, petrographic microscope, X-ray diffractometer, fluid inclusion and electron microprobe analyses. Special tools and machines are used in these methods to study and identify alteration minerals and their relationship qualitatively or quantitatively after samples are selected from the available and/or selected lithologic units.

Previous studies of hydrothermal alteration are temperature dependent and often relate well with the respective formation temperature (Franzson, 1994). As can be seen from Figure 4, a smectite-zeolite zone dominates at a wide temperature range between 50 and 200°C, then transforms downwards into mixed-layer clays in the range of about 200-230°C, where it transforms to chlorite at 230°C. Chlorite-epidote alteration forms at a temperature range between 240 and 280°C while epidote-actinolite forms between 280 and 350°C.

Previous studies showed that the resistivity characteristics of a high-temperature field are a low-resistivity cap underlain by a high-resistivity core as seen at Nesjavellir (Árnason et al., 1987). In Figure 5, the low resistivity is reflected in the smectite-zeolite zone, while the high resistivity is reflected in the chlorite zone and the chlorite-epidote zone. These changes conform to the transformation of smectite to chlorite which involves changes of crystal types and, most importantly, the rapid decrease in the water contents of the alteration assemblage. The resistivity of the formation has been related to a small amount of the conductive minerals contained in rocks which enhances the conductivity of the formation, causing the resistivity to be low. On the other hand, the open layer structure of smectite provides a good dimensional channel for ion conduction. Ions can migrate between layers under the action of adsorption of polar molecules, contributing to low resistivity, hence, the ionic change capacity in the crystals. The low-resistivity cap is a highly conductive layered silicate with a high ionic change capacity, whereas the chlorite and chlorite-epidote zones are bound in a more resistive crystalline lattice.

The main hydrothermal minerals in the Theistareykir high-temperature geothermal field are smectite, zeolite, chlorite, epidote, amphibole, feldspar and quartz (Anette K. Mortensen et al. at ÍSOR, unpublished work). The alteration pattern suggests a progressive increase in temperature with depth.

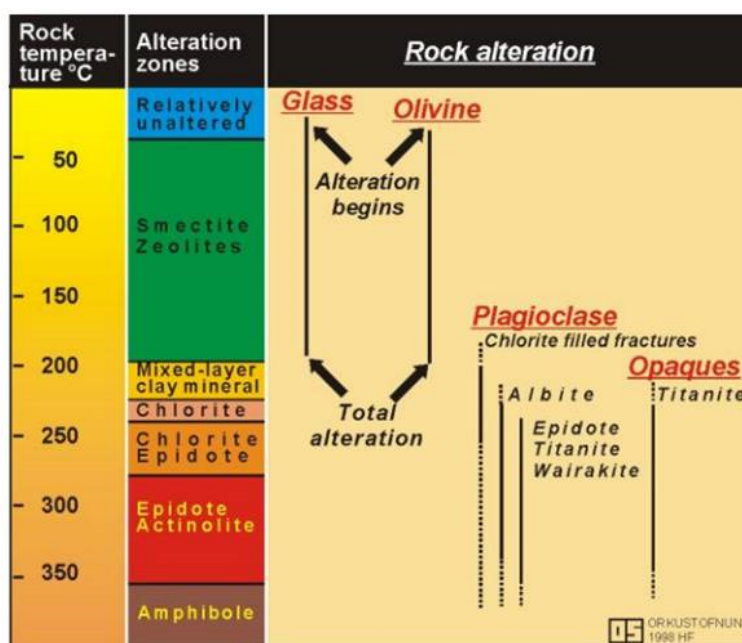


FIGURE 4: Rock temperature, alteration zones and the corresponding rock alteration (Franzson, 1994)

The strata observed in the wells shows thick basaltic sequences (tuff, breccias and dikes). The number of intrusions and possible intrusions increases with depth, especially at the lowest part of the wells.

3.3 Resistivity from surface exploration, TEM and MT

3.3.1 Resistivity of geothermal systems in Iceland

Resistivity found from the inversion of TEM and MT surface surveys of high-temperature geothermal systems in the basaltic rocks of the volcanic zones of Iceland generally reveals similar resistivity structures which correlate with the alteration mineralogy zoning (Árnason et al., 2000). A low-resistivity cap was observed on the upper margins of the reservoirs, underlain by a high-resistivity core. Extensive comparison of this resistivity structure to well data has revealed a consistent correlation to the zones of dominant alteration minerals, where the low-resistivity cap coincides with the smectite-zeolite zone and the transition to the high-resistivity core within the mixed layer clay zone. Within the high-resistivity core, chlorite and epidote are the dominant alteration minerals. The alteration mineralogy is, on the other hand, mostly related to temperature. This has the important consequence that the resistivity structure can be interpreted directly in terms of temperature while the alteration formed possibly by historic temperature. The upper boundary of the low-resistivity cap is generally found where the temperature is in the range of 50–100°C and the transition to a high-resistivity core occurs at temperatures in the range of 230–250°C (Árnason et al., 2000).

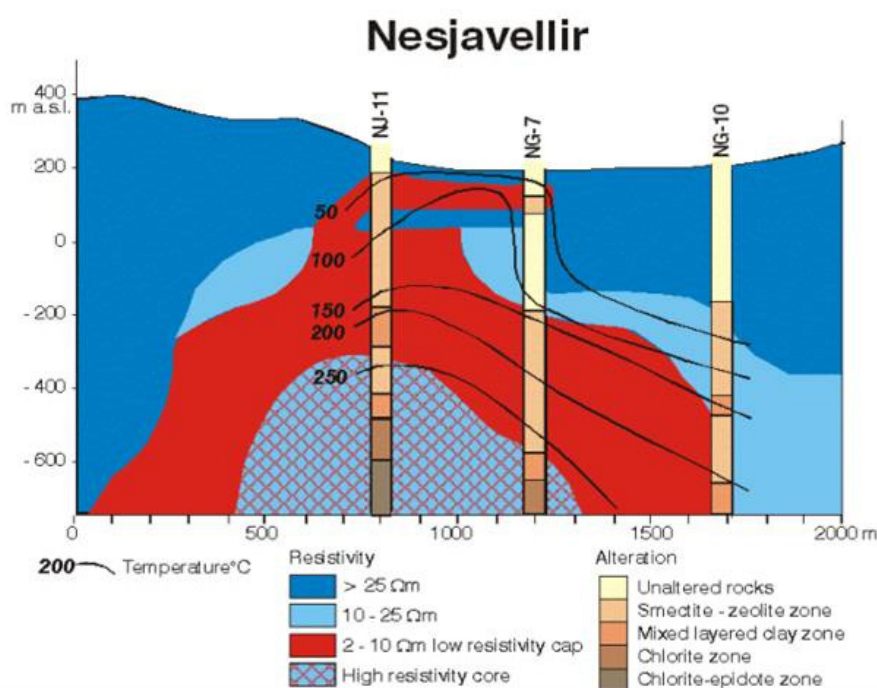


FIGURE 5: The relationship between resistivity, alteration zones and temperature (Árnason et al., 1987; 2000)

The magnetotelluric method uses time variations of the Earth's magnetic field to investigate the resistivity structure of the Earth's interior (Karlsdóttir et al., 2012). The time varying magnetic field represents electromagnetic waves that penetrate the earth. By simultaneously measuring natural variations, mutually perpendicular horizontal components of the magnetic and electric fields which are coupled through Maxwell's equations, the subsurface resistivity can be found by inversion. The electric and magnetic field variations are measured as a function of time i.e. as a time series. The time series are composed of a sum of harmonic (sinusoidal) components of different periods (frequencies). Short period (high frequency) waves are attenuated at a shallow depth, hence, do not penetrate deep, but the longer the period (lower the frequency) the deeper the waves probe into the earth. It means the electrical parameters must be measured on a longer period of fields to probe deeper into the earth. In processing the MT data, the time series are sorted into different frequencies (by Fourier transformation) and the relationship between the electric and magnetic fields gives information about the resistivity at different depths. MT can, therefore, penetrate from shallow depths to a depth of several tens of kilometres (Karlsdóttir et al., 2012).

Wherever MT measurements have been conducted in the volcanic zones in Iceland, a deep-seated low-resistivity layer at a 10–15 km depth has been seen. The upper boundary (10 Ωm) of this low-resistivity layer arches up to a depth as shallow as 2–3 km beneath high-temperature geothermal systems. As the low-resistivity layer is thought to reflect high temperatures, it is interpreted as providing information on the upwelling of heat into geothermal systems. Plume-like low-resistivity anomalies in limited areas beneath the deep low-resistivity layer, as seen in TEM and MT measurements at Upptyppingar (Vilhjálmsón et al., 2008), also support the idea of active heat up-flow.

The hydrothermal alteration reflects the alteration caused by the heating of the rocks and reflects the peak temperature experienced by the system at the present or in the past. Resistivity measurements reveal the alteration, hence, the temperature, provided there is equilibrium between the alteration and the present temperature. In case of cooling, the resistivity will reflect the temperature at which the alteration was formed. Whether the resistivity indicates the present temperature of the system will only be confirmed by drilling (Karlsdóttir and Vilhjálmsón, 2011).

3.3.2 Resistivity in Theistareykir geothermal field

Resistivity surveys have been undertaken with the TEM, AMT and MT methods at the Theistareykir high-temperature geothermal field on several occasions. The first survey was performed in the 1970s into the early 80s with DC methods (Grönvold and Karlsdóttir, 1975; Gíslason et al., 1984). The first TEM survey was performed by ÍSOR in 2004 with an addition in 2006 (Karlsdóttir et al., 2006). In the summer of 2007, Mannvit and KMS Technologies did an AMT/MT survey at Theistareykir (Yu et al. 2008a; 2008b) but the results could not be used due to insufficient recording of data in the field. Finally, ÍSOR made TEM and MT measurements in 2009 (Karlsdóttir and Vilhjálmsón, 2011) and continued with an MT survey of the area in 2009–2011, followed by 1D interpretation of the MT data along with the existing TEM data. The survey was done over two periods, 62 MT soundings during the summer of 2009 and 25 MT soundings during the summer of 2011. Furthermore, 14 new MT soundings were performed in the summer of 2012 and two of the 2011 soundings were repeated. The total number of MT sites is, therefore, 101 along with TEM sounding sites (Karlsdóttir et al., 2012).

A joint 1D inversion of the MT and TEM data was presented in 2011 by Karlsdóttir and Vilhjálmsón. The static shift corrected MT data was then inverted to 3D (Karlsdóttir et al., 2012). The 3D model indicates that a low-resistivity structure ($<10 \Omega\text{m}$) is located at a depth of 400–600 m, elongated in an east-west direction from Mt. Baejarfjall in the east towards Mt. Maelifell in the west. Below this low-resistivity structure, the resistivity increases sharply. Similar structures were detected by gravity and magnetic field studies (Ármannsson et al., 1986).

The 3D inversion of TEM/MT resistivity data from Theistareykir showed a conventional resistivity structure for a high-temperature system, a low-resistivity cap underlain by a high-resistivity core. The low-resistivity cap reaches the surface at Theistareykir, where also the highest elevation of the high-resistivity core is seen. A deep seated low-resistivity body, indicating the heat source of the geothermal system, is present under Ketilfjall, extending from there north and northeast. This is the most prominent low-resistivity body at depth and it domes up under the southern part of Ketilfjall up to 2 km b.s.l. depth. Other low-resistivity bodies are present at greater depths, under Stórahversmór and the southeast part of Baejarfjall. Two distinctive low-resistivity bodies extend from the low-resistivity cap in the northern part of the survey area down to 10 km depth b.s.l. It is tempting to connect these phenomena to the Húsavík Fracture Zone where it infiltrates the Theistareykir fissure swarm and even to crustal deformation detected in the area in 2007–2008 (Karlsdóttir et al., 2012).

Figure 6 shows an example of a 3D-presentation from Petrel software showing the 5 geothermal wells in the Theistareykir geothermal field in this study. The 64" resistivity for the selected wells is also shown on the well tracks.

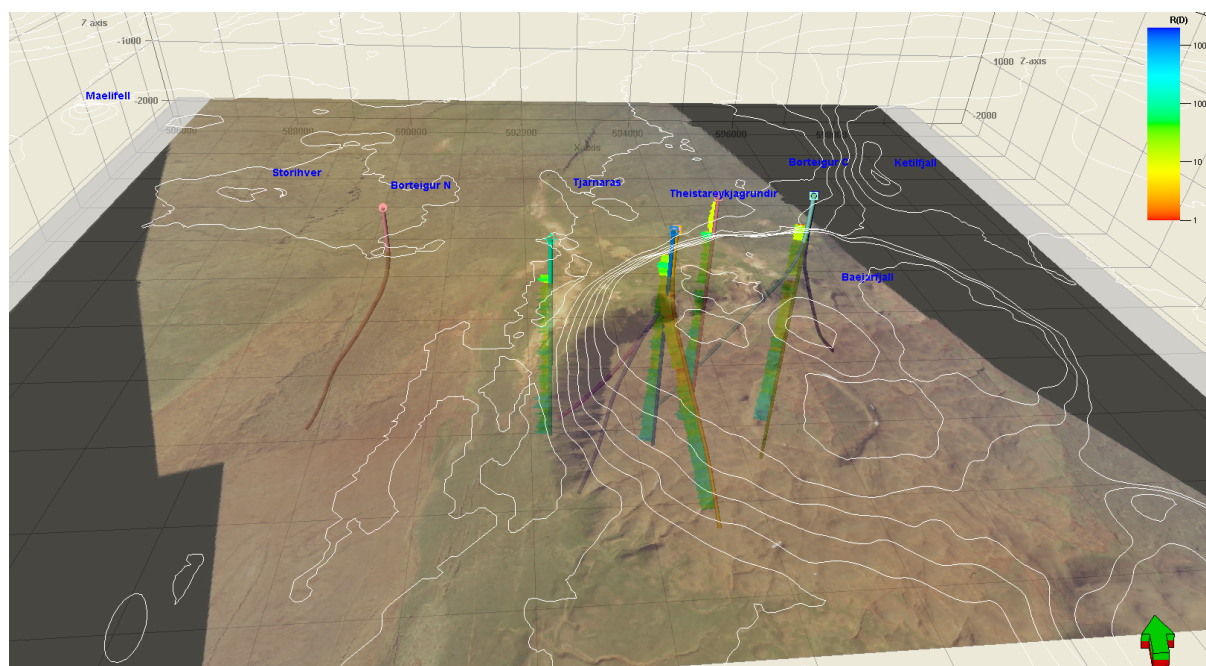


FIGURE 6: The 5 selected boreholes at Theistareykir with measured 64" resistivity from the project study; the resistivity scale (1-2000 Ωm) is logarithmic, shown in the upper right corner; the 1 Ωm is red, 10 Ωm yellowish, 100 Ωm green and 1000 Ωm blue

4. DATA PREPARATION

4.1 Correction of well logs

Geothermal wells are drilled either vertically or directionally. The exploration wells in Theistareykir high-temperature geothermal field are drilled in four stages where the casings are: surface casing, safety casing and production casing. The deepest part is the production part of the well cased with a slotted liner. Mud or water circulation is used while drilling down to the production part and water circulation applied in the production part of the wells. Cementing is needed in each section above the production part of the wells to anchor the casing to the formation. The height of the drill rigs and the casing depth with reference to flans, top of cellar or ground surface in different sections of each well at Theistareykir are revealed in Table 2.

Depth must be corrected in the resistivity measurements and other borehole measurements so that the measured depths of all measurements in a well are consistent and the ground surface is the common reference point. The main part of this project was to correct and prepare the well logs for further processing. In all of the well logs during drilling, the platform of the drill rigs was used as a common reference, but after drilling the ground surface was the common reference.

Following is a summary of significant corrections that were made:

- 1) The depths of measurements were adjusted from drilling platforms down to the ground surface. The depth of measurements from the drilling period needed to be corrected from the platform down to the surface. Well logs were measured from the platforms and their depths needed to be reduced by the height of the platforms. The heights of different drill rigs are shown in Table 2.

TABLE 2: Summary of the wells for correction in Theistareykir field

Well name	Section	Circulation fluid	Drill rig	Height of drill rig (m)	Casing depth w.r.t. flans (m)	Casing depth w.r.t. top of cellar or grs. (m)
ThG-01	Pre-drilling	mud	Sleipnir	6.0	69.1	69.9
	1	mud	Sleipnir	6.0	188.7	189.5
	2	water	Sleipnir	6.0	609.5	610.3
	3	water	Sleipnir	6.0	1924.2	1925.0
ThG-02	Pre-drilling	water	Sleipnir	6.0	101.5	102.3
	1	mud	Sleipnir	6.0	270.0	270.8
	2	water	Sleipnir	6.0	611.1	611.9
	3	water	Sleipnir	6.0	1704.9	1705.7
ThG-03	Pre-drilling	mud	Jötunn	6.9	—	—
	1	mud	Jötunn	6.9	247.8	248.6
	2	mud	Jötunn	6.9	756.7	748.9
	3	water	Jötunn	6.9	—	—
ThG-04	Pre-drilling	mud	Jötunn	6.9	—	66.2
	1	mud	Jötunn	6.9	262.1	262.9
	2	mud	Jötunn	6.9	823.7	824.5
	3	water	Jötunn	6.9	—	—
ThG-09	Pre-drilling	mud	Geysir	6.8	103.0	103.8
	1	mud	Geysir	6.8	296.8	297.6
	2	mud	Geysir	6.8	816.9	817.7
	3	water	Geysir	6.8	—	—

- 2) The casing depth needs to be known in order to make the adjustment of the depth measurements to the end of the casings, which could be detected in some of the well logs. The casing depth is, however, in some cases expressed in drilling reports based on drilling platforms, in some places compared to the edge of the basement or ground surface and in some cases it is assumed to be the borehole flans. The casing depths of different sections of each well can be seen in Table 2. In this project, the flans to the top of the cellar, in the design figure for Well ThG-03, is 0.800 m and was used for Wells ThG-01 to ThG-04. In the design figure for Well ThG-09, this seemed to be 0.811 m, only used for that well.
- 3) The resistivity logs were not corrected in this study but should be corrected for well Caliper, temperature and fluid conductivity. The circulation fluid used while drilling varies so its conductivity needs to be measured and given for a fixed temperature for the corrections. The resistivity of the fluid as well as the formations depends upon temperature. The ÍSOR software for correcting the resistivity can be used on a UNIX system only, which is not available for UNU Fellows.
- 4) Finally, the logs of similar kind from different sections in one well were put together in one file after the corrections were made. These continuous logs were imported into the Petrel 3D software where the data was connected to the well paths through their measured depth.

4.2 Petrel – previous work

The Petrel software was used in the presented project and its relevant features are described briefly below. Figure 6 shows an example of a 3D-presentation from Petrel software.

Petrel is a shared earth model tool developed by Schlumberger to discover reservoir patterns through a common data model (Schlumberger, 2008). In one application, geophysics, geology, petrophysics, production data and seismic events can be imported into Petrel to generate visual and easy access. The

powerful features of Petrel not only allow users to improve understanding of the internal details of the reservoir, but also describe the spatial distribution of the reservoir properties as well as seamlessly integrate data and a reservoir numerical simulator, all according to the inserted data for modelling.

4.2.1 A 3D resistivity model

Two resistivity models found by joint inversion of TEM and MT data had previously been inserted into Petrel. The 25×25 grid is with TEM and MT from a 1D inversion but the 250×250 from a 3D inversion, and the resolution is different in the two models. A 3D inversion of the MT data can give more reliable and detailed results than a 1D inversion (Karlsdóttir et al., 2012). Therefore, the 250×250 grid 3D model was used in this project.

Four resistivity maps from the report by Karlsdóttir et al. (2012) are presented in Figures 7-10 in order to show the character of the resistivity structure of the geothermal system, both horizontally and vertically, in Theistareykir high-temperature geothermal field. The geothermal system is characterized by a low-resistivity cap underlain by a high-resistivity core. The results also revealed a low-resistivity layer at depth, arching up under the centre of the geothermal system with the upper border ($10 \Omega\text{m}$) at 4–5 km depth.

The black dots show the locations of the TEM and MT stations in Figures 7 and 8. Figure 7 shows the resistivity at 250 m above sea level. It shows the low resistivity with red colour and the high resistivity with blue colour. In this case the blue colour represents the unaltered rocks on the surface outside the geothermal field, whereas the red colour shows the top of the emerging low-resistivity cap over the geothermal area.

Figure 8 shows the resistivity at 2000 m b.s.l. It shows the low-resistivity zone at depth appearing in the northeast part. There are several hints of low resistivity, such as Ketilfjall, Baejarfjall, Stórahversmór and the Tjarnarás area. Low resistivity a little to the right of the middle of the figure is under Ketilfjall, north of Baejarfjall (see Figure 2). Well ThG-03 (Figure 3) is located west of Ketilfjall. The prominent low resistivity bodies in the northwest part of the map are the anomalies allegedly connected to the Húsavík transform fault.

In Figure 9, a cross-section of resistivity through Theistareykir and Bóndhólsskard from west to east, (the green line 125 shown in Figure 2), indicates the low-resistivity cap that reaches the surface in the middle of the figure and tilts towards the east. The high-resistivity core covers the middle stratum and low resistivity appears again at depth in the eastern part which indicates the main heat source or the Ketilfjall resistivity anomaly. It also shows an anomaly at greater depth under Stórahversmór in the western part.

In Figure 10, a cross-section of resistivity through Theistareykir and Baejarfjall from south to north (the green line 1625 shown in Figure 2) shows the low-resistivity cap; the low resistivity is underlain by a high-resistivity core. It also shows the low resistivity at depth, i.e. the Ketilfjall anomaly or the main heat source to the north and a smaller anomaly at more depth under Baejarfjall.

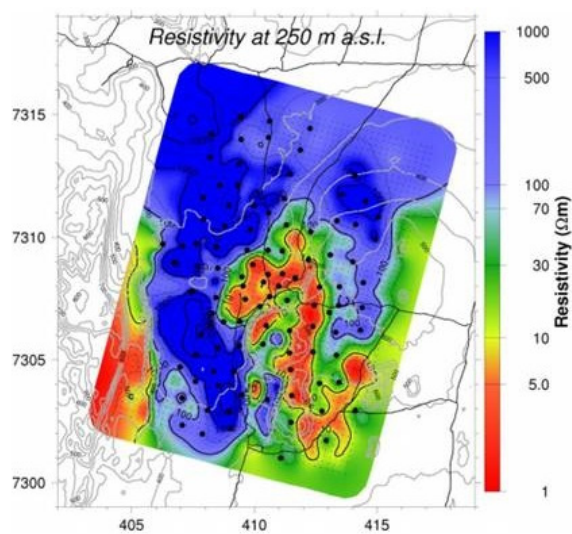


FIGURE 7: Resistivity at 250 m a.s.l.
(Karlsdóttir et al., 2012)

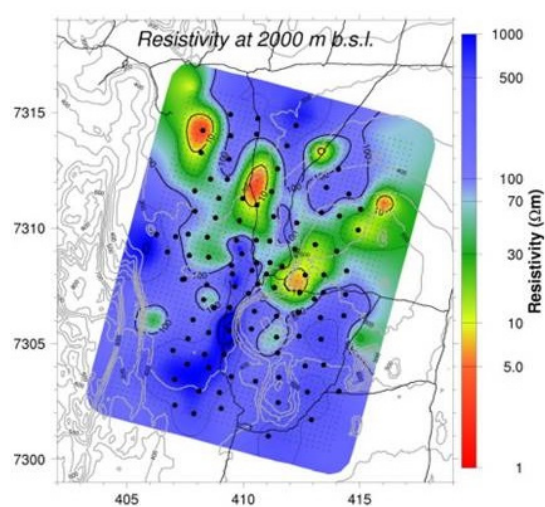


FIGURE 8: Resistivity at 2000 m b.s.l.
(Karlsdóttir et al., 2012)

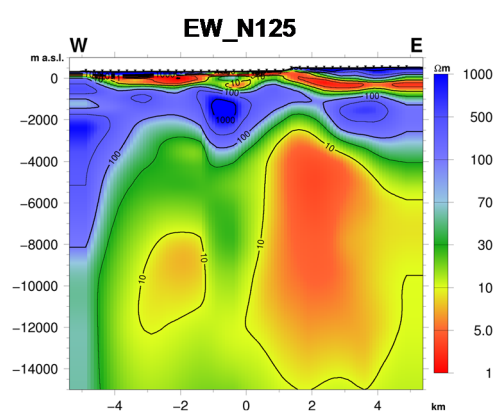
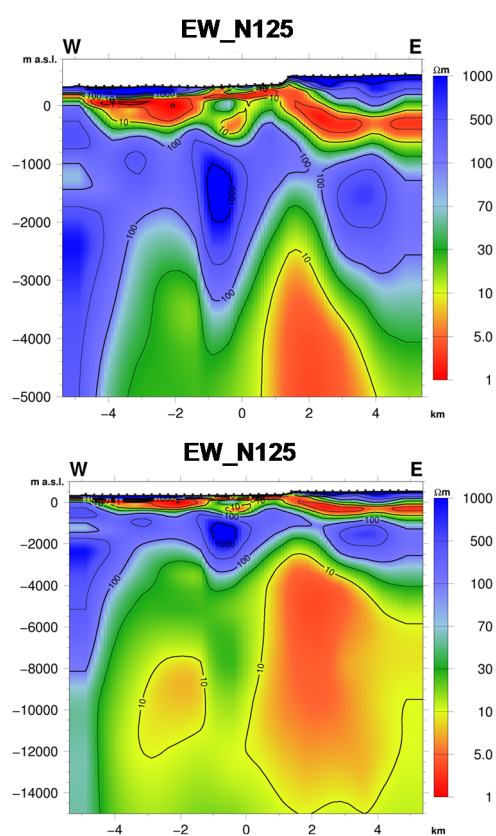


FIGURE 9: A W-E resistivity cross-section through Theistareykir and Ketilfjall down to 5 km depth (above) and down to 15 km depth (below) (Karlsdóttir et al., 2012)

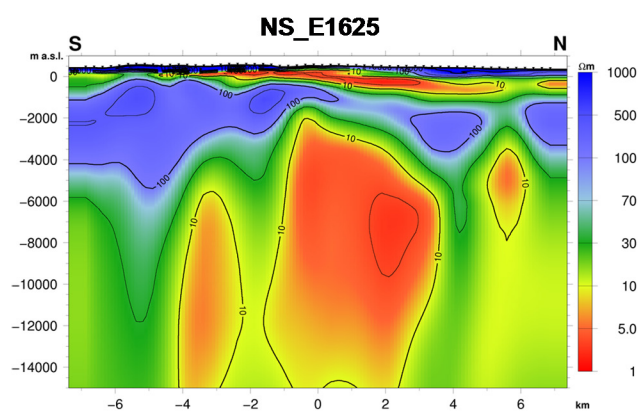
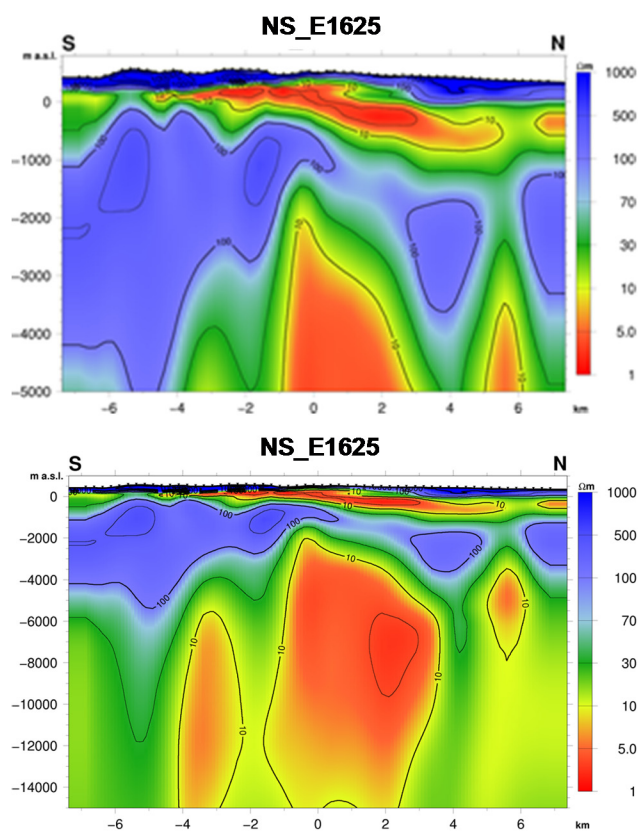


FIGURE 10: A resistivity cross-section from south to north, through Baejarfjall and Ketilfjall down to 5 km depth (above) and down to 15 km depth (below) (Karlsdóttir et al., 2012)

4.2.2 Alteration minerals

The information from drill cuttings and XRD-clay mineral research had already been analysed by employees at ÍSOR and inserted for each well into Petrel by Ms. Anette K. Mortensen (unpublished work at ÍSOR). Her work in Petrel includes geological sections, the layers of first appearance of alteration minerals, as well as alteration zonation.

Figures 11 and 12 show the first appearance of smectite-zeolite (forming at 50-200°C) and epidote-amphibole (forming at 280-350°C) layers (Franzson et al. 1994). The variation in depth of the first appearance of the smectite-zeolite and epidote-amphibole layers indicates that the formation temperature at Theistareykir tends to be highest in the central part of the area. The doming up of both of the layers (Figures 11 and 12), especially the epidote-amphibole layer, is close to where the heat source is assumed to be in recent modelling of the geothermal resources (Arnaldsson et al., 2011). It may be noticed in Figure 12 that the curvature can be large where the range of depths for the relevant mineral is high within a short distance. The well paths cut through the surface which appears as the first appearance of the minerals in the relevant well. There are only six samples in every layer to control the area. More detailed and accurate results will be concluded in further studies at ÍSOR.

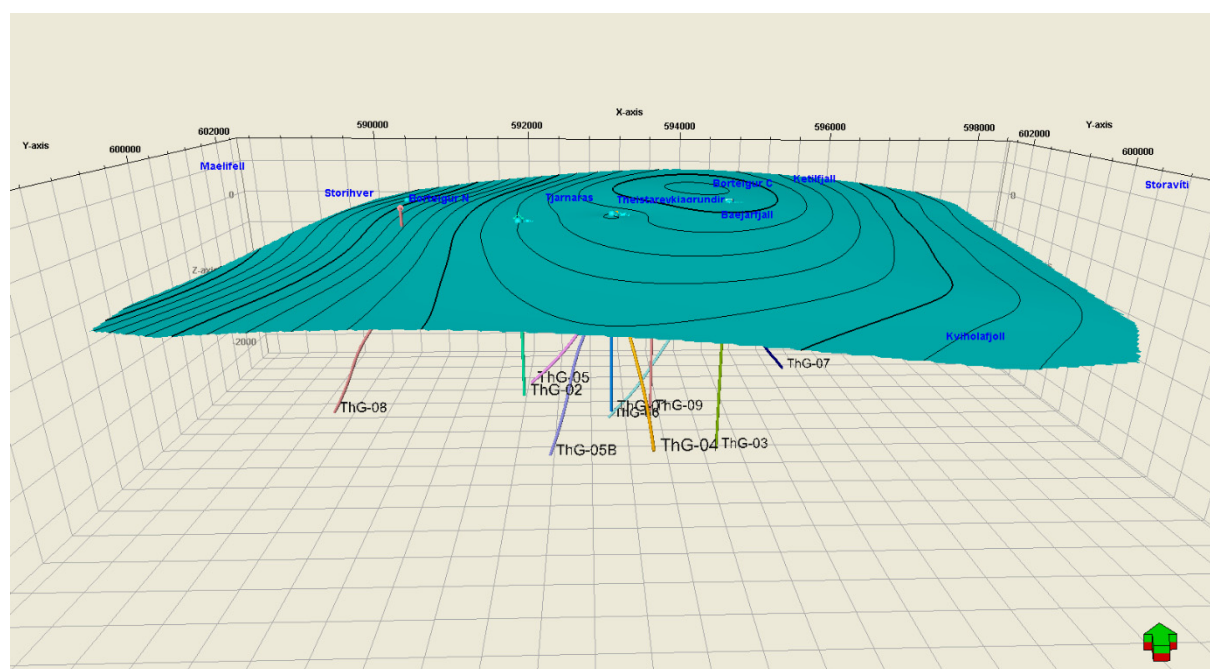


FIGURE 11: A layer made from the uppermost depth of detection of smectite-zeolite in 6 wells (adapted from Mortensen, unpublished work at ÍSOR)

5. RESULTS

5.1 Petrel – present study

The Petrel model of alteration minerals had already been done by Anette K. Mortensen, showing the layer of the first appearance of the alteration minerals which was used for comparison in this project. A 3D model from inversion of TEM and MT had been prepared (Karlsdóttir et al., 2012) and then inserted into Petrel by Gunnlaugur M. Einarsson at ÍSOR. The processes in Petrel in this project were the following:

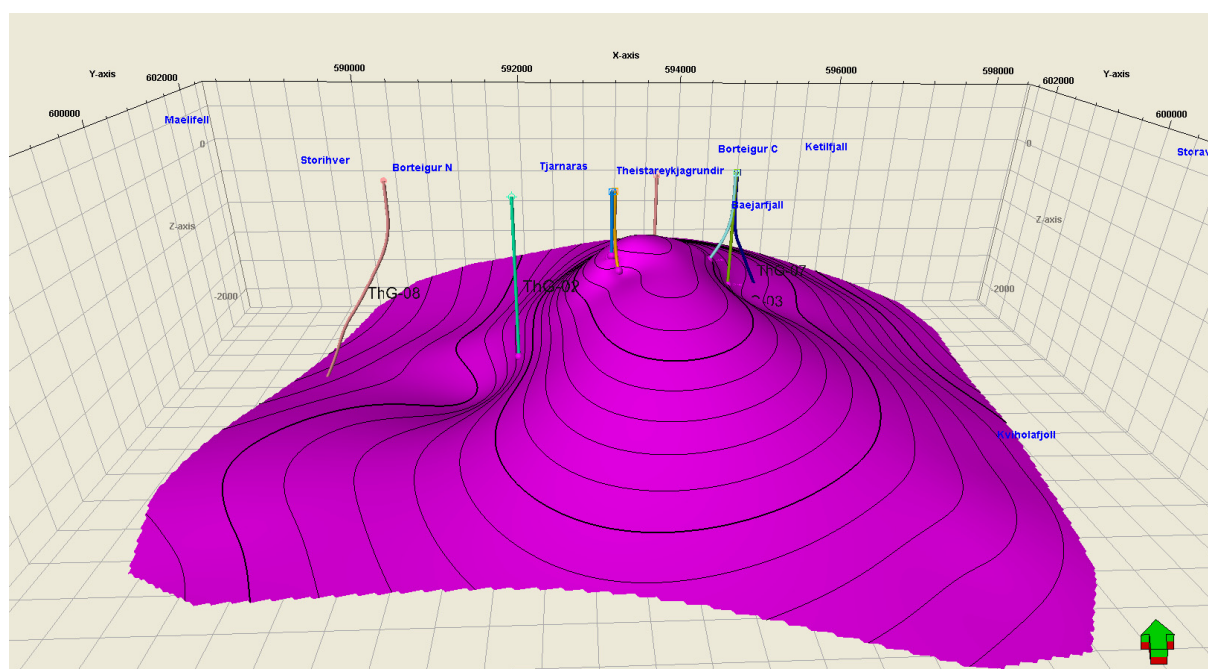


FIGURE 12: A layer made from the uppermost depth of detection of epidote-amphibole in 6 wells (adapted from Mortensen, unpublished work at ÍSOR)

- 1) Firstly, corrected 16" and 64" resistivity, Caliper, gamma and Neutron-Neutron well logs were inserted as measured depth and value and linked to the well paths.
- 2) Secondly, both 16" and 64" resistivity well logs were averaged to the same resolution as the 3D model from TEM and MT, using the Scale up property section in Petrel.
- 3) Finally, the measured 16" and 64" resistivity well logs, the averaged 16" and 64" resistivity and the "pseudo logs" from the TEM and MT model were combined in a log-plot in the main study in this project, as seen in Haraldsdóttir et al. (2010; 2012), with a similar scale for comparison. In addition, the alteration mineral zones and intrusions were included in the log-plots.

The depth is shown as true vertical depth (TVD) and the "pseudo logs", which are made from the TEM/MT model, have a different scale from the resistivity scales of the resistivity well logs, since the values are $\log(\text{resistivity})$. The scale of the well logs ranges from 1 to 2000 Ωm while the corresponding scale of the resistivity from the TEM/MT inversion and the deduced "pseudo logs" is 0 to 3.3. For example, for resistivity values 1 and 2000 Ωm , $\log 1=0$ and $\log 2000=3.3$. The plots were made similar by using log and linear scales for those.

5.2 Well logs in boreholes

The well logs were plotted together on a log plot to identify important information, e.g. geological sections, and to process for further analysis. In this study, one example of processed well logs from Well ThG-01 at Theistareykir is shown in Figure 13. The depth is the true vertical depth with respect to sea level. From left to right, the graph shows the alteration mineral zones, the geological sections, the intrusions and the formation temperature, caliper, gamma, and Neutron-Neutron, but the 64" resistivity and 16" resistivity are plotted together with a logarithmic scale in Figure 13.

The formation temperatures of Wells ThG-01, ThG-02, ThG-03, and ThG-04 had been found previously and are shown in Figure 14. The rock temperature in ThG-01 increases continuously with depth in Figures 13 and 14 up to 331.6°C. The alteration minerals indicate the geothermal temperature when they were formed, so comparing them with the present formation temperature indicates if a geothermal system is in balance, warming or cooling.

The Caliper logs of Wells ThG-01 and ThG-03 were measured with a 3 arm probe, whereas Wells ThG-02, ThG-04 and ThG-09 were measured with a 4 arm probe. For example, there is a cavity at 60 m b.s.l. where the caliper shows an obviously higher peak. From the gamma and Neutron-Neutron logs, several peaks with high values, e.g. at depth 580 m and 1360 m b.s.l., probably indicate acidic layers or intrusions intersecting basaltic rocks. In general, higher gamma ray represents acidic characteristic and higher Neutron-Neutron log indicates low porosity. The corresponding higher resistivity peaks in 16" and 64" resistivity logs are shown together in the last column in Figure 13.

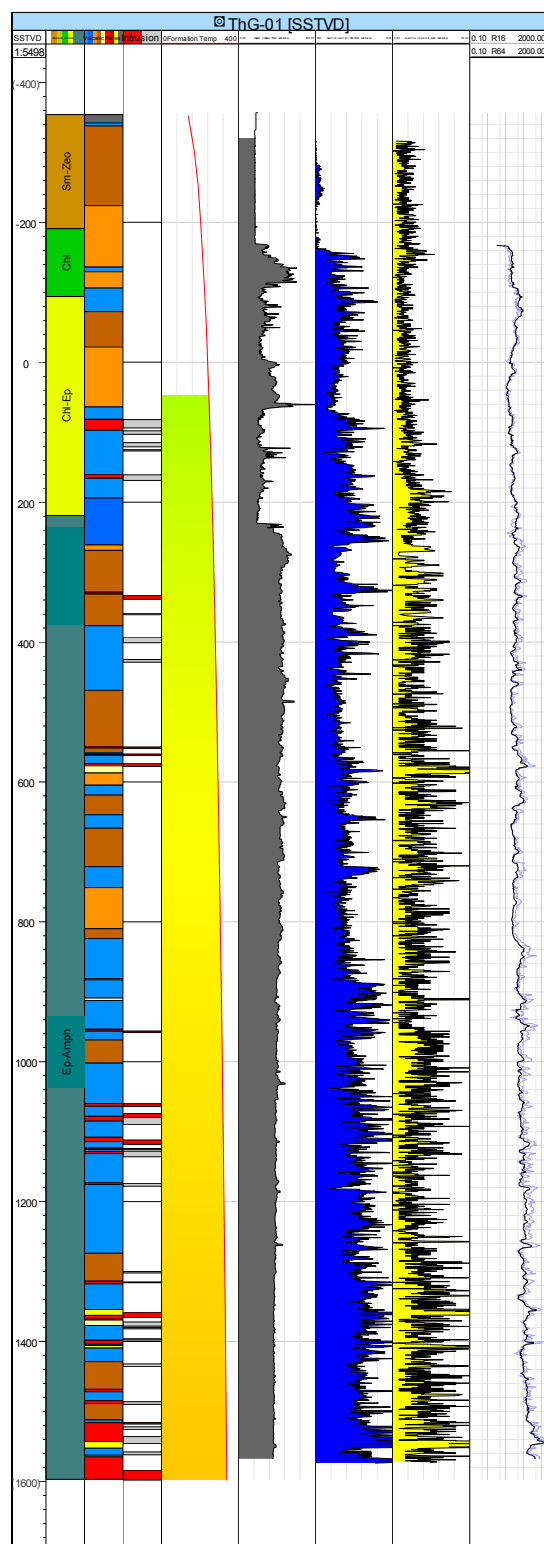


FIGURE 13: Well logs: Caliper, gamma, N-N, 16" and 64" resistivity of Well ThG-01 at Theistareykir, as well as alteration zones, geological sections, intrusions and rock temperature (Mortenson et al. at ÍSOR, unpublished work at ÍSOR)

5.3 Rock temperature in the Theistareykir geothermal system

The rock temperature in Wells ThG-01, ThG-02, ThG-03, ThG-04 and ThG-09 (ÍSOR database) is shown in Figure 14 for comparison with the resistivity and alteration temperature. Well ThG-02 is the coldest of the boreholes but is shallow with respect to other boreholes at Theistareykir. It is warmer at a deeper depth in Well ThG-05B which lies under Well ThG-02. Wells ThG-01, ThG-03, ThG-04 and ThG-09 are warmer than Well ThG-02 and their locations are in the centre and eastern part of the research area shown in Figure 3.

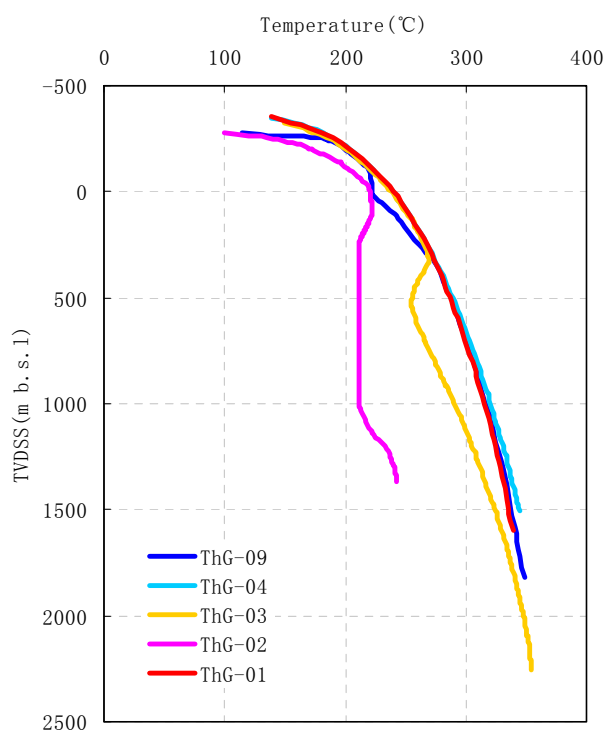


FIGURE 14: Estimated rock temperature in boreholes at Theistareykir

5.4 Comparison of borehole and surface resistivity as well as alteration minerals

5.4.1 Comparison of resistivity in boreholes and from surface exploration

Simplified log plots for the 5 selected wells are shown in Figures 15-19. The diagrams in the figures show alteration minerals, intrusions and possible intrusions, 64" resistivity, 16" resistivity, averaged 64" resistivity, averaged 16" resistivity and "pseudo-logs" from the TEM and MT electrical soundings, in that order. The averaged 64" and 16" resistivity and the "pseudo-logs" from the inversion of TEM/MT model have the same resolution. Wells ThG-01 and ThG-04 are located at the same drill pad. The upper part of a well is vertical down to the kick off depth. The upper parts of these two wells are vertical down to 200 m b.s.l. and, from Figures 15 and 18, the resistivity logs look similar to each other.

The 16" resistivity of Wells ThG-01, ThG-02, ThG-03 and ThG-04 is a little higher than the 64" resistivity. But 16" resistivity is lower than 64" resistivity at a depth from the top to 50 m a.s.l. in Well ThG-09, and inverses below 50 m a.s.l. The "pseudo-logs" from the inversion of TEM and MT electrical soundings has the same trend in these 5 wells, first lower than 16" and 64" resistivity and then higher at a certain depth of each well. On the whole, the 64" resistivity, 16" resistivity, averaged 64" resistivity, averaged 16" resistivity and the "pseudo-logs" have a slight difference but are a very good match.

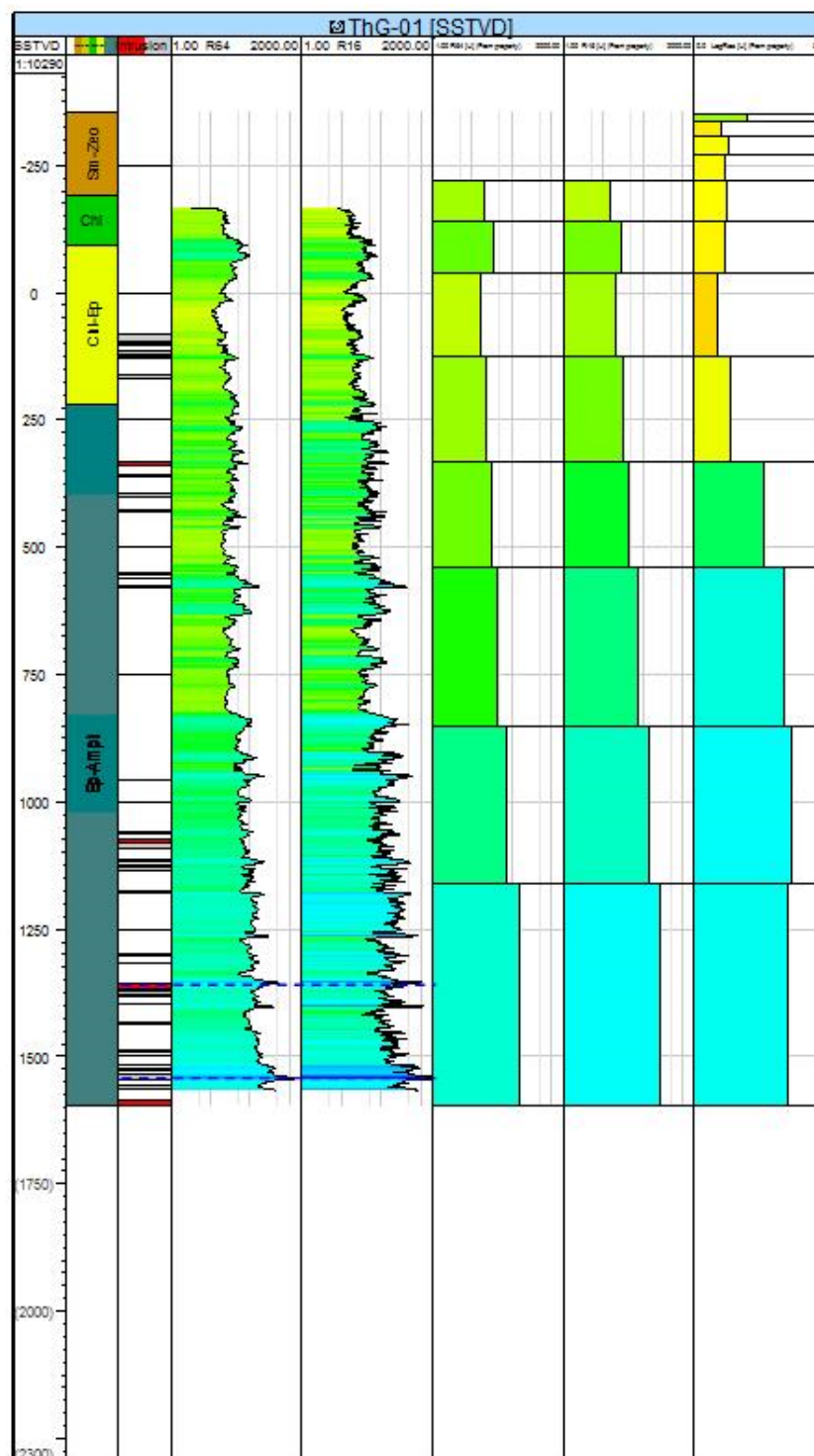


FIGURE 15: Well ThG-01: Alteration minerals, intrusions, 64" resistivity, 16" resistivity, averaged 64", averaged 16" and the "pseudo-logs" from TEM/MT; the resistivity colours scale is similar to the scale in Figure 4 (1-2000 Ωm). The resistivity scale is logarithmic from 1 to 2000 Ωm and the "pseudo log" scale is linear from 0 to 3.3 (see text)

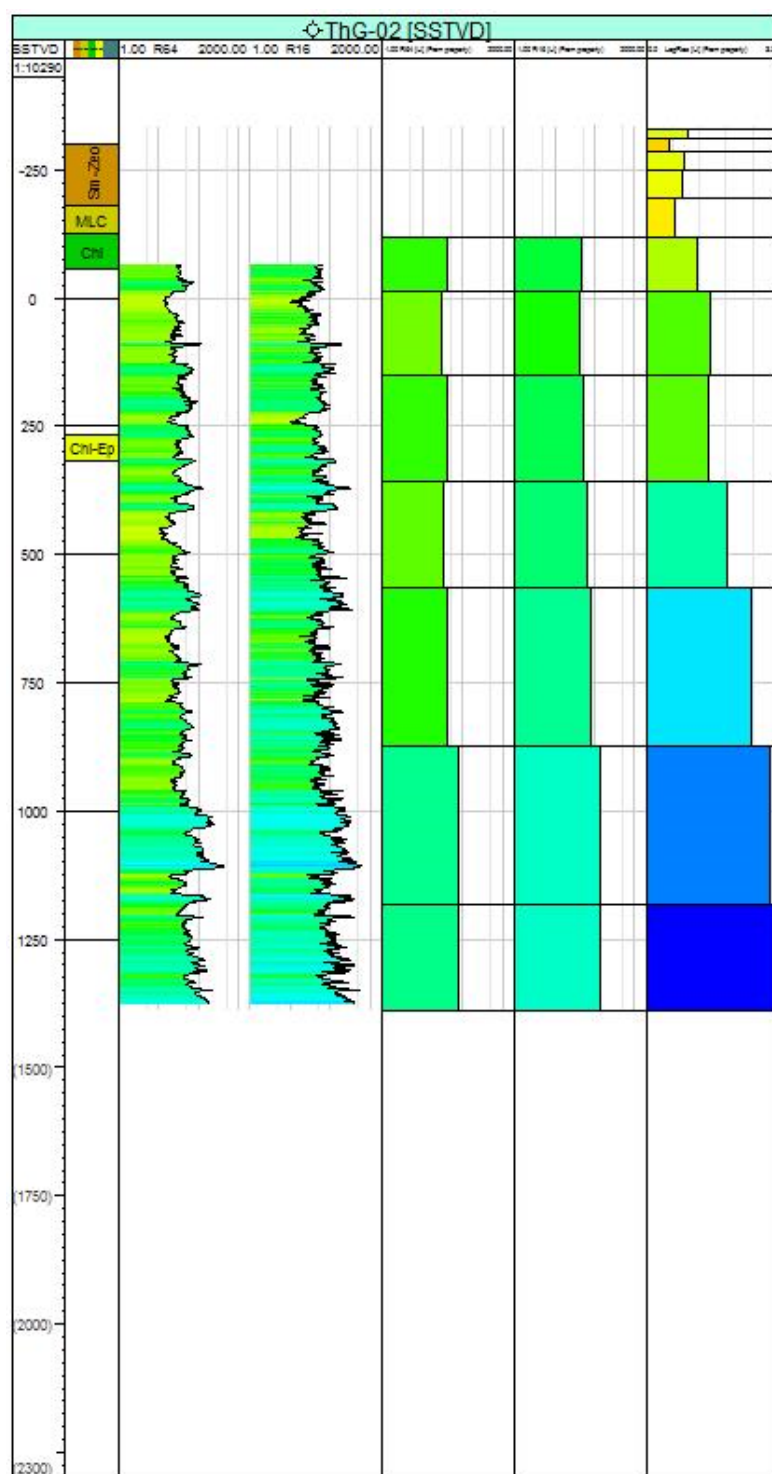


FIGURE 16: ThG-02: Alteration minerals, 64" resistivity, 16" resistivity, averaged 64", averaged 16" and the "pseudo-logs" from TEM/MT are shown side by side; the resistivity colours scale is similar to the scale in Figure 4 (1-2000 Ωm); the resistivity scale is logarithmic from 1 to 2000 Ωm and the "pseudo log" scale is linear from 0 to 3.3 (see text)

The 64" and 16" resistivity logs are high at different depths (e.g. at 1380 and 1540 m b.s.l. in Well ThG-01, at 950 and 1625 m b.s.l. in Well ThG-03 and at 100 and 375 m b.s.l. in Well ThG-04) and coincide with intrusions or possible intrusions shown with blue lines in the figures.

The comparison of averaged logs and the resistivity from TEM/MT shows that they match well with each other and have a similar variation trend with increasing depth. For example, the averaged 64" resistivity, averaged 16" resistivity and the "pseudo-logs" have lower values at a depth of around 50 m b.s.l. in Well ThG-01 (Figure 15). The values of the "pseudo-logs" are very low in the same well in the smectite-zeolite zone, but continue getting lower down to the grid cell at around 50 m b.s.l. Farther down, in the chlorite-epidote zone, the TEM/MT resistivity starts to increase and tends to be higher than the averaged resistivity which has different values. The resistivity in the epidote-amphibole zone increases with depth both in the "pseudo logs" and the averaged resistivity logs.

The comparison of averaged 64" and 16" resistivity and the "pseudo-logs" from TEM/MT model shows the change trend is a little bit different in Well ThG-02 (Figure 16).

The averaged 64" and 16" resistivity decreases at depth of around 100 m b.s.l. but the "pseudo-log" decreases at depth of around 250 m b.s.l., and is possibly shifted and should correspond to each other.

The averaged 64" resistivity decreases a little at a depth of around 500 m b.s.l. but the averaged 16" resistivity and the "pseudo-logs" increase. This is a very little increase and probably within the error limits of these averaged values. Resistivity and alteration minerals could not be compared due to a lack of alteration minerals in Well ThG-02.

The comparison of averaged resistivity logs and the "pseudo-logs" resistivity from TEM/MT for Well ThG-03 shows a little different pattern but still good correlation down to the grid around 1300 m b.s.l., but the TEM/MT shows the unusual behaviour of decreasing at that depth and decreasing even more farther down. This is the deepest of the 5 wells and probably is showing the top of a low-resistivity plume in the 3D TEM/MT model reaching up from depth. The changes in the averaged 16" and 64" resistivity do not coincide totally, but those changes are small. They both increase gradually from 800 m depth, whereas the TEM/MT pseudo log decreases. The borehole logs are more reasonable and valid due to more exact in situ measurements. Besides, the increase in the well logs at the deepest part of the well coincides with the increase in frequency of detected intrusions or possible intrusions from drill cuttings at that depth. The averaged resistivity logs increase a little from the chlorite to the chlorite-epidote zone and do not change much until they come into the epidote-amphibole where they increase as can be clearly seen in Figure 17.

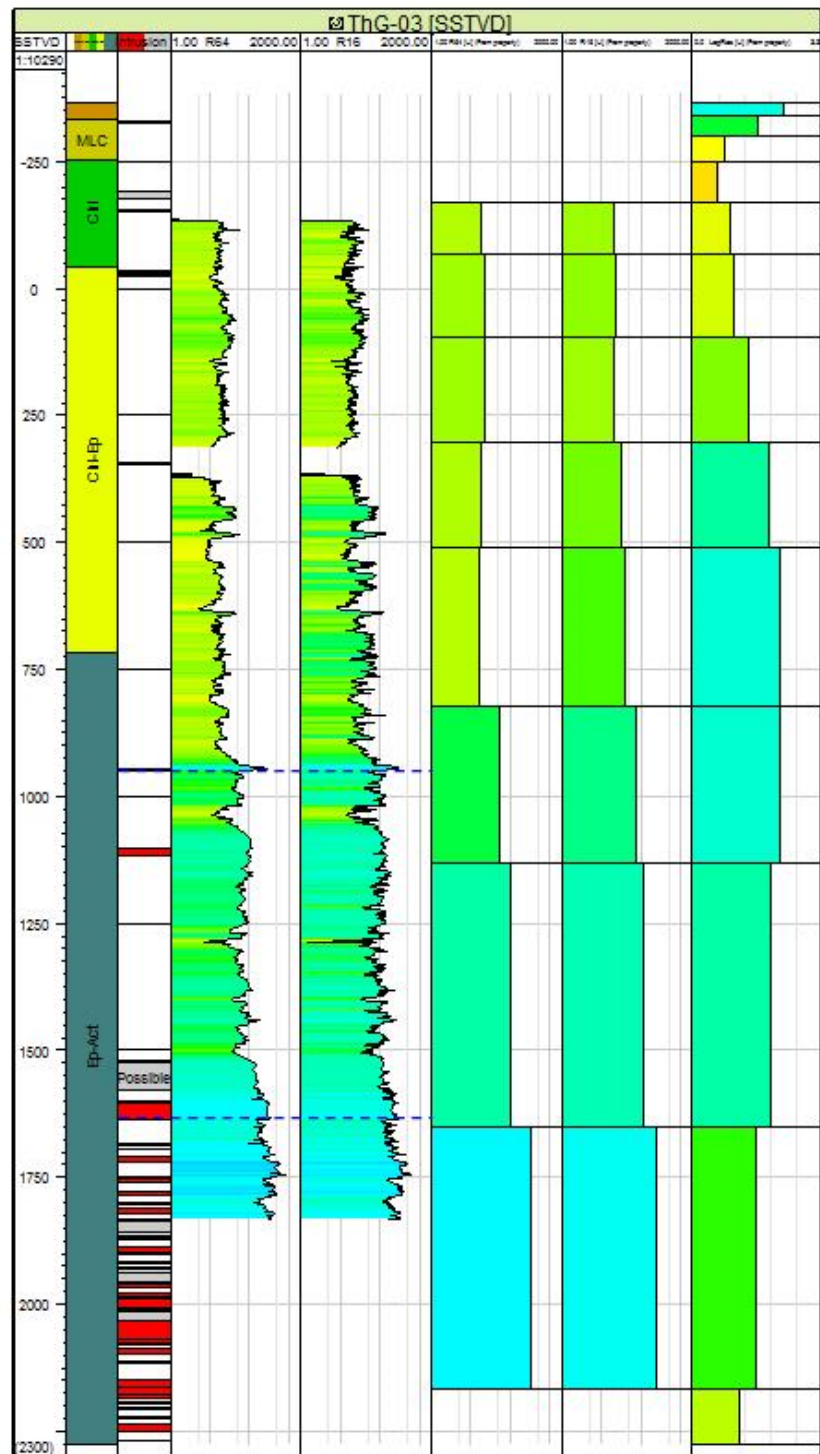


FIGURE 17: Well ThG-03: Alteration minerals, intrusions, 64" resistivity, 16" resistivity, averaged R64, averaged R16 and the "pseudo-logs" from TEM/MT are shown side by side; the resistivity colours scale is similar to the scale in Figure 4 (1-2000 Ωm); the resistivity scale is logarithmic from 1 to 2000 Ωm and the "pseudo log" scale is linear from 0 to 3.3 (see text)

The comparison of averaged logs and the resistivity from TEM/MT shows a very good corresponding relationship for Well ThG-04 in Figure 18, especially the changes at depths of around 50 m and 300 m b.s.l. The 64" and 16" resistivity are extremely low around a depth of 650 m b.s.l., but the averaged cell is so big that it disappears in the higher values. The “pseudo-log” resistivity appears lower at a depth of around 740 m b.s.l. which could correspond to the low resistivity in the measured logs a little higher. The “pseudo-log” resistivity is low and does not change much in the chlorite zone. The resistivities from the borehole and from surface exploration exhibit an increasing trend in the epidote-amphibole zone.

In Figure 19 the averaged 64" resistivity, the averaged 16" resistivity and the “pseudo-log” have a good correlation with increasing depth in Well ThG-09. The 64" and 16" resistivity logs, at depths of above 50 m a.s.l., is extremely low, probably caused by different scales or some problems with measurements. The averaged 64" and 16" resistivity decreases at a depth of around 250 m b.s.l., but the “pseudo-log” resistivity decreases at a depth of around 100 m b.s.l., probably corresponding to each other. The averaged resistivity and “pseudo-log” show similar patterns down the well from the cell around 1000 m b.s.l. but, as in Well ThG-03, the TEM/MT is decreasing, but only at the deepest cell.

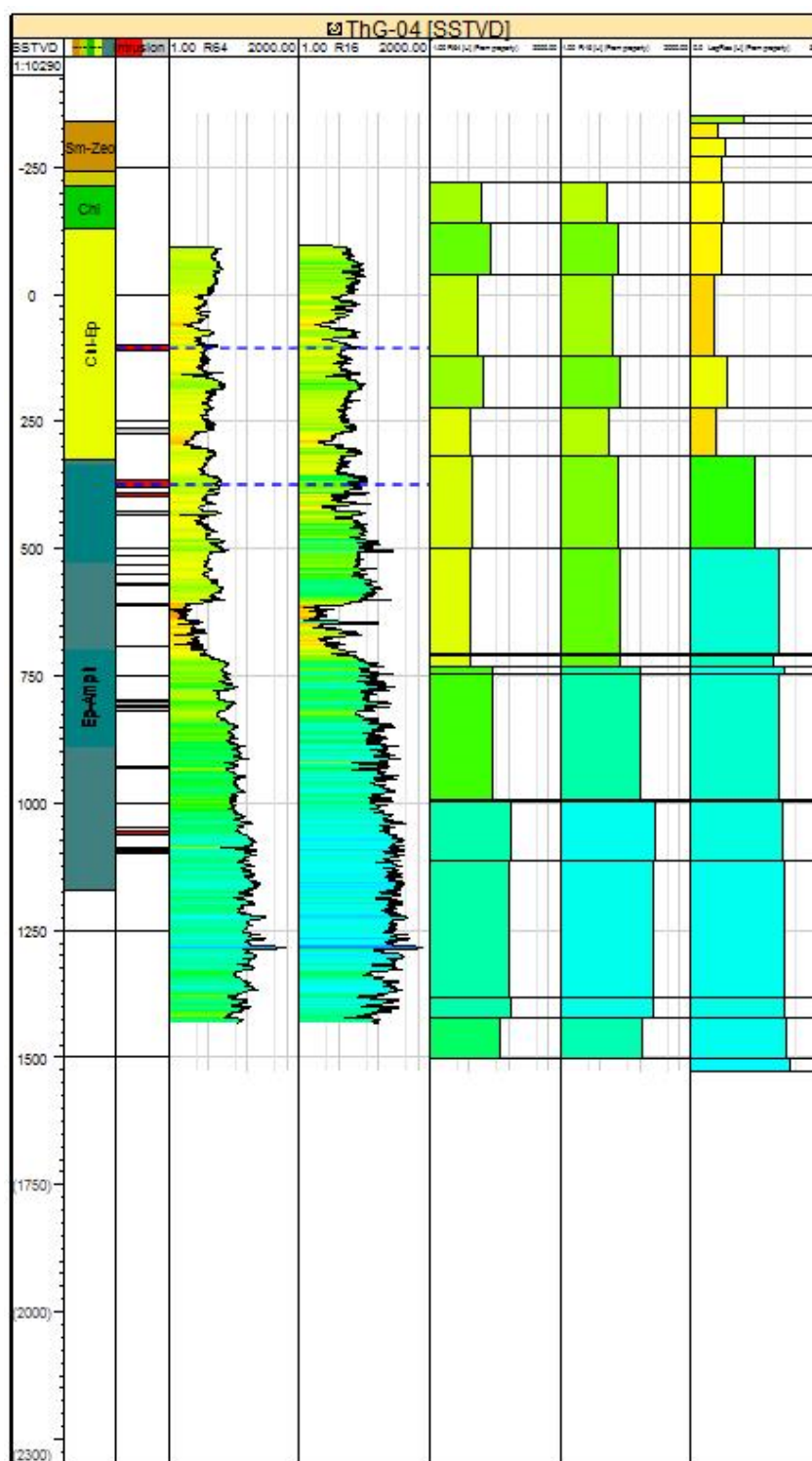


FIGURE 18: Well ThG-04: Alteration minerals, intrusions, 64" resistivity, 16" resistivity, averaged R64, averaged R16 and the “pseudo-logs” from TEM/MT; the resistivity colours scale is similar to the scale in Figure 4 (1-2000 Ω m); the resistivity scale is logarithmic from 1 to 2000 Ω m and the “pseudo log” scale is linear from 0 to 3.3 (see text)

5.4.2 Comparison of resistivity and alteration minerals

In Table 3 the alteration minerals are linked to the temperature during their formation (based on Kristmannsdóttir, 1979, and Franzson, 2010). The depths of the alteration zones in Wells ThG-01, ThG-03 and ThG-04 were used to get information about the rock temperature at similar depth. These are shown for comparison in Table 3.

The resistivity increases with increasing alteration (mixed-layer clay, chlorite, chlorite-epidote and epidote-amphibole), generally below the smectite-zeolite zone, but at different depths in different wells. In this project, the resistivity logs were not available from the first section of the wells where the smectite-zeolite zone is located (Figures 15-19). The resistivity increases below the chlorite in Wells ThG-01, ThG-02 and ThG-04, below the mixed-layer clay in Well ThG-03, but the resistivity changes from higher to lower at several intervals in the wells.

5.4.3 Well correlation

The wells in Figure 20 are in the eastern part of Theistareykir high-temperature geothermal field and lie from west to east (Figure 3), i.e. Wells ThG-02, ThG-01, ThG-04 and ThG-03. The first appearance of alteration minerals from drill cuttings and XRD analysis is shown with lines across the figure. The figure shows the alteration mineral zones, averaged 64", averaged 16", also including the well log on top of the relevant averaged logs and the “pseudo-logs” from the 3D model from the inversion of TEM/MT for each well. The low-resistivity layer can be seen in the “pseudo logs” from the TEM and MT 3D model, high

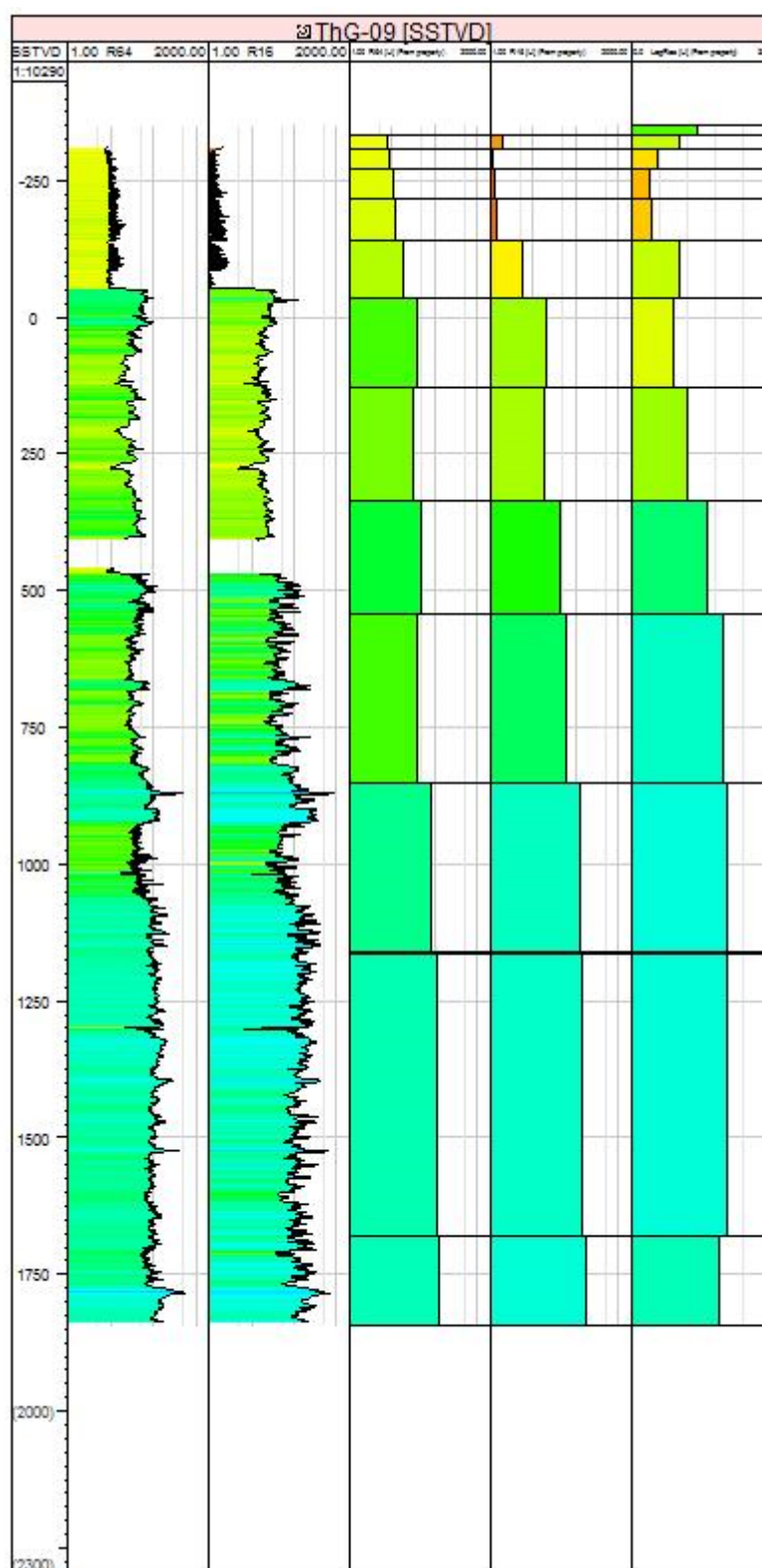


FIGURE 19: Well ThG-09: 64" resistivity, 16" resistivity, averaged R64, averaged R16 and the “pseudo-log” from TEM/MT; the resistivity colours scale is similar to the scale in Figure 4 (1-2000 Ωm); the resistivity scale is logarithmic from 1 to 2000 Ωm and the “pseudo log” scale is linear from 0 to 3.3 (see text)

up in the wells, but this is only an indication as the measured resistivity was not measured in the first section of the wells where the low-resistivity zone is located.

TABLE 3: Comparison of rock temperature and alteration temperature

Alteration minerals	Franzson's previous study (°C)	ThG-01 (°C)/Depth (m b.s.l.)	ThG-02 (°C)/Depth (m b.s.l.)	ThG-03 (°C)/Depth (m b.s.l.)	ThG-04 (°C)/Depth (m b.s.l.)
Smectite-zeolites	50-200	140-200 -354 to -190	100-170 -300 to -180	140-200 -368 to -333	140-200 -339 to -242
Mixed-layer clay	200-230	—	170-190 -180 to -125	155-185 -333 to -253	185 -242 to -212
Chlorite	240-250	200-220 -190 to -95	—	200-220 -253 to -41	200-220 -212 to -129
Chlorite-epidote	250-280	220-260 -95 to 219	—	220-260 -41 to 718	220-260 -129 to 326
Epidote-amphibole	280-350	260-340 219 to 1953	—	255-340 718 to 2659	260-340 326 to 1169

The first appearance of the alteration minerals in the chlorite zone appears at more depth in the western part (Well ThG-02) than in the middle of the area (Wells ThG-01 and ThG-04), and even at more depth farther northeast (Well ThG-03). The chlorite-epidote analysis in Well ThG-02 is incomplete due to lack of data and will, therefore, not be included. That zone does not show any great difference between the three remaining wells in the centre and northeast part of the area. On the other hand, its thickness appears to be greater towards the east based on the fact that epidote-amphibole appears at greater depths in Well ThG-04 than in Well ThG-01, and even deeper down in Well ThG-03 than in the other wells. The epidote-amphibole zone reaches to the bottom of each well, looking more extensive in Well ThG-04 than in the other wells because it is 800-1000 m deeper than the others.

5.5 Cross plot examples

A cross plot can be useful for checking the consistency of data for numerous datasets, as well as for each well individually, and even for finding errors (Haraldsdóttir et al., 2010). Figures 21 and 22 show the comparisons of measured 16" resistivity and 64" resistivity with a log-log scale from boreholes ThG-01 and ThG-09, respectively. The graphs in the figures relate variables from the same type of measurements. The points are spread linearly in the log-log plot of well ThG-01, and the situation is similar in Wells ThG-02, ThG-03 and ThG-04. The values of 16" resistivity are higher than for 64" resistivity. Neither has the temperature influence on resistivity nor the influence of the well fluid been corrected for. In Figure 23, there are several points where the values of 64" resistivity are relatively higher with respect to the 16" resistivity, in general; the difference can be seen in one of the sections. It also can be seen in Figure 19 above 50 m a.s.l. There might have been a bad cable or some problems with the scales in the measurements.

Figure 23 shows the cross plot of the “pseudo-logs” from the inversion of TEM and MT electrical soundings and averaged 64" resistivity from borehole measurements with the same resolution. Clearly there are much fewer points compared to the previous Figures 21 and 22 and are well-distributed around the 1:1 line. The values in the “pseudo-logs” are relatively higher than in the averaged 64" resistivity, possibly caused by the low resolution in the interpretation of the surface exploration, yet still have certain relevance.

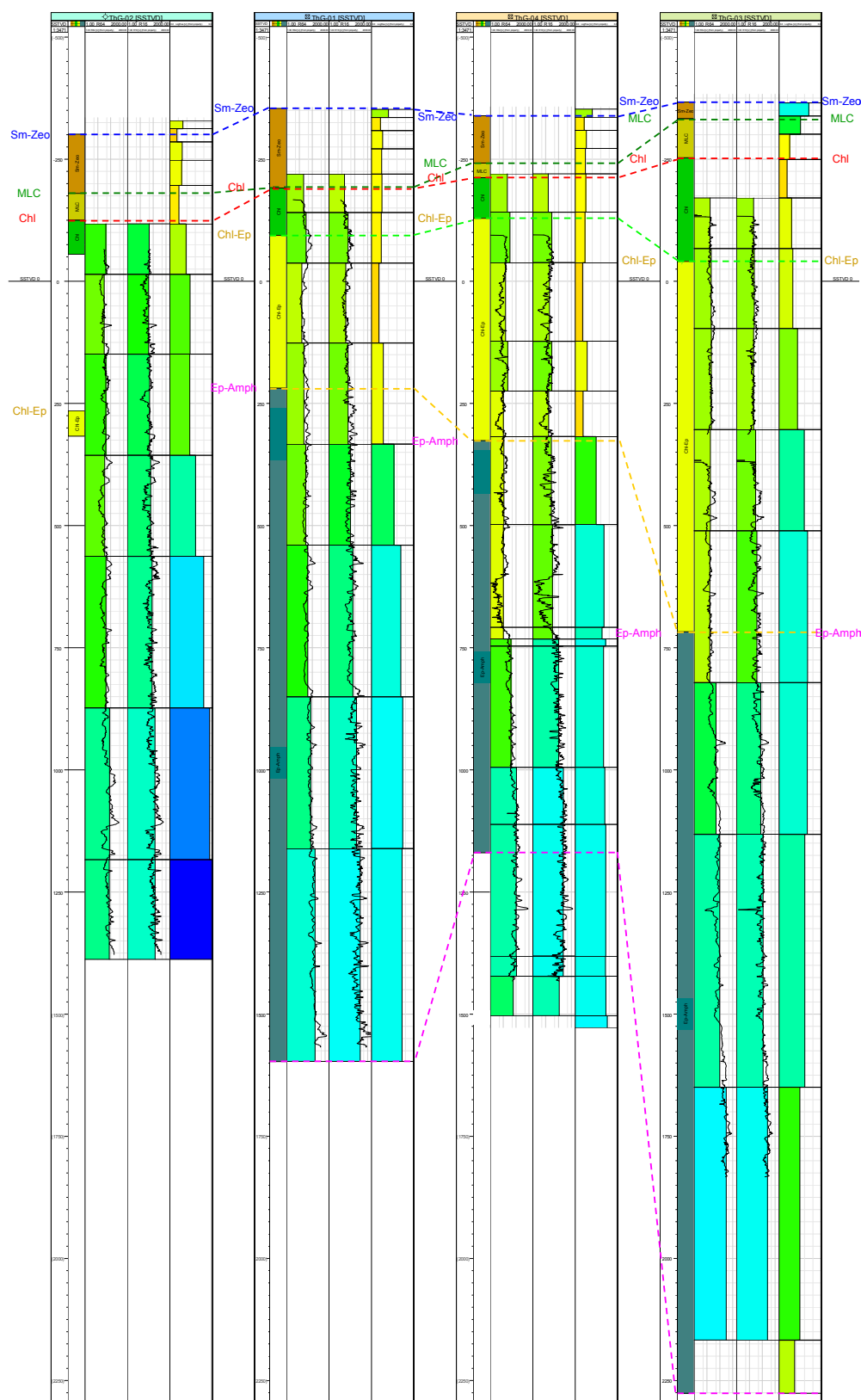


FIGURE 20: Correlation of Wells ThG-02, ThG-01, ThG-04 and ThG-03 at Theistareykir; alteration zones, 64" resistivity, averaged R64, 16" resistivity, averaged R16 and "pseudo-log" from the inversion of TEM/MT for each well, as well as connection lines for the first appearance of each alteration mineral; the colour scale is the same as that in Figure 4 (1-2000 Ωm)

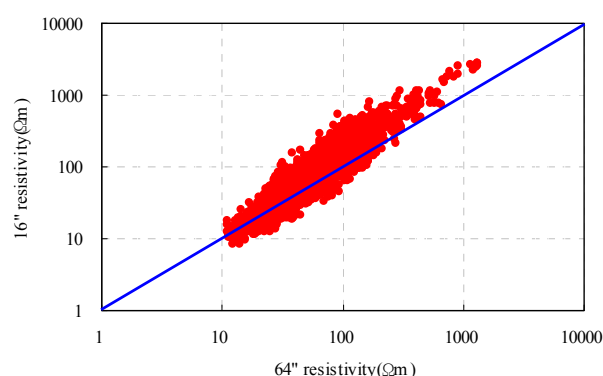


FIGURE 21: Well ThG-01: Comparison of measured 16" and 64" resistivity on a log-log scale

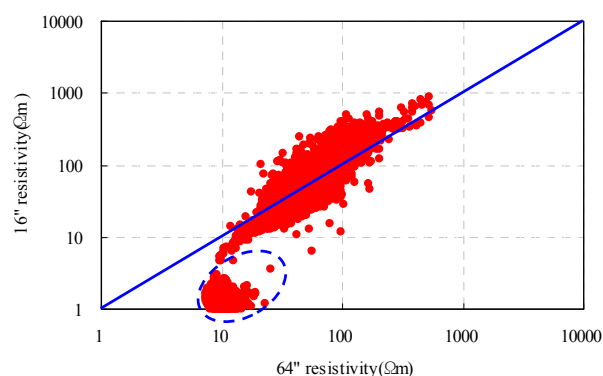


FIGURE 22: Well ThG-09: Comparison of measured 16" and 64" resistivity on a log-log scale

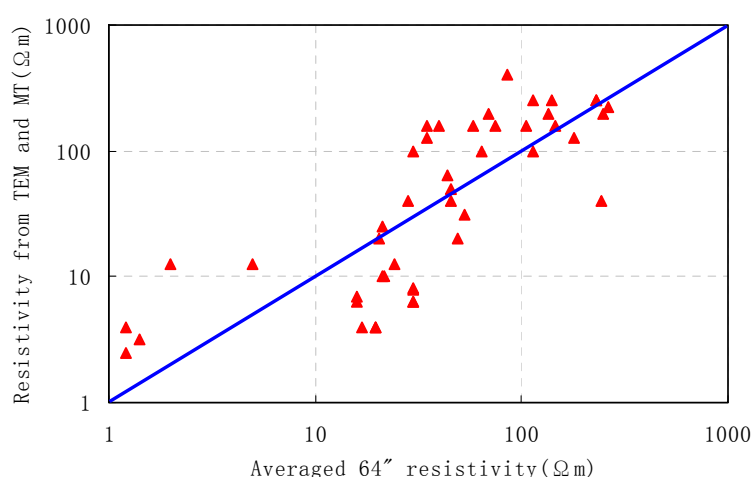


FIGURE 23: Comparison of the “pseudo-logs” from TEM and MT surface exploration and averaged 64" resistivity from 5 boreholes at Theistareykir on a log-log scale

6. CONCLUSIONS AND FUTURE SUGGESTIONS

The resistivity in boreholes and the resistivity from the inversion of TEM and MT data have slight differences but, in general, show a very good correlation. They show a high-resistivity core under a low-resistivity cap which reaches the surface in some of the wells at Theistareykir. The resistivity shown in the “pseudo-logs” from the inversion of TEM/MT decreases from the surface and increases with depth which also applies for the resistivity in Wells ThG-01, ThG-02 and ThG-03, as well as in Well ThG-09. In Well ThG-04, the averaged 16" and 64" resistivity logs as well as the TEM/MT data all show the same pattern in the changing increasing and decreasing resistivity. This is indeed a remarkably good correlation between different methods of measurements. The characteristics of some important layers disappear because of the low resolutions which cause loss of details in information for the selected wells.

The first appearance of temperature dependent alteration minerals from drill cuttings analysis is shown with the resistivity in a combined log-plot for Wells ThG-02, ThG-01, ThG-04 and ThG-03 from west to east at Theistareykir. It shows that the mixed-layer clay was not detected in the central area of Theistareykir, and the alteration zone of chlorite-epidote is thicker in the eastern part than in the central

part. The first detection of epidote-amphibole was lower in Well ThG-04 than in Wells ThG-01 and ThG-02, which indicates a lower state of alteration in the well further to the east.

The gamma ray, Neutron-Neutron and resistivity logs in Well ThG-01 show a good relationship for acidic layers and intrusions, based on evidence from high gamma values caused by acidic characteristics, and high Neutron-Neutron values due to low porosity and a high resistivity value. The corrections for the influence of Caliper, temperature and fluid on resistivity logs need to be done in order to obtain more consistent results.

Well ThG-02 has lower rock temperature than the other wells at similar depths. Resistivity and alteration minerals cannot be compared in that well due to a lack of information about the alteration minerals. More intense results will be found after studies with more data, such a study of the alteration minerals in Well ThG-09 in comparison with the other wells.

ACKNOWLEDGMENTS

I would like to express my sincere gratitude to the UNU-GTP director, Mr. Lúdvík S. Georgsson, and retiring director, Dr. Ingvar B. Fridleifsson, for giving me the opportunity to participate in the six month Geothermal Training Programme, as well as the other UNU-GTP staff, Ms. Thórhildur Ísberg, Mr. Ingimar G. Haraldsson, Ms. Málfríður Ómarsdóttir and Mr. Markús A. G. Wilde for their incredible support and assistance during the whole training in Iceland. Great thanks go to my supervisors, Dr. Svanbjörg Helga Haraldsdóttir and Ms. Ragna Karlsdóttir, for their patient supervision, instructions and guidelines throughout my project; I especially benefited from Svana's attitude towards the work. Special thanks to Ms. Anette K. Mortensen at ÍSOR for her useful and helpful information about my project, and Mr. Gunnlaugur M. Einarsson at ÍSOR for preparing the 3D model from the inversion of TEM and MT electrical soundings. Thanks to all lecturers, staff members of ÍSOR and Orkustofnun for their comprehensive presentations, sharing of their knowledge and experiences, as well as to all of my dear classmates for the great and wonderful life we spent together in Iceland.

Many thanks to Dr. Li Wenpeng, Dr. Guo Jianqiang, Dr. Sun Xiaoming, Dr. Cha Enlai and my institution (Centre for Hydrogeology and Environmental Geology Survey, which belongs to the China Geological Survey under the Ministry of Land and Resources) for approving and supporting me to attend the UNU training programme. Above all, I am very grateful to my family, especially my parents, for their full understanding, strong encouragement and continuous support for the whole period of my study and stay in Iceland.

REFERENCES

- Ármannsson, H., 2004: Chemical aspects of exploration of the Theistareykir high temperature geothermal area, N-E Iceland. *Proceedings of the 11th International Symposium on Water-Rock Interaction 2004*, Taylor & Francis Group, London, 63-67 pp.
- Ármannsson, H., 2011: The Theistareykir geothermal system, North East Iceland. Case history. *Paper presented at "Short Course VI on Exploration for Geothermal Resources", organized by UNU-GTP, GDC and KenGen, Lake Naivasha, Kenya*, 11 pp.
- Ármannsson, H., Gíslason, G. and Torfason H., 1986: Surface exploration of the Theistareykir high-temperature geothermal area with special reference to the application of geochemical methods. *Applied Geochemistry*, 1, 47-64.

Ármannsson, H., Kristmannsdóttir, H., Torfason, H. and Ólafsson, M., 2000: Natural changes in unexploited high temperature geothermal areas in Iceland. *Proceedings of the World Geothermal Congress 2000, Kyushu-Tohoku, Japan*, 521-526pp.

Arnaldsson, A. Halldórsdóttir, S., Kjaran, S.P. and Axelsson, G., 2011: *Mathematical model of the Theistareykir geothermal system and first assessment of production capacity*. ÍSOR – Iceland Geosurvey, Reykjavík, report ÍSOR-2011/049 (in Icelandic), 58pp.

Árnason, K., Karlsdóttir, R., Eysteinnsson, H., Flóvenz, Ó. G. and Gudlaugsson, S. Th., 2000: The resistivity structure of high-temperature geothermal systems in Iceland. Oral presentation at IGA, *Proceedings of the World Geothermal Congress 2000, Kyushu-Tohoku, Japan*, 923-928 pp.

Árnason, K., Haraldsson, G.I, Johnsen, G.V., Thorbergsson, G., Hersir, G.P., Saemundsson, K., Georgsson, L.S., Rögnvaldsson, S.Th. and Snorrason, S.P., 1987: *Nesjavellir–Ölkelduháls. Surface exploration*. Orkustofnun, Reykjavík, report OS-87018/JHD-02 (in Icelandic), 112 pp.

Björnsson, S., Gudmundsdóttir, I.D., and Ketilsson, J., 2010: Geothermal development and research in Iceland. Orkustofnun, Reykjavík, 39 pp, website: www.nea.is/media/utgafa/GD_loka.pdf.

Darling W.G. and Ármannsson H., 1989: Stable Isotopic aspects of fluid-flow in the Krafla, Námafjall and Theistareykir geothermal systems of Northeast-Iceland. *Chemical Geology*, 76-3/4, 197-213.

Franzson, H., 1994: *Nesjavellir. Details about alteration in a geothermal system*. Orkustofnun, Reykjavík, report OS-94021/JHD-06 (in Icelandic), 34 pp.

Franzson, H., Árnason, K., Saemundsson, K. and Gunnlaugsson, E., 2010: The Hengill geothermal system. *Proceedings of the World Geothermal Congress 2010, Bali, Indonesia*, 9 pp.

Gíslason G., Johnsen, G.V., Ármannsson, H., Torfason, H., and Árnason, K., 1984: *Theistareykir – geothermal prospecting in a high temperature field*. Orkustofnun, report OS-84089/JHD-16 (in Icelandic), 134 pp.

Gudmundsson, Á., Gautason, B., Lacasse, C., Axelsson, G., Thorgilsson, G., Ármannsson, H., Tulinius, H., Saemundsson, K., Karlsdóttir, R., Kjaran, S.P., Pálmarrson, S.Ó., Halldórsdóttir, S. and Egilson, Th., 2008: *Conceptual model of the Theistareykir field and a volumetric resource assessment*. ÍSOR – Iceland GeoSurvey, Mannvit Engineering and Vatnaskil Consulting Engineers, Reykjavík, report ÍSOR-2008/024, 67 pp.

Grönvold, K., and Karlsdóttir, R., 1975: *Theistareykir. An interim report on the surface exploration of the geothermal field*. Orkustofnun, Reykjavík, report OS-JHD-7501 (in Icelandic), 37pp.

Haraldsdóttir, S.H., Franzson, H. and Árnason, K., 2012: Preliminary study of down-hole resistivity from 72 boreholes in the S-Hellisheidi Geothermal Field, SW-Iceland, with respect to surface resistivity data and alteration minerals. *Proceedings 37th Workshop on Geothermal Reservoir Engineering, Stanford University, Stanford, Ca*, 10 pp.

Haraldsdóttir, S.H., Franzson, H., Árnason, K., Einarsson G.M., and Björnsson, H., 2010: Comparison of down-hole and surface resistivity data from the Hellisheidi geothermal field, SW-Iceland. *Proceedings of the World Geothermal Congress 2010, Bali, Indonesia*, 25-29.

Karlsdóttir R. and Vilhjálmsen, A.M., 2011: *MT and TEM survey at Theistareykir in 2009*. ÍSOR-Iceland GeoSurvey, Reykjavík, report ÍSOR-2011/021 (in Icelandic), 78 pp.

Karlsdóttir R., Vilhjálmsson A.M., Árnason K. and TeklesenbetB., A., 2012: *Theistareykir geothermal area, Northern Iceland, 3D inversion of MT and TEM data*, ÍSOR – Iceland GeoSurvey, Reykjavík, report ÍSOR-2012/046, 173 pp. (TeklesenbetB?)

Karlsdóttir, R., Eysteinnsson, H., Magnússon, I.Th., Árnason, K., and Kaldal, I., 2006: *TEM resistivity surveying at Theistareykir and Gjástykki in 2004-2006*. ÍSOR-Iceland GeoSurvey, Reykjavík, report ÍSOR-2006/028 (in Icelandic), 88 pp.

Kristmannsdóttir, H. Alteration of Basaltic Rocks by Hydrothermal-Activity at 100-300°C. *Developments in Sedimentology*, 1979 (17), 359-367.

Lu Q.H., Zhang X.X., and He Z.Y., 2012: Geothermal development and analysis home and abroad. *China Petrochemical 2012, abstracts*, 39.

Saemundsson, K., 2007: *Geology of the Theistareykir area*. ÍSOR-Iceland GeoSurvey, Reykjavík, report ÍSOR-07270, 23 pp.

Schlumberger, 2008. “*Petrel introduction course*”, Schlumberger, course material, 555pp.

Stefánsson, V. and Steingrímsson, B.S., 1990: *Geothermal logging I, an introduction to techniques and interpretation* (3rd ed.). Orkustofnun, Reykjavík, report OS-80017/JHD-09, 117 pp.

Steingrímsson, B., 2011a: Geothermal well logging: Cement bond and Caliper logs. *Paper presented at “Short Course on Geothermal Drilling, Resource Development and Power Plants”*, organized by UNU-GTP and LaGeo, Santa Tecla, El Salvador, 9 pp.

Steingrímsson, B., 2011b: Geothermal well logging: Geological wireline logs and fracture imaging. *Paper presented at “Short Course on Geothermal Drilling, Resource Development and Power Plants”*, organized by UNU-GTP and LaGeo, Santa Tecla, El Salvador, 11 pp.

Vilhjálmsson, A.M., Flóvenz, Ó.G., Karlsdóttir, R., Árnason, K., Eysteinnsson, H. and Saemundsson, K., 2008: Geophysical evidence for magmatic transport in the lower crust in Iceland. *Paper presented at AGU conference 2008, paper no.MR43A-1803*.

Yu G., He L.F., He Z.X., Strack, K.M. and Tulinus, H., 2008a: *Iceland Theistareykir 2-D MT survey. Data processing and interpretation*. Mannvit, Reykjavík, and KMS Technologies, report, 64 pp.

Yu G., He L.F., Yang Y.J., He Z.X., and Strack, K.M., 2008b: *Iceland Theistareykir magnetotelluric (MT) survey data processing and interpretation*. Mannvit, Reykjavík, and KMS Technologies, report, 103 pp.



BOREHOLE GEOLOGY AND HYDROTHERMAL MINERALISATION OF WELLS MW-09 AND MW-12, MENENGAI GEOTHERMAL FIELD, KENYA

Tito Plimo Lopeyok

Geothermal Development Company

P. O. Box 17700-20100

Nakuru

KENYA

tlopeyok@gdc.co.ke, titolopeyok@yahoo.com

ABSTRACT

Wells MW-09 and MW-12 are exploration/production wells located in the caldera of the Menengai volcano in the Menengai geothermal field. They are both vertical wells. Well MW-09 was drilled to a depth of 2077 m while Well MW-12 was drilled to a depth of 2042 m. This report presents data obtained from analysis of drill cuttings from both wells. Analytical techniques applied, include binocular analysis, petrographic analysis, XRD analysis, and fluid inclusion analysis. The rock units encountered in both wells consist predominantly of trachyte, tuffs, pyroclastics, and a syenitic intrusion at depth. The top section of the well consists of blocky post-caldera trachyte lavas overlain by a thin layer of pyroclastic deposits. A thick layer of tuff encountered at 200-300 m marks the boundary between pre- and post-caldera lavas. Hydrothermal minerals in Menengai occur as replacements of primary minerals or as vein and vesicle fillings. The main hydrothermal minerals observed in both wells include: zeolite, chalcedony, calcite, pyrite, quartz, wollastonite, and actinolite. Based on alteration mineral assemblages and clay analysis, three alteration mineral zones were identified. They are: smectite zeolite zone, quartz-illite zone, and actinolite-wollastonite-illite zone. The appearance of actinolite at 1364 m in Well MW-09 and at 1922 m in Well MW-12, indicates formation temperatures over 280°C.

1. INTRODUCTION

Menengai is a high-temperature geothermal field situated north of Lake Nakuru on the floor of the central Kenyan Rift (Figure 1). It is comprised of three volcanic centres: Menengai caldera, the Ol'rongai volcano to the northwest, and the Olbanita plains and parts of the Solai tectonovolcanic axis (TVA) to the northeast (GDC, 2010). Deep geothermal wells have been drilled in the Menengai caldera and proved the existence of a geothermal resource. At the time of writing this report, 15 wells have been drilled. Wells MW-09 and MW-12 are the ninth and twelfth exploration wells to be drilled in the Menengai geothermal field, respectively, both sited within the caldera. They are vertical wells drilled to depths of 2077 and 2042 m, respectively. Well MW-09 is located at coordinates E172848, N9977301 at an elevation of 2105 m a.s.l. Well MW-12 is located at coordinates E173573, N9976446 at an elevation 2132 m a.s.l. The wells were aimed at tapping from the NE-SW striking faults and the NNW-SSE structures associated with the Solai and Molo tectonovolcanic axes, respectively.

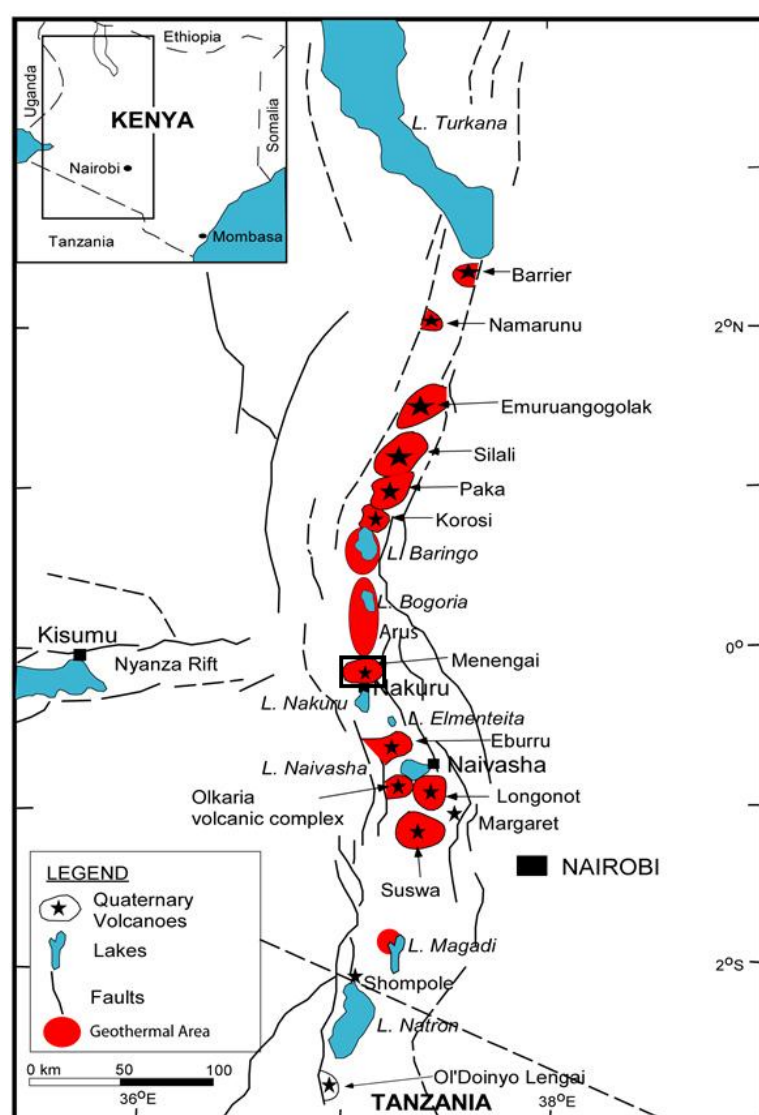


FIGURE 1: Map showing the location of Menengai (obtained and modified from Omondi, 2011)

2005). The graben basins are linked by intracontinental transforms and segmented by transfer zones and accommodation zones. The East African Rift system has two main branches: the western and eastern branches. The western branch runs over a distance of 2200 km from the Afar triple junction to Northern Tanzania while the eastern branch runs over 2100 km from Lake Albert in Uganda to Lake Malawi in Malawi.

Two mantle plumes occur beneath the East African Rift system. The northern plume corresponds to the Ethiopian dome while the southern one corresponds to the Kenyan dome. However, the number of mantle plumes influencing magmatism and tectonics in the East African Rift has generated an extensive debate but with most authors favouring a two plume model (Ebinger and Sleep, 1998; George et al., 1998; Rogers et al., 2000). There is a general consensus, from geophysical, petrological, and geochemical evidence, that the Afar mantle plume underlies the Ethiopian plateau. The uncertainty is mainly in regard to the Kenyan and Tanzanian segments of the Rift system. It is suggested that magmatism was related to the presence of hot mantle plume material beneath the site of the present rift with such a mantle having a potential temperature of up to 1500°C (Mechie et al., 1997). Figure 2 shows a map of Africa illustrating elevated grounds of more than 1200 m above sea level. The elevated areas are mainly associated with a mantle that influences magmatism and tectonics in the East African Rift system.

The objectives for drilling the wells was to further explore and determine subsurface geology, hydrothermal alteration, the nature of the reservoir, chemical characteristics, and the depth to the resource. This report presents data acquired from analysis of rock cuttings from both wells. The project report was carried out as a partial fulfilment of a six month training course at the United Nations University Geothermal Training Programme (UNU-GTP).

2. GEOLOGY

2.1 Regional geology

The East African Rift system is an active continental rift zone in East Africa that is characterized by intense tectonism and volcanism. It is a series of aligned successions of adjacent individual tectonic basins which are several thousand kilometres long. The basins are generally bordered by uplifted shoulders (Chorowicz, 2005). Each basin is controlled by faults and forms a graben or a trough, nearly one hundred kilometres long, and a few tens of kilometres wide, which is either empty or filled with sediments and/or volcanic rocks (Chorowicz,

The Kenya Rift Valley forms a segment of the eastern branch of the East African Rift system. It runs from Lake Turkana in the north to Lake Natron (Tanzania) in the south where the rift splays southwards to form the Northern Tanzanian divergence. Magmatism in the Kenyan Rift is mainly related to the rise of a plume that is focused beneath a weak zone that marks the boundary between the Tanzanian craton and the adjacent Proterozoic mobile belt (Smith, 1994). Along the 40-80 km wide rift graben, several Quaternary volcanic centres are formed. The volcanoes are

rooted on open fractures such as tension joints, tail-cracks or tensional releasing bends (Korme et al., 1997). Most of the volcanoes are eruptive with one or more explosive or effusive eruptions that initiated caldera collapse. Volcanic material from these volcanic centres coupled with Quaternary sediments virtually covers the whole rift floor. The evolution of the Kenyan Rift started in early Miocene (30-35 Ma) at the Turkana Rift in northern Kenya (Baker et al., 1971, 1972; Smith, 1994; Lagat et al., 2005). This is where the earliest volcanic rocks in the Kenyan Rift have been found (Macdonald et al., 2001). It marked the onset of magmatism that has since propagated towards the south through the Central Rift and the southern Kenyan Rift before finally reaching northern Tanzania 5-8 Ma ago (Baker and Wohlenberg, 1971; Baker et al., 1972). The high elevation at the central Kenyan Rift may be the result of dynamic or thermal uplift that is caused by an underlying mantle plume (Baker and Wohlenberg, 1971). Seismic studies also indicate crustal thickening resulting from intense magmatic activity that may also contribute significantly to the uplift (KRISP working group, 1987). Crustal thickness beneath the Kenyan Rift is estimated to be 30-35 km (e.g. Mechie et al., 1997).

The basement to the Kenyan Rift (Figure 3) is complex and is divided into three zones: the Archaean Tanzanian craton, the late Proterozoic Panafrikan Mozambique belt and a zone of craton margin which was reactivated during the Panafrikan orogeny (Smith and Mosley, 1993).

The Kenyan Rift is divided into three sectors: northern, central and southern rifts. The central Kenyan rift, at Menengai, is characterized by a sharp turn in rift direction. This marks the boundary between the northern Kenyan Rift Valley and the Central Rift. The Central Kenyan Rift segment is set in the middle of the Kenyan dome. The general elevations of the rift floor rise from 1050 m in the north, to 2100 m in the centre (Central Rift), and steps down progressively southwards to 600 m at Lake Natron. Smith and Mosley (1993) explain the sharp bend of the rift at Menengai to be an intersection of the rift with a large NW-striking basement structure called the Aswa lineament. Simiyu and Keller (1997) associate the sharp bend with the extent of contact between the Archaean Tanzanian craton and the orogenic belt. A N80°E trending Nyanza half-graben branches with the Central Kenyan Rift at Menengai (Figure 3), and disappears westward under Lake Victoria. The Menengai volcano is situated at a triple junction between the northern Kenyan, central Kenyan and Nyanza rifts, almost at the centre of the Kenya dome.

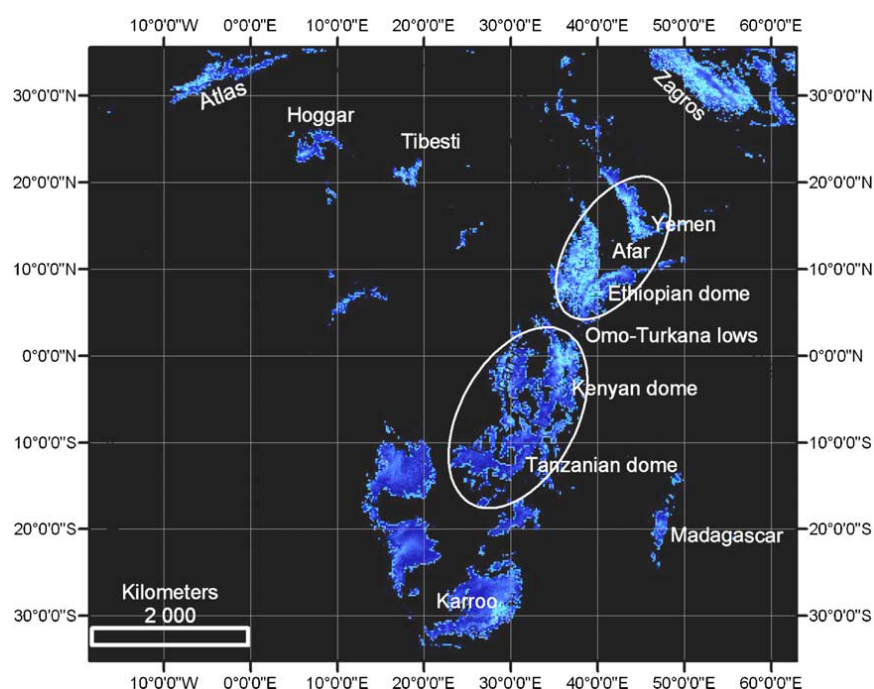


FIGURE 2: Map of Africa showing elevated surfaces higher than 1200 m; the two circles represent the Ethiopian and Kenyan domes (Chorowicz, 2005)

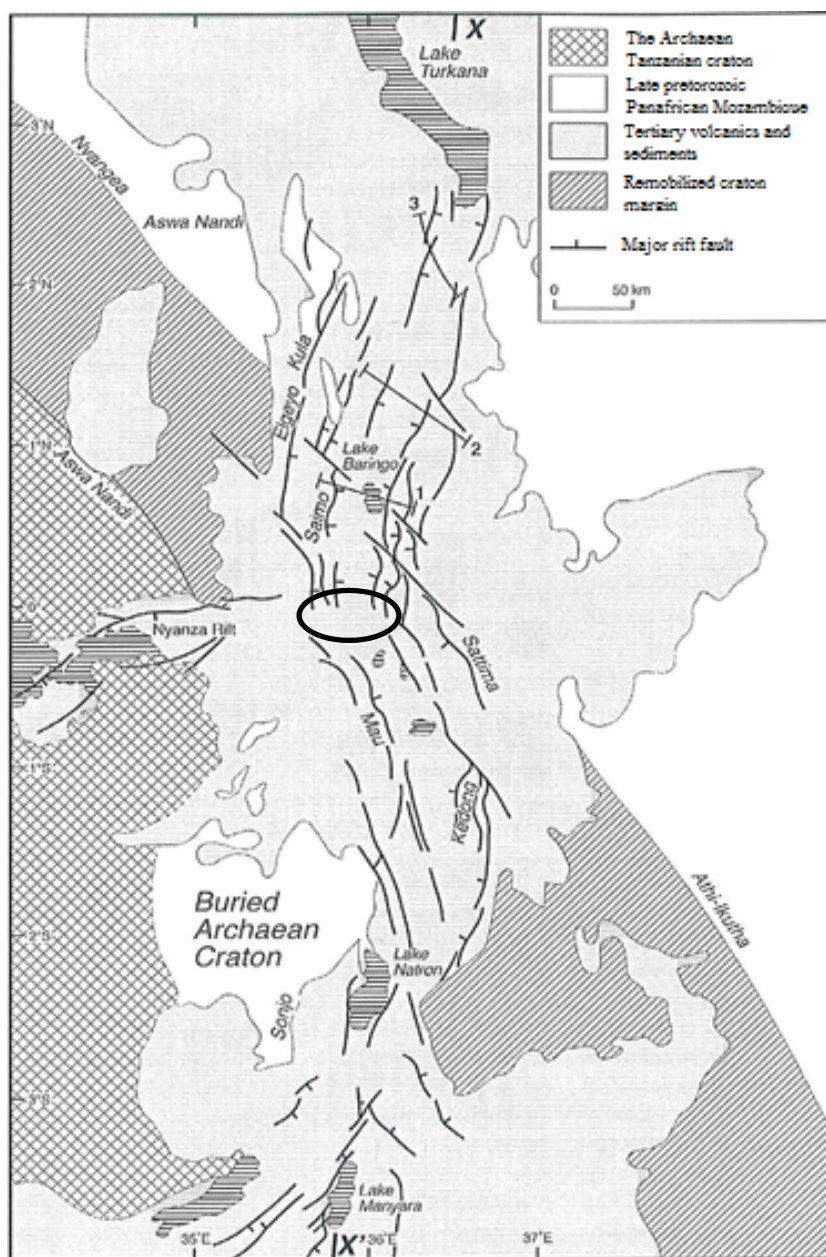


FIGURE 3: Structural framework of the Kenyan Rift; the circle marks the location of Menengai (modified from Smith and Mosley, 1993)

is associated with the formation of the shield and the eruption of lavas that preceded the collapse of the caldera. The pre-caldera lavas were covered by later syn- and post-caldera volcanics and are, therefore, not seen on the surface. The caldera wall, however, exposes a good sequence of the shield building lavas with minor airfall tuff intercalations. The oldest exposed pre-caldera lava yielded a K-Ar date of 0.18 ± 0.01 Ma (Leat, 1984). Based on the fact that the outcrop is exposed at an altitude 50 m higher than the inferred shield base, it is presumed that it must have been erupted during the early shield building stage. This, therefore, suggests that activity at Menengai started shortly before 0.18 Ma. On the north-western flank of the Menengai shield, scoraceous airfall tuffs of pre-caldera age are exposed around the Ol'rongai volcanic centre. The total volume of the pre-caldera volcanics is estimated to be 29 km^3 , mostly consisting of lava (Leat, 1984).

The second phase, the syn-caldera activity, is associated with the caldera collapse. The incremental caldera collapse is believed to have occurred in two episodes (Leat, 1984; Macdonald and Scaillet,

2.2 Geology of Menengai

The Menengai geothermal field region comprises Menengai volcano, the Ol’rongai volcanoes, the Olbanita plains, and parts of the Solai TVA to the northeast (GDC, 2010) covering an area of approximately 950 km² (Figure 4). Menengai is one of the Quaternary volcanoes formed on the axis of the Kenyan Rift (Figure 1). It is a trachytic central volcano that is underlain by a high-level magma chamber. The activity in the volcano started 0.2 Ma ago with the formation of a broad low angle trachytic lava shield (Leat, 1984). The activity continued in the Pleistocene, with the formation of a caldera, to more recent activity that has given rise to the flows on the caldera floor (Macdonald et al., 1970). The surface geology is dominated by recent (post-caldera) lavas especially within the caldera, pyroclastics and ignimbrite sheets on the northern flanks and alluvial sediments on the surrounding rift floor (Figure 4). The geology of Menengai can be divided into three main phases: pre-caldera volcanics, syn-caldera activity, and post-caldera activity. The first phase, the pre-caldera phase,

2006). The formation of the 11.5×7.5 km large caldera was accompanied by the eruption of two ash flow tuffs. Each of the tuff layers is underlain by a pumice deposit and separated by a thin layer of sediments, indicating a short quiescence period between the eruptions. The collapse is mainly associated with the second ash flow eruption. The ash flow tuffs covered an area of approximately 1350 km² with an estimated volume of 50 km³ (Leat, 1984). Ash samples (cores) of the syn-caldera activity have yielded a carbon date between 12,850-29,320 years BP. This, therefore, estimates the probable age of the Menengai caldera.

The third phase, the post-caldera activity, mainly involved an eruption of recent lavas and ash deposits from vents within the caldera. An estimated 23 km³ of lava from about seventy lava flows cover almost the entire caldera floor (Leat, 1984). The post-caldera lava pile is estimated to be about 300 m thick. Ash deposits cover areas around Menengai and are more widespread on the western flanks, probably due to westward direction of prevailing winds during the eruptions. The ash deposits are also interbedded with lava flows on the caldera floor. Other post-caldera units include lake sediments found inside the caldera and unconsolidated scoria erupted from trachytic cinder cones found in the southern part of the caldera floor and rim.

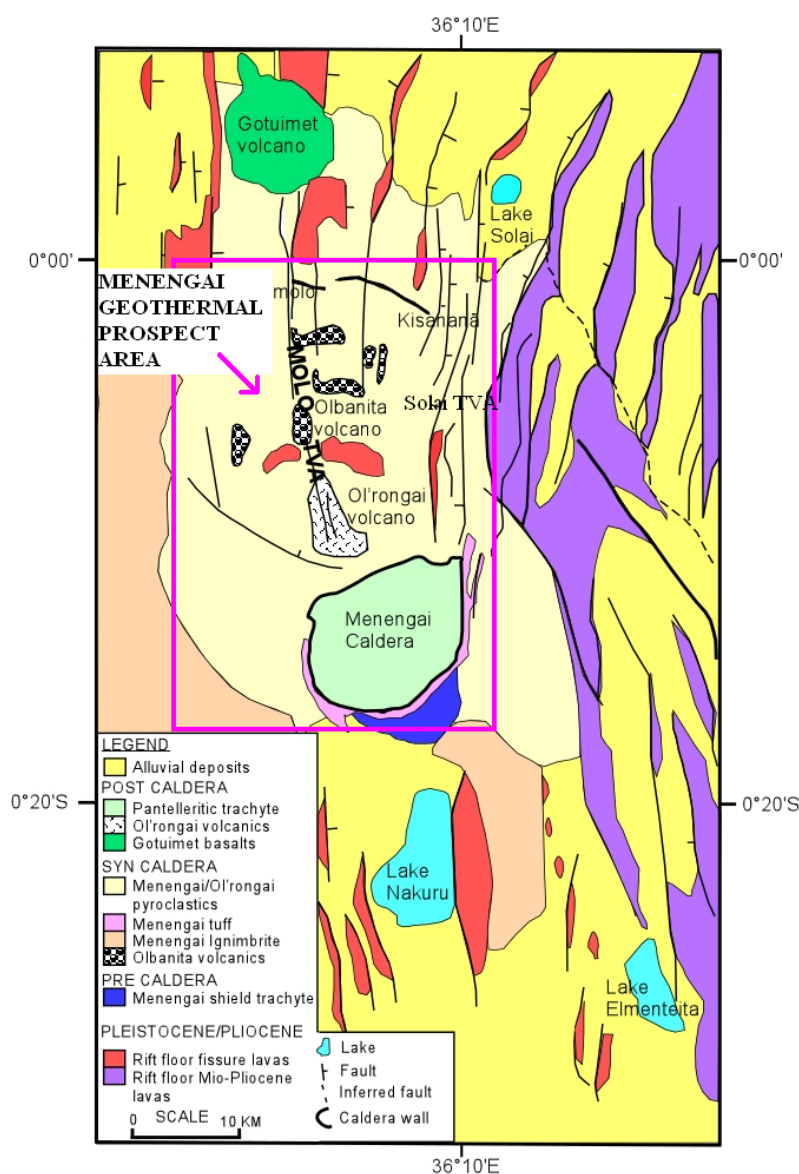


FIGURE 4: Geological map of Menengai (GDC, 2010)

2.3 Tectonic structures of Menengai

The tectonic setting of Menengai is complex. Menengai is set at a point where the Kenyan Rift abruptly takes a sharp change in direction. This change is associated with the contact between the Tanzanian craton and orogenic belts (Simiyu and Keller, 1997). The bend is also associated with the Aswa lineament intersecting the Kenyan Rift (Smith and Mosley, 1993). It also marks a triple junction where the Nyanza half-graben (failed rift) branches with the Kenyan Rift (Burke and Dewey, 1973).

According to Chorowicz, (2005), Menengai developed on a possible tail-crack end structure (Figure 5) at the southern end of a complex N-S striking fault zone. This N-S trending fault zone defines the Solai tectonovolcanic axis. Most of the post-caldera lava flows erupted from along the arched tail-crack structure that developed on the western part of the Solai TVA end. The Solai TVA is parallel to, and

continuous with, a swarm of young faults which cut the rift valley floor between Menengai and the equator (Leat, 1984). There is also an indication from the tail-crack structure that the N-S striking zone of normal faults has a dextral strike-slip throw component (Chorowicz, 2005).

Menengai caldera is an elliptical depression with major and minor axes measuring approximately 11.5 km and 7.5 km, respectively (GDC, 2010). The general NE-SW orientation (Figure 6) and elliptical shape depicts extensional tectonics in Menengai with the main rift trough trending N-S north of Menengai and NNW-SSE south of Menengai. Mibei (2012) relates the extensional tectonics on the caldera to spatial variations in the crustal stress regime, as illustrated by different orientations of faults north of the caldera.



FIGURE 5: Tail-crack end of the N-striking fault zone in Menengai (Chorowicz, 2005)

A NW-SE trending ridge on the northwest part of the Menengai shield defines the Ol'rongai tectonic structure that represents part of the larger Molo TVA (Geotermica Italiana, 1987). This structure extends northwards past the Goitumet volcanic centre and possibly southwards into the Menengai caldera. These two tectono-volcanic axes, Molo TVA and Solai TVA, are important in controlling the permeability in the geothermal system.

2.4 Geothermal exploration and geoscientific aspects of Menengai

A detailed study of the geothermal assessment of the Menengai field was carried out by KenGen and the Kenyan Ministry of Energy in 2004. The purpose of the investigations was to determine the existence of a geothermal system in Menengai and recommend locations for exploratory drilling. The study involved geological, geophysical and geochemical surveys. Integrated results of the studies indicated the existence of a hot, ductile, and dense body centred beneath the Menengai caldera. The study estimated that the high-temperature part of the resource covers an area of about 48 km² (KenGen, 2004). More detailed work involving all the geoscientific disciplines was carried out by the Geothermal Development Company (GDC) in 2010. Based on the results of the study, exploratory wells were sited. Drilling started in February 2011 and is still ongoing. At the time of writing this report, 15 wells have been drilled.

An iso-resistivity map plotted from 1D joint inversion of magnetotelluric (MT) and transient electromagnetic (TEM) data indicates a conductive body of less than 5Ωm at 2000 m.b.s.l, centred under the southern caldera floor, and a smaller anomaly at the centre of the caldera (Figure 7).

Result from micro-seismic studies indicated that seismic events are concentrated within the Menengai caldera, around the central to the southern part of the caldera, by the northeast caldera wall and the Olbanita area to the northwest of the Menengai caldera where the events are also shallow (Simiyu, 2010). The events occur along two trends. The first follows the rift axis in a NNW-SSE trend cutting through Olbanita, Menengai and towards Lake Nakuru in the southeast. The second trend is parallel to the Nyanza Rift axis in a NE-SW direction along the major axis of the caldera from Bahati on the Aberdare ranges, through the caldera, Nakuru town and Rongai. Figure 8 shows a NW-SE seismic event section with a depth distribution across Olbanita and Menengai caldera. V_p/V_s ratios indicate the caldera area to have lower velocity ratio formations with deeper horizons, suggesting a high temperature, low pore pressure and vapour dominated system (Simiyu, 2010).

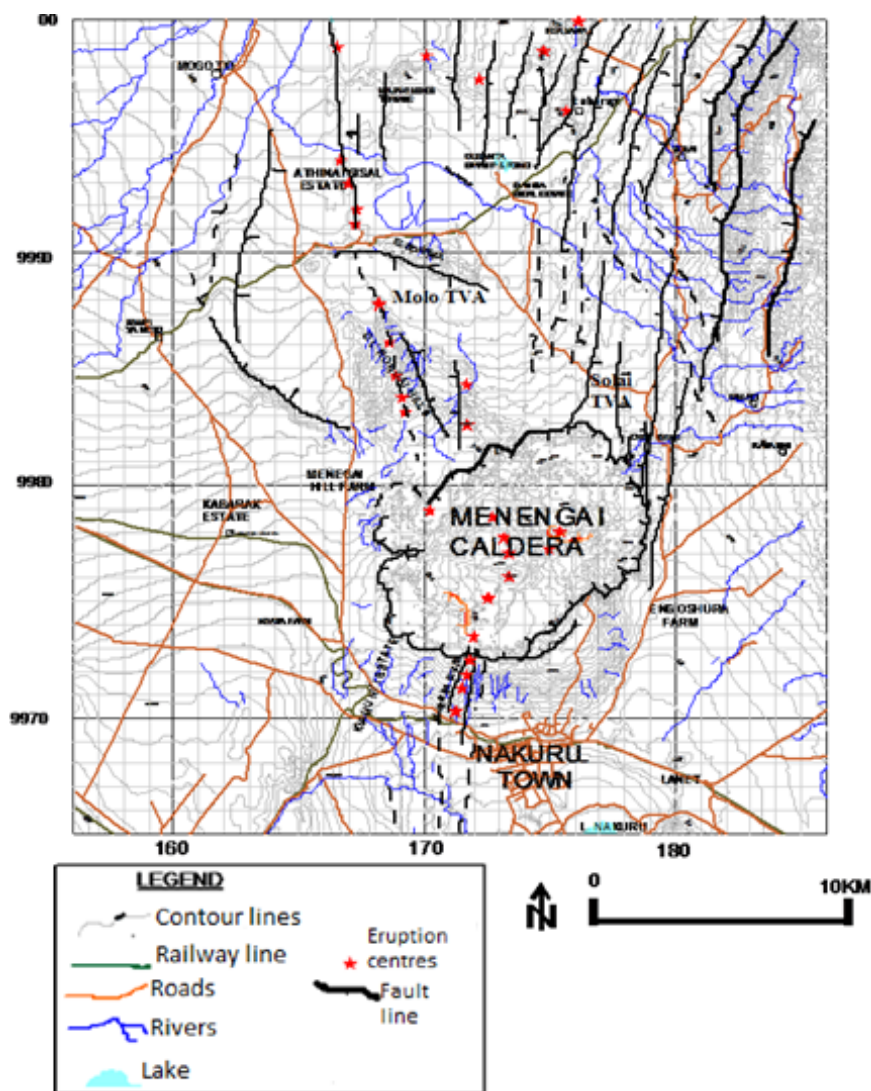


FIGURE 6: Structural map of Menengai (GDC, 2010)

The seismic activity is intense with shallow events centred on the Menengai caldera. This zone of shallow events is, therefore, presumed to indicate the heat source for the geothermal system.

Geochemical studies in Menengai revealed high CO_2 values ($>2.5\%$) along a narrow belt running NW-SE (along Molo TVA) while other areas exhibit values lower than 1 %. High carbon dioxide concentration in the soil gas was observed around Ol'rongai Hill, in the central part of the caldera and in the south-western part of the caldera, indicating good permeability. High absolute values of Rn-220 gases in the soil and fumaroles were measured in the northern and north-western parts of Menengai and in the caldera, indicating enhanced permeability. The ratio of the Rn-220/ CO_2 gases indicated high values in the northern parts of the field and within the caldera. These areas also showed high CO_2 and Rn-220 absolute values. The soil temperature measurements taken at a depth of 0.7 m showed a higher-temperature anomaly in the caldera, especially around the fumaroles. CO_2 , H_2 and H_2S gas geothermometry for the Menengai fumaroles gave calculated temperatures of above 250°C . From the temperature estimation using the gas geothermometers, it is presumed that the reservoir temperatures beneath Menengai caldera are over 250°C (GDC, 2010).

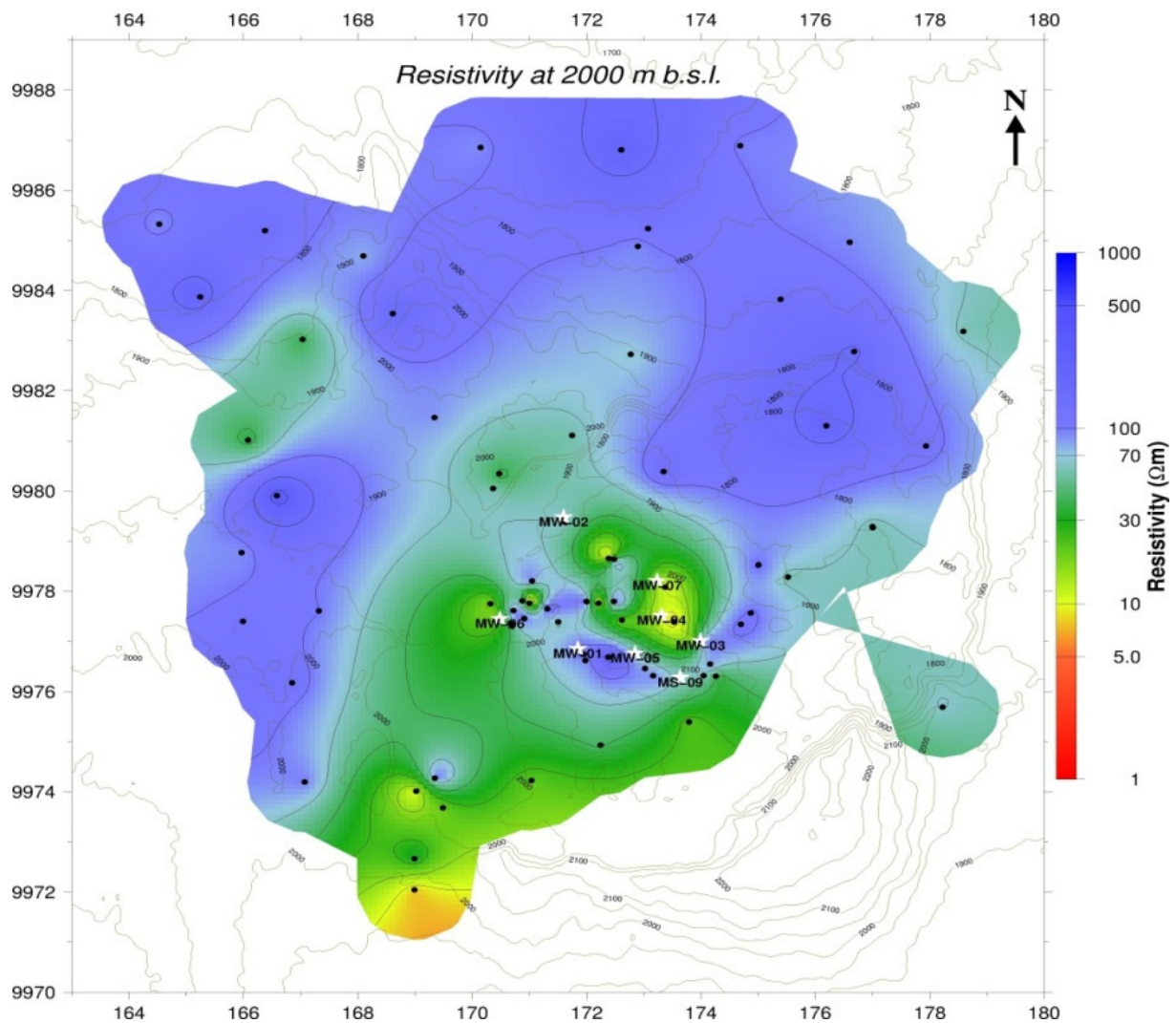


FIGURE 7: Iso-resistivity map at 2000 m.b.s.l. of the Menengai field; black dots denote 1D inversion models while the white stars represent Menengai wells (Gichira, 2012)

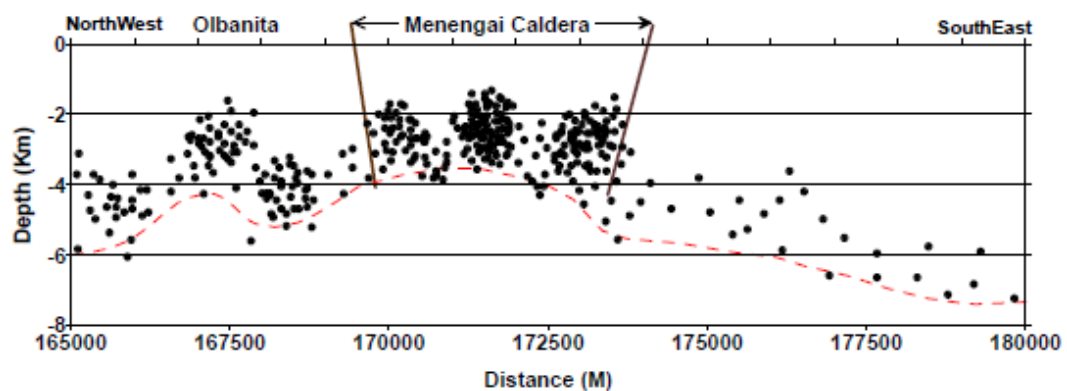


FIGURE 8: The distribution of seismic events in Menengai (Simiyu, 2010)

3. SAMPLING METHODOLOGY AND ANALYSIS

Cuttings from Menengai wells were sampled at two metre intervals during drilling after which a preliminary binocular analysis was performed at the rig site by the rig geologists. The main features identified include: the lithology penetrated, the rock texture, fractures, alteration minerals and the intensity of alteration. The results from the preliminary analyses supported the determination of casing depths as well as in advising the drilling crew and engineers on various geotechnical aspects. The samples were then taken to the GDC laboratory, washed, dried, packed and stored systematically for easy retrieval. Samples of interest from selected depths were identified and thin sections prepared for further petrographic analysis. For the purpose of this project, portions of cutting samples from all the available depths for Wells MW-09 and MW-12 were sent to the Iceland GeoSurvey (ISOR) laboratories in Iceland for detailed analyses. The four main analytical techniques employed were: binocular analysis, petrographic spectroscopy, X-ray diffraction analysis, and fluid inclusion analysis.

3.1 Binocular analysis

All the samples were prepared for binocular analysis. The samples were carefully washed with clean water to remove impurities and dust to enhance visibility. The aim of this analysis was to identify the lithology, texture, alteration mineralogy, degree of alteration, and fracturing. The samples were analysed using an Olympus SZX12 binocular microscope and the properties noted include: the colour of the rock, grain size, texture, vein filling if present, alteration mineralogy, and degree of alteration; from these observations, the rock types and their properties were identified. Samples of interest were selected for XRD analysis. Platy calcite and quartz grains from different depth ranges in both wells were picked for fluid inclusion geothermometry.

3.2 Petrographic microscopy

Based on preliminary binocular analysis performed at the rig site, representative samples from different depths and lithologic units in both wells were selected for petrographic analysis. A total of 66 thin sections, 21 from Well MW-09 and 45 from Well MW-12, were prepared at the GDC laboratories. The thin sections were analysed using a Leitz Wetzler petrographic microscope. The purpose was to confirm rock types, grain sizes, rock textures, and to identify additional alteration minerals that were not observed during the examination with the binocular microscope. The order at which the alteration minerals were formed was also noted when possible.

3.3 X-ray diffraction analysis

A total of 36 samples, 27 from Well MW-09 and 9 from Well MW-12, were selected for XRD clay analysis in order to identify the alteration zones. Untreated, glycolated and heated samples were evaluated to classify the clay types found in the wells. The clay analyses were carried out using a Bruker D8 focus XRD machine. Results of the XRD analysis for both wells are summarized in tables in Appendices I and II, and examples given in Appendix III.

Portions of cuttings from selected samples were scooped and mixed with water in test tubes. The mixtures were shaken for 4-5 hours to dissolve and extract clay from the cuttings. A few drops of water from each of the dissolved drill cutting samples were placed on separate glass slides which had been washed previously with an organic solvent, acetone and dipped in a glycol solution for 24 hours. The samples in the test tubes were left to settle for 12 hours. The clay samples were first run in the X-ray diffractometer and the peaks recorded. The glycolated samples were subsequently run in the X-ray diffractometer and the peaks were recorded. The clay samples were heated to 550°C before performing the third run in the X-ray diffractometer and the peaks were recorded. For each sample, three peaks, each from the corresponding runs, were recorded. The main aim for the analysis was to identify clays,

zeolites and actinolite alteration minerals, establish the alteration zonation and to further deduce the alteration temperatures.

3.4 Fluid inclusion analysis

Based on the measured temperature logs and binocular analysis, quartz and platy calcite mineral grains were selected from two depth ranges in each well. A fluid inclusion analysis for the mineral grains was undertaken to predict the temperatures at which the minerals were formed (primary mineral) or when the fractures healed (secondary mineral). The mineral grains were heated using a Linkam THSMG 94 stage and the temperatures at which bubbles disappeared were noted. The temperature measurements were recorded at 5°C intervals. The temperatures at which the bubbles disappeared corresponded closely to the temperature conditions at which the fluids were trapped in the crystal. This is referred to as the homogenisation temperature (T_h). Fluid inclusion geothermometry, when compared with results from alteration mineralogy and well temperature measurements, provides important information on the thermal history of a geothermal system. It provides evidence as to whether a geothermal system is heating, cooling or is in equilibrium.

4. BOREHOLE GEOLOGY

4.1 Drilling wells

Wells MW-09 and MW-12 are the ninth and twelfth wells, respectively, to be drilled in the Menengai geothermal field. They are both vertical wells located inside the caldera (Figure 9). The wells were

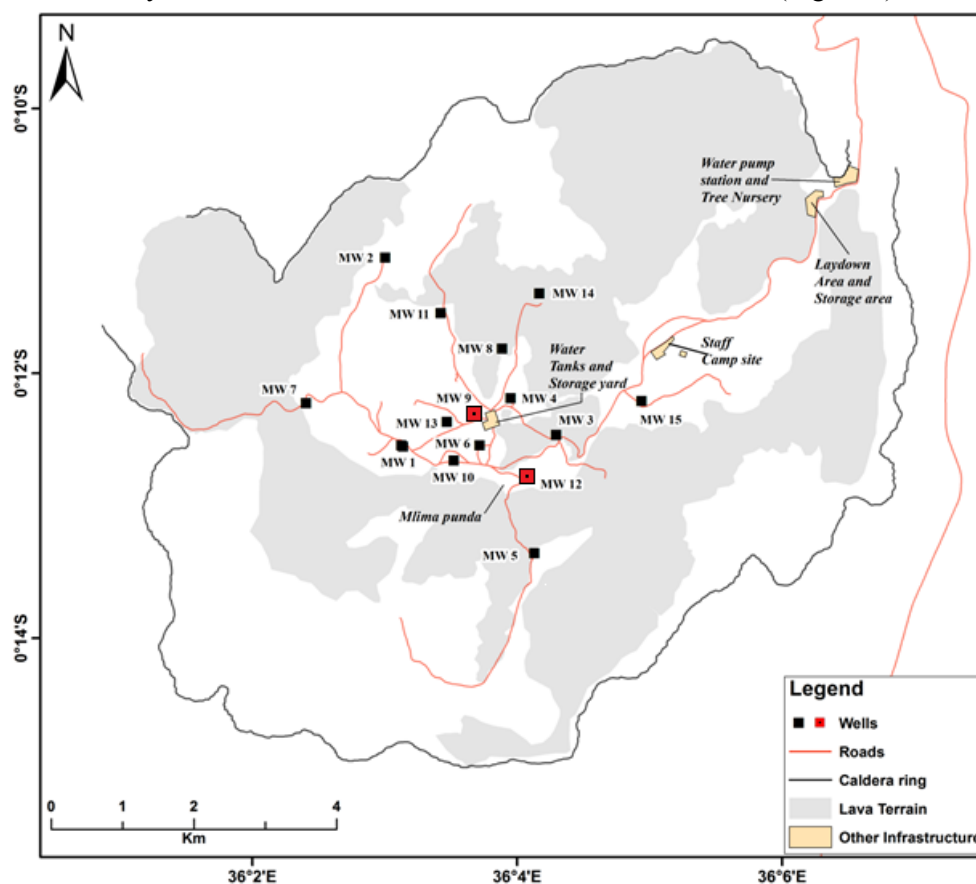


FIGURE 9: Locations of wells MW-09 and MW-12

aimed at tapping from the NE-SW striking faults and the NNW-SSE structures associated with Solai and Molo tectonovolcanic axes (Figure 6).

4.1.1 Well MW-09

The well was spudded on 17th July, 2012 and completed on 29th October, 2012. It took 105 days to complete drilling the well, reaching a depth of 2077 m from the cellar top (CT) (Figure 10). The target depth according, to the well prognosis, was set at 2200 m. However, the drilling was terminated at 2077 m after persistent circulation losses from 2036 to 2077 m, and a significant increase in torque. An effort was made to regain circulation by employing underbalanced drilling, but this proved to be futile. Based on experience from previously drilled wells within the field, it was found necessary to terminate the well at this point. The drilling of Well MW-09 was executed in four phases from the start to the successful completion (Table 1).

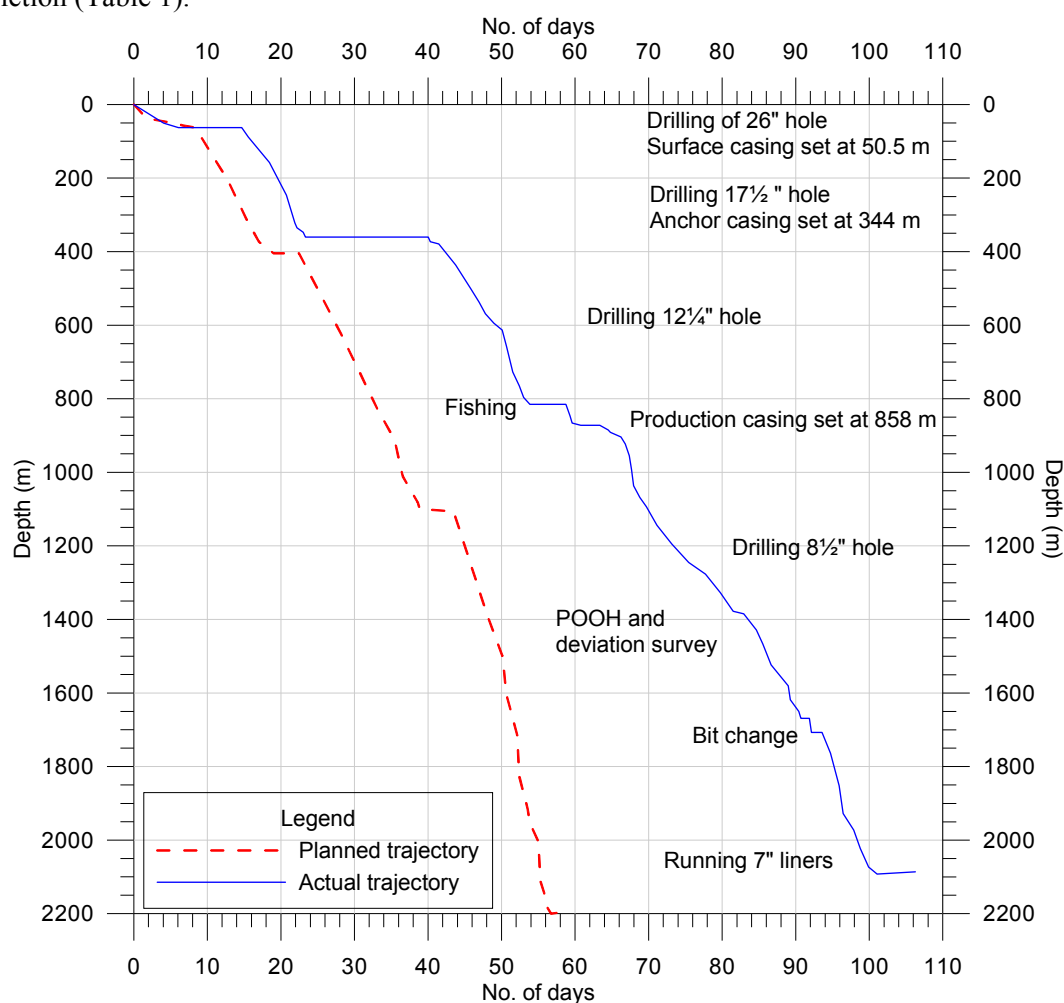


FIGURE 10: Drilling progress of Well MW-09

For the first phase, a 26" surface hole was drilled to a depth of 50 m CT. The drilling fluid used was mud for the first 10 m and thereafter changed to water with high viscosity mud sweeps at regular intervals. The 20" surface casing was set at 50 m. Total loss of

TABLE 1: Drilling phases and depths of Well MW-09

Drilling phase	Drill bit diameter	Casing diameter	Drilled depth (m)
First	26"	20"	50
Second	17 1/2"	13 3/8"	344
Third	12 1/4"	9 5/8 "	858
Fourth	8 1/2"	7" Slotted liners	2077

returns was experienced from 2-14 m and 16-26 m.

Circulation of returns was fairly good in the bottom half of the section. Primary and secondary cement jobs were done. Cement return was received on the surface after performing sixteen backfill cement jobs. A total of 180.34 tons of cement was consumed in this section.

For the second phase, a 17½” hole was drilled to a depth of 344 m CT where the 13⅜” casing was set. The upper part of this section was drilled with mud and thereafter with water and occasional mud sweeps to the bottom of the section. This intermediate section was characterized by partial losses from 50-131 m, total loss of circulation from 131-338 m and good circulation of returns from 338-344 m. Primary cementing was done and cement was received on the surface after performing nine backfill cement jobs, consuming a total of 110.75 tons of cement.

The 12¼” hole, the third phase, was drilled to a depth of 858 m CT and the 9⅝” production casing was set at 856 m. The drilling fluid used was mud from 344-800 m and water with gel sweeps at regular intervals from 800-858 m. A 9⅝” casing was run in to a depth of 858 m and a cement job was performed. Cement was received on the surface after the first backfill cement job, consuming 54 tons of cement. Circulation of returns was fairly good in this section except for a total loss experienced at 542-552 m and occasional intermittent losses. The fourth and final phase of drilling was the 8½” production section which was drilled to the total depth of 2077 m, after which the 7” slotted liner was run in. Circulation of returns in this section was relatively good except for intermittent losses and partial loss of circulation at 882-886, 890-892, 894-900, 902-904, 908, 950-954, 964-968, 1022, 1058, 1072, 1042, 1158, 1368, 1382, 1482, 1694-1700, 1722, 1862-1866, 1978, 1996, 2008, 2044, 2054, and a total loss from 2060 m to the bottom of the well. The liner was set hanging at 801 m, 55 m above the production casing shoe.

4.1.2 Well MW-12

The well was spudded on 14th October 2012 and completed on 16th January 2013. It took 93 days to complete drilling the well (Figure 11). The target depth was set at 2200 m but as the drill string got stuck, drilling was terminated at 2042 m. A summary of casing depths, bits and casing diameters for the four phases of well drilling is shown in Table

TABLE 2: Drilling phases and depths of Well MW-12

Drilling phase	Drill bit diameter	Casing diameter	Drilled depth (m)
First	26”	20”	48
Second	17 ½”	13⅜”	358
Third	12 ¼”	9⅝”	850
Fourth	8 ½”	7” Slotted liners	2042

2. The surface hole was drilled with mud to a depth of 48 m with good returns of circulation until 38 m depth where total loss of circulation was encountered and was persistent until the casing depth of 48 m had been reached. The 20” surface casing was run in and a cement job was performed. Cement returns were received on the surface after primary cementing and six backfill cement jobs. A total of 96.28 tons of cement was used in this section.

The second phase was drilled with a 17½” bit to a depth of 358 m, where the anchor casing was set. Mud was used as drilling fluid from 48 to 332 m and then water to the bottom of the section. Circulation returns were rather poor with frequent circulation losses that prompted ten cement plug jobs and/or use of lost circulation material (LCM) to heal the losses and regain circulation. A total volume of 164.68 tons of cement was consumed in this section, 76.89 tons for the casing and 87.79 tons for the plug jobs.

The third phase, a 12¼” hole, was drilled to a depth of 850 m and the production casing was set at 843 m. The section was initially drilled with mud to a depth of 444m, before switching to aerated drilling to the bottom of the section. Circulation of returns was generally not good in this section. Major circulation losses were encountered at 436-478, 526-552, 562-588, 594-616, 680-690, and 736-806 m while a total loss was encountered at 436-478 m. Cement plug jobs were performed where total loss was experienced

in an attempt to heal the loss. Primary cementing and two backfills were completed before returns were received on the surface. A volume of 96.86 tons of cement was consumed in this section. A volume of 79.69 tons of cement was used to cement the 9 $\frac{5}{8}$ " casing while 17.17 tons was used to perform plug jobs.

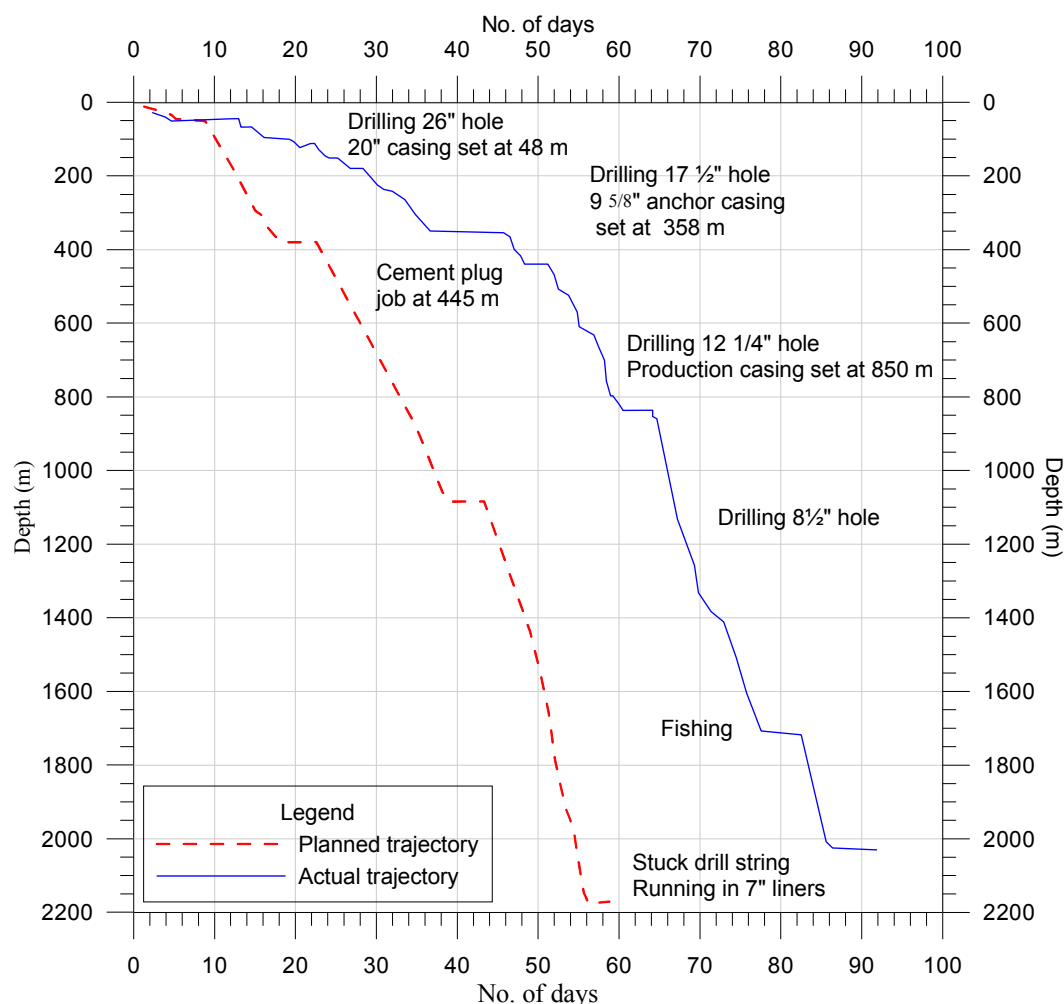


FIGURE 11: Drilling progress of Well MW-12

The final phase was drilled using an 8 $\frac{1}{2}$ " bit to a depth of 2042 m with aerated water and foam. Circulation returns were good throughout the column. No major geotechnical problems were encountered in this section. The drill string got stuck at 2042 m for four days before it was freed. After the string was unstuck, a 7" slotted liner was run in to the bottom of the hole. The liner was set hanging at 813 m, 30 m above the production shoe casing.

4.2 Stratigraphy

The stratigraphy of Menengai Wells MW-09 and MW-12 is dominated by trachyte with occasional tuff intercalations. Pyroclastics and a syenitic intrusion at the bottom section of the wells are the only other formations encountered.

Pyroclastics: These occurred at two levels in Well MW-09, on the surface (0-2 m) and from 342-346 m, and once in Well MW-12, from 8-12 m. They are brownish grey in colour, oxidized and unaltered. The rock contains a mixture of brownish tuff, pumice, trachyte, and obsidian (only in the top section). The tuff is vesicular with some of the vesicles filled with amorphous silica lining and zeolites.

Trachyte: In both wells trachytes occurred from the surface to the bottom of the well with intermittent tuff intercalations. Trachytes vary widely in terms of colour, texture and mineralogical composition. It varies from light grey, greenish grey, brownish grey to dark grey in colour, fine to medium grained in grain size. The texture varies from equigranular, to weakly porphyritic to strongly porphyritic. The porphyritic nature and their dissimilarity occur as a result of varying phenocryst sizes and quantity. The main phenocrysts are pyroxenes and sanidine feldspars. The groundmass is mainly made up of feldspars that show trachytic flow textures and, in some instances, spherulitic textures. The lower section of the wells is mainly composed of medium to fine grained trachytes.

In the upper sections of the wells, the trachyte is fresh, grey to dark grey in colour, fine grained and porphyritic. It is blocky in nature and highly fractured and, therefore, circulation fluid was lost in this section. The enormous amount of primary cement pumped during the surface casing and the number of backfills in the section gives a picture of how fractured the formation is. From 50 m, the rock is relatively fresh but with slight oxidation and a faint greenish colouration. The greenish colouration intensity tends to increase with increasing depth. From a depth of 550 m, the trachyte is characterized by large phenocrysts of sanidine, set in a fine feldspar rich groundmass. Alteration varies at various depths ranging from moderate to high alteration in the middle to lower sections of the wells. Sanidine is completely altered to albite at these depths and high-temperature minerals of actinolite and wollastonite appear from 1366 m in Well MW-09 and 1858 m in Well MW-12 and persist to the bottom of the wells. Calcite is rare in this unit, especially from the surface to 800 m, but occurs where there are tuff intercalations, and the amount increases significantly at depths from 800 m to the bottom. Pyrite occurs intermittently from the depth of 700 m to the bottom of the wells.

Tuff: is encountered on several occasions in both wells, either as thick layers or lenses, intercalated with trachytes. Tuffs intersections are closely associated with both partial or total losses and high penetration rates. The first occurrence of a tuff layer in Well MW-09 was at 120 m, a 12 m thick layer immediately followed by a major loss zone. After the 200 m loss zone, tuff occurred as lenses intercalating with trachyte from 342 m to 428 m. Other thick tuff layers in this well were at 346-368, 510-536, 688-700, 742-780, 1438-1454, and at 1688-1700 m.

In Well MW-12, substantial layers of tuff were intercepted at 210-270, 328-354 and 400-434 m.

Syenite: A thin sheet of a syenitic intrusion was intercepted at 1948-1960 m in Well MW-09 and at 1872-2028 m in Well MW-12. It is whitish in colour, medium to coarse grained and porphyritic with dark greenish pyroxenes and amphiboles phenocrysts.

4.2.1 Lithology of Well MW-09

The lithology of Well MW-09 is shown in Figure 12.

0-2 m Pyroclastics: The formation contains a mixture of brownish tuff, pumice, trachyte, and obsidian.

2-14 m: Circulation loss.

14-16 m Trachyte: Grey, fine grained porphyritic trachyte.

16-24 m: Circulation loss.

24-28 m Trachyte: Grey to dark grey, fine grained porphyritic trachyte.

28-50 m Trachyte: Light grey, hypocrySTALLINE trachyte with elongated phenocrysts of clinopyroxene.

50-72 m Trachyte: Light grey to brownish grey, fine grained, porphyritic trachyte. The formation is more oxidized than the overlying formation.

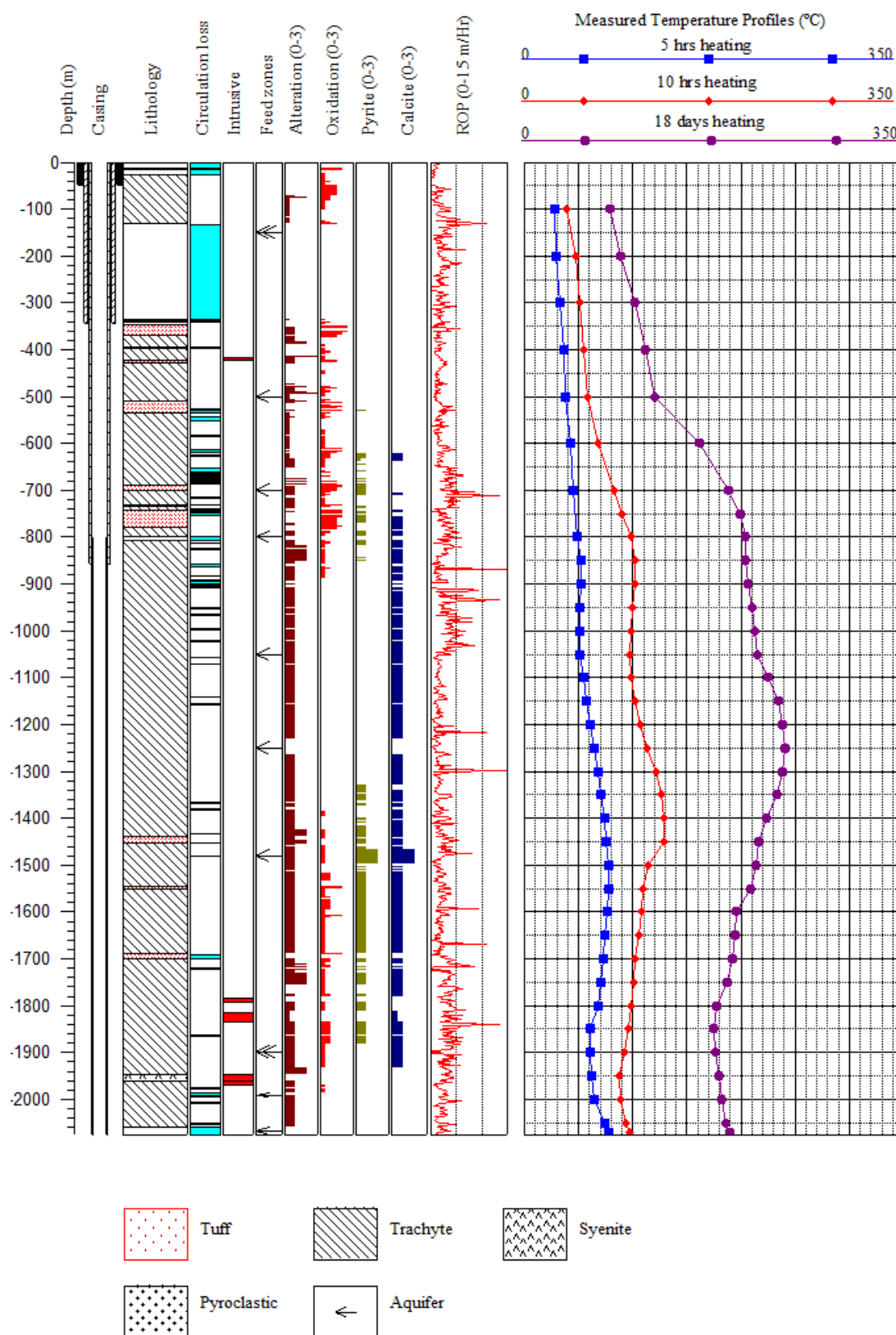


FIGURE 12: Lithology, alteration, ROP and temperature logs in Well MW-09

72-82 m Trachyte with tuff lenses: Light grey to greenish grey, fine grained trachyte. Few tuff fragments are observed at 76-82 m. The formation is fairly oxidized.

82-120 m Trachyte: Light grey to greenish grey, fine grained trachyte. The formations appear fresh but with a slight greenish coating.

120-132 m Tuff: Light grey, fine grained vesicular tuff. The vesicles are filled with amorphous silica and zeolites. The rock exhibits slight oxidation.

132-342 m: Circulation loss.

342-370 m Tuff: Brownish vesicular tuff with the vesicles being filled by amorphous silica and zeolites. The rock is slightly oxidized at the top and highly oxidized from 360-370 m. This unit is preceded by a major loss zone.

370-422 m Trachyte: Greenish grey fairly fresh, fine grained lava. It is porphyritic with phenocrysts of pyroxenes and feldspars. Pyrite is disseminated in the groundmass.

422-428 m Tuff: Reddish brown, fine grained vesicular rock unit with vesicles showing a silica lining. It is relatively oxidized. Fresh, fine grained trachyte grains were also observed.

428-510 m Trachyte: Light grey, fresh to greenish grey fine to medium grained rock, mainly composed of whitish feldspars and some pyroxenes. It is slightly altered to greenish clays. This unit exhibits some oxidation from 480-500 m.

510-526 m Tuff: Very light grey, fine grained rock that is fairly altered. The rock is vesicular with vesicles filled by silica. Reddish brown stains on the rock surface showed evidence of oxidation. Pyrite is disseminated in the groundmass. A few cuttings of trachyte were also noted at 526 m.

526-530 m: Circulation loss.

536-624 m Trachyte: Brownish grey, fine grained lava composed mainly of feldspars and pyroxene phenocrysts. The rock is altered. Occasional quartz veins are present. Pyrite is disseminated in the groundmass. Brownish grey lenses of fine grained tuff intercalations were observed between 536-552 m.

624-734 m Trachyte: Light grey fine, grained porphyritic lava composed of pyroxenes and large feldspar phenocrysts. The rock exhibits moderate oxidation and is slight alteration to light greenish clays. It contains a considerable amount of calcite and pyrite. Tuff lenses were observed within this unit, especially from 628-684 and 718-730 m. Intermittent losses were experienced at 624-628, 654-660, 684-684, 714-718, and 730-734 m.

734-780 m Tuff: Reddish brown, fine grained rock. It is vesicular at some instances with the vesicles being filled with calcite. Pyrite is disseminated in the groundmass. A few grains of trachyte were noted.

780-810 m Trachyte: Light grey, very fine grained, feldspar phyric trachyte. Some cuttings of brownish tuff were mixed with the trachyte. Losses were experienced at 784-790 m and 800-810 m.

810-864 m Trachyte: Grey to greenish grey, fine grained porphyritic rock with phenocrysts of feldspar and pyroxene. The rock is altered and has minor veins filled with quartz. Calcite also occurs as vesicle fillings. Pyrite is disseminated in the groundmass.

864-1300 m Trachyte: Light grey, medium grained feldspar porphyritic trachyte lava. Occasional phenocrysts of pyroxene are observed. The groundmass is almost 90% glassy. The rock exhibits slight alteration. Calcite is abundant across the unit and occurs as a vesicle infill. Pyrite was observed as disseminations on the groundmass and veinlet fillings from 810-854 m.

1300-1438 m Trachyte: Light grey to greenish grey, fine grained, porphyritic trachyte. This unit has abundant pyrite, chalcopyrite and calcite. High-temperature alteration minerals of actinolite and wollastonite appeared from 1366 m.

1438-1448 m Tuff: Brownish to light greenish grey, fine grained tuff with sanidine in the matrix. Calcite, pyrite and chalcopyrite were noted in this unit.

1448-1468 m Trachyte: Light to yellowish/greenish grey, fine grained trachyte. The rock is highly altered. It has significant amounts of wollastonite.

1468-1548 m Trachyte: Grey to greenish and brownish grey, fine grained, porphyritic, highly altered trachyte. This unit has abundant pyrite, chalcopyrite, calcite and wollastonite.

1548-1552 m Tuff: Reddish brown, fine grained, vesicular tuff. The vesicles are filled with calcite and pyrite. Abundant pyrite was disseminated in the groundmass.

1552-1946 m Trachyte: Light grey to greenish grey, fine to medium grained feldspar phyric lava exhibiting slight alteration to green and brownish clays. Pyrite is notably abundant and disseminated on the surface of the rock fragments. Actinolite and wollastonite minerals were also observed in the rock unit. Minor tuff lenses were encountered at 1574-1596 m, 1674, 1712 m, and 1778-1782 m. The rock is highly altered.

1948-1960 m Syenitic intrusion: Whitish with dark green specs, fresh feldspar rich, coarse grained rock.

1960-2060 m Trachyte: Light grey to greenish grey, fine grained, highly altered trachyte mixed with bluish tuff fragments.

4.2.2 Lithology of Well MW-12

The lithology of Well MW-12 is shown in Figure 13.

0-12 m Pyroclastics: Mixed cuttings of reddish brown and light greenish grey, vesicular rock and volcanic glass.

12-16 m: Circulation loss.

16-166 m Trachyte: Grey, fine grained, relatively fresh, highly fractured trachyte.

166-270 m Tuff: Reddish brown to yellowish brown, highly oxidized, fine grained vesicular tuff. The vesicles are filled with amorphous silica. Loss of returns was experienced from 174-186, and 238-242 m.

270-332 m Trachyte: Grey to greenish grey, fine to medium grained, porphyritic trachyte. It consists of phenocrysts of mainly pyroxenes and feldspars. Circulation losses were experienced at 320-322 m.

332-354 m Tuff: Reddish brown, fine grained, vesicular tuff. The vesicle walls were lined with amorphous silica.

354-360 m: Circulation loss.

360-836 m Trachyte: Light to dark grey, fine to medium grained, porphyritic trachyte with minor tuff intercalations at 400, 412, 554, and 674 m. The rock contains feldspar and pyroxene phenocrysts. The main alteration minerals are chalcedony, calcite and pyrite. A significant amount of pyrite was noted at

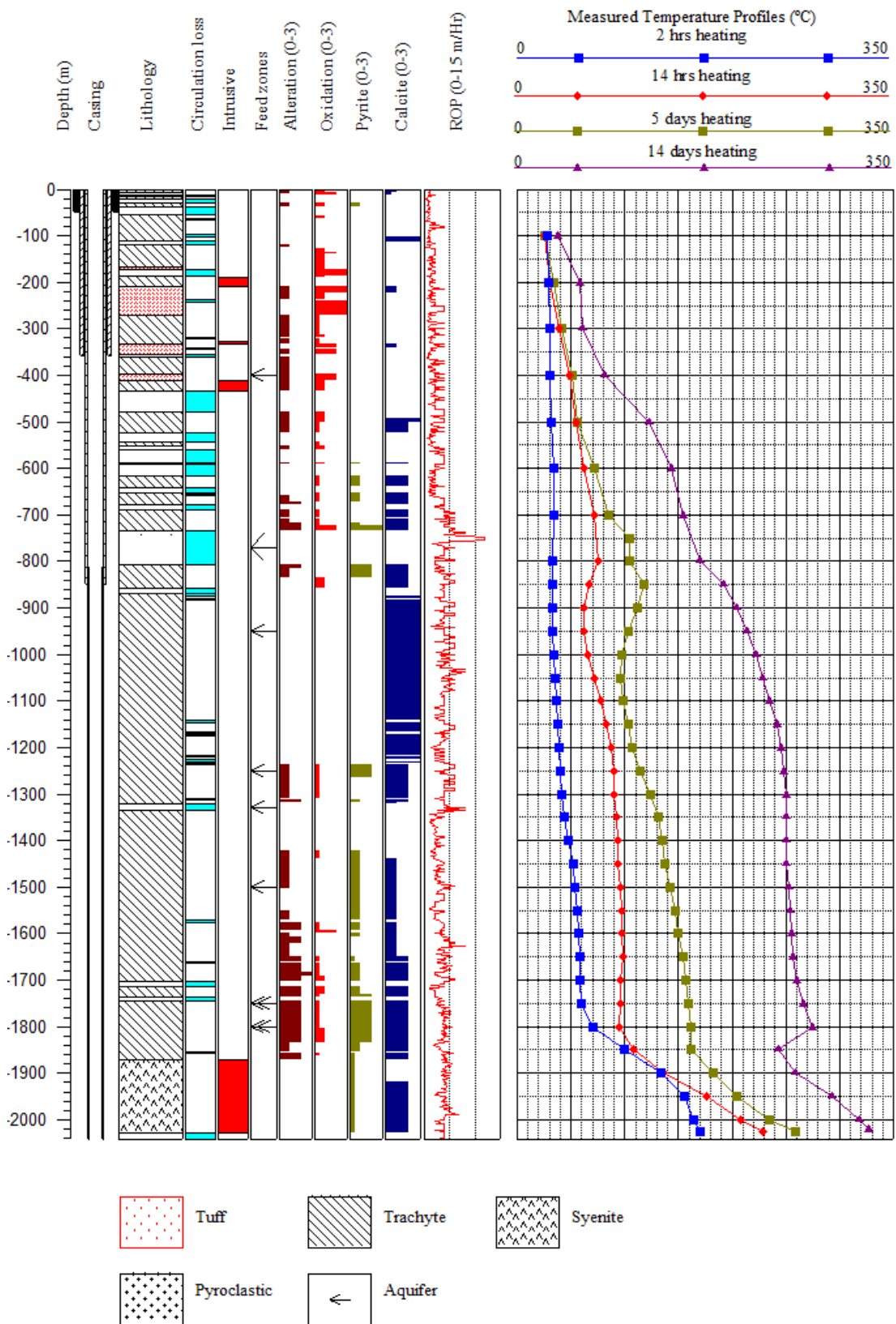


FIGURE 13: Lithology, alteration, ROP and temperature logs in Well MW-12

734 m. Calcite is present in this unit in varying extents. Major loss zones were encountered at 436-478, 562-588, 594-616, 642-652, 680-690, and 736-806 m.

836-1236 m Trachyte: Whitish, relatively fresh, medium to coarse grained porphyritic trachyte with phenocrysts of sanidine and occasionally augerine–augite. Calcite is abundant in this unit.

1236-1576 m Trachyte: Light grey to dark grey, fine to medium grained, porphyritic trachyte with large phenocrysts of sanidine and prismatic pyroxenes.

1576-1704 m Trachyte: Light grey to greenish grey, fine grained, porphyritic, moderately altered trachyte. Abundant pyrite was noted at 1594 m and 1600 m. The rock is intensely oxidized at 1600-1606 m. Chalcopyrite was noted from 1648-1704 m. The alteration intensity increases progressively with depth.

1704-1716 m: Circulation loss.

1716-1870 m Trachyte: Whitish to yellowish and greenish grey, fine grained highly altered trachyte. The rock shows abundant calcite and pyrite. Wollastonite appeared at 1858 m.

1870-2028 m Syenitic Intrusion: Light grey, coarse grained, massive and porphyritic syenite with large phenocrysts of sanidine and pyroxene. It exhibits low intensity of alteration and has abundant calcite.

4.3 Aquifers

In geothermal wells, faults and fractures in rocks enhance permeability. Geothermal wells are sited and drilled with the aim of intercepting high-temperature permeable zones. Aquifers in the Menengai wells were identified using temperature logs, hydrothermal alteration, circulation losses and the rates of penetration. Most of the permeable zones are associated with lithological contacts, characterized by intense oxidation and an abundance of calcite and pyrite. Possible locations of aquifers were identified in Well MW-09 at 150-350, 500, 700, 800, 1050, 1250, 1480, 1900, 1986-1996, and 2060-2077 m (Figure 12), summarized in Table 3.

TABLE 3: Inferred permeable zones in Well MW-09

Depth (m)	Evidence from geological observations, drilling observations and temperature monitoring profiles (logs)
150-350	Major circulation loss and increase in measured temperature
500	Lithological contact between tuff and trachyte, increase in measured temperature and oxidation intensity
700	Primary permeability in tuff, high oxidation intensity, abundance of pyrite, high rate of penetration
800	Circulation loss
1050	Increase in measured temperature
1250	Circulation loss, decrease (reversal) in measured temperature
1480	Lithological contact between tuff and trachyte, increase in alteration intensity, abundance of calcite and pyrite
1900	Fractured trachyte, increase in measured temperature
1986-1996	Circulation loss, increase in measured temperature
2060-2077	Circulation loss, increase in measured temperature

In Well MW-12, aquifers were encountered at 400, 740-800, 950, 1250, 1330, 1500, 1750, and 1800 m (Figure 13). The aquifers at 800 and 1350 m are associated with intense alteration and oxidation and preceded by circulation losses and high penetration rates. The aquifers at 1750 and 1850 m are the main feeders in the well and are associated with intrusive contacts. The host rock is intensely altered and oxidized and has abundant calcite and pyrite. Temperature measurements at this depth showed a sharp increase. Possible locations of aquifers in Well MW-12 are summarized in Table 4.

TABLE 4: Inferred permeable zones in Well MW-12

Depth (m)	Evidence from geological observations, drilling observations and temperature monitoring profiles (logs)
400	Primary permeability in tuff, increase in measured temperature
740-800	Major circulation zone, increase in rate of penetration, increase in measured temperature
950	Abundance of calcite, increase in measured temperature
1250	Fractured trachyte, increase in alteration intensity and oxidation, abundance of calcite and pyrite, increase in measured temperature
1330	Circulation loss, high penetration rate, increase in measured temperature
1500	Increase in measured temperature, increase in rate of penetration, abundance of pyrite and calcite
1750	Sharp increase in measured temperature, intense alteration, abundant pyrite and calcite
1850	Sharp temperature kick, high-alteration intensity, abundant calcite and pyrite, oxidation

5. ALTERATION AND HYDROTHERMAL MINERALOGY

5.1 Primary minerals

The primary minerals are rock forming minerals that were formed during the crystallisation of magma as it cooled. These minerals become unstable when subjected to hydrothermal conditions and are replaced by secondary minerals which are stable at the new temperatures and pressure conditions (Browne, 1978). The primary minerals observed in rock cuttings from Wells MW-09 and MW-12 includes: volcanic glass, pyroxene, olivine, amphibole, feldspar, and Fe-Ti oxides. As these minerals were exposed to alteration, they were subsequently replaced by several secondary minerals. A summary of the primary minerals and their corresponding secondary products is given in Table 5.

TABLE 5: Primary minerals and their secondary alteration products
(modified from Browne, 1982)

Primary minerals	Secondary mineral products
Volcanic glass, quartz, amorphous silica	Zeolites, quartz, clays, calcite
Olivine	Clays
Pyroxene, amphibole	Clays, pyrite, calcite, actinolite
Sanidine	Calcite, clay, albite
Fe-Ti oxide	Pyrite, sphene

Volcanic glass: Volcanic glass is common in the near surface formations in Wells MW-09 and MW-12. It is formed by the quenching of magma to form glassy obsidian fragments. They exhibit conchoidal fracturing and frequently have brownish tints of oxides.

Olivine: Olivine is rare in both wells and occurs as greenish glassy crystals. It is identified by its poor/lack of cleavage and high birefringence under the petrographic microscope. It alters to clays.

Pyroxene: These are relatively abundant in trachyte but rare in syenite and tuff in both wells. They are clearly identified in binocular microscope as dark prismatic minerals and by their near right angle (87°/93°) cleavage. These minerals exhibit little alteration near the surface but the intensity of alteration increases with depth. The pyroxenes mainly alter to amphiboles and actinolite at depth. The main type of pyroxene observed was augerine-augite.

Amphiboles: Amphiboles are identified by their strong pleochroism and perfect cleavage at 124°/56° under the petrographic microscope. They exhibit little alteration near the surface but the intensity of alteration increases with depth where they mainly alter to clays.

Sanidine: This is the main type of phenocryst found in Wells MW-09 and MW-12, easily identified using binocular and petrographic analyses. They alter to calcite, clays and albite at depth. When viewed under petrographic microscope, it is colourless in plane polarized light and grey in crossed polarized light. It is characterized by its distinctive Carlsbad twinning.

Fe-Ti Oxides: The most abundant opaques in the wells and are relatively resistant to alteration. These oxides occur as magnetite and mostly alter to sphene.

5.2 Hydrothermal minerals

Hydrothermal minerals in Menengai occur as replacements of primary minerals or as vein and vesicle fillings. Permeability and porosity of the rocks control the access of thermal fluids, which results in hydrothermal alteration of the rocks and precipitation of secondary minerals in open spaces (Lagat, 2004). Most of the hydrothermal minerals were identified by binocular analysis and subsequently confirmed using petrographic analysis. The main hydrothermal alteration minerals and their distribution in Wells MW-09 and MW-12 are shown in Figures 14 and 15 and are described below:

Zeolites are rare in both wells. The zeolite types identified were scolecite and mesolite. They occur as densely packed fibrous aggregates often radiating from several sources along vesicle walls, especially in tuff layers. Zeolites are generally thermodynamically metastable at 60-110 °C (Kristmannsdóttir, 1979). The first occurrence of zeolites in Well MW-12 was close to the surface. They also occurred at 8.82 and 402 m. In Well MW-09, they were only encountered at 82 and 122 m.

Pyrite is found in abundance in both wells. It was observed from 530-850 and 1350-1880 m in Well MW-09 and at 600-840, 1240-1260 m and from 1420 m to the bottom of Well MW-12. It occurs as cubic crystals with brassy yellow lustre in reflected light. It is mainly observed as fine disseminations and as large cubic crystals in the feldspathic groundmass in trachytes and to a lesser extent as deposits in fractures, vesicles and veins. Abundance of pyrite indicates good permeability (Lagat, 2008; Reyes, 2000). This is evident in both wells, where most of the inferred aquifers were characterized by an abundance of pyrite.

Chalcopyrite was observed from 400-500 and 1350 m to the bottom of Well MW-09 and 1650-1850 m in Well MW-12. It occurs as fine disseminations in the rock and as deposits in veinlets. It is distinguished from pyrite by a golden tinge to bronze colour and tetragonal crystal symmetry.

Albite occurs as an alteration mineral of sanidine feldspar. Albite alteration was observed under petrographic microscope from 660 m in Well MW-12 and 1860 m in Well MW-09 to the bottom of well columns. They indicate temperatures of above 180°C (Kristmannsdóttir, 1979) and appear as dirt on the surface of the sanidine feldspars.

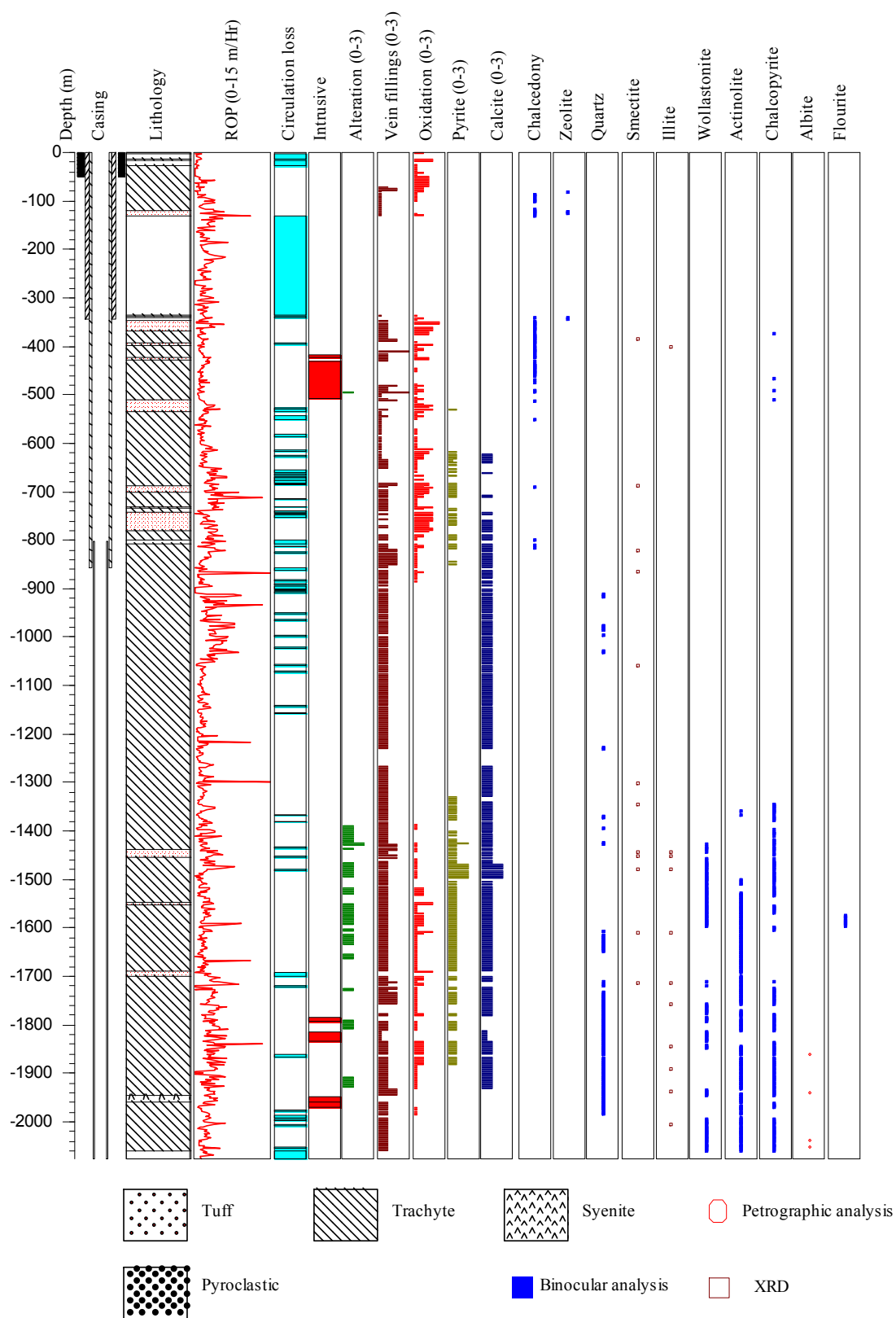


FIGURE 14: Alteration minerals and their distribution in Well MW-09

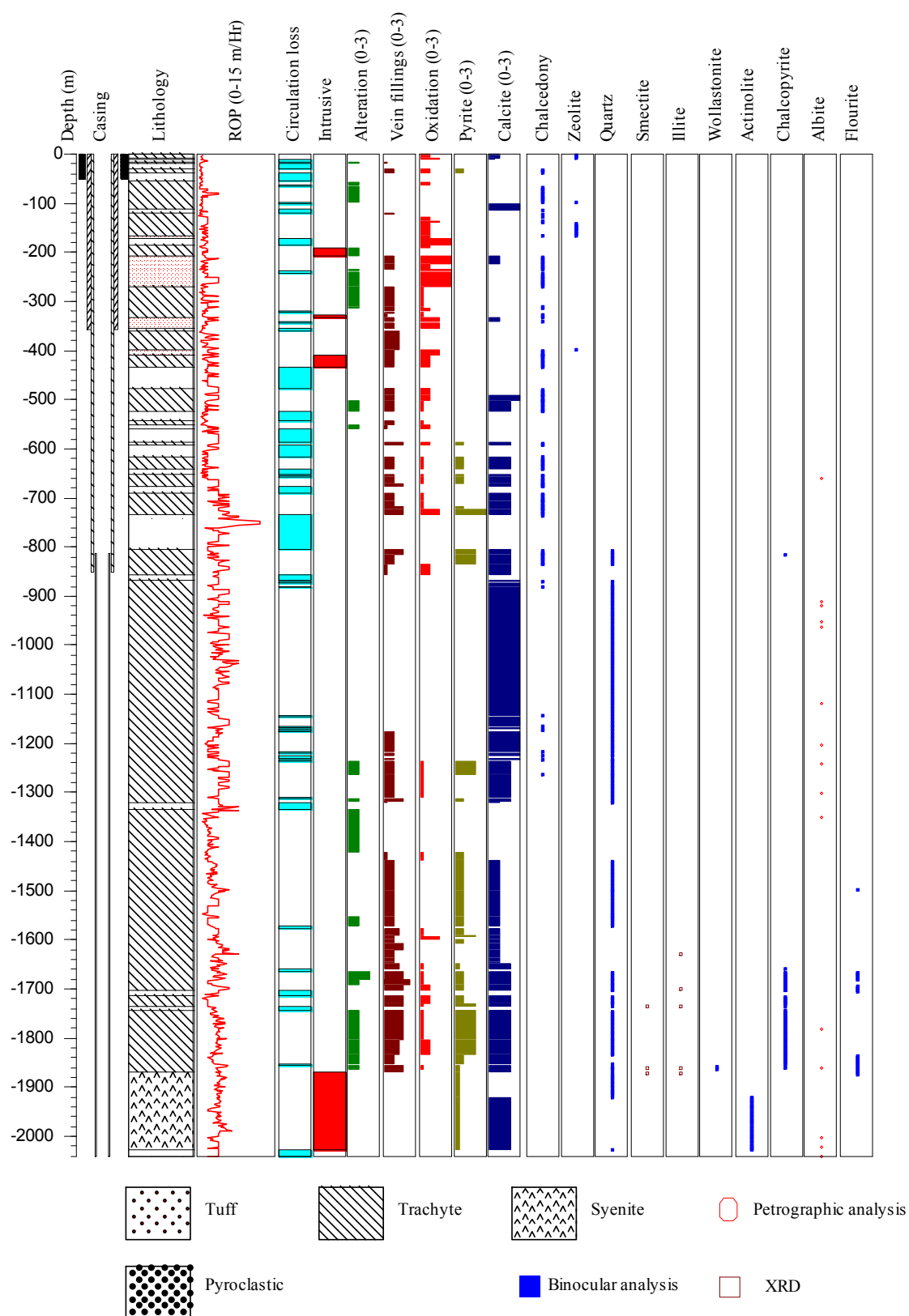


FIGURE 15: Alteration minerals and their distribution in Well MW-12

Opal occurs at shallow depths as a white or milky white lining in vesicles and veins, especially in the tuffs. Opal is a low-temperature silica mineral that is stable at temperatures between 20-100°C. In Well MW-09, it occurred from 86-130 m while in Well MW-12, it occurred from 32-226 m.

Chalcedony occurs intermittently in the wells, often as colourless to whitish globules on rock surfaces and as linings in vesicles and veins. It was observed from 126-800 m in Well MW-09 and from 226-1260 m in Well MW-12. Its presence indicates temperatures of above 100°C (Kristmannsdóttir, 1979). At depths where the formation temperature exceeds 180°C, chalcedony is replaced by quartz (Lagat, 1995).

Calcite occurs intermittently in varying amounts distributed down the well columns. In Well MW-09 it occurred from 512 m to 1992 m, where it disappeared. Calcite is stable at temperatures below 300°C and, therefore, its disappearance at 1992 m may signify temperatures exceeding 300°C below that depth. In Well MW-12, calcite occurred from the surface to the bottom of the well. The mineral occurs in vesicles, veins and disseminated in the groundmass where it replaces sanidine feldspar. Calcite presence is associated with carbon dioxide activity in the reservoir.

Oxides are mainly noted in the wells at shallow depths and where water interacts with the rocks. The most common ones are iron oxides. In both wells, oxidation occurrence was noted from the surface to around 900 m depth and from 1250 to 1900 m.

Quartz: Secondary quartz started to appear at 900 m and 800 m in Wells MW-09 and MW-12, respectively, and persisted almost to the bottom of both wells. At shallow depths, it occurs as a replacement product of chalcedony while at deeper depth it is deposited in veins and vesicles. Quartz is colourless to white in colour, and occurs as euhedral to subhedral crystals. It is easily recognized in petrographic analysis by its low relief, low birefringence and lack of cleavage or twinning. The presence of secondary quartz below 900 m depth indicates that the formation temperature is more than 180°C.

Wollastonite is a colourless, fibrous mineral when viewed both under the binocular and petrographic microscopes. It occurred from 1426 m depth to the bottom of Well in MW-09 and from 1858 m to 1864 m in Well MW-12. The presence of wollastonite is indicative of formation temperatures higher than 270°C (e.g. Njue, 2010).

Actinolite forms in close association with wollastonite. Actinolite appeared at 1508 m in Well MW-09 and at 1922 m in Well MW-12. It is green to greyish green in colour and grows as fibrous prismatic crystals. The mineral is formed as a replacement of pyroxene. The presence of actinolite is associated with temperatures exceeding 280°C (Reyes, 2000).

Clay minerals are alteration products of primary rock forming minerals. The type of clay formed depends on the temperature, fluid composition, pH and the permeability of the formation. Clay minerals are rare in Wells MW-09 and MW-12. Two types of clay minerals were identified by the use of the X-ray diffraction analysis (XRD). The clays encountered were:

Smectite occurred at 386 m and from 688-1714 m in Well MW-09. They displayed high peak values of 12.2-13.6 Å in untreated and 12.9-14 Å in glycolated samples and 10 Å when heated. In Well MW-12, smectite occurred from 1736 m and persisted to the bottom of the well. It displayed values of 12.8-17.7 Å in both untreated and glycolated samples, and 10.3 Å in the heated sample. The occurrence of smectites indicates temperatures lower than 200°C.

Illite forms at temperatures above 200°C. In Well MW-09, illite occurred at 400 m and from 1444 m to the bottom of the well. It displayed peaks between 10.3 Å in untreated, glycolated and heated samples. In Well MW-12, it occurred at 1630 m and from 1700 m to the bottom of the well.

5.3 Alteration mineral zonation

Based on the clay XRD, binocular and petrographic analysis of samples from Wells MW-09 and MW-12, an alteration mineral zonation model could be constructed. The main minerals used were zeolites, chalcedony, quartz, actinolite, wollastonite and clays. Clay minerals are very useful for the interpretation of thermal history of a geothermal system because of their quick response to temperature change (Kristmannsdóttir, 1979). From the hydrothermal mineral assemblages, three major alteration zones were identified in Wells MW-09 and MW-12 below an unaltered zone (Figure 16). The zones are:

Unaltered zone: The top 50-80 m of both wells is characterized by low alteration. The rocks are generally fresh but oxidation is due to interaction with the surface and cold groundwater.

Smectite-Zeolite zone: This zone is characterized by the first appearance of zeolites and chalcedony and the presence of low-temperature smectite clay. Zeolites and chalcedony were identified by binocular and petrographic microscopes while smectite was confirmed by XRD analysis. This mineralogical assemblage represents temperatures below 180°C.

Quartz-Illite zone: This zone is marked by the first appearance of quartz and the presence of high-temperature clays (illite). The mineralogical assemblage indicates temperatures of above 180°C.

Actinolite-Wollastonite-Illite zone: This zone is characterized by the first appearance of wollastonite and actinolite and the presence of illite. The occurrence of actinolite suggests formation temperatures of above 280°C (Reyes, 2000), and was seen from 1400 m in Well MW-09 and 1900 m in Well MW-12.

5.4 Fluid inclusion geothermometry

Fluid inclusion geothermometry is a powerful tool for outlining changes in temperature regimes in a geothermal system. Fluid inclusions are tiny bubbles of liquid and vapour that are formed when fluids are trapped in crystals and subsequently cooled due to differential thermal contraction of fluid and host

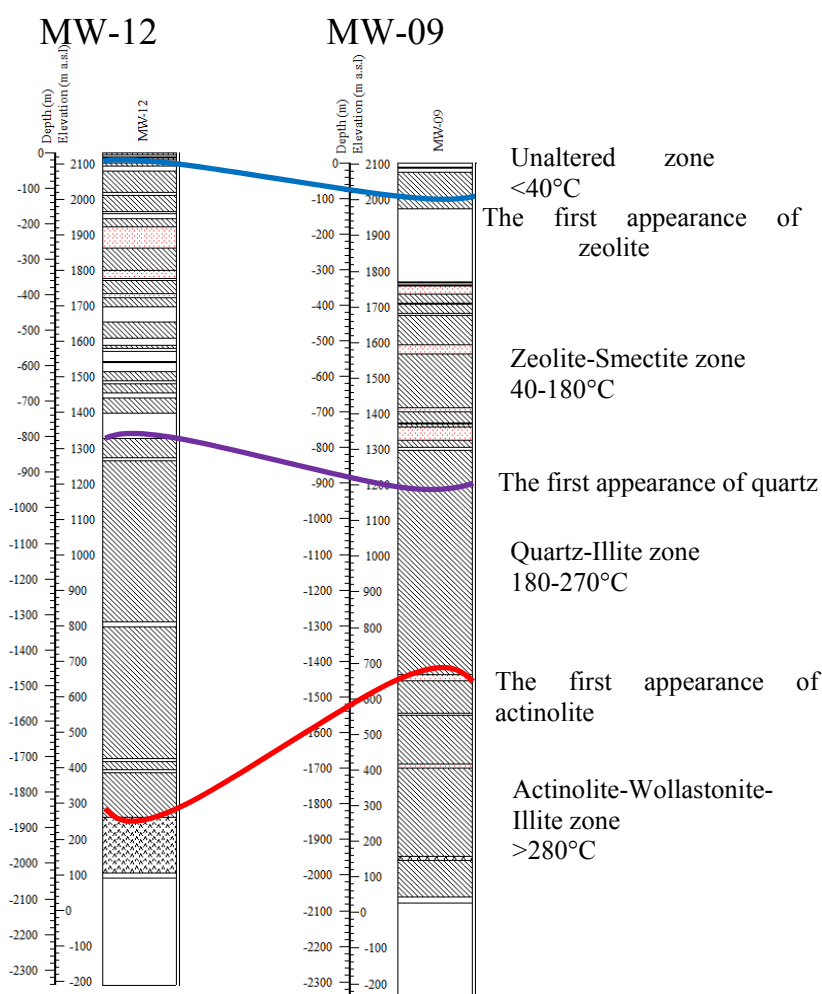


FIGURE 16: Alteration mineral zonation profile in Wells MW-09 and MW-12

mineral. Primary inclusions are formed during primary crystal growth, often concentrated along the first order of growth discontinuity or occur as isolated inclusions distributed within the crystal (Roedder, 1984). Secondary inclusions are formed after primary growth, often along healed micro-structures. The inclusions trapped in minerals during crystallization or recrystallization were analysed to determine the temperature at which the inclusions/vacuoles were formed.

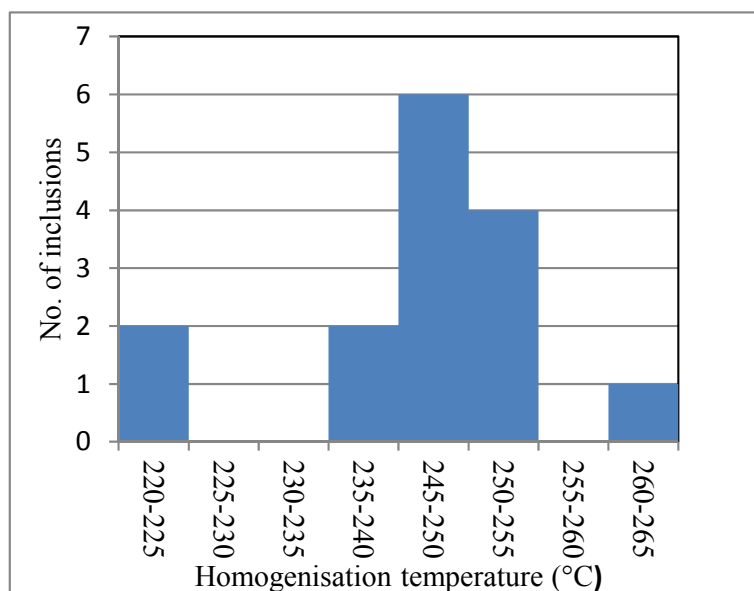


FIGURE 17: Fluid inclusion measurements from a calcite crystal at 1000-1100 m in Well MW-09

Mineral crystals from selected depth ranges from both wells were picked for fluid inclusion analysis. They were heated using a Linkam THSMG 94 stage and the temperatures at which the inclusions reached homogenisation temperature and the bubbles disappeared were noted. The temperature measurements were recorded at 5°C intervals. The temperatures at which the bubbles disappeared correspond to the temperatures at which the fluids were trapped in the crystal. This is referred to as the homogenisation temperature (T_h). A calcite crystal from 1000-1100 m depth range in

Well MW-09 and a quartz crystal from 874-884 m in Well MW-12 were used for the analysis of fluid inclusions and their temperatures of homogenisation were recorded. The homogenisation temperature values of fifteen fluid inclusions in a calcite crystal from Well MW-09 ranged from 220 to 260°C with an average of 245°C (Figure 17). Twenty nine fluid inclusions were identified and studied in a quartz crystal from Well MW-12. The homogenisation temperature values in the inclusions ranged from 250-345°C, with an average value of 300°C (Figure 18).

Correlations were made between measured temperatures, hydrothermal alteration temperatures, boiling depth curves, and fluid inclusion temperatures in both wells, presented in Figures 19 and 20. From the data, it is difficult to interpret whether the wells are in equilibrium or heating up. In Well MW-09, the alteration, measured and fluid inclusion temperatures plot within the same range from 210-245°C. The temperature measurements used in the comparison shown in

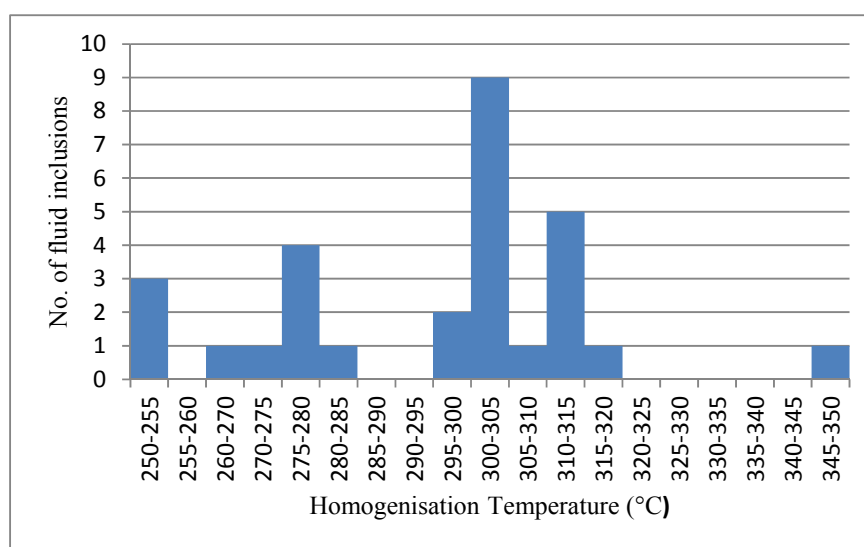


FIGURE 18: Fluid inclusion measurements from a quartz crystal from 874-884 m depth range in Well MW-12

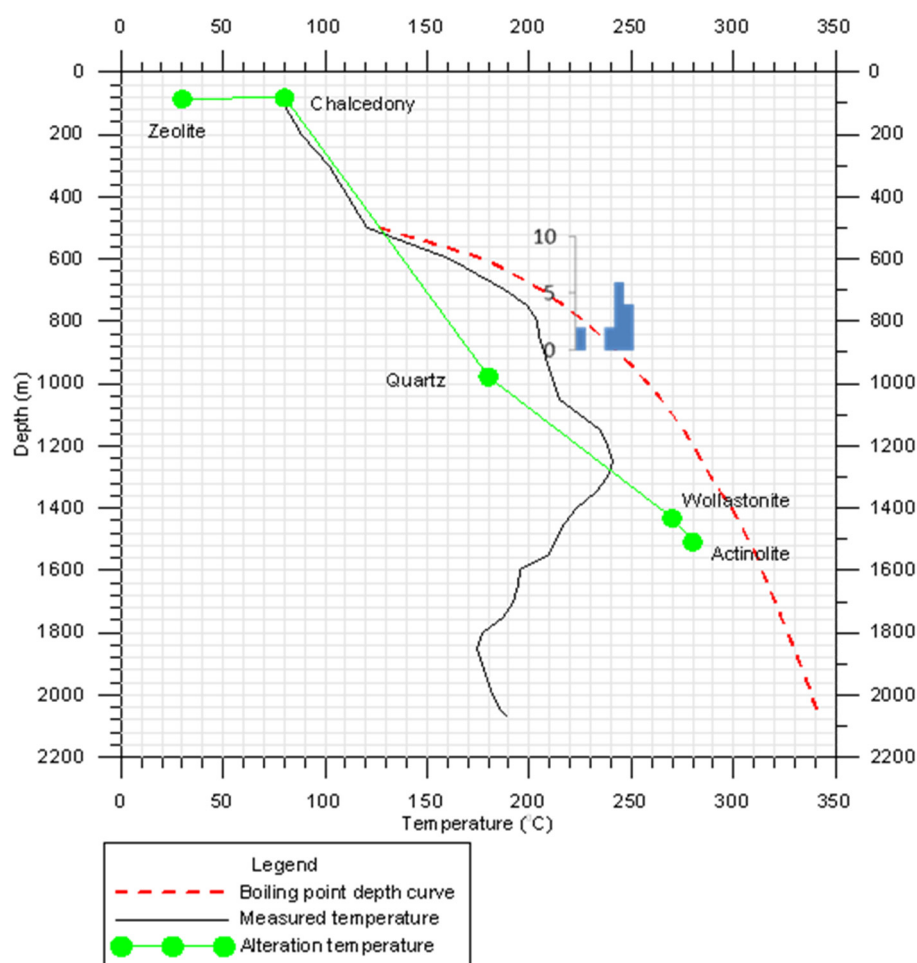


FIGURE 19: Comparison between fluid inclusion temperature, alteration temperature, measured temperature and the calculated boiling point depth curve in Well MW-09

Figure 19 were taken after 18 days of heating. The measured temperature, however, does not reflect the formation temperature after such a short time of heating up, i.e. the well has not yet recovered. The temperatures varied significantly in Well MW-12. At 880 m, the depth from where the quartz crystal for fluid inclusions was picked, the average homogenisation temperature is 300°C while the alteration temperature is 190°C and the measured temperature is 210°C. The temperature measurements plotted, were taken after 14 days of heating. Fluid inclusion temperatures in both wells, plotted along the boiling point depth curve and, therefore, represent boiling conditions. However, the measured well temperatures were generally higher than the alteration temperatures, and are still rising, indicating that the wells are heating up.

6. DISCUSSION

Menengai is located at the centre of the Kenya dome which is experiencing crustal thinning caused by a mantle plume. Tectonically, the central volcano is set at a triple junction where the Nyanza Rift branches from the main rift and developed on a potential tail-crack end structure at the southern end of the complex N-S striking Solai TVA (Chorowicz, 2005). A NNW-SSE trending ridge that is part of Molo TVA is believed to cut through the caldera. All of these structures play an important role in enhancing permeability in Menengai.

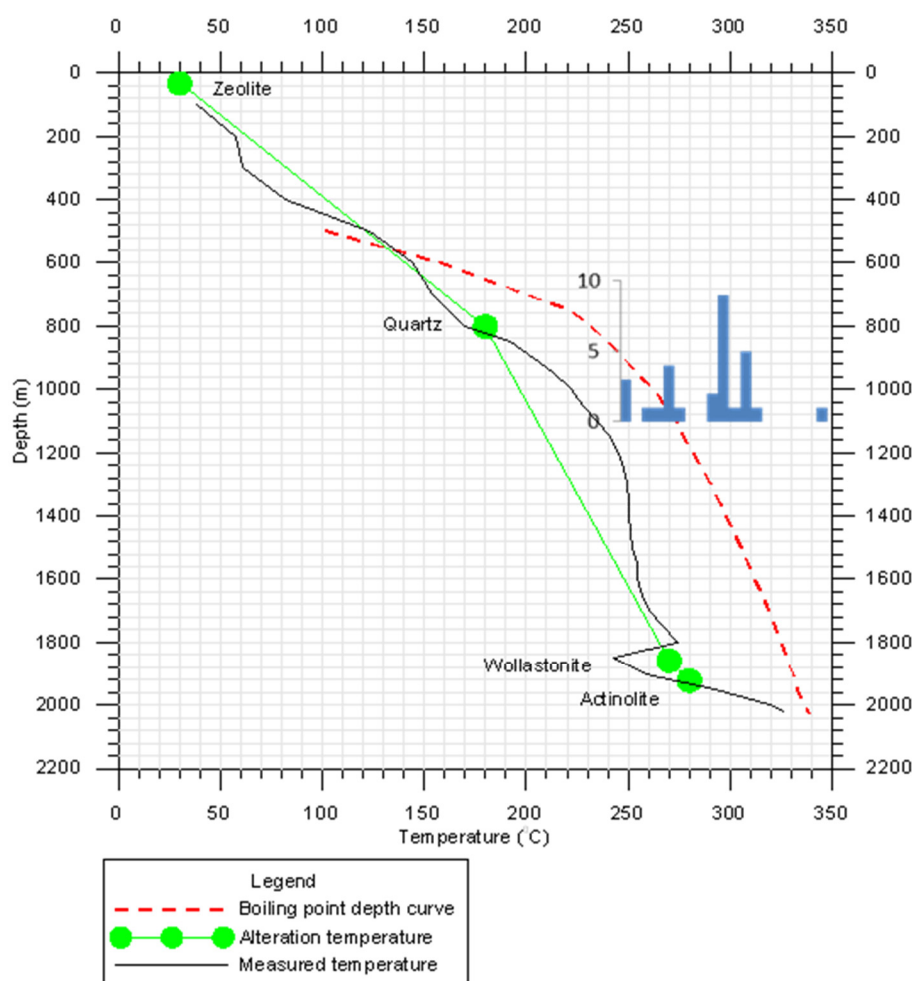


FIGURE 20: Comparison between fluid inclusion temperature, alteration temperature, measured temperature and the calculated boiling point depth curve in Well MW-12

The litho-stratigraphic units of Wells MW-09 and MW-12 generally show close similarity to the other wells previously drilled within the Menengai caldera (Omondi, 2011; Mibei, 2012; Kipchumba, 2013). The upper sections of the wells consist of a thin layer of pyroclastics underlain by a 50-80 m layer of blocky unconsolidated recent trachyte lavas and 100-200 m thick massive trachyte lavas. These form the post-caldera lavas erupted within the caldera. Thick tuff layers were encountered at 342-368 m in Well MW-09 and somewhat shallower, at 210-270 m, in Well MW-12. However, the tuff layer in Well MW-09 is probably shallower and thicker than indicated, as a major circulation zone preceded its occurrence. The tuff layer marks a boundary between the post-caldera and pre-caldera volcanics and cuts across all the other wells previously drilled in Menengai and is, therefore, an important marker horizon. Major circulation losses occurred either before or after the tuff layer and in some instances within the tuff layer. The middle sections of the wells mainly consist of trachyte lavas with occasional tuff intercalation.

The hydrothermal mineral distribution in both wells showed progressive temperature increase with depth. The analyses of sample cuttings indicate that low-temperature minerals like zeolites, chalcedony and low-temperature clays, dominate the upper sections of the wells. Moderately high to high-temperature hydrothermal minerals, ranging from 180 to >300°C, were encountered from the mid to the lower sections of the wells, based on the occurrence of secondary quartz, albite, wollastonite and actinolite. The abundance of pyrite and chalcopryrite signify that the wells are highly permeable. The hydrothermal mineralogy generally indicates that the wells are located in a high-temperature geothermal system.

The comparison between lithologic sequences across Wells MW-12, MW-09, MW-08 and MW-11 shows close similarities, but displays relative vertical displacements (Figure 21). The circulation losses experienced at the presumed tuff marker horizon associated with the caldera collapse makes stratigraphic correlations difficult.

Homogenisation fluid inclusion temperatures, measured temperatures and alteration temperatures indicate that the system may be in equilibrium or more likely, to be heating up. Fluid inclusion temperatures in both wells plot along the boiling point depth curve and, therefore, represent boiling conditions in the wells. However, correlation between measured and alteration temperatures, which represents the current condition, indicate that the wells may be heating up.

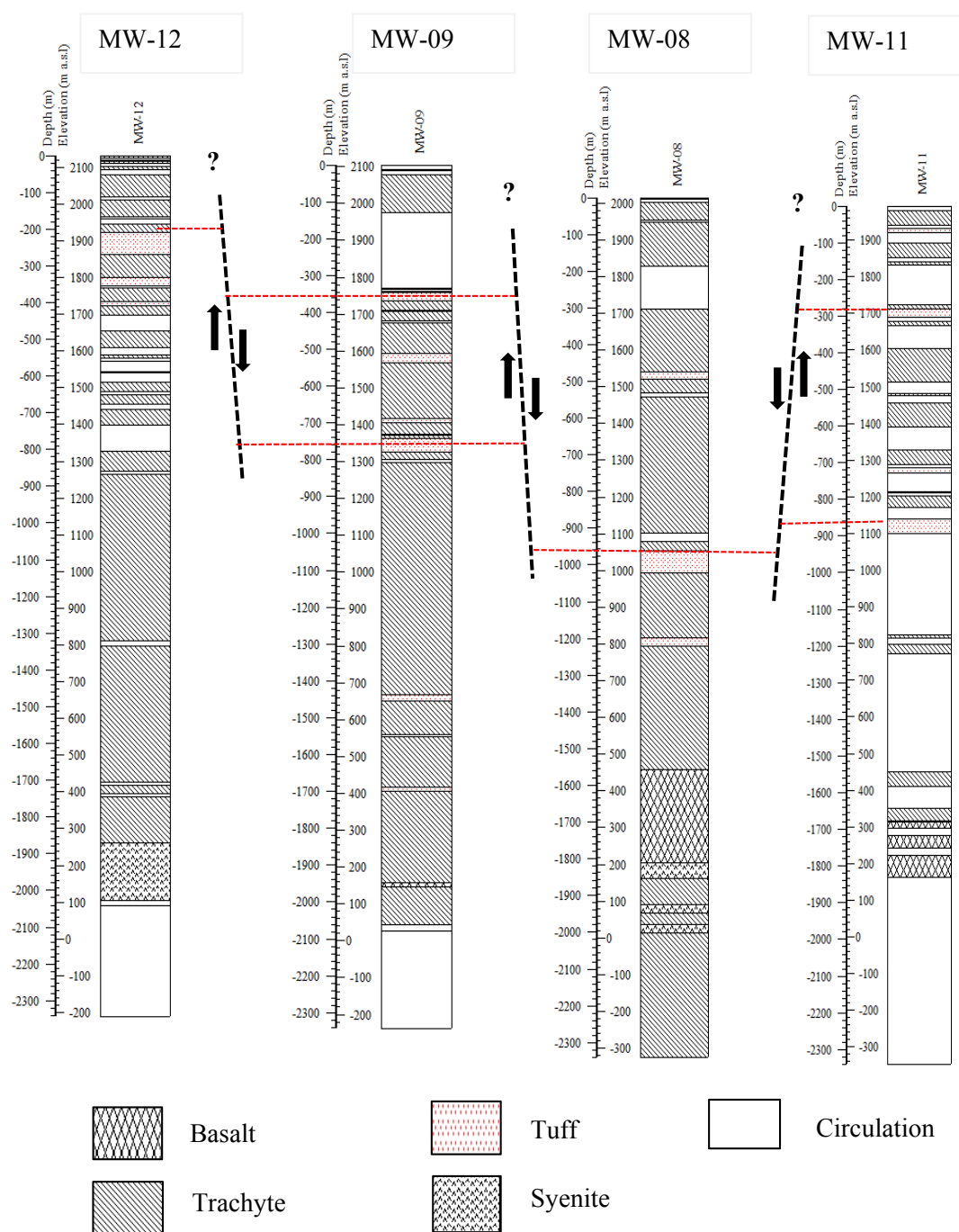


FIGURE 21: Stratigraphic correlation of Wells MW-12, MW-09, MW-08 and MW-11 (MW-08 and MW-11 from Kipchumba, 2013)

7. CONCLUSIONS AND RECOMMENDATIONS

1. Regional and local tectonics play an important role in enhancing permeability in Menengai geothermal system. Post-caldera lava flows issued from a postulated tail-crack structure that developed west of the N-S striking zone of normal faults has a dextral strike-slip throw component (Solai TVA).
2. The lithostratigraphy of Menengai wells is predominantly composed of trachytes and tuff layers.
3. Several aquifers were identified in Wells MW-09 and MW-12, based on temperature logs, hydrothermal alteration, circulation losses and the rates of penetration. Sources of permeability in the wells are fractures and faults, lithological contacts and primary permeability of tuffs.
4. Based on hydrothermal minerals assemblages, three alteration zones were defined below a zone free of alteration. These are: smectite-zeolite zone, quartz-illite zone and actinolite-wollastonite-illite zone.
5. The abundance of pyrite and chalcopyrite signifies that the wells are highly permeable. The permeable zones were also characterized by high alteration intensity and oxidation, especially at lithological contacts and high penetration rates.
6. The measured temperature logs do not reflect the true formation temperature since the wells had not recovered when the available temperature logs were taken. More temperature measurements should be carried to ascertain the recovery.
7. Results from fluid inclusion measurements are preliminary and relatively inconclusive. Therefore, further fluid inclusion analyses should be carried out, particularly at deeper levels in the wells.

ACKNOWLEDGEMENTS

I wish to express my sincere gratitude to the Government of Iceland and the United Nations University (UNU), for granting me a fellowship to undertake specialized training at the UNU-Geothermal Training Programme. Special thanks to Mr. Lúdvík S. Georgsson, the director, and Dr. Ingvar B. Fridleifsson, former Director, of UNU-GTP. I wish to acknowledge my employer, the Geothermal Development Company (GDC) for granting me permission to attend the course. I'm deeply indebted to my supervisors, Dr. Hjalti Franzson, Dr. Björn S. Hardarson and Ms. Anette K. Mortensen for their indispensable assistance and guidance in my project. To the Iceland GeoSurvey (ISOR) staff and all the lecturers, thank you so much for sharing your skills and knowledge. To the UNU-GTP staff, Ms. Thórhildur Ísberg, Mr. Markús A.G. Wilde, Mr. Ingimar G. Haraldson, and Ms. Málfríður Ómarsdóttir, thank you for your invaluable support during my stay in Iceland.

Special thanks to my wife, Eglah, my daughter, Cherop and my son, Ruto and the entire family for prayers, encouragement, support and for enduring my long absence.

I thank God for his sufficient grace, endless love and care.

REFERENCES

- Baker, B.H., and Wohlenberg, J., 1971: Structural evolution of the Kenya Rift Valley. *Nature*, 229, 538-542.
- Baker, B.H., Mohr, P.A., and Williams, L.A.J., 1972: Geology of the Eastern Rift System of Africa. *Geological Society of America, Special Paper 136*, 1-67.
- Baker, B.H., Williams, L.A.J., Miller, J.A., and Fitch, F.J., 1971: Sequence and geochronology of the Kenya Rift volcanics. *Tectonophysics*, 11, 191-215.
- Browne, P.R.L., 1978: Hydrothermal alteration in active geothermal fields. *Annual Review Earth & Planetary Sciences*, 6, 229-250.
- Browne, P.R.L., 1982: Permeability in geothermal fields and hydrothermal alteration. In: Hochstein, M.P. (ed.), *Introduction to geothermal prospecting*. Auckland University, Auckland, NZ, 50-54, and 85-89.
- Burke K., and Dewey J., F. 1973: Plume generated triple junctions: Key indicators in applying plate tectonics to old rocks. *J. Geol.*, 81, 406-433.
- Chorowicz, J., 2005: The mechanisms of the East African Rift System formation. *J. African Earth Science*, 43, 379-410.
- Ebinger, C. J., and Sleep, N. H., 1998: Cenozoic magmatism throughout east Africa resulting from impact of a single plume. *Nature*, 365, 788-791.
- GDC, 2010: *Menengai geothermal prospect, an investigation for its geothermal potential*. GDC, Nakuru, Kenya, Geothermal Resource Assessment Project, internal report, 66 pp.
- George, R.M.M., Rogers, N.W., and Kelley, S., 1998: Earliest magmatism in Ethiopia: evidence for two plumes in one flood basalts province. *Geology*, 26, 923-926.
- Geotermica Italiana Srl., 1987: *Geothermal reconnaissance survey in the Menengai - Bogoria area of the Kenya Rift Valley*. UN (DTCD)/GOK, report.
- Gichira, J.M., 2012: Joint 1D inversion of MT and TEM data from Menengai geothermal field, Kenya. Report 11 in: *Geothermal training in Iceland 2012*. UNU-GTP, Iceland, 137-167.
- KenGen, 2004: *Menengai volcano: Investigations for its geothermal potential*. KenGen and Ministry of Energy, Geothermal Resource Assessment Project, internal report.
- Kipchumba, J. L., 2013: Borehole geology and hydrothermal alteration of wells MW-08 and MW-11, Menengai geothermal field, Kenya. Report 10 in: *Geothermal training in Iceland 2013*. UNU-GTP, Iceland, 37.
- Korme, T., Chorowicz, J., Collet, B., and Bonavia, F.F., 1997: Volcanic vents rooted on extension fractures and their geodynamic implications in the Ethiopian Rift. *J. Volcanology & Geothermal Res.*, 79, 205-222.
- KRISP Working Group, 1987: Structure of The Kenya Rift from seismic refraction. *Nature*, 325, 239-242.
- Kristmannsdóttir, H., 1979: Alteration of basaltic rocks by hydrothermal activity at 100-300°C. In: Mortland, M.M., and Farmer, V.C. (editors), *International Clay Conference 1978*. Elsevier Scientific Publishing Co., Amsterdam, 359-367.

Lagat, J.K., 1995: Borehole geology and hydrothermal alteration of well OW-30, Olkaria geothermal field, Kenya. Report 6 in: *Geothermal Training in Iceland 1995*, UNU-GTP, Iceland, 135-154.

Lagat, J.K., 2004: *Geology, hydrothermal alteration and fluid inclusion studies of the Olkaria Domes geothermal field, Kenya*. University of Iceland, MSc thesis, UNU-GTP, Iceland, report 2, 71 pp.

Lagat, J.K., Arnórsson, S., Franzson, H., 2005: Geology, hydrothermal alteration and fluid inclusion studies of Olkaria Domes geothermal field, Kenya. *Proceedings of the World Geothermal Congress 2005, Antalya, Turkey*, 14 pp

Leat, P. T., 1984. Geological evolution of the trachytic caldera volcano Menengai, Kenya. *J. Geol. Soc. London*, 141, 1057-1069.

MacDonald, R., and Scaillet, B., 2006: The central Kenya peralkaline province: insights into the evolution of peralkaline salic magmas. *Lithos*, 91, 59-73.

MacDonald, R., Bailey, D. K., and Sutherland, D., 1970: Oversaturated peralkaline glassy trachyte from Kenya. *J. Petrology*, 11, 507-517.

MacDonald, R., Black, S., Fitton, J. G., Rogers, N. W., and Smith, M., 2001: Plume-lithospheric interactions in the generation of the basalts of the Kenya Rift, East Africa. *J. Petrology*, 42, 877-900.

Mechie, J., Keller, G.R., Prodehl, C., Khan, M.A., and Gaciri, S.J., 1997: A model for the structure, composition and evolution of the Kenya rift. *Tectonophysics*, 278, 95-119.

Mibei, G., 2012: Geology and hydrothermal alteration of Menengai geothermal field. Case study: wells MW-04 and MW-05. Report 21 in: *Geothermal training in Iceland 2012*. UNU-GTP, Iceland, 437-465.

Njue, L.M., 2010: Borehole geology and hydrothermal mineralisation of well HE-27, Hellisheidi geothermal field, SW-Iceland. Report 24 in: *Geothermal training in Iceland 2010*. UNU-GTP, Iceland, 463-492.

Omondi, C., 2011: Borehole geology and hydrothermal mineralisation of wells MW-01 and MW-02, Menengai geothermal field, Central Kenya Rift Valley. Report 30 in: *Geothermal training in Iceland 2011*. UNU-GTP, Iceland, 737-773.

Reyes, A.G., 2000: *Petrology and mineral alteration in hydrothermal systems. From diagenesis to volcanic catastrophes*. UNU-GTP, Iceland, report 18-1998, 77 pp.

Roedder, E., 1984: *Fluid inclusions*. Mineral. Soc. Am., Rev. Mineral., 12, Washington, DC, 644 pp.

Rogers, N., Macdonald. R., Fitton, J.G., George, R., Smith, M., Barreiro, B., 2000: Two mantle plumes beneath the East African rift system: Sr, Nd and Pb isotope evidence from Kenya Rift basalts. *Earth & Planet. Science Letters*, 176, 387-400.

Simiyu, S.M., 2010: Application of micro-seismic methods to geothermal Exploration: Examples from the Kenya rift. *Paper presented at "Short Course V on Exploration for Geothermal Resources"*, organized by UNU-GTP, GDC and KenGen, at Lake Bogoria and Lake Naivasha, Kenya, 27 pp.

Simiyu, S.M., and Keller, G.R., 1997: Integrated geophysical analysis of the East African Plateau from gravity anomalies and recent seismic studies. *Tectonophysics*, 278, 291-314.

Smith, M., 1994: Stratigraphic and structural constraints on mechanisms of active rifting in the Gregory Rift, Kenya. *Tectonophysics*, 236, 3-22.

Smith, M., and Mosley, P., 1993: Crustal heterogeneity and basement influence on the development of the Kenya Rift, East Africa. *Tectonics*, 12, 591-606.

APPENDIX I: Results of the XRD analysis for Well MW-09

Depth (m)	D(001) Untreated	D(001) Glycolated	D(001) Heated	Mineral	Type	Other minerals
76				No clay		8,6Å
386	~13.6	~13.6	Destroyed	Sm:sm	Smectite	Amphibole
400	10.3	10.3	10.3	Illite	Illite	Amphibole
482				No clay		Amphibole
512				No clay		Amphibole
636				No clay		
688	12.9	>12.9	~10	Sm:sm	Smectite	
820	13.6	14	10.2	Sm:sm	Smectite	
864	13.5	>13.5	~10	Sm:sm	Smectite	
1060	13.5	>13.5	~10	Sm:sm	Smectite	
1302	13.5	>13.5	~10	Sm:sm	Smectite	Amphibole
1344	13.5	>13.5	~10	Sm:sm	Smectite	Amphibole
1388				No clay		
1424				No clay		
1436				No clay		
1444	12.2/10	>12.2/10	~10	Sm: sm/ill	Smectite-Illite	Amphibole
1452	12.2/10	>12.2/10	~10	Sm: sm/ill	Smectite-Illite	Amphibole
1478	12.2/10	>12.2/10	~10	Sm: sm/ill	Smectite-Illite	Amphibole
1610	12.2/10	>12.2/10	~10	Sm: sm/ill	Smectite-Illite	Amphibole
1684				No clay		
1714	14.1/10.3	14.1/10.3	10.3	Sm: sm/ill	Smectite-Illite	Amphibole
1756	10.3	10.3	10.3	Illite	Illite	Amphibole
1844	10.3	10.3	10.3	Illite	Illite	Amphibole
1890	10.3	10.3	10.3	Illite	Illite	Amphibole
1936	10.3	10.3	10.3	Illite	Illite	Amphibole
1948	10.3	10.3	10.3	Illite	Illite	Amphibole
2006	10.3	10.3	10.3	Illite	Illite	Amphibole

APPENDIX II: Results of the XRD analysis for Well MW-12

Depth (m)	D(001) Untreated	D(001) Glycolated	D(001) Heated	Mineral	Type	Other minerals
590				No clay		Amphibole
810				No clay		
1498				No clay		Possible kaolinite, amphibole
1630	10.4	10.4	~10,4	Illite	Illite	Amphibole
1666				No clay		
1700	10.3	10.3	10.3	Illite	Illite	Amphibole
1736	13.4/10.3	13.4/10.3	~10	Sm: sm/ill	Smectite-Illite	Amphibole
1860	12.8/10.3	12.8/10.3	~10	Sm: sm/ill	Smectite-Illite	
1872	17.7/10.3	17.7/10.3	~10	Sm: sm/ill	Smectite-Illite	

APPENDIX III: XRD patterns for the clay minerals in wells MW-09 and MW-12

54605/MW-09 #08 UNT

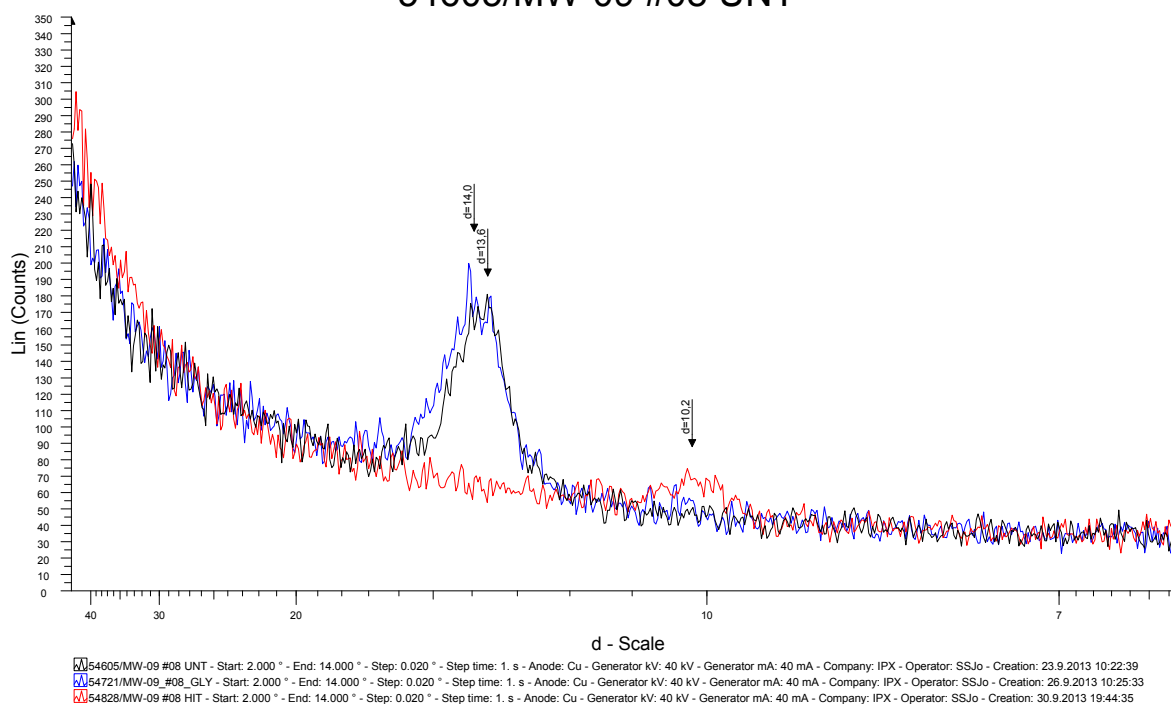


FIGURE 1: Smectite at 820 m

54620/MW-09 #23 UNT

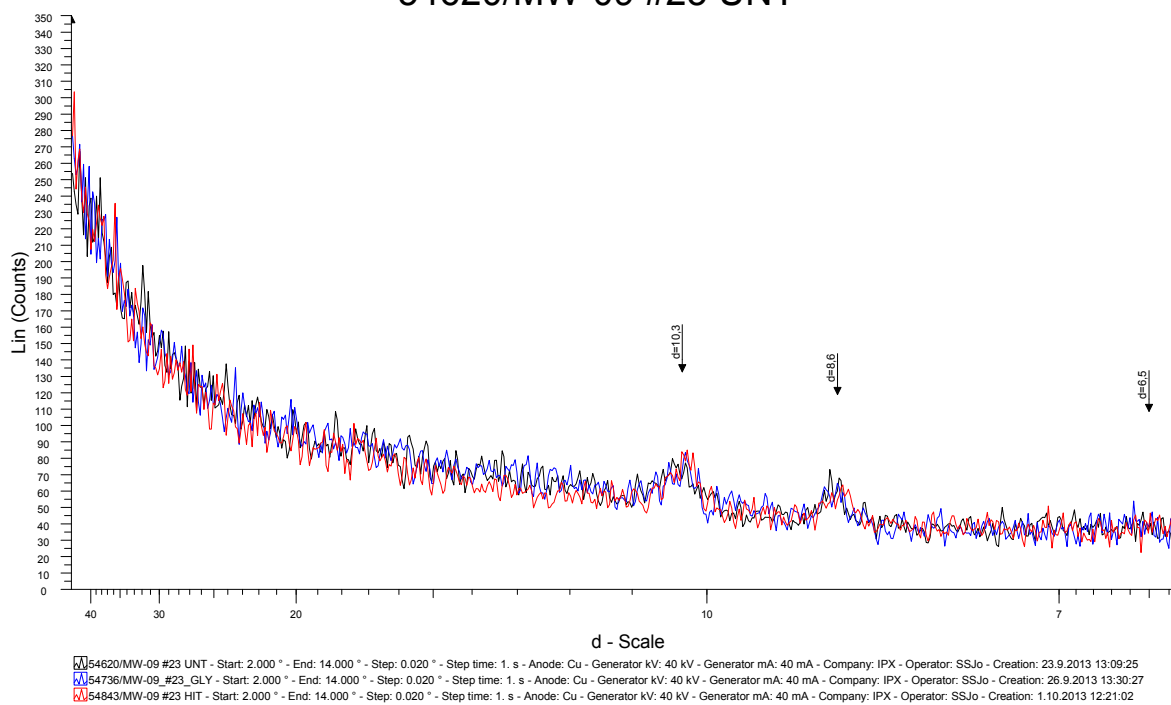


FIGURE 2: Illite, amphiboles and feldspars at 1844 m

54623/MW-09 #26 UNT

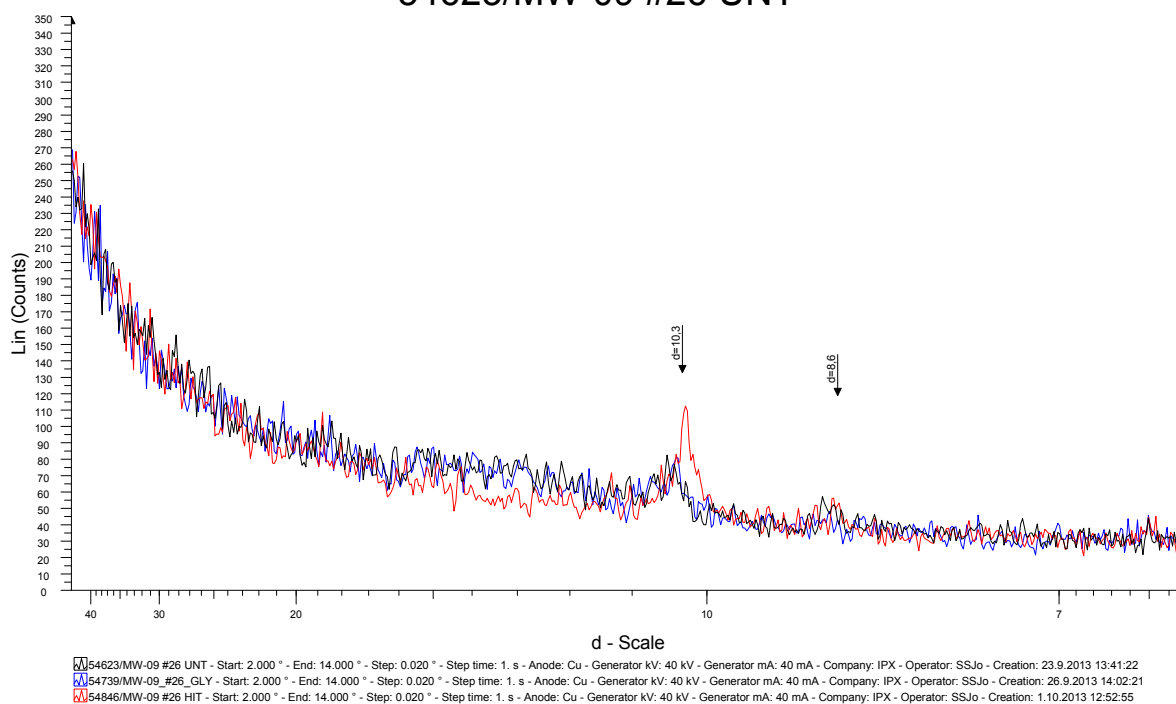


FIGURE 3: Illite and amphiboles at 1946 m

54639/MW-12 #06 UNT

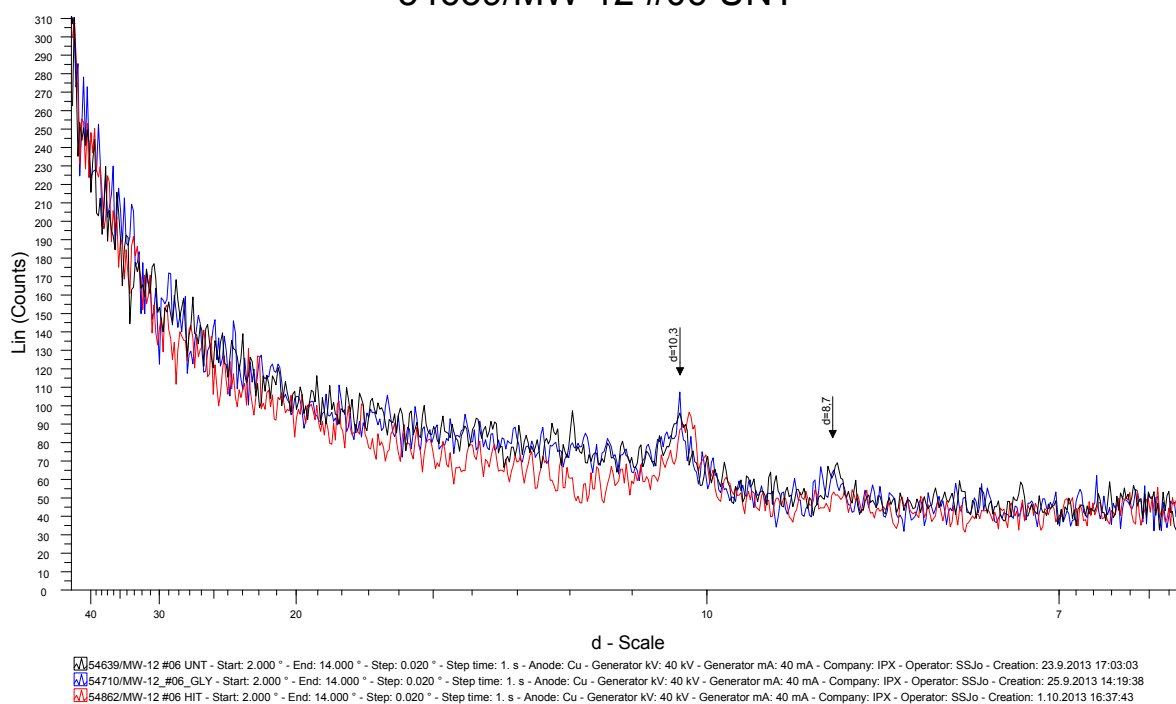


FIGURE 4: Illite and amphiboles at 1700 m

54641/MW-12 #08 UNT

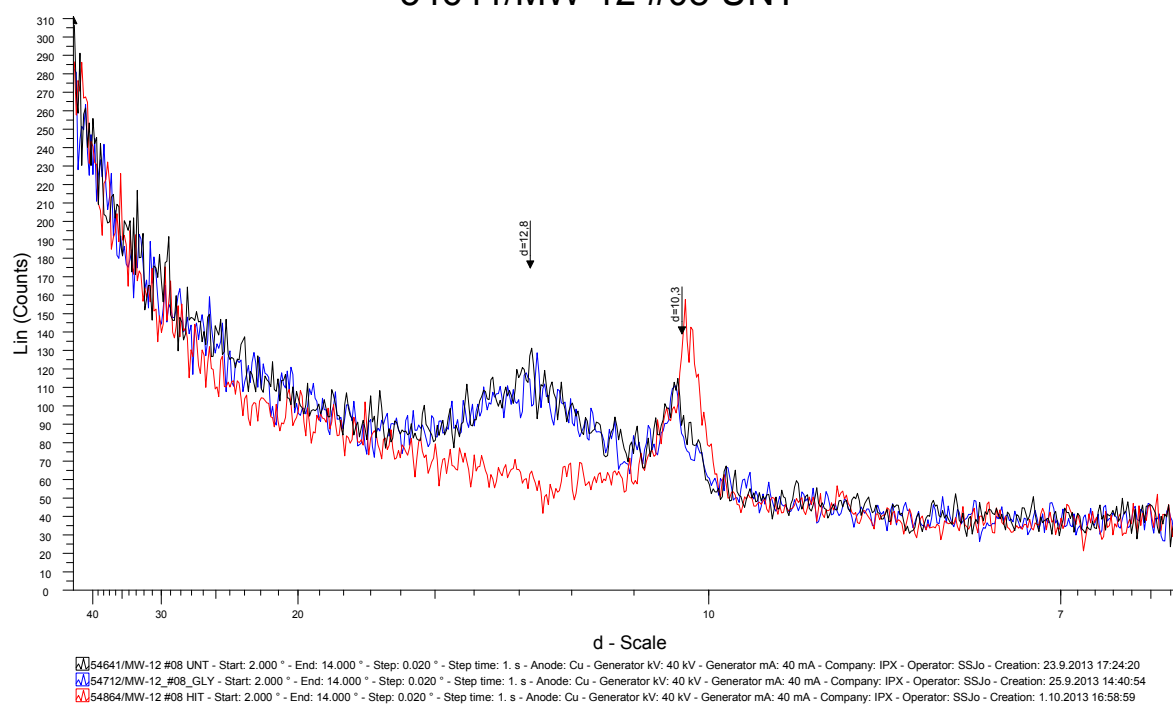


FIGURE 5: Illite and smectite at 1736 m



REDUCING GEOTHERMAL DRILLING PROBLEMS TO IMPROVE PERFORMANCE IN MENENGAI

Isaac Kipkoech Makuk

Geothermal Development Company – GDC

P.O. Box 17700

Nakuru – 20100

KENYA

imakuk@gdc.co.ke, imakuk@gmail.com

ABSTRACT

Drilling geothermal wells is one of the main construction activities of a geothermal project. The aim is to access the available steam in the production zone of a geothermal reservoir. The discharged wet steam is separated into steam that is channelled to a power plant, where it drives turbines to produce electricity, and water which is normally injected back into the reservoir. Several challenges are encountered while drilling geothermal wells. These challenges have resulted in drilling timelines not being met as well as increases in drilling costs. This report describes the causes of some of these challenges and how they can be minimized or reduced so as to improve performance. Challenges encountered in Menengai geothermal field in Kenya are the main subject of this study. These challenges are either natural or due to human error. This report found that drill string sticking accounted for 12% of the total drilling time in Menengai. Sticking is caused by poor well bore cleaning, especially when there is lost circulation and long or periodic waiting for water. Lost circulation is caused by intersecting fractures or permeable zones. Measures for mitigating problems of lost circulation so as to avoid sticking have been discussed. This report found that the most troublesome zone in Menengai is at a depth of 2100 m where the drill string got stuck in Wells MW03, MW04, MW07 and MW12. Wells MW01 and MW06 had drill string sticking at a depth of 2206 and 2202.96 m, respectively. A comparison was made with the 2104 m depth of an Iceland Deep Drilling Project well at Krafla in Iceland. An analysis indicated that the troubles were related to intersecting magma intrusions, shown by fresh glass in the cuttings that were observed at the shale shakers. The magma pushed the drill string up (large drop in hook load) and it got stuck, blocking the circulation at the same time. Temperature surveys later showed the fluid near the bottom was superheated. Metal fatigue was found to be another problem, as shown by shears that were experienced on cross-over box ends. To minimize this, the report suggests the use of drill string risk management for close monitoring of any defects.

1. INTRODUCTION

Drilling is an important activity in geothermal utilization for accessing geothermal reservoirs with hot water and steam. It is also used to refine a geothermal system's conceptual model which helps in assessment and management of the system for sustainable utilization and development. This, in turn,

insures that the reservoir and power plant are properly utilized. In drilling operations, we are in business only when we are drilling on the bottom (making a hole). Any activity, other than casing and waiting on cement to cure, is regarded as not only non-productive, but incurs undesirable costs. This is because the rig is hired at an hourly rate (or at times on a meter rate depending on the contract). Drilling problems have been encountered in the past and will continue to happen in the future. Attempts are constantly being made to avoid and reduce these problems. With technological and technical know-how advances, methods to tackle these problems should be greatly improved. Drilling costs associated with non-drilling time can be so high that it can reach 15 to 35% of the total well cost (Raja et al., 2011). Reducing these problems increases drilling performance and reduces well cost, thereby increasing the viability of a geothermal drilling project, such as Menengai (Figure 1).

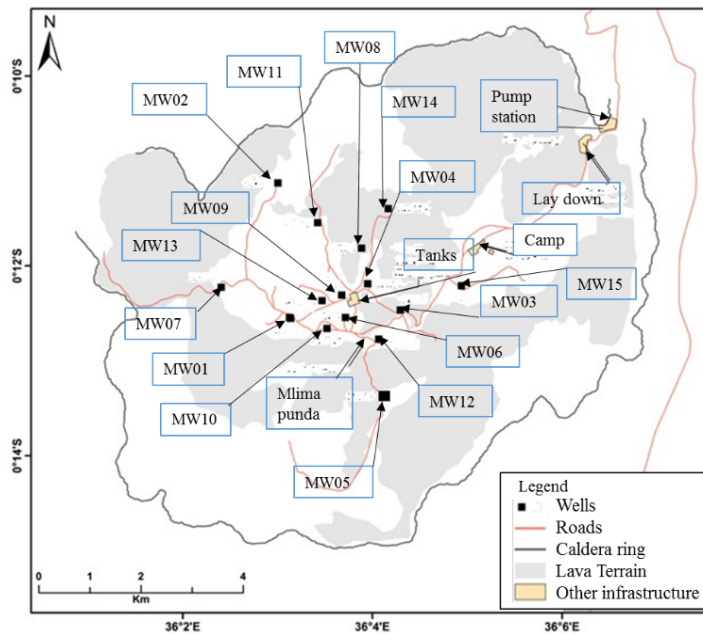


FIGURE 1: Map showing Menengai geothermal field and wells (GDC, 2013)

2. STUCK PIPE

Stuck drill pipes comprise one of the major drilling problems encountered at Menengai geothermal field in Kenya. This problem has also been experienced in Olkaria geothermal field in Kenya and almost all other drilling (oil and gas or geothermal) fields in the world. Drill pipe sticking is not only a waste of time and cost, but also may result in the loss of part of the bottom hole assembly (BHA) or drill string. When that happens, a decision may have to be made to place a cement plug in the well and sidetrack the well to bypass the “fish”, causing time delays and additional cost. Agarwal (2008) argues that 60% of sticking occurs in the drill collar section of the drill string. This is due to their higher outside diameter compared with the rest of the drill string and around the stabilizers.

During normal operations, the driller desires to drill on the bottom (make a hole), pull out of the hole (to change the bit) or run in hole (a new bottom hole assembly). The driller may also wish to make a wiper trip to clear any obstructions. When not able to do this, it can result in the drill string not rotating or moving up/down the hole; the drill string is then said to be stuck. When the drill string gets stuck, drilling fluid is not usually received at the surface, although sometimes it can be. This is an observation made by the author of this report while working at rigs in Menengai.

Drill string sticking is classified into three types, based on the overriding mechanism. These types are: geometry related, solids related and differential sticking (Devereux, 1998).

2.1 Geometry related sticking

The hole and BHA relative geometry have an impact on the ability of the drill string to get stuck. Either an inclination or diameter of the hole relative to the BHA will restrict the drill string in its course. It has

been found that the greater the hole inclination, the more the chances of the drill string getting mechanically stuck. The wells described in this report at Menengai are, however, all drilled vertically.

2.1.1 Under-gauge hole

Due to prolonged drilling through hard formations, the bit gets worn out and, as a result, its diameter is reduced, referred to as a loss of gauge. This implies that the hole's diameter may not be uniform for the entire hole section. This creates a tapered or tight hole which can cause mechanical sticking due to the hole geometry when running in with a new bit.

2.1.2 Key seat

Extensive work done by Lubinski (1950) indicates that doglegs cause drilling problems. As the drill string continuously rotates and rubs against one point on the wall of the hole, it finally results in the creation of a groove (key seat). This happens when the lateral force of the rotating string is higher than the formation strength at the point (or length) of contact. It is also possible for a key seat to be grooved into a casing (a metal) as opposed to a rock.

As the driller pulls out of hole, a certain section of a drill string cannot get past the key seat, depending on the outside diameter. The drill pipe body will only go past the key seat but the tool joint, as well as a drill collar will not, due to their larger outside diameter. It is interesting to note that a 2° nearly vertical spiral hole, as observed by Lubinski (Murphey, 1966) causes excessive key seats while a 3° straight inclined hole with deviation all in one direction does not have severe key seats and drilling problems. Therefore, they contend, perfectly vertical holes should be avoided so as to reduce incidences of stuck pipe. Figure 2 shows how key seats are generated.

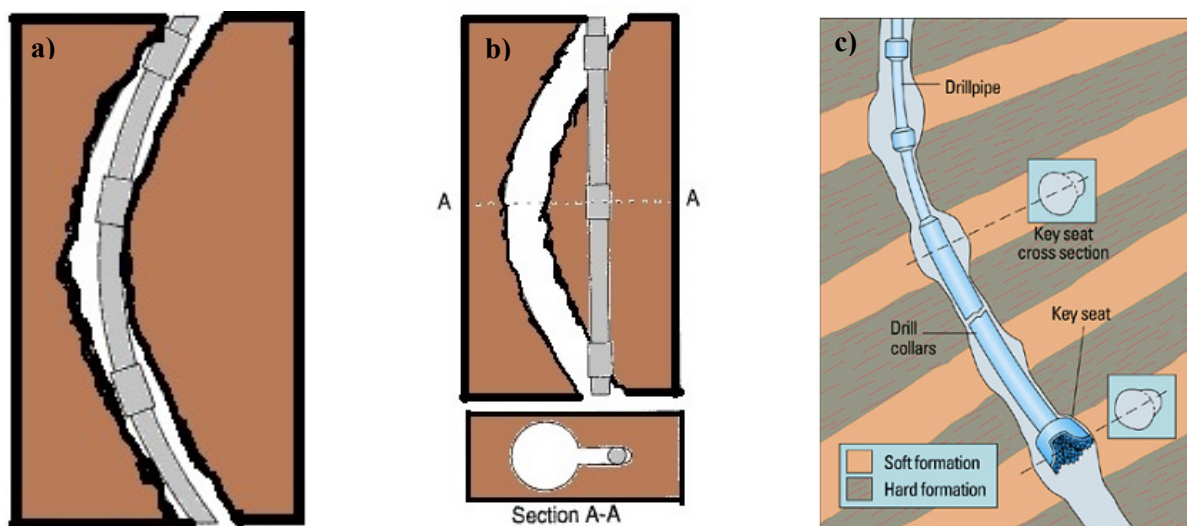


FIGURE 2: Key seat generation: a) Buckling and continuous rotation of drill pipe; b) A key seat has been generated; c) Key seat formed when going from hard to soft formation (Grace et al., 2008; Schlumberger, 2013)

2.2 Mobile formations

The mud hydrostatic pressure is meant to support the borehole wall. When this pressure is not sufficient, then the borehole wall can collapse due to the overlying overburden pressure acting on the formation as shown in Figure 3 (Pašić et al., 2007). The collapsed formation will eventually result in sticking. If there is an increase of water in the near-well bore vicinity, then the shale strength will reduce (Mody

and Hale, 1993; Van Oort et al., 1994). There are several methods in which water is transported into and out of the formation in the near-well bore region (Van Oort et al., 1995). The most overriding method, argues Van Oort et al. (1996, 1997), is the chemical potential difference as well as the wellbore/formation differential pressure. Water based muds are used instead of oil based mud, mainly due to environmental and economic concerns (Van Oort, 1996). For geothermal drilling, the problem is not exactly the same.

2.3 Geo-pressured formations

When fluid flows into a formation, and it is substantially restricted over long geological time, an overpressure develops (Hsu and Belaud, 1998). Additional sedimentary loading increases the pore pressure. If the mud hydrostatic pressure of a borehole is less than the pore pressure, then slivers of shale will be squeezed into the well bore due to the differential pressure. Without proper hole cleaning, this continues to the point where the drill string gets stuck. The sizes of the slivers are usually smaller at the surface than at the bottom of the hole due to breakup as it is being circulated.

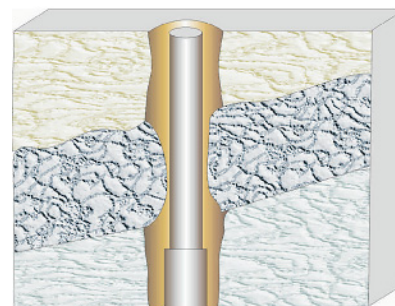


FIGURE 3: Mobile formation (Pašić et al., 2007)

On the other hand, abnormally low pressured formations can be encountered, as is the usual case for geothermal reservoirs. Either an abnormally low or high pressured formation causes drilling problems. In abnormally low pressured formations, lost circulation will be experienced. Highly depleted reservoirs (probably due to over-exploitation) have also been found to be a cause of abnormally low pressured formations (Barriol et al., 2005).

2.4 Unconsolidated formation

As a result of poor bonding between the rock particles, the formation becomes unconsolidated and poorly packed. This is common for sands, gravel and small river bed boulder formations at shallow depths of about 500 m (Bowes and Procter, 1997). Poor bonding makes the strength of the rocks weak and the rocks can easily yield due to overburden pressures. Any attempt to remove the previously supporting rock while drilling will cause the nearby rocks to fall into the well bore as shown in Figure 4. This eventually causes sticking of the drill string. Mud cake helps to prevent the poorly bonded rocks from collapsing into the well bore. Absence of, or too thin a mud cake will aggravate the collapse.

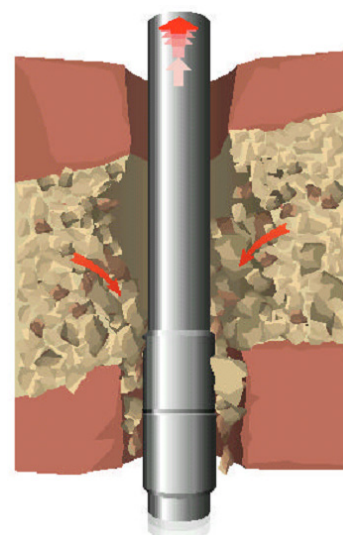


FIGURE 4: Unconsolidated formation (Bowes and Procter, 1997)

2.5 Naturally fractured formations

In a geothermal field, there are faults and naturally fractured rock formations (Devereux, 1998). The rock pieces divided by natural fractures as shown in Figure 5 can be small or large (Pašić et al., 2007). Unlike the collapse of pieces of rock due to poor bonding in unconsolidated formations, naturally fractured formations (whose rock might have a good bond) collapse due to the impact of the drill string vibrations. Formations with faults and dips have been found to have an effect on how vertical the well bore can be. Drilling

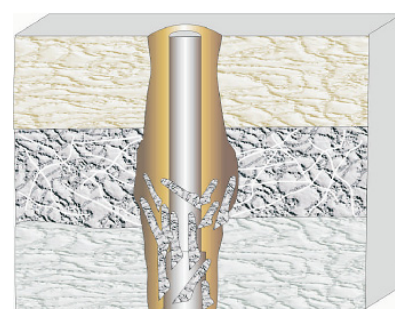


FIGURE 5: Naturally fractured formation (Pašić et al., 2007)

through faults and dip strata leads to a crooked hole as the drill bit tends to slide off or down the dips rather than going head-on through the strata. According to Gow (2005), crooked holes are also facilitated by drilling through different formations with alternating strength and resistance, with the bit deflecting from the perpendicular particularly when encountering hard formations.

2.6 Junk

Any material that is not drillable and finds its way into the well bore is regarded as junk. It may be part of the fishing tool that gets worn out and drops into the hole. Poor housekeeping at the rig floor, or around the cellar, can result in some junk getting into the hole. Items that are regarded as junk are: tong jaws or pins, broken pieces of guide shoe or milled fish fragments, bearings, and bolts falling down from the top drive. Bolts that were used for some repair and forgotten up the mast could also fall during vibrations. The junk can fall into the hole either during normal drilling or momentarily when there is no drilling, and the hole is open, and the rig floor men forget to cover the rotary table opening. If the mud pump screens are worn out and not replaced, they may allow pieces of metal dropped in the mud tanks to be sucked by the mud pumps and pumped all the way through the drill string to the bit. Small pieces of junk can also fall into the drill pipe bore when applying dope. Bit cones can also break off in the hole and become junk. Naturally occurring strong materials can also be regarded as junk.

2.7 Cement blocks

After setting the casing and the cement has cured, drilling out the cement follows. Devereux (1998) suggested that there is a possibility of a large pocket below the casing shoe. Cement in the pocket could fracture due to a lack of support. Upon resuming drilling on the bottom, the fractured cement can fall onto the drill string and cause the BHA to get stuck. The fallen heavy cement blocks will overwhelm the drilling fluid and will not be transported to the surface, as desired. This will, in effect, make cuttings accumulate in the annulus and contribute further to stuck pipe problems.

2.8 Green cement

Running in hole with a drill string too soon after cementing can be problematic. If a drill string is run into the hole at a high rate, it will cause a surge which results in a sudden pressure increase. This sudden pressure increase causes the green cement to flash set (Bowes and Procter, 1997). Consequently, the drill string gets stuck. Even if the speed of running in hole is not fast, and the cement has not fully set, then there is a high possibility of the drill string getting stuck in the cement. The weight on bit (WOB) indicator will not be able to detect wet cement when trying to tag on cement. This will result in the assumption that the top of cement has not been reached.

2.9 Collapsed casing

A properly designed casing should withstand the collapse pressures at the depth at which it is set. The burst pressure is the internal pressure inside the casing and assumes full reservoir pressure all along the wellbore. Collapse of the casing occurs when the external pressure is greater than the internal pressure. The external pressure is mainly due to the cement column while cementing the casing. A worst case scenario of collapse occurs when the casing has been cemented and the inside is completely empty. Research done by Skúlason et al. (2011) established that water pockets trapped in the casing-casing annulus after a cement job causes a casing collapse as shown in Figure 6 (drawn using ANSYS 11.0 finite element analysis software). The casing fails or collapses when its yield strength or collapse resistance is exceeded. However, the value of yield strength and collapse resistance reduces when these material properties change due to the effect of axial loading. Very high velocity steam can erode the

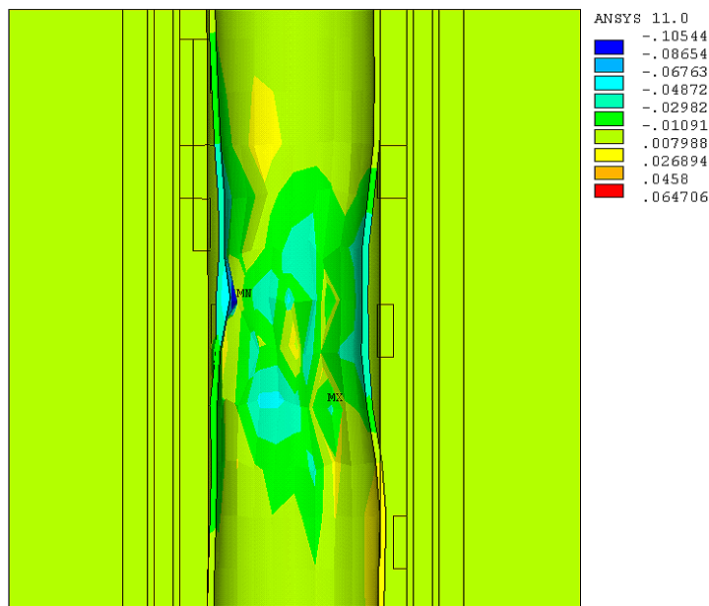


FIGURE 6: Casing collapse due to water pocket (Skulason et al., 2011)

induce stresses on the formation. Simulations and research done by Luo (2004) indicate that formation pore pressure increased as tectonic stress increased. The mechanism behind this increase is two-fold. Firstly, the lateral tectonic stress creates an increase in the compaction rate of the pores, leading to a volume decrease. Due to this, there will be disequilibrium between pore fluid expulsion and formation compaction, thereby facilitating natural over-pressuring. Secondly, due to compaction, the rock porosity will decrease and, correspondingly, permeability decreases. As formation permeability decreases, the formation pressure correspondingly increases (Osborne et al., 1997; He, 1999).

Drilling into highly tectonic stressed formations, argued Bowes and Procter (1997), causes the rocks to fall into the well bore. This is due to the substantial difference between the near wellbore stress and the mud hydrostatic pressure which is supposed to support and counteract the near wellbore pressure and prevent formation fluid or cuttings from coming in. These tectonically stressed formations occur on or around mountainous areas.

2.11 Reactive formations

Several mechanisms behind rock and fluid interaction have been advanced. They include: swelling pressure, osmosis, fractured shale, hydraulic, pressure diffusion, mechanical, fluid penetration and capillary pressure (Manohar, 1999). The water in the drilling fluid migrates to the formation and with time, causes swelling. Van Oort (2003) explained that this migration takes place in three phases. From the centre of the well bore (Figure 7), the mud pressure front goes out into the formation. This is followed by a solute/ion invasion front. The ions could be K^+ , Ca^{2+} , or Mg^{2+} or any other that are used as a swelling pressure inhibitor. The last phase of the fluid/formation interaction is the filtrate invasion front. Formation swelling, if not checked, can create stuck pipe problems.

casing, thereby compromising its strength due to reduced wall thickness. Corrosion caused by chemical properties of the well also reduces the strength and collapse resistance of the casing. Poor workmanship and aggressive running procedures can buckle the casing. Collapsed casing can not only jam the drill string, it can also reduce the wells output and can even render it non-productive.

2.10 Tectonically stressed formations

Geological studies have shown the existence of plate tectonic movements. The movements can either be separation, collision or shear. These create the formation of faults or folds. These crustal movements, due to plate tectonic activity,

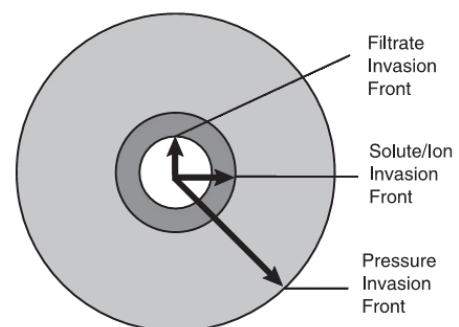


FIGURE 7: Drilling fluid invasion of a shale

2.12 Balling up

While drilling, the formation or mud may become sticky. Due to adhesive forces, the mud accumulates on the bit or drill assembly. When pulling out of hole, the accumulated mud becomes compacted and can cause sticking of the pipe. Problems associated with balling up have been encountered when drilling at high rates of penetration (Warren, 1940). This happens because the clay cuttings do not get sufficient time to hydrate to mud. Continuous drilling at this rate results in continuous accumulation of natural clay or sticky mud. If the mud filter cake is too thick, it may eventually reduce the well bore's diameter. As the drill string is being pulled out of the hole, it scrapes off the filter cake and, with time, it accumulates resulting in balling up.

2.13 Differential sticking

During drilling, either for oil and gas or geothermal steam, drilling fluid is used. The main purpose of drilling fluid is to maintain a well's hydrostatic pressure for well control and transport of cuttings from the bottom hole to the surface. This is made possible by the addition of materials that improve, among other properties, the viscosity and density of the drilling fluid. As the density of the drilling fluid is increased, the well hydrostatic pressure increases to a value that exceeds that of the formation pressure. On reaching this value, mud and filtrate are lost into the permeable formation due to the pressure gradient. This is followed by the formation of a filter cake as solids, present in the drilling fluid, are accumulated at the permeable wall. For geothermal drilling, a low density water-based mud made with bentonite is normally used, having a density of only 1.05 g/cm^3 .

The onset and development of filter cake is dependent upon the solids content of the mud. Figure 8 shows the stages through which a mud cake filter develops. At the beginning (Figure 8a), the drill string, ideally, rotates about the wellbore centre. With time, the dynamic or static mud and filtrate pass through the permeable wall of the well bore as described earlier. Concurrently, solids are deposited in the well, eventually forming a filter cake, as shown in Figure 8b. If efforts are not taken to immediately free the stuck pipe then, with time, the filter cake's thickness will increase, as shown in Figure 8c. The cake's thickness will increase with the square root of time as predicted by Darcy's law (Murrilo et al., 2009).

Studies have shown that the probability of differential sticking increases with time, due to an increase in filter cake thickness. Differential sticking is dependent on mud cake filtration properties that include: thickness, shear strength and lubricity. These properties, in turn, are dependent on the following variables:

- Mud solids content (either low or high-gravity solids);
- Fluid loss;
- Mud differential pressure; and
- Mud type.

An increase in the development of filter cake and its thickness can be interrupted by drill string rotation. Mud filter cake erosion can be experienced depending upon drill string rotation eccentricity. Due to this eccentricity, a section of the well bore's circumference is scrapped off. There are three scenarios of filter cake erosion. Figure 9a shows drill pipe erosion, which is caused by the lateral movement of the

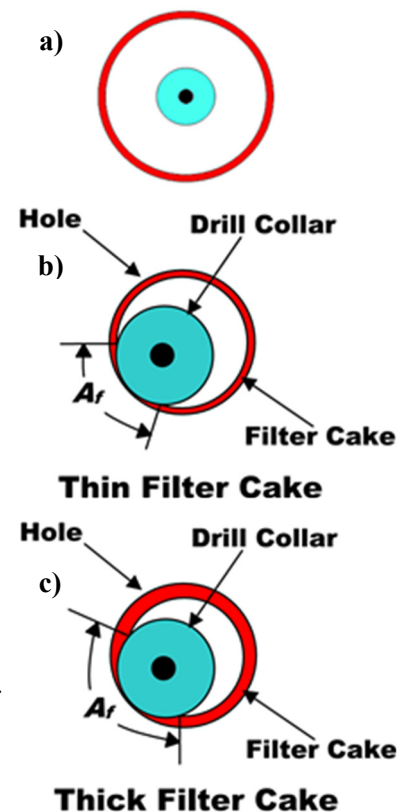


FIGURE 8: Development of a filter cake (Grace et al., 2008)

drill pipe. Figure 9b shows filter cake erosion caused by wiper trip. The third type of filter cake erosion is caused by reaming operations. The reaming erosion, as shown in Figure 9c, is more uniform than the other two types, because most of the cake has been scrapped off. If the drill string is left for some time without rotating it, then the filter cake will start to surround the drill collar as shown in Figure 9d. This results in bridging between the drill collar, or drill pipe, and the filter cake. Bridging, which increases the drill collar and filter cake contact area, further increases the differential sticking force.

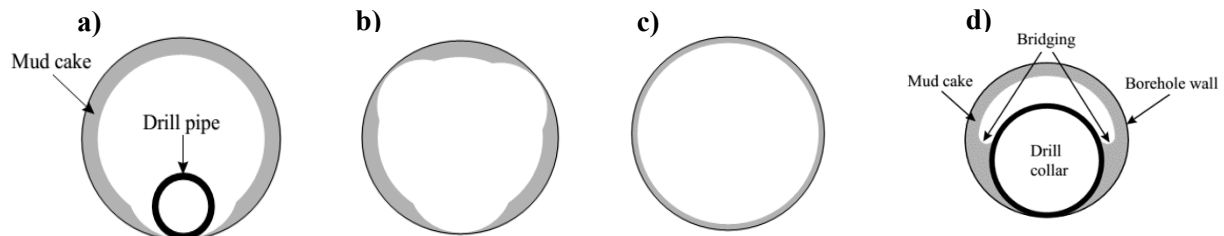


FIGURE 9: Mud cake erosion (Schlumberger, 1997): a) Drill pipe erosion; b) Wiper trip erosion; c) Reaming erosion; d) Bridging due to stationary drill collar

2.13.1 Mechanism of differentially stuck pipe

For differential sticking to occur, there has to be ‘differential pressure’. This is a phrase that is sometimes referred to in other literature as overbalance. Differential pressure is the amount of mud hydrostatic pressure less that of the formation pressure. A significant amount of differential pressure forces the drill string (either drill pipe or drill collars) against the well bore wall, due to the pressure gradient.

2.13.2 Permeable zone

Depending on drilling fluid properties, the permeable zone provides favourable conditions for the formation of mud cake. The thicker the mud cake, the higher the chances of getting differentially stuck. If the fluid loss (mud property) is high, then there are high chances of getting differentially stuck. This is because more fluid is lost to the formation as filtrate while more solids are deposited at the wall. The deposited solids are responsible for sticking.

2.13.3 Contact area

As shown in Figure 8a, sticking will not occur if there is no contact between the drill string and the well bore wall. The larger the arc length contact area, the higher the degree of differential sticking. The longer the depth of the contact area between the drill string and the mud cake, the higher the degree of sticking. This is because frictional forces associated with larger surface areas are higher compared to those of smaller surface areas.

The size and shape of the pipe also affects the contact area. Spiral and small outside diameter drill collars have a smaller contact area with the mud cake compared to un-spiralled larger outside diameter drill collars.

2.13.4 Stationary drill string

There are higher chances of getting stuck if the drill string is stationary, as shown in Figure 9d, as explained earlier. This is caused by too much time spent during connection/disconnection, especially when working with the Kelly system rig. Many stoppages when making connections of single joints increase the number of times and length of time of a stationary drill string. This is also common in the Kelly system rigs. An abrupt repair on a crucial rig component like the drawworks makes the drill string stationary. If the top drive motors fails, then the driller will not be able to rotate the drill string, thus

making it stationary for as long as he waits on repairs. Getting stuck also makes the drill string stationary.

2.13.5 Differential pressure

This is caused by high mud hydrostatic pressure compared to the formation pressure. Usually, the formation pressure is known by using pressure gradients determined in logs from other wells within the field. The driller or mud engineer has no control over the formation pressure. But he has control over the mud hydrostatic pressure. The only way to reduce the differential pressure to within safe limits is by reducing the mud hydrostatic pressure. This is achieved through mud density reduction. Mud or water used for geothermal drilling is always of low density. Figure 10 shows the process of differential sticking.

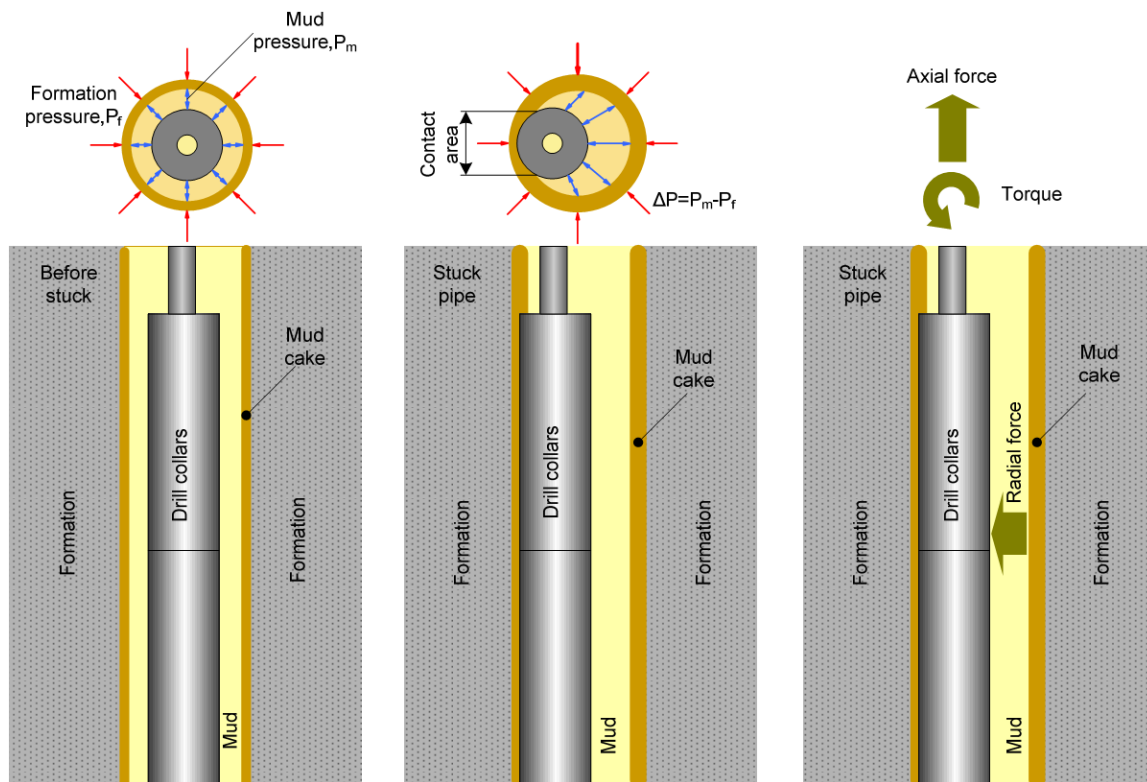


FIGURE 10: The process of differential sticking (Matanovic, 2011)

Mathematically, differential sticking is given by:

$$\Delta P = P_m - P_f \quad (1)$$

where ΔP = The differential pressure;
 P_m = The mud pressure; and
 P_f = The formation pressure.

When the pipe is stuck, then a pull out force is required to free it. This is mathematically given by the following equation:

$$F = \Delta P A_c \mu \quad (2)$$

where F = Pull out force (N);
 ΔP = Differential pressure (Pa);
 A_c = Contact area between the pipe and the mud cake; and
 μ = Coefficient of friction between the pipe and the mud cake.

The contact area depends on the arc length and length (depth) of the pipe in contact with the mud cake. The contact area is given by:

$$A_c = \psi_{arc} L_{ep} \quad (3)$$

where ψ_{arc} = Arc length; and
 L_{ep} = Embedded pipe length.

The arc length is given by:

$$\psi_{arc} = 2 \sqrt{\left(\frac{D_h}{2} - t_{mc}\right)^2 - \left(\frac{D_h}{2} - t_{mc} \frac{D_h - t_{mc}}{D_h - D_{op}}\right)^2} \quad (4)$$

where $2t_{mc} \leq D_{op} \leq (D_h - t_{mc})$.

D_h , t_{mc} and D_{op} represent the hole diameter, mud cake thickness and pipe outside diameter, respectively. Murrilo et al. (2009) studied the effect of the coefficient of friction and mud cake thickness on the pulling force of a stuck pipe. This he did by using the different coefficient of friction between the pipe and the mud cake as well as changing the length of the pipe embedded. He also studied the effect of mud cake thickness on the pulling force of a stuck pipe. He did this by changing the different mud cake thickness and lengths of embedded pipe for comparison purposes.

The different parameters used are shown in Tables 1 and 2. When the parameters in Tables 1 and 2 were inserted in the various equations, the resulting stuck pipe pull out force was as shown in the graphs in Figures 11 and 12, respectively (Murrilo et al., 2009). Note that the shape of Figure 12 is a typical square root function graph.

TABLE 1: Different friction coefficient and embedded pipe length

D_h	9 in
D_{op}	6 in
t_{mc}	1/32 in
L_{ep}	20,30,40 ft

TABLE 2: Different cake thickness and embedded pipe length

D_h	9 in
D_{op}	6 in
μ	0.25
L_{ep}	20,30,40 ft

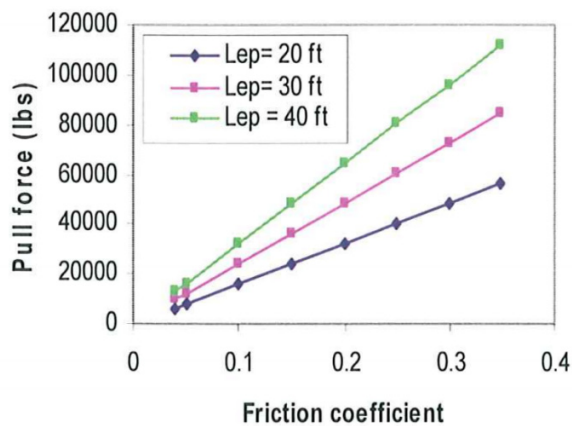


FIGURE 11: Effect of friction coefficient on pulling force (Murrilo et al., 2009)

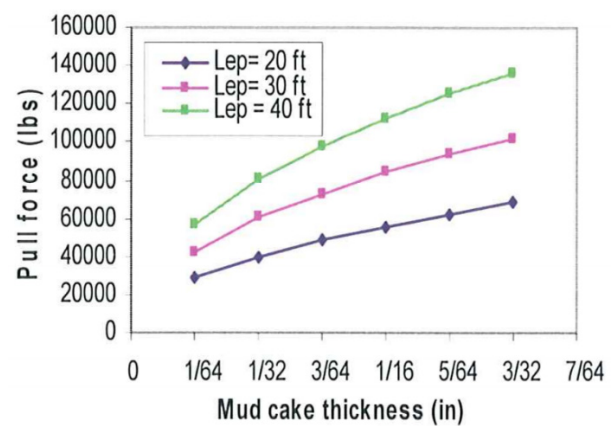


FIGURE 12: Effect of mud cake thickness on pulling force (Murrilo et al., 2009)

3. LOST CIRCULATION

Lost circulation is one of the major contributors to non-productive time in geothermal drilling. Attempts geared to cure lost circulation are costly because of the consumption of lost circulation materials and sometimes cement. Cost increase is also attributed to lost man hours while waiting cement to become hard. Studies done by Mohammed et al. (2012) found out that lost circulation was between 36% and 39% of non-productive time when drilling in Lobo field in South Texas, USA.

Lost circulation refers to the loss of drilling fluid or cement slurry, partially or completely, to highly permeable zones, cavernous and naturally or induced fractured formations as shown in Figure 13. This occurs while drilling or doing a cementing job. Lost circulation is caused by either poor drilling practices, or natural factors that are associated with the type of formation that is being drilled into (Shaker, 2008). Usually, the drilling fluid hydrostatic pressure is maintained at slightly higher than the formation pressure so as to prevent formation fluids from entering the well bore. That is also a key item in well control for avoiding blow-outs.

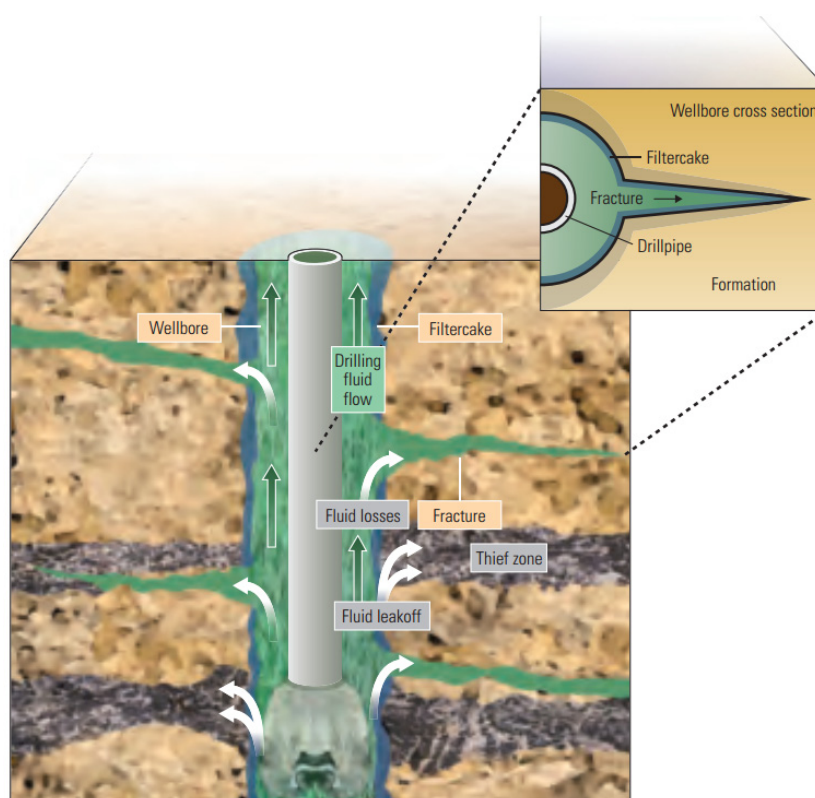


FIGURE 13: Lost circulation (Schlumberger, 2011)

Induced fractures occur whenever the drilling fluid hydrostatic pressure and pump pressure is much greater than the fracture gradient of the formation, as shown in Figure 13 (Cook et al., 2012). The green arrows in the Figure show the path taken by the drilling fluid back to the surface during normal drilling. The white arrows, on the other hand, show the path taken by the drilling fluid into the “thief zones” where fractures have been induced. If immediate remedial action is not taken to cure the loss, then larger and longer fractures will be created. This is because the pressure needed to propagate a fracture is usually less than that needed to initiate it. It should be noted that losses are caused by both original and induced porosities. In geothermal wells, cooling of the well during drilling often induces thermal fracturing which contributes to fluid loss.

3.1 Types of lost circulation

3.1.1 Seepage loss

This is a type of lost circulation in which the rate of loss is less than 4 m³/hr for water based mud (Abbas et al., 2003). The rate of this fluid loss depends on a number of factors that are either real, or apparent. High rates of penetration may seem, apparently, to be having seepage losses when they are actually not. Displacement of solids with fluids is a known cause of seepage loss. The nature of the formation dictates whether a fluid loss is seepage or not. The amount of overbalance also determines if a fluid loss is seepage or not.

Once the cause of seepage loss has been identified, then a solution is sought. If the losses are not severe, then the operator can drill ahead and hope that all will be fine. This is a strategy that has been used by other operators (Finger and Blankenship, 2010). This can save cost and time, especially when nearing casing setting depth. The low rates of fluid loss can be identified by trip tank measurements, smart electronic flow meters, or by looking at the returns flowing into the shale shakers.

Another solution to address seepage loss is to pull out of the hole and up past the diagnosed loss zone and shutting down the mud pumps. This is followed by giving the hole ample time to heal. As the hole is healing with time, other rig operations are carried out such as cut and slip, or preventive maintenance on the top drive system. This is done for about two hours and is intended to reduce non-productive time.

The most appropriate solution is to anticipate the loss and prepare for it in advance. This is done by preparing drilling mud with the proper properties. These properties are discussed in the 'Mud section' of this research. As drilling progresses, changes may occur in the formation that were not anticipated, and can lead to more losses than expected. When this happens, a reactive approach is applied as opposed to a proactive approach in managing lost circulation problems. This is done by the addition of lost circulation materials, discussed in the 'lost circulation materials' section.

3.1.2 Partial loss

Partial loss occurs when the losses are more than 4 m³/hr for water based mud. The partial loss is considered moderate if the rates of flow are less than 16 m³/hr. These losses are higher than seepage losses but some drilling fluid returns are still received on the surface. If remedial action is not taken to cure the losses, then this can lead to total loss.

One of the causes of partial loss is surge pressure. These (abnormal) pressures are exerted on the well bore wall when the drill (or casing) string is suddenly run into the hole and exceeds the formation fracture gradient thereby opening up fractures. These fractures are routes through which drilling fluids are lost. Partial losses are also caused by a considerable mud pressure overbalance that fractures the formation and enhances fluid loss. Most of the fractures or loss zones encountered while drilling geothermal wells are natural and cannot be avoided.

3.1.3 Total loss

Total loss occurs when no drilling fluid returns to the surface. The worst case is when there is no fluid column in the well bore after the mud pumps have been shut down. Losses of drilling fluids at the rate of more 16 m³/hr are accounted as total losses. Then formation fluids can flow into the well bore and may be difficult to control. Total loss is caused by the inability of the drilling mud to form a sufficient filter cake to seal off the zone. This may be a result of very high permeable formations. Another contributing factor to total loss is the use of too high a mud density. Other factors include excessive yield point (YP) and gel strength of the mud as they contribute to surge and swab pressures. Increasing pump pressure too quickly contributes to lost circulation. Total losses encountered in the production zone of geothermal wells are welcome, indicating a good production potential of the well, but can cause drilling problems.

3.2 Types of lost circulation zones

Lost circulation zones are classified as either vertical or horizontal zones. Vertical loss zones have fractures that are induced or natural. Horizontal loss zones, on the other hand, have fractures that are porous sand and gravel or cavernous. Horizontal loss zones can also have induced or natural fractures.

Porous sands and gravel zone

This type of loss zone is associated with a gradual drop in mud tank levels. Continuous drilling may lead to total loss.

Induced fractured zone

This loss zone is identified with a decrease in pump pressure. The loss is abrupt and may be followed by a complete loss. These fractures are induced when the mud weight exceeds 1.25 g/cm^3 . Induced fractures are also formed when there is a loss of circulation even though adjacent wells have not experienced losses. Microfractures are also induced by thermal contraction of the rock upon cooling by the drilling fluid.

Naturally fractured zone

This loss zone can be found in any type of formation. The loss can progress from partial to total loss if the same kind of formation is drilled through. An increase in loss is a result of more fractures being intersected.

Cavernous zone

This type of zone is usually associated with fractures of large proportions. Rough drilling followed by sudden and even total loss of returns is an indicator of this type of zone. The drill string can go down several feet followed by abrupt lost circulation.

Underground blowout zone

In this zone, fluids migrate from a lower active zone to an overlying zone. Underground blowouts are associated with fluctuating pressure readings as well as mud tank levels. Underground blowouts in a geothermal well can be quite dangerous and difficult to control. The well section in a blowout condition is ready to rush steam to the surface if the hydrostatic head cannot be maintained above the steam pressure.

Effects of lost circulation:

- Contributes to non-productive time which increases cost;
- Insufficient well hydrostatic pressure leading to kicks;
- Loss of mud and lost circulation material (LCM), thereby increasing costs;
- Drilling with aerated water (compressors) which is more expensive;
- Drilling with water and high viscosity polymer pills;
- Well collapse, sticking problems;
- Poor hole cleaning of cuttings and well fill-in, sticking problems, and
- Lack of formation information, no cuttings.

3.3 Mitigating lost circulation

Drilling fluid design is done with special considerations to specific parameters that will prevent lost circulation. These fluid parameters include rheology, density, fluid loss, solids content, and chemical parameters.

The use of well bore strengthening materials and mechanisms is another strategy that is used to prevent and reduce lost circulation. In this method, fracture propagation is restricted by particles that enter into the fracture and create a 'barrier'. This is implemented through the use of a particularly designed shape and size of particulate materials. Well bore strengthening mechanisms are also aimed at increasing the pressures at which lost circulation starts. This increases the drilling margin (Cook et al., 2012). The last effort to solve lost circulation is to cure. This is done through the use of lost circulation materials (LCM) or by cementing the loss zone.

3.3.1 Wellbore strengthening mechanisms

Fracture propagation resistance

Fracture propagation resistance is a mechanism in which lost circulation material goes into the fracture opening and forms a ‘barrier’ in the form of an external filter cake that seals off the fracture propagation tip (Figure 14).

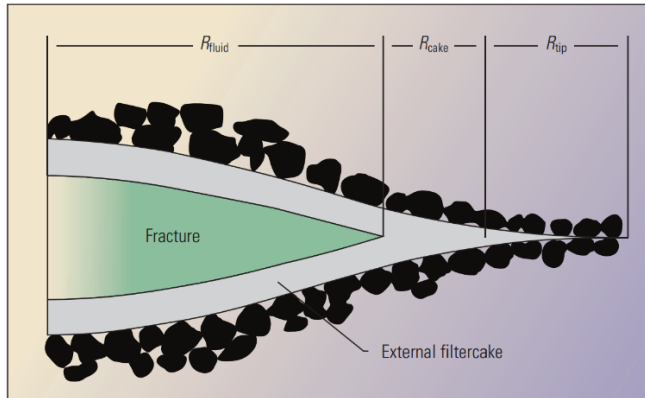


FIGURE 14: Fracture propagation (Cook et al., 2012)

R_{fluid} is the radial distance between the well bore's centre and the beginning of the filter cake wall. R_{cake} is the filter cake thickness and is the distance between the filter cake and the start of the fracture tip. R_{tip} is the distance between the end of cake thickness to the outer edge where the drilling fluid meets the formation. This enables the formation to resist further encroachment of the fracture. While rock strength is still the same, its ability to withstand fracturing has been increased. This is usually possible until new higher mud pressures start opening up a new fracture again after which the LCM penetration starts

the same process of fracture tip isolation. Stopping further fracture opening and propagation helps in preventing (any further) lost circulation.

Well bore isolation

This is a strengthening mechanism in which all efforts are made to ensure that the well bore is isolated when drilling. In order to achieve this, well bore strengthening materials (with strengths equal to or greater than that of the rock) have been designed with the aim of reducing rock permeability and hence ‘plastering’ it (Cook et al., 2012). This ‘plastering’ effect cuts off the pressure communication between the well bore and the rock (formation) as well as preventing drilling fluids from invading the formation. Other strategies of well bore isolation include the use of nano particles that help in a substantial reduction of permeability. These methods are generally not applied during geothermal drilling.

Hoop stress mechanism: The stress cage concept

The stress cage concept suggests that by adding a suitable well bore strengthening material (WSM) to a drilling fluid, it is possible to increase the hoop stress at the edge of the well bore. In dealing with lost circulation in this mechanism, an overbalanced WSM drilling fluid is circulated in an overbalanced state with the intention of creating shallow fractures. These fractures are then immediately filled and sealed

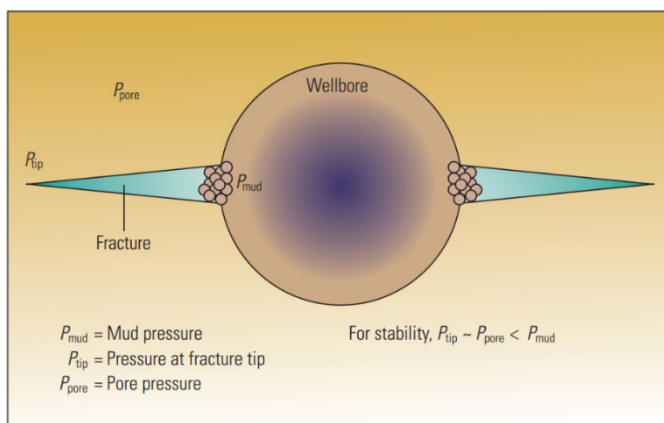


FIGURE 15: Stress cage concept (Schlumberger, 2011)

by WSM present in the drilling fluid. These WSM materials form small balls (shown in Figure 15) that accumulate, block, seal and form a bridge at the mouth of the fracture. This will, in essence, prevent further fracture propagation. The fluid in the fracture leaks off to the nearby rocks leading to pressure dissipation. The reduced pressure in the fracture opening causes it to close. However, this is limited by the bridge and wedge at the mouth of the fracture. When this happens, hoop stress (or stress cage) is established. Several shallow fractures formed by the hoop stress mechanism increase the rock's compressive strength.

This means that a higher well bore pressure is needed to fracture the rock. This helps in preventing formation collapse.

Fracture closure stress

The fracture closure stress mechanism is similar to that of the stress cage concept. The fracture propagation inhibition theory and the way it creates hoop stress in the well bore vicinity is the same. The difference is, while a fracture is initiated in the hoop stress mechanism, the fracture close stress mechanism acts on existing fractures. Mud treatment is used as high fluid-loss pills. The high fluid loss mud property that is desired allows the carrier fluid to be drained leaving behind a plug that breaks pressure communication between the fracture tip and the formation. The WSM used should be large particles of similar sizes. The similarity in sizes enables it to have higher permeability and hence higher fluid loss. It should also be noted that the larger the size, the greater the permeability.

4. DRILLING FLUIDS: FUNCTIONS AND TYPES

4.1 Functions of drilling fluids

Cuttings removal

A well bore is good to drill only if the cuttings removal is good. Drilling problems are aggravated if there is poor cuttings removal from the well. As the bit continues to drill into the formation, cuttings are generated and can accumulate. One of the major functions of drilling fluid is to transport these cuttings from the bit and other foreign objects in the annulus to the surface and finally to the solids control system. If this is not done properly, then these cuttings and foreign objects, if any, will accumulate around the bit or drill string, thereby increasing torque and eventually leading to a stuck pipe. By increasing the lifting capacity of the drilling fluid, the annular velocity will be able to lift the cuttings out of the hole. The main factor affecting hole cleaning is the upward annular velocity of the drilling fluid. When water is used it should be at a minimum 0.5-1.0 m/s but can be half of that while drilling mud is used. It has been shown that by increasing mud viscosity and reducing its weight, there will be substantial cost savings while achieving hole cleaning as if a heavier mud was used (Grace et al., 2008).

Bit cooling and cleaning

As the bit rotates and cuts the formation during drilling, heat is generated through friction. In addition, as the well is drilled deeper, temperature increases, depending on the formation temperature profile. High temperatures can damage the elastomer seals of a bit leading to loss of bearing lubricant and will, in the long run, lead to bearing failure and seizure of the bit. In order to avoid this problem, drilling fluid is used to cool the bit, as well as other downhole tools such as mud motors and MWD tools. It is important to maintain the circulation as during stops the well heats up. While running in hole the bit can be cooled at all times by circulation, if the rig has a top drive. The balling up (or bit balling) problem was described earlier in Section 2.13. To offset this problem, the drilling fluid cleans the cuttings that have been accumulated around the bit and BHA. This is facilitated by the mechanical energy of the mud pump.

Wellbore stability

The drilling mud helps to keep the well bore stable. This is because it builds up a mud cake that supports the well bore wall. This will, in effect, prevent the formation from collapsing. The drilling fluid, due to its hydrostatic pressure, prevents formation fluids from flowing into the well and probably damaging well control and surface equipment if it leads to a blow-out. A proper drilling fluid keeps the well bore stable by preventing the formation from swelling.

Suspend cuttings

When the mud pumps are switched off, circulation stops and this means that particle (or annular) velocity falls to zero. A good drilling fluid will be able to prevent the cuttings from falling down (by gravity) because of its thixotropic properties, and will keep the cuttings in suspension. If the drilling fluid is not able to do this, then cuttings will accumulate around the bit and stabilizers and, if this continues unchecked, then stuck pipe problems can be encountered. Water does not have the same capacity to support the cuttings during no flow and, thus, the well needs to be cleaned prior to adding a new drill pipe. This is done by circulating water for ~10 minutes or to circulate a high viscosity polymer pill, especially if there is loss of circulation in the well.

Drill string lubrication

Lubrication can help a lot, especially in deviated wells and those with dog leg severity. Of particular concern is when the drill string is lying on the well bore wall. This is because drag and torque increase with an increase in the length of contact between the drill string and the well bore wall. The addition of lubricant reduces the coefficient of friction between the two surfaces in contact, but usually the mud or water provides enough lubrication.

Grace et al. (2008) have, however, argued that mistakes have been made when something is added to the drilling fluid instead of removing it. Torque and drag are symptoms of poor hole cleaning and, instead of treating the problem, we are treating the symptom. The problem was poor cuttings removal, not torque and drag. Therefore, before a strategy is applied, the underlying problem ought to be critically analysed with an intention of coming up with the best option. It should be borne in mind that the application of a particular ‘good’ solution can result in an even bigger problem.

Assist in formation evaluation

A considerable source of drilling problems is related to the geological formations. This was discussed at length in Section 2. The best way to understand the well is by getting information on the geology. One of the functions of drilling mud is to provide us with this information. As the mud is circulated from the bit to the surface, it transports the generated cuttings. The cuttings are screened off at the solids control equipment and dumped appropriately to the mud pit. A small quantity of these cuttings is collected at a geologist’s sampling point at 2-5 meter intervals for analysis. These analyses give useful information regarding the formation being drilled. Apart from refining the field geological model, this information gives insight into potential drilling problems. This helps in better planning in dealing with formation related drilling problems.

Support of drill and casing strings

Drilling deep wells requires long drill strings and the longer the drill string the heavier the total weight. Surface equipment for handling drill strings is designed for a certain maximum load (hookload). By increasing the mud density, it is possible to increase its buoyancy factor, thereby increasing the buoyancy force. This will, in effect, reduce the drill string (apparent) weight. As geothermal wells use water and low density mud, the buoyancy factor stays virtually the same and most geothermal drilling employs rigs with ample hook load ratings (tonnes).

$$\text{Buoyancy factor, } k = 1 - \frac{\text{density of fluid (mud)}}{\text{density of object (steel 7.85 g/cm}^3\text{)}} \quad (5)$$

$$\text{Apparent weight} = \text{Weight in air} \times \text{Buoyancy factor} \quad (6)$$

Lowering of floating casing

When running in a casing string, there are occasions when it ‘floats’, if it is not filled up with water. This is indicated by lower than normal hook load as shown on the weight indicator. The driller and the rig floor men can see this quickly by looking at the elevator. As the casing string is lowered, it reaches a point where the elevator is coming down while the casing string is not moving. The cause of this is either the casing has hit an obstruction or it has ‘floated’. The solution to the ‘floating’ problem is to

completely fill up the casing with drilling fluid to counteract and overcome the buoyancy. If the problem is due to an obstruction, then the time-consuming solution is to pull out of hole and drill out or ream the obstruction.

Other functions of drilling fluids are:

- Cool the formation, particularly prior to cementing casings;
- Powering down-hole tools, mud motor and measurements while drilling (MWD);
- Retard or prevent corrosion;
- Assist in cementation; and
- Prevent adverse effects of H_2S and CO_2 .

4.2 Types of drilling fluids

The type of drilling fluid to be used has an impact on well bore drilling problems. The type of formation being drilled into also determines the type of drilling fluid to be used. The different types of drilling fluids available are: water-based mud, oil-based mud and aerated water (Figure 16). A drilling mud is composed of:

- A continuous phase (liquid phase);
- Colloidal phase (for example gel forming phase);
- Inert phased (for example a weighting material); and
- Chemical phase.

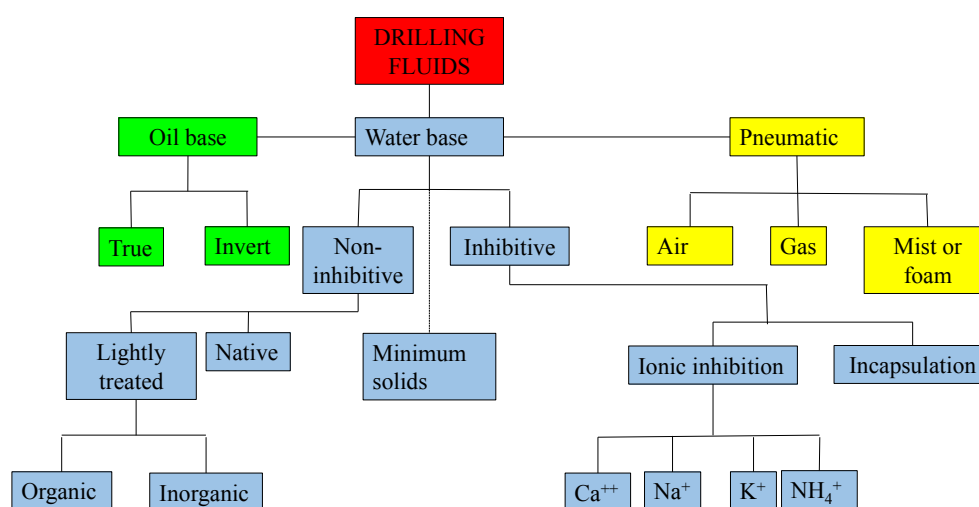


FIGURE 16: Classification of drilling fluids

4.2.1 Water-based drilling fluid

Clear water

Clear water is the least expensive among all other types of drilling fluids. Clear water can be used with occasional mud or polymer pills to reduce the costs. The water source can either be sea, lake or a permanent river, or a borehole depending on not only its proximity to the rig site but also its cost of pumping. Brine, which is fluid collected from discharging wells, can be used as a liquid phase in the drilling of geothermal wells after it has been cooled in a pond. It is recommended that a borehole be sunk next to the river, lake or sea. This helps to protect the pump from sucking in objects. During winter, the water surface can be frozen and, therefore, the pump is unable to pump, but access to warm water solves the problem.

When mixed with bentonite, water acts as the continuous phase with its main function being to provide the initial viscosity. This viscosity can be modified to suit desired rheological properties. The water liquid phase also helps to suspend the colloidal solids, like bentonite or other inert solids like weighting material (for example, barite).

Clear water has a poor lubrication property which can increase the torque. The other weakness of clear water is that there is no control over fluid loss and, consequently, there is no control over the filter cake. Clear water does not have good cuttings suspension capacity. This means that when the mud pumps are shut down, cuttings will fall down into the annulus and settle, causing a problem that it ought to have prevented. Fortunately, water is the least expensive drilling fluid and its poor suspension capacity can be improved by occasional mud sweeps. In spite of these disadvantages, drilling with water using the proper precautions is safe and it is the preferred drilling fluid for the open hole section of geothermal wells.

Water-based mud

To improve the cuttings suspension property of clear water, naturally occurring clay is added. The most common type of clay used is bentonite which is a member of the montmorillonite group. Bentonite mixed with water, 5-7% by weight, has a viscosity higher than that of clear water. It will also have better cuttings suspension capacity and can form a thin mud filter cake with very low permeability (US Army Corps, 2001). Water-based mud is classified either as non-inhibitive or inhibitive. Non-inhibitive mud, unlike inhibitive mud, has no chemical additives that would otherwise prevent the formation from absorbing water.

Inhibited mud

This type of mud is either ionically inhibited or encapsulated. Ionically inhibited mud has a chemical composition that is designed to reduce or prevent (inhibit) swelling of the formation. Dispersion can be improved using chemical dispersant additives (that de-flocculate the mud) so as to achieve high density muds with good rheological properties. However, care must be taken because solids-laden mud reduces the drilling rate of penetration and can cause well bore erosion. This erosion can cause well bore stability problems. Encapsulated mud has polymers that coat the cuttings and well bore wall to form a barrier. This barrier slows down water diffusion and, as a result, slows down hydration and disintegration.

4.2.2 Oil-based mud

Oil based muds are never used for geothermal drilling. If there is a desire to try them, these are the issues. Oil-based mud has oil as the continuous phase. The oil phase helps in the formation of thin walled mud cake which lowers the chances of getting a differentially stuck pipe. Its enhanced lubrication property reduces the drag and torque of the drill string. Oil-based mud must not be used where temperatures exceed their flash and fire points. Reduced water content in water-based mud ensures that swelling up of the well bore well is greatly reduced. Compared with inhibitive water-based mud, oil-based mud is more inhibitive. An oil continuous phase should be maintained at all times. This is because water wetting of weighting materials like barite can cause it to settle (Mohammed and Mohammed, 2009). The main disadvantage of oil-based mud is that it is not environmentally friendly.

4.2.3 Pneumatic drilling fluids

The use of aerated water and foam mixtures are highly recommended when drilling potentially productive formations. This is because, unlike mud, they don't plug and block the wellbore with filter cakes and cuttings (if an underbalance is properly maintained). This is beneficial in the sense that formation permeability and fissures are left open to allow producing fluid to pass through. For this reason, among others, compressed air has been incorporated as a drilling fluid to reduce geothermal drilling problems.

Aerated drilling fluids are divided into four types, as shown in Figure 17, depending on the percentage of air present in the mixture. Straight air has been used in dry steam dominated reservoirs like the Geysers in the United States. Its use has also been extended to high pressure reservoirs by the addition of denser fluids (Russell, 1987). To achieve this, air is injected into either water or mud at the standpipe with the purpose of reducing the drilling fluid density. This is desired so as to achieve an underbalance or pressure balance with the formation. This helps to reduce differential pressure which, in turn, prevents formation damage.

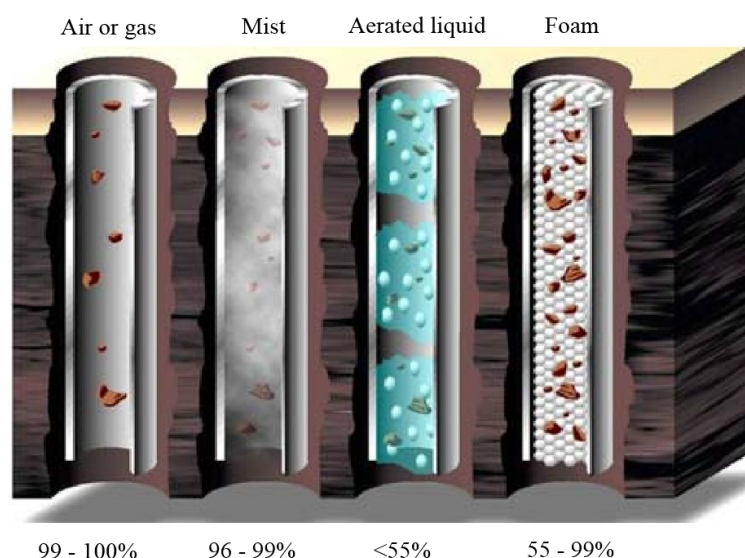


FIGURE 17: Types of air drilling fluids

Russell (1987) suggested that the use of aerated water fluid in a water-sensitive formation is possible because the high rates of penetration associated with aerated fluid enables faster drilling and casing before hydration of the formation takes place. Aerated drilling is a preventive measure for differential sticking because it balances the formation pressure.

Hole (2008) argues that many geothermal reservoirs are found in areas where geothermal and sedimentary rocks are interlayered. These reservoirs are associated with local as well as regional faults and fractures. This makes these zones permeable and, as a result, lost circulation is a common problem. To counter this problem, aerated fluids are used that ensure drilling fluids as well as cuttings are circulated out of the hole to the surface. This helps in avoiding stuck pipe problems and prevents formation damage. In addition, aerated fluids reduce skin damage caused by cuttings blocking up permeable zones. Aerated fluids, compared with those that are non-aerated, also help in improving reservoir production. In his study on a drilling campaign in Kenya, Hole (2008) found that the productivity of wells drilled using aerated fluids was on average, more than double that of wells drilled without air.

4.3 Lost circulation solutions

The problem of lost circulation was discussed in Section 3. When preventive measures are not successful, then curative measures are applied. These measures are divided into three categories and include: (1) bridging agents, (2) surface-mixed systems, and (3) down hole-mixed systems.

4.3.1 Bridging agents

Bridging agents, also referred to as lost circulation materials (LCM), are used to stop fluid flow by physically blocking the path through which fluid passes into the formation during the course of drilling, or when it is temporarily suspended. Different types of LCM are available and depend on sizes. These are: (1) Granular, (2) Flakes, (3) Fibrous and (4) Encapsulated.

Granular

Granular LCMs are chunky in shape and are prepared in different sizes. These types of LCM form a bridge either at the formation face, or inside the formation matrix. As drilling continues, there is axial as well as lateral movement of the drill string which, occasionally or continuously, rubs against the well bore wall. This causes abrasion of granular bridges deposited on the formation wall and finally its

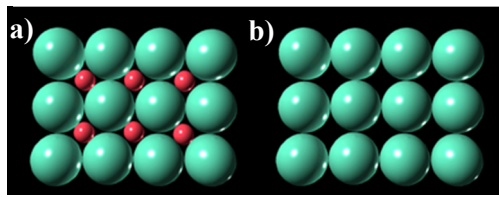


FIGURE 18: Effect of particle size distribution on porosity:

- a) Two sizes packing, porosity = 14%;
- b) Similar size packing, porosity = 48%

improves the chances of eliminating lost circulation. Examples of granular LCM are mica flakes, nut shells, cotton hulls and wood.

Flakes

This is a type of lost circulation material whose particles are thin and flat in shape, with a large surface area. They are not soluble in the mud which they are mixed in, and are available in different sizes. Examples of flake LCM are mica and plastic cellophane.

Fibrous

Where the formation is porous and highly permeable, fibrous LCM (with slender, long and flexible particles) are used to cure fluid losses because of their ability to form mat-like bridges. This helps the mud to form a filter cake since permeability is reduced. Fibrous LCM are also available in different sizes and lengths of fibre. Examples of fibrous LCM are cedar bark, shredded cane stalks, mineral fibre and hair.

4.3.2 Surface-mixed systems

These are systems that involve the use of cement slurries to stop lost circulation. Because of its thixotropic nature, cement slurry is pumped as a liquid and as it enters into a lost circulation zone the velocity of the leading edge reduces. This is followed by the forming of a gel that strengthens and starts to offer flow resistance. After pumping has stopped, resistance increases until the gel hardens, thereby preventing fluid loss. LCM, such as mica flakes, can be added to the cement slurry depending on lost circulation severity.

4.3.3 Down hole-mixed systems

These are systems in which two or more fluids are mixed in the well bore or in the lost circulation zone, after which it forms a viscous plug or a precipitate that seals the zone. One such method is the Flo-Check method where a solution of sodium silicate reacts with a calcium chloride brine to form a plug of calcium silicate down-hole. The mixing is delayed until the fluids are just in front of the loss zone. This is done by either pumping a spacer or simultaneously pumping one fluid through the string and the other through the annulus.

5. BOTTOM HOLE ASSEMBLY (BHA) DESIGN

Drill string contact with the well bore wall is not desired as it causes wear and key seats which can happen during buckling. Lubinski (1950) suggested that to counter this problem, efforts should be made to ensure that the drill string is subjected to tensile loading and the BHA be subjected to compressive loading. This is made possible by ensuring that the buoyed weight of the BHA (drill collars and heavy weight drill pipes) exceeds the maximum weight on the bit. This can be represented mathematically as follows:

$$\text{Required air weight of BHA} = \frac{\text{Maximum WOB} \times \text{safety factor}}{\text{bouyancy factor} \times \cos\theta} \quad (7)$$

where θ = Well bore inclination.

The safety factor should be at least 1.1 to allow for any drag due to friction.

6. FISHING – A BALANCE OF DECISIONS

After all the preventative and corrective measures have been applied, sticking can still occur. This is the time to unstick the stuck drill string. The most important thing to know is the depth of the free drill string to the stuck point (free point) as shown in Figure 19. This is determined mathematically, according to Hooke's law, as shown in Equation 8.

$$L = \frac{E \times A \times e}{F_2 - F_1} \quad (8)$$

where L = Length from the surface to the stuck point (m);
 A = Cross-sectional area of pipe body (m²);
 E = Young's modulus of steel (200 GPa);
 e = Length of stretch (m);
 F_1 = Force applied when pipe is in tension (N); and
 F_2 = Force applied to stretch pipe by "e" (N).

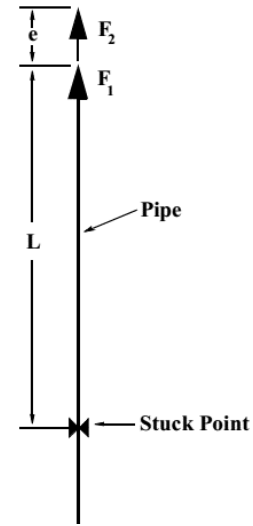


FIGURE 19: Stuck point location

The parameter e , the stretch distance used for calculating the stuck point location, is determined using the following procedure that is normally done on the rig floor:

- Ensure that the entire string is in tension, an upward force, F_1 greater than the total weight, is applied to the drill string;
- A datum line is drawn on the drill pipe, usually at the top of rotary table; and
- Another upward force, F_2 that is greater than F_1 is applied which causes the pipe to stretch by an amount "e" above the drawn datum in accordance with Hooke's law.

Having measure e , the stuck point location (SPL) can be easily calculated using Equation 8 and its value used as the first point for locating the free point indicator tool which gives a more exact value. Another method that is used to locate a fish is a drill pipe recovery log which uses an acoustical survey. This method is usually employed when the fish is very long. There are situations where unsticking is unsuccessful and time consuming. In such cases, a decision may be made to terminate and abandon the well or plug and side-track. Such a decision requires that the SPL be known. This is because it is the point at which the pipe will be backed-off and, if not possible, cut either mechanically, chemically or by use of explosives.

Mechanical cutting of pipes is hydraulically activated to make cutting arms contract and cut the pipe. Electrically driven cutting tools have also been developed. Chemical cutting, on the other hand, uses a strong acid that oxidises and cuts the pipe. When backing-off using the explosive method, the drill string is given a left-hand torque while locating the explosive at a tool joint closest to the SPL. This is followed by detonating the explosive causing the tool joint to unscrew. Backing off operations by explosives is the most common method and usually works on the first try.

After establishing the SPL, it is important to evaluate the next course of action, as shown in Figure 20. This decision is guided by economics. It should be noted that each decision made has an associated cost. If the equipment that is stuck has a large cost, then more fishing time should be allowed compared

to a shorter time for low cost equipment. It has been found that the maximum fishing time that should be allocated is given by Equation 9 below (Johnson et al., 2013).

$$D_f = \frac{V_f + C_s}{C_f + C_d} \quad (9)$$

where D_f = Number of days allocated for fishing;
 V_f = Value of the fish;
 C_s = Estimated cost of side tracking the well;
 C_f = Daily fishing tool rental and personnel charges; and
 C_d = Daily rig operating charges.

The steps one goes through when making a decision to free a stuck pipe are illustrated in Figure 20, adapted from Bowes and Procter (1997). The decision making process is triggered by a stuck pipe. The first line of action is to find out the SPL using the available method. This is followed by working the drill string up and down the hole. However, there is a limit on the amount of force used to pull up the string. This is important since there is a pulling force beyond which the weakest member of the drill string will fail, leading to a loss. This limiting force is known as maximum overpull and its value is calculated using Equation 10 below:

$$\text{Maximum Overpull} = (0.9 \times \text{Yield Strength}) - \text{Hookload} \quad (10)$$

$$\text{Hookload} = \text{Air Weight} \times \text{Buoyancy Factor} \quad (11)$$

The allowable tensile loading in practice is 90% (safety factor) of the pipe's yield strength value which is obtained from API RP7G or drilling data handbooks. If, after working, the pipe is free, normal drilling operations resume and, if not, another decision is made. This could either be continuously working up the drill string or trying alternative methods which could be spotting diesel ('black magic') or corn oil. The addition of diesel or oil reduces torque and drag. A decision can also be made at this stage to cut the pipe. The most effective method to cut the drill string is by high-energy explosives lowered on a wireline to the point of detonation. If all decisions made are not successful, then it is high time the well is plugged and side-tracked or terminated.

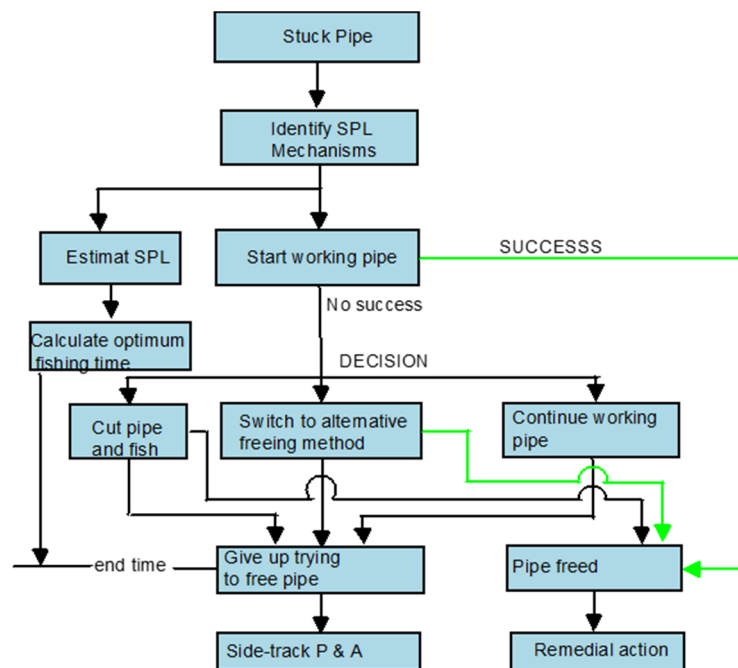


FIGURE 20: Freeing stuck pipe flow chart
(Bowes and Procter, 1997)

6.1 Fishing tools

A number of fishing tools are available that are intended to engage the fish internally or externally. They come in a number of sizes, shapes and with different material properties. Other fishing tools are meant to trap and collect foreign objects that have either fallen into the well bore or that have broken in the course of fishing, drilling or logging. Fishing tools are mainly available commercially although they may also be fabricated to suit particular needs or in order to reduce time delays associated with procurement procedures. Some of the most commonly used fishing tools are illustrated in Figure 21. Figure 21a shows a junk mill that is used to grind junk into smaller pieces so that it can be lifted by the

circulating fluid. The material of the grinding surface at the bottom of the mill is made of tungsten carbide. Different designs and sizes of junk mills are available depending on the application. The flat surface mills have concavity that guide and centre the junk below the mill (Johnson et al., 2013). Figure 21b shows an impression block whose purpose is to help in knowing the dimensions of the upper part of the fish in the well bore. This tool also shows the fish's position with respect to the well bore. Knowing the fish's dimensions and its position, the fisherman selects the best size of catching accessories and tools. For example, if the fish is leaning on the wall of the well bore, then a wall hook guide will be required to pull the fish and guide it to a catching tool. The material of the bottom of an impression block is made of soft lead. An impression block is connected at the bottom of a fishing string then lowered to contact the fish, thereby creating a dent (or impression) on the soft lead. It is then pulled back to the surface for examination.

Figure 21c shows a junk magnet which is used to attract and remove ferrous materials that are too heavy to be lifted by the circulating fluid. At the top of this tool is a box joint that is connected to the drill string while a magnet is attached to its bottom. Figure 21d shows a taper tap. A smaller variation of its design is the pin tap. A taper (or pin) tap is used in catching a fish internally. This is done by connecting it at the end of a fishing string and lowering it to contact the fish. This is followed by applying a small weight (recommended by the manufacturer) and rotating it to wedge the tap threads into the fish. A guide can be attached to the tap if the well bore diameter is considerably larger than that of the fish. This helps in preventing the tap from bypassing the fish. A safety joint is normally used to enable the fishing string to be backed off, just in case the tap and fish become permanently stuck.

Figure 21e shows an overshot which is an external tool. This is the most common tool used to fish a broken drill string. It is used in a conjunction basket or spiral grapple that latches onto the fish externally. The overshot is lowered while washing over the top of the fish until there is a slight reduction in weight which shows the overshot has contacted the fish. A guide shoe at the bottom, directs the overshot to engulf the fish. This is followed by rotating the overshot to the right which makes the grapple open to engage the fish. Pulling the fish without rotating it causes the grapple to retract inside the tapered bowl and latch onto the fish. A mill control packer may be used in conjunction with the overshot to grind any flared fish top before it is directed to the grapple. After this, the fish is pulled out of the well bore (Johnson et al., 2013).

Figure 21f shows a reverse circulating junk basket which is used after a fishing operation. While fishing, metal fragments either from the overshot guide or from grinding of the flared fish top may fall down the well bore. Also, other ferrous materials may have not been picked up by the junk magnet. As the circulating fluid is pumped, it flushes fragments at the bottom hole and carries them through the reverse circulating junk basket where the fragments are deposited on a catcher as the fluid exits the basket on its way to the surface. The basket is finally pulled out of the well bore and the fragments in the barrel are disposed of.

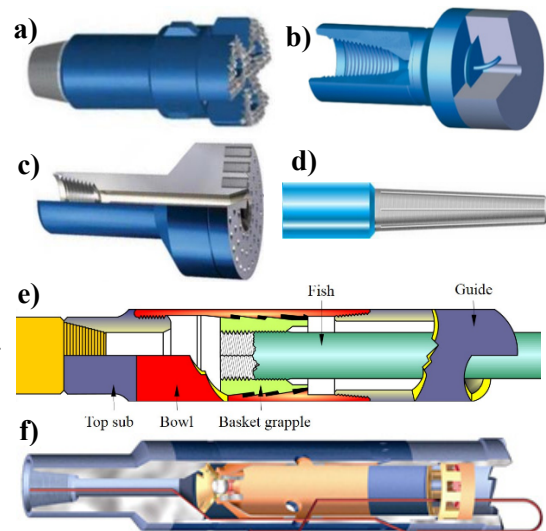


FIGURE 21: Commonly used fishing tools,
a) Junk mill (Schlumberger, 2012);
b) Impression block;
c) Junk magnet (Schlumberger, 2012);
d) Taper tap (Nov, 2013);
e) Overshot (Matanovick, 2011);
f) Reverse circulating junk basket
(Pioneer Oil Tools Ltd, 2013)

7. THE CASE OF MENENGAI

Several wells have been drilled in Menengai geothermal field where serious sticking related problems have been encountered. Table 3 shows a series of activities that occurred before and during sticking in different wells. The activities were looked into with a view to correlating them with subsequent drill string sticking. The knowledge of possible causes of sticking helps in strategizing the most appropriate

TABLE 3: Activities related to sticking of different wells in Menengai

Well	Activity
MW01	114.37 to 124.5 m drilled using water with partial returns. String stuck at 124.5 m. Freed after 3 hrs. Drilled from 137.8 to 400.5 m using water, no returns. Got stuck while pulling out of hole (POOH) when sounding hole. Got free. Got stuck at 378 m while running in hole (RIH) 13 3/8 casing (csg), but successfully landed. Drilled from 2184 to 2206 m. Pressures then went up and got stuck. Pipe freed after 8 hrs. Some pipes bent and twisted.
MW02	Wait on water for 4 days. Reaming 88 to 132 m without returns. Major obstruction at 116 and 131 m. Got stuck at 133 m but freed. Experienced total loss at 206.5 m then followed by stuck drill string which was freed. No returns from 206.5 to 213 m then got stuck again but pipe freed. Reamed from 168 to 218 m then got stuck during connection. Stuck for 3 days.
MW03	Drilled from 95.18 to 113 m using water with returns. Got stuck for 45 min. Drilled from 130 to 167.2 m with no returns. Got stuck for 30 min. Reamed from 2064 m to 2093.54 m while experiencing high torque. Then POOH and got stuck for 9 days.
MW04	There were no lost circulation problems. However drill string, without warning, got stuck at 2117 m. Then freed after 9 days.
MW06	2036-2039, 2097, 2124 to 2137, 2143-2151, 2164.5, 2132, 2143-2151, 2164 and 2186 m no returns received on surface. Drilling ahead using aerated water and foam at 2202.96 m while receiving returns on surface, then got stuck.
MW07	Drilled from 112.6 to 120.11 m using brine with returns. On lifting bit off bottom, got stuck at 105 m but pipe was freed. Drilled from 120.11 to 149.25 m with intermittent partial/full returns. Drilled from 134 to 138 m and experienced drilling break with cuttings fully flowing out. Circulated hole at 149 m. While lifting string off the bottom, got stuck with high torque and SPP. Worked string up and down, then introduced air. A tension of 160 kN applied. Thereafter, no rotation and circulation. Then no SPP. All fluids pumped got lost into the formation. Pumped LCM repeatedly and introduced air. SPP rose to 800 psi and pipe got free. Drilled from 149.25 to 150.56 m using brine with no returns. Suddenly torque and SPP increased followed by stuck pipe which was freed. POOH from 1205 to 1184 m while back reaming. Pump went off while trying to connect back a stand that had been removed. Saver sub got damaged then installed circulating head. On connecting back saver sub, realised string got stuck but with returns. After 3 days it was freed. Drilled from 1996.98 to 2135.93 m using aerated brine and foam with no returns. This was followed by stuck pipe at 2135.93 m which was then freed.
MW08	Drilled from 150 to 178.7 m using water and mud sweeps then 6 5/8 × 4 1/2 cross-over sheared at the box end. Drilled from 179 to 210 m using water and mud sweeps then POOH to inspect bit. It was found out that an 8" drill collar sheared at the box end of its tool joint. Wait on water for 17 days due to failed transformer at the pump station. Then drilled out cement from 378.9 to 407.1 m. Continued to drill ahead to 458.77 m. On POOH, it was realised part of the BHA was left down hole which was successfully fished out on the 7 th day. Drilled ahead from 2162 to 2355.56 m using aerated brine and foam with returns. POOH to RIH liners. It was realised part of the BHA was left down hole.

TABLE 3 cont.: Activities related to sticking of different wells in Menengai

Well	Activity
MW09	Drilled from 701 to 706 m and encountered soft formation. Returns ok. Drilled ahead from 706 to 812.86 m using mud with returns. Drastic decrease in SPP and hook load noted with increase in WOB. Then POOH from 812.86 m to inspect drill string. It was noted the DP that joins HWDP had sheared 1.05 m from the box end of the tool joint. The fish was successfully retrieved on the 4 th day. Most of the collars showed defects on the box end. Drilling ahead from 1741.81 to 1950 m with partial returns (partial), then got stuck but freed after 1 hr.
MW10	Drilled from 113.26 to 310 m with water and occasional mud sweeps with no returns. Then sudden hook load drop POOH to inspect drill string. It was noted that a 6 $\frac{5}{8}$ \times 4 $\frac{1}{2}$ cross over sub had parted leaving fish down hole which was freed after 4 days. Drilled from 392 to 740.77 m using water and occasional mud sweeps and periodic wait on water for 8 hrs. This took place over a period of 10 days. Then hook load dropped followed by POOH to inspect drill string. It was noted a 6 $\frac{5}{8}$ \times 4 $\frac{1}{2}$ cross over sub between HWDP and 8" DC had parted.
MW11	At 574.78 m, pulled drill string to the shoe for repairs. Tried to circulate through the bit but unsuccessful. Then POOH and found the bit clogged to the bit sub. 1842.37 m. Wait on water for 3 days. Got stuck while reaming at 1842.37 m then did fishing for 26 days.
MW12	Drilled from 49 m using water without returns. Then waited 3 hrs for repairs. Resumed drilling to 57.14 m when there was a power failure followed by stuck pipe after which it was freed. Drilled from 1912 to 2054 m using aerated water and foam with returns. Then got stuck suddenly due to an increase in WOB and torque. The string was freed on the 5 th day.

measures to avoid them. In doing so, time spent in unsticking or fishing will be minimized. This will further avoid BHA (or parts of drill pipe) losses in the hole. As a result, drilling costs will be reduced and drilling performance increased.

Table 4 shows the break-down of drilling wells in Menengai. Table 5 shows the average rate of penetration used to drill a section of a well which is also shown graphically in Figure 22. Table 5 shows the average rate of penetration in meters per day to drill each section. Table 6 shows the depths where sticking occurred in different wells and Figure 23 shows the average sticking time per section. Well MW10 was only drilled to a depth of 740.77 m and then abandoned due to drilling problems. Figure 24 shows the actual drilling progress for 11 wells in Menengai.

TABLE: 4: Time break-down of drilling wells in Menengai (days)

Section	Well											
	MW01	MW02	MW03	MW04	MW06	MW07	MW08	MW09	MW10	MW11	MW12	Average
Surface	10	14	16	12	24	12	12	16	12	15	14	14
Intermed.	17	41	16	18	19	33	37	25	21	26	33	26
Production	22	12	12	18	14	37	28	24	100	41	19	30
Main hole	27	54	56	33	38	50	46	39		48	27	42
Total	76	121	100	81	95	132	123	104	133	130	93	

TABLE: 5: Average rate of penetration per section (m/day)

Section	Well											
	MW01	MW02	MW03	MW04	MW06	MW07	MW08	MW09	MW10	MW11	MW12	Average
Surface	8	6	5	7	3	5	5	4	5	5	4	5
Intermed.	19	8	20	18	17	9	8	12	13	8	9	13
Production	20	34	58	39	49	23	20	21	4	15	26	28
Main	50	44	18	31	29	19	31	31		20	44	27

TABLE: 6: Sticking depth (m) per section

MW01	MW02	MW03	MW04	MW06	MW07	MW08	MW09	MW10	MW11	MW12
Surface hole										
					59	58				57
Intermediate hole										
114	109	113			105			310	176	367
125	133	167			149					
378	135				151					
	207									
	213									
	218									
Production hole										
					1184	458	813	741		
Main hole										
2206		1187 2112	2117	2203	1957 2136		1950		1842	2054

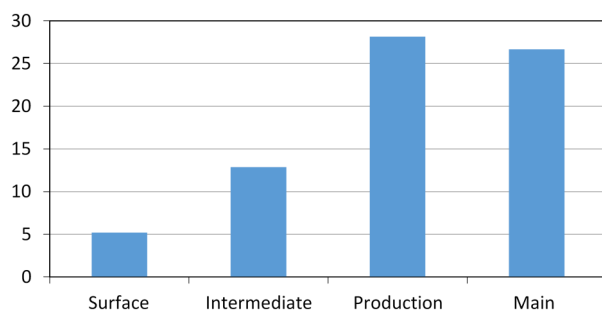


FIGURE 22: Average rate of penetration in different hole sections (m/day)

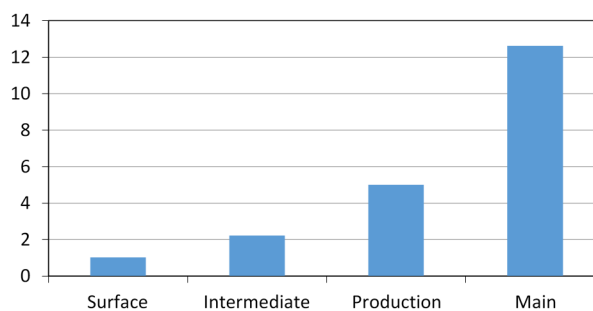


FIGURE 23: Average sticking time for each section of the well (days)

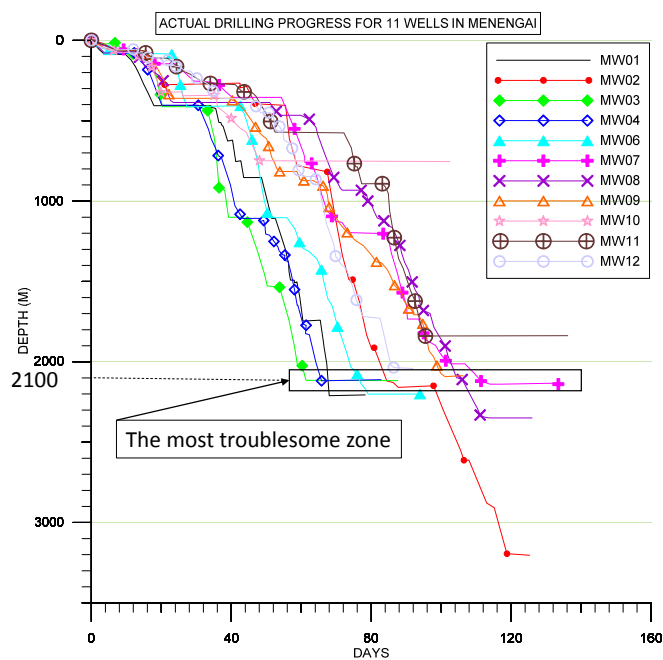


FIGURE 24: Drilling progress curves showing the most troublesome zone in Menengai at ~2100 m

8. DISCUSSION

8.1 Changes in drilling parameters

Zooming in to the Easy View program graph display, whose screenshot is shown in Figure 25, shows that drill string sticking in Well MW06 took place at around 02:40 hrs on the 13th of January, 2012. The drilling parameters, shortly before and after sticking occurred in this well, are shown in Table 7.

The possible causes of changes in drilling parameters shortly before sticking occurred include, but are not limited to the following reasons:

Hook load

The hook load was reduced suddenly from 888.1 to 748.3 kN at the time the drill string got stuck. This shows that there is a sudden force acting upwards on the string which is opposite to the direction of the hook load. This upward acting force could probably be due to magma being thrust up into the well before being rapidly quenched. Hook load drop due to a sheared pipe is usually accompanied by a standpipe pressure drop. In this case, there was a hook load drop accompanied by a standpipe pressure increase, meaning the pipe did not shear. However, after 11 days of fishing, the fish was retrieved and part of the drill string was found to have sheared due to the fishing effort. The pipe sheared above the free point and the upper part of the drill string was recovered. After sticking occurred, hook load increased (Figure 25) upon hoisting, which is an indication of the sticking. A drastic drop in hook load due to shear was also confirmed in Well MW09, as described in Table 3.

TABLE 7: Drilling parameters shortly before and after sticking of Well MW06

Parameter	Shortly before sticking	Just before sticking
Drilled depth (m)	2202.91	2202.91
Rotary Torque (kNm)	14.7	0.3
Pipe pressure (MPa)	6.18	7.06
Hook load (kN)	888.1	748.3
Rotation (RPM)	61.36	6.51
Weight on bit (kN)	54.6	186.2

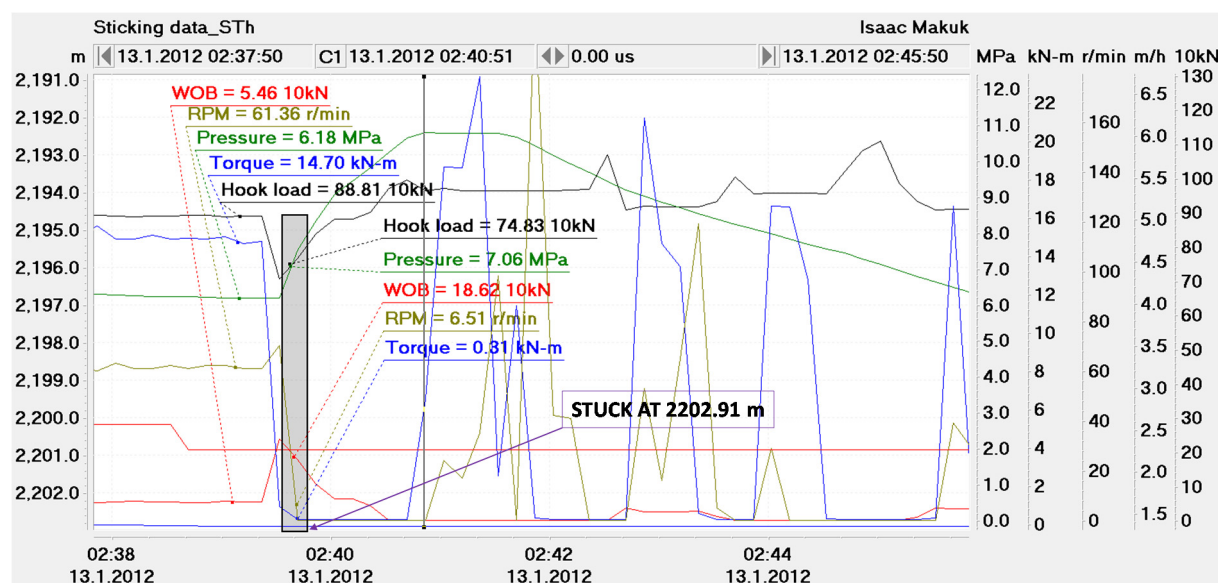


FIGURE 25: Easy View programme screenshot showing drilling parameters shortly before and after sticking took place in Well MW06

Rotary torque

The rotary torque decreased from 14.7 to 0.3 kNm, as shown in Table 7. This happened as the drill string rotation stopped due to the sticking. The rotary torque then went up when rotation was attempted and there was no circulation of drilling fluid as the jets got plugged.

Standpipe pressure

In Table 7, it can be seen that the standpipe pressure increased from 6.18 to 7.06 MPa. The pressure increase was a result of the drill bit being blocked. The mud pump was cut off shortly after.

Weight on bit

The weight on bit increased from 54.6 to 186.2 kN as shown in Table 7. Weight on bit is given by drill string weight minus hook load. Due to conservation of mass, the drill string weight is constant. Hook load keeps changing depending on the weight on bit and upthrust due to buoyancy or, in this special case, magma being thrust up the well. This means that if the hook load decreases, then the weight on bit increases, as shown in Figure 25.

8.2 Fatigue

Depending on the well bore curvature, part of the drill string can be subjected to a bending moment. As the drill string is being rotated, it wobbles as it revolves around inside the well bore. This causes changes in forces acting on a particular point in the drill string from compressive to tensile. This is repeated many times until the drill string is lowered, or the well bore geometry changes. This cyclic loading compromises the mechanical strength of the drill string. Fatigue failure is, in the initial stages, initiated by the formation of crystallographic defects. If these defects grow and increase their density, then it will reach a critical stage where slip movement of the defective planes takes place, resulting in the formation of microscopic cracks. As the number of cracks increase, the fatigue life of the drill string point reduces. If crack propagation is accelerated, for example due to vibrations, the drill string component will experience fatigue failure.

On pulling out of hole the last joint of heavy weight drill pipe in Well MW09, it was found that the 6 $\frac{3}{8}$ ×4 $\frac{1}{2}$ cross-over sub had parted, with 120 mm of the box side coming out of the hole and the rest remaining inside the hole. Note that the box length of a shouldered connection is 130 mm (Gabolde and Nguyen, 2006). This shows that the crossover sub most probably parted at the last thread, which happens to be the point with the lowest fatigue life, as observed in finite element analysis (FEA) and discussed by Ellis et al. (2008). There were three similar occasions in which 6 $\frac{3}{8}$ ×4 $\frac{1}{2}$ cross-overs failed. Apart from the cross-overs, there were instances in which the drill collars sheared, for example in Well MW08 as described in Table 3. In order to minimize fatigue failure, the following measures should be applied:

- Avoid prolonged fishing operations by repeated overpull and rotation of a stuck drill string;
- Minimize curvature and buckling;
- Apply proper thread compound to protect critical areas;
- Optimize well trajectory; and
- Regular non-destructive testing (NDT) of drill string and its risk management that ensures close monitoring of running hours and any defect(s). Especially important is frequent ultrasonic inspection of the box and pin on the drill collars and subs.

8.3 Rotary slip setting position

After a drop in standpipe pressure and hook load occurred in Well MW09, indicating a brake, the drill string was pulled out of hole to inspect it. It was observed that a drill pipe joining the heavy weight drill pipe had sheared 1.05 m from the tool joint as described in Table 3. This happens to be the rotary slip setting position on the drill pipe. Rotary slips are used to hold the drill pipe when making or breaking a

connection. Continuous gripping of the drill pipe at the same position by slip could have initiated a point of weakness through ‘small creep loading’. This could have been made worse by poor handling, for example, setting the slip before the pipe was stopped which results in pipe deformation. Pulling out of well with drag could have caused a sufficient force to propagate a fracture and the final shear of the drill pipe at the slip setting position. To avoid this scenario, the drill pipe slip setting position should be changed on a rotational basis. This could be done by removing one joint, then pulling out of hole the rest of the joints in stands.

8.4 The top section

Low average rates of penetration were experienced in the surface top section of wells in Menengai, as shown in Figure 22. This is attributed to the hard and fractured rock in this section. The severe vibrations encountered led to waiting for repairs which further reduced the drilling rate. Top drive rigs have been mostly affected in the surface casing section of the well because of mechanical breakdowns and failures due to vibrations. Top drive guide rails have to be realigned to ensure the well bore is maintained vertically. To minimize the wait on repairs and increase the average rates of penetration, the top surface has been drilled using the Kelly system rather than the top drive. The use of air hammers (DTH) should also be investigated for this section as they would work well in very hard and fractured formations near the surface. The rigs have air compressors and pumps for the drilling soap, so only the 26" bit and DTH hammer are required.

8.5 The 2100 m depth

The 2100 m depth in Menengai is the most troublesome zone, as shown by the concentration of flat spots in Figure 24. This is not surprising as the wells intersected magma. Well MW16 (not shown in Figure 24) also got stuck at a depth of 2084 m after which the fish was retrieved. On average, sticking time takes 12% of the total drilling time in Menengai. The troublesome zone is the main contributor to the high sticking time of the main hole, as shown in Figure 23.

Interestingly, there was also a 2100 m troublesome zone during the drilling of an Icelandic Deep Drilling Project (IDDP I) well at Krafla in Iceland, as shown in Figure 26. The problem at this depth was

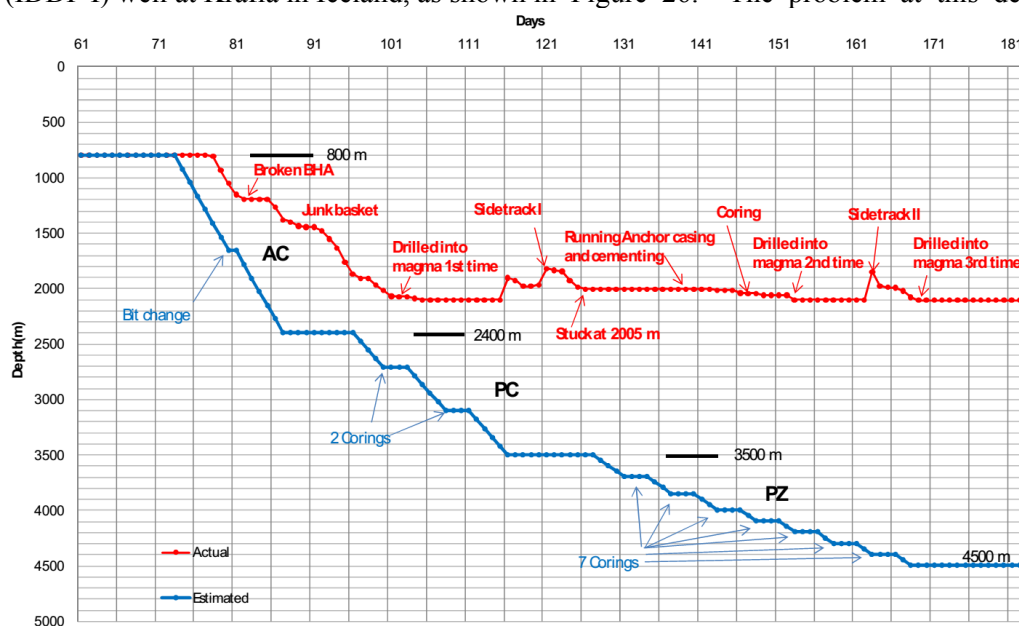


FIGURE 26: Drilling progress showing a troublesome 2104 m depth for IDDP I at a well in Krafla, Iceland (Hólmgæirsson et al., 2010)

attributed to intersecting magma which the drill bit drilled into at 2104 m depth. That was followed by the observation of quenched glass cuttings at the shale shakers, whose temperature was estimated to have been at 1050°C before cooling (Hólmgeirsson et al., 2010). However, previous interpretation of magnetotelluric data suggested that a magma chamber was located deeper than 4.5 km. The magma intrusion that was drilled into at IDDP 1 showed that the geophysical methods used did not have sufficient resolution to identify it (Elders and Fridleifsson, 2009).

While drilling Wells MW04 and MW06 in Menengai, fresh glass was found in the cuttings at depths of 2082 and 2174 m, respectively, indicating a possible intersection of magma intrusions. Since glass is susceptible to alteration and especially at such depths and in a high temperature geothermal system, it ought to have been completely altered. The fresh glass, therefore, is believed to have been rapidly chilled magma by the drilling fluid. Extremely high temperatures, as well as sticking problems, were recorded at these depths for these wells (Mibei, 2012). To avoid problems associated with intersecting magma intrusions, the drill string should immediately be pulled out of hole whenever glass cuttings are seen at the shakers and further drilling stopped, but the experience is that there is no advance warning.

8.6 Reddish soils

Over a long period of time, soil forms on the ground. When a volcanic eruption occurs, the lava flows over the soil and bakes it, thereby changing its colour to an anomalous red colour. After another long period of time, soil forms again on top of the lava and the cycle continues as long as the eruptions do. This forms a sequence of layers of reddish soil and lava. While drilling Well MW06, reddish sample cuttings were collected between 1614 and 1638 m, depicting the presence of reddish soils in Menengai. These soils, when they come into contact with drilling fluid, disintegrate rapidly and lead to the formation of huge cavities in the well bore (Mibei, 2012). These cavities enhance the formation collapse as well as compromise efficient circulation and the transport of cuttings. This results in the accumulation of cuttings which increases torque and subsequent sticking problems. This is believed to have happened in Well MW01 when reddish brownish returns were seen shortly before sticking. To avoid this, whenever reddish returns are seen at the shakers, the drill string should immediately be pulled out by one stand and run in hole slowly while rotating and cleaning the hole with a mud or high-viscosity pill and checking for torque increase. Should torque increase, the drill string should be pulled out again the same way until the well bore is safe.

8.7 Fishing operation in Menengai

Fishing operations have been successfully carried out in Menengai, but there are also cases of losing a part of the drill string. Several fishing tools have been used including an overshot dressed with a spiral or basket grapple, complete with a mill control packer. Other tools include a junk mill, a junk magnet, a junk basket and an impression block. More fishing equipment is needed. This includes a sufficient assortment of spiral and basket grapples as well as taper taps. Problems were experienced while trying to back off a stuck drill string in Well MW10. The problems were both technical and time delays. Waiting on fishing tools was a contributing factor to time delays. This was because tools needed for backing off and cutting the drill string were not available on site. Acquisition of these tools was time consuming due to procurement procedures. It is recommended that backing off tools, including explosives, be available in abundance. Legal, security and safety problems associated with the storage of explosives at the rig site can be solved by acquiring and storing them in a police station or military barracks closest to Menengai. This idea is borrowed from fishing operations at rigs in Iceland where backing off explosives are under the custody of the Coast Guard that avail them whenever needed. This will reduce the time of backing off a stuck drill string and contribute to better performance. In addition to fishing equipment, directional drilling equipment should also be available in abundance to allow for quick side tracking. Subcontracting of fishing and directional services will help in quick solutions to these problems. This is because, the more time a drill string is stuck, the less chance of unsticking it.

9. CONCLUSIONS

This report identified that 12% of drilling time was spent on drill string sticking activities in Menengai. This increases drilling costs and reduces drilling operations performance because of the extended drilling time spent in fishing activities. The sticking occurrences were caused by formation challenges that included lost circulation and collapses. Most unexpected and extreme was intersecting magma at 2100 m which resulted in the drill string getting stuck and blocking the circulation, without any advanced warning. Well bore geometry related to sticking, like key holes, was also encountered in Menengai. In addition, differentially stuck pipe was experienced. To reduce time spent on fishing activities and subsequently improving drilling performance, a number of suggestions have been given. Sufficient well bore cleaning is the best way to avoid sticking. This is achieved through the use of proper drilling fluids. Different types of drilling fluids were discussed. Mud is used when drilling a large diameter hole to achieve good cleaning and the mud cake is beneficial in the cased sections of the well as it stops small losses. The effectiveness of this can be improved through the addition of lost circulation materials. When this is still not sufficient, then cement plugs can be placed to heal the loss. The emphasis on avoiding lost circulation is to have drilling fluid all the time that ensures the hole is cleaned properly to avoid the accumulation of cuttings that cause sticking. It should be noted that mud should not be used in the production zone since this will adversely affect the permeability. In the open hole section of the well, it is important to have large losses as it indicates good future production. Cuttings find their way into formation fractures when returns are not received on the surface and, to counteract that, air is added to the drilling fluid for pressure balance. Very high rates of penetration should be avoided to give cuttings time to be carried up to the surface and to avoid sticking. Menengai geothermal field has a troublesome zone at 2100 m depth in Wells MW03, MW04, MW07 and MW12 that is traced to probable intersecting magma, just as in the IDDP well at Krafla. The sequence of getting stuck, the fresh glass cuttings and superheated steam above the critical temperature once the well had heated up, are all indications. Reddish soils were also found to contribute to sticking, due to their formation collapsing tendencies. Suggestions have been made to immediately pull out of hole whenever reddish brownish returns are received and run in hole slowly while ensuring good circulation. It is also recommended that the drill string be pulled out of hole immediately if glass cuttings are seen on the shale shakers and to terminate drilling operations, as the cuttings may indicate proximity to magma. To save time and cost, a formula for calculating the maximum allowable time spent on fishing based on economics has been highlighted in this report as a basis for making a decision as to whether to continue with fishing operations or not.

ACKNOWLEDGEMENTS

I wish to sincerely thank Mr. Lúdvík S. Georgsson, the director of the United Nations University Geothermal Training Programme and Dr. Ingvar Birgir Fridleifsson, the former director, as well as the management of the geothermal development company (GDC) for giving me an opportunity to come and study here in Iceland. I thank the United Nations University and the government of Iceland for providing funds for my study. I am grateful to Mr. Ingimar G. Haraldsson, Ms. Thórhildur Ísberg, Ms. Málfríður Ómarsdóttir and Mr. Markús A. G. Wilde who made my stay in the office and home here in Iceland very comfortable and conducive for learning.

I am greatly indebted to my supervisor, Mr. Sverrir Thórhallsson, who was always eager to give me knowledge of drilling technology in class, and his huge support and guidance in my project. I thank all the UNU lecturers who taught me and the UNU Fellows for their good company and support.

I thank my wife Mercy and son Maurice for their moral support and for accepting my being away from them for six months. I thank the Almighty God for loving and caring for me.

REFERENCES

- Abbas, R., Jarouj, H., Dole, S., Junaidi, E.H., El-Hassan, H., Francis, L., Hornsby, L., McCraith, S., Shuttleworth, N., van der Plas, K., Messier, E., Munk, T., Nødland, N., Svendsen, R.K., Therond, E., and Taoutaou, S., 2003: A safety net for controlling lost circulation. *Oilfield Review*, 15-4, 20-27.
- Agarwal, N., 2008: Drill collars with auto-release sleeves. *Paper presented at IADC/SPE Asia Pacific Drilling Technology Conference and Exhibition, Jakarta, Indonesia*, 7 pp.
- Barriol, Y., Glaser, S.K., Pop, J., Bartman, B., Corbiell, R., Eriksen, O.K., Laastad, H., Laidlaw, J., Manin, Y., Morrison, K., Sayers, M.C., Romero, T.M., and Volokitin, Y., 2005: The pressures of drilling and production. *Oilfield Review*, 17-5, 22-41.
- Bowes, C., and Procter, R., 1997: *1977 drillers stuck pipe handbook*. Procter & Collins Ltd., Ballater, Scotland, 71 pp.
- Cook, J., Growcock, F., Quan, G., Hodder, M., and Van Oort, E., 2012: Stabilizing the wellbore to prevent lost circulation. *Oilfield Review* 23-4, 26-35.
- Devereux, S., 1998: *Practical well planning and drilling*. Pennwell, Oklahoma, OK, United States, 524 pp.
- Elders, W., and Fridleifsson, G.Ó., 2009: Iceland deep drilling project finds magma. *GRC Bulletin, July/August 2009*, 31-32.
- Ellis, S., Wadsworth, T., Lee, K., Gerdes, M., Altizer, S., 2008: Connection fatigue index (CFI): An engineered solution for connection selection and a replacement for BSR. *Paper presented at the 2008 IADC/SPE Drilling Conference*, Orlando, FL, United States, 8 pp.
- Finger, J., and Blankenship, D., 2010: *Handbook of best practices for geothermal*. Sandia National Laboratories, report SAND2010-6048, 84 pp.
- Gabolde, G., and Nguyen, J.P., 2006: *Drilling data handbook* (8th edition). Institut Francais P'etrole Publications Paris, France, 576 pp.
- Gow, A., 2005: *Roughnecks, rock bits and rigs: the evolution of oil well drilling technology in Alberta, 1880-1970*. University of Calgary press, Alberta, Canada, 674 pp.
- Grace, D., Shursen, J., and Carden, R., 2008: *Drilling practices*. Petroskills, Oklahoma, OK, USA, 774 pp.
- He, J., 1999: Multiple tectono-thermal modelling of Liaohe basin in the Cenozoic. *Chinese J. Geophysics*, 42-1, 62-68.
- Hole, H. 2008: Drilling fluids for drilling of geothermal wells. *Paper presented at "Petroleum Engineering Summer School", Workshop 26, Dubrovnik, Croatia*, 8 pp.
- Hólmgeirsson, S., Gudmundsson, Á., Pálsson, B., Bóasson, H., Ingason, K., and Thórhallsson S., 2010: Drilling operations of the first Iceland deep drilling well (IDDP). *Proceedings of the World Geothermal Congress 2010, Bali, Indonesia*, 10 pp.
- Hsu, K., and Belaud, D., 1998: Integration application of real-time LWD sonic for overpressure detection and seismic. *Overpressure Proceedings Workshop 1998, Pau, France*, 221-226.

Johnson, E., Lee, M., and Robertson, R., 2013: Landing the big one – The art of fishing. *Oilfield Review*, 24-4, 26-35.

Lubinski, A., 1950: *A study of the buckling of rotary drilling strings*. Drilling and Production Practice, American Petroleum Institute, 37 pp.

Luo, X., 2004: Quantitative analysis on overpressuring mechanism resulted from tectonic stress. *Chinese J. Geophysics*, 47-6, 1223-1224 (in Chinese).

Manohar, L., 1999: Shale stability: Drilling fluid interaction and shale strength. *Proceedings of SPE Asia Pacific Oil and Gas Conference and Exhibition 1999, Jakarta, Indonesia*, 10 pp.

Mibei, G., 2010: Geology and hydrothermal alteration of Menengai geothermal field. Case study: wells MW-04 and MW-05. Report 21 in: *Geothermal training in Iceland 2012*. UNU-GTP, Iceland, 437-465.

Mody, F.K., and Hale, A.H., 1993: A borehole stability model to couple the mechanics and chemistry of drilling fluid/shale interaction. *J. Petr. Technol.*, 1093-1101.

Mohammed, A., Abolle-Okoyeagu, I., and Okeke, C., 2012: A comparative analysis of the trouble time for conventional and casing drilling wells: A case study on the Lobo Trend. *Internat. J. Science & Technology*, 1-11, 584-588.

Mohammed, M., and Mohammed, S., 2009: Effect of additives on rheological properties of invert emulsions. *Iraqi J. Chemical & Petroleum Engineering*, 10-3, 31-39.

Murphey, C., 1966: Hole deviation and drill string behaviour. *SPE Journal*, 6-1, 44-54.

Murrilo, A., Neuman, J., and Samuel, R., 2009: Pipe sticking and avoidance using adaptive fuzzy logic and neural network modelling. *Proceedings of SPE Production and Operation Symposium*, 2009, Oklahoma, OK, United States, 244-258.

Osborne, J., Swarbrick, E., 1997: Mechanisms for generating overpressure in sedimentary basins: A re-evaluation. *AAPG Bull*, 81-6, 1023-1041.

Pašić, B., Gaurina-Međimurec, N., and Matanović, D., 2007: Wellbore instability: Causes and consequences. *Rudarsko-Geološko-Naftni Zbornik*, 19, 87-98.

Raja, H., Sørmo, F., and Morten, L., 2011: Case-based reasoning: Predicting real-time drilling problems and improving drilling performance. *Proceedings of SPE Middle East Oil and Gas Show and Conference, Manama, Bahrain*, 12 pp.

Russell, M., 1987: The use of aerated fluids in geothermal drilling. *Proceedings of 9th Geothermal Workshop, Auckland, NZ*, 153-157.

Schlumberger, 1997: *Stuck-pipe prevention. Self learning course*. Schlumberger Anadrill, 65 pp.

Schlumberger, 2013: *Keyseat*. Schlumberger Ltd., website: <http://www.glossary.oilfield.slb.com/en/Terms.aspx?LookIn=term%20name&filter=keyseat>

Shaker, S., 2008: Loss of circulation: Causes and consequences in geopressed systems. *Paper presented at AADE Fluids Conference and Exhibition, 2008, Houston, TX, United States* 5 pp.

Skúlason, G.K., Johnsson, M.T., Pálsson, H., Karlsdóttir S.N., and Thorbjörnsson, I.O., 2011: Load history and buckling of the production casing in a high temperature geothermal well. *Proceedings of the 36th Workshop on Geothermal Reservoir Engineering, Stanford University, Stanford, CA, United States*, 9 pp.

U.S. Army Corps of Engineers, 2001: *Geotechnical investigations*. U.S. Army Corps of Engineers, Engineering and Design, website: publications.usace.army.mil/publications/eng-manuals/EM_1110-1-1804_sec/EM_1110-1-1804.pdf

Van Oort, E., 1997: Physico-chemical stabilisation of shales. *Proceedings of SPE International Symposium on Oilfield Chemistry 1997, Houston, TX, United States*, 523–538.

Van Oort, E., 2003: On the physical and chemical stability of shales. *J. Petroleum Sci. & Engineering*, 38, 213-235.

Van Oort, E., Hale, A.H., and Mody, F.K., 1994: Critical parameters in modelling the chemical aspects of borehole stability in shales and in designing improved water-based shale drilling fluids. *Proceedings of SPE Annual Technical Conference and Exhibition 1994, New Orleans, LA, United States*, 25-28.

Van Oort, E., Hale, A.H., and Mody, F.K., 1995: Manipulation of coupled osmotic flows for stabilisation of shales exposed to water-based drilling fluids. *Proceedings of SPE Annual Technical Conference and Exhibition 1995, Dallas, TX, United States*, 497-509.

Van Oort, E., Ripley, D., Ward, I., Chapman, J.W., Williamson, R., and Aston, M., 1996: Silicate-based drilling fluids: Competent, cost-effective and benign solutions to wellbore stability problems. *Proceedings of IADC/SPE Drilling Conference, 1996, New Orleans, LA, United States*, 189-204.

Warren, E., 1940: Causes, preventions, and recovery of stuck drill pipe. *Paper presented at the Drilling and Production Practice Conference, New York, NY, United States*, 10 pp.



GEOTHERMAL GRADIENT AND GEOLOGY OF HOFFELL LOW-TEMPERATURE FIELD, SE-ICELAND

Mohammed Masum

Geological Survey of Bangladesh
153, Pioneer Road, Segunbagicha
Dhaka-1000
BANGLADESH
Masum613@yahoo.com

ABSTRACT

The study area is a part of the Geitafell central volcano in southeast Iceland. This area has been studied extensively for the exploration of geothermal resources, in particular low-temperature, as well as for research purposes. A geological map is the foundation on which a geothermal exploration is based. All other data need to be interpreted in view of the observed or known geological features. During geothermal exploration, geothermal maps should emphasize on young igneous rocks that could act as heat sources at depth. They also show the distribution and nature of fractures and faults, and the distribution and type of hydrothermal alteration. This report describes the results of a geothermal and geological mapping project in a low-temperature geothermal field in SE-Iceland. The aim of the study was to familiarize the author with geothermal gradient mapping, interpretation of geological information, including tectonic structures and low-temperature geothermal manifestations, as well as to study the site selection for production/exploration well drilling. Another goal of this study was to make geological and geothermal maps of a volcanic field and to analyse whether some relationship could be established between the tectonic setting and the geothermal alteration of the study area. The geothermal model of the drilled area is consistent with the existence of a structurally controlled low-temperature geothermal reservoir at various depths ranging from 50 to 600 m. Televiewer data showed that Wells ASK-29, ASK-50, ASK-56, ASK-82, and ASK-83 drilled in the area have open fractures and show a comparatively high geothermal gradient, indicating that further drilling for exploration/production should be executed. A geothermal map is presented on which possible drilling targets for a production well are suggested.

1. INTRODUCTION

1.1 Location, topography and climate of the study area

The study area, located in SE-Iceland (Figures 1 and 2), is home to a low-temperature geothermal field, which is about 400 km east of Reykjavik, the capital city of Iceland. It is located at 64°42'20"N – 64°44'20"N and 15°04'20"E – 15°06'30"E. Within the region the extinct central volcano of Geitafell is found, but it was active five million years ago (Fridleifsson, 1983a).



FIGURE 1: Map showing the location of the study area

between 1100 and 2100 mm per year. Winter is cold with a mean daily temperature in the range between -2 and -4°C . Summers are fairly warm, with a mean monthly temperature of about 8 – 10°C (Einarsson, 1991). The weather is highly unpredictable since rainfall may occur at any time, and snowfall can prevail in the winter. There are two glacial rivers, Austurfljót and Sudurfljót, draining the area. These are braided river systems which flow across a sandur plain, known as Hoffellssandur, on which the mountain of Svínafell (323 m) is located.

1.2 Background and objectives

Bangladesh is one of the poor and developing countries which suffer from a serious shortage of electricity. About 40% of the country has electricity coverage. Frequent power cuts also cause severe problems. In order to improve the electrical supply, the Geological Survey of Bangladesh (GSB) initiated a drilling programme in 2010, exploring possible geothermal resources in the north-western part of the country. During the exploration phase of geothermal prospects, geological mapping of surface geothermal manifestations and low-temperature surveys are essential for evaluating geothermal resources. Therefore, on the request of GSB, The Geothermal Training Programme of the United Nations University (UNU-GTP) in Iceland kindly approved the present author to attend the programme in the specialized field of geological exploration in 2013. This study is a part of a six month training course at the UNU-GTP in Iceland in 2013 which commenced in April. The first 2–3 months were used for course work, field excursions and practical training in various geothermal disciplines. The remaining 3 months were used for practical training in geothermal exploration, the results of which are described in this report. The objective of the study was to provide the author with training in geothermal mapping, using the volcanic field at Hoffell in SE-Iceland as a study area. This is a low-temperature geothermal field and the author was trained in exploring such an area and how to analyse, interpret and present the data which was gathered.

Today the roots of the volcano can be seen, due to glacial erosion. The topography comprises mountains of volcanic rocks and a valley mostly covered by alluvium and vegetation. The altitude is between 30 and 500 m above sea level. Since the study area is close to the Atlantic Ocean, it is affected by the Irminger current, which greatly moderates the climate along Iceland's southern and western coasts. The climate of the area is characterized by a fairly cold winter and a moderate summer. The area receives a relatively high mean annual precipitation,

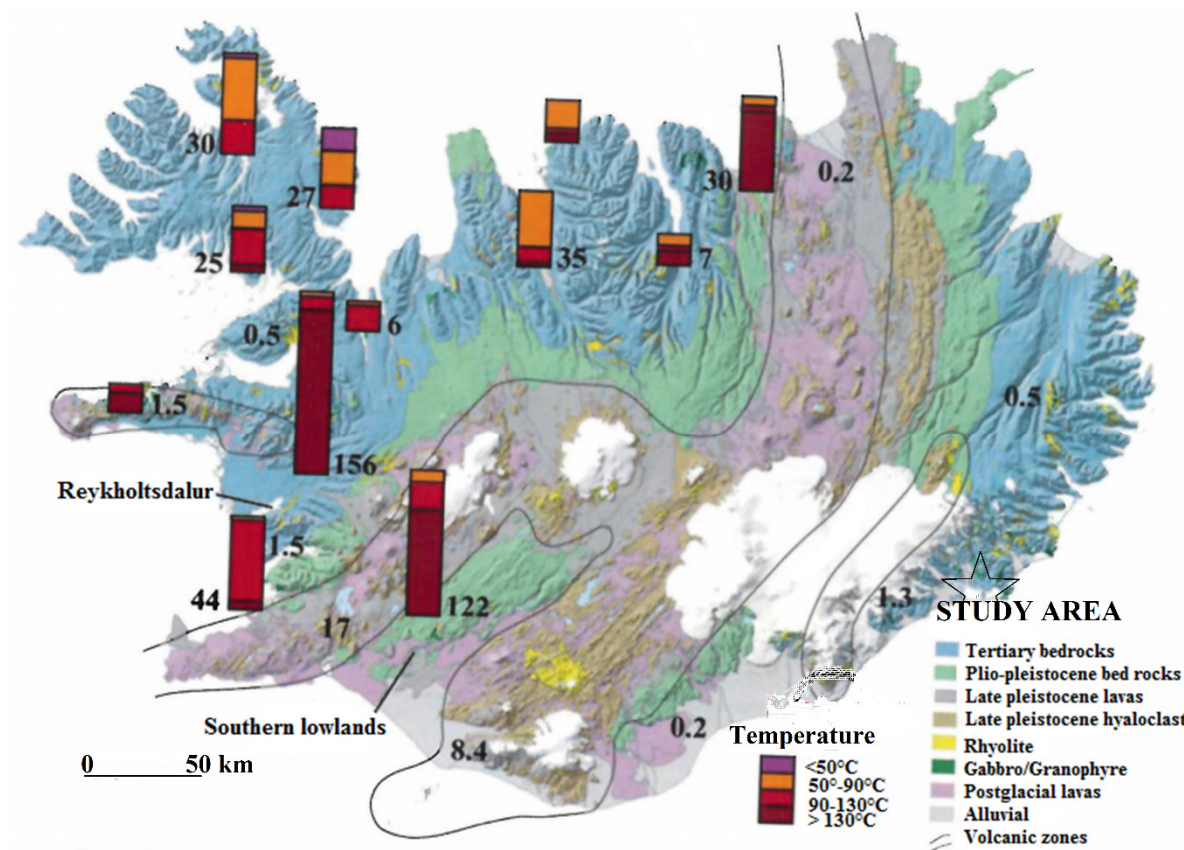


FIGURE 2: Geological map of Iceland (modified from Jóhannesson and Saemundsson, 1999)

1.3 Previous work

The geothermal area is mentioned in several reports but the first comprehensive study of the geology of the area appeared in the PhD thesis of Guðmundur Ómar Fridleifsson (1983a). The field was explored for geothermal applications in 1992 when the first wells were drilled. Later Stapi- Geological Services (1993, 1994, 2002, 2005, and 2006) did geothermal studies in the area on the basis of the temperature gradients of the region. Hjartarson et al. (2012) went through all existing data and made suggestions regarding further work in the area. Árnadóttir et al. (2013) used a televiwer in order to better acquire indications of the direction and angle of fissures and faults in 7 wells. Also, temperature, dimensional, neutron and gamma measurements were completed in the same research. Based on these results, exploration/production Well HF-01 was sited and drilled. The results from that well confirm the existence of an 80°C geothermal field (Kristinsson et al., 2013). Besides these, some studies were also completed about the surrounding study area. Burchardt and Guðmundsson (2009) worked on the infrastructure of Geitafell volcano, southeast Iceland. Three-dimensional modelling of Geitafell volcano was done by Burchardt et al. (2011).

2. GEOLOGY AND TECTONIC SETTING OF ICELAND

2.1 Geology

Iceland is geologically a young country. It is located on the spreading boundary of the Mid-Atlantic Ridge, where the American and Eurasian tectonic plates are diverging at an average rate of 2 cm per year (Figure 3). Iceland is formed by the coincidence of the spreading boundary of these plates and a

hotspot or mantle plume. As the plates move apart, excessive volcanism caused by the mantle plume construct the island. Iceland is the largest island on the Mid-Atlantic Ridge because of the additional volcanism caused by the plume, which is stationary. However, the NW movement of the plate system as a whole, relative to the plume, has caused several rift jumps to the east throughout the geological history of the island (Hardarson et al., 1997). The oldest rock formations date back to the late Tertiary basaltic lava pile, which is predominantly exposed in the eastern and northwest quadrants of the island (Figure 2). The oldest rocks are dated at approximately 16 Ma in the extreme northwest region (Hardarson et al., 1997). The Quaternary rocks are composed of sequences of basalt lavas and hyaloclastites that are exposed along the volcanic zones. The nature of the volcanic products during this period was strongly controlled by climatic conditions. The volcanism is divided into interglacial (ice-free) volcanism and subglacial (glacial) volcanism (Saemundsson, 1979, 1980). The ice free volcanism is categorized into inter- and post-glacial volcanism, and the rock types erupted under this climatic condition are represented by subaerial eruptions forming lava flows, pyroclastic scorias and welded lavas. The glacial volcanism is divided into sub- and supraglacial volcanism, and eruptions are characterised by phreato-magmatic deposits and the formation of hyaloclastites. The surface geology is entirely made up of volcanic rocks with basalts being 80-85% of the volcanic pile, and acid and intermediate rocks 10%. The amount of sediments of volcanic origin is 5-10% in a typical Tertiary lava pile, but may locally be higher in Quaternary rocks (Saemundsson, 1979; Jakobsson and Gudmundsson, 2008).

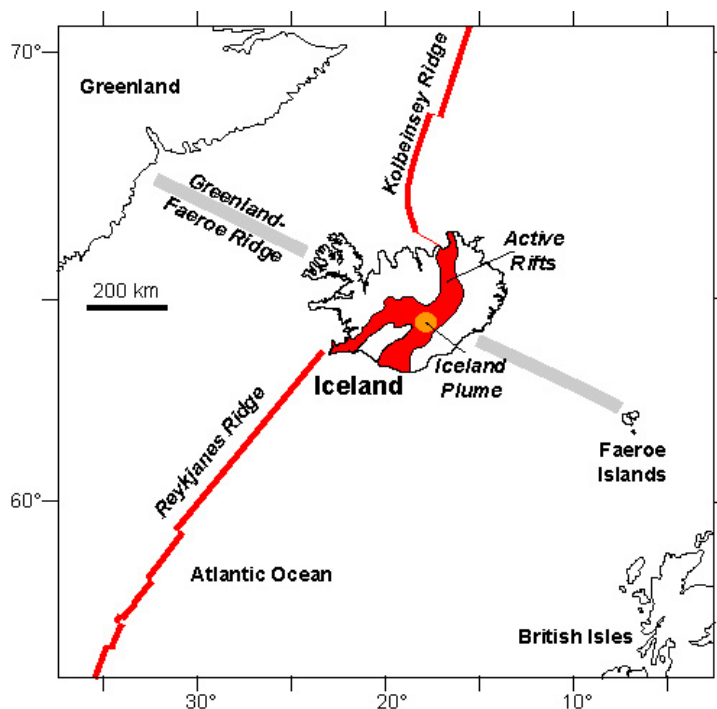


FIGURE 3: Tectonic systems of Iceland
(modified after Keck Junior Research Project, 2004)

2.2 Tectonic setting

Iceland lies astride the Mid Atlantic Ridge on the diverging North American and Eurasian Plates (Figure 3). The tectonic plates move apart, towards southeast and northwest, and both the North American and the Eurasian systems move to the northwest across the stationary hot spot. On top of hot spots, generally a 20-100% molten layer is found at a depth of 5-20 km, which supplies sufficient material for eruptions (Bjarnason, 2008). Iceland is home to more than 100 volcanoes, over 25 of which have erupted in recent history (Jakobsson and Gudmundsson, 2008). Eruptions occur about every 5-10 years and primarily consist of basaltic lava and tephra. A few long-lived centres, such as Mt. Hekla, erupt more silicic magmas (Blake, 1970). Iceland is by

far the biggest subaerial part of the Mid Atlantic Ridge and, while the North Atlantic is spreading symmetrically away from the mid-ocean ridge (Hjartarson, 2009), the ridge itself migrates over the plume and repeatedly shifts its spreading axis through rift jumping (Hardarson et al., 1997). The Mid Atlantic Ridge is a constructive plate boundary while the Greenland-Iceland-Faeroes Ridge is thought to be the trail of the Icelandic mantle plume, which has been active from the time of the opening of the North Atlantic Ocean 60 million years ago to the present (Sigmundsson and Saemundsson, 2008). The mantle plume is seen to be located below Central East Iceland (Figure 3), close to the volcanic rift zone which crosses Iceland from southwest to northeast (Figures 2 and 4) and is divided into two parallel branches in South Iceland (Pálmason and Saemundsson, 1974). In South and North Iceland, the Mid

Atlantic Ridge has been displaced to the east by transform faults which are defined as fracture zones (Óskarsson et al., 1985). The southern fracture zone is called the South Iceland Seismic Zone (SISZ) while the northern one is called the Tjörnes Fracture Zone (TFZ), shown in Figure 4. The volcanic rift zone is about one-third of the area of Iceland. The volcanic rift zone is a zone of active rifting and volcanism and is characterised by well-developed extensional structures such as tension fractures, normal faults and grabens with dykes and normal faults occurring at deeper levels (Gudmundsson, 1998). According to Gudmundsson (1992), a fissure swarm associated with a central volcano may be up to 5-10 km wide and 40-80 km long and make up most of the volcanic rift zone.

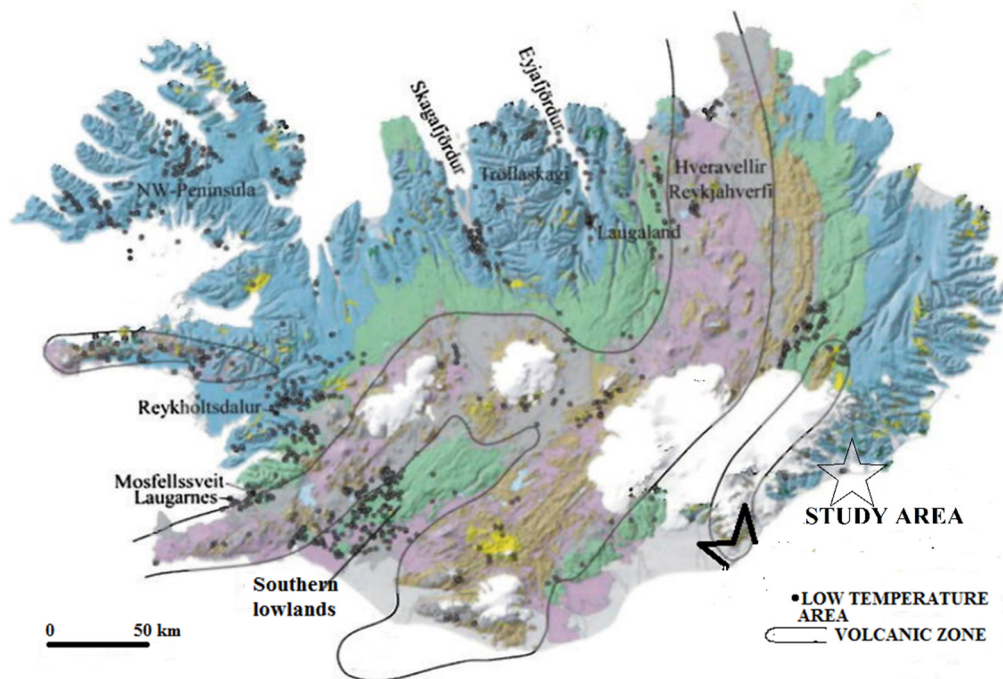


FIGURE 4: Map showing the distribution of low-temperature areas in Iceland; the volcanic zones are enclosed by a dark line (modified from Jóhannesson and Saemundsson, 1999)

3. GEOTHERMAL ACTIVITY IN ICELAND

Iceland is one of the most volcanically active places on earth, resulting in a large number of volcanoes and hot springs. Earthquakes are frequent, but rarely cause serious damage. More than 200 volcanoes are located within the active volcanic zone stretching through the country from the southwest to the northeast, and at least 30 of them have erupted since the country was settled (Arnórsson et al., 2008). It is characterised by high heat flow due to its geological location on a divergent plate boundary. The regional heat flow ranges from 80 to 200 mw/m², furthest away from and near the spreading zone, respectively (Neuhoff et al., 1999). Geothermal activity in Iceland has been classified as high-temperature and low-temperature fields. Surface activity in the low-temperature geothermal areas is distinctly different from that of the high-temperature areas as described below.

3.1 High-temperature activity

The high-temperature fields are defined by temperatures above 200°C at 1 km depth in the crust and they are located in the belts of active volcanism within the rift zone (Figure 4). The heat sources of high-temperature geothermal fields are high level magma chambers and magmatic intrusions. Most of the high-temperature geothermal fields lie astride active fissure swarms where the fissures intersect the

lithospheric plate boundary. Central volcanic complexes have formed at some of these points and calderas have developed in several of them. Geothermal manifestations of high-temperature fields are characterised by the occurrence of fumaroles, mud pools, hot springs, and geysers. They are mainly used for the production of electricity but also for hot water.

3.2 Low-temperature activity

The low-temperature areas are fracture and fault dominated deriving their heat from convection within the cooling lithospheric plate. According to Arnórsson and Gíslason (1991) low-temperature geothermal activity in Iceland is the consequence of one or more of the four following scenarios:

- a) Deep circulation of groundwater from higher to lower elevation along fractures or other permeable structures, driven by a hydraulic head.
- b) Convection in young fractures formed by deformation of older crust.
- c) Drift of high-temperature geothermal systems out of the active volcanic belts, accompanied by cooling due to displacement from the magmatic heat source.
- d) Intrusion of magma into fractures or other permeable formations by the margins or outside the volcanic belts.

The heat-source for low-temperature activity in Iceland is believed to be the island's abnormally hot crust, but faults and fractures, which are kept open by on-going tectonic activity, also play an essential role by providing channels for the water that circulates through the systems and mines the heat. Outside the volcanic zones, the temperature gradient varies from about 150°C/km near the margin to about 50°C/km farther away (Arnórsson et al., 2008). There are more than 250 separate low-temperature areas with temperatures, not exceeding 150°C in the uppermost 1,000 m, mostly in the areas away from and flanking the active volcanic zones (Figure 4) (Burchardt and Gudmundsson, 2009).

3.3 Utilization of low-temperature geothermal energy

Low-temperature geothermal energy has been utilized for many purposes, both for direct use and for binary power plants. Initially in Iceland it was used for bathing and washing. The first trials to use geothermal energy for space heating were made in the middle of the 18th century in Iceland. Direct heating in all its forms is far more efficient than electricity generation and places less demanding temperature requirements on the heat resource. Heat may come from co-generation with a geothermal electrical plant or from smaller wells or heat exchangers buried in shallow ground. As a result, geothermal heating is economical over a much greater geographical range than geothermal electricity. Where natural hot springs are available, the heated water can be piped directly into radiators. Low-temperature geothermal heat is also used for swimming pools, fish farming, to heat greenhouses and by many companies to dry products like fish heads and wood. The study area at Hoffell in SE-Iceland is home to low-temperature geothermal energy. The main use of this energy is for space heating and bathing (Figure 5) in the adjoining region.



FIGURE 5: Low-temperature geothermal water being used for bathing at Hoffell

4. GEOTHERMAL AREA OF THE GEITAFELL CENTRAL VOLCANO, SE ICELAND

4.1 Introduction

The study area is partly related to the extinct Geitafell central volcano. The total thickness of strata from the volcano is 2700 m which indicates that the volcano was a high mountain. The volcano has two major structural elements: 1) a caldera fault and 2) a flexure zone. It was active about 5 million years ago but glacial erosion has since exposed its core (Fridleifsson, 1983a). The study area by Hoffell (Figure 6) is outside the caldera fault as can be seen on the geological map in Figure 7. The volcano is located northwest of the town Höfn (Figure 1) and has been deeply carved and eroded by the glaciers of the last glaciation.



FIGURE 6: Photograph showing the study area around the Hoffell farm

4.2 Geology and tectonic setting of the study area

The Geitafell central volcano was formed within a rift zone (Saemundsson, 1979). The study area is located within this volcanic complex. It was active five to six million years ago and activity lasted for about a million years (Fridleifsson, 1983a). The area consists mostly of tholeiitic rocks of which 60% are basaltic lavas and 30% hyaloclastites (Figure 7). Several gabbro bodies are exposed in its core, representing the uppermost part of an extinct crustal magma chamber surrounded by a dense swarm of inclined sheets. Intrusive rocks of the Geitafell volcano are composed of several gabbro, granophyre and felsite intrusions, together with dyke and sheet swarms. A dense swarm of inclined (cone) sheets is in direct contact with the chamber (Fridleifsson, 1983a). The sheets and basaltic dykes range from aphyric porphyritic dolerites to aphyric and fine grained, porphyritic basalt. The overall pattern of the tectonics relates to divergent movement of crustal plates and is accompanied by inflow of magma to all crustal levels. The general characteristics of the dilation tectonics involved are open fissures and grabens at the surface but normal faulting at depth (Fridleifsson, 1983a).

4.3 Stratigraphic units of this volcanic area

The research area is separated into 7 major stratigraphic units. The stratigraphic division is described below (Fridleifsson, 1983a):

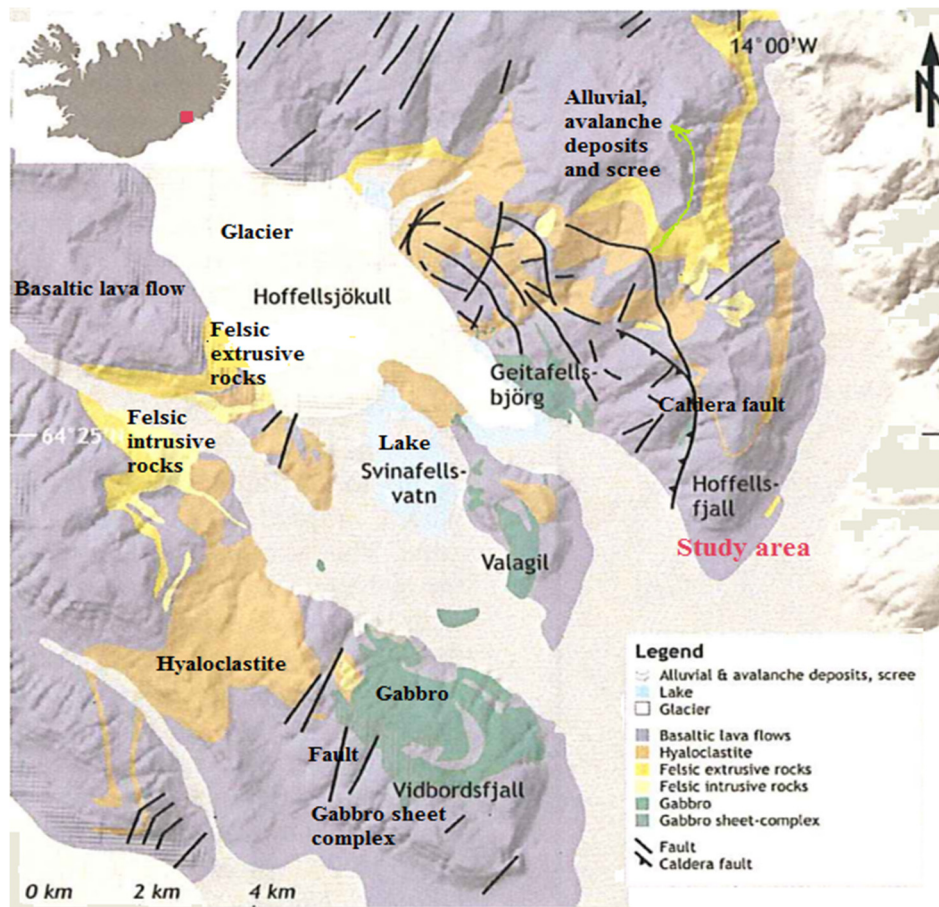


FIGURE 7: Geological map of the study area (modified from Fridleifsson, 1983a)

Basaltic lava unit-I (B-I): This unit is mainly composed of tholeiitic lavas. The unit is divided into three sub-units. B-I unit thickens towards the centre of a hypothetical NE-SW striking fissure-swarm crossing the Geitafell central volcano. The maximum thickness of this unit is 750 m.

Rhyolite unit-I (R-I): This unit is located within the basaltic lava unit-I the volcano which comprises mixed composition. An altered pitchstone layer, granophyric intrusion and acid tuff are found in this unit. Maximum thickness of this unit is 50 m.

Hyaloclastite unit-I (H-I): Mainly composed of aphyric basalt clasts, but acid clasts also occur in some locations. Basic pillow lava is not found within this unit but pillow fragments occur in many places. This unit is heavily intruded and highly brecciated by sheets.

Basaltic lava unit-II (B-II): This unit comprises thick tholeiite, olivine tholeiite, feldspar tholeiite, and feldspar porphyritic basalt flows. Most of the lavas are believed to have been erupted outside the Geitafell central volcano. The maximum thickness of this unit is 700 m.

Hyaloclastite unit-II (H-II): This unit consists mainly of aphyric basalt fragments and reworked, porphyritic, boulder beds as well as feldsparphyric tuff. In addition, some highly vesicular interbedded lava flows may be found. This unit is maximum 300 m thick.

Rhyolite unit-II (R-II): The unit comprises three rhyolitic lavas. Acid tuff beds with two thinner rhyolitic lavas are interbedded in the base of lava unit III.

Basaltic lava unit-III (B-III): The unit comprises thick tholeiite, olivine tholeiite and feldspar porphyritic basalt flows, some of which also contain phenocrysts of pyroxene and olivine. Most of the lavas are regarded as having been erupted outside the Geitafell central volcano.

4.4 Stratigraphy of the study area

The study area is mainly composed of tholeiitic lavas which lie under the basaltic unit-I (B-I). Heavily intruded and highly brecciated by sheets as well as aphyric basalt clasts and acid clasts bearing older hyaloclastite units are included in this area. Feldsparphyric basalt lava under the unit of basaltic lava unit-II (B-II) is also found in the study area (Figure 7). According to Fridleifsson (1983a), the intrusive rocks of this volcanic area have been divided into 12 phases which are described below:

Intrusive phase-1: This phase is regarded as a feeder dyke system to basaltic lava units I and II, rhyolite unit I and hyaloclastite unit II. Acid intrusives are regarded as belonging to intrusive phase I and are only found within rhyolite unit I on the east side of Mt. Hoffellsfjall.

Intrusive phase-2: The Geitafell central volcano, as well as contemporaneous gabbros, constitutes the phase. The gabbro has hypidiomorphic granular texture in which mineral phases are bytownite-labradorite, calcite, augite, and titanomagnetite. Olivine and orthopyroxene are most often completely pseudomorphed, mainly to talc, chlorite and magnetite.

Intrusive phase-3: Feldsparphyric dykes are common in this phase and they are slightly younger than the Geitafell gabbro and apparently related to the same intrusive episode. Only a few members are found to belong to phase-3.

Intrusive phase-4: Acid veins crosscut the pegmatite veins in the gabbro and brecciate the gabbro near the southern end.

Intrusive phase-5: This phase consists of a doleritic cone-sheet swarm, the sheets being 0.5-1.5 m thick. The doleritic sheet swarm is characteristically greyish green and thus differs from all other intrusive phases except intrusive phase-7.

Intrusive phase-6: A Feldsparphyric dolerite sheet swarm is dominant in this phase. The feldspar phenocrysts are bytownite, zoned to labradorite, and a dolerite matrix which is slightly finer grained than in intrusive phase-5.

Intrusive phase-7: It is characterized by a dyke swarm, sometimes feldsparphyric with thickness commonly less than 1 m. The grain size of this phase is similar to that of phase-5.

Intrusive phase-8: A fine grained basaltic sheet swarm forms this phase. The thickness of these sheets varies from 0.3 m to 1 m and is most common in Efstafellsnes, Efstafell area.

Intrusive phase-9: The dykes of this phase are thicker than the sheets. This phase is petrographically similar to phase-8.

Intrusive phase-10: This phase is characterized by highly feldspar porphyritic dykes and sheet swarms which are found with apparently contemporaneous gabbro intrusions in Vidbordsfjall, Kráksgil and Litla Dímon. Phase-10 is believed to have occurred during the caldera formation.

Intrusive phase-11: Large felsitic intrusions, rhyolite or pitchstone dykes and veins constitute the phase. Rhyolite unit-II was probably fed by intrusive phase-11. A close association is seen between intrusive phases 10 and 11.

Intrusive phase-12: Thick dolerite dykes characterize phase-12 with thicknesses varying from 0.5 to 6 m but most of the dykes are close to 2 m across. Unlike the other intrusive phases, the dykes are commonly columnar jointed and relatively fresh but develop characteristic brown weathered surfaces.

5. MINERALOGICAL EVOLUTION AND TECTONICS OF THE GEITAFELL AREA

5.1 Mineralogical evolution

The mineralogical distribution within the Geitafell hydrothermal system is represented by the five mineralogical zones (Figure 8). The five mineral zones all relate to the formerly active high-temperature geothermal system (Fridleifsson, 1983a, 1983b). They are:

- 1) Chlorite zone (Chl)
- 2) Epidote zone (Ep)
- 3) Androdite zone (Gr)
- 4) Actinolite zone (Act)
- 5) Sulphide zone

In particular, four of these zones (chlorite→epidote→garnet→actinolite) show the progressive appearance of the index minerals within both the host rocks and the intrusive rocks (including phase-11). Four to six major mineral vein systems were formed in the volcano. Upon progressive rise in the geothermal gradient within the volcano, the vein mineral deposition changed to silica precipitates (jasper→chalcedony→quartz) and smectite→chlorite. A high-temperature system then became active upon the emplacement of the central gabbros (IP-2) at shallow depths and a sharp change in vein deposits took place. The veins, formed after the IP-2 emplacement, show distinctive depth and spatially related variation, generally involving higher temperature mineral assemblages at depths and towards the volcanic centre. The types of minerals formed in veins related to the high-temperature system within the actinolite zone include epidote, quartz, calcite, actinolite, androdite, and albite (see photo in Figure 9). In the overlying mineral zones, actinolite, quartz, albite, and wairakite sequentially disappear from the vein system, while within the upper part of the epidote zone, epidote and prehnite are more or less restricted to mineral veins and wall rock zones within and in the vicinity of some members of a particular intrusive phase-10 (IP-10) and or in the vicinity of the caldera fault. The last vein systems invariably contain zeolites, chiefly, stilbite and heulandite, related to cooling of the high-temperature system (Fridleifsson, 1983b).

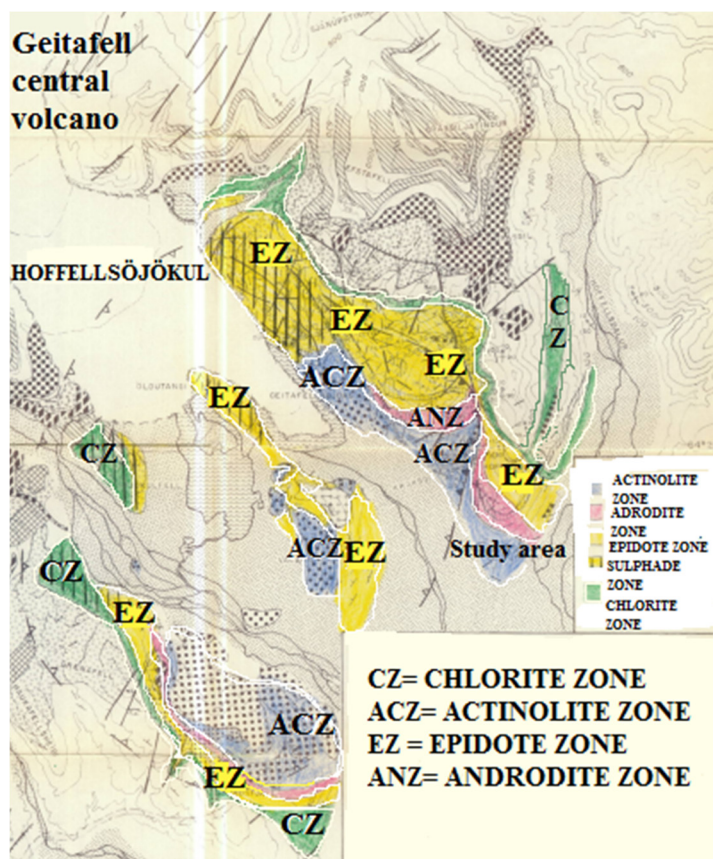


FIGURE 8: Map showing the mineralogical alteration zones around the study area (modified from Fridleifsson, 1983b)

5.2 Intrusive phases

The study area is mainly composed of tholeiitic lavas and dykes but sheets and faults are also found (see photo in Figure 10). The strike direction is north-west and the dip direction is north-east (65-80°NE). According to the description of several intrusive phases, it may be suggested that the study area of Hoffell is under the intrusive phase-5. Dolerite sheets are most common in intrusive phase-5 which is also found randomly near the Hoffell farm area (Fridleifsson, 1983a). Three main mineral zones are found in the study area. Epidote, androdite and actinolite are most common; chlorite zone is also found but scarcely. The study area is mainly composed of a gabbro sheet complex with some felsic extrusives. Dykes and cone sheets, which sometimes cut each other, are also to be noted in this area. This area also forms part of intrusive phases 6, 10 and 12 (Fridleifsson, 1983a).

5.3 Fractures and veins

Fracture systems act as conduits for fluids and play an important role in the extraction of geothermal energy in both liquid- and vapour-dominated fields. Several types of fractures can developed in a rock formation. Several types of vein fillings were observed in the study area which are directly related to the low-temperature geothermal field.

5.4 The hydrothermal system of the Geitafell central volcanic complex

Low-temperature geothermal areas are fed by regional groundwater systems and withdraw heat from a large volume of warm country rocks. The state of any hydrothermal system through time depends upon the interactions of different lithologies, moving fluids, transfer and availabilities of heat and the tectonic scenario within the systems. The way in which these parameters interact with one another is shown in Figure 11. The origin of hydrothermal fluids may be juvenile, magmatic, meteoric, connate, metamorphic, and oceanic; in the Geitafell hydrothermal system, most of the fluids are meteoric or oceanic or a mixture of the two (Fridleifsson, 1983b).

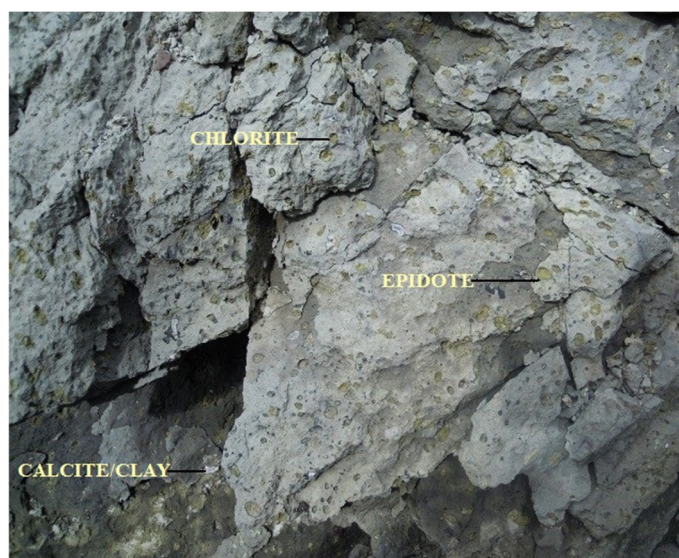


FIGURE 9: Photograph showing vein fillings in a rock found in the study area by Hoffell; green colours indicate chlorite, yellowish green is epidote and white colour indicates calcite or clay mineral



FIGURE 10: Photograph showing dykes in the Hoffell farm area

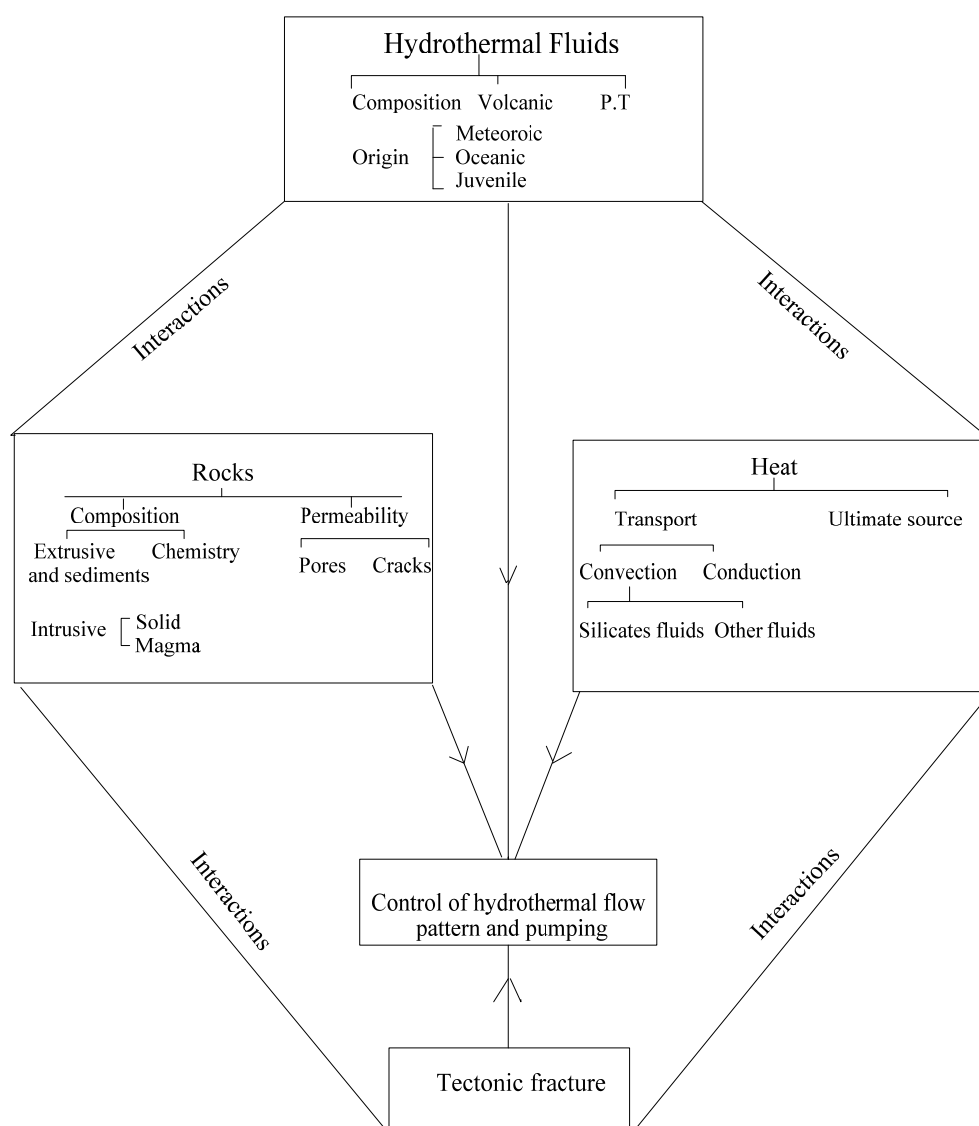


FIGURE 11: Diagram showing the hydrothermal system of the Geitafell central volcano and the adjoining study area (after Fridleifsson, 1983b)

6. WELL HF-1

6.1 Stratigraphy of Well HF-1

Iceland GeoSurvey (ÍSOR) conducted a drilling programme for a deep exploration well in the study area near the farm of Hoffell. The well (HF-1) was drilled down to 1608 m, the main purpose being to confirm the existence of an 80°C hydrothermal system. A detailed lithological description of Well HF-1 is presented below and shown in Figure 12, according to Kristinsson et al. (2013).

Gravel (0-18 m): This layer acts as an aquifer in the area. Mixed rock fragments, basaltic, and acidic, of different grain sizes. The unit represents river deltas and coastal environments.

Lava pile (18-90 m): Eight to nine tholeiitic lava flows separated by scoria.

Sediments (90-92 m): Slightly rounded basalt and glass fragments.

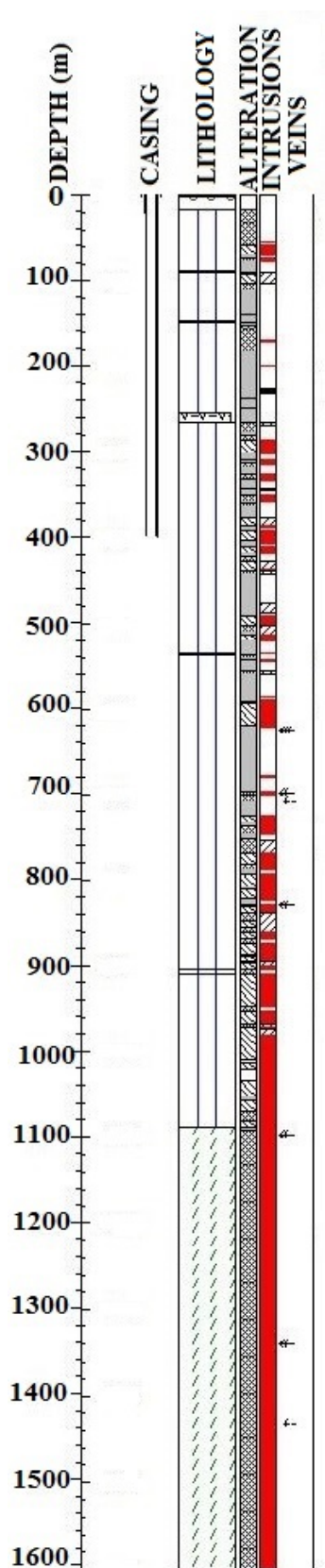


FIGURE 12: Lithology and their description of Well HF-1 at Hoffell farm area, SE-Iceland (modif. from Kristinsson et al., 2013)

Lava pile (92-147 m): The top part is porous and includes some scoria. The pile becomes less porous with depth. Five separated tholeiitic lava flows were observed. Red interlayers are present in between the lavas. The rocks are mainly fine-medium grained and aphyric.

Sediments (147-150 m): Basalt rock fragments and sedimentary grains.

Lava pile (150-256 m): Tholeiitic lava flows (10-12 in number), usually aphyric but plagioclase is found at 204-213 m depth.

Tuff (256-267 m): Oxidized tuff mixed with ash and scoria.

Lava pile (267-537 m): Mostly fine grain tholeiitic lavas. Plagioclase and pyroxene are observed at 315-320 m but otherwise the lavas are mostly aphyric. Pyroxene is found at 359-366 m, and at 420-428 m olivine tholeiite is observed.

Lava pile (537-904 m): The top layer is plagioclase phyrlic. At 554-565 m plagioclase and pyroxene are found but it is inconclusive if this is lava or an intrusion. Otherwise, this is mostly a fine to medium grained basalt pile of tholeiites and olivine tholeiites. The largest feed-zone in the well is at 626 m depth which also shows significant washout. Some plagioclase is observed at 680-685 m but otherwise the pile is mostly aphyric. Scoria is found between the lava flows. Below 720 m intrusions seem to become common, indicated by NN and resistivity loggings.

Sediments (904-905 m): The nature of this sediment is unclear. It is very fine grained, darkish with glassy crystals which seem to be pore fillings or rounded phenocrysts, in disequilibrium with the magma. The rock is fairly porous.

Intrusions (905-1608 m): Below 905 m the lithology consists almost entirely of intrusive rocks, even though occasionally lavas may be observed. Below 905 m a granophyre intrusive is encountered which extends to the bottom of the well (1608 m).

6.2 Intrusions

In the study area, several types of intrusions are found. These are mainly gabbro intrusions associated with a large number of intrusive sheets.

Gabbro intrusions: The intrusion has a diapiric form with a steeply plunging feeder and pronounced tabular jointing. This gabbro is the most extensively studied where it rises from the sandur plain. Seven main mineral vein systems were emplaced within the Geitafell gabbro (Fridleifsson, 1983b).

Dykes: The ratio of dykes in the area is high, in some areas they make up to 40% of the strata. The strike is 55°-70°NW and they

dip steeply to the southwest (65-80°SW). There are two main types of dykes, regional dykes, usually 1.5-2 m thick, and steeply dipping cone sheets, usually about 0.6 m thick (Fridleifsson, 1983a). Cone sheets and dykes (Figure 10) are fine-grained basalt to coarse dolerite (Annels, 1967).

Cone sheets: The cone-sheet swarm is of doleritic composition, the dykes usually being 0.5-0.7 m thick but sometimes up to 1.5 m (Annels, 1967). They are greyish green in colour and are readily distinguished from other cone sheets of other intrusive phases. The sheet swarm is widely distributed in the area dipping towards the southwest or northwest. Some sheets are almost vertical as they intrude through the lava pile.

7. GEOTHERMAL MAPPING USING GRADIENT WELLS

A geothermal or temperature gradient is a physical property that describes in which direction and at what rate the temperature changes in units of degrees (on a particular temperature scale) per unit length. The rate of change in temperature in a given direction, especially in altitude, is a temperature gradient of the change of temperature with depth. Geothermal energy is heat from underground or is the energy stored in the form of heat beneath the earth's surface. In this energy, the temperature gradient is the most important and common element. Heat flow is directly related to the temperature gradient. There are no surface manifestations in this area, so the gradient method was applied to locate geothermal anomalies and prepare a geothermal map. Drilling a gradient well is a method used in exploration of both high- and low-temperature geothermal fields. Low permeability is a prerequisite for the method to give reliable results. It is important to avoid disturbances from the internal flow inside the well. In fracture controlled low-temperature fields, shallow wells give the best results. The regional geothermal gradient (Figure 13) must also be known as a baseline for recognizing thermal anomalies (Saemundsson 2007).

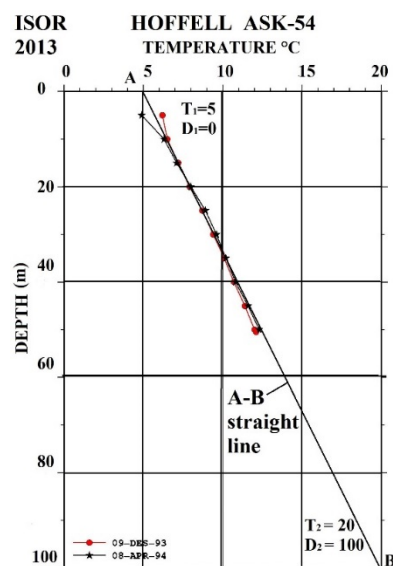


FIGURE 14: Temperature versus depth relationship

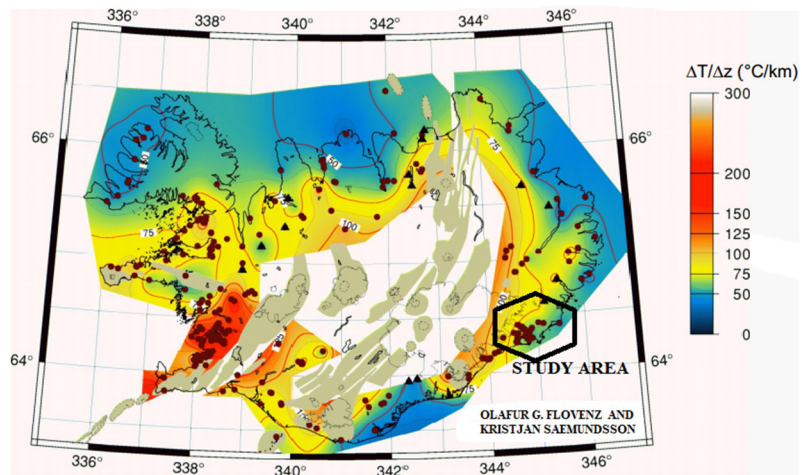


FIGURE 13: Geothermal gradient map of Iceland showing the regional gradient 40-60°C/km in the study area (Flóvenz and Saemundsson, 1993)

There are no surface manifestations in this area, so the gradient method was applied to locate geothermal anomalies and prepare a geothermal map. Drilling a gradient well is a method used in exploration of both high- and low-temperature geothermal fields. Low permeability is a prerequisite for the method to give reliable results. It is important to avoid disturbances from the internal flow inside the well. In fracture controlled low-temperature fields, shallow wells give the best results. The regional geothermal gradient (Figure 13) must also be known as a baseline for recognizing thermal anomalies (Saemundsson 2007).

7.1 Gradient calculation

The gradient calculation was conducted based on Equation 1 as well as with the help of Figure 14, clearly described below. In Figure 14 the relationship between temperature and depth is shown. An A-B straight line was drawn which cuts the maximum points of temperature versus depth points. Then the dt and dz were calculated from Figure 14.

$$G = \frac{dt}{dz} = \frac{T_2 - T_1}{D_2 - D_1} \quad (1)$$

where G = Temperature gradient ($^{\circ}\text{C}/\text{km}$)
 T_1 = Starting temperature of straight line ($^{\circ}\text{C}$);
 T_2 = Ending temperature of straight line ($^{\circ}\text{C}$);
 D_1 = Starting depth of straight line (m);
 D_2 = Ending depth of straight line (m);

With: $T_1 = 5^{\circ}\text{C}$; $T_2 = 20^{\circ}\text{C}$; $D_1 = 0$ m; $D_2 = 100$ m, Equation 1 yields:

$$G = \frac{20 - 5}{100 - 0} = 0.15^{\circ}\frac{\text{C}}{\text{m}} = 150^{\circ}\text{C}/\text{km}$$

The temperature gradient of ASK-54 is $150^{\circ}\text{C}/\text{km}$ as calculated by the above formula. The temperature gradient was calculated for several wells in the Hoffell area, using the same formulas. After the calculation, the gradient was plotted for a certain well location on a map and isotherm lines were drawn, resulting in a gradient map.

7.2 Geothermal gradient map of the study area

Figure 15 shows the location of all the wells in the area. The depth of the wells varies from 50 to 600 m and the temperature gradient varies from 100 to $210^{\circ}\text{C}/\text{km}$ (Well ASK-29). The contour lines were drawn with respect to certain temperature intervals, creating the geothermal gradient map in Figure 16. In addition, a heat map was made based on the measurements of the same gradient wells at Hoffell. The heat map shows temperature conditions at 50 m depth (Figure 17). Three different temperature zones are shown in the two maps. The red colour-bounded zones represent the highest temperature gradient, $>200^{\circ}\text{C}/\text{km}$ (Figure 16) and the highest temperature, $>15^{\circ}\text{C}$ (Figure 17).

Figure 18 illustrates a comparison between the temperature map and the gradient map. It shows that the highest gradient zone (dark colour bounded) is within the larger highest temperature zone (red colour bounded). It clearly shows the N-S trend of maximum heat, while on a more regional scale, the anomaly is more east or southeast trending indicating flow towards these directions.

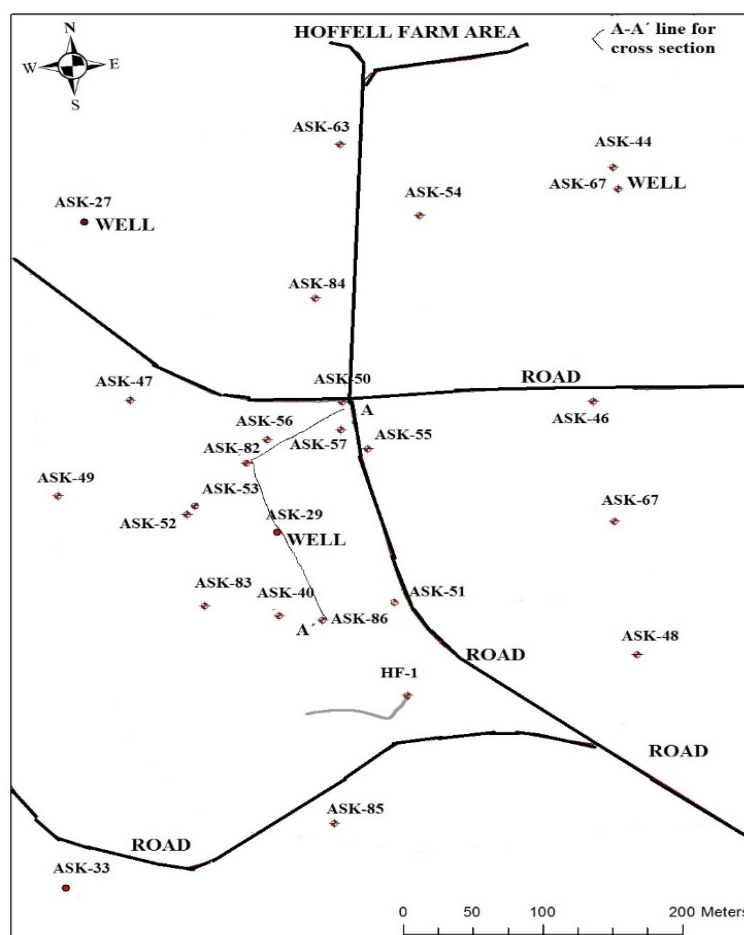


FIGURE 15: Map showing the location of different wells and roads in the study area

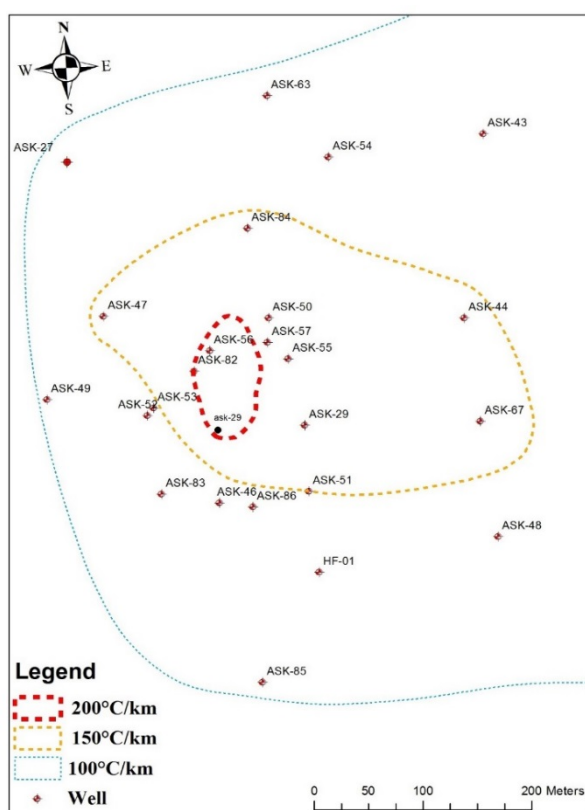


FIGURE 16: Map showing the temperature gradient in the wells of the Hoffell area

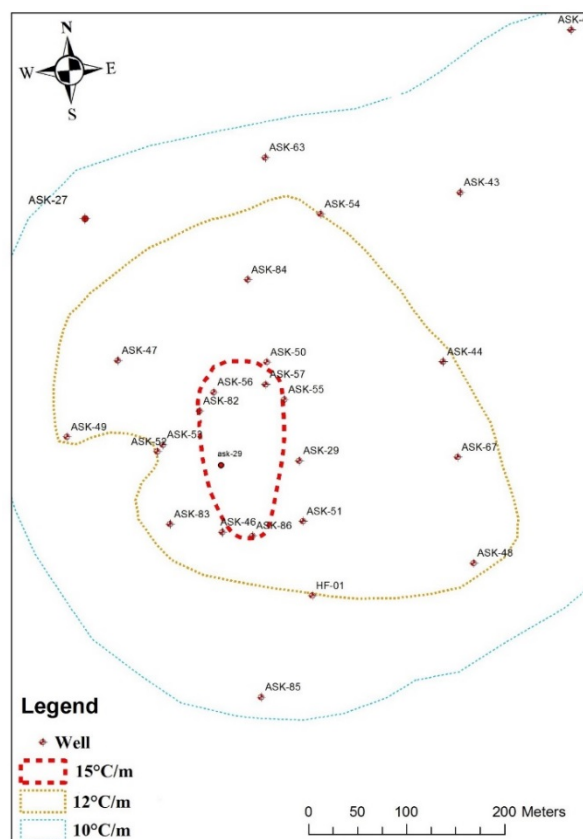


FIGURE 17: Map showing the temperature in the wells of the Hoffell area at 50 m depth

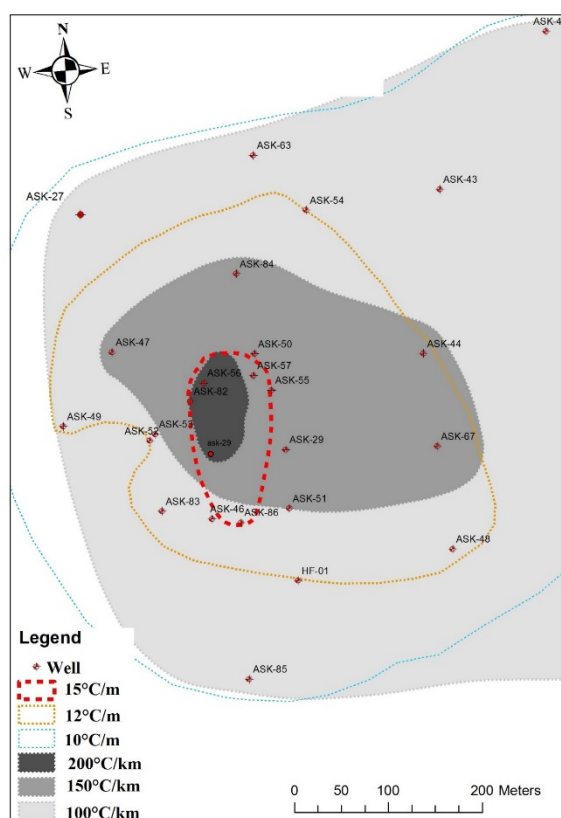


FIGURE 18: Comparison between temperature and gradient maps of the Hoffell area

8. INTERPRETATION OF FRACTURES AND VEINS IN SEVERAL WELLS

In all, the temperature gradients of 23 wells in the study area were measured, and in some of them open veins as well as open fractures could be seen in televiewer measurements, which indicates a good reservoir. Figure 19 shows the main structural trends and directions of open fractures in the measured wells. Grouping these, the open fractures-fault zones trend in NNE-SSW and W-E WSW-ENE directions (Figure 19). Also seen are four main structural trends, NE-SW to NNE-SSW, W-E and NW-SE (Figure 19). The wells within the area of maximum temperature have been demarcated (Wells ASK-29, ASK-50, ASK-57, ASK-82 and ASK-86). Some of these are described below regarding open fractures (Table 1). Only in Wells ASK-29 and ASK-85 insufficient data was collected with televiewer.

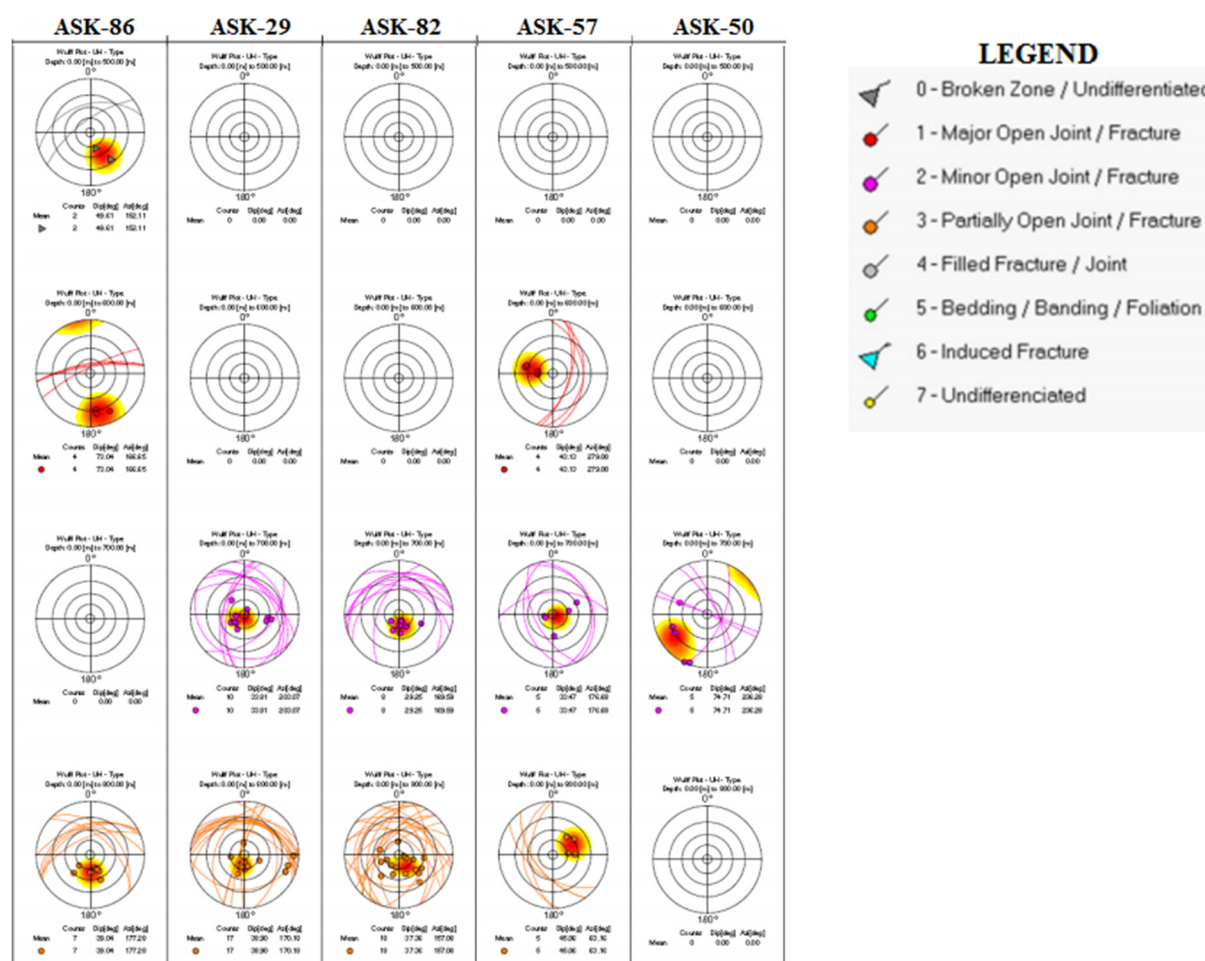


FIGURE 19: Map showing the main structural trends and direction of open fractures in the measured wells (modified from Árnadóttir, 2013)

TABLE 1: Short summary of veins seen in Wells ASK-29, ASK-50, ASK-57, ASK-82, ASK-85 and ASK-86 that appeared in the televiewer measurements at Hoffell study area, and other veins in the same wells (modified from Árnadóttir, 2013)

Well no.	Veins appearing in televiewer measurement		Other veins defined but above the teleview. measurements
ASK-29			126 m, 129 m
ASK-50	74 m	Viewed as open fractures	
ASK-57	465 m	Viewed as large open fractures at the depth of 458 m	113 m, 121 m, 296 m
ASK-82	180 m	Viewed as open fractures	
ASK-86	485 m	Viewed as large open fractures at a depth of 486.35 m	228 m, 300 m

Well ASK-29. The temperature gradient of this hole is 210°C/km hole. Ten large open fractures and their dip direction S33°W were seen. Seventeen partially open fractures were also found with a dip direction of almost 40°S (Figure 19). The highest temperature gradient (210°C/km) was calculated for this well. This well and the adjoining area may be a high-temperature prospect zone. The well is 150 m deep with a feed zone at shallow depth, clearly seen in the well's cross-section. This well is the shallowest well among all the measured wells.

Well ASK-50. The temperature gradient of this well is 150°C/km. This well is also in the high-temperature region. From the televiewer data (Figure 20), the vein is at 74 m depth, where an open fracture is seen. Five major open fractures were counted, with an average dip direction of S 74°W, and no minor/partially open fractures were found in this well. Feed zones were found at shallow depth. This is a 150 m deep well and the shallowest open fracture well.

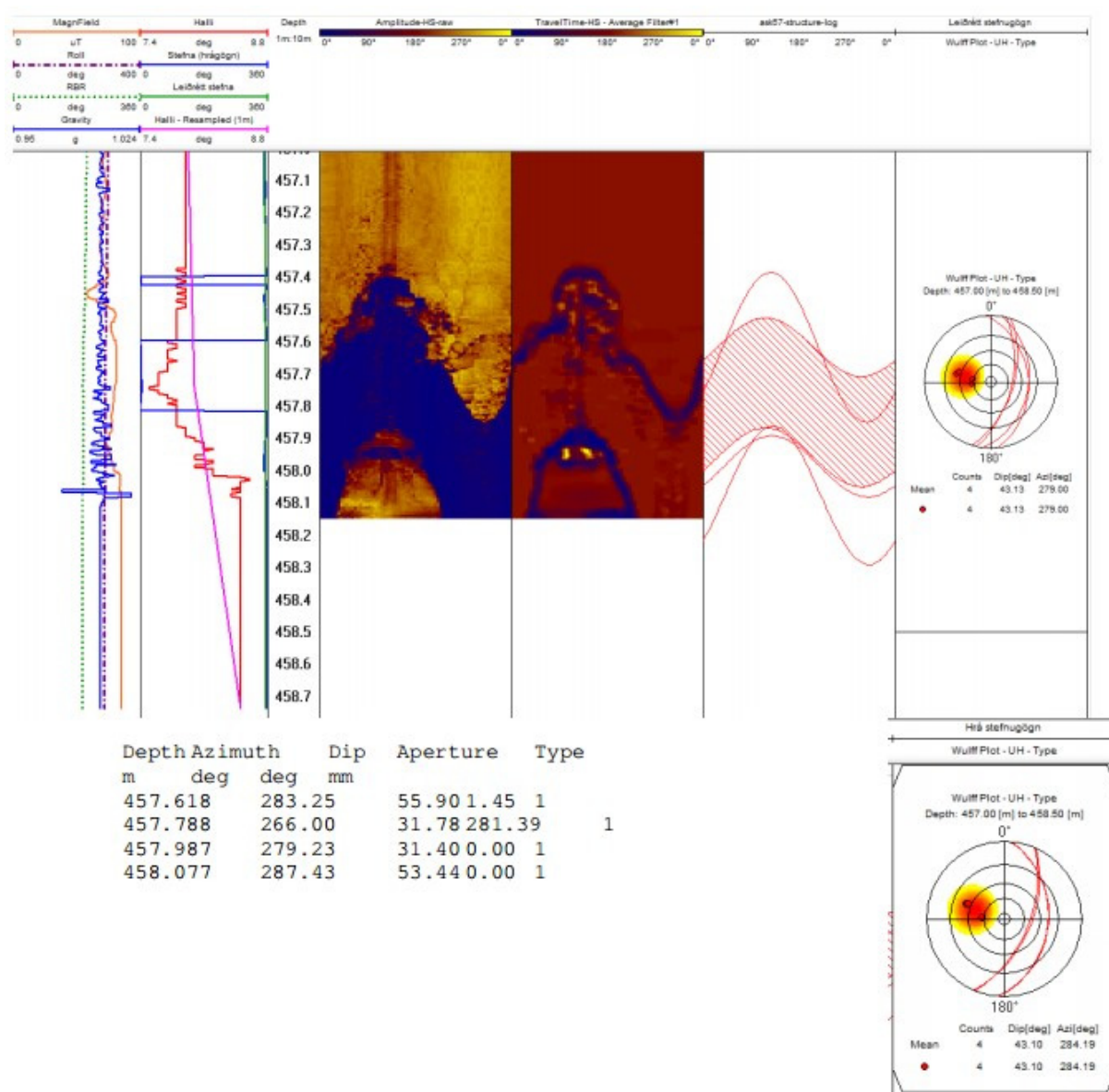


FIGURE 20: Televiewer measurement data of Well ASK-50 showing veins, open fractures and their dip direction (Árnadóttir, 2013)

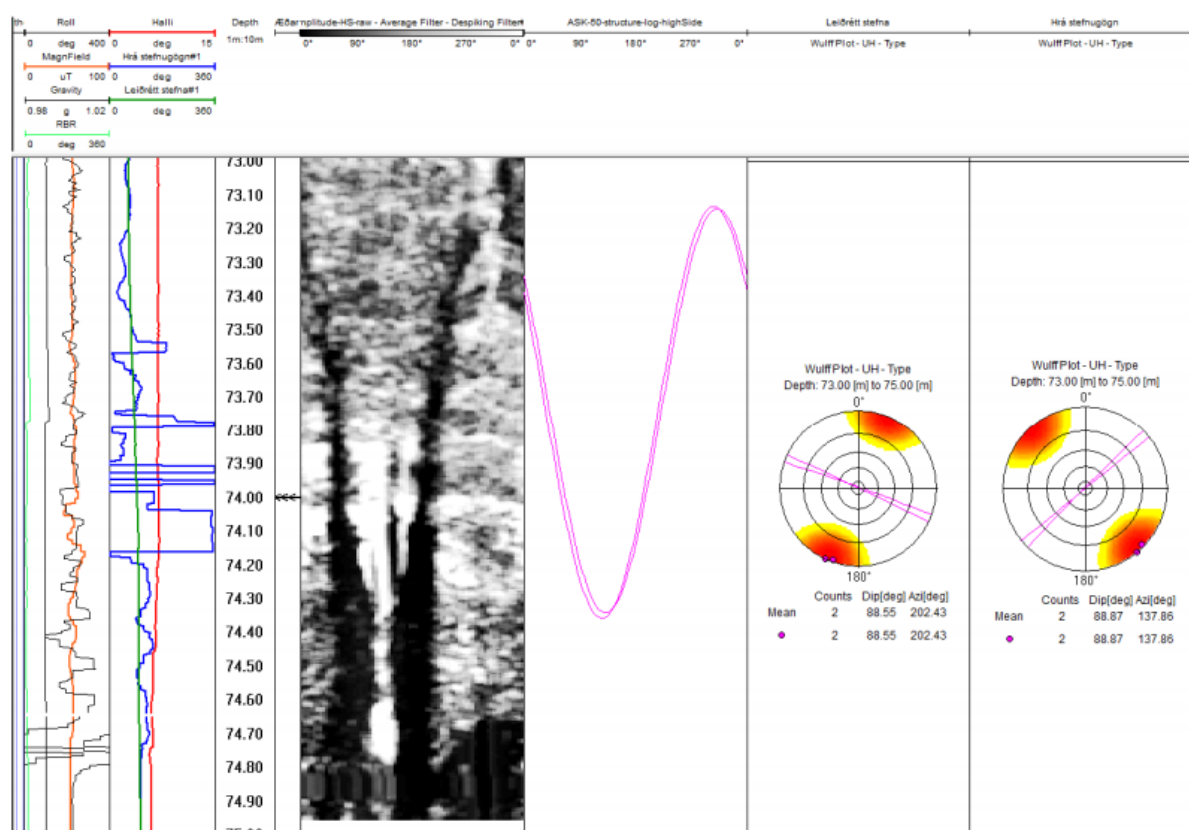


FIGURE 21: Televiewer measurement data of Well ASK-57 showing veins, open fractures and their dip direction (Árnadóttir, 2013)

Well ASK-57. The temperature gradient of this well is 169°C/km. Well ASK-50 is about 50 m north of this well and shows 160°C/km. Well ASK-55 is 55 m southeast of Well ASK-57 and shows 173°C/km. So ASK-57 is in a comparatively high temperature region. From the televiewer data (Figure 21), a vein is at 458.14 m depth, which shows a large open fracture. Here the measuring device was set at 465 m. Four major open fractures were counted with an average dip direction 43°, almost west. 5 minor fractures were observed and their dip angles are S 33°E. Five partially open fractures were also found with a dip direction of N45°E. This is a deep well with a deep feed zone.

Well ASK-82. The temperature gradient of this well is 210°C/km which is in the highest temperature gradient. From the televiewer data (Figure 22), the vein is at 180 m depth, which shows a large open fracture. This is an artesian type well in the middle part of the study area. Two major open fractures were found with a dip direction of almost 30°S, so it is difficult to identify if it is a contact or joint or fault. 18 partially open fractures were also observed and their dip direction is S37°E. A feed zone was observed at a shallow depth.

Well ASK-86. The temperature gradient of this well is 180°C/km. From the televiewer data (Figure 23), the vein is at 485 m depth, and shows a large open fracture. Here the measuring device was set at 486.35 m. Four major open fractures (S73°E) and seven partially open fractures were also found with a dip direction of almost 39°S (Figure 23). A feed zone was also found at greater depth (Figure 24). This is a deep well.

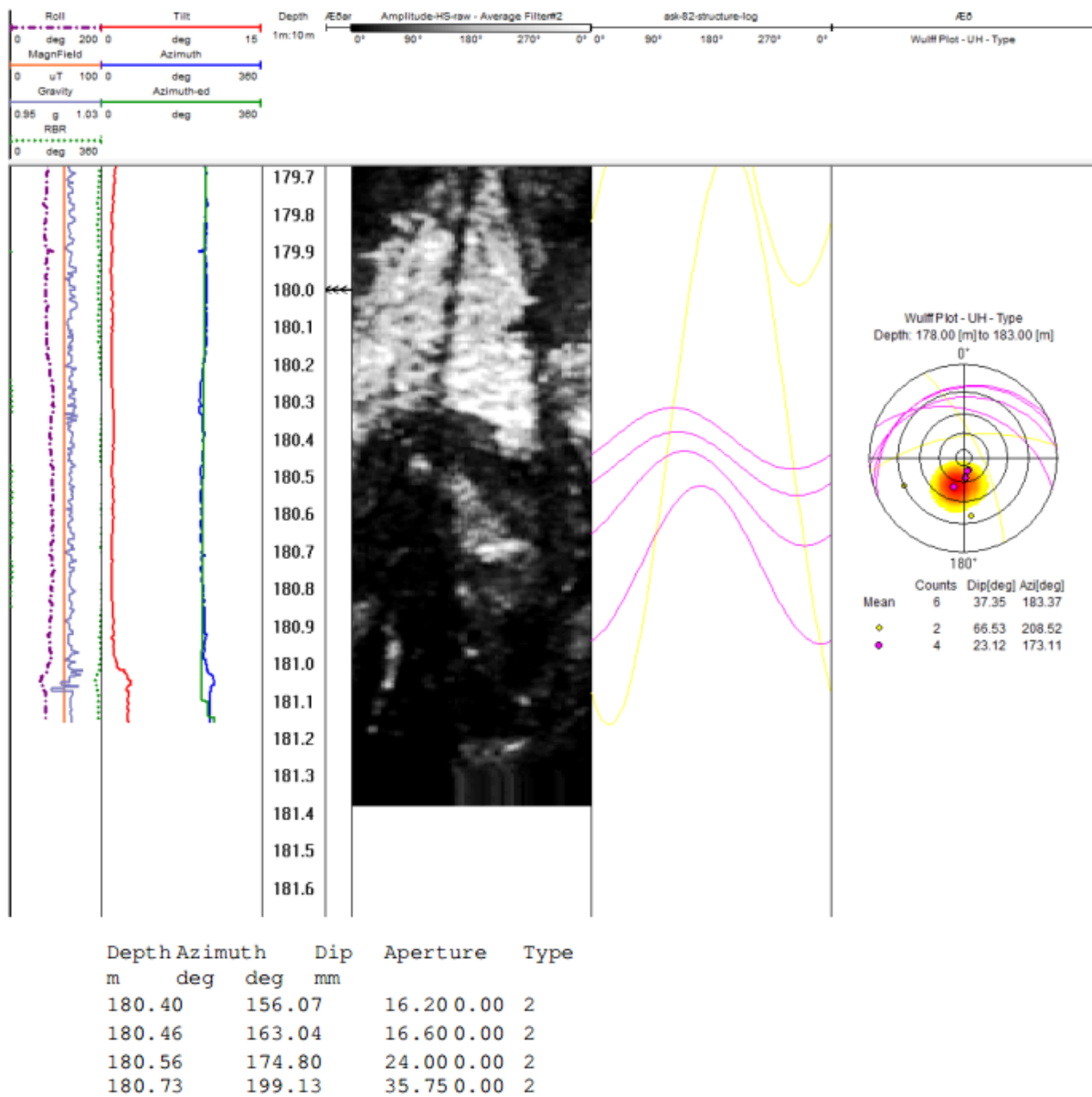


FIGURE 22: Televviewer measurement data of Well ASK-82 showing veins, open fractures and their dip direction (Árnadóttir, 2013)

Figure 24 shows a cross-section from Well ASK-86 to Well ASK-50, showing the feed zones registered in the wells on the cross-section.

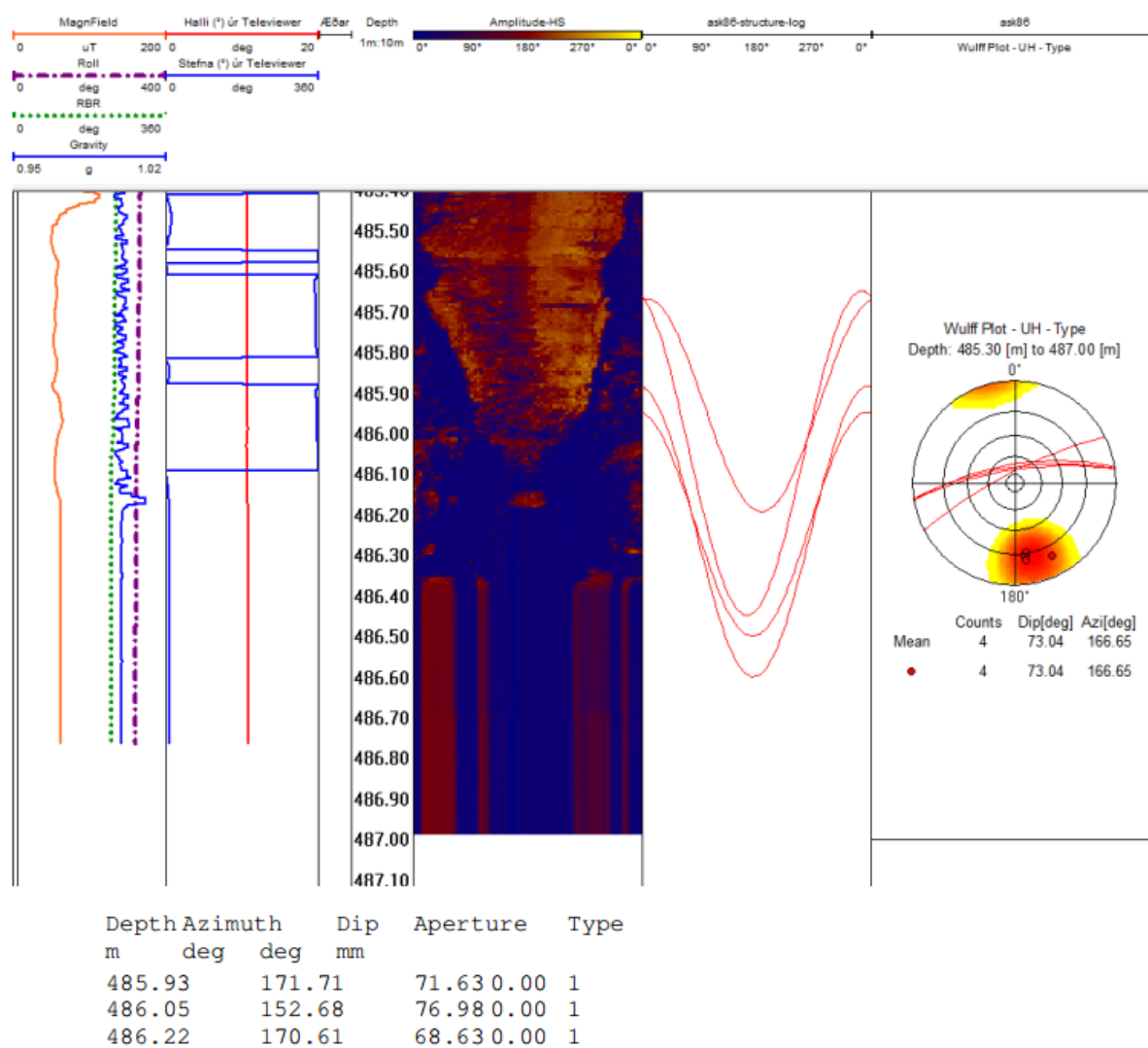


FIGURE 23: Televiewer measurement data of Well ASK-86 showing veins, open fractures and their dip direction (Árnadóttir, 2013)

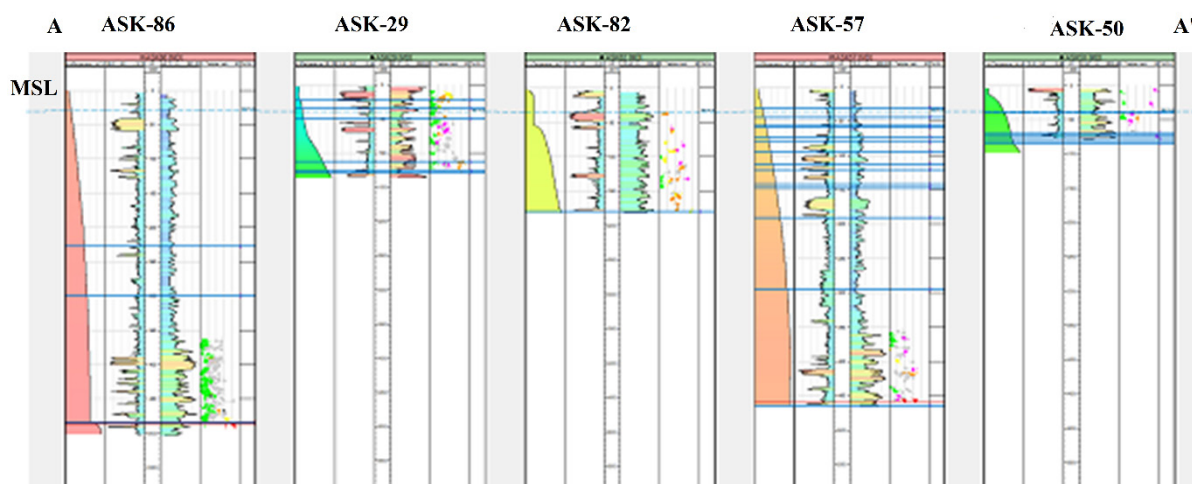


FIGURE 24: Cross-section from Well ASK-86 to Well ASK-50 (location see Figure 15); blue lines indicate feed zones (modified from Árnadóttir, 2013)

9. CONCLUSIONS AND RECOMMENDATIONS

The study area is in the south-eastern part of the Geitafell central volcano in southeast Iceland. It is important on account of the low-temperature geothermal field in an area where the regional gradient is 40-60°C/km. The area was mainly studied with respect to the temperature gradient but also for geological information. The volcanic complex is deeply eroded due to glacial erosion. The stratigraphy is mainly composed of tholeiitic rocks of which 60% are basaltic lavas and 30% hyaloclastites. The general characteristics of the dilation tectonics involved are open fractures and graben at the surface and normal faulting at depth. During the study period, 23 wells were investigated and their temperature gradients measured to establish the subsurface temperature of the area. In this area, heat flow gradually increases from the N-S striking centre to the eastern side.

From the measured temperature gradient of different wells, as well as the televiwer data, is clear that Wells ASK-29, ASK-56, ASK-82, ASK-57 and their adjoining area show the highest temperature zone. This data also illustrates several veins at specific depths or open fractures striking NNE-SSW and W-E WSW-ENE. The highest zone showed more than a 200°C/km gradient. Even though there are no surface manifestations, it is clear that the subsurface temperatures are abnormal in this region. Based on these results, in case of further drilling, I would propose to site the wells in the eastern part of the zone with the highest temperatures,

The surveyed area is a large region which is geologically controlled by the structures from the Geitafell central volcano. It is probably the most important area in SE-Iceland with respect to geothermal energy and its potential use. Therefore, it is proposed that further geological exploration and geophysical surveys should be carried out to get a clearer picture of the geothermal and geological conditions, as well as the tectonic framework, in an area of great importance to the communities in that quarter of Iceland.

ACKNOWLEDGEMENTS

I would like to express my heartiest gratitude to Dr. Ingvar Birgir Fridleifsson, retiring director, and Mr. Lúdvík S. Georgsson, director, of the UNU Geothermal Training Programme for their hospitality and selfless dedication to the UNU Fellows. I especially want to extend my unreserved gratitude to my supervisor, Mr. Sigurdur Gardar Kristinsson, senior geologist of ISOR-Iceland GeoSurvey, for his excellent technical support, lectures and friendliness. At the same time, I am grateful to my second supervisor, Dr. Björn S. Hardarson, geologist of ISOR-Iceland GeoSurvey, who shared his knowledge and for valuable information that he gave me either in the field or in the office as well as for his help in preparing the report. For excellent guidance during fieldwork in Geitafell and Hoffell, I would like to thank Dr. Guðmundur Ómar Fridleifsson for his great input.

Additionally, I would like to thank all the lecturers and the staff members at Orkustofnun and ISOR for the knowledge, assistance and valuable comments given to us during the lecture sessions. I also thank the UNU Fellows of 2013 for their unbelievable friendship and cooperation during our training time, especially the borehole geology and geological exploration group.

My deepest, heartiest and grateful thanks also go to the UNU-GTP staff, Mrs. Thórhildur Ísberg, Mrs. Málfríður Ómarsdóttir, Mr. Markús A. G. Wilde, for their continuous help during this course.

I would like to give heartiest thanks and gratefulness to Mr. Ingimar Gudni Haraldsson, project manager of the UNU-GTP, for his good cooperation, instructions and cordial helpfulness during the training period as well as in report preparation. I am also thankful to UNU Fellows Mr. M.M. Tharanga, N.B. Munasinghe, from Sri Lanka for supporting me during these 6 months.

I am grateful to DG of Geological Survey of Bangladesh, Energy and Mineral Resources Division, Government of the People's Republic of Bangladesh, for allowing me to attend the course.

Finally, I would express my thankfulness and gratefulness to my branch chief, Dr. Md. Nehal Uddin, director of the Geological Survey of Bangladesh, for his valuable suggestions and guidance during the six months training period.

REFERENCES

- Annels, A.E., 1967: *The geology of the Hornafjörður region, southeast Iceland*. University of London, PhD thesis, 120 pp.
- Árnadóttir, S., Egilson, Th., Blischke, A., Stefánsson, H.O., and Jóhannesson, H., 2013: *Televiwer and well measurements at Hoffell and Midfell in Nesjar and the location of well HF-1*. ÍSOR – Iceland GeoSurvey, Reykjavík, report ÍSOR-2013/017 (in Icelandic), 81 pp.
- Arnórsson, S., and Gíslason, G., 1993: Introduction to igneous petrology (in Icelandic). *Náttúrufræðingurinn*, 62, 181-205.
- Arnórsson, S., Axelsson, G., and Saemundsson, K., 2008: Geothermal system in Iceland, *Jökull*, 58, 269-302.
- Bjarnason, I. Th., 2008: An Iceland hotspot saga, *Jökull*, 58, 3-16.
- Björnsson, A., Saemundsson, K., Einarsson, P., Tryggvason, E., and Grönvold, K., 1977: Current rifting episode in North Iceland. *Nature*, 266, 318-323.
- Blake, D.H., 1970: Geology of the Álftafjörður volcano, a Tertiary volcanic centre in south-eastern Iceland. *Sci. Iceland*, 2, 43-63.
- Burchardt, S. and Gudmundsson, Á., 2009: The infrastructure of Geitafell volcano, Southeast Iceland. In: Thórdarson, Th., Self, S., Larsen, G., Rowland, Höskuldsson, S.K. (eds.), *Studies in volcanology: The Legacy of George Walker*. GSL on behalf of IAVCEI publications, 349-369.
- Burchardt, S., Tanner, D., Troll, V., Krumbholz, M., Gustafsson, L., 2011: Three-dimensional geometry of concentric intrusive sheet swarms in the Geitafell and the Dyrkjöll Volcanoes, Eastern Iceland. *Geochemistry Geophysics Geosystems*, Q0AB09. Accessed through website: [dx.doi.org/10.1029/2011GC003527](https://doi.org/10.1029/2011GC003527).7-12.
- Einarsson, M., 1991: Temperature conditions in Iceland 1901-1990. *Jökull*, 41, 1-19.
- Fridleifsson, G.Ó., 1983a: *The geology and the alteration history of the Geitafell Central Volcano, southeast Iceland*. University of Edinburgh, Grant Institute of Geology, PhD thesis, 324.
- Fridleifsson, G.Ó., 1983b: Mineralogical evaluation of a hydrothermal system. *Geothermal Resources Council, Trans.*, 7, 147-152.
- Flóvenz, Ó.G., and Saemundsson, K., 1993: Heat flow and geothermal processes in Iceland. *Tectonophysics*, 225, 123-138.
- Gudmundsson, Á., 1992: Formation and growth of normal faults at the divergent plate boundary in Iceland. *Terra Nova*, 4, 464-471.
- Gudmundsson, Á., 1998: Magma chambers modelled as cavities explain the formation of rift-zone central volcanoes and their intrusion and extrusion frequencies. *J. Geophys. Res.*, 103, 401-412.

- Hardarson, B.S., Fitton, J.G., Ellam, R.M., and Pringle, M.S., 1997: Rift-relocation - a geochemical and geochronological investigation of a palaeo-rift in NW Iceland. *Earth Planet. Sci. Lett.*, 153-3, 181-196.
- Hjartarson, Á., Flóvenz, Ó.F., and Ólafsson, M., 2012: *Probability of geothermal resources near Hoffell and Midfell in Nesjar: research and material examined*. ÍSOR – Iceland GeoSurvey, Reykjavík, report ÍSOR-2012/002 (in Icelandic), 23 pp.
- Jakobsson, S.P., and Gudmundsson, M.T., 2008: Subglacial and intraglacial volcanic formations in Iceland. *Jökull*, 58, 179-196.
- Jóhannesson H., and Saemundsson, K., 1999: *Geological map 1:1.000.000*. Icelandic Institute of Natural History.
- Keck Junior Research Project, 2004: Contrasting Tertiary central volcanoes in NW Iceland. Website: sunburst.usd.edu/~Brennan.Jordan/IcelandKeck2004.html.
- Kristinsson, S.G., Helgadóttir, H.M., Stefánsson, H.O., Tryggvason, H., Pétursson, F., and Ólafsson, M., 2013: *Drilling well HF-1: drilling history, geology and capacity measurements*. ÍSOR – Iceland GeoSurvey, Reykjavík, report ÍSOR-013/030 (in Icelandic), 49 pp.
- Neuhoff, P.S., Fridriksson, Th., Arnórsson, S., and Bird, D.K., 1999: Porosity evolution and mineral paragenesis during low-grade metamorphism of basaltic lavas at Teigarhorn, eastern Iceland. *Am J. Sci.*, 299, 467–501.
- Óskarsson N., Steinthórsson S. and Sigvaldason G.E., 1985: Iceland geochemical anomaly: origin, volcanotectonics, chemical fractionation and isotope evolution of the Crust. *J. Geophys. Res.*, 90, 111-125.
- Pálmason, G., and Saemundsson K., 1974: Iceland in relation to the Mid-Atlantic Ridge. *Annual Review Earth Planet. Sci.*, 2, 25-50.
- Saemundsson, K., 1979: Outline of the geology of Iceland. *Jökull* 29, 7-28.
- Saemundsson, K., 1980: Application of geology in geothermal research in Iceland (in Icelandic with English summary). *Náttúrufræðingurinn*, 50- 3/4, 157-188.
- Saemundsson, K., 2007: Geology and gradient wells. *Presented at Short Course II on Surface Exploration for Geothermal Resources, organized by UNU-GTP and KenGen, Naivasha, Kenya*, 11 pp.
- Sigmundsson, F., and Saemundsson, K., 2008. Iceland: a window on North-Atlantic divergent plate tectonics and geologic processes. *Episodes*, 31, 92-97.
- Stapi Geological Services, 1993: *Geothermal exploration in East-Skaftafellssýsla in 1992*. County committee of East-Skaftafellssýsla, report, 88 pp.
- Stapi Geological Services, 1994: *Geothermal exploration in East-Skaftafellssýsla in the years 1993-1994*. County committee of East-Skaftafellssýsla, report, 200 pp.
- Stapi Geological Services, 2002: *Hornafljörður-Hoffell. Geothermal exploration in 2002*. County committee of East-Skaftafellssýsla, report, 18 pp.
- Stapi Geological Services, 2005: *Hornafljörður-Hoffell. Geothermal exploration in 2003-2004*. County committee of East-Skaftafellssýsla, report, 19 pp.
- Stapi Geological Services, 2006: *Geothermal exploration by Hoffell in 2005-2006*. County committee of East-Skaftafellssýsla, report, 9 pp.



VOLUMETRIC, LUMPED AND 2-D NUMERICAL MODELS OF THE MOMOTOMBO RESERVOIR, NICARAGUA

Idalia Araceli Matus Pravia

Nicaraguan Electricity Company

Geochemistry Laboratory

Intersección Pista Juan Pablo II y Prolongación Ave. Bolívar

Managua

NICARAGUA

imatus@enel.gob.ni

ABSTRACT

The production capacity of the Momotombo geothermal field has declined over time when production wells were damaged by scaling and suffered from cooling. The reservoir is characterized by a deep, vertical upflow zone of 280-320°C feeding a shallow horizontal reservoir at 300-500 m depth and 180-240°C temperature. Geothermal fluid was observed on the surface in hot springs and fumaroles. The chloride concentration in most of the production wells has been decreasing because of the incursion of cold water into the reservoir, presumably entering the reservoir by the hot spring conduits. The proven and possible production capacity for 25 years was estimated using the Monte Carlo volumetric method at 20 MW and 50 MW, respectively. The total production data and pressure drawdown were simulated satisfactorily by a one- and two-tank open lumped model. The two-tank open model yielded a reservoir volume in the 4 km³ range, the same as the estimated proven reservoir volume in the Monte Carlo method. The permeability of the lumped model ranged from 75 to 230 mD. A 2D numerical model was developed and calibrated using the code iTOUGH2, allowing for the study of the chloride concentration changes over time. The thin 2D slice could be heated up by 3.3 kg/s of 330°C water. The highest permeability of 340 mD complies well with the inner 230 mD permeability of the lumped model. The results of the simulation indicated that chloride concentration is a good parameter for future studies. Decreases in chloride concentration imply intrusion of low temperature and fresh groundwater into the reservoir. Intrusion of low-temperature groundwater into the reservoir and extensive boiling in the shallow reservoir due to pressure drawdown induced cooling in the reservoir and these are regarded here as the main reasons for the operational problems encountered in the wellfield management.

1. INTRODUCTION

1.1 The Momotombo developmental history

The Momotombo geothermal field is located on the southwest flank of the Cordillera Los Marrabios, on the northern shore of Lake Managua, at the foot of the Momotombo stratovolcano (Figure 1).

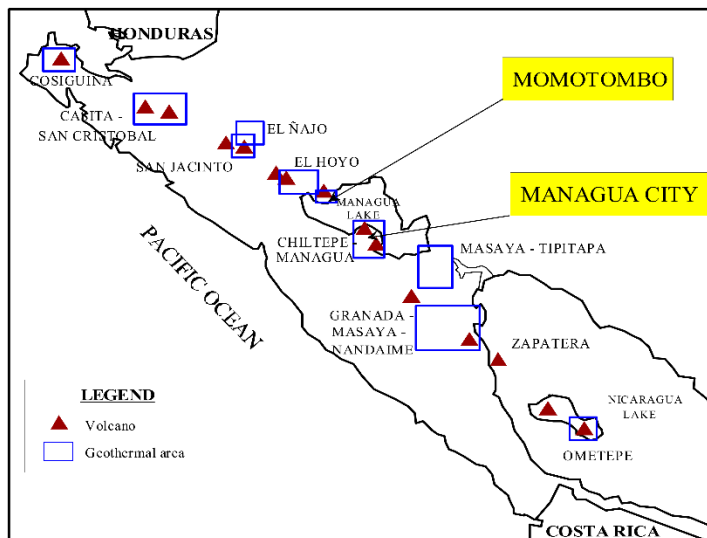


FIGURE 1: Location map of Momotombo (Porrás, 2008)

Momotombo is currently the most intensely studied geothermal field in Nicaragua, with a long production history.

The field began producing electricity in 1983 with an installed capacity of 35 MWe. In 1989, another 35 MWe unit was commissioned. Soon thereafter the increased steam production rate led to downhole scaling and lost enthalpies, mainly due to a decline in well productivity caused by either temperature and pressure drops in the reservoir or scaling in the wellbore and formation. This field's behaviour led to a production history which declined from a short peak of 69 MWe in 1991 to 9 MWe in 1999 (Björnsson, 2008).

During this period, production well output decreased rapidly, showing marked changes in temperature and pressure, paralleled by changes in the consistency and chemistry of the geothermal fluids and the enthalpy (Porrás and Björnsson, 2010). All these changes are attributed to excessive exploitation of the proven resource, low injection volumes, maintenance challenges, and rapid infiltration of cold lake water into the reservoir.

This resource management problem was largely mitigated when Ormat took over field operations, led by mechanical work-overs (acid stimulation, calcite scaling inhibition, full reinjection and drilling of deep wells) in order to recover steam production. In 2002, an organic unit Rankine cycle Ormat Energy Converter (OEC) was commissioned with a 7 MWe installed capacity, increasing the total installed capacity to 77 MWe. Nowadays, the power production in Momotombo power plant has stabilized at 25 MWe.

1.2 Goal of the present study

The main objectives of the present study are:

- 1) To carefully review available literature of Momotombo and identify data sources of value for reservoir engineering studies;
- 2) To collect and plot with time the chloride concentrations history from the Momotombo geothermal production wells to shed light on the nature of the reservoir's outer boundaries;
- 3) To estimate the proven and possible production for 25 years of plant life of the Momotombo geothermal field by using the Monte Carlo volumetric method;
- 4) To calibrate a simple lumped parameter model simulating the reservoir pressure drawdown history and compare this model's properties with the Monte Carlo volumetric method; and
- 5) Study changes in the Momotombo reservoir due to exploitation by a 2D numerical model of the system using the iTOUGH2 simulator. Particularly make an effort in calibrating the model for both single and double water equations of state to accommodate for the rapid chloride decline observed after peak production.

2. BACKGROUND

2.1 Data sources

The exploration, development and field operations of the Momotombo geothermal field were carried out by the government of Nicaragua through the National Energy Authority with the collaboration of several international institutions and cooperating countries. Substantial numbers of papers are available in the public geothermal literature. For example, the International Geothermal Association (IGA) gives access to 16 papers, and 3 papers have been published by the UNU-GTP (González B., 1990; González S., 1990; Porras, 1991). Therefore, the data available for this study come from several sources. Chemical data from the period between 1980 and 2013 were provided by Empresa Nicaragüense de Electricidad (ENEL), initially called Instituto Nicaragüense de Energía (INE). The chemical analyses were reported by Arnórsson et al. (1996) and entered into the database of ENEL. Many of the data sets of temperature, pressure, enthalpy, production, and reinjection water used in this report for the assessment of changes in the Momotombo geothermal field come from Enrique Porras' PhD dissertation (2005). Finally, the above mentioned publications in the IGA database have been carefully reviewed and used to identify topics of interest for this study.

2.2 Momotombo production history

The Momotombo geothermal field started production in 1983 when the first turbine unit of 35 MWe was commissioned. As shown in Figure 2, the power output was relatively stable at about 35 MWe from 1983 to 1986. During this time period, this unit was fed from five shallow wells (MT9, MT12, MT20, MT23 and MT27). At the end of 1986, the output started decreasing because Well MT9's casing collapsed (Porras, 2006).

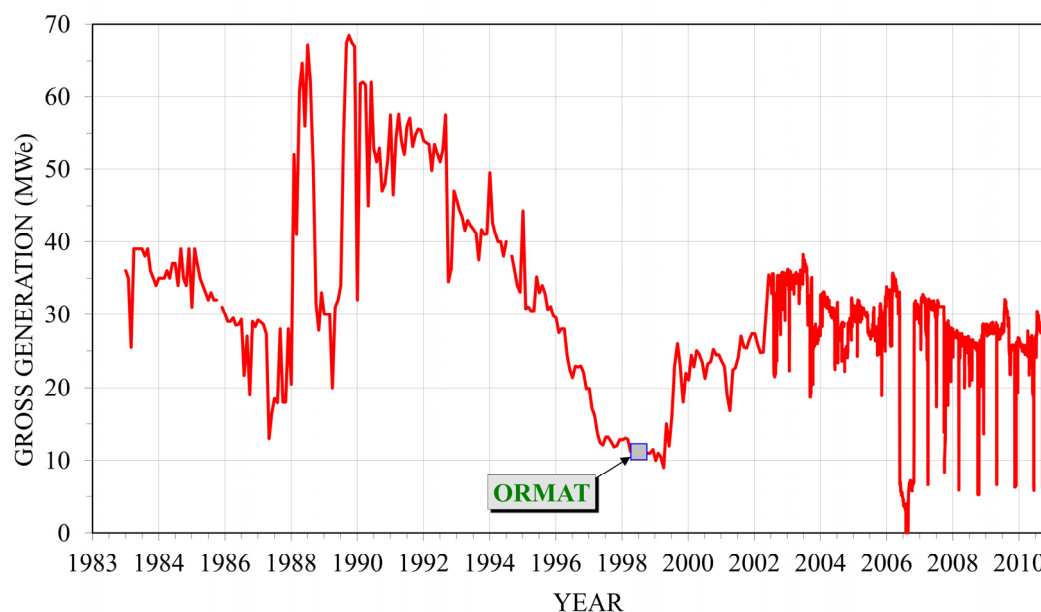


FIGURE 2: Power generation history of the Momotombo geothermal field (Porras, 2012)

Six years after the start of production, in 1989, a second 35 MWe unit was installed, tapping steam from an additional six shallow wells. When the second unit started to work, the output reached about 66 MWe for a short period, then fell back to 30 MWe because of generator and/or turbine vibrations. Also, Well MT36 dropped out of operation early after commissioning the second unit because of a high concentration of non-condensable gases in the produced steam (Porras, 2006).

The highest peak of power output, 69 MWe, was reached in 1990 after the turbine vibration issue had been resolved. However, from 1990 to 1999, the power output declined steadily to about 9 MWe (Figure 2). From 1992 until 1997, three new wells were drilled to make up for the loss in power output but, unfortunately, this effort was unable to mitigate the productivity decline of other wells.

In 1999, the power output had declined to about 9 MWe. Only 7 wells were producing, mainly because the shallow wells located in the central part of the field were damaged by scaling while other shallow production wells, located in the eastern part of the wellfield, were suffering from cooling (Porrás, 2006).

In July 1999, Ormat took over management of the field with the goal to rehabilitate the Momotombo geothermal power plant. Rehabilitation consisted of work-overs, acid stimulation, calcite scaling inhibition, repairing mechanical failures, cementing jobs, full reinjection and mitigating the cooling effect of re-injection by pushing the injected mass to the eastern wellfield boundary and, finally, drilling deep wells in order to evaluate the possibility of recovering steam production. Figure 2 shows a sizeable recovery of power output in 2000.

In 2002, an organic unit Rankine cycle Ormat Energy Converter (OEC) was commissioned with a 7 MWe installed capacity, fed by separated brine at a temperature of 155°C; the brine is cooled down to about 100°C before being reinjected. This increased the total installed capacity to 77 MWe.

In 2003, the power output peaked at 35 MWe, but then started to decline due in part to enthalpy losses arising from cold fluid intrusion into the shallow feedzone reservoir. This hampered considerably the steam and flow rates of four shallow production wells. This decrease might also have been affected by plugging; removing calcite scale after mechanical cleaning could result in skin damage in the vicinity of the well (Porrás, 2006).

The current Momotombo wellfield has 47 wells, of which 11 are for production, 7 are reinjection wells and 3 are monitoring wells. 17 wells failed and 9 are dry wells no longer producing; these were drilled during the four drilling stages (1974-1978, 1981-1985, 1992-1996 and 2000-2002). The well depths range from 300 to 2839 m (Porrás, 2005). Figure 3 shows the location of all the wells.

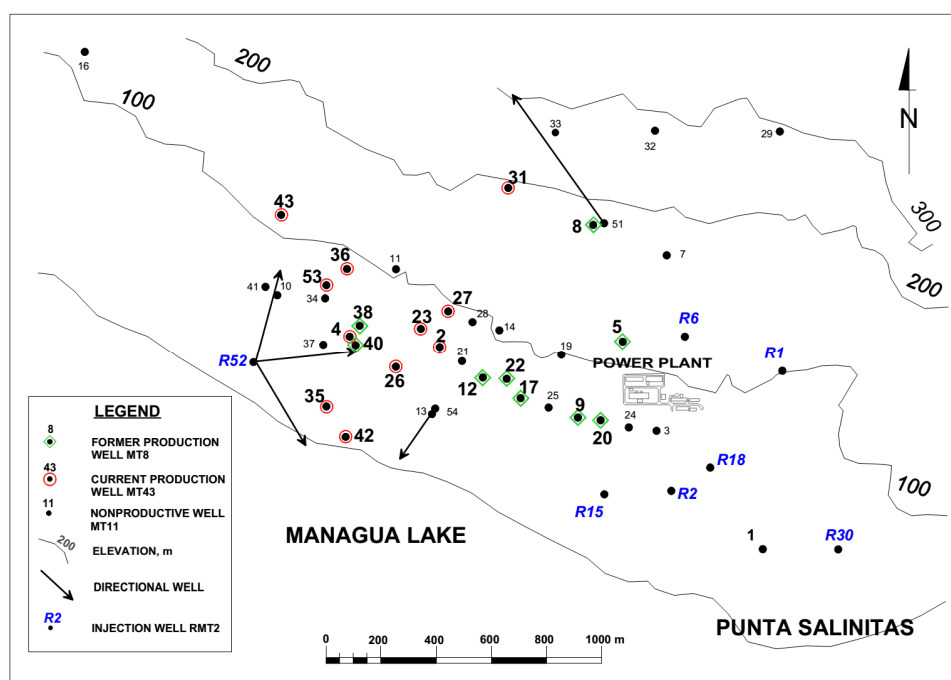


FIGURE 3: Location map of production and reinjection wells of Momotombo (Porrás and Björnsson, 2010)

Initially, the Momotombo power plant was fed by 24 production wells. Nowadays, the power plant has only 11 production wells connected. Table 1 lists the current production wells with information about their location, depth, casing depth and elevation.

TABLE 1: Current production wells in Momotombo (Porrás, 2005)

Well name	Coordinates		Depth (m)	Casing depth (m)	Elevation (m)
	East	North			
MT-2	549096	1370355	490	356	60
MT-4	548776	1370397	1435	665	74
MT-23	549027	1370428	864	260	71
MT-26	548941	1370286	640	266	49
MT-27	549126	1370486	442	368	87
MT-31	549360	1370933	582	338	202
MT-35	548686	1370235	1295	603	56
MT-36	548755	1370634	1653	650	97
MT-42	548755	1370047	2093	1420	42
MT-43	548536	1370845	2500	1682	128
OM-53	548693	1370583	2053	1103	88

Reinjection is a very important part of any geothermal development and is often a key factor in the success or failure of many power projects. Momotombo geothermal field began operating a limited reinjection system during the period 1983-1989, but the scheme has changed in terms of the magnitude of the amount of reinjection as well as the reinjection water temperature. Most of the separated water was discharged into Managua Lake until 1999. The location of the reinjection wells is shown in Figure 3 with names that start with R; these wells are located mainly in the eastern part of the well field. In this report these reinjection wells are also referred to as RMT followed by the identification number.

The separated water was sent to these wells either pressurized by pump or as gravitational flow (Porrás, 2005). Initially, the temperature of the reinjected water was 170°C, but it gradually decreased to 155°C in 2003, and is now just about 100°C after commissioning the binary unit. Figure 4 shows the histories of brine production and reinjection at Momotombo from the beginning in 1983 until 2009. We can see in the figure that the re-injected fraction increased substantially after 1999.

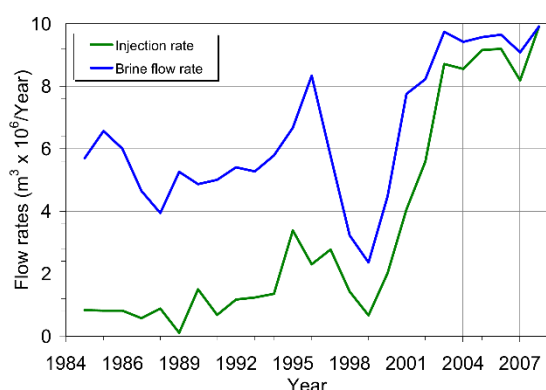


FIGURE 4: Brine production and reinjection

In 2002-2003 two tracer tests were conducted to identify the hydrological flow paths and the rate of return prior to installation of the OEC, thereby supporting a revised injection strategy for the well field. The analysed tracer tests suggested that there is a direct connection between the East wellfield and the production wells and indicates high permeability, most likely characterized by fractures in the shallow reservoir (Björnsson, 2008).

The analysis revealed that Well RMT15 has a good connection with the production wells, Well RMT6 can be used as an injector with a low risk of the production wells cooling, and that Wells RMT2 and RMT18 are good reinjection wells. A revised geological model of the field suggests a south-north boundary separating Wells RMT2 and RMT18 from the rest of the wells (Kaplan, 2004).

A new injection strategy was adopted since installation of the binary unit began in 2003, with limited injection into Well RMT15, and maximizing injection into Wells RMT2, RMT18 and RMT30.

2.3 Geological setting

The Momotombo geothermal field is located on the southwest flank of the Cordillera Los Marrabios which has several high temperature geothermal resources on the northern shore of Lake Managua at the foot of the Momotombo stratovolcano. The field was developed in the scope of the Nicaragua depression within which the Momotombo volcanic complex is located. The volcanic complex consists of several small volcanic cones and a large caldera located adjacent to and northwest of the Momotombo volcano.

The area of the Momotombo geothermal field is characterized mainly by three fault systems: NW-SE, NE-SW and N-S (Figure 5). Regional faults are aligned in a N-S direction; the Momotombo fault and the SR fault are the principal NW-SE trending faults, and in the centre part of the wellfield, the NE-SW trending Björnsson's fault is the principal fault. These sets of faults allow the circulation of fluids in a hydrothermal system. The most productive shallow wells are located in a zone corresponding to structural crossings in a fractured zone formed in the intersection of the faults of these three systems (Porras, 2009).

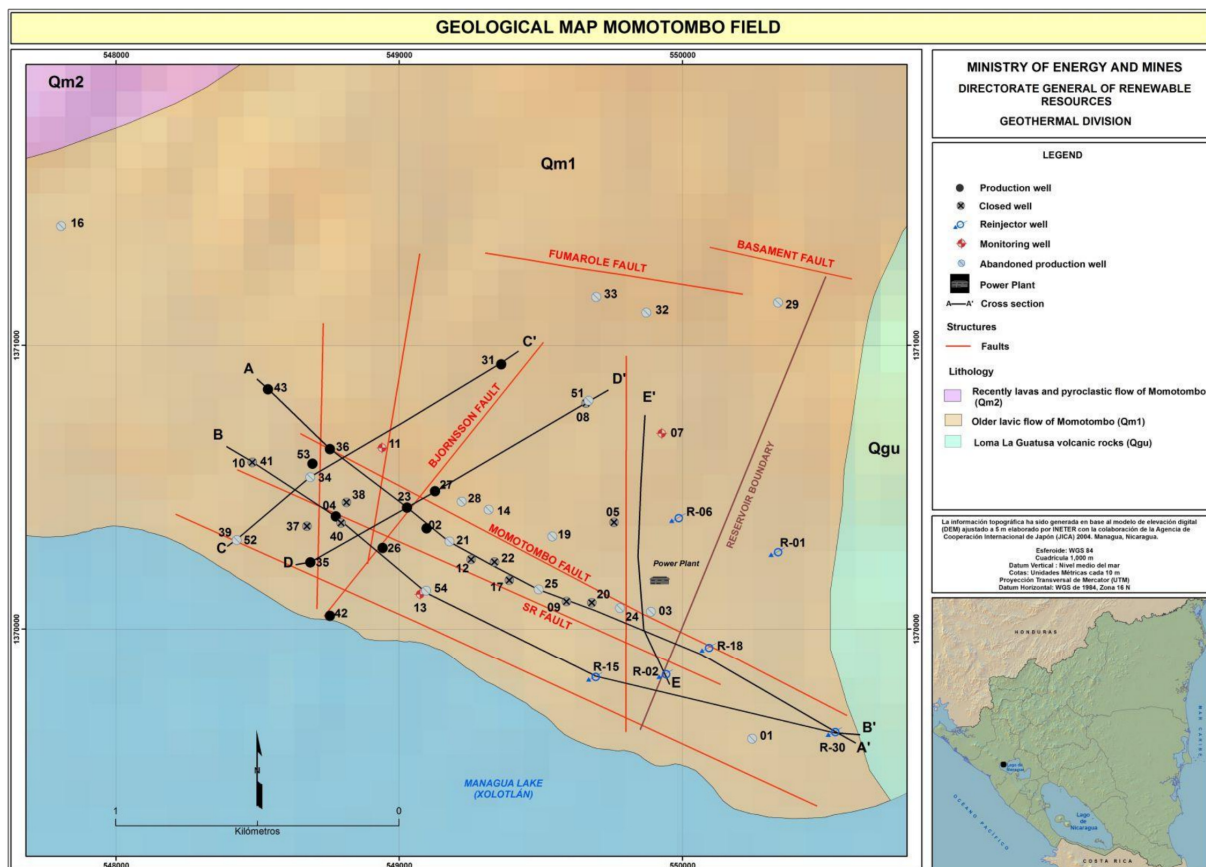


FIGURE 5: Geological map of Momotombo field (Egilsson et al., 2012)

The petrographic study by Combredet et al. (1987) showed that the lithology of the Momotombo geothermal field has been divided into the six units: unit I: 0-260 m b.s.l.; unit II: 260-600-800 m b.s.l.; unit III: 600-800 m b.s.l.; unit IV: 1600-2000 m b.s.l.; unit V: 360 m thick; and unit VI: 2300 m b.s.l. These formations consist of andesite and andesite-basaltic volcanic products, volcano-clastic deposits, different kinds of tuffs, volcano-sedimentary and sedimentary deposits, and some sub-intrusive bodies and dikes. This study suggests that a long period of volcanic activity took place in this area and that the formations were formed during early Miocene to the Quaternary age. The volcanic and volcano-clastic deposits have a total thickness of about 1700 m.

The rocks of the Momotombo geothermal reservoir consist of an interlayered sequence of lavas, tuff and pyroclastics down to a depth of 1500-1700 m and range in composition from basaltic to dacitic. Below this there are ignimbrites with minor tuffs. Light grey silty sediments underlie the ignimbrites. Andesitic dykes occur in the sediments (Arnórsson et al., 1996).

The wells in the Momotombo field are distributed in an area of about 3 km², but most of them are concentrated in an area of only 1.5 km².

2.4 The conceptual reservoir model

A conceptual model of Momotombo has been published in several articles (López et al., 1980; Porras et al., 2005; Björnsson, 2008; Porras and Björnsson, 2010). The model has not changed drastically through the years but has been refined as more data became available. The early conceptual models of the Momotombo geothermal field were developed by different consulting companies and after each exploration stage a thorough study of all technical data was generated. The 4 stages are described by Córdón (1980):

Stage 1: This model was developed by Texas Instruments in 1971. The objective was to delineate the field using geological and geophysical methods, and to confirm the presence of high temperature at depth.

Stage 2: This model was developed by the United Nations Development Program in 1973. Its most important contribution was to provide geochemical data that strongly suggested an upflow of thermal water originating in a deep and high-temperature reservoir. Sveinn S. Einarsson, then advisor to the United Nations, revised this model in 1977, based on analyses of the temperature distribution in drillholes (Einarsson, 1977).

Stage 3: The Electroconsult model was developed by Electroconsult in 1977 and isotope analyses suggested the existence of two reservoirs, in a convective cell, developing within permeable formations and some cold water inflow from the east partially feeding the shallow reservoir.

Stage 4: This model was developed by California Energy Company in 1979. This study included an analysis of temperature measurements and geological observations from 33 wells. Also, the first stratigraphic column was presented.

The IECO (International Engineering Company) model was developed from analyses of subsurface temperature distribution and from previous findings by various companies. This model found that the shallow reservoir is controlled by fracture permeability within the 200 m to 500 m depth range and that the deep reservoir extends to the west with increasing depth, but has an abrupt temperature drop near the eastern margin of the fracture zone due to cold water inflow.

The concept of two geothermal reservoirs was later applied to Momotombo, based on the depths to the production zones: one is a shallow reservoir and the other is a deep reservoir (González, 1990). There are three permeable horizons: a shallow permeable layer (200-700 m b.s.l.) and two layers located around 700-1500 and 1500-2000 m b.s.l. (Porras, 2012).

It is evident that the Momotombo field (Figure 6) is not a geothermal reservoir in which fluids are heated by conduction, but rather this field is part of a hydrothermal convective system (Goldsmith, 1980). The geothermal reservoir is hosted in andesitic flows and tuffs; the permeability of these rocks is controlled by faults and associated fracture zones. Some of these faults correspond to the lateral boundaries of the reservoir (Porras, 2005).

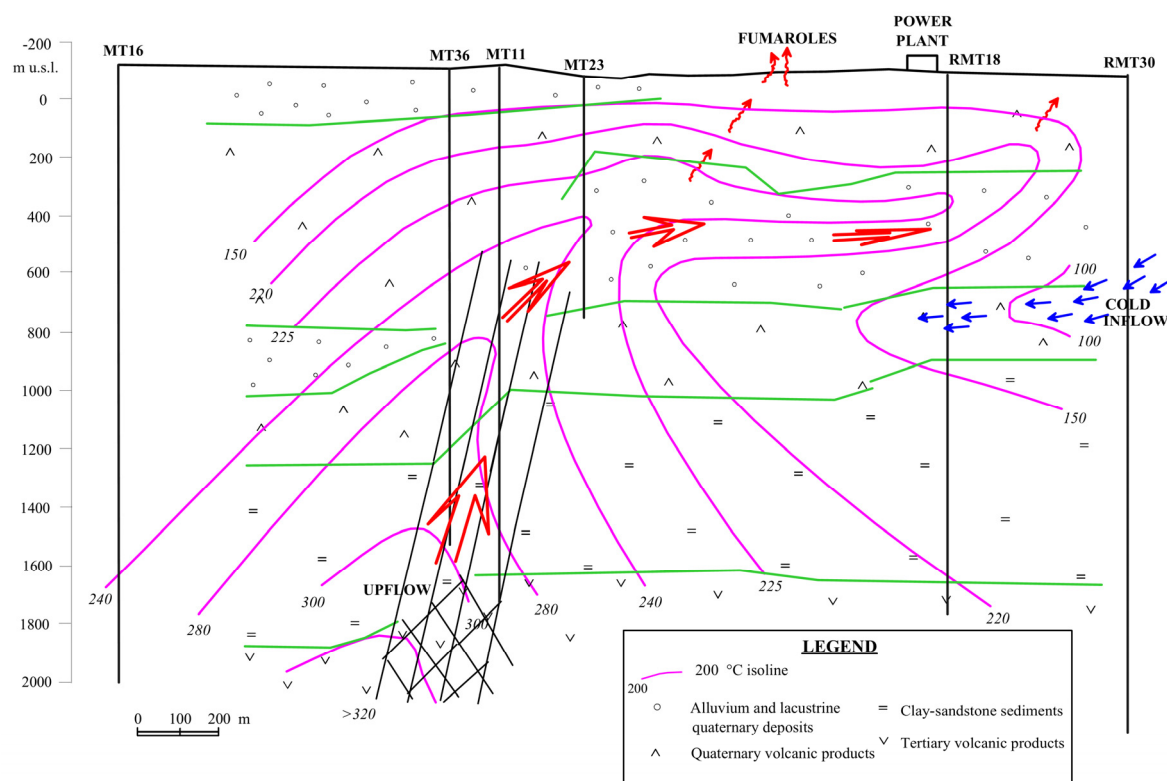


FIGURE 6: Temperature cross-section and a conceptual model of the Momotombo geothermal field (Porras and Björnsson, 2010)

The steady state condition of the Momotombo reservoir was a liquid single phase but then changed to a liquid-steam two phase reservoir soon after fluid production started in 1983. The two phase zone was developed mainly in the shallow reservoir when more fluid was produced for the second unit in 1989 (Porras, 2006).

The current conceptual model was most recently published by Porras and Björnsson (2010). This model is a review of previous models, based on information derived from deep drilling and the production history. Figure 6 shows this conceptual model as a temperature cross-section from west to east with a vertical upflow zone as a prominent feature. Most of the shallow production wells located in the middle of the field present 225-250°C feeding zones at intermediate depths. Wells drilled in the eastern part of the field encountered temperature inversions below this high temperature zone. Waters with temperatures below 100°C were found at intermediate depths, suggesting inflow (recharge) from either Lake Managua or from shallow cold water aquifers. The conceptual model is limited in that very few wells reach 500 m b.s.l., which makes the temperature distribution at deep levels less certain than at shallow levels. Geochemical studies have not conclusively determined whether Lake Managua is the source of this low-temperature inflow (Arnórsson et al., 1996). The production wells in the eastern half of the field were initially fed by a shallow lateral flow of boiling water from the major upflow (Arnórsson et al., 1996).

3. CHANGES IN FLUID CHEMISTRY WITH TIME

The dynamic production history of Momotombo is largely attributed to fast pressure and enthalpy changes resulting from up to 69 MW of steam generation from only 1-2 km² of proven wellfield. The pressure and enthalpy changes are described in detail in earlier publications (Porras, 2005). The geochemical changes, which are considerable have, however, received less attention. This chapter is

to give some highlights of these changes, later to be revisited in this study by an iTOUGH2 numerical study.

3.1 Chloride concentration history of produced fluid

The Momotombo geothermal reservoir is a sodium-chloride liquid dominated system. It has two reservoirs with an inflow of cold water from the east and an upflow of hot water from the central west. The changes observed in chemical composition between 1983 and the present are related to rapid infiltration of local and cold meteoric water into the shallow aquifer. Additionally, some of the declines in production were due to the encroachment of reinjected water into the production zone, and boiling in the reservoir as a result of extensive exploitation (Verma et al., 1996).

Chloride is amongst the most useful non-reactive chemical species used in geochemical analysis of liquid dominated geothermal reservoirs. Initially, reservoir water of Momotombo contained about 2700-3300 ppm Cl (Arnórsson et al., 1996). It is evident that chloride concentrations in many of the well discharges have changed with time, especially in the shallow wells (less than 600 m deep) in the eastern part of the production field (MT2, MT12, MT17, MT20 and MT22). Wells MT23, MT26, MT35 and MT38 are of intermediate depth (600-1300 m) and showed a moderate decline in chloride concentrations with time. Well MT36 is the deepest producing well and has maintained chloride levels the same as shallow Well MT27. Verma and Arnórsson both concluded that the decreasing chloride concentrations are caused by the incursion of cold water into the geothermal reservoir in response to the pressure loss accompanying its exploitation.

According to a report by Quijano (1989) using data from four production wells (MT12, MT20, MT23 and MT27) and hot springs near the area, chloride concentrations of springs before exploitation of the field were similar to weirbox water from the wells. This indicated that springs were a direct discharge of the reservoir. Boiling occurs at the shallower levels of the reservoir (300-500 m deep) in response to exploitation. Formation boiling also occurred at deeper levels of the reservoir where the permeability was less (Wells MT31 and MT35).

Figure 7 gives a better understanding of chloride behaviour in the reservoir with time and how it correlates to the exploitation history of the field. The figure shows how chloride concentrations

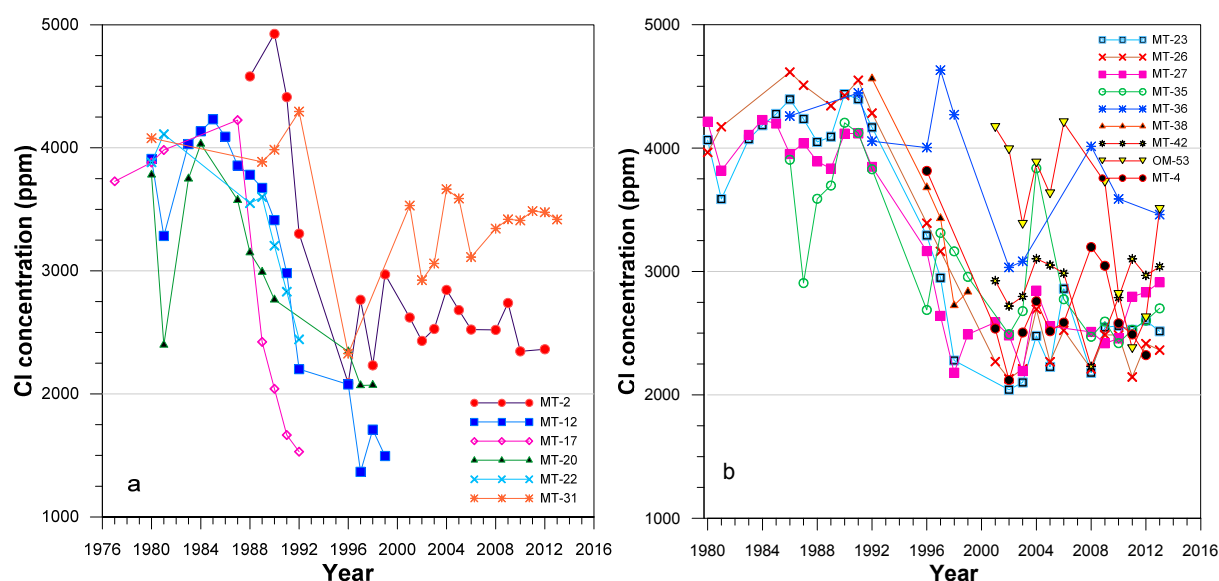


FIGURE 7: Average annual chloride concentrations: a) Cl concentrations of shallow wells located at the edge of the shallow reservoir with time; b) Cl concentrations for shallow and deep production wells located in the western part of the wellfield with time

decreased rapidly in early times, most evident in the shallow wells. Initially all the shallow wells had a chloride concentration of around 4000 ppm but this changed over time, decreasing to about 2000 ppm with the exception of the shallow wells MT2 and MT31.

Well MT31 maintained a stable concentration of chloride between 1980 and 1992. Then it experienced a decrease in concentration. In 2006 the chloride concentration reached about 3000 ppm and has remained semi stable until today. Well MT2 showed similar behaviour, with a rapid decline until 1996 and then maintained a constant concentration of chloride of about 2500 ppm.

Wells MT23, MT26 and MT27 showed relatively stable values of around or above 4000 ppm until 1992 followed by a drastic decline to values of about 2000 ppm. These wells are located on the Björnsson fault. When Well MT42 came online in 1997, it showed values of around 3000 ppm but declined to around 2000 ppm in 2008, while in 2012 it again recovered to about 3000 ppm. Well MT36 showed a constant concentration of about 4000 ppm until 2002. Wells MT4, MT35 and MT38 showed a gradual decline from around and above 4000 ppm to around 2500 ppm. Well OM53 started with a concentration of about 4000 ppm in 2001 but fluctuated around this value until 2008 and between 2009 and 2011 the concentration declined to around 2500 ppm. In 2013, Well OM53 had a chloride concentration of about 3500 ppm.

After the 1990-1996 period of rapidly declining chloride concentration, most wells reached a relatively constant value between 2000 and 3000 ppm with the exception of Wells MT31 and MT36 which had values of about 3500 ppm.

As a note of caution, this study was unable to definitely confirm if the chloride concentrations in Figure 7 are that of the reservoir or in the weir box. In the latter case, the chloride values in Figure 7 need to be converted to a slightly lower value, a task which is beyond the scope of this report.

4. MONTE CARLO VOLUMETRIC ASSESSMENT

Geothermal resource assessment is a process for estimating the amount of thermal energy that can be extracted from a geothermal reservoir, evaluating all available data from surface discharge and downhole. These data are evaluated along with other geoscientific information obtained from geological, geophysical and geochemical measurements. The main focus of this assessment is to confirm that there exists a geothermal resource and this gives a certain capacity for a certain period with well-defined fluid characteristics and resource management strategies to ensure production sustainability over a long term period (Sarmiento and Steingrímsson, 2011).

The Monte Carlo simulation is a numerical volumetric modelling technique that uses variables that are often shrouded in uncertainty, making it necessary to define a probability distribution for these variables. By using such random values for the most sensitive volumetric model parameters, a probability distribution can be assessed for the reservoir power generation capacity. The discrete distribution for the outcome is quantified or divided into intervals of proven, probable and possible reserves, giving the upside potential and downward risk in sizing up the field power potential (Sarmiento and Steingrímsson, 2008).

4.1 Thermal energy calculation

The volumetric method refers to the calculation of the thermal energy in the rock and the fluid. It is based on the volume and temperature of a reservoir. The equation used in calculating the thermal energy for a liquid dominated reservoir is as follows:

$$Q_T = Q_r + Q_w \quad (1)$$

and

$$Q_r = A * h [\rho_r * C_r * (1 - \phi) * (T_i - T_f)] \quad (2)$$

$$Q_w = A * h [\rho_w * C_w * \phi * (T_i - T_f)] \quad (3)$$

where Q_T = Total thermal energy (kJ);
 Q_r = Heat in rock (kJ);
 Q_w = Heat in water (kJ);
 A = Area of the reservoir (m²);
 h = Average thickness of the reservoir (m);
 C_r = Specific heat of rock at reservoir conditions (kJ/kgK);
 C_w = Specific heat of liquid at reservoir conditions (kJ/kgK);
 ϕ = Porosity;
 ρ_r = Rock density (kg/m³);
 ρ_w = Water density (kg/m³);
 T_i = Average temperature of the reservoir (°C); and
 T_f = Final or rejection temperature (°C).

When the reservoir has a two-phase zone, it is necessary to calculate the heat component of both liquids. A comparison made by Sanyal and Sarmiento (2005) indicates that if only water is produced from the reservoir, only 3.9% of the stored heat is contained in the fluids; the rest is in the rock matrix. If only steam is produced from the reservoir, only 9.6% is contained in the fluids. If both water and steam are produced from the reservoir, between 3.9 and 9.6% of the heat is contained. Conclusively, all the fluids are in the rock and it doesn't matter whether one distinguishes between the stored heat in the water and steam, respectively.

The possible size of a new power plant that could be supported by the resource in question is based on the following equation:

$$P = \frac{Q_t * R_f * C_e}{P_f * t} \quad (4)$$

where P = Power potential (MWe);
 R_f = Recovery factor;
 C_e = Conversion efficiency;
 P_f = Plant factor; and
 t = Time in years (economic life).

The *recovery factor* refers to the fraction of the stored heat in the reservoir that could be extracted to the surface. It is dependent on the fraction of the reservoir that is considered permeable and on the efficiency by which heat could be swept from these permeable channels. The *conversion efficiency* takes into account the conversion of the recoverable thermal energy into electricity. The *economic life* of the project is the period it takes the whole investment to be recovered within its target internal rate of return. This is usually 25-30 years. The *plant factor* refers to the plant availability throughout the year, taking into consideration the period when the plant is scheduled for maintenance, or whether the plant is operated as a base-load or peaking plant. The good performance of many geothermal plants around the world places the availability factor to be between 90 and 97 %.

The Monte Carlo simulation is used to determine the proven, probable and possible or inferred reserves based on the resulting percentiles obtained from the cumulative frequency or the probability density function, where the proven reserves will have a P90 (90 percentile) probability, P50 for the proven + probable reserves, and P10 for the proven + probable + possible reserves. The percentile value indicates the probability value that the quantity of the reserves to be covered will equal or exceed the proven reserves. The accuracy of this method depends on the type, amount and quality of

geoscientific and engineering data and the accuracy increase when the field has wells and production data become available (Sarmiento and Steingrímsson, 2008).

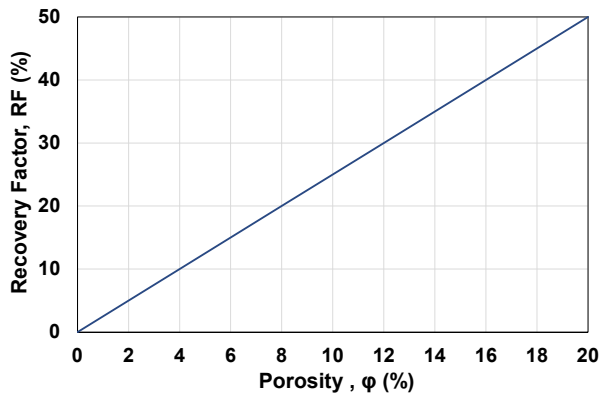


FIGURE 8: Correlation between porosity and recovery factor (from Muffler, 1979)

4.2 Recovery factor

The recovery factor cannot be measured directly, but a constant value (0.25) was often applied in earlier reservoir assessment and sometimes this is estimated to be a function of the reservoir porosity (Muffler, 1979). In Figure 8, we can see the theoretical geothermal recovery factor as a function of reservoir porosity.

Nowadays it is generally believed that the recoverable fraction of the stored energy was overestimated at least for fractured reservoirs (Williams, 2007).

4.3 Parameter evaluation

In this study, the Momotombo reservoir area was estimated by taking into account the resistivity contours, temperature contours and geophysical exploration of the current wellfield. These are used to define the proven reservoir. As there may be an existing reservoir sector still to be discovered, another scenario of double the proven resource is studied, here called the possible reservoir. The thickness of the reservoir was taken from the correlation of temperature and pressure profiles of the wells and petrographic analysis (Figure 6). The temperature of the reservoir was defined by the temperature profiles, indicating that the reservoir temperature increased in the western part of the well field, where the highest temperature above 320°C was found for Well MT43 below 2250 m b.s.l. (Figure 6). The most likely recovery factor was conservatively estimated as 15% for the calculation of thermal energy available in a volume of porous media, based on the volcanic nature of the reservoir. The 10% most likely porosity assumption will, for example, give 25% recovery, using Figure 8.

The assessment analysis of the potential of the field, using the Monte Carlo volumetric method was explained above and the parameters used in this analysis are summarized in Table 2.

TABLE 2: Parameters used to estimate probability distribution for the Monte Carlo simulation

Parameters and units	Proven (P_{90})			Possible (P_{10})			Type of distribution
	Min	Most likely	Max	Min	Most likely	Max	
Surface area (km ²)	1	2.5	3	3	5	7	Triangular
Thickness (m)	1000	2000	3000	1000	2000	3000	Triangular
Rock density (kg/m ³)		2500			2500		Single value
Porosity (%)	5	10	15	5	10	15	Triangular
Rock specific heat (J/kg°C)		900			900		Single value
Temperature (°C)	200	250	320	200	250	320	Triangular
Fluid density (kg/m ³)		799.2			799.2		f(temp)
Fluid specific heat (J/kg°C)		4870			4870		f(temp)
Recovery factor (%)	10	15	25	10	15	25	Triangular
Conversion efficiency (%)		11			11		f(temp)
Plant life (years)		25			25		Single value
Rejection temperature (°C)		150			150		Single value

4.4 Results of production capacity

The results obtained through the Monte Carlo volumetric method are shown in Figure 9 which shows the frequency distribution and the cumulative probability distribution of the proven and possible reservoir. Figures 9a and 9b indicate that the proven reservoir has a mean value of capacity of 26 MWe with a standard deviation of 11 MWe, while the most likely value of the power production capacity is 20 MWe for 25 years of plant life. We can also see that the estimated power production will be in the range of 13-41 MWe and the cumulative distribution shows that the resource capacity will be at least 10 MWe. Figures 9c and 9d indicate that the possible reservoir's estimated capacity of the Momotombo geothermal field has a mean value of 60 MWe with a standard deviation of 24 MWe, and the most likely value of the power production capacity is 50.5 MWe for 25 years of plant life. We can also see that the estimated power production will be in the range of 32-93 MWe and the cumulative distribution shows that the resource capacity will be at least 40 MWe. Note that the volume of the proven reservoir is 5 km³.

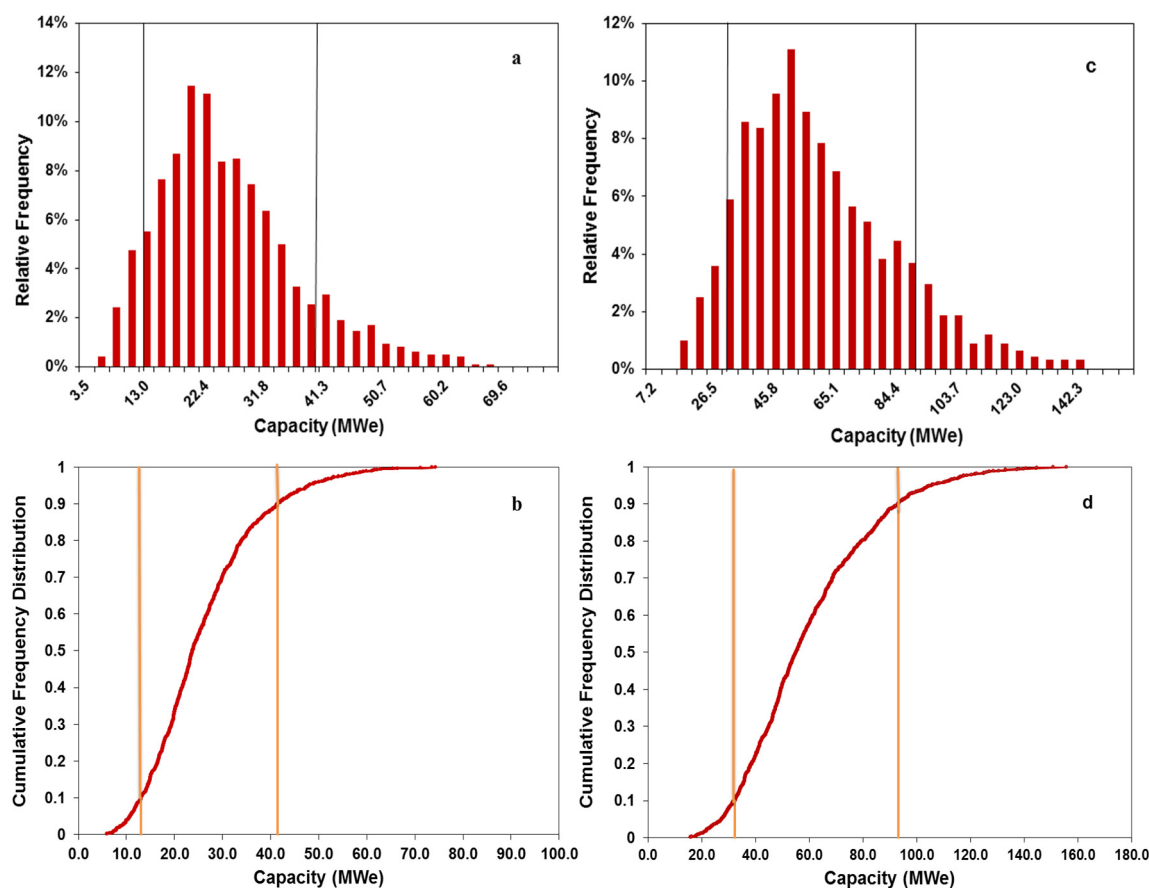


FIGURE 9: Comparison between assessment of proven and possible reserves of the Momotombo field: a) Relative frequency of power production capacity of proven assessment; b) Cumulative frequency of power production capacity of proven assessment; c) Relative frequency of power production capacity of possible assessment; d) Cumulative frequency of power production capacity of possible assessment

Comparing the proven and possible assessments, we can see that the difference is 30 MWe; this is because the values of the surface area are different. In Tables 3 and 4, the values obtained from the Monte Carlo volumetric assessment are summarized.

TABLE 3: Most likely estimate from Monte Carlo simulation

	Proven		Possible	
	Most likely	Random pick	Most likely	Random pick
Total energy (TJ)	1207	1074	2414	3900
Total recoverable energy (TJ)	181	180	362	832
Electric power	20	25	50	116

TABLE 4: Monte Carlo simulation results

	Proven	Possible
	MW _e	MW _e
Mean electric power (MW _e)	26	60
Median electric power (MW _e)	24	55
Standard deviation (MW _e)	11	24
90% above (P ₁₀ MW _e)	13	32
90% below (P ₉₀ MW _e)	41	93

5. SIMPLE LUMPED PARAMETER MODEL

The lumped parameter modelling approach constitutes an efficient method of simple modelling used to simulate pressure response data from a liquid dominated geothermal reservoir and provide information on the corresponding properties of the geothermal system in question. The principal purpose of such modelling is to estimate the production potential of geothermal systems through pressure response predictions and to estimate benefits of different management options.

In simple models, the real structure and spatially variable properties of a geothermal system are greatly simplified, such that analytical mathematical equations, describing the response of the model to energy production, may be derived.

5.1 Model description

Lumped models consist of a few tanks which are connected by conductors or resistors. Fluid is produced from the innermost-tank and the pressure response to production is also monitored here. The method tackles the simulation as an inverse problem and can simulate the pressure response very accurately. It automatically fits the analytical response functions to the observed data by using a nonlinear iterative least squares technique for estimating the model parameters.

In Figure 10 we can see a general lumped parameter model; the first-tank simulates the production part of the geothermal reservoir, the second and third-tanks simulate the outer parts of the system. The

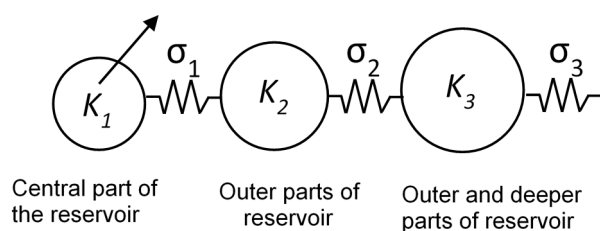


FIGURE 10: General lumped parameter model (Axelsson et al., 2005)

third-tank is connected by a resistor to a constant pressure source, which supplies recharge in the long run. Lumped models can either be open or closed. The model in Figure 10 is open; without the connection to the constant pressure source the model would be closed.

When a model is open it may be considered optimistic, since equilibrium between production and recharge will eventually always be reached

during long term production, causing the water level drawdown to stabilize. A closed model may be considered pessimistic, since no recharge is allowed for such a model and the water level declines steadily with time during long term production (Axelsson et al., 2005).

The tanks simulate the storage capacity of different parts of the reservoir in question, whereas the resistors simulate the permeability. A tank in a lumped model has the mass storage coefficient κ when it responds to a load of liquid mass m with a pressure increase by $p=m/\kappa$. The mass conductance of a resistor is given by σ when it transfers $q=\sigma\Delta p$ units of liquid mass per unit time, at a pressure differential Δp .

The basic equation describing the pressure response p of an open lumped model with N -tanks, to a constant production Q since time $t = 0$ is given by the following equation (Axelsson and Arason, 1992):

$$p(t) = - \sum_{j=1}^N Q \frac{A_j}{L_j} (1 - e^{-L_j t}) \quad (5)$$

The pressure response of an equivalent N -tank closed model is given by the equation:

$$p(t) = - \sum_{j=1}^{N-1} Q \frac{A_j}{L_j} (1 - e^{-L_j t}) + QBt \quad (6)$$

where p = Pressure (Pa);
 Q = Flow rate (kg/s);
 A_j = Coefficient of the model;
 L_j = Coefficient of the model;
 B = Coefficient of the model; and
 t = Time (s).

The coefficients A_j , L_j and B are functions of the storage coefficients of the tanks (κ_j) and the conductance coefficients of resistors (σ_j) of the model. The storage coefficient of a tank is defined by the equation:

$$\kappa = Vs \quad (7)$$

where s = $\rho_w(\emptyset C_w + (1 - \emptyset)C_r)$, storativity of the reservoir (kg/Pa m³);
 ρ_w = Density of water at specific reservoir conditions (kg/m³);
 C_w = Compressibility of geothermal fluid (Pa⁻¹);
 C_r = Compressibility of rock matrix (Pa⁻¹);
 \emptyset = Porosity of reservoir; and
 V = Volume of different tanks (m³).

One can envisage the lumped models as several concentric cylinders of radius R_i . This allows for converting the capacitors K_i to geometrically similar cylinders provided a reservoir thickness H is known. Thus:

$$R_1 = \sqrt{\frac{V_1}{\pi H}}; R_2 = \sqrt{\frac{V_1 + V_2}{\pi H}}; R_3 = \sqrt{\frac{V_1 + V_2 + V_3}{\pi H}} \quad (8)$$

Therefore:

$$r_1 = \frac{R_1}{2}; r_2 = R_1 + \frac{(R_2 - R_1)}{2}; r_3 = R_2 + \frac{(R_3 - R_2)}{2} \quad (9)$$

where R = Radius of different tanks (m);
 H = Thickness of the reservoir (m); and

r = Half radius of different tanks (m).

For one and two dimensional flow, the conductance is defined by the following equations:

$$\sigma = \frac{Ak}{Lv} \quad (10)$$

$$\sigma = \frac{2\pi Hk}{\ln(r_2/r_1)v} \quad (11)$$

where A = Flow area (m²);
 k = Permeability (m²);
 L = Length of resistor (m); and
 v = Kinematic viscosity (Pa s).

Thus, one can estimate the volume of the lumped reservoir model with Equation 7. The reservoir permeability can then, in turn, be estimated by Equations 10 or 11. Finally, with a fully calibrated model at hand, it may be used to predict the pressure changes in the reservoir in the future for given production scenarios.

5.2 Simulation results

Axelsson and Arason (1992) developed the simulation program Lumpfit to obtain pressure changes in hydrological reservoirs. This lumped model methodology was used to obtain information about reservoir properties of the Momotombo field; the model was based on the observed pressure changes resulting from the actual production history 1983-2004. In this case, the total production history was digitized from Figure 3.7 in Porras (2005). Likewise, the pressure change histories in Wells MT11 and MT13 were digitized from Figures 3.7 and 3.9 in Porras (2005) to construe a pressure response curve. In this case the total production was used instead of the net production since reinjection was insignificant until the year 2000.

The procedure for finding the best fitting parameters for a specific lumped model is as follows: in the first step a one-tank open model was used and then a two-tank open model. The results of the simulation for total production are shown in Figure 11, the model parameters are shown in Table 5 and the properties of the Momotombo reservoir are summarize in Table 6.

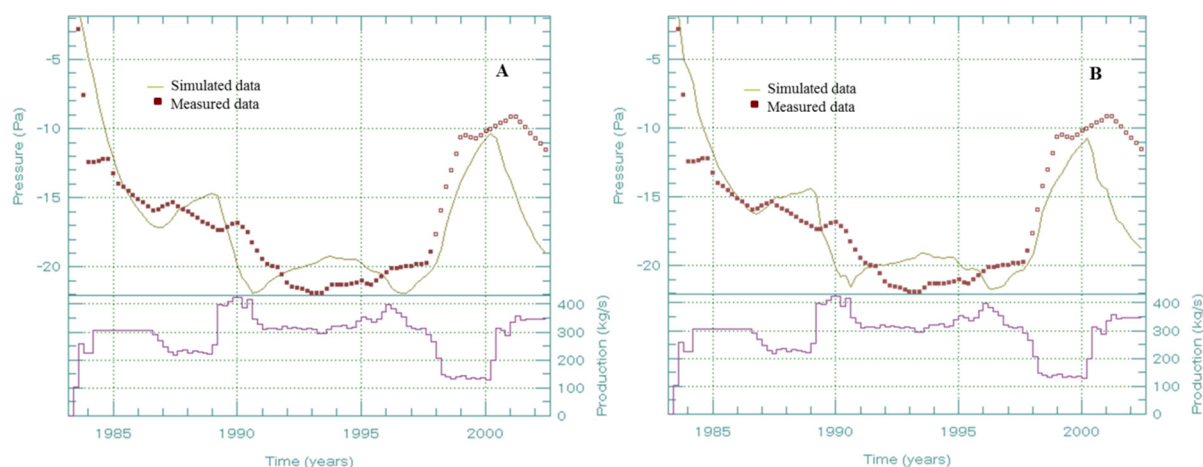


FIGURE 11: Total production and pressure response data of the Momotombo geothermal field simulated by a lumped parameter model: a) One-tank open model; b) Two-tanks open model

TABLE 5: Parameters of the simulation by lumped model

Parameters	Total production	
	Open, one-tank	Open, two-tank
A_1	0.504570×10^{-1}	0.303737
L_1	0.817232	25.9474
A_2		0.304736×10^{-1}
L_2		0.613834
B		
κ_1 (ms ²)	6250.08	943.596
κ_2 (ms ²)		9913.23
σ_1 (10 ⁻³ ms)	0.161966	0.707262
σ_2 (10 ⁻³ ms)		0.211813
Coeff.of determin. (%)	65.1	70.4
Misfit standard deviation (bars)	2.16	2.02

TABLE 6: Properties of the reservoir according to lumped model

Properties	Model	First-tank	Second-tank
Reservoir volume (km ³)	Two-tanks open	0.4	4.2
Permeability (mD)		232	75

Using a two-tank open model resulted in a satisfactory fit between the measured and simulated pressure (Figure 11b). One assumption, however, was necessary to attain this match, namely neglecting pressure data collected after 2000 when large scale injection commenced. The first-tank can be considered the innermost part of the geothermal reservoir and the second acts as the surrounding recharge area of the system.

The best fitting lumped model reveals a storage coefficient of the main area κ_1 and the recharge area κ_2 as 943.6 and 9913.2 ms², respectively. The conductivity σ_1 and σ_2 is 0.71×10^{-3} and 0.21×10^{-3} ms, respectively. Using the storativity published by Porras (2005) and Equation 7, the volume of the first-tank and the volume of the second-tank were calculated as 0.4 and 4.2 km³, respectively.

Assuming two-dimensional flow and using the most likely parameters of the Monte Carlo volumetric method (Table 2), the thickness of the reservoir is 2 km, the radius of the first-tank equals 250 m and the radius of the second tank equals 850 m. Therefore, $r_1 = 124.57$ m and $r_2 = 551.93$ m. Using Equation 11, the permeability estimated for the first tank is 232 mD and 75 mD for the second tank.

6. A 2D DISTRIBUTED PARAMETER MODEL BY iTOUGH2

The present study concludes by using the simulator iTOUGH2 (Finsterle, 1999) to calibrate a 2D vertical slice model of the Momotombo reservoir. iTOUGH2 was developed on top of the TOUGH2 (Pruess et al., 1999) simulator code for adding inverse modelling capabilities. This automates the process of repeatedly improving parameters to obtain a better fit to data and adjusts in a direction that minimizes the differences between observed and calculated values.

6.1 Governing equations

TOUGH2 is a numerical simulation program for multi-dimensional, multi-component and multi-phase flow of mass and heat in porous and fractured media. The TOUGH2 architecture is based on a model mesh that consists of a number of elements connected to each other. For each of these elements, we need to set up a number of equations defining the accumulated mass and heat, fluxes of heat and mass through all surfaces and generation points where applicable.

The governing equations of mass and heat are discretized and solved between consecutive time steps by the Newton-Raphson iteration scheme. The basic mass and energy balance equation solved by TOUGH2 has the general form (Pruess, 1999):

$$\frac{d}{dt} \int_{V_n} M^\kappa dV_n = \int_{\Gamma_n} F^\kappa \cdot n d\Gamma_n + \int_{V_n} q^\kappa dV_n \quad (12)$$

The first term (M) of Equation 12 represents mass or energy accumulation in sub-volume V , where κ can denote 1 water, 2 air, 3 heat, 4 tracer, 5 CO₂ ...etc. The second term (F) represents mass or heat fluxes through the surface of our sub-volume V and the last term (q) represents sources and sinks of mass and heat. The normal vector is denoted by n on surface element $d\Gamma_n$, pointing inward into V_n .

The mass accumulation term is specified as:

$$M^\kappa = \emptyset \sum_{\beta} S_{\beta} \rho_{\beta} X_{\beta}^{\kappa} \quad (13)$$

where M^κ = Total mass of component κ (kg);
 \emptyset = Porosity;
 S_{β} = Saturation of phase β ;
 ρ_{β} = Density of phase β (kg/m³); and
 X_{β}^{κ} = Mass fraction of component κ present in phase β .

The heat accumulation is written as:

$$M^{N\kappa+1} = (1 - \emptyset) \rho_R C_R T + \emptyset \sum_{\beta} S_{\beta} \rho_{\beta} U_{\beta} \quad (14)$$

where ρ_R = Grain density of the rock (kg/m³);
 C_R = Specific heat of the rock (J/kg °C);
 T = Temperature (°C); and
 U_{β} = Specific internal energy in phase β (J/kg).

Advective mass flux is specified as a sum over phases:

$$F^\kappa|_{adv} = \sum_{\beta} X_{\beta}^{\kappa} F_{\beta} \quad (15)$$

And individual phase fluxes are given by a multiphase version of Darcy's law:

$$F_{\beta} = \rho_{\beta} u_{\beta} = -k \frac{k_{r\beta} \rho_{\beta}}{\mu_{\beta}} (\nabla P_{\beta} - \rho_{\beta} g) \quad (16)$$

where u_{β} = Darcy velocity in phase β (m/s);
 k = Absolute permeability (m²);
 $k_{r\beta}$ = Relative permeability to phase β (-);
 μ_{β} = Dynamic viscosity (kg/ms);
 P_{β} = $P + P_{c\beta}$, fluid pressure in phase β (Pa);
 P = Pressure of a reference phase (usually a gas phase) (Pa);

$P_{c\beta}$ = Capillary pressure (≤ 0) (Pa); and
 g = Vector of gravitational acceleration (m/s^2).

The heat flux contains both conductive and convective components:

$$F^{NK+1} = -\lambda \nabla T + \sum_{\beta} h_{\beta} F_{\beta} \quad (17)$$

where λ = Thermal conductivity ($\text{W/m } ^\circ\text{C}$); and
 h_{β} = Specific enthalpy in phase β (J/kg).

6.2 Development of a 2D numerical model

As discussed in an earlier section concerning the chemistry changes in Momotombo, it is of interest to see if these can be observed in distributed parameter numerical models. Particularly, it would be good to determine the cause of the chloride concentration changes shown in Figure 7. Therefore a 2D numerical model study using the iTOUGH2 platform was conducted and is presented below.

6.2.1 Model mesh and boundary conditions

A rectangular area of 3000 m length by 2500 m depth and 200 m thickness was selected as the basis for the 2D numerical model and then adjusted to the conceptual model shown in Figure 6. The model selected has 540 elements with 11 wells and is divided into 9 rock types. In Figure 12 we can see the model mesh and the rock type distribution calibrated for iTOUGH2. The different colours mean the following: red is the basement, yellow represents the surface, green is a shallow reservoir, light blue is the vertical permeable zone feeding model hot springs on the surface, orange is a deep vertical up flow zone, blue represents cold water inflow from the east, grey is the western boundary and pink is the eastern boundary.

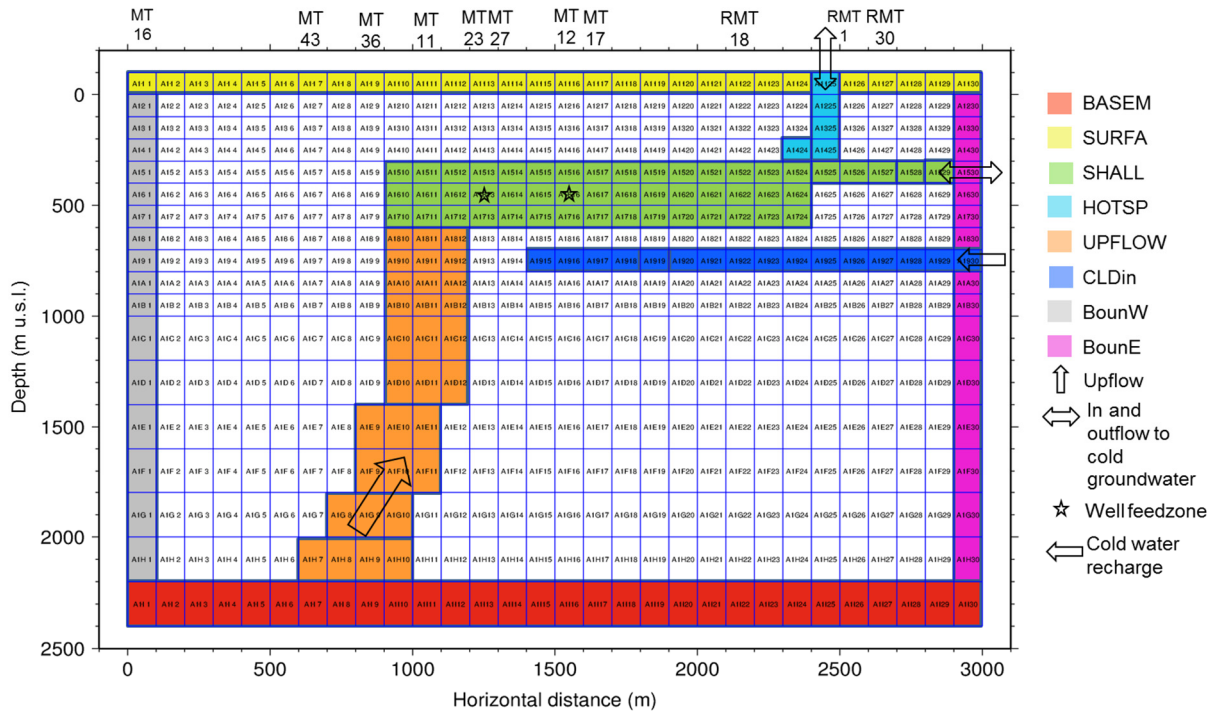


FIGURE 12: Mesh of the 2D numerical model of the Momotombo reservoir

The model's top and eastern constant pressure boundary conditions is regarded here as Lake Managua that has a chloride concentration of around 200 ppm (Parello et al., 2008). The numerical model was designed such that this low temperature lake water is able to flow into the deep model, if its pressure declines during production while discharging fluid to the surface under natural state conditions. The top, bottom, east and west boundary layers were defined as inactive; they remain at constant pressure and temperature at all times. This was actually not the case in the early model calibration, when the two outer vertical boundaries were assigned the steady state temperature profiles of Wells MT16 (BounW) and RMT30 (BounE). Their pressure could, however, change and were only set as steady state when the model pressure satisfactorily matched the observed initial pressure of Well MT11.

The top SURFA layer was centred at 50 m a.s.l. and given a fixed pressure of 4 bars and about 1 mD vertical permeability to the layer below. The bottom BASEM layer, on the other hand, was given very low vertical permeability but the temperature distribution was in line with the temperatures shown in Figure 6. Heat could, therefore, flow vertically between this base layer and the active layers above, while mass flow was negligible.

6.2.2 Sources and sinks

The 2D Momotombo model is heated by a constant mass inflow of around 1500 kJ/kg enthalpy into the deepest orange coloured upflow elements shown in Figure 12. This mass rises up to 300-500 m depth where it enters the horizontal shallow reservoir. The fluid here will move laterally to the east where two flow channels allow it to escape from the model. One is by the hot spring upflow zone called HOTSP while the other is to a constant pressure and temperature element in the 5th layer of the BounE rock column. Note that both connections deliberately allowed for either outflow or inflow, subject to the model pressure.

In addition to the mass upflow and outflow boundary conditions at the surface, only two production wells were introduced to study the model enthalpy, pressure and chloride changes with time after 1983. These were Wells MT27 and MT12. Both produce at a constant arbitrary 10 kg/s flow rate, Well MT27 from 1983, while Well MT12 was put online in 1989 when the second 35 MW unit was commissioned. This assumption greatly simplified the actual production history of the Momotombo field, but was deemed necessary and reasonable for a two month long study exercise. For those interested in a more detailed reservoir model, the PhD thesis of Porras (2005) is an appropriate reference.

6.2.3 Modelling chloride changes with time

In the present model, substantial effort was put into imitating the declining chloride concentrations of the wells with time (Figure 7). For this endeavour, the two water option of TOUGH2 was applied. The basic assumption is that the deep and hot geothermal inflow consists of 99% of water 1 while the top ground water layer is, on the other hand, 99% mass fraction of water 2. As the model execution took off, the two waters mixed in the model and their mass fractions were constantly updated by the TOUGH2 mass balance equations.

A simple linear relation was used to convert the mass fraction of water 1 to chloride concentration in ppm, namely, by multiplying the mass fraction by 4000, which is the initial chloride concentration of the deeper and hotter Momotombo wells (Figure 7).

6.2.4 Observations in calibrating the model

A total of 12 observation data sets were used in calibrating the model mesh shown in Figure 12. These grouped firstly into the initial temperature profiles in Wells MT11, 12, 17, 23, 36, 43, RMT1 and 18, and an initial pressure profile in Well MT11. These profiles were digitized from Figures 2.11 and 2.17 in Porras's (2005) PhD thesis. Secondly, the pressure drawdown history in Figure 11 was imported to

an element close to Well MT11. Thirdly, the observed enthalpy history of Well MT27 was digitized from Figure 3.4 in Porras (2005) and served as a constraint for allowing this well to temporarily flash into formation with an accompanying temporary rise in enthalpy. Last, but not least, the chloride history of Well MT27 (Figure 7) was imported to the inverse file of iTOUGH2 to see if the cold model boundary to the east and the surface hot spring would recharge fresh water to the shallow reservoir and, hence, result in declining chloride in the well with time.

6.2.5 Calibration of the model

The calibration in iTOUGH2 requires an inversion technique of numerical simulation. The first step is to make a model forward file. This file includes parameters of the different rock types, the model elements, connections, initial conditions and generation points. For the mesh generation, the inbuilt mesh maker of TOUGH2 was applied. Secondly, an inverse input file had to be developed, consisting of a parameter block which defined the model parameters to be inverted for, an observation block which defined the times when the code compared measured and computed values; this block also incorporated the measurements extracted from Porras's (2005) thesis. In this study, 14 model parameters were inverted for, 11 horizontal and vertical permeability, the cold water recharge rate to the CLDin layer (Figure 12), and the rate and enthalpy of the deep inflow. Finally, a computation block was written for controlling the numerics of the inversion. Of special convenience is the STEADY STATE SAVE feature of iTOUGH2 which allowed for matching both steady state and production date in the same execution.

The simulator automates the process of repeatedly improving the parameters to obtain a better fit with the data and adjusts these parameters in a direction that minimizes the differences between observed and calculated data. This misfit boils down to a single number called the objective function. It is the sum of the square of all residues of measured and computed values, divided with the standard deviation of each dataset.

Inverse calculations were required to adjust parameter block lists, including temperature, pressure, enthalpy and drawdown of the different elements of the grid. Block lists of observation times and values were used for calibration and a block list of computational options.

6.2.6 Rock properties

After creating the model mesh, it was necessary to assign rock properties to each element in the system. The rock properties are density, porosity, permeability, thermal conductivity and heat capacity. In Table 7, the rock properties of the mesh are summarized for the best model calibrated by the inverse method against the 12 datasets at hand.

TABLE 7: Rock properties for each grid in the system

Rock	Density (kg/m ³)	Porosity (%)	Permeability (m ²)			Thermal conduct. (W/m°C)	Heat cap (J/kg°C)
			k ₁	k ₂	k ₃		
Unknw	2650	0.20	1.000E-17	1.000E-15	7.749E-17	2.50	1.00E+03
SURFA	2650	0.20	10.00E-15	1.000E-14	1.013E-13	2.50	1.00E+03
BASEM	2650	0.10	1.000E-14	1.000E-35	1.000E-35	2.50	1.00E+03
UPFLO	2650	0.10	7.400E-15	5.000E-14	6.709E-14	2.50	1.00E+03
SHALL	2650	0.20	3.420E-13	1.000E-14	1.025E-13	2.50	1.00E+03
HOTSP	2650	0.20	4.300E-14	2.500E-13	1.882E-13	2.50	1.00E+03
CLDin	2650	0.20	1.450E-13	1.000E-14	5.081E-15	2.50	1.00E+03
BounW	2650	0.10	1.000E-15	1.000E-14	7.749E-17	2.50	1.00E+50
BounE	2650	0.10	1.000E-15	1.000E-14	7.749E-17	2.50	1.00E+50

Rock features are explained as follows: SURFA rock type was assigned to the top of the model and BASEM rock type was assigned to the base of the reservoir, both defined as inactive; UPFLO rock type was assigned at depth, SHALL rock type was assigned to shallow reservoir between 300 and 400 m, HOTSP rock type was assigned to the outflow of hot springs, CLDin rock type was assigned to cold recharge from east, and BounW and BounE rock types were assigned to the boundary located in the western and eastern part of the field, respectively. Note that the most productive reservoir volume, SHALL, is of 340 mD permeability and complies nicely with the 230 mD estimated in the lumped model.

6.2.7 Simulation results for natural state

The iTOUGH2 model match to the observed steady state data is shown in different graphs in this section. The initial setting of the parameters is very important because it causes remarkable changes in the simulation. One of the most important parameters is permeability; the rate at which fluid passes through the material depends on three basic factors in addition to the intrinsic permeability: porosity, density affected by temperature, and pressure to which the fluid is subjected.

In Figures 13-20, a comparison is done on measured and simulated temperature profiles of one monitoring well (MT11), five production wells (MT12, 17, 23, 36 and 43), and two reinjection wells (RMT1 and 18). Production Wells MT12, MT17, MT36 and MT23 are reasonably matched although Well MT23 showed a shallow steam zone. Well MT43 showed a result near the boiling point curve. Reinjection wells RMT1 and RMT18 showed a temperature inversion both in the field data and in the model. In Figure 21 we can see initial pressure in Well MT23 and a good match between measured and simulated pressure.

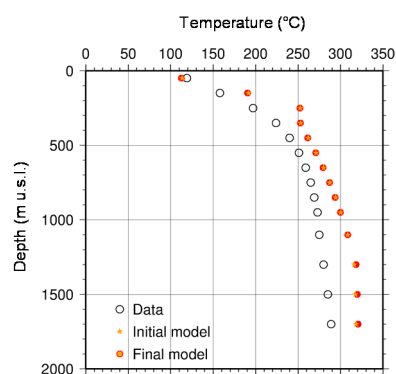


FIGURE 13: Temperature measured and simulated in Well MT11

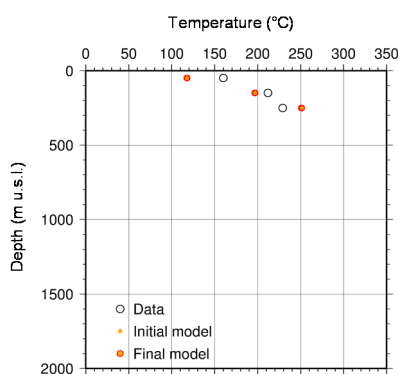


FIGURE 14: Temperature measured and simulated in Well MT12

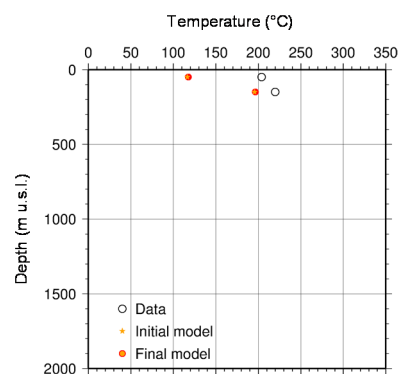


FIGURE 15: Temperature measured and simulated in Well MT17

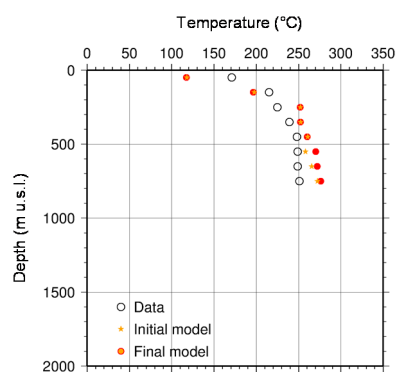


FIGURE 16: Temperature measured and simulated in Well MT23

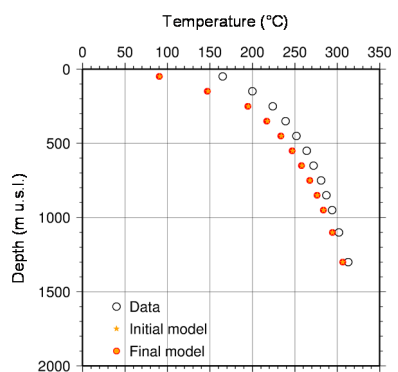


FIGURE 17: Temperature measured and simulated in Well MT36

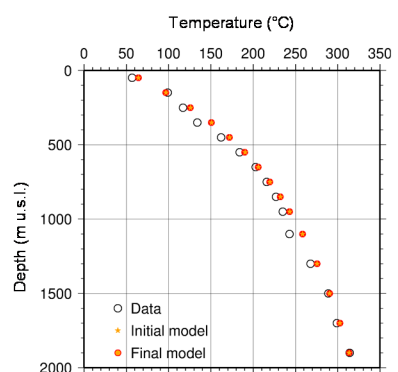


FIGURE 18: Temperature measured and simulated in Well MT43

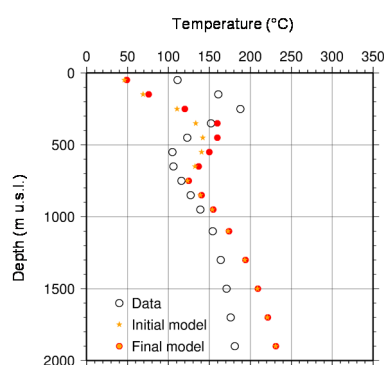


FIGURE 19: Temperature measured and simulated in Well RMT1

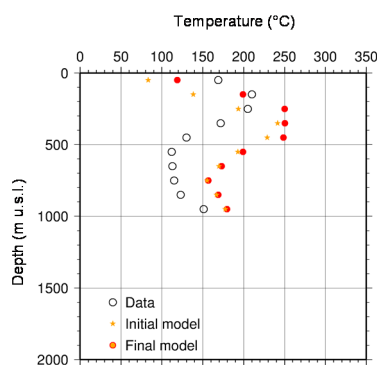


FIGURE 20: Temperature measured and simulated in Well RMT18

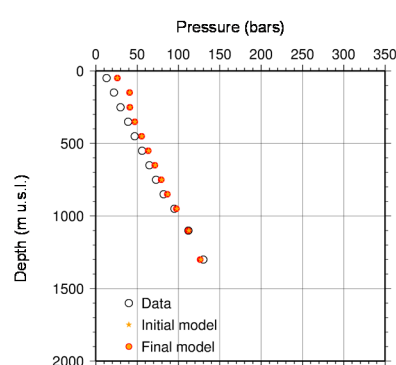


FIGURE 21: Pressure measured and simulated in Well MT23

In the natural state model, 3.3 kg/s of 1504 kJ/kg enthalpy and 330°C temperature were needed to match the temperature and pressure data presented above. The cold water lateral recharge into CLDin in the east was estimated as 0.55 kg/s of 101°C fluid.

Figure 22 presents a cross-section of the initial temperature distribution in the 2D model and the mass fraction of the deep geothermal water component in the natural state. Additionally, the graph shows that the computed model is filled by geothermal water with the exception of its shallow east corner where some free convection of the cold groundwater takes place.

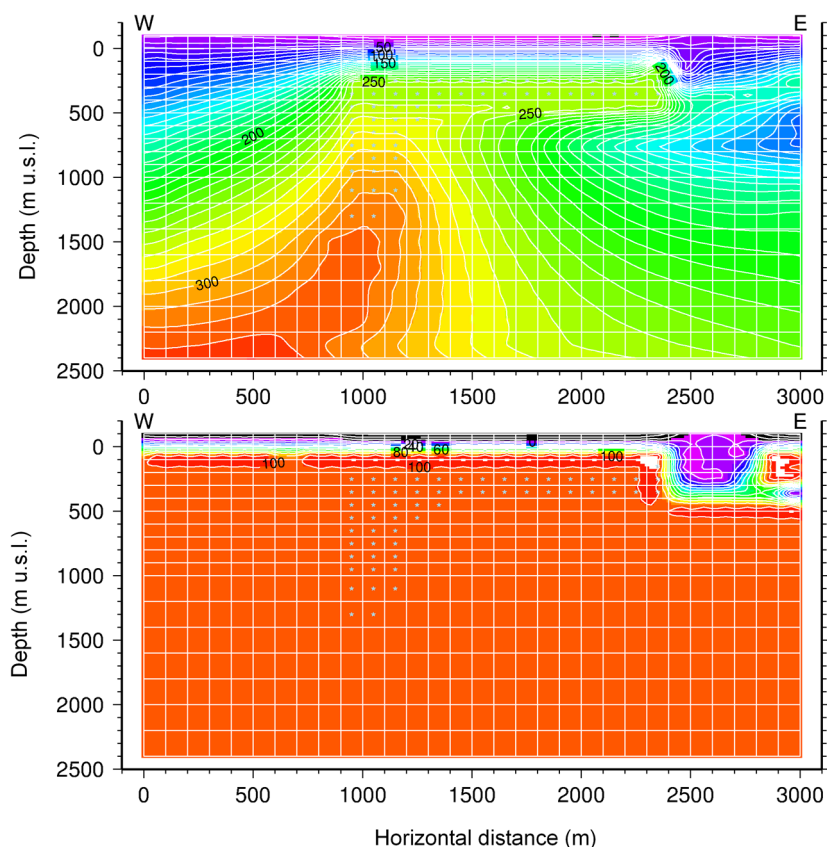


FIGURE 22: Cross-section of the initial temperature distribution and the mass fraction of the deep geothermal water component

6.2.8 Simulation results for production data

Figure 23 shows a cross-section of the final (end of year 2012) temperature distribution, mass fraction of the original geothermal water and computed reservoir cooling. A prominent feature is the invasion of fresh water from the surface near the east boundary into the shallow reservoir. It is evident that this incursion caused dilution in the chloride concentration of the production wells located in the shallow reservoir. The cross-section in Figure 23 supports the theory that many shallow wells suffer in temperature due to invasion of cold water into the reservoir.

The re-injected brine has a higher chloride concentration than the geothermal reservoir fluid and continued recirculation of the brine will result in gradually increasing the chloride concentration of the produced brine. The chloride concentration when production started was high, indicating that before the freshwater incursion started to affect the composition of the reservoir fluid, it was being affected by progressive boiling.

In Figure 24 we can see enthalpy with time of Well MT12 gradually decreasing. In Figure 25 we can see enthalpy with time of the shallow production Well MT27; when production in the second unit started, the enthalpy increased but then decreased, possibly due to fast inflow of low-temperature groundwater.

In Figure 26 we can see the pressure drawdown of the monitoring Well MT11 that is located above the upflow zone. The match between measured and simulated pressure drawdown is reasonable and can only be improved by a more thorough description of the well's flow history in a 3D model.

The chloride concentration with time was used to detect mixing of groundwater with deep recharge fluid. Decreases in the chloride concentration implied intrusion of low-temperature and low-salinity groundwater into the reservoir. Intrusion of low-temperature ground water into the reservoir and extensive boiling in the shallow reservoir due pressure drawdown induced cooling in the reservoir.

In Figure 27 we can see that the computed chloride concentration decreased with time in line with observations. This observation is, therefore, apparently of value in numerical model calibrations and should be of value in future numerical models made for Momotombo.

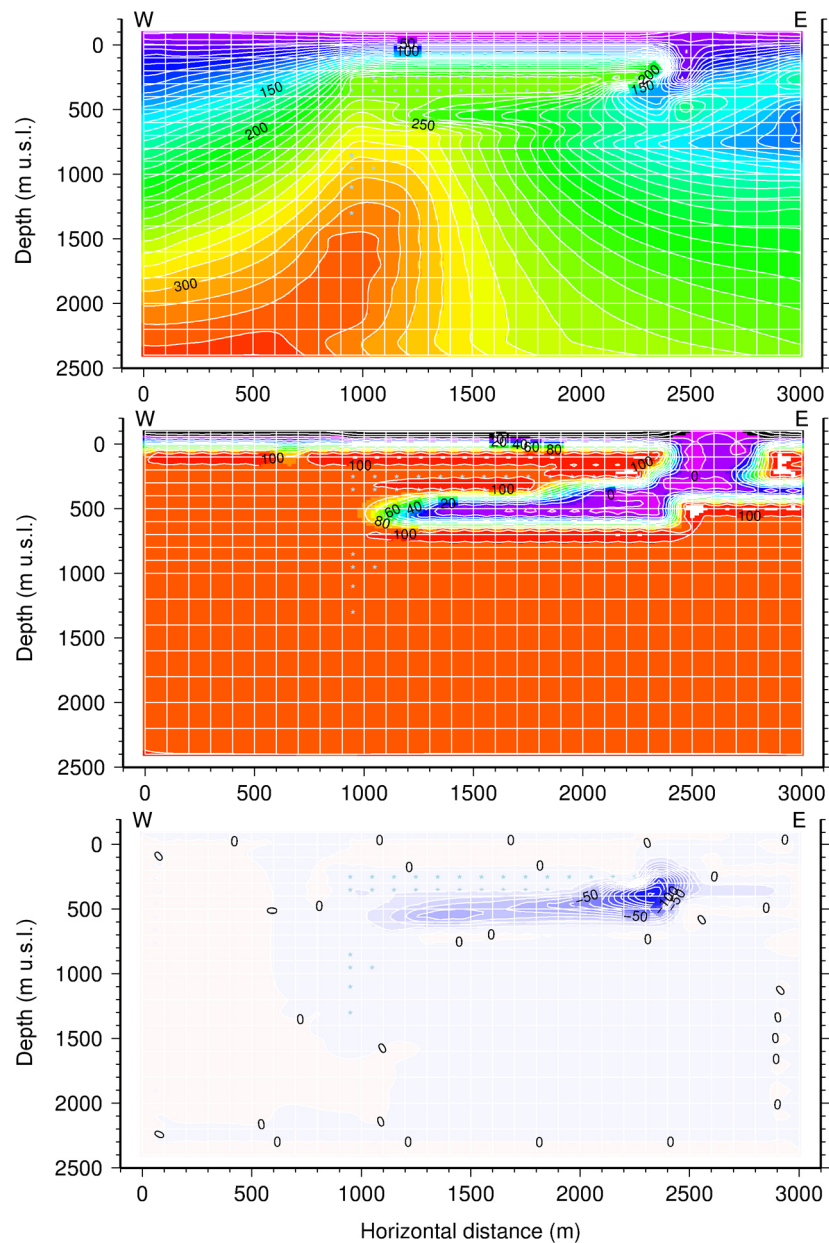


FIGURE 23: Cross-section of the final temperature distribution, mass fraction of the groundwater component and cooling model

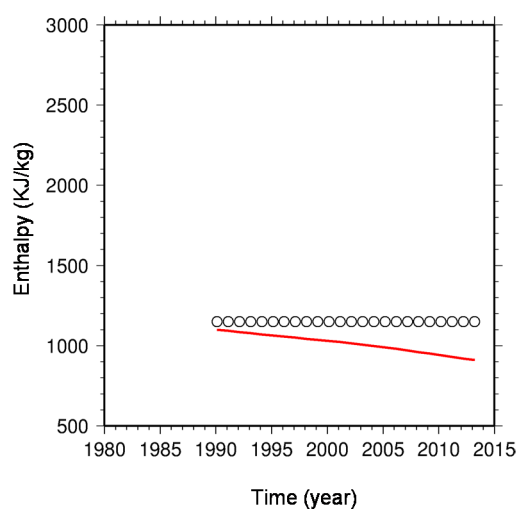


FIGURE 24: Enthalpy in Well MT12

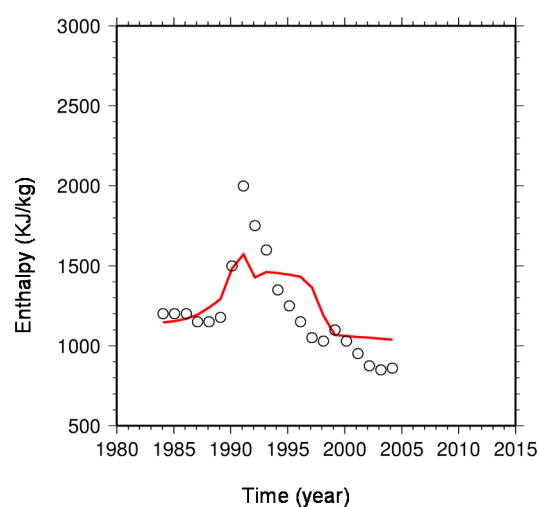


FIGURE 25: Enthalpy in Well MT-27

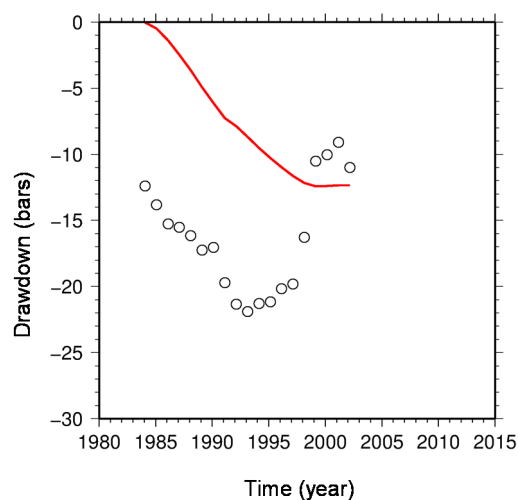


FIGURE 26: Pressure drawdown, measured and simulated, in Well MT11

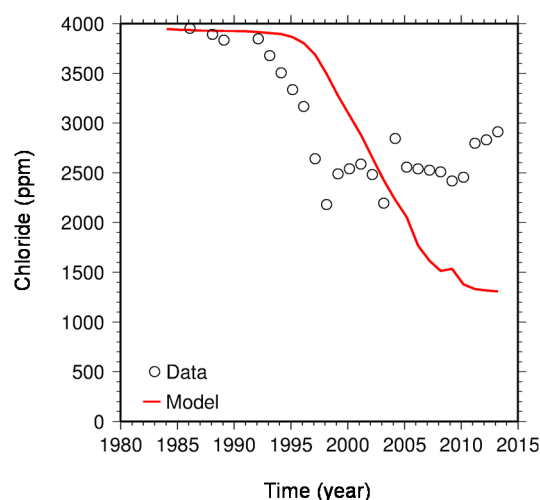


FIGURE 27: Chloride concentration in Well MT27

7. CONCLUSIONS

The main purpose of the present work was to verify the generating capacity estimates by modelling and to see if chloride changes could support the calibration of a 2D iTOUGH2 model.

The main conclusions of this work are as follows:

1. The large data base at hand allowed for simple lumped volumetric and distributed parameter numerical modeling.
2. The Monte Carlo volumetric method was used to assess the proven and possible production. The most likely values of the power production capacity is 20 MWe and 50.5 MW, respectively, for 25 years of plant life.
3. The volumetric assessment indicated that the current 30 MW production complies with the proven reservoir size.
4. More power production is a scenario only if the proven resource area can be increased.
5. The total production data and pressure drawdown could be simulated satisfactorily by one and two-tank open models.

6. The two-tank open models yielded a reservoir volume in the 4 km³ range, the same as the estimated proven reservoir volume in the Monte Carlo method. Reservoir permeability ranges from 75 to 230 mD.
7. iTOUGH2 simulation indicated that chloride concentration is a good parameter for future studies. Decreases in chloride concentration imply intrusion of low-temperature and low-salinity groundwater into the reservoir. Intrusion of low-temperature groundwater into the reservoir and extensive boiling in the shallow reservoir due pressure drawdown induced cooling in the reservoir.
8. The chloride concentration simulation infers that about half of the current reservoir fluid is diluted by cold water invasion from Lake Managua.
9. This cold fluid invasion is the primary origin of the various wellfield operational challenges faced in Momotombo.

It is recommended that a 3D model should be simulated to study the change in chloride concentration over time in all the production wells; such a model would complement the existing study by Porras (2005) while being better constrained for assessing the impact of the cold water inflow. This is a sizeable endeavor which would require man and computer power. But such a study would assist in optimizing the power production in the near future.

ACKNOWLEDGEMENTS

I want to extend my sincere gratitude to the Government of Iceland, the United Nations University Geothermal Training Programme and the Government of Nicaragua for giving me the opportunity to participate in this training. My heartfelt gratitude goes to Dr. Ingvar B. Fridleifsson and Mr. Lúdvik S. Georgsson for their support in completing this training. I also thank very much Ms. Thórhildur Ísberg, Mr. Ingimar Gudni Haraldsson, Mr. Markús A. G. Wilde and Ms. Málfríður Ómarsdóttir for their help during these six months and for making me feel welcome in Iceland. I convey my good wishes to all the lecturers and staff of Orkustofnun and ÍSOR.

Sincere thanks to my supervisor, Mr. Grímur Björnsson for being an excellent guide in the development of this report. I also want to thank Ms. Saeunn Halldórsdóttir and Dr. Gudni Axelsson for their help. Thanks so much to all UNU Fellows class 2013 for their support during the last six months, especially Claudia and Angel for their friendship, encouragement and for making this the best experience away from home.

I would like to express my appreciation to my company, Empresa Nicaragüense de Electricidad for allowing me to participate in this training and I extend my thanks to my boss, Ms. Melba Sú, for her support and confidence in me and to all my colleagues at the Geochemistry Laboratory for their valuable assistance.

Finally, I want to thank God for giving me wisdom, strength and knowledge to be able to finish my final project. Thanks to all my family, especially my mom; without your love and dedication, nothing would have been possible. Thanks, CM; love you.

REFERENCES

Arnórsson, S., Sánchez, M., Miranda, K., 1996: *Interpretation of geochemical and isotopic data from well discharges in the Momotombo Geothermal Field, Nicaragua, with recommendations on monitoring studies*. IAEA, 41 pp.

Axelsson, G., and Arason, P., 1992: *LUMPFIT, automated simulation of pressure changes in hydrological reservoirs. Version 3.1, user's guide*. Orkustofnun, Reykjavík, 32 pp.

Axelsson, G., Björnsson, G. and Quijano, J., 2005: Reliability of lumped parameter modeling of pressure changes in geothermal reservoirs. *Proceedings of the World Geothermal Congress 2005, Antalya, Turkey*, 8 pp.

Björnsson, G., 2008: Review of generating capacity estimates for the Momotombo geothermal reservoir in Nicaragua. *Geothermal Resources Council Transactions*, 32, 341-346.

Combredet, N., Guilhaumou, N., Cormy, G. and Martínez, E. 1987: *Petrographic correlation and analysis of fluid inclusions in hydrothermal quartz crystals in four wells in the Momotombo geothermal field, Nicaragua*. Instituto Nicaragüense de Energía, Managua, Nicaragua, internal report (in Spanish), 32 pp.

Cordón, U., 1980: Momotombo field models at six stages in time. *Geothermal Resources Council Transactions*, 4, 443-446.

Egilsson, Th., Halldórsdóttir, S., Espinales, A., Ruiz, F., Matus, I., Gonzalez, M., Ruiz, J., and Quintero, R., 2012: *Assessment of the Momotombo geothermal field in Nicaragua*. ÍSOR -Iceland GeoSurvey, report ÍSOR-2012/010, 225 pp.

Einarsson, S.S., 1977: Study of the temperature distribution in the geothermal reservoir at Momotombo and its implications. U.N.O.T.C. technical report NIC/74/003.

Finsterle, S., 1999: *iTOUGH2 User's guide*. Lawrence Berkeley National Laboratory, Berkeley, California, United States, Report LBNL-40040.

González B.M., 1990: *Analysis of wellbore temperatures and pressure in the Momotombo geothermal field, Nicaragua*. UNU-GTP, Iceland, report 5, 29 pp.

González S.M., 1990: *Initial temperature of Momotombo geothermal field*. UNU GTP, Iceland, report 6, 43 pp.

Kaplan, U., 2004: Geothermal cold brine injection. Two years experience in the Momotombo Field, Nicaragua. *Geothermal Resources Council Transactions*, 28, 59-64.

López, C.V., and Eckstein, Y., 1980: Six month production test at Momotombo. Preliminary results. *Geothermal Research Council Transactions*, 4, 357-360.

López, C.V., Hoyt, B.R. and Eckstein, Y., 1980: Subsurface temperature distribution and structure of the geothermal reservoir at Momotombo, Nicaragua. *Geothermal Research Council Transactions*, 4, 459-462.

Muffler, L.P.J. (editor), 1979: *Assessment of geothermal resources of the United States - 1978*. USGS Circular 790, Arlington, VA, United States, 163 pp.

Parello, F., Aiuppa, A., Calderon, H., Calvi, F., Cellura, D., Martinez, V., Militello, M., Vammen, K., and Vinti, D., 2008: Geochemical characterization of surface waters and groundwater resources in the Managua area (Nicaragua, Central America). *Applied Geochemistry*, 23, 914-931.

Porras, M.E., 1991: *Production characteristics of the Momotombo geothermal field, Nicaragua*. UNU-GTP, Iceland, report 10, 54 pp.

Porras, E., 2005: *Development of numerical model of the Momotombo geothermal field, Nicaragua*. Kyushu University, Fukuoka Japan, PhD thesis, 207 pp.

Porras, E., 2006: The Momotombo reservoir performance upon 23 years of exploitation and its future potential. *Paper presented at "Workshop for Decision Makers on Geothermal Projects in Central America", organized by UNU-GTP and LaGeo in San Salvador, El Salvador*, 10 pp.

Porras, E., 2008: Twenty five years of production history at the Momotombo geothermal field, Nicaragua. *Paper presented at "30th Anniversary Workshop of the United Nations University Geothermal Training Programme", organized by UNU-GTP in Reykjavik, Iceland*, 7 pp.

Porras, E., 2009: Geophysical exploration of the Momotombo Geothermal Field, Nicaragua. *Paper presented at "Short course on surface exploration for geothermal resources", organized by UNU-GTP and LaGeo in Ahuachapán and Santa Tecla, El Salvador*, 9 pp.

Porras, E., 2012: Stimulating wells – The experience in the Momotombo geothermal field, Nicaragua. *Paper presented at "Short Course on Geothermal Development and Geothermal Wells", organized by UNU-GTP and LaGeo in Santa Tecla, El Salvador*, 8 pp.

Porras, E., and Björnsson, G., 2010: The Momotombo reservoir performance upon 27 years of exploitation. *Proceedings of the World Geothermal Congress 2010, Bali, Indonesia*, 5 pp.

Pruess, K., Oldenburg, C., and Moridis, G., 1999: *TOUGH2 User's guide, version 2.0*. Lawrence Berkeley National Laboratory, report LBNL 43134, Berkeley, CA, United States, 197 pp.

Quijano, J.L., 1989: *Chemical and isotopic composition of the production fluids in the Momotombo field, Nicaragua*. INE, Nicaragua, internal report, 15 pp.

Sanyal, S.K., and Sarmiento, Z.F., 2005: Booking geothermal energy reserves. *Geothermal Resource Council Transactions*, 29, 467-474.

Sarmiento, Z.F., and Steingrímsson, B., 2008: Computer programme for resource assessment and risk evaluation using Monte Carlo simulation. *Paper presented at "Short course on Geothermal Project Management and Development", organized by UNU-GTP, KenGen, DGSM, in Entebbe, Uganda*, 11 pp.

Sarmiento, Z.F., and Steingrímsson, B., 2011: Resource assessment I: Introduction and volumetric assessment. *Paper presented at "Short course on Geothermal Drilling, Resource Development and Power Plants", organized by UNU-GTP and LaGeo, in Santa Tecla, El Salvador*, 15 pp.

Verma, M.P., Martínez, E.M., Sánchez, M., Miranda, K., Gerardo, J.Y., and Araguas, L., 1996: Hydrothermal model of the Momotombo geothermal system, Nicaragua. *Proceedings of the 21st Workshop on Geothermal Reservoir Engineering, Stanford University, Stanford, CA, United States*, 29–34.

Williams, C.F., 2007: Updated methods for estimating recovery factors for geothermal resources. *Proceedings of the 32nd Workshop on Geothermal Reservoir Engineering, Stanford University, Stanford, CA, United States*, 7 pp.



1D JOINT INVERSION OF TEM AND MT DATA: SUSWA GEOTHERMAL FIELD, RIFT VALLEY, KENYA

Yussuf N. Mohamud

Geothermal Development Company, Ltd. – GDC
P.O. Box 17700 – 2010
Nakuru
KENYA
ynoor@gdc.co.ke

ABSTRACT

Suswa geothermal prospect is the southernmost trachyte shield volcanic complex at the base of the Kenyan Rift floor. It is located about 15 and 30 km to the south of Mt. Longonot and Olkaria Domes, respectively, and is characterized by 2 nested calderas. The last volcanic activity in the area occurred less than 400 years ago in the inner caldera. Geothermal surface indicators are in the form of fumaroles, alterations, young lavas and geothermal grass. Unique to Mt. Suswa among the volcanic complexes in the rift axis is its phonolitic composition in addition to trachyte and pyroclastic formations. The main structures in the area trend N-S, ENE-WSW and along the caldera ring structures. The main recharge is from the rift flanks to the east and west of the prospect area.

The result from resistivity surveys using 1D joint inversion of MT and TEM data indicates the presence of a deep conductor at 4000 m b.s.l. in the Kisharo area, a dominant resistive structure at sea level (0 m) and a conductive layer between 1000 m a.s.l. and 1500 m a.s.l. The deep conductor below the caldera could be the heat source of the prospect. A profile (profile 2) across the southern slopes of Mt. Suswa reveals a deep lying conductor in pockets between 7500 and 3000 m b.s.l., while above 0 m, near parallel conductive layers are prominent.

In the Kisharo area at the floor of the outer caldera, with intense fumarolic activities, the resistivity is high near the surface, probably due to dry steam associated with a deep groundwater table.

1. INTRODUCTION

Suswa geothermal prospect is located in the southern part of the Kenyan Great Rift floor in a chain of geothermal prospects along major tectonic structures extending from Lake Turkana in the north to Lake Magadi in the south (Figure 1). At the southernmost exit of the volcanic shield complex is Mt. Suswa, a large trachytic shield volcano with two nested summit calderas that erupted trachyte, phonolite lavas and tuffs from 240 to >100 ka (White et al., 2012). The inner caldera is composed of an annular ring, and a central resurgence block (island block) which formed as a result of uplift. It is about 4 km in diameter. The outer caldera measures 12 by 10 km, oriented ENE-WSW (Lagat, 2003). The prospect area extends more than 700 km² and stands 800 m above the rift floor with the highest elevation point

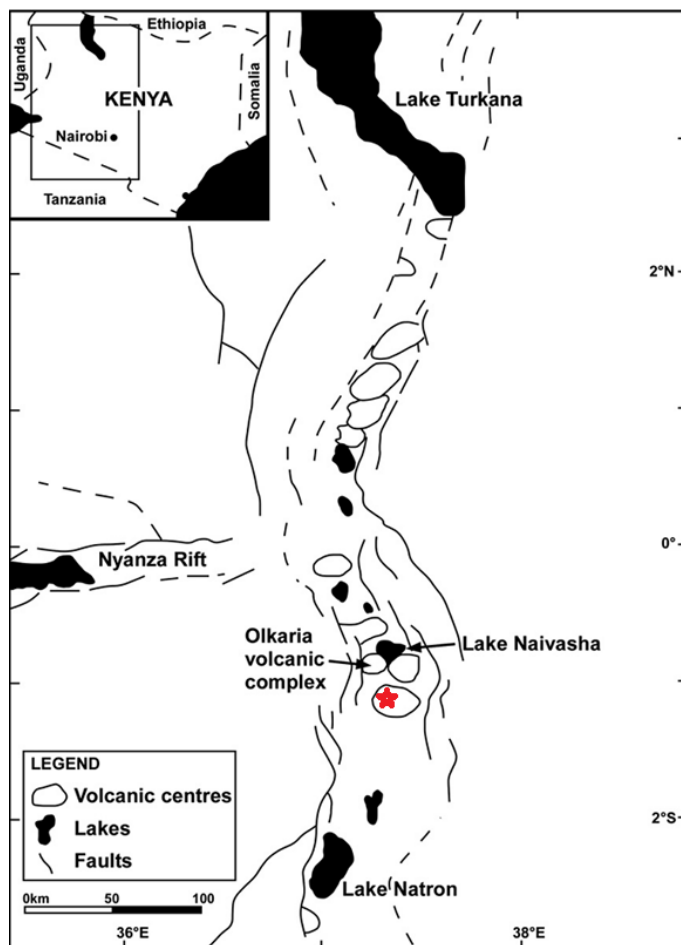


FIGURE 1: Map of the Kenya Rift faults showing the major Quaternary central volcanoes and the location of the Suswa volcanic shield complex (red star) (modified from Karingithi et al., 2010)

resistivity survey methods were used due to their direct relationship to the properties of the subsurface that characterize a geothermal reservoir such as salinity, temperature, permeability, porosity, water rock interaction and alteration (Hersir and Björnsson, 1991).

The main objective of this work is to process the data collected in Suswa using magnetotelluric (MT) and transient electromagnetic methods (TEM), 1D joint inversion of TEM data and statically shift corrected MT data, and to generate iso-depth maps and cross-sections using *TemX* and *TEMTD* Linux based programs developed at Iceland GeoSurvey (ISOR) by Árnason (2006a and 2006b).

2. RESISTIVITY OF ROCKS

Electrical resistivity is the most powerful geophysical method in geothermal prospecting and uses the basic Ohm's law in detecting geothermal signatures in subsurface rocks. The common principle of all electric methods is to induce currents into the ground and monitor the signal generated at the surface by current distribution (Hersir and Björnsson, 1991). These are detected because of resistivity contrasts caused by several factors in the otherwise resistive rock. Geothermal fluids, altered rocks, recharge conduits and heat sources are all characterized by low resistivity. However, since apparent resistivity is measured, it needs to be transformed into specific resistivity which depends on the material.

of 2356 m above sea level. The annular ring is phonolitic in composition and it is where the latest volcanic activity took place less than 400 years before the present (BP) (GDC, 2013).

The presence of young lava and fumaroles indicates a thermally active surface at depth. McCall and Bristow (1965) attributed extensive fumarolic activity in Suswa at the present time to emitted steam, probably derived from meteoric water but charged with CO₂ and probably nitrogen. The manifestations are found within the outer caldera floor, caldera walls and on the slopes of the volcano, especially the southern slopes in Soitamurt where they occur in the form of altered grounds, steaming grounds and fumaroles. The hottest fumarolic activities occur along the wall of the inner caldera (GDC, 2013).

Surface studies by Omenda (1997), Geothermal Development Company in 2013 and KenGen in 1993-94 all indicated possibilities of a high-temperature field in Suswa despite the fact that no exploration wells have yet been drilled in the area.

Geophysical methods as part of geoscientific exploration techniques are the key to geothermal resource assessment before drilling. In Suswa, MT and TEM

The specific resistivity, ρ , defined through Ohm's law, states that the electrical field strength E (V/m) at a point in a material is proportional to the current density, j (A/m²):

$$E = \rho j \quad (1)$$

Resistivity ρ (Ωm) is also defined as the ratio of potential difference ΔV (V) to the current I (A) across a material with a cross-sectional area of 1 m² which is 1 m long:

$$\rho = \Delta V / I \quad (2)$$

Solid rocks are natural insulators unless their properties are altered to a porous media by geophysical or geochemical processes, thereby increasing their conductivity level. The main determinants of rock conductivity near earth surfaces are porosity and conductivity of fluid, dependent on salinity and temperature which changes with depth and region (Vozoff, 1990). Additionally, the type of fluid and saturation level, degree of alteration and mineral assemblages further affect the conductivity of a porous rock. The conduction mechanisms in a geothermal system are due to free ions and fluids in the porous rock and electrons in minerals at the water-rock interface (Flóvenz et al., 2012).

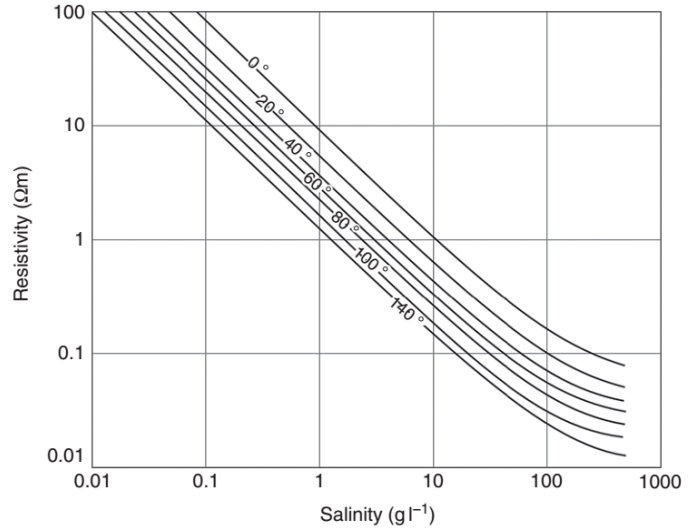


FIGURE 2: The resistivity of solutions of NaCl as a function of concentration and temperature (Flóvenz et al., 2012; based on Keller and Frischknecht, 1966)

Porosity is defined as the ratio of pores to the total volume of the rock. The degree of its interconnectedness (effective porosity) affects its effectiveness in enhancing conductivity in the rock matrix. Electric conduction in water-saturated porous rocks occurs mainly along pores of interconnected fractures in a volcanic zone. The resistivity of porous rock is correlated to porosity by the inverse square given by Archie's law (Archie, 1942):

$$\rho = \rho_w a t \varphi_t^{-n} \quad (3)$$

where ρ = Bulk (measured) resistivity (Ωm);
 ρ_w = Resistivity of the pore fluid (Ωm);
 φ_t = Fracture porosity as a proportion of the total volume;
 a = Empirical parameter ($^{\circ}\text{C}^{-1}$);
 t = Temperature ($^{\circ}\text{C}$);
 n = Cementing factor, an empirical parameter.

2.1 Salinity

Equivalent salinity of NaCl is used to illustrate the relationship between conductivity and salinity at different temperatures since NaCl is the dominant conductive species in geothermal fluids at depth (Ussher et al., 2000). The conduction is by mobile ions in a salt solution. Figure 2 shows the linear relationship between salinity and conductivity as expressed in Equation 4:

$$\sigma \approx \frac{C}{10} \quad (4)$$

where C (g l⁻¹) is the concentration of NaCl until at very high salinities beyond that of a geothermal reservoir.

2.2 Temperature

Resistivity of an aqueous solution at temperature 0-200°C decreases with increasing temperature, due to the increasing mobility of the ions caused by a decrease in the viscosity of the water (Figure 3).

For temperatures above 150°C, the mobility of free charges is affected by changes in viscosity, density and dielectric permittivity of the water causing conductivity to diverge from a linear relationship (Figure 2) and decreases with increasing temperature above 250°C (Flóvenz et al., 2012).

As depth increases, porosity and permeability decrease due to an increase in pressure. Pore fluid in the rock enters into a vapour phase because of the high temperature and pressure. Hence, at great depth in the crust and mantle, water is not a major medium of conduction. In most of the minerals, at depth, conductivity increases exponentially with an increase in temperature but decreases with pressure (Vozoff, 1990); this relationship was given in an Arrhenius formula and is illustrated in Figure 3:

$$\sigma = \sigma_0 e^{-\left[\frac{(E_a + P\Delta V)}{kT}\right]} \quad (5)$$

where σ = Matrix conductivity (S/m);
 σ_0 = Conductivity at infinite temperature (S/m);
 E_a = Activation energy (J);
 P = Pressure (Pa);
 ΔV = Activation volume (m³);
 k = Boltzmann's constant (m² kg/s²K⁻¹);
 T = Absolute temperature (K).

When basalts are subjected to a temperature in the range of 400-900°C in a laboratory study, it gives E_a (0.8) and σ (300). This indicates that the rock resistivity is in the order of 1000 Ωm at 400°C and decreases to 10 Ωm at 800°C. Further increase in temperature will cause partial melts in the rock matrix and decrease the resistivity. In a geothermal environment where temperatures above 400°C are expected in the root of the system, the matrix conductivity will influence the overall conductivity (Flóvenz et al., 2012).

2.3 Resistivity of high-temperature areas and alterations

In a typical high-temperature geothermal system, resistivity is high in unaltered cold formations near the surface. As temperature progressively increases from 50 to 100°C with depth, low-temperature mineral alterations such as smectite and zeolites are formed making the rocks conductive due to their loosely bound cations. Resistivity increases again at moderately high temperatures of about 230-240°C, where the clay minerals are gradually replaced by chlorite as the dominant alteration minerals in the transition zone of mixed-clay layers. At higher temperatures exceeding 250°C, epidote and chlorite dominate, and the system is more resistive due to the bounded ions in the crystal lattice (Árnason et al., 2010).

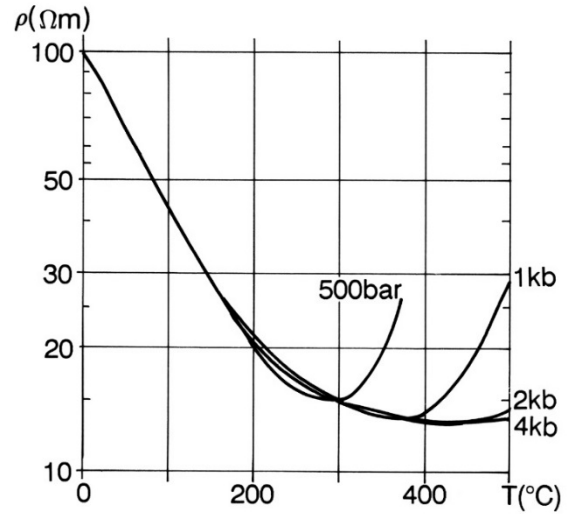


FIGURE 3: Resistivity of a NaCl solution as a function of temperature and pressure (Flóvenz et al., 2012; based on Quist and Marshall, 1968)

The primary minerals in the host rock matrix are transformed into different minerals because of water–rock interaction and chemical transport by the geothermal fluids. Formation of alteration minerals depends on temperature, the types of primary minerals and the chemical composition of the geothermal fluid while the intensity of alteration is controlled by porosity and permeability (Flóvenz et al., 2012). The relationship between resistivity, temperature, alteration and the conduction mechanism in a typical high-temperature basalt-dominated volcanic geothermal field is synopsized in Figure 4.

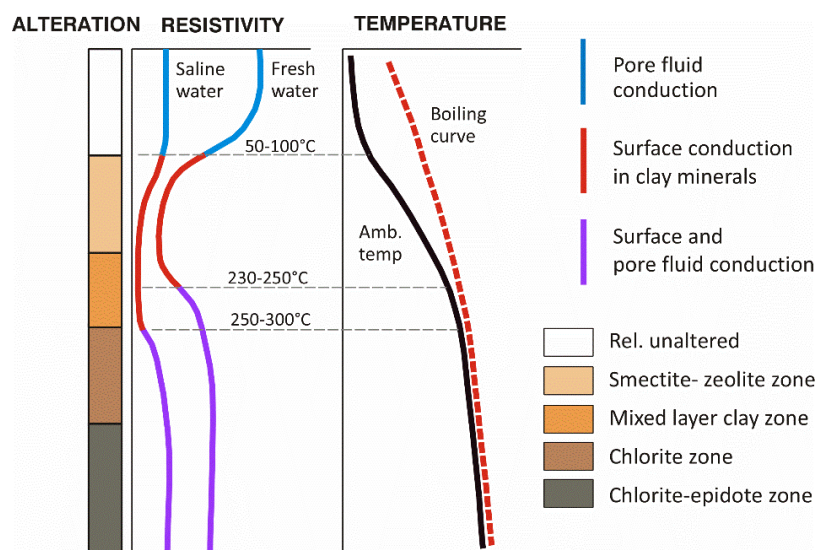


FIGURE 4: General subsurface resistivity, hydrothermal alteration, temperature, and conduction mechanism of the basaltic crust in Iceland (Flóvenz et al., 2012; based on Flóvenz et al., 2005)

For a long time researchers all over the world were puzzled by the high-resistivity core at depth which could not really be explained. It was expected that resistivity would decrease with an increase in temperature at depth until the late 80s when the cause of the resistive core at depth was established as being due to high-temperature alteration minerals; this became a model to be used all over the world in high-temperature volcanic systems (Figure 5). If the temperature that formed alteration minerals prevails, then subsurface temperature can be projected from resistivity structures. Thus, a resistivity structure is regarded as exhibiting the ultimate temperature since alteration is not affected by cooling in general. When alteration minerals indicate lower temperature than that measured in a well, it shows an immature system still undergoing heating up with alteration lagging behind, hence, not being in thermal equilibrium yet. However, when alteration minerals show higher temperature than that measured in a well, it is an indication of cooling in the system (Árnason et al., 2010 and Flóvenz et al., 2012). It is, therefore, prudent to not only confirm the shallow conductors and the resistive core but more importantly the deep-sited heat source before drilling to confirm the resources during geophysical surveys.

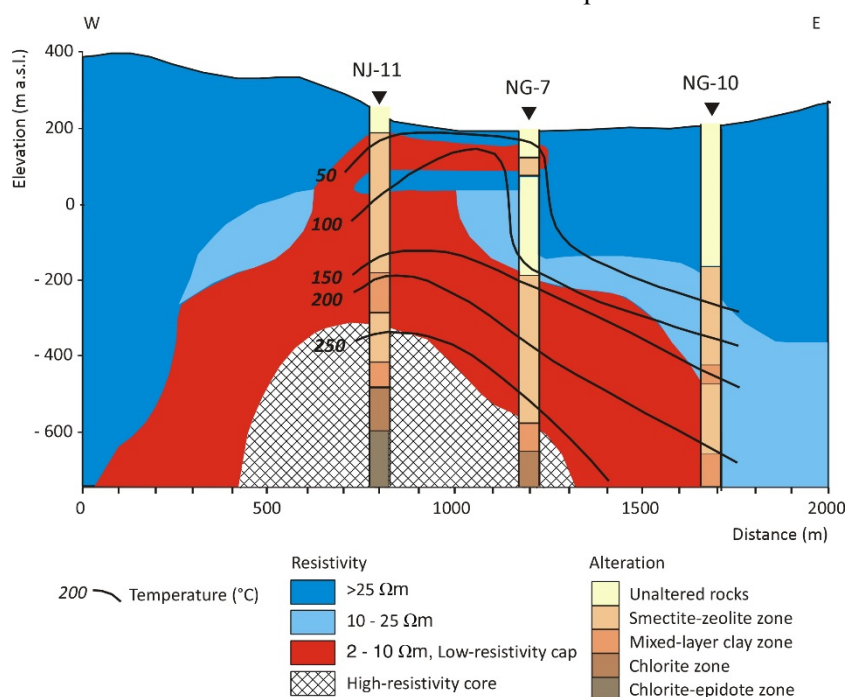


FIGURE 5: Classic example of a high-temperature geothermal system showing a resistivity cross-section from Nesjavellir geothermal field, SW-Iceland, alteration zoning and temperature (Árnason et al., 1987)

Hersir and Árnason (2009) indicated that similar resistivity structures in high-temperature geothermal fields hosted in volcanic rocks were globally characterized by convex structures. The general picture is of a low-resistivity zone doming up in the outer margin of a reservoir, underlain by higher resistivity and a resistive core. This is shown in Figure 5, which comes from a DC resistivity survey conducted in the Nesjavellir area, SW-Iceland in 1985 and 1986, detailing the picture of the resistivity structure in the uppermost 1 km compared with data from nearby boreholes.

3. RESISTIVITY SURVEY AND DATA COLLECTION

The use of resistivity methods in geothermal research started in the 1940s; by the 1960s these were the most important geophysical methods in surface exploration, delineating geothermal resources and production fields. The parameter of interest is the electrical resistivity which, in geothermal areas, gives information on temperature and rock alteration with depth, the major factors for understanding geothermal systems (Georgsson and Karlsdóttir, 2009).

The main principle common to all electrical methods is that electrical current is induced into the earth either directly (DC) or indirectly from a control source (TEM) or a natural source (MT) which generates an electromagnetic signal that is monitored at the surface (Georgsson and Karlsdóttir, 2009). In mapping resistivity variations with depth, sounding methods are used while profiling is applied to measure lateral variation of resistivity along a profile. The most important methods currently in use will be discussed in this chapter.

3.1 DC methods: Schlumberger sounding

Current is injected into the earth through electrodes at the surface (Figure 6a) generating an electrical field measured in square wave response (Figure 6b). Based on the geometry of the set-up, the electrical resistivity of the rock structures below is calculated from Ohm's law, (Equation 1). For a homogeneous earth and a single current source, the relevant equation for the electrical potential, V , at a distance, r , from the current source I , becomes:

$$V_r = \frac{\rho I}{2\pi r} \text{ or } \rho = 2\pi r \cdot V_r / I \quad (6)$$

However, the earth is not homogeneous and what is measured is an average resistivity of the subsurface down to a certain depth penetrated by the current, called the apparent resistivity (ρ_a). Using Equation 6 above, the apparent resistivity can be derived:

$$\rho_a = \frac{\Delta V}{I} \cdot \frac{(S^2 - P^2)\pi}{2P} = K \Delta V / I \quad (7)$$

where $S = AB/2$ and $P = MN/2$, ΔV is the potential difference and K is a geometrical factor.

The basis of operation in Schlumberger soundings lies in the configuration array shown in Figure 6a where the pairs of potential electrodes (MN) are maintained around the centre of the array. Moving MN is not recommended unless it is absolutely necessary to boost the measured signal while maintaining 20% of the distance between current electrodes (Georgsson and Karlsdóttir, 2009). The current electrodes (AB) diverge from the centre in equi-distance in both directions while the distance is increased in steps until the desired current length is reached. The depth of penetration increases with an increase in distance between A and B, which is about 1/3 of the distance between the current electrodes. The results from the response are plotted on a log-log scale for apparent resistivity as a function of $AB/2$ with increasing distance of separation for interpretation.

3.2 TEM method

The principle of operation in the TEM method is well explained in reports by Árnason (1989) and McNeill (1994). It involves transmitting a steady current sourced from a generator or battery pack into an insulated large square loop (300 m × 300 m) laid on the ground (Figure 7) that builds up a magnetic field of known strength. The current in the loop is abruptly turned off in a fraction of a second before it is turned on again. When the current is off, the built-up magnetic field in the loop starts to decay. The resultant decaying primary magnetic field induces secondary electrical currents (eddy currents) in the ground which further induce a secondary magnetic field decaying with time. The current distribution and decay rate of the secondary magnetic field depends on the subsurface resistivity structure of the earth (Árnason, 1989) and the response is monitored on the ground surface by measuring induced voltage in a receiver coil at the centre of the transmitter loop in time gates, as shown in Figure 8. The induced currents are shallow at early time (initial time when a strong eddy current is formed immediately after turn off, close to the transmitter loop) when the current is confined to the transmitter loop, while at late time (when the eddy current has decayed, weakened and travelled down with time) it radiates deeper and away from the loop. Current travels faster in resistive media and slows down within conductive layers (Rowland, 2002).

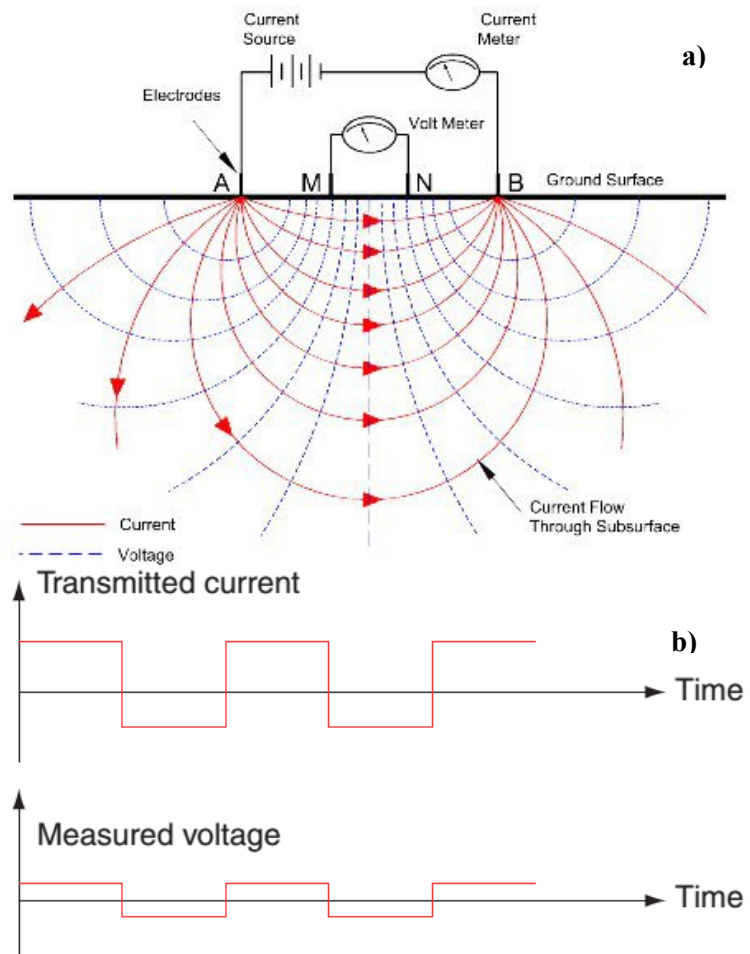


FIGURE 6: a) Field layout Schlumberger (NGA, 2013);
b) typical half-duty square wave current and the corresponding potential signal (Flóvenz et al., 2012)

TRANSMITTER WAVEFORM:

3 Amps.
300 Hz to 3 Hz

TRANSMITTER:
Timing and Switching
Electronics

Tx

RECEIVER ANTENNA:
1m Diameter
Multi-turn, Air Core Coil

RECEIVER:
Sampling and
Stacking Electronics

Rx

TRANSMITTER LOOP:
Single Conductor 10 Gauge Wire

20-200m
(60-600 ft.)

FIGURE 7: TEM field layout (Rowland, 2013)

The depth of penetration depends on the length of induction in the receiver coil after the current is turned off before it get noisy, and the resistivity of the subsurface stratum (Árnason, 2006a; McNeill, 1994). Thus, a low-resistivity stratum will require a longer period of time than the high-resistivity stratum to probe the same depth. Current is turned off linearly in a designated (TOFF) time interval measured by the transmitter and fed to the receiver manually to minimize infinite voltage induction in the source loop when turn off is sudden (Árnason, 1989).

3.2.1 Response curves for a homogeneous earth

The induced voltage in a receiver coil at late time in a homogeneous half space of conductivity, σ , is given by Árnason (1989):

$$V_{t,r} = I_o \frac{C(\mu_o \sigma r^2)^{3/2}}{10\pi^{1/2} t^{5/2}} \quad (7)$$

where

$$C = A_r n_r A_s n_s \frac{\mu_o}{2\pi r^3} \quad (8)$$

where t = Elapsed time after the transmitter current is turned off (s);
 r = Radius of the transmitter loop (m);
 A_r = Cross-sectional area of the receiver coil (m²);
 n_r = Number of windings in the receiver coil;
 μ_o = Magnetic permeability in vacuum (H/m);
 A_s = Cross-sectional area of the transmitter loop (m²);
 n_s = Number of windings in the transmitter loop;
 I_o = Transmitted current (A);
 $V_{t,r}$ = Measured voltage (V).

Equation 8 simulates characteristics of decaying induced voltage through time. The response measured in the receiver coil in a 1, 10 and 100 Ωm resistivity half space is shown in Figure 9 where the induced voltage is steady earlier in time but decreases with time until it reaches late time when induced voltage (V_t) decreases linearly as a function of time (t) logarithmically with a gradient of -5/2. Thus, induced voltage $V(t)$ in a receiver for a late time homogeneous half space with conductivity (σ) is proportional to $t^{-5/2}$ and $\sigma^{3/2}$ as seen in Equation 8. The response in early times depends on resistivity because it increases with an increase in resistivity (Árnason, 1989).

Figure 10 shows apparent resistivity approaching true resistivity of a homogeneous half space at late time as resistivity values reduce and the receiver voltage increases due to the presence of all the current after turn off. Apparent resistivity is based on the time behaviour of the receiver coil output voltage at

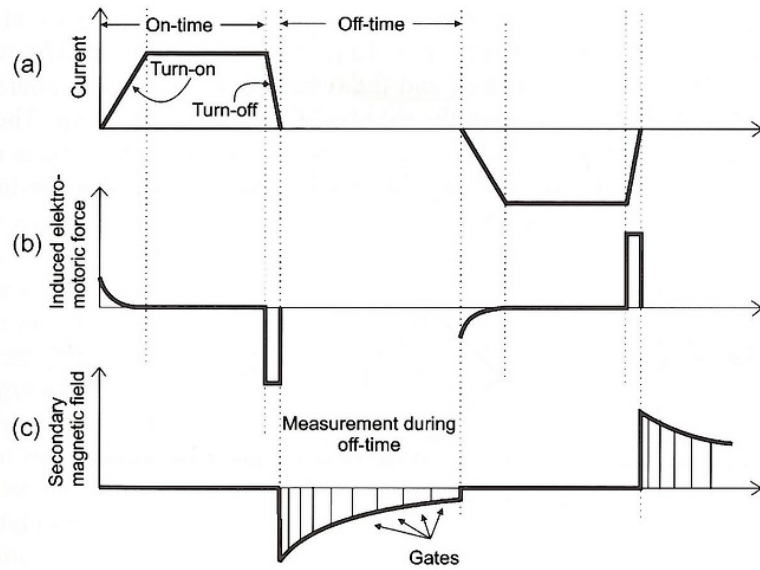


FIGURE 8: Basic principles of TEM method: a) Current flow in the transmitter loop; b) Induced e.m.f. in the ground; c) Secondary magnetic field measured after the current is turned off in the receiver coil assumed to be at the centre of the transmitter loop (Christensen et al., 2006)

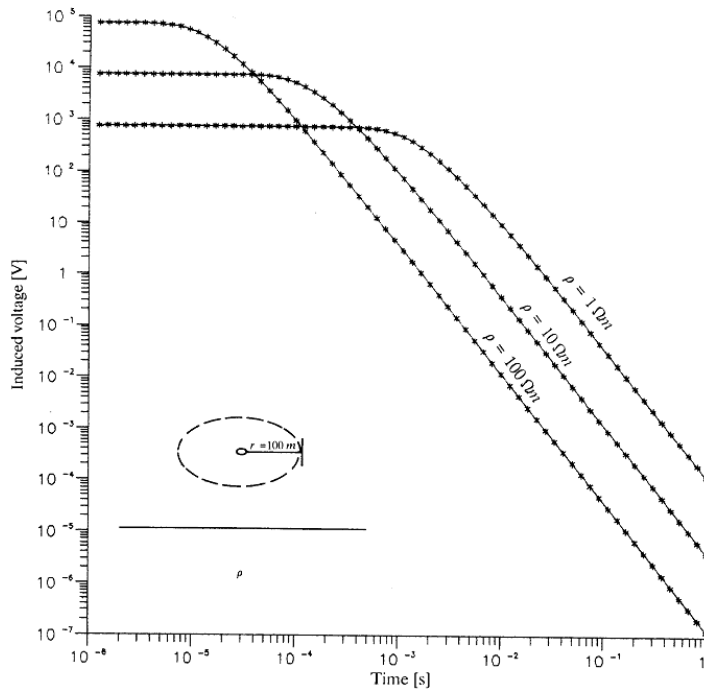


FIGURE 9: Voltage response for a homogeneous half-space (Árnason, 1989)

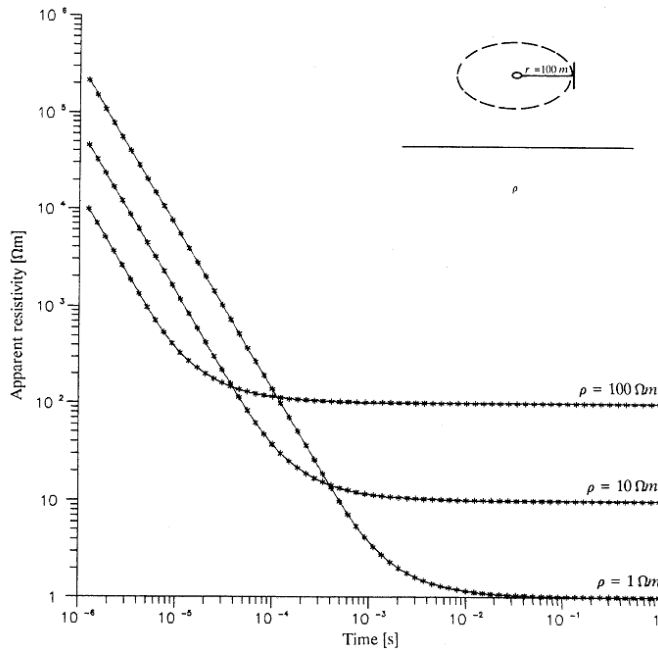


FIGURE 10: Late time apparent resistivity for a homogeneous half-space (Árnason, 1989)

late time when it decays as $t^{-5/2}$. At early time when current is entirely in the upper layers, the receiver voltage is too low, thus apparent resistivity is too high (McNeill, 1994). Apparent resistivity, ρ_a , of a homogeneous half-space in terms of induced voltage at late times after the source current is turned off is given by (Árnason, 1989):

$$\rho_a = \frac{\mu_0}{4\pi} \left[\frac{2\mu_0 A_r n_r A_s n_s I_0}{5t^{5/2} V_{t,r}} \right]^{\frac{2}{3}} \quad (9)$$

3.2.2 TEM data acquisition

The TEM data from Suswa field were collected using equipment from Zonge and Phoenix Geophysics (V8). The setup is shown in Figure 7. A loop of 300 m \times 300 m was laid out on the ground by at least two field crew members in a square configuration from a common point where the current source is located. Transmitter and receiver are synchronized using crystal clocks (in-built) so that the receiver knows the exact current turn off time (generated when synchronizing and manually fed into the receiver by the surveyor) to begin recording the decaying voltage. The transmitter and receiver were set to the same frequency while the loop was being laid out to ensure cross communication between them in transmitting and receiving signals. Once the loop was connected, the generator was turned on to transmitted current (10 A) to build-up a strong magnetic field in the loop. The receiver loop and coil were transferred to the centre of the loop, located 212 m from the transmitter for 300 m by 300 m, and 140 m for 200 m by 200 m loop. At the centre of the loop where the readings were recorded through the receiver coil, data were acquired in low and high frequencies. At low frequency, the TEM probes much

deeper and is less influenced by near surface cultural noise, while at high frequencies it measures at shallow depths. Before changing to high frequency reading, the transmitter frequency is manually adjusted before proceeding with data collection in the next frequency phase to ensure the signals transmitted are received at the same frequencies or else no data are collected.

Different coil sizes were used to maximize the receiver readings at different frequencies. A small coil was used to probe at shallow depths at high frequency without saturating the voltage since the current

induced was less. At low frequency reading, the bigger loop induces more current and measures the response at depth in the late time before the signal weakens and is drowned into noise. In shallow depths, a small loop is more effective than a bigger loop, while at great depth the bigger loop is more advantageous. The data were automatically saved in the receiver to be downloaded and processed for inversion and interpretation.

3.3 MT Method

Magnetotelluric (MT) was pioneered by Tikhonov (1950) and Cagniard (1953) in Russia and France, respectively. It is an electromagnetic method that probes electro-stratigraphic structures of the earth from shallow depths to hundreds of kilometres (Hersir and Árnason, 2010). Thus, the basic application of the MT method is to determine the subsurface electrical conductivity of the complex earth from measurements of natural transient magnetic (**H**) and electric (**E**) fields on the surface in orthogonal direction (Hersir and Árnason, 2010).

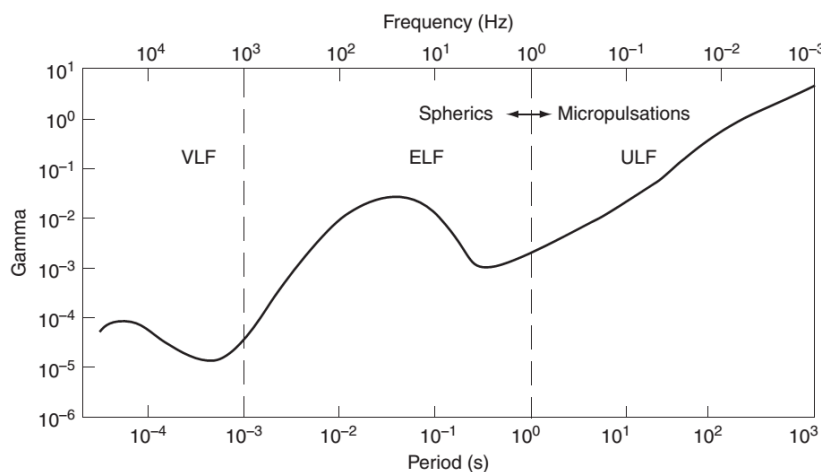


FIGURE 11: Electromagnetic frequency ranges (Flóvenz et al., 2012)

MT superiority over the rest of electrical methods is due to its great depth of subsurface penetration which depends on the range of period it operates in. The longer the period of measurement, the higher is the depth of penetration. Thus, three main categories of 5 channel Magnetotelluric units are classified according to ranges of frequencies/periods they operate in which also determine the depth of penetration (Figure 11). MT operates in the range of 400

Hz – 0.0001 Hz, Audio-MT 100 Hz – 10 kHz and LMT - long period (1000 – 10,000 s). The MT method is passive and uses natural magnetic variations in the geomagnetic field of the earth as its signal source and has no external source of power in its operation except for the data logger powered by batteries.

3.3.1 Sources of the earth's electromagnetic fields

The spectrum of the earth's electromagnetic field varies widely between high and low frequencies. The source of low frequencies (long periods) is ionospheric and magnetospheric currents due to solar wind interference with the earth's magnetic field while high frequencies (short periods) greater than 1Hz are caused by thunderstorms near the equator and distributed as guided waves between the earth and the ionosphere (Hersir and Árnason, 2010).

3.3.2 Field setup and data acquisition

The know-how on instrumentation (Figure 12), data acquisition, processing and interpretation is the fundamental step in the effective use of magnetotelluric equipment which will be highlighted in this report. The main components of a 5-channel

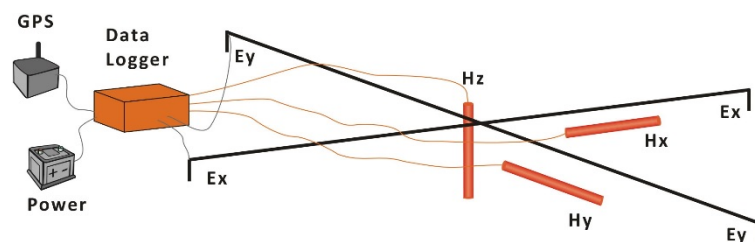


FIGURE 12: Magnetotelluric setup for data acquisition (Flóvenz et al., 2012)

MT data acquisition unit instrument (MTU-5) from Phoenix Geophysics are a data logger (MTU), 2 pairs of electric lines (E_x and E_y) which measure the electric potential differences between the electrode pairs, and 3 magnetic coils (H_x , H_y and H_z) which are sensors for measuring magnetic variations. One pair of electric lines (E_x) is oriented in the N-S magnetic direction while the (E_y) lines are oriented along the E-W magnetic direction. Porous pot electrodes with porous ceramic bottoms at the end of each electric line with $PbCl_2$ solutions installed in wet pits with a solution of NaCl to reduce ground resistance and noise is well illustrated in Phoenix Geophysics' users guide manual (2005). A Global Positioning System (GPS) satellite synchronizes the data, which are recorded and saved onto a data logger in time series digital format into a memory flash card (Flóvenz et al., 2012). A fully charged 12 V battery powers the data logger over the period of data collection, mostly overnight.

In addition to the setup shown in Figure 12, a waterproof canvas is required to cover the battery and data logger to protect the duo from direct contact with water and dust. A compass for orienting the magnetic and electric sensors in horizontal and orthogonal directions and markers (stick) to enhance alignment when orienting electric and magnetic lines are vital. To ensure the magnetic sensors are horizontally laid (H_x and H_y) and that H_z is vertical, a spirit level is used.

MT equipment is calibrated before the start of a new field survey to ensure the equipment is in good working condition and is normalized to the environment for the survey. Both the box (MTU) and magnetic coil sensors are calibrated.

3.3.3 Basic principles

In principle, a naturally occurring time varying fluctuating magnetic field induces an electrical field which further induces an eddy current in the ground, measured on the surface in horizontal (E_x) and orthogonal (E_y) directions. The electric fields are induced by the corresponding source magnetic fields ($E_x H_y$ and $E_y H_x$) orthogonally (Flóvenz et al., 2012); thus, by measuring variations in the magnetic and electrical fields on the surface, subsurface resistivity and phase as a function of the frequency of the electromagnetic field are determined using the four basic Maxwell equations given below:

Faraday's law:

$$\nabla \mathbf{E} = \mu \frac{\partial \mathbf{H}}{\partial t} \quad (10)$$

Ampere's law:

$$\nabla \mathbf{H} = \mathbf{j} + \varepsilon \frac{\partial \mathbf{E}}{\partial t} \quad (11)$$

Gauss's law (electric field):

$$\text{div } \mathbf{D} = \eta \quad (12)$$

Gauss's law (magnetic field):

$$\text{div } \mathbf{B} = 0 \quad (13)$$

where \mathbf{E} = Electrical field (V/m);
 \mathbf{B} = Magnetic intensity (A/m);
 \mathbf{j} = Electrical current intensity (A/m²), and
 $\mathbf{j} = \sigma \mathbf{E}$;
 μ = Magnetic permeability (H/m);
 ε = Electric permittivity (F/m);
 $\mathbf{D} = \varepsilon \mathbf{E}$; and
 $\mathbf{B} = \mu \mathbf{H}$.

3.3.4 Impedance tensor and dimensionality

The impedance tensor (Z) relates the orthogonal components of the horizontal electric and magnetic fields using Maxwell equations to generate resistivity of a homogeneous half space. The phase difference between E_x and H_y is equal to $\frac{\pi}{4} = 45^\circ$.

$$\begin{pmatrix} E_x \\ E_y \end{pmatrix} = \begin{pmatrix} Z_{xx} & Z_{xy} \\ Z_{yx} & Z_{yy} \end{pmatrix} \begin{pmatrix} H_x \\ H_y \end{pmatrix} \quad (\mathbf{E} = \mathbf{ZH}) \quad (14)$$

$$E_x = Z_{xx}H_x + Z_{xy}H_y \quad (15)$$

$$E_y = Z_{yx}H_x + Z_{yy}H_y \quad (16)$$

$$Z_{xy} = \frac{E_x}{H_y} = \sqrt{\omega\mu\rho} e^{i\pi/4} \text{ and } Z_{yx} = \frac{E_y}{H_x} = -Z_{xy} \quad (17)$$

where Z = Impedance tensor;
 $\pi/4$ = Phase difference between the electric and the magnetic field;
 Z_{xy} and Z_{yx} = Characteristic impedance in x and y directions;
 ω = Angular frequency ($2\pi f$) where f is frequency (Hz);
 μ = Magnetic permeability (H/m);
 E_{xy} = Electric field intensity (V/m) in x, y direction;
 H_{xy} = Magnetic field intensity (A/m) in x, y direction.

Each component of the impedance tensor, Z_{ij} , is composed of real and imaginary parts. They have both magnitude and phase.

Resistivity of a homogeneous half space is given by:

$$\rho_{xy} = \frac{1}{\omega\mu} |Z_{xy}|^2 = \rho_{yx} = \frac{1}{\omega\mu} |Z_{yx}|^2 = \rho \quad (18)$$

For an inhomogeneous earth, the apparent resistivity (ρ_a) and phase (θ_a) as a function of frequency can be defined as if the earth was homogeneous using this same formula. In an inhomogeneous earth, the resistivity, ρ , in the Equation above can be written as:

$$\rho_a = 0.2T|Z|^2; \theta = \arg(Z) \neq 45^\circ \quad (19)$$

The apparent resistivity calculated from the off-diagonal elements of the impedance tensor in Equations 18 and 19 are the same for a homogeneous 1D earth. Rotating the impedance tensor for a non-1D earth will change the resistivity values of ρ_{xy} and ρ_{yx} . Thus, during the inversion process, they will give two different models, neither of them necessarily being the correct one. Hence, the rotationally invariant determinant of the impedance tensor, which is a kind of an average value of the apparent resistivity and phase, is used here in the inversion to produce the model (Badilla, 2011). The determinant of the apparent resistivity and phase is calculated by:

$$\rho_{det} = \frac{1}{\omega\mu} |Z_{det}|^2 = \frac{1}{\omega\mu} \left| \sqrt{Z_{xx}Z_{yy} - Z_{xy}Z_{yx}} \right|^2; \theta_{det} = \arg(Z_{det}) \quad (20)$$

3.3.5 Skin depth

The depth below the surface of the conductor where the electromagnetic field has decreased to e^{-1} of its original value is called the skin depth. It is expressed as:

$$\delta = 500\sqrt{\rho T} \quad (\text{m}) \quad (21)$$

where δ is the skin depth (m), ρ is the resistivity of the medium (Ωm) and T is the period (s).

The expression indicates estimated depth of penetration and depends on resistivity and period; the larger the period the deeper the sounding detects the subsurface resistivity.

3.3.6 2D earth

In a 2D earth environment, resistivity varies with depth and in one lateral direction. It is constant in the other horizontal direction (along the electrical strike). MT impedance tensor data are mathematically rotated with one axis perpendicular to the electrical strike and the other axis is parallel to it, by minimizing the off diagonal elements of the impedance tensor. So $Z_{xx} = Z_{yy} = 0$, like in the 1D case, but the difference is that, in 2D, $Z_{xy} \neq -Z_{yx}$:

$$Z_{2D} = \begin{pmatrix} Z_{xx} & Z_{xy} \\ Z_{yx} & Z_{yy} \end{pmatrix} \text{ rotated to give } Z_{2D} = \begin{pmatrix} 0 & Z_{xy} \\ Z_{yx} & 0 \end{pmatrix} \quad (22)$$

In 2D the field is split into two independent impedance tensor modes: E- and B-polarization. Transverse Electric (TE) mode or E-polarization is when the electric field is parallel to the electromagnetic strike and Transverse Magnetic (TM) mode or B-polarization is when the magnetic field is parallel to the electromagnetic strike.

In a 3D case, resistivity varies in all three directions, that is $Z_{xx} \neq Z_{yy}$ and $Z_{xy} \neq -Z_{yx}$ with no possible rotational direction that minimizes the diagonal components to zero (0) at the same time.

Swift skew is expressed below and gives an indication of 1D, 2D or 3D subsurface environment depending on the calculated value of S. Large S value indicates 3D and a small value indicates 1D and 2D:

$$\text{Skew} = S = \frac{|Z_{xx} + Z_{yy}|}{|Z_{xy} - Z_{yx}|} \quad (23)$$

3.3.7 Strike analysis

The electrical strike direction shown in Figure 13 is an indication of where the resistivity changes least often in the same direction as the geological strike direction of the survey area. The figure shows alignment along the low-resistivity anomaly within the caldera rim, indicating ring structures (e.g. see Figure 29). The Z-strike is achieved by minimizing the diagonal impedance tensor elements (Z_{xx} and Z_{yy} or maximizing the off diagonal elements Z_{xy} and Z_{yx}). However, there is 90° ambiguity in geoelectric strike (i.e. Z-strike) which is fixed

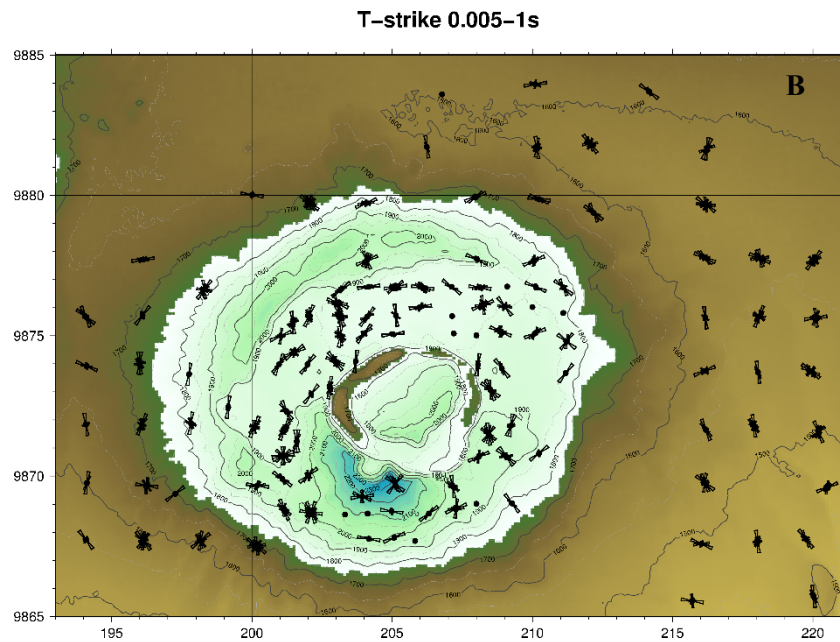


FIGURE 13: Rose diagram for electrical strike direction based on Tipper strike at 0.005-1 s

by measuring H_z and calculating the Tipper strike as shown in Equation 24 (Hersir et al., 2013) and Figure 14:

$$H_z = T_x H_x + T_y H_y \quad (24)$$

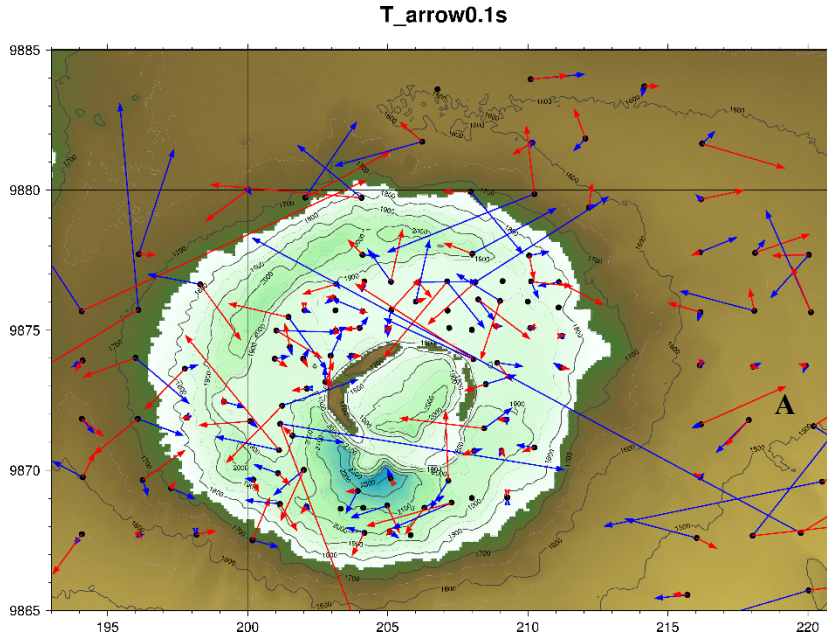


FIGURE 14: Induction arrows at shallow depth (0.1 s) pointing away from the caldera rim

Figure 14 is an example of induction arrows; the blue arrows are the real and the red are the imaginary part. The blue arrows point away from the conductor at shallow depth within the ring structure.

3.3.8 Static shift

The static shift problem is common in resistivity methods that measure voltage (electric field) over a short distance on the earth's surface and are due to inhomogeneities in resistivity close to the electrodes, like DC soundings and MT. The apparent resistivity is distorted by a multiplicative constant, S , which displays a shift when

data are presented on a log scale as shown in Figure 15. In Suswa field, most MT data were shifted down (on average 0.8), shown on the histogram in Figure 16, due to near surface conductive bodies. Above the conductive bodies, the static shift multiplier (S) was less than 1, and the apparent resistivity curve shifted downward resulting in decreased depth to the boundaries. S higher than 1 results in higher resistivity and increased depth to the boundaries, causing an upward shift of apparent resistivity over resistive bodies (Árnason, 2008).

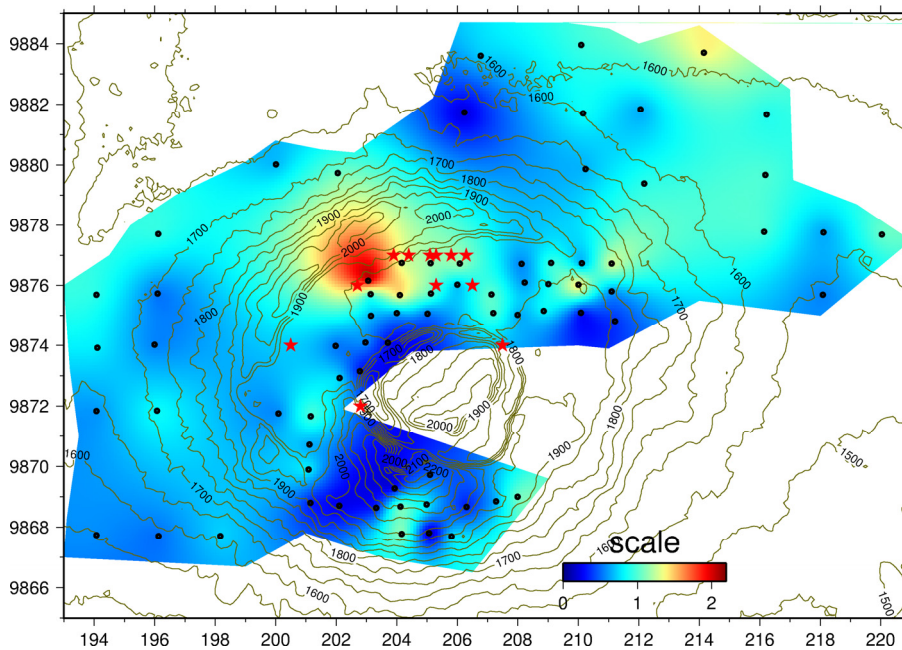


FIGURE 15: Static shift distribution map, black circles are MT/TEM locations and red stars are fumaroles

Two main causes of static shift are electric field and current distortion due to the near-surface contrast in topography that causes channelling effects that are common in a geothermal environment. In the upflow zone where conductive clay minerals form convex structures surrounded by resistive lava,

distortion may be common. The solution is to correct static shift in MT and DC data using transient electromagnetic data which are not affected by this problem (Árnason et al., 2010).

4. PROCESSING AND INVERSION OF MT AND TEM DATA

4.1 MT data processing

The collected time series data downloaded from the MT equipment are quality scrutinized using the time series viewer option in the *SSMT2000* software (Phoenix Geophysics, 2005). This will give a first indication of the data quality that influences decision making on whether to repeat the sounding or not. Then parameter files (tbl) are edited to reflect the setup for the collected data. The resulting time series are Fourier transformed to the frequency domain, and then the different auto- and cross-powers are calculated using the robust processing method (RPM). The data are graphically edited using *MTEditor* Phoenix geophysics software by masking the outliers to achieve apparent resistivity and phase curves and other relevant parameters. The resulting MT parameters are all saved as EDI files ready for export to the interpretation software (see SEG, 1991). Figure 17 illustrates processed MT apparent resistivity and phase curves from the Suswa prospect. At periods below 0.1 s, it exhibited a 1D response where apparent resistivity values and phase decreased with increasing period. For periods above 0.1 s, the curves separated indicating a non-1D environment with one apparent resistivity increasing as the other decreased.

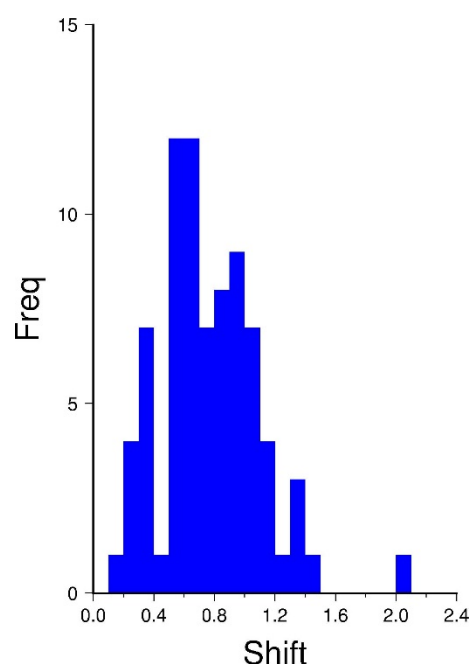


FIGURE 16 : Static shift histogram

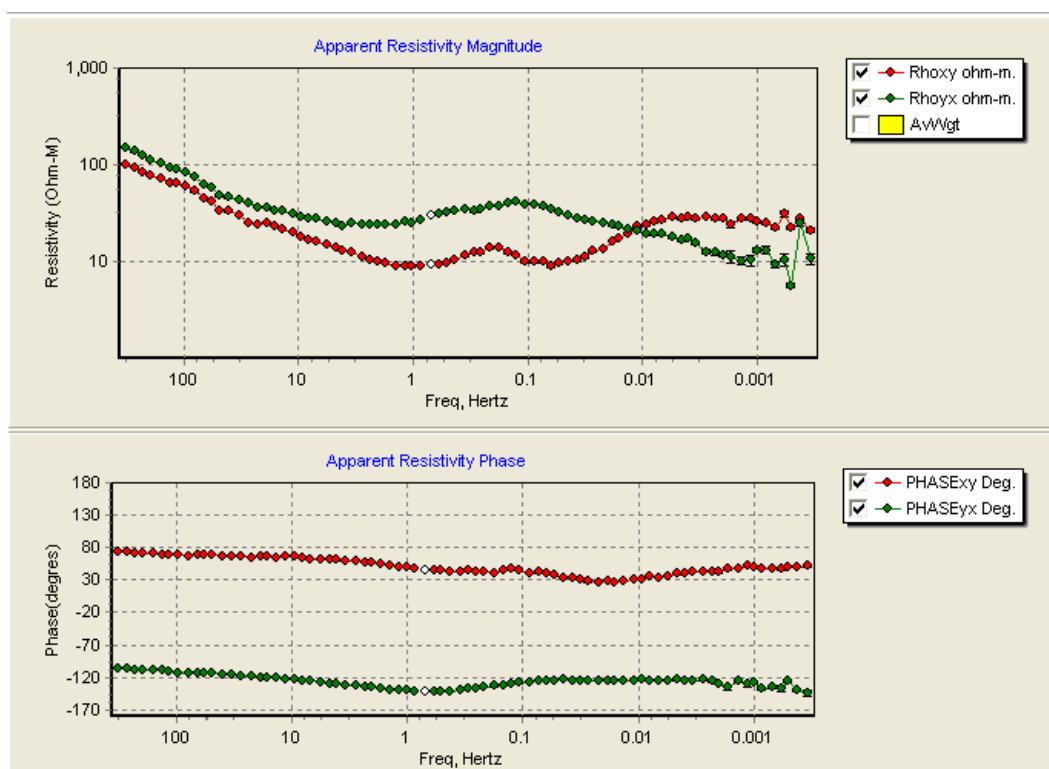


FIGURE 17: MTEditor output showing apparent resistivity and phase curves of Suswa sounding SUSMT94

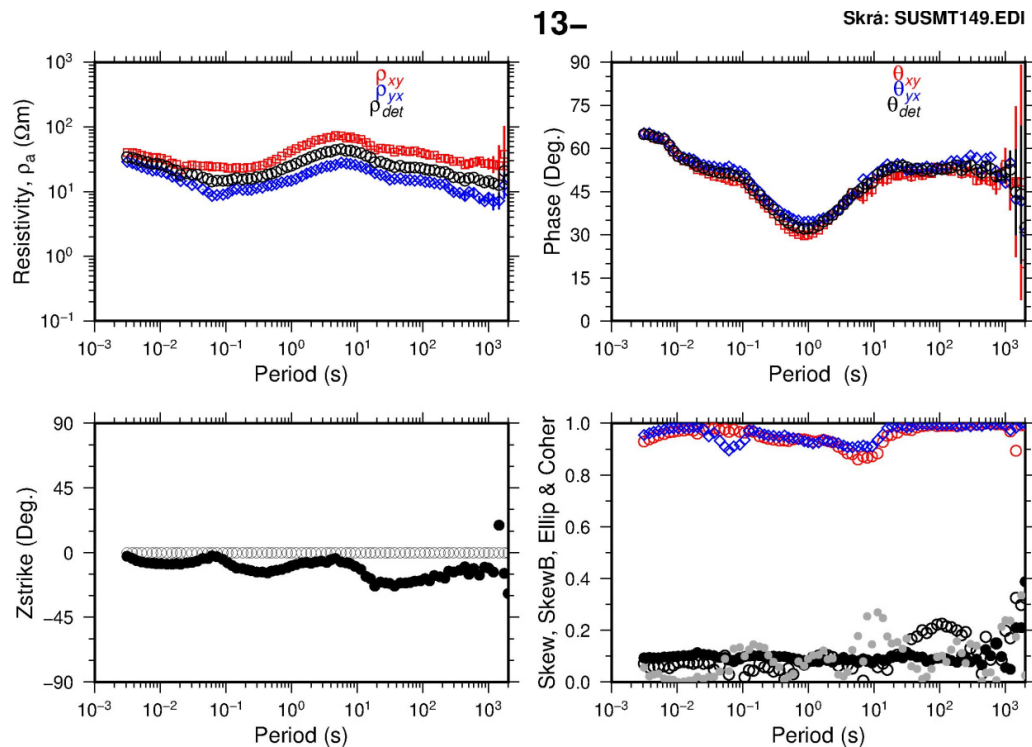


FIGURE 18: Processed MT data for sounding 149 (SUSMT149) from Suswa geothermal prospect, Kenya; The plots show the apparent resistivity and phase derived from the xy (red) and yx (blue) components of the impedance tensor and the determinant invariant (black), the Z-strike or Swift angle (black dots), and multiple coherency of xy (red) and yx (blue), and skew (black dots) and ellipticity (grey dots)

The Electronic Data Interchange (EDI) files produced by *MTEditor* are run through scripts developed at ISOR: *dos2unix*, changes the edi files from a window based environment to a Linux readable format and *spect2edi* calculates various parameters and produces the result in the standard EDI format which is ready for inversion in the *TEM TD* programme. Suswa data were also run through *edidatum* script to change the coordinates taken by GPS from WGS84 datum to Arc1960 for Kenya and *edi2ps* to generate PostScript graphs. Finally *ps2raster* transforms postscript files to PNG or JPEG figures. Figure 18 shows MT sounding SUSMT149 which has been run through the aforementioned Linux scripts, ready for *TEM TD* inversion software and is explained below. The remaining soundings are given in Appendix II (Mohamud, 2013).

4.3 1D inversion of TEM data

Figure 19 shows a typical inversion process. In the beginning only measured data and a guessed initial model are available. The initial model is run to test if the response fits the measured data. If the fit is good it becomes the final model and if not, the model is subjected to an iterative algorithm, where the parameters resistivity and thicknesses are adjusted. The inverted model is run again in a forward algorithm and compared several times in an iteration process which improves the model in a successive iteration until a good fit is obtained. In Árnason (1989), the details of the inversion algorithm are discussed. The TEM TD program uses damping parameters to smooth sharp steps and oscillations in the model values. Minimum structure Occam inversion is performed, where the number of layers and thicknesses are kept constant while the resistivity variation is

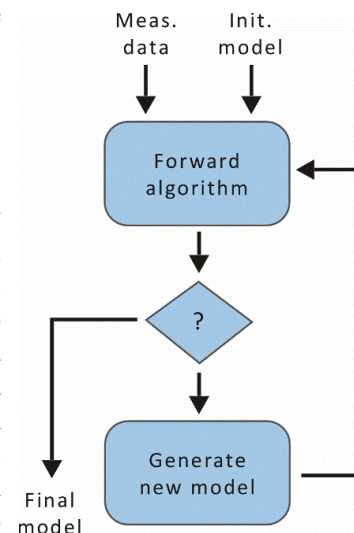


FIGURE 19: Sequence of the inversion process (Flóvenz et al., 2012)

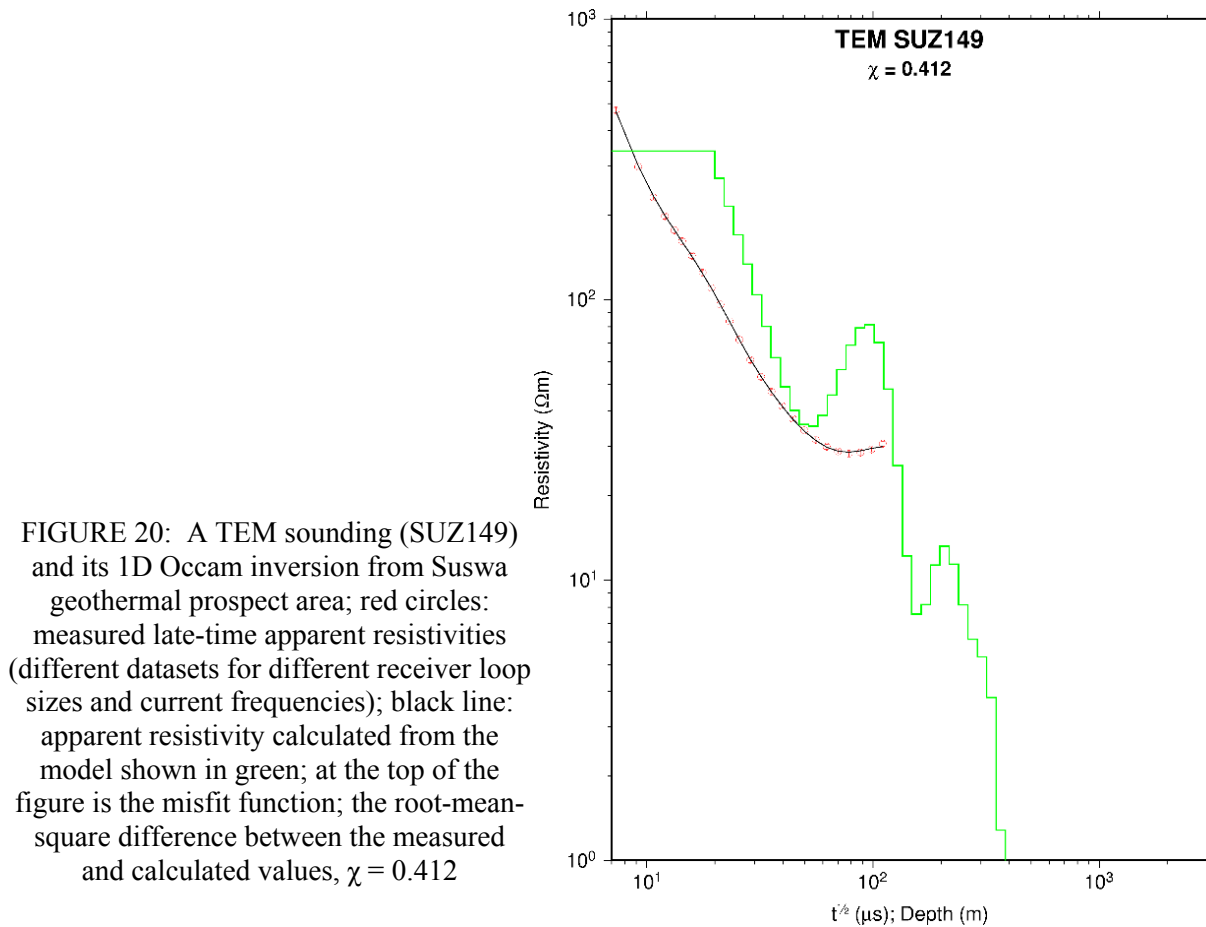


FIGURE 20: A TEM sounding (SUZ149) and its 1D Occam inversion from Suswa geothermal prospect area; red circles: measured late-time apparent resistivities (different datasets for different receiver loop sizes and current frequencies); black line: apparent resistivity calculated from the model shown in green; at the top of the figure is the misfit function; the root-mean-square difference between the measured and calculated values, $\chi = 0.412$

smoothed with damping parameters. Árnason (2006b) gives a detailed step by step procedure on 1D inversion of MT and TEM using *TEMTO* software developed at ISOR.

In this report, 72 TEM soundings from Suswa geothermal prospect were 1D inverted. An example is given in Figure 20. All of them can be found in Appendix I (Mohamud, 2013).

4.4 Joint inversion of MT and TEM data

To correct the static shift problem in MT data already discussed in the previous chapter, the MT inversion is run jointly with TEM data which is not affected by the static shift as it uses magnetic rather than electrical fields during data acquisition. The shift parameter is one of the parameters that is inverted for in *TEMTO*. Either an MT or TEM initial model is run from inverted or processed measured data to get started; then, from the model, an inversion algorithm is run as explained in Figure 19. Several parameters are adjusted until a good fit between MT and TEM curves are obtained. An example is given in Figure 21. The remaining jointly inverted soundings can be found in Appendix III (Mohamud, 2013).

In a perfectly static-shift free situation, the shift which is the ratio of MT to TEM distance of separation is 1. However, the earth is heterogeneous and in a low-resistivity near-surface environment the curves are shifted downwards with an S factor less than 1, and in a high-resistivity environment the curves shift upwards with an S value exceeding 1. The distance recommended between MT and TEM soundings to be used in joint inversion should not exceed 50-100 m.

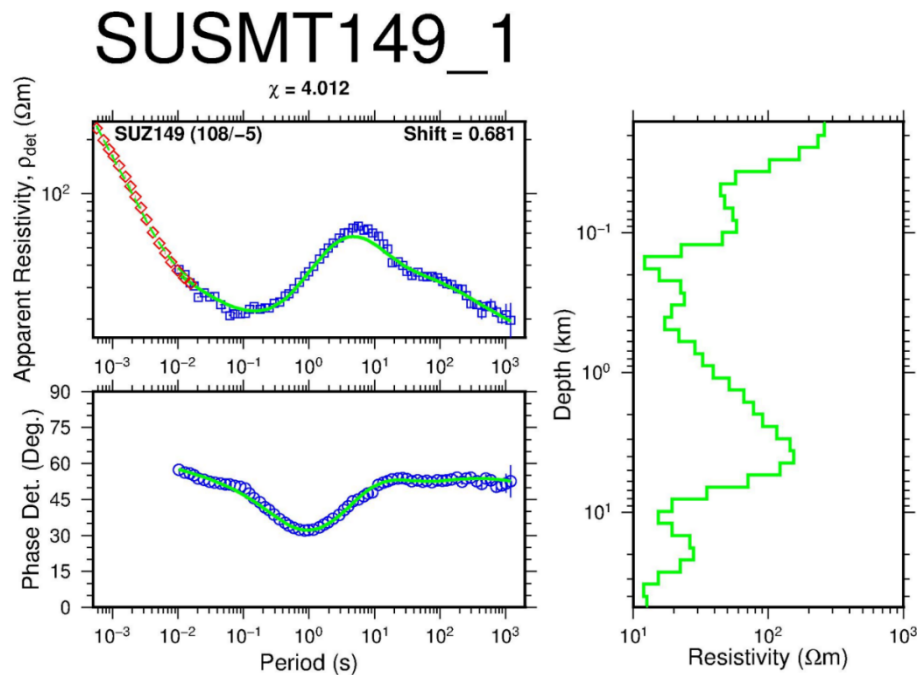


FIGURE 21: Joint 1D inversion of TEM and MT data: SUSMT149_1 is the MT station corresponding to TEM station SUZ149; red diamonds: measured TEM apparent resistivity; blue squares: measured MT determinant apparent resistivity; blue circles: apparent phase derived from the determinant of MT impedance tensor; green lines: on the right show the 1D resistivity inversion model, and to the left are its synthetic MT apparent resistivity and phase response; numbers in parentheses (108/-5) indicate the two stations were 108 m apart and their elevation difference was 5 m (- sign means TEM station is at higher elevation than MT); Chi square χ (4.012) is the misfit between the measured and calculated values in the models while 0.681 is the shift value

5. SUSWA GEOTHERMAL AREA

5.1 Geological and structural setting

The Kenya Rift is a volcano tectonic axis of continental scale that stretches from the Afar junction in the north to southern Africa. The Rift started 30 million years ago (Omenda, 1997). During the last 2 million years, intense volcanic activities in the Rift axis formed large shield volcanoes associated with high-temperature geothermal prospects in the Kenya Rift. The young volcanic formations in the Rift graben host shallow magmatic bodies beneath them which enhance the occurrence of geothermal activities in the rift zone (Omenda, 2007). Mt. Suswa is the southernmost volcano of the Kenya Dome (Figure 1), located 30 km south of Greater Olkaria Domes. The main surface geology in Suswa is trachyte, phonolite, ignimbrite, and volcanic ash.

The chronological occurrence of volcanic episodes in Mt. Suswa area was summarized by White et al. (2012) and discussed by several others (Espejel-García, 2009; and Omenda, 1997) in three major phases. The first phase was the initial eruption of predominantly trachyte lava flows derived from a central source with some phonolite that led to the formation of a shield volcano. The second phase was during cauldron subsidence (syn-caldera) that produced abundant pumice and thick lava flows from a ring fracture zone outside the caldera. The third eruptive phase is post caldera lavas that filled the caldera and resulted in Ol Doinyo Nyukie volcano. A collapse in the form of a concentric graben formed inside the older caldera towards the end of the last eruptive episode, seen in Figure 22.

The main structures in the area are N-S trending faults aligned with the main rift graben (Figure 23). The calderas form the main visible ring structures that seem to control the fumarolic activities on the walls of the outer caldera in the Kisharo area. Tandamara fault dissects the calderas into two halves oriented in a N-S direction, inferred from trachytic lava domes aligned on the northern slopes of Mt. Suswa (Omenda, 1997).

5.2 Geothermal manifestations

Surface geothermal manifestations in Suswa are in the form of altered and hot grounds, the presence of geothermal grass, cinder cones, young lavas and fumaroles (GDC, 2013). The manifestations are located along the rim of the inner and outer caldera walls and on the floor and slopes of the outer caldera (see Figure 23). The fumarolic activities are stronger on the rim of outer caldera wall suggesting the presence of a structurally controlled hydrothermal system. However, manifestations outside the ring structures are weak fumaroles with low alteration and temperatures readings. The Mt. Suswa local community harvests water from condensed fumaroles as their source of water for domestic use.

5.3 Previous work

An interferometry synthetic aperture radar (InSAR) study by Biggs et al. (2009) between 1997 and 2008, to detect surface displacement of high resolution, showed subsidence of about 5 cm at Mt. Suswa between 1997 and 2000, indicative of an existing active magmatic system beneath it. Changing pressures within the crustal magma reservoirs caused by magma and/or volatile fluxes produce changes in volcano shape on the scale of centimetres to metres.

Gravity data analysis and interpretation by Cantini et al. (1990) indicated a NE-SW trending positive anomaly beneath the southern edge of the caldera with an amplitude of 30 mGal. The anomaly is presumably related to the heat source, postulated to be of basaltic melt magma directly beneath the caldera. The study also related identified linear positive anomalies showing structurally controlled shallow bodies in the basement of the Suswa volcanic activity.

Passive seismic data collected and analysed by Simiyu (1999) over a seismic network in the Suswa geothermal prospect area showed low seismic velocity values, interpreted to mean high heat flow,

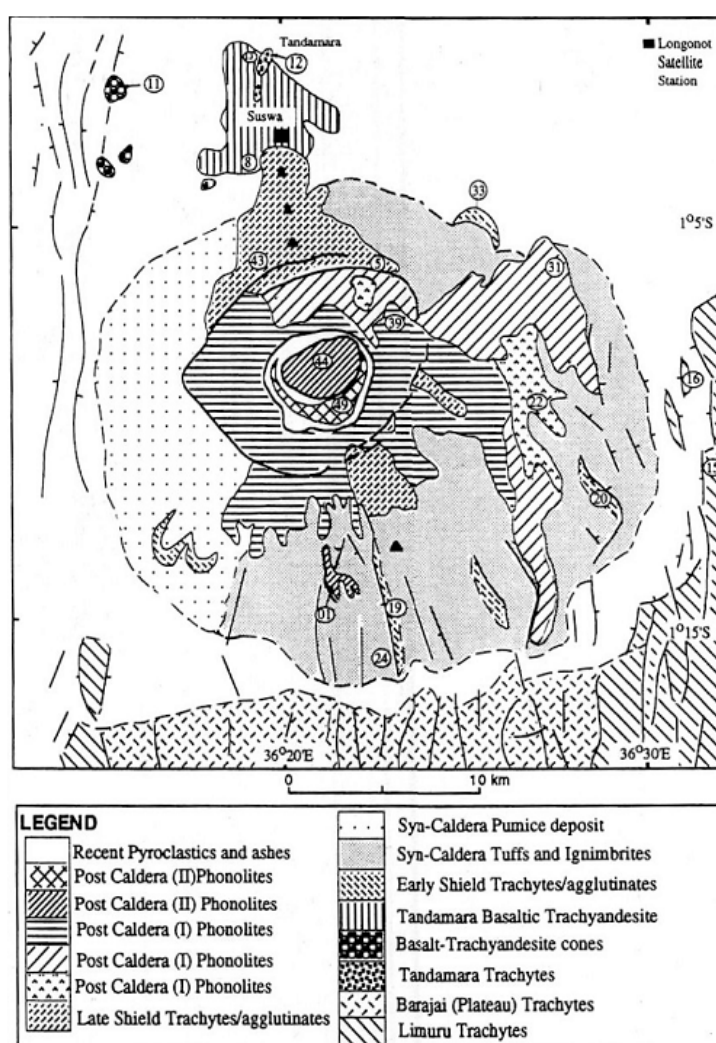


FIGURE 22: Suswa geology (Omenda, 1998)

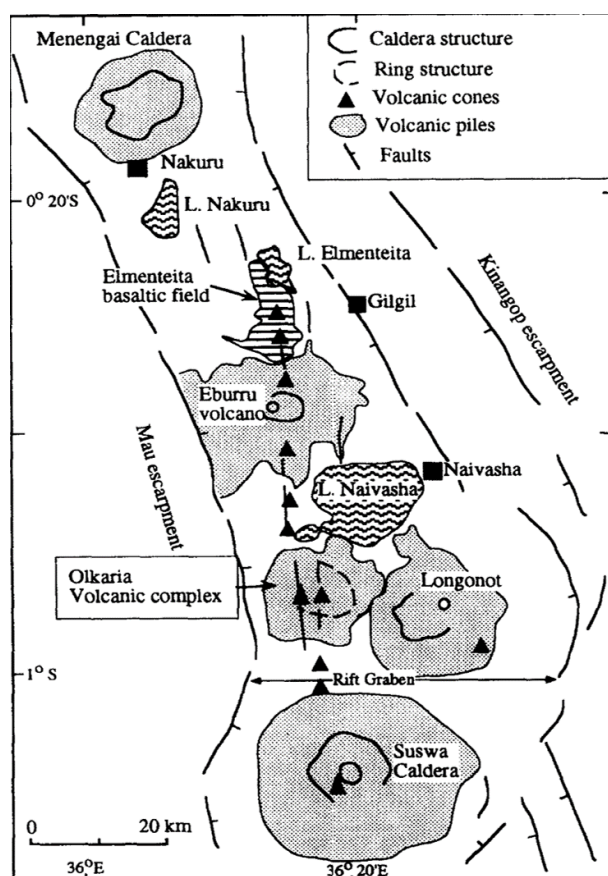


FIGURE 23: Structures of Suswa (Omenda, 1998)

fracturing of rocks and steam saturation. Simiyu (1999) further indicated seismicity gaps within the field mark zones, inferred to be hot magmatic intrusions that have raised the temperature above the brittle-ductile transition temperature of above 450°C.

Simiyu and Keller (1997) also indicated from research carried out by the Kenya Rift International Seismic Project (KRISP) in 1985 and 1990 that seismic events are at shallower depth and smaller on the axis but larger and deeper on the rift flanks south of Lake Naivasha, an area that encompasses Suswa. Figure 24 shows a high V_p velocity zone below the Suswa prospect.

Results from an integrated resistivity survey (MT and DC), Onacha et al. (2009) identified three anomalous areas: the southwest part of the caldera, the eastern slope and the northwest corner of the caldera close to the anticipated heat source. High-resistivity values noted from Suswa caldera rocks in comparison to Olkaria and Longonot areas were ascribed to lower alteration, lower bulk permeability and varied lithology. They further anticipated high vertical permeability due to recent caldera reactivation.

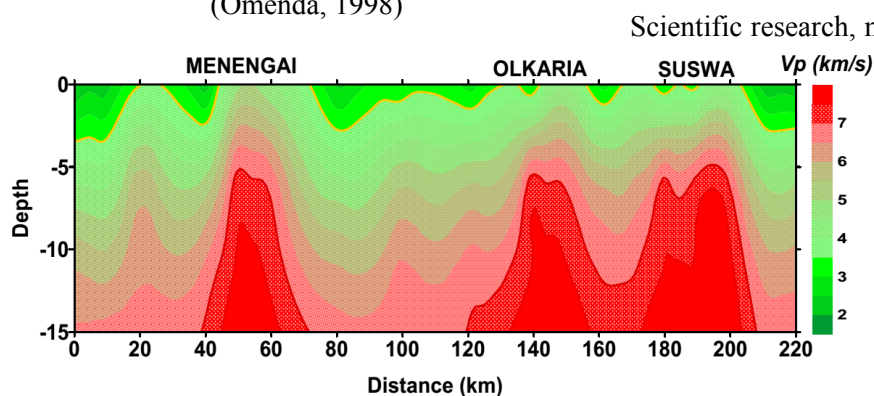


FIGURE 24: Seismic velocity model along the Rift axis showing high-velocity zones beneath Menengai, Olkaria and Suswa volcanic centres based on the KRISP 1985-1990 axial model by Simiyu, 2010, based on Simiyu and Keller, 2000

Scientific research, mainly in geology, have been carried out by different entities from PhD and Masters dissertations to geoscientific researches by Kenya Electricity Generating Company (KenGen) and more recently Geothermal Development Company (2013) in the search for geothermal resources. The current data used for this project are a part of 150 MT and 103 TEM soundings collected in a survey conducted in 2013.

In this report, 72 data points of both MT and TEM soundings in the same location or within 200 m of each other were used. TEM was used for static shift correction of the MT data in 1D joint inversion of TEM and MT as described in the next chapter.

5.4 Suswa MT and TEM survey area

The survey points for both MT and TEM data, fumaroles and profiles for the cross-sections are shown in Figure 25. MT data were collected using Phoenix Geophysics equipment (MTU-5A) for a period of

about 22 hours. The survey was conducted between December 2012 and February 2013, covering 150 MT and 103 TEM soundings. In this survey two types of TEM equipment were used. Phoenix Geophysics V8 equipment with a transmitter loop size (200 by 200 m) collected the data at 5 and 25 Hz frequencies. The Zonge TEM (300 by 300 m) transmitter loop was used to collect at 4 and 16 Hz frequencies and 10 A current. The areas around the outer caldera walls and the inner caldera were not surveyed due to challenges in accessibility.

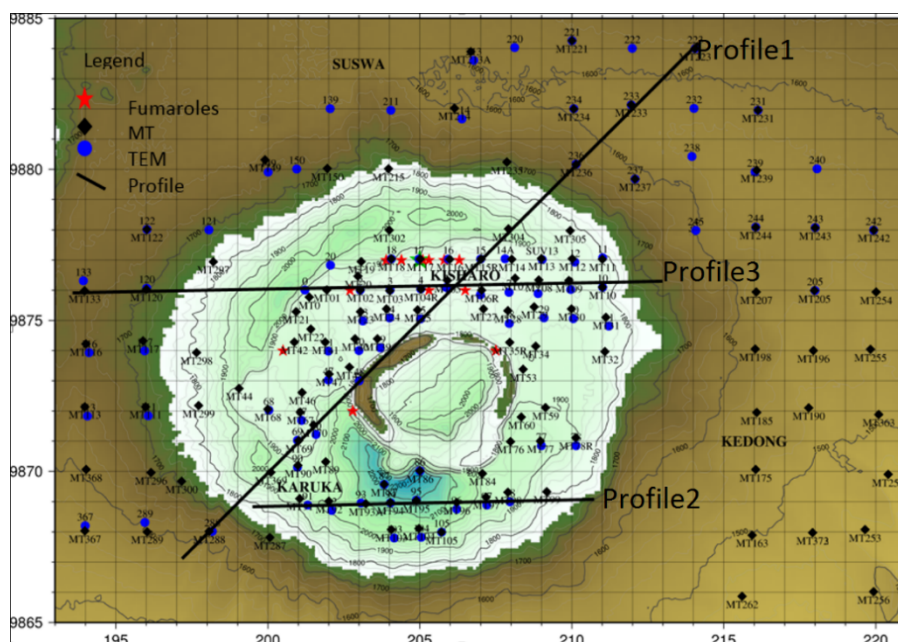


FIGURE 25: Sounding locations: Blue circles are TEM soundings, black diamonds are MT stations, red stars are fumaroles, and solid lines denote profiles

6. RESULTS OF MT AND TEM SURVEYS

The outcome of the joint 1D inversion of MT and TEM data is presented as cross-sections and iso-depth resistivity maps. Due to a large data gap between the soundings, attention should be given only to the area where the soundings are located and not the interpolated area between them for effective interpretation. Resistivity cross-sections were plotted by the TEMCROSS programme developed at ÍSOR (Eysteinnsson, 1998). The program calculates the best line between the selected sites on a profile and plots resistivity iso-lines based on the 1D model generated for each sounding. It is actually the logarithm of the resistivity that is contoured so that the colour scale is exponential, but the numbers at the contour lines are resistivity values (Barkaoui, 2011).

Three cross-sections were generated down to a depth of 10,000 m b.s.l., and down to sea level (1800 m below ground surface) while iso-depth resistivity slices were generated at 1600 and 1000 m a.s.l., sea level, and 4000 and 8000 m b.s.l.

6.1 Cross-sections

The cross-sections in Figures 26, 27 and 28 (see the location in Figure 25) point to subsurface signatures common to volcanic geothermal environments. In Figure 26 a and b (profile 1) the cross-section runs SW-NE cutting the rims and outer caldera floor. A low-resistivity anomaly in the top section to the northeast is due to sedimentary deposits associated with air fall ash during the eruption of the Suswa calderas and sequential weathering and erosion from both Mt. Longonot and Suswa. At a depth of about 3000 m b.s.l., a conductor ($< 10 \Omega\text{m}$) persists to the end of the 10 km vertical depth in this profile. This low-resistivity anomaly at depth below the sedimentary plain to the north-northeast and east of Mt. Suswa could be due to layers of sedimentary fillings in the rift since its inception. In addition to lake sediments in the rift basin, the rift is tectonically active with micro-seismic activities that continuously

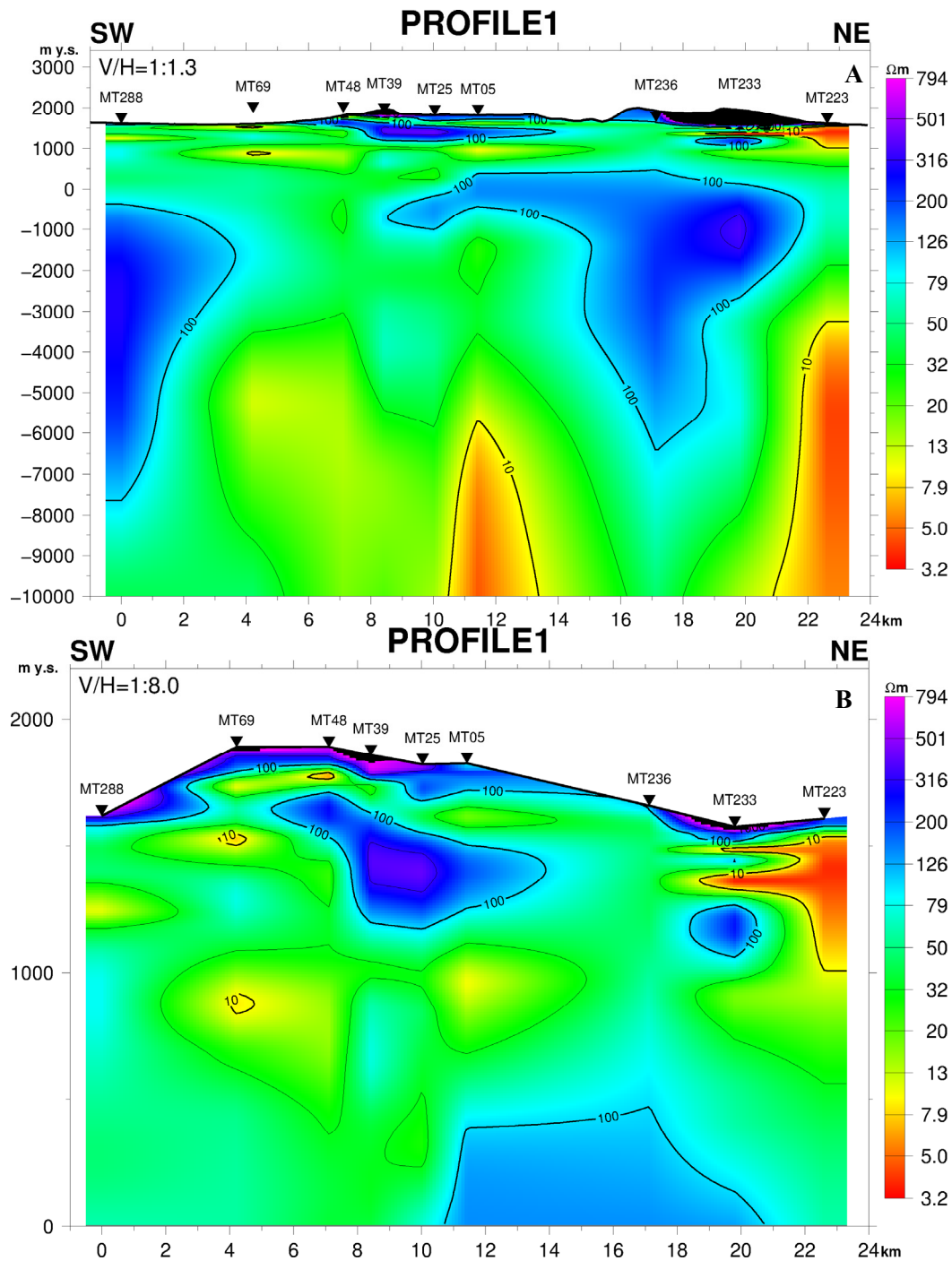


FIGURE 26: Resistivity cross-section profile 1;
a) Down to 10,000 m b.s.l.; b) Down to sea level

open up fractures enhancing permeability and porosity to the deep lying sedimentary formations. Increase in pressure and temperature with sediment depth, the highly fractured rift basin, fine lake sediments, a porous media and a high-temperature gradient from the tectonically active rift system may have influenced the low resistivity in the basin. The low-resistivity anomaly common to Kenya rift below the sedimentary basin at depth is, however, not well understood. Geothermal origins have been associated with East African rift sedimentary deposits as in the case of Tendaho in Ethiopia, which could be the case in Kenya, subject to confirmation by more geoscientific research.

Below the outer caldera floor, at about 1000 m a.s.l., a low-resistivity anomaly probably caused by low-temperature alteration minerals (zeolite/ smectite) is shown in Figure 25. Above this layer, a deep

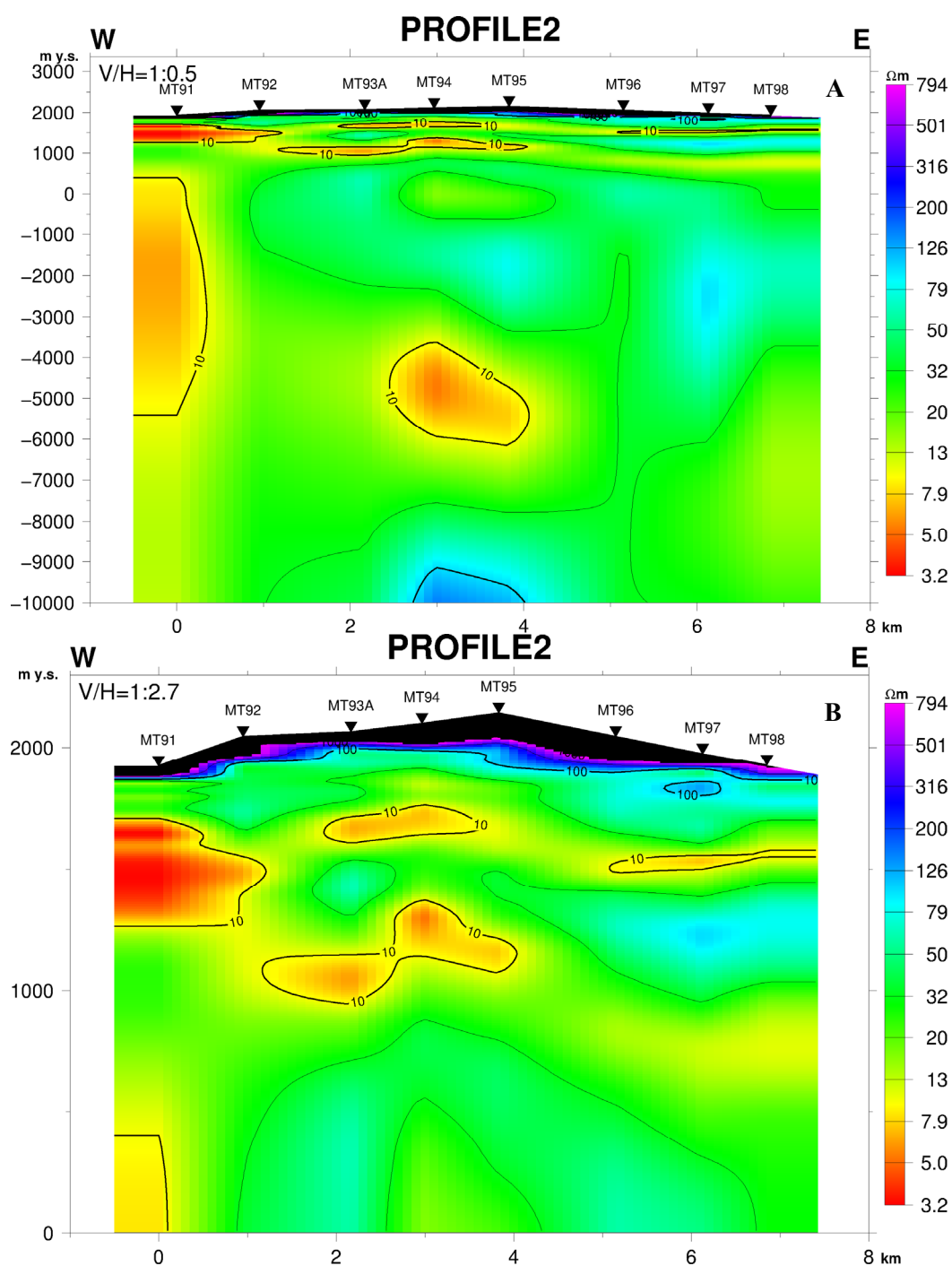


FIGURE 27: Resistivity cross-section profile 2:
a) Down to 10,000 m b.s.l.; b) Down to sea level

groundwater table could be inferred from the high resistivity. It is associated with fumaroles which are presumably due to dry steam. The near surface high resistivity is caused by remnants of unaltered rocks. High resistivity oriented vertically below the rims of the caldera clearly demarcate the caldera walls both in depth and breadth and probably the extent of the geothermal field. The resistive core at sea level (0 m) below the conductive cap (see Figure 26) is most likely caused by high-temperature alteration minerals consistent across the Suswa caldera. Below the resistive core is the deep seated doming conductor ($< 10 \Omega\text{m}$), presumed to be connected to the heat source.

Figure 27 shows a profile across the southern slope of the outer caldera. High resistivity near the surface is unaltered formations associated with recent phonolitic lava flow from the most recent eruptions, below

which are conductive layers (about 1000 m a.s.l.), associated with volcanic ash deposits from pre-caldera eruptions and low-temperature mineral alterations. At depths between 3000 and 6500 m b.s.l., a pocket of conductive bodies is found in the centre of the profile which could be part of the heat source. At the western corner (below sounding MT91), a much closer conductor (1500 m a.s.l.) prominent near the surface and at depth between 500 m a.s.l., and 5500 m b.s.l., could probably be due to the sedimentary basin deposits discussed above.

Figure 28 shows profile 3 across the floor of the northern caldera and the western rim of the outer caldera and western slopes. The profile shows similar features as seen in profile 1 inside the caldera and profile

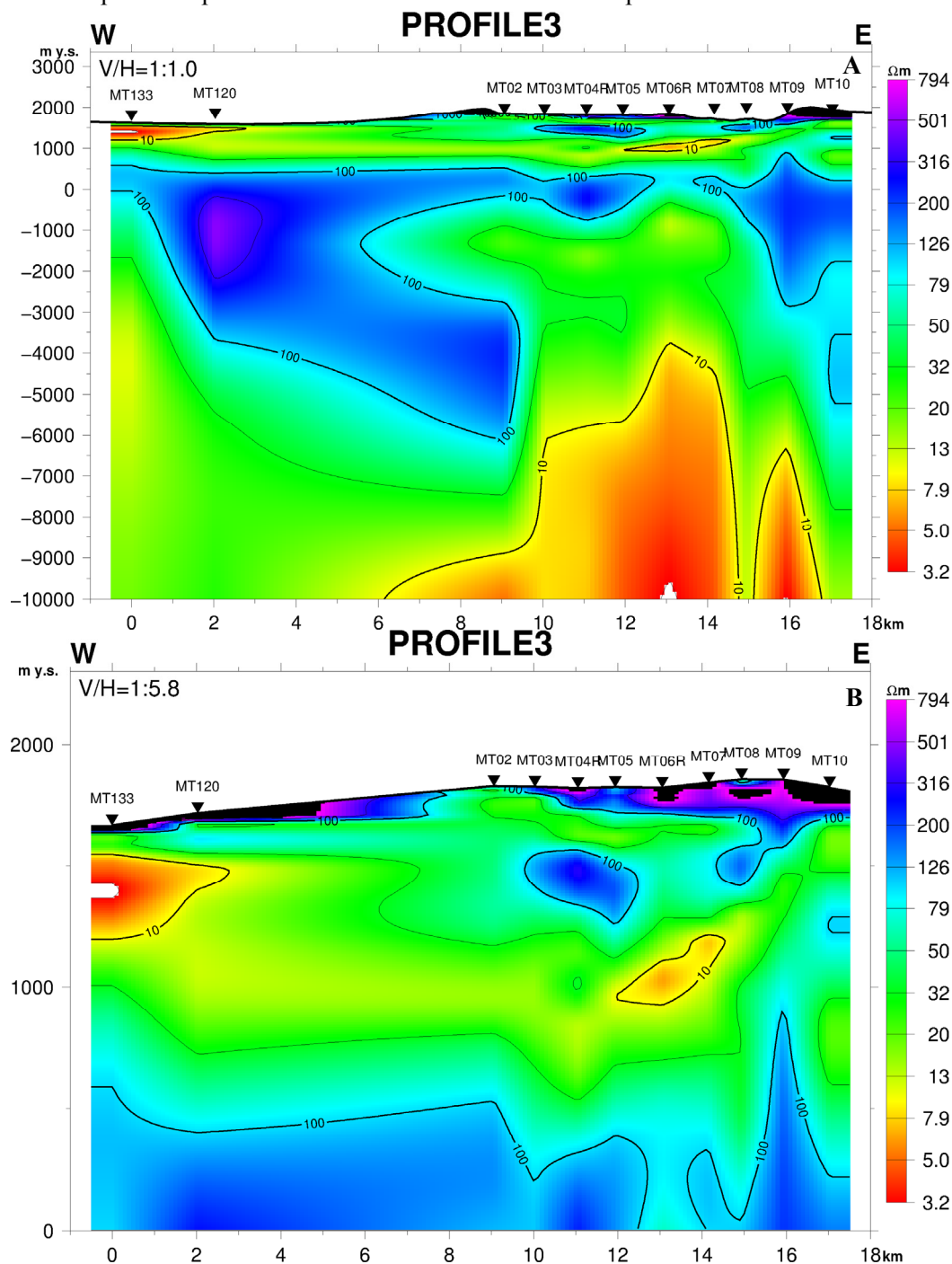


FIGURE 28: Resistivity cross-section profile 3:
a) Down to 10,000 m b.s.l.; b) Down to sea level

2 to the western side. The high-resistivity core at sea level is confined between low resistivity above 500 m a.s.l., related to low-temperature alteration minerals and a deeper conductor below 4000 m b.s.l., presumed to be the heat source. The heat plume is right below the caldera.

6.2 Iso-resistivity maps

Iso-resistivity depth maps (Figures 29-33) were generated using the *TEMRES* programme (Eysteinnsson, 1998) from 1D Occam models at different elevations, contoured and coloured in a logarithmic scale. Figure 29 is at a depth of 1600 m a.s.l., and shows a shallow conductive layer attributed to weathering, volcanic ash and sedimentary deposits to the south. The high-resistivity area below the fumarolic areas may have resulted from unaltered formation and a low level of water-rock interaction because of the high steam level in the fumaroles attributed to a deep groundwater table in Suswa. Thus, the absence of near surface geothermal fluids and dry steam causes a resistivity high in fumarolic areas in the northern floor of the outer caldera.

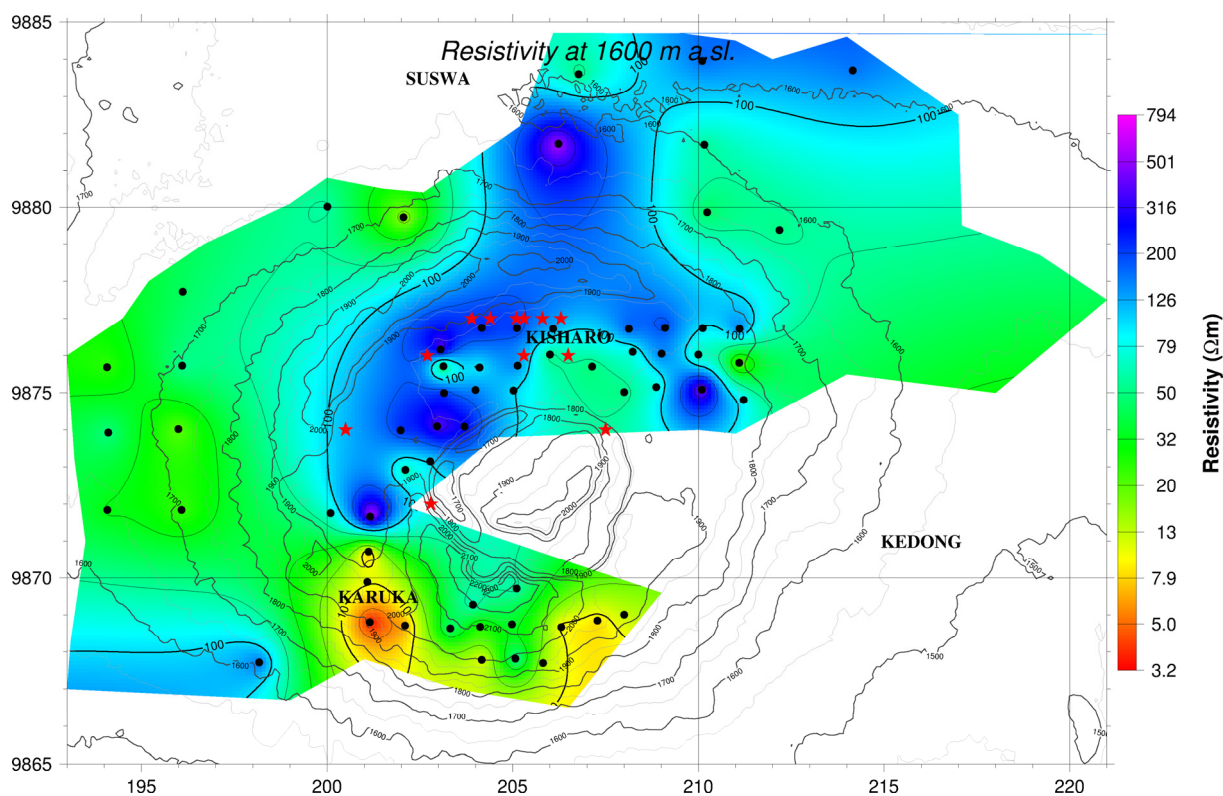


FIGURE 29: Resistivity map at 1600 m a.s.l.; black dots denote MT soundings and red stars are fumaroles

In Figure 30, a low-resistivity anomaly is now evident at 1000 m a.s.l., which could be the result of low-temperature alteration minerals.

Figure 31 shows high resistivity at sea level (0 m), attributed to high-temperature alteration minerals common to high-temperature volcanic geothermal systems. Resistivity highs also demarcate the caldera walls at the rims and at depth. A less resistive zone bordering the inner caldera ring and oriented in a NE-SW direction could indicate a structural alignment following the caldera axis. This structure could be the main conduit of the geothermal fluid and is associated with the upflow zone of the system below the calderas.

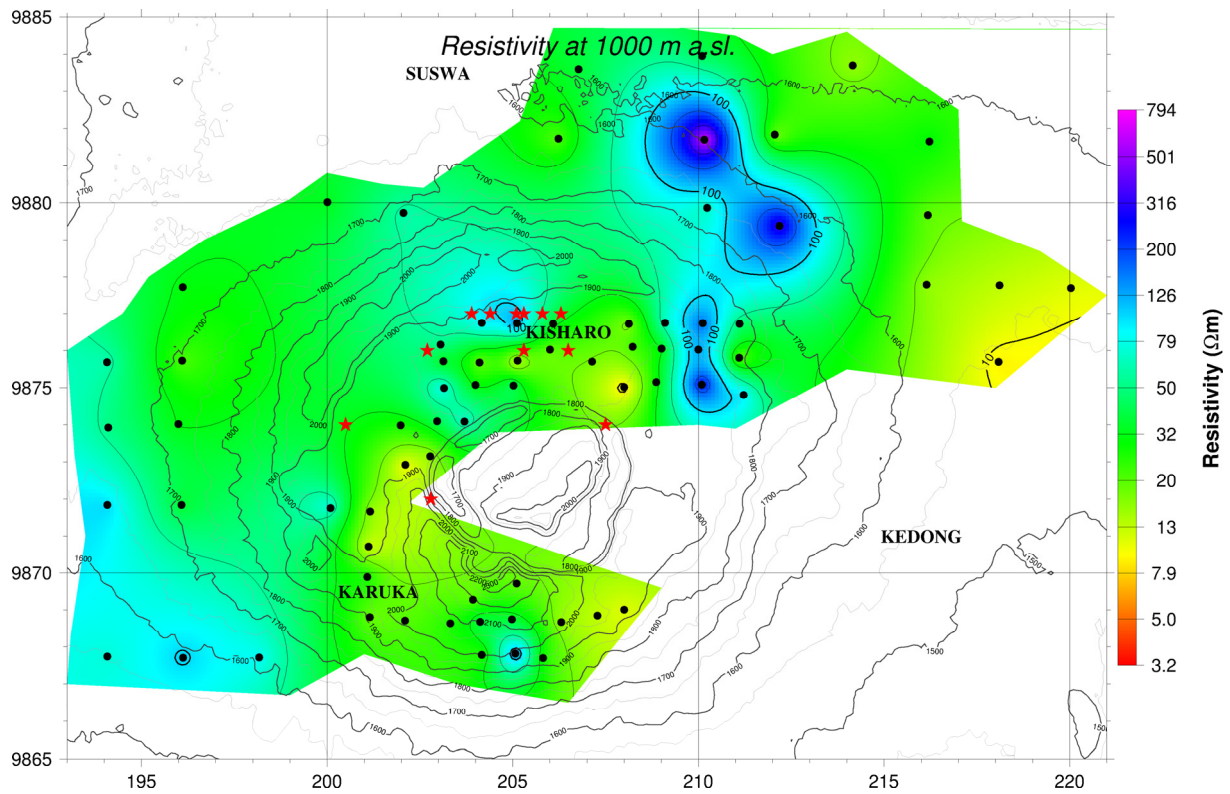


FIGURE 30: Resistivity map at 1000 m a.s.l.

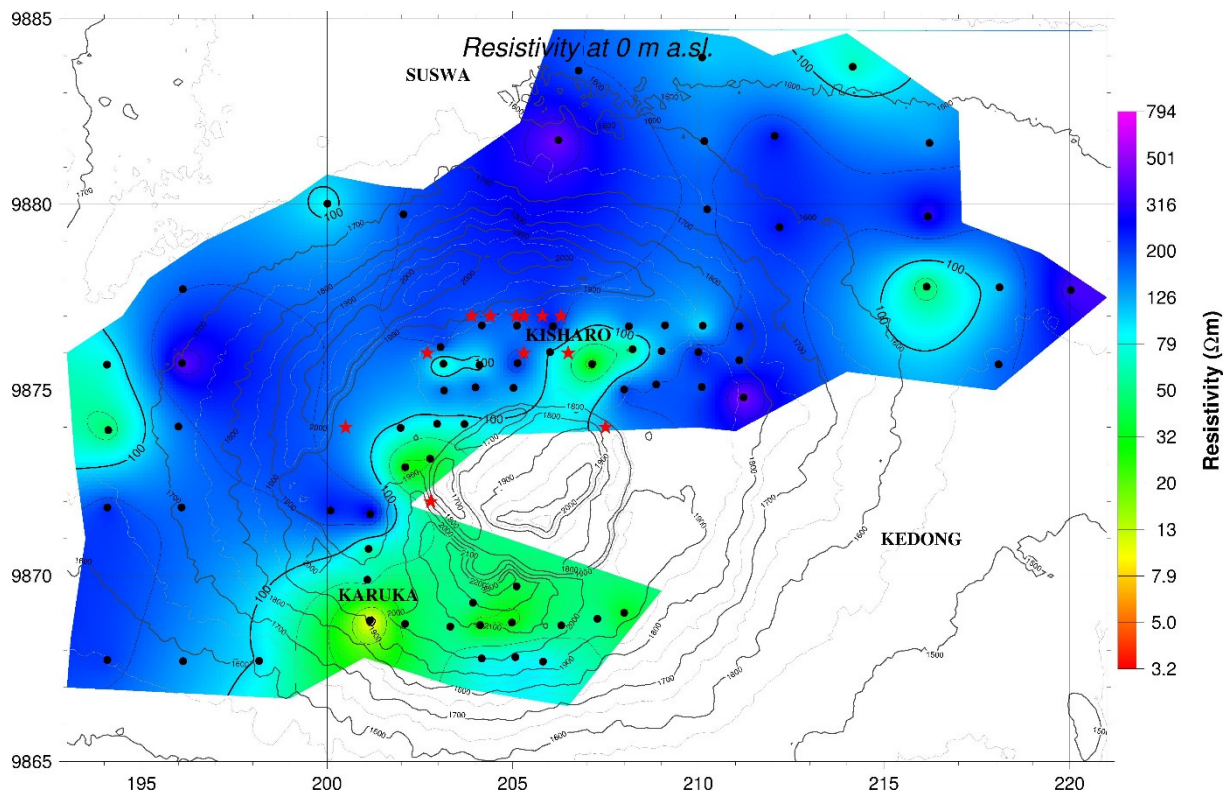


FIGURE 31: Resistivity map at sea level

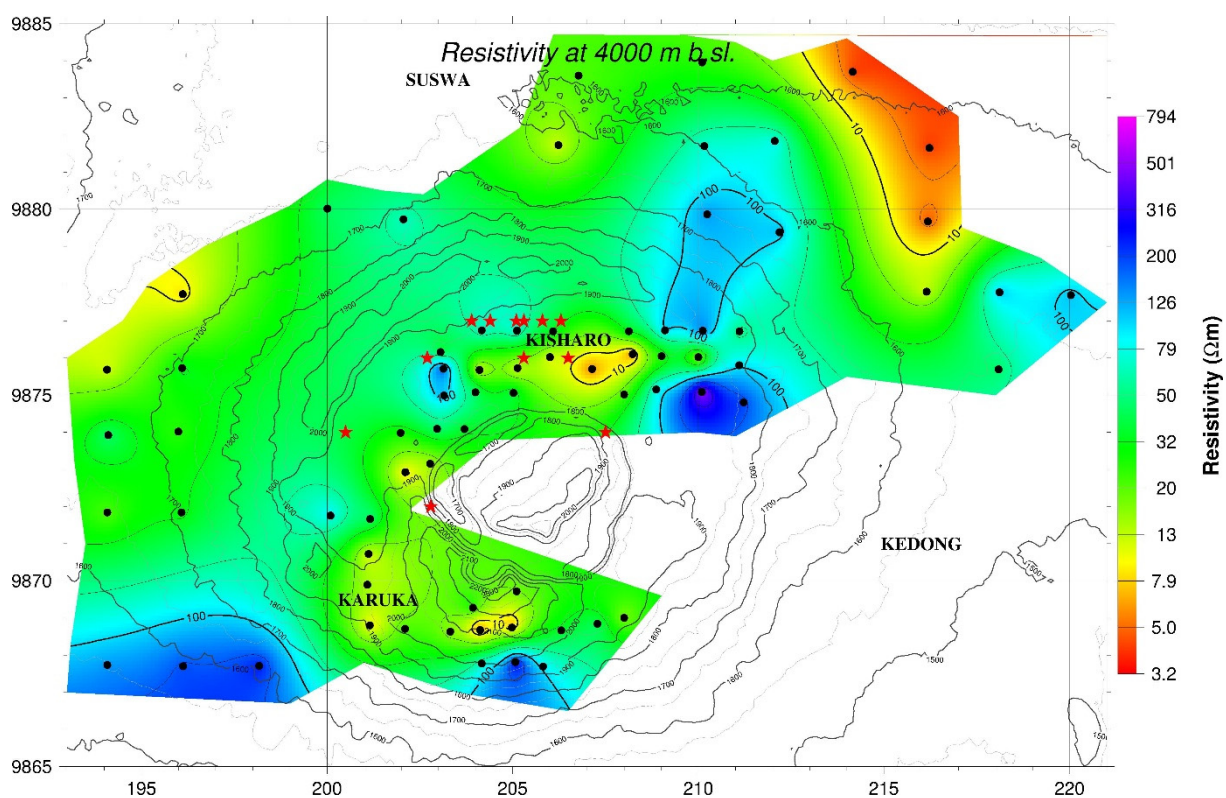


FIGURE 32: Resistivity map at 4000 m b.s.l.

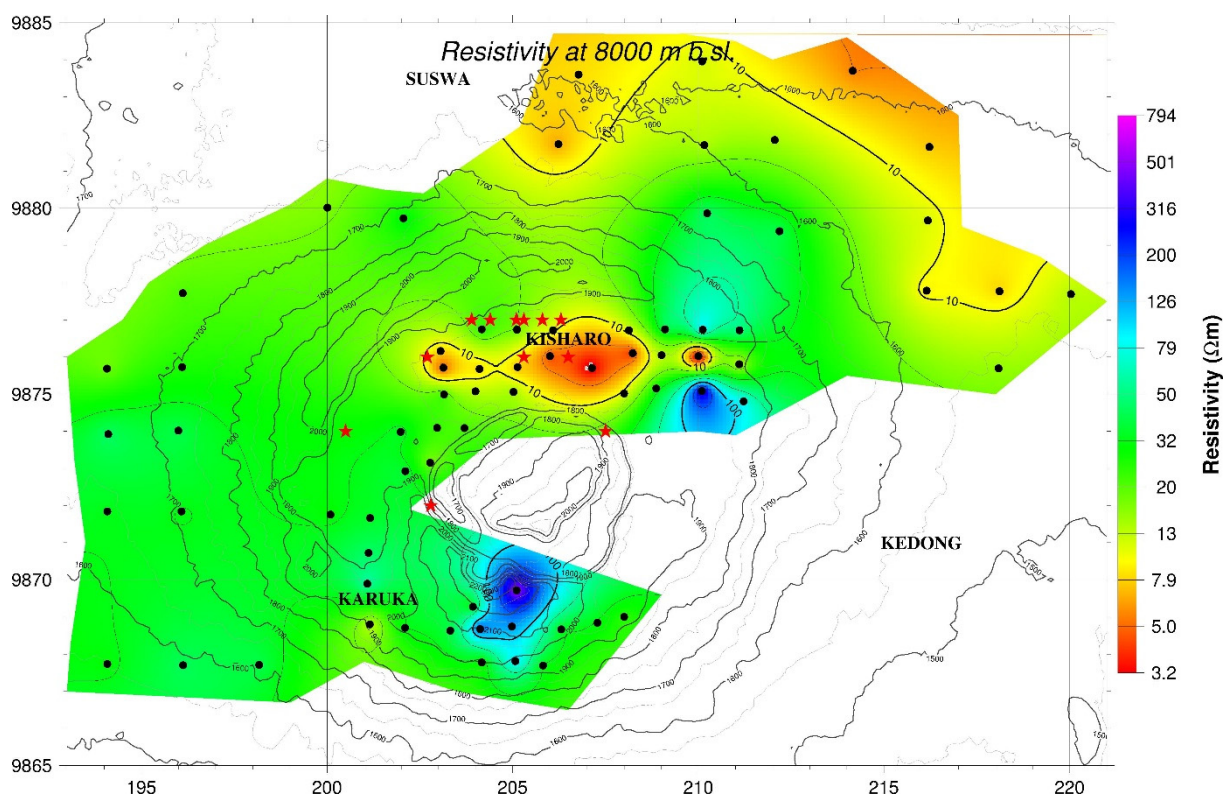


FIGURE 33: Resistivity map at 8000 m b.s.l.

Figure 32 shows the top of the deep conductors at 4000 m b.s.l, which together presumably form the heat source. These conductors are seen to the north, south and west of the inner caldera. However, there are no data in the inner caldera to establish if the heat sources are connected or discrete. The NE-SW structural alignment of conductive bodies encircling the inner caldera is obvious. It must be noted that the conductors are very pronounced, oriented along the dense fumaroles in the caldera. The low-resistivity anomaly to the northeast is outside the caldera in a sedimentary basin between Suswa, Domes and Longonot, as discuss above.

Figure 33 shows an iso-depth map at 8000 m b.s.l. showing conductive bodies ($< 10 \Omega\text{m}$) at the floor of the outer caldera in the north, trending W-E and to the north and north-northeast of the outer caldera in the sedimentary plain. The conductive area increases with an increase in subsurface depth and seems to merge (12,000 m b.s.l. not shown in this report). The deep conductors cannot be established south and west of the caldera at depths below 6000 m b.s.l., probably due to their formation in pockets with a source below the inner caldera where the last eruption occurred. The persistence of the main conductive body below the fumaroles in the north, oriented W-E, could be the main source of heat for Suswa prospect.

7. CONCLUSIONS AND RECOMMENDATIONS

Suswa has a geothermal potential, as shown by the resistivity cross-sections and iso-depth maps and strike analysis. The classical high-low-high-low pattern common in volcanic regions with a geothermal system is displayed, i.e. surface highs due to resistivity caused by unaltered rocks, followed by low resistivity at around 1000 m a.s.l, due to low-temperature alteration minerals. At sea level (0 m) a resistive core was found, most likely associated with high-temperature alteration minerals. Deep conductors below 4000 m b.s.l. could be the heat source for the Suswa geothermal system. The independent strike analysis of induction arrows and Tipper strike based on H_z confirms resistivity structures, generated from the two electrical and magnetic components.

The low resistivity in the sedimentary basin at depth could be due to deep conductive lake sediments, porous media, and a highly fractured rift basement due to active tectonic and micro-seismic activities that permeate fluids within the rift sedimentary structures.

7.1 Recommendations

- 1) A resistivity survey of the inner caldera would delineate the source of the deep conductors seen in the south as pockets and would probably show if they are connected to deep conductors in the north.
- 2) A resistivity survey of the north-northeast and eastern sedimentary plain (Kedong Ranch) connecting Suswa to Domes and Longonot area could establish geothermal signatures to the east of Suswa town.
- 3) More TEM infill should be conducted for the sites where MT surveys have already been done.
- 4) 3D inversion of MT data for Suswa prospect would give better resolution in delineating the resource signatures.
- 5) Additional surface exploration work could lead to the creation of a conceptual model of the area.

ACKNOWLEDGEMENTS

I wish to acknowledge the UNU-GTP and Icelandic Government for the six month UNU Fellowship award, ÍSOR - Iceland GeoSurvey and Orkustofnun - the Icelandic National Energy Authority for their outstanding teaching staff and provision of support materials and Geothermal Development Company for providing the data and granting me a study leave.

Many thanks go to Dr. Ingvar Birgir Fridleifsson (former director), current director Mr. Lúdvík S. Georgsson, Ms. Thórhildur Ísberg, Mr. Ingimar G. Haraldsson, Ms. Málfríður Ómarsdóttir and Mr. Markús A.G. Wilde, for their terrific support and facilitation of the training programme.

Special thanks to my supervisors, Mr. Gylfi Páll Hersir and Mr. Knútur Árnason for their assistance, availability and open door policy and advice during the study time. I wish to give my thanks to Mr. Arnar Már Vilhjálmsen and Mr. Andemariam Teklesenbet for their assistance with my project.

More thanks to colleagues at UNU-GTP in Geophysical Exploration section for their fruitful discussions and sharing of knowledge. To the entire UNU-GTP fellows of 2013, much thanks. To my colleagues at GDC geophysics section, my utmost gratitude for your support especially in data acquisition.

To my family, your support during these six months away was paramount. Most importantly, thanks to the Almighty Allah who taught mankind by the pen what they didn't know. Certainly I have learnt much in this training.

REFERENCES

Archie, G.E., 1942: The electrical resistivity log as an aid in determining some reservoir characteristics. *Trans. AIME*, 146, 54-67.

Árnason, K., 1989: *Central loop transient electromagnetic sounding over a horizontally layered earth*. Orkustofnun, Reykjavík, report OS-89032/JHD-06, 129 pp.

Árnason, K., 2006a: *TemX short manual*. ÍSOR – Iceland GeoSurvey, Reykjavík, internal report, 17 pp.

Árnason, K., 2006b: *TEMTD (Program for 1D inversion of central-loop TEM and MT data)*. ÍSOR – Iceland GeoSurvey, Reykjavík, short manual, 16 pp.

Árnason, K., 2008: *The magnetotelluric static shift problem*. ÍSOR - Iceland GeoSurvey, report ÍSOR-08088, 16 pp.

Árnason, K., Eysteinnsson, H., and Hersir, G.P., 2010: Joint 1D inversion of TEM and MT data and 3D inversion of MT data in the Hengill area, SW Iceland. *Geothermics*, 39, 13-34.

Árnason, K., Haraldsson, G.I., Johnsen, G.V., Thorbergsson, G., Hersir, G.P., Saemundsson, K., Georgsson, L.S., Rögnvaldsson, S.Th., and Snorrason, S.P., 1987: *Nesjavellir-Ölkelduháls. Surface exploration*. Orkustofnun, Reykjavík, report OS-87018/JHD-02 (in Icelandic), 112 pp.

Badilla E., D., 2011: Resistivity imaging of the Santa Maria sector and the northern zone of Las Pailas geothermal area, Costa Rica, using joint 1D inversion of TDEM and MT data. Report 8 in: *Geothermal training in Iceland 2011*. UNU-GTP, Iceland, 85-118.

Barkaoui, A.E., 2011: Joint 1D inversion of TEM and MT resistivity data with an example from the area around the Eyjafjallajökull glacier, S-Iceland. Report 9 in: *Geothermal training in Iceland 2011*. UNU-GTP, Iceland, 119-148.

Biggs, J., Anthony, E.Y., and Ebinger, C.J., 2009: Multiple inflation and deflation events at Kenyan volcanoes, East African Rift. *Geology*, 37-11, 979–982.

Cagniard, L., 1953: Basic theory of the magneto-telluric method of geophysical prospecting. *Geophysics*, 18, 605-635.

Cantini, P., Cataldi, A., and Pinna, E., 1990: Gravity study of the structure of Suswa volcano and basement in the Kenya Rift. *Geothermics*, 19-4, 367–384.

Christensen, A., Auken, E., and Sorensen, K., 2006: The transient electromagnetic method. *Groundwater Geophysics*, 71, 179-225.

Espejel-García, V., 2009: *Suswa volcano, Kenya rift: Evidence of magma mixing, Na-F complexing and eruptions triggered by recharge*. University of Texas, El Paso, PhD thesis, 115 pp.

Eysteinnsson, H., 1998: *TEMMAP, TEMRES and TEMCROSS plotting programs*. ÍSOR – Iceland GeoSurvey, Reykjavík, unpublished programs and manuals.

Flóvenz, Ó.G., Spangenberg, E., Kulenkampff, J., Árnason, K., Karlsdóttir, R., and Huenges E., 2005: The role of electrical conduction in geothermal exploration. *Proceedings of the World Geothermal Congress 2005, Antalya, Turkey*, CD, 9 pp.

Flóvenz, Ó.G., Hersir, G.P., Saemundsson, K., Ármannsson, H., and Fridriksson Th., 2012: Geothermal energy exploration techniques. In: Syigh, A., (ed.), *Comprehensive renewable energy*, vol. 7. Elsevier, Oxford, 51-95.

GDC, 2013: *Suswa geothermal prospect*. GDC, unpublished report, 107 pp.

Georgsson, L.S., and Karlsdóttir, R., 2009: Resistivity methods - DC and TEM with examples and comparison from the Reykjanes peninsula and Öxarfjörður, Iceland. *Paper presented at “Short Course on Surface Exploration for Geothermal Resources”, organized by UNU-GTP and LaGeo, in Ahuachapan and Santa Tecla, El Salvador*, 14 pp.

Hersir, G.P., and Árnason, K., 2010: Resistivity methods - MT. *Paper presented at „Short Course V on Exploration for Geothermal Resources“, organized by UNU-GTP, GDC and KenGen at Lake Bogoria and Lake Naivasha, Kenya*, 7 pp.

Hersir, G.P., Árnason, K. and Steingrímsson, B., 2009: Exploration and development of the Hengill geothermal field. *Paper presented at “Short Course on Surface Exploration for Geothermal Resources”, organized by UNU-GTP and LaGeo, in Ahuachapan and Santa Tecla, El Salvador*, 14 pp.

Hersir, G.P., Árnason, K., and Vilhjálmsson, A.M., 2013: 3D inversion of magnetotelluric (MT) resistivity data from Krýsuvík high temperature geothermal area in SW Iceland. *Proceedings of the 38th Workshop on Geothermal Reservoir Engineering, Stanford University, Stanford, Ca*, 14 pp.

Hersir, G.P., and Björnsson, A., 1991: *Geophysical exploration for geothermal resources. Principles and application*. UNU-GTP, Iceland, report 15, 94 pp.

Karingithi, C., Arnórsson, S., and Grönvold, K., 2010: Processes controlling aquifer fluid compositions in the Olkaria geothermal system, Kenya. *J. Volcanology & Geothermal Research*, 196, 57–76.

Keller, G.V., and Frischknecht, F.C., 1966: *Electrical methods in geophysical prospecting*. Pergamon Press Ltd., Oxford, 527 pp.

Lagat, J., 2003: Geology and the geothermal systems of the southern segment of the Kenya Rift. *Proceedings of the International Geothermal Conference IGC2003 "Multiple integrated uses of geothermal resources"*, Reykjavik, S12, 33-40.

McCall, G.J.H., and Bristow, C.M., 1965: An introductory account of Suswa volcano, Kenya. *Bulletin Volcanologique*, 28-1, 333-367.

McNeill, 1994: *Principle and application of time domain electromagnetic techniques for resistivity sounding*. Geonics Ltd., Ontario, technical note TN 27, 15 pp.

Mohamud, Y.N., 2013: Appendices to the report "*ID joint inversion of TEM and MT data: Suswa geothermal field, Rift Valley, Kenya*". UNU-GTP, Iceland, report 19 appendices, 92 pp.

NGA, 2013: *Geophysical methods*. Northwest Geophysical Associates, Inc., website: www.nga.com/Geo_ser_DC_tech.htm.

Omenda, P.A., 1997: *The geochemical evolution of Quaternary volcanism in the south central portion of the Kenya rift*. University of Texas, El Paso, PhD thesis, 217 pp.

Omenda P.A., 1998: The geology and structural controls of the Olkaria geothermal system, Kenya. *Geothermics*, 27-1, 55-74.

Omenda, P.A., 2007: Status of geothermal exploration in Kenya and future plans for its development. *Paper presented at "Short Course II on Surface Exploration for Geothermal Resources"*, organized by UNU-GTP and KenGen, at Lake Naivasha, Kenya, 13 pp.

Onacha, S., Shalev, E., Malin, P., and Leary, P., 2009: Joint Geophysical Imaging of fluid-filled fracture zones in geothermal fields in the Kenyan Rift Valley. *Geother. Resource Council, Trans.*, 33, 465-471.

Phoenix Geophysics, 2005: *Data processing user guide*. Phoenix Ltd., users guide.

Quist, A.S., and Marshall, W.L., 1968: Electrical conductances of aqueous sodium chloride solutions from 0 to 800°C and at pressures to 4000 bars. *J. Phys. Chem.*, 72, 684-703.

Rowland, B.F., 2002: *Time-domain electromagnetic exploration*. Northwest Geophysical Associates, Inc., 6 pp.

SEG, 1991: *MT/EMAP data interchange standard*. Society of Exploration Geophysicists, 112 pp.

Simiyu, S.M., 1999: Seismic velocity applications to geothermal evaluation and exploitation, Southern Lake Naivasha. *Proceedings of the 24th Workshop on Geothermal Reservoir Engineering, Stanford University, Stanford, Ca.*, 131-139.

Simiyu, S.M., 2010: Application of micro-seismic methods to geothermal exploration: examples from the Kenya Rift. *Paper presented at Short Course V on Exploration for Geothermal Resources, organized by UNU-GTP, GDC and KenGen, at Lake Bogoria and Lake Naivasha, Kenya*, 27 pp.

Simiyu, S.M., and Keller, G.R., 1997: Integrated geophysical analysis of the East African Plateau from gravity anomalies and recent seismic studies. *Tectonophysics*, 278, 291-314.

Simiyu S.M., and Keller G.R., 2000: Seismic monitoring within the Olkaria geothermal field. *J. Volcanology & Geothermal Research*, 95, 197-208.

Tikhonov, A.N., 1950: Determination of the electrical characteristics of the deeper strata of the earth's crust. *Dokl. Akad. Nauk, USSR*, 73, 295-297 (in Russian).

Ussher G., Harvey C., Johnstone R., and Andersson E., 2000: Understanding the resistivities observed in geothermal systems. *Proceedings of the World Geothermal Congress 2000, Kyushu-Tohoku, Japan*, 1915-1920.

Vozoff, K., 1990: Magnetotellurics: principles and practice. *Proceedings of the Indian Academy of Sciences-Earth and Planetary Sciences*, 99, 441-471.

White, J.C., Espejel-García, V.V., Anthony, E.Y., and Omenda, P.A., 2012: Open system evolution of peralkaline trachyte and phonolite from the Suswa volcano, Kenya rift. *Lithos*, 152-1, 84-104.



GEOTHERMAL BINARY CYCLE POWER PLANT PRINCIPLES, OPERATION AND MAINTENANCE

Angel Fernando Monroy Parada

LaGeo S.A de C.V

15 Avenida Sur, Colonia Utila

Santa Tecla, LaLibertad

EL SALVADOR

amonroy@lageo.com.sv

ABSTRACT

Binary cycle power plants play an important role in the world, generating electricity from low and medium temperature geothermal temperature resources. This report describes a thermodynamic model of a binary cycle power plant and its components. A basic binary cycle and a binary cycle with a recuperator for different turbine inlet pressures are modelled. How the addition of a recuperator in the cycle shifts the maximum point of turbine work output, increasing the turbine work output for a given reinjection temperature and helping when the reinjection temperature is limited by the geothermal water chemistry, is analysed. The report shows that Isopentane and n-Pentane are the working fluid options for the Berlin binary cycle power plant in El Salvador. The parasitic loads for wet and air cooling systems are influenced by the seasonal fluctuations of the ambient temperature. The maintenance of binary cycle power plants is highly influenced by different factors, such as the nature of the geothermal fluid used in the primary loop, the nature of the working fluid, the technology and location of the plant, climate and weather. The operation and maintenance in both Svartsengi and the Berlin binary cycle power plants are presented.

1. INTRODUCTION

Geothermal energy resources have often been associated with the movements of tectonic plate boundaries. El Salvador, a small country in Central America, with an area of 21,040 km² and a population of 6.2 million, is located on the Pacific coast of Central America along the “Pacific ring of fire” where the Cocos and the Caribbean plates interact. The volcanic activity and seismicity associated with the plates are important for geothermal potential development in the country. El Salvador was the first Central American country to exploit geothermal sources. Electricity generation using geothermal energy started in El Salvador in 1975. Development reached a total capacity of 204.2 MW. In El Salvador, the geothermal resource management, exploitation and production of geothermal energy was developed by LaGeo S.A. de C.V. and the installed capacity is distributed mainly in two geothermal fields: 95 MW in Ahuachapán geothermal field and 109.2 MW in Berlin geothermal field. Figure 1 shows the location of El Salvador in Central America, together with its geothermal fields.



FIGURE 1: Location of El Salvador in Central America and its geothermal fields

geothermal field consists of two single flash condensing turbines and one double flash condensing turbine, while Berlin geothermal field utilizes three flash condensing turbines and one binary cycle power plant. A project for increasing the capacity of the Berlin power plant started in 2005. The plant now has an increased capacity by the addition of a 44 MW condensing unit and a 9.2 MW binary unit. The binary power unit has a source temperature of 180°C, obtained from the separated water of the production wells. The total installed capacity of El Salvador is forecast to be about 290 MW by 2015 (Bertani, 2012).

Geothermal fields, systems and reservoirs are classified by temperature, enthalpy and physical state, among other factors. According to the temperature classifications, geothermal sources vary from temperatures below 150°C to temperatures above 200°C, and can be a mixture of steam and water, mainly steam or mainly water. The temperature of the geothermal resource defines the type of technologies required to exploit the available heat and the utilization of the geothermal fields. As mentioned above, El Salvador has two geothermal fields; both are classified as high-temperature geothermal fields: Ahuachapán shows temperatures between 230 and 250°C and Berlin shows a temperature of 300°C. Generally, the high temperature fields are mainly exploited for the generation of electricity, as is the case in El Salvador. The technology utilized for exploiting the Ahuachapán

Electricity generation from geothermal energy made a modest start in 1904 at Larderello in the Tuscany region of northwest Italy with an experimental 10 kW-generator (Lund, 2004). Since then, there has been interest in developing and exploiting geothermal resources around the world and, today, electricity from geothermal energy (a worldwide renewable energy source) has grown to 10,898 MW in 24 countries, producing an estimated 67,246 GWh/yr. The development of worldwide geothermal power production can be seen in Figure 2. The number of geothermal countries is expected to increase from 24 in 2010 to 46 in 2015. Binary power plant technology plays a very important role in the modern geothermal electricity market (Bertani, 2012). The first geothermal binary power plant was put into operation at Paratunka near the city of Petropavlovsk on Russia's Kamchatka peninsula, in 1967. It was rated at 670 kW. It ran successfully for many years, proving the concept of binary plants as we know it today. Nowadays, binary plants are the most widely used type of geothermal power plant with 162 units in operation in May 2007, generating 373 MW of power in 17 countries. They constitute 32% of all geothermal units in operation, but generate only 4% of the total power. Thus, the average power rating per unit is small, only 2.3 MW/unit, but units with ratings of 7–10 MW are coming into use with advanced cycle design (DiPippo, 2007).

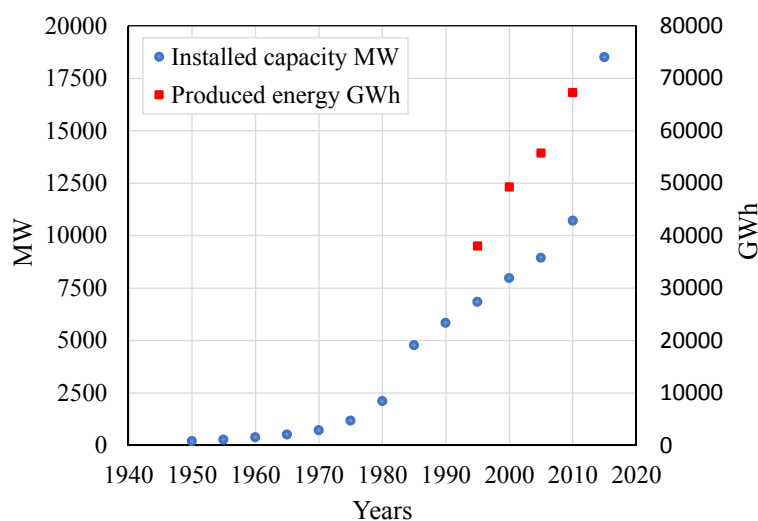


FIGURE 2: Development of worldwide geothermal power production (Bertani, 2012)

El Salvador has played a role in the worldwide development of binary power plants, with the first installed binary power plant in the country located in Berlin geothermal field. In this first unit, the organic Rankine cycle was used to generate electricity using Isopentane as a working fluid. The binary power plant was designed to utilize remnant heat from the geothermal water (waste brine) to evaporate Isopentane. This unit is currently producing electricity, however, there have been operational challenges causing tripping of equipment and even resulting in unit shut-down. Since the unit started running, maintenance and overhaul measures have been developed, and some modifications were executed on the equipment to ensure continuous operation of the plant at maximum capacity and efficiency. LaGeo has experience with this technology and is still learning about it. However, it has been a first great step for the development of electricity production using low and medium temperature geothermal energy in El Salvador.

2. GEOTHERMAL BINARY CYCLE POWER PLANTS

2.1 General characteristics of geothermal fields for utilization of binary cycle power plants

As mentioned in the introduction, the geothermal resource temperature defines the technologies required to exploit the available heat for the utilization of geothermal fields. Table 1 summarizes the classifications of geothermal fields, based on temperatures and physical states. Generally, the high temperature fields are mainly exploited for electricity generation, using dry steam and flash steam technologies. For medium and low temperature geothermal fields, binary cycle power plants show good performance. Nowadays, binary cycle power plants are the most common technology for utilizing low temperature geothermal sources for electricity generation.

TABLE 1: Classification of geothermal fields based on temperature and physical state
(modified from Saemundsson, 2009)

Temperature classification	Physical state classification
Low-temperature geothermal fields have reservoirs with temperature below 150°C at a depth of 1 km. These fields are often characterized by hot or boiling springs.	Liquid-dominated geothermal fields with the water temperature below the boiling point at the prevailing pressure; the liquid phase controls the pressure in the reservoir. Some steam may be present.
Medium-temperature geothermal fields have reservoirs with temperatures between 150- 200°C at a depth of 1 km.	Two-phase geothermal fields where steam and water co-exist and the temperature and pressure follow the boiling point curve.
High-temperature geothermal fields have reservoirs with temperature above 200°C at a depth of 1 km. The fields are characterized by fumaroles, steam vents, mud pools and highly altered ground.	Vapour-dominated geothermal fields where temperature is above the boiling point at the prevailing pressure and the vapour phase controls the pressure in the reservoir. Some liquid water may be present.

In a geothermal binary cycle power plant, the thermal energy of the geothermal fluid is transferred through a heat exchanger from the geothermal fluid to the working fluid which is then vaporized and used to run the turbine coupled to a generator to produce energy. The geothermal and working fluids are confined in separate systems and never come into contact. In this way, the geothermal fluid does not contact the moving parts (mainly the turbine and all rotary equipment in the power plant), thus reducing the negative effects of potential scaling and erosion observed when the geothermal fluid is used as a working fluid. Most binary cycle power plants operate with pumped wells. The pumps are

located below the flash level in a well to prevent flashing by raising the pressure above the saturation pressure for fluid temperature (Elliott et al., 1998).

Binary cycle power plants can be used to generate additional electricity from the geothermal fluid after its utilization in flash power plants. Such binary cycle power plants are known as bottoming plants. With the inclusion of a binary cycle in the geothermal system, the total energy efficiency increases. The geothermal water (brine) exiting from the primary utilization still has sufficient potential to produce turbine work output using a binary power unit as a bottoming cycle for the overall plant. No additional well costs are associated with such electricity generation from binary power plants.

Electricity can now be generated from resources below 100°C where the binary power plant using an organic Rankine cycle process is used in combination with other utilization, as in district heating projects (Lund, 2004). Binary cycle power plants are useful for harnessing low and medium temperature resources and raising the exploitability of geothermal potential worldwide (Bertani, 2012).

2.2 El Salvador geothermal power plants

The major utilization of geothermal energy in El Salvador is for power generation, but some direct uses have been implemented on a small scale, such as for drying grains and fruits. At present, there are two geothermal fields with power plants in operation in El Salvador: Ahuachapán and Berlin. The temperatures in these fields are 230°C in Ahuachapán and 300°C in Berlin. The depth range for the wells varies from 800 m in the shallow areas of Ahuachapán to 2,800 m in Berlin.

Geothermal energy production in El Salvador first started in 1975 at Ahuachapán. Ahuachapán has three condensing units, two 30 MW single flash units and one 35 MW double flash unit. The separated water from the production wells is totally re-injected into the field, using pumps. The pumping station is known as RTA.

Berlin started production in 1992 with two back pressure units of 5 MW each. Currently, Berlin has four units, two 28 MW condensing - single flash units, one 44 MW condensing – single flash unit and one 9.2 MW binary unit used as a bottoming plant. To generate electricity from this binary unit, the separated water is used as a heat source. After heat removal from the separated water coming from the production wells, the separated water is totally re-injected into the reservoir. The reinjection is done using pumps and gravity. The pumping station is known as RTB. Currently the total installed capacity is 95 MW in Ahuachapán and 109.2 MW in Berlin.

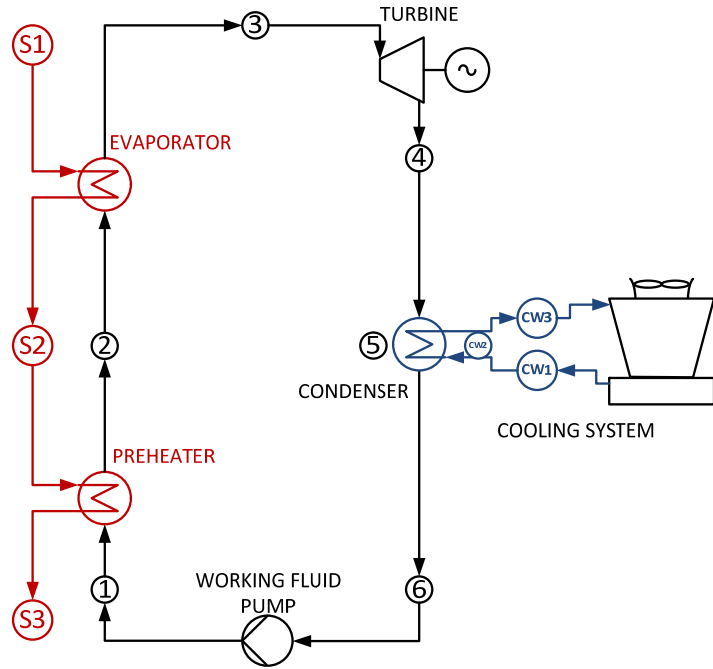
In Berlin, the amount of additional power that could be generated from the separated water in a binary unit depends on how much heat can be removed from the separated water before scaling becomes a problem. The geothermal water from Berlin's liquid dominated reservoir has about 1% of total dissolved solid (TDS) with an appreciable amount of calcium and boron (100 to 200 ppm). When the water is separated in cyclone separators at 10 bars and 185°C, the water contains 800 ppm of silica. And for this condition, the separated water has a silica saturation index (SSI) of 0.95 %. Additionally, when the separated water is cooled, the SSI increases, for example to 1 at 180°C and to 2.2 at 100°C (at 2.2, silica is oversaturated). A research study was conducted to minimise the scaling potential in the re-injection system, and the results recommended 130°C as the lowest temperature value and implementing acid dosing to maintain a pH between 5.5 and 6.0 (SKM, 2004).

3. BASIC BINARY CYCLE

The concept of a binary cycle power plant, known as an organic Rankine cycle (ORC), is a modification of a Rankine cycle where the working fluid is an organic fluid which has a lower boiling point and higher vapour pressure than water along all state points that compound the thermodynamic cycle.

The geothermal binary cycle power plant is formed by two cycles: the primary cycle that contains the geothermal fluid, and a secondary cycle where the organic working fluid is enclosed. The primary cycle starts at the production wells and ends in the re-injection wells. In the primary cycle, the temperature and the desired flow rates of geothermal fluid are determined by the reservoir's field properties. The geothermal fluid can be either water or steam. When the geothermal fluid is water or brine, it is kept at a pressure above its flash point at fluid temperature along the primary cycle in order to avoid flashing of geothermal fluid in the heat exchangers. The geothermal fluid temperature, at the end of the primary cycle, is not allowed to drop to the silica scaling point.

The main components of a basic geothermal binary cycle power plant are the preheater, evaporator, turbine, condenser and working fluid pump. The schematic diagram in Figure 3 shows the main components of the cycle. The basic thermodynamic process of binary cycles is the Rankine cycle, where the vapour reaches a dry saturated condition in the evaporator and is condensed in the condenser. A simple method for describing a binary power cycle is to follow the T-s diagram shown in Figure 4. The thermodynamic states of the working fluid in the secondary cycle are shown in the P-h diagram in Figure 5. Such a diagram helps in understanding the thermodynamic cycle and different states of the working fluid.



The binary cycle (Figure 3) consists of the following four processes:

FIGURE 3: Schematic diagram of a basic binary power cycle

- 6 – 1 Isentropic compression in the working fluid pump;
- 1 – 2 – 3 Constant pressure heat addition in preheater and evaporator;
- 3 – 4 Isentropic expansion in a turbine; and
- 4 – 5 – 6 Constant pressure heat rejection in a condenser.

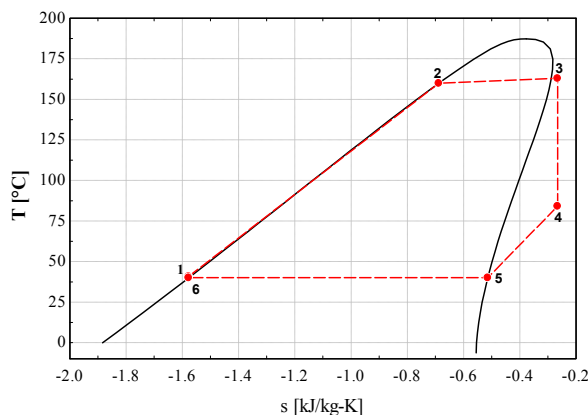


FIGURE 4: T-s diagram for a binary cycle using Isopentane as a working fluid

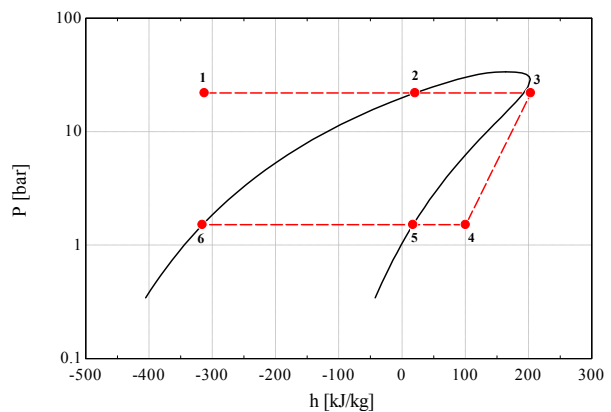


FIGURE 5: P-h diagram for a binary cycle using Isopentane as a working fluid

In the secondary cycle, the working fluid enters the pump at state 6 as a saturated liquid and is compressed isentropically to the operating pressure of the evaporator. The working fluid temperature increases during the isentropic compression process, due to a slight decrease in the specific volume of the working fluid. The working fluid enters the preheater as a compressed liquid and leaves the evaporator as a saturated vapour at state 3. Typically, in the heating-evaporating process, in the preheater the working fluid is delivered to its boiling point. The preheater and evaporator are basically large heat exchangers where the heat coming from the geothermal fluid is transferred to the working fluid at a constant pressure. The evaporator is the section where the working fluid is vaporized at a constant temperature. This saturated condition ensures that no liquid droplets enter the turbine. The saturated vapour at state 3 enters the turbine where it expands isentropically and produces work by rotating the turbine shaft connected to an electric generator. The pressure and the temperature of the vapour drop during this process to the values at state 4, where vapour enters the condenser. At this state, vapour is usually superheated. In the condenser, vapour is condensed at a constant pressure by rejecting heat into the environment. The working fluid leaves the condenser as saturated liquid and enters the working fluid pump, completing the cycle. The efficiencies of the turbine and the working fluid pumps modify the expansion and compression process and are used to determine the real work in both components.

Binary cycle power plants can be cooled by water or air; these methods of cooling are called wet and air cooling systems, respectively. In areas where water is valuable, and/or not easily accessible or conserved, dry cooling systems are used.

It is important to note that the area under processes 1-2-3 represents the heat transferred to the working fluid in the preheater and evaporator, and the area under the processing curve of states 4-5-6 represents the heat rejected in the condenser. The difference between these two areas is the network produced by the cycle (the area enclosed by the cycle curve).

4. BINARY CYCLE COMPONENTS AND ENERGY ANALYSIS

All five components associated with the basic binary cycle (preheater, evaporator, turbine, condenser and pump) are steady flow devices and can be analysed as steady flow processes. In this analysis, the kinetic and potential energy changes are usually small relative to the work and heat transfer terms and are usually neglected. The heat exchangers do not involve any work, and the pump and the turbine are assumed to be isentropic. The heat exchangers are assumed to be well insulated, and all the heat transfer is between the geothermal fluid and the working fluid. The following presents the main equations for energy analysis along with a short discussion of the main components.

4.1 Preheater and evaporator

The preheater and evaporator (Figure 6) are the first components in a binary power cycle. They receive the fluid from the geothermal production wells. These components are heat exchangers where the geothermal fluid, as a heat source, transfers some of its energy to the cold working fluid of the binary cycle.

Point S1 is the entry of the geothermal fluid to the evaporator; at this point, the temperature and mass flow of the fluid are determined by the geothermal reservoir properties. Point S3 is the outlet of the geothermal fluid from the preheater and this point has two temperature design criteria. The first criterion is applied when the fluid coming from the preheater is considered for further utilization. A good example of this is in a district heating system, with an inlet temperature of around 80 - 85°C. The

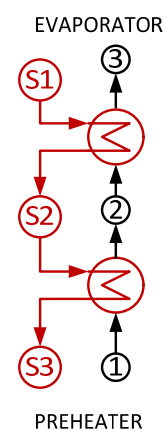


FIGURE 6:
Schematic
diagram for a
preheater and
evaporator

second criterion is associated with scaling problems; the outlet temperature must be kept as high as possible in order to avoid scaling on the geothermal fluid side in the heat exchangers.

Point 1 is the entry of the working fluid, fed by the working fluid pump, into the preheater; point 3 is the outlet of the working fluid vapour towards the turbine. The condition at point 3 is determined by the cycle and turbine requirements; for a binary cycle, this point would be saturated or slightly superheated.

Considering the entire package as a thermodynamic system where the amount of heat transfer to the working fluid is equal to the heat losses from the geothermal fluid, the energy balance equation is given as:

$$\dot{m}_{gf}(h_{S1} - h_{S3}) = \dot{m}_{wf}(h_3 - h_1) \quad (1)$$

where \dot{m}_{gf} = Mass of geothermal fluid;
 \dot{m}_{wf} = Mass of working fluid; and
 h = Values of enthalpies at each specific point.

If the heat capacity of the geothermal fluid is assumed to be known, in the energy balance the enthalpy difference may be replaced by the difference in temperature:

$$\dot{m}_{gf}Cp_{gf}(T_{S1} - T_{S3}) = \dot{m}_{wf}(h_3 - h_1) \quad (2)$$

where Cp_{gf} = Specific heat of geothermal fluid; and
 T = Temperatures at each specific point.

The temperature-heat transfer or temperature-enthalpy difference diagrams play a central role in the design of heat exchangers (preheater, evaporator and condenser). Figure 7 provides a diagram for a hot geothermal fluid and a cold working fluid in the preheater and evaporator. The hot fluid must be cooled from the inlet temperature (TS1) to the outlet temperature (TS3), whereas the cold working fluid must be heated from the inlet temperature (T1) to the outlet temperature (T3). The direction of these processes is indicated by the arrows in the figure. The temperatures and mass flow rates are assumed to be fixed. The abscissa represents the total amount of heat that is passed from the geothermal fluid to the working fluid. It can be shown either in percentages or in heat units. The minimum temperature difference in the heat exchanger, between the geothermal fluid and the working fluid, is called the pinch-point, and the value of that difference is designated the pinch-point temperature difference, ΔT_{pp} . In the analysis of this diagram, points 1, 2 and 3 are known from the cycle thermodynamics analysis. Therefore, the preheater and evaporator may be analysed as follows:

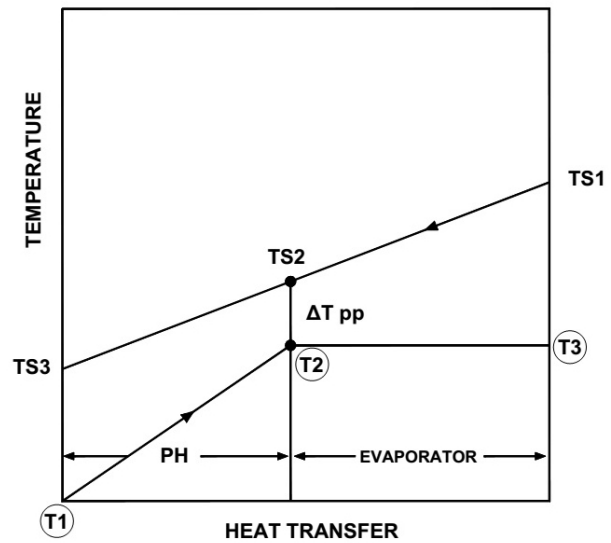


FIGURE 7: Temperature – heat transfer diagram for preheater (PH) and evaporator; Points 1-2-3 correspond to T1, T2 and T3 and are known values obtained from the working fluid process

Preheater

$$\dot{m}_{gf}Cp_{gf}(T_{S2} - T_{S3}) = \dot{m}_{wf}(h_2 - h_1) \quad (3)$$

Evaporator

$$\dot{m}_{gf}Cp_{gf}(T_{S1} - T_{S2}) = \dot{m}_{wf}(h_3 - h_2) \quad (4)$$

The pinch-point temperature difference is generally known from the manufacturer's specifications; this allows TS2 to be found from the known value for T2 as follows:

$$T_{S2} = T_2 + \Delta T_{pp} \quad (5)$$

where ΔT_{pp} = Pinch-point temperature difference.

While it is theoretically possible for the pinch-point to occur at the cold end of the preheater (TS3), this practically never happens (DiPippo, 2007).

4.2 Turbine

The binary cycle turbine converts the vapour thermodynamic energy of the working fluid to mechanical work on the turbine shaft; this shaft is coupled to the generator where electricity is produced. The thermodynamic analysis of the turbine in binary cycles follows the same assumption as for steam turbines. Figure 8 show the turbine from the cycle flow diagram for reference in the following analyses. Point 3 is the vapour inlet to the turbine, and point 4 is the turbine exit. The ideal turbine is isentropic, that means the entropy at the inlet point is the same as at the outlet point. The vapour enthalpy change in the real turbine is the enthalpy change in the ideal turbine multiplied by the turbine isentropic efficiency. The work output of the real turbine is this enthalpy change multiplied by the working fluid mass flow through the turbine.

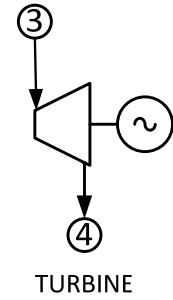


FIGURE 8:
Schematic
diagram for a
turbine

$$\dot{W}_T = \dot{m}_{wf}(h_3 - h_4) = \dot{m}_{wf} \eta_t (h_3 - h_{4s}) \quad (6)$$

where \dot{W}_T = Work output of the turbine; and
 η_t = Turbine isentropic efficiency.

It is important to note that the selection of the working fluid defines some parameters in the turbine design.

4.3 Condenser

The condenser is another heat exchanger in the binary cycle. The condenser exchanges heat between the cooling fluid cycle and the working fluid vapour. The turbine exhaust vapour exits the turbine and is led to the condenser where it is condensed by the cooling fluid. The condenser may be water or air cooled. This process occurs at a constant pressure (isobaric condensation).

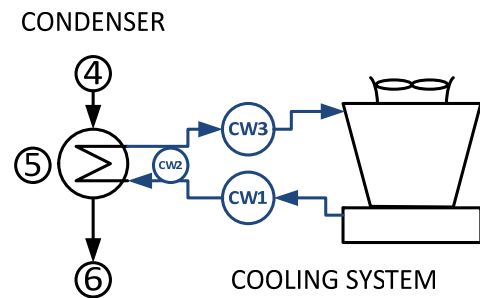


FIGURE 9: Schematic diagram for a
condenser and a wet cooling system

Figure 9 shows the condenser scheme from the cycle flow diagram for reference in the following analyses. The calculations for the condenser are roughly the same in both cases as the temperature profile of cooling fluid (air or water) is very close to linear. At point 4, the vapour comes from the turbine. At point 5, the vapour reaches the dew point and it is at this point that the condensation process starts. Point 6 is the condensed fluid, normally saturated liquid, moving towards the working fluid pumps. Point CW3 is the entry of the cooling fluid and CW1 is the outlet of the cooling fluid, to and from the cooling tower.

The condenser heat transfer between the working fluid and the cooling fluid can be expressed as follows:

$$\dot{m}_{CF} (h_{CW3} - h_{CW1}) = \dot{m}_{wf} (h_4 - h_6) \quad (7)$$

where \dot{m}_{CF} = Mass of cooling fluid.

The cooling fluid may be taken as having a constant specific heat C_{P-CF} for the small temperature range from inlet to outlet. To dissipate the required amount of waste heat, a cooling tower with a specified range, TCW3 – TCW1, will need a mass flow rate determined by the following equation:

$$\dot{m}_{CF} C_{P-CF} (T_{CW3} - T_{CW1}) = \dot{m}_{wf} (h_4 - h_6) \quad (8)$$

where C_{P-CF} = Specific heat of cooling fluid.

In the thermodynamics analysis of the condenser, the increase in the outlet temperature of the cooling fluid and the condenser pinch point temperature are assumed.

4.4 Binary cycle with a recuperator

The binary cycle can be modified with the incorporation of a recuperator. The recuperator is another heat exchanger and represents one additional piece of equipment in the binary cycle power plant. The incorporation of a recuperator is shown in Figure 10. The figure shows the position of the components in the cycle. The recuperator increases the temperature of the working fluid at the preheater entry (point 2) and thus leads to a higher temperature (point S3) of the geothermal fluid for re-injection. This means that the heat obtained from the geothermal fluid is replaced by the recovered heat. The recovered heat in the working fluid, at point 2, is removed from the working fluid at the turbine exhaust condition, at point 5.

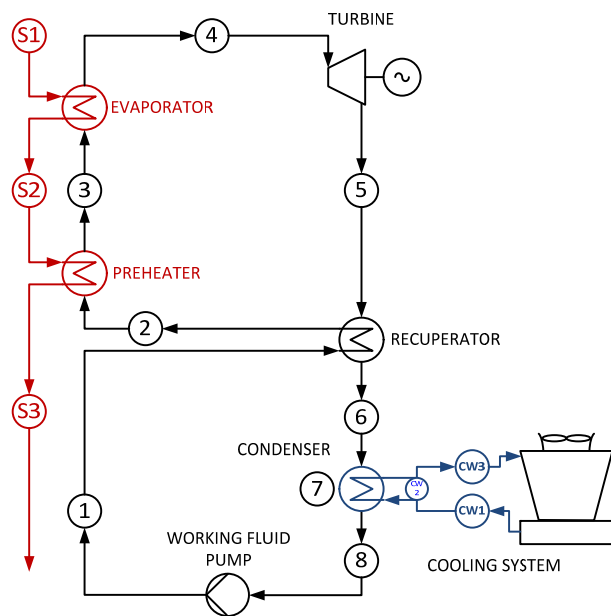


FIGURE 10: Schematic diagram of the binary power cycle with a recuperator

As mentioned in Section 4.1, point S3 is the outlet of the geothermal fluid from the preheater. This point has design temperature limits imposed by the risk of scaling or the requirements of a secondary process.

In this report, the EES computer program was used for thermodynamic calculations for different cycle simulations. This program is a general equation solver that solves thousands of algebraic and differential equations. The program provides a high accuracy thermodynamic property database for the fluids used in this research (F-Chart Software, 2012).

Figures 11 and 12 show the simulation results for a basic binary cycle and a binary cycle with a recuperator for different reinjection temperatures. The simulation for both cycles was done using Isopentane and n-Pentane as a working fluid with an inlet temperature of 180°C geothermal fluid. For the calculations, 221 kg/s of geothermal fluid and 40°C as a condensing temperature were assumed. In the recuperator, the available heat is the heat which can be removed from the turbine exit vapour until the vapour reaches the dew point. After that, the vapour temperature is the same as the condensation temperature and the recuperation process is complete. The calculation is based on an ideal binary cycle.

The addition of a recuperator causes no change in the maximum turbine work output of the binary cycle, as shown in Figures 11 and 12. The recuperation process does not increase the turbine work output, but the efficiency increases as a result of less heat input from the geothermal fluid (Valdimarsson, 2011).

The addition of a recuperator, however, causes a shift in the maximum point of turbine work output of the cycle with respect to the reinjection temperature.

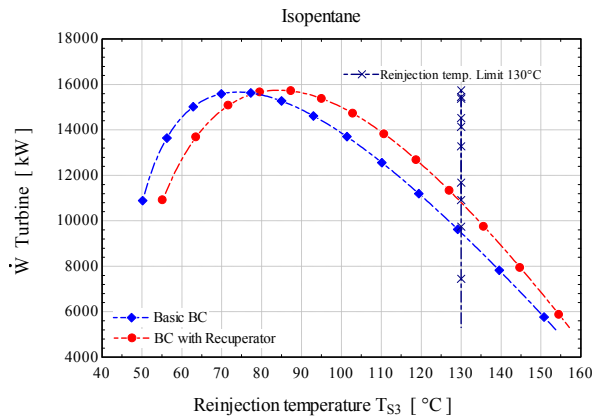


FIGURE 11: Variation of turbine work output with reinjection temperature for Isopentane

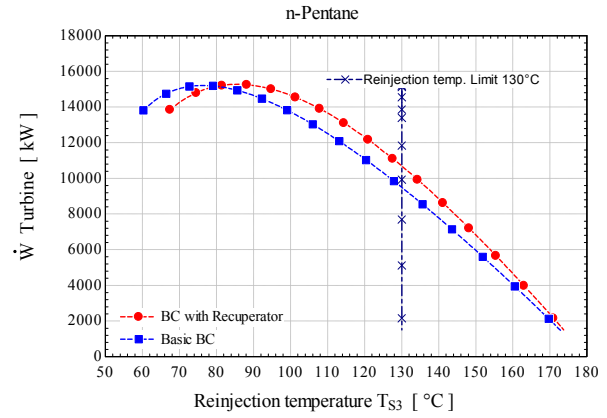


FIGURE 12: Variation of turbine work output with reinjection temperature for n-Pentane

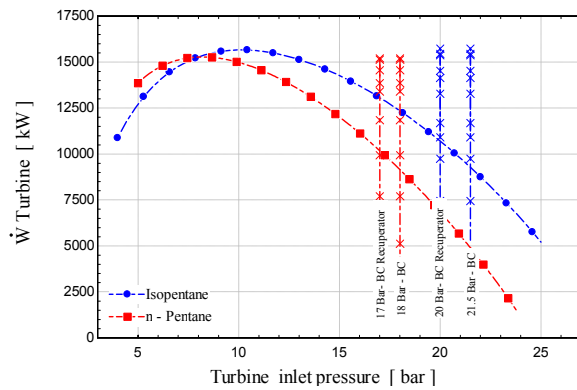


FIGURE 13: Turbine work output against turbine inlet pressure for Isopentane and n-Pentane at the same reinjection temperature ($T_{S3} = 130^{\circ}\text{C}$)

As shown in the figures, for the Isopentane, the maximum turbine work output point is moved 20°C and the re-injection temperature is moved from 65°C to 85°C . And for n-Pentane, the maximum point is moved 10°C and the reinjection temperature is moved from 75°C to 85°C .

When the reinjection temperature is limited by the geothermal water's chemistry, adding a recuperator serves to increase the turbine work output for a given reinjection temperature. Figures 11 and 12 show that the turbine work output increases by 15% at 130°C reinjection temperature. Figure 13 shows the pressure value that fits for 130°C when Isopentane and n-Pentane are used in a basic binary cycle and a binary cycle with a recuperator.

Figures 14 and 15 show the simulation results of a basic binary cycle and a binary cycle with a recuperator for different turbine inlet pressures. The simulation uses the same parameters and

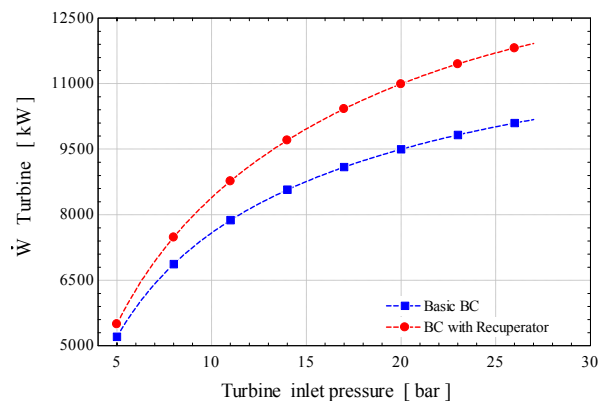


FIGURE 14: Variations of turbine work output with turbine inlet pressure for Isopentane

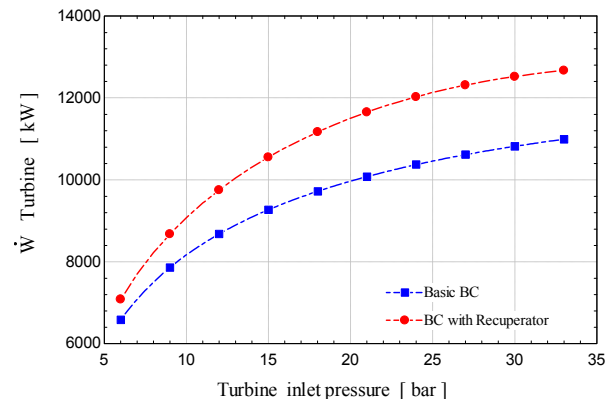


FIGURE 15: Variation of turbine work output with turbine inlet pressure for n-Pentane

assumptions as for the previous simulation and at a constant reinjection temperature of 130°C. With a constant reinjection temperature in both simulations, the same amount of available heat that could be exchanged in the preheater and the evaporator was simulated.

4.5 Heat exchanger sizing and estimated equipment cost

The geothermal binary cycle requires different sizes of heat exchangers for heat transfer processes. Each heat exchanger has its own ability to exchange the amount of heat according to its function during the process and it is this amount of heat exchange which defines the size of the equipment. The size of the heat exchanger is expressed in terms of the area needed to exchange heat, expressed in m². The heat transfer in the heat exchangers involves the concepts of convection and conduction and, for determining the area of the heat exchanger, it is convenient to work with the total heat transfer coefficient U that considers the effect of these two concepts (Table 2). Additionally, the log mean temperature difference (LMTD) method is applied to determine the heat transfer area.

TABLE 2: Values assumed for the total heat transfer coefficient (Ahangar, 2013)

Component	U (W/m ² °C)
Preheater	1000
Evaporator	1600
Recuperator	400
Condenser	800

The area of the heat exchanger surfaces (A), expressed in terms of the rate of heat transfer (Q), the heat transfer coefficient (U) and the log mean temperature difference (LMTD), can be written as follows:

$$A = \frac{Q}{U * LMTD} \quad (9)$$

and

$$LMTD = \frac{\Delta T_1 - \Delta T_2}{\ln\left(\frac{\Delta T_1}{\Delta T_2}\right)} \quad (10)$$

where ΔT_1 = Temperature difference between the fluids at the inlet of the heat exchanger; and
 ΔT_2 = Temperature difference between the fluids at the outlet of the heat exchanger.

Table 3 shows the values for the areas for heat exchangers used in a basic binary cycle and a binary cycle with a recuperator. These areas were calculated assuming Isopentane as a working fluid, the geothermal fluid temperature available at 180°C, a mass flow rate of 221 kg/s and 40°C as a condensing temperature.

The cost for the heat exchangers used in a binary cycle with a recuperator, compared with a basic binary cycle, follows the heat exchanger area. For an investment in heat exchangers for a binary cycle with recuperator, considering the energy cost at 120 \$/MW and the operation and maintenance cost at 5% of annual income, the payback time is 1.71 years.

An overall conclusion can be drawn that when the recuperator is added, compared with a basic binary cycle, the total plant cost becomes higher. When some limit in the outlet temperature of the primary loop exists, like geothermal fluid chemistry or district heating applications, the recuperator helps to overcome these limitations and generate more turbine work output. As the basic binary cycle has a lower cost, in general, this option is the best when no such constraints exist.

In order to evaluate the area required for heat exchangers for different working fluids, a simulation was carried out. The results are shown in Figure 16. The simulations used a basic binary cycle and calculations assumed a geothermal fluid temperature of 180°C, a mass flow rate of 221 kg/s and 40°C as the condensing temperature. Figure 16 shows the variations in turbine work output with the total area required for the heat exchangers used in binary power plants. The total area required for a heat

exchanger to generate the corresponding turbine work output is influenced by the properties of the working fluid selected for the binary cycle

TABLE 3: Areas and cost for a heat exchanger for a binary cycle and a binary cycle with a recuperator

Working fluid	Turbine inlet pressure		Reinjection temperature (TS3)		
Isopentante	22 bar		130°C		
		Basic binary		Binary with recuperator	
	Turbine output	9722 kW		11309 kW	
	Unit cost (US\$/m ²)	Area (m ²)	Cost (US\$/m ²)	Area (m ²)	Cost (US\$/m ²)
Preheater	450	1144	\$ 514,800	1401	\$ 630,450
Evaporator	500	1197	\$ 598,500	1326	\$ 663,000
Recuperator	400	0	-	2677	\$ 1,070,800
Condenser	600	1775	\$ 1,065,000	4212	\$ 2,527,200
Total		4116	\$ 2,178,300	9616	\$ 4,891,450
Output difference (MW)	Annual generation (MWh)	Energy cost (US\$/MWh)	Annual income (US\$)	Areas cost difference (US\$)	Payback (years)
1.587	13902	\$ 120	\$ 1,668,254	\$ 2,713,150	1.71

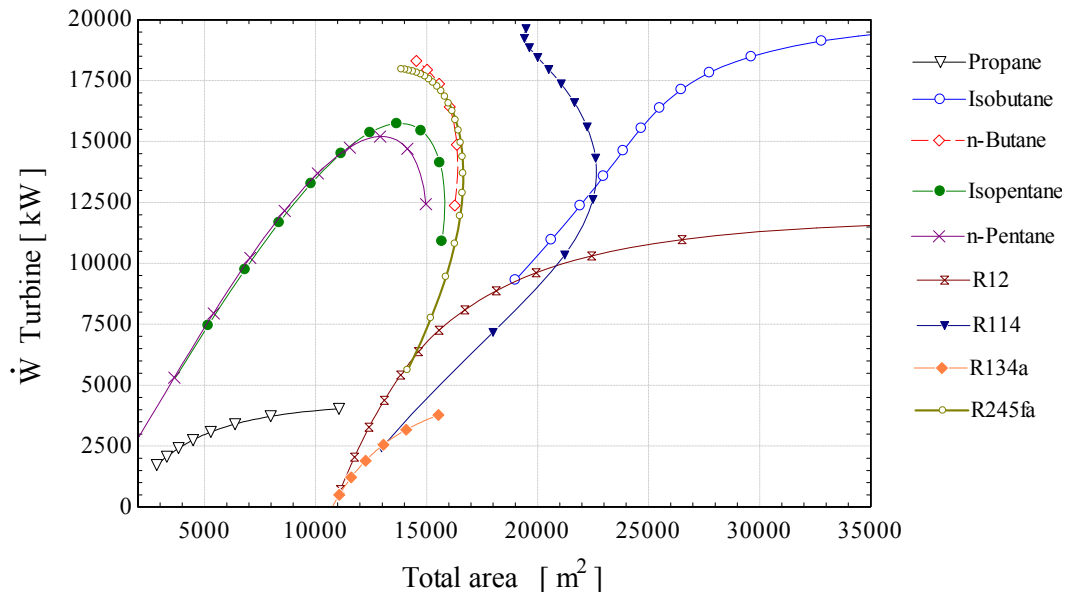


FIGURE 16: Variations of the total area required for a heat exchanger in a basic binary cycle using different working fluids

4.6 Cooling system

Cooling systems are used to reject the heat from the cycle. In binary cycle power plants, the component responsible for dissipating the heat load is the condenser. In the condenser, the vapour phase of the working fluid is condensed at a constant temperature and the heat load is rejected to the environment.

For binary cycle power plants, three types of cooling systems can be applied: the options are a water cooling system, a wet air cooling system and an air cooling system. The water cooling system consists of a shell and tube heat exchanger; this type of cooling system is used mainly when the binary power plant is located in areas with easy access to water. The good range of temperatures for the cooling water used in this cooling system can be from 5 to 25°C. Normally, horizontal double pass shell and tube heat exchangers are components in binary cycle power plants.

The wet air cooling systems use water and air as the cooling fluid, and consist of a condenser and a cooling tower. In wet cooling systems, the vapour of the working fluid from the turbine is condensed in shell and tube heat exchangers. The vapour is condensed by removing the heat and transferring it to the cooling water flowing in the condenser tubes. The cooling water, after removing the heat from the working fluid vapour in the condenser, is pumped to a cooling tower where the heat is transferred to ambient air flowing through the cooling tower. For the evaporation losses and blow down effects, make-up water is required to compensate. For a binary power plant, the most common types of cooling towers are the cross-flow and counter flow types. The typical temperature difference between the inlet and outlet cooling water is 10°C (Mendrinós et al., 2006).

In air cooling systems, air is used to condense the working fluid vapour and reject the heat to the environment. The air cooling system included in this report is also known as an air cooled condenser system. In this air condenser, the working fluid vapour flows through the tubes; the tubes form the condenser area; the heat is rejected to the ambient air via conductive heat transfer. The conductive heat transfer is created by fans that blow ambient air across the outside surface of the tubes. In an air cooling system, no water supply is necessary. A useful graph, shown in Figure 17, plots the air temperature leaving the air condenser as a function of the inlet air temperature (Mishra et al., 2010). The air cooling system is one option when the binary power plant is located in an area with little or no water, where access to water is strictly regulated, and where extremely low ambient temperature conditions exist.

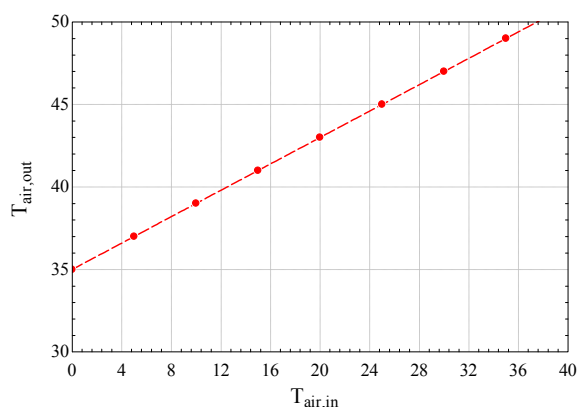


FIGURE 17: Behaviour of outlet temperature as a function of inlet temperature for the air cooled condenser (modified from Pieve and Salvadori, 2011)

Figures 18 and 19 show the variations of parasitic loads for wet and dry cooling systems with ambient temperature for a basic binary cycle. For calculations, Isopentane was used as a working fluid and the available geothermal fluid temperature was 180°C. The mass flow rate of geothermal fluid was 221

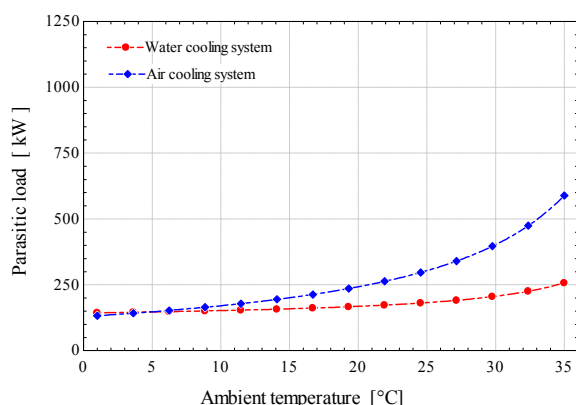


FIGURE 18: Variations of parasitic loads for cooling systems with ambient temperature

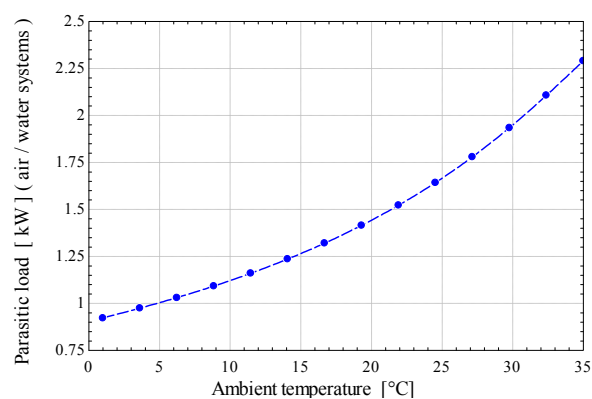


FIGURE 19: Variations of specific parasitic work for cooling systems

kg/s and 40°C was the condensing temperature. Figure 18 shows an almost constant parasitic load of the wet cooling system with respect to the ambient temperature. Figure 19 shows variations of the parasitic work ratio for air cooling and water cooling with ambient temperature. In general, the performance of the cooling systems is influenced by the seasonal fluctuation of the ambient temperature. The heat sink temperature for the cycle is the air temperature and affects the overall cycle performance.

5. WORKING FLUIDS

Organic fluids are used as working fluids in binary cycles. The right selection of a working fluid in binary cycle power plants is very important as it has a primary effect on the efficiency of the power plant, the sizes of power plant components, the design of the expansion turbine, power plant stability, safety, performance, economy and environmental concerns. Because of the low temperature of the heat source, thermodynamic losses occurring in heat exchangers have a significant impact on the overall efficiency of the cycle. These inefficiencies are highly dependent on the thermodynamic properties of the working fluid. A common characteristic of all working fluids used in binary cycle power plant is their low boiling point. They also have critical temperatures and pressures lower than water. Because of the low critical temperature, some organic working fluids can operate under supercritical conditions in geothermal binary cycles. This allows for a better match between the temperatures of the two fluids in heat exchangers. Numerous fluids can be used as a working fluids in binary cycle power plants, except for those having too high or low critical temperature. The working fluid options include: hydrocarbons (HCs), perfluorocarbons (PCFs), chlorofluorocarbons (CFCs), hydrofluorocarbons (HFCs), hydrofluoroolefins (HFOs), hydrochlorofluorocarbons (HCFCs), alcohols, siloxanes, fluorinated ether, and ether. With reference to the thermodynamic characteristics, the most practical options are hydrocarbons, hydrofluorocarbons, hydrochlorofluorocarbons, perfluorocarbons, and chlorofluorocarbons. Nevertheless, when a working fluid is selected, factors such as safety, health and environmental impact issues should be considered. Because of their strong effect on the ozone layer depletion, fluorocarbons were forbidden to be used in binary cycle power plant applications (Lukawski, 2009).

The determination of appropriate working fluids for use in binary cycle power plants is a complex task and has a direct relationship with the heat recovery process in the thermodynamic cycle. The working fluids can be classified according to their saturation vapour states, one of the most important characteristics for working fluids in binary cycles.

Figures 20, 21 and 22 show three types of vapour saturation curves in a temperature-entropy (T-s) diagram: a wet working fluid with negative slopes; an isentropic working fluid with nearly infinitely

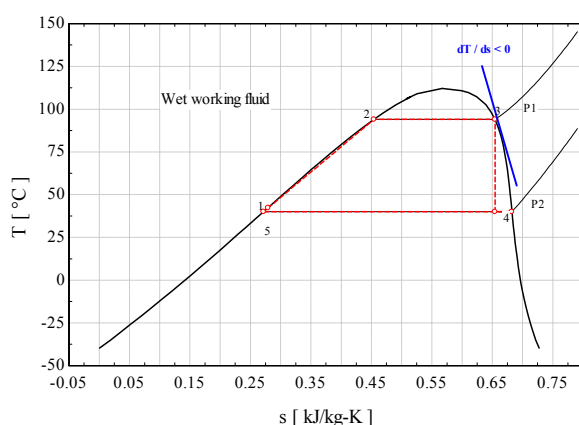


FIGURE 20: T-s diagram for wet working fluids ($dT/ds < 0$)

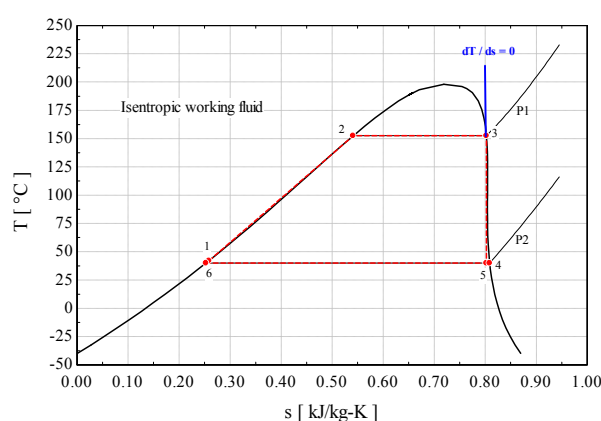


FIGURE 21: T-s diagram for isentropic working fluids ($dT/ds = 0$)

large slopes; and a dry working fluid with positive slopes (dT/ds). It is observed from the T-s diagram that for wet working fluids, a superheater is employed to superheat the vapour, and after isentropic expansion in the turbine, the wet working fluid becomes a mixture of liquid and vapour. The saturated vapour of a dry working fluid becomes superheated after isentropic expansion in the turbine. An isentropic working fluid has an almost vertical vapour saturation curve. Since the vapour expands along a vertical line on the T-s diagram, vapour saturated at the turbine inlet will remain saturated throughout the turbine without condensation. The saturation condition persists during expansion in the turbine. The fact that there is no need for installing a recuperator makes isentropic working fluids ideal working fluids for binary cycle power plants. As mentioned above, because of the negative slope of the saturation vapour curve for a wet working fluid, after isentropic expansion in the turbine, the working fluid exists in two phases. Typically, when a wet working fluid is used in the cycle, the minimum dryness fraction at the outlet of a turbine is kept above 85%, for preventing erosion and damage to the turbine blades. The problems of erosion and damage to the blades are more severe with steam turbines. To satisfy the minimum dryness fraction after isentropic expansion in the turbine, wet working fluid at the inlet of the turbine should be superheated. Isentropic and dry working fluids do not need superheating, so the concerns about liquid droplets on the turbine blades are reduced (Bao and Zhao, 2013). Therefore, the dry or isentropic working fluids are more suitable for binary cycle power plants. These types of fluids are known as a retrograde fluids. Table 4 shows a list of different working fluids.

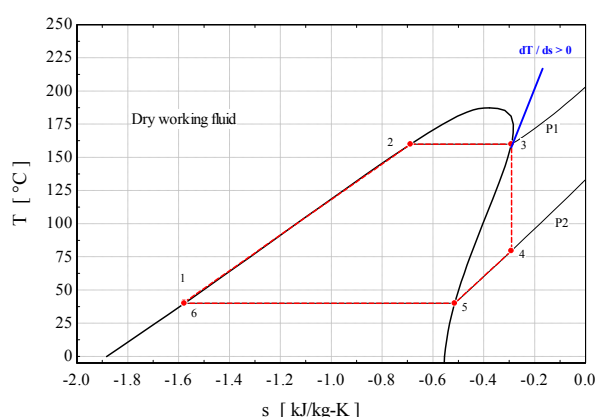


FIGURE 22: T-s diagram for dry working fluids ($dT/ds > 0$)

TABLE 4: Thermodynamics, health and environmental properties of some candidate working fluids for geothermal binary cycles (Modified from DiPippo, 2007)

Fluid	Formula	Critical temp. (°C)	Critical pressure (bar)	Molar mass (kg/kmol)	Toxicity	Flammability	ODP*	GWP**
Propane	C ₃ H ₈	96.95	42.36	44.09	Low	very high	0	3
i-Butane	i-C ₄ H ₁₀	135.9	36.85	58.12	Low	very high	0	3
n-Butane	C ₄ H ₁₀	150.8	37.18	58.12	Low	very high	0	3
i-Pentane	i-C ₅ H ₁₂	187.8	34.09	72.15	Low	very high	0	3
n-Pentane	C ₅ H ₁₂	193.9	32.40	72.15	Low	very high	0	3
R-12	CCl ₂ F ₂	112.0	41.14	120.9	non-toxic	non-flam.	1.0	4,500
R-114	C ₂ Cl ₂ F ₄	145.7	32.89	170.9	non-toxic	non-flam.	0.7	5,850
R134a	CH ₂ FCF ₃	101.0	40.59	102.0	Low	non-flam.	0	1,430
R254fa	C ₃ H ₃ F ₅	154.0	36.51	134.0	Low	non-flam.	0	1030
Ammonia	NH ₃	133.6	116.27	17.03	Toxic	Lower	0	0
Water	H ₂ O	374.1	220.89	18.02	non-toxic	non-flam.	0	-

*Ozone Depletion Potential

** Global Warming Potential

In order to evaluate the performance of different working fluids, a simulation was carried out. The results are shown in Figures 23 and 24. The simulations use a binary cycle with a recuperator and calculations assume a geothermal fluid temperature at 180°C, a mass flow rate of 221 kg/s and 40°C as a condensing temperature.

Figure 23 shows the variations of turbine inlet pressure with the reinjection temperature of the geothermal water. For temperatures ranging from 80°C to 160°C, only Isopentane and n-Pentane can be selected as a working fluid. These types of working fluids are selected when the reinjection temperature is limited by the geothermal water chemistry or another design condition. For reinjection

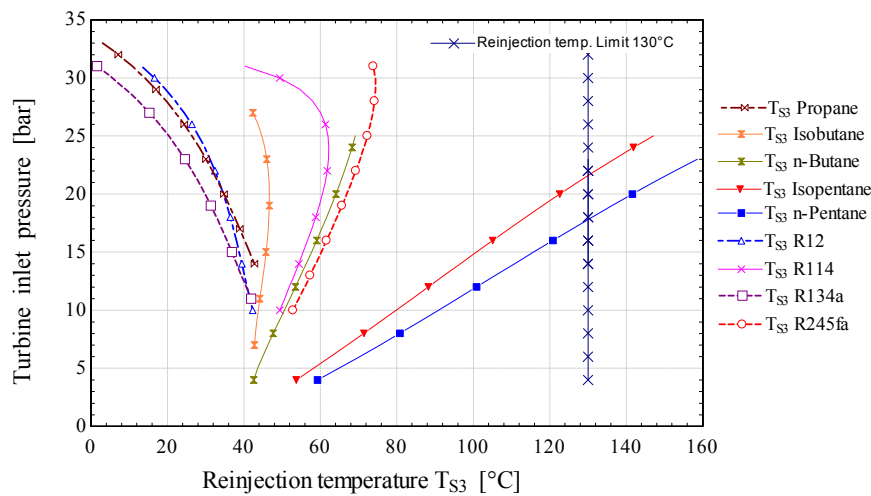


FIGURE 23: Variation of the turbine inlet pressure of different working fluids with the reinjection temperature of geothermal water

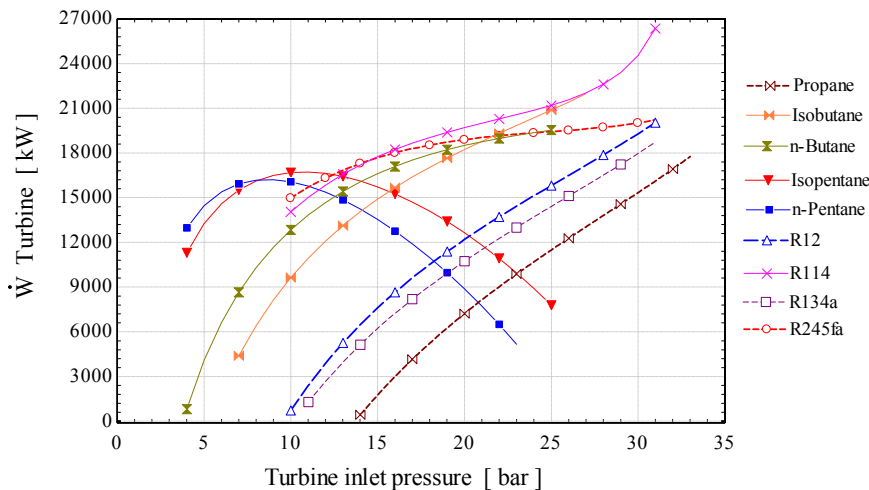


FIGURE 24: Turbine work output for different turbine inlet pressures with different working fluids

shown, the turbine work output increases at higher turbine inlet pressure until its critical pressure is reached; the complete opposite behaviour is observed for Isopentane and n-pentane. Finally, to make a working fluid selection, the following parameters must be known: the temperature available from the geothermal fluid (heat source), the reinjection temperature limit, if it exists, for the application, and the turbine inlet pressure which is defined by the manufacturer. Also, consideration concerning safety, health and environmental factors should be taken into account.

6. WORLDWIDE BINARY CYCLE POWER PLANTS

Binary cycle power plants play an important role in the world for generating electricity from low geothermal temperature fields. The number of countries utilizing geothermal energy is increasing every year, with many countries focusing on electricity generation using binary cycle technology. According to Bertani (2012), in 2010, 1.1 GW was generated using binary cycle power plants. However, binary cycle power plants are 44% of the total geothermal power plants. Appendix I shows the binary power plants installed around the world.

temperatures between 40 and 80°C, the working fluid options are Isopentane, n-pentane, isobutane, n-butane, R114 and R245fa. These fluids can be selected when the geothermal fluid has no limitations on temperature and can be cooled down approaching the condensing temperature. Once the working fluid has been evaluated in accordance with the desired reinjection temperature, the next step in the selection is to evaluate the turbine work output that can be obtained. Figure 24 shows the variation of turbine work output for different values of turbine inlet pressures. As seen from the figure, Isopentane and n-pentane have a maximum point of turbine work output, and the maximum work occurs in the range between 9 -10 bars. R245fa shows an increasing stable behaviour for the turbine work output, from 15 to 30 bars. For R114, isobutane and the other working fluids

7. GENERAL DESCRIPTION AND OPERATION OF SVARTSENGI AND BERLIN BINARY POWER PLANTS

7.1 Svartsengi binary units

Svartsengi power plant is located on the Reykjanes Peninsula in Iceland. The geothermal power plant is located at the high-temperature field near the town of Grindavík. Svartsengi power plant supplies electricity to the national grid and district heating water, serving 20,000 people (Thórólfsson, 2005). Svartsengi began to generate electricity in 1976 when the first combined heat and power plant started (Power Plant 1). In 2008 the last phase (Power Plant 6) was finished. This power plant was built in six phases (Table 5); the production capacity in Svartsengi is 75 MWe and 150 MWt (HS Orka, 2013).

TABLE 5: Installed capacity in Svartsengi power plant at each phase (HS Orka, 2013)

Phase	Building years	Technology	Units	MWe/Unit	MWt/Unit
Plant 1	1976 - 1979	Back pressure steam turbine	2	1	0
Plant 2	1979 – 1980	Heat exchanger	3	0	25
Plant 3	1980	Back pressure steam turbine	1	6	0
Plant 4	1989 – 1993	Isopentane binary units	7	1.2	0
Plant 5	1998 – 2000	Extraction-condensing steam turbine	1	30	75
Plant 6	2006 - 2007	Condensing steam turbine	1	30	0

In Svartsengi, Plant 4 consists of binary power units, as shown in Table 5. There are a total of 7 binary units, designed by Ormat, using Isopentane as a working fluid and each unit generates 1.2 MW. The binary units at Svartsengi are known as Ormat4 to Ormat10 (Figure 25). The heat source for those units comes from the low pressure geothermal steam exhaust of a back pressure steam turbine (Plant 3). The amount of exhaust steam available from Plant 3 is 38.5 kg/s saturated steam at 1.2 bars (Verkís, 2013). The temperature corresponding to these conditions for the exhausted steam is 103°C. As mentioned above, the power from each unit is the same, but they have different condensing systems. Those condensing systems are air systems and water systems. In the air condensing systems, the vapour of the working fluid goes directly to the air cooled condenser. The air cooled condenser is a heat exchanger with tubes fixed at the ends to inlet and outlet header boxes with a passage in-between for the flow of air blown by fans. In Svartsengi, Ormat 7, 8, 9 and 10 units are air cooled.

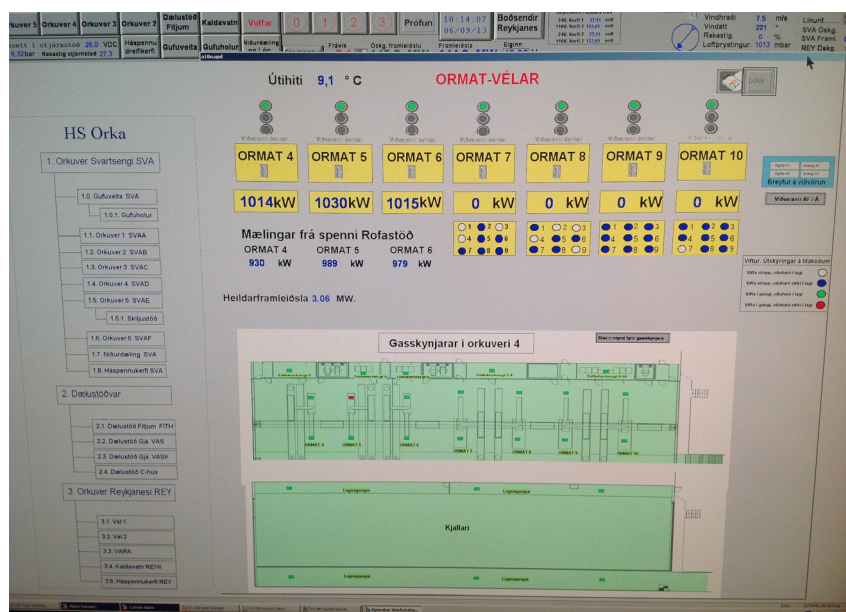


FIGURE 25: Screen from control room in Svartsengi power plant

The water condenser systems are comprised of shell and tube heat exchangers. The exhaust working fluid vapour from the turbine is passed to the shell side of the condenser where it is condensed by cooling water circulating through the tubes. The cooling water enters the condenser at a temperature of 5°C and leaves the condenser at 22°C. In Svartsengi, ORMAT 4, 5 and 6 units are water cooled.

The Ormat units are based on the organic Rankine cycle and consist of the following components: preheater/evaporator, separator, condenser, turbine, gearbox, generator, feed or working fluid pumps and a power and control cabinet. Figure 26 shows the P&ID diagram and a photo of one binary Ormat unit where the components can be identified. The saturated steam passes through the tubes of the preheater-evaporator to heat and evaporate the working fluid (Isopentane) in the shell side of the evaporator. The vapour of the working fluid then moves into the separator where droplets are removed. The level of the working fluid in the evaporator is regulated automatically by a controlled feed valve. In normal operation conditions, the vapour from the separator passes through the main valve to the turbine. The level of the working fluid in the evaporator is regulated automatically by a controlled feed valve. In normal operation conditions, the vapour from the separator passes through the main valve to the turbine.

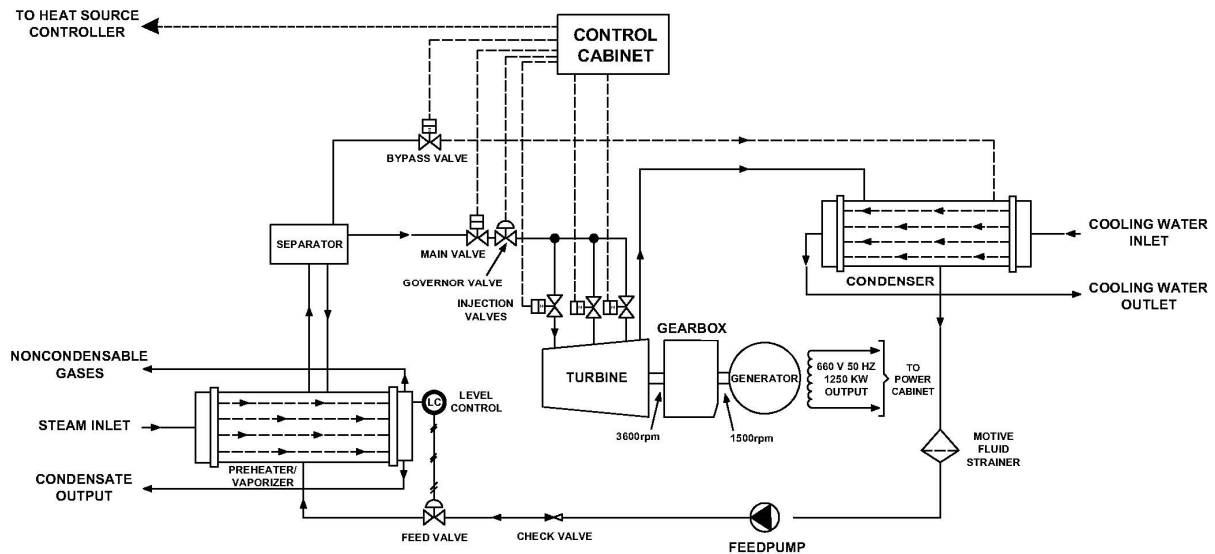


FIGURE 26: Binary Ormat unit at Svartsengi, water cooled condenser

The working fluid vapour expands in the turbine, and the turbine drives the generator using a gearbox at 3600/1500 rpm. The units have a bypass that, in case of a stop or under abnormal operating conditions, allows the vapour from the evaporator to reach the condenser directly. The generator has a nominal power output of 1300 kW at 660 V and 50 Hz. The exhaust working fluid vapour is cooled and condensed to liquid by the condenser system. The working fluid is removed from the condenser by the working fluid pump and returned to the preheater/evaporator to complete the heat cycle. The unit is

controlled by control devices and circuits contained in a power and control cabinet. In Table 6, the operating parameters, type of equipment, and other important characteristics of the preheater-evaporator and turbine that are part of the binary units are summarized.

TABLE 6: Technical data of the preheater-evaporator and turbine

Preheater-evaporator and separator		Turbine	
Type	Shell and tube heat exchanger	Type	Impulse
Fluid at tube side	Saturated steam	Stages	Single
Fluid at shell side	Working fluid (Isopentane)	Working fluid	Isopentane
Evaporator outlet pressure	5.5 bar	Net power output	1,200 kW
Heat source inlet temp.	103°C	Vapour inlet pressure	6.2 to 8.3 bar
Heat source outlet tem.	95°C	Vapour inlet temp.	95°C
Saturated steam flow	5 kg/s	Vapour outlet temp.	44°C
Working fluid flow	25 kg/s	Speed	3600 rpm
		Mechanical seal	Oil lubricated
Other	Evaporator fitted with a safety relief valve	Other	Turbine has capacity to operate at partial or full capacity

The gearbox is used to reduce the turbine shaft's speed from 3600 to 1500 rpm and to drive the generator. The gearbox uses two double – helical gears placed in a cast iron housing. The gearbox has an independent lubrication system for cooling and to lubricate the gear mesh and its bearings. The oil temperature in the gearbox should be 40 +/- 10°C. For cooling the oil used in the gearbox, the cooling arrangement is integrated into the lubrication system which uses 1.2 kg/s of water at a maximum 25°C. The gearbox has protection against high temperature and low pressure failures in the lubrication system.

The working fluid pumps (Figure 27) that remove the Isopentane from the condenser are vertical, centrifugal and multistage type. Each pump has 10 stages; the impellers are made of bronze, and the housing is made of cast iron. The working fluid pumps are driven by a three phase electrical motor. The outlet pressure of the pumps is 6.3 bars.

The generators are designed for continuous operation and, as was mentioned, they are driven by the turbine via a gearbox. The generators are three phase, brushless revolving field synchronous type for the units with a water condenser system, and an asynchronous type for units with an air cooled condenser system. The generator design construction has two bearings for placing the shaft in the generator. The generator is cooled by a heavy fan, mounted on one end of the shaft, and also has an extra cooling system to maintain the air temperature at the required temperature level. This extra cooling system is provided by air – water cooler heat exchangers. The power and control cabinets contain all the control devices and electrical circuits required for controlling the units.



FIGURE 27: Isopentane pump belonging to the water cooled binary Ormat units at Svartsengi; it shows the Isopentane return pipeline from the condenser to the pump

The units have auxiliary systems which allow automatic control and monitoring of the binary cycle generation process. The auxiliary systems are the pneumatic, lubrication, instrument and control

systems. The pneumatic systems use compressed air to feed the actuators on the automatic valves. The lubrication system mainly supplies oil to the turbine and generator bearings, as well as supplying the seal oil in the turbine's mechanical seal; the pressure in the mechanical seal chamber is 8.2 bars. The pump used in the lubrication systems is a gear pump type and the maximum discharge pressure is 15 bar. The instrument and control system's purpose is to control the start-up procedure, normal operations and shutdown procedures. This system has a program, measuring instruments and input devices, auxiliary controls and relays, indication lights and a synoptic panel.

In Svartsengi power plant, the operation is totally automatic and remotely monitored. According to the operation manual for a binary unit (Ormat, 1992), these units have the following operating procedures: preconditions for startup, start up, normal operation, normal shutdown and automatic shutdown procedure (Tesema, 2002).

The shift operator in the power plant is responsible for troubleshooting and carrying out emergency maintenance. For operating the binary units there are only two workers, the operator and the daily maintenance manager.

7.2 Berlín binary power plant

The Berlín binary cycle power plant is located at Berlin, Usulután in El Salvador. The Berlín binary cycle power plant is located at the platform of Well TR-9 in Berlín geothermal field, and is called Unit 4. The Berlín geothermal field has 4 power plants; the developmental history is summarized in Table 7. The Berlín binary cycle started its construction in 2005 and was commissioned in 2007. The goals of this binary power plant were to generate electricity and to supply the demand with a geothermal resource, increase the efficiency of the Berlín geothermal field and contribute to local sustainable development. The binary cycle power plant technology was used for the first time in El Salvador in this unit.

TABLE 7: Berlin geothermal field development in El Salvador (Guidos and Burgos, 2012)

Phase	Building years	Technology	Units	MWe/Unit
Well head units	1992	Back pressure steam turbine	2	5, Out of operation
Units 1 & 2	1999	Condensing steam turbine	2	28
Unit 3	2005	Condensing steam turbine	1	44
Unit 4	2007	Isopentane binary cycle unit	1	9.2

In Berlin, the geothermal wells produce a two phase fluid, geothermal water and steam. The steam is used to feed the turbines in the flash steam power plant and the geothermal water is re-injected in the wells, downstream of the production wells and power plant. The binary cycle power plant in Berlín is designed to remove internal energy from the geothermal water before reinjection, which has a temperature of 180°C, to generate electricity. The geothermal water used in this unit comes from Wells TR4/5 and TR2/9; the steam from these wells is used to generate electricity in units 1 and 2. The Berlin binary cycle power plant is a good example of a bottoming power plant.

The organic Rankine cycle is utilized to generate electricity. This binary power plant uses Isopentane as its working fluid. The gross power output is 9.2 MWe and its own energy consumption for the circulation pumps, cooling water pumps, cooling tower fans and other electrical and auxiliary equipment is taken from the same generation. Therefore, the net power production delivered to the grid is 7.8 MWe.

In Berlin binary cycle power plant, the process is divided into three loops. The first loop is the geothermal water circulation, the heat source. The second loop is the working fluid process, and the third loop is circulation of cooling water. In the first loop of this binary power plant, the heat source comes from two reinjection systems; one pipeline collects the geothermal water from wells TR2 and TR9. The system is called TR2/9. Another pipeline collects the geothermal water from wells TR4 and TR5 and the system is called TR4/5. Figure 28 shows the process diagram for the first loop. System TR4/5 carries 221 kg/s of hot water at 22 bars. System TR2/9 carries 79 kg/s at 11 bars. The geothermal water exchanges heat with the working fluid in the preheaters and the evaporators; this exchange takes place in both systems and the vapour of the working fluid leaves the evaporators at 22 bars. The geothermal water is cooled down from 180 to 140°C before being re-injected.

The second loop is the Isopentane process cycle; the mass flow of working fluid used in the Berlin power plant is 123.3 kg/s. Table 8 shows the changes along the loop and the parameters of the working fluid under design conditions.

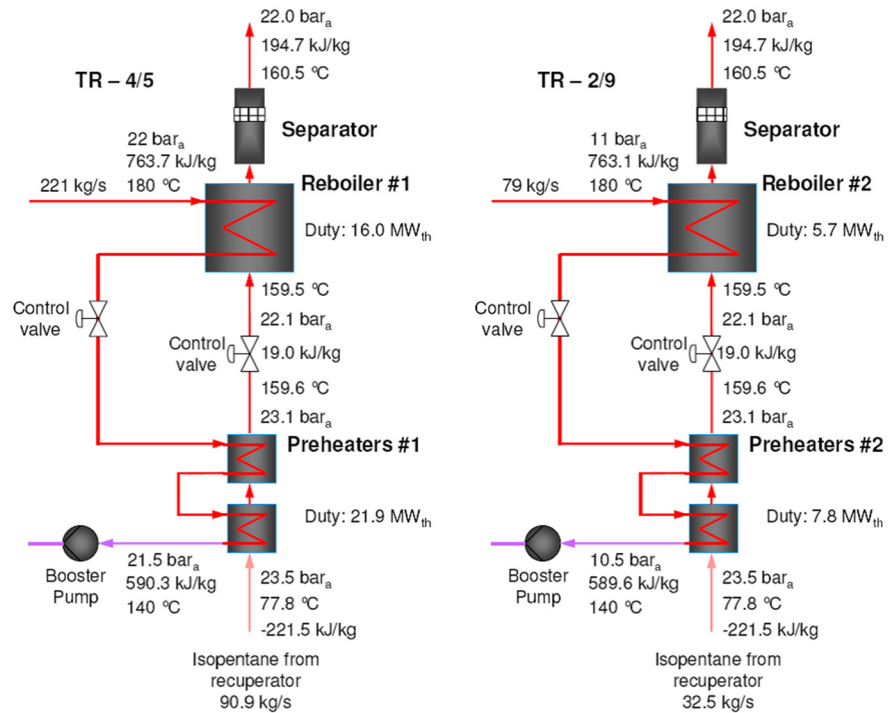


FIGURE 28: Preheaters, evaporators and the first loop process diagram (Enex, 2007)

The third loop corresponds to the cooling water cycle; the flow of water in this cycle is 1,013 kg/s. In this loop, the water removes the heat from the working fluid through the condenser, which is a shell and tube heat exchanger type. The water evaporates the removed heat into the atmosphere in the cooling tower. A set of pumps is used to circulate the water from the condenser to the cooling tower. Due to evaporation during the heat exchange, blow down, and drift, constant make-up water is needed. The make-up pumps deliver 20.3 kg/s of condensate water from the pond of the condensation units.

In the Berlin binary cycle, the turbine-gearbox-generator is mounted on a structural steel skid. In the turbine, the working fluid expands from the inlet to the outlet pressure in two steps: The first step takes place in the inlet guide vanes (IGV; variable nozzles) and the final steps take place in the radial wheel or rotor (Figure 29). The turbine converts the kinetic energy into

TABLE 8: Design condition for the working fluid at each step of the cycle's process

Working fluid phase change	Parameters		
Evaporation:	Temperature	159.5	°C
	Turbine inlet pressure	22	bar
Expansion:	Turbine outlet pressure	1.85	bar
	Turbine inlet temp.	160.5	°C
	Turbine outlet temp.	92.9	°C
Cooling:	Recuperator outlet temp.	52.6	°C
Condensation:	Condenser pressure	1.8	bar
	Condenser outlet temp.	44.8	°C
Compression:	Pump discharge pressure	23.78	bar
	Pump discharge temp.	46.1	°C
Heating in recup.:	Outlet temperature	77.7	°C
Heating in preheat:	Outlet temperature	159.5	°C

mechanical work, transmitted by the shaft to the generator via the gearbox (GE-Energy, 2013). The turbine case is sealed at the shaft by a dry face mechanical seal. Nitrogen and air are injected as a sealing and cooler fluid. The mechanical seal has an internal division in the labyrinth seal: a front labyrinth (working fluid) side and a back labyrinth (lubrication oil) side. The nitrogen goes through the front labyrinth side and is mixed with the vapour, to ensure that the working fluid is retained in the turbine.



FIGURE 29: Inlet guide vanes (IGV) and radial wheel of turbine (GE-Energy, 2013)

The mix of air and purged nitrogen goes through the back labyrinth side of the mechanical seal and flows toward the vent cavity; this mix removes any heat generated in the mechanical seal and ensures that the lubrication oil mist does not migrate to the expander process side. The gearbox is connected to the turbine through a power shaft and connected to the generator through a low speed coupling. This gearbox reduces the turbine shaft speed from 6490 to 1800 rpm. The generator is a brushless excitation type ABB unit with a horizontally mounted rotor and air to water closed circuit cooling. It produces a voltage of 13.8 kV and 60 Hz.

The heat exchangers in the Berlin binary cycle are used to transfer heat between different fluids. Figure 30 shows the arrangement of all the shell and tube heat exchangers in this plant. Basically, the heat exchanger transfers heat from the geothermal water to the working fluid in the preheater and evaporator, transfers heat between the exhaust vapour and the liquid working fluid in the recuperator, and transfers heat from the working fluid to the cooling water in the condenser. The working fluid along the process flows in the shell side in this equipment.

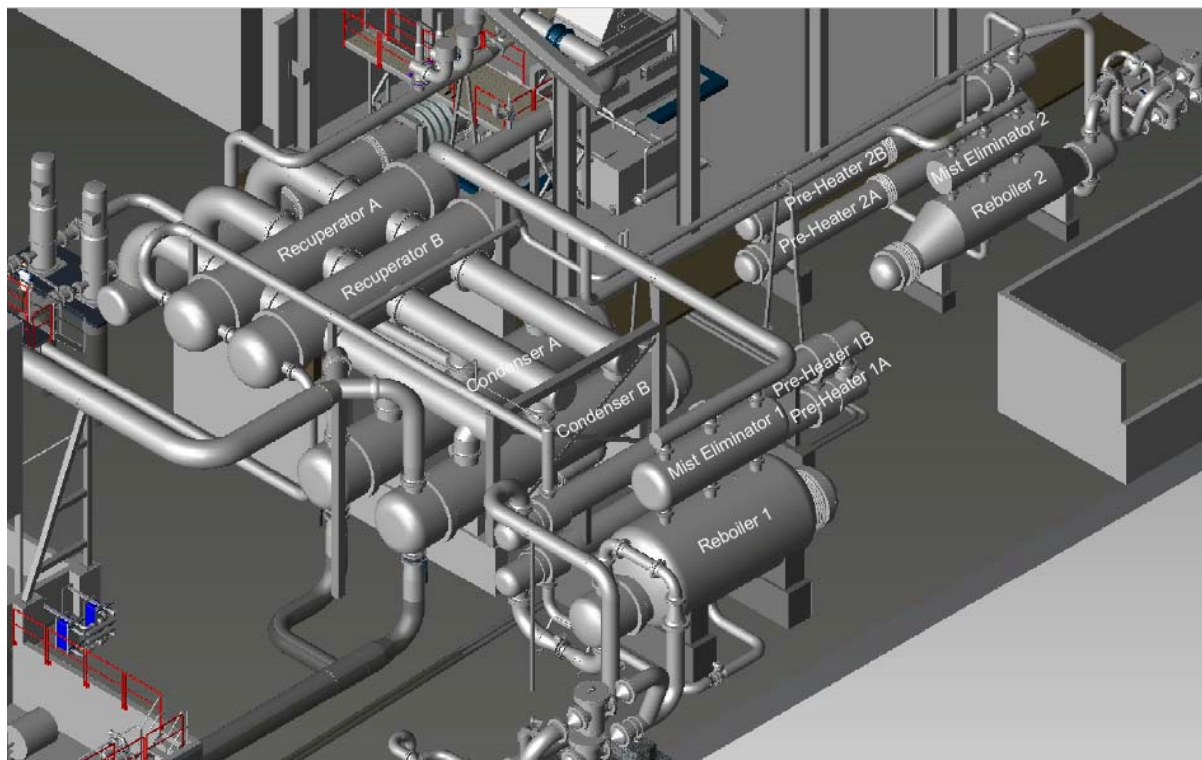


FIGURE 30: Shell and tube heat exchanger in Berlin binary plant (Enex, 2007)

The cooling tower's main function is to remove the heat from the water used in the condenser. The cooling tower acts as a final heat sink in the process by delivering this heat into the environment. This cooling tower is a counter-flow type and has two fans that draw air upward against the flow of water falling from the top. Operating under design conditions, the tower can handle a flow of up to 4,122

m³/hr. The water from the condenser to the cooling tower is pumped by centrifugal pumps that are designed as a single stage, double suction and horizontal split volute type.

The working fluid pumps are of the vertical, centrifugal and multistage type. The pumps are equipped with a mechanical seal, with a cartridge design that allows changing the seal without taking the pumps apart. The mechanical seal is flushed by an American Petroleum Institute (API) plan. The API helps to select the type and control for a mechanical seal application. For working fluid pumps in the Berlin binary unit, the temperature at the seal should be a maximum of 10°C above the pumped working fluid temperature. The working fluid pumps are driven by a three phase electrical motor.

As mentioned above, the mechanical seal used in the turbine casing works with nitrogen on the working fluid side; both fluids exist as a mix in the outlet of the turbine. To remove the non-condensable nitrogen from the working fluid, a nitrogen extraction system was installed in the condenser, where the working fluid liquefies and the nitrogen remains in the gas phase which is ejected to the atmosphere from a gas separator.

The units have auxiliary systems which allow for automatic control and monitoring of the Berlin binary cycle. These include the nitrogen generator system, pneumatic, ventilation, fire protection, inhibitor, auxiliary cooling water for the generator-gearbox-turbine set, lubrication, instrument and control systems.

In the Berlin binary cycle power plant, the operation is totally automatic, locally and remotely monitored. Figure 31 shows the actual screen for the process that is used by the operator to monitor the cycle. According to the operation manual for a binary unit (Enex), these units have the following operation procedures: preconditions for start-up, start-up, turbine start-up, turbine warm start, normal operation, normal shutdown, turbine trip and trip of the working fluid cycle. For operation of the Berlin binary plant, there is only one operator in each shift. The operator is responsible for monitoring all the parameters of the unit, troubleshooting and executing start-ups and shutdown procedures. The operators work in 8 hour shifts.

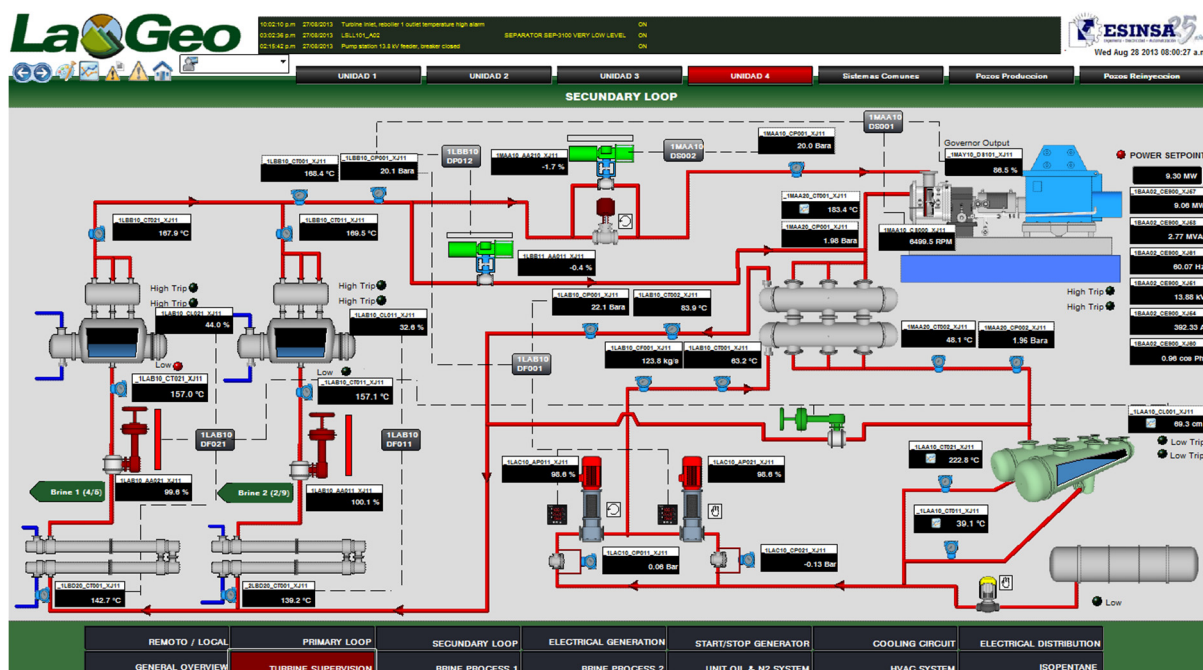


FIGURE 31: Screen of second loop in Berlin binary cycle power plant

8. BINARY CYCLE MAINTENANCE WORK AND EXPERIENCES

The maintenance of a binary cycle power plant includes a series of activities carried out on each component of the binary plant in order to ensure its continuous performance. The maintenance of binary cycle power plants is highly influenced by different factors, such as: the nature of the geothermal fluid used in the primary loop, the nature of the working fluid, the technology and location of the plant, climate and weather. In order to operate a binary cycle power plant as a base load unit, a perfect maintenance programme configured to ensure high availability and reliability is a challenge. Corrosion and scaling are the most common problems in binary power plants.

To develop the maintenance activities, a maintenance management programme is needed to help in coordination, control, planning, implementing and monitoring the necessary activities required for each component of the binary plant. There are a variety of maintenance programmes and methods dealing with the following basic maintenance strategies: corrective, preventive, predictive and proactive maintenance. The best maintenance programme analyses and applies the correct combination of strategies for each component of the whole power plant. Also, nowadays software is available that can help to manage these activities; examples of these tools are Dynamic Maintenance Management (DMM), used in Svartsengi power plant, and Maximo software, used in the Berlin power plant. These software programmes have been designed to manage assets and help to automate all aspects of maintenance. These software programmes have the following common functions: machine history, preventive maintenance schedules, work orders, condition monitoring, condition based flagging, time accounting, fault reports, improved safety, expense tracking, procurements, trending and performance reports (DMM,2013; Projetechn, 2013).

In this report, the basic maintenance strategies are summarized, and the major mechanical maintenance activities carried out on the turbine, heat exchangers, pumps and cooling towers of the binary cycle power plants are described. The report also describes certain experiences from Svartsengi and Berlin binary cycle power plants during their operation and maintenance.

As was mentioned above, the basic maintenance strategies are corrective, preventive, predictive and proactive maintenance. A corrective maintenance strategy proposes running the machinery until it fails. This strategy seems to be economic because the manpower requirements and their costs are minimal. But, when the machinery fails at some unexpected time, it is required to schedule manpower at the site for emergency shifts, have a complete stock of parts available in a warehouse, and make a contract with a specialist in case of emergency. The shut down time depends on the magnitude of the failure. In addition, an unexpected failure can lead to an unsafe environment or conditions, both to personnel and the facilities. All these factors need to be considered for a corrective maintenance strategy; since failures cannot be predicted so the cost will be high.

Preventive maintenance consists of scheduling maintenance activities aimed at preventing failures and breakdowns in the machinery. The main goal of this strategy is to prevent the failure before it occurs. The preventive maintenance activities consist of equipment checks, lubrication, oil changes, looking for leaks, tightening bolts, mechanical adjustments, partial or complete overhauls, etc. At the same time, the operating hours, according to the manufacturer's recommendations, are scheduled for the change of worn parts before they really fail. This strategy has the advantage that during maintenance, the workers can identify if the machinery needs maintenance; also, they can record the deteriorations in machinery and suggest/schedule the next maintenance. The associated costs for this technique are related to long availability and the service life of the machinery. The strategy helps in controlling the shut down time period of the machinery. The disadvantage of this strategy includes unnecessary maintenance and incidental damage to components while the risk of unexpected failures still prevails. Preventive maintenance includes the predictive strategy maintenance.

The predictive maintenance strategy mainly focuses on measuring the operating conditions of the machinery and ascertaining if the machinery is working under certain standard conditions.

Measurements are logged over time. The strategy suggests taking corrective measures when the measurements go beyond standard operation limits. This strategy requires new tools, software and specialized technicians to obtain and analyse the data, as well as to predict when the machinery must be repaired. Vibration monitoring conditions are the most common technique used to monitor operating conditions (for example, the continuous monitoring systems installed on the bearing pedestals on the turbine-gearbox-generator set). But, the vibration technique is limited to monitoring mechanical conditions; therefore, other monitoring and diagnostic techniques that can be useful for maintaining reliability and efficiency of the machinery include: an acoustic analysis, motor analysis technique, thermography, tribology, process parameter monitoring, visual inspections and other non-destructive testing techniques.

Proactive maintenance focuses its work on reducing the failure recurrence or unexpected failure, determining the root cause of previous failures (Asaye, 2009).

In a binary cycle power plant, besides the different maintenance practices that are summarized above, major overhauls are carried out according to the manufacturer's recommendations. The common major overhaul period for a binary cycle power plant is between 40,000 to 48,000 hours. The principal mechanical maintenance activities developed during the major overhauls of the main equipment, as well as the experiences of maintenance and development, in Svartsengi and Berlin binary cycle power plants, are mentioned below:

8.1 Turbine

The turbine is a key component in binary cycles. For this component, the maintenance activities include the following:

- Disassemble the turbine wheel and nozzle ring;
- Check condition of turbine wheel and nozzle ring;
- Check condition of turbine mechanical seal, o-rings and bearings;
- Check and clean the oil tank filter and change oil;
- Check the gearbox; and
- Perform non-destructive testing, such as liquid penetrant, magnetic particles and ultrasonic.

The objectives during the major overhaul include looking for wear, cracks and damage in the movement parts; furthermore, some critical parts should be replaced according to the manufacturer's recommendations.

Since operations began in Svartsengi binary power plant, the major corrective maintenance activity was associated with the mechanical seal. The mechanical seal showed failures on the seal faces caused by using the wrong type of lubrication oil. Nowadays, the mechanical seal is working well and the failure was eliminated by lubricating the mechanical seal with high thermal resistance oil. Figure 32 shows the mechanical seal damages.

In the Berlin binary cycle power plant, the mechanical seal is of the dry face seal type; this type of seal has a disadvantage. The disadvantage is the requirement for the injection of seal gas during operations and even during shutdown time. It is required in order to dissipate heat generated by the dry face seal and for avoiding contact of the seal faces with the

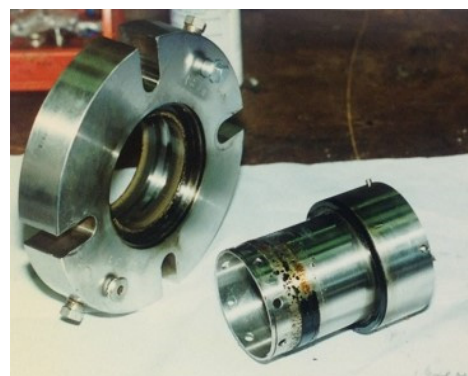


FIGURE 32: Mechanical seal, contaminated and damaged (Svartsengi binary power plant)

lubricating oil and oil mist on one side, and working fluid on the other. Figure 33 shows mechanical seal damage.

When the mechanical seal is damaged, the amount of seal gas flowing to the working fluid side increases the discharge pressure and decreases the turbine work output, because of the presence of incondensable seal gas flowing in the process.

In the Berlin binary cycle power plant, the nozzle ring of the turbine was changed because of erosion and jamming problems. The change included a new design for the nozzle ring.



FIGURE 33: Mechanical seal, contaminated and damaged (Berlin binary cycle power plant)

8.2 Heat exchangers

The heat exchangers are the components in which the geothermal fluid, the working fluid and the cooling fluid interact. The major maintenance work on heat exchangers is cleaning the heat exchange area, depending on the processing conditions. As is known, the geothermal fluid flows through the tubes, so the major problems found in the heat exchangers are associated with the chemistry of the fluid, and scaling problems. The working fluid side, theoretically, does not require a cleaning process. The cleaning process can be carried out with pressurized water and chemical cleaning. A recommended practice is to run a pressure test to verify the seal of the heat exchanger, to avoid contamination of the working fluid.

In Svartsengi, the geothermal fluid used in the binary power plant is steam, and there have been no major problems. However, in the Berlin binary cycle power plant, geothermal water is used in the primary loop, and scaling problems associated with the chemistry of the fluid are present. In Berlin, both chemical and pressurized water cleaning processes are used during maintenance work. A pressure test was done in the Berlin binary cycle, to ensure the tightness of the heat exchanger. During this test, when tubes were identified with leakages, in order to avoid contamination of the working fluid with geothermal fluid, these tubes were blocked.

8.3 Working fluid pumps

The working fluid pumps are the components that circulate the working fluid in the binary cycle. For these components, the maintenance activities are as follows:

- Check the intermediate bearing sleeves and bushing against wear;
- Check the shaft and impellers;
- Check the causing wear ring and the impeller wear ring for any wear;
- Check the parts for corrosion and erosion;
- Carefully check the coupling for any wear;
- Check the bearing cage for any wear;
- Check the run out of the shaft;
- Check condition of pump mechanical seal and o-rings;
- Change oil; and
- Check the coupling alignment.

In Svartsengi binary power plant, a major overhaul is carried out for the working fluid pumps after every 40000 hours and, during this work, the shaft, sleeves, bushing, wear ring, bearing, mechanical seal and

shaft are replaced. The pump is equipped with a single mechanical seal and the cartridge design allows for changing the mechanical seal without taking it apart.

In the Berlin binary cycle power plant, the working fluid pumps have the same overhaul schedule as in Svartsengi. The mechanical seal in Berlin binary cycle power plant has been changed from a single to a double seal type. The advantage of the double mechanical seal is that it eliminates leakage of the working fluid into the atmosphere, and working fluid losses are eliminated during a failure of the seal. The cartridge design allows for changing the mechanical seal without taking it apart.

8.4 Cooling systems

The main function of the cooling system is to condense the working fluid and dissipate the removed heat to the environment. The condensers in Svartsengi are water and air coolers; the maintenance activity is to clean the heat exchange areas and check the seals in the system. In Svartsengi power plant, if the air cooled condenser has a leak, the leakage will be stopped by installing a short sleeve inside each tube where it ends in the end of header box. These sleeves will be installed using hydraulic tube expansion technology. The sleeve will be expanded for tight contact with the parent tube in the header box. Figure 34 shows the air condenser, the leakage zone and the sleeves that used to seal the condenser.



FIGURE 34: Air condenser and the leakage zone

The Berlin binary cycle has a wet cooling system, and mechanical maintenance work is carried out on the circulating water pumps, gearbox and fans. For these components, the maintenance activities are as follows:

- Check the intermediate bearing and bushing against wear;
- Check the shaft and impellers;
- Check the parts for corrosion and erosion;
- Carefully check the coupling for any wear;
- Check condition of pump mechanical seal and o-rings;
- Check the coupling alignment;
- Check the gears for any wear;
- Check the fan blades; and
- Change the gearbox oil.

In the Berlin binary cycle power plant, the circulation water pumps were changed after corrosion problems were found. The construction material of these pumps was changed from cast iron to stainless steel, and the stuffing box was changed to a mechanical seal. The corrosion was caused by the chemistry of the condenser water that was used as a cooling fluid.

9. CONCLUSIONS

The production of electricity from binary cycle power plants is useful for harnessing low and medium temperature resources and raising the total exploitable geothermal potential worldwide. The number of countries utilizing geothermal energy is increasing every year, with many countries focusing on electricity generation using binary cycle technology.

The concept of a binary cycle power plant, known as an organic Rankine Cycle (ORC), is a modification of the Rankine cycle where the working fluid, instead of water, is an organic fluid having a lower boiling point and a higher vapour pressure than water.

Dry or isentropic working fluids are more suitable for binary cycle power plants than wet working fluid. To select a working fluid, the temperature of the geothermal fluid, the reinjection temperature limit, the turbine inlet pressure, and considerations of safety, health and environmental factors should be known.

The addition of a recuperator causes no change in the maximum turbine work output of the binary cycle, but causes a shift in the maximum point of the turbine work output of the cycle with respect to the reinjection temperature. However, when the reinjection temperature is limited by the geothermal water chemistry, or by other design constraints such as district heating applications, adding a recuperator serves to increase the turbine work output for a given reinjection temperature and helps to overcome these limitations.

The addition of a recuperator causes an increase in the condenser area required for cooling. The total area for a binary cycle using a recuperator increases by 42% over that of a basic binary cycle. The cost for heat exchangers using a recuperator, when compared with a basic binary cycle, increases almost by the same ratio.

The overall economic conclusion can be drawn that when the recuperator is added, the total plant cost is higher. As the basic binary cycle has a lower cost, in general, this option is the best when no constraints exist.

When the reinjection temperature is in the range of 80°C to 160°C, according to this research Isopentane and n-Pentane are the most suitable working fluids. In El Salvador, Isopentane is the working fluid in the binary power plant. However, n-pentane is another working fluid option for designing binary cycle units for the Berlin power plant.

The best option for the cooling system of a binary cycle is the wet cooling system. The dry cooling system is an option when the binary power plant is not located near water, or water is strictly regulated, or for where extremely low ambient temperature conditions exist.

The primary working fluid can be either water or steam. The advantage of using steam is that scaling problems are minimized.

The maintenance of binary cycle power plants is highly influenced by different factors such as: the nature of the geothermal fluid used in the primary loop, the nature of the working fluid, the technology and location of the plant, climate and weather. Corrosion and scaling are the most common problems in binary power plants.

To develop the maintenance activities, it is necessary to have a maintenance management programme to help in coordination, control, planning, implementing and monitoring the necessary activities required for each component of the binary plant.

ACKNOWLEDGEMENTS

I want to especially thank my employer, LaGeo S.A. de C.V., for giving me the opportunity to attend this training to strengthen my knowledge in geothermics for the near future. My most sincere thanks go to Mr. Lúdvík S. Georgsson and Dr. Ingvar B. Fridleifsson, current and former director, respectively, of the United Nations University Geothermal Training Programme (UNU-GTP), for inviting me and giving me the opportunity to participate, grow academically and personally in this course. Thanks go to the staff of the UNU-GTP, Ms. Málfríður Ómarsdóttir, Ms. Thórhildur Ísberg, Mr. Markús A. G. Wilde, and Mr. Ingimar G. Haraldsson, for their enthusiastic help and support during my stay in Iceland. I want to give special thanks to my supervisors, Dr. Páll Valdimarsson, Mr. Geir Thórólfsson, and Ms. María Gudjónsdóttir, for their dedication, availability, support and guidance while working on this geothermal report.

I want to thank all 2013 UNU Fellows; special thanks go to my friends, Claudia, Idalia and Mariela for an unforgettable friendship, memorable moments and times during these six months. For my utilization colleagues and friends, I want to say “thank you so much”.

This report is dedicated to my family, especially my wife, Xochilt, for her love, patience and support.

My gratitude goes to the people who gave me their invaluable support for attending this training. These include Mr. Jorge Burgos, Ms. Evelyn de Velis, Mr. David Lopez, Mr. Jorge Castillo, and Mr. José Luis Henríquez.

Last, but not least, I owe my deepest gratitude to J. Estevez, A. Rugamas, C. Melgar, and O. Cideos for helping me with technical information, commenting on my manuscript and answering my questions.

REFERENCES

Ahangar, F.A., 2012: Feasibility study of developing a binary power plant in the low-temperature geothermal field in Puga, Jammu and Kashmir, India. Report 6 in: *Geothermal training in Iceland 2012*. UNU-GTP, Iceland, 1-24.

Asaye A.M., 2009: *Evaluation of maintenance management through benchmarking in geothermal power plants*. University of Iceland, MSc thesis, UNU-GTP, Iceland, report 3, 60 pp.

Bao J., and Zhao Li, 2013: A review of working fluid and expander selections for organic Rankine cycle. *Renewable and Sustainable Energy Reviews*, 24, 325–342.

Bertani, R., 2012: Geothermal power generation in the world 2005 – 2010 update report. *Geothermics*, 41, 1-29.

DiPippo, R., 2007: *Geothermal power plants: Principles, applications, case studies and environmental impact* (2nd edition). Butterworth Heineman, Elsevier, Kidlington, United Kingdom, 493 pp.

DMM, 2013: *DMM Software*. Dynamic Maintenance Management, website: www.dmm.is.

Elliott, C.T., Chen, K., and Swanekamp, C.R., 1998: *Standard handbook of power plant engineering* (2nd edition). McGraw-Hill, New York, United States, 1248 pp.

Enex, 2007: *Binary plant Berlin, operation and instruction manual*.

F-Chart Software, 2012: *EES, Engineering equation solver*. F-Chart Software, website: www.fchart.com.

GE-Energy, 2013: *Turboexpander-generators. Products & Services – Turboexpander*. GE Energy, website: www.ge-energy.com.

Guidos, J., and Burgos, J., 2012: Geothermal activity and development in El Salvador – Producing and developing, El Salvador. *Paper presented at “Short Course on Geothermal Development and Geothermal Wells”, organized by UNU-GTP and LaGeo, Santa Tecla, El Salvador*, 12 pp.

HS Orka, 2013: *Svartsengi plant IV*. HS Orka, Ltd., website: www.hsorka.is.

Lukawski, M., 2009: *Design and optimization of standardized organic Rankine cycle power plant for European conditions*. University of Iceland & the University of Akureyri, MSc thesis, 87 pp.

Lund, J.W., 2004: 100 years of geothermal power production. *Geo-Heat Center, Bulletin, September 2004*, 11-19.

Mendrinós, D., Konloléontos. E., and Karystas, C., 2006: Geothermal binary plants: water or air cooled? *Proceedings of Workshop 5 on Electricity generation from Enhanced Geothermal Systems, Strasbourg, France*, 10 pp.

Mishra, G.S., Glassley, W., and Yeh, S., 2010: *Analysis of life cycle water requirements of energy & transportation fuels: electricity from geothermal resources*. University of California, Institute of Transportation Studies, Davis, CA, United States, 59 pp.

Ormat, 1992: *Maintenance manual for 1300 kW nominal output Ormat Energy Converter*.

Pieve, M., and Salvadori, G., 2011: Performance of an air-cooled steam condenser for a waste-to-energy plant over its whole operating range. *Energy Conversion & Management*, 52, 1908-1913.

Projetechn, 2013: *Maximo asset management by IBM*. Projetechn, website: www.projetechn.com.

Saemundsson, K., 2009: Geothermal systems in global perspective. *Paper presented at “Short Course IV on Exploration for Geothermal Resources”, organized by UNU-GTP, KenGen and GDC, Lake Naivasha, Kenya*, 11 pp.

SKM, 2004: *Berlin geothermal field, binary cycle power plant project. Silica polymerization and deposition trials at TR4/5 and TR2/9 brine lines*. SKM, unpublished report.

Tessema A., 2002: Geothermal binary plant operation and maintenance systems with Svartsengi power plant as a case study. Report 15 in: *Geothermal training in Iceland 2002*. UNU-GTP, Iceland, 287-306.

Thórólfsson, G., 2005: Maintenance history of a geothermal plant: Svartsengi, Iceland. *Proceedings of the World Geothermal Congress 2005, Antalya, Turkey*, 7 pp.

Valdimarsson, P., 2011: Geothermal power plant cycles and main components. *Paper presented at “Short Course on Geothermal Drilling, Resource Development and Power Plants”, organized by UNU-GTP and LaGeo, Santa Tecla, El Salvador*, 24 pp.

Verkís, 2013: *Power plant OV4 – Svartsengi, Iceland*. Verkís Consulting Engineers, website: www.verkis.is.

APPENDIX I: Binary power plants installed in the world

China							
Plant		Year	Type	MW-rated	N° Units	MW-Total	Comments
Dengwu	Unit 2	1977	Binary	0.2	1	(0.2)	Retired
Huailai		1971	Binary	0.285	1	(0.285)	Retired
Wentang		1971	Binary	0.05	1	(0.05)	Retired
Xiongyue		1978	Binary	0.1	1	(0.1)	Retired
Tuchang		1985	Binary	0.3	1	(0.3)	Inactive
Nagqu	Unit 1	1993	Binary	1	1	1	
Totals					1	1	
Iceland							
Plant		Year	Type	MW-rated	N° Units	MW-Total	Comments
Svartsengi	Unit 4	1989	Binary	1.3	3	3.9	Kalina Cycle
	Unit 4	1993	Binary	1.2	4	4.8	
Husavik	Extension	2000	Binary	2	1	2	
Totals					8	10.7	
Italy							
Plant		Year	Type	MW-rated	N° Units	MW-Total	Comments
Travale 21		1991	Binary	0.7	1	0.7	
Totals					1	0.7	
Japan							
Plant		Year	Type	MW-rated	N° Units	MW-Total	Comments
Otake Pilot		1978	Binary	1	1	(1)	Retired
Hatchobaru 3		2003	Binary	2	1	2	
Takigami Binary		1997	Binary	0.49	1	0.49	
Nigorikawa Pilot		1978	Binary	1	1	(1)	Retired
Totals					2	2.49	
Mexico							
Plant		Year	Type	MW-rated	N° Units	MW-Total	Comments
Los Azufres	Units 11&12	1993	Binary	1.5	2	3	
Maguarichic	Piedras de Lumbre	2001	Binary	0.3	1	0.3	
Totals					3	3.3	
New Zealand							
Plant		Year	Type	MW-rated	N° Units	MW-Total	Comments
Wairakei	Bottoming Unit	2005	Binary	5	3	15	
Kawerau	TaraweraOrmat	1989	Binary	1.3	2	2.6	
	TG2	1993	Binary	3.9	1	3.9	
	Mokai I	2000	Flash-Binary	25.5	1.6	55	
Mokai	Mokai II	2006	Flash-Binary	34.8	1.1	44	
Ngawha		1998	Flash-Binary	4.5	2	9	
	Combined cycle	1997	Flash-Binary	13,4.5	1.3	26.5	
Rotokawa	Extension	2003	Flash-Binary	4.5	1	4.5	
Totals					13	160.5	

Philippines							
Plant		Year	Type	MW-rated	N° Units	MW-Total	Comments
Luzon:	Binary I, II, III	1994	Binary	3	5	15	
Makiling-Banahaw	Binary	1994	Binary	0.73	1	0.73	
Leyte	Upper Mahiao Units 4-7	1996	Flash-Binary	34,12,5.5	5	142	
Totals					11	157.73	
Russia							
Plant		Year	Type	MW-rated	N° Units	MW-Total	Comments
Paratunka	Unit 1	1967	Binary	0.68	1	(0.68)	Retired
Totals					0	0	
United States: California							
Plant		Year	Type	MW-rated	N° Units	MW-Total	Comments
East Mesa	GEM I	1979	Binary	13.4	1	(13.4)	Dismantled Original Plant
	ORMESA I	1987	Binary	0.923	26	(24)	
	ORMESA I	2003	Binary	10.1	4	22	
	ORMESA II	1988	Binary	0.825	20	16.5	
	ORMESA IE	1988	Binary	0.8	10	8	
	ORMESA IH	1989	Binary	0.542	12	6.5	
Heber	Binary Demo	1985	Binary	45	1	(45)	Dismantled Orig. SIGC
	Heber 2	1993	Binary	2.75	12	33	
	Gould	2006	Binary	2.5	4	10	
Totals					62	96	
Casa Diablo							Aka Mammoth
	MP-I	1984	Binary	3.5	2	7	
	MP-II	1990	Binary	5	3	15	
	PLES-I	1990	Binary	3.3	3	10	
Totals					8	32	
Honey Lake	Wineagle	1985	Binary	0.35	2	0.7	
	Amedee	1988	Binary	0.8	2	1.6	
Totals					4	2.3	
United States: Nevada, Utah, Hawaii, Idaho and Alaska							
Plant		Year	Type	MW-rated	N° Units	MW-Total	Comments
Nevada	Wabuska 1	1984	Binary	0.5	1	0.5	Aka San Emidio
	Wabuska 2	1987	Binary	0.7	1	0.7	
	Desert Peak 2	2007	Binary	6	2	12	
	Empire	1987	Binary	0.9	4	3.6	
	Steamboat I	1986	Binary	0.86	7	6	
	Steamboat IA	1988	Binary	0.55	2	1.1	Orig. Galena 1
	Steamboat 2	1992	Binary	7	2	14	
	Steamboat 3	1992	Binary	7	2	14	
	Burdette	2006	Binary	10	2	20	
	Galena 2	2007	Binary	10	1	10	
	Soda Lake 1	1987	Binary	1.2	3	3.6	
	Soda Lake 2	1991	Binary	2	6	12	
	Stillwater I	1989	Binary	0.93	14	13	
	Brady II	2002	Binary	3	1	3	
Totals					48	113.5	
Utah	Cover Fort 1	1985	binary	0.5	4	(2)	Inactive
Totals					0	0	
Hawaii	Puna PGV-1	1992	Flash-Binary	2.5	10	25	
Totals					10	25	

Idaho	Raft River Raft River Phase 1	1981	Binary	5	1	(5)	Dismantled, 1982
		2007	Binary	13	1	13	
Totals					1	13	
Alaska	Chena Hot Springs	2006	Binary	0.2	2	0.4	
Totals					2	0.4	
Australia							
Plant		Year	Type	MW-rated	N° Units	MW-Total	Comments
Mulka	Unit 1	1986	Binary	0.02	1	(0.02)	Inactive
Birdsville	Unit 1	1992	Binary	0.15	1	0.15	
Totals					1	0.15	
Austria							
Plant		Year	Type	MW-rated	N° Units	MW-Total	Comments
Blumau: Rogner Hotel & Spa		2001	Binary	0.25	1	0.25	
Altheim	Unit 1	2002	Binary	1	1	1	
Totals					2	1.25	
Costa Rica							
Plant		Year	Type	MW-rated	N° Units	MW-Total	Comments
Miravalles	Unit 5	2004	Binary	9.5	2	19	
Totals					2	19	
El Salvador							
Plant		Year	Type	MW-rated	N° Units	MW-Total	Comments
Berlín	Bottoming Unit	2007	Binary	9.3	1	9.3	
Totals					1	9.3	
Germany							
Plant		Year	Type	MW-rated	N° Units	MW-Total	Comments
Neustadt- Glewe	Unit 1	2003	Binary	0.2	1	0.2	
Totals					1	0.2	
Guatemala							
Plant		Year	Type	MW-rated	N° Units	MW-Total	Comments
Zunil	Orzunil Unit 1	1999	Flash- Binary	3.5	7	24.6	
Amatitlán	Unit 1	2007	Flash- Binary			20	
Totals					7	44.6	
Kenya							
Plant		Year	Type	MW-rated	N° Units	MW-Total	Comments
Olkaria III	Phase I	2000	Flash- Binary	6	2	12	Aka West Olkaria Flower Company
Oserian	Unit 1	2004	Binary	1.8	1	1.8	
Totals					3	13.8	
Nicaragua							
Plant		Year	Type	MW-rated	N° Units	MW-Total	Comments
Momotombo	Unit 3	2002	Binary	7.5	1	7.5	
Totals					1	7.5	

Portugal							
Plant		Year	Type	MW-rated	N° Units	MW-Total	Comments
Ribeira Grande	Phase A	1994	Binary	2.5	2	5	
	Phase B	1998	Binary	4	2	8	
Totals					4	13	
Thailand							
Plant		Year	Type	MW-rated	N° Units	MW-Total	Comments
Fang	Unit 1	1989	Binary	0.3	1	0.3	
Totals					1	0.3	
Turkey							
Plant		Year	Type	MW-rated	N° Units	MW-Total	Comments
Salavath	Dora 1	2006	Binary	7.4	1	7.4	
Totals					1	7.4	
Argentina							
Plant		Year	Type	MW-rated	N° Units	MW-Total	Comments
Copahue	Unit 1	1988	Binary	0.67	1	(0.67)	Retired in 1996
Ethiopia							
Plant		Year	Type	MW-rated	N° Units	MW-Total	Comments
Langano	Unit 1	1998	Flash-Binary	3.9,4.6	2	(8.5)	Inactive
Zambia							
Plant		Year	Type	MW-rated	N° Units	MW-Total	Comments
Kapisya		1986	Binary	0.1	2	(0.2)	Not Connected to transmission line



GEOTHERMAL EXPLORATION IN GUFUDALUR, HVERAGERDI, SW-ICELAND

M.M Tharanga N.B Munasinghe
Geological Survey and Mines Bureau
No. 569, Epitamulla Road
Pitakotte
SRI LANKA
tharanga_muna@yahoo.com

ABSTRACT

The Hveragerdi geothermal field is located on the eastern margin of the western rift zone and the western margin of the South Iceland Seismic Zone (SISZ). Earthquakes with epicentres in the Hveragerdi central volcano are quite common; most of these are smaller than 4 on the Richter scale. The most recent earthquakes in the SISZ occurred on the 29th of May 2008 with two major earthquakes with magnitudes of 6.3 and 5.5 between the towns of Selfoss and Hveragerdi. It is believed that the first earthquake triggered the second one. These major earthquakes affected the Hveragerdi geothermal field. Many sudden changes regarding surface manifestations were observed. Visible fractures on the surface, the appearance of new fumaroles, hot springs, and many surface manifestations in the Hveragerdi geothermal field changed due to these earthquakes. The main purpose of this study on the valley of Gufudalur, Hveragerdi, is to map the surface manifestations, alteration and soil temperatures and correlate the manifestations with structures such as faults, fractures and lineaments. In addition, the results are compared with previous geothermal maps from the same area to pinpoint any changes caused by the earthquakes in 2008. More than 450 GPS locations of geothermal manifestations were taken and divided into 12 separate active areas. Present geothermal activity was compared with studies done in 1995 and soon after the earthquakes in 2008.

The present study reveals that the earthquakes which occurred in 2008 created new geothermal manifestations and the geothermal activity increased. New surface manifestations are still forming in the Gufudalur, Hveragerdi area. Alignment of geothermal manifestations along preferred directions indicates structural features, like lineament expression of underlying geological structures such as faults/fractures/lineaments. The major structural trends that control the geothermal manifestations are oriented NE-SW, although N-S and NW-SE oriented faults and fractures are also present. On the basis of geothermal mapping, it was concluded that the geothermal manifestations are controlled by the geological structures and topography.

1. INTRODUCTION

1.1 Study area and background

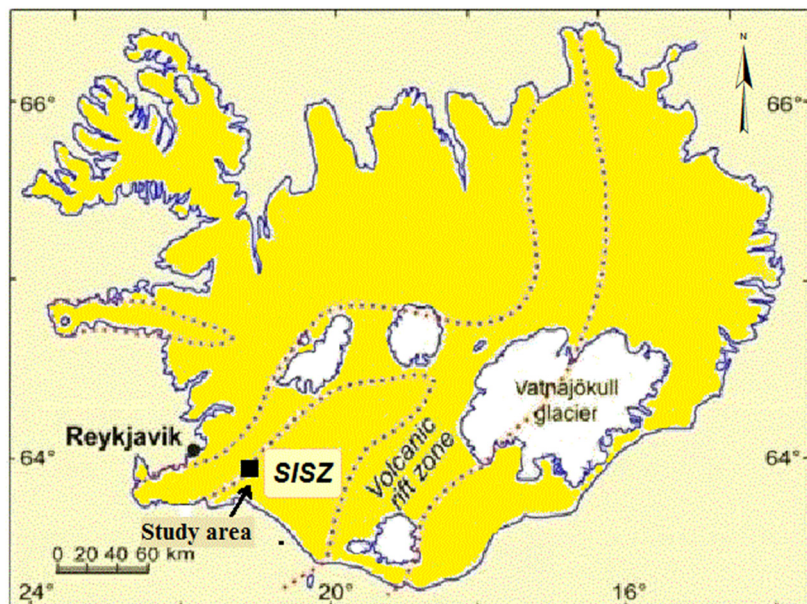


FIGURE 1: Location of the study area

Hveragerdi geothermal field is located on the eastern margin of the western volcanic (rift) zone (Figure 1). With respect to the tectonic setting of Iceland, seismic activity is common. The study area of Gufudalur valley in the Hveragerdi district is located in the South Iceland Seismic Zone (SISZ). The area is geothermally highly active and surface manifestations such as fumaroles, hot springs, mud spots and hot ground are common. Fumaroles and hot ground dominate in the northern part of the system and hot springs are common below 100 m elevation in the southern part (Geirsson and Arnórsson, 1995).

With the occurrence of an earthquake in southern Iceland, of magnitude 6.3 on the Richter scale, on the 29th May 2008, the geothermal activity in the area changed overnight. The epicentre was located 8 km west-northwest of the town of Selfoss. The impact of the earthquake affected the Hveragerdi geothermal field and many sudden changes in the system were observed. Visible fractures on the surface and the appearance of new fumaroles and hot springs were observed; many surface manifestations in the Hveragerdi geothermal field changed due to the earthquake. Even sudden pressure drops or increases in the wells in the area caused changes in the water levels of geothermal wells in the area (Thorbjörnsson et al., 2009).

With respect to the location of the Hveragerdi geothermal field relative to the active volcanic belt of Iceland (Figure 1), and in conjunction with it drifting out of the volcanic belt, the field is probably in the process of changing from a high- into a low- temperature geothermal system (Arnórsson, 1995a and b).

Since the major earthquake in 2008, several studies have been done in the surrounding area to identify changes in the region, but few detailed geothermal mapping projects have been executed to identify changes in the Gufudalur, Hveragerdi valley. The main purpose of this study is to map all surface manifestations, alteration and soil temperatures, and correlate the manifestations with structures such as faults, fractures and lineaments. In addition, the results are compared to older geothermal maps from the same area in order to pinpoint any changes caused by the earthquakes in 2008.

1.2 South Iceland Seismic Zone (SISZ)

The active volcanic rift zone which lies across Iceland is the surface expression of the Mid Atlantic Ridge and it is divided into two parallel branches in South Iceland (Figure 1). The block between does not show evidence of active deformation or volcanism and earthquake epicentres are completely lacking (Einarsson, 2008). This block appears to fulfil the criteria of a micro plate and has been termed the Hreppar microplate. The southern boundary of the Hreppar Microplate is marked by the South Iceland

Seismic Zone (SISZ), where large strike-slip earthquakes occur (Einarsson, 2008). These fracture zones and faults are seismically very active and earthquakes are experienced regularly (Figure 2). Accumulated strain in the SISZ is released during strike-slip earthquakes and such a type of earthquakes, as large as magnitude 7, take place at intervals of decades to centuries (Einarsson, 1991).

The SISZ shows widespread evidence of Holocene fracturing. Glaciated surfaces, alluvial plains and postglacial lava flows are fractured along the 15 km wide, 70 km long, E-W trending seismic zone (Einarsson and Eiríksson, 1982; Einarsson et al., 1981, 2002; Clifton and Einarsson, 2005). A map of all detectible Holocene fault structures is shown in Figure 2a.

Earthquakes with epicentres in the Hveragerdi central volcano are fairly common. Most of these are smaller than 4 on the Richter scale, like in 1991 and in 1995, involving episodes of intense seismic activity. Many such earthquake episodes are known from this century and, in two of these, significant changes in surface hydrothermal activity took place, i.e. in 1915 or 1916 and in 1947. (Saemundsson and Fridleifsson, 1992). The SISZ was hit by a series of earthquakes in June 2000, two of which caused considerable damage (Stefánsson et al., 2003). The earthquakes followed a pattern previously observed in large historical earthquakes in this zone. The activity began on June 17 with a magnitude 6.5 event in the eastern part of the zone. This immediately triggered activity along about a 90 km long stretch of the plate boundary to the west, including three events with magnitudes larger than 5 on the Reykjanes peninsula oblique rift (Clifton et al., 2003; Pagli et al., 2003; Árnadóttir et al., 2004). The pattern of faulting during the 2000 earthquake sequence is compatible with the model of “bookshelf faulting” for the SISZ. It was furthermore demonstrated that bookshelf faulting continued to the west, along the Reykjanes peninsula oblique rift (Árnadóttir et al., 2004).

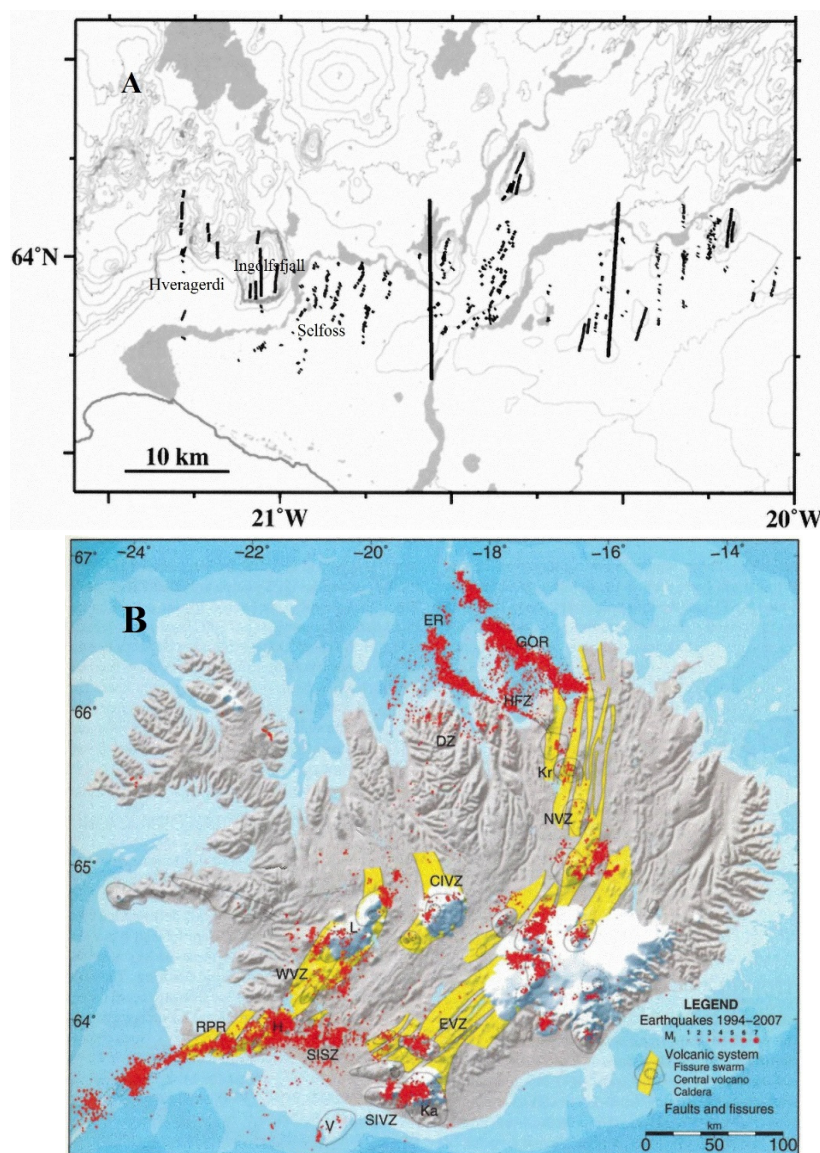


FIGURE 2: a) Mapped Holocene faults in South Iceland Seismic Zone; The heavy N-S lines show the source faults of the June 17 and 21, 2000 earthquakes; b) Red dots on the map shows earthquake epicentres 1994-2007 (Einarsson, 2008)

The most recent major earthquake in the SISZ occurred on the 29th of May 2008, with a magnitude of 6.3. Its location was between the towns of Selfoss and Hveragerði (Figures 2a and 3). The epicentre of the first earthquake was by the southwest end of Mt. Ingólfsfjall (Figures 2 and 3) and immediately afterwards, another earthquake occurred, about 5 km west of the first earthquake. The epicentre of the second earthquake was on a N-S fault about 8 km west-northwest of Selfoss, and about 2 km southeast of Hveragerði. It is believed that the first earthquake of 5.5, triggered the second one of 6.3 (Figure 3) (Icelandic Meteorological Office, 2008; Thorbjörnsson et al., 2009; Brandsdóttir, et al., 2010).

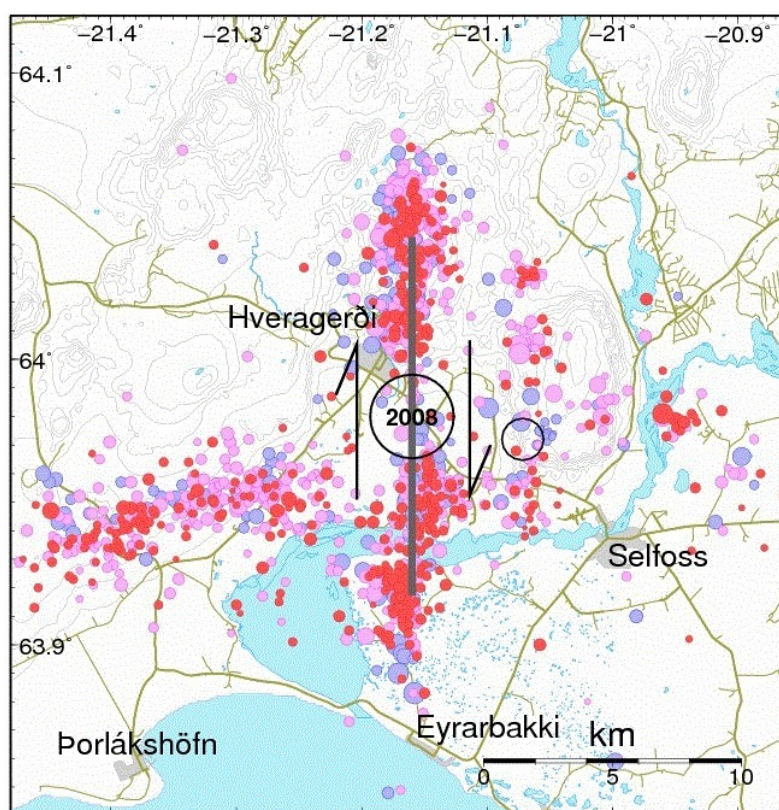


FIGURE 3: The epicenters of the earthquakes which occurred 29th May 2008; Rings represent the two major earthquake epicenters and small dots indicate minor earthquakes that occurred during the following three days (Icelandic Meteorological office, 2008)

1.3 Previous studies

The first systematic mapping of the Hengill area, including Hveragerði and Gufudalur, was published in 1967 (Saemundsson, 1967). In the 1970s, the area was mapped in relation to drilling activities at Hveragerði. Later, by combining previous work, the Hveragerði central volcano was outlined and many of the formations from which it is composed were established. Jónsson (1989) undertook some research in the area, mostly on Upper Pleistocene and Holocene lavas. During 1989 and 1990, the geological mapping of this area was finalized, the emphasis being on the lithostratigraphy, tectonics, the geothermal activity and alteration of the area (Saemundsson and Fridleifsson, 1992, 1996). The Hveragerði central volcano was mapped in detail some years ago by Orkustofnun, in co-operation with Hitaveita Reykjavíkur (Reykjavik District Heating) (Saemundsson and Fridleifsson, 1992). The maps were later combined with maps of the Hengill central volcano and published (Saemundsson, 1995a and b). Walker (1992) mapped the volcano with respect to its eruptive units and their petrology. A conceptual model of the Hveragerði geothermal reservoir, based on chemical data, was published by Geirsson and Arnórsson in 1995. All this work was combined in a map of the Hengill central volcano in a scale of 1:50,000 (Saemundsson, 1995). Geothermal exploration of the Hveragerði-Graendalur area was also done by the UNU-GTP fellow Kyagulanyi (1996) and, the same year, geothermal exploration of the Saudá valley north of Hveragerði was carried out by UNU-GTP fellow Malik (1996). Kristjánsson and Fridriksson (2003) published a geothermal map of the Ölfus area, partly based on research done by Saemundsson (1993a and b). Heat measurements in the soil and fractures in Hveragerði were completed by Saemundsson and Kristinsson in 2005. Thorbjörnsson et al. (2009) investigated the effects of the earthquakes of 29th May 2008 on the groundwater level, geothermal activity, fractures and pressure in boreholes in the Hveragerði area.

2. GEOLOGY, TECTONIC SETTING AND GEOTHERMAL ACTIVITY IN ICELAND

2.1 Geology and tectonic setting of Iceland

Iceland is a geologically young island and owes its existence to the uprising Icelandic mantle plume and crustal accretion at the diverging American and Eurasian lithospheric plates. The relative movement of the lithospheric plate boundary in relation to the stationary mantle plume is responsible for the complicated tectonic and volcano-stratigraphic structure of Iceland, compared to the Mid Atlantic Ridge to the north and south of the country, and for the eastward shifting of the volcanic belts in Iceland (Ward and Björnsson, 1971; Saemundsson, 1974; Jóhannesson, 1980; Óskarsson et al., 1985; Einarsson, 1989; Hardarson et al., 1997). It is believed that the general tectonic trends in Iceland as seen today have remained the same for at least 24 Ma (Saemundsson, 1980). Even though the American and Eurasian lithospheric plates of the North Atlantic Ocean are spreading (2 cm/yr.) symmetrically, the whole region is drifting slowly to the northwest with respect to the Iceland plume (Hardarson et al., 2008). During Anomaly 6 (24–19 Ma ago), the Mid Atlantic Ridge axis moved on top of the mantle plume and then gradually west of it (Vink, 1984). However, as the spreading ridge system in Iceland continues to drift NW with respect to the plume, it is periodically recaptured by the plume through the process of rift relocation or ridge jumping. This plume ridge interaction has been a dominant process in the formation and tectonic evolution of Iceland (Hardarson et al., 1997, 2008).

The volcanic belts in Iceland run SW-NE across the country (Figure 4). The plate spreading across the island is accommodated by several volcanic rift zones and two main transcurrent slip zones. In the south of the island, the Reykjanes segment of the Mid Atlantic Ridge comes on shore at the Reykjanes peninsula oblique rift zone and branches into the Western Volcanic Zone (WVZ).

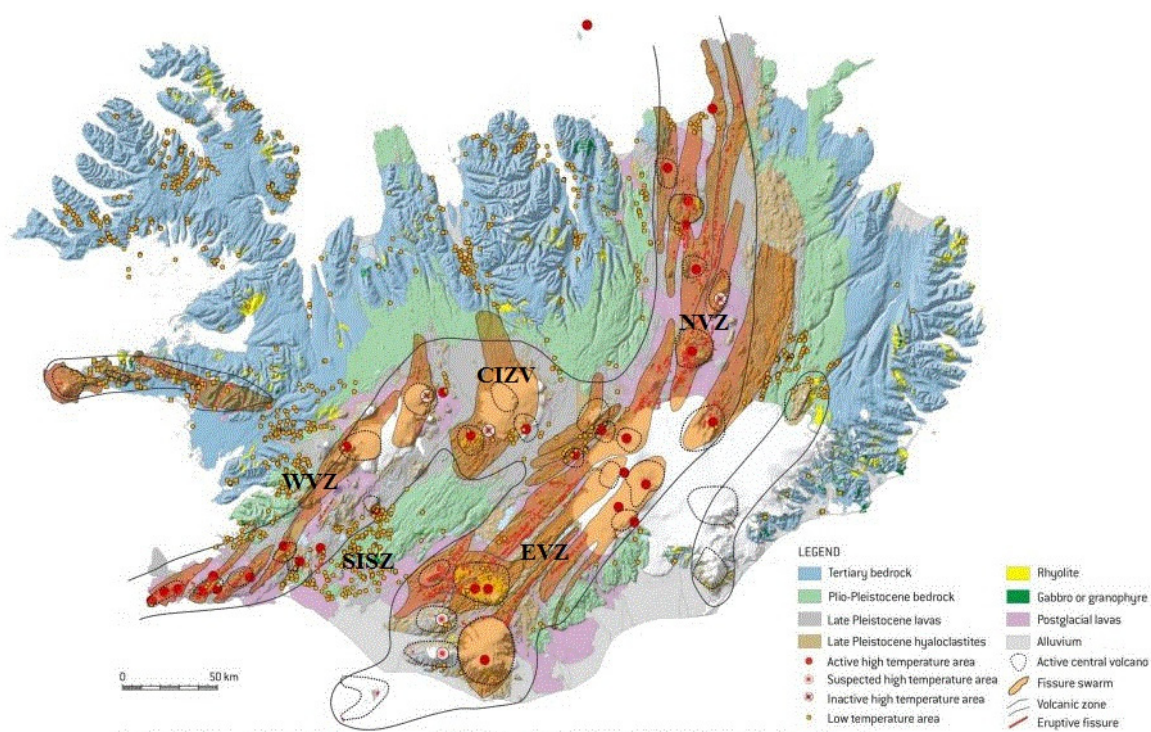


FIGURE 4: Geological map of Iceland showing the main rock formations, the volcanic zones and the geothermal areas; WVZ=Western Volcanic Zone, EVZ=Eastern Volcanic Zone, CIZV=Central Iceland Volcanic Zone, NVZ=Northern Volcanic Zone, SISZ=South Iceland Seismic Zone (Jóhannesson and Saemundsson, 1999)

Plate spreading across South Iceland in the WVZ and the Eastern Volcanic Zone (EVZ) is accommodated by left-lateral E-W transform motion across the South Iceland Seismic Zone (SISZ) which connects two volcanic zones (Figure 4). The EVZ extends northward and continues as the Northern Volcanic Zone (NVZ) (Árnadóttir et al., 2008). These main fault structures, volcanic zones and belts that lie within these zones are called volcanic rift zones, which are characterised by intense volcanic, seismic and high temperature geothermal activity (Gudmundsson and Jacoby, 2007; Thórdarson and Larsen, 2007).

Icelandic rocks are mainly composed of Tertiary plateau lavas, Plio-Pleistocene lavas and hyaloclastites, formed subglacially, and Holocene lavas (Figure 4). Approximately 85-90% of the volume of Iceland above sea level is igneous rocks, while some 10-15% is consolidated sediments. Due to the shallow erosion level of the volcanic pile, volcanic rocks predominate; less than 0.5% of the surface is intrusive and plutonic rocks (Saemundsson, 1980; Jóhannesson and Saemundsson, 1998). The geological formations in Iceland have conveniently been divided into four formations (Saemundsson, 1980): Holocene (< 0.01 Ma); Late-Pleistocene (0.01-0.78 Ma); Plio-Pleistocene (0.78-3.3 Ma); and Tertiary (3.3-16 Ma) (Hardarson et al., 2008).

Icelandic rocks are predominantly of basaltic composition. About 75% of the rocks are basalt, 14% intermediate rocks and 11% silicic rocks, which is close to a recent estimate of the production of volcanic rocks during the last 1100 years in Iceland (Jakobsson et al., 2008). The oldest rocks exposed on land in Iceland are only about 16 million years old (Moorbath et al., 1968; Watkins and Walker, 1977; McDougall et al., 1984; Hardarson et al., 1997).

2.2 Geothermal activity

Geothermal activity in Iceland is common due to the tectonic setting of the country as it is located on the Mid Atlantic spreading ridge, making the island a natural laboratory for geothermal research. Geothermal areas can be identified by surface manifestations such as hot springs, fumaroles, etc. while some areas may show no surface indications. Depending on their temperature, geothermal fields can be utilized in many ways from direct use to electricity generation.

Geothermal activity is mainly classified into high- and low-temperature fields and this classification is based on the geological setting and on temperature data from drill holes (Böðvarsson, 1961). At present, it is considered that low-temperature areas show temperatures of less than 150°C in the 1000 m depth, but above 200°C in the 1000 m depth are high-temperature areas (Fridleifsson, 1979). The areas within the active rifting zones (Figure 4) are considered high-temperature fields, characterized by active volcanoes and fissure swarms. Their heat sources are cooling intrusions or other significant magma bodies. Low-temperature areas are mainly found outside the volcanic rift zones, such as in Quaternary and Tertiary formations. They are often fracture dominated systems, and derive their heat from the hot crust conducted and pushed upwards along structures such as faults, fractures and dykes. Away from the fractures, the bedrock is less permeable and heat transfer is dominated by conduction. Few Icelandic geothermal fields have reservoir temperatures in the obvious temperature gap in the definition above but those are sometimes called medium-temperature fields (Saemundsson et al., 2009).

3. MAPPING OF GEOTHERMAL MANIFESTATIONS

3.1 Methodology

The main objective of this project is mapping the surface geothermal manifestations in the Gufudalur area north of the village of Hveragerdi (Figures 2 and 3). The mapping of surface manifestations involves determining the surface characteristics of the manifestations and plotting their GPS locations

on a map. The aim is to compare the data with results obtained before and soon after the 2008 earthquake episode and map any observable changes in geothermal activities which were caused by the quakes. In addition, an effort is made to correlate any changes with structures formed during this seismic event.

Geothermal phenomena in the research area are manifested in the form of warm, hot or boiling springs, fumaroles steam vents, solfataras, and warm and hot ground, mud pools, silica and other encrustations and hydrothermal alteration (altered ground). The temperatures of individual surface manifestations were measured using a digital thermometer and their locations were plotted on a basemap using specific symbols for each phenomenon. The areas, where geothermal activity was observed as being clustered, are marked as zones of active geothermal area by giving a location number and are discussed briefly.

The springs were classified according to their temperature and any surface effects caused by the springs, such as precipitates or deposits, where noted. In addition, if a spring was located near a larger stream or river, the stream or river temperature was measured.

Altered grounds were identified and mapped. Several temperature measurements were performed to determine the temperature distribution within the hot or altered ground. Special notice was given to the colour of the altered ground and its form. The form of the precipitates and taste was noted to try to distinguish between silica and some form of mineral salt; samples were collected and analysed using XRD.

3.2 Characteristics of geothermal manifestations

3.2.1 Springs

Springs are the most common hydrothermal manifestations in the study area and they have a wide range of temperatures. Based on their temperature, the springs were divided into four categories: (i) cold springs with temperatures below 10°C; (ii) moderately warm (tepid) springs with temperatures between 10 and 30°C; (iii) warm springs with temperatures between 30 and 70°C; and (iv) hot springs with temperatures above 70°C.

A hot spring is a spring that is produced by the emergence of geothermally heated groundwater from the Earth's crust. There are geothermal hot springs in many locations and silica and other mineral coatings can be observed in the rocks along the flow paths.

3.2.2 Fumaroles/steam vents, mud pools and boiling hot springs

These forms of geothermal manifestations are grouped together and, in many cases, they are found interlinked in the same location. Fumarole/steam vents are often found in active geothermal areas, emitting steam and gases such as carbon dioxide, sulphur dioxide, hydrogen chloride and hydrogen sulphide (Figure 5). The steam is created when hot water turns to steam as pressure drops and subsequently emerges from the ground. The term solfataras, from the Italian solfo, meaning sulphur, is given to fumaroles that emit sulphurous gases. Fumaroles may occur along tiny cracks or long fissures, in unsystematic clusters or fields, and on the surfaces of lava flows and thick deposits of pyroclastic flows. A fumarole field is an area of thermal springs and gas vents where magma or hot igneous rocks at shallow depth release gases or interact with groundwater. From the perspective of groundwater, fumaroles could be described as hot springs that boiled off all water and the resultant steam reaches to the surface.



FIGURE 5: Fumarole found in the study area



FIGURE 6: Mud pool found in the study area



FIGURE 7: Steaming ground with white precipitates and mineral salts



FIGURE 8: Yellowish green moss in the warm ground

Mud pools and mud pots form in high-temperature geothermal areas where water is in short supply (Figure 6). The little water that is available rises to the surface at a spot where the soil becomes rich in grey coloured clay and other fine particulates. The viscosity of the mud usually changes with seasonal changes of the water table.

3.2.3 Hydrothermal alteration, minerals, salt precipitation and warm grounds

Rock alteration due to hydrothermal fluids basically means changing the mineralogy of the rock by passing hot water through the rocks and changing their composition by adding, removing or redistributing the components of the rocks. The fluids carry metals in solution, either from a nearby igneous source, or by leaching nearby rocks. The primary minerals are replaced by secondary minerals because of changes in the prevailing conditions subjected to the rock. These changes could be changes in temperature, pressure, or chemical conditions or any combination of these factors.

Extinct alteration is much more widespread and is expressed by grey clays of kaolinitic, smectitic and chloritic types. Silica and mineral salt precipitations are actively formed in areas of present geothermal activity (Figure 7). In some of these areas, alteration and precipitation mostly occurs along fractures within the rock mass. The process of sintering is sometimes manifested in the form of a thin crust of mineral salts and silica, accompanied by sulphur deposition.

Yellowish green moss characterizes warm grounds (Figure 8). This is the only vegetation which can thrive above 35°C in this climate and soil type but, below 27°C, grass will grow. Rising temperature is usually manifested in dying or drying-away of the thick green grass. Typically, black soil is observed in the hot grounds or where progressively increasing heat is being transferred to the surface.

4. TECTONIC SETTINGS AND CONNECTIONS TO THE THERMAL ACTIVITY OF HVERAGERDI

4.1 The relationship between surface manifestations and the geology and tectonics

Geothermal manifestations are surface indications of geothermal activity in the subsurface. Geothermal manifestations such as hot springs, fumaroles/steam vents, altered or hot ground, steaming grounds,

steam jets and sulphur depositions, must be mapped and their extent measured and correlated to geological structures.

Faults and fractures always indicate movements within the earth's crust. Faults can be distinguished from each other by lateral or vertical displacement; open fissures are common in most rock formations, but some are covered by erosional material. Therefore, they are often difficult to ascertain. Geological structures like fracture zones, shear zones, faults, fractures and fissures may not always be obvious on the surface. Rock slides, landslides, avalanches and erosional material can cover the surface geological features. However, in some situations, geothermal manifestations may indicate subsurface conditions, even though they are not apparent on the surface. For example, such manifestations may be oriented in a linear direction which only becomes obvious once a map is compiled. Alignment of geothermal manifestations along preferred directions indicates structural features like lineament expression of an underlying geological structure such as faults and fractures. These lineaments may indicate fracture zones, shear zones or intrusions such as dykes.

Tectonic movements within the Hveragerdi central volcano and its immediate surroundings are chiefly of four types: 1) tilting towards NW; 2) faulting; 3) formation of open seismic fissures and hot spring fissures; and 4) fracturing of rocks with little or no displacement (Saemundsson and Fridleifsson, 1992). The tilting is most intense furthest to the northwest, up to 8°, decreasing eastwards, only being 1-2° east of the volcano. The progressive increase in tilting towards the NW, towards the Hrómundartindur- and Hengill volcanic centres, and the relatively young age of the tilting, indicates that the tilting is caused by progressively increased burial of the younger volcanics in the rift zone to the west. Most commonly, faults in the area strike NE-SW or N-S and show 10 to 20 m displacement. A well-known seismic fissure striking N20°E extends from Hveragerdi across the Varmá river, towards Badstofuhver and the extinct hot spring, Svadi. After the 1947 earthquake, a narrow open fissure was seen in the terrace above Hverahvammur. The banks of the Varmá river (Figure 9) are scree covered but, just east of it, several NE-SW fissures with hot water are exposed. A N-S fissure is found west of Saudá (on the east side of Klóarmelar) in the centre of the valley. It is characterized by a long line of hot springs distributed along the fissure. The third open fissure is found in Földalháls, several tens of m long with a line of depressions occurring along it. The longest seismic fissures of this type, all of which relate to present day activity of the South Iceland Seismic zone, extend about 1 km. NE-SW striking fractures are common as are NW-SE. N-S trends are also seen in the Hveragerdi central volcano area (Saemundsson and Fridleifsson, 1992). According to the conceptual model of the Hveragerdi high-temperature geothermal field, a stream of geothermal water enters the Hveragerdi field from the north and the temperature of the water is 240-250°C. The water flows south and, on the way, the water cools due to mixing with cold groundwater (Geirsson and Arnórsson, 1995).

4.2 General geology of the Gufudalur area

The Gufudalur valley area is located in the extinct Hveragerdi volcano, which drifted about 5 km away from the rift axis to the west during the last 500,000 to 1 million years (Fridleifsson, 1979). The extinct Hveragerdi volcano and the presently active Hengill volcanic system developed on the western branch of the volcanic rift zone in SW-Iceland, which is characterized by tensional stress parallel to the spreading direction. The Hengill central volcano is intersected by a fracture system trending N30-35°W, forming geothermal manifestations such as fumaroles and hot springs, which are distributed in a zone from Hveragerdi centre to the Hengill centre, transecting the main fissure swarms (Fridleifsson, 1979). The main heat source of the Hveragerdi system is from the volcanic rift zone through the faults and fissure swarms connecting to the Hengill central volcano (Fridleifsson, 1979). Fissures/faults and the hydrothermal activity are interconnected with the seismic activity. Rock slides are a prominent surface feature in the study area, mostly caused by large earthquakes related to the South Iceland Seismic Zone since the Holocene.

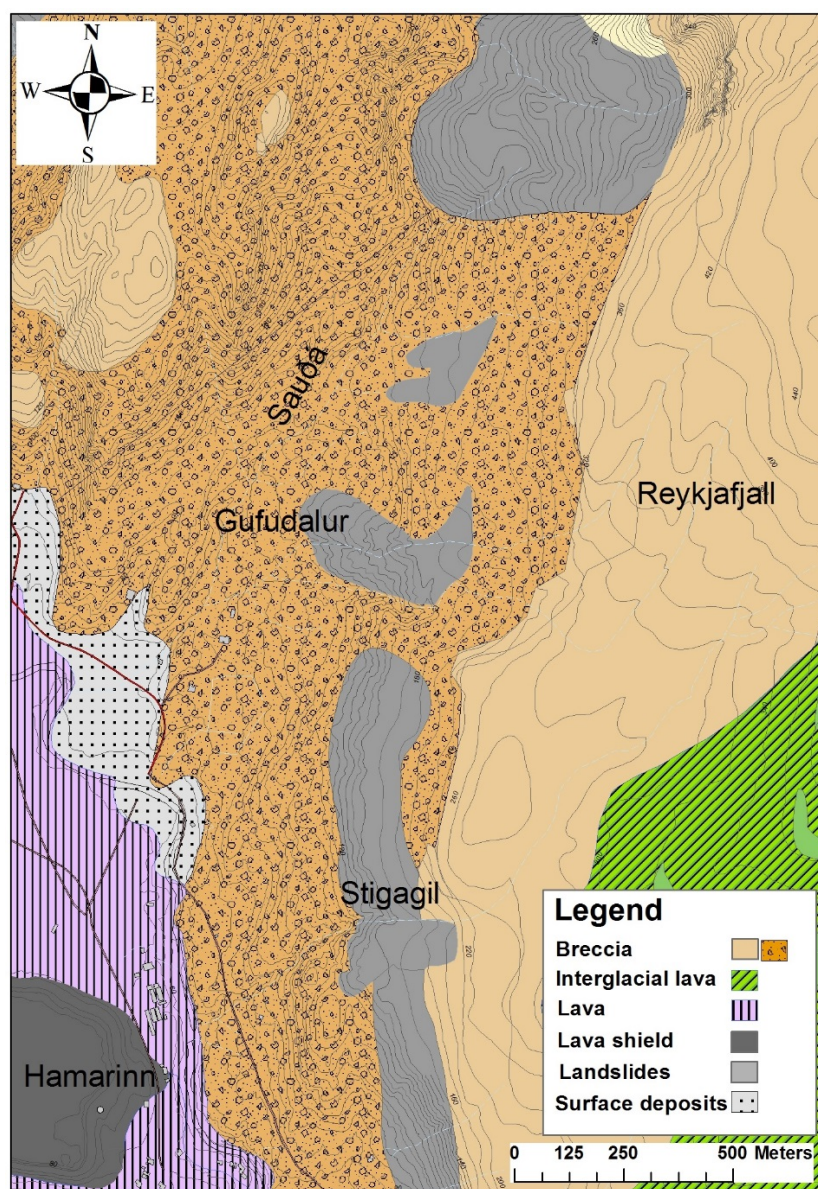


FIGURE 9: Map showing the general geology of the Gufudalur area

hydrothermal alteration are considered as being the older series and the main units are hyaloclastite of quartz tholeiite composition, termed the Varmá formation, and of olivine tholeiite composition, termed the Tindar and Saudá formations (Saemundsson and Fridleifsson, 1992). The alteration degree reaches the smectite/chlorite alteration zone locally (indicated by the pale green colour of the rocks) in the stratigraphically lower Varmá formation. The regional blackish to brownish colouring of the Tindar and Saudá units suggests a smectite alteration-zone (Saemundsson and Fridleifsson, 1992). The less altered rock units are categorized by younger rock series that occurred at higher levels in the hills north and east of the Saudá valley. The main units are a group of lavas termed the Kvíar basalts and a group of hyaloclastites higher up, extending to Mt. Reykjafjall (Figure 9), east of Saudi (Saemundsson and Fridleifsson, 1992).

The volcanic rocks in the area are mostly of basaltic composition and are mainly composed of various lithofacies of subglacially formed hyaloclastites and interglacial lava flows (Figure 9). They range from olivine tholeiite to tholeiite; some basaltic andesites also occur. The hyaloclastites range from glassy fine grained tuffs to coarse breccias and pillow lavas. Sometimes these pass into lava flows. The units have textures ranging from aphyric, fine or coarse grained to variably porphyritic. The hyaloclastites in the volcano form NE-SW striking ridges; the younger ones also show N-S strikes. The rocks are slightly tilted towards WNW or NW, and the maximum tilt reaches up to 8° in Dalaskard in the northwest. The tilt is much less in the south and east. Numerous dykes are found in the centre, some of these forming dyke swarms, and most of them are of the same composition as the extrusive rocks (Saemundsson and Fridleifsson, 1996).

Rocks in this area can be divided into two main rock series. The rocks that have been affected by strong

4.3 Details of geothermal manifestations

East of the Gufudalur valley area (Figure 9), geothermal manifestations consist mainly of steaming grounds, steam vents/fumaroles, hot springs, and warm and hot grounds. It was seen that several manifestations were noticeable after the earthquakes in 2008 and it was also observed that activity had increased since the earthquakes in 2008. The map in Figure 10 shows the location of old and present geothermal manifestations in the Hveragerdi central area and the areas containing a large number of manifestations can be observed as clusters of points on the map. They were divided into 12 localities which are described briefly. The map also shows previous geothermal exploration/mapping carried out in the area by Saemundsson (1995b), and soon after the earthquakes in 2008 by Thorbjörnsson et al. (2009). Among the twelve locations on the map, localities No. 13-04 and 13-07 are new geothermal manifestations; they were not identified in previous studies. Increased geothermal activity was observed in areas shown at locations No. 13-01, 13-02, 13-05, 13-06, 13-10, 13-11 and 13-12, while areas shown at locations No. 13-03, 13-08 and 13-09 appear stable when compared to the geothermal activity in 1995 and 2008. The alignment of geothermal manifestations striking NE-SW are also shown on the map.

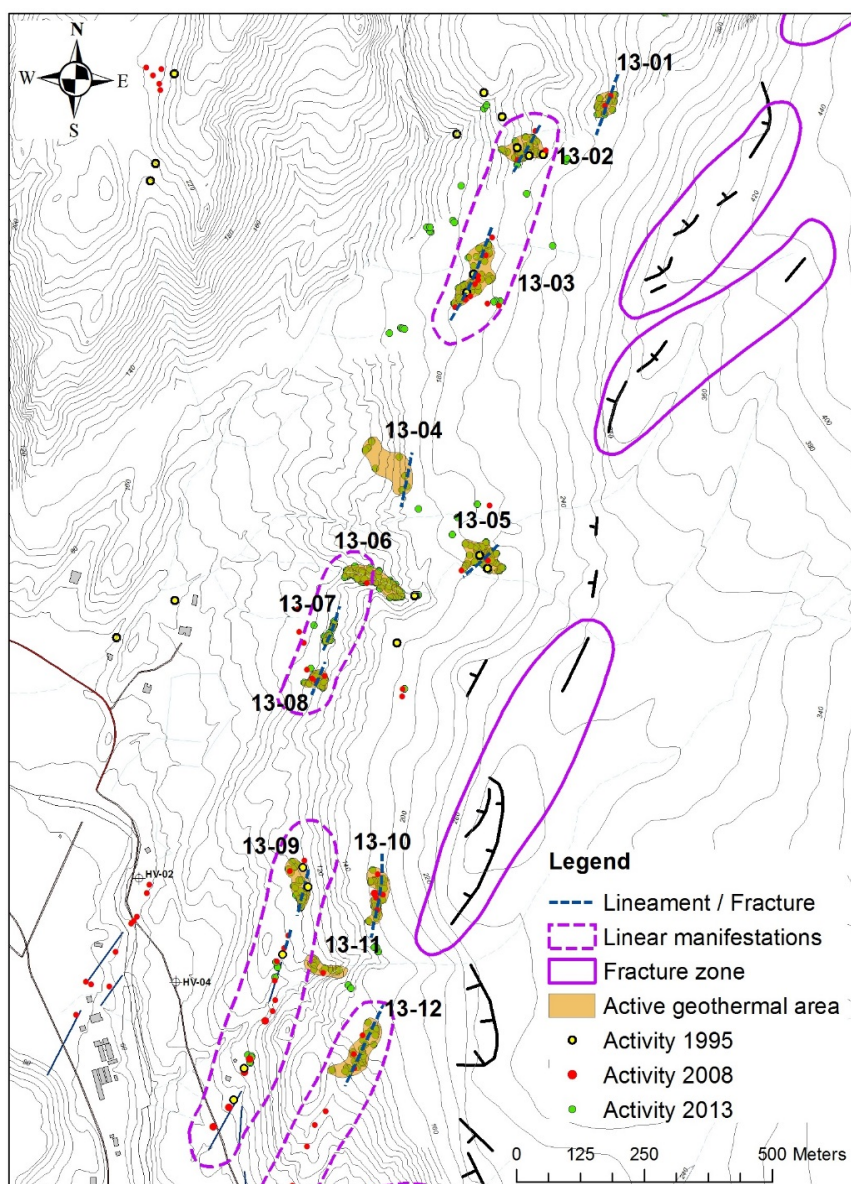


FIGURE 10: Map showing the location of geothermal manifestations and geological structures in the Gufudalur, Hveragerdi area; the geothermal activity in 1995, 2008 and 2013 is shown in different colours; active geothermal areas are shown in 12 location zones; linear manifestations and fracture/lineament in NE-SW direction are also shown on the map; geothermal activity mapped in 1995 and 2008 was completed by Saemundsson (1995) and Thorbjörnsson et al (2009); activity in 2013 refers to the present study



FIGURE 11: Warm and steaming grounds in Location No. 13-01



FIGURE 12: The intense geothermal activity in the area of Location No. 13-02



FIGURE 13: The geothermal activity in the area at Location No. 13-03

Location No. 13-01: The geothermal activity is recent and centred in a 2 x 2 m size steaming ground at temperatures of about 97°C, surrounded by warm grounds covered by yellowish green moss (Figure 11). The steaming ground is covered with white and yellow mineral precipitates. The total area is about 25 × 10 m in size and extends NE-SW.

Location No. 13-02: Intense geothermal activity is present in this area (13 x 20 m) and consists mainly of a large area of steaming ground with steam vents with temperatures greater than 90°C. White, yellow precipitates and mineral salts are present and give off H₂S (sulphur) smells. Also found was a combined 2 × 2 m size boiling mud pool and fumarole. Steaming and hot grounds in the active area are circled by yellowish green moss (Figure 12).

Location No. 13-03: Highly altered steaming ground covered with white and yellow mineral precipitates (Figure 13). Seven fumaroles were identified while a 1 x 1 m size grey colour clay filled boiling mud pool was located in this gently sloping area; their temperatures exceed 97°C. A small hot spring is located in the same area.

Location No. 13-04: This area is mostly warm ground (>20°C) covered by rock slide gravel in a 40 x 10 m area and contains several warm and hot springs (up to 82°C) having <5 l/s flow. Run-off water in the area is in the temperature range of 27-55°C.

Location No. 13-05: This area is on a steep slope having six moderately warm springs with very low flow rates and three boiling springs (98°C) with low flow rates. Two mud pools and one fumarole are located in the steaming ground. H₂S odour is noticeable and the vegetation is spoiled due to the hot and steaming grounds. Yellowish green moss covers most of the warm grounds (see Figure 14). One sample of precipitates in the warm spring area (Sample No. 6) was analysed by XRD and identified the presence of calcite.

Location No. 13-06: The area is in a gully with a large number of geothermal manifestations aligned along the gully (Figure 15), mostly composed of steaming grounds with mineral precipitates such as silica and calcite. Five fumaroles with temperatures exceeding 97°C were found. H₂S odour is noticeable. Also, a number of hot springs with low flow rates were seen running into the stream running through the gully. Most of the hot and warm grounds are located on the slopes inside the gully.

The extent of the geothermal activity in Locations No. 13-05, 13-06 and No. 13-07 are shown in Figure 16. Also shown are the types of manifestations found in the zones. Location No. 13-06 had several sites of activity before the earthquakes in 2008, but the geothermal activity has increased, extending in a NW direction. Location No. 05 increased activity compared to activity in 1995 and 2008. The area shown in Location No. 13-07 is new activity, not yet identified after the earthquakes in 2008 by the mapping done by Thorbjörnsson et al. in 2009. The direction of the lineament/fracture is NE-SW and the direction of the activity in location No. 13-06 is controlled by the topography.

Location No. 13-07: Two patches of yellowish green moss could be observed with a temperature range of 20-69°C. The warm grounds are 15 x 10 m and 9 x 5 m, extending N10°E. This is fresh activity, not recorded in previous studies (Figure 17).

Location No. 13-08: Steaming ground with two hot springs and one fumarole on a steep slope near abandoned Well SP-01 (Figure 18). The area also shows layers of precipitates of an extinct geyser (Spýtir); two samples (Samples No. 1 and 7) of mineral salts and precipitates were tested by XRD and identified the presence of gypsum and anhydrite.

Location No. 13-09: Evidence of an extinct geyser and a combination of large boiling springs, boiling mud pools, and fumaroles were found at this location, shown on the map in Figure 21, along with steaming grounds, hot and warm grounds shown in Figure 19. A boiling spring with about a 3 x 4 m size pool and water rising in a geyser for about 20-50 cm were seen. Seven boiling mud pools are distributed in this area surrounded by brownish and grey coloured clay, the largest one extending 5 x 5



FIGURE 14: Geothermal activity in Location No. 13-05



FIGURE 15: The geothermal activity along the gully area of Location No. 13-06

m. 25 x 25 m; hot and warm ground with hot, warm springs and a warm water pool are located a few metres to the north of the old geyser area.

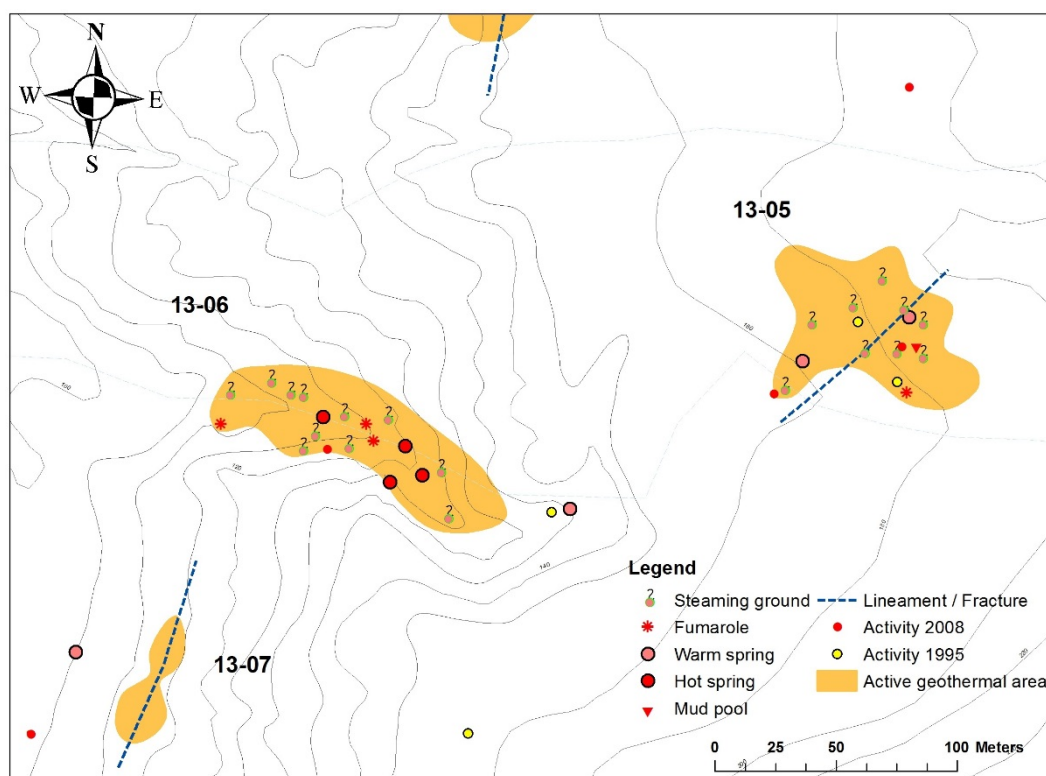


FIGURE 16: Map showing Locations No. 13-05, 13-06 and 13-07



FIGURE 17: The yellowish green moss in the warm ground at Location No. 13-07

Location No. 13-10: This recently active area is located in the rock fall area; steaming grounds are about 10 m in width and extend several tens of metres to the south, as shown in Figure 21. The steaming grounds contain white and yellow precipitates and three samples were tested (Samples No. 2, 3 and 4) in the laboratory using XRD which identified the presence of amorphous silica (opal), gypsum and anhydrite. One fumarole and one small mud pool are present and steaming ground gives rise to H_2S odour. Although the subsurface structures are covered by a rock fall/surface deposits, geothermal activity at the surface indicates a sub-surface structure with a lineament/fracture striking NE-SW.

Location No. 13-11: The area contains 20 x 10 m size warm ground (temperatures up to $70^{\circ}C$) covered with yellowish green moss and several warm springs with temperatures ranging from $50-60^{\circ}C$, including

a warm spring (38°C) having a flow-rate of 1 l/s. Another 10 × 10 m size warm ground is located close to the major spring area and the activity of this area started after the earthquakes in 2008 and has increased since then. The area is presented in Figure 21 and shows a NW-SE trend. A sample collected by the spring (Sample No. 5) for XRD analysis indicates the presence of calcite.

Location No. 13-12: A number of steaming grounds with temperatures greater than 95°C are scattered in this area. A large area of warm grounds is observed surrounding the steaming grounds (Figure 20). The activity in this area started after the earthquakes in 2008 and currently geothermal activity in the area is increasing, trending N10°E.

The map shown in Figure 21 shows the geothermal manifestations representing the areas of geothermal activity. The general trend of the manifestations is aligned in the direction of NE-SW. The geothermal activity in the areas of Locations No. 13-10, 13-11 and 13-12 was new and started soon after the earthquakes in 2008, and activity is still increasing. In 1995, no geothermal activity in this area was reported. Location No. 13-09 shows old geothermal activity and has evidence of an extinct geyser.

5. DISCUSSION

Mapping of surface manifestations on the east side of Gufudalur valley, Hveragerdi, has revealed new manifestations which were created after major earthquakes struck in 2008. When comparing the author's study to previous studies carried out in 1995 by Saemundsson, and soon after the earthquakes (Thorbjörnsson et al., 2009), new manifestations are revealed in the area and there has



FIGURE 18: The geothermal activity at Location No. 13-08



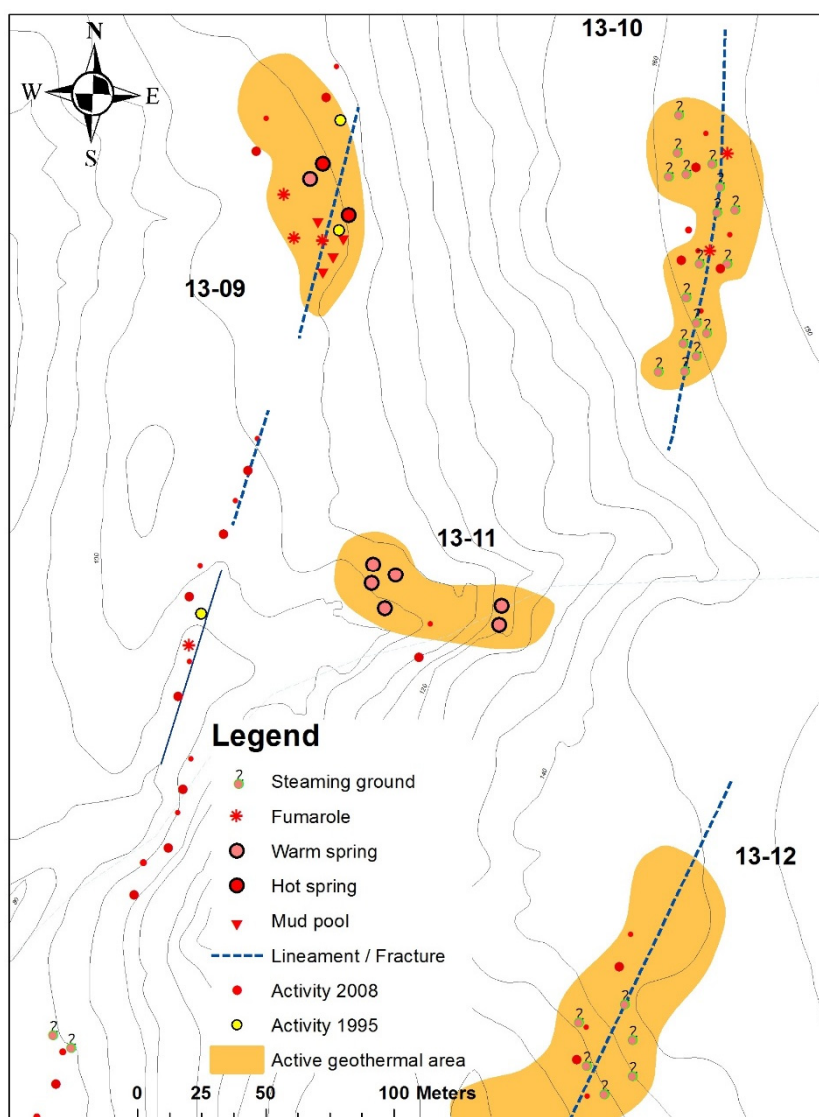
FIGURE 19: At Location No. 13-09 there is an extinct geyser area having several mud pools, boiling spring/gyser and steaming grounds



FIGURE 20: Steaming grounds and warm grounds in the area of Location No. 13-12

been an increase in geothermal activity from 2008 to 2013. New surface manifestations such as fumaroles/steam vents, hot springs, boiling springs, warm grounds, hot grounds and steaming grounds were identified towards the high elevated areas on the east slopes of the valley, indicating that new lineaments/fractures had opened, virtually parallel to the old fractures.

Some parts of the study area are covered by landslides and rock slides and, therefore, most of the geological features are covered by surface deposits, but in some locations geothermal activity has been powerful enough to manifest itself at the surface, revealing the subsurface conditions, and the manifestations indicate a pattern of alignment striking NE-SW and NNE-SSW.



6. CONCLUSIONS

FIGURE 21: Map showing the extent of geothermal activities at Locations No. 13-09, 13-10, 13-11 and 13-12

Detailed geothermal mapping

of surface manifestations was carried out in the Gufudalur valley, Hveragerdi geothermal field, which indicated that the geothermal manifestations are the result of large earthquakes affecting tectonic structures.

The east side of the Gufudalur valley area is characterized by widespread geothermal manifestations having variable temperatures, and variable degrees of alteration, controlled by structural elements such as faults and fractures. The alignment of geothermal manifestations is in preferred directions indicating geological structures derived from tectonic activity and structural control. The major faults represent several fractures on the surface while the fractures unite in the sub surface.

By investigating the new geothermal surface manifestations, new lineaments/fractures were identified on the eastern side of the valley, trending N-S and NE-SW, which were formed by two earthquakes which occurred in Hveragerdi and Selfoss on 29th May 2008. The major structural trends that control the geothermal manifestations are oriented NE-SW, but NW-SE and N-S oriented lineament/fractures and faults are also present. The earthquakes in 2008 created new, or renewed, geothermal activity; the geothermal activity has intensified and new surface manifestations are still appearing in the Gufudalur, Hveragerdi area.

On the basis of geothermal mapping, the geothermal manifestations are controlled by the tectonics and topography. Some parts of the study area are covered by rock falls, landslides or avalanche deposits. Therefore, the presence at the surface of geothermal phenomena may be heavily dependent on the individual sizes of the rock falls, landslide blocks and their thickness. Consequently, the faults and fractures that control the flow of the hydrothermal fluids may be hidden underneath major landslides and rock falls.

The local groundwater level can change seasonally, affecting the appearance of geothermal manifestations like hot springs, mud pools and steam vents in such a way that when the groundwater table is high, it forms boiling/hot springs, but they can change to mud pits and eventually to steam vents when the ground water level is low.

Colour changes in the vegetation in warm grounds, such as yellow to green moss and grass, reflect temperature distribution and vegetation over the dyed vegetation, indicating changes of the phenomena due to heating or cooling.

Seven samples were tested in the XRD to identify the mineral precipitates and salts found in the steaming grounds (Samples No. 1, 2, 3, and 4), warm springs (Samples No. 5 and 6), and extinct geyser deposits (Sample No. 7). The laboratory results indicate the presence of amorphous silica (opal) in Samples No. 3, 4 and 7; calcite was found in Samples No. 5 and 6; gypsum and anhydrite minerals were found in Samples No. 1 and 2. The results are shown in Appendix I.

7. RECOMMENDATIONS

- Geothermal manifestations indicate that new faults/fractures were formed by the two major earthquakes in 2008, showing that geological structures such as faults, shear zones, fissures and lineaments are derived from active tectonic activities.
- The type of geothermal mapping for geothermal exploration completed in this study can be applied in the prospect for utilizing geothermal energy for small scale, binary power generation in Sri Lanka.
- It is essential to create and increase awareness amongst decision makers and politicians on the importance of geothermal energy as a clean renewable energy source, as opposed to fossil fuel burning power stations.
- More people should undergo training in various disciplines relevant to geothermal development for the purpose of increasing the number of qualified geothermal personnel in Sri Lanka.
- The mobilization of funds for detailed geothermal resource assessments in potential geothermal areas of Sri Lanka is highly recommended.

ACKNOWLEDGEMENTS

I would like to express my gratitude to Dr Ingvar B. Fridleifsson, retiring director of the UNU Geothermal Training Programme and Mr. Lúdvík S. Georgsson, director, for giving me the great opportunity to attend this special training, and also for their generous advice and assistance throughout the training program. I would also like to thank Mr. Ingimar G. Haraldsson, Ms. Málfríður Ómarsdóttir, Ms. Thórhildur Ísberg and Mr. Markús A.G. Wilde for their kindness and efficient help during the training.

My deepest thanks go to my supervisors, Dr. Björn S. Hardarson and Mr. Sigurdur G. Kristinsson for their help and instruction during training and field work, which made this report possible. Thanks are

also given to the other members of the Iceland GeoSurvey (ÍSOR). I also want to thank the UNU-GTP Fellows of 2013 for our unforgettable relationship.

Special thanks goes to Mr. B. A. Peiris, director general, Dr. N.P. Wijayananda, former chairman, Dr. W.K.B.N. Prame, deputy director (Geology), Mr. K.T.U.S. de Silva, assistant director (Geology), Mr. Nalin de Silva and other colleagues of Geological Survey and Mines Bureau, Sri Lanka, for their support.

Finally, I am deeply grateful to my parents, brother and my wife, Dinali Lecamwasam, for their love and support during these six months.

REFERENCES

Árnadóttir, T., Geirsson, H. and Einarsson, P., 2004: Co-seismic stress changes and crustal deformation on Reykjanes peninsula due to triggered earthquakes on June 2000. *J. Geophys. Res.* 109-B09307, 12 pp.

Árnadóttir, T., Geirsson, H., and Jiang, W., 2008: Crustal deformation in Iceland: Plate spreading and earthquake deformation. *Jökull*, 58, 67 pp.

Arnórsson, S., 1995a: Geothermal systems in Iceland; structures and conceptual models I, high-temperature areas. *Geothermics*, 24, 561-602.

Arnórsson, S., 1995b: Geothermal systems in Iceland: Structure and conceptual models II. Low-temperature areas. *Geothermics*, 24, 603-629.

Bödvarsson, G., 1961: Physical characteristics of natural heat resources in Iceland. *Jökull*, 11, 38pp.

Brandsdóttir, B., Parsons, M., White, R.S., Gudmundsson, O., Drew, J. and Thorbjarnardóttir, B.S., 2010: The May 29th 2008 earthquake aftershock sequence within the South Iceland Seismic Zone: Fault locations and source parameters of aftershocks, 2008, *Jökull*, 60, 23-46.

Clifton, A.E., and Einarsson, P., 2005: Styles of surface rupture accompanying the June 17 and 21, 2000 earthquakes in the South Iceland seismic zone. *Tectonophysics*, 396, 159 pp.

Clifton, A.E., Pagli, C., Jónsdóttir, J.F., Eythórsdóttir, K., and Vogfjörð, K., 2003: Surface effects of triggered fault slip on Reykjanes Peninsula, SW Iceland. *Tectonophysics*, 369, 145-154.

Einarsson, P., 1989: Earthquake focal depth in Iceland and conclusions on crustal structure and temperatures. *Abstracts from the Conference of the Icelandic Geological Society on the Crust of Iceland, Reykjavík* (in Icelandic), 7 pp.

Einarsson, P., 1991: Earthquakes and present-day tectonism in Iceland. *Tectonophysics*, 189, 261-279.

Einarsson, P. 2008: Plate boundaries, rifts and transforms in Iceland. *Jökull*, 58, 35-58.

Einarsson, P., and Eiríksson, J., 1982: Earthquake fractures in district and Rangárvellir in south Iceland seismic zone. *Jökull*, 32, 113-119.

Einarsson, P., Böttger, M., and Thorbjörnsson, P., 2002: *Faults and fractures of south Iceland Seismic zone near Thjórsá*. Landdsvirkjun, Reykjavík, report LV-2002/090, 8pp.

Einarsson, P., Björnsson, S., Foulger, G., Stefánsson, R., and Skaftadóttir, T., 1981: Seismic pattern in south Iceland seismic zone. In: Simpson, D., and Richards, P. (eds.), *Earthquakes prediction – An international review*, Am. Geophys. Union, Maurice Ewing Series 4, 151 pp.

Fridleifsson, I.B., 1979: Geothermal activity in Iceland. *Jökull*, 29, 47-56.

Geirsson, K. and Amorsson, S., 1995: Conceptual model of the Hveragerdi geothermal reservoir based on chemical data. *Proceedings of the World Geothermal Congress 1995, Florence, Italy*, 2, 1251-1256.

Gudmundsson, M.T., and Jacoby, W., 2007: Hotspot Iceland: An introduction. *J. Geodynamics*, 43-1, 1-5.

Hardarson, B.S., Fitton, J.G., and Hjartarson, A., 2008: Tertiary volcanism in Iceland. *Jökull*, 58, 161-178.

Hardarson, B.S., Fitton, J.G., Ellam, R.M., and Pringle, M.S., 1997: Rift relocation-a geochemical and geochronological investigation of a paleo-rift in northwest Iceland. *Earth Planet. Sci. Lett.*, 153, 181-196.

Jakobsson, S.P., Jónsson, K., and Sigurdsson, I.A. 2008: The three igneous rock series of Iceland. *Jökull*, 58, 117-138.

Jóhannesson, H., 1980: Structure and evolution of volcanic zones in W-Iceland. *Náttúrufræðingurinn*, 50, (in Icelandic), 13-31.

Jóhannesson, H. and Saemundsson, K., 1998: *Geological map of Iceland 1:500.000* (2nded.). Náttúrufræðistofnun Íslands and Landmaellingar Íslands.

Jóhannesson, H., and Saemundsson, K., 1999: *Geological map of Iceland 1:1.000.000*. Náttúrufræðistofnun Íslands.

Jónsson, J., 1989: *Hveragerdi and surroundings, geological overview*. Rannsóknarstofnunin Nedri Ás, report 50 (in Icelandic), 56 pp and map.

Kristjánsson, B.R., and Fridriksson, Th., 2003: *State Horticultural School, Reykjum in Ölfus. Geothermal map*. ISOR-Iceland GeoSurvey. Report 2003-01 (in Icelandic), 4pp.

Kyagulanyi, D., 1996: Geothermal exploration in the Hveragerdi Graendalur area, SW-Iceland. Report 8 in: *Geothermal training in Iceland 1996*. UNU-GTP, Iceland, 161-176.

Malik, A.H., 1996: Geothermal exploration of Saudá valley north of Hveragerdi, SW-Iceland. Report 9 in: *Geothermal training in Iceland 1996*. UNU-GTP, Iceland, 177-195.

McDougall, I., Kristjánsson, L., and Saemundsson, K., 1984: Magnetostratigraphy and geochronology of northwest Iceland. *J. Geophys. Res.*, 89(B8), 7029-7060.

Meteorological Office, 2008: *Information on earthquakes*. Meteorological Office of Iceland, Reykjavík, website: en.vedur.is/#tab=skjalftar.

Moorbath, S., Sigurdsson, H., and Goodwin, R., 1968: K-Ar ages of oldest exposed rocks in Iceland: *Earth & Planet. Science Letters*, 4, 197-205.

Óskarsson, N.S., Steinthórsson, S., and Sigvaldason, G.E., 1985: Iceland geochemical anomaly: origin, volcanotectonics, chemical fractionation, and isotope evolution of the crust. *J. Geophys. Res.*, 90, 10011-10025.

Pagli, C., Pedersen, R., Sigmundsson, F., and Feigl, K.L., 2003. Triggered fault slip on June 17, 2000 on the Reykjanes Peninsula, SW Iceland captured by radar interferometry. *Geophys. Res. Lett.*, 30-6, 1273.

Saemundsson, K., 1967: *Vulkanismus und Tektonik des Hengill-Gebietes in Sudwest-Island*. Acta Nat. Isl., II-7, (in German), 195 pp.

Saemundsson, K., 1974: Evolution of the axial rifting zone in northern Iceland and Tjörnes fracture zone, *Geol. Soc. Am. Bull.*, 85, 495-504 pp.

Saemundsson, K., 1980: Outline of geology of Iceland. *Jökull*, 29, 28 pp.

Saemundsson, K., 1993a: *Hveragerdi – geothermal activity*. Orkustofnun, Reykjavík, report KS-93/20, 33 pp.

Saemundsson, K., 1993b: *Geothermal map of Hveragerdi and Reykir*. Orkustofnun, Reykjavík, report JHD-JFR8716, 54 pp.

Saemundsson, K., 1995a: *Geological map of the Hengill area 1:50,000*. Orkustofnun, Reykjavík.

Saemundsson, K., 1995b: *Geothermal and hydrothermal map of the Hengill area, 1:25,000*. Orkustofnun, Reykjavík.

Saemundsson, K., and Fridleifsson, G.Ó., 1992: *The Hveragerdi central volcano, geological description*. Orkustofnun, Reykjavík, report OS-92063/JHD-35 B (in Icelandic), 25 pp.

Saemundsson, K., and Fridleifsson, G.O., 1996: The Hveragerdi central volcano. An extended English abstract from Saemundsson, K., and Fridleifsson, G.Ó., 1992: *The Hveragerdi central volcano, geological description*. Orkustofnun, Reykjavík, report GOF-KS-96/03, 10 pp.

Saemundsson, K., and Kristinsson, S.G., 2005: *Hveragerdi. Temperature measurements in earth and fractures*. ÍSOR – Iceland GeoSurvey, report ISOR-2005/041 (in Icelandic), 16 pp + 2 maps.

Saemundsson, K., Axelsson, G., and Steingrímsson, B., 2009: Geothermal systems in global perspective. *Proceedings of a “Short Course on Surface Exploration for Geothermal Resources, organized by UNU-GTP and LaGeo, Santa Tecla, El Salvador*, 16 pp.

Stefánsson, R., Gudmundsson, G. and Halldórsson, P., 2003: *South Iceland earthquakes 2000- a change for earthquakes prediction*. Meteorological Office, Reykjavík, report VI-R03017, 21pp.

Thórdarson, Th. and Larsen, G., 2007: Volcanism in Iceland in historical time: Volcano types, eruption styles and eruptive history. *J. Geodynamics*, 43, 118-152.

Thorbjörnsson, P., Saemundsson, K., Kristinsson, S.G., Kristjánsson, B.R, and Ágústsson, K., 2009: Southern lowland earthquakes 29th May 2008, effect of groundwater level, geothermal activity and fractures. (in Icelandic), 44 pp.

Vink, G.E., 1984: A hotspot model for Iceland and the Voring Plateau. *J. Geophys. Res.*, 89, 9949-9959.

Walker, C., 1992: *The volcanic history and geochemical evolution of the Hveragerdi region, SW-Iceland*. Ph.D. thesis, University of Durham, Durham, 356 pp.

Ward, P., and Björnsson, S., 1971: Micro earthquakes, swarms and the geothermal areas of Iceland. *J. Geophys. Res.*, 76, 953-982.

Watkins, N.D., and Walker, G.P.L., 1977: Magnetostratigraphy of Eastern Iceland. *Am. J. Sci.*, 277, 513-584.

APPENDIX I: XRD results of seven samples of mineral precipitates

54928/UNU S-01

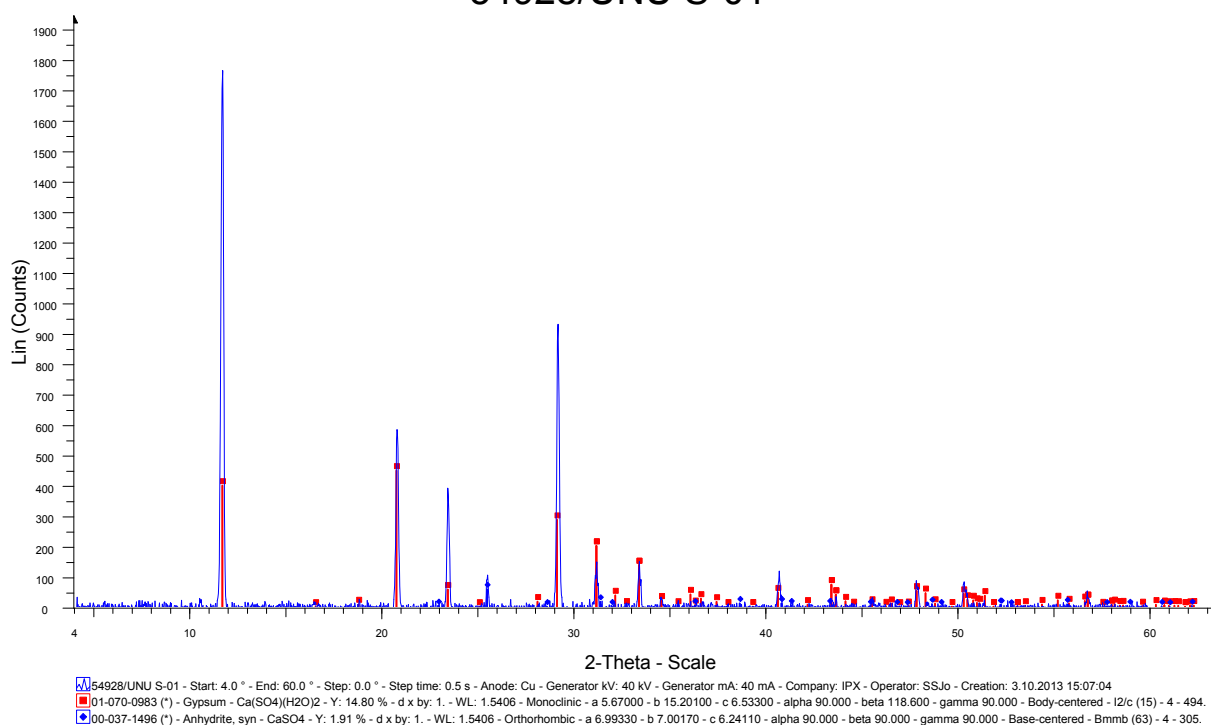


FIGURE 1: XRD graph showing the presence of gypsum and anhydrite minerals in Sample No. 1 collected in steaming ground at Location No. 13-8

54929/UNU S-02

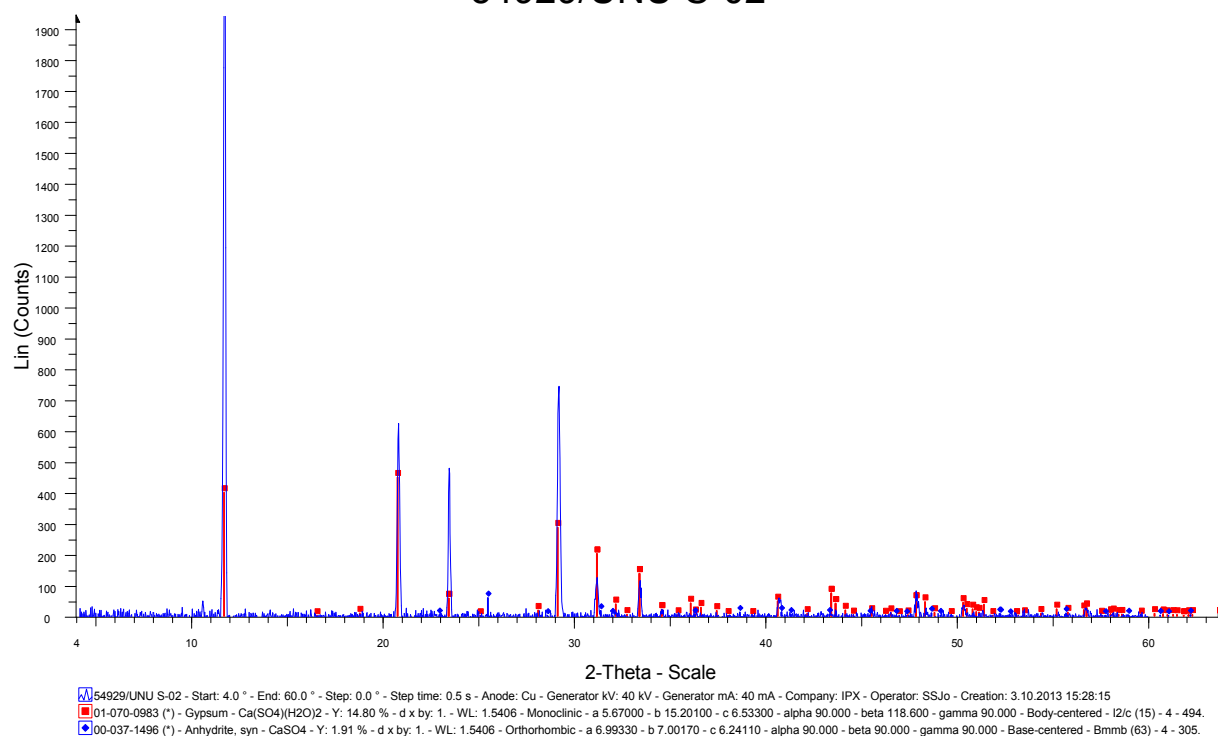


FIGURE 2: XRD graph showing the presence of gypsum and anhydrite minerals in Sample No. 2 collected in steaming ground at Location No. 13-10

54930/UNU S-03

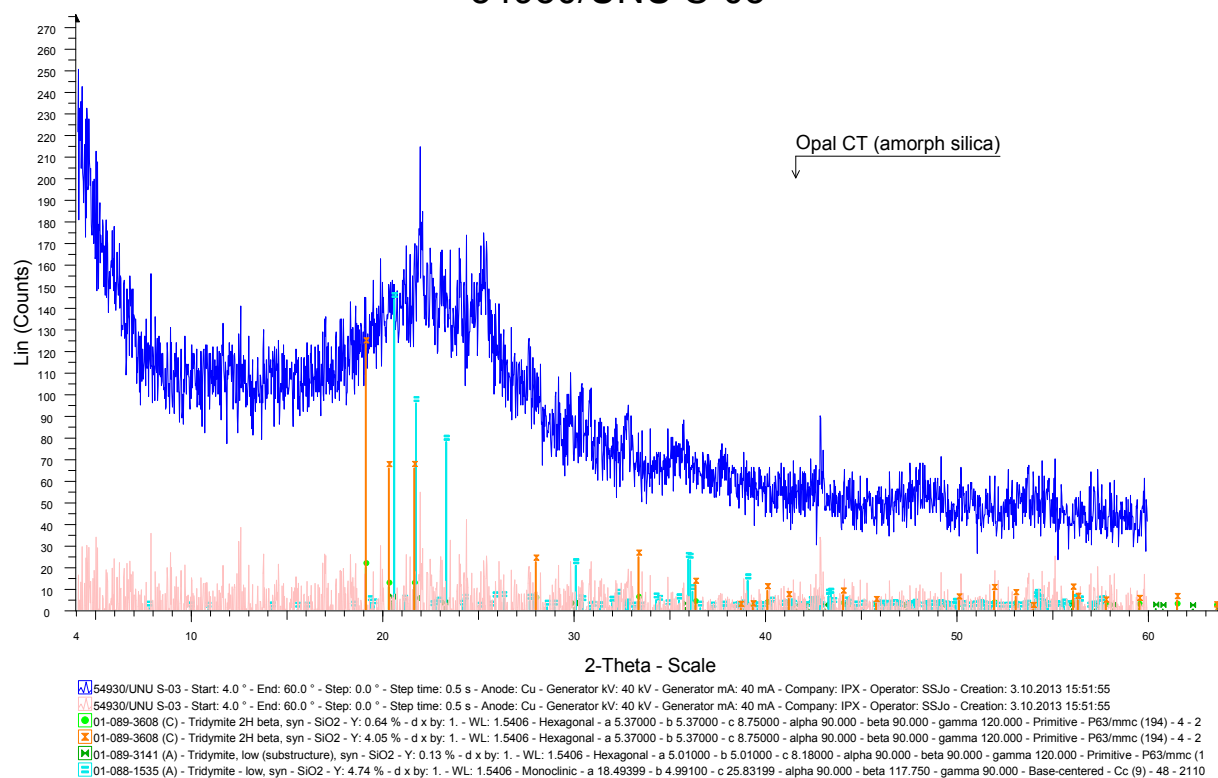


FIGURE 3: XRD graph showing the presence of amorphous silica (opal) in Sample No. 3 collected in steaming ground at Location No. 13-10

54931/UNU S-04

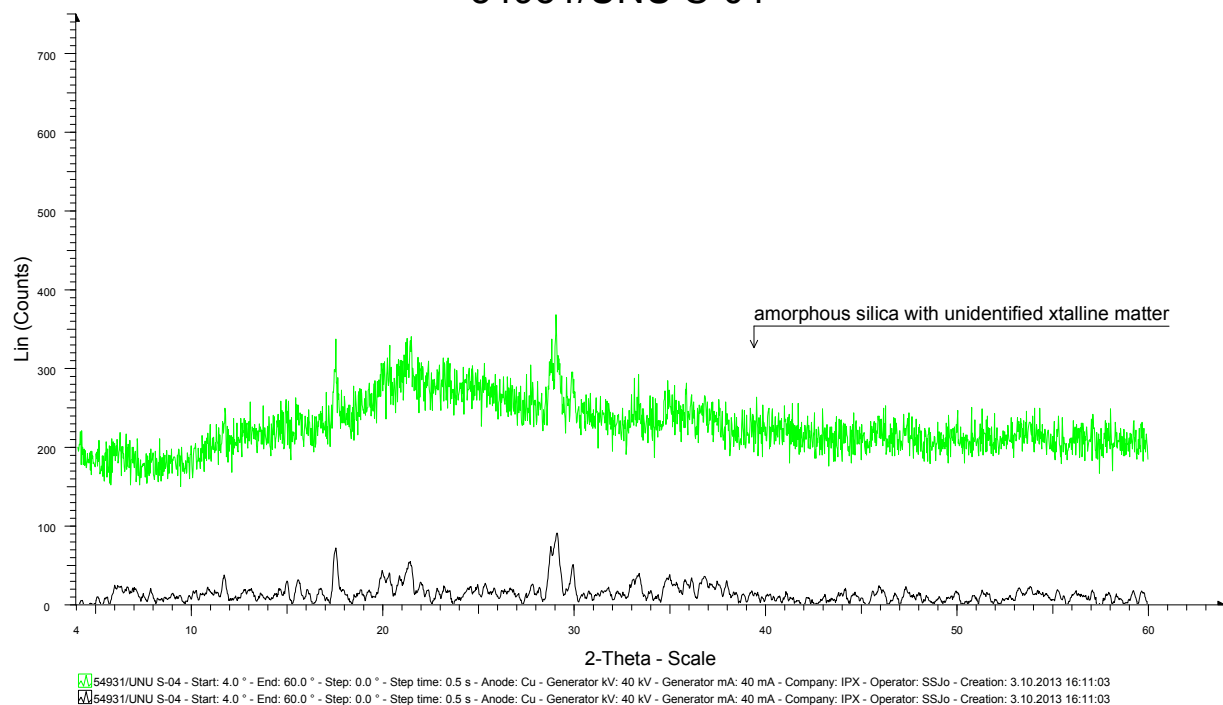


FIGURE 4: XRD graph showing the presence of amorphous silica (opal) in Sample No. 4 collected in steaming ground at Location No. 13-10

54932/UNU S-05

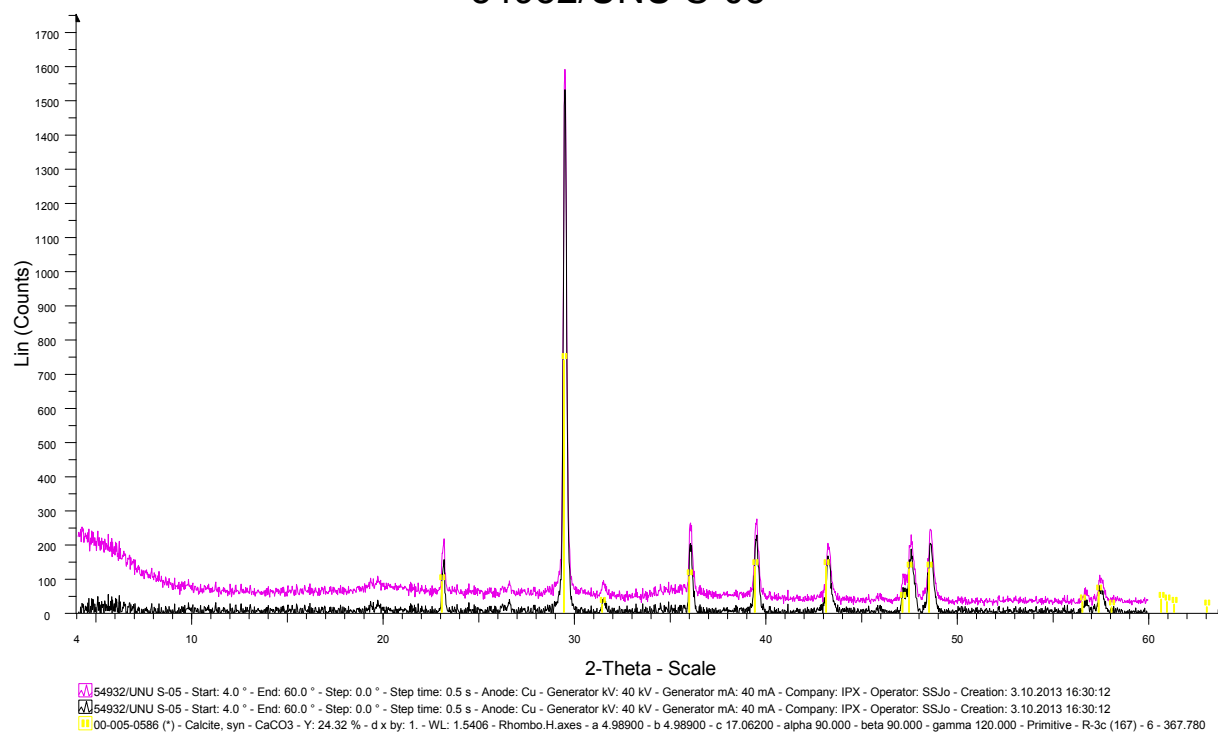


FIGURE 5: XRD graph showing the presence of calcite in Sample No. 5 collected in warm spring at Location No. 13-11

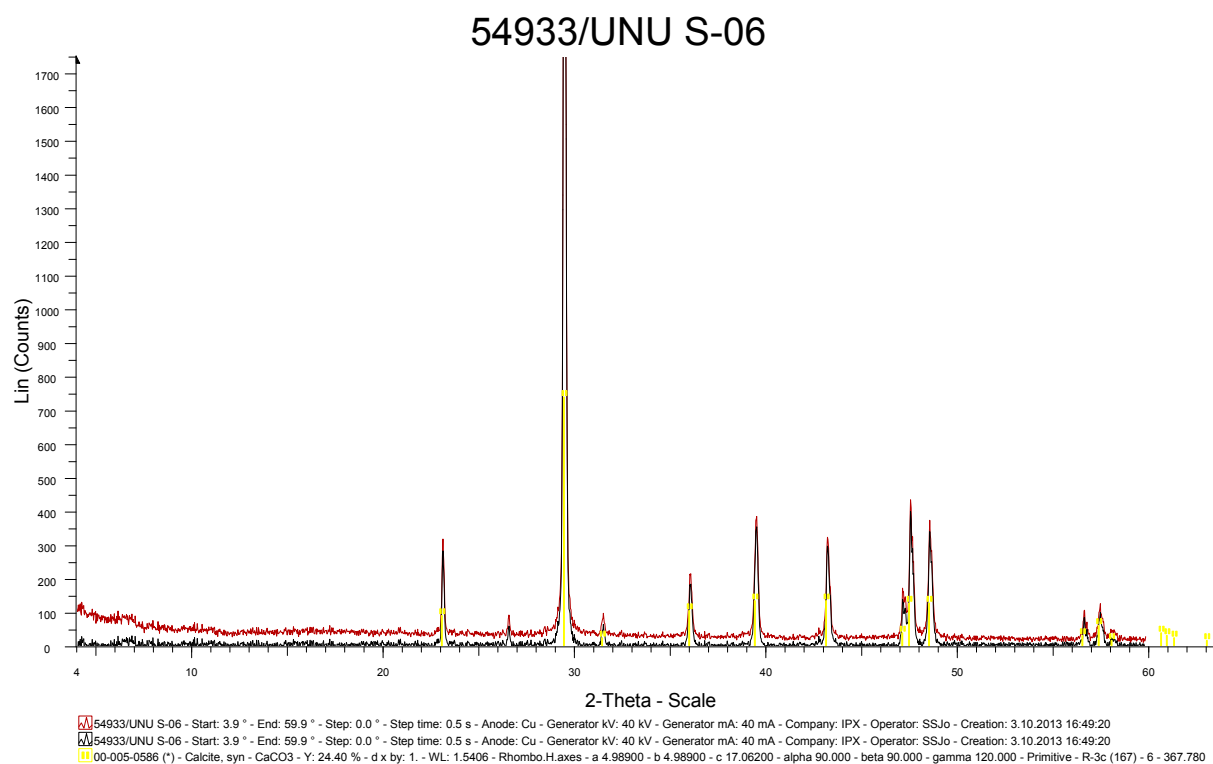


FIGURE 6: XRD graph showing the presence of calcite in Sample No. 6 collected in warm spring at Location No. 13-05

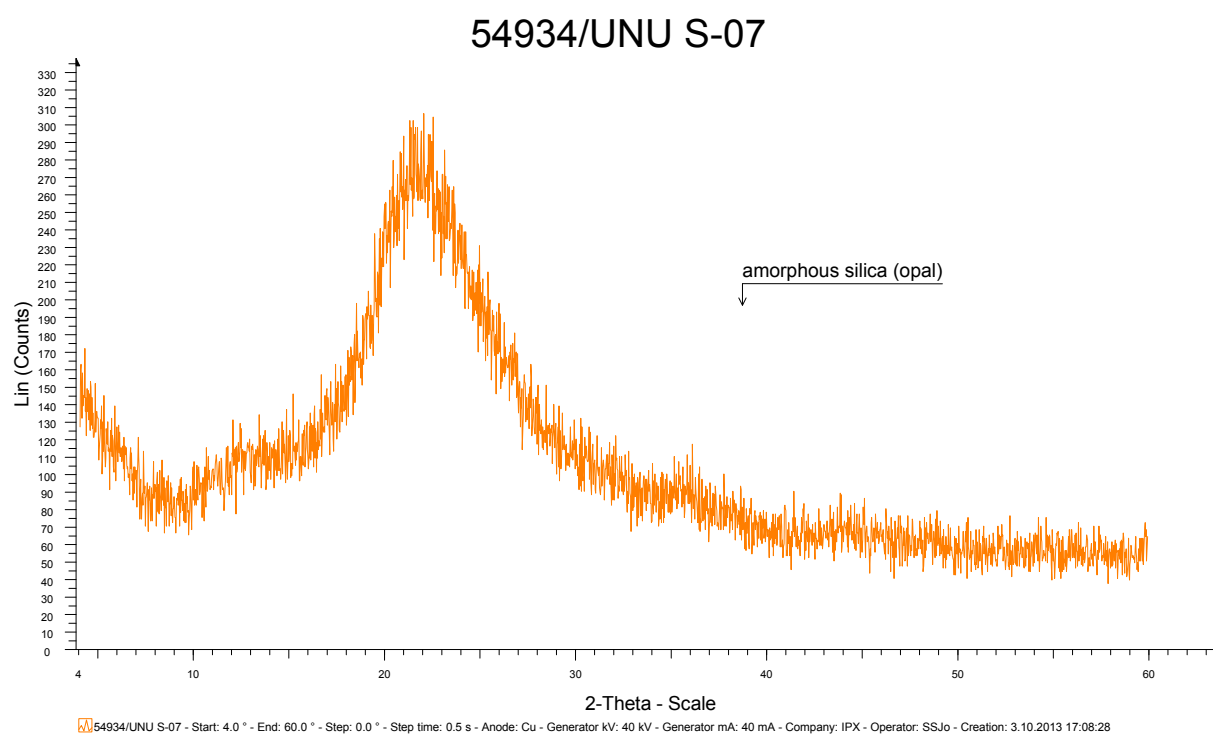


FIGURE 7: XRD graph showing the presence of amorphous silica (opal) in Sample No. 7 collected in extinct geyser deposit at Location No. 13-8



COMPARATIVE ANALYSIS OF GEOTHERMAL POWER PLANT DESIGNS SUITABLE FOR MALAWI'S CHIWETA GEOTHERMAL FIELD

Tufwane Mwagomba

Malawi Energy Regulatory Authority
Private Bag B-496
Lilongwe
MALAWI
tufwane@gmail.com

ABSTRACT

Energy is the engine that drives the economy of a country. Unfortunately, Malawi experiences insufficient electricity generation capacity to support its economic activities. Located within the East African Rift System (EARS), which is one of the hottest geothermal zones in the world, Malawi is deemed to have significant potential geothermal energy resources that could be utilized. However, despite its favourable location, Malawi has been slow in developing production from its geothermal resource. Geological studies indicate that a geothermal system is located in Malawi with a subsurface reservoir temperature range of 169-249°C, which has been manifested through hot springs. Studies of hot springs like Chiweta indicated that the resource could be developed for electricity generation as well as direct utilization. Based on Lindal's diagram of geothermal utilization (Ragnarsson, 2006), the Chiweta geothermal field temperature falls in the category suitable for electricity generation. This report analysed the various geothermal power plant designs suitable for development in Malawi. The analysis covered both technical and economic factors. The report proposes the power plant designs best suited for Chiweta field in Malawi: the basic binary power plant at reservoir temperatures below 210°C; and the basic hybrid power plant at a reservoir temperature of 240°C.

Further studies are proposed to confirm the resource and its subsequent development as well as other potential utilization methods for the resource.

1. INTRODUCTION

1.1 General overview of geothermal energy

Geothermal energy is defined as a natural heat flow from the earth. It is estimated that at the base of the continental crust, temperatures are in the range of 200-1000°C and that, at the centre of the earth, temperatures may be in the range of 3500-4500°C (Fridleifsson et al., 2008). Geothermal energy is considered to be a clean and renewable resource, compared to other sources of energy like fossil fuels and coal, since it emits much less of greenhouse gasses like CO₂ (Hunt, 2001). Geothermal resources are being exploited around the world in a variety of applications and resources. Geothermal resources

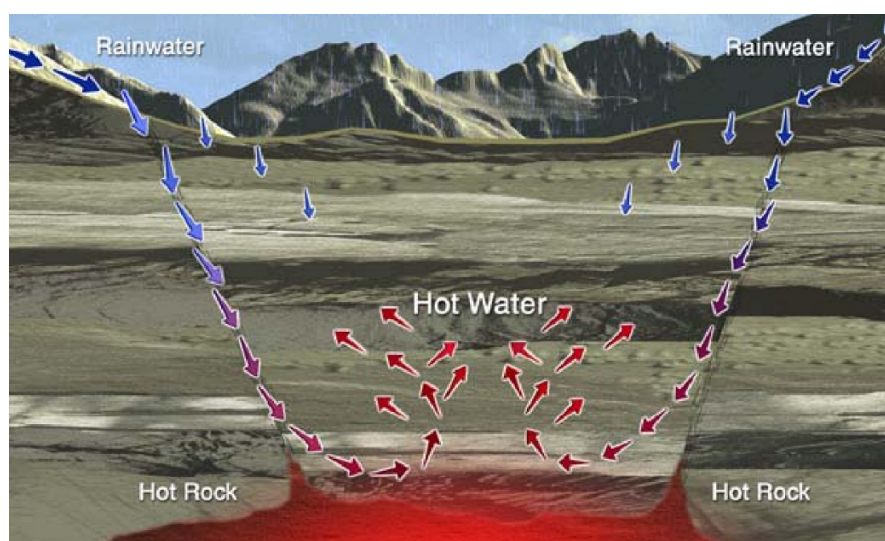


FIGURE 1: Geothermal reservoir formation (Blodgett and Slack, 2009)

can be observed through surface manifestations such as hot springs, fumaroles, surface alteration, geysers, mud pools, etc., depending on the type of reservoir in the subsurface region and the geology of the area. Even though geothermal energy is considered a renewable resource because the heat is transferred from the interior of the earth, which is essentially in abundance, the extent of its exploitation challenges the resource's future exploitation. If the resource is exploited more than the resource's ability to naturally recharge itself, the utilization sustainability of the resource is obstructed.

A geothermal system (Figure 1) consists of a heat source, permeable rock, and an inflow of water. The heat source is mostly an intrusion of magma that is close to the earth's surface. When the water inflow is heated through the heat source, the hot water or steam can be trapped in the permeable and porous rocks, forming a geothermal reservoir. Geothermal reservoir temperature normally increases with an increase in depth into the earth's crust.

Generally, geothermal resources are classified by their temperature or enthalpy as low, medium and high temperature/enthalpy resources, according to their reservoir fluid temperatures. The temperature is used as a classification parameter because it is easy to measure. Temperature also gives an indication of the energy content of the fluid to be extracted from the subsurface. High temperature fields have reservoir temperatures of more than 180°C, and middle to low temperature fields have temperatures below 180°C (Fridleifsson et al., 2008). The theory of plate tectonics states that the earth is made of plates that are floating above the mantle. Where these plates meet, there can be volcanic activity and most of the high temperature geothermal fields are located along these plate boundaries.

1.2 Geology of Malawi

Location: Malawi is a country in southeast Africa, located between latitudes 9° S and 17° S and longitudes 32° E and 36° E. It has boundaries with Tanzania in the north and northeast, Mozambique in the east, south and southwest and with Zambia in the west and northwest.

Geology: Malawi is within the Great Rift Valley which extends from Djibouti to Mozambique and lies at the southern end of the western branch of the East African Rift system (Figure 2). According to Gondwe et al. (2012), the major geological units that make up Malawi are Precambrian to lower Palaeozoic high metamorphic rocks with shaly and semi-shaly affinities. Intercalated within these are calc-silicate units and marbles. Ortho-gneissic rocks include calc-alkaline and ultra-basic rocks. In general, Karoo and Cretaceous to recent sedimentary rocks are distinguished. Karoo volcanism was observed in the form of basaltic and diabasic lava flows. Upper Jurassic to lower Cretaceous magmatic activity is ascribed to the Chilwa alkaline province. This is a suite of alkaline igneous rocks including carbonatites and related rocks, syenites and granites. The province is well developed to the south of the country and is related to the rift system.

Structural control of Lake Malawi Rift is believed to be dominated by a series of segmented N-S rifts controlling normal faults. The Lake has been subdivided into three linked half graben basins, which are the Karonga, Nkhata-bay and Nkhotakota sub-basins; these alternate in polarity along the axis of the lake, each controlled by a major bounding fault system (Gondwe et al., 2012).

1.3 Geothermal resource studies for Malawi

Malawi has porous sedimentary horizons at depth, limited to the small fault-bounded Karoo Basin sediments and the young Neogene rift floor deposits, which hold water and may act as good aquifer. Unpublished studies for Malawi's geothermal potential, conducted by Malawi's geological surveys department, have been going on for some time but are not very detailed.

From the studies done, it was stipulated that Malawi geothermal resources are manifested in hot springs that are located mostly along or near the intersections of major faults. There are over 60 hot springs that have been identified and documented and geochemical analyses have been done for some of them in order to understand the nature of the underlying reservoir, its temperature and the origin of the water in the system. Surface temperatures of the hot springs are between 28°C and 79°C. Further, geochemical studies suggest that most of the water, with some isolated exceptions, is immature and has not attained equilibrium, thereby presenting some degree of uncertainty about the system. This might be either a result of thermal water mixing with fresh groundwater or might mean the system is permeable and fast at recharging. Subsurface temperature studies, done with some level of confidence, deduced a reservoir temperature range of 169-249°C. The majority of the hotter springs in Malawi occur in the northern part of the country, with a more promising field in Chiweta. The Chiweta area provides the highest surface temperature of 79°C and the highest geothermometry temperature of 249°C. The chemistry of the Chiweta water shows that the water is rich in chloride, indicating a high input of geothermal fluid. It can, therefore, be concluded that Malawi has a geothermal resource, especially when focusing on Chiweta, but needs further detailed studies to ascertain the resource's size and characteristics.

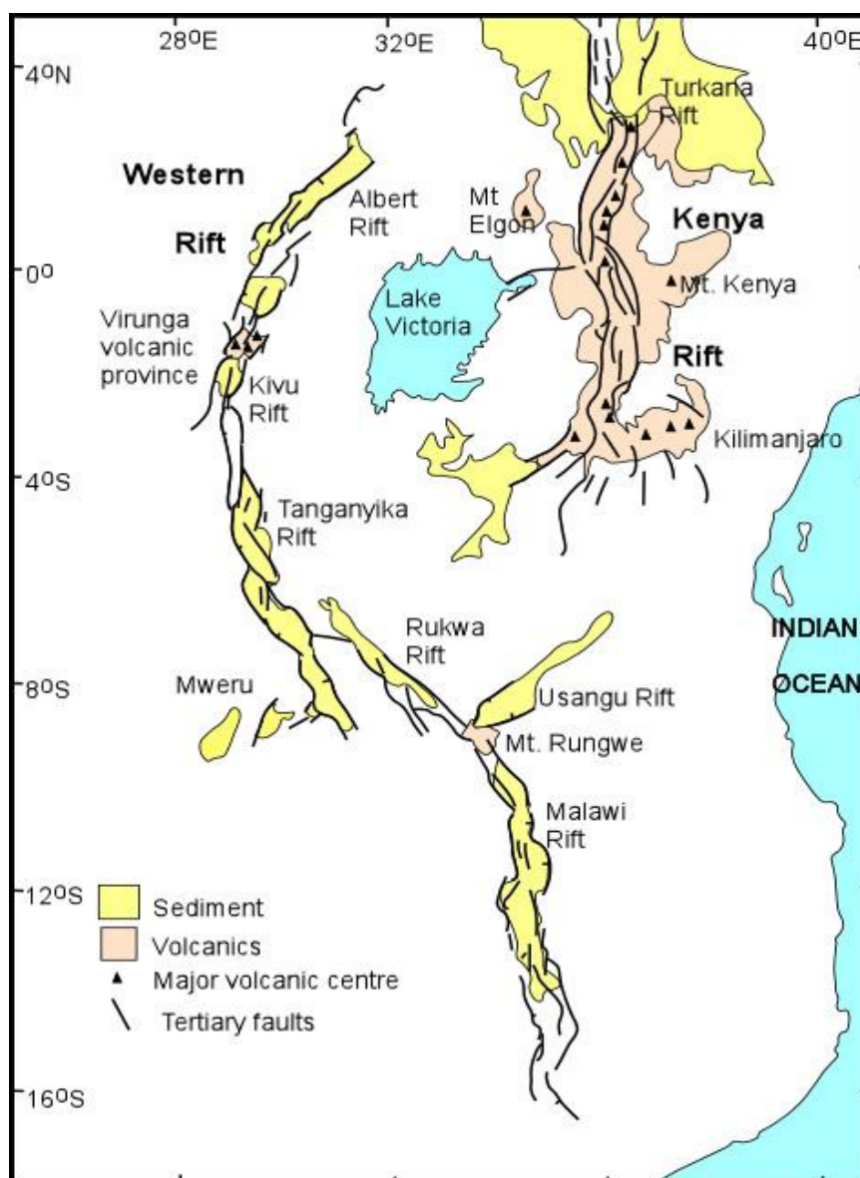


FIGURE 2: The East African Rift System (Omenda, (2005)

2. POTENTIAL GEOTHERMAL APPLICATIONS FOR MALAWI

Geothermal utilization involves the extraction of fluid and heat from a reservoir in various ways and means. For many centuries all around the world, geothermal water was used primarily for bathing, cooking and heating. Today's utilization of geothermal resources is done at various ranges of temperature as proposed by the Lindal diagram (Figure 3) by using advances in geothermal utilization

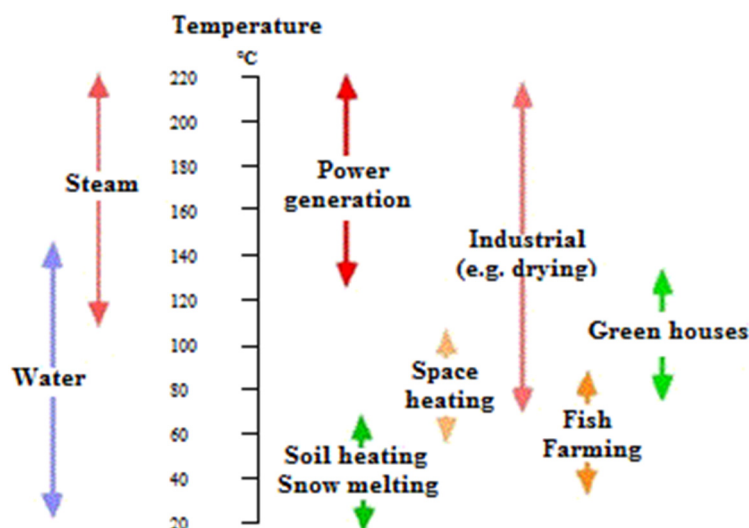


FIGURE 3: Lindal's geothermal utilization diagram

technologies. In broader terms, geothermal utilization is divided into two categories, direct utilization and indirect utilization. Direct utilization includes space heating, bathing, agricultural, aquaculture and some industrial uses, where the thermal energy of the fluid is used directly. Indirect utilization of geothermal energy is mostly concerned with the production of electricity, where the thermal energy of the fluid is converted into electrical power. The current common trend in geothermal development is utilizing a geothermal resource through cascading in a power plant along with other possible direct applications.

2.1 Power generation

Electricity generation via a geothermal resource is commonly applied to fluid temperatures around 150°C and higher where generation is commercially viable (Figure 3). But with the advancement in technology, considerably lower temperatures could also be used with the application of binary fluids and binary power plants, providing hope for accelerating the development of geothermal energy worldwide (Bertani, 2010).

In Malawi, generally hydro power stations generate the electricity, accounting for 95% of the total electricity generation, which is 285.85MW. All the major power stations are located in the southern part of Malawi along a single river, Shire that runs out of Lake Malawi (Figure 4). One small hydro station is located in the northern part of the country. Because of the geographical locations of the stations, Malawi's electricity system suffers instability due to transmission distances and insufficient generation capacity.

Malawi's electricity sector is dominated by a state owned electric company called the Electricity Supply Corporation of Malawi (ESCOM). The country has an installed capacity of 285.85 MW and mostly operates at 275MW with respect to a non-conventional spinning reserve. The current projected electricity demand is about 340MW, even though this is a suppressed figure rendering to the daily load shedding of electricity. Malawi experiences an average load shedding of 20MW at peak every day. Because of insufficient generation capacity, the Malawi system operates with a spinning reserve of about 10MW, putting a lot of stress on already insufficient generation capacity.

The population of Malawi is estimated to be 13 million people according to population census report of 2008 (NSO, 2010). Of this population, it is estimated that about 7.6% of the population has access to

the national grid electricity (MCA – Malawi, 2010). With such enormous numbers of the inhabitants not able to access grid electricity, the majority of the population depends on other alternative sources of energy for their daily needs.

According to the department of energy affairs, the current Malawi energy mix is predominantly dependent on biomass in the form of firewood and charcoal (Table 1). The current status of the energy mix poses a big challenge for the natural vegetation of Malawi as trees are wantonly cut for an energy source. The Malawi government came up with the National Energy Policy (2003) which, among other things, focuses on improving the efficiency and effectiveness in energy supply industries and improving security and reliability of energy supply systems, as well as mitigating environmental impacts of energy production and utilization. The spirit behind the policy is to reduce the dependency of the population on firewood by providing environmentally friendly alternatives so that the energy needs of the population are met in a sustainable manner.

In line with Malawi's energy policy objectives and concern with the power shortage that the country experiences, the country is reviewing the role of generating electricity from sources other than hydro, based on the country's available resources. With geothermal being one of the resources that the country has with the potential for generating power, and with reference to the Lindal diagram in Figure 3, Malawi needs to scale up its studies in order to develop the resource and meet the growing energy demand. This study, therefore, focuses on assessing appropriate power plant designs for Malawi's geothermal resource that the country may adopt for development.



FIGURE 4: Map of Malawi

TABLE 1: Energy mix projections in Malawi 2000 – 2050
(National energy policy for Malawi, 2003)

	2000	2010	2020	2050
Biomass	93%	75%	50%	30%
Liquid Fuels	3.50%	5.50%	7%	10%
Electricity	2.30%	10%	30%	40%
Coal	1%	4%	6%	6%
Renewables	0.20%	5.50%	7%	10%
Nuclear	0%	0%	0%	4%
TOTAL	100%	100%	100%	100%

In order to maximise the economies of scale from a given geothermal resource, integration of geothermal power generation projects with agricultural production, farm processing, and distillation or dehydration facilities is rapidly growing in popularity. The trend is as a result of advancements in the generation of electricity from moderate temperature geothermal resources with temperature ranges of 100°-150°C. There is an economic advantage in full utilization of the resource in such a way. Worldwide, geothermal developers are evaluating building projects for optimal resource utilization and a reduction in waste heat rejection, with reference to the various economic activities happening around the prospective geothermal resource.

2.2 Fish farming with geothermal

Located in a tropical region with an abundance of sunlight and fresh water including Lake Malawi, Malawi is home to hundreds of different tropical fresh water species of fish. Among the many species available, tilapia (locally called chambo) is found in Lake Malawi and is the most liked fish from the lake. Chambo have been taken from the lake and bred into various fish ponds across the country, using extensive aquaculture. Thus, the fish are stocked in ponds and then feed on each pond's natural vegetation. Temperature and sunlight enhance the production of aquatic plants through photosynthesis. The aquatic plants, which are mostly algae and related plants, are consumed by smaller animals such as zooplanktons. The zooplanktons are then eaten by the fish, thus making an aquatic ecosystem. Studies have shown that tilapia and other tropical fish breeding, using geothermal heat, has been a success in many areas with examples from Japan, China and USA. A special example is given in the state of Oregon in the USA where chambo from Lake Malawi was successfully bred using geothermal water (Kiruja, 2012). Geothermal water at about 90°C is mixed with colder water into the fish pond for an optimal pond temperature of about 28°C which is maintained year round. Here, geothermal heat is used for better control of pond temperature, thereby leading to optimal fish growth. This results in yields that are encouraging. The quality of water and the control of diseases are critical in the breeding of fish using geothermal resources.

Even though the atmospheric temperatures in Malawi are of a typical tropical type, temperature differences during the day and night, coupled with seasonal changes, are significant. Such factors have an impact on chambo breeding in ponds such that production is not at its best. Malawi could, therefore, incorporate geothermal energy into chambo breeding in various fish ponds for optimal production.

2.3 Other potential applications of geothermal resource utilization in Malawi

One of the industrial uses of geothermal energy is the distillation of ethanol. Ethanol in Malawi is locally produced from by-products of sugar production. Some of the geothermal prospect areas in Malawi are close to the sugar producing area in the central region district of Nkhosha. Attempts were made in the USA to produce ethanol (alcohol fuel) using geothermal energy. These attempts were not successful, as the economics were marginal (Lund, 2005) in the early days. However, further studies now prove that production using geothermal energy could be viable. Global fuel prices have been on the rise, and that rise is felt by most developing countries' economies. Malawi is a landlocked nation with no direct access to the sea; this factor, with regard to the transportation of goods and services within the country and outside, coupled with rising fuel prices, makes the economy volatile. Currently, Malawi uses a 20:80 blending ratio of ethanol to petrol in its petrol supplies with an aim to reducing carbon emissions, as well as cutting import bills on fuel. With the increase in fuel demand, ethanol production has been challenged as it operates under capacity versus demand. Malawi could, therefore, attempt to increase ethanol production using geothermal energy. Development of ethanol production plants could be done by taking advantage of the proximity of the prospective geothermal areas to the sugar producing factories.

3. GEOTHERMAL POWER PLANT TECHNOLOGIES SUITABLE FOR MALAWI

3.1 Overview of power plant technologies

The power plants that are developed for geothermal resource exploitation are divided into two main categories which are steam cycle and binary cycle (Valdimarsson, 2010). The steam cycle plants are those that utilise the geothermal fluid directly to produce electricity; binary cycle plants are those that use e.g. organic fluid that obtain heat from the geothermal brine in order to produce electricity. The different types of power plants that are commonly developed are: single-flash steam plants, double-flash steam plants, binary organic Rankine cycle, binary Kalina cycle, combined single flash with ORC plant, and combined ORC cascade. The characteristics of a geothermal field are crucial in determining the appropriate type of power plant suitable for the field. Various sources in the literature propose that conventional steam turbines require a particular range of fluid temperatures, depending on field characteristics; the same applies to a binary plant that utilizes a secondary working fluid that requires a certain range of fluid temperature. The temperature ranges are mostly within the proposal of the Lindal diagram. Outside such temperature ranges, the cycles become uneconomical.

One of the good things about geothermal power plants is that when the plant is fully automated, it can operate unmanned and can go through a self-start procedure after they have tripped off line due to faults unrelated to the power plant. The plants can be monitored and started remotely if required. Examples of such plants are the Reykjanes and Svartsengi geothermal power plants in Iceland.

It is estimated that the availability of geothermal power plants, measured with respect to hours in a set time period, is mostly over 95% (Kagel, et al., 2007). This characteristic makes geothermal power plants base load plants.

3.2 Steam-flash plants

In designing a flash steam plant (either single or double flash), it is assumed that the geothermal fluid is a saturated water from the reservoir. This common assumption comes with the fact that, generally, dry steam reservoirs are very rare (DiPippo, 1999). Where vapour dominated reservoirs exist, direct-steam plants are used; otherwise the assumption holds. With reference to Figure 5, as the fluid travels towards the surface through the production well, it experiences a flashing process along the way. Flashing of the fluid means that the fluid pressure decreases and steam forms from the saturated water. The fluid is directed to the power plant from wells via pipelines. The two-phases, water and steam, are separated by a separator directing the steam towards the inlet of a turbine for electricity generation. The separated brine is directed to reinjection or, where need and brine characteristics allow, for further utilization such as for district heating. This is called a single-flash power plant. Even though experimental machines have tried to use two-phase fluid for running the turbine, the general approach has mostly been to separate the two phases (DiPippo, 1999). The water phase from the separator may be flashed again for a low pressure turbine, making the cycle a double-flash power plant. Double-flash power plants are normally associated with high-enthalpy geothermal fields with temperatures in excess of 240°C.

After passing through and driving the turbine for electricity generation, the steam exits into either a condenser, where it is condensed and cooled by a chosen cooling medium for a condensing plant, or is exhausted into the environment for a back-pressure plant.

Experience has shown that the flashing process is an appropriate power generation process where resource temperatures are above 150°C. However, some developments in studies seem to indicate that flashing technology can be employed at temperatures as low as 120°C or less, and at a cost significantly lower than that of a similarly sized binary plant (Pritchett, 1996). Such studies are trying to work out scaling problems that are major barriers to flash plant development at lower temperatures. These technological studies could result in more efficient utilization of geothermal energy in the future.

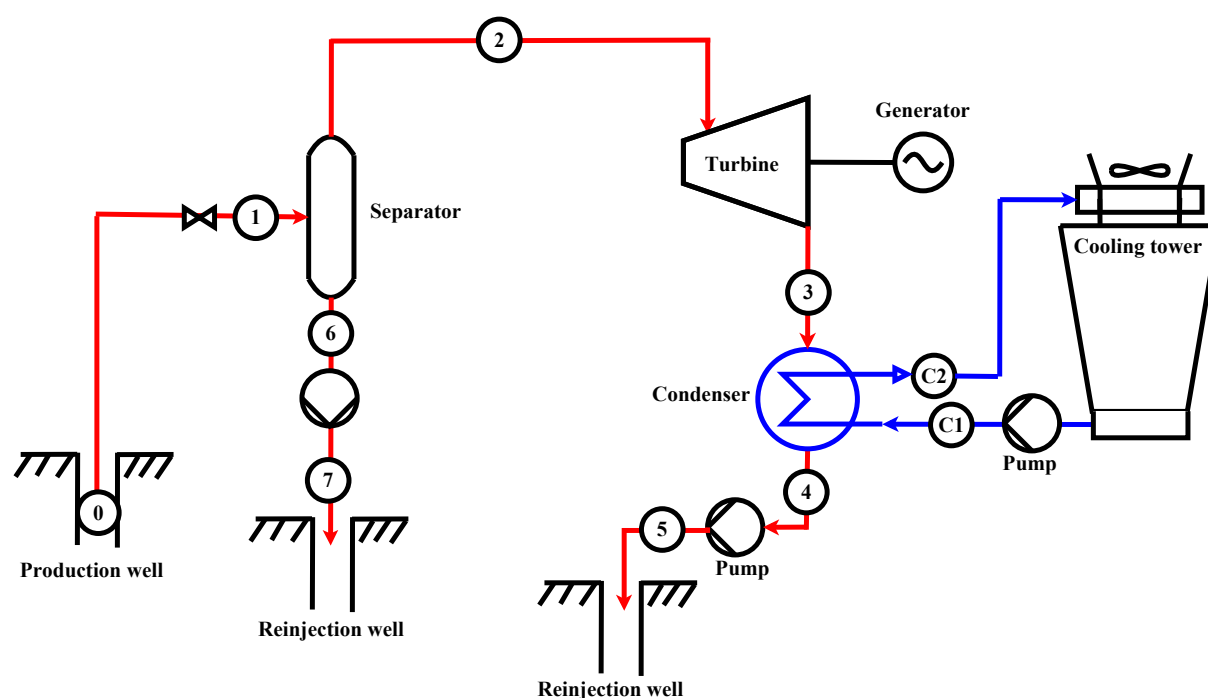


FIGURE 5: Single-flash power plant process diagram

3.3 Binary cycle power plants

The primary objective in developing binary cycle power plants was to generate electricity from low to medium temperature geothermal resources and to increase the utilization of the geothermal fluid through recovery of heat from waste fluid. Binary power plants utilize a secondary working fluid for power generation. The working fluid, which is usually an organic fluid, has a low boiling point and high vapour pressure at low temperatures, when compared to geothermal fluid. Binary power plants are mostly utilized for geothermal resource temperatures of 150°C and less (DiPippo, 2008). From various studies conducted among geothermal energy resources, it is believed that the medium- and low-temperature liquid-dominated systems are the most abundant sources occurring around the world (Franco and Villani, 2009). This makes the use of binary power plants popular in electricity generation applications for geothermal utilization. In a binary plant, the thermal energy of the geothermal fluid in the primary cycle is transferred to the secondary working fluid via a heat exchanger for use in the Organic Rankine Cycle (Figure 6) or the Kalina Cycle (Figure 7). The vaporized working fluid is expanded through a turbine which, in turn, drives a generator for electricity generation. The vapour is then condensed in the condenser and returned to the heat exchanger through a pump in a closed loop, and the process continues in the cycle. Efficient use of heat in the binary cycle can lead to an outlet temperature of the geothermal fluid that can be further utilized in other applications, depending on the fluid's characteristics.

In recent years, there has been development of an improved binary cycle called the Kalina Cycle (Figure 7). Kalina power plants utilize an ammonia and water mixture as its working fluid in the binary cycle with geothermal fluid as its primary cycle just like in the basic binary power plant. The working fluid from the vaporizer passes through a separator which separates liquid fluid and steam. The working fluid steam is expanded through the turbine in a superheated condition. As the steam goes to the condenser from the turbine, it mixes with the fluid from the separator before rejecting some heat in a recuperator. The fluid then passes through a condenser where it is condensed. From the condenser the fluid passes through the recuperator for the first pre-heating and then to the pre-heater and evaporator. The fluid in the recuperator is heated by the fluid (with a higher enthalpy) that comes from the separator and turbine. As such, a Kalina cycle has the advantage in that it allows a higher heat exchange effectiveness to be achieved over and above the traditional binary plant. Literature and studies estimate that Kalina power

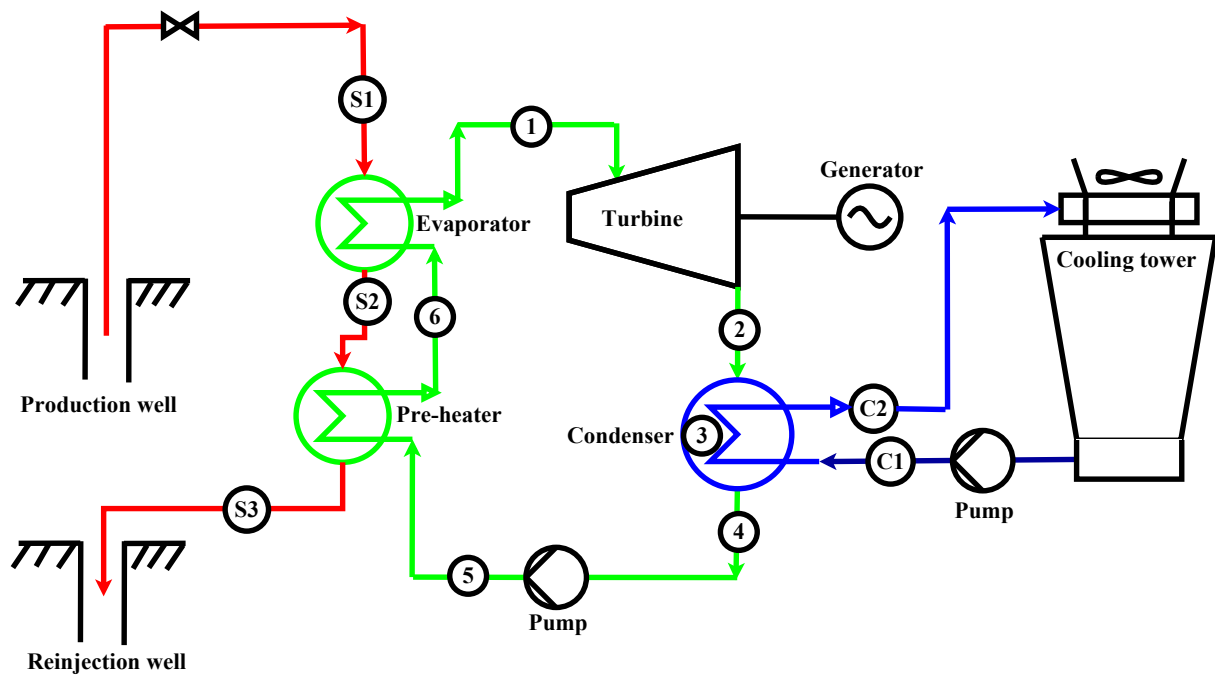


FIGURE 6: Binary power plant process diagram

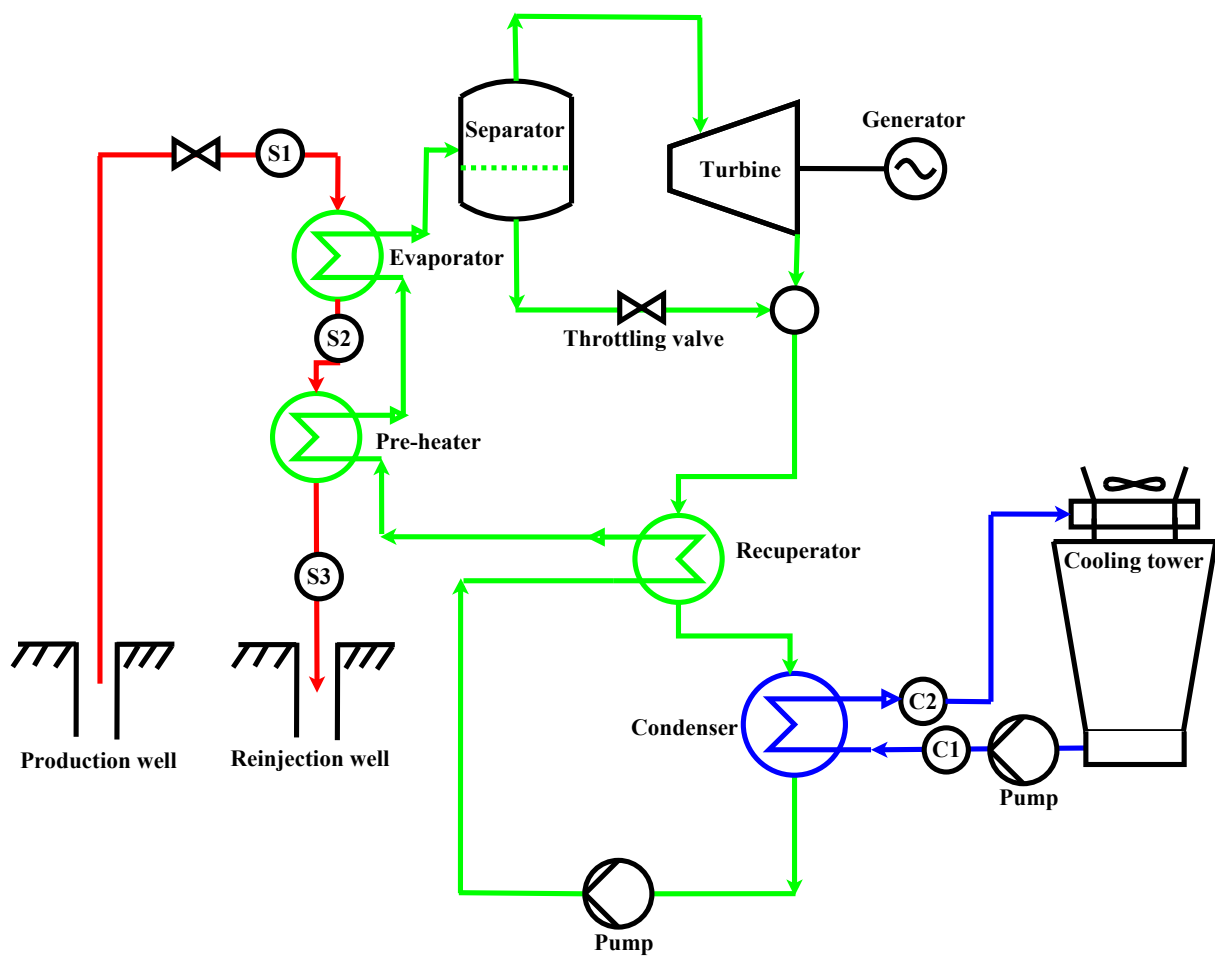


FIGURE 7: Kalina power plant process diagram

plants are about 40% more efficient (Dickson and Fanelli, 2003) compared to the traditional binary power plants, even though they are not yet as popular as the traditional binary plants.

Binary power plants are usually constructed in small modular units of the order of a few kWe to a few MWe capacity which, when added together, create a power plant of a few MWe. This mode makes binary power plants cost effective and a reliable means of geothermal electricity generation for medium to low temperature geothermal resources.

3.4 Hybrid power plants

A hybrid power plant (Figure 8) is a combination of steam flash and binary cycles. The configuration may be such that it combines single flash with a binary cycle or a double flash with binary, depending on the levels of field enthalpy. The cascaded binary cycle may get its primary fluid heat from either brine coming from the flash cycle's separator or from the steam from the exhaust from the turbine of a back pressure steam flash cycle. The binary bottoming that uses steam from a back pressure turbine as a heat source has some advantages, as Thórhallsson (2005) explained, as it would be free of scaling problems. An example is the Svartsengi plant in Iceland. The rest of the cycles are as mentioned earlier.

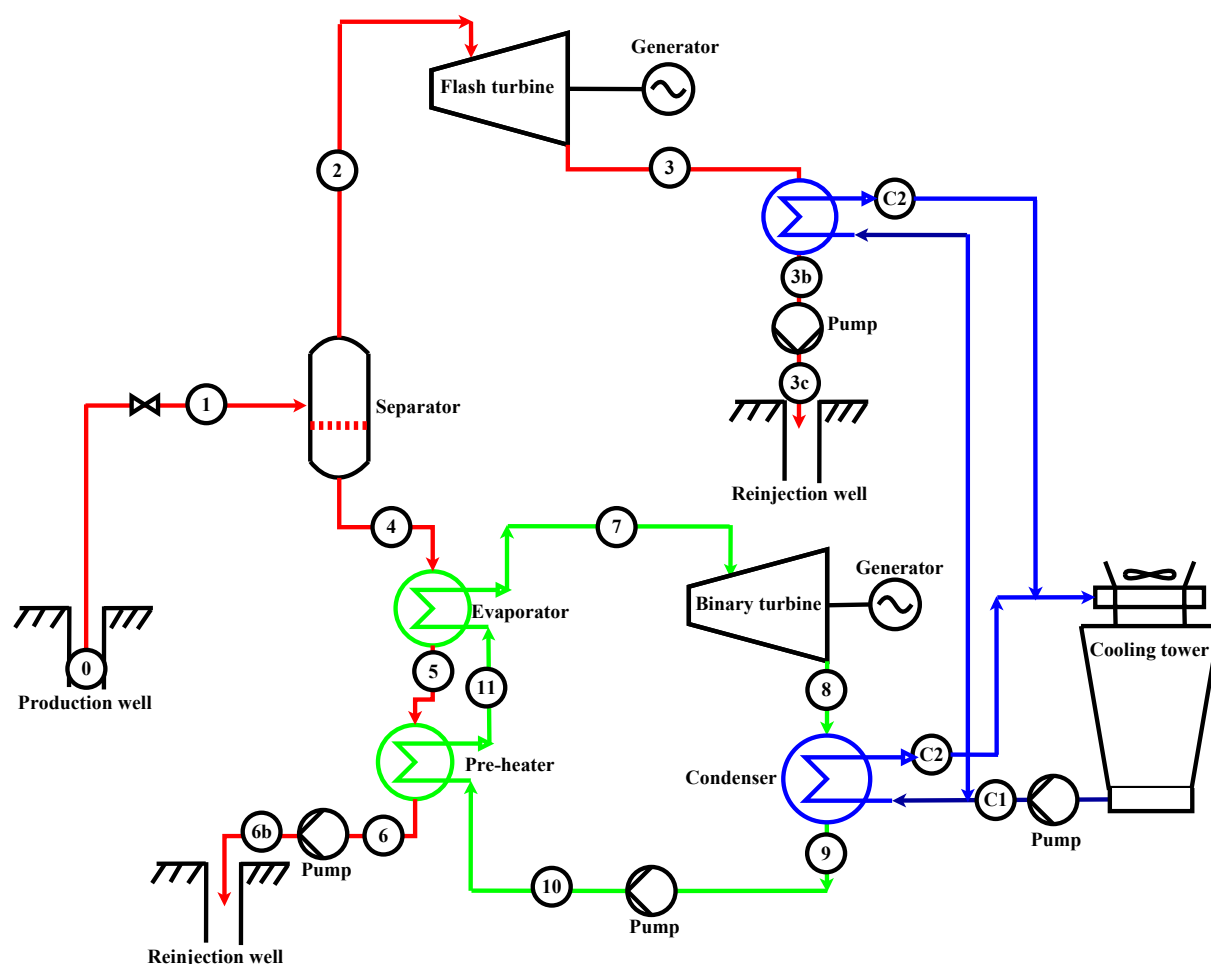


FIGURE 8: Hybrid power plant process diagram

A suitable power plant design for any field is the one that: matches with the expected geothermal production well parameters; is reliable; and is environmentally friendly while giving assurance of its economic viability. Based on the geochemical data available for Malawi and using the Lindal geothermal resource utilization diagram, three possible proposals for Malawi's development of its

geothermal resource are: through a single flash power plant, a binary power plant, or a hybrid of the single flash and binary cycle power plant. The power plant could then be cascaded with other direct various applications, depending on the characteristics of the geothermal brine that may come from power plant utilization. The proposed cycles are presented in the assessments below to find the most suitable option for Malawi, in terms of both technical analysis and economic analysis.

4. THERMODYNAMIC DESIGN CONSIDERATIONS FOR POWER PLANTS

4.1 Single-flash power plant - thermodynamic considerations

The assessment of the thermodynamic design considerations for a single flash power plant is based on the single-flash diagram in Figure 5. From Figure 5 it is assumed that, at stage 0 which is the geothermal reservoir, the fluid is in single state liquid form at a saturated pressure with respect to the T-s diagram in Figure 9. This also assumes that there is no heat loss along the way to the surroundings or that the heat lost is negligible; therefore, an adiabatic process from 0 to 1 is assumed. Therefore:

$$h_0 = h_1 \quad (1)$$

It is also assumed that there is no loss of mass along the way from 0 to 1 or that the loss is negligible; hence, the mass balance at point 1:

$$\dot{m}_0 = \dot{m}_1 \quad (2)$$

The fluid is throttled into the separator through a valve at the wellhead. The process of throttling the geothermal fluid results in a pressure decrease at point 1 of the T-s diagram in Figure 9. Due to pressure reduction the fluid starts boiling, meaning that the temperature is dependent upon the separator pressure (Valdimarsson, 2011a). At the separator, there is a separation of steam and liquid. The level of the separator pressure and enthalpy determines how much steam is produced. The lower the separator pressure, the more the steam produced, hence there is less liquid. The higher the separator pressure, the less steam is produced, hence there is more liquid. For the single-flash plant, the target is to get the optimum steam flow and enthalpy, so an optimal separator pressure for this purpose was reached by following the relationship of separator pressure and turbine output. This indicates that the selection of the separator pressure is crucial in designing a geothermal power plant. This pressure, coupled with the wellhead pressure, determines whether boiling starts in the formation or not. If boiling starts in the

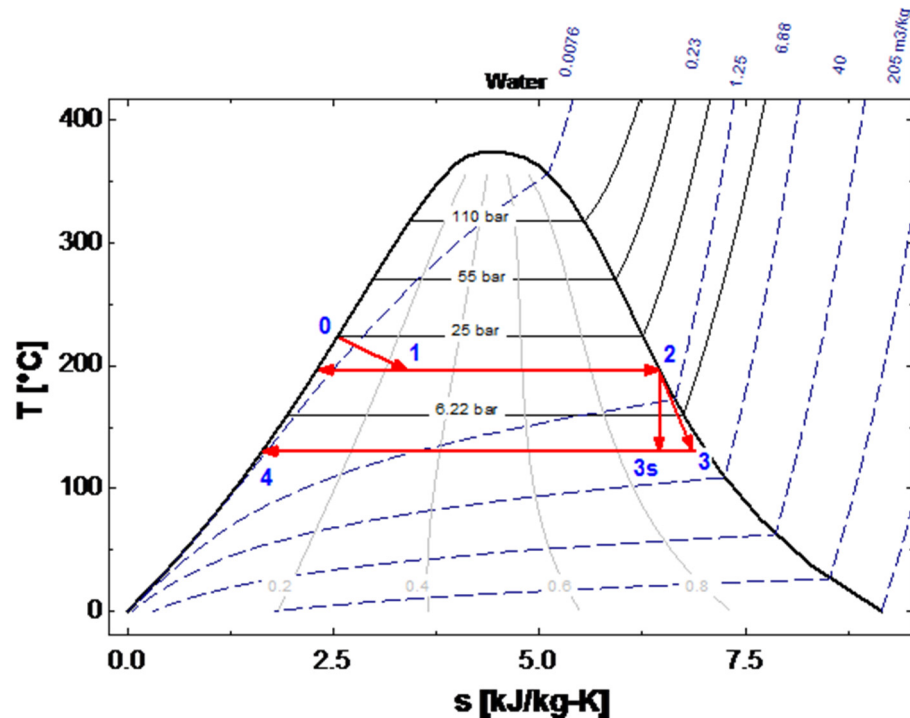


FIGURE 9: T-s diagram for a single-flash cycle

The lower the separator pressure, the more the steam produced, hence there is less liquid. The higher the separator pressure, the less steam is produced, hence there is more liquid. For the single-flash plant, the target is to get the optimum steam flow and enthalpy, so an optimal separator pressure for this purpose was reached by following the relationship of separator pressure and turbine output. This indicates that the selection of the separator pressure is crucial in designing a geothermal power plant. This pressure, coupled with the wellhead pressure, determines whether boiling starts in the formation or not. If boiling starts in the

formation, it can lead to scaling along the fluid's path, thereby reducing/blocking the fluid's flow passage in the formation. This may lead to a shorter lifespan of the well.

The steam fraction at the entry point of the separator is defined as follows:

$$x_1 = \frac{h_1 - h_6}{h_2 - h_6} \quad (3)$$

where x_1 is the steam fraction at the separator's entrance,
 h_x is the fluid enthalpy at point x .

Looking at the mass balance at the separator's entry point, the total mass flow rate entering the separator (\dot{m}_1) is equal to the sum total of the mass flow rate of the fluid leaving the separator. This is represented by:

$$\dot{m}_1 = \dot{m}_2 + \dot{m}_6 \quad (4)$$

But at point 2, the fluid is saturated steam and at point 6 is saturated water (Figure 10). Therefore, with the mass flow rate for steam (\dot{m}_2) and the mass flow rate for water (\dot{m}_6) at these respective points, and with respect to \dot{m}_1 , the steam fraction becomes:

$$\dot{m}_2 = x_1 \dot{m}_1 \quad (5)$$

$$\dot{m}_6 = (1 - x_1) \dot{m}_1 \quad (6)$$

where x_1 is the steam fraction at the separator's entrance.

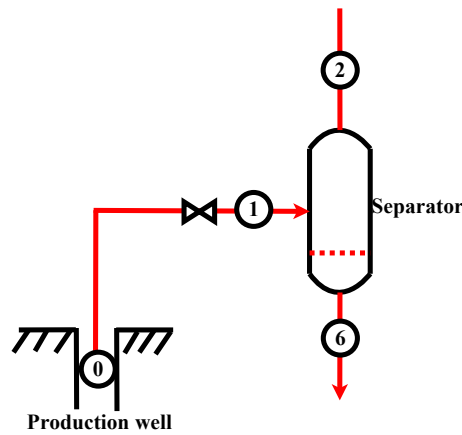


FIGURE 10: Separator point

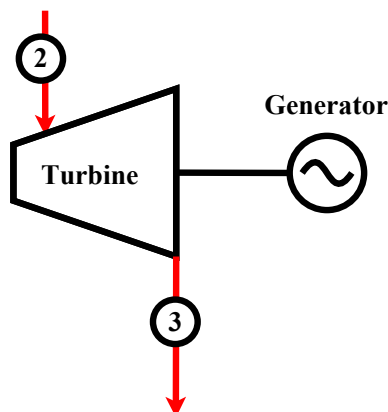


FIGURE 11: Turbine point

The fluid from point 6 is either reinjected into the field or further utilized, depending on the fluid characteristics in terms of temperature and chemistry. The steam from point 2 is directed to the turbine entrance through a demistifier/mist eliminator.

The steam from point 2 is expanded through a turbine producing mechanical power that is used in turning the turbine to generate electricity. The steam at the turbine entry is in the same state as when exiting the separator, with some pressure drop due to transportation in the piping system. The work done by the steam, in turning the turbine, causes a drop in enthalpy at point 3 (Figure 11). It is ideally perceived that the process of expansion of steam in the turbine is isentropic, i.e. the entropy at the output of the turbine is the same as the entropy at the turbine inlet. However, in real application, the process is not isentropic since the expansion is irreversible and the process increases fluid entropy. Therefore, both the isentropic enthalpy h_{s3} and the real enthalpy h_3 are assessed at point 3. The relationship between enthalpy and isentropic turbine efficiency is given by the following equation:

$$\eta_{tur} = \frac{h_2 - h_3}{h_2 - h_{s3}} \quad (7)$$

where η_{tur} is the turbine isentropic efficiency;
 h_{s3} is the isentropic enthalpy at point 3.

However, in calculating the work done by the turbine, the isentropic enthalpy, together with the isentropic turbine efficiency (η_{tur}), is

commonly used. The efficiency is provided by the turbine's manufacturer and, in common practice, this efficiency is 85%.

From the equations above, the work done by the steam which is the mechanical power output from the turbine is given by turbine efficiency, the mass flow rate of the fluid passing through the turbine, and the enthalpy drop across the turbine. This relationship is presented in the following equation:

$$\dot{W}_{tur} = \eta_{tur} * \dot{m}_2(h_2 - h_{s3}) \quad (8)$$

where \dot{W}_{tur} is the mechanical power output of the turbine.

From the turbine, the steam is led to atmospheric exhaust and into the atmosphere for a back pressure system. In a condensing system, the steam from the turbine is led to a condenser which changes the fluid from a vapour state to a liquid state. Pressure at this point is kept as low as possible in order to extract more energy from the turbine process. The condenser is one of the most important facilities in the cycle because it assists the turbine in obtaining maximum efficiency in its energy conversion. The condenser is coupled to a cooling system which commonly either uses freshwater access or a circulation process with a cooling tower. The lower the temperature of the condenser, the more efficient the turbine process becomes. A cooling tower cools the water from the condenser using air. This means that the condenser temperature can be partly dependent on the local average temperature of the area.

Basically, there are two types of condensers, the direct contact condenser and the surface condenser (most often a shell and tube heat exchanger). The direct contact condensers are designed in such a way that production steam directly contacts the cooling water which cools the steam down and forms liquid. This condenser is applicable in flash plants but not in binary plants since a closed loop secondary fluid is used there. The surface condenser allows for two separate fluids to exchange heat without directly coming into contact with each other. In the case of geothermal plant, such condensers require more fresh water for the effectiveness of the system. The surface condensers are more applicable in binary cycles where secondary fluid does not come into contact with the water. They can also be used in flash systems, depending upon the characteristics of the fluid in use.

The cooling system can either be water cooled or air cooled. The air cooled system uses fans that are electrically driven to cool the working fluid. The water cooled system uses water that can either be sprayed in direct contact condensers or passed through the shell and tube condensers. It is more economical to use a water-cooled system in the case of a flash power plant; in a binary power plant, the air cooling system can be considered where access to water is limited. In Malawi, where a source of cooling water is not a problem as water bodies are close to the geothermal prospective areas, the water cooled system is proposed. Therefore, in this study, the cooling system will use the water cooling tower.

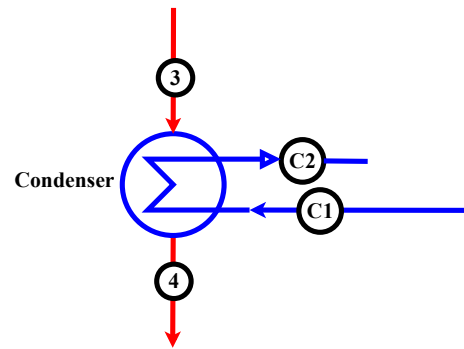


FIGURE 12: Condenser point

The heat rejected (\dot{Q}_{wf_cond}) from the working fluid to the cooling medium in the condenser is found by the mass flow rate of the fluid and the enthalpy drop across the condenser (Figure 12). In a single flash plant, the working fluid is the geothermal steam itself. The relationship is presented in the following equation:

$$\dot{Q}_{wf_cond} = \dot{m}_{wf}(h_3 - h_4) \quad (9)$$

The rejected heat from the working fluid is transferred to and accepted by the cooling water as \dot{Q}_{cw} , hence the relationship is as follows:

$$\dot{Q}_{wf_cond} = \dot{Q}_{cw} \quad (10)$$

Where \dot{Q}_{cw} is a relationship between the cooling water mass flow rate and the enthalpy change in the cooling water across the condenser. This relationship is given by the following equation:

$$\dot{Q}_{cw} = \dot{m}_{cw}(h_{c2} - h_{c1}) \quad (11)$$

Or

$$\dot{Q}_{cw} = \dot{m}_{cw}cp_{cw}(T_{c2} - T_{c1}) \quad (12)$$

where h_{cx} is cooling water enthalpy at point x ;
 cp_{cw} is the specific heat capacity for cooling water;
 T_{cx} is the cooling water temperature at point x .

The hot water from the condenser is sprayed in the cooling tower where it comes into contact with ambient air. The process converts some amount of water into vapour which is released into the environment and, hence, there is an exchange of both heat and mass between the water and the air.

In direct contact condensers, during the condensing process, part of the cooling water is sent back to the condenser after it is cooled by air in the cooling tower. The excess water may be sent for reinjection for sustainable production and environmental mitigation just like the brine from the separator, or it may be directly rejected into the environment, depending on the fluid chemistry.

The cooling water is sourced from various sources like nearby streams, boreholes for cooling water and part of the condensed steam from the geothermal fluid in the direct contact condensers, as mentioned earlier.

The heat that is collected from the condenser via cooling water is rejected into the atmosphere by evaporation through the cooling tower. When the cooling water reaches the cooling tower, it is allowed to come into direct contact with the ambient air, thereby rejecting the heat to the air. The cooling towers can be designed either with forced air counter flow or induced air cross flow.

4.1.1 Consideration of potential scaling

When the geothermal fluid is flashed, non-condensable gases (NCGs) emerge. The natural characteristics of these gases are such that they do not change state; neither do they dissolve, so some attention is required. If left unattended, the NCGs collect in the condenser steam space and generally increase pressure at the turbine exit side which, in effect, reduces the efficiency of the turbine, resulting in low generation capacity and can lead to a turbine trip if left unattended. It is for this reason that the NCGs are supposed to be removed. The gasses, therefore, must be extracted from the condenser by a vacuum gas extractor which should not affect the turbine efficiency through pressure increase.

Reinjection needs to be done with proper studies of the field and the fluid. The field studies are supposed to suggest an appropriate location for reinjection wells where reinjection will not cause short-circuiting of cold water into the reservoir, thereby lowering the production temperature. Tracer testing is one of the tools used to understand the connection between the production wells and the reinjection wells.

Studies of the fluid chemistry are meant to provide knowledge about the chemical composition of the fluid. This assists in ascertaining the probability of scaling at various temperature levels, both in the surface equipment and in the reinjection wells. It is recommended that the silica solubility curve (Figure 13) be consulted to ascertain safe working reinjection temperatures, with respect to the silica content in the geothermal brine. For Malawi, with reference to Figure 12, and a sub-surface temperature range of 169-249°C, the safe reinjection temperature that can avoid silica scaling is around 70°C for 169°C, and around 110°C for 249°C when both flashing the brine and using a binary cycle. The project has observed these considerations where necessary.

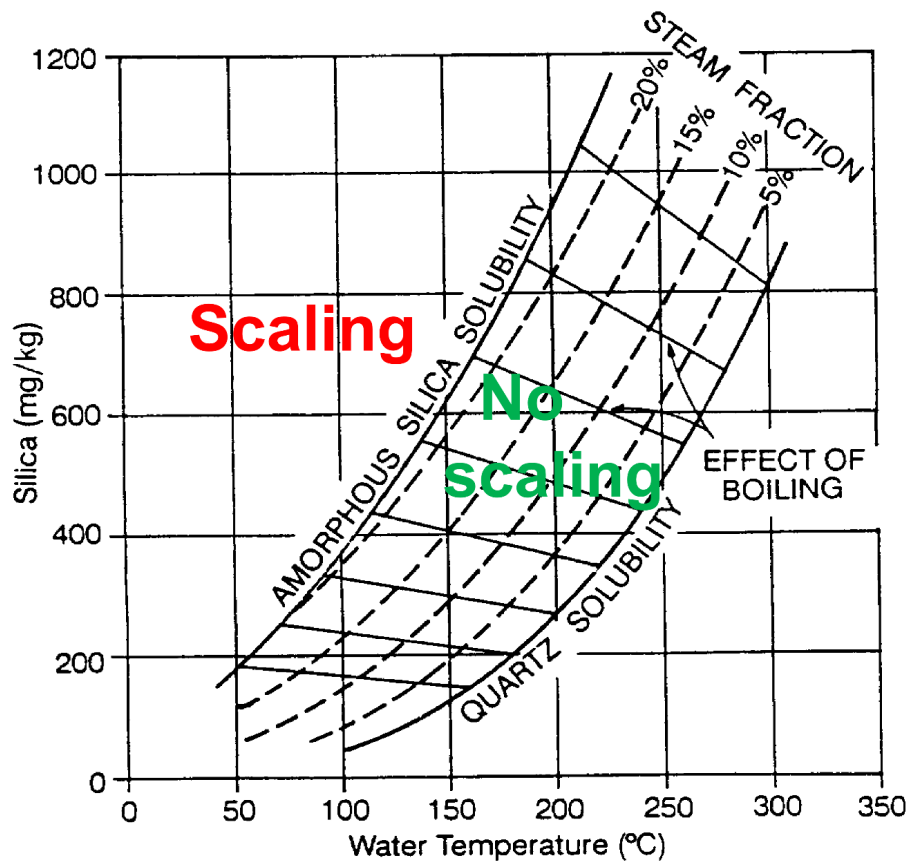


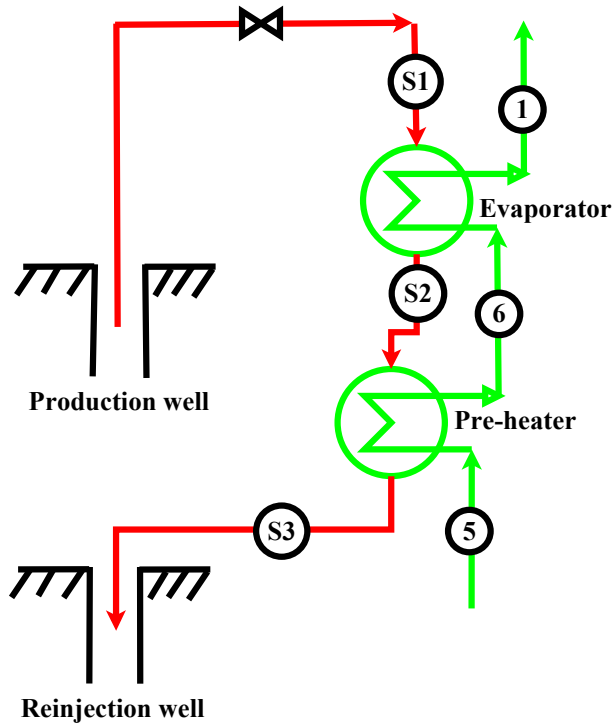
FIGURE 13: Amorphous silica solubility curve (Thórhallsson, 2013)

4.2 Binary power plant thermodynamic design considerations

With the advancement in technology and the demand for cleaner energy that geothermal resources offer, Binary power plants (or Organic Rankine Cycle units – ORC) are becoming popular in areas where the reservoir has low-enthalpy characteristics. Binary plants are also being implemented for further utilization of geothermal brine from flash power plants where temperature allows. They are mostly considered to be viable energy conversion systems, both technically and environmentally, in the cases above. A binary cycle power plant consists of two fluid systems for the generation of electricity, i.e. the primary and the secondary systems. The primary system is the hot open loop geothermal fluid system which is the source of the energy. The secondary system is the closed loop working fluid system that is in contact with the turbine and gets its heat from the hot geothermal fluid of the primary system. The fluid used in the secondary system is usually an organic fluid that has a low boiling point and a high vapour pressure, when compared to water, at a common given temperature.

The thermodynamic analysis of a binary power plant is based on the basic binary diagram in Figure 6. The heat from the geothermal water is transferred to a secondary working fluid through heat exchangers and the cooled geothermal water is reinjected back into the reservoir.

The geothermal fluid enters the primary cycle at point S1 (Figure 14), and vaporizes the working fluid in the evaporator. The geothermal fluid then leaves the evaporator and enters the pre-heater through point S2. The geothermal fluid heats the working fluid in the pre-heater and then leaves the pre-heater through point S3 (Figure 14).



Conversely, the working fluid in the secondary cycle enters the pre-heater through point 5 and is heated by the geothermal fluid. The working fluid then leaves the preheater as saturated liquid and enters the evaporator through point 6. In the evaporator, the fluid is vaporized and leaves the evaporator through point 1 directed towards the turbine (Figure 14).

The process of heat exchange is designed such that the heat rejected by the geothermal fluid in both the evaporator and the pre-heater is received by the working fluid at these respective points. The thermodynamic assessment is, therefore, as follows:

$$\dot{Q}_b = \dot{Q}_{wf} \quad (13)$$

where \dot{Q}_b is the total heat rejected by geothermal brine; and

\dot{Q}_{wf} is the total heat received by the working fluid.

FIGURE 14: Pre-heater and evaporator point

The total heat rejected by the brine is the sum of the heat rejected in both the evaporator and the pre-heater and is given by the equation:

$$\dot{Q}_b = \dot{m}_b (h_{S1} - h_{S3}) \quad (14)$$

where \dot{m}_b is the brine mass flow; and
 h_x is the enthalpy at point x .

Using temperatures instead of enthalpy, Equation 14 becomes:

$$\dot{Q}_b = \dot{m}_b * c_{pb} (T_{S1} - T_{S3}) \quad (15)$$

where c_{pb} is the brine specific heat capacity;
 T_x is the temperature at point x .

The mass balance across the primary and secondary cycle then becomes:

$$\dot{m}_b * c_{pb} (T_{S1} - T_{S3}) = \dot{m}_{wf} (h_1 - h_4) \quad (16)$$

where \dot{m}_{wf} is the working fluid mass flow.

The mass balance across the pre-heater and the evaporator then becomes:

$$\text{Pre-heater:} \quad \dot{m}_b * c_{pb} (T_{S2} - T_{S3}) = \dot{m}_{wf} (h_5 - h_4) \quad (17)$$

$$\text{Evaporator:} \quad \dot{m}_b * c_{pb} (T_{S1} - T_{S2}) = \dot{m}_{wf} (h_1 - h_5) \quad (18)$$

Temperatures at point 5 and S2 recognise the effect of the pinch point in the heat exchanger. Their relationship is, therefore, given with respect for the heat exchanger pinch as follows:

$$T_{S2} = T_5 + T_{pp} \quad (19)$$

where T_{pp} is the heat exchanger pinch temperature as provided by the heat exchanger's manufacturer:

Beyond the evaporator, the thermodynamic assessment of the binary cycle is similar to that of the basic flash cycle, as discussed in the single-flash assessment. It must be mentioned, though, that binary power plants do not use direct-contact condensers, as the secondary cycle is a closed loop.

An ideal binary power plant is considered to have no emissions to the atmosphere, hence it is environmentally friendly. However, where the secondary fluid is not handled properly, in terms of leakages, emissions into the atmosphere become significant. The geothermal fluid never comes into contact with the turbine and is fully re-injected after heat extraction. By not letting the geothermal fluid come into contact with the turbine, it provides the turbine and the associated equipment a corrosion free operation, hence guaranteeing a longer life span. It also helps the binary power plants avoid the release of greenhouse gasses and related toxic elements, such as CH_4 and CO_2 , which are common in flash power plants.

4.2.1 Choice of working fluid in binary plant

The type of working fluid to be used in a binary power plant is of importance and the process of choosing it requires the consideration of several factors. The working fluid's thermodynamic properties have a large effect on the performance of the plant, and its cost also affects the overall cost of the power plant. The parameters that need to be considered when choosing a working fluid include: the critical temperature of the fluid, critical pressure, the environmental impact of the fluid, health and safety of the fluid and the cost of the fluid. DiPippo (2008) compared different working fluids that could be used in a binary power plant. The fluids were compared according to their critical temperature, critical pressure, toxicity, flammability, Ozone Depletion Potential (ODP) and Global Warming Potential (GWP). The GWP was considered to be relative to the amount of heat that could be trapped by a similar mass of carbon dioxide as to the working fluid being analysed. The choice of an appropriate working fluid is based on a best fit with the thermodynamic conditions and the cost, with a preference for retrograde fluids (fluids with a positive slope saturation curve in a T-s diagram). The comparison of the fluids is summarized in Table 2.

The fluids in Table 2 show that they have lower values for the critical temperature and pressure than those for water.

TABLE 2: Properties of binary plant working fluids (modified from DiPippo, 2008)

Fluid	Formula	Critical temp. [°C]	Critical pressure [bar]	Toxicity	Flammability	ODP	GWP	Molecular wt.
Propane	C_3H_8	96.6	42.36	Low	Very high	0	3	44.09
i-Butane	$\text{i-C}_4\text{H}_{10}$	134.9	36.85	Low	Very high	0	3	58.12
n-Butane	C_4H_{10}	152	37.18	Low	Very high	0	3	58.12
i-Pentane	$\text{i-C}_5\text{H}_{12}$	187.8	34.09	Low	Very high	0	3	72.15
n-Pentane	C_5H_{12}	193.9	32.4	Low	Very high	0	3	72.15
Ammonia	NH_3	133.65	116.27	Toxic	Lower	0	0	17.03
Water	H_2O	374.14	220.89	Non-Toxic	Non-flam.	0	0	18

Working fluids are further divided into three types according to their saturation vapour curves in the T-s diagram (see Figure 15). The three types are: wet fluids, isentropic fluids and dry fluids. According to Bao and Zhao (2013), the dry fluids exhibit a positive slope of a saturation curve in a T-s diagram (Figure 15c) while the wet fluids have a negative slope of the same, with examples of ammonia and water as the wet fluids. The isentropic fluids exhibit a nearly infinitely large slope, which is almost vertical (Figure 15b). Examples of isentropic fluids include fluorinol 85 and R11. The isentropic fluids remain in a vapour saturated state while expanding through the turbine, since the expansion occurs along the vertical line of the T-s diagram. This results in the fluid not condensing at the turbine outlet; hence, there is an absence of liquid droplets inside the turbine.

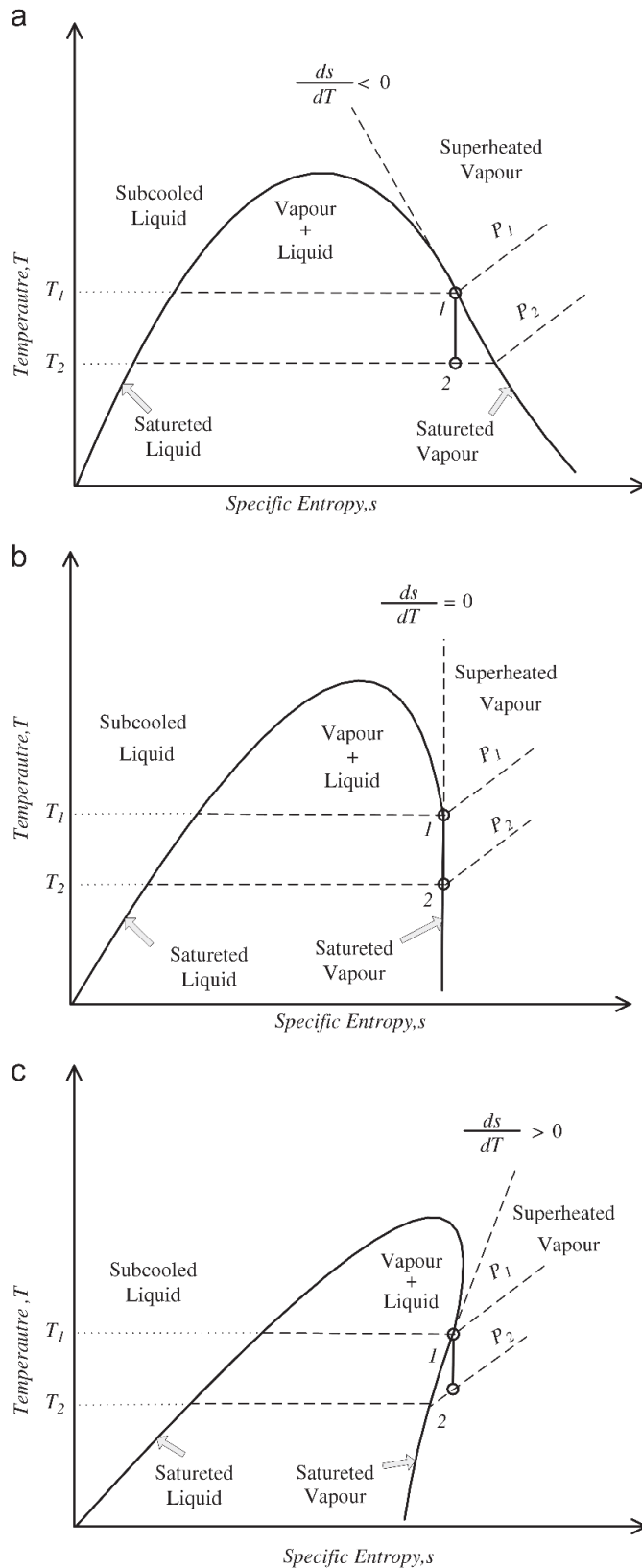


FIGURE 15: T-s for working fluids, (a) wet fluid, (b) isentropic fluid and (c) dry fluid (Bao and Zhao, 2013)

For the wet fluids, the outlet of the turbine normally contains some level of saturated liquid. This is due to their negative saturation vapour curve (Figure 15a); these could damage the turbine blades. To sustain operations with wet fluids, the fluid is normally superheated at the turbine inlet and the dryness fraction of the fluid is kept at a minimum of 85%, beyond which damage to the turbine blades becomes severe. The isentropic and dry fluids do not need superheating and a minimum dryness fraction since they are already in the vapour saturated phase at the turbine exit. This is the reason why, in most binary applications, the dry fluids and the isentropic fluids are the ones commonly used; they do not condense after going through the turbine.

The choice of a working fluid is then a function of its critical temperature in relation to the geothermal fluid temperature, and the state of the fluid after exiting the turbine, as it is not desirable to have a fluid that condenses as it expands through the turbine.

The process of choosing a working fluid for this project was based on a literature review which recommended retrograde fluids (dry fluids). Isopentane and Isobutane have been frequently used in many instances. These two fluids were tested in a binary model, at 6 bar well head pressure and reservoir temperature of 180°C , to determine the better choice. The analysis varied the turbine inlet pressure. With this analysis, it was observed that Isopentane reached its maximum work output at a lower turbine pressure than Isobutane. This meant that Isopentane exhibited a higher turbine work output than Isobutane at lower pressures, while Isobutane exhibited a higher turbine work output than Isopentane at higher pressures. Beyond some critical pressure, Isobutane's behaviour was unpredictable (Figure 16). However, reinjection temperature analysis revealed that the peak turbine work for Isobutane appears at a lower reinjection temperature than the peak turbine work for Isopentane (Figure 17). As the silica solubility curve

has already been alluded to, the use of Isobutane to get optimal turbine work within the reservoir

temperatures of Chiweta would require the introduction of scaling inhibitors in the reinjection process. Isopentane turbine work output appears to be within the safe working zone for scaling. With this outcome, the choice of Isopentane was made as a working fluid for all the binary models under study in this project.

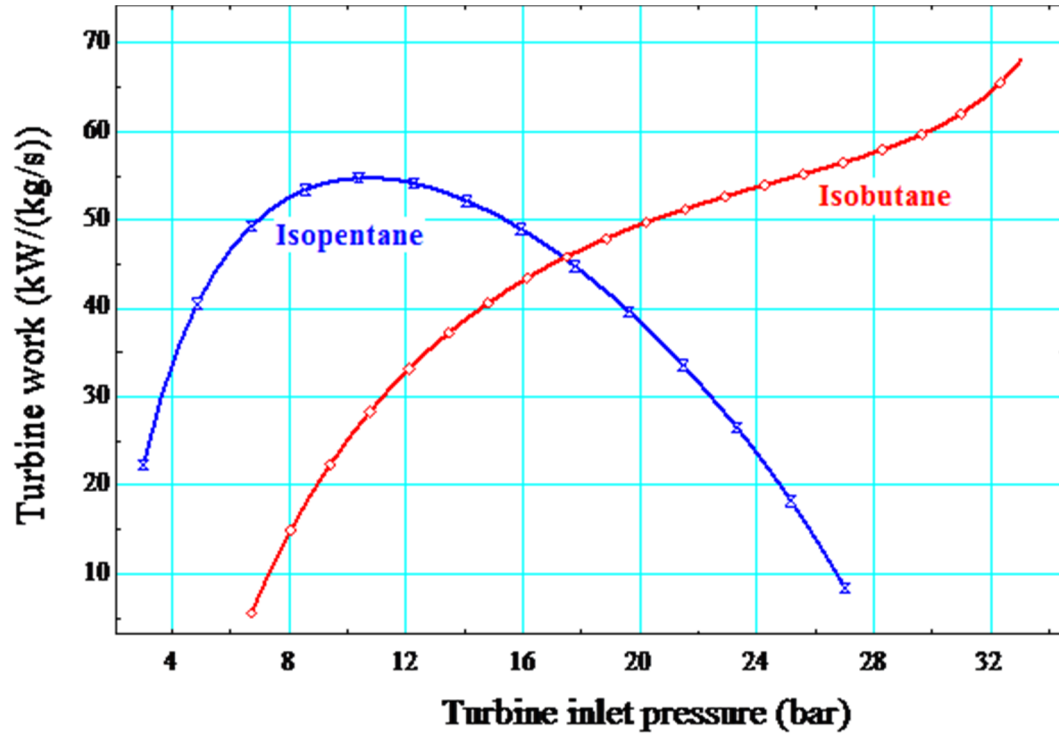


FIGURE 16: Working fluid turbine inlet pressure

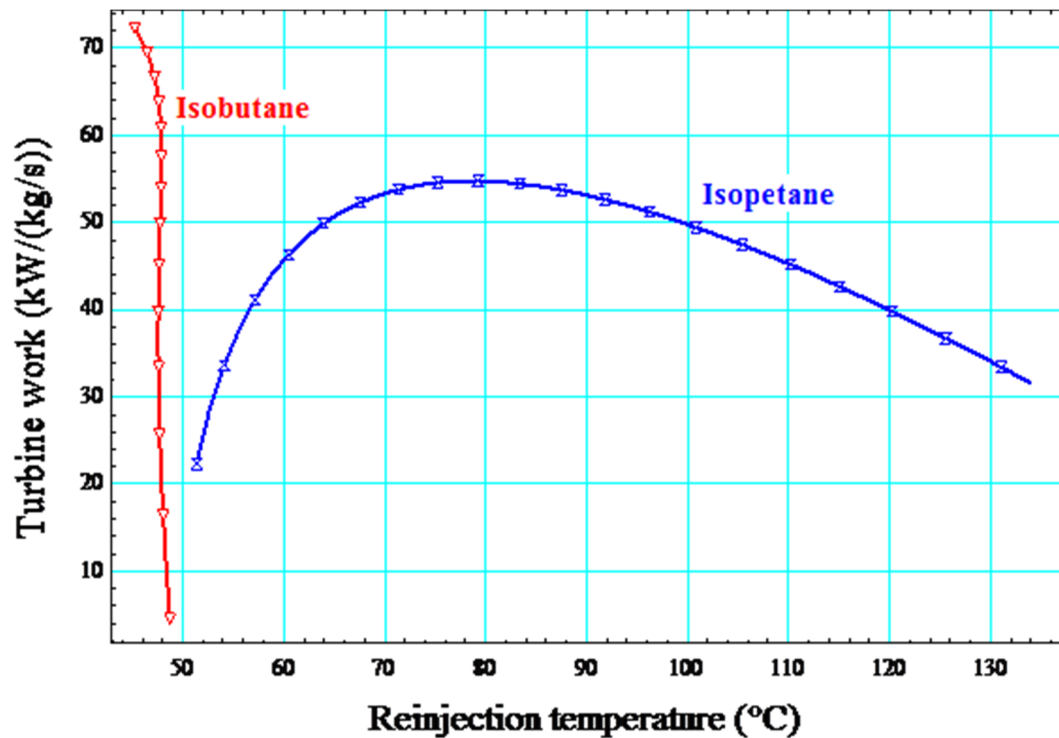


FIGURE 17: Working fluid reinjection temperature

4.3 Recuperator effect in a binary power plant

When a recuperator was incorporated into the binary model, two things were observed about its behaviour in the new binary cycle. The parameters observed were the brine reinjection temperature and the turbine inlet work. These parameters were observed with varying turbine inlet pressure. When the temperature difference in the primary cycle, between the reservoir and reinjection point, was controlled to be common in both a binary model with a recuperator and in a binary model without a recuperator, it was observed that the turbine work output for the recuperative model was higher than the work output from the basic binary model without a recuperator while the turbine inlet pressure was varied (Figure 18). When the reinjection temperature was not controlled but the turbine inlet pressure was varied, it was observed that the model with a recuperator reached its maximum turbine work at a higher reinjection temperature than the model without a recuperator. Based on these observations, in both models the maximum turbine work was the same (Figure 19), with a shift in reinjection temperature.

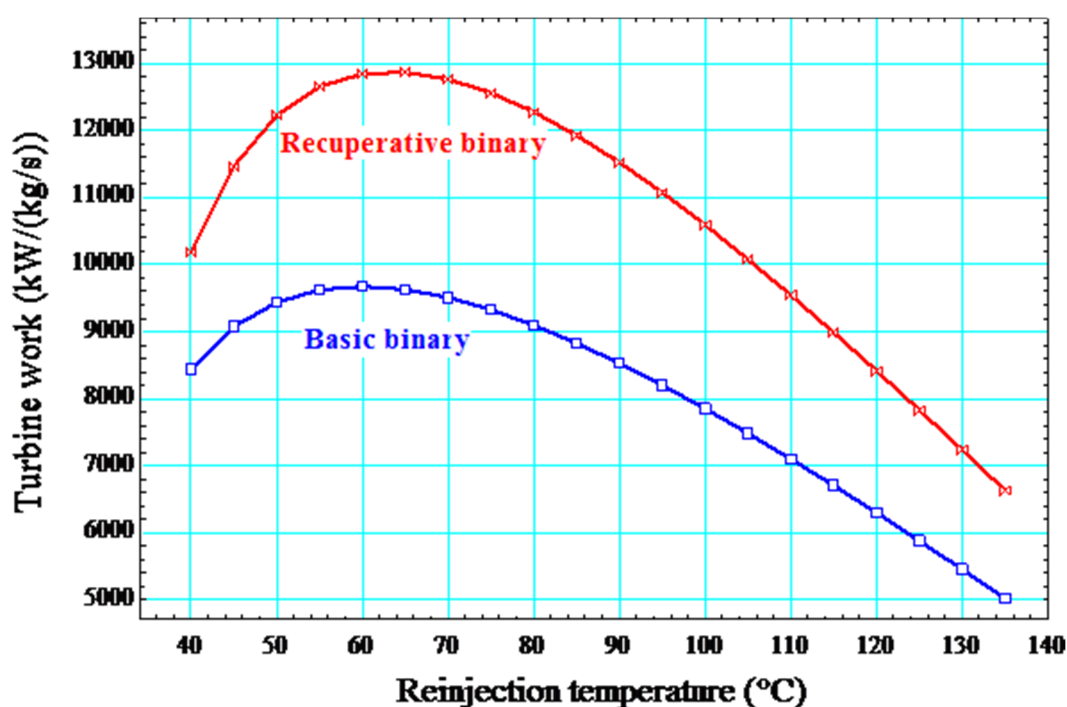


FIGURE 18: Impact of a recuperator on models under controlled reinjection temperature

It can be concluded, therefore, that depending on the desire of the model, the recuperator can either be used for improved turbine work output or to reinject brine at a higher temperature, while maintaining turbine work output where chemistry restrictions prevail. Valdmarrsson (2011a) suggested that a recuperator be used where chemical conditions demanded a higher reinjection temperature in order to get optimal benefits from a resource. The addition of a recuperator to a system increases the capital cost of the system in the sense that additional heat exchanger area is needed in the recuperative model than in the basic model.

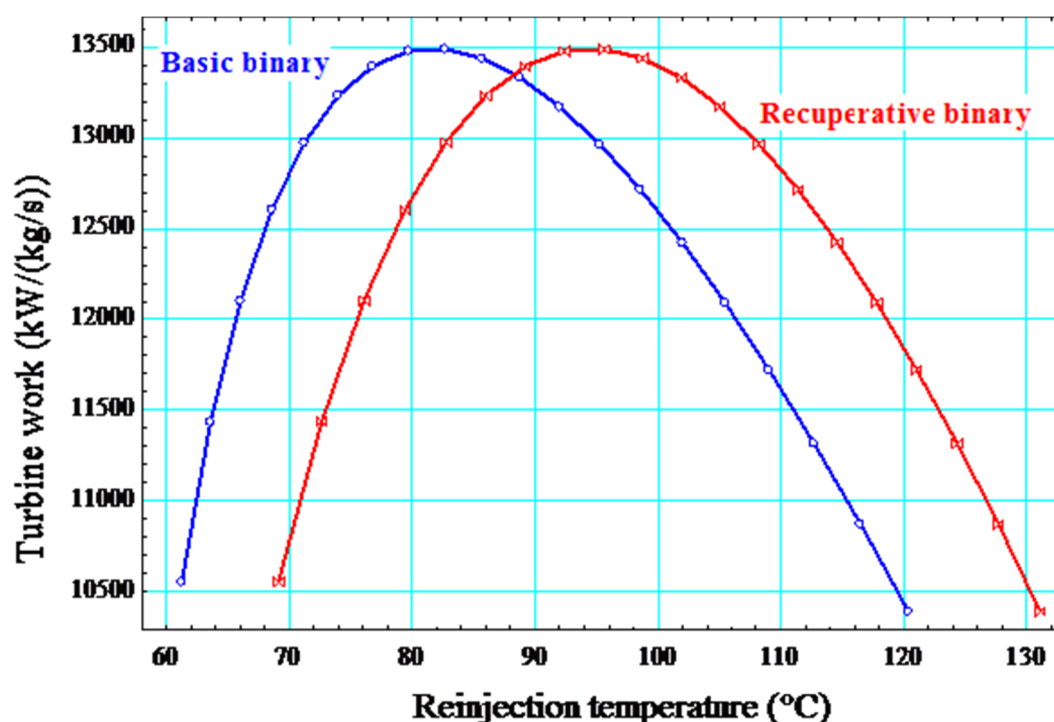


FIGURE 19: Impact of a recuperator on models under free reinjection temperature

5. MODELLING OF GEOTHERMAL POWER PLANTS USING EES

From the discussions above, the power plants were modelled using Engineering Equations Solver (EES) software. This software assists in analysing the thermodynamics of various fluids in a power plant to give desired outputs in terms of turbine work, cycle efficiency and more. Programmes for each power plant model, as mentioned earlier, were produced and analysed. Since Malawi has not done many studies to ascertain field characteristics that would fully satisfy in creating model parameters, some assumptions were used in all the analyses. Wherever applicable, the assumptions followed the general characteristics of the Chiweta field. The following are the parameters and assumptions used in the analyses:

- Heat exchanger pinch temperature: 4°C
- Ambient temperature: 25°C
- Geothermal fluid mass flow: 1 kg/s (*in order to calculate specific power output*)
- Turbine efficiency : 85%
- Pump efficiency : 75%
- Binary working fluid : Isopentane
- Heat transfer coefficients (U) (Ahangar, 2012)
 - $U_{\text{Evaporator}} = 1600 \text{ W/m}^2\text{°C}$
 - $U_{\text{Pre-heater}} = 1000 \text{ W/m}^2\text{°C}$
 - $U_{\text{Recuperator}} = 400 \text{ W/m}^2\text{°C}$
 - $U_{\text{Condenser}} = 800 \text{ W/m}^2\text{°C}$
- Plant lifespan: 30 years
- Discount rate: 15%
- Operation and maintenance cost: 4% of gross income
- Cost of steam gathering system: US\$250/kW (Hance, 2005)
- Electricity tariff: US\$0.09/kWh (ESCOM, 2013)
- Plant components Unit Cost (UC) (Ahangar, 2012)
 - $UC_{\text{Evaporator}} = \text{US\$}500/\text{m}^2$
 - $UC_{\text{Pre-heater}} = \text{US\$}450/\text{m}^2$
 - $UC_{\text{Recuperator}} = \text{US\$}400/\text{m}^2$
 - $UC_{\text{Condenser}} = \text{US\$}600/\text{m}^2$
 - $UC_{\text{Turbine}} = \text{US\$}500/\text{kW}$
 - $UC_{\text{Pump}} = \text{US\$}450/\text{kW}$

The reservoir temperature was split into three levels for the model analyses. The three reservoir temperature levels were at 180, 210 and 240°C in accordance with the range of subsurface temperatures in Malawi. The reinjection temperatures, according to the amorphous silica solubility curve in Figure 13 were, therefore, 70, 110 and 130°C, respectively.

All the models were first optimised to get the best fit of parameters at a given point with optimal model output. The process of optimization involved the turbine inlet pressure and the wellhead pressure while observing the conditions that gave the highest possible turbine output within the allowable reinjection temperature range of a given reservoir temperature. The pinch temperature was conveniently assumed for the sake of the analyses. Of interest to the observations were the thermal efficiency, exergetic efficiency, turbine work output and the specific gain from the model. Thermal efficiency is the ratio of the power produced in a power plant to the heat transferred to that power plant (Valdimarsson, 2011b). Thermal efficiency is given by Equation 20.

$$\eta_{th} = \frac{\dot{W}_{tur}}{\dot{Q}_b} \quad (20)$$

Exergy is the portion of heat from a heat source which can be converted into work (Valdimarsson, 2011b). Therefore exergetic efficiency is the ratio of the power produced in a power plant to the portion of heat available which can be converted into work. The heat available for work conversion is given as a function of the local environmental conditions. Exergetic efficiency (η_{ex}) is given by Equation 21.

$$\eta_{ex} = \frac{\dot{W}_{tur}}{\dot{Q}_{av}} \quad (21)$$

where \dot{Q}_{av} is the available heat as a function of local environmental conditions.

The turbine work output is the amount of energy (kW) obtained from the turbine in a given model. Since hybrid models consist of two turbines, the sum of the work of the two turbines was considered; the gross turbine work was used in the analysis. A specific turbine work was obtained in a given model as a result of using a unit mass flow from the well of 1kg/s, hence the specific work was given by kW/(kg/s). The specific gain defines the amount of work that can be obtained per dollar of the cost of the total power plant cost (kW/US\$). Specific gain is given by the total cost of a model and the turbine work output of the model as given in Equation 22.

$$Specific\ gain = \frac{\dot{W}_{tur}}{Plant\ cost} \quad (22)$$

In all the observations above, the principle of ‘the bigger the better’ applied in selecting a suitable model. The following were the findings from the analyses.

5.1 Technical comparative analysis of power plants

5.1.1 Single-flash plant model - technical analysis

From the single-flash model analysis, it was observed that the plant improved its performance with an increase in reservoir temperature (Figure 20). The thermal efficiency and exergetic efficiency of the model increased in the same proportion as the resource temperature increased. Of significant note was that turbine work output increased more as reservoir temperature increases from 210 to 240°C. It was also observed that the specific gain of the plant was relatively higher at high temperature with an increase in work output compared to lower temperature. This is because the plant becomes efficient at higher temperatures and more economical than at lower temperature. This confirms the understanding that single-flash models are more viable at higher reservoir temperatures than at lower reservoir temperatures.

5.1.2 Basic binary plant model - technical analysis

From the analysis of the basic binary plant, the model showed that its performance increased with the first increase in reservoir temperature from 180 to 210°C (Figure 21). At this level, the thermal efficiency as well as the turbine work output increased. The exergetic efficiency slightly decreased because at this point the reinjection temperature was fixed as opposed to a reinjection temperature of 180°C. The cost of generation at this level is relatively lower and there is more benefit of work from a dollar input, thus an increase in specific gain. As the reservoir temperature increased from 210 to 240°C, the performance of the cycle decreased in such a way that thermal efficiency, exergetic efficiency and turbine work reduced. The reinjection temperatures observed at the three reservoir temperature level were 78, 110 and 130°C. The cost of generation at these levels was relatively lower and the specific gain was almost the same to what was gained at 210°C, signifying that the cost of the power plant at this level was higher than at 210°C. This confirms the understanding that binary cycle models are more economically viable at low to medium reservoir temperatures than at higher reservoir temperatures.

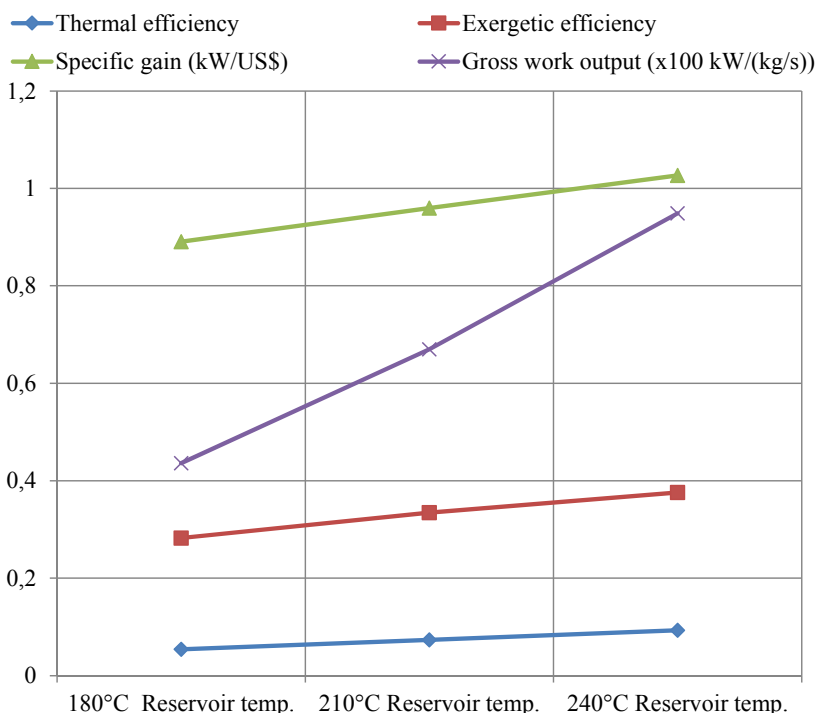


FIGURE 20: Single-flash performance with reservoir temperature

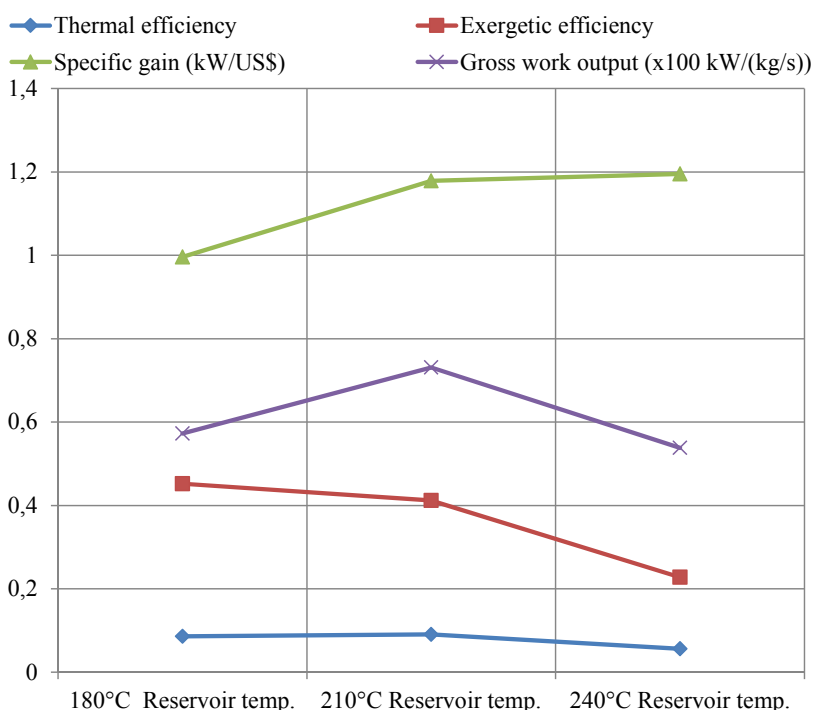


FIGURE 21: Basic binary cycle performance with reservoir

5.1.3 Recuperative binary plant model - technical analysis

From the analysis of the impact of a recuperator on a basic binary and a recuperative binary plant, the analysis of a recuperative binary plant model showed that at a reservoir temperature of 180°C, the

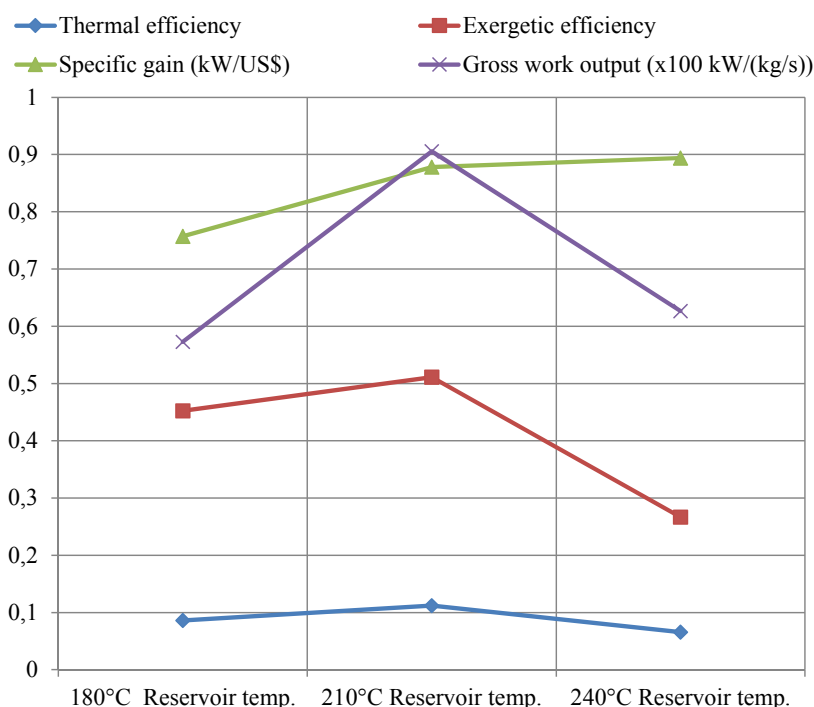


FIGURE 22: Recuperative binary cycle performance with reservoir temperature

compared to the basic binary cycle, the specific gain at this level was relatively lower as there was less benefit of work per dollar input with regard to the basic binary cycle. This signifies that the cost of a recuperative power plant is higher than the basic binary plant. With further increase of reservoir temperature from 210° to 240°C, the performance of the cycle decreased such that thermal efficiency, exergetic efficiency and turbine work reduced in the basic binary cycle. However, in the recuperative binary plant, there was slightly higher exergetic efficiency and turbine work than in the basic binary plant. The reinjection temperatures observed at the three reservoir temperature levels were 89°, 110° and 130°C. The specific gain in the recuperative plant was observed to be lower than in the basic binary plant, signifying that the cost of the recuperative plant was higher than for the basic binary. The overall general analysis showed that the recuperative binary cycle models were more viable at low to medium reservoir temperatures than at higher reservoir temperatures and that the benefits of that model over the basic cycle were generally traded in. The areas for the condenser and the pre-heater in the recuperative binary plant increased compared to the basic binary plant and this caused the overall cost of the cycle to increase, thus reducing the benefits.

5.1.4 Basic hybrid and recuperative hybrid power plant - model technical analysis

The hybrid that was used in this project was the one with binary bottoming, using brine from the separator of a single-flash plant, taking into consideration the fact that the proposed Chiweta field is a medium to low-enthalpy field and flashing is at low pressure. The hybrid under study used both a basic binary cycle and a recuperative binary cycle. The principle behind the hybrid cycle under study was to optimise the use of the geothermal resource even further, after flashing. Therefore, the first line of optimization is the single-flash cycle cascaded with the binary cycle.

From the model's analysis, it was observed that the basic hybrid plant's performance was better than that of the single-flash plant (Figure 23). The hybrid plant exhibited more turbine work output and higher exergetic efficiency than the single-flash plant at 180°C reservoir temperature. However, at this level of temperature, the specific gain was almost the same as for the single-flash plant. This is because

performance exhibited the behaviour seen in Figure 15. The reinjection temperature at 180°C was higher than the reinjection temperature of a basic binary plant with the same turbine work output. The recuperative reinjection temperature was 89°C. As the reservoir temperature increased from 180° to 210°C, the performance improved more than in the basic binary plant (Figure 22). At this level, the thermal efficiency as well as the turbine work output increased and their increase was much higher than in the basic binary cycle. At this level, the exergetic efficiency was also observed to increase. Even though the turbine work was high at this level,

of the simultaneous increase in turbine work output with increase in plant cost. The basic hybrid plant's performance and specific gain improved with an increase in reservoir temperature. The thermal efficiency and exergetic efficiency of the model tended to be relatively stable unlike the increase observed in the single-flash cycle. This is the result of a combination of a single flash that increases efficiency with an increase in reservoir temperature, and a binary plant that decreases in efficiency with an increase in temperature. As in the single-flash cycle, of significant note was that the turbine work output increased more as reservoir temperature increased from 210° to 240°C with a corresponding increase in plant specific gain. The hybrid plant becomes cheaper at higher temperatures than at lower temperature as it is delivered more turbine work than at lower temperature while maintaining efficiency.

Similar observations were noted when a recuperative hybrid cycle was analysed (Figure 24). Notable changes in behaviour were that a recuperative hybrid was more stable in efficiency than the basic hybrid across reservoir temperature changes. It was also observed that the recuperative hybrid delivered slightly higher turbine work output at higher reservoir temperatures of 210° and 240°C than the basic hybrid plant. However, the specific gain in the recuperative hybrid model was lower than for the basic hybrid model. This was caused by the addition of a recuperator to the plant, which generally increases the plant's cost.

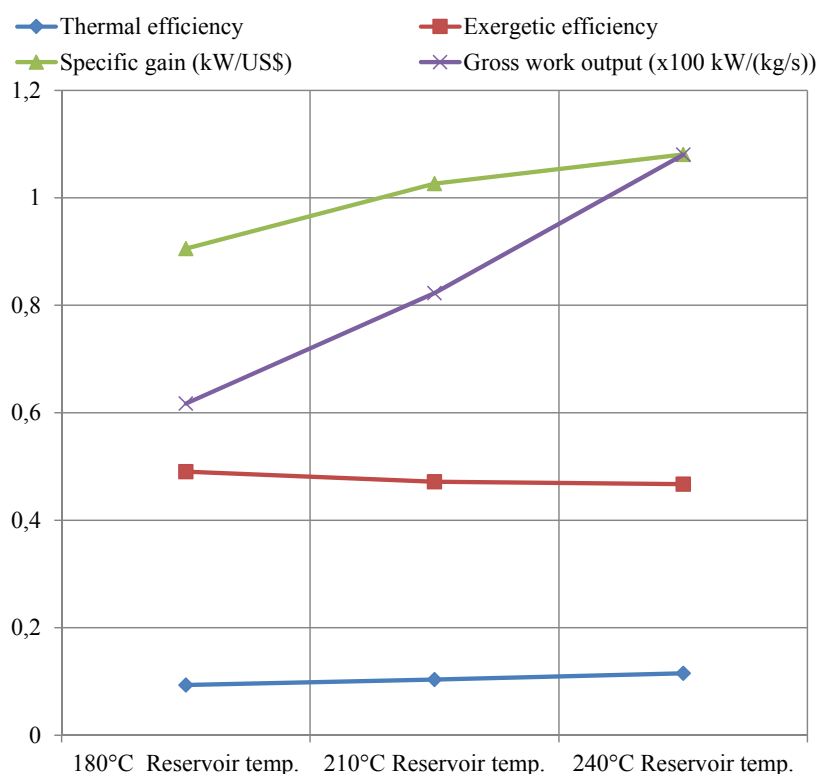


FIGURE 23: Basic hybrid cycle performance with reservoir temperature

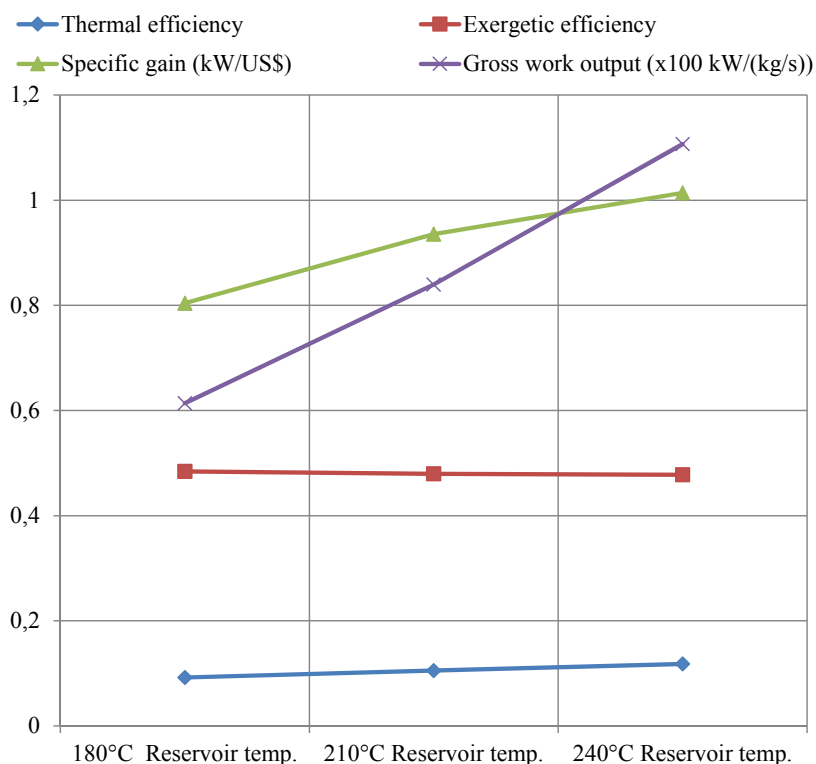


FIGURE 24: Recuperative hybrid cycle performance with reservoir temperature

5.2 Economic analysis of the modelled power plants

The electricity tariff regime for Malawi segregates customers depending on the type of use implemented by the country's sole electricity service provider ESCOM. Among others, the segregation considers whether the customer is connected at either a single-phase for domestic use, or connected at a three-phase for domestic and industrial uses. The current electricity tariff in Malawi, with respect to the customer type, is in the range of US\$0.06 – 0.12 per kWh (ESCOM website). This report used the mid-range tariff for economic analysis which is US\$0.09. The economic analysis compares the payback period of the models as well as the Net Present Value (NPV) of the models. The analysis assumes a uniform tariff over a 30 year life span of the power plant; thus, a constant annual cash income was assumed and not all cost factors were included.

5.2.1 Payback period analysis

Payback period is the length of time required for a project's cash inflow to recover the original cash outlays required by the project's initial investment (Bejan, et al., 1996). This is considered the period where the net cash inflow of the project is zero. The principle of a payback period advises choosing a project that gives the least payback period among projects under consideration. The payback period is found by using Equation 23:

$$T_{PB} = \frac{TDI}{ANCF} \quad (23)$$

where T_{PB} is the payback period;
 TDI is the total depreciable investment;
 $ANCF$ is average annual net cash inflow (Bejan, et al., 1996).

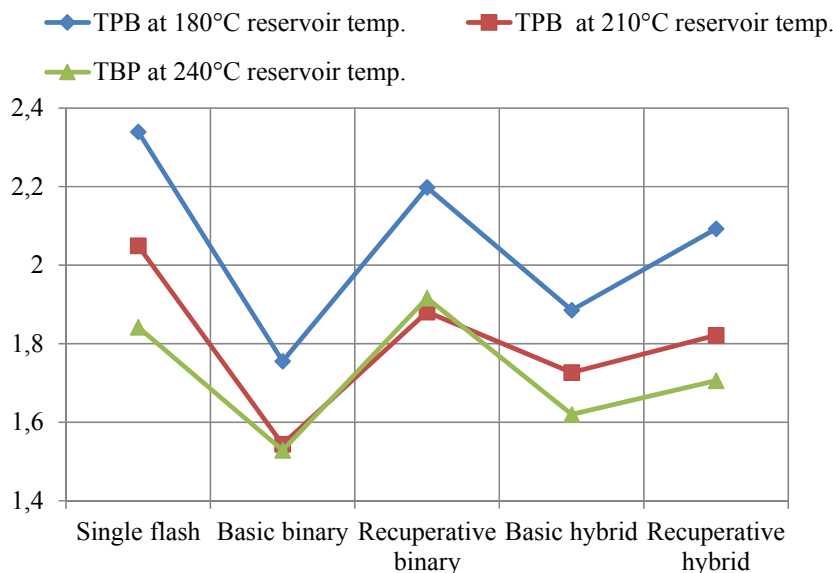


FIGURE 25: Payback period analysis

payback period at all levels (Figure 25). It was also observed that there is a bigger variation in the payback period at lower reservoir temperature than at higher reservoir temperature. This is due to the fact that there is more work delivered at higher reservoir temperature than at lower reservoir temperature, thereby significantly increasing the annual revenue and thus reducing the payback period.

For purposes of comparison in this analysis, TDI was assumed to be the cost of the power plant and $ANCF$ is the plant's annual net income. The analysis focuses on power plant components and the unified cost of steam gathering. The net cash inflow does not considered tax deductions, loan interest payments and related expenses. Subjecting all the models at every reservoir temperature level to the payback period analysis, it was observed that basic binary plants and the basic hybrid plants are the ones that exhibit a relatively lower

5.2.2 Net Present Value (NPV) analysis

Where the NPV principle is used, it advises that a project should be chosen if it has a positive NPV, otherwise the project should be rejected. It is also further recommended to choose a project with a higher NPV among projects with positive NPV under consideration. The NPV formula is given in Equation 24:

$$NPV = \sum_{z=0}^{BL} Y_z(1-i)^{-z} \quad (24)$$

where Y_z is the net cash flow at the end of z^{th} time period;
 BL is the book life of the project;
 i is the effective discount rate (Bejan, et al., 1996).

The net cash flow does not consider tax deductions, loan interest payments and related expenses. The book life of the project is assumed to be 30 years and the discount rate is 15%. From the NPV analysis, all the power plants exhibited a positive NPV (Figure 26). At 180°C, a single-flash plant showed the lowest NPV of all the models, while the rest of the models showed NPV within the same range of US\$150,000-200,000. At 210°C reservoir temperature, the single-flash plant had the least NPV followed by a basic binary, while the rest were within the same range around US\$250,000. At 240°C reservoir temperature, the basic binary and the recuperative binary plants exhibited the lowest NPV, while the basic hybrid and the recuperative hybrid plants exhibited the highest NPV. The single flash was observed to be in between the two ranges.

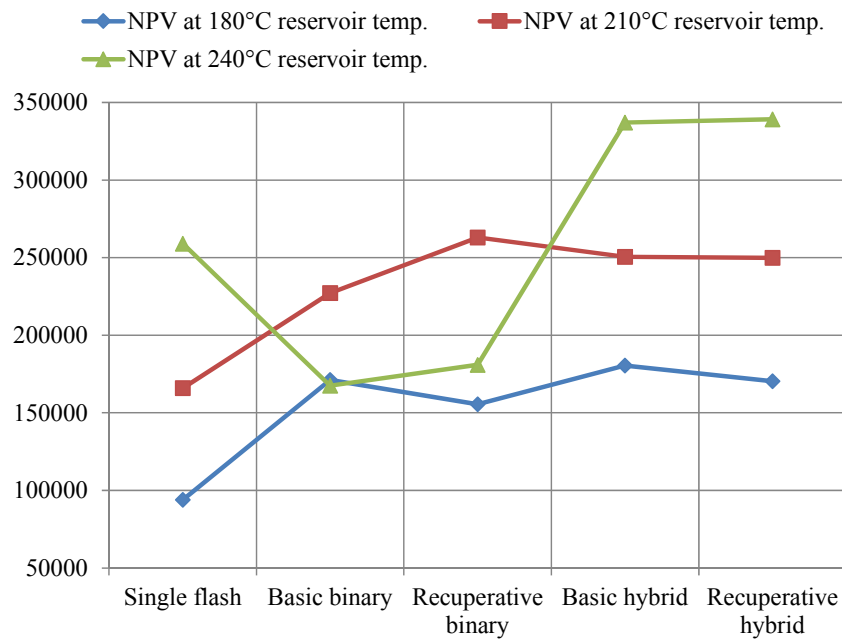


FIGURE 26: NPV analysis

6. RECOMMENDED DESIGN FOR CHIWETA FIELD

Based on the analyses done, recommendations are given for the three values of reservoir temperature.

- At a reservoir temperature of 180°C, the recommended design is the basic binary plant. The design has a higher specific gain than the other models; it also requires the shortest payback period and has a relatively higher NPV. The thermal efficiency and exergetic efficiency of a basic binary plant at this level do not vary significantly from that of the other models, however it was more efficient than the single flash. Overall, the model turbine work output was almost the same as for recuperative binary, basic hybrid and recuperative hybrid plants but the basic binary is the cheapest of them all.

- At a reservoir temperature of 210°C, the recommended design is the basic binary plant. The design has the highest specific gain of all the models; it also requires the shortest payback period among the models. Even though the model does not give the highest NPV, the model's NPV is higher than that of a single flash cycle and is also closer to the higher NPV of the other models. The thermal efficiency and exergetic efficiency of the basic binary cycle at this level do not vary significantly from that of the other models.
- At a reservoir temperature of 240°C, the recommended design is the basic hybrid plant. The design has a higher specific gain than the other models; it comes in second after the basic binary plant but offers more turbine work output than the basic binary model. The model also gives a shorter payback period among the models, coming in second best after the basic binary model. The model exhibits a higher NPV, second best after the recuperative hybrid model but relatively cheaper than it. The thermal efficiency and exergetic efficiency of the basic hybrid at this level were relatively higher than for the other models, almost the same as the recuperative hybrid model.

7. CONCLUSIONS

From the preceding study, it can be concluded that Malawi could develop either a basic binary or a basic hybrid power plant for the utilization of its Chiweta geothermal field. These power plant models proved to be more technically and economically viable than the other plants that have similar development potential in Malawi. In as much as the study has suggested the mentioned power plants for development, there is a need for Malawi to conduct detailed studies for the fields to obtain meaningful data that could lead to development of the resource. Since geothermal development is multi-disciplinary, there is need for further studies to be carried out using MT and TEM soundings to find the geophysical properties of the Malawi resource. Exploratory wells could then be drilled to confirm the obtained data from the geochemical and geophysical explorations.

The integration of power production with other direct utilization programmes does significantly improve the economic viability of using lower temperature geothermal fluids and could result in a much higher overall efficiency than could be achieved with just producing power or just direct use projects. The proposed utilizations should be studied further for potential integration and for optimizing resource efficiency.

ACKNOWLEDGEMENTS

Appreciation should go to the leadership of UNU-GTP, Mr. Lúdvík S. Georgsson and Dr. Ingvar Birgir Fridleifsson, and the entire UNU-GTP team, Ms. Thórhildur Ísberg, Ms. Málfríður Ómarsdóttir, Mr. Markús A. G. Wilde and Mr. Ingimar G. Haraldsson, for according me such an opportunity to study geothermal utilization for the benefit of Malawi and making sure that my stay in Iceland realizes its cause in a comfortable manner. Without the support of the team, I could hardly have achieved the strides made so far.

My supervisors, Ms. María Sigríður Guðjónsdóttir and Dr. Páll Valdimarsson – P.V., were passionate in sharing as much knowledge on the area under study as possible with me, to the best of their abilities. Their efforts are much appreciated.

The management team of MERA is also appreciated for allowing me to participate in this course. I also appreciate the efforts of my wife and family who had to deal with my absence for the period of the course but continued to offer much needed moral support. To God be the glory.

REFERENCES

- Ahangar, F.A., 2012: Feasibility study of developing a binary power plant in the low-temperature geothermal field in Puga, Jammu and Kashmir, India. Report 6 in: *Geothermal Training in Iceland 2012*. UNU-GTP, Iceland, 1-24.
- Bao, J., and Zhao, L., 2013: A review of working fluid and expander selections for Organic Rankine Cycle. *Renewable and sustainable Energy review*, 24, 325-342.
- Bejan, A., Tsatsaronis, G., and Moran, M., 1996: *Thermal design and optimization*. John Wiley & Sons, NY, 542 pp.
- Bertani, R., 2010: Geothermal power generation in the world, 2005–2010, update report. *Proceedings of the World Geothermal Congress 2010, Bali, Indonesia*, 41pp.
- Blodgett, L., and Slack, K., 2009: *Basics of geothermal energy production and use*. Geothermal Energy Association, Washington, DC, 55pp.
- Dickson, M.H., and Fanelli, M. (eds.), 2003: *Geothermal Energy: Utilization and technology*. UNESCO Renewable Energy Series, 205 pp.
- DiPippo, R., 1999: Small geothermal power plants: Design, performance and economic. *Geo-Heat Center Bulletin* 1999, June, 1-8.
- DiPippo, R., 2008: *Geothermal power plants. Principles, applications, case studies and environmental impact*. Elsevier Ltd., Kidlington, UK, 493 pp.
- ESCOM, 2013: *Tariffs on electricity*. ESCOM, website: www.escom.mw/tariffs.php.
- Franco, A., and Villani, M., 2009: Optimal design of binary cycle power plants for water-dominated, medium-temperature geothermal fields. *Geothermics*, 38, 379–391.
- Fridleifsson, I.B., Bertani, R., Huenges, E., Lund, J. W., Ragnarsson, A., and Rybach, L., 2008: The possible role and contribution of geothermal energy to the mitigation of climate change. In: Hohmeyer, O., and Trittin, T., (Eds.) *Proceedings of IPCC Scoping Meeting on Renewable Energy Sources 2008*, Luebeck, Germany, 36pp.
- Gondwe, K., Allen, A., Georgsson, L.S., Loga, U., and Tsokonombwe, G., 2012: Geothermal development in Malawi – a country update. *Proceedings of the 4th African Rift Geothermal Conference, ARGeo C-4, Nairobi, Kenya*, 7pp.
- Hance, C.N., 2005: *Factors affecting costs of geothermal power development*. Geothermal Energy Association, Washington, DC, USA, 64pp.
- Hunt, T.M., 2001: *Five lectures on environmental effects of geothermal utilization*. UNU-GTP, Iceland, report 1-2000, 109pp.
- Kagel, A., Bates, D., and Gawell, K.A., 2007: *A guide to geothermal energy and the environment*. Geothermal Energy Association, Washington, DC, 75pp.
- Kiruja, J., 2012: Direct use of geothermal energy in USA: *Proceedings at “Short course VII on Exploration for Geothermal Resources”, Lake Naivasha, Kenya 2012*, 5pp.

Lund, J.W., 2005: *Direct heat utilization of geothermal resources Worldwide 2005*, Oregon Institute of Technology, Geo-Heat Center, Klamath Falls, OR, 14pp.

MCA – Malawi, 2010: Public private partnerships on electricity generation for rural areas, 2011 – 2016. MCA, Lilongwe, Malawi.

National Energy Policy for Malawi, 2003: *National energy policy*. Republic of Malawi, January, 2003.

NSO 2010: *2008 population and housing census report*. Republic of Malawi, report, 30pp.

Omenda P.A., 2005: The geology and geothermal activity of the East African Rift System. *Proceedings of “Workshop for Decision Makers on Geothermal Projects and Management”*, organized by UNU-GTP and KenGen, Naivasha, 9 pp.

Pritchett, J.W., 1996: A study of electrical generating capacities of self-discharging slim holes. *Proceedings of the 21st Workshop on Geothermal Reservoir Engineering Stanford University, Stanford, Ca*, 55-66.

Ragnarsson, Á., 2006: Geothermal utilization, direct use and power generation. *Paper presented at ICEIDA short course on Geothermal Capacity Building, Nicaragua*, 24pp.

Thórhallsson, S., 2005: Common problems faced in geothermal generation and how to deal with them. *Paper presented at “Workshop for Decision Makers on Geothermal Projects and Management”*, organized by UNU-GTP and KenGen in Naivasha, Kenya, 12 pp.

Valdimarsson, P., 2010: Production of electricity from a geothermal source. In: Popovski K. (ed.), *Geothermal Energy*, MAGA, Macedonia 150-180.

Valdimarsson, P., 2011a: Geothermal power plant cycles and main components. *Paper presented at “Short Course on Geothermal Drilling, Resource Development and Power Plants”*, organized by UNU-GTP and LaGeo, St. Tecla, El Salvador, 24 pp.

Valdimarsson, P., 2011b: Thermodynamics of geothermal power production - Overview. *Paper presented at “Short Course on Geothermal Drilling, Resource Development and Power Plants”*, organized by UNU-GTP and LaGeo, St. Tecla, El Salvador, 9pp.



**UNITED NATIONS
UNIVERSITY**

GEOHERMAL TRAINING PROGRAMME
Orkustofnun, Grensasvegur 9,
IS-108 Reykjavik, Iceland

Reports 2013
Number 23

GEOCHEMISTRY OF THERMAL WATER FROM THE THEISTAREYKIR GEOTHERMAL FIELD IN NE-ICELAND COMPARED TO THAT OF THE GEOTHERMAL PROSPECTS IN NW-RWANDA

Jean Pascal Niyigena

EWSA – Energy, Water and Sanitation Authority
P.O. Box 537
Kigali
RWANDA
niyigena2011@gmail.com

ABSTRACT

Geochemical methods were applied to the Theistareykir field in NE Iceland and the geothermal prospects in NW Rwanda. The results were then compared. Theistareykir was subjected to production drilling a decade ago, while in NW Rwanda, exploratory drilling started in August 2013. In Theistareykir field, Wells ThG-2, ThG-3, ThG-4 and ThG-5b discharge the characteristic enthalpy of a mixture of liquid and vapour (917 - 2661 kJ/kg). The discharged fluid was classified as mature Na-Cl-HCO₃ water and the maximum subsurface temperature calculated by the WATCH programme was 300°C. The chemical composition of the wells and warm springs suggests the presence of more than one aquifer drawing fluid from a single base reservoir; warm springs are the result of super-heated shallow water. When boiled, the deep liquid becomes super-saturated with amorphous silica; calcite saturation has been reached in most wells.

The geochemistry of the warm springs in the geothermal prospects in NW Rwanda suggests that the water is Na-HCO₃ water that has not attained full equilibrium. The thermal water might be steam heated groundwater, not necessarily reflecting subsurface properties.

Both in the Theistareykir field and the geothermal prospects in NW Rwanda there are warm springs on the surface which do not necessarily reflect the deep reservoir properties. Their presence simply indicates that the prevailing reservoir of the geothermal system is composed of many aquifers, some shallow, others deep.

1. INTRODUCTION

Geochemistry has a key role in the geothermal industry from earlier investigations, to utilization, and through development. Its application is only meaningful by assuming that the natural geothermal fluid arising to the surface preserves the signature of the deep subsurface where it formed. Most chemical species in aqueous solution are in equilibrium with their host rock minerals. As thermal fluid mines heat from the rock reservoir and the equilibrium is said to be temperature dependent, so it is possible

to predict the reservoir temperature based on the chemistry of the fluid collected at the surface. In the initial stages of surface investigations, geochemistry gives information on the sub-surface temperature with the help of geothermometers. Geochemistry is used for the classification of geothermal water and for the location of areas with enhanced permeability, by measuring carbon dioxide gas fluxes and performing radon counts. The origin of the fluids can be traced by analysing the fluids and looking into the composition of conservative constituents or isotope ratios. The geochemical data obtained during the production phase are used to predict the future response of the reservoir due to pressure decline, production load, boiling and recharge. Geochemical data are also used to forecast naturally occurring problematic geothermal processes such as scaling, corrosion and cooling of geothermal systems (Arnórsson, 2000). In this report, geochemical data from wells and hot springs in the Theistareykir geothermal field, NE Iceland, and some hot and warm springs in the NW-Rwanda geothermal areas are reviewed and interpreted to evaluate the surface and deep geothermal waters, mineral equilibrium conditions, and to estimate the subsurface temperatures. The results from the two geothermal fields are then compared.

Theistareykir is one of the high-temperature geothermal systems in Iceland situated in the northeast. This field has been subjected to several geothermal surface surveys and exploration drilling. Based on the outcomes of the surface studies, Ármannsson et al. (1986) presented a conceptual model of the Theistareykir field and divided it into five sub-areas out of which three are suitable for further geothermal development. The ongoing plan is to set up a geothermal plant of 90 MW electrical power by 2015 in the area. Four water samples from discharging wells and 2 from discharging springs were used in this study to characterize the chemistry of this field.

The northwest part of Rwanda is believed to host a substantial geothermal resource for generating economically viable electrical power. Yet, its development is still at an early stage. After extensive surface investigations, it was divided into three prospects, namely Karisimbi, Kinigi and Gisenyi. Exploration drilling started in the Karisimbi prospect in 2013 and is still going on. The drilling results will be used to conceptualize the reservoir regime that governs the geothermal system. Six samples from hot, warm and cold springs were selected to study this area.

The purpose of this paper is to apply geochemical methods to the results obtained from drilling and the information gained from surface springs to describe the properties of the deep aquifers. Theistareykir is a geothermal field where surface water properties do not reflect the reservoir conditions, as has been proven through the drilling results. Drilling was initiated at Theistareykir based on the results of studies on fumaroles. By comparing Theistareykir's characteristics to the geothermal prospects in NW Rwanda, where only information from surface water is available, the Theistareykir experience can lead to a better understanding of the reservoir properties of the geothermal system in Rwanda.

2. BACKGROUND OF THE GEOTHERMAL FIELDS STUDIED

2.1 The Theistareykir geothermal field NE-Iceland

Geological studies at Theistareykir have been carried out by several authors but the results were summarized by Gautason et al. (2010). Theistareykir is a high-temperature geothermal system situated in NE-Iceland (Figure 1). It lies in a fissure swarm some 25 km north of Lake Mývatn in NE-Iceland. The intense volcanic activity is very pronounced in the centre of the system, yet a true caldera structure has not developed. The most active parts of the area are related to active fractures which increase permeability and enable geothermal fluids to circulate and reach the surface. The bedrock in the area is divided into hyaloclastite ridges formed by subglacial eruptions during the Ice Age, interglacial lava flows, and recent lava flows (younger than 10,000 yrs), all of which are basaltic. Acidic rocks are found on the western side of the fissure swarm, originating from subglacial eruptions up to the last glacial period. Rifting is still active in the fissure swarm.

Geothermal interest in the Theistareykir area, as presented by Ármannsson (2012a), dates back several centuries to the mining of sulphur that was used for the fabrication of gun powder for the Danish king. Surface exploration started in 1972-1974, and a major geothermal assessment was carried out in 1981-1984. From 1991-2000, the area was occasionally monitored.

The findings of the surface exploration showed that the area has a reservoir of good permeability. Calculated heat loss and geothermometers were used to estimate the temperature of the aquifer and it was found to be at least 280°C. The recharge zone was located in the southeast, and the origin of the fluid is probably far to the south (Ármannsson et al., 1986; Ármannsson 2012a). The results of surface exploration in the Theistareykir area suggest that it can be divided into 5 distinct sub-areas (Figure 2), of which three (A, C and D) are suitable for drilling.

Based on the drill sites suggested by Gautason et al. (2000), the first well, Well ThG-1, was drilled in area C in the autumn of 2002 to a depth of 1953 m, with a casing to 614 m depth. The major inflows are at 620-640 m depth and 1620-1640 m depth. The measured enthalpy at the surface was 2180 kJ/kg and the total flow from the well was 16-17 kg/s. The calculated steam fraction at depth at 280°C was 0.611. In 2003, the second well, Well ThG-2, was drilled to 1720 m depth. This well made drilling a challenge with loss of circulation at several different depths. Extreme loss of circulation was encountered at 260 m depth, and inferred a powerful aquifer. In 2006, Well ThG-3 was drilled to a depth of 2659 m and the maximum temperature recorded was 380°C. Its flow oscillated with enthalpy varying from about 1600 to 2600 kJ/kg, but approached the higher value with time and eventually settled as a high enthalpy steam well, giving 10-12 kg/s of high temperature steam. In 2007, Wells ThG-4 and ThG-5 were both drilled directionally from the same well pad as Well ThG-1. The first one is a high enthalpy steam well with a steam flow of 30 kg/s of high temperature steam, but well ThG-5 is a low enthalpy well, similar to well ThG-2, with a large liquid water flow. In 2008, Well ThG-5 was redrilled as Well ThG-5b under



FIGURE 1: Location of Theistareykir geothermal field in NE-Iceland (modified from Georgsson et al., 2005)

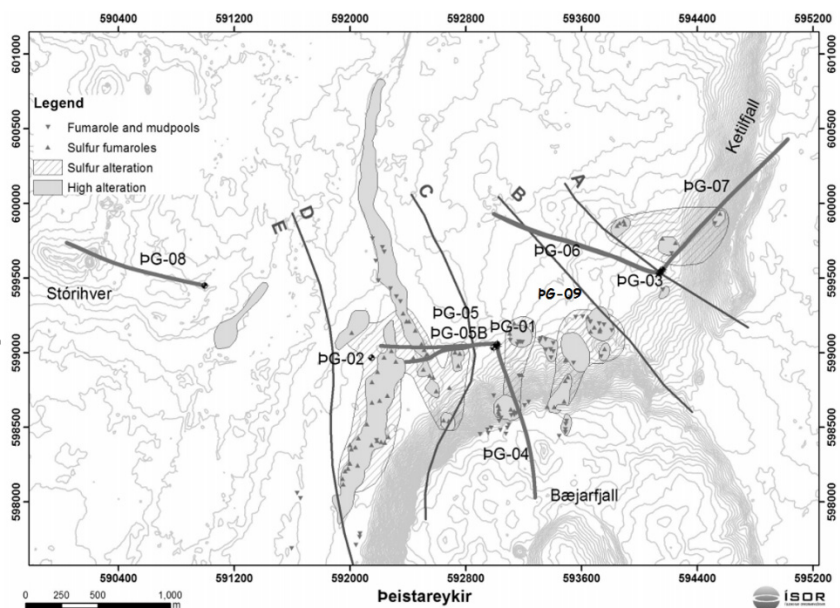


FIGURE 2: Location of deep wells and division of Theistareykir into five sub-areas (from Óskarsson et al., 2013)

a sharper angle and Well ThG-6 was drilled directionally from the well pad of Well ThG-3. The maximum temperature in Well ThG-5b was 300°C and 312°C in Well ThG-6 with respective enthalpies of 1485 and 2663 kJ/kg. Well ThG-7 was drilled in 2011 to a depth of 2509 m, with the highest measured temperature of 292°C. The enthalpy is about 2400 kJ/kg. Its isotopic characteristics suggest that it may produce from a different reservoir than the other wells in the area. Well ThG-8 was drilled in 2011, too, to a depth of 2503 m; it proved to be cool and has not been discharged. The latest is Well ThG-9, drilled in 2013 to a depth of 2194 m; its highest measured temperature was 338.5°C, with an enthalpy of about 2600 kJ/kg. Due to a short discharge period, representative samples have not been obtained (Óskarsson et al., 2013). Chemical compositions of ThG-2, ThG-3, ThG-4 and ThG-5b well fluids are discussed in this report as well as data from two warm springs. The current plan of Landsvirkjun (Iceland's National Power Company) and Theistareykir Ltd. (a jointly-owned municipal development company) is to build a geothermal power plant, with an electrical power capacity of 90 MW, at Theistareykir in two stages, starting in mid-2015.

2.2 Geothermal prospects in NW Rwanda

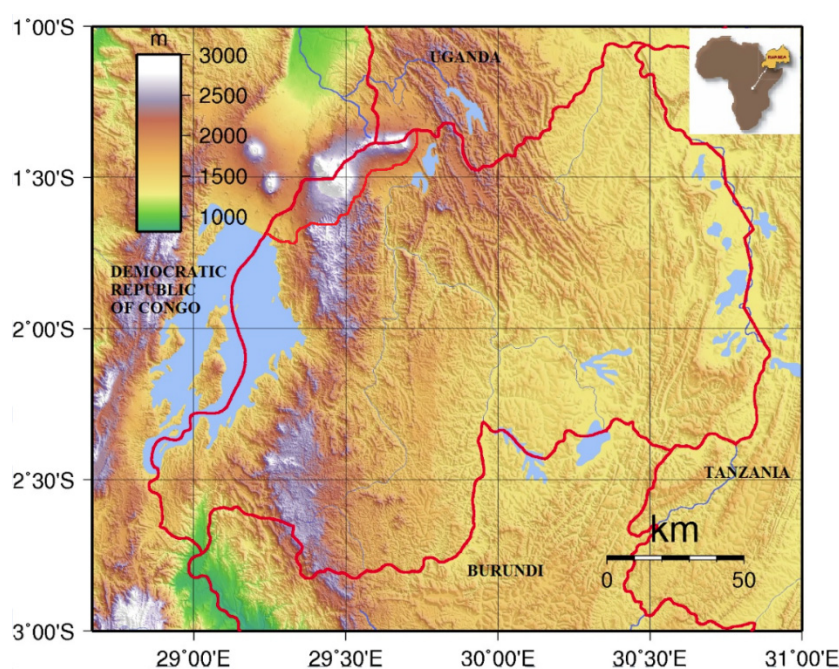


FIGURE 3: Topographic map showing the location of Rwanda and the geothermal area in the northwest

The geothermal prospects in NW-Rwanda (Figure 3) lie on the slopes of the Volcano National Park (VNP) and cover an area of 600 km², comprising 5 Strato volcanoes, i.e. Karisimbi, Bisoke, Sabyinyo, Gahinga and Muhabura, dating from the Quaternary period. Those massive volcanoes are a part of the Virunga Volcanic Range that forms a transverse chain in the western branch of the East African Rift (EAR). Those volcanoes were not active in historical time. Yet the Karisimbi volcano, the highest in the Virunga Volcanic Range with an elevation of 4507 m above sea level, is located approximately 22 km from

Nyiragongo and 30 km from Nyamuragira, both volcanoes in the eastern DRC that erupted in 2002 and 2010, respectively.

The geology of the geothermal prospects in NW-Rwanda, as well as the geology of the western branch of the EAR in general, is characterized by the abundance of potassic alkaline rocks that consist of basanites, leucitites, nephelinites, K-mugearites, K-benmoreiites and K-trachytes and other intermediate lavas in the Virunga area (Omenda, 2011). The geological setting consists of granite, migmatites, gneisses and mica schists of the Paleoproterozoic Ruzizian basement, overlain by the Mesoproterozoic Kibaran belt. The Kibaran belt, composed of folded and metamorphosed sediments, mainly schist and quartzite intruded by granite, covers most of Rwanda (BGR, 2009).

The geothermal prospects in NW Rwanda do not display many conventional surface geothermal manifestations. The thermal areas of Gisenyi and Karago are the only places where hot springs discharge water at the surface at 73 and 64°C, respectively. There is also a large amount of carbon

dioxide discharged through cold water springs in several places in both the Karisimbi and Kinigi prospects. Evidence of a large amount of carbon dioxide discharged in the past is expressed in the form of thick deposits of travertine exposed close to some springs in Musanze. However, the lack of surface manifestations does not mean a lack of potential geothermal conditions at depth. This is particularly true where an overlying non geothermal groundwater horizon masks the geothermal system. Where the top of a geothermal system is intersected by a large cold water aquifer, the heat will be swept down. Therefore, either no evidence of the geothermal system will appear on the surface, or large-volume warm springs may appear at large distances from the source (Gupta and Roy, 2007).

Reconnaissance surveys for geothermal energy in Rwanda were carried out in the 1980s, mapping areas of geothermal potential. Two prospective areas (Figure 4, associated with the Western Branch of the East African Rift), were identified and these comprise: the prospects in the northwest that are related to the Virunga volcanic chain, and the Bugarama prospect in the southwest of the country. Gisenyi and Mashuza hot springs, with surface temperatures of 73 and 53°C, respectively, were mapped as natural occurrences of surface manifestations. Intense exploration in the northwest area, which lies on the slope of the VNP from Lake Kivu in the west to Lake Ruhondo in the east, commenced in 2006. Since then, quite a number of geochemical, geophysical and geological investigations have been carried out in the above mentioned prospect and later led to the demarcation of the above field into 3 prospects, namely Karisimbi, Kinigi and Gisenyi, based on their developmental ranking (Figure 4). In early 2013, a geothermal review meeting was held in Kigali with the aim of integrating all existing data on the northwest prospect into one refined conceptual model. The data concerned was collected from the field in 2009 by the Kenya Electricity Generating Company (KenGen), and in 2011 by the Institute of Earth Science and Engineering (IESE) from New Zealand and KenGen (Mariita, 2010; Shalev et al., 2012). The outcome of this meeting was the siting of 3 geothermal exploration wells in the Karisimbi prospect, based on the conceptual model while

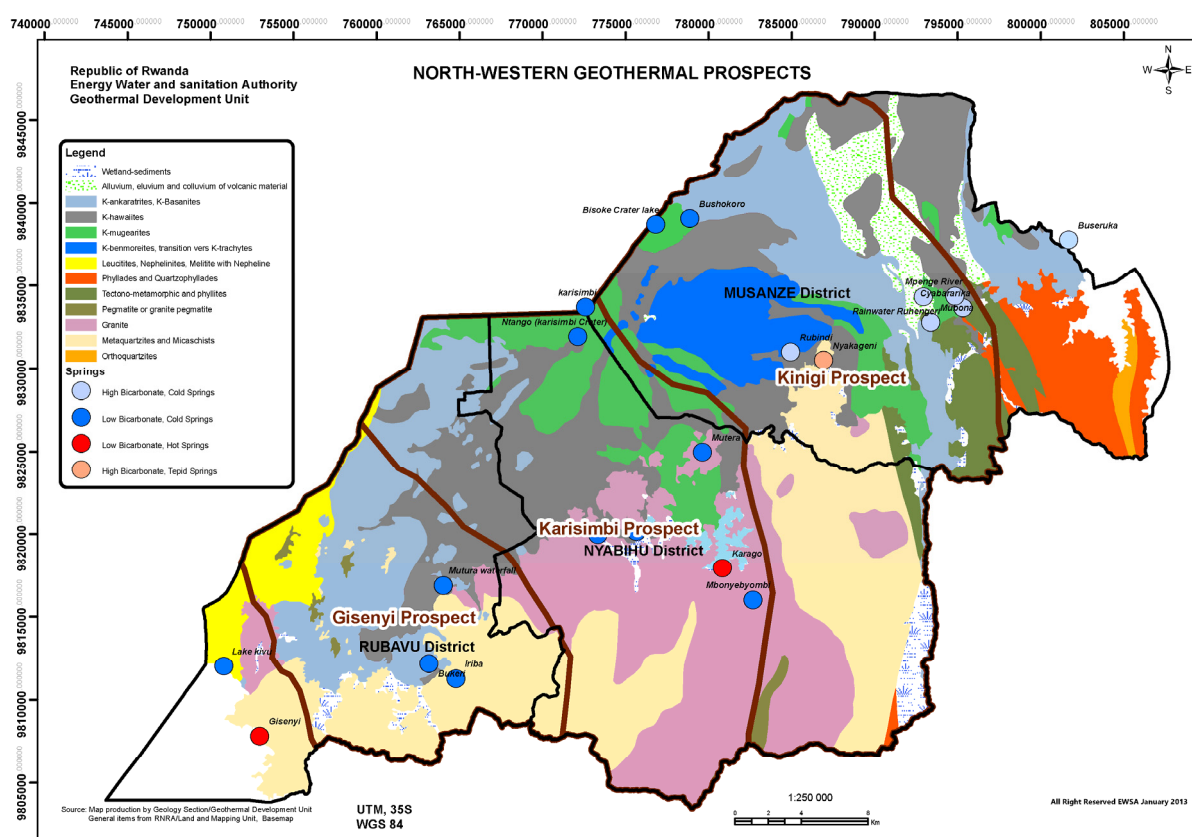


FIGURE 4: Geological map of geothermal prospects in NW-Rwanda

considering environmental aspects and infrastructure access. In mid-July 2013, Rwanda started drilling the first exploration wells (3 km deep) in the Karisimbi prospect and, hence, joined Kenya and Ethiopia in promoting the green and renewable energy resource in the region.

3. THERMAL WATER COMPOSITION IN THEISTAREYKIR AND NW-RWANDA

3.1 Thermal water composition in the Theistareykir field

The analytical data used in this report (Table 1) to classify the thermal water in the Theistareykir field consist of four composite samples from discharging wells (ThG-2, ThG-3, ThG-4 and ThG-5b) obtained from ÍSOR's database and two samples from warm springs from Ármannsson et al. (1986). Sampling and analysis were carried out by ÍSOR in conformity with sampling procedures described by Ármannsson and Ólafsson (2006). The wells discharged at the characteristic enthalpy of a mixture of liquid and vapour. Excess enthalpy for a discharging well is caused by boiling and phase segregation, explained in the following section. The water composition shows that Wells ThG-2 and ThG-5b tap fluid from a different aquifer than the rest of wells. The warm spring water is shallow steam heated groundwater.

3.1.1 Fluid aquifer assessment

After the collection of both water and steam samples with the aid of a Webre separator and recording the separation pressures, the steam fraction (water/steam ration) was calculated from the well discharge enthalpy. The aquifer fluid composition from wet-steam well data was assessed in two scenarios. In the first one, the well was considered to be a thermodynamically isolated system (no mass and heat transfer). In this case, only liquid water exists in the aquifer and the first level of boiling occurs within the well. The enthalpy of the total well discharge and its composition is the same as that of the water entering the well. Such situations are not always the case. When extensive boiling starts in a well's producing aquifers, both the discharge enthalpy and the total discharge composition may depart from those of the aquifer fluid. Under such circumstances, specific models are needed to connect well discharge and aquifer fluid composition (Arnórsson and Stefánsson, 2005).

The second scenario, in which the fluid is not regarded as an isolated system, may either be considered closed (heat is not conserved) or open (neither heat nor mass is conserved). In the former, the enthalpy is not a conserved quantity. Excess enthalpy (the discharge enthalpy is higher than that of liquid water at the aquifer temperature) would be produced by conductive heat flow from the aquifer rock to the fluid. In the latter, excess discharge enthalpy could result from the segregation of the flowing water and the steam in the aquifer. Difficulties in evaluating the relative importance of processes that result in excess discharge enthalpy lead to uncertainties in the calculation of the chemical composition of the aquifer fluid based on analytical data on water and steam samples collected at the wellhead (Arnórsson and Stefánsson, 2005; Arnórsson et al., 2007).

$$X = \frac{h^t - h^l}{h^v - h^l} \quad (1)$$

where X = Steam fraction;
 h^t = Total enthalpy of the fluid entering the well (kJ/kg);
 h^v = Enthalpy of vapour phase (kJ/kg); and
 h^l = Enthalpy of liquid phase (kJ/kg).

The steam fraction X is then used to calculate the deep liquid composition by using the following mass balance equation:

To calculate the steam fraction the Equation 1 is used:

$$C_i^t = C_i^v X + C_i^l(1 - X) \quad (2)$$

where C_i^t = Total concentration;
 C_i^v = Concentration in the vapour phase;
 C_i^l = Concentration in the liquid phase; and
 i = Chemical component of interest.

Some speciation and reaction path programs have been developed to compute concentrations of all chemical species present in deep aquifers. Among them are the WATEQ, PHREEQE, SOLVEQ and WATCH series. The last one was used in this report for the above mentioned purpose. WATCH is a computer programme that calculates the fluid aquifer composition based on the chemical analyses of samples collected at the surface and a reservoir temperature that may be arbitrary, measured or due to a suitable geothermometer. It computes the initial concentration of the chemical species present in the aquifer before they start ascending to the surface. Thus, it is possible to predict which minerals are likely to form or not from the knowledge of log Q (reaction quotient) and log K (equilibrium constant) values, calculated by WATCH. The programme gives two options for simulating the composition of aquifer fluids, i.e. by conductive cooling or boiling. The WATCH (version 2.4) technique was originally developed by Arnórsson et al. (1983), but the latest version is described by Bjarnason (2010).

3.1.2 Classification of geothermal water

It is useful to classify geothermal water before subjecting it to geochemical methods. The reason is that the water may not satisfy the premises of the geochemical computations. There are two common ways of classifying geothermal water, i.e. by the use of the Cl-SO₄-HCO₃, and the Na-K-Mg ternary diagrams (Giggenbach, 1991). The main purpose of this classification is to assess whether the sub-surface temperature can be predicted by the use of solute geothermometers. Geothermometers provide conclusive information if applied to what is denoted as “mature waters” that have reacted with bed rock minerals and reached equilibrium with them. They are characterized by high Cl concentrations compared to those of SO₄ and HCO₃. Cl is a conservative element that does not take part in mineral deposition and dissolution equilibria in geothermal fluids. Chloride-rich waters are generally found near the up-flow zones of geothermal systems. High SO₄ steam-heated waters are often encountered over the more elevated parts of a field. This diagram can be also used to assess possible mixing of groundwater and geothermal fluid as the degree of separation from the Cl corner towards the HCO₃ corner is the result of interaction of the CO₂ charged fluids at lower temperatures (Arnórsson, 2000).

TABLE 1: Representative chemical composition of wet-steam well discharges and springs in the Theistareykir high-temperature

Sample	Sample no				SP bar-g	h kJ/kg	Cond mS/cm	Liquid phase										Vapour phase							
	CO ₂ ppm	H ₂ S ppm	B ppm	SiO ₂ ppm				TDS ppm	Na ppm	K ppm	Mg ppm	Ca ppm	F ppm	Cl ppm	SO ₄ ppm	CO ₂ ppm	H ₂ S ppm	H ₂ %	N ₂ %	CH ₄ %					
ThG-2	20040276	6	917	636	66.1	29.7	0.53	380	750	139	14.5	0.003	0.83	0.73	43.7	40.6	2470	176	4.95	90.24	2.9				
ThG-3	20070023	25	1943	892	13.6	29.8	2.22	747	1258	166	41.2	0	1.34	0.76	225	5.53	1330	1177	94.89	4.36	0.58				
ThG-4	20080095	15.7	2661	432	24.4	26.5	3.95	663	978	76.1	17.1	0.019	0.22	1.42	88.3	3.22	155	820	94.38	5.47	0.04				
ThG-5b	20080503	15.3	1485	580	20.7	45.6	0.74	718.5	1027	120	30	0.002	0.37	1.07	49.3	18.3	4205	394	21.7	76.02	1.12				
V-1	19820630				191	0.1		104	400	76.3	7.48	11	49	0.1	9.3	105									
V-1					56.01	0.1		35.5	124	7.45	0.63	5.22	12.1	0.06	13.5	5.01									

SP = Sampling pressure; h = Enthalpy; ThG = Well; V = Spring

In the Theistareykir field, the samples from the warm springs exhibit bicarbonate waters. They plot in the peripheral waters zone, as shown in Figure 5. The presence of Mg in the springs indicates that they result from a mixture of thermal water and groundwater (Figure 6). Water samples from the wells plot at equilibrium and may be classified as Cl waters, except for the samples from Well ThG-2 which has HCO₃ water. The substantial HCO₃ concentration in the well water suggests that the water may derive from CO₂-rich steam condensing or mixing with water. This is sometimes the case with old geothermal waters or on the peripheries of geothermal areas in outflows. Such waters are commonly at equilibrium and may be used to predict subsurface properties (Ármannsson, 2012b).

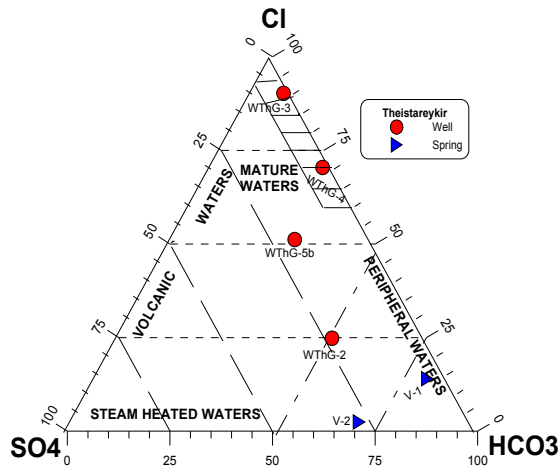


FIGURE 5: Cl-SO₄-HCO₃ ternary diagram for selected samples from the Theistareykir field

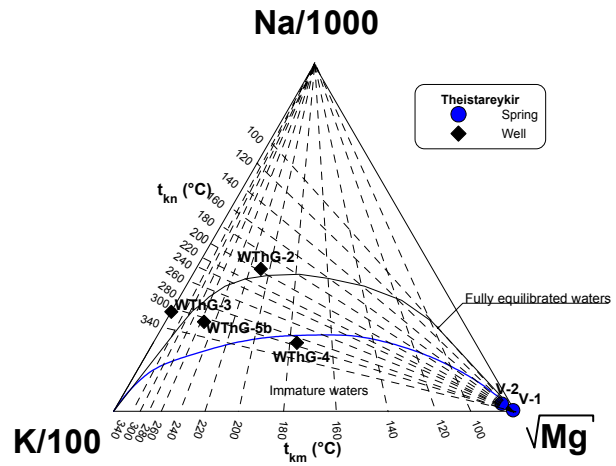


FIGURE 6: Na-K-Mg equilibrium diagram for Theistareykir water samples

3.1.3 Subsurface temperature estimation

Geothermometry is a technique used to predict sub-surface temperature in geothermal systems. It is based on the assumption that there is a temperature dependent equilibrium of the fluid in the aquifer with the rock for a given chemical or isotope composition that has been reached. A large number of geothermometers has been developed by several authors; the most used ones are the silica (quartz and chalcedony), Na/K and Na-K-Ca geothermometers (Árnórsson, 2000). The reservoir temperature was estimated by the help of WATCH and below there is a list of the geothermometers used in this report:

Chalcedony geothermometer, 20-330°C (Árnórsson et al., 1983):

$$t^{\circ}C = \frac{1112}{4.91 - \log S} - 273.15 \quad (3)$$

Quartz geothermometer, 20-330°C (Fournier and Potter, 1982):

$$t^{\circ}C = \frac{1309}{5.19 - \log S} - 273.15 \quad (4)$$

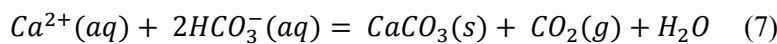
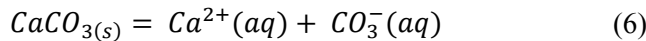
Na/K geothermometer, 25-250°C (Árnórsson et al., 1983):

$$t^{\circ}C = \frac{993}{0.993 + \log(Na/K)} - 273.15 \quad (5)$$

The values for subsurface temperatures (Table 2) range from 200 to 300°C for the wells and from 55 to 199°C for the springs. The chalcedony geothermometer yielded slightly low values, whereas the Na/K geothermometer produced relatively high values, except for Well ThG-2. For wells, the quartz geothermometer seemed to provide a reliable temperature, close to equilibrium with the deep liquid composition. Hence, Theistareykir area can be categorised as a high-temperature geothermal field.

3.1.4 Silica and calcite scaling assessment

Scaling is one of the problems encountered during geothermal utilization, caused by the nature of the fluid aquifer; the magnitude varies from one field to another. The best known scales are amorphous silica and calcite in producing wells, surface equipment and reinjection wells. Calcite starts to form within the well when boiling starts and its solubility decreases with an increase in temperature, contrary to silica solubility. The calcite solubility is dictated by Equation 6 while the precipitation reaction of calcite can be described by Equation 7.



Once the boiling has become intense, the CO_2 enters into a vapour phase, raising the pH of the fluid. When the fluid becomes oversaturated with respect to CaCO_3 , scales start to form. The dissolved silica in a geothermal system can lead to quartz and amorphous silica precipitation. However, it has been found that scaling from quartz never occurs because of its slow formation process. On the other hand, amorphous silica is of considerable concern in surface equipment and reinjection wells.

From the WATCH program results, it can be predicted whether a given mineral is likely to form or not by using the equation:

$$SI = \log\left(\frac{Q}{K}\right) \quad (8)$$

where SI = Saturation index;
 Q = Quotient of ionic activities; and
 K = Solubility product constant (function of temperature or pressure).

If $SI < 0$ under-saturated, mineral dissolves;
 $SI = 0$ saturated exactly, no mineral reaction; and
 $SI > 0$ supersaturated, mineral precipitates.

The water samples from the Theistareykir field have been scrutinized with respect to amorphous silica and calcite scaling and all probable scenarios were drawn in Figures 7 and 8. The saturation index was calculated for temperature values ranging from 100 to 287°C. The fluid from Well ThG-2 remains under-saturated with respect to amorphous silica for both adiabatic boiling and conductive cooling processes. However, upon adiabatic boiling, it became supersaturated with calcite; scaling is likely to occur in the well if the fluid boils at a temperature higher than 198°C.

Amorphous silica and calcite saturation with respect to the fluid is reached at 178°C and 220°C, respectively, in Well ThG-3 for adiabatic boiling. If the fluid is boiled below 178°C, amorphous silica scaling may take place, and calcite scaling at temperatures higher than 220°C. Conductive cooling below 150°C is likely to cause amorphous silica scaling. Regarding Well ThG-4, no calcite scaling is expected to take place; only boiling the fluid to below 160

TABLE 2: Calculated composition (in ppm) of the deep liquid for the representative samples from the Theistareykir field

	T (°C) Qtz	T (°C) Chal	T (°C) Na/K	B	SiO ₂	Na	K	Mg	Ca	F	Cl	SO ₄	Al	CO ₂	H ₂ S	NH ₃	H ₂	O ₂	CH ₄	N ₂	TDS
ThG-2	218	201.8	204.8	0.5	336.3	123.0	12.8	0.0	0.7	0.6	38.7	35.9	1.0	342.8	46.5	0.0	0.1	0.0	0.4	21.4	663.7
ThG-3	287.3	271.6	290.7	1.9	632.9	140.6	34.9	0.0	1.1	0.6	190.6	4.7	1.3	712.4	638.7	0.0	22.8	0.0	1.1	14.5	1065.8
ThG-4	270.3	257.2	301.3	3.4	566.2	65.0	14.6	0.0	0.2	1.2	75.4	2.8	1.6	146.0	765.6	0.0	36.4	0.0	0.1	29.2	835.3
ThG-5b	273.6	260	300.1	0.6	592.1	98.9	24.7	0.0	0.3	0.9	40.6	15.1	1.7	1370.0	158.0	1.4	1.1	0.0	0.4	52.2	846.3
V-1	139	112.3	199.2																		
V-1	86.8	55.3	184.9																		

T (°C) Qtz = Quartz geothermometer; T (°C) Chal = Chalcidony geothermometer; T (°C) Na/K = Na/K geothermometer

and 140°C may cause amorphous silica scaling for boiling and cooling, respectively. Finally, for Well ThG-5b, scaling by amorphous silica is possible for both boiling and conductive cooling below 160 and 140°C, respectively. Calcite is supersaturated, with respect to the fluid, up to 160°C upon boiling and to 240°C upon conductive cooling.

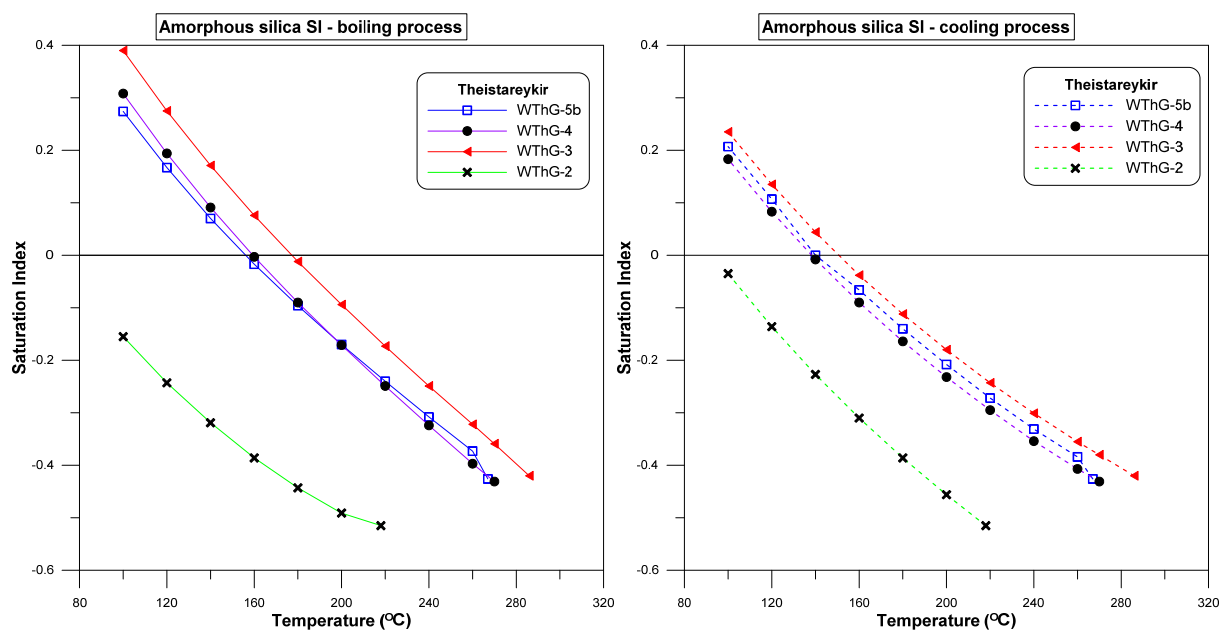


FIGURE 7: Amorphous silica, SI vs. temperature diagram for fluid from Theistareykir field

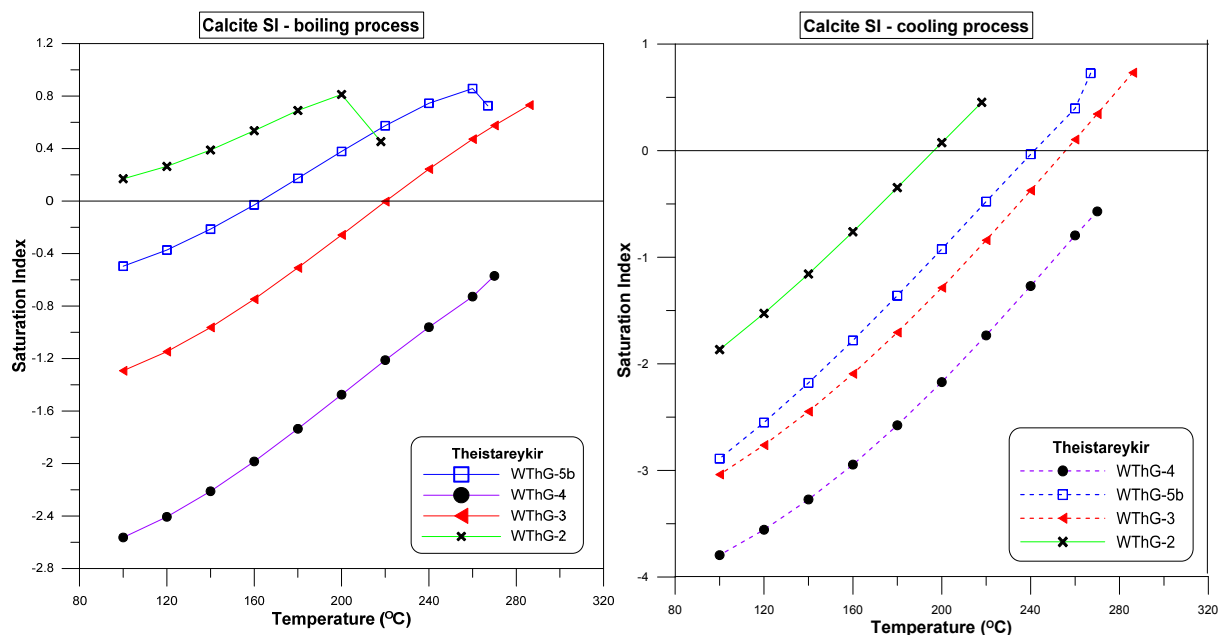


FIGURE 8: Calcite, SI vs. temperature diagram for fluid from Theistareykir field

3.2 Geochemistry of geothermal water in NW-Rwanda

The spring water samples, from northwest Rwanda, that were used in this report were collected by the Federal Institute for Geosciences and Natural Resources (BGR), Germany, in 2008 and were analysed by Iceland GeoSurvey (ÍSOR). The analytical data (Table 3) are reviewed and interpreted in this section.

TABLE 3: Water composition of selected springs in NW-Rwanda;
the concentrations are in mg/kg, unless otherwise stated

Sample	T°C	pH	Na	K	Ca	Mg	SiO ₂	B	Cl	Al	F	SO ₄	HCO ₃	Fe	Mn	δ ¹⁸ O	δ ² H
Gisenyi	73.1	6.68	495	38	35	11.2	56.2	2.1	195	0.016		55.8	1140	0.3		-3.5	-9.7
Karago	64.1	7.12	253	15	21	2.4	84	0.3	77	0.011		77.9	537	0	0.17	-3.72	-12.4
Mpatsi	31.2	6.75	208	23	144	16.8	86.3	1.3	41	0.006		31.2	1050	0.2	0.14	-3.61	-11.2
Iriba	22.3	7	394	17	77	23.2	58.3	0.4	287	0.051		67	846	2.2	0.23	-3.44	-8.8
Mbonyebyombi	34.5	7.04	187	12	20	2.4	60.3	0.2	52	0.02	5.48	44.2	414	0.7	0.16	-3.86	-12.8
Nyakageni	20.5	6.9	229	43	71	23.2	62.7	0.7	73	0.444	3.1	31.5	854	12	0.3	-2.7	-5.7

According to the classification of geothermal water made by Giggenbach (1991), the selected springs are mainly characterized by HCO₃⁻ rich waters and low Cl, as shown in the Cl-SO₄-HCO₃ ternary diagram (Figure 9). Thus, the springs are probably the result of a heated geothermal fluid from the deep reservoir reaching the surface and mixing with shallow groundwater. This is confirmed by the presence of magnesium in the spring water (see Na-K-Mg diagram in Figure 10). Depleted in geothermal water, its presence reveals the cold groundwater inflow into the system. The water classification above does not confirm whether the given water is of geothermal origin or not. However, when waters are classified as Cl-rich or mature, there is an increased assurance that the use of geothermometers to estimate the reservoir temperature will give reliable results. This classification of hot and warm springs from NW Rwanda is consistent with the classification made by Ármannsson and Eyjólfsson (2009).

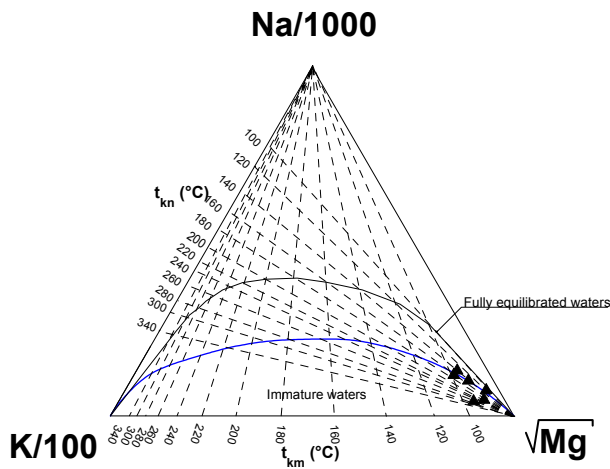


FIGURE 9: Cl-SO₄-HCO₃ Ternary diagram for selected springs in NW Rwanda

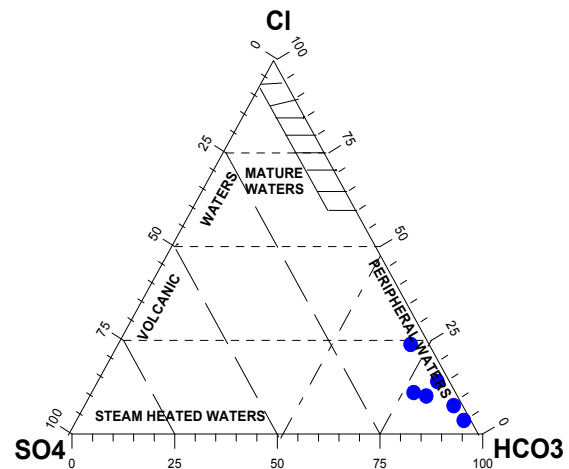


FIGURE 10: Na-K-Mg Ternary diagram for selected springs in NW Rwanda

The quartz (Fournier and Potter, 1982) and chalcedony (Fournier, 1977) geothermometers gave temperature values ranging from 80 to 129°C. The Na/K geothermometer (Árnórsson et al., 1983) yielded higher values from 142 to 270 °C. The discrepancy could arise because the selected water samples may not yet have reached full equilibrium, confirmed in Figure 10. The temperature values for the selected samples are shown in Table 4. In most cases, the chalcedony geothermometer seems to give reliable temperature values, as it is close to equilibrium with all waters.

The results of the stable isotope determinations (δ¹⁸O and δ²H) suggest that the spring water is of meteoric origin as they plotted near the world meteoric line and the Kenya rain line in Figure 11. This means that the thermal water was derived from local surface water that infiltrated deep layers and then mined the heat from the host rocks (Craig, 1963). However, the isotope composition of NW Rwanda waters needs to be studied to improve the accuracy of these analyses because the meteoric lines used might not tell the whole story. In order to estimate the thermal water content of the mixed water, we

used the silica enthalpy model (Figure 12). Unfortunately, the results plot horizontally, making them unsuitable for use in the model. Drilling results will help to elucidate the thermal water composition.

TABLE 4: Measured surface temperatures and calculated subsurface temperatures for selected springs in NW Rwanda

Sample	Measured T (°C)	Qrtz T (°C)	Chal T (°C)	Na/K T (°C)
Gisenyi	73.1	107.7	77.8	172.7
Karago	64.1	127.8	99	142
Mpatsi	31.2	129	101.6	212.5
Iriba	22.3	109.4	79.7	122.2
Mbonyebyombi	34.5	111	81.4	149.2
Nyakageni	20.5	112.9	83	270.4

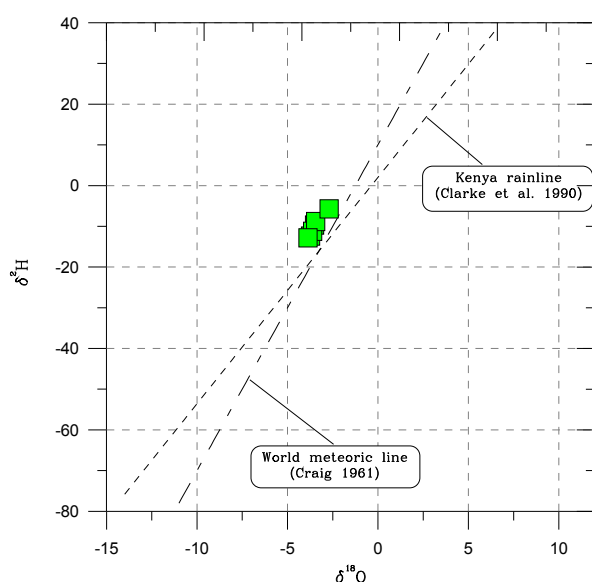


FIGURE 11: Isotopes for selected springs in NW Rwanda

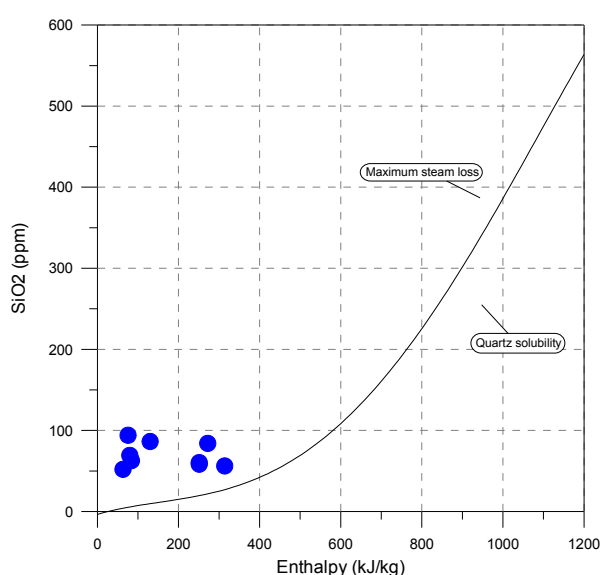


FIGURE 12: Silica mixing model for selected springs in NW Rwanda

4. RESULTS, DISCUSSION AND COMPARISON

In the Theistareykir field there is a fundamental difference between the water composition of the warm springs and the discharge wells. The spring waters are rich in Mg and HCO_3 whereas well waters are not. The presence of Mg implies groundwater origins, but the fact that the springs' temperatures at the surface are 24 and 34°C suggests that the springs are getting their water from steam-heated groundwater. This difference has been proven by isotope analysis where the warm spring water plots close to local rainwater and the geothermal fluid is not of local origin, as discussed by Darling and Ármannsson (1989). The thermal water is considered to originate from precipitation far to the south, flowing along the fissure swarm and conductively heated. There were differences in the water composition between the wells, suggesting that different aquifers provided their fluid. Thus, there are shallow and deep aquifers in the Theistareykir system. This is in agreement with the subdivision of Theistareykir into 5 sub areas, dependent on the discharge fluid and the conceptual model of the system (Gudmundsson et al., 2008).

On the other hand, the thermal water from the northwest prospects of Rwanda appears to originate from local precipitation, as indicated by isotope analysis. Two scenarios may explain the thermal activity of the few warm springs encountered there. In the first one, the warm water may result from heated groundwater, as is the case in Theistareykir field. The second scenario proposes the mixing of shallow groundwater with geothermal fluid ascending from a deep aquifer. The nature of the water samples did not allow any use of common mixing models to estimate the amount of the hot water content in the mixed waters. When trying to use the silica enthalpy model, all samples plotted horizontally, making it difficult to apply this model. Presently, the two scenarios remain debatable. Most likely the drilling results will help to decide which model is applicable.

4.1 Comparison between the Theistareykir field and the geothermal prospects in NW-Rwanda

The reservoir regime of the Theistareykir field is complex; there exist several aquifers, all drawing fluid from the same reservoir. In addition, there is mixing of geothermal fluid and shallow ground water in some aquifers. Water discharged at the surface by springs is different from that of the deep fluid. In the geothermal prospects in NW Rwanda, the surface manifestations do not seem to reflect deep aquifer properties. A convective geothermal system may have been formed in such a tectonically active environment. The high rainfall and pronounced rock permeability in this volcanic prospect could certainly suppress the surface manifestations of a geothermal system below.

In contrast with the Theistareykir field, where the geothermal activity is related to the most recent volcanic activity in the area which took place some 2500 years ago (Óskarsson et al., 2013), the prevailing geothermal systems in the prospects in NW Rwanda are associated with Quaternary activity. The geothermal fluid would probably be derived from local precipitation, which is not the case for Theistareykir. The drilling results in NW Rwanda will give a considerable clarification, as far as similarities and dissimilarities with regard to Theistareykir are concerned.

5. CONCLUSIONS

The chemical composition of spring waters and well discharges in Theistareykir shows that the geothermal water can be classified as Na-Cl or HCO_3 rich water, in general. All wells and springs discharge distinct fluid in chemical composition. This simply indicates that the prevailing reservoir of the geothermal system consists of many aquifers, some shallow, others deep. The warm water in the springs might be steam-heated shallow water. The subsurface temperatures confirm Theistareykir as a high-temperature geothermal field, as the calculated temperatures for the geothermal fluids are higher than 270°C , except for those from ThG-2 which draws fluid of 218°C , taking the quartz geothermometer temperature as the reference temperature. From the WATCH programme calculations, scaling from amorphous silica on surface materials and in reinjection wells is, in most cases, likely to take place if the fluid is separated at temperatures below 160°C . Calcite may pose problems in wells, too.

The thermal waters from the geothermal prospects in NW Rwanda are characterized as Na- HCO_3 waters that have not reached full equilibrium. The significant HCO_3 and Mg concentrations suggest the water to be of groundwater origins. The thermal water might be steam heated groundwater and may not necessarily reflect subsurface properties. Mixing of geothermal fluid with shallow water is not excluded from the likely scenarios, unless drilling results prove otherwise. When trying to apply mixing models, the results were not conclusive.

The Theistareykir field and the geothermal prospects in NW Rwanda host warm springs at the surface that do not necessarily reflect the deep reservoir properties. Mixing of geothermal fluid with shallow groundwater may take place in NW Rwanda.

ACKNOWLEDGEMENTS

I am very eager to thank the Government of Iceland and the United Nations University Geothermal Training Programme (UNU-GTP) under the leadership of Mr. Lúdvík S. Georgsson (Director) and Dr. Ingvar B. Fridleifsson (former Director) for awarding me the UNU Fellowship in the Chemistry of Thermal Fluids. My acknowledgement goes also to the Energy, Water and Sanitation Authority (EWSA), my employer, for allowing me to attend this training. I am thankful to my supervisors, Dr. Halldór Ármannsson and Dr. Thráinn Fridriksson, for their valuable advice, suggestions and for sharing their knowledge for my project. Many thanks go to Ms. Thórhildur Ísberg, Ms. Málfríður Ómarsdóttir, Mr. Ingimar G. Haraldsson and Mr. Markús A. G. Wilde, UNU-GTP staff, for their daily assistance and training facilitation through the 6 months. I wish to extend my gratitude to all lecturers for their informative presentations; I have been inspired by each and every one of you.

My heartfelt thanks go to my wife, Nirere M. Grace, for her moral support, patience and continuous care of our son, Mpano N. Franklin, for the period I have been away from home.

REFERENCES

- Ármannsson, H., 2012a: The Theistareykir geothermal system, North East Iceland: Case history. *Paper presented at "Short Course VII on Surface Exploration for Geothermal Resources", organized by UNU-GTP, GDC and KenGen, at Lake Bogoria and Lake Naivasha, Kenya*, 11 pp.
- Ármannsson, H., 2012b: Geochemical aspects of geothermal utilization. In: Sayigh, A. (ed.), *Comprehensive renewable energy*, vol. 7. Elsevier, Oxford, 95-168.
- Ármannsson, H., and Eyjólfsson, I.E., 2009: *Interpretation of geochemical data for Rwanda*. ÍSOR – Iceland GeoSurvey, Reykjavík, report ISOR-2009/022, prepared for BGR, 18 pp.
- Ármannsson, H., and Ólafsson, M., 2006: *Collection of geothermal fluids for chemical analysis*. ÍSOR, Reykjavík, report ISOR-2006/016, 17 pp.
- Ármannsson, H., Gíslason, G., and Torfason, H., 1986: Surface exploration of the Theistareykir high-temperature geothermal area, with special reference to the application of geochemical methods. *Applied Geochemistry*, 1, 47-64.
- Arnórsson, S. (ed.), 2000: *Isotopic and chemical techniques in geothermal exploration, development and use. Sampling methods, data handling, interpretation*. International Atomic Energy Agency, Vienna, 351 pp.
- Arnórsson, S., and Stefánsson, A., 2005: Wet-steam well discharges. II. Assessment of aquifer fluid compositions. *Proceedings of the World Geothermal Congress 2005, Antalya, Turkey*, 11 pp.
- Arnórsson, S., Gunnlaugsson, E., and Svavarsson, H., 1983: The chemistry of geothermal waters in Iceland III. Chemical geothermometry in geothermal investigations. *Geochim. Cosmochim. Acta*, 47, 567-577.
- Arnórsson, S., Stefánsson, A., and Bjarnason, J.Ö., 2007: Fluid-fluid interaction in geothermal systems. *Reviews in Mineralogy & Geochemistry*, 65, 229-312.
- BGR, 2009: *Geothermal potential assessment in the Virunga geothermal prospect, Northern Rwanda*. Federal Institute for Geosciences and Natural Resources (BGR), final report, 104 pp.

Bjarnason, J.Ö., 2010: *The speciation program WATCH, Version 2.4, user's guide*. The Iceland Water Chemistry Group, Reykjavík, 9 pp.

Clarke, M.C.G., Woodhall, D.G., Allen, D.J., and Darling, W.G., 1990: *Geological, volcanological and hydrogeological controls on the occurrence of geothermal activity in the area surrounding Lake Naivasha, Kenya*. Kenyan Ministry of Energy and British Geological Survey, 138 pp.

Craig, H., 1961: Isotopic variations in meteoric waters. *Science*, 133, 1702-1703.

Craig, H., 1963: The isotopic geochemistry of water and carbon in geothermal areas. In: Tongiorgi, E. (ed.), *Nuclear geology on geothermal areas*. Consiglio Nazionale delle Ricerche, Laboratorio di Geologia Nucleare, Pisa, 17-53.

Darling, W.G., Ármannsson, H., 1989: Stable isotopic aspects of fluid flow in the Krafla, Námafjall and Theistareykir geothermal systems of Northeast Iceland. *Chemical Geology*, 76, 175-196.

Fournier, R.O., 1977: Chemical geothermometers and mixing model for geothermal systems. *Geothermics*, 5, 41-50.

Fournier, R.O., and Potter, R.W., 1982: An equation correlating the solubility of quartz in water from 25° to 900°C, at pressures up to 10,000 bars. *Geochim. Cosmochim Acta*, 46, 1969-1973.

Gautason, B., Ármannsson, H., Árnason, K., Sæmundsson, K., Flóvenz, Ó.G., and Thórhallsson, S., 2000: *Thoughts on the next steps in the exploration of the Theistareykir geothermal area* (In Icelandic). Orkustofnun, report BG-HÁ-KÁ-KS-ÓGF-STh-2000/04, 11 pp.

Gautason, B., Gudmundsson, Á., Hjartarson, H., Blischke, A., Mortensen, A.K., Ingimarsdóttir, A., Gunnarsson, H.S., Sigurgeirsson, M.Á., Árnadóttir, S., and Egilson, Th. 2010: Exploration drilling in the Theistareykir high-temperature field, NE-Iceland: Stratigraphy, alteration and its relationship to temperature structure. *Proceedings of the World Geothermal Congress 2010, Bali, Indonesia*, 5 pp.

Georgsson, L.S., Sæmundsson, K., and Hjartarson, H., 2005: Exploration and development of the Hveravellir geothermal field, N-Iceland. *Proceedings of the World Geothermal Congress 2005, Antalya, Turkey*, 10 pp.

Giggenbach, W.F., 1991: Chemical techniques in geothermal exploration. In: D'Amore, F. (coordinator), *Application of geochemistry in geothermal reservoir development*. UNITAR/UNDP publication, Rome, 119-144.

Gudmundsson, Á., Gautason, B., Lacasse, C., Axelsson, G., Thorgilsson, G., Ármannsson, H., Tulinius, H., Sæmundsson, K., Karlsdóttir, R., Kjaran, S.P., Pálmarsson, S.Ó., Halldórsdóttir, S., and Egilson, Th., 2008: *Conceptual model of the Theistareykir geothermal area and the evolution of the geothermal resource by the volumetric method*. ÍSOR – Iceland GeoSurvey, Mannvit and Vatnaskil, report ÍSOR-2008/024, MV-049 and Vatnaskil 08.05 (in Icelandic), 67 pp.

Gupta, K., and Roy, S., 2007: *Geothermal energy, an alternative resource for the 21st century*. Elsevier, New York, NY, United States, 293 pp.

Mariita, N.O. (ed.), 2010: *Geothermal potential appraisal of Karisimbi prospect, Rwanda*. KenGen, Kenya, report, 150 pp.

Omenda, P.A., 2011: The geology and geothermal activity of the East African Rift. *Paper presented at "Short Course V on Exploration for Geothermal Resources", organized by UNU-GTP, GDC and KenGen, at Lake Bogoria and Lake Naivasha, Kenya*, 18 pp.

Óskarsson, F., Ármannsson, H., Ólafsson, M., Sveinbjörnsdóttir, Á.E., and Markússon, S.H., 2013: The Theistareykir geothermal field, NE Iceland: fluid chemistry and production properties. *Procedia Earth and Planetary Science*, 7, 644-647.

Shalev, E., Brown, P., Wameyo, P., Hochstein, M., Palmer, J., and Fenton, R., 2012: *Geoscientific survey of Rwandan Kalisimbi, Gisenyi and Kinigi geothermal prospects*. University of Auckland, Institute of Earth Science and Engineering (IESE), report, 209 pp.



BOREHOLE GEOLOGY AND HYDROTHERMAL ALTERATION MINERALOGY OF WELL OW-39A, OLKARIA GEOTHERMAL PROJECT, NAIVASHA, KENYA

Joyce Atieno Okoo

Kenya Electricity Generating Company, Ltd.
Olkaria Geothermal Project
P.O. Box 785-20117, Naivasha,
KENYA
jokoo@kengen.co.ke

ABSTRACT

Well OW-39A is a directional well drilled to the south at an azimuth of 180° and inclination of 20° to a measured depth (MD) of 3066 m, adjacent to the Ololbuttot N-S trending eruptive fissure. Comprehensive binocular and petrographic analyses of cuttings from the well indicate that the lithology of the well comprises five rock units, i.e. pyroclasts, rhyolites, tuffs, basalts, and trachytes and then intrusions of rhyolitic, syenitic, basaltic, and granitic composition. Trachyte forms the main reservoir rock and it is the dominant rock below 900 m. These rock units host secondary hydrothermal mineral assemblages which are dependent on temperature, permeability and rock type. Mineral deposition sequences in the well show systematic evolution from low to high temperature conditions with depth, as observed from alteration minerals in veins and vesicles. Five alteration zones were identified: an unaltered zone (0-134 m), a zeolite- smectite-illite zone (134-578 m), a chlorite-illite zone (578-748 m), an epidote-chlorite-illite zone (748-896 m) and an actinolite-epidote-wollastonite zone (896-3066). The appearance of epidote at 750 m and actinolite at 896 m indicates temperatures of 250 and 280°C, respectively, at these depths. A comparison of fluid inclusion analyses, alteration and formation temperature indicates two geothermal episodes, one of a high temperature geothermal system below 700-800 m depth and a recent second phase of cooling. Permeability is observed in the cuttings by the intensity of oxidation, veining, alteration intensity, circulation losses, the presence of calcite, and an abundance of pyrite. Eight feed zones are identified in the well starting from 750 down to 2750 m, deduced from the shape of temperature profiles, and their locations correlate with the cutting data as mentioned above. The intermediate feed zone at 1100 and the major feed zone at the 2100 m are considered the dominant ones in the well.

1. INTRODUCTION

1.1 General information

The Greater Olkaria Geothermal Area (GOGA) is situated southwest of Lake Naivasha in the eastern arm of the African Rift Valley in Kenya (Figure 1). The rift is part of the East African Rift system that

runs from the Afar triple junction at the Gulf of Aden in the north to Beira, Mozambique in the south (Lagat 2004).

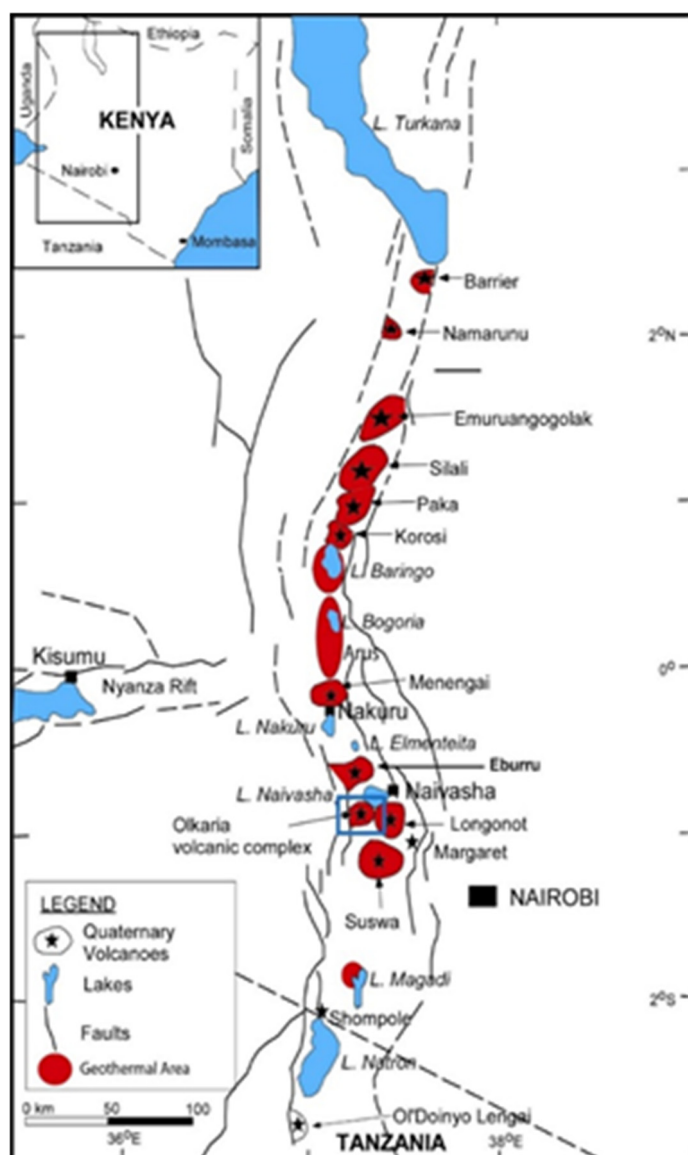


FIGURE 1: Map of Kenya showing the location of Olkaria geothermal field and other Quaternary volcanoes along the rift axis

MWe. Currently, construction is underway for Olkaria I (140 MWe) units 4 and 5 in Olkaria East field and Olkaria IV (140 MWe) units 1 and 2 in Domes field (Figure 2).

1.2 Well OW-39A

Well OW-39A is located in the Olkaria East production field, (Figure 2) defined by UTM E 0198168, N 9901777 and an elevation of 2158 m a.s.l. It is a directional well drilled to the south at an azimuth of N 180°E and an inclination of 20° to a measured depth (MD) of 3066 m. The surface, anchor and production casings were set at 50.2, 292, and 750 m, respectively. It was designed as a production well with the aim of tapping steam from Ololbutot fissure, which is a N-S trending eruptive fissure, and also to confirm the importance of this structure, given the fact that it is associated with the most active surface manifestations in Olkaria.

This segment of the eastern arm of the rift, also called the Kenyan Rift, extends from Lake Turkana in Northern Kenya, where the earliest volcanic rocks in the Kenyan Rift have been found (MacDonald et al., 2001), to Lake Natron in northern Tanzania. The Rift is part of a divergent zone where spreading occurs, resulting in thinning of the crust, eruption of lavas and associated volcanic activities. It crosses two regions of topographic uplift, the Ethiopian and Kenyan Domes, both regarded as the surface manifestation of underlying mantle plumes (Thiessen et al., 1979). The Kenya Dome is associated with more than 1 km of uplift, but is apparently in isostatic equilibrium, supported by the loading of an anomalous mantle within the underlying lithosphere (Smith, 1994). The Olkaria volcanic complex is bounded to the north by the Eburru complex and to the east and south by the Longonot and Suswa volcanoes, respectively. Olkaria geothermal field is divided into smaller sectors (Figure 2) namely: East, Northeast, West, South, Domes and Central Olkaria, all relative to the position of the Olkaria volcanic centre and for ease of development. Power production started in Olkaria East field in 1981 where the first 15 MWe power plant was commissioned. Currently, the production is 45 MWe. Olkaria II power plant, located in the Olkaria Northeast field, was opened in 2003 and currently produces 105 MWe. The third plant, located in Olkaria Northwest field, owned by OrPower, an independent power producer, generates 48

2. GEOLOGY

2.1 Geological setting

According to Baker et al. (1971, 1972) and Smith and Mosley (1993), the African Rift is structurally controlled and was formed due to tectonic activities involving faulting and fracturing at the collisional zones between the Archean Tanzania craton and the Proterozoic orogenic belts. The Greater Olkaria volcanic complex, which is located in the African Rift, is characterized by numerous volcanic centres of Quaternary age (Macdonald et al., 1987; Marshall et al., 2009). These volcanic centres appear as steep-sided domes formed by successions of lavas and/or pyroclastic rocks, or as thick lava flows of restricted lateral extent. Magmatic activities, associated with this complex, commenced during the late Pleistocene and continue to Recent times, as indicated by the Ololbutot comendite lava, which has been dated at 180 ± 50 yrs B.P (Clarke et al., 1990). It is the only occurrence of surface comendite within the Kenya Rift (Lagat, 2004).

Other Quaternary volcanic centres adjacent to the Olkaria Volcanic complex include Longonot volcano to the east, Suswa caldera to the south, and the Eburru volcanic complex to the north (Figure 1). Whereas the other volcanoes are associated with calderas of varying sizes, the Olkaria volcanic complex does not have a clear caldera subsidence structure. The presence of a ring of volcanic domes in the east, south, and southwest (Figure 3) has been used to invoke the presence of a buried caldera (Naylor, 1972; Virkir, 1980; Clarke et al., 1990; Mungania, 1992). Seismic wave attenuation studies for the whole of the Olkaria area have also indicated an anomaly in an area coinciding with the proposed caldera (Simiyu et al., 1998). Other studies on Olkaria have not identified the existence of the caldera, e.g. resistivity studies did not map a clear discontinuity at the margin of the proposed caldera (Onacha, 1993). Ignimbrite flows that could have been associated with the caldera collapse have not been positively identified in Olkaria (Omenda, 1998). Furthermore, petrochemistry of lavas within the Olkaria area shows that they were produced from discrete magma chambers (Omenda, 2000). Another explanation for the proposed caldera hypothesis is that the ring structure was formed by magmatic stresses in the Olkaria “magma chamber” with the line of weakness being loci for volcanism (Omenda, 2000).

2.2 Structural geology

The geological structures (Figure 3) within the Greater Olkaria volcanic complex include: the ring structure, rift fault systems, the Ol’Njorowa gorge, and dyke swarms. The faults trend ENE-WSW, N-

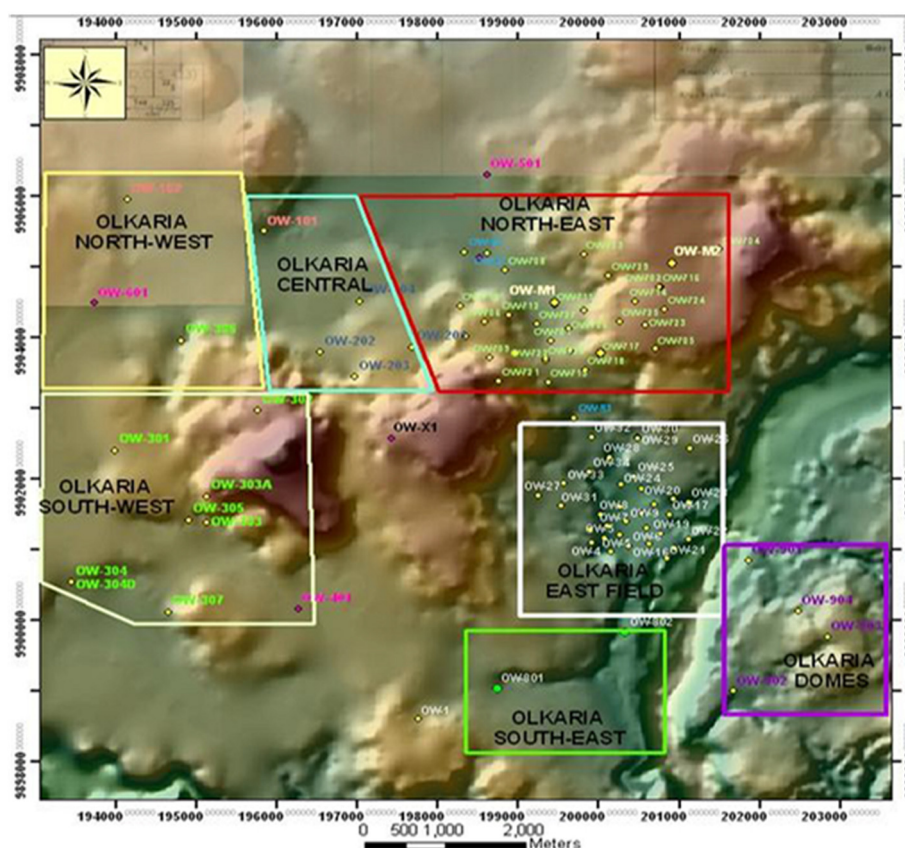


Figure 2: Location map of Well OW-39A and geothermal fields in the Greater Olkaria geothermal area (KenGen, 2000)

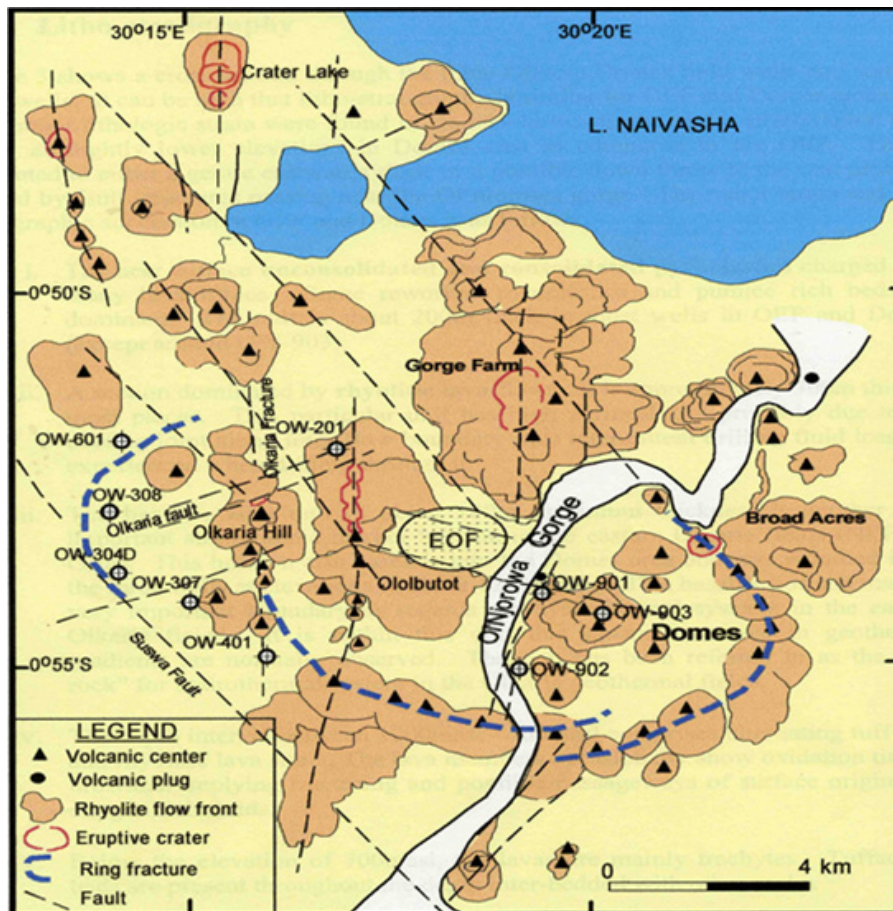


FIGURE 3: Structural map of Greater Olkaria geothermal area (modified from KenGen, 2000)

S, NNE-SSW, NW-SE and WNW-ESE. These faults are more prominent in the East, Northeast and West Olkaria fields, but are scarce in the Olkaria Domes area, possibly due to the thick pyroclastic cover (Lagat, 2004). The NW-SE and WNW-ESE faults are thought to be the oldest fault system and they link the parallel rift basins to the main extensional zone (Wheeler and Karson, 1994). Gorge Farm fault is the most prominent of these faults. It bounds the geothermal fields in the northeast part and extends to the Olkaria Domes area. The most recent structures are the N-S (Ololbutot eruptive fissure) and the NNE-SSW faults. Dyke swarms exposed in the Ol'Njorowa gorge trend

in a north-northeasterly direction, further attesting to the recent reactivation of faults with that trend. The development of the Ol'Njorowa gorge was initiated by faulting along the trend of the gorge but the feature, as it is seen today, was mainly formed due to a catastrophic outflow of Lake Naivasha during its high stands (Clarke et al., 1990). Volcanic plugs (necks) and felsic dykes occurring along the gorge further attest to the fault control in the development of this feature. Subsurface faults have been encountered in most Olkaria wells, as reported in geological well reports (Ryder, 1986; Lagat, 1998, 2004; Muchemi, 2000; Otieno and Kubai, 2013; Mwanja et al., 2013). Hydroclastic craters located on the northern edge of the Olkaria Domes area mark magmatic explosions which occurred in submerged country (Mungania, 1999). These craters form a row along which the extrapolated caldera rim trace passes.

2.3 Subsurface and surface geology

The subsurface geology of the Olkaria geothermal field can be divided into five broad lithostratigraphic groups (Figure 4) based on age, tectono-stratigraphy and lithology, as revealed by data from more than eighty deep wells in the geothermal area (Omenda, 2000). The formations are: the Proterozoic "basement" formations; Mau tuffs; Plateau Trachytes; Olkaria Basalt; and Upper Olkaria Volcanics.

The basement consists mainly of Proterozoic amphibolite grade gneiss, schists and associated marble and quartzites of the Mozambiquan group (Shackleton, 1986; Mosley, 1993; Smith and Mosley, 1993). The rocks are not exposed in Olkaria. Reflection seismic, gravity and geological correlations indicate that the depth to the "basement" is about 5-6 km in the Central Kenya Rift (Simiyu, 1996; Simiyu and

Keller, 1997). Seismic and gravity studies indicate the presence of a high-density magmatic intrusion in the metamorphic “basement” rocks (Baker and Wohlenberg, 1971; Baker et al., 1971; Simiyu, 1996). The Pre-Mau formation is composed of trachytes, basalts and ignimbrites and is not exposed in the area, but there are outcrops on the rift scarps in parts of the southern Kenya Rift. These rocks are directly overlain by the Mau tuffs that are Pliocene in age.

Mau tuffs are the oldest rocks that are exposed in the Olkaria area. These rocks are common in the area west of Olkaria Hill (Figure 3), but are absent in the east due to an east dipping high angle normal fault that passes through Olkaria Hill (Omenda 1994, 1998). The rocks vary in texture from consolidated to ignimbritic tuffs and are the main geothermal reservoir rocks in the Olkaria west field (Lagat, 2004).

Plateau trachytes have been encountered in Olkaria wells and consist mainly of trachytic lavas with intercalations of basalt, tuff and rhyolite. These are of Pleistocene age and occur in the area east of Olkaria Hill where a graben existed prior to their eruptions (Omenda, 1994, 1998). These rocks act as host rock for the Olkaria geothermal field (Ogoso-Odongo, 1986; Omenda, 1994, 1998; Lagat, 2004).

Olkaria basalt is also of Pleistocene age and the formation consists of basaltic flows, separated by thin tuff layers, minor pyroclastic deposits, trachytes and occasional rhyolites. It varies in thickness from 100 m to 500 m, underlying the Upper Olkaria volcanics. From reservoir modelling (Haukwa, 1984; Ambusso and Ouma, 1991) and hydrothermal studies (Browne, 1984; Leach and Muchemi, 1987; Muchemi, 1992; Omenda, 1998) the formation is believed to form the cap-rock of the Olkaria geothermal system.

Upper Olkaria volcanics, which are of mid Pleistocene to Recent age, occur from the surface down to about 500 m depth. They consist of comendite lavas and their pyroclastic equivalents, ashes from Suswa and Longonot volcanoes and minor trachytes and basalts (Thompson and Dodson, 1963; Clarke et al., 1990; Omenda, 1998). Comendite is the dominant rock in this formation. The youngest of these lavas is the Ololbutot comendite, which has been dated at 180 ± 50 yrs (Clarke et al., 1990).

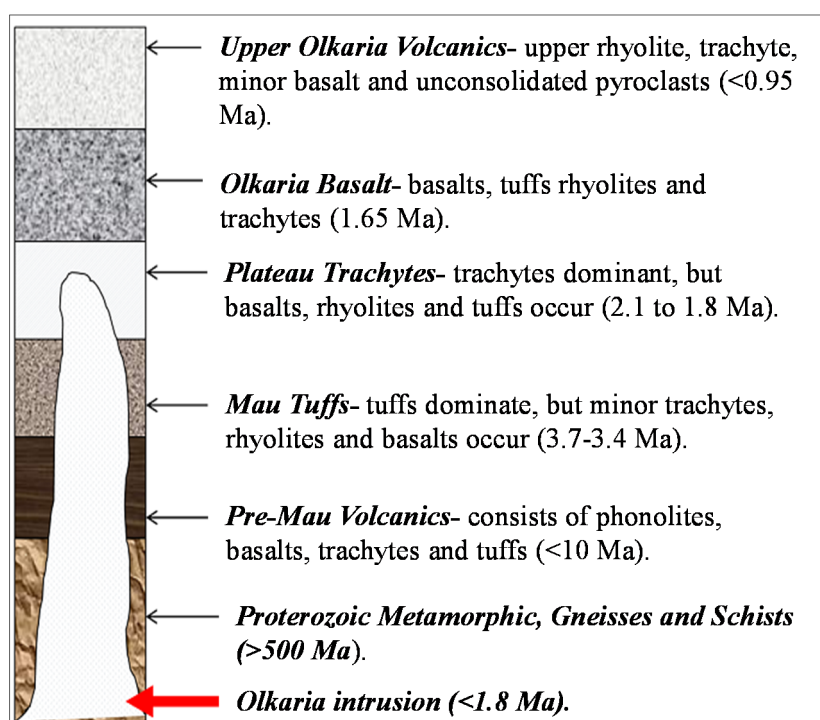


FIGURE 4: Stratigraphic column of the Olkaria volcanic complex (modified from Omenda, 2000)

3. SAMPLING AND ANALYTICAL METHODS

3.1 Sampling

Samples of cuttings from Well OW-39A were taken at each 2 m interval at the drill site during drilling, but in cases where the sample was too small, up to a 4 m depth interval was sampled. Preliminary analysis was done at the rig site by the use of a binocular microscope, to enable the geologists and drillers to understand the subsurface geological formations and conditions, which assisted in applying the right drilling procedures. Representative samples of the rock units encountered in the well were then selected for detailed laboratory analysis of hydrothermal alteration minerals and fluid inclusion studies.

3.2 Analytical methods

3.2.1 Stereo microscope analysis

Drill cuttings sampled at 2 m intervals were scooped from the sample bags using a petri dish. The sample was then washed thoroughly with clean water to remove impurities and dust. Water added onto the cuttings to enhance visibility of the sample and obscure features such as finely disseminated sulphides, e.g. pyrite. The sample was then placed on the mounting stage of an Olympus SX16 binocular microscope for analysis by noting essential features such as: colour(s) of the cuttings, rock type(s), grain size, rock fabrics, original mineralogy, alteration mineralogy and intensity.

3.2.2 Petrographic microscope analysis

Representative samples from selected lithological units encountered in the well were selected and 72 thin sections were prepared for petrographic studies. The thin sections were then mounted on a Leica petrographic microscope for analysis. Petrographic analysis is used to study the mineralogical evolution, confirm the rock type(s), the alteration minerals, and any additional alteration minerals not observed by the binocular microscope.

3.2.3 X-ray diffraction analysis

Samples were selected from representative lithological units and analysed for clays. The <2 microns fractions were prepared for X-ray diffraction by crushing the rock into a fine powder. The crushed sample was placed in a test tube, distilled water was added to dissolve the constituents, then the test tube was shaken and left in a rack so that the <2 microns phyllosilicates were left in suspension. A few drops were placed on a marked glass slide and left to dry so that the sample could be analysed using the XRD equipment. Ethylene glycol was added to the air dried sample and then the sample was heated to between 500-550°C. The samples were analysed in the XRD equipment after each treatment to identify the different types of clays based on the peak locations and the intensity in the XRD spectra.

3.2.4 Fluid inclusion analysis

Fluid inclusions are "bubbles" of fluid trapped within the host mineral during its deposition from its parent hydrothermal fluid. Fluid inclusions can be either primary or secondary. Primary fluid inclusions are trapped in the crystal lattice during growth while secondary fluid inclusions are trapped along healed cracks (Roedder, 1984). Fluid inclusions were identified in the prepared sample by use of a petrographic microscope. Double-polished thin sections (approximately 70 microns) of cuttings from Well OW-39A, which contained abundant quartz, were prepared for fluid inclusion analysis. The thin sections were mounted on a Linkam THS MG 94 heating stage for analysis. The inclusions were heated slowly until the fluid homogenization temperatures (i.e. the bubble disappears) were obtained. Homogenization temperatures of individual inclusions were measured at least twice and the results were recorded in 5°C intervals.

4. RESULTS

4.1 Lithology

The preliminary geological logs of Well OW-39A were done at the rig site where the samples were analysed using binocular microscope, confirmed later in the laboratory using thin section analysis. The lithological column (Figure 5) of the well is composed of unconsolidated pyroclastics forming a thin layer at the top, overlaying a volcanic sequence consisting of tuffs, trachytes, rhyolites, basalt, and some rhyolitic, basaltic, syenitic and granitic intrusions. A summary of the lithology of Well OW-39A are described below.

Pyroclasts 0-14 m

The pyroclastics are unconsolidated and yellowish to brown, light grey and form the upper 14 m in the well. The rock unit consists of lithic fragments of rhyolite, trachyte and pumice. The rock is dominated by volcanic ash, and crystals of glass, quartz, feldspars, obsidian and pumice.

Rhyolites 14-208 m

A 190 m thick formation characterised by rhyolitic lavas and from 100 m depth rhyolitic tuffs. The rhyolitic lava at 14-44 m is whitish to creamish lava microcrystalline with quartz in a fine grained matrix. The lava is slightly quartz and arfvedsonite porphyritic with quartz intergrowth. This is followed by two rhyolitic tuff layers at least 60 m in thickness. The upper tuff is brown in colour and heterogeneous with a lot of quartz in an ashy matrix. The lower tuff is greyish with quartz phenocrysts in a fine matrix. At 158 m depth is a 40 m thick rhyolitic lava, which is white to creamish in colour and well crystallized. The lava is feldspar and quartz rich with phenocrysts of quartz.

Tuffs 232-368 m

This layer consists of a 136 m thick layer of medium grained rhyolitic tuff formation. From 232 to 250 m it is light grey to whitish homogeneous rock with vesicles partially filled. Between 250 to 268 m it is brownish, while from 268-368 m it is greenish heterogeneous rock with lithic fragments of quartz in a fine grained matrix. The rock shows slight oxidation; there is a minor loss between 368 to 374 m.

Basalts 374-414 m

The top 374 to 394 m is composed of a homogeneous non-porphyritic basaltic tuff that is highly fractured, vesicular and there is increased oxidation, veining and an abundance of pyrite. It overlies a 20 m thick basaltic layer characterised by dark brown colour and is fine grained with plagioclase phenocrysts and a lot of magnetite in the matrix. Abundant pyrite appears as cubes embedded in the matrix. Loss of returns was experienced between 414 and 424 m.

Trachyte 424-696 m

This layer is composed of variable trachytic lava. The top 424 to 550 m is brownish fine grained massive and homogeneous non porphyritic lava. The matrix is composed of pyroxenes and microcline laths. Between 550 to 588 m the lava is slightly porphyritic with sanidine and pyroxene. The lava shows veining and the amount of pyrite decreases with depth. This is underlain by ~90 m thick porphyritic layer with a typical trachytic texture. There was a loss of returns between 696 to 748 m.

Basalt 748-762 m

The rock unit is composed of 14 m thick basaltic lava with a loss of returns between 750-758 m. It is dark grey mafic fine to medium grained porphyritic with plagioclase and pyroxenes in a rich very fine grained plagioclase lath. The rock is highly altered and oxidised. Abundant calcite was seen in the vesicles. A medium aquifer is located in this rock unit at 750 m. There was a major loss of returns between 762 to 802 m.

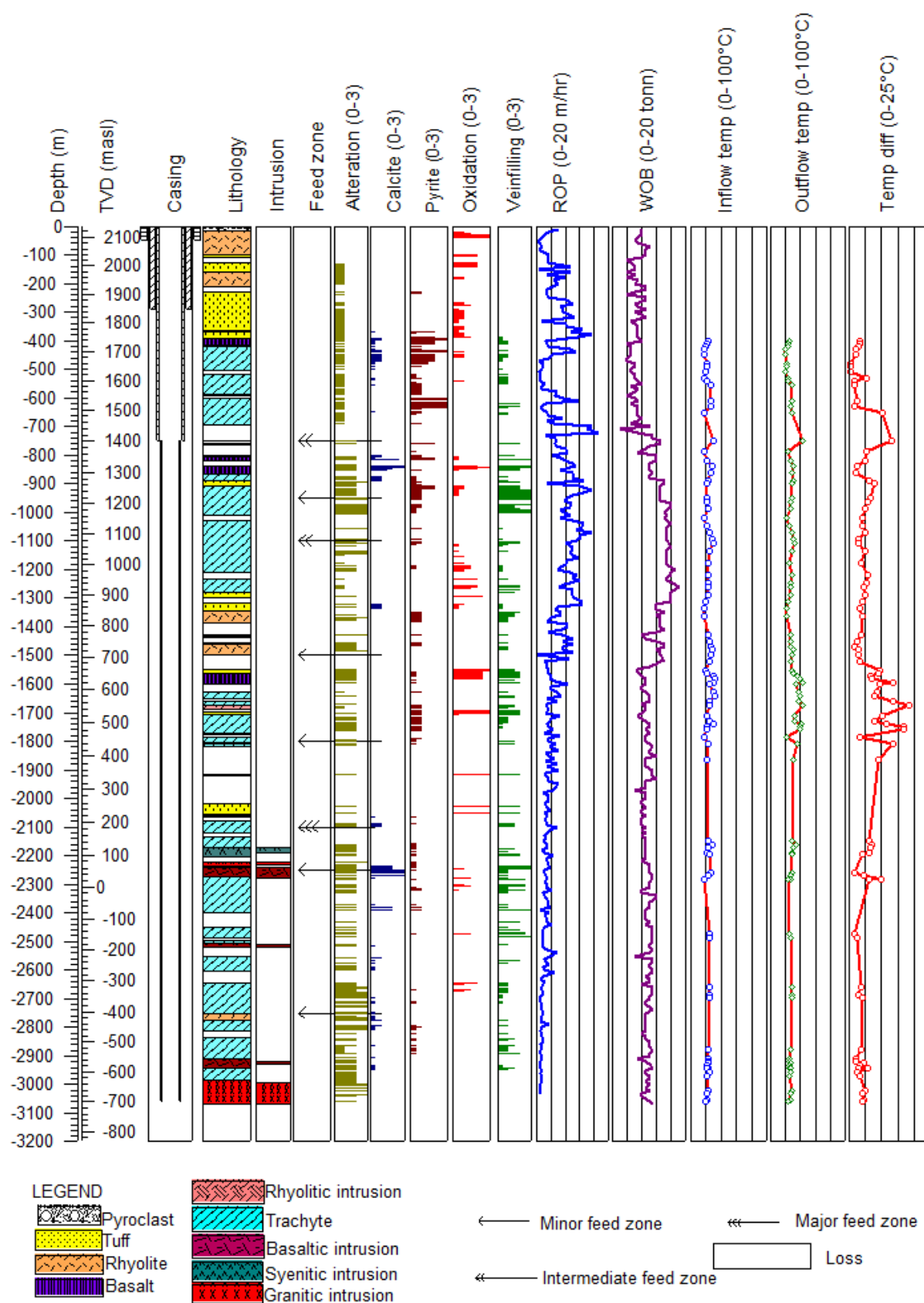


FIGURE 5: Stratigraphy and drilling parameters of Well OW-39A

Trachyte/Basalt 802-1008 m

The top 16 m of this unit is composed of medium grained highly vesicular and homogeneous lava with sanidine phenocrysts. The lava exhibits the flow orientation in the matrix. Pyrite is a common mineral with minor calcite. Veining is common. This unit is underlain by a 40 m thick basaltic layer between 836 and 876 m. The basalt is dark brown, brownish grey fine to medium grained highly oxidised phyric with plagioclase. There is abundant calcite in vesicles and veins. Magnetite is common in the matrix. It is highly altered with an increased abundance of epidote with depth. From 876 to 1008 m the rock is light grey, to light brown medium grained feldspar rich lava sanidine and pyroxene porphyritic, showing increased veining and magnetite with depth. It is intercalating with an 18 m thick heterogeneous highly oxidised and vesicular basaltic tuff between 890 to 908 m.

Trachyte and basaltic tuff 1028-1340 m

This layer consists of trachyte intercalating with less than 50 m thick layers of trachyte. The top depth is a 200 m thick trachyte layer which is a fine to medium grained highly altered grey light grey, light brown feldspar rich lava. It is porphyritic with sanidine and becomes more crystalline with depth. The lava is underlain by a ~50 m dark brown basaltic tuff between 1296 to 1344 m, fine to medium grained with lithic fragments of plagioclase and quartz in the matrix, porphyritic with plagioclase and slightly oxidised. There was a minor loss of returns from 1340 to 1344 m.

Rhyolite 1344-1500 m

This layer is light brown medium grained crystalline less porphyritic with quartz and pyroxenes (augerine). The matrix is composed of quartz; pyrite is disseminated in the matrix and a magnetite vein was noted. The lava is highly altered between 1460 to 1472 m. Between 1500 to 1550 m there was a loss of returns.

Basalt 1550-1602 m

The lava is approximately 40 m thick. The first 12 m is basaltic tuff which is reddish brown heterogeneous with angular grains, highly vesicular and fractured, underlain by a dark brown homogeneous fine to medium grained porphyritic basaltic layer. The rock unit is fractured and veined.

Trachyte 1628-1674 m

Light grey fine to medium grained partially crystalline phyric lava with sanidine and abundant pyroxenes and feldspars in the matrix. It shows flow texture and the feldspar are altered to albite.

Trachyte/basalt 1692-2054 m

Trachyte lava intercalates with thin layers of basalt. Between 1692 to 1710 m is a basaltic layer which is reddish brown, fine grained tuffaceous rock that is highly oxidised. Below this layer lies a trachyte layer which is ~ 200 m thick. The lava is greyish brown, greyish, partially crystalline and porphyritic with quartz, feldspars and pyroxenes. It shows slight oxidation with pyrite disseminated in the matrix. The rock is more altered at 1762-1772 m. The feldspars are altered to albite. At 1916-1920 m and 2020-2054 m is a reddish brown tuffaceous rock with medium heterogeneous angular grains, characterised by high fracturing, veining and oxidation. There is a major loss between 1818-1916 m and 1920-2018 m.

Trachyte 2066-2148 m

Between 2066-2090 m, the lava is light grey, fine grained and less porphyritic. Spherulitic texture is observed and the matrix is composed of feldspars and pyroxene. It is massive and lacks the trachytic texture. The lava is characterised by high fracturing and veining. From 2090 to 2148 m the lava is grey to dark grey, highly porphyritic, shows flow banding and slight oxidation. Abundant epidote was also noted in this layer. Losses occurred at 2120-2134 m.

Trachyte 2240-2750 m

Greyish brown medium grained porphyritic highly altered lava, characterised by a trachytic texture, high veining and fracturing, this layer is 8 m thick (2240-2246 m), overlaying a basaltic intrusion (2248-2274 m described below under intrusives). Beneath the intrusion is a thick layer of trachytic lava (2274-

2750 m) greyish, greyish brown to greyish green, crystalline, highly porphyritic with sanidine and pyroxene (augerine-augite) and shows a flow texture. The matrix is composed of microcline laths and pyroxenes and with abundant veins which are completely filled and it is highly altered between 2274 and 2336 m.

Rhyolite 2750-2774 m

Whitish felsic feldspar and quartz rich lava. It is glassy to fine grained with quartz and riebeckite phenocrysts. The lava has a high intensity of alteration.

Trachyte 2774-2986 m

This rock unit is fine to medium grained and varies in colour from greyish to brownish. Between 2774 and 2866 m the lava is highly porphyritic with sanidine, quartz and pyroxenes (augerine-augite) and shows typical trachytic texture. From 2866 to 2908 the lava is light grey in colour, more altered and fractured and veined. This lava overlies a ~28 m thick basaltic layer (described below under intrusives). At 2942 -2986 m the lava is greyish brown, medium grained. Veins in this rock unit have been filled. Between 2986 and 3066 m exists a granitic intrusion (discussed below under intrusions).

Intrusions

Intrusions were encountered at depth in the well. They are identified as being relatively fresh compared to the highly altered surrounding host and the chilled margins. The existence of intrusives is indicative of a heat source in a geothermal system. Intrusives encountered in the well are as follows:

Basaltic intrusions

Basaltic intrusives were encountered at 2252-2274, 2504-2518, and 2914-2940 m depth. The intrusives are fine to medium grained, weakly to moderately altered, with glassy margins. They are porphyritic with plagioclase feldspars, and highly fractured. The fresh intrusives are dark grey to black while the altered ones appear grey.

Syenitic intrusion

Syenite occurs at 2170-2190 m. It is light grey to whitish in colour, massive, medium grained and porphyritic with large sanidine phenocrysts. It shows a trachytic texture and the matrix is composed of pyroxenes and feldspars. This intrusion is associated with the major aquifer in the well.

Granitic intrusion

Granite occurs to the bottom of the well from 2992 to 3066 m. It is light grey to whitish, medium to coarse grained with granular and phaneritic texture. The contact with the host rock is glassy and highly altered. The rock is porphyritic with quartz and feldspars and occasionally some individual crystals of quartz form very large phenocrysts. It is massive and fresh with abundant quartz and riebeckite in the matrix.

Rhyolitic intrusion

A rhyolitic intrusion was encountered between 1674 and 1686 m. It is a whitish to light grey in colour, medium- to coarse grained, crystalline rock consisting of notable quartz crystals. Arfvedsonite-riebeckite and augerine-augite are common in the matrix. The rock is fractured and has veins filled with abundant pyrite.

4.2 Hydrothermal alteration mineralogy

4.2.1 Alteration of primary minerals

Primary minerals are minerals that form during the solidification and crystallization of the rock. These minerals include both the essential minerals used to assign a classification name to a rock and they form in a sequential group as dictated by the physico- chemical conditions under which the magma solidifies.

These minerals become unstable at temperatures prevailing in a geothermal system and, therefore, alter to secondary minerals when subjected to hydrothermal conditions (Browne, 1978). The common primary minerals (Table 1) in this well include volcanic glass, olivine, pyroxene, amphibole, plagioclase, sanidine, microcline and opaques (Fe-Ti oxides).

TABLE 1: Primary minerals; order of replacement and alteration products of Well OW-39A (modified from Browne, 1984)

Most susceptible ↓ Least susceptible	Primary minerals	Alteration product
	Volcanic glass	Zeolites, clays, chalcedony quartz, calcite
	Olivine	Clays, calcite, chlorite, actinolite
	Plagioclase	Calcite, albite, quartz, illite, epidote, sphene
	Sanidine, microcline	Albite, adularia, clays
	Pyroxene	Chlorite, illite, calcite, quartz, albite, epidote
	Opaques	Hematite, pyrite, sphene

4.2.2 Hydrothermal minerals

A number of hydrothermal minerals are highly temperature dependant and are, thus, extensively used to map the temperature regimes of geothermal systems (Browne, 1978, 1984; Omenda, 1998). The hydrothermal alteration minerals appear both as replacements of primary minerals, and as fillings in vesicles, vugs and fractures. The distribution and abundance of the hydrothermal minerals were characterised from binocular microscopic studies, and petrographic and XRD analysis of the drill cutting samples taken at 2 m intervals. Although hydrothermal alteration changed the primary minerals in different ways and magnitude, the original textures and minerals are often still recognizable. The distribution and kind of mineral assemblages present in hydrothermal systems is influenced by factors such as permeability, rock and water composition, temperature, pressure and duration of hydrothermal alteration (Browne and Ellis, 1970; Reyes, 2000). The main hydrothermal minerals encountered in Well OW-39A were oxides (hematite and magnetite), zeolites (scolecite), quartz, calcite, epidote, pyrite, adularia, wollastonite, fluorite, sphene, albite, actinolite, prehnite and clays (smectite, chlorite, illite, mixed layer clays). The distribution of hydrothermal minerals in Well OW-39A is shown in Figure 6, and a description is given here below:

Hematite was observed as silver-grey, brown to reddish brown in colour. Hematite can form in environments associated with colder in-flow that is more oxygen-rich by the oxidation of magnetite or iron-rich minerals in the formation. In this well, hematite was observed between 274 and 1568 m and is abundant in silver grey below 900 m.

Magnetite is an iron oxide. The reduction of hematite to magnetite at high temperatures and pressures in the presence of water causes the precipitation of stable magnetite from a hydrothermal fluid in a hydrothermal system in vesicles and veins (Mathews, 1976), while magnetite precipitation can also be associated with intrusions. The oxide was first observed at 968 m as a black to brown black cubic mineral filling in veins and occasionally in vesicles.

Zeolites can be distinguished by their shape: mainly fibrous/acicular, tabular/prismatic and granular (Saemundsson and Gunnlaugsson, 2002). The zeolites were observed as white to light brown fibrous and radiating minerals. In this well, zeolites occurred from 134 to 460 m. Zeolites are not common and only scolecite was identified.

Chalcedony is a cryptocrystalline form of silica commonly referred to as the amorphous form of silica. It was observed as translucent white to grey, grey to greyish blue and some were in shades of brown. It was observed in trachyte, basalt and tuffs at the upper parts of the well from 250 m to a depth of about 624 m. Below this depth, it became unstable and recrystallized to quartz. It is a low-temperature

mineral, observed in the well as fillings in veins and vesicles, indicating formation temperatures of ~110 to 180°C.

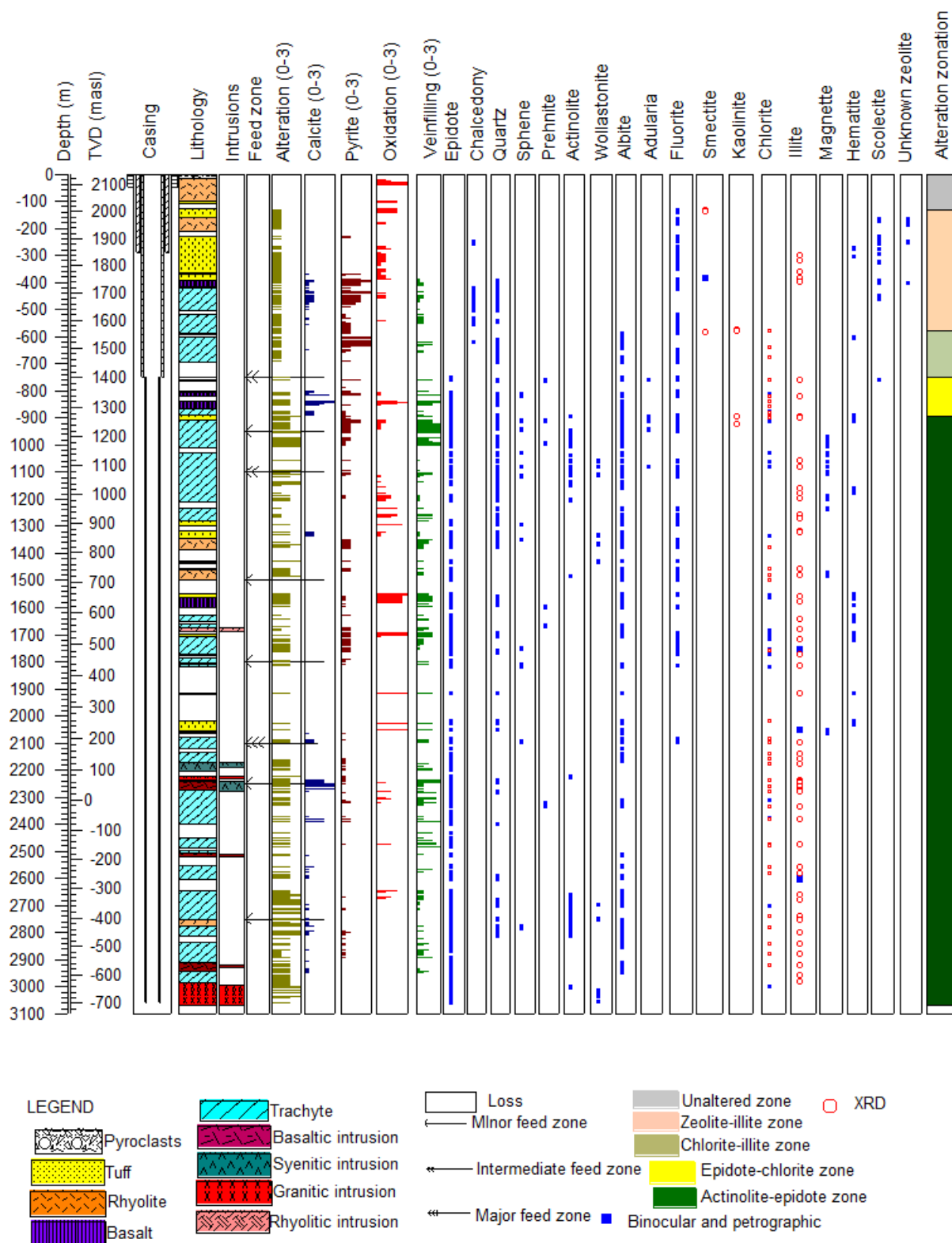


FIGURE 6: Lithology, distribution of hydrothermal minerals and mineral zones in well OW-39A

Quartz first occurred at 400 m as a secondary mineral and was not observed as such below 2812 m. It is colourless and occurs in euhedral to subhedral crystals. It has conchoidal fracturing, indistinct cleavage, and undulating extinction under the microscope which makes it easily identifiable. It occurs as an infilling in both vesicles and veins. The first occurrence of quartz indicates formation temperature greater than 180°C.

Calcite occurs intermittently from 250 m and disappears completely below 2950 m. It is abundant between 836 and 850 m in basaltic rock and 2234 and 2264 m in a fractured trachytic rock at the contact with a basaltic intrusion (2240-2276 m). The major aquifer in this well (2100 m) is associated with calcite in trachytic lava, indicating that the zone is permeable. Calcite replaces feldspars and volcanic glass, and is also seen as an infill in vesicles, fractures and veins. It is abundant in the basaltic formations with minor occurrences in tuffs and trachyte. Browne and Ellis (1970) stated that relatively high carbon dioxide concentrations in solution in the presence of a mineral pH buffer causes calcite to form in place of other calcium aluminosilicates. Therefore, calcite formation in this well could be related to carbon dioxide (CO₂) concentrations in the reservoir fluids. Platy calcite was observed in the vesicles as composite crystals formed of numerous paper thin subcrystals. It was common in the basaltic and trachytic layers between 392 to 750 m and also at 760 m. Its presence in the well indicates possible boiling conditions and high porosity (Browne, 1984; Omenda, 1998; Muchemi, 1992; Simmons and Christenson, 1994). Calcite also disappears at temperatures >300°C (Simmons and Christenson, 1994).

Pyrite occurs as euhedral cubic crystals with shiny brassy yellow lustre. The mineral was first observed at 232 m in the well. Well-formed cubic pyrite crystals were deposited in fractures, vesicles and veins and as disseminations in the groundmass. An abundance of pyrite indicates high activity of sulphur, good permeability and past or present boiling regimes (Lagat, 1998), hence its abundance in the well coincided with intermediate aquifers at 750 and 1100 m, and also a minor aquifer at 950 m, indicating good present and past permeability and also boiling zones at these depths.

Epidote first appeared at 748 m; from there, crystalline epidote persisted to the bottom of the well. The mineral is identified from rock cuttings by its yellow to greenish yellow colours. In thin sections, it is pleochroic with pale green, pale yellow and greenish brown colours exhibiting high relief with parallel extinction. It was found filling fractures, vesicles, and replacing primary plagioclase and pyroxene and, in most cases, formed mineral associations mainly with quartz, chlorite, calcite, actinolite and prehnite and sometimes pyrite. The presence of well-crystallized epidote indicates temperatures of more than 250°C (Omenda, 1990; Gylfadóttir et al., 2011).

Albite forms by the replacement of primary feldspars and plagioclase phenocrysts into hydrothermal albite. It is identified by its colour, which is cloudy white or greyish white. It is an anisotropic mineral showing uneven fracturing. It appears as striated, anhedral to subhedral crystals. It was observed in the well from 588 m down to the bottom; albite replaces feldspars at temperatures of 180°C and above (Reyes, 2000).

Fluorite is a very common mineral in this well. It was first observed at 134 m and was then common down to 2750 m. It is identified in a petrographic microscope by its very low relief, two perfect cleavages and its pale brown to colourless colour in thin section, while it is isotropic under crossed nicols.

Sphene is not a common mineral in this well. It was first encountered at 812 m and appearing intermittently down to 2786 m, where it disappeared completely. It occurs mainly as irregular grains but rarely as clear euhedral crystals having acute rhombic sections. The mineral forms mainly as a result of alteration of Fe-Ti-oxides.

Prehnite was first noted in the well at 758 m. It has a high relief and is colourless in plane polarised light which changes to green yellow and orange in crossed nicols. It is identified by its sheaf like bow-tie texture and strong birefringence. It occurs as vein and vesicle filling in association with epidote and chlorite. Prehnite indicates minimum formation temperatures of about 250°C (Reyes, 2000).

Wollastonite is a rare mineral in this well and appeared first at 1058 m. It is white to colourless, sometimes grey, with a distinct crystal habit appearing as fibrous and radiating aggregates. In thin section it is colourless and has moderately high relief. It forms in vesicles in association with epidote and actinolite. Its presence in the well indicates formation temperatures above 270°C (Reyes, 2000).

Actinolite is pale green, green and sometimes dark green in colour and occurs as fibrous, radial crystals and massive to granular aggregates in the groundmass. In thin sections, it shows moderate relief with weak pleochroism of pale yellow, deep green blue and pale green colours. The first occurrence of actinolite was at 894 m and from there actinolite is persistent to the bottom of the well, filling in vesicles and sometimes seen in veins. The mineral is formed as a replacement of pyroxenes. In most cases it forms mineral associations with quartz, pyrite, wollastonite and epidote. This mineral indicates formation temperatures above 280°C (Lagat, 2007; Gylfadóttir et al., 2011).

Clay minerals

Clay minerals are the most common and dominant hydrothermal alteration minerals that were observed in Well OW-39A. They are finely crystalline or metacolloidal and occur as flake-like or dense aggregates of varying types (Pendon, 2006). Their occurrence in a geothermal system is an indication of changes in the chemical environment, such as the presence of acidic fluids in a relatively neutral environment, while their distribution depends on the ability of fluids to approach equilibrium in host rocks at any scale during the hydrothermal processes (Harvey, 1998) and also as temperature indicators (Kristmannsdóttir, 1979; Franzson, 1998). Four types of clays were identified from the surface to the bottom of the well, based on binocular analysis, petrographic analysis and XRD analysis. A brief description is given below; some XRD analyses are shown in Appendix I.

Smectite is a low temperature clay and it is seen as fine grained brown to green aggregates, recognized by the first order birefringence colour. It was observed at shallow depths, identified by its characteristic extinction sun feature in thin section (384 m). Its occurrence indicates temperatures of less than 200°C (Franzson, 2013) and also an alkaline fluid environment. Smectite is unique in that it swells when ethyl glycol is added to it and, when heated, it shrinks. In this regard, it shows characteristic peaks of 14.78 Å-16.33 Å, 18.37 Å-19.58 Å and 10.50 Å-10.98 Å for air-dried/untreated, glycolated and heated samples, respectively.

Kaolinite is bright green to white in colour, replaces K-feldspar, and occurs as a vein and vesicle filling mineral. It was identified by XRD analysis with a peak of 7.15 Å for the untreated and glycolated samples, and completely collapsed after being heated to 550°C. It occurs in low intensity alteration below 572 m. Kaolinite is associated with acid alteration and low temperatures up to 180°C (Reyes, 2000).

Chlorite is pale green to dark green in cuttings, but in thin sections it is pale green and occasionally shows anomalous brown colour. It is fine to coarse grained weakly to non-pleochroic and shows low birefringence. It exhibits small intergranular patches in the shallow depths while at deeper levels it forms radial aggregates. The mineral occurred as a filling in vesicles, veins and fractures in association with epidote, quartz and calcite. XRD analyses of chlorite showed conspicuous peaks at 7.0-7.2 Å and 14.0-14.5 Å in the untreated, glycolated and oven heated samples, differentiating it from kaolinite whose peak collapses when heated to 550°C.

Illite is a common clay mineral extensively distributed in this well. It is colourless to brown under petrographic microscope. It was observed as a vein filling and as an alteration product of sanidine. Under XRD analyses, it showed strong peaks of between 9.9 and 10.4 Å in untreated, glycol treated and heated samples (Appendix I). It was first observed at 298 m in XRD analysis. Its appearance indicates temperature above 200°C (Kristmannsdóttir, 1979).

4.3 Hydrothermal alteration mineral zonation

Hydrothermal minerals are known to form at specific temperatures in a geothermal system (Browne, 1978, 1984; Omenda, 1998). The distribution of the hydrothermal minerals with depth in Well OW-39A is dependent on temperature. In this well, the mineralization pattern shows five distinct zones, as shown in Table 2. The top zone is the unaltered zone (0-134m) and has no alteration related to geothermal activity, suggesting the temperatures were <40°C. The second zone (zeolite –smectite-illite zone) extends from 134 to 578 m. This is the lowest grade mineral alteration zone, indicating a temperature range of 40-200°C. The upper boundary of this zone coincides with the first occurrence of zeolites at about 134 m. The third zone (Chlorite- illite zone) occurs between 578 to 748 m and is characterised by high oxidation in the upper parts at 600-640 m depth. The upper boundary is marked by the first appearance of chlorite in XRD analysis at 578 m, suggesting the alteration temperatures could be above 230°C. The fourth zone (epidote-chlorite-illite) extends from 748 to 896 m. It is characterised by an abundance of epidote, suggesting that alteration temperatures are above 250°C. Other minerals present in this zone include albite, sphene, quartz, chlorite, illite and calcite. The fifth zone extends from 896 m to the bottom of the well. It is marked by first appearance of actinolite at 896 m, indicating alteration temperatures above 280°C below this depth. It is characterised by mineral assemblages of actinolite, wollastonite, epidote and prehnite. Other minerals in this zone include pyrite, calcite, fluorite, chlorite, illite, and oxides.

TABLE 2: Alteration mineral zones in Well OW-39A

Depth (m)	Alteration	Temp range (°C)
0-134	Unaltered	<40
134-578	Zeolite-smectite-illite	40-200
578 -748	Chlorite-illite	230-250
748-896	Epidote-chlorite-illite	250-280
896-3066	Actinolite-epidote-wollastonite	>280

4.4 Stratigraphic and alteration mineralogical correlation of Wells OW-39A, OW-37A and OW-35A

4.4.1 Stratigraphic correlation

A geological cross-section extending from the southwest at Well OW-39A, through Well OW-37A and to Well OW-35 in the northwest (Figure 7) is shown in Figure 8. The lithology of the three wells shows the same type of rocks as those observed in other Olkaria wells (Musonye, 2012; Mwangi, 2012; Ronoh, 2012; Njathi, 2012). The top formation is composed of pyroclastic rock, which is very thin in Well OW-39A but thicker in Wells OW-37A and OW-35, indicating there could have been a flow forming thicker layers in the low lying areas of Wells OW-37A and OW-35. These pyroclasts overlie rhyolitic lavas in all the wells with subsequent layers of tuff, trachyte and basalt. Tuffs are common rocks in the three wells above 800 m, intercalating with basalt, rhyolite and trachyte; this could indicate that this area experienced phreatic episodes of eruptions in the past. Basalt occurs in the three wells with a thickness less than 50 m. Trachytes dominate the bottom depths in all the wells below 900, 750 and 700 m in Wells OW-39A, OW-37A and OW-35, respectively, intercalating with tuffs, rhyolite, basalts and minor intrusions. This could indicate the onset of the Plateau trachytes in these wells. The intrusions are only encountered in Wells OW-39A and OW-35. Basaltic and granitic intrusions occur only in Well OW-39A, whereas rhyolitic and syenitic intrusions occur in both wells (OW-39A and OW-35). There are no intrusions encountered in Well OW-37A. The occurrence of the intrusions in specific wells may imply that these intrusions are dykes. As has been discussed by earlier researchers on the subsurface geology of Olkaria (Browne, 1984; Leach and Muchemi, 1987; Muchemi, 1992; Omenda, 1998), a basaltic lava flow coincides with the cap rock of the reservoir and has been used as a marker horizon, as it is widespread. The basaltic lava was encountered at 808 m in Well OW-39A, 640 m in Well OW-37A;

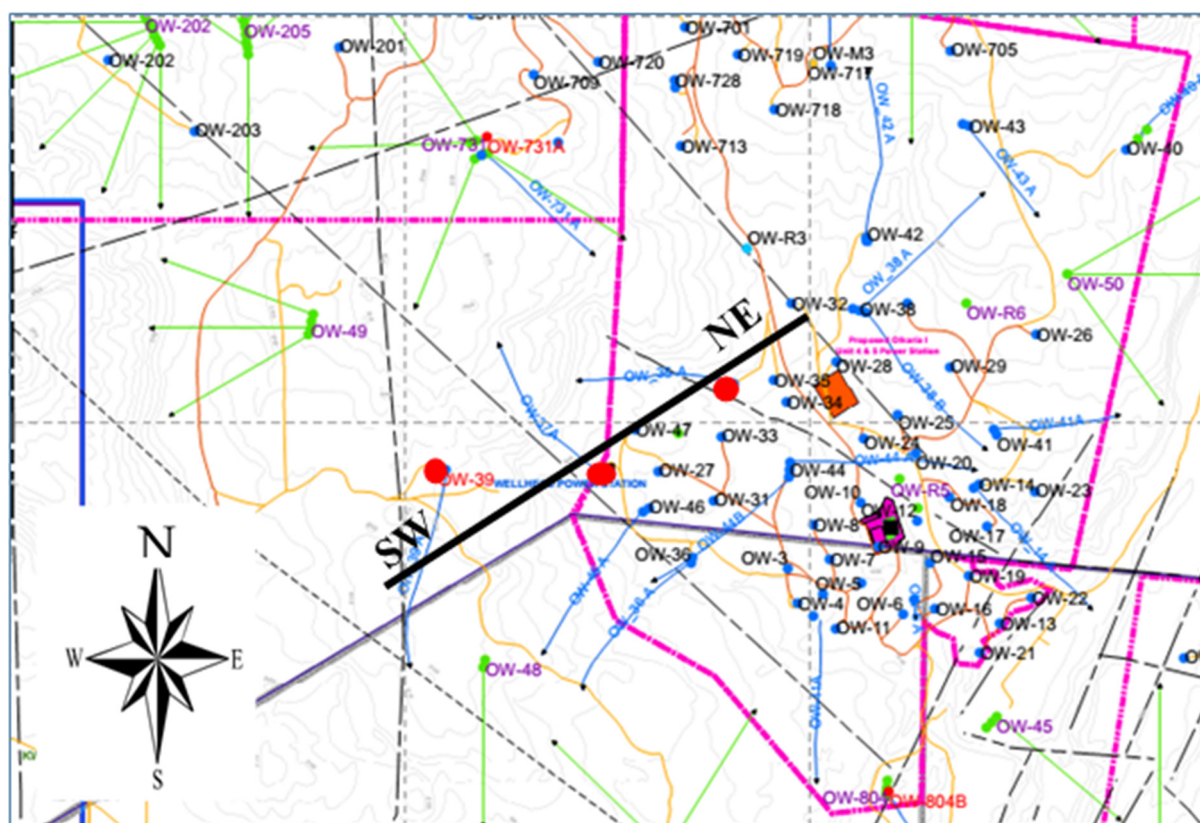


FIGURE 7: Cross cutting of correlation direction between Wells OW-39A, OW-37A and OW-35A

OW-35 shows slightly variable depths of occurrence which may imply minor faulting. This, therefore, reveals the possible existence of a fault between Wells OW-39A and OW-37A, with the down throw towards Well OW-39A. The other fault could exist between Wells OW-37A and OW-35, with the down throw towards Well OW-35 (Figure 8).

4.4.2 Alteration mineral correlation

Isograds give a general picture of the temperature distribution in a geothermal system as they delineate the first appearance of an index mineral. The first appearance of index minerals was plotted (Figure 9) in all three wells and five distinct alteration zones were identified in all three. The top zone (unaltered zone) is quite thin in all the wells. The zeolite-smectite-illite zone appears at 2004 m a.s.l. in Well OW-39A, 1919 m a.s.l. in Well OW-37A and 1768 m a.s.l. in Well OW-35. This zone is thicker in Wells OW-39A and OW-37A and thinner in Well OW-35. The chlorite-illite zone appears at 1560 m a.s.l. in Well OW-39A, 1388 m a.s.l. in Well OW-37A and 1768 m a.s.l. in Well OW-35. This zone is thicker in Wells OW-37A and OW-35 but thinner in Well OW-39A. The first appearance of chlorite at these depths indicates alteration temperature of $\approx 230^{\circ}\text{C}$. The first appearance of epidote is in basaltic lava at 1390 m a.s.l. in Well OW-39A, in a trachytic lava at 845 m a.s.l. in Well OW-37A and in tuff at 1288 m a.s.l. in Well OW-35, indicating that the alteration temperatures at these depths in the wells is 250°C . This temperature (250°C) is shallower in Wells OW-39A and OW-35 while deeper in Well OW-37A. The epidote zone is thinner in Well OW-39A and thicker in Well OW-35. Actinolite first appears in Well OW-39A at 1242 m a.s.l. Well OW-37A at 467 m a.s.l. and in Well OW-35 at 342 m a.s.l. The plots indicate that this zone is shallowest in Well OW-39A, indicating hotter shallow depth of alteration temperatures above 280°C . The correlation indicates elevation of the hydrothermal alteration in the area around Well OW-39A, implying the proximity of an upflow zone. Formation and alteration temperatures are within a similar range in Wells OW-37A and OW-35 but, in Well OW-39A, the formation and alteration temperatures are the reverse of each other, that is, the alteration temperature

indicates the proximity of upflow while the current formation temperature indicates marked cooling of the same structure. This might indicate a flow reversal of a specific permeability structure from a geothermal outflow to an inflow of cooler fluid into the geothermal system.

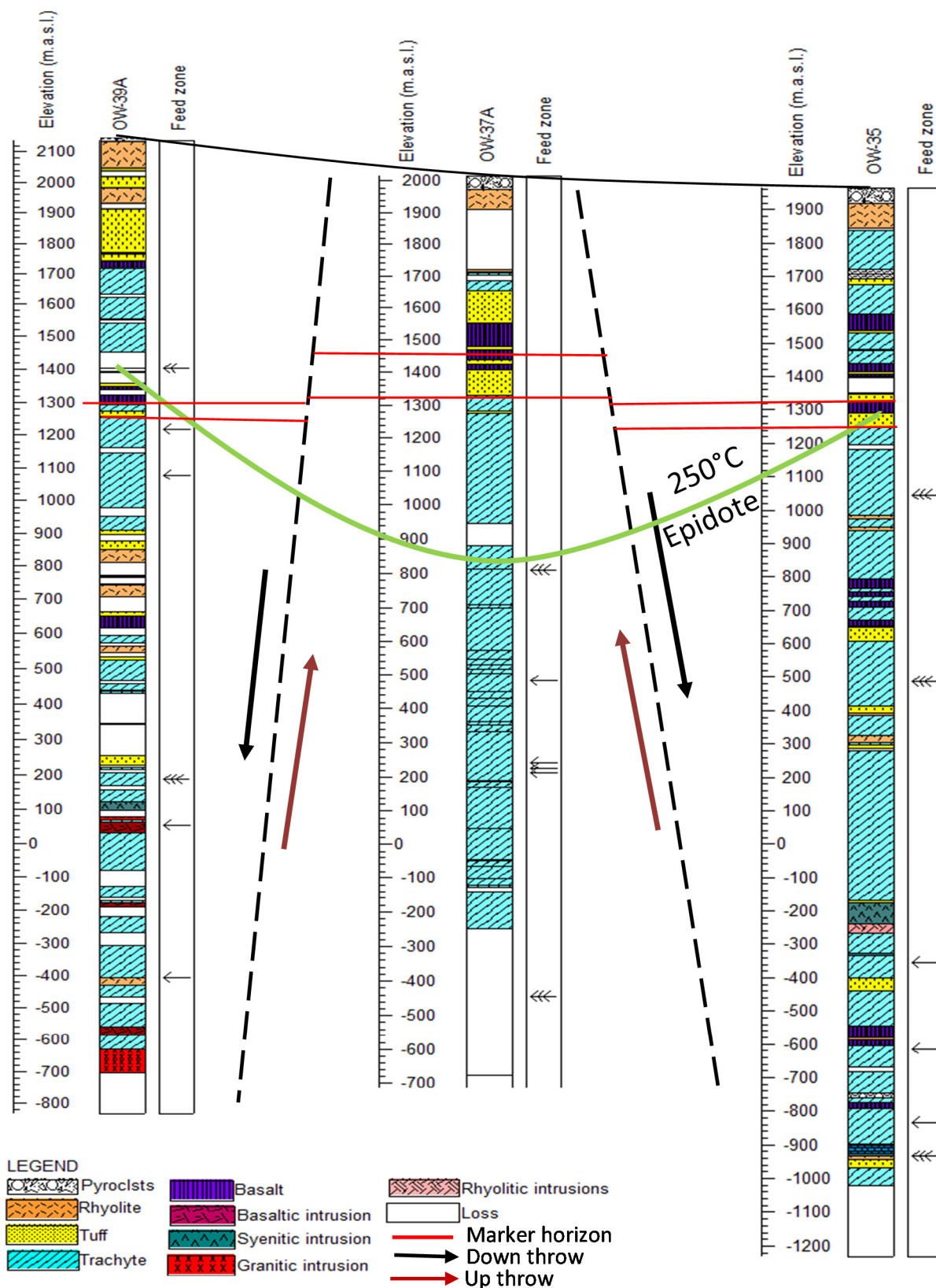


FIGURE 8: Stratigraphic correlation between Wells OW-39A, OW-37A and OW-35

4.5 Mineralogical evolution

The paragenetic sequences in hydrothermal systems are identified from cross-cutting veins and amygdale infilling sequences (Lagat, 2004). Paragenesis is the successive order in which minerals in a rock or a vein have crystallized. This successive sequence of mineral deposition is influenced by variations in pressure, temperature and the chemical composition of hydrothermal fluids that result in the precipitation of different hydrothermal alteration minerals at different times as conditions change in a geothermal reservoir. Therefore, compiling a paragenetic sequence with depth in a geothermal system assists in deciphering the detailed geologic geothermal history of the system. The mineral deposition sequence in vesicles and veins in Well OW-39A indicates a systematic increase in alteration temperatures, revealed by the deposition of low temperature minerals first, followed by high temperature ones. It was also observed that sequences at shallow depths consisted of low temperature minerals while high temperature mineral sequences were found at deeper levels. Table 3 shows the depositional sequences of hydrothermal alteration minerals in cuttings from Well OW-39A.

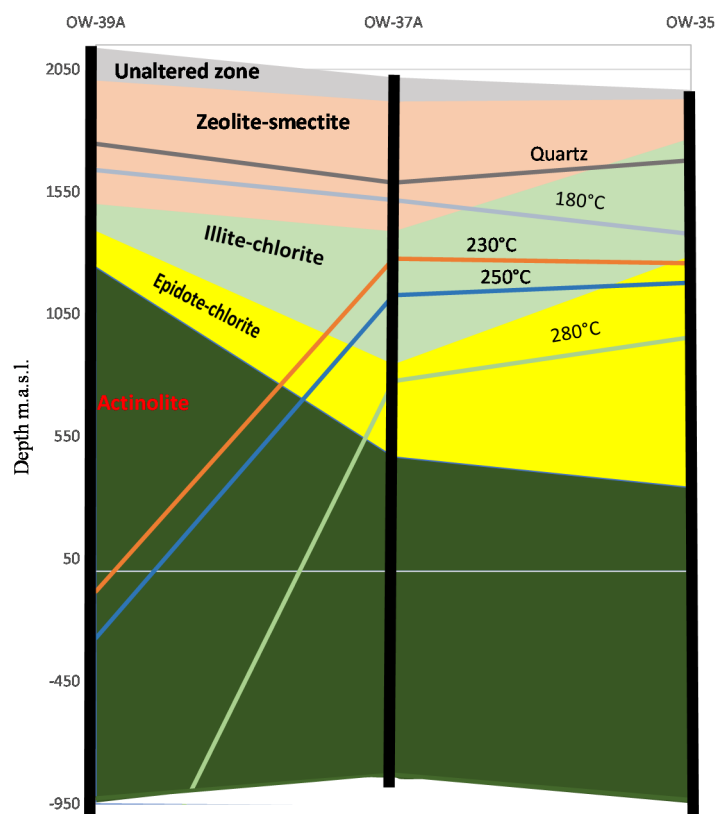


FIGURE 9: Alteration mineral correlation between Wells OW-39A, OW-37A and OW-35

4.6 Fluid inclusion geothermometry

Fluid inclusion analyses in Well OW-39A were done in quartz crystals. Fluid inclusion homogenization temperatures give the entrapment temperature of a fluid in a mineral (Roedder, 1984). This temperature, combined with other geochemical techniques, constrains potential sources and migration pathways and assists in deciphering the thermal history of a geothermal system. The homogenization temperatures (T_h) of the inclusions were measured in quartz crystals picked from 810 m depth and the results are presented in Figure 10. The T_h values ranged from 210-285°C in the quartz, apparently from two populations. The lower T_h value range is 210-215°C while the higher one ranges from 280-285°C. The lower range T_h values appear to be formed in healed fractures in the crystal and may have formed at a later stage than the higher ones which appeared more primary in nature. The high values may, therefore, be from an earlier phase, thus indicating that cooling had taken place in the geothermal system at this location.

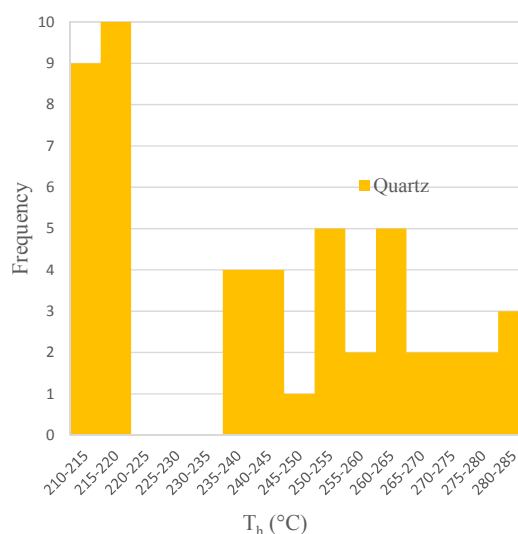


FIGURE 10: Histogram showing temperature and distribution of fluid inclusion

TABLE 3: Depositional sequences of hydrothermal alteration minerals in Well OW-39A

Depth (m)	Older younger Sequence	Type
250	Zeolite » illite	Vein
402	Fluorite » illite	Vein
404	Zeolite » calcite » quartz » pyrite	Vesicle
438	Chalcedony » quartz » illite » platy » calcite	Vesicle
442	Zeolite » chalcedony » zeolite » quartz	Vein
448	Zeolite » calcite » clays	Vein
450	Pyrite » calcite	Vesicle
452	Chalcedony » zeolite	Vesicle
814	Quartz » chlorite » calcite	Vein
860	Chlorite » calcite	Vein
890	Chlorite » quartz » epidote	Vein
958	Quartz » chlorite	Vein
970	Quartz » chlorite	Vesicle
1114	Quartz » chlorite	Vein
1702	Quartz » epidote	Vein
2030	Quartz » chlorite » epidote	Vein
2240	Epidote » quartz	Vesicle
2288	Quartz » epidote	Vesicle
2602	Epidote » actinolite	Vesicle
2678	Epidote » actinolite	Vesicle
2698	Epidote » wollastonite	Vesicle

4.7 Comparison of measured, hydrothermal and fluid inclusion temperatures for Well OW-39A

Comparison of fluid inclusion, formation and alteration temperatures of Well OW-39A was done by plotting the formation temperature, mineral alteration temperatures and fluid inclusion data as shown in Figure 11. Comparisons between formation and alteration temperatures in a well are an important tool in determining the present geothermal condition of the well; they can indicate whether the well is cooling down, heating up or in equilibrium. In this well, alteration temperatures at 270, 392, 580, 748 and 896 m are 130, 180, 230, 250 and 280°C, respectively. The formation temperatures at 270, 392, 580, 748 and 896 m are 100, 150, 195, 205 and 210°C, respectively. The alteration temperatures at 270, 392, 580, 748 and 896 m are 30, 30, 45, 60 and 70°C, respectively, higher than the formation temperature, indicating the well is cooling. This difference increases with depth.

The homogenization temperature (T_h) values at 812 m in the well ranged from 210-285°C in the

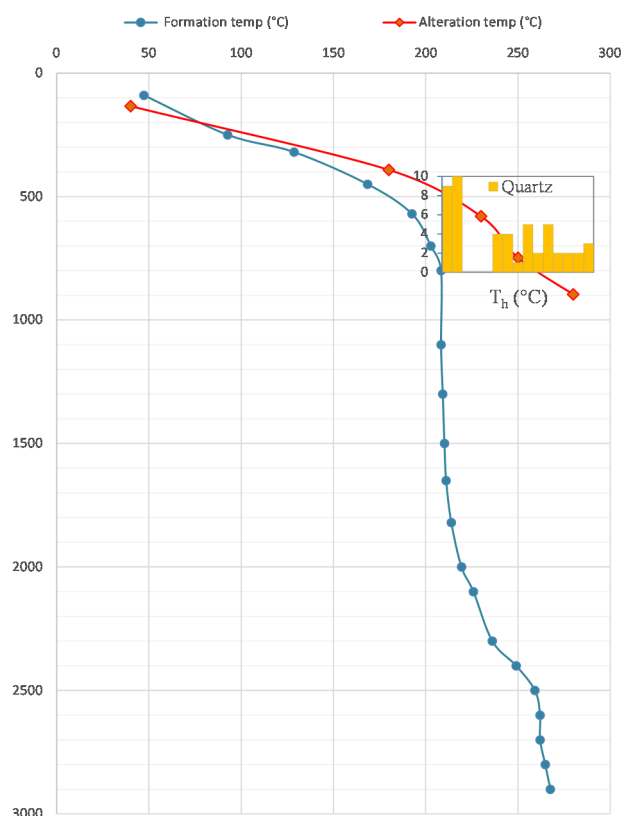


FIGURE 11: Comparison between fluid, fluid inclusion, alteration and formation temperatures of Well OW-39A

quartz, as discussed above. The formation temperature at this depth is 208°C. The lowest T_h value range is 210-215°C while the highest is 280-285°C. These measurements indicate the inclusions (with lower T_h range 210-215°C) are near equilibrium with the current formation temperatures, whereas the high temperature range inclusions are far above the formation temperature. The formation temperature at 812 m is 208°C, indicating that the lower T_h range is in equilibrium with the current formation temperature, whereas the highest T_h range is far above the formation temperature. The two sets of T_h temperatures reveals two geothermal histories of the well; at one time elevated temperature existed, succeeded by cooling. In this discussion, we assume that the measured temperature conforms to the formation temperature.

4.8 Aquifers and permeable zones

The main sources of permeability in the Greater Olkaria volcanic complex are lithological contacts, intrusive boundaries and major faults and fractures (Lagat, 2004; Gylfadóttir et al., 2011). Permeability and feed zones in Well OW-39A (Table 4) were identified and interpreted by monitoring the loss of circulation fluid during drilling, hydrothermal alteration mineralogy patterns, changes in circulating fluid temperature and temperature recovery tests (Figure 12). The temperature logs and alteration intensity reveal that the well is highly permeable above 2250 m. The feed zones in this well were identified in the production zone and are classified as major, minor, and intermediate. Four minor aquifers occurring at 950, 1500, 1800, 2250 and 2750 m are marked by high intensity of alteration fracturing and loss of returns. Two intermediate aquifers occur at 750 and 1100 m. At 750 m, there is a marked loss of circulation and high intensity of alteration while at 1100 m, there is high alteration intensity, veining and fracturing. The major aquifer at 2100 m is marked by lithological contact between intrusions, loss of circulation and fracturing.

TABLE 4: Interpreted permeable zones / aquifers based on geological observations

Depth (m)	Evidence geological observation
696	Loss of circulation
748	Loss of circulation with high intensity of rock alteration calcite and pyrite deposition, fracturing of trachyte lava
950	Alteration intensity and highly fractured rock, veining and oxidation
1008	Loss of circulation
1100	High intensity of alteration, increase in oxidation and fracturing
1500	Loss of circulation
1550	Primary porosity, and high intensity of alteration
1602	Loss of circulation
1800	Loss of circulation, fracturing
2100	Lithological contact between syenite and trachyte, intrusion, veining and fracturing alteration
2250	Lithological contact between basaltic intrusion and trachyte, veining, fracturing and increased amount of calcite
2750	Lithological contact between rhyolite and trachyte

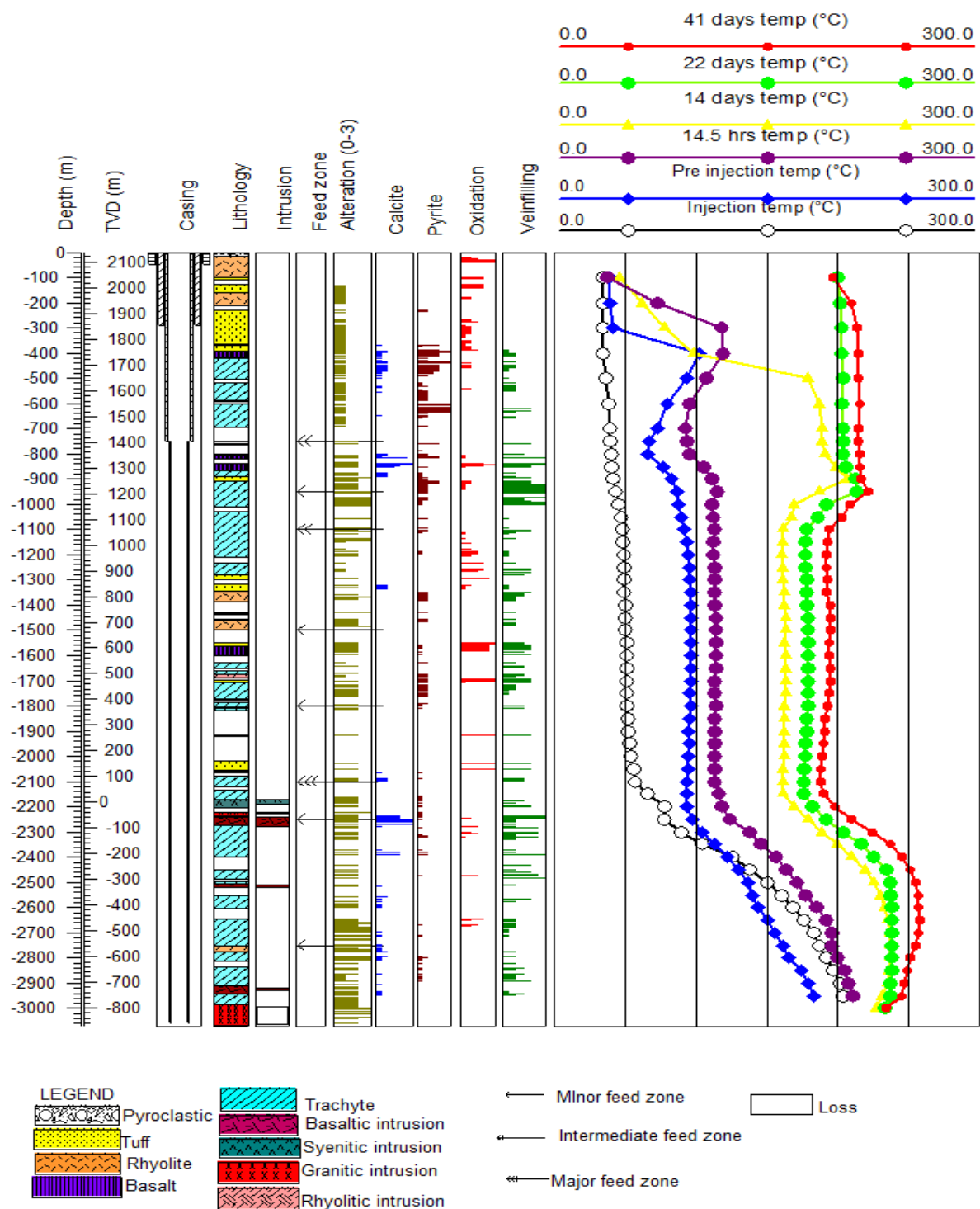


FIGURE 12: Feed zones in Well OW-39A in relation to the geological evidence and the recovery and circulation fluid temperature measurements

5. DISCUSSION AND INTERPRETATION

The lithology of Well OW-39A was interpreted by analysis of the drill cuttings from the well, using binocular and petrographic microscopes. From these analyses, five main rock types, namely pyroclastics, tuffs, rhyolites, basalts and trachytes, were encountered in the well. Pyroclastic rocks form the uppermost 14 m; the underlying rhyolites extend to 98 m and correspond to the Olkaria comendites. Rhyolitic tuffs and basalts dominate the upper 400 m of the stratigraphic column of the well, representing the Upper Olkaria volcanics, while Plateau trachytes dominate at depth and form the main reservoir formation. Hence, the stratigraphy of Well OW-39A relates well with the general stratigraphic column of the Greater Olkaria volcanic complex (Shackleton, 1986; Ogo-Odongo, 1986; Omenda, 2000).

Stratigraphic correlation between Wells OW-39A, OW-37A and OW-35 show that the pyroclastic deposit forms a very thin layer in Well OW-39A, but is thicker (44-48 m) and of almost equal thickness in Wells OW-37A and OW-35, implying the pyroclastic deposit could have been a flow deposit formed by erosion of a higher elevated area (Well OW-39A) resulting in thicker layers in the low lying areas (Wells OW-37A and OW-35). Rhyolites appear near the surface in all three wells, underlying the pyroclasts and extending to 98 m in Well OW-39A, 304 m in Well OW-37A and 122 m depth in Well OW-35. These are the comenditic lavas and their occurrence conforms to the Olkaria stratigraphic column. Tuff is a common rock in the three wells above 800 m. It first occurs below the rhyolites in Well OW-39A and below the trachytes in both Well OW-37A and Well OW-35, intercalating with basalt, rhyolite and trachyte; this could indicate that this area experienced phreatic eruptions in the past. Basalt occurs in the three wells with a thickness of less than 50 m. The uppermost occurrence was first noted at 392 m in Well OW-39A, 468 m in Well OW-37A and 380 m in Well OW-35. This basalt layer can be used as a marker horizon when carrying out analyses of drill cuttings to infer buried faults in this area. However, the depth of the basalt also often corresponds to the cap rock of the geothermal reservoir. Below the Olkaria basalts, trachyte is the dominant rock in the wells. At greater depth, it was observed to be the dominant rock below 900, 750 and 700 m in Wells OW-39A, OW-37A and OW-35, respectively, intercalating with minor thin layers of tuff, basalt and rhyolite along with minor intrusives, although intercalations of tuffs, basalts, rhyolites and intrusives were absent in Well OW-37A. This also relates to the Plateau trachytes which were noted to occur in the Olkaria geothermal complex at a depth between 1000 and 2600 m. Intrusives were only encountered in Wells OW-39A and OW-35 at depth. Apart from the granitic intrusion encountered at the bottom of Well OW-39A, the other intrusives ranged from 8 to 30 m in apparent thickness. Basaltic and granitic intrusions occur only in Well OW-39A, whereas rhyolitic and syenitic intrusions occur in both wells (OW-39A and OW-35). There was no intrusion encountered in Well OW-37A. The occurrence of the intrusions in specific wells could probably imply that some of these intrusions are dykes. The occurrence of fresh rhyolitic dykes implies a young age, possibly related to the Ololbutot eruptive fissure. The presence of a thick granitic intrusion (~80 m) at depth could signify a more substantial intrusion and serve as a local heat source at depth, as was postulated by Gylfadóttir et al. (2011) when interpreting possible heat sources (below Olkaria hill, Gorge farm volcanic centre and domes), based on the seismic attenuation data of the Olkaria geothermal system.

Taking into consideration the topographic correction between the wells, true vertical depth with reference to the elevation of each well was used. Stratigraphic correlation of the basalt layers between the three wells indicates the possible existence of normal faults between Wells OW-39A/OW-37A and OW-37A/OW-35, with downthrows towards Wells OW-39A and OW-35, respectively. Also the appearance of dominant trachyte below 900, 750 and 700 m in Wells OW-39A, OW-37A and OW-35, respectively, correlates well with the probable existence of normal faults, as shown in Figure 8, and hence conforms to observations made by Lagat (2004).

Permeability in Well OW-39A is very high, characterised by high fracturing, veining, the intensity of alteration, and circulation losses. The presence of calcite and the abundance of pyrite in this well indicate high past or present permeability. The well also shows high oxidation, indicating there were

channels/fractures of oxygen rich fluid flow in the rocks. Aquifer information is determined through the analysis of temperature logs run during and after completion of the well. Circulation losses/gains and alteration data play important roles in positioning aquifers. The aquifers in Well OW-39A were determined from temperature logs and are mainly associated with a high intensity of alteration, lithological boundaries, fractures and highly fractured rocks. Two intermediate aquifers occur at 750 and 1100 m. At 750 m, the aquifer is marked by a loss of circulation and high intensity of alteration, while at 1100 m (in trachyte), the aquifer is defined by high alteration intensity, veining and fracturing. From the interpretation of the temperature profile, this aquifer (1100 m) could be a channel of cold fluids into the well. A major aquifer at 2100 m is associated with an intrusion of syenitic composition, but fracturing was observed at the intrusion contact. In Well OW-37A, major aquifers were noted in trachyte at 1250 m, marked by circulation losses, fracturing and high intensity of alteration and at 2600 m, by loss of circulation. In Well OW-35, three major aquifers were identified. At 980 and 1480 m, the aquifers were marked by high intensity of alteration, an abundance of pyrite, oxidation and veining, while at 2900 m the aquifer was marked by fracturing, intrusives, veining and lithological contact between rhyolite and syenitic intrusions.

Hydrothermal alteration minerals were observed in the veins, vugs and vesicles and as a replacement of primary minerals. Their distribution in active geothermal fields depends on the ability of fluid to approach equilibrium in host rocks at any scale during the hydrothermal processes. In this well (OW-39A), the appearance of smectite (134, 384 m) and kaolinite (572 m) indicate temperatures of less than 200°C, whereas kaolinite indicates the presence of acidic fluids. Illite and chlorite are the dominant clay minerals in this well, appearing down to the well bottom.

The study of the hydrothermal distribution pattern shows five distinct alteration zones with the first appearance of the index minerals coinciding with the upper boundary of each zone. These are: the unaltered zone (0-134 m) that has no alteration related to geothermal activity, suggesting temperatures of <40°C. The second zone (zeolite-smectite zone) that extends from 134 to 578 m is the lowest grade mineral alteration zone, indicating alteration temperatures of <200°C. It is characterised by high oxidation and abundant zeolites. The third zone (chlorite-illite zone), which is marked by the first appearance of chlorite, occurs between 578 and 748 m. The zone is fractured as evidenced in the veining and is characterised by an abundance of pyrite and calcite, suggesting the zone is highly permeable. Epidote-chlorite-illite is the fourth zone, extending from 748 to 896 m. The top depth is marked by the first appearance of epidote and is characterised by high oxidation, veining, high intensity of alteration, and an abundance of pyrite and calcite, indicating that the zone is also highly permeable. The appearance of epidote in this zone indicates that the alteration temperature at 748 m and below could be above 250°C. Other minerals present in this zone include albite, prehnite, sphene, quartz, chlorite, illite, fluorite, pyrite, calcite and oxides. The fifth zone extends from 896 m to the bottom of the well. It is marked by the first appearance of actinolite at 896 m, indicating temperatures above 280°C below this depth. It is characterised by the mineral assemblage of actinolite, wollastonite, epidote and prehnite. Other minerals in this zone include pyrite, calcite, fluorite, chlorite, illite, and oxides. The absence of actinolite for a long interval between 1488 and 2210 m in the well could indicate the absence of favourable conditions, such as high temperature, for the formation of actinolite.

Successive sequences of mineral deposition in vesicles and veins is influenced by variations in pressure, temperature and the chemical composition of hydrothermal fluids that result in the precipitation of different hydrothermal alteration minerals at different times (Reyes, 2000). In Well OW-39A, it was observed that sequences at shallow depths consisted of low temperature minerals while a high temperature mineral sequence was found at depths below 890 m. The mineral deposition sequence in the veins and vesicles showed systematic gradation from low to high temperature minerals throughout the well, implying that the low temperature minerals were older as they were deposited first and the subsequent high temperature minerals were younger. This reveals that during the deposition of these minerals, the geothermal system around the well was heating up.

The homogenization temperature (T_h) values, analysed from fluid inclusions in a quartz vein from 812 m in Well OW-39A, ranged from 210 to 285°C, but formed two populations; the lower T_h value range is 210-220°C, while the higher one is 235-285°C. For comparison, the measured (formation) temperature at this depth is 208°C. Inclusions in the healed fractures had a T_h range of 210-220°C, representing current conditions, while the primary inclusions had a T_h range of 235-285°C. These measurements indicate that the inclusions with lower T_h range (210-220°C) are near equilibrium with the current formation temperatures, whereas the high-temperature range (235-285°C) inclusions are far above the formation temperature, but in equilibrium with the alteration temperature. The wide range in T_h temperature reveals two geothermal phases in the proximity of the well, meaning the temperature was higher than 280°C at one point in time, but has since cooled to ~210°C. Alteration temperature is far above the formation temperature below 392 m (Figure 10) indicating the reservoir is cooling below this depth.

The alteration mineral correlation between Wells OW-39A, OW-37A and OW-35 (Figure 9) indicates that the chlorite-illite zone is thinner in Well OW-39A while it is thicker in Wells OW-37A and OW-35, implying a higher temperature gradient with depth in Well OW-39A. Epidote occurs at a shallower depth in Wells OW-39A (1390 m a.s.l.) and OW-35 (1288 m a.s.l.), but deeper in Well OW-37A (845 m a.s.l.). This zone is thicker in Well OW-35 than in the other two wells. Actinolite appears at the shallowest depth in Well OW-39A and deeper in Well OW-35A, hence the actinolite zone is thicker in Well OW-39A. The plots indicate that this shallow zone in Well OW-39A indicates higher alteration temperatures at shallow depth, possibly caused by an upflow zone and higher permeability around Well OW-39A. Formation and alteration temperatures are within the same range, i.e. almost at equilibrium in Wells OW-37A and OW-35 but, in Well OW-39A, formation and alteration temperature are reversed. That is, the alteration temperature indicates a previous upflow zone in the vicinity around this well, while the current formation temperature indicates a reversal in temperature, probably due to cold water inflow and mixing.

Well OW-39A was drilled directionally to the south, adjacent to the Ololbutot fault which is a N-S trending eruptive fissure which erupted approximately 180±50 yrs. (Clarke et al., 1990). Gylfadóttir et al. (2011) noted that this fault appears to represent a long term groundwater flow structure breaking through the hydrological barrier that the Olkaria region forms, south of Lake Naivasha. Permeability connected to the groundwater systems can also shape the alignment of the thermal reservoir, as is postulated as being the cause of the separation between Olkaria West and East (Ololbutot fissure). Observations made from oxidation trends, veining and temperature logs in Well OW-39A indicate that the well is highly fractured and that these fractures act as groundwater flow channels in the rock formations. Also, the reversal in alteration (through fluid inclusion analysis) and formation temperatures (Figure 12) observed in the well indicates that the fluid flow in the area around the well has been reversed using the same geothermal structure, implying an old hot geothermal structure reversed to a “cold geothermal barrier” which has resulted in cooling of Well OW-39A. Observations made from hydrothermal alteration mineralogy and a mineral deposition sequence do not show a temperature reversal, hence, signs of cooling are not evident. This could probably imply that the cooling of the area around the well is a recent event.

6. CONCLUSIONS

- The lithology of Well OW-39A is composed of pyroclastics, tuffs, rhyolites, basalts, trachytes and minor basaltic, rhyolitic, syenitic and granitic intrusions. The rock types conform to the general geology of Olkaria.
- The thick (~80 m apparent thickness) granitic intrusion could originate from a deeper granitic body which may be a heat source.
- Stratigraphic correlation of Wells OW-39A, OW-37A and OW-35 indicates the possible existence of a normal fault between Wells OW-39A and OW-37A, and Wells OW-37A and OW-35.

- Hydrothermal alteration mineral assemblages and their distribution in the well are mainly controlled by temperature, rock type, fluid composition and permeability. Low temperature minerals were found in the upper part while high temperature minerals reside in the deeper part.
- Mineral depositional sequences in vesicles and veins in the well show systematic gradation of hydrothermal alteration minerals, ranging from low temperature to high temperature, indicating a history of heating in the reservoir.
- Five alteration zones were identified, based on hydrothermal mineral assemblages. These include: an unaltered zone (0-134 m); a zeolite-smectite-illite zone (134-578 m); a chlorite-illite zone (578-748 m); an epidote-chlorite zone (748-896 m); and an actinolite-epidote-wollastonite zone (896-3066 m).
- Temperature profile monitoring and geological evidence indicate Well OW-39A is highly permeable above 2250 m.
- Aquifers in this well show a close association with circulation losses, fractured formations, and lithological contacts between the formation and intrusions at depth. High past and present permeability in this well is indicated by the high abundance of pyrite and calcite, high alteration intensity, high oxidation, fracturing and the high occurrence of veins. High oxidation in this well may also indicate groundwater flow in the fractures in the area around the well.
- Comparison between fluid inclusion, alteration, and formation temperature indicate evidence of two geothermal phases in proximity to the well; the first phase of elevated temperatures is succeeded by a cooling phase. Hence, the well is cooling.
- Alteration zones in Well OW-39A show a marked elevation compared to neighbouring Wells OW-37A and OW-35, suggesting that the well is nearer to an upflow zone than the others. However, a comparison of the formation temperatures of the same wells show much lower temperatures in Well OW-39A, indicating that the upflow channel in proximity to the well may now be acting as an inflow of cooler fluids from outside of the geothermal system. An assumption was made that the measured temperature in the well is the same as the formation temperature.
- Observations made from hydrothermal alteration mineralogy and the mineral deposition sequence did not show a temperature reversal, hence, signs of cooling were not evident. This might imply that the cooling of the area around the well is a recent event, possibly younger than the Ololbutot eruptive fissure.

ACKNOWLEDGEMENTS

My first sincere gratitude is expressed to the United Nations University Geothermal Training Programme (UNU-GTP) and the Government of Iceland for granting me this opportunity to study and widen my understanding of geothermal energy. Special thanks go to the former director of the UNU-GTP, Dr. Ingvar B. Fridleifsson, Mr. Lúdvík S. Georgsson, director, Ms. Thórhildur Ísberg, Mr. Ingimar G. Haraldsson, Mr. Markús A. G. Wilde and Málfríður Ómarsdóttir, for their coordinated assistance to smoothly see me through this course. I extend my gratefulness to my supervisors, Ms. Anette K. Mortensen, Dr. Björn S. Hardarson and Dr. Hjalti Franzson, for their tireless technical assistance, dedication and availability during the entire project time. Thanks go to Sigurdur Sveinn Jónsson for his assistance in interpretation of X-RD data and to all other ISOR staff.

I would also like to thank my employer, Kenya Electricity Generating Company (KenGen), for granting me the opportunity to attend this course. Special thanks go to my fellow borehole geologists, Tito, Loice and Claudia, for their immense support during the project. To the 2013 UNU fellows, thanks for creating a conducive environment that made me feel at home.

Special thanks go to parents, my husband, and my children for their endless love, moral support, encouragement and prayers during the six months period.

Finally, I wish to express my heartfelt gratitude to the almighty God for giving me strength and for how far he has brought me.

REFERENCES

- Ambusso, W.J. and Ouma, P.A., 1991: Thermodynamic and permeability structure of Olkaria Northeast field: Olkaria fault. *Geothermal Resource Council, Trans.*, 15, 237-242.
- Baker, B.H., and Wohlenberg, J., 1971: Structural evolution of the Kenya Rift Valley. *Nature*, 229, 538-542.
- Baker, B.H., Mohr, P.A., and Williams, L.A.J., 1972: Geology of the Eastern Rift System of Africa. *Geological Society of America, Special Paper 136*, 1-67.
- Baker, B.H., Williams, L.A.J., Miller, J.A., and Fitch, F.J., 1971: Sequence and geochronology of the Kenya Rift volcanics. *Tectonophysics*, 11, 191-215.
- Browne, P.R.L., 1978: Hydrothermal alteration in active geothermal fields. *Annual Review Earth & Planetary Sciences*, 6, 229-250.
- Browne, P.R.L., 1984: Subsurface stratigraphy and hydrothermal alteration of the eastern section of the Olkaria geothermal field, Kenya. *Proceedings of the 6th New Zealand Geothermal workshop*, Geothermal Institute, Auckland, 33-41.
- Browne, P.R.L., and Ellis, A.J., 1970: The Ohaki-Broadlands hydrothermal area, New Zealand: mineralogy and related geochemistry. *Am. J. Sci.*, 269, 97-131.
- Clarke, M.C.G., Woodhall, D.G., Allen, D., and Darling G., 1990: Geological, volcanological and hydrogeological controls on the occurrence of geothermal activity in the area surrounding Lake Naivasha, Kenya, with coloured 1:100 000 geological maps. Ministry of Energy, Nairobi, 138 pp.
- Franzson, H., 1998: Reservoir geology of the Nesjavellir high-temperature field in SW-Iceland. *Proceedings of the 19th Annual PNOC-EDC Geothermal Conference, Manila*, 13-20.
- Franzson, H., 2013: *Borehole geology*. UNU-GTP, Iceland, unpublished lecture notes.
- Gylfadóttir, S.S., Halldórsdóttir, S., Arnaldsson, A., Ármannsson, H., Árnason, K., Axelsson, G., Einarsson, G.M., Franzson, H., Fridriksson, Th., Gudlaugsson, S.Th., Gudmundsson, G., Hersir, G.P., Mortensen, A.K. and Thordarson, S., 2011: *Revision of the conceptual model of the Greater Olkaria geothermal system-phase I*. Mannvit/ÍSOR/Vatnaskil/Verkís Consortium, report, Reykjavík, 100 pp.
- Harvey, C.C., 1998: *The application of clay mineralogy to the exploration and development of hydrothermal resources*. Geothermal Institute, University of Auckland, NZ, unpublished lecture notes.
- Haukwa, C.B., 1984: *Recent measurements within Olkaria East and West fields*. Kenya Power Co., internal report, 13 pp.
- Kristmannsdóttir, H., 1979: Alteration of basaltic rocks by hydrothermal activity at 100-300°C. In: Mortland, M.M., and Farmer, V.C. (editors), *International Clay Conference 1978*. Elsevier Scientific Publishing Co., Amsterdam, 359-367.
- Lagat, J.L., 1998: *Borehole geology of well OW-801, Olkaria South East Field*. KenGen, Kenya, internal report, 12 pp.

Lagat, J.L., 2004: *Geology, hydrothermal alteration and fluid inclusion studies of Olkaria domes geothermal field, Kenya*. University of Iceland, MSc thesis, UNU-GTP, Iceland, report 2, 71 pp.

Lagat, J., 2007: *Borehole geology of OW-904A*. KenGen, Kenya, internal report.

Leach, T.M., and Muchemi G.G., 1987: Geology and hydrothermal alteration of the North and West exploration wells in the Olkaria geothermal field, Kenya. *Proceedings of the 9th New Zealand Geothermal Workshop, Geothermal Institute, Auckland*, 187-192.

MacDonald, R., Black, H.E., Fitton, J.G., Marshall, A.S., Nejberr, K., Rodgers, N.W., and Tindle, A.G., 2008: The roles of fractional crystallization, magma mixing, crystal mush remobilization and volatile melt interactions in the genesis of a young basalt-peralkaline rhyolite suite, the Greater Olkaria volcanic complex, Kenya Rift Valley. *J. Volcanology*, 49-8, 1515-1547.

MacDonald, R., Black, S., Fitton, J.G., Rogers, N.W., and Smith, M., 2001: Plume-lithospheric interactions in the generation of the basalts of the Kenya Rift, East Africa. *J. Petrology*, 42, 877-900.

MacDonald, R., Davies, G.R., Bliss, C.M., Leat, P.T., Bailey, D.K., and Smith, R.L., 1987: Geochemistry of high silica peralkaline rhyolites, Naivasha, Kenya rift valley. *J. Petrology*, 28, 979-1008.

Marshall, A.S.L., Macdonald, R., Rogers, N.W., Fitton, J.G., Tindle, A.G.N., Nejberr, K., and Khinton, R.W., 2009: Fractionation of peralkaline silicic magmas: The Greater Olkaria volcanic complex, Kenya Rift valley. *J. Petrol.*, 50, 323-359.

Mathews, A., 1976: Magnetite formation by the reduction of hematite with iron under hydrothermal conditions. *American Mineralogist*, 61, 927-932.

Mosley, P.N., 1993: Geological evolution of the late Proterozoic “Mozambique belt” of Kenya. *Tectonophysics*, 221, 223-250.

Muchemi, G.G., 1992: *Geology of the Olkaria North East field KPC*. KenGen, Kenya, internal report.

Muchemi, G.G., 2000: *Conceptual model of Olkaria geothermal field*. KenGen, Kenya. KenGen, internal report.

Mungania, J., 1992: *Preliminary field report on geology of Olkaria volcanic complex with emphasis on Domes area field investigations*. Kenya Power Company, internal report.

Mungania, J., 1999: *Geological report of well OW-714*. Kenya Power Company, Kenya, internal report.

Musonye, X.S., 2012: Borehole geology and alteration mineralogy of well OW-914A, Domes area Olkaria geothermal field. Report no 23 in: *Geothermal training in Iceland*, 501-540.

Mwangi, D. W., 2012: Borehole geology and hydrothermal mineralization of well OW-916, Domes geothermal field. Report no 24 in: *Geothermal training in Iceland*, 541-571.

Mwania, M., Munyiri, S., and Okech, E., 2013: Borehole geology and hydrothermal mineralisation of well OW-35, Olkaria East geothermal field, Central Kenya Rift Valley. Report 1 in: *Geothermal training in Kenya*. UNU-GTP, Iceland, 1-56.

Naylor, W.I. 1972: *The geology of Eburru and Olkaria geothermal prospects*. UNDP project report, KPC, 58 pp.

- Njathi, D.W., 2012: Borehole geology and hydrothermal mineralization of well OW-911A, Olkaria Domes geothermal field, Kenya. Report no 25 in: *Geothermal training in Iceland*. UNU-GTP, Iceland, 573-600.
- Ogoso-Odongo, M.E., 1986: Geology of Olkaria geothermal field. *Geothermics*, 15, 741-748.
- Omenda, P. A., 1990: *Geological report for Olkaria well OW-305*. KPC internal report.
- Omenda, P.A., 1994: The geological structure of the Olkaria west geothermal field, Kenya. *Proceedings of the 19th Stanford Geothermal Reservoir Engineering Workshop, Stanford, Ca*, 125-130.
- Omenda, P.A., 1998: The geology and structural controls of the Olkaria geothermal system, Kenya. *Geothermics*, 27-1, 55-74.
- Omenda, P.A., 2000: Anatectic origin for comendite in Olkaria geothermal field, Kenya Rift; Geochemical evidence for syenitic protholith. *African J. Science and Technology. Science and Engineering Series*, 1, 39-47.
- Omenda, P.A., 2007: The geothermal activity of the East African rift. *Presented at Short Course II on Surface Exploration for Geothermal Resources, organised by UNU-GTP and KenGen, at Lake Naivasha, Kenya*, 12 pp.
- Onacha, S.A., 1993: *Resistivity studies of the Olkaria-Domes geothermal project*. Kenya Power Company, internal report.
- Otieno, V., and Kubai, R., 2013: Borehole geology and hydrothermal mineralisation of well OW-37A, Olkaria East geothermal field. Report 2 in: *Geothermal training in Kenya*. UNU-GTP, Iceland, 57-105.
- Pendon, R.R., 2006: *Borehole geology and hydrothermal mineralisation of well HE-22, Ölkelduháls field, Hengill area, SW-Iceland*. Report 17 in: *Geothermal training in Iceland 2006*. UNU-GTP, Iceland, 357-390.
- Reyes, A.G., 2000: *Petrology and mineral alteration in hydrothermal systems. From diagenesis to volcanic catastrophes*. UNU-GTP, Iceland, report 18-1998, 77 pp.
- Roedder, E., 1984: *Fluid inclusions*. Mineral. Soc. Am., Rev. Mineral., 12, Washington, DC, 644 pp.
- Ronoh, I.J., 2012: Borehole geology and hydrothermal alteration of well OW-912B, Olkaria Geothermal field, Central Kenya Rift Valley. Report no 25 in: *Geothermal training in Iceland*, 695-732.
- Ryder, A.J.D., 1986: *Geological report of well OW-701 Olkaria geothermal field, Kenya*. KenyaPower Company report, prepared by GENZL.
- Saemundsson, K., and Gunnlaugsson, E., 2002: *Icelandic rocks and minerals*. Edda and Media Publishing, Reykjavík, Iceland, 233 pp.
- Shackleton, R.M., 1986: Precambrian collision tectonics in Africa. In: Coward, M.P., and Ries, A.C., *Collision Tectonics, Geological Society Special Publication*, 19, 329-249.
- Simiyu, S.M., 1996: *Integrated geophysical study of the southern Kenya rift*. University of Texas, El Paso, PhD thesis.
- Simiyu, S.M., and Keller, G.R., 1997: Integrated geophysical analysis of the East African Plateau from gravity anomalies and recent seismic studies. *Tectonophysics*, 278, 291-314.

Simiyu, S.M., Oduong, E.O., and Mboya, T.K., 1998: *Shear wave attenuation beneath the Olkaria volcanic field*. KenGen, Kenya, internal report, 29 pp.

Simmons, S F., and Christenson, B.W., 1994: Origins of calcite in boiling geothermal system. *American Journal of Science*, 294 361-400.

Smith, M., 1994: Stratigraphic and structural constraints on mechanisms of active rifting in the Gregory Rift, Kenya. *Tectonophysics*, 236, 3–22.

Smith, M., and Mosley, P., 1993: Crustal heterogeneity and basement influence on the development of the Kenya rift, East Africa. *Tectonics*, 12, 591-606.

Thiessen, R., Burke, K. and Kidd, W.S.F., 1979: African hotspots and their relation to the underlying mantle. *Geology*, 7, 263-266.

Thompson, A.O., and Dodson, R.G., 1963: *Geology of the Naivasha area*. Geological Survey of Kenya, Kenya, report 55.

Wheeler, W.H., and Karson, J.A., 1994: Extension and subsidence adjacent to a “weak” continental transform: an example of the Rukwa Rift, East Africa. *Geology*, 22, 625-628.

Virkir Consulting Group, 1980: *Geothermal development at Olkaria*. Report prepared for Kenya Power Company.

APPENDIX I: XRD analysis from Well OW-39A

OW-39A_#07_UNT (572 m)

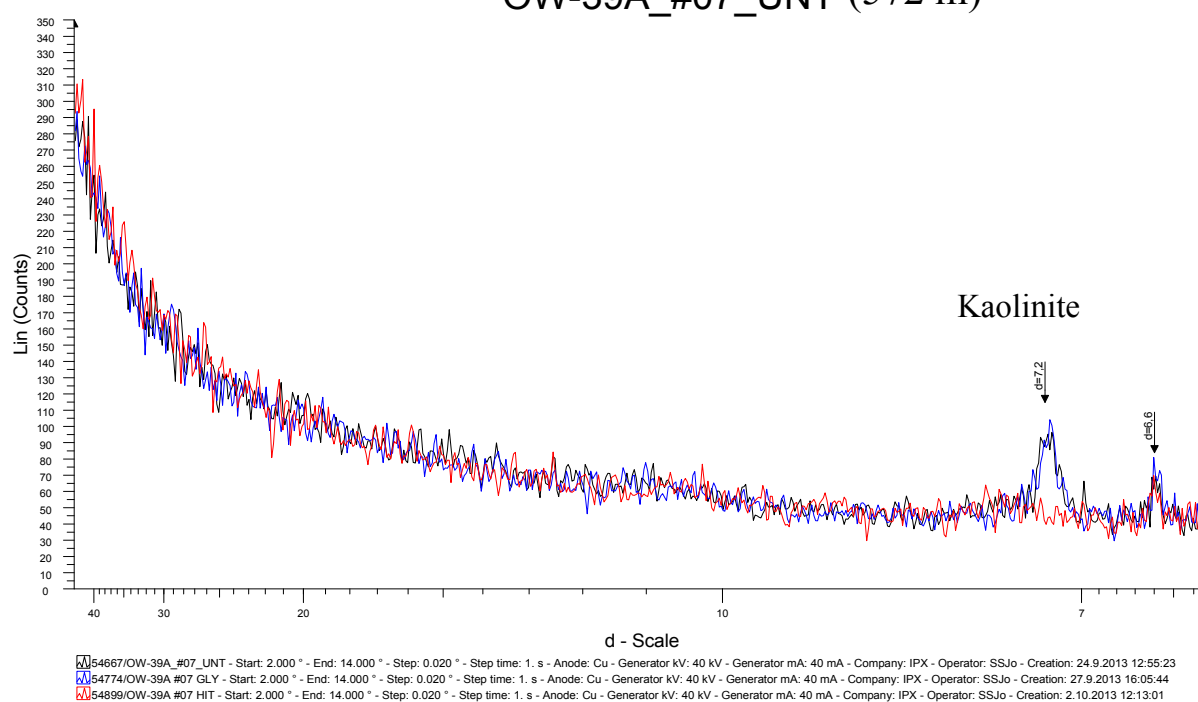


FIGURE 1: XRD analysis showing kaolinite peak

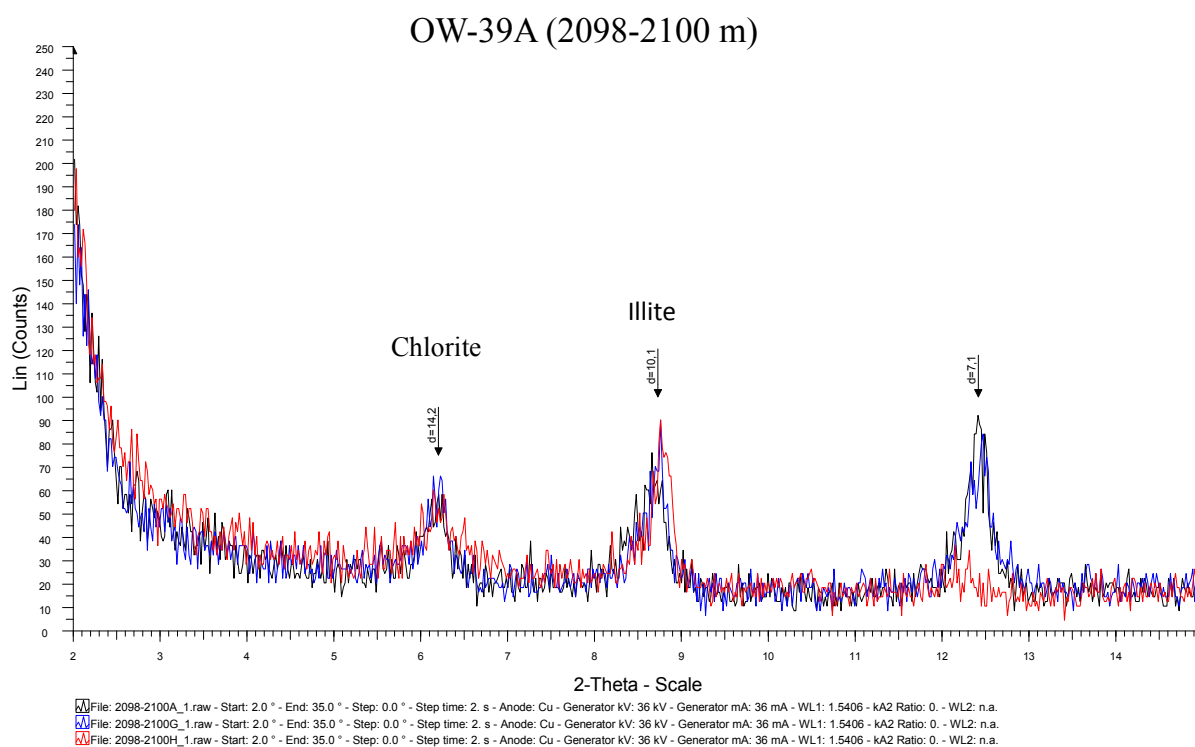


FIGURE 2: XRD analysis showing chlorite and illite peaks



**UNITED NATIONS
UNIVERSITY**

GEOTHERMAL TRAINING PROGRAMME
Orkustofnun, Grensasvegur 9,
IS-108 Reykjavik, Iceland

Reports 2013
Number 25

GEOTHERMAL DRILLING TIME ANALYSIS: A CASE STUDY OF MENENGAI AND HENGILL

Lilian Aketch Okwiri

Geothermal Development Company, Ltd. - GDC
P.O. Box 17700 - 20100
Nakuru
KENYA
lokwiri@gdc.co.ke

ABSTRACT

Drilling operations are run on tight schedules and drilling time delays come at a high cost. A large part of drilling workdays is spent on making the wellbore, and activities that support drilling, contribute to productive time (PT), while a significant part of the time is spent on drilling problems, and activities aimed at finding solutions and solving these problems. This contributes to non-productive time (NPT). Problems occurring during drilling can be avoided sometimes but, on other occasions, they are beyond the drilling crew's control; the causes are numerous and their effects are undesirable. This paper evaluates the extent of NPT associated with 15 wells drilled in Menengai, as well as identifying their causes and effects, and finally suggests recommendations aimed at increasing PT while reducing NPT to make the drilling process more effective. Data from 19 wells in Iceland were used for comparison. Workdays were analysed for 12 activities including: actual drilling, casing, cementing casings, cementing losses, equipment repair, wait on water, logging, changing the bit and bottom hole assembly (BHA), fishing, stuck pipe, reaming and 'other' activities. 'Other' activities were mostly waiting on materials, instructions and personnel. Blow out preventers (BOP) and wellhead installation and any other equipment installed after spading was included in this category. The analysed data was obtained from completion reports and drilling logs.

Because of the challenging geological conditions, drilling wells in Menengai took longer time than planned. In addition, the field was new and the crew did not know what to expect. The crew members were also new to each other and had to become accustomed to working together. Lost circulation was the major formation problem experienced, resulting in further problems of stuck pipe and drillstring failure. Drilling problems due to the formation increased with depth, with major challenges experienced at depths of about 2200 m, with a stuck pipe topping the list of drilling problems. It was concluded that productive time in Menengai could be increased through a change in technology, especially bit technology, while activities such as cementing could be accelerated with more knowledge of the subsurface conditions through logging and a thorough job of managing the loss zone. It is not possible to totally eliminate NPT, but minimizing it and increasing PT will result in a shorter project implementation time and reduce drilling costs.

1. INTRODUCTION

The objective of drilling a geothermal well is to drill a fit-for-use well, in a safe manner, using the available technology while minimising the overall cost. To control well costs, it is important to improve drilling efficiency and cut down on drilling time. Time analysis of drilling a well is important as it will eventually influence the economic analysis of a drilling project.

Drilling operations are not always completed on schedule. There are many factors and events that come into play, such as drilling problems and some technical and non-technical non-productive time (NPT), pushing the drilling operation behind schedule, hence, increasing the cost of the wells. It is almost certain that problems will occur while drilling a well, even in very carefully planned wells. For example, in areas in which similar drilling practices are used, hole problems may be reported where no such problems existed previously, because the formations are non-homogeneous. Therefore, two wells near each other may have totally different geological conditions (PetroWiki, 2013a).

The most common drilling problem in geothermal wells leading to NPT has always been formation related, leading to stuck pipes and bottom hole assembly failure. In some cases, efforts to retrieve the string are unsuccessful and this leads to the expensive process of side-tracking or, in the worst case, abandoning the well when further work is no longer considered economically viable. Such wells bring the drilling company into time overruns and eventually cost overruns. Other common causes of NPT in drilling geothermal wells include, but are not limited to, lost circulation, formation damage and rig equipment failure. Personnel experience and available technology may also influence drilling time.

This paper presents an analysis of the drilling time of 15 wells drilled in Menengai geothermal field and compares them to 19 wells drilled in Hengill field in Iceland. Time spent on different activities was analysed and how they, in turn, affected the drilling performance with an emphasis on NPT as the major cause of drilling time extension. The aim of this paper is to identify the NPT affecting wells drilled in Menengai field, using wells drilled in Hengill area for comparison, determine their causes and effects and attempt to come up with solutions to reduce them and positively influence drilling performance. The activities analysed included actual drilling, running casing, cementing casing and circulation losses, logging, reaming, fishing, stuck drill pipe, repairs, wait on water and 'other' activities.

1.1 Menengai

Menengai is a major Quaternary caldera volcano forming one of fourteen geothermal sites in Kenya. It is located within the axis of the central segment of the Kenya Rift just north of Nakuru town and a few kilometres south of the equator. The Menengai geothermal field is characterized by complex tectonic activity associated with two rift floor tectono-volcanic axes (TVA), Molo and Solai, that are important in controlling the geothermal system (Njue, 2011).

Geothermal drilling in Menengai field started in February 2011. The aim was to determine geothermal resource availability, hydrothermal capacity and the chemical characteristics of the resource. The project was initiated following a detailed exploration conducted in 2004 that pointed to the existence of an exploitable geothermal resource within the caldera. Currently, drilling of production wells is ongoing following the completion of exploration and appraisal wells. By July 3, 2013, fifteen wells had been completed. The location of these wells within the caldera is shown in Figure 1.

Drilling in Menengai is carried out using four rigs (Simba 1, Simba 2, Kifaru 1 and Kifaru 2) owned by Geothermal Development Company (GDC) in Kenya. Simba 1 and Kifaru 2 are top drive rigs, while Simba 2 and Kifaru 1 are rotary driven. All the rigs have the capacity to reach a depth of 7000 m with a maximum hook load of 4500 kN. Menengai geothermal wells have targeted depths of 2500 m, drilled in four sections, as shown in Figure 2. The casings are usually screwed together. The 26" hole is drilled using a tri-cone roller mill tooth bit down to 80m, while the other hole sections are drilled with a tri-

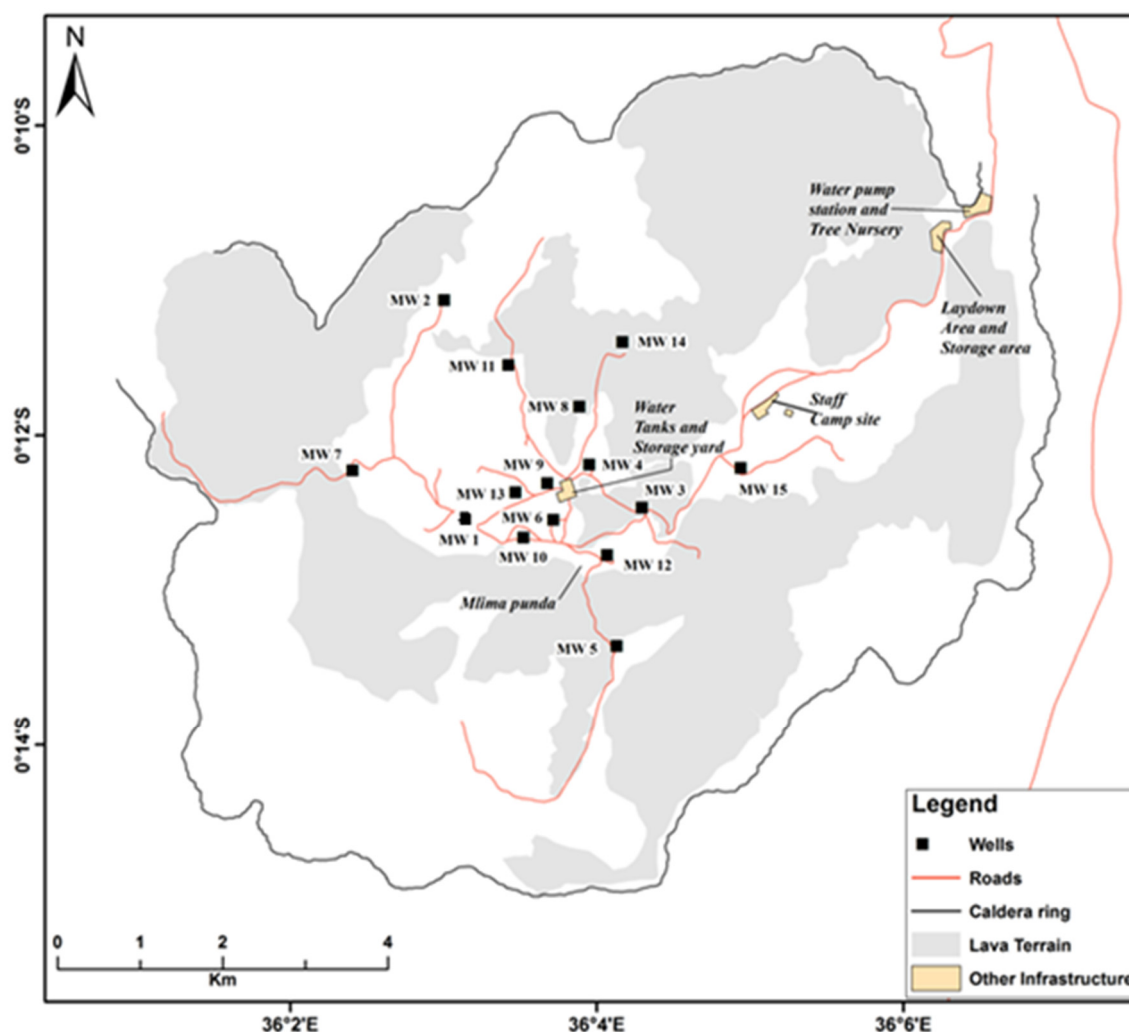


FIGURE 1: Location of wells in Menengai

cone roller tungsten carbide insert bit. Cementing is done using the single stage method where cement is pumped through the casing with backfills through the annulus, with 8 hours setting time in between cementing jobs. The drilling fluid used in the upper parts of the well is simple water-based bentonite mud. When fractured zones are encountered above the production casing shoe depth, attempts are made to seal these losses using Loss of Circulation Materials (LCM) and, in extreme cases, cement plugs are used. The final hole section is drilled with water and, in areas of lost circulation, aerated water and foam are used. The majority of well logging is carried out during well completion but a few are carried out during drilling. The well logs are usually temperature, pressure, injection tests and a full set of lithological logs when the wells are completed.

1.2 Hengill

The Hengill high-temperature field rates as one of the largest in Iceland. It is located 30 km east of Reykjavik on the eastern border of the Reykjanes Peninsula, SW-Iceland. The Hengill volcanic system is composed of crater rows and a large fissure swarm. It has a 100 km long NE-SW axis, 3-16 km wide. The Hengill central volcano covers an area of about 40 km² (Björnsson et al., 1986).

Hengill wells were drilled in four successive sections. Two small rigs with a hook-load capacity of 50 tonnes (t) were used for the initial drilling to 90 m depth. An intermediate size rig (100 t) was used for the shallow sections (1 and 2) of a few wells. Four larger rigs (179-300 t) were used for the main drilling. A total of seven drill rigs owned by the Iceland Drilling Ltd were used in the drilling effort. All the rigs

are hydraulic with a top-drive and the large ones have automatic pipe handling. The initial drilling (21" hole) in Hengill is performed with air hammer and foam or tricone bits with tungsten carbide inserts, using mud and water as circulation fluids. Rotary drilling techniques with tricone bits were applied in Section 1 from 90-300 m depth, but in section 2 from 300-800 m depth a mud motor was used to rotate the bit and a Measurement While Drilling (MWD) tool was inserted in the drillstring to monitor the direction (azimuth) and inclination of the well. In section 3 from the 800 m production casing to the total depth, no mud was used; drilling was carried out with water only as long as there were no severe circulation losses. Most wells were then switched over to aerated water by compressed air for pressure balance until the total depth was reached (Sveinbjörnsson and Thórhallsson, 2013). The casing programme for Hengill wells is as shown in Figure 3. Logging was done in all four sections of the Hengill wells when casing depths had been attained. Logs carried out were usually temperature and pressure; injection tests were generally carried out when a final depth had been reached to estimate the permeability of the well and to decide whether it should be protected with a perforated liner or whether it should be drilled deeper. Caliper logs were carried out before cementing casing and loss zones and cement bond logging (CBL) was carried out after cementing. A full set of lithological logs were carried out when a well was completed.

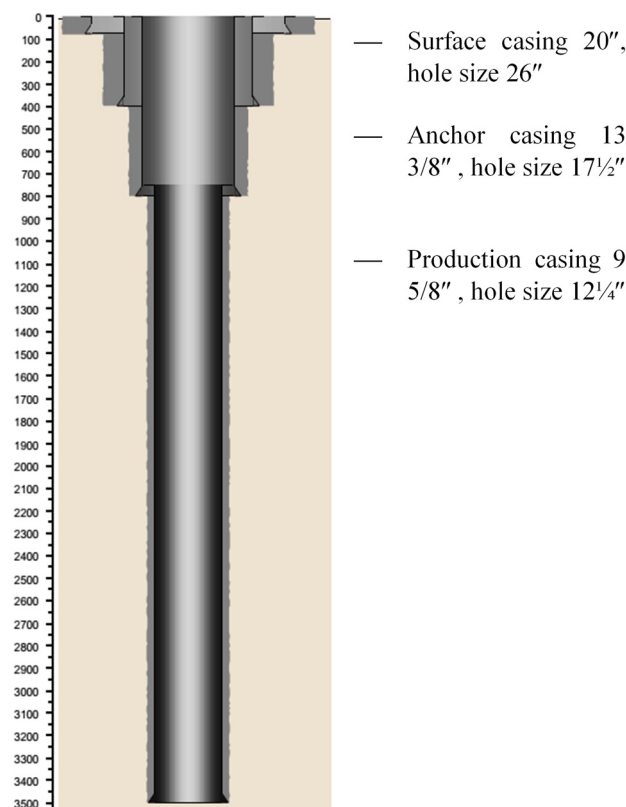


FIGURE 2: Casing programme for Menengai wells
(Figure generated in RIMDrill)

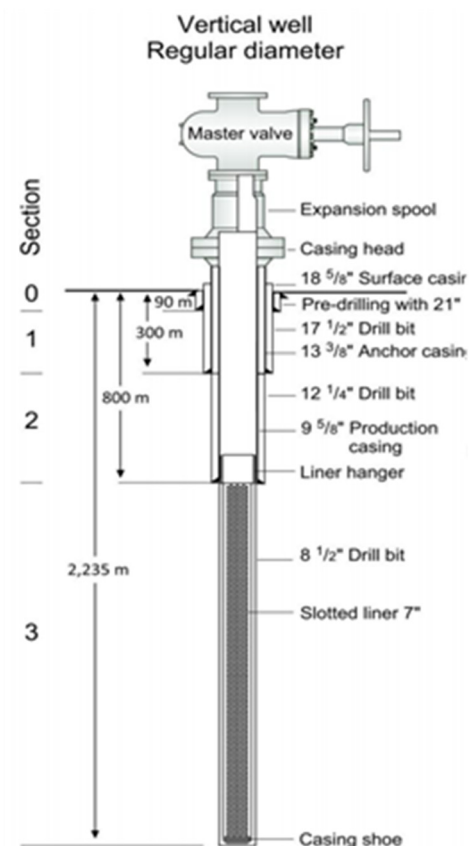


FIGURE 3: Casing programme for Hengill wells (Figure from ISOR)

2. DRILLING TIME ANALYSIS

2.1 Factors influencing drilling time

The time taken to drill and complete a well directly influences the cost of any geothermal project. Hence, completing a well in time is cost effective and essential. Noerager (1987) stated that the measured depth is the most important factor in predicting the time it will take to drill a well. But this is not always the case as drill rates are often constrained by factors that the driller does not control (Kaiser, 2007). These

factors include geologic conditions at the drill site where Rate of Penetration (ROP) is controlled by the hardness or softness of the formation, available weight on the bit, location of the target reservoir, physical characteristics and prevailing reservoir conditions. Exogenous events such as stuck pipe, adverse weather, and mechanical failure cannot be predicted and can have a significant impact on the time and cost to drill a well (Kaiser, 2007). Other factors such as wellbore quality, experience and preferences of the driller cannot be quantified. The technology and resources used also contribute to drilling rates. All these factors influence drilling performance metrics.

2.1.1 Geological conditions

The most obvious aspect of the downhole environment that influences drilling difficulty is the physical characteristics of the rock (lithology). Drilling through hard and very hard, abrasive formations results in the most difficult problems in the drilling industry, despite the developments and improvements of drilling tools, equipment, machines and techniques. Soft formations are easily eroded by the drilling fluid or mechanical abrasion caused by the drilling fluid, resulting in large cavities in the well bore. Cementing this type of formation is problematic and may result in an increase in the cementing time. Loose formations that collapse easily add to hole cleaning time and could end up causing a stuck pipe, while a fractured formation will result in lost circulation problems.

Information on the geology is obtained from drill chips/cuttings and lithology logs. Lack of knowledge of the change in hardness of the formation may cause several problems during a drilling operation. These unfortunate incidents may occur on the borehole wall, down in the hole or could lead to equipment wear and eventually equipment failure. Too little knowledge about the formation being drilled may lead to the wrong choice of bit. Incorrect bit type causes low ROP and eventually equipment failure (Solberg, 2012). Having the right information on the geology of the area is paramount in making sound decisions in planning for the well.

2.1.2 Prevailing reservoir conditions

Downhole pressure, temperatures and reservoir fluids affect the way a well is drilled. They provide information for locating the productive zones and, hence, influence where casings are set and how cementing is done. Formation pressure influences how much drilling fluid is pumped into the wellbore. Choosing the right pump rate is of great importance as higher formation pressure that overrules wellbore pressure will lead to kicks and eventually blowouts if not controlled. Higher wellbore pressures may cause formation damage and lost circulation problems, resulting in greater problems such as stuck pipes.

2.1.3 Available technology

Recent advancements in technology have benefitted the drilling industry and the choice lies with the operator to suit his preference. Top drive, power swivels, air/foam balanced drilling, PDC bits, horizontal drilling, casing while drilling, reverse circulation cementing, logging while drilling, environmentally safe fluid formulations, micro drills, and coiled tubing are all good examples of these improvements (Dumas et al., 2012). The use of current technology has revolutionised how drilling is carried out and increased drilling progress efficiency and safety. In addition, implementation of new technologies has led to a reduction in drilling time and cost. Even so, technology comes with its own challenges. For example, the sensitive nature of technologically advanced equipment such as a top drive predisposes them to more breakdowns, especially when drilling in areas with lots of vibration. This means more downtime for repairs for rigs with top drives than those without.

2.1.4 Equipment and consumables availability

Drilling operations are run on tight schedules and costs are based on the number of days needed to complete the operations. Therefore, drilling companies have invested in expensive equipment. It is important to ensure that this equipment is always available for efficient drilling. When equipment breaks

down, it is essential to restore it quickly through repair and replacement of parts. Spare parts for drill rigs are a complicated and important task to be handled. To avoid having to stop the drilling operations, it is very important to have a functioning system which can provide spare parts if and when a component breaks down or needs maintenance (Samland, 2011). It should be noted that the integrity of drilling equipment and its maintenance are major factors in minimizing drilling problems. Proper rig hydraulics (pump power) for efficient bottom and annular hole cleaning, proper hoisting power for efficient tripping out, proper derrick design loads and drilling line tension load to allow safe overpull in case of a sticking problem, and well-control systems (ram-, annular- and, internal preventers) that allow kick control under any kick situation are all necessary for reducing drilling problems. Proper monitoring and recording systems that monitor trend changes in all drilling parameters and can retrieve drilling data at a later date, proper tubular hardware specifically suited to accommodate all anticipated drilling conditions, and effective mud-handling and maintenance equipment that will ensure that the mud properties are designed for their intended functions are also necessary (PetroWiki, 2013b).

Drilling materials and consumables such as cement, fuel, drilling detergent, drilling mud and even water are also important; without these, drilling cannot proceed. Drilling operations will be greatly compromised without proper planning for these materials.

2.1.5 Personnel experience

Given equal conditions during drilling operations, personnel are the key to the success or failure of those operations (PetroWiki, 2013a). Drilling is an industry of learning by doing and it takes years to build the experience necessary for the industry. Experience will make a difference on how efficient a drilling job is carried out, in that operations will be safer and drilling performance improved. Other than experience, it is important to continue training personnel on new technologies and new engineering practices as the drilling industry is changing fast, with increased automation and better procedures intended to improve performance.

2.1.6 Well specification

Well specifications affect how much time is spent on a particular well. There may not be much time difference in drilling directional and vertical wells (Sveinbjörnsson, 2013), but directional wells do come with their own unique challenges, different from those encountered in vertical wells. More surveys must be carried out. It is not possible to apply desired weights or rotary speeds as it is in vertical wells. Other factors on well specification may include the number of casing strings and where they are set. Correct determination of where casing strings are set to shield against problematic zones, such as lost circulation zones, will ensure a reduction in drilling problems. Bit and casing size selection can mean the difference between a well that must be abandoned before completion and a well that is an economic and engineering success. Improper size selection can result in holes so small that the well must be abandoned because of drilling problems (PetroWiki, 2013a).

2.2 Drilling time

Drilling time is the time required to drill the wellbore to maximum depth. It includes productive time (PT) spent on activities that actually contribute towards the construction of the wellbore, and were planned for, and non-productive time (NPT) spent on activities that had to be done, but were not planned for. This information is presented in Table 1, showing a summary of PT and NPT activities, adapted from previous work done by Adams et al. (2009) to fit this study. Drilling time for a particular well or project can be identified through reports generated from drilling and logging wells in an area. This data is able to detect trends and irregularities in drilling time and delineate problematic areas. Proper analysis of drilling data will provide insight on expected characteristics and problems to be encountered in the well, which is important in planning for any well.

TABLE 1: Productive Time, PT, and Non-Productive Time, NPT, activities

Activity	PT	NPT
Drilling	Actual drilling Tripping in drill	Stuck pipe BHA change Reaming Fishing Circulating to clean well
Casing	Running in casing	Stuck casing\hung up casings Lay down damaged casing joints
Logging	Running in logging tool Actual logging	Stuck tool string
Cementing	Cementing casing	Cementing loss\plug jobs Cement backfills\top ups
Equipment	Equipment service	Equipment breakdown
Others	Nippling up BOP and Blowie line	Wiper tripe Tripping in for other reasons other than drilling Wait on materials, spares, fuel and personnel, water and instructions

2.2.1 Non-productive time (NPT) defined

Drilling time studies have been undertaken by companies for some time. All have different names for NPT. Amoco refers to this time as Unscheduled Events; BP calls it 'Non-Productive Time'; Mobil and Superior both call it 'Accountable Lost Time'; Dome refers to it as 'Problem Time'; while Exxon and Tenneco call it 'Trouble Time' (Kadaster et al., 1992).

NPT is any occurrence which causes a time delay in the progression of planned operations. It includes the workdays required to resolve that problem, and the time to bring the operation back to the point or depth at which the event occurred. NPT is, thus, anything that you did not intend to do but are required to do anyway. Therefore, anything that occurs outside of the well's original plan should be counted as NPT (Kadaster et al, 1992). Hsieh (2010) defines NPT as time periods during which the drilling operation is ceased or the penetration rate is very low; it is not a performance metric of what has gone wrong but a way to identify things that can be improved.

As companies consider the definition of NPT differently, activities considered to be non-productive are varied. It should be considered though that any activity that is carried out during drilling time without progress being made on the wellbore should fall into the NPT category.

2.2.2 The Causes of NPT

Causes of NPT in drilling are varied; they can be due to unforeseeable events that the drilling crew cannot control, or be due to inadequate planning for a job.

2.2.3 Effects of NPT

Time overrun affects the progress of drilling, leading to fewer wells being drilled by the end of the stipulated drilling project period. Time overrun means the drilling crew could not carry out their work within the scheduled period. It is important that the drilling time be reviewed at the completion of the well; knowledge built on the causes of the delays can be applied to the next wells to be drilled to improve efficiency.

Cost overrun: arises when the cost of the well surpasses the budget allocation. This could be due to overhead costs required to solve the problems that caused NPT and kept the crew on the rig for extra days. Drilling problems such as sticking and fishing may require the involvement of a fishing specialist which will increase the drilling cost. Cost overrun is related to time overrun; once a project cannot be completed on time, it will most certainly incur extra cost.

Change of well plan| side-tracking: When skill and force fail in retrieving a drillstring lost in a well, sometimes the only solution is to abandon the stuck portion and drill a sidetrack around it, changing the drilling program completely and potentially adding millions of dollars to the well cost (Aldred et al., 1999). Other reasons for sidetracking could be to get past a problematic zone such as a circulation loss zone that cannot be healed, or be an incompetent formation that keeps collapsing or a fishing challenge. This may be justified by the high investment already in that particular well, in terms of time and money, or the belief that the well will be a good producer. This is a consequence of NPT, as the change in plan always comes after time has been spent on trying to solve the problem.

The drilling plan may also be changed when drilling problems do not allow drilling to proceed. This may be due to harsh wellbore conditions, such as extreme temperatures, and pressures causing drillstring failure, leading to a reduction in the target depth to depths that the drillstring can perform.

Total abandonment: A well is abandoned when it is deemed no longer economically viable, in terms of time and cost, to continue putting resources into it, even when the well is at an advanced stage. Other reasons for abandoning a well are the same as those for changing a well plan or side tracking. Problematic wells that are advanced in depth may still be used for production, even if drilling is terminated before the target depth is reached.

3. DATA ANALYSIS

Of the total time it takes to drill a geothermal well, only 30-40% is actually spent in making a hole by rotating the drill bit on the bottom. The rest of the time is spent on: rig-up and down, installing cement casings, installing valves, logging, operations to solve drilling problems related to loss zones, instable formation or for “fishing” when the drill string becomes stuck or breaks. A good way to assess what the problem may be is to look at a curve plotting depth vs. days that the job has taken for each well. Any “flat spots”, where there is no advance in depth for several days, show up clearly and will indicate that there may be a problem (Thórhallson, 2006).

Figure 4 shows drilled depths vs. workdays for the Menengai wells. Wells MW10 and MW14 were abandoned at 740 and 750 m, respectively, following a stuck pipe. In both cases, attempts to free the string resulted in drillstring failure. The fishing exercise was unsuccessful. Well MW13 had a long flat time due to equipment breakdown. More than half of the wells had a long flat time at the end because of sticking.

Well construction activities and drilling problems affecting overall drilling time were considered for 15 wells drilled in Menengai and 19 wells drilled in Hengill to compare the total time for the wells. These wells are presented in Table 2. In the analysis of activities sections, more wells in Hengill were used to strengthen the data set.

TABLE 2: Summary of wells studied; note that section 0 is excluded in workdays

Icelandic wells				Kenyan wells			
Well no.	Total drilled depth (m)	Section 1 - 3		Well no.	Total drilled depth (m))	Section 1-3	
		Drilled depth (m)	Workdays			Drilled depth (m)	Workdays
HE-03	1,887.0	1,797.6	39	MW-01	2,207.0	2,126.3	70
HE-04	2,008.0	1,936.4	45	MW-02	3,200.0	3,120.0	112
HE-05	2,000.0	1,909.5	44	MW-03	2,112.5	2,031.5	85
HE-06	2,013.0	1,940.0	37	MW-04	2,117.0	2,035.1	72
HE-07	2,270.0	2,162.0	47	MW-05	2,095.7	2,034.7	89
HE-08	2,808.0	2,668.0	38	MW-06	2,203.0	2,122.0	73
HE-13	2,397.0	2,324.0	42	MW-07	2,135.9	2,076.9	109
HE-20	2,002.0	1,901.0	72	MW-08	2,355.6	2,290.5	113
HE-21	2,165.0	2,070.0	32	MW-09	2,089.0	2,027.5	92
HE-26	2,688.0	2,596.0	51	MW-10	740.8	679.4	94
HE-36	2,808.0	2,703.0	61	MW-11	1,842.0	1,771.5	122
HE-51	2,620.0	2,522.2	33	MW-12	1,842.0	1,783.0	82
HE-53	2,507.0	2,437.5	57	MW-13	2,012.1	1,950.8	141
HE-54	2,436.0	2,342.0	34	MW-14	750.1	687.8	117
HE-55	2,782.0	2,685.0	34	MW-15	1,679.6	1,603.6	68
HE-57	3,118.0	3,023.0	41				
NJ-23	1,751.0	1,659.0	45				
NJ-24	1,929.0	1,849.7	35				
NJ-25	2,098.0	1,993.0	31				
Average	2,330.9	2,237.8	43.1		1,958.8	1,889.4	95.9

The activities analysed included actual drilling, casing, cementing casing, cementing loss, repairs, sticking, fishing, change of BHA, wait on water and logging. Evaluation was made on the time taken for each activity, assuming NPT to be the main reason for the extended drilling time. Trip time was considered as part of the activity that was being tripped for, i.e., tripping time for BHA change was considered a part of the BHA change time, while tripping time for logging was considered as logging time. 'Other' activities referred to include time spent waiting on materials, fuel and instructions, installation of BOP and wellhead and any other activity time that was not captured in the analysis, most of them being NPT activities. To compare the drilling time for different activities, the respective numbers of workdays were normalized to the same reference well both for Menengai and Hengill wells.

Section 0 was excluded from the data in comparison for the total time because there was a difference in width of the surface hole, 26" in Menengai and 21" in Hengill, some of the data for Hengill wells was not available, and a small 50 t rig was used to drill them. Average depth drilled per day in sections 1, 2 and 3 for Hengill wells was 52 m/day and 22 m/day for wells drilled in Menengai. The average meters per day for Menengai wells were calculated without Wells MW10 and MW14, as the last section for these wells was never drilled. The sections used from Hengill wells were from both vertical and directional regular diameter wells because a former time analysis of directional and vertical wells resulted in no significant difference (Sveinbjörnsson, 2010). Table 3 shows the reference well used in normalisation of the data used in the analysis. The rest of the analysis was carried out, included more wells from Hengill including injection wells and wells whose designs were changed from large to regular diameter because of problems. These additional wells included six in section 0, six in section 1, four in section 2 and three in section 3.

TABLE 3: Reference well

	Depth
section 0	80
section 1	400
section 2	850
section 3	2000

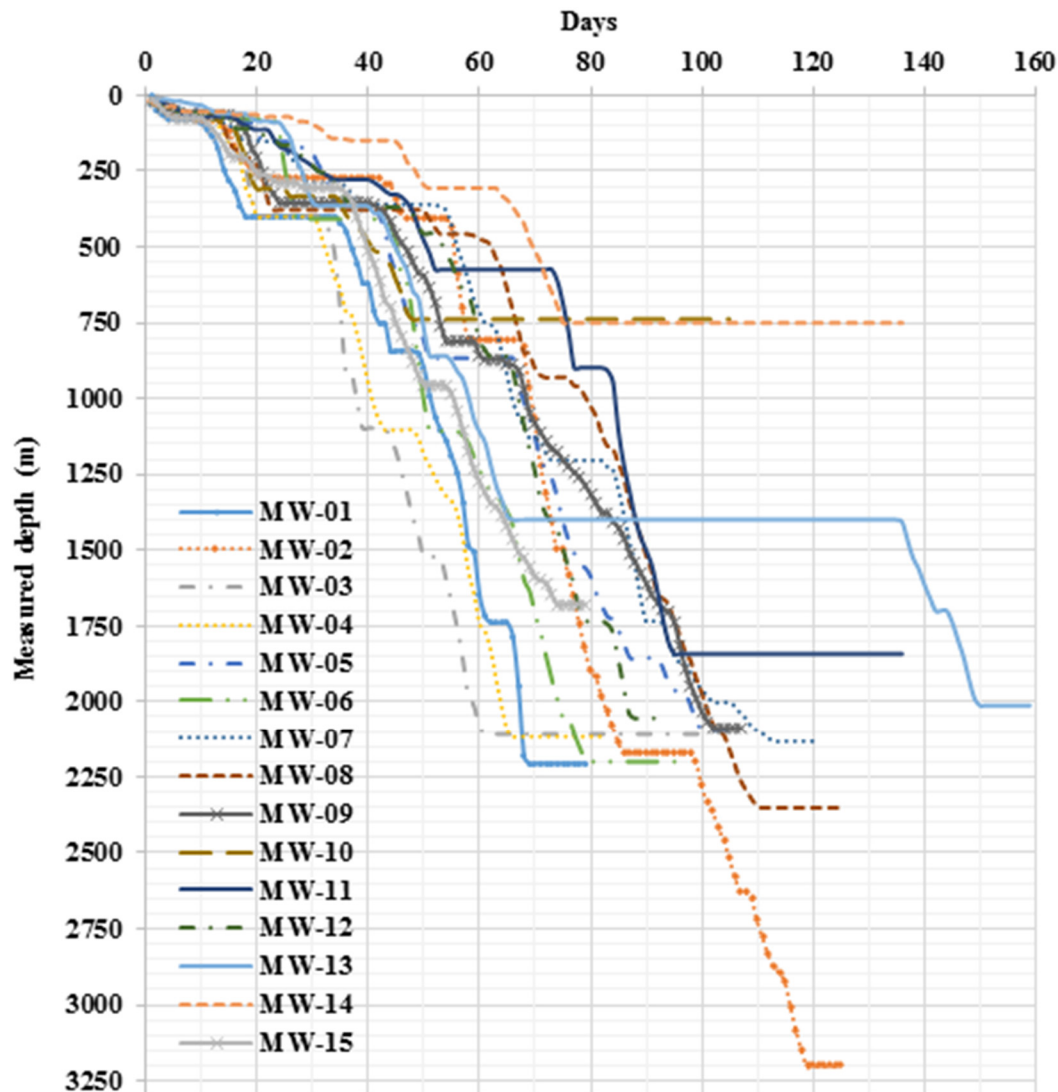


FIGURE 4: Depth vs. days graphs for Menengai wells MW01 to MW15

Equation 1 below was used for normalization of the drilling time data for different activities (Sveinbjörnsson, 2010).

$$T_i = \frac{\text{Drilled reference depth}}{\text{Actual drilled depth}} \times t_i \quad (1)$$

where T_i = The normalized number of workdays for section i ; and
 t_i = The actual number of days spent on section i .

Tables 4 and 5 show normalised data for each section and the overall average working days for Menengai and Hengill, respectively.

TABLE 4: Normalized days for activities in Menengai

Section	Total	Active drilling	Placing casing	Cementing casing	Cementing loss	Stuck	Reaming	Fishing	Wait on water	Changing bit	Repair	Logging	Other
0	16.7	6.5	0.5	2.6	0.9	0.2	0.5	0.1	0.6	0.1	0.6		4.1
1	31.0	10.4	1.0	3.5	2.5	0.7	1.5	0.8	3.1	0.5	0.9	0.4	5.8
2	16.1	8.1	0.6	2.4	0.5	0.1	0.3	0.9	0.2	0.7	0.4	0.2	1.7
3	45.3	20.1	1.3		0.0	5.1	1.2	2.3	0.7	2.0	5.6	1.2	6.0
Total	109.0	45.1	3.3	8.4	3.9	6.0	3.4	4.0	4.7	3.3	7.6	1.8	17.6

TABLE 5: Normalized days for activities in Hengill

Section	Total	Active drilling	Placing casing	Cementing casing	Cementing loss	Stuck	Reaming	Fishing	Wait on water	Changing bit	Repair	Logging	Other
0	5.10	2.53	0.65	0.81	0.59	0.05	0.25	0.05		0.08	0.02	0.09	
1	10.62	5.03	1.35	1.66	1.00	0.51		0.03				0.91	0.12
2	7.41	3.55	0.71	0.86	0.62	0.26	0.05		0.17	0.01	0.10	1.05	0.03
3	15.58	8.69	0.96		0.67	0.54	0.62	0.14	0.12	0.46	0.26	3.02	0.09
Total	38.7	19.8	3.7	3.3	2.9	1.4	0.9	0.2	0.3	0.6	0.4	5.1	0.2

Figures 5 and 6 show graphs of the workdays spent per well for actual drilled depths in each field, together with the average time. The data here excludes section 0 for reasons explained above. For the 3 sections used in the graph, the longest time spent on a well in Menengai was 141 days and the average time per well in Menengai was 94.5 days. The Hengill wells took an average of 43 days and the well with the most workdays took 72 days. These graphs were produced from raw data before normalisation.

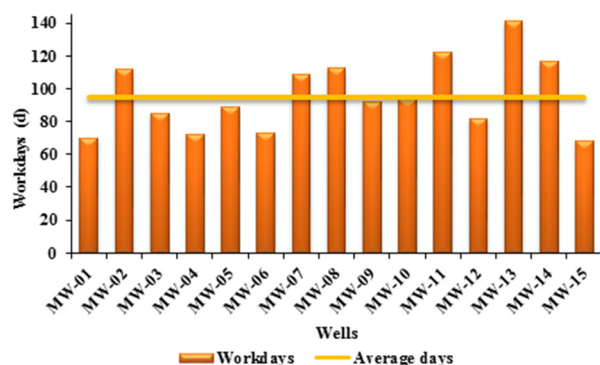


FIGURE 5: Menengai wells: actual workdays for actual drilled depths excluding section 0

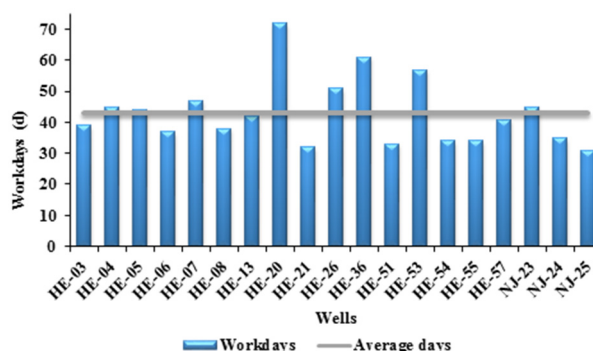


FIGURE 6: Hengill wells: actual workdays for actual drilled depths excluding section 0

Figures 7 and 8 are pie charts representing the percentage distribution of activities in Menengai and Hengill. 44% of the time in Menengai was spent on actual drilling, accounting for 45.1 days out of 109 days, while the category “other activities” took the second highest time with 14%, accounting for 17.6 days. 52% of the total time in Hengill was spent on actual drilling, accounting for 19.8 days, with logging taking up 16% of the total time, accounting for 5.1 days. The category ‘Other’ was lowest for Hengill with 1% accounting for 0.2 days, while logging was lowest for Menengai with 2% accounting for 1.8 days. Figure 9 is a bar graph comparing the two fields; the values were weighted by the average of activity time per section.

Figures 10 and 11 are pie chart representations of the NPT distribution in each field. The ‘other activities’ was the largest contributor of NPT in Menengai, with 37%, while cementing loss zones was the largest contributor of NPT in Hengill wells with 49%. The activities considered here as NPT were cementing loss, sticking, fishing, wait on water, changing bit, equipment repair and ‘other’ activities. These activities contributed to NPT as their occurrence hindered wellbore progress. The rest of the activities were considered as PT as they contributed directly to well creation. Figures 12 and 13 are pie chart representations of the ratio of PT to NPT in the two fields. Menengai wells experienced a larger

NPT. 40% of the total drilling days were spent on NPT which equals 43.7 days. Hengill wells experienced lesser NPT with only 14% of the total workdays, amounting to 5.4 days.

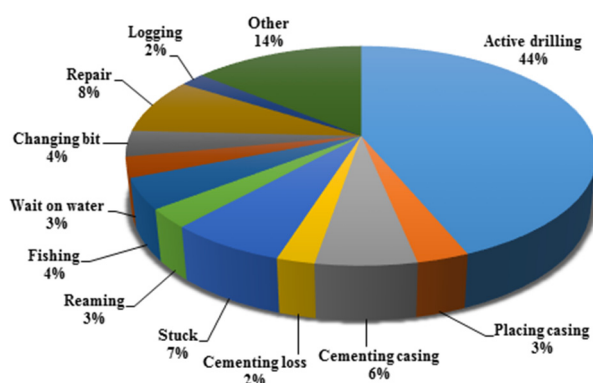


FIGURE 7: Percentage distribution of activities in Menengai

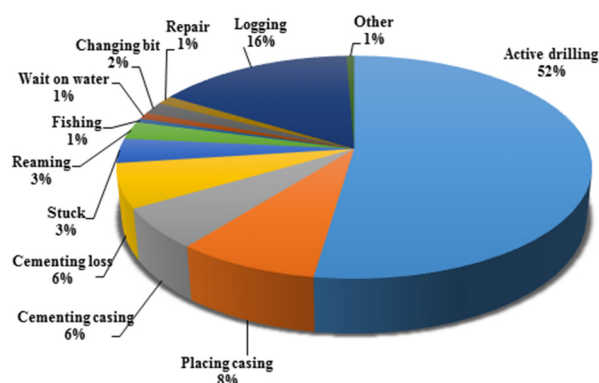


FIGURE 8: Percentage distribution of activities in Hengill

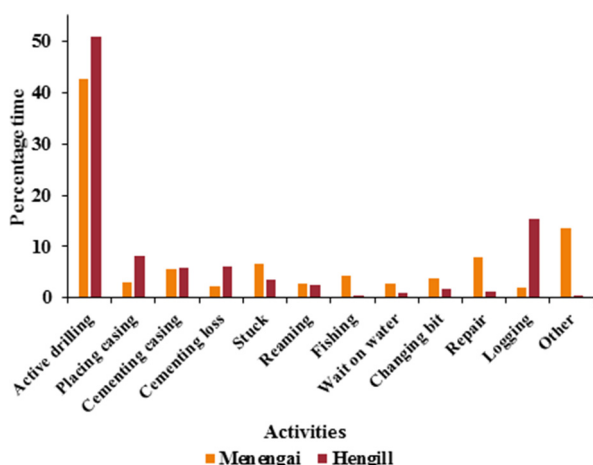


FIGURE 9: Weighted average of percentage per activity for Menengai and Hengill

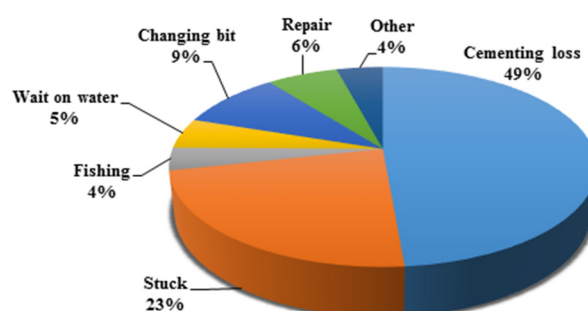


FIGURE 10: Percentage representation of NPT distribution in Hengill

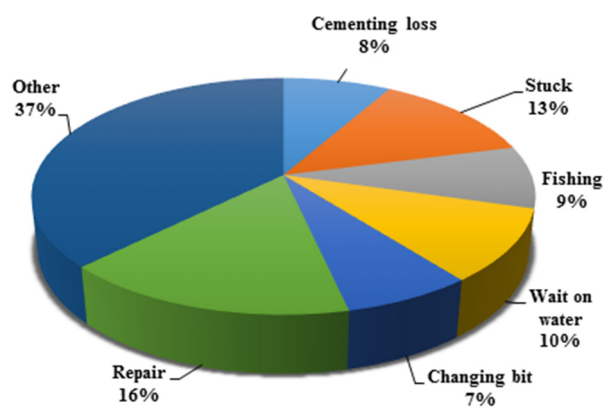


FIGURE 11: Percentage representation of NPT distribution in Menengai

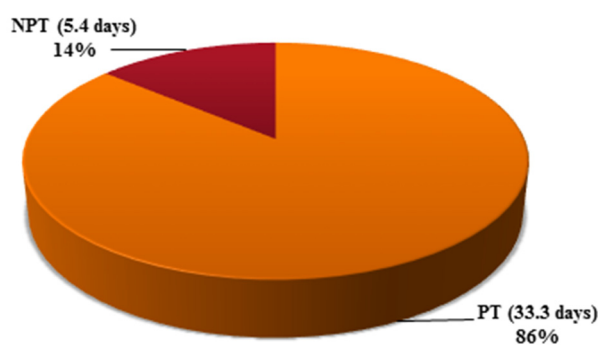


FIGURE 12: Productive time compared to non-productive time in Hengill

4. DISCUSSION

Using the normalised data on the reference well, wells drilled in Hengill took an average of 38.7 days to complete the well to 2000 m, while wells drilled in Menengai took an average of 109 days. Therefore, it took almost three times longer to complete similar wells in Menengai as in Hengill. From the raw data analysis, it was found that the average depth per day was 52 m/day in Hengill while it was 22.9 m/day in Menengai. The actual rate of penetration with the bit on bottom was 102 m/day in Hengill and 46 m/day in Menengai. There was more NPT in Menengai wells, amounting to 40% the total work time while Hengill wells incurred a NPT of 14.7% of the total work time.

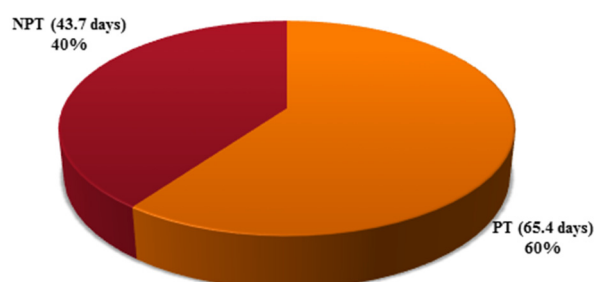


FIGURE 13: Productive time compared to non-productive time in Menengai

4.1 Actual drilling

45.1 days were spent on actual drilling in Menengai and 19 days in Hengill which was 42.7 and 51.0% of the workdays, respectively. It is possible that the length of time spent in drilling Menengai wells could be due to hard formations as the rate of penetration was relatively low. Section 0 in Menengai took 6.5 days, while in Hengill it took 2.5 days. This can be explained by the fact that in Menengai this section was drilled using a tricone bit that depends on rotary action to drill. The problem results from the shallow nature of the hole in this section; the rigs had no room for collars, hence the weight on the bit was far too low and large vibrations were experienced. In Hengill, this section is generally drilled with an air hammer, making the drilling faster; furthermore, the diameter of the hole in Menengai is usually large while a regular diameter is used in Hengill. The actual cause of a longer drilling time for the rest of the sections is not clear, other than the hard formation. It could also be considered that Menengai is a new field and the crew was also new to each other and had yet to become accustomed to working together.

It can be said that the drilling rate depends largely on the hardness or softness of the formation being drilled on. This goes to show that bit selection is an important factor and so is the weight on bit and the RPM applied in determining drilling time.

4.2 Casing

Casing time for both fields was relatively low, with 3.3 days in Menengai and 3.7 days in Hengill. The size of the casings and depths did not influence the casing time much, considering section 0 in Menengai had a large diameter. On considering the percentages, Menengai wells spent 3% of the total time in placing casing, while 8% of the total time was spent in placing casings in the Hengill wells. This could be attributed to the fact that the 18½" casing was welded and the other casings were screwed together.

4.3 Cementing casing

Cementing in Menengai took longer, with an average of 8.4 days, while in Hengill an average of 3.3 days was spent on cementing. This indicates that most of the cementing jobs for the Hengill wells were done in the first step, thereby reducing backfills. The use of caliper logs ensured shorter cementing time for Hengill wells. Caliper measurements give approximate wellbore diameters that were used to accurately calculate the amount of cement to be used. A rule of thumb in planning cementing jobs in

Hengill: twice the theoretical volume of slurry is calculated based on the bit size used. It should also be noted that cementing methods also play a role in the cementing time. In Hengill, the cementing is done using the inner string method which allows cement slurry to be pumped until returns are obtained on the surface and has a reduced cement displacement time. However, a single stage method is used in Menengai. Single stage cementing has shortfalls such as an increased risk of cement settling within the casing, resulting in large amounts of cement being drilled out, adding to the drilling workdays. Figure 14 is a pie chart representing the total casing cement job carried out in Menengai. Backfills took four times longer than primary cementing, as there was no information on the cement volume needed.

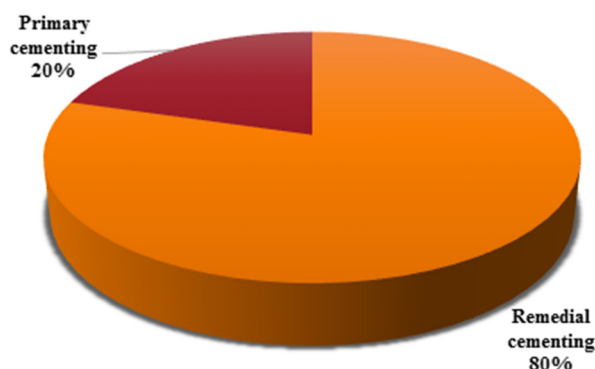


FIGURE 14: Ratio of primary cementing to remedial cementing time in Menengai

4.4 Cementing loss

Cementing loss time in Menengai was 3.9 days, while in Hengill it was 2.9 days. This translates to 2% of the total workdays in Menengai and 6% of the total workdays in Hengill. Considering that a caliper log is usually run before a plug job is done in Hengill, while in Menengai plugging is done without actual knowledge of the wellbore area being plugged, then plugging in Menengai may not be sufficient. A loss circulation problem is pronounced in Menengai; this is due to the fractured nature of the Menengai formation. Drilling practices may also lead to induced fractures aggravating loss circulation problems. If not managed, loss circulation can cause other problems in the well bore.

4.5 Logging

Hengill wells were logged more often than the Menengai wells. 16%, equivalent to 5.1 days of the total workdays in Hengill, was spent on logging. 2%, equivalent to 1.8 day, was spent on logging in Menengai. Several logs were carried out throughout the course of drilling the wells in Hengill while, in Menengai, most of the well logs were carried out during well completion. These logs usually included temperature, pressure, caliper, cement bond log (CBL) and other well completion logs. The caliper and CBL logs were not carried out in Menengai. The frequency of logging was also low in Menengai compared to Hengill.

Well logs are the only link to bottom hole conditions and, therefore, their importance cannot be over-emphasised. The more information available about the reservoir conditions, the easier it is to make accurate decisions on drilling and to develop solutions to drilling problems, such as areas to case off to avoid cold zones, and in making decisions on how to treat loss zones. Caliper logs and CBL logs are important for cementing job integrity.

4.6 Bottom hole assembly (BHA) change

Hengill spent 0.6 days in BHA change while Menengai spent 3.3 days. Most of the BHA change time was spent in tripping out to change worn-out bits. Reducing the number of BHA trips will eventually reduce this part of the NPT. The drill bit is the single equipment component that most impacts the rate at which a well progresses to total depth. Improved bit life determines how often a bit must be changed and often eliminates the incremental bit trip, and resultant delays and lost time. Changing lithologies at various depths, such as those in Menengai, also create a set of variables that affect bit durability. Other

factors influencing ROP and durability include drilling fluid condition, weight on the bit (WOB), and rotary speed (RPM) of the bit. Drilling challenges are overcome with improved drill bit technology (Cochener, 2010).

4.7 Fishing

Fishing time was longer in Menengai wells, with an average of 4 days; in Hengill wells, the average was 0.2 days. Most of the fishing time experienced in Menengai was a result of drillstring failure from a stuck pipe. In the effort to free the stuck pipe, the drillstring was subjected to high torque and large over-pull, causing it to strain and eventually fail. Excessive tension from over pull and fatigue from repeated stress can also lead to drillstring failure.

To reduce the number of drillstring failures, it is important to ensure drill pipes and other tubes are inspected for faults and defects as required.

4.8 Stuck pipe

On average, Menengai wells were stuck for 6 days, while Hengill wells were stuck for 1.4 days. Both drillstrings and casing strings experienced sticking. There was more sticking in section 3 than in all the other sections. In Menengai, most of the sticking followed a period of problematic circulation and a moment of stopped circulation such as after pipe connection. There were also cases where the sticking occurred when drilling resumed after a period of waiting on water. Due to lost circulation, most of the cuttings were not removed from the hole and were left suspended; as a result, these cuttings fell to the bottom and onto the string. Loss of circulation results in poor hole cleaning and, if enough efforts are not made to regain it, sticking is inevitable.

Poor hole cleaning may not be the only cause for a stuck pipe. Some of the wells that experienced sticking in Menengai, especially in section 3, had good circulation returns with cuttings being received on the surface when sticking occurred. According to Mibei (2012), chilled fresh glass was encountered at 2,174 m in well MW05 (now named MW06), indicating a possible intrusion of magma. Glass is susceptible to alteration and at such depths in a high temperature geothermal system such as Menengai, it would have altered completely unless it was a very recent intrusion that was chilled by the drilling fluid. Drilling challenges were experienced at these depths, i.e. sticking of the drillstring. Anomalously high temperatures were recorded at the bottom of these wells. This is probably due to a high heat flow influx from the magmatic intrusion into the country rocks. Figure 15 shows the drilling parameters for Menengai Well MW06 at the time of sticking at 2202m. The sticking was sudden and there were no signatures of sticking observed prior to sticking. Other wells experienced similar sticking around the same depth.

Sticking is an expensive NPT occurrence in drilling, especially when the drillstring fails during efforts to free it, resulting in the loss of the bottom hole assembly. In such a case, much of the well will be blocked by the lost pipe. It requires either drilling a long sidetrack or performing time-consuming fishing operations to clear the hole.

4.9 Other activities

Other activities referred to here include: top drive, wellhead and BOP installation, and wait on fuel, material and instructions. Any activity that had to be carried out and was not planned for was included in this category. These activities took 17.6 days in Menengai and 0.2 days in Hengill. This was the second largest time of the total Menengai workdays and the largest NPT. Top drive installation was included here since, in Menengai, it is not used until after section 0. This is because the top section is

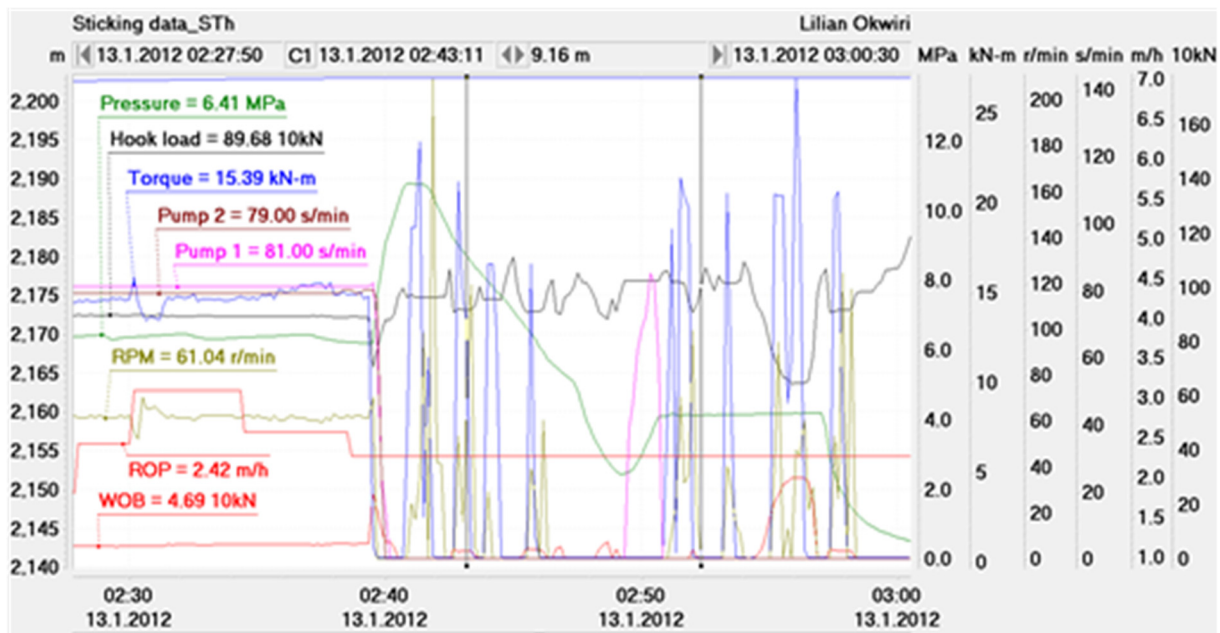


FIGURE 15: Drilling parameters at the time of sticking in Well MW06

usually characterised by a hard formation. Low ROP causes high string vibration, leading to frequent top drive breakdown. In Hengill, the top drive is rigged up on the big rig after section 0 is done. BOP installation took a relatively longer time to install in Menengai and materials took longer to be delivered to the site. Significant time was spent waiting for instructions which could signify planning was not sufficient in the first place. A consideration should be made on planning for trouble time when planning for the well. This will ensure that when drilling problems occur, the crew will know how to proceed even if further instructions are given later.

4.10 Repairs

Repairs were the third largest time consumer in Menengai wells, accounting for 7.6 days, while in Hengill, 0.4 days were spent on repairs. The larger part of equipment repairs was due to waiting for spare parts, as the procurement process is long and some of the spares had to be sourced from abroad. The big question is, is it economically viable to have in storage expensive spare parts/equipment that may not fail for years or risk not having it and incur the cost of waiting for days, even weeks, when it fails. According to Samland (2011), the costs of having a drill rig wait for several days and the consequences of a serious accident while drilling are of such magnitude that expensive equipment, advanced monitoring, redundant systems and other safety measures may often be worthwhile. To complicate the planning of spare parts further, many parts have an unpredictable demand, some parts will become unavailable, new manufacturers and brands are introduced and delivery times may vary from the stated values.

4.11 Reaming

On average, 3.4 days were spent on reaming in Menengai while 0.9 days were spent in Hengill. Reaming is usually done to straighten a crooked hole or to enlarge a tapered or tight well bore. If it is left uncorrected, it will cause problems during running in the casings. The crooked hole is a result of a change in formation that is beyond the control of the driller but, with the right choice of BHA, it can be minimised; a tapered wellbore is usually a result of under gauge bit.

4.12 Wait on water

Wait on water days were 4.7 in Menengai, while 0.3 in Hengill. In Menengai, this was necessitated by the severe loss of circulation encountered throughout the drilling process. Loss of circulation meant that water in the mud tanks and the pond were depleted fast and the replenishing rate was not as fast. Four rigs drill in the Menengai caldera and all four depend on the same supply. Water in Menengai is supplied from drilled wells, and sometimes brine from discharging wells. The formation in Menengai is highly fractured and drilling crews experience frequent long lost circulation periods. This means that there should be a constant supply of drilling fluids at the drilling sites. The use of fluids such as drilling mud and lost circulation materials is not advised in production zones because of their sealing properties which could end up compromising productivity. Therefore, water is used in drilling blind in this section.

The importance of water on a geothermal drilling site cannot be over emphasised. It is the basic drilling fluid in geothermal drilling; it can be used on its own and can be used to mix mud and can even be used when drilling with aerated foam. It is used in cementing and also in quenching a well during kicks and blowouts.

5. OPPORTUNITIES TO REDUCE NPT

It is not possible to completely eliminate NPT but it can be minimised to an extent that it does not impact drilling time so much. Process improvement and change of drilling practices are fundamental in ensuring that inefficiencies in the drilling process have been taken care of.

5.1 Acceleration of other drilling activities

Actual drilling is mostly dependent on the formation being drilled and to some extent the experience of the driller and the drilling technology used. Having the best of the three does not always guarantee a faster ROP. To reduce drilling time, other drilling activities can be accelerated to fast track drilling time. Figure 16 is a scatter plot showing NPT against workdays for Menengai wells. Statistically, there is a low correlation between the time it took to complete a well and the time spent on NPT; therefore, as much as NPT adds to drilling time, there are other

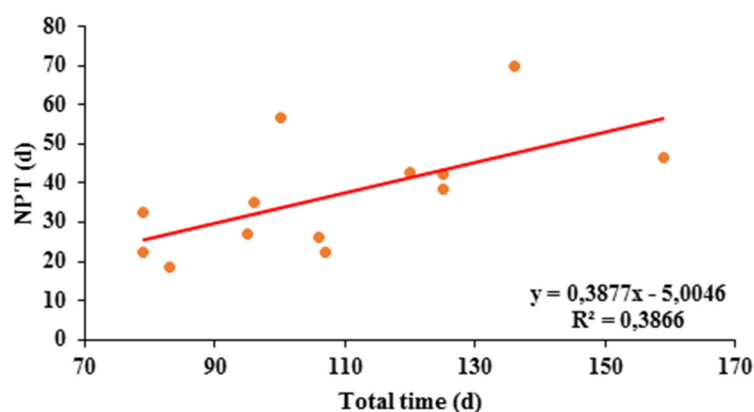


FIGURE 16: Non-productive time vs. total time in Menengai

causes for time overruns. As previously observed, cementing is one of those activities to be fast tracked, by reducing the time spent on backfills and carrying out the bulk cementing in the primary cementing. Planning for early delivery of materials, spares and equipment, ensures the drilling progress will be uninterrupted. Changing bit technology to achieve one bit per section for the upper shallower depths and fewer bit changes for the deeper production section will reduce bit trip time. The use of an air hammer to accelerate drilling the top hole will reduce drilling time for this section.

5.2 Learning curve analysis

It is important to study the performance of successful wells to identify success factors, and to attempt to duplicate the success. A learning curve involves learning from the experience of the first few wells and incorporating those lessons into planning the next well to reduce drilling time and increase performance in subsequent wells. Drilling is a repetitive job, therefore, the more wells drilled the more learning takes place. Knowledge is acquired and a set of skills required for the job are improved with every new well drilled; this leads to a reduction in the drilling time for new wells. Figures 17 to 20 attempt to analyse whether learning took place as more wells were drilled in these fields.

Figures 17 and 18 are scatter plots showing drilling time against the order of drilled wells. The correlation of workdays to wells drilled was 0.00 in Hengill and 0.07 in Menengai. Statistically, neither field showed any correlation between drilling time and the order of drilling. These figures show that the drilling time is constant for all the wells drilled in these fields, with a slight increase in time on wells drilled in Menengai.

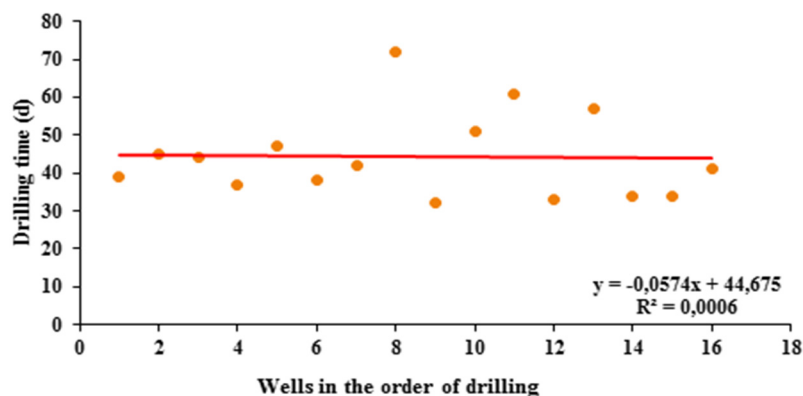


FIGURE 17: Drilling time vs. order of drilling for Hengill wells

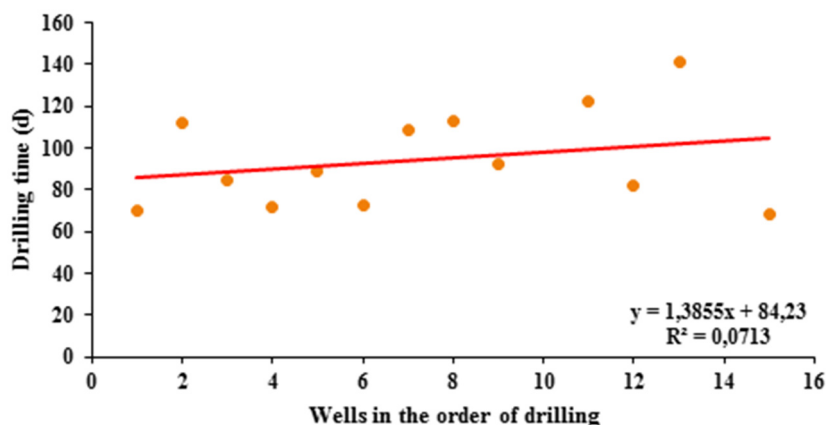


FIGURE 18: Drilling time vs. order of drilling for Menengai wells

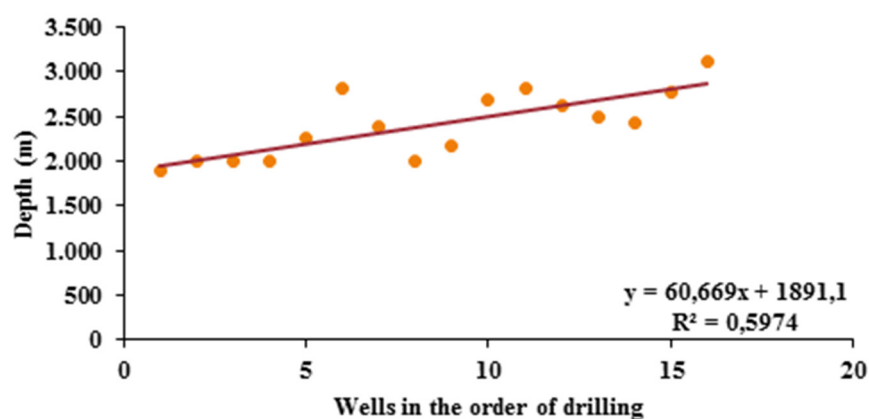


FIGURE 19: Depth vs. order of drilling for Hengill wells

Figures 19 and 20 are scatter plots showing drilled depth against wells in the order of drilling in the two fields. In Hengill, a positive correlation of 0.5974 was found between depth and wells in order of drilling. A correlation of -0.421 was found for Menengai wells. Statistically, the depths for wells drilled in Hengill increased as more wells were drilled. This can, therefore, explain Figure 17. In as much as the drilling time remained constant, the depths increased. Unfortunately, for the wells drilled in Menengai, the depths reduced as more wells were drilled in the same field.

The graphs show that if all wells drilled in Hengill were of the same depth, then the overall amount of workdays would reduce for the latest wells. There is an indication that learning took place in this field

as more wells were drilled. There was an increase in experience while drilling more wells and increased knowledge of the field. This was not so for Menengai. Drilling time was constant with an increased number of wells drilled. There is need for learning in Menengai field through a transfer of knowledge and experience from one well to another. This would ensure that best practices were carried forward and drilling mistakes in one well were not repeated in another.

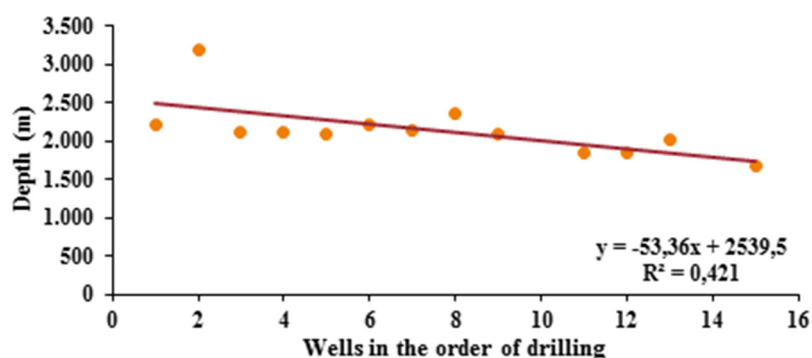


FIGURE 20: Depth vs. order of drilling for Menengai wells

Reduction in well time is realised as learning takes place, rapidly improving efficiency and performance on subsequent wells as lessons are learnt and technology is applied more effectively. Ensuring that personnel work with their experienced counterparts while incorporating training and retraining on the job instills the learning process. Training comes at a cost but the trade-off is realised when drilling efficiency is increased. Drilling data gathered during drilling should be analysed to build knowledge on what works and what does not. The information obtained will also play a key role in planning subsequent wells and the transfer of lessons learnt will improve drilling performance.

5.3 Planning

An efficient drilling process depends on continual planning for normal drilling activities and for unforeseeable occurrences in drilling. Having a plan to handle common drilling problems will see drilling problems solved faster and some even prevented. Studies of previous drilling performance will give insight as to where planning was not sufficient. Therefore, proper planning for a new well should involve collecting and analysing data from previous wells, identifying root causes of problems encountered in those wells and developing solutions. This means that sound records should be kept as this will be a guideline not only of what went wrong but for what could be done better. The planning process should be flexible, incorporating new ideas and technologies as the drilling process demands.

Proper planning ensures that even the most complex of wells can be drilled efficiently and safely. Drilling times would be reduced, irrespective of well specifications with proper planning. Figures 21 and 22 are scatter plots of time against depth for Hengill and Menengai, respectively. Time versus depth had a correlation of 0.56 in Hengill and 0.056 in Menengai. Statistically, there was no correlation between time and depth in both fields. This goes to show that even the deepest wells can be drilled in the

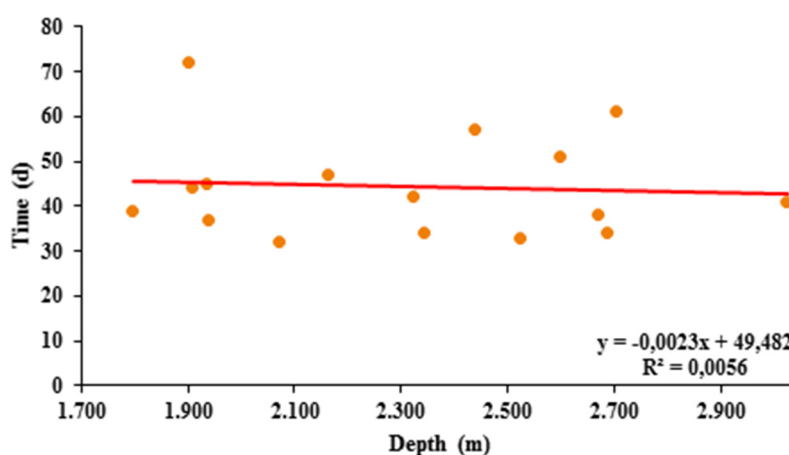


FIGURE 21: Time vs. depth for Hengill wells

shortest time possible if well planned for. It should be noted that the data sets used herein were small; it would be interesting to learn the outcome if more data was added.

Successful drilling hinges on developing a sound plan, continually updating it in light of new information, and keeping involved personnel informed on a timely basis. The plan must include procedures to follow under normal circumstances and methods for

dealing with the most likely and most severe problems that may be encountered. With proper training, a well-defined drilling process, sufficient data and tools for interpretation, successfully drilling a well should be a routine process (Aldred et al., 1999).

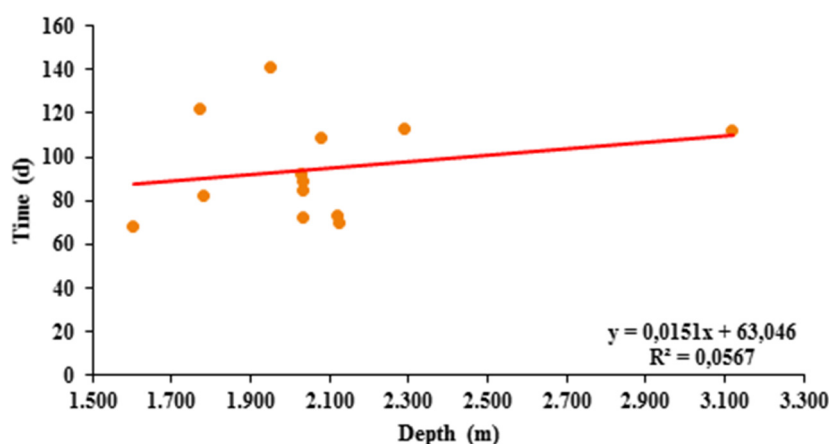


FIGURE 22: Time vs. depth for Menengai wells

5.4 Innovations

Innovation involves the deliberate application of new or different solutions that meet new requirements and lead to better results. Today's drilling technology has greatly improved and most of the industry's problems are routinely being solved. Applying different technology already existing in the market in problematic areas could be the solution to NPT. Time spent on activities such as tripping for bit and BHA change and also reaming due to a tapered formation could be greatly reduced through investing in better quality bits. Cementing time could be greatly reduced through logging before any cement job. A little more time might be spent on logging but the trade-off is much less time spent on cementing which would be of great help in reducing the NPT.

6. CONCLUSIONS

The geology in Menengai presents the biggest challenge to drilling, slowing down drilling activities and creating drilling problems. It contributed a larger part of NPT experienced in this field and leads to extended drilling days.

Menengai wells experienced more challenges and deviated from the original time schedule, incurring significant time overruns. Formation geology of the site played a major role in the problems experienced, considering the amount of time spent on stuck pipes, reaming, cementing losses and the time it took to drill the reference well, compared to Hengill. Initial problems experienced such as a stuck pipe led to other problems that also contributed to NPT, such as drillstring failure and equipment (i.e. top drive) breakdown, owing to overpull and high torques applied during stuck pipe and fishing operations. Drilling problems related to wellbore pressure such as lost circulation, and stuck pipe increased significantly with depth.

Time spent on activities such as tripping for bit and BHA change and also reaming due to a tapered formation could be greatly reduced through investing in better quality bits. Air hammers should be considered for drilling section 0 as this would greatly reduce the drilling time and equipment breakdown caused by vibrations.

Cementing time could be greatly reduced through logging before any cement job. Caliper logs would aid in determining how much cement to pump while cement bond logs would ensure that the cement job was done right. A little more time might be spent on logging but the trade-off is a better cementing job and much less time spent on cementing. Considering a change in the cementing method to the inner string method could also make a difference. Despite the use of cement plugs to cure losses in sections 1 and 2, lost circulation related problems were still experienced. A thorough job should be done to ensure that the loss zones are sealed and do not disturb the drilling process.

‘Other’ activities accounted for 17.6% of the total drilling time at Menengai. These were mostly waiting on materials, consumables and instructions. There is a need to change how the materials and consumables are planned for. Adequate planning from the beginning of the drilling process would ensure that unscheduled events or problem time would not be a surprise and, therefore, drilling progress would not be halted while waiting for instructions.

Drilling has been problematic as the 2200 m depth is approached. Eight wells got stuck at these depths and some resulted in loss of BHA. The wells are, however, productive and it may, therefore, not be desirable to attempt drilling deeper.

ACKNOWLEDGEMENTS

I wish to thank the Government of Iceland and the United Nations University Geothermal Training Programme for the opportunity to participate in this training programme. My sincere gratitude goes to the former Director, Dr. Ingvar B. Fridleifsson and the current Director, Mr. Lúdvík S. Georgsson, for their direction and guidance throughout this training. My appreciation goes to the staff of UNU-GTP: Ms. Thórhildur Ísberg, Mr. Ingimar G. Haraldsson, Ms. Málfríður Ómarsdóttir and Mr. Markús A. G. Wilde, for their guidance and support during my stay in Iceland, not forgetting Rosa for ensuring I had all the reading materials I needed. I am grateful to my dedicated supervisor, Björn Már Sveinbjörnsson; this report could not have been completed without his guidance and input. I acknowledge the assistance and advice from Mr. Sverrir Thórhallson.

Special thanks to Geothermal Development Company, Ltd. of Kenya for giving me the opportunity to participate in this programme. My sincere gratitude goes to Mr Michael Mbevi, the Drilling operations Manager at GDC, for believing in my capabilities. My colleagues Abraham, Cyrus, Billy, James and Eric: I am grateful for your support in terms of data collection. Special thanks to my family, mum and dad, Charles, Felix and David for their love, support, encouragement and their prayers which helped me in accomplishing this training. Finally, my gratitude goes to God, for without God I wouldn’t have made it this far.

REFERENCES

- Adams, A.J., Gibson, C., and Smith, R., 2009: Probabilistic well time estimation revisited. *Paper presented at SPE/IADC Drilling Conference and Exhibition, 2009, Amsterdam*, 30pp.
- Aldred, W., Plumb, D., Bradford, I., Cook, J., Gholkar, V., Cousins, L., Minton, R., Fuller, J., Goraya, S., and Tucker, D., 1999: Managing drilling risk. *Oilfield reviews, Summer 1999*, 18 pp.
- Björnsson, A., Hersir, G.P., and Björnsson, G., 1986: The Hengill high-temperature area SW-Iceland: Regional geophysical survey. *Geoth. Res. Council, Trans.*, 10, 205-210.

Cochener, J., 2010: *Quantifying drilling efficiency*. Office of Integrated Analysis and Forecasting, U.S. Energy Information Administration, report, 16 pp.

Dumas, P., Antics, M., and Ungemach, P., 2012: *Report on geothermal drilling*. GEOELEC, report (version 2), 10 pp.

Hsieh, L., 2010: *Rig NPT: The ugly truth 2010 - operators call on contractors to improve maintenance, vendors to simplify designs*. Drilling Contractor, website: www.drillingcontractor.org/rig-npt-the-ugly-truth-6795.

Kadaster, A.G., Townsend, C.W., and Albaugh, E.K., 1992: Drilling time analysis: a total quality management tool for drilling in the 1990's. *Proceedings of the 67th Annual Technical Conference and Exhibition of SPE, Washington, DC*, 1-16.

Kaiser, M.J., 2007: A survey of drilling cost and complexity estimation. *Internat. J. Petroleum Science & Technology*, 1-1, 1-22.

Mibei, G., 2010: Geology and hydrothermal alteration of Menengai geothermal field. Case study: wells MW-04 and MW-05. Report 21 in: *Geothermal training in Iceland 2012*. UNU-GTP, Iceland, 437-465.

Njue, L. M., 2011: Stratigraphy and hydrothermal mineralogy of well MW-02, Menengai geothermal field. *Proceedings of the Kenya Geothermal Conference KGC2011*, Nairobi, Kenya, 5 pp.

Noerager, J.A., and White, J.P., 1987: Drilling time predictions from statistical analysis. *SPE/IADC drilling conference*, New Orleans, La, 12 pp.

PetroWiki, 2013a: *Drilling problems and solutions*. PetroWiki, website: petrowiki.org/PEH%3ADrilling_Problems_and_Solutions.

PetroWiki, 2013b: *Introduction to Well Planning*. PetroWiki, website: petrowiki.org/PEH%3AIntroduction_to_Well_Planning.

Samland R., 2011: *Drilling spare parts: Identifying and evaluating critical Parameters*. University of Stavanger, Norway, MSc thesis, 54 pp.

Solberg S.M., 2012: *Improved drilling process through the determination of hardness and lithology boundaries*. Norwegian University of Science and Technology, Trondheim, MSc thesis, 96 pp.

Sveinbjörnsson, B.M., 2010: Estimate of costs and uncertainties in high-temperature drilling in the Hengill area. Reykjavik University, MSc thesis, 170 pp.

Sveinbjörnsson, B.M., 2013: Drilling performance and productivity of geothermal wells - a case history of Hengill geothermal area in Iceland. *Proceedings from the 47th Rock Mechanics/Geomechanics Symposium, 2013, San Francisco, Ca, ARMA-13-386*, 10 pp.

Sveinbjörnsson, B.M., and Thórhallsson, S., 2013: *Drilling performance, injectivity and productivity of geothermal wells*. *Geothermics (2014)*, 50, 76–84.

Thórhallsson S., 2006: New developments in geothermal drilling. *Paper presented at Workshop for Decision Makers on Geothermal Projects in Central America, organized by UNU-GTP and LaGeo in San Salvador, El Salvador*, 8 pp.



RESISTIVITY STRUCTURE OF THE EBURRU GEOTHERMAL FIELD, KENYA, DEPICTED THROUGH 1D JOINT INVERSION OF MT AND TEM DATA

Ammon Ojwang Omiti

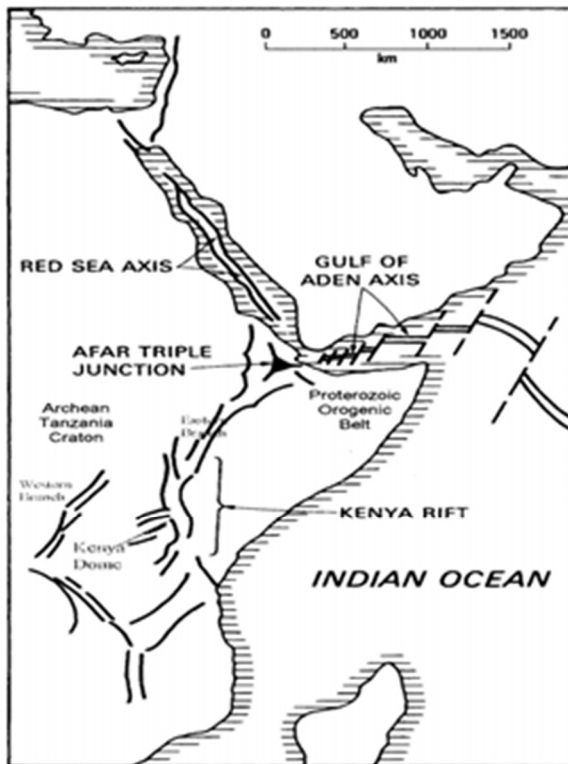
Kenya Electricity Generating Company Ltd. - KenGen
Geothermal Resource Development
P.O. Box 785
Naivasha 20117
KENYA
aomiti@kengen.co.ke

ABSTRACT

Eburru is one of the geothermal fields in Kenya, producing 2.5 MWe from one of the six exploratory wells. In order to drill production wells, a total of 36 additional MT and TEM soundings were carried out in 2013 to delineate the geothermal resource field of Eburru. This report discusses and presents the results of earlier soundings and soundings from 2013 which brought the total number to 43 MT and 43 TEM soundings. The TEMTD program was used for joint 1D inversion of MT and TEM data, the program calculates the shift factor. The MT data are, therefore, corrected for static shift. Data used in this report were acquired by the KenGen staff team using a data logger MTU-5A made by Phoenix Ltd. for acquiring MT data and TerraTEM made by Monex GeoScope Ltd. for TEM data. MT data were processed using SSMT2000 and MTeditor before jointly inverted with TEM data. The results discussed in this report present 1D joint inversion, resistivity cross-sections and iso-resistivity maps down to a few kilometres. The reservoir in Eburru geothermal field is located at about 2500 m b.g.l. according to the sub-surface resistivity structure.

1. INTRODUCTION

Eburru geothermal field is located in the great East African Rift System (EARS) which is a major tectonic structure stretching about 6100 km starting from the Red Sea in the north to Mozambique in the south. The Rift starts from a triple junction, evident in Ethiopia; at this point, two branches are in contact with the Red Sea and the Gulf of Eden while the third passes through Ethiopia to the south. Eburru is located in the eastern arm of the EARS stretching through Eritrea, Ethiopia, Kenya, and all the way down to Mozambique (Figure 1). The Great Africa Rift system forms more or less a linear like zone where the continental plate is being pulled apart with the rifting between. A widened mantle plume probably began under east Africa creating the three arms which are: The East Africa Rift, The Gulf of Eden Rift and The Red Sea Rift (Omenda and Karingithi, 1993). The heat flow from the asthenosphere along the rift zones led to volcanism and the formation of domes, as can be seen in Olkaria to the south of Eburru (Figure 2). The eastern branch is believed to be much older and is considered to have developed about 13-23 million years earlier than the western branch; this is supported by the discovery of preserved vertebrate fossils and volcanic ash which are believed to be about 23 million years old (Velador et al., 2002).



2.2 Porosity

Fractional porosity, ϕ_τ , is defined as the fraction of void space of a given total volume of a rock material or the measure of the ability of a given rock material to hold fluid:

$$\phi_\tau = \frac{V_\theta}{V} \quad (2)$$

where ϕ_τ = Fractional porosity;
 V_θ = Volume of void;
 V = Total volume of the material.

Archie's law has been used for relating the conductivity of a reservoir rock and the conductivity of the fluid contained in the pores. It describes the resistivity dependence on porosity if ionic conduction in the pore fluid dominates other conduction mechanisms in the rocks. For normal rocks, the law is valid only if the resistivity of pore fluid is 2 Ωm or less and it is a very good approximation if the resistivity is dominated by the saturating fluid (Archie, 1942):

$$\rho = \rho_w a \phi_\tau^{-n} \quad (3)$$

where ρ_w = Resistivity of the pore fluid (Ωm);
 ϕ_τ = Fractional porosity;
 a = Empirical parameter;
 n = Cementing factor.

2.3 Temperature

Resistivity of an electrolyte and temperature are related as shown in Figure 3. The resistivity of rock decreases with increasing temperature, more ions are set free and a decrease in the viscosity of the electrolytic solution makes them more mobile. At higher temperatures, above 300°C, a decrease in dielectric permittivity of water results in a decrease in the number of dissociated ions in the solution, hence, an increase in fluid resistivity.

Dakhnov (1962) described the relationship between temperature and resistivity of an electrolyte for temperatures in the range of 0 to about 200°C with the formula:

$$\rho_w = \frac{\rho_{wo}}{1 + \alpha(T - T_0)} \quad (4)$$

where ρ_w = Resistivity (Ωm) of the fluid at temperature T ;
 ρ_{wo} = Resistivity (Ωm) of the fluid at temperature T_0 ;
 T_0 = Room temperature ($^\circ\text{C}$);
 α = Coefficient temperature of the resistivity, $\alpha \approx 0.023^\circ\text{C}^{-1}$ for $T_0 = 25^\circ\text{C}$.

The importance of temperature variation of electrolytes on the resistivity of rocks is greatest at temperatures below 150°C but decreases with an increase in temperatures due to mineral alteration.

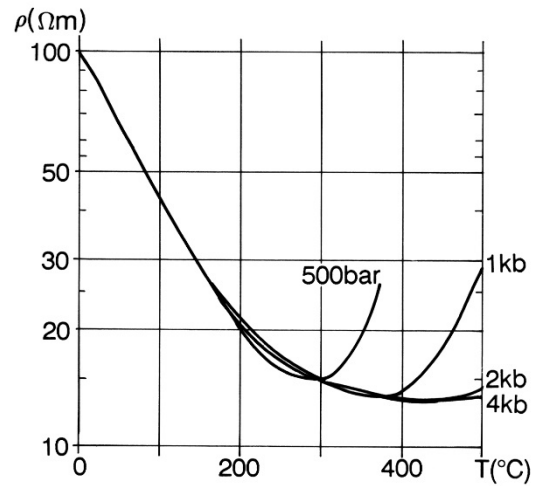


FIGURE 3: Electrical resistivity of NaCl solution as a function of temperature at different pressures (Hersir and Björnsson, 1991; based on Quist and Marshall, 1968)

2.4 Salinity of pore fluid

Dissolved salts in water normally break into negatively and positively charged ions. In saline water, positively charged ions are calcium (Ca^+), sodium (Na^+), Magnesium (Mg^+) and potassium (K) while the negatively charged ions are sulphate (SO_4^{-2}), carbonate (CO_3^{-2}), chloride (Cl^-) and bicarbonate (HCO_3^-). Salinity is the practical measure of the amount of dissolved salts in water. The relationship between conductivity and salinity is described by the equation below (Zhdanov and Keller, 1994):

$$\sigma = \frac{1}{\rho} = F \cdot (c_1 q_1 m_1 + c_2 q_2 m_2 + \dots) \quad (5)$$

where σ = Conductivity (S/m);
 F = Faraday's number (9.65×10^4 C/mole);
 c_i = Concentration of ions;
 q_i = Valence of ions;
 m_i = Mobility of ions.

Conductivity of the rock increases with increased salinity of the pore fluid.

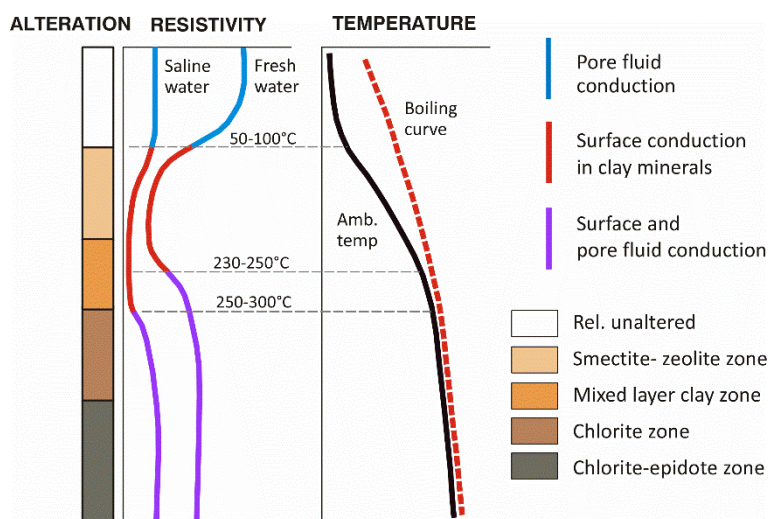


FIGURE 4: A summary of general resistivity structure of high temperature fields in Iceland (Flóvenz et al., 2012; based on Flóvenz et al., 2005)

At temperatures greater than 300°C (Figure 4) epidote and actinolite become common.

The resistivity of the reservoir rock is dependent on the minerals present. The resistivity of the chlorite-epidote zone increases due to low mobility of ions bound in a crystal lattice.

2.5 Water rock interaction

The interaction between hot fluids and rocks results in the formation of secondary minerals which is called geothermal alteration. The main factors determining which type of alteration is formed are fluid composition, permeability and temperature (Henley and Ellis, 1983). The secondary minerals at medium to low temperature in basalt are commonly dominated by clays (smectite and illite), zeolites, oxides (Meheganet al., 1982), and hydroxides. At temperatures of about 200-250°C a zone of mixed clays is formed, then replaced by chlorite and epidote at 250-300°C.

3. ELECTRICAL RESISTIVITY METHOD

Electrical resistivity methods are used to measure the resistivity structure of the subsurface. Current is induced into the ground and signals are monitored at the surface. The following are the most common resistivity methods:

- DC resistivity methods
- Electromagnetic methods

3.1 Direct current resistivity method

The direct current (DC) resistivity method is one of the techniques used to measure the earth's resistivity; by making a measurement on the ground surface, the true resistivity of the ground can be estimated. Current is driven into the ground and the resulting voltage is measured at the surface.

Figure 5 describes the basic principles of DC resistivity measurements. Current is injected through a pair of electrodes (A and B) which are short metallic stakes driven about two feet into the ground; two additional electrodes (M and N) are then used to measure the resulting potential difference (V) generated by the current (I).

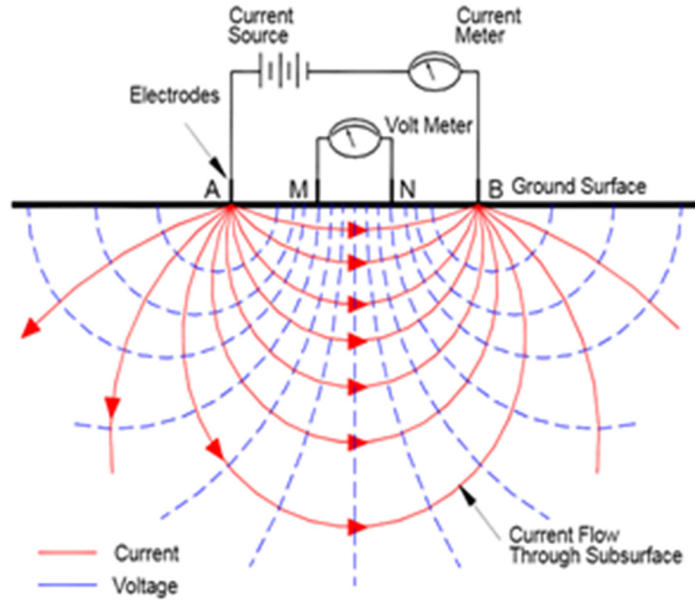


FIGURE 5: Illustrating schematic basic concept of direct current resistivity measurement

Readings obtained from the instrument (current and voltage) are normally reduced to apparent resistivity values. Apparent resistivity is defined as the resistivity of the earth that would produce the observed instrument result or response for a given distance of electrode spacing and is normally plotted on a log-log graph.

Ohm's law is a fundamental physical law governing the flow of current in the ground:

$$\mathbf{J} = \sigma \mathbf{E} = \frac{1}{\rho} \mathbf{E} \quad (6)$$

where \mathbf{J} = Current density (A/m^2);
 \mathbf{E} = Electric field intensity (V/m);
 σ = Conductivity of the medium (Ωm^{-1});
 ρ = Resistivity (Ωm).

The potential from a point source is given by:

$$V(r) = \frac{\rho I}{2\pi r} \quad (7)$$

where V = Potential (V);
 r = Distance to the current electrode (m);
 I = Total current flow (A).

Potentials measured at M and N in Figure 5 in a linear array are given by:

$$V_M = \frac{\rho I}{2\pi} \left(\frac{1}{AM} - \frac{1}{MB} \right) \quad (8)$$

$$V_N = \frac{\rho I}{2\pi} \left(\frac{1}{AN} - \frac{1}{NB} \right) \quad (9)$$

Total potential difference between electrode M and N is, thus:

$$V_{MN} = V_M - V_N = \frac{\rho I}{2\pi} \left[\left(\frac{1}{AM} - \frac{1}{MB} \right) - \left(\frac{1}{AN} - \frac{1}{NB} \right) \right] \quad (10)$$

The above equation can be rearranged to yield:

$$\frac{2\pi}{K} = \left[\left(\frac{1}{AM} - \frac{1}{MB} \right) - \left(\frac{1}{AN} - \frac{1}{NB} \right) \right] \quad (11)$$

The resistivity is, therefore, equal to:

$$\rho = \frac{V_{MN}}{I} K = \frac{V_{MN}}{I} \pi \left[\frac{S^2 - P^2}{2P} \right] \quad (12)$$

where S = Half distance between A and B (m);
 P = Half distance between M and N (m).

For a non-homogeneous earth, Equation 12 is used to define the apparent resistivity which is a function of S and P . For the Wenner array there is equidistance separation between the electrodes a ; the geometric factor of the Wenner array assumes a simple form, $K = 2\pi a$, hence the apparent resistivity is equal to:

$$\rho_{Wenner} = \left(\frac{V_{MN}}{I} \right) 2\pi a \quad (13)$$

3.2 Electromagnetic methods

In electromagnetic measurements, an alternating magnetic field is used to induce measurable current in the subsurface. The method includes time domain electromagnetic and frequency domain electromagnetic methods. Primary fields are generated by passing alternating current (AC) through long wires or loops, inducing eddy currents which generate secondary fields depending on the resistivity of the subsurface rocks.

3.2.1 Transient electromagnetic method (TEM)

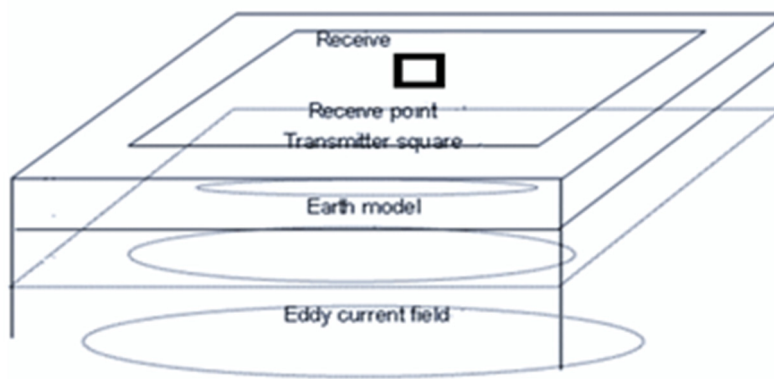


FIGURE 6: Central loop TEM sounding configuration

The transient electromagnetic method (TEM) is used to measure the electrical resistivity of the subsurface down to a depth of several hundreds of metres. The measurements can be conducted on the ground (Figure 6) or can be air-born (skyTEM) to cover a large area over a short period of time. The TEM is executed by passing current into the ungrounded TX-loop to build up a known constant magnetic field, termed the primary magnetic

field. The current is abruptly turned off and the change in the primary magnetic field induces electromotive force which results in eddy currents in the surroundings which, again, result in a secondary magnetic field.

The secondary magnetic field from the eddy currents decreases with time as the eddy currents diffuse downwards and outwards. The resistance of the country rocks weakens the current with time, converting the electrical energy to heat. The decay rate of the magnetic field is measured as the voltage induced into the receiver coil at the centre of the transmitter loop.

Maxwell's equations are used to define the fundamental law of the electromagnetic field (Kaufman and Keller, 1983):

$$\nabla \times \mathbf{E} = -\frac{\partial \mathbf{B}}{\partial t} \quad (14)$$

$$\nabla \times \mathbf{H} = \mathbf{j} + \frac{\partial \mathbf{D}}{\partial t} \quad (15)$$

$$\nabla \cdot \mathbf{B} = 0 \quad (16)$$

$$\nabla \cdot \mathbf{D} = \eta \quad (17)$$

For isotropic medium the described fields above are linked with:

$$\mathbf{D} = \varepsilon \mathbf{E} \quad (18)$$

$$\mathbf{B} = \mu \mathbf{H} \quad (19)$$

$$\mathbf{j} = \sigma \mathbf{E} \quad (20)$$

where \mathbf{E} = Electrical intensity (V/m);
 η = Electric charge density of free charges (C/m³);
 \mathbf{D} = Electric displacement vector (C/m²);
 \mathbf{B} = Magnetic flux density (T);
 \mathbf{j} = Electric current density (A/m²);
 \mathbf{H} = Magnetic field (A/m);
 μ = Magnetic permeability (H/m);
 ε = Electric permittivity (F/m);
 σ = Electrical conductivity (S/m).

In a homogeneous half space of conductivity (σ), the induced voltage in the receiver coil at late times is (Árnason, 1989):

$$V(t, r) \approx I_o \frac{C(\mu_o \sigma r^2)^{\frac{3}{2}}}{10\pi^{\frac{1}{2}} t^{\frac{5}{2}}} \quad (21)$$

where $C = A_r n_r A_s n_s \frac{\mu_o}{2\pi^3}$;
 t = Time elapsed after the transmitter current is turned off (s);
 A_r = Cross-sectional area of the receiver loop (m²);
 A_s = Cross-sectional area of the transmitter loop (m²);
 n_s = Number of windings in the transmitter loop;
 r = Radius of the transmitter loop;
 $V(t, r)$ = Transient voltage (V);
 I_o = Current in the transient loop (A).

The late time apparent resistivity (ρ_a) is defined by solving Equation 21, leading to Equation 22:

$$\rho_a = \frac{\mu_o}{4\pi} \left[\frac{2I_o \mu_o A_r A_s n_r n_s}{5t^{\frac{5}{2}} V(t, r)} \right]^{2/3} \quad (22)$$

3.2.2 Magnetotelluric method (MT)

The magnetotelluric method (MT) is a passive electromagnetic method that measures the electrical properties below the earth's surface. Natural variation in the earth's magnetic field is the source of energy for the magnetotelluric technique. The primary magnetic field, which is the external energy, is generated by variations in the earth's magnetic field transferred in a wide and continuous spectrum of electromagnetic waves. On reaching the earth's surface, some are reflected and the remaining part penetrates into the earth and induces currents (telluric current) into the earth. The telluric currents produce a secondary magnetic field which is measured on the earth's surface providing information on the conductivity of the subsurface up to hundreds of kilometres in depth.

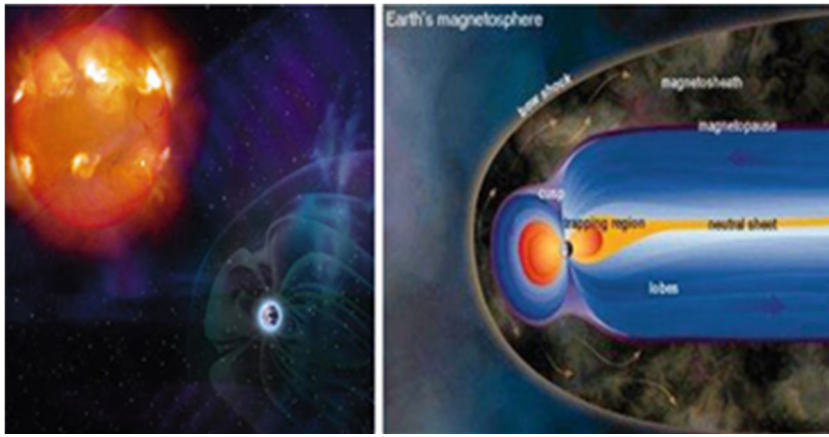


FIGURE 7: Solar wind interaction with the magnetosphere (Encyclopaedia Britannica, 2010)

Frequencies above 1 Hz are generated by lightning discharge along equatorial regions and frequencies lower than 1 Hz are generated by the interaction of the earth's magnetosphere and solar winds (Figure 7). Solar wind is a continual stream of plasma radiating mainly protons and electrons from the sun and when it encounters magnetopause, they are deflected in opposite directions, establishing an electric field.

Maxwell's equations describe the electromagnetic field within a material (Equations 14-17), and have solutions as a linear combination of harmonic waves:

$$E = E_0 e^{i(\omega t + kr)} \quad (23)$$

$$B = B_0 e^{i(\omega t + kr)} \quad (24)$$

where ω = Angular frequency of electromagnetic oscillations (rad/s);
 t = Time (s);
 k = Wave number (m^{-1});
 r = Position vector (m).

In a homogeneous structure the electric component takes the form:

$$E = E_0 e^{i\omega t} \cdot e^{-i\beta z} \cdot e^{-\alpha z} \quad (25)$$

where $\beta = \sqrt{\mu\sigma\omega/2}$ (m^{-1}).

The first factor of Equation 25 is wave amplitude, the second and third factors are sinusoidal time and variation in depth, respectively, and the last one is exponential decay.

Skin depth can be defined as the depth where the electromagnetic field has been reduced to e^{-1} of the original value. The decay can be expressed by skin depth, δ (m), and for the value of z which in this case decays to $1/e$ (Vozoff, 1991):

$$\delta = \sqrt{(2/\mu_0)\sigma\omega} = 500\sqrt{\rho T} \text{ (m)} \quad (26)$$

The skin depth permits the characterization of the investigated depth to increase according to the square root of the product of period and resistivity.

Uniform half space

If a uniform half space is impinged upon by a vertically propagating (along z-axis) plane electromagnetic wave $\partial E/\partial x = \partial H/\partial x = \partial E/\partial y = \partial H/\partial y = 0$, and the fields obey equations like:

$$\frac{\partial^2 E_x}{\partial z^2} = k^2 E_x \quad (27)$$

where $k^2 = i\mu\sigma\omega$.

From Maxwell's equations we get:

$$H_y = -\frac{1}{i\mu\omega} \frac{\partial E_x}{\partial z} \quad (28)$$

The orthogonal components of the field satisfy:

$$Z = \frac{E_x}{H_y} = \frac{i\omega\mu}{k} = -\frac{E_y}{H_x} \quad (29)$$

The relationship between the electric and magnetic fields is, therefore:

$$\begin{pmatrix} E_x \\ E_y \end{pmatrix} = \begin{pmatrix} 0 & Z \\ -Z & 0 \end{pmatrix} \begin{pmatrix} H_x \\ H_y \end{pmatrix} \quad (30)$$

where

$$Z = \sqrt{(i\omega\mu)/\sigma} \quad (31)$$

A magnetic field lags behind the electric field by $\pi/4$ in a completely homogeneous and isotropic half space with true resistivity equal to:

$$\rho = \frac{|Z|^2}{\omega\mu} = \frac{T}{2\pi\mu} |Z|^2 \quad (32)$$

where T = The period (s).

This can be expressed as (Cagniard, 1953):

$$\rho = 0.2 T \frac{|E_x|^2}{|H_y|^2} \quad (33)$$

where ρ = Resistivity (Ωm);

T = Period (s);

E = Horizontal electric field (mV/km);

H = Orthogonal horizontal magnetic field in γ = Tesla $\cdot 10^{-9}$.

For inhomogeneous half space, the above equation is used to define the apparent resistivity:

$$\rho_a = 0.2 T |Z|^2 = \frac{|E|^2}{|H|^2} \quad (34)$$

Z also has a phase:

$$\varphi = \tan^{-1} \frac{(\text{image } \left[\frac{E_x}{H_y} \right])}{(\text{Real } \left[\frac{E_x}{H_y} \right])} \quad (34)$$

Tensor impedance

1D impedance tensor: The conductivity of a 1D layered earth changes only with depth. The impedance tensor, Z , in this case is expressed as:

$$Z_{1D} = \begin{pmatrix} 0 & Z_{xy} \\ -Z_{xy} & 0 \end{pmatrix} \quad (35)$$

The apparent resistivity and phase in a layered earth are defined as:

$$\rho_a(\omega) = \frac{1}{\omega\mu_o} |Z(\omega)|^2 \text{ and } \varphi = \tan^{-1} \left[\frac{\text{Im}Z_{xy}}{\text{Re}Z_{xy}} \right] \quad (36)$$

2D impedance tensor: The conductivity for a 2D earth changes in one lateral direction and with depth but is constant in strike the direction:

$$Z_{2D} = \begin{pmatrix} Z_{xx} & Z_{xy} \\ Z_{yx} & Z_{yy} \end{pmatrix} \quad (37)$$

The horizontal axes of the field layout are normally not aligned along the electromagnetic strike. The diagonal elements $Z_{xx} = -Z_{yy}$ are equal in amplitude but have opposite signs; the off diagonal Z_{xy} and Z_{yx} are independent values. If the x direction is parallel to the strike direction, Z_{2D} impedance tensor becomes:

$$Z_{2D} = \begin{pmatrix} 0 & Z_{xy} \\ Z_{yx} & 0 \end{pmatrix} \quad (38)$$

The strike direction in a 2D earth is obtained by rotating the coordinates system to the direction minimizing the diagonal elements of the tensor, Z_{xx} and Z_{yy} . The 90° ambiguity in the electric strike is resolved by calculating the Tipper strike from H_z .

3D impedance tensor: The conductivity in a 3D earth varies in all directions (x, y and z). The impedance tensor in this case is expressed as:

$$Z_{3D} = \begin{pmatrix} Z_{xx} & Z_{xy} \\ Z_{yx} & Z_{yy} \end{pmatrix} \quad (39)$$

All the elements of the 3D impedance tensor must all be considered, because they are non-zero irrespective of rotation.

According to Flóvenz et al. (2012), it is very essential in a 1D dimension to invert for some rotational invariants defined in such a way that it averages over directions. Then one does have to deal with the question of rotation. Three such invariants exist:

$$Z_B = \frac{Z_{xy} - Z_{yx}}{2} \quad (40)$$

$$Z_{det} = \sqrt{Z_{xx}Z_{yy} - Z_{xy}Z_{yx}} \quad (41)$$

$$Z_{gm} = \sqrt{-Z_{xy}Z_{yx}} \quad (42)$$

All these parameters give the same values for a 1D earth response. For 2D, Z_{det} (determinant) and Z_{gm} (geometric mean) reduce to the same value, but Z_B (arithmetic mean) is different. For 3D responses, all these parameters are different (Flóvenz et al., 2012).

Tipper

For a non-1D earth, a part of the magnetic field tips into the vertical. The vertical magnetic component H_z is expressed as a linear combination of horizontal magnetic field components H_x and H_y (Everett and Hyndman, 1967), where:

$$H_z = AH_x + BH_y \quad (43)$$

The Tipper magnitude is given by:

$$T = \sqrt{A^2 + B^2} \quad (44)$$

For a 1D earth, $A = B = 0$. For a 2D earth the structure can be rotated such that the x-axis is in the strike direction where $A = 0$, but $B \neq 0$. This is done by properly minimizing $|A|$. This strike direction is called the Tipper strike.

Shift

Static shift is frequency independent off-set or shift of the apparent resistivity curves when plotted on a log-scale (constant multiplicative factor on a linear scale) scaled by a real factor. It results from distortion of the amplitude of the electric field due to the presence of shallow and local bodies of non-homogeneities. The scaling factor of shift cannot be determined from MT data collected at one station. A reliable indicator that static shift is present in the data is a parallel shift of apparent resistivity curves for ρ_{xy} and ρ_{yx} . Lack of parallel shift of apparent resistivity does not guarantee absence of static shift since the scaling factor of the two curves might be equal.

Interpretation of MT data via 1D modelling without considering the static shift will shift the depths of conducting bodies by the square root of the shift factors, and modelled resistivity will be wrong by a factor of S.

4. INSTRUMENTATION OF MAGNETOTELLURIC AND TRANSIENT ELECTRO-MAGNETIC EQUIPMENT

4.1 Magnetotelluric (MT) equipment

Magnetotelluric (MT) equipment is used for data acquisition and the main aim is to collect high quality data over a broad period range. The equipment consists of three magnetic sensors, five electrodes, five telluric cables each at least 30 m long, magnetic cables and one data logger; usually a five channel logger is used to measure the time components of the electromagnetic field, E_x , E_y , H_x , H_y and H_z . The deployment of MT equipment is done in reference to the x and y-axis in magnetic north and east, respectively. The E-fields are measured as voltage between rounded electrodes about 60 m (2×30 m) apart. The electrode at the centre is used to ground the data logger (Figure 8). The magnetic coil for H_x is oriented along the magnetic N-S direction with the connected side facing the instrument (Figure 9); H_y is oriented along the magnetic E-W direction and H_z is the vertical component. The electrodes are connected to the MTU data logger. The electrodes are made of KCl or PbCl₂ in solution enclosed in a ceramic container. Wet bentonite is applied on the outside of the electrodes to ensure good contact with the soil. The three magnetic coils measure the natural time varying magnetic fields at the earth's surface which are caused by electromagnetic waves radiated from the sun and from distant electrical storms (Vozoff, 1991). The soundings were made by computing the impedance for a range of frequencies ranging from 320 to 0.001 Hz from data acquired over 18-26 hours.

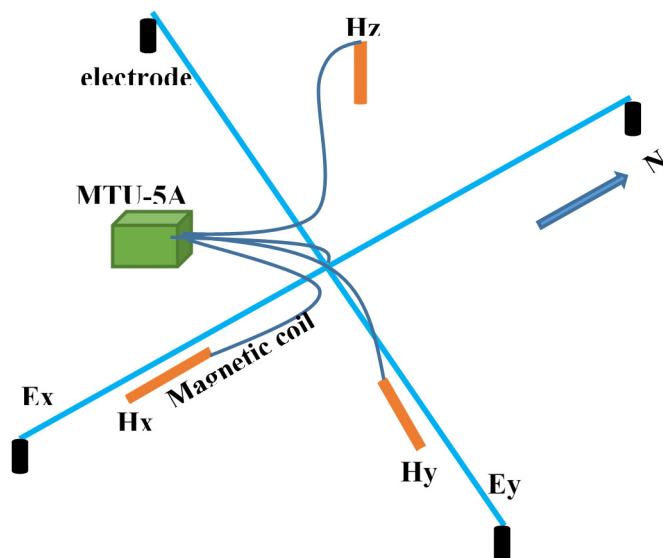


FIGURE 8: Layout of MT equipment (each electrode is placed 30 m from centre of the array)

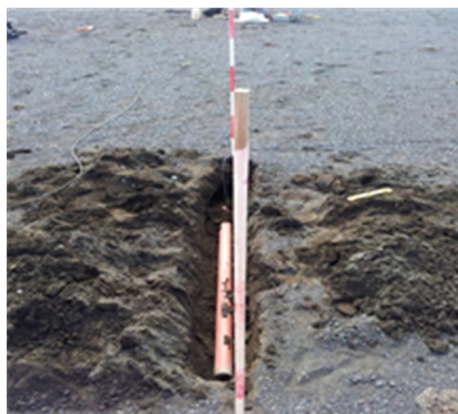


FIGURE 9: Magnetic N-S trending magnetic coil

the data collected by TerraTEM were processed using TerraTEM software and stored in USF form before being taken to TEMTD for inversion.

4.2 Transient electromagnetic method (TEM)

The instrument used in the acquisition of the analysed data was TerraTEM, developed by MonexGeoScope Pty Ltd. TerraTEM is made up of a transmitter (TX), receiver (RX), a 100×100 m loop and a battery pack. The transmitter is connected to the loop and the receiver placed at the centre is also connected to the transmitter with a synchronization cable (Figure 10).

The data used in this report were acquired according to the method developed by Monex Ltd. The locations of the loops were always chosen depending on area topography, avoidance of cultural interference and accessibility. The loop was laid out using compass directions to measure the sides precisely. All

5. GEOTHERMAL SURVEY AT EBURRU GEOTHERMAL FIELD

5.1 Geology of Eburru

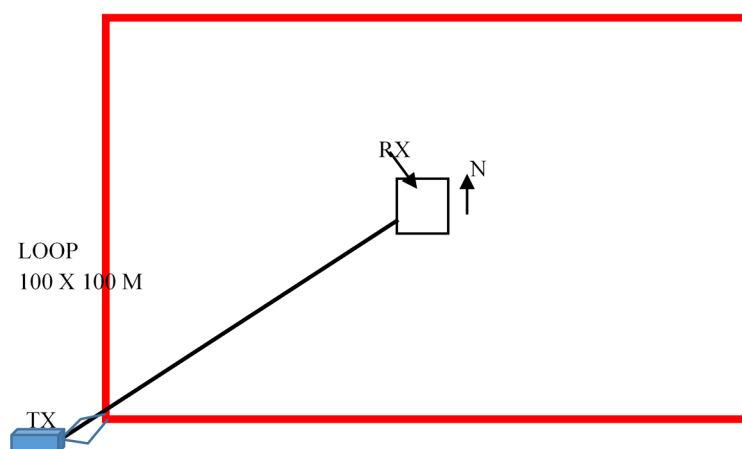


FIGURE 10: Schematic diagram of TerraTEM equipment deployed in the field

basalts are the most abundant rocks in the area and trachytes are mainly pantelleritic. The western older sector of Eburru is covered by upper trachytes which are underlain by lower pantellerite while the caldera on the eastern side is composed of upper pantellerite and upper trachytes. The eastern pantellerites are considered to be the youngest rocks, dating about 400 years (Clarke et al., 1990). The presence of syenite below the entire Kenyan Rift has been suspected, including in Eburru geothermal field; the drilled cores collected from Eburru confirmed a syenitic body at about 2400 m below ground level. The volcanic cones and domes have been referred to as a caldera (Omenda, 1997).

Eburru geothermal field is located within the Great Rift Valley system to the south of Menengai and north of Olkaria geothermal fields. In the 1980s, geoscientific studies were done in Eburru leading to the drilling of six exploratory wells between 1986 and 1990 with an average depth of 2.5 km. The elevation reaches 2800 m above sea level and is the highest topography within the Rift valley floor. Eburru structures mainly trend in N-S direction with west and east volcanic centres. Eburru has been active since Pleistocene. Rhyolite, trachytes and

Six wells have been drilled in Eburru (Figure 11). Three out of the six wells discharged and one well, EW-1, is used for production of 2.5 MWe. The fluid chemistry from well EW-1 indicates that Eburru reservoir is non-boiling with a high amount of non-condensable gases and high-salinity brine. Low magnesium and calcium content in the brine reduces the scaling problem in this well with a high chloride level of 956-1976 ppm compared to Olkaria (KPC, 1990).

5.2 The resistivity survey

The geophysical methods applied during the early 1980s included DC soundings (Schlumberger) and gravity leading to the siting of the exploratory wells. In 2006 to 2007, the more advanced geophysical methods, comprising transient electromagnetics (TEM) and magnetotellurics (MT), were applied. A total of 7 TEM and 7 MT soundings were carried out using the Zonge TEM system and MTU-5A Phoenix MT equipment, respectively (Figure 12). The latest survey of April 2013 added 36 MT and 36 TEM soundings using two sets of TerraTEM system and four sets of MTU-5A Phoenix MT equipment.

A total of 43 TEM and 43 MT soundings were analysed to improve the conceptual model of Eburru geothermal field.

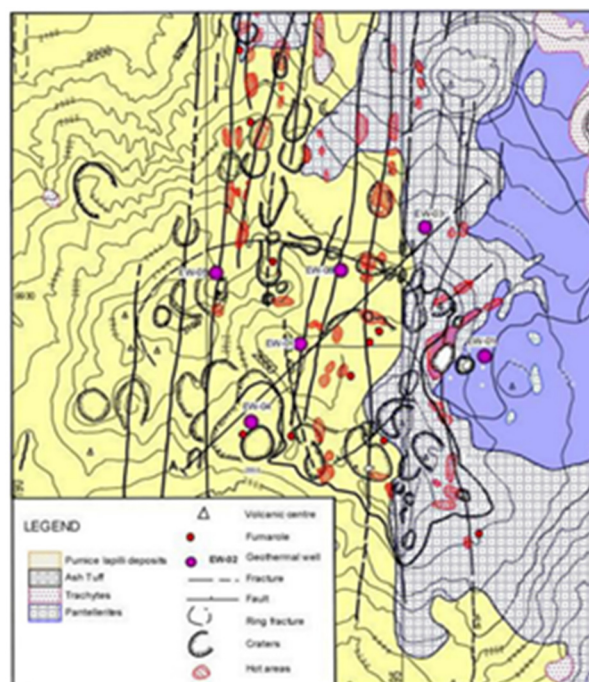


FIGURE 11: Eburru geological map with structures (Omenda and Karingithi, 1993)

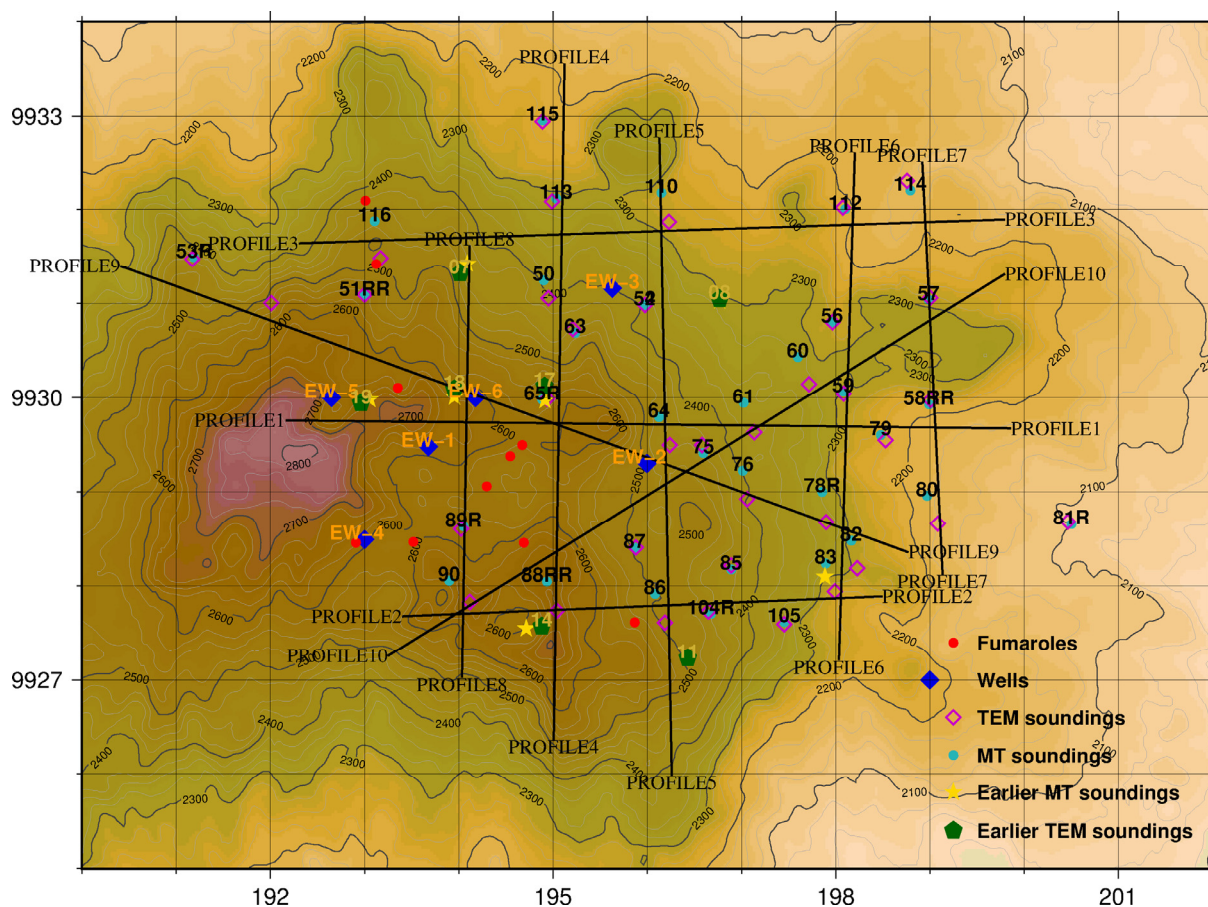


FIGURE 12: Location of MT soundings (black dots) and TEM soundings (inverted triangles); black lines are the cross-sections used in interpreting the resistivity structure of Eburru

6. PROCESSING AND INVERSION OF EBURRU FIELD DATA

MT and TEM data processing is specifically done to suppress various types of noise that affect measurements. It was found that the method used in processing these data could recover response functions from noisy field data. The processed data used in defining the subsurface resistivity structure of the Eburru geothermal field were high-quality data except for a few which were used as bench marks to test the quality of the software in case the field data were noisy.

6.1 Transient electromagnetic data processing

The TerraTEM data collected in Eburru were processed by TemxUSF program, a new version of TEMX for TerraTEM equipment. The program reads the USF file output of TerraTEM and enables a visual editing of data by masking outlier points before the data are used in TEMTD for inversion (Árnason, 2006a).

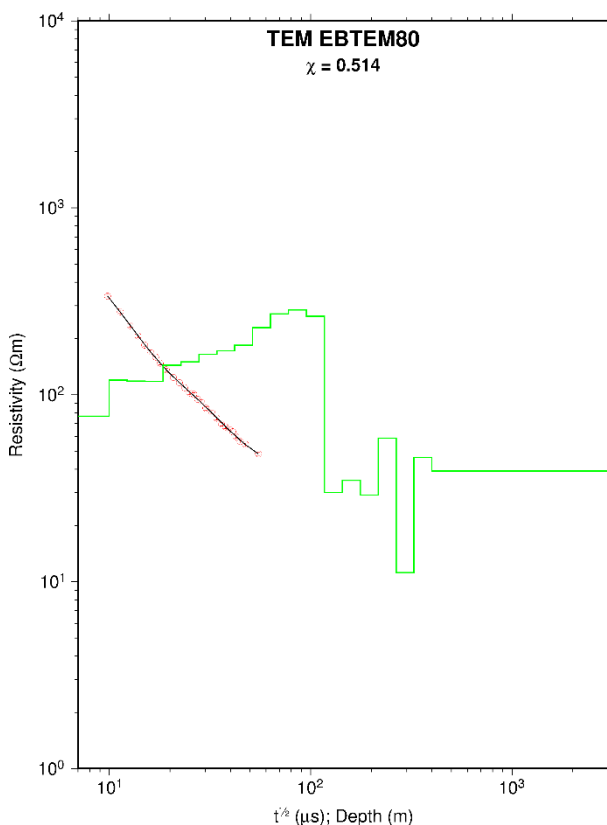


FIGURE 13: 1D inversion of a TEM sounding; χ shows the fit between measured and calculated data

The TEMTD program was used for the Eburru data to perform 1D inversion. In 1D inversion it is assumed that the earth consists of horizontal layers with different resistivity and thicknesses (Figure 13). The program runs on a Linux operational system and can be used for joint inversion of MT and TEM, or inversion of MT or TEM alone. For joint inversion, the program is used to determine the best static shift for MT data and indicate the static shift value, hence solving the shift problem. 1D inversion calculates the layered model and determines how its response best fits the measured data. All the TEM soundings curves and the associated 1D models are given in Appendix I (Omiti, 2013).

6.2 Magnetotelluric data processing

The MT data analysed in this report were acquired using magnetotelluric equipment MTU-5A made by Phoenix Geophysics, Canada. Data were acquired with three different sets of equipment. The initial processing was done by SSMT2000 from Phoenix Geophysics (2005). The software was provided by the equipment manufacturer. This involved editing the parameter file to reflect the setup of the data acquisition and Fourier

transforming the resulting time series data to the frequency domain. The MTeditor program was then used to display the phase curves, the apparent resistivity and the auto- and cross powers used to calculate each point of the curve. The program was also used to edit or smooth the data further by removing outliers, considered as noisy data points, on the phase or apparent resistivity curve. The final results from MTeditor were stored in EDI format (Electromagnetic data interchange), ready for inversion in the TEMTD program (Figure 14). Processed data of all the MT soundings are shown in Appendix II (Omiti, 2013).

6.3 Eburru strike analysis

Rose diagrams for the electrical strike, based on the Tipper strike for different period ranges, were analysed for this report. Tipper strikes at shallow depths 0.001-1 s, and greater depths, 1-1000 s, are shown in Figures 15 and 16. The Tipper strike is consistent with the results of 1D joint inversion models with the low resistivity at the centre and the Tipper strike aligned around the low resistivity.

6.4 TEMTD 1D inversion

TEMTD is a program used for 1D inversion of MT data and joint inversion of MT and TEM data. The TEMTD program was written by Knútur Árnason of ISOR (Árnason, 2006b). The program is capable of inverting the apparent phase derived from the MT off-diagonal element tensor (yx and xy modes) and the apparent resistivity (Figure 17). It is also able to calculate the static shift multiplier needed to fit both the TEM and MT data with the same model in joint inversion. It is capable of doing smooth Occam inversion with increasing but fixed layered thicknesses with depth as well as with inverting for resistivity values and thicknesses of layered models. A complete set of all the 1D joint inversion results of each sounding is shown in Appendix III (Omiti, 2013).

6.4.1 Joint Inversion of MT and TEM

As discussed in the next section, MT apparent resistivity is frequently shifted by a multiplicative factor. The shift is constant at all frequencies with no effect on the phase data (Jones, 1988). The amount of static shift depends on the resistivity characteristics beneath the area of study (Berdichevsky and Dmitriev, 1976).

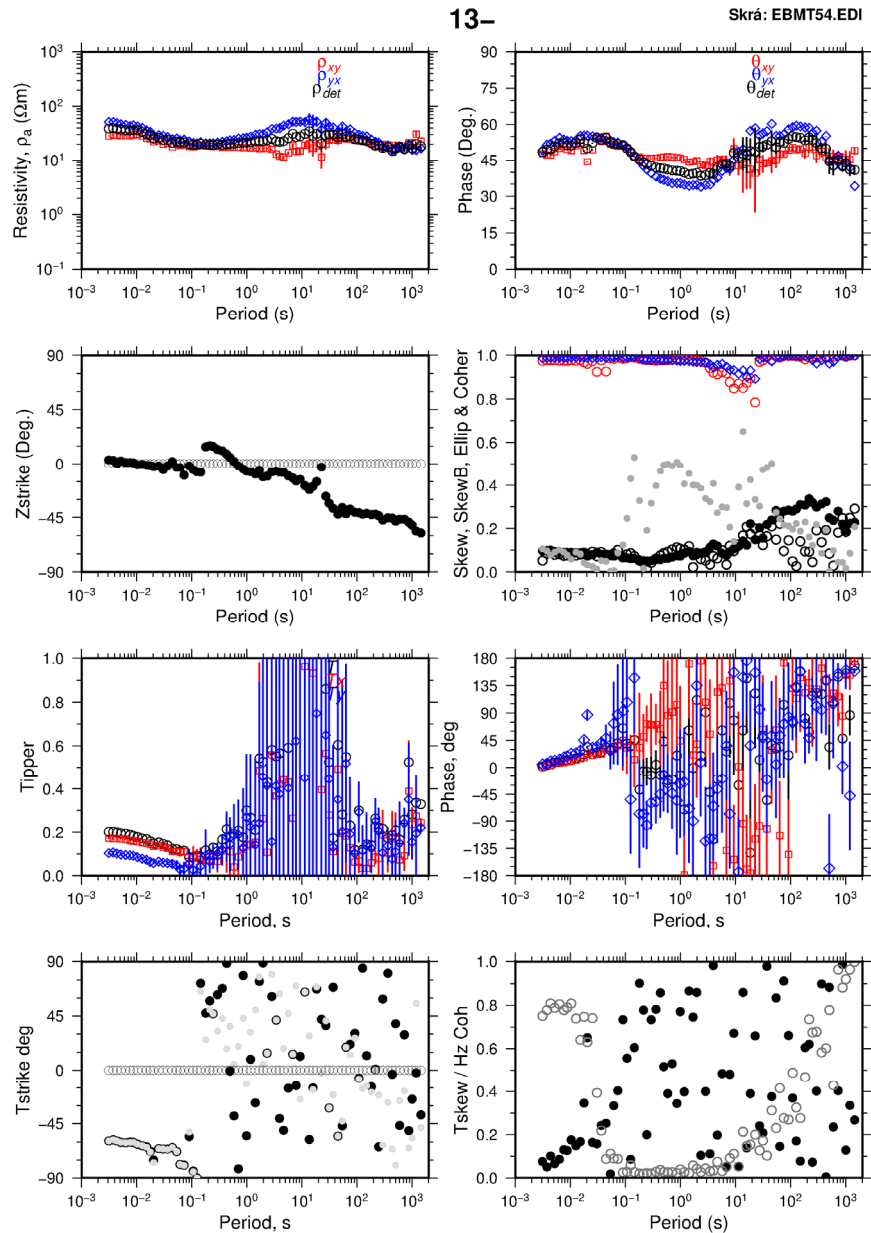


FIGURE 14: MT parameters as extracted from EDI file: apparent resistivity, phase in xy and yx direction and the determinant, electrical strike direction Zstrike, coherence, skew, Tipper, Tipper phase, Tstrike and Tskew

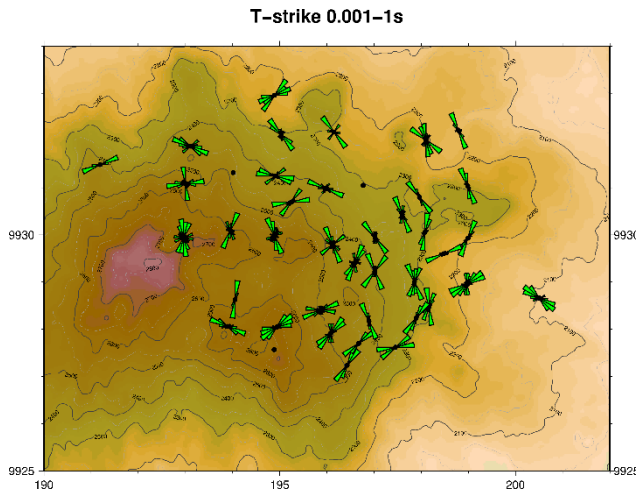


FIGURE 15: Rose diagram for the electrical direction based on the Tipper strike at 0.001-1 s

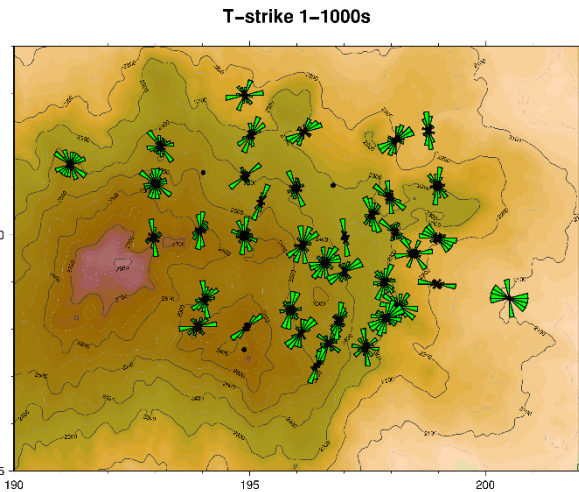


FIGURE 16: Rose diagram for the electrical direction based on the Tipper strike at 1-1000 s

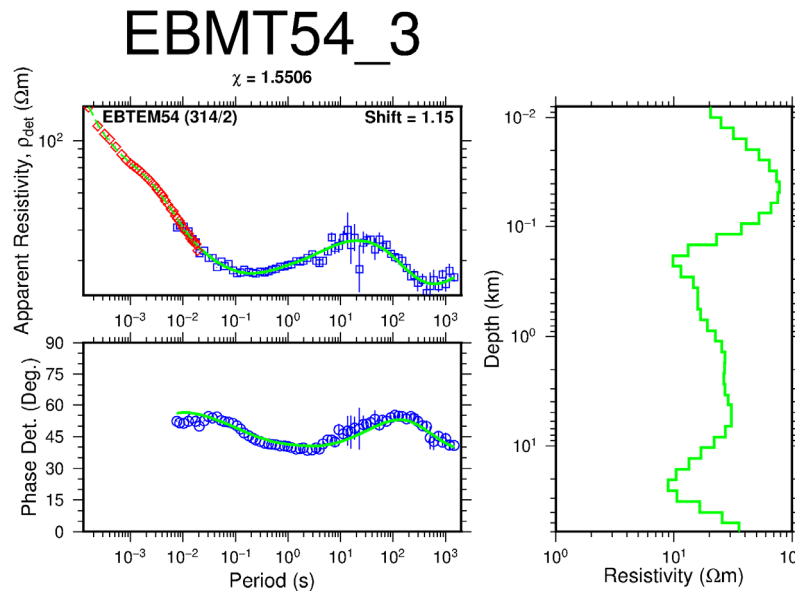


FIGURE 17: 1D Joint inversion of MT and TEM soundings; red and blue symbols on the top left represent the TEM apparent resistivity and the determinant apparent resistivity of the MT soundings, respectively; the bottom panel shows the determinant apparent phase of the MT sounding; the right box shows the results of 1D resistivity inversion model, the green line is the fit of TEM and MT data

TEM TD software was used for jointly inverting MT and TEM data for correction of static shift. Joint 1D Occam inversion of MT and TEM data was performed and the best multiplicative factor or shift parameter of all the MT soundings in Eburru were determined (see Figure 17).

6.5 Static Shift

Near surface inhomogeneities result in the build-up of charges which cause electric field distribution or galvanic distortion to affect the MT data (Chave and Smith, 1994). The distortion manifests itself as a frequency independent and unknown multiplier factor (shift on a log-scale) of the apparent resistivity. The phase, however, is not affected. TEM soundings do not

experience the static shift problem; therefore, TEM data are used for static shift correction of MT data collected at the same site. Apparent resistivity processed from MT data can be scaled to fit the TEM curve data or jointly inverted with TEM data.

A total of 43 MT soundings were jointly inverted with TEM data. Figure 18 shows a histogram of shift parameters from the Eburru geothermal field. Most of the MT shifts are less than one, indicating a conductive body underlying the area. All the MT data were shifted, showing the importance of TEM at every MT station. Figure 19 shows a map of the spatial distribution of static shift parameters in Eburru geothermal field, dominated by low shift parameters.

7. RESULTS AND DISCUSSION

Resistivity interpreted from electromagnetic methods or direct current method has been used for geothermal exploration for several years. The correlation between resistivity and drilling results has been done in many drilled geothermal field and shows that the resistivity method can be used to “x-ray” the earth’s subsurface (Árnason et al., 2000). The indirect correlation of temperature and resistivity is controlled by the degree of hydrothermal alteration. High-temperature

geothermal systems are normally associated with low resistivity resulting from mineral alteration (Árnason et al., 2000). The possibility of using the resistivity method to interpret temperature, permeability and alteration in a geothermal system sometimes resolves the geometry of the geothermal reservoir.

The study of low-resistivity zones is very essential in the delineation of high-temperature zones targeted for geothermal drilling. The interpretation of Eburru data will take into consideration the structures, the geological setting and the alteration pattern that might influence the area’s resistivity distribution. The final models are presented here in two different ways, as iso-resistivity maps for different elevations (depths) and as resistivity cross-sections.

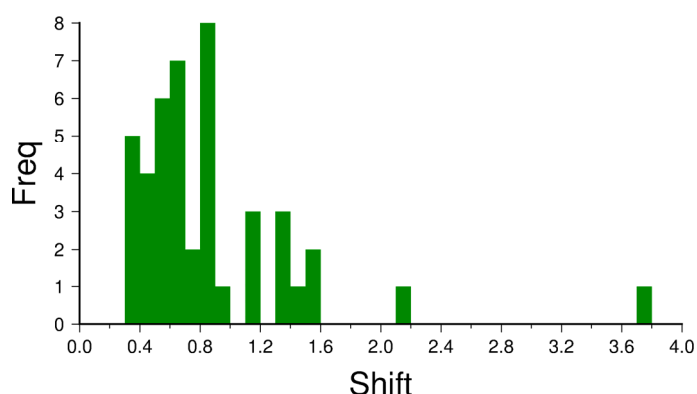


FIGURE 18: A histogram of the static shift parameters for Eburru field

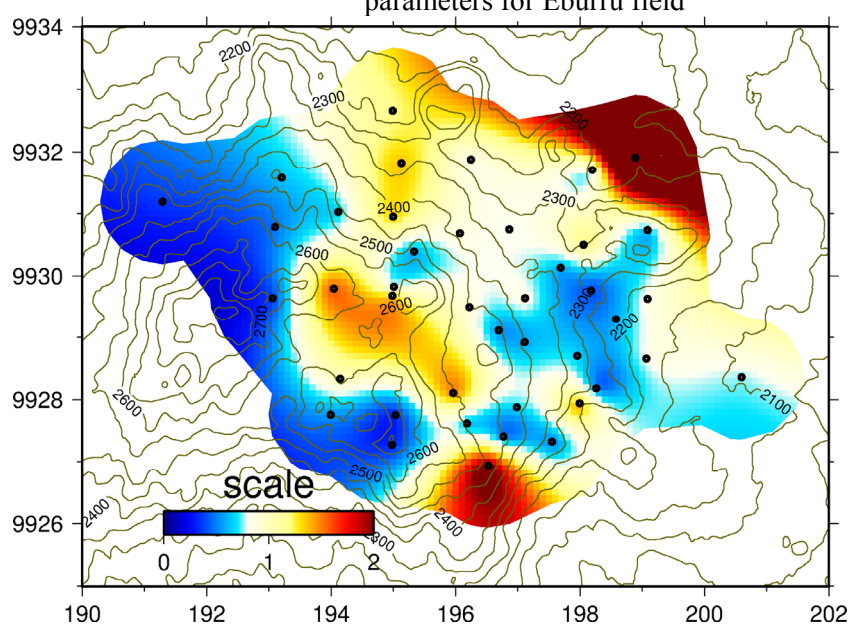


FIGURE 19: Spatial distribution of static shift parameters for determining apparent resistivity in Eburru geothermal field

7.1 Cross-sections

Several cross-sections were made in the area, with the locations shown in Figure 12 above. Three cross-sections are in an east-west direction, five in a north-south direction, one in a northeast-southwest direction and the last one in a southeast to northwest direction (Omiti, 2013, Appendix IV). The cross-sections were plotted by the TEMCROSS program (Eysteinnsson, 1998) developed at ISOR – Iceland GeoSurvey. The programme plots the resistivity obtained from the 1D inversion.

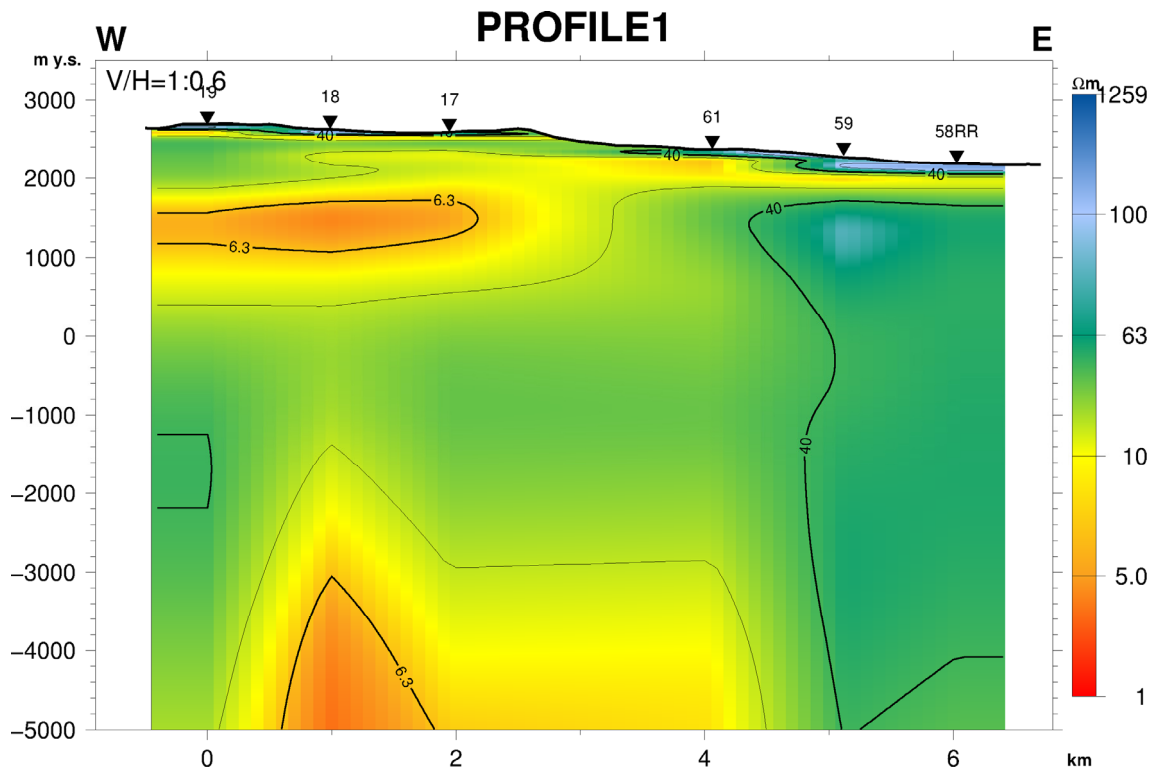


FIGURE 20: Resistivity cross-section in Eburru along profile 1 based on 1D joint inversion of MT and TEM data

Cross-section along profile 1 (Figure 20) has six soundings and is about 7 km long (cuts across well EW-5 and EW-6): It shows a thin resistive layer near the surface along the profile interpreted as unaltered formations underlain by low resistivity less than 10 Ωm , interpreted as due to the effect of geothermal manifestations such as fumaroles. Below this, at 900-1800 m a.s.l., is a conductive cap beneath soundings 19, 18, and 17, of resistivity less than 6 Ωm , interpreted as hydrothermal alteration minerals like zeolites and smectite formed in the temperature range of 100-230°C. It is then underlain by a resistive body, interpreted as high-temperature alteration minerals associated with chlorite and epidote with a formation temperature range between 250 and 300°C. Up-doming low resistivity at 3000 m b.s.l. below soundings 19, 18, and 17 is probably associated with the heat source of Eburru geothermal field. Soundings 59 and 58RR mark the eastern boundary of Eburru geothermal field. A thin conductive layer near the surface is interpreted as the presence of sediments and groundwater and is not associated with geothermal activity. The underlying high resistivity is described as the regional resistivity outside a geothermal field.

The cross-section along profile 2 (Figure 21) is to the south of well EW-4, 2 km south of profile 1, cuts across five soundings and extends for 5 km. The resistivity distribution of the top layer varies from west to east with a medium resistivity of 10-30 Ωm seen near the surface beneath sounding numbers 90, 88R and 86, interpreted as near surface alteration, and a resistive layer of 100 Ωm beneath soundings 85 and 83, interpreted as unaltered formation near the surface. The low resistivity to the west continues downwards and is underlain by a resistive body of about 50 Ωm at 900 m a.s.l. down to 2100 m b.s.l., interpreted as a chlorite-epidote zone due to high-temperature geothermal alteration. The eastern part below soundings 85 and 83 shows a very thin layer of low resistivity at about 2200 m a.s.l., interpreted as being due to sedimentary deposits and groundwater effect. It is then underlain by high resistivity down to a depth beyond 10,000 m b.s.l., interpreted as normal resistivity outside the geothermal field and, hence, outside the boundary of the resource area to the east.

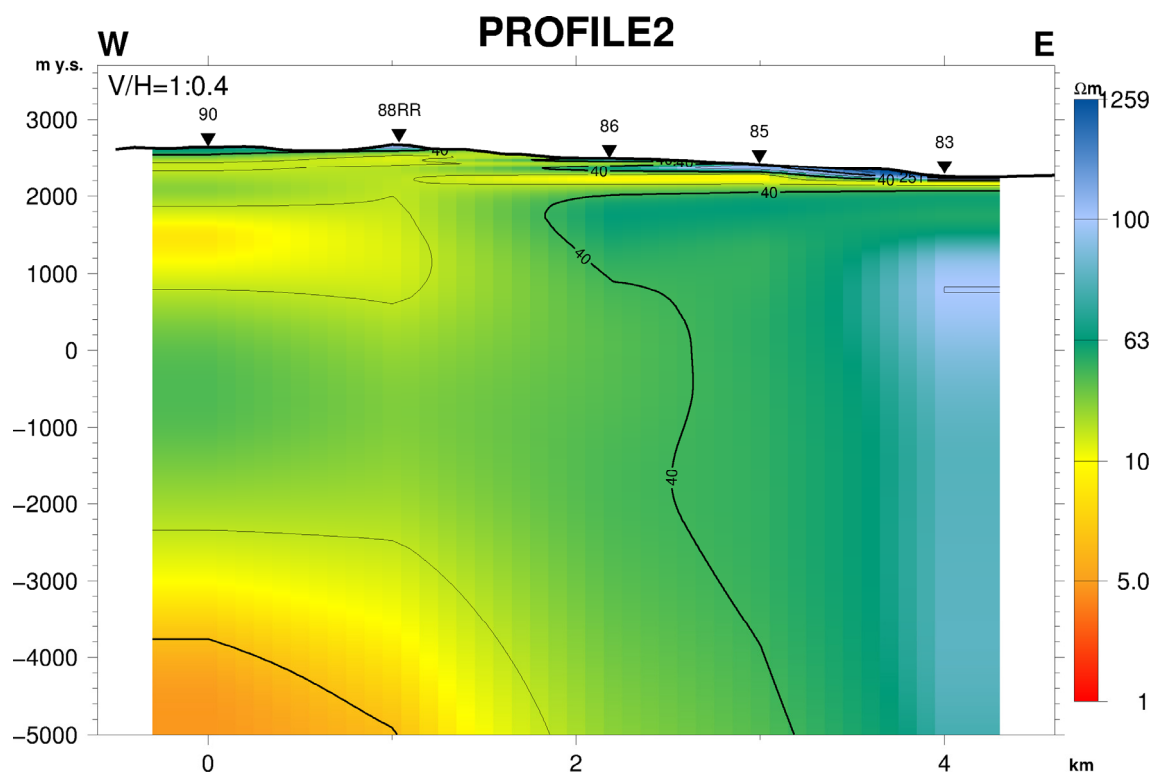


FIGURE 21: Resistivity cross-section in Eburru along profile 2
based on 1D joint inversion of MT and TEM data

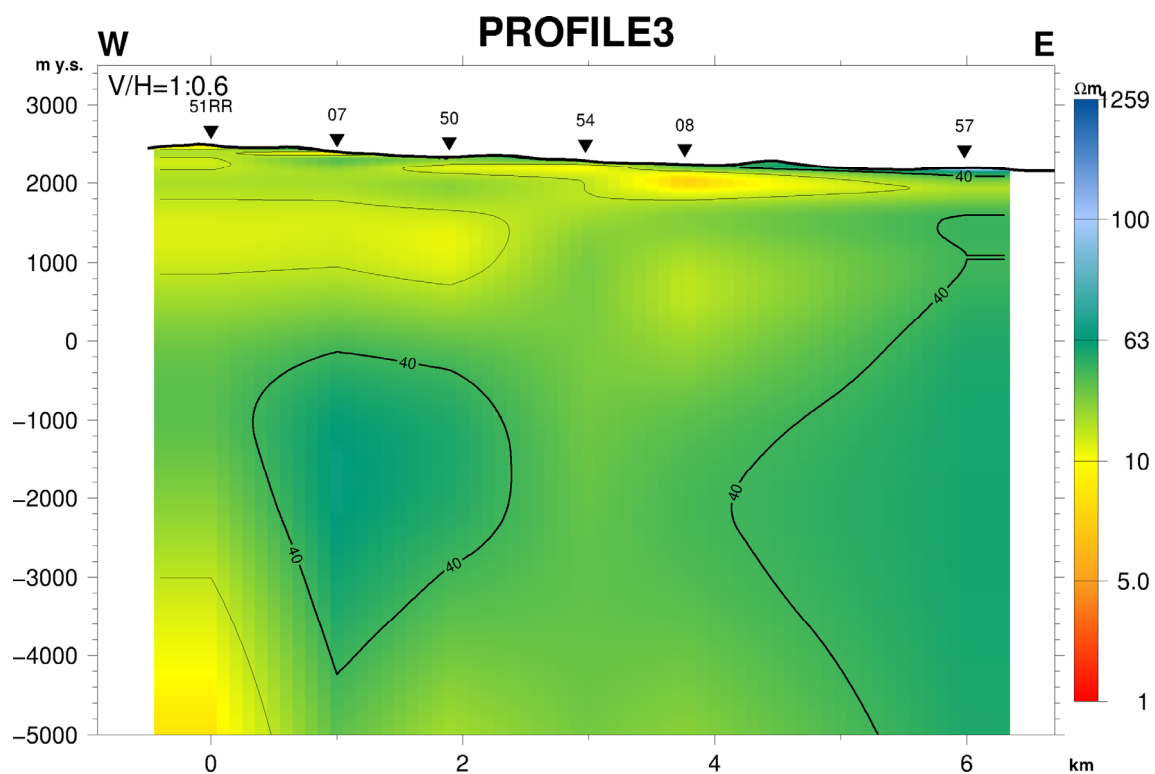


FIGURE 22: Resistivity cross-section in Eburru along profile 3
based on 1D joint inversion of MT and TEM data

The cross-section along profile 3 (Figure 22) dissects the area in a west-east direction, cutting across six soundings in the northern part of the study area, close to well EW-3. The resistivity pattern of the area

indicates a close proximity to the northern boundary of the geothermal field. Resistivity pattern related to low- and high-temperature alteration minerals is not as well evident in the western side of the cross-section as in profile 1. The eastern side shows the regional resistivity outside the geothermal field, indicating the boundary.

Profile 4 cross-section (Figure 23) cuts the area in a north-south direction. It is about 6 km long and includes seven soundings. The resistivity pattern shows the northern boundary below soundings 115 and 113. The southern part has a thin layer of high resistivity near the surface, indicative of unaltered minerals, overlying a uniform fairly low resistivity of about 10 Ωm , indicative of altered minerals due to steam condensate from a hot upflow from the underlying resistive layer, interpreted as high-temperature altered rock.

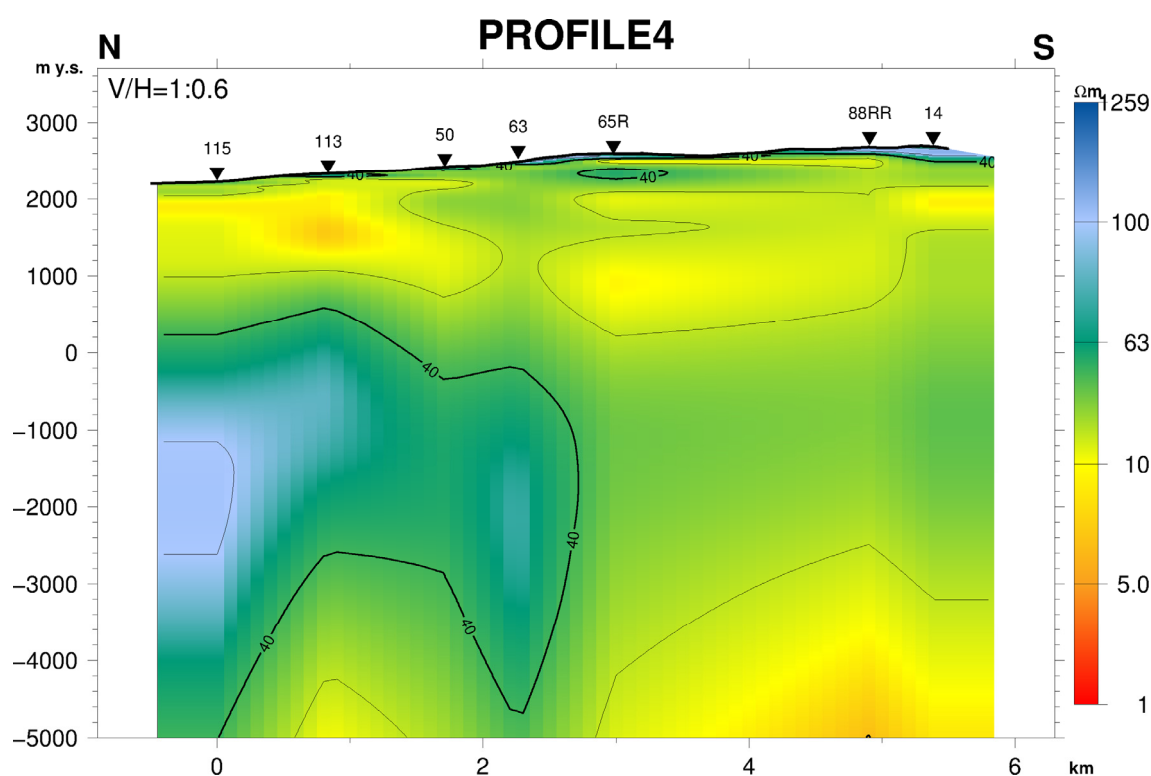


FIGURE 23: Resistivity cross-section in Eburru along profile 4 based on 1D joint inversion of MT and TEM data

The cross-section along profile 8 (Figure 24) is about 4.5 km long. It includes four soundings in a north-south direction and passes close to well EW-1 and EW-6. The distribution of the resistivity in this cross-section clearly depicts resistivity of a high-temperature field. At the top is a thin layer of high resistivity near the surface, signifying unaltered rocks overlying the low resistivity of about 10 Ωm , interpreted as resulting from geothermal activity. A pocket of low resistivity ($< 5 \Omega\text{m}$) below soundings 18 and 89R, interpreted as a smectite-zeolite zone, could indicate low-temperature alteration from a hot upflow condensate from an underlying resistive layer, interpreted as a chlorite-epidote zone associated with high-temperature alteration minerals, is in agreement with the temperature log in well EW-1. The temperature in well EW-4 is in disagreement with the subsurface resistivity presumably due to the fossil effect in the reservoir towards the southern boundary, indicating cooling of the reservoir. All the cross-sections are shown in Appendix IV (Omiti, 2013).

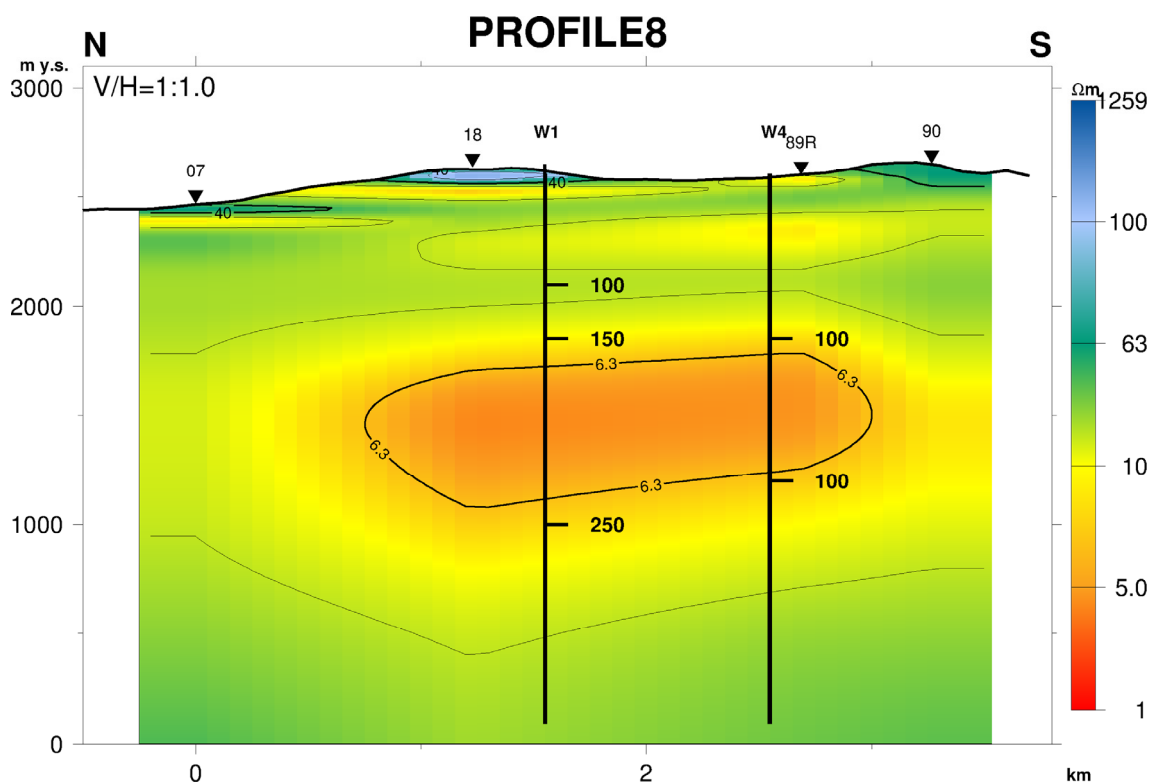


FIGURE 24: Resistivity cross-section in Eburru along profile 8 based on 1D joint inversion of MT and TEM data

7.2 Iso-resistivity maps

Iso-resistivity maps were constructed from TEMMAP program (Eysteinsson, 1998) to display the resistivity at different depths in Eburru. Analysis of the conductance, which is a product of the resistivity and thickness, was also done.

Resistivity map at 2000 m a.s.l. (Figure 25): At about 500 m below the ground level, the map shows a fairly uniform resistivity of about 10 Ωm . The fairly low resistivity can be interpreted as due to hydrothermal alterations lining fractures in rocks. Low resistivity on the eastern, northern and northwest boundaries is due to sediments and groundwater effect.

Resistivity map at 1500 m a.s.l. (Figure 26): At about 1500 m below the ground level, this map shows a fairly low resistivity ($< 10 \Omega\text{m}$) except for the eastern boundary. The fairly low resistivity is interpreted as low-temperature alteration minerals like smectite or zeolites and also confirms the presence of geothermal fluid.

Resistivity map at 500 m a.s.l. (Figure 27): At about 2500 m below the ground level, this map shows high resistivity defining the reservoir of Eburru. The high resistivity of $> 40 \Omega\text{m}$ in the central part is interpreted as due to the high-temperature alteration minerals, chlorite and epidote. The southeast, northeast and northwest parts show very high resistivity, of $> 100 \Omega\text{m}$, defining areas outside the geothermal system.

Resistivity map at 1500 m b.s.l. (Figure 28): At about 4000 m below the ground level, low resistivity spreads from the southwest, interpreted to be connected to the heat source of Eburru geothermal field. The high resistivity of the outer layer persists downward, an indication of the boundary and areas outside the geothermal system.

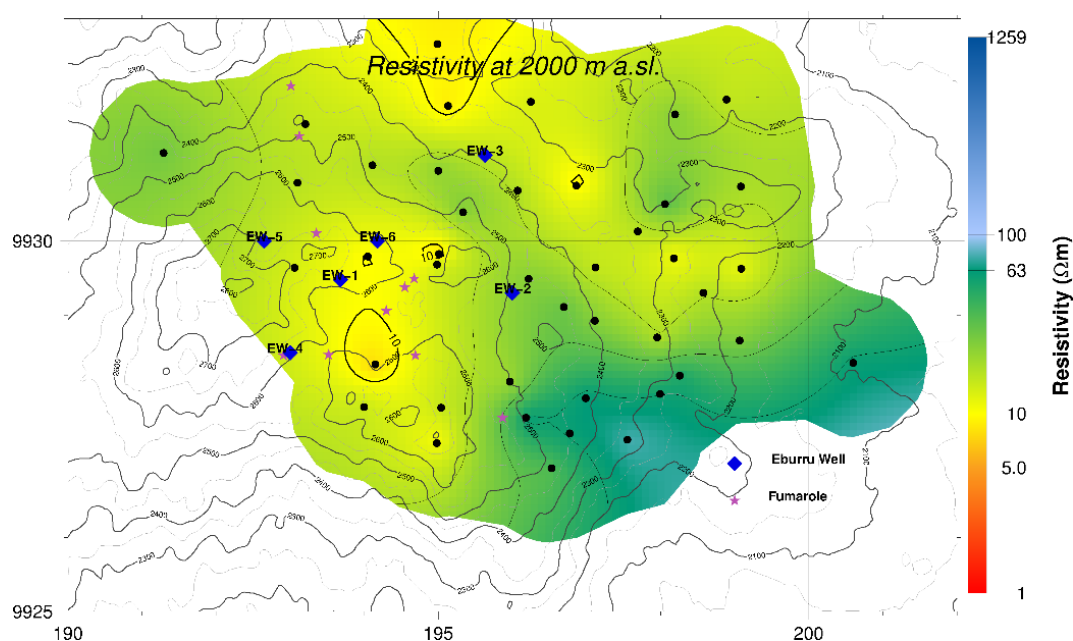


FIGURE 25: Resistivity iso-map at 2000 m a.s.l. of Eburru geothermal field, black dots denote MT soundings

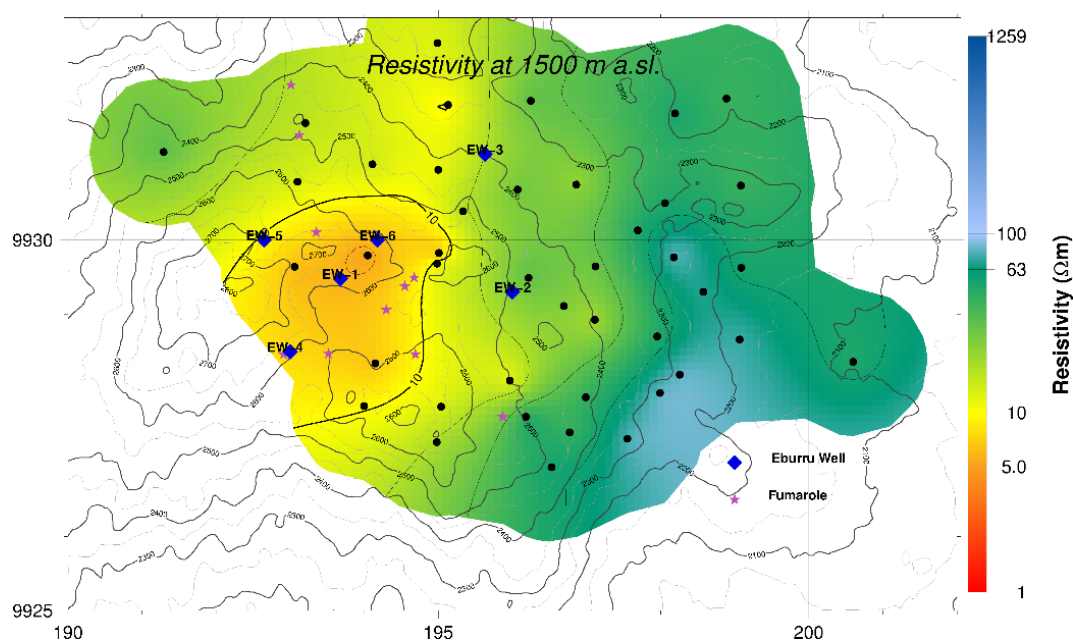


FIGURE 26: Resistivity iso-map at 1500 m a.s.l. of Eburru geothermal field

Resistivity map at 2500 m b.s.l. (Figure 29): At about 5000 m below the ground level, the central delineated low resistivity is associated with the heat source of Eburru geothermal field. The boundary of the resource is evident in the boundary between the low resistivity and high resistivity, with the very high resistivity defining areas outside the geothermal system.

Resistivity map at 10,000 m b.s.l. (Figure 30): At about 12,500 m below the ground level, there is not as much change as in Figure 29 except for the persistent decrease of resistivity in the southwest side of the centre, an indication of an increase in the conductor downwards towards the suspected deep seated heat source (magma chamber) within the volcano. Three wells drilled above the heat source discharged (EW-

1, EW-6 and EW-4) and the remaining three wells drilled outside the heat source did not discharge, indicating the importance of a geophysical survey before exploration drilling.

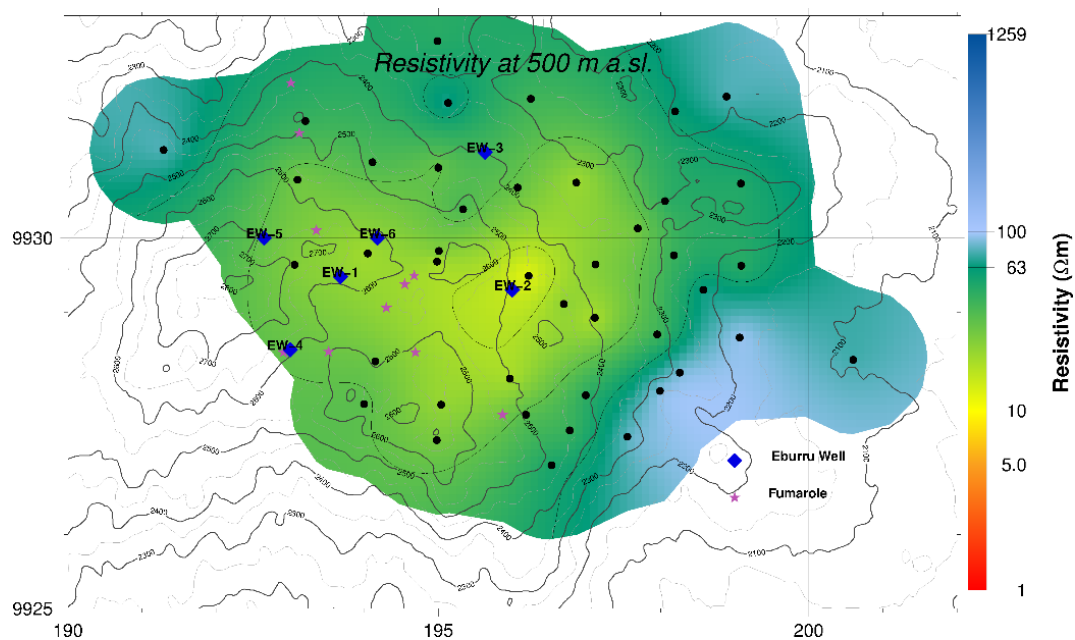


FIGURE 27: Resistivity iso-map at 500 m a.s.l. of Eburru geothermal field

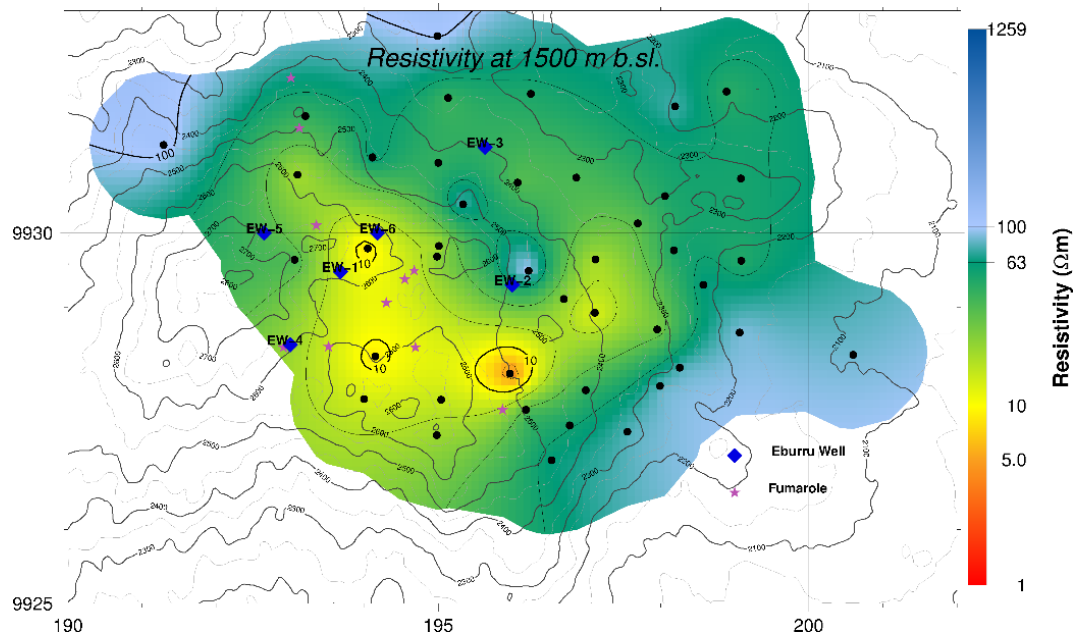


FIGURE 28: Resistivity iso-map at 1500 m b.s.l. of Eburru geothermal field

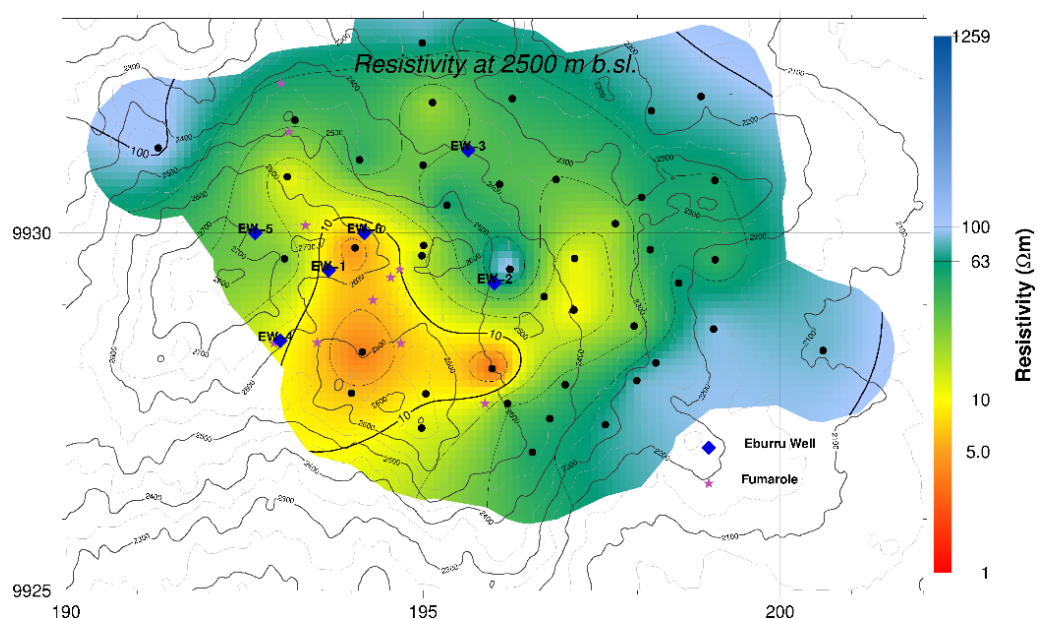


FIGURE 29: Resistivity iso-map at 2500 m b.s.l. of Eburru geothermal field

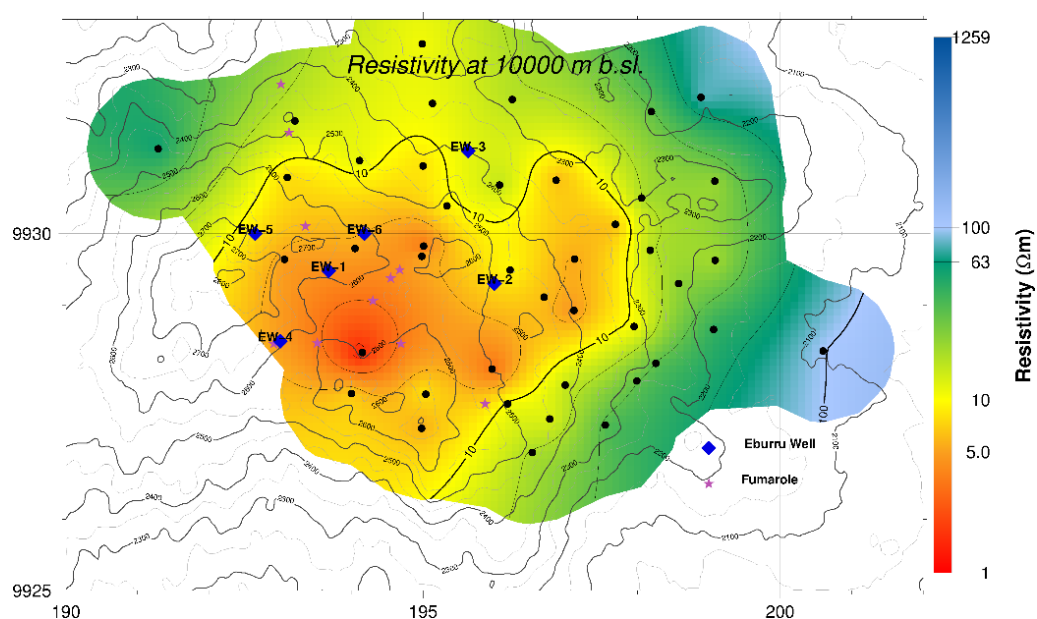


FIGURE 30: Resistivity iso-map at 10,000 m b.s.l. of Eburru geothermal field

8. CONCLUSIONS AND RECOMMENDATIONS

From the Eburru integrated data interpretation of 1D joint inversion of MT and TEM data, the following resistivity layers were observed in cross-sections and iso-maps:

- A very thin layer of high near-surface resistivity ($> 60 \Omega\text{m}$) covering almost the entire area, interpreted as unaltered formations and superficial deposits;
- It is followed by a uniform near-surface low-resistivity layer ($< 10 \Omega\text{m}$) resulting from geothermal activity, such as fumaroles;
- A second layer of low resistivity ($< 6 \Omega\text{m}$) is evident in the central and southwest parts, associated with smectite and zeolite alteration which formed as a result of hydrothermal alteration;

- It is followed by a resistive layer ($> 30 \Omega\text{m}$) at about 2500 m b.g.l., associated with resistive high-temperature alteration minerals like epidote and chlorite which define the geothermal system of Eburru;
- A good deep conductor ($< 10 \Omega\text{m}$), indicating the probable heat source of Eburru geothermal field, is well evident in the southwest towards the centre.

The interpreted data clearly delineates the Eburru geothermal resource boundary except to the southwest where the resource seems to be close to the surface. It is, therefore, recommended that more MT and TEM data be collected in the western and southwest parts of the study area in order to delineate the exact boundaries of the resource field.

ACKNOWLEDGEMENTS

I owe my sincere appreciation to outgoing Director, Dr. Ingvar Birgir Fridleifsson, and the new Director, Mr. Lúdvík S. Georgsson, for awarding me this scholarship. I would also like to thank Ms. Málfríður Ómarsdóttir, Mr. Ingimar G. Haraldsson, Mr. Markús A.G. Wilde, Ms. Thórhildur Ísberg and all of the ISOR staff for helping and guiding me during the training period. Special thanks go to my supervisors, Mr. Gylfi Páll Hersir and Mr. Knútur Árnason, for always being there for me and working with me full time during this research work. I would also like to express my gratitude to my classmates - we had fruitful discussions. To my family, thanks for your prayers and love throughout my entire training in Iceland. Lastly and the greatest of all, thanks go to God, for care and sustenance throughout my work.

REFERENCES

- Archie, G.E., 1942: The electrical resistivity log as an aid in determining some reservoir characteristics. *Trans. AIME*, 146, 54-67.
- Árnason, K., 1989: *Central loop transient electromagnetic sounding over a horizontally layered earth*. Orkustofnun, Reykjavík, report OS-89032/JHD-06, 129 pp.
- Árnason, K., 2006a: *TemX short manual*. ÍSOR – Iceland GeoSurvey, Reykjavík, internal report, 17 pp.
- Árnason, K., 2006b: *TEM TD, a programme for 1D inversion of central-loop TEM and MT data*. Short manual. ÍSOR – Iceland GeoSurvey, Reykjavík, internal report, 17 pp.
- Árnason, K., Karlsdóttir, R., Eysteinnsson, H., Flóvenz, Ó.G., and Gudlaugsson, S.Th., 2000: The resistivity structure of high-temperature geothermal systems in Iceland. *Proceedings of the World Geothermal Congress 2000, Kyushu-Tohoku, Japan*, 923-928.
- Berdichevsky, M.N., and Dmitriev, V.I., 1976: Distortion of magnetic and electric fields by near-surface lateral inhomogeneities. *Acta Geodaet. Geophys. et Montanist. Acad. Sci. Hung.*, 11, 447-483.
- Cagniard, L., 1953: Basic theory of the magneto-telluric method of geophysical prospecting. *Geophysics*, 18, 605-635.
- Chave, A.D., and Smith, J.T., 1994: On electric and magnetic galvanic distortion tensor decomposition. *J. Geophys. Res.*, 99-B3, 4669-4682.
- Clarke, M.C.G., Woodhall, D.G., Allen, D., and Darling G., 1990: *Geological, volcanological and hydrogeological controls on the occurrence of geothermal activity in the area surrounding Lake Naivasha, Kenya, with coloured 1:100 000 geological maps*. Ministry of Energy, Nairobi, 138 pp.
- Dakhnov, V.N., 1962: Geophysical well logging. *Q. Colorado Sch. Mines*, 57-2, 445 pp.

Encyclopaedia Britannica, 2010: Solar wind. Encyclopaedia Britannica Online, webpage: www.britannica.com/EBchecked/topic/1589681/Solar-Dynamics-Observatory.

Everett, J.E., and Hyndman, R.D., 1967: Geomagnetic variations and electrical conductivity structure in southwestern Australia. *Phys. Earth Planet. Inter.*, 1, 24-34.

Eysteinnsson, H., 1998: *TEMRES, TEMMAP and TEMCROSS plotting programs*. ÍSOR - Iceland GeoSurvey, unpublished programs and manual.

Flóvenz, Ó.G., Hersir, G.P., Saemundsson, K., Ármannsson, H., and Fridriksson Th., 2012: Geothermal energy exploration techniques. In: Sayigh, A., (ed.), *Comprehensive renewable energy*, vol. 7. Elsevier, Oxford, 51-95.

Flóvenz, Ó.G., Spangenberg, E., Kulenkampff, J., Árnason, K., Karlsdóttir, R., Huenges, E., 2005: The role of electrical interface conduction in geothermal exploration. *Proceedings of the World Geothermal Congress 2005, Antalya, Turkey*, 9 pp.

Henley, R.W., and Ellis, A.J., 1983: Geothermal systems ancient and modern - a geochemical review. *Earth-Science Reviews*, 19-1, 1-50.

Hersir, G.P., and Björnsson, A., 1991: *Geophysical exploration for geothermal resources. Principles and applications*. UNU-GTP, Iceland, report 15, 94 pp.

Jones, A.G., 1988: Static shift of magnetotelluric data and its removal in a sedimentary basin environment. *Geophysics*, 53-7, 967-978.

Kaufman, A.A., and Keller, G.V., 1981: *The magnetotelluric sounding method*. Elsevier Scientific Publishing Co., Amsterdam, 595 pp.

Kaufman A.A., and Keller, G.V., 1983: *Frequency and transient sounding. Methods in Geochemistry and Geophysics*, 16. Elsevier Scientific Publishing Co., Amsterdam, 685 pp.

KPC, 1990: *Olkaria West field information report*. STRM, Kenya Power Company, Ltd., internal report, 240 pp.

Mehegan, J.M., Robinson, P.T., and Delaney, J.R., 1982: Secondary mineralization and hydrothermal alteration in the Reydarfjörður drill core, eastern Iceland. *J. Geophysical Research*, 87-Nb8, 6511-6524.

Omenda, P.A., 1997: *The geochemical evolution of Quaternary volcanism in south-central portion of the Kenya Rift*. University of Texas, El Paso, PhD thesis, 218 pp.

Omenda, P.A., and Karingithi, C.W., 1993: Hydrothermal model of Eburru geothermal field, Kenya. *Geoth. Res. Council, Trans.*, 17, 155-160.

Omiti, A.O., 2013: *Appendices to the report: "Resistivity structure of the Eburru geothermal field, Kenya, described through 1D joint inversion of MT and TEM data"*. UNU-GTP, Iceland, report 26 appendices, 104 pp.

Phoenix Geophysics, 2005: *Data processing user guide*. Phoenix Ltd., users guide.

Quist, A.S., and Marshall, W.L., 1968: Electrical conductances of aqueous sodium chloride solutions from 0 to 800°C and at pressures to 4000 bars. *J. Phys. Chem.*, 72, 684-703.

Velador, J.M., Omenda, P.A., and Anthony, E.Y., 2002: Geology and the origin of trachytes and pantellerites from the Eburru volcanic field, Kenya Rift. *Paper presented at the AGU Fall Meeting 2002*.

Vozoff, K., 1991: The magnetotelluric method. In: Nabighian, M.N (ed.), *Electromagnetic methods. Applied Geophysics*, 2, 641-711.

Zhdanov, M.S., and Keller, G.V., 1994: *The geoelectrical methods in geophysical exploration*. Elsevier Scientific Publishing Co., Amsterdam, 873 pp.



DIRECTIONAL WELL DESIGN, TRAJECTORY AND SURVEY CALCULATIONS, WITH A CASE STUDY IN FIALE, ASAL RIFT, DJIBOUTI

Farah Omar Farah

Ministry of Energy and Natural Resources

P.O. Box 10010

Djibouti

DJIBOUTI

farahwalioullah@gmail.com

ABSTRACT

Djibouti plans to drill 4 new geothermal wells for its future production in the Lava Lake or Fialé, within the Asal Rift segment. These wells are planned to be directionally drilled and the targets are based on six previous wells (Asal 1 - 6) drilled in the late 1980s in this rift segment. These 6 wells were drilled in an area which has high temperature potential, but problems of low permeability and high salinity were encountered. This paper presents directional well planning for these new wells and calculations for: (a) the trajectory and survey, (b) the well path, (c) the vertical depth. Two case studies are presented for Fialé and the resulting well path, using the build and hold type of directional wells. A simple BHA with two-stabilizers is proposed with an optimal weight on bit. Based on the casing plan, the kick-off point should be lowered to 430 m depth rather than 350 m as proposed by the pre-feasibility study, which is about 30 m below the casing shoe of the intermediate casing. Another option is drilling vertical wells, which would provide the same subsurface information as directional wells. However, a thorough cost analysis of drilling, survey tools, and equipment is needed to determine whether directional or vertical drilling is financially advantageous for the exploration wells. Directional drilling would not require new permitting or much geological and geophysical studies as such studies were done in the pre-feasibility phase in 2008. Drilling pads and targets for vertical drilling would, however, require further studies and a permit to drill inside of Fialé crater.

1. INTRODUCTION

Directionally drilled wells represent an efficient way to reach special targets that are difficult to reach using vertically drilled wells. A drawback of directional drilling is higher cost, but the advantage is that surface construction may be minimized while still reaching the intended targets. The main factor in the cost of a directional well is the horizontal distance to the target. The objective of the present study is to present the calculations that show the well path in a 3D space, and to develop the model that gives the minimum drilling length for these wells. The project of constructing and operating a geothermal power plant is divided into four phases from the exploration phase to production. The Asal project is currently in the exploration phase, which involves drilling four exploration and appraisal wells, followed by a

resource appraisal period, and finally by drilling seven to nine additional production wells. Information attained through the drilling of the exploration wells and during the appraisal of the second phase will be used for the conceptual design of the power plant. The true vertical depth (TVD) departure from the end of the built section, and the well path in a build and hold well profile is calculated.

Although the focus of this work is directional drilling, vertical drilling should not be excluded as a perfectly viable option. Therefore, this topic is also presented in a separate section and compared with directional drilling.

1.1 Background

The objective of steering a well trajectory in the right direction and hitting a geological target many kilometers downhole has forced the drilling industry to really focus on tools and methods to identify wellbore location and its path during drilling. In the early days of drilling exploration, it was common to set the drilling rig right above the target and drill a vertical well into it. Later, it became necessary to drill wells to reach targets that were deviated from the reference location at the surface. Throughout the years, many tools and methods have been developed for directional drilling. There are several companies offering tools to deflect and steer wellbores in the right direction and to measure wellbore inclination and azimuth.

The directional survey measurements are given in terms of inclination, azimuth and 3D coordinates, TVD, northing and easting at the depth of the survey station. For many applications, the accurate position and direction of the borehole should be determined at depths which may not coincide with the depth of survey stations. A mathematical tool for interpolating between survey stations is then required.

1.2 Objective

The objective of this paper is to show the calculation methods needed for directional well path design and to show the usage of trajectory and survey calculation methods by designing the well path of two wells in Asal Fialé. The emphasis is on the following:

- Calculate the true vertical depth (TVD) and departure from the vertical, at the end of the build-up (EOB) section and the total depth (TD) to the bottom of the hole, in a build and hold well profile.
- Calculate directional coordinates.
- Describe formulas used to describe and calculate the well trajectory for different methods: Tangential; balanced tangential; average angle; radius of curvature; and minimum curvature.
- Outline the procedure for calculating survey results.
- Calculate the northing, easting, TVD, vertical section and dogleg severity of a survey station using the minimum curvature method.
- Determine the exact bottom hole location of the well.
- Monitor the actual well path while drilling to ensure the target is reached.
- Orient deflection tools (such as directional drilling assemblies) in the required direction when making corrections to the well path.
- Design the bottom hole assembly (BHA) including the buoyed weight (or hook load) in a vertical hole and the required BHA weight in air.

1.3 Scope

The minimum curvature method was chosen for trajectory calculations of the well. The scope of this work is based on:

- Literature review on directional drilling and survey calculation methods; and
- Trajectory and survey calculations methods.

1.4 Literature review

The following directional drilling methods are covered in the following books: *Applied drilling engineering* by Bourgoyne, Millhem, Chenevert, and Young (1991); *Directional drilling and deviation control technology* by the French Oil and Gas Industry Association (1990); and *Directional drilling* by Inglis (1987). Other references are indicated where used. It is pertinent to note that this literature is focused towards petroleum drilling practices. Other sources are:

- 1957: J.E. Edison presents the average angle method;
- 1968: G.J. Wilson presents the radius of curvature method;
- 1971: J.E. Walstrom presents the balanced tangential method;
- 1973: W.A. Zarembo presents the minimum curvature method;
- 1991: Xiushan Liu presents the constant curvature method;
- 1994: Wong et al., and Morita and Whitebay elaborate on the design of wells.
- 2004: S.J. Sawaryn and J.L. Thorogood present their SPE paper named *A compendium of directional calculations using the minimum curvature method*.

2. DIRECTIONAL WELL DESIGN

2.1 Directional drilling

Directional drilling is described as the deflection of a wellbore in order to reach a pre-determined objective below the surface of the earth". Figure 1 shows the main parameters of a directional well.

2.1.1 Definitions and terminology

Directional drilling is the methodology for directing a wellbore along a predetermined trajectory to a target. Vertical wells are usually defined as wells with an inclination within 5° . Wells with an inclination greater than 60° are referred to as highly deviated wells. Wells with a section having an inclination greater than 85° for a significant distance are called horizontal wells. The following terminology is used:

- *Azimuth*: The angle ($^\circ$) between the north direction and the plane containing the vertical line through the wellhead and the vertical line through the target.
- *Build-up rate*: The angle from the kick-off point is steadily built up. This is the build-up phase. The build-up rate ($^\circ/30$ m) is the rate at which the angle is built.
- *Drop-off point*: The depth where the hole angle begins to drop off (i.e. tending to vertical).
- *Displacement*: The horizontal distance between the vertical lines passing through the target and the wellhead.
- *Inclination*: Angle ($^\circ$) made by the tangential section of the hole with the vertical.
- *Kick-off point (KOP)*: The depth at which the well is first deviated from the vertical.
- *Measured depth (MD)*: Depth (length) of the well along the well path.

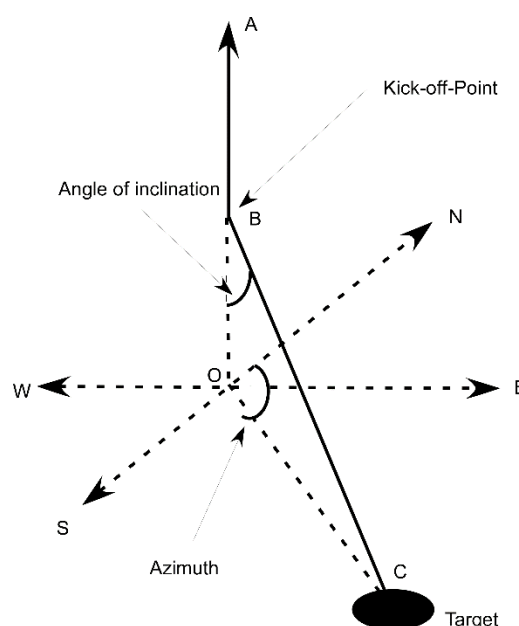


FIGURE 1: Measurement parameters of a directional well (modified from Gabolde and Nguyen, 1991)

- *Tangent section*: Section of a well where the well path is maintained at a certain inclination, with the intent of advancing in both TVD and vertical section. Short tangential sections are built for housing submersible pumps for example.
- *True-vertical depth (TVD)*: Vertical distance between *kelly bushing (KB)* and survey point.
- *Vertical Section (VS)*: Pre-defined azimuth angle along which the VS is calculated, usually the angle between north and a line uniting the wellhead and the total depth, measured on a plan view.
- *Well path*: The trajectory of a directionally drilled well in three dimensions.

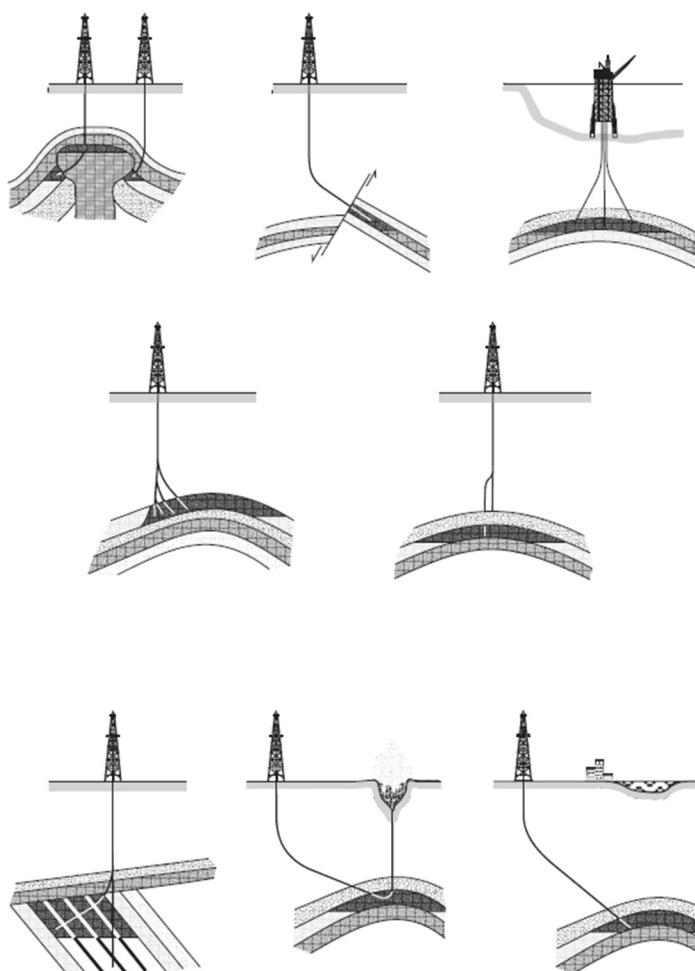


FIGURE 2: Several applications of directional drilling as common in the oil industry (Bourgoyne et al., 1991)

potential for damaging the casing can be minimized by drilling parallel to a fault and then changing the direction of the well to cross the fault into the target.

c) Inaccessible locations. Vertical access to a producing zone is often obstructed by some obstacle at the surface (e.g. river estuary, mountain range, city). In this case, the well may be directionally drilled into the target from a rig site some distance away from the point vertically above the required point of entry into the reservoir.

d) Side-tracking and straightening. It is, in fact, quite difficult to control the angle of inclination of any well (vertical or deviated) and it may be necessary to 'correct' the course of the well for many reasons. For example, it may be necessary in the event of the drillpipe becoming stuck in the hole to simply drill around the stuck pipe (or fish), or plug back the well to drill to an alternate target.

2.1.2 Application

The directional well is planned along a predetermined trajectory to hit a subsurface target. The target may be geometric and even adjusted in real time based on *logging while drilling (LWD)* measurements.

There are many reasons for drilling a non-vertical (deviated) well. Some typical applications of directionally controlled drilling are shown in Figure 2.

a) Multi-well platform drilling is widely employed in the North Sea. The development of these fields is only economically feasible if it is possible to drill a large number of wells (up to 40 or 60) from one location (platform) without moving it. The deviated wells are designed to intercept a reservoir over a wide area. Many oil fields (both onshore and offshore) would not be economically feasible without directional drilling.

b) Fault drilling. When a well is drilled across a fault, the casing may be damaged by fault slippage. The

e) *Salt dome drilling.* Salt domes (called diapirs) often form hydrocarbon traps in what were overlying reservoir rocks. In this form of trap, the reservoir is located directly beneath the flank of the salt dome. To avoid potential drilling problems in the salt (e.g. severe washouts, moving salt, high pressure blocks of dolomite) a directional well can be used to drill alongside the diapir (not vertically down through it) and then at an angle below the salt to reach the reservoir.

f) *Relief wells.* If a blow-out occurs and the rig is damaged, or destroyed, it may be possible to kill the “wild” well by drilling another directionally drilled well (relief well) to intercept or pass within a few feet of the bottom of the “wild” well. The “wild” well is killed by circulating high density fluid down the relief well, into and up the wild well.

2.1.3 Directional well types

There are several types of wellbore profiles. Below there is a description and an illustration of the most common profiles:

- *Build and hold profile* (Type 1) is the most common and simplest. The well is vertical until the KOP where it is kicked off and an angle is built. When the desired inclination is reached, the well path is kept tangent or straight until the target is reached.
- *Build, hold and drop profile* (Type 2), also called *shaped wells*, is the same in the upper section as the build and hold well profile. The well is kept vertical until KOP and an inclination is built and the tangent section is drilled. After the tangent section, a drop-off section is drilled where the inclination is reduced and the well path is almost vertical as it hits the target.
- *Deep build/kick-off* (Type 3) is a type of wellbore drilled when there is a hindrance, such as a salt dome, or when the well has to be side-tracked. The well is drilled vertically to a deep KOP and then inclination is built quickly to the target. Horizontal well profile and Horizontal Drain hole well profile are other types of wellbore trajectories. Theoretically, there are more than ten types of wellbore profiles.

These well trajectories are shown in Figure 3.

2.2 Planning the well profile

The first step in planning a directional well is to design the wellbore path, or trajectory, to intersect a given target. The initial design should consider the various types of paths that can be drilled economically.

2.2.1 Parameters defining the well path

There are three specific parameters which must be considered when planning one of the trajectories shown in Figure 3. These parameters combine to define the trajectory of the well:

- *Kick-off point*, is the long hole measured depth at which a change in inclination of the well is initiated and the well is oriented in a particular direction (in terms of north, south, east and west). In general, the most distant targets have the shallowest KOPs in order to reduce the inclination of the tangent section of the well (Figure 3). It is generally easier to kick off a well in shallow formations than in deep formations. The kick-off should also be initiated in formations which are stable and not likely to cause drilling problems, such as unconsolidated clays.
- *Build-up and drop off rate* (in degrees of inclination) are the rates at which the well deviates from the vertical (usually measured in degrees per 30 m or 100 ft). The build-up rate is chosen on the basis of previous drilling experience in the location and the tools available, but rates between 1° and 3° per 30 m or 100 ft of hole drilled are most common in conventional wells. Since the build-

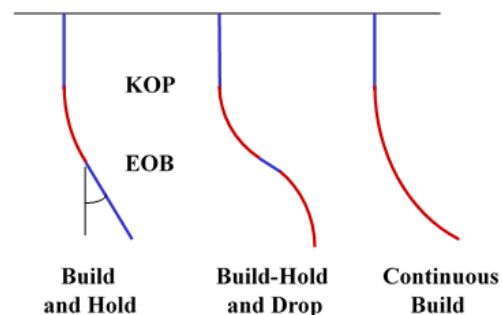


FIGURE 3: Most common types of wellbore profiles

up and drop off rates are constant, these sections of the well, by definition, form the arc of a circle. Build up rates in excess of $3^\circ/30$ m are likely to cause doglegs when drilling conventional deviated wells with conventional drilling equipment. The build-up rate is often termed the dogleg severity (DLS).

- *Tangent angle* of the well (or drift angle) is the inclination (in degrees from the vertical) of the long straight section of the well after the build-up section of the well. This section of the well is termed the tangent section because it forms a tangent to the arc formed by the build-up section of the well. The tangent angle will generally be between 10° and 60° since it is difficult to control the trajectory of the well at angles below 10° and it is difficult to run wire line tools into wells at angles greater than 60° .

2.2.2 Target and geography

The trajectory of a deviated well must be carefully planned so that the most efficient trajectory is used to drill between the rig and the target location and ensure that the well is drilled for the lowest cost. When planning, and subsequently drilling the well, the position of all points along the well-path trajectory is considered in three dimensions (Figure 4). This means that the position of all points on the trajectory must be expressed with respect to a three dimensional reference system. The three dimensional system that is generally used to define the position of a particular point along the well path is:

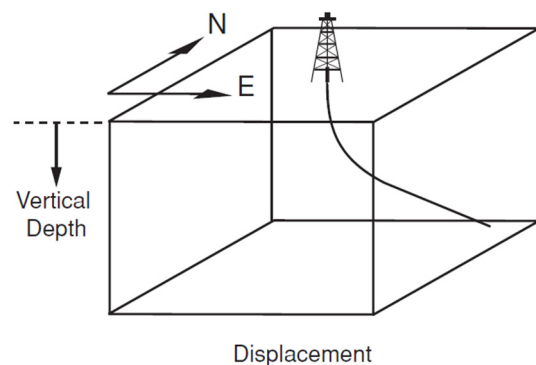


FIGURE 4: Well planning reference systems

- The vertical depth of the point below a particular reference point.
- The horizontal distance traversed from the wellhead in a northerly direction.
- The distance traversed from the wellhead in an easterly direction.

The depth of a particular point on the well path, referred to as true vertical depth (TVD) is expressed in metres (feet) vertically below a reference (datum) point. The northerly and easterly displacement of the point horizontally from the wellhead is reported as Northing/easting or longitude/latitude.

2.2.3 Defining the well path

Having fixed the target and the rig position, the next stage is to plan the geometrical profile of the well to reach the target. The most common well trajectory is the build and hold profile, which consists of 3 sections - vertical, build-up and tangent. The trajectory of the wellbore can be plotted when the following points have been defined:

- KOP kick-off point (selected by engineer);
- TVD and horizontal displacement of the end of the build-up section; and
- TVD and horizontal displacement of the target (defined by position of rig and target).

Since the driller will only be able to determine the long hole depth of the well, the following information will also be required:

- A long hole depth (AHD) of the KOP (same as TVD of KOP);
- Build up rate for the build-up section (selected by engineer);
- Direction in which the well is to be drilled after the KOP in degrees from north (defined by position of rig and target);
- AHD at end of build (EOB) and the tangent section commences; and
- AHD of the target.

These depths and distances can be defined by a simple geometrical analysis of the well trajectory.

2.3 Well path calculation

2.3.1 Build-and-hold

The following information is required:

- Surface (slots) coordinates;
- Target coordinates;
- True vertical depth of target;
- True vertical depth to KOP;
- Build-up-rate.

The choice of slot depends on a number of factors including target location and the proximity of other wells. The target coordinates and depth are selected by the geologist. The choice of KOP and build-up rate has to be made by the directional engineer (Bourgoyne, et al., 1991):

Figures 5 and 6 show a build-and-hold wellbore trajectory intersecting a target at a true vertical depth (TVD) of TVD_3 and at a horizontal departure of D_h (point D). The kickoff point is at a TVD of depth TVD_1 , where the rate of inclination angle build-up is q in degrees per unit length.

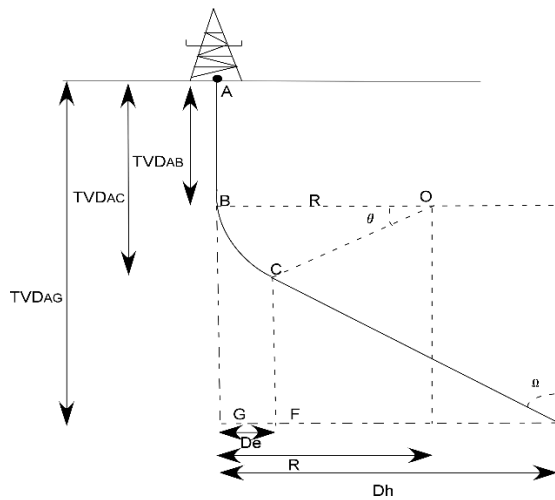


FIGURE 5: Geometry of build-and-hold type well path for $D_h > R$

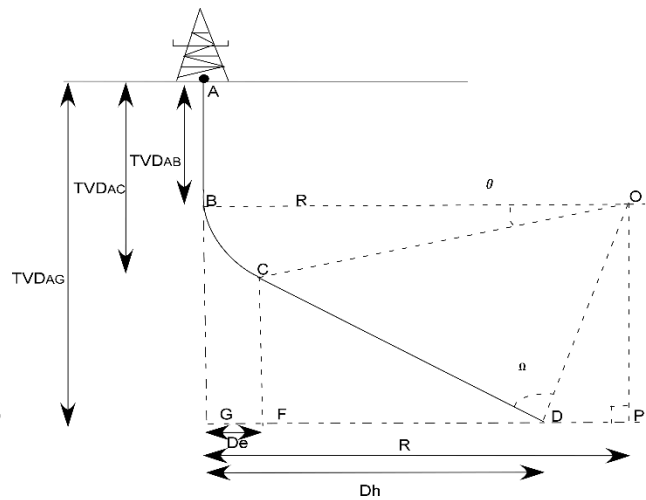


FIGURE 6: Geometry of build-and-hold type well path for $R > D_h$ (same definitions as for Figure 5)

- TVD_{AB} : Distance from the surface location to the KOP;
 $B-D$: Distance from KOP to the bottom of hole;
 D_h : Deviation of the wellbore from the vertical (Horizontal displacement);
 TVD_{AG} : True vertical depth;
 $MD (A-D)$: Well measured depth; and
 q : Build up rate ($^{\circ}/30$ m).

For the following formula, note that $TVD_3 = TVD_{AG}$, $TVD_2 = TVD_{AC}$, $TVD_1 = TVD_{AB}$. The radius of curvature, R , is thus:

$$R = \frac{180^{\circ}}{\pi} * \frac{1}{q} \quad (1)$$

where q is the build-up rate in $^{\circ}/30$ m.

To find the maximum inclination angle, θ , consider in Figure 6 that:

$$90^\circ = \theta + (90^\circ - \Omega) + \tau$$

or:

$$\theta = \Omega - \tau \quad (2)$$

The angle τ can be found by considering the triangle OPD, where (case $R > D_h$):

$$\tan \tau = \frac{DP}{PO} = \frac{R - D_h}{TVD3 - TVD2} \quad (3a)$$

and

$$\tau = \arctan\left(\frac{R - D_h}{TVD3 - TVD1}\right) \quad (3b)$$

Angle Ω can be found by considering ODC, where:

$$\sin \Omega = \frac{R}{OP} \quad (4)$$

and

$$Lob = \sqrt{(R - D_h)^2 + (TVD3 - TVD1)^2}$$

Substituting OP into Equation 4 gives:

$$\sin \Omega = \frac{R}{\sqrt{(R - D_h)^2 + (TVD3 - TVD1)^2}} \quad (5)$$

The maximum inclination angle, θ , for the build-and-hold case where $D_h < R$ is:

$$\theta = \arcsin\left[\frac{R}{\sqrt{(R - D_h)^2 + (TVD3 - TVD1)^2}}\right] - \arctan\left(\frac{R - D_h}{TVD3 - TVD1}\right) \quad (6)$$

The length of the arc, section BC, is:

$$L(BC) = \frac{\pi}{180^\circ} * R * \theta \quad (7)$$

or:

$$L(BC) = \frac{\theta}{q} \quad (8)$$

The length of the trajectory path, CD, at a constant inclination angle can be determined from triangle DCO as:

$$\tan \Omega = \frac{CO}{Lcb} = \frac{R}{Lcb} \quad (9)$$

and

$$Lcb = \frac{R}{\tan \Omega} \quad (10)$$

The total measured depth, D_M , for a true vertical depth of $TVD3$ is:

$$D_M = TVD1 + \frac{\theta}{q} + \frac{R}{\tan \Omega} \quad (11)$$

where D_M equals the vertical section to kickoff plus build section plus constant inclination section (Figures 6 and 7).

The horizontal departure GF (D_E) at the end of the build can be determined by considering D'CO, where:

$$D_E = R - R \cos \theta = R(1 - \cos \theta) \quad (12)$$

To find the measured depth and horizontal departure along any part of the build before reaching maximum angle θ , consider the intermediate inclination angle θ' , the inclination angle at C', which will yield a new horizontal departure, D_n .

The preceding derivation is valid only when $D_h < R$. Another way of expressing the maximum inclination angle, θ , in terms of R , $TVD1$, $TVD3$, and D_h for $D_h > R$ is:

$$\theta = \arctan\left(\frac{TVD3 - TVD1}{R - D_h}\right) - \arccos\left[\left(\frac{R}{TVD3 - TVD1}\right) * \sin\left(\arctan\left(\frac{TVD3 - TVD1}{R - D_h}\right)\right)\right] \quad (13)$$

2.3.2 Build-hold and drop

The second type of trajectory is the build, hold, and drop or S shape curve, which is depicted in Figure 7, for the cases where $R < D_h$ and $R + R1 > D_t$, and in another case where $R < D_h$ and $R + R1 < D_t$. In all of these cases, the maximum inclination is reduced to zero at D_t with drop radius $R1$, which is derived in the same manner as the build radius, R .

- TVD_{BG} : Distance from the surface location to the KOP;
- TVD_{AG} : True vertical depth of well (TVD);
- $B-D$: Distance from KOP to the bottom of hole (MD);
- $G-D$: Deviation of the wellbore from the vertical to the end of tangent section;
- $G-P$: Deviation of the wellbore from the vertical to the end of drop section;
- $A-G$: True vertical depth;
- $A-P$: Measured depth; and
- D : End of tangent section.

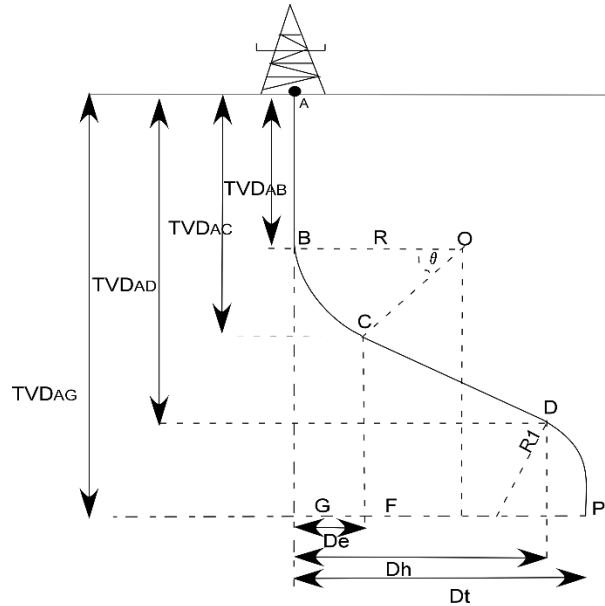


FIGURE 7: Geometry of build-hold and drop type well path for $R > D_h$ and $R + R1 < D_t$

The following equations are used to calculate the maximum inclination angles for $R + R1 > D_t$ and $R + R1 < D_t$:

$$\theta = \arctan\left(\frac{TVD4 - TVD1}{R + R1 - D_t}\right) - \arccos\left[\left(\frac{R + R1}{TVD4 - TVD1}\right) * \sin\left(\arctan\left(\frac{TVD3 - TVD1}{R + R1 - D_t}\right)\right)\right] \quad (14)$$

$$\theta = 180^\circ - \arctan\left(\frac{TVD4 - TVD1}{R + R1 - D_t}\right) - \arccos\left[\left(\frac{R + R1}{TVD4 - TVD1}\right) * \sin\left(\arctan\left(\frac{TVD3 - TVD1}{R + R1 - D_t}\right)\right)\right] \quad (15)$$

2.4 Directional drilling tools

There are a number of tools and techniques which can be used to change the drilling direction of the bit. These tools and techniques can be used to change the inclination or the azimuthal direction of the wellbore or both. All of these tools and techniques work on one of two basic principles. The first principle is to introduce a bit tilt angle into the axis of the BHA just above the bit; the second is to introduce a side force to the bit (Figure 8). The introduction of a tilt angle or side force to the bit will result in the bit drilling off at an angle from the current trajectory. This is currently the most used method in geothermal drilling.

The major tools currently used for this purpose are:

- *Steerable positive displacement motor*, currently used mostly in geothermal;
- *Non-rotating steerable drilling systems*;
- Rotary steering system;
- Directional *bottom hole assemblies (BHA)*; and
- *Whipstocks*, mostly used for sidetracks.

The most commonly used technique for changing the trajectory of a geothermal wellbore uses a piece of equipment known as a positive displacement (mud) motor. The end of the motor may be set at an angle to introduce tilt to the bit. The motor is powered by the drilling fluid being pumped down the drill string and it rotates the drill bit. The end of the motor may be set at a small angle to deflect the bit and thus gain trajectory deflection. By “sliding” (i.e. drilling without rotation) the motor turns the bit and the set angle allows deflection of the wellbore. In between the well is drilled by rotating the drillstring and thus a straight wellbore trajectory is obtained. By mixing these both methods the well trajectory may be deflected, without introducing too high a dogleg.

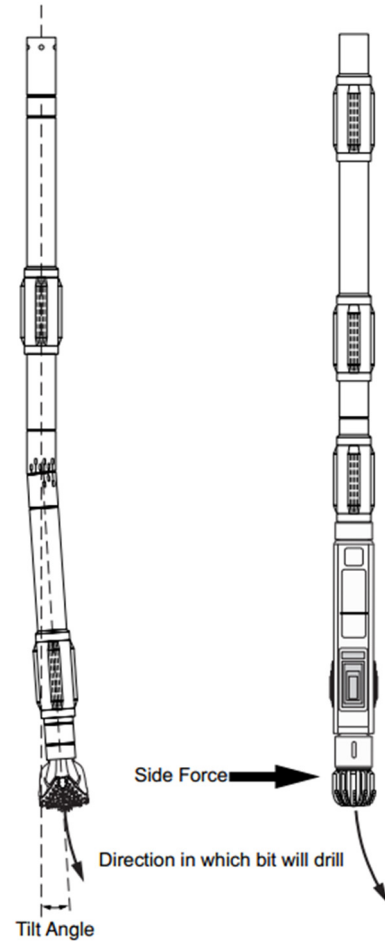


FIGURE 8: Bit tilt angle and side force (Baker Hughes INTEQ, 1995)

Sidetrack is when a new well path is to be obtained out of a previous one. The main sidetrack methods used in directional drilling are:

- Whipstocks, the retrievable, open-hole whipstock is only used in special applications, e.g. rigs with small pumps, and sidetracks in deep, very hot holes. The whip-stock is pinned to a limber BHA which includes a small bit. A typical BHA is:
 - Motors, in this method, a bent sub is run directly above a PDM. A typical BHA is as follows: Bit + PDM + bent sub + float sub + orienting sub (UBHO) + non-magnetic DCs + HWDP + DP.
 - Whip-stock + pilot bit + stabilizer + shearpin sub + 1 joint of drill pipe + UBHO + non-magnetic DC.
- Jetting, this technique is used to deviate the wellbore in soft and friable formations. The well can be kicked off and built up to maximum inclination using one BHA. A typical jetting BHA is:

- Bit + near-bit stab. + UBHO (universal bottom hole orientation) + MWD + NMDC (non-magnetic drill collar) + stab + DC + stab., etc.

2.5 Well surveying

During drilling it is close to impossible to make the actual trajectory precisely match the designed well path. For that reason, it is important to monitor the well trajectory and take corrective actions as the well is being drilled. To achieve this goal there must be reliable survey measurement tools and techniques that determine inclination, azimuth and perhaps the tool face orientation at different points along the well path. Survey tools only provide an incremental departure from a known starting point. The known point is referred to as the tie-on, or ties line. The first survey station is recorded deeper than the tie-on. The tools measure inclination and azimuth, the MD is known. The points of measurements are called survey stations. The measured parameters are then used to calculate the wellbore position in terms of the 3D coordinates N, E and TVD. Inclination angle is measured with respect to the vertical while azimuth is measured with respect to either magnetic or true north. But azimuth is typically reported in reference to true or grid north. As a result, the azimuth needs to be corrected before being reported or used in calculations. True north is the absolute north reference. Magnetic Declination is the angle from true north to magnetic north, and Grid Convergence is the angle from true north to grid north.

2.5.1 Application

When planning a 3D well trajectory, one of the most important considerations is torque and drag. If the torque and drag are not carefully considered, the drill string might fail. The torque and drag model used makes special assumptions that simplify the analysis and are used to model real drill strings. The most important factor influencing the torque and drag forces is the hole curvature. The well path should be redesigned with a smaller build-up rate if the drill string seems to fail when simulating these forces during the design stage. There are many causes for excessive torque and drag such as: sliding friction, tight hole, collapsing or swelling clay/shale, key seats, differential sticking and cuttings build-up. The minimum curvature method assumes the bending part in the equilibrium equation used to calculate torque and drag is discontinuous at survey stations. Some authors mean this is one of the main weaknesses of using the minimum curvature method. Due to the missing bending stresses, the method might not represent the real drill string configuration.

2.5.2 Survey calculation methods

There are several methods of computing directional surveys (Figure 9). However, only four are commonly used today. The main methods are:

- Average angle;
- Tangential;
- Balanced tangential (rarely used);
- Radius of curvature; and
- Minimum curvature.

The tangential method gives significant errors throughout the wellbore path, as well as the bottom hole location. The balanced tangential method is included as it is the basis for the minimum curvature method. These methods use inclination and azimuth at a specified measured depth. The difference between these methods is how they process the raw survey

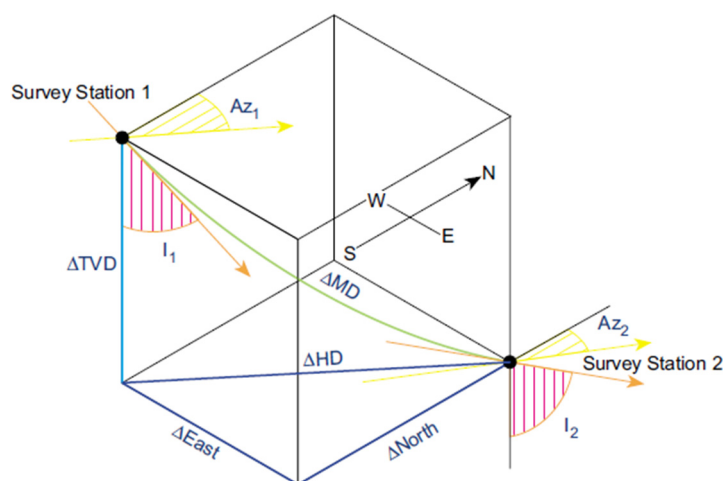


FIGURE 9: Survey

These methods use inclination and azimuth at a specified measured depth. The difference between these methods is how they process the raw survey

data of inclination, azimuth, and measured depth. The following paragraphs are a description of these methods (Sperry-Sun, 2001).

A. Average angle method

The average angle method (Figure 10) uses the average of the inclinations and azimuths measured at the upper and lower survey stations. The average of the two sets of angles is assumed to be the inclination and the azimuth over the incremental measured depth. The wellbore path is then calculated using simple trigonometric functions.

Average angle calculations:

$$\Delta_{NORTH} = \Delta MD * \sin \left(\frac{I1 + I2}{2} \right) * \cos \left(\frac{Az1 + Az2}{2} \right) \quad (16)$$

$$\Delta_{EAST} = \Delta MD * \sin \left(\frac{I1 + I2}{2} \right) * \sin \left(\frac{Az1 + Az2}{2} \right) \quad (17)$$

$$\Delta_{TVD} = \Delta MD * \cos \left(\frac{I1 + I2}{2} \right) \quad (18)$$

where MD = Measured depth between surveys (m);
 $I1$ = Inclination (angle) at upper survey (°);
 $I2$ = Inclination (angle) at lower survey (°);
 $Az1$ = Azimuth direction at upper survey (°); and
 $Az2$ = Azimuth direction at lower survey (°).

B. Tangential method

The tangential method (Figure 11) uses the inclination and azimuth at the lower end of the course length to calculate a straight line that represents the well bore, and passes through the lower end of the course length. The wellbore is assumed to be a straight line throughout the course length. This method is the most inaccurate of the methods discussed and should not be used in the determination of survey results unless the course lengths are not longer than the length of the survey tool.

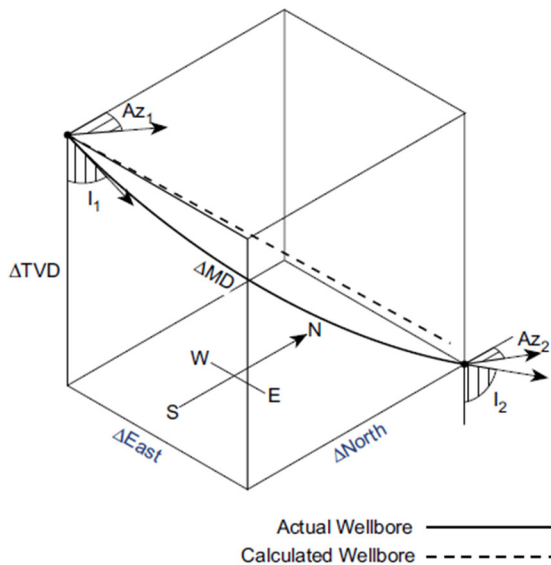


FIGURE 10: Average angle method

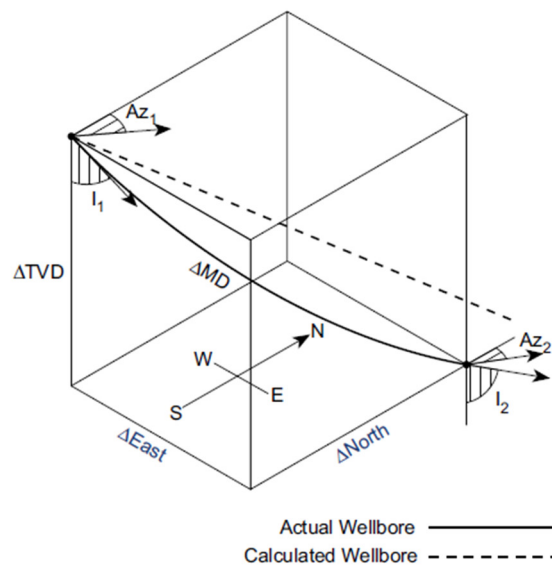


FIGURE 11: Tangential angle method

Tangential calculations:

$$\Delta_{NORTH} = \Delta MD * \sin I2 * \cos Az2 \quad (19)$$

$$\Delta_{EAST} = \Delta MD * \sin I_2 * \sin Az_2 \quad (20)$$

$$\Delta_{TVD} = \Delta MD * \cos I_2 \quad (21)$$

where MD = Measured depth between surveys (m);
 I_2 = Inclination (angle) of lower survey ($^\circ$); and
 Az_2 = Azimuth direction of lower survey ($^\circ$).

C. Radius of curvature method

The radius of curvature method (Figure 12) uses the inclination and azimuth measured at the upper and lower ends of the course length to generate a circular arc when viewed in both the vertical and horizontal planes. This method assumes that the well path lies on a cylinder whose axis is vertical, and has a radius equal to the radius of curvature in the horizontal plane. It determines the length of the arc between the upper and lower ends of the course length in the horizontal plane. The cylinder can then be “unwrapped” to calculate the length of the circular arc along the cylinder surface. Consequently the incremental TVD is unaffected by changes in azimuth.

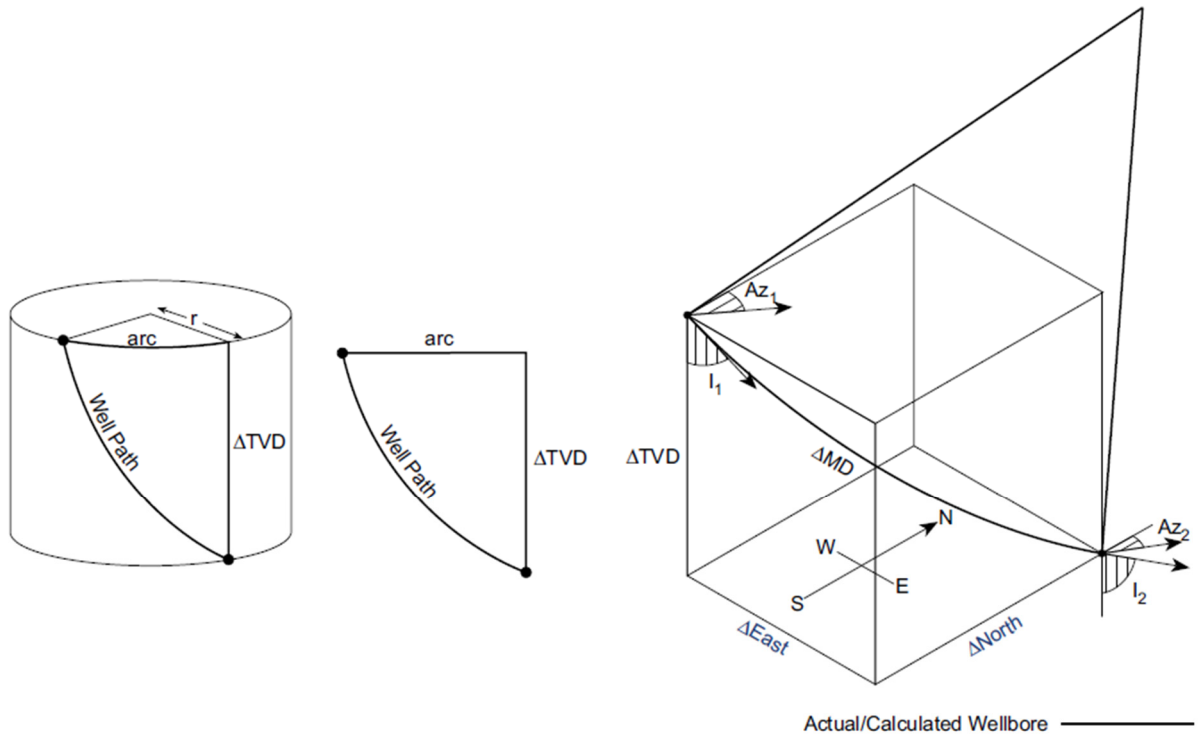


FIGURE 12: Radius of curvature method

Radius curvature calculations:

$$\Delta_{NORTH} = \frac{\Delta MD * [(\cos I_1 * \cos I_2) + (\sin Az_2 * \sin Az_1)]}{(I_2 - I_1) * (Az_2 - Az_1)} \quad (22)$$

$$\Delta_{EAST} = \frac{\Delta MD * [(\cos I_1 * \cos I_2) + (\cos Az_1 * \cos Az_2)]}{(I_2 - I_1) * (Az_2 - Az_1)} \quad (23)$$

$$\Delta_{TVD} = \frac{\Delta MD * (\sin I_2 - \sin I_1)}{(I_2 - I_1)} \quad (24)$$

where MD = Measured depth between surveys (m);
 $I1$ = Inclination (angle) at upper survey ($^{\circ}$);
 $I2$ = Inclination (angle) at lower survey in degrees ($^{\circ}$);
 $Az1$ = Azimuth direction at upper survey ($^{\circ}$); and
 $Az2$ = Azimuth direction at lower survey ($^{\circ}$).

D. Minimum curvature method

This model takes the space vectors defined by inclination and direction measurements and smooths them onto the wellbore curve (Figure 13). This method is really a modification of the balanced tangential method. Instead of approximating the wellbore path with two straight lines, the minimum curvature replaces these lines with a circular arc. This arc is calculated by using a dogleg scale factor based on the amount of angular change over the course length. The plane of the arc is at an oblique angle.

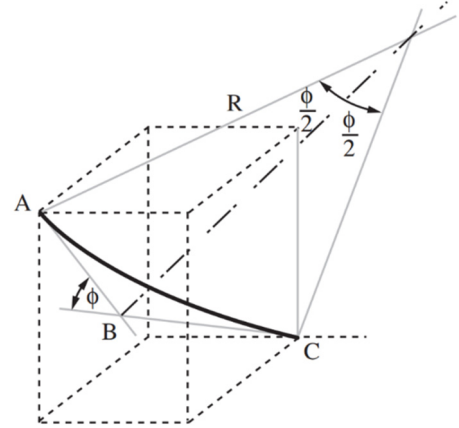


FIGURE 13: Minimum curvature method

Minimum curvature calculation:

$$\Delta_{NORTH} = \frac{\Delta MD}{2} * [(\sin I1 * \cos Az1) + (\sin I2 * \cos Az2)] * RF \quad (25)$$

$$\Delta_{EAST} = \frac{\Delta MD}{2} * [(\sin I1 * \sin Az1) + (\sin I2 * \sin Az2)] * RF \quad (26)$$

$$\Delta_{TVD} = \frac{\Delta MD}{2} * (\cos I1 + \cos I2) * RF \quad (27)$$

where

$$RF = \frac{2}{\theta} * \tan \frac{\theta}{2} \quad (28)$$

and

$$\cos \theta = \cos(I2 - I1) - \sin I1 * \sin I2 * (1 - \cos(Az2 - Az1)) \quad (29)$$

Also MD = Measured depth between surveys (m);
 $I1$ = Inclination (angle) of upper survey ($^{\circ}$);
 $I2$ = Inclination (angle) of lower survey ($^{\circ}$);
 $Az1$ = Azimuth direction of upper survey ($^{\circ}$);
 $Az2$ = Azimuth direction of lower survey ($^{\circ}$);
 RF = Ratio factor.

2.5.3 Surveying tools

When drilling a directional well, the actual trajectory of the well must be regularly checked to ensure that it is in agreement with the planned trajectory. This is done by surveying the position of the well at regular intervals. These surveys will be taken at very close intervals (~12 m, or every connection) in the critical sections (e.g. in the build-up section) of the well. While drilling the long tangential section of the well, surveys may only be required every 36 m (or every third connection). The surveying programme will generally be specified in the drilling programme. If it is found that the well is not being drilled along its planned course, a directional orientation tool must be run to bring the well back on course. In general, the earlier such problems are recognised the easier they are to correct. Surveying therefore plays a vital role in directional drilling.

A. Measurement while drilling (MWD) tools

The inputs for the above mentioned methods are MD, inclination and azimuth. MWD tools are a reliable and a fast way to measure these parameters and steer a well in the desired direction while keeping track of the wellbore trajectory. MWD tools use accelerometers which measure local acceleration and magnetometers that measure the earth's magnetic field. When drilling with the OnTrak MWD system, surveys are taken after every stand (approximately every 10-30 m). The pumps are shut down and, when a new connection is made up and pumps are turned back on, the tool's directional sensors measure Inclination and Azimuth. The OnTrak (inclination measurements) system needs to be stationary and non-rotating to take an accurate survey. The AutoTrak, which has a directional sensor that measures inclination continuously, is capable of accurately measuring inclination while being rotated. This makes it an ideal tool to use when for instance Geosteering. The inclination measured can then be compared to the OnTrak inclination measurements to get a more accurate wellbore position. Many companies, such as Baker Hughes, offer different types of MWD tools. One of the most used MWD tools is the Baker Hughes AutoTrak G3 rotary steerable system which consists of an AutoTrak steering unit with an OnTrak system for real-time MWD/LWD measurements.

B. Gyro measurement while drilling

Gyro measurement while drilling was introduced as an alternative to the gyro single shot tool for some applications. While the gyro single shot is run on the wire line, the gyro MWD is a real-time tool run alone or with a regular MWD tool on the drill pipe. Gyro MWD is commonly used in the top sections to get a more accurate magnetic interference measurement. This will, in turn, reduce the risk of colliding with an existing wellbore when drilling from a platform. The gyro-MWD technology is also used for orienting and setting whipstocks for side-tracking wells where regular MWD tools may be affected by magnetic interference.

3. CASE STUDY IN THE ASAL RIFT

Six wells have been drilled in the Asal Rift (1986-1987), recorded by Italian consultants (Aquater, 1989). These wells are vertical. Wells A1 and A2 were drilled in 1975. A1 produced geothermal fluid at 250°C with salinity of 130 g/l from a depth of 1070 m. A2 was not productive. Wells A3 to A6 were drilled from June 1987 to June 1988. Of these wells, wells A3 and A6 encountered a productive aquifer at 1100-1300 m depth. A new prefeasibility study was carried out in 2007 in the Asal Rift by Icelandic consultants from Iceland GeoSurvey and Reykjavik Energy Invest (REI) (Figures 14 and 15). The geological (Khodayar, 2008) and geophysical (Árnason et al., 2008) results

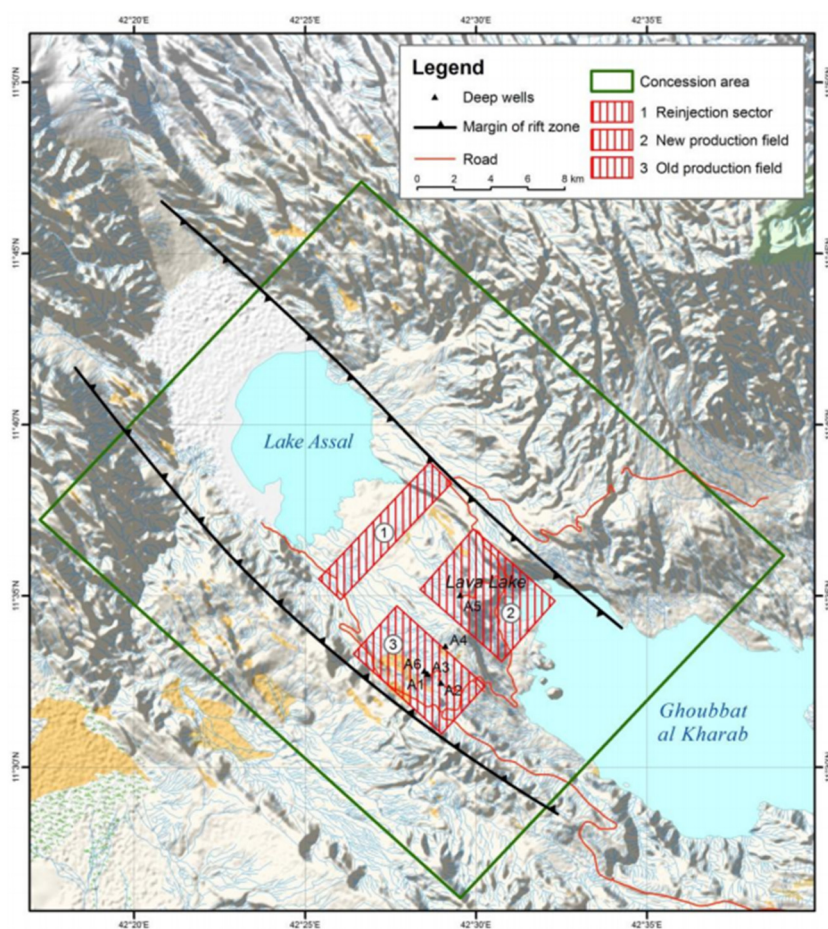


FIGURE 14: Asal Field, concession area for drilling (REI, 2009)

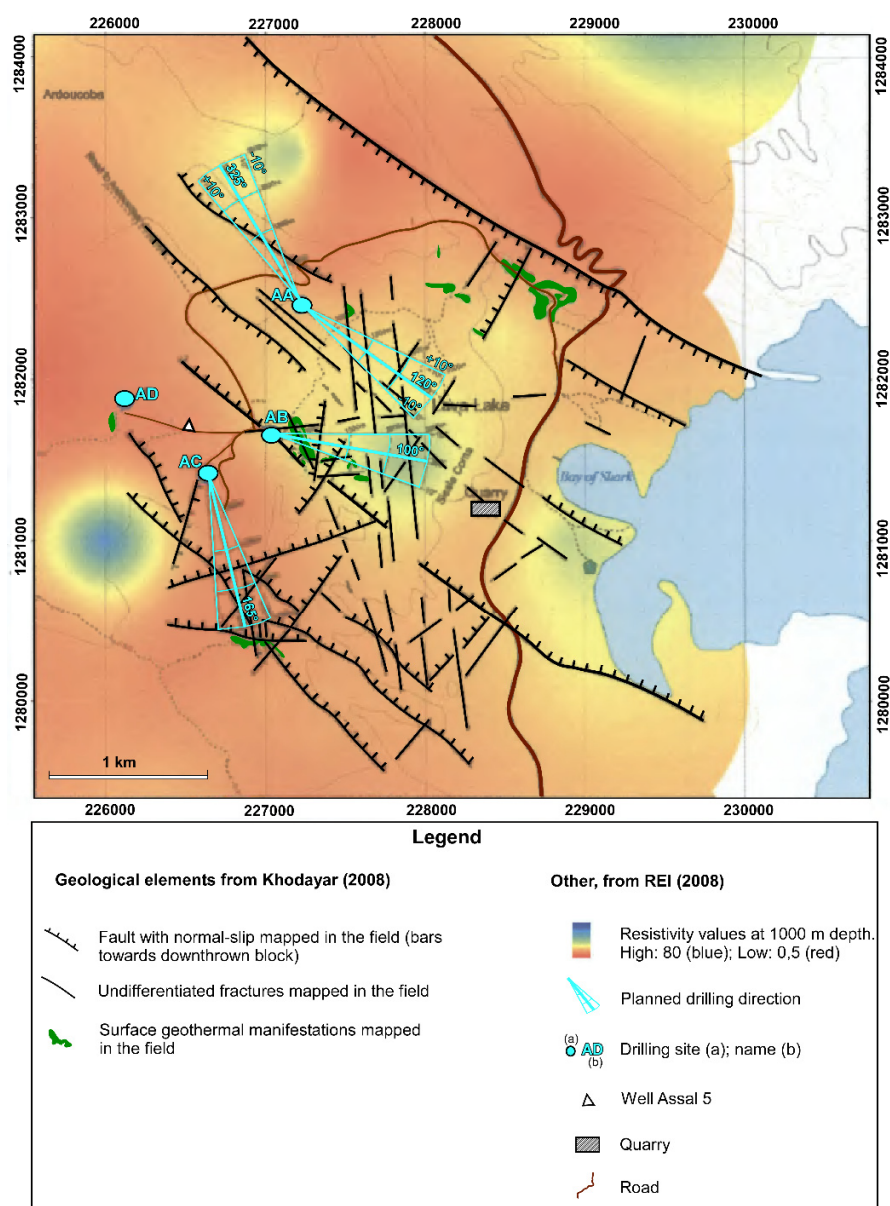


FIGURE 15: Well path of four targets inside and outside of the Lava Lake (Fialé) for directional drilling, as suggested by REI (2009)

of the pre-feasibility phase identified Fialé in the Asal Rift as a favourable production sector due to its impressive faulting, massive magma deposition and active steam fumaroles on the surface (Figure 14); the production section of well A5 of the former Asal drilling project is located within the sector. Well A5 was unproductive and penetrated both cold and hot formations. This resource behaviour suggests firstly that there are active flow channels of fresh seawater that recharge a deep reservoir. These faults should provide pressure support and more favourable fluid chemistry than observed in the old well (field sector A). The high downhole temperature confirms a large heat reserve. Based on these results, four new wells (AA to AD) from four drill pads were suggested by REI (REI, 2009), aiming at targets within and in the immediate surroundings of Fialé (Figure 15).

3.1 Objective

The geothermal wells planned by REI are to be drilled down to 2500 m depth and they are all to be directional. In order to reach the drilling targets, the drill sites were chosen to be located where discharge brine could be disposed of and where disturbances to the pristine environment would be at a minimum.

If the geothermal resource proves accessible, it is expected that more wells, perhaps as many as 5, will be drilled from the same drill pads. In this way, the roadwork and surface piping could be kept to a minimum. A storage place will be set up at the drill site, most likely between sites AC and AD. This is a flat area where drilling material and equipment are stored after having been shipped to Djibouti and transported to the Fialé drilling area. Part of the storage area will be fenced and a part of it will be roofed for protection against the sun. The four wells (AA to AD) are planned to be drilled vertically using percussion and rotary drilling assemblies, as applicable, to a kick off point (KOP) at approximately 350

m depth (Rotary Kelly Bushing). Inclination is to be built at a uniform rate of 3°/30 m to an inclination of 30°, with a specified nominal azimuth, which shall be maintained to the final well depth. The kick-off and initial build will be achieved with a mud motor and MWD equipment until the desired inclination and direction have been achieved. Once inclination and direction have been achieved, rotary assembly and electronic multi-shot measurement tools will be utilised. However, vertical drilling should be considered as an option, and its technical and cost aspects are briefly discussed in Section 3.5.

3.2 Geological context of the planned wells

The four planned wells are within the Asal Rift segment, which is one of the five rift segments in Djibouti. The other four are Alol, Gaggade, Hanle, and Goba'ad, all with geothermal potential. The five rift segments have a NNW to WNW strike. They are narrow elongated depressions, surrounded by elevated plateau and massifs. Their altitudes vary from 0 to 300 m a.s.l., except for the Asal segment which, at its northwest tip, drops to -150 m b.s.l. in the Asal Lake. These segments are among the major tectonic elements of the Afar depression. They have a complex geology since the Miocene period (Varet, 1978; Gaulier and Huchon, 1991) that includes: (a) successive volcano tectonic events related to the opening of the Red Sea, East African Rifts and Aden Ridge; (b) the shift of a rift from the Red Sea to the Afar Depression; (c) westward propagation of the Aden-Tadjourah ridges; (d) rift jumps and simultaneous activity of several rift segments; (e) the rotation of the Danakil Horst; and (f) complex kinematics and relative plate motion. Successive rifting since Miocene resulted in the accumulation of a vast basaltic trap and rhyolites in Afar, deposition of thick intercalated marine sediments as well as thinner lacustrine sediments filling the five rift segments. Magmatic and tectonic processes of the plate boundaries are the origin of geothermal activity in this part of Africa.

The Asal Rift itself (Figure 14) extends from the Gulf of Goubet in the southeast to Lake Asal in the northwest, bounded by major WNW striking normal faults. Due to its accessibility, this segment has been studied quite extensively, demonstrating that the rift is bounded by WNW striking major normal faults. The most active part of the Asal segment is the Inner Rift, which is about 3 km wide and is located to the southeast. The Inner Rift hosts most of the recent volcanism, with the last eruption dating from 1978. The most prominent feature of the Inner Rift is the Lava Lake, also called Fialé. The Lava Lake is an apparent crater about 1.3 km wide whose floor is covered by recent basaltic lavas.

The high geothermal potential of the Asal Rift is known from high-temperature exploration wells drilled over the past decades. While previous studies demonstrated the importance of the WNW normal faults of the rift, the recent geological pre-feasibility study shows two additional pieces of information on which grounds Fialé has been chosen as the target site (Khodayar, 2008): (a) there are more sets of fractures than the WNW set present within the rift; (b) Fialé could be a caldera, hosting the most significant surface geothermal manifestations of the Asal Rift segment.

3.2.1 Asal 5: An example of a well profile

Well Asal-5 (Figure 16) is the deepest well (2105 m) drilled in the Asal Rift and is unproductive as it penetrates both cold and hot formations. Data from this well (Árnason and Flóvenz, 1995) indicate a possible shallow hot reservoir (160°C) at 500-550 m depth, then a cold zone (about 60°C) down to 1200 m depth. Below 1200 m, temperature increases and the bottom temperature is about 333°C at 2105 m. The well has never been discharged. This temperature profile suggests firstly that there are active flow channels of fresh seawater recharging a deep reservoir. Secondly, the downhole high temperature confirms a large heat reserve. After the well became unsuccessful, Icelandic scientists familiar with the strategic research of similar geothermal fields joined the exploration of Asal Geothermal Field. The geological investigations of the Asal Field (Saemundsson, 1988) indicated that Well Asal-5 was not correctly sited as it would be about 700-1000 m from the geothermal up flow zone. Shortly thereafter, resistivity studies were undertaken using the TEM method (Transient Electromagnetics) in the Inner Rift (Árnason et al., 1988). The survey indicated the existence of an up flow zone of geothermal fluid

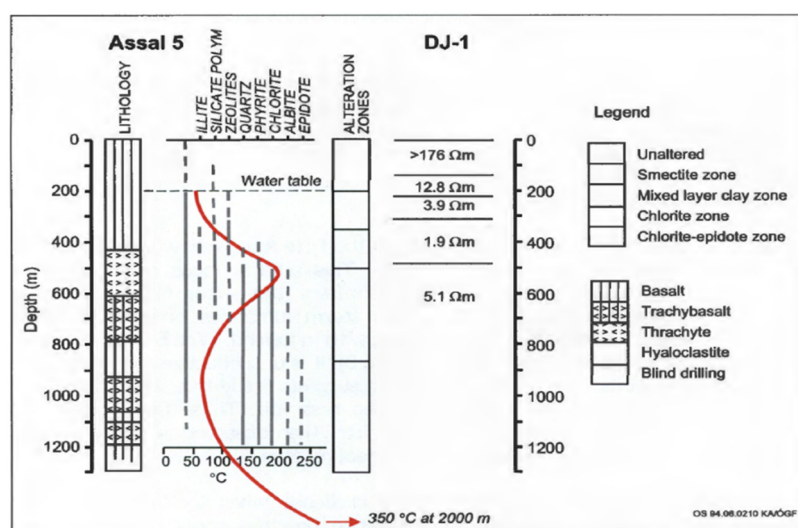


FIGURE 16: Temperature profile, geology, thermal alteration and TEM based resistivity model for well 5 (modified from Árnason and Flóvenz, 1995)

2008). Resistivity, in general, is indicative of past or present secondary (altered) minerals rather than the hydrology or the real subsurface temperatures. In particular, the map at 3000 m b.s.l. (Figure 17) delineates several low resistivity bodies, three of which (zones A, B and C) are the suggested potential geothermal sites. Area A is Fialé, whereas areas B and C are by the western flank of the rift segment. By analogy with Icelandic fields, the resistivity studies also infer the salinity of these areas so that there could be more open low salinity systems under the Lava Lake (Fialé), while areas B and C might be highly saline (Figure 17).

It is interesting to note that the salinity of wells A1 to A6 (115-130 g/l) is high (between 1000 and 1300 m), that of Ghoubet is very low (39.3 g/l at 25 m depth), while the Asal Lake to the northwest has the highest salinity (276.5 g/l at the surface and is

under the Lava Lake, as had been mentioned by Saemundsson (1988). These results showed this area to be the most promising for future exploratory wells.

3.2.2 Geophysical and geological results

The recommendations of REI for drilling in the Asal Rift (Figure 15) are based on the results of geophysical and geological pre-feasibility studies (Figures 17 and 18). Geophysical investigations within the rift segment show different high and low resistivity zones from 0 to 9000 m b.s.l. (Árnason et al.,

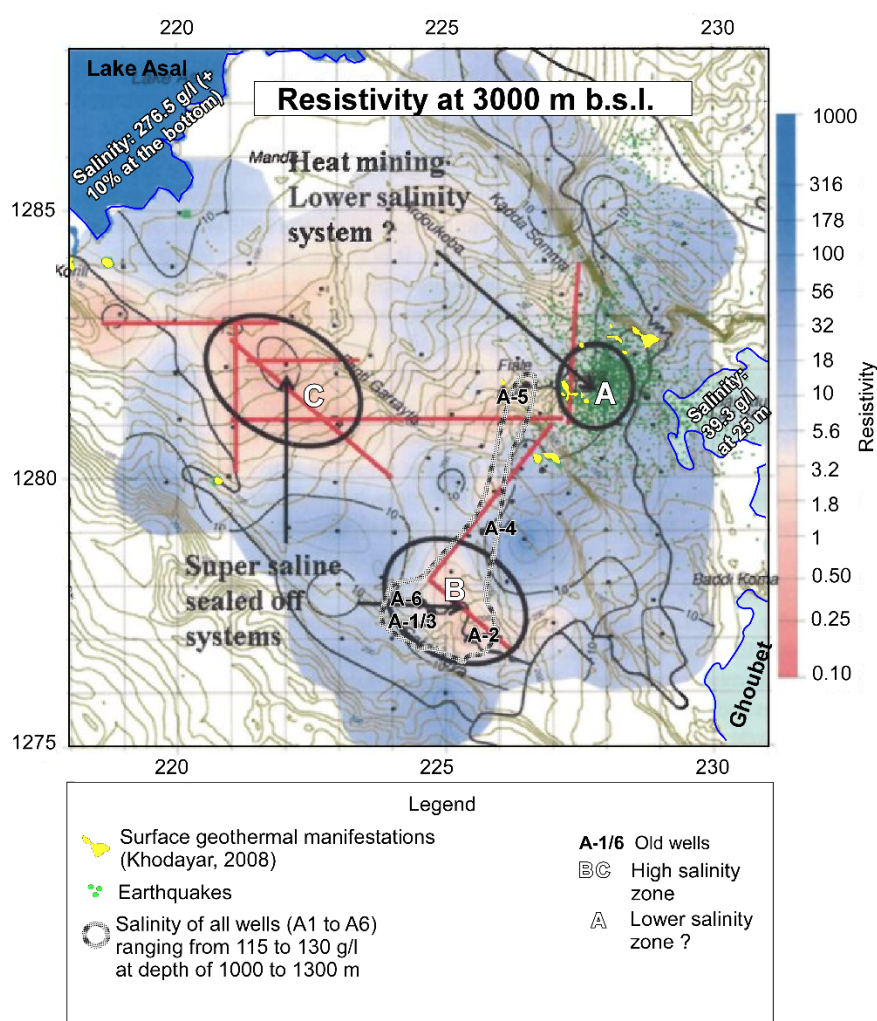


FIGURE 17: Resistivity 3000 m below sea level (modified from Árnason et al., 2008)

10% higher at the bottom) (Virkir-Orkint, 1990). This raises the question of the provenance of the saline water and the subsurface hydrology through rocks and/or open fractures.

The pre-feasibility geological field studies focused on Fialé, but a short investigation was also made in Korili/Gale le Kôma to the southwest of the Asal Lake (Khodayar, 2008). Results suggested both areas as having high potential. The detailed mapping of geology, tectonic and surface geothermal manifestations in Fialé identified three sub-areas (A, B, and C in Figure 18).

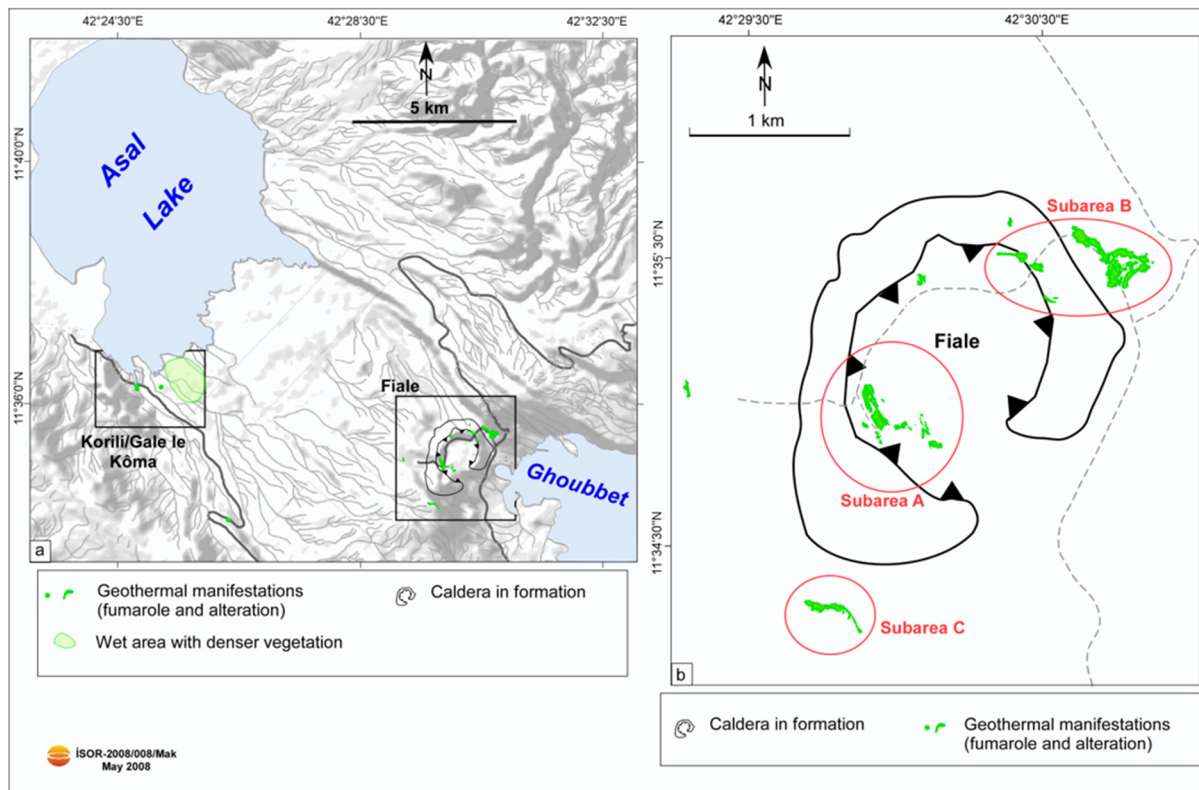


FIGURE 18: Location map of geothermal areas studied in the field (Khodayar, 2008)

The sub-area A to the west of Fialé has the highest potential as it has the most evidence of geothermal activity. The first target zone there is an altered zone with fumaroles and hot wet soil up to 91°C along an open NNW fracture. This fracture is seismically active and is monitored instrumentally. The second target zone is adjacent to the NNW fracture on the inner slope of Fialé where the hot wet soil reaches 75.5°C. In sub-area B to the east of Fialé (Figure 18), most alterations are aligned in WNW and ENE zones that coincide with the underlying WNW and ENE fractures. The WNW and ENE altered zones are respectively parallel to the adjacent inner rift boundary fault and to the trace of a major fault stretching from west-southwest of Fialé towards sub-area B. Sub-area C is high up on a rifted block above the outer slope of Fialé to the west. Along with the WNW faults of the rift, sets of fractures striking NNW, ENE and E-W were also mapped in and around the Lava Lake (Khodayar, 2008). Evidence of these fractures is also seen in geophysical results, and constitutes some of the targets chosen by REI for directional drilling (Figure 15). Finally, geological investigations suggested that Fialé might be a caldera (Khodayar, 2008), which is likely since seismicity is highest under the Lava Lake (Figure 18) and could be indicative of a magmatic body at depth.

3.2.3 Exploration wells

The proposed location of the four drill pads (shown in Figure 15) in Asal Fialé by REI (REI, 2008), are the following:

- a) Well AA is located on the outer slopes of the Lava Lake rim. The drilling target from drilling site AA is the inner part of the Lava Lake, especially the intersections of various fault lines identified by geological mapping. The horizontal distance from a drill pad is about 1000 m, making the drilling targets within the Lava Lake reachable from Site AA. Facing the site to the northwest, at the foot of the slope, is a flat area which could in the future be the location of a separation station and/or power house.
- b) The location of drill pad AB is on a flat plane bordered by low ridges with NW-SE directions. To the southeast the plane connects to the Lava Lake through a depression in the crater rim. The current track to the Ardoukoba crater ascends here from Lava Lake and traverses the drill site. From Site AB the main fumarole area could be reached by directional drilling towards the east, and by a southerly direction the main fault plane of the Fialé area could be penetrated.
- c) Parallel to the plane of Site AB, but to the southwest, is another flat area, bordered by a low ridge to the northeast and the high cliff of the main plane to the southwest. This plane is hidden from view and is large enough to accommodate drill pads, a separation station and a power house. Wells drilled from a pad in the southeast corner of the plain could reach drilling targets under Lava Lake and the important fault planes of the Fialé area.
- d) The location is farthest to the east, and is reserved as an option for the last exploration well if the drilling of the first well shows that the Lava Lake target is less promising than the area between the Lava Lake and the eastern fault boundary of the Inner Rift. This area could accommodate a few wells aimed at the faults of the eastern border of the Inner Rift. This drill pad would only be prepared if the other drill sites were found to be less suitable than currently anticipated.

3.2.4 Surface locations and targets

Four drill pads have been planned by REI, based on recommendations from the recent geological and geophysical studies from ISOR (Iceland GeoSurvey). The surface and target coordinates are shown in Tables 1 and 2.

TABLE 1: Surface coordinates of the proposed wells

Well	X (Easting) m	Y (Northing) m	Latitude/Longitude (Degrees/Minutes/ Seconds)	Latitude/Longitude (Degrees/ Decimal)	Elevation (m)
AA	227212.1	1282455	11°35'25.31"N 42°29'54.85"E	11.590364 N 42.498569 E	104
AB	227030.3	1281667	11°34'59.63"N 42°29'49.08"E	11.583235 N 42.496967 E	124
AC	226651.5	1281424	11°34'51.64"N 42°29'36.65"E	11.581009 N 42.493515 E	109
AD	226121.2	1281879	11°35'6.27"N 42°29'19.13"E	11.585078 N 42.488619 E	118

3.3 Planning the well path

TABLE 2: Target coordinates

The normal method for determining a well path is to ascertain coordinates by using some type of surveying instrument to measure the inclination and the direction at various depths (stations) and then calculate the trajectory. Appendix I shows the expected lithology and the scheduled design for Wells AA and AB.

	Target zone coordinates
Well AA	N120° or N325° (two propositions) N100° N165°
Well AB	
Well AC	

3.3.1 Trajectory calculations

In Asal, the plan is to drill under the Lava Lake to the locations designated as the four targets. For these wells, a build-and-hold trajectory will be used. Horizontal departure to the target zone is 1015 m at a TVD of 2247.2 m. The recommended rate of build is 3°/30 m. The kick-off depth is 350 m. We have to determine (1) the radius of curvature, R ; (2) the maximum inclination angle, θ ; (3) the measured depth to the end of the build; (4) the total depth measured; (5) the horizontal departure to the end of the build. The surface and target coordinates are shown in Section 3.2.4. *Please note that these trajectory calculation results are the same for all four wells; only survey calculations using the target zone are different.*

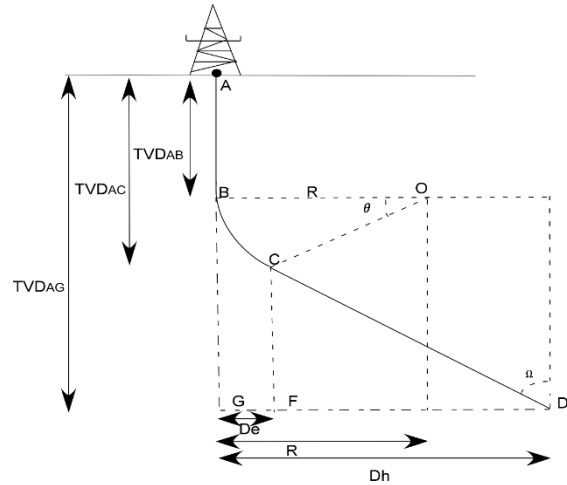


FIGURE 19: Geometry of build-and-hold type well path for $D_h > R$

Figure 19 shows the necessary parameters for the calculations. First the radius of the curvature is calculated. Note, $D_h > R$.

$$R = \frac{180}{\pi} * \frac{1}{\frac{3^\circ}{30 \text{ m}}} = 573 \text{ m}$$

For this case, $D_h > R$. A way of expressing the maximum inclination angle, θ , in terms of R , $TVD1$, $TVD3$, and D_h for $D_h > R$ is:

$$\begin{aligned} \theta &= 180^\circ - \arctan\left(\frac{TVD3 - TVD1}{D_h - R}\right) \\ &\quad - \arccos\left[\frac{R}{TVD3 - TVD1} * \sin\left(\arctan\left(\frac{TVD3 - TVD1}{D_h - R}\right)\right)\right] \end{aligned} \quad (30)$$

$$\begin{aligned} \theta &= 180^\circ - \arctan\left(\frac{2247 - 350}{1015 - 573}\right) \\ &\quad - \arccos\left[\frac{573}{2247 - 350} * \sin\left(\arctan\left(\frac{2247 - 350}{1015 - 573}\right)\right)\right] = 30.21^\circ \end{aligned}$$

The length of the arc, section BC, is calculated using Equation 7:

$$L(BC) = \frac{\pi}{180} * 573 * 30.21 = 302.12 \text{ m}$$

The measured depth to the end of build at an inclination of 30.21° is:

$$L(C) = TVD1 + \frac{\pi * R * \theta}{180} \quad (31)$$

$$L(C) = 350 + \frac{\pi * 573 * 30.12^\circ}{180^\circ} = 651.22 \text{ m}$$

The horizontal departure to the end of the build is calculated using Equation 12:

$$D_E = 573 * (1 - \cos 30.22^\circ) = 77.36 \text{ m} \approx 78 \text{ m}$$

The total measured depth to the target is:

$$L(d) = TVD1 + \frac{\pi * \theta * R}{180^\circ} + \frac{TVD3 - TVD1 - R * \sin \theta}{\cos \theta} \quad (32)$$

$$L(d) = 350 + \frac{\pi * 30.12^\circ * 573}{180^\circ} + \frac{2247 - 350 - 573 * \sin 30.12^\circ}{\cos 30.12^\circ} = 2512 \text{ m}$$

The total measured displacement depth to the target (maximum) is:

$$D_h = L(d) - TVD1 * \sin \theta \quad (33)$$

$$D_h = 2512 - 350 * \sin(30.12^\circ) = 1085 \text{ m}$$

A trajectory worksheet is shown in Figure 20.

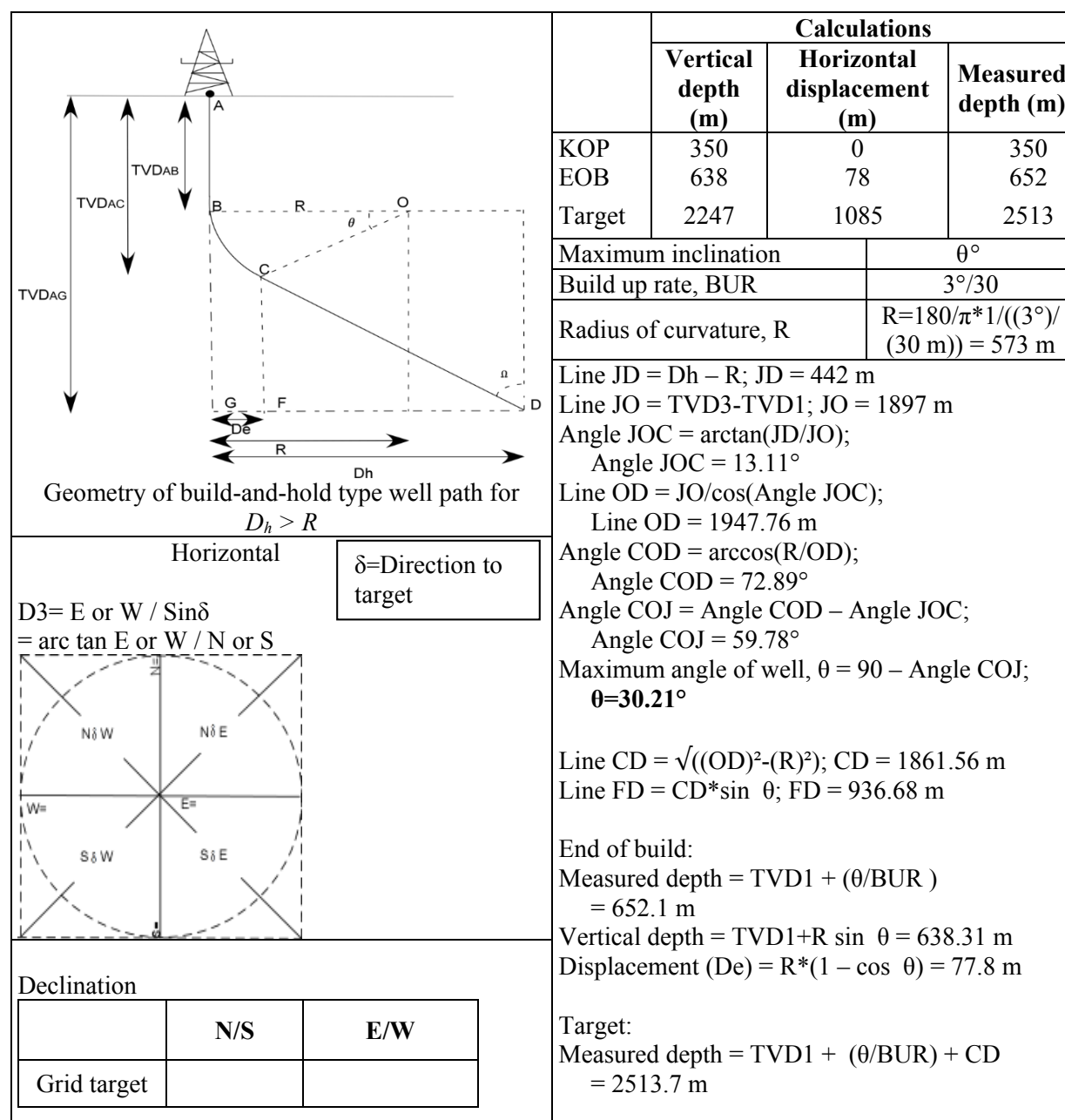


FIGURE 20: Trajectory worksheet

3.3.2 Directional survey calculations

The normal method for determining the well path is to ascertain the coordinates by using some survey method to calculate the inclination and direction at various depths (stations) and then calculate the trajectory. There are 18 or more calculation techniques for determining the trajectory of the wellbore. The main difference in all these techniques is that one group uses straight line approximations and the other assumes the wellbore is more of a curve and is approximated with curved segments. For this case, the minimum curvature method will be used (Figure 21) which is the most accurate and commonly used. Whilst drilling a deviated well, the measured depth, inclination and azimuth of the well are measured at station 2 (see survey data below). The north and east co-ordinates, TVD, vertical section and dogleg severity, of the next station are calculated according to the minimum curvature method.

This method smooths the two straight-line segments of the balanced tangential method using the *ratio factor*, RF. The survey information of measured depth, inclination, and azimuth are entered in the appropriate columns (i.e. measured depth-total, inclination, and azimuth-observed) in Table 3.

For Well AA:

At first, the dogleg angle, calculated from Equation 29:

$$\cos \theta = \cos(27^\circ - 3^\circ) - \sin 3^\circ * \sin 27^\circ * (1 - \cos(325^\circ - 325^\circ)) = 0.9135$$

$$\theta = \arccos 0.9135 = 24.00^\circ = 0.4188 \text{ radians}$$

Then, the ratio factor is obtained from Equation 28 ($\theta = B$ and must be radians):

$$RF = \frac{2}{0.4188} * \tan\left(\frac{24.0^\circ}{2}\right) = 1.0631$$

The East is calculated using Equation 26:

$$\Delta_{EAST} = \frac{620 - 380}{2} * ((\sin 3^\circ * \sin 325^\circ) + (\sin 27^\circ * \sin 325^\circ)) * 1.0631 = -35.81 \text{ m}$$

The North is calculated from Equation 25:

$$\begin{aligned} \Delta_{NORTH} &= \frac{620 - 380}{2} * ((\sin 3^\circ * \cos 325^\circ) + (\sin 27^\circ * \cos 325^\circ)) * 1.0631 \\ &= 51.15 \text{ m} \end{aligned}$$

The vertical (TVD) is obtained using Equation 27:

$$\Delta_{TVD} = \frac{620 - 380}{2} * (\cos 3^\circ + \cos 27^\circ) * 1.0631 = 233.5 \text{ m}$$

For Well AB:

The parameters of Well AB are shown in Table 4.

At first, the dogleg angle:

$$\cos \theta = \cos(27^\circ - 3^\circ) - \sin 3^\circ * \sin 27^\circ * (1 - \cos(100^\circ - 100^\circ)) = 0.9135$$

$$\theta = \arccos 0.9135 = 24.00^\circ = 0.4188 \text{ radians}$$

Then, the ratio factor:

$$RF = \frac{2}{0.4188} * \tan\left(\frac{24.0^\circ}{2}\right) = 1.0631$$

The East:

$$\Delta_{EAST} = \frac{620 - 380}{2} * ((\sin 3^\circ * \sin 100^\circ) + (\sin 27^\circ * \sin 100^\circ)) * 1.0631 = 61.49 \text{ m}$$

The North:

$$\Delta_{NORTH} = \frac{620 - 380}{2} * ((\sin 3^\circ * \cos 100^\circ) + (\sin 27^\circ * \cos 100^\circ)) * 1.0631 = -10.84 \text{ m}$$

The vertical (TVD):

$$\Delta_{TVD} = \frac{620 - 380}{2} * (\cos 3^\circ + \cos 27^\circ) * 1.0631 = 233.5 \text{ m}$$

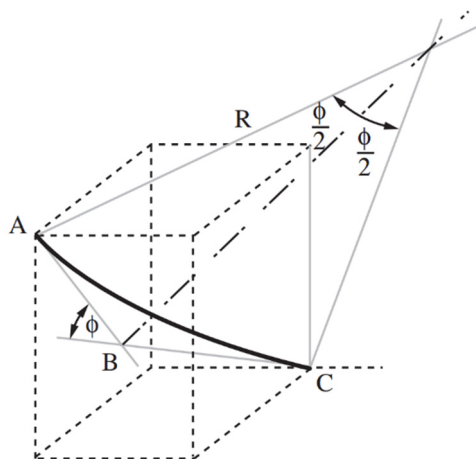


FIGURE 21: Minimum curvature method

TABLE 3: Parameters of Well AA

Station	MD	INC	AZI	TVD
02	380	3	325	379.83
09	620	27	325	609.96

TABLE 4: Parameters of Well AB

Station	MD	INC	AZI	TVD
02	380	3	100	379.83
09	620	27	100	609.96

3.3.3 Well path

Other calculation methods sometimes used are the balanced tangential method, the radius of curvature method, and the average angle method. The three-dimensional geometrical representation of the trajectory for Well AA is presented below, where the wellbore is deflected at point B. The well was turned clockwise for the N325° and N100° target zone, presented in Table 5:

TABLE 5: Target coordinates

	Target zone coordinates
Well AA	N120° or N325° (two propositions)
Well AB	N100°
Well AC	N165°

The different views of Well AA are presented in Figures 22 and 23.

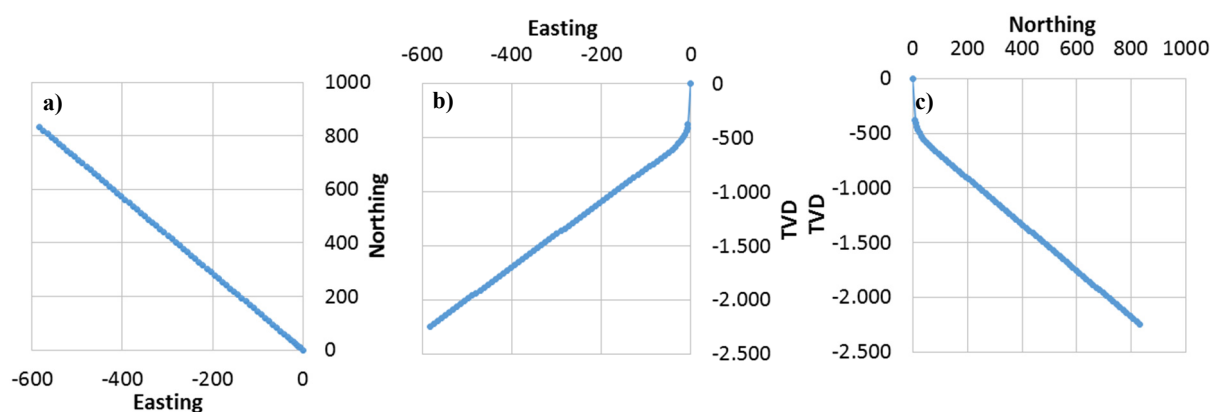


FIGURE 22: a): Horizontal displacement (D_h); b) A view from the south on the TVD projected on a vertical W-E plane; and c) A view from the east on the TVD projected on a vertical S-N plane

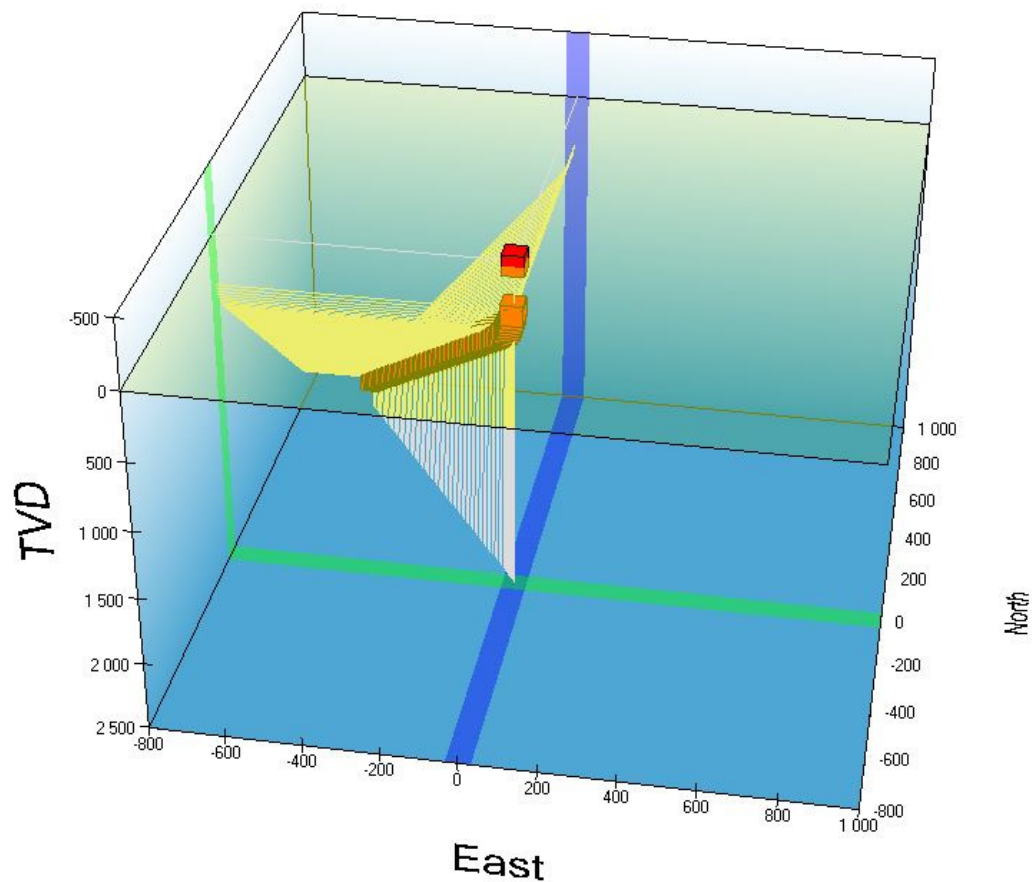


FIGURE 23: A 3D view trajectory of Well AA

The different views of Well AB are presented in Figures 24 and 25.

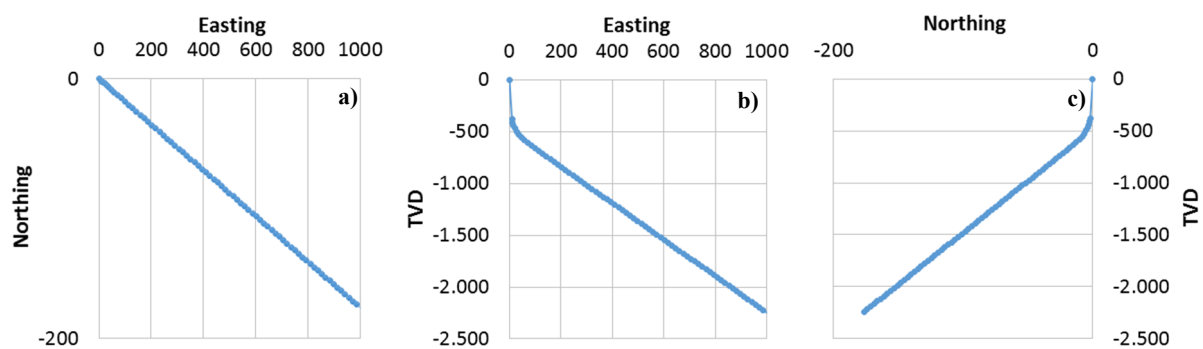


FIGURE 24: a) Horizontal displacement; b) A view from the south on the TVD projected on a vertical W-E plane; and c) A view from the east on the TVD projected on a vertical S-N plane

As to which method yields the most accurate results, Table 6 compares the four different calculation methods using data taken from a planned well. An example for comparison is Well AA.

Note that the tangential method shows considerable difference. This is why the tangential method is rarely used. The differences between the average angle, the minimum curvature, and the balanced tangential methods are so small that any of the methods could be used for calculating the trajectory. Several calculation methods are summarised in an excel worksheet for an overview (see Table 7).

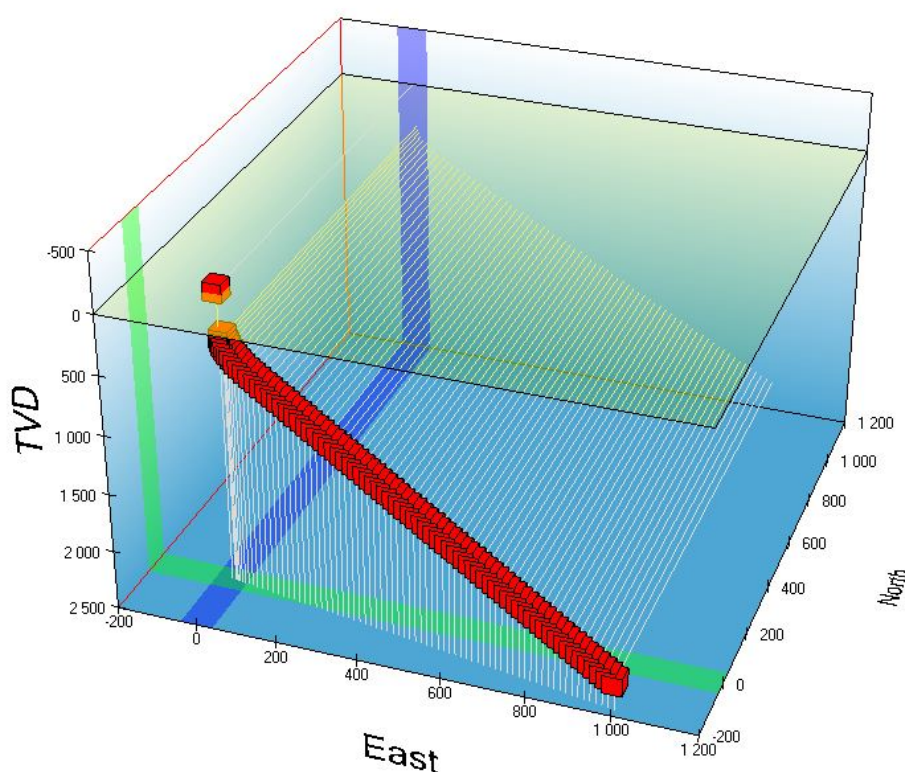


FIGURE 25: A 3D view trajectory of Well AB

TABLE 6: Comparison of the accuracy of various calculation methods

Case 1:		Well AA	
Direction:		Due north	
Survey interval:		240 m	
Rate of build:		3°/30 m	
Total inclination:		30° at 650 m	
Azimuth:		325°	
Calculation method	Total vertical depth (m)	North displacement (m)	
Minimum curvature	233.50	51.15	
Balanced tangential	226.75	49.77	
Angle-averaging	231.82	50.88	
Tangential	213.84	89.25	

3.3.4 Drill string design (limitations)

The drill string is defined here as the drill pipes with tool joints and drill collars that reach from the rig down to the drill bit. The drill stem consists of the drill string and other components of the drilling assembly that includes the Kelly, subs, stabilizers, reamers as well as shock absorbers, and drilling jars used in certain drilling conditions. The lowermost part of the drill string with the drill collars etc. is called the bottom hole assembly (BHA) (Figure 26).

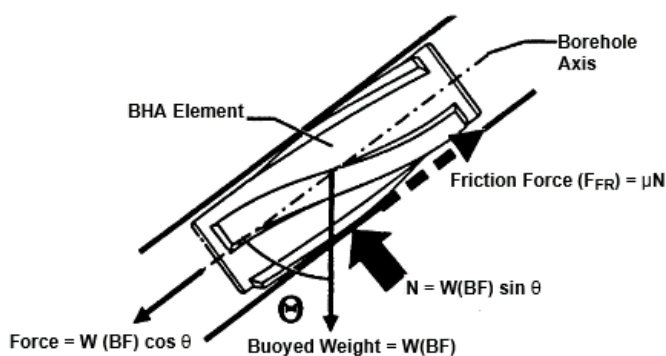


FIGURE 26: BHA weight for rotary assemblies

TABLE 7: Excel worksheet, comparison between calculation methods

Well AA								
Measured depth	Hole dev	Dev azi	Avg. tangential method			Balanced tangential method		
			North	East	TVD	North	East	Tvd
0	0	325	0	0	0	0	0	0
380	3	325	8.18	-5.72	379.87	8.17	-5.72	379.74
410	6	325	10.10	-7.07	409.78	10.10	-7.07	409.64
...
2510	30	325	832.23	-508.33	2247.20	832.21	-582.72	2246.98
Measured depth	Hole Dev	Dev Azi	Minimum curvature			Radius of curvature		
			North	East	TVD	North	East	TVD
0	0	325	0	0	0	0	0	0
380	3	325	8.17	-5.72	379.83	0	0	379.74
410	6	325	10.10	-7.07	409.73	0	0	409.64
...
2510	30	325	832.22	-582.73	2247.13	0	0	2247.33
Well AB								
Measured depth	Hole dev	Dev azi	Avg tangential method			Balanced tangential method		
			North	East	TVD	North	East	TVD
0	0	100	0	0	0	0	0	0
380	3	100	-1.73	9.83	379.87	-1.73	9.83	379.74
410	6	100	-2.74	12.14	409.78	10.10	-7.07	409.64
...
2510	30	100	-176.42	872.78	2247.20	-176.42	1000.50	2246.98
Measured depth	Hole dev	Dev azi	Minimum curvature			Radius of curvature		
			North	East	TVD	North	East	TVD
0	0	100	0	0	0	0	0	0
380	3	100	-1.73	9.83	379.83	0	0	377.84
410	6	100	-2.14	12.15	409.73	0	0	407.82
...
2510	30	100	-176.42	1000.52	2247.13	0	0	2247.33

There are four basic requirements which must be met when designing a drill string:

- The burst, collapse and tensile strength of the drill string components must not be exceeded;
- The bending stresses within the drill string must be minimised;
- The drill collars must be able to provide all of the weight required for drilling; and
- The BHA must be stabilised to control the direction of the well.

In order to design the BHA to hit the bottom target, the following will be determined:

- Length of BHA necessary for a desired weight on bit (WOB);
- Length of drill pipe and drill collar to be used with a specific bottom hole assembly; and
- Design of a drill string for the conditions specified.

Design parameters:

Depth	= 2510 m
Hole size	= 8½"
Mud weight	= 1.08
Desired MOP	= 30.10 ³ daN = 30 600 kg
Safety factor in collapse	= 1.15
Size and weight of drill collars	= (6½ in. x 2¼ in.) = 147.92 kg/m
Weight on bit (WOB)	= 10 tonnes

The buoyancy factor needs to be calculated:

$$BF = \frac{W_s - W_m}{W_s} \quad (34)$$

where BF = Buoyancy factor;
 W_s = Weight of steel (7.85 g/l); and
 W_m = Weight of mud or completion brine fluid (1.05 g/l).

$$BF = \frac{7.85 - 1.05}{7.85} = 0.8662$$

Then the length of drill collar necessary for 10 tons of WOB:

$$L(DC) = \frac{10^5 WOB}{\cos(\alpha) * F_{PN} * P_{DC} * k} \quad (35)$$

where $L(DC)$ = Length of drill collars (m);
 WOB = Maximum weight on bit (t);
 α = 3° (hole angle from vertical);
 F_{PN} = 85% (neutral point position as percentage of the total drill collar string length);
 P_{DC} = Weight per meter of drill collar (kg/m); and
 k = Buoyancy factor.

$$L(DC) = \frac{10 * 10^5}{(0.998) * (85) * (147.92) * (0.8662)} = 92 \text{ m} \approx 10 \text{ DC}$$

Pipe size, weight and grade used are:

4½" = 20.00 lb/ft, Grade g105, IEU, Range 2 (9.1 m);
 P_{DP} = 29.76 kg/m (weight per meter of drill collar);
 T_{el} = $120 \cdot 10^3$ daN (tensile yield strength); and
 P_{ct} = 30 000 kPa (limit collapse pressure).

No drill pipes are used to apply weight on the bit. All the weight comes from the drill collars, 85% of the DC weight, as shown before. Table 8 summarizes the BHA design for a depth of 2510 m.

TABLE 8: Dimensions and weight for the BHA

Hole size (inches)	Bit sizes (Inches)		Weight on bit (kg)	Length of drill collar (m)	Weight of BHA for tangent section (kg)
8½"	6½" OD	2¼" ID	10000	92	130258.18

3.4 Scenario of vertical drilling

Directional drilling is the same as vertical drilling until the kickoff point at 350 m depth, at which depth the well is deviated gradually from the vertical (Figures 27 a and b). Vertical well drilling operations differ from directional well drilling operations. A non-exhaustive comparison between these two types of drilling methods highlights the main technical aspects such as engineering, environmental issues, subsurface data collection, and costs (Table 9). Three main points can be taken from this correlation:

- A target depth of 2000 m has been chosen in this comparison as an example, which is within the depth range suggested by REI for directional drilling. This short comparison shows that each type of drilling has its pros and cons. The costs of drilling alone are clearly higher for directional drilling, due to the longer length of the well to reach the target. If the costs of survey tools and equipment are added, then directional drilling may be up to 30% more expensive than vertical

TABLE 9: Non-exhaustive comparison between directional and vertical drilling for a target at a depth of 2000 m as example; note that the differences between the two drilling types are presented in italics

Well features, data collection, and others	Directional drilling	Vertical drilling
Engineering and environmental issues	Needs casing	Needs casing
	<i>140 t. hook load of rig</i>	<i>80-100 t. hook load of rig</i>
	<i>Pad size: 12,140-24,280 m²</i>	<i>Pad size: 4,046-12,140 m²</i>
	Multiple well pads and side tracking	Multiple well pads and side tracking
	<i>Accessing target from distance, therefore, smaller well pads and sites constructions with reduced cost of water well supply, well track profile planning, rig shifting, steam gathering system, access roads, pipelines, site rehabilitation, brine disposal, etc., resulting in less environmental issues</i>	<i>Accessing target precisely from above, therefore, more well pads and construction sites with higher cost of water well supply, well track profile planning, rig shifting, steam gathering system, access roads, pipelines, site rehabilitation, brine disposal, etc., resulting in more environmental issues</i>
	<i>More expensive tools and supervision</i>	<i>Less expensive tools and supervision</i>
Length of time for drilling	45 m/day	45 m/day
Well length to reach a target at 2000 m	<i>~ 2310 m</i>	<i>2000 m</i>
Subsurface data collection	Alteration/mineral assemblage	Alteration/mineral assemblage
	Salinity	Salinity
	Rock permeability	Rock permeability
	Fractures/broken zones	Fractures/broken zones
	Heat	Heat
	Stress and strain	Stress and strain
	Earthquake location	Earthquake location
Further studies to locate targets	<i>Available</i>	<i>Required</i>
Permit	<i>No drilling permit needed inside Lava Lake</i>	<i>Drilling permit needed inside Lava Lake</i>
Unit cost of drilling without tools, equipment, and supervision	<i>~ 1500-2000 \$/m</i>	<i>~ 1500-2000 \$/m</i>
Total drilling cost without tools, equipment, supervision, and site constructions	<i>3,465,000-4,620,000 \$</i>	<i>3,000,000-4,000,000 \$</i>

drilling. On the other hand, the costs of multiple well pads can change the outcome. A detailed cost analysis of multiple well pads is needed to see the total costs of each type of drilling and which one would be financially sound.

- From an environmental view point, the constructions related to multiple well pads, as well as the water waste, chemical products, and mud from the wells are major concerns. Due to these main concerns, drilling in the Lava Lake is not permitted at this point. Considering that vertical drilling must be carried out above the target(s), i.e. inside the Lava Lake for potential targets there, the

existence of the permit is an issue that has to be dealt with should vertical drilling be revealed as the preferred choice for targets inside the Lava Lake.

- From geological and geophysical points of view, information regarding the subsurface can be obtained equally from directional and vertical drilling (Table 9), but the ultimate choice depends on the total costs for each type of drilling. As to the well production, cases are known worldwide where directional drilling has been 2.5-7 times more productive than vertical drilling. This higher production rate may partly be due to the fact that directional drilling intersects several fractures or a wider broken zone with higher permeability (Figure 27a). But as indicated, pre-feasibility studies are not precise enough to accurately locate potential targets for vertical drilling outside or inside the Lava Lake of Fialé. Considering that knowledge of the dip direction of a target fracture is critical for vertical drilling (Figure 27b), further geological studies are required to estimate the potential fracture targets as well as the risks, especially concerning seismically active fractures such as the NNW fault in the western part of Fialé.

Due to a lack of further geological and geophysical studies, at this stage the best suggestion for vertical drilling would be to aim at the same targets as recommended by REI for directional drilling (Figure 28), given that permission can be obtained to drill inside the Lava Lake. To offer more choices in the site of well AA, a few fractures have been reported from the pre-feasibility study (Khodayar, 2008). According to that study, these fractures were identified from aerial photographs only. Their exact locations on maps may be more or less displaced due to distortions between the old aerial imageries and the old topographical maps on which the fractures were reported at the time of that study. In general, vertical drilling could be located on both sides of an individual fracture to obtain its dip direction, or at fracture intersections. It is important to keep in mind that the above suggestion is, in no way, a thorough site selection of targets for vertical drilling; further studies are necessary.

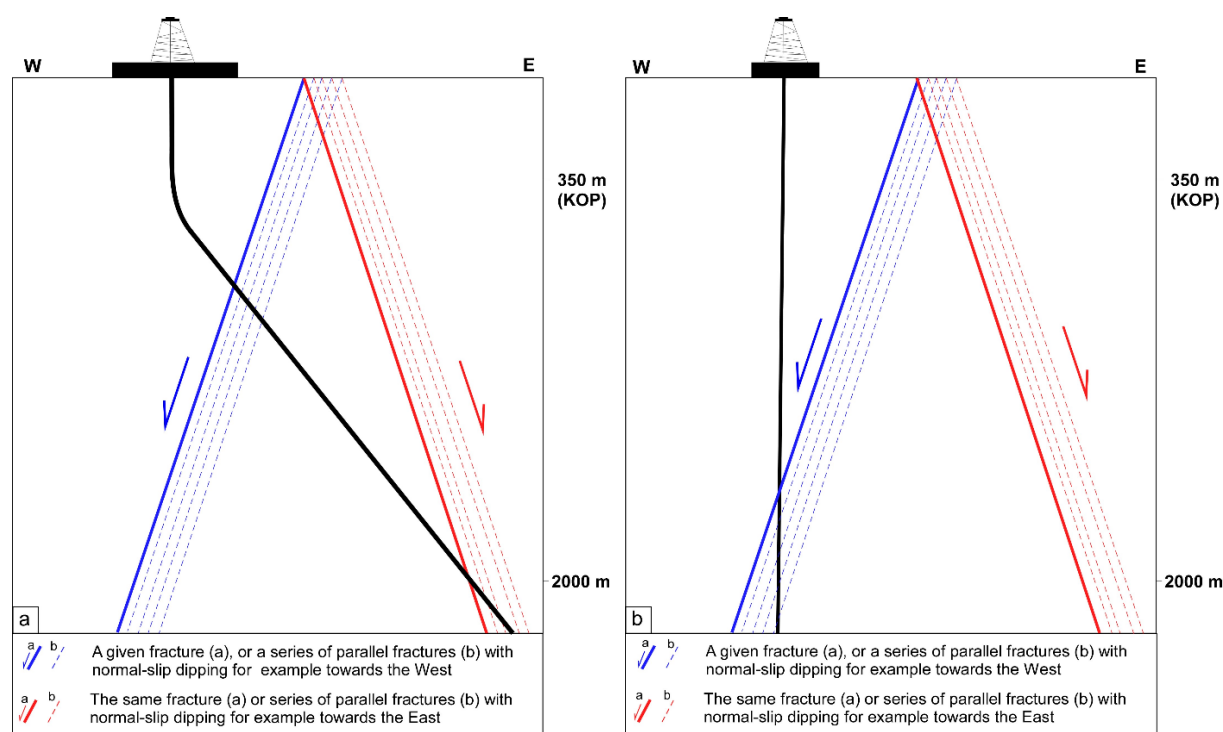


FIGURE 27: Directional and vertical drilling

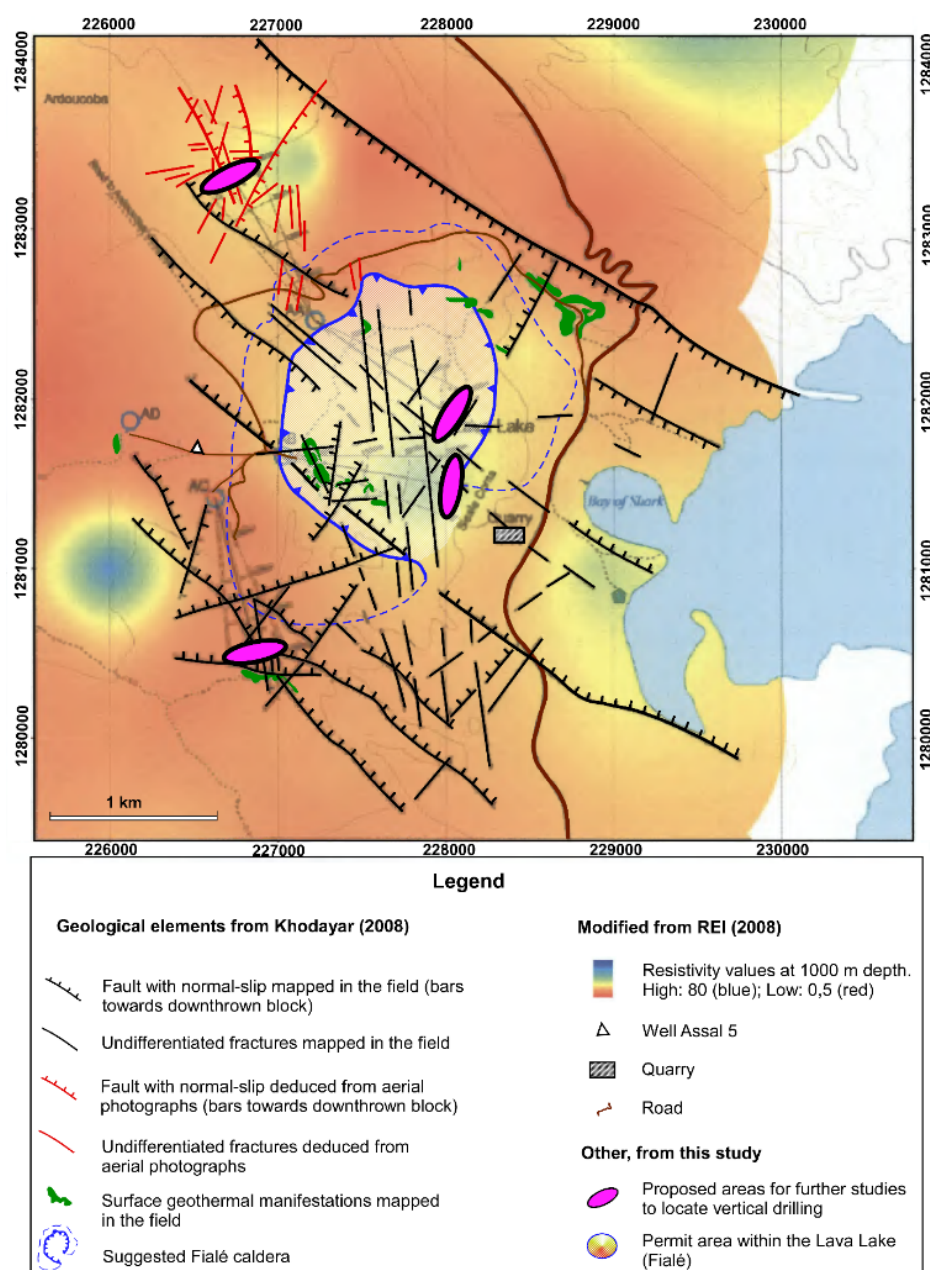


FIGURE 28: Proposed areas requiring further studies to locate vertical drilling inside and outside of the Lava Lake (Fialé)

4. CONCLUSIONS AND RECOMMENDATIONS

Based on the calculations in the case studies of directional drilling, the build and hold program is the most attractive approach for the production wells in Asal Fialé. Simple two-stabilizer building assemblies could be used with optimal WOB. Because the BHA could always be building the angle, the effects of the formation forces could be controlled easily by adjustment of the second stabilizer, either closer to or farther from the lead stabilizer. Drilling through the abrasive sandstone at the base of the cretaceous would require 3-point roller reamers instead of stabilizers. These reamers would also be necessary in hard limestone. To drill through these wells, regular spiral or straight-bladed stabilizers could be used. The risk in the build and hold program is that the build might close in the harder limestone and motors would be needed to complete the hole.

The foregoing approaches are only a few of the possibilities that could be deduced from the principles presented in the report. There is no absolute way of drilling a directional well. However, there are better, optimal ways to drill any well (good planning and careful selection of the bit, mud system, etc.) that should minimize the risks. Assuming the previous results (trajectory and survey calculations), with REI's proposal to make the KOP at 350 m, it is proposed here that the kick off point should be at least 30 meters below the casing shoe. Thus, all directional wells in the future in Asal should have a kickoff point at 430 m depth at least with a 400 m intermediate casing.

Vertical drilling is another option. Based on the results of the pre-feasibility studies, the best suggestions for vertical drilling at this stage are to drill down to 2000 m into the targets recommended by REI (2009) (Figure 28). Such vertical exploration wells would be best placed on both sides of individual fractures or at their intersections. For potential targets inside of the Lava Lake of Fialé, a permit has to be obtained. However, additional geological and geophysical surveys are required to accurately select the targets for vertical drilling. Such studies should also estimate the risks related to seismic faults, in particular for those target fractures inside the Lava Lake where shallow magmatic bodies could be present at depth. Drilling inside the Lava Lake would have the advantage of determining whether that area as a whole is indeed less saline than the two other target areas suggested by REI (Figure 17).

The concluding remarks and recommendations can be summarised as follows:

- All subsurface information can be gathered by either vertical or directional drilling.
- The choice of drilling method depends mostly on the cost, for which a thorough cost estimate of: (a) survey tools and equipment for directional drilling, (b) multiple well pads, and (c) drilling, will determine whether vertical or directional drilling is the better option.
- For directional drilling, no further studies or permits are required at this stage. But if vertical drilling is favoured, then further studies are required to understand and choose the targets before drilling, and a permit must be obtained to drill inside the Lava Lake of Fialé.

ACKNOWLEDGEMENTS

The success and final outcome of this project required a lot of guidance and assistance from many people and I am extremely fortunate to have gotten this for the completion of my project work. That I have done this is only due to such guidance and assistance and I will not forget to thank them. I wish to thank Dr. Ingvar B. Fridleifsson, the outgoing director of the UNU Geothermal Training Programme, and Mr. Lúdvík S. Georgsson, the present director of the UNU GTP, for their organization of the training and the follow up of our learning. Many thanks to Mr. Ingimar Gudni Haraldsson, Ms. Málfríður Ómarsdóttir, Mr. Markus A. G. Wilde, and Ms. Thórhildur Ísberg for their support and help in the programme. I wish also to thank my supervisors for their help in different parts of my report: Hannes Sverrisson (from Mannvit) for directional well design, Sverrir Thórhallsson (from ÍSOR) for bottom hole assembly, and Dr. Maryam Khodayar (from ÍSOR) for vertical drilling, and the insightful discussions, valuable advice, and their support during the whole period of the study, and especially for their patience and guidance during the writing process. I am grateful to the UNU Fellows for the wonderful time we had together during this 6 months.

I hope my friends and colleagues, too numerous to thank individually, will forgive me for not compiling a huge list here.

Lastly, I thank almighty, my parents, brother, and sisters for their constant encouragement without which this assignment would not be possible. To the love of my life, Samia!

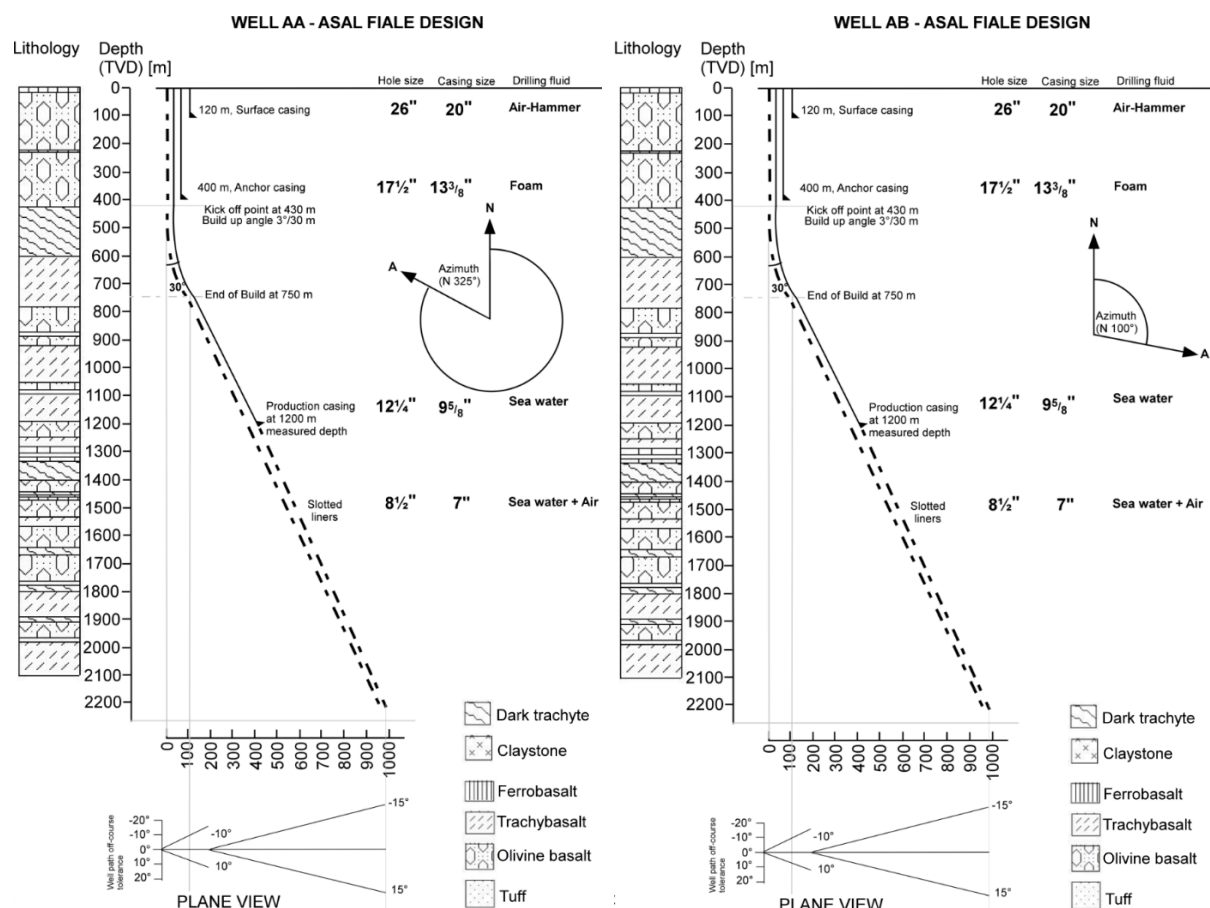
Above all, I praise God, the almighty for providing me this opportunity and granting me the capability to proceed successfully.

REFERENCES

- Aquater, 1989: *Djibouti geothermal exploration project, Republic of Djibouti, final report*. Aquater, Italy, report, 159 pp.
- Árnason, K., and Flóvenz, Ó.G., 1995: Geothermal exploration by TEM-Soundings in the Central Asal Rift in Djibouti, East Africa. *Proceedings of the World Geothermal Congress 1995, Florence, Italy*, 933-938.
- Árnason, K., Eysteinnsson, H., and Vilhjálmsson, A.M., 2008: *The Asal geothermal field, Djibouti. Geophysical surface exploration, 2007-2008*. ÍSOR - Iceland GeoSurvey, report ISOR-2008/019, prepared for REI (confidential), 74 pp.
- Árnason, K., Björnsson, G., Flóvenz, Ó.G., Haraldsson, E.H., 1988: *Geothermal resistivity survey in the Asal rift, volume I: Main text*. Orkustofnun, Reykjavík, report S-88031/JHD-05, prepared for the UND-OPS and ISERST, 48 pp.
- Baker Hughes INTEQ, 1995: *Drilling engineering workbook. A distributed learning course*. Baker Hughes INTEQ Inc., 410 pp.
- Bourgoyne, A.T., Millheim, K.K., Chenevert, M.E., and Young, F.S. Jr., 1991: *Applied drilling engineering*. SPE Textbook Series, 2, 502 pp.
- French Oil and Gas Industry Association, 1990: *Directional drilling and deviation control technology*. Editions technic, Paris, France, 137 pp.
- Gabolde, G., and Nguyen, J.P., 1991: *Drilling data handbook*. Gulf Publishing Co., Houston, TX, United States, 542 pp.
- Gaulier J.M., and Huchon, P., 1991: Tectonic evolution of Afar triple junction. *Bull. Soc. Géol. France*, 126, 451-464.
- Inglis, T.A., 1987: *Directional drilling*, vol. 2. Graham & Totman, Ltd., London, 260 pp.
- Khodayar, M., 2008: *Results of the 2007 surface geothermal exploration in the Asal Rift and transform zones, Djibouti: Tectonics and geothermal manifestations* (revised version, May 2008). Iceland GeoSurvey, report ÍSOR-2008/008, prepared for REI (confidential), 81 pp + 5 maps.
- REI, 2008: *Drilling and testing of geothermal exploration wells in the Assal Area, Djibouti: Environmental management plan*. Reykjavik Energy Invest, report REI-2008/Assal 1, 58 pp.
- REI, 2009: *Geothermal pre-feasibility study in the Asal Rift, Djibouti: Project status after completions of surface exploration studies and environmental impact assessment*. Reykjavik Energy Invest, confidential report, REI-2008, 20 pp.
- Saemundsson, K., 1988: *Djibouti geothermal project. Analysis of geological data pertaining to geothermal exploration of Asal rift*. UNDP, 18 pp.
- Sperry-Sun, 2001: *Directional surveying fundamentals*. Sperry-Sun Training Department, a Halliburton Company, Houston, TX, United States, 108 pp.
- Varet, J., 1978: *Geology of central and southern Afar (Ethiopia and Djibouti Republic)*. Centre National de la Recherche Scientifique, Paris, France, 124 pp.

Virkir-Orkint, 1990: *Djibouti geothermal scaling and corrosion study, final report*. Virkir-Orkint Consulting Group Ltd, Iceland, report prepared for Electricité de Djibouti, 273 pp.

APPENDIX I: Expected lithological profiles and designs for Wells AA and AB, Asal, Fiale





GEOTHERMAL WELL DESIGN

Abdirasak Omar Moumin

Ministry of Energy and Natural Resources

P.O. Box 10010

Djibouti

DJIBOUTI

abdirasak@hotmail.fr

ABSTRACT

This report describes the geothermal well design for the future 4 wells in the Lava Lake area in Fiale Caldera in Djibouti. Various geophysical studies in the framework of different projects have confirmed the presence of a magmatic heat source potentially useful for the production of geothermal energy. The present work includes: the casing design, the wellhead pressure estimate, and cementing of the casings to prevent contamination of fresh water and maintain well integrity during exploitation. An Excel based programme was developed for the casing design. Also, the Viking engineering programme calculated the reduced collapse resistance and assisted the Excel programme. The criteria for the casing design were as follows: preliminary selection based on burst and collapse pressure, selection based on tension, and finally the biaxial correction. Since the reservoir pressures and temperatures of Wells AA, AB, AC and AD are not known, the reservoir pressure and temperature of Well Asal 5 were used to design the 4 wells and it is expected that the same casing string design will be used.

1. INTRODUCTION

The formation pressures, geology, hole depth, formation temperature and other factors are important for the final selection of casing grades and weights of a geothermal well. The casing design process consists of selecting the casing sizes, weight, grades and setting depths. This is done by calculating the burst, collapse, and axial loads affecting the casing during drilling of the well and also while the well is in production. Other factors such as corrosion must also be taken into account. The casing design is of utmost importance for the success of the well. The cost of the casing constitutes a considerable part of the total cost of the well, approximately 20%.

The first wells, in total six (Asal 1, 2, 3, 4, 5 and 6), were drilled in 1975 and 1987/1988 in the Lake Asal area to depths of 1316-2105 m, with temperatures up to 350°C (Elmi, 2005). Asal 5 will be used as a reference for designing the new wells AA, AB, AC and AD. The hydrostatic pressure profile for Asal 5 can be seen in APPENDIX III. The lithology from Asal 5 is better than what was expected for the Lava Lake in Fiale area. Asal 5 was drilled in the Inner Rift, about 1 km west of Lava Lake. The drilling of Well Asal 5 started on 7th January 1988 and finished on March 3, 1988. The final depth is 2,105 m and the temperature at the bottom is 350°C. It is unproductive and penetrates both cold and hot formations. In March 1988, Dr. Kristjan Saemundsson made a geological survey in the Asal Field, where he indicated that Well Asal 5 was not correctly sited, as it would be about 700-1000 m from the

geothermal upflow zone (Saemundsson, 1988). In June 1988, a resistivity survey using the TEM method (Transient Electromagnetics) was carried out in the "Inner Rift" (Árnason et al., 1988). The survey indicated the existence of an upflow zone of geothermal fluid under the Lava Lake, as had been predicted by Saemundsson (1988). These results show this area to be most promising for siting future exploratory wells.

2. WELL SITE GEOLOGY

The well design shall be based on a geological prognosis comprised of the expected stratigraphy and lithology. Geological conditions and fresh water aquifers are important factors for selecting the number of casing strings, casing setting depths and to select optimum drilling targets.

Wells AA, AB, AC, and AD will be sited in the Fiale area (Figure 1), specifically north of the Lava Lake about 70 km west of Djibouti city. The project area is estimated to be 2.5 km². The sector is favoured because of its impressive faulting, massive magma deposition and active steam fumaroles on the surface. The Asal rift zone is dominated by very recent volcanic rocks and is characterized by a diverging plate boundary and continuous microseismic earthquakes. The last volcanic eruption took place in 1978 at Ardoukoba, southeast of Lake Asal. From 1975 to 1988 studies of the area were conducted. They proved that there is a heat source (350°C) in the area and that the fluids are highly saline (Virikir-Orkint, 1990). The Asal area is between Ghoubbet El Kharab and Lake Asal. The Fiale area is the southeast part of the Inner Rift. The Lava Lake is a circular depression in the centre of the Fiale area (REI, 2008). Djibouti is located where three major extensional structures, the Red sea, the East African Rift and the Gulf of Aden, meet and form the Afar Depression (Varet, 1973; Stieltjes, 1976).

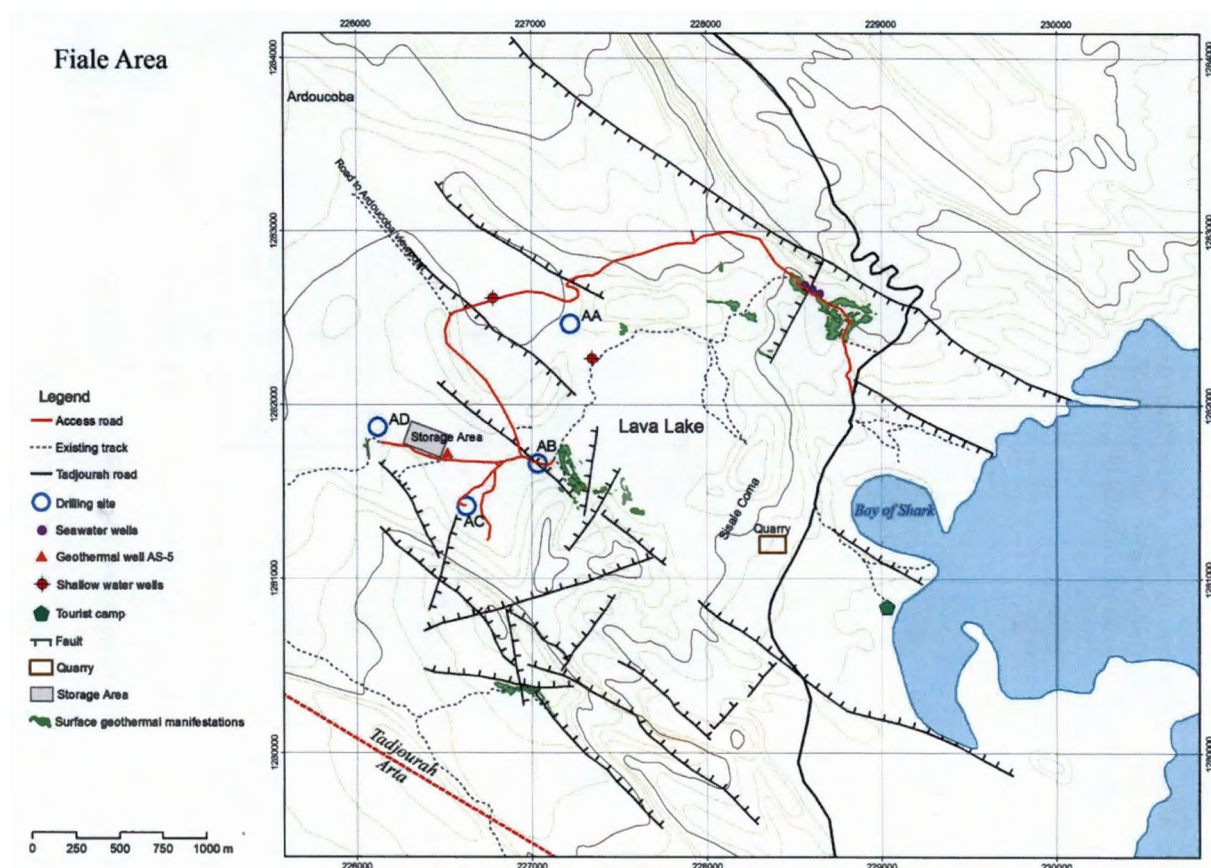


FIGURE 1: Map of Fiale area (REI, 2008)

The area could be impermeable. Significant fractures and faults are under the Lava Lake and it is a geological anomaly that should be protected. Therefore, the wells will not be drilled directly above the Lava Lake. To cut major faults, the technique of directional drilling will be used. The tectonic map is important for siting the wells and for targeting the faults.

2.1 Lithological logs

As already mentioned, the lithology of Well Asal 5 is expected to be similar to that of the new drilling site. The Italian company Aquater (Aquater, 1989) made lithological studies of Well Asal 5 and, in doing so, collected cuttings every 5 m. The cuttings were studied using a binocular microscope. Thin sections of the cuttings were collected every 10 m or when necessary every 5 m. The thin sections were studied using a polarizing microscope. The stratigraphic series was reconstructed and the hydrothermal alteration paragenesis was studied. The lithological sequence is quite monotonous, and most of the encountered rock type can be classified in the following units: ferrobasalt, olivine basalt, tuff, trachy-basalt, dark trachyte, sand or slit, and claystone (Figure 2).

2.2 Alteration zones

The hydrothermal mineral assemblages presented in Well Asal 5 indicate high-temperature geothermal activity. Six hydrothermal alteration zones were established based on the progressive alteration of the rock (Figure 3). These zones are as follows (Khairah, 1989): unaltered zone; smectite zone (this zone indicates a temperature range of up to 200°C); mixed layer clay zone (this zone is found at a

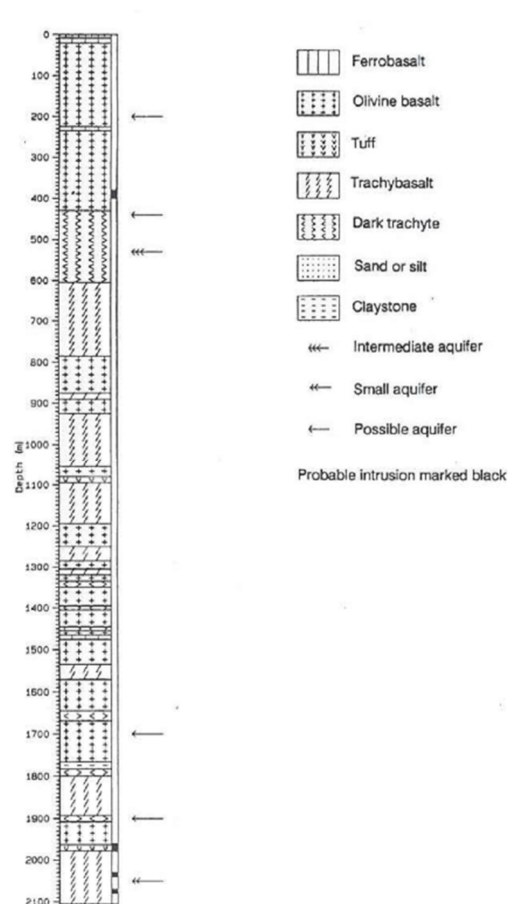


FIGURE 2: Lithological sequence expected for the Lava Lake in the Fiale area

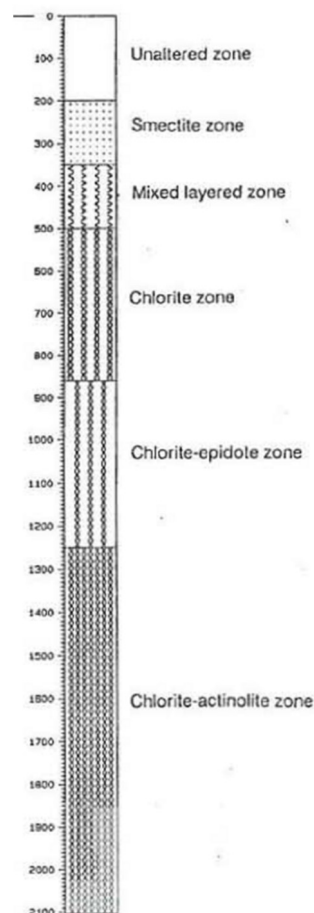


FIGURE 3: Alteration zones for the Lava Lake in the Fiale area

temperature range of about 200-230°C); chlorite zone (the zone measures a temperature range of about 230-240°C); chlorite-epidote zone (this zone falls in the temperature range of 230-280°C); and chlorite-actinolite zone (this zone is correlated with temperatures exceeding 280°C).

2.3 Temperature profiles

Well Asal 5 showed a sharp increase in temperature below 200 m b.s.l., with a maximum of about 180°C at 500 m. Between 500 and 1000 m depth, the rocks drastically cooled down with temperatures as low as 60-70°C. After 1000 m depth, the temperature increased rapidly, reaching more than 350°C at 2100 m (Figure 4). The significant inversion on the temperature profile of Well Asal 5 might be explained by the superficial underground flow toward Lake Asal which goes deeper in this well (Jalludin, 2010). For wellhead design purposes, the temperature in the part that penetrates the cold formations was reversed and a maximum temperature of 312°C at 2050 m was assumed (Figure 5). If, during drilling, temperatures exceed this temperature according to cutting samples and temperature readings, drilling should be halted and a flow test conducted.

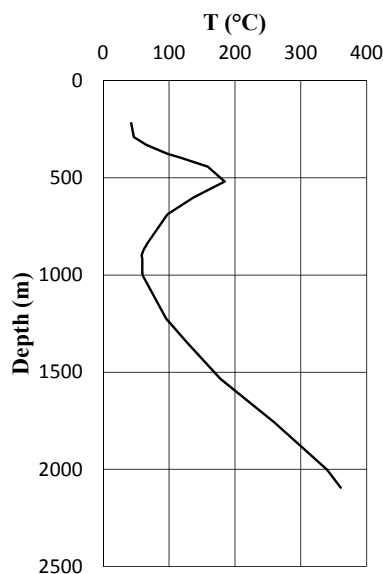


FIGURE 4: Temperature profile of Well Asal 5

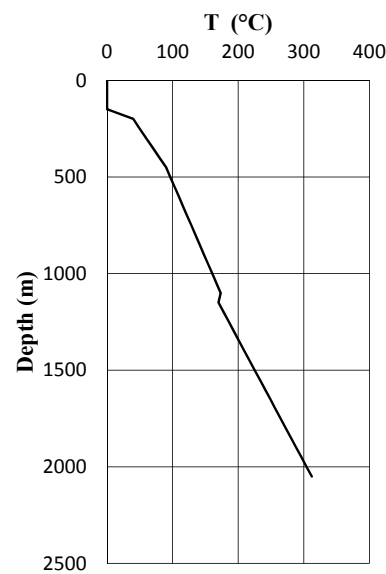


FIGURE 5: Expected temperature profile in the new wells

3. CASING DESIGN

The well design defines the desired final status of the well. Geothermal well designs and drilling practices are similar worldwide (Hosseini-Pourazad, 2005). The casing design is the same, whether the well is drilled vertically or directionally. Casings are designed to accomplish two different tasks. The first is to allow safe drilling of the well and to resist any force or conditions that are imposed upon it during drilling, without sustaining significant damage. The second is to meet the well's objectives without requiring a workover during the well's lifetime. Therefore, the main functions of the casing in any well are: to maintain hole integrity, to prevent contamination of near fresh water zones, to provide a suitable connection for the wellhead equipment and a hole of known diameters and depth to facilitate the running of test and completion equipment, to provide a conduit for well production, and to optimize well cost. Since pressure varies along each section of the hole, different casing sizes are employed; this arrangement gives a final tapered shape to the finished well. It is possible to run a casing string having the same outside diameters but with different thickness or strength properties. Thus, a heavy or high grade casing could be run along the section of the hole containing high pressures, or near the surface where tensile stresses are high. Multiple intervals of casing are successively placed within previous casings in geothermal wells. The typical casings used are:

The conductor pipe is the first casing to be put in place, and is often installed before the rig is mobilized. The conductor pipe can be excavated for or it can be driven with a hammer. It has the largest diameter and it is generally set at approximately 1-10 m below ground level. The conductor casing is used to seal off unconsolidated formations at shallow depths to prevent cave-ins.

The surface casing is the first casing string used after the conductor pipe. It supports the wellhead and BOP (Blow Out Preventer) equipment and other casings. The surface casing is used to seal off any fresh water zones and is generally set at approximately 50-200 m below ground level.

The anchor casing is run in deeper wells where kick tolerance or troublesome formations make it unsafe or undesirable to drill from the surface casing all the way to the production casing's setting depth in the hole section.

The production casing is the last casing string. It is run to isolate the producing zones, to provide reservoir fluid control, and to permit selective production in multi-zone production. It should be cemented to the top like the other casings. This is the string through which the well will be completed.

A liner is a casing string that does not reach the surface and is suspended from the inside of the previous casing string by a device known as a liner hanger or is allowed to stand on the bottom of the well. The liner hanger is usually attached to the second or third joint of the casing string. In liner completions, both the liner and the production casing act as the production string, but the liner can also be perforated and is then set in the production section, intended to keep the well from collapsing and remain permeable so that the geothermal fluid can flow into the well.

3.1 Casing materials

Other than the threaded connections used to connect together the individual joints of steel pipe for each casing string, various other items are required for the cementing operation; a reinforcement to the bottom joint of the casing and a connection for the wellhead may also be included in the casing string.

Guide (float) shoe or casing shoe: is attached to the bottom of the first casing joint and protects the casing bottom end from damage (during running of the casing) and the casing string from the impact associated with landing the casing on the bottom. To prevent the cement slurry from flowing back up the casing, the guide shoe has a non-return valve as a precaution.

Liner hanger allows the liner to be suspended from the previous casing; it is attached to the top of the liner. The choice of hangers will be limited to those compatible with the casing programme.

Float collar is normally installed one or two joints above the float- or guide shoe. The float collar prevents the cement being pumped into the casing/wellbore annulus from re-entering the casing after cementing operations and contains a non-return valve. When using an inner string, cementing the stab-in at the end of the cementing string is connected to the float collar.

Scratchers are devices attached to the outside of the casing, to remove the mud cake and break up gelled mud left by the drilling mud. They are sometimes run through the production zone.

Centralisers are installed on the casing string as it is run; a typical programme might be: 1 centraliser immediately above the shoe, 1 on every joint on the bottom 3 joints, 1 every joint through the production zone, 1 every 3 joints elsewhere. Their function is to reduce the friction between the casing string and the borehole and to centre the casing to ensure a cement sheath of sufficient thickness all around the casing. They are particularly required in deviated wells. Centralizer spacing depends on hole straightness and the clearance between the casing and bore.

3.2 Casing properties

Casing is usually specified by the following parameters: outside diameter, wall thickness, weight per unit length, type of connection, type of coupling, length joint, and grade of steel. The casings which

are most used have been standardised by the American Petroleum Institute (API). Appendix I lists the API specifications, standards and bulletins referred to in this report.

3.2.1 Casing size

TABLE 1: Drift mandrels

The size of the casing refers to the outside diameter (O.D.) of the main body of the tubular (not the connector). Casing sizes vary from 4.5" to 36" diameter. Tubulars with an O.D. of less than 4.5" are called tubing. API

Casing diameter (in)	Mandrel length		Mandrel diameter	
	(in)	(mm)	(in)	(mm)
< 9 5/8	6	152	ID-1/8	ID-3.18
9 5/8 to 13 5/8	12	305	ID-5/32	ID-3.97
13 3/8 and larger	12	305	ID-3/16	ID-4.76

ID: Inside diameter

recommended dimensions of drift mandrels, which are used to determine the pipes inner roundness, are as follows: the drift diameter (Table 1) is the maximum size of a drill bit that can safely be run through the casing.

3.2.2 Joint length

TABLE 2: Length range of a casing joint - API

The length of a joint of casing has been standardised and classified by the API (Table 2). The precise length of each joint has to be measured. The length is measured from the top of the connector to a

Range	Length		Average length	
	(feet)	(m)	(feet)	(m)
1	16-25	4.9-7.6	22	6.7
2	25-34	7.6-10.4	31	9.45
3	Over 34	Over 10.4	42	12.8

reference point on the pin at the other end of the casing joint. Casing is run most often in Range 3 lengths to reduce the number of connections in the string. Since casing is made up of single joints, Range 3 lengths can be handled easily by most rigs.

3.2.3 Casing weight

The weight per foot of the casing is representative of the wall thickness of the pipe. There are, for instance, three different weights of 20" casing; see the *Drilling data handbook* (Gabolde and Nguyen, 2006).

3.2.4 Connections

The casing is fabricated in joints and is delivered to the rig. The casing joints are joined together by threaded connections. They exist in a wide variety of threaded connections. In the API standard 5B, the connection between the joints is carried out by coupling; it (coupling or casing collar) is threaded internally (female) and is installed on one end of each joint before it is delivered to the rig. Contrary to coupling, the casing joints are threaded externally at either end. The standard types of API threaded and coupled connections are:

- Short thread connection (STC);
- Long thread connection (LTC); and
- Buttress thread connection (BTC).

3.2.5 Casing grade

API defines the characteristics of various steels and assigns letters to identify those grades (the chemical composition of the material); the number refers to the minimum yield strength of the material, e.g. N-80 casing has the minimum yield strength of 80000 psi and K-55 has the minimum yield strength of 55000 psi; refer to API specification 5CT for complete definitions. Table 3 shows the different grades of steel classified by API. Certain manufacturers produce non-API materials.

Both seamless and welded tubulars are used as casing although seamless casing is the most common type of casing and usually only H and J grades are welded.

TABLE 3: Tensile requirements for casing and tubing

Grades		H40	J55	K55	N80	L80	C90	C95	T95	P110
Properties										
Grades color codes		1 black	1 green	2 green	1 red	1 red 1 brown	1 purple	1 brown	1 silver	1 white
Min. yield strength	Bar Psi	2760 40000	3790 55000	3790 55000	5520 80000	5520 80000	6210 90000	6550 95000	6550 95000	7580 110000
Max. yield strength	Bar Psi	5520 80000	5520 80000	5520 80000	7580 110000	6550 95000	7240 105000	7580 110000	7580 110000	9650 140000
Min. ultimate tensile strength	Bar Psi	4140 60000	5170 75000	6550 95000	6890 100000	6550 95000	6890 100000	7240 105000	7240 105000	8620 125000

3.3 Safety factor

The exact values of loadings are difficult to determine; the safety factor is used to allow and to ensure that the rated performance of the casing is always greater than any expected load. Safety factors are arbitrary figures that have evolved with experience. Each operating company uses its own values for safety factors for specific situations. The minimum acceptable casing design factors (NZS, 1991) are:

- Internal yield (burst) design factors 1.5 -1.8;
- Collapse design factors 1.2;
- Tensile design factors 1.5 – 1.8; and
- Compressive factor 1.2.

3.4 Casing design criteria

Generally, the casing design process involves three distinct steps: The selection of the casing sizes and setting depths; the definition of the operational scenarios which will result in burst, collapse and axial loads being applied to the casing; and the calculation of the magnitude of these loads and selection of an appropriate weight and grade of casing. The load inside any particular string will differ from those inside the other strings. Each string of casing must be carefully designed to withstand the anticipated loads to which it will be exposed during installation, when drilling the next hole section, and when producing from the well.

Radial loads (burst and collapse) and axial (tensile and compressive) loads to which the casing will be exposed during the lifetime of the well will dictate the depth of the casing shoe. The casing design should be calculated using the true vertical depth. The majority of the equations used in this section have been extracted from Baker Hughes INTEQ (1995), BG Group (2001), and Heriot-Watt University (2010).

3.4.1 Collapse

Collapse pressure originates from the column of mud used during drilling and the column of cement used to cement the casing in place. The collapse load at any point along the casing can be calculated from:

$$P_c = P_e - P_i \quad (1)$$

where P_c = Collapse pressure;

- P_e = External pressure due to mud or cement; and
 P_i = Internal pressure due to mud, water or cement.

Before designing each casing string, it is important to define the hypotheses to be considered:

- While running casing and designing for the collapse pressure, the internal pressure is zero ($P_i=0$) because the surface, anchor and production casings are assumed to be empty (full evacuation).
- At the surface we assume that the collapse pressure is zero ($P_c = 0 = P_e$).
- At the shoe of each casing string, the maximum collapse pressure is calculated. The collapse pressure increases with depth, going from zero at surface to the maximum value at the shoe.

The equation for the collapse pressure while running the casing generally is as follows:

$$\begin{aligned} \text{At surface} \quad & P_c = 0 \\ \text{At shoe} \quad & P_c = P_e = \rho \times g \times \text{CSD} \end{aligned} \quad (2)$$

- where P_c = Collapse pressure;
 P_e = External pressure (due to drilling mud or other drilling fluid);
 g = Force of gravity;
 CSD = Casing setting depth; and
 ρ = Density of drilling mud.

In *metric units*, the collapse pressure is given by:

$$P_c = \rho \times 0.0981 \times \text{CSD} \quad (3)$$

- where P_c = Collapse pressure (bar);
 CSD = Casing setting depth (m); and
 ρ = Density of current drilling mud (kg/l).

while in *imperial units*, the collapse pressure is given by:

$$P_c = \rho \times 0.052 \times \text{CSD} \quad (4)$$

- where P_c = Collapse Pressure (psi);
 CSD = Casing Setting Depth (feet);
 ρ = Density of current drilling mud (ppg).

After running the casing and when designing for the collapse pressure, the column of cement imposes the external pressure, and the casing is assumed to be full of water.

The density of fluid inside the casing is equal to 1 kg/l, hence:

$$P_e = \rho[\text{cement}] \times g \times \text{CSD} \quad (5)$$

$$P_i = \rho[\text{fluid inside the casing}] \times g \times \text{CSD} \quad (6)$$

$$\text{At shoe} \quad P_c = [\rho[\text{cement}] - \rho[\text{fluid inside the casing}]] \times g \times \text{CSD} \quad (7)$$

$$\text{At surface} \quad P = 0$$

The collapse pressure due to the mud column ($P_i = 0$, inside casing totally empty) is higher than the collapse pressure due to the cement column ($P_i \neq 0$, casing full of displacement fluid); that is why the collapse pressure due to the mud column is used for the design of the collapse resistance. Then the design factor, discussed in Section 3.3, is added.

3.4.2 Burst

The burst pressure design must ensure that the pressure inside the casing does not exceed the casing burst pressure limit. The top section of each casing string and wellhead shall be designed to resist the pressure and temperature conditions. The pressures at the surface and at the casing shoe are calculated by the equation defined below:

$$P_b = P_i - P_e \quad (8)$$

When designing for the burst pressure, to optimize the casing's resistance, it is assumed that at the surface the internal pressure is due to the hydrostatic pressure minus the weight of the gas. The external pressure is assumed to be $P_e = 0$.

Burst at surface:

$$P_e = 0 \quad (9)$$

$$P_i = P_h - \text{NHTD} \times \rho_2 \times 0.0981 = P_b \quad (10)$$

The hydrostatic pressure is given by the following equation:

$$P_h = \text{NHTD} \times \rho_1 \times 0.0981 \quad (11)$$

where P_b = Burst pressure at surface (bar);
 P_i = Internal pressure at surface (bar);
 P_e = External pressure at surface (bar);
 P_h = Hydrostatic pressure at NHTD (bar);
 ρ_1 = Density of saturated liquid;
 ρ_2 = Gas density at NHTD; and
 NHTD = Next hole total depth (m).

For more details, see Section 6 where the hydrostatic pressure is calculated for every 50 m.

Burst at shoe:

$$P_e = \text{CSD} \times 0.105 \quad (12)$$

The gradient of salt water is 0.105 bar/m or 0.465 psi/ft.

$$P_i = P_p + \rho_c \times L_c \times 0.0981 + L_w \times \rho_w \times 0.0981 \quad (13)$$

$$P_b = P_i - P_e \quad (14)$$

where P_b = Burst pressure at shoe (bar);
 P_i = Internal pressure at shoe (bar);
 P_e = External pressure at shoe (bar);
 P_p = Applied pressure pumping (bar);
 ρ_c = Cement slurry density (kg/l);
 ρ_w = Density of displacement fluid (kg/l);
 L_c = Height of cement column inside casing (m); and
 L_w = Height of water column inside casing (m).

3.4.3 Axial loads: tension load

The axial load that may be exerted on the casing string is the tension and compression that occur under the following conditions (Figure 6): the tension is due to the weight of the casing and the cooling of the well, and the compressive loads are due to thermal expansion during heating-up of the well.

Casings are mostly in tension except for conductor pipes. Tension loads are determined by: the forces due to the buoyed weight, the bending force in deviated wells, the shock load and the force due to pressure testing. The design factor for all axial tensile and compressive loading shall not be less than 1.2 (NZS, 1991). If the yield strength of casing is exceeded during running and cementing of the casing, then casing failure is likely.

Calculation of buoyed weight:

The weight of casing in air is given by:

$$W_a = W_p \times \text{CSD} \quad (15)$$

where W_p = Nominal unit weight of casing (lb/ft); and
 W_a = Weight air (lb).

Therefore, the buoyant weight of casing is given by:

$$W_b = W_a \times \text{BF} \quad (16)$$

$$\text{BF (Buoyancy factor)} = 1 - \frac{\rho}{\rho_s} \quad (17)$$

where ρ_s = Steel density (7.85 kg/l);
 ρ = Density of fluid (fluid displacement or mud or cement) (kg/l); and
 W_b = Buoyant weight (lb).

Hence

$$\text{Buoyancy force} = W_a(1 - \text{BF}) \quad (18)$$

Calculation of buoyed weight in different liquids (inside and annular):

Here, the buoyant weight is determined by using the buoyancy factor from the following equation:

$$\text{BF} = \frac{\left[1 - \frac{\rho_e}{\rho_s}\right] - \frac{\text{ID}^2}{\text{OD}^2} \times \left[1 - \frac{\rho_i}{\rho_s}\right]}{1 - \frac{\text{ID}^2}{\text{OD}^2}} \quad (19)$$

where ID = Inside diameter (in);
OD = Outside diameter (in);
 ρ_i = Density of fluid inside casing (kg/l); and
 ρ_e = Density of fluid outside casing (kg/l).

When the cement is inside the casing, the tensile force at the surface from the casing weight (buoyant weight) is at its maximum value and the minimum value of the tensile force at the surface from the casing weight is attained when the entire volume of cement is displaced outside the casing.

Bending force:

Bending force arises if casing is run in deviated wells or in wells with severe dogleg. In the deviated wells, the bends must be considered. The bending force can be computed from the following:

$$B_f = 63 \times W_p \times \text{OD} \times \theta \quad (20)$$

where OD = Outside diameter (in);
 θ = Dogleg severity, degrees/100 ft;

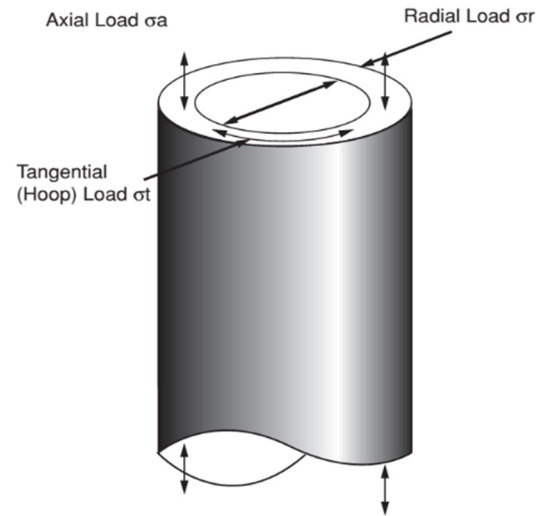


FIGURE 6: Casing loads

W_p = Nominal unit weight of casing (lb/ft); and
 B_f = Bending force (lb).

Shock loads:

The casing string experiences shock loads when it is decelerated or accelerated while setting or unsetting the casing slips. The shock load is given by:

$$\text{Shock load} = 3200 \times W_p \quad (21)$$

To recap, the preliminary casing selection is based on burst and collapse, and the safety factor in tension during pressure testing must be more than 1.5 – 1.8; it is given by the relationship below. The casing should be tested to the maximum pressure for which it has been designed.

$$\text{Safety Factor in tension} = \frac{\text{Yield Strength}}{\text{Total Tensile loads}} \quad (22)$$

$$\text{Total tensile loads} = W_b + B_f + \text{Shock load} + \text{Force due to pressure testing} \quad (23)$$

$$\text{Force due to pressure testing} = \frac{\pi}{4} \times ID^2 \times \text{testing pressure} \quad (24)$$

where Testing pressure = 60% (depends on the company involved) \times Burst pressure.

Axial loading applied to the liner:

The perforated liner in the production section of the well is not cemented and is not supported or constrained. Therefore, the extreme compressive stress, due to the thermal expansion and bending forces concerning the perforated liner, is given by:

$$F_{ec} = L_z \times W_p \times g \left[\left[\frac{1}{A_p} \right] + \left[\frac{OD \times e}{L_p} \right] \right] \quad (25)$$

where F_{ec} = Extreme compressive stress (N);
 L_z = Length of the liner (m);
 W_p = Nominal weight of casing (kg/m);
 g = Acceleration due to gravity ($m\ s^{-2}$);
 A_p = Cross-section area of pipe (m^2);
 OD = Outside diameter (m);
 e = Eccentricity (actual hole diameter minus OD) (m); and
 L_p = Net moment of inertia of the pipe section, allowing for perforation ($kg\ m^2$).

After the well has been completed, the tensile axial load in the top section of the casing, below the wellhead, applied by the fluid in the well is:

$$F_w = \frac{\pi}{4} P_w ID^2 \quad (26)$$

where F_w = Lifting force due to wellhead pressure (N);
 P_w = Maximum wellhead pressure (Pa); and
 ID = Inside diameter of production casing (m^2).

3.4.4 Axial loads: compression

The compressive loads due to thermal expansion during heating-up of the well when the casing is constrained both longitudinally and laterally by cement is:

$$F_c = C_t \times [T_2 - T_1] \times A_p \quad (27)$$

where F_c = Compressive loads (N);

- C_t = $E \times a$, thermal stress constant for casing steel (MPa/°C);
 T_2 = Maximum expected temperature (°C);
 T_1 = Neutral temperature (temperature at time cement is set (°C);
 A_p = Cross-section area of pipe (m²);
 E = Modulus of elasticity; and
 a = Coefficient of linear thermal expansion.

Casing string design shall allow for the changes in casing properties at elevated temperatures, as shown in Table 4. The modulus of elasticity can be assumed to be constant over the temperature range; the value is 200×10^6 MPa. The coefficient of linear, thermal expansion should be taken as $12 \times 10^{-6}/^\circ\text{C}$. Normally the coefficient of linear, thermal expansion is not constant, particularly at low temperature and pressures, and must be determined by reference to the steam tables. Therefore, the thermal stress constant for casing steel is: $C_t = 2.4$ MPa/°C.

TABLE 4: Temperature effects (NZS) on casing properties (K-55)

	Temperature (°C)			
	20 (°C)	100 (°C)	200 (°C)	300 (°C)
API yield strength	1	0.95	0.95	0.95
Tensile strength	1	0.97	1.02	1.07
Modulus of elasticity	208	208	200	192

3.4.5 API rated capacity of casing

The API bulletin 5C3 defines four formulas for calculating the collapse resistance of casings (Rabia, 1987). The API collapse formulas predict acceptable minimum collapse values, not average values. They are determined by yield strength of axial stress (see Section 3.6.5) and OD/t. They are given by the following equations:

The theoretical *elastic collapse pressure*, P_c , may be determined from the following equation in imperial units:

$$P_c = \frac{46.978 \times 10^6}{\left[\frac{OD}{t} \left[\frac{OD}{t} - 1 \right]^2 \right]} \quad (28)$$

where P_c = Elastic pressure (psi);
 OD = Outside diameter (in); and
 t = Wall thickness (in).

And in metric units:

$$P_c = \frac{3.304 \times 10^6}{\left[\frac{OD}{t} \left[\frac{OD}{t} - 1 \right]^2 \right]} \quad (29)$$

The elastic collapse pressure equation (Equation 28) is applicable where the following relationship is satisfied:

$$\frac{OD}{t} \geq \frac{2 + \frac{B}{A}}{3 \times \frac{B}{A}} \quad (30)$$

where

$$A = 2.8762 + 0.10679 \times 10^{-5} Y_p + 0.21301 \times 10^{-10} Y_p^2 - 0.53132 \times 10^{-16} Y_p^3 \quad (31)$$

$$B = 0.026233 + 0.50609 \times 10^{-6} Y_p \quad (32)$$

and Y_p = Minimum yield strength of the casing (psi).

The *transition collapse pressure* (P_t) is given by:

$$P_t = Y_p \times \left[\frac{C}{\frac{OD}{t}} - D \right] \quad (33)$$

where C and D are constants given by the following relationship:

$$C = \frac{46.95 \times 10^6 \left[\frac{3\frac{B}{A}}{2+\frac{B}{A}} \right]^3}{Y_p \left[\frac{3\frac{B}{A}}{2+\frac{B}{A}} \right] \left[\frac{3\frac{B}{A}}{2+\frac{B}{A}} \right]^2} \quad (34)$$

$$D = \frac{CB}{A} \quad (35)$$

Equation 33 is applicable if:

$$\frac{Y_p[A - C]}{E + Y_p[B - D]} \leq \frac{OD}{t} \leq \frac{2 + \frac{B}{A}}{3\frac{B}{A}} \quad (36)$$

where

$$E = -465.93 + 0.030867Y_p - 0.10483 \times 10^{-10}Y_p^2 + 0.36989 \times 10^{-13}Y_p^3 \quad (37)$$

The plastic *collapse pressure* may be calculated from the following equation:

$$P_p = Y_p \left[\frac{A}{\frac{OD}{t}} - B \right] - E \quad (38)$$

Equation 38 is applicable if the following relationship is verified:

$$\frac{[A - 2]^2 + 8 \left[B + \frac{E}{Y_p} \right]^{1/2} + [A - 2]}{2 \left[B + \frac{E}{Y_p} \right]} \leq \frac{OD}{t} \leq \frac{Y_p[A - C]}{E + Y_p[B - D]} \quad (39)$$

The *yield strength collapse pressure*, P_y , is calculated by:

$$P_y = 2Y_p \left[\frac{\frac{OD}{t} - 1}{\left(\frac{OD}{t} \right)^2} \right] \quad (40)$$

The range of OD/t is:

$$\frac{OD}{t} \leq \frac{[A - 2]^2 + \left[B + \frac{E}{Y_p} \right]^{1/2} + [A - 2]}{2 \left[B + \frac{E}{Y_p} \right]} \quad (41)$$

3.4.6 Biaxial loads

The radial stress is often negligible compared to the axial and tangential stresses. The manufacturer provides the collapse resistance for casing under zero axial load. Under field conditions, this is never the case. Considering the axial stress, the new yield strength is given by:

$$Y_{pa} = \left[\sqrt{1 - 0.75 \times \left[\frac{S_a}{Y_p} \right]^2} - 0.5 \times \frac{S_a}{Y_p} \right] Y_p \quad (42)$$

where Y_{pa} = Yield strength considering axial stress, psi or MPa;
 Y_p = Minimum yield strength of the casing, psi or MPa; and
 S_a = Axial stress, psi or MPa.

$$S_a = \frac{\text{Axial load(lb)}}{\text{Cross section area(in}^2\text{)}} \quad (43)$$

The result from Equation 42 will be used for calculating burst and collapse (see above). The minimum burst resistance of the casing is calculated by using Barlow's equation:

$$P = 0.875 \times \left[\frac{2 \times Y_{pa} \times t}{OD} \right] \quad (44)$$

And the minimum collapse resistance is calculated by the following steps:

- Calculate the axial stress (S_a) at the section of casing under consideration;
- Determine (Equation 42) the yield strength considering the axial stress, Y_{pa} ;
- Calculate the ratio OD/t;
- Using Equations 31, 32, 34, 35 and 37, calculate the constants A, B, C, D and E and determine the range for which OD/t is applicable (Equations 30, 36, 39 and 41); and
- Determine the appropriate equation for calculating the reduced collapse resistance from OD/t.

Viking Engineering, LG, has developed an Excel based programme to calculate collapse resistance. The input data are: OD, pipe weight per foot, grade, the yield strength considering the axial stress (Y_{pa}), and t (thickness). The output of the programme is A, B, C, D, F (in the programme, C=F and D = G), and the collapse resistance.

3.4.7 Triaxial loads

In the most critical case, one needs to take into consideration triaxial stress analysis. To calculate it, the radial, tangential, and axial stresses need to be calculated. Often, the triaxial stress analysis is not used but, in reality, the casing string is submitted to triaxial loading. In the casing design of wells AA, AB, AC and AD, we do not consider the triaxial stress analysis.

4. CASING DESIGN PROGRAMME FOR WELLS AA, AB, AC, AD

In this part, the casing design for wells Asal A, Asal B, Asal C and Asal D are presented. To do this, an Excel based programme was used as well as the Viking Engineering programme, which was used to calculate the reduced collapse resistance.

Step 1: Preliminary selection of weight and grade, based on burst and collapse pressure

The program calculates the burst pressure at the shoe and at the surface, as well as the collapse pressure at the shoe and at the surface for each casing string. The input data for the programme is namely the casing setting depth, the mud programme, the hydrostatic pressure, the temperature and the gas density.

Step 2: Selection based on tension

After step 1, the burst and collapse requirements are known, and the weight and grade of the casing are selected. Therefore, the tension can be calculated. The input data for the programme is the specifications of the casing string given by the manufacturer. The programme determines the total

tensional load, the safety factor for the casing in tension, and the safety factor in tension during pressure testing. If the safety factor is more than 1.6, the preliminary selection grade and weight is approved. Otherwise, replace and choose heavier casing string and check the calculation again.

Step 3: Viking engineering programme; Axial stress, yield strength of axial stress equivalent grade and reduced collapse pressure

The last step determines the effect of tensile load on collapse resistance, yield strength and the burst resistance. This calculation is done by the Viking programme. The input data is given by the principal programme.

4.1 Hole and casing sizes

The first decision required is the diameter of the production casing; then the other casing strings are chosen according to the availability of standard casing and bit sizes, rig equipment or other factors that give the desired clearances (Devereux, 1998). The considerations in selecting the diameter of the production casing are: the desired size of the production or test tube, and the requirements for logging or for gathering information from the well. Worldwide, in most high-temperature wells two basic designs are used: regular diameter wells with a production casing of 9 5/8" and a slotted liner of 7"; and large diameter wells with a casing of 13 3/8" and a slotted liner of 9 5/8".

In the environmental impact assessment report (Meinken and Schüle, 2012), it was decided to drill wells AA, AB, AC and AD with a 9 5/8" production casing. Figure 7 shows the sequence of casing and bit sizes planned for the 4 wells.

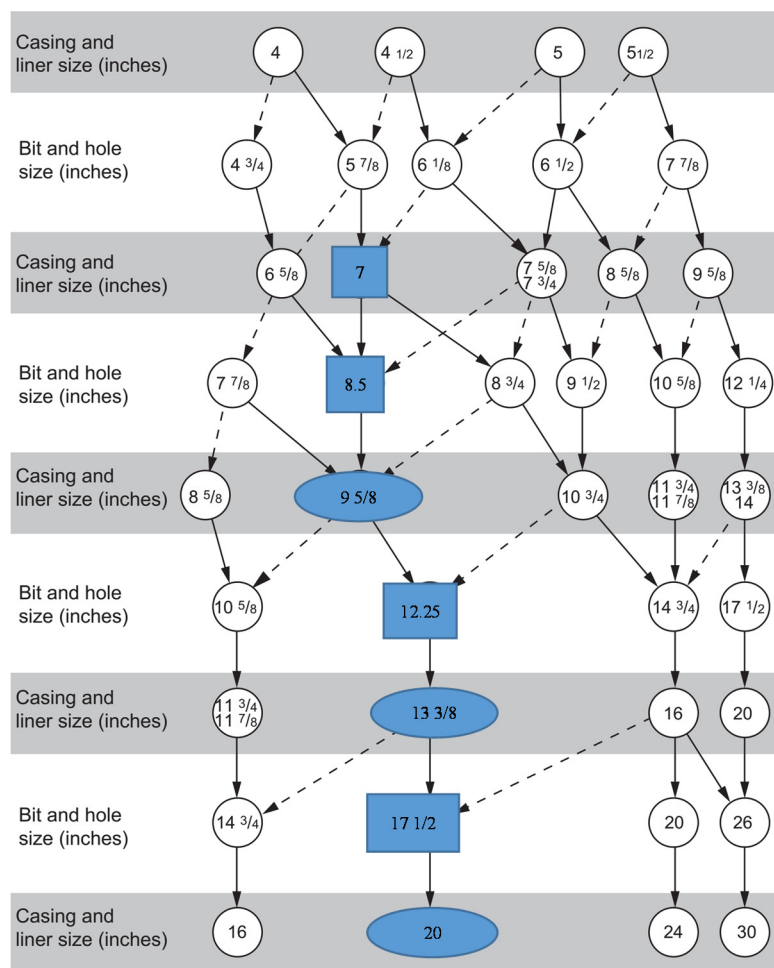


FIGURE 7: Casing programme for Wells in the Fiale area
Casing sequence (blue ,ellipse)), bit sizes (blue, box).

4.2 Casing setting depth

When designing the casing setting depths, several different factors need to be taken into account: geological information, lithological column, pore pressure gradients and fracture gradients of the formations to be penetrated, and any other available data. Often, in high-temperature areas the casing strings are: conductor casing, surface casing, anchor casing and production casing. In the open section of the hole, there is also the liner which can be hung from the production casing or set on the bottom of the well.

The New Zealand standard method was used for designing the casing setting depths for Wells AA, AB, AC and AD. It is a method for determining the minimum casing depth for high-temperature geothermal wells. As already mentioned, the presence of a strong circulation of cold sea water close to Well Asal 5 between 500 and 1100 m depth could affect the production zone planned for the 4 wells. So, to protect the production zone, the production casing depth is set at 1210 m and the surface and anchor casing depths are deduced using the New Zealand standard method. The drilling programme for Wells AA, AB, AC and AD is summarized in Table 5.

TABLE 5: Drilling programme: Wells AA, AB, AC and AD

	Surface Casing	Anchor Casing	Production Casing	Liner
Nominal size (OD):				
inches	20	13.375	9.625	7
mm	508	339.73	244.48	177.8
Diameter hole/bit:				
inches	26	17.5	12.25	8.5
mm	660.4	444.5	311.15	215.9
Casing setting depth:				
m	160	480	1210	2050
feet	525	1575	3970	6726
Drilling fluid:	Foam	Sea water based mud	Sea water based mud	Sea water/aerated
Density drilling fluid:				
kg/l	0.6	1.05	1.05	NA
ppg	5.01	8.76	8.76	NA

4.3 Selection of grade and weight

With an Excel worksheet, the burst and the collapse loads were calculated to select an appropriate weight and grade for surface, anchor and production casings. It is assumed that the casings are totally empty due to losses of drilling fluid and the applied pumping pressure is neglected. For the design, the effects of temperature on the casing properties (discussed in Section 3.4.4) were not considered. Tables 6 and 7 give the results of the burst and collapse calculations for each casing. The liner does not undergo burst or collapse loads because it is perforated.

The burst and collapse resistance of the available grade in API must be higher than the collapse and burst loads. The appropriate grade and weight for Wells AA, AB, AC and AD are:

- Surface casing: 20" 94.0 lb/ft K55;
- Anchor casing: 13.375" 54.50 lb/ft K55; and
- Production casing: 9.625" 40 lb/ft K55.

It is possible to use the grade and weight above but, to be on the safe side, because the anchor and production casings are set rather deep and to anticipate added pressures due to cementing pumping pressures, 68 lb/ft for the anchor casing and 47 lb/ft for the production casing were selected. The liner is perforated and, therefore, there is no burst or collapse pressure acting on it. A 7" 26.0 lb/ft perforated liner is sufficient, using Equation 27. Using Halliburton eRedbook, a drawing of the wellbore for the wells was made (Figure 8). For each casing, the collapse pressure was drawn between 0 at the surface and the maximum value at the casing setting depth. The collapse and burst resistance values were plotted as vertical lines, as shown in Figures 9, 10 and 11.

TABLE 6: Results of burst pressure calculations for each casing

Surface casing				
CSD	160.00	m	524.93	ft
Next hole total depth	480.00	m	1574.80	ft
Height of cement column inside casing	76.57	m	251.20	ft
Height of water column inside casing	83.43	m	273.73	ft
Density of current drilling mud	0.60	kg/l	5.01	ppg
Density of displacement fluid	1.00	kg/l	8.35	ppg
Density of cement (class G)	1.90	kg/l	15.86	ppg
Gas density at NHTD	0.0005	kg/l	0.00442	ppg
Gradient of salt-saturation	0.105	bar/m	0.465	psi/m
Force of gravity	0.0981			
Applied pumping pressure	14.13	bar	204.89	psi
Hydrostatic pressure at NHTD	29.00	bar	420.62	psi
<i>Burst at surface</i>	28.98	bar	420.25	psi
Burst at surface by safety factor 1.5	43.46	bar	630.38	psi
Pe at surface	0	bar	0	psi
Pi at surface	28.98	bar	420.25	psi
<i>Burst at shoe</i>	19.78	bar	286.92	psi
Burst at shoe by safety factor	29.67	bar	430.39	psi
Pe at shoe	16.80	bar	243.67	psi
Pi at shoe	36.58	bar	530.59	psi
Calculation of height of water and cement inside the casing				
Capacity of cylinder 20"	202.70	l/m		
Capacity of surface casing 20"	32432	l	32.43	m3
Volume of slurry	38800	l	38.80	m3
60% freshwater	23280	l	23.28	m3
40% cement (class G)	15520	l	15.52	m3
Anchor casing				
CSD	480	m	1574.80	ft
Next hole total depth	1210	m	3969.82	ft
Height of cement column inside casing	218.33	m	716.31	ft
Height of water column inside casing	261.67	m	858.49	ft
Density of current drilling mud	1.05	kg/l	8.76	ppg
Gas density at NHTD	0.005	kg/l	0.04173	ppg
Applied pumping pressure	42.38	bar	614.67	psi
Hydrostatic pressure at NHTD	92.00	bar	1334.37	psi
<i>Burst at surface</i>	91.41	bar	1325.76	psi
Burst at surface by safety factor 1.5	137.11	bar	1988.64	psi
Pe at surface	0.00	bar	0.00	psi
Pi at surface	91.41	bar	1325.76	psi
<i>Burst at shoe</i>	58.34	bar	846.22	psi
Burst at shoe by safety factor	87.52	bar	1269.33	psi
Pe at shoe	50.40	bar	731.00	psi
Pi at shoe	108.74	bar	1577.22	psi
Calculated height of water and cement inside the casing				
Capacity of cylinder 13.375"	90.64	l/m		
Capacity of anchor casing 13.375"	43507.20	l	43.51	m3
Volume of slurry	49474.00	l	49.47	m3
60% freshwater	29684.40	l	29.68	m3
40% cement (class G)	19789.60	l	19.79	m3

TABLE 6 cont.: Results of burst pressure calculations for each casing

Production casing				
CSD	1210	m	3969.82	ft
Next hole total depth	2050	m	6725.72	ft
Height of cement column inside casing	454.16	m	1490.04	ft
Height of water column inside casing	755.84	m	2479.78	ft
Density of current drilling mud	1.05	kg/l	8.76	ppg
Gas density at NHTD	0.0565	kg/l	0.47150	ppg
Applied pumping pressure	106.83	bar	1549.48	psi
Hydrostatic pressure at NHTD	158.20	bar	2294.55	psi
<i>Burst at surface</i>	146.84	bar	2129.75	psi
Burst at surface by safety factor 1.5	220.26	bar	3194.62	psi
Pe at surface	0	bar	0	psi
Pi at surface	146.84	bar	2129.75	psi
<i>Burst at shoe</i>	138.58	bar	2009.96	psi
Burst at shoe by safety factor	207.87	bar	3014.94	psi
Pe at shoe	127.05	bar	1842.73	psi
Pi at shoe	265.63	bar	3852.70	psi
Calculated height of water and cement inside the casing				
Capacity of cylinder 9.625"	46.94	l/m		
Capacity of anchor casing 9.625"	56797.40	l	56.80	m3
Volume of slurry	53296.00	l	53.30	m3
60% freshwater	31977.60	l	31.98	m3
40% cement (class G)	21318.40	l	21.32	m3

TABLE 7: Results of collapse pressure calculations for each casing

Surface casing				
<i>Collapse pressure during running of the casing</i>				
<i>Collapse at surface</i>	0	bar	0	psi
<i>Collapse at shoe</i>	9.42	bar	136.59	psi
Collapse at shoe by safety factor 1.2	11.30	bar	163.91	psi
Pe at shoe	9.42	bar	136.59	psi
Pi at shoe	0	bar	0	psi
<i>Collapse pressure after running the casing</i>				
<i>Collapse at surface</i>	0	bar	0	psi
<i>Collapse at shoe</i>	14.13	bar	204.89	psi
Collapse at shoe by safety factor 1.2	16.95	bar	245.87	psi
Pe at shoe	29.82	bar	432.54	psi
Pi at shoe	15.70	bar	227.65	psi
Anchor casing				
<i>Collapse pressure during running of the casing</i>				
<i>Collapse at surface</i>	0	bar	0	psi
<i>Collapse at shoe</i>	49.44	bar	717.11	psi
Collapse at shoe by safety factor 1.2	59.33	bar	860.54	psi
Pe at shoe	49.44	bar	717.11	psi
Pi at shoe	0	bar	0	psi
<i>Collapse pressure after running the casing</i>				
<i>Collapse at surface</i>	0	bar	0	psi
<i>Collapse at shoe</i>	42.38	bar	614.67	psi
Collapse at shoe by safety factor 1.2	50.86	bar	737.60	psi
Pe at shoe	89.47	bar	1297.63	psi
Pi at shoe	47.09	bar	682.96	psi

TABLE 7 cont.: Results of collapse pressure calculations for each casing

Production casing				
<i>Collapse pressure during running the casing</i>				
<i>Collapse at surface</i>	0	bar	0	psi
<i>Collapse at shoe</i>	124.64	bar	1807.72	psi
Collapse at shoe by safety factor 1.2	149.56	bar	2169.27	psi
Pe at shoe	124.64	bar	1807.72	psi
Pi at shoe	0	bar	0	psi
<i>Collapse pressure after running the casing</i>				
<i>Collapse at surface</i>	0	bar	0	psi
<i>Collapse at shoe</i>	106.83	bar	1549.48	psi
Collapse at shoe by safety factor 1.2	128.20	bar	1859.37	psi
Pe at shoe	225.53	bar	3271.11	psi
Pi at shoe	118.70	bar	1721.64	psi

For hydrostatic pressure at each section see Section 6, Table 10

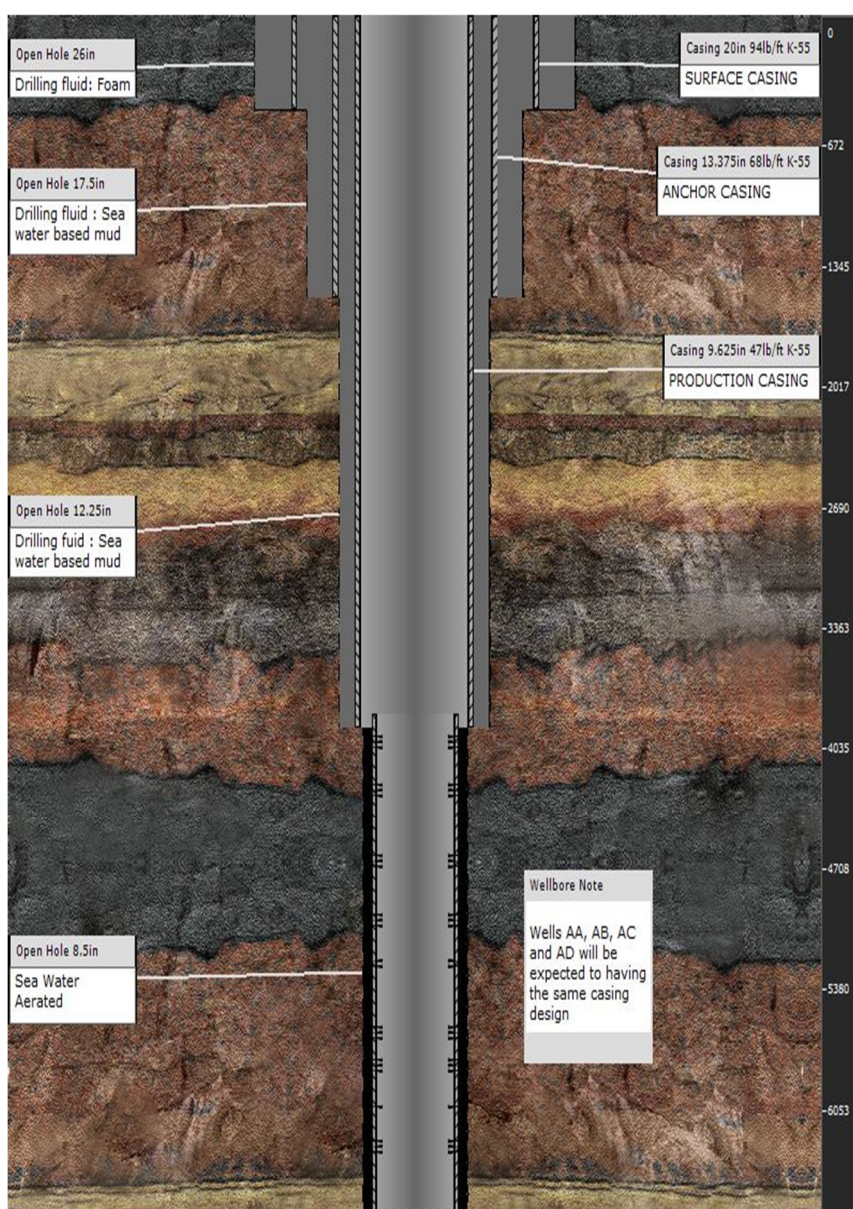


FIGURE 8 : Wellbore schematic, Fiale area

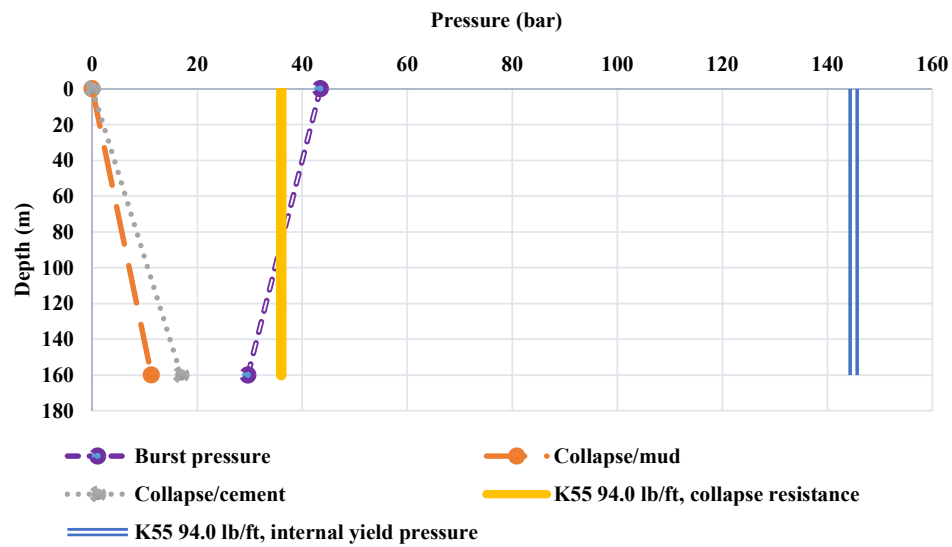


FIGURE 9: 20" casing design

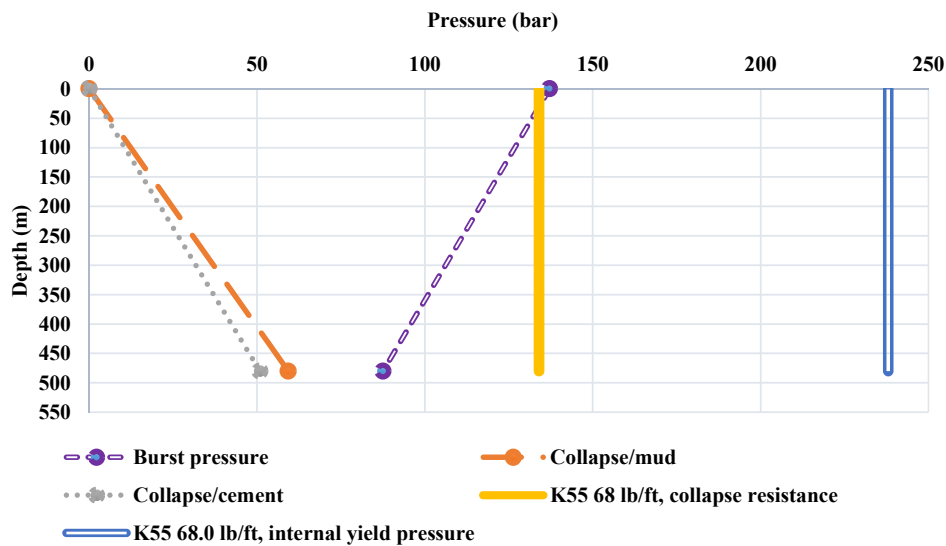


FIGURE 10: 13 3/8" casing design

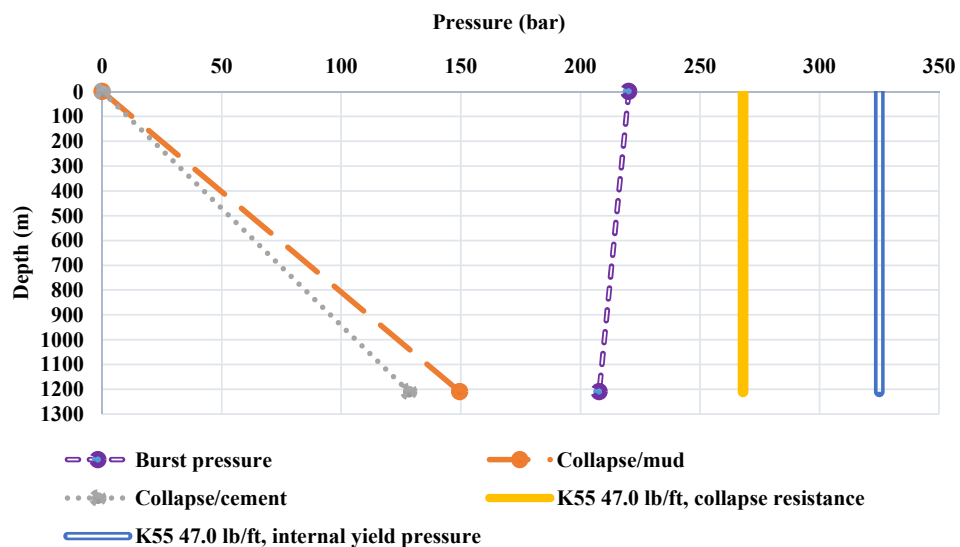


FIGURE 11: 9 5/8" casing design

4.4 Casing design in deviated Wells AA, AB, AC and AD

From the sections above, the general method for casing design was applied to directional wells by simply converting the measured depth (MD) to true vertical depth. The collapse, burst and tension criteria were then applied and the appropriate casing grades were selected. Finally, in the deviated sections of the well, the vertical lengths of selected grades were converted to the measured depth (MD) lengths by simply dividing the vertical depth by $\cos(\text{angle of deviation})$ (see Appendix II, which shows the well trajectories).

Basic design data:

Kick off point for Wells AA, AB, AC and AD = 480 m;

Deviation angle = 30°;

TVD = 2050 m; and

Measured depth (MD) = 2250 m.

The selection of grade and weight provides the basis for checking for tension. The tensile loads are to be included in the design of the casings string. In Table 8, the total tensile load and the safety factor for each section were determined to assure that the safety factor for the tension loads was equal or above 1.5 – 1.8. The entire volume of cement is outside the casing and the casing inside is full of displacement fluid. When the casing is cemented, the effects of shock loading disappear; therefore, a safety factor of 1.4 in tension in the production section could be tolerated. Table 9 shows the compressive loads on the casing due to thermal expansion during heat-up.

TABLE 8: Tensile loads

Selected grade and weight	Max. buoyant weight in 1000 daN	Bending force in 1000 daN	Shock load in 1000 daN	Lifting force due to wellhead pressure in 1000 daN	Force due to pressure testing in 1000 daN	Total tensile load in 1000 daN	Safety factor
Surface casing 20" 94.0 lb/ft K55	19.2		133.8		161.3	314.1	2.1
Anchor casing 13.375" 68.0 lb/ft K55	41.6		96.8	36.4	125.84	300.2	1.6
Production casing 9.625" 47.0 lb/ft K55	72.5	31.71	66.9		68.8	239.9	1.4

TABLE 9: Compressive loads due to thermal expansion during heating-up

	Surface casing	Anchor casing	Production casing
Compressive loads in 1000 daN	156	352	508

Biaxial correction is resolved using an equation from the *Viking Engineering* programme (Appendix IV) for reducing the collapse rating in the presence of axial tension. The collapse resistance of the casing in the presence of axial stress is calculated by reducing the yield strength in accordance to the axial stress, giving:

Surface casing: 20 " 94.0 lb/ft K55

Axial stress = 1599.5 psi

Reduced yield strength due to axial stress: 54.2 ksi

Reduced collapse pressure: 520 psi

Anchor casing: 13.375 " 54.50 lb/ft K55

Axial stress = 4804.4 psi

Reduced yield strength due to axial stress: 52.4 ksi

Reduced collapse pressure: 1900 psi

Production casing: 9.625 " 40 lb/ft K55

Axial stress = 11096 psi

Reduced yield strength due to axial stress: 48.6ksi

Reduced collapse pressure: 3600 psi.

5. CEMENTING PROCESS

In this section, the cement job for each casing will be calculated. The casings of Wells AA, AB, AC, and AD will be cemented in place with a single-stage cementing operation with a cementing head (single-stage cementing), which is the most common type of cementing operation when there is no loss of circulation (Bett, 2010). Other common cementing methods in geothermal wells can be used such as multiple-stage and inner-string cementing. The single-stage procedure follows the following steps (Figure 12):

- Installation of the cementing head;
- Cleaning out the mud in the annulus;
- Release wiper plug, to clean the inside of the casing and to maintain the spacer front;
- Pump spacer into the casing;
- Pump cement;
- Release shut-off plug; and
- Stop the displacement process when the plug reaches the float collar.

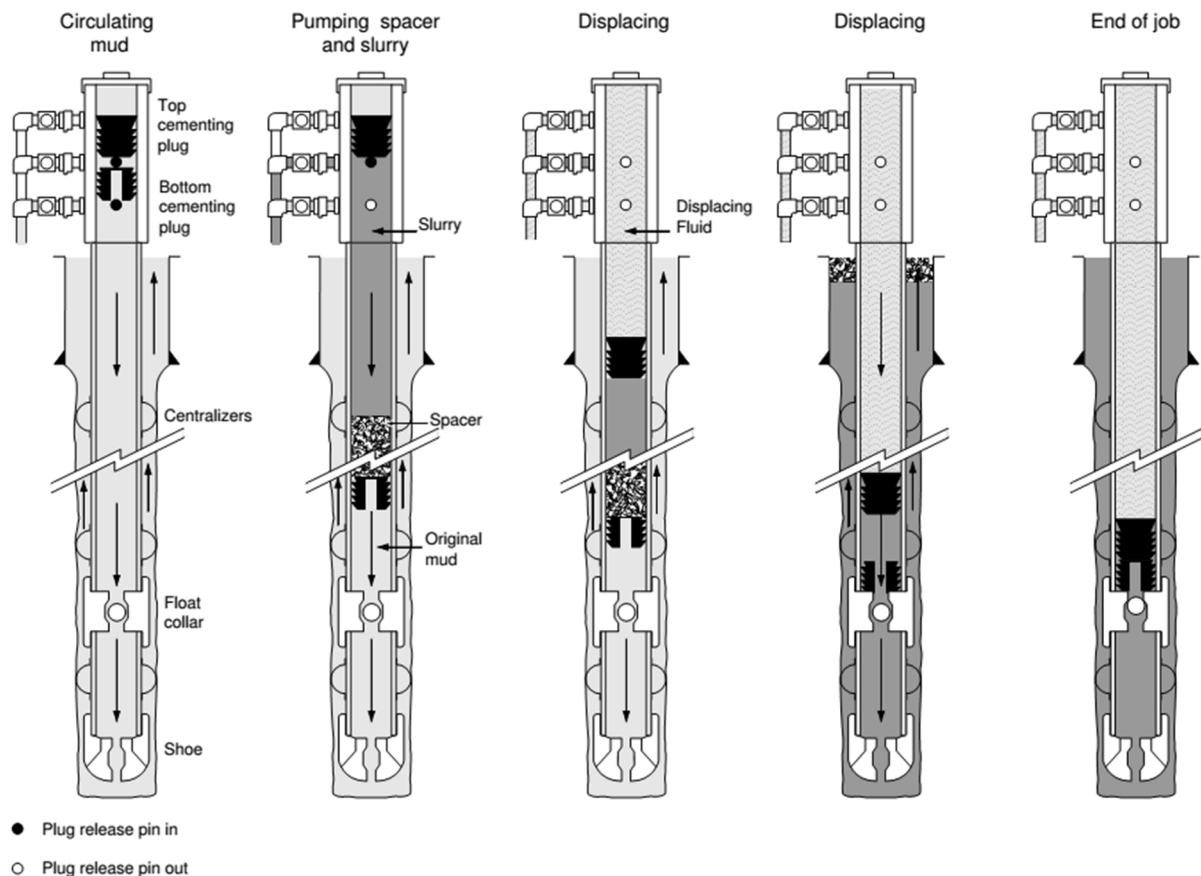


FIGURE 12: Single-stage cementing operation

5.1 Cementing calculations for Asal Wells AA, AB, AC and AD

All casings are fully cemented back to the surface. For each casing, the total slurry volume is the sum of four volumes: slurry volume between the casing and the open hole, slurry volume left inside the casing below the float collar, slurry volume in the rathole, and slurry volume in the annulus between the casing and the previous casing (Figure 12). The duration of the operation can be calculated using a displacement rate of 24 l/s and a mixing and pumping rate of 20 l/s (Thórhallsson, 2013).

Conductor casing, 30"

V = Volume of an annular space between open hole (28") and conductor casing:

Slurry	0.4	m ³
Plus 60% excess	0.64	m ³

Surface casing: 20" 94.0 lb/ft K55

<u>Casing 20" 94.0 lb/ft K55</u>	<u>Open hole 26"</u>
Capacity 185.32 l/m	Capacity 342.5 l/m
Displacement 202.68 l/m	Depth of open hole 156 m
CSD 160 m	

<u>Previous casing 30"</u>	<u>Rathole</u>
Capacity 456 l/m	Depth of rathole 2 m
Previous CSD 2 m	Capacity 342.5 l/m

- Slurry volume between casing and hole:
 $V1 = \text{Depth of open hole} \times (\text{Capacity of open hole (26")} - \text{Casing displacement (20")}) = 22 \text{ m}^3$.
 Assume gauge hole, add 60% excess in open hole, $V1 = 35 \text{ m}^3$.
- Slurry volume in the rathole:
 $V2 = \text{Depth of rathole} \times \text{Capacity of open hole (26")} = 0.7 \text{ m}^3$.
 Assume gauge hole, add 60% excess in open hole, $V2 = 1.1 \text{ m}^3$.
- Slurry volume below the float collar, shoe track:
 $V3 = \text{Depth of shoe track (10 m)} \times \text{Casing capacity (20")} = 1.85 \text{ m}^3$.
- Slurry volume between casing:
 $V4 = \text{Depth of previous casing} \times (\text{Casing capacity 26"} - \text{Casing displacement 20"}) = 0.51 \text{ m}^3$.

The total cement required for the surface casing is 38.8 m³. The duration of the cementing operation is given by:

$$\text{Duration} = \frac{\text{Slurry volume}}{\text{Pumping and mixing rate}} + \frac{\text{Displacement volume}}{\text{Displacement rate}} + \text{Contingency (1hr)} \quad (44)$$

The displacement volume is the slurry volume inside the casing between the cementing head and the float collar. Therefore, the displacement volume is calculated from the volumetric capacity of the casing and the depth of the float collar in the casing (volumetric capacity of casing \times depth of float collar).

- Displacement volume = $(150+12 \text{ (depth landing joint)}) \times 185.32 \text{ l/m} = 30.02 \text{ m}^3$.
- Duration of operation = 113 minutes.

Anchor casing: 13.375" 54.50 lb/ft K55

Casing 13.375" 68.0 lb/ft K55

Capacity 78.1 l/m
 Displacement 90.65 l/m
 CSD 480 m

Open hole 17.5"

Capacity 155.2 l/m
 Depth of open hole 318 m

Previous casing 20"

Capacity 185.32 l/m
 Displacement 202.68 l/m
 Previous CSD 160 m

Rathole

Depth of rathole 2 m
 Capacity 155.2 l/m

- a. Slurry volume between casing and open hole:
 $V1 = \text{Depth of open hole} \times (\text{Capacity open hole (17.5")} - \text{Casing displacement (13.375")}) = 21 \text{ m}^3$.
 Assume gauge hole, add 60% excess in open hole, $V1 = 33 \text{ m}^3$.
- b. Slurry volume in the rathole:
 $V2 = \text{Depth of rathole} \times \text{Capacity of open hole (17.5")} = 0.3 \text{ m}^3$.
 Assume gauge hole, add 60% excess in open hole, $V2 = 0.5 \text{ m}^3$.
- c. Slurry volume below the float collar, shoe track:
 $V3 = \text{Depth of shoe track (10 m)} \times \text{Casing capacity (13.375")} = 0.78 \text{ m}^3$.
- d. Slurry volume between casing:
 $V4 = \text{Depth of previous casing} \times (\text{Casing capacity 20"} - \text{Casing displacement 13.375"}) = 15.15 \text{ m}^3$.
 The total cement required for the anchor casing is 49.5 m^3 .
- e. Displacement volume = $(470+12 \text{ (depth landing joint)}) \times 78.1 \text{ l/m} = 37.64 \text{ m}^3$.
- f. Duration of operation = 127 minutes.

*Production casing 9.625" 47 lb/ft K55*Casing 9.625" 68.0 lb/ft K55

Capacity 38.19 l/m
 Displacement 46.94 l/m
 CSD (=length) 1290 m

Open hole 12.25"

Capacity 76.04 l/m
 Depth of open hole 808 m

Previous casing 13.375"

Capacity 78.1 l/m
 Displacement 90.65 l/m
 Previous CSD 480 m

Rathole

Depth of rathole 2 m
 Capacity 76.04 l/m

- a. Slurry volume between casing and open hole:
 $V1 = \text{Depth of open hole} \times (\text{capacity of open hole (12.25")} - \text{casing displacement (9.625")}) = 24 \text{ m}^3$.
 Assume gauge hole, add 60% excess in open hole, $V1 = 38 \text{ m}^3$.
- b. Slurry volume in the rathole:
 $V2 = \text{Depth of rathole} \times \text{capacity of open hole (12.25")} = 0.15 \text{ m}^3$.
 Assume gauge hole, add 60% excess in open hole, $V2 = 0.24 \text{ m}^3$.
- c. Slurry volume below the float collar, shoe track:
 $V3 = \text{Depth of shoe track (10 m)} \times \text{casing capacity (9.625")} = 0.4 \text{ m}^3$.
- d. Slurry volume between casing:
 $V4 = \text{Depth of previous casing} \times (\text{casing capacity 13.375"} - \text{casing displacement 9.625"}) = 15 \text{ m}^3$.
 The total cement required for production casing is 53 m^3 .
- e. Displacement volume = $(1280+12 \text{ (depth landing joint)}) \times 38.19 \text{ l/m} = 49 \text{ m}^3$.
- f. Duration of operation = 139 minutes.

6. WELLHEAD DESIGN

Wellheads include several pieces of equipment; the most important is the master valve which is used to isolate the well. Other equipment include the casing head flange, gaskets, bolts, kill valves and the expansion spool. A typical permanent wellhead can be seen in Figure 13. Wellhead pressure (WHP) can be proportional to the reservoir pressure; when the reservoir pressure is high, the wellhead pressure will likely also be high. The phases of the fluid at the wellhead vary. There can be different phases: saturated water, saturated steam, or gas that accumulates in the well when it is shut in. The surface conditions are never equal to the bottom hole conditions due to the column of the fluid in the well but in some cases, they can be similar. The different wellhead components should be designed to withstand the maximum pressure and temperature exposure under static and flowing conditions. The wellhead should be designed according to the practice codes. The master valve is often chosen by using pressure ratings of flanges, conforming to ANSI b16.5 and to API 6A (Hole, 1996). The top section of the anchor casing, from the surface to around 25 m depth, should also comply with the ASME B31.1 Power piping code.

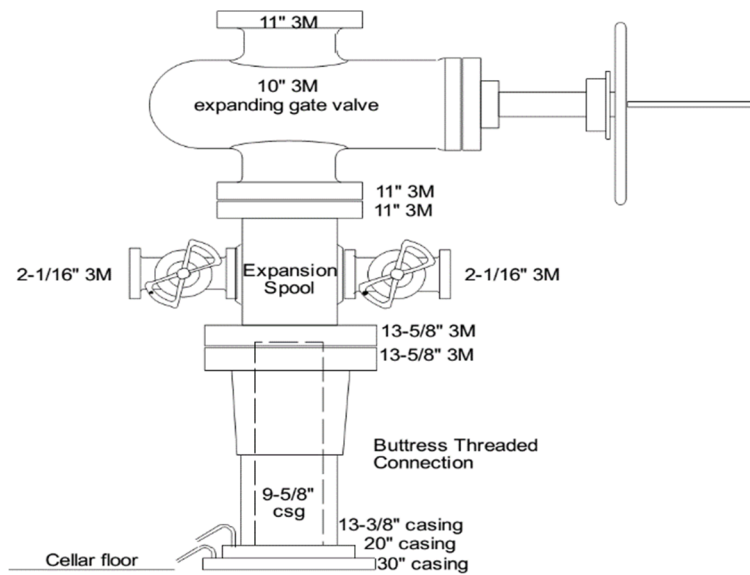


FIGURE 13: Typical complete wellhead

6.1 Wellhead pressure estimate and class

In Table 10, the wellhead pressure is calculated using the density of the saturated liquid. Then one can calculate the hydrostatic pressure and the density of saturated steam in order to calculate the pressure of the steam column in the production section back to the surface and the wellhead. First the hydrostatic pressure is calculated from 200 m (water level) to the bottom of the well at 2000 m at every 50 m. Secondly, the boiling point (1100 m) is determined. From this point, the pressure of the steam column in the production section and to the surface and the wellhead is calculated. The class of the wellhead shall be API 3000; it was chosen by using the pressure ratings of flanges conforming to ANSI b16.5 and to API 6A (Figure 14).

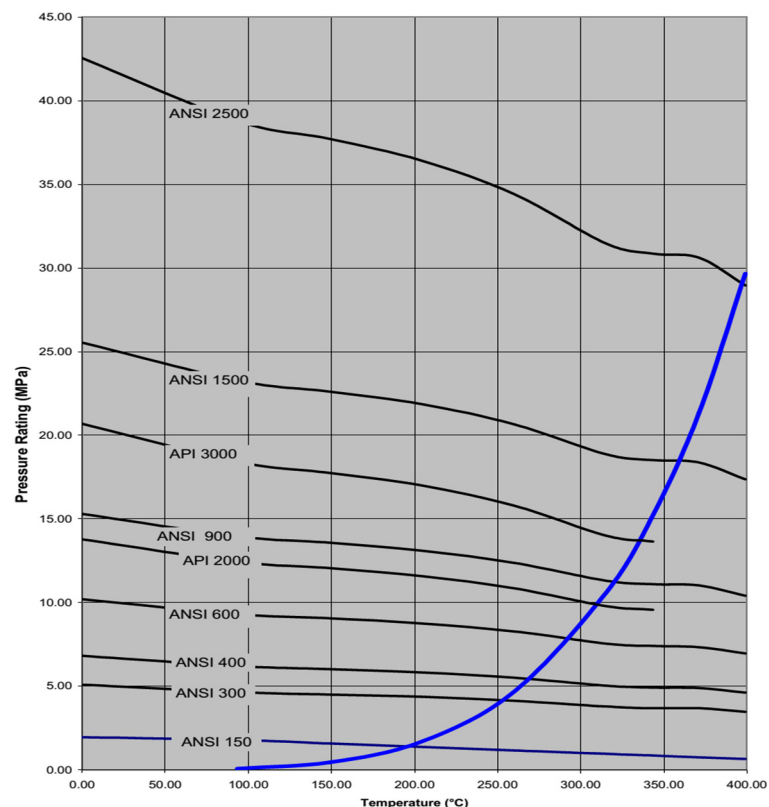


FIGURE 14: Pressure rating of wellhead

TABLE 10: Wellhead pressure estimate

Vertical depth	Temp	Boiling Point	Density		Hydrostatic pressure	Steam column production-section
			Sat. liquid	Sat. vapour		
(m)	(°C)	(bar)	(kg/m ³)	(kg/m ³)	(bar)	(bar)
0.0	0.0					94.585
50.0	0.0					94.863
100.0	0.0					95.140
150.0	0.0					95.417
200.0	40.0	0.1	992.2	0.1		95.694
250.0	50.0	0.1	988.0	0.1	4.8	95.971
300.0	60.0	0.2	983.2	0.1	9.7	96.248
350.0	70.0	0.3	977.7	0.2	14.5	96.525
400.0	80.0	0.5	971.8	0.3	19.2	96.802
450.0	90.0	0.7	965.3	0.4	24.0	97.079
500.0	96.4	0.9	960.9	0.5	28.7	97.356
550.0	102.9	1.1	956.3	0.7	33.4	97.634
600.0	109.3	1.4	951.5	0.8	38.0	97.911
650.0	115.7	1.7	946.5	1.0	42.7	98.188
700.0	122.1	2.1	941.4	1.2	47.3	98.465
750.0	128.6	2.6	936.0	1.4	51.9	98.742
800.0	135.0	3.1	930.5	1.7	56.5	99.019
850.0	141.4	3.8	924.9	2.0	61.0	99.296
900.0	147.9	4.5	919.0	2.4	65.5	99.573
950.0	154.3	5.3	913.0	2.8	70.0	99.850
1000.0	160.7	6.3	906.8	3.3	74.4	100.127
1050.0	167.1	7.4	900.4	3.9	78.8	100.405
1100.0	173.6	8.6	893.8	4.5	83.2	100.682
1150.0	170.0	7.9	897.5	4.1	87.6	100.959
1200.0	177.9	9.6	889.2	4.9	92.0	101.236
1250.0	185.8	11.4	880.7	5.8	96.3	101.513
1300.0	193.7	13.6	871.9	6.9	100.6	
1350.0	201.6	16.1	862.8	8.1	104.8	
1400.0	209.5	18.9	853.4	9.5	109.0	
1450.0	217.4	22.0	843.6	11.0	113.1	
1500.0	225.3	25.6	833.4	12.8	117.2	
1550.0	233.2	29.6	822.9	14.8	121.3	
1600.0	241.1	34.1	811.9	17.1	125.2	
1650.0	248.9	39.1	800.4	19.6	129.2	
1700.0	256.8	44.6	788.5	22.5	133.0	
1750.0	264.7	50.6	776.1	25.7	136.8	
1800.0	272.6	57.3	763.0	29.3	140.6	
1850.0	280.5	64.7	749.3	33.5	144.3	
1900.0	288.4	72.7	734.9	38.1	147.9	
1950.0	296.3	81.5	719.6	43.4	151.4	
2000.0	304.2	91.1	703.3	49.5	154.8	
2050.0	312.11	101.513	685.892	56.494	158.212	

7. CONCLUSIONS

The casing programme is vital to the success and safety of the well drilling process and to the integrity and life of the well. The design of Wells AA, AB, AC and AD was oversized to avoid any risk. After drilling the first well, the first useful geotechnical data for the new drilling site will be available; then the design of the other three wells can be optimized.

Generally, drilling can be done with foam or mud. The choice of drilling fluid will depend on the geology and the surrounding terrain. In the Fiale area, it is most likely that the drilling fluid used will consist of seawater based drilling mud. But in the production section, using aerated drilling should be considered because of possible low permeability.

ACKNOWLEDGEMENTS

I would first like to thank my supervisor, Arnar Bjarki Árnason, for teaching me to be more independent throughout this project. I also would like to thank my teachers at UNU-GTP.

I especially want to thank Mr. Ingimar Gudni Haraldsson, Ms. Málfríður Ómarsdóttir, Mr. Markús A. G. Wilde and Ms. Thórhildur Ísberg, all of whom dedicated their time to me during my stay in Iceland. Finally, I express my sincere gratefulness to the now retired director, Dr. Ingvar Birgir Fridleifsson, and the new director, Mr. Lúdvík S. Georgsson.

REFERENCES

Aquater, 1989: *Asal 5 well report - final report*. Aquater, Italy, 64 pp.

Árnason, K., Björnsson, G., Flóvenz, Ó.G., Haraldsson, E.H., 1988: *Geothermal resistivity survey in the Asal rift, volume 1: Main text*. Orkustofnun, Reykjavík, OS-88031/JHD-05, prepared for the UND-OPS and ISERST, 48 pp.

Baker Hughes INTEQ, 1995: *Drilling engineering workbook. A distributed learning course*. Baker Hughes INTEQ Inc., 410 pp.

Bett, E.K., 2010: Geothermal well cementing, materials and placement techniques. Report 10 in: *Geothermal training in Iceland 2010*. UNU-GTP, Iceland, 99-130.

BG Group, 2001: *Well engineering and production operations management system – Casing design manual*. B.G. Group, document number WSD CD 01, 51 pp.

Devereux, S., 1998: *Practical well planning and drilling*. Pennwell, Oklahoma, OK, United States 524 pp.

Elmi, H.D., 2005: Analysis of geothermal well test data from the Asal rift area, Republic of Djibouti. Report 6 in: *Geothermal training in Iceland 2005*. UNU-GTP, Iceland, 39-59.

Gabolde G., and Nguyen, J.P., 2006: *Drilling data handbook* (8th edition). Institut Française du Pétrole Publications, Paris, 552 pp.

Heriot-Watt University, 2010: *Drilling engineering*. Heriot-Watt University, Department of petroleum engineering, 539 pp.

Hole, H.M., 1996: Geothermal Energy New Zealand, Ltd. *Seminar on Geothermal Drilling Engineering, Jakarta, Indonesia, Seminar handbook.*

Hosseini-Pourazad, H., 2005: High-temperature geothermal well design. Report 9 in: *Geothermal training in Iceland 2005*. UNU-GTP, Iceland, 111-123.

Jalludin, M., 2010: State of knowledge of the geothermal provinces of the Republic of Djibouti. *Paper presented at "Short Course V on Exploration for Geothermal Resources" organized by UNU-GTP, KenGen and GDC, Lake Naivasha, Kenya*, 14 pp.

Khaireh, A.E., 1989: *Borehole geology of well Asal-5, Asal geothermal field, Djibouti*. UNU-GTP, Iceland, report 6, 31 pp.

Meinken, W., and Schüle, S., 2012: *Geothermal resources evaluation project Djibouti, environmental and social impacts*. Fichtner GmbH and Co., final report, 14 pp.

NZS, 1991: *Code of practice for deep geothermal wells*. Standards New Zealand, NZS 2403:1991, 96 pp.

Rabia, H., 1987: *Fundamentals of casing design, vol. 1*. Graham & Trotham, London, United Kingdom, 285 pp.

REI, 2008: *Drilling and testing of geothermal exploration wells in the Asal area, Djibouti: Environmental management plan*. Reykjavik Energy Invest, report REI-2008/Assal 1, 58 pp.

Saemundsson, K., 1988: *Djibouti geothermal project. Analysis of geological data pertaining to geothermal exploration of Asal rift*. United Nations Development Programme, 18 pp.

Stiltsjes, L., 1976: Research for a geothermal field in a zone of oceanic spreading: Examples of the Asal Rift. *Proceedings of the 2nd UN Symposium on the Development and Use of Geothermal Resources, San Francisco, CA, United States*, 1, 613-623.

Thórhallsson, S., 2013: *Geothermal drilling technology*. UNU-GTP, Iceland, unpublished lecture notes.

Varet, J., 1978: Geology of central and southern Afar (Ethiopia and Djibouti Republic). Centre National de la Recherche Scientifique, Paris, France, 124 pp.

Virkir-Orkint, 1990: *Djibouti, geothermal scaling and corrosion study*. Virkir-Orkint, Reykjavík, report, 109 pp.

APPENDIX I: API specifications, standards and bulletins

API SPEC 5CT, "Specification for casing and tubing": Covers seamless and welded casing and tubing, couplings, pup joints and connectors in all grades. Processes of manufacture, chemical and mechanical property requirements, methods of test and dimensions are included.

API STD 5B, "Specification for threading, gauging, and thread inspection for casing, tubing, and line pipe threads": Covers dimensional requirements on threads and thread gauges, stipulations on gauging practice, gauge specifications and certifications, as well as instruments and methods for the inspection of threads of round-thread casing and tubing, buttress thread casing, and extreme-line casing and drill pipe.

API RP 5A5, “Recommended practice for filed inspection of new casing, tubing and plain-end drill pipe”: Provides a uniform method of inspecting tubular goods.

API RP 5B1, “Recommended practice for thread inspection on casing, tubing and line pipe”: The purpose of this recommended practice is to provide guidance and instructions on the correct use of thread inspection techniques and equipment.

API RP 5C1, “Recommended practice for care and use of casing and tubing”: Covers use, transportation, storage, handling, and reconditioning of casing and tubing.

API RP5C5, “Recommended practice for evaluation procedures for casing and tubing connections”: Describes tests to be performed to determine the galling tendency, sealing performance and structural integrity of tubular connections.

API BULL 5A2, “Bulletin on thread compounds”: Provides material requirements and performance tests for two grades of thread compound for use on oil-field tubular goods.

API BULL 5C2, “Bulletin on performance properties of casing and tubing”: Covers collapsing pressures, internal yield pressures and joint strengths of casing and tubing and minimum yield load for drill pipe.

API BULL 5C3, “Bulletin on formulas and calculations for casing, tubing, drill pipe and line pipe properties”: Provides formulas used in the calculations of various pipe properties, also background information regarding their development and use.

API BULL 5C4, “Bulletin on round thread casing joint strength with combined internal pressure and bending.” Provides joint strength of round thread casing when subject to combined bending and internal pressure.

APPENDIX II: Calculated hole trajectories for Wells AA, AB, AC and AD

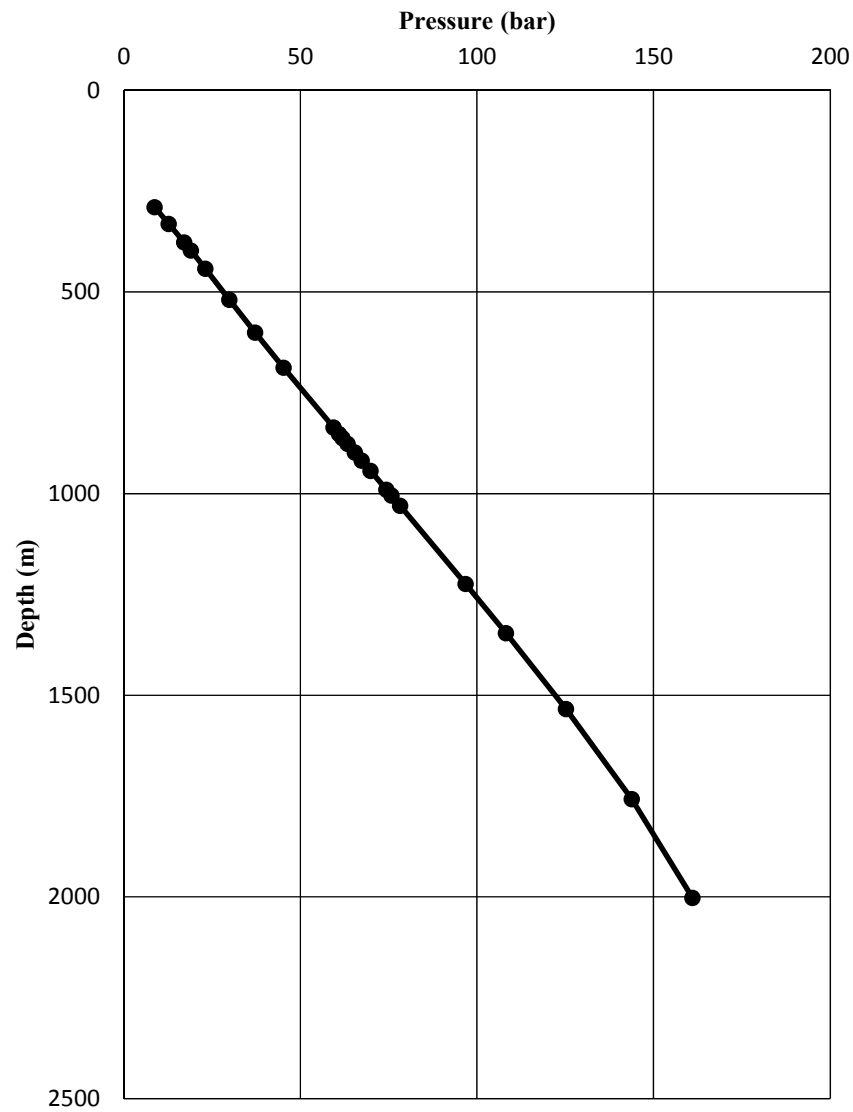
Dogleg severity: 2.5 degrees/30 ft., Deviation angle 30 degrees

MD (m)	Inclination (°)	TVD (m)	Displacement (m)
0	0	0	0
30	0	30	0
60	0	60	0
90	0	90	0
120	0	120	0
150	0	150	0
160	0	160	0
180	0	180	0
210	0	210	0
240	0	240	0
270	0	270	0
300	0	300	0
330	0	330	0
360	0	360	0
390	0	390	0
420	0	420	0
450	0	450	0
480	0	480	0


MD (m)	Inclination (°)	TVD (m)	Displacement (m)
510	2.5	510.0	0.7
540	5	539.9	2.6
570	7.5	569.8	5.9
600	10	599.4	10.4
630	12.5	628.8	16.3
660	15	658.0	23.4
690	17.5	686.8	31.8
720	20	715.2	41.5
750	22.5	743.1	52.3
780	25	770.6	64.4
810	27.5	797.5	77.7
840	30	823.8	92.1
870	30	849.8	107.1
900	30	875.8	122.1
930	30	901.7	137.1
960	30	927.7	152.1
990	30	953.7	167.1
1020	30	979.7	182.1
1050	30	1005.7	197.1
1080	30	1031.6	212.1
1110	30	1057.6	227.1
1140	30	1083.6	242.1
1170	30	1109.6	257.1
1200	30	1135.6	272.1
1230	30	1161.6	287.1
1260	30	1187.5	302.1
1290	30	1213.5	317.1
1320	30	1239.5	332.1
1350	30	1265.5	347.1
1380	30	1291.5	362.1
1410	30	1317.4	377.1
1440	30	1343.4	392.1
1470	30	1369.4	407.1
1500	30	1395.4	422.1
1530	30	1421.4	437.1
1560	30	1447.3	452.1
1590	30	1473.3	467.1
1620	30	1499.3	482.1
1650	30	1525.3	497.1
1680	30	1551.3	512.1
1710	30	1577.2	527.1
1740	30	1603.2	542.1
1770	30	1629.2	557.1
1800	30	1655.2	572.1
1830	30	1681.2	587.1
1860	30	1707.1	602.1
1890	30	1733.1	617.1
1920	30	1759.1	632.1
1950	30	1785.1	647.1
1980	30	1811.1	662.1
2010	30	1837.1	677.1
2040	30	1863.0	692.1

MD (m)	Inclination (°)	TVD (m)	Displacement (m)
2070	30	1889.0	707.1
2100	30	1915.0	722.1
2130	30	1941.0	737.1
2160	30	1967.0	752.1
2190	30	1992.9	767.1
2220	30	2018.9	782.1
2250	30	2050	797.1

APPENDIX III: Hydrostatic pressure in Well Asal 5



APPENDIX IV: Reduced collapse resistance, production casing

		
API Collapse		
Input		
D (in)	9,625	Pipe Outside Diameter
Weight (lb/ft)	47	Pipe Weight Per Foot
Grade	K55	Pipe Grade
Yield Strength (ksi)	48,6	Pipe Yield Strength
Wall (in)	0,472	Pipe Wall Thickness
Nominal ID (in)	8,681	Nominal Inside Diameter
Collapse Resistance (psi)	3600	Calculated Collapse Rating
Collapse Calculations		
D/t	20,39	
A	2,970661	
B	0,050525	
C	995,6239	
F	2,011316	
G	0,034209	
Yield Strength Collapse (psi)	4480	Collapse Ratings Based on D/t
D/t	15,44	
Plastic Collapse (psi)	3570	Collapse Ratings Based on D/t
D/t	25,89	
Transition Collapse (psi)	3090	Collapse Ratings Based on D/t
D/t	39,53	
Elastic Collapse (psi)	6130	Collapse Ratings Based on D/t
This calculator calculates API collapse resistance for a specific pipe.		



BOREHOLE GEOLOGY AND HYDROTHERMAL ALTERATION OF WELL SV-5A, SAN VICENTE GEOTHERMAL FIELD, EL SALVADOR, C.A.

Claudia Mercedes Pichardo López

LaGeo S.A. de C.V.
15 Avenida Sur, Colonia Utila
Santa Tecla, La Libertad
EL SALVADOR
cpichardo@lageo.com.sv

ABSTRACT

Well SV-5A is an exploration well located in El Salvador in the San Vicente geothermal field. It is a directional well, drilled to a depth of 1798.5 m. The drill cuttings of the well were analysed through a binocular microscope and through a petrographic microscope in thin sections. The lithology of Well SV-5A consists of andesite lava flows, basalt-andesite, dacite and three different types of tuffs: crystal tuff, lithic tuff and crystal-lithic tuff. The alteration minerals show that temperature increases with depth. Mineralogical assemblages reflect five zones of alteration: a smectite-zeolite zone at 386-750 m, a mixed layer clay zone at 750-920 m, a chlorite zone at 920-1200 m, a chlorite-epidote zone at 1200-1242 m, and an epidote-actinolite zone at 1500-1798.5 m. Four aquifers were identified in the production section of the well, based on the temperature profiles and circulation losses during drilling. When the first appearance of alteration minerals and the results of the analysis of fluid inclusions were compared, equilibrium was observed, reflecting a temperature of 280°C at 1500 m depth. The formation temperature estimated at that same depth in the well is 240°C. By comparing the formation temperature with fluid inclusions and the alteration mineralogy, a cooling of about 40°C has occurred in the geothermal system. According to the calculated Horner temperature, the well was still in a thermal recovery process during the last temperature log, which showed an increase of 5°C, which means that the formation temperature of the well could possibly reach 245°C.

1. INTRODUCTION

El Salvador is located in Central America, has a territorial extension of 20,742 km² and a population of 6.2 million. Geologically the country is part of the Pacific Ring of Fire and is situated in an environment of convergent tectonic plate boundaries, which promotes the formation of volcanic arcs and active geothermal systems.

El Salvador has significant geothermal potential and since the early 1960s many areas have been studied with geothermal interest. The geothermal power generation in El Salvador started in 1975 and has been increasing steadily since. Currently, there are two developed fields, Berlin and Ahuachapán, with an

installed electrical capacity of 204.4 MW. The geothermal power station in Ahuachapán has three units and a total installed capacity of 95 MW; the total installed capacity in Berlin (four units) is 109.4 MW.

El Salvador has an estimated geothermal resource of 791 MW in areas of high and low enthalpy, so the use of this energy is only 25%. Recent studies have shown that geothermal energy is the best option to meet future demands and to diversify the country's energy matrix, as this would greatly reduce the energy dependence based on fossil fuels and, thus, the vulnerability induced by high oil prices that the country has had to face since the last oil crisis.

The geothermal field of San Vicente is located in the central part of El Salvador (Figure 1), about 60 km from the capital, San Salvador. This field is located by the San Vicente volcano (Chichontepeque), with no history of recent volcanic activity. Indications of an active geothermal system are found in three active fumaroles located on the northern flank of the volcano.

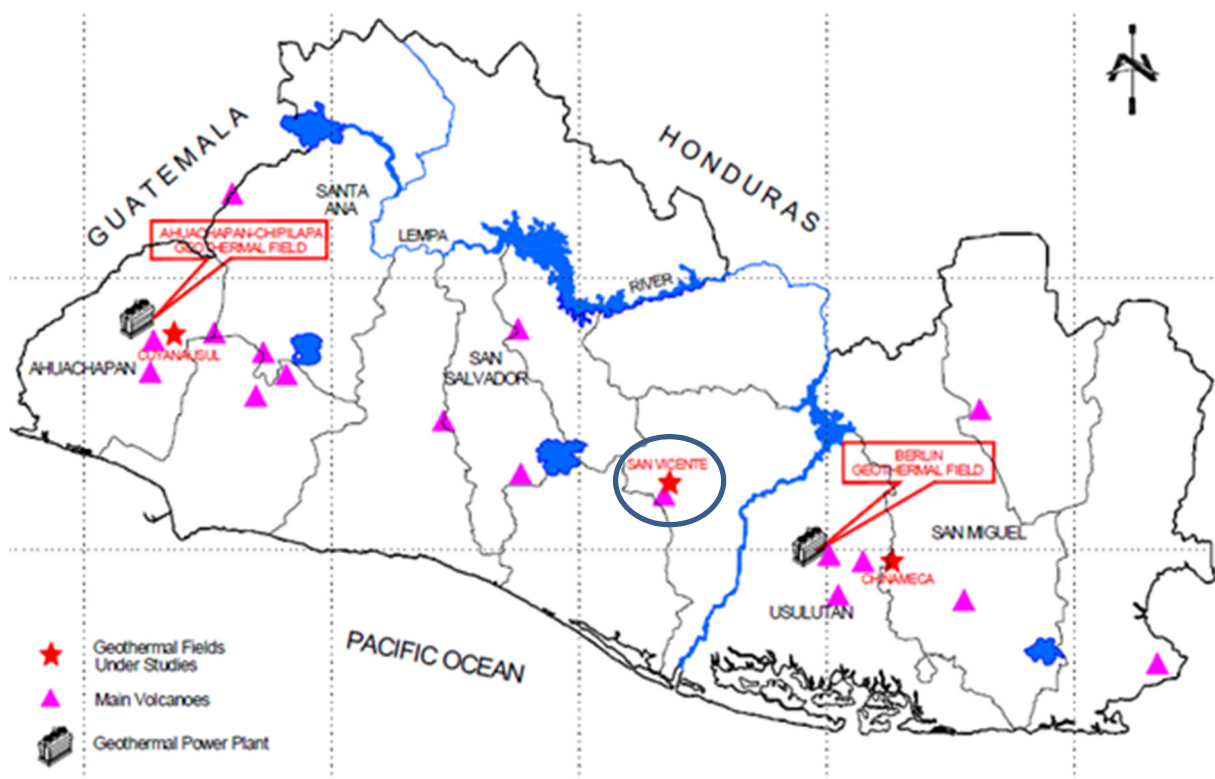


FIGURE 1: Location map of the geothermal fields and exploration fields of El Salvador (CNE, 2012). San Vicente is shown within the circle.

The geothermal area of San Vicente volcano has been the subject of several studies since the early sixties, when PNUD assessed the major geothermal areas of El Salvador. At the end of the 1970s, the Comisión Ejecutiva Hidroeléctrica Del Rio Lempa de El Salvador, CEL (CEL, 1992), carried out the first geophysical exploration studies in the San Vicente area. Based on their results, it was proposed that exploration drilling should be conducted to confirm the existence of a geothermal reservoir in the San Vicente volcano.

Following the first exploration drilling (which did not show good results), the project was put on hold and it was not until the year 2004 that LaGeo S.A de C.V. obtained the concession field and continued with superficial exploration studies and exploratory drilling. During the years 2006-2007 three exploration Wells SV-1A, SV-2A and SV-3 were drilled (Figure 2); of the three, only the first confirmed the existence of a geothermal reservoir, but with low permeability. Consequently, LaGeo decided to drill exploration Well SV-5A to the southwest of well SV-1 with the aim of finding better permeability.

This report is focused on the characterization of the geology of Well SV-5A, which was drilled from October 2012 until January 2013, based on the analysis of the cuttings and the two cores obtained during drilling.

1.1 Tectonic setting of El Salvador

The study area is located in the central-eastern Salvadoran territory, which, from the point of view of plate tectonics, is within the Caribbean Plate. The main morpho-tectonic features are produced by the subduction of the Cocos Plate under the Caribbean Plate (Middle America Trench) and the interaction of the Caribbean Plate with the North American Plate (System-Polochic-Motagua fault) (Figure 3).

The Salvadoran territory is bound to the north by a regional structure called the Central Graben, which runs through the country and extends from Guatemala to Nicaragua, where it is known as the "Depression of Nicaragua". This structure is the largest and most influential in the surface geology of the region. In fact, much of the recent volcanic edifices are arranged through this structure.

The transcurrent component of the movement between the Cocos and the Caribbean plates is probably accommodated on land by a slip along a major E–W trending dextral transcurrent fault system (El Salvador Fault Zone, ESFZ) (Martínez-Díaz et al., 2004) which runs along the volcanic front and represents the source of the strong strike-slip seismicity. Between the dextral ESFZ and the sinistral Motagua fault system, a series of N–S trending grabens testify to the existence of a broad zone of nearly E–W extension (Agostini et al., 2006).

The main structures belonging to the ESFZ have an approximate E–W strike, and are characterized by right-lateral kinematics. These faults, running sub-parallel to, and north of, the volcanic front, affect late Pleistocene and Holocene deposits and present a strong morpho-tectonic signature, testifying to very recent activity (Corti et al., 2005). The active tectonics of the ESFZ are further corroborated by the

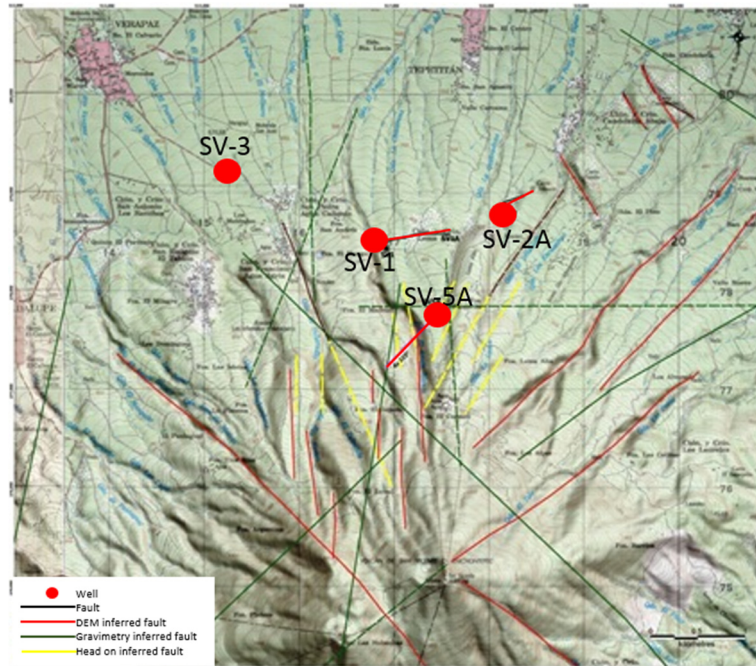


FIGURE 2: Map location of the wells drilled in the geothermal field of San Vicente (modified from LaGeo, 2013b)

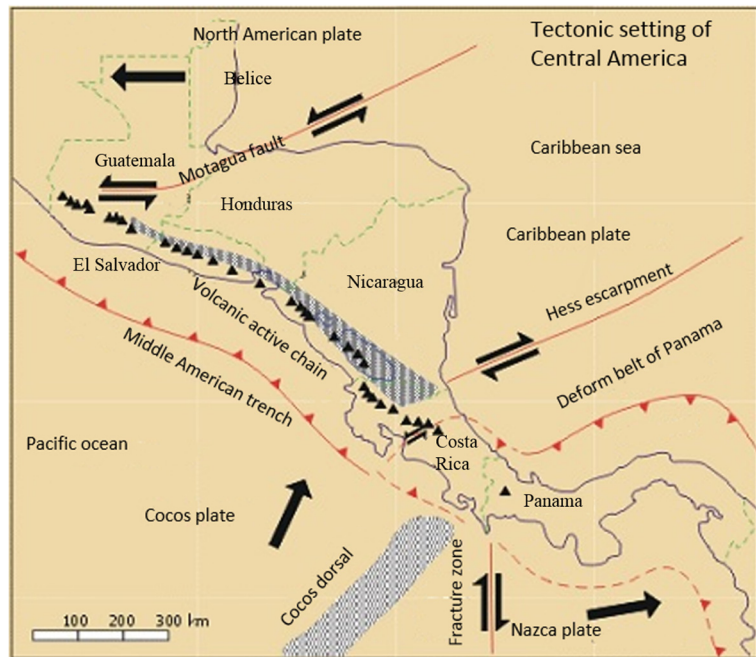


FIGURE 3: Regional tectonic framework of Central America (modified from LaGeo, 2005)

strong transcurrent crustal seismicity associated with this fault zone (Martínez-Díaz et al., 2004). In particular, the major upper crustal seismic events that have taken place since 1912 in El Salvador occur parallel to, and north of, the volcanic front (Martínez-Díaz et al., 2004). Reliable focal mechanisms indicate strike-slip events with one of the planes oriented E–W. At least six of the major destructive earthquakes ($M \geq 6$) along the volcanic front seem to be related to a slip along the ESFZ segment located between River Lempa and Lake Ilopango (Martínez-Díaz et al., 2004; Agostini et al., 2006).

1.2 Regional geology

El Salvador is very active tectonically, as it lies within the area of an interaction between the Cocos Plate and the Caribbean Plate, where the former is subducted beneath the latter. Geologically, El Salvador is a very young country, mainly composed of rocks of Quaternary and Tertiary age, in addition to a small portion of Cretaceous age rocks (Figure 4).

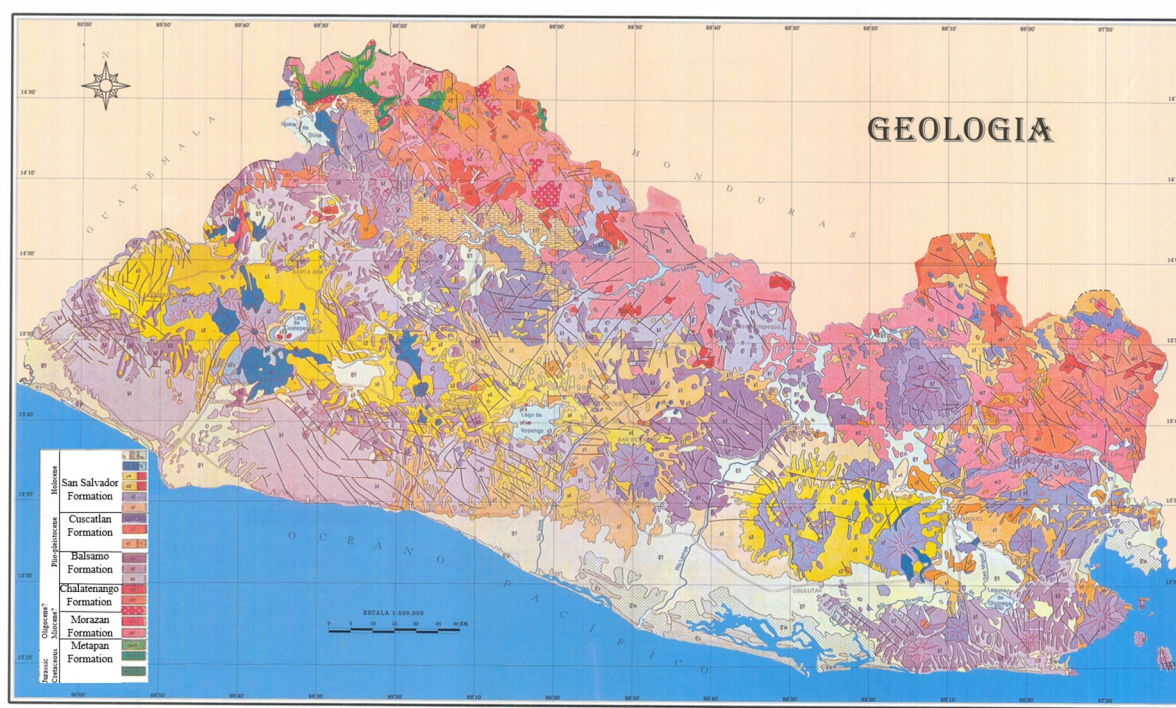


FIGURE 4: Geological map of El Salvador (modified from German Geological Mission, 1970)

The oldest rocks of El Salvador are sedimentary rocks corresponding to the Metapan formation, where limestone, marl and shale are intercalated. These rocks outcrop in the northwest part of El Salvador. The Tertiary rocks are of volcanic origin and are located in the north, as they belong to an ancient volcanic system. They are mainly composed of basalts, andesites, rhyolites and extensive ignimbritic flows. Intrusives of acid composition, related to the old volcanic structure, are also found. Many hot springs, as well as hydrothermal alteration in this area (Figure 5), are associated with the old magmatic chamber and possibly with the last intrusions of this extinct volcanic arc. The geothermal fields in this area are medium to low temperature ($<180^{\circ}\text{C}$).

The Quaternary rocks owe their origin to the great structure that crosses the country parallel to the coastline of El Salvador, the central graben, where volcanic activity has emerged recently. The present active volcanic arc of El Salvador is located in this structure, which has given rise to many volcanoes, mainly of basaltic and andesitic composition. Additionally, it has given rise to large calderas, evidenced by dense ignimbritic flows. Currently all high-temperature geothermal fields ($>200^{\circ}\text{C}$) are related to the active volcanic arc and many hot springs and hydrothermal manifestations can be observed along this structure.

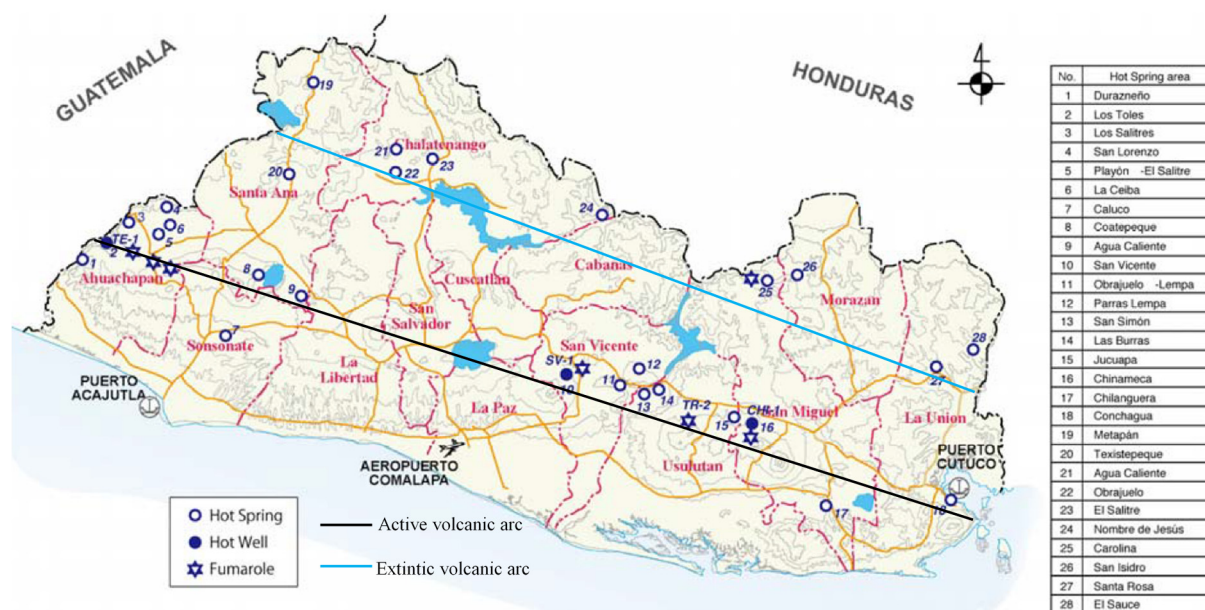


FIGURE 5: Location of volcanic systems in El Salvador (modified from CNE, 2012)

2. LOCAL GEOLOGY

2.1 San Vicente geothermal field

The San Vicente geothermal field is located in the central part of El Salvador, almost 5 km away from the city of San Vicente and approximately 60 km from the capital, San Salvador. Interest in the geothermal potential in the San Vicente volcano has been demonstrated since the 1960s when PNUD included the area in its campaign to assess the various geothermal prospects in El Salvador. The total area of concession, which was granted by the General Superintendence of Electricity and Telecommunications (SIGET), was approximately 100 km² (Figure 6). The project is currently at a prefeasibility stage, which includes the drilling of two more exploration wells.

2.2 Background of the San Vicente geothermal field

The geothermal area of the San Vicente volcano has been the subject of several studies since the early 1960s, when PNUD assessed the major geothermal areas of El Salvador. In the years 1977 to 1979, CEL conducted the first geophysical exploration study in the San Vicente, consisting of vertical electrical soundings AB / 2 = 1500. The penetration of these soundings was limited to the first 500 m. The results of these studies became the basis for delimiting the area for future investigations.

In 1978-79, exploration Wells SV-1, PSV-1 and PESV-2 were drilled, reaching depths of 1346.5, 551 and 506.5 m, respectively. SV-1 penetrated a permeable zone that can be considered part of a potential geothermal reservoir. In 1992-1993, CEL conducted a second exploration campaign with a suite of geoscientific studies including surface geological mapping, gravity and Schlumberger surveys and geochemical sampling of surface waters.

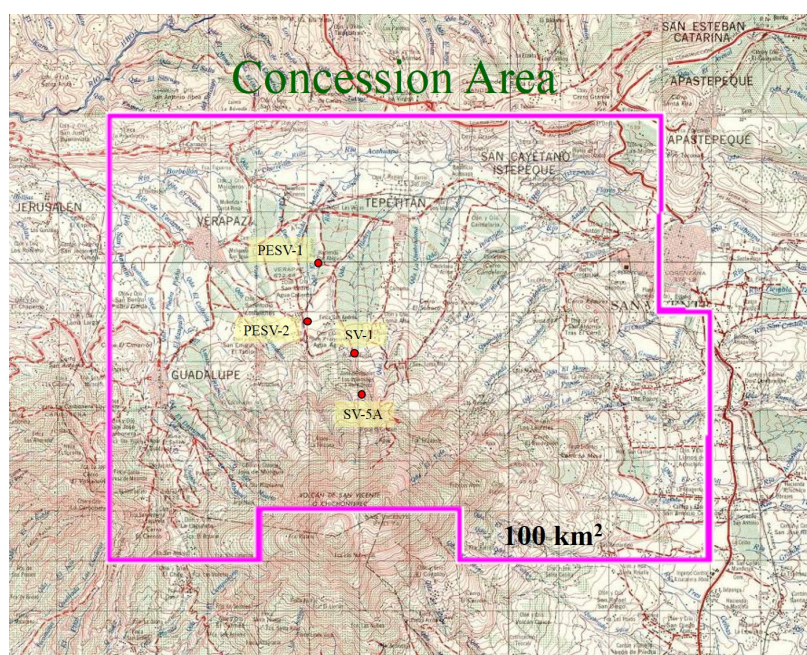


FIGURE 6: Concession map of San Vicente geothermal field (modified from LaGeo, 2005)

In late 2004, LaGeo SA de CV acquired the concession for studies of the San Vicente geothermal area. Until the beginning of 2005, LaGeo performed complementary studies of geology, geochemistry and geophysics. Based on their results, it was proposed that three exploration wells be drilled, two directional (Wells SV-1A and SV-2A) and one vertical (Well SV-3).

During the years 2006 and 2007, Wells SV-1A, SV-2A and SV-3 were drilled. However, the results were not as expected and in November of 2009, LaGeo engaged Iceland GeoSurvey (ISOR) in reviewing and evaluating the conceptual model of the San Vicente geothermal

field and the results of the deep exploration drilling. Included was an estimate of the electric potential of the field and a feasibility assessment of continuing with further deep exploration drilling and the identification of new drilling targets. In the year 2012, LaGeo proposed the drilling of exploration Well SV-5A.

2.3 Geology of the San Vicente Volcano

The San Vicente volcano is an andesitic, composite volcano, the second most voluminous in El Salvador, covering 130 km³ (Carr et al., 1981). It is located approximately 60 km east of the capital city, San Salvador.

Chichontepec is a paired volcano whose eastern crater (elevation: 2180 m) appears to be morphologically younger while the western crater (elevation 2105 m) seems older. The remnants of an older volcanic centre lie immediately west of the main volcanic edifice (Figure 7) which consist of a series of pronounced hills arranged in a semicircle (La Carbonera hills).

The beginning of La Carbonera volcano's activity is poorly defined according to Rotolo and Castorina (1998), but the onset is considered to be 2.2 ± 0.4 and 1.2 ± 0.2 Ma. La Carbonera volcano experienced a pyroclastic eruption that led to the collapse of the edifice, thereby giving rise to a caldera, which is referred to as the La Carbonera caldera (CEL, 1992). From this caldera numerous pyroclastic events occurred, beginning with a deposit of ignimbrite and followed by a sequence of dacitic pumice falls. According to Rotolo and Castorina (1998), the isopach pattern of dacitic pumice deposits locates the vent's position inside the annular structure, which is outlined by the La Carbonera hills.

The renewed volcanic activity, following the pyroclastic stage, formed a considerable volume (130 km³) of thick (~20 m) lava flows, which built up the Chichontepec edifice inside the La Carbonera caldera. Lavas on the northern and southern flanks of the volcano were probably emitted from a central vent, while those of the eastern flank were emitted from a parasitic vent, which is located to the east of the summit craters (Rotolo and Castorina, 1998).

The most recent activity of this complex is dominated by effusive volcanic eruptions, a moderately fluid magma and low gas content. The lava flows that formed the San Vicente volcano are mainly of intermediate composition, predominantly andesitic lava flows with some alternating basaltic lava flows. These lavas have a high content of xenoliths, mainly of basic and intermediate composition.

In 2005, LaGeo conducted rock sampling with the purpose of defining the surface rocks in more detail, resulting in the discovery of a dacitic dome which is located in the West cone (Figure 8). The discovery of this structure in the San Vicente volcano is of great importance since it suggests a magmatic differentiation and, therefore, the possibility of a shallow magmatic chamber.

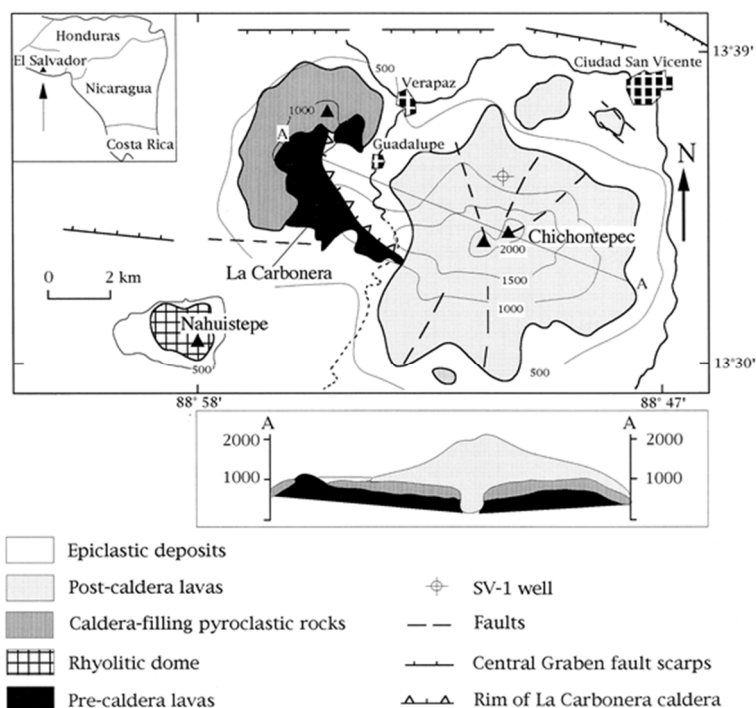


FIGURE 7: Generalized geological map of the Chichontepec volcanic centre (Rotolo and Castorina, 1998)

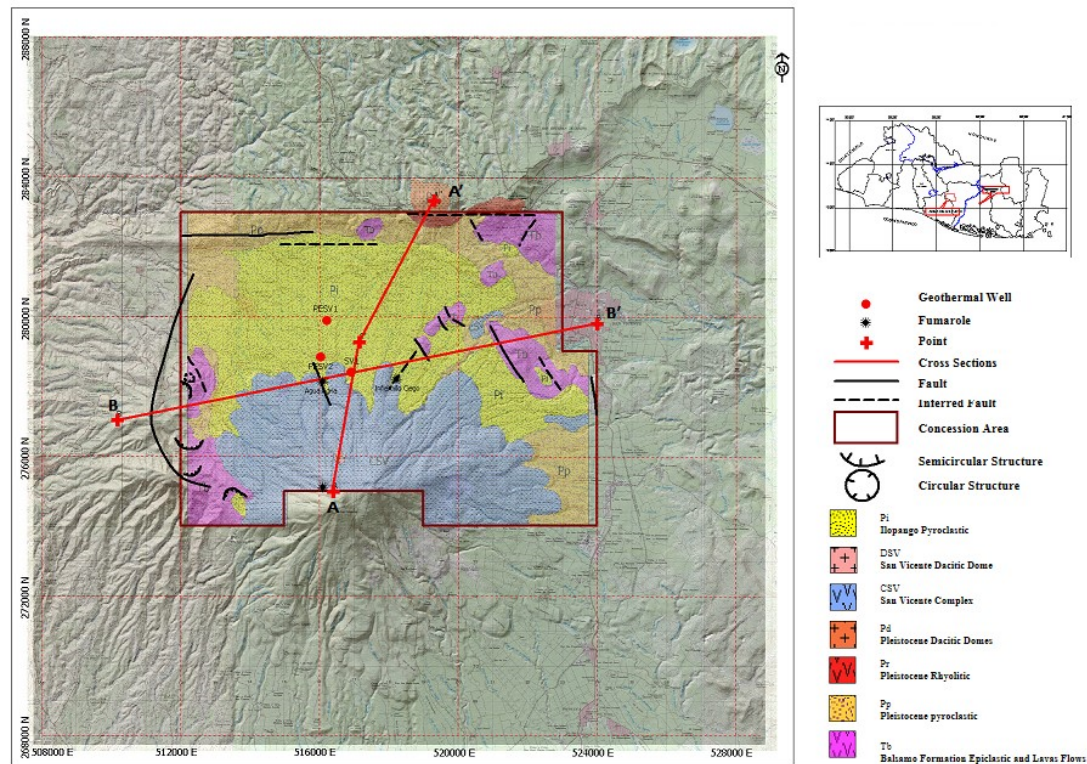


FIGURE 8: Geological map of San Vicente geothermal field (modified from LaGeo, 2005)

The age of this dome is uncertain, but the morphological characteristics and its location indicate that it may be the last event in the formation of the volcano. Furthermore, the fumaroles and hot springs of the geothermal system are close to the dome (LaGeo, 2005).

2.4 Geological structures

The study area is located within the most active areas of the country. The tectonics are related to regional forces associated with the subduction of the Cocos Plate beneath the Caribbean Plate. The area is dominated by a nearly E-W directional pattern, characterized by dominant right-lateral kinematics. This transcurrent movement is produced by horizontal stresses σ_1 and σ_3 oriented NNW-SSE and ENE-WSW, respectively (LaGeo, 2005).

The E-W fault system corresponds to the Central Graben system fault. The majority of the important structures in the San Vicente geothermal field have this orientation, and the most representative is the Agua Agria fault, which is directly related to the geothermal system. This fault is associated with the most fumarolic activity in the field.

The system of NW-SE faults is associated with an extension zone generated by the Central Graben. This pattern of faults is evident in the Infiernillo Ciego ravine and in the Agua Agria fumaroles. Many geological structures that cut San Vicente volcano have this orientation.

3. BOREHOLE GEOLOGY

This report is based on the borehole geology of exploration Well SV-5A in the San Vicente geothermal field. For the realization of this report, it was necessary to analyse drill cuttings and thin sections of selected cutting samples from the well.

Well SV-5A has the Lambert coordinates of 517.434N and 277.746E, situated at an elevation of 986.70 m a.s.l. on the northern flanks of the San Vicente volcano. The main objectives in drilling Well SV-5A were to confirm the existence of a geothermal reservoir and to find good permeable conditions.

The well was drilled from 4 m to 1798.50 m. In total, 600 samples were collected at 2 m intervals, from 4 m to 1242 m, after which the well experienced a total loss of circulation. Two cores were obtained, the first at a depth of 1500 m and the second at 1750 m.

3.1 Drilling history of Well SV-5A

Well SV-5A is a directional well with a final depth of 1798.50 m. The drilling company was Perforadora Santa Barbara (PSB), S.A. de C.V. using the drill rig, Massarenti 4000. The onset of drilling was October 13th, 2012 and drilling finished on January 7th, 2013.

This well was initially designed to be drilled in four sections. The first section was intended to be vertical and the second where deviation of the well took place. The third and the fourth sections were to be drilled directionally. However, during the progress of the well and due to early circulation losses, it was decided to continue to the fourth section of drilling with the same drilling diameter.

Drilling of Well SV-5A started with a vertical section with diameters of 26" and 17½" to 388 m, followed by deviation to the southwest, which ended with an azimuth of 231° and an inclination of 30.5°, with a horizontal displacement of 614.06 m at the final depth of 1798.50 m MD (1636.33 m TVD). A short description of the drilling activities is presented below and can also be seen in Figure 9:

First section: Drilling from the surface to 109.3 m was done with a 26" bit followed by RIH (run in hole) of the 20" surface casing down to 107.22 m depth. Small circulation losses were recorded at the end of this stage, from 93 to 109.30 m; two cement plugs were placed to control the circulation losses.

Second section: The formation was drilled from 109.30 to 756.50 m with a 17½" bit; the 13⅜" casing was placed at 752.43 m. Many circulation losses occurred between 110 m and 250 m, and 10 cement plugs were placed to control them. These partial and total losses were associated with changes in the formation and fractures in the host rocks. The deviation of the well started at 388 m.

Third section: The formation was drilled from 956.50 to 1798.50 m with a 12¼" bit, followed by the run in of a 9⅝" slotted liner. Total loss of circulation occurred at 1094 m; at 1116 m there was partial loss of circulation, and at 1244 m total loss was associated with the geothermal reservoir. After drilling the well, the BOP was removed to install the master valve.

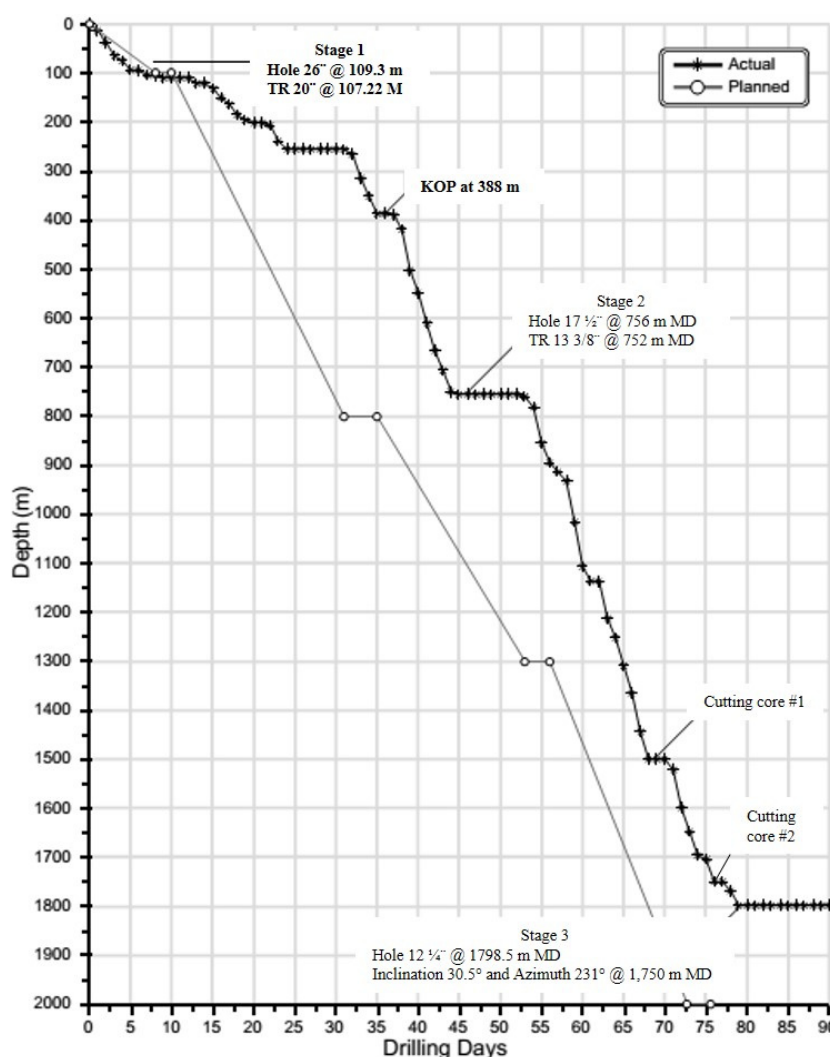


FIGURE 9: Drilling programme of Well SV-5A
(modified from LaGeo, 2013a)

3.2 Analytical method

Four main techniques were employed to formulate the lithological and mineralogical descriptions of Well SV-5A:

Binocular microscope was used for the analysis of drill cuttings. The analysis consisted of identifying the properties of the rocks, mainly: rock type, grain size, primary mineralogy, texture, alteration mineralogy, vein fillings, and the intensity of hydrothermal alteration of the rocks. A total of 180 samples of drill cuttings were analysed by this technique, using an Olympus 12 binocular microscope.

Petrographic microscope was used to describe in more detail the properties of the rocks. It was helpful in identifying alteration minerals that could not be seen under the binocular microscope. It was also necessary to study the depositional sequence of secondary minerals by which it is possible to determine the state of the geothermal system from a mineralogical point of view. A total of 66 thin sections were analysed at intervals of 20 m with an Olympus SZ12 petrographic microscope.

X-ray diffractometer analysis: This technique is mainly used for detailed identification of the clay groups and to establish, with greater accuracy, the mineralogical boundaries between low and high temperature. Eighteen samples of clays were selected for this analysis, between 400 and 1242 m depths.

Fluid inclusion analysis provides us with the temperatures that the geothermal system has experienced through time. This technique involves heating the fluid inclusions trapped in the crystals (calcite, quartz

or wairakite) and measuring the temperature of homogenization as the bubble within the fluid inclusion and the fluid itself merge. Microthermometric measurements were performed at one interval in the well (at 1500 m depth) using a Linkam THMSG-600 stage.

3.3 Stratigraphy

The stratigraphy of Well SV-5A is based on the analysis of the drill cuttings. The first stage consisted of binocular microscopic analysis and the second stage of the petrographic analysis, to confirm and define more precisely the types of rocks. As is common in volcanic environments, the well shows an intercalation of lava flows and tuffs. These lavas were classified as basaltic andesites, andesites and dacites, based on the contents of phenocrysts (pyroxene, plagioclase, olivine and hornblende), and on the texture, matrix type and degree of crystallisation of the rocks. The tuffs that were found were classified according to the matrix, crystal contents and lithic contents, and ranged from lithic tuffs to crystal tuffs and crystal lithic tuffs. A detailed description of the main formations is found below, but Figure 10 shows the stratigraphic column together with some drilling parameters.

Volcanoclastic deposits (6-18 m): Fine grained rock, sub-rounded to sub-angular grey-pink-yellow fragments composed of andesite, basaltic-andesite and oxidized fragments, crystals of plagioclase, pyroxene, magnetite and fresh glass. In the cuttings, limonite was observed in oxidized fragments.

Basaltic andesitic lava (18-30 m): Medium grained rock, dark grey, with vesicular porphyritic texture and phenocrysts of pyroxene, plagioclase, magnetite and some olivine. Petrographic analysis showed a hyalopilitic-porphyritic matrix. Fragments of xenoliths (dolerite) were also observed.

Andesitic lavas (30-260 m): Sequences of andesitic lavas interspersed with small amounts of generally oxidized scoria, due to contact between the flows. These lavas have a high content of xenoliths which, by means of petrographic analysis, were identified as two types: the most common is dolerite with phenocrysts of plagioclase, pyroxene, magnetite and small olivine. Diorite xenoliths were also observed with phenocrysts of plagioclase, pyroxene and opaque minerals which had been oxidized to hematite.

36-88 m: Andesitic lava, dark grey to light grey towards the bottom, with porphyritic texture, phenocrysts of pyroxene, plagioclase, magnetite and fresh glass.

88-146 m: Andesitic lava, grey to reddish grey towards the bottom, medium grained with porphyritic texture, phenocrysts of pyroxene, plagioclase, magnetite and fresh glass.

160-168 m: Andesitic scoreaceous, reddish grey, coarse grained, porphyritic texture, phenocrysts of pyroxene, plagioclase and magnetite. Some minerals of magnetite were replaced by hematite.

168-188 m: Andesitic lava, light grey, coarse to medium grained, porphyritic texture with phenocrysts of pyroxene, plagioclase and magnetite. Some minerals of magnetite had been replaced by hematite. Fresh glass was also observed.

202-270 m: Andesitic lava, reddish grey, medium grained, porphyritic texture, with phenocrysts of pyroxene, plagioclase and magnetite. Some magnetite minerals had been replaced by hematite. At the top and at the bottom, Fine grained and scoreaceous rock was seen.

Crystal tuff (270-278 m): Crystal tuff, beige with many crystals of plagioclase, pyroxene, yellow feldspar and magnetite. Fresh glass was observed.

Dacitic lavas (278-368 m): Sequence of dacitic lava flows, beige to light grey towards the bottom, coarse to medium grained and fine grained towards the bottom. The rock has porphyritic texture with

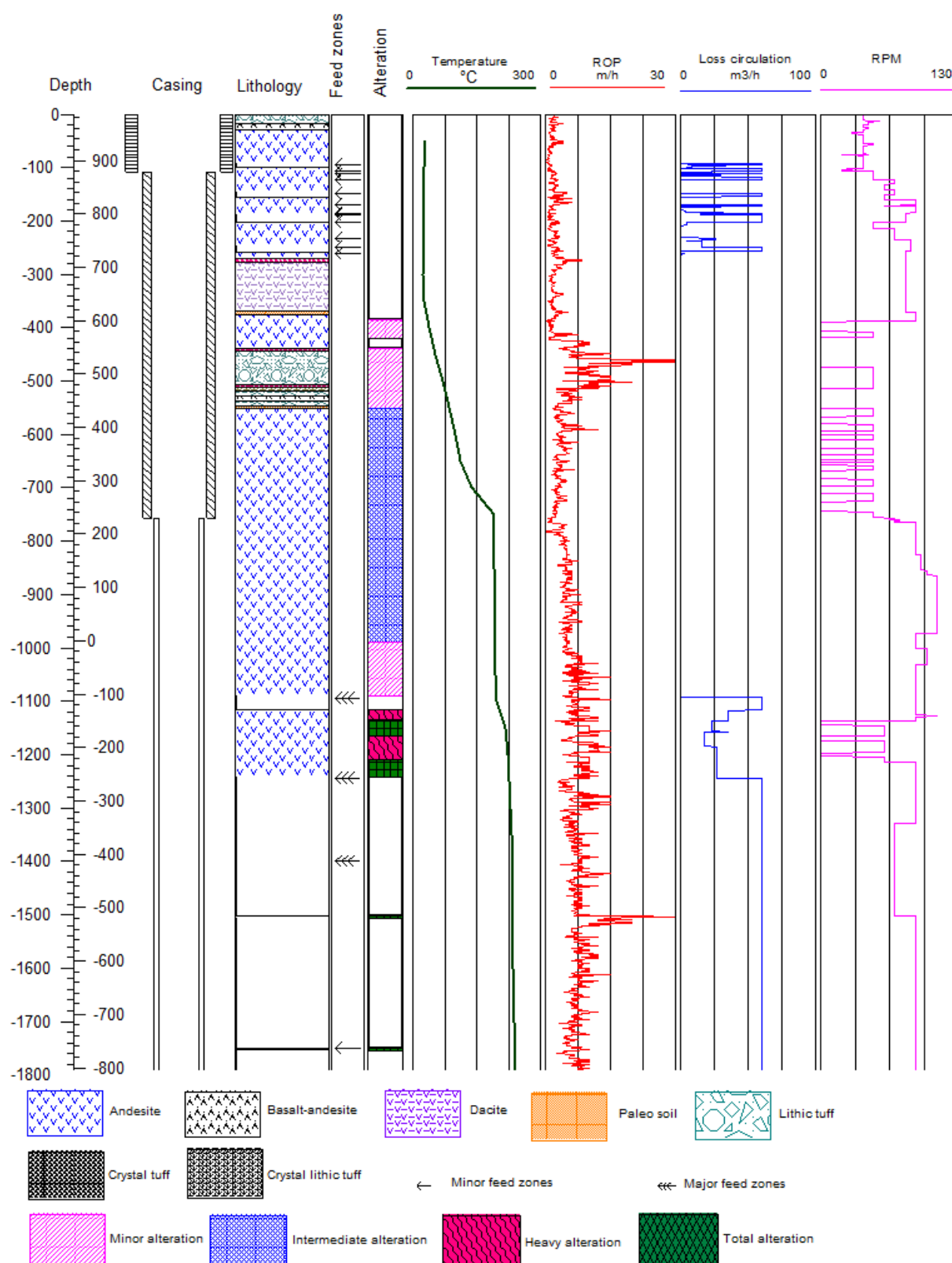


FIGURE 10: Stratigraphic section and drilling parameters in Well SV-5A

phenocrysts of plagioclase, pyroxene, hornblende and magnetite, some of which had been replaced by hematite. Dolerite and diorite xenoliths were observed.

Paleo soil (368-376 m): Fine rounded fragments, reworked. Opal and yellow clays were observed, considered to represent the beginning of low-temperature alteration.

Andesitic lavas (376-438 m): Andesitic lava, grey, medium to coarse grained, porphyritic texture, phenocrysts of plagioclase, pyroxene and magnetite. Some magnetite minerals had been replaced by hematite. Calcite, opal and smectite clays were observed. Small veins filled with opal and smectite clays were also noted. At the top and at the bottom, scoreaceous and fine grained rocks were seen.

Crystal tuff (438-450 m): Crystal tuff, dark grey, with some lithics of scoria and andesite and crystals of plagioclase, pyroxene and magnetite. Fresh glass was observed. Opal, calcite and smectite clays were noted.

Lithic tuff (450-506 m): Lithic tuff, grey-yellow, medium to coarse grained, with lithic andesite, dacite, pumice and scoria. There was some pyrite seen towards the bottom. Alteration minerals included calcite, opal and smectite clays.

Crystal tuff (506-512 m): Crystal tuff, dark grey, crystals of plagioclase, pyroxene and magnetite. Fresh glass was observed. Opal, calcite, smectite clays and some lithic pyrite were observed.

Crystal lithic tuff (512-518 m): Crystal lithic tuff, grey, medium grained with crystals of pyroxene, plagioclase and magnetite. Lithics of andesite were seen (very rounded) and some pyritized lithics. Opal, calcite and smectite clays were observed, representing alteration mineralogy.

Lithic tuff (518-528 m): Fine fragments, rounded, and crystals of plagioclase, pyroxene and magnetite. Opal, calcite and smectite clays were observed.

Andesitic lavas (528-538 m): Scoreaceous andesite, dark, coarse grained, with porphyritic texture, phenocrysts of plagioclase, pyroxene and magnetite. Calcite, opal and smectite clays were observed in pores.

Lithic tuff (538-546 m): Lithic tuff, dark grey, medium grained, with lithics of andesite and few crystals of plagioclase and pyroxene. Alteration minerals included calcite, smectite clays and opal.

Paleo soil (546- 552 m): Matrix of fine grained rocks of brown colour with some lithics of andesite and scoria. Calcite, opal, smectite clays and oxidation were observed.

Andesitic lavas (552-1242 m): Andesitic lava sequence with trachytic matrix. At the top, the formation is pink, and towards the bottom it is light grey.

552-740 m: Andesitic lavas, very altered, medium to coarse grained, displaying a scoreaceous texture and a trachyte matrix with phenocrysts of plagioclase and opaque minerals (magnetite) and a few crystals of pyroxene. Clays, calcite, opal and zeolites (heulandite) were observed in pores.

740-920 m: Andesitic lavas, grey to greenish grey, fine to medium grained, somewhat porphyritic with trachyte matrix and phenocrysts of plagioclase and opaque minerals (magnetite) and a few crystals of pyroxene. The mineralogy alteration consisted of mixed layer clays, calcite, tridymite, opal, oxidation, and smectite clays.

920-1090 m: Andesitic lavas, grey to greenish, grey at the top and some reddish grey grains towards the bottom. Fine to medium grained, somewhat porphyritic with a trachyte matrix and phenocrysts of plagioclase and opaque minerals (magnetite). The mineralogy alteration consisted of calcite,

mixed layer clays, chlorite, quartz and sphene. Towards the bottom the amount of alteration minerals decreased and oxidation increased.

1116-1242 m: Andesitic lavas, much altered, light grey to greenish grey towards the bottom, fine grained, with a trachyte matrix. The amount of alteration minerals increased consisting of calcite, quartz, chlorite, epidote, sphene, illite, prehnite and wairakite.

4. HYDROTHERMAL ALTERATION

Hydrothermal alteration depicts changes in the mineralogy, texture and chemistry of the rocks, produced in the presence or movement of hydrothermal solutions.

Hydrothermal alteration minerals are secondary minerals deposited in vesicles (holes, cavities) and fractures and replace primary minerals.

Several hydrothermal alteration assemblages occur in the cuttings and cores from the San Vicente wells. In most cases, the alteration followed a pro grade trend of increasing rank and intensity with depth. At low temperatures, the subsurface mineral assemblages were characterised by various smectites and zeolites that, with increasing temperature, are replaced by e.g. chlorite, epidote, prehnite and actinolite. Alkali-feldspars, sulphides, quartz and calcite were found independent of temperature (Markússon and Stefánsson, 2011).

4.1 Primary rock minerals

The San Vicente hydrothermal system has altered the volcanic rocks in the area, resulting in the development of new mineral assemblages and a redistribution of certain elements through hydrothermal fluid circulation (Table 1). The primary minerals in the rocks are unstable at high temperature and pressure, leading to their replacement by new minerals that are stable in the new formation environment (Browne, 1978).

TABLE 1: Alteration of the primary rock minerals in Well SV-5A

Primary rock minerals	Alteration mineral products
Plagioclase	Clays, calcite, epidote, quartz, heulandite, wairakite, actinolite.
Pyroxene	Oxides, calcite, clays.
Opaque minerals	Sphene.
Olivine	Clays.

Different minerals have different susceptibilities to alteration, depending on the pressure and temperature conditions to which rocks are exposed. Primary minerals are present in all the rocks in Well SV-5A, being mainly plagioclase, pyroxene, opaque minerals and olivine, as well as hornblende in lower proportions.

Olivine is one of the basic rock forming minerals found in basaltic andesite lavas. Olivine was observed in two flows, the first at 20 m, where it had altered to iddingsite and the second at 528 m where small olivine crystals were completely replaced by smectite clays.

The plagioclases are the most common minerals in the rocks, and are mainly observed as phenocrysts in andesitic lava flows and the basaltic andesite. Plagioclases are also common in crystal rich tuffs, where they have been partly replaced by calcite, clays and opal from 400 to 750 m, and by chlorite,

quartz, calcite, epidote and wairakite below 750 m and towards the bottom. The matrix of the lavas is mainly composed of feldspars which are slightly albitized in the lower part of the well.

The pyroxenes were found as phenocrysts in lava flows and crystal rich tuffs; through petrographic analysis, two types of alteration mineral replacements of pyroxene were identified. The first was noted at 20 m down to 400 m where pyroxenes were replaced by iron oxides, and the second at 400-1242 m where they were replaced by calcite, mixed layer clays and chlorite.

Opaque minerals were observed in large amounts in the lava flows, both as phenocrysts and as part of the matrix, primarily as magnetite which had, in many cases, been replaced by hematite. From 1000 m to 1242 m, the opaque minerals were partially replaced by sphene.

4.2 X-ray analysis

The X-ray analysis is used to quantify the proportions of different minerals, mainly in clay groups, and to identify different zones of clay minerals.

A total of 18 samples were analysed from 400 to 1242 m in Well SV-5A. The data is shown in Table 2 showing that, from 506 to 860 m, the clays correspond to the low temperature smectite group. At 880 to 920 m, the mixed layered clays appear.

From 1122 to 1242 m two types of high temperature clays were analysed: chlorite and illite. These clays are associated with high temperature minerals like epidote, actinolite and prehnite.

TABLE 2: Results of the XRD analysis of clay minerals in Well SV-5A;
Sm: smectite; MLC: mixed layer clay (smectite/chlorite); Chl: chlorite
Ill: illite; Chlunst: unstable chlorite

Sample #	Depth(m)	d(001) UNT	d(001) GLY	d(001) HIT	d(002)	Mineral	Type	Remarks	Other minerals	Depth(m)
#1	400					no clay				400
#2	506	15.9	17.9	10.1		Sm:sm	Sm			506
#3	528	15.9	17.9	10.1		Sm:sm	Sm			528
#4	564	15.6	17.9	10.1		Sm:sm	Sm			564
#5	600	13/15	17	10.1		Sm:sm	Sm			600
#6	640	15.9	16.8	10.1		Sm:sm	Sm			640
#7	740	15.5	17.9	10.1		Sm:sm	Sm			740
#8	800	12.8	13.5	10.1		Sm:sm	Sm			800
#9	860	14.9	15.7	10.1		Sm:sm	Sm			860
#10	880	32,5/14,9	34,7/16,1	11.8	~7,4	MLC: sm/chl	MLC			880
#11	920	30,8/14,8	33,0/16	11.7	7.3	MLC: sm/chl	MLC			920
#12	1000					No clay				1000
#13	1080					No clay				1080
#14	1122	~14,5/11	~14,5/11	~14/11	~7,2	Chl: ill.	Chl: ill	uncertain	Illite	1122
#15	1160					No clay				1160
#16	1200					No clay				1200
#17	1220	14,6/10	14,6/10	~14/10	7,2 hit=0	Chl. Unst.	Chlunst.		Illite	1220
#18	1242	14,6/10	14,6/10	~14/10	7,2 hit=0	Chl. Unst.	Chlunst.		Illite	1242

4.3 Distribution of hydrothermal minerals

Figure 11 shows the distribution of the hydrothermal alteration in the well, but a detailed description of the occurrence of the various alteration minerals is given below.

Calcite started to appear at 386 m, gradually increasing down to 1090 m, and mainly replacing plagioclase. At 1116 and down to 1242 m a strong increase in calcite was presented, replacing plagioclase and pyroxene and filling small veins. In the two cores obtained at 1500 and 1750 m, excessive depositional calcite was observed, which could indicate that the fluid is probably in a state of boiling.

Opal was observed from 374 to 740 m, generally associated with clays, filling small veins and cavities of andesitic lavas.

Pyrite first appeared promptly at 500 m, only appearing again at 1116 m, persisting down to the bottom of the well. It is usually disseminated in the matrix, forming perfect cubic crystals, and in the cores it was also observed as vein fillings. Generally, the appearance of pyrite in large quantities indicates good permeability.

Zeolites: This group belongs to the sodium-calcium-alumina hydrosilicates which are generally found as secondary minerals in the cavities of igneous rocks, replacing plagioclase or through decomposition of volcanic glass. Two varieties of zeolites were found: heulandite and wairakite, which are described below:

Heulandite was observed in the range from 620 to 700 m, as small acicular and feathery crystals. In thin section they were observed in fractures and some cavities.

Wairakite: This high temperature zeolite (200°C) was identified through thin sections, from 1220 m to the bottom of the well, usually associated with calcite, replacing plagioclase and filling cavities. In the cores obtained in the well, the wairakite was associated with quartz and epidote filling the fractures. This zeolite is indicative of good permeability.

Smectites clays: This group of clays (associated with temperatures less than 200°C) started to appear at 400 m and was seen down to 740 m, mainly associated with opal. It was also found in the matrix of the tuffs and replacing plagioclase in the matrix lava flows.

Mixed layer clays were observed continuously from 740 to 1040 m, mainly filling cavities and associated with calcite crystals. These minerals are a transition between the group of smectites and chlorites, indicating 200-230°C temperatures.

Chlorite (230°C) began to appear at 920 m and persisted down to the bottom of the well, replacing primary minerals such as plagioclase and pyroxene and also filling cavities and small veins. In thin section it was observed as grey coloured with feathery and fibrous appearance. In the cores it was seen pervasively substituting the matrix.

Quartz (180°C) was observed from 900 m down to the bottom of the well, beginning as deposits in small veins and some cavities in the lava flows. In the two cores, microcrystalline quartz was observed. In the second core the highest amount was found where the matrix was entirely replaced by quartz.

Sphene first appeared at 1000 m and was seen down to 1240 m. It was recognized through thin sections and found disseminated in the rock matrix replacing the iron oxides.

Epidote (230-250°C) began to appear at 1180 m and was seen all the way to the bottom of the well. At the beginning it was pale yellow in colour and was observed replacing plagioclase crystals, associated

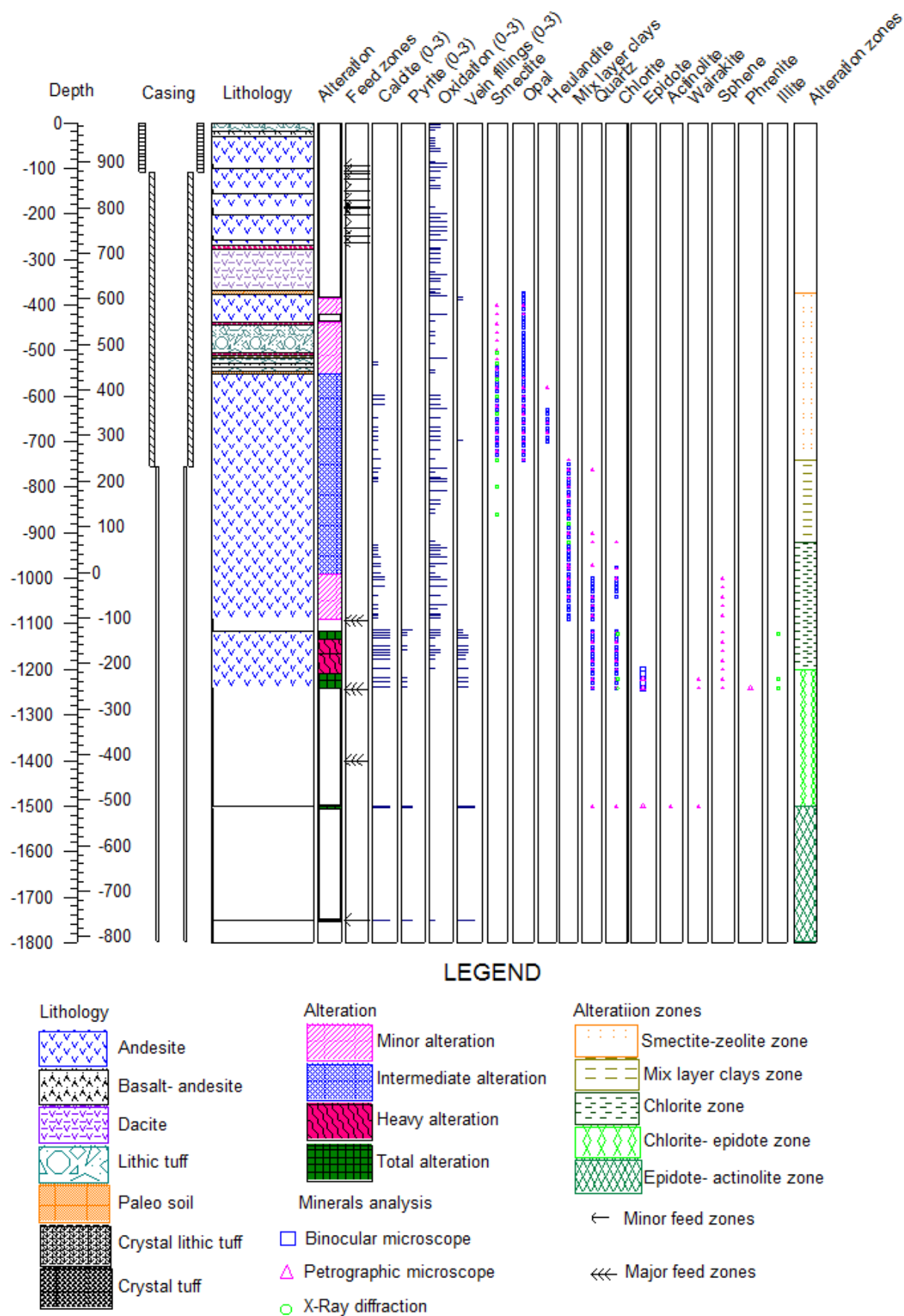


FIGURE 11: Distribution of hydrothermal alteration minerals in Well SV-5A

with prehnite, chlorite and wairakite. In the cores it exhibited yellow-green colours, with fibrous and radial forms, filling veins associated with calcite, wairakite and actinolite.

Prehnite (240°C) appeared only at 1240 and 1242 m, just before the loss of circulation. Tiny crystals were associated with epidote and it was only identified in thin section. It is characterized by high interference colours.

Actinolite appeared at 1500 m in the core obtained at this depth. The crystals were fibrous, with high relief and high interference colours. This amphibole mineral is associated with high temperature of more than 280°C in geothermal fields.

Illite (230°C) appeared first at 1220 m depth according to XRD analyses. It is the product of alteration of feldspar minerals and could be found in the groundmass in andesitic lavas flows.

4.4 Vein fillings

At the top of the well, no vein or vesicle fillings were observed. From 386 m it was possible to see small veins in lava flows that were filled with low-temperature minerals such as opal and clays of the smectite group.

From 560 m there was an increase in the deposition of low-temperature minerals, mainly in vesicles, most of them filled by opal, clays of the smectite group, calcite and zeolites of the heulandite type. Small veins filled with heulandite were also seen between 620 and 700 m.

Below 750 m there was a decrease in depositional alteration minerals both in vesicles and in veins. Small vesicles were filled with mixed layer clays and some veins with calcite. Then at 900 m the deposition increased again in vesicles and small veins which were filled with quartz, calcite and mixed layer clays. At 1000 m, the deposition of chlorite as vesicle fillings was observed. However, from 1040 to 1090 m deposition in veins and vesicles decreased again.

Between 1116 and 1242 m, a steady increase of high temperature alteration minerals was observed in small veins and vesicles, mainly calcite, pyrite and quartz. At 1240 m tiny vein fillings with wairakite and epidote were noted.

In core # 1 at 1501 m, most of the veins were filled with calcite, epidote, actinolite, wairakite, pyrite, and quartz. However, in core # 2 at 1750 m, there was a slight decrease in vein fillings compared to core # 1. The main veins were filled with calcite, quartz and iron oxides, which may infer cold water inlet into the geothermal system.

4.5 Alteration mineral zones

The mineralogical facies of Well SV-5A were determined through the hydrothermal alteration minerals observed by the three techniques (macroscopic, petrographic and x-ray diffraction) used for identification.

It is known that secondary minerals produced in a geothermal system are stable at certain pressures and temperatures (e.g. Browne, 1978; Franzson, 2013). That is why it is possible to determine the mineralogical facies that occur in a geothermal well and to estimate, according to the mineralogy assemblage, the temperature of the well.

The smectite-zeolite zone begins at 376 m and extends down to 750 m. This area is characterized by the presence of low-temperature minerals such as opal, clays of the smectite group, calcite and, towards the

bottom of that interval, by the appearance of low-temperature zeolites of the heulandite type. This assemblage of minerals suggests a temperature of approximately 40-180°C.

The mixed layer clay zone starts at 750 m and extends to 920 m. in this section we observe the development of the mixed layer clays together with calcite and, from 780 m, the appearance of quartz. The development of this assemblage of minerals indicates a temperature of >180°C.

The chlorite zone is characterized mainly by the appearance and development of chlorite, which begins to appear at 920 m according to the petrographic analysis. This is slightly higher than the X-ray diffraction analysis of chlorite, reflecting the details accounted for in the thin sections, which can be missed from the XRD. From 1000 m, sphene began to develop. A good association of the minerals chlorite, calcite, quartz, pyrite, sphene, and illite was observed. This association of minerals indicates a temperature of around 230°C.

The chlorite-epidote zone developed from 1200 to 1242 m (due to loss of circulation, it cannot be determined further down) and was characterized by the appearance of epidote, which is associated with chlorite, sphene, calcite, quartz, illite, wairakite, prehnite, and pyrite. According to this association of minerals, the estimated temperature should be around 240°C.

The epidote-actinolite zone was observed in core # 1 at 1501-1507 m, characterized by the appearance of well developed actinolite filling fractures. At this depth, the association of epidote, actinolite, wairakite, pyrite, quartz, calcite, and chlorite was found, which indicates a temperature of at least 280°C.

4.6 Mineral deposition sequence

The deposition of secondary minerals produced by hydrothermal alteration, induced by geothermal systems, depends largely on the fluid temperature. However, we know that during the development of a geothermal system, the chemical and physical properties of the fluid can vary with time; this is evidenced in the depositional sequence of the secondary minerals, which in turn is of great importance for recognising the current status of the system.

The analysis of the depositional sequence of secondary minerals from Well SV-5A was carried out by means of petrographic analysis and binocular analysis of the cuttings (Table 3).

TABLE 3: Depositional sequences of hydrothermal alteration minerals in Well SV-5A

Depth (m)	Depositional sequence	Filling type
400	Smectite-opal	Vein
460	Iron oxides-smectite-calcite	Vesicle
760	Iron oxides-mixed layer clays	Vesicle
760	Calcite-mixed layer clays	Vesicle
780	Smectite-mixed layer clays	Vein
970	Iron oxides-calcite-chlorite	Vesicles
1220	Chlorite-epidote	Vesicle
1240	Prehnite-epidote	Vesicle
1501	Calcite-quartz	Vein
1501	Calcite-wairakite-epidote	Vein
1501	Wairakite-epidote-actinolite	Vein

At the top of the well, where deposition of secondary minerals starts, vein fillings were observed with clays of the smectite group and opal, suggesting a sequence of low temperature minerals. In the intermediate part of the well, a relative evolution in the mineralogy was observed. In some vesicles deposition of calcite followed by mixed layer clays was noted, as well as iron oxides followed by mixed layer clays. At 780 m the deposition of smectite before mixed layer clay suggests increasing temperature.

At 970 m other mineral sequences could be seen which evidenced an increase in temperature, where some vesicles presented a deposition from iron oxides to calcite and finally chlorite. At 1240 m

deposition of prehnite, followed by epidote, was noted in vesicles, both high-temperature minerals reflecting a stable depositional system.

In core # 1 is an excellent deposition evidence of high-temperature minerals in the veins. At this depth, three main sequences were identified: the first with a deposition of calcite followed by quartz, the second deposition with calcite followed by wairakite and then epidote, and the third with deposition of wairakite followed by epidote and lastly actinolite. These depositions evidence a stable behaviour within the current geothermal system.

5. AQUIFERS

Well SV-5A crossed high permeability zones during drilling (Table 4). These total and partial losses were due to formation changes, fractures in the host rocks and were also associated with the geothermal reservoir (e.g. increased alteration and major faults). Figure 12 shows the lithology together with the experienced permeable zones in the well.

TABLE 4: Loss of circulation during the drilling of Well SV-5A

Stage	Depth (m)	Type of loss	Geological description
26"	93-94	PPC	Andesite scoreaceous oxidized
	95-96.5	PPT	Andesite scoreaceous oxidized
	96.5-100	PPC:	Andesite partially oxidized
	106.5-109.3	PTI	Andesite partially oxidized
17 1/2"	112.5-122	PTC	Andesite
	123	PPC	Andesite
	149-154.5	PTC	Andesite
	170-185	PTI	Andesite
	185.5-188	PPC	Andesite
	189-202	PTC	Andesite scoreaceous oxidized
	203-208	PPC	Andesite scoreaceous oxidized
	232-250	PPC:	Andesite scoreaceous oxidized
	250-256	PTC	Andesite
	262	PPC:	Andesite scoreaceous
12 1/4"	1094-1115	PTC	Andesite
	1116-1244	PPC:	Andesite
	1245-1798.5	PTC	Andesite

PTC: Total loss of circulation, PTI: total losses intermittent, PPC: Partial loss of circulation

In the first section of the 26" width, partial and total losses were associated with change in the lithology (e.g. scoria between lava flows). In the second section of the 17 1/2" width, partial losses were associated with formation changes and total losses were associated with fractures in the host rock. In the 12 1/4" production part of the well, total losses of circulation were associated with the geothermal reservoir.

For the determination of aquifers, temperature profiles from the well were used, from 7 to 81 days of thermal recovery (Figure 11). Based on the logs, it was concluded that the well crosses four hot aquifers, the first at 1100 m where there was total loss of circulation, coinciding with a sharp increase in the hydrothermal alteration.

At 1250 m there is another hot aquifer which coincides with total loss in circulation and, just before the loss of circulation, wairakite crystals were observed. Wairakite is associated with good permeability zones and aquifers (Reyes, 2000).

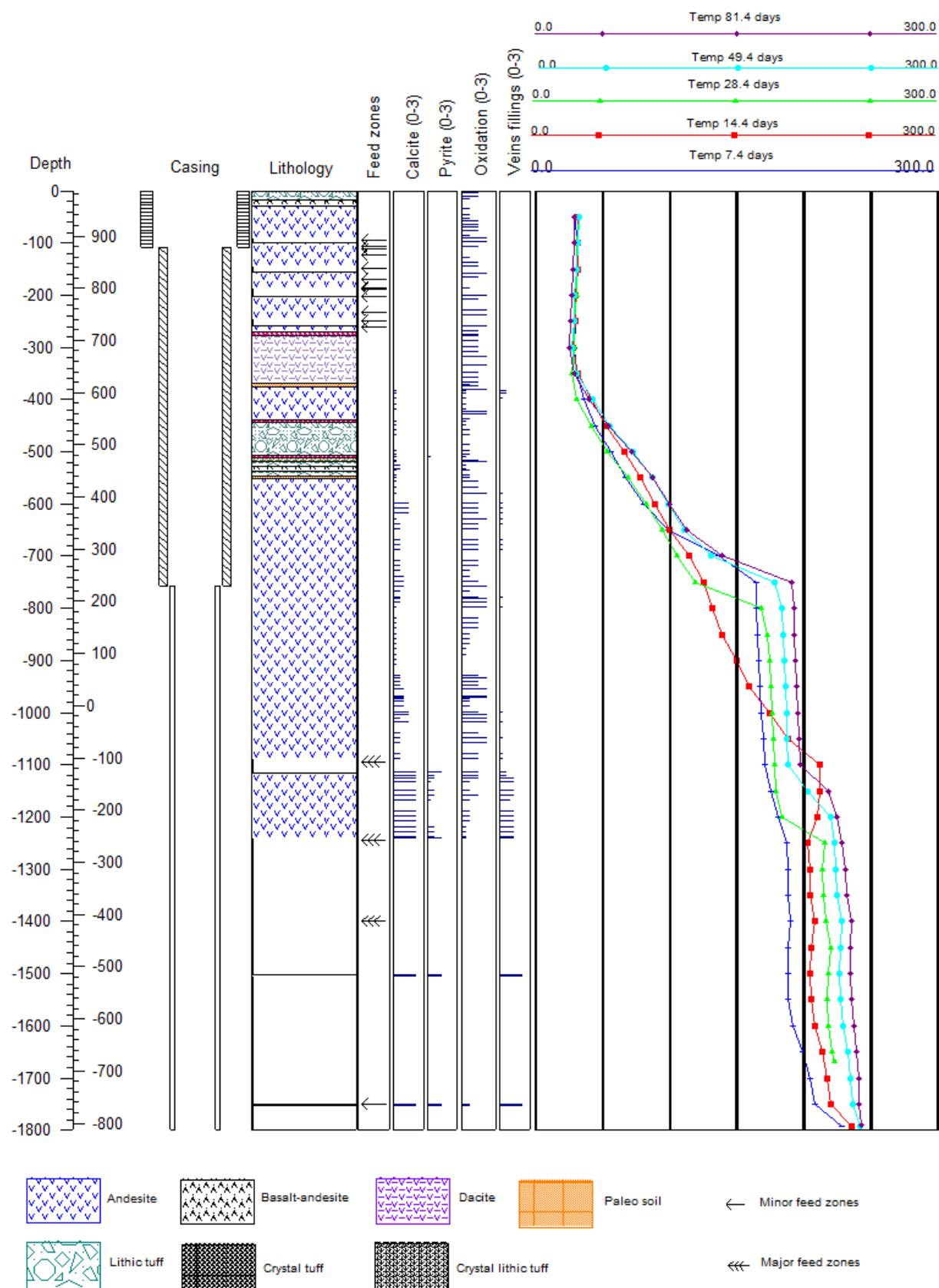


FIGURE 12: Lithology and permeable zones in Well SV-5A

At 1400 m another hot aquifer was observed, identified by means of temperature logs, where there is an input zone that continues to heat up. In this area, it was not possible to correlate with the alteration mineralogy because there were no cutting samples at this depth.

Towards the bottom of the well at 1750 m, yet another aquifer was observed in the temperature logs, which is evidenced in core # 2 by a breccia of faults. There are also many fractures found filled with high temperature minerals and with iron oxide of the hematite type as a last deposition.

The deposition of hematite in the fractures could indicate the presence of cold water. Cold water contains more oxygen than hot water and, upon contact with rocks, the process of oxidation between minerals and oxygen occurs, forming hematite in the fractures.

6. FLUID INCLUSIONS AND FORMATION TEMPERATURE

Fluid inclusions, trapped during the growth of minerals, provide important information on the temperature conditions in a geothermal system. Two main types of fluid inclusions from hydrothermal fluids exist: primary inclusions and secondary inclusions.

The primary inclusions are vapour and liquid portions trapped in the fluid during the crystallization of minerals, representing a small sample of the original hydrothermal solution of the geothermal system. The secondary inclusions were trapped after the growth of the crystal and formed in micro fractures and crystal imperfections. This type of inclusions is very important because it shows the current state of the geothermal system. When steam inclusions are heated and observed through a microscope, the vapour bubbles merge with the fluid (disappear) at a certain temperature and when this happens, the homogenization temperature has been obtained, giving information about the temperature at which the fluid was captured.

Fluid inclusions were analysed in two calcite crystals from core # 1 at 1501 m. A total of 70 fluid inclusions were analysed (Figure 13). The type of fluid inclusions in the crystals could, however, not be determined. It was not possible to analyse the crystals from the cuttings since the grains were too fine.

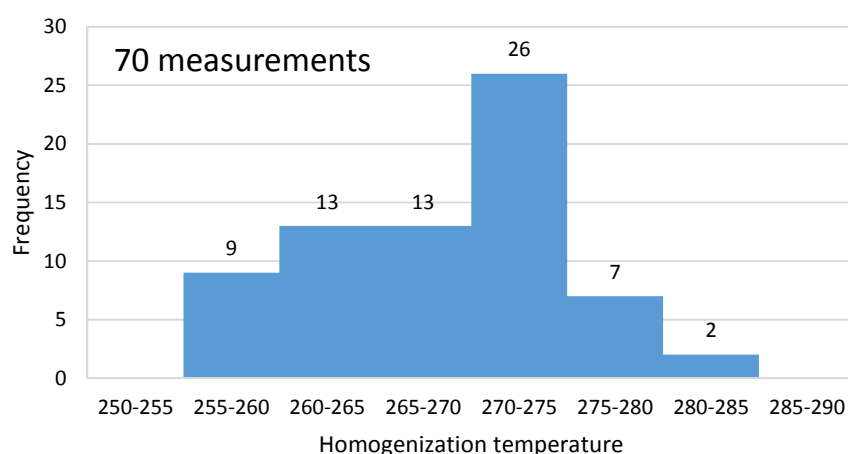


FIGURE 13: Fluid inclusion measurements from 1501 m depth in Well SV-5A

The homogenization temperature of the fluid inclusions ranged between 255 and 285°C. The highest concentration of measurements was in the range 270-275°C. Temperatures up to 285°C were measured, possibly indicating the initial fluid temperature, which is also supported by the appearance of actinolite, which forms at temperatures of 280°C. Furthermore, many

inclusions were measured ranging between 255 and 270°C, possibly reflecting a conductive cooling within the geothermal system. However, the homogenization temperature seems to be in balance with the deposition of alteration minerals, further suggesting that some cooling of up to 40°C has occurred in the system since the estimated formation temperature at that depth is somewhat lower than the alteration temperature (see Section 7).

7. DISCUSSION

The stratigraphy of Well SV-5A is based on the analysis of drill cuttings, consisting primarily of lava flows and some pyroclastic sequences. The identified rocks vary in composition from basaltic andesite, andesite, dacite and a variety of lithic tuffs, crystal tuffs and a combination of the two. This variety of rocks reflects an evolved magma chamber under the volcanic complex of San Vicente.

However, from 556 to 1800 m, a thick series of andesitic flows were observed, all very similar chemically and texturally. At 438-556 m there is a sequence of tuffs that possibly originated from the collapse of the old volcanic structure of San Vicente and, from 4 m down to 438 m, there are sequences of dacite lava flows. In the lower part of that depth interval, a lot of andesites with xenoliths of basic composition could be seen, possibly meaning that beneath the San Vicente volcano lies a large intrusive of basic composition that may have been emplaced just after the volcano collapsed.

Aquifers and feed zones were identified by means of temperature logs, an abundance of alteration minerals and circulation losses experienced during drilling. The aquifers found in Well SV-5A at the top are related to changes in the formation and with natural fractures in the lava flows. By contrast, the aquifers within the geothermal reservoir are associated with large faults, indicated by the loss of circulation at 1094 m which is associated with a fault zone identified at the surface by a digital elevation model. The aquifer is also associated with the abrupt change in alteration mineralogy observed at that depth. Furthermore, at 1750 m in core # 2, a highly faulted and fractured area was noted which corresponds to an aquifer identified by means of the temperature logs. In both zones, a large amount of wairakite was identified, which is associated with good permeability zones.

Evidence of hydrothermal alteration started at 400 m, where mainly low temperature minerals such as opal, clays of the smectite group and calcite were deposited and at 620 m the low temperature zeolite heulandite was observed. Below 750 m there was a change in the mineralogical temperature, with the appearance of mixed layer clays and quartz and, at 920 m, another change was seen with the appearance of chlorite and sphene. However, the most drastic change in the alteration occurred below 1094 m where a high temperature mineral association was observed with pyrite, calcite, quartz, chlorite, epidote, wairakite, prehnite, and sphene. The maximum alteration associated with the geothermal reservoir was found at 1500 m where core # 1 was obtained, where a mineral assemblage of 280°C was found with the appearance of actinolite together with epidote, wairakite, quartz, chlorite, calcite, and pyrite. This distribution of alteration minerals, from low temperature minerals increasing with depth to high temperature minerals which appeared towards the bottom of the well, indicates a progressive increase in the deposition of these minerals.

In accordance with the mineralogical assemblage and the first appearance of certain temperature dependent minerals such as quartz, chlorite, epidote, and actinolite, it was possible to define five alteration zones: from 376 to 750 m the smectite-zeolite zone; from 750 to 920 m the mixed layer clay zone; from 920 to 1200 m the chlorite zone; at 1200 m the chlorite-epidote zone appeared; and at 1500 m the epidote-actinolite zone. These alteration zones reflect a normal deposition in the geothermal system, and the occurrence of high temperature minerals such as epidote, actinolite, wairakite, and prehnite suggest temperatures up to 280°C.

The analysis of fluid inclusions suggested temperatures up to 280°C, which is consistent with the alteration minerals found in the well, specifically in core # 1, where actinolite was identified. However, when these results are compared with the 240°C formation temperature measured in the well, a cooling of around ~40°C was noted. Figure 14 suggests that the temperature is at equilibrium down to 750 m and, below this depth, an imbalance between the alteration mineralogy and the formation temperature can be seen.

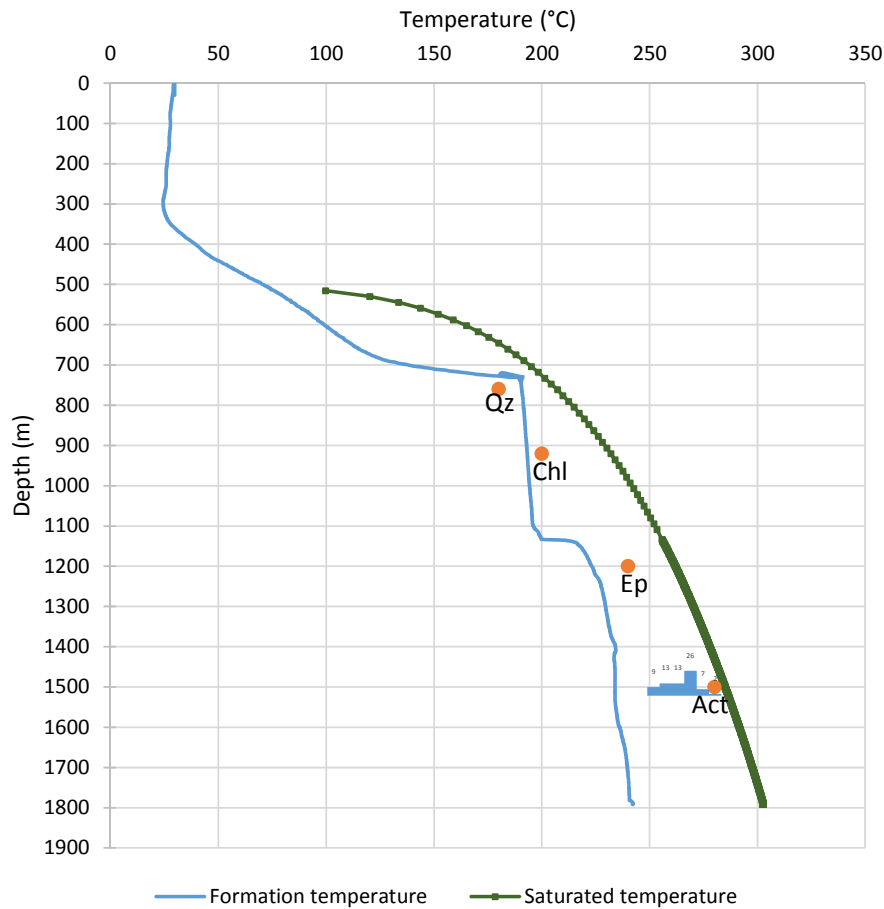


FIGURE 14: Comparison of the fluid inclusion, formation temperature, boiling curve and alteration minerals of Well SV-5A

8. CONCLUSIONS

- The lithology of Well SV-5A is composed of lithic tuff, crystal tuff, crystal lithic tuff, andesite, basalt-andesite, and dacite.
- According to binocular and petrographic analyses, the depositional sequence of alteration minerals in vesicles and veins show a normal gradation of hydrothermal alteration minerals from low- to high-temperature.
- Five alteration zones were identified, based on the hydrothermal mineral assemblages: from 376 to 750 m, the smectite-zeolite zone; from 750 to 920 m, the mixed layer clay zone; from 920 to 1200 m, the chlorite zone; from 1200 to 1242 m, the chlorite-epidote zone; and from 1500 m, the epidote-actinolite zone.
- The permeability at the top is controlled by fractured formations and lithological contacts between formations.
- The permeability within the geothermal reservoir is mainly associated with fractures and fault zones, where an increase in high temperature alteration mineralogy was observed as well as with a general high abundance of pyrite and calcite.
- The fluid inclusions at 1501 m depth reflect temperatures between 255 and 280°C, which are in concordance with the alteration mineralogy, reflecting temperatures of 280°C as seen by the appearance of actinolite.
- According to the calculated Horner temperature, the well should reach a temperature of 245°C, reflecting a cooling of ~40°C in the geothermal system.

ACKNOWLEDGEMENTS

I want to especially thank my employer, LaGeo S.A de C.V., for giving me the opportunity to attend this training to strengthen my knowledge for the near future. My most sincere thanks go to Dr. Ingvar B. Fridleifsson and Mr. Lúdvík S. Georgsson, directors of the United Nations University Geothermal Training Programme (UNU-GTP), for inviting me and giving me the opportunity to participate in this course. Thanks go to the staff of the UNU-GTP, Ms. Thórhildur Ísberg, Ms. Málfríður Ómarsdóttir, Mr. Markús A. G. Wilde and Mr. Ingimar G. Haraldsson, for all their assistance during the training, their patience and the help they gave me during my stay in Iceland. I want to give special thanks to my supervisors, Ms. Helga Margrét Helgadóttir, Ms. Anette K. Mortensen, Dr. Björn S. Hardarson and Dr. Hjalti Franzson for their dedication, availability, support and guidance while working on this report. My sincere gratitude goes to all the staff of Iceland GeoSurvey (ÍSOR) and other professionals who gave lectures during this training, for passing on their knowledge and for always being available when needed.

I want to thank all 2013 UNU fellows for an unforgettable time during these six months, especially Angel Monroy, Idalia Matus and my borehole geology group: Tito, Loyce and Joyce for all the discussions and the fun times we had together.

This report is dedicated with all my love to my family, most especially to my beloved husband, Raymundo Quintanilla, for giving me all his love, support and wise counsel, my mother Luz Argentina Lopez Herrera for giving me her support and unconditional love, my brothers Javier Antonio, Christian D. and Christian M., my sisters of heart, Maria Jose, Margine, Nohelia and Marjorie for forever being with me when I needed them the most, and for their support and unconditional friendship.

REFERENCES

- Agostini, S., Corti, G., Doglioni, C., Carminati, E., Innocenti, F., Tonarini, S., Manetti, P., Di Vincenzo, G., and Montanari, D., 2006: Tectonic and magmatic evolution of the active volcanic front in El Salvador: insight into the Berlin and Ahuachapán geothermal areas. *Geothermics*, 35, 368–408.
- Browne, P.R.L., 1978: Hydrothermal alteration in active geothermal fields. *Ann. Rev. Earth and Planet. Sci.*, 6, 229–250.
- Carr, M.J., Mayfield, D.G., and Walker, J.A., 1981: Relation of lava compositions to volcano size and structure in El Salvador. *J. Volcanol. Geotherm. Res.*, 10, 35–48.
- CEL, 1992: *Partial synthesis of the volcanologic area, San Vicente geothermal field*. CEL, Geothermal Division, Santa Tecla, El Salvador, internal report (in Spanish).
- CNE, 2012: *Master plan for the development of renewable energy in the republic of El Salvador*. CNE, direccion de desarrollo de recursos renovables, internal report (in Spanish).
- Corti, G., Carminati, E., Mazzarini, F., Garcia, M.O., 2005: Active strike-slip faulting in El Salvador (Central America). *Geology*, 33, 989–992.
- Franzson, H., 2013: *Borehole geology*. UNU-GTP, Iceland, unpublished lecture notes.
- German Geological Mission, 1970: *Geological map of El Salvador*. Webpage: www.snet.com.sv
- LaGeo, 2005: *Geological exploration report on geothermal field of San Vicente*. LaGeo S.A de C.V., geological Department, Santa Tecla, El Salvador, internal report (in Spanish).
- LaGeo, 2013a: *Drilling report on well SV-5A*. LaGeo S.A de C.V., Drilling Department, Santa Tecla, El Salvador, internal report (in Spanish).
- LaGeo, 2013b: *Geological report on well SV-5A*. LaGeo S.A de C.V., Geological Department, Santa Tecla, El Salvador, internal report (in Spanish).

Markússon, S., and Stefánsson, A., 2011: Geothermal surface alteration of basalts, Krýsuvík Iceland- Alteration mineralogy, water chemistry and the effects of acid supply on the alteration process. *J. Volcanol. Geotherm. Res.*, 206, 46–59.

Martínez-Díaz, J.J., Alvarez-Gómez, J.A., Benito, B., and Hernández, D., 2004: Triggering of destructive earthquakes in El Salvador. *Geology*, 32, 65–68.

Reyes, A.G., 2000: *Petrology and mineral alteration in hydrothermal systems: from diagenesis to volcanic catastrophes*. UNU-GTP, Iceland, report 18-1998, 77 pp.

Rotolo, S.G., and Castorina, F., 1998: Transition from mildly-tholeiitic to calc-alkaline suite: the case of Chichontepec volcanic centre, El Salvador, C. America. *J. Volcanol. Geotherm. Res.* 86, 117-136.

APPENDIX I: Characteristic XRD patterns for the clay minerals of Well SV-5A

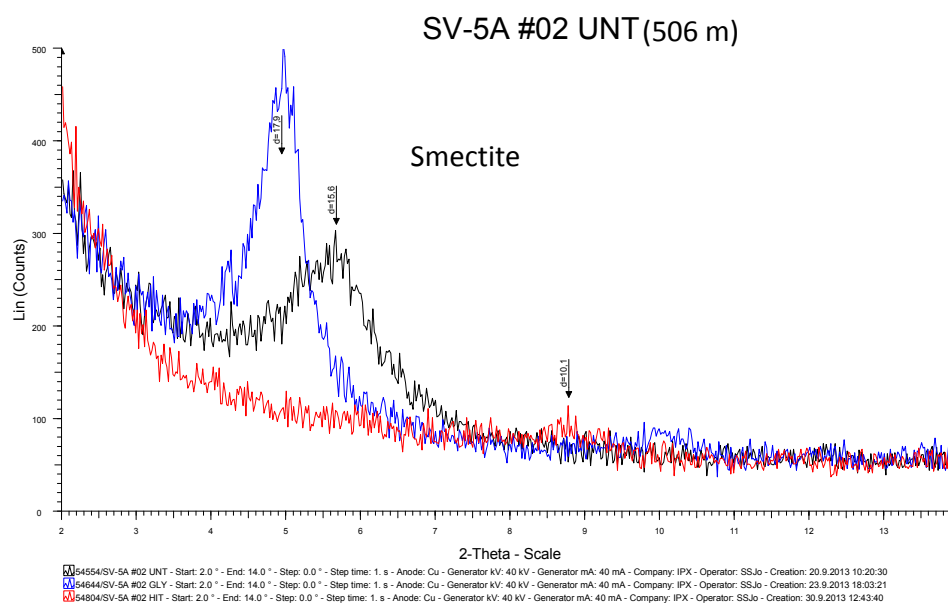


FIGURE 1: XRD analysis showing presence of smectite

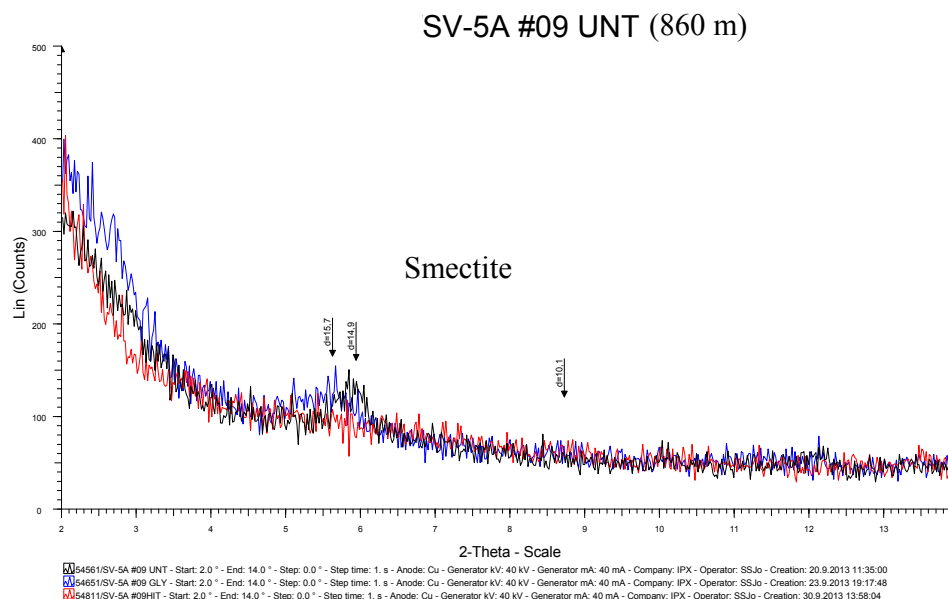


FIGURE 2: XRD analysis showing presence of smectite

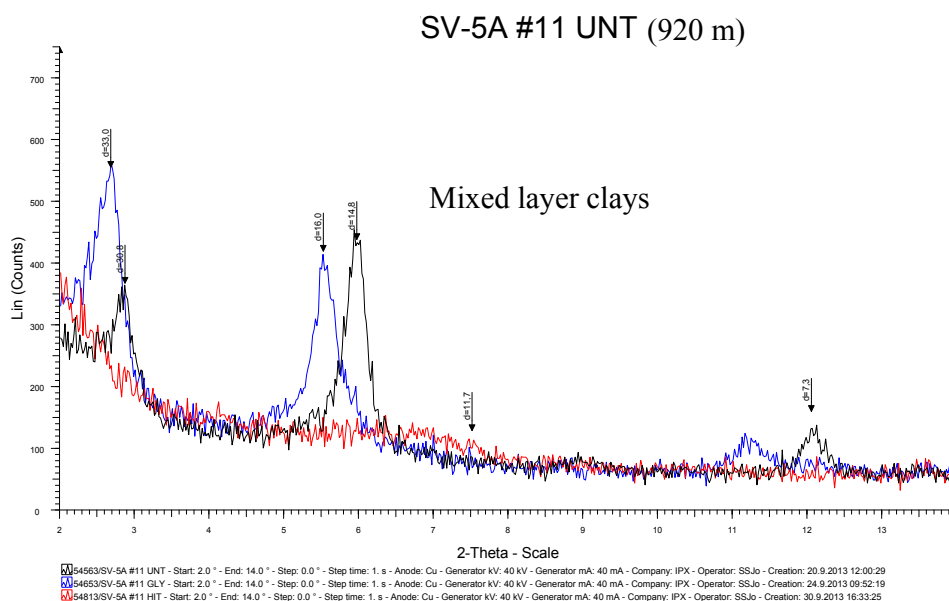


FIGURE 3: XRD analysis showing presence of mixed layered clays

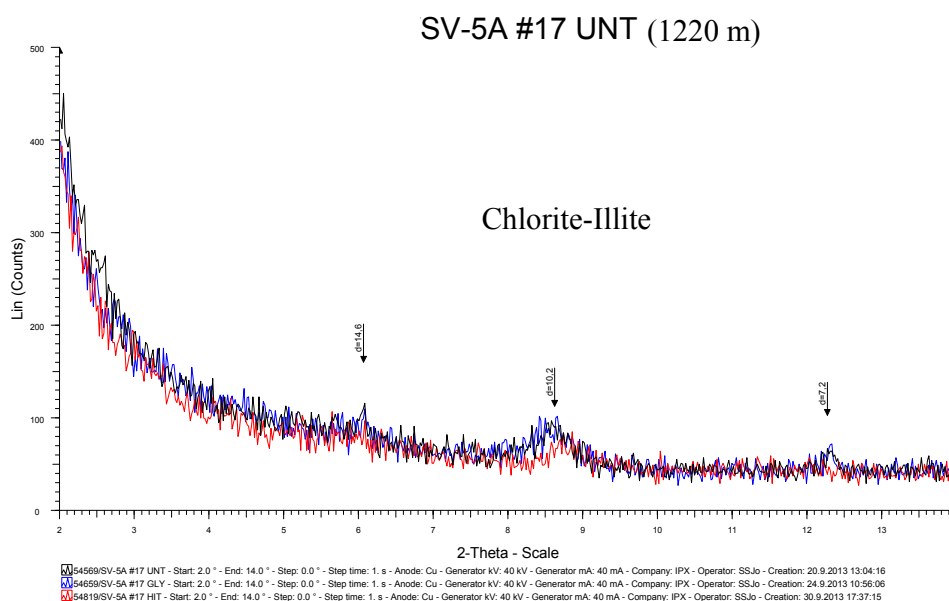


FIGURE 4: XRD analysis showing presence of chlorite and illite



ANALYSIS OF GEOTHERMAL CASING THINNING RATE OF LEYTE GEOTHERMAL PRODUCTION FIELD

Anthony S. Ponce

Energy Development Corporation - EDC
38/F One Corporate Center Building
Julia Vargas corner Meralco Avenue
OrtigasCenter, Pasig City, 1605
PHILIPPINES
ponce.as@energy.com.ph

ABSTRACT

Corrosion is one of the technological problems that geothermal management faces in the operation of geothermal wells. The primary cause of corrosion in geothermal wells is exposure to geothermal brine where conductive and convective heat transfer happens from the reservoir to the surface. The geothermal well supplies the motive two-phase steam fluid from the reservoir to the surface fluid collection facility, and then to the separator where steam is separate from brine. The casing of the well is the first equipment that encounters the field's geothermal fluid. The flow of geothermal brine from the reservoir causes the casing to deteriorate by way of corrosion. The impact of turbulence, corrosion and erosion significantly reduce the integrity of the casing. Thus, monitoring these facilities is vitally important to minimize the risks to geothermal operations. Caliper measurements are taken to monitor the thickness of the casing for safety and environmental concerns. The effective management of a geothermal well necessitates a very thorough knowledge of the extent to which the aforementioned factors contribute to casing degradation. In this paper, the contribution of factors affecting the thinning rate of a geothermal casing, such as temperature, flow velocity, pH, well geometry and corrosion species, was studied. The effects of several corrosive species on casings were also studied. The corrosive species and the factors affecting the thinning rate of the production wells of the Leyte geothermal production field were analysed with multiple linear regression models in order to determine the dependency of the thinning rate on these parameters. Fluid discharge measurements and sampled chemistry concentrations at the surface were simulated at downhole conditions using software HOLA and WATCH. The results were analysed statistically using ANOVA, a P value test, and multiple regression coefficients. Adjusted R^2 of the regression analysis and mean absolute percentage error (MAPE) aided in selecting a good regression model. The study showed that fluid discharge characteristics such as temperature, velocity, pH, steam fraction and geometry of the well contribute about 56.71% to the thinning rate of the casing. The predicted thinning rate model also shows similar trending of the average thinning rate compared to the measured thinning rate for the first and second surveys of repeatedly measured wells.

1. INTRODUCTION

The objective of this study is to determine the significant factors and corrosive species that predominantly affect the thinning rate of production casing and to predict the thinning rate of the casing. This study is relevant in putting in place a systematic program for monitoring the casing conditions of a geothermal well. This study aims to provide an idea on the average thinning rate of the casing based on surface measured data of the well. The results of the study may also help to prioritize wells by programming caliper measurements for monitoring the rate of corrosion in the well casings. The study is limited to the production wells of Leyte geothermal production field (Figure 1) and concentrate only on the internal corrosion of the well.

After a geothermal production well is drilled and utilized to extract heat energy from a reservoir, certain problems occur and one of these problems is corrosion. Casing corrosion is one of the challenging technological problems in managing a geothermal production field. Scaling is another technological problem during geothermal utilization.

Geothermal fluids contain CO_2 , H_2S , NH_3 and chloride ions that can cause the corrosion of metallic materials. The fluid characteristics change over time as heat extraction takes place. Thus, it is important to put in place a systematic procedure for monitoring the fluid chemistry of every geothermal well in operation.

The casings of geothermal wells, when exposed to the flow of geothermal brine flow, experience thinning. The thinning of the casing, primarily a result of material loss, compromises the casing's

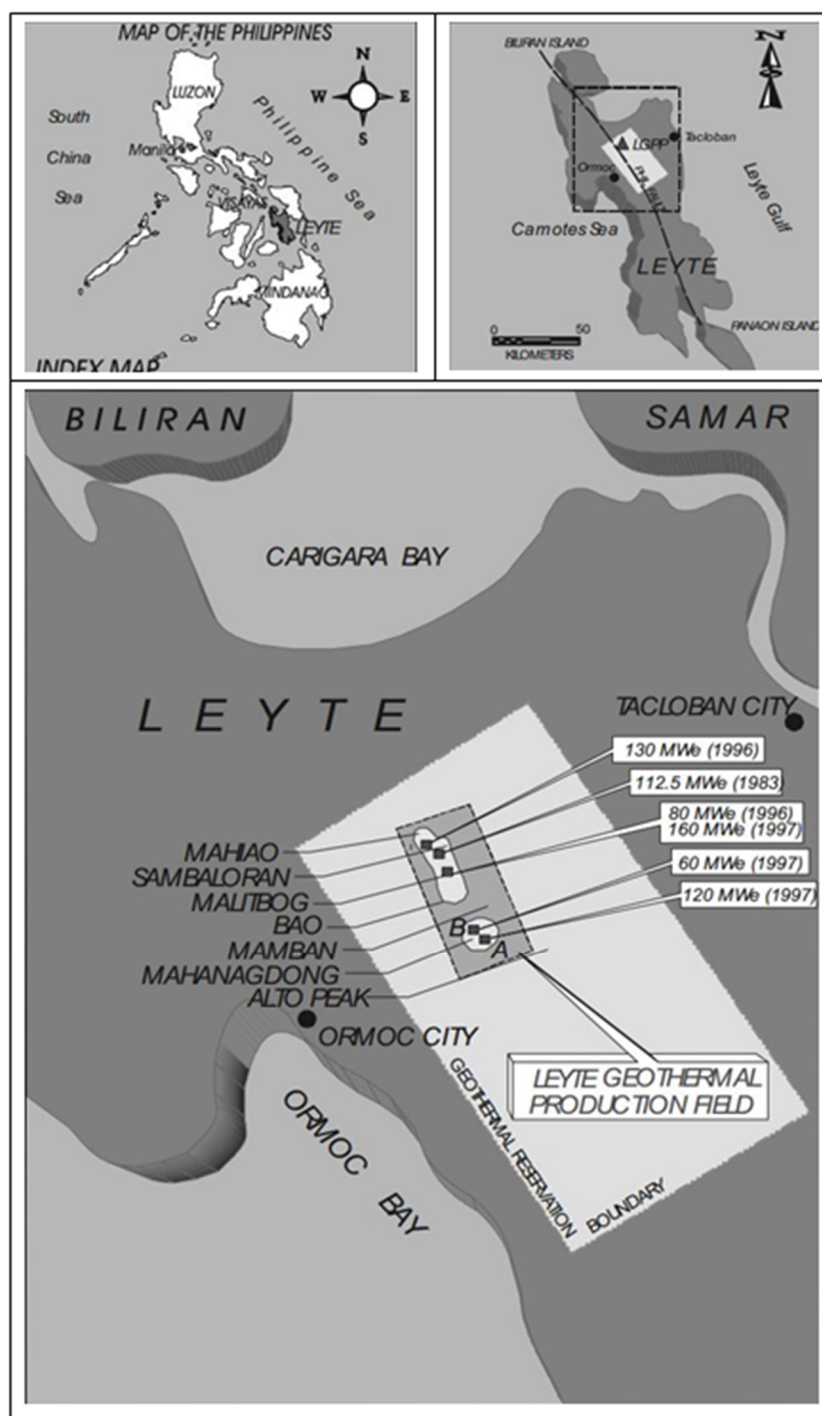


FIGURE 1: Location map of Leyte geothermal production field

integrity; this may eventually lead to casing breaks and casing collapse and, consequently, a reduction of well output. Casing breaks at shallow depths may cause steam to leak into the formation and within the pad. The steam leak within the overlap of the anchor casing and the production casing may lead to an underground blowout. The high risk involved with unreliable casing conditions requires systematic monitoring of the casing's integrity. This is for environmental and safety concerns and to ensure continuous geothermal well operation. The integrity of the casing is inspected by using downhole-logging tools such as caliper tools, electromagnetic tools, acoustic tools or video cameras; these tools are used to examine the condition of the casing.

The production casing in the geothermal fields of Cerro Prieto in Mexico experienced serious corrosion, both internal and external, after several years of production. To some extent, due to the extent of the corrosion of the casing, modifications, of both the grades of steel used and the thickness of the casing, were implemented in order to prolong usage of the well. In cases where the corrosion was extensive, the casings lasted only for two and a-half years after utilization (Ocampo-Diaz et al., 2005).

In the Krafla geothermal field, the carbon steel liner at the bottom of Well KJ-39 fractured and was severely corroded, caused by the aggressive nature of the fluid. Metallurgic examination of the liner indicated damage due to hydrogen embrittlement. Karlsdóttir and Thorbjörnsson (2012) found that abrupt changes in the environment had occurred at 1600 m, resulting in damage to the liner. The changes were a result of mixing two different transition systems: very hot dry steam containing H_2S , CO_2 and HCl , flowing upward; and a colder two-phase fluid. The mix resulted in a highly acidic fluid at the transition point.

A casing inspection caliper checked the condition of the casings of the production wells in the Leyte geothermal production field (Figure 1). In the Mahanagdong sector, the brine produced from the production wells has a very low pH. Hence, periodically, and using caliper surveys, the well casings were monitored for thinning. After several years of utilization, one of the production wells in the Mahanagdong area was plugged and then abandoned; the cause was severe corrosion.

The high-enthalpy single-phase steam-dominated wells of the Leyte geothermal production field were monitored using caliper measurements. There is severe corrosion in these wells because of the presence of a high quantity of suspended solids. The results of the caliper surveys served as a baseline for well utilization and intervention strategies in order to mitigate further deterioration of the casings.

The data, from the caliper surveys of production wells in Leyte geothermal production field, were used to study the thinning rate of the casings. The characteristics of the fluid discharge, such as fluid velocity, temperature, pH, and fluid chemistry concentration, were used to study the effects of the thinning rate on the casings.

2. CORROSION IN GEOTHERMAL WELLS

Corrosion is a damaging occurrence due to chemical or electrochemical action on the surrounding environment. It is detrimental to the appearance of metals and causes degradation of the equipment and material failure if kept unchecked. The corrosion process may assume several forms. On the overall surface of the metal, the reaction takes place slowly and reduces the thickness of the metal. In isolated areas, the corrosion may be localised. In some cases, the corrosion occurs on the weakest part of the metal where a difference in resistance to corrosive destruction is present. The differences in resistance in the metals are due to impurities and possible non-uniform treatment of the metal during manufacturing.

In a geothermal environment, the corrosion process depends upon the chemical composition of the geothermal fluid or brine. The geothermal brine has a wide range of composition, from strongly acidic

brine that corrodes most common alloys to the more usual neutral pH waters that may lay protective scales on the metal's surface (Elguedri, 1999).

In a high-temperature geothermal field, brine flashes inside the wellbore and changes from single-phase to two-phase due to the drop in pressure while the well is being flowed. Wahl (1977) discussed the effect of flashing on brine composition as the geothermal well produces steam. The flashing of the brine causes two main changes on the chemical concentration. First, evaporating some of the water in the brine achieves a higher concentration of the remaining components while the brine is flashed at a sufficiently low pressure. The ratio of the brine between after flashing and before flashing is dependent upon the weight fraction of the water flashed. Second is the effect of flashing on the chemistry of the brine. Flashing removes certain constituents such as carbon dioxide or hydrogen sulphide. As carbon dioxide is the dominant gas in the fluid mix, this will have the most significant effect on the chemistry of the fluid. The effect of CO₂ release is, in principle, the change in fluid pH. The next most significant is the reduction of dissolved CO₂ in the brine. When CO₂ dissolves in water, a small portion of it reacts chemically with H₂O to form carbonic acid. In water, carbonic acid dissociates rapidly to form H⁺ ion and HCO₃⁻, so it affects carbonate equilibrium and pH values change as a result. The release of CO₂ from the solution will result in release of carbonate ions, causing the pH of the fluid to increase.

2.1 Corrosive species in geothermal brine

There are key chemical species that produce significant corrosion effects on metallic materials. Conover, et al. (1979) generalized the corrosive effects of these chemical species:

- *Hydrogen ion (H⁺)* - Increasing the concentration of hydrogen (decrease in pH) will result in an increase in the rate of general corrosion for carbon steel, especially when fluid has a pH below 7. The metal in a fluid with pH higher than pH 7, (low concentration of hydrogen ion), forms a protective layer or film which minimizes the rate of corrosion. However, when the protective layer is broken, serious localized corrosion occurs which can cause pitting, crevice corrosion and stress corrosion cracking.
- *Chloride ion (Cl⁻)* – The chloride ion causes the local breakdown of passive films that protect the metal from uniform corrosion, thus resulting in pitting, crevice corrosion, or stress corrosion cracking. An increase in chloride concentrations can also lead to an increase in uniform corrosion, but this is not as critical as the localized effect.
- *Hydrogen sulphide (H₂S)* – This corrosive specie is more severe for copper and nickel alloys. The effect of H₂S on iron-based materials is less predictable. It accelerates corrosion on the metal but, in some cases, it inhibits corrosion. High strength steels are often subject to sulphide stress cracking, which is a form of hydrogen embrittlement. The oxidation of hydrogen sulphide, in aerated geothermal process streams, increases the acidity of the streams. A low concentration of hydrogen sulphide may have serious detrimental effects, especially when oxygen is present.
- *Carbon dioxide (CO₂)* – In the acidic region, i.e. as in carbonic acid (H₂CO₃), it can accelerate the uniform corrosion of carbon steel. Carbon dioxide largely controls the pH of geothermal fluids and process streams. Carbonates and bicarbonates can display mild inhibitive effects.
- *Ammonia (NH₃)* – It can cause stress corrosion cracking of copper alloys and accelerate uniform corrosion in mild steels.
- *Sulphate (SO₄⁻)* – It plays a minor role in most geothermal fluids. However, in low chloride fluids, sulphate becomes the main aggressive anion; it rarely causes the same severity of the localized corrosion as the chloride ion.
- *Oxygen (O)* – Oxygen is present in low concentrations in geothermal brine. Inadvertent intrusion of even traces of this gas into geothermal brine has led to serious accelerated corrosion. The addition of minor quantities of oxygen to a geothermal system can increase the chances of severe localized corrosion of normally resistant alloys. The corrosion of carbon steels is sensitive to trace amounts of oxygen.

- *Transition metal ions* – Transition metal ions could also be included as a key species. Some oxidized forms of transition metals (Fe^{3+} , Cu^{2+} and others) are corrosive, but these ions are present in the lowest oxidized state in geothermal fluids. When transition metals are exposed to oxygen by aeration or mixing with water of different quality, oxygen can convert Fe^{2+} to Fe^{3+} , which is another reason for scrubbing oxygen from geothermal streams.

2.2 Types of corrosion encountered in geothermal systems

There are several types of corrosion attacks found in equipment used in a geothermal environment (Conover, et al., 1979). Some of the main modes of corrosion that occur in geothermal systems are as follows:

- *Uniform corrosion*. It is a general overall attack on the metal surface, often promoted by chloride, carbon dioxide, oxygen or ammonia.
- *Pitting*. This type of corrosive attack is localized which results in the development of small pits in the metal surface. Pits are associated with the breakage of the protective film on the surface of the metal. It is susceptible to increases in the chloride and hydrogen ion content of the fluid.
- *Crevice corrosion*. It is a localized type of corrosion, similar to pitting. This depends on geometry and forms in the crevices of the equipment.
- *Stress corrosion cracking*. This is a catastrophic type of failure promoted by a combination of tensile stress and the presence of chloride in the environment. The severity of the stress corrosion cracking increases with increasing temperature and in the presence of oxygen.
- *Sulphide stress cracking*. Similar to stress corrosion cracking, sulphide stress cracking is also a catastrophic type of failure that results from exposure under stress of susceptible materials to a hydrogen sulphide environment in an aqueous phase. Contrary to the stress corrosion cracking, sulphide stress cracking decreases in severity with increasing temperature, but low pH may greatly accelerate the failure.
- *Hydrogen blistering*. This is the rupture of a metallic material, caused when hydrogen is trapped in voids and accumulates at a sufficient pressure. This occurs in low strength alloy steel in aqueous solutions containing hydrogen sulphide. The material does not need to be stressed in order for hydrogen blistering to occur.
- *Intergranular corrosion*. This is a regional type of corrosion, which occurs around grain boundaries, or in the neighbour grains of metallic materials, with little or no attack on the bodies of the grains. The alloy disintegrates, loses its strength, or both.
- *Galvanic corrosion*. It occurs by electrical conduction of two different metals. The corrosion of a less noble material accelerates in this kind of corrosion. During material selection, the order of the galvanic series is a reference used for preventing galvanic corrosion.
- *Fatigue corrosion*. This is a premature fracture caused by fluctuating stress exposed in a corrosive environment. The fatigue corrosion limit is the largest stress applied under a given condition of stress, temperature, and corrosive environment, without causing the material to fail for a given number of cycles.
- *Erosion-corrosion*. It is the accelerated corrosion of one metal exposed to a corrosive fluid. This occurs when fluid flows faster than the critical velocity familiar to that metal. It is the abrasion of the metallic material by high velocity fluids on the hanging solid materials or particles. Metal exposed to this kind of corrosion does not form corrosive products on its surface.

2.3 Other factors affecting the rate of corrosion

Aside from the chemical species present in geothermal fluids that significantly affect the rate of corrosion of metal, there are other factors. Some of these other factors lead to types of erosion-corrosion,

where fluid contacts the metallic material and damages the protective film created from the initial corrosive reaction. These factors are related to hydrodynamic parameters such as the temperature, pH, fluid velocity, two-phase flow quality, geometry of the flow, and the pipe material component, which influence the erosion-corrosion mechanism (Petric and Ksiazek, 1997). Several studies and laboratory experiments have concentrated on the effect of environmental factors on the corrosion of materials.

Effect of pH. Low pH affects the uniform corrosion rate of low carbon and low alloyed steels. According to Ikeuchi et al. (1982), the corrosion rate of a material is: a) inversely proportionally to pH when the pH is in the range of 1 to 4 due to the active dissolution of materials; and b) is independent of pH when pH is in the range of 4 to 10. In flow accelerated corrosion, as the hot pH in the system become more acidic, the relative rate increases. The influence of pH on the erosion-corrosion is more serious than on corrosion alone.

Effect of velocity. According to Sanada et al. (1998), the rate of corrosion is independent of the flow rate when the flow rate ranges from 70 to 100 m/s. However, as the velocity increases, the corrosion rate increases. When the velocity approaches the velocity of sound, the material is damaged remarkably by cavitation-erosion (Ikeuchi et al., 1982).

Effect of temperature. Rates of corrosion are significantly dependent on temperature (Sanada et al., 1998). The effect of temperature is high for alloys that have intermediate performance. However, the pH still has the dominant effect on the rate of corrosion.

Effect of pipe geometry. Shape and size of a piping geometry has a significant impact on flow-accelerated corrosion. This factor affects localized velocities and turbulence within the pipe component. A complex geometry could increase the localized velocity in a given section by two to three times compared to the bulk velocity (Petric and Ksiazek, 1997).

Effect of fluid quality. In a two-phase flow, the fluid flows along the pipe wall. The temperature and pressure determine the amount of steam, according to the mass fraction of the quality of the water/steam mixture. The steam quality determines the distribution of the voids within the flow stream; that distribution, in turn, affects the mass transfer and rate of the flow-accelerated corrosion.

Effect of metal alloy content. The amount of alloy material present in the metal affects the stability and solubility of the oxide layer on the surface. Traces of molybdenum, copper and particularly chromium can have a significant impact on the rate of corrosion. The influence of pH on the rate of corrosion in a two-phase fluid shows the dependence of a material's composition on pH, as shown in the experiment by Sanada et al., (1995), wherein carbon and low alloy steels severely corroded at a pH less than 3.5.

3. GEOCHEMISTRY OF THE PHILIPPINE GEOTHERMAL FIELDS

The downhole pH and sulphur chemistry, as a function of boiling point temperatures, were determined for a number of wells from different fields; these could be linked to the sulphide mineralogy of rocks recovered from the acid Cl-SO₄ wells (Lichti et al., 1998). The produced fluids are classified as three types: low CL, high SO₄ with Na+K>Cl; high Cl, high SO₄ with CL>Na+K; and high Cl, high SO₄ with Na+K>Cl.

The Leyte geothermal production field in North Central Leyte is the largest geothermal area in the Philippines. It is a liquid-dominated high temperature geothermal field and its brine has neutral to low pH. The brine from the Mahanagdong sector of the Leyte geothermal production field has a pH ranging from 3 to 8, based on actual samples taken from the wells. It is inferred that the temperature of the aquifers in Mahanagdong ranges from 250 to 300°C; the aquifers have higher concentrations of H₂S and H₂ in the initial aquifer fluids (which are assumed to be purely liquid), than those at equilibrium with

the hydrothermal mineral assemblage (Angcoy, 2010). The Mahanagdong field discharges low pH fluid with high salinity and has either high or low sulphate concentrations. The reservoir fluids with high sulphate acidic fluids have a high concentration of the HSO_4 species that dissociates at a lower temperature, resulting in an acidic fluid discharge at the wellhead (Cabahug and Angcoy, 2013).

4. RESEARCH METHODOLOGY

4.1 Data preparation

The data obtained from the casing inspection caliper runs, conducted on geothermal wells of Leyte geothermal production field, were used for statistical analysis. The thinning rate (TR) of the casings was calculated using Equation 1, based on the measured pit depth, obtained from the multifinger arm caliper tool. Table 1 summarizes the caliper survey conducted on the two-phase and dry wells of the Leyte geothermal production field.

$$TR = \frac{\text{pitdepth (mm)}}{\text{time (years)}} \quad (1)$$

TABLE 1: Summary of the caliper survey conducted on the two-phase and dry wells of Leyte geothermal production field

	Two-phase wells	Dry wells
No. of wells surveyed	19	16
Length of cased hole	739 - 1948 m	475 - 1657 m
Casing diameter	177.80 - 339.73 mm	244.48 - 339.73 mm
Total mass flow	5-55 kg/s	3 - 25.2 kg/s
Enthalpy	1056 -2536 kJ/kg	~ 2700kJ/kg

The multi-finger caliper used is the memory type 30-finger arms caliper shown in Figure 2. Its 30-feeler arms record the radii of the casing and provide a complete representation of the well casing condition. The mechanical caliper is among the simplest and most accurate tools available on the market for measuring the internal diameter of the casing. It is useful for analysing internal corrosion damage, scale build-up, collapsed and parted casing breaks. The tool consists of a centralizer to put the tool in-centre inside the casing, and a caliper finger arm, which reaches out to the inside of the casing wall. Caliper finger arms are made of tungsten carbide, tipped for wear. A mechanical tripper opens the memory-type caliper tool. From the 30 radii recorded, the maximum measured inner diameter of the casing was used to represent the minimum thickness of the casing at depth.



FIGURE 2: Photo of a 30-arm Multifinger caliper tool

The downhole temperature, fluid velocity, and steam fraction were obtained by wellbore simulation, using the software package, HOLA. HOLA reproduces the measured flowing temperature and pressure profiles in flowing wells and determines the relative contribution of each feedzone for a given discharge condition (Björnsson et al., 1993). The simulator can handle both single and two phase flows in vertical pipes and calculates the flowing temperature and pressure profiles in a well. It solves numerically the differential equations that describe the steady-state energy, mass and momentum flow in a vertical pipe.

The flow within the well was assumed to be in steady state at all times, but the reservoir pressure was allowed to vary with time. Top-down simulations were conducted where the downhole well conditions were simulated based on given wellhead conditions, such as mass flowrates and enthalpy values. There was no comparison made between the simulated temperature and pressure profiles and the measured flowing temperature and pressure profiles of all the wells, because flowing surveys were not available for all of them. To simplify the simulation process and since the cased hole section is the main point of interest, it was assumed that the depth of the feedzone was at the production casing shoe with the properties of the flow discharge. Table 2 shows the well discharge data used at wellhead conditions, while Table 3 summarizes the simulated downhole results given by HOLA.

TABLE 2: Fluid discharge data of two-phase and dry wells studied for predicting the thinning rate of the casing

Well name	Date sampled	WHP	MF	H	Well name	Date sampled	WHP	MF	H
Well 1	6-May-12	1.10	48.5	1736	Well 20	30-Oct-11	1.1	18.4	2779
Well 2	11-May-11	1.10	4.7	2435	Well 21	4-May-11	1.0	7.5	2777
Well 3	4-Nov-10	1.10	36.8	1687	Well 22	15-Sep-11	1.0	6.8	2777
Well 4	8-Dec-11	1.10	28.0	1611	Well 23	23-Jul-11	1.0	16.7	2777
Well 5	27-Nov-10	1.10	24.0	1632	Well 24	26-Jan-12	1.0	3.0	2777
Well 6	22-Aug-12	1.1	55.2	1056	Well 25	28-Apr-11	1.5	19.1	2788
Well 7	3-Apr-12	1.1	40.6	1085	Well 26	2-Sep-11	1.8	20.0	2796
Well 8	30-Oct-10	1.1	50.6	1315	Well 27	13-Sep-11	1.23	25.2	2787
Well 9	11-Nov-10	1.1	54.4	1194	Well 28	12-Aug-11	1.02	8.5	2779
Well 10	19-Jun-09	1.1	39.1	1178	Well 29	10-Mar-11	1.1	9.9	2781
Well 11	4-Nov-12	1.3	32.2	1659	Well 30	9-Aug-12	1.4	13.6	2787
Well 12	26-Feb-11	1.22	29.1	1283	Well 31	4-Sep-10	1.4	23.9	2549
Well 13	13-Sep-11	1.25	42.4	2476	Well 32	26-Jan-13	1.5	5.3	2778
Well 14	26-Nov-12	1.11	30.04	1165	Well 33	7-Dec-11	1.5	19.6	2697
Well 15	20-May-11	1.8	20.9	1482	Well 34	13-Oct-10	1.45	14.2	2789
Well 16	22-Dec-12	1.35	18.86	2413	Well 35	11-Jan-12	1.2	6.5	2789
Well 17	11-Nov-12	1.7	26.4	1325					
Well 18	11-Aug-12	1.42-1.55	25.1	2536					
Well 19	23-Jul-12	1.2	10.6	2312					

WHP: Wellhead pressure; MF: Mass Flow; H: Enthalpy

TABLE 3: Summary of simulated downhole data using software HOLA

Type	No of wells	Range of temperature (°C)	Range of fluid velocity (m/s)
Two-phase well	19	188 – 288	3.5 - 110
Dry well	16	184 – 236	13 - 98

The software WATCH simulated the fluid chemistry concentrations of pH, Cl, SO₄, H₂S, CO₂ and H₂ in the geothermal brine at downhole conditions. The Icelandic Water Chemistry group presented the software WATCH as a chemical speciation program for UNU fellows in 1993. It interprets the chemical composition of geothermal fluids. The program reads the chemical analyses of water, gas and steam condensate samples, collected at the surface, and computes the chemical composition of downhole or aquifer fluids. This includes the pH, aqueous speciation, partial pressures of gases, redox potentials, and activity products for mineral dissolution reactions (Arason et al., 2003). Figures 3 and 4 shows the water and gas chemistry data of each well surveyed, while Table 4 summarizes the simulated downhole results given by WATCH.

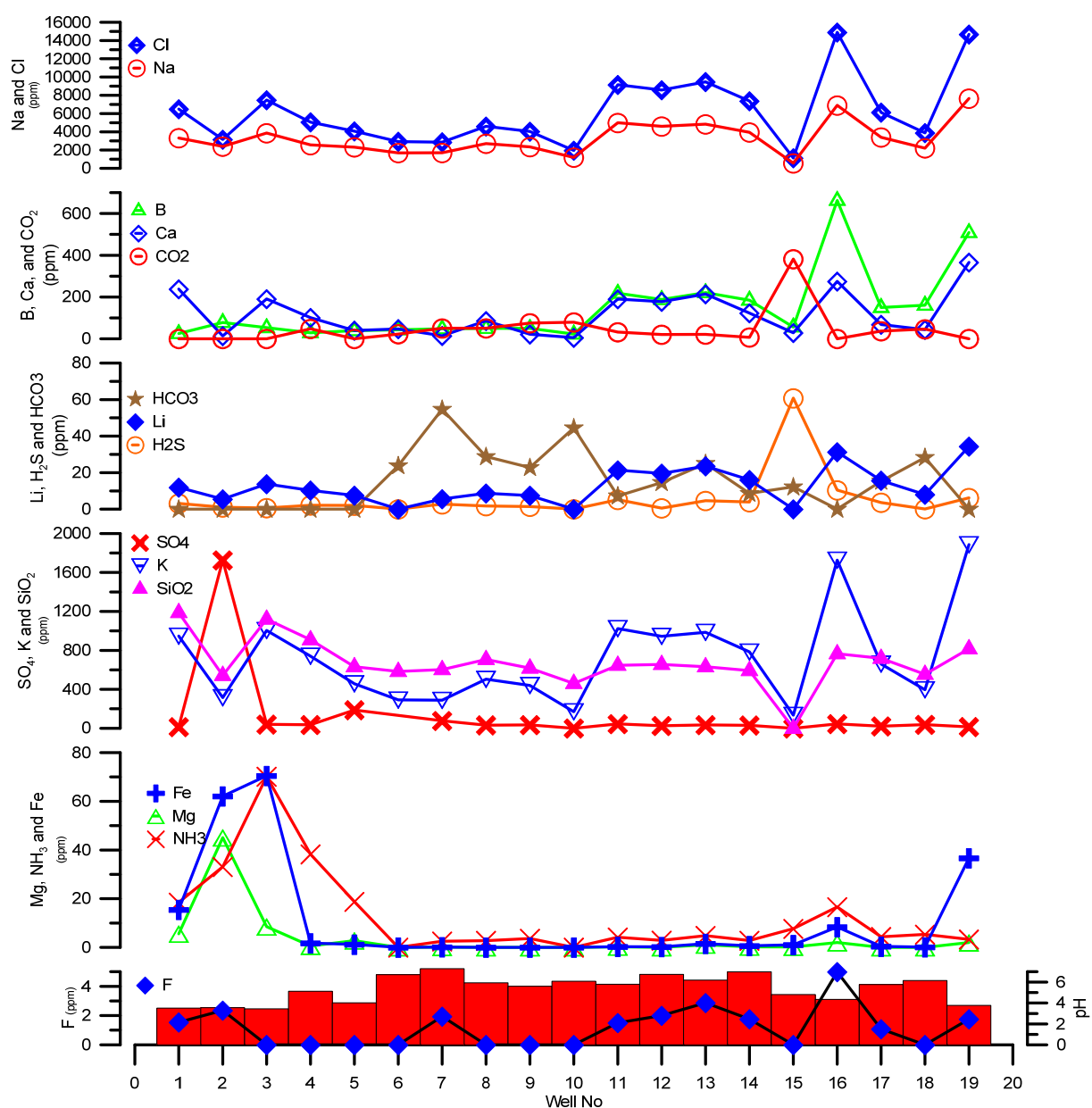


FIGURE 3: Sampled water chemistry data of two-phase wells

TABLE 4: Summary of simulated concentrations of corrosive species using software WATCH

Range of simulated downhole chemistry of the well studied							
Cl _w (ppm)	SO _{4w} (ppm)	CO _{2w} (ppm)	H ₂ S _w (ppm)	CO _{2g} (ppm)	H ₂ S _g (ppm)	H ₂ g (ppm)	Range of fluid pH
970 -15097	0 - 1701	11 - 1205	Feb-54	3578 – 56071	176 - 1534	0.1 - 7.13	3.6 - 6.9

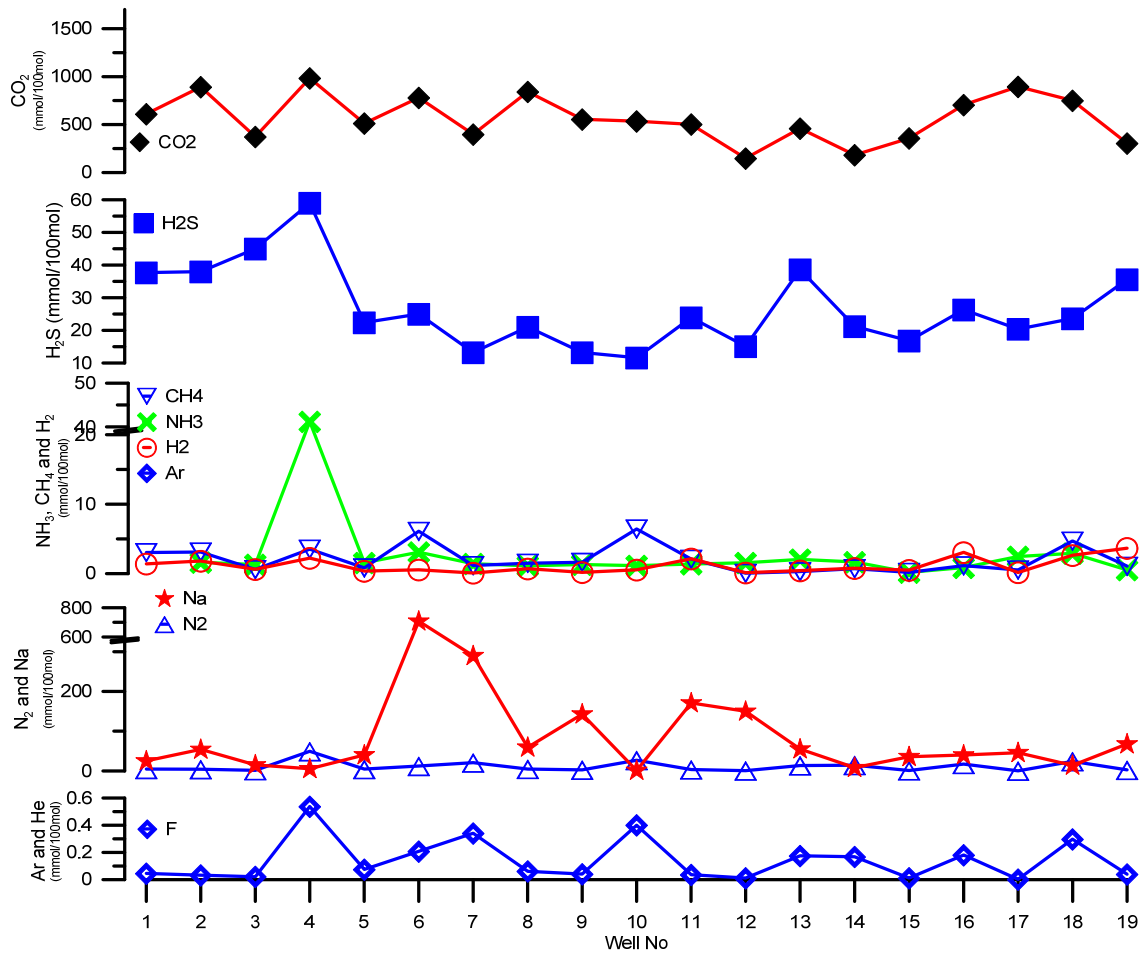


FIGURE 4: Sampled gas chemistry data of two-phase wells

Table 5 summarizes the total suspended solids (TSS) data, measured at the surface. This parameter was not included in the simulation. It was assumed that the TSS concentration at the surface was constant throughout the cased hole. The simulation of TSS is very complex because, aside from the particles coming from the open hole section, the eroded particles from the casing could be contributing to the measured TSS at the surface.

TABLE 5: Measured total suspended solids (ppm) in dry wells

Well 20	Well 21	Well 22	Well 23	Well 24	Well 25	Well 26	Well 27	Well 28	Well 29	Well 30	Well 31	Well 32	Well 33	Well 34	Well 35
10.5	2.5	2.96	29.6	2.5	2.5	6.7	2.5	2.5	2.5	9.6	45.4	2.5	2.72	9.9	2.5

The effect of well geometry on the impact of flow particles as a function of well inclination θ was obtained using the equation given by Finnie et al. (1992). The well inclination of the well was taken from the deviation survey of the well.

For $\theta \leq 18.5^\circ$:

$$f(\theta) = (\sin 2\theta - 3\sin^2\theta) \quad (2)$$

And for higher inclinations, $\theta > 18.5^\circ$:

$$f(\theta) = \frac{\cos^2\theta}{3} \quad (3)$$

4.2 Development of a corrosion model

The thinning rate of the casing can be expressed as a function of the factors affecting the rate of corrosion according to the following:

$$TR = f(T, V_s, pH, X, f(\theta)) \quad (4)$$

$$TR = f(Cl_w, H_2S_w, SO_{4w}, CO_{2w}, H_{2g}, H_2S_g, CO_{2g}) \quad (5)$$

where	TR	= Average thinning rate of casing joint (mm/year);
	T	= Simulated downhole temperature (°C);
	V_s	= Simulated fluid velocity (m/s);
	pH	= Fluid pH;
	X	= Steam fraction;
	$f(\theta)$	= Effect of well inclination;
	TSS	= Total suspended solids (ppm);
	Cl_w	= Chloride concentration in water (ppm);
	H_2S_w	= Hydrogen sulphide in water (ppm);
	CO_{2w}	= Dissolved Carbon dioxide in water (ppm);
	SO_{4w}	= Sulphate in water (ppm);
	H_2S_g	= Hydrogen sulphide gas (ppm);
	CO_{2g}	= Carbon dioxide gas(ppm);
	H_{2g}	= Hydrogen gas (ppm).

To model the effect of the above-mentioned factors on the thinning rate of the casing, a linear regression model was developed. Regression analysis is a statistical process used for estimating the relationships between variables. Regression analysis seeks to determine the causal effect of one variable upon another. The regression analysis helps in understanding how the typical values of dependent variables change when any one of the independent variables is varied, and the rest of the independent variables are kept constant.

The regression equation used for predicting the impact of the factors affecting the casing's thinning rate was based on the mathematical model for flow-accelerated corrosion, in which the affecting factors are interrelated, as shown in Equation 6 (Petric and Ksiazek, 1997).

$$WR = F(MT) * F(G) * F(X) * F(pH) * F(O_2) * F(T) * F(AC) \quad (6)$$

where	WR	= Wear rate
	$F(MT)$	= Factor for mass transfer effect
	$F(G)$	= Factor for geometry effect
	$F(X)$	= Factor for void fraction (steam quality)
	$F(pH)$	= Factor for pH effect
	$F(O_2)$	= Factor for Oxygen effect
	$F(T)$	= Factor for temperature effect
	$F(AC)$	= Factor for alloy content effect

Logarithmic transformation of data was used to set up the multiplicative factors to form a linear equation. This was done by taking the logarithmic form of both sides of Equation 7 and the identity of the logarithm of (A * B) which is log A + log B. The multiplicative function can be expressed in a linear equation, as shown in Equation 8, which can be used for linear regression as shown in Equation 9:

$$TR = A * T * V_s * pH * X * f(\theta) \quad (7)$$

$$\ln(TR) = \ln(A * T * V_s * pH * X * f(\theta)) \quad (8)$$

$$\ln(TR) = \ln(A) + \ln(T) + \ln(V_s) + \ln(pH) + \ln(X) + \ln(f(\theta)) \quad (9)$$

Different cases of regression equations were used. For the corrosive species, an additive form and multiplicative forms were used. The additive form is the simplest model form for a regression. The multiplicative form for a regression for the corrosive species was included as a check to see if the interrelated model of the corrosion species would provide a better model for predicting the thinning rate of the casing. The list of cases for the regression analysis, the corrosive species, and the relevant factors included in the regression are summarized in Table 6.

TABLE 6: Regression equation for two-phase wells in predicting the thinning rate of the casing using the affecting factors

Case	Regression model
1	$Ln(TR) = \beta_{10} + \beta_{11}Ln(T) + \beta_{12}Ln(V_s) + \beta_{13}Ln(pH)$
2	$Ln(TR) = \beta_{20} + \beta_{21}Ln(T) + \beta_{22}Ln(V_s) + \beta_{23}Ln(pH) + \beta_{24}Ln(f(\theta))$
3	$Ln(TR) = \beta_{30} + \beta_{31}Ln(T) + \beta_{32}Ln(V_s) + \beta_{33}Ln(pH) + \beta_{34}Ln(X) + \beta_{35}Ln(f(\theta))$
4	$TR = \beta_{40} + \beta_{41}Cl_w + \beta_{42}H_2S_w + \beta_{43}SO_{4w} + \beta_{44}CO_{2w} + \beta_{45}H_{2g} + \beta_{46}H_2S_g + \beta_{47}CO_{2g}$
5	$Ln(TR) = \beta_{50} + \beta_{51}Ln(Cl_w) + \beta_{52}Ln(H_2S_w) + \beta_{53}Ln(SO_{4w}) + \beta_{54}Ln(CO_{2w})$ $+ \beta_{55}Ln(H_{2g}) + \beta_{56}Ln(H_2S_g) + \beta_{57}Ln(CO_{2g})$
6	$Ln(TR) = \beta_{60} + \beta_{61}Ln(V_s) + \beta_{62}Ln(f(\theta)) + \beta_{63}Ln(T) + \beta_{64}Ln(TSS)$

where β_{i0} and β_{ik} are the normal and slope coefficients due to the affecting factors, and corrosive species ($T, V_s, pH, X, f(\theta), Cl_w, H_2S_w, SO_{4w}, CO_{2w}, H_{2g}, H_2S_g, CO_{2g}$). The regression model of cases 1 to 6 can be written as a single matrix equation, as shown in Equation 10:

$$y_{(n+1)} = x_{(nk+1)}\beta_{(k+1)} \quad (10)$$

where $x = (T, V_s, pH, X, f(\theta), Cl_w, H_2S_w, SO_{4w}, CO_{2w}, H_{2g}, H_2S_g, CO_{2g})$, and $y = (TR_1, TR_2, \dots, TR_{1n})$, which is a vector of the measured thinning rate at different levels of the affecting parameters (x variables).

Affected parameters in the thinning rate can be shown in matrix form X ,

$$x = \begin{bmatrix} 1 & x_{11} & \dots & x_{1k} \\ 1 & x_{21} & \dots & x_{2k} \\ \vdots & \vdots & \ddots & \vdots \\ 1 & x_{n1} & \dots & x_{nk} \end{bmatrix} \quad (11)$$

where $\beta = (\beta_0, \beta_1, \beta_2, \dots, \beta_k)'$ values contain the regression coefficients due to the factors affecting the thinning rate. The residual sum of squares is solved by including an error factor (e) in Equation 10.

The transformation equations leading to a normalized form of the equation are given in Equation 14:

$$\begin{matrix} x'x\beta & = & xy' \\ (k+1) \times (k+1) & & (k+1) \times 1 \end{matrix} \quad (12)$$

$$x'x = \begin{bmatrix} n & \sum x_{i1} & \sum x_{i2} & \dots & \sum x_{ik} \\ \sum x_{i1} & \sum x_{i1}^2 & \sum x_{i1}x_{i2} & \dots & \sum x_{i1}x_{ik} \\ \sum x_{i2} & \sum x_{i1}x_{i2} & \sum x_{i2}^2 & \dots & \sum x_{i2}x_{ik} \\ \vdots & \vdots & \vdots & \ddots & \vdots \\ \sum x_{ik} & \sum x_{i1}x_{ik} & \sum x_{i2}x_{ik} & \dots & \sum x_{ik}^2 \end{bmatrix} \quad (13)$$

$$xy' = \begin{bmatrix} \sum y_i \\ \sum x_{i1}y_i \\ \sum x_{i2}y_i \\ \vdots \\ \sum x_{ik}y_i \end{bmatrix} \quad (14)$$

The solution of the normalized Equation 12 provides a solution of the independent coefficients of the operating parameters and is given in Equation 15:

$$\beta = (x'x)^{-1}xy' \quad (15)$$

The multiple regression and the analysis of variance (ANOVA) test were performed at a 95% confidence level in order to examine the combined effects of temperature, fluid velocity, fluid pH, well geometry, steam fraction, and corrosive species such as chloride, sulphate, hydrogen, carbon dioxide and hydrogen sulphide on the thinning rate of the geothermal well casing.

4.3 Selection of a good model

In selecting a good model for predicting the thinning rate casing, two criteria are used. The first criterion is use of the adjusted coefficient of determination (R_a^2) and the second is the mean absolute percentage error.

The adjusted coefficient of determination, (R_a^2), is a variation of R^2 , which is proportional to the variation of the response variable.

$$R_a^2 = \left(\frac{MS_{Tot} - MS_{error}}{MS_{Tot}} \right) \quad (16)$$

where MS = Mean of squares.

This kind of variation or R^2 includes a penalty for unnecessarily explanatory variables. It measures the proportion of the observed spread in the responses explained by the model. The higher value of adjusted R^2 illustrates a good correlation.

Another criterion used in selecting the model is the mean absolute percentage error (MAPE). It is a measure of the accuracy of a method for constructing fitted values in statistics, specifically for estimation. MAPE is expressed as a percentage as shown in Equation 17. The model with lower MAPE is a good prediction model.

$$MAPE = \frac{1}{n} \sum_i^n \left| \frac{Actual_i - Predicted_i}{Actual_i} \right| R_a^2 = \left(\frac{MS_{Tot} - MS_{error}}{MS_{Tot}} \right) \quad (17)$$

5. RESULTS AND DISCUSSION

The correlation results of the thinning rate in the casing as a dependent variable, and the factors affecting it ($T, V_s, pH, X, f(\theta),$), are summarized in Table 7.

TABLE 7: Correlation results of the thinning rate in the casing

Case model	Multiple R	R ²	Adjusted R ²	Standard error	Observation
1	0.7247	0.5252	0.5240	0.8870	1188
2	0.7467	0.5576	0.5561	0.8566	1188
3	0.7543	0.5689	0.5671	0.8459	1188
4	0.7415	0.5499	0.5472	0.1910	1188
5	0.6627	0.4391	0.4358	0.9657	1188
6	0.4101	0.1682	0.1634	0.9484	700

The coefficient of determination R² ranges from 0.5252 to 0.5689 for cases 1 to 3, while the adjusted R² ranges from 0.5240 to 0.5671. This implies that a combination of factors such as temperature, fluid velocity and fluid pH, contributes 52.40% to the thinning rate of the casing of geothermal well. On the other hand, a combination of the temperature, fluid velocity, steam fraction, well geometry and fluid pH factors contributes 56.71% to the thinning rate. For the regression of the corrosive species found in the two-phase wells, 54.72% was the additive term of the species' contribution to the thinning rate of the casing. The adjusted R² of the regression for dry wells shows that 16.34% of the thinning rate comes from the effects of velocity, temperature, well geometry and total suspended solids, which is a very low correlation on the thinning rate of the casing.

The low value of coefficient determination could be the result of the effects of other factors, such as the condition of the casing used in the geothermal well. It is possible that the casing had pitting inside before it was installed in the borehole. Well stimulation conducted on the geothermal well, like a drilling work-over, for example by the drill bit as it is run in hole inside the well during mechanical clearing operations, could significantly affect the condition of the casing. During clearing operations, a casing joint section located at a high inclination could be much affected by the drill pipe.

Higher residuals were observed for cases 1 to 3, 5 and 6, mainly because they were logarithmically transformed, when compared to case 4. Since the coefficient of determination of the resulted regression is low, the residual of the regression is high. In addition, since the data is log-transformed, any error or change in the value of an outcome variable is presented as a percentage of the value. The percentage of change was multiplied for each term of the variable; this makes the residual value of the model high.

Table 8 shows ANOVA results of the thinning rate of the casing and all of the relevant factors. All of the regression cases were highly significant to the thinning rate of the casing. Intuitively, the thinning rate can be determined using the factors used. However, the adjusted R² (please refer to Table 7) values are still low, indicating that the model needs further improvement; the model can be used as a good prediction model.

The P value of the variables shows that the coefficient of the factors for cases 1 to 6 has values lower than 0.05, using a 95% confidence interval for all variables as shown in Table 9. This shows that the test is statistically significant. Case 4 of the regression model shows that the corrosive species CO_{2w} and H₂S_w are not significant in the additive terms of the regression model of the thinning rate. The case 4 regression model was reduced to the form of Equation 18, and the result of the regression is shown in Table 10.

TABLE 8: Summary of ANOVA for the casing thinning rate and affecting factors

Case model		df	SS	MS	F	Significance
1	Regression	3	1030.3319	343.4440	436.4842	6.57×10^{-191}
	Residual	1184	931.6205	0.7868		
	Total	1187	1961.9524			
2	Regression	4	1093.9418	273.4854	372.7296	1.08×10^{-207}
	Residual	1183	868.0106	0.7337		
	Total	1187	1961.9524			
3	Regression	5	1116.2291	223.2458	312.0128	4.80×10^{-213}
	Residual	1182	845.7234	0.7155		
	Total	1187	1961.9524			
4	Regression	7	52.5885	7.5126	205.9238	1.70×10^{-199}
	Residual	1180	43.0495	0.0365		
	Total	1187	95.6380			
5	Regression	7	861.5407	123.0772	131.9789	2.23×10^{-143}
	Residual	1180	1100.4117	0.9326		
	Total	1187	1961.9524			
6	Regression	4	126.3930	31.5982	35.1316	9.61×10^{-27}
	Residual	695	625.1012	0.8994		
	Total	699	751.4942			

Case 4 (reduced form):

$$TR = \beta_{40} + \beta_{41}Cl_w + \beta_{42}SO_{4w} + \beta_{43}H_{2g} + \beta_{44}H_2S_g + \beta_{45}CO_{2g} \quad (18)$$

The parameter estimates of the variables shown in Tables 9 and 10 were analysed. Cases 1 to 3 of the factors affecting the thinning rate of the two-phase wells such as temperature, fluid velocity and fluid pH have negative coefficients, indicating a decreased effect on the thinning rate as the value of variables is increased. The increase in the steam fraction and well inclination corresponds to an increase in the thinning rate of the casing, as interpreted from the coefficient of the parameter estimates.

The plot of the average thinning rate of the wells, vis-a-vis the temperature at the wellhead, is shown in Figure 5. The plot shows a decreasing trend in the average thinning rate of the casing as the temperature of the wells at the surface increases for the 19 two-phase wells that were included in the study. The trend of the maximum thinning rate of the two-phase wells against simulated temperature at depth showed no apparent change in the trend between the temperature ranges. However, when only two-phase wells with higher pH ranging from 5 to 6 were considered, a decreasing trend was found in the thinning rate of the well with increasing temperature, shown in Figure 6. It is possible that within the well studied, as the fluids were boiled, the pH of the fluid decreased and moved to the surface. The temperature of the fluid decreases due to pressure drop as the fluid flows to the surface. The resultant decrease in pH fluids corrodes the casing of the well. This was observed by Lichti et al. (1998): in the potential-pH Pourbaix diagram of Mahanagdong well MG-9D, as the temperature decreased in the two-phase flow, small changes in

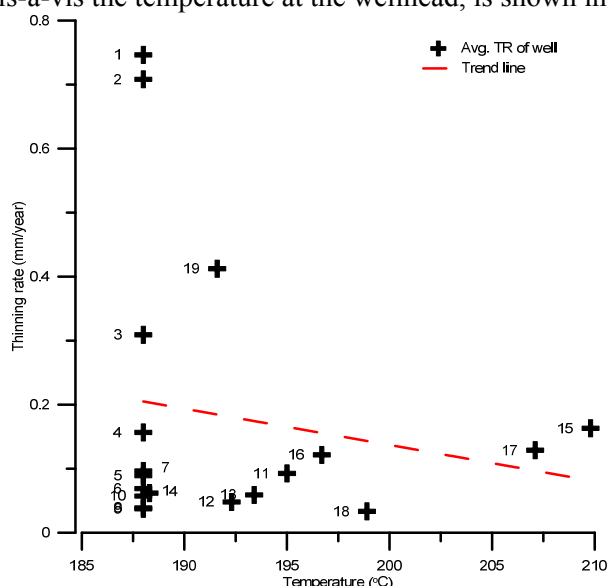


FIGURE 5: Plot of average thinning rate of two-phase wells against temperature at the wellhead

TABLE 9: Summary of parameter estimates

Case model	Variables		Coefficients	Standard error	t Stat	P-value
1	Intercept	β_{10}	29.4158	1.7118	17.1841	2.92×10^{-59}
	$\ln(T)$	β_{11}	-3.6181	0.2898	-12.4852	1.07×10^{-33}
	$\ln(V_s)$	β_{12}	-0.7349	0.0433	-16.9838	4.59×10^{-58}
	$\ln(pH)$	β_{13}	-5.9338	0.1658	-35.7958	8.72×10^{-191}
2	Intercept	β_{20}	30.8487	1.6602	18.5816	7.98×10^{-68}
	$\ln(T)$	β_{21}	-4.1648	0.2859	-14.5655	2.50×10^{-44}
	$\ln(V_s)$	β_{22}	-0.5784	0.0450	-12.8427	1.95×10^{-35}
	$\ln(pH)$	β_{23}	-5.1166	0.1826	-28.0276	5.59×10^{-133}
	$\ln(f(\theta))$	β_{24}	0.0720	0.0077	9.3109	5.97×10^{-20}
3	Intercept	β_{30}	23.4251	2.1111	11.0959	2.77×10^{-27}
	$\ln(T)$	β_{31}	-3.0741	0.3434	-8.9522	1.32×10^{-18}
	$\ln(V_s)$	β_{32}	-0.7261	0.0518	-14.0303	1.77×10^{-41}
	$\ln(pH)$	β_{33}	-4.5885	0.2036	-22.5374	7.44×10^{-94}
	$\ln(X)$	β_{34}	0.3005	0.0538	5.5811	2.96×10^{-08}
	$\ln(f(\theta))$	β_{35}	0.0529	0.0084	6.3153	3.81×10^{-10}
4	Intercept	β_{40}	2.61×10^{-02}	0.0241	1.0815	2.80×10^{-01}
	Cl_w	β_{41}	-1.09×10^{-05}	0.0000	-5.0462	5.22×10^{-07}
	H_2S_w	β_{42}	-3.18×10^{-03}	0.0019	-1.6717	9.49×10^{-02}
	SO_{4w}	β_{43}	2.80×10^{-04}	0.0000	20.1761	5.22×10^{-78}
	CO_{2w}	β_{44}	1.11×10^{-05}	0.0001	0.0951	9.24×10^{-01}
	H_{2g}	β_{45}	4.86×10^{-02}	0.0058	8.4308	9.89×10^{-17}
	H_2S_g	β_{46}	3.73×10^{-04}	0.0000	7.8152	1.21×10^{-14}
	CO_{2g}	β_{47}	-4.94×10^{-06}	0.0000	-3.1630	1.60×10^{-03}
5	Intercept	β_{50}	-4.4051	1.4990	-2.9387	3.36×10^{-03}
	$\ln(Cl_w)$	β_{51}	-0.7249	0.0555	-13.0570	1.71×10^{-36}
	$\ln(H_2S_w)$	β_{52}	0.9019	0.2729	3.3046	9.80×10^{-04}
	$\ln(SO_{4w})$	β_{53}	0.0653	0.0087	7.4773	1.48×10^{-13}
	$\ln(CO_{2w})$	β_{54}	-1.3214	0.2644	-4.9968	6.71×10^{-07}
	$\ln(H_{2g})$	β_{55}	0.4364	0.0419	10.4157	2.30×10^{-24}
	$\ln(H_2S_g)$	β_{56}	0.6935	0.2239	3.0976	2.00×10^{-03}
	$\ln(CO_{2g})$	β_{57}	0.7771	0.2765	2.8102	5.03×10^{-03}
6	Intercept	β_{60}	-19.8154	3.7784	-5.2444	2.08×10^{-07}
	$\ln(V_s)$	β_{61}	-0.2237	0.0884	-2.5311	1.16×10^{-02}
	$\ln(f(\theta))$	β_{62}	0.0718	0.0137	5.2574	1.95×10^{-07}
	$\ln(T)$	β_{63}	3.5387	0.7192	4.9203	1.08×10^{-06}
	$\ln(TSS)$	β_{64}	0.1368	0.0445	3.0745	2.19×10^{-03}

the stability of iron sulphide were observed. However, due to a continuing decrease in pH, the corrosion reaction moved from the limits of FeS into Fe⁺⁺, which is free of corrosion. This signifies that the pH of the fluid predominantly controls the thinning rate of the casing and is in agreement with the experimental results of Sanada et al. (1998); thus, the pH of the fluid predominantly controls the rate of corrosion.

The thinning rate of the casing is also higher in the low velocity range, as shown in Figure 7. The velocity of the fluid at downhole increases as the fluid phase changes from single to two-phase, as induced by boiling. The observed trend of a higher thinning rate at lower fluid velocity implies that thinning of the casing occurs at the velocity where the fluid is in a liquid phase condition. Slow velocity of the fluid results in longer residency time; this gives more time for thinning reactions at the surface of the casing. Most of the wells with higher thinning rates were wells with low pH fluid (Wells 1, 2, 3, 19, 16 and 15).

TABLE 10: Regression analysis, ANOVA and parameter estimate of reduced form of case 4

Case model	Multiple R	R ²	Adjusted R ²	Standard error	Observation	
4 (reduced form)	0.7401	0.5478	0.5459	0.1913	1188	
Case model		df	SS	MS	F	Significance
4 (reduced form)	Regression	5	52.3903	10.4781	286.3757	8.82E-201
	Residual	1182	43.2477	0.0366		
	Total	1187	95.6380			
Case model	Variables		Coefficients	Standard error	t Stat	P-value
4 (reduced form)	Intercept	β_{40}	0.04718	0.02057	2.29370	2.20E-02
	Cl_w	β_{41}	-0.00001	0.00000	-4.89714	1.11E-06
	SO_{4w}	β_{42}	0.00030	0.00001	26.33232	1.26E-120
	H_{2g}	β_{43}	0.05119	0.00566	9.04524	5.98E-19
	H_2S_g	β_{44}	0.00030	0.00002	12.23086	1.78E-32
	CO_{2g}	β_{45}	-0.00001	0.00000	-7.10980	2.01E-12

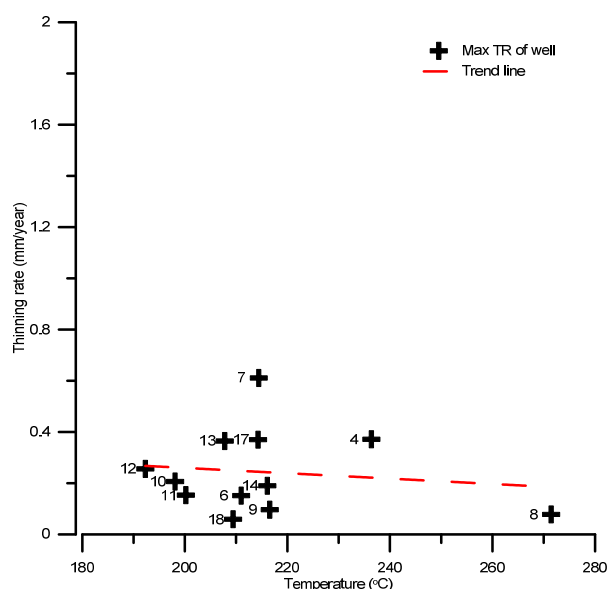


FIGURE 6: Maximum thinning rate of two-phase wells with pH > 5 plotted against its corresponding downhole temperature

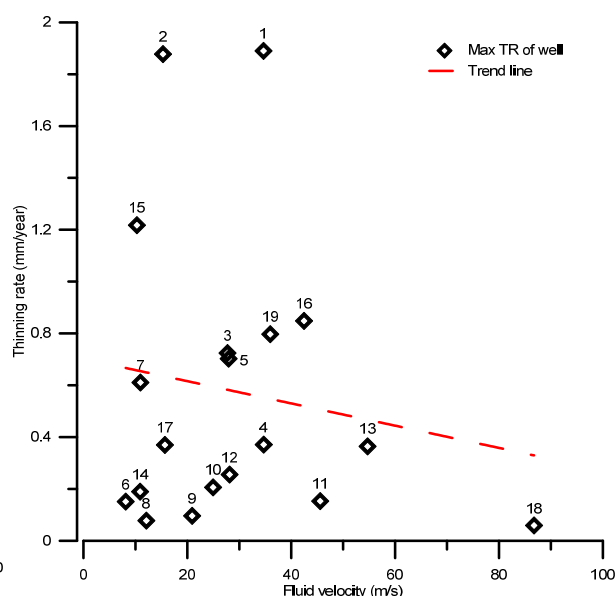


FIGURE 7: Plot of maximum thinning rates of wells with corresponding fluid velocity

The results of the regression for the two-phase wells were analysed. The parameter estimates of fluid pH showed a trend of a decreasing rate of corrosion as the pH of the fluid increased. This is in agreement with the findings from the corrosion study by Sanada et al. (1998) which said that a higher corrosion rate occurs at low pH. The plot of the maximum thinning rate with corresponding pH with depth is shown in Figure 8.

The plot of the maximum thinning of the casing with its corresponding steam fraction illustrates a trend of an increasing thinning rate in relation to the steam fraction, as shown in Figure 9. The result of the regression of the steam fraction shows that the thinning rate of the casing increases with increased steam fractions. The plot demonstrates that the maximum thinning rates were found in wells with low pH fluid. The flashing of the geothermal brine changed the concentration of the dissolved gasses and these resulted in a decrease in pH in the wells studied.

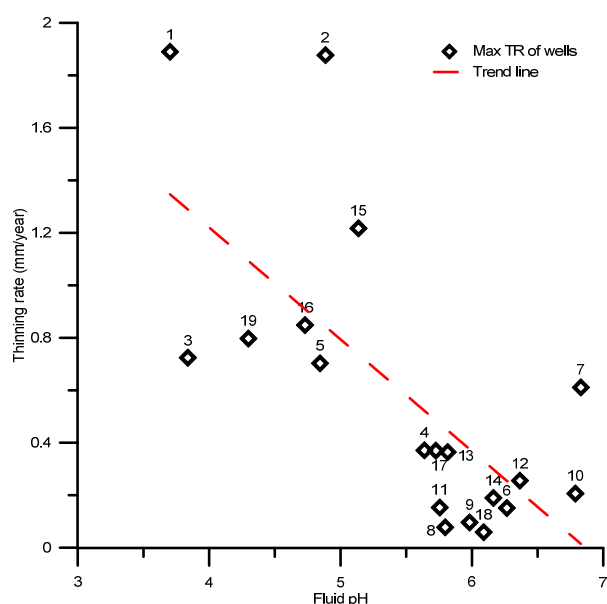


FIGURE 8: Plot of maximum thinning rate of well with its corresponding fluid pH

Based on the regression analysis, the deviated well geometry shows an increased effect in the thinning rate. However, the contribution of this factor to the thinning rate is very low when compared to other factors. A deviated well geometry will cause more turbulence in fluid flow. The rate of corrosion is much higher for a turbulent flow having a low pH concentration (Sanada et al., 1998).

Parameter estimates of the corrosive species of the reduced form of case 4 shows that for the studied wells, species of H_2S gas and H_2g significantly contribute to the thinning rate of the casing. Figure 10 illustrates a trend of an increasing thinning rate with respect to an increase in H_2S gas concentration. The casings used in most of the geothermal wells are carbon steel K55. This type of casing has a small percentage of copper and nickel; when hydrogen sulphides are present, the corrosion is severe.

High concentrations of H_2 gas in the wells lead to an increased thinning rate of the casing, as shown in Figure 11. Increased hydrogen concentrations lower the pH of the fluid. The casing experiences stress corrosion cracking at higher concentrations of hydrogen gas. On the other hand, low concentrations of hydrogen gas in the well result in the formation of scales, which protects the casing from the corrosive fluid and slows down corrosion of the casing. Metals become brittle because of the absorption and diffusion of hydrogen at the molecular level. The embrittlement is much more severe when hydrogen sulphide is present (Praselia et al., 2010).

For two-phase wells, the thinning rate decreased with increased chloride concentrations, but not significantly, as shown in Figure 12. The parameter estimate of chloride in case 4 was also too small to have an effect on the reduction of the thinning rate, compared to the impact of hydrogen sulphide gas.

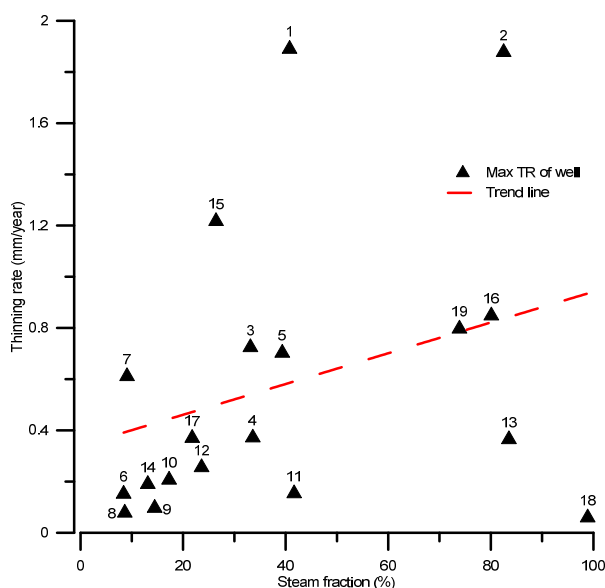


FIGURE 9: Plot of maximum thinning rate with its corresponding steam fraction

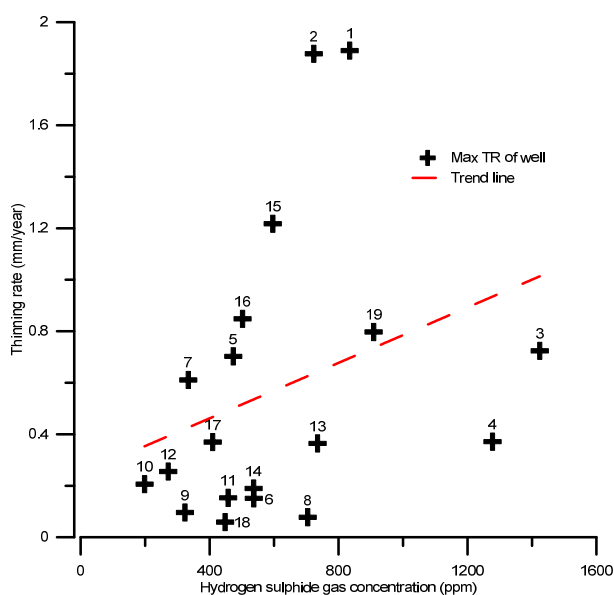


FIGURE 10: Plot of maximum thinning rate with its corresponding H_2S gas concentration

There was a small decline in the trend on the plot. The chloride ion breaks the passive film formed in the metal, which results in pitting. An increasing trend in the thinning rate was expected. However, a reversal in this trend could be attributed to the use of particular data sets from wells with low pH and low chloride concentrations. Downhole simulation of the chemistry of the fluid led to the observation of increasing chloride concentrations as the fluid flows upward with a corresponding decrease in the fluid pH. The regression results imply that the trend of the thinning rate is independent of the chloride concentrations but is dependent on the fluid pH of the well studied.

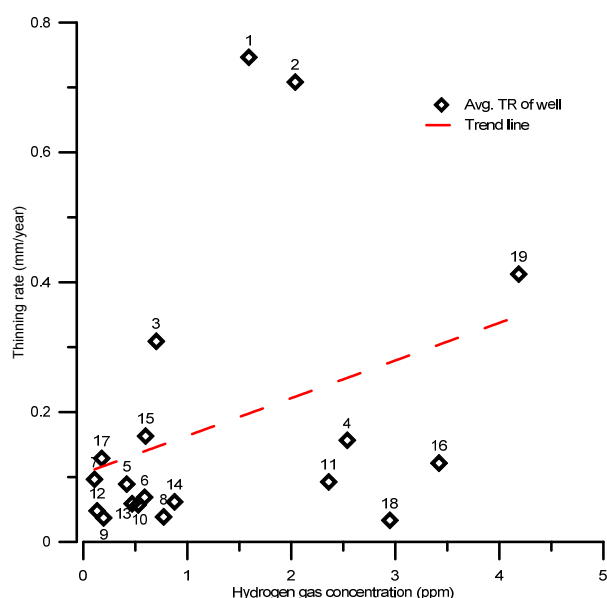


FIGURE 11: Plot of average thinning rate of the casing with minimum H_2 gas concentrations in each well

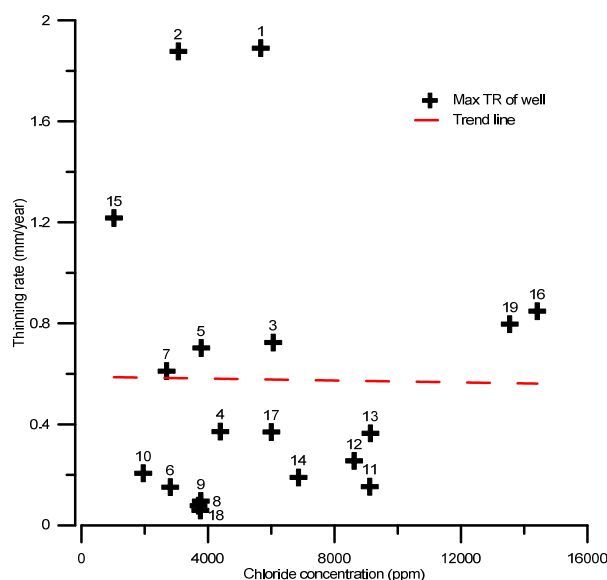


FIGURE 12: Plot of maximum thinning rate with its chloride concentration

The maximum thinning rate of the studied wells with the corresponding sulphate concentrations is plotted in Figure 13. An increase in the thinning rate is evident, based on the results of the regression model for case 4. Fluid with high sulphate concentrations and with low chloride concentrations becomes the more aggressive anion in the corrosion reaction. The decrease in pH may be due to higher concentrations of the sulphur species (H_2S and SO_4) in the datasets.

Parameter estimates of case 5 show a different interpretation of the model. Here, they show that all corrosive species are significant in the model. The CO_{2g} and H_2S_g have high contributions to the thinning rate of the casing. However, in the water phase, the decreasing concentration of CO_{2w} and increasing concentration of H_2S_w , results in an increased thinning rate. The trend of the thinning rate was plotted, based on the maximum and average thinning rates of the casing of each well, as shown in Figures 14 and 15. The increased concentration of dissolved CO_2 in the water contributes to the development of scales, such as calcium carbonate, which shields the casing from corrosion. Fluid, with a low concentration of dissolve CO_2 in the water but with an increasing concentration of dissolved H_2S in the water, contributes to the thinning of the casing. The presence of H_2S inhibits the formation of an oxide film on the steel surface (Banas et al., 2007).

According to Lichti et al. (1981), geothermal fluids with significant concentrations of H_2S and CO_2 often experience the formation of thick adherent layers of corrosive products. This film of corrosive products consists of iron sulphides; the growth rate of these sulphides is directly related to the rate of corrosion. The thinning of the casing becomes apparent when these corrosive products are removed.

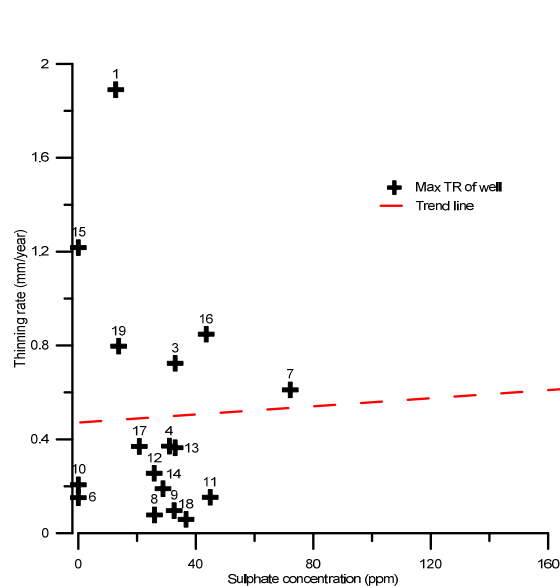


FIGURE 13: Plot of maximum thinning rate with its sulphate concentration

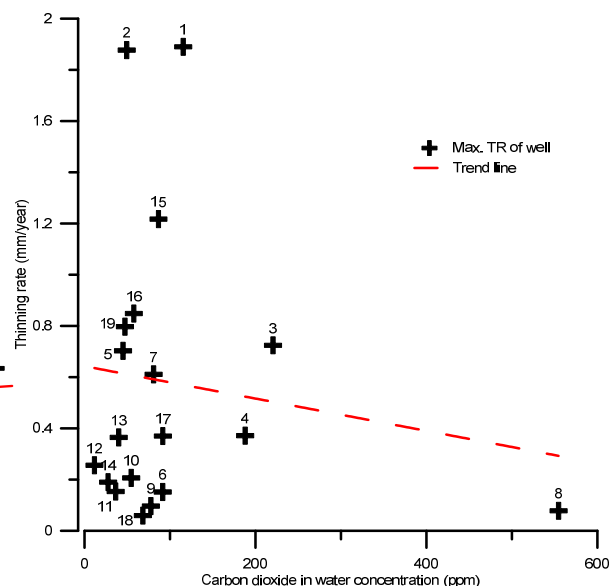


FIGURE 14: Plot of maximum thinning rate with its dissolved CO₂ concentration in water

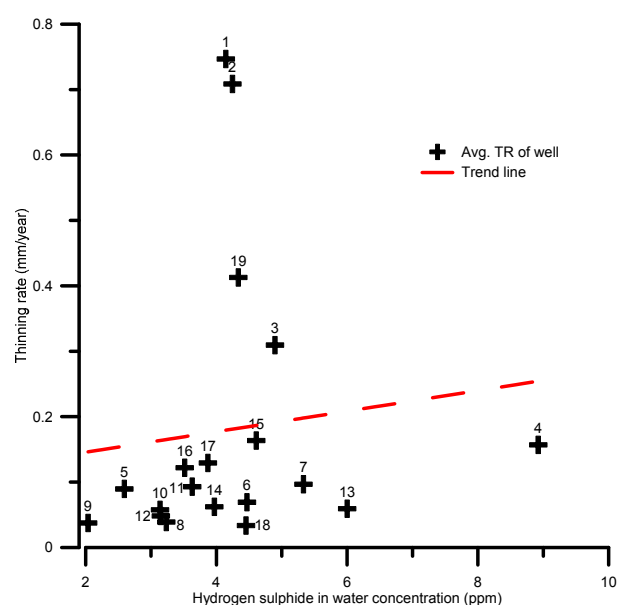


FIGURE 15: Plot of average thinning rate with minimum H₂S concentration in water of each well

Case 6 of the regression showed that temperature significantly affects the thinning rate of the casing, followed by TSS and then well geometry. The coefficient of the determination for case 6 is very low, which shows that there are other factors contributing to the thinning rate of the casing for dry wells. In some geothermal fields, the presence of volatile chloride in steam severely corrodes equipment such as well casings, the wellhead, pipeline and turbines (Hirtz et al., 1991). Even when no traces are found at the surface, it is possible that low pH fluid condensates corrode the casing of most dry wells.

The results of the mean absolute percentage error and the adjusted R² of the regression model are shown in Table 11. Of the three cases, case 3 suggests the best model because it has the highest adjusted R² and the lowest MAPE. Case 6 of the regression model has a high MAPE value, as expected for a low adjusted R². This shows that the model is limited and is lacking other variables that control the thinning rate of the casing.

Concerning the regression of corrosive species in predicting the thinning rate, case 4 results have a higher adjusted R² than case 5, but case 5 has a lower MAPE than case 4.

For choosing the better of the two models, the Akaike information criterion (AIC) was used; AIC is a measure of the relative quality of a statistical model for a given set of data. AIC provides a mean of model selection, and deals with the trade-off between actual data and how well the model fits with the actual data: the lower the value of AIC, the better the fit. The AIC is defined as:

TABLE 11: Mean absolute percentage error (MAPE) and adjusted R^2 of regression model

Case model	Adjusted R^2	MAPE
1	0.5240	170.78
2	0.5561	170.41
3	0.5671	166.76
4 (reduced form)	0.5459	209.50
5	0.4358	149.81
6	0.1634	213.77

$$AIC_i = -2\log L_i + 2V_i \quad (19)$$

where L_i = Maximum likelihood for the candidate model i ;
 V_i = Free parameters.

The AIC rewards descriptive accuracy through maximum likelihood and penalizes lack of parsimony according to the number of free parameters, as shown by Equation 19 (Wagenmakers and Farrell, 2004).

The reduced form of case 4 results in lower AIC values, which illustrates a good fit between the predicted values and the observed values, as shown in Table 12.

TABLE 12: Result of Akaike information criterion (AIC) validation between reduced form of case 4 and case 5

Case model	Degree of freedom	AIC
4 (reduced form)	7	-3921.94
5	9	-1504.5

Figures 16-18 show plots for the observed thinning rate of the casing and the predicted value of the thinning, using the affecting factors and the corrosive species for two-phase wells and dry wells. The plots show that the observed thinning rates of two-phase wells are scattered for wells with low pH fluid.

Most of the predicted values for case models 3 to 5 were unable to match the wells with low pH fluid. In addition, the predicted value for some of the wells did not fit the observed values for wells that were mechanically clearing obstructions.

The coefficients of the parameter estimates, listed in Tables 9 and 10, were used to develop a set of linear regression equations for the thinning rate of geothermal casings.

Case 3:

$$\begin{aligned} \ln(TR) = & 23.4251 - 3.0741\ln(T) - 0.7261\ln(V_s) - 4.5885\ln(pH) \\ & + 0.3005\ln(X) + 0.0529\ln(f(\theta)) \end{aligned} \quad (20)$$

Case 4 (reduced form):

$$\begin{aligned} TR = & 0.04718 - 0.00001Cl_w + 0.0003SO_{4w} + 0.0511H_{2g} \\ & + 0.0003H_2S_g + -0.00001CO_{2g} \end{aligned} \quad (21)$$

A second set of caliper surveys for Wells 1 to 3 were used to compare the predicted thinning rate, using case models 3 and 4. The average thinning rate of the casings from these surveys was compared with the average predicted thinning rate of the casings.

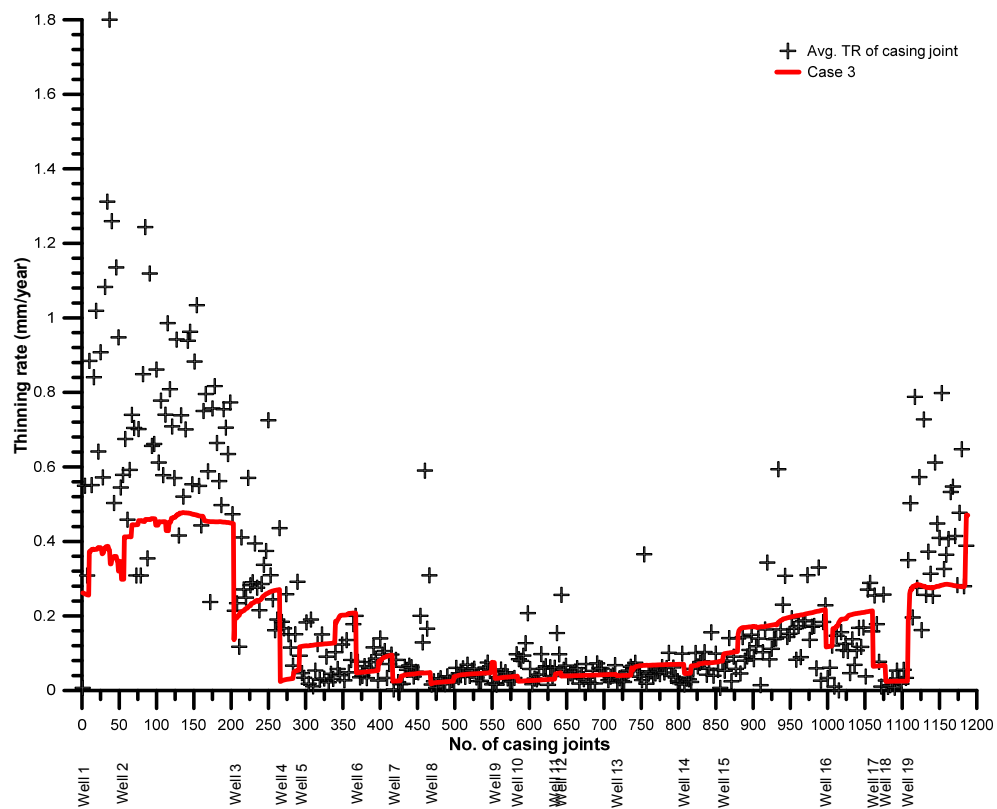


FIGURE 16: Plot of observed and predicted thinning rate, using case 3 model

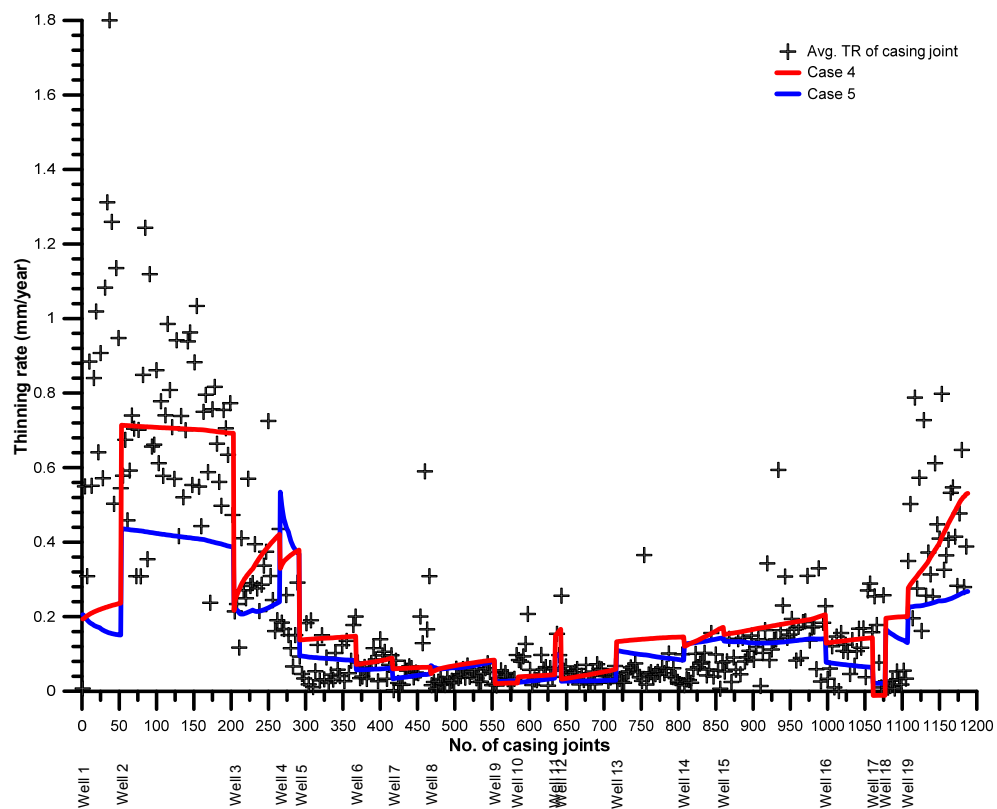


FIGURE 17: Plot of observed and predicted thinning rate, using case 4 and 5 models

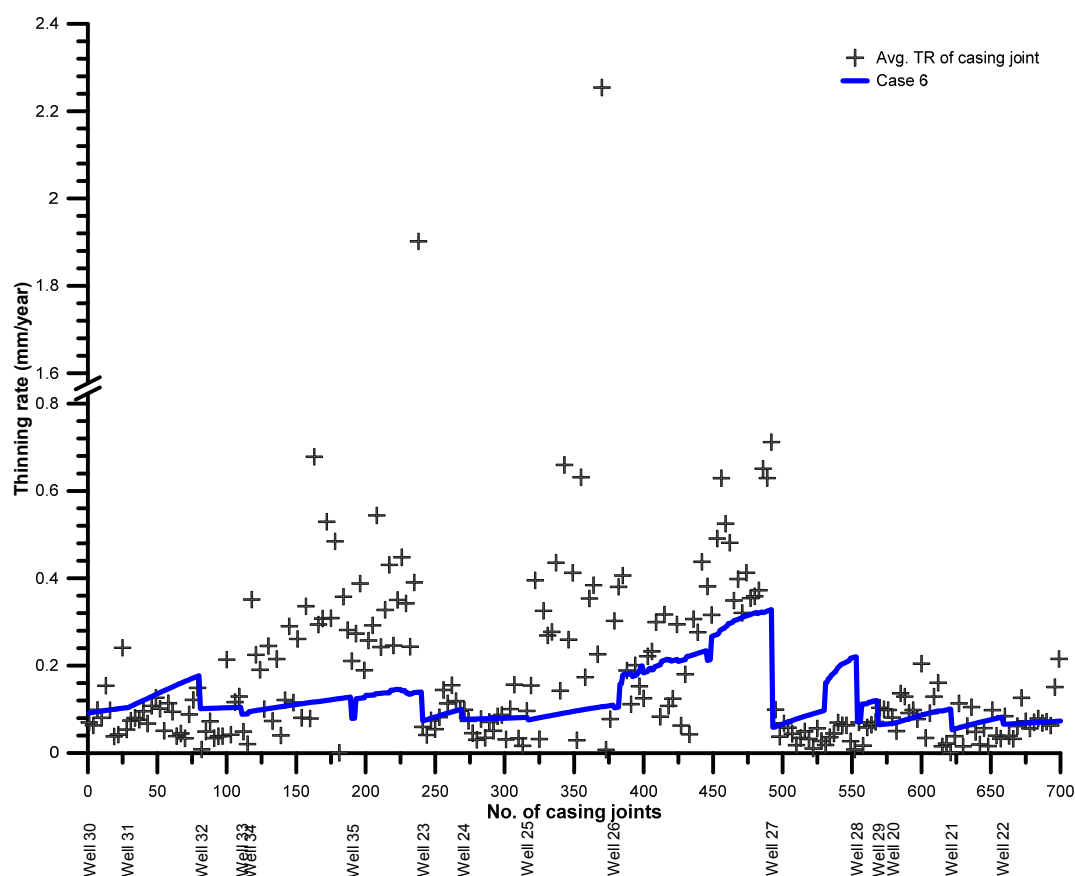


FIGURE 18: Plot of predicted value against observed value of thinning rate for case 6

Reduced case 4 in Well 3 almost predicted the average thinning rate of the caliper surveys, shown in Figure 19. Wells 1 and 2 have large differences between the measured and the predicted average thinning rate of the casing. This was expected, since the predicted value of the regression did not match the observed value in the regression model plot.

Comparing the first and second surveys, the change in the thinning rate for the three wells shows a similar trend in the predicted thinning rate of the casing, using case 3 and 4 models, shown in Figure 20. Even the average predicted thinning rate of the case model did not match the observed average thinning rate from the caliper survey. Despite this, the model can be used as a tool for determining candidate wells to be surveyed. Knowing the thinning rate trend of the casings for specific wells, (based on results from the prediction model), those wells with a high risk of corrosion should be monitored more frequently. Moreover, mitigating actions should be performed on those wells in order to alleviate the high risk associated with their utilization.

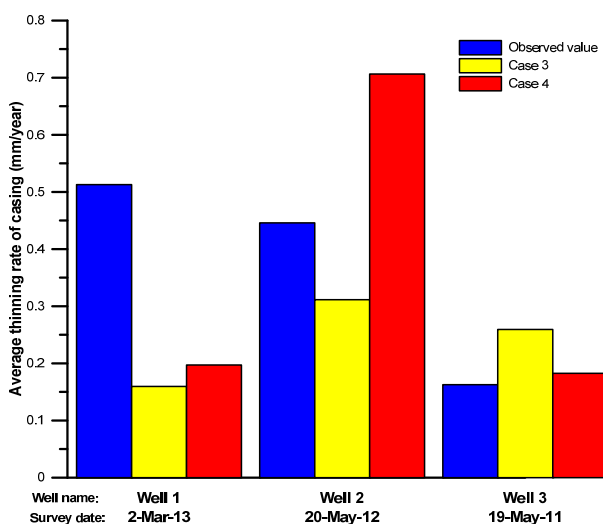


FIGURE 19: Bar chart of average casing thinning rates of measured second caliper surveys and average predicted thinning rate of Wells 1 to 3

The model regression of case 6 was used to predict the average thinning rate of the dry wells, shown in Figure 21. The predicted average thinning rate of the casing conforms to the observed average thinning rate of Wells 21 and 24. These wells showed good matches on the regression model plots, as shown in Figure 18. Well 26 had a low predicted value against the measured value. However, the thinning rate trend between the first and second surveys in the model prediction for dry wells was similar to the regression model for two-phase wells.

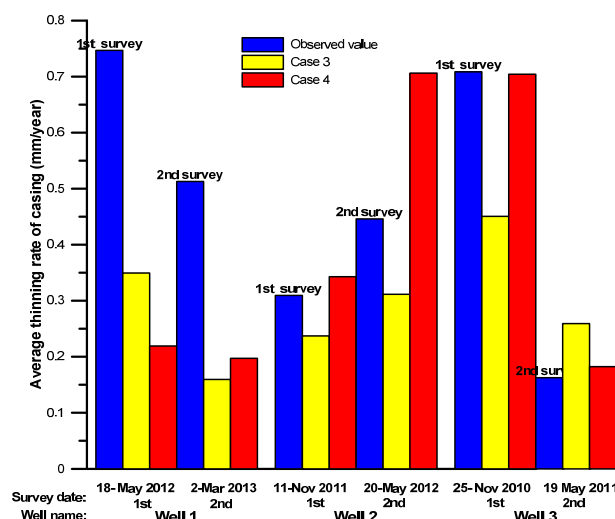


FIGURE 20: Comparison of the average casing thinning rate of the observed and predicted rates of the first and second surveys for Wells 1 to 3

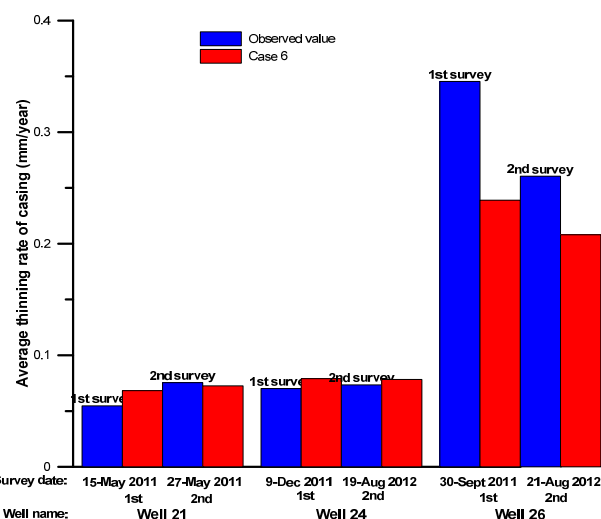


FIGURE 21: Comparison of the average casing thinning rate, both measured and predicted, of the first and second surveys for dry Wells 21, 24 and 26

6. SUMMARY AND CONCLUSIONS

Monitoring the thinning rate of the geothermal well casing is essential in managing the geothermal production field. The loss of integrity of the casing due to thinning could result in high risk in operational safety, environmental damage and loss of profit. The main cause of thinning of the casing is its exposure to fluid discharge.

Regression modelling was used to study the thinning rate of geothermal casing in Leyte Geothermal Production Field. Using software HOLA and WATCH, field data, such as fluid discharge measurements and samples of fluid chemistry from the wellhead, were simulated to obtain the downhole condition. The simulated data were used as datasets for the regression model of the thinning rate of the casing. The results of caliper inspection surveys, conducted on the well casings, were used as response variables in the regression model.

The regression analysis showed that fluid discharge characteristics such as temperature, velocity, pH, steam fraction and the geometry of the well are highly significant on the thinning rate of the geothermal casing for two-phase wells. These factors contribute 56.71% on the thinning of the casing. The prediction of the thinning rate of casings for dry wells, using temperature, fluid velocity, concentration of total suspended solids and the geometry of the well, was found to be significant to the model, but these factors contributed only 16.34% to the thinning of the casing.

The model was inadequate for accurately predicting thinning of the casing. Other factors needed to be considered in order to improve the reliability of the model for predicting casing thickness in dry wells.

The effects of corrosive species, such as Cl_w , H_2S_w , SO_{4w} , CO_{2w} , H_{2g} , H_2S_g , CO_{2g} , were also studied. Regression results on the thinning rate, using the concentrations of corrosion species, showed that these corrosion species contributed from 43.6 to 54.7 % to the thinning of the casing. An additive and a multiplicative term of the corrosive species were also included in the regression. The regression models of corrosion species used the Akaike Information Criterion (AIC) in order to select a good model for prediction. Based on the results of the selection test, and using the different models, the additive term of the corrosion species provided a good prediction model for the thinning rate of the casing.

Among the corrosion species considered, H_2S and H_2 gases have a significant effect on the thinning of the casing. The presence of these corrosion species in high concentrations could cause hydrogen embrittlement and sulphide stress cracking for wells with high temperature ranges. High sulphate concentrations were present in two-phase wells with a high thinning rate. This illustrates the contribution of sulphur species (H_2S and SO_4) in the thinning of the casing, correlating to a decrease in fluid pH in most of the wells studied.

The study revealed the behaviour of thinning of the casing, comparing regression modelling of the measured thinning rate to the simulated downhole condition. The following were the observed behaviours of the thinning rate:

- Fluid pH predominantly controls the thinning rate of the casing. A low pH geothermal fluid results in a high thinning rate of the casing.
- The thinning rate of the casing increases as the steam fraction of the fluid increases. It is more severe when casing is exposed to acidic geothermal fluids.
- Most of the maximum thinning rates of the well casings included in this study occurred at lower velocity ranges. This could be due to the fluid's long residence time with which to react with the casing.
- A complex well geometry could result in fluid turbulence that can cause an increase in the thinning rate. However, the effect of well geometry is low, based on the data coming from the wells included in this study. Flow turbulence greatly affects the rate of thinning of the casing when fluid pH is low.
- For the temperature range of 188°C to 280°C, the average thinning rate of the casing decreased as the temperature range of the wells increased. A change in the chemistry of reservoir fluid with high sulphate content as it flashed and moved to the surface, yielding a low pH discharge, might be responsible.
- Concentrations of total suspended solids significantly affect the thinning of the casing in dry wells.

The regression model needs further refinement before it can provide accurate predictions of a casing's thinning rate. The model reflects low pH wells. The model should be tested on high pH wells, in order to validate the model further and to test its reliability in predicting the thinning rate of casings. In the meantime, the model can be used to determine if a casing's thinning rate is increasing or decreasing, which can then be used as a criterion for selecting wells for casing inspection.

The condition of the casing before it was installed in the borehole could be responsible for the low coefficient of determination (adjusted R^2) of the regression model. The well stimulation activities conducted on some of the wells included in this study have a significant bearing on the results of the regression modelling.

In order to mitigate an increase in the thinning rate, the following measures are recommended:

- The application of a corrosion and scaling inhibitor;
- The use of corrosion resistant metal alloy for areas with low pH fluid;
- The application of an anti-corrosion chemical coating agent to the casing;
- The application of cathodic protection.

7. RECOMMENDATIONS AND FUTURE WORK

The model was not tested on wells with high pH, due to the unavailability of a repeat survey or data from a high pH two-phase well. Therefore, the model needs to be validated, using new field data from wells with high pH fluid, in order to determine the reliability of the model for predicting the casing-thinning rate. The regression model for the thinning rate should be applied to data from other geothermal fields in order to compare the results with that from the Leyte geothermal production field.

The regression model needs to be improved by segmented linear regression to increase the predicting capability of the model, in which independent variables are partitioned into intervals, for example grouping the data according to low pH and high pH. The effects of partial pressure of CO₂ and H₂S on the thinning rate can be include in the regression model, upon which most studies of corrosion rates in oil and gas are concentrated. Shear stress analysis of the fluid flow to the casing can also be a future focus of the study. The shear stress on the wall surface induced by flowing fluid can prevent film formation or may destroy the protective film that has formed.

Historical data of fluid discharge could be used to monitor changes in the thinning rate of the casing with time.

ACKNOWLEDGMENTS

The author would like to express his deepest gratitude to the following:

... the UNU-GTP family under the dedicated and esteemed staff of Dr. Ingvar Birgir Fridleifsson (retired), Mr. Lúdvík S. Georgsson, Director of UNU-GTP, Mr. Ingimar Gudni Haraldsson (Project Manager), Ms. Málfríður Ómarsdóttir (Environmental Scientist), Ms. Thórhildur Ísberg, and Mr. Markús A. G. Wilde. Thank you for giving me the opportunity to attend the six months training programme and to gain more knowledge about the geothermal industry.

... to his supervisors, Dr. Einar Jón Ásbjörnsson, Mr. Hörður Halldórsson, Mr. Benedikt Steingrímsson and Mr. Halldór Örvar Stefánsson, for guidance and support in completing the research study.

... to Mr. Halldór Ármannsson, Mr. Finnbogi Óskarsson and Dr. Jón Örn Bjarnason, for their support in explaining the behaviour of the corrosion species and their assistance in using software WATCH.

... to Mr. Sverrir Thórhallsson for his opinions regarding corrosion in geothermal wells.

... to the management of Energy Development Corporation: President Richard B. Tantoco; and Senior Vice-President of Technical Services Sector, Manuel S. Ogena, for giving me the opportunity to take part in the training programme.

... to his superiors: Mr. Francis Xavier M. Sta. Ana, Mr. Dave Yglopaz and Mr. Edson Emoricha: thank you for nominating the author to take up this specialized course to enhance his technical capabilities on his present line of work.

... to Mr. Jaime Jemuel Austria for his advice in making the research project.

... to his colleagues: Sir Richie Angcoy, Sir Danny Dacillo, Mam Kat Belas-Dacillo, Regina Cabahug, Jansell Jamero, Gary Mondejar, Hazel Colo, Rowena Abapo, and Suzette Labao for providing the data needed for the study, even with their heavy workloads.

... to his parents, Mr. Armando C. Ponce and Mrs. Aurora S. Ponce, and to his siblings for their love and emotional support, inspiring the author to give his best in everything he does.

... to the UNU fellows for all the memories in the training and wonderful experiences that were shared in Iceland.

...finally to GOD for HIS blessings for all of us.

REFERENCES

- Angcoy, E., 2010: *Geochemical modelling of the high-temperature Mahanagdong geothermal field, Leyte, Philippines*. University of Iceland, MSc thesis, UNU-GTP, report 1, 79 pp.
- Arason, Th., Björnsson, G., Axelsson, G., Bjarnason, J.Ö., and Helgason, P., 2003: *The geothermal reservoir engineering software package ICEBOX, user's manual*. Orkustofnun, Reykjavík, report, 48 pp.
- Björnsson, G., Arason, P., Bödvarsson, G.S., 1993: *The wellbore simulator HOLA. Version 3.1. User's guide*. Orkustofnun, Reykjavík, 3 pp.
- Banas, J., Lelek-Borkowska, U., Mazurkiewics, B., and SolarSKI, W., 2007: Effect of CO₂ and H₂S on the composition and stability of passive film on iron alloys in geothermal water. *Electrochimica Acta*, 52, 5704-5714.
- Cabahug, M.R.S., and Angcoy, E.C. Jr., 2013: Modeling the reservoir fluids of acidic geothermal wells in Mahanagdong, Leyte, Philippines. *Procedia Earth & Planetary Science*, 7, 105-108.
- Conover, M., Ellis, P., and Curzon, A., 1979: Material selection guidelines for geothermal power systems. An overview. In: Casper, L.A., and Pinchback, T.R. (eds.), *Geothermal scaling and corrosion*. American Society of Testing Materials, Philadelphia, PA, 262 pp.
- Elguedri, M., 1999: Assessment of scaling and corrosion problems in the Kebili geothermal field, Tunisia. Report 1 in: *Geothermal Training in Iceland 1999*. UNU-GTP, Iceland, 1-40.
- Finnie, I., Stevick, G.R. and Ridgely, J.R., 1992: The influence of impingement angle on the erosion of ductile metals by angular abrasive particles. *Wear*, 152, 91-98.
- Hirtz, P., Buck, C., and Kunzman, R., 1991: Current techniques in acid-chloride corrosion control and monitoring at the Geysers. *Proceedings 16th Workshop on Geothermal Reservoir Engineering, Stanford University, Stanford, Ca*, 83 pp.
- Ikeuchi, J., Sanada, N., Asano, O., Kurata, Y., Odawara, O., and Okahara, Y., 1982: Corrosion and erosion-corrosion of iron based alloys in a geothermal resource area (Onikobe) in Japan. *Proceedings of the International Conference on Geothermal Energy, Florence, Italy*, 1, 383-394.
- Karlsdóttir, S. and Thorbjörnsson, I., 2012: *Hydrogen embrittlement and corrosion in high temperature geothermal well*. NACE international – The Corrosion Society, website: www.nace.org/ctsm/store/product.aspx?id=cd5f691f-82ed-e111-ac69-0050569a007e
- Lichti, K., Soylemeszoglul, S. and Cunlife, K., 1981: Geothermal corrosion and corrosion products. *Proceedings of the New Zealand Geothermal Workshop 1981*, 103-108.
- Lichti, K., White, S. and Sanada, N., 1998: Corrosion in deep and acidic geothermal wells. *Proceedings of the 19th PNOC-EDC Geothermal Conference*, 199-212.
- Ocampo-Diaz, J., Valdez-Salaz, B., Shorr, M., Saucasa-M, I., and Rosas-Gonzales, N., 2005: Review of corrosion and scaling problems in Cerro Prieto geothermal field over 31 years of commercial operations. *Proceedings of the World Geothermal Congress 2005, Antalya, Turkey*, 5 pp.
- Petric, G., and Ksiazek, P., 1997: Flow-accelerated corrosion in industrial steam and power plants. *Proceedings of the Engineering & Papermakers Conference 1997*, 1537-1542.
- Prasetia, A.E., Salazar A.T.N. and Toralde, J.S.S., 2010: Corrosion control in geothermal aerated fluids drilling projects in Asia Pacific. *Proceedings of the World Geothermal Congress 2010, Bali, Indonesia*, 7 pp.
- Sanada, N., Kurata, Y., Nanjo, H. and Ikeuchi, J., 1995: Material damage in high velocity acidic fluids. *Geothermal Resources Council, Trans.* 19, 359-363.
- Sanada, N., Kurata, Y., Nanjo, H., Ikeuchi, J. and Kimura, S., 1998: Corrosion in acidic geothermal flows with high velocity. *Proceedings of the 20th New Zealand Geothermal Workshop*, 121-126.

Wagenmakers, E-J., and Farrell, S., 2004: AIC model selection using Akaike weights. *Psychonomic Bulletin & Review*, 2004, 192-196.

Wahl, E, 1977: *Geothermal energy utilization*. Wiley & Sons, Inc., NY, 26-43.

APPENDIX I: Summary of calliper surveys conducted and water and gas chemistry in two-phase wells in the Leyte geothermal field

TABLE 1: Summary of the calliper survey conducted in two-phase wells of Leyte geothermal production field

Well name	Survey date	Years in service (ref. to date survey)	No of casing joints	Size of production casing (mm)	Casing thickness (mm)	Average thinning rate (mm/year)
Well 1	18-May-12	1.05	52	244.475	11.99	0.7467
Well 2	24-Nov-11	1.40	151	244.475	11.05	0.7086
Well 3	25-Nov-10	1.40	62	177.8	9.19	0.3094
Well 4	14-Jan-12	6.69	26	177.8	9.19	0.1569
Well 5	23-Nov-10	8.05	76	244.475	11.99	0.0895
Well 6	1-Feb-12	14.21	49	339.725	12.19	0.0691
Well 7	14-Jun-12	14.57	51	244.475	11.05	0.0967
Well 8	5-Dec-10	12.72	86	177.8	9.19	0.0390
Well 9	8-Dec-10	12.56	31	244.475	11.05	0.0375
Well 10	27-Nov-10	13.02	50	244.475	11.05	0.0575
Well 11	11-Sep-12	14.97	8	244.475	11.05	0.0929
Well 12	18-Jan-11	13.14	74	244.475	11.05	0.0483
Well 13	5-Sep-11	14.75	91	244.475	11.05	0.0592
Well 14	17-Dec-12	18.09	53	244.475	11.99	0.0622
Well 15	12-Aug-11	5.09	137	244.475	11.99	0.1634
Well 16	12-Dec-12	8.09	63	244.475	11.05	0.1218
Well 17	9-Sep-12	3.47	17	244.475	11.05	0.1291
Well 18	13-Aug-12	12.88	30	244.475	11.05	0.0336
Well 19	26-Aug-12	1.28	81	177.8	9.19	0.4127

TABLE 2: Summary of calliper survey conducted in dry wells of Leyte geothermal production field

Well name	Survey date	Years in service (ref. to date survey)	No of casing joints	Size of production casing (mm)	Casing thickness (mm)	Average thinning rate of cas. joints (mm/year)
Well 20	30-Nov-11	13.98	42	244.475	11.05	0.1033
Well 21	15-May-11	28.30	37	177.8	9.19	0.0547
Well 22	3-Dec-11	12.41	42	244.475	11.05	0.0869
Well 23	21-Aug-11	12.74	29	244.475	11.05	0.1099
Well 24	9-Dec-11	13.04	47	244.475	11.05	0.0701
Well 25	1-Mar-11	1.70	62	244.475	11.05	0.2895
Well 26	30-Sep-11	2.67	114	244.475	11.05	0.3455
Well 27	3-Sep-11	14.81	61	244.475	11.99	0.0481
Well 28	15-Aug-11	15.00	15	339.725	12.19	0.0529
Well 29	26-Feb-11	13.13	11	244.475	11.99	0.0829
Well 30	8-Jun-12	12.94	27	244.475	11.05	0.1118
Well 31	14-Dec-10	11.68	53	244.475	11.05	0.0906
Well 32	19-Dec-12	13.48	30	244.475	11.05	0.0641
Well 33	14-Oct-11	13.18	5	339.725	12.19	0.0458
Well 34	21-Nov-10	4.46	74	244.475	11.99	0.2483
Well 35	4-Feb-12	2.87	51	244.475	11.99	0.3608

TABLE 3: Sampled water chemistry of two-phase wells in Leyte geothermal production field

Well name	Sampling date	Wellhead pressure	Sampling pressure	Enthalpy	Surface concentration (ppm)															
					pH	Li	Fe	HCO3	SO4	Cl	F	Ca	Mg	K	Na	SiO2	B	NH3	H2S	CO2 Total
Well 1	6-May-12	1.01	0.991	1742	3.5	12	16	0	14.6	6495	1.5	238	5.6	947	3327	1188	25	18.5	3.18	0
Well 2	20-Aug-12	1	1	2399	3.6	5.5	62	0	1727	3157	2.4	14	45	315	2400	543	78	33.1	1.08	0
Well 3	29-May-10	1.08	1.06	2265	3.4	14	71	0	40.7	7479	0	191	8.5	1005	3864	1120	53	70.2	0.68	0
Well 4	7-Jun-09	1.03	0.95	1822	5.1	10	1.8	0	35.8	5064	0	101	0.6	741	2561	909	29	38.3	2.17	47.8
Well 5	19-Jan-11	1.03	0.87	1558	4	7.5	1.2	0	188	4066	0	40	2.8	458	2324	632	39	18.8	2.03	0
Well 6	15-Jul-10	1.26	1.23	1232	6.7	0	0	23.8	0	2933	0	47	0	291	1694	583	43	0	0	22.6
Well 7	26-Sep-12	1.2	1.082	1078	7.3	5.6	0.1	54.7	77	2870	1.9	14	0.1	288	1703	603	48	2.53	2.76	50.2
Well 8	1-Jun-10	1.29	1.14	1441	5.9	8.7	0	28.8	32.3	4603	0	86	0	504	2715	707	50	2.79	1.78	50.7
Well 9	1-Jun-10	1.24	1.12	1222	5.6	7.5	0	22.8	34.9	4035	0	21	0	440	2349	618	50	3.62	1.47	75.3
Well 10	3-Sep-08	1.393	1.383	1115	6.1	0	0	44.5	0	1953	0	5.3	0	170	1195	461	23	0	0	79.2
Well 11	23-Jun-12	1.41	1.41	1539	5.8	21	0.3	7.26	45.1	9151	1.5	190	0.3	1024	4987	646	218	4.17	5.19	32.1
Well 12	10-Feb-11	1.37	1.29	1264	6.8	20	0.2	14.6	25.7	8573	2	178	0	945	4601	655	188	2.88	0.57	20.2
Well 13	29-Oct-11	1.4	1.395	2476	6.2	24	1.5	25	34.2	9475	2.9	214	1.1	986	4836	632	221	4.83	4.61	20.8
Well 14	26-Apr-12	1.19	1.052	1212	7	16	0.7	8.62	31	7375	1.8	123	0.3	784	3952	593	185	2.8	3.92	6.93
Well 15	13-Jun-11	1.66	1.4	1409	4.8	0	1.1	12.2	0	1128	0	29	0.2	134	563	0	56	7.68	60.8	382
Well 16	25-Jul-12	1.5	1.453	2463	4.4	31	8.4	0	45	14897	5	275	2	1727	6899	765	663	16.6	10.4	0
Well 17	11-Jan-12	1.73	1.657	1351	5.8	16	0.4	15.3	21.2	6129	1.1	68	0	660	3404	718	150	4.37	3.64	36.9
Well 18	26-Aug-10	1.55	1.5	2536	6.2	8	0.1	28.3	37.9	3884	0	44	0	396	2214	554	161	5.34	0.11	46.1
Well 19	23-Jul-12	1.32	1.129	2370	3.8	34	37	0	14.9	14679	1.8	366	2	1886	7655	817	509	3.32	6.22	0

TABLE 4: Sampled gas chemistry of two-phase wells in Leyte geothermal production field

Well name	Sampling date	WHP	Sampling pressure	Surface concentration (mmol / 100 mol)									
				H	CO ₂	H ₂ S	NH ₃	He	H ₂	Ar	N ₂	CH ₄	Na
Well 1	6-May-12	1.01	0.991	1742	610	37.7		0	1.4	0.05	4.5	3.03	25.1
Well 2	20-Aug-12	1.01	0.01	2399	892	38	1.62	0	1.81	0.03	4.08	3.11	54.1
Well 3	29-May-10	1.08	1.06	2265	374	45	1.31	0	0.62	0.02	1.54	0.58	15.1
Well 4	7-Jun-09	1.03	0.95	1822	984	59	41.2	0	2.23	0.54	49.3	3.53	5.32
Well 5	19-Jan-11	1.03	0.87	1558	513	22.4	1.56	0	0.36	0.08	4.44	0.83	40.2
Well 6	23-Aug-10	1.27	1.24	1232	780	25	3.08	0	0.55	0.21	12.2	6.09	708
Well 7	14-Sep-12	1.16	1.082	1078	399	13.2	1.41	0	0.09	0.34	20.7	1.16	290
Well 8	20-Aug-10	1.25	1.16	1441	843	21	1.12	0	0.69	0.06	4.82	1.5	59.5
Well 9	30-Aug-10	1.21	1.06	1222	556	13.2	1.31	0	0.18	0.04	2.8	1.63	143
Well 10	19-Nov-08	1.403	1.393	1088	536	11.6	1.15	0	0.54	0.4	26.8	6.43	1.06
Well 11	23-Jun-12	1.41	1.41	1539	503	23.9	1.38	0	2.14	0.04	3.39	2.09	171
Well 12	10-Feb-11	1.37	1.29	1264	148	15.1	1.56	0	0.12	0.01	0.61	0.05	150
Well 13	29-Oct-11	1.4	1.395	2476	460	38.6	2.05	0	0.42	0.18	13.5	0.28	54.9
Well 14	26-Apr-12	1.19	1.052	1212	183	21.2	1.68	0	0.77	0.17	14.5	0.71	8.28
Well 15	13-Jun-11	1.66	1.4	1409	358	16.8	0.18	0	0.5	0.01	0.99	0.19	35.8
Well 16	25-Jul-12	1.5	1.4	2463	706	26.3	0.86	0	3.06	0.18	17.2	1.14	40
Well 17	11-Jan-12	1.73	1.4	1351	895	20.4	2.46	0	0.16	0	0.32	0.52	45.9
Well 18	26-Aug-10	1.55	1.4	2536	750	23.6	2.92	0	2.63	0.3	24	4.69	13.9
Well 19	23-Jul-12	1.32	1.4	2370	306	35.6	0.53	0	3.66	0.04	2.42	1.06	67.7



INJECTION AND PRODUCTION WELL TESTING IN THE GEOTHERMAL FIELDS OF SOUTHERN HENGILL AND REYKJANES, SW-ICELAND AND THEISTAREYKIR, N-ICELAND

Wondwossen Redie Kewiy
Geological Survey of Ethiopia
Geothermal Energy Department
P.O. Box 2302
Addis Ababa
ETHIOPIA
rediewondwossen@yahoo.com

ABSTRACT

In this paper, different approaches and methods are used for analysing well test data. Well testing is performed in order to monitor the pressure response in a reservoir when it is subjected to injection or production. The main purpose is to evaluate the properties that govern the nature of the reservoir, flow characteristics and deliverability of the well. The project emphasis is on well completion and flow test data from Hellisheidi, Reykjanes and Theistareykir geothermal areas. An analysis of data from step-rate injection tests, temperature and pressure profiles was conducted in Hellisheidi, Reykjanes and Theistareykir geothermal areas as well as a discharge test in Reykjanes. Four wells were selected: Wells HE-04, HE-09, RN-28 and ThG-09. Well Tester software was used for the step rate injection test analysis. Temperature and pressure profiles were analysed to estimate the formation temperature and the initial reservoir pressure. The ICEBOX software was applied to get the Horner plot of rock temperature at selected depths in HE-04 and ThG-09 well, using a program called BERGHITI, and the BOILCURVE program was used to acquire the boiling curve. During the production test, measurements were made from which the fluid flow and its energy content were deduced and chemical characteristics were measured. The Russel James method can be used to determine the flow characteristics with a simple weir-box being used to measure the liquid flow.

1. INTRODUCTION

The aim of this project is to study examples of injection and production well testing at southern Hengill, Reykjanes and Theistareykir high temperature geothermal fields in Iceland. Before describing the well testing activities, the geological structure of Iceland will be reviewed in general.

The country is located in the active mid-oceanic ridge system. It is one of a few areas in the world where the mid-oceanic ridge rises above sea level. Central volcanoes and fissure swarms characterize the volcanic zones. A tectonic and active volcanic zone crosses the country from southwest to northeast (Figure 1). The high-temperature areas are narrowed to the active zones of volcanism. The Mid-Atlantic Ridge is a divergent plate boundary along which the North American plate and the European plate are

drifting away from each other in the northern part of the Atlantic Ocean. The Reykjanes Ridge, southwest of Iceland, and the Kolbeinsey Ridge, to the north, are segments of the Mid-Atlantic Ridge. The spreading rate is around 2 cm/year. Iceland is formed as a result of widespread volcanism along this ridge.

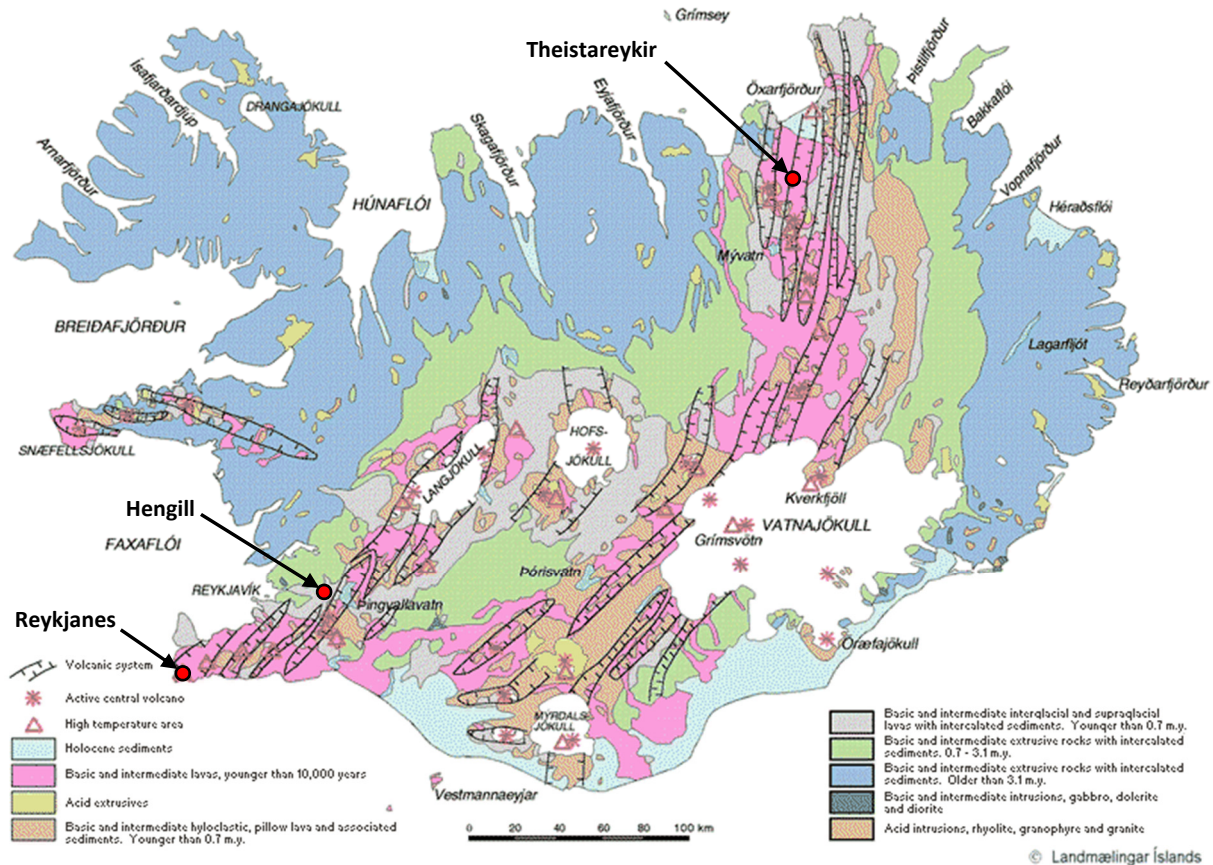


FIGURE 1: Geological map of Iceland showing the oldest Tertiary rocks, older Plio-Pleistocene eruptives, Holocene rocks and other young formations; volcanic systems follow the oceanic ridge (adopted from Jóhannesson and Saemundsson, 1999)

2. GEOLOGY OF ICELAND

Iceland is located on the Mid-Atlantic Ridge, the boundary between the North American and the Eurasian plate. Iceland is the product of an interaction between a spreading plate boundary and a hot mantle plume, the source of additional volcanism under the country; the country is moving slowly northwest across the hot spot (Vink, 1984). The spreading is approximately 8-20 mm/year or 2 cm/year according to Árnadóttir (2008). The creation of Iceland in its current form is thought to have begun some 24 million years ago (Saemundsson, 1979). The oldest rocks are 16-14 million years old and are exposed in the extreme northwest and east, while the youngest rocks are located within the volcanic rift zone (Jóhannesson and Saemundsson, 1999).

The geological formations of Iceland can be divided into the following four major groups: Tertiary (16 to 3.3 Ma - Miocene-Pliocene); Plio-Pleistocene (3.3 to 0.8 Ma); Upper Pleistocene (0.8 to 0.011 Ma); and Postglacial (11,000 to present). Iceland is mainly composed of basalts (80-85%) and intermediate to acidic rocks (10%) while sedimentary rocks of volcanic origin represent only 5-10%. The Pleistocene

rocks are confined mainly to a broad SW-NE trending zone between the Tertiary plateau basalt areas, and are also exposed within the Tjörnes, Snaefellsnes and Skagi peninsulas.

3. GEOTHERMAL ENERGY

Geothermal energy is the natural heat contained within the earth that can be recovered and exploited. Heat flows from the interior of the earth to the surface, either by convection through hot water mass transfer or by heat conduction. The most obvious appearances of the earth's thermal energy are in areas of recent volcanism and tectonic activity. The temperature increases with depth and the volcanoes, geysers, hot springs, etc. are, in a sense, the visible or tangible expression of the heat which originates in the interior of the Earth.

According to Muffler and Cataldi (1978), a geothermal resource is what should more specifically be called the accessible resource base, that is, all of the thermal energy stored between the Earth's surface and a specified depth in the crust, beneath a specified area and estimated with respect to the local mean annual temperature.

A geothermal reservoir is usually defined as the section of an area of geothermal activity that is hot and permeable so that it can be exploited economically for the production of fluid and heat (Grant and Bixley, 2011).

Low-temperature and high-temperature reservoirs: Low-temperature geothermal systems have a reservoir temperature below 150°C, and high-temperature systems have reservoir temperatures above 200°C at 1000 m depth. The intermediate system between these two systems has a temperature between 150 and 200°C.

Liquid-dominated, vapour-dominated and two phase geothermal reservoirs: Geothermal reservoirs are conveniently categorized as either liquid-dominated or vapour-dominated. In each case, the name refers to the phase which controls the pressure in the reservoir in its undisturbed state. When one phase is dominant, the other phase may also be present and partially mobile. A reservoir where steam and water co-exist is called a two-phase geothermal reservoir. In high-temperature reservoirs, a decline in pressure caused by exploitation may initiate boiling in parts of the reservoir making a liquid-dominated reservoir become a vapour reservoir.

4. THE THEISTAREYKIR, S-HENGILL AND REYKJANES GEOTHERMAL AREAS

4.1 Theistareykir

The Theistareykir high-temperature geothermal area lies in the Theistareykir fissure swarm in NE-Iceland (Figures 1 and 2). The geothermal activity covers a 10.5 km² area (Sæmundsson, 2007) and the most intense activity is on the northwest and northern slopes of Mt. Bæjarfjall and in the pastures extending northwards to the western part of Mt. Ketilfjall. If the old alteration in the western part of the swarm is considered to be a part of the thermal area, its coverage is nearly 20 km².

The bedrocks in the area are divided into breccias (hyaloclastites) from sub-glacial eruptions during the Ice Age, interglacial lava flows, and recent lava flows (younger than 10,000 years), all of which are basaltic rock. Acid rocks are only found on the western side of the fissure swarm, from a sub-glacial eruption during the last glaciation. Rifting is still active in the fissure swarm, its faults and fractures active in recent times (Ármannsson et al., 1986).

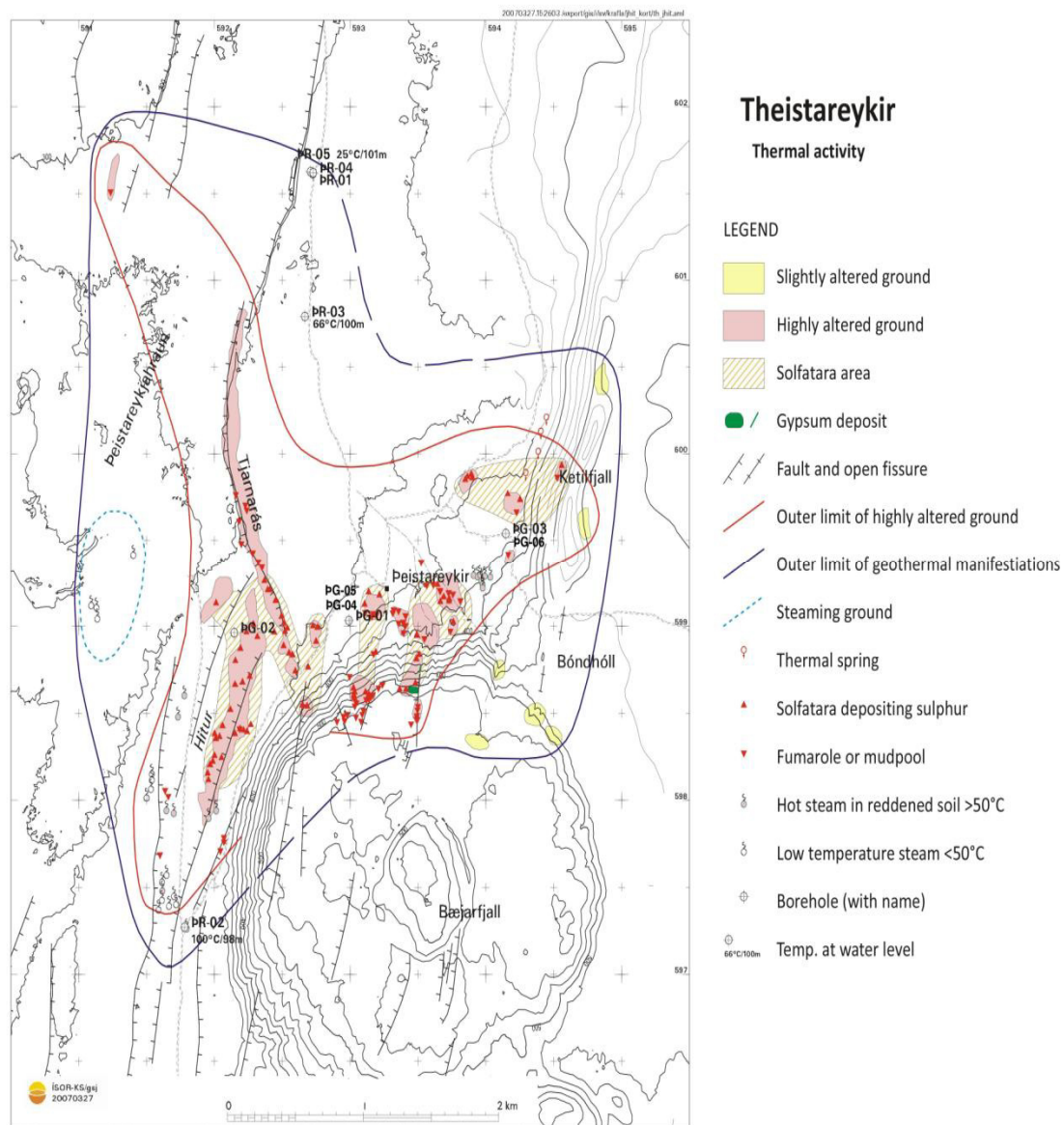


FIGURE 2: Thermal activity at Theistareykir (Ármansson, 2008)

4.2 S-Hengill

The Hengill geothermal system lies in the middle of the western volcanic zone in Iceland, on the plate boundary between N-America and the European crustal plates. It is one of the largest high-temperature geothermal areas in the country. The geothermal activity of this area is connected to three volcanic systems. The geothermal area in Reykjadalur, Hveragerdi, belongs to the oldest system, called the Grensdalur system. North of this is a volcanic system named after Mt. Hrómundartindur, which last erupted about 10,000 years ago.

The geothermal area in Ölkelduháls is connected to this volcanic system. West of this volcanic system lies the Hengill volcanic system, with intense tectonic and volcanic NE-SW fractures and faults extending from Lake Thingvallavatn to Nesjavellir and further to the southwest through Innstidalur, Kolvidarhóll, Hveradalir (hot spring valley) and Hellisheidi (Figure 3). The bedrock in the Hengill area consists mostly of palagonite formed by volcanic eruptions below glaciers during the last ice ages. For this project, wells HE-04 and HE-09 were selected to study temperature and pressure profiles and well tests.

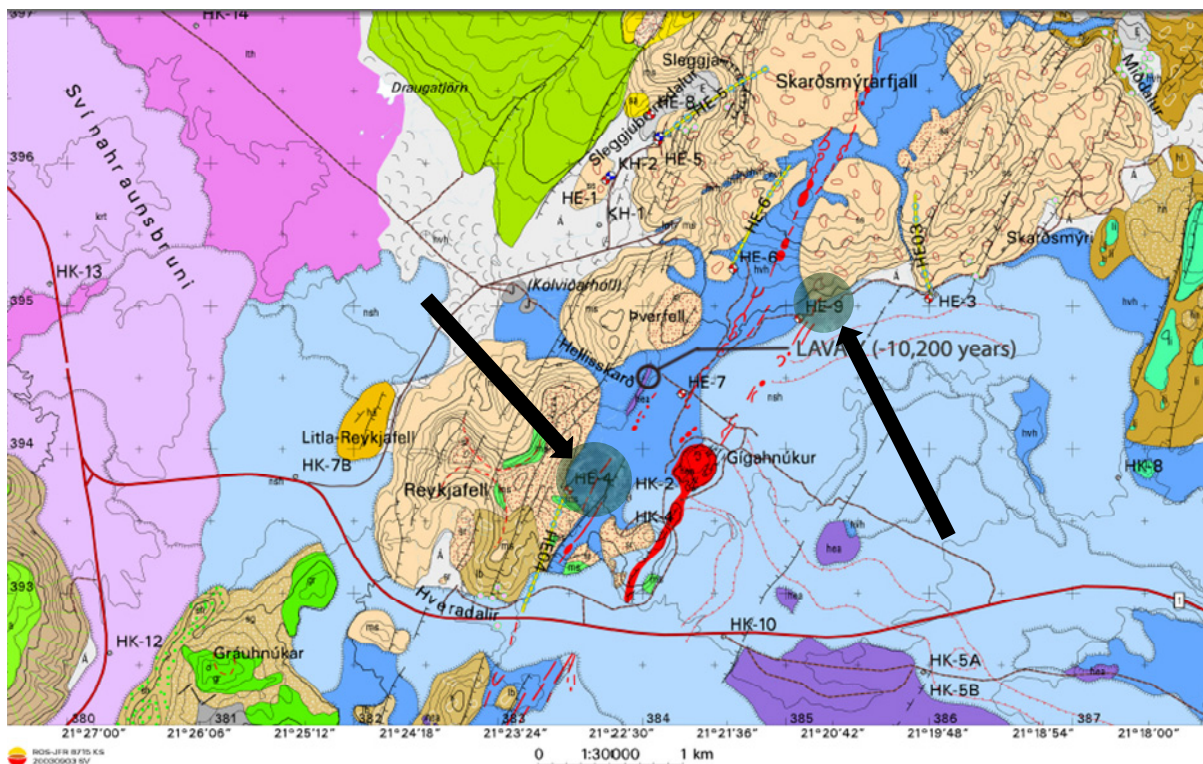


FIGURE 3: Geological map of S-Hengill showing the locations of wells HE-04 and HE-09 (Saemundsson, 1995)

4.3 Reykjanes

The Reykjanes geothermal system is located on the Reykjanes Peninsula, SW-Iceland. It is constructed of young, highly permeable basaltic formations, transected by an intense NE-SW trending fault zone, and is tectonically active. The volcanic activity on the peninsula is concentrated along fissure swarms. High-temperature geothermal systems occur in all of the Reykjanes Peninsula fissure swarms (Figure 4).

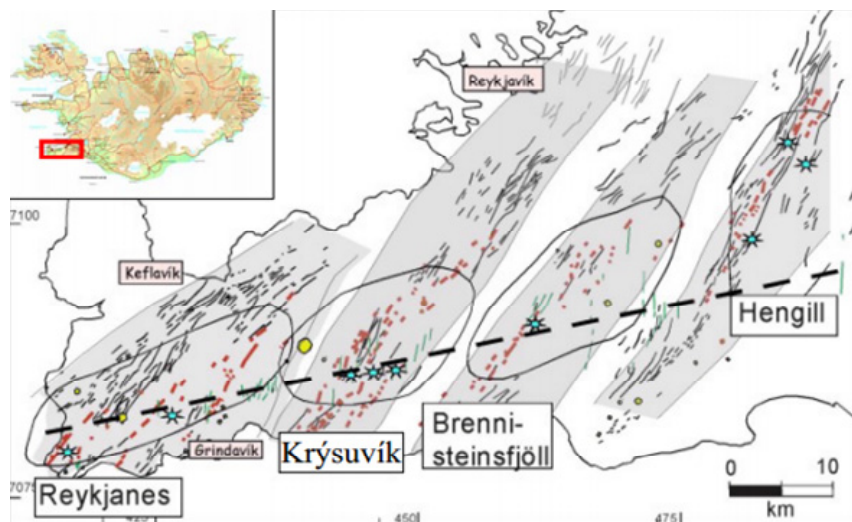


FIGURE 4: Tectonic map of Reykjanes peninsula showing fissure swarms, eruptive fissures, geothermal centres and approximate location of the plate boundary (dashed line) (modified from Clifton, 2007)

The Reykjanes geothermal area is located at the centre of active fault swarms that facilitate hydrologic convection. High-level magma chambers have apparently not formed in the Reykjanes volcanic systems and sheeted dike complexes are likely to serve as the magmatic heat source for geothermal activity. Surface geothermal manifestations occur over an area of 1 km², but observations from more than 30 drill holes and several activity surveys indicate that the subsurface area of the active system is at least 2 km².

5. THEORY OF WELL TESTING

The first step for a reservoir engineer is to estimate the relevant reservoir and wellbore parameters by a transient pressure test. This information is needed to confirm whether a well is satisfactorily drilled and to decide how to exploit the reservoir. The important reservoir and wellbore parameters are the permeability, the storativity, and the skin factor. The type of reservoir (porous and fractured) and the type and location of the reservoir boundaries are also important.

In practice, well testing (pressure transient tests) consists essentially of changing the well's flow rate by injection into the well and measuring the well's response as a function of time. A model is used to simulate the data and the reservoir and well parameters are deduced from the model (Figure 5).

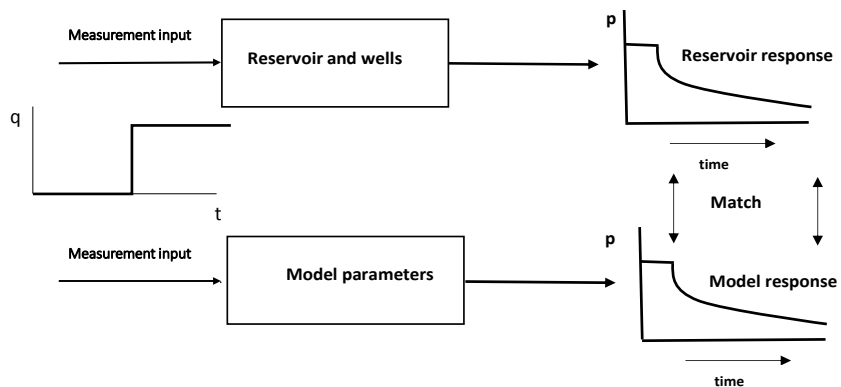


FIGURE 5: Well testing procedure (Horne, 1995)

Types of well tests

Examples of the possible types of tests are shown in Figure 6. Note that q is positive for production and negative for injection.

During well tests, fluid is extracted to the surface or injected into the well at controlled rates. A program of flow and shut-in periods is used to establish deliverability and completion efficiency of the well. Tests can involve a single well or many wells. Depending on test objectives and operational considerations, a range of well tests can be carried out.

Build-up test: This test is conducted in a well that has been producing for some time at a constant rate and is then shut-in. The build-up down hole pressure is then recorded for a given time.

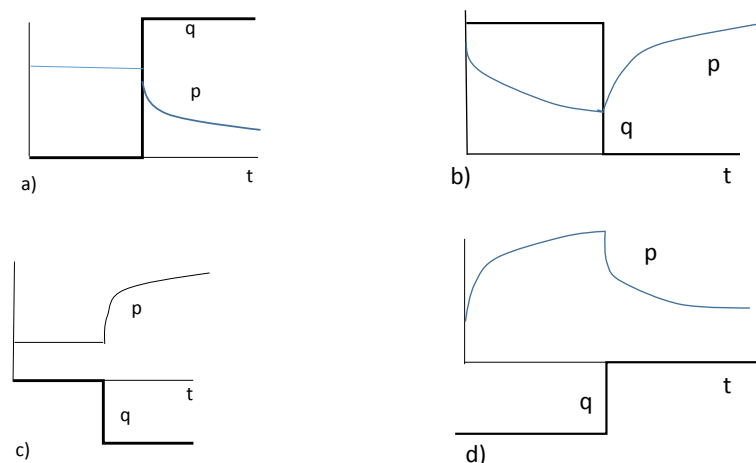


FIGURE 6: Types of well tests: a) Drawdown test; b) Build-up test; c) Injection test; and d) Falloff test (Horne, 1995)

Drawdown test: This test is conducted when a well has flowed at a constant rate. The down hole pressure and the production rate are measured as functions of time and analysed to estimate the reservoir properties. The major difficulty of the drawdown is the inability to maintain a constant flow rate.

Injection test: This test is identical to a drawdown test, except that the flow is into the well rather than out of it. Fluid is injected into the well at a constant rate, and the injection rate and the down hole pressure are measured as functions of time.

Falloff test: This test is analogous to a build-up test and it measures the pressure decline as a function of time subsequent to shut-in or the reduction of an injection.

5.1 Injection test

The injection well test is a field test method where fresh water is injected into the well to raise the water level until a steady height is attained, and the pressure or water level change in the well is recorded. The hydrogeological parameters (such as permeability) of the test layer can be determined by analysing the injection well test data. Its theoretical basis is that the water flow from the well to the stratum shall conform to the laws of seepage flow in a porous medium.

5.1.1 Theoretical background of injection well testing

When a well is subjected to injection in order to monitor the pressure response in a reservoir, it is used to evaluate the properties that govern flow characteristics and the well. The parameters that are deduced by modelling are permeability, storativity, transmissivity, wellbore skin, well bore storage, initial pressure and reservoir boundaries. To estimate all these parameters, mathematical models are used to simulate the reservoir response.

The pressure diffusion equation is used to calculate the pressure in the reservoir after a given time and at a certain distance from an injection or production well receiving or producing fluid at a specific rate. The following assumptions are made to simplify the derivation of the equation (Horne, 1995):

- Horizontal radial flow;
- Darcy's Law;
- Homogeneous and isotopic reservoir and isothermal conditions;
- Single phase flow and small pressure gradient;
- Uniform thickness of the reservoir;
- Constant permeability (k), porosity (ϕ), fluid viscosity (μ) and small and constant total compressibility (c_t); and
- Gravity and thermal effects are negligible.

The pressure diffusion equation is derived by combining the equations from the three laws that govern it:

- a) Law of conservation of mass (mass in - mass out = mass rate of change):

$$\left(\rho Q + \frac{\partial(\rho Q)}{\partial r} dr \right) - \rho Q = 2\pi r dr \frac{\partial(\rho \phi h)}{\partial t} \quad (1)$$

- b) Darcy's law (conservation of momentum):

$$Q = \frac{2\pi r h k}{\mu} \frac{\partial p}{\partial r} \quad (2)$$

- c) Fluid compressibility (equation relates the pressure to density at a constant temperature):

$$c_t = \phi c_w + (1 - \phi) c_r \text{ where } c_r = \frac{1}{1 - \phi} \frac{\partial \phi}{\partial p} \text{ and } c_w = \frac{1}{\rho} \frac{\partial \rho}{\partial p} \quad (3)$$

This is reduced to:

$$\frac{1}{r} \frac{\partial}{\partial r} \left(r \frac{\partial p}{\partial r} \right) = \frac{\mu c_t}{k} \frac{\partial p}{\partial t} = \frac{S}{T} \frac{\partial p}{\partial t} \text{ or } \frac{\partial^2 p}{\partial r^2} + \frac{1}{r} \frac{\partial p}{\partial r} = \frac{\mu c_t}{k} \frac{\partial p}{\partial t} = \frac{S}{T} \frac{\partial p}{\partial t} \quad (4)$$

$$S = c_t h \text{ and } T = \frac{k h}{\mu} \quad (5)$$

where ρ = Density (kg/m³);
 Q = Volumetric flow rate (m³/s);
 ϕ = Porosity (-);

c_t	= Total compressibility (Pa^{-1});
c_r	= Rock compressibility (Pa^{-1});
c_w	= Water compressibility (Pa^{-1});
T	= Transmissivity ($\text{m}^3 / (\text{Pa s})$);
S	= Storativity ($\text{m/Pa} = (\text{m}^3 / (\text{m}^2 \text{Pa}))$);
μ	= Dynamic viscosity (Pa s);
k	= Permeability (m^2); and
h	= Reservoir thickness (m).

5.1.2 Initial parameters

The deduced parameters found by the simulation of a well test (Júliússon et al., 2007) are explained in the report as given by the software, and follow below almost word for word.

The *storativity* has great impact on how fast the pressure movement can travel within the reservoir. Also, the storativity varies significantly between reservoir types: liquid-dominated, two-phase or dry steam. The variation is because of its dependence on fluid compressibility. The storativity common values for liquid-dominated geothermal reservoirs are around $10^{-8} \text{ m}^3 / (\text{Pa} \cdot \text{m}^2)$ while for two-phase reservoirs it might have values on the order of $10^{-5} \text{ m}^3 / (\text{Pa} \cdot \text{m}^2)$.

The *transmissivity* describes the ability of the reservoir to transmit fluid, hence mainly affecting the pressure gradient between the well and the reservoir. The transmissivity can vary by a few orders of magnitude but common values from injection testing in Icelandic geothermal reservoirs are on the order of $10^{-8} \text{ m}^3 / (\text{Pa} \cdot \text{s})$.

During an injection test, the *injectivity index* (II) is often used as a rough estimate of the connectivity of the well to the surrounding reservoir. Here it is given in units of $(\text{L/s})/\text{bar}$ and is defined as the change in the injection flow rate divided by the change in the stabilized reservoir pressure:

$$II = \frac{\Delta Q}{\Delta P} \quad (6)$$

Where II = Injectivity $(\text{l/s}/\text{bar})$;
 ΔQ = Change of flow rate (l/s) ; and
 ΔP = Change in pressure (bar) .

By using the injection well test, the main characteristics of the reservoir and the well which can be determined are:

- 1) The permeability;
- 2) The transmissivity;
- 3) The storativity;
- 4) The boundary properties; and
- 5) The skin.

The skin is a variable used to quantify the permeability of the volume immediately surrounding the well (Figure 7). This volume is often affected by drilling operations, being either damaged (because of drill cuttings blocking the fractures) or stimulated (due to extensive fracturing around the well). For damaged wells, the *skin factor* is positive, and for

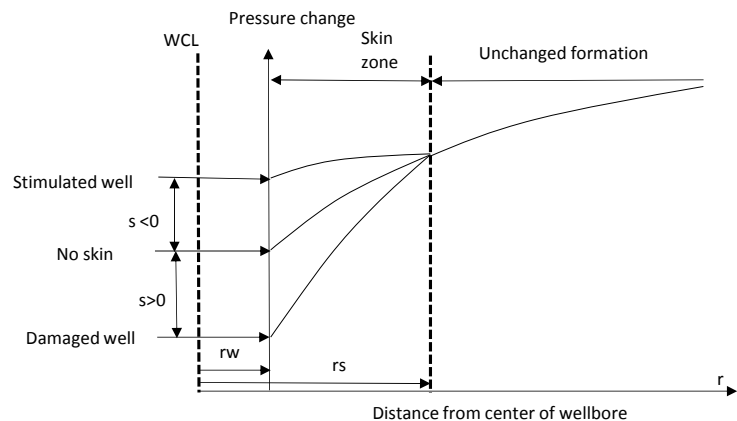


FIGURE 7: Pressure changes in the vicinity of a well due to a skin effect (WCL = well centre line; r_w = well radius; r_s = radius of skin) (Hjartarson, 1999)

stimulated wells it is negative. The skin factor (s) in Icelandic geothermal reservoirs is commonly around -1, though values may range from about -5 to 20. When $s < 0$, the well reacts as a wider well would (stimulated); if $s > 0$, the well seems narrower (damaged).

Different types of boundaries are shown in Figure 8.

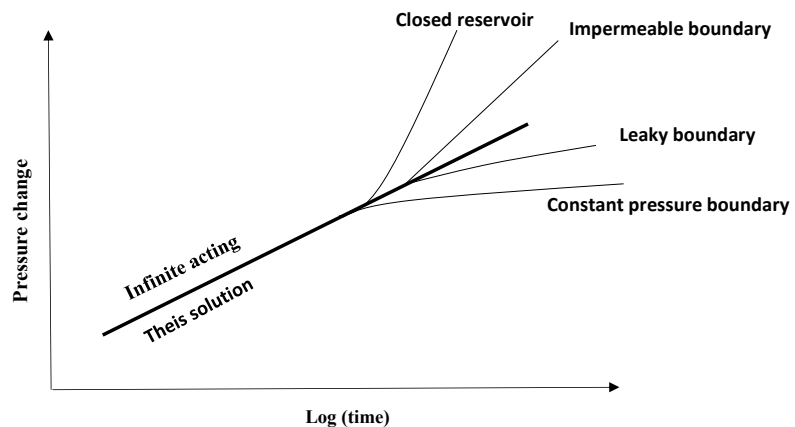


FIGURE 8: Typical pressure responses for different reservoir models (Böðvarsson and Witherspoon, 1989)

5.2 Production well testing

5.2.1 Theoretical background

Production well tests in high-temperature geothermal wells are conducted to determine the production capacity and to analyse the flow characteristics of a well. The tests are done after a geothermal well has been drilled and allowed to warm up for some time or stopped after producing for a while. Then a discharge test is conducted by starting the well's flow, followed by measurements to calculate the fluid flow at different wellhead pressures. The well is discharged into a silencer which is designed to reduce the noise level resulting from the discharge. In addition, the silencer acts as a water-steam separator at atmospheric pressure. Figure 9 shows the setup for production well testing and the example and formulas here are adjusted to Reykjanæs, where the separator and equipment were moved to the well to be monitored. The lip pressure is measured at the end of the discharge pipeline as it enters the silencer, and measurement of water separated from the silencer is done in a V-notch weir while the steam is allowed to escape into the atmosphere.

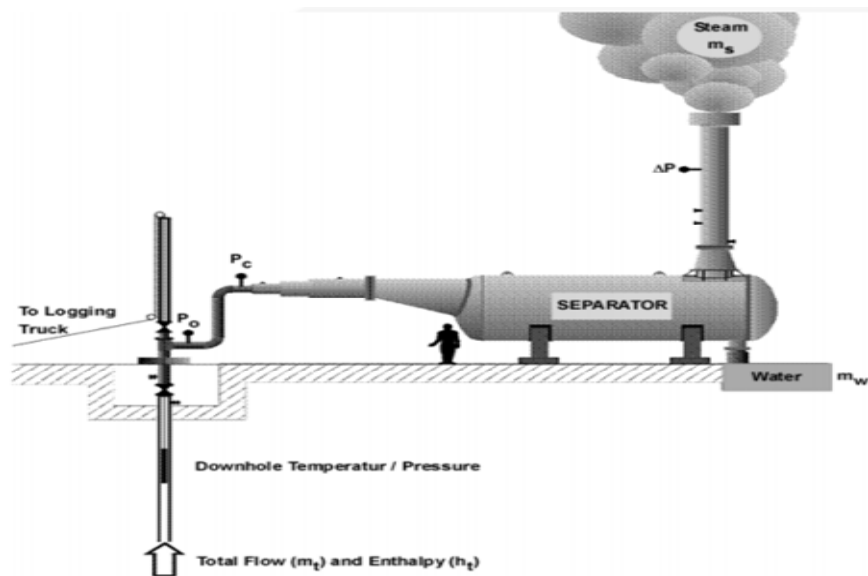


FIGURE 9: Flow and enthalpy separator measurements (Haraldsdóttir, 2013)

Russell James's formula is an empirical formula developed in 1960 which relates mass flow, enthalpy, discharge pipe area and lip pressure as follows:

$$Q_t = KA \frac{P_c^{0.96}}{H^{1.102}} \quad (7)$$

where Q_t = Mass flow (kg/s);
 K = 184 for A in cm^2 ;
 H = Total enthalpy (kJ/kg);

A = Cross section area of the pipe (cm²); and
 P_c = Lip pressure (bar-a).

The mass ratio of steam to the the total flow and the total enthalpy as a function of the enthalpy of steam and enthalpy of water can be written as:

$$X = \frac{Q_s}{Q_t} \quad \text{and} \quad H = XH_s + (1 - X)H_w \quad (8)$$

where X = The steam mass fraction;
 Q_s = Mass flow of steam (kg/s);
 H_s = Enthalpy of steam (kJ/kg); and
 H_w = Enthalpy of water (kJ/kg).

The separated water flow Q_w is the water separated at atmospheric pressure from the total well flow with enthalpy H . Therefore,

$$Q_t = Q_w \frac{H_s - H_w}{H_s - H} \quad (9)$$

where Q_w = Mass flow of water (kg/s);

Combining Equations 7 and 9 gives:

$$\frac{Q_w}{AP_c^{0.96}} = \frac{184}{H_t^{1.102}} \frac{H_s - H}{H_s - H_w} \quad (10)$$

The enthalpies H_s and H_w can be found in a steam-table for corresponding pressure or temperature and the only unknown is H_t from which the electric power can be calculated.

6. INJECTION WELL TESTS FROM FOUR HIGH-TEMPERATURE WELLS IN ICELAND

An injection test is mostly performed in high-temperature wells at the end of drilling. Injection tests for four wells are studied in this project. When water is injected into the well, the pressure response can be monitored. The injection rate is changed in steps during the test, increasing or decreasing the rate in order to observe the different pressure responses in the well. It is possible to estimate different parameters of the well and the surrounding reservoir by simulating the pressure response to the injection, such as the injectivity index, storativity, transmissivity and skin effect, from the information gathered. The processing of the data and the Well Tester simulations are described for each of the three steps in Well HE-04, but only the results are shown for the other wells.

6.1 Well HE-04

Well HE-04 is a vertical well which was drilled in 2001 to a measured depth of 2008 m. The injection test in Well HE-04 was performed after completion of drilling on 12 Oct. 2001. All three steps in the injection test were performed the same day. The injection rates changed from 40 to 20.5 l/s; 20.5 to 30.8 l/s; and 30.8 to 45 l/s (Figure 10). The injection test was done in 7 hours and 18 minutes.

The pressure gauge was located at 1600 m which was believed to be close to the main feed zones in the well. Before the injection test started on 12 Oct. 2001, injection was constant at 40 l/s of water, to wash the formation from offensives of filtrate and cuttings formed during drilling, to improve the skin effect and achieve a stabilized flow rate before the injection test. At 02:15, injection was decreased to 20.5 l/s, and at 04:06 the injection was increased to 30.8 l/s.

From Figure 10, it can be seen that in step 1 the pressure drops after it seems to be stabilizing; this is probably due to instable injection or problems with the measuring device, but could indicate a small opening in the reservoir. But steps 2 and 3 show an increase in pressure. In step 3, the end of the injection test, the injectivity index is increased to 14.2 (l/s)/bar.

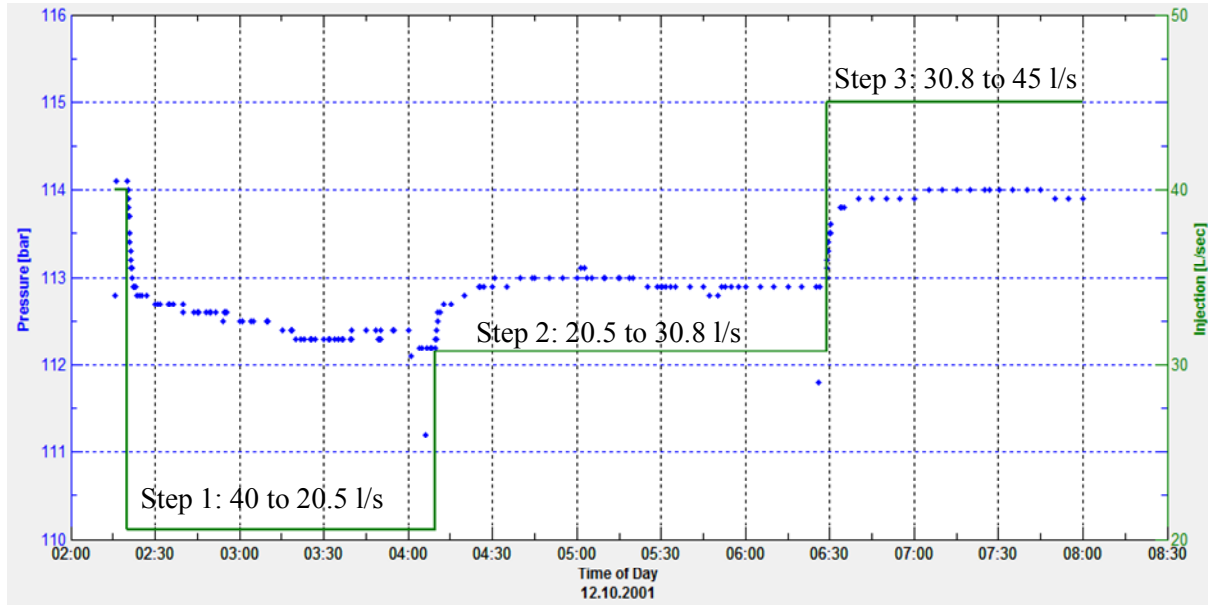


FIGURE 10: Pressure and injection as a function of time at 1600 m depth in Well HE-04 during an injection well test

To model the data (pressure vs. time) during the injection test, a software called Well Tester was used. Well Tester was developed at ISOR (Iceland GeoSurvey). The well test model selected for Well HE-04 assumed a homogenous reservoir, constant pressure boundary (Figure 8), constant skin and well bore storage for all of the steps.

The reservoir temperature was inserted into Well Tester as well as the wellbore radius r_w , the dynamic viscosity of the reservoir fluid μ , the total compressibility c_t , and the porosity ϕ , partly by choosing the default values in Well Tester. All parameter values are shown in Table 1, as well as the initial pressure which Well Tester deduced from the data file with time and pressure.

TABLE 1: Summary of the initial parameters given in Well Tester for Well HE-04

Parameter name	Parameter value	Parameter unit
Estimated reservoir temperature	230	°C
Estimated reservoir pressure	113	bar
Wellbore radius (r_w)	0.11	m
Dynamic viscosity of reservoir fluid (μ)	1.18×10^{-4}	Pa·s
Total compressibility	1.3×10^{-10}	1/Pa
Porosity (ϕ)	0.10	-

The dynamic viscosity was updated by Well Tester for the selected temperature.

The Well Tester software was used to simulate each step separately, and the parameters were calculated for each step. The results from Well Tester are shown in Table 2 and explanations of the data processing and modelling with Well Tester follow for Well HE-04.

TABLE 2: Summary of the results from the non-linear regression parameter estimate using injection test data from Well HE-04

	Storativity S ($\text{m}^3/(\text{Pa}\cdot\text{m}^2)$)	Transmissivity T ($\text{m}^3/(\text{Pa}\cdot\text{s})$)	Skin factor s	Wellbore storage C (m^3/Pa)	Permeability thickness kh (Dm)	Injectivity Index II ($(\text{l/s})/\text{bar}$)
Step 1	1.5×10^{-10}	6.4×10^{-8}	-3.4	1.4×10^{-5}	7.5	11.4
Step 2	4.4×10^{-8}	5.7×10^{-8}	-3.5	3.0×10^{-5}	6.7	11.3
Step 3	1.9×10^{-8}	1.5×10^{-7}	-0.7	1.0×10^{-5}	17.9	14.2

Modelling step 1:

Using the Theis model, non-linear regression analysis was performed to find the parameters that best fit the selected data. The results are shown graphically for step 1 in Figure 11. Here the decrease in injection caused the pressure to decrease from 114.1 to 112.4 bar, which is a change of 1.7 bar. The total time was 1 hour and 15 minutes. Figure 12a shows additional plots of the same data on a log-linear scale and (b) a log-log scale. Figure 12b also shows the derivative of the pressure response, multiplied with the time passed since the beginning of the step. This is used to determine which type of model is most applicable for the observed data.

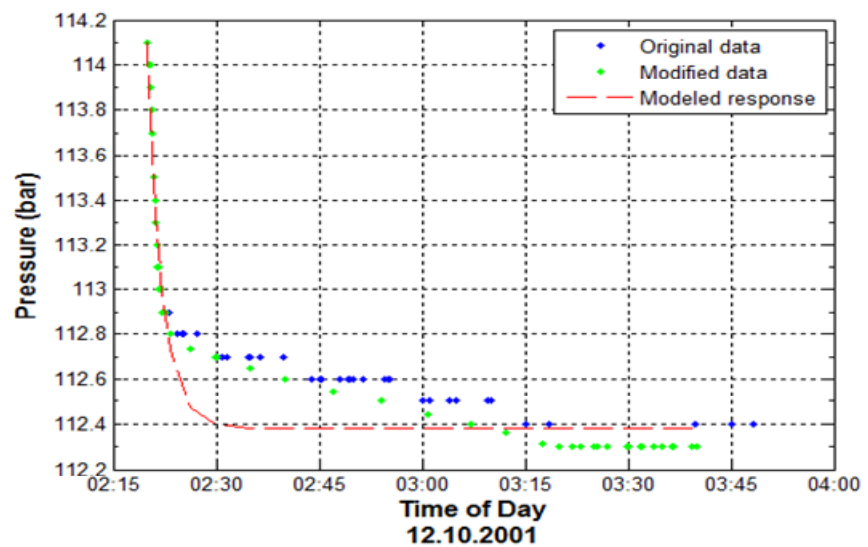


FIGURE 11: The model results and the selected data for step 1 in Well HE-04

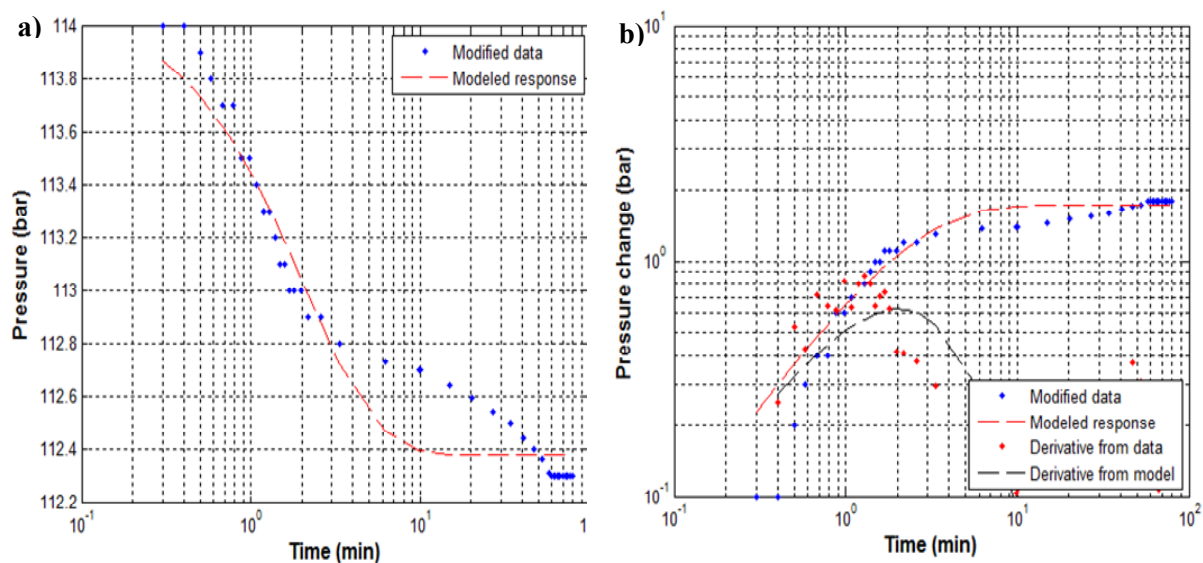


FIGURE 12: The model results and the selected data for step 1 in HE-04 on; a) a log-linear scale, and b) a log-log scale; the derivatives in (b) are commonly used to determine the most appropriate type of model

Modelling step 2:

The regression analysis results are shown graphically for step 2 in Figure 13. The modelled response and the modified data show a good fit. The pressure increases by 0.9 bar during 2 hours and 15 minutes. Figure 14 shows an additional plot of the same data on a) a log-linear scale and b) a log-log scale. In the log-linear scale, the modelled response fits quite well with the modified data.

In the log-log scale model, the derivatives from the data are scattered on Figure 14 (b).

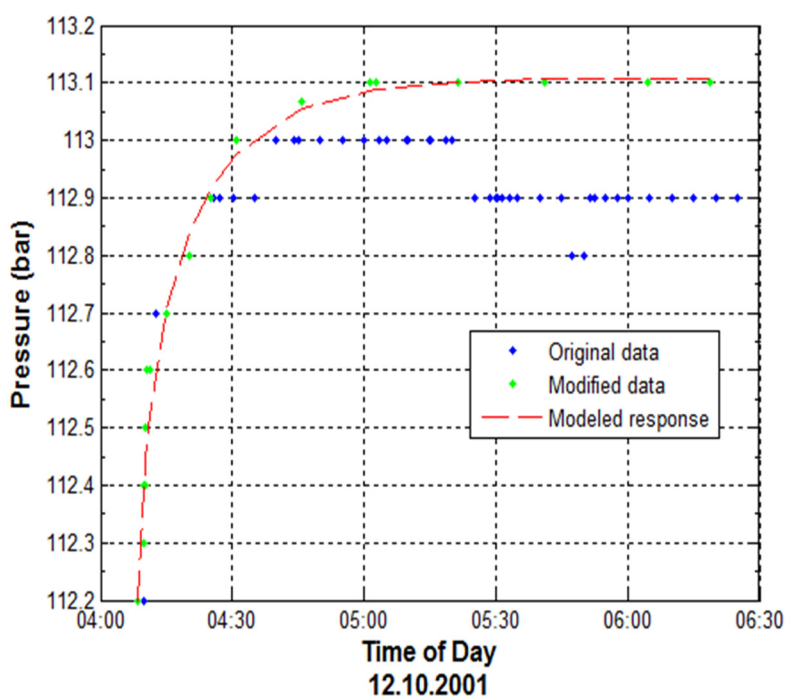


FIGURE 13: The model results and selected data for step 2 in Well HE-04

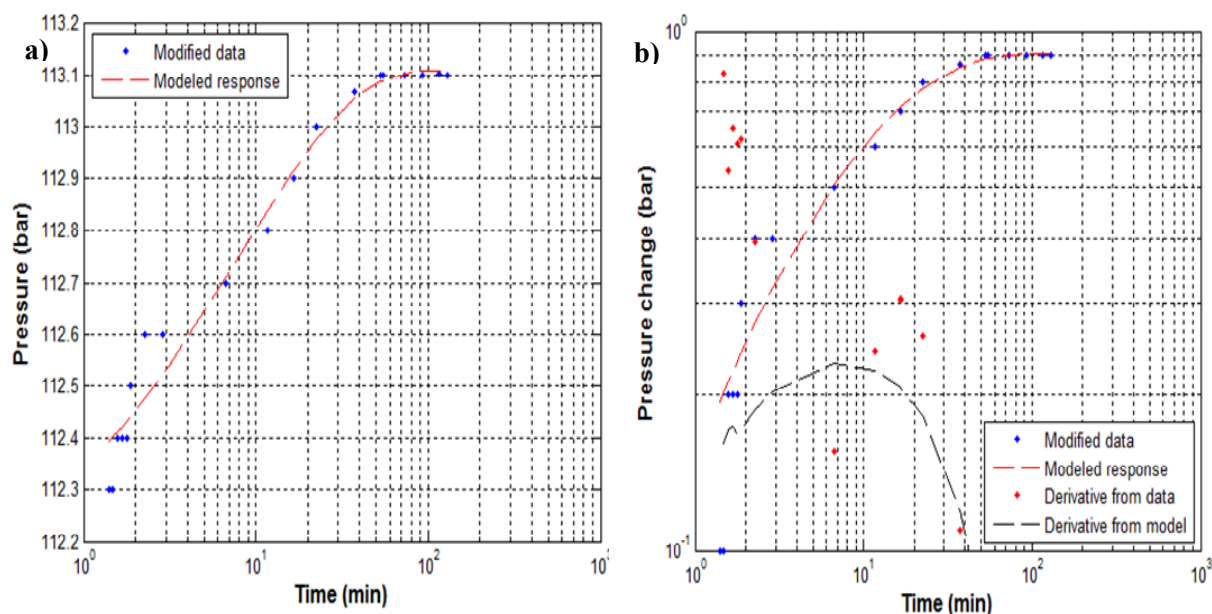


FIGURE 14: The model results and selected data for step 2 in Well HE-04 on: a) a log-linear scale, and b) a log-log scale, where the derivative plot is also shown

Modelling step 3:

The results from the regression analysis are shown graphically for step 3 in Figure 15. The modelled response and the modified data show a good fit. The injection well test showed a pressure increment from 113.0 to 114.0 bar, which is a change in 1.0 bar for a total time of 1 hour and 10 minutes. In Figure 16 (a), the graph shows a fitted modelled response and modified data for log-linear scale, and in (b) the log-log plot shows a good fit of model and data; the derivative plot from the model follows well the derivative points of the selected data.

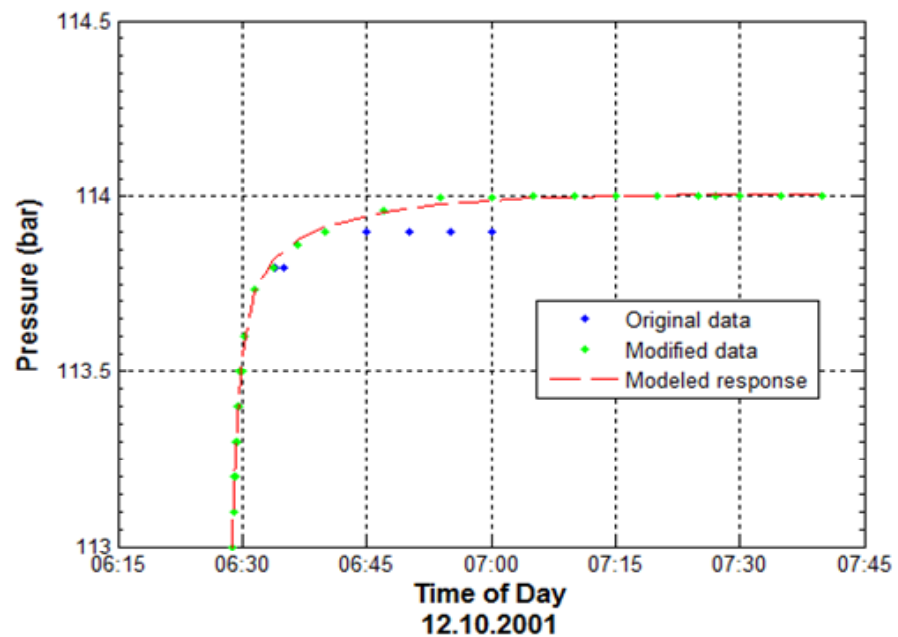


FIGURE 15: The model results and selected data for step 3 in Well HE-04

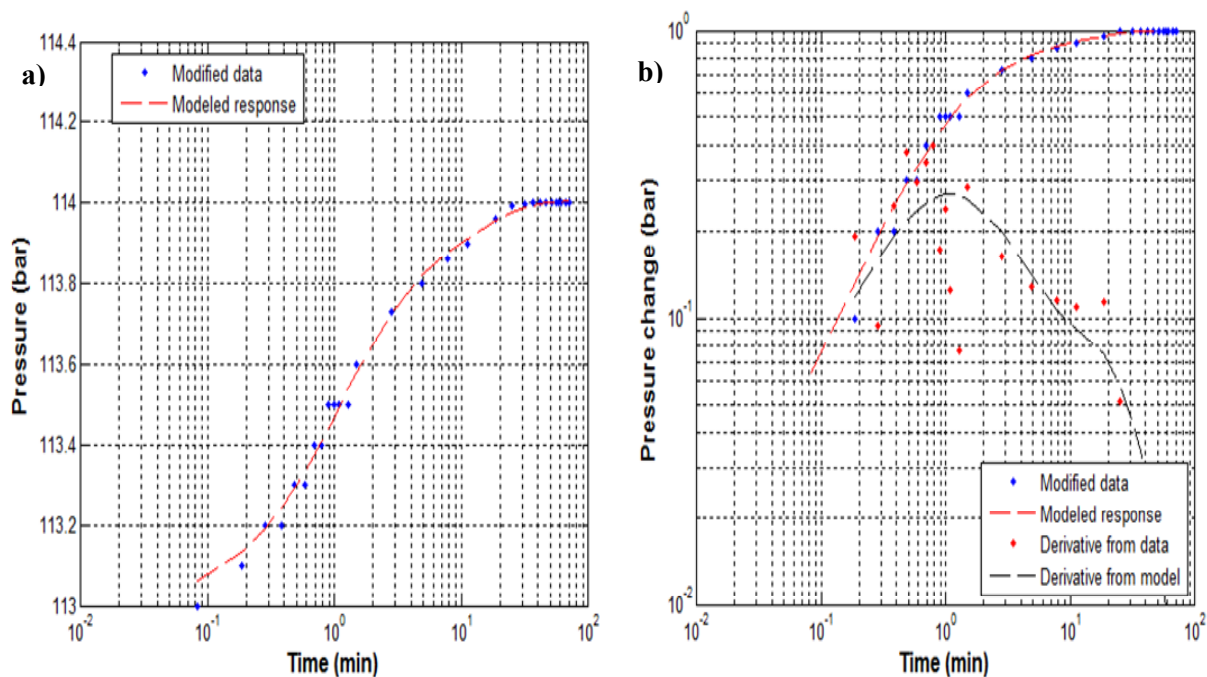


FIGURE 16: The model results and the selected data for step 3 in Well HE-04 on:
a) a log-linear, and b) a log-log scale

6.2 Well HE-09

Well HE-09 is a vertical well, drilled in 2003 to a measured depth of 1604 m. The injection test in Well HE-09 was performed after completion of drilling on 22 June 2003. During the three steps, the injection rates were changed from 25.2 to 35.4 l/s; 36.3 to 55.4 l/s; and 55.9 to 25.3 l/s, respectively (Figure 17).

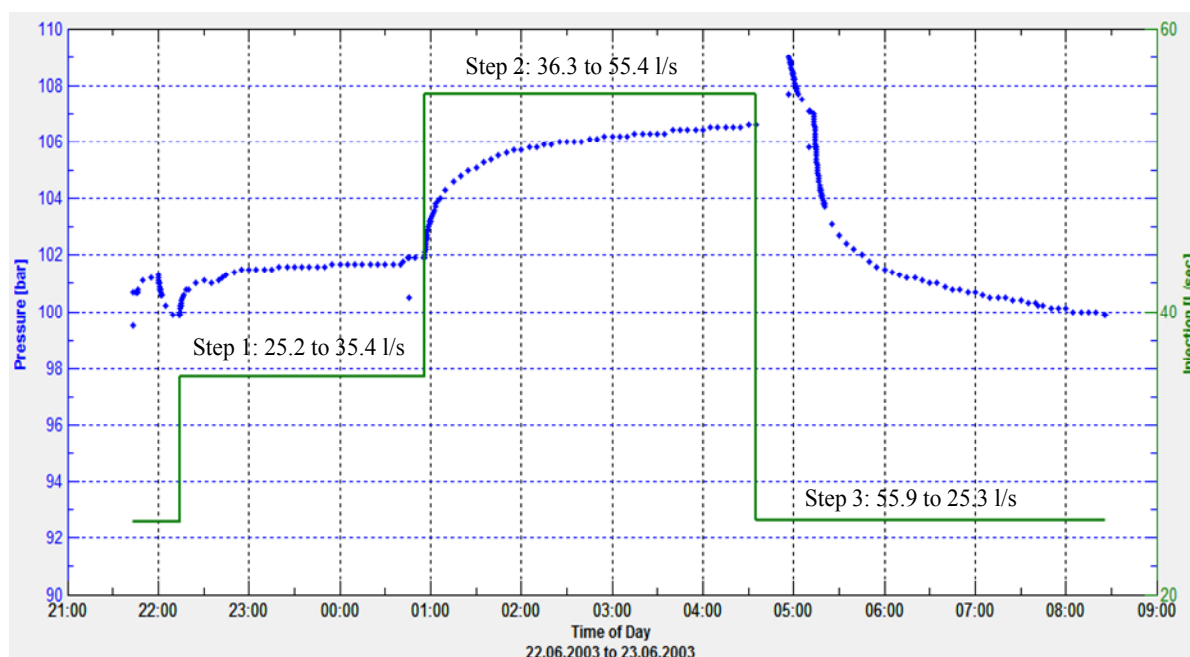


FIGURE 17: Pressure and injection as a function of time in Well HE-09 during an injection well test

The total injection test was done in 10 hours and 8 minutes with a pressure gauge being lowered to a depth of 1200 m. The results for Well HE-09 from the non-linear regression in Well Tester are listed in Table 3.

TABLE 3: Summary of the initial parameters given in Well Tester for Well HE-09

Parameter name	Parameter value	Parameter unit
Estimated reservoir temperature	295	°C
Estimated reservoir pressure wellbore	103	bar
Radius (r_w)	0.16	m
Dynamic viscosity of reservoir fluid (μ)	8.86×10^{-5}	Pa·s
Total compressibility	2.93×10^{-10}	1/Pa
Porosity (ϕ)	0.10	-

The initial parameters for Well HE-09 are listed in Table 3. At a temperature of 295°C, the dynamic viscosity was 8.86×10^{-5} Pa·s; the reservoir pressure deduced by Well Tester from the pressure data was 103 bar. It was assumed that the reservoir is homogenous, the boundary has constant pressure, and the well has a constant skin and well bore storage. The results from Well Tester are shown in Table 4.

TABLE 4: Summary of the results from the non-linear regression parameter estimate using injection test data from Well HE-09

	Storativity S ($\text{m}^3/(\text{Pa} \cdot \text{m}^2)$)	Transmissivity T ($\text{m}^3/(\text{Pa} \cdot \text{s})$)	Skin factor s	Wellbore Storage C (m^3/Pa)	Permeability thickness kh (Dm)	Injectivity Index II ($(\text{l/s})/\text{bar}$)
Step 1	5.4×10^{-10}	2.3×10^{-8}	-3.6	6.8×10^{-6}	2.00	5.3
Step 2	7.9×10^{-8}	1.6×10^{-10}	-3.7	7.6×10^{-6}	0.014	4.3
Step 3	7.2×10^{-10}	2.3×10^{-8}	-2.9	1.1×10^{-5}	2.05	4.3

6.3 Well ThG-09

Well ThG-09 is a vertical well, drilled in 2012 to a measured depth of 2194 m. The injection test in Well ThG-09 was performed after completion of drilling on 14 December 2012. During the three steps the injection rates were changed from 20 to 30 l/s; 30 to 40 l/s; and 40 to 25 l/s, respectively (Figure 18). The total injection test was done in 10 hours and 15 minutes with a pressure gauge being lowered to a depth of 1760 m. The initial parameters in Well Tester are shown in Table 5 and the results for Well ThG-09 from the non-linear regression parameters are listed in Table 6.

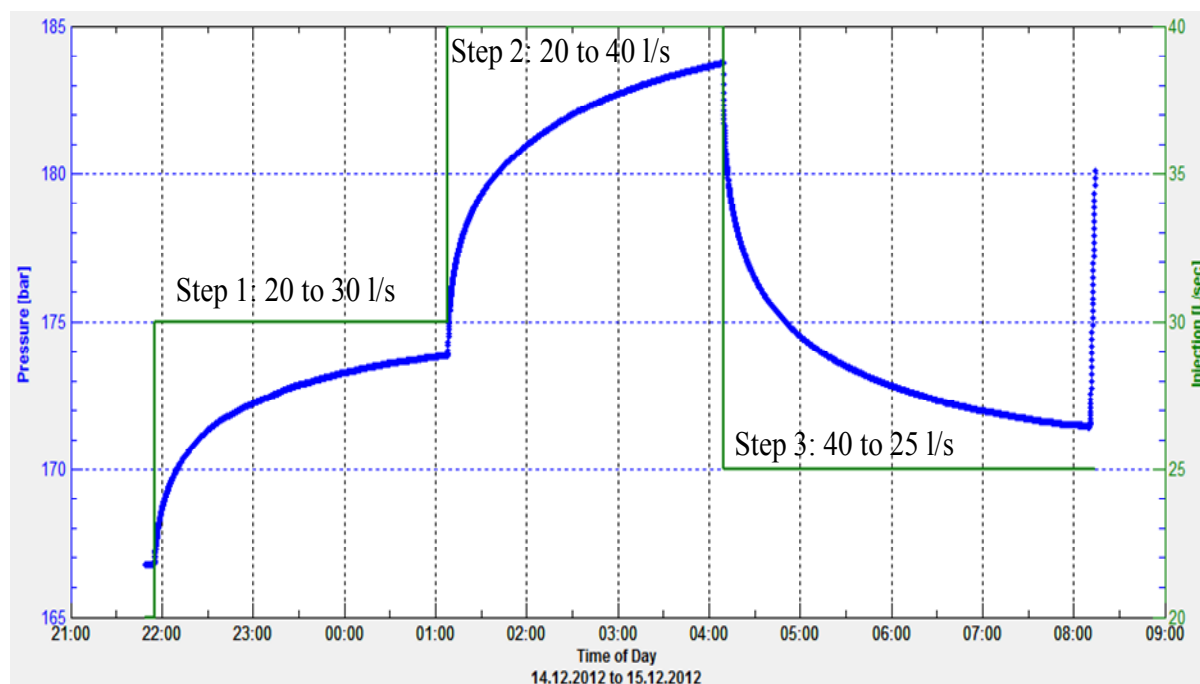


FIGURE 18: Pressure and injection as a function of time in Well ThG-09 during an injection test at 1760 m depth

TABLE 5: Summary of the initial parameters given in Well Tester for Well ThG-09

Parameter name	Parameter value	Parameter unit
Estimated reservoir temperature	280	°C
Estimated reservoir pressure	173	bar
Wellbore radius (r_w)	0.16	m
Dynamic viscosity of reservoir fluid (μ)	9.69×10^{-5}	Pa·s
Total compressibility	2.03×10^{-10}	1/Pa
Porosity (ϕ)	0.10	-

TABLE 6: Summary of the results from the non-linear regression parameter estimate using injection test data from Well ThG-09

	Storativity S ($\text{m}^3/(\text{Pa} \cdot \text{m}^2)$)	Transmissivity T ($\text{m}^3/(\text{Pa} \cdot \text{s})$)	Skin factor s	Wellbore storage C (m^3/Pa)	Permeability thickness kh (Dm)	Injectivity index II ($(\text{l/s})/\text{bar}$)
Step 1	5.0×10^{-8}	5.2×10^{-9}	-3.5	5.9×10^{-6}	0.50	1.4
Step 2	8.2×10^{-8}	3.1×10^{-9}	-3.4	9.7×10^{-7}	0.30	1.0
Step 3	8.4×10^{-8}	5.0×10^{-9}	-3.0	6.0×10^{-7}	0.49	1.2

The initial parameters for Well ThG-09 are listed in Table 5. At a temperature of 280°C, the estimated reservoir pressure was 173 bar at a depth of 1760 m. For all steps, it was assumed that the reservoir is homogenous, the boundary is constant pressure, and the well has a constant skin and well storage.

6.4 Well RN-28

The injection well test data for Well RN-28 could not be analysed by the Well Tester software. The reason is that, as seen from Figure 19, for each step as the injection rate increased, the pressure decreased. It was supposed to increase if the right data were used. Additionally, in step 3 as the injection flow rate decreased from 50 l/s to 10 l/s, the pressure increased as shown in Figure 19. So the behaviour of this well was different from the usual case and could not be explained with the injection changes. Notice that the pressure changes were very small.

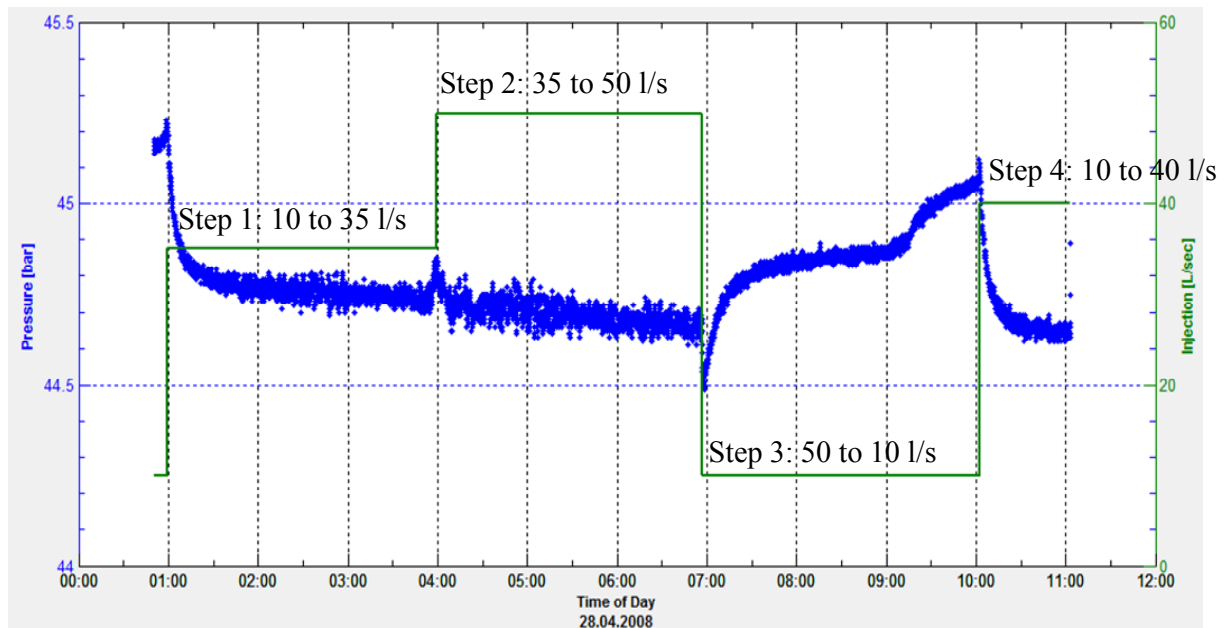


FIGURE 19: Pressure as a function of time in Well RN-28 during an injection test with 4 steps

7. PRODUCTION WELL TEST FROM THE HIGH TEMPERATURE GEOTHERMAL FIELD AT REYKJANES

7.1 Well RN-28 production test

The production test analysis is presented in Table 7. For the production testing of Well RN-28, five steps were taken with lip pipe diameter 16 cm. The water height in the V-notch weir box for step 1 is 1.2 cm and for step 2 it is 1.45 cm, while for the rest of the steps it is 0 which means the water is on the bottom of the V-notch weir box.

To obtain the flow rate and enthalpy from the measurements of the steam and water flow values for the Reykjanes separator, the Russel-James formula (Equation 7) was used.

The water flow can be found by:

$$Q_w = 0.0146 * W^{2.47} \quad (11)$$

TABLE 7: Measurements of pressure, lip diameter and water height for Well RN-28

Step	Water height W (cm)	Well head pressure P_o (bar-g)	Critical pressure P_c (bar-g)	Change in pressure ΔP (mbar)	Bottom pressure P_b (bar-g)	Well head temperature T_o (°C)
1	1.2	46.2	0.8	22.4	50.3	261
2	1.45	46.0	3.0	77.4	50.0	260
3	0	45.5	3.8	93.3	49.8	259
4	0	44.0	4.9	143.3	49.6	257
5	0	46.2	1.9	35.8	49.9	261

where Q_w = Water flow (kg/s); and
 W = Water height in V-notch or weirbox (cm).

And the steam flow for the Reykjanes separator is:

$$Q_s = 2.733\sqrt{\Delta P} \quad (12)$$

where Q_s = Steam flow (kg/s); and
 ΔP = Change in pressure (mbar), over an orifice in the outlet pipe for the steam.

Using the LIP program and manual calculations, the values of Q_s (the steam flow) and Q_w (the water flow) were found. The total flow rate is the sum of Q_s and Q_w . The ratio of the steam flow rate and the total flow rate is represented by X as a percentage rate:

$$X = \frac{Q_s}{Q_t} \quad (13)$$

Additionally, for finding the energy value from the power plant, the constant total flow rate of Reykjanes was taken as 1.68 kg/s for the production of 1 MWe. The results for the flow rate and enthalpy for RN-28 are stated in Table 8. For a well head pressure of 44 bar-g, the flow rate is 32 kg/s and the power is 19 MWe.

TABLE 8: Results of flow rate and enthalpy for Well RN-28

Step	Q_w (kg/s)		Q_s (kg/s)		Q_t (kg/s)		X (%)	Enthalpy H (kJ/kg)	Power (MWe)
	Lip	Manual	Lip	Manual	Lip	Manual			
1	0.03	0.02	10.9	13.38	10.9	13.4	99.8	2670	8
2	0.04	0.04	23.5	23.48	23.5	23.52	99.8	2672	14
3	0	0	28.3	26.88	28.3	26.88	100	2676	16
4	0	0	34.1	31.92	34.1	31.92	100	2676	19
5	0	0	17.3	16.8	17.3	16.8	100	2676	10

8. FORMATION TEMPERATURE AND INITIAL PRESSURE IN A WELL

Formation temperature serves as the basis for conceptual models and is important in decision making on well completion. For this reason, the formation temperature of Wells HE-04 and ThG-09 were evaluated from the warm up temperature logs by considering the condition of the well during measurements and then extrapolating the data at each depth. The ICEBOX program (Arason et al., 2004) Berghiti was used to estimate the formation temperature and compare it to the warm-up temperature values at different depths. The Horner plot was used to estimate the formation temperature using this program.

8.1 The boreholes drilled at Hellisheidi and Theistareykir

Information obtained from pressure and temperature logs are used to determine thermal gradients and heat flow, location of aquifers, reservoir temperature, the physical state of a reservoir, flow patterns, in blow out risk evaluation, and management of geothermal fields. The rate of change during circulation gives some idea about the flow rate and the time for warm up. The main problem with down hole measurements during disturbed conditions is that temperature and pressure in the wellbore do not match those in the reservoir.

An analysis of temperature and pressure profiles that were measured in two boreholes, Wells HE-04 at Hellisheidi and ThG-09 at Theistareykir is presented in this section. The locations of these wells and their casing depths are presented in Table 9.

TABLE 9: Overview of parameters for the two wells

Borehole no.	Drilled depth (m)	Casing depth (m)
HE-04	2008	779
ThG-09	2194	825

8.2 Formation temperature and pressure in Well HE-04

The warm-up temperature data for Well HE-04 were analysed using the Horner plot method to determine the formation temperature. The evaluations of the formation temperature and the initial pressure for Well HE-04 were based on pressure and temperature logs, measured after injection testing after completion of the well and the consequent warm-up period as shown in Figure 20. The warm-up temperature profiles got closer and closer as the warm-up period increased, implying that the well was approaching thermal equilibrium after a short time, which was also reflected in the formation temperature evaluated using the Horner method. The dynamic temperature profile reflected the formation temperature at the bottom of the hole. There is no down flow of fluid in the well during dynamic conditions (Björnsson, 2004).

The warm-up profiles show the location of several feed points. After a rapid warming-up for 13 days, the temperature increased more slowly and became more stable, even after 26 and 62 days, at a measuring depth between 680 m and 760 m, as seen in Figure 20. In the measuring depth range of 760

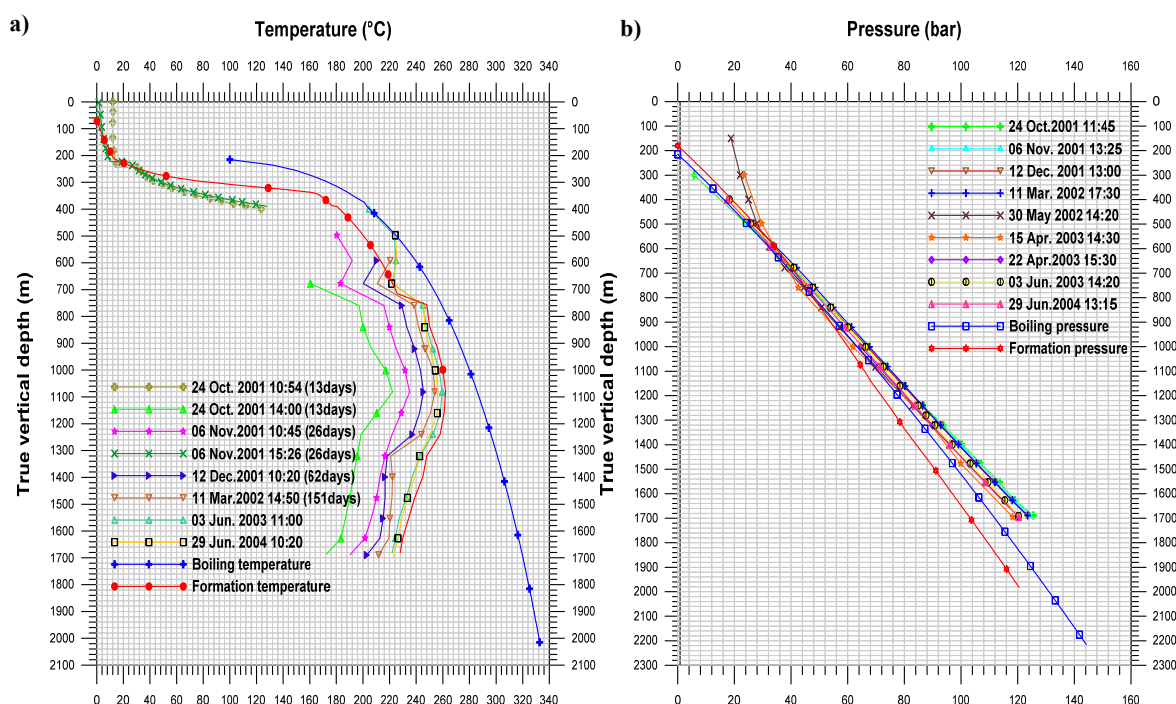


FIGURE 20: Well HE-04: a) Formation temperature; b) Formation pressure

m to 1080 m after 151 days warming up, the formation temperature curve converged and the temperature value decreased slightly. The maximum temperature measured in Well HE-04 was 262°C at a depth of 1080 m. The formation temperature never reached the boiling curve, therefore, the well is liquid dominated.

From the plots of pressure profiles during the warm-up period, the pivot point in Well HE-04 was determined to be at 765 m depth. This indicates that the controlling feed zone of the well is located at about this depth. As the well warms up, the pressure gradient decreases. Pressure profiles revolve around a pivot point that can indicate the location of either a single feed point or the main feed point of a well. Above the pivot point, the formation pressure is greater than the boiling pressure, but below the pivot point it is the reverse.

8.3 Formation temperature and pressure in Well ThG-09

The assessment of formation temperature and initial pressure for Well ThG-09 was based on pressure and temperature logs measured during the warm-up period, shown in Figure 21. The warm-up profiles show the location of several feed points. All temperature profiles in the upper part of the well up to 350 m drilled depth (vertical depth) follow the boiling curve. The most recent profile follows the boiling point curve (Figure 21).

As the well warms up, the pressure gradient increases. Pressure profiles revolve around a pivot point which can indicate the location of either a single feed point or the main feed point of a well. For Well ThG-09, the pivot point is located around 1148 m (92 bar) drilled depth. The initial pressure is almost the same as the boiling pressure throughout the well.

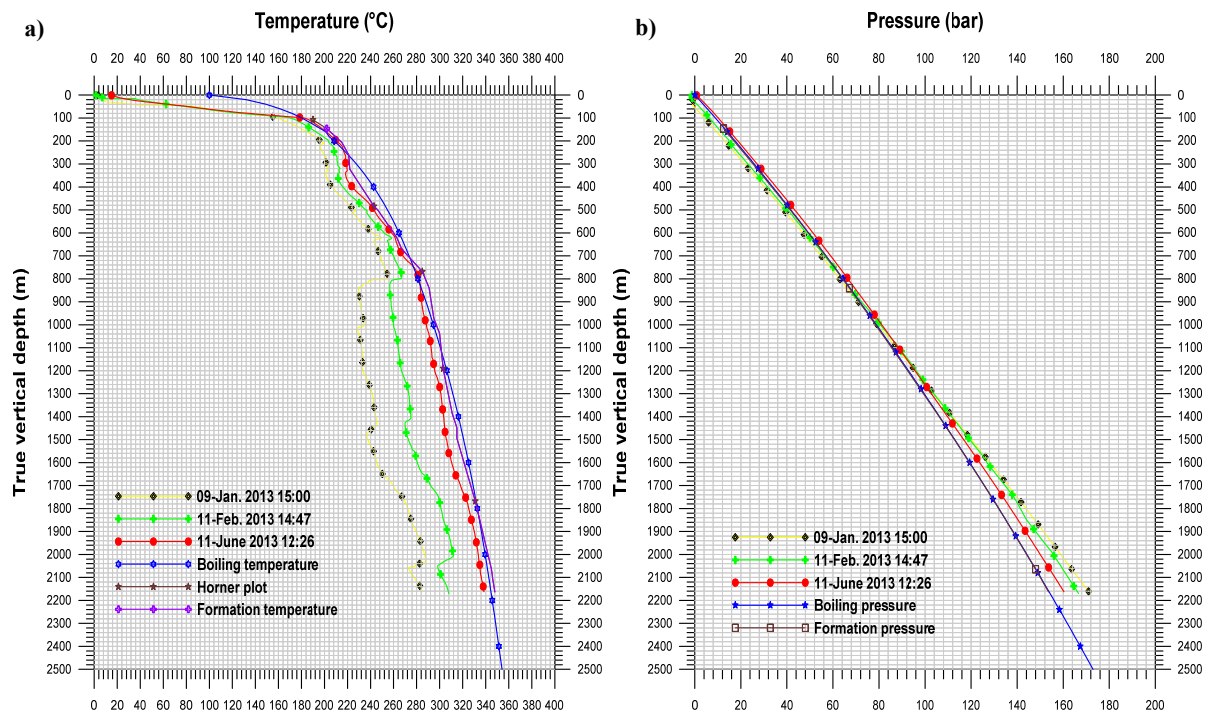


FIGURE 21: Well ThG-09: a) Formation temperature graph; b) Formation pressure graph

9. CONCLUSIONS AND RECOMMENDATIONS

The main goal of this project was to analyse the temperature and pressure characteristics of four wells in Hellisheidi, Reykjanes and Theistareykir geothermal fields. Analysis of temperature and pressure profiles as well as injection and production well tests were the main methodologies applied in characterising the various aspects of the geothermal systems. The following conclusions can be made from the combined observations of the aforementioned analysis.

During temperature and pressure log analysis for Well HE-04, two main feed zones were recognized at depths of 765 and 1400 m; smaller feed zones were identified as well. The highest rock temperature of 262°C was obtained at a depth of 1080 m. The formation temperature is far from the boiling curve which indicates that the reservoir is liquid dominated. The pivot point of this well was 45.7 bar at 765 m.

For borehole Well ThG-09, the analysis led to the conclusion that the number of feedzones was greater than in Well HE-04. These were at a depth of 797-845, 1408-1478 and 2005-2064 m, with additional smaller feedzones. The highest temperature of Well ThG-09 was recorded at a depth of 2064 m with a value of 345°C. The formation temperature follows the boiling curve. The pivot point is located at 1148 m (91.9 bar).

Injection well test conclusions for Wells HE-04, HE-09 and ThG-09, respectively, are:

1. The transmissivity calculated values are 7.8×10^{-8} , 2.8×10^{-8} and 1.0×10^{-8} m³/(Pa·s), respectively. According to this the ability of a reservoir to transmit fluid for Well HE-04 was greater than for Wells HE-09 and ThG-09.
2. The storativity values can be compared as 1.6×10^{-8} , 0.1×10^{-8} and 6.3×10^{-8} m³/(Pa·m²), respectively, highest in Well ThG-09.
3. The connectivity of the well with the surroundings or the injectivity index (II) was great for Well HE-04 at 13.2 (l/s)/bar; second was Well HE-09 at 4.6 (l/s)/bar. Well ThG-09 was third with a value of 1.2 (l/s)/bar.
4. The permeability thickness of the above three wells is 10.7, 1.4 and 0.43 Dm, respectively.

Well RN-28's production well test gave a range of values for the electrical production capacity of the well, from the steps examined. This well could produce up to 19 MWe for 19 bar separator pressure.

ACKNOWLEDGEMENTS

I would like to express my sincere gratitude to my supervisors Dr. Svanbjörg H. Haraldsdóttir and Ms. Saeunn Halldórsdóttir for introducing me to injection and production well tests; for teaching me software like Well Tester, ICEBOX (PREDYP, Boiling Curve, BERGHITI, LIP); for teaching me in detail about geothermal reservoir engineering; for their patient supervision and valuable discussions during my work to complete my report successfully.

Special thanks to Orkuveita Reykjavíkur, Landsvirkjun, HS Orka and ÍSOR companies for the data from Wells HE-04, He-09, RN-28 and ThG-09, the basement and backbone of my project.

My sincere and profound thanks go to all the administrative staff members who created a comfortable and adequate work environment during my six months stay in Iceland and to all lecturers involved in transferring their precious knowledge. Finally, I would like to express my appreciation to all my UNU-GTP 2013 colleagues for our wonderful friendship.

REFERENCES

Afeworki O.M., 2010: Analysis of temperature and pressure characteristics of the Hverahlíd geothermal field in the Hengill geothermal system, SW-Iceland. Report 6 in: *Geothermal training in Iceland 2010*, UNU-GTP, Iceland, 1-28.

Arason, Th., Björnsson, G., Axelsson, G., Bjarnason, J.Ö., and Helgason, P., 2004: *ICEBOX – geothermal reservoir engineering software for Windows. A user's manual*. ISOR, Reykjavík, report 2004/014, 80 pp.

Ármannsson, H., 2008: The Theistareykir geothermal system, North east Iceland. *Paper presented at „Short Course IV on Exploration for Geothermal Resources“, organized by UNU-GTP, KenGen and GDC at Lake Naivasha, Kenya*, 11 pp

Ármannsson, H., Gíslason, G., and Torfason, H., 1986: Surface exploration of the Theistareykir high-temperature geothermal area, with special reference to the application of geochemical methods. *Applied Geochemistry*, 1, 47-64.

Árnadóttir, Th., Geirsson, H., Jiang, W., 2008: Crustal deformation in Iceland: Plate spreading and earthquake deformation. *Jökull*, 58, 59-74.

Björnsson, G., 2004: *Using temperature and pressure logs to determine reservoir condition and well status*. UNU-GTP, Iceland, unpublished lecture notes.

Bödvarsson, G.S., and Witherspoon, P.A., 1989: Geothermal reservoir engineering, part 1. *Geotherm. Scie & Tech*, 2-1, 1-68.

Grant, M.A., and Bixley, P.F., 2011: *Geothermal reservoir engineering*, 2nd edition. Academic Press, New York, 359 pp.

Haraldsdóttir, S.H., and Jónsson, P., 2013: *Production well testing*. UNU-GTP, Iceland, unpublished lecture notes.

Horne, R.N., 1995: *Modern well test analysis, a computer aided approach* (2nd ed.). Petroway Inc., United States, 257 pp.

Jóhannesson H., and Saemundsson, K., 1999: *Geological map 1:1.000.000*. Icelandic Institute of Natural History.

Júlíusson, E., Grétarsson, G., Jónsson, P., 2007: *Well Tester 1.0b, User's guide*. ÍSOR – Iceland GeoSurvey, report ÍSOR-2008/063, 26 pp.

Muffler, P., and Cataldi, R., 1978: Methods for regional assessment of geothermal resources. *Geothermics*, 7, 53-89.

Saemundsson, K., 1979: Outline of the geology of Iceland. *Jökull* 29, 7-28.

Saemundsson, K., 1995: *Geological map of the Hengill area 1:50,000*. Orkustofnun, Reykjavík.

Vink, G.E., 1984: A hotspot model for Iceland and the Voring Plateau. *J. Geophys. Res.*, B 89, 9949.



INTERPRETATION OF RECENT TEMPERATURE AND PRESSURE DATA AND UPDATED CONCEPTUAL MODEL OF THE GREATER OLKARIA GEOTHERMAL SYSTEM, KENYA

Eric Rop

Kenya Electricity Generating Company, Ltd. – KenGen
Olkaria Geothermal Project
P.O. Box 785-20117, Naivasha,
KENYA
erop@kengen.co.ke

ABSTRACT

Optimal development and utilisation of geothermal resources is dependent on the understanding of their size and nature, both in the natural undisturbed state as well as the dynamic response as a result of utilisation, hence the need to develop a conceptual model.

The conceptual model is the main input for the complex field numerical modelling for resource estimates and field development plans. The temperature and pressure models are used as the basis for geothermal field concept development as well as geothermal well discharge characteristics such as enthalpy, mass flow and chemistry. The geology, geochemistry, geophysical information, surface geology and borehole geology play a significant role in understanding the heat source, the permeability, flow patterns and the origin of hot and cold recharge of a geothermal system.

The Olkaria Conceptual model has been updated several times, since the first simple one was presented by Sweco and Virkir in 1976, as new data was acquired. The present model was presented by the consortium of Mannvit/ÍSOR/Vatnaskil/Verkís during the field optimisation study in 2012.

This report presents the updated temperature and pressure model of the Greater Olkaria geothermal system, based on newly acquired temperature and pressure data through ongoing drilling operations in the field. The perceived change in the conceptual model of the field as result of this new data is also pointed out and recommendations made on further drilling sites to give a better understanding of the Olkaria geothermal resource.

1. INTRODUCTION

The Greater Olkaria geothermal field is a high temperature geothermal system located in the Kenya Rift Valley which is part of the tectonically active East African Rift valley, extending from the Afar triple junction at the Gulf of Eden in Mozambique, to the south. The Rift valley splits into the Western Rift system and the Eastern Rift system on entering the Eastern Africa region. Seventeen volcanic centres

have been identified in the Kenya Rift system and geothermal activity has been found associated with eleven of them. Figure 1 shows the location of the Greater Olkaria Geothermal field within the Kenya Rift valley.

The field is divided into sectors as shown in Figure 2. These sectors are: Olkaria East, Olkaria Northeast, Olkaria South West, Olkaria Central, Olkaria North West, Olkaria South East and the Olkaria Domes field. Three power plants are currently operating: Olkaria I and II, operated by KenGen, are generating a total of 155 MWe, including a 5 MWe well head unit pilot plant, while Olkaria III, operated by OrPower 4 Inc., is generating a total of 84 MWe. At present, power plants with a generating capacity of 280 MWe are under construction, utilising steam both from Olkaria East (Olkaria I) and Domes geothermal fields.

The wells in the North West part of the field are utilised by the Oserian farm for domestic power generation and direct heating of green houses. Spa facilities and heated swimming pools are also under construction to utilise the steam and hot water from Olkaria II power station for heating purposes.

The recent optimisation study, carried out in 2011 by the Mannvit/ÍSOR/Vatnaskil/Verkís consortium, divided the Olkaria geothermal resource into two parts:

1. The heavily explored part;
2. The periphery and less explored parts.

The *Heavily explored part* is defined as the part of the Olkaria field where good geophysical and reservoir information was available at the time of the study. Through extensive drilling and long term utilization data, the production response in this part of the field is well defined and understood. Hence, a more representative conceptual model was developed (Mannvit/ÍSOR/Vatnaskil/Verkís, 2011).

The electrical generating capacity of the heavily explored part of KenGen's concession area in Olkaria is estimated to be about 630 MWe based on volumetric resource assessment, lumped parameter pressure response modelling and detailed numerical modelling (Mannvit/ÍSOR/Vatnaskil/Verkís, 2012a and b). This includes the 150 MWe already installed and the 280 MWe currently in the final stages of power plant construction.

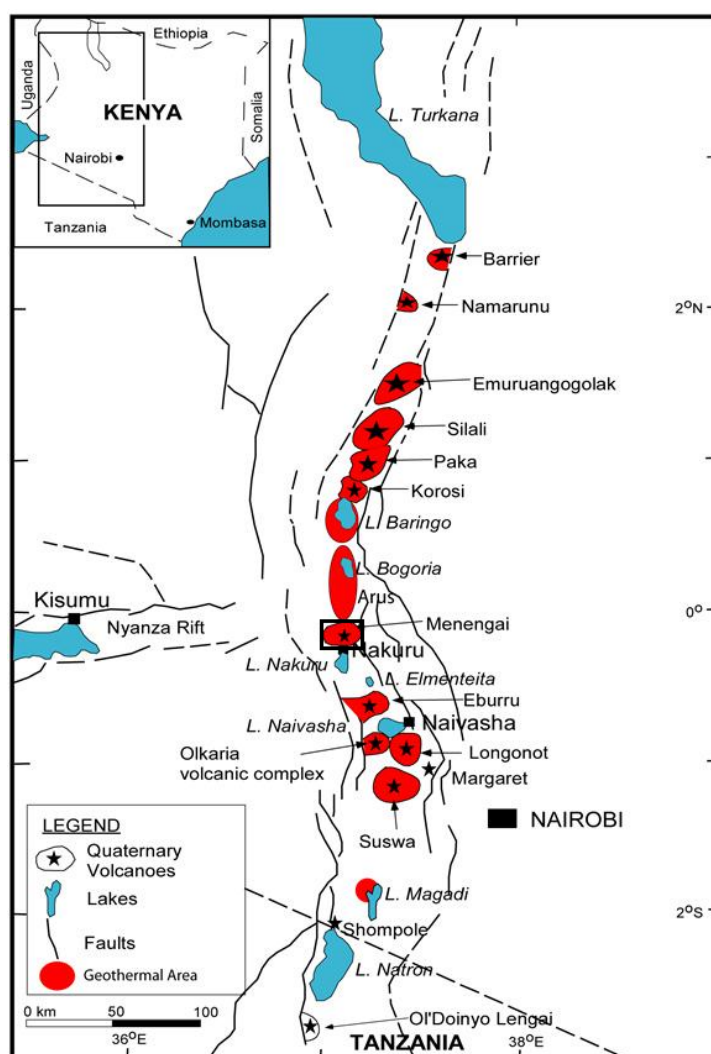


FIGURE 1: Map showing the Greater Olkaria Geothermal prospect within the Kenyan Rift Valley

The less explored part, on the other hand, is explained as where drilling has been limited and mainly indirect indications of an exploitable resource exist. Therefore, the model for this part is deduced as being very speculative. The electrical generating capacity of the less explored part is estimated to be 300 MWe, based on a volumetric assessment (Mannvit/ÍSOR/Vatnaskil/Verkís, 2012a). The consortium recommended that the anticipated resources in the less explored parts be further explored through comprehensive surveying and drilling.

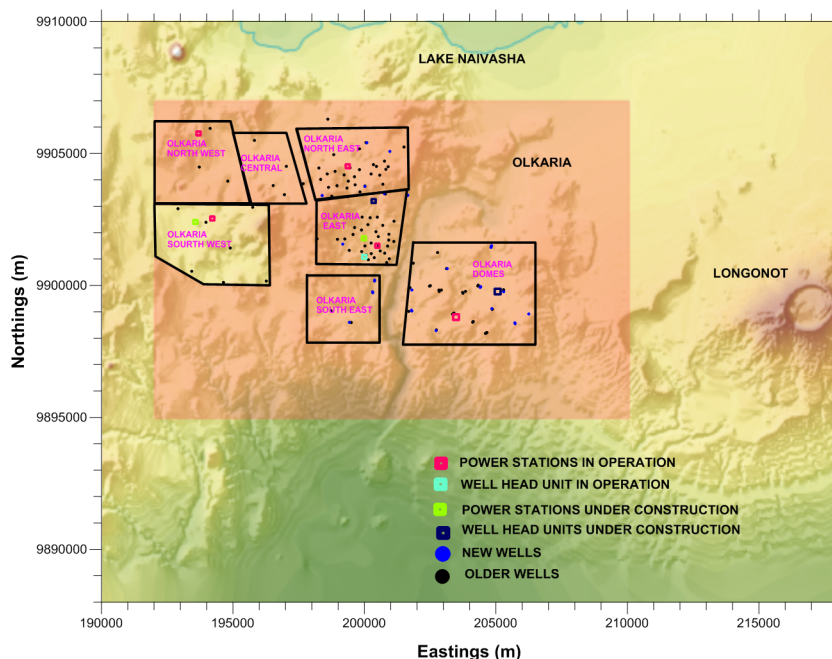


FIGURE 2: The Greater Olkaria geothermal field and subsectors

Upon recommendations of the present optimisation study, KenGen embarked on extensive drilling of more production wells in the heavily explored parts and step out drilling in the less explored parts in an effort to try and delineate the extent of the resource. As a result of this drilling, new data has been obtained which requires analysis and interpretation to aid in updating the present conceptual model of the less explored part, thus providing more understanding of the geothermal field. The new data was acquired quickly from present drilling operations which involved 8 drilling rigs. It is imperative that the data analysis and interpretation be kept at pace with the drilling operations so as to guide the operation and aid the management in making critical decisions regarding the optimised development of the field.

An effort is, therefore, made in this report to update the temperature and pressure models of the Greater Olkaria Geothermal field, critical input in calibrating the natural state geothermal reservoir model as well as for formulating a field development plan. An effort is also made to point out the effects of the newly acquired data on the present conceptual model.

2. THE GREATER OLKARIA GEOTHERMAL SYSTEM

The rift system has experienced repeated upwarping volcanism of mostly rhyolitic and trachytic rocks which started 20 million years ago. Upwelling of the asthenosphere provides the driving mechanism for the lithospheric uplift and extension (Clarke et al., 1990). Structures of the rift valley vary both perpendicularly and along the rift.

2.1 Geology

Olkaria geothermal system is believed to have been active from late Pleistocene to Holocene Age (Clarke et al., 1990). The geothermal field is inside a major volcanic complex cut by N-S normal rifting faults, trending NW-SE and WNW-ESE. It has numerous rhyolitic domes forming a ring structure associated with the major fractures and magmatic activity. The ring structure is more pronounced in the eastern and southeast parts of the Domes field. The ring structure breaks into outer and inner parts in the southeast part. The most prominent volcanic structures are the Ol’Njorowa gorge, N-S trending

Ololbutot fault, NE trending Olkaria fault, the Olkaria fracture, Suswa fault, and the Gorge Farm fault (Muchemi, 1999). Figure 3 below shows a geological map of the Olkaria volcanic system.

Eruptions associated with the Olkaria volcano and the Ololbutot fault zone have produced rhyolitic and obsidian flows. Much of the surface manifestations have been concealed by pyroclastic ash eruptions from the Longonot and Suswa volcanoes, making it difficult to predict the throws and offset of fractures from the surface. Several geothermal manifestations occur along these fractures and faults. The clustered ring structures may indicate several magma sources, but of the same geological age as evident from the surface (Mungania, 1999).

Stratigraphic information indicates that the subsurface is dominated by rhyolitic tuffs and breccias with subordinate trachytes followed by a series of basaltic lavas of various thicknesses, intercalated with trachytes. These are followed by a thick series of trachytic lavas, subordinate basalt and acidic volcanic rocks which are replaced by the Mau tuffs in the western part of the field. Intrusions which are believed to be associated with permeability are rarely encountered in Olkaria wells, as the dipper stratigraphy is mainly dense trachytic lavas (Muchemi, 1999).

The basaltic series found in the Olkaria wells are excellent marker beds forming a sub-horizontal landscape for tectonic faults. The boundary between the rhyolitic pyroclastic succession and the underlying trachytes with the intercalating basalt series marks the onset of the Olkaria volcano (Mannvit/ÍSOR/Vatnaskil/Verkís, 2011). The level of basalt is observed to be similar between the tectonically quiet East field, but is more pronounced in the Domes field, inferring NE-SW faulting and may coincide with the proposed inner caldera fracture.

2.2 Geophysical survey

The gravity survey of the shallow crust beneath Olkaria shows a general gravity high tending north-northwest and in line with regional geological structures. However, there are local highs that trend northeast in line with recent fault trends. These local gravity highs are interpreted as dyke intrusions which are heat sources in some areas while in others, e.g. along the Ololbutot fault zone, they act as hydrological barriers between fields (Maarita, 2009).

Some earlier geological studies suggested the presence of a caldera at Olkaria marked by the eastern ring of domes (Naylor, 1972; Mungania, 1992; Clark et al., 1990). Gravity and seismic data do not show any indications of the presence of any caldera structure at Olkaria (Simiyu et al., 1998a; Ndombi, 1981). The occurrence of magmatic and gravity anomalies at the intersections of NE and NW rift faults is an

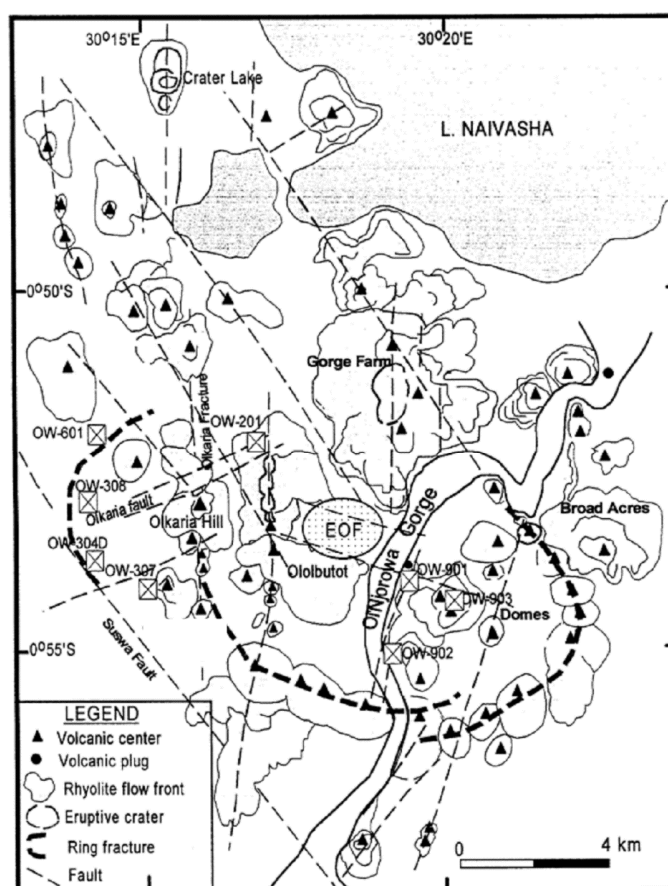


FIGURE 3: Map of the Greater Olkaria volcanic complex showing volcanism and tectonics (Muchemi, 1999)

indication of distinct near surface heat sources controlling the reservoir characteristics of the geothermal system.

Micro-earthquake monitoring for epicentre and hypocentre locations, Figure 4, shows that Olkaria is a high temperature geothermal field characterised by a high level of micro earthquake activity. The Olkaria West area has shallow high frequency events and deep low frequency events. The shallow events occur at the intersection of the Olkaria and Suswa faults. The shallow events are associated with an up-flow zone at the Olkaria West field. Shallow high frequency tectonic events and deeper low volcanic tectonic events occur within the East production field and NE-Olkaria along a NW-SE linear trend. The tectonic events that occur near the surface are associated with fluid movements and these volcanic tectonic events occur at the intersection of the Ololbutot fault zone and the Olkaria fault. Medium to deeper events occurring along the Ololbutot fault are linked to fluid movement at depth. Analysed temperature and pressure measurements, as well as the resistivity and the geochemical analysis, have shown that the fault is a recharge zone.

The S-wave attenuating bodies from the Micro seismic data collected during monitoring in the period 1996-1998 is an indication of the presence of partially molten material at depth. They coincide clearly with high productivity and the temperature regions of the Olkaria field as shown in Figure 5 (Mannvit/ÍSOR/Vatnaskil/Verkís, 2011).

A resistivity anomaly is clearly seen in the East, Northeast and West sectors in Olkaria (Figure 6). Low-resistivity anomalies are associated with up-flow zones where geothermal fluids flow along high permeability fracture zones. Resistivity structures show distinct northeast and northwest linear trends that are most likely due to alteration caused by geothermal fluid circulation along aligned fluid-filled fractures (Onacha et al., 2009).

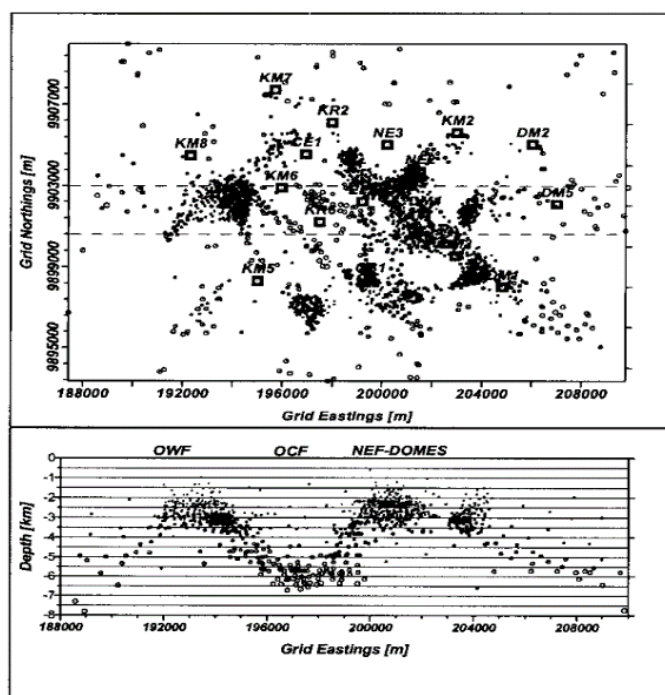


FIGURE 4: Location of microseismic events in the Olkaria field, recorded during a monitoring campaign in 1996-1998 (Simiyu, 2000)

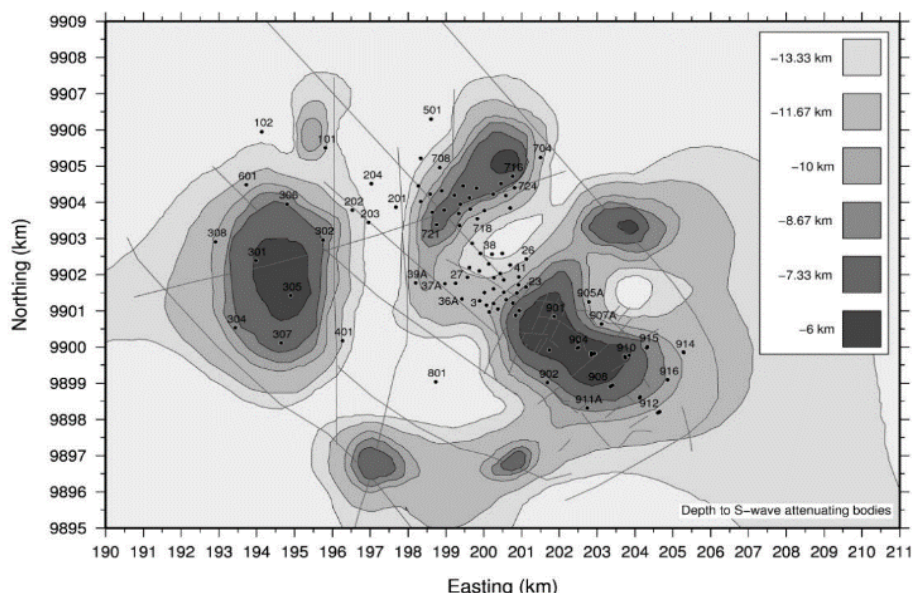


FIGURE 5: Depth to top of S-wave attenuating bodies in Olkaria geothermal field (adapted from Simiyu, 1998) (Mannvit/ÍSOR/Vatnaskil/Verkís, 2011)

The resistivity anomaly distribution at shallow depths is known to be in line with surface geothermal alteration. It is clear that a resistivity anomaly with NW-SE and NE-SW directions is structurally controlled. This explains that the structures that control geothermal fluid circulation are in the NW-SE and NE-SW directions. The shallow low resistivity anomaly is due to low temperature alteration followed by a resistive layer due to high temperature minerals and then a lower resistivity is interpreted as the heat source. Low resistivity anomalies, at depths of 1000 m a.s.l., define the geothermal resource. Some of the high resistivity coincides with the recharge areas associated with the NE-SW and NW-SE trending faults which act as conduits for cold water flow from the rift valley scarps. The geothermal fluid up-flow zones occur at the intersections of these regional faults and areas near the heat source. The resistivity anomaly in the Domes area does not manifest itself clearly with a weaker manifestation southwest of Olkaria (Maarita, 2009).

New resistivity data both for MT and TEM for Olkaria Domes field was analysed by Wanjohi in 2011 and the resistivity model is shown in Figures 6 and 7. This model indicates the extension of the geothermal resource in the southeast part of Olkaria because of the high resistivity mapped below the low resistivity (Wanjohi 2011), a common observation in high-temperature resources due to the high-temperature alteration.

2.3 Conceptual model development

The first conceptual model of the Olkaria geothermal field was developed by Sweco and Virkir (1976), based on data available at the time. The model was very simple because few wells had been drilled at the time. Sweco and Virkir postulated a boiling geothermal reservoir covered by a steam zone and restrained on the top by tuffaceous cap rock.

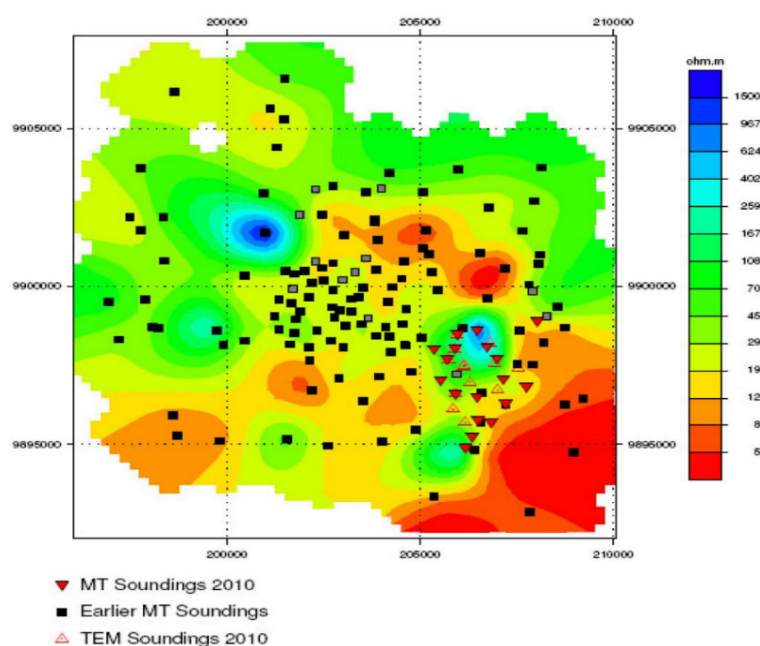


FIGURE 6: Resistivity map of Olkaria Domes field at -400 m a.s.l. (Wanjohi, 2011)

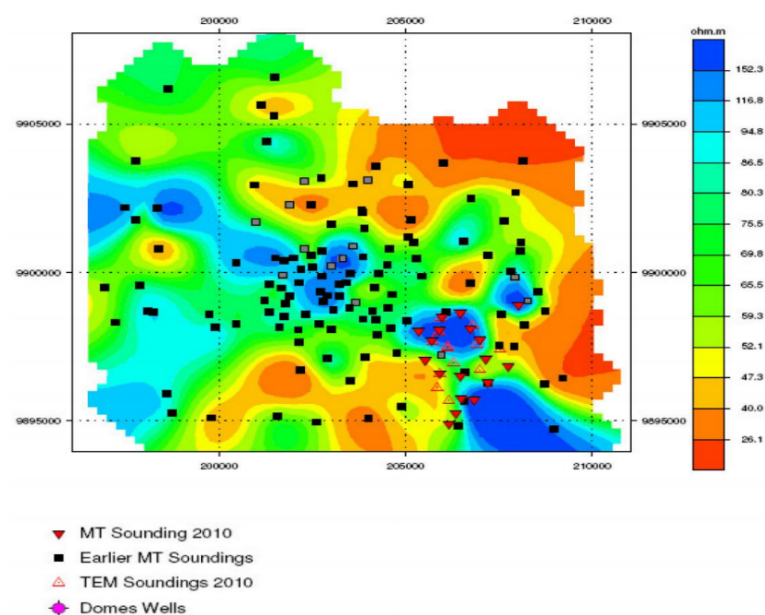


FIGURE 7: Resistivity map of Olkaria Domes field at 1600m a.s.l. (Wanjohi, 2011)

The recharge was believed to be meteoric water percolating down to 1600 m b.s.l. where it was heated to about 320°C. The hot water was then assumed to rise and eventually boil, with steam condensing below the cap rock; then the fluid fell to lower layers due to density differences where it was reheated in a convective cycle as shown in Figure 8.

Ofwona amended the model in 2002 by proposing two up-flow zones, one in the Olkaria Northeast field and another in the Olkaria East field, while the recharge was from all sides of Olkaria. Ofwona indicated that the Olkaria West field was not connected to the Olkaria East field but was separated by a low-temperature zone in central Olkaria. Extensive boiling also occurred in the up-flow zones to form steam caps below the cap rock. Figure 9 below shows the amended conceptual model by Ofwona.

West-JEC (West Japan Engineering Consultants, Inc.) further revised the conceptual model in 2009 (Figure 10) while undertaking a field optimisation study. They considered the origin of the heat source in the Olkaria geothermal system to be a magma chamber responsible for the volcanic activity in Olkaria. The magma chamber peaks in several locations, creating convective heat transfer and providing hot recharge to different parts of the geothermal system. They proposed an up-flow for the Domes sector through the R1 fault. The chemical model of all fields east of Ololbutot fault suggested that the fluids of all three sectors, East, Northeast and Domes field, had a common origin at depth, water between approximately 325-340°C in temperature with a chlorine concentration at ~450 mg/l. They explained that a common SE-NW trending structure, R1, may connect all three up-flow zones at great depths and may be extending northwards.

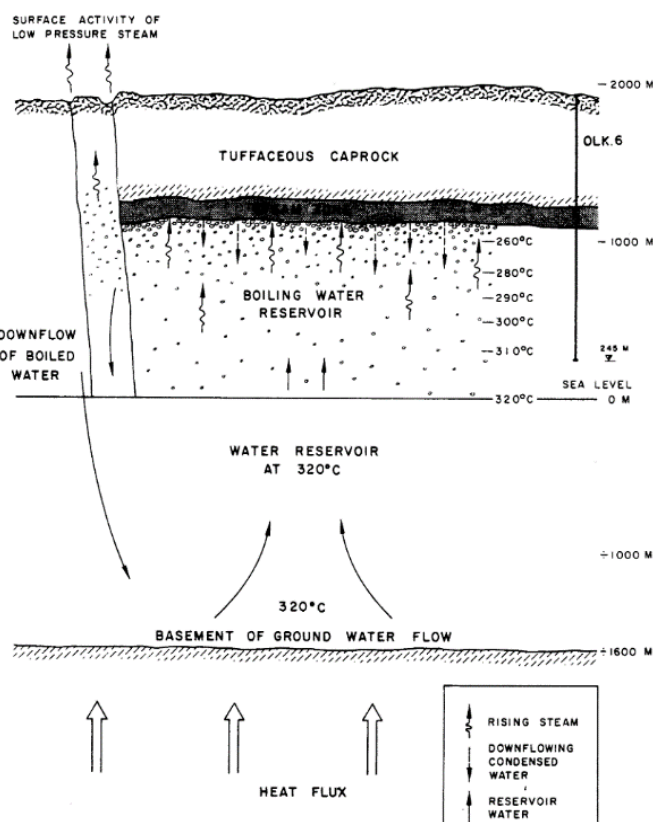


FIGURE 8: A simple conception model of the Olkaria Geothermal field (SWECO and Virkir, 1976)

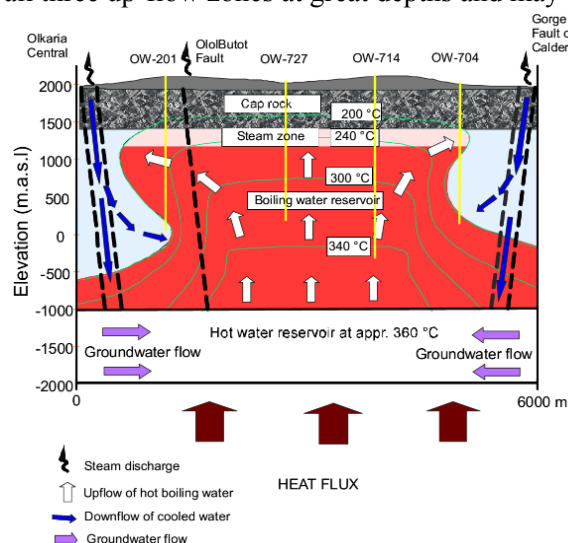


FIGURE 9: Olkaria conceptual model as presented by Ofwona (2002)

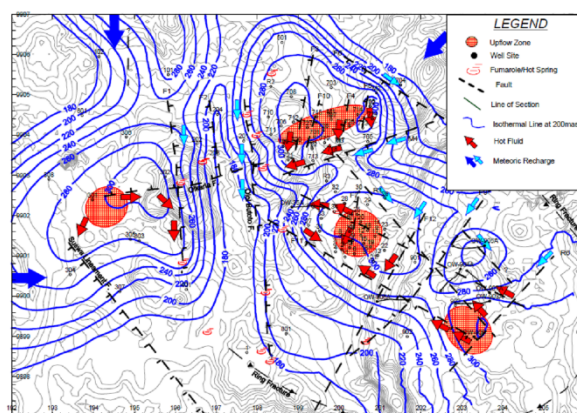


FIGURE 10: Olkaria conceptual model as presented by West-JEC (2009a)

The present conceptual model of the Olkaria geothermal system (Figure 11) was presented in 2012 by a consortium of Mannvit/ÍSOR/Vatnaskil/Verkís who undertook a field optimisation study as explained by Axelsson et al. (2013).

According to this model, the heat source is believed to be deep seated magma chamber or chambers with three intrusions 6-8 km from the surface, lying beneath the Olkaria hill, the Gorge farm volcanic centre and in the Olkaria Domes area. Four major up-flow zones were identified. The first feeds the Olkaria West field, believed to be connected with the heat source beneath Olkaria Hill.

Two major up-flow zones were identified as being connected to the Gorge farm heat source, one feeding the Northeast production field and another feeding the East field and the northeast corner of the Domes field. The fourth up-flow zone is associated with the ring structure in the Domes field, connected to the heat source identified below that area.

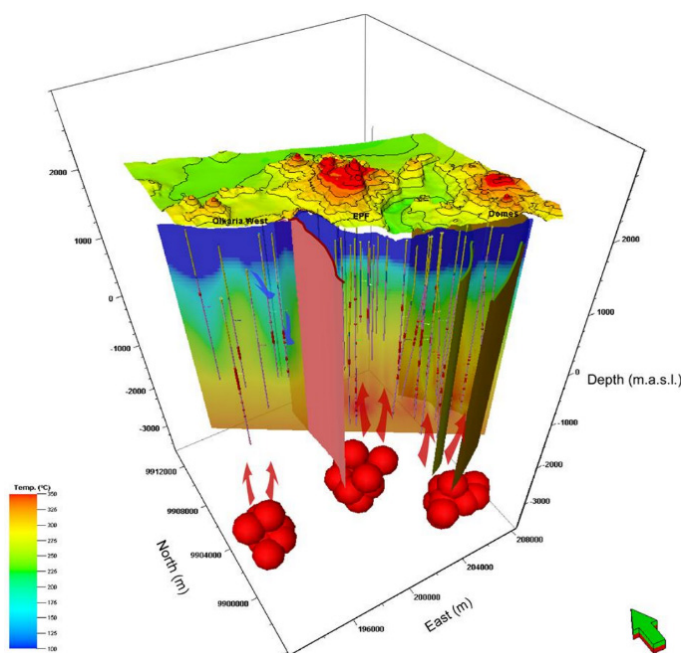


FIGURE 11: The present Olkaria conceptual model (Mannvit/ÍSOR/Vatnaskil/Verkís, 2011)

Permeability is believed to be controlled by NW-SE, NE-SW trending faults as well as the ring structure. Cold water flows into the system through the N-S trending Ololbutot fault which is a flow barrier between the western and eastern parts of the field. Water inflow into the Olkaria Domes area is believed to originate from the northeast part of the Domes field. They then concluded that the geothermal resource extended southeast of the field, based on the geochemistry, pressure and temperature data, and the geophysical data. They pointed out a possible resource in the south central and south west parts of Olkaria, indicated by limited geophysical data and surface manifestations.

From the discussions above, it is evident that the Olkaria field conceptual model underwent a transformation from a simple model presented by Sweco and Virkir (1976) to the more complex current model because of the continued collection of data, which gave a deeper understanding of the geothermal system. It is worth noting that the transformation underwent improvement, with the initial concept holding throughout the transformation process.

3. REVISION OF THE OLKARIA CONCEPTUAL MODEL

Optimal utilisation and expansion of geothermal resources is mainly dictated by reliable conceptual models which are updated with continued development and utilisation. They are the basis of field development plans and geothermal reservoir modelling (Axelsson et al., 2013). Conceptual models are descriptive or qualitative models, incorporating and unifying all available exploration, drilling and testing data (Grant et al., 1982).

Therefore, conceptual models are developed based on geological, geophysical, reservoir temperature and pressure as well as geochemical data. Monitoring data collected over time, during utilisation of geothermal resources, are used in updating conceptual models. The conceptual model explains the nature of the heat source, and the recharge zones; it describes the main flow channels as well as the general flow patterns in the reservoir.

3.1 New temperature and pressure data

Physical measurements made in geothermal wells provide the primary information from which the physical properties of a geothermal resource can be evaluated. The most important measurements are the temperature, pressure and the mass flow, made either in the well-bore or at the surface. During the first stages of resource development, an understanding of the resource in terms of its undisturbed state, size, rock characteristics, and pressure as well as temperature distribution is essential (Grant and Bixley, 2011).

New data has been acquired from the ongoing step out drilling operations and well testing in the Greater Olkaria Geothermal field. This includes both temperature and pressure measurement data as well as injection well test data. The discharge test data for a few wells are also available while most of the wells are still warming up after drilling. The temperature and pressure data for 28 wells has been analysed for this report. The drilling well data, such as the casing depth, casing shoe and conversion of the temperature and pressure measured depth to the true vertical depths, is also essential in understanding well design. The temperature and pressure profiles in this report are presented at the measured depth, while the elevations for the formation temperature and pressure are done in true vertical depth to allow comparison with the results of other reports on the field.

The temperature and pressure data were acquired through different well test operations using the Kuster temperature and pressure mechanical gauges. The temperature gauge uses a bimetal where the temperature expansion of the bimetal indicates the temperature. In this type of tool, the temperature measurements are not real time but recorded in a temperature probe on a clock driven recorder. An accuracy of more than $\pm 1^\circ\text{C}$ of the value is not achievable with the sensor, but they are superior to other sensors in that they can operate at higher temperatures, or up to 360°C . Pressure mechanical gauges, on the other hand, use the Bourdon tube where the fluids are in contact, hence sensing the pressure of the geothermal fluid at the measuring points. Their accuracy is between ± 1 and ± 0.1 bar of the measured value. These mechanical tools are regularly calibrated using a calibrating oil bath to ensure the accuracy of the measured data. A wire line assembly is used to lower the tools to the measuring depths.

The data used was obtained from various well test operations including well completion tests and temperature and pressure measured periodically during the warm up period. The well completion test involves first a temperature and pressure run immediately after stopping the water circulation in the drilling operation; it helps in understanding the temperature and pressure state of the well. This is followed by an injection test with pressure build-up and a pressure fall-off test to monitor the pressure response of the system due to changes in injection. This operation is commonly known as pressure transient analysis. The temperature and pressure profile, during pumping, maps out the zones of water loss during injection which corresponds to the points where the well is connected to the reservoir and may later indicate feed zones during production. The well's permeability can then be evaluated indirectly as well as the well's storativity.

3.2 Methodology

It is not possible to directly measure the subsurface well characteristics that are needed to assess a geothermal resource, as is the case in groundwater and the petroleum industry. An interpretation or an inference is made from the information available from a well test programme. The temperature and pressure were analysed, based on different models. The temperature models can be conductive, convective, isothermal, boiling conditions and one dimensional convection flows.

After well completion, geothermal wells are given time to recover from the cooling effect of the drilling fluids and to reach equilibrium with the formation. The temperature recovery behaviour is monitored during the warm up period so as to obtain information on the location of feed zones; the time series obtained are later analysed to estimate the natural undisturbed temperature of the system. The rate of

temperature recovery is dependent on the properties of the particular well as to whether the aquifers are warming up faster than the impermeable part of the well or vice versa. Usually, in static wells without internal flows or boiling conditions, the aquifers warm up more slowly than other parts of the well because of the cooling effects of the circulating drilling fluid.

Cross flow scenarios occur commonly in closed wells between the upper aquifers and the lower ones where flow comes into the well from upper aquifers and out through the lower aquifers. This type of well is characterised by a fairly constant temperature profile over a large depth interval in the well.

High-temperature wells sometimes experience boiling, where the fluid follows the boiling point with depth curve at some points in the well. Steam bubbles are formed and pushed upwards, warming the upper zones of the well where they are condensed and fall back by gravity, exhibiting one-dimensional convection behaviour.

Negative temperature gradient behaviour is also observed in geothermal wells. This is a situation where the temperature decreases with depth as a result of non-vertical water flow in the wells. This information can be used to locate horizontal flow patterns in geothermal fields (Stefánsson and Steingrímsson, 1990).

Formation temperature is an important parameter when understanding the nature of geothermal reservoirs during exploration, drilling, logging, well completion and reservoir analysis. The subsurface temperature available from borehole well logs is always lower than the true or static formation temperature, because of the cooling effect of drilling fluids. In Olkaria, it is not always possible to allow sufficient time for the wells to heat up before discharge because of operational constraints. Furthermore, penetration of a steam zone during drilling results in the masking of temperatures at shallower depths, hence making it difficult to estimate the true formation temperature in this region.

Various techniques have been developed to obtain true formation temperatures from transient data (Dowdle and Cobb, 1975; Barelli and Palama, 1981). James N. Albright developed a method (Albright method) for calculating the formation temperature during economical interruptions of drilling operations while a geothermal test well was being drilled for the *Hot Dry Rock geothermal energy project* conducted by the Los Alamos scientific laboratory. Further details of this method can be obtained from The User's Manual by Arason et al. (2004).

A simple and effective method was published by Roux et al. (1979), based on the Horner time. The basic concept is the straight line relationship on a semi logarithmic scale of measured temperature versus the ratio of the Horner time, τ :

$$\tau = \frac{\Delta t}{(t_c + \Delta t)} \quad (1)$$

where Δt is the time in hours after stopping circulation and t_c is the circulation time in hours.

The static formation temperature, T_{ws} is extrapolation from the straight line relationship to Horner time $\tau = 1$.

Berghiti (Arason et al., 2004.), a computer program based on the Horner time method, was used for this project during the formation temperature estimation. The following procedure was used on making a decision on the applicable part of the geothermal wells:

1. The temperature values of the well less than 50 m from the well bottom were not used because circulation might not have been effective in this region;
2. Only sections of conductive heat transfer were considered;
3. Sections with indications of flow between different sections, internal circulation and cross-flow in the wellbore were not used.

The condition of geothermal fluids at zones penetrated by some of the wells is liquid at greater depths and is at specific temperatures referred to as the saturation temperature. As the fluid flows up the wells, the pressure reduces until a saturation temperature is reached where boiling occurs. This means that the formation temperature can be assumed to follow the saturation curve at depths where the fluid is believed to be at the saturation temperature. The pressure in geothermal wells is equivalent to the hydrostatic gradient plus the dynamic gradient at some point in the well where the liquid is at saturation temperature. The dynamic gradient is much smaller than the hydraulic gradient and the pressure can be approximated by Equation 2 below:

$$\frac{dp}{dz} = \rho_w g \quad (2)$$

Equation 2 can be used to calculate the boiling point depth curve for the saturation conditions by numerically solving Equation 3 (Arason et al., 2004):

$$P(z) = P_0 + g \int_{z_0}^z \rho_{\text{sat}} dz \quad (3)$$

The formation pressure can therefore be determined from the formation temperature for the part of the well which is at boiling conditions by calculating the saturation pressures at that temperature. The boiling point depth curve was formulated in this report by considering the water level and using BOILCURVE, a computer program in Icebox (Arason et al., 2004) for calculating the boiling point curve. PREDYP, another program in Icebox (Arason et al., 2004), which calculates the pressure in a static water column as a function of measured temperature and water density, was also used to estimate the formation pressure.

3.3 Updated temperature and pressure models

The temperature and pressure models discussed in the previous chapter were formulated based on all the available temperature and pressure measurements for a given well. The effects of boiling and internal flows are taken into account while estimating the initial temperature and pressure at the point of the system in the well. The new wells drilled in the Greater Olkaria geothermal field used in the project are shown in blue in Figure 12. Also shown are the older wells

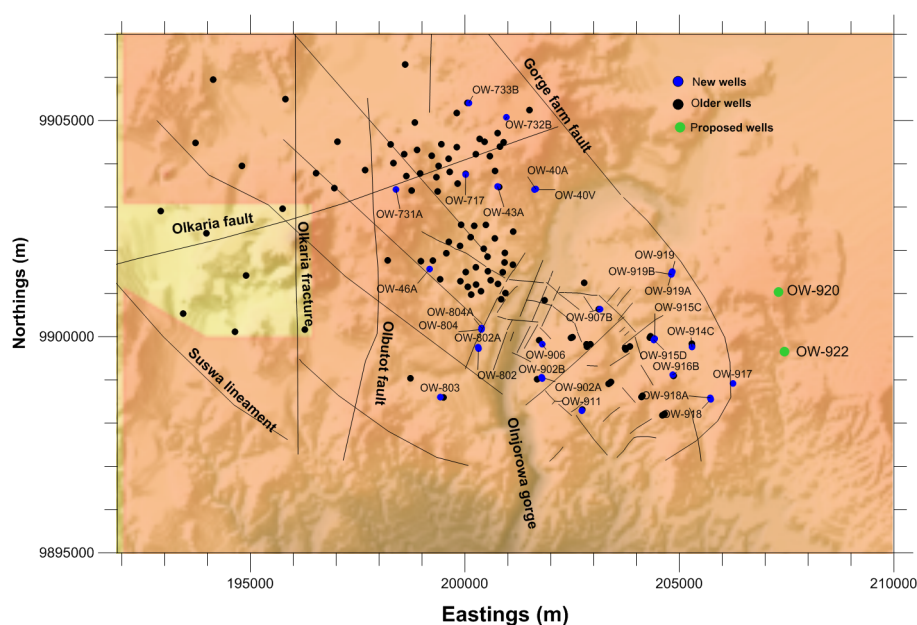


FIGURE 12: Geothermal wells in the Greater Olkaria geothermal field

which were analysed earlier. The temperature and pressure profiles of the new wells incorporated with their estimated formation temperatures are shown in Appendix I, with a few examples discussed below.

Figures 13, 14 and 15 give the temperature and pressure estimates in Wells OW-918A, OW-917 and OW-918, respectively, located in the southeast part of Olfaria Domes field as shown in Figure 12.

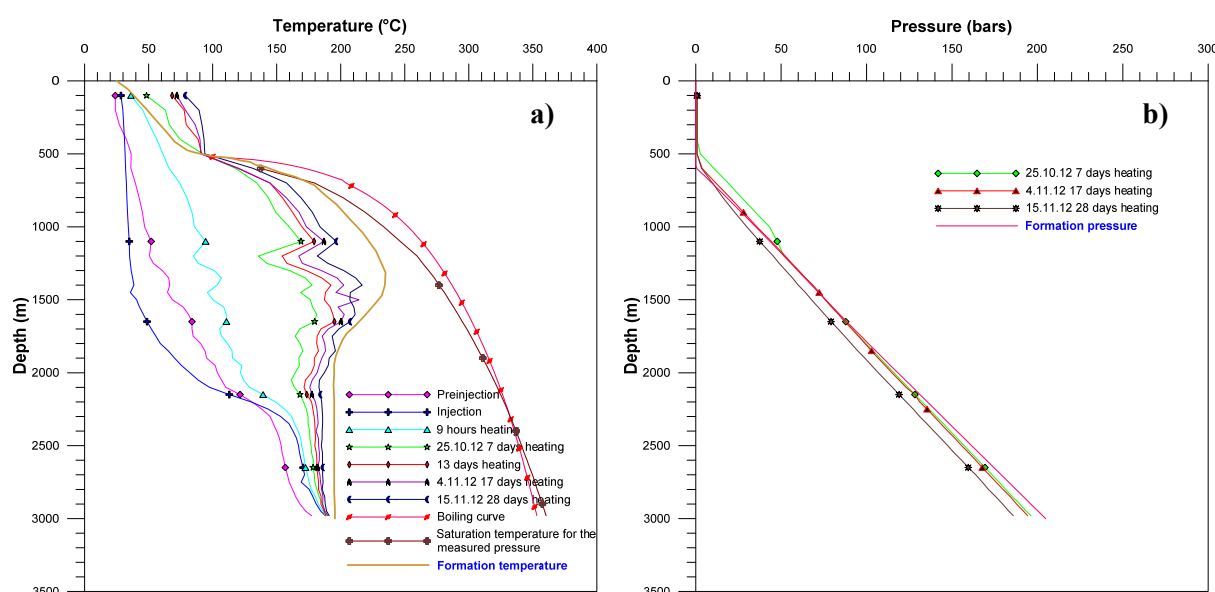


FIGURE 13: Well OW-918A: a) Temperature profile; and b) Pressure profile

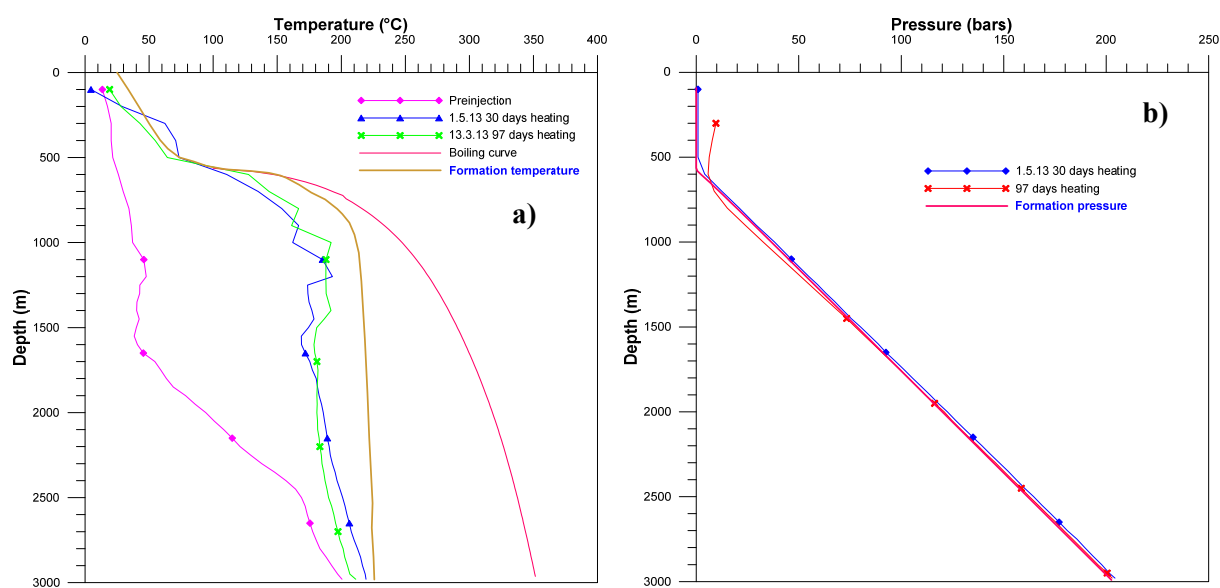


FIGURE 14: Well OW-917: a) Temperature profile; and b) Pressure profile

The temperature profile in Well OW-918A shows a high gradient up to a depth of 1300 m from the surface, then a temperature reversal to the well bottom. The formation temperature estimates to about 250°C at 1300 m and then reduces to 210°C at the well's bottom.

Conductive heating is evident in Well OW-917 to the well bottom, which is an indication of poor permeability. Well OW-918 also shows conductive temperature recovery to about 1300 m, then isothermal conditions to 2150 m, followed by a slight temperature reversal before another level of conductive heating to the well bottom.

The pressure profiles in Wells OW-918A and OW-917 show a water table at around 600 m, while in Well OW-918 a water table at around 500 m was observed. In Wells OW-918A and OW-917, estimated formation pressure shows a water table at around 600 m, while in Well OW-918, a water table at around 500 m was observed.

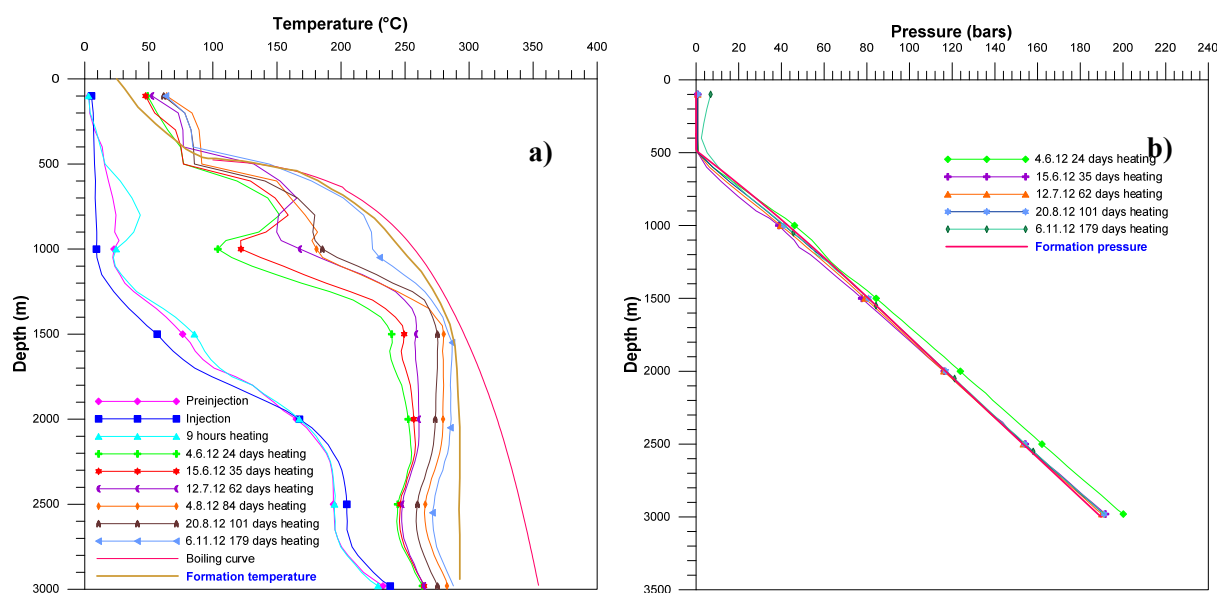


FIGURE 15: Well OW-918: a) Temperature profile; and b) Pressure profile

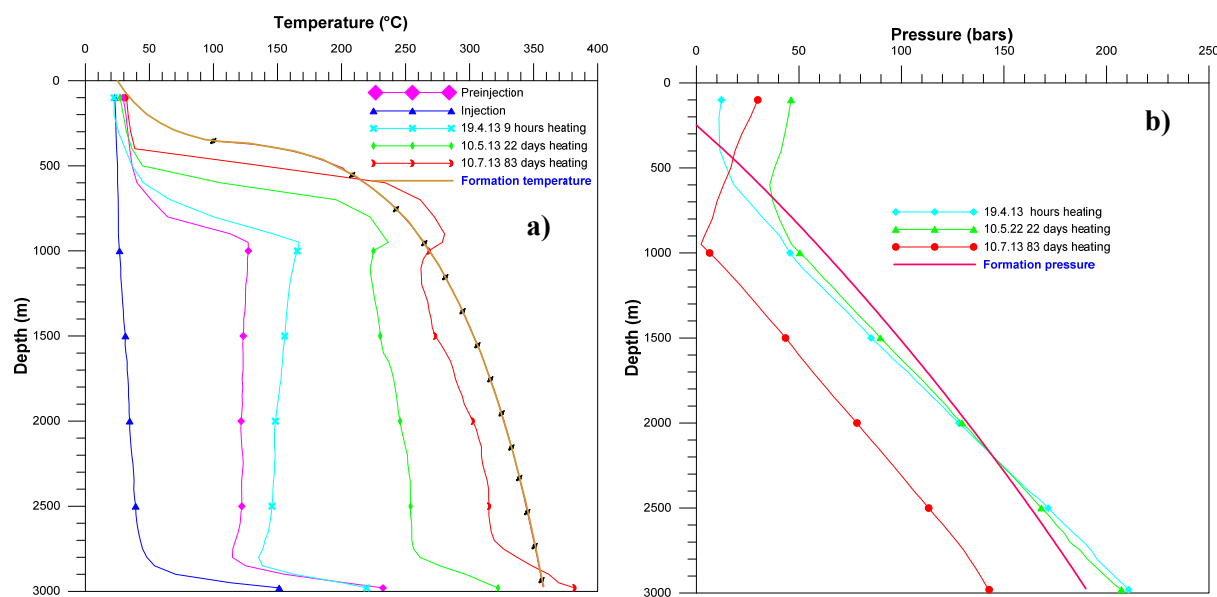


FIGURE 16: Well OW-919A: a) Temperature profile; and b) Pressure profile

Well OW-919A is a very hot well drilled in the eastern part of the Olkaria Domes field with temperatures of about 350°C at the well bottom and a pressure close to 200 bars (Figure 16). The formation temperature in the well follows the boiling point curve to the well bottom.

Figure 17 and Figures 1 and 2 in the Appendix I show the temperature profiles in Wells OW-731A, OW-717, and OW-732B, respectively, located in the NE production field as shown in Figure 12. The temperature is observed to increase to a peak of 230°C at around 1100 m, then reverses sharply to 190°C, followed by normal temperature gradient to the well bottom in Well OW-731A.

A temperature reversal is also seen in Well OW-732A where the estimated formation temperature increases to about 300°C at around 2000 m from the surface, then suffers a reduction to 250°C at the well bottom with a low discharge enthalpy of 1060 kJ/kg. Well OW-717 also records lower temperatures

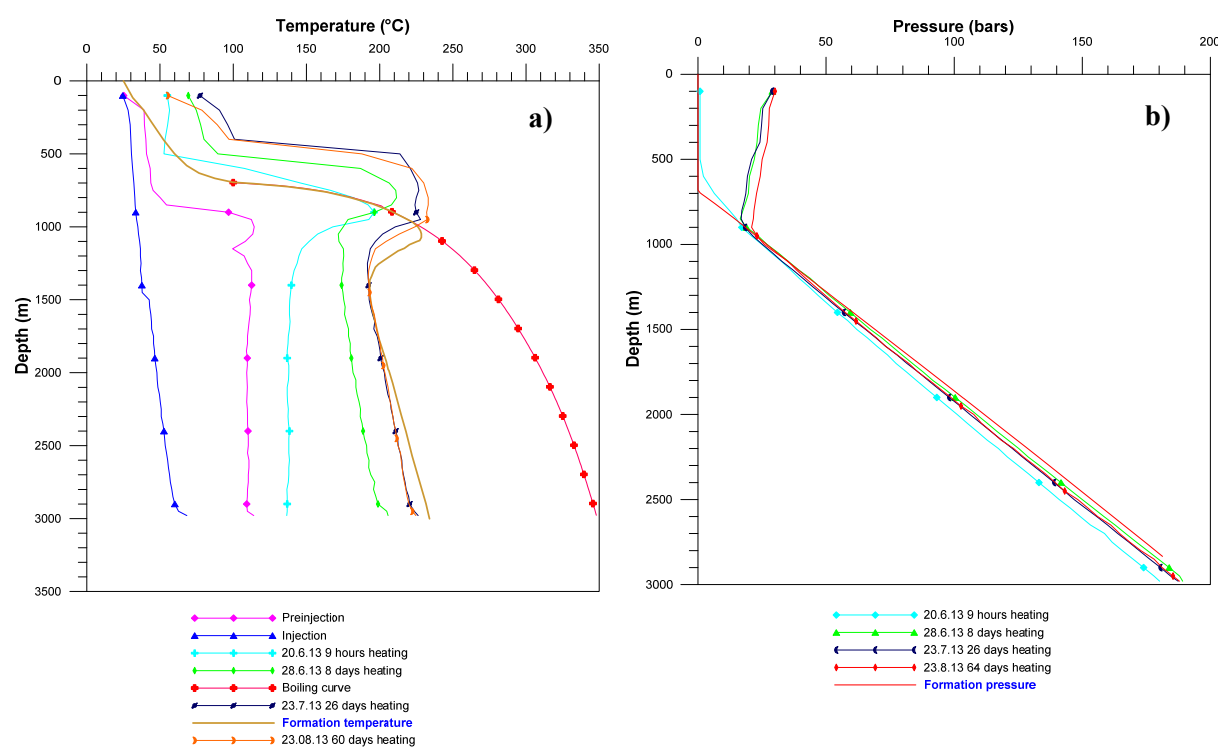


FIGURE 17: Well OW-731A: a) Temperature profile; and b) Pressure profile

than nearby, but shallower, wells with a low enthalpy of 1580 kJ/kg, similar to old Well OW-717 which was drilled in the same region.

Well OW-733B (Figure 18) in the northern part of the Olkaria Northeast field shows high temperatures of close to 370°C at the well bottom with the estimated formation temperature following the boiling curve

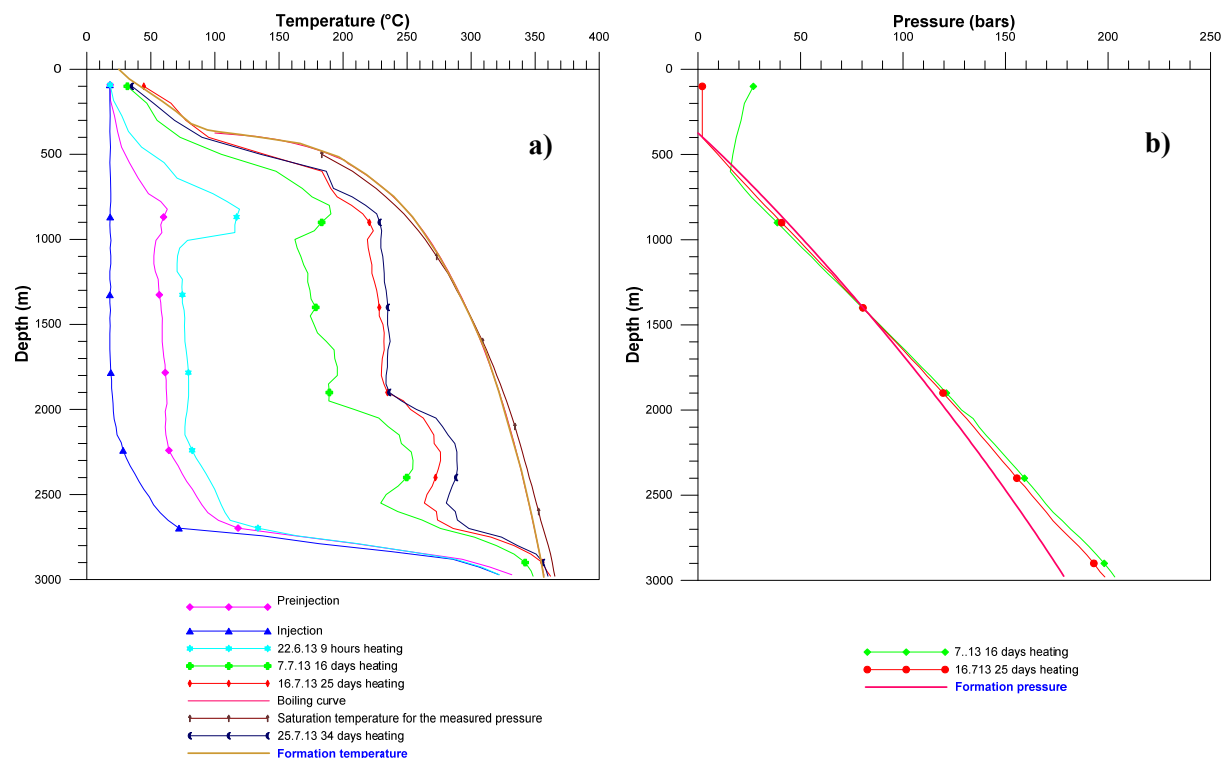


FIGURE 18: Well OW-733B: a) Temperature profile; and b) Pressure profile

point by depth curve. Wells OW-43A and OW-46A (Figures 3 and 4, respectively, in Appendix I) in the Olkaria East field show boiling conditions at 800 m depth and high discharge enthalpy of 2428 and 2085 kJ/kg recorded, respectively, thus the formation temperatures were interpreted to follow the boiling point with depth curve. Wells OW-40V and OW-40A were drilled in the eastern part of the East production field, bordering the Northeast production field, as shown in Figure 12 above. Low temperatures were recorded in these wells with alteration minerals showing inflow of cold water into Well OW-40V. However, slightly higher temperatures were observed in Well OW-40A which was drilled directionally to the east; the well has high pressures and good permeability to a few metres from the well bottom. Figures 5 and 6 in Appendix I show the temperature and pressure plots in Wells OW-40V and OW-40A, respectively.

The temperature and pressure profiles for the Southeast field are shown in Figures 7-11 in Appendix I. Generally, low pressures were recorded in the wells. Well OW-802 recorded temperatures of up to 290°C at the well bottom with the estimated formation temperature following the boiling point with depth curve to around 1450 m. Boiling was observed in Well OW-802A above 1000 m and the main feed zone shown by the injection temperature profile is located at around 1950 m. Conductive heating is generally observed in Well OW-803 while Well OW-804 also shows boiling above 1000 m.

The temperature and pressure models are presented as cross-sections across selected areas considered to be of interest and where additional data was acquired. Five planar sectional views were also made so as to understand the heat and pressure distributions at different elevations in the field. The formation temperature and initial pressure estimates done by the Mannvit/ÍSOR/Vatnaskil/Verkís consortium in 2011 and 2012a were also included so as to have a clearer picture of the field.

Figures 1 and 2 in Appendix II show temperature and pressure contour maps for the Olkaria geothermal field at 1200 m a.s.l., respectively, while Figures 19-26 show the temperature and pressure iso-maps across the Olkaria field at 800, 400, 0 and -400 m a.s.l., respectively. In

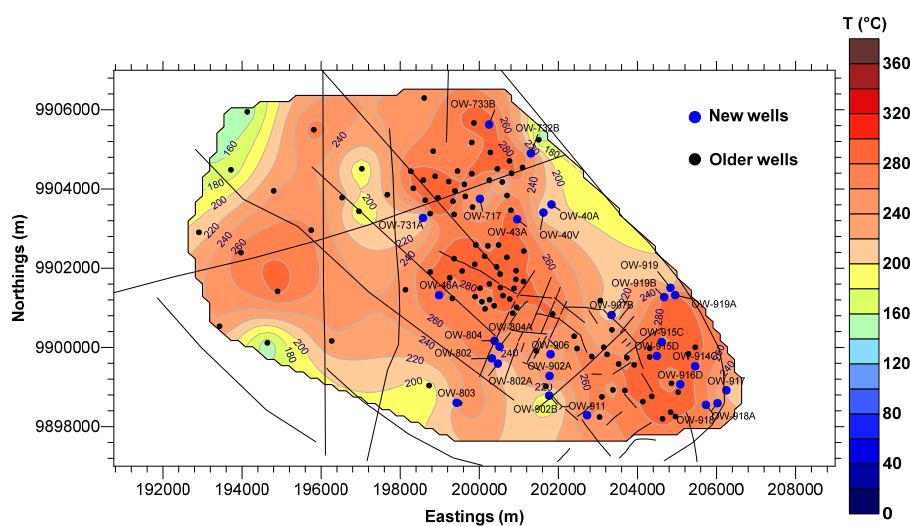


FIGURE 19: Temperature distribution at 800 m a.s.l. elevation

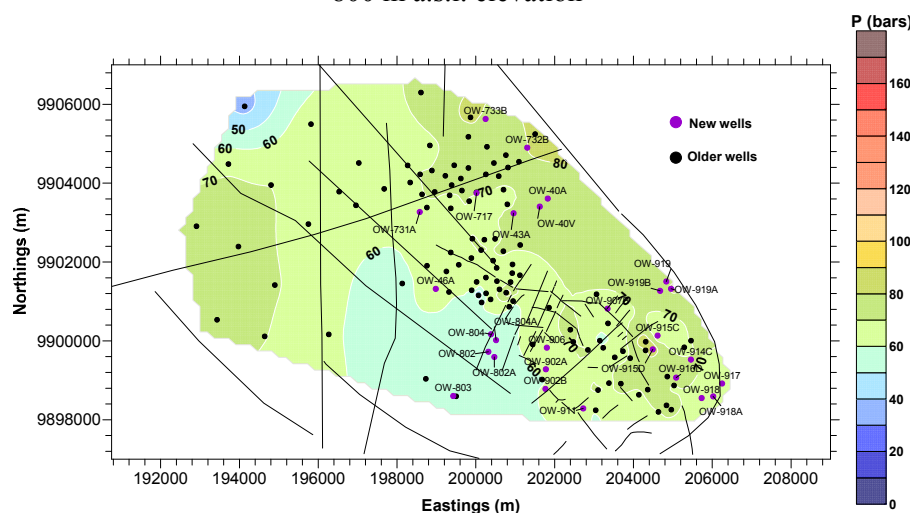


FIGURE 20: Pressure distribution at 800 m a.s.l. elevation

the figures below, the new wells are shown in blue and the older wells are shown in black.

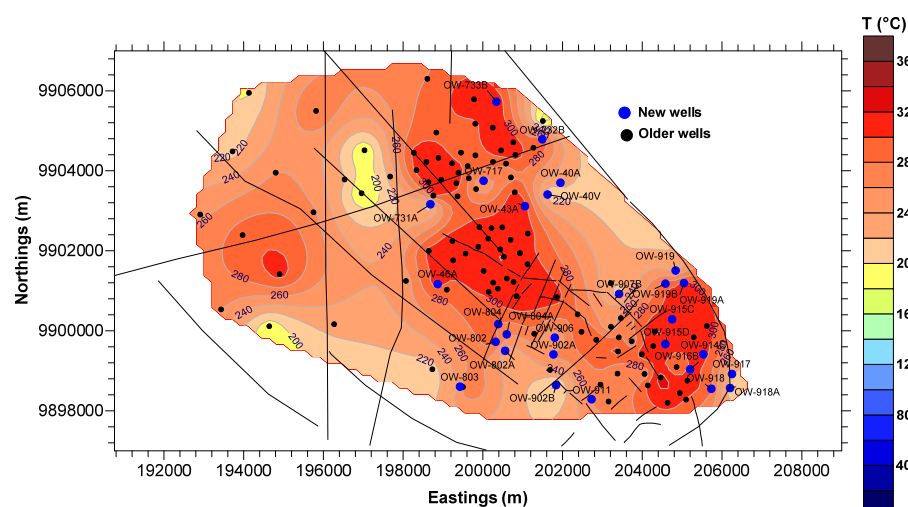


FIGURE 21: Temperature distribution at 400 m a.s.l. elevation

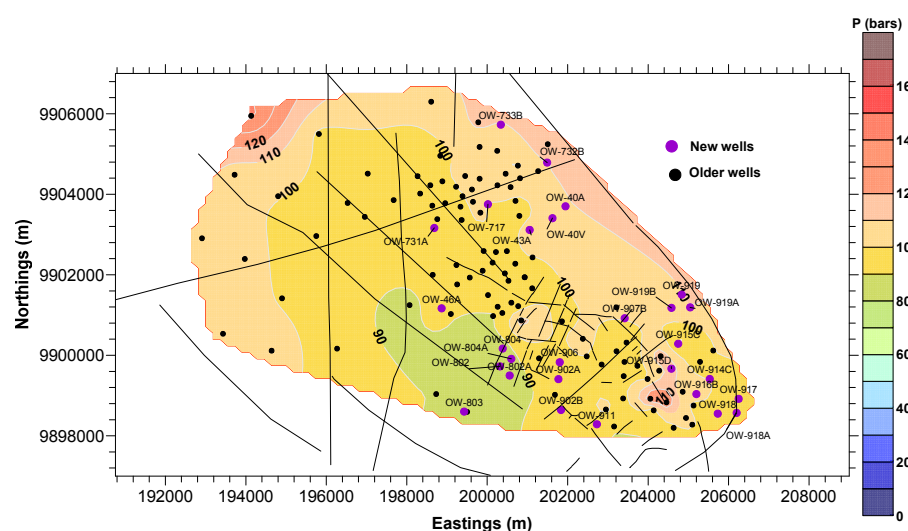


FIGURE 22: Pressure distribution at 400 m a.s.l. elevation

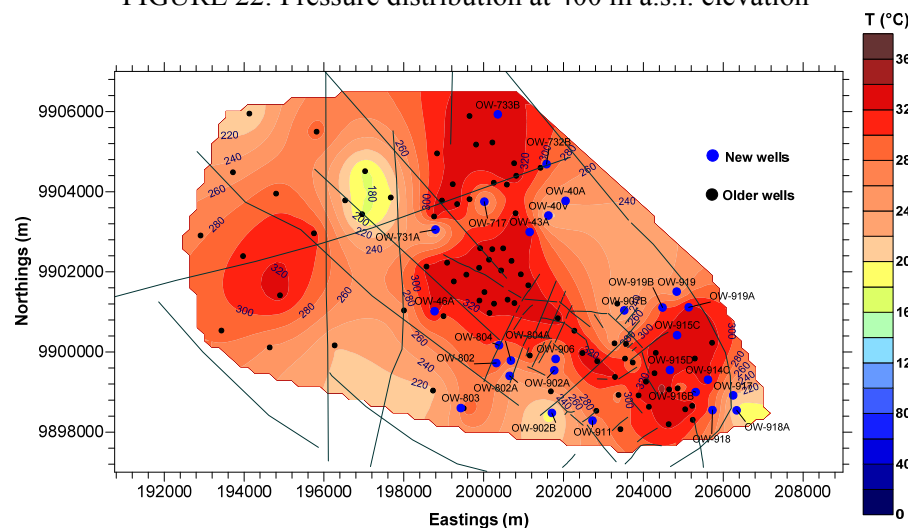


FIGURE 23: Temperature distribution at sea level

The temperature distribution in the field at an elevation of 800 m a.s.l. shows cooling around Well OW-731A which could be close to the boundary of the cold Ololbutot fault around Well OW-201 and the Northeast production field. Slight cooling is evident towards Well OW-717 which could mark the boundary of the Northeast and East production fields along the Olkaria fracture to Wells OW-40V and OW-40A. This trend is also observed at elevations of 400, 0, and -400 m a.s.l. The isotherms in the southern part show high temperature around this area, separated from the Domes field by a lower temperature around Well OW-902B.

The southeast part of Domes shows cooling around Well OW-918A where the isotherms are observed to move gradually to a few depths from the surface from all other parts of the Domes field area towards the location of Wells OW-914 and OW-915 and extend eastward, indicating that the main up-flow zone for Olkaria Domes field is located in the region. Slight cooling was observed around Wells OW-910 and OW-909.

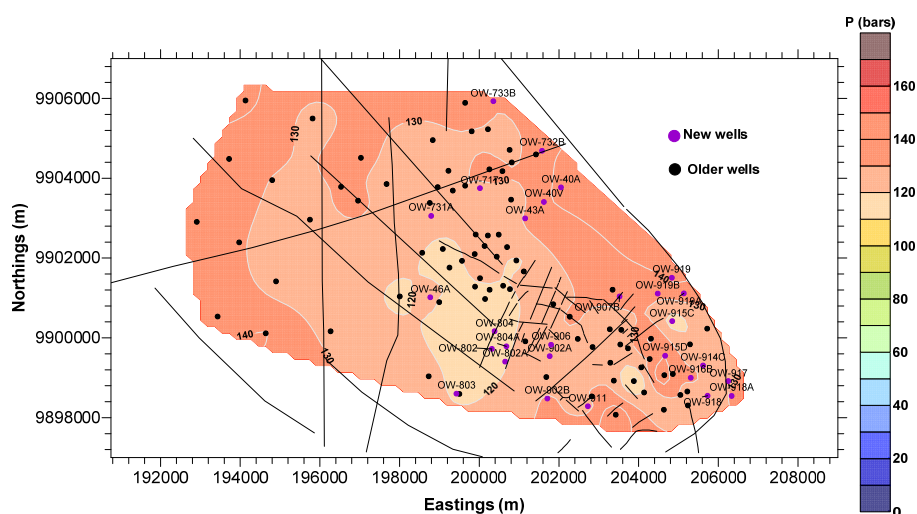


FIGURE 24: Pressure distribution at sea level

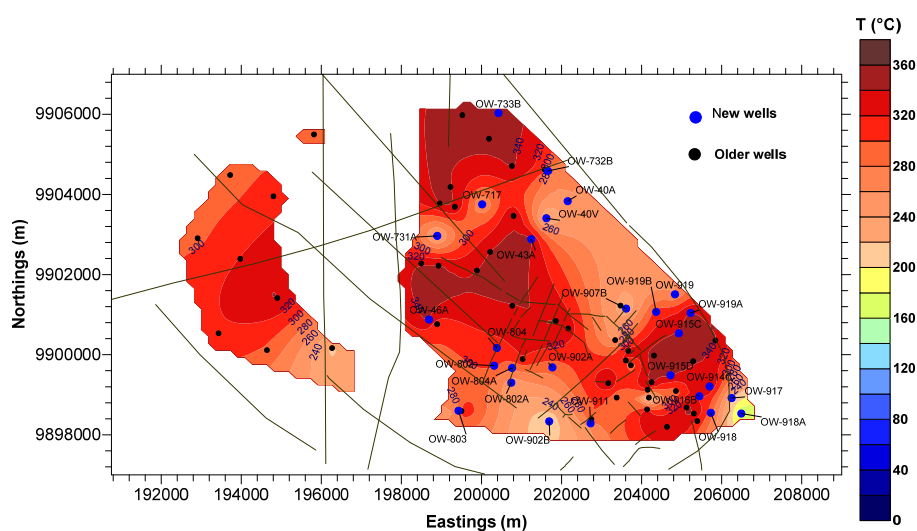
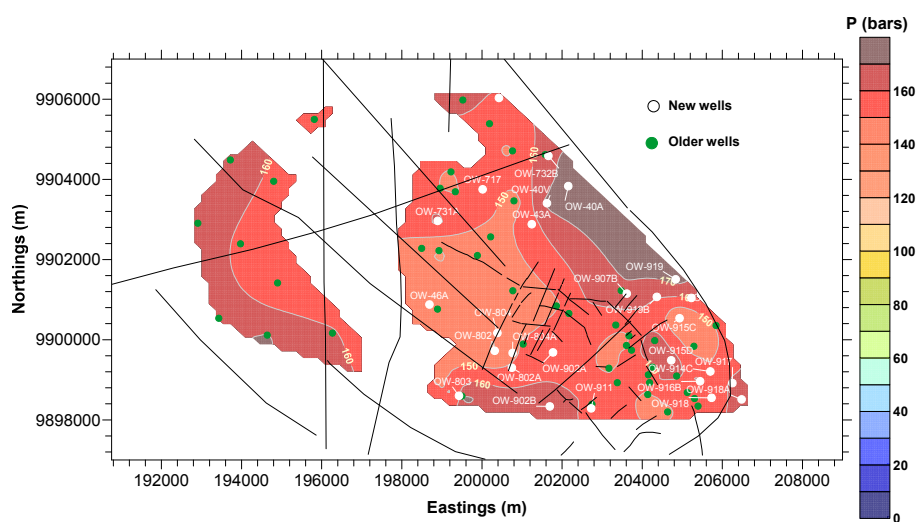
FIGURE 25: Temperature distribution at
-400 m a.s.l. elevation

FIGURE 26: Pressure distribution at -400 m a.s.l. elevation

It is also evident, from the isotherms at 1200 m a.s.l. and 800 m a.s.l., that a higher temperature region is shallower in the East production field than in the Domes field. The isomaps show the pressure is lowest in the southern part of the Olkaria field.

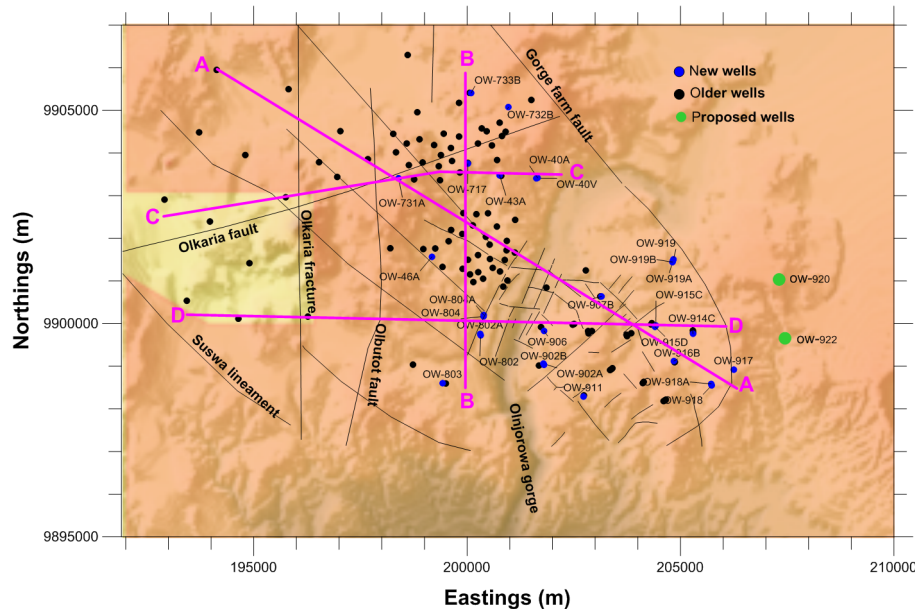


FIGURE 27: Map showing well locations and cross-sections across the Olkaria geothermal field

Four cross-sections were made for the analysis of the vertical temperature and pressure models of the Olkaria geothermal system. Figure 27 shows the location of the different cross-sections, AA, BB, CC, and DD.

Figure 28 shows the temperature and pressure in cross-section AA from Well OW-102 in the Olkaria South West field through to Wells OW-731A and OW-38 to OW-917 in the southeast part of

Olkaria Domes field. The isotherms are depressed west of Olubutot fault with the 160°C isotherm reaching a depth of 0 m a.s.l., indicating cooling in that part of the field. A possible cooling was also observed around Well OW-731A.

The isotherms drastically rose to a shallower depth as the Northeast production field was crossed with the 200°C isotherm at around 1650 m a.s.l. The isotherm went slightly deeper as the East field was crossed to a depth of 1500 m a.s.l. around Wells OW-38 and OW-41, located at its main up-flow zones. The isotherms are then depressed to a depth of around -100 m a.s.l., crossing Well OW-907A in the Domes production field. Moving to the main up-flow zone in the Domes field, located around Wells OW-915 and OW-916, the temperature line approaches the surface at a depth of 1650 m a.s.l. Cooling is possibly occurring in around Well OW-918A in the southeast Domes, as indicated by the depressed 201°C isotherm at a depth of around -600 m a.s.l.

The pressure isolines for cross-section AA (Figure 28b) display the same pattern, peaking at the perceived up-flow zones and dipping at the regions experiencing cooling.

Cross-section BB runs from Well OW-803 in the south to Well OW-733B in the north, passing through Well OW-717. Figure 29 shows a slight movement of the isotherms near the surface as you cross from the south to the centre of the East production field. Slight cooling was observed around Well OW-717 but the isotherms move close to the surface in the north. A similar pattern was observed in the pressure contour lines (Figure 29b).

Figure 30 shows cross-section CC, starting at Well OW-308 in the west reaching to the northeast to Well OW-717, then to the east to Well OW-40A. Cooling was also observed to the west of the Olubutot fault with slight cooling around Well OW-717 (Figure 30a). Another indication of cooling was seen in Well OW-40V but the hot contour moved to a shallower level as it approached the Gorge farm fault through Well OW-40A.

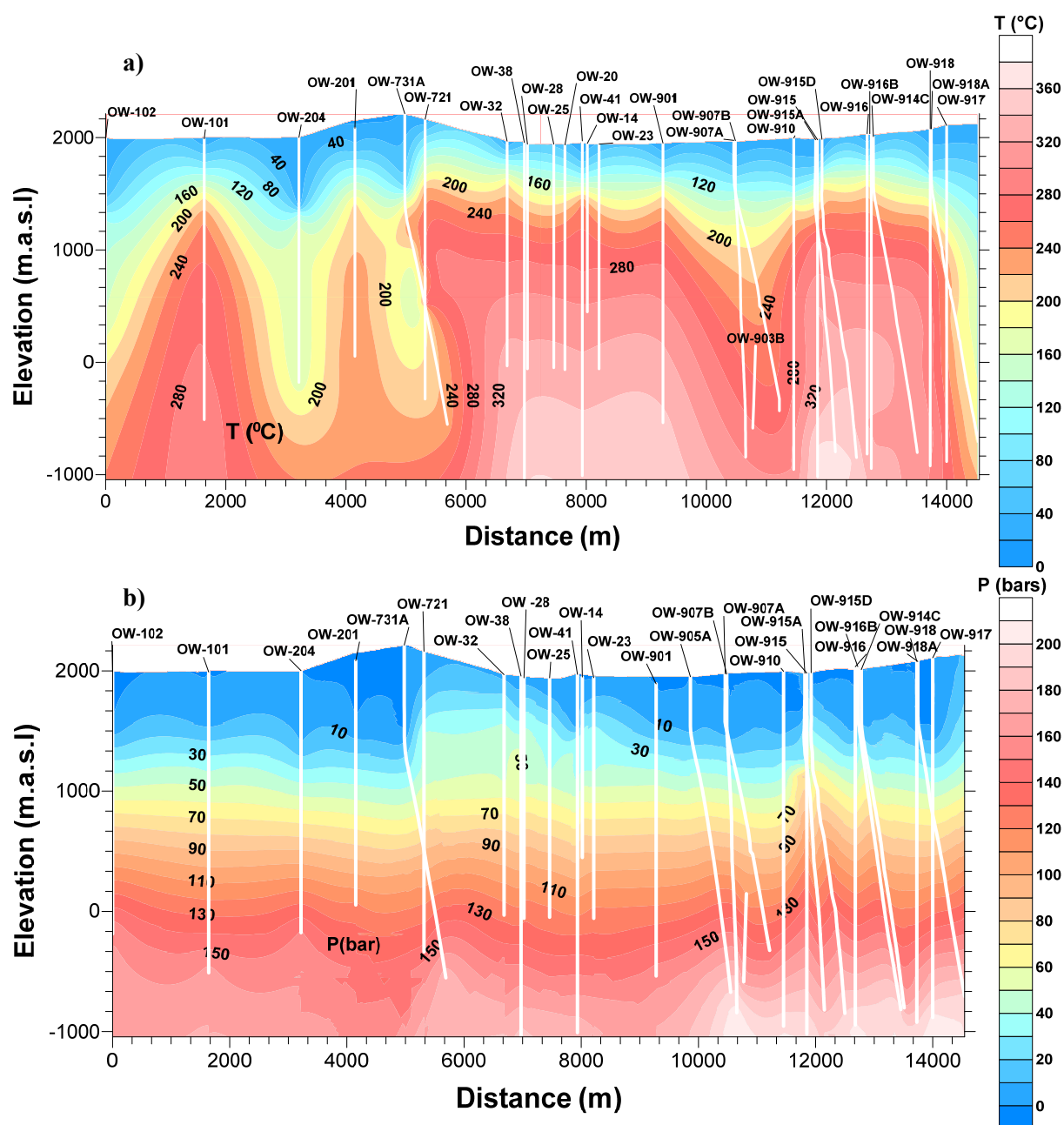


FIGURE 28: Cross-section AA: a) temperature profile; and b) pressure profile

Another cross-section of interest is section DD (Figure 31) from Well OW-304 in the West field to Well OW-914 in the Domes field. Figure 31a shows that cooling was observed to the west of the Ololbutot fault, as observed in the previous sections, but moved gradually closer to the surface from Well OW-802 to Well OW-914 in the East field. A similar pattern was observed with the isobars dipping near the Ololbutot fault (Figure 31b).

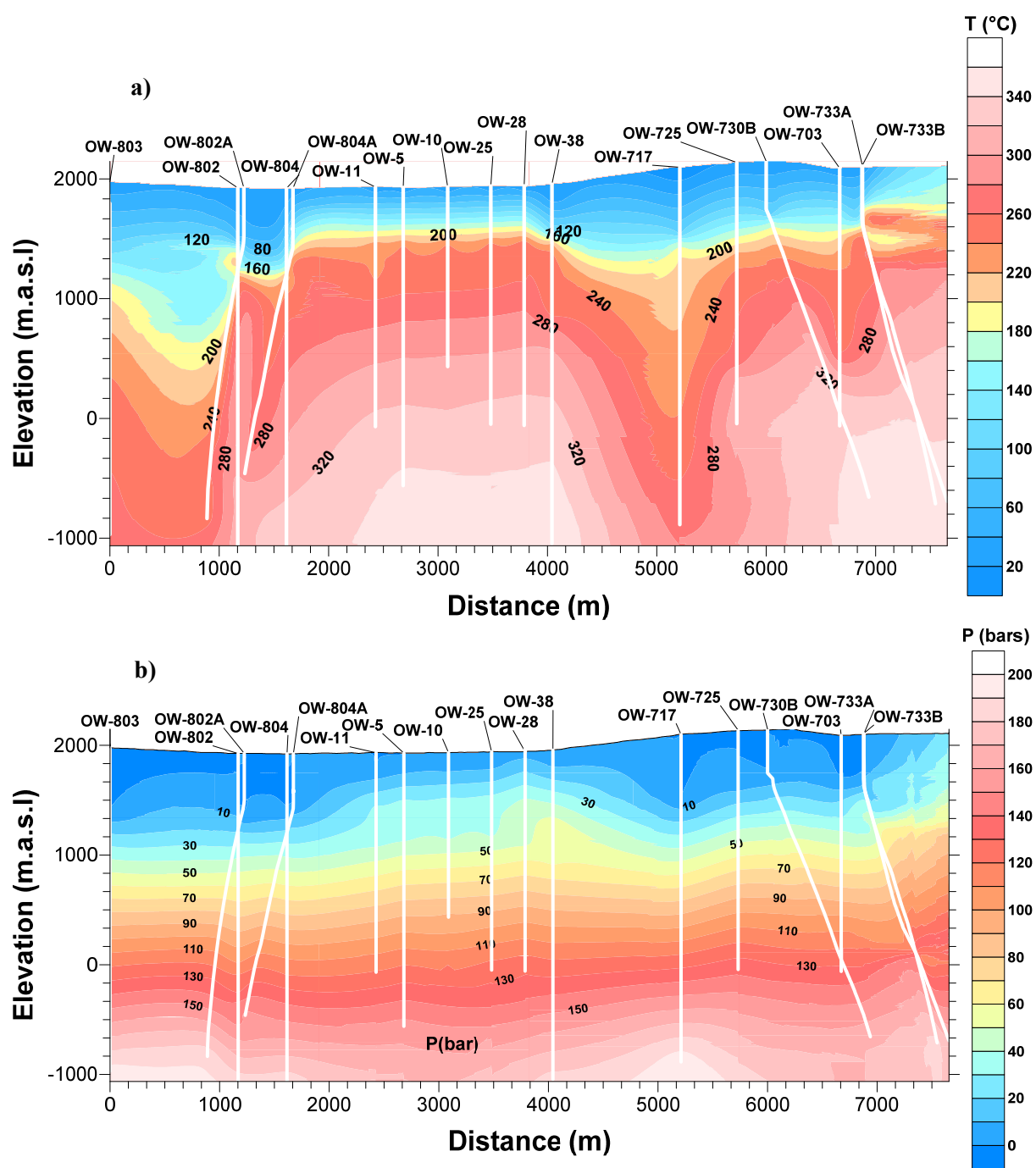


FIGURE 29: Cross-section BB: a) temperature profile; and b) pressure profile

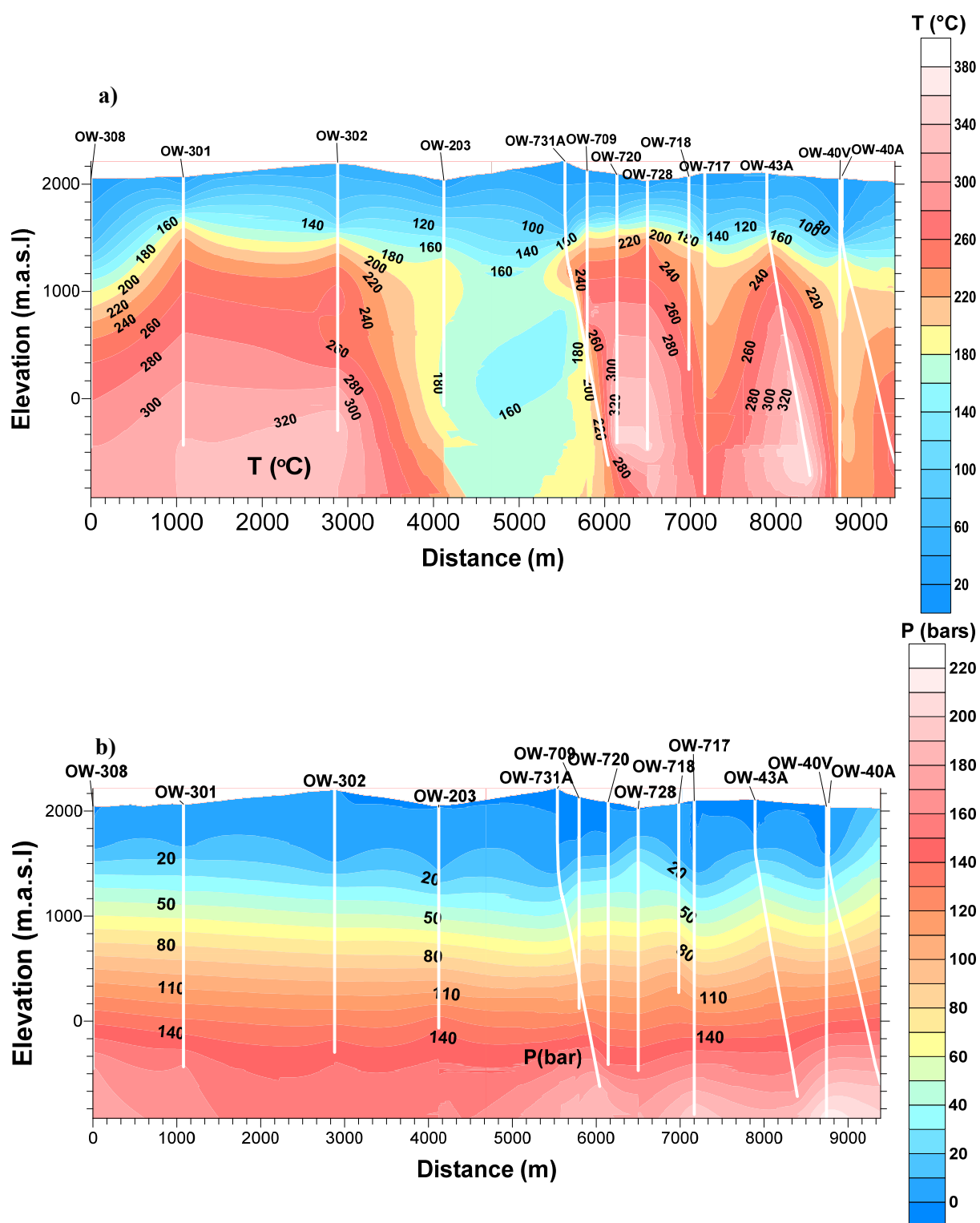


FIGURE 30: Cross-section CC: a) temperature profile; and b) pressure profile

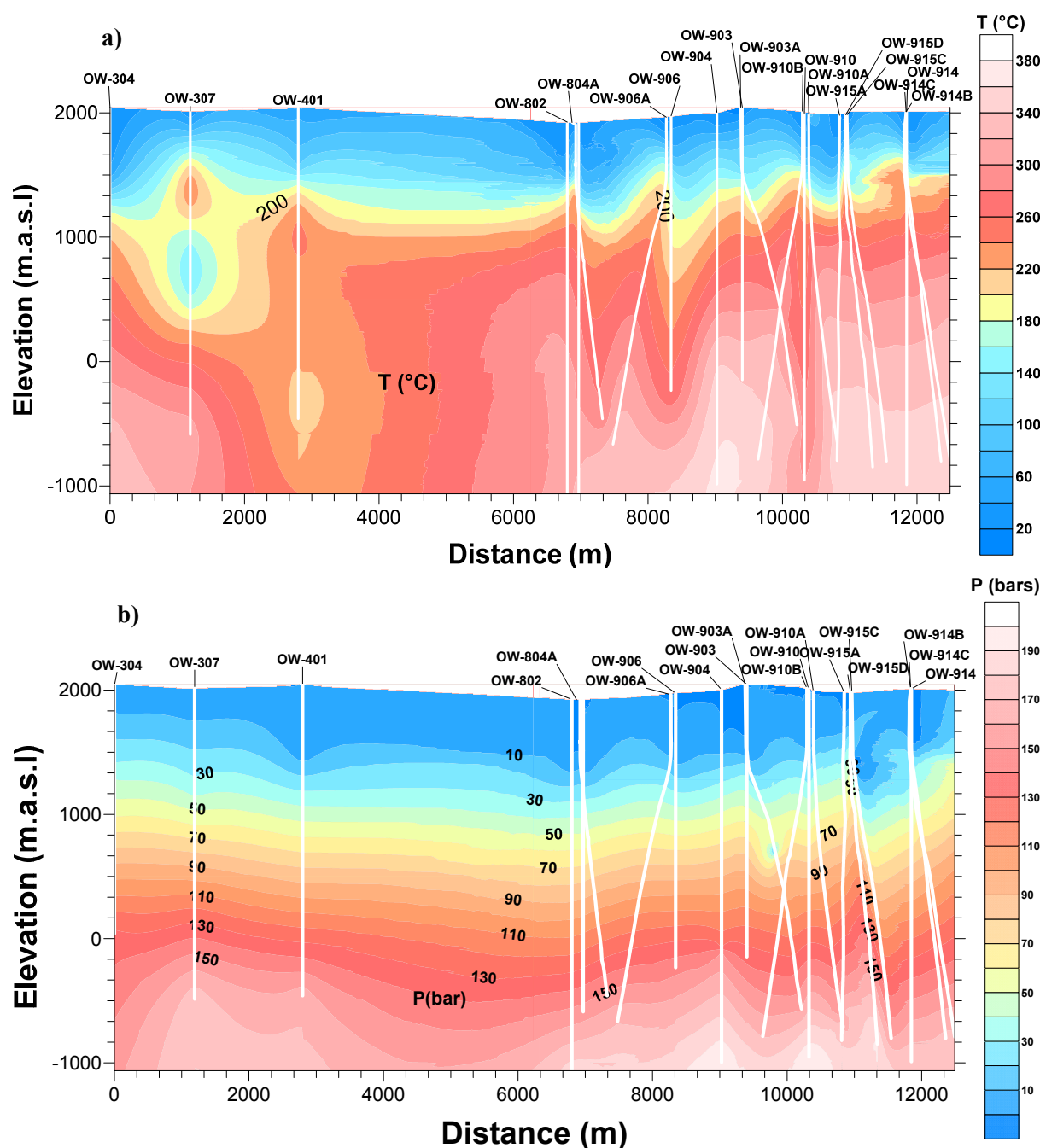


FIGURE 31: Cross-section DD: a) temperature profile; and b) pressure profile

3.4 Revision of the conceptual model

The development of reliable conceptual models requires a multi-disciplinary approach where the varying dimensional concepts of different geosciences involved in the exploration and development are put together. Conceptual model development requires the understanding of the nature and size of the heat source, the fluid recharge to the system and the up-flow zones, the main permeable regions of the system, the initial temperature and pressure conditions of the system and the nature of the boundary conditions.

The present work looks at the possible changes in the Olkaria geothermal field conceptual model as developed by the consortium of Mannvit/ÍSOR/ Vatnaskil/Verkís, based on the interpretation of newly

acquired temperature and pressure data and the accompanying updated temperature and pressure model. The geology and the geophysical information, as analysed and described by Mannvit/ÍSOR/Vatnaskil/Verkís (2011), played a key role in interpreting the data as well as in developing the temperature and pressure models. New additions to the conception model are pointed out as follows:

1. The geothermal resource possibly extends north of the Olkaria Northeast production field, confirmed by very high temperatures of over 360°C in Well OW-733B, newly drilled in the area.
2. The immediate eastern part of the East production field is possibly a down-flow zone or low temperature region but, further east towards the Gorge farm fault, temperatures are increasing, indicating a possible up-flow zone.
3. The area near Wells OW-717 and OW-731A indicates a down flow zone that could indicate the boundary of the East field and the Northeast field, as well as cooling in the region.
4. The eastern part of Domes field is a high-temperature and pressure up-flow zone; the boundary was not demarcated by Wells OW-914B and OW-914C, recently drilled in the area. Both wells show high temperatures, as seen in Figure 31a.
5. The wells already drilled in the southeast part of the Olkaria Domes field indicate very poor permeability in a small area, as shown by the localised high-resistivity anomaly in Figure 6 in Section 2.2. Further east of the spot with a high resistivity anomaly, down-flow conditions are encountered. Well OW-918A, drilled across the ring structure southeast of Domes field across an area where the ring structure curves towards the west, indicates a temperature reversal at the well bottom, a result of a possible horizontal flow in the region. Further southeast, a low resistivity anomaly is encountered which could be the result of a possible up-flow zone.

Figure 32 shows a pictorial view of the revised conceptual model.

It is believed that three major heat sources are within the Olkaria geothermal system. These are magma intrusions from deep lying magma to a depth of 6-7 km from the surface. The heat sources are located below the Olkaria hill, the Gorge farm volcanic centre, and below Olkaria Domes field. The one below the Olkaria hill is responsible for the up-flow zone in the western part of the field and is shown in Figure 32, marked in red to the left.

The heat source located at the Gorge farm volcanic centre is associated with the up-flow zone for Olkaria East and Olkaria Northeast fields, as shown by the red arrow in Figure 32, indicating conduction from this heat source to the Olkaria East up-flow zone. The red body to the right in Figure 32 represents the heat source beneath Olkaria Domes field. Heat is then conducted to a deep reservoir located near the up-flow zones for each field, as shown by the orange arrows. Cold down flow is proposed to come from the Ololbutot fault and the ring structure in the southeast part of the Domes field down to this hot region, thus forming a hot water reservoir beneath each up-flow zone for the different fields.

Four major up-flow zones are connected to this deep reservoir through NW-SE and NE-SW trending faults. These four major up-flow zones are confirmed by the temperature and pressure contour maps in Section 3.3. The pressurised hot water flows upwards through faults and fractures and some move all the way to the surface as fumaroles and hot springs. The reduced pressure in Olkaria East and Olkaria Northeast fields, as the water rises to shallower levels, results in boiling, thus forming a steam cap near the cap rock.

In the wells drilled in the Domes field, which had a chance of intersecting these fractures, the pressurised water enters the wells and boils in the wells as they rise up when the wells are opened, yielding two phase steam and water on the surface.

Another up-flow zone is proposed beyond the down flow in the southeast part of the Domes field that may be associated with the heat source beneath the Olkaria Domes field. There could be fractures and faults that connect to a possible hot water reservoir associated with this heat source, thus forming a reservoir in this part of the field. This is shown by the low resistivity of 12-29 Ωm in the vicinity of a conductive zone of 0-12 Ωm , associated with good productive areas in the Olkaria Domes field.

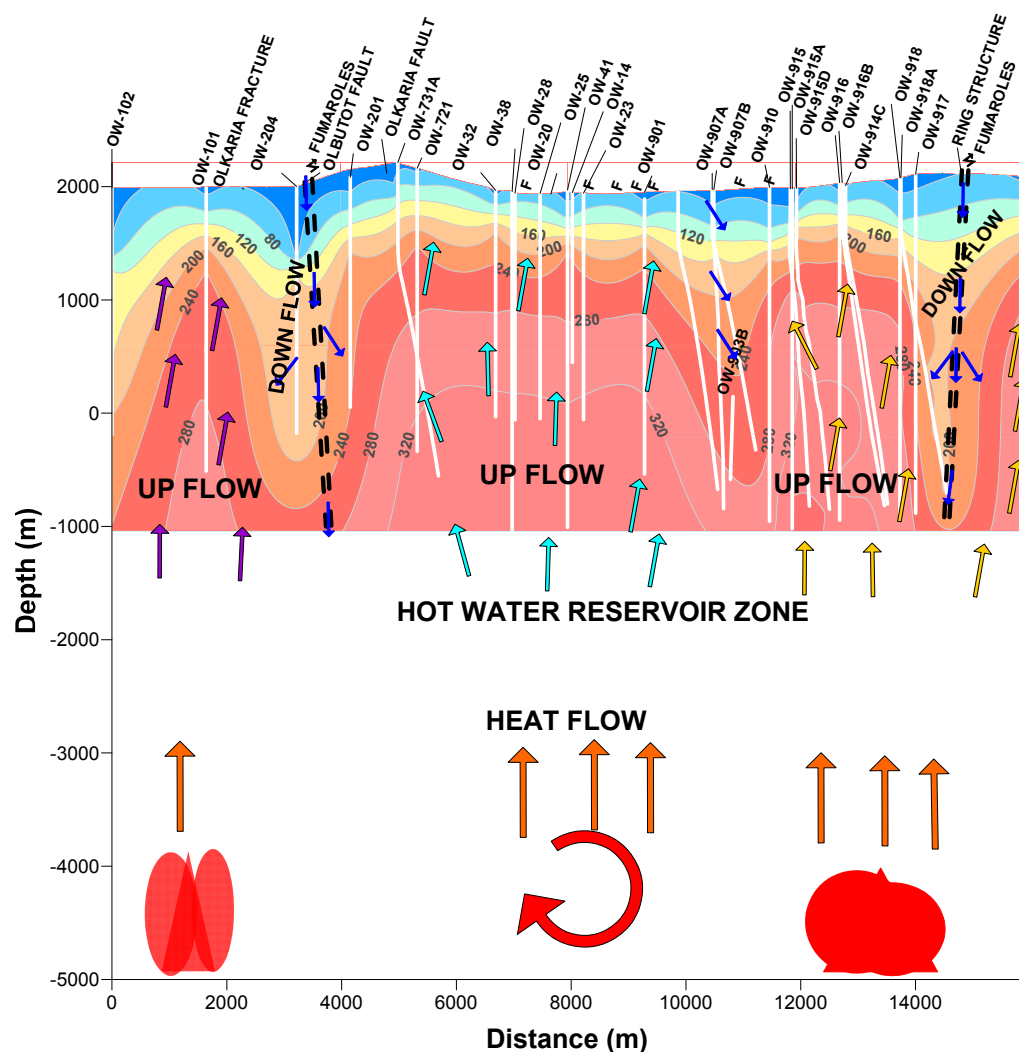


FIGURE 32: Revised conceptual model

Gas geothermometers indicated a temperature of 250°C; surface manifestations such as fumaroles, altered grounds and steaming grounds indicate the likelihood of good permeability.

4. DISCUSSION

Figure 33 shows a map of Olkaria with the structures and location of the newly drilled wells, together with the old wells. Areas with resistivity of interest are also marked, based on the resistivity analysis at -400 m of Olkaria Domes done by Wanjohi in 2011, shown in Figure 6. Also mapped are the centres at 6 km depth to the top of seismic wave attenuating bodies, presented by Mannvit/ ÍSOR/Vatnaskil/Verkís (2011), shown in Figure 5.

The high temperature of 362°C encountered in Well OW-733B at the well's bottom suggests that the well penetrated an up-flow zone near the Gorge farm volcanic centre, believed to be associated with the heat source for the Olkaria Northeast and the Olkaria East production fields. Very high temperatures of close to 381°C were also encountered in Well OW-919A in the Domes field at a depth of 2980 m from the surface. This well was directionally drilled towards the centre of the area, believed to be above the heat source for the Olkaria Domes field.

The horizontal sections confirm the location of four major up-flow zones for the Olkaria field, shown by the pattern of high temperature areas moving from a horizontal section at 1200 to -400 m a.s.l. (Figures 19-25 and Figure 1 in Appendix II).

Cooling was witnessed around new Well OW-717 in the NEPF, with a temperature reversal in Wells OW-731A and OW-732B. The temperature reversal in Well OW-731A was confirmed by alteration

minerals which indicate a cold inflow and low temperatures. Low enthalpies of 1060 and 1580 kJ/kg were encountered in Wells OW-732B and OW-717 which may further confirm cooling in the region. Temperature reversals may suggest horizontal inflow of colder fluids at upper zones and out flow in the lower formations. This indicates that there could be a fracture taking in cold fluids either from the Ololbutot fault or re-injection Well R3 to these areas. It could also suggest that Well OW-731A is located at the boundary of the colder zone and the East field, separated by the Ololbutot fault. It is worth noting that this cooling was observed along the Olkaria fault as the wells are aligned along this fault.

There is also a possibility of the colder water being re-injected in Well R-3 finding its way through the fracture that is near it, all the way to the Olkaria fault and then eastwards. This could explain the colder zone shown in the 0 m a.s.l. contour map (Figure 23), separating the Northeast production field and the East production field.

The low temperature witnessed in Well OW-40V may confirm that the well is far from any heat source, as shown in Figure 5 and mapped in Figure 33. The heat source near this well, as shown in Figure 5, is deeper than 13 km and may not have strike fractures connected to other up-flow zones. The increase in temperature in Well OW-40A, which was drilled directionally eastwards from the same well pad, may confirm increasing temperatures eastwards near the heat source centre located to the east of Well OW-40V, which is near the Gorge farm fault, shown in Figure 33. It is also important to note that Well OW-40A encountered high down-hole pressures. This could indicate that an exploitable geothermal resource could possibly exist east of the Olkaria Northeast field, due to its proximity to the Gorge farm fault.

Temperature and pressure were observed to increase gradually from Well OW-804 in the Southeast production field to the Domes area, and then suddenly rise as the up flow zone near Well OW-914 was crossed. This explains why the upper and central parts of the Southeast production field had good temperatures. It also shows that the up-flow zone in the Domes field extends to the east and temperature in the newly drilled wells there, Wells OW-914C and OW-914D, showed no evidence of a boundary.

A temperature cross-section from the south to the east showed an up-flow zone, as was expected, in the East production field, then slight cooling around Wells OW-731A and OW-717, followed by an up-flow

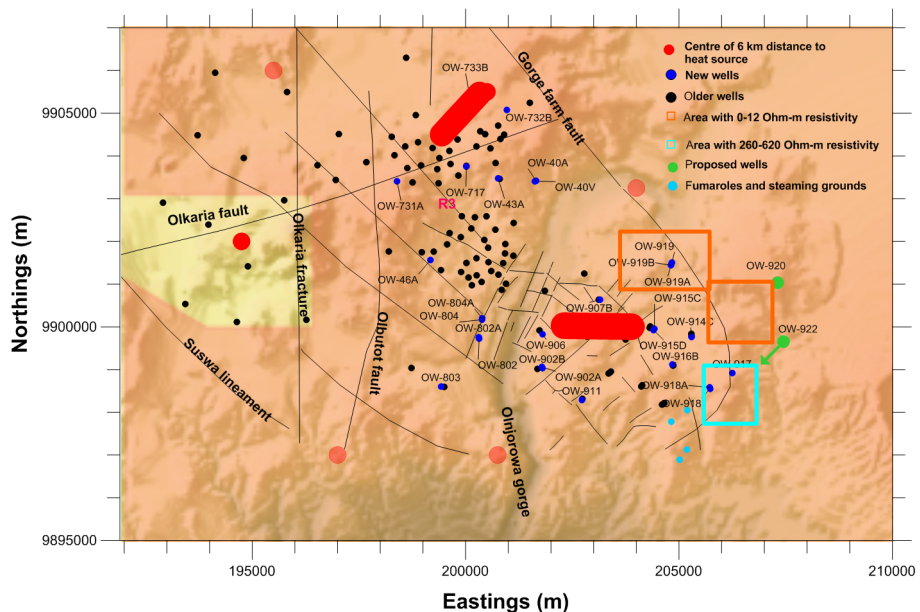


FIGURE 33: Map of the Olkaria geothermal system, showing faults and fractures; main and proposed heat sources and areas mapped from the resistivity

zone associated with the Northeast production field. The boundary in the north has not yet been delineated by present drilling and it is possible that the geothermal resource extends northwards.

Well OW-918A, drilled across the southeast corner of the ring structure in the Domes field, showed a temperature reversal at 1700 m from the surface. Well OW-917 drilled near it showed conductive heating to the well bottom and Well OW-918 showed conductive heating to about 1500 m depth, confirming poor permeability in the area penetrated by these wells. The resistivity survey discussed earlier in this section shows a high resistivity anomaly in the range of 260-620 Ωm . This could indicate impermeable rock.

The lithology shows that the dominant rock is trachyte (Musonye, 2013). The temperature reversal witnessed in Well OW-918A suggests a horizontal flow in the vicinity of this well. Low-temperature alteration minerals were encountered, confirming cold water inflow. A temperature regime of cold-hot-cold from an analysis of the alteration minerals and calcite deposition on fractures, also confirmed the horizontal cold flow in this region.

The resistivity of the Olkaria Domes (Figure 6) showed a resistivity of 12-19 Ωm bordering a region of very low resistivity, 0-12 Ωm , in the vicinity of the heat source, as shown in Figure 32, suggesting a potentially good production zone. The high conductivity could be due to water filled fractures with good permeability. Figure 33 illustrates that this region of high conductivity follows the ring structure. The higher resistivity bordering the low resistivity could be due to high-temperature alteration minerals. The southeast part of the Domes field has the same characteristics with the highly conductive region, likely following the outer ring structure. This could imply that the geothermal resource could possibly extend to the southeast and east of Domes field, as earlier suggested. The above discussion explains the conceptual model, as shown in Figure 32, in Section 3.4.

5. CONCLUSIONS

The temperature and pressure model of the Greater Olkaria geothermal field has been updated, based on newly acquired well temperature and pressure data. The resulting additions to the present conceptual model have also been pointed out. It can, therefore, be concluded that:

1. The heat source for the Olkaria geothermal system is, as previous theorized, explained by Mannvit/ÍSOR/Vatnaskil/Verkís who did the field optimisation study shown in Figure 5.
2. Four major up-flow zones have been confirmed, feeding the Olkaria West, Olkaria East, Olkaria Northeast and the Olkaria Domes fields.
3. The geothermal resource extends further north and to the east of the KenGen concession area in Olkaria.
4. Possible resources also exist east of the Northeast field and the southeast part of Domes field.
5. Permeability is believed to be controlled by NW-SE, NE-SW trending faults as well as the ring structure.
6. Cooling of the system was observed around Wells OW-731A, OW-732B and OW-717.
7. Down flow is likely occurring along the ring structure in the southeast part of the Olkaria Domes field, which could possibly be a cold recharge zone. Ololbutot fault has been confirmed as being responsible for the cold water recharge to the field.

Based on the above conclusions, it is further recommended:

1. That a well be sited outside the high-resistivity anomaly experienced near the ring structure in the southeast part of the Domes field and east of Well OW-914C, so as to gain a better understanding

of that area. The proposed Wells OW-922 and OW-920 are located in the region and the study supports the siting of these wells.

2. To consider another area in the northern part of the Northeast production field where indications of a boundary have not yet been encountered.
3. To conduct further investigations to better understand the cooling around Well OW-717 and to explain the origins of the cooling.

ACKNOWLEDGEMENTS

I take this opportunity to sincerely thank the United Nations University Geothermal Training Programme and the Government of Iceland for granting me an opportunity to improve my skills in geothermal energy development. Special thanks go to the outgoing director of the UNU-GTP, Dr. Ingvar B. Fridleifsson, the present director Mr. Lúdvík S. Georgsson, Ms. Thórhildur Ísberg, Mr. Ingimar G. Haraldsson, Mr. Markús A. G. Wilde, and Ms. Málfríður Ómarsdóttir for their assistance throughout the course. I extend my gratitude to my supervisors, Ms. Saeunn Halldórsdóttir, Ms. Sigríður Sif Gylfadóttir from ÍSOR and Mr. Andri Arnaldsson. Special thanks to all other ÍSOR staff, especially Dr. Gudni Axelsson and Mr. Benedikt Steingrímsson, for guidance and their valuable time in reviewing my project report together with Mr. Benedikt Steingrímsson, for guidance and their valuable time in reviewing my project report.

I am indebted to Kenya Electricity Generating Company (KenGen) management for granting me leave to attend this informative course and for allowing me use of the company's data for my project. I also thank my colleagues in the company for their assistance in the provision of good data for my project. I say thank you to the 2013 UNU Fellows for their company and fruitful discussions during my stay in Iceland. I would also like to take this opportunity to thank my family and wife for giving me moral support, love, prayers and encouragement.

Finally, I want to thank God for the good health, strength and his blessings during my stay in Iceland.

REFERENCES

- Arason, T., Björnsson, G., Axelsson, G., Bjarnason, J.Ö., and Helgason, P., 2004: *ICEBOX – geothermal reservoir engineering software for Windows. A user's manual*. ISOR, Reykjavík, report 2004/014, 80 pp.
- Axelsson, G., Arnaldsson, A., Gylfadóttir, S.S., Halldórsdóttir, S., Mortensen, A.K., Bore, C., Karingithi, C., Koech, V., Mbithi, U., Muchemi, G., Mwarania, F., Opondo, K., and Ouma, P., 2013: Conceptual model and resource assessment for the Olkaria geothermal system, Kenya. *Proceedings of the "Short Course V on Conceptual Modeling of Geothermal Systems"*, organized by UNU-GTP and LaGeo, Santa Tecla, El Salvador, 21 pp.
- Barelli, A., and Palama, A., 1981: New method for evaluating formation equilibrium in holes during drilling. *Geothermics*, 10-2, 95-102.
- Clarke, M.C.G., Woodhall, D.G., Allen, D., and Darling G., 1990: *Geological, volcanological and hydrogeological controls on the occurrence of geothermal activity in the area surrounding Lake Naivasha, Kenya, with coloured 1:100 000 geological maps*. Ministry of Energy, Nairobi, 138 pp.

Dowdle, W.L., and Cobb, W.M., 1975: Static formation temperature from logs - an empirical method. *J. Petroleum Technology*, 27-11, 1326-1330.

Grant, M.A., and Bixley, P.F., 2011: *Geothermal reservoir engineering*, 2nd edition. Academic Press, New York, 359 pp.

Grant, M.A., Donaldson, I.G., and Bixley, P.F., 1982: *Geothermal reservoir engineering*. Academic Press, New York, 369 pp.

Mannvit/ÍSOR/Vatnaskil/Verkís Consortium, 2011: Revision of the conceptual model of the Greater Olkaria Geothermal System-Phase I. Mannvit/ÍSOR/Vatnaskil/Verkís, Reykjavík, 100pp.

Mannvit/ÍSOR/Vatnaskil/Verkís Consortium, 2012a: Volumetric resource assessment and lumped parameter pressure response modelling of the Greater Olkaria Geothermal System-Phase I. Mannvit/ÍSOR/Vatnaskil/Verkís, Reykjavík, March, 43pp.

Mannvit/ÍSOR/Vatnaskil/Verkís Consortium, 2012b: Development of the numerical model of the Greater Olkaria Geothermal System-Phase I. Mannvit/ÍSOR/Vatnaskil/Verkís, Reykjavík, June, 111pp.

Mariita, N.O., 2009: Exploration history of Olkaria geothermal field by use of geophysics. *Paper presented at "Short course IV on exploration for geothermal resources", UNU-GTP, KenGen and GDC, Lake Naivasha, Kenya*, 13 pp.

Muchemi, G.G., 1999: *Conceptualised model of the Olkaria geothermal field*. The Kenya Electricity Generating Company, Ltd., internal report, 46 pp.

Mungania, J., 1992: *Geology of the Olkaria geothermal complex*. Kenya Power Company, Ltd., internal report, 38 pp.

Mungania, J., 1999: *Summary of updates of the geology of the Olkaria Domes geothermal field*. Kenya Electricity Generating Company, Ltd., unpublished report.

Musonye, X.S., 2013: *Borehole geology and alteration mineralogy of well OW-917, Domes area, Olkaria geothermal field, central Kenya rift*. The Kenya Electricity Generating Company, Ltd., internal report, 33 pp.

Naylor, W.I., 1972: *Geology of the Eburru and Olkaria prospects*. U.N. Geothermal Exploration Project, report.

Ndombi, J.M., 1981: The structure of shallow earth beneath the Olkaria Geothermal field, Kenya, deduced from gravity studies. *J. Volcanol. & Geothermal Research*, 9, 237-251.

Ofwona, C.O., 2002: *A reservoir study of Olkaria East geothermal system, Kenya*. University of Iceland, M.Sc. thesis, UNU-GTP, Iceland, report 1, 74 pp.

Onacha, S.A., Shalev, E., Malin, P., and Leary, P., 2009: *Joint geophysical imaging of fluid-filled fracture zones in geothermal fields in the Kenya Rift valley*. Auckland University, Institute of Earth Science and Engineering, NZ, 6 pp.

Roux, B., Sanyal, S.K., and Brown, S.L., 1980: An improved approach to estimating the reservoir temperature from transient temperature data. *Paper presented at 50th Annual Regional Meeting of the Society of Petroleum Engineers of AIME, Los Angeles*, 5 pp.

Simiyu, S.M., and Malin, P.E., 2000: A “volcano-seismic” approach to geothermal exploration and reservoir monitoring: Olkaria, Kenya and Casa Diablo, USA. *Proceedings of the World Geothermal Congress 2000, Kyushu-Tohoku, Japan*, 1759-1763.

Simiyu, S.M., Oduong, E.O., and Mboya, T.K., 1998a: *Shear wave attenuating beneath the Olkaria volcanic field*. The Kenya Electricity Generating Company, Ltd., internal report, 30 pp.

Stefánsson, V., and Steingrímsson, B.S., 1990: *Geothermal logging I, an introduction to techniques and interpretation* (3rd ed.). Orkustofnun, Reykjavík, report OS-80017/JHD-09, 117 pp.

Sweco and Virkir, 1976: *Feasibility report for the Olkaria geothermal project*. Sweco and Virkir, report prepared for United Nations and Government of Kenya.

Wanjohi, A., 2011: *Geophysics report, east of Olkaria Domes (Akira) geothermal field*. The Kenya Electricity Generating Company Ltd, internal report, 34 pp.

West-JEC, 2009: *The Olkaria optimisation study (phase II) – final reservoir analysis report*. West Japan Engineering Consultants, Inc., 301pp.

APPENDIX I: Temperature and pressure profiles with formation temperatures in recently drilled wells in Olkaria

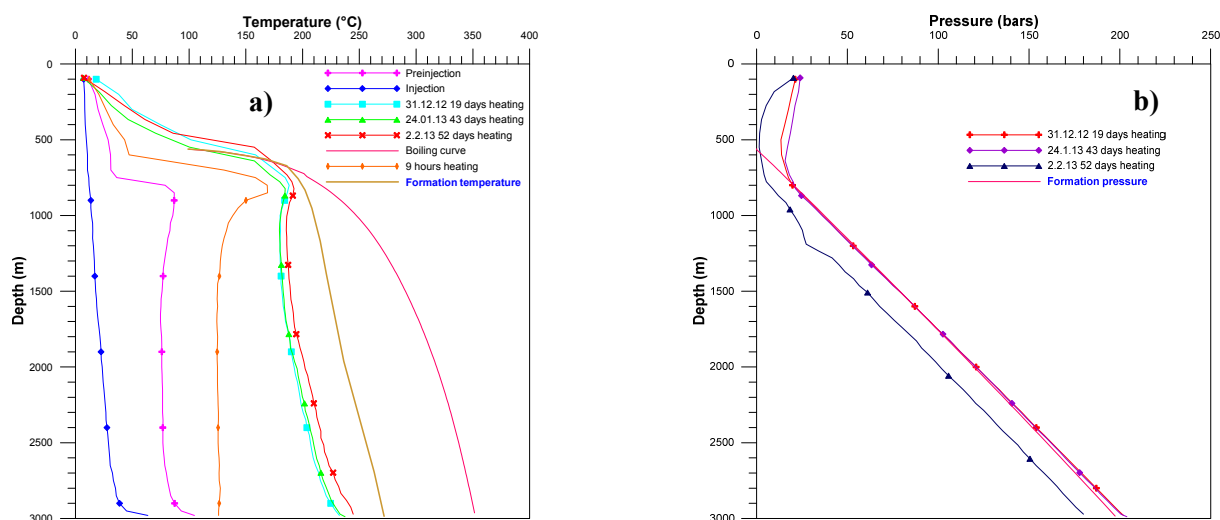


FIGURE 1: Well OW-717: a) Temperature profiles; b) Pressure profiles

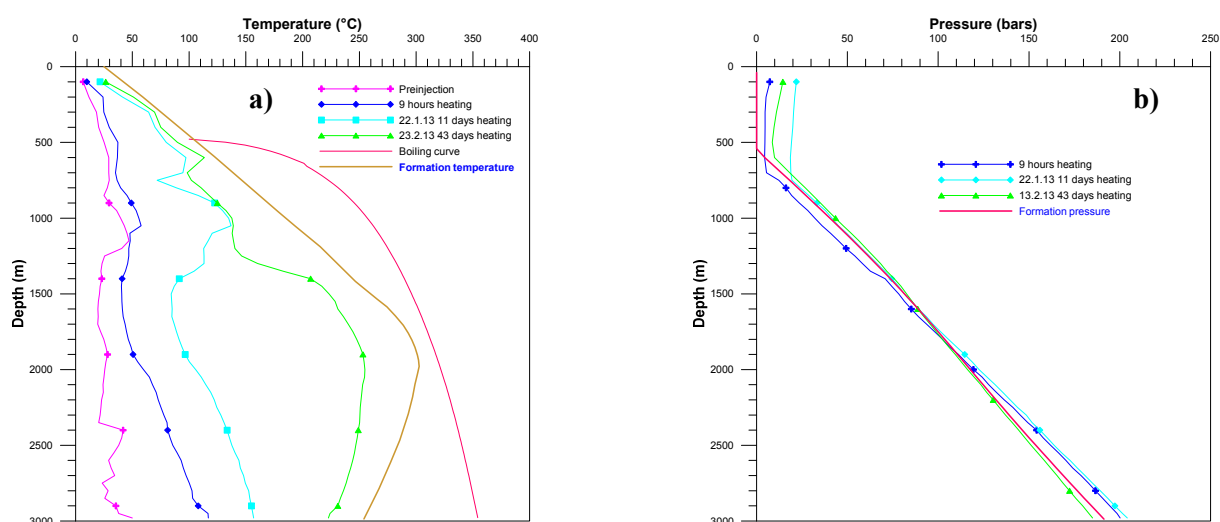


FIGURE 2: Well OW-732B: a) Temperature profiles; b) Pressure profiles

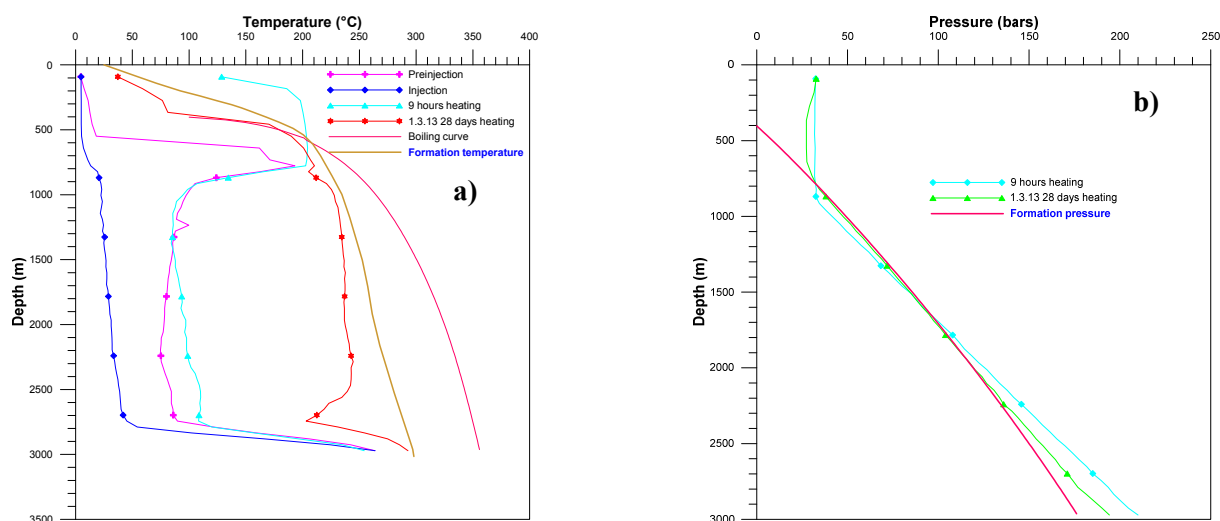


FIGURE 3: Well OW-43A: a) Temperature profiles; b) Pressure profiles

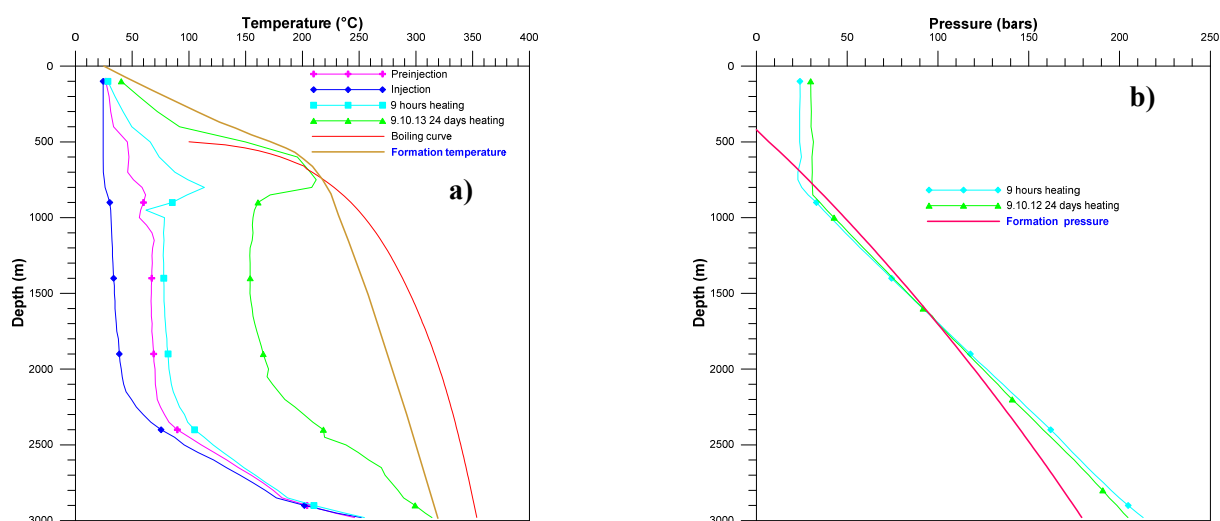


FIGURE 4: Well OW-46A: a) Temperature profiles; b) Pressure profiles

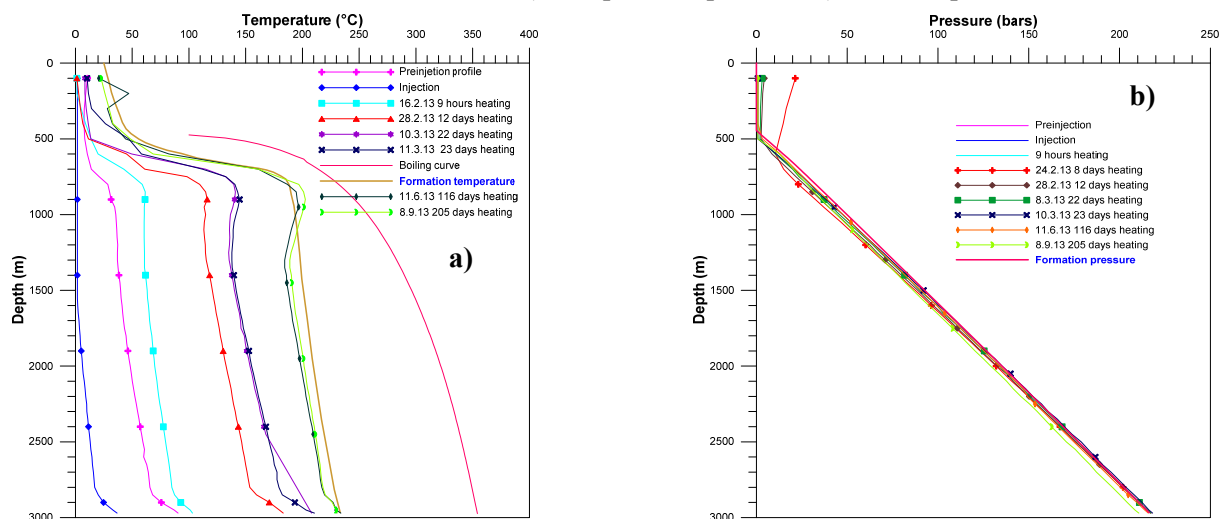


FIGURE 5: Well OW-40V: a) Temperature profiles; b) Pressure profiles

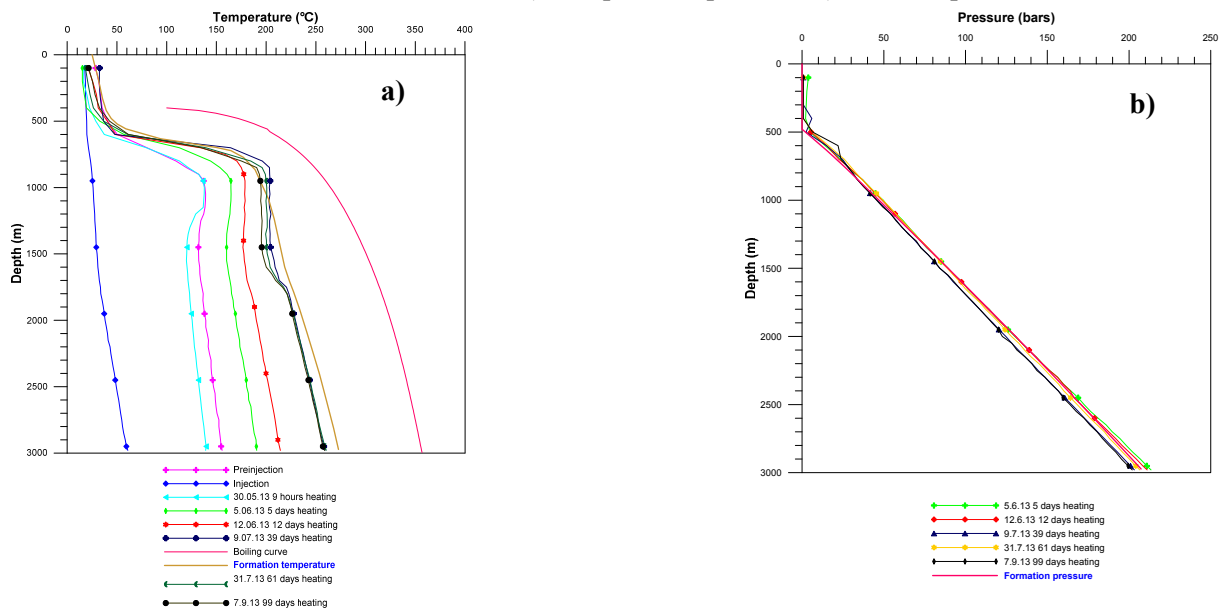


FIGURE 6: Well OW-40A: a) Temperature profiles; b) Pressure profiles

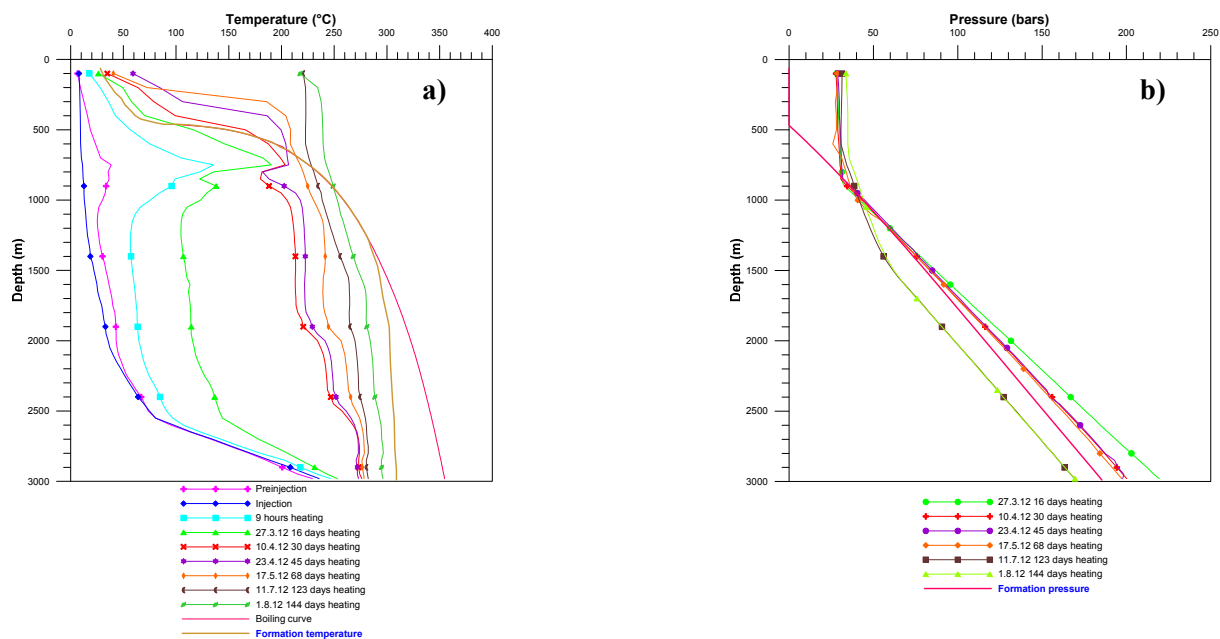


FIGURE 7: Well OW-802: a) Temperature profiles; b) Pressure profiles

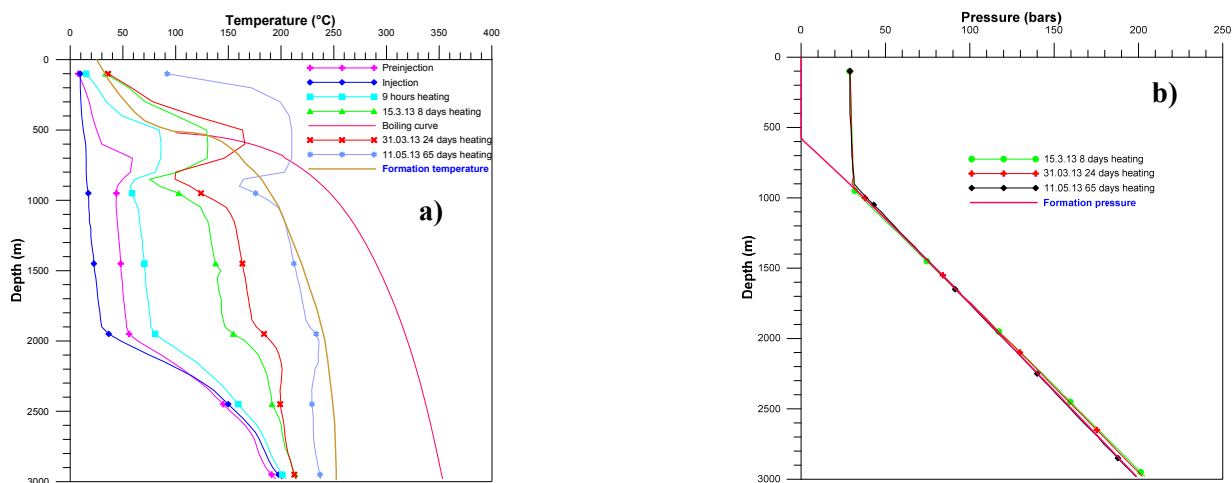


FIGURE 8: Well OW-802A: a) Temperature profiles; b) Pressure profiles

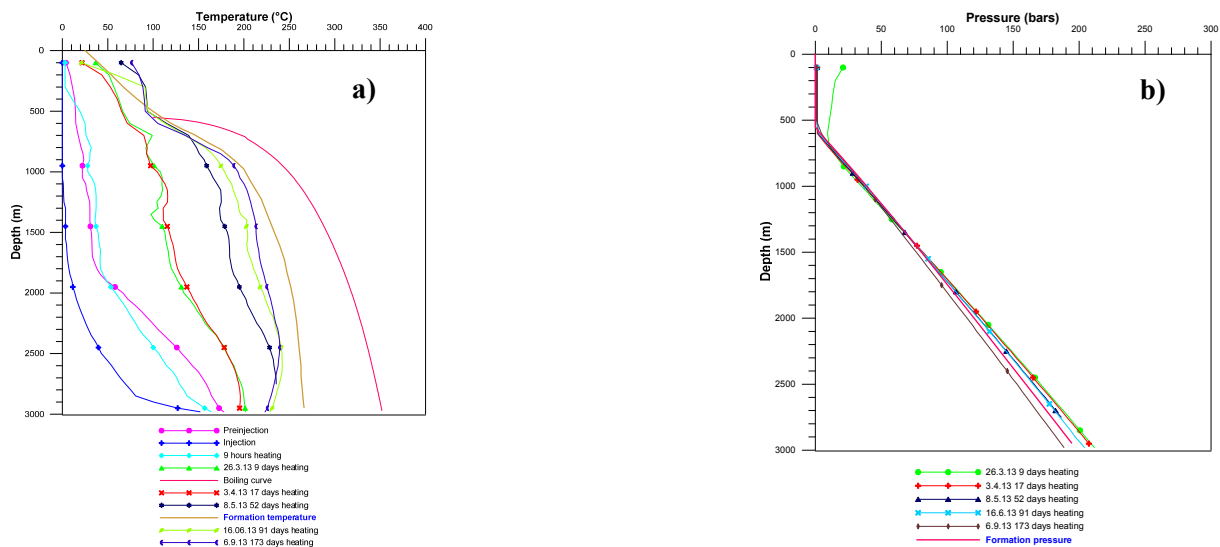


FIGURE 9: Well OW-803: a) Temperature profiles; b) Pressure profiles

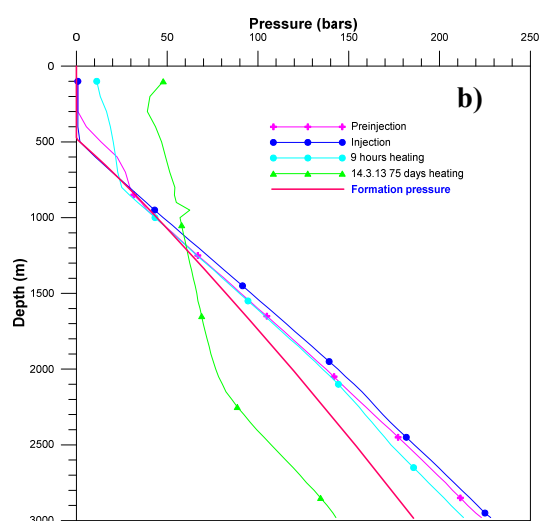
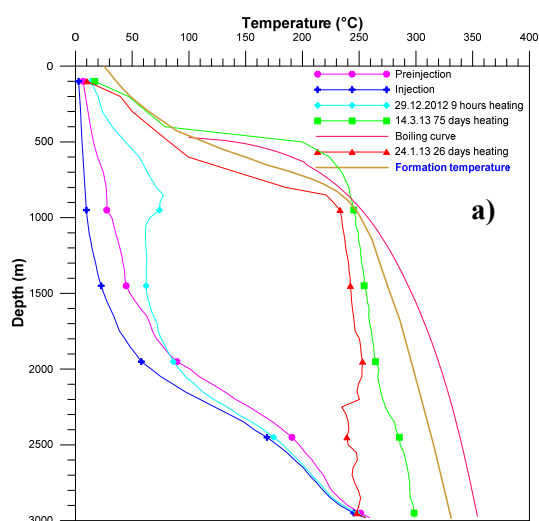


FIGURE 10: Well OW-804: a) Temperature profiles; b) Pressure profiles

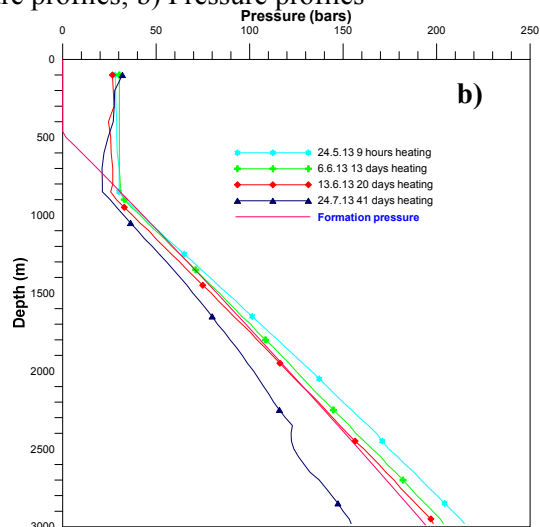
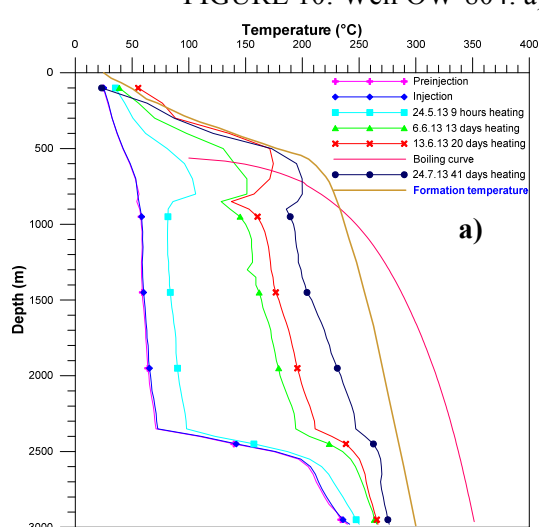


FIGURE 11: Well OW-804A: a) Temperature profiles; b) Pressure profiles

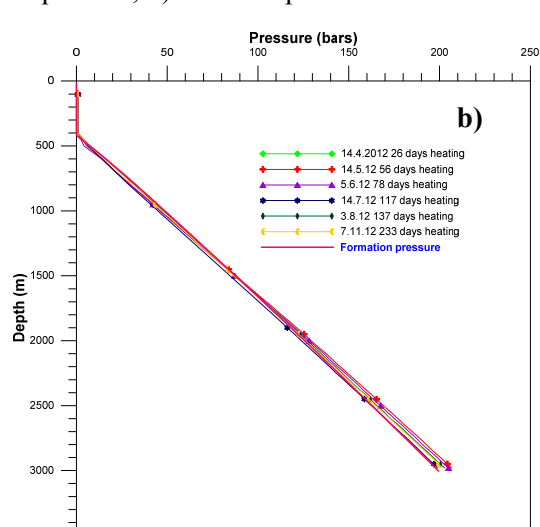
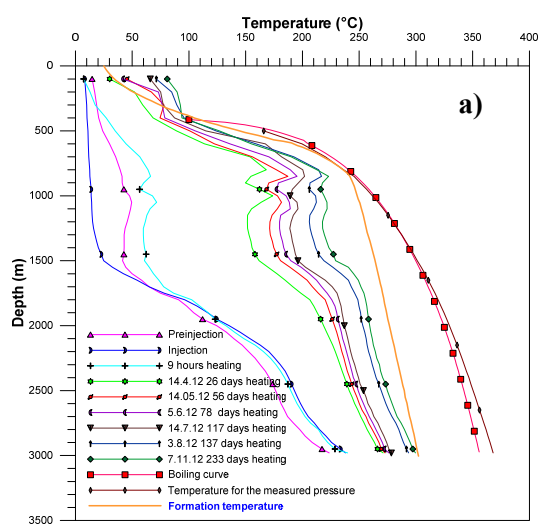


FIGURE 12: Well OW-902A: a) Temperature profiles; b) Pressure profiles

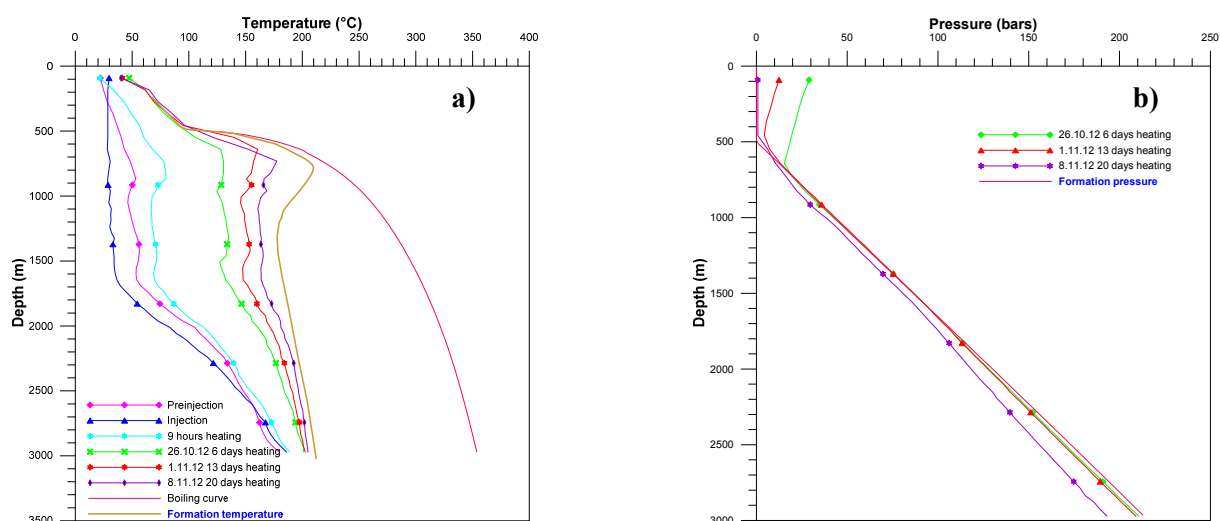


FIGURE 13: Well OW-902B: a) Temperature profiles; b) Pressure profiles

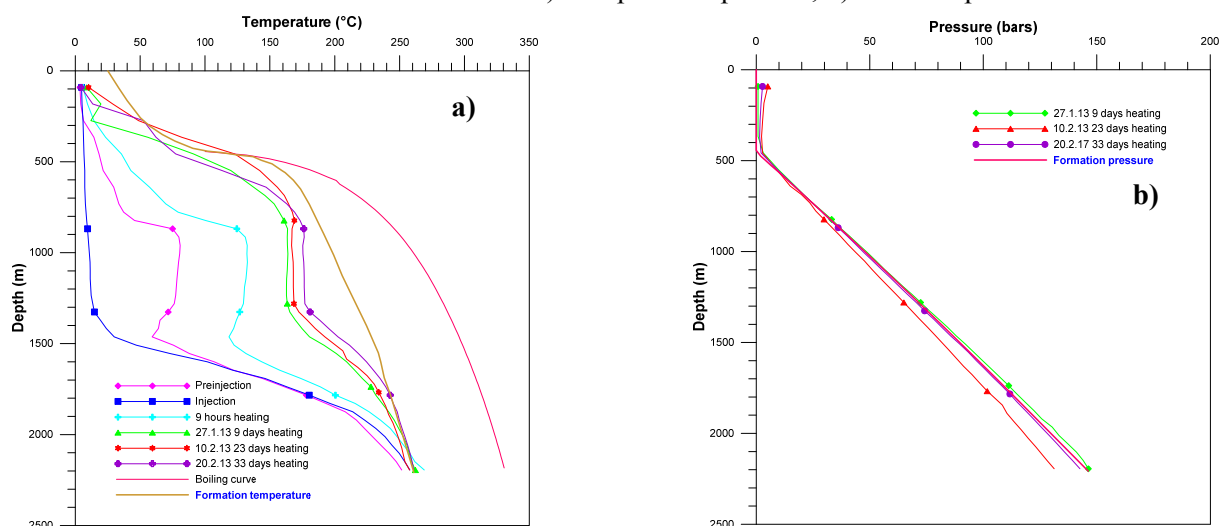


FIGURE 14: Well OW-906: a) Temperature profiles; b) Pressure profiles

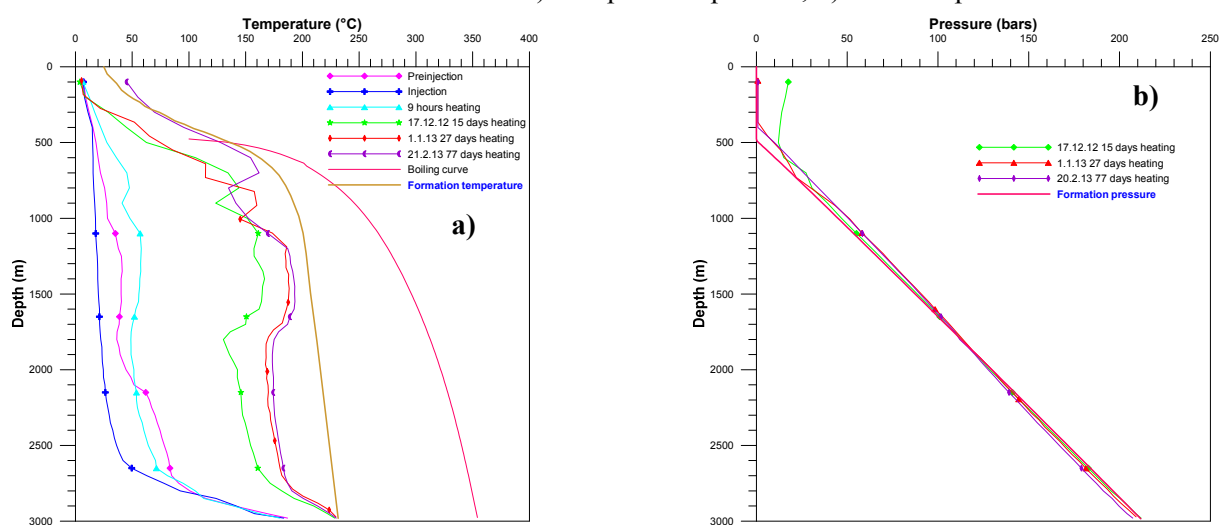


FIGURE 15: Well OW-907B: a) Temperature profiles; b) Pressure profiles

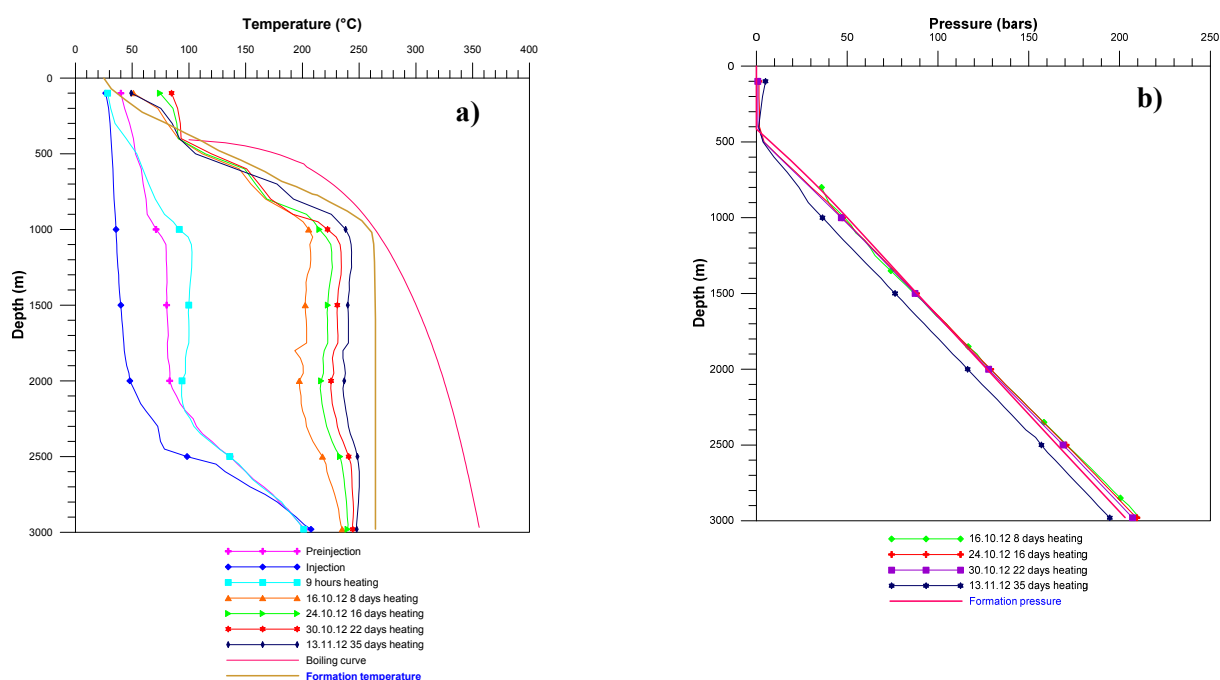


FIGURE 16: Well OW-911: a) Temperature profiles; b) Pressure profiles

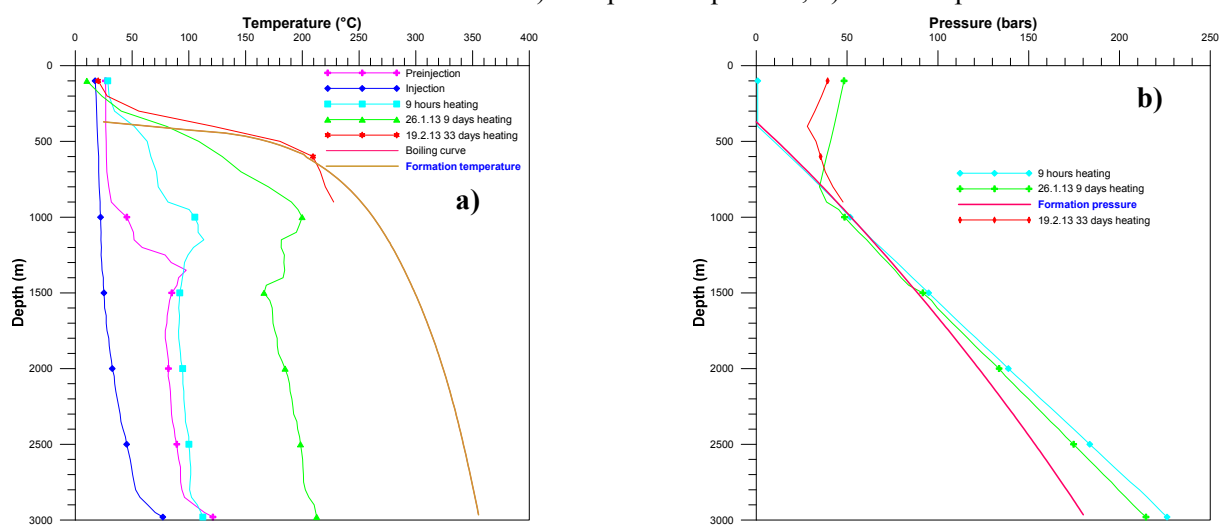


FIGURE 17: Well OW-914C: a) Temperature profiles; b) Pressure profiles

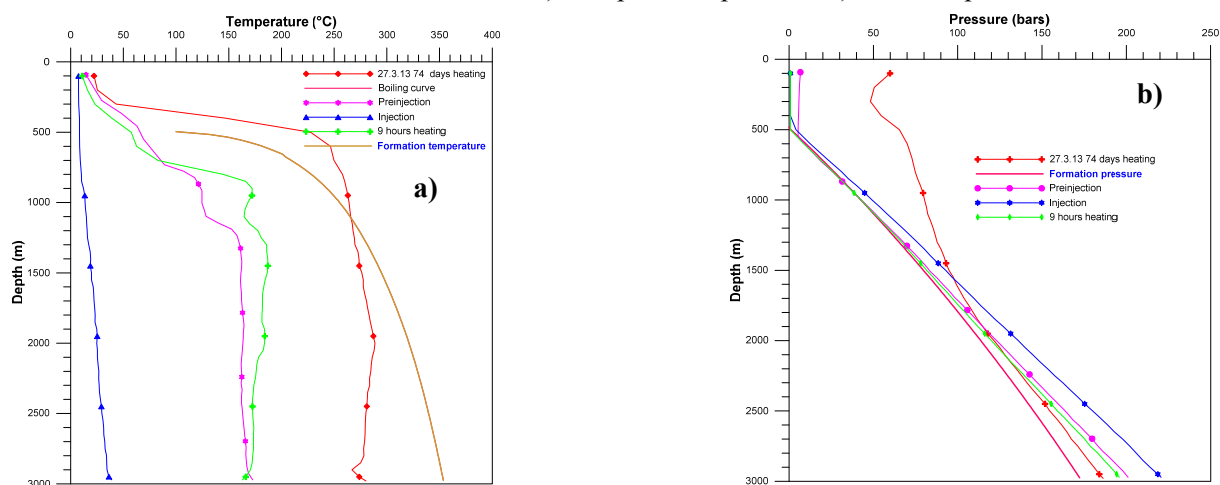


FIGURE 18: Well OW-915C: a) Temperature profiles; b) Pressure profiles

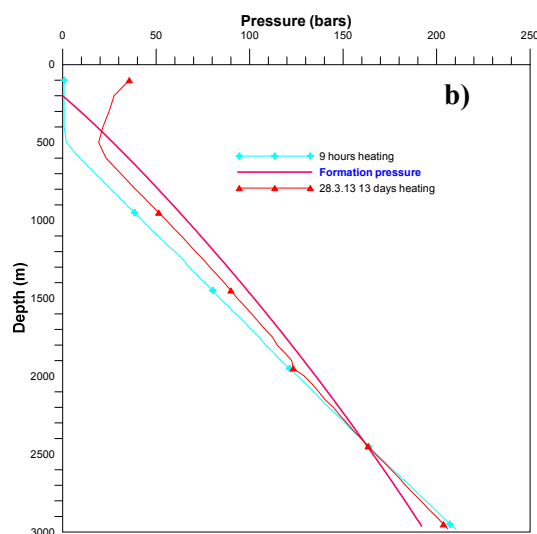
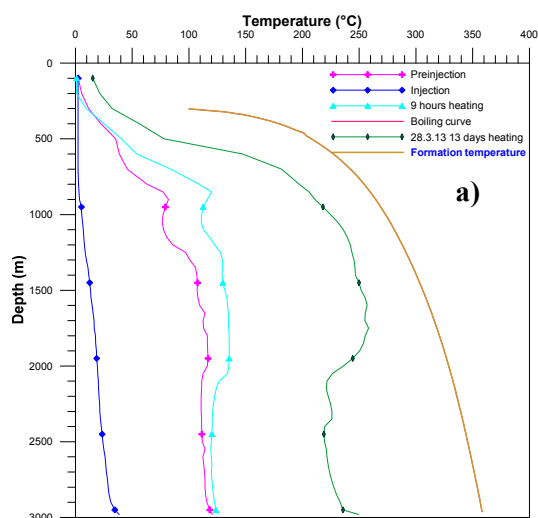


FIGURE 19: Well OW-915D: a) Temperature profiles; b) Pressure profiles

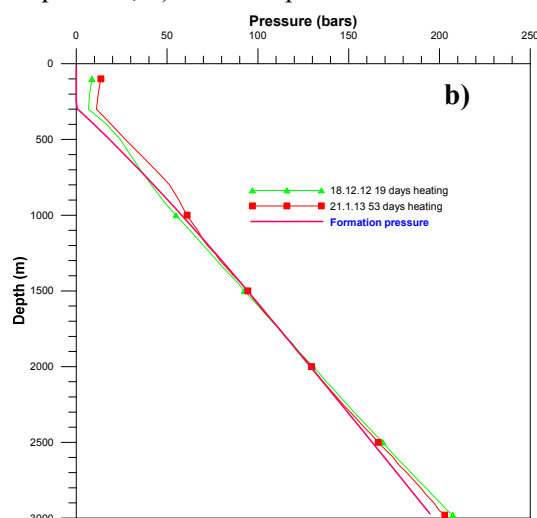
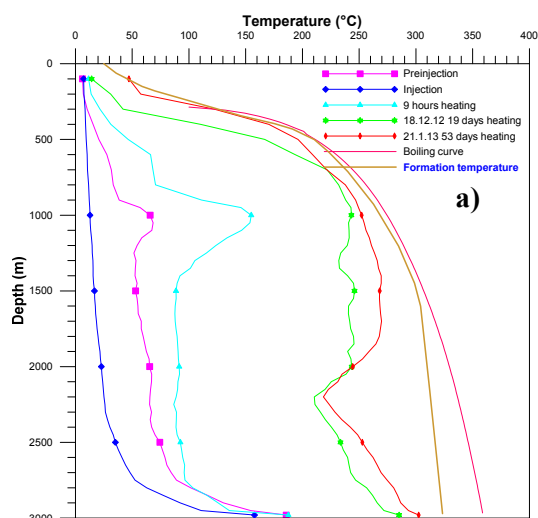


FIGURE 20: Well OW-916B: a) Temperature profiles; b) Pressure profiles

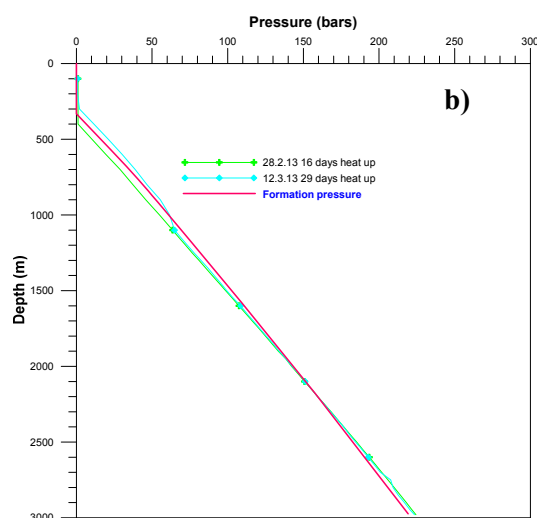
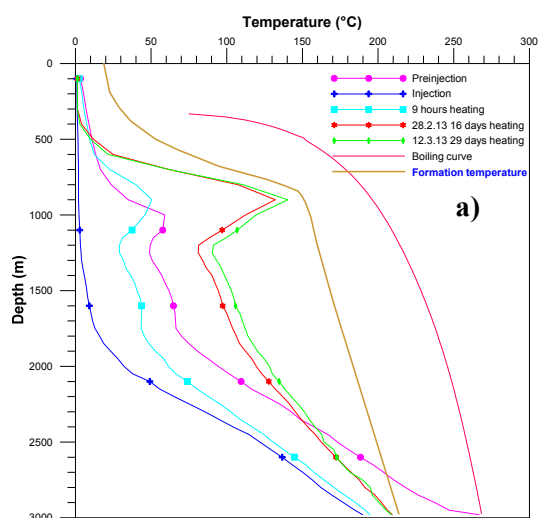


FIGURE 21: Well OW-919: a) Temperature profiles; b) Pressure profiles

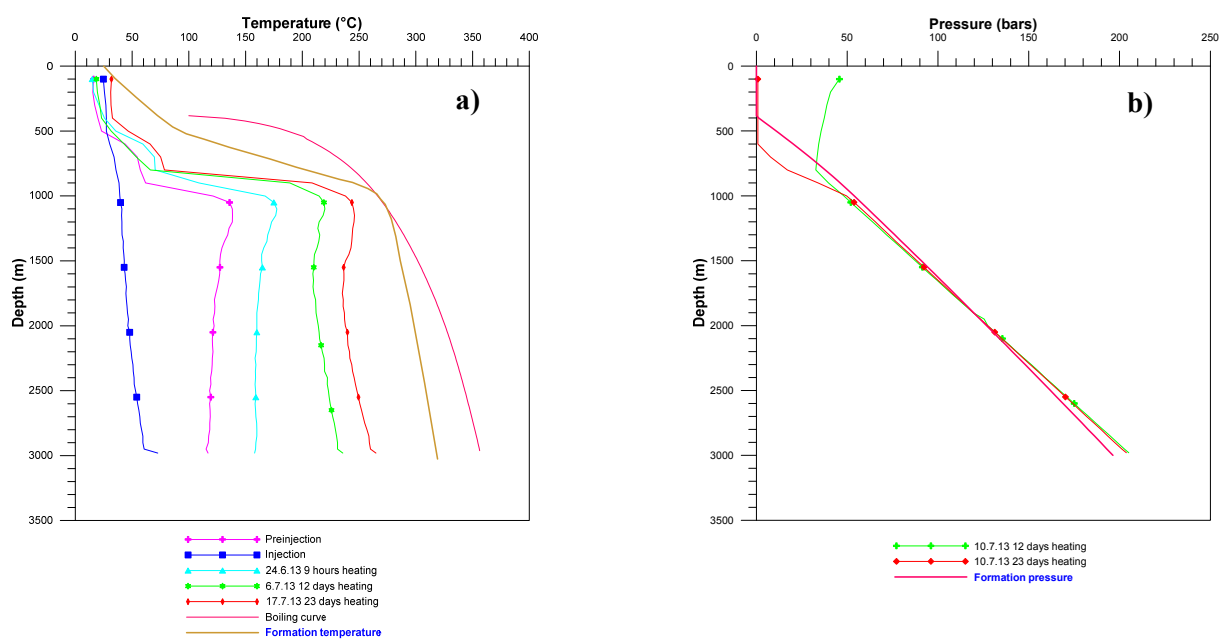


FIGURE 22: Well OW-919B: a) Temperature profiles; b) Pressure profiles

APPENDIX II: Temperature and pressure contour maps for Olkaria at 1200 m a.s.l.

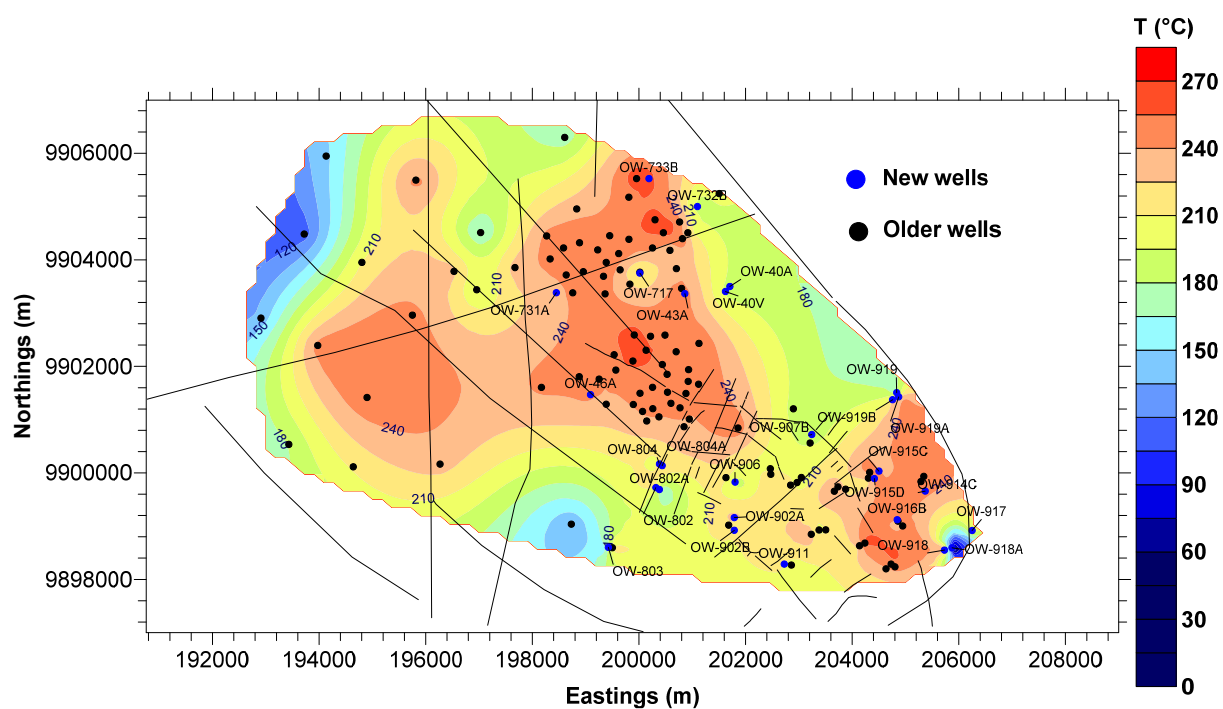


FIGURE 1: Temperature distribution at 1200 m a.s.l.

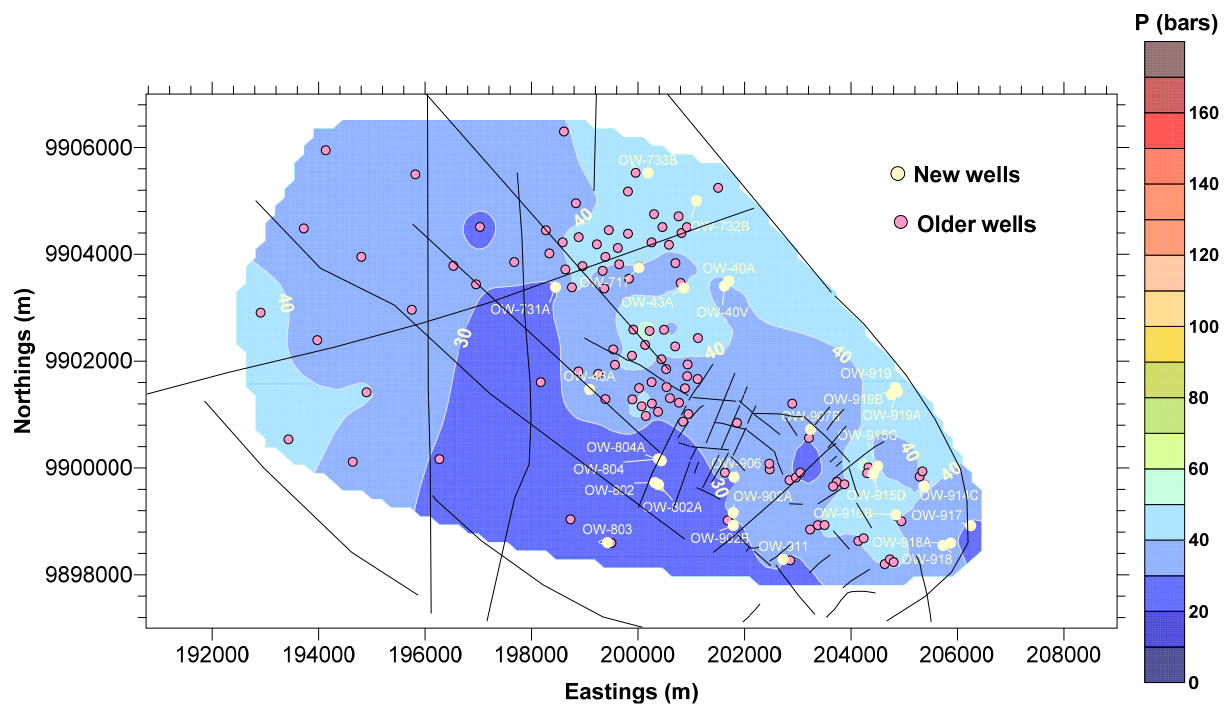


FIGURE 2: Pressure distribution at 1200 m a.s.l.



SYNTHESIS OF WELL TEST DATA AND MODELLING OF OLKARIA SOUTH EAST PRODUCTION FIELD

Daniel S. Saitet

Kenya Electricity Generating Company, Ltd. – KenGen
Olkaria Geothermal Project
P.O. Box 785-20117, Naivasha,
KENYA
dsaitet@kengen.co.ke

ABSTRACT

Well data was analysed and reservoir parameters were interpreted, then the two were unified, incorporating the entirety of the known knowledge and information into a single simplified conceptual model. The analysed wells are highly permeable with convective zones appearing below 1 km depth in the zone immediately adjacent to Ololbutot lava flow. No independent magmatic heat sources were interpreted for the system, rather NW-SE and NNE-SSE trending faults act as fluid conduits, allowing the fluid to percolate into the deep reservoir rock where it collects heat, and upwells where localized upflow zones, in the vicinity of Well OW-802, appear along permeable structures. The HOLA well bore simulator is used to predict well output curves for deep wells in the field. Most of the wells are fed by a single phase liquid reservoir; therefore, low outputs are expected. A resource assessment was carried out using the Monte Carlo simulation which showed average power output was likely to be produced in the area, about 42 MWe, and the maximum possible output was shown to be in the region of 73 MWe, using conventional flash power plant cycles. A natural state model for the field was constructed using TOUGH2. The model places plausible resource prospect areas along known structures in the area.

1. INTRODUCTION

Olkaria, a large volcanic complex, located at the axis of the Great East African Rift Valley, has been the focus of geothermal exploration in Kenya for many years. Reconnaissance studies were commissioned to explore the area for geothermal resources in the early fifties. Numerous surface manifestations that are prevalent in the area, including fumaroles, altered grounds and sulphur deposits, are believed to have attracted initial explorers to the area. It was not until 1956 that drilling started in the area. Two wells, Wells OW-X1 and OW-X2, were drilled to 950 m depth with no success. The two wells were located close to an area which was most probably easily accessible and with great surface activity. Their failure to sustain discharge discouraged further drilling activity until the oil crisis when exploration for alternative energy sources gathered momentum. By this time, the government and the United Nations Development Program entered into cooperation to support additional exploration studies. Extensive geo-scientific studies were carried out and proved the existence of exploitable resources at Olkaria.

The next well, located southeast of Olkaria Hill, was drilled to a kilometre depth. Well OW-1 was not able to discharge despite being located in a geologically plausible location at the intersection of two major faults. A decision was then made to concentrate drilling efforts eastwards near the most recent lava flow. Well OW-2 was drilled next with great success. The well encountered temperatures above 280°C and discharged high enthalpy fluids. Deep exploration wells were drilled thereafter near this well and culminated in the commission of a 45 MWe plant at Olkaria 1, which was fully operational by 1985.

For further development in the area, a decision was reached to subdivide the large field into seven sectors namely: Olkaria West (OWPF), Olkaria North West (ONWPF), Olkaria Central (OCPF), Olkaria North East (ONEPF), Olkaria East (OEPF), Olkaria South East (OSEPF) production fields and Olkaria Domes. The locations of the field sectors (Figure 1) were decided relative to Olkaria Hill.

Further drilling activities were concentrated in the Olkaria West and Northeast fields where power plants with 84 MWe and 105 MWe were subsequently built. Drilling at Olkaria Domes did not start until 1998 when the first well was drilled there. To date, many wells have been drilled in the Domes field and a power plant is presently under construction.

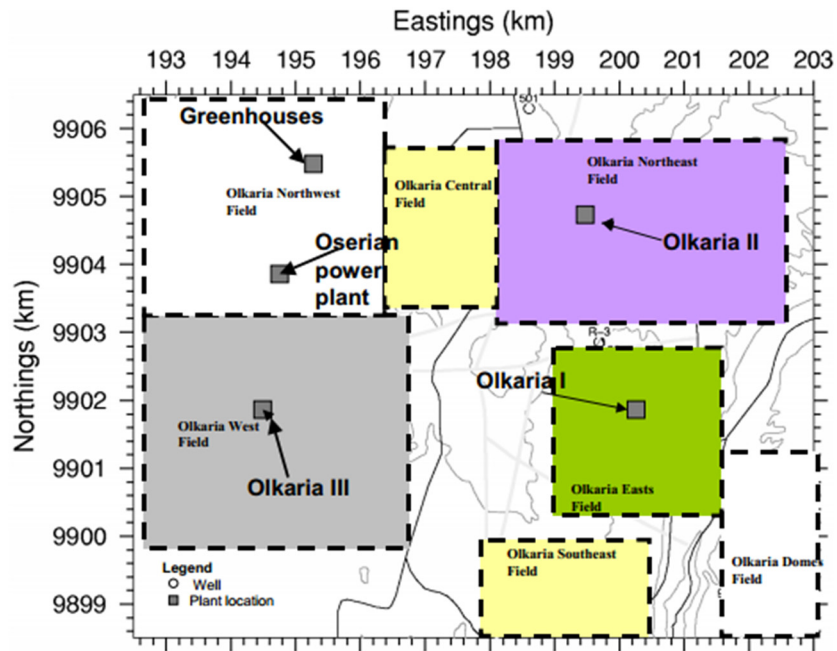


FIGURE 1: Olkaria geothermal field showing seven production sectors

Olkaria South East is the subject of this work. Prior to drilling deep wells, the area was thought to be an outflow zone (Ouma, 2009) from the nearby Olkaria East field and, therefore, was somewhat ignored in the exploration for high-temperature geothermal resources. A decision to re-inject hot brine from the Olkaria East production field into this area was also envisaged more recently. To this end, two shallow re-injection wells were drilled near unproductive Well OW-801. These wells were meant to be used in case sites for re-injection near the field were either unavailable or as part of a dynamic reinjection plan, envisaged to become necessary upon completion of an additional 140 MW power plant which is also under construction.

However, recent deep drilling, commenced with the drilling of Well OW-802, revealed that this field could be productive. Well OW-11A, drilled from the Olkaria East production field, directed under the Ololbutot lava flow, turned out to be very impressive. More wells have now been sited and drilled in the area, all giving positive results. It is unfortunate that, to date, none of these wells has been flow tested. It is expected that further appraisal drilling will continue in this area, at least in the near future, before current wells can be flow tested. A critical review of available data is, therefore, necessary if drilling is to continue.

This project, consequently, is focussed on synthesising available well test data to attempt to understand the properties, geometry and nature of the reservoir there. This work, apart from attempting to model reservoir conditions at depth, is also aimed at estimating the productivity of the wells already drilled and the resource capacity.

2. GEOLOGY AND STRUCTURAL SETTING

2.1 Geological setting

Olkaria is located at the floor of the central Kenyan Rift about 150 km northeast of Nairobi. The area is both geologically and structurally complex. The volcanic system is associated with an old central volcano which collapsed, leaving a large caldera rim of approximately 5 km which is defined, in part, by a ring fracture and by pumice domes. Rocks occurring on the surface are predominantly quaternary comendites, pumice fall and ash deposits of late Pliocene to Holocene. Some trachytic flows appear to the south of the geothermal area below thick pyroclastic covers associated with Longonot and Suswa eruptive material. Minor volcanic glass material also appears in a few localities.

Volcanic centres are structurally controlled. The main eruptive centre is the Olkaria hill, with major structural features contributing significantly. The Ololbutot and Gorge farm faults are such eruptive fissures. The most recent volcanic episode is associated with the Ololbutot fault which produced rhyolite flows dated about 250 years BP, based on charred wood found under it (Clarke et al., 1990).

The lithostratigraphic structure in the area is nearly horizontal (Muchemi, 1999; and Brown, 1984). Based on rock cutting and cores, the general lithostratigraphy of the greater Olkaria complex can be divided into two, with the axis separating the western sector from the eastern sector passing through Olkaria hill. Omenda (1998) discussed these formations and proposed nomenclature: Mau tuffs, Plateau trachytes, Olkaria basalts and Upper Olkaria volcanics. Mau tuffs were found to be unique to the western sector, while the trachytes and basalts are unique to the eastern sector.

Geothermal manifestations are structurally controlled. Hot grounds and fumaroles are located along fractures, with intense activity found at their intersections. Production wells sited at these intersections prove to be particularly good.

2.2 Structures

Olkaria is a complex grid faulted area located in the vicinity of western rift boundary faults of the Rift system. Tectonic activity is associated with extensional rifting and consequent tension created North-South faulting along the axis of the rift. The dominant structures at Olkaria are the Ololbutot fault (North-South), the Gorge farm fault (North East-South West), the Olkaria Fault (East North East-West South West) and the Suswa fault (North East-South West). An alignment of eruptive domes is prominent to the east of the field, probably demarcating a caldera rim, and was mapped elsewhere around the greater volcanic complex. Many other buried faults with similar trends have been inferred by analysis of drill cores and rock cuttings. (Muchemi, 1998; Omenda, 1998). Micro-seismic monitoring of Olkaria geothermal field showed lineaments of epicentres similar to mapped structures (Simiyu and Keller, 1999). Intersections of these lineaments are associated with shallower and less prominent seismic events suspected to be consequent to fluid flow in the subsurface.

Olkaria South East field (OSEPF) is traversed by the Ololbutot fault to the west, a North West-South East trending fault passing through the Ololbutot recent lava flow, and is bounded to the east by the Olchorro Oirowua gorge. Another prominent structure trends NNE-SSW, intersecting with NW-SE fault in close vicinity to Well OW-804 in the OSEPF. A shorter parallel fault is also intersected by Wells OW-804A and OW-802A which were drilled directionally to the southeast. The inferred alignment of eruptive centres offers a natural boundary for the field to the south. The field is juxtaposed with the Olkaria East production field, which has produced for more than 30 years, and the Domes field, which is currently in the development phase. Figure 2 shows the structural map of the greater Olkaria geothermal field.

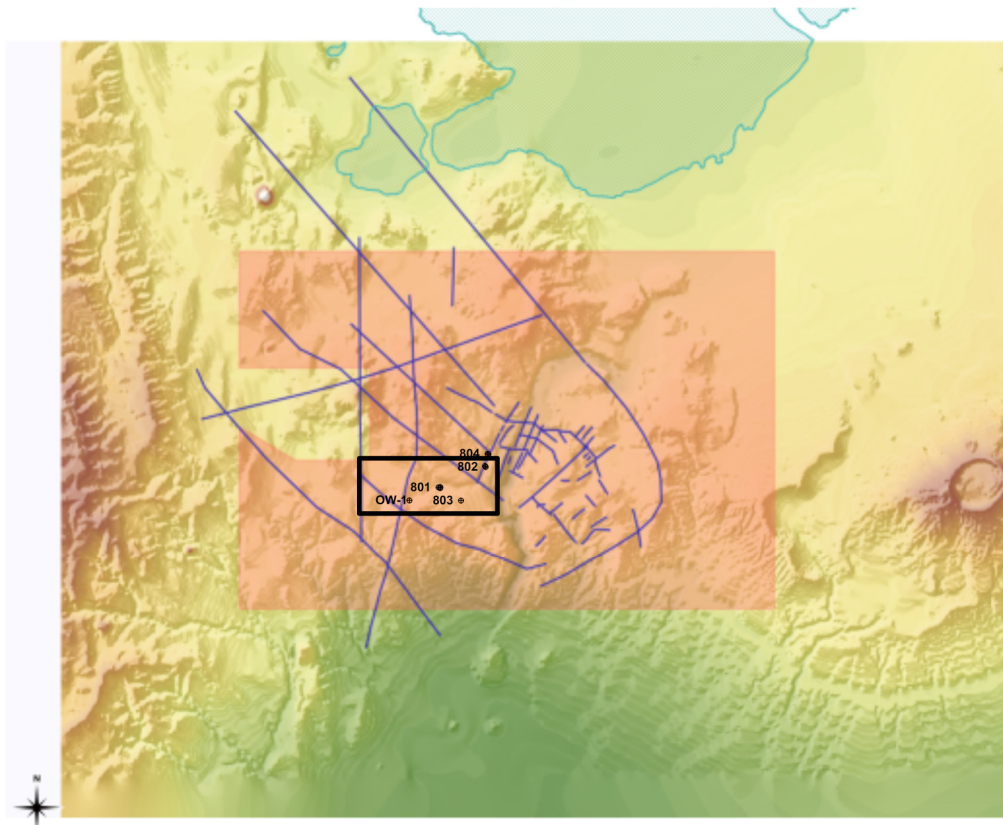


FIGURE 2: Structural map of Olkaria geothermal field; inset is the Olkaria Southeast production field; black dots show locations of drilled wells

3. ANALYSIS OF TEMPERATURE AND PRESSURE PROFILES

Drilling involves pumping large volumes of cold water or air into a well for a long time. This destabilizes the thermodynamic conditions of a well and the formations in the near vicinity. After geothermal wells are completed, temperature and pressure profiles are taken during warm-up. Temperature measured in the well during the period of thermal recovery is useful in determining feed zones of the well, physical conditions such as boiling, head transfer mechanisms, fluid flow patterns and in estimating formation temperatures of the undisturbed reservoir. However, it is important to note that drilling does change the conditions of the reservoir such that we can never know the exact initial prevailing conditions. The feed zones in the well tend to accept drilling fluids, thus cooling them significantly and these feed zones will, consequently, recover more slowly than their surroundings. Profiles, taken while injecting fluids into the well, show these points as fluid loss zones, represented by rapid changes in the thermal gradient. Later, as the well recovers from drilling effects, such changes in thermal gradients are associated with aquifer feed points.

An important aspect in the analysis of temperature profiles is the determination of the physical conditions and processes occurring in the well and its immediate surroundings. In determining the physical conditions of the well fluid, it is obviously important to determine the boiling conditions. In the case of high temperature wells, the question of whether boiling processes occur in the well or in the reservoir is answered. Boiling temperature increases with increases in pressure. Fluids at greater depth are, therefore, expected to boil at higher temperatures. In evaluating estimated boiling temperatures, the effects of salinity and impurities in the water are ignored. In ICEBOX, a program called Boilcurv is available for finding the boiling point with depth curve. The program computes the boiling point curve

from a reference pressure provided by the user, based on the integral formula of pressure (Equation 1) that follows the water saturation density with depth (Arason et al., 2004).

$$P(z) = P_o + g \int \rho_{sat}(P(z))dz \quad (1)$$

where $P(z)$ = Pressure at any depth;
 P_o = Pressure at initial elevation;
 ρ_{sat} = Density in a column of single phase fluid at saturation pressure;
 g = Gravitational acceleration;
 z = Depth.

Thermal transfer mechanisms in the well are identifiable from temperature profiles. Essentially, only conduction and convective heat transfer occur in geothermal wells. The two mechanisms are easily identifiable in geothermal wells. Conductive heat transfer is commonly represented by high gradient profiles in a straight line in impermeable rock formations. In contrast, convective heat transfer manifests when temperature profiles show isothermal conditions at small to greater depths. This usually results in vertical temperature profiles. Convection is very important in geothermal studies as it points out permeability in geothermal reservoirs. Identifying areas with conduction and convection heat transfer is very important in identifying the components of the reservoir. The cap rock is commonly dominated by conduction with a steep gradient while convective zones denote the reservoir. Obviously, wells should be cased at the reservoir to avoid the incursion of colder fluids.

Using the temperatures recorded during the warm-up period, one is able to estimate formation temperatures. In some cases, it involves fitting a curve to later profiles if the temperature stabilizes over a reasonably long time. Some wells stabilize in temperature rather quickly. In many cases, two phase well conditions may follow the boiling point curve. Semi analytical methods are available today for better estimation of these temperatures. There are two widely used methods for doing this. The Horner method (Dowdle and Cobb, 1975; Takai et al., 1994) and the Albright method (Albright, 1976). The Albright method is useful for short term heating such as in determining formation temperature during drilling for blow out prevention. The Horner method is more appropriate for longer heating up periods, such as when a well is warming up after drilling. Temperatures recorded at a point for different warm-up times are plotted against the Horner time and a line is fitted to the points whose extrapolation to long times gives the estimate of the formation temperature. It is important to fit the straight line to latter points when it is expected that the well has somewhat approached full recovery. Arason et al. (2004) presented a robust software, Berghiti, included in ICEBOX, for performing this task.

Pressure in the reservoir is directly related to the reservoir fluid. It is the reservoir fluid that mines and transports the heat that is present in the rock to the surface. Its importance cannot, therefore, be over-emphasised. Pressure gradients are the driving forces for fluid flow in the reservoir. Pressure gradient in a flowing geothermal well can be described by three terms (Equation 2). The first term is associated with frictional forces as the fluid travels up the well; the second is associated with acceleration of the fluid; and the last term is due to the pressure potential. In hydrostatic wells, only the third term is non-zero.

$$\frac{dP}{dz} = \left[\frac{dP}{dz} \right]_{\text{fric}} + \left[\frac{dP}{dz} \right]_{\text{acc}} + \left[\frac{dP}{dz} \right]_{\text{pot}} \quad (2)$$

where P = Pressure;
 z = Depth.

Pressure changes during warm up as fluid becomes lighter, and the pressure profiles are expected to revolve around a point of constant reservoir pressure known as the “best feedzone”. This point is commonly referred to as the pivot point and is the best connection to the reservoir, representing reservoir pressure at that depth. Pressure is stable here since the volume concerned is ideally very big; therefore, heating does not result in significant density variations. The method employed to evaluate initial

formation pressure involves calculating a hydrostatic profile based on a formation temperature profile and then fitting the so calculated hydrostatic pressure profile through the pivot point observed during warm up. In this work, the program Predyp, presented by Arason et al. (2004) was used to calculate the initial pressure from estimated formation temperature profiles.

3.1 Heat-up profiles

Well OW-1 was the first well drilled in the UNDP project of 1975 after unsuccessful attempts at the initial two sites much earlier. It is located in the vicinity of two intersecting fault zones in an area dominated by intense surface activity. Well OW-1 was drilled to a depth of 1003 m, reaching temperatures of 126°C at the bottom. This well was abandoned without a wellhead valve and is still open to the atmosphere. Vertical permeability is evident in this area, especially slightly east of Well OW-1 where fumarolic activity is most intense. No pressure measurements were recorded in this well.

Well OW-801 was drilled near the Ololbutot lava flow in 1996. It is assumed that this well has equilibrated with formation conditions after about 8 years of heating up. The well intersected vertical flows of fluid of more than 200°C from about 1300 m depth to the bottom (2000 m), where it achieves a stable temperature of 215°C (Figure 3a). With the casing set at 847 m depth, the well feed point is located at 950 m where colder inflows are expected; minor ones are found at 1350 m. This well is, therefore, unproductive and has no wellhead pressure. No boiling occurs in the well. The pressure profiles (Figure 3b) are hydrostatic and show the water level at 575 m depth.

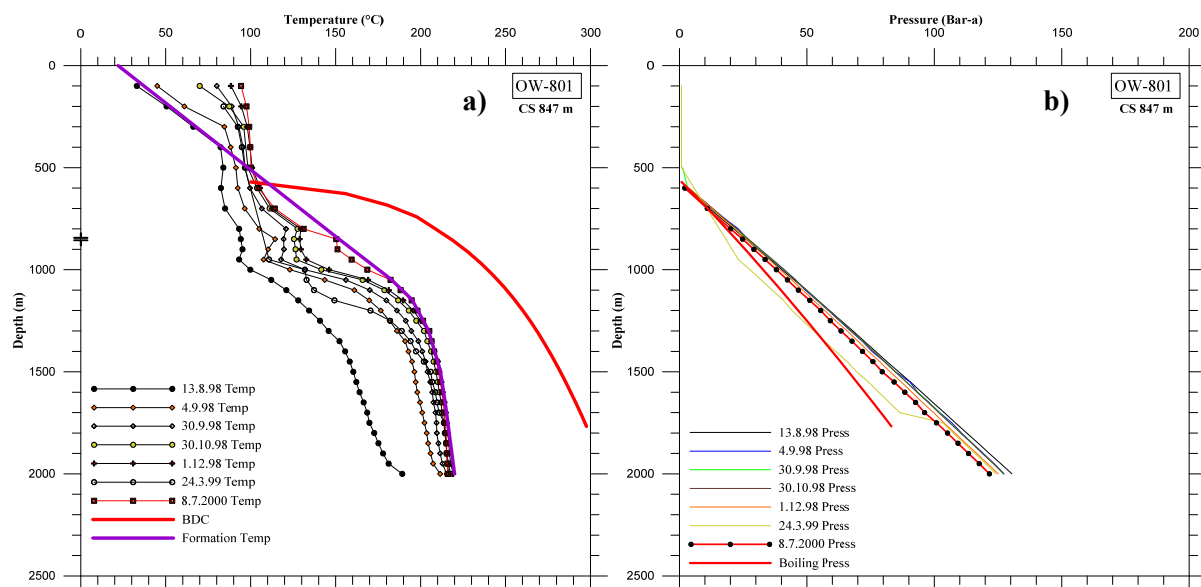


FIGURE 3: Well OW-801: a) Temperature profiles; b) Pressure profiles

Wells OW-801R1 and OW-801R2. Two shallow wells were drilled on Well OW-801's well pad, originally meant for possible shallow reinjection. These wells are located side by side at 50 m separation. The temperature profiles (Figures 4a) in Well OW-801R1 show a cold well cased at 190 m with feed points at 300, 350 and 500 m. The main feed zone was interpreted to be at 350 m. The well was drilled to 600 m, achieving about 90°C at the bottom, measured after twenty days of heating up. Similarly, Well OW-801R2 (Figures 5a) intersects permeable feed points at 350, 500 and 550 m. The well is cased at 266.7 m depth and reached 103°C at the bottom (640 m) after thirty three days of heating up. Pressure profiles for Well OW-801R1 (Figure 4b) and Well OW-801R2 (Figure 5b) are predominantly hydrostatic, with water levels located at 370 and 520 m, respectively, based on the latest profiles.

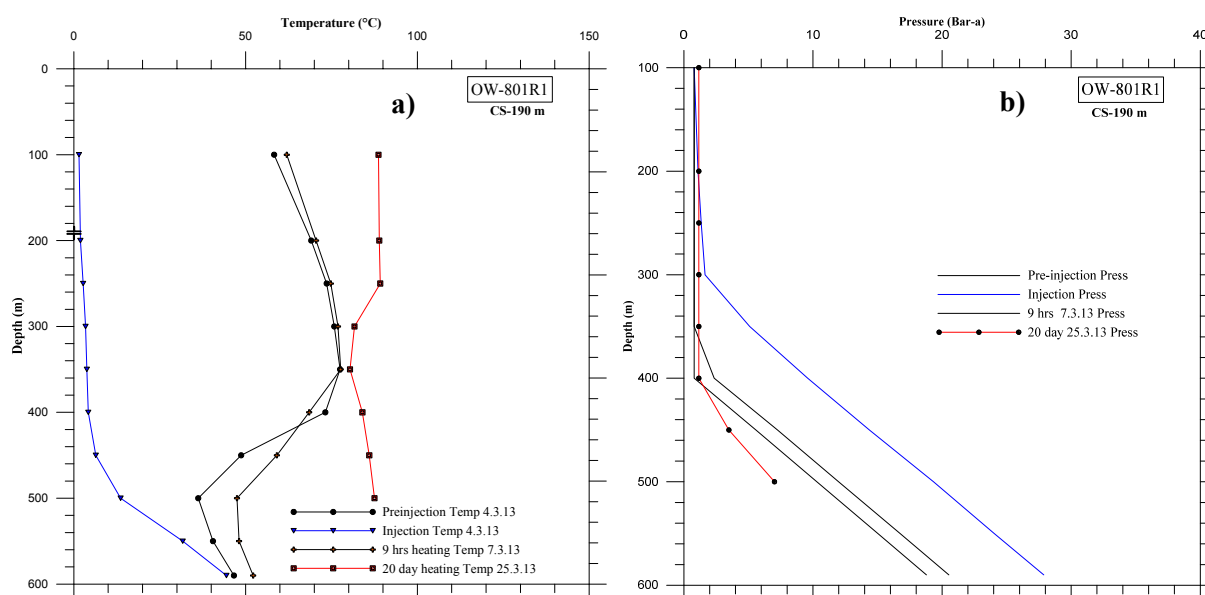


FIGURE 4: Well OW-801R1: a) Temperature profiles; b) Pressure profiles

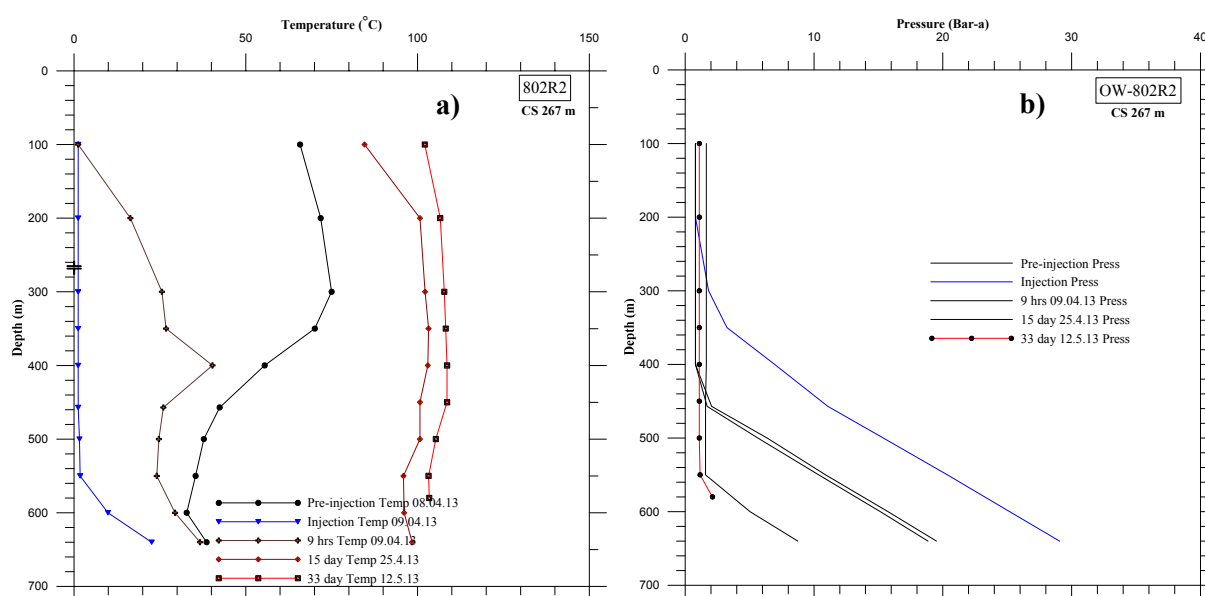


FIGURE 5: Well OW-801R2: a) Temperature profiles; b) Pressure profiles

Well OW-802, drilled to 3000 m depth, intercepted hot aquifers at 850, 1050, 1800 and 2000 m with cross flows between them. The temperature (Figure 6a) reached about 280°C at the bottom of the well. The best feed zone was estimated to be at 1050 m. Boiling occurs inside the well at 1300 m depth. Pressure profiles (Figure 6b), taken for up to 144 days of heating, show the pressure pivot point in the region of 1150 m depth. The latest profile indicates possible wellhead pressures of 33.1 bar-g down from 170 bar at the well bottom.

Well OW-802A was drilled directionally (N137°E) to a depth of 3000 m and intercepts hot aquifers at 850, 1800 and 2500 m (Figure 7a). The main aquifer intersected by Well OW-802 is located at about 1800 m in this well and contributes a significant part of fluid into the well at about 237°C. Later temperature measurements appear to approximate near vertical isotherms increasingly heating up. Boiling occurs just above the casing depth. The formation temperature follows the shape of the boiling

point temperature. Pressure profiles (Figure 7b) show 200 bar-a at the bottom and suggest 28.2 bar-g can be expected at the well top and a hydrostatic level at 500 m. A unique and prominent pressure control point is not clear in this well. However, a pivot point is suggested at 1500 m depth.

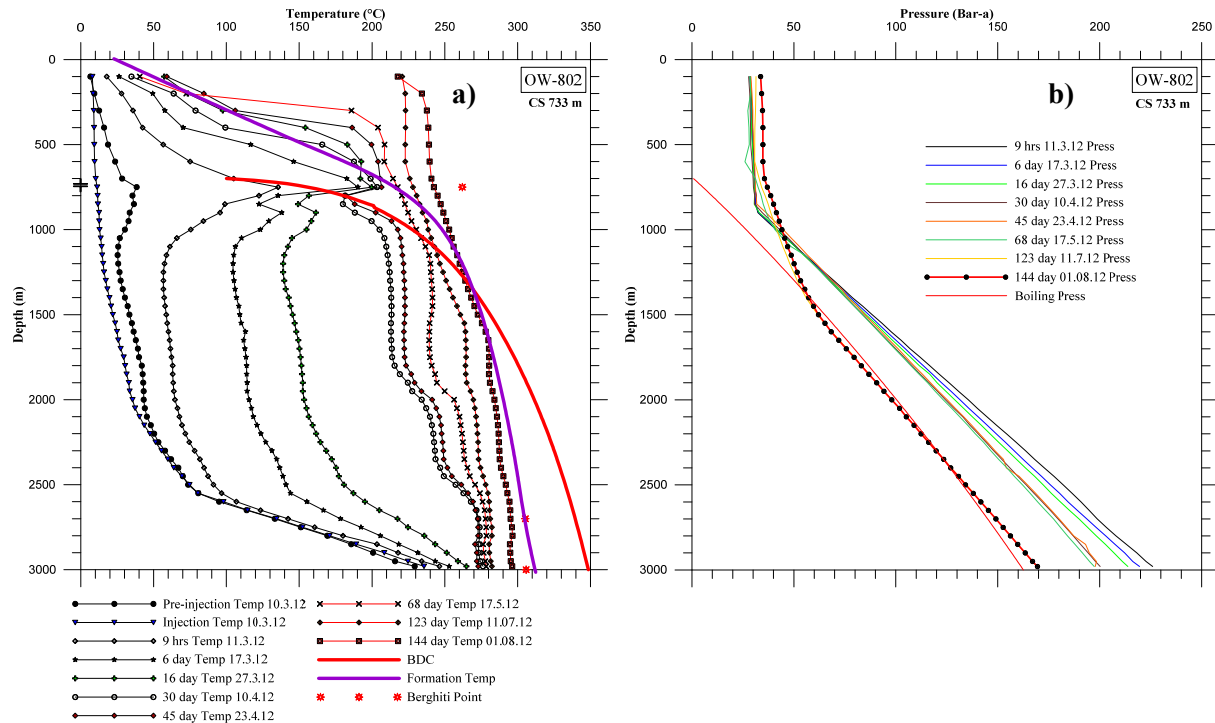


FIGURE 6: Well OW-802: a) Temperature profiles; b) Pressure profiles

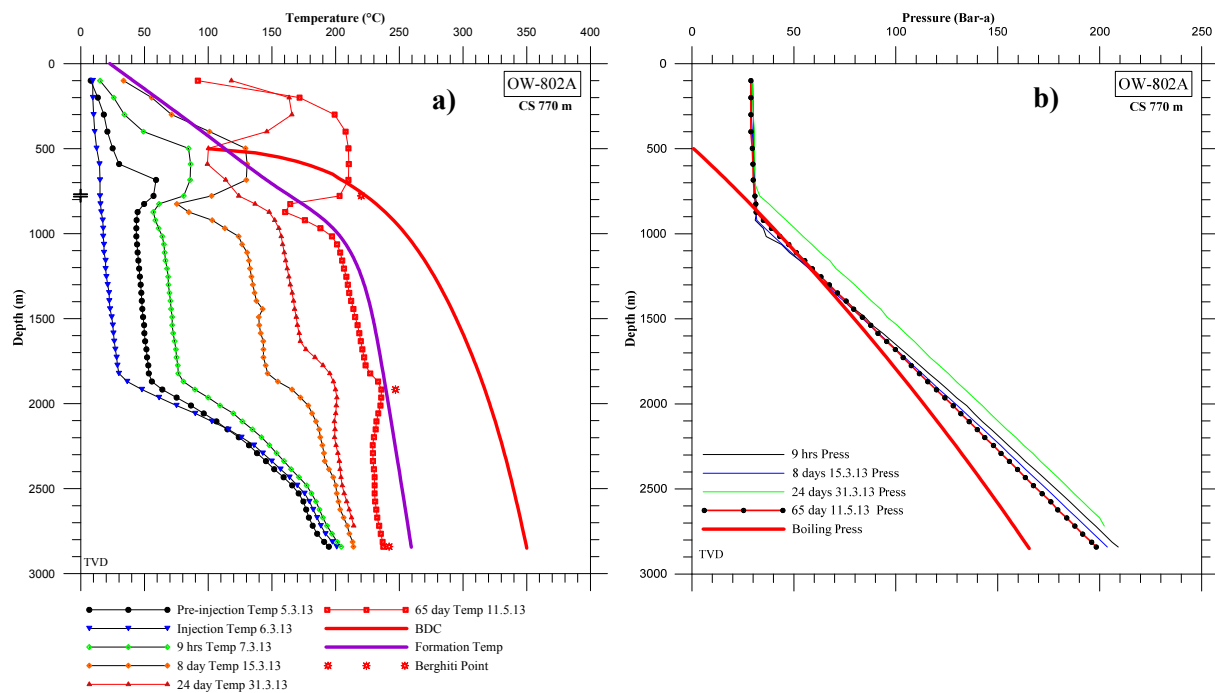


FIGURE 7: Well OW-802A: a) Temperature profiles; b) Pressure profiles

Well OW-803. In this well, feed points are located at 1300, 1500, 1800, 2500 and 2850 m, delivering fluids of about 230°C after about three months of heating up (Figure 8a). The formation temperature

follows the boiling point curve. A temperature reversal occurs near the bottom and is attributable to a bottom feedzone that is slowly recovering from the effects of drilling. Eventually, this effect is expected to disappear as stable formation temperatures are reached. Pressure profiles (Figure 8b) taken in this well show a non-artesian well with a hydrostatic level at 575 m with pressure profiles slowly revolving around 1500 m depth where a pivot point is located. The well reaches pressures above 200 bar-a at the bottom.

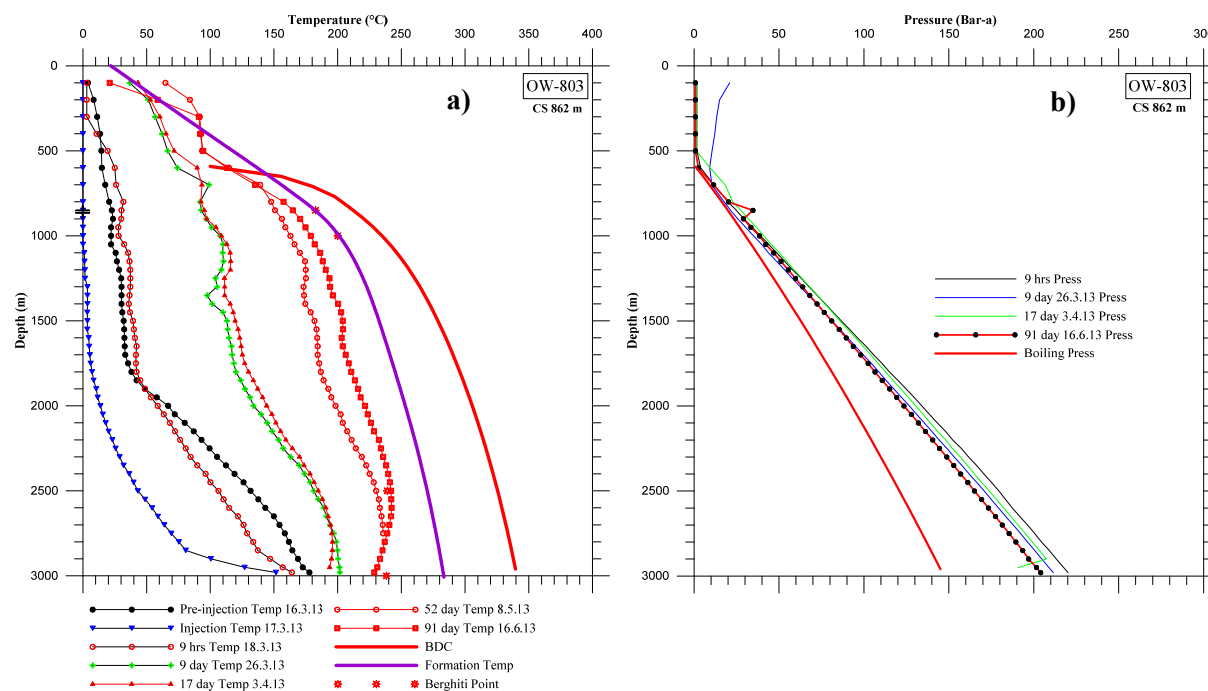


FIGURE 8: Well OW-803: a) Temperature profiles; b) Pressure profiles

Well OW-804 is the hottest well in this field at present. The well intersects hot feeder zones at 850, 1500, 1900, 2200 and 2900 m and reaches temperatures over 300°C at the bottom (Figure 9a). Gas pressure accumulates at the well's top and as steam condenses, as evidenced by drastic cooling in the shallower cased off regions. Most of the reservoir is shown to be a vertical isotherm of 250°C which shifts closer to 300°C towards the final one third of the well. In determining the boiling temperature in this well, the pressure profile was used to calculate the corresponding boiling temperature. Pressure profiles (Figure 9b) collected from this were not consistent with the temperature, as the tool was reported to leak or fail completely. Consequently, these measurements were dropped from this analysis. Initial pressures taken just after drilling showed higher pressures at the bottom, which eventually even out to about 140 bar-a after 75 days of heating up. It is difficult to evaluate a pivot point with so few pressure profiles. However, a depth of 1200 m is suggested by available data.

Well OW-804A is directionally drilled (N145°E) and intersects hot feed zones at 1200, 1300, 1450, 2250 and 2450 m with relative contribution probably highest at 2250 m. The formation temperature follows the boiling point temperature with flashing occurring only inside the casing, and reaches over 310°C at the bottom (Figure 10a). Pressure profiles (Figure 10b) show a hydrostatic level at 575 m depth. The well bottom is at 150 bar-a pressure, and 31 bar-g is expected at the wellhead.

3.1.1 Summary

Feedzones:

Table 1 summarizes the temperature situation in all the wells in this field as well as feed zone locations. Wells OW-802, OW-804 and OW-804A encounter temperatures above 280°C while Wells OW-802A and OW-803 reached temperatures in the range of 230-240°C for the latest measured bottom-hole

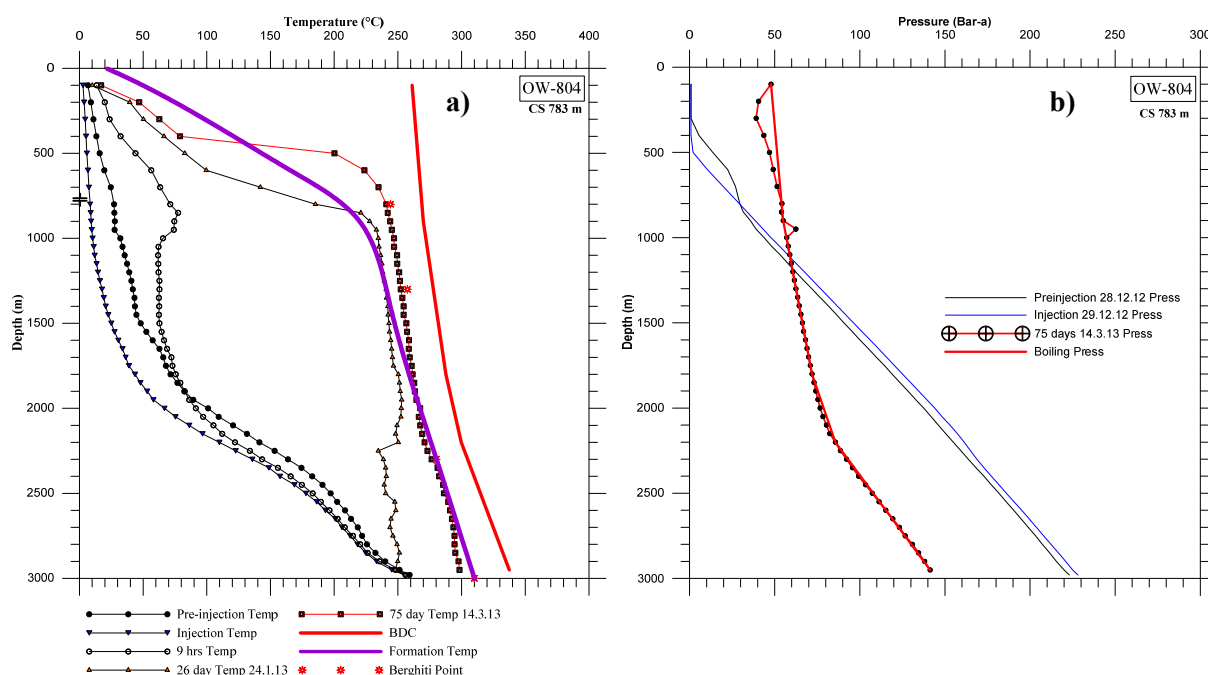


FIGURE 9: Well OW-804: a) Temperature profiles; b) Pressure profiles

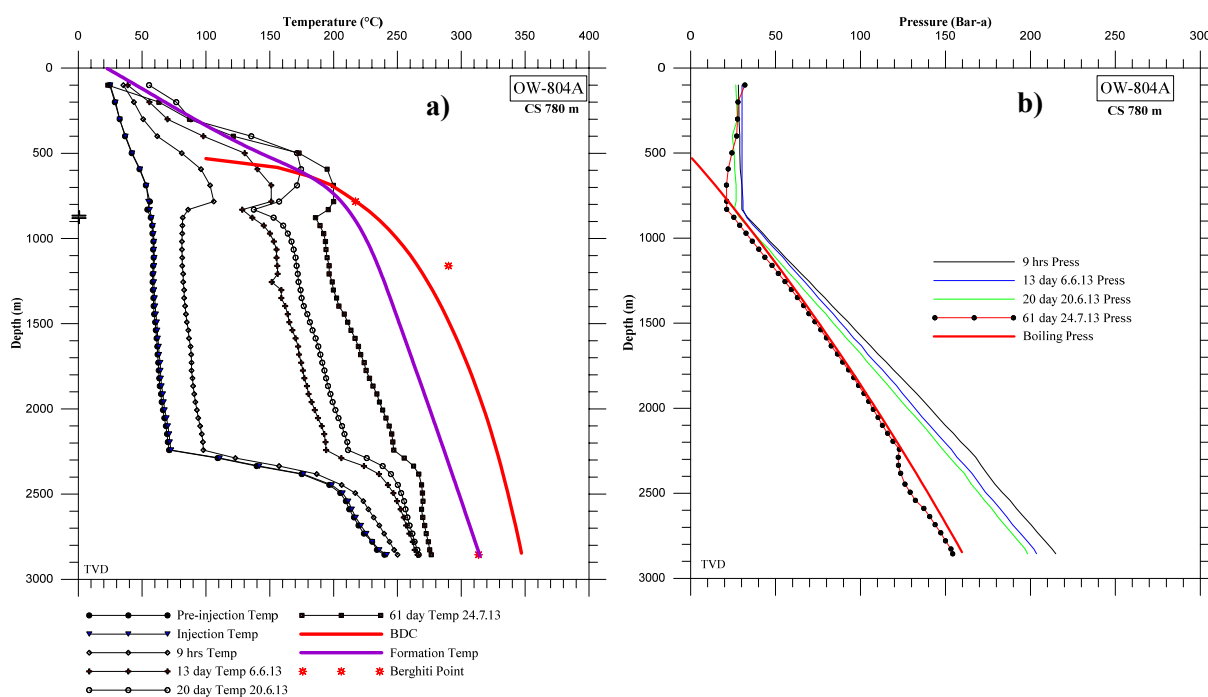


FIGURE 10: Well OW-804A: a) Temperature profiles; b) Pressure profiles

temperatures (BHT). All these temperatures are considered high and are not significantly lower than those encountered elsewhere in Olkaria. However, in the adjacent Olkaria East production field, most wells produce from steam fed reservoirs at shallow depths, and liquid zones at greater depths. This does not seem to be the case in these wells, except for Well OW-802, which bears a resemblance. Deliverability of these wells could be limited by this fact. In some cases, at the Olkaria Domes field, marginal wells with similar profiles as these have turned out to be poor wells. However, wells in this field have appreciably higher permeability than their counterparts in the margins of the Domes field. A

good example is seen in Wells OW-917, OW-918 and OW-918. Pressure situations in Olkaria Southeast wells closely resemble observations elsewhere in Olkaria.

TABLE 1: Summary of well temperature and feed zones

Well name	Type	DepthTVD (m)	Casing shoe TVD (m)	Measured BHT (°C)	Main feed zone TVD (m)	Other feed zone TVD (m)
OW-1	Vertical	1003	418	126
OW-801	Vertical	2000	847	215	950	1350
OW-801 R1	Vertical	600	190	87	350	300 500
OW-801 R2	Vertical	640	266.7	103	500	350 550
OW-802	Vertical	3000	732.7	280	1050	850 1800 2000 2500
OW-802A	Directional N137°E	2860	785.3	220	1800	850 2500
OW-803	Vertical	3000	861.68	230	1500	1300 1800 2500 2850
OW-804	Vertical	3000	782.65	300	1900	850 1500 2200 2900
OW-804A	Directional N145°E	2870	796.7	280	2250	1200 1300 1450 2450

Physical conditions:

The early wells drilled in the Olkaria Southeast field were shallow and only penetrated into the sharp thermal gradient of the reservoir cap rock. Well OW-801 achieved some convective character at depth but that occurred at non-commercial temperatures. More recent deep drilling has proved the existence of a resource, at least in the northeast margins of the field closest to known structures. The wells presently under study are located near significant structures in the area and are therefore likely to be reasonable producers. Reservoir temperature ranges from 230 to 360°C with the highest located near known structures. Reservoir fluids are likely to be liquid dominated with boiling processes commencing only at the wellbores of Wells OW-802, 802A, 803, and 804A. It is notable, however, that most of these wells have seldom reached stable formation conditions and, therefore, physical conditions may change with more recovery. Figure 11 shows the formation temperatures calculated from available warm up profiles. Some corrections were performed to compensate for the effects of convection in the wellbores and short warm-up periods in a few cases.

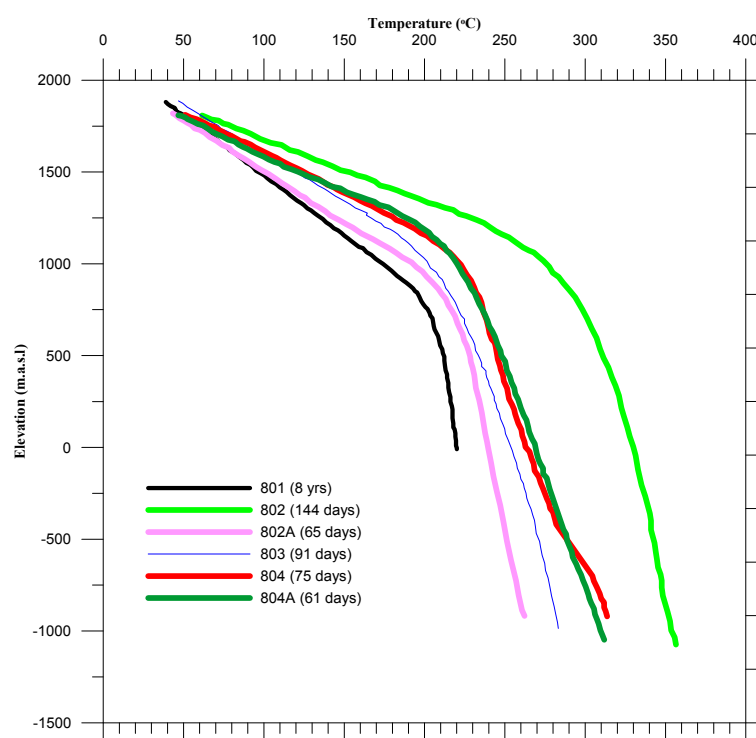


FIGURE 11: Formation temperature profiles

3.1.2 Temperature gradient analysis

It is necessary to characterize the reservoir in this field to find out its probable size, nature, geometry and physical conditions. This is the ultimate goal of the drilling exercise which is currently on-going.

With only limited data available during the course of writing this project, the task can still be accomplished reasonably well. However, data is limited to the south of Ololbutot and covers only a small fraction of the possible resource area. The approach taken here is to collate available information to study the similarities and lack thereof to the adjacent Olkaria East field whose reservoir is well studied. The Olkaria East reservoir is two-phase with a shallow (<1000 m) steam cap formed after more than thirty years of production. Recent wells drilled from the East field under the Ololbutot lava flow proved to be good producers. Such a well is Well OW-11A which delivers two phase fluids in excess of 23 kg/sat discharge enthalpy of 1950 kJ/kg. The main production of the well is located deep in the well and is associated with the North-West trending fault. The same fault controls permeability and fluid movement distribution in the Olkaria Southeast field. Other minor faults trending north-northeast intersect with this fault further south.

The first question addressed here, therefore, is how similar or different is the reservoir at Olkaria Southeast field from those already well known in the greater Olkaria field. To begin with, a filtering analysis is necessary to determine how its temperature relates to some common standard. Axelsson and Gunnlaugsson (2000) arbitrarily defined high-temperature geothermal fields as those reaching temperatures above 200°C at one kilometre depth. Well temperature profiles were filtered by assuming a steep conductive thermal gradient reaching 200°C at 1000 m, which defines a high-temperature system. The convective part of the system was also filtered according to the boiling point curve.

The results show the field is well above the threshold of a high-temperature geothermal field up to a depth of 1000 m. However, the oldest wells in the field, namely Wells OW-1 and OW-801, do not meet this threshold. It appears that the thermal gradient falls quite drastically from Well OW-801 towards Well OW-1 and increases sharply in a North-North-East direction, reaching a peak at Well OW-802. This indicates the existence of a system with the hottest region centred on Well OW-802 and which is deeper than that at the nearby OEPPF. It is argued here that perhaps the system could actually be joined at depth, and that two up flows exist, one on either side of the North West-South East fault, passing through the Ololbutot lava flow. The sharp contrast in the temperatures at the conductive depth defines the location of the shallowest up flow to be closest to the wellpads of Wells OW-802 and OW-804. Away from the fault, the system cools as it gets farther away from the hot area in the direction of Well OW-1.

The convective part of the system suggests the reservoir either follows the boiling point curve or a fraction of it. Some of the wells considered here have not fully recovered from drilling and, therefore, may reach temperatures slightly higher than those found in the present study. Well OW-801 is shallowest and has fully heated up, reaching about 80% of the boiling point curve at depths below 1500 m. Well OW-802 has temperatures much higher than the boiling point while its neighbour, Well OW-802A, which was drilled SSE, reaches only 85% of the boiling point. Well OW-803 is currently the most southerly of the new cluster of wells and has temperatures following 90% of boiling point. Both wells in the 804 pad closely approximate the boiling point at about 95%. Well OW-804A was also drilled SSE with a trajectory closer to Well OW-802A and intersects more permeable zones.

The possibility of these wells discharging two phase fluids is, therefore, apparent from these results. This reservoir, however, lacks the traditional shallow steam zone commonly intersected in the neighbouring field. In most wells, moderately hot aquifers are encountered near the casing shoe before reaching the mature convective cell.

It is proposed here that the NW-SE fault passing through Ololbutot lava flow acts as a hydro-geological barrier, separating the fields while providing conduits to sustain a constant pressure boundary.

3.2 Temperature distribution

It is important in the analysis of well temperature profiles not only to study each well individually but also to study the spatial distribution. Temperature distribution in space helps in characterizing the field,

especially in locating up flow and inflow zones. Drill-hole locations are usually targeted in up flow areas. Local temperature distribution also helps to map permeability distribution. It should be noted here that there are few drill holes in the area and they are somewhat stacked together in the northeast margin of the field. The isotherms presented here, therefore, should be looked at with this limitation in mind.

Temperature iso-maps

Horizontal maps of temperature distribution were made at five elevations: 1000, 500, 0, -500 and -750 m a.s.l.

Temperature at 1000 m a.s.l. At this depth, the temperature rises in the eastern half of the field reaching its maximum around Well OW-802 (Figure 12). A shallow colder incursion into the area is observable, trending in a NW fashion, which corresponds roughly to the main structure in the region. Sparse data to the west shows a progressively colder region away from the hotter zone. The 200°C contour reveals a NS trending thermal anomaly with a significant structural barrier passing in between well pads 802 and 804. Well OW-803 is located at the westernmost margin of this anomaly.

Temperature at 500 m a.s.l. Temperature is distributed in a similar fashion as that observed at 1000 m a.s.l. with the anomaly now covered by the 230°C contour line (Figure 13).

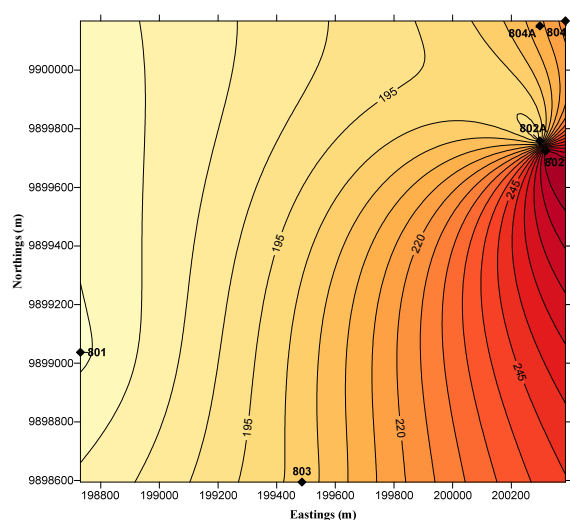


FIGURE 12: Temperature contour map at 1000 m a.s.l.

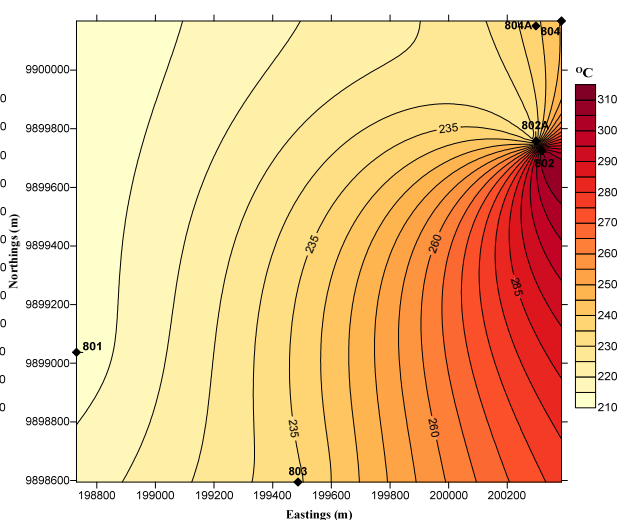


FIGURE 13: Temperature contour map at 500 m a.s.l.

Temperature at 0 m a.s.l. (sea-level). This level corresponds approximately to 2 km depth in this field. Three quarters of the area lies under the 240°C contour line with the same area discussed earlier being under a significantly higher thermal anomaly. The cold incursion attributed to a NW trending structure lessens but its effect is still clear (Figure 14).

Temperature at -500 m a.s.l. Only the newly drilled wells reach these depths. Figure 15 shows that the temperature distribution follows an already observed trend.

Temperature at -750 m a.s.l. At this depth, the thermal anomaly observed earlier is defined by

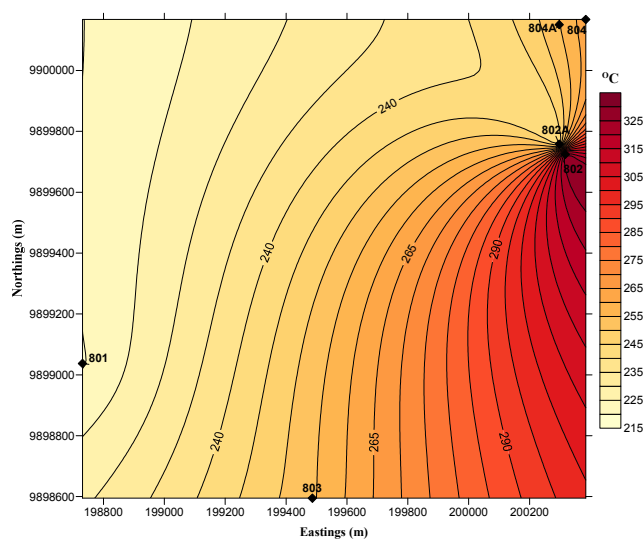


FIGURE 14: Temperature contour map at sea-level

temperature above 275°C. A strong N-S trend is observable here and the incursion of the colder area is more defined in a NW fashion (Figure 16).

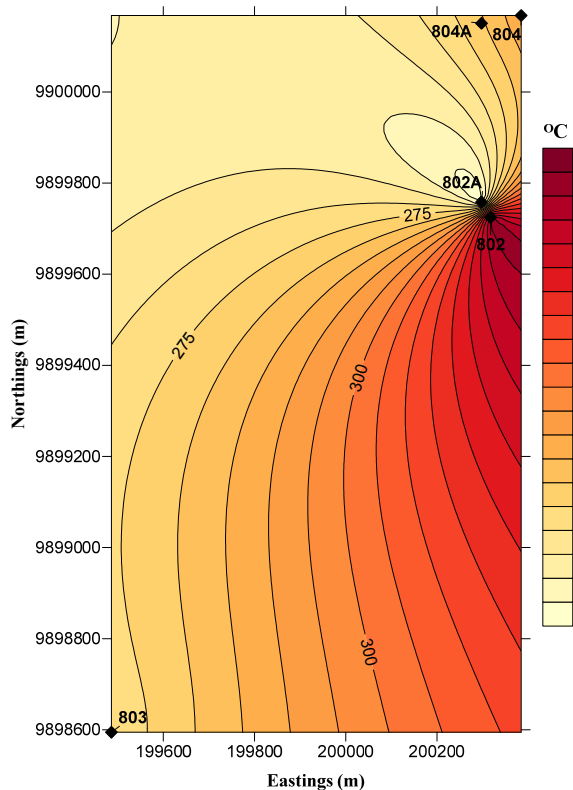


FIGURE 15: Temperature contour map at -500 m a.s.l.

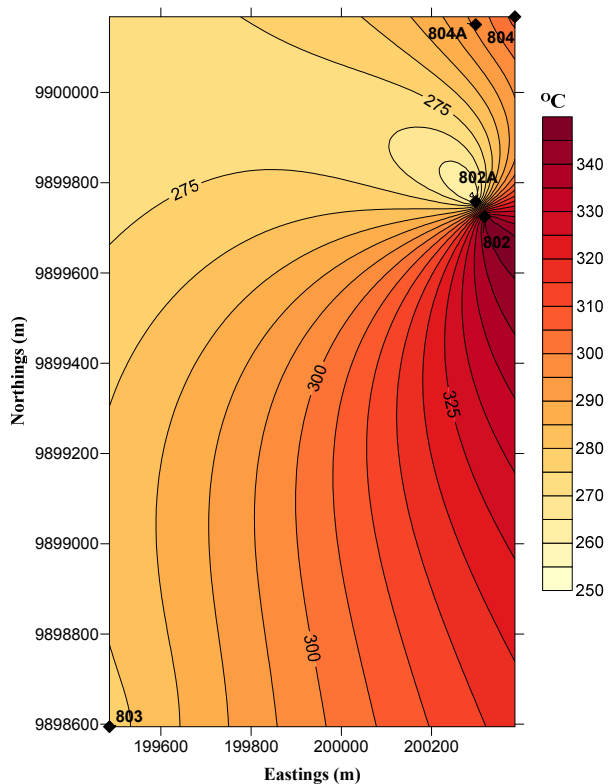


FIGURE 16: Temperature contour map at -750 m a.s.l.

Temperature profiles

Four profiles or cross-sections were taken across the field to study the temperature distribution at depth in selected directions. The first two profiles were taken across the field E-W (Profile 1) and N-S (Profile 2), and the next two were chosen to intersect selected wells in the field: Well OW-1 through OW-804 (Profile 3), and Well OW-803 through Well OW-804 (Profile 4).

Profile 1 shows typical geothermal reservoir temperature behaviour with capping at about 1100 m a.s.l. and the mushroom doming up from great depths into the shallow crust at temperatures above 240°C (Figure 17). The mushroom is strongly vertical and narrow; it is centred between the wellpads of Wells OW-803 and OW-802. It is elongated diagonally, getting deeper to the west. There exists a barrier traversing through the area just east of Well OW-804's pad which strongly suggests a deep fault responsible for a downthrown profile and a temperature reversal in the directional Well OW-804A.

Profile 2. Temperature variations in the N-S profile (Figure 18) suggest the reservoir is centred on Well OW-802 and upwelling of fluids from a deep reservoir is vertically controlled. The hottest region appears not to reach the bottom of Well OW-804A which was drilled directionally to the southeast, suggesting it leaves the centre of the up flow at depth. Temperature decreases to the southern margins of the study area. However, temperature rises considerably to the extreme southerly Well OW-803, showing perhaps good temperatures may exist in that direction. The likely interpretation of this behaviour is that fluid upwelling is strongly controlled by N-S and NNW-SSE trending structures which Well OW-801 does not seem to intersect. Towards Well OW-803, the well intersects a significant permeable zone.

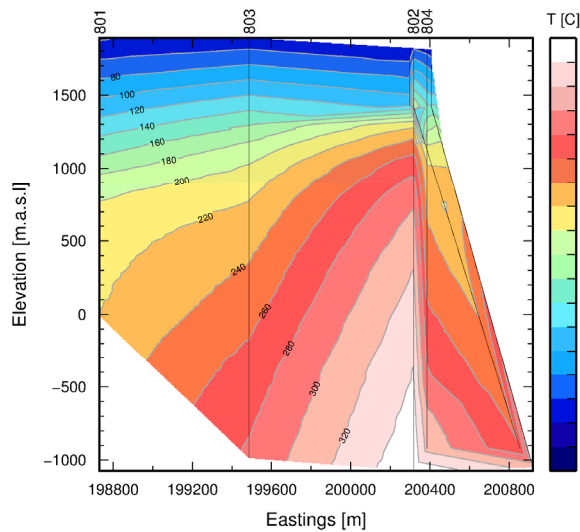


FIGURE 17: Temperature cross-section along profile 1

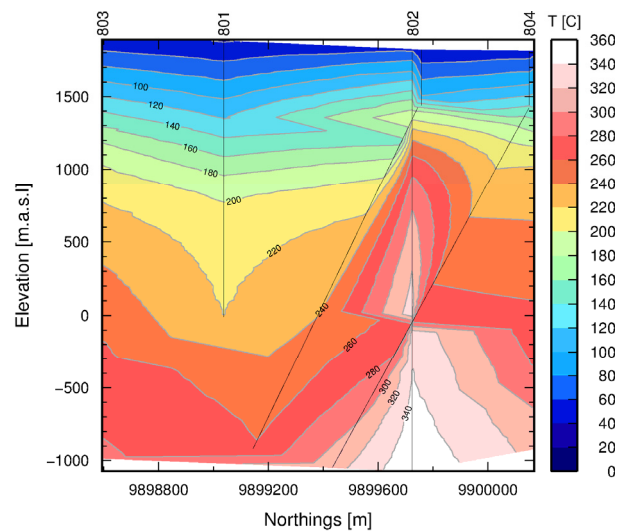


FIGURE 18: Temperature cross-section along profile 2

Profile 3 (Figure 19) is taken from Well OW-1 and elongates in a northeasterly direction, ending at Well OW-804. The profile considers vertical wells falling in between. The temperature distribution along this profile is mushroom shaped, centred at Well OW-802. The reservoir is capped around 1200 m a.s.l. corresponding to about 700 m depth where temperature rises sharply reaching over 300°C, just half a kilometre deeper. The hotter region gradually falls to greater depths towards the start of the profile. It can be generally confirmed here that temperature falls with distance away from Well OW-802 in the direction traversed by profile 3. The existence of a deeper temperature barrier in the opposite direction is observable as well with slight temperature reduction observed in Well OW-804, which corroborates well with the situation in profile 1.

Profile 4 strikes in a north-northeast direction from Well OW-803 and traverses through Well OW-802 and ends at Well OW-804, covering close to two kilometres. The narrow reservoir temperature distribution is clearly conserved here (Figure 20). Considering the 280°C contour, the bottom of the mushroom covers over 2 km and narrows upwardly. The reservoir cap is consistently located at about 700 m depth and is deeper in the regions of Well OW-803, away from the main fault.

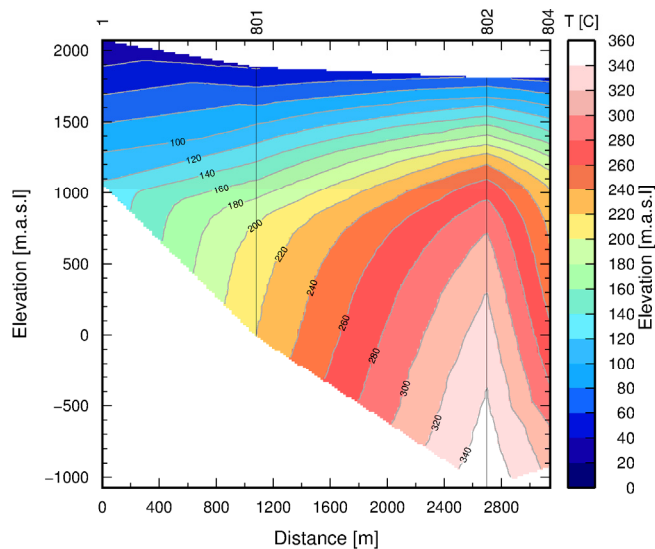


FIGURE 19: Temperature cross-section along profile 3

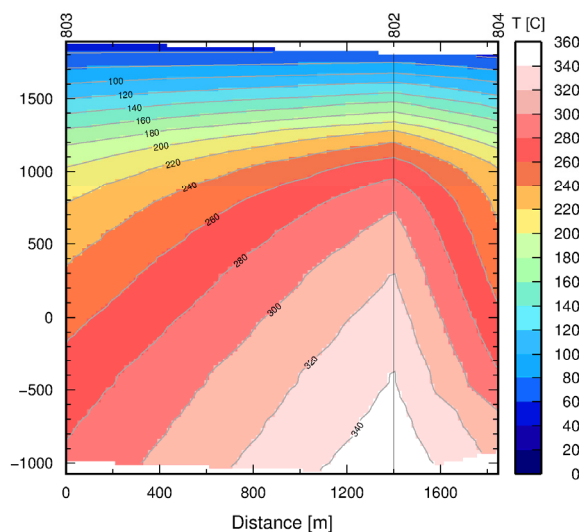


FIGURE 20: Temperature cross-section along profile 4

3.3 Pressure distribution

Evaluation of initial pressure in this field shows all deep drill holes are in a somewhat similar pressure regime. Figure 21 shows the pressure profiles which lie approximately in the same range as in the Olkaria East field. Well OW-802, however, departs slightly at great depths due to the influence of steam in the wellbore as it has heated up the longest. Well OW-802 is also located at the centre of the upflow region. Comparatively, these pressures agree reasonably well with the initial reservoir pressures evaluated during injection testing and which are reported in the next chapter.

Pressure iso-maps

Pressure gradients are the driving force of geothermal fluids up the wellbore. It is very common for high pressure wells to deliver more at the wellhead. Pressure potentials drive fluids between aquifers. Understanding pressure distribution in space is, therefore, very important in deducing the flow directions of geothermal fluids. Similar depths investigated for temperature in Section 3.2 were also studied to understand the spatial pressure behaviour in the field. It should also be noted here that at present only a few drill holes have been drilled in the area and their locations are stacked in the northeast margin of the field.

Pressure at 1000 m a.s.l. High-pressure regimes are located in the southeast margin of the study area and a northwest trend was deduced for possible fluid movement at this depth (Figure 22). Of importance to note is the most pressurized region is located around Well OW-803. The high-pressure regime then eases outwardly in the direction of Well OW-801 and northwards.

Pressure at 500 m a.s.l. The highest pressure regime is localized at Well OW-803 and eases outwardly in all directions (Figure 23). At this depth, which corresponds to depths in excess of 1400 m, pressures in the region of 80 bar-a are prevalent. Likely fluid movements at this depth are, therefore, deduced to be in a northeast direction.

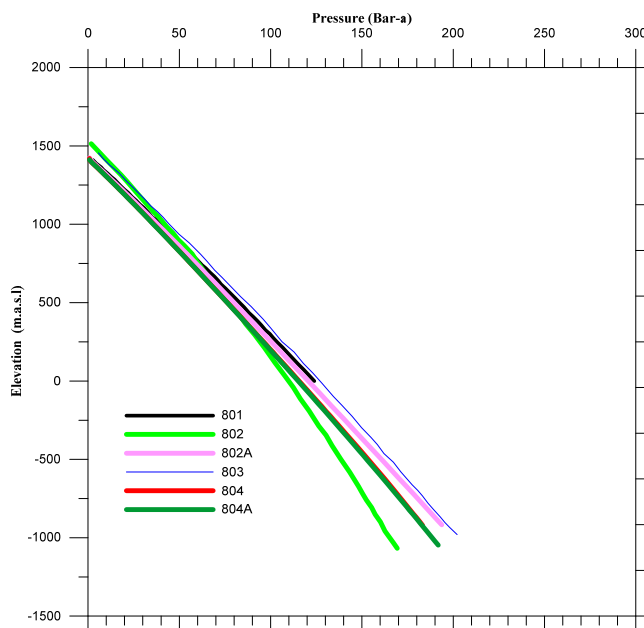


FIGURE 21: Initial pressure profiles

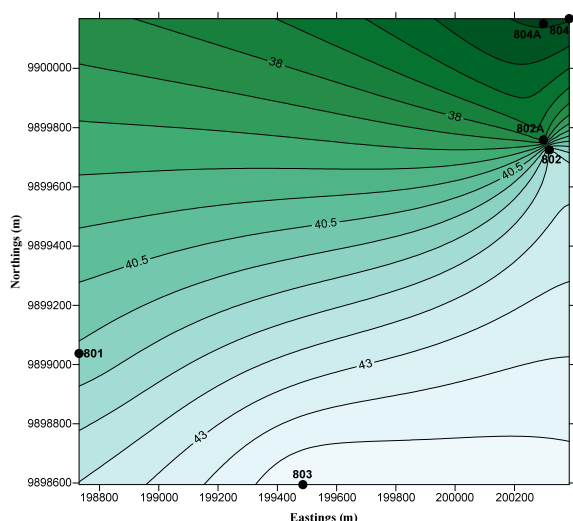


FIGURE 22: Pressure contour map at 1000 m a.s.l.

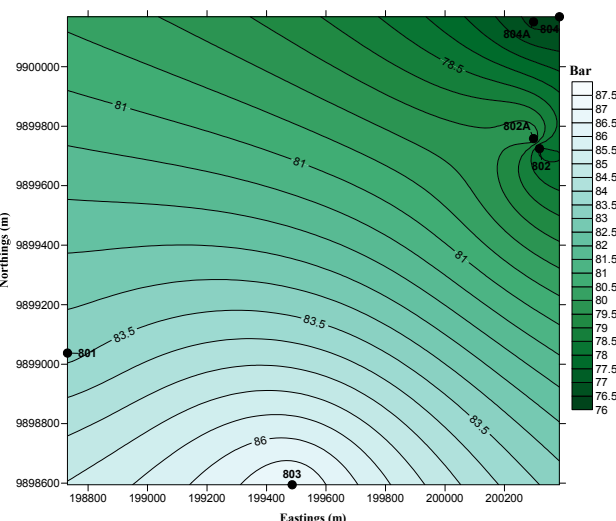


FIGURE 23: Pressure contour map at 500 m a.s.l.

Pressure at 0 m a.s.l. (sea-level). A significant pressure gradient exists between the two non-artesian wells located in the southern and southwest parts of the field and their counterparts to the northeast (Figure 24).

Pressure at -500 m a.s.l. At this depth, a strongly NW-SE trending high-pressure region is evident in the vicinity of the wells on the 802 well pad (Figure 25). The highest pressure observed in Well OW-803 persists at this depth.

Pressure at -750 m a.s.l. A similar situation persists as already observed at -500 m a.s.l. with increasing pressure gradient observable (Figure 26). Fluid flow directions at well bottoms are particularly directed toward Well OW-802, interpreted as the centre of the upflow area.

Pressure profiles

The same profiles or cross-sections considered for the temperature distribution (Section 3.2) were also considered for a pressure analysis.

Profile 1. Pressure distribution along this profile shows doming of a high-pressure region, peaking at Wells OW-802 and OW-804 and elongating to the west. The western part show uniform distribution between Wells OW-801 and OW-803, suggesting a boundary of the high-pressure regime. The highest pressure region at depth is located just at the bottom of both wells drilled on the 804 pads and 802 pads (Figure 27).

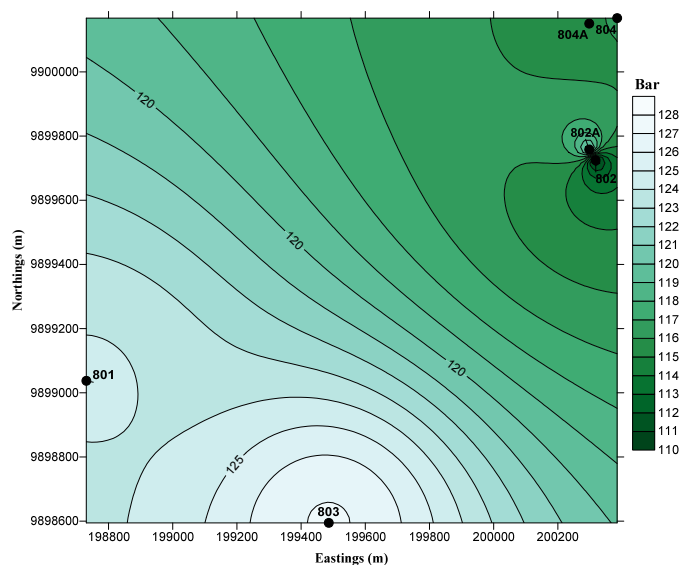


FIGURE 24: Pressure contour map at sea-level

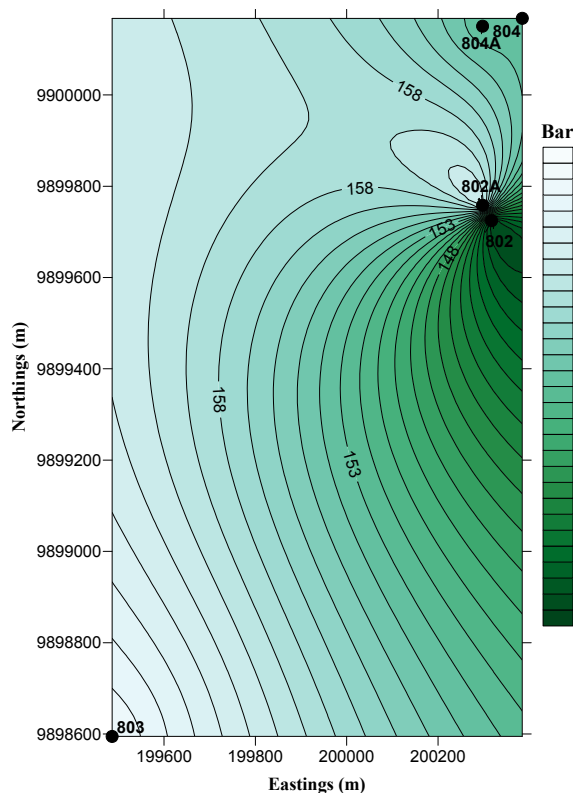


FIGURE 25: Pressure contour map at -500 m a.s.l.

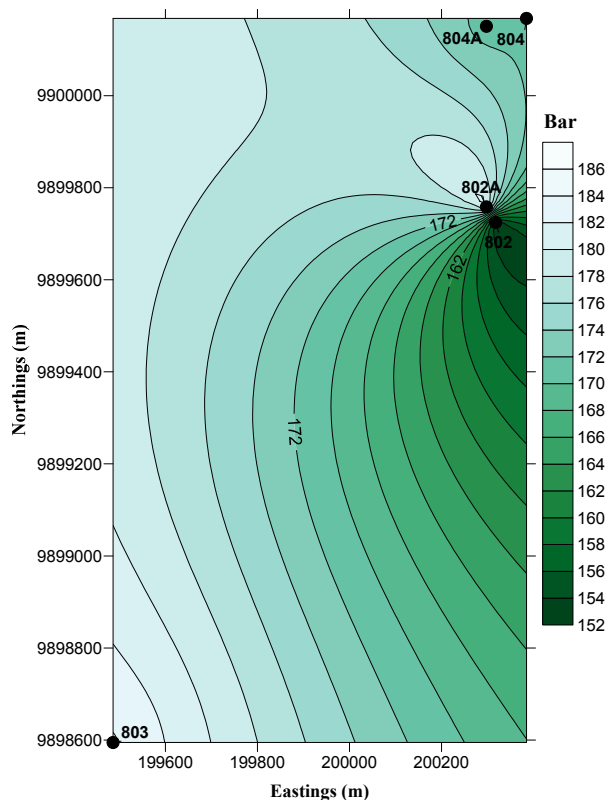


FIGURE 26: Pressure contour map at -750 m a.s.l.

Profile 2. High pressure regimes exist in the northernmost margins of the field and stretch to the central part of the field before decreasing almost drastically as you move away from the structures near Ololbutot lava flow (Figure 28). This structure suggests a down flow associated with the margins of the mushroom shaped structure of the temperature profile. Hot water rises at the centre of the mushroom centred near Well OW-802 and flows away to great depths to the west and southwest of the area. The up doming of fluids in Well OW-803, already seen in temperature profile 2, is attributable to an intersection of another permeable structure.

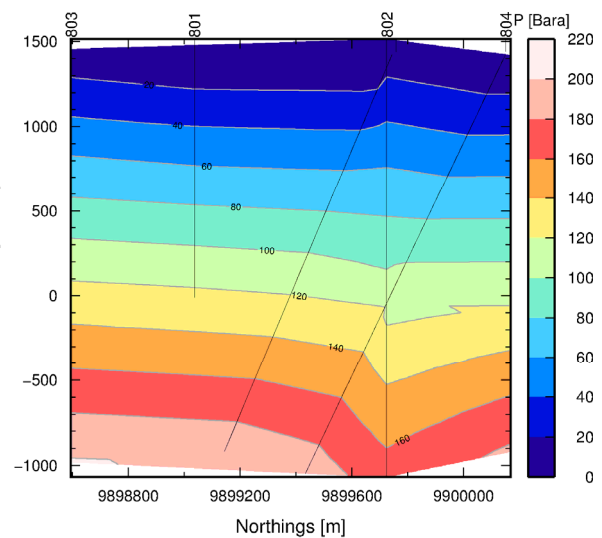
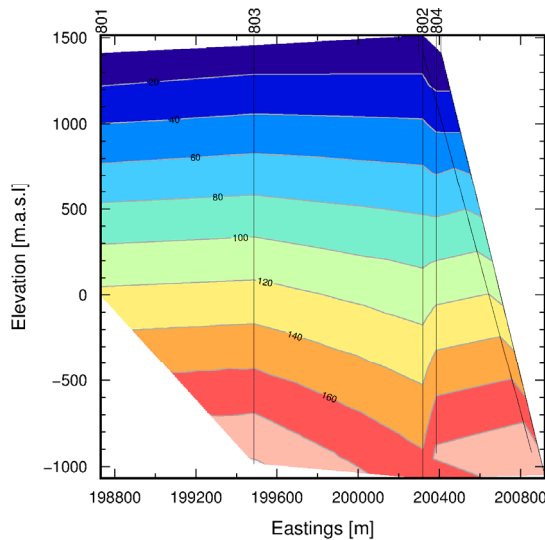


FIGURE 27: Pressure cross-section along profile 1 FIGURE 28: Pressure cross-section along profile 2

Profile 3 (Figure 29) is limited by the absence of measured pressure at Well OW-1 and, therefore, shows a similar distribution as that of temperature only beginning at Well OW-801. A similar trend is observed where high-pressure regimes fall towards the end of the profile and decline in pressure towards the opposite side.

Profile 4. The pressure distribution is consistent with all other profiles rising towards the fault and diminishing in the opposite direction quite drastically (Figure 30). The main production in Well OW-803 is actually deeper where the most permeability exists and at locations where higher pressures are intersected in the region. This attribute is typical for the marginal areas of the mushroom temperature behaviour in geothermal reservoirs.

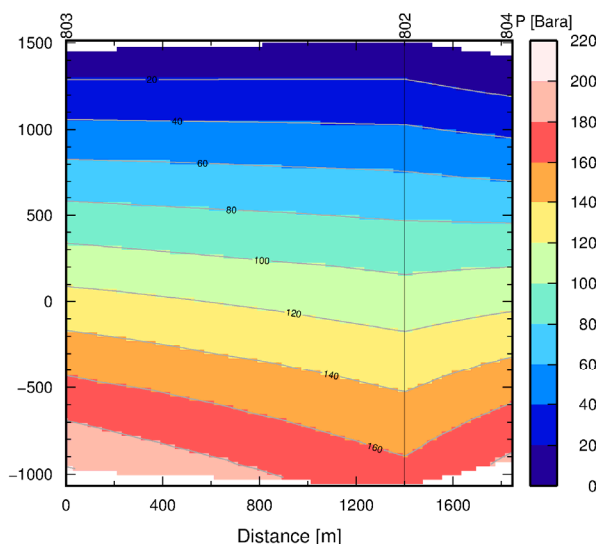
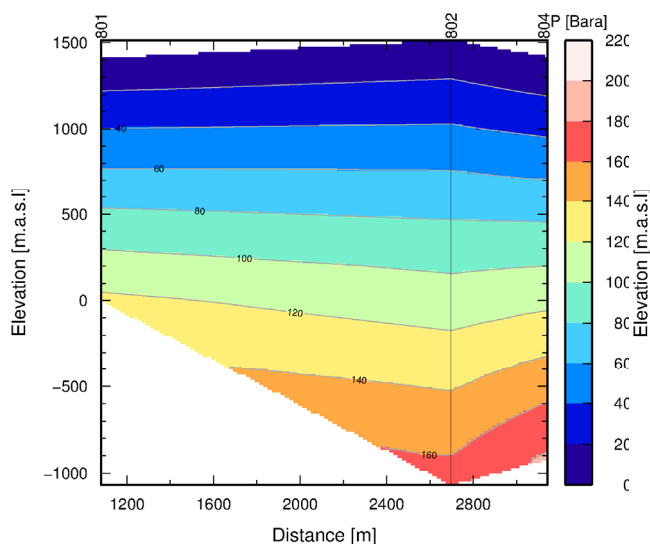


FIGURE 29: Pressure cross-section along profile 3 FIGURE 30: Pressure cross-section along profile 4

3.4 Alteration mineralogy

Composition of geothermal fluids is controlled by temperature dependent reactions between the rock and fluid. The resulting hydrothermal alteration products are affected by temperature, pressure, rock type (at low temperatures), permeability, fluid composition and duration (Brown, 1978). These minerals provide a historical evolution of temperatures in the system.

Particular alteration minerals have been employed in different fields as a kind of geothermometer. While this is mainly field dependent, the Olkaria experience (Omenda, 1998) with mineral formation temperature does not differ largely with those observed elsewhere, e.g. Reyes (2000), and are, therefore, adopted here.

In this study, two minerals were chosen for this purpose. The first appearance of epidote maps formation temperatures of 240°C being encountered, and that of actinolite-biotite gives temperatures in excess of 280°C. The first appearances of these minerals were plotted alongside established temperature profiles in the field. Figure 31 shows reasonable correlation between the two thermometers to the east of the field, and a departure in the colder part of the field, mainly in Wells OW-801 and OW-803. In this section of the study area, temperatures shown by mineralogy are much lower than the actual measurements in drill holes. This is a consequence of cooling further away from the established upflow and known fluid conduits in the area.

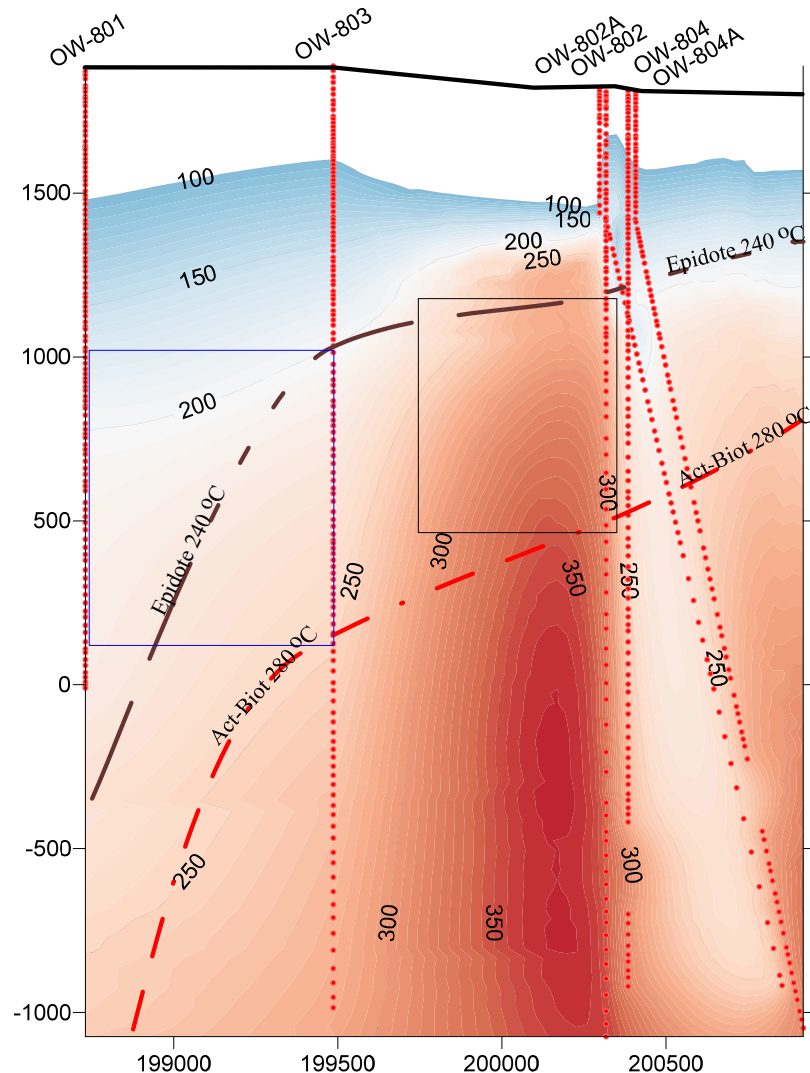


FIGURE 31: Relationship between formation temperature and alteration mineralogy at OSEPF; Black dotted line shows first appearance of epidote; red dotted line shows first appearance depths of actinolite or biotite; blue rectangle shows regions of cooling; black one shows regions of either equilibrium or heating

3.5 Well simulation

3.5.1 Theory

The flow of geothermal fluid flowing vertically in a well can be expressed by using two sets of mathematical equations. Between the feed zones, the flow is represented by one dimensional steady state equations of momentum, energy and mass flux equations. In the case of a feed zone being encountered, mass and energy balances are then required between the fluid already in the wellbore and the incoming fluid. By applying boundary and initial conditions that fully describe the problem, the

governing equations can then be solved numerically. The solutions to these equations involve taking small finite sections of the pipe from the origin of the fluid to the top, thus a continuum from the feed zone to the wellhead is solved. It is also possible to solve the equations from top to bottom, as well, with an appropriate description of the flow.

The governing steady-state equations for mass, momentum and energy flux for a vertical flowing well is set up in Equations 3, 4, and 5.

$$\frac{d\dot{m}}{dz} = 0 \quad (3)$$

$$\frac{dP}{dz} - \left\{ \left[\frac{dP}{dz} \right]_{\text{fric}} + \left[\frac{dP}{dz} \right]_{\text{acc}} + \left[\frac{dP}{dz} \right]_{\text{pot}} \right\} = 0 \quad (4)$$

$$\frac{dE}{dz} \pm Q = 0 \quad (5)$$

where \dot{m} = Total mass flow;
 z = Depth;
 P = Pressure;
 E = Total energy flux;
 Q = Ambient heat loss over unit distance.

In case a feed zone is encountered, flow between the well and the reservoir gives the governing equation of the form:

$$\dot{m}_{\text{feedzone}} = PI \left[\frac{k_{rl}\rho_l}{\mu_l} + \frac{k_{rs}\rho_{rs}}{\mu_s} \right] (P_r - P_l) \quad (6)$$

where \dot{m} = Flow rate from feed zone;
 PI = Productivity index of feed zone;
 k_{rl} = Relative permeability in liquid phase;
 k_{rs} = Relative permeability in steam;
 ρ_l = Density of liquid;
 ρ_{rs} = Density;
 μ_l = Dynamic viscosity of liquid;
 μ_s = Dynamic viscosity of steam;
 P_r = Reservoir pressure;
 P_l = Well pressure.

The HOLA well simulator presented by Björnsson (1987) solves these equations for vertical wells from the bottom feed zone up the well. The bottommost feed zone need be at the bottom of the well and the flow into the well is defined as positive; the flow from the well outwardly into the formation takes the negative sign. Different computation modes are available in HOLA for simulations with different known parameters.

In this work, computation mode 2 was applied for predicting the output curves, given known relative feed zone flow rates and calculated enthalpy conditions. The Orkiszewski velocity model (Orkiszewski, 1967) was assumed to describe the phase velocity in the wells.

3.5.2 Results

The program HOLA was used to estimate the productivity curve for candidate wells in OSEPF. The thermodynamic parameters used were calculated from observed pressure and temperature conditions during warm up, discussed in Section 3.1. The well productivity indices were estimated by taking the assumption that it equals a third of the well's injectivity indices (Grant and Bixley, 2011) and relative contributions assigned to the feed zones in the well.

Results show liquid wells producing at low pressure regimes with moderate deliverability (Figure 32).

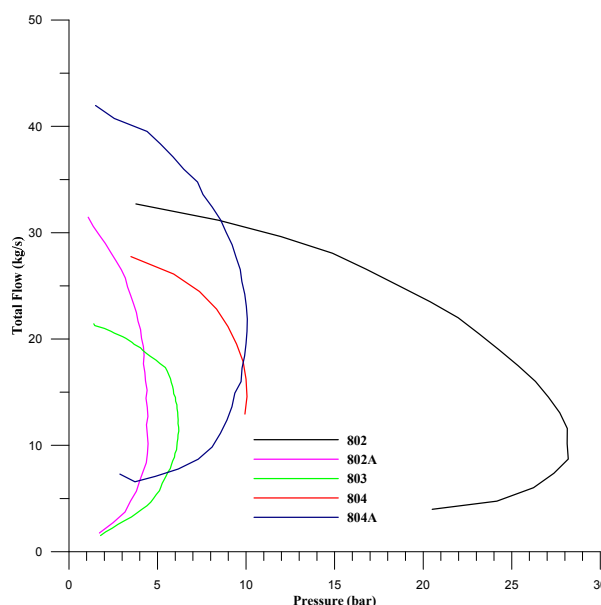


FIGURE 32: Calculated output curves

4. PRESSURE TRANSIENT ANALYSIS

4.1 Theoretical background

The basis of pressure transient analysis lies in the partial differential equations describing single phase flow in porous media. However, we are concerned with only a limited part of the problem involving describing pressure responses in the reservoir as measured in the vicinity of a well penetrating into the reservoir. In geothermal situations, fractures play a more important role in controlling reservoir permeability than porous rock. Darcy's law is used to describe fluid flow in a porous media. The resulting equation can be extrapolated to fractured media since, on a large scale, such as the case of geothermal reservoirs, fractures behave as porous rock. We expect to see immediate wellbore effects and gradually transit to boundary effects at later times in a well test. The pressure diffusion equation (Equation 7) describes the flow within the infinite acting reservoir with appropriate boundary conditions applied to describe flow in the outer margins. The pressure diffusion equation takes the form of a heat diffusion equation in all respects. The two processes are, therefore, comparable.

$$S \frac{\partial p}{\partial t} = \frac{k}{\nu} \nabla^2 p - f(x, y, z) \quad (7)$$

where S = Storativity;
p = Pressure;
t = Time;
k = Permeability;
ν = Kinematic viscosity of water;
f(x, y, z) = Mass source density.

4.2 Description of injection tests at Olkaria

Pressure response is measured by injecting cold water at varying rates at the top of a well soon after the well is completed and cased. The availability of the rig on site is important as they often have good pumping capability and reliable water supply. There are cases where warm brine is used to supplement cold water. The two waters are mixed together in collection tanks so that no significant thermal contribution from injected water is envisaged.

A typical well completion test program involves taking temperature and pressure profiles in the beginning as soon as the slotted liner is lowered into the well. This profile is mainly used to locate appropriate permeable zones from where to monitor pressure response during injection. The location of such points is chosen depending on permeability contrast between different feed zones and pressure tolerance of the measuring tool for the length of pressure monitoring. The measuring tool is then lowered to the chosen depth and step rate injection begins. Typically, there are three injection steps of 5 l/s, from 16.67, to 31.67 l/s, each lasting for three hours. The initial injection at 16.67 l/s is usually four hours long and seldom has any observable effects on reservoir pressure. After three hours of injection at the greatest pumping rate (31.67 l/s), another temperature and pressure profile is taken without stopping the injection. There is, therefore, a significant gap between this last injection step and the next step where continuous pressure monitoring at the selected depth is discontinued.

Following a successful step rate test, an eight hour long monitoring of pressure draw-down is measured at the same depth where injection response was monitored. This last step is done without any injection into the well at all. This usually gives reasonable pressure draw-down curves despite the drastic pressure fall at the beginning when the pumps are switched off. This is arguably unimportant as more often wellbore storage effects dominate the well and the transition to the infinite acting reservoir response happens at least an hour into the test. By neglecting the apparent sudden drop at the beginning, this paper shows the reservoir and its boundary effects can be successfully modelled.

4.3 Reservoir properties

In this section, common parameters associated with well test analysis are discussed and their relationships with common hydrological parameters of interest in characterizing geothermal reservoir are deduced. The aim of the analysis in a well test is to deduce hydrological parameters that characterize the reservoir penetrated by the well. These parameters are then interpreted to build a hydrological picture of the larger reservoir under study.

Parameters

The *estimated reservoir pressure* (P_{est}) and *estimated reservoir temperature* (T_{est}) are average estimates for the part of the reservoir that is being investigated in the well test. These values are used to calculate approximate values of the dynamic viscosity of the reservoir fluid and the total compressibility of the rock matrix and the fluid.

Wellbore radius (r_w) is the average radius of the well at the reservoir depth, given in meters.

Dynamic viscosity of the reservoir fluid (μ) is the estimated average viscosity of the fluid at reservoir conditions. In cases where the fluid is in two phases, the average viscosity can be taken as the harmonic average of the two phases, weighted by the mass fraction of each phase, i.e. $\mu_t = (x_w/\mu_w + x_s/\mu_s)^{-1}$, where x_w is the mass fraction of water and x_s is the mass fraction of steam (Horne, 2006).

Total compressibility (c_t) describes the ability of the fluid and reservoir rock to compress or expand as a function of pressure. Formulations for computing compressibility will be slightly different depending on the physics of the fluid and the reservoir, but a further discussion on that can be found in Grant et.al. (1982). Total compressibility will typically be on the order of 10^{-9} Pa⁻¹ for a liquid-dominated reservoir, 10^{-7} Pa⁻¹ for a dry-steam reservoir, and 10^{-6} Pa⁻¹ for a two-phase steam-water reservoir.

Porosity (ϕ) is the volume fraction of the rock which is capable of holding water.

Transmissivity (T), based on volumetric flow, has the SI unit [m³/Pas]. It describes the ability of the reservoir to transmit fluid, hence largely affects the pressure gradient between the well and the reservoir. Its physical formulation is (kh/μ) , where k is the effective permeability of the reservoir, h is the reservoir thickness, and μ is the dynamic viscosity of the active reservoir fluid. The transmissivity can

vary by a few orders of magnitude but common values from injection testing in geothermal reservoirs are on the order of $10^{-8}[\text{m}^3/\text{Pa}]$.

Storativity (S) has the SI unit $[\text{m}^3/\text{Pa m}^2 \text{ or } \text{m}/\text{Pa}]$ and defines the volume of fluid stored in the reservoir, per unit area, per unit increase in pressure. Hence, it has great impact on how fast the pressure wave can travel within the reservoir. The general formulation of storativity is $S = c_t h$, where c_t is the total compressibility of the rock and the reservoir fluid, and h is the reservoir thickness. Storativity varies greatly between reservoir types (i.e. liquid-dominated vs. two-phase or dry-steam) because of its dependence on fluid compressibility (Grant et al., 1982).

Skin factor (s) is a variable used to quantify the permeability of the volume immediately surrounding the well. This volume is often affected by drilling operations, being either damaged (e.g. because of drill cuttings clogging the fractures) or stimulated (e.g. due to extensive fracturing around the well). For damaged wells the skin factor is positive, and for stimulated wells it is negative. The typical skin factor in geothermal wells is considered to be in the range -5 - 5 , although values may range from about -5 - 20 . The skin factor can also be described in terms of the effective wellbore radius, i.e. the apparent radius of the wellbore caused by the skin effect. The effective radius is given by $r_{eff} = r_w e^{-s}$ where r_w is the measured wellbore radius (Horne, 1995). It should be noted that the skin factor and storativity are quite strongly correlated in most well test models, hence the relative accuracy of each parameter will be lowered when both are included.

Wellbore storage (C) is a property that accounts for the difference between the wellhead flow rate, and the “sand face” flow rate (i.e. the flow into or out of the actual formation). Wellbore storage effects can occur in several ways, but most commonly by changing the liquid level and fluid expansion. In injection testing, the most dominant cause for wellbore storage is changing liquid level. The storage effect is caused by the volume in the wellbore itself being emptied or filled. In the case of fluid expansion, consider a drawdown test. When the well is first opened to flow, the pressure in the wellbore drops and the fluid in the wellbore expands, providing the initial production volume (Horne, 1995). Typically under single phase liquid conditions, the wellbore storage, because of fluid expansion, is negligible. However, in a geothermal well where the wellbore fluid changes from a single phase liquid to a two-phase steam-water, the expansion effect can be very significant.

Radius of investigation (r_e) is the approximate distance at which the pressure response from the well becomes undetectable. Hence, this radius defines the area around the well being investigated, although the value of the parameter should be viewed more qualitatively. When boundary conditions are seen in the data, the approximate distance to the boundary will define the radius of investigation.

The *injectivity index (II)* is often used as a rough estimate of the connectivity of the well to the surrounding reservoir. Here it is given in the units $[(\text{l/s})/\text{bar}]$ and it is defined as the change in the injection flow rate divided by the change in the stabilized reservoir pressure (Equation 8).

$$II = |\Delta Q / \Delta P| \quad (8)$$

Here $\Delta Q = Q_f - Q_i$ and $\Delta P = P_f - P_i$ where i refers to the initial value and f refers to the final value. In Well Tester software (Júlíusson et al., 2007), the pressure values used to calculate II are taken from the modelled response, not the actual data collected.

Deduced parameters

Two specific parameters of interest in reservoir physics can be deduced by combining the initial parameter estimates and the well test results. The parameters estimated in the well test are the transmissivity (T) and storativity (S) and, given the porosity (ϕ), total compressibility (c_t) and dynamic viscosity (μ), one can estimate the reservoir thickness and the effective permeability from Equation 9.

$$h = \frac{S}{\phi c_t} \quad \text{and} \quad k = \frac{T\mu}{h} \quad (9)$$

However, it should be noted that the error in these estimates is influenced by the combined error in the underlying parameters so, as a general rule, the results should only be viewed as a qualitative cross check on the well test results.

The *effective permeability* (k) is a measure of the ability of the reservoir rock to transmit fluid. Permeability has the SI units [m^2] but is commonly referred to using Darcy units, i.e. $1 \text{ D} \approx 10^{-12} \text{ m}^2$. Permeability in geothermal reservoirs is generally on the order of 1 to 100 mD (milliDarcy), i.e. $10^{-15} - 10^{-13} \text{ m}^2$.

Reservoir thickness (h) is the estimated thickness of the formation that is actively exchanging fluid with the wellbore.

4.4 Results of step rate injection tests at Olkaria South East Field

Step-rate injection tests are carried out in all newly drilled wells. Pressure transient data were collected for different injection rates and analyses using Well Tester software. The results of these analyses are tabulated in Table 2. In general, the injection tests were considered successful despite there being few pressure recordings, a common limitation of mechanical tools. Pressure response of data is important in diagnostic exercises to deduce the nature of reservoirs, their sizes and existing boundary conditions. For simplicity, deep reservoirs were considered to be at an average of 240°C with a pressure range of 160-180 bar-a. The area actively exchanging reservoir fluids can be difficult to determine. An estimate of an average 500 m was considered reasonable for the purpose of this study. However, shallower wells had different reservoir thicknesses and expected temperatures.

In the analysis of the injection tests, two kinds of models were considered for the reservoir, on one hand a homogeneous reservoir and on the other hand a dual porosity reservoir. Three different boundary conditions were used in the modelling: an infinite reservoir, a reservoir with constant pressure at the boundary, and finally a no-flow boundary in which case the fluid cannot flow freely across the boundary; but, in that case, the pressure continues to increase with time when the injection rate is kept steady. Best results from the tests showed that the reservoir conforms to the homogeneous reservoir with a constant pressure boundary, and a constant skin with wellbore storage.

TABLE 2: Well test analysis

Well Name	Depth TVD (m)	Main Feedzone TVD (m)	II(all steps) (l/sbar)	Best step	Transmis- sivity $\times 10^{-8}$ $\text{m}^3/(\text{Pa}\cdot\text{s})$	Storativity $\times 10^{-8}$ $\text{m}^3/(\text{Pa}\cdot\text{m}^2)$	Skin factor	Well bore storage $\times 10^{-4}$ m^3/Pa	II (best step) (l/s bar)
OW-801 R1	600	350	4.75	4	3.06	1.14	-6.14	1.12	12.23
OW-801 R2	640	500	4.27	4	2.66	1.41	0.76	1.4	3.47
OW-802	3000	1050	6.95	1	0.74	6.65	-5	0.72	5.34
OW-802A	2860	1800	3.34	3	1.75	6.65	-1.87	0.47	2.92
OW-803	3000	1500	1.12	5	0.84	6.95	-3.15	0.59	1.75
OW-804	3000	1900	4.87	4	3.23	6.75	-2.08	5.55	7.51
OW-804A	2870	2250	4.28	4	6.3	6.75	0.41	5.56	7.23

Well OW-801R1 was modelled with homogenous-infinite-constant-skin with wellbore storage for a 200 m thick reservoir. The injection steps fitted the reservoir model fairly well. Step 4 was considered the best fitted step (Figure 33) which gives injectivity of 12.23 l/s bar and effective permeability of $4.61 \times 10^{-14} \text{ m}^2$. Estimates of the injectivity index were, however, lowered when all steps were considered.

Well OW-801R2 was modelled with similar model parameters as Well OW-801R1, and with step 4 returning the best results with an injectivity index of 3.47 l/s bar and effective permeability of $4.75 \times 10^{-14} \text{ m}^2$. Figure 34 shows the fit for Step 4.

Well OW-802. Four injection steps were studied for this well. The first step with a homogeneous, constant pressure and wellbore storage with constant skin, fitted well (Figure 35). An injectivity index of 5.34 l/s bar and effective permeability of $1.70 \times 10^{-15} \text{ m}^2$ were obtained for this step.

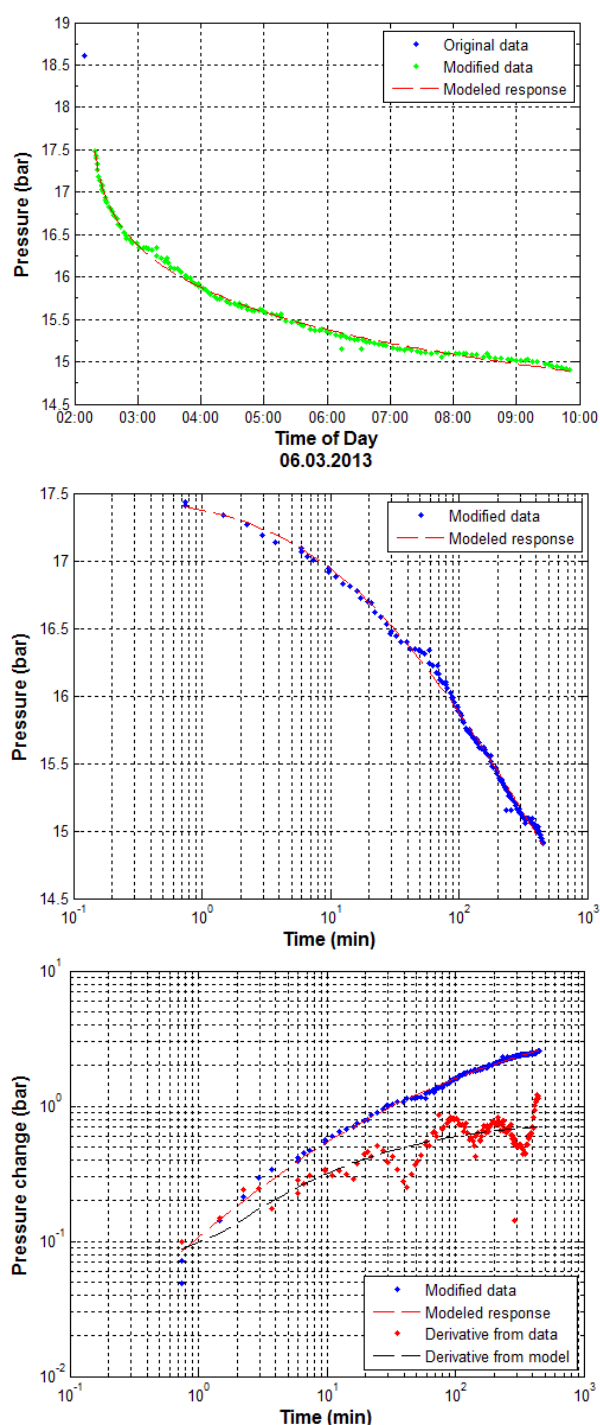


FIGURE 33: Fit between model and collected data in linear, semi-log and log-log scale for step number 4 for Well OW-801R1

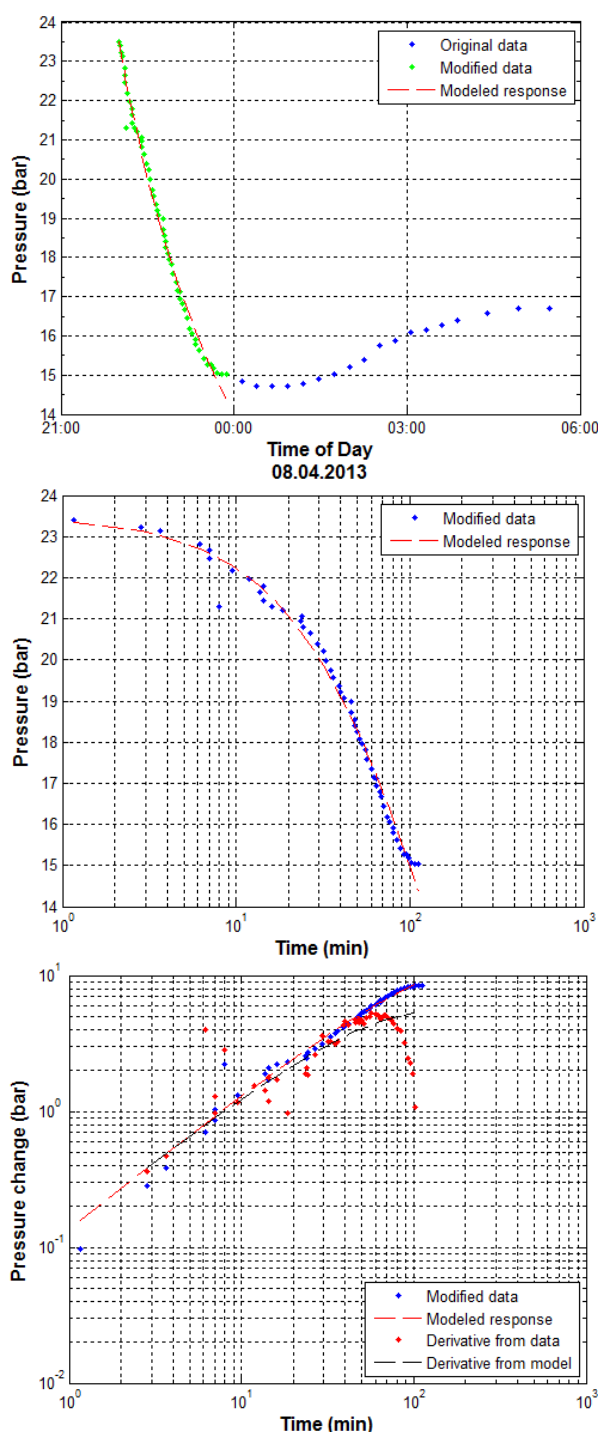


FIGURE 34: Fit between model and collected data in linear, semi-log and log-log scale for step number 4 for Well OW-801R2

Well OW-802A. Three injection steps were considered for this well for a constant pressure bounded homogeneous reservoir with wellbore storage and constant skin. Of the three steps considered, the third step obtained the best fit to the model (Figure 36) with an injectivity index of 2.92 l/s bar and effective permeability of $1.99 \times 10^{-15} \text{ m}^2$.

Well OW-803. Five steps were considered in this well. The first and last steps were successfully modelled with homogeneous, constant pressure and constant skin with wellbore storage reservoir model. In a few steps, the reservoir tended to demonstrate no flow boundaries. However, the dominant

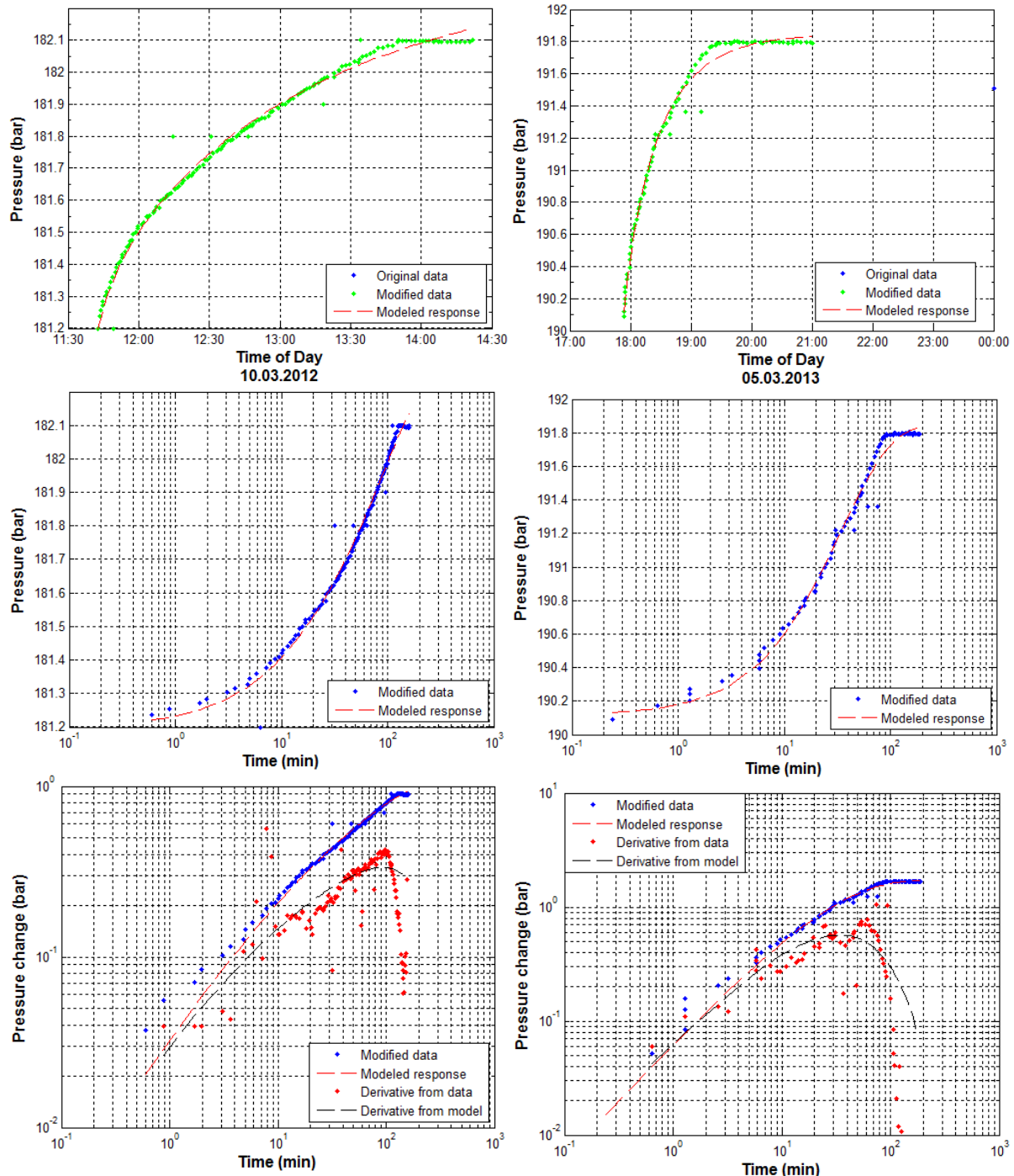


FIGURE 35: Fit between model and collected data in linear, semi-log and log-log scale for step number 1 for Well OW-802

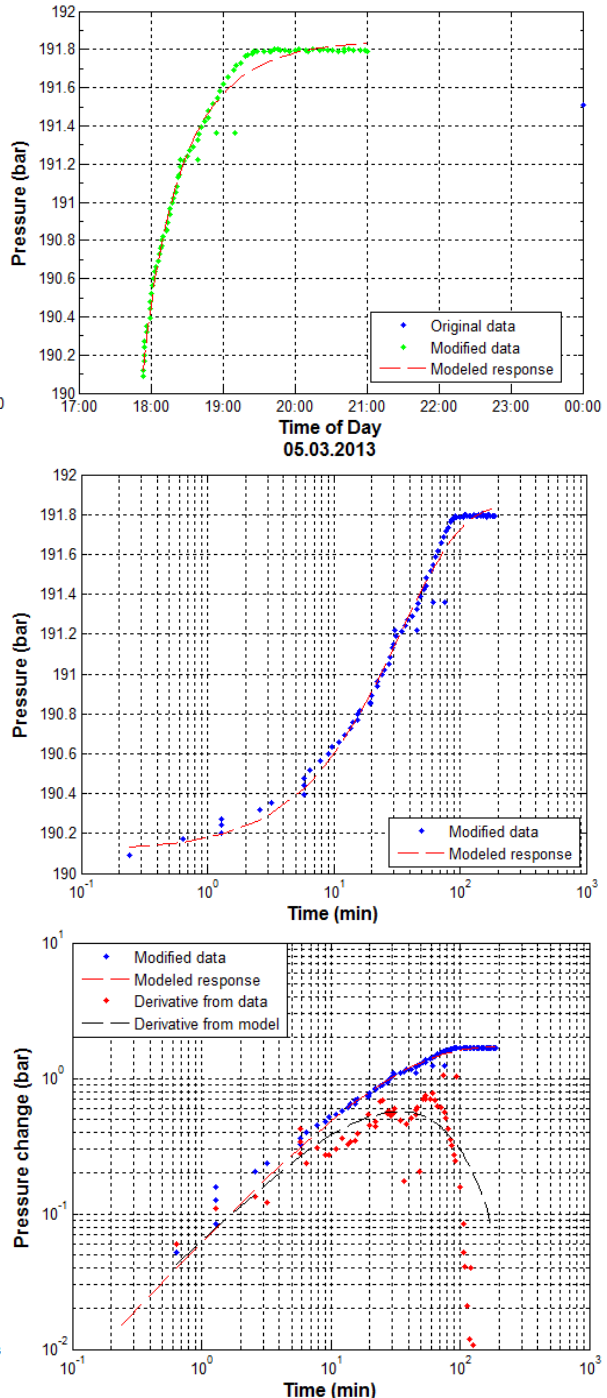


FIGURE 36: Fit between model and collected data in linear, semi-log and log-log scale for step number 3 for Well OW-802A

behaviour was constant pressure with the probable effect of low permeability. The fit in the last step was exceptionally good and returned a low injectivity index of 1.75 l/s bar and effective permeability of $1.74 \times 10^{-15} \text{ m}^2$. Figure 37 shows the fit obtained for step 5.

Well OW-804. Four injection steps were modelled as homogeneous, constant pressure and constant skin with wellbore storage reservoir, with step 4 considered the best step based on its fit. Figure 38 shows the linear, semi-logarithmic and logarithmic plots obtained for pressure transient analysis for step 4. The step obtained an injectivity index of 7.51 l/s bar and effective permeability of $7.37 \times 10^{-15} \text{ m}^2$.

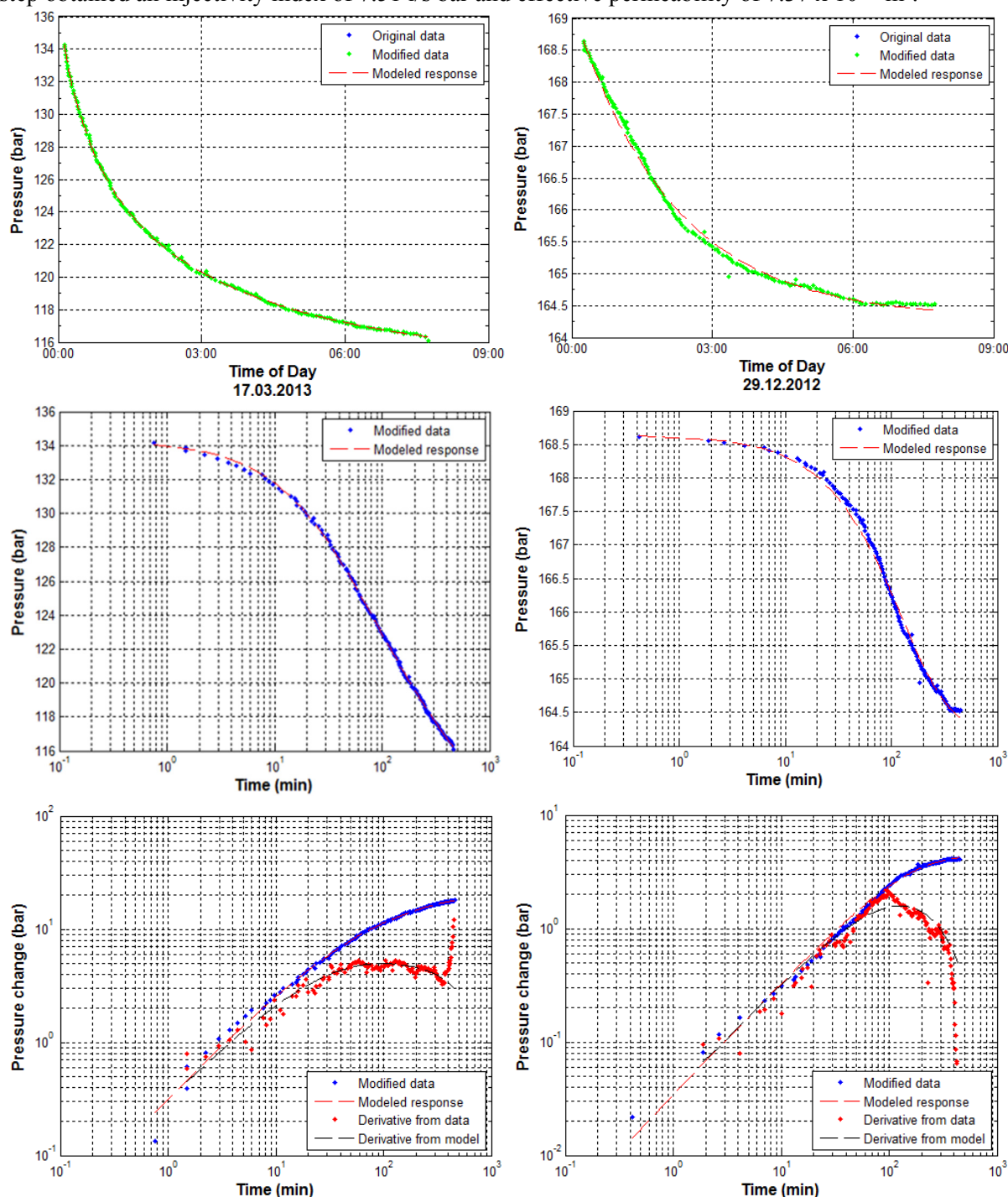


FIGURE 37: Fit between model and collected data in linear, semi-log and log-log scale for step number 5 for Well OW-803

FIGURE 38: Fit between model and collected data in linear, semi-log and log-log scale for step number 4 for Well OW-804

Well OW-804A. Of the four injection steps considered for analysis, the fourth step fitted best to a homogeneous, constant pressure and constant skin with wellbore storage reservoir model. The step returned an injectivity index of 7.23 l/s bar and effective permeability of $1.44 \times 10^{-14} \text{ m}^2$. Figure 39 shows the fit obtained for step 4.

5. CONCEPTUAL MODEL OF THE FIELD

Grant and Bixley (2011) defined conceptual models as descriptive models of geothermal systems incorporating, and unifying the essential parts of physical features of the system. A conceptual basis is constructed by unified interpretation of data available for a particular field. Incorporation of ideas and viewpoints from various disciplines and expertise are essential in this task. Variable datasets are used in the construction of these models and depend on the phase of development and, therefore, the amount of data available. Fields under exploration rarely have any datasets beyond surface geo-scientific data. In the case of fields that have some or many drill-holes, conceptual models involve the interpretation of a lot more data and are, therefore, considerably more detailed.

The Olkaria geothermal field has been studied extensively over the decades. New information is increasingly acquired with drilling of additional and deeper wells, all of which have dramatically increased knowledge of the system. Down-hole data is of paramount importance in providing calibrations to models developed earlier with little or no information about the different sectors of the field, its geometry, nature and boundaries. The Olkaria conceptual model proposed by West-JEC (2009) and improved by Mannvit/ÍSOR/Vatnaskil/Verkís Consortium (2011) describes the heat source of the system as being of magmatic origin lying at shallow (6 km) depth with dyke intrusions which, in turn, are responsible for at least four up flow areas: one below the Olkaria Domes, another below the East field, still another below the Northeast field and a fourth below the West field. Meteoric water from the high rift scarps percolate deep via deep seated faults dipping into the centre of the rift, are heated on their way, and up-well along permeable structures.

A simple localized model of the Olkaria Southeast production field was developed and is presented in Figure 40. The analyses of temperature and pressure data in Sections 3 and 4 of this work were used to construct a conceptual model of the field. Geothermal fluids permeate through the Ololbutot fracture

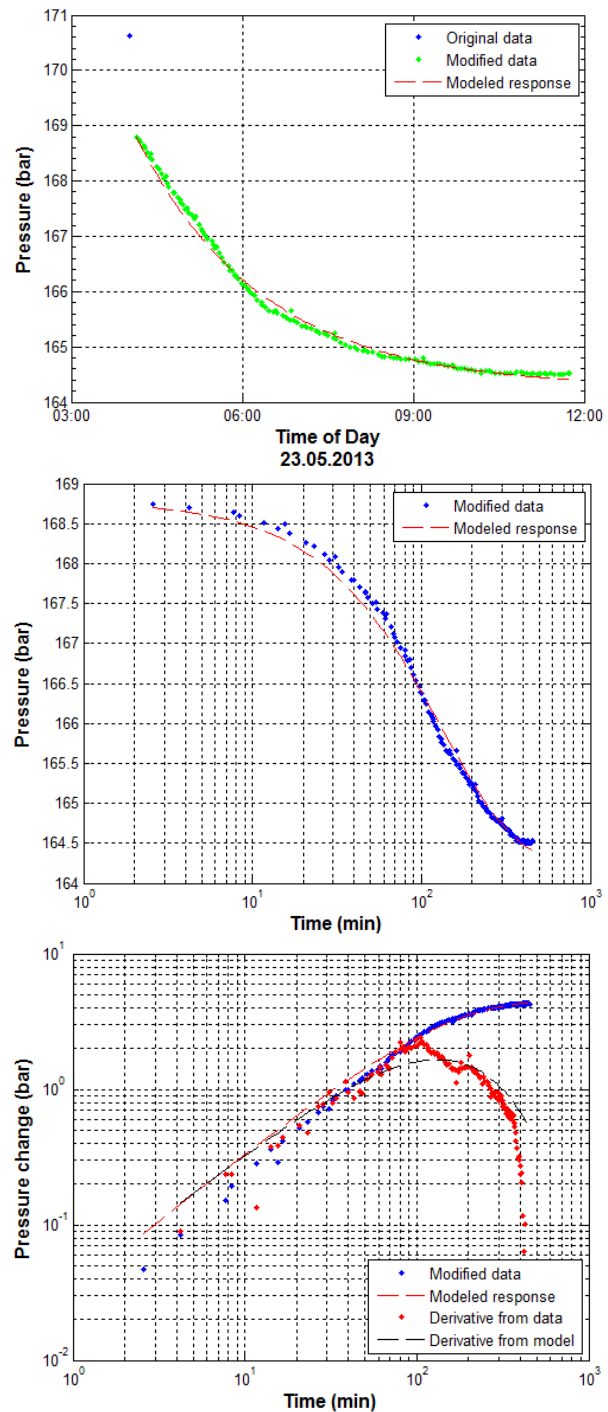


FIGURE 39: Fit between model and collected data in linear, semi-log and log-log scale for step number 4 for Well OW-804A

zone and the NW-SE faults intersecting it, allowing water to percolate deep into the hot crust. The waters are heated, become lighter and flow towards the surface through permeable zones and structures. The greatest and hottest up flow is located near Well OW-802. The up-welled waters reach the impermeable cap rock above it where it is dispersed on either side of the mushroom-shaped upflow.

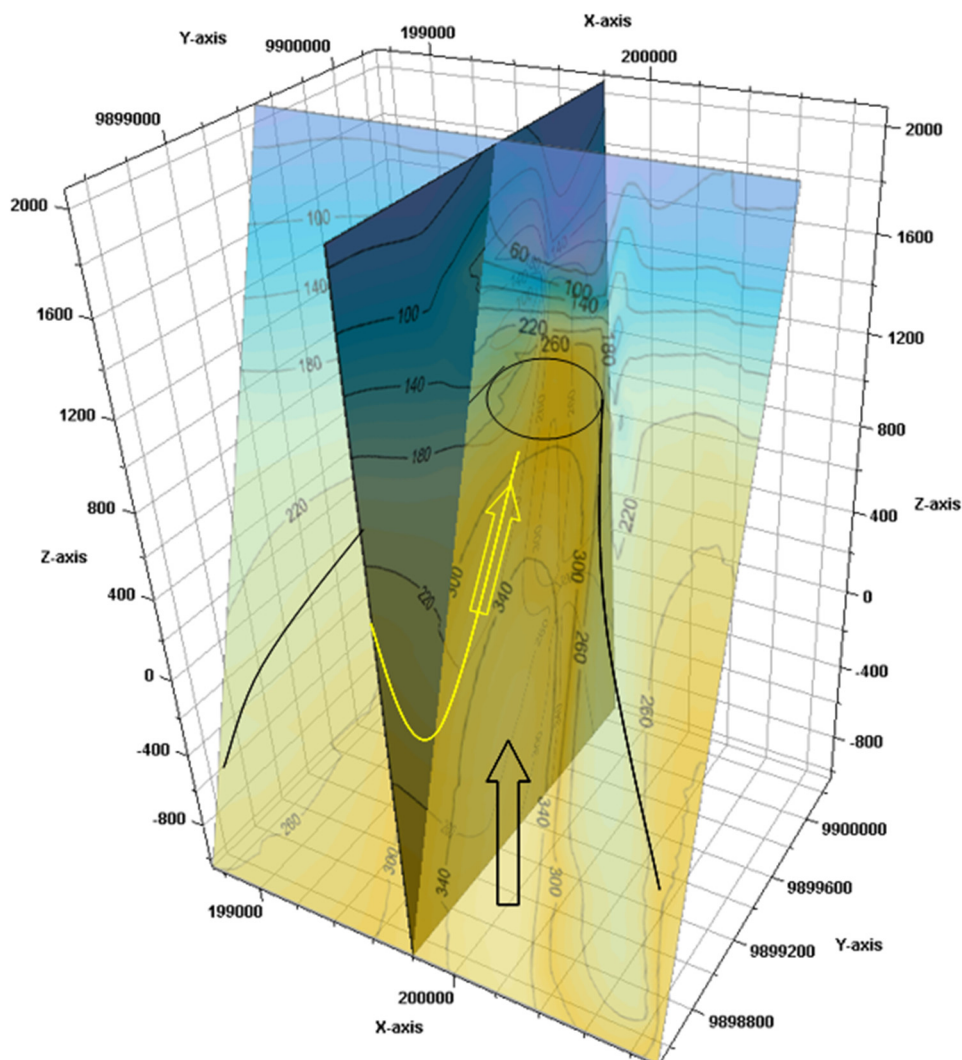


FIGURE 40: Conceptual model of the Olkaria South East production field

6. VOLUMETRIC ASSESSMENT

6.1 Theoretical background

The volumetric assessment method is a static modelling technique mainly used in the mining and petroleum industries. It was more commonly used in geothermal fields in the past than it is today. The Monte Carlo technique is used for repeat multivariable simulation of random variables to generate random inputs from appropriate probability distributions. Essentially, this method approaches the complex question of geothermal resource estimates rather heuristically. For each input variable (except those with lesser uncertainty) in a particular field or situation, computational algorithms are used to sample thousands or more possibilities.

The volumetric assessment is useful in the early stages of development of geothermal fields when little information is available to support more detailed numerical models. In geothermal resource estimation, a resource area is first estimated, then calculations proceed to estimate thermal energy stored in the rock matrix and in the fluid present in rock interstitial spaces. The geometry of the system, its dynamic response to production/injection and hydrologic parameters are not considered. The main benefit of this method, however, is that it offers an early reconnaissance for likely capacity with only limited information.

In the volumetric method, an estimate of the surface area of the resource and its thickness (volume) is required to estimate the thermal heat in place. In many cases, this information is usually deduced from geo-scientific studies of the area. Geophysical surveys, such as MT/TEM, are particularly important in defining resource areas and estimate their probable dimensions before drilling is done. In the absence of these, geological and geochemical data may be used. In drilled prospect areas, better estimates can be obtained from temperature measurements.

The total energy (E_{total}) in the reservoir equals the stored energy in the rock matrix (E_r) and in the pore space volume (E_l) (Equation 10). Usable energy is calculated using a reference temperature, T_{ref} referring to the cut off temperature for a specific utilization of the energy.

$$E_{\text{total}} = E_r + E_l \quad (10)$$

where

$$E_r = V (1 - \phi) \rho_r \beta_r (T - T_{\text{ref}})$$

$$E_l = V \phi \beta_l \rho_l (T - T_{\text{ref}})$$

and

V	= Reservoir volume;
Φ	= porosity;
ρ_r	= Rock density;
ρ_l	= Density water;
β_r	= Specific heat capacity of rock;
β_l	= Specific heat capacity of water;
T	= Reservoir temperature.

Not all available energy is usually accessible. Limits to accessibility are widely variable and may depend on many factors. The accessibility factor, A , is incorporated to discount inaccessible energy from the calculations. The recovery factor, R , defines the proportion of accessible energy that can be technically recovered using available technology. The recoverable energy (E_{rec}) then becomes as shown in Equation 11.

$$E_{\text{rec}} = A * R * E_{\text{total}} \quad (11)$$

Electrical conversion efficiency, η is then introduced to give an amount of energy that can be converted in a conventional turbine generator.

$$E_e = \eta E_{\text{rec}}$$

$$P_e = \frac{E_e}{\Delta t}$$

where

E_e	= Total electrical energy;
P_e	= Electrical power potential for generation over time, Δt .

6.2 Model parameters

Surface area. A conclusive anomaly is not apparent in resistivity measurements in a few stations in the area. The surface activity is concentrated along major structures. This is construed to indicate vertical permeability associated with these structures and cannot reliably map out the extent of a viable high temperature resource. It is, however, clear that the up flow zone elongates at least 2-3km (profile 3) and is not more than 750 m thick (profile 2); an area of 2 km² is a reasonable lower estimate of proven steam resources. The fact that the temperature diminishes away from the present up flow area indicates that its extent is probably quite limited. In the absence of localized heat sources, the system is expected to be quite narrow with structures being the most important controls. The upper limit is taken to be 6 km² which is a guess between the proven resource and the total area available for exploitation.

Thickness. The reservoir is located not less than 1000 m depth. Most of the wells in this area are cased at about 700 m depths; therefore, the maximum production depth is only 2300 m in the deepest well. It is evident that some potentially productive aquifers were already cased off. The bottom of the reservoir has not yet been reached. It was, therefore, decided to take a thickness of 2500 m to represent the upper boundary and 1000 m should reflect the least thickness. It is clear however that the likely thicknesses are closer to the upper limit.

Temperature. Reservoir temperatures taken were between 240 and 360°C. A limit of 240°C was taken as wells this deep may not sustain discharge below this temperature. The choice of this temperature was influenced by recent observations in the marginal wells located in Domes field. It is expected that well discharges are likely to produce fluids at an average of 260°C. The rejection temperature is set at flashing conditions commonly adopted for condensing plants at Olkaria.

Recovery factor. A higher recovery factor was selected, based on the determination of the likely resource area. Since the proven resource area was considered, it is reasonable to elevate the recovery factor. High permeability is observed in this field and, therefore, a higher energy recovery is further justified.

6.3 Monte Carlo simulation

Table 3 summarises the input parameters for the Monte Carlo simulation while the results of simulations for the above input are presented in Table 4. The production capacity of the field is estimated at 42 MWe. Frequency distribution for electrical power potential shows a mean of 45 MWe. 10% of the cumulative probability predicts a 23 MWe output while 90% on the other hand predicts an output of 73 MWe (Figure 41). Sarmiento and Steingrímsson (2011) presented the proposition that 90% of the outcomes represent the maximum possible outcome inclusive of proven, probable and possible resource, while the 10% marker represents the proven resources only.

TABLE 3: Summarized input parameter estimates for Monte Carlo simulation

Input variable	Units	Minimum	Most likely	Maximum	Distribution
Surface area	(km ²)	2	3	6	Triangle
Thickness	(m)	1000	2500	2500	Triangle
Rock density	(kg/m ³)		2700		Fixed
Porosity	(%)	8	--	12	Uniform
Rock specific heat	(J/kg°C)		950		Fixed
Temperature	(°C)	240	260	360	Triangle
Fluid density	(kg/m ³)		900		Fixed
Fluid specific heat	(J/kg°C)		4200		Fixed
Recovery factor	(%)	5	15	20	Triangle
Conversion efficiency	(%)		12		Fixed
Plant life	(years)		30		Fixed
Rejection temperature	(°C)		150		Fixed

TABLE 4: Result of Monte Carlo simulation

Parameter	Units	Result
Most likely estimate		
Energy in place	(TJ)	2216
Total recoverable	(TJ)	332.5
Monte Carlo simulation		
Median electrical power	MWe	42
Mean electrical power	MWe	45
Standard deviation	MWe	20
90% above (<i>proven</i>)	MWe	23
90% below (<i>max. possible</i>)	MWe	73

7. NUMERICAL MODEL

7.1 Background

Numerical models are distributed models, where many variables are simulated to understand the dynamic nature of systems. By simulating the long term response of fields to exploitation, the models can be a very reliable means for modelling geothermal systems.

In numerical models, a conceptual model is relied upon to offer a general understanding of the nature, geometry and size of the system in question. It is important for this conceptual model to sufficiently incorporate all information, usually in many bits and pieces, as presented by various professional disciplines working in the field. The challenge is usually to unify the basic concepts into one single coherent understanding of the field. Each information-set may be found to be extremely important in providing constraints to numerical models. With a qualitative model, largely descriptive, the task and challenge of modelling is henceforth to transform this understanding into a mathematical model which is as close to reality as possible. It is seldom possible to describe the many minor details put into these models, but the main concepts are largely the target of this exercise.

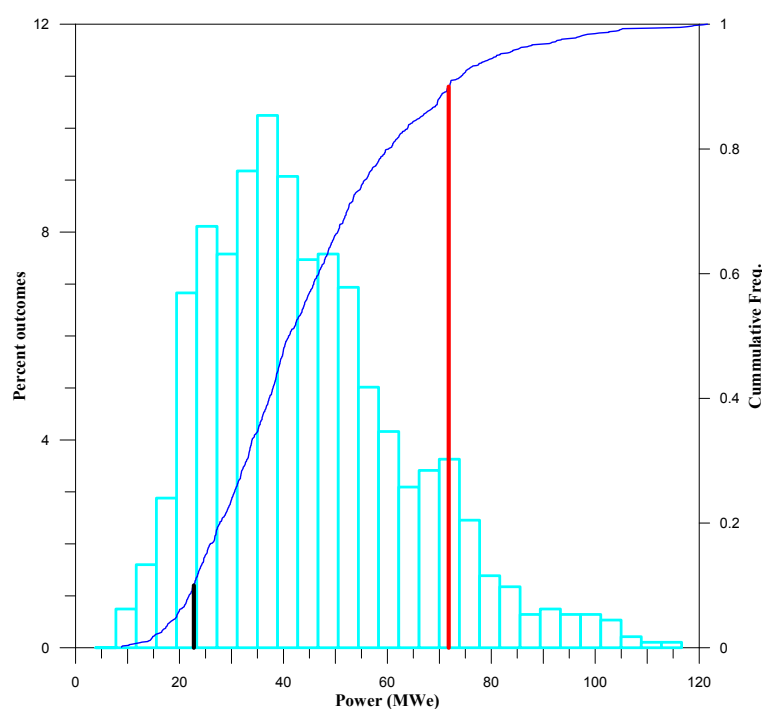


FIGURE 41: Probability distribution and cumulative probability for power output

A natural state model is developed to simulate the conditions prevailing in an area or reservoir before exploitation commences. Primary variables to fit into this simulation are the formation temperature and initial pressure data which are estimated from available temperature and pressure measurements. These data can sufficiently describe the important physical state qualities necessary for describing mass and energy fluxes and the balance in the reservoir. Variable data sets may be used here, as well, such as the

7.3 Initial conditions

Initial conditions were calculated for the permeability and heat conductivity allowed for each domain. Simulations were then run to obtain steady state conditions for each element. Initial temperature and pressure conditions observed in well measurements were matched quite closely in this model. Layer A (topmost layer) was initially assigned a temperature of 19.1°C and pressure 5 bar; based on a uniform thermal gradient of 80°C/km, temperature and pressure were assigned to all other layers as shown in Figure 43.

7.4 Natural state model

Fluid sources are located in elements in the vicinity of established intersecting structures known to control fluid movements. Mass sources are assigned strengths of between 5-10 kg/s and steady state conditions are calculated where changes in the primary variables are small on the time-scale of several thousand years. Fumarolic activity located in the vicinity of Ololbutot fault to the southeast margin of the field was simulated with a mass sink located in the vicinity of Well OW-1, discharging at -0.0001 kg/s at 2500 kJ/kg. The temperature distribution at depth was matched to the key qualities evaluated in the preceding analysis of pressure and temperature by

experimenting with different values for permeability and heat inflow to the system. The reservoir cap was set at about 1000 m a.s.l., where onset of convection was observed. The convective temperatures varied, relative to the well location with respect to the centre of the upflow. Well OW-802, for example, showed convection at about 320°C, while Well OW-804 showed convection at 280°C. On the other hand, Well OW-801, which is located outside this upflow, only reached around 200°C.

An equilibrated model returned the conditions shown in Figure 44 for element A178, located in the vicinity of Well OW-804, element A217 located near Well OW-802, and element A146 which is located near Well OW-801.

Figure 45 shows the modelled temperature distribution for Layer F (sea-level). High-temperature spots are seen in the northeast margins of the field where a NNE-SSW trending anomaly is mapped.

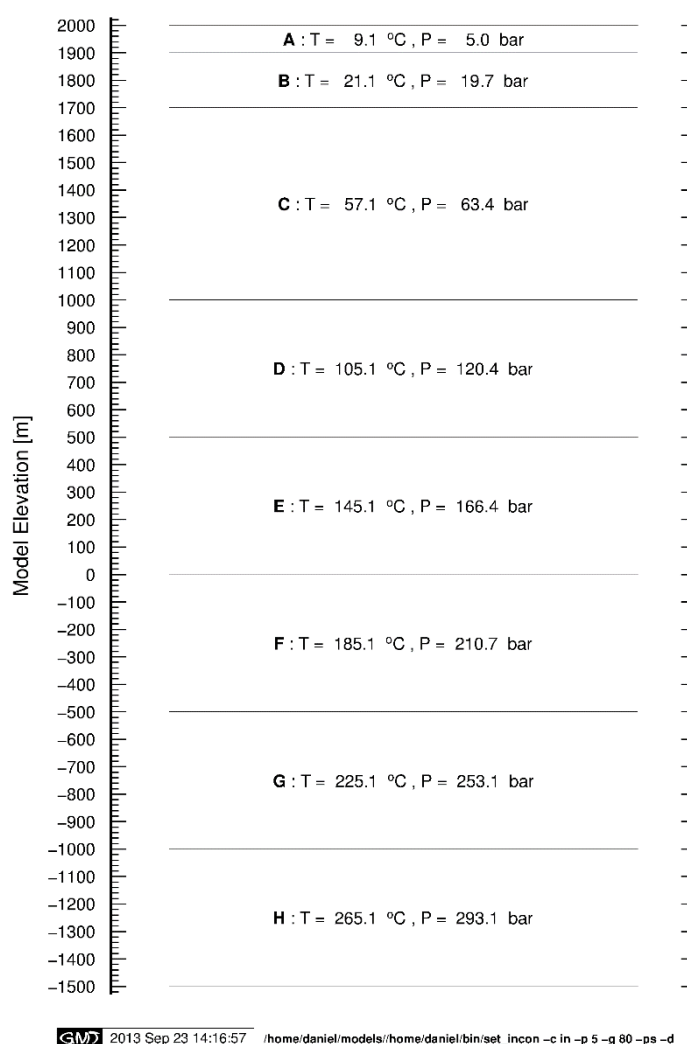


FIGURE 43: Vertical section of the grid showing initial conditions for each layer

Minor hot zones are also shown to exist in the northwest part of the field, aligned N-S and at the southwest margins. The fluid in this part of the field is associated with the Suswa fault zone and the ring fracture inferred by its close proximity.

8. CONCLUSIONS AND RECOMMENDATIONS

The Olkaria Southeast production field consists of an upflow zone located beneath Well OW-802, which domes to shallow depths at high temperatures and is aligned in a NE-SW fashion. The system is narrow and is highly structurally controlled. The region west of Well OW-803 is shown to be cooling and Wells OW-801 and OW-1 are outside the high-temperature geothermal system.

The reservoir is a homogeneous one with constant pressure boundaries, interpreted to be sustained by recharge from the main structures in the field. Contrary to earlier hypotheses, the geothermal system is not sustained by outflow from the Olkaria East field. On the contrary, it consists of an independent hydrological system controlled mainly from fluid moving from the south northwards, with NW-SE trending structure-dominated fluid movement at depths.

No localized and independent magmatic heat sources were interpreted for this system, but rather were associated with similar magma heat under Olkaria East field. Fluids travelling in the fractures present in the field encounter great heat at depth in the vicinity of the field and upwell at the intersections of grid faults located in the area. The hotter fluids are associated with the NW-SE trending structures passing through Ololbutot lava flow and cool away from it as permeability decreases. Cooler fluid is present in the NE-SW fault intersected by Wells OW-802A and OW-804A but contributes to significant convective zones in these wells.

Plausible drilling targets are along the NW-SE trending faults. This work shows another possible drilling target in the southwest margin of the field, immediately west of the Ololbutot fault. This location is thought to contain hot fluids associated with the Suswa fault zone and the ring fracture.

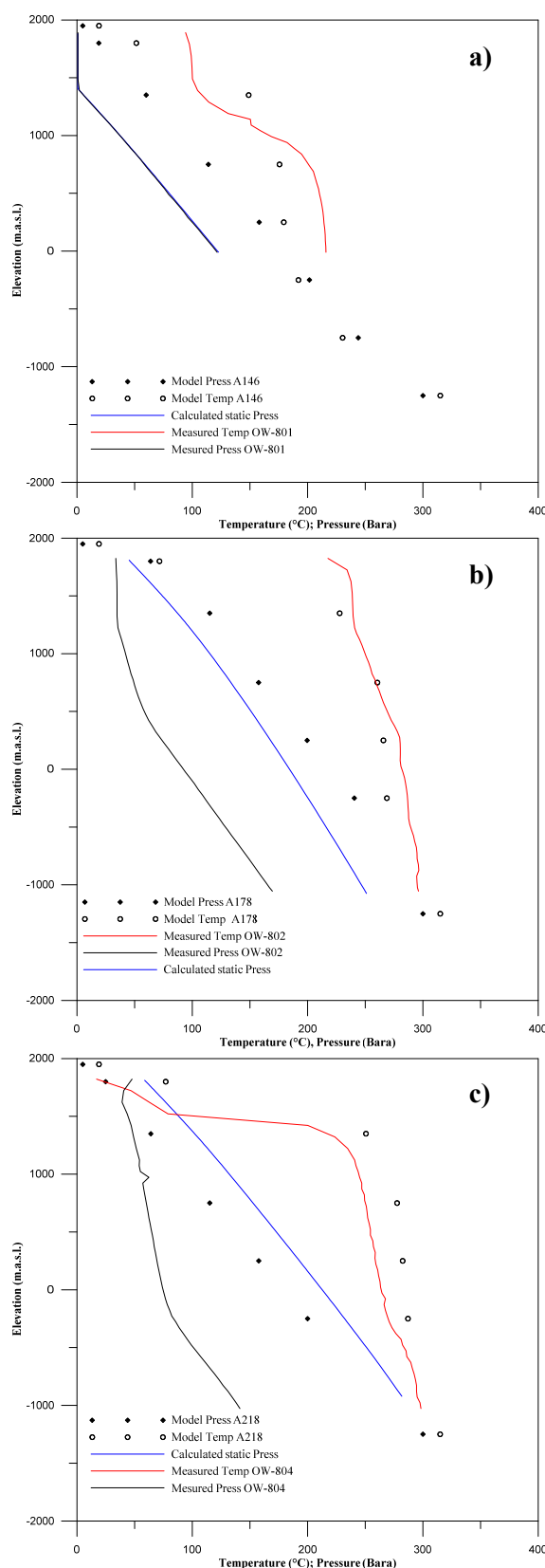


FIGURE 44: Match between well temperatures and pressure and vertical column through elements A146 (a), A178 b), and A218 (c) in the model

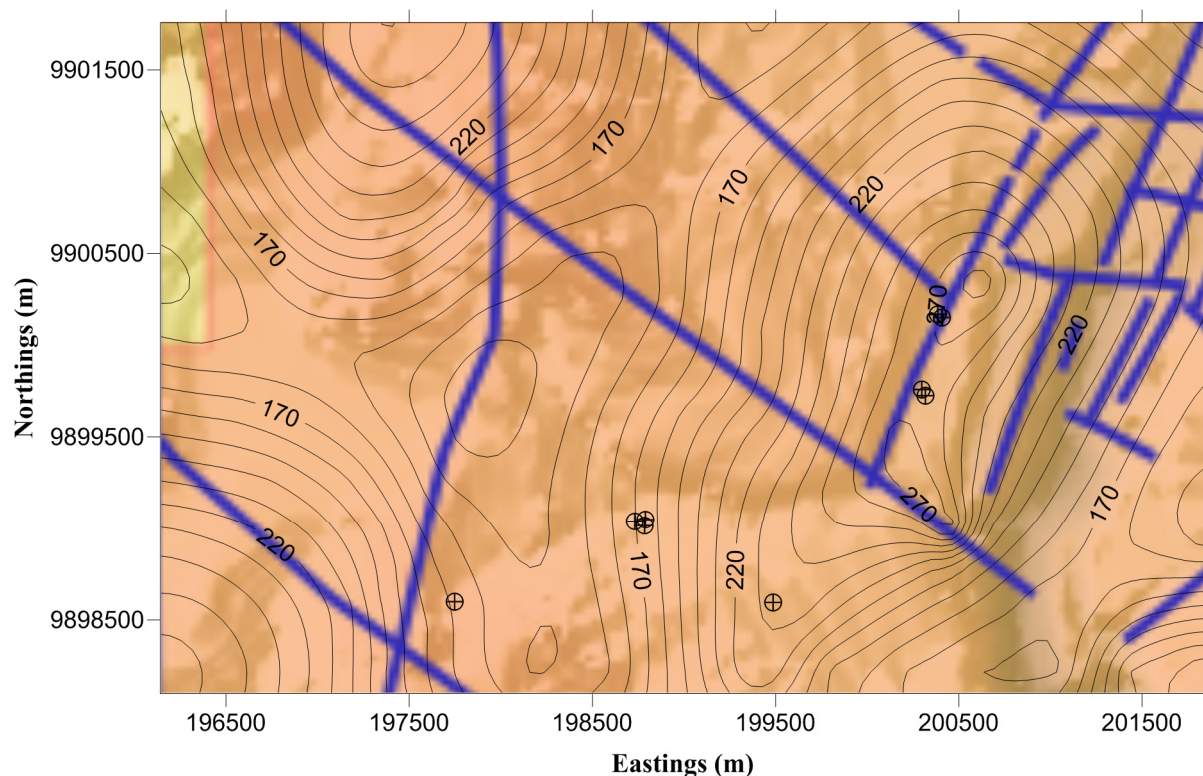


FIGURE 45: Model temperature contours at Layer F (sea level)

REFERENCES

Albright, J.N., 1976: A new and more accurate method for the direct measurement of earth temperature gradients in deep boreholes. *Proceedings of the 2nd United Nations Symposium on the Development and Use of Geothermal Resources, San Francisco*, 847-851.

Arason, Th., Björnsson, G., Axelsson, G., Bjarnason, J.Ö., and Helgason, P., 2004: *ICEBOX – geothermal reservoir engineering software for Windows. A user's manual*. ISOR – Iceland GeoSurvey, Reykjavík, report 2004/014, 80 pp.

Axelsson, G., and Gunnlaugsson, E., (convenors) 2000: *Long-term monitoring of high and low enthalpy fields under exploitation*. World Geothermal Congress 2000, Short Course, Kokonoe, Kyushu district, Japan, 226pp.

Björnsson, G., 1987: *A multi-feedzone geothermal wellbore simulator*. Lawrence Berkeley Laboratory, report LBL-23546, 8-19.

Brown, P.R.L., 1978: Hydrothermal alteration in active geothermal fields. *Annual Review in Earth and Planetary Sciences*, 6, 229-250.

Brown, P.R.L., 1984: Subsurface stratigraphy and alteration of the Eastern section of the Olkaria geothermal field, Kenya. *Proceedings of the 6th New Zealand Geothermal Workshop, University of Auckland, NZ*, 33-42.

Clarke, M.C.G., Woodhall, D.G., Allen, D., and Darling, G., 1990: *Geological, volcanological and hydrogeological controls of the occurrence of geothermal activity in the area surrounding Lake Naivasha, Kenya*. Ministry of Energy, Kenya and British Geological Survey, 138 pp.

Dowdle, W.L., and Cobb, W.M., 1975: Static formation temperature from well logs – an empirical method. *J. Petrol. Tech.*, 27, 1326-1330.

Grant, M.A., Donaldson, I.G., and Bixley, P.F., 1982: *Geothermal reservoir engineering*. Academic Press, New York, 369 pp.

Grant, M.A. and Bixley, P.F., 2011: *Geothermal reservoir engineering* (2nd ed.). Academic press, Burlington, USA, 359pp.

Horne, R.N., 1995: *Modern well test analysis, a computer aided approach* (2nd ed.). Petroway, Inc., USA, 257 pp.

Júlíusson, E., Grétarsson, G., Jónsson, P., 2007: *Well Tester 1.0b. User's guide*. ÍSOR – IcelandGeoSurvey, report 2008/063, 26 pp.

Mannvit/ÍSOR/Vatnaskil/Verkis Consortium, 2011: *Revision of the conceptual model of the Greater Olkaria geothermal system – Phase I*. Mannvit/ÍSOR/Vatnaskil/Verkís, Reykjavík, report, 100 pp.

Muchemi, G.G., 1998: Geothermal exploration in the Kenyan rift. In: Georgsson, L.S. (ed.), *Geothermal training in Iceland, 20th Anniversary Workshop 1998*. UNU-GTP, Iceland, 121-130.

Muchemi, G.G., 1999: *Conceptualised model of the Olkaria geothermal field*. The Kenya Electricity Generating Company, Ltd., internal report, 46 pp.

Omenda, P.A., 1998: *The geology and structural controls of the Olkaria geothermal system, Kenya*. *Geothermics*, 27-1, 55-74.

Orkiszewski, J., 1967: Predicting two-phase pressure drop in vertical pipe, *J. Petrol. Technol.*, 19, 829-838.

Ouma, P.A., 2009: Geothermal exploration and development of the Olkaria geothermal field. *Paper presented "Short Course IV on Exploration for Geothermal Resources"*, organized by UNU-GTP, GDC and KenGen, at Lake Naivasha, Kenya, 16 pp.

Pruess, K., Oldenburg, C., and Moridis, G., 1999: *TOUGH2, user's guidance version 2.0*. Lawrence Berkeley National Laboratory, 197 pp.

Reyes, A.G., 2000: *Petrology and mineral alteration in hydrothermal systems: from diagenesis to volcanic catastrophes*. UNU-GTP, Iceland, report 18-1998, 77 pp.

Sarmiento, Z.F., and Steingrímsson, B., 2011: Resource assessment I: introduction and volumetric assessment. *Paper presented at "Short Course on Geothermal Drilling, Resource Development and Power Plants, organized by UNU-GTP and LaGeo, in Santa Tecla, El Salvador*, 15 pp.

Simiyu, S.M., and Keller, G.R., 1999: Seismic monitoring of the Olkaria geothermal area, Kenya Rift Valley. *J. Volcanology & Geothermal Research*, 95, 197-208.

Takai, K., Hyodo, M., and Takasugi, S., 1994: Estimation of equilibrium formation temperature by curve-fitting method and its problems. *Proceedings of the 19th Workshop on Geothermal Reservoir Engineering*. Stanford University, Stanford, Ca, 65-73.

West JEC, 2009: *Olkaria optimization study (phase II). Final report*. West JEC, report made for KenGen, 64pp.



**UNITED NATIONS
UNIVERSITY**

GEOTHERMAL TRAINING PROGRAMME
Orkustofnun, Grensasvegur 9,
IS-108 Reykjavik, Iceland

Reports 2013
Number 34

DESIGN OF A COOLING SYSTEM FOR STORAGE OF AGRICULTURAL PRODUCTS WITH EMPHASIS ON IRISH POTATOES

Jane Uwera

Ministry of Infrastructure
EWSA – Energy, Water and Sanitation Authority
P.O. Box 537
Kigali
RWANDA
kamanzijn@yahoo.com

ABSTRACT

This project focuses on the design of a cooling system for storage of agricultural products. It compares the efficiency of a vapour compression cycle powered by electricity from a binary geothermal power plant, and an absorption refrigeration unit which uses a geothermal heat source to drive the absorption cycle in a chilling process, both in a 25°C environment with a compartment temperature of 5°C. These two cycles are to provide the same cooling to the cold storage with a heat load equivalent to 140 kW. The parameters that were mainly monitored for comparison are COP, the power required to run the cycles, and the required mass flow of a geothermal fluid. After mathematical and thermodynamic analysis of the cycles, it was found that the overall efficiency of a binary plant coupled to the compression refrigeration is a bit low, or 0.432, as it must include both the thermal efficiency of the plant and the COP of the compression cycle, and that of the absorption refrigeration cycle is 0.471, but can go as high as 0.6 when a heat exchanger is used.

1. INTRODUCTION

Geothermal energy is a sustainable form of energy that can be used directly as heat or indirectly by conversion to other forms of energy. The method of its utilization is highly dependent on thermodynamic properties and the fluid chemistry. The high temperature resources are mainly used for power generation while the lower temperature resources can be used partially for power generation and other direct use applications. Geothermal resources in the range of 80-150°C can preferably be used to power the heat driven processes, such as cooling systems, and in absorption refrigeration system which uses thermal energy as the heat source. Resources within this temperature range are probable to be found in Rwanda's geothermal fields. Karisimbi, which began drilling activities recently, is one of them.

Rwanda is an East African country located along the Western Branch of the East African Rift system with a surface area of 26,338 km² and a population estimate of 11 million inhabitants (NISR, 2012). Rwanda is an agricultural country with about 90% of the population engaged in subsistence agriculture, with few natural resources. The primary foreign exports are tea and coffee, while tourism is the third

largest source of foreign exchange. Irish potatoes are the most common food crop produced on large scale in the Northern Province where most of Rwanda's geothermal fields are located.

The term refrigeration refers to cooling of an area or a substance below the environmental temperature, and therefore involves the process of removing heat. Mechanical refrigeration uses the evaporation of a liquid refrigerant to absorb heat. The refrigerant goes through a cycle so that it can be re-used. The main cycles include vapour-compression, absorption, steam-jet of steam ejector, and air.

This report discusses the design of a cooling system for storage of agricultural products using geothermal energy, with a case study on the Karisimbi geothermal field, Rwanda.

1.1 Objective of the study

The purpose of this study is to assess two different refrigeration processes and model the systems by analysing the thermodynamic properties of the working fluids and setting up the cooling units. There are two well-known refrigeration systems which are vapour compression and vapour absorption cycles. Comparison of the performance of these two systems will be observed, operating from a proposed geothermal heat source. The vapour compression cycle will be integrated with a binary power plant for the supply of electricity to run the compressor motors while the vapour absorption cycle will be powered by the typical geothermal heat source.

2. GEOTHERMAL IN RWANDA

2.1 Geological and structural settings

Rwanda hosts two prospective areas: the National Volcanoes Park and the faults associated with the East African Rift near Lake Kivu. The National Volcanoes Park was identified as a potential host for large, high-temperature geothermal systems, while the rift provides an environment for small, low-to moderate-temperature resources. The current study involves the northwest part of Rwanda that includes the National Volcanoes Park. The main structural trends of this area are controlled by the older basement structures. The Nyiragongo volcano to the west of the area has been erupting periodically. This signifies that a heat source for a geothermal system could exist around the major volcanoes. The area of exploration is between Nyiragongo volcano to the west, Muhabura volcano to the east and Gisenyi to the south. The major structural trends, as summarized by the German Institute of Geosciences and Natural Resources (BGR, 2009), show that the older rift border faults have a predominantly northwesterly trend while the younger eastern rift border faults have a northeasterly trend. Other important structures include an accommodation zone, which marks the boundary between the basement rocks and volcanic rocks. It is anticipated that this structural pattern is probably buried below the younger volcanic rocks (Onacha, 2008).

2.2 Geothermal fields

The geothermal areas in the western region cover an area of about 900 km² and it has been further subdivided into the three regions of Karisimbi, Gisenyi and Kinigi. The Karisimbi geothermal prospect is found on the southern slopes of the Karisimbi Volcano. Karisimbi field is part of the National Volcanoes Park. No geothermal manifestations such as fumaroles or alteration have been reported in this area. However, a couple of hot springs are located south and out of the volcanic field, as shown in Table 1, with the highest temperature of 64°C at Karago (located in the southern part of Karisimbi geothermal prospect).

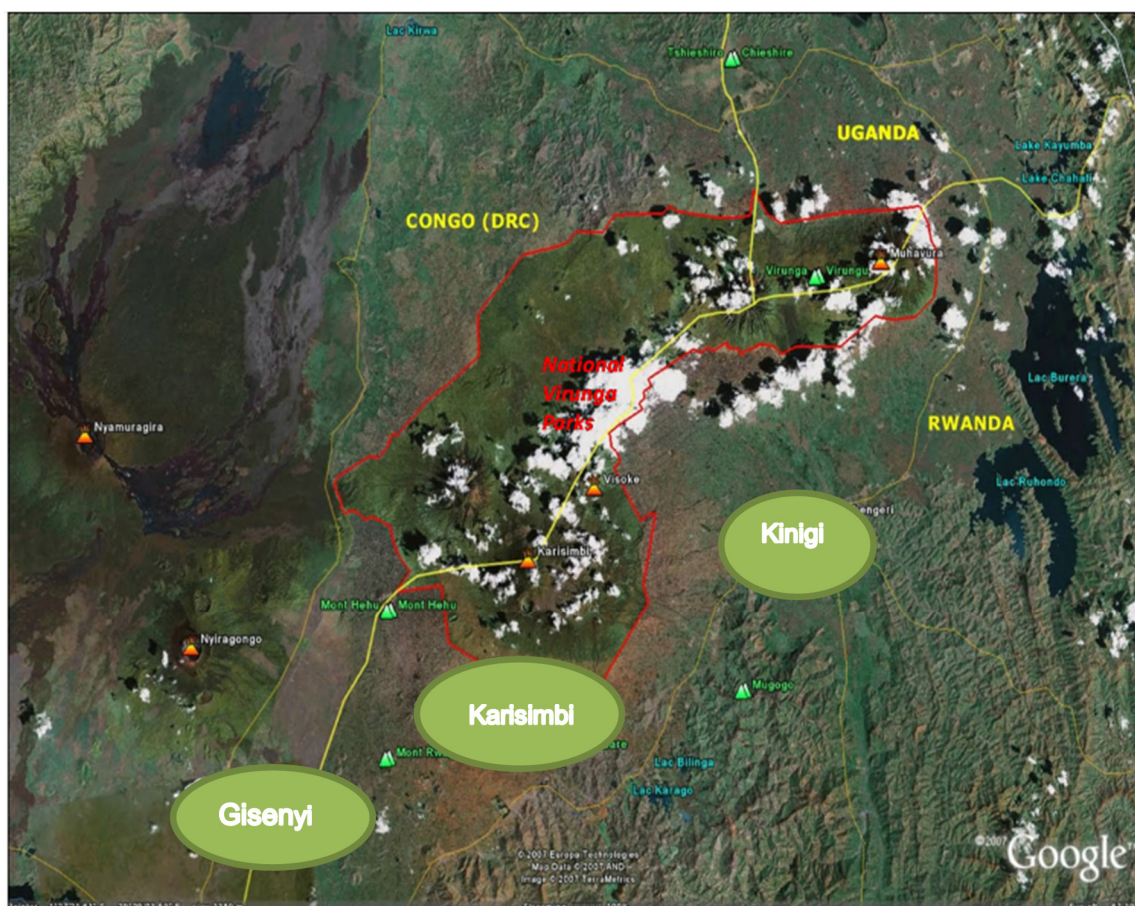


FIGURE 1: Map showing the geothermal fields in northwest Rwanda (modified from Namugize, 2011)

2.3 Karisimbi geothermal field

Karisimbi geothermal field is situated in the western province and occupies an area of about 200 km². The prospect lies to the south of the National Volcanoes Park (NVP). This area has very fertile soils suitable for agricultural activities, with a heavy downpour and an annual rainfall average of 800 mm. The proposed sites for exploration drilling are found to the north of Mukamira. The calculated temperature ranges from the geothermometers are very low (Table 1), probably due to the nephelinites absorbing silicate hot springs which produce sodium bicarbonate water with temperature between 70-75°C. The flow rates from all the vents are estimated to be 2-5 kg/s and are controlled by fractures. It is postulated that some of the vents could be buried below the lake's surface. Based on fluid geothermometers, the reservoir temperature is estimated to be between 150 and 210°C. (Newell et al., 2006; BGR, 2009).

TABLE 1: Surface temperatures and calculated temperature based on fluid chemistry

Location	Surface temp. (°C)	Quartz temp. (°C)	Na/K temp. (°C)	Temperature range (°C)
Karago	64	126	147	120-140
Gisenyi	70-72	107	175	105-210

Figure 2 shows the expected weather conditions in Karisimbi.

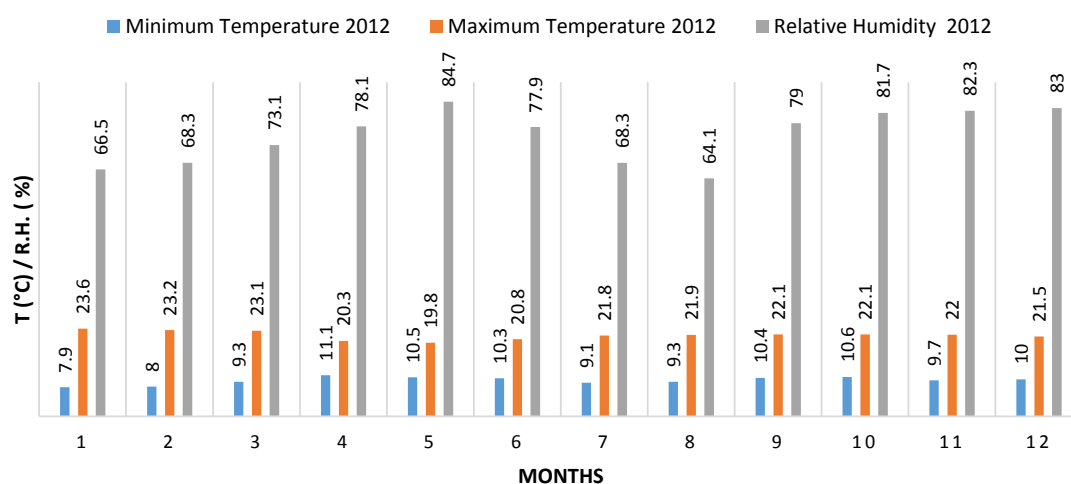


FIGURE 2: Weather conditions in Karisimbi in 2012 on a monthly basis

2.4 Geothermal utilization and direct use opportunities

The Government of Rwanda (GoR), through the Ministry of Infrastructure (MinInfra) and the newly formed Electricity Water and Sanitation Authority (EWSA), has plans to explore and develop over 300 MWe from geothermal resources by 2017. The immediate goal is the establishment of the viability of the geothermal resources by drilling wells in one of the geothermal prospects. Drilling operations for the three first exploration wells are now ongoing and the next three prospects will follow immediately. Rwanda has identified four geothermal prospects; once drilling is successful, the immediate plan is the connection of wellhead generating units for early power generation and feasibility studies for direct use applications of geothermal energy. The GoR also intends to develop direct utilization of geothermal resources in the agricultural sector using greenhouses, and drying rice and fish. Other direct uses will include the uses of geothermal heat in pyrethrum processing and for drying tea and coffee. Geothermal energy could also be used in industrial processes such as mineral processing and cooling systems applications (Onacha, 2011).

3. CASE STUDY ON IRISH POTATOES

3.1 Irish potatoes value chain in Rwanda

The potato has become an important food crop in Rwanda with about 133,000 hectares under cultivation; more than 1 million metric tonnes (MT) of potatoes are produced annually (Agri, 2012). The Irish potato requires a relatively cool and moist climate to achieve the best results. Musanze, Burera, Gicumbi and Nyabihu districts account for 90% of the national potato production in Rwanda. A significant portion of the Irish potatoes produced are consumed in the areas of production and there is no potato storage or processing in Rwanda yet. Most potatoes are transported to the markets almost immediately after harvest, generally unwashed in large bags. In most cases, the farmer does not know the price he will receive for his potatoes before reaching the main market; this becomes a challenge for them in terms of marketing and economic planning. The potato production and selling prices are summarized in Table 2.

TABLE 2: Potato production cost and selling prices in Rwanda

Potato	Size and units	Value
Production cost	USD/ha	1,068-2,595
Selling price	USD/kg	0.099-0.46
Average production cost	USD/kg	0.13
Average yield	kg/ha	9,400
Average crop value	USD/ha	1,277

3.2 Potato growing seasons

There are basically two seasons (A and B) for potato growing in Rwanda, as shown in Figure 3, with the first season (A) extending from September to December and the second season (B) extending from February to May.

Potato Season A									Pl.	Growing		H
Potato Season B		Pl.	Growing		H							
	J	F	M	A	M	J	J	A	S	O	N	D

FIGURE 3: Potato growing seasons in Rwanda; **Pl** stands for planting, and **H** for harvesting

3.3 Statement of the problem and need for the study

The potato production cycle in Rwanda is quite short, about 3-4 months, and follows two main growing seasons (Figure3), however, in some regions it is possible to extend the growing cycle beyond those seasons if sufficient moisture is available in the soil. The lack of storage and processing facilities makes it necessary for Rwandan potato farmers to sell their produce almost as soon as it is harvested; this is the current weakness of the Rwanda potato sector. The big challenge is the lack of storage facilities for their produce on a large scale and leads to the immediate sale of most of the harvest to neighbouring countries like Burundi and others at low prices. Yet, if they had some storage facilities, potatoes could be stored for some time and sold at competitive prices.

3.4 Potato storage conditions

3.4.1 Mid and long-term storage

The objective of long-term storage is to maintain a consistent, ideal environment for the duration of the storage period. Long-term storage demands more critical control than short-term storage. Recommended storage temperatures depend upon crop condition, variety and intended end use. General recommendations for storage temperatures are listed in Table 3.

TABLE 3: Potential storage duration of potatoes

Potatoes	Temperature (°C)	RH (%)	Potential storage duration
Fresh market	4-7	95-98	10 months
Processing	8-12	95-98	10 months
Seeds	0-2	95-98	10 months

3.4.2 Storage design parameters and related heat load calculations

It is desired to design a cooling system for storage of agricultural products with an emphasis on potatoes. This storage is proposed to be built in the northern province of the country in the Musanze district near most of the geothermal fields in Rwanda, in order to make use of the geothermal heat. It has a capacity for storing 312 tonnes of potatoes, using wooden storage bins. The other detailed dimensions and conditions are summarized in the tables below along with the related refrigeration load calculations.

3.4.3 Refrigerated cold storage

Figure 4 shows the location of a cooling unit in the cold storage, together with the proposed wooden storage bins (Figure 5).

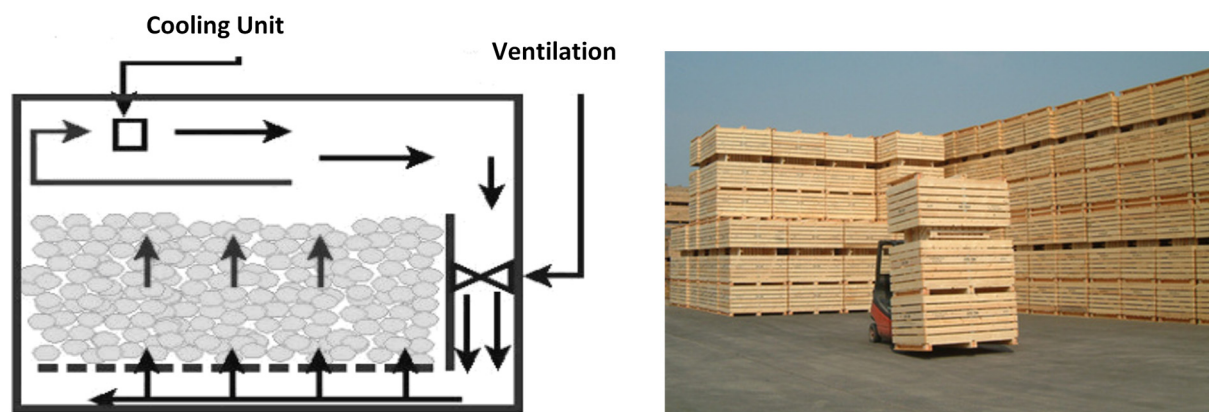


FIGURE 4: Cooling unit connected to cold store and proposed 1000 kg storage bins (PalletLink, 2013)

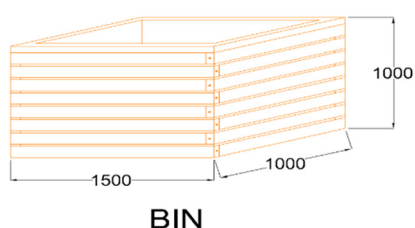


FIGURE 5: A potato storage bin

3.4.4 Wooden storage bins

The storage bins under this design (Figure 5) are made of cypress timber. The major advantages of wooden bins are low cost, superior strength, and having been the industrial standard for a long time. Wood bin kits are produced and assembled locally which minimizes transportation cost from manufacturer to end users. Their dimensions are summarized in Table 4.

TABLE 4: Wooden bin details

Wooden storage bins	Units	Value
Number of bins	Piece	312
Bin dimensions	m	L=1.5 ,W=1, H=1
Bin weight	kg	90
Total weight of bins	kg	28,080
Storage capacity of the bin	kg	1000
Specific heat of the bin	kJ/kg°C	0.5

3.4.5 Dimensions for potatoes cold storage

Many different things must be considered while planning the construction of cold warehousing facilities and it requires an enormous degree of precision and attention to details. One of the most important things to consider is which concrete floor to use. Not all concrete floors are made alike, and there are many different methods that can be used to install them. The chilled room must also consider the sealing system which best fits the needs of the cold storage and the corresponding concrete walls and roof. Homogeneous insulation is assumed. Enough space must be left above the storage bins for lights and other cooling system ducts. Table 5 shows the details of the cold room.

3.4.6 Description of storage construction materials and insulation

The insulation materials used are wood fibre, which includes residue and waste wood to produce a suitable low density wood fibre board which is easy, safe to work with and cost-effective. It is designed

to be used inside the building as it offers additional insulation when used in interior walls, floors and ceilings. Wood fibre insulation can absorb moisture and has high vapour diffusion capabilities, allowing the panels to act as a breathable structure. This helps to improve the indoor air quality by absorbing and releasing heat back later when the temperature decreases (see Figure 6 and Table 6 for working and storage conditions).

TABLE 5: Details of the cold room for potato storage

Potatoes	Units	Quantity
Storage capacity	bins	312
Store dimensions	m	L=25, W=16, H=5.5
Volume (V)	m ³	2,200
Surface area including the floor (A)	m ²	1,294
Temperature difference, ΔT	(°C)	20
Specific heat of potatoes	kJ/kg°C	0.82
Rate of respiration	W/kg	0.028
Overall coefficient of transmission	W/m ² °C	1.6

TABLE 6: Working conditions and assumptions for the design system; uniform insulation is assumed on the walls, ceiling and floor

Loading weight and time:	104 bins (104,000 kg of potatoes); 3 days to fill		
Cooling rate:	1 st day, 20 to 10°C; 2 nd day, 10 to 5°C		
Air changes from door opening during cooling	times per day	6	
Air changes from door opening during storage °C	times per day	1.8	
Heat load to lower air from 20 (90% RH) to 10°C (95% RH)	kW/m ³	0.45	
Heat load to lower air from 10 to 5°C (95% RH)	kW/m ³	0.087	

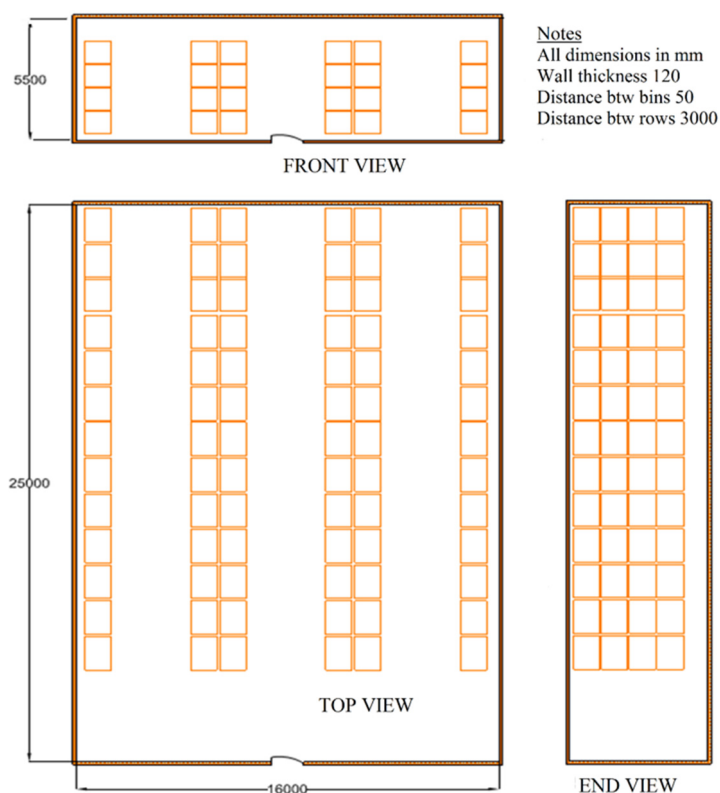


FIGURE 6: Overview of the bins in the chilled room

3.4.7 Storage heat load calculations

Heat load determination. The total heat load consists of the amount of heat to be removed from the refrigerated room during a certain period. It is dependent on two main factors: heat leakage or heat transfer load, and heat usage or service load, respectively. Thus, the following types of heat loads were considered in the design of this cold room.

Building transmission load. The building transmission load is the total amount of heat that leaks through the walls, windows, ceiling, and floor of the refrigerated room per unit of time (usually kW or kJ/s). Heat leakage, therefore, is affected by the amount of the exposed surface, thickness and the kind of insulation used, and the temperature difference between the inside and the outside of the refrigerated room. Thus, it is the heat transfer from the outside into the refrigerating space via the insulated walls of the refrigerator:

$$\text{Building transmission load} = A * U * \Delta T \quad (1)$$

where A = The outer surface area of the building (m^2);
 U = The overall coefficient of transmission ($\text{W}/\text{m}^2\text{°C}$); and
 ΔT = The temperature difference (°C).

Air change heat load. Air that enters a refrigerated space must be cooled. Air needs to be renewed, and consequently there is a need for ventilation. When air enters the refrigerated space, heat must be removed from it. Air which enters the refrigerated space usually cools and reduces in pressure. If the refrigerated room is not air tight, air will continue to leak in. Also, each time a service door or walk-in door is opened, the cold air inside, being heavier, will spill out the bottom of the opening, allowing the warmer room air to move into the refrigerated room. The actions of moving materials in or out of the refrigerated room, and a person going into or leaving the refrigerated room, result in warm air moving into the refrigerated space through the process of air infiltration. Hence, the air change heat load is the heat transfer due to closing and opening of the refrigerator doors and subsequent changes in the air-heat content in the refrigerated space.

$$ACL = V_s * \rho(h_o - h_i) * ACD \quad (2)$$

where ACL = Air change load due to door opening, infiltration and ventilation etc. (kW);
 V_s = Volume of the cold room (m^3);
 h = Enthalpy of air (kJ/kg);
 ρ = Density of air (kg/m^3);
 ACD = Air change per day, number of times; and
 Subscripts o and i denote out and in, respectively.

Miscellaneous heat loads. All sources of heat not covered by leakage, product cooling, and respiration load are usually listed as miscellaneous loads. Some of the more common miscellaneous loads are lights, electric motors and people. These are small loads estimated to be 4,4 kW in total.

Product heat load. Any substance that is warmer than the refrigerator is placed where it will lose heat until it cools to refrigerator temperature. Respiration heat is the heat given off by living things, especially plant products, in this case potatoes. Potato tubers from immature lands are susceptible to bruising and skinning which can have high respiration rates. The use of a cooler temperature and/or higher air inflow is an effective method for improving their conservation. The respiration rate of potatoes is shown in table 7 (Trevor et al., 2013).

TABLE 7: Heat load calculations

Temperature (°C)	ml CO_2 /kg·h	Average respiration rate (W/kg)
5	6-8	0.000336
10	7-11	0.000432
15	7-16	0.000552
20	9-23	0.000768

$$PHL = W * c_p * \Delta T/t \quad (3)$$

where PHL = The product heat load (kW);
 W = The potato weight (kg); and
 c_p = The specific heat of potatoes (kJ/kg °C).

3.5 Heat usage load

The heat usage or service load is the sum of the following heat loads per unit of time: cooling the content of the refrigerated room temperature, cooling of air changes, removing respiration heat from potatoes, removing heat released by electric lights, electric motors, and the like, and heat given off by people entering and/or working in the refrigerated room. Usage, or the service load of the refrigerated room, was determined by the temperature of the articles that were put into the refrigerator, their specific heat, generated heat, and latent heat as the requirement demanded. Another consideration is the nature of the

service required. This involved air changes (determined by number of times per day that the doors of the refrigerator would be opened) and the heat generated inside by fans, lights and other electrical devices.

Heat load calculations are divided into two cases: consideration of the peak refrigeration load, especially in filling up and emptying the store, and consideration of the heat load when the room has attained the room storage temperature.

3.5.1 Scenario A (peak refrigeration)

The storage room took 3 days to fill and the temperature was reduced as shown in Table 8 to reach storage room temperature (20-10-5°C).

TABLE 8: Peak refrigeration load capacity

Parameter	Value (kW)
Building transmission load	11.5
Air change load from door openings	10.2
Product cooling	71.2
Miscellaneous heat loads	4.4
Heat of respiration during cooling potatoes	24.5
Maximum heat accumulated in storage before cooling completed	4.9
Subtotal	126.7
Design margin (10%)	12.6
Total required refrigeration	140

The total heat load calculated for the chilled room is 140 kW.

3.5.2 Scenario B (Storage temperature)

The total refrigeration for a completely chilled storage room is 34 kW as shown in Table 9.

TABLE 9: Storage temperature refrigeration load capacity

Parameter	Value (kW)
Building transmission load	11.6
Air change load from door openings	3
Miscellaneous heat loads	4.4
Respiration rate	12
Subtotal	31
Design margin 10%	3.1
Total required refrigeration	34

Scenario A (peak refrigeration) operates at 140 kW while scenario B needs 34 kW, which is the load after the room has reached a constant temperature.

4. THEORY OF REFRIGERATION SYSTEMS

A refrigeration is a process of removing heat from one location, mainly in a confined space, and rejecting the unwanted heat into a specific preferable environment; in other words, the refrigeration process is a

method for lowering the temperature of an object. There are two common refrigeration systems that are widely used: vapour Absorption Refrigeration Systems (ARS) and vapour Compression Refrigeration (CR) systems. This project will mainly focus on the comparison between these two cycles by evaluating their efficiency (Table 10).

TABLE 10: Absorption system compared to compression system

	Absorption	Compression
A	Uses low-grade energy like heat. Therefore may be worked on exhaust system from I.C. engines, etc.	Uses high-grade energy like mechanical work
B	Moving parts are only in pump which is a small element of the system. Hence operation is smooth.	Moving parts are in compressor, therefore, more wear, tear and noise
C	The system can work on lower evaporator pressures also without affecting the COP	The COP decreases considerably with decrease in evaporator pressure
D	No effect of reducing the load on performance	Performance is adversely affected at partial-loads
E	Liquid traces of refrigeration present in piping at the exit of evaporator constitute no danger	Liquid traces in suction line may damage the compressor
F	Automatic operation for controlling the capacity is easy	Is difficult

4.1 Vapour absorption cycle

Absorption refrigeration systems are much like vapour compression cycles but the compressor is replaced by a generator and the absorber (Figure 7). Refrigerant enters the evaporator in the form of a cool, low-pressure mixture of liquid and vapour (4). Heat is transferred from the relatively warm water to the refrigerant, causing the liquid refrigerant to boil. The absorber draws in the refrigerant vapour (1) to mix with the absorbent. The pump pushes the mixture of refrigerant and absorbent up to the high pressure side of the system. The generator delivers the refrigerant vapour (2) to the rest of the system. The refrigerant vapour (2) leaving the generator enters the condenser, where heat is transferred to water at lower temperature, causing the refrigerant vapour to condense into a liquid. This liquid refrigerant (3) then flows to the expansion device, which creates a pressure drop that reduces the pressure of the refrigerant to that of the evaporator. The resulting mixture of liquid and vapour refrigerant (4) travels to the evaporator to repeat the cycle.

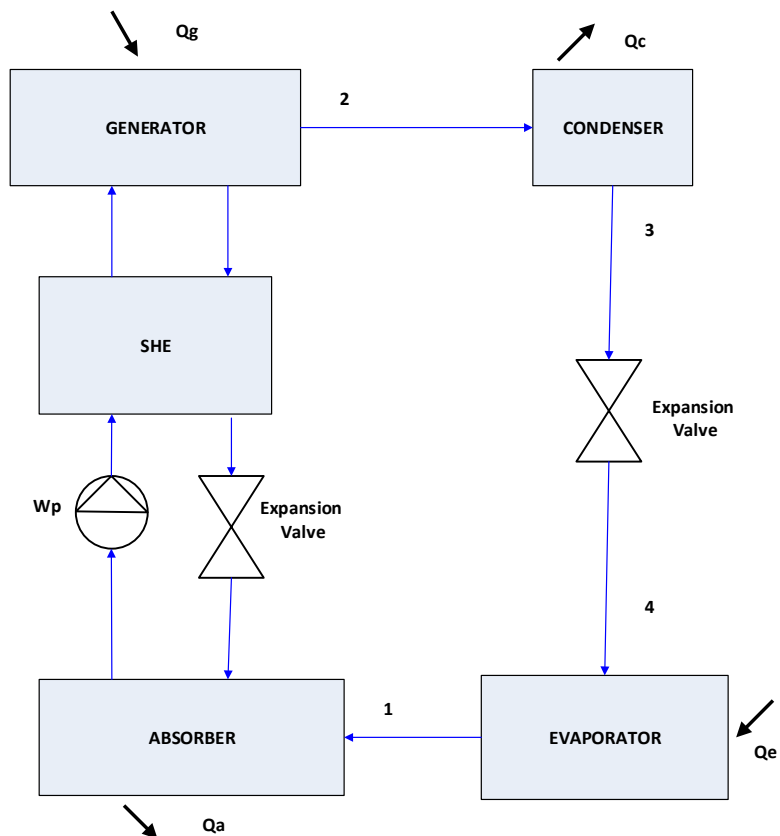


FIGURE 7: Schematic diagram of a simple absorption refrigeration system

4.1.1 Principle of operation

The most common principle of operation for a simple absorption system is based on principles first developed by the French scientist Ferdinand Carré (about 1860). More details on absorption systems were given by Nibergall (1959), Bäckström (1970) and ASHRAE (1996). As a vapour compression system, an absorption system of this type consists of the following components (Figure 8):

Condenser	Where the refrigerant is condensed to liquid
Expansion valve	Where the pressure of the refrigerant liquid is reduced from condensing pressure to the pressure in the evaporator
Evaporator	Where the refrigerant evaporates, for which process heat is supplied – from the compartment/room to be cooled

Instead of a mechanically operated compressor in the vapour compression cycle, the absorption system has a “thermal compressor” involving the following components:

Absorber	Where the refrigerant vapour is absorbed, and forms a <i>liquid</i> solution. During this process, heat is released, which means that the absorber must be cooled. The heat released is equivalent to the heat of condensation plus a heat of solution (or mixing) pertinent to the combination of refrigeration and the absorption medium.
Pump	By which the solution leaving the absorber is given a pressure equivalent to the pressure in the generator (same as in the condenser).
Generator	Where the refrigerant is separated from the solution by a distillation process. In a simple case, this is done by just “boiling” off the refrigerant from the solution. Heat (equal to the operating energy of the system) must be supplied for this process.
Regulating valve	Where the “poor” solution from the generator is passing on its way from the generator to the absorber. The valve is necessary since the pressures in these two components are different.

In order to decrease the demand for operating heat, and thus improve the efficiency, it is beneficial to use a heat exchanger, where heat is recovered from the hot “poor” solution leaving the generator, and used for preheating the “rich” solution from the absorber before it enters the generator.

4.1.2 System efficiency and coefficient of performance

Efficiencies of absorption chillers are described in terms of coefficient of performance (COP), which is defined as the refrigeration effect divided by the net heat input. Single-effect absorption chillers have COPs of approximately 0.6-0.8 out of an ideal 1.0. Since the COPs are less than one, the single-effect chillers are normally used in applications that recover waste heat, such as waste steam from power plants or boilers. Double-effect absorption chillers have COPs of approximately 1.0 out of an ideal 2.0. While not yet commercially available, prototype triple effect absorption chillers have calculated COPs of 1.4 to 1.6 (Southern California Gas Company New Buildings Institute, 1998).

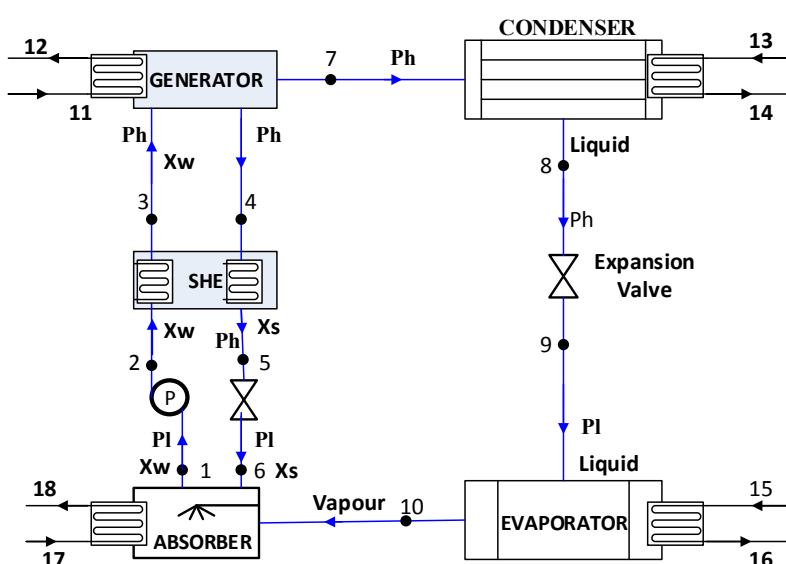


FIGURE 8: NH₃-H₂O absorption refrigeration system

Compared with mechanical chillers, absorption systems have a low coefficient of performance. However, absorption chillers can substantially reduce operating costs because they are powered by low-grade waste heat.

It is recommended to use a solution heat exchanger in absorption systems as it allows the solution from the absorber to be preheated before entering the generator by using the heat from the hot solution leaving the generator. Therefore, the COP is improved as the heat input at the generator is reduced.

Moreover, the size of the absorber can be reduced as less heat is rejected. Experimental studies show that the COP can be increased up to 0.6 when a solution heat exchanger is used.

The temperature of the heat source is the most important factor in the thermal efficiency of an absorption chiller. The higher the temperature of the heat source, the better the COP. Also, the efficiency of an absorption machine quickly deteriorates as soon as the temperature of the heat source drops below the design figure.

Efficiency of an absorption refrigeration system can be expressed by the coefficient of performance (COP), which is defined as the ratio between the amounts of heat/energy absorbed from the environment by the evaporator and the heat/energy supplied to the generator to operate the cycle.

$$COP = \frac{\text{Cooling capacity } (Q_e)}{\text{Heat used to drive the chiller } (Q_g)} \quad (4)$$

4.1.3 Working media

There are several refrigerant compounds that are usually used in refrigeration systems, but the most common are $\text{H}_2\text{O}/\text{NH}_3$ and $\text{LiBr}/\text{H}_2\text{O}$. $\text{LiBr}/\text{H}_2\text{O}$ is mainly used in cooling/air conditioning applications where the temperature goes as low as 0°C . $\text{LiBr}/\text{H}_2\text{O}$ is then used as the absorbent, and water as the refrigerant (Ratlamwala et al., 2012).

Aqueous Lithium Bromide is a salt solution substance where the salt component will start to precipitate when the mass fraction of the salt exceeds the maximum allowable solution solubility. Since the temperature and the mass fraction of the solution impact the solution solubility more than the pressure, these two components will affect the crystallization process significantly. Most of the available literature (e.g. ASHRAE Handbook of Fundamentals etc.) provides crystallization behaviour down to only 10°C . The typical evaporating temperature for an absorption chiller system is usually lower than 10°C . Hence, it is essential to have an accurate prediction of the crystallization temperature in this range during the design phase in order to avoid crystallization.

In the $\text{H}_2\text{O}/\text{NH}_3$ solution, NH_3 is the refrigerant in the mixture. It has a freezing point of -77°C and has high latent heat from vaporization. In this report, $\text{H}_2\text{O}/\text{NH}_3$ is used for absorption cycle applications as it has a low freezing point, and is low in cost (Srikhirin et al., 2001).

Ammonia is toxic, gaseous, an irritant, and is corrosive to copper alloys. With an ammonia refrigerant, the ever present risk of an escape brings with it a risk to life. However, data on ammonia escapes have shown this to be an extremely small risk in practice; consequently, there is no control on the use of ammonia refrigeration in densely populated areas and buildings in almost all jurisdictions in the world. However, in most cases, a secondary circuit with glycol to transport heat from the cooled storage to the working fluid is employed, so that leakages will not come in contact with the stored goods.

Due to the working principle of the absorption refrigeration cycle a pair of media is needed. The traditional combination is the pairing of ammonia and water, the ammonia being the refrigerant and water the absorption medium. The essential reasons for why this pair is suitable to use are the facts that ammonia is a good refrigerant and that the saturation vapour pressure of ammonia in a water solution is

considerably lower than that of pure ammonia (refer to Appendix I, Figure 1). The pairing of ammonia and water has interesting thermodynamic properties: both fluids have good heat transfer characteristics. One drawback, however, is that the vapour formed in the generator contains not only ammonia, but also, to certain extent, water vapour. In order to decrease the water content in the refrigerant, a “water separator”, or rectifier, is installed along with the generator. In large plants, the generator is designed as a distillation column.

4.1.4 Necessary conditions for the selection of working fluids

The performance of the cycle depends mainly on the chemical and thermodynamic properties of the working fluids. The following elements influence the performance of the working fluid:

- Refrigerant should have high vaporization heat, and a high concentration within the absorbent in order to maintain a low circulation rate between the generator and the absorber per unit of cooling capacity;
- It is recommended that the fluid be chemically stable, non-toxic and non-explosive;
- The liquid phase must have a margin of miscibility within the operating temperature range of the cycle;
- The difference in boiling temperature between the pure refrigerant and the mixture at the same pressure should be as large as possible;
- Properties such as viscosity, thermal conductivity, and the diffusion coefficient should be taken into account; and
- Refrigerant and absorbent should be non-corrosive, environmental friendly and low in cost.

4.1.5 Thermodynamic analysis of the system

A schematic of a typical water–ammonia absorption refrigeration system is illustrated in Figure 8. The system includes a generator, absorber, condenser, evaporator, and a solution heat exchanger. The determination of the thermodynamic properties of each state point in the cycle, the amount of heat transfer in each component, and the flow rates at different lines depend on the generator temperature, evaporator temperature, condenser temperature, absorber temperature, liquid-liquid heat exchanger effectiveness, and the refrigeration load.

For carrying out a thermodynamic analysis of the proposed vapour absorption refrigeration system, the following assumptions were made:

- No pressure changes except through the flow pump and pressure expansion valve.
- At point 1, 4 and 8, there is only saturated liquid.
- At point 10, there is only saturated vapour. Pumping is isentropic. Assume a weak solution contains a larger percentage of refrigerant and a smaller percentage of absorbent and a strong solution contains a larger percentage of absorbent and a smaller percentage of refrigerant. The percentages of the weak solution at state 1, 2 and 3 and the percentages of the strong solution at state 4, 5 and 6 will remain same. The temperatures at thermodynamic states 11, 12, 13, 14, 15, 16, 17 and 18 are the external circuit for water which is used to input heat for the components of the system shown in Figure 8.
- This system has two pressure limits; one is a high-pressure limit and the other is the low-pressure limit.
 $P_1 = P_6 = P_9 = P_{10} = \text{Low pressure.}$
 $P_2 = P_3 = P_4 = P_5 = P_7 = P_8 = \text{High pressure.}$

Energy analysis

Generator:

On balancing the energy across the generator:

$$Q_g + Q_3 = Q_4 + Q_7 \quad (5)$$

And:

$$Q_3 = \dot{m}_3 * h \quad (6)$$

$$Q_4 = \dot{m}_4 * h_4 \quad (7)$$

$$Q_7 = \dot{m}_7 * h_7 \quad (8)$$

where Q = Heat flow (kW);
 \dot{m} = Mass flow (kg/s);
 h = Enthalpy (kJ/kg).

Balancing the concentration across the generator:

$$\dot{m}_3 * X_3 = \dot{m}_4 * X_4 + \dot{m}_7 * X_7 \quad (9)$$

$$\dot{m}_1 = \frac{\dot{m}_4 * X_s}{X_w} \quad (10)$$

where X = Ammonia content in working media.

Combining Equations 9 and 10:

$$\dot{m}_6 = \frac{-\dot{m}_{10}}{1 - \frac{X_6}{X_1}} \quad (11)$$

Using Equations 6-8:

$$Q_g = (\dot{m}_7 * X_7) + (\dot{m}_4 * X_4) - (\dot{m}_3 * X_3) \quad (12)$$

Heat supplied to the generator is:

$$Q_g = \dot{m}_6 * C_{p_{water}} = \pi r^2 * (T_{12} - T_{11}) \quad (13)$$

$$\dot{m}_{11} = \frac{(\dot{m}_7 * X_7) + (\dot{m}_4 * X_4) - (\dot{m}_3 * X_3)}{C_{p_{water}} * (T_{12} - T_{11})} \quad (14)$$

Condenser:

On balancing the energy across the condenser:

$$Q_c + Q_8 = Q_7 \quad (15)$$

$$Q_8 = \dot{m}_8 * h_8 \quad (16)$$

$$Q_7 = \dot{m}_7 * h_7 \quad (17)$$

$$Q_c = (\dot{m}_7 * h_7) - (\dot{m}_8 * h_8) \quad (18)$$

Heat supplied to the condenser is:

$$Q_c = \dot{m}_{15} * C_{p_{water}} (T_{15} - T_{16}) \quad (19)$$

On comparing Equations 12 and 13, we can get \dot{m}_{15} :

$$\dot{m}_{15} = \frac{(\dot{m}_7 * h_7) - (\dot{m}_8 * h_8)}{C_{p_{water}} (T_{15} - T_{16})} \quad (20)$$

Evaporator:

On balancing the energy across the evaporator:

$$Q_e + Q_9 = Q_{10} \quad (21)$$

$$Q_9 = \dot{m}_9 * h_9 \quad (22)$$

$$Q_{10} = \dot{m}_{10} * h_{10} \quad (23)$$

On putting the energy values for points 9 and 10 into Equation 21:

$$Q_e = (\dot{m}_{10} * h_{10}) - (\dot{m}_9 * h_9) \quad (24)$$

Knowing that heat extracted from the evaporator is:

$$e = \dot{m}_{17} * C_{p_{water}} * (T_{18} - T_{17}) \quad (25)$$

Comparing Equations 17 and 18:

$$\dot{m}_{17} = \frac{(\dot{m}_{10} * h_{10}) - (\dot{m}_9 * h_9)}{C_{p_{water}} * (T_{18} - T_{17})} \quad (26)$$

Absorber:

On balancing the energy across the absorber:

$$Q_a + Q_1 = Q_6 + Q_{10} \quad (27)$$

And:

$$Q_1 = \dot{m}_1 * h_1 \quad (28)$$

$$Q_6 = \dot{m}_6 * h_6 \quad (29)$$

$$Q_{10} = \dot{m}_{10} * h_{10} \quad (30)$$

We have already found out m_1 and m_6 by using Equations 10 and 11 for calculating T_5 ; we can use the relation of effectiveness of the heat exchanger:

$$T_5 = -\varepsilon - \frac{T_4}{(T_4 - T_2)} * (T_4 - T_2) \quad (31)$$

Using Equations 21-23, we can get Q_1 , Q_6 and Q_{10} .

By putting energy values for 1, 6 and 10 into Equation 21, we get:

$$Q_a = (\dot{m}_6 * h_6) + (\dot{m}_{10} * h_{10}) - (\dot{m}_1 * h_1) \quad (32)$$

We also know that the heat transfer from the absorber is:

$$Q_a = \dot{m}_{13} * C_{p_{water}} (T_{14} - T_{13}) \quad (33)$$

On comparing Equations 26 and 27, we can get m_{13} ; similarly by using the energy balance, we can get:

$$\dot{m}_{13} = \frac{(\dot{m}_6 * h_6) + (\dot{m}_{10} * h_{10}) - (\dot{m}_1 * h_1)}{C_{p_{water}} * (T_{14} - T_{13})} \quad (34)$$

Heat exchanger:

The requirement of the heat exchanger area for the absorption system was calculated using the log mean temperature difference method. Since the rate of heat transferred is a linear function of the overall coefficient of heat transfer, the heat transfer area of the heat exchanger and the log mean temperature difference for the heat transfer process could be derived from Equation 29:

$$Q = U * A * LTMD \quad (35)$$

$$LMTD = \frac{(T_4 - T_3) - (T_5 - T_2)}{\ln \left(\frac{(T_4 - T_3)}{(T_5 - T_2)} \right)} \quad (36)$$

Heat exchange efficiency becomes:

$$\eta_{she} = \ln \left(\frac{(T_4 - T_3)}{(T_5 - T_2)} \right) \quad (37)$$

$$\dot{m}_4(T_4 - T_5) = \dot{m}_2(T_2 - T_3) \quad (38)$$

4.2 Vapour compression cycles

In the vapour-compression refrigeration cycle (Figure 9), refrigerant enters the evaporator in the form of a cool, low-pressure mixture of liquid and vapour (4). Heat is transferred from the relatively warm air or water to the refrigerant, causing the liquid refrigerant to boil. The resulting vapour (1) is then pumped from the evaporator by the compressor, which increases the pressure and temperature of the refrigerant vapour. The hot, high-pressure refrigerant vapour (2) leaving the compressor enters the condenser where heat is transferred to ambient air or water at a lower temperature. Inside the condenser, the refrigerant vapour condenses into a liquid. This liquid refrigerant (3) then flows through the expansion valve, which creates a pressure drop that reduces the pressure of the refrigerant to that of the evaporator. At this low pressure, a small portion of the refrigerant boils (or flashes), cooling the remaining liquid refrigerant to the desired evaporator temperature. The cool mixture of liquid and vapour refrigerant (4) travels to the evaporator to repeat the cycle.

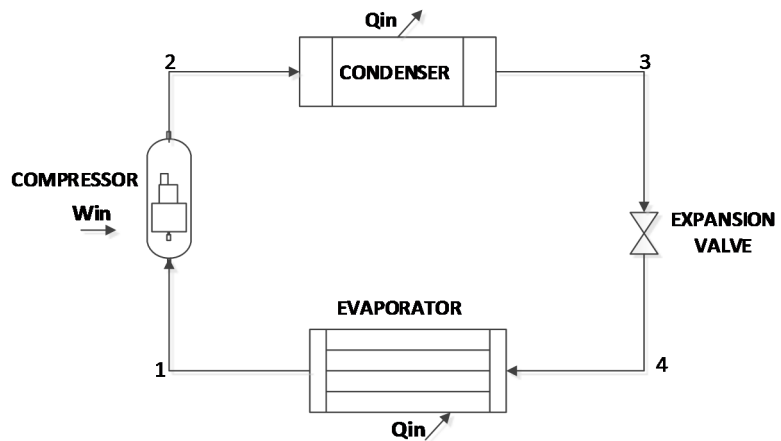


FIGURE 9: Schematic diagram of a simple compression refrigeration system

Figure 10 shows in few steps how a compressor systems work. The process from 1 to 2 is when the compressor increases the pressure of the evaporated refrigerant vapour to raise its temperature. On the

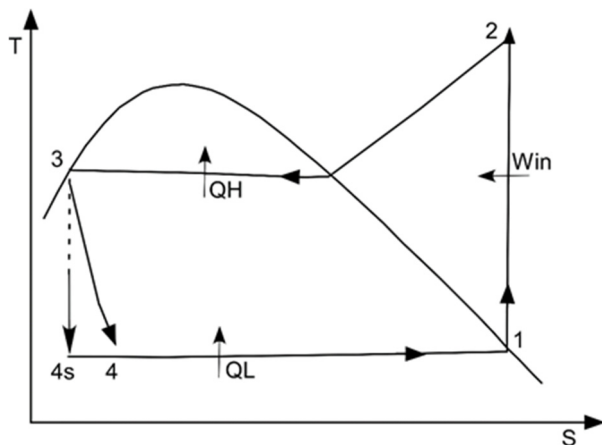


FIGURE 10: T-S diagram for a simple compression system

suction side, the compressor keeps the pressure of the liquid refrigerant low, causing the refrigerant to operate at a lower temperature. In the following step, from 2 to 3, the fluid enters the condenser and heat is rejected while the pressure stays constant. From 3 to 4 an expansion occurs under a throttling process where the enthalpy is constant. The pressure drops down as well as the temperature of the refrigerant. The final step is from 4 to 1. When the cold liquid enters the evaporator, heat is added and the liquid evaporates. This is the part where the cooling takes place (Wulfinghoff, 1999). In Figure 10, the relationship between temperature and entropy is shown in different positions in the compression cycle where the curve shows saturation for the working fluid.

4.2.1 Analysis of the cycle

The thermodynamic analysis of the compression cycle is performed using the following assumptions:

- The system is in steady state;
- The vapour is saturated at the inlet of the compressor;
- The isentropic efficiency of the compressor is 75%; and
- There is no pressure loss along the pipe and in the valves.

Table 11 shows the mass and energy balance of the compression refrigeration system.

TABLE 11: Mass balance and energy balance of a vapour compression refrigeration system; refer to Figure 9 for orientation

Component	Mass balance	Energy balance
Compressor	$\dot{m}_1 = \dot{m}_2$	$W_{comp} = \dot{m}_1 h_1 - \dot{m}_2 h_2$ $W_{comp\ isent} = \dot{m}_1 (h_{isent} - h_1)$
Condenser	$\dot{m}_2 = \dot{m}_3$	$Q_{cond} = \dot{m}_2 h_2 - \dot{m}_3 h_3$
Expansion valve	$\dot{m}_3 = \dot{m}_4$	$h_3 = h_4$
Evaporator	$\dot{m}_4 = \dot{m}_1$	$Q_{ev} = \dot{m}_1 h_1 - \dot{m}_4 h_4 = (\text{refrigeration effect})$

The technology in this cycle uses electricity to compress the working fluid and the cycle is relatively effective. The coefficient of performance (COP), as a measure of system efficiency, is defined as the ratio between the amounts of heat absorbed in the evaporator to the power given to the compressor:

$$COP_c = \frac{\text{Cooling capacity}}{\text{Required input}} = \frac{Q_E}{W_c} \quad (39)$$

where W_c = The work input into the compressor.

4.2.2 Refrigerant selection criteria

Selection of refrigerant for a particular application is based on the following requirements:

- Thermodynamic and thermo-physical properties;
- Environmental and safety properties; and
- Economics.

4.2.3 Thermodynamic and thermo-physical properties

The requirements are:

- Suction pressure:** At a given evaporator temperature, the saturation pressure should be above atmospheric pressure to prevent air or moisture ingress into the system and for ease of leak detection.
- Discharge pressure:** At a given condenser temperature, the discharge pressure should be as small as possible to allow light-weight construction of the compressor, the condenser, etc.
- Pressure ratio:** Should be as small as possible for high volumetric efficiency and low power consumption.
- Latent heat of vaporization:** Should be as large as possible so that the required mass flow rate per unit cooling capacity will be small.

4.2.4 Choice of refrigerant R134a

The refrigerant R134a was selected to be used in the proposed vapour compression cycle for the following reasons: It is an almost odourless liquid with a low boiling point of -26°C at atmospheric pressure. It has a low specific volume of vapour with a good volumetric efficiency. It is non-toxic, non-corrosive, and non-flammable. Its ozone depletion potential is zero with little global warming potential. More importantly, its cost is comparatively low, and it produces a relatively good refrigerating effect at moderate and economical operating conditions. Also, its leakage can be easily detected by using a soap solution.

5. THE BASIC CONCEPT OF ENERGY CONVERSION IN AN ORGANIC RANKINE CYCLE POWER PLANT

The simple organic Rankine cycle power plant follows the scheme shown in Figure 11. The working fluid is an organic fluid, also called refrigerant.

5.1 The simplified schematic basis of ORC power plant

The geothermal fluid heat enters the system through a series of heat exchangers, in which heat is transferred to the working fluid. Typically, there are two stages of heat exchange: one occurring in a preheater, where the temperature of the working fluid is raised to its bubble point, and the other in an evaporator, where the working fluid is vaporized. However, in cases where the fluid must reach a superheated state, a third heat exchanger – a super heater – is added. After isobaric heat addition, which occurs between states 5 and 1, high-pressure vapour is expanded in the turbine (1-2). The exhaust vapour of the organic fluid from this process is superheated, which is a result of the characteristic retrograde shape of the working fluid saturation line. The superheated stream of the exhaust gas may be sent directly to the condenser where it is cooled to T_3 and condensed. However, if economically feasible, exhaust from the turbine may lead to another heat exchanger-regeneration which recovers part of the sensible heat. After leaving the condenser, the working fluid enters the pump, where its pressure is increased to P_4 and is returned directly, or through the regenerator, to the preheater. The working fluid operates in a sealed, closed-loop cycle. The thermodynamic process undergone by the working fluid is shown in commonly used temperature-entropy and pressure-enthalpy diagrams (Lukawski, 2009) in Figure 12.

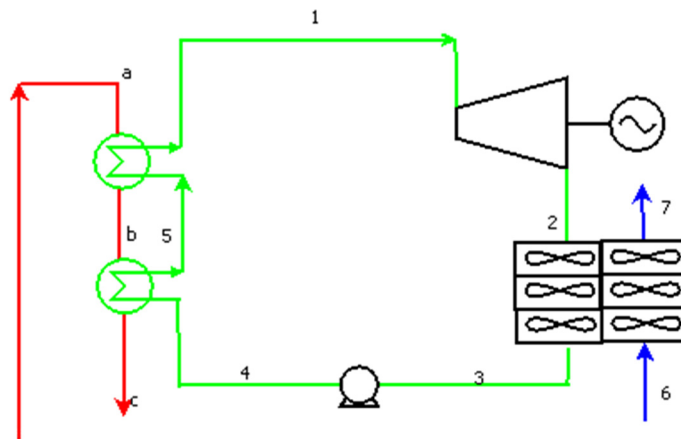


FIGURE 11: Simplified schematic of basic ORC power plant

Preheater and evaporator:

The analysis for the above two components are well described in many engineering books. Standard methodology assumes:

1. Steady state operating conditions;
2. No heat losses from heat exchangers not connected with the transfer of mass;
3. Pure concentration flow in heat exchangers;
4. Constant overall heat transfer coefficient;
5. Constant specific heat of heat source fluid; and
6. Changes of kinetic and potential energy of fluid is negligible.

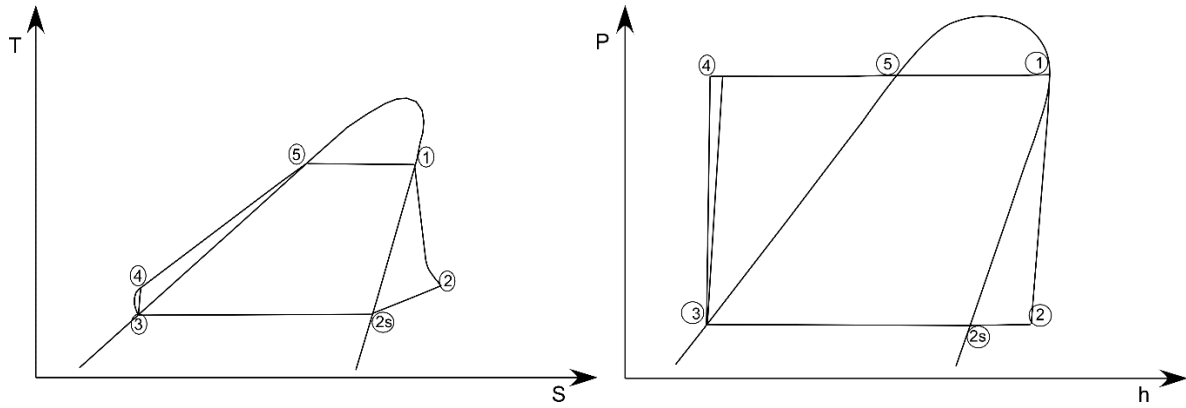


FIGURE 12: Temperature–entropy and pressure–enthalpy diagrams for a binary power plant

As heat losses in heat exchangers are neglected, the amount of heat added to the working fluid is equal to the heat extracted from the heat source.

$$Q = \dot{m}_{hs}(h_{hs,ev,in} - h_{hs,ph,out}) \quad (40)$$

$$Q = \dot{m}_{wf}(h_{wf,ev,out} - h_{wh,ph,in}) \quad (41)$$

where the subscript ‘hs’ refers to heat source fluid, ‘wf’ to working fluid, ‘ph’ to preheater and ‘ev’ to evaporator.

In the temperature-heat exchange diagram of a heat exchanger, the place where the minimum temperature difference between two fluids occurs is called the pinch. The location of the pinch point and the value of the pinch point temperature is one of the major parameters influencing the performance of ORC power plants and will be investigated and optimized in this study.

Turbine:

The purpose of the turbine is to change the potential of pressurized gas into rotational kinetic energy. The stream of high-pressure vapour of an organic fluid expands in the turbine, causing its internal parts to rotate. The rotor is connected by a shaft to the generator which changes rotational kinetic energy into electricity. The expansion process is considered adiabatic and a steady state of operation is assumed. Knowing the isentropic efficiency of the turbine (η_t), which is given by the manufacturer, the generated power can be calculated as follows (DiPippo, 2008).

$$W_{gen} = \dot{m}_{wf}(h_1 - h_2) = \dot{m}_{wf} \eta_t (h_1 - h_{2s}) \quad (42)$$

where η_t is the isentropic efficiency of the turbine and state 2s corresponds to an ideal isentropic turbine.

The heat dissipation system is of great importance for binary power plants because of significantly bigger quantities of rejected heat per unit of electricity output compared to other sources of energy, as well as the high sensitivity for temperature variations of the heat sink. The heat dissipated from the cycle is primarily heat from condensation of the working fluid and can be defined in terms of the thermal efficiency of the cycle as:

$$Q_{rej} = Q_{in}(1 - \eta_{th}) \quad (43)$$

Where Q_{in} is the heat input to the cycle, in this case, the sum of the heat rates of the preheater and the evaporator, and η_{th} stands for the thermal efficiency of the cycle. The amount of heat that has to be rejected to the atmosphere per unit of work output is:

$$Q_{rej} = \frac{W(1 - \eta_{th})}{\eta_{th}} \quad (44)$$

where W = Power generated by the turbine.

Cooling tower:

To improve the net power output of the plant, it is very important to develop a cooling system that cools the steam leaving the turbine. This system is composed of an air cooled surface condenser which condenses the working fluid before it enters the pump. While transferring heat to the cooling air, the working fluid changes phase, from gaseous to liquid. The power consumed by the cooling tower fan is given by:

$$W_{fan} = \frac{V_{air} * \Delta p}{\eta_{fan}} \quad (45)$$

where V_{air} = Volumetric flow of the air through the fan;
 Δp = Pressure increase over the fan; and
 η_{fan} = The efficiency of the fan and its electric motor.

Because heat losses in exchangers are neglected, the amount of heat added to water is equal to that which is extracted from the working fluid.

$$\dot{m}_{wf}(h_{wf,cond,in} - h_{wf,cond,out}) = \dot{m}_{cw}C_{p,cw}(T_{cw,out} - T_{cw,in}) \quad (46)$$

Pump:

Using the same assumptions that were used for the turbine, power consumed by the feed pump can be calculated as:

$$W_p = \dot{m}_{wf}(h_5 - h_4) = \dot{m}_{wf} \left(\frac{h_{5s} - h_4}{\eta_p} \right) \quad (47)$$

where η_p is the isentropic pump efficiency and state 5s corresponds to an ideal isentropic pump.

Net power output:

Net power output of the power plant, also known as power output, can be calculated by subtracting all auxiliary power requirements from the gross power produced by the turbine.

$$W_{net} = W_t - (W_{fan} + W_p) \quad (48)$$

The most common and widely used working fluids are hydrocarbon based fluids such as isopentane or propane. A good design and selection of a working fluid gives optimal efficiency, both technically and economically for a given geothermal fluid condition.

5.2 Working fluids

Power plants for generating electricity from hydrothermal resources can be divided into two types: binary and steam. As the word “binary” indicates, there are two cycles in binary plants. The two cycles in such plants are the primary cycle, with the geothermal fluid, and the secondary cycle with the working fluid. The most commonly used fluids are refrigerants and hydrocarbons and, in some cases, a mixture of the two. The Kalina binary power plant is the best example, using a mixture of ammonia and water as a working fluid. The choice of the working fluids depends mainly on the thermodynamic properties of fluids, as well as considerations of health, safety and environmental impacts (DiPippo, 2008).

TABLE 12: Thermodynamic properties of one of the candidate working fluids for binary plants (DiPippo, 2008)

Working fluid	Formula	Crit. temperature (°C)	Crit. pressure (kPa)
Isopentane	i-C ₅ H ₁₂	187.80	3,409

This study only considers isopentane as a working fluid, and the thermodynamic properties of the geothermal brine and boundary conditions. See Table 12 for the thermodynamic properties of isopentane.

6. SYSTEMS MODELLING

6.1 Single-effect water-ammonia absorption system

A single-effect absorption refrigeration technology, water-ammonia absorption refrigeration, is selected for modelling. A single geothermal well feeds the system directly as the heat source, while a machine refrigerates a stream of water for a specific cooling load. The performance of this machine is analysed with variable system components to achieve the best performance. This model is calculated and analysed based on steady state conditions, with the assumptions:

- Heat exchanger is well insulated from the surroundings;
- Potential and kinetic energy changes during heat exchange and at all fluid streams are ignored;
- Modelling the absorption refrigeration system using a geothermal heat source is done by Engineering Equation Solver (EES).

6.2 Absorption refrigeration system description and mathematical modelling

Geothermal fluids for heating a $\text{NH}_3\text{-H}_2\text{O}$ solution have the following technical specifications, as shown in Table 13. Geothermal hot water at 150°C , 30 bar was used in this study under the following two scenarios.

- Power generation in binary cycle where part of the power produced is used to run compressors in a vapour compression refrigeration; and
- Heat production to run a vapour absorption refrigeration cycle.

TABLE 13: Initial design parameters for single-effect ARS

A typical water–ammonia absorption refrigeration system (ARS) is illustrated in Figure 8. The system includes a generator, an absorber, a condenser, an evaporator, and a solution heat exchanger. The determination of the thermodynamic properties of each state point in the cycle, the amount of heat transfer in each component, and the flow rates at different lines, depend upon the generator temperature, evaporator temperature, condenser temperature, absorber temperature, liquid-liquid heat exchanger effectiveness, and the refrigeration load.

A single effect absorption refrigeration system, complete with a solution heat exchanger, is modelled for a water-ammonia system.

In this refrigeration system, the absorption machine provides a cooling effect for the cold storage room with a refrigeration load of 140 kW refrigeration/evaporator capacity. It was assumed that the absorption machine was fed by 150°C geothermal brine from a well at a pressure of 30 bars. The effect of the solution concentration on refrigeration performance is obtained by monitoring the strong and weak concentration differences in a certain range. It was assumed that the generator produced ammonia refrigerant with an ammonia concentration of 99.9 %. A complete list of initial design parameters is displayed in Table 13. Other parameters were freely figured to achieve a preferable machine performance.

T_{source}	150°C
\dot{m}_{source}	3.8 kg/s
Q_{ref}	140 kW
η_{pump}	0.95
η_{she}	0.60
ΔT_{pinch}	5°C
$\Delta T_{\text{evaporator}}$	5°C
$T_{\text{condenser}}$	38.9°C
T_{absorber}	25°C
P_{high}	15 bar
P_{low}	2 bar
$T_{\text{reinjection}}$	114.4°C
$T_{\text{cond inlet}}$	25°C
$T_{\text{cond outlet}}$	33.9°C

6.3 Simulation results of vapour absorption cycle

Table 14 shows the main parameters that were monitored during the analysis of the cycle.

TABLE 14: Heat transfer rates of the system, COP, power consumption and required mass flow

Components	Duty
Generator (Q_g)	295.9 kW
Condenser (Q_c)	215.5 kW
Absorber (Q_a)	221.7 kW
Q_{ref}	140 kW
COP	0.471
Total power required (W-equivalent heat)	91.57 kW
Required mass flow	3.8 kg/s

TABLE 15: Inputs and output parameters for the cycle

Parameters	Compression cycle
Condenser inlet temperature	25°C
Condenser outlet temperature	33.59°C
Pressure high	7.7 bar
Pressure low	2.4 bar
Compressor work	28.12 kW
Electrical power consumed	29.86 kW
COP	4.688

kinds depending on the source of the heat/energy being used to run the cycle. There are heat driven systems, ARS, which are said to be the most effective systems, especially when coupled with refrigeration systems. The design of heat operated systems can be based on different principles. Consider the combination of a (heat operated) binary power station and an electrically operated vapour compression system for refrigeration (Figure 13). On the whole, the combination represents a heat operated system: the primary energy source for operation is the heat supplied in the power station. In Figure 13, it is obvious that there is one “power generating process” and one “refrigeration” process in the system. There are different ways to combine the cycles or to integrate the processes with one another. An obvious combination (from Figure 13) is to build a “double loop system” based on two Rankine cycles. However, the most common example of a heat operated system is the absorption cycle, based on the principle of Carré where the moving part of such a system is, in principle, a liquid pump. This system has some general comments on the coefficient of performance, COP_h of heat operated systems. We can define the COP_h as the ratio between the achieved refrigeration capacity, Q_2 , and, necessary heating energy for its operation, Q_b , (shown in Figure 13).

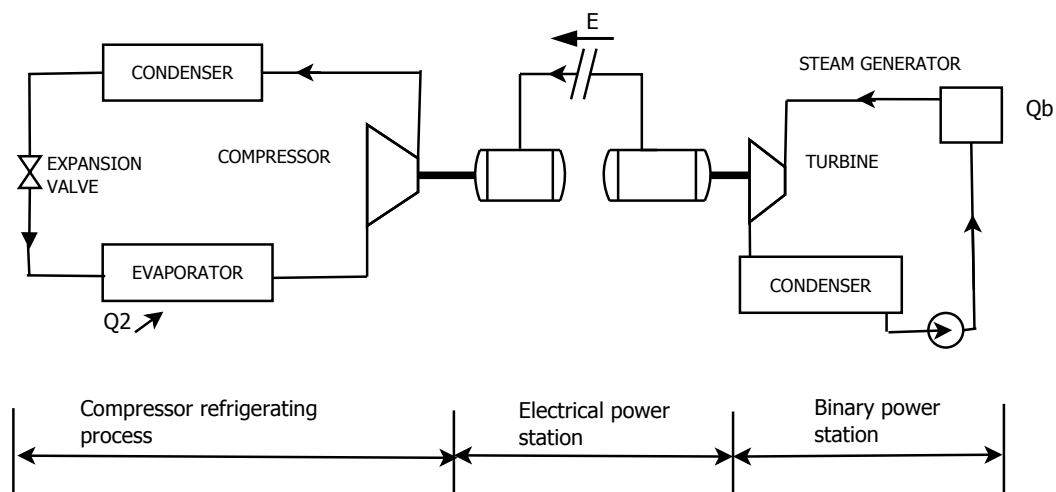


FIGURE 13: A vapour compression refrigeration plant coupled to a binary cycle

6.4 Simulation results for vapour compression cycle

The thermodynamic properties of the system at various state points (refer to Appendix I, Table 1) were calculated using R134a as a refrigerant by using the equations presented in Table 11. The results given in Table 15 were analysed at $T_3 = 30^\circ\text{C}$ and at $T_4 = -5^\circ\text{C}$, which are the condenser and evaporator temperatures, respectively. The thermodynamic properties of the state points for a compression refrigeration cycle are shown in Appendix I, Table 1.

6.5 Binary cycle integrated with compression refrigeration

Cooling systems are of different

$$COP_h = \frac{Q_2}{Q_b} \quad (49)$$

Notice that this relationship differs from that used in the definition of the COP_2 , of the regular vapour compression cycle, by that fact that it defines the ratio between two terms expressing “heat energies”. Returning to the example given in Figure 13, the COP_h includes not only the refrigeration system, but also the efficiency of the power station. Let us use the symbol η_t for the overall power station and COP_2 for the coefficient of performance of the refrigerating system. It is obvious that the following relationship must prevail.

$$COP_h = \eta_t * COP_2 \quad (50)$$

The COP_h of a heat operated system can always be expected to be smaller than the COP_2 of a system which is based on mechanical (electric) energy for the operation. This observation also implies that, for a given cooling capacity, the heat operated system must be equipped with heat exchangers of larger capacities than a mechanically operated system. This is also an indication that a heat operated system may become more costly to build than an electrical system of the same capacity. However, this comparison is sensitive to the ratio between the cost of an electric motor and compressors in comparison to the heat exchangers (Granryd et al., 2005).

The basic idea of this integrated system was to have a closed loop system for binary power plant power generation where part of it will be used to drive the compression cycle for refrigeration purposes. The integrated system would utilize the heat from a liquid-dominated geothermal well of 150°C geothermal fluid temperature, which is enough to operate a binary cycle geothermal power plant. The system was set to run in a tropical country which has a 25°C ambient temperature.

6.5.1 Binary cycle simulation results

Table 16 shows the simulation results for the thermodynamic properties and heat transfer rates of each component, respectively (refer to Appendix I, Table 2). In this simulation, calculations were performed for a 140 kW cooling load. The results are mostly based on the parameters that were being monitored which are turbine power output, fan and pump inputs and a few others, as shown in Tables 16 and 17.

TABLE 16: Inputs and outputs for binary cycle

Input parameters	Units	Values	Output parameters	Units	Values
Isopentane as working fluid			Net power output	kW	29.86
Mass of the brine	kg/s	0.9	Pump and fan input	kW	1.6
Mass of the working fluid	kg/s	0.52	Thermal efficiency (η_{th})		0.1282
Reservoir temperature	°C	150			
Reservoir pressure	bar	30			

TABLE 17: Comparison between an integrated binary cycle with compression refrigeration and an absorption refrigeration cycle

Input parameters to the cycle	Integrated binary cycle coupled to vapour compression refrigeration	Stand-alone absorption refrigeration system
Thermal power required to run cycle	323.8 kW	295.9 kW
Mass flow of the brine	0.911 kg/s	1.947 kg/s
Re-injection temperature	89.84°C	114.4°C
COP	0.432	0.471

6.5.2 Comparison between integrated binary cycles with compression refrigeration and absorption refrigeration processes

The comparison between these two cycles was mainly based on the efficiency, the thermal power required to run the cycle, the mass flow rates and re-injection temperatures. Basing such a comparison on COP only can sometimes be misleading, as the heat that can be extracted from geothermal brine in a binary cycle is much higher than the heat extracted by the generator in an absorption cycle; other parameters were also compared.

6.6 Discussion on the results

In this simulation process, three cycles, a binary cycle, a compression cycle and an absorption cycle, were analysed. Using input parameters, the thermodynamic properties at the various state points, the energy flow rate at various components of the cycles, the coefficient of performance and the mass flow rates of the system were calculated through the mathematical model by Engineering Equation Solver Software (EES). The results of the EES model are shown in Figures 1-3 in Appendix II. Latent heat of refrigerants and the heat requirement to increase the solution temperature are the main factors that affect the performance of a refrigerant. It was revealed that the absorption refrigeration system should be properly designed to achieve its maximum performance; different amounts of a heat source and cooling loads affect refrigeration parameters. It is also very important to mention that the higher the temperature of the heat source, the better the COP. Also, the efficiency of an absorption machine quickly deteriorates as soon as the temperature of the heat source drops below the design temperature.

7. CONCLUSIONS

The results from the comparison done between a binary cycle integrated with compression refrigeration and vapour absorption refrigeration cycles, for a heat load of 140 kW cold storage, indicate that the binary cycle coupled with compression refrigeration has a lower COP of 0.432, compared to 0.471 for the absorption cycle. Also, the geothermal fluid mass flow required to drive the absorption cycle is higher than that required to drive a binary cycle coupled to a compression cycle for the same cooling effect. The thermal power required to drive the binary cycle is 323.8 kW, while that of an absorption cycle is 295.9 kW, which combines the power required for the pump work done by the absorber, condenser and evaporator.

8. RECOMMENDATIONS FOR FUTURE WORK

Changing more variables in the optimization process is one possibility in order to achieve a higher system performance. In a binary cycle, this can be applied by varying the well head pressure. By changing this pressure, especially if different mass flows are applied, the system performance can be further optimized. For the absorption refrigeration cycle, the addition of a separator (rectifier) to the cycle may be worked on to increase system efficiency. An overview of system performance based on exergetic efficiency could be analysed to measure the potential work and final work output relative to environmental conditions. Finally, the economic performance of absorption chillers could be analysed, even if it is known that a heat operated system (chillers) may become more costly to build than an electrical system of the same capacity due to more components of the cycle; such a comparison would be sensitive to the ratio between the cost of an electric motor and compressors in comparison to the heat exchangers.

ACKNOWLEDGEMENTS

This is a great opportunity to express my respect for all those who aided me in completing this six month program. I am pleased to thank the Government of Iceland through the United Nations University for the financial support. My gratitude goes to Mr. Lúdvík S. Georgsson, the director of UNU-GTP, for the fellowship, and Dr. Ingvar Birgir Fridleifsson, the outgoing director; also to all the UNU-GTP staff, Mr. Ingimar G. Haraldsson, Ms. Thórhildur Ísberg, Ms. Málfrídur Ómarsdóttir and Mr. Markús A. G. Wilde, for their continuous help. I am very grateful to my advisors, Mr. Thorleikur Jóhannesson and Mr. Davíð Örn Benediktsson, for encouraging and supervising me. Thank you for the time and the discussions. I also would like to extend my appreciation to all staff and lecturers of Orkustofnun and Iceland GeoSurvey - ÍSOR, for sharing their experience with us. I would also like to thank all the UNU Fellows for our memorable time and friendship.

This report is especially dedicated to my parents and my family, in general; thanks for the moral support, prayers and care.

REFERENCES

- Agri, 2012: *Knowledge centre*. Banque Populaire, Rwanda, Ltd.
- ASHRAE, 2009: *ASHRAE handbook - Fundamentals*. American Society of Heating Refrigerating and Air-conditioning Engineers, Atlanta, GA, United States, 880 pp.
- Bäckström, M., 1970: *Kylteknikern* (in Swedish). Svenska kyltekniska föreningen, 928 pp.
- BGR, 2009: *Geothermal potential assessment in the Virunga geothermal prospect, Northern Rwanda*. Federal Institute for Geosciences and Natural Resources (BGR), final report, 104 pp.
- DiPippo, R., 2008: *Geothermal power plants. Principles, applications, case studies and environmental impact*. Elsevier Ltd., Kidlington, United Kingdom, 493 pp.
- Granryd, E., Ekroth, I., Lundqvist, P., Melinder, A., Palme, B., and Rohlin P., 2005: *Refrigerating engineering*. Stockholm.
- Hauksson, Th., 2013: *Utilization of absorption cycles for Nesfiskur and Skinnfiskur*. University of Iceland, Reykjavík, MSc thesis, 97 pp.
- Lukawski, M., 2009: Design and optimization of standardized organic Rankine cycle power plant for European conditions. RES - the School for Renewable Energy Science in affiliation with the University of Iceland and the University of Akureyri, Akureyri, MSc thesis, 87 pp.
- Namugize, J.N., 2011: Preliminary Environmental Impact Assessment of geothermal exploration and development in Karisimbi, Rwanda. Report 28 in: *Geothermal training in Iceland 2011*. UNU-GTP, Iceland, 669-708.
- Newell, D., Rohrs, D., and Lifa, J., 2006: *Preliminary assessment of Rwanda's geothermal energy development potential*. Chevron Corporation, Indonesia, report, 27 pp.
- NISR, 2012: *Statistical yearbook, 2012*. National Institute of Statistics, Rwanda, 187 pp.
- Onacha S.A., 2008: *Geothermal resources exploration programme in Rwanda*.

Onacha S.A., 2011: Rwanda geothermal resources development, country update. *Proceedings of the Kenya Geothermal Conference KGC 2011, Nairobi*, 6 pp.

PalletLink, 2013: *Storage box design*. PalletLink, website: www.palletlink.com/potato-boxes/box-design/

Planck, R., and Niebergall, W., 1959: *Handbuch der Kältetechnik: Sorptions-Kältemaschinen*, 7. Springer Verlag, Berlin, Germany, 559 pp.

Ratlamwala, T., Dincer, I., and Gadalla, M.G., 2012: Thermodynamic analysis of a novel integrated geothermal based power generation-quadruple effect absorption cooling-hydrogen liquefaction system. *Internat. J. Hydrogen Energy*, 37-7, 5840–5849.

Soslow, T.V., Trevor, V., and Voss, R., 2013: *Potato – recommendations to maintain post harvest quality* (in French). UC Davis, website: postharvest.ucdavis.edu/L%C3%A9gumes/Pomme_de_Terre/

Southern California Gas Company New Buildings Institute, 1998: *Absorption chillers*. Advanced Design Guideline Series, 97 pp.

Srikhirin, P., Aphornratana, S., and Chungpaibulpatana, S., 2001: A review of absorption refrigeration technologies. *Renewable and Sustainable Energy Reviews*, 5, 343-372.

Tesha, 2009: *Absorption refrigeration system as an integrated condenser cooling unit in a geothermal power plant*. University of Iceland, MSc thesis, UNU-GTP, Iceland, report 1, 68 pp.

Wulfinghoff, D.R. 1999. *Energy efficiency manual*. Energy Institute Press, 1536 pp.

APPENDIX I: Thermodynamic graphs and properties

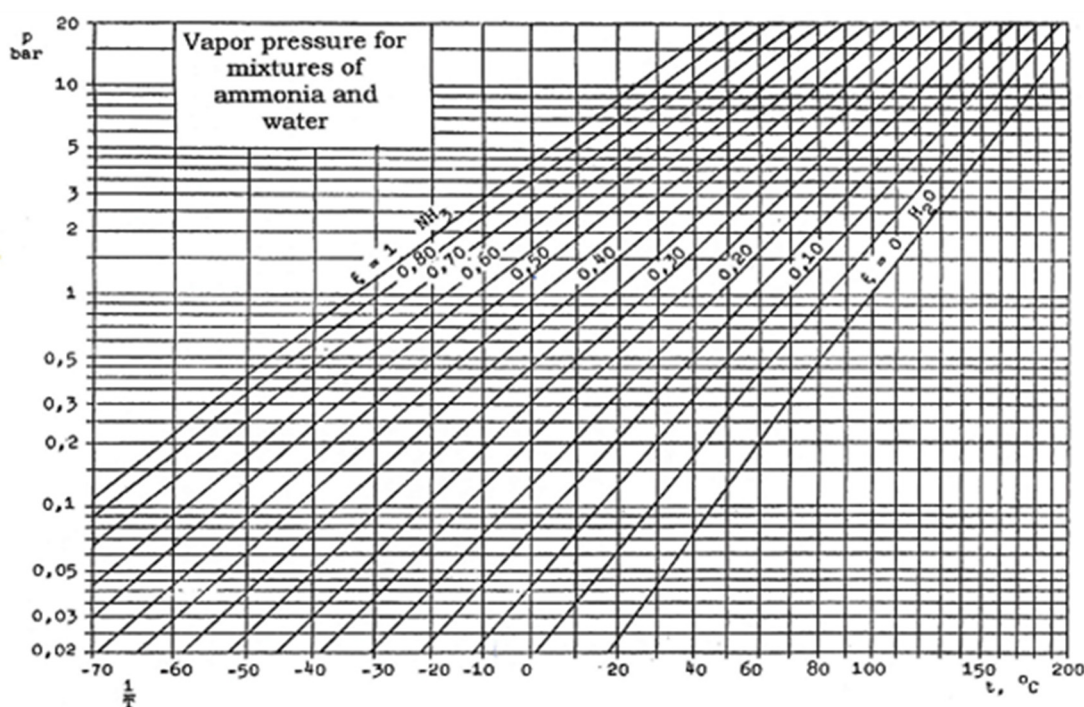


FIGURE 1: Saturation vapour pressure of $\text{NH}_3\text{-H}_2\text{O}$ solutions (data from Planck and Niebergall, 1959)

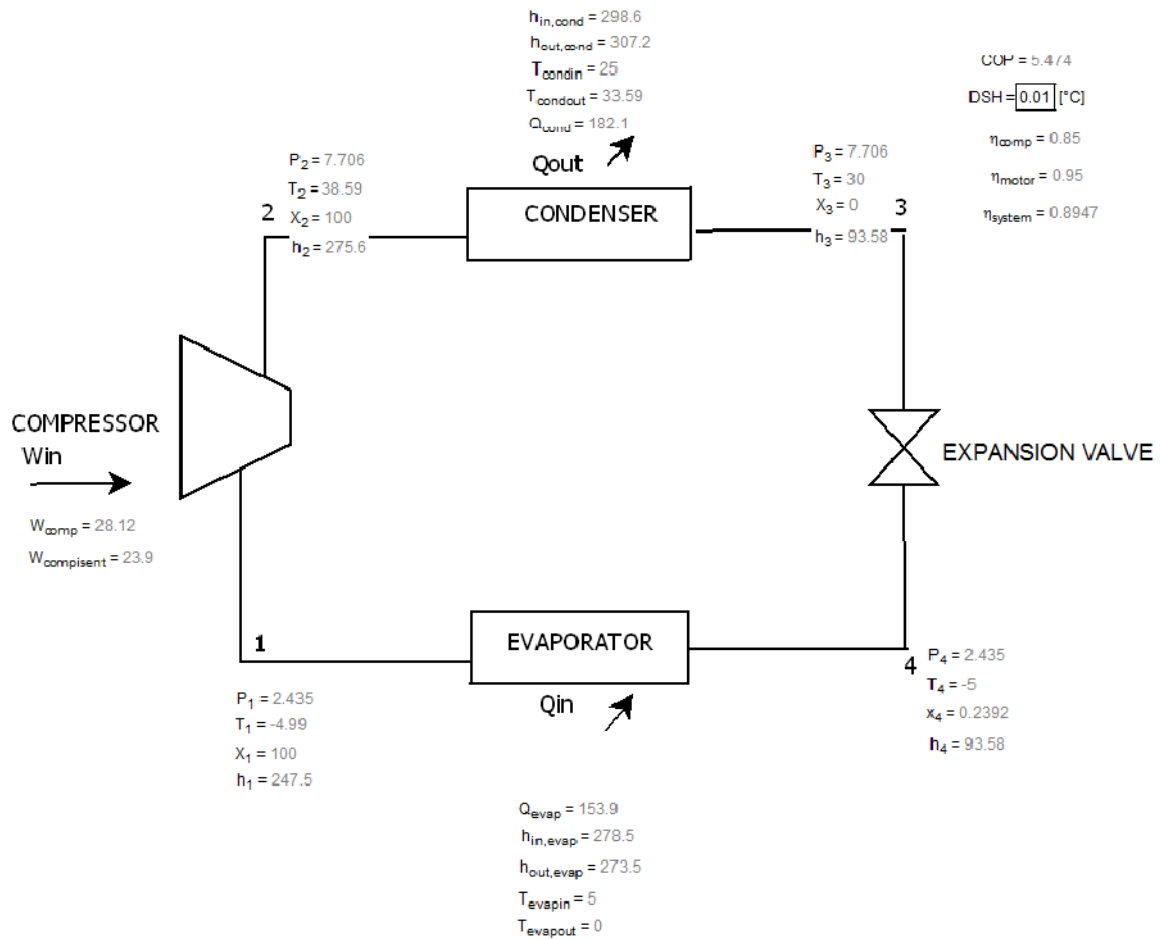


FIGURE 2: Compression cycle, EES simulation

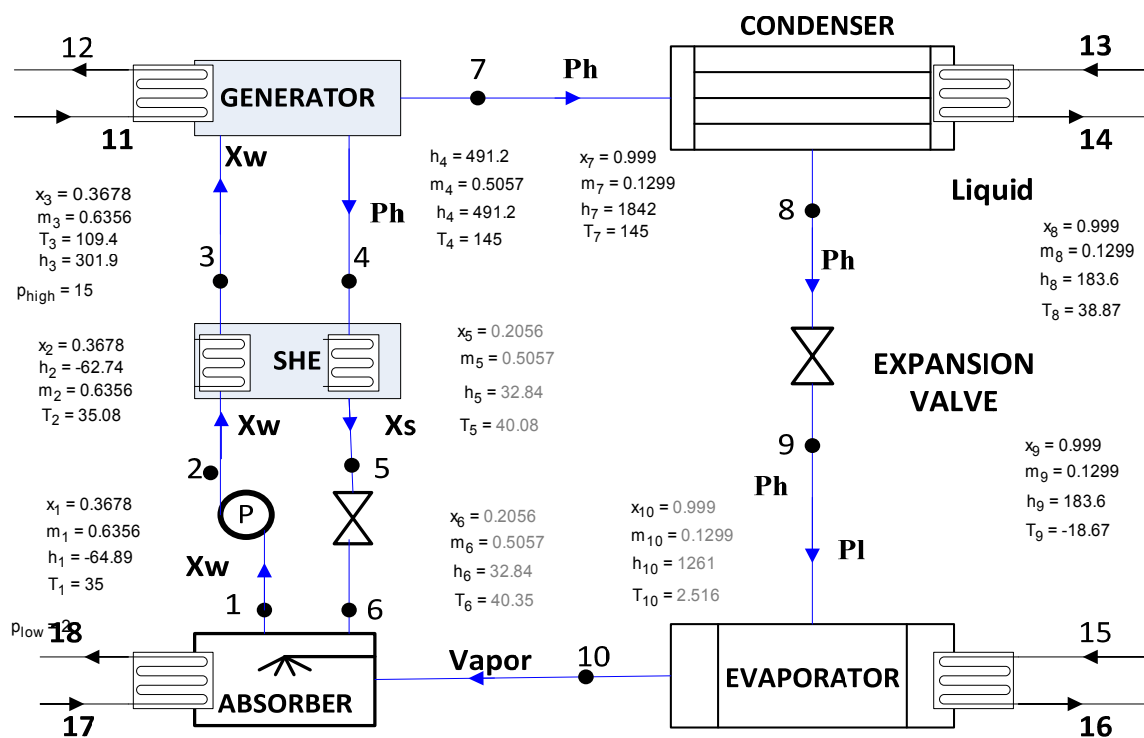


FIGURE 3: Absorption cycle, EES simulation



**UNITED NATIONS
UNIVERSITY**

GEOTHERMAL TRAINING PROGRAMME
Orkustofnun, Grensasvegur 9,
IS-108 Reykjavik, Iceland

Reports 2013
Number 35

DETECTION AND DELINEATION OF GEOTHERMAL RESOURCES USING 1D JOINT INVERSION OF MT AND TEM DATA WITH PRACTICAL APPLICATIONS FROM REYKJANES GEOTHERMAL FIELD, SW-ICELAND

Ronald Togo Verave

Mineral Resources Authority
Geological Survey Division
Mining Haus, Poreporena Freeway
P.O. Box 1906, Port Moresby, 121
PAPUA NEW GUINEA
rverave@mra.gov.pg

ABSTRACT

Geophysical exploration is a vital part of geothermal prospecting, particularly during the initial stages of development. When conducted alongside geological and geochemical work, a better understanding of the subsurface of the geothermal resource and its characteristics can be obtained. The resistivity methods in geophysical exploration are considered the most powerful geophysical tool in prospecting for high-temperature geothermal resources. This is because the subsurface distribution of resistivity can tell about the parameters that directly influence the geothermal system. A typical alteration distribution in a high-temperature geothermal field is expected but it is subject to the elevation of the area and its distance to the coast. Systems close to the coast do not tend to have as sharp a correlation between alteration and subsurface resistivity (e.g. Reykjanes, SW-Iceland) as systems further away from the coast; this is due to the high salinity in the geothermal fluids. 1D joint inversion of TEM and MT data was done to remove the static shift of the MT data from the Reykjanes geothermal field. Results from the 1D joint inversion revealed a homogeneous low resistivity at shallow depths as was discovered by past studies in the area. An iso-resistivity map at a depth of 10,000 m revealed two heat sources, one to the southwest and another to the northeast. They are associated with deep seated intersecting fractures and faults.

1. INTRODUCTION

The global geothermal energy outlook is gaining momentum as it is becoming more feasible to develop today than it used to be in the past. An increase in knowledge and technology in exploration, drilling and reservoir engineering has resulted in advancements in geothermal electrical generation and exploration. The advancements were driven by technologies used in oil and gas prospecting and also from mining.

Geothermal energy is the heat energy produced in the core of the earth that can be harnessed to generate electrical energy or for a wide range of direct uses such as district heating, bathing etc.

The main objective in the early stages of geothermal energy development is detecting and defining the extent of a geothermal resource, siting wells and understanding the characteristics of the geothermal reservoir. This information is usually obtained during the initial stages of geothermal development where geophysical exploration, geological surface exploration and geochemical exploration are carried out.

Geophysical exploration plays an important role in achieving these objectives. Resistivity methods and thermal methods are proven to be the most powerful geothermal tools in geothermal prospecting because they detect parameters that are directly influenced by geothermal activity.

This report focuses mainly on two resistivity methods, Transient Electromagnetics (TEM) and Magnetotellurics (MT). TEM and MT are the two resistivity methods most intensely used for geothermal prospecting in the world. It discusses the process involved in 1D joint inversion of TEM and MT data, their results and interpretations using examples from the Reykjanes high-temperature geothermal field, SW-Iceland. TEM and MT field procedures and data acquisition are also discussed with some fundamental concepts presented in the background section of this report.

2. BACKGROUND

2.1 Resistivity and geothermal systems

In high-temperature geothermal systems, subsurface resistivity is used to describe the relationship between the parameters that characterize the geothermal system and its history. It is one of the most valuable physical properties of materials and has proven to be the most useful geophysical parameter in the search for geothermal resources (Ussher et al., 2000). Therefore, it is paramount to gain a better understanding of the resistivity of rocks and the parameters that correlate to the geothermal activity (Georgsson, 2013).

2.1.1 What is resistivity?

Specific resistivity, ρ , is defined through Ohm's law. The electrical field strength, \vec{E} [V/m] at a point in a material is proportional to the current density, \vec{j} [A/m²]:

$$\vec{E} = \rho \vec{j} \quad (1)$$

The proportionality constant, ρ , depends on the material and is called the specific resistivity, measured in Ωm . The reciprocal of resistivity is conductivity ($1/\rho = \sigma$).

Resistivity can also be defined as the ratio of the potential difference, ΔV [V/m], to the current, \vec{I} [A], across a material which has a cross-sectional area of 1 m² and is 1 m long.

$$\rho = E/j = \Delta V/L \cdot S/I \text{ and since } E = \Delta V/L \text{ and } j = I/S \text{ then } \rho = \Delta V/I \quad (2)$$

2.1.2 Electrical resistivity of water bearing rocks

The conductivity of most rocks reflects the electrolytic conduction by the aqueous solution of common salts present in the pores of rocks and conduction at the rock-water boundary. The resistivity is controlled by parameters listed below:

- *Porosity and pore structure of the rock*
Porosity is basically the ratio of the pore volume and the total volume of a material. There are three main types:

- intergranular, where the pores are formed as spaces between grains or particles in compact materials like sediments and volcanic ash
- joints-fissures or fractures, where the pores are formed by a net of fine fissures caused by tectonics or cooling of the rocks (igneous rocks, lava)
- vugular porosity, where big and irregular pores have been formed due to the dissolution of material evident in limestone formations.

In order for conduction to occur through the pores, the pores must be interconnected and water filled or saturated. Water saturated pores conduct electricity along the connected pores and the relationship is that the pores in a formation are resistive if the voids are free from water. The reverse happens when the pores are filled and are interconnected.

- *Conductivity of the rock matrix*

In geothermal conditions, the rock matrix itself acts as an insulator at reservoir temperatures and has poor conductivity. The only way conduction is possible is through the presence of fluid and ions in rocks and by electrons in minerals at the rock-water interface. This is contrary to conditions of very high temperature where rocks first start to melt. Here we see the matrix conductivity follows the Arrhenius formula:

$$\sigma_m(T) = \sigma_0 e^{-E/kT} \quad (3)$$

Flóvenz et al. (2012) showed, based on work done by Scarlato et al. (2004), that basalts and related materials over the temperature range of 400-900°C give values of 0.80 for E and 300 for σ_m , which means that the matrix resistivity of basaltic rocks is in the order of 1000 Ωm at 400°C and decreases to 10 Ωm at 800°C.

Partial melt will still increase conductivity at high temperatures. For instance, in the roots of geothermal systems where temperatures exceed 400°C, the matrix conductivity is basically responsible for the overall conductivity.

- *Water rock interaction and the mineral assemblage, alteration*

In high-temperature geothermal systems, water-rock interaction produces alteration (secondary) minerals. The type of minerals formed depends upon the chemical composition of the host-rocks, pore fluid and temperature.

The amount of alteration depends upon time, permeability and the chemical composition and texture of the rocks. The alteration minerals lining the walls of the fractures seem to control, to a large extent, the electrical resistivity in rocks up to temperatures of 200-250°C.

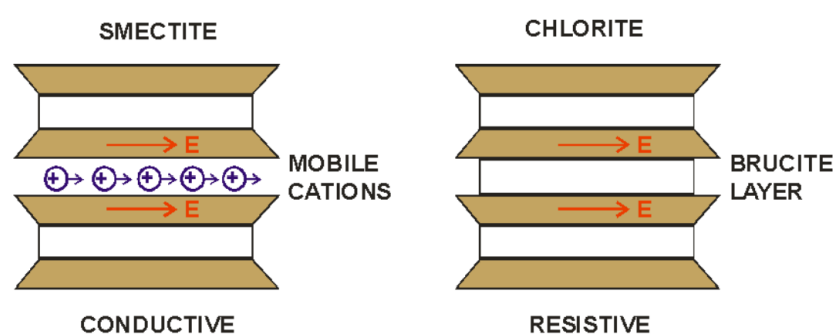


FIGURE 1: Smectite and chlorite mobile cations distributions (Hersir, 2013)

Some of the alteration minerals are conductive while others are less conductive or resistive (see Figure 1). Smectite/zeolites have loosely bound cations that make them conductive. In chlorite, the ions are bound in a crystal lattice, making them resistive.

- CEC (cation-exchange capacity) for smectite is: 0.8-1.5 meq/g
- CEC for chlorite is: 0.01 meq/g

- *Temperature*

The relationship between temperature and the resistivity of an aqueous solution is described by Dakhnov (1962) through the equation below:

$$\rho_w = \frac{\rho_{wo}}{1 + \alpha(T - T_0)} \quad (4)$$

ρ_{wo} (Ωm) is the resistivity of the fluid at temperature T_0 , α is the temperature coefficient of resistivity, where the value of α is approximated to 0.023°C^{-1} at $T_0 = 25^\circ\text{C}$.

It is generalised that, at temperatures of 0 – 200°C , resistivity of aqueous solutions decreases with increasing temperature. This is caused by increasing mobility of the ions caused by a decrease in the viscosity of the water. At high temperatures, a decrease in the dielectric permittivity of the water results in a decrease in the number of dissociated ions in the solution. This starts to increase fluid resistivity, usually above 300°C (Quist and Marshall, 1968), as shown in Figure 2 (at left).

- *The degree of fluid saturation*

Below the ground water table, the rocks in geothermal areas are generally saturated by water and steam. Thus, the groundwater table is the mark at which conductivity is prominent, thereby indicating significant water saturation. The layers above the groundwater table could be partially saturated and the resistivity there depends upon the degree of saturation in the rocks.

- *Salinity of pore fluid*

Salinity of fluids in high-temperature geothermal systems is expected and it affects resistivity measurements to some degree. There is a nearly linear relationship between salinity and resistivity as seen in Figure 2 (at right).

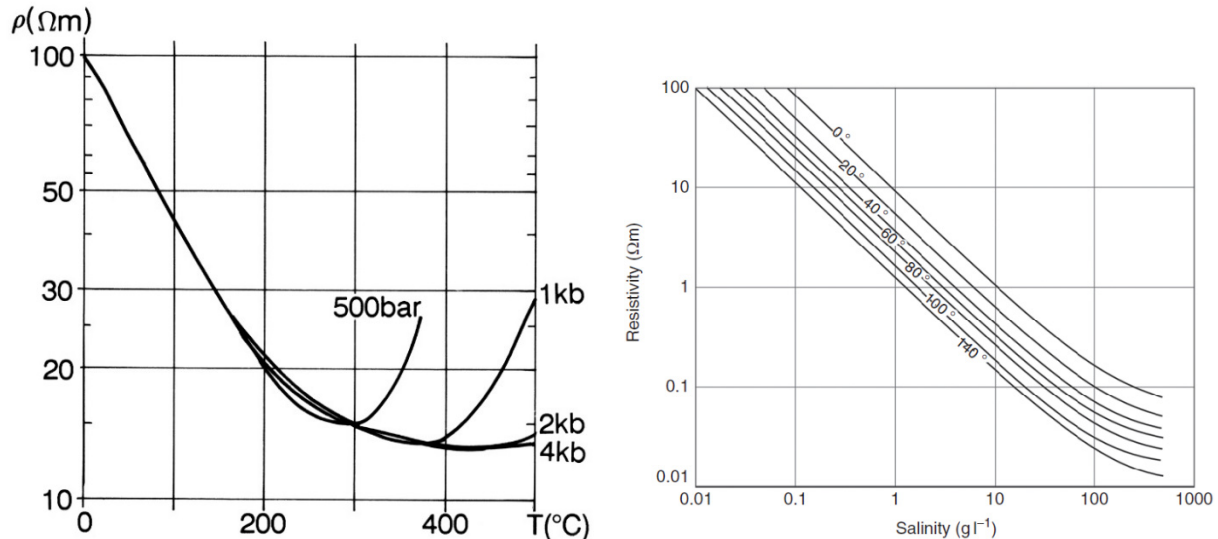


FIGURE 2: Left – electrical resistivity as a function of temperature at different pressures (Flóvenz et al., 2012; based on Quist and Marshall, 1968); Right – resistivity as a function of salinity (Flóvenz et al., 2012; based on Keller and Frischknecht, 1966)

These parameters are described in detail by Flóvenz et al. (2012) who generalised that at typical reservoir temperatures, the conduction in the rock matrix is normally negligible. The main contributors to the electrical conduction in geothermal reservoirs are conduction by dissolved ions in the pore fluid (pore-fluid conduction) and conduction by absorbed ions on the pore surface (interface or surface conduction).

Electrical conductivity in minerals and solutions takes place by the movement of electrons and ions. Most rocks near the earth's surface have low conductivity. Conduction of electricity is mostly through groundwater contained in rock pores and along surface layers at the contact of rocks and solution.

2.1.3 Association between high temperature and clay alteration

Hydrothermal alteration has successfully been used to define several parameters of geothermal systems such as the temperature distribution, permeability and thermal evolution. The association between temperature and clay alteration arrangements is well established and can be used as a tool for predicting temperature during drilling. Inferred correlations between alteration types and resistivity can extend this further to enable better prediction of reservoir temperature from surface geophysical measurements.

In a high-temperature geothermal field in volcanic areas, geothermal fluids are sometimes saline and hydrothermal alterations cause pervasive changes to the natural resistivity of rocks in which the system develops. Generally, the salinity and the clay alteration, combined with the high temperatures produced by the geothermal activity, tend to create a lower overall resistivity in geothermal systems.

Commonly noticed as we gradually progress from surface to deeper levels, is a high resistivity above the low-temperature zone; this is interpreted as a zone that may tend to have poor water-saturation, minimal hydrothermal alteration and little reduction of resistivity by temperature. This can be referred to as the cool upper part of the system where there is no alteration at temperature less than 70°C.

The highly conductive zone at intermediate temperatures is widely known as a characteristic of geothermal systems. Low resistivity in this zone is correlated with clay hydrothermal alteration predominantly made up of smectite/zeolite minerals (Árnason et al., 1987a). This low-resistivity zone in the past was often regarded as being associated with the hot saline fluids of the geothermal systems (Ussher et al., 2000). This may have been true for high-salinity reservoirs such as those in western USA. Temperatures of 70-230°C were encountered there with low resistivity of the order of 1-10 Ωm .

At still deeper levels, the higher resistivity found in the core of the system is correlated with some vapour-dominated reservoirs but is characteristic of most low-moderate salinity reservoirs. This layer is below the overlying conductive zone and the high resistivity is due to the rock matrix being less conductive than the saturated fluids, because low conductivity alteration products dominate mineralisation. Temperatures here are above 230°C, and typical resistivity values are greater than 10 Ωm (Ussher et al., 2000).

Figure 3 shows a resistivity cross-section taken from the Nesjavellir high-temperature geothermal field in SW-Iceland. It depicts the resistive structure of a high-temperature geothermal field in association with the alteration

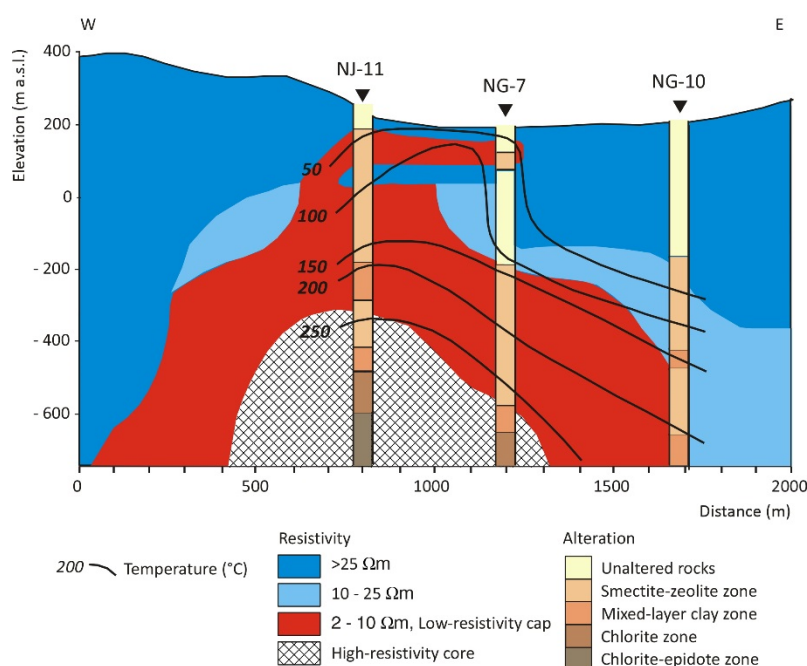


FIGURE 3. Typical resistivity structure of a high-temperature geothermal reservoir showing a high-resistivity core beneath a low-resistivity cap based on 2D interpretation of a detailed multi-method DC resistivity survey from 1985 and 1986 (Árnason et al., 1987b)

temperatures and minerals as described above. The up-doming low-resistivity cap is predominantly controlled by highly conductive alteration minerals, like smectite and zeolite which have a high cation exchange capacity (CEC). The alteration temperatures smectite/zeolite dominate the temperature interval between 100 and 230°C. The highly resistive core below is contained by the conductive cap where alteration minerals such as chlorite and epidote are dominant. The presence of these minerals makes these layers more resistive because the ions in chlorite and epidote are bound in crystal lattices, making them resistive. The low CEC of chlorite contributes immensely to the resistive nature of chlorite.

To tell whether the system is fossil or young cannot be answered by uncovering the subsurface resistivity distribution alone. Delineating resistivity anomalies in high-temperature geothermal fields reflects the subsurface alterations but not necessarily the temperature within the system. The alteration temperatures and the formation temperature have to be at equilibrium in order to infer temperatures through subsurface resistivity. In a younger geothermal system, the alteration temperature lags behind the formation temperature, while in a fossil geothermal system the alteration temperatures are higher than the formation temperature.

2.2 Geophysical exploration methods in geothermal prospecting

Geophysical exploration of geothermal resources deals with the measurement of the physical properties of the earth. In geothermal exploration the resistive property of the earth and its thermal distribution are most useful entities which can describe parameters that are directly influenced by geothermal activity. Resistivity and thermal methods are, therefore, called the direct methods while other methods, referred to as indirect or structural methods, explore the physical parameters of the host rock, such as magnetic properties, density and seismic velocity.

In the following discussion, the emphasis is on the resistivity methods, particularly TEM and MT, and their application in geothermal exploration. Although it must be clear that it is important to combine different methods to obtain adequate information to give a better understanding of the geothermal system.

The idea behind all resistivity methods is to induce an electrical current into the earth and monitor signals, normally at the surface, generated by the current distribution. The three main resistivity electrical sounding methods are the DC sounding method, TEM and MT.

The DC Schlumberger method was extensively used in the 1970s and 1980s. In conventional direct current soundings, such as Schlumberger soundings, this is done by injecting current into the ground through electrodes at the surface; the signal measured is the electric field (the potential difference over a short distance) generated at the surface. In magnetotellurics (MT), the current in the ground is induced by time variations in the earth's magnetic field, and the signal measured is the electric field at the surface. In transient electromagnetics (TEM), the current is also induced by a time-varying magnetic field but, in this case, the current source is not the natural field; the source is of a controlled magnitude generated by current in a loop or a grounded dipole and the monitored signal is the decaying magnetic field at the surface.

2.2.1 Basic theory of TEM

There exist several methods of TEM measurements, varying only by source type (loop source or dipole source) and the positioning of the receiver in relation to the source (Flóvenz et al., 2012). This record describes a configuration of the central-loop TEM setup where the receiver is placed in the middle of the source loop. TEM was introduced into the geothermal exploration realm in the 1980s with refinements done during the decade. The central loop TEM method was first tested for geothermal exploration in Iceland in the summer of 1986 (Árnason et al., 1987b).

TEM makes use of a magnetic field to induce currents in the earth. In the central loop TEM sounding method, a constant magnetic field is built up by transmitting strong current through a big loop (Figure 4). Then the current is abruptly turned off. The decaying magnetic field induces secondary currents and a secondary magnetic field, decaying with time. The decay rate of the secondary field is monitored by measuring the voltage induced in a receiver coil (or small loop) in the centre of the transmitting loop. Current distribution and the decay rate are recorded as a function of time dependent on the resistivity of structures in the earth, and can be interpreted in terms of the subsurface resistivity structure (Georgsson, 2013).

ρ_a is a function of several variables. This includes measured voltage; time elapsed from turn off; area of loops/coils; number of windings in loops/coils; and magnetic permeability.

For a homogeneous half-space, the apparent resistivity ρ_a , is expressed in terms of induced voltages at late times (Figure 5) after the source current is turned off and is given by:

$$\rho_a = \frac{\mu_0}{4\pi} \left[\frac{2\mu_0 A_r n_r A_s n_s I_0}{5t^{5/2} V(t, r)} \right]^{2/3} \quad (5)$$

where t = Time elapsed after the transmitter current is turned to zero (s);
 $V(t, r)$ = Measured voltage in the receiver loop (V);
 A_r = Cross-sectional area of the receiver loop (m²);
 n_r = Number of windings in the receiver loop;
 A_s = Cross-sectional area of the transmitter loop (m²);
 n_s = Number of windings in the transmitter loop;
 μ_0 = Magnetic permeability in vacuum (H/m);
 r = Radius of transmitter loop (m).

To see how Equation 5 is derived, the reader is referred to Árnason (1989).

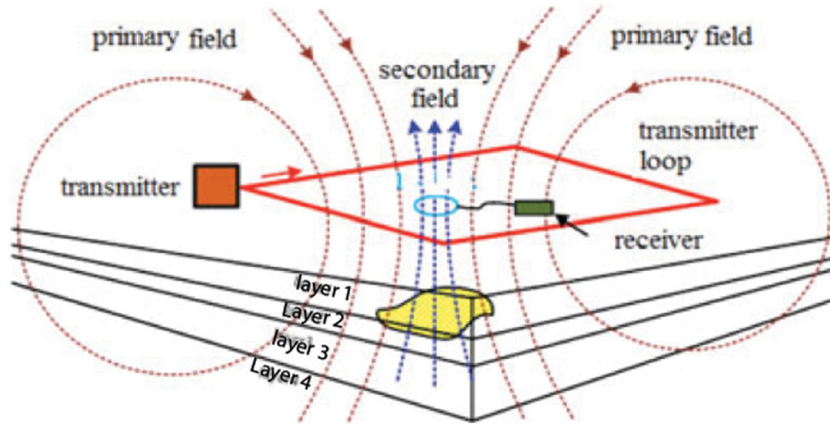


FIGURE 4: Layout of TEM field configuration (modified from Xue et al., 2013)

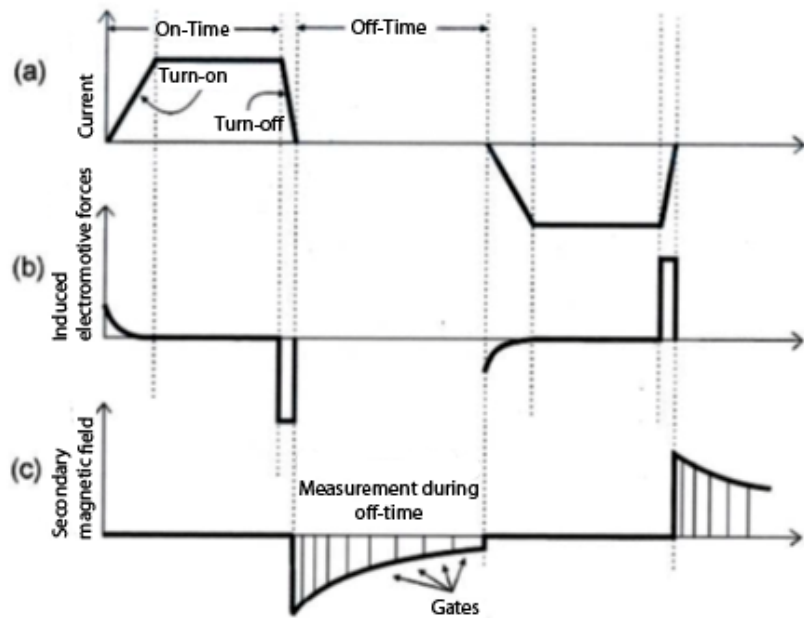


FIGURE 5: Time gates showing pattern during early time and late time responses (modified from Rowland, 2002)

2.2.2 Basic theory of MT

The magnetotelluric method or magnetotellurics (MT) is an electromagnetic geophysical exploration technique that images the electrical properties (distribution) of the earth at subsurface depths. The energy for the magnetotelluric technique is from natural sources of external origin. When this external energy, known as the primary electromagnetic field, reaches the earth's surface, part of it is reflected back and the remaining part penetrates the earth. Earth acts as a good conductor, thus, electric current (known as telluric currents) are induced, in turn producing a secondary magnetic field.

The MT method was first introduced by Tikhonov (1950) and Cagniard (1953) and further by Cantwell (1960) and Vozoff (1972, 1991). Measurements from the horizontal component of the natural electromagnetic field are used to construct the full complex impedance tensor, Z , as a function of the frequency. The relationships between the electrical and the magnetic field can be best described by assuming the following equation which was taken from (Hersir et al., 2013):

$$\begin{bmatrix} E_x \\ E_y \end{bmatrix} = \begin{bmatrix} Z_{xx} & Z_{xy} \\ Z_{yx} & Z_{yy} \end{bmatrix} \begin{bmatrix} H_x \\ H_y \end{bmatrix} \quad (6a)$$

or in matrix form:

$$\vec{E} = Z\vec{H} \quad (6b)$$

where \vec{E} and \vec{H} are the electrical and magnetic field vectors (in the frequency domain), respectively, and Z is a complex impedance tensor which contains information on the subsurface resistivity structure.

For a homogeneous and 1D earth, $Z_{xy} = -Z_{yx}$ and $Z_{xx} = Z_{yy} = 0$. For a 2D earth, resistivity varies with depth and in one horizontal direction, it is possible to rotate the coordinate system such that $Z_{xx} = Z_{yy} = 0$, but $Z_{xy} \neq Z_{yx}$. For a 3D earth, all the impedance tensor elements are different.

From the impedances, the apparent resistivity (ρ) and phases (θ) for each frequency can be calculated as:

$$\rho_{xy} = 0.2T|Z_{xy}|^2 = 0.2T \left| \frac{E_x}{H_y} \right|^2; \theta_{xy} = \arg(Z_{xy}) \quad (7a)$$

$$\rho_{yx} = 0.2T|Z_{yx}|^2 = 0.2T \left| \frac{E_y}{H_x} \right|^2; \theta_{yx} = \arg(Z_{yx}) \quad (7b)$$

How deep the MT soundings can probe is dependent on the wavelength of the recorded EM fields and the subsurface resistivity structure. The longer the period T , the deeper it penetrates and vice versa. Skin depth, sometimes referred to as the penetration depth (δ), describes the relationship between the varying magnitude of the period T and the depth of penetration and is given by:

$$\delta(T) \approx 500\sqrt{T\rho} \text{ (m)} \quad (8)$$

where the EM fields have attenuated to a value of e^{-1} (0.37) of their surface amplitude. ρ is the average resistivity of the subsurface down to that depth (Flóvenz et al., 2012).

Time series data acquired are transformed into the frequency domain, and auto- and cross-power spectra are calculated to estimate the impedance tensor as a function of frequency. The determinant of the impedance tensor, which is also called the effective impedance, Z_{DET} (Pedersen and Engels, 2005), is defined as:

$$Z_{DET} = \sqrt{Z_{xx}Z_{yy} - Z_{xy}Z_{yx}} \quad (9)$$

The effective impedance can be used to compute the determinant apparent resistivities and phase. For all current directions, a useful average of the impedance is best derived from the determinant data.

2.2.3 Static shifts

The presence of near surface resistivity inhomogeneities can distort the electrical field, since the field is not continuous across resistivity boundary. This galvanic distortion effect is known as static shift. This effect shifts the MT apparent resistivity sounding curve (i.e., $\log \rho_a$ vs. $\log T$) by some constant scale factor. Static shift does not affect the phases of the MT impedance tensor. Since a magnetic field is relatively unaffected by surface inhomogeneities, controlled-source magnetic-field soundings such as Central-loop Transient Electromagnetic (TEM) soundings can be used to correct for static shifts. The MT sounding curve is shifted vertically so that the high frequency part of the MT curve agrees with the TEM curve. The low-frequency MT curves then provide an undistorted picture of the deep resistivity section (Jones, 1988).

2.3 Inversion theory

Geophysical data are modelled and interpreted in terms of subsurface parameters in two ways: a direct way, known as forward modelling, and an indirect way, known as inverse modelling. In the forward modelling, the response functions are estimated from the model parameters of the subsurface. On the other hand, in the inverse method, a guessed initial model of the subsurface is assumed and a theoretical geophysical response is computed for the assumed model and compared with the observed data. This process is repeated for various models through an iterative process until a minimum difference between the computed and the observed response is achieved. The result is the statistically best solution with conclusive estimates of the model parameters, and it groups the parameters into well determined parameters and poorly determined ones and calculates how the estimates may be interrelated. It also indicates which data points contain relatively important information necessary to resolve the model parameters.

The forward algorithm for MT is the standard complex impedance 1D recursion algorithm. For TEM, the forward algorithm uses standard recurrence relationships to calculate the kernel function for the vertical magnetic fields, due to an infinitesimal grounded dipole with harmonic current on the surface of a horizontally layered earth (Árnason, 1989; Ward and Hohmann, 1987).

The inversion algorithm used in TEMTD is the Levenberg-Marquardt non-linear least square inversion described by Árnason (1989). The misfit function is the root-mean-square difference between measured and calculated values ($chisq$), weighted by the standard deviation of the measured values. In fitting values, it is a matter of choice for the user whether to use apparent resistivity or measured voltages.

Further on in the program used for inversion (TEMTD), it has the capability of smoothing models. This occurs with respect to resistivity variations between layers (actual logarithm of conductivity) and layer thicknesses (actual logarithm of ratios of depth to top and bottom of layers). Damping is done on “first derivatives” and “second derivatives”. The former counteracts sharp steps in the model while the latter counteracts the oscillations in the model values (log scale). The minimised function in this process is the weighted root-mean-square misfit ($chisq$), and also the “potential”:

$$Pot = chisq + \alpha \cdot DS1 + \beta \cdot DS2 + \gamma \cdot DD1 + \delta \cdot DD1 \quad (10)$$

DS1 and DS2 are the first and second order derivatives of log-conductivities in the layered model, and DD1 and DD2 are the first and second order derivatives of the logarithms of the ratios of layer depths. The coefficients α , β , γ and δ are the relative contributions of the different damping terms and are specified by the user.

2.4 Reykjanes high-temperature geothermal field

The Reykjanes peninsula is situated on the southwest tip of Iceland. The region has several high-temperature areas. This report discusses results from 1D joint inversion of TEM and MT data taken from the Reykjanes high-temperature area (Figure 6), which is situated on the outer Reykjanes peninsula along with Eldvörp and Svartsengi to the east. These high-temperature areas are situated directly in the path where the Mid Atlantic Ridge comes ashore.

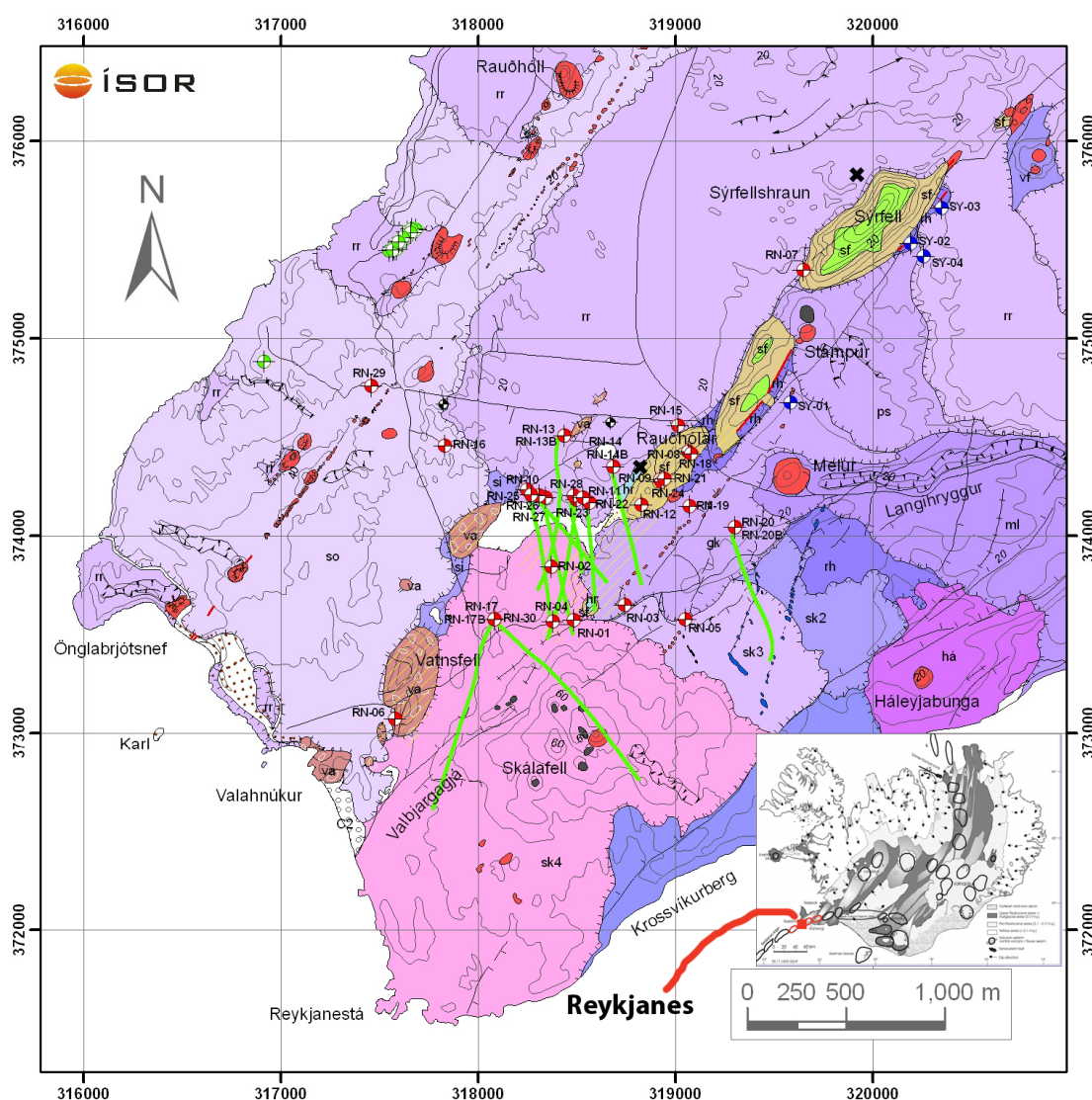


FIGURE 6: Geology of the Reykjanes high-temperature field (modified from ISOR database)

2.4.1 Geology and tectonics of the Reykjanes system

The history and geology of the Reykjanes system is well established by a lot of research and studies done in the area. Sigurdsson (2010) gave a detailed overview of the geology and surface manifestations of the Reykjanes high-temperature field, partly based on some findings/work by Fridleifsson and Albertsson (2000). Figure 6 shows the geology and the surface manifestations of the area. Sigurdsson (2010) described it as being entirely covered by sub aerial lavas of Holocene age, whereas hyaloclastites ridges of late Pleistocene age poke the lava fields, with the same NE-SW strike as the volcanic crater rows, faults and fissures. Parts of the hyaloclastite ridges and lava fields are hydrothermally altered,

and are centred within manifestations of fumaroles, mud pools and hot springs. The youngest fissure eruptions date back to 1226 at the crater row Stampar on the northwest side of Reykjanes, while the 2nd youngest is about 2000 years old. Within this fissure zone, at least 4 volcanic eruptions occurred in the Holocene period. Sigurdsson (2010) further points out the older fissure zone situated on the southeast side of Reykjanes, close to the Skálafell fissure zone. Frequent movement of faults and fissures over time have reactivated the hydrothermal manifestations, which are mostly located between these two eruptive zones.

The peninsula experiences high seismicity, characterised by normal faulting on northeast striking planes or strike-slip on north or east trending planes (Einarsson, 1991). Seismicity mostly occurs at between 1 and 5 km depth and the oblique motion appears to cause bookshelf deformation, whereby parallel N-S trending, right-lateral strike-slip faults accommodate the overall left-lateral transform motion.

Previous geophysical work using DC Schlumberger methods in the 1970s revealed a continuous elongated zone of resistivity below 6 Ωm (low-resistivity zone) in the Reykjanes peninsula (Georgsson, 1981). Later surface resistivity surveys include TEM and most recently MT. The measurements delineated a low-resistivity area interpreted as altered rocks due to high temperatures (see Sigurdsson, 2010 and references therein). The interpreted low-resistivity sheet has an aerial extension of around 11 km² at 800 m depth (Figure 7). A profile with MT and TEM measurements along the Reykjanes peninsula in 2008 revealed resistivity anomalies at depth under the Reykjanes high-temperature field, as well as other locations connected with geothermal activity (see Sigurdsson, 2010 and references therein). In 2010, more MT measurements were done in all TEM measured locations in the area. The results from 1D joint interpretation of the TEM and MT soundings showed the existence of a low-resistivity body down to 8-10 km's depth under the high-temperature field in Reykjanes.

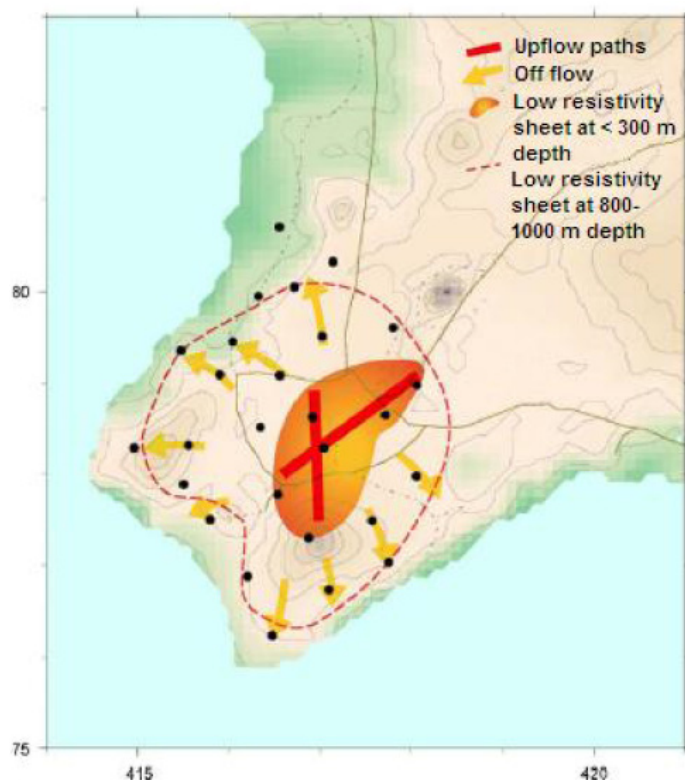


FIGURE 7: Areal extent of the low-resistivity body at 800 m depth (Sigurdsson, 2010)

Earlier exploration dates back to 1956 when the first well was drilled to 162 m depth, reaching temperatures of up to 185°C. It was soon discovered (Björnsson, 1971) that the salinity of the geothermal fluid was from seawater which made up the brine extracted in the area.

The Reykjanes geothermal field went through many developmental stages. From the 1970s through to the 1990s, it was mainly exploited for a salt factory. In the late 1990s, further investigations resulted in the drilling of well 10, and plans for developing the field for electrical generation. The power plant came online in May 2006, generating 100 MWe from two 50 MWe double flow turbines, with seawater cooled condensers (Sigurdsson, 2010).

3. FIELD PROCEDURES AND DATA ACQUISITION

It is essential to record field procedures as they differ in application and configuration from country to country and also differ depending on the aim of survey. The procedures and configurations used in my discussion are entirely based on ISOR's (Iceland GeoSurvey's) configurations and standards, applied to geothermal exploration in Iceland.

Before deploying MT and TEM equipment and their components, it is important to make sure that they are properly tested and checked. This section of the paper is written based on practical hands on experience on data acquisition and equipment setup of both TEM and MT during a field campaign at Hágöngur/Thórisvatn.

At this point, the location of all sounding stations had been planned and mapped out such that the factors outlined below were avoided and/or minimised to have a better chance for acquiring quality data.

- 1) *Topography*: EM soundings generally require setup on regular terrain.
- 2) *Power lines & electrical fences*: Soundings must be located at least 500 m away from these objects to avoid uncontrolled high frequency signals.
- 3) *Accessibility*: Preferably accessible by vehicle. Mainly to save time.
- 4) *Seasons*: Avoid seasons that bring thunderstorms which generate a lot of disturbance by injecting high-frequency and noisy signals into the area.
- 5) *Human population and environmental factors*: Movement of people and vehicles can be a source of noise in the area and, furthermore, people have the tendency to interfere with the stations in a more drastic manner. Landforms such as rivers and lakes and even geothermal manifestations are not favourable places at which to acquire quality data.

3.1.1 MT setup

Prior to an MT survey and before setting up an MT sounding (Figure 8), it is necessary that calibrations be done on MT equipment. During this field campaign, calibrations were done before the setup of the MT soundings.

Three control units consisting of two 5 channel/component control units and one 2

Channel/component control unit were used (Figure 9). The process is delicate, particularly in dealing with the magnetic coils which require care when handling. They were placed parallel and 3 m from each other (Figure 9a). Calibration involved establishing communication between the field computer and the control unit, thus, all necessary components mainly coils, global positioning system (GPS) and ground electrode had to be connected. A start-up file containing information like gains, filters, acquisition time and calibration was loaded onto the field computer using the SSMT2000 program. At this stage, the status of the data acquisition unit and its components was visually inspected before it was instructed to calibrate and store the start-up file onto a flash disk. During the same process all units were time synchronized using GPS satellites.

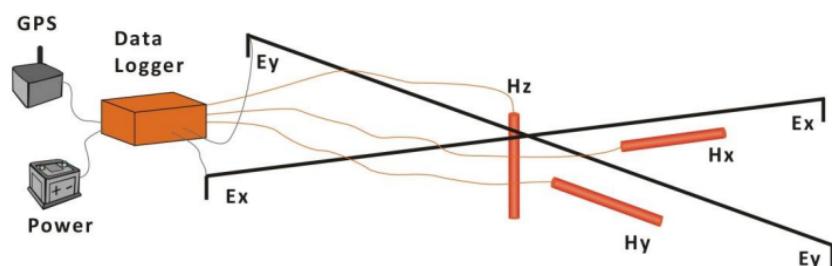


FIGURE 8: MT layout (Flóvenz et al., 2012)

To reduce the noise, particularly local cultural noise, a remote station was set up some tens of kilometres away from the survey area during data acquisition. The idea is that the magnetic field generally is the same over a large area and local cultural noise recorded at MT stations may not be recorded at the remote station. Therefore, remote stations are needed to correct for bias in the MT data as the noise part of the signals is not coherent at the two sites.

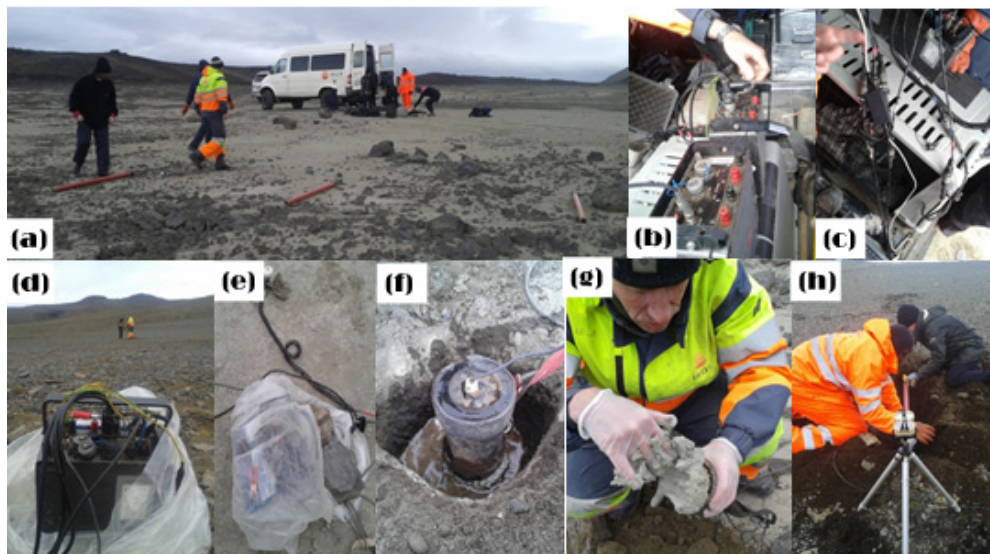


FIGURE 9: MT a) Laying out coils 3 m apart in preparation for calibration; b) Setting up recorders for calibration; c) Showing computer cable connection to recorders; d) Recorder placed facing north; e) Recorder placed in plastic bag covering; f) Planting of electrode into the earth; g) Placing bentonite on to the ceramic bottom of the electrode; and h) Burying magnetic coil component with precise orientation (N-S and E-W)

When setting up an MT sounding, the location of the station was scouted before choosing the area with a surface which typically had no more than 20 degrees of slope and was free from factors mentioned earlier. In this survey, a 5 channel MT data acquisition system (MTU-5P) from Phoenix Geophysics was used. The MT setup is made up of a data recorder, 5 non-polarising electrodes, a GPS, a 12 V battery, a flash memory card, three induction coils (telluric), a clinometer/ Brenton compass, levelling devices (3 bubbles), spades, a plastic bag for the recorder, a tripod and co-axial cables.

The typical layout for an MT sounding is shown in Figure 8, which shows the electrodes aligned in magnetic NS and EW directions, and the magnetic components in an orthogonal manner. It is customary to have the x-direction pointing to magnetic north. The recorder is placed at the centre and is usually facing north.

Firstly, the centre of the site is determined using a levelling device dropped from the tripod. The tripod is used to set up the bearings, marked with stakes by which the electrode cables are fastened to the centre pole and are moved, accordingly, to their respective placing (Figure 9).

The four electrode dipoles are buried 50 m away from the centre and 40 cm deep. The porous ceramic base of the electrode is coated with bentonite (Figure 9g) and buried with electrolytic solution salt. These measures enhance the conduction between the electrode and the ground.

The magnetic coils are extremely sensitive to noise from wind, people walking, or trucks, thus they are buried to prevent movement. The magnetic coils are precisely aligned N-S and E-W, respectively, making sure that they are properly levelled (Figure 9h) and the horizontal coil is buried upright, levelled at a 90° angle.

3.1.2 MT data acquisition

At each MT station, five measurements (channels) are recorded. They are the magnetic field in the two horizontal directions and in the vertical direction, and the electric field in the horizontal directions. In the MT method, the natural fluctuations of the earth's magnetic field are used as the signal source. Those fluctuations induce currents in the ground which are measured on the surface (E_x and E_y). The magnetic field is measured in three orthogonal directions (H_x , H_y and H_z) (Figure 8).

The electric and magnetic fields are measured as a function of time. The four channels are E_x , E_y , H_x , H_y . From basic physics, the electric field in the x direction (E_x) should correlate with the magnetic field in the y direction (H_y), and similarly E_y correlates with H_x . H_z is recorded to give information about the electric strike. E_x , H_y , E_y and H_x can be used to get information about the subsurface resistivity.

The data are synchronized with GPS signals and by comparing these data with another station's simultaneous recording, noise can be identified and reduced. This method, known as "remote referencing," allows the data at one station to be compared to data at another station, recorded at exactly the same time, and compared for coherency. Any non-coherent data are thrown out and are considered to be noise. This greatly improves data quality. Recording at each station takes 6-18 hours, depending on signal strength and survey parameters.

For a homogeneous or layered earth the electrical field is induced by (coherent with) its orthogonal source magnetic field (i.e. E_x correlates with H_y , and E_y with H_x). For more complicated resistivity structures, these relationships become more complex. The magnetic field was measured with induction coils and the electrical field by a pair of led-chlorite filled electrodes. The MT instruments used are from Phoenix Geophysics in Canada (2009), MTU type, and can measure the MT signals in the frequency range from about 400 Hz to 0.0000129 Hz.

In each sounding the MT units were deployed for recording and picked up the following day, giving about 20 hours of continuous time series. The short-period MT data (high frequency) mainly reflect the shallow structures due to their short depth of penetration, whereas long period data mainly reflect the deeper structures. The MT method has the greatest exploration depth of all resistivity methods, some tens or hundreds of kilometres, depending on the recorded periods, and is practically the only method for studying deep resistivity structures. In this survey, the exploration depth of the MT soundings was around 30 km, but varied considerably depending on resistivity and in particular on data quality.

3.1.3 TEM setup and data acquisition

Because of static shift problems in MT data in volcanic geothermal fields, care is taken when conducting TEM surveys so that they are placed at the same spot as the MT sounding (within 50-100 m). TEM equipment owned by ISOR was used for this and consisted of a PROTEM receiver and a TEM57-MK2 transmitter from Geonics, Ltd. It also had a power module (current booster), a small receiver loop (100 m²), a big receiver loop (5613 m²) and a reference cable. To produce higher and stable currents (25 A) ISOR uses a 5 kV generator.

Before setup for TEM, it is imperative to synchronize the crystal clocks in both the transmitter and the receiver. Usually they are heated up for half an hour or more. While waiting for the synchronization to complete, the TEM layout can be done. First the square transmitter loop is laid out; the size of loop is dependent on the depth of interest (to probe a depth of 1000 m, 300×300 m² is sufficient). Then the centre of the transmitter loop is marked for layout of the 10×10 m receiver loop.

Before data acquisition, current from the transmitter is sent through the transmitter loop and measured at low frequency (2.5 Hz). Extra current needed for the process is taken from the power modules, included among the equipment. Current values are registered on the transmitter when it becomes stable. Turn of time (TOT) is measured in micro-seconds at high frequency (25 Hz). This information is required in order to calibrate the receiver before measuring TEM data.

The transmitter current, usually 18-22 A, is transmitted at a high frequency of 25 Hz and a low frequency of 2.5 Hz. For each frequency, 20 measuring time gates were evenly spaced on a log-scale from 0.09-7 ms for the high frequency, and 0.9-70 ms for the low frequency, after current turn off. Repeated transients were stacked and stored in the computer memory of the receiver and later downloaded to a personal computer, ready for further processing.

4. DATA PROCESSING AND INVERSION

This section of the report describes the process and steps involved in preparing the MT and TEM raw data, using various programs used by ISOR. Processing of MT data involved the use of SSMT2000 software by Phoenix while the TEM raw data were processed using an in-house program TemX, which was developed by ISOR (Árnason, 2006a). SSMT2000 is a Windows-based software used in a Windows XP platform, while the TemX is a UNIX based program.

TEM and MT data used in this section were borrowed from HS Orka for this project exercise and consisted of 17 TEM soundings and 17 MT soundings. The measurements of TEM and MT data were made in the years 2008, 2010 and 2012. For joint inversion purposes, the TEM and MT had to be paired so they were measured approximately in the same location to give better results.

Inversion of both TEM and MT was done using TEMTD (Árnason 2006b), developed by ISOR. The program has the capability of inverting both TEM and MT, independently or even jointly.

4.1.1 Processing of MT data

Raw data from MT were imported into SSMT2000 where the calibration files and also the remote station data were used for processing. The digitally recorded times series were Fourier transformed from the time domain into the frequency domain, then the robust processing method provided by the SSMT2000 was used to calculate the auto and cross powers.

The output files, consisting of average cross and auto powers, were imported into MTeditor (program from Phoenix) where manual editing was done. Manual editing is only necessary if a visual inspection of the data is unsatisfactory in the eyes of the experienced geophysicist. The processed sounding is saved as a standard EDI file format which can then be used as an input file for the inversion process.

The MT data must go through a series of steps following the above, where conversion of the EDI file to a UNIX format is required in order to invert the apparent resistivity and phase contained in the auto and cross powers. The following steps were followed:

- 1) Input files RKN018.mth and RKN018.mtl are automatically formed by the MTeditor which are used to produce the file RKN018.mpk.
- 2) Using MT-Editor, we converted for EDI (universal data standard for MT) using RKN018.mpk file. The file, at this stage, will have the extension .edi which is in ASCII format.
- 3) The next step is to convert the file in ASCII format to BINARY format so that the .edi can be used in UNIX. This step is required because all programs used for inversion were developed in the UNIX background. The conversion is done using the command *dos2unix* which is executed in terminal mode in UNIX.
- 4) *spect2edi* command is then executed on the resulting file from the last step, where the file format is rearranged and calculations of various MT parameters and GPS coordinates are converted from degrees to wgs84. The product from this step is a standard EDI file format with the extension **.EDI**.

The file produced (RKN018.EDI) at the end of this process is now the input for TEMTD which is a UNIX based program used to invert MT and TEM data. Figure 10 shows a typical processed MT data, generated using the TEMTD command *edi2ps*.

4.1.2 Processing TEM data

TEM data measured by the PROTEM-D3 receiver were extracted and loaded into TemX program for visual inspection and editing. TemX calculates averages and standard deviations for repeated transient voltage measurements and calculates late time apparent resistivity as a function of time. These are

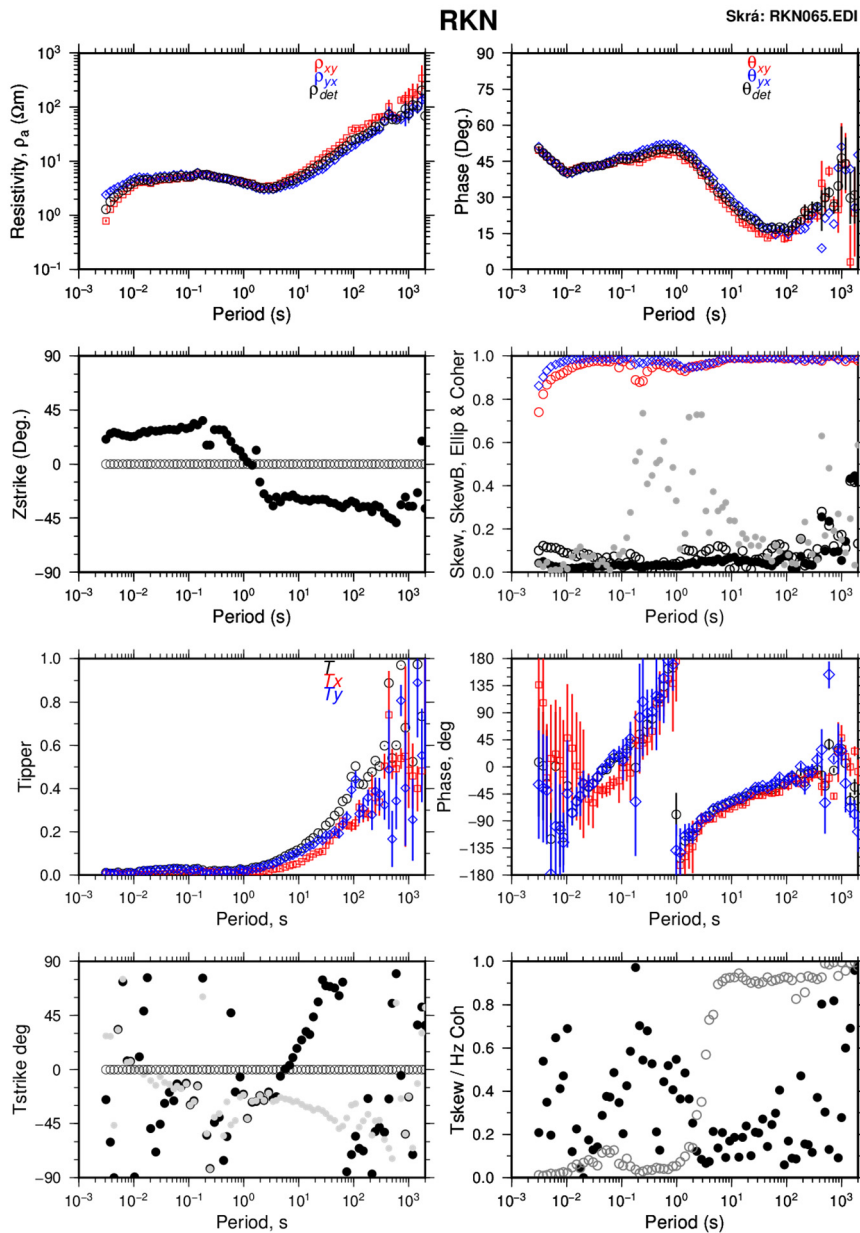


FIGURE 10: Processed MT data: The top row shows apparent resistivity denoted by ρ_{xy} (red) and ρ_{yx} (blue) which is also depicted in the associated Phase diagram to the right; The ρ_{det} (black) dots denote the determinant invariant; The second row of diagrams shows the Z-strike (Swift angle) denoted by black dots on the left side; on the right is shown the coherency dots in red and blue for ρ_{xy} and ρ_{yx} respectively; The black dots depict skew and the grey dots are the ellipticity; The bottom two rows of diagrams show various forms of Tipper data

All masking is done at the voltage plot where stacking of voltages at the same time is performed. Once satisfied, the TEM data file header is modified, by adding information about the data. Information such as coordinates of the sounding, elevation, personnel involved in the survey, site of the sounding, sounding name and the datum used at that time are then inserted. For this case, the datum used was UTM-WGS84. The TEM data is now complete and saved as an .INV file which will be the input file to the program TEMTD.

displayed visually using a graphical-user interface (GUI); the program is also user interactive where the outliers or noise readings can be masked out by the click of a mouse. For my project, 8 TEM soundings were processed using TemX while the rest were already processed INV files. To process TEM data using TemX, the file is loaded using TemX in a UNIX terminal.

Upon loading TEM data, the turn off time and the drift values recorded in field note books are given where necessary. This is needed to correct for turn-off time and drift time recorded off the PROTEM-D3 transmitter during the survey. TemX displays the TEM data, as shown in Figure 11, where on the left, the transient voltages are plotted versus time, and the right shows apparent resistivity plotted versus time. In the apparent resistivity plot, the blue dots represent the high frequency data recorded at early times, while the red and green dots are the late time data recorded at low frequency.

4.2 Inversion of TEM and MT data

Inversion of TEM and MT data was done using the TEMTD program. TEMTD performs 1D inversion with horizontal layered earth models or Occam inversion of central-loop Transient Electro-Magnetics (TEM) and Magnetotelluric (MT) data. It can be used to invert either TEM or MT data, or jointly invert both TEM and MT data, by which the best static shift parameter for the MT data is determined. The program assumes, for TEM data, a source loop of square shape and that the receiver loop is at the centre of the source loop. Waves forms of the current are assumed to be half-duty bipolar semi waves (equal current-on and current-off segments), with exponential current turn-on and linear current turn-off. For MT data, the program assumes standard EDI for impedance and/or apparent resistivity and phase data. The program runs under UNIX/LINUX operating systems and is written in ANSI-C. It uses the gnuplot graphics program to display graphics from the inversion.

For this report, at the start only TEM data were inverted using 1D (layered earth) Occam (minimum structure) inversion; final models (.plo files) were set aside for use in the joint inversion of TEM and MT. During this process, the rotationally invariant determinant apparent resistivity and phase of the MT and TEM soundings were inverted. Figure 12 shows a typical result of such inversion. The best estimate of the shift parameter for this sounding is $S = 0.686$, i.e. the MT apparent

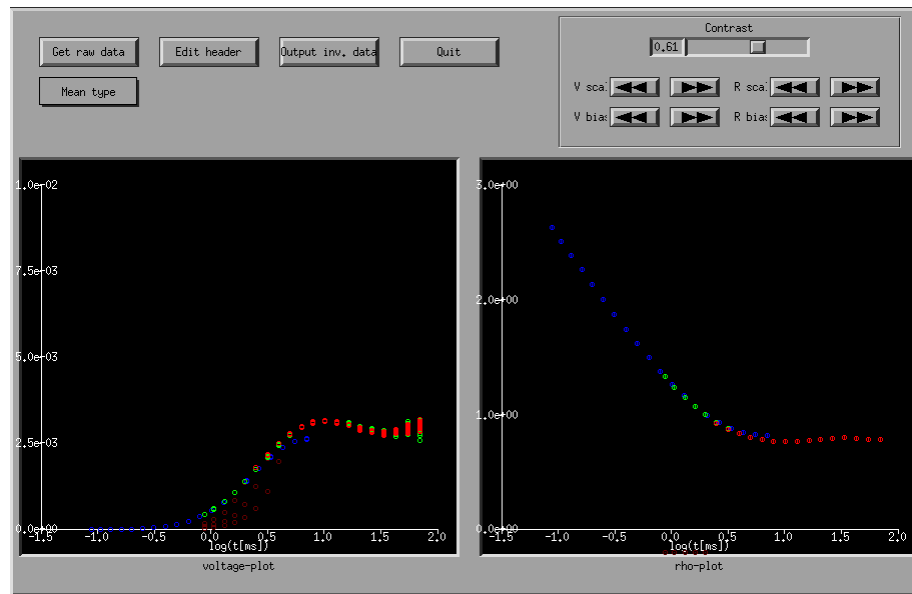


FIGURE 11: TemX GUI used to visualize TEM data and edit outliers/noise

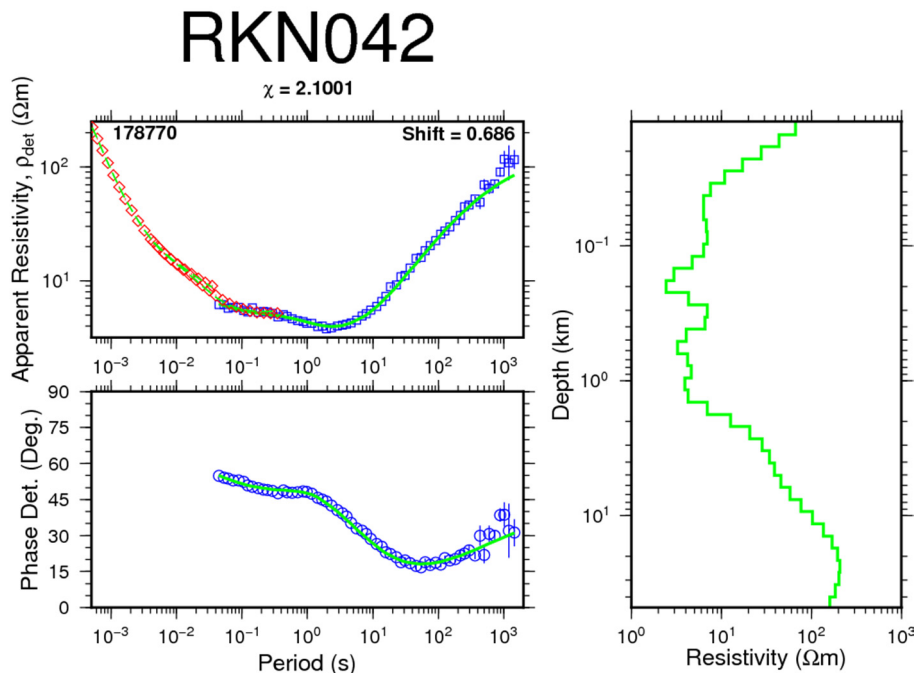


FIGURE 12: A typical result of 1D joint inversion of TEM and MT soundings; red diamonds: TEM apparent resistivities transformed to a pseudo-MT curve; blue squares: measured apparent resistivities; blue circles: apparent phase derived from the determinant of MT impedance tensor; light blue symbols to the left of the green curve: data not used in the inversion; green lines: on the right are results of the 1D resistivity inversion model and to the left are its synthetic MT apparent resistivity and phase response; vertical blue line: error bars

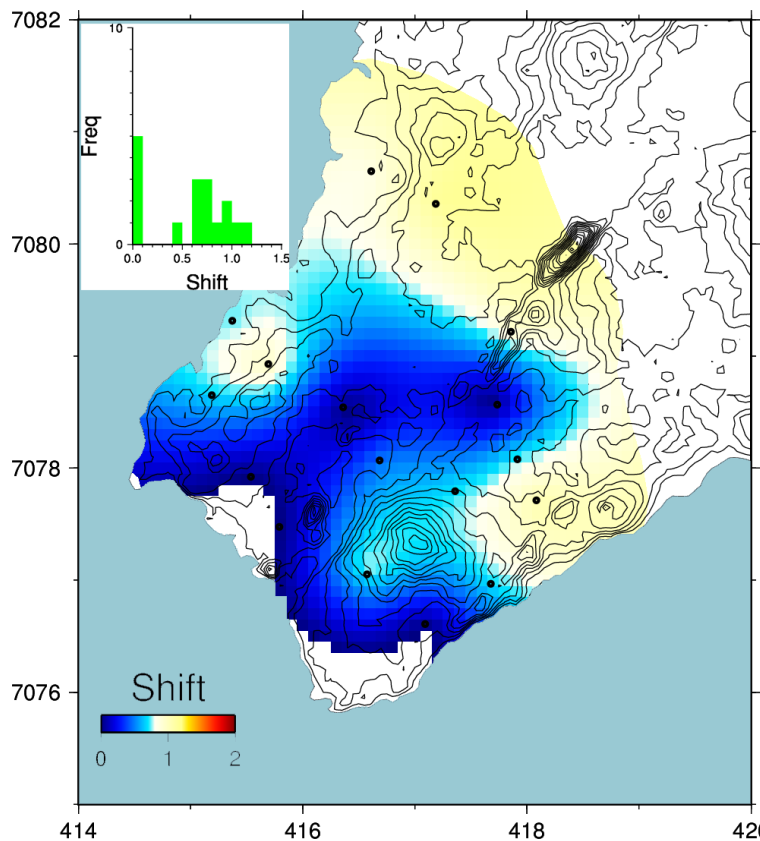


FIGURE 13: Spatial distribution of static shift parameters for the determinant apparent resistivity in the Reykjanes area; black dots denote TEM and MT sounding locations

5. RESULTS AND INTERPRETATION

From the 1D joint inversion of TEM and MT data, associated programs written by ISOR were used to generate: cross-sections, iso-resistivity maps, shift maps, rose diagrams and induction arrows, which are given in the Appendix section of the report (Verave, 2013). Due to technical issues, rose diagrams, induction arrows and Tippers were not produced. In all, 17 TEM and MT soundings were jointly inverted. Four profiles, shown in Figure 14, were used to extract cross-sections to a depth of about 20 km. The map also shows surface manifestations and wells used to correlate with subsurface resistivity.

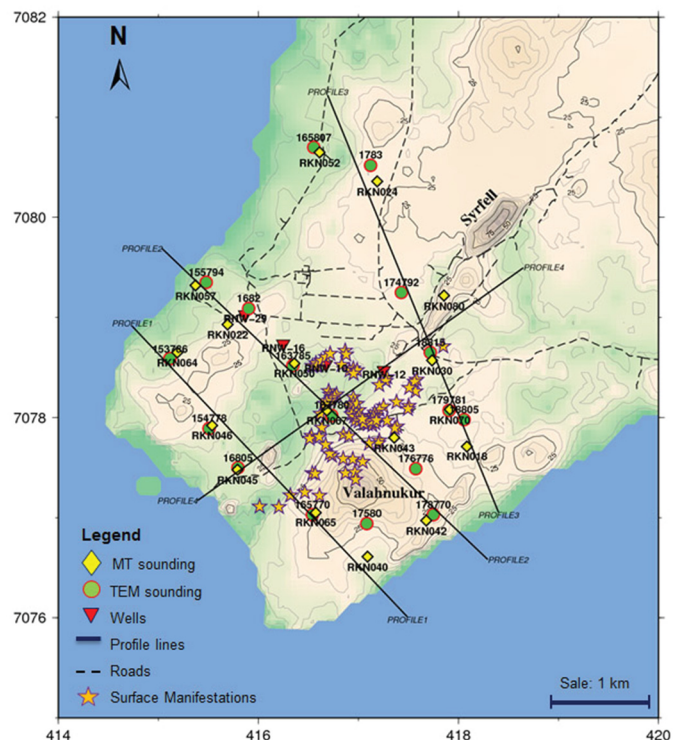


FIGURE 14: Locality map of TEM and MT soundings

resistivity has to be divided by 0.686 to be consistent with the TEM sounding. In Figure 12, the TEM data were plotted as a function of the period (T) by using the transformation $T = t/0.2$ (Sternberg et al., 1988) which differs from what happens in the inversion of TEM only.

A histogram of all shift multipliers for all 17 soundings is given in Figure 13 as an insertion. It is seen that they are in the range 0.1-1.2, and that the static shift multipliers lower than one are more common than those higher than one. Shifts lower than 1 are within the vicinity of surface manifestations. The shift values greater than 1 are located further away from the low-resistivity anomaly and the surface manifestations (Figure 13). It is, therefore, important to calculate and map out the shift distributions.

5.1 Resistivity cross-sections

Profile 1 runs approximately 3.5 km NW-SE and is situated in the southwesternmost part of the Reykjanes geothermal field. Figure 15 shows two cross-sections taken from this profile where five TEM and MT soundings were used. Cross-section A reveals subsurface resistivity distribution down to 5000 m. A low-resistivity layer is well defined in the upper most part of cross-section A, spanning from 0 to 1800 m depth below sea level (b.s.l.), with resistivity values ranging from 1 to 10 Ωm . The lowest resistivity value of 1 Ωm was seen below MT sounding RKN046 at a depth of 500-1000 m. The appearance of the conductive cap of low resistivity is consistent with previous resistivity surveys which observed a continuous homogeneous low-resistivity anomaly in the Reykjanes field (see Sigurdsson, 2010 and references therein). Beneath this conductive cap below 1800 m, we see a gradual increase in resistivity down to about 4000-5000 m b.s.l. where the subsurface becomes more resistive. Resistivity values of up to a 100 Ωm are observed at this depth.

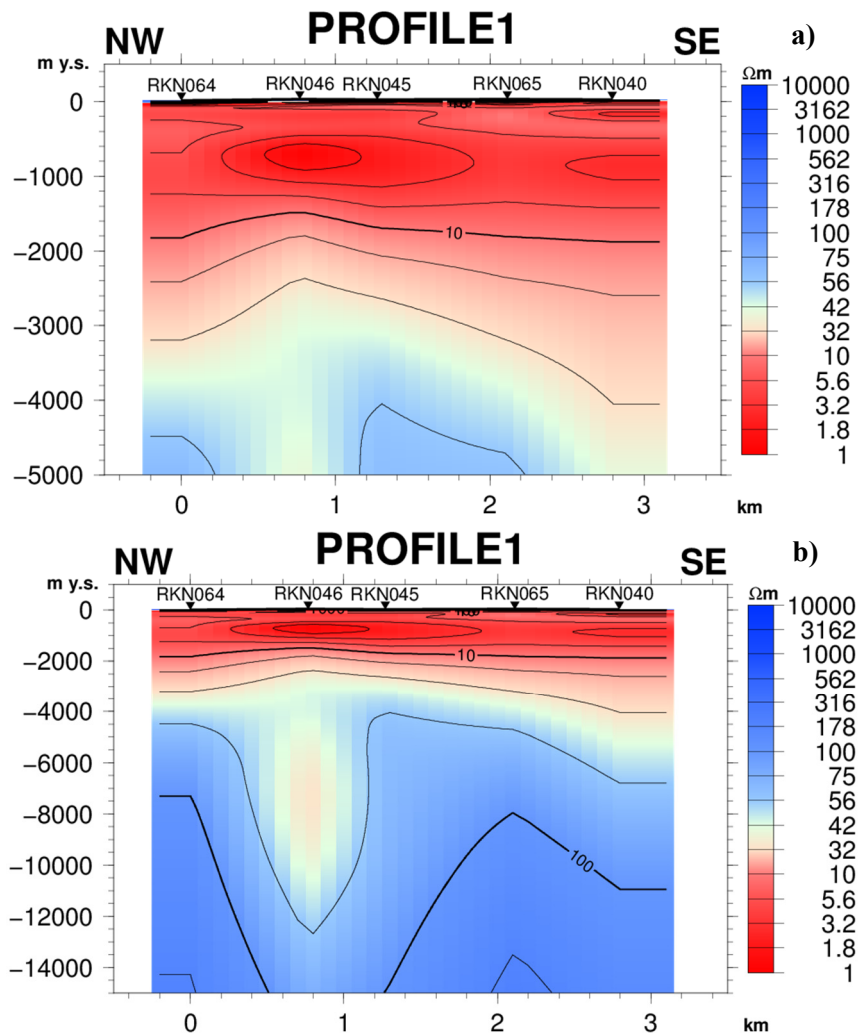


FIGURE 15: Profile 1 showing a resistivity cross-section, a) to a depth of 5000 m; and b) to a depth of 15,000 m

Cross-section B shows the deep resistivity structure beneath profile 1 down to 15000 m, where an anomalous low-resistivity body is prominent. It is directly below MT sounding RKN046 and extends from 4000 to 12000 m, i.e. through the high-resistivity body. The resistivity in this body may be up to 40 Ωm . This presumably could be due to low-resistivity alteration minerals that have precipitated in fractures and filling beneath MT sounding RKN46. It is also observed that the conductive cap is thinner in the northwest and broadens toward the southeast (controlled by surface activity).

Profile 2, (Figure 16), runs NW-SE, and is located between profile 1 and profile 3 (Figure 14) and passes through the area of main surface manifestations. It spans across the centre of the high-temperature area, for 3.8 km, including 6 TEM and MT soundings. Cross-section A of profile 2 shows a similar resistivity distribution as profile 1, with a homogeneous low-resistivity cap extending from 0 to 2000 m depth. The lowest resistivity values of 1 Ωm was observed beneath MT sounding RKN067 and extends a little southeast directly under MT sounding RKN043 and is encountered at a shallow depth of 200 m and extends to about 800 m. The 10 Ωm resistivity contour clearly defines the transition from the low-resistivity zone to increasing resistivity. Cross-section B of profile 2 does not show the anomalous low-

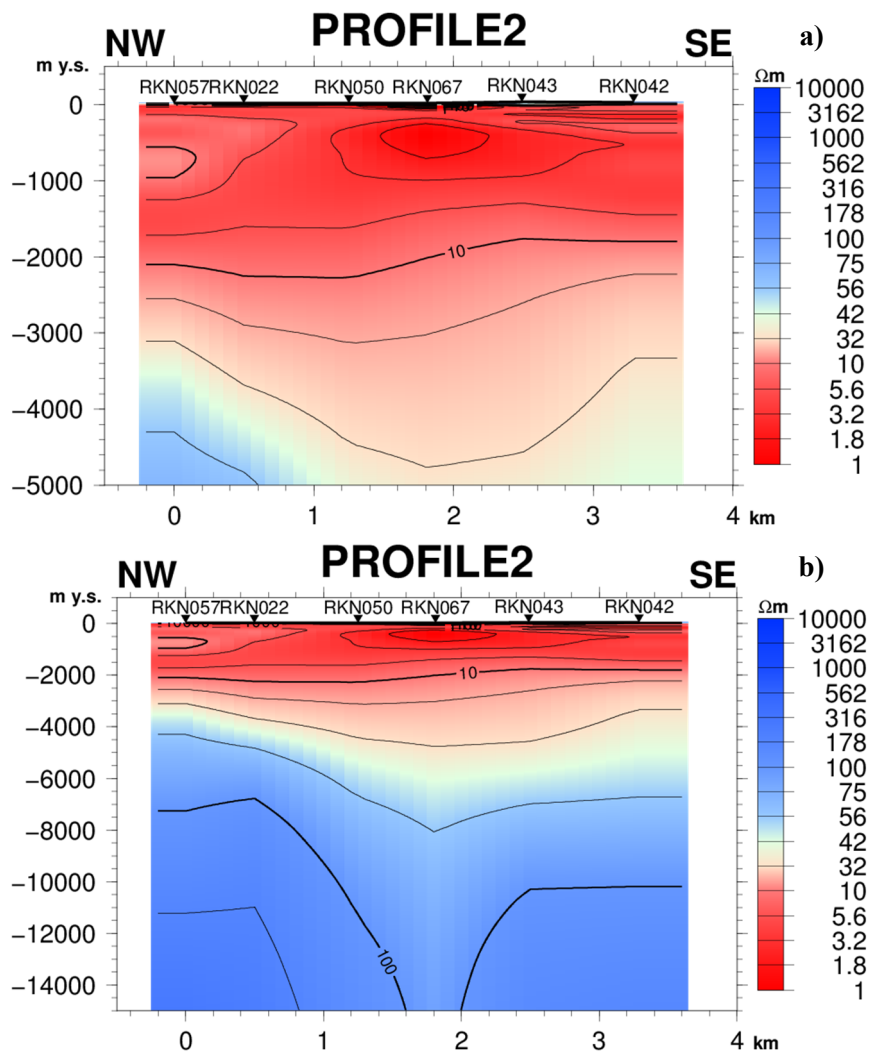


FIGURE 16: Profile 2 showing resistivity cross-section, a) to a depth of 5000 m; and b) to a depth of 15,000 m

resistivity pocket observed in Profile 1. This could be due to the quality of MT data taken from this profile.

Profile 3 (Figure 17) runs also NW-SE, and is located away from the centre of the geothermal field towards the northeast corner. It consists of 6 MT and TEM soundings that make up a profile of more than 4 km in length. The area it covers has little or no surface manifestations. The only manifestations found are located near MT soundings RKN80 and RKN30. Cross section A probes to a depth of 5000 m. The low-resistivity cap at shallow depth is consistent with what has been seen in the previous profiles. However, here the lateral resistivity distribution is not as continuous as observed previously. The resistivity contour shows irregularities and is not well connected laterally. Directly below MT

sounding RKN030, the lowest resistivity of 1 Ωm was observed; it is laterally continuous towards the southeast of profile 3 between 200 and 1200 m depth. Northwest of profile 3, there is a break in the lateral continuity of low resistivity, caused by the upward appearance of a 10 Ωm resistivity value.

Cross-section B of profile 3 shows a low-resistivity body at 12,000 m below sea level, similar to that observed in profile 1. The low-resistivity body is encountered at a greater depth than that shown in profile 1 and is directly beneath MT sounding RKN030.

Profile 4 (Figure 18) cuts through the centres of profiles 1, 2 and 3 in a SW-NE direction and covers MT soundings RKN045, RKN067, RKN030 and RKN080 (Figure 14). Cross-section A of profile 4 clearly shows a laterally continuous low-resistivity cap extending from 0 to about 1800 m where the high-resistivity boundary is found. A pocket of very low resistivity is imminent below soundings RKN067 and RKN030, which are situated directly within the area of surface manifestations (Figure 14). Cross-section B shows the subsurface distribution to a depth of 15000 m and reveals a low-resistivity anomaly around the same depth as that observed in profile 3 (12000 m). This low-resistivity anomaly appears to be at the intersection of profiles 3 and 4.

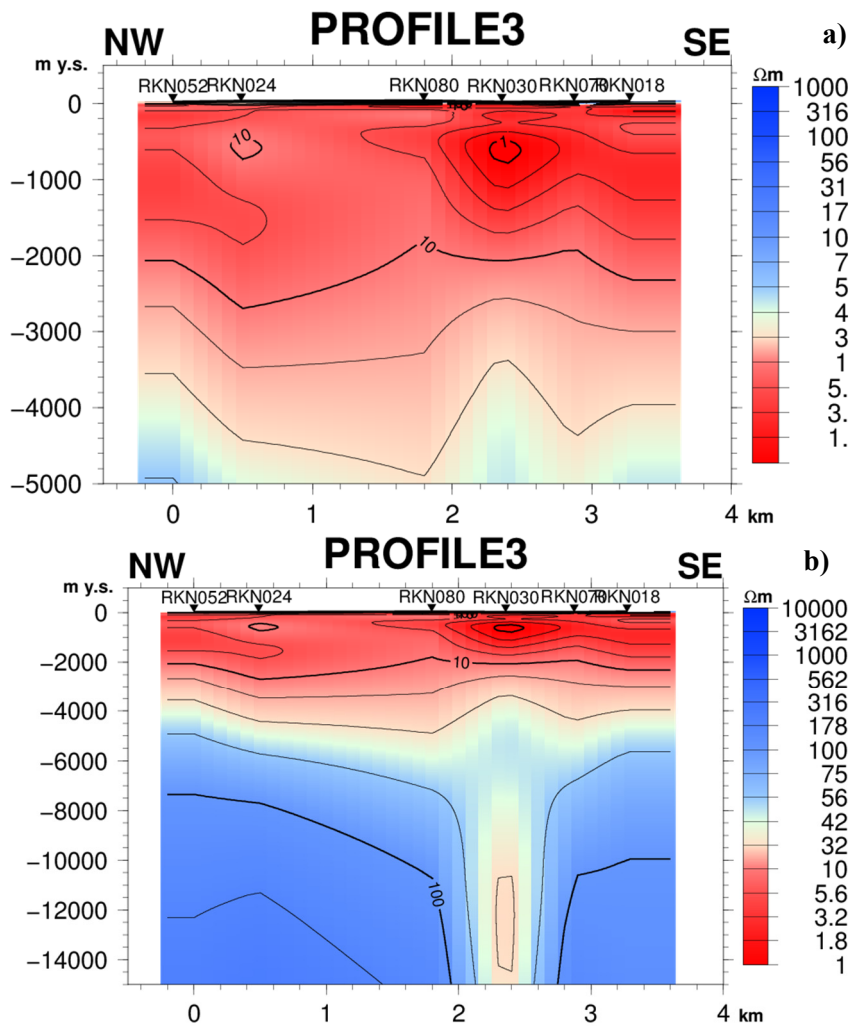


FIGURE 17: Profile 3 showing resistivity cross-section, a) to a depth of 5000 m; and b) to a depth of 15,000 m

5.2 Iso-resistivity maps

Figure 19 shows iso-resistivity maps at 500 and 2500 m b.s.l. The areal extent of resistivity at 500 m was interpreted as a low-resistivity sheet which covers the whole Reykjanes geothermal field. Resistivity values range from 1 to 10 Ωm with the lowest resistivity found in the central part of the geothermal system and higher resistivity values, mainly towards the fissure swarm in northwest. A resistivity patch of 1 Ωm is located directly below sounding RKN030 and it elongates towards the sea in the west where sounding RKN046 is situated (Figure 19a). This may indicate some connectivity below the two soundings. The area of very low resistivity correlates well with the location of surface manifestations.

At 2500 m (Figure 19b) the resistivity is considerably higher with values ranging from 30 to 40 Ωm . Lower resistivity values are prominent in the northeast but resistivity increases toward the southwest part of the geothermal field. At this depth, the conductive cap (sheet) has already diminished.

Figure 20 shows the resistivity distribution at 10,000 m b.s.l. High resistivity values of 100 Ωm dominate the extent of the geothermal field with two patches of low-resistivity bodies protruding the high-resistivity layer. Judging by the resistivity contours, the two low-resistivity anomalies seem to be connected. A similar connecting trend is seen in Figure 19a. Coincidentally, the two low-resistivity

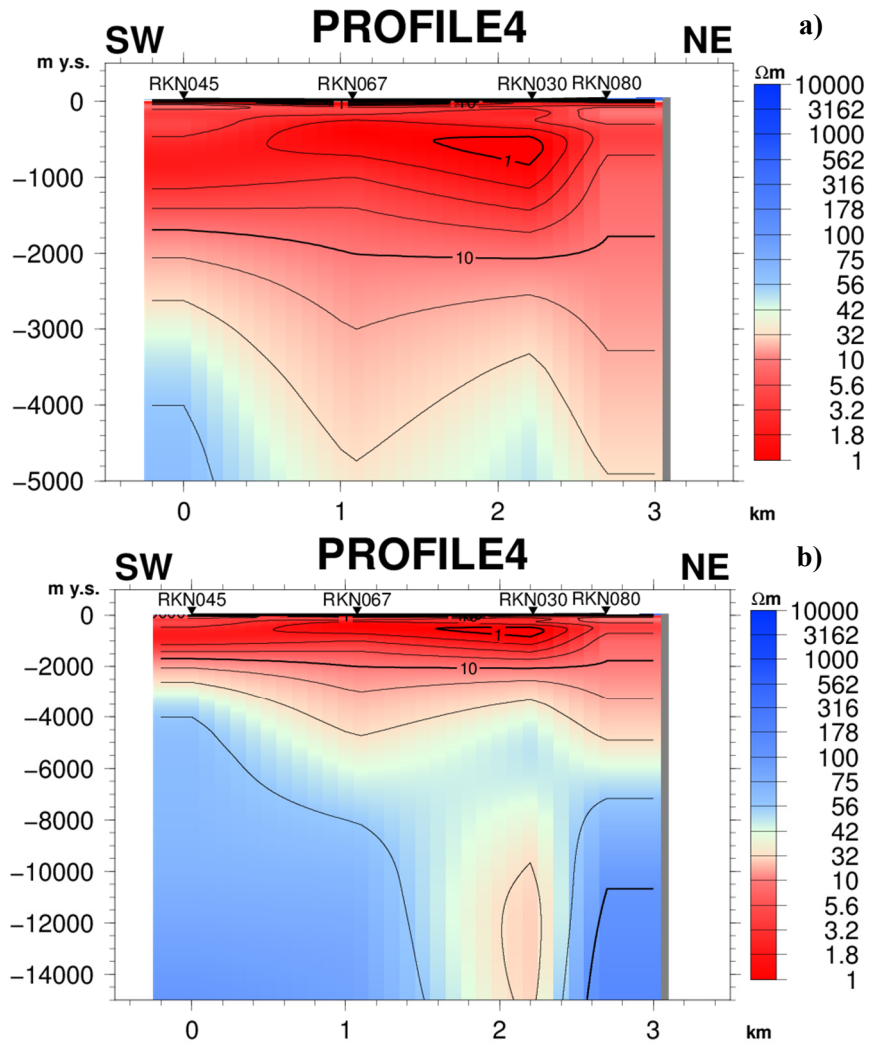


FIGURE 18: Profile 4 showing resistivity cross-section, a) to a depth of 5000 m; and b) to a depth of 15,000 m

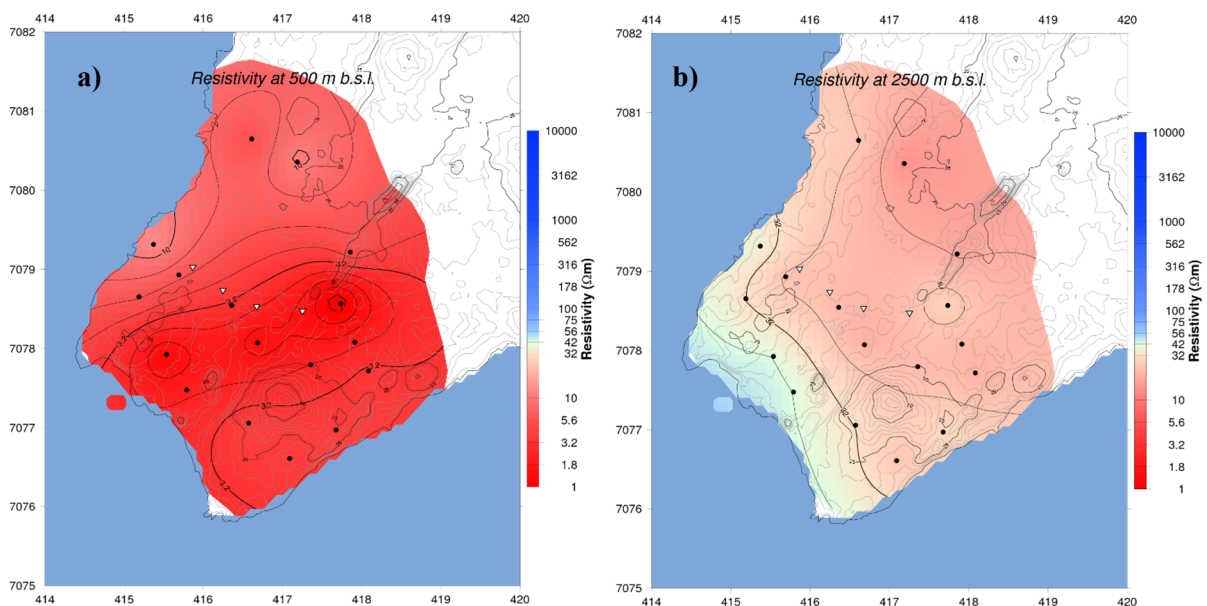


FIGURE 19: Iso-resistivity maps at a) 500, and b) 2500 m b.s.l.

anomalies fall directly beneath soundings RKN030 and RKN046. The low-resistivity anomaly below sounding RKN030 is more prominent than that seen below sounding RKN046. The anomaly could be associated with a heat source at this depth.

5.3 Correlating resistivity cross-sections and hydrothermal alteration

For practicing purposes, two cross-sections, from profile 2 and profile 4, were used to show hydrothermal mineral alteration as revealed in cuttings from the boreholes. Well data and information for well 10 were taken from Franzson et al. (2002) and are reliable. Information from wells 16 and 29 were estimates of alteration occurrences at various depths.

Figure 21a shows profile 2 with wells 10, 16 and 29 plotted with their alteration information. Well 10 shows smectite/zeolite from the top and down to 500 m. A thin layer chlorite zone sits below the smectite/zeolite zone with a thickness of 100 m. From 600 to 1100 m, the chlorite/epidote zone is found with epidote/amphibole dominating below 1100 m. The estimated depth and alteration sequences of wells 16 and 29 are similar, only differing in thickness and depth of occurrence. The sequences of the two latter wells are as follows: they start with an unaltered layer at the top followed by a thick layer of smectite/zeolite, a thin mixed-clay layer (100 m). At the bottom of the well, epidote/amphibole dominates.

Using information from well 10, it can be seen that the resistivity cross-section does not correlate sharply with the alteration sequence. While saying that, we can still see

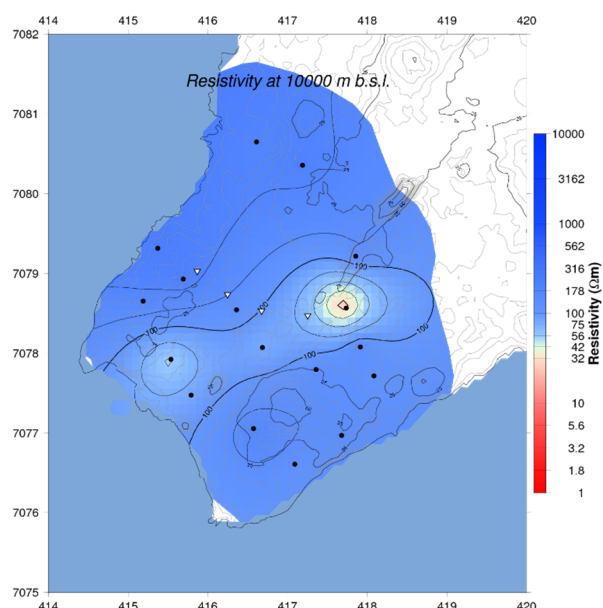


FIGURE 20: Iso-resistivity map showing areal distribution of resistivity at 10,000 m b.s.l.

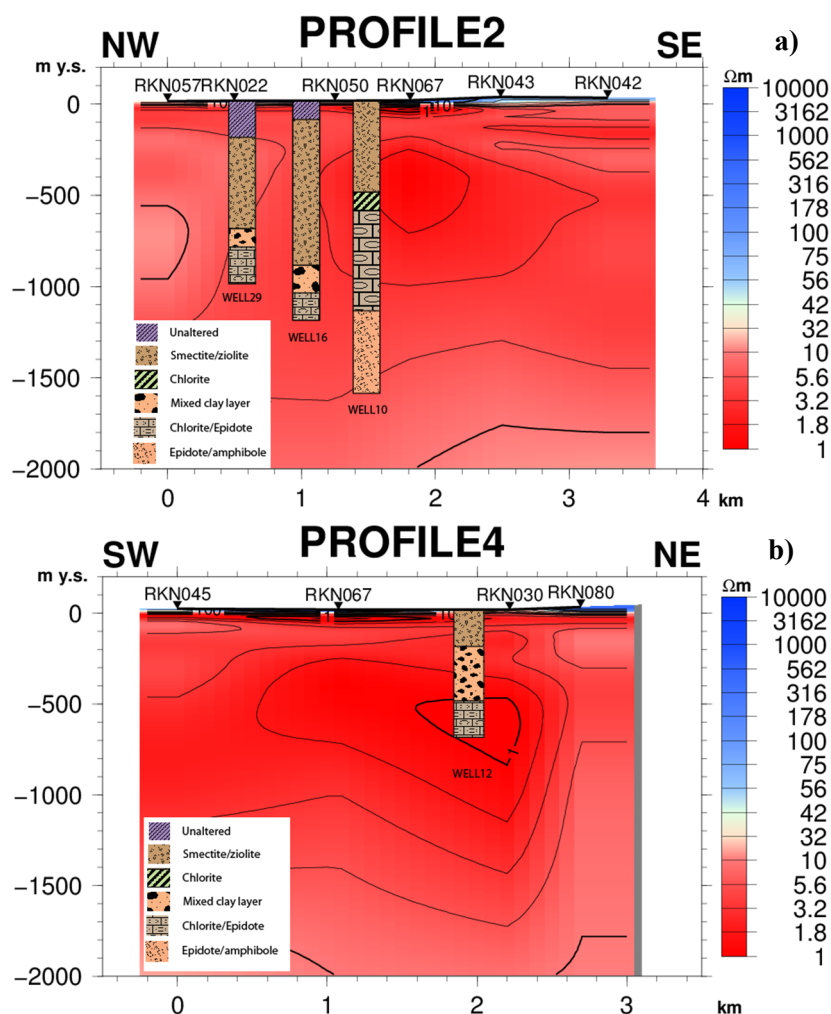


FIGURE 21: Correlation between subsurface resistivity and alteration minerals down to 2000 m; a) Profile 2; and b) Profile 4

some correlation. The smectite/zeolite zone fits well with the resistivity values of 1-3 Ωm which are found below soundings RKN050 and RKN067 at a depth of 500 m. A chlorite zone is found within this low-resistivity anomaly, which may infer the transitional boundary of low to higher temperatures. The chlorite/epidote zone is found within the low-resistivity anomaly and extends down and out of the low-resistivity pocket. The colour gradient of the resistivity begins to change at depths where epidote/amphibole are found. Higher resistivity values up to or greater than 10 Ωm can be seen and resistive minerals such as epidote and amphibole are dominant. The explanation for the average correlation of the alteration and resistivity distribution can be attributed to the colour pallettes used to display the resistivity distribution and/or are due to the high seawater salinity in the system.

Profile 4 cross-section (Figure 21b) shows well 12 with information of alteration minerals acquired from borehole data given by ISOR. The well penetrates through a region of a low-resistivity patch at a depth range of 500-1600 m. The smectite/zeolite layer is found at resistivity values of 3.5-5 Ωm , while the mixed-layer clays are found at a resistivity range of 1-3.5 Ωm . The bottom sequence of chlorite/epidote begins at 1 Ωm and extends downwards and away from the low-resistivity layer. The alteration and resistivity correlation does not agree very well in this case.

5.4 2D layout of profile

All profiles produced were finally arranged in such a way as to give a 2D view of their relative position (Figure 22). The aim was to compare the deep-resistivity distribution and anomaly found in all four profiles at once, and come up with an explanation to questions that might arise from this 2D view. From Figure 22 we see a low-resistivity anomaly at depths of up to 10,000 m in the centre of all three profiles that run through the geothermal field in a NW-SE direction. It is, however, not prominently shown in profile 2 and this could be due to the quality of the sounding above the expected anomaly. Profile 4, in contrast, runs in a SW-NE direction and cuts through the other profiles (as shown by a yellow block), and shows the anomaly at a similar depth but further toward the northeast. There is some linearity about the anomaly which, at depth, is prominent. The low-resistivity anomaly at greater depths may be attributed to the main fractures, running SW-NE, caused by the Mid-Atlantic spreading. The low-

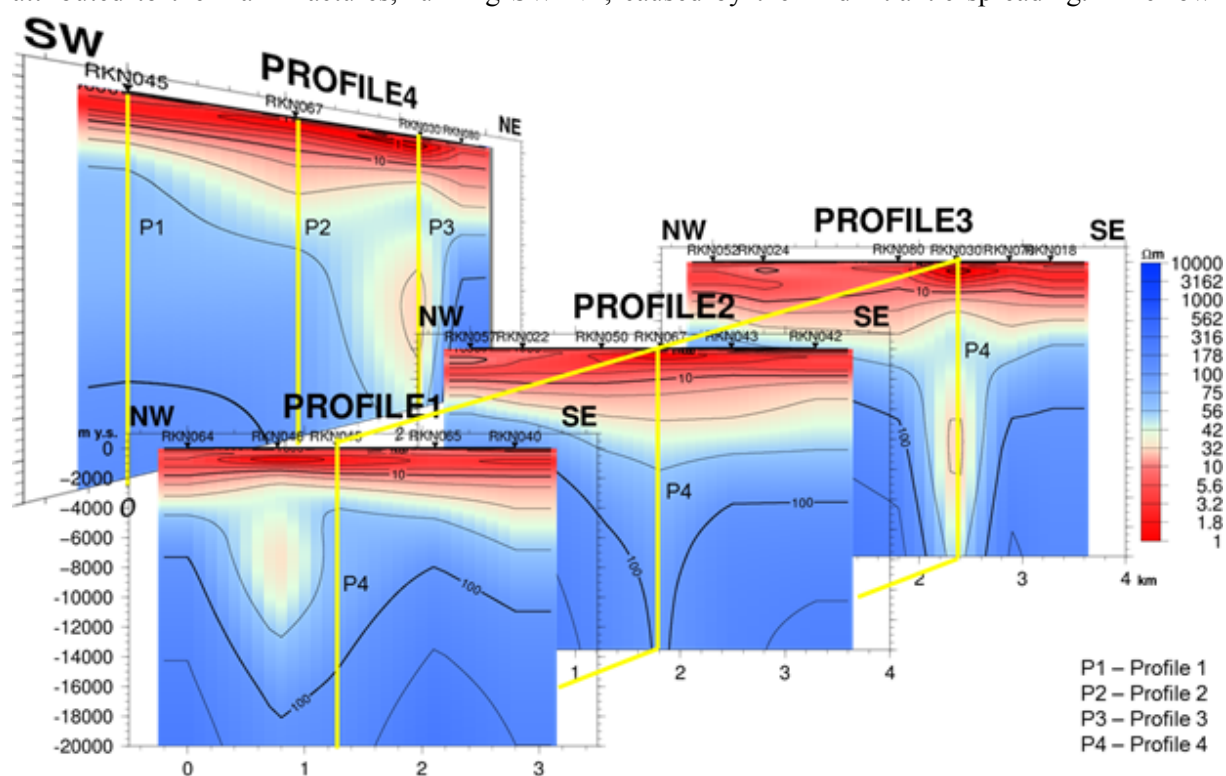


FIGURE 22: 2D layout of a cross-section depicting the deep resistivity distribution of Reykjanes

resistivity values of 10-42 Ω m at the anomaly, protrude the much more resistive surrounding formation and the resistivity values may be caused by the appearance of less resistive alteration minerals. In addition, profile 4 shows the same anomaly found in profile 3 and it is much broader than in profile 3; this could be because it cuts through a large portion of the intersection of two fractures described by Sigurdsson (2010).

6. DISCUSSION AND CONCLUSIONS

1D joint inversion of TEM and MT data was performed, based on 17 TEM and MT soundings leased from HS Orka for the purpose of my training. The results obtained and interpreted cannot be considered conclusive. Using more data would have helped in giving better results, but the main idea was to become acquainted with the skills and knowledge involved in producing the results presented in this report.

The results of all cross-sections derived from all the profiles were strikingly similar. A homogenous low-resistivity layer exists above a high-resistivity body. The low resistivity is associated with the presence of conductive minerals, such as smectite and zeolite, and the higher resistivity below the conductive cap is caused by resistive minerals such as chlorite, epidote and amphibole. The anomalously low resistivity values are mainly influenced by the seawater salinity present in the geothermal field.

A low-resistivity anomaly, relatively speaking, at deeper parts of the geothermal system, found in profiles 3 and 1, shows resistivity values that indicate the presence of alteration minerals epidote and amphibole, which may have been left behind by the upflow of geothermal fluid. However, it is more likely that this low resistivity is due to different alteration found here in fractures and linings of the walls. This could also mean that the anomaly seen here could be activated by deep fractures where there is good permeability. This is also evident in the iso-resistivity map taken at a depth of 10,000 m b.s.l.

In conclusion, the application of 1D joint inversion of TEM and MT data to detect and delineate geothermal resources is evidently supreme. The results from 1D joint inversion of TEM and MT data can be correlated with the main parameters that influence the geothermal reservoir.

Inversion of MT alone is subject to static shift problems and, therefore, it is recommended that TEM data must be jointly inverted with MT to give a more reliable result, especially in high-temperature volcanic systems.

ACKNOWLEDGEMENTS

I would like to thank the United Nation University and the government of Iceland for this wonderful opportunity to be one of the 2013 UNU-GTP Fellows. I would also like to extend my appreciation to Mineral Resource Authority for releasing me for this training, particularly Mr. Nathan Mosusu, for his support and encouragement leading up to the training.

My modest and sincere gratitude is extended to my supervisors, Mr. Gylfi Páll Hersir, Mr. Andemariam Teklesenbet and Mr. Knútur Árnason for their excellent help, guidance, advice, tireless work and the knowledge passed during the project season.

My heartfelt thanks are extended to the outgoing Director, Dr. Ingvar Birgir Fridleifsson, and his successor, Mr. Lúdvík S. Georgsson, for their encouraging words and support from start to finish of this training. Special thanks to Ms. Thórhildur Ísberg, Mr. Markús A.G. Wilde, Ms. Málfríður Ómarsdóttir

and Mr. Ingimar G. Haraldsson, for their help in getting things done administratively and for personal matters.

I am also thankful to the class of 2013 UNU-GPT for friendship and help through the highs and lows of life in Iceland.

Lastly, I wish to acknowledge my wife for the commitment and patience during the 6 months of training, and to whom I dedicate this work.

REFERENCES

Árnason, K., 1989: *Central loop transient electromagnetic sounding over a horizontally layered earth*. Orkustofnun, Reykjavik, report OS-89032/JHD-06, 146, 54-67.

Árnason, K., 2006a: *TEMX (A graphical interactive program for processing central-loop TEM data, short manual)*. ISOR Iceland GeoSurvey, Reykjavik, 10 pp.

Árnason, K., 2006b: *TEMTD (Program for 1D inversion of central-loop TEM and MT data)*. ISOR Iceland GeoSurvey, Reykjavik, short manual, 16 pp.

Árnason, K., Flóvenz, Ó.G., Georgsson, L.S., and Hersir, G.P., 1987a: Resistivity structure of high-temperature geothermal systems in Iceland. *International Union of Geodesy and Geophysics (IUGG) XIX General Assembly, Vancouver Canada, Abstracts V*, 477.

Árnason, K., Haraldsson, G.I., Johnsen, G.V., Thorbergsson, G., Hersir, G.P., Saemundsson, K., Georgsson, L.S., Rögnvaldsson, S.Th., and Snorrason, S.P., 1987b: *Nesjavellir-Ölkelduháls, surface exploration 1986*. Orkustofnun, Reykjavik, report OS-87018/JHD-02 (in Icelandic), 112 pp + maps.

Björnsson, S. (ed.), 1971: Reykjanes, final report on the exploration of the geothermal field. Orkustofnun, report (in Icelandic), 190 pp.

Cagniard, L., 1953: Basic theory of the magneto-telluric method of geophysical prospecting. *Geophysics*, 18, 605-635.

Cantwell, T., 1960: *Detection and analysis of low-frequency magnetotelluric signal*. PhD thesis, M.I.T., Department of Geology and Geophysics, Cambridge, Ma. USA, 171 pp.

Dakhnov, V.N., 1962: Geophysical well logging. *Q. Colorado Sch. Mines*, 57-2, 445 pp.

Einarsson, P., 1991: Earthquakes and present-day tectonism in Iceland. In: Björnsson, S., Gregersen, S., Husebye, E.S., Korhonen, H., and Lund, C.E. (editors), *Imaging and understanding the lithosphere of Scandinavia and Iceland. Tectonophysics*, 189, 261-279.

Flóvenz, Ó.G., Hersir, G.P., Saemundsson, K., Ármannsson, H., and Fridriksson Th., 2012: Geothermal energy exploration techniques. In: Sayigh, A., (ed.), *Comprehensive renewable energy*, vol. 7. Elsevier, Oxford, 51-95.

Franzson, H., Thórdarson, S., Björnsson, G., Gudlaugsson, S.Th., Richter, B., Fridleifsson, G.Ó., and Thórhallsson, S., 2002: Reykjanes high temperature field, SW-Iceland, geology and hydrothermal alteration of well RN-10, *Proceedings of the 27th Workshop on Geothermal Reservoir Engineering*, Stanford University, Stanford, Ca, SGP-TR-171, 8 pp.

Fridleifsson, G.Ó., and Albertsson, A., 2000: Deep geothermal drilling at Reykjanes Ridge: Opportunity for an international collaboration. *Proceedings of the World Geothermal Congress 2000, Kyushu-Tohoku, Japan*, 3701-3706.

Georgsson, L.S., 1981: A resistivity survey on the plate boundaries in the western Reykjanes peninsula, Iceland. *Geothermal Resources Council, Trans.*, 5, 75-78.

Georgsson, L.S., 2013: *Geophysical exploration*. UNU-GPT, Iceland, unpublished lecture notes.

Hersir, G.P., 2013: *Resistivity of rocks*. UNU-GTP, Iceland, unpublished lecture notes.

Hersir, G.P., Árnason, K., and Vilhjálmsson, A.M., 2013: 3D inversion of magnetotelluric (MT) resistivity data from Krýsuvík high temperature geothermal area in SW Iceland. *Proceedings of the 38th Workshop on Geothermal Reservoir Engineering, Stanford University, Stanford, Ca*, 14 pp.

Jones, A.G., 1988: Static shift of magnetotelluric data and its removal in a sedimentary basin environment. *Geophysics*, 53-7, 967-978.

Keller, G.V., and Frischknecht, F.C., 1966: *Electrical methods in geophysical prospecting*. Pergamon Press Ltd., Oxford, 527 pp.

Pedersen, L.B., and Engels, M., 2005: Routine 2D inversion of magnetotelluric data using the determinant of the impedance tensor. *Geophysics* 70, 33-41.

Phoenix Geophysics, 2009: *User's guide*. Phoenix Ltd., manual.

Quist, A.S., and Marshall, W.L., 1968: Electrical conductances of aqueous sodium chloride solutions from 0 to 800°C and at pressures to 4000 bars. *J. Phys. Chem.*, 72, 684-703.

Rowland, B.F., 2002: *Time-domain electromagnetic exploration*. Northwest Geophysical Associates, Inc., 6 pp.

Scarlato, P., Poe, B.T., Freda, C., and Gaeta, M., 2004: High pressure and high temperature measurements of electrical conductivity of basaltic rock from Mount Etna, Sicily, Italy. *J. Geophys. Res.*, 109-B02210, 11 pp.

Sigurdsson, Ó., 2010: The Reykjanes seawater geothermal system – Its exploration under regulatory constraints. *Proceedings of the World Geothermal Congress 2010, Bali, Indonesia*, 2 pp.

Sternberg, B.K., Washburne, J.C., and Pellerin, L., 1988: Correction for the static shift in magnetotellurics using transient electromagnetic soundings. *Geophysics*, 53, 1459-1468.

Tikhonov, A.N., 1950: Determination of the electrical characteristics of the deeper strata of the earth's crust. *Dokl. Akad. Nauk, USSR*, 73, 295-297 (in Russian).

Ussher, G., Harvey, C., Johnstone, R., and Andersson, E., 2000: Understanding the resistivities observed in geothermal systems. *Proceedings of the World Geothermal Congress 2000, Kyushu-Tohoku, Japan*, 1915-1920.

Verave, R.T., 2013: *Appendices to the report: "Detection and delineation of geothermal resources using 1D joint inversion of MT and TEM data with practical applications from Reykjanes geothermal field, SW-Iceland."*. UNU-GTP, Iceland, report 35 appendices, 71 pp.

Vozoff, K., 1972: The magnetotelluric method in the exploration of sedimentary basins. *Geophysics* 37, 98-141.

Vozoff, K., 1991: The magnetotelluric method. In: Nabighian, M.N (ed.), *Electromagnetic methods. Applied Geophysics*, 2, 641-711.

Ward S.H., and Hohmann G.W., 1987: Electromagnetic theory for geophysical applications In: Nabighian, M.N. (ed.), *Electromagnetic methods in applied geophysics, volume I, theory*. Society of Exploration Geophysicists, Tulsa, OK, 131-311.

Xue, G.Q., Gelius, L.-J., Xiu, L., Qi Z.P., and Chen, W.Y., 2013: 3D pseudo-seismic imaging of transient electromagnetic data – a feasibility study. *Geophysical Prospecting*, 61 (suppl. 1), 561-571.



**UNITED NATIONS
UNIVERSITY**

GEOTHERMAL TRAINING PROGRAMME
Orkustofnun, Grensasvegur 9,
IS-108 Reykjavik, Iceland

Reports 2013
Number 36

PRELIMINARY STUDY OF BINARY POWER PLANT FEASIBILITY COMPARING ORC AND KALINA FOR LOW-TEMPERATURE RESOURCES IN RUSIZI VALLEY, BURUNDI

Ferdinand Wakana

Ministry of Energy and Mines
Avenue of Revolution
P.O. Box 745
Bujumbura
BURUNDI
wakanafer@yahoo.fr

ABSTRACT

Low-temperature resources are located in many areas and represent a high potential as energy resources. The most efficient and cost effective way to exploit this type of resource is based on binary cycle technology. This study addresses the preliminary feasibility assessment of a binary power plant utilizing low temperature geothermal resources in the Rusizi valley in Burundi. The focus is on the selection of a working fluid, evaluating the net power output, the performance of the working fluid, and the economic analysis and comparison of an Organic Rankine Cycle and a Kalina cycle. The potential resource temperatures are in the range from 90°C to 140°C, and the mass flow of the geothermal fluid ranges between 20 kg/s and 80 kg/s. Models of the Organic Rankine Cycle and the Kalina cycle were developed and analysed by using the EES program. The obtained results revealed the feasibility of a binary power plant under various geothermal field conditions.

1. INTRODUCTION

The East Africa Rift System (EARS) has the largest geothermal potential of the continent. It is one of the major tectonic structures of the earth where the heat energy of the interior of the earth escapes to the surface. Burundi is one of the countries located along the East Africa Rift system. According to previous studies, 15 hot springs with surface temperatures measured from 20 to 68°C were found in the western part of the Rift System in Burundi. The hottest geothermal system is expected to be in the Rusizi valley and the most likely reservoir temperature for this system could be in range of 100 to 140°C (Fridriksson et al., 2012).

Electricity production in Burundi is totally dominated by hydro power and diesel generators. With climate change and oil price fluctuations, the country faced a serious energy crisis in 2010 and 2011, because of power load shedding during which some quarters of Bujumbura town spent three to four consecutive days without electricity. This paralyzed the activities of small and medium-sized businesses. The electricity production is mostly handled by the national water and electricity utility, REGIDESO, which has an installed capacity of 45.8 MW, of which 30.8 MW are hydropower plants and 15.5 MW are thermal units, constituting 97 per cent of the nationally installed capacity. In addition to the capacity mentioned above, is the importation of 3 MW from the Rusizi I hydropower plant,

through a purchasing contract between REGIDESO and the Congolese National Electricity Company (SNEL), and another 13.3 MW from Rusizi II, managed by the international society for electricity in the great lakes region (SINELAC).

The government of Burundi decided to respond to those challenges by making long term investments in energy installations to ensure continuous economic growth and by developing renewable energy. The development of geothermal energy is one of the sustainable solutions that the government adopted (Ministry of Energy and Mining of Burundi, 2012). According to the preliminary available data reported by ISOR in 1982 and 2012, binary power plant technology might be possible in the Rusizi valley system at Burundi if the detailed study is proven (Fridriksson et al., 2012).

This report concerns a tentative design of a binary power plant with consideration of the Rusizi valley resource, making use of a temperature range of 90 to 140°C. The design analyses the thermodynamic parameters of different ORC and Kalina cycles, optimizing the net power output and analysing the economic feasibility. As necessary data for this study, such as fluid mass flow and the chemistry of the reservoir, are not yet available, a calculation model was made by assuming some parameters.

2. GEOTHERMAL ENERGY IN WORLD

Geothermal energy is known as a clean, renewable and environmentally benign energy source based on heat from the earth. It is number four of the renewable energy sources in the world used for electricity production after hydro, biomass and wind. It is followed by solar and wave energy. Electricity has been generated commercially by geothermal steam since 1913, and geothermal energy has been used on a scale of hundreds of MW for five decades, both for electricity generation and direct use. Utilization has increased rapidly over the last three decades. Geothermal resources have been identified in some 90 countries; there are quantified records of geothermal direct utilization in 78 countries and electricity production in 24 countries (Fridleifsson et al., 2008). The thirteen countries with the highest geothermal electricity production in 2010 are shown in Table 1.

TABLE 1: The thirteen countries with highest geothermal electricity production in 2010 (Fridleifsson, 2013)

Country	GWh/Year
USA	16,603
Philippines	10,311
Indonesia	9,600
Mexico	7,047
Italy	5,520
Iceland	4,597
New Zealand	4,055
Japan	3,064
Kenya	1,430
El Salvador	1,422
Costa Rica	1,131

3. PRINCIPLES OF GEOTHERMAL ENERGY

Geothermal energy is energy that comes from deep within the earth (Figure 1). Radioactive elements within the earth experience ongoing decay and release heat with a very high temperature. The high temperature heat is constantly released to space through a thick layer of rock. This heat flow produces energy called “geothermal energy” and is generated by a temperature difference between deeper hotter zones and shallower colder zones. Geothermal resources are characterized by features such as volcanoes, hot springs, geysers, and fumaroles. Most however, cannot be seen as they are deep underground. There may be no clues above ground that a geothermal reservoir is present. Geologists use different methods to find geothermal reservoirs. The only way to be sure there is a reservoir is to drill a well and test the temperature deep underground.

At present, geothermal production wells are commonly 2 km deep, and rarely more than 3 km deep. The rocks have to be permeable in order to allow water to flow through and transfer heat from the hot

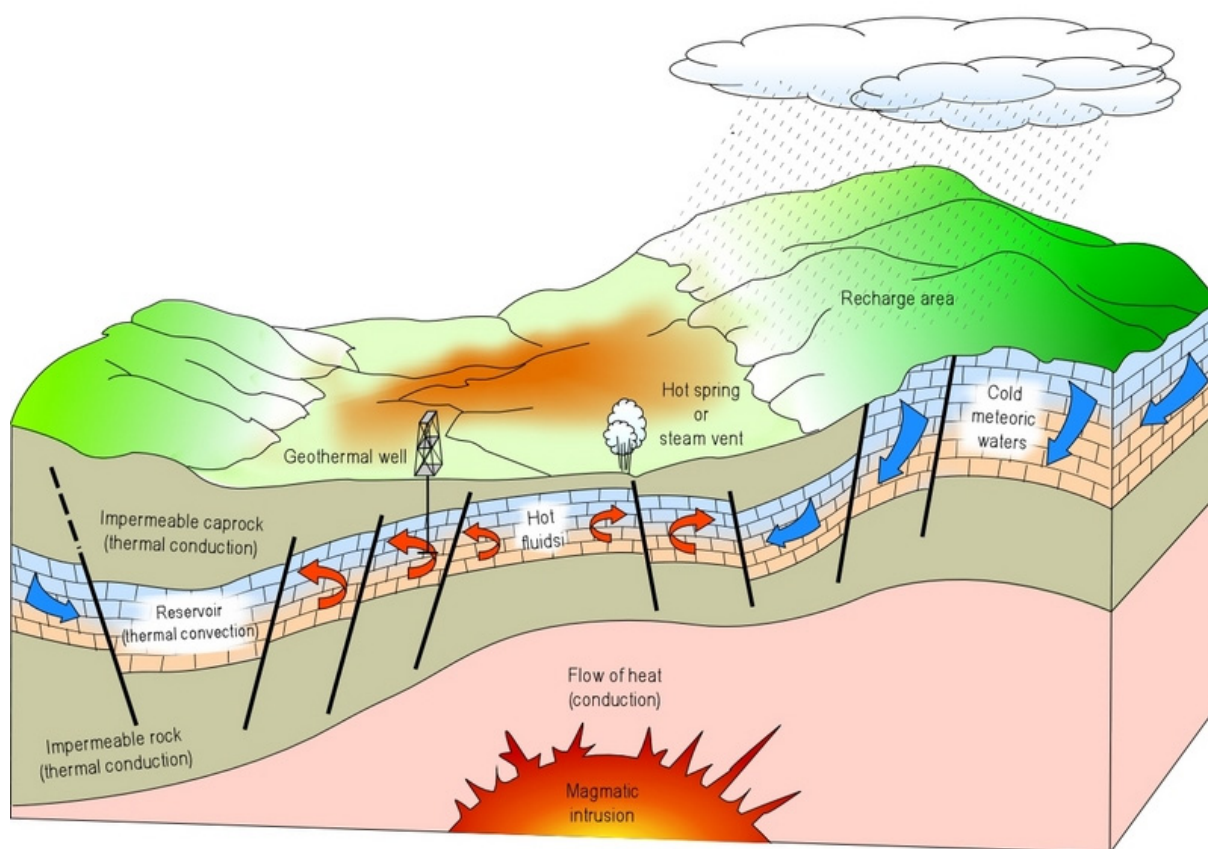


FIGURE 1: Schematic representation of a geothermal system (Dickson and Fanelli, 2003)

rock formations to the reservoirs at depths manageable for commercial drilling. Geothermal energy has, at present, considerable economic potential only in areas where thermal water or steam is concentrated at depths less than 3 km in restricted volumes, analogous to oil in commercial oil reservoirs. The drilling technology for geothermal fluid is similar to that for oil. But as the energy content of a barrel of oil is much greater than the equivalent amount of hot water, the economic requirements for permeability of the formations and the productivity of the geothermal wells are much higher than for oil wells. Exploitable geothermal systems occur in a number of geological environments (Uhorakeye, 2008). They can be divided broadly into two groups depending on whether they are related to young volcanoes and magmatic activity or not. High temperature fields used for conventional power production (with temperatures $>150^{\circ}\text{C}$ at 1 km depth) are confined to the former group, but geothermal fields exploited for direct applications of the thermal energy can be found in both groups. The temperature of thermal systems varies from place to place, depending on the local conditions (Fridleifsson and Freeston, 1994). The most active geothermal resources are usually found along major plate boundaries where earthquakes and volcanoes are concentrated.

4. DIFFERENT TYPES OF GEOTHERMAL POWER PLANTS AND ENERGY CONVERSION SYSTEMS

There are several types of geothermal power generation systems. The technology used to convert geothermal energy into forms usable for human utilization can be categorized into three groups. According to the temperature of the geothermal resources, the system may be classified broadly as high temperature (greater than 170°C), moderate temperature ($90\text{--}170^{\circ}\text{C}$), and low temperature (less than 90°C). High temperature systems are often exploited for electricity generation, while low temperature systems are more suited for direct use applications. High and moderate temperature systems may be

used for both electricity generation and direct use applications (Geoscience Australia and ABARE, 2010).

The technology required to tap a geothermal system is determined by its temperature. For low to moderate temperature systems ($<170^{\circ}\text{C}$), the electricity is often generated using “binary or ORC technology”. The geothermal fluids are transported to the surface in the production wells and the produced water is then piped to a power plant. The geothermal water flows through a heat exchanger, which causes the vaporization of the organic fluid. The cooled brine is re-injected in the injection well and the vapour drives a turbine which produces electricity. The expanded vapour is condensed in the condenser and pressurized again with the condensate pump to complete the cycle (Smeets, 2012).

For a high-temperature system ($>170^{\circ}\text{C}$), electricity is most often produced by passing the geothermal steam directly through a condensing steam turbine. The geothermal fluid from a reservoir reaches the surface as a mixture of steam and brine, due to boiling of the fluid. The steam is then separated from the brine, either by a cyclone effect in a vertical separator or by gravity in a horizontal separator. The dry steam is directed to a turbine which is connected to a generator to generate electricity, while the separated brine is piped back into the reservoir through reinjection wells. The power generation is called single flash (Nugroho, 2011).

If the geothermal fluid from the well is at high pressures, double flash configuration is possible. In double flash configuration the geothermal fluid is first separate from the brine in high pressure separator, then second flashing of the brine is possible from the first separator. The resulting high pressure steam is directed to a high pressure turbine and the separated brine, which still contains reasonably high enthalpy, is throttled and directed to the low pressure separator for additional steam production. Steam from the high pressure turbine is mixed with the steam from the low pressure separator and then directed to the low pressure turbine to generate extra power. The brine from a low pressure separator is piped to the reinjection wells (Nugroho, 2011).

Different combinations of cycles can be made in order to maximise the output power from a system. Among these are: binary cycle with a single-flash cycle using a back pressure turbine, a single flash using a condensing turbine and a binary cycle and a single flash back pressure cycle, a binary cycle utilizing separated brine and a binary cycle utilizing the exhaust steam from the back pressure unit, etc. (Nugroho, 2011).

5. OVERVIEW OF THE GEOTHERMAL RESOURCE IN BURUNDI

The East Africa Rift System (EARS) is known as one of the major tectonic structures of the earth where the heat energy of the interior of the earth escapes to the surface. This energy flow takes place in the form of volcanic eruptions, earthquakes and the upward transport of heat by hot springs and natural vapour emissions. The estimated geothermal energy resource potential in the East Africa Rift System is more than 15,000 MWe (Teklemariam, 2012). Geothermal resource manifestations exist in many locations in the western part of Burundi. This western part of Burundi is connected to the East Africa Rift system (EARS) in the western branch (Figure 2). Many reports have been made in Burundi, describing the geothermal manifestation since 1878 by Stanley, e.g. in 1968, 1972, and 1981, and by UNDP. Some reports described the locations and the chemical analyses. By request of the Ministry of Public Works, Energy and Mines of Burundi in 1981, the Icelandic International Development Agency carried out a reconnaissance survey in 1982.

During the reconnaissance mission of 1982, Ármannsson and Gíslason visited 14 geothermal sites, comprising all known geothermal locations in the country. These are all sites of hot springs with temperatures ranging from near ambient (22°C) to 63°C . All the geothermal sites are located in the

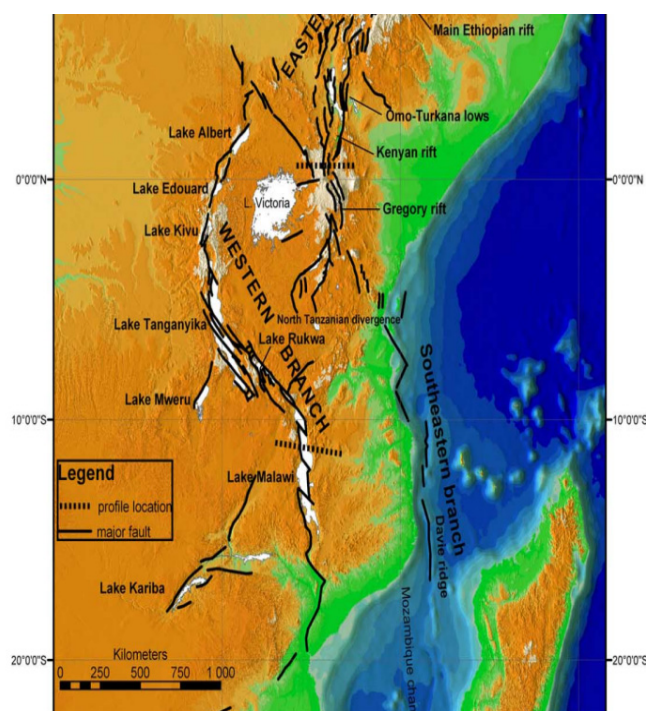


FIGURE 2: Main structures of the EARS; main faults are marked with black lines



FIGURE 3: Geothermal sites in Burundi and the main tectonic structures

western part of the country (Figure 3); six (6) are located within the western branch of the Eastern Africa Rift valley. The hottest springs are all located in the Rift Valley and the three (3) hottest ones, Ruhwa, Gasenyi and Ruhanga, are located in the Rusizi Valley, north of Lake Tanganyika. Of the remaining eight, seven are located less than 40 km east of the Rift Valley and one, Mashuha, is located some 60 km east of the Valley (Fridriksson et al., 2012).

5.1 Geological context

The Rift System may be divided into two main branches, i.e. the eastern branch and the western branch. The western branch runs over a distance of 2100 km, from Lake Albert in the north to Lake Malawi in the south (Figure 4). The central segment of the rift, trending NW-SE, includes Lake Tanganyika (773 m a.s.l.) with a surface area of 32,600 km², about 650 km long and up to 70 km wide. The maximum thickness of the sediment fill is 4-5 km in the Tanganyika basin. The sediments started to accumulate in Miocene or early Pliocene. The Tanganyika basin is divided on the western side by normal faults with a curved trace (Fridriksson et al., 2012), and into several asymmetric sub-basins by NW-striking faults. On the northern part of Lake Tanganyika, these faults are accompanied by geothermal activity.

In the western branch of the East Africa Rift Valley, volcanic activity is more widespread than in the eastern branch. In the adjacent province of the neighbouring countries, such as DRC and Rwanda, the geochronological and petrological data suggest that volcanism associated with the western rift began ~11 Ma ago in the Virunga region, north of Lake Kivu, ~10 Ma ago in the Bukavu Province, south of Kivu, and 9 Ma ago in the Rungwe region, east of Lake Tanganyika. In each of these three provinces, volcanism began before the initial subsidence of the local sedimentary basins. However, in the Tanganyika basin or Burundi, there is no related subaerial volcanism, but there are some indications of under plating of magma below the Tanganyika basin (Fridriksson et al., 2012). Tholeiites, which originated in the Bukavu Province, south Kivu, are found in the north-westernmost part of Burundi, on the borders of Rwanda and DRC (Ármansson and Gíslason, 1983).

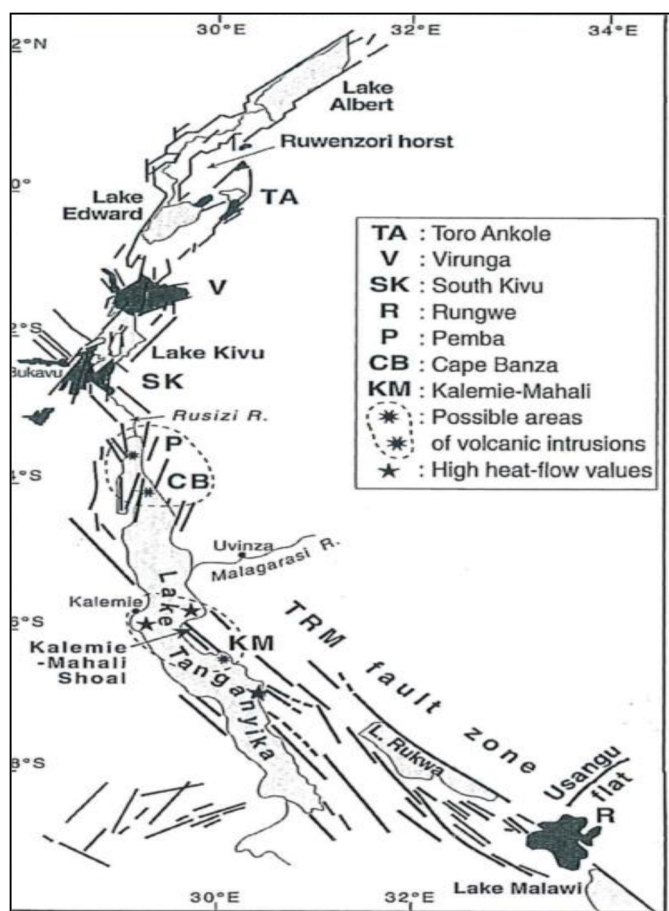


FIGURE 4: Distribution of Cenozoic lavas in the Kivu Province and neighbouring areas

Tanganyika Rift in Rusizi are generally characterized by low porosity and permeability (Ármansson and Gíslason, 1983).

The map in Figure 4 indicates that the lavas entered the NW tip of Burundi. The Burundian bedrock is mostly composed of Precambrian formation and complexes. Dominant rock types are quartzite, gneiss, granite, dolomite, schist, sandstone and conglomerate. The Rusizi valley is filled with thick sequences of alluvium formed during the Holocene. Sediments from Pleistocene, mostly lithified sandstone and conglomerates, are characteristic of the area east of the Rusizi valley, overlying Precambrian formations. Tertiary tholeiitic and alkali lavas are found in NW Burundi (covering some 30 km²), originating from the volcanic zone of south Kivu in Rwanda. The age of the lava flows is estimated to be 6-8 Ma (Ármansson and Gíslason, 1983).

According to several researchers, the hot springs in NW Burundi do not seem to be directly associated with the Cenozoic basalts found in that area, but they infer that under plating of magma might be an important process beneath the Tanganyika Rift (Fridriksson et al., 2012) on the western shore of Lake Tanganyika, along the N-S major faults with NW-SE trending faults (Fridriksson et al., 2012). The geothermal systems within the sediments of the

5.2 Geochemical analytical context

The highest source temperatures were suggested to be in the Rift Valley according to the Icelandic GeoSurvey reports produced in 1983 and 2012. Three sites of highest temperatures were estimated at locations in the Rusizi valley. All discharges in the Rusizi Valley were carbon dioxide rich. This could indicate the presence of a powerful heat source. The high carbon dioxide concentrations lead to super saturation with respect to calcium carbonate, in some cases, so that care would have to be exercised in avoiding calcium carbonate deposition in the event of exploitation.

The chemical compositions in Ruhwa are classified as CO₂-rich Na-HCO₃ waters and are very similar to the results of the Mashyuza samples in Rwanda. The chemical compositions are characteristic of all the geothermal resources in the Rusizi Valley in Burundi, i.e. Ruhwa, Ruhanga, Cibitoke and Gasenyi (Fridriksson et al., 2012).

Using chemical geothermometers to assess the likely temperature in the reservoir, the highest was found in Ruhwa with 102°C, slightly lower than the 110°C observed for the 1983 sample. This temperature is low for electricity production with conventional flashing technology, but a binary unit is a possible option.

6. GEOTHERMAL BINARY POWER PLANT DESIGN

6.1 Introduction

The low to medium temperature sources are unusable for generating electricity with conventional methods. These resources are a water-dominated system and they cannot flash the steam for driving the turbine to generate power. In order to generate electricity from low-to-medium temperature sources and to increase the utilization of thermal resources by recovering waste heat, binary technologies have been developed. The binary plant technologies use a secondary working fluid. Intense research has been done on binary technologies and it shows promising results for converting low and medium temperature resources into electricity. The technology is still being developed to enhance the overall net conversion efficiency (Paci et al., 2009).

Generally, there are two main types of binary cycles, the Organic Rankine Cycle (ORC) and the Kalina cycle. The ORC commonly uses hydrocarbons as the appropriate working fluid and Kalina uses a water-ammonia mixture (typically around 85-15 weight by percentage) (Kopunicova, 2009). The Kalina cycle achieves a thermodynamic efficiency (brine effectiveness) that is approximately 50% greater than that of standard binary Rankine plants (Dickson and Fanelli, 2003). The objectives of this design are:

- To analyse the feasibility of a binary power plant with the parameter conditions of the Rusizi area, using an Organic Rankine Cycle; and
- To compare a net power output (efficiency) by using an Organic Rankine cycle and a Kalina cycle.

6.2 Technical overview of binary geothermal power plants

6.2.1 Organic Rankine Cycle power plant

Binary cycle geothermal power plants are close in thermodynamic principle to conventional fossil or nuclear plants in that the working fluid is in a closed cycle. The binary working fluid is contained completely within pipes, heat exchangers and the turbine, so that it never comes in chemical or physical contact with the environment (DiPippo, 2008).

A binary system has two fluid streams: first is the heat exchange of the geothermal fluid where the working fluid of the ORC absorbs heat from the geothermal fluid via the heat exchanger; the second is the ORC working cycle. These two fluid streams are separated and the heat transfer takes place through the heat exchangers; normally, shell-and-tube heat exchangers are applied.

The simple organic Rankine Cycle power plant follows the scheme shown in Figure 5. The organic fluid receives heat from the geothermal fluid in a heat exchanger (5-6) and finally is vaporized (6-1) before entering the turbine to produce mechanical work and eventually electricity in the generator. After isobaric heat addition, which occurs between states 5 and 1, high-pressure vapour is expanded in the turbine (1-2). After expansion, the organic fluid is sent to a condenser where it is cooled and condensed (2-4) and then pumped (4-5) again in a closed circuit to be vaporized again.

Binary power plants usually have a separate cooling medium that can be fresh water or air. Air cooled condensers are usually a solution for power plants with no fresh water availability. After the heat from the geothermal fluid has been utilized in the heat exchangers the temperature of it is lower and it is re-injected in a injection well for recharge to the reservoir.

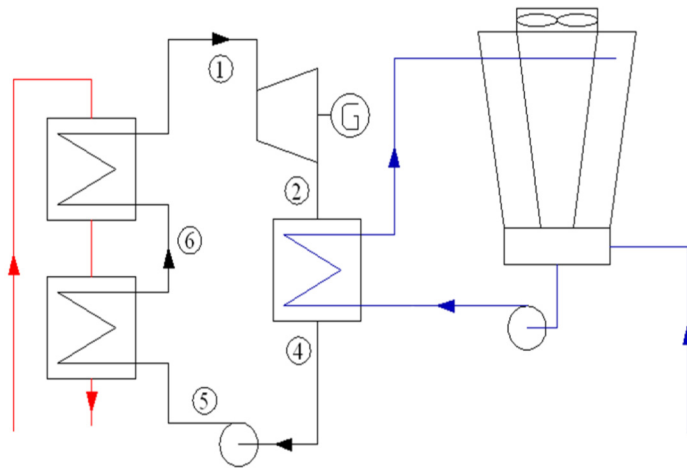


FIGURE 5: Simplified schematic of a basic ORC power plant

6.2.2 Parameters of the Organic Rankine Cycle

Parameters of the preheater and evaporator:

The preheater and evaporator are components that are used to transfer heat from the geothermal fluid to the working fluid. These component are often referred to as heat exchangers and in some cases these two components are one unit.

In this case, the preheater and evaporator are separated. The preheater heats the working fluid before it enters the evaporator. When the boiling point is approached, the organic fluid is

transferred to the evaporator to evaporate before being sent to the turbine.

The heat losses through the heat exchanger to the environment are neglected and the total amount of heat added to the organic fluid is equal to the heat extracted from the geothermal fluid. This transfer is described below:

$$Q_{exchanger} = m_{geo}(h_a - h_c) \quad (1)$$

$$Q_{exchanger} = m_{wf}(h_1 - h_5) \quad (2)$$

where m_{geo} = Mass flow of geothermal fluid (kg/s);
 m_{wf} = Mass flow of organic fluid (kg/s);
 h_a = Enthalpy of geothermal fluid entering the evaporator (kJ/kg);
 h_c = Enthalpy of geothermal fluid leaving the preheater (kJ/kg);
 h_1 = Enthalpy of organic fluid leaving the evaporator (kJ/kg);
 h_5 = Enthalpy of organic fluid entering the evaporator (kJ/kg);
 w_f = Organic fluid; and
 geo = Geothermal fluid.

Hence, the thermodynamic heat balance is:

$$m_{geo}(h_a - h_c) = m_{wf}(h_1 - h_5) \quad (3)$$

And in a case where the geothermal fluid contains low dissolved gases and solids, the previous equation becomes:

$$m_{geo}c_p(T_a - T_c) = m_{wf}(h_1 - h_5) \quad (4)$$

where c_p = Specific heat capacity of water at constant pressure (kJ/kg°C);
 T_a = Temperature of geothermal fluid entering the evaporator (°C); and
 T_c = Temperature of geothermal fluid leaving the preheater (°C).

Considering the constant geothermal fluid heat capacity, the energy balance in the evaporator and the preheater can be described by the following equations

For evaporator:

$$m_{geo}c_p(T_a - T_b) = m_{wf}(h_1 - h_6) \quad (5)$$

For preheater:

$$m_{geo}c_p(T_b - T_c) = m_{wf}(h_6 - h_5) \quad (6)$$

where T_b = Temperature of geothermal fluid between evaporator and preheater (°C); and
 h_6 = Enthalpy of geothermal fluid between evaporator and preheater (kJ/kg).

In this design, the heat exchanger's function is demonstrated in the temperature – heat transfer, or T-Q, diagram (Figure 6). The abscissa represents the total amount of heat that is passed from the geothermal fluid to the organic fluid. The preheater provides sufficient heat to raise the organic fluid to its boiling point (1-2). The evaporation occurs from states 6-1 (referring to Figure 5) along an isotherm for a pure organic fluid (2-3 in Figure 6). The place in the heat exchanger where the geothermal fluid and the organic fluid experience the minimum temperature difference is called the pinch point, and the value of

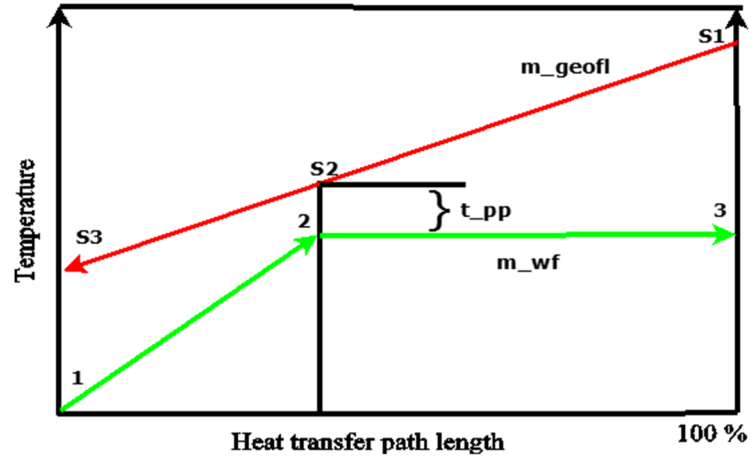


FIGURE 6: Preheater and evaporator temperature distribution (modified from DiPippo, R., 2008)

that difference is designated the pinch point temperature difference ΔT_{pp} (DiPippo, 2008). The pinch point location and the value of the pinch point temperature difference are two major parameters influencing the performance of the heat exchanger. The pinch point temperature is generally known from the heat exchanger manufacturer's specifications. The total amount of heat transferred in the heat exchanger is given by the following equation (DiPippo, 2008):

$$Q = U \cdot A \cdot LMTD \quad (7)$$

Where U = Overall heat transfer coefficient (W/m²K);
 A = Total heat transfer area (m²); and
 $LMTD$ = Logarithmic mean temperature difference (K).

LMTD can be expressed by the following equation:

$$LMTD = \frac{(T_{hot,in} - T_{cold,out}) - (T_{hot,out} - T_{cold,in})}{\ln\left(\frac{T_{hot,in} - T_{cold,out}}{T_{hot,out} - T_{cold,in}}\right)} \quad (8)$$

where $T_{hot,in}$ = Temperature of geothermal fluid at heat exchanger inlet (K or °C);
 $T_{cold,out}$ = Temperature of geothermal fluid at heat exchanger outlet (K or °C);
 $T_{hot,out}$ = Temperature of organic fluid at heat exchanger outlet (K or °C); and
 $T_{cold,in}$ = Temperature of organic fluid at heat exchanger inlet (K or °C).

Parameters of the turbine and generator:

The turbine is a device that converts the thermal energy from the organic fluid into electrical energy through the generator. The pressurized vapour steam of organic fluid expands in the turbine and leads to rotation of the rotor. The rotor is connected to a generator which changes rotational kinetic energy into electricity. The expansion process in the turbine is considered adiabatic and steady state of the operation is assumed. The efficiency of the turbine (η_{th}) is isentropic and is given by the manufacturer. The power generated by the turbine can be calculated by the following equation in accordance with Figure 5 (DiPippo, R., 2008):

$$W_{turbine} = m_{wf}(h_1 - h_2) \quad (9)$$

$$W_{turbine} = m_{wf} \eta_{th} (h_1 - h_{2s}) \quad (10)$$

where h_1 = Enthalpy of organic fluid at turbine inlet (kJ/kg);

- h_2 = Enthalpy of organic fluid at turbine outlet (kJ/kg);
 h_{2s} = Enthalpy of organic fluid at turbine outlet assuming isentropic expansion (kJ/kg);
 η_{th} = Efficiency of the turbine.

Parameters of the condenser:

The condenser is a heat exchanger between the hot vapour from the turbine and the cooling medium (either water or air) of the cycle. The calculation of the condenser is roughly the same in both cases. The working fluid comes from the turbine to the inlet of the condenser through point 2 (Figure 5) and from the outlet of the condenser at point 4. The cooling fluid comes from the cooling system for entry into the condenser at point C1 and from the outlet condenser at point C2, as shown in Figure 7. A good cooling system improves the net power of the plant and can cool the working fluid to an optimal pressure and temperature. It also controls the reinjection temperature of the geothermal fluid. There are two types of cooling systems (Khairah, 2012).

Wet cooling system:

The wet cooling system uses both water and air (Figure 7). The system is composed of a surface condenser which condenses the working fluid before entering the pump. While transferring heat to the cooling water, the working fluid changes phases and then goes directly to the pump. The main technology used in geothermal plants is mechanical draft induced with a fan instead of natural draft. There are two main tower configurations available, indicating the direction of the air flow in relation to the water flow:

- Counter flow; and
- Cross flow.

The cold water from the cooling system is used to dissipate heat stored in the condenser. After going through the exchanger, the hot water from the condenser passes through a cooling tower and is cooled down by a fan, using outside air. A supply of make-up water (C3) is needed to compensate for evaporation losses. A wet cooling system is commonly used in many geothermal plants for high efficiency, but presents some disadvantages, like the large amount of water needed, water vapour plumes and also some corrosion in the fan due to the chemistry.

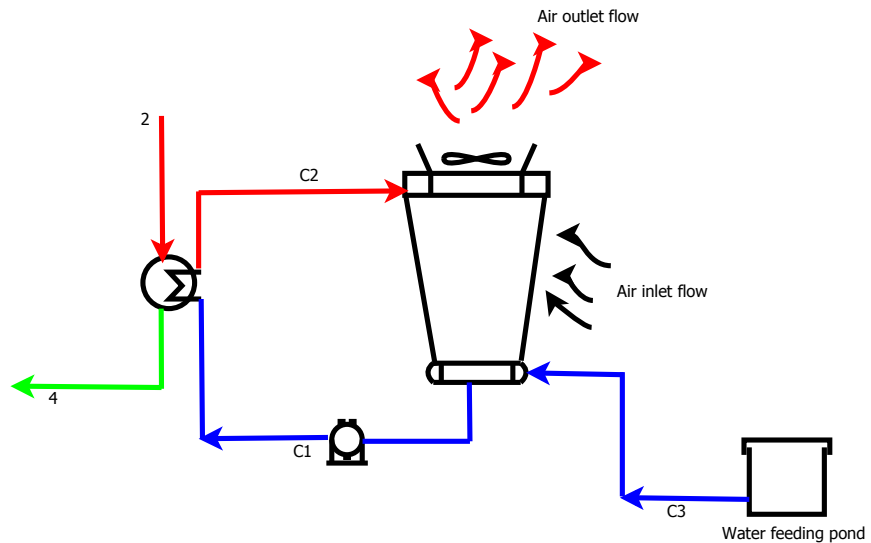


FIGURE 7: Wet cooling system (modified from Khairah, 2012)

Most geothermal plants use an induced drafted fan on top of the tower, for a better cooling process. The energy balance of the wet cooling system requires complex equations due to the numerous parameters involved. It takes account of the air entering and leaving, as well as the water entering and leaving the condenser and the make-up water supply. These equations are expressed below.

Mass balance for dry air:

$$m_{ain} = m_{aout} = m_{air} \quad (11)$$

- where
- m_{ain} = Mass flow of cold air entering cooling system (kg/s);
 - m_{aout} = Mass flow of hot air leaving cooling system (kg/s); and
 - m_{air} = Mass flow of air used by cooling system (kg/s).

Mass balance for water and the vapour content in the air stream:

$$m_{vin} + m_{c2} + m_{c3} = m_{c1} + m_{vout} \quad (12)$$

where m_{vin} = Mass flow of water vapour entering cooling system (kg/s);
 m_{vout} = Mass flow of water vapour leaving cooling system (kg/s);
 m_{c1} = Mass flow of water entering the condenser (kg/s);
 m_{c2} = Mass flow of water leaving the condenser (kg/s); and
 m_{c3} = Mass flow of makeup water entering the cooling system (kg/s).

The relationships between the dry air and the vapour stream entering and leaving are:

$$m_{vout} = m_{aout}\omega_{out} \quad (13)$$

$$m_{vin} = m_{ain}\omega_{in} \quad (14)$$

where ω_{out} = Specific humidity of cold air entering the cooling system (kg water/kg dry air); and
 ω_{in} = Specific humidity of hot air leaving the cooling system (kg water/kg dry air).

The equation for energy balance, taking Equation 12 into consideration, is:

$$(m_{vin}h_{vin} + m_{ain}h_{in}) + m_{c2}h_{c2} + m_{c3}h_{c3} = m_{c1}h_{c1} + m_{vout}h_{vout} + m_{aout}h_{out} \quad (15)$$

where h_{in} = Enthalpy of dry air entering the cooling system (kJ/kg);
 h_{out} = Enthalpy of dry air leaving the cooling system (kJ/kg);
 h_{vin} = Enthalpy of water vapour entering the cooling system (kJ/kg);
 h_{vout} = Enthalpy of water vapour leaving the cooling system (kJ/kg);
 h_{c1} = Enthalpy of cold water leaving the cooling tower system (kJ/kg);
 h_{c2} = Enthalpy of hot water entering the cooling tower system (kJ/kg); and
 h_{c3} = Enthalpy of makeup water (kJ/kg).

For a unit of dry air, Equation 15 becomes:

$$\left(\frac{m_{vin}}{m_{ain}} * h_{vin} + h_{in}\right) + \frac{m_{c2}}{m_{ain}} * h_{c2} + \frac{m_{c3}}{m_{ain}} * h_{c3} = \frac{m_{c1}}{m_{ain}} * h_{c1} + \left(\frac{m_{vout}}{m_{ain}} * h_{vout} + h_{out}\right) \quad (16)$$

Using Equations 13 and 14, Equation 16 becomes:

$$(\omega_{in} * h_{vin} + h_{in} + \frac{m_{c2}}{m_{ain}} * h_{c2} + \frac{m_{c3}}{m_{ain}} * h_{c3} = \frac{m_{c1}}{m_{ain}} * h_{c1} + \omega_{out} * h_{vout} + h_{out} \quad (17)$$

$$(\omega_{in} * h_{vin}) + \frac{m_{c2}}{m_{ain}} * h_{c2} + \frac{m_{c3}}{m_{ain}} * h_{c3} = \frac{m_{c1}}{m_{ain}} * h_{c1} + (\omega_{out} * h_{vout}) + (h_{out} - h_{in}) \quad (18)$$

The inflow of dry air is unchanged in the tower, but there are water losses due to evaporation, as well as drift losses in droplets carried out of the cooling tower with exhaust air. To prevent scaling and to avoid an accumulation of impurities, an amount of water is blown out from the basin. The mass flow of evaporation, m_e , is given (El-Wakil, 1984) by:

$$m_e = m_{air}(\omega_{out} - \omega_{in}) \quad (19)$$

The drift losses, m_{drift} , can be estimated by the following equation (Perry and Green, 2008):

$$m_{drift} = 0.0002m_{c2} \quad (20)$$

And the blow down for mass flow is calculated by the formula (Perry and Green, 2008):

$$m_{bl} = \frac{m_e + (cycle - 1) + m_{drift}}{cycle - 1} \quad (21)$$

where m_{bl} = Blowdown consistent unit (kg/s); and
 $cycle$ = Ratio of dissolved solids in the recirculation water to dissolved solids in make-up water, normal range between 3 to 5 cycles.

Therefore, the make-up water required is found by the equation:

$$m_{c3} = m_e + m_{drift} + m_{bl} \quad (22)$$

Dry cooling system:

The dry cooling system uses air to condense steam from the turbine by forcing ambient air over a bundle of finned tubes containing the steam inside. It is often used where a water supply is not available near the power plant. Mostly, in geothermal plants, the dry air cooling system is a mechanical draft type using fans with motors driven by electrical power. There are two main configuration of the placement of fan in mechanical dry cooling system:

1. The induced draft configuration has a mechanical fan on top of the tower. The fan pulls air over the tube bundles and blows it away reducing risk of recirculation. High power is needed if the ambient temperature is high, due to low inlet air velocities.
2. The forced draft configuration has a mechanical fan on the bottom of the tower, to force air into circulating over the bundle tubes. Air is circulated uniformly in the tower due to the low discharge air velocities from the bundle tube and has more of recirculating the air than induced draft. The forced draft configuration is more impacted by cold climatic conditions.

The dry cooling system is very sensitive to ambient temperature variations, which directly affect the output of the power plant. Unlike with wet cooling systems, the need for a make-up water supply is eliminated as are water freezing problems, and water vapour plumes. The maintenance and operation requirements and costs are low due to fewer components being used. The energy balance in the dry cooling system condenser, Figure 8, is represented by the following equation:

$$m_{wf}(h_2 - h_3) = m_{air}c_{p,air}\Delta T \quad (23)$$

where ΔT is the difference between the air temperature entering and leaving the cooling system.

Equation 23 can be expressed as:

$$m_{wf}(h_2 - h_3) = m_{air}c_{p,air}(T_{c2} - T_{c1}) \quad (24)$$

where m_{wf} = Mass flow of working fluid (kg/s);
 m_{air} = Mass flow of air flowing inside the condenser (kg/s);
 $c_{p,air}$ = Specific heat capacity of air (kJ/kg K);
 T_{c1} = Temperature of the ambient air entering the cooling system ($^{\circ}\text{C}$); and
 T_{c2} = Temperature of the ambient air leaving the cooling system ($^{\circ}\text{C}$).

The power used by the fans to move air through the cooling system is found by the following equations:

$$w_{fan} = \frac{v_a \Delta P}{\eta_{fan,motor}} \quad (25)$$

$$v_a = \frac{m_a}{\rho_{a,out}} \quad (26)$$

$$P_{fan,motor} = \frac{P_{fan}}{\eta_{fan,motor}} \quad (27)$$

where w_{fan} = Mechanical work of fan;
 v_a = Volume flow of air;
 ΔP = Static head of fan;
 $\eta_{fan,motor}$ = Efficiency of fan motor;
 m_a = Mass flow of air; and
 $\rho_{a,out}$ = Density of air.

The feed pump:

The feed pump is used increase the pressure of the working fluid and push it from the condenser to the preheater. The process of pumping is assumed to be isentropic. The power used by the feed pump is expressed with the following equation:

$$W_{fp} = m_{wf}(h_5 - h_4) = \frac{m_{wf}(h_{5s} - h_4)}{\eta_p} \quad (28)$$

where W_{fp} = Work of the feed pump (kW);
 h_{5s} = Enthalpy of the working fluid assuming isentropic process; and
 η_p = Isentropic pump efficiency.

The net power output and thermal efficiency of the binary cycle:

The net power output depends upon the components of the power plant, like preheater and evaporator efficiency. Another parameter to be considered is the cooling system and circulation pump which consume a great fraction of the generated power. The circulation pumps use generally between 2 and 10% of the gross power of the plant and the cooling tower fans can vary between 10 and more than 30% of the gross power (Franco and Villani, 2009). The relationships below give the net power output of the binary power plant:

$$W_{net} = W_{turbine} - W_{pump} - P_{fan,motor} \quad (29)$$

where W_{net} = Net power output of power plant;
 $W_{turbine}$ = Power produced by turbine;
 W_{pump} = Power used by all pumps in cycle; and
 $P_{fan,motor}$ = Power used by cooling fans.

The thermal efficiency is found by using the first law of thermodynamics; here the division of the work produced by the turbine and the heat extracted from the geothermal fluid in the preheater and evaporator. The heat extracted from the heat exchanger (preheater and evaporator) is given by Equation 2, and the thermal efficiency of the cycle is given by the following equation:

$$\eta_{cycle} = \frac{W_{turbine}}{Q_{exchanger}} \quad (30)$$

Working fluid selection:

The working fluid needs to be carefully selected, based on the geothermal brine temperature and the fluid's thermodynamic properties. The working fluid has great influence on the performance of the power plant. There are many working fluids, but the choice must have a lower boiling point than water, and have no negative impacts on health, safety and the environment (DiPippo, 2008). Hydrocarbons and refrigerants are the most common fluids used. In this study, three hydrocarbons, one refrigerant and a mixture of ammonia-water are considered, as shown in Table 2, to optimize the efficiency and net power output of a binary power plant.

TABLE 2: Properties of the working fluid

Fluid	Formula	Critical temperature T_c (°C)	Critical pressure P_c (bar)	Molecular weight, M (g/mol)
Isobutane	$(CH_3)_3CH$	135	36.85	58.12
Isopentane	C_5H_{12}	187.20	33.78	72.149
Propane	C_3H_8	96.6	42.36	44.10
R134a	CF_3-CH_2F	101	40.59	102

Scaling prevention:

Different types of scales are found in various geothermal areas. The major scaling species in geothermal brine typically include calcium, silica and sulphide compounds. Calcium compounds frequently

encountered are calcium carbonate and calcium silicate. Metal silicate and metal sulphide scales are often observed in high temperature resources. Silica can present even more difficulties, as it will form an amorphous silica scale that is not associated with other cations. Calcium carbonate scale frequently causes operational problems in the brine handling system. It typically forms as a result of the decrease of solubility of CO_2 in the liquid phase. The solubility of CO_2 decreases any time a pressure drop occurs and corresponds with increasing pH (Stapleton and Weres, 2011). At elevated temperatures, even small amounts of calcium in the brine will precipitate with pH increase. Calcium carbonate scale can form in production wells, plant vessels and equipment, and injection lines and wells.

Silica related scale is one of the most difficult scales occurring in geothermal operation. Silica is found essentially in all geothermal brine and its concentration is directly proportional to the temperature of the brine. As brine flows through the well to the surface, the pressure drops and the temperature of the brine decreases. This entails that silica solubility decreases correspondingly and the brine phase becomes over saturated. Under these conditions, silica precipitates as either amorphous silica or it will react with available cations (e.g. Fe, Mg, Ca, Zn) and form co-precipitated silica deposits. These deposits are extremely tenacious and can occur throughout the production field, plant and injection systems.

Effective scale prevention in geothermal operations is often critical to the success of a project. The scale prevention methods are related to site-specific conditions in the field. These conditions dictate the type of scale prevention method that will be feasible. Calcium carbonate scaling may be prevented by:

- a) Acting on carbon dioxide partial pressure;
- b) Acting on the pH of the solution; and
- c) Using chemical additives (scale inhibitors).

Pressure and temperature manipulations of the geothermal fluid can be achieved quite easily by pumping a geothermal well instead of relying on its natural flow. Adding HCl to the geothermal fluid in order to decrease the pH below a certain value at which no calcite scaling can form is technically possible but expensive. The utilization of scale inhibitors is the most common and promising method of combating scaling problems. The main problem is to select the most suitable inhibitor among the hundreds of different chemicals on the market (Stapleton and Weres, 2011).

Thermodynamic modelling of an Organic Rankine Cycle:

In this study, the model presented in Figure 8 is a simple binary cycle using an organic working fluid, such as isopentane, isobutane, propane or R134a. The working cycle components are the preheater, evaporator, turbine, condenser, and pump. The condenser is cooled by a dry cooling system. The cooling system uses a fan and motor to supply and remove air. The cooling system was chosen with regard to the Rusizi area conditions. In this area, there are two rivers, Rusizi River and Ruhwa River. These two rivers are shared by the Democratic Republic of Congo and Rwanda. The use of these rivers required an agreement between these countries.

The geothermal water is pumped from a well in order to pressurize it. Using Engineering Equation Solver (EES) software, a thermodynamic model of the binary plant cycle was developed for all working fluids and the parameters of the cycle were analysed. The EES program is given in Appendix I. The objectives were optimization of the efficiencies of different working fluids and obtaining the net power output with a temperature range of 90-140°C and a geothermal flow rate of 20-80 kg/s. The ranges used refer to the reconnaissance study report of the geothermal areas in Burundi, produced in September 2012. These ranges were estimated using the geothermometer analysis method. Many input data were

estimated during the development of the thermodynamic cycle of the binary plant, because of the lack of sufficient data being available from the field. Table 3 shows the assumptions that were made.

Optimization of turbine inlet pressure of working fluid cycle:

The optimal design of a binary geothermal power plant can be considered as a multi-objective, multi-variable constrained optimization problem. Three main temperatures can be considered as constraints, i.e. the geothermal fluid, rejection, and ambient temperatures. The whole optimization problem can be reformulated into manageable sized sub-problems. The results from the high optimization level represent the input data for the detailed design. The effects of the optimum component design (pressure losses, pumping power) are iterated at the system level (Franco and Villani, 2009).

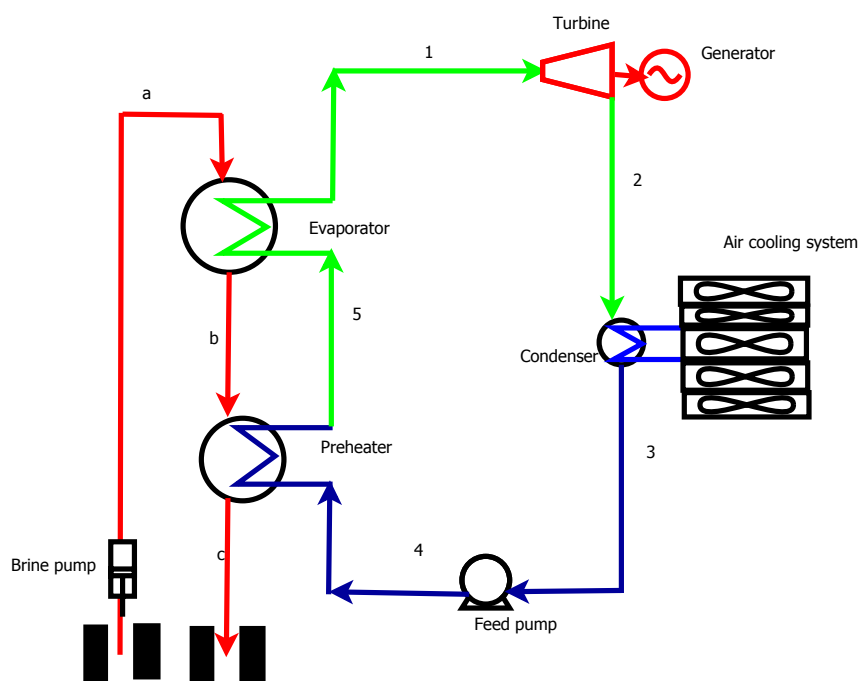


FIGURE 8: Binary cycle with air cooling system

The whole optimization problem can be reformulated into manageable sized sub-problems. The results from the high optimization level represent the input data for the detailed design. The effects of the optimum component design (pressure losses, pumping power) are iterated at the system level (Franco and Villani, 2009).

TABLE 3: Design parameters assumed for the binary cycle power plant

Parameters	Unit	Minimum value	Maximum value
Mass flow rate of geofluid	kg/s	20	80
Temperature of geofluid from the well	°C	90	140
Pressure of geofluid from the well	bar	30	
Reinjection temperature	°C	70	
Ambient temperature of Rusizi area (Ndayirukiye, 1986)	°C	30	
Turbine efficiency	%	85	
Feed pump efficiency	%	75	
Fan efficiency	%	65	
Atmospheric pressure	bar	1.02	
Relative humidity (Ndayirukiye, 1986)	%	70	
Pinch point of vaporizer	°C	5	
Air temperature leaving the cooling system assumed equal to ambient temperature plus 12°C	°C	42	
Working fluids: isobutane, isopentane, propane and R134a	kg/s		
Vaporizer pressure	bar	Optimized	Optimized
Temperature of condenser	°C	45	

In this study, the turbine inlet optimum pressure required for every working fluid was considered for a temperature resource in the range between 90 and 140°C; the pressure was optimized to obtain a good output from the binary power plant design. The turbine inlet pressure plays an important role in producing mechanical force for driving a generator. The net power output was considered a parameter in this optimization as was the reinjection temperature, in order to prevent possible calcite carbonate

scaling that could occur during operation. The optimization of the inlet turbine pressure was achieved by using a computer code. EES software was helpful in creating the code to resolve thermodynamic problems. It was used in this study to optimize different parameters of the design cycle, including the pressure inlet into the turbine for the temperature range 90°C and 140°C, with respect to the reinjection temperature while other parameters were constant. The optimization was done for all working fluids and analysed to find the highest work output. The behaviour and work output of the working fluid at different pressures allowed the selection of the optimum pressure. Figure 9 shows the optimum pressure for each working fluid at different temperatures.

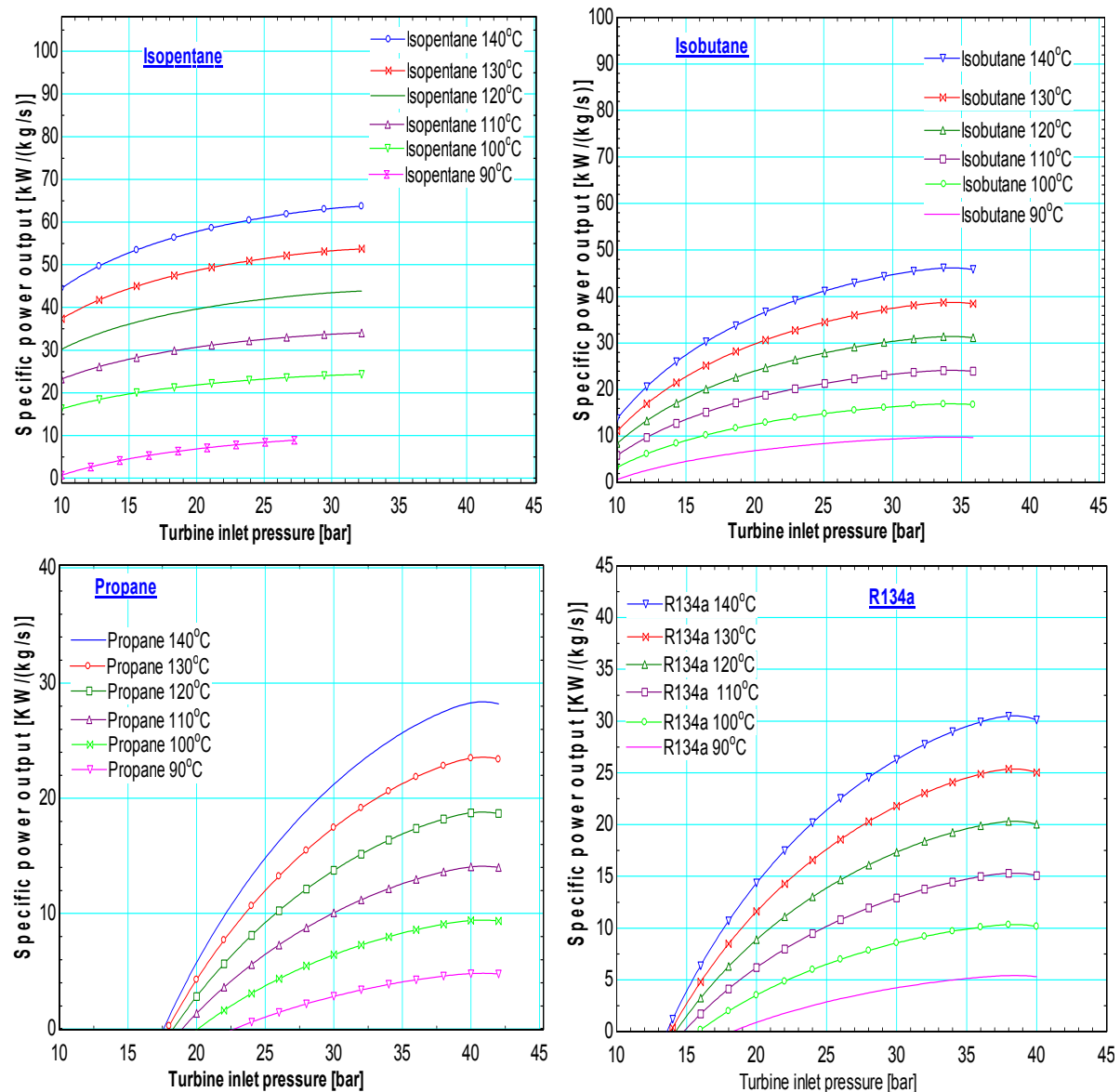


FIGURE 9: Power plant output with turbine inlet pressure

After optimization, it was observed that some working fluids showed a different optimal pressure at different temperatures or the same optimal pressure in a certain temperature range. One working fluid, R134a, gave an optimal output at the same pressure throughout the temperature range considered, and needs high pressure to generate an optimal output. A summary of the results of different optimum pressures for all working fluids at the various temperatures considered is shown in Tables 4-7.

Power plant performance analysis:

The first and second law efficiencies are usually used to assess the performance of binary power plants. These two parameters can help to compare the various available combinations of the source, rejection and condensation temperatures, and give indications about the specific power of the plant. Another important parameter to be considered is the mass flow rate used to generate a fixed power output.

In this study, the thermodynamic parameters of the binary model cycle were developed and the EES program was used to estimate the parameter values of a model binary cycle. Knowing the pressure of the turbine inlet, the temperature of the geothermal resource, the ambient temperature, the reinjection temperature and the condenser temperature, other parameters could be calculated by EES. The calculation was done with a geothermal mass flow input of 1 kg/s as the heat source. The reinjection temperature used in this study was fixed at 70°C, considering the low enthalpy of the geothermal resource according to Alessandro and Marco Villani and the September 2012 reconnaissance study report of the geothermal resource in the Rusizi Valley. For a geothermal field that has temperatures between 110 and 160°C, it is difficult to use rejection temperatures lower than 70-80°C; the latter temperature is a crucial parameter in plant design (Franco and Villani, 2009). The condenser temperature was fixed at 45°C because the ambient temperature is very high, with an average of 30°C. Results of the analyses for a binary power plant model for all working fluids chosen are presented in Tables 4 to 7. The performance results are given as the exergy efficiency value as a function of temperature. The exergy efficiency, using the second law of thermodynamics, assesses the extraction of heat from a geothermal resource in regards to maximum theoretical work output. Figure 10 shows the behaviour of the exergy efficiency at different pressures and different temperatures of the geothermal resource. Among the working fluids used in this study, isopentane is better than the other working fluids, followed by isobutane.

The first law efficiency and the exergy efficiencies with optimum turbine inlet pressure were calculated to assess the performance of different configurations. This assessment shows the losses in the cycle. The analysed results are illustrated in Tables 4-7. The exergy efficiency, the first law efficiency and the mass flow of the working fluid indicate the thermodynamic performance of a binary cycle. The objective is to extract more heat and gain the highest power output for the least cost. The investment is another parameter to be considered in binary power plant design. The results show that isopentane is better than the other working fluids tested. Figure 11 illustrates the behaviour of various working fluids used for an Organic Rankin cycle.

TABLE 4: Properties of isopentane

T_{geo} (°C)	T_{inj} (°C)	Power output (kW/kg·s)	η_{th}	η_{exerg}	m_{wf} (kg/s)
90	70	12.57	0.14	0.50	0.17
100	70	22.7	0.17	0.68	0.255
110	70	31.8	0.18	0.78	0.338
120	70	42.6	0.20	0.85	0.424
130	70	52.2	0.20	0.86	0.511
140	70	62.0	0.20	0.87	0.599

TABLE 5: Properties of isobutane

T_{geo} (°C)	T_{inj} (°C)	Power output (kW/kg·s)	η_{th}	η_{exerg}	m_{wf} (kg/s)
90	70	8.2	0.096	0.32	0.34
100	70	15.8	0.125	0.487	0.33
110	70	23.8	0.141	0.58	0.56
120	70	30.09	0.146	0.55	0.70
130	70	38.13	0.149	0.57	0.69
140	70	45.4	0.152	0.58	0.81

TABLE 6: Properties of propane

T_{geo} (°C)	T_{inj} (°C)	Power output (kW/kg·s)	η_{th}	η_{exerg}	m_{wf} (kg/s)
90	70	3.8	0.045	0.15	0.28
100	70	9.07	0.071	0.27	0.43
110	70	14.05	0.083	0.34	0.60
120	70	18.7	0.088	0.37	0.76
130	70	23.4	0.091	0.38	0.91
140	70	28.3	0.094	0.39	1.078

TABLE 7: Properties of R134a

T_{geo} (°C)	T_{inj} (°C)	Power output (kW/kg·s)	η_{th}	η_{exerg}	m_{wf} (kg/s)
90	70	5.4	0.064	0.21	0.56
100	70	10.3	0.081	0.31	1.14
110	70	15.3	0.09	0.34	1.03
120	70	20.3	0.095	0.36	1.42
130	70	25.5	0.099	0.38	1.71
140	70	30.3	0.101	0.39	2.01

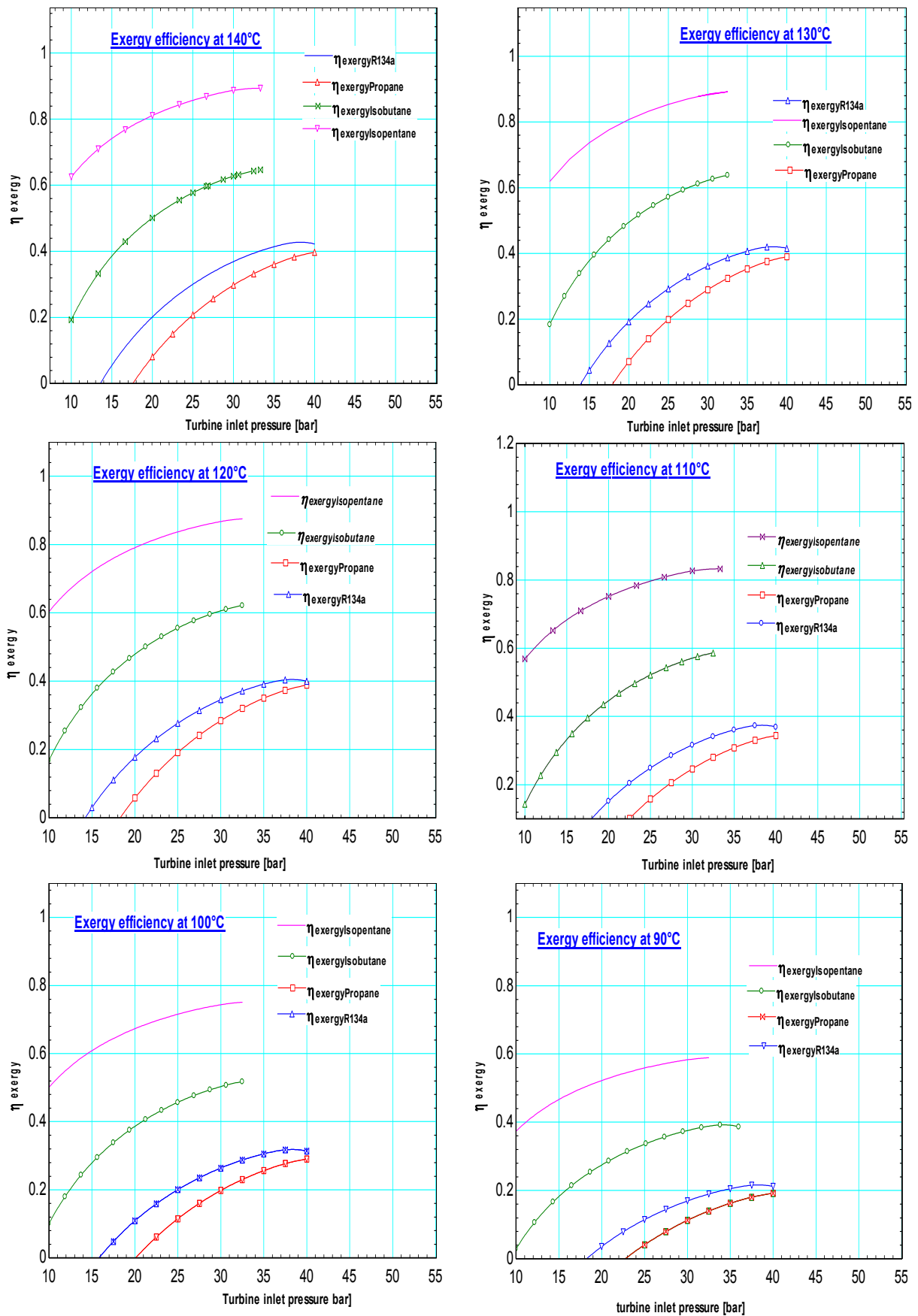


FIGURE 10: Exergy efficiency with turbine inlet pressure for different working fluids

6.2.3 Investment cost estimation of Organic Rankine Cycle

It is difficult to make accurate estimates of project costs at the conception stage. The cost estimates at this stage generally have a large margin of error. The level of accuracy of the cost estimates depends upon the information available. Capital cost of geothermal projects is very site and resource specific. The source temperature will determine the power conversion technology as well as the overall efficiency of the power system. Site accessibility and topography, local weather conditions, land type and ownership are additional parameters affecting the cost and the time required to bring the power plant online. This means that the costs of geothermal projects vary from site to site, as well as the cost of financing. In this study, the cost estimate is only a part of the total investment. The total cost considers the investment of the exploration phase, drilling wells and reservoir stimulation. The base costs of main equipment are estimated based on the experience of experts, as seen in Table 8. The costs are assumed to be thumb values, although best estimates should be obtained through vendor quotations. The parameters used to estimate the cost of purchased equipment include the surface area, power or capacity.

To estimate the cost of equipment, calculations were done for one kilogram of geothermal water mass flow. The cost takes into consideration the area of the evaporator, the preheater, and the condenser, a feed pump, cooling tower and fan, turbine and well pump. The cost is shown in Figure 12 for the range of temperatures considered. The fixed capital investment is divided into two: direct cost (DC) and indirect cost (IC). The direct cost concerns: the purchased equipment cost (PED); purchased equipment installation (33% of PED); piping (35% of PED); instrumentation and controls (12% of PEC); electrical equipment and materials (13% of PEC); civil, structural and architectural work (21% of PEC); and service facilities (35% of PEC). The indirect costs include: engineering and supervision (8% DC); construction costs and contractor's profile (15%); and 15% is added as a contingency to the DC and IC sums (Bejan et al., 1996).

TABLE 8: Assumed thumb values for equipment costs

Equipment	Unit size	Base cost / unit size (USD)
Preheater	m ²	450
Evaporator	m ²	500
Condenser	m ²	600
Turbine	kW	500
Pump	kW	450
Motor	kW	450

The first estimate of equipment cost, illustrated in Figure 12, showed the need for more investment for propane and R134a, compared to isopentane and isobutane. The highest cost was influenced by the biggest condenser area required for propane, followed by R134a and isobutane to lower the high temperature of the working fluid from the turbine to the low condenser temperature. Knowing the estimated cost of the equipment, one should be able to estimate other investment costs required for a binary power plant cycle. For estimation of the total cost of investment for a binary cycle power plant installation (Table 9), the assumptions above were used to calculate the fixed capital costs.

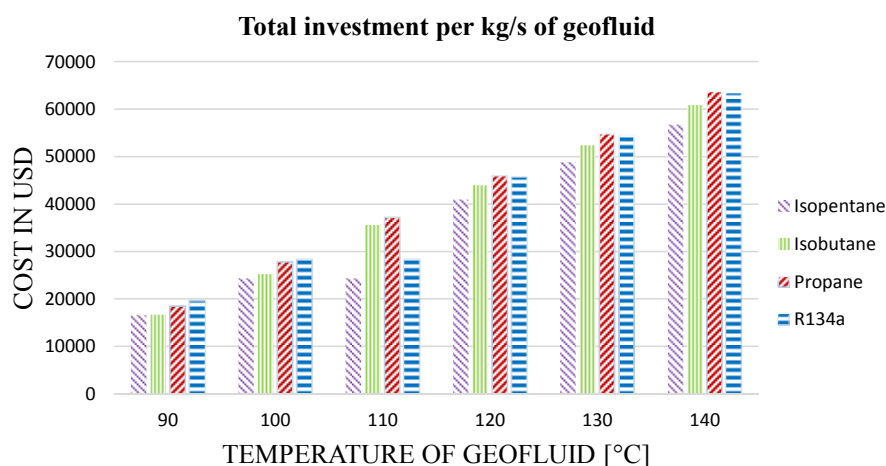


FIGURE 12: Comparison of estimated equipment costs for the ORC at different temperatures with one kg/s of geothermal mass flow

TABLE 9: Total cost of ORC for 1 kg/s of geofluid in USD, evaluated for various temperatures of geofluid

Temperature (°C)	Isopentane (USD)	Isobutane (USD)	Propane (USD)	R134a (USD)
90	16,579	16,690	18,504	19,637
100	24,313	25,204	27,807	28,315
110	24,313	35,560	37,227	28,315
120	40,962	43,925	45,988	45,704
130	48,801	52,345	54,806	54,473
140	56,713	60,844	63,705	63,323

6.2.4 Economic analysis of Organic Binary Cycle model

Considering the price of electricity (0.18 USD/kWh in March 2012) (Ministry of Energy and Mining of Burundi, 2012) from REGIDESO which is responsible for the production and distribution of water and electricity in Burundi, the annual cost of energy was calculated, and ten years was considered the time needed for a return of investment. The cost of operation and maintenance was estimated as 6% of the annual revenue. Two scenarios assuming 10% and 15% interest rates were analysed. The baseline for the calculation used was the thermal design and optimization book (Bejan et al., 1996). The mass flow of the geothermal resources was estimated to be in the range of 20-80 kg/s. The results of the calculation are presented below; the following equation was used:

$$F = P(1 + i)^n \quad (31)$$

where F = Future value in n years;
 P = Present value that is equal to total cost of investment;
 i = Earning rate (%) in interest per year; and
 n = number of years for investment return.

Annual cost of energy = 0.18 USD/kWh * value of power * value hours per days * number of days per year.

The annual revenue is the difference between the annual energy cost and the cost of maintenance and operation. In this study, tax depreciation was neglected. The results of the analysis are shown in Figure 13. The results show the behaviour for different temperatures in two scenarios with the same price charged by REGIDESO and with augmentation of the energy price. Isopentane was shown to be economical in all ranges of geothermal temperature in both scenarios. Isobutane was economical in the range between 100 and 140°C for an interest rate of 15% at REGIDESO prices. Propane and R134a showed an economical result in the range 120-140°C when the price was increased by 39%.

6.2.5 Kalina cycle power plant

The first version of the Kalina cycle was invented and proposed by Eng. Alexander Kalina in 1980. A Kalina cycle is a modified organic cycle using a mixture of ammonia-water as a secondary working fluid in specific ratios and may be the preferred choice for geothermal resources with temperatures below 140°C (Oguz, 2011). Ammonia-water used as working fluid was the most preferred among several organic mixtures which yielded maximum geothermal water utilization. The technology of a Kalina cycle has developed over the last two decades; however, commercial marketing of the technique started only a few years ago (Lolos and Rogdakis, 2009).

The innovative technology has undergone intense development, optimisation and large-scale demonstrations, based on the initial version, with significant power generation in the industrial world. The first Kalina cycle was constructed between 1991 and 1997 at Canoga Park, California, for demonstration purposes with a 6.5 MW installed capacity and ran for a total of 8600 hours. This period

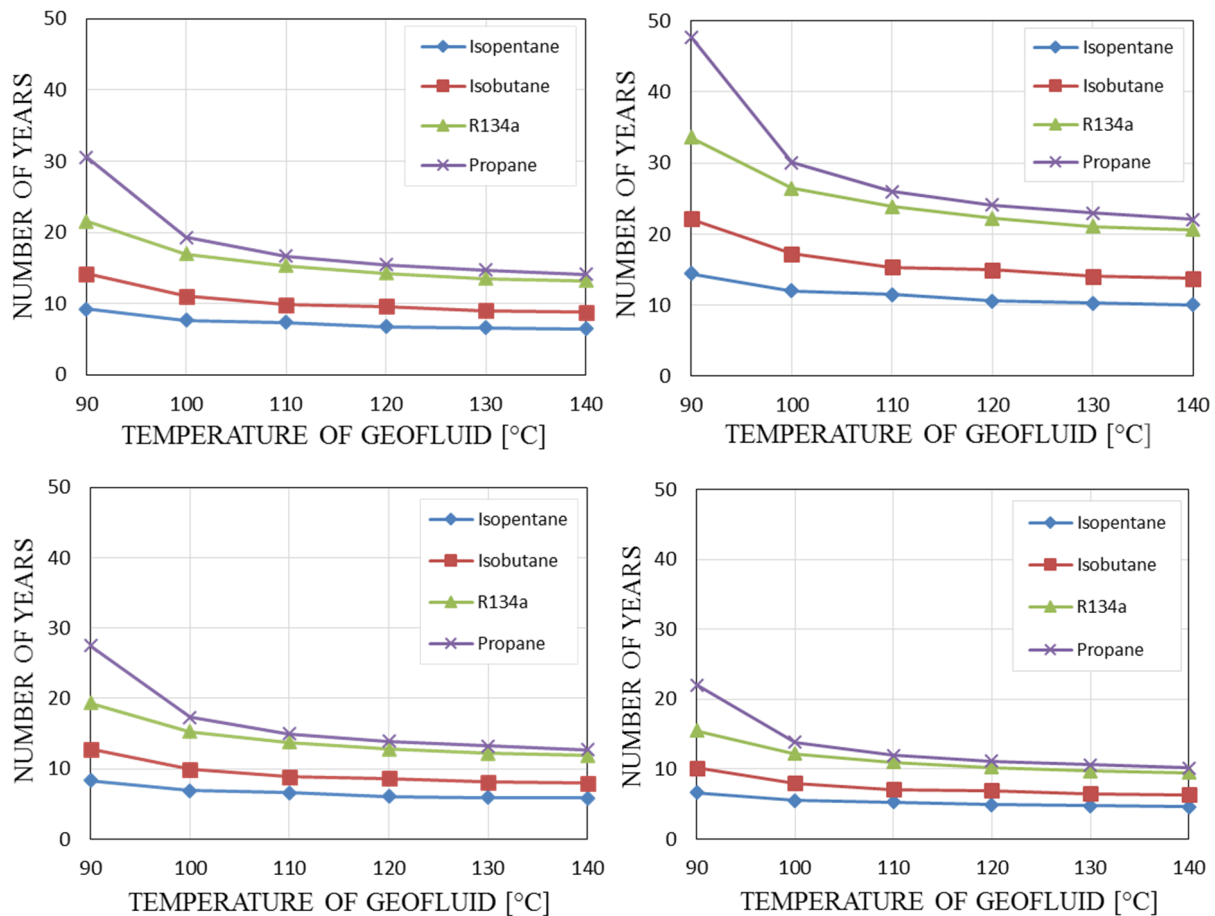


FIGURE 13: Comparison of economic analysis of ORC for different working fluids showing actual time for return of investment as a function of geofluid temperature: a) Interest rate = 10%, price of electricity = 0.18 USD/kWh; required time for return on investment = 10 years; b) Interest rate = 15%, price of electricity = 0.18 USD/kWh; required time for return on investment = 10 years; c) Interest rate = 15%, price of electricity = 0.2 USD/kWh; required time for return on investment = 10 years; d) Interest rate = 10%, price of electricity = 0.25 USD/kWh; required time for return on investment = 10 years

included tests to demonstrate and verify efficiency gains in heat and combined cycle operation (DiPippo, 2005). Three new commercial Kalina cycle power plants were commissioned in 1999 in Iceland and Japan, with a 4.5 MW waste-to-energy demonstration facility and a 3.5 MW waste heat power plant at Sumitomo Steel in Japan, and a 2.0 MW geothermal power plant in Húsavík, in N-Iceland.

Kalina power plant principles and modelling:

The Kalina cycle is principally a modified Organic Rankin Cycle, and was developed in an attempt to reduce the losses incurred by the use of a pure substance working fluid. The goal of the Kalina cycle is that by using a mixture of ammonia and water as the working fluid, the temperature profile of the working fluid will more closely follow the temperature profile of the heat source and sink. There are several variations of the basic Kalina cycle, based on the application (Jones, 2011). A mixture of fluids has been proposed to substitute steam in a Kalina cycle, where a mixed working fluid of variable composition is used to provide a better match between the temperatures of hot and cold flows. The composition of the fluid is changed in the cycle at different points. In most Kalina cycle studies, a mixture of water and ammonia has been used. The ammonia in the mixture begins to vaporize first and, as it boils off, the liquid mixture ammonia concentration decreases, and the boiling temperature of the liquid mixture increases. By adjusting the mass fraction of ammonia in the mixture, the Kalina cycle can be optimized based on the input conditions. Figure 14 shows a basic conceptual illustration of the Kalina cycle. The EES program for the Kalina cycle is given in Appendix II.

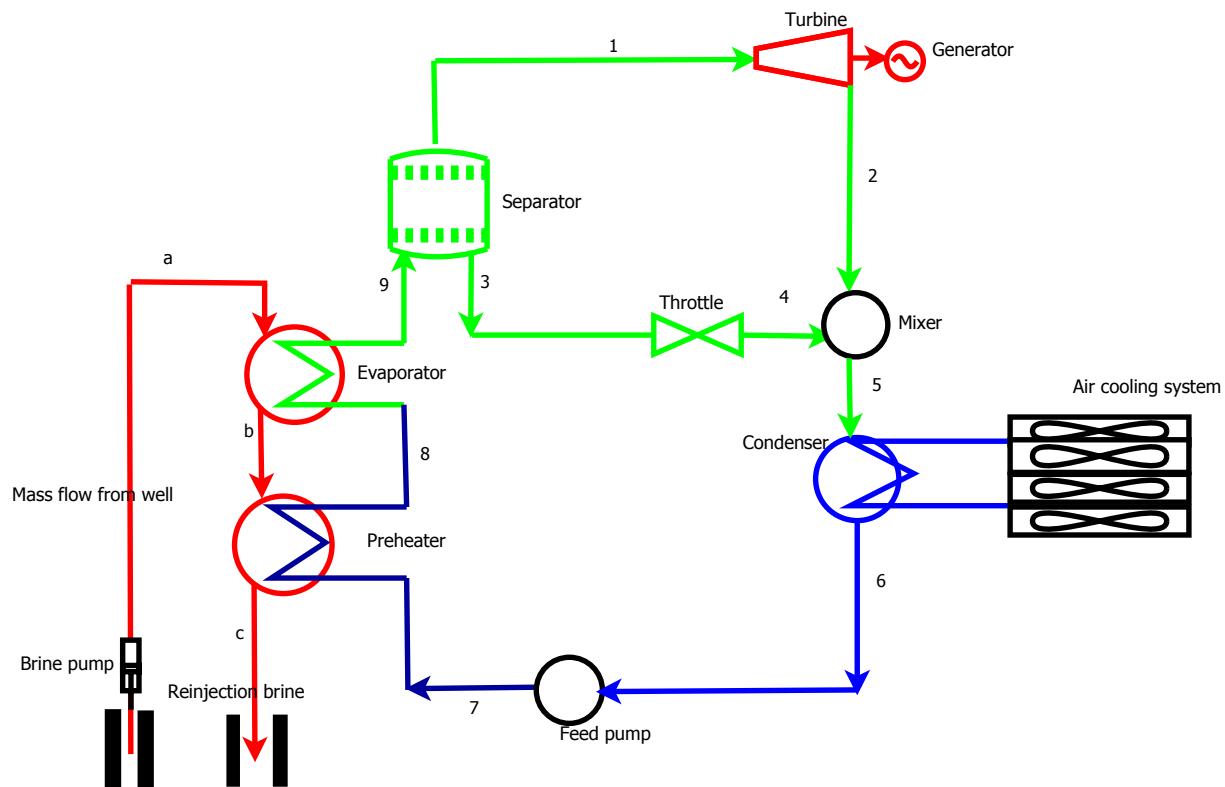


FIGURE 14: Schematic of a basic Kalina cycle

The working fluid (ammonia-water) leaves the evaporator or boiler as a saturated mixture. The quality of the mixture is a function of the concentration of ammonia in the working fluid mixture, the temperature of the heat source, and the pressure of the working fluid. Once the working fluid mixture leaves the evaporator, it enters the phase separator.

The task of the phase separator is to separate the working fluid into two separate streams. The saturated vapour portion of the working fluid is an ammonia rich mixture that passes through the separator to state 1 (Figure 14). The saturated vapour continues on to the turbine where it undergoes an isentropic expansion to produce work. The saturated vapour is expanded into a saturated mixture and exits the turbine. The saturated mixture is at state 2. The mass fraction of the working fluid that did not vaporize in the evaporator leaves the separator as a saturated liquid at state 3. The saturated liquid portion of the working fluid is a weaker ammonia mixture than the saturated vapour portion of the working fluid. The hot saturated liquid is sent to the mixer (or absorber) at a low pressure with a throttling valve, where it is mixed with the saturated mixture leaving the turbine at the same low pressure. The recombined mixture leaves the mixer at state 5 and passes through the condenser where heat is rejected and the working fluid is brought back to a saturated liquid. The saturated liquid leaves the condenser at state 6. A pump is then used to isentropically compress the working fluid mixture to the maximum pressure of the cycle at state 7. The cold working fluid then enters the preheater and absorbs heat and leaves the preheater at state 8. The preheated working fluid mixture then enters the evaporator to start the process all over again.

Thermal efficiency and net power output of a Kalina cycle power plant:

The thermal efficiency of the power plant cycle is of upmost importance in order to produce an economically viable system, and can be used as the primary evaluation parameter. The utilization of the first law efficiency of thermodynamics, allows the measurement of the cycle performance. It is a direct measure of the heat transfer requirements in the boiler and condenser. A cycle with a high first law efficiency would have a much smaller boiler heat transfer area requirement per unit work output.

However, several other factors such as the transfer coefficients and pressures play a role in the size of the equipment.

The evaluation of the first law of thermodynamic is the most common way of evaluating the Organic Rankine Cycle using a working fluid such as water or a hydrocarbon. The efficiency of the Kalina cycle system was calculated by varying the pressure and the fraction of ammonia in the water. The calculation was carried out for the entire range of temperatures between 90 and 140°C in order to find the optimum operation. The same procedure was used to calculate the net power output for different pressures and fractions of ammonia. The results are presented in Figure 15. The results show that ammonia water as a working fluid can be used at different pressures by changing the concentration of ammonia mixture in the water. Figure 15 shows the behaviour of the water ammonia mixture as a working fluid at different pressures and with different ratios of ammonia in the mixture.

The optimum pressure determined by the pinch point of the heat exchanger was 30 bar for the entire temperature range considered, with a mixture fraction of 90% ammonia. The results are given in Table 10.

TABLE 10: Optimum operating conditions of power plant for ranged temperature resource

Temperature (°C)	Ammonia fraction	High pressure (bar)	Low pressure (bar)	Cycle efficiency	Exergy efficiency	Specific power output (kW/kg·s)
90	0.8	15	5	3%	10%	2.5
100	0.8	15	5	6%	21%	6
110	0.8	15	2	12%	50%	20.6
120	0.8	15	2	13%	51%	25.9
130	0.9	20	2	16%	68%	40.4
140	0.9	30	2	19%	81%	57.6

Investment cost estimation of Kalina cycle model equipment:

Based on the same principles of ORC and considering that the cost per unit size is the same, the total cost of equipment was calculated. However, the calculation did not include the separator and mixer costs as there was no baseline for the calculation or estimation. The calculated cost is shown in Table 11. The total cost for the equipment listed above includes the cost of: a fan, a feed pump, a turbine and a well pump for different temperatures in a range between 90 and 140°C. The results are shown in Table 12.

TABLE 11: Area of different components of Kalina cycle model (without mixer and separator)

Temperature (°C)	Area condenser (m ²)	Area evaporator (m ²)	Area preheater (m ²)
90	13.67	11,06	1,209
100	12,43	14,86	1,446
110	12,35	18,27	1,63
120	12,44	21,54	1,79
130	12,64	24,85	1,91
140	12,93	28,32	2,01

TABLE 12: Total equipment cost of Kalina cycle model (without mixer and separator)

Temperature (°C)	Total equipment cost of Kalina model (without separator and mixer) (USD)
90	20,690
100	24,364
110	28,554
120	32,727
130	36,846
140	40,895

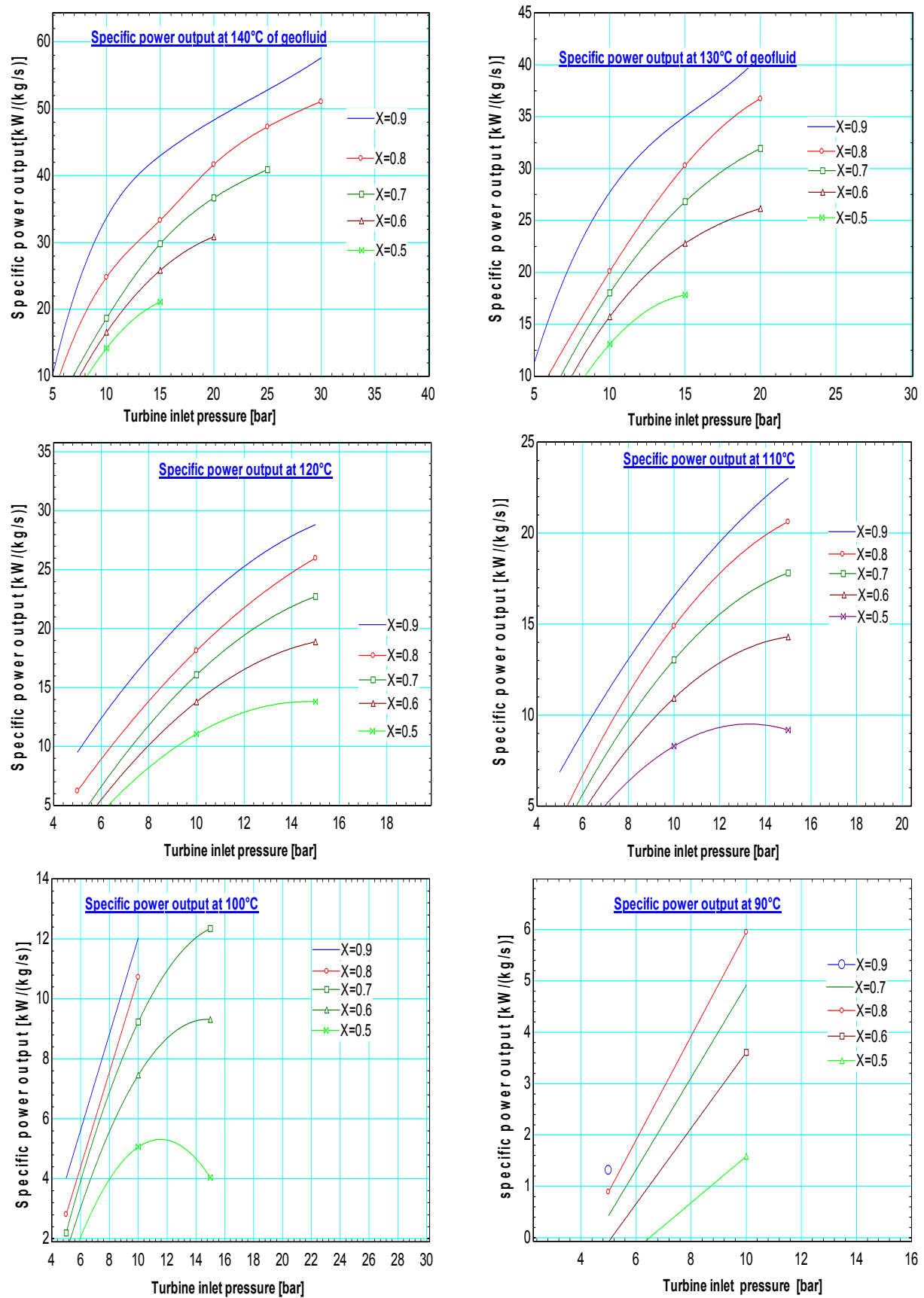


FIGURE 15: Comparison of net power output for different pressure and fraction of ammonia in mixture

7. COMPARISON OF ORGANIC RANKINE CYCLE AND KALINA CYCLE

A simple model of a geothermal power plant was made to compare the thermodynamic performance of the two cycles. The main comparison consisted of power outputs and cycle efficiency. The two cycles utilized a secondary fluid for obtaining heat energy through a heat exchanger from a geothermal source. The difference between the ORC and Kalina cycle is in the working fluid and the equipment components. The Organic Rankine Cycle utilizes a hydrocarbon or refrigerant as a working fluid in a closed loop. The Kalina cycle has specific parameters due to its mixture of ammonia and water. The optimum turbine inlet pressure in the Kalina cycle depends on the ammonia fraction in the water-ammonia mixture and the temperature of geothermal fluid. These factors influence the optimum output and the heat extraction efficiency. The advantages of the Kalina cycle are being able to increase or decrease the power output by adjusting the fraction of ammonia in the mixture without changing any equipment. Theoretically, Kalina has a higher efficiency when the heat source stream has a finite heat capacity. But, ORC and Kalina are similar when the source is condensing steam (Valdimarsson, 2003).

In this study, the ORC and Kalina cycles were analysed in regard to the first and second laws of efficiency. The performance of the Kalina cycle is similar to that of ORC. With temperatures below 100°C, the ORC cycle is a more favourable option than the Kalina Cycle. However, an increase in the temperature of the geothermal fluid leads to an increase in Kalina efficiency and power output. At 140°C, the efficiency and power output of Kalina are about the same as that of isopentane in the ORC, with the highest efficiency and power output. With the increase in geothermal fluid temperature, Kalina efficiency and power output might be higher than ORC at geothermal fluid temperatures above 140°C. That means that Kalina cycle performance at temperatures below 140°C has the same performance as ORC with the right working fluid. This result agrees with some authors who said that the Kalina cycle permits a gain in performance with respect to ORC. The adoption of the Kalina cycle, at least for low power levels and medium-high temperature thermal sources, does not seem to be justified by a gain in performance with respect to a properly optimized ORC. The gain is very small and is obtained with a complicated plant scheme, large surface heat exchangers and particularly high pressure resistant and non-corrosive materials, both expensive and unproven (Bombarda et al., 2010). The results on the performance of all the Organic Rankine Cycle working fluids used and the working fluid for the Kalina cycle are summarized in Tables 4-7 and 10.

Considering the models, the Kalina cycle has many more components than the Organic Rankine Cycle and sometimes the setup is very complex. This increases the cost of a power plant. The comparison of equipment shows high costs for the Kalina cycle, without adding the cost of separator and mixer. The calculation was done using the same baseline for the ORC. Regarding power output for all ORC cycles used and for the Kalina cycle, isopentane gave the highest output followed by isobutane, R134a, propane and then the Kalina cycle at temperatures less than 100°C. But, between 100-120°C, the Kalina cycle produced higher power output than propane and R134a. At 130-140°C, output from the Kalina cycle increased quickly and gave the highest power output of the working fluids considered, except for isopentane. At 140°C, Kalina gave a power output near the power output given by isopentane. This means that if the temperature is higher than 140°C, the Kalina cycle would give higher power output than the isopentane. Looking at the energy input and power output in the modelled systems, the answer is clear. For temperatures lower than 100°C, the Kalina cycle performance is less than that of ORC. But, for temperatures between 100 and 140°C, the performance of Kalina and ORC is similar, depending on the working fluid selected for ORC.

Again, ammonia is toxic and highly corrosive, which has to be taken into account in material selection. In this study, ORC was appreciated for its efficiency if the working fluid was chosen properly. Isopentane gave a good performance with this type of geothermal resource. It should be taken into consideration if all assumptions are proven in the future with detailed studies.

8. CONCLUSION AND RECOMMENDATIONS

After analysing several parameters of the two cycles, the ORC was considered the best for use in Burundi for its low temperature resource. The ORC showed good efficiency. It has been used for a long time and still shows improvement and it is reliable and safe in operation. The Kalina cycle technologies are very complex and relatively new compared to ORC. In many cases of research, the Kalina cycle was shown to be the most efficient. However, for low temperature resources, the Kalina cycle's highest efficiency is questioned by some authors. ORC's power output is very similar to that of the Kalina cycle for geothermal fluid temperatures in the range of 110 and 140°C, and the Kalina cycle shows less power output for resource temperatures lower than 100°C.

The Kalina cycle can be appreciated for its thermodynamic properties. Its working fluid is a mixture that has variable boiling temperature that allow it to decrease or increase the power output without changes in equipment components. But, it is expensive compared to ORC because it requires a large area for the condenser and evaporator. For temperatures higher than 140°C, the Kalina cycle might give a better performance than ORC with regard to the first and second laws of thermodynamics. Economic analysis showed the feasibility of a binary power plant of low temperature in Rusizi Valley in Burundi, if future studies prove the assumptions considered in this study. However, the working fluid must be well selected to reach the economic goal. In this study, isopentane was shown to be economical if used for such low temperature geothermal fluid. Isobutane for temperatures superior to 120°C was shown to be economical. The maximum power output at 140°C and a geofluid mass flow rate of 80 kg/s could reach 4.9 MW, and a minimum at the same temperature with a mass flow rate of 20 kg/s is around 1.2 MW, using isopentane as the working fluid. At 90°C, the maximum power output that could be reached is 1 MW with a mass flow of 80 kg/s, and a minimum 0.3 MW with a mass flow rate of 20 kg/s, using isopentane.

As this study was done based on assumptions, detailed exploration is needed to gather more information on the subsurface. With that information, the results of this work could be improved.

ACKNOWLEDGEMENTS

I would like to express my sincere gratitude to the UNU-GTP and the Government of Iceland for awarding me this scholarship to participate in the six month training programme. I also would like to express my gratitude to the officials of the Burundian Ministry of Energy and Mines for supporting and granting permission. Many thanks go to the Geothermal Training Programme staff, Dr. Ingvar B. Fridleifsson, outgoing director, Mr. Lúdvík S. Georgsson, director, Thórhildur Ísberg, administrator, Ingimar G. Haraldsson, project manager, Málfríður Ómarsdóttir, environmental scientist and Markús A. G. Wilde, for their assistance and support during my stay in Iceland. Intense gratitude also goes to all lecturers. Great thanks go to Dr. Páll Valdimarsson and Mrs. María Sigríður Guðjónsdóttir, for their help during the training and the preparation of this report. I wish to express my thanks to my supervisor, Heimir Hjartarson, for his assistance and help during the preparation of this report.

Special thanks go to my family and friends for their support, encouragement and prayers during my stay in Iceland. Geothermal Utilization Engineers class 2013 and all colleague UNU Fellows: I enjoyed meeting and being with you.

REFERENCES

Ármansson, H., and Gíslason, G., 1983: *Geothermal resources of Burundi – Report on a reconnaissance mission 1982.08.30-09.13*. Orkustofnun, report OS-83025/JHD-06, 102 pp.

Bejan, A., Tsatsaronis, G., and Moran, M., 1996: *Thermal design and optimization*. John Wiley & Sons, USA, 560 pp.

Bombarda, P., Invernizzi, C.M., Pietra, C., 2010: Heat recovery from diesel engines: A thermodynamic comparison between Kalina and ORC Cycles. *Appl. Therm. Eng.*, 30, 212-219.

Dickson, M.H., and Fanelli, M., 2003: *Geothermal energy. Utilization and technology*. UNESCO, Renewable Energy Series, 205 pp.

DiPippo, R., 2005: *Geothermal power plants: Principles, applications and case studies*. Elsevier Ltd., Kidlington, UK, 450 pp.

DiPippo, R., 2008: *Geothermal power plants. Principles, applications, case studies and environmental impact*. Elsevier Ltd., Kidlington, UK, 493 pp.

El-Wakil, M.M., 1984: *Power plant technology*. McGraw-Hill Companies, USA, 861 pp.

Franco, A., and Villani, M., 2009: Optimal design of binary cycle power plants for water-dominated, medium temperature geothermal fields. *Geothermics*, 38-4, 379-391.

Fridleifsson, I.B., 2013: *Geothermal utilization*. UNU-GTP, Iceland, unpublished lecture notes.

Fridleifsson, I.B., and Freeston, D.H., 1994: Geothermal energy research and development. *Geothermics*, 23-2, 175-214.

Fridleifsson, I.B., Bertani, R., Huenges, E., Lund, J.W., Ragnarsson, Á., and Rybach, L., 2008: The possible role and contribution of geothermal energy to the mitigation of climate change. In: *IPCC Scoping Meeting on Renewable Energy Sources - Proceedings, Luebeck, Germany*, 191 pp.

Fridriksson, Th., Sigurgeirsson M.Á., Ármannsson, H., 2012: *Reconnaissance study of geothermal areas in Burundi: geoscientific studies*. ÍSOR – Iceland GeoSurvey, Reykjavik, report ÍSOR-2012/053, 37 pp.

Geoscience Australia and ABARE, 2010: *Australian energy resource assessment*. Commonwealth of Australia, Canberra, 357 pp, website: www.ga.gov.au/image_cache/GA16725.pdf.

Jones, D.A., 2011: *A study of the Kalina cycle system II for the recovery of industrial waste heat with heat pump augmentation*. Auburn University, MSc thesis, 93 pp.

Khairah A., 2012: Cooling system design for a binary power plant in North-Goubhet field, Djibouti. Report 18 in: *Geothermal training in Iceland 2012*. UNU-GTP, Iceland, 371-395.

Kopunicova, 2009: *Feasibility study of binary geothermal power plants in Eastern Slovakia: Analysis of ORC and Kalina power plants*. RES - the School for Renewable Energy Science in affiliation with the University of Iceland and the University of Akureyri, MSc thesis, 71 pp.

Lolos, P.A., and Rogdakis, E.D., 2009: A Kalina power cycle driven by renewable energy sources. *Energy*, 34-4, 457-464.

Ministry of Energy and Mines of Burundi, 2012: *Investment opportunities in renewable energy Burundi*. MEM, Burundi, 52 pp.

Ndayirukiye, S., 1986: *La plaine occidentale du Burundi - Etude régionale*. Géographie-Aménagement, Nice, France, PhD thesis (in French), 721 pp.

Nugroho, A.J., 2011: *Optimization of electrical power production from high-temperature geothermal fields with respect to silica scaling problems*. University of Iceland, MSc thesis, UNU-GTP, report 2, 57 pp.

Oguz, A., 2011: Power generation from medium temperature geothermal resources: ANN-based optimization of Kalina cycle system-34. *Energy*, 36-5, 2528-2534.

Paanu, T., Niemi, S., and Rantanen, P., 2012: *Waste heat recovery – bottoming cycle alternatives*. Proceedings of the University of Vaasa, Finland, report 175, 26 pp.

Paci, M., Fastelli, I., and Rossi, 2009: *Advanced systems for power production from geothermal low temperature resources*. Enel Ingegneria e Innovazione, Pisa, Italy, 14 pp.

Perry, R., and Green, D., 2008: *Chemical engineers handbook*. McGraw-Hill, New York, United States, 2735 pp.

Smeets, J.R., 2012: *Geothermal power production*. IF Technology.

Stapleton, M., and Weres, O., 2011: Recent developments in geothermal scale control. *Proceedings of the International Workshop on Mineral Scaling 2011, Manila, Philippines*, 69-76.

Uhorakeye, T., 2008: Feasibility design of an integrated single-flash binary pilot power plant in NW-Rwanda. Report 27 in: *Geothermal training in Iceland 2008*. UNU-GTP, Iceland, 519-538.

Teklemariam, M., 2012: Overview of geothermal resource exploration and development in the East African Rift system. *Presented at Short Course VII on Exploration for Geothermal Resources, organized by UNU-GTP, GDC and KenGen, at Lake Bogoria and Lake Naivasha, Kenya*, 10 pp.

Valdimarsson, P., 2003: *ORC and Kalina: Analysis and experience*. Washington State University, lecture notes, website: northwestchptap.org/NwChpDocs/ORC_and_Kalina_Analysis_and_experience.pdf.

APPENDIX I: The EES program for the Organic Rankine Cycle

```
{Fluid$:"Isobutane"}
T_delta =12
T_pp=5
Cp=4.19
Cp_air=1.02

"--- Brine conditions ---"

{m_dot_geof=80}
{T_a=140 }{ temperature well}
{P[0]=30 }{ pressure from well}
{T_c=70 }{ re-injection}
"--- Constant assume ---"
{P[1]=32 }{pressure goes to turbine}
eta_turb=0.85
eta_pump=0.75
eta_pumpcool=0.75
eta_fan=0.65
eta_motor=0.75
T_ambient=30
P_atm= 1.02
RH=0.70

"--- Point 1 ---"
{Turbine}
T[1]=T[6]
h[1]=Enthalpy(Fluid$,P=P[1],x=1)
s[1]=Entropy(Fluid$,h=h[1],P=P[1])

"--- Point 2 ---"
{outturbine}
P[2]=P[3]
s[1]=s[2] {isentropic}
h_2s=Enthalpy(Fluid$,s=s[2],P=P[2])
h[2]=h[1]-((h[1]-h_2s)/eta_turb)
```


T[2]=Temperature(Fluid\$,P=P[2],s=s[2])

W_turbine= m_dot_wf*(h[1]-h[2])

"--- Point 3 ---"

{condenser of cycle}

{T_condenser=28}

P[3]=Pressure(Fluid\$,T=T_condenser,x=0)

h[3]=Enthalpy(Fluid\$,T=T_condenser,x=0)

s[3]=Entropy(Fluid\$,T=T_condenser,h=h[3])

Cp_air*(T_cool_OUT-T_wb)
m_air=(m_dot_wf(h[2]-h[3]))

{using cooling air}

T_cool_OUT=T_ambient+T_delta

Q_cond=(m_dot_wf*(h[2]-h[3]))

T[3]=T_condenser

"--- Point 4 ---"

{feed pump of cycle}

s[3]=s[4]

P[4]=P[1]

h_4s=Enthalpy(Fluid\$,s=s[3],P=P[4])

h[4]=h[3]+((h_4s-h[3])/eta_pump)

T[4]=Temperature(Fluid\$,P=P[4],s=s[4])

W_p=m_dot_wf*(h[4]-h[3])

"--- Point 5 ---"

{preheater of cycle}

P[5]=P[1]

h[5]=Enthalpy(Fluid\$,x=0,P=P[1])

s[5]=Entropy(Fluid\$,P=P[1],h=h[5])

T[5]=T_b-T_pp

"--- Point 6 ---"

{evaporator}

cp[1]=Cp(Water,T=T[0],P=P[0])

T[0]=T_a

h[0]=Enthalpy(Water,T=T[0],P=P[0])

P[6]=P[1]

T[6]=T[5]

h[6]=Enthalpy(Fluid\$,P=P[1],x=1)

s[6]=Entropy(Fluid\$,h=h[6],P=P[6])

m_dot_geof*cp[1]*(T_b-
T_c)=m_dot_wf*(h[5]-h[4])

(m_dot_geof*cp[1]*(T_a-
T_b)=m_dot_wf*(h[1]-h[5]))

".....{Power for cooling condenser}....."

P_inair=P_atm

T_wb=WetBulb(AirH2O,T=T_ambient,r=R
H,P=P_inair)

h_inair=Enthalpy(AirH2O,T=T_ambient,r=
RH,P=P_inair)

P_dp=0.121

rho=Density(AirH2O,T=T_ambient,r=RH,P
=P_inair)

P_fan=(P_dp*m_air)/(rho*eta_fan)

W_fan=P_fan*eta_pumpcool

W_t= W_turbine-

(W_p+W_fan+P_pumpmotor)

{balance the heat exchange}

Q_a=m_dot_geof*cp[1]*(T_a-T_b)

Q[1]=m_dot_wf*(h[1]-h[5])

Q_b=m_dot_geof*cp[1]*(T_b-T_c)

Q[2]=m_dot_wf*(h[5]-h[4])

Q_tot=m_dot_geof*cp[1]*(T_a-T_c)

{Energy for well pump}

H=250

g=9.81

P_pumpmotor=(H*m_dot_geof*g)/(eta_pu
mp*eta_motor*1000)

eta_cycle=W_t/Q_tot

".....{Analysis of Exergy}....."

h_ingeowater=Enthalpy(Water,T=T_a,P=P
[0])

s_ingeowater=Entropy(Water,h=h_ingeow
ater,P=P[0])

h_steadstate=Enthalpy(Water,T=30,P=1.0
2)

s_steadstate=Entropy(Water,h=h_steadst
ate,P=1.02)

Exergy1=m_dot_geof*((h_ingeowater-
h_steadstate)-303*(s_ingeowater-
s_steadstate))

eta_exergy= W_t/Exergy1

".....{Overall heatp}....."

{evaporator}

LMTD_ev=((T_a-T[1])-(T_b-T[5]))/B[1]

B[1]=ln((T_a-T[1])/(T_b-T[5]))

```

U_evap=1600
{w/m^2 °C}
A_evap=(Q_a*10^3)/(U_evap*LMTD_ev)

```

```

{preheater}

```

```

LMTD_preh=((T_b-T[5])-(T_c-T[4]))/B[2]
B[2]=ln((T_b-T[5])/(T_c-T[4]))
U_preheater=1000
{w/m^2 °C}
A_preheater=(Q_b*10^3)/(U_preheater*L
MTD_preh)

```

```

{condenser}

```

```

LMTD_cond=((T[2]-T_cool_OUT)-
(T_condenser-T_ambient))/B[3]
B[3]=ln((T[2]-T_cool_OUT)/(T_condenser-
T_ambient))
U_condenser=800
{w/m^2 °C}
A_condenser=(Q_cond*10^3)/(U_condens
er*LMTD_cond)

```

```

{+++Cost of Power plant components +++}
{Unit area cost}

```

```

UC_Eva=500
UC_Preh=450
UC_Sup=500
UC_fan=400
UC_Cond=600
UC_Tur=500
UC_Pump=450

```

```

Cost_Cond=A_Condenser*UC_Cond
Cost_Preh=A_Preheater*UC_Preh
Cost_Eva=A_Evap*UC_Eva
Cost_Turbine=W_turbine*UC_Tur
Cost_Feed_Pump=W_P*UC_Pump
Cost_well_Pump=P_pumpmotor*UC_Pum
p
Cost_fan=W_fan*UC_fan

```

```

Cost_total=(Cost_Cond+Cost_Preh+Cost_
Eva+Cost_Turbine+Cost_Feed_Pump+Co
st_well_Pump+Cost_fan)

```

APPENDIX II: The EES program for the Kalina cycle

```

{Kalina program}

```

```

",,,Assume data,,,"

```

```

m_dot_geo=1
{used for optimization 1kg/s}
{T_a= 120[°C]}{used variation of
temperature between 90 to 140°C}
{T_c=70}
P_geo=30[bar]
eta_turbine=0.85
eta_pump=0.75
eta_fan=0.65
eta_pumpcool=0.75
eta_motor=0.75
P_atm=1[bar]
RH=0.70
{relative humidity}
{P_high=30[bar]}
{P_low=5[bar]}{vary between 2 to 5bar}
T_air=30[°C]
{ambient temperature}
Cp_air=1.02
T_p_hotwell=15[°C]
T_p_vaporizer=5 [°C]
{vary between 2 to 5°C}

```

```

x_mixture=0.9

```

```

{Variation between 0.1 to 0.9}

```

```

",,,6,,,"

```

```

{Analysis outlet condenser and inlet pump}

```

```

T[6]=T_air+T_p_hotwell
P[6]=P_low
x_m[6]=x_mixture
Qa[6]=0
Tk[6]=T[6]+273.2
Call NH3H2O(138, Tk[6], x_m[6], Qa[6]:
Tk_6, P_6, x_m_6, h[6], s[6], u[6], v[6],
Qa_6)

```

```

",,,7,,,"

```

```

{Analysis outlet feed pump}

```

```

P[7]=P_high
x_m[7]=x_m[6]
dh_pump=((P[7]-P[6])*v[6])*(100000/1000)
[kJ/kg]
h[7]=h[6]+dh_pump
Call NH3H2O(234, P[7], x_m[7], h[7]:
Tk[7], P_7, x_m_7, h_7, s[7], u[7], v[7],
Qa[7])
Tk[7]=T[7]+273.2

```

""",8,""

{Point 8 is the bubble point, which means that boiling margin in preheater is zero}

{Analysis outlet preheat}

P[8]=P[7]

x_m[8]=x_m[7]

Qa[8]=0

Call NH3H2O(238, P[8], x_m[8], Qa[8]:

Tk[8], P_8, x_m_8, h[8], s[8], u[8], v[8],

Qa_8)

T[8]=Tk[8]-273.2

""",9,""

{Analysis over preheater}

T[9]=T_a-T_p_vaporizer

Tk[9]=T[9]+273.2

P[9]=P[8]

x_m[9]=x_m[8]

Call NH3H2O(123, Tk[9], P[9], x_m[9]:

Tk_9, P_9, x_m_9, h[9], s[9], u[9], v[9],

Qa[9])

""",1,""

{Analysis inlet turbine}

{saturated vapor point}

Tk[1]=Tk[9]

P[1]=P[9]

Qa[1]=1

Call NH3H2O(128, Tk[1], P[1], Qa[1]:

Tk_1, P_1, x_m[1], h[1], s[1], u[1], v[1],

Qa_1)

T[1]=Tk[1]-273.2

vap_ratio*x_m[1]+liq_ratio*x_m[3]=x_m[9]

vap_ratio+liq_ratio=1

""",3,""

{saturated liquid point}

Tk[3]=Tk[9]

P[3]=P[9]

Qa[3]=0

Call NH3H2O(128, Tk[3], P[3], Qa[3]:

Tk_3, P_3, x_m[3], h[3], s[3], u[3], v[3],

Qa_3)

T[3]=Tk[3]-273.2

""",2,""

{Analysis outlet turbine}

{isentropic}

P[2]=P[5]

x_m[2]=x_m[1]

Call NH3H2O(235, P[2], x_m[2], s[1]:

Tk_2s, P_2s, x_m_2s, h_2s, s_2s, u_2s,

v_2s, Qa_2s)

eta_turbine=(h[1]-h[2])/(h[1]-h_2s)

Call NH3H2O(234, P[2], x_m[2], h[2]:

Tk[2], P_2, x_m_2, h_2, s[2], u[2], v[2],

Qa[2])

T[2]=Tk[2]-273.2

""",4,""

h[4]=h[3]

P[4]=P[5]

x_m[4]=x_m[3]

Call NH3H2O(234, P[4], x_m[4], h[4]:

Tk[4], P_4, x_m_4, h_4, s[4], u[4], v[4],

Qa[4])

T[4]=Tk[4]-273.2

""",5,""

{Analysis inlet condenser}

h[5]=vap_ratio*h[2]+liq_ratio*h[4]

P[5]=P[6]

x_m[5]=x_m[6]

Call NH3H2O(234, P[5], x_m[5], h[5]:

Tk[5], P_5, x_m_5, h_5, s[5], u[5], v[5],

Qa[5])

T[5]=Tk[5]-273.2

{Point b}

c_p_geo=Cp(Water,T=T_a,P=P_geo)

{T_b=T[8]+T_p_vaporizer}

Q_dot_rhs=m_dot_geo*c_p_geo*(T_a-

T_b)

Q_dot_rhs=m_dot_wf*(h[9]-h[8])

{Point c}

Q_dot_rhi=m_dot_geo*c_p_geo*(T_b-T_c)

Q_dot_rhi=m_dot_wf*(h[8]-h[7])

Q_dot_heat=m_dot_wf*(h[9]-h[7])

"....."

{Power pproduction analysis}

W_turbine=

m_dot_wf*vap_ratio*x_m[1]*(h[1]-h[2])

W_pump=m_dot_wf*(h[7]-h[6])

{feeding pump}

{Power air cooling analysis}

P_inair=P_atm

T_wb=WetBulb(AirH2O,T=T_air,r=RH,P=

P_inair)

```

h_inair=Enthalpy(AirH2O,T=T_air,r=RH,P
=P_inair)
P_dp=0.121
rho=Density(AirH2O,T=T_air,r=RH,P=P_in
air)
T_cool_OUT=T_air+ 5 {T_p_hotwell}
Cp_air*(T_cool_OUT-T_wb)
*m_air=(m_dot_wf*(h[5]-h[6]))
{using cooling air}
{T_cool_OUT=T_air+T_delta}
P_fan=(P_dp*m_air)/(rho*eta_fan)
W_fan=P_fan*eta_pumpcool

{Energy for well pump}
H=250
g=9.81
P_pumpmotor=(H*m_dot_geo*g)/(eta_pu
mp*eta_motor*1000)

```

```

{Net power}
W_t= W_turbine-
(W_pump+W_fan+P_pumpmotor)

```

```

{Cycle Efficiency}

```

```

eta_cycle= W_t/Q_dot_heat

```

```

",,,{Analysis of Exergy},,,

```

```

h_ingeowater=Enthalpy(Water,T=T_a,P=P
_geo)
s_ingeowater=Entropy(Water,h=h_ingeow
ater,P=P_geo)

```

```

h_steadstate=Enthalpy(Water,T=30,P=1.0
2)
s_steadstate=Entropy(Water,h=h_steadst
ate,P=1.02)
Exergy1=m_dot_geo*((h_ingeowater-
h_steadstate)-303*(s_ingeowater-
s_steadstate))

```

```

Eta_exergy= W_t/Exergy1

```

```

"...{Overall heatp}..."

```

```

{evaporator}
LMTD_ev=((T_a-T[9])-(T_b-T[8]))/B[1]
B[1]=ln((T_a-T[9])/(T_b-T[8]))
U_evap=1600
{w/m^2 °c}
A_evap=(Q_dot_rhs*10^3)/(U_evap*LMT
D_ev)

```

```

{preheater}

```

```

LMTD_preh=((T_b-T[8])-(T_c-T[7]))/B[2]
B[2]=ln((T_b-T[8])/(T_c-T[7]))
U_preheater=1000
{w/m^2 °c}
A_preheater=(Q_dot_rhi*10^3)/(U_preheat
er*LMTD_preh)

```

```

{condenser}
Q_cond=(m_dot_wf*(h[5]-h[6]))
LMTD_cond=((T[5]-T_cool_OUT)-(T[6]-
T_air))/B[3]
B[3]=ln((T[5]-T_cool_OUT)/(T[6]-T_air))
U_condenser=800
{w/m^2 °c}
A_condenser=(Q_cond*10^3)/(U_condens
er*LMTD_cond)

```

```

{+++Cost of Power plant components +++}

```

```

{Unit area cost}

```

```

UC_Eva=500
UC_Preh=450
UC_Sup=500
UC_fan=400
UC_Cond=600
UC_Tur=500
UC_Pump=450

```

```

Cost_Cond=A_Condenser*UC_Cond
Cost_Preh=A_Preheater*UC_Preh
Cost_Eva=A_Evap*UC_Eva
Cost_Turbine=W_turbine*UC_Tur
Cost_Feed_Pump=W_pump*UC_Pump
Cost_well_Pump=P_pumpmotor*UC_Pum
p
Cost_fan=W_fan*UC_fan
Cost_total_equipment=(Cost_Cond+Cost_
Preh+Cost_Eva+Cost_Turbine+Cost_Fee
d_Pump+Cost_well_Pump+Cost_fan)

```



PROCESSING AND 1D INVERSION OF MAGNETOTELLURIC DATA FROM DUBTI AREA IN TENDAHO GEOTHERMAL FIELD, ETHIOPIA

Behailu Woldeesemayet

Geological Survey of Ethiopia
Geothermal Energy Department
P.O. Box 2302, Addis Ababa
ETHIOPIA
msemayet@yahoo.com

ABSTRACT

Electromagnetic methods are one of the most effective geophysical methods in geothermal exploration. They enable imaging the subsurface conductivity. Magnetotelluric (MT) and transient electromagnetic methods (TEM) are the most successful methods in identifying geothermal resources prior to drilling. The MT method uses the natural source of the electromagnetic field to screen out the resistivity structure down to a depth of several kilometers, whereas TEM uses an artificial source field to image the near-surface resistivity variations down to a depth of around one kilometre. Data collected by these methods are processed. The processed data are used for a 1D Occam inversion to create a resistivity model. This report discusses the processing and inversion of magnetotelluric (MT) data from the Dubti area in Tendaho geothermal field, NE-Ethiopia. TEM soundings from the Krýsuvík area in SW-Iceland are used as an example of the processing and inversion of transient electromagnetic data.

1. INTRODUCTION

Geophysical exploration is one of the applied branches of geophysics which includes measurements on the surface, above the surface in the air, and within the earth in boreholes. It measures the physical properties of the earth's subsurface. These physical properties show discontinuities from place to place in a geothermal field. These properties include the propagation of waves, density, magnetic susceptibility, thermal conductivity and electrical conductivity. Geophysical methods are classified into direct methods and indirect or structural methods. Direct methods are thermal and electrical methods. Structural methods are seismics, gravity and magnetics. These methods are helpful in exploring geothermal resources. The electromagnetic methods are especially powerful in exploring geothermal resources. They include a variety of techniques, survey methods applications and interpretation procedures. The electromagnetic methods include the magnetotelluric (MT) and transient electromagnetic (TEM) methods. These methods are used to describe the resistivity structure beneath the surface of the earth. In this report, the main electromagnetic methods, the MT method and the TEM method, are discussed. In addition, 1D modelling of MT data from the Dubti area in Tendaho geothermal field in NE-Ethiopia and the inversion of TEM data from the Krýsuvík geothermal field in SW-Iceland are discussed.

2. LITERATURE REVIEW

2.1 Geophysical methods for geothermal prospecting

Geophysical methods play a big role in geothermal exploration. They are able to determine what is found beneath the earth's surface, describing the structure of the earth under the surface. The structure of the earth in a certain geothermal field is known through the property of rocks. These properties include the propagation of waves, density, magnetic susceptibility, thermal conductivity and electrical conductivity of rocks which can be measured directly or indirectly. Geophysical methods are classified into, direct and indirect (structural) methods (Hersir and Björnsson, 1991). Direct methods are thermal and electric methods, whereas structural methods are gravity, magnetics and seismic methods. The basic electric methods in modern geothermal exploration, TEM and MT, are discussed in Section 4, and their basis, the electrical resistivity, is discussed in Section 3.

2.2 Indirect (structural) methods

Gravity surveys are used to study geological formations through variations of density between subsurface rocks. The density of the rock depends on mineral composition and porosity. This is shown by the Bouguer anomaly. It is used to show geological information that may reveal magmatic bodies, i.e. the heat source. A gravity survey can also be used in groundwater exploration and mineral exploration.

Magnetics are used to measure the variations in the earth's magnetic field. They can be measured using a handheld magnetometer or from the air, that is an aeromagnetic survey. The measurements indicate the variations in the magnetic properties of the subsurface rocks. They may help in mapping faults and dykes.

Seismic waves are pulses of strain energy that propagate in solids and fluids. They are divided into two classes: passive seismic methods and active seismic methods (Lemma, 2007). Active seismic waves are a controlled generation of elastic waves from a seismic source, which can provide an image of the subsurface. Active seismic methods cover all seismic waves having an artificial source, whereas passive seismic methods include natural sources of waves, like an earthquake produced by faulting.

3. ELECTRICAL PROPERTIES OF ROCKS

All rock materials have intrinsic properties. One of the intrinsic properties of rocks is its electrical property. The electrical property of rocks can be described by the resistivity. The resistivity of a material is dependent on the geometric parameters and the type of the material it is made of. Consider the conductive material shown in Figure 1. The resistivity, ρ (Ωm), of a material is inversely proportional to its length (l) and directly proportional to the cross-sectional area (A). Therefore:

$$\rho = R \frac{A}{l} \quad (1)$$

where R = Resistance of the material (Ω);
 l = Length of the material (m);
 A = Cross-sectional area of the material (m^2);
 ρ = Resistivity (Ωm).

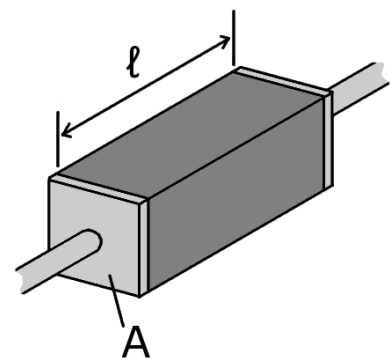


FIGURE 1: A conductive material

According to Ohm's law, electrical resistivity can also be defined as the ratio of the potential difference ΔV to the current I , across a material which has a cross-sectional area of 1 m^2 and is 1 m long. This is shown as:

$$\rho = \frac{\Delta V}{I} \quad (2)$$

where ρ = Resistivity (Ωm);
 ΔV = Potential difference (V);
 I = Current flow through the material (A).

The electrical conductivity, σ (S/m), of the material is the reciprocal of the resistivity, i.e.:

$$\sigma = \frac{1}{\rho} \quad (3)$$

The major conduction mechanisms in rocks are as follows:

- *Pore fluid conduction*: Takes place through ions dissolved in the pore fluid.
- *Surface conduction*: Conduction takes place on the surface of the pores by absorbed ions.
- *Mineral conduction*: Rock matrix creates this type of conduction.

The electrical resistivity of rocks depends mostly on salinity, porosity, temperature, water rock interaction and alteration (Hersir and Árnason, 2009).

3.1 Salinity

Conductivity of the pore fluid depends on the salinity and mobility of ions in the solution. The conductivity of a solution, σ , may be determined by considering the current flow through a cross-sectional area of 1 m^2 at a voltage of 1 V/m . This can be described by the equation (Hersir and Björnsson, 1991):

$$\sigma = F (c_1 q_1 m_1 + c_2 q_2 m_2 + \dots). \quad (4)$$

where F = Faraday's number ($9.649 \times 10^4 \text{ C/mole}$);
 c_i = Concentration of ions;
 q_i = Valence of ion;
 m_i = Mobility of different ions.

Figure 2 shows the relationship between the resistivity of NaCl solutions as a function of salinity at different temperatures. From Figure 2, it is seen that the conductivity of an aqueous solution increases with increasing temperature because of the increase in the mobility of the ions, caused by the lowering of the viscosity of the water. Increasing salinity increases conductivity.

3.2 Porosity/permeability

Porosity is the ratio between the pore volume and the total volume of a material. There are three types of porosity: intergranular, joints-fissures and vugular (Hersir and Árnason, 2009). The porosity of a rock can be determined by the equation:

$$\Phi_t = \frac{V_v}{V_T} \quad (5)$$

where Φ_t = Porosity;
 V_v = Volume of void space (m^3);
 V_T = Total bulk volume of the material (m^3).

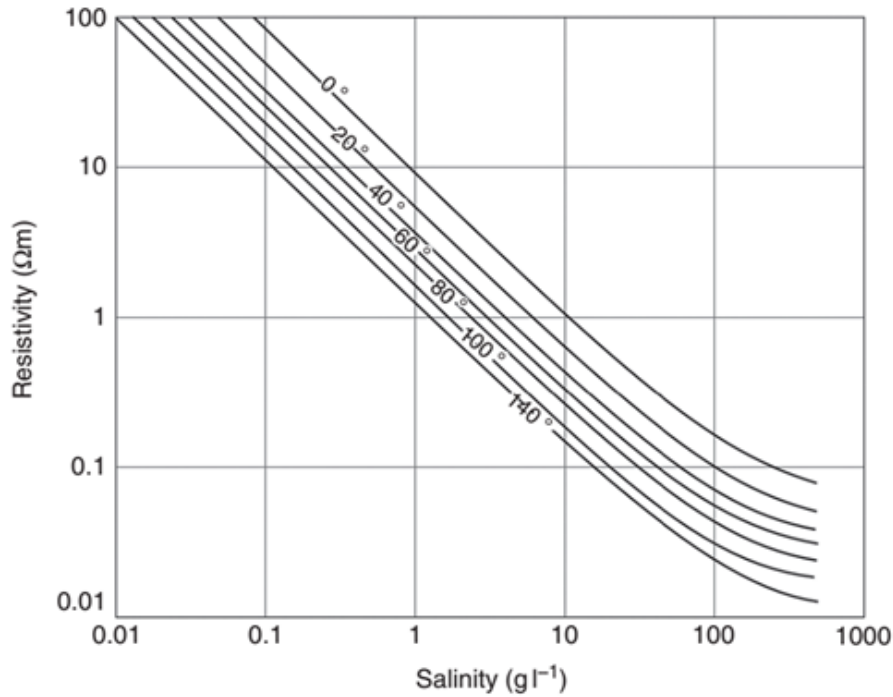


FIGURE 2: The resistivity of solutions of NaCl as a function of concentration and temperature (Flóvenz et al., 2012; based on Keller and Frischknecht, 1966)

The electrical conductivity of rocks is dependent on porosity. The resistivity of water-saturated rocks is related to the porosity according to Archie's law (Archie, 1942) as follows:

$$\rho = \rho_w a \Phi_t^{-n} \quad (6)$$

where ρ = Bulk resistivity (Ωm);
 ρ_w = Resistivity of the pore fluid (Ωm);
 Φ_t = Porosity;
 a and n = Empirical constants.

Archie's law is valid only for pore fluid resistivity, $\rho_w \leq 2 \Omega\text{m}$ (Lemma, 2007).

In some rocks, part of the pore space may be occupied by air (above the water table) or by natural gas, carbon dioxide or petroleum, all of which are insulators. In such cases, Archie's law is modified as follows (Zhdanov and Keller, 1994):

$$\rho = \rho_w a \Phi_t^{-n} f^c \quad (7)$$

where f = Fraction of pores containing water of resistivity, ρ_w ;
 c = Empirical constant.

Permeability is the ability of fluids to move within the rock matrix. Permeability depends on the link between pore spaces within the whole rock rather than the porosity of the rock. It is also affected by packing, shape and arrangement of granular materials. Rocks may have high porosity but if the pores are not interconnected then the fluid cannot flow. Therefore, the rock is impermeable even if it has high porosity. The permeability of the rock can be found by the following equation:

$$K = \frac{Q\eta L}{AP} \quad (8)$$

where K = Permeability (m^2);
 Q = Fluid flow rate (m^3/s);

η	= Fluid viscosity (Pa·s);
L	= Length of the rock (m);
A	= Cross-sectional area available for flow (m ²);
P	= Pressure drop (Pa).

3.3 Temperature

At moderate temperatures, 0-200°C, resistivity of aqueous solutions decreases with increasing temperature. Temperature has a direct effect on the mobility of ions. Dakhnov (1962) has explained this relationship as:

$$\rho_w = \frac{\rho_{wo}}{1 + \alpha(T - T_o)} \quad (9)$$

where ρ_{wo}	= Resistivity of the fluid at temperature T_o (Ωm);
α	= Temperature coefficient of resistivity ($^{\circ}\text{C}^{-1}$);
T	= Final temperature ($^{\circ}\text{C}$);
T_o	= Reference temperature ($^{\circ}\text{C}$).

At high temperatures, a decrease in the dielectric permittivity of the water results in a decrease in the number of dissociated ions in the solution. Above 300°C, this starts to increase fluid resistivity.

3.4 Interaction of water with rocks (alteration)

Resistivity of rocks decreases due to rock-fluid interaction. The bulk resistivity is decreased by surface conduction along the interface between the rock and water. This can be expressed by Equation 10 (Hersir and Björnsson, 1991):

$$\sigma = \left(\frac{1}{F}\right) \sigma_w + \sigma_s \quad (10)$$

where σ	= Bulk conductivity (S/m);
F	= Formation factor;
σ_w	= Conductivity of pore fluid (S/m);
σ_s	= Interface conductivity (S/m).

If the rocks are fresh and unaltered, then conduction takes place through the pore fluid only. There are relationships between alteration, subsurface resistivity, temperature and the conduction mechanism in high-temperature geothermal systems. Figure 3 shows these relationships for high-temperature geothermal systems in Iceland. The hydrothermal alteration of minerals is affected by hydrothermal water that causes mineral alteration, producing e.g. different clay minerals. The type of minerals formed depends on the temperature and the type of the original rock. Alteration starts at temperatures around 100°C. Below this temperature, there are no altered minerals. In the unaltered zone the conduction mechanism is pore fluid conduction.

There is a change in alteration starting from 100°C. In the range of temperatures from 100 to 250°C, the dominant alteration minerals are smectite-zeolites and mixed-layer clay. Smectites and zeolites exist at temperatures below 200°C, while mixed-layer clays are found between 200 and 250°C. The main conduction in this region is surface conduction in the clay minerals. This zone shows clearly the variation of resistivity with alteration. From 250 to 300°C, mixed-layer clays and chlorite become the dominant alteration minerals. In the high-resistive core (chlorite-epidote), we have surface and pore fluid conduction. Resistivity reflects alteration – in case of fossil system (cooling – alteration temperature is higher than the rock temperature) alteration remains and so does the resistivity structure – the rock temperature is lower than expected. In young systems where the alteration lags behind, the

alteration temperature is lower than the rock temperature. And, there are variations in resistivity in both saline and fresh water. Saline water systems are more conductive in all zones than fresh water systems. There is also a change in the conduction mechanism in both systems. At temperatures between 250 and 300°C, conduction mechanisms in salinewater systems are surface conduction in clay minerals, in fresh water systems it is both surface and pore fluid conduction. In other zones, similar conduction mechanisms take place. The original rocks, which consist of minerals, are changed to different types of minerals due to water-rock interaction and chemical transport due to geothermal fluids (Flóvenz et al., 2012). Different zones of mineralization from top to bottom can be seen in Figure 3. The variation of minerals in each zone also has a variation in resistivity because different minerals have different resistivity. In general, the interaction of water with rocks affects the conductivity of the subsurface of a geothermal system.

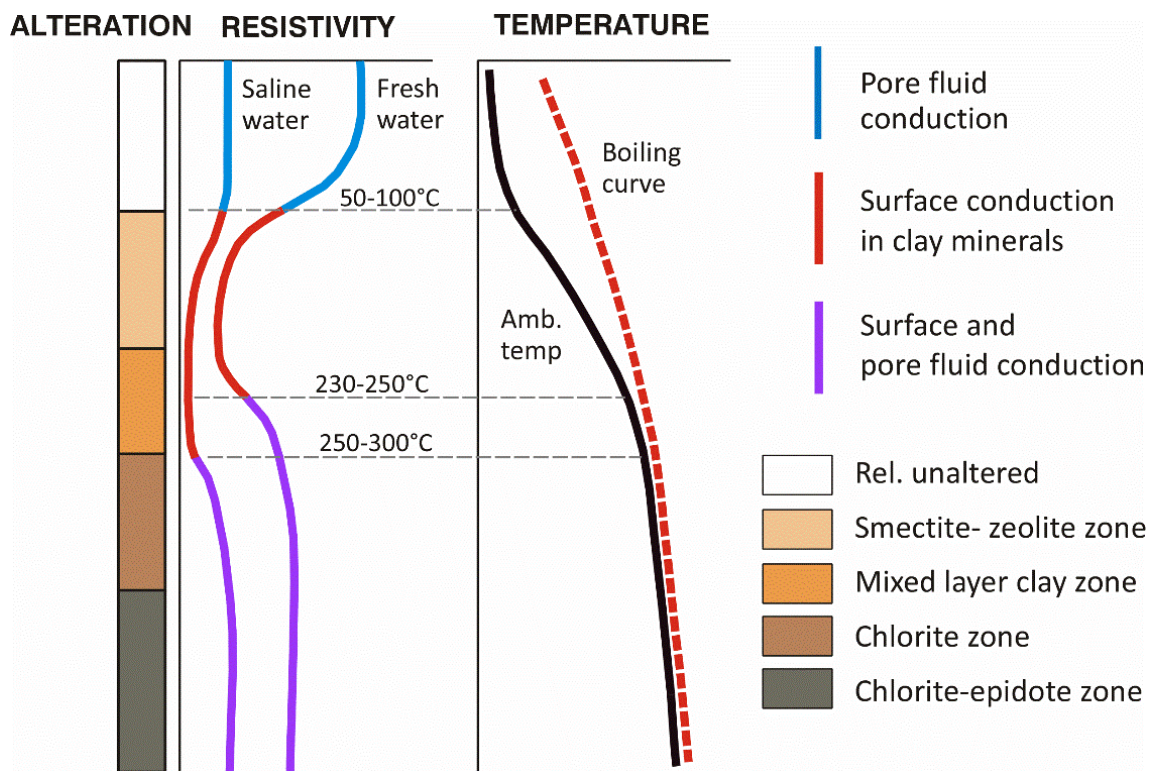


FIGURE 3: General resistivity structure of high-temperature areas in Iceland (Flóvenz et al., 2012; based on Flóvenz et al., 2005)

4. THEORY AND SETUP OF MT AND TEM

4.1 Theory of TEM

The transient electromagnetic method is a time domain electromagnetic method. It is classified as a grounded dipole or loop source method, depending on how the current from the source is introduced into the ground (Kebede, 2001). Figure 4 shows the central loop method. TEM uses an artificial time-varying magnetic field to induce currents into the earth. A loop of wire is placed on the ground and a constant current is applied to produce a fixed magnetic field. The current is automatically turned off; then the field is decaying in the ground. The decaying field creates a current at great depth. The fluctuation of the decaying magnetic field can be monitored by the receiver coil. The receiver measures the voltage as a function of time. The current distribution and the decay rate of the secondary magnetic field depend on the resistivity structure of the earth. The decay rate as a function of time can be realized in terms of the subsurface resistivity structure (Teklesenbet, 2007). Figure 4 shows a loop of wire placed

on the ground, and a constant magnetic field of known value is built up by transmitting a current into the loop.

The depth of penetration of central loop TEM is controlled by how long the induction in the receiver coil can be traced before it is drowned by noise. The induced voltage $V(t, r)$ in the receiving coil in a homogeneous half space of conductivity σ is given by (Árnason, 1989):

$$V(t, r) = I_o \frac{C(\sigma \mu r^2)^{3/2}}{10 \pi^{1/2} t^{5/2}} \quad (11)$$

where $C = A_r n_r A_s n_s \frac{\mu}{2\pi r^3}$;
 A_r = Cross-sectional area of the receiver coil (m^2);
 n_r = Number of turns on the receiver coil;
 A_s = Area of transmitting loop;
 n_s = Number of turns in the transmitter loop;
 t = Time elapsed after the current in the transmitter is turned off (s);
 μ = Magnetic permeability (H/m);
 $V(t, r)$ = Transient voltage (V);
 r = Radius of the transmitter loop (m);
 I_o = Current in the transmitting loop (A).

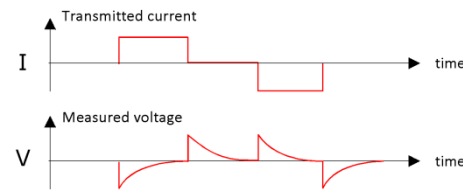
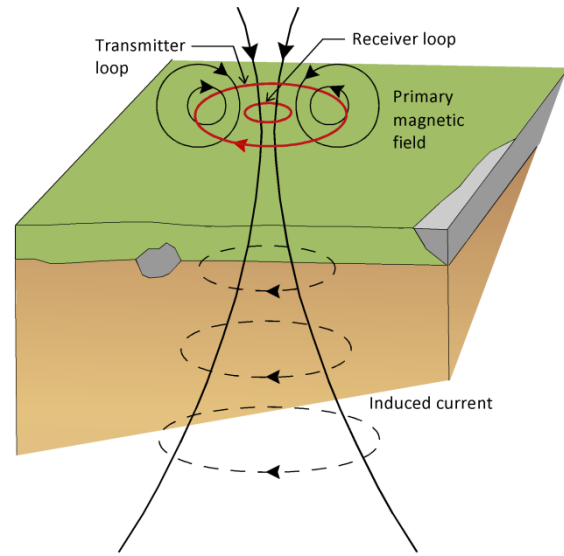


FIGURE 4: TEM sounding setup; the receiver coil is in the center of the transmitter loop; Transmitted current and the measured voltages are shown (Flóvenz et al., 2012)

The result of TEM measurements is calculated as apparent resistivity as a function of time after the current is turned off. The substitution of $\sigma = 1/\rho$ gives the resistivity as:

$$\rho_a = \frac{\mu_o}{4\pi} \left[\frac{2\mu_o I_o A_r n_r A_s n_s}{5t^2 V(t, r)} \right]^{2/3} \quad (12)$$

where ρ_a = Late time apparent resistivity (Ωm).

The curve of the apparent resistivity is inverted to a model with an assumption of homogeneous isotropic layers. The model helps to represent and interpret the data. It leads to a 1D Occam (minimum structure) inversion of the sounding. TEM soundings have better resolution than other artificial source electromagnetic methods because the source loop covers a wide area. However, they are sensitive to other artificial sources of electromagnetic fields such as noise.

4.2 Field setup of TEM

TEM instruments are produced by different companies. They have the same function but operate differently. Two of the mostly widely used ones are PROTEM from Geonics, and Zonge from Zonge Engineering and Research Organization. A wire is placed on the ground in a square loop as a transmitter coil. The square loop can be e.g. $200 \text{ m} \times 200 \text{ m}$ or $300 \text{ m} \times 300 \text{ m}$. The transmitter coil is connected to the transmitter. Another rectangular loop of size $10 \text{ m} \times 10 \text{ m}$ is placed at the centre of the square loop, the receiver loop.

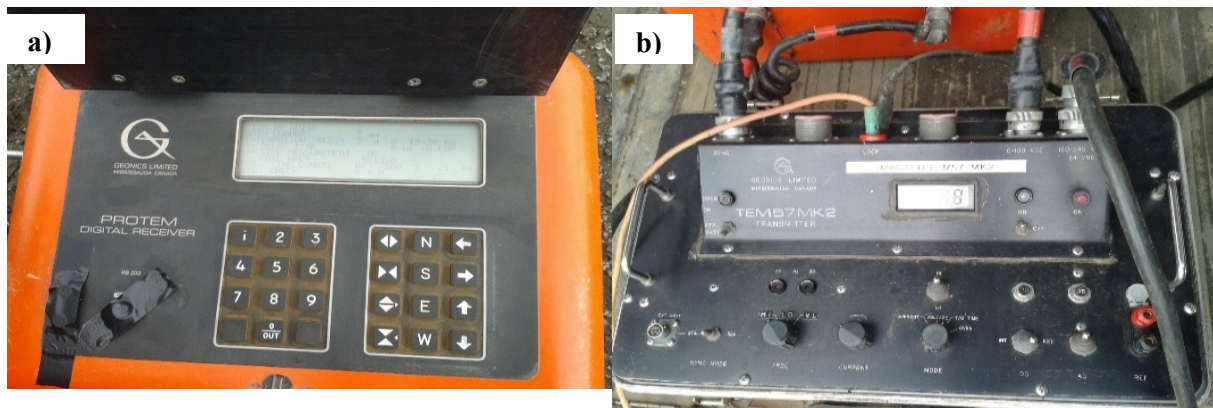


FIGURE 5: TEM equipment: a) Receiver; b) Transmitter

The transmitter and receiver (see Figure 5) are synchronized with crystal clocks so that the receiver knows exactly when the current is ejected through the transmitter loop by the transmitter, which is connected to a signal generator. It produces a magnetic field around the loop. Figure 6 shows the set-up for the TEM method. When the current is turned off automatically, the magnetic field produced by the transmitter loop induces a voltage through the conductive ground. Then the ground again induces a magnetic field in the receiver loop. The magnetic field induced in the secondary coil is vertical in the centre of the transmitter loop. The induced magnetic field produces an electromotive force. The receiver measures this signal as a function of time. The signal is measured at different frequencies by the receiver. At the time when the current through the transmitter is turned off, the current in the ground will be close to the surface, which gives information on the resistivity of the upper layer of the earth. There is always noise in geophysical measurements. Here, there is also noise which comes from lightning and power lines. This noise is reduced by taking repeated measurements.

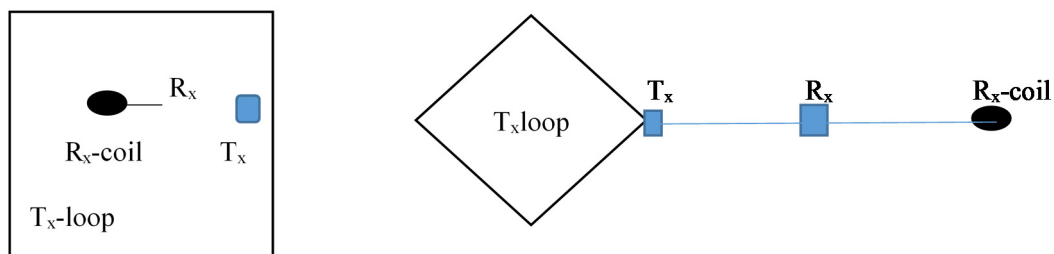


FIGURE 6: Configuration of the TEM method

4.3 Theory of MT

The magnetotelluric (MT) method is a passive electromagnetic method. It involves measuring fluctuations in the natural electric \mathbf{E} and magnetic \mathbf{B} fields in orthogonal directions on the surface of the earth. It is a means of determining the conductive structure of the earth at depths ranging from a few tens of metres to several hundreds of kilometres (Simpson and Bahr, 2005). There are two sources which give rise to the MT signal (Teklesenbet, 2012):

1. At low frequencies, less than one cycle per second, the source of the signal originates from the interaction of the solar wind with the earth's magnetic field. Solar wind is a stream of charged particles released from the upper atmosphere of the sun. It consists of protons and electrons. They face the earth's magnetic field and are deflected in opposite directions, thereby producing an electric field.
2. Electromagnetic fields which have frequencies higher than 1 Hz originate from meteorological activities, such as lightning discharges. These signals are called sferics.

The behaviour of electromagnetic fields at any period is defined accurately by Maxwell's equations (Simpson and Bahr, 2005). These equations are as follows:

$$\nabla \times \mathbf{E} = -\frac{\partial \mathbf{B}}{\partial t} \quad (13)$$

$$\nabla \times \mathbf{H} = \mathbf{j} + \frac{\partial \mathbf{D}}{\partial t} \quad (14)$$

$$\nabla \cdot \mathbf{B} = 0 \quad (15)$$

$$\nabla \cdot \mathbf{D} = \eta \quad (16)$$

where \mathbf{E} = Electric field (V/m);
 \mathbf{B} = Magnetic induction (T);
 \mathbf{D} = Electric displacement (C/m²);
 \mathbf{j} = Electric current density owing to free charges (A/m²);
 η = Electric charge density owing to free charges (C/m³).

The depth of the electromagnetic responses can be estimated by using the electromagnetic skin depth. It is defined as the depth where the electromagnetic field has reduced to e^{-1} of its original real value at the surface (Simpson and Bahr, 2005):

$$\delta(T) = \left(\frac{T}{\pi\mu\sigma}\right)^{\frac{1}{2}} \quad (17)$$

where $\delta(T)$ = Electromagnetic skin depth (m);
 T = Period (s);
 σ = Average conductivity of the medium (S/m);
 μ = Magnetic permeability.

Usually, μ is assigned its free space value ($\mu_0 = 4\pi \times 10^{-7} \text{Hm}^{-1}$) and Equation 17 can be approximated as:

$$\delta(T) \approx 500\sqrt{T\rho} \quad (18)$$

where ρ = The apparent resistivity or average resistivity of the medium (Ωm).

Great depths can be screened by the MT method, which is the advantage of this method in comparison to other electromagnetic methods.

The impedance, \mathbf{Z} , can be defined as:

$$\begin{bmatrix} E_x \\ E_y \end{bmatrix} = \begin{bmatrix} Z_{xx} & Z_{xy} \\ Z_{yx} & Z_{yy} \end{bmatrix} \begin{bmatrix} H_x \\ H_y \end{bmatrix} = \mathbf{Z} \quad (19)$$

This can be realized as the magnetic field being applied to the earth and producing an electric field through electromagnetic induction. The components of the impedance tensor are complex and can be expressed as $Z_{ij} = \text{Re}(Z_{ij}) + \text{Im}(Z_{ij})$ in Cartesian form.

The transfer function in Equation 19 can be minimized into specific expressions, depending on the distribution of electrical conductivity being considered. For a 1D earth, there is no electric field induced parallel to the induced field, and thus, $Z_{xx}=0$ and $Z_{yy}=0$ and $Z_{xy} = -Z_{yx}$, or:

$$\begin{bmatrix} E_x \\ E_y \end{bmatrix} = \begin{bmatrix} 0 & Z_{xy} \\ Z_{yx} & 0 \end{bmatrix} \begin{bmatrix} H_x \\ H_y \end{bmatrix} \quad (20)$$

For a 1D earth, the same impedance is measured regardless of the orientation of the x and y axis.

Apparent resistivity is an average resistivity for the volume of the earth at which a particular period of the electromagnetic field penetrates (Castells, 2006). The apparent resistivity can be derived from the impedance tensor as follows:

$$\rho = \frac{1}{\omega\mu} |Z|^2 = \frac{T}{2\pi\mu} |Z|^2 \quad (21)$$

where T = The period;
 Z = Impedance.

Using another system of units, the above equation can also be written as follows:

$$\rho = 0.2T \frac{|E_x|^2}{|H_y|^2} \quad (22)$$

where ρ = Resistivity (Ωm);
 E_x = Horizontal electric field (mV/km);
 H_y = Orthogonal horizontal magnetic field (gamma);
 T = Period (s).

The impedance phase gives additional information about the conductive structure. It can be determined as the tangent inverse of the ratio of the imaginary component of the impedance tensor to the real component of the tensor:

$$\varphi = \tan^{-1} \left[\frac{\text{Im}Z}{\text{Re}Z} \right]$$

The Tipper is defined as:

$$H_z = T_x H_x + T_y H_y \quad (23)$$

In 1D earth model fields, the Tipper, for the x and y components, is zero.

For 2D earth, the conductivity is constant in one horizontal direction, but varies in the vertical and the other horizontal direction. The impedance can be rotated mathematically into the strike direction such that the diagonal elements of Equation 19 are both equal to zero, but the off diagonal elements are not the same, i.e.:

$$Z_{xx} = Z_{yy} = 0; \quad \text{and} \quad Z_{xy} \neq Z_{yx}$$

For a 3D earth, the resistivity varies in all three directions. All the impedance tensor elements in Equation 19 are different and the components of the impedances are not equal and non-zero.

4.4 Field set-up of MT

The set-up of a MT sounding is shown in Figure 7. It consists of three magnetic coil sensors (H_x , H_y and H_z), a data logger, four porous pot electrodes, a battery and a GPS antenna. A group of 3 or 4 people can do the field work of an MT survey. Before setting up the survey sites, calibration must be done. There are two things to be calibrated: the instrument and the sensors. This helps in learning the functionality of the instrument and sensors. Calibration of the instrument takes 10-20 minutes. When calibrating the sensors, they are put parallel to each other, 3 m apart. The sensors are connected to the data logger. Then the data logger is started. Recording the data takes 1-2 hours. When the calibration is done, the survey site can be set.

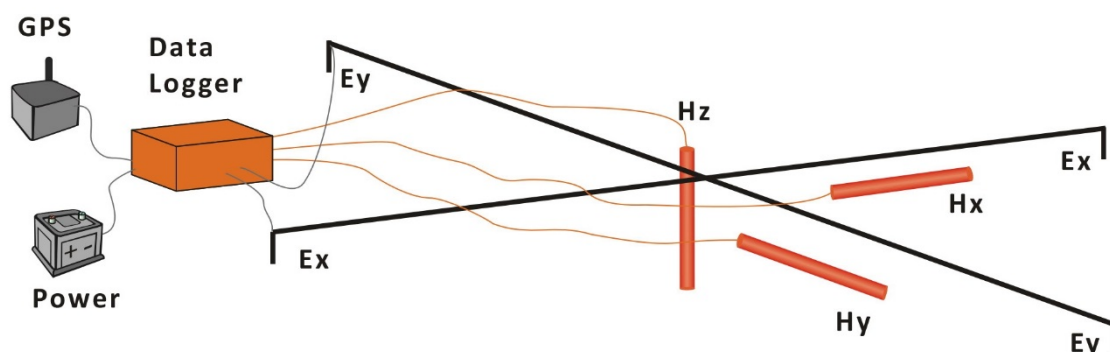


FIGURE 7: Set-up of a magnetotelluric sounding (Flóvenz et al., 2012)

To put up the site, the centre of the site has to be located. Once the site is located, the electrodes and the coil sensors are buried, the electrodes and the sensors are connected to the data logger and the GPS is connected. To do this, the following procedure is followed: First locate the four directions: North, South, East and West using a compass and a tripod. Then align the electrodes towards each direction, 50 m from each if possible. Then dig 30-50 cm for burying the electrodes. Before burying the electrodes, use baked bentonite and put them at the bottom sides of the electrodes to make a good contact with the ground. Figure 8 shows how to bury the electrodes. Four of them are



FIGURE 8: Buried MT electrode



FIGURE 9: Arrangement of an MT coil

buried in the same way. Then connect the cables to the MTU-5 unit, called the data logger. Besides this, there are three sensor coils which must be buried: one in a North-South direction, the other in an East-West direction, and the third one vertically down. Put the coil some distance from the centre in a north direction, following the path of the electrodes. Align the coil in a N-S direction and make a mark on the ground. Take the coil and bury it in a 40 cm deep horizontal ditch, as shown in Figure 9. Bury the second coil horizontally in an east-west direction; this is checked by using a leveller. Bury the third coil vertically in a 1.5 m hole. Connect the cables which extend from the coils to the unit. Finally, the GPS is connected to the unit.

The unit is powered by switching a red button to on and releasing it. The LED indicator between the North and South E-line terminals blinks at first and, after a slight delay, it will light steadily. After around 30 seconds, the unit starts up and begins finding satellites. It blinks four

times when it has acquired at least four satellites. It also registers the electric dipole length, pot resistance, potential difference and the alignment of the coils. Then it starts to record the data. It is compulsory to stay until it finishes all these things. The data logger is left as it is, with a plastic cover for safety. Data are continuously recorded on a flash card inside the unit until the next day. After checking if the unit recorded data, it is switched off by the user. The flash card is removed from the unit and connected to the computer. Then data are copied to the computer and are ready for processing using SSMT2000 software.

5. PROCESSING AND 1D INVERSION OF TEM SOUNDINGS

5.1 Processing of TEM soundings

Processing of TEM soundings here requires the use of a UNIX computer operating system. It is a multipurpose operating system which has many users. In this system, there is software called TemX (Árnason, 2006a). TemX downloads data. It operates the voltage data as a function of time after the current turn off with respect to the current in the transmitter. Moreover, it also considers the area covered by the antenna and the gain. Those parameters are displayed on the screen of the receiver, graphically and analytically. This helps the user to remove the outliers and calculate the mean value of the data. It also evaluates the apparent resistivity. A PROTEM receiver is used to retrieve the data. The raw data files are called: .fru. They are extracted by TemX. When data are recorded by the receiver, there may be errors made by the crystal clocks. In addition to this, there may be missing data of the turn off time. These two things can be corrected for when opening the raw data. Data are represented in a graphical form as shown in Figure 10. There are two plots on the screen. On the right is resistivity versus logarithmic time, and on the left, voltages multiplied by $t^{5/2}$ vs. logarithmic time. On both graphs there

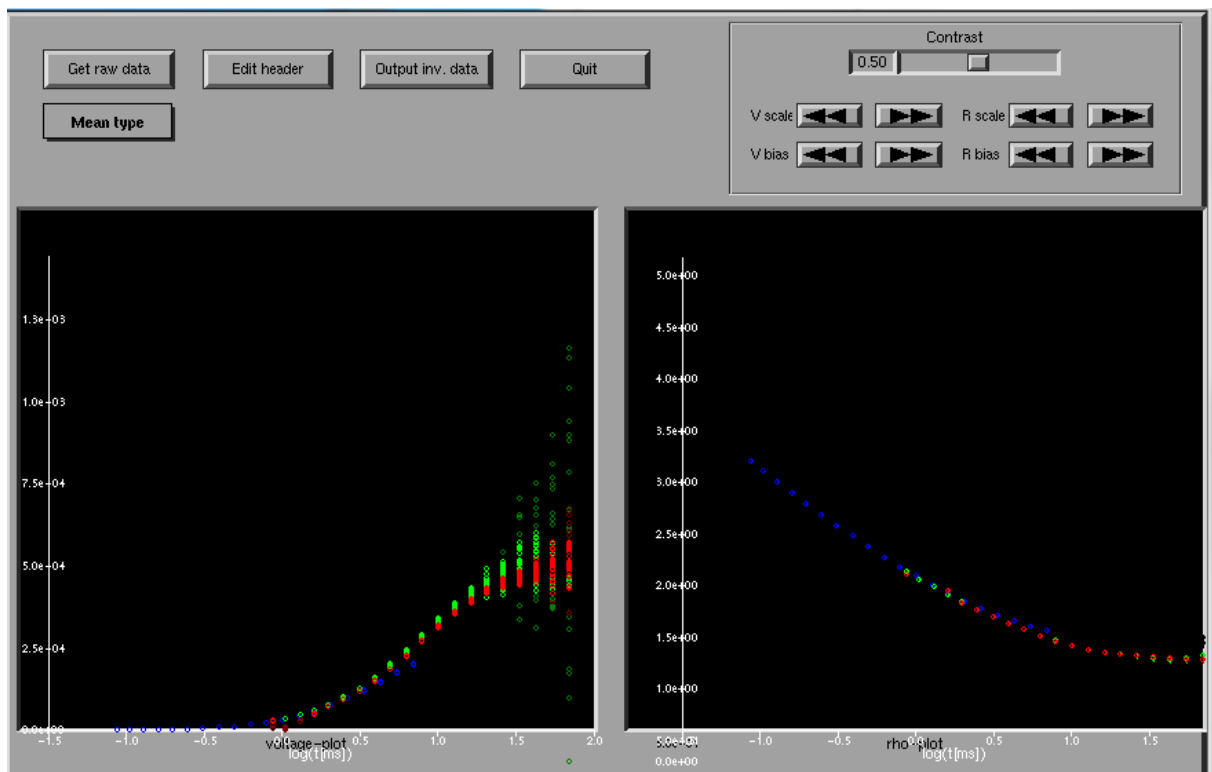


FIGURE 10: Edited raw data from a TEM sounding

are three colored curves. The blue curve is for high-frequency data from the small receiver loop. The green one is for high-frequency data from the small receiver loop and the red curve is for low-frequency data from the big receiver loop. There are points which deviate from the relatively smooth graph line (outliers); these points are edited or masked. Once this editing work is done, click on the edit header to edit the UTM coordinates, the area where the sounding was done, etc. Then click on quit. This saves what was edited. Click on the output .inv file and save the output data of this sounding. Then this sounding is ready for inversion in the TEMTD program.

5.2 1D inversion of TEM soundings

The inversion of TEM soundings involves a software called TEMTD which works in a UNIX environment (Árnason, 2006b). Data are prepared in TemX and fed into TEMTD using a script with an initial model. Once the model inversion is produced, that model is used in the Occam inversion to produce the final model. Figure 11 shows the resistivity vs. depth of TEM 1D Occam (minimum structure) inversion. These data are from the Krýsuvík area in SW-Iceland. The area is one of the high-temperature geothermal fields in SW-Iceland. Different parameters can be changed in the script to get a smoother curve. On top of Figure 11, there are two numbers: TEM443962 is the name of the sounding; the other number is the misfit function, i.e. the difference between the measured data and the calculated data. The misfit value should be as low as possible so that the measured and the calculated data are close to each other. Here the value is 0.366.

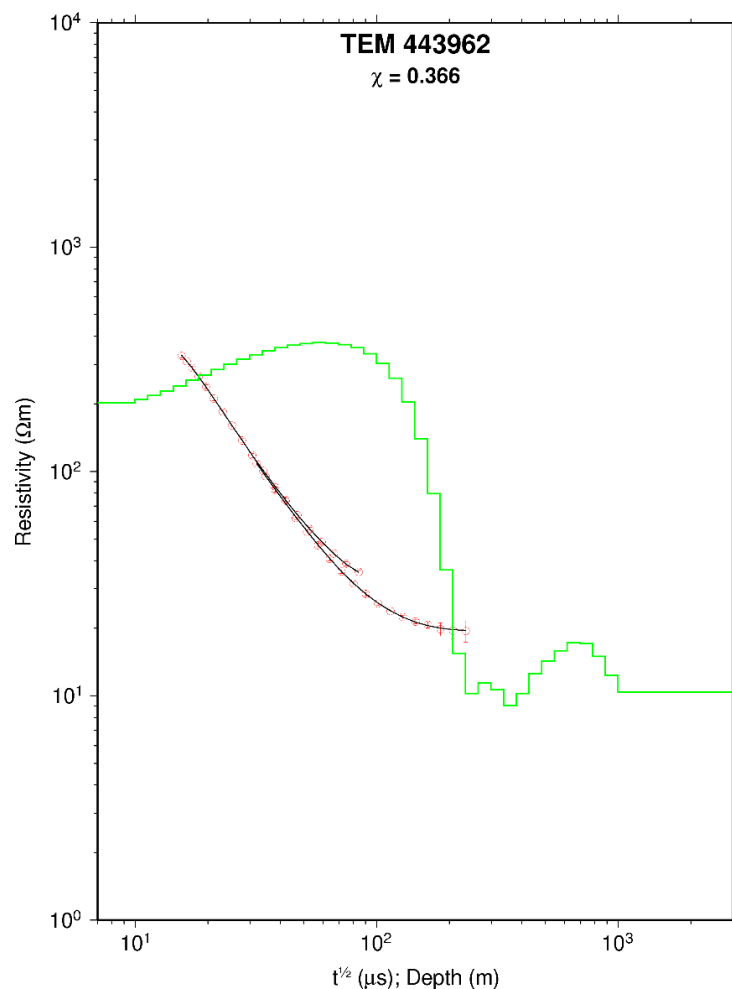


FIGURE 11: 1D inversion of a TEM sounding from the Krýsuvík area, SW-Iceland; Red circles: measured late-time apparent resistivity (different datasets for different receiver loop sizes and current frequencies); black line: apparent resistivity calculated from the model shown in green; Below the name of the TEM station (TEM 443962) at the top of the figure is the misfit function, the root-mean square difference between the measured and calculated values ($\chi=0.366$)

6. PROCESSING AND 1D INVERSION OF MT SOUNDINGS FROM THE DUBTI AREA IN TENDAHO

6.1 Processing MT soundings from the Dubti area

Tendaho geothermal field is one of sixteen geothermal fields found in the Ethiopian rift. It is located in the northeast part of Ethiopia in the Afar Regional State, in Dubti Wereda. Potential sites of Tendaho geothermal field are Ayrobera, Dubti and Alallobad. Ayrobera and Alallobad are in the surface

exploration stage. Much work has been done in the Dubti area. Figure 12 shows the location of Tendaho geothermal field. The Dubti shallow geothermal resource is located at about 600 km distance northeast of Addis Ababa, and is found in the northwest part of the Tendaho Graben, central Afar depression. The nearest town in the project area is Semera, which is the recent capital city of Afar. Tendaho Graben is transected by an excellent tarmac highway that serves as the main transport route for Ethiopian's foreign trade through Djibouti. Accessibility to the project area is very good. It is possible to reach the area from Addis Ababa along two main highways: the Addis Ababa – Nazareth – Awash – Semera and Addis Ababa – Kombolcha – Semera routes. These are mainly asphalt roads and partly weathered road, shown by a green line in Figure 12. This area is mainly covered with vegetation that is common with arid climatic conditions. The geologic outline of this area is unique because of its location at the juncture of three major rifts: the main Ethiopian rift, the Red sea and the Gulf of Aden rift. It is a place where continental drift takes place. Repeated tectonic activity, volcanism and sedimentation accompanied by tectonics, erosion and eoline activities made their own contributions to the present structure of the area. This low lying flat land is formed mainly by Fluvo-lacustrine and eoline sediment and recent central fissure axial volcanics. Asphalt roads that can be used within the study area are the Semera – Aysiata, Semera – Dobi and Semera – Logiya roads for the Dubti & Ayrobera surface manifestations and the Logiya fossil hydrothermal deposit, respectively. Access within the Dubti surface manifestation area is possible along an abandoned state farm road (Dubti Cotton plantation shown in red box in Figure 12). One can drive on plain land to reach Ayrobera after turning away from the Semera-Dobi asphalt road (~17 km from Semera), although sandy ground makes accessibility more difficult. A local guide is necessary to avoid the sandy ground. There are numerous foot trails in the study area (the entire plain land that dominates the study area can be used as a foot trail, see Figure 13).

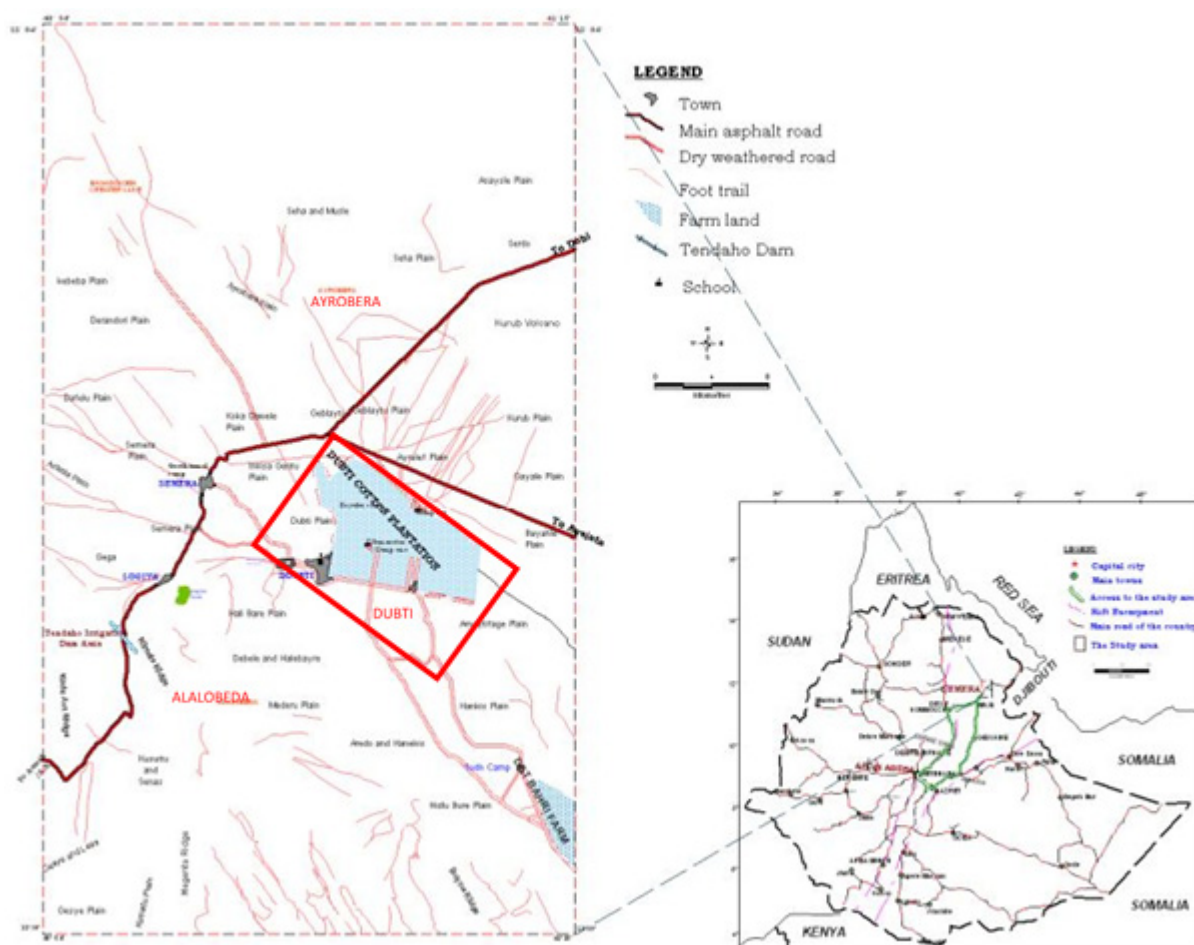


FIGURE 12: Location of the Tendaho Dubti geothermal field
(Megersa and Getaneh, 2006)

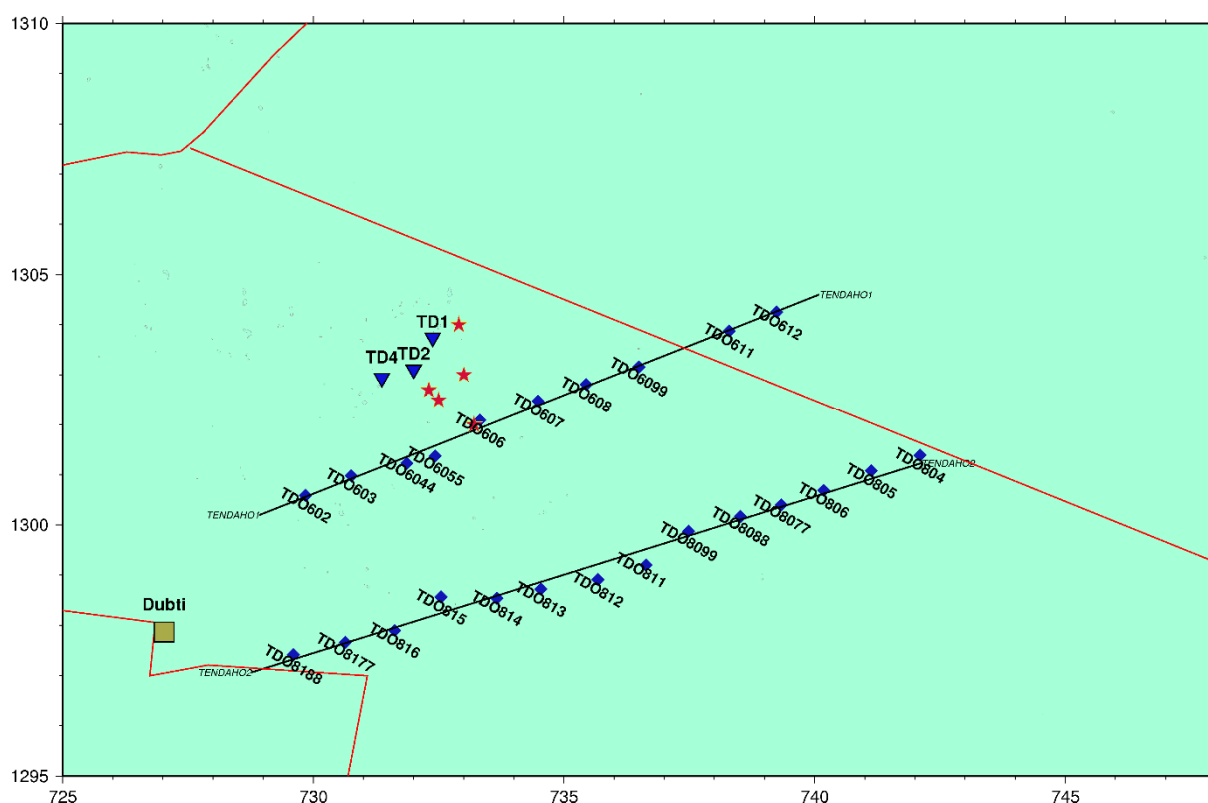


FIGURE 13: Location of MT soundings in the Dubti area (UTM37, datum: ADINDAN Ethiopia, in km); blue diamonds denote MT soundings, red stars are fumaroles, and blue triangles are wells; red lines are roads

6.1.1 Review of previous work

The first reconnaissance survey was done by UNEP-EIGS in 1973 (Megersa and Getaneh, 2006). The survey indicated the existence of geothermal resources. Following the recommendations given by the survey and other studies, an agreement was reached between the Ethiopian and Italian governments to try and locate the resources in the Tendaho area. In the first phase geologic, hydrogeology, geochemistry and preliminary geophysics studies were carried out in 1979. The second phase continued in 1980 by including geophysics and drilling of shallow temperature boreholes. The aim of these studies was discovering economically exploitable reservoirs. The results of the study showed significant geothermal resources.

With capital from the Italian government, exploration drilling was carried out between 1993 and 1995. Three deep wells (TD1-TD3) were drilled to a depth of 1.5 to 2 km and one shallow well (TD4) to a depth of 0.5 km. The Geological Survey of Ethiopia drilled additionally two shallow wells (TD5 and TD6). The results of the deep drilling showed a high temperature of 200-270°C. The reservoir is liquid-dominated and shallow, characterized by low-salinity non-condensable gasses. Out of the six wells, four of them could supply enough steam to operate a pilot power plant of 5 MWe.

6.1.2 MT survey

MT surveys were carried out to further delineate the resource. The MT surveys were conducted in 2010-2013. The surveys conducted in 2013 in the Dubti area were done by the Geological Survey of Ethiopia. More than 80 soundings were done in Tendaho geothermal field that year. Among these are 30 soundings on two profiles from the Dubti area. The area is covered by a sugarcane plantation. The soundings were done in this plantation. Figure 13 shows the location of the soundings with the two profiles.

The instruments used for MT data collection were two Phoenix units. The system has the following components:

- Five channel MTU-5 unit (data logger);
- Coil sensors;
- Porous pot electrodes of dipole length 100 m;
- Batteries of 12 V;
- GPS tripod;
- Extra cables.

The components are connected in a site as discussed in the setup of MT method in Figure 7. Data are recorded and saved on a flash card which is placed in the data logger. On the next day, the flash card is taken out of the unit and connected to the computer to transfer data to the computer, to process and store. Once the data are transferred to the data logger, the data on the flash card are erased to make it ready for the next station. Raw time series data were recorded in the Dubti area in the Tendaho geothermal field. A total of 24 soundings were carried out in the field. The time series data were downloaded into a program called SSMT2000 from Phoenix.

6.1.3 Data processing

The first step of MT data processing involves Fourier transformation from the time domain to the frequency domain. To do a Fourier transform, Window-based software called SSMT2000 was used. It takes raw time series data, calibration files and site parameter files as inputs. All sites to be processed have identical frequency parameters. Soundings which have to be processed are selected. The calibration files are also selected together with the site parameter file. Click the TS to FT button on or select from the processing menu. Then the program starts to transform the time series to Fourier coefficients. In robust processing, the auto- and cross-powers are calculated. Finally, these are edited in the Phoenix programme MTEditor, masking outliers. The product is exported as edi-files (SEG, 1991), later to be used as an input to the TEMTD program.

6.2 1D Occam inversion of MT soundings

TEMTD is a program which inverts MT and TEM data alone or it inverts jointly MT and TEM data (Árnason, 2006b). Here, it was used for the inversion of MT data. First, data are converted for access in a UNIX operating system, applying the script dos2unix. This makes the files ready to run in the UNIX environment. Then spect2edi is applied to transform the data into .EDI form. The .EDI files are fed into the TEMTD programme. Initially, a model file should be produced. Then, using the model file, an Occam inversion is run using scripts in Unix. To achieve a good fit, some parameters can be changed or improved according to the fit. It is also possible to vary the number of layers to get a good fit. Furthermore, many more iterations can be used in order to get a good fit. Figure 14 shows the 1D Occam inversion of one sounding. It shows apparent resistivity versus period, phase versus period and depth versus resistivity. The depth is estimated to be 30 km.

6.2.1 Static shift

Static shift is caused by near-surface resistivity inhomogeneities close to the electric dipoles. It is common in geothermal fields in volcanic areas. There are two things that produce static shifts. These are: voltage distortion (dependence of the electric field on the resistivity where the voltage is measured); and current distortion or current channeling (Árnason, 2008). These two phenomena scale the magnitude of the electric field at the surface by a certain unknown factor. It has no effect on the phase of the electric field. The scale of the electric field also affects the measured apparent resistivity in volcanic geothermal systems. In sedimentary areas like Tendaho geothermal field, static shift has until now not been regarded as a problem because near the surface and at shallow depth the geology of the

area is sedimentary deposits and sedimentary formations. Moreover, previous data show that there is little shift in the magnitude of the apparent resistivity. The scaling of the magnitude of the electric field (resistivity) is almost one. The solution to this phenomenon is doing joint inversion of MT and TEM data. Since inhomogeneities are at shallow depth, joint inversion helps to resolve the shift factor (Árnason, 2008).

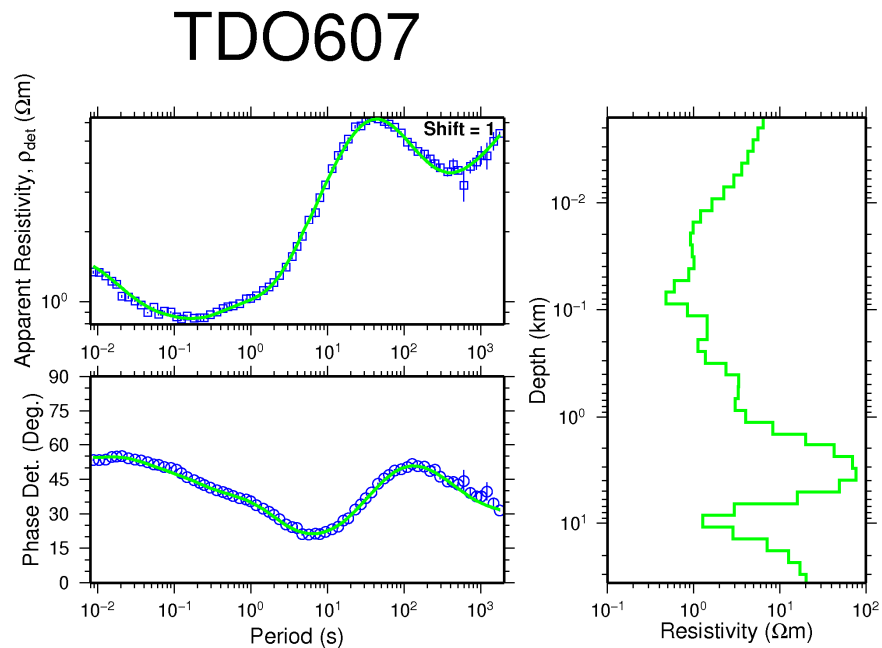


FIGURE 14: 1D Occam inversion of an MT sounding; blue squares: measured apparent resistivity; blue circles: apparent phase – both derived from the determinant of the MT impedance tensor; green lines: on the right, results of the 1D resistivity inversion model, to the left its synthetic MT apparent resistivity and phase response

7. INTERPRETATION OF THE INVERSION

7.1 Cross-sections

Figure 13 shows the location of two MT cross-sections which run from southwest to northeast. The two cross-sections are parallel, 1 km apart. To plot the results of the inversion, the scripts TEMCROSS and TEMRESD were used (Eysteinnsson, 1998). These programs run in a UNIX environment.

Figure 15 shows cross-section Tendaho 1, which runs from southwest to northeast. It is characterized by a low-resistivity anomaly of $< 1 \Omega\text{m}$, reaching from the surface down to a depth of around 300 m b.s.l. At a depth of 1.9 km, the resistivity has become quite high. Below sounding TDO606, there is higher resistivity near the surface than below the neighbouring soundings. This is probably due to static shift or three dimensional variations of the resistivity. There is a well between MT sounding TDO605 and TDO606. This is well TD2, directionally drilled. The depth of the well is 2100 m and it is productive. The kick off point of the well is at 885 m. The formation temperature of the well increases from the surface down to a depth of 650 m (Amdeberhan, 1998), as shown in Figure 15. Near the surface, the temperature is 100°C . Then, at a depth of 160 m, the temperature is 200°C , and at a depth of 380 m it is 240°C . In the cross-section, this depth shows a low-resistivity anomaly. This is presumably related to the smectite–zeolite zone. There is a high-resistivity layer below the low resistivity. This high-resistivity anomaly is most likely the chlorite-epidote zone. Figure 16 shows cross-section Tendaho 1 down to a depth of 10,000 m. Below the high resistivity layer, there is a low-resistivity zone at a depth of 6000 m b.s.l. The high resistivity extends through the low resistivity below MT sounding TDO606. This could be due, as mentioned earlier, to static shift. Therefore, it is necessary to do TEM in that area to correct for the shift.

Figure 17 shows cross-section Tendaho 2 down to a depth of 2500 m, which runs parallel to cross-section Tendaho 1. It includes 13 soundings. There is a low-resistivity anomaly $< 0.7 \Omega\text{m}$ from the

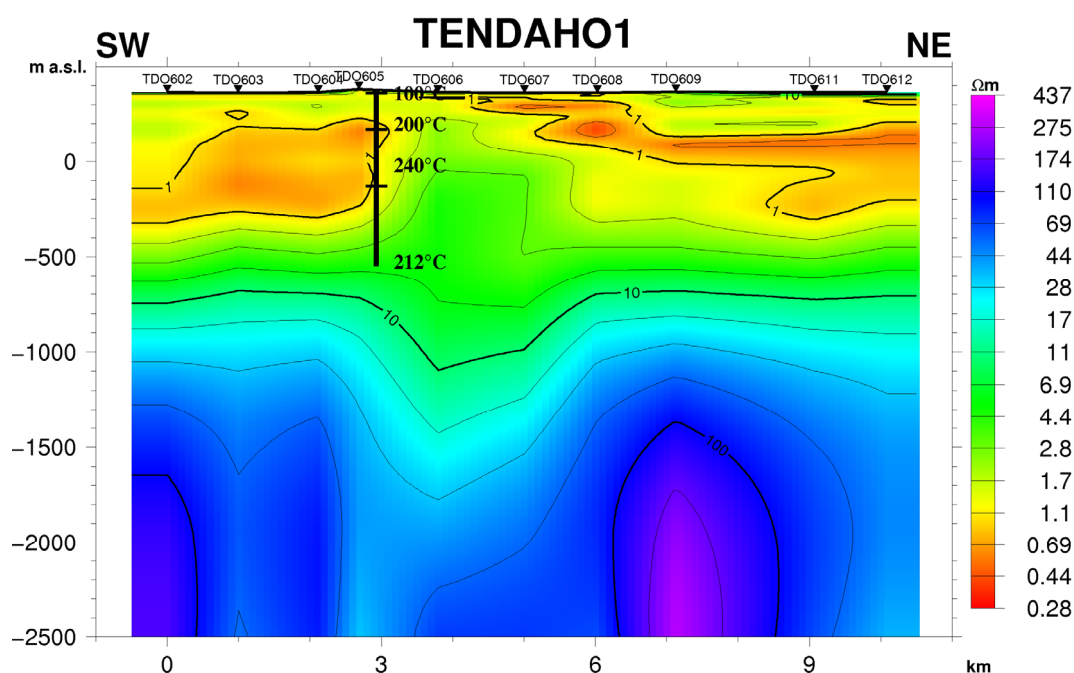


FIGURE 15: MT resistivity cross-section TendaHo1 down to a depth of 2500 m;
for location see Figure 13

surface down to a depth of 800 m. Below MT sounding TDO807, there is a zone of higher resistivity than in the neighbouring soundings. This could be due to static shift of the area or three dimensional variations of the resistivity. The low resistivity near the surface is presumably the smectite-zeolite hydrothermal alteration zone. Below the low-resistivity anomaly there is a high-resistivity zone, clearly seen in Figure 18, which shows the cross-section of TendaHo2 down to a depth of 10,000 m. High resistivity starts at a depth of 1000 m and extends to 4000 m b.s.l. This high-resistivity zone is most likely the chlorite-epidote zone. Below the high-resistivity zone there is a low resistivity $< 1.1 \Omega\text{m}$, probably connected to the heat source.

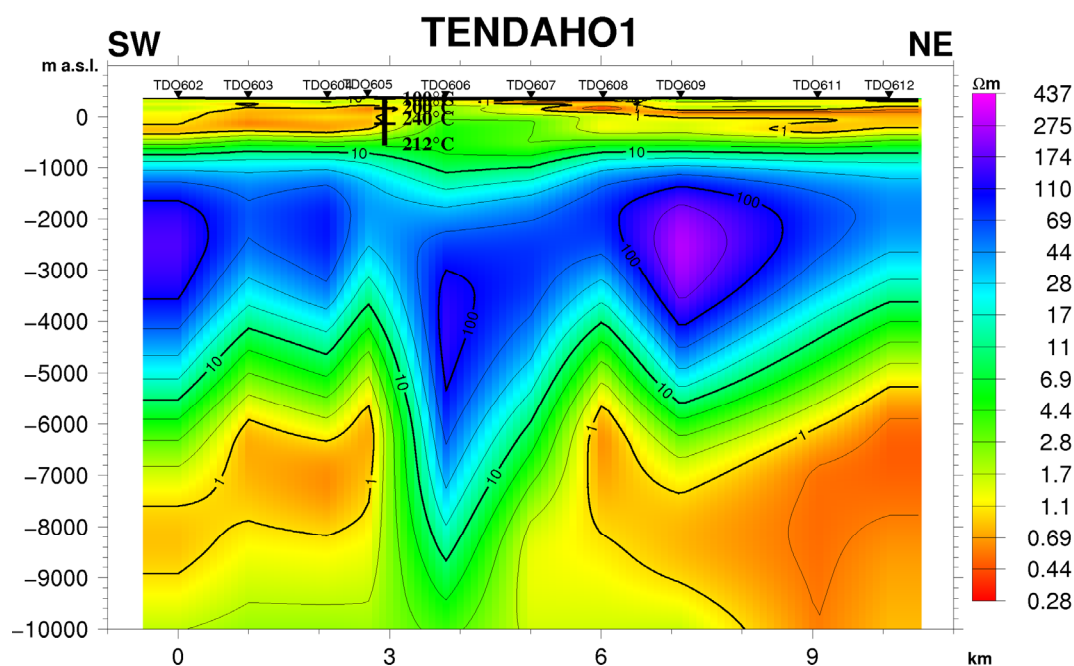


FIGURE 16: MT resistivity cross-section TendaHo1 down to a depth of 10 km;
for location see Figure 13

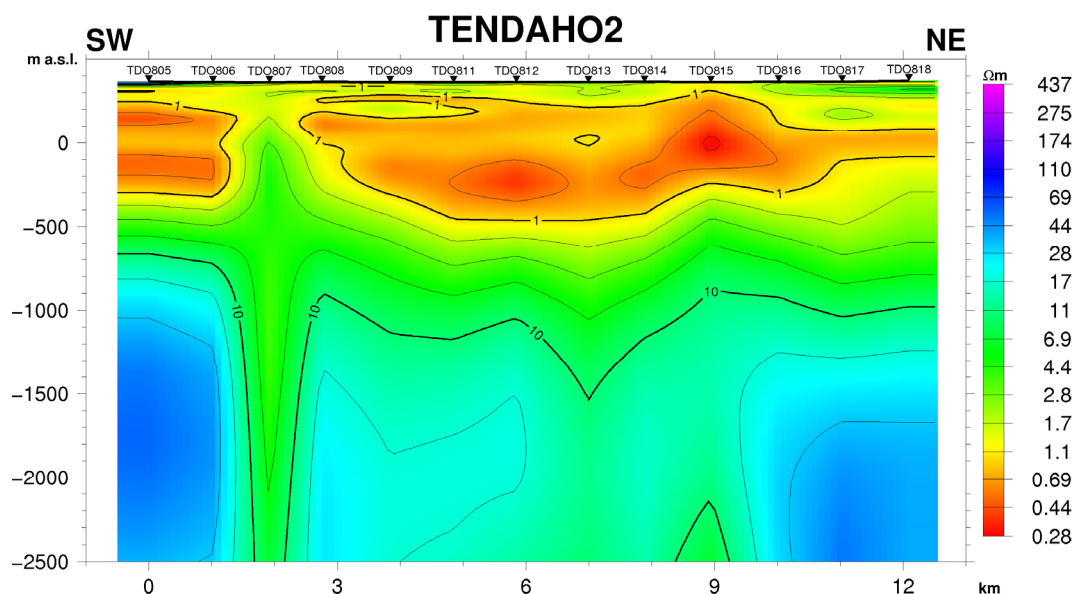


FIGURE 17: MT resistivity cross-section TendaHo 2 down to a depth of 2500 m; for location see Figure 13

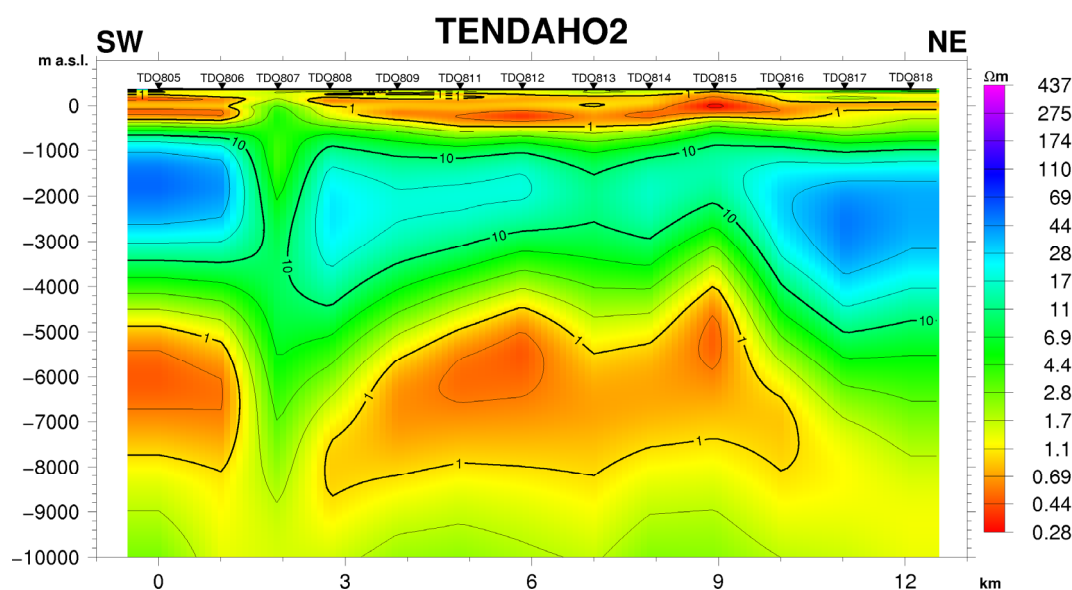


FIGURE 18: MT resistivity cross-section TendaHo 2 down to a depth of 10 km; for location see Figure 13

These resistivity cross-sections can be related to the geological stratigraphy of the wells. Figure 19 shows the borehole geological stratigraphy of wells TD2, TD4 and TD1. From the surface down to a depth of 1100 m, it is composed of sediments, both fine and coarse. There are also recent basalts in this zone. Below 1200 m, the geological structure is made up of the Afar Stratoid basalts.

7.2 Iso-resistivity maps

An iso-resistivity map shows the lateral resistivity variations at a certain depth below the surface. Figure 20 shows resistivity variations at sea level. The resistivity is a bit higher near the surface manifestations. In general, the map shows low resistivity. This is seen clearly on the cross-section, as well, showing low resistivity at this depth, which correlates to the smectite-zeolite zone.

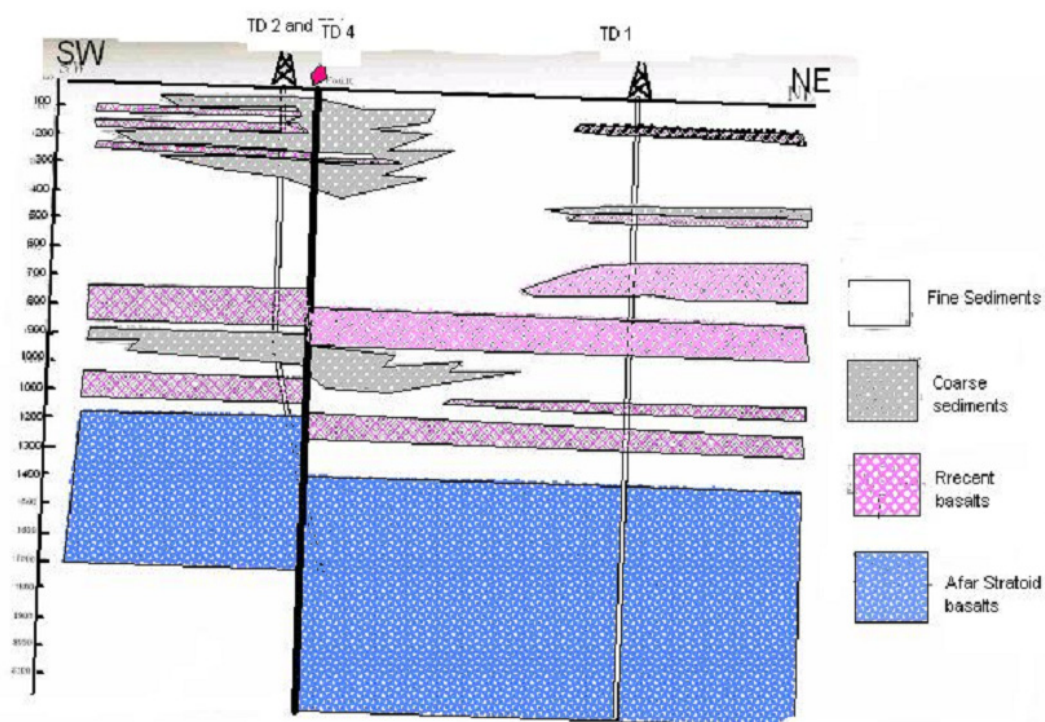


FIGURE 19: Geological stratigraphy of wells TD2, TD4 and TD1
(for location see Figure 13)

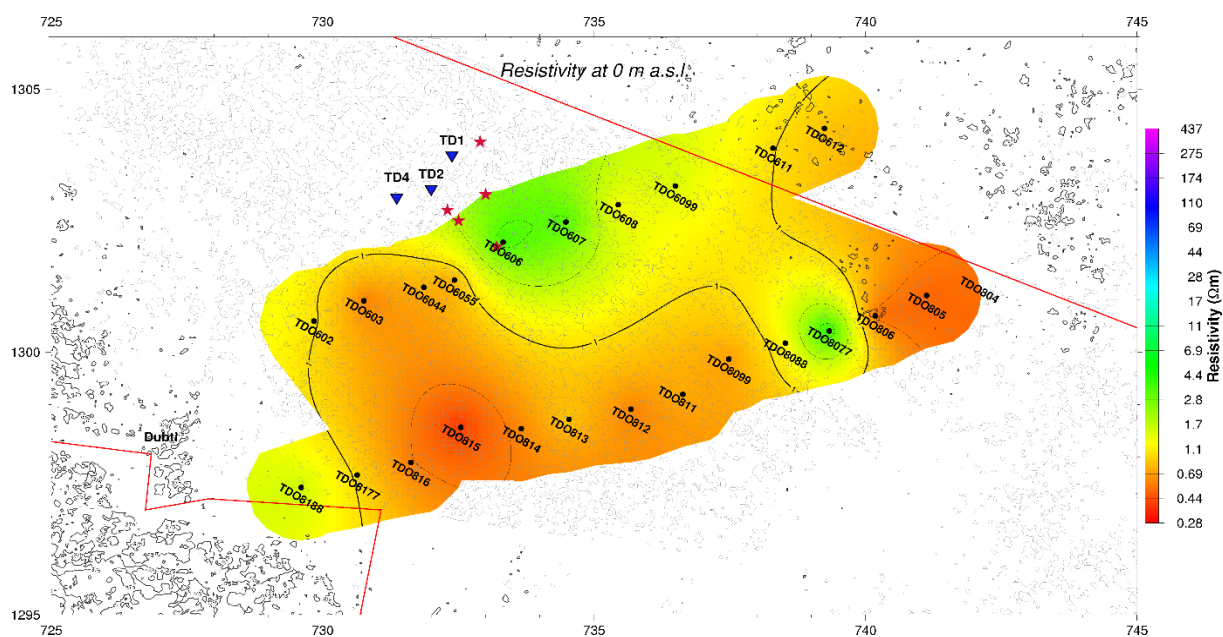


FIGURE 20: Iso-resistivity map at sea level; black dots denote MT soundings,
red stars are fumaroles and blue triangles are wells; red lines are roads

Figure 21 shows the resistivity at 2500 m below sea level. Here, there is a higher resistivity, which can also be seen in profiles Tendaho 1 and Tendaho 2. This section of the map fits with both cross-sections at this depth. The resistivity is related to the chlorite-epidote alteration zone.

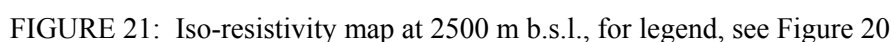
[illegible]

FIGURE 22: Iso-depth resistivity map at 6500 m b.s.l., for legend, see Figure 20

Cross-sections Tendaho 1 and Tendaho 2 show the same features. They show similar resistivity values at similar depths, starting from low resistivity ($<1 \Omega\text{m}$) near the surface down to a depth of 800 m which is followed by a fairly high resistivity ($> 40 \Omega\text{m}$) with a thickness of about 4 km. Below it, low resistivity

is found. This structure could be related to the geological stratigraphy seen in the wells. In the geological stratigraphy, the upper layers are mostly sedimentary down to a depth of 1000 m below the surface. Therefore, the low-resistivity layer close to the surface down to a depth of 800 m could be related to sedimentary deposits and formations or altered mineralizations with rock temperature of around 200-230°C. This is the smectite-zeolite zone. The higher resistivity below the low resistivity relates to the Afar Stratoid basalts. This is seen in Figure 19. At a depth of 6000 m there is low resistivity; this may be related to the main fracture zone, upflow of geothermal fluids or even the heat source.

There are resistivity variations near the surface. These variations are seen in MT soundings TDO606 and TDO807 and are probably caused by static shift. To reduce the static shift effect, transient electromagnetic (TEM) measurements are advisable, followed by joint inversion of MT and TEM data.

ACKNOWLEDGEMENTS

I would like to thank the United Nations University Geothermal Training Programme and the Government of Iceland for giving me this opportunity to participate in this specialized training. Special gratitude goes to the former director of UNU-GTP, Dr. Ingvar B. Fridleifsson, and the new director, Mr. Lúdvík S. Georgsson, for offering me the opportunity to participate in the Geothermal Training Programme. Thanks to all staff members of UNU-GTP for their guidance and support. Special thanks to my advisors, Mr. Gylfi Páll Hersir, Mr. Knútur Árnason and Mr. Andemariam Teklesenbet, for their valuable time, special lectures, guidance and treatment. All lecturers, Orkustofnun and ISOR staff members, are greatly acknowledged for sharing their knowledge and experience. I am also grateful to the Geological Survey of Ethiopia for supporting my studies in Iceland.

Finally, I would like to thank the Almighty God for all his help.

REFERENCES

- Amdeberhan, Y., 1998: A conceptual reservoir model and production capacity estimate for the Tendaho geothermal field, Ethiopia. Report 1 in: *Geothermal training in Iceland 1998*. UNU-GTP, Iceland, UNU-GTP, 1-24.
- Archie, G.E., 1942: The electrical resistivity log as an aid in determining some reservoir characteristics. *Trans. AIME*, 146, 54-67.
- Árnason, K., 1989: *Central loop transient electromagnetic sounding over a horizontally layered earth*. Orkustofnun, Reykjavík, report OS-89032/JHD-06, 129 pp.
- Árnason, K., 2006a: *TemX, short manual*. ISOR, Reykjavík, internal report, 17 pp.
- Árnason, K., 2006b: *TEMED (program for 1D inversion of central-loop TEM and MT data)*. ISOR, Reykjavík, internal report, 16 pp.
- Árnason, K., 2008: *The magnetotelluric static shift problem*. ISOR - Iceland GeoSurvey, report ÍSOR08088, 16 pp.
- Castells, A.M., 2006: *A magnetotelluric investigation of geoelectrical dimensionality and study of the central Betic crustal structure*. University of Barcelona, Spain, PhD thesis, 45 pp.
- Dakhnov, V.N., 1962: Geophysical well logging. *Q. Colorado Sch. Mines*, 57-2, 445 pp.

Eysteinnsson, H., 1998: *TEMRES, TEMMAP and TEMCROSS plotting programs*. ÍSOR- Iceland GeoSurvey, unpublished programs and manual.

Flóvenz, Ó.G., Spangerberg, E., Kulenkampff, J., Árnason, K., Karlsdóttir, R., Huenges, E., 2005: The role of electrical interface conduction in geothermal exploration. *Proceedings of the World Geothermal Congress 2005, Antalya, Turkey*, 9 pp.

Flóvenz, Ó.G., Hersir, G.P., Saemundsson, K., Ármannsson, H., and Fridriksson Th., 2012: Geothermal energy exploration techniques. In: Sayigh, A., (ed.), *Comprehensive renewable energy*, vol. 7. Elsevier, Oxford, 51-95.

Hersir, G.P., and Árnason K., 2009: Resistivity of rocks. *Paper presented at "Short Course on Surface Exploration for Geothermal Resources"*, organized by UNU-GTP and LaGeo, Santa Tecla, El Salvador, 8 pp.

Hersir, G.P., and Björnsson, A., 1991: *Geophysical exploration for geothermal resources. Principles and applications*. UNU-GTP, Iceland, report 15, 94 pp.

Kebede, Y., 2001: Application of the resistivity method in the Krísuvík geothermal area, Reykjanes peninsula, SW-Iceland. Report 6 in: *Geothermal training in Iceland 2001*. UNU-GTP, Iceland, 115-142.

Keller, G.V., and Frischknecht, F.C., 1966: *Electrical methods in geophysical prospecting*. Pergamon Press Ltd., Oxford, 527 pp.

Lemma, Y., 2007: Magnetotelluric and transient electromagnetic methods in geothermal exploration, with an example from Tendaho geothermal field, Ethiopia. Report 11 in: *Geothermal training in Iceland 2007*. UNU-GTP, Iceland, 225-256.

Megersa, G., and Getaneh, E., 2006: *Geological surface hydrothermal alteration and geothermal mapping of Dubti-Semera area, Tendaho geothermal field*. Geological Survey of Ethiopia, unpublished report, 65 pp.

SEG, 1991: *MT/EMAP data interchange standard*. Society of Exploration Geophysicists, 112 pp.

Simpson, F., and Bahr, K., 2005: *Practical magnetotellurics*. Cambridge University Press, Cambridge, UK, 254 pp.

Teklesenbet, A., 2007: Transient electromagnetic and magnetotelluric geophysical methods in the Hengill area, SW-Iceland. Report 22 in: *Geothermal training in Iceland 2007*. UNU-GTP, Iceland, UNU-GTP, 521-554.

Teklesenbet, A., 2012: *Multidimensional inversion of MT data from Alid geothermal area, Eritrea; comparison with geological structures and identification of a geothermal reservoir*. University of Iceland, MSc thesis, UNU-GTP, Iceland, report 1, 92 pp.

Zhdanov, M.S., and Keller, G.V., 1994: *The geoelectric methods in geophysical exploration*. Elsevier, Amsterdam, 873 pp.



UNITED NATIONS
UNIVERSITY

GEOTHERMAL TRAINING PROGRAMME
Orkustofnun, Grensasvegur 9,
IS-108 Reykjavik, Iceland

Reports 2013
Number 38

CHEMICAL ASSESSMENT OF ICELANDIC GEOTHERMAL FLUIDS FOR DIRECT APPLICATIONS

Md. Shakhin-Uz-Zaman

Geological Survey of Bangladesh
153, Pioneer Road, Segunbagicha
Dhaka 1000
BANGLADESH
skngsb@gmail.com

ABSTRACT

This research deals with the chemical assessment of geothermal fluids for direct applications from low-temperature geothermal fields in Iceland. In addition, geothermal brine, geothermally heated groundwater, cold spring water, seawater or a mixture of two of these different fluids were evaluated for direct use or for use via a heat exchanger for space heating, balneotherapy, agriculture, aquaculture, and industrial applications. In order to fulfil the objectives, all the water samples were analysed and compared with the standards and guidelines for physicochemical parameters as well as for trace elements. The results revealed that, in some cases, there is the possibility of scaling and corrosion from low-temperature geothermal waters, brine and heated groundwater. The risk of amorphous silica scaling was observed only for brine water and the risk of magnesium silicate scaling was observed both for low-temperature geothermal water and heated groundwater. No scaling is likely to occur due to the mixing of brine water from Svartsengi and cold groundwater from Lágar at 40°C and 15°C, which are the ideal temperatures for balneotherapy and agriculture. Geothermal brine is effective for balneotherapeutic applications. A mixture of 37% brine and 63% cold groundwater at a temperature of 40°C also appears to be effective for this purpose as is sea water if it is heated to a temperature of 40°C. Some geothermal waters are permissible for agricultural application with respect to EC, TDS, sodium percent, SAR, boron toxicity and trace elements. Brine and sea water should not be used for this purpose. Dissolved H₂S gas in geothermal fluids was identified as a major limiting factor for aquaculture applications, even after mixing with 90% cold groundwater. Geothermal fluids that contain H₂S are not suitable for food processing industries because of their taste and odour and sometimes because of high concentrations of trace elements such as fluoride and boron. Cold spring waters are suitable for this purpose.

1. INTRODUCTION

The rapid acceleration of geothermal development in recent years has coincided with growing public awareness about potential problems connected to direct exploitation of geothermal fluids as well as with health issues. Geothermal fluids contain different concentrations of a wide variety of dissolved constituents. The amount and nature of the dissolved chemical species in geothermal fluids are function of temperature and the local geology. In addition to providing beneficial minerals, geothermal fluids

may give rise to undesirable or toxic properties through the deficiency or excess of various elements. Use of geothermal fluids must be subject to certain guidelines prescribed for different physicochemical parameters for different direct applications such as space heating, balneotherapy, agriculture, aquaculture, and industrial uses.

The principal direct use of geothermal fluids in Iceland is for space heating. However, during utilization, the space heating systems sometimes face problems such as corrosion and scaling in the supply pipes. Scaling and the possibility of corrosion can be predicted by using the mineral equilibria and chemistry. For geothermal water, it is important to evaluate the chemical characteristics, not only for different applications but also when making decisions on the selection of proper reinjection sites to avoid affecting the quality of the groundwater. Water that people drink to slake their thirst may also supply major and especially minor or trace elements which are nutritionally essential to good health (Keller, 1978). However, it is most important to realise that whatever the element, it is the dosage that is critical, as even essential elements can cause ill health if taken in excessive amounts.

On the other hand, high dissolved solid and gas concentrations in geothermal water, termed mineral water, are thought to give certain health benefits (Skapare, 2010). From a balneological point of view, trace elements could have pharmacological benefits (Manuel, 2010). In agriculture, a number of trace elements known as micronutrients are essential to plants, albeit in very small quantities. Often their deficiency can cause devastating effects (Gandouzi, 1999). However, in most irrigation situations, the primary water quality concern is the salinity. An excess or deficiency of dissolved salts and trace elements such as micronutrients in water can limit its use for agricultural applications. According to available guidelines, some elements are essential to fish growth while others are very toxic. Temperature, pH, dissolved oxygen, hydrogen sulphide, ammonia and carbon dioxides are the most frequently recorded physicochemical components that may cause harm in aquaculture (Svobodová, 1993). Trace elements can be concentrated in fish tissues to a level that may be unsafe for human consumption (Roberts, 1975). Even some chemical characteristics of water might be suitable for one species of fish but not for others. Therefore, the aim of this work is to study the chemical characteristics of geothermal fluids in order to evaluate their suitability for major direct applications.

2. DIRECT APPLICATIONS OF GEOTHERMAL FLUIDS

Geothermal energy is a renewable, clean and cost effective energy, an alternative to conventional fuels for heat and power generation. The source of the geothermal energy is the earth's internal heat. Electric power generation and direct utilization are two applications of geothermal energy in Iceland. Direct application of geothermal fluids is one of the most common, versatile and oldest forms of utilization. It usually uses geothermal energy with temperatures below 150°C (Lund, 2007). In Iceland, the major area of direct utilization for space heating includes district heating systems; swimming, bathing and balneology; agricultural applications such as greenhouse and soil heating; aquaculture applications such as pond and raceway water heating; and industrial processes such as mineral extraction, food and grain drying. Other applications include ice melting in the winter season.

The use of geothermal energy for space heating in Iceland was initiated in 1907 when a farmer ran a concrete pipe from a hot spring that led steam to his house. It started on a small scale in Reykjavik in 1930. Now, space heating is the principal direct application of geothermal energy in Iceland. It distributes geothermal water through piping systems to homes and other buildings. It is estimated that 89% of all houses in the country have access to geothermal or geothermally heated water (Ragnarsson, 2010) and about 90% of the country's inhabitants are connected to a district heating service (Gunnlaugsson, 2004). About 30 separate geothermal district heating systems are operated in towns and villages and an additional 200 smaller systems in rural areas.

Geothermal water has been used for bathing for thousands of years. In balneology, the practice of using natural mineral water for the cure of diseases and ailments has a long history. The important factors to be considered in balneology are the temperature of the water and the mineral content. In this modern age, geothermal swimming pools and hot baths have been constructed in several places around the world, including Iceland. Swimming pools and hot baths are typically supplied with warm water direct from a low-temperature geothermal system. Among the approximately 163 swimming centres in Iceland, 134 use geothermal water (Orkustofnun, 2010). These are mainly for recreational and social purposes. Swimming has been gaining in popularity in Iceland and the attendance for swimming increases year by year.

The main uses of geothermal energy in agriculture are greenhouse heating, soil disinfection, soil heating and drying crops. Geothermal heating of greenhouses started in Iceland in 1924. Before that, warm soil had been used for growing potatoes and vegetables. A greenhouse produces different types of vegetables (tomatoes, cucumbers, peppers, herbs, and berries), flowers, potted plants and even bananas for the domestic market. Soil heating has been used since the 1970s when the systems for soil heating became economical and applicable for modern cultivation with the appearance of plastic pipeline materials (Gunnlaugsson, et al., 2003). Soil disinfection uses only a minor part of the total energy used in agriculture.

The main use of geothermal fluid in aquaculture is to adjust the water to a suitable temperature for fish growth. Geothermal heat allows better control of pond temperature, thus optimising growth. Geothermally heated aquaculture ponds are common in Iceland. In Iceland, fish farming is mainly practised in shore-based plants, although some plants are on dry land. Geothermal water, commonly at 20-50°C, is used to heat fresh water directly or in heat exchangers. In 2008, there were about 50 registered fish farms in Iceland (Ragnarsson, 2010).

The uses of geothermal fluid for industrial processes in Iceland are very diverse. It has been used for drying fish, seaweed, hardwood, wool washing and cement blocks, retreading car tires, baking bread etc. However, the most important water consuming sectors are food processing industries such as for drying food, salt and grain and for the dairy, beverage, fat and margarine industries. Commercial liquid carbon dioxide is also produced from geothermal fluid. Next to the geothermal power plant in Svartsengi, a plant produces methanol from CO₂ gas exhausted by the power plant. Several other industrial processes have been operated in the past such as a diatomite plant and salt production from geothermal brine.

3. DESCRIPTION OF THE SAMPLE LOCATIONS AND FLUID CHEMISTRY

The chemical composition of 14 different water samples was taken from the ÍSOR database for evaluation of direct applications. Among them, 6 water samples are from low-temperature geothermal waters, 2 are from geothermal brine, 1 from geothermally heated groundwater, 3 from cold groundwater and 2 from sea water. The proximity of cities, communities, existing and potential direct applications and municipal water supply systems were considered for the sample selection. The reasons behind the selection of cold water sources are due to cold water being heated with geothermal water by means of a heat exchanger, and sometimes by mixing with geothermal water for different direct applications. Figure 1 shows the sample locations and Table 1 gives a summary of all the samples.

3.1 Reykir, Reykjabraut, Hrolleifsdalur, Ósbrekka, Laugar, and Urridavatn low-temperature geothermal areas

The Reykir (in Hjaltdalur), Reykjabraut and Hrolleifsdalur low-temperature geothermal areas are located in northwest Iceland, in an area which is entirely composed of Tertiary basalt, characterised by high mountains, deep fjords and valleys. Several geological studies have shown that most of the formations consist of a number of tholeiitic lava flows of varying thickness interbedded with soil layers, several sedimentary horizons and a number of extinct volcanic systems. The geothermal waters in these areas are used for space heating, greenhouse heating, bathing and swimming. Ósbrekka is situated within the Laugarengi low-temperature geothermal field at Ólafsfjörður in NE-Iceland. Several geological maps have shown that Tertiary basaltic layers extend deep into the formation. There are sedimentary layers and scoria beds between the lava layers with horizontal intrusions (Sbterev, 1994). The water is used for space heating and swimming. Laugar is situated southeast of the town of Sudureyri within the West fjords peninsula in northwest

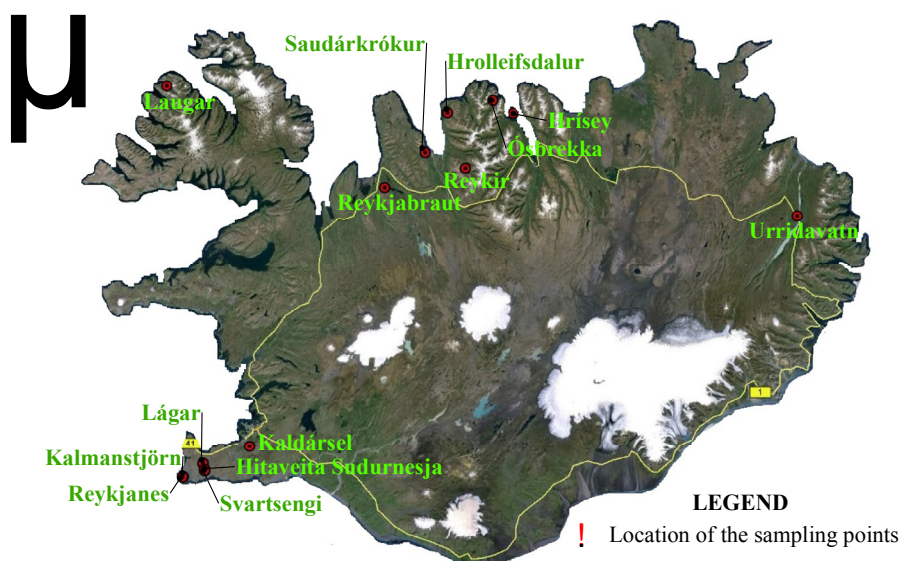


FIGURE 1: Map of Iceland showing the locations of all samples

TABLE 1: Description of all the water samples

No.	Location name	Location type	Sample type
1.	Laugar	Borehole	Low-temperature
2.	Urridavatn	Borehole	Low-temperature
3.	Reykjabraut	Borehole	Low-temperature
4.	Reykir	Borehole	Low-temperature
5.	Ósbrekka	Borehole	Low-temperature
6.	Hrolleifsdalur	Borehole	Low-temperature
7.	Reykjanes	Pipeline	Brine
8.	Svartsengi	Pipeline	Brine
9.	HS Orka	Pipeline	Heated
10.	Lágar	Spring	Cold
11.	Kaldársel	Spring	Cold
12.	Hrísey	Borehole	Cold
13.	Kalmanstjörn	Borehole	Seawater
14.	Saudárkrókur	Pipeline	Seawater

Iceland. The volcanic rocks there are also Tertiary, but relatively older than the rest of the country. The lack of flat lowlands in this area makes it unsuitable for agriculture activities, except for sheep farming, but fishing is vital for the local economy. Three exploration wells and two production wells have been drilled in the Laugar field for district heating, swimming and fish drying purposes. The Urridavatn geothermal field is a low-temperature geothermal field located in Tertiary formations in east Iceland, outside the neo-volcanic zone below Lake Urridavatn. It is situated on the flanks of active volcanic zones. Many faults pass through the area, actually part of a graben (Haddadin, 1995). The production of hot water from the field started in 1980; the water is utilized for district heating service in the towns of Egilsstaðir and Fellabaer.

3.2 Reykjanes and Svartsengi high-temperature geothermal areas

The Reykjanes high-temperature geothermal field is located at the southwest tip of the Reykjanes peninsula. This peninsula is elongated, oriented in forming an oblique segment of the constructive plate margin. The formation history of this peninsula can be explained by the geodynamic processes which are responsible for an anomalously large extrusion rate of magma to its maximum just south of central Iceland (Jakobsson, et al., 1978). It is characterised by extensive postglacial lava fields and steep-sided mountains and ridges of pillow lavas, pillow breccias and hyaloclastites which protrude through the lava fields. The exploited geothermal system is hosted by basaltic rocks, sub-glacial hyaloclastites, breccias and pillow lavas as well as tuffaceous sediments. The aquifer is liquid dominated but has developed a steam cap since production started at the 100 MWe Reykjanes power plant in 2006. The geothermal brine has seawater salinity and is believed to have originated as seawater. The sample was collected from the effluent channel to the ocean and is a mixture of geothermal brine (~10%), condensate (~10%) and seawater coolant (~80%) (Hardardóttir and Óskarsson, 2012). The Svartsengi high-temperature geothermal field is associated with an active rift zone on the Reykjanes peninsula in southwest Iceland. The accumulated rocks are of basaltic composition and formed in two different environments: lava flow sequences erupted from volcanoes during interglacial periods, and the hyaloclastite formation erupted under ice during glacial periods (Franzson, 1983). The boundaries of this field are thought to follow the boundaries of the westernmost fissure swarm on the Reykjanes peninsula and extend to the southwest in connection with the Eldvörp geothermal area. The Svartsengi system is liquid dominated and also has a steam cap. The salinity of the geothermal brine is about 2/3 that of seawater salinity. The sample was collected from the brine pipeline to the reinjection well and is a mixture of geothermal brine (~50%), condensate and cooling water (Gudfinnsson and Óskarsson, 2012).

3.3 Lágar, Kaldársel and Hrísey cold groundwater sample areas

Kaldársel is located in the Hafnarfjörður area in southwest Iceland. This spring is located where tectonic fissures cross low hills of pillow lava breccia, and is most likely the main aquifer (Sigbjarnarson, 1982). This area is protected as it provides the Hafnarfjörður municipal water supply for drinking purposes. Lágar is situated about 5 km northwest of the Svartsengi power plant. In 1976, Hitaveita Sudurnesja Ltd. (now HS Orka) constructed the first phase of six of its existing cogeneration power plants at Svartsengi on the Reykjanes peninsula. The plant uses geothermal steam for power generation and produces hot water by heating cold water from Lágar with geothermal water in thermal exchangers and by injecting geothermal steam. The hot water is used for space heating, swimming and industrial purposes. The cold water from Lágar is also used for drinking water in the neighbouring communities of Grindavík and Reykjanesbaer. The water is pumped from a freshwater lens that floats atop a more saline water body (Gudfinnsson and Óskarsson, 2012). Hrísey is an island in the Eyjafjörður fjord in N-Iceland, and is a remnant of an old plateau of lavas that covered the area before the fjord was carved out by glaciers on either side of the island. The cold water comes from a 130 m deep well that was drilled in 1987 and produces from a fresh water layer atop more saline water. The well supplies the hamlet on the island with drinking water.

3.4 Kalmanstjörn and Saudárkrókur seawater sample areas

The seawater wells at Kalmanstjörn are situated in the Reykjanes peninsula, a few km north of the Reykjanes power plant. These wells are rather shallow (50-60 m deep), drilled very near the coast, and draw seawater from the surrounding lava and hyaloclastite formations. The water is used as cooling water for the Reykjanes power plant. Saudárkrókur is the largest town in northwest Iceland and the second largest town on the north coast of Iceland, with a population of about 2600. The seawater pipeline from which this sample is drawn is used by a local shrimp factory.

3.5 Fluid chemistry

The chemical composition of geothermal water from low-temperature geothermal boreholes, geothermal brines, heated water used for district heating pipelines, and cold water from springs and the sea, used in this report is given in Appendix I. The concentration of all elements is in mg/l. Geothermal waters from Laugar, Urriðavatn, Reykjabraut, Reykir, Ósbrekka, and Hrolleifsdalur have been characterised as follows: low temperature (61.9 to 88.2°C), fresh (185 to 596 mg/l TDS), alkaline (9.29 to 10.22 of pH), and soft (6.3 to 51.8 mg/l of total hardness or TH as CaCO_3), and contains Ca^{2+} (2.5 to 20.5 mg/l), SO_4^{2-} (6.01 to 149 mg/l), HCO_3^- (9.8 to 27.7 mg/l); Na^+ (35.5 to 153 mg/l) and Cl^- (8.4 to 191 mg/l). The relative ion concentration level for cations is the same in all the geothermal water samples, namely $\text{Na}^+ > \text{Ca}^{2+} > \text{K}^+ > \text{Mg}^{2+}$. Cl^- is the predominant anion for Laugar, Urriðavatn and Hrolleifsdalur, SO_4^{2-} is the predominant anion for Reykjabraut, and HCO_3^- is the predominant anion for Ósbrekka. Brine waters from Reykjanes and Svartsengi have been characterised as follows: salty (27600 and 12958 mg/l of TDS), neutral (7.76 and 6.75 of pH) and very hard (4860 and 1540 mg/l TH as CaCO_3), contains Ca^{2+} (526 and 617 mg/l), SO_4^{2-} (1790 and 15.2 mg/l), HCO_3^- (73.5 and 10.9 mg/l), Na^+ (8650 and 3940 mg/l) and Cl^- (15810 and 7510 mg/l). The relative ion concentration level for cations is $\text{Na}^+ > \text{Mg}^{2+} > \text{Ca}^{2+} > \text{K}^+$ for Reykjanes, and $\text{Na}^+ > \text{Ca}^{2+} > \text{K}^+ > \text{Mg}^{2+}$ for Svartsengi. For anions, it is $\text{Cl}^- > \text{SO}_4^{2-} > \text{HCO}_3^-$ for both. Sea water from Saudárkrókur and Kalmanstjörn has been characterised as follows: cold (8.6 and 8.3°C), salty (15400 and 30682 mg/l of TDS), slightly alkaline (8.6 and 8.3 of pH) and very hard (6540 and 5200 mg/l of TH as CaCO_3), contains Ca^{2+} (728 and 341 mg/l), SO_4^{2-} (2060 and 2240 mg/l), HCO_3^- (10.8 and 113.7 mg/l); Na^+ (8260 and 8720 mg/l) and Cl^- (16350 and 16190 mg/l). The relative ion concentration levels for cations and anions are the same in both sea water samples, which is $\text{Na}^+ > \text{Mg}^{2+} > \text{Ca}^{2+} > \text{K}^+$ and $\text{Cl}^- > \text{SO}_4^{2-} > \text{HCO}_3^-$. Cold groundwater from Kaldársel, Hrísey and Lágar has been characterised as follows: cold (3.4 to 5.7°C), fresh (88 to 178 mg/l of TDS), neutral to alkaline (7.02 to 8.94 of pH) and soft (20 to 57.7 mg/l of TH as CaCO_3), contains Ca^{2+} (24.9 to 9.08 mg/l), SO_4^{2-} (2.4 to 10.4 mg/l), HCO_3^- (28.3 to 42.3 mg/l); Na^+ (9.39 to 39.5 mg/l) and Cl^- (8.4 to 80.4 mg/l). The relative ion concentration level for cations is the same in all the cold water samples, namely; $\text{Na}^+ > \text{Ca}^{2+} > \text{Mg}^{2+} > \text{K}^+$. HCO_3^- is the predominant anion for Kaldársel and Hrísey, whereas Cl^- is the predominant anion for the Lágar water sample. The heated water for the district heating system of Hitaveita Sudurnesja is characterised as follows: low temperature (70°C), fresh (165 mg/l of TDS), alkaline (9.01 of pH) and soft (47.8 mg/l of TH as CaCO_3), contains Ca^{2+} (7.89 mg/l), SO_4^{2-} (10.2 mg/l), HCO_3^- (13.9 mg/l), Na^+ (32.5 mg/l) and Cl^- (74.7 mg/l). The relative ion concentration levels for cations and anions are $\text{Na}^+ > \text{Ca}^{2+} > \text{Mg}^{2+} > \text{K}^+$ and $\text{Cl}^- > \text{HCO}_3^- > \text{SO}_4^{2-}$. This water actually comes from the Lágar cold groundwater. The chemical composition did not change much after being heated except for the pH value, which increased from 7.46 to 9.01, due to degassing of CO_2 , which decreased from 13.5 to 10.5 mg/l.

The chloride-sulphate-bicarbonate ternary diagram was used for distinguishing between the different types of water described by Giggenbach (1991). According to Giggenbach, chloride rich waters are general found near the up-flow zone of geothermal systems. High sulphate steam-heated waters are generally encountered over the more elevated parts of a field. The degree of separation between data points from high chloride and bicarbonate waters may give an idea of the relative degree of interaction of the carbon dioxide charge of the fluid at lower temperatures, and of the bicarbonate concentrations, which increase with time and the distance travelled underground. The $\text{Cl-SO}_4\text{-HCO}_3$ ternary plot (Figure 2) shows that the geothermal waters from Laugar and Hrolleifsdalur are chloride waters, and the waters from Urriðavatn and Reykir are mixed chloride-sulphate and chloride-sulphate-bicarbonate waters, respectively. Geothermal water from Ósbrekka tends toward the bicarbonate corner, possibly suggesting a peripheral nature of thermal water, whereas geothermal water from Reykjabraut is classified as a sulphate water. Brine waters from Reykjanes and Svartsengi, sea waters from Saudárkrókur and Kalmanstjörn, and heated water from Hitaveita Sudurnesja, plot close to the chloride corner and close to the field of mature geothermal water although that is certainly not the case. Water from the cold spring in Lágar also plots close to mature geothermal water, but the other two samples from Kaldársel and Hrísey plot in the peripheral water of bicarbonate type. The difference between the Lágar water and the Kaldársel and Hrísey water is most likely due to slight mixing with the underlying seawater in Lágar.

The geothermal waters from Laugar, Urriðavatn, Reykjabraut, Reykir, Ósbrekka, and Hrolleifsdalur appear to be in equilibrium at temperatures less than 100° to 120°C, according to the Na–K–Mg ternary plot of Giggenbach (1988) (Figure 3). They all fall within the full equilibrium field. The reservoir temperatures indicated by the calculated chalcedony geothermometer are close to the measured temperatures but the sodium-potassium geothermometer gives considerably lower values. One brine sample from Svartsengi falls into the full equilibrium field; the other one from Reykjanes, along with the sea water samples, falls under the partially equilibrated and mixed water field. All spring water from Kaldársel, Hrísey and Lágar and the heated water from Hitaveita Sudurnesja form a group at the Mg corner, which means they are immature waters. This is not unexpected as these are groundwater samples, not geothermal water.

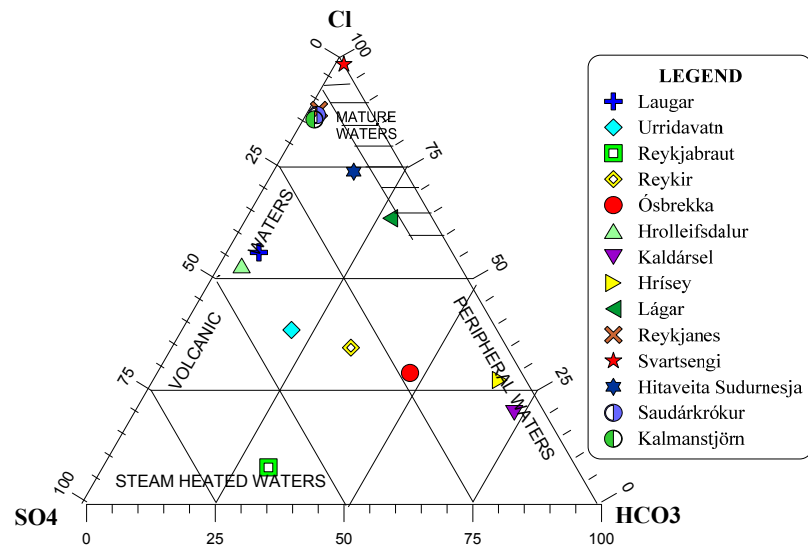


FIGURE 2: Cl–SO₄–HCO₃ ternary plot of all the water samples

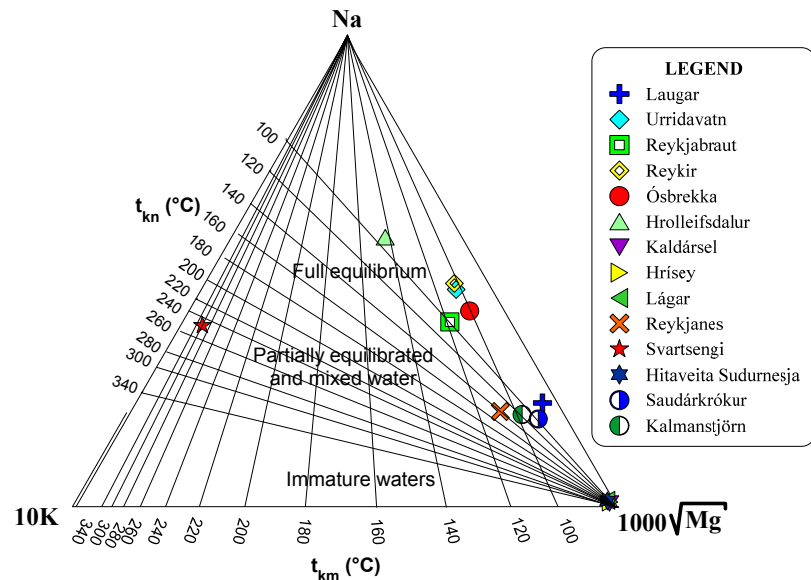


FIGURE 3: Na–K–Mg ternary plot of all the water samples

4. CHEMICAL ASSESSMENT FOR SPACE HEATING APPLICATIONS

The most important direct applications of geothermal fluid in Iceland is space heating which includes district heating systems, greenhouse and soil heating, heating of swimming pools, drying of fish, vegetables and food products, and other industrial purposes where direct heat applications are necessary. Almost 90% of all houses in Iceland are currently heated by geothermal water. Low-temperature geothermal fields are the main source of water for this utilization, although geothermally heated groundwater is also common. Corrosion and scaling problems have occurred in some cases. Sometimes, scaling and corrosion processes are interactive and complex. There is no single index for the interpretation of these processes.

Corrosion has been experienced in association with water containing dissolved oxygen at temperatures less than 80°C, and with carbon dioxide in water below 100°C with high concentrations of chloride. An inadvertent intrusion of oxygen into geothermal water may lead to greatly accelerated corrosion. An increase of dissolved oxygen can reduce hydrogen sulphide (H₂S) or vice versa. For this reason, geothermal steam is usually injected into heated groundwater, causing H₂S in the steam to remove the

dissolved oxygen and, thus, protect pipelines from corrosion. The primary effects of carbon dioxide in geothermal systems involve carbonate species and pH changes. Waters with pH below 6.5 are likely to be severely or extremely corrosive to steel and moderately corrosive to alloys such as brass. Theoretically, a high uniform corrosion rate is due to the presence of carbon dioxide and sodium chloride up to about 80°C. There is significant localized damage, at least to iron and steel, when the carbon dioxide concentration exceeds 20 mg/l. Chloride ions cause the local breakdown of passive films and increase the solubility of iron in geothermal water by forming highly soluble complexes with the ferric ion (Elguedri, 1999).

Icelandic geothermal water is normally not corrosive due to its low dissolved oxygen level (<0.003 mg/l) and high pH value (>9) (Richter et al., 2007). All the geothermal water samples from Laugar, Urridavatn, Reykjabrut, Reykir, Ósbrekka, and Hrolleifsdalur and the district heating water from Hitaveita Sudurnesja were high in pH value (>9) and low dissolved oxygen concentrations (<0.001 mg/l), except for the samples from Laugar and Ósbrekka, with 0.10 and 0.06 mg/l of dissolved oxygen, respectively. Problems due to corrosion have been encountered in the communities that use water from those two fields. The pH values in brine water from Reykjanes and Svartsengi are 7.7 and 6.7, respectively, which are suitable values, but the CO₂ content is higher in Reykjanes with a concentration of 65.8 mg/l. Chloride concentrations are also very high in the samples from Reykjanes and Svartsengi. The CO₂ value in the samples from Reykjabrut is 21.2 mg/l, which is slightly higher than the damaging mark of 20 mg/l; all other samples have lower values, excluding cold waters which were not considered for corrosion assessment.

Troublesome scaling can be encountered during the utilization of geothermal fluid, although in most cases there are ways to control it. The most common precipitates from low-temperature geothermal fluids are calcium carbonate (CaCO₃), amorphous silica (SiO₂) and magnesium silicate (MgSiO₃·H₂O). The solubility of calcite increases with decreasing temperature. Therefore, cooling of geothermal water does not cause calcite scaling. But if the water boils or mixes with saline water, calcite scales may form. The mixing of the inflow from two or more different sources, with different chemistries and temperature, often affects the solubility of calcite towards super saturation. In this case, equilibrium may occur, again precipitating calcite.

Deposition of magnesium silicate may form when fresh water is mixed with geothermal water. The groundwater is high in magnesium compared to geothermal water which, on the other hand, is high in silica. The mixing of geothermal water with fresh groundwater results in high magnesium concentrations. The solubility of magnesium silicates is very low at high pH values. Therefore, high magnesium and high pH values are favourable for magnesium silicate scaling. To determine the scaling potential, the saturation indices (log Q/K) were calculated using the computer program WATCH (Bjarnason, 1994) for the measured temperature, and by cooling the samples down to 25°C from the measured temperature in 5°C intervals. The speciation technique was only applied to the hot water samples.

Saturation indices were calculated for the amorphous silica, calcite and magnesium silicate (chrysotile) minerals. A positive saturation index for a mineral means that the solution is super saturated with respect to that particular mineral and, theoretically, this means it would start to precipitate. However, production data for low-temperature geothermal waters in Iceland show that calcite normally does not instantaneously precipitate until the log Q/K value reaches more than about 0.40 (Bai Liping, 1991).

Calculated calcite saturation indices vs. temperature are shown in Figure 4. The figure shows that there does not appear to be a risk of calcite scaling in any of the geothermal waters from Laugar, Urridavatn, Reykjabrut, Reykir, Ósbrekka, and Hrolleifsdalur or the heated water from Hitaveita Sudurnesja (HS) or the brine water from Svartsengi. In the sample from Reykjanes, the saturation index of calcite was higher than the 0.32 value at a temperature above 50°C. For a saturation index between 0.32 and 0.50,

calcite scaling may or may not occur, depending on other factors (Bai Liping, 1991). On the other hand, supersaturation of magnesium silicate (chrysotile) was calculated in the water samples from Laugar, Reykir, Ósbrekka, Reykjanes, and HS above 25°C, and from Reykjabraut only above 60°C (Figure 5). This may cause scaling. The geothermal brine water sample from Svartsengi showed a risk of amorphous silica scaling at temperatures below about 73°C (Figure 6).

To observe the scaling potential after mixing geothermal water with cold water, the mixing of cold groundwater (5.7°C) from Lágur and hot geothermal brine water (99°C) from nearby Svartsengi power plant was calculated. The fractions of the cold water in the mixture were 63% and 90%, intended to yield mixture temperatures of 40 and 15°C, which are optimum temperatures for balneotherapeutic and aquaculture applications, respectively. The mixing ratios were calculated using Equation 1. The chemical composition of the mixed water was determined assuming a pH value of 6.75, which is the value of the Svartsengi sample, due to its higher buffer capacity. The calculated saturation indices (log Q/K) for amorphous silica, calcite and magnesium silicate (chrysotile) of mixed water were calculated using the WATCH program. At 40°C, the log(Q/K) for amorphous silica, calcite and chrysotile were -0.17, -1.14 and -7.00, respectively, all negative. At 15°C, the log(Q/K) values were -0.39, -18.56 and -9.88, respectively, which are also negative. Therefore, there should be no risk of amorphous silica, calcium carbonate or magnesium silicate precipitation in this mixed water.

$$X \cdot 5.7 + (1 - X) \cdot 99 = 40 \quad (1)$$

$$\text{or,} \quad X = 63 \% \quad (2)$$

where X = Cold water fraction.

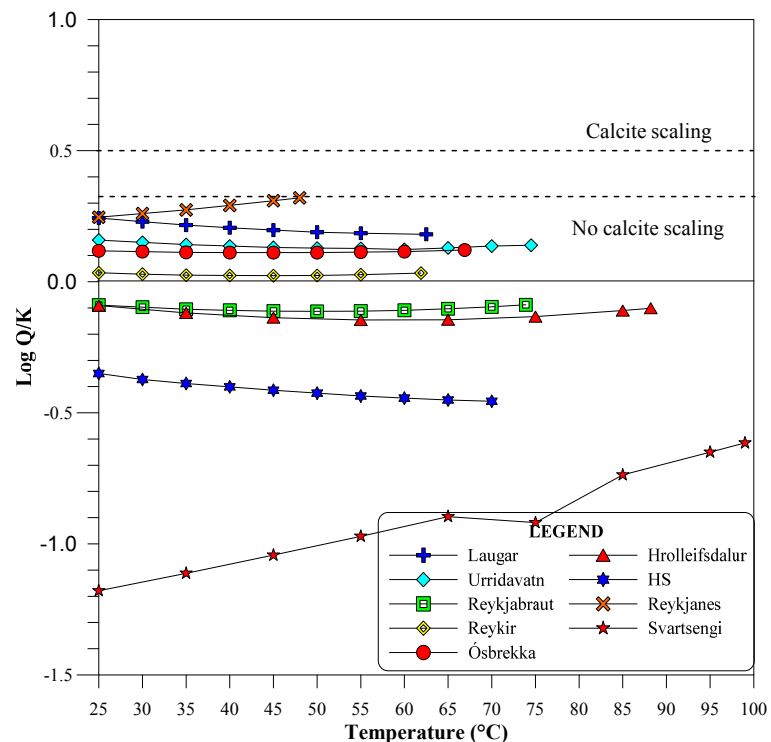


FIGURE 4: Calcite saturation index

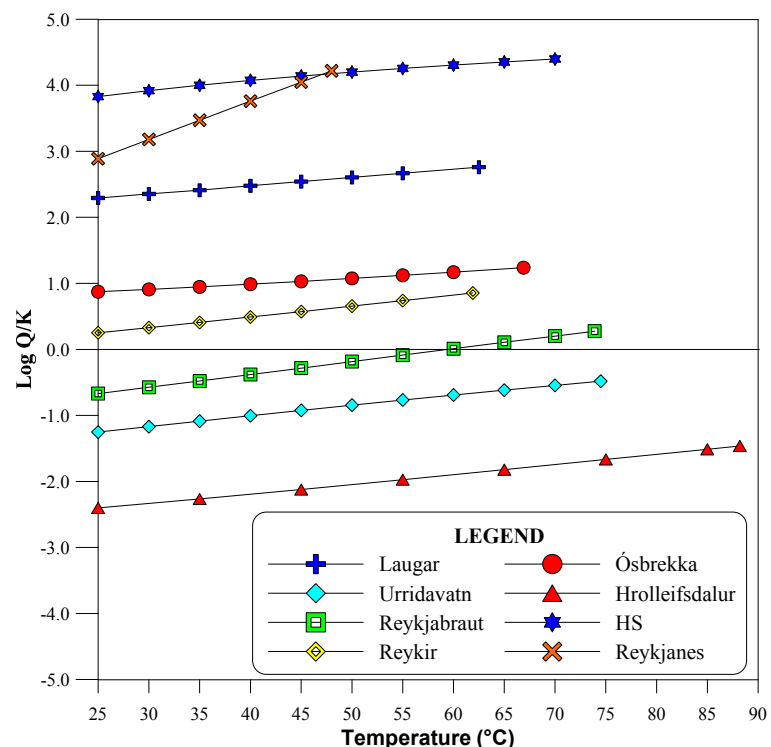


FIGURE 5: Magnesium silicate (chrysotile) saturation index

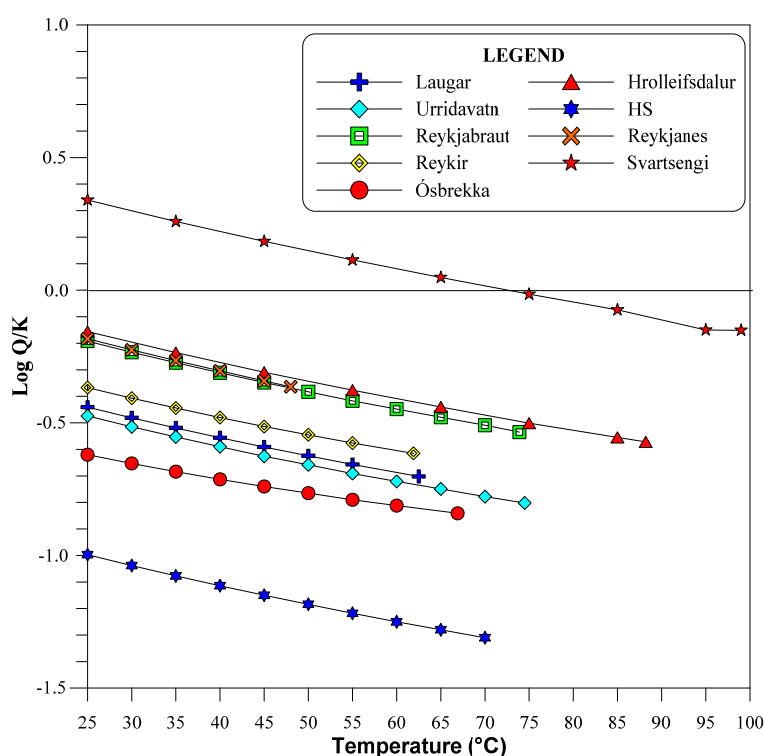


FIGURE 6: Magnesium silicate saturation index from Svartsengi high-temperature field

5. CHEMICAL ASSESSMENT FOR BALNEOTHERAPEUTIC APPLICATIONS

Geothermal fluid in balneotherapy is the oldest known type of application in Iceland. This culture goes back to ancient times. In Iceland, there are numerous swimming pools, several hot springs as well as recreation centres such as the Blue Lagoon, Mývatn Nature Baths, and the Nauthólsvík geothermally heated beach, which are visited by tens of thousands of guests every year. Improving health and appearance, getting away from stress to refresh and revitalize the body and mind are the main reasons for taking a geothermal water bath, and this culture is an important part of Icelandic life.

Thermal water having curative properties is termed as mineral water. Though there is no internationally accepted definition of mineral water, certain common criteria are found in all commonly used definitions. According to Komatina (2004), mineral water can be classified on the basis of total mineralization, ion and gas composition, content of active therapeutic components, acidity or alkalinity and temperature. According to the classification of the International Society of Medical Hydrology, the Societe International de Technique Hydrothermale (SITH), the International Association of Spas, Health Resort and Balneology and the German Health Resorts Association, a water source can be classified as curative if it possesses one or more of the following properties: more than 1500 mg/l of TDS, 20 mg/l of Fe (iron metal water), 1 mg/l of I (iodine mineral water), 1 mg/l of H_2S (hydrogen sulphide water), 18 nCi/l (nano-curie) of radon (radon water), 1 mg/l of fluoride (fluoride rich water) and if the temperature exceeds 27°C.

The actions of the geothermal water on humans are generated by three factors: thermal, chemical and mechanical factors. The net benefit of immersion in mineral water is probably the result of a combination of these factors (Sukenik et al., 1999). A water temperature of 36-37°C has various beneficial healing effects such as increasing the heart rate and cardiac flow, decreasing blood pressure, controlling contractions and muscular spasms by relaxing skeletal muscles and reducing soft tissue pain

(Fracas, 2005). The evaluation for balneotherapeutic applications of all water samples, as well as for the mixed water, is given in Table 2. A mixed water composition was calculated using 37% geothermal water at a temperature 99°C from Svartsengi and 63% cold water at a temperature 5.7°C from Lágar, so that the mixed water temperature was 40°C, which is an optimal temperature for balneotherapeutic applications. Mineral waters that are classified on the basis of temperature and a balneotherapeutic standpoint, fall into one of the following groups: cold (below 20°C), hypothermal (20-37°C), thermal (37-42°C), and hyperthermal (above 42°C) (Matz et al., 2003). According to this classification, all the geothermal waters, brine waters and heated water are hyperthermal. It is evident that the effects of thermal water are increased vasodilation in the veins of the, skin thereby accelerating the metabolic processes and oxygen supply and improving blood circulation in the cells of the skin (GTC and VO, 1988).

TABLE 2: Chemical parameters of all the water samples compared with the standards

Parameters	Unit	EU (2009) and US spa standards	Sample codes														
			1	2	3	4	5	6	7	8	9	10	11	12	13	14	15
pH	-	7.2 -7.6	E	E	E	E	E	E	E	B	S	E	B	E	S	E	B
Temperature	°C	29-35	E	E	E	E	E	E	B	B	B	E	E	E	B	B	S
EC	μS/cm	>2308	B	B	B	B	B	B	B	B	B	NA	NA	B	S	NA	NA
TDS	mg/l	>1500	B	B	B	B	B	B	NA	B	B	S	S	B	S	S	S
Ca	mg/l	>150	B	B	B	B	B	B	B	B	B	S	S	B	S	S	S
Mg	mg/l	>50	B	B	B	B	B	B	B	B	B	S	B	B	S	S	B
Na	mg/l	>200	B	B	B	B	B	B	B	B	B	S	S	B	S	S	S
K	mg/l	0-90	S	S	S	S	S	S	S	S	S	E	E	S	E	E	E
F	mg/l	>1.0	B	B	S	S	B	B	B	B	B	B	B	B	B	B	B
Cl	mg/l	>200	B	B	B	B	B	B	B	B	B	S	S	B	S	S	S
SO ₄	mg/l	>200	B	B	B	B	B	B	B	B	B	S	B	B	S	S	B
HCO ₃	mg/l	>600	B	B	B	B	B	B	B	B	B	B	B	B	B	B	B
H ₂ S	mg/l	>1.0	B	B	S	B	NA	B	B	NA	B	B	B	B	NA	B	B
Al	mg/l	0.02	S	S	S	S	S	S	S	B	B	B	S	B	B	B	B
As	mg/l	6 x 10 ⁻⁶	B	B	B	B	B	B	B	B	B	B	B	B	B	B	B
Ba	mg/l	0.08	B	B	B	B	B	B	B	B	B	S	S	B	S	S	S
B	mg/l	0.08	S	S	S	S	B	S	NA	B	B	S	S	S	B	S	S
Cd	mg/l	3 x 10 ⁻⁶	B	S	B	B	B	B	B	S	B	B	B	B	S	B	B
Cr	mg/l	35 x 10 ⁻⁵	B	B	B	B	S	S	S	B	S	S	S	S	B	S	S
Cu	mg/l	5 x 10 ⁻⁶	S	S	S	S	S	S	S	S	S	S	S	S	S	S	S
Fe	mg/l	>1.0	B	B	B	B	B	B	B	B	B	B	B	B	B	B	B
Hg	mg/l	7 x 10 ⁻⁶	B	B	B	S	B	S	B	B	B	B	B	B	B	B	B
Mn	mg/l	0.023	B	B	B	B	B	S	B	B	B	S	S	B	S	B	S
Pb	mg/l	<4.0	S	S	S	S	S	S	S	S	S	S	S	S	S	S	S
Sr	mg/l	5.3	B	B	B	B	B	B	B	B	B	S	B	B	S	S	B
Zn	mg/l	<5.0	S	S	S	S	S	S	S	S	S	S	S	S	S	S	S

1: Laugar; 2: Urriðavatn; 3: Reykjabraut; 4: Reykir; 5: Ösbrekka; 6: Hrolleifsdalur; 7: Kalársel; 8: Hrísey; 9: Lágar; 10: Reykjanes; 11: Svartsengi; 12: Hitaveita Sudurnesja (HS); 13: Saudárkrókur; and 14: Kalmanstjörn; 15: Mixed water (40°C); S: Suitable for balneotherapeutic use; E: Exceeding the standard value; B: Below the standard value; NA: No available data

The chemical factors determine the curative properties of water for skin disease and other kinds of therapeutic uses (Manuel, 2010). In this study, the physicochemical parameters, including trace elements, were compared with the standards for spas in the European Union (2009) and the USA. In comparison with the standard limits, it should be noted here that the standard usually refers to the minimum value, except in the case of Pb and Zn for which it defines a maximum value. Figure 7 shows that one spring sample from Lágar and one sea sample from Saudárkrókur showed pH values within the standard limit of 7.2-7.6. Other samples showed either higher or lower pH. The pH has a direct impact on users only at very low or very high values. Primarily, irritation of the skin and eyes appears to be

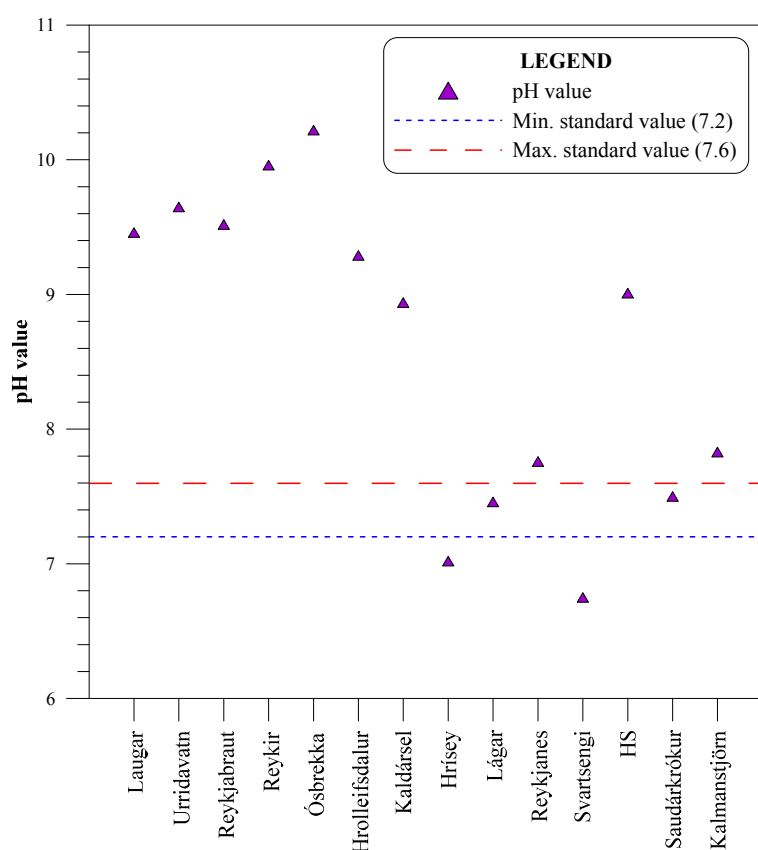


FIGURE 7: pH values compared with the EU (2009) and US spa standards

linked to high or low pH. Water with high pH could have an adverse effect on hair by causing the hair fibres to swell and by cleaving the cystine bridges between adjacent polypeptide chains of the hair protein. The graph in Figure 8 compares the relevant physicochemical parameters of all water samples with the standard values. In terms of TDS, brine waters from Reykjanes and Svartsengi, sea waters from Saudárkrókur and Kalmanstjörn and mixed water are mineral rich waters (TDS>1500 mg/l), suitable for balneological purposes. These samples are also rich in Na^+ , Ca^{2+} , Mg^{2+} , Cl^- and SO_4^{2-} except for the SO_4^{2-} concentration in Svartsengi, as well as in the mixed water which was below the standard value. Others samples show lower than the recommended values of the above mentioned parameters. Ca^{2+} , Mg^{2+} , Na^+ , Cl^- , and SO_4^{2-} are the most common constituents for waters considered to have therapeutic properties (Skapare, 2001).

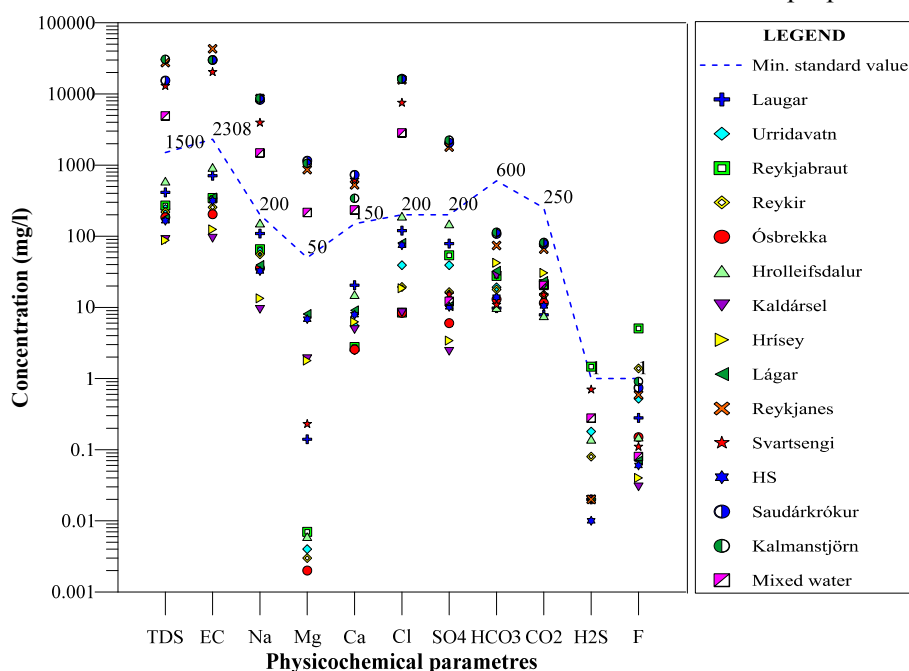


FIGURE 8: Physicochemical parameters compared with the EU (2009) and US spa

Among the various mineral salts present in geothermal water, HCO_3^- is known to be important, but all the samples contained less than the minimum amount of HCO_3^- (600 mg/l), and the same applied to CO_2 . However, therapeutic activities of CO_2 water baths (700 to 1300 mg/l) are explained by a synergism between hydrostatic pressure and the chemical properties of CO_2 which acts directly on the blood vessels of the skin, causing vasodilation and increased

oxygen utilization (Hartmann et al., 1997). Waters from Reykjabraut and Reykir are mineral waters in terms of F^- content. The F^- concentrations of these two samples were 5.08 and 1.39 mg/l, respectively.

The main diseases recommended for treatment by mineral water are as follows: degenerative joint diseases of the locomotive system, nervous system functional disorders, overweight problems, etc. (Bojadgieva et al., 2002). Hydrogen sulphide (H_2S) affects the microcirculation in the body, markedly dilating peripheral vessels and enhancing vascular motion (Skapare, 2001). The sulphur that penetrates the skin is oxidized and evokes various physiological responses in the skin, such as vasodilation in the microcirculation; it also has an analgesic influence on the pain receptors, and inhibits the immune response. It also interacts with oxygen radicals in the deeper layers of the epidermis; it may be transformed into pentathionic acid which could be the source of the antibacterial and antifungal activity of sulphur water (Matz et al., 2003). Only the sample from Reykjabraut contained 1.47 mg/l of H_2S , making it suitable for this category.

Trace elements such Al, As, Cu, Fe, Mn and Zn give medicinal properties to mineral water (Saman, 2000). Figure 9 shows the concentrations of trace elements in comparison with standard values. All geothermal waters, brine water from Svartsengi and the mixed water contained higher values of Al than the minimum required standard value of 0.02 mg/l, suitable for balneotherapeutic use. Samples from Urridavatn, Saudárkrókur and Hrísey showed suitable concentrations of Cd, and Ósbrekka, Hrolleifsdalur, Reykjanes, Hitaveita Sudurnesja (HS) showed suitable concentrations of Cr. In terms of Hg, Reykir and Hrolleifsdalur showed the presence of permissible concentrations. Almost all the waters, including the mixed water, were characterised by a high concentration of B, except for the geothermal water from Ósbrekka, the district heating water from HS and the waters from cold springs, where the B values were less than 0.08 mg/l. Brine waters from Reykjanes and Svartsengi, mixed water and one sea water sample from Saudárkrókur showed Mn values above the minimum required value of 0.02 mg/l, and sea waters from Saudárkrókur and Kalmanstjörn and brine water from Reykjanes showed Sr values that were above the minimum required value of 5.3 mg/l. In all water samples, Pb and Zn values were within the permissible limits of 4 and 5 mg/l, respectively.

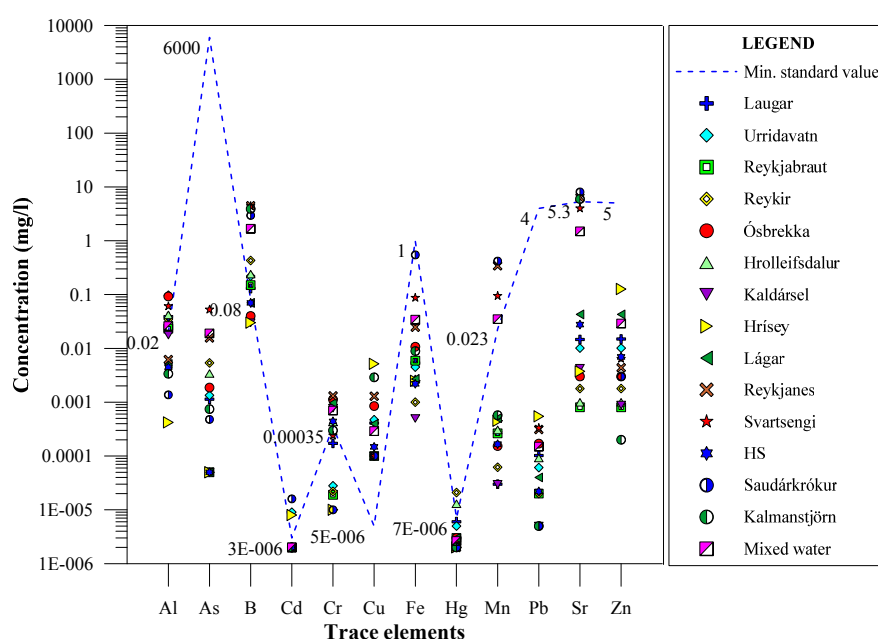


FIGURE 9: Trace element concentrations compared with the EU (2009) and US spa standards

6. CHEMICAL ASSESSMENT FOR AGRICULTURAL APPLICATIONS

The suitability of water for irrigation purposes depends upon the effects of the various chemical constituents. The chemical composition of water varies, depending on the origin of the water as well as time and space. Generally, all types of natural water contain dissolved salts due to the interaction of water and rock. The combinations of different types of salts present in the water limit the suitability of the water for irrigation purposes. The concentration of salts and other dissolved chemical substances increases with evaporation. High concentrations of some of these chemical substances are toxic to plants. The general parameters for assessing the irrigation water quality are: total salinity determined

from electrical conductivity (EC), relative proportions of Na^+ , sodium adsorption ratio (SAR) and boron toxicity. However, a number of trace elements can be found in water which may further limit its use for irrigation purposes.

6.1 Electrical conductivity (EC) and sodium percentage (% Na^+)

When evaluating irrigation water, the primary water quality concern is usually salinity due to its effect on both the plants and soil. Most salinity problems in agriculture result from salts carried by water for irrigation. Water with high salinity is toxic to plants. However, salinity alone does not determine the suitability of water for irrigation water, other factors must be considered. Electrical conductivity (EC) is a good measurement of saline hazards to crops. Total dissolved solid (TDS) is sometimes referred to as the total salinity.

Five classes of irrigation water based on EC and TDS are defined in Table 3 (Texas A&M University, 2003). In terms of EC and TDS, all the water samples from low-temperature geothermal boreholes, springs and heated water are within the excellent or good water classes with EC values from 21.4 to 709 $\mu\text{S}/\text{cm}$ and TDS values from 88 to

TABLE 3: Irrigation water classification based on EC and TDS

Class	Category	Electrical conductivity ($\mu\text{S}/\text{cm}$)	TDS (mg/l)
Class 1	Excellent	<250	<175
Class 2	Good	250 to 750	175 to 525
Class 3	Permissible	750 to 2000	525 to 1400
Class 4	Doubtful	2000 to 3000	1400 to 2100
Class 5	Unsuitable	>3000	>2100

414 mg/l, except for one sample from a low-temperature geothermal borehole in Hrolleifsdalur which falls under the permissible water class with EC and TDS value of 926 $\mu\text{S}/\text{cm}$ and 596 mg/l, respectively. Samples from sea and geothermal brine water have TDS in the range from 12958 to 30682 mg/l. Consequently, all the samples from sea and brine water are unsuitable for irrigation use.

Not only EC but also the relative proportion of Na^+ and K^+ are very important in classifying irrigation water. The primary effect of a high relative proportion of Na^+ is a reduction in the osmotic activity of plants, thus less absorption of water and nutrients from the soil. Therefore, water with low EC but a relative high Na^+ concentration may be considered less suitable for irrigation than water with the same measured EC but a more balanced diet of cations. The relative proportion of Na^+ concentrations in irrigation water is usually denoted as % Na^+ and can be determined by the formula (Wilcox, 1955) given below, where the concentrations are expressed in meq/l:

$$\% \text{Na} = \frac{(\text{Na}^+ + \text{K}^+) \times 100}{(\text{Ca}^{2+} + \text{Mg}^{2+} + \text{Na}^+ + \text{K}^+)} \quad (1)$$

All samples were classified based on $\text{Na}\%$ and EC in the Wilcox diagram (Figure 10). The figure shows that all the samples from springs in Kaldársel, Hrísey and Lágar and the heated pipeline sample from HS are in the excellent to good water classes. Samples from the low-temperature geothermal fields in Laugar, Urridavatn, Reykir, Reykjabrut, and Ósbrekka fall under permissible to doubtful, and Hrolleifsdalur belongs to the doubtful to unsuitable water classes for irrigation. Samples from brine and sea water were not plotted in this diagram due to their extremely high values; all of those waters are unsuitable for this application. A comparison of Figure 10 and Figure 3 shows that mature geothermal water would, in most cases, be considered unsuitable for irrigation due to the high Na^+ ratio.

6.2 Sodium adsorption ratio (SAR)

The sodium adsorption ratio (SAR) is an important parameter for determining the suitability of groundwater for irrigation. It is like the % Na^+ , a measure of alkali or sodium hazard which relates to

an infiltration problem. The higher the SAR values in the water, the greater the risk of Na^+ adsorption to the soil, which leads to the development of an alkali soil. When the concentration of Na^+ is high in irrigation water, Na^+ tends to be adsorbed to clay particles, displacing magnesium and calcium ions, reducing the soil's permeability and eventually resulting in soil with poor internal drainage. Ca^{2+} and Mg^{2+} are important due to their counter effects to sodium. Continued use of water with a high SAR value leads to a breakdown in the physical structure of the soil. When the soil is dry, it becomes hard and compact and eventually impervious to water penetration. Fine textured soil, especially high in clay, is most subject to this action. It can be calculated from the concentrations of Na^+ , Ca^{2+} and Mg^{2+} according to Hem (1989):

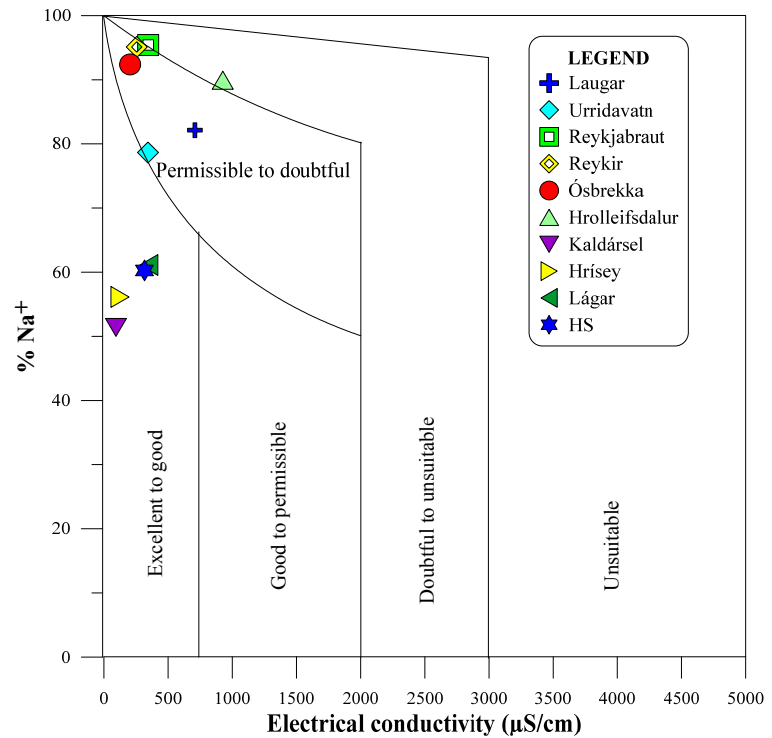


FIGURE 10: Suitability of irrigation water (from Wilcox, 1955)

$$\text{SAR} = \frac{\text{Na}^+}{\sqrt{\frac{\text{Ca}^{2+} + \text{Mg}^{2+}}{2}}} \quad (2)$$

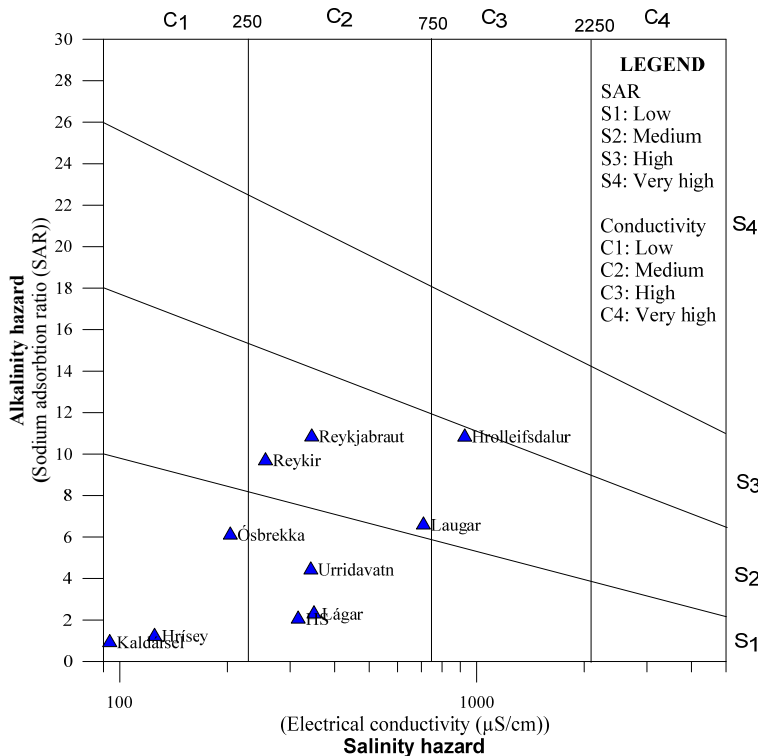


FIGURE 11: Classification of irrigation water (from Richard, 1954)

The plot of the data on the SAR diagram (Richard, 1954), in which EC is taken as the saline hazard and SAR as the alkaline hazard, is shown in Figure 11. Geothermal water from Ósbrekka shows low hazard in terms of both alkalinity and salinity, Urriðavatn shows a low alkalinity hazard but a medium salinity hazard, Laugar, Reykjabaut and Reykir show medium alkalinity and salinity hazards and Hrolleifsdalur shows medium alkalinity but a high salinity hazard. Samples from spring water in Hrísey and Kaldársel show low alkalinity and salinity hazard, while Lágur shows low alkalinity but medium salinity hazard. The sample from Hitaveita Sudurnesja (HS) district heating water shows a medium alkalinity and salinity hazard.

6.3 Boron toxicity

TABLE 4: Plant tolerance of boron (modified after Texas A&M University, 2003)

A number of elements in water can cause toxic reactions to plants when present in high concentrations. Boron is the greatest concern after sodium. Boron is present in water as boric acid, which may be toxic to plants even at very low concentrations. It can also accumulate in the soil. The high boron concentration in many geothermal systems is derived from boron rich rock. When the rock within the crust becomes sufficiently heated, boron is extracted into the surrounding formation water, and moves to the surface through faults and fractures (Smith, 2002). Plant species differ in their tolerance to boron. Some of them are listed with tolerance in Table 4. Samples from sea water in Saudárkrókur and Kalmanstjörn and geothermal brine water from Reykjanes and Svartsengi have high concentrations with 4.5, 4.4, 2.9 and 3.9 mg/l of boron, respectively (Figure 12). Other samples appear to be within the recommended limit of 1 mg/l of B for sensitive plants. Boron toxicity causes different effects on plants, such as altered metabolism, reduced root cell division, lower leaf chlorophyll content and photosynthetic rates (Nable et al., 1997). However, turf grass is not particularly sensitive to high levels of boron. Table 5 gives a summary of the water suitability for irrigation.

Sensitive (1.0 mg/l of B)	Semi-tolerant (2.0 mg/l of B)	Tolerant (3.0 mg/l of B)
Walnut	Sunflower	Athel
Navy bean	Potato	Asparagus
Plum	Cotton	Palm
Pear	Tomato	Datepalm
Apple	Sweet pea	Sugarbeet
Grape	Robin rose	Mangel
Persimmon	Olive	Gardenbeet
Cherry	Barley	Alfalfa
Peach	Wheat	Gladiolus
Apricot	Corn	Broadbean
Blackberry	Oat	Onion
Orange	Pumpkin	Turnip
Avocado	Bell pepper	Cabbage
Grapefruit	Sweet potato	Lettuce
Lemon	Limabean	Carrot

TABLE 5: Suitability of water for irrigation based on several classifications

Value	Water class	Sample location
Based on electrical conductivity (EC) (µS/cm)		
<250	Excellent	Ósbrekka, Kaldársel and Hrísey.
250-750	Good	Laugar, Urriðavatn, Reykjabaut, Reykir, Lágur and HS.
750-2000	Permissible	Hrolleifsdalur.
2000-3000	Doubtful	-
>3000	Unsuitable	Reykjanes, Svartsengi, Saudárkrókur and Kalmanstjörn.
Based on total dissolve solid (TDS) value (mg/l)		
<175	Excellent	Hrísey and HS.
175-525	Good	Laugar, Urriðavatn, Reykjabaut, Reykir, Ósbrekka and Lágur.
525-1400	Permissible	Hrolleifsdalur.
1400-2100	Doubtful	-
>2100	Unsuitable	Reykjanes, Svartsengi, Saudárkrókur and Kalmanstjörn.
Based on alkalinity hazard or sodium adsorption ratio (SAR) (Richards,1954)		
<10	Low	Laugar, Urriðavatn, Reykir, Ósbrekka, Kaldársel, Hrísey, Lágur & HS.
10-18	Medium	Reykjabaut and Hrolleifsdalur.
18-26	High	-
>26	Very high	Reykjanes, Svartsengi, Saudárkrókur and Kalmanstjörn.
Based on boron concentration (mg/l)		
<1.00	Excellent	Laugar, Urriðavatn, Reykir, Reykjabaut, Ósbrekka, Hrolleifsdalur, Hrísey, Lágur and HS.
1.00 to 2.00	Good	-
2.00 to 3.00	Permissible	-
3.00 to 3.75	Doubtful	-
>3.75	Unsuitable	Reykjanes, Svartsengi, Saudárkrókur and Kalmanstjörn.

6.4 Trace elements

Some trace elements such as copper (Cu), iron (Fe), manganese (Mn), zinc (Zn), molybdenum (Mo) and nickel (Ni) have been considered plant nutrients for a long time. They must be available in soil for good growth and production. If the soil is not able to supply them to the plants, they will show deficiency symptoms and growth will be affected as well as production. However, sometimes trace elements such as arsenic may be taken up

in high amounts and accumulate in plants (bioaccumulation). This applies particularly to trace elements in the form of organic compounds and accumulates in tissues after being dissolved. High concentrations of trace elements are not only hazardous for plants and soil but, through the food chain, hazardous for human health, too. In Figure 12, the values of trace elements in all the samples were compared with the recommended limits given by Rowe and Abdel-Magid (1995) for irrigation water.

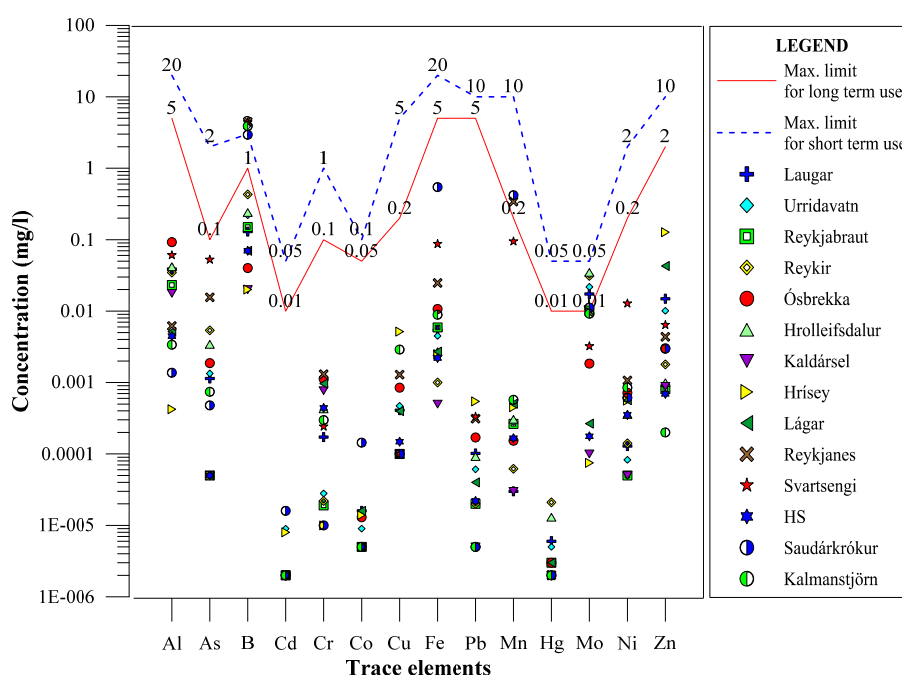


FIGURE 12: Trace element concentrations compared with recommended limits

High concentrations of aluminium (Al) inhibit root growth (Delhaiz and Ryan, 1995). The recommended value for Al is 5 mg/l for short term and 20 mg/l for long term irrigation. Al concentrations are within the recommended limit in all the water samples. Arsenic (As) is non-essential and is generally toxic to plants; it may trigger a sequence of reactions leading to growth inhibition, disruption of photosynthetic and respiratory systems (Grag and Singla, 2011). All the samples are within the recommended limit of 0.1 mg/l of As for long term irrigation use. High concentrations of chromium (Cr) give rise to severe chlorosis, necrosis and a host of other growth abnormalities and anatomical disorders (Samantaray et al., 1996). Cadmium (Cd) interferes with the metabolic processes within plants. Cr and Cd concentrations in all the water samples were lower than the maximum recommended limit of 0.1 mg/l and 0.01 mg/l, respectively, for long term irrigation use. High concentrations of copper (Cu), manganese (Mn), and zinc (Zn) result in chlorosis, a reduction in leaf size, foliage and necrosis. Both the samples from geothermal brine in Reykjanes and Svartsengi and one sample from the sea water in Saudárkrókur, had Mn concentrations of 0.34, 0.94 and 0.40 mg/l, respectively, exceeding the maximum recommended value of 0.02 mg/l for long term irrigation use. But, they are within the limits for short term use. Four out of six samples that were collected from low-temperature boreholes in Laugar, Urriðavattn, Reykir and Hrolleifsdalur had Mo concentrations of 0.02, 0.02, 0.03 and 0.03 mg/l, respectively; one sample from seawater in Saudárkrókur had a Mo concentration of 0.01 mg/l, which is at the margin of the recommended value of 0.01 mg/l for long term irrigation use. Mo toxicity is not thought to be significant to plants and does not produce harmful effects. All the low-temperature samples were within the limits for short term irrigation use (0.05 mg/l) with respect to Mo. Concentrations of other measured elements were within the recommended limits for both short and long term irrigation purposes.

7. CHEMICAL ASSESSMENT FOR AQUACULTURAL APPLICATIONS

According to the Food and Agriculture Organization, aquaculture is understood to mean the farming of aquatic organisms including fish, molluscs, crustaceans and aquatic plants. The term aquaculture is only applied to fish farming in this paper. Conditions are excellent in Iceland with regard to unpolluted seawater, abundant spring water and economical geothermal water. The main limiting factor in locating a fish farm is the availability of suitable water. Suitable water for the desired species means proper ionic, gaseous and metal content as well as temperature. Geothermal water may be utilized in three ways in aquaculture: direct use in a fish pond, mixing with cold water, and heating a fish pond by using a heat exchanger. A handful of fish production facilities are presently using geothermal water, in part, or totally for fish culture. In the utilization of warm water of geothermal origin, temperature regulation is of prime importance. A constant water supply of suitable temperature leads to increased fish production. According to the L ndal diagram (L ndal, 1973), it is recommended that the temperature of the geothermal water be in the range between 20 and 66 C for potential use in aquaculture. In cold countries, including Iceland, besides cold water species, geothermal water makes the farming of warm water species viable. Each fish species has a different temperature at which optimal development occurs, but a common optimal temperature is 15 C (Svobodova et al., 1993). In addition to the water samples, a water mixture, composed of 10% geothermal water from Svartsengi and 90% cold water from L gar, yielding a temperature of 15 C, was evaluated for the suitability of aquaculture applications. In addition to temperature, physicochemical parameters as well as trace element content of the water are important when evaluating the suitability of the water for aquacultural applications. In Table 6, all the samples were compared with the standard values provided by Svobodova et al. (1993); Wedemeyer (1977), and Piper (1982).

TABLE 6: Comparison of all the water samples with the aquaculture water quality standards (modified from Svobodova et al., 1993; Wedemeyer, 1977; and Piper, 1982)

Water quality for aquaculture			Sample codes														
Parameters	Min. value (mg/l)	Max. Value (mg/l)	1	2	3	4	5	6	7	8	9	10	11	12	13	14	15
pH*	6.5	8.5	E	E	E	E	E	E	E	S	S	S	S	E	S	S	S
TDS	-	3000	S	S	S	S	S	S	NA	S	S	E	E	S	E	E	S
TH *	10	400	S	S	B	B	B	S	S	S	S	E	E	S	E	E	S
Alkalinity *	10	400	B	S	S	S	S	B	S	S	S	S	B	S	S	S	S
Al	-	0.52	S	S	S	S	S	S	S	S	S	S	S	S	S	S	S
As	-	3	S	S	S	S	S	S	S	S	S	S	S	S	S	S	S
Cd	-	0.0002	S	S	S	S	S	S	S	S	S	S	S	S	S	S	S
Cr	-	7.5	S	S	S	S	S	S	S	S	S	S	S	S	S	S	S
Cu	-	0.01	S	S	S	S	S	S	S	S	S	S	S	S	S	S	S
Fe	-	0.2	S	S	S	S	S	S	S	S	S	S	S	S	E	S	S
Hg	-	0.002	S	S	S	S	S	S	S	S	S	S	S	S	S	S	S
Mn	-	0.01	S	S	S	S	S	S	S	S	S	E	E	S	E	S	S
Ni	-	0.1	S	S	S	S	S	S	S	S	S	S	S	S	S	S	S
Pb	-	0.7	S	S	S	S	S	S	S	S	S	S	S	S	S	S	S
Zn	-	0.1	S	S	S	S	S	S	S	E	S	S	S	S	S	S	S
DO	> 6	-	B	B	B	B	B	B	B	NA	NA	NA	NA	NA	B	NA	NA
CO ₂	-	10	S	E	E	E	E	S	E	E	E	E	E	E	E	E	E
H ₂ S	-	0.002	S	E	E	E	S	E	NA	NA	NA	NA	E	NA	NA	S	NA

1: Laugar; 2: Urridavatn; 3: Reykjabrut; 4: Reykir; 5:  sbrekka; 6: Hrolleifsdalur; 7: Kald rsel; 8: Hr sey; 9: L gar; 10: Reykjanes; 11: Svartsengi; 12: Hitaveita Sudurnesja (HS); 13: Saud rkr kur; 14: Kalmanstj rn; 15: Mixed water (15 C); S: Suitable for potable water; E: Exceeding the maximum permissible limit; B: Below minimum permissible limit; and NA: No available data; pH*: Unitless; TH and alkalinity *: mg/l as CaCO₃.

7.1 Physicochemical parameters

Fish are cold blooded creatures and their body temperature is more or less the same as that of the water in which they live, usually no more than 0.5 to 1°C above or below. The metabolic and immune system of the majority of fish species has an optimum performance at a water temperature of about 15°C (Svobodova et al., 1993). Cold-water fish can maintain a similar metabolic rate at comparatively low temperature, but above 20°C they usually became less active and consume less food. Raising the temperature of the water lowers the saturation levels of dissolved gases. Consequently, heated water is supersaturated in dissolved gases and is deleterious to the fish (Robert, 1975). Super saturation of dissolved gases may cause fish death as a result of blockage of major arteries and the erosion of fins. For salmonids, the optimal growing temperature is 10°C (Fridleifsson et al., 1995). Water temperature also influences the initiation and course of a number of fish diseases. The samples from cold springs and sea water ranged from 3.4 to 8.6°C. All other geothermal water samples ranged from 48 to 99°C. Considerable progress can be achieved in warm water fish cultures using geothermal water. Techniques for water temperature control enable maintaining optimal conditions so that the fish can fully utilize their growth potential to achieve maximum weight gains. The pH balance is essential to fish metabolism. The optimal pH range is from 6.5 to 8.5. Values above 9.2 and below 4.8 can damage and kill some species such as salmonids. Water pH can be changed when mineral acids and hydroxides or other acidic or alkaline substances are discharged or leach into water courses, ponds or lakes.

Samples from all low-temperature boreholes in Laugar, Urriðavatn, Reykjabraut, Reykir, Ósbrekka, and Hrolleifsdalur had elevated pH values ranging from 9.29 to 10.22, which is higher than the optimal range (Figure 13). The high pH values of low-temperature geothermal water are due to interaction with the basaltic host rock. The sample from Kaldársel and the heated water sample from HS had less alkaline pH, 8.94 and 9.01, respectively. The pH values in all other samples were within the optimal limit, ranging from 7.04 to 7.83. Total hardness (TH) is an important factor relating to the growth of the fish. Hard water is usually well buffered while soft water is usually less buffered. Soft water may cause bone deformities due to a lack of Ca. Water can be classified as soft (0 to <75 mg/l), moderately hard (75 to 150 mg/l), hard (150 to 300 mg/l) and very hard (>300 mg/l) in terms of TH with CaCO₃. Samples from sea and brine

waters were very hard, range from 4360 to 6540 mg/l, whereas samples from low-temperature geothermal and spring waters were soft, ranging from 6.25 to 57.7 mg/l in terms of TH of CaCO₃. The hardness value for mixed water was 205 mg/l of CaCO₃, which is hard water. Alkalinity is also important in fish farming because it protects the fish from a rapid change in pH values. It has the capacity to neutralise acid without lowering the pH value. This measure of an acid-neutralizing capacity is important in figuring out how buffered the water is against sudden changes in the pH value. The

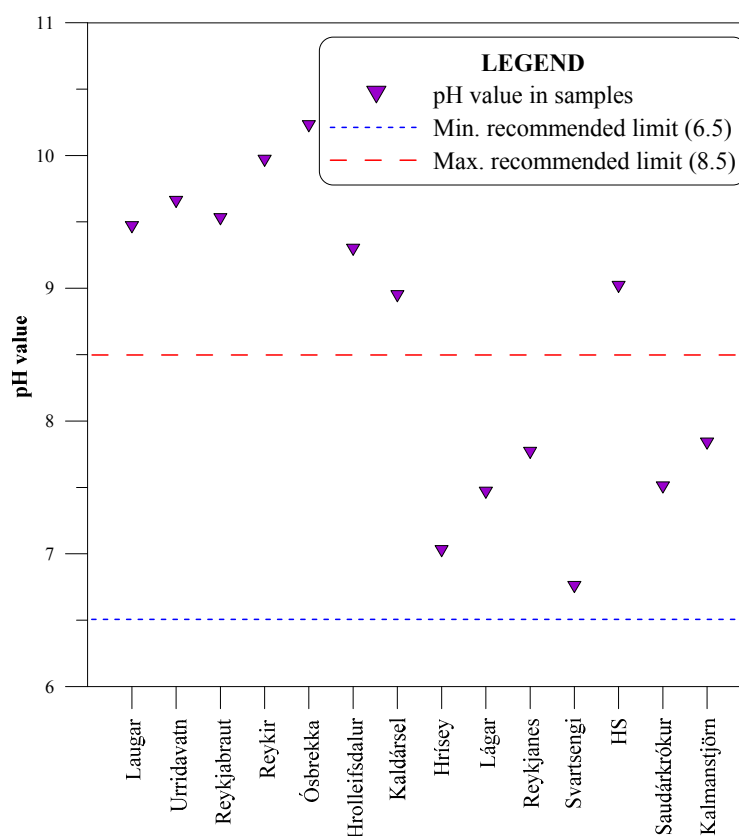


FIGURE 13: pH values of the selected samples compared with the standards

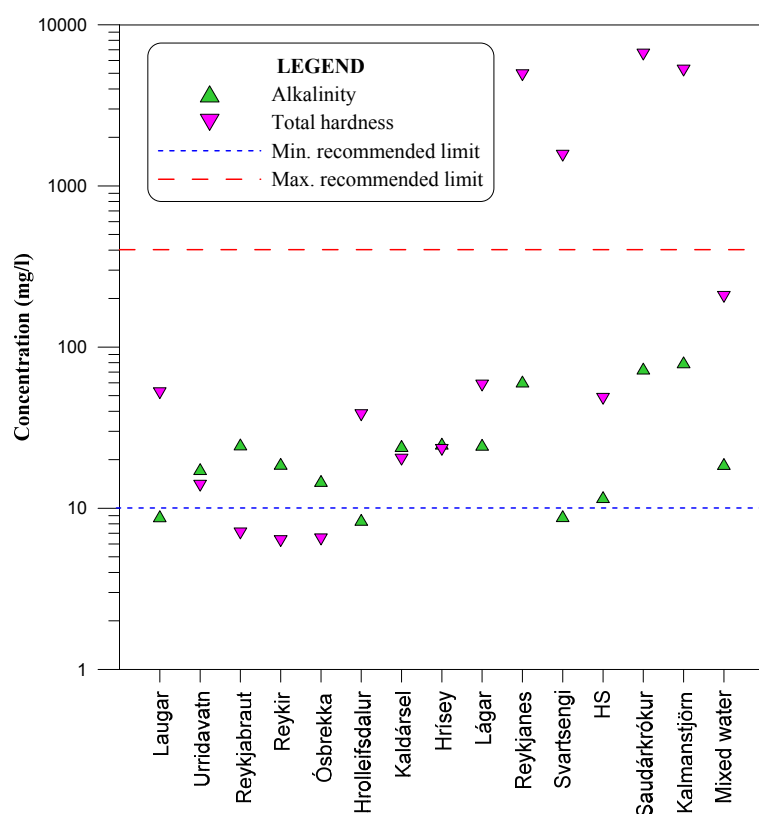


FIGURE 14: Alkalinity and hardness (as CaCO_3) of the selected samples compared with the standards

maximum and minimum limits for both hardness and alkalinity are 10 and 400 mg/l as CaCO_3 . Samples from Reykjanes, Svartsengi, Saudárkrókur, and Kalmanstjörn appeared to be above the limit in terms of TH; samples from Laugar, Hrolleifsdalur and Svartsengi appeared to be below the limit in terms of alkalinity. To some extent, the high pH of the samples makes up for the low alkalinity. Other samples were within the standard limit of both the TH and alkalinity (Figure 14).

Dissolved oxygen (DO) is a crucial water quality parameter in both flow and circulation of aquaculture systems. Hypoxia, or oxygen depletion, is a phenomenon that occurs in aquatic environments as dissolved oxygen becomes less available. Fish exposed to oxygen deficient water do not take food, gasp for air, gather at the inflow to ponds where the oxygen levels are

higher, become torpid, fail to react to irritation, lose their ability to escape capture and ultimately die. Significant differences in oxygen demand are found for different species, for example salmonids have a higher requirement for oxygen (8 to 10 mg/l) than other species. The major parameters for assessing the oxygen requirements of fish are temperature, the average individual weight, and the total weight of fish per unit volume of water. Oxygen requirements increase at a higher temperature (e.g. an increase in water temperature from 10 to 20°C at least doubles the oxygen demand), a higher total weight of fish per unit volume of water can lead to increased activity and, thus, increased respiration as a result of overcrowding. The oxygen requirements of fish also depend on other factors, including the temperature, pH and CO_2 level in the water. The recommended minimum DO requirement is 6 mg/l. DO, in all the low-temperature geothermal water samples, was less than 0.01 mg/l. The sea water sample measured in Saudárkrókur showed 0.05 mg/l O_2 . DO values in all the other water samples were unavailable, but it may be assumed that the geothermal water has less than 0.001 mg/l of O_2 . However, this problem can be solved by aerating the water with O_2 .

High concentrations of H_2S are very toxic to fish; the lethal concentration for different species ranges from 0.4 (salmonids) to 4 mg/l (carp, tench and eel). H_2S exerts its toxicity by forming sulphides with the active groups of different metallo-enzymes in cell and blood pigments, thereby interrupting cellular respiration (Miron and Kristensen, 1993). The toxicity of H_2S decreases with increasing water pH because of a reduction in the ratio of the non-dissociated toxic H_2S to the less toxic HS^- ions. The optimum concentration should be less than 0.002 mg/l. In Figure 15, four samples out of six samples from low-temperature geothermal water showed H_2S values ranging from 0.08 to 1.47 mg/l, higher than the optimum range (0.002 mg/l); two samples show less than 0.03 mg/l. On the other hand, those samples had some dissolved O_2 , so it is very unlikely that there is also H_2S in the samples. Samples from brine water in Svartsengi and the mixed water showed 0.7 and 0.1 mg/l of H_2S , respectively, not suitable for aquaculture. The H_2S values in all other samples were less than 0.03 mg/l, but exact values are unknown; therefore, comparison with the optimum value is difficult. H_2S reacts with O_2 to form

SO₄, so that the small amounts of H₂S present in the low-temperature geothermal water may be removed, either by aerating or dilution with cold air-saturated water.

The toxic action of carbon dioxide (CO₂) is either direct or indirect. Direct action is an excess of CO₂, which can cause a reduction in CO₂ diffusion from the fish blood into the respiratory water. However, CO₂ rarely causes direct toxicity in fish. The indirect effect is its influence on the pH value. The free CO₂ released during respiration reacts with the water, producing carbonic acid (H₂CO₃), and the pH value is lowered and limits the capacity of the fish blood to carry oxygen by lowering the blood pH at the gills. The maximum tolerable range of CO₂ is 10 mg/l. All the kinds of water sampled showed higher concentrations of CO₂ ranging from 15 to 82 mg/l, except for two samples from the geothermal waters in Laugar and Hrolleifsdalur. The concentrations of CO₂ in Laugar and Hrolleifsdalur were 7.9 and 7.6 mg/l, respectively.

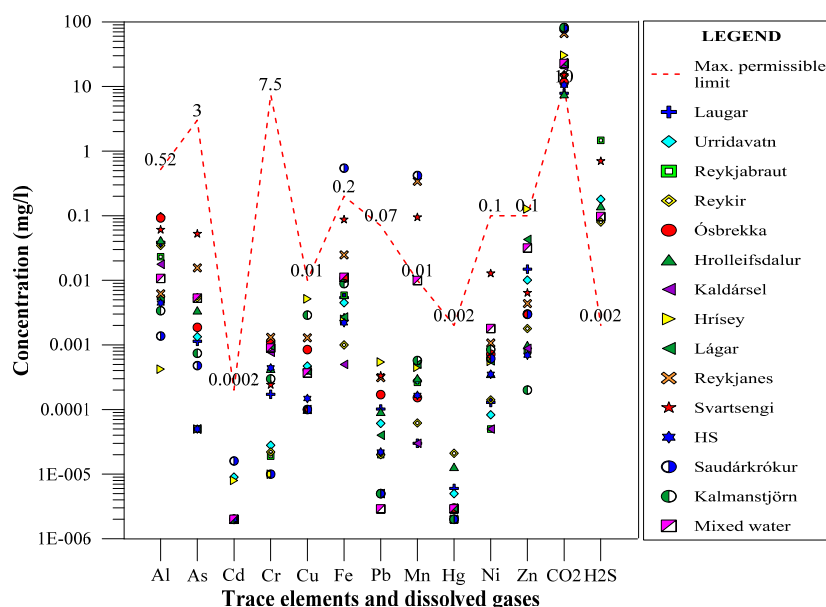


FIGURE 15: Trace elements and dissolved gas concentrations compared with the standards

7.2 Trace element toxicity

The metals found to be of the greatest importance for fish are aluminium (Al), chromium (Cr), iron (Fe), nickel (Ni), copper (Cu), zinc (Zn), arsenic (As), cadmium (Cd), mercury (Hg) and lead (Pb) (Svobodova et al., 1993). The graph in Figure 15 shows how these metals compare with standard values. Starting at a concentration of 0.1 mg/l, Al is toxic to fish in acidic, un-buffered waters. It influences gill permeability and damages the surface cells of the gill. Al is mainly toxic to fish at pH values 5.0 to 5.5. Al ions accumulate on the gills and clog them with a slimy layer which limits breathing. High concentrations of Al cause reduced growth and consequently the productivity of a fish farm is reduced. The tolerable limit of Al is as low as 0.5 mg/l. In all the water samples and mixed water, the concentrations of Al were less than 0.1 mg/l which is suitable for fish. Fe is vital to the life of all aquatic creatures. Fe is not deadly to any aquatic animals at normal levels, but at higher levels when iron does not dissolve in water, fish cannot process all the iron they take in from water or food. The iron can build up in the internal organs of fish, eventually killing them. The standard limit of Fe contents for fish is determined based on the fish type. In all fish species, it is generally accepted that the concentration of Fe should not exceed 0.2 mg/l; but for salmonids, the limit should not exceed 0.1 mg/l. The concentrations of Fe were less than 0.1 mg/l in all water samples along with the mixed water, except for one seawater sample from Saudárkrókur in which the Fe concentration was 0.55 mg/l. Fe, as well as Al, toxicity may be augmented with increasing acidity. Even in slightly acidic water, the increase in the concentrations of these metals will make the water more harmful to fish (Vuorinen et al., 1998). Precipitation of iron compounds and tufts of the iron bacteria in the water reduces the gill area for respiration.

The recommended limit for Mn is up to 0.01 mg/l. Brine waters from Reykjanes, Svartsengi, and the sea water from Saudárkrókur showed higher values of Mn. However, Mn toxicity in fish is not extensive. As may accumulate in large quantities in fish tissues. Therefore, it can enter into the human

body through the food chain. All the water samples and mixed water had a low concentration of As with values less than 0.01 mg/l. High concentrations of Ni compounds are of medium toxicity to fish. According to the standard value, Ni concentrations should be less than 0.1 mg/l. The toxic exposure to Ni turns mucus and lamellae in the gill chambers to a dark red colour, reduces breathing and may cause liver damage, depending on the accumulation in the tissues. Ni concentrations in all the samples were less than 0.01 mg/l, including the mixed water.

High concentrations of Cu and Zn in the water can be harmful, although at lower levels they are essential elements for fish. The characteristic symptoms of toxicity caused by copper ions and compounds are breathing difficulties. The maximum admissible Cu concentration in water for the protection of fish is in the range of 0.001 to 0.01 mg/l, depending on the physical and chemical properties of water and on the species of fish (Svobodova et al., 1993). All water samples and the mixed water contained less than the maximum admissible value of Cu concentrations, and are consequently considered safe in terms of Cu toxicity. Zn poisoning of fish is most frequently encountered; small fish are extremely sensitive to Zn. The poisoning effects on fish are similar to those found for copper. Zn toxicity in fish can be greatly influenced by both water hardness and the pH value (Everall et al., 1989). All the water samples and the mixed water were within the permissible limit of 0.1 mg/l for Zn, except a slightly higher concentration, 0.13 mg/l, in one sample from a cold water well in Hrísey.

Cd effects are similar to that of other toxic metals; Cd can cause damage to the reproductive organs, as well as to the central nervous system. The maximum admissible Cd concentration in water is 0.0002 mg/l. Cd concentrations recorded in all the water samples and the mixed water were less than 0.00001 mg/l. Consequently, all the water samples are suitable in terms of Cd.

Hg can cause damage to some vital tissues and organs in fish and may also have a harmful effect on reproduction by reducing egg production. For fish, in general, the maximum admissible concentration of Hg has been suggested to be as low as 0.002 mg/l. All water samples and the mixed water had much lower values of Hg (<0.00002 mg/l).

Pb toxicity is characterised by damage to the gills, so fish are killed by suffocation. The maximum admissible Pb concentration in water is 0.007 mg/l. The contents of Pb in all the water samples and the mixed water were within the permissible limit. The toxicity of Cr is similar to Pb. The concentrations of Cr appeared to be very low (<0.00001 mg/l) in all the water samples.

8. CHEMICAL ASSESSMENT FOR INDUSTRIAL APPLICATIONS

Diverse water quality is required for different types of industries. However, food drying and processing is the most important hot water consuming industrial sector in Iceland. The industries within this sector are: fish, meat, vegetable and potato industries; the dairy industry; beverage and breweries industry, and the margarine and fat industry. The food industries have a high demand for potable water due to the wide variety of components added to the product during processing where water comes into contact with the product. An EU directive has strictly prohibited the use of non-potable water in food industries. In Iceland, about 95% of the country's potable water is untreated groundwater, extracted from springs and boreholes, and less than 5% from the surface (Gunnarsdóttir, 2012). The largest groundwater resources are in the volcanic zone and the high porosity of surface layers and bedrock is often characterized by thin layers of soil. The natural geochemistry of ground and surface water, resulting from interaction with rocks, creates widespread health problems in many parts of the world. The deficiency, excess or imbalances of different chemical species present in potable water are well known to have an influence on human health. Therefore, it is important to evaluate the chemical characteristics of potable water. At the same time, the chemical composition of groundwater is important for decision makers when it comes to the selection of sites for geothermal reinjection wells, in order to avoid affecting the quality of the groundwater. The World Health Organization (WHO), European Union (EU) and other

organizations have set guidelines with recommended levels for different chemical species in potable water. The concentrations of all the chemical species of all the water samples were compared with WHO (2004) guidelines for potable water (Table 7).

TABLE 7: Water quality of all the water samples compared with the WHO (2004) guidelines

Parameters	WHO (2004) guidelines		Sample codes													
	Most desirable limit (mg/l)	Max. Allowable limit (mg/l)	1	2	3	4	5	6	7	8	9	10	11	12	13	14
pH *	-	6.5-8.5	E	E	E	E	E	E	S	E	S	S	S	E	E	S
TDS	500	1500	S	S	S	S	S	S	NA	S	S	E	E	S	E	E
Ca	75	200	S	S	S	S	S	S	S	S	S	E	E	S	E	E
Mg	50	150	S	S	S	S	S	S	S	S	S	E	S	S	E	E
Na	-	200	S	S	S	S	S	S	S	S	S	E	E	S	E	E
K	-	12	S	S	S	S	S	S	S	S	S	E	E	S	E	E
F	>0.05	<1.5	B	S	S	S	B	S	B	B	B	E	B	B	B	S
Cl	200	600	S	S	S	S	S	S	S	S	S	E	E	S	E	E
SO ₄	200	400	S	S	S	S	S	S	S	S	S	E	S	S	E	E
H ₂ S	0.05	0.1	S	E	E	E	NA	E	S	NA	S	S	E	S	NA	S
Al	-	0.2	S	S	S	S	S	S	S	S	S	S	S	S	E	S
As	-	0.01	S	S	S	S	S	S	S	S	S	E	E	S	E	S
Ba	-	0.7	S	S	S	S	S	S	S	S	S	S	E	S	S	S
Cd	-	0.003	S	S	S	S	S	S	S	S	S	S	S	S	S	S
Cr	-	0.05	S	S	S	S	S	S	S	S	S	S	S	S	S	S
Cu	-	2	S	S	S	S	S	S	S	S	S	S	S	S	S	S
Fe	-	0.3	S	S	S	S	S	S	S	S	S	S	E	S	E	S
Hg	-	0.001	S	S	S	S	S	S	S	S	S	S	S	S	S	S
Mn	-	0.05	S	S	S	S	S	S	S	S	S	S	E	S	S	S
Mo	-	0.07	S	S	S	S	S	S	S	S	S	S	S	S	S	S
Ni	-	0.02	S	S	S	S	S	S	S	S	S	S	S	S	S	S
Pb	-	0.01	S	S	S	S	S	S	S	S	S	S	S	S	S	S
Zn	-	3	S	S	S	S	S	S	S	S	S	S	S	S	S	S
B	-	0.05	S	S	S	S	S	S	NA	S	S	S	E	S	E	E

1: Laugar; 2: Urridavatn; 3: Reykjabrut; 4: Reykir; 5: Ósbrekka; 6: Hrolleifsdalur; 7: Kaldársel; 8: Hrísey; 9: Lágur; 10: Reykjanes; 11: Svartsengi; 12: Hitaveita Suðurnesja (HS); 13: Saudárkrókur; and 14: Kalmanstjörn; S: Suitable for potable water; E: Exceeding the WHO guideline values; B: Below WHO guideline values; and NA: No available data; pH*: Unitless.

8.1 Physicochemical parameters

The water samples from the springs in Kaldársel, Hrísey and Lágur and from sea water in Saudárkrókur and Kalmanstjörn are cold water with temperatures ranging from 3.4 to 8.6°C. Low-temperature geothermal waters from Laugar, Urridavatn, Reykjabrut, Reykir, Ósbrekka, and Hrolleifsdalur, heated water from Hitaveita Sudurnesja, and brine waters from Reykjanes and Svartsengi are hot waters with temperatures ranging from 48 to 99°C. Temperature has an impact on the solubility of a number of inorganic constituents and chemical contaminants that may have impact on health. Warm water temperatures may enhance the growth of micro-organisms and may increase problems related to colour, odour and taste. Figure 16 shows that the pH values of low-temperature geothermal boreholes vary between 9.29 and 10.22, which indicates the extent of the interaction between the hot water and the basaltic rocks; these pH values are higher than the desirable range (6.5 to 8.5) according to WHO (2004). In addition, one sample collected from a spring in Kaldársel and the heated pipeline from HS showed higher pH values than the desirable range. The values were 8.94 and 9.01, respectively. The pH values in all the other samples were within the desirable range. However, the Icelandic and EU regulations on

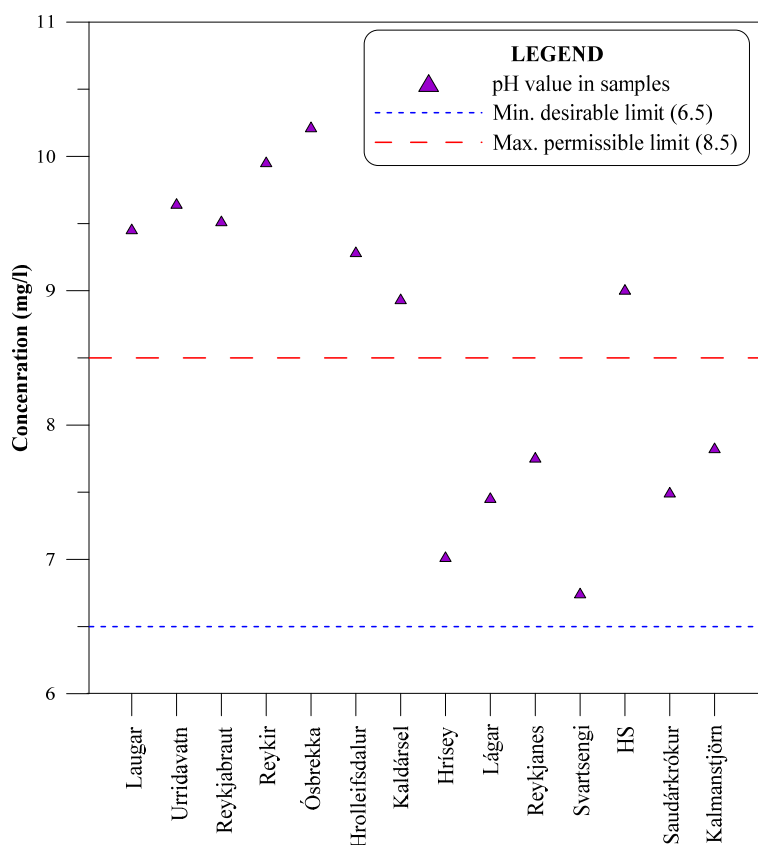


FIGURE 16: pH values compared with the guidelines

water range from 88 to 178 mg/l, which is also within the desirable limit. All the samples from the brine and sea water showed much higher values of TDS, ranging from 15400 to 30682 mg/l. TDS greater than 1000 mg/l results in a salty taste, and water with extremely low TDS may be considered unacceptable because of its flat and insipid taste (WHO, 2004). The high TDS in potable water may cause gastrointestinal irritation in humans. The concentrations of Ca^{2+} in brine and sea waters range from 341 to 728 mg/l, higher than specified as most desirable and way beyond the maximum permissible

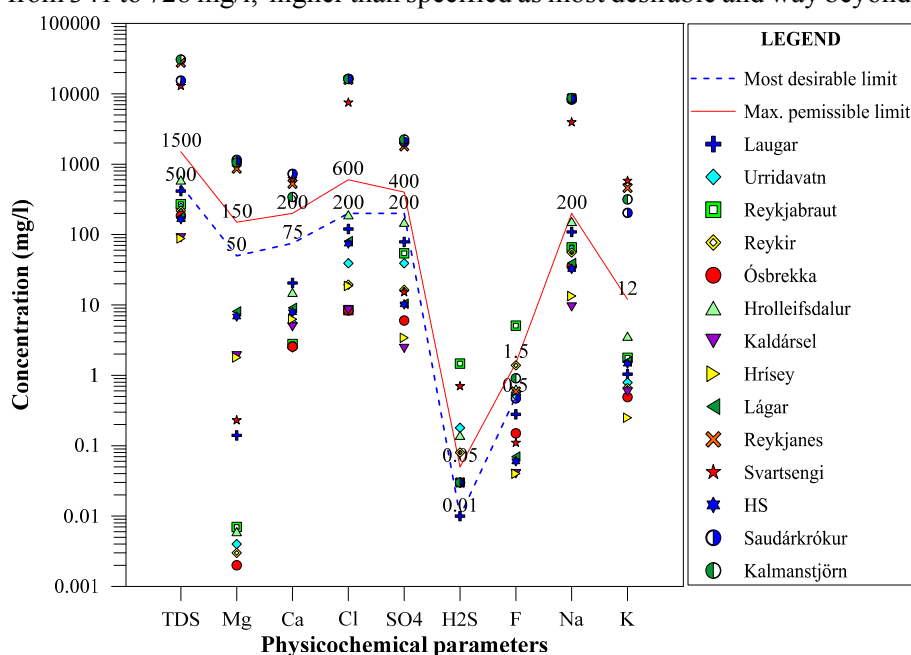


FIGURE 17: Physicochemical parameters compared with the guidelines

potable water allow a pH of 6.5 to 9.5. The pH has no direct impact on consumers but it does affect the effectiveness of water disinfection and clarification. Low pH may cause corrosion of water mains and pipes in water supply systems, as well as an increase in bacterial growth. Failure to minimize corrosion can result in the contamination of drinking-water and adverse effects on its taste and appearance.

All the physicochemical parameters were compared with WHO (2004) guidelines. According to the guidelines, a total dissolve solid (TDS) value of 500 mg/l is the most desirable and up to 1000 mg/l is the maximum permissible limit for potable water. Figure 17 shows that the TDS values ranged from 185 to 596 mg/l in the low-temperature geothermal waters so these waters are within the permissible limit.

Samples from springs and heated limit of 75 and 200 mg/l, respectively. Ca^{2+} concentrations in other samples varied from 2.5 to 20.5 mg/l.

The concentrations of Mg^{2+} in both the samples from sea water from Saudárkrókur and Kalmanstjörn were more than ten times higher than the desirable limit of 50 mg/l. One sample from brine water in Reykjanes showed a Mg^{2+} concentration of 0.23 mg/l, which is within the desirable limit for potable water

but the other sample from Svartsengi had a higher Mg^{2+} concentration of 864 mg/l. The concentrations of Mg^{2+} in the rest of the samples were within the permissible limit. Both Ca^{2+} and Mg^{2+} are essential to human health. Low intakes of Ca^{2+} have been associated with risks of osteoporosis, nephrolithiasis, colorectal cancer, hypertension, coronary artery disease, insulin resistance and obesity (WHO, 2006). When the absorbed Ca^{2+} is in excess of need, the excess is excreted by the kidney in most healthy people. A low Mg^{2+} level in the human body has been associated with endothelial dysfunction, increased vascular reactions, high circulating levels of reactive protein and decreased insulin sensitivity (WHO, 2006). The major effect of excess Mg^{2+} intake is renal insufficiency associated with a significant decrease in the ability to excrete magnesium. Potable water with high concentrations of Mg^{2+} with high SO_4^{2-} may have a laxative effect, although consumers may adapt to these levels as exposure continues (WHO, 2011). In general, an increase of both Ca^{2+} and Mg^{2+} concentrations in water results in an increase in the total hardness (TH).

Water can be classified as soft (< 75 mg/l), moderate (75 to 150 mg/l), hard (150 to 300 mg/l) and very hard (>300 mg/l), based on the TH as CaCO_3 (Sawyer and McCarty, 1967). Samples collected from brine and sea water fell under the very hard water class. Other samples from low-temperature geothermal boreholes, springs and heated pipeline fell under the soft water class. Long term consumption of hard water may cause urological problem or urolithiasis, pre-natal mortality, cancer and cardiovascular disorders (Agrawal and Jagetai, 1997). A guideline value of 200 mg/l was established by WHO, based on taste considerations. Samples from brine and sea water have high concentrations of Na^+ , ranging from 3940 to 8720 mg/l. Na^+ concentrations in the samples from low-geothermal boreholes, springs and heated pipelines were within acceptable limits, ranging from 9.39 to 153 mg/l. The excess of Na^+ is thought to cause hypertension, congenial diseases and kidney disorders, but there is no firm evidence that can support the theory (WHO, 2004).

As per the standard guidelines, the maximum permissible limit for K^+ is 12 mg/l. The K^+ concentrations range from 0.25 to 3.6 mg/l in all the water samples, except in the brine and sea waters where it ranges from 203 to 579 mg/l. The high concentrations of K^+ in brine waters are due to the fact that both geothermal brines originate from seawater.

The most desirable limit for Cl^- is 200 mg/l and the maximum permissible limit is 600 mg/l. The concentrations of Cl^- in all samples were lower than the most desirable limit, ranging between 8.36 and 191 mg/l, except in the brine and sea water samples, which ranged between 7510 and 16350 mg/l. A high concentration of Cl^- in drinking water causes a salty taste and has a laxative effect.

The concentrations of SO_4^{2-} are also high in brine and sea water, ranging from 1790 to 2240 mg/l, except for one sample from a brine water sample from Svartsengi which had a SO_4^{2-} concentration of 15.2 mg/l. Samples from all other sources had a SO_4^{2-} concentration of between 2.41 and 149 mg/l, within the most desirable limit of 200 mg/l. SO_4^{2-} ingestion in excess of the maximum allowable limit of 400 mg/l in potable water may have gastrointestinal effects (WHO, 2004).

The F^- content in all the water samples ranged from 0.05 to 5.08 mg/l. F^- is an essential element for health. Deficiency or low concentration (<0.5 mg/l) in potable water leads to dental caries. However, a high intake of F^- over 1.5 mg/l may cause skeletal and dental fluorosis (WHO, 1998). Therefore, it is essential to have a safe limit of F^- concentrations in between 0.5 and 1.5 mg/l in potable water. Samples from low-temperature boreholes in Urriðavatn, Reykir and Hrolleifsdalur showed F^- concentrations within the recommended guidelines, Laugar and Ósbrekka showed lower concentrations of F^- of 0.28 and 0.15 mg/l, respectively, and Reykjabrut showed a higher concentration, 5.08 mg/l, than the recommended limit for F^- .

All the spring waters and heated water of HS showed lower values for F^- (< 0.07 mg/l) than the recommended limit. F^- concentrations in the sea water samples appeared to be within the permissible limit. F^- concentration in one brine water sample from Reykjanes was within the permissible limit, but

the one from Svartsengi was lower than the permissible limit. The concentrations of these two samples were 0.59 and 0.11 mg/l, respectively.

The taste and odour thresholds of hydrogen sulphide (H_2S) in water were estimated to be between 0.05 and 0.1 mg/l. The rotten eggs odour of hydrogen sulphide may be noticeable in the distribution system due to oxygen depletion. Almost all the waters from the low-temperature boreholes exceeded the value of the taste and odour threshold except for two samples from Laugar and Ósbekka which showed less than a 0.03 mg/l concentration of H_2S . The brine water sample from Svartsengi showed a higher value of 0.7 mg/l of H_2S concentration. All other samples showed less than 0.03 mg/l of H_2S concentration.

8.2 Trace elements

The levels of trace elements in water and their significance in terms of health are of particular importance in potable water. Some elements are non-essential to human health and above certain limits they are toxic, such as aluminium (Al), arsenic (As), cadmium (Cd), mercury (Hg), lead (Pb), boron (B), silver (Ag), radium (Ra), radon (Rn) and uranium (U). However, some elements are essential at trace levels but can exhibit toxic properties in excess levels of concentrations such as beryllium (Be), vanadium (V), chromium (Cr), manganese (Mn), iron (Fe), cobalt (Co), nickel (Ni), zinc (Zn), selenium (Se), molybdenum (Mo), antimony (Sb) and barium (Ba). Many other elements have no effect on human health. The comparison between all the measured trace element concentrations in all the water samples with the WHO (2004) guideline is given in Figure 18.

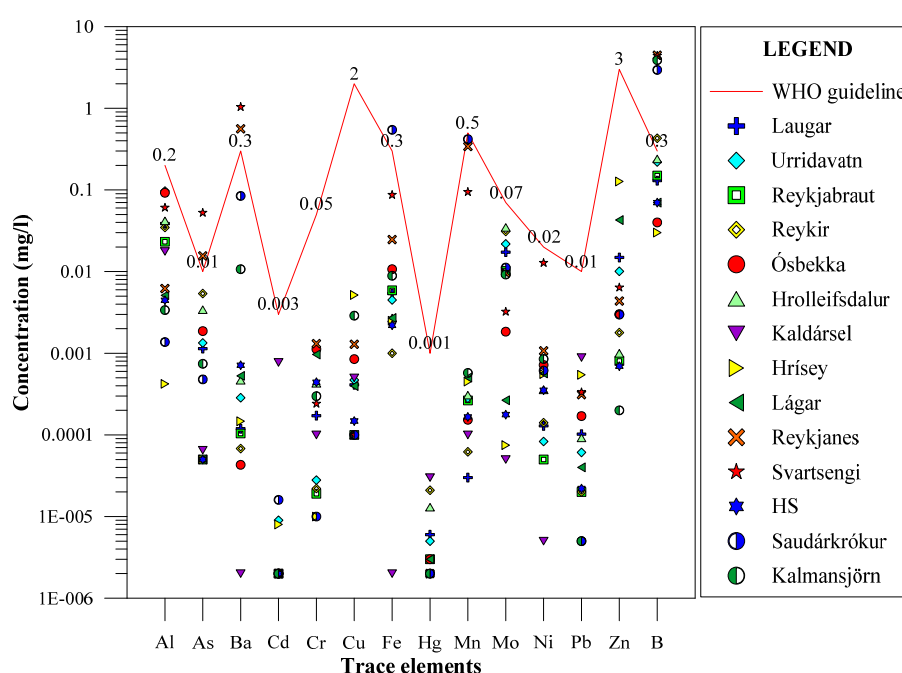


FIGURE 18: Trace element concentrations compared with the guidelines

There is no health-based guideline value recommended for Al. However, a concentration of Al of 0.2 mg/l in drinking-water provides a compromise between the practical use of Al salts in water treatment and discoloration of distributed water (WHO, 1998). The metabolism of Al in humans is not well understood; it is poorly absorbed and most of the absorbed Al is rapidly excreted in urine. Al concentrations in all the waters were within the recommended limit.

There is no health-based guideline value recommended for Al. However, a concentration of Al of 0.2 mg/l in drinking-water provides a compromise between the practical use of Al salts in water treatment and discoloration of distributed water (WHO, 1998). The metabolism of Al in humans is not well understood; it is poorly absorbed and most of the absorbed Al is rapidly excreted in urine. Al concentrations in all the waters were within the recommended limit.

The tolerable limit for As is 0.01 mg/l for humans. The As concentrations were higher than the guideline value in the brine waters from Reykjanes and Svartsengi. The As concentrations of these two samples were 0.015 and 0.05 mg/l, respectively. All other water samples had As concentrations of less than 0.005 mg/l. The common symptom of chronic As poisoning is conjunctivitis, melanosis, depigmentation and keratosis. The connection between As exposure and skin and internal cancers is well established (Dissanyaake and Chandrajith, 1999). Numerous studies have examined the risk of cancers associated with arsenic ingestion through potable water. There is overwhelming evidence that

consumption of high levels of arsenic through potable water was causally related to the development of cancer at several sites (WHO, 2004).

Ba is present as a trace element in both igneous and sedimentary rocks. A health-based guideline value of 0.7 mg/l was derived for barium, based on concerns regarding the potential of Ba to cause hypertension (WHO, 2001). One brine water sample from Reykjanes had a Ba concentration of 0.56 mg/l, which is within the tolerable limit; another brine water sample collected from Svartsengi contained 1.04 mg/l of Ba, which is higher than the tolerable limit. All other samples had Ba concentrations of less than 0.1 mg/l. It should be noted that excess water-soluble Ba may cause hypertension (WHO, 2004).

The tolerable limit of B is 0.5 mg/l. B concentrations were high for both the brine and sea waters. B concentrations from brine water in Reykjanes and Svartsengi were 4.47 and 4.40 mg/l, respectively. From sea water samples in Saudárkrókur and Kalmanstjörn, B concentrations were 2.95 and 3.90 mg/l, respectively. Concentrations in all the other water samples were less than the maximum tolerable limit, range from less than 0.03 to 0.43 mg/l. Naturally occurring boron was present in water, primarily as a result of leaching from rocks and soils containing borates and boro-silicates (WHO, 1998). B can accumulate in bodies and may infect the stomach, liver, kidney and brain of the human body. B is rapidly and almost completely absorbed by the human body. Long-term exposure of humans to B compounds leads to mild gastrointestinal irritation (WHO, 1998).

Fe is a central component of haemoglobin in the blood. Excessive intake has no serious impact on health. There is usually no noticeable taste at concentrations below 0.3 mg/l Fe. The sea water sample from Saudárkrókur and the brine water sample from Svartsengi had slightly higher concentrations of Fe than is recommended in terms of taste. The sample from Svartsengi was also slightly elevated in Mn. Mn is one of the most abundant metals in the earth's crust and usually occurs together with Fe. It is an essential trace element for humans. Neuro-toxic effects due to excessive intake of Mn in potable water have been observed (WHO, 2004). The values of all other measured elements were within the permissible limits.

9. SUMMARY AND CONCLUSIONS

Water from different sources is of different types and is variable in chemical composition due to mixing with sea water, volcanic activity, geothermal alteration, water-rock interaction and various other factors. From 14 samples from different sources, geothermal waters showed various types of water such as chloride, bicarbonate and mixed chloride-sulphate and chloride-sulphate-bicarbonate type and appeared to be fully equilibrated. The brine and sea waters were of chloride type and were either in full or partial equilibrium with rock. Spring and heated waters were, in all cases, considered to be immature waters, even though chloride might be the dominant cation.

Geothermal waters from Laugar and Ósbrekka may be corrosive in space heating applications, due to the presence of dissolved oxygen. The brine characteristics from Reykjanes and Svartsengi are also corrosive, due to carbon dioxide, especially the water from Reykjanes. In some cases, scaling may occur. Amorphous silica can precipitate from the brine water from Svartsengi when cooled to below 73°C. Several geothermal waters from low-temperature geothermal fields and geothermally heated water showed the possibility of magnesium silicate scaling. No scaling should be observed after mixing Lágar cold groundwater and Svartsengi hot brine water at 15°C and 40°C, with 63% and 90% cold water fractions, respectively. A summary of the results is given in Table 8.

TABLE 8: Summary of the results

Sample location	Space heating applications	Balneotherapeutic applications	Agricultural applications	Aquaculture applications	Industrial applications
Laugar	P	S	P	US	S
Urridavatn	S	S	P	US	US
Reykjabraut	P	S	P	US	US
Reykir	P	S	P	US	US
Ósbrekka	P	S	P	US	US
Hrolleifsdalur	S	S	US	US	US
Reykjanes	P	S	US	US	US
Svartsengi	US	S	US	US	US
Hitaveita Sudurnesja (HS)	P	US	S	US	S
Lágar	NA	US	S	S	S
Kaldársel	NA	US	S	P	S
Hrísey	NA	US	S	S	S
Kalmanstjörn	NA	S*	US	S	US
Saudárkrókur	NA	S*	US	S	US
Mixed water	S	S	NA	US	NA

S: Suitable; S*: Suitable after heating; P: Permissible; US: Unsuitable; and NA: Not assessed.

For the assessment of balneotherapeutic applications, waters from brine and sea are classified as mineral waters, along with some geothermal waters such as from Reykir and Reykjabaut, in terms of H₂S and fluoride. All geothermal waters are suitable for balneotherapeutic applications in terms of temperature. However, sea waters are not thermal waters, but mineral rich in terms of TDS. They can be used either after heating with geothermal water in thermal heat exchangers, or by mixing with geothermal water. Reykjanes and Svartsengi brine waters are considered to be well matched with spa specifications, as is the mixed water that results from mixing 63% cold groundwater with geothermal brine water; consequently, these waters are suitable for balneotherapeutic use.

For the assessment of the quality of irrigation water, EC, TDS, sodium percent, SAR, boron toxicity and trace elements are important parameters. Temperature was not considered for this evaluation. According to EC, TDS, sodium percent and SAR, all springs and heated water fell under the excellent to good water class. All geothermal waters are permissible for agricultural purposes, except water from the Hrolleifsdalur geothermal area, which is considered unsuitable for irrigation. All geothermal, cold and heated groundwater are suitable, in terms of boron and trace elements. Brine and sea waters are not suitable for irrigation purposes in terms of EC, TDS, sodium percent, SAR and boron values.

Various physicochemical parameters (excluding temperature), dissolved gas and trace element concentrations in water were considered in assessing the water's suitability for aquaculture. None of the geothermal waters were considered suitable for aquaculture due to high pH. Spring and sea waters are suitable for aquaculture, though some exceed the limits for hardness, CO₂, Fe and Mn, which have no major effects on fish. H₂S concentrations in geothermal and brine waters are higher than the maximum recommended limit. H₂S concentrations are also high after mixing brine water with 90% cold water. Consequently, geothermal, brine and mixed waters are not suitable for aquaculture, unless aerated with O₂ to remove H₂S.

For the assessment of the water quality for the applications of drinking or food processing industries, the WHO guidelines were followed. Waters from all springs and the heated pipeline are of potable quality in terms of all physicochemical parameters and trace elements except for pH. None of the sea and brine waters are potable due to high salinity. Most of the geothermal waters are not suitable in terms of pH, H₂S and, in some cases, fluoride and boron.

ACKNOWLEDGEMENTS

I would like to express my deepest gratitude to Dr. Ingvar B. Fridleifsson, Former Director, and Mr. Lúdvík S. Georgsson, Director, of the United Nations University, Iceland, for giving me the opportunity to take part in the Geothermal Training Programme in 2013.

I am sincerely grateful to my supervisor, Mr. Finnbogi Óskarsson, for his supervision and valuable suggestions throughout this research work. I would like to thank Mr. Ingimar Gudni Haraldsson, Mrs. Málfríður Ómarsdóttir, Ms. Thórhildur Ísberg and Mr. Markús A. G. Wilde, for their advice and assistance during the training programme.

I thank all the teachers for the introductory and specialized training lectures and all the UNU Fellows for friendship and good cooperation. Finally, I thank the Director General of the Geological Survey of Bangladesh for approving my attendance in this training programme.

REFERENCES

- Agrawal, V., and Jagetai, M., 1997: Hydrochemical assessment of groundwater quality in Udaipur city, Rajasthan, India. *Proceedings of National conference on dimensions of environmental stress in India*, 151–154.
- Bai Liping, 1991: Chemical modelling programs for predicting calcite scaling, applied to low temperature geothermal waters in Iceland. Report 3 in: *Geothermal training in Iceland 1991*. UNU-GTP, Iceland, 45 pp.
- Bjarnason, J.Ö., 1994: *The speciation program WATCH, version 2.1*. Orkustofnun, Reykjavík, 7 pp.
- Bojadgieva, K., Dipchikova, S., Benderev, A., and Koseva, J., 2002: Thermal water and balneology in Bulgaria. *GHC Bulletin, Volume 23, No 1*, 18–25.
- Delhaize E. and Ryan P.R., 1995: Aluminium toxicity and tolerance in plants. *Journal of Plant Physiology* 107, 315–321.
- Dissanayake, C.B., and Chandrajith, R., 1999: Medical geochemistry of tropical environments. *Elsevier Science, Earth-Science reviews* 47, 213–258.
- Elguedri, M., 1991: Assessment of scaling and corrosion problems in the Kebili geothermal field, Tunisia. Report 1 in: *Geothermal training in Iceland 1999*. UNU- GTP, Iceland, 1–39.
- European Union, 2009: Directive 2009/54/EC of the European parliament and the council, 2009, on the exploitation and marketing of natural mineral waters. *Official Journal of the European Union, OJL 164*, 58pp.
- Everall, N.C., MacFarlane, N.A.A., and Sedgwick, R.W., 1989: The interactions of water hardness and pH with acute toxicity of zinc to brown trout, *S. trutta*, L. *J. Fish Biology*, 35. 27–36.
- Fracas, D.M., 2005: Therapeutic effects of the geothermal water in the Felix spa, Romania. *Proceedings of World Geothermal Congress 2005. Antalya, Turkey*, 4pp.
- Franzson, H., 1983: The Svartsengi high-temperature field, Iceland, subsurface geology and alteration. *Geothermal Resources Council, Transactions*, 7, 141–145.

Fridleifsson, G.Ó., Benediktsson, B., Georgsson, L.S., Ólafsson, M., Matthíasson, J., and Jóhannsson, I., 1995: Very low-temperature geothermal utilization in fish farming in Iceland - A Case history from the Silfurstjarnan Ltd., Iceland. *Proceedings of the World Geothermal Congress 1995, Florence, Italy*, 2299pp.

Gandouzi, M.A., 1999: Geothermal waters in greenhouses in Tunisia: use of computers to control climate and fertigation with cooled geothermal water. Report 3 in: *Geothermal training in Iceland 1991*. UNU-GTP, Iceland, 71–95.

Garg N., and Singla P., 2011: Arsenic toxicity in crop plants: physiological effects and tolerance mechanisms. *Environmental Chemistry Letters* 9, 303–321.

Giggenbach, W.F., 1988: Geothermal solute equilibria. Derivation of Na-K-Mg-Ca geoindicators. *Geochim. Cosmochim. Acta*, 52, 2749–2765.

Giggenbach, W.F., 1991: Chemical techniques in geothermal exploration. In: D'Amore, F., (coordinator), *Application of geochemistry in geothermal reservoir development*. UNITAR/UNDP publication, Rome, 119–142.

Gudfinnsson, G.H., and Óskarsson, F., 2012: *Svartsengi power plant. Steam and water quality in 2011*. Iceland GeoSurvey, ÍSOR-2012/016. 59 pp.

Gunnarsdóttir, M.J., 2012. *Safe drinking water: Experience with water safety plans and risk factors*, PhD dissertation, Faculty of Civil and Environmental Engineering, University of Iceland. 128pp.

Gunnlaugsson, B., Agustsson M.A., and Adalsteinsson, S., 2003: Sustainable use of geothermal energy in Icelandic horticulture, *International Geothermal Conference 2003, Reykjavik, Iceland*, 20–24.

Gunnlaugsson, E., 2004: Geothermal district heating in Reykjavik, Iceland. *International geothermal days in Poland 2004, Zokopane, Poland*, 162-169.

GTC and VO, 1988: *Health hotel program in Hungary*. Geo-Thermal Cooperative and Virkir-Orkint Ltd., Budapest, Report, 30 pp.

Haddadin, G., 1995: Borehole geophysics and geology of the Urridavatn geothermal area, E-Iceland. Report 5 in: *Geothermal training in Iceland 1991*. UNU-GTP, Iceland, 113–134.

Hardardóttir, V., and Óskarsson, F., 2012: *Reykjanes power plant. Steam and water quality in 2011*. Iceland GeoSurvey, ÍSOR-2012/017, 50 pp.

Hartmann, B.R., Bassenge, E., and Pittler, M., 1997: Effect of carbon dioxide-enriched water and fresh water on the cutaneous microcirculation and oxygen tension in the skin of the foot. *J. Angiology*, 48, 337–343.

Hem, J.D., 1989: Study and interpretation of the chemical characteristics of natural water. *USGS Water Supply Paper*, 2254, 263pp.

Jakobsson, S.P., Jónsson, J., and Shido, F., 1978: Petrology of the Western Reykjanes Peninsula, Iceland. *J. Petrology*, 19, 669–705.

Keller, W.D., 1978: Drinking water: A geochemical factor in human health. *Geological Society of America Bulletin* 1978, no. 3, 334–336.

Komatina, M., 2004: *Medical geology: effects of geological environments on human health*. Chapter 2 in: Geological factors, Elsevier, 2004, 488pp.

Líndal, B., 1973: Industrial and other applications of geothermal energy, except power production and district heating. In: Armstead, H.C.H. (eds.) *Geothermal energy*. Paris, UNESCO, LC 7297, 135–148.

Lund, J.W., 2007: *Characteristics, development and utilization of geothermal resources*. Geo-Heat Centre Bulletin, Geo-Heat Centre, Oregon Institute of Technology, 9pp.

Manuel, A.V.C., 2010: Chemical assessment of water prospects for direct applications in Nicaragua. Report 31 in: *Geothermal training in Iceland 1991*. UNU-GTP, Iceland, 675–709.

Matz, H., Orion, E., and Wolf, R., 2003: *Balneotherapy in dermatology*. Dermatologic Therapy, Blackwell Publishing, Inc. U.S.A 16, 132–140.

Miron, G., and Kristensen, E., 1993: Behavioural response of three nereid polychaetes to injection of sulfide inside burrows. *Marine Ecology-progress Series*, 101, 147–147.

Nable, R.O., Bañuelos, G.S., and Paull, J.G., 1997: Boron toxicity. *Plant and Soil*, 193, 181–198. (Is Paull with one L or 2 LL?)

Orkustofnun, 2010: *Geothermal Development and research in Iceland*. Orkustofnun, Reykjavík, Iceland, 39pp.

Piper, R.G., 1982: Fish hatchery management. *USDI, U.S Fish Wildlife and Service, Washington, D.C.* 517 pp.

Ragnarsson, Á., 2010: Geothermal development in Iceland 2005-2009. *Proceedings of World Geothermal Congress 2010, Bali, Indonesia*, 12pp.

Richards, L.A., 1954: *Diagnosis and improvement of saline alkaline soils*. US Department of Agriculture, Hand Book 60, 160pp.

Richter, S., Thórarinsdóttir, R.I., and Jónsdóttir, F., 2007: On-line corrosion monitoring in geothermal district heating systems. II. Localized corrosion. *Elsevier Science, Corrosion Science* 49, 1907–1917.

Roberts, P.A., 1975: *Fish culture utilization of geothermal energy*. Energy Research and Development Administration, Idaho National Engineering Laboratory, 50pp.

Rowe, D.R. and Abdel-Magid, I.M., 1995: *Handbook of wastewater reclamation and reuse*. CRC Press, Inc. 550pp.

Saman, J., 2000: *The properties of the curative water and its uses for therapeutic treatment in Jordan*. Berichte der Geologischen Bundesanstalt, Geomedicine Seminar, Vienna, 29–37.

Samantaray S., Rout, G.R., and Das, P., 1996: Role of chromium on plant growth and metabolism. *Acta Physiologiae Plantarum*, 20-2, 201–212.

Sawyer, C.N., & McCarty, D.L., 1967: *Chemistry of sanitary engineers*, McGraw-Hill, New York. 2nd edition. 518pp.

Sbterev, D., 1994: Assessment of the Olafsfjörður low-temperature geothermal field, N-Iceland. Report 12 in: *Geothermal training in Iceland 1991*. UNU-GTP, Iceland, 291–310.

Sigbjarnarson, G., 1982: *Selection of sites for groundwater exploitation in south-western Iceland*. Orkustufnun, Iceland, 15pp.

Skapare, I., 2001: Utilisation of geothermal water in the Riga/Jurmala region of Latvia for recreation and health. Pre-feasibility study for an outdoor thermal swimming pool. Report 11 in: *Geothermal training in Iceland 2001*. UNU-GTP Iceland, 237–266.

Smith, R.A., 2001: Basic geology and chemistry of borate. *American Ceramic Society, Bulletin*, 22(2), 64pp.

Sukenik, S., Flusser, D., & Abu-Shakra, M., 1999: *The role of SPA therapy in various rheumatic diseases*. Rheumatic Disease Clinics of North America, 25, 883–897pp.

Svobodová, Z., Lloyd, R., Máchová, J., and Vykusová, B., 1993: *Water quality and fish health*. EIFAC Technical Paper 54, FAO, Rome, 71pp.

Texas A&M University, 2003: *Irrigation water quality standards and salinity management strategies*. Produced by Agriculture Communication, 8pp.

Vuorinen, P.J., Keinänen, M., Peuranen, S., and Tigerstedt, C., 1998: Effects of iron, aluminium, dissolved humic material and acidity on grayling (*Thymallus thymallus*) in laboratory exposures, and a comparison of sensitivity with brown trout (*Salmo trutta*). *Boreal Environment Research* 3, 405–419.

Wedemeyer, G.A., 1977: Environmental requirements for fish health. In: *Proceedings of the International Symposium on Diseases of Cultured Salmonids*, Tavolek, Inc., Seattle, Wash., 41–55.

WHO, 1998: *Guidelines for drinking-water quality, Vol. 2* (2nd ed.), *Health criteria and other supporting information*. World Health Organization, Geneva, 127pp.

WHO, 2001: *Barium and barium compounds*. World Health Organization, Geneva, Concise International Chemical Assessment Document 33, 52 pp.

WHO, 2004: *Guidelines for drinking-water quality, Vol. 1, recommendations* (3rd ed.), World Health Organization, Geneva, 515pp.

WHO, 2006: *Meeting of experts on the possible protective effects on hard water against cardiovascular disease, Washington, D.C.* World Health Organization, Geneva, 13pp.

WHO, 2011: Hardness in Drinking-water. *Background document for development of WHO Guidelines for Drinking-water Quality*. World Health Organization, Geneva, 11pp.

Wilcox, L.V., 1955: *Classification and use of irrigation waters*. U.S. Department of Agriculture, Washington, D.C., Circular 969, 19pp.

APPENDIX I: Chemical composition of all the water samples

Parameters	Laugar	Urridavatn	Reykjabaugur	Reykir	Ösbrekkja	Hvölsfjallur	Kaldársel	Hrísey	Lágar	Reykjanes	Svartsengi	HS	Saudarkrókur	Kalmatstjörn
Location type	Borehole	Borehole	Borehole	Borehole	Borehole	Borehole	Spring	Spring	Spring	Pipeline	Pipeline	Pipeline	Pipeline	Borehole
Water type	Low-T	Low-T	Low-T	Low-T	Low-T	Low-T	Cold	Cold	Cold	Brine	Brine	Heated	Sea	Sea
Temperature ¹	62.5	74.5	73.9	61.9	66.9	88.2	3.5	3.4	5.7	48	99	70	8.6	8.3
pH ¹	9.46	9.65	9.52	9.96	10.22	9.29	8.94	7.02	7.46	7.76	6.75	9.01	7.5	7.83
pH-Temperature ¹	22.2	21.3	22.1	19.6	20.5	22	21.7	21.4	21.6	22	22.3	22.7	22.5	22.1
EC at 25°C ²	709	343	345	256	204	926	93.7	125.1	350	65.8	15	316	30000	-
CO ₂	7.87	15	21.2	15	11.5	7.6	20.4	30.5	23.5	65.8	15	10.5	77.8	82
H ₂ S	<0.03	0.18	1.47	0.08	<0.03	0.14	<0.03	-	<0.03	<0.03	0.7	<0.03	-	<0.03
O ₂	0.1	<0.001	<0.001	<0.001	0.06	<0.001	-	-	-	-	-	-	0.05	-
B	0.13	0.22	0.15	0.43	0.04	0.24	-	<0.03	0.07	4.47	4.4	0.07	2.951	3.9
SiO ₂	57.5	59.3	104.7	98.3	77.8	102	23.4	16.4	14.8	79.1	256	13.2	13.8	8.1
Na	109	61.3	65.8	55.7	35.5	153	9.39	13.4	39.5	8650	3940	32.5	8260	8720
K	1.04	0.79	1.77	0.66	0.49	3.6	0.582	0.25	1.58	461	579	1.47	203	316
Mg	0.14	0.004	0.007	0.003	0.002	0.006	1.9	1.79	8.1	864	0.23	6.85	1150	1060
Ca	20.5	3.52	2.78	2.5	2.56	15.1	4.89	6.27	9.08	526	617	7.89	728	341
F	0.28	0.52	5.08	1.39	0.15	0.64	<0.05	0.04	0.07	0.59	0.11	0.06	0.47	0.91
Cl	120	39.1	8.44	19.4	8.36	191	8.44	18.6	80.4	15810	7510	74.7	16350	16190
SO ₄	78.8	39.1	54.2	16.4	6.01	149	2.41	3.41	10.4	1790	15.2	10.2	2060	2240
Al	0.0389	0.0968	0.0232	0.0347	0.0923	0.0418	0.0177	0.00422	0.00513	0.0062	0.0607	0.00446	0.00137	0.00338
As	0.00114	0.00134	<0.00005	0.00338	0.00187	0.00342	<0.00005	<0.00005	<0.00005	0.0156	0.0525	<0.00005	0.000478	0.000743
Ba	0.000119	0.000285	0.000104	0.00068	0.000043	0.000467	0.00065	0.000147	0.000529	0.561	1.04	0.000714	0.0844	0.0107
Cd	<0.000002	0.000009	<0.000002	<0.000002	<0.000002	<0.000002	<0.000002	0.000008	<0.000002	<0.000002	<0.000002	<0.000002	0.000016	<0.000002
Co	0.000016	0.000009	<0.000005	<0.000005	0.000013	<0.000005	<0.000005	0.000014	0.000016	<0.000005	<0.000005	<0.000005	0.000144	<0.000005
Cr	0.000172	0.000028	0.000019	0.000022	0.00112	0.000428	0.000771	<0.00001	0.000968	0.00131	0.000241	0.000441	<0.00001	0.000298
Cu	0.00041	0.000471	<0.0001	<0.0001	0.000848	<0.0001	<0.0001	0.00317	0.000397	0.00129	<0.0001	0.000148	<0.0001	0.000289
Fe	0.0054	0.0045	0.0059	0.001	0.0107	0.0027	0.0005	0.0025	0.0027	0.0247	0.0871	0.0022	0.545	0.0089
Hg	0.000006	0.000005	0.000003	0.000021	0.000003	0.000013	<0.000002	<0.000002	0.000003	<0.000002	0.000002	<0.000002	<0.000002	<0.000002
Mn	<0.00003	0.000282	0.000264	0.00062	0.000153	0.000306	<0.00003	0.000451	0.000505	0.341	0.0945	0.000166	0.419	0.000374
Mo	0.0173	0.0218	0.0102	0.0311	0.00184	0.0348	0.0001	0.000075	0.000266	0.00963	0.00322	0.000177	0.0112	0.0092
Ni	0.000129	0.000083	<0.00005	0.000141	0.000718	0.000356	<0.00005	0.000558	0.000566	0.00107	0.0128	0.000352	0.000614	0.000851
Pb	0.000102	0.000061	0.00002	0.00002	0.00017	0.000092	<0.000005	0.000545	0.00004	0.000311	0.000333	0.000022	<0.000005	<0.000005
Sr	0.0146	0.0296	0.0444	0.00382	0.00869	0.0439	0.00427	0.00375	0.0305	6.32	3.99	0.0276	8.06	5.95
Zn	0.0149	0.0101	0.00805	0.00179	0.00301	0.000998	0.000885	0.127	0.0428	0.00437	0.0064	0.000695	0.00297	<0.0002
TDS	414	241	270	219	185	596	-	88	178	27600	12958	165	15400	30682

1: °C; 2: Unitless; 3: µS/cm and other element concentrations are in mg/l.